CODEN: JASMAN

THE JOURNAL of the Acoustical Society of America

ISSN: 0001-4966

Vol. 101, No. 4 April 1997

MEETING PROGRAM SUMMARY **JOINT ASA/NOISE-CON MEETING** **15–20 JUNE 1997**
State College, PA
(see pp. 1791–1792)

(Continued)

CONTENTS—*Continued from preceding page*

(Continued)

CONTENTS—*Continued from preceding page*

(Continued)

CONTENTS—*Continued from preceding page*

ACOUSTICAL NEWS—USA

Elaine Moran
Acoustical Society of America, 500 Sunnyside Boulevard, Woodbury, New York 11797

Editor's Note: *Deadline dates for news items and notices are 2 months prior to publication.*

New Fellows of the Acoustical Society of America

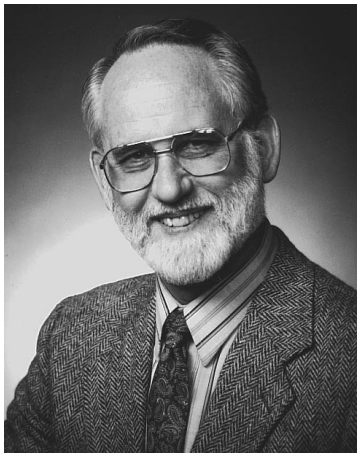

David A. Nelson—For contributions to clinical psychoacoustics.

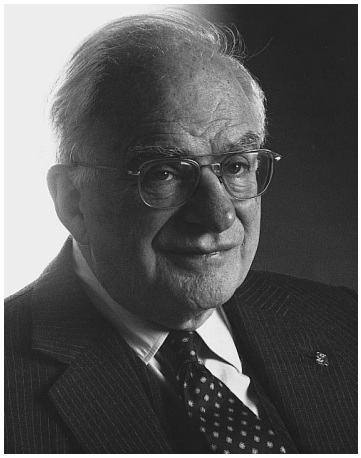

Norman C. Pickering—For contributions to violin acoustics and high-fidelity reproduction of music.

Patrick M. Zurek—For contributions to binaural hearing and signal processing for improved hearing aids.

News from the Robert Bradford Newman Student Award Fund

[*Editor's Note:* The Newman Fund is sponsored by the Greater Boston Chapter of the Acoustical Society of America in cooperation with the Society's Technical Committees on Architectural Acoustics and Noise and the ASA Committee on Education.]

Eight Newman Medals awarded to students during 1996

In 1996, the eleventh year of the Robert Bradford Newman Student Award Medal program, eight students were selected to receive the medal ''For Merit in Architectural Acoustics.'' Two of this year's recipients attend architectural schools not previously represented on the awards list—the University of Waterloo in Ontario and the École d'Architecture de Paris, Belleville, France.

Following is a list of the recipients of medals and their projects:

Katherine Bambrick Ambroziak
Princeton University
Outdoor Performing Area of the Boys Choir of Harlem

Fiorella Dinoi
University of Waterloo, Ontario
Acoustics in Atrium Spaces

Jennifer Drain
Roger Williams University
Priscilla Beach Performing Arts Center
Plymouth, MA

Joseph Louis King
Clemson University
Acoustic Solutions for an AIDS Inpatient Environment

Robert M. Lilkendey
University of Florida
Noise Exposure and Hearing Conservation Programs for Construction Workers

Thomas J. McGraw
University of Kansas
An Acoustical Survey of Selected Lecture Halls at the University of Kansas

Marie-Catherine Sklavenitis
École d'Architecture de Paris
Rénovation de la salle Popesco du Théâtre Marigny à Paris

Deirdre Terzian
Massachusetts Institute of Technology
The Movement of Sound Through the Galleries at the Davis Museum

David Eplee Fund to provide Beranek Book for future medalists

A special fund was established in 1996 in memory of David Eplee, a medalist in 1989, who designated that the Newman Student Award Fund should be the recipient of a gift from his estate.

The Advisory Committee has chosen to utilize this fund to give an autographed copy of Leo L. Beranek's new book, *Concert and Opera Halls: How They Sound* to all medalists in 1997 and henceforth. The Beranek book is available through the ASA Books^{+} program and is published by the Acoustical Society of America.

1996 Schultz Grant awarded to Gary W. Siebein

Gary W. Siebein, Professor and Director, Architectural Technology Research Center, at the University of Florida, in Gainesville, has been awarded the fourth Theodore John Schultz Grant, sponsored by the Newman Student Award Fund.

 0001-4966/97/101(4)/1751/8/$10.00

Professor Siebein, a Principal of Siebein Associates, was selected from a group of applicants considered for this grant which is awarded every year or two to teachers of architectural acoustics. Professor Siebein was also the recipient of the first Schultz Grant in 1990.

The grant will be used to prepare ''An Acoustical History of Theaters and Concert Halls, Parallel Developments in Music, Performance Spaces and the Orchestra.'' The multi-media presentations that will be the product of this study will be available in the future at no cost to the schools of architecture.

Schultz grant for 1997 announced

The Advisory Committee has also announced that a fifth Schultz Grant will be awarded in 1997. The grant provides partial support to the development of improved teaching methods, new curricula, or research in architectural acoustics education. Applicants must have teaching experience in acoustics and should manifest a strong desire to develop improved methods of teaching architectural acoustics.

Applicants for this grant should send a curriculum vitae, a letter describing how the grant will be used, and an outline budget indicating expenses for which support is being sought. Applications and attachments should be postmarked no later than 30 June 1997, and mailed to: Schultz Grant, c/o Newman Student Award Fund, P.O. Box 6349, Lincoln Center, MA 01773.

For further information, applicants are encouraged to contact Carl Rosenberg (617-499-8052) or Bill Cavanaugh (508-443-7871).

Eleven-year review of medalists, at 31 schools

1996 marked the eleventh year of Newman Student Award Medal program. During these years, medals have been given ''For Merit in Architectural Acoustics'' to a total of 101 students.

In addition to these medals, ASA books—which will now include Beranek's *Concert and Opera Halls*—have also been presented to all medalists. They are:

Halls for Music Performance, Two Decades of Experience, edited by Talaske, Wetherill & Cavanaugh (1982)

Acoustics of Worship Spaces, edited by Lubman & Wetherill (1985).

Theaters for Drama Performance, Recent Experience in Acoustical Design, edited by Talaske & Boner (1987)

Acoustical Design of Music Education Facilities, edited by McCue & Talaske (1990)

Approximately one-third of the projects for which students have been recognized have involved research projects, whereas the remainder have related to specific building applications. Approximately two-thirds of these building applications have focused on listening and performance spaces.

The 31 schools that have participated in this program include 5 architectural schools outside of the United States and one music school, the Berklee College of Music, in Boston, a school that offers a full course in Architectural Acoustics.

The following is a list of these 31 institutions. The number of students who have been awarded the Newman medals during the past 11 years is also indicated:

UNITED STATES

Schools of Architecture

Boston Architectural Center	6
California Polytechnic State University	1
Clemson University	12
Cornell University	1
Georgia Institute of Technology	1
Harvard Graduate School of Design	2
Iowa State University	4
Kent State University	1
Massachusetts Institute of Technology	4
Oklahoma State University	6
Pennsylvania State University	6
Princeton University	6
Rhode Island School of Design	8
Roger Williams University	2
Southern California Institute of Architecture	1
University of Arizona	1
University of California, Los Angeles	1
University of Florida	11
University of Illinois	1
University of Kansas	5
University of Maryland	3
University of North Carolina, Charlotte	3
University of Texas, Arlington	1
Virginia Polytechnic Institute	1

Music Schools

Berklee College of Music	1

INTERNATIONAL

Çambridge University, England	1
École D'Architecture de Paris, France	1
University of Aukland, New Zealand	6
University of Ricardo Palma, Peru	2
University of Waterloo, Canada	1
University of Western Australia	1

Further information on the fund's activities is available from the fund's headquarters. Please address correspondence to: RBN Student Award Fund, P.O. Box 6349, Lincoln Center, MA 01773, Telephone: 617-259-9299, Fax: 617-259-8136.

Regional Chapter news

Delaware Valley: On Wednesday, 13 November 1996, the Delaware Valley Chapter of ASA met with the Philadelphia Section of AES at the Studios of WHYY-TV and FM, the Public stations in Philadelphia. Don Carlson of Industrial Acoustics spoke about modular studios. IAC has built hundreds of such studios for radio, television, and recording use since 1952. They are favored today by owners who occupy rental space, as they can be disassembled and moved. The new Quad Series VIII studio was introduced at NAB and AES this year and features 65-dB noise isolation, and choice of absorbing and diffusing interior panels. After this presentation, Dr. John Barry of USDOL–OSHA introduced a Russian visitor, Alexander Bogachov, Director of Dynamic Technologies, Ltd., Moscow. Mr. Bogachov gave a short talk on the state of acoustics in Russia today. During the Soviet era, he and many colleagues were employed by government funded institutes doing acoustics research. Today, he is a private consultant engaged in such projects as noise control in apartment buildings, and testing of audio systems. Other acoustical engineers are less fortunate: one distinguished colleague, he said, is in the business of importing tea. The group enjoyed a sandwich and fruit buffet prepared by Sharon Sank, who does mailings for the ASA Chapter and the AES Section.

JON R. SANK

USA Meeting Calendar

Listed below is a summary of meetings related to acoustics to be held in the U.S. in the near future. The month/year notation refers to the issue in which a complete meeting announcement appeared.

1997

13–16 April	23rd International Symposium on Acoustical Imaging, Boston, MA [Sidney Lees, Bioengineering Dept., Forsyth Dental Ctr., 140 Fenway, Boston, MA 02115; FAX: 617-262-4021; E-mail: slees@forsyth.org]. *7/96*
12–14 May	Third AIAA/CEAS Aeroacoustic Conference, Atlanta, GA [Dr. Stephen Engelstad, Lockheed Martin Aeronautical Systems, D/73-47, Z/0-685, Marietta, GA 30063, Tel.: 770-494-9178; FAX: 770-494-3055; E-mail: sengelstad@fs2.mar.1mco.com].
9–13 June	Acoustic Emission Workshop Group (AEWG) 40th Regular Meeting and Primer, Evanston, IL [David W. Prine, Program Chair, 40th AEWG Meeting, Infastructure Technology Inst., Northwestern Univ., 1801 Maple

Ave., Evanston, IL 60201-3140, Tel.: 847-491-2873; FAX: 847-467-2056; E-mail: dprine@nwu.edu].

15–20 June — Eighth International Symposium on Nondestructive Characterization of Materials, Boulder, CO [Debbie Harris, The Johns Hopkins University, Ctr. for Nondestructive Evaluation, 102 Maryland Hall, 3400 N. Charles St., Baltimore, MD 21218, Tel.: 410-516-5397; FAX: 410-516-7249, E-mail: cnde@jhuvms.hcf.jhu.edu].

15–17 June — NOISE-CON 97, State College, PA [Institute of Noise Control Engineering, P.O. Box 320, Arlington Branch, Poughkeepsie, NY 12603, Tel.: 914-891-1407; FAX: 914-463-0201].

16–20 June — 133rd meeting of the Acoustical Society of America, State College, PA [ASA, 500 Sunnyside Blvd., Woodbury, NY 11797, Tel.: 516-576-2360; FAX: 516-576-2377; E-mail: asa@aip.org, WWW: http://asa.aip.org].

9–13 July — International Clarinet Association, Texas Tech Univ., Lubbock, TX [Keith Koons, Music Department, Univ. of Central Florida, P.O. Box 161354, Orlando, FL 23816-1354, Tel.: 407-823-5116; E-mail: kkoons@pegasus.cc.ucf.edu].

7–11 Sept. — American Academy of Otolaryngology—Head and Neck Surgery, San Francisco, CA [American Academy of Otolaryngology—Head and Neck Surgery, One Prince St., Alexandria, VA 22314, Tel.: 703-836-4444; FAX: 703-683-5100].

22–24 Sept. — Second Biennial Hearing Aid Research and Development Conference, Bethesda, MD [National Institute of Deafness and Other Communication Disorders, 301-907-3844; FAX: 301-907-9666; E-mail: hearingaid@tascon.com].

1–5 Dec. — 134th meeting of the Acoustical Society of America, San Diego, CA [ASA, 500 Sunnyside Blvd., Woodbury, NY 11797, Tel.: 516-576-2360; FAX: 516-576-2377; E-mail: asa@aip.org, WWW: http://asa.aip.org].

1998

21–26 June — Thirteenth U.S. National Congress of Theoretical and Applied Mechanics, Gainesville, FL [Martin A. Eisenberg, AeMES Dept., Univ. of Florida, P.O. Box 116250, Gainesville, FL 32611-6250, Tel.: 352-392-0961; FAX: 352-392-7303; E-mail: meise@eng.ufl.edu].

22–26 June — 135th meeting of the Acoustical Society of America/16th International Congress on Acoustics, Seattle, WA [ASA, 500 Sunnyside Blvd., Woodbury, NY 11797, Tel.: 516-576-2360; FAX: 516-576-2377; E-mail: asa@aip.org, WWW: http://asa.aip.org].

13–17 Sept. — American Academy of Otolaryngology—Head and Neck Surgery, San Francisco, CA [American Academy of Otolaryngology—Head and Neck Surgery, One Prince St., Alexandria, VA 22314, Tel.: 703-836-4444; FAX: 703-683-5100].

12–16 Oct. — 136th meeting of the Acoustical Society of America, Norfolk, VA [ASA, 500 Sunnyside Blvd., Woodbury, NY 11797, Tel.: 516-576-2360; FAX: 516-576-2377; E-mail: asa@aip.org, WWW: http://asa.aip.org].

Revisions to Membership List

New Associates

Akiyama, Iwagz, Shonan Inst. of Technology, Electrical Engineering, 1-1-25 Tsujido-nishikau-gun, Fujisawa 251, Japan

Albano, Leoni F., CIRASS, Univ. Di Napoli, v. Porta Di Massa 1, Napoli I-80133, Italy

Arai, Takayuki, Electrical Engineering, Oregon Graduate Inst., P.O. Box 91000, Portland, OR 97291-1000

Asaki, Thomas J., Los Alamos National Lab., MS K764, Los Alamos, NM 87545

Austin, Thomas C., 23 Wampum Rd., East Falmouth, MA 02536

Baffoni, Frank A., 65 Ann Dr., East Greenwich, RI 02818

Bastaki, Mahmood A., P.O. Box 52669, Dubai, United Arab Emirates

Behler, Gottfried K., Iw Winkel 16, Roetgen 52-159, Germany

Benjamin, Kim C., 55 Cedar Ave., Portsmouth, RI 02871

Bernstein, Larry S., Spectral Sciences, Inc., 99 South Bedford St., Burlington, MA 01803

Bliss, Donald B., Mechanical Engineering and Materials Sci., Duke Univ., Hudson Hal, Science Dr., Durham, NC 27708

Bonneau-Chareau, Anne, CRIN-CNRS, Campus Scientifique BP 239, Vandoeuvre les Nancy 54506, France

Brenner, Michael P., Mathematics Dept., Massachusetts Inst. of Technology, 77 Massachusetts Ave., Cambridge, MA 02139

Bronsdon, Robert L., Walt Disney Imagineering, 1401 Flower St., Glendale, CA 91221

Bruno, Anthony B., P.O. Box 1447, New London, CT 06320

Bucka, Michael P., Acoustical Analysis Associates, Inc., 22148 Sherman Way, Ste. 206, Canoga Park, CA 91303

Campbell, Nick, ATR, ITL, Seika-cho, Hikari-dai 2-2, Kyoto 619-02, Japan

Causse, Rene E., IRCAM, 1 place Igor Stravinsky, Paris 75004, France

Chadwell, C. David, Marine Physical Lab., Scripps Inst. of Oceanography, 9500 Gilman Dr., La Jolla, CA 92093-0205

Challis, Louis A., Challis and Associates, 246/248 Dowling St., Kings Cross, Sydney, NSW 2011, Australia

Chang, Enson, Dynamics Technology, Inc., 21311 Hawthorne Blvd., #300, Torrance, CA 90503

Cheeke, David, Physics Dept., Concordia Univ., 1455 de Maisonneuva Blvd., West, Montreal, PQ H3G 1M8, Canada

Choi, Singhoon, Dept. of Supercomputer Applications, Samsung Advanced Inst. of Tech., P.O. Box 111, Suwon 440-600, Korea

Christensen, Claus L., Dept. of Applied Acoustics, DTU, Bygning 352, Lyngby 2200N, Denmark

Chung, Sang K., Jet Propulsion Lab., MS 183-401, 4800 Oak Grove Dr., Pasadena, CA 91109

Connor, Laurence N., AOP & E, Woods Hole Oceanographic Inst., MS #9, Woods Hole, MA 02543

Copmann, Kathryn S., Speech Language Pathology/Audiology, Loyola College, 4501 North Charles St., Baltimore, MD 21210

Crossland, Linda S., 4526 Tarantella Ln., San Diego, CA 92130

De la Fuente Garcia, Rebeca, Multifamiliar IMSS edit. 26, D. Col. Narvarte 03020 DF, Mexico

De Mori, Renato, School of Computer Science, McGill Univ., 3480 Univ., Montreal, PQ H3A 2A7, Canada

DeJaco, Jerome F., 9990 Scripps Vista Way, #87, San Diego, CA 92131

DiIorio, Daniela, SACLANTCEN, CMR 436, APO, AE 09613-5000

Duenas, Alberto D., DMV Ltd., Gamma House, Enterprise Rd., Chilworth, Hampshire SO16 7NS, U.K.

Duncan, Stephen F., School of Music, Eastern New Mexico Univ., Station 16—ENMU, Portales, NM 88130

Dunlop, John I., Physics Dept., Univ. of South Wales, Barker St., Kennington, Sydney, NSW 2033, Australia

Dupont, Peirre E., Aerospace and Mechanical Engineering, Boston Univ., 110 Cummington St., Boston, MA 02215

Duraiswami, Ramani, 6005 Cloudy April Way, Columbia, MD 21044

Edgerton, Michael E., Waisman Center #469, Univ. of Wisconsin—Madison, 1500 Highland Ave., Madison, WI 53705-2280

Farrara, Katherine W., 215 Lake Clab Court, #203, Charlottesville, VA 22902

Filippi, Paul J. T., CNRS-LMA, 31 Chemin Joseph Aiguier, Marseille, Cedex 20, 13402, France

Fischer, Sven, Rollnerstr. 134, Neurnberg 90408, Germany

Frederiksen, Erling, Egebaekveg 23, Holte DK-2840, Denmark

Friberg, Anders K., Speech, Music and Hearing, KTH, Box 70014, Stockholm S-100 44, Sweden

Gascon, Francisco, Univ. de Sevilla, Fisica Aplicada, Reina Mercedes 2, Sevilla 41012, Spain

Gelman, Leonid M., National Tech. Univ. of Ukraine, Dept. of Non-Destructive Testing, pr. Peremogy 37, Kiev 252056, Ukraine

Girolami, Gerard M., Equize Acoustique, Univ. de Corse, Corte 20250, France

Gold, Martin A., Univ. of Florida, 231 ARCH, Gainesville, FL 32611

Gramtorp, Johan, Bruel and Kjaer, Transducers R & D, Skodsborgvej 307, Nerum 2850, Denmark

Habault, Dominique M. L., CNRS-LMA, 31 Chemin J. Aiguier, Marseille, Cedex 20, 13402, France

Hallgren, Asa V., Telia Research AB, Strategic Knowledge, Marinens v. 30, Haninge 13680, Sweden

Hamilton, David A., Noise and Vibration, Cummins Engine Co., M/C 71400 Box 3005, Columbus, IN 47202-3005
Haresign, Tim, Dept. of Natural and Mathematical Sciences, Jimmy Leeds Rd., Pomona, NJ 08240
Harun, Mokhtar, Electrical Engineering, Univ. of Technology Malaysia, FKE, UTM 81300, Skudai Johor, Malaysia
Hayes, Bruce P., Dept. of Linguistics, UCLA, Los Angeles, CA 90095-1543
Heffner, Rickye S., Psychology Dept., Univ. of Toledo, 2801 Bancroft, Toledo, OH 43606
Helweg, David A., NCCOSC, RDT&E Division, Code D-351, 53560 Hull St., San Diego, CA 92152-5001
Hofmans, Geert C. J., Noederlandplein 85, Eindhoven 5620 AH, The Netherlands
Holmes, Peter R., 10 Wattle Rd., Hawthorn VIC 3067, Australia
Holzrichter, John F., Lawrence Livermore Lab., L-3, 700 ''E'' Ave., Livermore, CA 94550
Honda, Kiyoshi, Waisman Center, Univ. of Wisconsin, 1500 Highland Ave., Madison, WI 53705
Hoole, Philip A., Inst. fur Phonetik, Ludwig-Maximiliang Univ., Schellingstr. 3, Munich D-80799, Germany
Kam, Yiu-Kee, Block B, 2/F Braemar Terrace, Pak Fuk Rd., North Point, Hong Kong
Kamiirisa, Hikaru, Information & System Engineering Div., Akishima Laboratories, Inc., Tsutsujigaoka 1-1-50, Akishima, Tokyo 196, Japan
Ke, Liu, Inst. of Acoustics, No. 17, Zhongguancun St., Beijing 100080, China
Keren, Gilad, US Waves, Inc., c/o Shelly Henry, 6716 Central Ave. Pike, Knoxville, TN 37912
Kondic, Ljubinko, Mathematics Dept., New York Univ., 251 Mercer St., New York, NY 10012
Laney, Hyru W., Science Applications International Corp., 1710 Goodridge Dr., McLean, VA 22102
Lanza, Gregory M., 12042 Gardengate Dr., St. Louis, MO 63146
Le Boeuf, Burney J., Biology Dept., Univ. of California, Rm. A332, EMS Bldg., Santa Cruz, CA 95064
Lea, Wayne A., Speech Science Inst., 201 West Burnsville Parkway, Ste. 156, Burnsville, MN 55337
Lee, Dong Hoon, Mechanical Engineering, Seoul National Polytechnic Univ., 172, Kongneung-dong, Nowon-gu, Seoul 139-743, Korea
Leep-Apolloni, Laurine, Computer Aided Engineering, Ford Motor Co. Research Lab., P.O. Box 2053, MD 2122-SRL, Dearborn, MI 48121
Li, Jing-Fang, #106-8675 French St., Vancouver BC V6P 4W5, Canada
Lohse, Detlef, Dept. of Physics, Univ. of Marburg, Renthof 6, Marburg 35032, Germany
Long, Russel K., WJ Gould Voice Research Center, Denver Center for the Perfomring Arts, 1245 Champa St., Denver, CO 80204
Lu, Ya Yan, Mathematics Dept., City Univ. of Hong Kong, 83 Tat Chee Ave., Kowloon, Hong Kong
Lunde, Per, Industrial Instrumentation, Christian Michelsen Research AS, Fantoftvegen 38, Fantoft-Bergen N-5036, Norway
Manning, Jason F., EVG, Applied Research Laboratories, 10000 Burnet Rd., Austin, TX 78713
Mariani, Joseph J., LIMSI-CNRS, BP 133, Orsay, Cedex 91403, France
Masaki, Shiobu, ATR Human Information Processing Research Laboratories, Dept. 4, 2-2 Hikaridai, Seika-cho, Soraku-gun, Kyoto 619-02, Japan
Masters, W. Mitchell, Zoology Dept., Ohio State Univ., 1735 Neil Ave., Columbus, OH 43210
Moren, Per, National Defence Research Est., Dept. 64, Stockholm 172-90, Sweden
Morgan, Dennis R., 4 Sycamore Ln., Morristown, NJ 07960
Morris, Robert L., NRaD, Code D44213, 53245 Patterson Rd., San Diego, CA 92152
Naganuma, Daisuke, 3-23 Nishifuna 6, Funabashi, Chiba 273, Japan
Nakashima, Hirotake, 5-2-48 Seiwadai-higashi, Kawanishi, Hyogo 666-01, Japan
Narahara, Yoshimasa, Dept. of Human Development, School of Humanities and Culture, Tokai Univ., 1117 Kitakaname, Hiratsuka-shi, Kanagawa-ken 259-12, Japan
Nielsen, Jesper R., GN Danavox AS, Technical Audiology, Markarvej 2A, Taastrup 2630, Denmark
Nielsen, Rudolf M., R. M. Nielsen Assoc. & Rep. Ltda., Rua Armando Barbedo 480 s. 402, Porto Alegre RS 91920-520, Brazil
Orduna-Bustamante, Felipe, Centro de Instrumentos, UNAM, Seccion de Acustica, Circuito Exterior CI, Mexico DF CP 04510, Mexico
Ozaki, Shunji, Oki Electric Industry Co., Ltd., Electronic & Communication Systems Lab., 10-3 Shibaura, 4-chome, Minato-ku, Tokyo 108, Japan
Pare, Serge, 11380 Royale Ave., Beaupre, PQ G0A 1E0, Canada
Paul, James G., Acoustics and Security Systems, Lockheed Martin Canada, 3001 Solandt Rd., Kanata, ON K2K 2M8, Canada
Pavel, Michael, Electrical Engineering, Oregon Graduate Inst., P.O. Box 91000, Portland, OR 97291-1000
Pawlowicz, Richard A., Dept. of Earth and Ocean Sciences, Univ. of British Columbia, 6270 Univ. Blvd., Vancouver, BC V6T 1Z4, Canada
Peil, Christopher, ReSound Corporation, 220 Saginaw Dr., Redwood City, CA 94063
Perrier, Pascal H. L., 10 Chemin des Marronnieres, Sassenage F-38360, France
Perry, James M., 132 Harrow Rd., Westfield, NJ 07090
Pihl, Jorgen N. B., Trastbacken 11, Spanoa S-16354, Sweden
Piwakowski, Bogdaw, Ecole Centrale de Lille, Lab. de Physique des Vibrations et d'Acoustique, Cite Scientifiqued, BP 48, Villeneuve d'Ascq 59651, France
Power, Jeff, 22 Cambridge Rd., Oakington, CB4 5BG, England
Proud, William G., Physics Dept., Univ. of Cambridge, PCS Group, Cavemdish Lab., Madingley Rd., Cambridge, Cambridgeshire CB3, OHE, U.K.
Ramstrum, Gunnar G., NRaD, 53245 Patterson Ave., San Diego, CA 92152
Raveendra, Satha T., Comet Development, Automated Analysis Corporation, 2805 South Industrial Highway, Ste. 100, Ann Arbor, MI 48104
Richards, Simon D., Defence Research Agency, SSPS5, DRA Winfrith, Winfrith Technology Centre, Dorset DT2 8XJ, UK
Roitblat, Herbert L., Psychology Dept., Univ. of Hawaii, 2430 Campus Rd., Honolulu, HI 96822
Rouat, Jean, Sciences Appliquees, Univ. du Quebec a Chicoutimi, 555 Boul. Universite, Chicoutimi PQ, G7H 2B1, Canada
Ryden, Leif S., Ingemansson Technology AB, Vattholmavagen 6, Uppsala S-754 23, Sweden
Saint-Vincent, Stephen, Naval Systems, Etrema Products, Inc., 2500 North Loop Dr., Ames, IA 50010
Sanghvi, Narendra T., Physiology & Biophysics, Indiana Univ. School of Medicine, 635 Barnhill Dr., Indianapolis, IN 46202
Savard, Jacques, 6398 De Gaspe, Montreal, PQ H2S 2X7, Canada
Schmidt, Jon, ReSound Corporation, 220 Jaginaw Dr., Redwood City, CA 94063
Schwartz, Bruce C., 4117 Brittany Dr., Redding, CA 96002
Sheu, Ming J., 22080 Perth Court, Novi, MI 48374
Simmer, Klaus U., Theresenstrasse 11, Bremen D-28203, Germany
Slack, Philip D., Aqua Enviroment, Inc., 3100 Kesner Blvd., Ste. N, San Rafael, CA 94901
Smith, Jerome A., Scripps Inst. of Oceanography, MPL/PORD, Code 0213, La Jolla, CA 92093-0213
Stafford, Kathleen M., CIMRS, Oregon State Univ/NOAA PMEL, 2115 SE OSU Dr., Newport, OR 97365
Stottlemyer, Thomas R., 22 Burrows St., Mystic, CT 06355
Sullivan, Patrick K., Oceanit Laboratories, Inc., 1100 Alakea St., 31st Floor, Honolulu, HI 96813
Takala, Tapio I., Helsinki Univ. of Technology, Computer Science, Otakaari 1, Espoo 02150, Finland
Thomas, Bazil, 46916 Amberwood, Shelby Township, MI 48317
Thompson, Daniel M., Berklee College of Music, Music Production and Engineering, 1140 Boylston St., Boston, MA 02115
Thwaites, Suszanne, 19 Booraba Ave., Lindfield, NSW 2070, Australia
Tuori, Timo K., Technical Research Centre of Finland, P.O. Box 1603, Jyvaskyla 40101, Finland
Umemura, Shin-ichiro, Hitachi Advanced Research Lab., Hatoyama, Saitama 350-03, Japan
Usagawa, Tsuyoshi, Dept. of Computer Science, Kumamoto Univ., 2-39-1 Kurokami, Kimamoto 860, Japan
Veilleux, Nanette M., Computer Sciences/Metropolitan College, Boston Univ., 755 Commonwealth Ave., Boston, MA 02215
Villar, Borja Z., c/Prim 47-3, San Sebastian, Guipuzcoa 20006, Spain
Vogel, Alfred, Medical Laser Center Luebeck, Peter-Monnik-Weg, Luebeck 23562, Germany
Vroomen, Jean H. M., Psychology Dept., Univ. of Tilburg, Warandelaan 2, P.O. Box 909153, Tilburg 5000LT, The Netherlands
Wakumoto, Masahiko, Dept. 4, ATR Human Information Processing, Research Lab., 2-2 Hikaridai, Seika-cho, Soraku-gun, Kyoto 619-02, Japan
Waters, Jeff H., 7642 Trailbrush Terrace, San Diego, CA 92152
Wiggins, John T., 818 Williams Ln., Chaddsford, PA 19317

Yamasaki, Yoshio, Advanced Research Center for Science and Engineering, Waseda Univ., 3-4-1 Okubo, Shinjuko-ku, Tokyo 169, Japan
Yaremchuk, Alexey I., Theoretical Dept., Andreyev Acoustics Inst., Shvernika 4, Moscow 117036, Russia
Yehia, Hani C., ATR-HIP, Dept. 4, 2-2 Hikari-dai, Seika-cho, Soraku-gun, Kyoto 619-02, Japan
Zavtrak, Sergei T., Inst. for Nuclear Problems, Bobruiskaya Str. 11, Minsk 220050, Belarus
Zhao, Yunxin, Electrical and Computer Engineering, Univ. of Illinois, 405 North Mathews Ave., Urbana, IL 61801
Zhou, Hsiao-Ling, 3215 Moss Oak Dr., Doraville, GA 30340

New Students

Ainsworth, Ron E., 585 North 400 East, #9, Provo, UT 84006
Basu, Debashis, Civil Engineering, State Univ. of New York at Buffalo, 212 Ketter Hall, Amherst, NY 14260
Bruce, Jerry W., II, Electrical & Computer Engineering, Univ. of Nevada, Las Vegas, 4505 Maryland Parkway, Box 454026, Las Vegas, NV 89154-4026
Burch, Holly A., Scripps Inst. of Oceanography, Marine Physical Lab., 0238, 9500 Gilman Dr., La Jolla, CA 92093-0238
Castasnet, Sabine, 701 NW 13th St., C-1, Boca Raton, FL 33486
Choe, Seokyun, 1163 Leahy Rd., La Mesa, Monterey, CA 93940
de Oliveira, Marcus W. N., Rua Encontro Marcado, 265, Jardim Clarice, Rio De Janeiro 22753-360, Brazil
Dudko, Yuriy V., Dept. of Ocean Engineering, Massachusetts Inst. of Technology, 77 Massachusetts Ave., Cambridge, MA 02139
Guedes, Renata, Rue Pio Correia 136/101, Rio de Janeiro 22461-240, Brazil
Hajda, John M., 1295 Federal Ave., #10, Los Angeles, CA 90025
Ham, William H., Linguistics, Cornell Univ., Morrill Hall, Ithaca, NY 14853
Hilnor, Rune P., Telecommunications/Acoustics, The Norwegian Univ. of Science and Technology, O. S. Bragstads Plass 2B, Trondheim N-7034, Norway
Jackson, Philip J. B., Dept. of Electronics and Computer Science, Univ. of Southampton, Southampton SO17 1BJ, U.K.
Kim, Sea-Moon, Dept. of Mechanical Engineering, KAIST, Yuseong-gu, 373-1, Kuseong-dong, Tae-Jon 305-701, Korea
Ladak, Hanif M., Dept. of Biomedical Engineering, McGill Univ., 3775 Univ. St., Montreal, PQ H3A 2B4, Canada
Lammers, Marc O., Marine Mammal Research Program, Hawaii Inst. of Marine Biology, P.O. Box 1106, Kailua, HI 96734
Lopez-Larrosa, Albert, Republica Argentina 167-171 2-1, Barcelona 08023, Spain
MacEachern, Margaret S., Linguistics, UCLA, 405 Hilgard Ave., Los Angeles, CA 90024
Mack, Michael J., 217 Monterey Blvd., San Francisco, CA 94131
Makashay, Matthew J., Dept. of Linguistics, Ohio State Univ., 222 Oxley Hall, 1712 Neil Ave., Columbus, OH 43210
Mar, Lindsay W., 14 Yarwood St., Marsfield, Sydney, NSW 2122, Australia
Mohammad, Mohammad A. S., 11 Bealing Close, Bassett, Southampton SO16 3AW, U.K.
Pang, Hee-Suk, Applied Acoustics Lab., Inst. of New Media and Communications, Seoul National Univ., Seoul 151-742, Korea
Perales, Olegario, 39 Gillman, Irvine, CA 92612
Philips, Jennifer D., Marine Mammal Research Program, Hawaii Inst., of Marine Biology, P.O. Box 1106, Kaneohe, HI 96734
Pray, Carl M., 2150 Lakeview Dr., Apt. 245, Ypsilanti, MI 48198
Rossi, Lucile S., Res. Belozizonte Bat. H, Quiartier Pietralba, Ajaccio 20090, France
Roy, Shiladitya, P.O. Box U-975, Univ. of South Alabama, Mobile, AL 36688-0001
Silva, Carlos A., Carlos Alberto Pinto de Abreu 141, 1 Direito, Coimbra 3040, Portugal
Smith, Steven S., 201 Vairo Blvd., Apt. 266, State College, PA 16803
Southall, Brandon L., Schusterman Lab., Long Marine Lab., UC Santa Cruz, 100 Shaffer Rd., Santa Cruz, CA 95062
Storms, Russell L., 1478A Kimball Ave., Seaside, CA 93955
Sullivan, Erin, 3301 Nittany Apts., 600 East Pollack Rd., State College, PA 16801
Sweeney, Aaron D., 3891 Miramar St., Apt. E, La Jolla, CA 92037
Tsao, Feng-Ming, Speech and Hearing Sciences, Univ. of Washington, Seattle, WA 98105
Vilar, Leonardo, 2 East 8th St., Apt. 2112, Chicago, IL 60605
Wallace, Kirk D., Lab. for Ultrasonics, Washington Univ., Dept. of Physics, 1 Brookings Dr., Campus Box 1105, St. Louis, MO 63130
West, Matthew K., Nuclear Engineering, Univ. of Missouri, E2433 Engineering Blvd. East, Columbia, MO 65211
Yoneyama, Kiyoko, Dept. of Linguistics, Ohio State Univ., 222 Oxley Hall, 1712 Neil Ave., Columbus, OH 43210
Yuan, River H., 6331 Alexander Dr., St. Louis, MO 63105
Zellner, Brigitte, LAIP, Faculte des Lettres, Univ. de Lausanne, Lausanne, 1015, Switzerland
Zhou, Shuliang, Nihon Univ., Atomic Energy Research Inst., 7-24-1 Narashinodai, Funabashi, Chiba 274, Japan

Members Elected Fellows

P. S. Beddor, L. R. Bernstein, J. S. Bolton, R. C. Coffeen, C. P. de Moustier, D. Deutsch, A. Freedman, L. M. Goldstein, J. P. Koester, A. Lofqvist, J. F. Lynch, A. L. Nuttall, R. C. Olson, N. C. Pickering, T. J. Plona, S. H. Ridgway, R. A. Roy, T. Shipp, T. Yamamoto, S. W. Yoon, P. M. Zurek

Associates Elected Members

Y. I. Bobrovnitskii, T. J. Carlson, P. A. Chinnery, D. B. Creamer, P. O. A. L. Davies, A. A. Doinikov, G. Ya Dymkin, M. P. Ekstrom, K. Grosh, Q. Hu, M. A. Kallistratova, J. B. Lawrie, J. J. Lee, A. R. Leyman, Y. Ma, A. G. Munin, K. Nakayama, D. J. Parzych, S. Santoboni, Y. Shigong, H. M. Tavossi, M. Yamashita, R. Venkatachalam, S. Zeroug, J. W. Zhang

Students to Associates

E. W. Andrews, P. T. Bangayan, C. Bartels, G. R. Bashford, H. A. Beveridge, M. W. Bonilha, P. J. Book, N. M. Carbone, M. J. Carley, D. J. Caswell, M. Conti, K. A. Doherty, A. Fujikawa, P. L. Gleason, H. E. Gockel, J. T. Goh, P. C. Guiod, A. M. Hepfer, M. Jessen, M. A. Johnson, E. J. Kim, S. A. Kleinknecht, C. L. Kussmaul, G. D. Larson, D. J. Levitin, W-L. Lin, A. J. Lotto, J. Lyzenga, M. W. Macon, I. Magrin-Chagnolleau, C-M. Mak, S. M. Meyouhas, D. C. Perrone, V. H. Poblete, B. Rapids, Z. M. Rhea, H. M. Rodriguez-Davila, A. K. Rogers, E. J. Ryerson, T. Sadralodabai, A. J. Schafer, J. Slovacek, A. E. Smith, P. E. Souza, J. Sun, R. P. Szwerc, X. Tang, K. Tom, M. E. Trainer, J. M. Trogolo, C-M. Wu

Associate to Student

L. M. Hinkelman

Reinstated

R. K. Coulson, K. G. Munhall, J. M. Niemiec—*Members*

D. E. Capine, J. L. Curtis, J. R. Dubberley, D. D. Gurdak, C. Herman, G. Krishnan, M. F. Morrison, L. J. White—*Associates*

K. D. Frampton—*Student*

Resigned

G. R. Garrison, D. F. Gordon—*Fellows*

L. E. Bergeron, W. Clayman, A. H. H. Cops, J. H. Delk, D. F. Gingras, K. M. Goudie-Marshall, A. C. Grippo, S-L. Hall, G. E. Liddiard, G. A. Lynch, H. A. J. Rynja, C. A. Sheridan, F. L. Striffler, J. P. Walsh—*Members*

J. W. Carre, D. R. Edwards, J. Franken, W. C. Nowlin, B. L. Patterson, P. R. Vandermeulen, L. D. West, A. S. Wright, J. R. Yarnall—*Associates*

M. L. Anderson—*Student*

Deceased

M. B. Gardner, F. E. Hale, O. E. Mattiat, H. L. Rich, H. F. Schuknecht, W. Dixon Ward—*Fellows*

C. J. Hemond, Jr., D. J. Karbo, W. T. Rawley, K. Ross, D. M. Sherwood, C. Stromsta, D. Thompson—*Members*

H. G. Beaver, I. S. Goodman, R. Hetu, R. W. Krug, H. E. Rodman—*Associates*

M. C. Isaac—*Student*

Fellows	799
Members	2765
Associates	2871
Students	871
	7306

ACOUSTICAL NEWS—INTERNATIONAL

Walter G. Mayer
Physics Department, Georgetown University, Washington, DC 20057

International Conference on the Divine Bell of King Songdok—Seoul, November 1996

Foremost among the many fine temple bells in Korea is the King Songdok (''Emille'') bell in Kyungju, which is a national symbol. Cast during the Silla dynasty (771 A.D.), it stands 3.66 m high and has a mass of nearly 20 000 kg. To honor this national treasure, the Korean Acoustical Society and the Kyungju National Museum organized an international conference with invited speakers from Korea, China, Japan, and the United States. It was a distinct privilege for me to participate in the event (see Fig. 1).

FIG. 1. The author and a small bell at the speakers' podium.

The conference was held in the beautiful Sejong Conference Center in Seoul. The conference was efficiently organized by Professor Yong Ohk Chin, Kyung Hee University, and his colleagues with support from the Chong Kun Dang Corporation, a pharmaceutical company. Papers dealt with the various scientific and historical studies on the King Songdok bell as well as comparisons of Korean bells with bells in other cultures. Attendees at the joint ASA/ASJ meeting in Honolulu will recall the interesting video tape (in the Acoustics Gallery exhibit) showing the results of acoustical holographic studies of radiation from the King Songdok bell by Professor Kim Yang-Hann and his colleagues at the Korean Advanced Institute of Science and Technology. The conference papers were published (in Korean) in a conference proceedings.

THOMAS D. ROSSING
Physics Department
Northern Illinois University
DeKalb, Illinois 60115

Papers published in JASJ(E)

A listing of Invited Papers and Regular Papers appearing in the latest issue of the English language version of the Journal of the Acoustical Society of Japan, JASJ(E), was published for the first time in the January 1995 issue of the Journal. This listing is continued below.

The January issue of JASJ(E), Vol. 18, No. 1 (1997) contains the following papers:

L. Hu, S. Imai, and C. Furuichi ''Phonemic segmentation for continuous Mandarin speech recognition''
K. Ozawa, Y. Suzuki, H. Uematsu, and T. Sone ''Effects of aural combination tones on the loudness of a pure tone masked by an inharmonic pure tone''
M. Takasu ''Vocalness of the female singing voice''
K. Miura and Y. Yasuno ''Long term sensitivity changes in electret condenser microphones''
S. Saito ''Nonlinearly propagating focused sound transmitted through solid plates''

International Meetings Calendar

Below are announcements of meetings to be held abroad. Entries preceded by an * are new or updated listings with contact addresses given in parentheses. Month/year listings following other entries refer to issues of the *Journal* which contain full calendar listings or meeting announcements.

April 1997

2–4	**International Symposium on Simulation, Visualization, and Auralization for Acoustic Research and Education**, Tokyo. *2/96*
7–9	**Acoustics 97**, Windermere. *2/97*
14–18	**Fourth French Congress on Acoustics**, Marseille. *6/96*
16–19	**2nd European Conference on Protection against Noise**, London. *2/97*
21–24	**International Conference on Acoustics, Speech, and Signal Processing—ICASSP 97**, Munich. *10/95*
21–25	**International Conference on Shallow-Water Acoustics**, Beijing. *10/96*

May 1997

12–16	**FASE Symposium on Hydroacoustics and Ultrasonics**, Jurata/Gdańsk. *4/96*
21–23	**Italian Acoustical Association Annual Meeting**, Perugia. *8/96*

June 1997

3–5	**8th International Meeting on Low Frequency Noise & Vibration**, Gothenburg. *2/97*
4–6	***International Conference on Computational Acoustics and its Environmental Applications**, Terni, Italy. (L. Morton, Wessex Institute of Technology, Ashurst, Southampton S040 7AA, UK; Fax: +44 1703 29 28 53; E-mail: lynn@wessex.witcmi.ac.uk)
5–7	**Conference on ICP and Inner Ear Pressure**, Bath. *4/96*
18–21	**3rd European Conference on Audiology**, Prague. *12/96*
23–25	**1st International Conference on Marine Electromagnetics**, London. *2/97*
24–27	**1st European Conference on Signal Analysis and Prediction**, Prague. *8/96*
25–27	**12th Echocardiology Symposium and 9th Meeting of the International Cardiac Doppler Society**, Rotterdam. *6/96*
25–27	**5th International Congress of the International Society of Applied Psycholinguistics** (ISAPL '97), Porto. *10/96*

July 1997

2–4	**Ultrasonics International '97**, Delft. *4/96*

 0001-4966/97/101(4)/1759/2/$10.00

14–17 **6th International Conference on Recent Advances in Structural Dynamics**, Southampton. *2/97*

21–25 ***4th International Conference on Natural Physical Processes Related to Sea Surface Sound**, Chilworth Manor, Hampshire, UK. (ISVR Conference Secretary, University of Southampton SO17 1BJ, UK; Fax: +44 11703 59 30 33; E-mail: mzs@isvr.soton.ac.uk)

August 1997

18–22 **3rd EUROMECH Solid Mechanics Conference**, Stockholm. *10/96*

19–22 **International Symposium on Musical Acoustics**, Edinburgh. *8/96*

21–23 **ACTIVE 97 Inter-Noise Satellite Symposium**, Budapest. *6/96*

24–27 **1997 World Congress on Ultrasonics**, Yokohama. *4/96*

25–27 **Inter-Noise 97**, Budapest. *2/96*

September 1997

1–4 **Modal Analysis Conference** (IMAC-XV Japan), Tokyo. *10/96*

10–12 **Biennial Conference New Zealand Acoustical Society**, Christchurch. *4/96, 12/96*

9–12 **31st International Acoustical Conference ''Acoustics-High Tatra 97''**, High Tatra. *10/96*

10–12 **Biomechanics of Hearing**, Stuttgart. *10/96*

15–18 **3rd EUROMECH Fluid Mechanics Conference**, Göttingen. *10/96*

18–19 ***4th Mexican Congress on Acoustics**, Gunnajuato, Gto., Mexico. (The Mexican Institute of Acoustics, P.O. Box 7805.07300, Mexico City, Mexico; Fax: +52 5 523 4742; E-mail: sberista@vmredipn.ipn.mx)

18–20 **Intonation: Theory, Models and Applications**, Athens. *2/97*

22–25 **5th European Conference on Speech Communication and Technology**, Patras. *2/96*

23–26 **Fluid-structure Interaction in Acoustics**, Delft. *10/96*

October 1997

7–10 **1997 IEEE Ultrasonics Symposium**, Toronto. *2/96*

8–10 **Acoustics Week in Canada 1997**, Windsor. *12/96*

23–26 **Reproduced Sound 13**, Windermere. *2/97*

November 1997

19–21 **WESTPRAC'97**, Hong Kong. *10/96*

20–23 **IOA Autumn Conference: Environmental Noise**, Windermere. *2/97*

December 1997

15–18 **5th International Congress on Sound and Vibration**, Adelaide. *10/96*

March 1998

23–27 **DAGA 98** (German Acoustical Society Meeting), Zürich. *8/96*

May 1998

25–27 **Noise and Planning 98**, Naples. *2/97*

June 1998

8–10 **EAA/EEAA Symposium ''Transport Noise and Vibration,''** Tallinn. *10/96*

November 1998

16–18 **Inter-Noise 98**, Christchurch. *4/96*

23–27 **ICBEN 98: Biological Effects of Noise**, Sydney. *12/96*

REVIEWS OF ACOUSTICAL PATENTS

Daniel W. Martin
7349 Clough Pike, Cincinnati, Ohio 45244

The purpose of these acoustical patent reviews is to provide enough information for a Journal reader to decide whether to seek more information from the patent itself. Any opinions expressed here are those of reviewers as individuals and are not legal opinions. Printed copies of United States Patents may be ordered at $3.00 each from the Commissioner of Patents and Trademarks, Washington, DC 20231. [S0001-4966(97)04604-3]

Reviewers for this issue:

GEORGE L. AUGSPURGER, *Perception Incorporated, Box 39536, Los Angeles, California 90039*
SAMUEL F. LYBARGER, *101 Oakwood Road, McMurray, Pennsylvania 15317*
D. LLOYD RICE, *11222 Flatiron Drive, Lafayette, Colorado 80026*
ERIC E. UNGAR, *Bolt, Beranek, and Newman Incorporated, 50 Moulton Street, Cambridge, Massachusetts 02238*

5,528,234

43.28.Tc TRAFFIC MONITORING SYSTEM FOR DETERMINING VEHICLE DIMENSIONS, SPEED AND CLASS

Siva A. Mani, Lexington, MA and Arunachalam Balaraman, Groton, MA
18 June 1996 (Class 340/933); filed 1 February 1994

This traffic monitoring system has monitoring stations **10A** distributed along many roads. Each station contains a pair of sonar modules **12A**, **B** that are spaced apart along the road, that measure the height of the vehicle **19** and the time it takes for travel between the two modules. A microcontroller **14A** at each station divides the separation distance by the travel time to

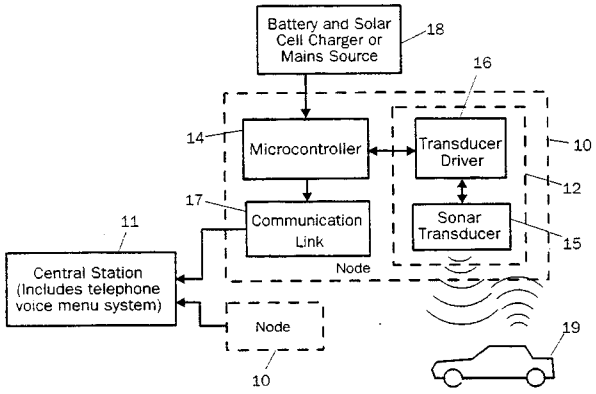

calculate vehicle speed. Vehicle length is estimated by multiplying calculated speed by the time taken for a vehicle crossing, and the class of vehicle is estimated from a probability table relating vehicle dimensions with vehicle classes. Information is transmitted to a central station **11** for overall traffic analysis.—DWM

5,528,224

43.28.Vd OPTICAL AND ACOUSTIC WEATHER IDENTIFICATION SYSTEM

Ting-I Wang, assignor to Scientific Technology, Incorporated
18 June 1996 (Class 340/583); filed 19 May 1995

An optical weather identification system is equipped with an additional channel in which a microphone beneath a solid dome transmits the noise of precipitation falling upon the dome. For sleet or hail, the noise spectrum transmitted by the microphone contains more high-frequency content than for rain, producing a separate classification for sleet or hail in addition to prior optical distinctions for rain and snow.—DWM

5,569,888

43.35.Zc ULTRASONIC ELEVATOR DOOR SAFETY SYSTEM

Sanjay Kamani and John K. Salmon, assignors to Otis Elevator Company
29 October 1996 (Class 187/317); filed 26 May 1994

An ultrasonic transmitter/receiver **60** positioned out of reach above and to the side of elevator doors **63**,**64** transmits a beam into the open-door space **65** by focused reflection from concave reflector **61**. A presence (e.g., a person) in the doorway reflects the beam back to the receiver, signaling the

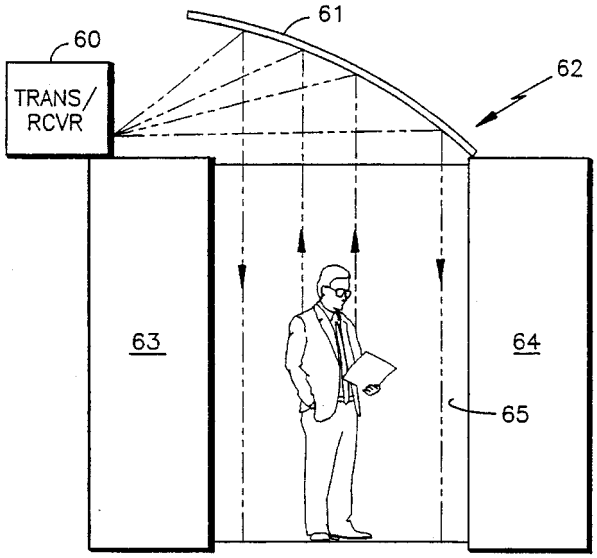

doors to remain open until the presence moves in or out. Stated advantages include lack of wear, dirt, and freedom from vandalism. The system is also usable for circular elevators with curved doors.—DWM

5,451,726

43.38.Ja OMNIDIRECTIONAL SPEAKER SYSTEM

Ted L. Haugum, assignor to Eclipse Research Corporation
19 September 1995 (Class 181/150); filed 25 April 1994

So-called omnidirectional radial horns typically project an intense

 0001-4966/97/101(4)/1761/9/$10.00

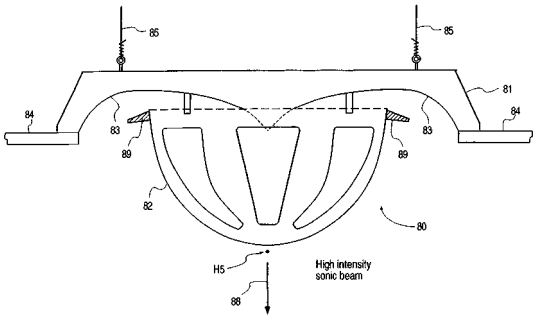

beam along the axis of rotation **88**. The patented system attempts to minimize this effect by adding an absorptive foam ring **89**.—GLA

5,526,441

43.38.Ja FULL RANGE CONVEX ELECTRODYNAMIC LOUDSPEAKER

Basilio Codnia and Juan P. Codnia, both of New Orleans, LA
11 June 1996 (Class 381/202); filed 18 August 1994

This loudspeaker appears to be a full-range cousin of Allison's pulsating dome tweeter (not referenced). The patent document is rather vague about its operating principles, but the reader can infer that stiff dome **13** will

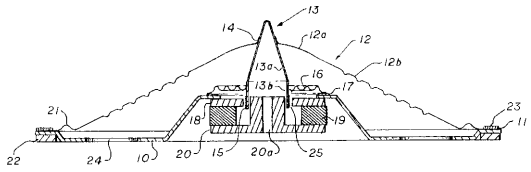

indeed reproduce high frequencies while the softer inverted cone **12** will operate as a piston at lower frequencies. The goal is to provide hemispherical radiation of sound at all audible frequencies.—GLA

5,561,717

43.38.Ja LOUDSPEAKER SYSTEM

Michael E. Lamm, assignor to American Trading and Production Corporation
1 October 1996 (Class 381/89); filed 15 March 1994

The patent explains, quite rightly, that multiple woofers can be oriented such that their inertial forces cancel out, thus minimizing cabinet vibrations. A number of commercial systems make a point of this feature.—GLA

5,412,734

43.38.Lc APPARATUS AND METHOD FOR REDUCING ACOUSTIC FEEDBACK

Samuel L. Thomasson, Gilbert, AZ
2 May 1995 (Class 351/83); filed 13 September 1993

The patent discloses a method for reducing howlback in a public address system or a hearing aid. The electrical signal from a microphone is tagged by adding an inaudible FM replica of itself. ''Any sound travelling from the speaker back to the microphone has an FM component containing the original sound. The FM component is demodulated, reconstructing the original sound. The reconstructed original sound is subtracted from the signal from the microphone, thereby removing the echo and canceling feedback.'' Somehow this sounds like an inverse perpetual motion scheme, but the patent makes interesting reading.—GLA

5,498,996

43.38.Lc HIGH-POWER, HIGH-FIDELITY TUBE AMPLIFIER

Scott G. Frankland, assignor to Wavestream Kinetics
12 March 1996 (Class 330/118); filed 21 November 1994

Each of the paralleled output tubes in this power amplifier has its own direct-coupled driver tube. Three groups of parasitic suppression components (ferrite beads) are included to maintain stability. No bypass capacitors are used.—GLA

5,509,081

43.38.Lc SOUND REPRODUCTION SYSTEM

Juha Kuusama, assignor to Nokia Technology GmbH
16 April 1996 (Class 381/103); filed in Finland 21 October 1992

This scheme, for automatic loudness control in the sound system of a vehicle, monitors and adjusts the gain of several frequency bands to compensate for frequency dependent masking.—GLA

5,566,240

43.38.Lc METHOD AND APPARATUS FOR ENHANCING THE QUALITY OF SOUND FROM ELECTRICALLY POWERED AUDIO EQUIPMENT

Ping-Cheung Lau, Hong Kong, Hong Kong
15 October 1996 (Class 381/124); filed in the United Kingdom 30 May 1991

It is an article of faith among the upper rank of ''golden ears'' that audio cables must be broken in. The patent states that ''This break-in period is as necessary for audio equipment as it is for a new car engine.'' The apparatus is a neat little box that stresses cables with square waves of various amplitudes and frequencies...in the preferred direction of signal flow, naturally. Thus, the consumer can buy audio cables that sound good right out of the box. Sometimes the benefits of modern technology are almost overwhelming.—GLA

5,521,663

43.38.Ne SOUND SYSTEM FOR STILL FILM PHOTOGRAPHY

Wyamn J. Norris III, San Jose, CA
28 May 1996 (Class 354/106); filed 22 July 1994

This still camera contains a microphone from which sound signals (titles, commentary, special effects) can be stored after conversion into digital binary form. As the film advances between exposures, this binary code is recorded on the film in the form of black and transparent bars adjacent to the picture image. After the film is developed for picture projection, a binary reading device in the projector makes the recorded audio audible when the corresponding picture is shown.—DWM

5,410,595

43.38.Si APPARATUS AND METHOD FOR NOISE REDUCTION FOR A FULL-DUPLEX SPEAKERPHONE OR THE LIKE

Sangil Park and Dion M. Funderburk, assignors to Motorola, Incorporated
25 April 1995 (Class 379/410); filed 12 November 1992

Complicated full-duplex teleconference setups using multiple microphones and loudspeakers require correspondingly complicated echo canceling devices, which tend to be noisy and time consuming to set up. What is described here is a system that measures certain acoustical qualities, calcu-

lates the minimum number of filter coefficients needed for desired results, and stores the coefficients for various microphones. During operation the coefficients are constantly updated.—GLA

5,559,855

43.38.Si SYSTEM AND METHOD FOR RECOGNIZING AND ROUTING TELEPHONE CALLS INVOLVING HEARING OR SPEECH IMPAIRED PERSONS

Jac P. Dowens and Elvis Hernandez, assignors to Lucent Technologies
24 September 1996 (Class 379/52); filed 29 November 1994

''A caller places a local, intra-LATA, or inter-LATA telephone call by adding a three digit prefix to a called party number (CPN); the prefix identifies the call as one in need of routing to an Operator Services for the Deaf (OSD) or Tele-communications Relay Services (TRS) center. The call is first routed to a switching network where a query is sent to a Universal Subscriber Data Structure database using the caller's Automatic Number Identification (ANI) and the CPN of the called party. The database responds

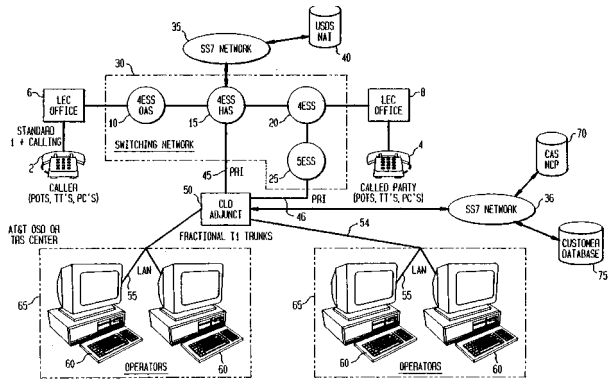

with the caller's and the called party's profiles. Thereafter, the call is routed to an adjunct which connects the call to an appropriate OSD or TRS center, whereupon the conversation can be relayed between the hearing or speech impaired person and the voice party.'' Patents 5,559,856 and 5,559,857, issued to the first inventor above and the same assignee, are closely related.—SFL

5,568,516

43.38.Si VERY LOW POWER CORDLESS HEADSET SYSTEM

Gene M. Strohallen and Robert F. Young, assignors to Phonic Ear, Incorporated
22 October 1996 (Class 375/259); filed 3 October 1994

The patent describes a cordless headset requiring very low power, using time variant modulation (TVM) for reception of a magnetic signal and TVM of radio frequency or infrared as the transmitter. The headset communicates with a base station that includes a TVM transmitter and loop. The receiver circuits in both the base station and the headset automatically adjust to variances in signal strength. Details of waveforms and circuitry are given.—SFL

5,438,623

43.38.Vk MULTI-CHANNEL SPATIALIZATION SYSTEM FOR AUDIO SIGNALS

Durand R. Begault, assignor to the United States of America
1 August 1995 (Class 381/17); filed 4 October 1993

By sensing a listener's head movement and applying appropriate pinnae-related transfer functions, virtual sound sources can be created that are stable in space. Such a technique might be used for video games, entertainment, or to enhance the intelligibility of several overlapping communications channels. The patent describes a practical method for deriving synthetic head-related transfer functions and imposing reprogrammable spatial cues to a number of audio signals received simultaneously.—GLA

5,418,335

43.40.Ph SYNCHRONIZED ACOUSTIC SOURCE

Graham A. Winbow, assignor to the Exxon Production Research Company
23 May 1995 (Class 181/106); filed 25 July 1994

The patent describes an apparatus for generating seismic waves with an improved signal-to-noise ratio. Oil and gas exploration techniques make use of seismic waves generated in boreholes by one means or another. Because a borehole makes an efficient acoustic waveguide, most of the energy is dissipated in ''tube waves'' rather than producing the desired P- and S-waves. However, by synchronizing the phase and amplitude of several acoustic sources it is possible to minimize the propagation of tube waves. The patent document includes a full description of underlying theory and is a good example of clear technical writing.—GLA

5,524,709

43.40.Ph METHOD FOR ACOUSTICALLY COUPLING SENSORS IN A WELLBORE

Robert J. Withers, assignor to Atlantic Richfield Company
11 June 1996 (Class 166/250.1); filed 4 May 1995

When a geophone is to be lowered into a wellbore for transmitting underground signals from one wellbore to others, it is advantageous to insure good acoustical coupling from the geophone through the walls of the wellbore into the surrounding earth. This patent describes a reversible method for obtaining good acoustical coupling by flowing a soluble cement into the wellbore around the geophone, allowing it to harden before signal radiation, and flowing a solvent into the wellbore to uncouple the geophone for subsequent removal.—DWM

5,518,347

43.40.Tm TUNED DAMPING SYSTEM FOR SUPPRESSING VIBRATIONS DURING MACHINING

William T. Cobb, Jr., assignor to Design and Manufacturing Solutions, Incorporated
21 May 1996 (Class 4009/141); filed 23 May 1995

This vibration attenuation system is intended for use in a boring bar or other extended tool support element that may be set into vibration during metal cutting. The system consists of a cylindrical mass that is placed into the boring bar, with some clearance between the mass and the cavity that houses it. The mass has conically chamfered ends that engage elastomeric O-rings which provide a resilient support for the mass in the cavity, so that the system acts much like a classical vibration absorber or tuned damper. In the device described in this patent there is provided an end cap that can be adjusted so as to vary the compression of the O-rings, thereby changing their stiffness and thus the resonance frequency of the damper.—EEU

5,517,357

43.40.Vn ANTI-VIBRATION OPTICAL DEVICE

Atsushi Shibayama, assignor to Nikon Corporation
14 May 1996 (Class 359/547); filed in Japan 30 March 1993

This device includes an optical vibration compensation unit that is actuated via a controller. This controller processes two signals: one that is derived from a vibration sensor attached to the objective lens system; and one derived from a detector that measures the shift in the optical axis direction of the shiftable lens of the objective lens system.—EEU

5,513,533

43.40.Yq DETECTION OF VIBRATIONAL ENERGY VIA OPTICAL INTERFERENCE PATTERNS

Bradford A. Wheeler and Antonio L. Deus, assignors to the United States of America
7 May 1996 (Class 73/657); filed 15 April 1993

A thin transparent film is applied to a surface of a structure that is subject to vibration. Changes in the film's thickness are measured by observing the interference patterns that result from a beam of coherent light being reflected from the top and bottom surfaces of the film. The frequency content of the vibration can be determined from the detected rate of change of the fringe pattern by means of standard mathematical techniques.—EEU

5,515,730

43.40.Yq APPARATUS FOR DETECTING THE AMPLITUDE, FREQUENCY OR MODES OF VIBRATION OF A VIBRATING PANEL

Shahamat Manzouri, assignor to British Aerospace PLC
14 May 1996 (Class 73/655); filed in the United Kingdom 23 November 1992

The apparatus depends on the phenomenon of Moire fringes, which are formed when coherent light incident on a diffraction grating is viewed through another identical grating. If the lines of the two gratings are parallel and one grating is displaced along a line normal to the lines of the gratings, then shades of gray are observed that vary cyclically as the displacement is increased. If the lines of one grating are projected onto a surface, the observed lines can be used to determine the motion of the surface normal to itself. In the apparatus, coherent light is projected onto a panel through a diffraction grating and the light reflected from the panel is detected by an array of photodiodes positioned behind a second diffraction grating. Signals from these diodes are analyzed by conventional means to produce the desired amplitude, frequency, and mode shape information.—EEU

5,521,840

43.50.Yw DIAGNOSTIC SYSTEM RESPONSIVE TO LEARNED AUDIO SIGNATURES

Fred H. Bednar, assignor to Westinghouse Electric Corporation
28 May 1996 (Class 364/508); filed 7 April 1994

This patent describes a system for diagnosing the presence of loose parts **22** in a pipe **32** through which liquid flows, ''such as a cooling circuit of a pressurized water nuclear reactor.'' Vibration pickup **42**, positioned

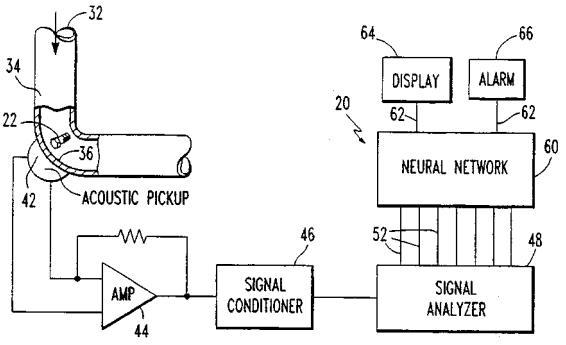

outside the bend **36** of the pipe, responds to the impact of part **22**, and the signal is analyzed and compared to previously stored signal analyses, causing a display or alarm to be operated when a match occurs.—DWM

5,570,426

43.66.Vt METHOD AND APPARATUS FOR INTRACRANIAL NOISE SUPPRESSION

William A. Gardner, Yountville, CA
29 October 1996 (Class 381/71); filed 7 December 1994

A method and apparatus are shown for active cancellation of vibrational noise produced by a medical or dental instrument in the head of a patient. Vibrations of the instrument and those in the head are sensed and

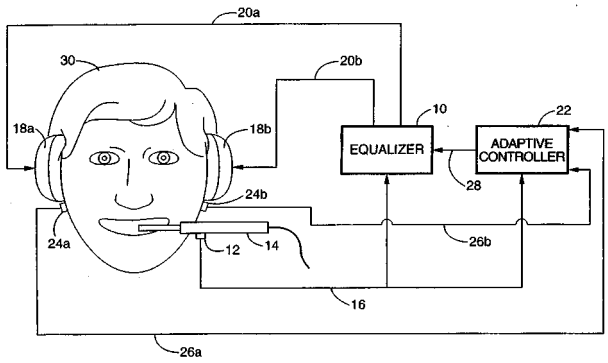

processed to generate canceling noise waves that are delivered to the patient via earphones or bone vibrators.—SFL

5,524,173

43.72.Ar PROCESS AND DEVICE FOR MUSICAL AND VOCAL DYNAMIC SOUND SYNTHESIS BY NON-LINEAR DISTORTION AND AMPLITUDE MODULATION

Miller Puckette, assignor to France Telecom
4 June 1996 (Class 395/2.77); filed in France 8 March 1994

A technique or model is described for parametrizing a sound which consists of multiple second-order formant envelopes excited by the harmonics of a pulsed fundamental signal. Such a model clearly applies to speech and is also said to be applicable to a number of musical sounds. Formants are characterized in terms of center frequency and decay bandwidth (or amplitude). A carrier signal is somehow time-modulated to produce the speech or musical sound.—DLR

5,528,725

43.72.Ar METHOD AND APPARATUS FOR RECOGNIZING SPEECH BY USING WAVELET TRANSFORM AND TRANSIENT RESPONSE THEREFROM

Siew K. Hui, assignor to Creative Technology Limited
18 June 1996 (Class 395/245); filed in the United Kingdom 13 November 1992

A method is presented for speech analysis and parametrization for use in a recognition system. Use of a wavelet transform of the digitized speech reduces the size of the frame vectors needed for a good representation. The wavelet coefficient sets are then further reduced by keeping only a two-bit deviation from the mean energy level for each coefficient.—DLR

5,530,768

43.72.Ew SPEECH ENHANCEMENT APPARATUS

Yoshiyuki Yoshizumi, assignor to Technology Research Association of Medical and Welfare Apparatus
25 June 1996 (Class 381/94); filed in Japan 6 October 1993

This speech enhancement device operates by increasing the amplitude briefly during the onset of the voiced portion following a consonant closure. Two smoothing filters with different time constants operate on the rectified

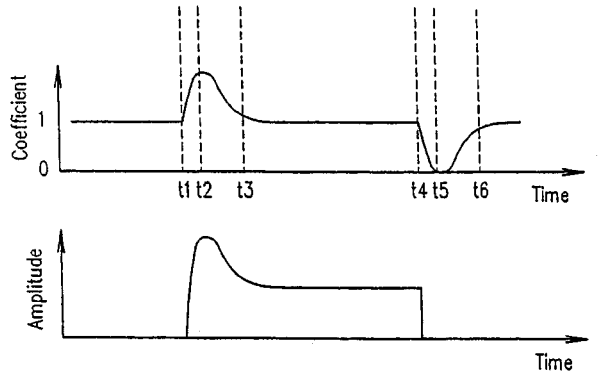

amplitude envelope signal. The ratio of these two filter outputs then controls a fast acting gain control. Various alternatives use additional smoothing filters to generate other gain control profiles.—DLR

5,524,279

43.72.Gy METHOD AND APPARATUS FOR IMPROVING PERCEIVED QUALITY OF A STORED VOICE MESSAGE IN A COMMUNICATION RECEIVER

James M. Keba and Clinton C. Powell, II, assignors to Motorola, Incorporated
4 June 1996 (Class 455/52.1); filed 24 May 1993

This communication link includes a mechanism to fill in brief missing speech segments which have been lost due to fading, interference or other such reasons. The idea is said to be effective when the intervals of reception failure are very short, on the order of a millisecond or so. In that case, the output is supposedly improved by storing signal portions during times of good reception and using these to fill the gaps during signal loss. No attempt is made to determine the acoustic properties of the missing portions from the context.—DLR

5,526,366

43.72.Gy SPEECH CODE PROCESSING

Kari Jarvinen and Janne Vainio, assignors to Nokia Mobile Phones Limited
11 June 1996 (Class 371/31); filed in Finland 24 January 1994

Prior packet-based speech transmission systems have used error detection codes to flag received packets containing erroneous data. Typically, the receiver produces either silence or a duplication of the preceding correct packet to fill in the gap. In this patent, a gradual degradation is produced by observing both the number of errors in a received packet and the ''freshness'' of the latest correct material, producing a sort of weighted composite replacement.—DLR

5,526,464

43.72.Gy REDUCING SEARCH COMPLEXITY FOR CODE-EXCITED LINEAR PREDICTION (CELP) CODING

Paul Mermelstein, assignor to Northern Telecom Limited
11 June 1996 (Class 395/228); filed 29 April 1993

A quadrature mirror filter bank (QMF) consists of a sequence of half-band filters in which the sample rate is reduced by half with each step down the band. At each band, a high-pass filter produces the band signal, while a mirror-image low-pass filter produces the drive for all lower bands. This code-excited LP vocoder promises fast searching of small codebooks by passing the extracted residual through a QMF bank. The highest frequency bands typically have very small codebooks. The lower bands, with larger codebooks, operate at much lower sample rates, resulting in significant computational savings.—DLR

5,528,723

43.72.Gy DIGITAL SPEECH CODER AND METHOD UTILIZING HARMONIC NOISE WEIGHTING

Ira A. Gerson and Mark A. Jasiuk, assignors to Motorola, Incorporated
18 June 1996 (Class 395/2.2); filed 28 December 1990

Many types of speech coders, but particularly code-excited LP coders, commonly use a method of noise weighting such that noise due to quantization errors is concentrated at the formant regions, leaving the valleys between formants relatively noise free. This patent applies a similar idea to the long-term, or pitch-frequency, filter. In that case, the strategy is to minimize noise at the harmonic frequencies, locating it instead in the troughs between harmonics.—DLR

5,528,727

43.72.Gy ADAPTIVE PITCH PULSE ENHANCER AND METHOD FOR USE IN A CODEBOOK EXCITED LINEAR PREDICTION (CELP) SEARCH LOOP

Yi-Sheng Wang, assignor to Hughes Electronics
18 June 1996 (Class 395/2.32); filed 2 November 1992

A modification is described for the excitation control system of a code-excited LP vocoder. The vocoder described uses an adaptive codebook in which the latest computed excitation vector is stored back into the codebook, replacing the oldest or least-used vector. In this system the computed vector is enhanced by taking each sample to a power slightly greater than one, and then rescaling to maintain the energy level before that vector is used to update the adaptive codebook.—DLR

5,528,726

43.72.Ja DIGITAL WAVEGUIDE SPEECH SYNTHESIS SYSTEM AND METHOD

Perry R. Cook, assignor to the Leland Stanford Junior University
18 June 1996 (Class 395/2.7); filed 27 January 1992

Variable-area-section tube models of the vocal tract were proposed for speech synthesis in the 60's and 70's. This patent builds on that work by combining in one model a variety of features individually explored and published by various working groups. Such features include explicit model-

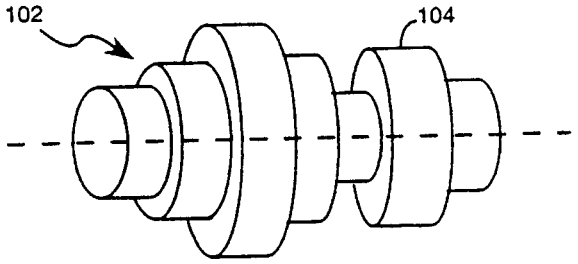

ling of the acoustic flow at tube branches, injection of noise at various section boundaries, specific articulator motion models to represent coarticulatory effects, and a detailed plan for producing a variety of glottal excitation effects.—DLR

5,524,172

43.72.Ja PROCESSING DEVICE FOR SPEECH SYNTHESIS BY ADDITION OF OVERLAPPING WAVEFORMS

Christian Hamon, assignor to The Ministry of Posts Telecommunications and Space Centre National d'Etudes des Telecommunications
4 June 1996 (Class 395/2.77); filed in France 2 September 1988

This patent presents a method intended to reduce the computational effort of synthesis from phonetic transcription while maintaining reasonable output voice quality. For each phonemic unit, a pair of diphone (entry and

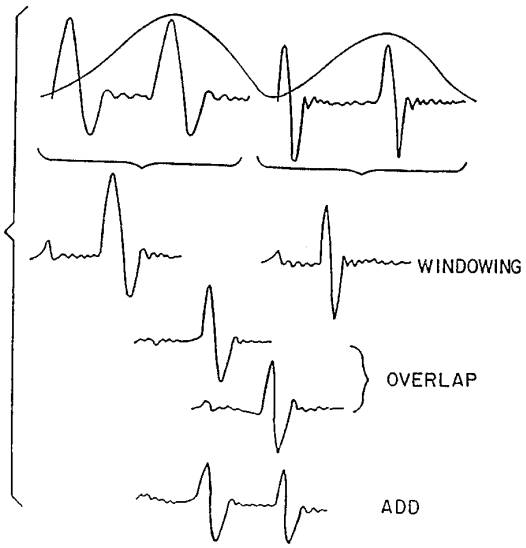

exit) waveforms is extracted from a database. These are overlapped by an amount dependent on the fundamental period and then summed to produce a ''phoneme-specific'' waveform.—DLR

5,530,738

43.72.Ja ELECTRIC POWER MEASURING INSTRUMENT WITH SPEECH SYNTHESIS FEATURE

Alexander McEachern, assignor to Infrastructure Instruments, Incorporated
25 June 1996 (Class 379/88); filed 21 November 1994

This instrument is a power meter monitoring attachment which includes a telephone connection and speech synthesis electronics. The system is able to place calls to specific stored numbers, and to detect rings and pick

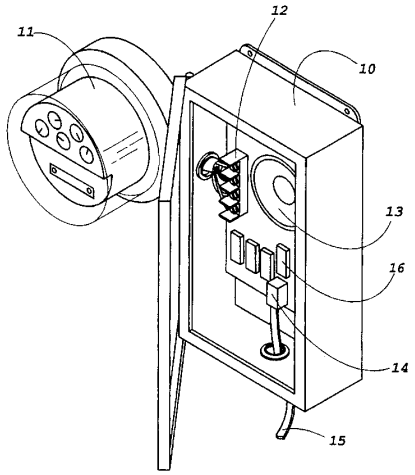

up the line to receive calls. A modem connection may be used for direct transfer of power system data or DTMF/voice interaction may be used to query or modify power meter parameters.—DLR

5,526,463

43.72.Ne SYSTEM FOR PROCESSING A SUCCESSION OF UTTERANCES SPOKEN IN CONTINUOUS OR DISCRETE FORM

Laurence S. Gillick and Robert S. Roth, assignors to Dragon Systems, Incorporated
11 June 1996 (Class 395/2.6); filed 22 June 1990

The patent describes a speech recognition system which smooths multiple frames of acoustic feature data, then clusters the smoothed frames into groups of phonetically similar items. An unknown utterance to be recognized is similarly smoothed, allowing the recognizer to narrow quickly the search to a small subset of the stored vocabulary. A similar idea is said to be applicable to continuous speech recognition systems. However, all descriptions are for discrete word systems.—DLR

5,526,466

43.72.Ne SPEECH RECOGNITION APPARATUS

Yumi Takizawa, assignor to Matsushita Electric Industrial Company
11 June 1996 (Class 395/2.62); filed in Japan 14 April 1993

For use in a phoneme-oriented, large-vocabulary recognition system, this technique would use phoneme or segment durations, often ignored, as a significant element in determining the recognition score. The justification for this is that matching the expected duration of each segment unit against the duration of the matching unknown segment helps eliminate errors in which a single segment is falsely matched with a sequence of segments from the unknown utterance.—DLR

5,528,728

43.72.Ne SPEAKER INDEPENDENT SPEECH RECOGNITION SYSTEM AND METHOD USING NEURAL NETWORK AND DTW MATCHING TECHNIQUE

Yoshihiro Matsuura and Toby Skinner, assignors to Kabushiki Kaisha Meidensha; Adaptive Solutions, Incorporated
18 June 1996 (Class 395/2.41); filed 12 July 1993

This speaker-independent speech recognition system uses a neural network to classify mel-scale spectral parameters into phonetic segment units and dynamic time warping to group strings of candidate phonetic units into

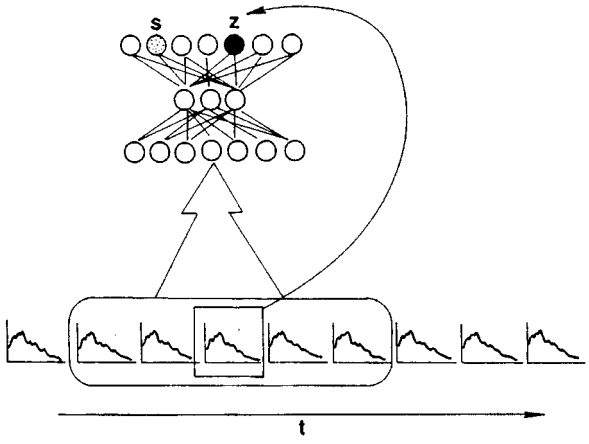

phoneme symbols. A typical dictionary of phonemic transcriptions of vocabulary items is used to convert the phoneme symbol strings into words.—DLR

5,528,731

43.72.Ne METHOD OF ACCOMMODATING FOR CARBON/ELECTRET TELEPHONE SET VARIABILITY IN AUTOMATIC SPEAKER VERIFICATION

Richard M. Sachs and Max S. Schoeffler, assignors to AT&T Corporation
18 June 1996 (Class 395/2.55); filed 19 November 1993

This nonlinear speech processing technique is intended to increase the similarity of utterances produced by the same speaker using different microphones. In particular, when one of the microphones is a carbon granule element, such as used in a telephone, the corresponding signal will be compressed in a characteristic manner. This method approximates that nonlinearity with a sample value input–output mapping as shown in the figure. The idea is that a signal already having this compression is little changed by a pass through the filter. Thus, all mic outputs are made to look like a carbon mic output.—DLR

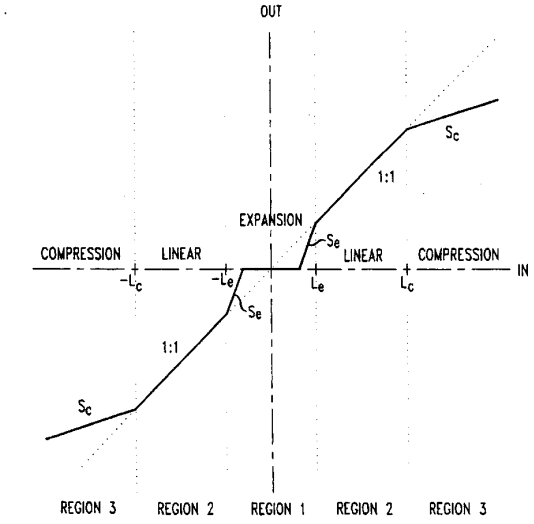

5,569,863

43.75.De TONE ENHANCER ATTACHMENT FOR STRING-MUSICAL INSTRUMENTS

Donald J. Lem, Scarsdale, NY
29 October 1996 (Class 84/312R); filed 6 March 1995

The tone ''enhancer'' **10** consists of absorptive pads **20** compressed between curved plates which clamp strings **91**, **92**, **93**, and **94**, thereby loading the strings and damping their vibration between bridge **60** and tailpiece **70** of a stringed musical instrument. This damping action eliminates sympathetic vibration of the string segments beyond the bridge, leaving the bowed segments on the other side of the bridge relatively unaffected. The attachment is easily applied or removed by using the catch and release mechanism **40**.—DWM

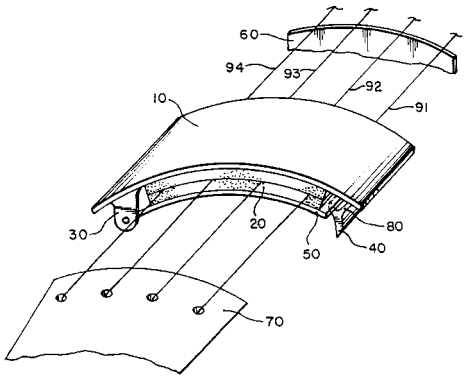

5,542,331

43.75.Ef SOUND-PRODUCING REED FOR WIND INSTRUMENTS

Harry Hartmann and Dieter Hahn, Stuttgart, Germany
6 August 1996 (Class 84/383A); filed in Germany 4 May 1992

This reed for wind instruments is laminated from fiber-reinforced plastic with some of the strands having different material characteristics from others, for the purpose of damping reed vibrations in a manner resembling wood reed vibrations.—DWM

5,569,864

43.75.Fg MUTE ATTACHED TO BRASS INSTRUMENT WITHOUT CHANGE OF PITCH OF SOUND

Shinji Hamanaga and Yoshihiko Matsukuma, assignors to Yamaha Corporation
29 October 1996 (Class 84/400); filed in Japan 14 November 1994

This patent discloses several mutes **10** for brass wind instruments which can be inserted into the bell **11** of the instrument, which have their inner surface **10d** so shaped that the instrument's standing waves normally generated in the absence of the mute are hardly changed by the presence of the mute. The intent is to avoid changing tonal frequency when the mute is used. The first patent reference cited is an expired patent of the reviewer, whose device was intended to avoid changing both frequency and spectrum of the tone.—DWM

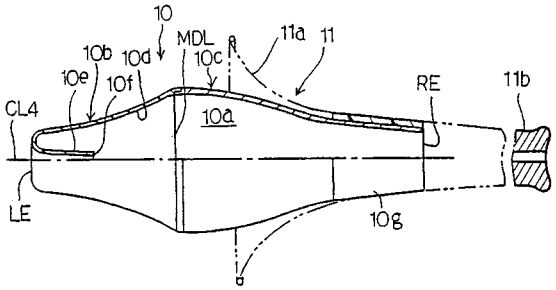

5,503,054

43.75.Gh MUSICAL INSTRUMENT BRIDGE

Lynn K. Ellsworth and John D. Shaneyfelt, assignors to 2TEK Corporation
2 April 1996 (Class 84/307); filed 29 April 1994

The bridge **50** of this guitar is supported from the back face **16**. The bridge structure provides independent cantilever ''fingers'' that support the termination of each string **22** separately, thereby reducing interstring coupling. The fingers are designed to allow freer vibration in the horizontal plane than in the vertical. Tuning of the finger resonance frequency is said to

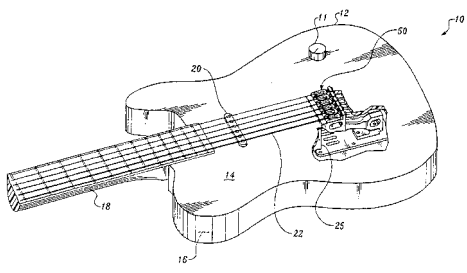

be ''somewhat a matter of taste. However, it has been determined that if the resonant frequency of the finger is the same as the pitch of the string, the finger will dampen the motion of the string as it is played, thereby producing little or no sound. Thus, the fingers should not have a resonant frequency that is exactly the same as the pitch of the string.''—DWM

5,542,329

43.75.Gh DEVICE FOR IMPROVING SOUND IN GUITARS AND SIMILAR STRINGED INSTRUMENTS

Shin H. Chen, Chicago, IL
6 August 1996 (Class 84/291); filed 6 September 1990

Inside the body of this guitar is mounted a rather complex wishbone shaped lever structure intended to improve the guitar tone. A post secured to a cross rib on the inside of the back panel drives the wishbone arms that extend laterally to points near the inside walls of the instrument, in order to excite a larger portion of the instrument body. According to the patent, the structure causes the soundboards ''to flap in unison,'' but how this is done is not explained clearly.—DWM

5,520,083

43.75.Hi CUSHIONED SUPPORT FOR DRUM

Jeff R. Falkner, Jr., assignor to Drum Workshop, Incorporated
28 May 1996 (Class 84/421); filed 24 January 1995

The circular flange **14** on which the drumhead **12** is supported is connected to the cylindrical drum shell **11** by multiple threaded rods **36** to a retainer ring **50** wrapped around the drum shell. Elastomer cushions **52** are inserted between the ring and the drum shell at each rod location, in order to

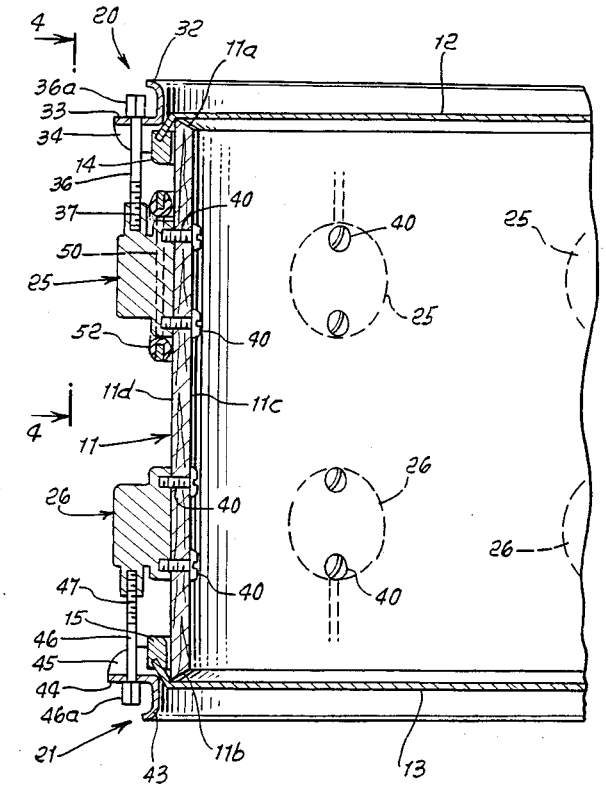

damp drum shell resonances and to isolate the drum shell mechanically from the drumhead circular flange. The purpose is to prevent drum shell resonances from affecting drum tone significantly.—DWM

5,561,254

43.75.Hi DEVICE FOR MODIFYING THE SOUND OF A DRUM

Scott Huffer, assignor to The Bohning Company
1 October 1996 (Class 84/411M); filed 19 June 1995

This patent discloses gelled plastisol discs which can be sealed to a drumhead at multiple locations near the edge of the stretched membrane to modify the sound of the drum through damping drumhead vibration. These flexible discs have a very smooth lower surface that is intended to seal to the membrane without the use of an adhesive so that the discs can be removed when the normal drumhead characteristics are to be restored.—DWM

5,520,089

43.75.Np WATER ORGAN

John G. Prentiss, Sante Fe, NM
28 May 1996 (Class 84/330); filed 12 October 1994

This patent mentions pneumatic organs driven by compressed air, and aeolian harps in which turbulent air flow excites tuned strings, then proposes the use of resonant air columns of different frequency, excited by controlled water streams so that ''the user may play a musical composition having a distinctly aqueous character.'' Hollow tubes **17a–d** of different tuned length have their lower ends immersed in reservoir **20** drained at notch **24** to

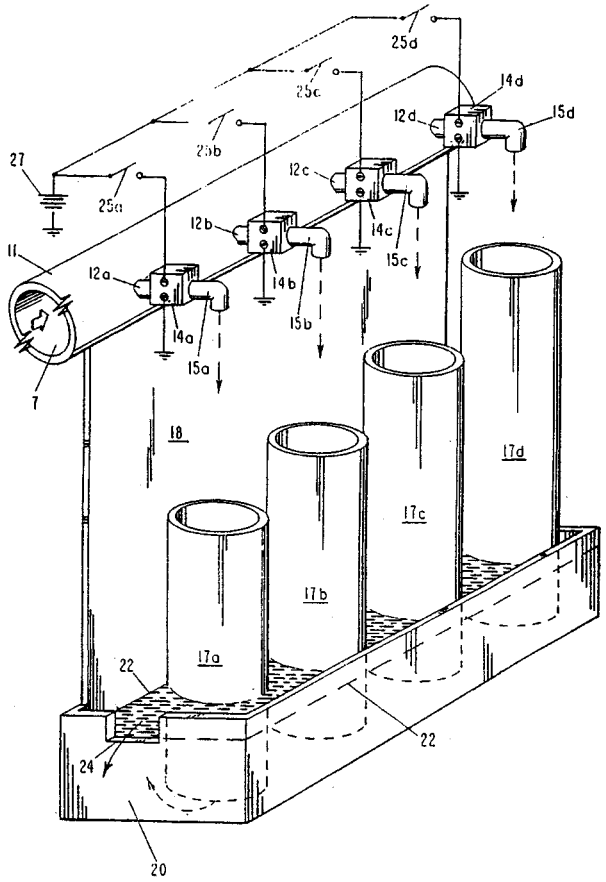

maintain a constant water level **22** that defines the lower end of the acoustically resonant air columns. Key switches **25a–d** can be played by a musician for selectively controlling valves **14a–d** to turn on water flow from nozzles **15a–d** from water pipe **11**, producing a musical tune or harmony, depending upon the number of keys played simultaneously.—DWM

5,539,146

43.75.St PERFORMANCE INFORMATION ANALYZER AND CHORD DETECTION DEVICE ASSOCIATED THEREWITH

Yutaka Tohgi, assignor to Yamaha Corporation
23 July 1996 (Class 84/650); filed in Japan 9 April 1993

This electronic musical instrument is provided ''with a performance information analyzer and a chord detection apparatus...which includes a central processing unit or CPU **1** arranged to use a working area of a working memory **3** for executing a control program stored in a program memory **2** in the form of a read-only memory. The electronic musical instrument has a keyboard **4** to be played by a user for keyboard performance and an automatic accompaniment apparatus to be activated under control of the CPU **1** for harmonizing automatic accompaniment with the keyboard performance. When applied with a key-code with a key-on signal or a key-off

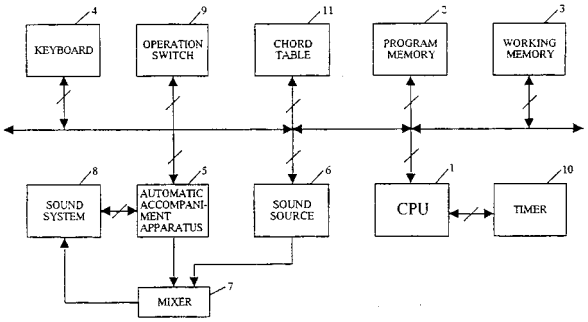

signal in response to depression or release of keys on the keyboard **4**, the CPU **1** applies the key-code with a note-on or a note-off to a sound source **6** for generating or muting a musical tone in accordance with the keyboard performance. The automatic accompaniment apparatus **5** is arranged to memorize a plurality of accompaniment patterns in accordance with the style of a musical tune and to select the memorized accompaniment patterns in response to a start signal applied thereto from the CPU **1** for effecting automatic performance at the selected pattern.''—DWM

5,508,472

43.75.Tv METHOD AND APPARATUS FOR EMULATING THE PITCH VARYING EFFECTS OF PIPE ORGAN WIND SYSTEMS AND ACOUSTIC COUPLING IN AN ELECTRONIC MUSICAL INSTRUMENT

W. Lawrence Hawkins, assignor to Rodgers Instrument Corporation
16 April 1996 (Class 84/653); filed 11 June 1993

This electronic organ system is designed to emulate tonal changes occurring in pipe organs as a result of wind pressure variations and acoustical coupling among pipes. In the block diagram shown, played key switches of keyboard **42** and selected stop switches of stop controls **64** exert two types of control. (a) Through lines **58** and **62**, respectively, they control which tone frequencies and tone wave forms are generated by generator control **56**, a normal function. Voice generators **66** and **68** are exemplary

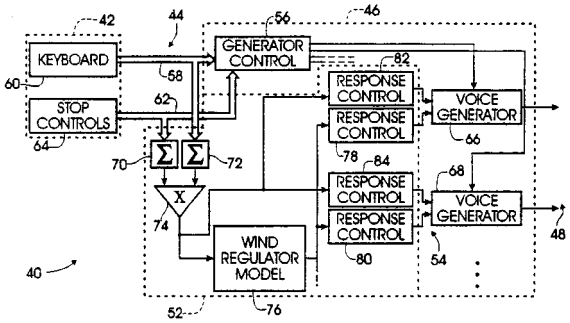

selections. (b) Signals from lines **58** and **62** are also supplied to accumulators **70** and **72** which measure the number of keys and voices selected, which are then multiplied. The product signal corresponds to the ''wind usage'' in a pipe organ. This product is applied directly to response controls **82** and **84** which effect detuning for chorus effect, and also through wind regulator model **76** to affect overall tuning on the time sale, much as it would be affected by changes in wind pressure of a typical pipe organ.—DWM

5,508,473

43.75.Tv MUSIC SYNTHESIZER AND METHOD FOR SIMULATING PERIOD SYNCHRONOUS NOISE ASSOCIATED WITH AIR FLOWS IN WIND INSTRUMENTS

Christopher D. Chafe, assignor to Leland Stanford Junior University
16 April 1996 (Class 84/659); filed 10 May 1994

In order to mimic the noise component of the sounds produced by acoustic wind instruments, this music synthesizer ''includes a vopex noise generator, an edge tone nonlinearity function driven by the differential between a blowing pressure signal and a feedback signal from the resonator. The vopex noise generator feeds its noise output signal back into itself so as to generate a noise ''votex.'' The vopex noise generator furthermore modulates the spectral content of the generated noise fluctuations in a manner that is period synchronous with the resonator output signal. As a result, the noise vopex signals mimic the turbulence associated with air blown into wind instruments by switching between structured and chaotic modes of operation in a manner that is period synchronous with the resonator output signal.''—DWM

5,561,275

43.80.Qf HEADSET FOR ELECTRONIC STETHOSCOPE

Gary Savage and Michel Swift, assignors to Delstar Services Informatiques, Incorporated
1 October 1996 (Class 181/131); filed 28 April 1994

The headset has hollow, relatively stiff arms, curving outwardly, to which ear tips can be attached at the upper end. At the lower end of the arms there is a more flexible section that allows the arms to spread for fitting to the ears, and that provides the force needed to hold the headset in place. Sound from the stethoscope chestpiece enters the lower end of the headset.—SFL

Smart foam for applications in passive–active noise radiation control

C. A. Gentry, C. Guigou, and C. R. Fuller
Vibration and Acoustics Laboratories, Virginia Polytechnic Institute and State University, Mechanical Engineering Department, Blacksburg, Virginia 24061-0238

(Received 19 April 1996; revised 8 October 1996; accepted 25 November 1996)

The development of a smart foam for passive–active noise control is discussed. The smart foam consists of cylindrically curved sections of PVDF film embedded in partially reticulated polyurethane acoustic foam forming a very thin, compact arrangement. The device is designed to reduce sound by the simultaneous action of the passive absorption of the foam (effective at high frequencies) and the active input of the PVDF element driven by an oscillating electrical input (effective at low frequencies). The PVDF actuator is configured to behave in a linear sense and to couple in-plane strain associated with piezoelectric effect with out-of-plane motion needed to radiate sound from the foam surface. The performance of the passive–active device is studied for controlling sound radiation from a vibrating piston. A feedforward LMS controller is used to minimize the signal from a far-field error microphone. Results of harmonic and broadband control are presented. The potential of the smart foam for globally reducing sound radiation in the low- and high-frequency range is demonstrated.
[S0001-4966(97)03704-1]

PACS numbers: 43.10.Ln, 43.50.Gf, 43.50.Ki [PJR]

INTRODUCTION

In the last few years, there has been increased interest in the reduction of sound and/or vibrations by use of hybrid active–passive control techniques. There are two general types of active–passive noise control approaches: the adaptive–passive techniques and active–passive hybrid techniques. The adaptive–passive techniques are essentially passive devices whose static properties are adapted or changed to optimize their performance.[1]

An example of an adaptive–passive control system uses electro-rheological fluids (ER), which undergo significant changes in their mechanical properties, such as their mass distribution, and energy dissipation characteristics, when subjected to electric fields. These fluids can be embedded in voids in structural materials enabling the global static properties (i.e., damping, stiffness, etc.) of the structure to be controlled.[2] Another adaptive–passive method utilizes adaptively tuned vibration absorbers[3] (whose simple form is a spring–mass system), which are being studied for aircraft applications to limit fuselage response to engines and propeller excitations.[4]

Active–passive hybrids use both active and passive elements in either series or parallel. The passive device usually carries the primary vibration attenuation characteristic, while the active component is used to enhance the performance of the passive system or overcome the limitations of the passive system. The active–passive approach is used in this paper to develop an active smart foam. The smart foam design integrates a distributed piezoelectric polymer actuator (the active component) between individual layers of sound-absorbing foam (the passive component). Smart foam can be bonded directly to a vibrating structure and act as an active surface coating, which provides reduction of structural sound radiation. Further details concerning active–passive surface coatings will be given but first a brief overview of passive sound reduction techniques is needed.

Porous sound-absorbing materials are commonly implemented for a large range of applications (such as buildings, machinery enclosures and aircraft) to reduce sound propagation. The use of a polyimide foam layer has been investigated for reducing sound transmission.[5] In noise control applications, which employ passive sound absorbers, the air molecules in the interstices of the porous material oscillate with the frequency of the exciting sound wave. This oscillation results in frictional losses. Changes in flow direction and expansions and contractions of the flow throughout irregular pores result in a loss of momentum in the direction of wave propagation. These two phenomena account for most of the energy losses in the high-frequency range.[6] However, a porous layer can absorb a large amount of acoustic energy only if its thickness is comparable to the wavelength of the incident sound. This implies that such a passive technique is not very efficient in the low-frequency region.

Active control techniques can be used to enhance the sound reduction of passive sound absorbing materials in the low frequencies. Bolton *et al.*[7] presented analytical results demonstrating that the low-frequency performance of a finite-depth layer of elastic porous material may be enhanced by applying an appropriate force to the solid phase at the front surface of the layer. They showed that at any angle of incidence, the solid phase of the foam may be forced so as to create a perfect impedance match with the incident plane wave, thus causing the sound to be completely absorbed. However, no physical implementation of such a device was discussed. An active–passive piezocomposite actuator has been experimentally developed and tested for underwater sound reduction.[8] The design of the active coating prevents an incident sound wave from reflecting off the acoustic

boundary of an object submerged in a heavy fluid. The acoustic energy associated with the incident disturbance is absorbed out of the medium through a piezocomposite device in the coating and dissipated by internal electrical means. This elastomer coating consists of a piezoelectric actuator and piezoelectric sensors embedded in an elastomer and controlled by an analog feedback network. The actuator was tested in a water-filled pulse tube and echo reduction levels were measured over an extended frequency band for tonal excitations. Good reduction was achieved and results clearly indicate how the active component of the device overcomes the limitations of a purely passive elastic coating. The results also indicate that by optimizing the embedded sensor location one can tune the piezocomposite coating to yield maximum echo reduction in a certain frequency band.

Another example of an active surface coating is actively controlled constrained layer damping (ACLD), which is an active–passive hybrid composed of a visco-elastic damping material sandwiched between two piezoelectric layers.[9] The three layer composite ACLD when bonded to a vibrating surface acts as a smart constraining layer damping treatment with built in sensing and actuation capabilities. The sensing is provided by the piezoelectric layer, which is directly bonded to the vibrating surface. The actuation is provided by the other piezoelectric layer driven by a control voltage. With appropriate strain control, the shear deformation of the visco-elastic damping layer can be increased, the energy dissipation mechanism can be enhanced, and the structural vibration damping ratio is increased. Analytical results involving beam vibration control show the ACLD treatment is superior to conventional active control damping, particularly in the low-frequency range (first three vibration modes of the beam). Recently, a smart foam to be used as an active–passive sound absorber has been implemented by incorporating a piezoelectric polymer PVDF (polyvinylidene fluoride) film within a foam layer.[10] This work provided the basis of the present study. The smart foam differs from previous work on sound reduction coatings in that it is designed to be used in air and incorporates a PVDF film embedded in a blown polyurethane foam. These materials are chosen because their impedance is closer to that of air when compared to the materials used to construct active surface coatings in underwater sound reduction applications. The PVDF film thus acts as an acoustic actuator to enhance the low-frequency sound absorption of the foam.

The concept of the smart foam is to combine active and passive control strategies such that the sound attenuation can be efficiently achieved over a broad range of frequencies. In this paper, the smart foam noise suppression device, combining a lightweight, distributed active layer and a passive acoustic damping material, is developed for the purpose of minimizing structural acoustic radiation. A schematic of the smart foam is shown in Fig. 1. Such a device consists of a layer of cylindrically curved piezoelectric polymer PVDF film embedded in partially reticulated polyurethane foam. As mentioned previously, it is usually impractical to rely on a purely passive sound absorption system in the low-frequency range. Therefore, the PVDF element is incorporated and serves as the active input to contribute to the low-frequency

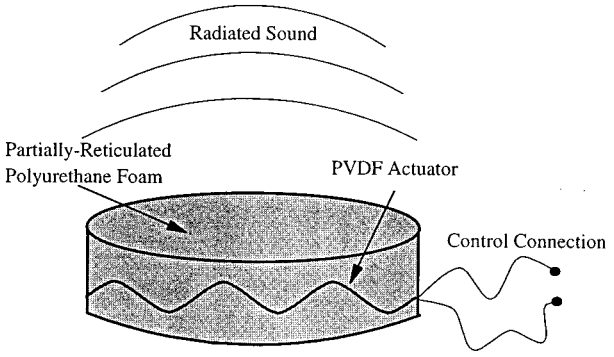

FIG. 1. Smart foam.

sound attenuation. The smart foam device differs from the ASAC control methods (see Ref. 11 for a discussion of ASAC) in that it adaptively modifies the acoustic impedance of a vibrating surface without the use of secondary control inputs directly mounted on the structure. It is also significantly different from common ANC techniques that use secondary acoustic sources (loud speakers) in arrays around the primary noise source because the smart foam is actually located on the surface of the vibrating structure. The goal of implementing smart foam is to modify the acoustic radiation impedance in order to yield a net decrease in the far-field sound power radiated by the vibrating noise source. While the most important advantage of implementing such a hybrid device in noise control applications is improved low-frequency performance, other positive attributes of active–passive noise control devices are increased robustness, increased stability, and decreased control spillover. It should also be mentioned that the passive–active device proposed in this paper is relatively lightweight, which makes it a good candidate for aircraft noise control applications.

In this paper, the construction of the smart foam is first described. The PVDF actuator is cylindrically curved to couple the in-plane strain associated with the piezoelectric effect with the out-of-plane motion needed to radiate sound from the foam surface. The actuator is then configured such that nonlinear effects associated with the film curvature are minimized. The PVDF active layer is bonded between the two foam halves forming a very thin, compact arrangement. The performance of the active–passive device is then demonstrated for controlling sound radiation from a vibrating piston. The problem of suppressing piston sound radiation is addressed because it represents a simple source and generates a monopolelike radiation pattern. A successful solution to this simple noise control problem using smart foam has two advantages. It will provide insight into the fundamental method of operation of smart foam and represent an important step in the progression toward implementing smart foam in more complex noise control problems. One can interpret the vibration pattern of complex structures as a finite sum of multiple monopole sources. Therefore, an array of smart foam can be employed to attenuate the sound generated by a complex structural noise source. A feedforward LMS controller[12] is used to minimize the signal from a far-field error microphone. Results of harmonic and broadband con-

trol are presented. The potential of the smart foam for globally reducing sound radiation in the low- and high-frequency range is demonstrated.

I. SMART FOAM CONSTRUCTION

A sound-absorbing material, known as partially reticulated polyurethane foam, provides the passive element of smart foam and it dissipates incident acoustic wave energy through friction associated with the coupling of the liquid and solid phases of the foam. Partially reticulated polyurethane foam is an acoustical grade, open cell, flexible ester based urethane foam designed to give maximum sound absorption per given thickness.[13] Since passive sound control is only significant at high frequencies, a PVDF film is embedded in the foam to implement the active control, which is most effective at low frequencies. Note that the actuator forces both the fluid and solid phases of the acoustic foam and acts in a speakerlike fashion. The main physical characteristic of the PVDF actuator is that it is intentionally curved to couple the predominantly in-plane strain associated with the piezoelectric effect and the out-of-plane motion, which is required to accelerate fluid particles and hence radiate sound away from the surface of the foam. A simple analytical model for a curved PVDF actuator revealed that, for a given input voltage, as the PVDF actuator (of constant dimensions) is changed from a flat configuration (infinite radius of curvature) to a half-cylinder configuration, the resulting out-of-plane displacement is increased. Since an increase of out-of-plane displacement yields an increase of sound radiation, a PVDF actuator curved into a series of half-cylinders was chosen for the smart foam design.

In a preliminary experiment, the smart foam included a continuous, homogeneous layer of 28-μm Ag metallized PVDF, which was curved into a series of four half-cylinders as shown in Fig. 2(a). Silver-electroded PVDF film was chosen as it can sustain high voltage amplitudes required for actuator applications. An electrical voltage of magnitude 30 V/μm can be then applied to the PVDF actuator without electrical breakdown. Driving the actuator with an ac voltage across the top and bottom electrode [without changing polarity, as shown in Fig. 2(a)] resulted in poor radiation efficiency of the active–passive device. When electrically excited, cell 1 and 3 experienced a positive upward displacement. Conversely, cell 2 and 4 experienced a negative downward displacement. The net result is an inefficient sound source at low frequencies with dipole-type radiation characteristics. In addition, the corresponding asymmetry of operation under positive and negative voltage caused asymmetry in the mechanical coupling between the out-of-plane displacement and the strain in the uni-axial direction of the film. This nonlinear dynamic behavior appeared in the form of higher-order harmonic distortion in the acoustic frequency response spectrum.

These undesirable characteristics were overcome using an arrangement first suggested by Tibbets.[14] Two improved PVDF actuator configurations are shown in Fig. 2(b) and (c). Each actuator is configured by dividing the continuous layer of PVDF film into several individual transducers by a chemical etching process. The etching process involves chemically

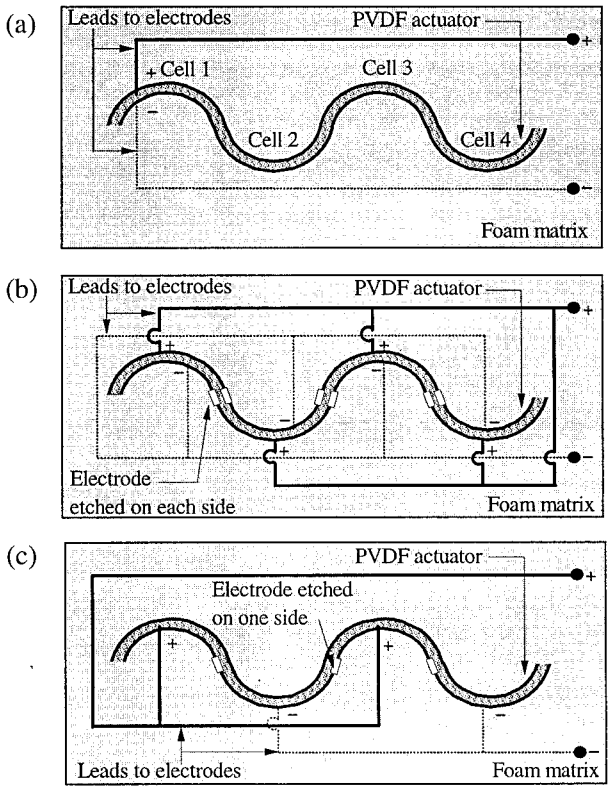

FIG. 2. PVDF actuator configuration. (a) Original; (b) parallel; (c) series-parallel.

removing or erasing thin portions of PVDF film electrodes at the boundaries where the physical polarity (curvature) of the actuator changes. The actuator is then composed of several individual transducers, which can be driven with different voltages (same amplitude with 180° phase difference). In the parallel actuator arrangement, as presented in Fig. 2(b), the top and bottom electrodes are then connected in parallel with phase reversal. Therefore, the PVDF film is activated such that neighboring cells are driven by the same voltage amplitude with an 180° phase difference. The resulting effect is that each cell moves in the same out-of-plane direction yielding a net volumetric source strength and as a consequence an increase in sound radiation as compared to the preliminary PVDF configuration illustrated in Fig. 2(a). The series-parallel actuator configuration, illustrated in Fig. 2(c), requires that only the bottom electrode is divided into independent transducers, which are then wired 180° out of phase. This arrangement also results in a more efficient radiator as compared to the original configuration as the PVDF film is moving as a whole in the out-of-plane direction. A detailed comparison of the effectiveness of these improved PVDF actuators as sound radiators will be discussed in a subsequent section of this paper. Note that the periphery of the PVDF film actuator was etched as well to prevent arcing effects. Electrical leads were attached to the PVDF actuator with a copper foil adhesive tape reinforced with silver epoxy glue. To complete the construction process of the active–passive control device, the PVDF element was embedded in a layer of polyurethane foam. Note that the piston used in performance testing of smart foam was 15 cm in diameter and

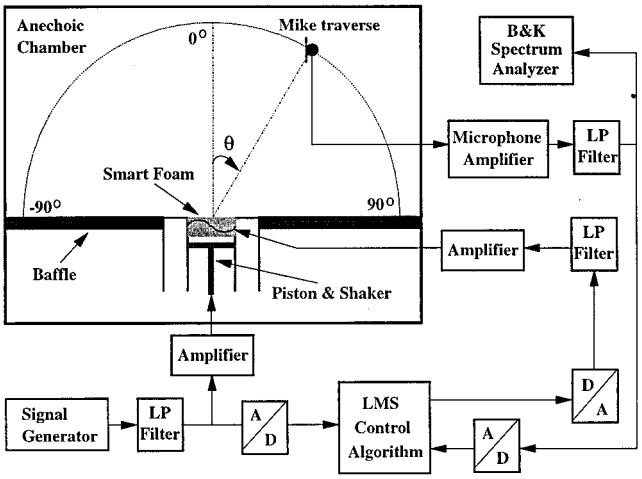

FIG. 3. Radiation control experimental setup.

dictated the size of the smart foam element to be fabricated. A series of four half-cylinder cells measuring approximately 2 cm in radius were cut through the cross section of a slab of foam measuring 15 cm in diameter and 5 cm thick. From a simple analytical model for the curved PVDF actuator, it was obtained that the largest radius possible for the PVDF actuator is optimal in terms of inducing out-of-plane displacement. Therefore, a 2 cm radius is used for each cell as it represents the largest that can be embedded within 5 cm of foam while allowing a minimum of $\frac{1}{2}$ cm of foam on the top and bottom surface of the device for protection of the piezoelectric layer. The PVDF actuator was bonded between the two circular foam halves retaining its curved shape and yielding a smart foam similar to that illustrated in Fig. 1. Silicon adhesive was chosen to bond the PVDF actuator because it is readily available and remains flexible once dry.

II. EXPERIMENTAL SETUP AND PROCEDURE

The radiation control experimental setup is shown in Fig. 3. The smart foam was manufactured as described in the previous section, and positioned on the surface of an oscillating piston mounted in a rigid baffle inside an anechoic chamber. The piston excitation was produced by a shaker driven by an external signal generator. A feedforward filtered-x LMS algorithm[12] was used to determine the appropriate control signal necessary to minimize the radiated sound at an error microphone. This error microphone was located in the far field at 1.5 m in the perpendicular direction from the device surface (direction $\theta=0°$ in Fig. 3). The control algorithm was implemented with a TMS320C30 DSP board resident in a personal computer. Note that the feedforward controller used the signal sent to the piston shaker as a reference signal (however, a signal from an accelerometer on the piston could also be used). A microphone located on a stepper motor driven traverse swept from $-90°$ to 90° at a radial distance of 1.5 m from the rigid baffle plane for 21 equally spaced measurement points. The far-field pressure levels were measured under three conditions:

(1) the bare piston operating alone (*piston*);
(2) the piston with smart foam and no control signal applied (*passive control*);
(3) the piston with smart foam and control signal applied (*active–passive control*).

The recorded sound-pressure levels (SPL) in dB relative to 20 μPa are presented for these three conditions to evaluate the efficiency of the passive–active device. A 20-μPa reference is used in all subsequent sound-pressure level calculations. The mechanical shaker used to drive the piston appeared to have two resonant frequencies at 290 and 472 Hz in the frequency band studied. Harmonic control was performed at 290 and 1000 Hz, respectively. These frequencies were chosen to illustrate how the smart foam has the ability to successfully attenuate low- and high-frequency sound. Broadband control was also investigated and in this case, the piston was driven with band limited random noise 0–1600 Hz. Note that for broadband control, a 15-ms delay was added to the disturbance path to make the system more causal. This enabled the controller to adapt the coefficients necessary to compensate the nonminimum phase zeros of the control and error path. It should also be mentioned that, in the following discussion, the term ''global'' means ''for all radiation angles $-90°\leqslant\theta\leqslant 90°$'' and ''global sound level'' refers to the average of the squared sound pressure measured at the 21 equally spaced microphone positions between $\theta=-90°$ to $\theta=90°$ and converted to dB relative to 20 μPa.

III. COMPARISON OF VARIOUS ACTUATOR CONFIGURATIONS

Linearization of the PVDF actuator dynamic response proved to be an important achievement in the smart foam development because it is associated with an increased radiation efficiency of the smart foam and therefore an increased sound reduction capability. To illustrate and compare the performance of the different actuator configuration referred to as the original PVDF actuator, the parallel actuator, and the series-parallel actuator, a simple experiment was performed in the anechoic chamber. The smart foam was positioned near the surface of the piston and in this case, was used as a noise source (i.e., the piston was stationary). For the different configurations, the PVDF actuator was driven at 290 Hz using an input voltage of 25, 50, 75, and 100 V rms. Note that the maximum voltage allowed to drive the PVDF actuator is about 300 V rms. The far-field sound-pressure level (SPL) was measured at the driving frequency as well as at the first and second harmonic frequencies with a microphone positioned normal to the foam surface (at a radial distance of 1.5 m in the direction $\theta=0°$) for each voltage increment.

Figure 4(a) presents the SPL for the three different actuator configurations using an input voltage of 100 V rms at 290 Hz. It can be seen that the series-parallel and parallel actuators are more than 15 dB louder than the original actuator. The parallel configuration yields an SPL about 6 dB higher than the series-parallel as it uses the both sides of PVDF electrode. The parallel actuator corresponds to the best configuration for increasing the SPL radiated by the smart foam. The linearity of the system with respect to the

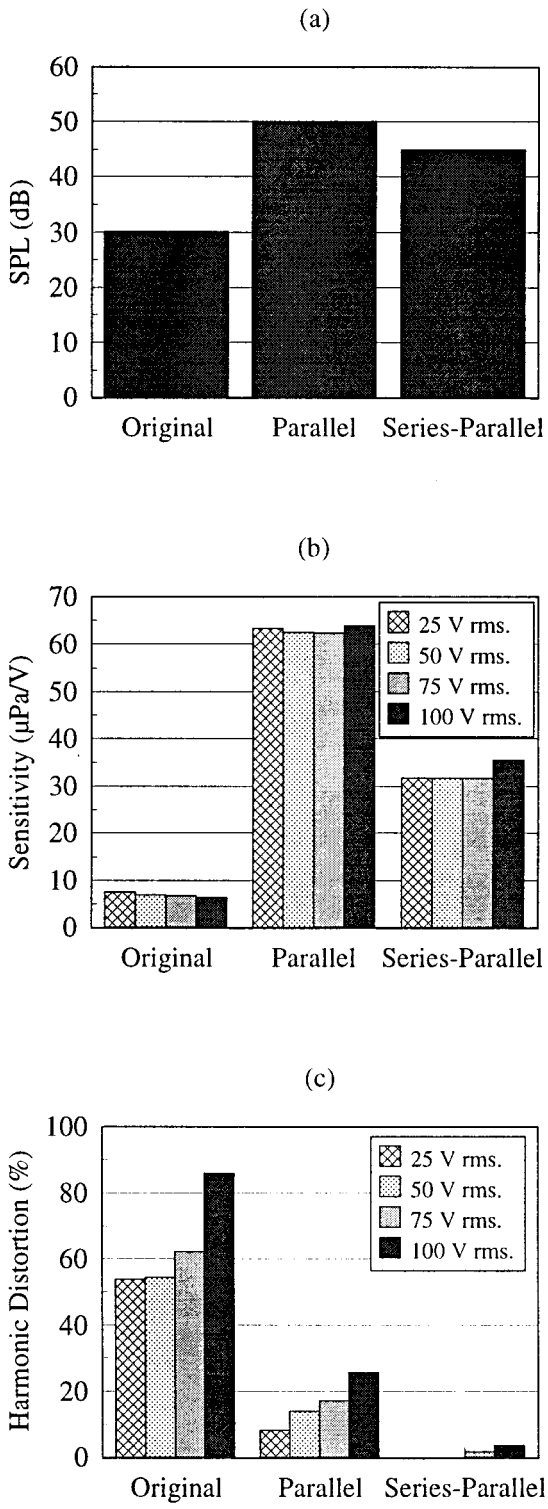

FIG. 4. Smart foam behavior at 290 Hz for different PVDF actuator configurations: (a) SPL under 100 V rms input voltage; (b) sensitivity; (c) harmonic distortion.

driving voltage or sensitivity is studied next. The sensitivity defined as the rms pressure divided by the input voltage is presented in Fig. 4(b). At the driving frequency, the sensitivity should ideally be a constant (as doubling the driving voltage is expected to double the radiated rms pressure). Indeed, the sensitivity is virtually constant for the three actuator configurations showing that the smart foam is linear with respect to the input voltage. It should also be noted that the sensitivity for the parallel configuration is the highest as it corresponds to the loudest system [see Fig. 4(a)] and is twice that of the series-parallel configuration. Finally, the nonlinear behavior in the form of harmonic distortion is investigated for the different actuator configurations. Harmonic distortion[15] is a measure of the pressure amplitude distortion and refers to the deviation from correspondence between the acoustic output wave and the electrical input wave that results from nonlinear effects in the smart foam. It is defined as the ratio of the pressure amplitude of the harmonics to those of the fundamental and the harmonics, i.e.,

$$\text{Distortion (in percent)} = 100\sqrt{\frac{p_2^2+p_3^2+p_4^2+\cdots}{p_1^2+p_2^2+p_3^2+\cdots}},$$

where p_1 represents the pressure at fundamental frequency, p_2 the pressure at the second harmonic, and so on. It can be seen in Fig. 4(c) that the original actuator configuration is associated with large harmonic distortion (more than 85% when driven with 100 V rms) compared to the other two PVDF actuator configurations. It is also observed that the distortion level is increased as the input voltage to the PVDF actuator is increased. The series-parallel actuator corresponds to the best configuration for minimizing the harmonic distortion of the smart foam. Note that the harmonic distortion associated with the original PVDF actuator configuration was observed in the experiments presented in Ref. 10.

It can be deduced that the parallel and series-parallel actuator PVDF configurations greatly improve the acoustic response of the smart foam. Both PVDF arrangements yield increased sound output and much less harmonic distortion than the original PVDF configuration. It is also believed that the nonlinear characteristic (predominantly in the form of harmonic distortion) can be further decreased by using a much thinner bonding layer to embed the PVDF actuator within the foam (i.e., the use of spray glue instead of silicon adhesive is under investigation). Silicon adhesive has a high viscosity compared to spray glue adhesive. This high viscosity induces a shearing effect in the smart foam, which promotes a nonlinear coupling of the PVDF in-plane strain and the displacement in the normal direction.

IV. PASSIVE EFFECT OF SMART FOAM ON SOUND RADIATION

In this section, the passive sound attenuation associated with the smart foam is studied and compared to that of a similar configuration of homogeneous plain acoustic foam. It is of interest to observe the effect of the PVDF actuator as well as the glue layer (used to bond the PVDF film to the foam) on the passive sound attenuation. Ideally, the passive sound control performance should not be reduced by the active layer embedded in the acoustic foam. A plain, homogeneous layer of acoustic foam (same dimensions as the smart foam) was used for comparison of passive performance. The piston was then driven by broadband random noise (0–1600 Hz) and the global sound level (as previously defined) was obtained. Figure 5 presents the global sound level for the

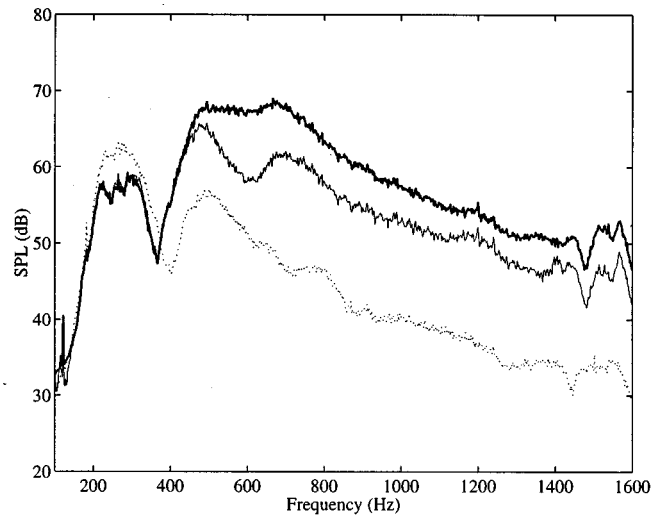

FIG. 5. Passive effects of embedded PVDF layer on global sound level: — piston; — plain foam; ---- smart foam.

bare piston (noise source without sound control treatment), for the piston with a plain layer of foam (noise source with common passive sound control treatment), and for the piston with smart foam (no control signal applied to PVDF actuator). Above 350 Hz, the active layer enhances the passive performance of the acoustic foam. Indeed, in this frequency range, the passive sound attenuation associated with the smart foam is about 15 dB (with respect to the untreated piston source) and that associated with the plain foam is around 6 dB. Obviously, the combined mass of the PVDF and glue layers enhances the passive performance of the acoustic foam as it causes a portion of the energy carried by incident acoustic waves to be reflected back towards the source. In the low-frequency range (below 350 Hz), the plain foam has no effect on the sound radiated by the piston. This is expected due to the longer wavelength of the incident acoustic wave relative to the foam thickness. However, the passive smart foam enhances sound radiation between 200 and 350 Hz. This may be attributed to a modification of the radiation impedance (increase of the resistive impedance) of the system due the presence of the PVDF and glue layers within the passive smart foam. In spite of this negative effect in the low-frequency range, the smart foam yields considerable passive sound reduction over the studied frequency band.

V. HARMONIC RADIATION PASSIVE/ACTIVE CONTROL RESULTS

Harmonic control of piston radiation was investigated for two different excitation frequencies. Control results are shown in Fig. 6(a) and (b) for 290 and 1000 Hz, respectively. A 290-Hz excitation frequency corresponds to a resonant frequency of the piston shaker and lies within a frequency range where the smart foam does not provide any passive attenuation. On the other hand, the 1000-Hz driving frequency was chosen because the smart foam provides more than 10 dB of passive sound attenuation in this frequency range. In general, the control results show that even if the sound radiation is

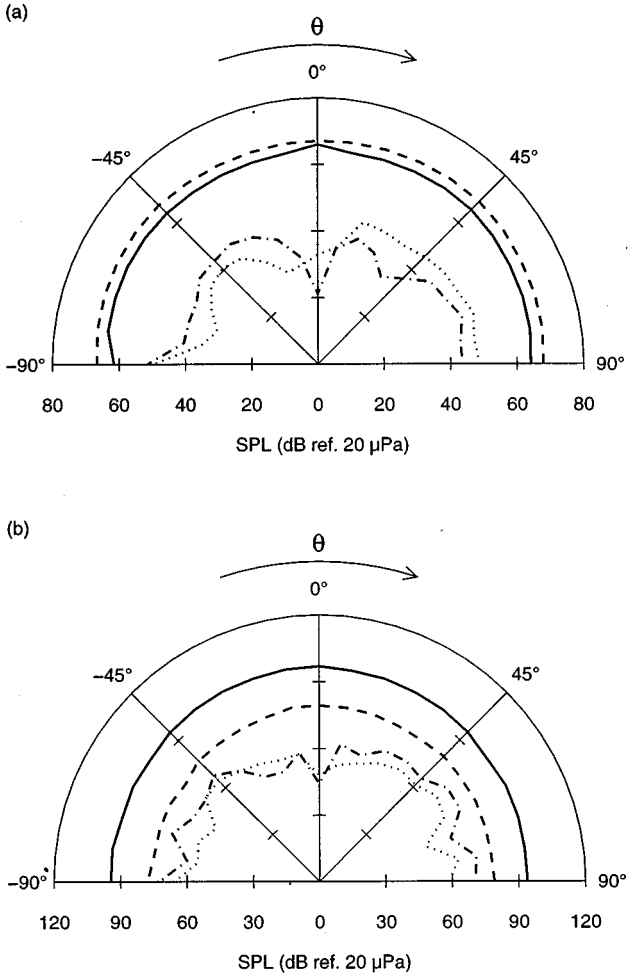

FIG. 6. Harmonic control results at (a) 290 Hz and (b) 1000 Hz: — piston; – – passive; -·-· passive–active series-parallel configuration; ··· passive–active parallel configuration.

minimized at only one location in space (direction $\theta=0°$), the sound attenuation under control is global. In Fig. 6(a), the global sound level is decreased by about 20 dB at 290 Hz using the series-parallel actuator. The parallel actuator yields a 16-dB global sound reduction. It is also observed that at this frequency, the passive smart foam causes a 1.5-dB increase in the far-field radiation. The reason for this behavior has been discussed in the previous section. Figure 6(b) shows results for a 1000-Hz excitation frequency. About 10-dB passive sound reduction is observed while a further 10-dB global reduction is attributed to the active PVDF actuator. The global noise cancellation was obtained as the smart foam is able to change the radiation impedance seen by the vibrating piston. The attenuation achieved by both PVDF actuator configurations is comparable at this frequency. Radiation control at other harmonic excitation frequencies was investigated and indicated that the series-parallel actuator performed best at reducing the piston sound radiation. However, it is important to note that the control voltage required by the series-parallel configuration is greater than that needed by the parallel actuator. For example, for a 290-Hz drive frequency, the series-parallel actuator required about 1.5 times more voltage than the parallel

actuator to minimize the piston radiation. This observation was expected as Fig. 4 illustrated that the parallel actuator was a more efficient sound radiator than the series-parallel actuator. At 1000 Hz, where passive sound absorption is evident, the control voltage required to drive the PVDF actuator was much lower than at 290 Hz. Therefore, as the piston excitation frequency increases, the passive absorption provided by the smart foam increases and the voltage required to drive the PVDF actuator decreases. Applying the maximum allowable control voltage (i.e., 300 V rms) would allow the smart foam to radiate a 60-dB sound-pressure level at 1.5 m at 290 Hz using the parallel configuration. For the same type of excitation, a 71-dB sound-pressure level could be generated by the smart foam at 1000 Hz. These experimental results reveal the benefits of implementing a composite active/passive system for acoustic radiation control.

VI. BROADBAND PASSIVE/ACTIVE CONTROL RESULTS

The second control case involves broadband control of piston radiation. The piston was excited with band-limited random noise between 0 and 1600 Hz. The error microphone was again located in the direction perpendicular to the surface of the foam (1.5 m away in direction $\theta=0°$). This error microphone position represents the location of maximum directivity. The performance of the smart foam for minimizing broadband radiation at the error microphone is presented in Fig. 7(a). Below 350 Hz, an active sound attenuation of about 10–15 dB is achieved for both actuator configurations. In this frequency range, it is important to note that the active component (PVDF actuator) is able to compensate for the poor performance of the passive smart foam. Above 350 Hz, the series-parallel actuator configuration performs better than the parallel one. This is believed to be related to the nonlinear behavior associated with the parallel configuration [as seen in Fig. 4(c)]. Above 350 Hz, about 15-dB attenuation can be attributed to the passive effect of the foam, while 10–15 dB attenuation is associated with the active contribution of the PVDF element for the series-parallel configuration. It was again noticed that the control signal used to drive the PVDF actuator (for all configurations) decreases in amplitude as frequency increases. Global sound levels associated with the passive/active device are presented in Fig. 7(b). It can be observed that in the low-frequency region, global active sound attenuation is achieved while using only one error microphone. For the series-parallel configuration, global active sound attenuation of about 10 dB is achieved up to 1200 Hz. The smart foam modifies the resistive radiation impedance of the source yielding global noise cancellation. However, above 1300 Hz, the amount of active reduction for both PVDF configurations seems to decrease and slight control spillover occurs. This may be attributed to the fact that the number of coefficients in the FIR filters used in the implementation of feedforward LMS controller was not sufficient to model the system response in the high-frequency range. However, even though control spillover is present, the levels never increase above that of the untreated piston. Thus, the passive sound absorption associated with the passive–active device provides some failsafe control. The

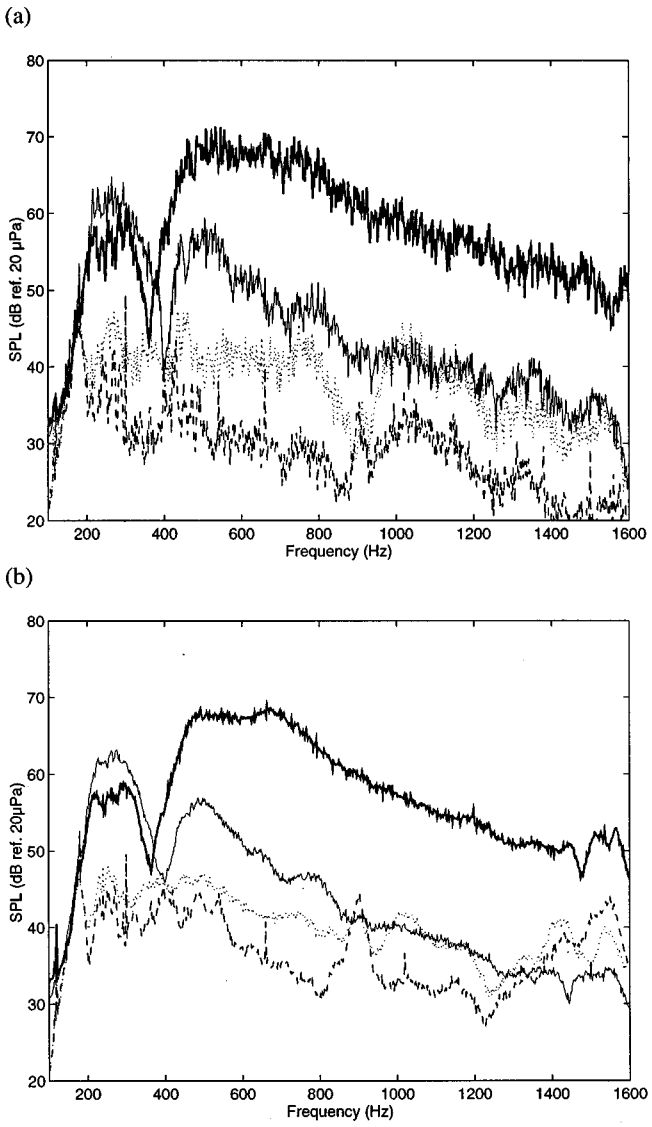

FIG. 7. Broadband control results (a) at the error microphone; (b) global sound level; — piston, — passive, ---- passive–active series-parallel configuration; ···passive–active parallel configuration.

complimentary nature of performing active–passive control is evident as the active part controls the low-frequency range while the passive component performs best at high frequencies.

VII. CONCLUDING DISCUSSION

In this paper, a smart foam has been introduced as a active–passive noise control device, which has many advantages over conventional noise attenuation systems. The smart foam consists of cylindrically curved sections of PVDF film embedded in partially reticulated polyurethane acoustic foam. The device is designed to reduce sound by the action of the passive absorption of the foam (effective at high frequencies) and the active input of the PVDF element driven by an oscillating electrical input (effective at low frequencies). The PVDF actuator was configured to behave in a linear sense as well as to increase its sound radiation effi

ciency. Global cancellation of harmonic and broadband noise induced by a vibrating piston was successfully achieved by the smart foam. The passive–active device was able to modify the radiation impedance observed by the piston over a wide range of frequencies. The potential of smart foam to globally reduce low- and high-frequency sound radiating from a vibrating piston was demonstrated.

Further research will concentrate on increasing the control authority of the device (i.e., the radiation efficiency and output of the PVDF actuator). With the current configuration of smart foam, it is possible to generate a 60-dB sound-pressure level at 1.5 m in the low-frequency region (≈300 Hz) when excited by the maximum allowable voltage. A multi-layer PVDF configuration and modification of the foam shape are two issues that are being studied to improve smart foam. The use of different error sensors (a far-field microphone is in general impractical) is also under study. The combination of completed analytical models for the porous foam and the curved PVDF film for the purpose of simulating a smart foam radiation control experiment is currently being investigated. Radiation control of more complex vibrating structures using a smart foam array will be a major area for future research.

ACKNOWLEDGMENTS

The authors gratefully acknowledge the support of this work by the Office of Naval Research under Grant No. ONR N00014-94-1-1140, the Army Research Office under Grant No. DAA H04-95-1-0037, and the NASA Langley Research Center.

[1] K. W. Ng, ''Applications of active control,'' The 1995 International Symposium on Active Control of Sound and Vibration, Active 95, Newport Beach, California, Supplemental paper, July 1995.
[2] M. V. Gandhi and B. S. Thompson, *Smart Materials and Structures* (Chapman & Hall, London, England, 1992), p. 74.
[3] A. H. von Flotow, A. Beard, and Don Bailey, ''Adaptive tuned vibration absorbers: tuning laws, tracking agility, sizing, and physical implementations,'' Proceedings of Noise-Con 94, Fort Lauderdale, Florida, May 1994, pp. 437–454.
[4] C. R. Fuller, J. P. Maillard, M. Mercadal, and A. H. von Flotow, ''Control of aircraft interior noise using globally detuned vibration absorbers,'' Proceedings of First Joint CEAS/AIAA Aeroacoustics Conference, Germany, Volume 1, 1995, pp. 615–624.
[5] Y. J. Kang, W. Tsoi, and J. S. Bolton, ''The effect of mounting on the acoustical properties of finite-depth polyimide foam layers,'' Proceedings of Noise-Con 93, Williamsburg, Virginia, 1993, pp. 285–290.
[6] L. Beranek and L. Ver, *Noise and Vibration Control Engineering: Principles and Applications* (Wiley, New York, 1992), p. 204.
[7] J. S. Bolton and E. R. Green, ''Smart foams for active absorption of sound,'' Second Conference on Recent Advances in Active Control of Sound and Vibration, Blacksburg, Virginia, 1993, pp. 139–149.
[8] T. R. Howarth, V. K. Varadan, X. Boa, and V. Varadan, ''Piezocomposite coating for active underwater sound reduction,'' J. Acoust. Soc. Am. **91**, 823–831 (1992).
[9] A. Baz, ''Active Constrained Layer Damping,'' Proceedings of Damping 93 Conference, San Francisco, California, February 1993.
[10] C. R. Fuller, M. J. Bronzel, C. A. Gentry, and D. E. Whittington, ''Control of Sound Radiation/Reflection with Adaptive Foams,'' Proceedings of Noise-Con 94, Fort Lauderdale, Florida, May 1994, pp. 429–436.
[11] C. R. Fuller, S. J. Elliott, and P. A. Nelson, *Active Control of Vibration* (Academic, London, 1996).
[12] P. A. Nelson and S. J. Elliott, *Active Control of Sound* (Academic, London, 1992).
[13] Polymer Technology Inc., Technical Data Sheet: ''Acoustical Products—An Overview,'' published by Polymer Technology Inc., Newark, Delaware.
[14] G. C. Tibbets, ''Transducers having piezoelectric film arranged with alternating curvatures,'' U. S. Patent No. 4,056,742 (November 1977).
[15] L. Beranek, *Acoustical Measurements* (Acoustical Society of America, Cambridge, MA, 1988), pp. 674–676.

An introduction to statistical energy analysis

Courtney B. Burroughs
Graduate Program in Acoustics, The Pennsylvania State University, State College, Pennsylvania 16804

Raymond W. Fischer
Noise Control Engineering, Incorporated, Billerica, Massachusetts 01821

Fred R. Kern
Atlantic Applied Research Corporation, Burlington, Massachusetts 01803

(Received 28 April 1993; revised 4 September 1996; accepted 20 November 1996)

The basic concepts and underlying assumptions of Statistical Energy Analysis (SEA) are reviewed. Using coupled simple oscillators as models for resonant modes, power balance equations are derived. Equipartition of energy among modes within a subsystem, and strong versus weak coupling between subsystems are discussed. Input requirements for exercising SEA power balance equations are defined and methods of obtaining the required input are outlined. Examples of the applications of SEA are presented and discussed. © *1997 Acoustical Society of America.*
[S0001-4966(97)07404-3]

PACS numbers: 43.10.Ln, 43.40.At [DWM]

INTRODUCTION

Designers are often required to comply with noise specifications in a complex system of acoustical and structural subsystems with several broadband sources of noise and vibration. In such systems, noise problems need to be identified early in the design stage so that treatments can be effectively integrated into the design. This requires the capability to accurately predict vibration and noise propagation throughout a system which involves coupled subsystems. At frequencies above the first few frequencies of resonance of subsystems, it is difficult, if not impossible, to use classical analytic models which involve modal expansions, or numerical methods which require large numbers of finite elements. Often it is necessary to predict the average vibration and/or noise levels in various frequency bands. Thus models that make predictions at single frequencies need to be exercised repeatedly to cover the range of frequencies in each frequency band of interest. To address the need to predict average vibration or noise levels in frequency bands for complex systems of inter-connected subsystems, Statistical Energy Analysis (SEA) methods were developed. Since its early conception, SEA has been widely used, primarily in the aerospace industry. The purpose of this article is to outline the basic principles behind SEA, review the development of SEA, present examples of its application, and examine input parameters as an introduction to SEA. This article can not satisfy all of the needs for the development of comprehensive models for the application of SEA to complex systems. The reader seeking more detailed information is referred to the book by Lyon and DeJong.[1]

SEA is statistical in that the frequencies of resonance for each subsystem are assumed to be uniformly distributed in frequency within each of the frequency bands used in the analysis. Since it is assumed that energy resides only in resonance modes, the total energy in each subsystem is the sum of the energies in the modes. This energy is assumed to be distributed equally among the modes in each subsystem and analysis band. By definition, subsystems are structural or acoustical entities that have modes which are similar in nature and, as will be shown later, have equal modal energies. Different subsystems typically have different modal energies. The primary variable of interest in SEA is energy. For steady-state conditions, a power balance is derived in each analysis band in which the input power to the subsystem(s) is either dissipated within the subsystem(s) or coupled to other subsystems where it is dissipated or radiated to the acoustic farfield. The energy is distributed among the subsystems to establish a balance in the power flow into and between subsystems such that the subsystem energies times their coupling, damping, and radiation loss factors account for all of the power input to the subsystems. From subsystem energies, other parameters, such as average vibration and sound pressure levels, are obtained. Because equal distribution of energy over space within each subsystem is assumed, only average vibration and noise levels in each subsystem can be obtained in each analysis band. Neither frequency distributions of the levels within each band, nor spatial distributions of the levels of the modal energy within a subsystem can be obtained from SEA. In most situations with multiple noise sources and paths, average levels are all that are required. This makes SEA an ideal tool that provides the required information with a minimum level of modeling complexity and detail. Its relatively simply equations and outputs can provide insight in developing an understanding of the important paths in designing required noise control treatments.

The mathematical basics and assumptions for SEA are outlined in Sec. I. In Sec. II, methods for obtaining the parameters required to exercise the power balance equations used in SEA for predicting the energy distribution within a system are reviewed. Examples of the application of SEA are presented in Sec. III, followed by a summary in Sec. IV.

I. BASICS OF SEA

SEA is used to predict the response of a dynamic system to external power input. A system will refer to the entire

 0001-4966/97/101(4)/1779/11/$10.00

complement of coupled structures and acoustic spaces under consideration. The system is then divided into subsystems which consist of a collection of similar resonant modes within a structure or acoustic space. For example, a bounded acoustic space is usually treated as a subsystem containing acoustic modes. Bending waves in a plate and longitudinal waves in the same plate may each be treated as separate sets of modes and therefore as separate subsystems. Once identified, subsystems are then coupled via coupling loss factors in the development of power balance equations that serve as the backbone of SEA.

The basic concepts of SEA are:

(1) Power flow between subsystems is proportional to the differences in the modal energies of the coupled subsystems. This is supported by mathematical modeling, outlined below, that begins with the coupling of two simple oscillators. The coupling of two oscillators becomes the building block for coupling of multimode resonant subsystems where each oscillator serves as a modal model.
(2) Power input or transmitted to a subsystem is either dissipated in the subsystem or transmitted to adjacent subsystems via junctions of structures or interfaces between structures and acoustic spaces. Thus a complete account of all of the power is taken.
(3) Energy resides only in resonance modes, so that the more modes a subsystem has in the analysis band, the greater the capacity of the subsystem to accept and store energy. Within each analysis band, the energy in a subsystem is uniformly divided among the modes. The net power coupled between subsystems is proportional to the difference in their modal energies and only passes from the subsystem with higher modal energy to those of lower modal energy. When modes have equal energy, it is referred to as an equipartition of energy.

There are several assumptions that are generally made in the development of SEA models.

(a) The input power spectra is broadband, i.e. there are no strong pure tones in the input power spectra.
(b) Energy is not created in the couplings between subsystems. Energy may be dissipated in junctions between subsystems, such as in isolation mounts, but generally this effect is added to subsystem damping loss factors.
(c) The damping loss factor is equal for all modes within a subsystem and analysis band.
(d) Modes within a subsystem do not interact except to share an equipartition of energy. The coherent effects between modes are ignored so that power sums apply.

A. Coupled simple oscillator

Two simple oscillators are shown in Fig. 1 coupled via a spring and gyroscope. The coupling forces transmitted through the spring are proportional to the differences in the displacements, ξ_1 and ξ_2, of the two masses in the oscillators. Coupling forces transmitted through the gyroscope are proportional to the velocities, $\dot{\xi}_1$ and $\dot{\xi}_2$, of the two oscillator masses. Arms connecting the oscillator masses to the top of the gyroscope slide in a fixed trough and are assumed to be inflexible along their axes. The bottom of the gyroscope is hinged in a ball socket. The displacement of the mass away from the base of the oscillator is taken as positive in each oscillator. A positive velocity for oscillator 1 results in a positive force on oscillator 2, and a positive velocity for oscillator 2 results in a negative force on oscillator 1. Adding the coupling forces by the spring and gyroscope between the oscillators to the equations of motion for the two oscillators yields

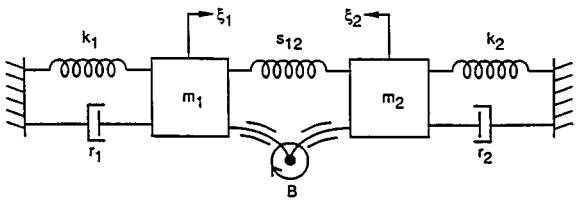

FIG. 1. Model of coupled simple oscillators.

$$
\begin{aligned}
&m_1\ddot{\xi}_1+r_1\dot{\xi}_1+k_1\xi_1+B\dot{\xi}_2+s_{12}(\xi_2-\xi_1)=F_1,\\
&m_2\ddot{\xi}_2+r_2\dot{\xi}_2+k_2\xi_2-B\dot{\xi}_1+s_{12}(\xi_1-\xi_2)=F_2,
\end{aligned}
\tag{1}
$$

where m_1 and m_2 are the masses of the oscillators, r_1 and r_2 are the viscous damping coefficients, k_1 and k_2 are the oscillator spring constants, B is the gyroscopic constant, s_{12} is the coupling spring constant, and F_1 and F_2 are the magnitudes of the harmonic forces applied to the oscillator masses. Grouping terms in Eq. (1) and defining $s_1=k_1-s_{12}$ and $s_2=k_2-s_{12}$, gives

$$
\begin{aligned}
&m_1\ddot{\xi}_1+r_1\dot{\xi}_1+s_1\xi_1+B\dot{\xi}_2+s_{12}\xi_2=F_1,\\
&m_2\ddot{\xi}_2+r_2\dot{\xi}_2+s_2\xi_2-B\dot{\xi}_1+s_{12}\xi_1=F_2.
\end{aligned}
\tag{2}
$$

These are the equations given by Cremer *et al.* (p. 478).[2] Therefore, we can now follow Cremer *et al.*

With harmonic time dependence, $e^{i\omega t}$, of the applied forces, Eqs. (2) reduce to algebraic equations which can be solved for the velocities of the oscillator masses:

$$
\begin{aligned}
\nu_1=i\omega\xi_1=&\frac{-i\omega}{m_1m_2D(\omega)}\{m_2(\omega^2-2i\omega\delta_2-\omega_2^2)F_1\\
&+(i\omega B+s_{12})F_2\},\\
\nu_2=i\omega\xi_2=&\frac{-i\omega}{m_1m_2D(\omega)}\{(-i\omega B+s_{12})F_1+m_1(\omega^2\\
&-2i\omega\delta_1-\omega_1^2)F_2\},
\end{aligned}
\tag{3}
$$

where

$$
\begin{aligned}
D(\omega)=&\omega^4-2i\omega^3(\delta_1+\delta_2)-\omega^2\left(\omega_1^2+\omega_2^2+4\delta_1\delta_2\right.\\
&\left.+\frac{B^2}{m_1m_2}\right)+2i\omega(\delta_1\omega_2^2+\delta_2\omega_1^2)-\frac{s_{12}}{m_1m_2}\\
&+\omega_1^2\omega_2^2.
\end{aligned}
\tag{4}
$$

In Eqs. (3) and (4), $\omega_i = (s_i/m_i)^{1/2}$ are the natural frequencies of the uncoupled oscillators, and $\delta_i = r_i/2m_i$ are related to the half-power bandwidths of the oscillators about their natural frequencies. Of interest is the power flow between the oscillators, which can be described as

$$P_{12} = \tfrac{1}{2}\,\mathrm{Re}\{F_{12}\nu_2^*\}, \tag{5}$$

where F_{12} is the force applied by oscillator 1 to oscillator 2, given by the last two terms in the second part of Eqs. (2), and the star (*) denotes the complex conjugate. Combined with the velocity given in Eqs. (3), this yields

$$P_{12} = \frac{\omega^2 s_{12}^2 + \omega^4 B^2}{m_1^2 m_2^2 |D(\omega)|^2}\,(m_2\delta_2|F_1|^2 - m_1\delta_1|F_2|^2). \tag{6}$$

This is the power flow at the single frequency, ω. For broadband excitation, the total power flow given by Eq. (6) must be integrated over the frequency bandwidth, $\Delta\omega$, of interest. If we assume that the natural frequencies of the oscillators are far from both limits of the frequency band, then the integration can be extended to $\pm\infty$ without significant loss in accuracy. The integral can be easily evaluated using integral tables [for example, see Ref. 3, p. 218, Eq. 3.112.5]. The result of the integration over frequency is

$$\overline{P_{12}} = \frac{\pi}{2\Delta\omega}\left[\frac{|F_1|^2}{\delta_1 m_1} - \frac{|F_2|^2}{\delta_2 m_2}\right] \times \frac{(\delta_1\omega_2^2 + \delta_2\omega_1^2)B^2 + (\delta_1+\delta_2)s_{12}^2}{m_1 m_2 Q}, \tag{7}$$

where

$$Q = (\omega_1^2 - \omega_2^2)^2 + 4(\delta_1+\delta_2)(\delta_1\omega_2^2 + \delta_2\omega_1^2) + (\delta_1+\delta_2) \times \left(\frac{\omega_1^2}{\delta_2} + \frac{\omega_2^2}{\delta_1}\right)\frac{B^2}{m_1 m_2} + \frac{(\delta_1+\delta_2)^2 s_{12}^2}{\delta_1\delta_2 m_1 m_2}. \tag{8}$$

In the derivation of Eq. (7), it was assumed that the input forces are independent of frequency, i.e. the excitations are broadband with a flat frequency spectra. Next, we would like to relate the power flow between the oscillators, given in Eq. (7), to the differences in the energies in the two oscillators. The energy, $\overline{W_i}$, in ith oscillator in $\Delta\omega$ bandwidth is given by

$$\overline{W_i} = \frac{m_i}{2\Delta\omega}\int_{-\infty}^{+\infty} \nu_i(\omega)\,\nu_i^*(\omega)\,d\omega. \tag{9}$$

In Eq. (9), we have made the same assumption on the limits of the bandwidth, relative to the natural frequencies of the oscillators, made in deriving Eq. (7) for the power flow. The integral of the terms involving the product F_1F_2 vanishes when we assume that the input forces are independent. For oscillator 1, we obtain

$$\overline{W_1} = \frac{\pi}{2\Delta\omega}\left\{\frac{|F_1|^2}{m_1\delta_1}\left[\frac{\tfrac{1}{2}(\omega_1^2-\omega_2^2) + (\delta_1+\delta_2)(\delta_1\omega_2^2+\delta_2\omega_1^2)}{Q}\right] + \frac{[s_{12}^2(\delta_1+\delta_2) + B(\delta_1\omega_2^2+\delta_2\omega_1^2)][m_2|F_1|^2 + m_1|F_2|^2]}{2m_1^2 m_2^2\delta_1\delta_2 Q}\right\}. \tag{10}$$

For oscillator 2, the energy is given by Eq. (10) with the indices interchanged. Taking the difference in the energies gives

$$\overline{W_1} - \overline{W_2} = \frac{\pi}{2\Delta\omega}\left[\frac{|F_1|^2}{m_1\delta_1} - \frac{|F_2|^2}{m_2\delta_2}\right] \times \left[\frac{\tfrac{1}{2}(\omega_1^2-\omega_2^2)^2 + (\delta_1+\delta_2)(\delta_1\omega_2^2+\delta_2\omega_1^2)}{Q}\right], \tag{11}$$

where the second term in Eq. (10) drops out because it is symmetric with respect to the two indices. Dividing Eq. (11) into Eq. (7) yields

$$\overline{P_{12}} = \beta(\overline{W_1} - \overline{W_2}), \tag{12}$$

where

$$\beta = \frac{2}{m_1 m_2}\,\frac{(\delta_1\omega_2^2 + \delta_2\omega_1^2)B^2 + (\delta_1+\delta_2)s_{12}^2}{(\omega_1^2-\omega_2^2)^2 + 2(\delta_1+\delta_2)(\delta_1\omega_2^2+\delta_2\omega_1^2)}. \tag{13}$$

Equation (13) is a function of the parameters of the oscillators (δ_1, δ_2, ω_1, and ω_2) and coupling factors (B and s_{12}) and not the energies in the oscillators. The reason we have gone into so much detail in the development of Eq. (12) is because it forms the basis for some of the underlying principles of SEA and its derivation illustrates some of the fundamental assumptions behind SEA. Equation (12) underpins SEA. It shows that power flow between two coupled oscillators, excited by broadband uncorrelated sources, is:

(1) Proportional to the differences in the energies in the oscillators or, as seen later, the modal energies for multimodal subsystems;
(2) The constant relating the power flow to the energy differences is a function of the coupling parameters and properties of the oscillators;
(3) The direction of power flow is from the oscillator with the higher (modal) energy to the oscillator with the lower (modal) energy.

Assume that only oscillator 1 is excited by a broadband source. Then, the net power flow from oscillator 1 to oscillator 2 must be dissipated in oscillator 2 to achieve a power balance. Thus

$$\overline{P_{12}} = \beta(\overline{W_1} - \overline{W_2}) = P_{2d}. \tag{14}$$

Since

$$\overline{W_i} = \tfrac{1}{2}m_i\overline{|\nu_i|^2}, \quad P_{2d} = \tfrac{1}{2}r_2\overline{|\nu_2|^2}, \tag{15}$$

Eq. (14) becomes

$$\frac{m_2\overline{|\nu_2|^2}}{m_1\overline{|\nu_1|^2}} = \frac{1}{1 + r_2/m_2\beta}. \tag{16}$$

Since $r_2/m_2\beta > 0$, Eq. (16) shows that the energy in the undriven oscillator 2 can not be greater than the energy in the driven oscillator 1. For small damping in oscillator 2 and strong coupling between the oscillators, i.e. $r_2/m_2\beta \ll 1$, Eq. (16) becomes

$$m_2\overline{|\nu_2|^2}=m_1\overline{|\nu_1|^2}. \tag{17}$$

The energy is equally divided between the two oscillators. The oscillators are said to be strongly or tightly coupled, and, as Eq. (17) shows, we have equipartition of energy between the oscillators when they are strongly coupled. Power can be viewed as passing back and forth between the oscillators to a much greater extent than it is dissipated in the oscillators.

For weak coupling and large damping in oscillator 2, $r_2/m_2\beta \gg 1$, and Eq. (16) becomes

$$m_2|\nu_2|^2 \ll m_1|\nu_1|^2. \tag{18}$$

Little of the power input to oscillator 1 gets into oscillator 2, and that power that does get into oscillator 2 is quickly dissipated, so that there is little energy built up in oscillator 2.

B. Coupled multiresonant subsystems

Now consider two coupled subsystems. In a given analysis band, subsystem 1 has N_1 modes and subsystem 2 has N_2 modes. The power flow from the m_1th mode in subsystem 1 to the m_2th mode in subsystem 2 is similar to that for two coupled oscillators, since each of the two modes act like a simple oscillator with inertial (mass), elastic (spring), and dissipative (dashpot) elements. Thus

$$\overline{P_{m_1m_2}}=\beta_{m_1m_2}(\overline{W_{m_1}}-\overline{W_{m_2}}), \tag{19}$$

where $\overline{P_{m_1m_2}}$ is the power flow from the m_1th mode in subsystem 1 to the m_2th mode in subsystem 2, $\beta_{m_1m_2}$ is the coupling parameter analogous to Eq. (13), and $\overline{W_{m_1}}(\overline{W_{m_2}})$ is the modal energy in the m_1th (m_2th) mode in subsystem 1 (subsystem 2). The bars over the variables in Eq. (19) denote an average over a frequency band. If we assume that all of the modes in subsystem 1 are strongly coupled, then the energy in subsystem 1 is equally divided among all of the modes within the analysis band. Strongly coupled modes can be thought of as modes that are all directly responsive to the same broadband excitation, such as the acoustic modes in a room responding to a broadband acoustic source in the room. The energy is equally divided among the modes when the damping loss factor is the same for all of the modes.

The coupling of the N_1 modes in subsystem 1 to the m_2th mode in subsystem 2 can then be expressed as

$$\overline{P_{1m_2}}=\langle\beta_{m_1m_2}\rangle_{N_1}N_1(\overline{W_{m_1}}-\overline{W_{m_2}}), \tag{20}$$

where $\langle\ \rangle_{N_1}$ indicates an average over the N_1 modes in subsystem 1. Extending this to include the N_2 modes in subsystem 2, we have

$$\overline{P_{12}}=\langle\beta_{m_1m_2}\rangle_{N_1N_2}N_1N_2(\overline{W_1}-\overline{W_2}), \tag{21}$$

where $\overline{P_{12}}$ is the net power flow from subsystem 1 to subsystem 2 in a frequency band. Defining

$$\eta_{12}=\frac{\langle\beta_{m_1m_2}\rangle_{N_1N_2}N_2}{\omega}, \tag{22a}$$

and

$$\eta_{21}=\frac{N_1\eta_{12}}{N_2}, \tag{22b}$$

where ω is the center frequency of the analysis band, then Eq. (21) can be written as

$$\overline{P_{12}}=\omega[\,\eta_{12}W_1-\eta_{21}W_2], \tag{23}$$

where $W_1=N_1\overline{W_{m_1}}$ and $W_2=N_2\overline{W_{m_2}}$ are the total energies in subsystems 1 and 2, respectively, and η_{12} and η_{21} are the coupling loss factors. The first term in Eq. (23) is the power lost by subsystem 1 to subsystem 2 and the second term in Eq. (23) is the power lost by subsystem 2 to subsystem 1. With the modal densities in subsystems 1 and 2 given by $n_1 = N_1/\Delta\omega$ and $n_2 = N_2/\Delta\omega$, respectively, we can write Eq. (22b) as

$$\eta_{21}=\frac{n_1\Delta\omega\,\eta_{12}}{n_2\Delta\omega}=\frac{n_1}{n_2}\,\eta_{12}. \tag{24}$$

Thus the coupling loss factor for subsystem 2 to subsystem 1 is greater than for subsystem 1 to 2 when the modal density in subsystem 1 is greater than the modal density in subsystem 2. The higher the modal density, the more modes there are to store energy within a fixed frequency band. Since modal densities are often easier to estimate than coupling loss factors, Eq. (24) can be used to reduce the effort required in obtaining estimates for the coupling loss factors, since only one of the two coupling loss factors for two coupled subsystems needs to be calculated.

The power input to subsystem 1 must either be transmitted to subsystem 2 or dissipated in subsystem 1. That is

$$\overline{P_{1\,\mathrm{input}}}=\overline{P_{1d}}+\overline{P_{12}}. \tag{25}$$

The power dissipated in subsystem 1 is given by

$$\overline{P_{1d}}=\omega\,\eta_1W_1, \tag{26}$$

where η_1 is the damping loss factor, which is the ratio of the power dissipated per radian of motion to the total energy. Using Eqs. (23) and (26) in Eq. (25),

$$\overline{P_{1\,\mathrm{input}}}=\omega\{(\,\eta_1+\eta_{12})W_1-\eta_{21}W_2\}. \tag{27}$$

Likewise, for the power input to subsystem 2,

$$\overline{P_{2\,\mathrm{input}}}=\omega\{(\,\eta_2+\eta_{21})W_2-\eta_{12}W_1\}. \tag{28}$$

Equations (27) and (28) are the power balance equations for two subsystems. In Eqs. (27) and (28) the reason for defining the coupling loss factors as in Eq. (22) can be seen. The coupling loss factor serves an analogous role to that of the damping loss factor. The damping loss factor is a measure of the rate at which energy is lost or dissipated within a subsystem, whereas the coupling loss factor is a measure of the rate at which energy in one subsystem is transmitted, and thereby lost, to another subsystem through their mutual coupling, when the energy in the other system is zero, i.e. it acts as an energy sink.

If power is input only to subsystem 1, then Eq. (28) leads to

$$\frac{W_2}{W_1}=\frac{\eta_{12}}{\eta_{21}+\eta_2}. \tag{29}$$

This is a useful relation for evaluating treatments for the reduction of energy (i.e., noise) in subsystem 2. Using Eq. (24) in Eq. (29) yields

$$\frac{\overline{W_{m_2}}}{\overline{W_{m_1}}} = \frac{\eta_{21}}{\eta_{21}+\eta_2}, \tag{30}$$

which indicates that for $\eta_{21} \gg \eta_2$, the modal energies in subsystems 1 and 2 are nearly equal and the two subsystems may be combined into one subsystem.

Equations (27) and (28) can be extended to N subsystems to obtain the set of N equations given by P. W. Smith Jr.:[4]

$$\overline{P_{i,\text{input}}} = \omega\left\{\left(\eta_i + \sum_{j\neq i}^{N} \eta_{ij}\right) W_i - \sum_{j\neq i}^{N} \eta_{ji} W_j\right\}, \tag{31}$$

for $i = 1,2,\ldots,N$. Equations (31) are the power balance equations for N coupled subsystems that form the basis for SEA. The unknowns are the energies, W_i, in the subsystems. The inputs are the coupling loss factors, η_{ij}, the damping loss factors, η_i, and the power inputs, $\overline{P_{i,\text{input}}}$. The power balance equations are solved for the energies in each frequency analysis band. Each analysis band must be wide enough to contain several modes in each subsystem.

Two key assumptions made in deriving the power balance equations were equipartition of energy and that resonant modes act like simple oscillators. In support of the validity of these assumptions, we once again follow Cremer *et al.*,[2] and consider a finite subsystem (e.g., a closed acoustic space or a finite beam, plate, or shell) that has resonant modes, $\phi_n(x)$, such that the response can be expressed in a modal (eigenfunction) expansion

$$\nu(x) = \sum_n \nu_n \phi_n(x) \tag{32}$$

where x denotes spatial location. The mode functions are orthogonal, i.e.

$$\int_s m\,\phi_n(x)\,\phi_m(x)\,dx = \begin{cases} \Lambda_n, & n=m, \\ 0, & n\neq m, \end{cases} \tag{33}$$

where Λ_n is the normalization constant for the nth mode and m is the mass distribution. For a single localized source modeled by

$$p(x) = F_0\,\delta(x-x_0), \tag{34}$$

we have

$$\nu_n = \frac{i\omega F_0 \phi_n(x_0)}{[\omega_n^2(1+i\eta)-\omega^2]}, \tag{35}$$

where $\delta(\cdot)$ is the Dirac delta function. The spatial average of the response is

$$\overline{\nu^2} = \frac{1}{M}\int_s m|\nu(x)|^2\,dx, \tag{36}$$

where M is the total mass of the subsystem. Using Eq. (32) in Eq. (35), we obtain

$$\overline{\nu_2} = \frac{1}{M}\sum_n \frac{\omega^2 F_0^2 \phi_n^2(x_0)}{[(\omega_n^2-\omega^2)^2+\eta^2\omega_n^4]\Lambda_n}, \tag{37}$$

where we have applied orthogonality [Eq. (33)]. For uniformly distributed point sources (''rain on the roof''), we integrate over source locations.

$$\overline{\overline{\nu_2}} = \frac{1}{M}\frac{1}{S}\int_S \sum_n \frac{\omega^2 F_0^2 \phi_n^2(x_0)\,dx_0}{[(\omega_n^2-\omega^2)^2+\eta^2\omega_n^4]\Lambda_n}. \tag{38}$$

Using Eq. (33)

$$\overline{\overline{\nu^2}} = \frac{\omega^2 F_0^2}{M^2}\sum_n \frac{1}{(\omega_n^2-\omega^2)^2+\eta^2\omega_n^4}. \tag{39}$$

Equation (39) shows that, for independent localized sources (or random broadband excitation), the input energy to all modes is uniform. Also, Eq. (39) indicates that the response of a subsystem to random broadband excitation is dominant at the resonance frequencies, ω_n.

Averaging over a frequency band $\omega_2-\omega_1=\Delta\omega$, which contains the modes n_1 to n_2, we obtain

$$\nu_{\Delta\omega}^2 = \frac{F_{\Delta\omega}^2}{M^2}\sum_{n=n_1}^{n_2}\frac{1}{\Delta\omega}\int_{\omega_1}^{\omega_2}\frac{\omega^2\,d\omega}{(\omega_n^2-\omega^2)^2+\eta^2\omega_n^4}, \tag{40}$$

where $F_{\Delta\omega}^2$ is the average of the forces within the frequency band. Assuming that $\omega_n \simeq \omega$, i.e., the range of resonance frequencies is small compared to the center frequency of the frequency band and that the damping loss factor is small so that the half-power bandwidths about resonant peaks remain well within the frequency band, then Eq. (40) becomes

$$\nu_{\Delta\omega}^2 = \frac{F_{\Delta\omega}^2}{M^2\Delta\omega}\sum_{n=N_1}^{N_2}\frac{\pi}{2\eta\omega_n}. \tag{41}$$

Again, applying the assumption that $\omega_n \simeq \omega$ for all n

$$v_{\Delta\omega}^2 \approx \frac{F_{\Delta\omega}^2}{M^2}\frac{\pi}{2\eta\omega}\frac{\Delta N}{\Delta\omega}. \tag{42}$$

For a simple oscillator,

$$\nu = \frac{i\omega F}{m[\omega_0^2-\omega^2+i\eta\omega_0^2]}. \tag{43}$$

Averaging Eq. (43) over a frequency band containing the natural frequency, ω_0, yields

$$\nu_{\Delta\omega}^2 = \frac{F_{\Delta\omega}^2}{m^2\Delta\omega}\frac{\pi}{2\eta\omega_0}. \tag{44}$$

Comparing Eqs. (42) and (44) shows that, when a multiresonant subsystem is excited by random broadband sources, the modal response is similar to the response of a simple oscillator and that the energy is equally distributed among the modes, such that the subsystem energy in a frequency band is directly proportional to the number of modes in the band. This is the basis of Eqs. (20) and (21) where we simply multiplied by the number of modes in each subsystem.

The power transmitted into a subsystem by a pressure field, $p(x)$, is given by

$$P=\frac{1}{2}\,\mathrm{Re}\left\{\int_S p(x)\,v^*(x)\,dx\right\}, \tag{45}$$

where the star (*) denotes the conjugate of the complex velocity, $v(x)$, which includes amplitude and phase, and $\mathrm{Re}(\cdot)$ denotes the real part of the complex quantity. Using the same method used in deriving Eq. (41) yields

$$P_{\Delta\omega}=\frac{F_{\Delta\omega}}{2}\,\frac{\pi}{2M}\,\frac{\Delta N}{\Delta\omega}. \tag{46}$$

This shows that the power transmitted into a subsystem is proportional to the modal density.

Adding Eqs. (27) and (28) for a system with two coupled subsystems yields

$$P_{1,\mathrm{input}}+P_{2,\mathrm{input}}=\omega\{\eta_1 W_1+\eta_2 W_2\}, \tag{47}$$

which shows that all of the power input to the system is dissipated. This is a simple power balance and is true regardless of the strength of the coupling, so that

$$\eta_1 W_1+\eta_2 W_2=\eta_1 W_1'+\eta_2 W_2', \tag{48}$$

where the primes denote the energies in the subsystems when the subsystems are strongly coupled. For strong coupling, the damping loss factors, η_1 and η_2, are much smaller than the coupling loss factors, η_{12} and η_{21}, so that Eq. (27) becomes

$$P_{1,\mathrm{input}}=\omega(\eta_{12}W_1'-\eta_{12}W_2'). \tag{49}$$

In the limit as we increase the coupling loss factors while maintaining a constant input power, Eq. (49) leads to

$$\eta_{12}\overline{W_1'}=\eta_{21}\overline{W_2'}. \tag{50}$$

Using Eq. (22b)

$$\frac{W_1'}{n_1}=\frac{W_2'}{n_2}, \tag{51}$$

which is equipartition of energy, which applies to strongly coupled subsystems.

From Eq. (48),

$$W_1=W_1'+\frac{\eta_2}{\eta_1}\,(W_2'-W_2). \tag{52}$$

Using Eq. (50) in Eq. (52), and the result in Eq. (28) yields

$$W_2-W_2'=\frac{P_{2,\mathrm{input}}/\eta_2-W_2'}{\eta_{12}/\eta_1+\eta_{21}/\eta_2+1}. \tag{53}$$

A similar equation can be derived for the energy in subsystem 1, so that,[4]

$$W_i-W_i'=\frac{P_{i,\mathrm{input}}/\eta_i-W_i'}{1+\gamma},\quad \text{for } i=1,2, \tag{54}$$

where

$$\gamma=\frac{\eta_{12}}{\eta_1}+\frac{\eta_{21}}{\eta_2} \tag{55}$$

The transition from weak coupling, where $\gamma\ll 1$ and $W_i=P_{i,\mathrm{input}}/\eta_i$, to strong coupling, where $\gamma\gg 1$ and $W_i=W_i'$, can be seen in Eq. (55) for two coupled subsystems. Equations (54) and (55) show that coupling between two subsystems is strong when the ratio of the coupling to damping loss factors for either subsystem is large.[4]

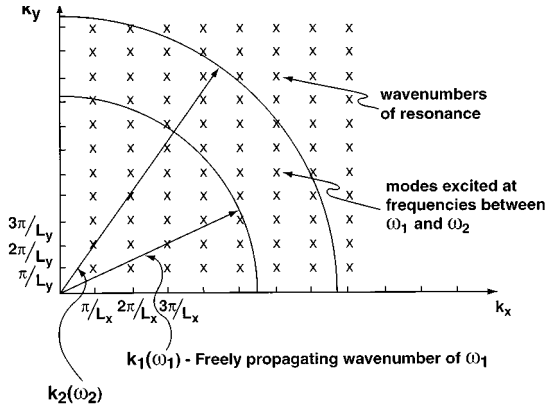

FIG. 2. Illustration of wave-number plot for estimating modal density of a simply-supported rectangular plate of dimensions L_x and L_y.

II. REQUIRED INPUT FOR POWER BALANCE EQUATIONS

The inputs required for the power balance equations are damping and coupling loss factors, subsystem masses, input powers, and modal densities. With these inputs, the power balance equations become algebraic equations with known coefficients which can be solved for the unknown energies in each of the subsystems. The average vibration and sound pressures are then computed from predictions of the subsystem energies. It is assumed that the input powers are known or can be computed based on force or displacement inputs and subsystem admittances. Damping loss factors for untreated structures, where the dissipation is in the material of the structure, must rely on measured data or experience for built-up structures. Mathematical expressions have been developed for coupling loss factors, modal densities, and damping loss factors for structures with added damping treatments. However, space does not permit the discussion of expressions for the parameters for all types of acoustical spaces and structures. We will, therefore, restrict ourselves to the consideration of rectangular flat plates, straight beams, and rectangular acoustical spaces.

A. Modal densities

Modal densities may be estimated from plots of wave numbers of resonance in the form of a grid pattern as illustrated in Fig. 2 for a simply-supported plate. Since the effect of boundary conditions reduces for higher-order modes, the simply-supported plate can be a good model for plates for purposes of estimating modal densities. The number of modes within a frequency band from ω_1 to ω_2 is then estimated by counting the modes that fall in between the two circles with radii equal to the wave numbers for freely propagating waves at the upper and lower frequencies of the band. Mathematical expressions can also be obtained by dividing the area inside the two circles by the area associated with each mode. In Fig. 2, this area is $\pi^2/L_xL_y=\pi^2/A$, where A is the area of the plate.

With the lower frequency set to zero, an estimate of the total number of modes, N, that exist below a given frequency (ω) is obtained. The modal density is then

$$n(\omega)=\frac{\partial N(\omega)}{\partial \omega}. \tag{56}$$

Also, the mean-value theory[5] may be used to estimate modal densities from measurements of the drive-point admittance as a function of frequency. The mean value of the measured drive-point admittance versus frequency (Y_c) is related to the modal density (n_n) as

$$Y_c=\frac{\pi n_n}{2M_n}, \tag{57}$$

where M_n is the modal mass. For one-dimensional structures, the modal mass is approximately one-half the total mass for the higher-order modes, and for two-dimensional structures, one-quarter the total mass.

B. Damping loss factors

Damping loss factors for energy dissipated by the material of the structure must rely on measurements or tables of representative damping loss factors. Typical ranges of damping loss factors are given in Figure 12.5 of Ref. 6. Damping treatments, such as free-layer and constrained-layer damping treatments, are often added to structures to reduce vibrations. Estimates of damping loss factors for treated structures are given in Section III.6 of Ref. 3.

C. Coupling loss factors

Coupling between in-plane (longitudinal and shear) and bending waves occurs at all junctions of structures except end-to-end junctions where there is no change in direction. Longitudinal waves have low dissipative losses, even in the presence of most damping treatments, and have longer wavelengths than bending waves. Thus longitudinal waves can provide an effective means of transmitting energy in structures over long distances. The energy in longitudinal waves can be coupled at junctions to bending waves which are dominant sources of radiated noise. Therefore, both longitudinal and bending waves need to be considered in the development of coupling loss factors for junctions of plates and beams to represent both multiwave type transmission and radiation.

There are two approaches for deriving expressions for coupling loss factors for structures; the modal and wave approaches. In the modal approach, the coupling between individual modes is computed and an average taken over the modes in each frequency band. In the wave approach, the coupling loss factor can be related to the power transmissibility for semi-infinite structures, which is often easier to estimate than the average of the couplings between modes of finite structures. The power transmitted from the first to the second structure through the junction is then energy lost by the first structure via the coupling. Since the coupling loss factor has been defined as the energy lost per radian of motion relative to the total energy in the structure, and the source of energy loss is transmission through the junction at the boundary of the first structure, it is possible to relate the coupling loss factor to the power transmission coefficient (τ_{12}) as follows,

$$\tau_{12}=\frac{P_{\text{trans}}}{P_{\text{inc}}}=\frac{\omega\eta_{12}W_{\text{tot}}}{W_{\text{tot}}(c_g/l_f)}=\frac{\omega\eta_{12}l_f}{c_g}, \tag{58}$$

where P_{trans} is the power transmitted through the junction, P_{inc} is the power incident on the junction, l_f is the mean-free path length between incidences on the junction, and c_g is the group velocity, i.e., the velocity of energy propagation. For beams, $c_g=2c_B$ where c_B is the wave phase speed and $l_f=L$, the length of the source beam, so that

$$\eta_{12}=\frac{2c_B}{\omega L}\,\tau_{12}. \tag{59}$$

For plates, $l_f=\pi A/L_{12}$, where L_{12} is the length of the junction, so that

$$\eta_{12}=\frac{2L_{12}}{\pi k_p A}\,\tau_{12}, \tag{60}$$

where k_p is the wave number for freely propagating bending waves in the source plate.

For beams or plates, expressions for the power transmissibility can be obtained by matching the transverse and angular velocities, and the shear forces and bending moments at the junction, or relating the transmissibility to the blocked forces generated by the incident wave, the impedances relating the blocked forces to the velocities at the junction, and the transmitted waves generated by the velocities at the junction. In plates, waves that comprise resonance modes are not all normally incident at junctions nor are all junctions of right angles. With the inclusion of a large number of modes in an analysis frequency band, the angles of incidence may be distributed over all possible incidence angles. In this case, expressions for the transmissibility as a function of incident angle must be derived and averaged over all incident angles, which adds greatly to the complexity of the calculations and results. Unfortunately, the additional complexities introduced by oblique incidence preclude simple expressions for the average transmissibility required for coupling loss factors for plates coupled at right angles. Although the temptation is to use normal incident transmissibilities to approximate averaged transmissibilities, coincidences at incident angles, where wave-number matching occurs, result in high transmissibilities. Furthermore, cutoff angles above which transmissibility vanishes could result in the introduction of significant errors with the use of normal incident transmissibility in coupling loss factors for plate. An example of the transmissibilities for bending-to-bending, bending-to-longitudinal and bending-to-shear waves for L junctions of two plates of equal thickness[2] is given by Fig. 3. For the thicknesses of the plates in this example, the bending-to-bending transmissibility peaks for an incidence angle of 31 deg. The cutoff angle for bending-to-longitudinal wave transmissibility is 18 deg and for bending-to-shear wave transmissibility, 28 deg. This example illustrates the complexities of the coupling loss factors as a function of incidence angle and the need to include all angles of incidence in computing coupling loss factor for junctions of structures.

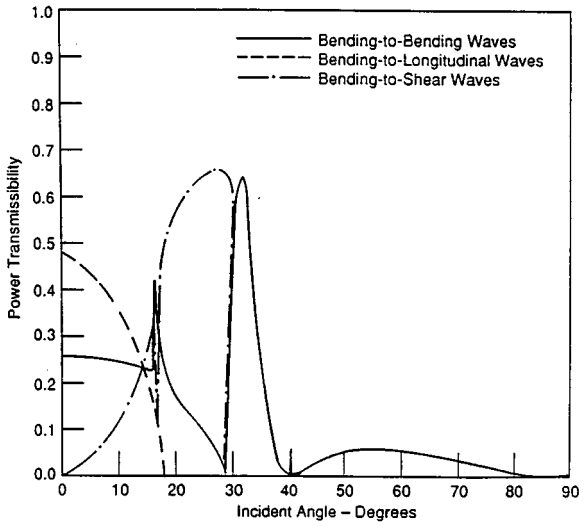

FIG. 3. Power transmissibilities for bending waves incident at a right angle L junction of two plates as a function of incidence angle.

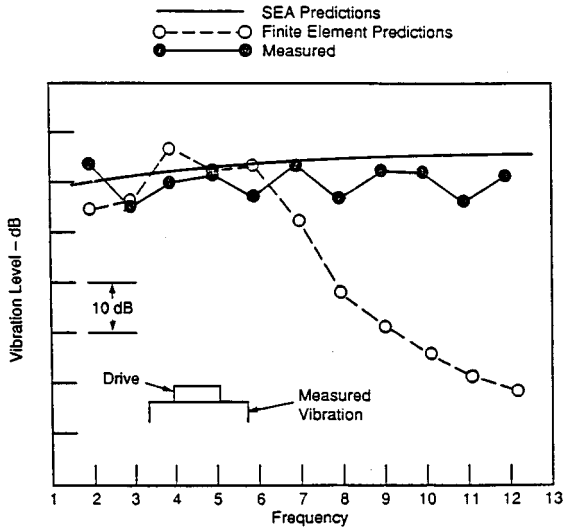

FIG. 4. Comparison of SEA and finite element model predictions to measured vibration levels for a six-plate system.

Because of the complexities involved in deriving meaningful expressions for coupling loss factors for structures, coupling loss factors have been the subject of a number of studies and incorporated into SEA computer codes. For more details, see Refs. 7–24.

The coupling loss factor (η_{sa}) for a plate radiating into an acoustic space is related to the radiation efficiency of the plate, σ_{rad}, by

$$\eta_{sa}=\frac{\rho_0 c_0 S \sigma_{\text{rad}}}{\omega M_s}, \tag{61}$$

where S is the radiating area of the plate and M_s the mass of the plate. Expressions for radiation efficiencies may be found in Ref. 25, Chapter 2 of Ref. 26, and Section 9.6 of Ref. 6.

D. Assembling an SEA model

The best approach to the definition of subsystems is to start with subsystems that extend to junctions that cause significant reflections. Bear in mind that different wave types often require subsystems of differing physical size. For example, since longitudinal wavelengths are larger than bending wavelengths, longitudinal subsystems may extend over a number of bending subsystems. If the coupling loss factors between two subsystems are such that they are strongly coupled in both directions, then these subsystems can be combined into one subsystem without loss of accuracy. Smaller models of the most complex part of the structure can sometimes aid in checking for strong coupling and simplification of the overall model.

For a first pass, it is useful to hypothesize strong coupling. The relationship between the assumed damping and coupling loss factors should be reviewed as the model is developed. The user not familiar with coupling loss factors should consider bounding these factors as a starting point for the power balance equations, and refining them as additional information becomes available and as the model is exercised and compared to measurements of predictions for similar systems.

Larger structures will contain more modes, allowing for a more accurate analysis at lower frequencies. The results for smaller structures will only be valid when there are several modes present, which may be limited to mid- to high-frequency ranges.

III. EXAMPLES OF THE APPLICATIONS OF SEA

For a system of six coupled fat plates, Lu *et al.*[27] conducted measurements on the broadband vibration levels in 1-kHz bands. The measured vibration levels are compared in Fig. 4 to predictions made using a finite element model and an SEA model. The configuration of the plates with the drive and measurement locations are also shown in Fig. 4. A single shaker was used to excite the system. At frequencies below 7 kHz, the predictions by both the finite element and SEA models are in good agreement with the measured levels. At 7 kHz and above, the finite element predictions show poor agreement with the measurements, while the SEA predictions continue to show good agreement. The limitation on the number of degrees of freedom in the finite element model led to the poor agreement with the measured levels at 7 kHz and above. The agreement shown in Fig. 4 illustrates the validity of SEA broadband predictions at high frequencies where finite element models are too costly to run. In finite element models, each plate must have a number of elements at least four times the number of wavelengths of the plate in each direction while the number of SEA subsystems is given by the number of wave types in the structural element, which is usually less than four.

A scale model of a Diesel engine foundation and ship bottom structure was modeled with twelve plates by Tratch[28] in an SEA model. SEA predictions were generated by Tratch using bending waves only, and using both bending and longitudinal waves in the plates and at the junctions. An ex-

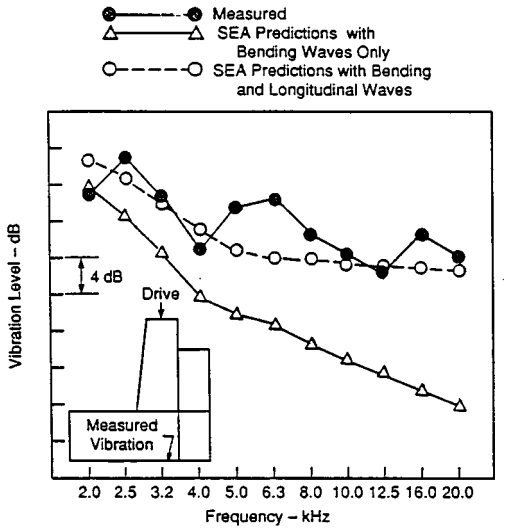

FIG. 5. Comparison of SEA predictions for a 12-plate system, with and without longitudinal waves, to measured vibration levels.

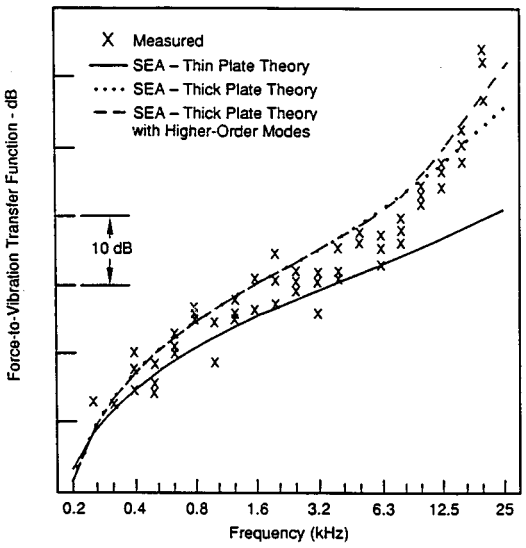

FIG. 6. Comparisons of SEA predictions with thin and thick plate theory coupling loss factors to measurements.

ample of comparisons between the SEA predictions and measured levels presented by Tratch[28] and Lyon[29] is given in Fig. 5, along with a sketch of the SEA 12-plate model. At frequencies above 2 kHz, the SEA predictions made without including longitudinal waves in the plates show poor agreement with the measured levels. As shown in Fig. 5, including longitudinal waves in the SEA model improved the predictions to the point where good agreement of the predictions with the measured levels was obtained up to 20 kHz. Thus accurate SEA predictions require the inclusion of longitudinal waves, particularly when the system has several structural elements and predictions are made at high frequencies. For additional discussion of this model, see Chapter 15 of Ref. 1. For thick plates at high frequencies, it also becomes necessary to incorporate thick plate theory to account for the higher modal densities of bending waves due to the lower wave speeds which occur in thick plate theory. This is illustrated in Fig. 6, where SEA predictions using thin and thick plate theory coupling loss factors are compared to measurements.[30]

Measurements of the transfer functions from the applied force in machinery spaces to vibrations levels in the hull plating of the USNS HAYES, a research ship used to conduct acoustical measurements, are compared to SEA predictions in Fig. 7.[31] The measurements were taken in narrowbands and the predictions generated for one-third octave bands. Because both the measurements and SEA predictions are of transfer functions, the results, except for band averaging, are not sensitive to bandwidths, so that direct comparisons can be made in Fig. 7. For the transfer of forces applied by the propulsor motor and in the generator room to the vibration of the hull plating, agreement between the measured and predicted levels in Fig. 7 is good, with only two exceptions; from 7 to 10 kHz for the propulsion motor transfer function and from 10 to 20 kHz for the generator room transfer function, where the differences are slightly above 10 dB. The structural losses were larger than predicted indicating that the structural loss factors were larger than predicted. All of the coupling loss factors for the HAYES were based on analytic models.

Results from an SEA model were presented by Burkewitz[32] for the propagation of sonar ping noise in the forward third of the USS GLOVER (FF 1098). The concern was the prediction of airborne noise in ship spaces. A total of 425 structural subsystems and 1513 junctions were included in the model. The first set of predictions, in which only bending waves in the structures were included, produced unsatisfactory agreement with the measured levels for the noise in the ship spaces generated by sonar pings. The inclusion of longitudinal waves improved agreement between the SEA predictions and measured levels. Figure 8 shows a compari-

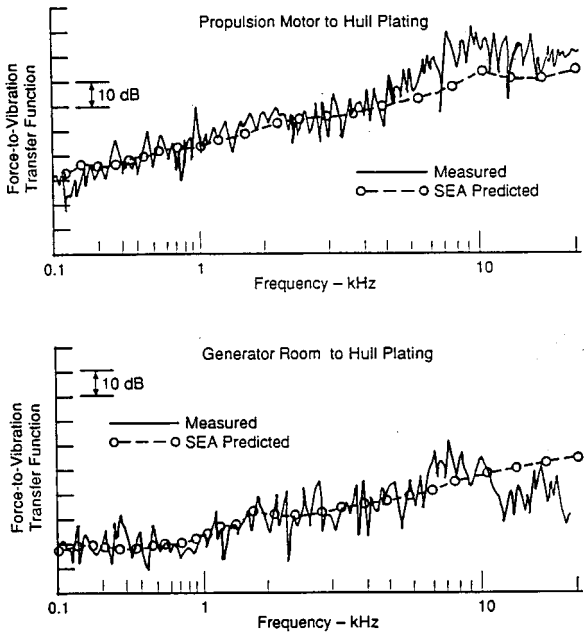

FIG. 7. Comparisons of SEA predictions to measured force-to-vibration transfer functions on the USNS HAYES.

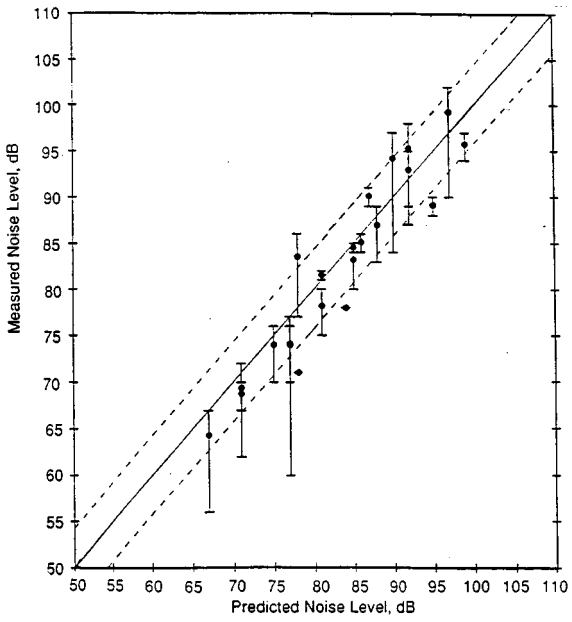

FIG. 8. SEA predictions versus measured cabin noise levels generated by sonar pings on the USS GLOVER.

son between the predicted and measured levels for twenty two cases. Agreement within ± 3 dB occurred when the dots fall inside the dashed lines in Fig. 8. The range in the measured levels taken during repeat pings are indicated by the horizontal lines through the dots. The agreement shown in Fig. 8 indicates that SEA can be used effectively to predict noise levels in complex systems with a large number of subsystems. However, the SEA model for the GLOVER was developed by validating coupling and damping loss factors with measurements conducted on the GLOVER. It would be risky to use the model developed for the GLOVER for other similar ships without some experimental verification of loss factors.

IV. SUMMARY

The basic concepts and assumptions behind Statistical Energy Analysis (SEA) are presented. Starting with the simple oscillator as a model of a resonant mode, coupling between resonant modes in subsystems is shown to be proportional to the differences in the energies in the modes. Classical modal expansions are used to justify equipartition of energy among modes in a subsystem and the assumption that each mode can be modeled as a simple oscillator. Power balance equations for coupled subsystems are derived, which can be solved for the energies in each of the subsystems. The required inputs to the power balance are the input powers to subsystems, modal densities, masses and damping loss factors for each subsystem, and coupling loss factors between subsystems. Methods for estimating modal densities are presented. Power inputs are specified by the user of the SEA power balance equations or computed for simple force or displacement inputs. Damping loss factors are usually obtained from measurements of the materials or typical structures used in the subsystems. The derivation of accurate expressions for coupling loss factors presents the greatest challenge to the SEA user. Coupling loss factors for structures are related to power transmissibility, which is usually easier to predict. Coupling between structures often requires the inclusion of in-plane (longitudinal and shear) as well as bending waves which makes the derivation of accurate coupling loss factors beyond the scope of this paper. Comparison of predictions from SEA models to measured levels, presented here, show that SEA is capable of providing accurate predictions of broadband noise and vibration levels in complex systems.

To be successful in providing accurate predictions, SEA models must:

(1) Be capable of predicting the input power to all subsystems from applied input forces, moments, velocities, or acoustic pressures. Measurements of input power is also acceptable but is frequently as difficult as a prediction.
(2) Represent all important mode types which occur within the modeled subsystem in the frequency range of interest, such as bending (thin and thick plate and beam) torsional, transverse shear, and longitudinal for structural elements; and one, two and, three dimensional modes for acoustical spaces, and each subsystem must contain several modes down to the lowest frequency band of interest.
(3) Have valid coupling loss factors for all mode types which interact at junctions of subsystems, such as structural joints, mounts, and radiating surfaces. Damping loss factors must also be known or predicted.
(4) Provide the output energies or derived vibration levels for those modes which are of interest, or will be measured.

Because of the relative simplicity of the SEA equations and power and energy outputs, SEA models can provide great insight to the dynamic system and can provide useful guidance for noise control treatment design and optimization.

Several organizations have prepared SEA computer codes. Three of these codes have been developed commercially. SEAM,[33] developed by Cambridge Colloborative Inc., was the first SEA computer code to become commercially available. Recently, AutoSEA,[34] developed by Vibro-Acoustic Sciences Ltd., has been made commercially available. AARCSEA,[35] which has been used in several naval vehicle and architectural designs, is available on an application basis to end user customers.

[1] R. H. Lyon and R. G. DeJong, *Theory and Application of Statistical Energy Analysis* (Buttersworths-Heimann, Boston, MA, 1995).
[2] L. Cremer, M. Heckl, and E. E. Ungar, *Structure-Borne Sound: Structural Vibrations and Sound Radiation at Audio Frequencies* (Springer-Verlag, New York, 1988), 2nd ed.
[3] I. S. Gradshteyn and I. M. Ryzhik, *Tables of Integral, Series, and Products* (Academic, New York, 1965).
[4] P. W. Smith, Jr., ''Statistical models of coupled dynamical systems and the transition from weak to strong coupling,'' J. Acoust. Soc. Am. **65**, 695–698 (1979).
[5] E. Skudrzyk, ''The mean-value method of predicting the dynamic response of complex vibrators,'' J. Acoust. Soc. Am. **67**, 1105–1135 (1980).
[6] L. L. Beranek and I. L. Ver (Eds.), *Noise and Vibration Control Engineering* (Wiley, New York, 1992).

[7] J. H. Wendel and B. L. Scott, ''Calculation of SEA Coupling Factors Using the Wave Approach-Results for Plates,'' Cambridge Collaborative Inc. Report 89-10-21610-2 (1989).
[8] V. V. Tyutekin, ''Reflection and refraction of flexure waves at the boundary of separation formed by two plates,'' Sov. Phys. Acoust. **8**(2), 180–183 (Oct.–Dec. 1962).
[9] S. V. Budrin and A. S. Nikiforov, ''Wave transmission through assorted plate joints,'' Sov. Phys. Acoust. **9**(4), 333–336 (April–June 1964).
[10] T. Kihlman, ''Sound transmission in building structures of concrete,'' J. Sound Vib. **11**(4), 435–445 (1970).
[11] W. Wohle, Th. Beckmann, and H. Schreckenbach, ''Coupling loss factors for statistical energy analysis of sound transmission at rectangular structural slab joints, Part I,'' J. Sound Vib. **77**(3), 323–334 (1975).
[12] W. Wohle, Th. Beckmann, and H. Schreckenbach, ''Coupling loss factors for statistical energy analysis of sound transmission at rectangular structural slab joints, Part II,'' J. Sound Vib. **77**(3), 335–344 (1975).
[13] V. A. Veshev and D. P. Kouzov, ''Influence of the medium on the vibrations of plates joined at right angles,'' Sov. Phys. Acoust. **23**(3), 206–211 (May–June 1977).
[14] Y. Irie and T. Nakamura, ''Random incidence energy transmission of bending waves at junctions,'' J. Acoust. Soc. Am. Suppl. 1 **64**, S26 (1978).
[15] G. Rosenhouse, H. Ertel, and F. P. Mechel, ''Theoretical and experimental investigations of structureborne sound transmission through a ''*T*'' joint in a finite system,'' J. Acoust. Soc. Am. **70**, 492–499 (1981).
[16] M. J. Sablik, ''Coupling loss factors at a beam *L*-joint revisited,'' J. Acoust. Soc. Am. **72**, 1285–1288 (1982).
[17] J. F. Doyle and S. Kamle, ''An experimental study of the reflection and transmission of flexural waves at an arbitrary *T*-joint,'' J. Appl. Mech. **54**, 136–140 (1987).
[18] R. C. N. Leung and R. J. Pinnington, ''Wave propagation through right-angled joints with compliance-flexural incident wave,'' J. Sound Vib. 31–46 (1990).
[19] R. S. Langley, ''Elastic wave transmission through plate/beam junctions,'' J. Sound Vib. **143**(2), 241–253 (1990).
[20] M. D. McCollum and J. M. Cuschieri, ''Bending and in-plane wave transmission in thick connected plates using statistical energy analysis,'' J. Acoust. Soc. Am. **88**, 1480–1485 (1990).
[21] J. A. Moore, ''Vibration transmission through frame of beam junctions,'' J. Acoust. Soc. Am. **88**, 2766–2776 (1990).
[22] J. L. Horner and R. G. White, ''Prediction of vibrational power transmission through bends and joints in beam-like structures,'' J. Sound Vib. **147**(1), 87–103 (1991).
[23] I-T. Lu, H. L. Bertoni, and H-Y. Chen, ''Coupling of plate waves at joints,'' J. Acoust. Soc. Am. **92**, 510–526 (1992).
[24] R. C. N. Leung and R. J. Pinnington, ''Wave propagation through right-angled joints with compliance: longitudinal incidence wave,'' J. Sound Vib. **153**(2), 223–237 (1992).
[25] G. Maidanik, ''Response of ribbed panels to reverberant acoustic fields,'' J. Acoust. Soc. Am. **34**, 809–826 (1962).
[26] F. Fahy, *Sound and Structural Vibration: Radiation, Transmission and Response* (Academic, New York, 1985).
[27] L. K. H. Lu, W. J. Hawkins, D. F. Downard, and R. G. DeJong, ''Comparisons of statistical energy analysis and finite element analysis vibration predictions with experimental results,'' Shock and Vib. Bull. **53**(4), 145–153 (1983).
[28] J. Tratch, Jr., ''Vibration transmission through machinery foundation and ship bottom structure,'' MS thesis, MIT, 1985.
[29] R. H. Lyon, ''In-plane contribution to structural noise transmission,'' Noise Control Eng. J. **26**(**1**), 22–27 (1986).
[30] A. C. Aubert, J. H. Wendell, and F. R. Kern, ''AARCSEA statistical energy analysis program—tutorial manual,'' AARC Report 126 (1991).
[31] R. W. Fischer, F. R. Kern, and I. Cross-Whiter, ''Preliminary test report—impedance measurements on machinery foundations aboard the HAYES,'' Atlantic Applied Research Corp. Tech. Memo 028 (1988).
[32] B. L. Burkewitz, ''The update and validation of the USS GLOVER (FF 1098) statistical energy analysis model for analysis of ping-noise due to operation of low-frequency, hull-mounted transmitter,'' BBN Systems and Technologies, Inc. Report No. 7469 (1990).
[33] Contact J. Manning, Cambridge Collaborative Inc., 689 Concord Avenue, Cambridge, MA 02138, Telephone (617) 876-5777 for more information on SEAM.
[34] Contact P. Bremmer, Vibro-Acoustic Science, Inc., 5355 Mira Sorrento Place, Suite 100, San Diego, CA 92121, Telephone (619) 597-7535 for more information on AutoSEA.
[35] Contact F. Kern, Atlantic Applied Research Corp., 4 A Street, Burlington, MA 01803, Telephone (617) 273-2400 for more information on AARC-SEA.

Acoustic radiation from membranes at high frequencies: The quantum chaos regime

Dominique Delande
Laboratoire de Spectroscopie Hertzienne de l'ENS, Université Pierre et Marie Curie, 4 Place Jussieu, 75005 Paris, France and X-RS, PARC-CLUB, 28 rue Jean Rostand, 91893-Orsay Cedex, France

Didier Sornette
Laboratoire de Physique de la Matière Condensée, CNRS URA 190, Université de Nice-Sophia Antipolis, 06108 Nice Cedex 2, France and X-RS, PARC-CLUB, 28 rue Jean Rostand, 91893-Orsay Cedex, France

(Received 7 February 1994; revised 25 September 1996; accepted 26 September 1996)

An efficient and reliable numerical scheme is developed to compute the radiation directivity and total power radiated by isolated eigenmodes and by finite bandwidth excitations of a membrane of arbitrary shape over the whole frequency domain. Results are presented for the case of a membrane having the shape of a stadium, this shape having been studied intensively in the literature concerned with the correspondence between classical geometrical ray trajectories and high-frequency vibrations, the so-called ''quantum chaos'' problem. Localization of the radiation directivity is shown to be due to ''scars'' of eigenmodes made by resonance on periodic ray orbits. The dependence of the radiation efficiency as a function of the ratio c_M/c of the membrane wave velocity c_M over the air sound speed c and its important fluctuations from mode-to-mode is explained by the theory of random matrices. [S0001-4966(97)02702-1]

PACS numbers: 43.20.Bi, 43.20.Fn, 43.40.Dx [JEG]

INTRODUCTION

We address the problem of acoustic radiation[1,2] from a vibrating membrane, observed at large distances from it. Our goal is first to develop an efficient and reliable numerical computation scheme for obtaining the properties of the acoustic radiation of membranes of arbitrary shapes over the whole frequency domain. The properties that will be described below are the total radiated power and the radiation directivity both in the case of the excitation of a single eigenmode or of a finite bandwidth. Second, we aim to understand the numerical results thus obtained using the concepts and theory of the emerging field of ''quantum chaos.'' [3]

In the last few years, there has been much interest and progress in the area of chaos and quantum physics.[3] On the one hand, one deals with a ''wave'' or Schrödinger equation in the quantum regime. (Note that we consider here quantum theory in the reduced meaning of ''quantum wave'' theory, which is nothing but a particular wave problem. It is in this sense that the analogy between ''quantum chaos'' and the problem of high-frequency vibrations in acoustics holds.[4,5]) On the other hand, in the classical limit, classical orbits describe the Hamiltonian motion. In acoustic language, this corresponds to the geometrical ray asymptotics regime described by the eikonal equation. The general semiclassical problem is to relate these two descriptions and to determine the effect of classical chaos on the quantum or wave behavior in the semiclassical or high-frequency regime. This regime occurs when the (de Broglie) wavelength λ is much smaller than any other characteristic length L of the problem. In this case, expansions in powers of λ/L can be developed and allow predictions for the structure of spectra and groups of eigenmodes. The advances which have been made in this subject are, however, all basically restricted to the Schrödinger wave equation. Recently,[4,5] it has become clear that the concepts and methods of quantum chaos also evidently apply to the Helmholtz equation in acoustics and electromagnetism, which is nothing but the stationary Schrödinger equation. Its relevance to thin plate vibration problems and elastodynamics has also been reasserted[6,7] after a long oblivion, following early suggestions.[8]

Thus, our purpose here is to show that it is possible to account for both the small-scale fluctuations of the radiation directivity using the theory of random matrices[9] as well as its large specific structures using the theory of periodic orbits of Gutzwiller.[3,10,11] In this theory which allows us to understand the structure of the eigenmodes of a membrane, a given eigenmode, or a suitable average over a few neighboring eigenmodes can be written as a sum over the different contributions of all periodic ray orbits, each with its period and amplitude (related to its stability). In particular, the ''scars'' on eigenmodes,[12] which are remnant resonances on periodic ray orbits, will be shown to largely control the large-scale structure of the radiation directivity diagram.

Our different results have been obtained for the case of a stationary vibrating membrane obeying the Helmholtz equation. However, most of our conclusions are easily generalized to the case of a vibrating plate. The main difference between the membrane and the plate problem appears in the behavior of the radiation efficiency, which is qualitatively different in the two cases due to the dispersive nature of the waves in the plate problem. Notwithstanding the fact that our first concern lies in the high-frequency regime, which is the least known, our method of calculation and the general con-

clusions also applies to the intermediate and low-frequency ranges.

In Sec. I, we describe briefly our method of calculation of the acoustic radiation directivity and of the total radiated power emitted by a membrane vibrating on one of its eigenmode (see also the Appendix). We then present in Sec. II our results obtained for a membrane having the shape of a stadium. In the wave-ray (quantum-classical) correspondence, the classical limit corresponds to the deterministic propagation of geometrical rays in straight lines which are specularly reflected by the boundaries (law of mirror reflection: angle of incidence equals angle of reflection). In the chaos literature, this corresponds to the ''billiard'' problem. In this context, the stadium billiard[13] has been one of the most studied.[3] It is made of two half-circles of unit radius and separated by a rectilinear portion of length 2. It is then known that almost all trajectories are chaotic in the strongest sense of the term, namely, ergodic, mixing, and *K*-complex. It is also for this shape that a large number of works have studied the quantum-classical or wave-ray correspondence. Using the same shape, we will thus be able to develop a coherent interpretation of the numerical results using the concepts derived in the field of ''quantum chaos'' (''scars'' of periodic ray orbits,[10] universal and nonuniversal behaviors, etc...). In Sec. III, we study the case of a membrane which is excited, not on a single eigenmode, but on a finite bandwidth, and discuss how the previous results are modified. In Sec. IV, we address in more details the properties of the fluctuations of the total radiated power, and more generally of any dissipation mechanism, as a function of frequency. We restrict our attention to the weak dissipation regime. We then summarize and conclude in Sec. V.

I. CALCULATION OF THE ACOUSTIC RADIATION OF A VIBRATING MEMBRANE

We consider a plane vibrating membrane limited by a closed boundary on which the amplitude of vibration is imposed to vanish. This so-called Dirichlet boundary condition corresponds to the baffled condition. We assume that the membrane is in contact with a light fluid (air, for instance) such that the total power radiated by the membrane is sufficiently weak. By this we mean that the eigenmodes of the membrane must be weakly perturbed by the loss. In the case of a heavy fluid (as occurs for instance in underwater applications) or at very high frequencies, the presence of the fluid induces non-negligible intermodal couplings and the notion of an eigenmode has no more any meaning.

The domain of validity of the ''light fluid'' regime is such that the loss due to radiation can be neglected. Quantitatively, any appreciable loss of the membrane energy W due to radiation must occur on a time scale much larger than the inverse of the local modal density. If we call P_{tot} the total radiation power loss, W decays as a function of time according to the equation

$$\frac{dW}{dt} = -P_{\text{tot}},$$

which yields $W = W_0 e^{-t/\tau}$. The characteristic decay time τ is obtained as follows: The total power radiated by the membrane can be estimated from the following formula:

$$P_{\text{tot}} \approx \frac{1}{2}\,\rho c \int\int \left[\frac{\partial w}{\partial t}\right]^2 dx\, dy,$$

where w is the vertical displacement of the membrane at (x,y,t) (the membrane is embedded in the plane $0xy$), ρ is the fluid density, and c is the sound velocity in the fluid. This equation can be seen to derive from Eqs. (6), (7), and (10) below when the radiation efficiency σ approaches one. Our purpose in starting with this equation is to provide a simple approximate but nevertheless enlightening estimation of the conditions under which the single unperturbed mode approximation holds. The total vibration energy stored within the membrane reads[14]

$$W = \mu \int\int \left[\frac{\partial w}{\partial t}\right]^2 dx\, dy,$$

using the viriel theorem according to which the elastic potential energy is equal to the kinetic energy, and thus the total energy stored in the membrane is twice its kinetics energy. Here, μ is the surface density of the membrane (mass per unit surface). We thus find that W decays as a function of time according to the equation $dW/dt = -P_{\text{tot}}$, which yields $W = W_0 e^{-t/\tau}$ with $\tau \approx 2\mu/\rho c$. Taking typically $\rho = 1$ kg/m^3, $c = 340$ m/s, and, for instance, $\mu = 0.5$ kg/m^2 yields $\tau \approx 3\times 10^{-3}$ s. In order for the ''light fluid'' approximation to hold, the frequency broadening of each eigenfrequency given by $(2\tau)^{-1}$ must be small compared to the spacing between consecutive eigenfrequencies.

As a basis of decomposition, we will use the eigenmodes of vibration of the membrane in vacuum. For a given eigenmode at pulsation ω, the amplitude of vibration $w(x,y)$ of the membrane [the temporal dependence $\exp(-j\omega t)$ is implicit in the following] obeys Helmholtz equation:

$$(\Delta + k_M^2) w(x,y) = 0$$

$$\text{with } w(x,y) = 0 \text{ on the boundary,} \tag{1}$$

and with $k_M = \omega/c_M$, $c_M = \sqrt{T/\mu}$ is the wave velocity in the membrane, and T is the membrane tension.

In the weak coupling regime studied here, each mode radiates essentially independently from each other. We thus first address the radiation by a single eigenmode. At large distances from the membrane, the radiated acoustic pressure in the fluid is given by Rayleigh's formula (using spherical coordinates where the axis z is normal to the plane of the membrane):[15]

$$p(R,\theta,\varphi) = -\rho\omega^2 \frac{e^{-jkR}}{2\pi R} \times \int\int w(x,y) e^{j(\lambda x + \mu y)}\, dx\, dy,$$

with

$$\lambda = k \sin\theta \cos\varphi, \quad \mu = k \sin\theta \sin\varphi.$$

Here, $k=\omega/c$ is the wave number of sound in the fluid. Introducing the Fourier transform of $w(x,y)$:

$$\hat{w}(\lambda,\mu)=\frac{1}{2\pi}\int\int w(x,y)e^{j(\lambda x+\mu y)}\,dx\,dy, \tag{2}$$

the radiated acoustic pressure can be expressed as

$$p(R,\theta,\varphi)=-\rho\omega^2\frac{e^{-jkR}}{2\pi R}\hat{w}(k\sin\theta\cos\varphi,\ k\sin\theta\sin\varphi). \tag{3}$$

The radiated acoustic pressure is directly related to the Fourier transform of the amplitude of vibration of the membrane. Physically, this means that spatial coherence effects between different points on the membrane play a major role. In practice, the numerical determination of this quantity (3) for arbitrary membrane shapes is a difficult problem, precisely due to the presence of these subtle spatial coherence effects, especially at high frequencies for which the spatial structure of eigenmodes is particularly complex (see below). The method that we have used to solve this problem is described in the Appendix. The results exhibit good converging properties and are very reliable.

The total power radiated by a given eigenmode in a given direction is proportional to the square of the radiated acoustic pressure. It reads[14,15]

$$\frac{dP}{d\Omega}=\frac{R^2|p(R,\theta,\varphi)|^2}{2\rho c}=\frac{\rho\omega^4}{2c}|\hat{w}(k\sin\theta\cos\varphi,\ k\sin\theta\sin\varphi)|^2. \tag{4}$$

The total energy radiated by a given eigenmode is obtained by integrating expression (4) over all directions:

$$P_{\text{tot}}=\int\frac{dP}{d\Omega}\,d\Omega=\frac{\rho\omega^4}{2c}\int\int|\hat{w}(k\sin\theta\cos\varphi,\ k\sin\theta\sin\varphi)|^2\times\sin\theta\,d\theta\,d\varphi, \tag{5}$$

which can also be written as

$$P_{\text{tot}}=\frac{\rho\omega^3}{2}\int_{r=0}^{r=k_Mc_M/c}\int_{\varphi=0}^{2\pi}|\hat{w}(r\cos\varphi,\ r\sin\varphi)|^2\times\frac{r\,dr}{\sqrt{(k_Mc_M/c)^2-r^2}}\,d\varphi, \tag{6}$$

this two-dimensional integral being taken over a disk of radius $k=k_Mc_M/c$. In order to make explicit the physical content of Eq. (6), let us introduce the radiation efficiency, also called the radiation factor, σ, a dimensionless quantity defined by the following equation:[15]

$$\sigma=\frac{P_{\text{tot}}}{\rho c\,\frac{1}{2}\int\int\left(\frac{\partial w}{\partial t}(x,y)\right)^2dx\,dy}. \tag{7}$$

The two-dimensional integral in the denominator of expression (7') is proportional to the mean-square velocity of an element of the membrane. For a given eigenmode at pulsation ω, we have

$$\int\int\left(\frac{\partial w}{\partial t}(x,y)\right)^2dx\,dy=\omega^2\int\int|w(x,y)|^2\,dx\,dy. \tag{8}$$

The integral in the rhs of Eq. (8) can be expressed as a function of the integral of its Fourier transform as follows:

$$\int\int|w(x,y)|^2\,dx\,dy=\int_{r=0}^{\infty}\int_{\varphi=0}^{2\pi}|\hat{w}(r\cos\varphi,\ r\sin\varphi)|^2r\,dr\,d\varphi. \tag{9}$$

Using Eqs. (3), (6)–(9), the radiation efficiency can be expressed as

$$\sigma=\frac{\int_{r=0}^{r=k=k_Mc_M/c}\int_{\varphi=0}^{2\pi}|\hat{w}(r\cos\varphi,\ r\sin\varphi)|^2\frac{r\,dr}{\sqrt{1-r^2/k^2}}\,d\varphi}{\int_{r=0}^{\infty}\int_{\varphi=0}^{2\pi}|\hat{w}(r\cos\varphi,\ r\sin\varphi)|^2r\,dr\,d\varphi}. \tag{10}$$

The integral in the numerator is defined over the disk of radius $k=k_Mc_M/c$, whereas the integral in the denominator is over the whole plane. Expression (10) suggests the radiation efficiently σ be interpreted as the average of $(1/\sqrt{1-r^2/k^2})$ weighted by the Fourier transform $\hat{w}^2$ of the membrane vibration amplitude.

Equation (7) then allows us to simply express the attenuation of an eigenmode due to acoustic radiation. Using our previous reasoning, this yields the characteristic decay time of an eigenmode:

$$\tau=\frac{2\mu}{\sigma\rho c}. \tag{11}$$

If $\sigma=1$ (as occurs for large values of the ratio c_M/c, see below), we recover our previous heuristic result. The corresponding broadening of the eigenfrequencies is then

$$\Delta\nu=\frac{\sigma\rho c}{\mu}. \tag{12}$$

Our approach is valid in the low attenuation regime where eigenmodes are well isolated, i.e., when the broadening $\Delta\nu$ is small compared to the frequency difference between two consecutive eigenfrequencies. If this is not the case, coupling between modes must be taken into account.

The typical eigenfrequency $\Delta\nu'$ spacing can be simply obtained from the smooth average modal density and reads

$$\Delta\nu'=\frac{2c_M}{k_MS},$$

where S is the total surface of the membrane. Eigenfrequencies are not overlapping on average if $\Delta\nu<\Delta\nu'$, i.e., for

$$k_M<\frac{2\mu}{\rho S}\frac{c_M}{\sigma c}.$$

The dimensionless parameter $c_M/\sigma c$ is studied in the sequel and is found larger than 1 for c_M/c much larger as well as much smaller than one. When $c_M/c \approx 1$, this parameter is minimum and can go slightly below 1 when σ becomes larger than 1 (see below). The condition on k_M can be written as

$$\lambda_M > \frac{\pi \rho S}{\mu},$$

where the wavelength is $\lambda_M = 2\pi/k_M$. The number of modes which do not overlap due the radiation broadening is then of the order of $(\mu/\rho)^2/S$, which has a simple geometrical interpretation. This ratio $(\mu/\rho)^2/S$ can be written as the ratio of the square of two lengths: $(\mu/\rho)^2/S = (D_0/D)^2$, where D is a typical dimension of the membrane and D_0 is the height of the air column whose mass is equal to that of the membrane (for the same section).

II. ANALYSIS AND INTERPRETATION OF THE RESULTS

A. Radiation diagram

1. The global picture: Summary of known results obtained from our formulation

To understand how our new results obtained for irregular modes can be integrated within common knowledge on acoustic radiation, we first summarize the basic properties which can be derived directly from the above formulation. We consider here the free radiation characteristics of the eigenmodes and do not consider the additional mechanisms that arise in the forced radiation case.

A very important property of the radiation directivity can be easily understood without any calculation. A given eigenmode can be decomposed as the linear superposition of plane waves having all the same modulus $k_M = \omega/c_M$ of the wave vector, but with *a priori* arbitrary directions (see the Appendix and Refs. 3d and 3e). The contribution of each plane wave to the Fourier transform of the vibration amplitude is close to a Dirac function centered on the corresponding wave vector (in fact, this would be exactly the case for an infinite membrane). As a consequence, the Fourier transform of the amplitude of vibration presents a nonvanishing value only in the close vicinity of the circle of radius k_M. A typical example is given in Fig. 1.

The diagram of acoustic radiation can be obtained from a simple geometrical projection, as shown in Fig. 2: the square of the Fourier transform of the amplitude of vibration of a given mode must be projected vertically along $0z$ on the sphere of radius $k = \omega/c$. This clearly shows the importance of the ratio $k/k_M = c_M/c$ of the wave velocity c_M in the membrane by the sound velocity c in the fluid. Depending on the value of this ratio, one observes the following regimes:

(i) if $c_M/c < 1$, the circle of radius k is smaller than the circle of radius k_M on which the Fourier transform $\hat{w}^2$ is not small. The radiated power is weak ($\sigma \ll 1$). The radiation diagram is obtained from the interior domain of the Fourier transform. It is more or less isotropic with important fluctuations from mode to mode (see Sec. IV for a discussion of the fluctuations). Physically, this corresponds to a sound velocity

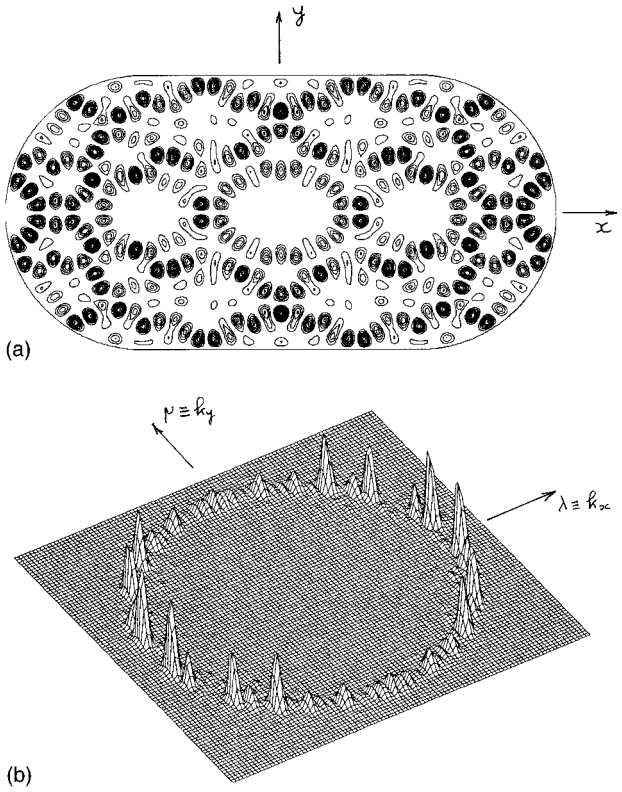

FIG. 1. (a) Eigenmode of vibration of a membrane having the shape of a stadium (the length of linear part equals the diameter of the circular caps=2) whose eigen-wave number is $k_M = 32.831$ in units where the radius is 1 (corresponding to approximately the 600th excited mode). Note that the amplitude of vibration is relatively well homogeneously spread over the whole surface of the membrane, with no obvious localization. (b) In contrast, the square of its Fourier transform (proportional to the directional radiated acoustic power) is very clearly localized in the vicinity of the circle of radius k_M. This implies that acoustic radiation is highly localized in a cone whose axis is perpendicular to the surface of the membrane.

in the fluid which is larger than the wave speed within the membrane. Different points of the membrane are therefore spatially incoherent. In a typical high-frequency eigenmode of a ''chaotic'' membrane[16] (i.e., such that the classical limit

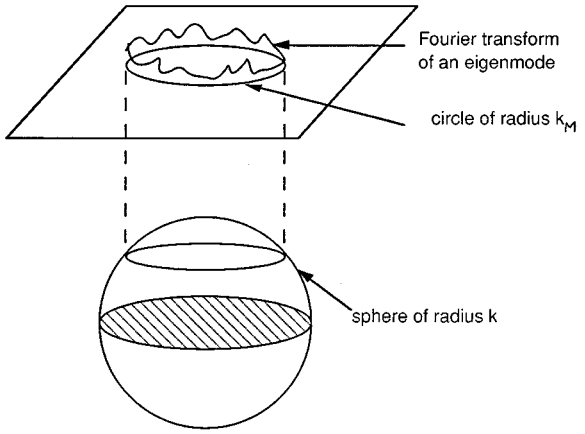

FIG. 2. The acoustic radiation diagram of an eigenmode of vibration is simply given by the vertical projection along z of the square of the Fourier transform $|\hat{w}|^2$ of the amplitude of vibration onto the sphere of radius k [see Eq. (4)].

gives a chaotic billiard), the correlations between the amplitudes and phases of vibration of different points are weak: this explains the weak radiation of such modes. In the limit $c_M \ll c$, the radius of the integral in Eq. (10) is smaller than the typical range of variation of $\hat{w}$ and σ is simply proportional to $|\hat{w}(0,0)|^2$. Thus, the monopolar moment provides the dominating contribution to the radiation, but it is very weak for high-frequency eigenmodes which exhibit alternative regions of positive and negative amplitudes.[16] This gives a very weak radiation.

(ii) If $c_M/c > 1$, the circle of radius k contains the circle of radius k_M on which the Fourier transform of an eigenmode amplitude is concentrated. This circle can thus be projected onto the sphere of radius k (see Fig. 2): This corresponds to a strong radiation, mainly on a cone of the axis perpendicular to the membrane plane and of half-opening angle equal to

$$\theta = \text{Arccos}\,\frac{c}{c_M}. \tag{13}$$

Physically, this situation corresponds to constructive interferences between different points of the membrane in certain directions, leading to a large increase of the radiated power. Such a mode is said to be radiating in a very anisotropic way. In the limit $c_M \gg c$, the radiation is essentially concentrated in the direction normal to the membrane surface.

(iii) If c_M/c is close to 1, the wave velocity of the membrane is close to the sound velocity of the fluid. The radiation is therefore mainly concentrated tangentially to the membrane [see Eq. (13)]. The solid angle effect increases the radiated power: the mode is hyper-radiating.

Note that for a membrane, the ratio k/k_M is exactly equal to the ratio c_M/c and does not depend on the eigenfrequency. This means that all modes are either simultaneously radiating ($c_M/c > 1$) or nonradiating ($c_M/c < 1$). In the case of a thin plate, the dispersion relation is no longer linear (ω is proportional to k^2) and the wave speed of the membrane increases linearly with k_M. This implies that low-frequency modes are nonradiating and high-frequency modes are all radiating. The eigenmodes at coincidence ($c_{\text{Plate}}/c \approx 1$) are hyper-radiating. Apart from this important difference, the behavior of plates and membranes are similar and use can be made of the correspondence found in Ref. 7 to exploit and adapt the present results obtained for membranes to plates.

2. Fluctuations in the radiation diagram and relation with periodic orbits ''scarring'' of eigenmodes

In the sequel, we focus our attention on the radiating regime ($c_M/c > 1$). This is more important for practical applications. In this regime, the main effect is the concentration of the radiation of the cone of the half-open angle given by Eq. (13). However, there are, in general, additional important localizations of radiation within this cone, corresponding to special preferred directions of radiation in space. In Fig. 3, we show the radiation diagram in the plane (λ,μ), which is proportional to the square of the Fourier transform of the membrane amplitude, for six consecutive eigenmodes of a membrane having the shape of a stadium. One can observe

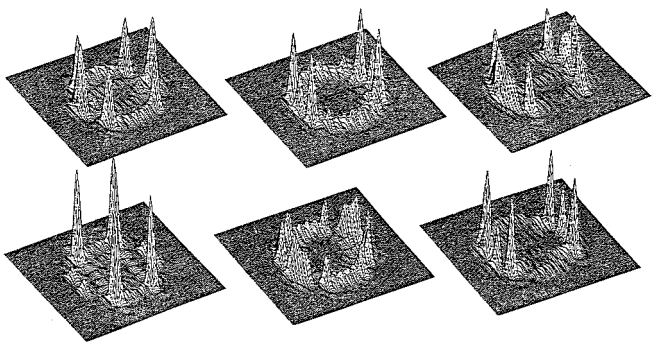

FIG. 3. Radiation diagram of six consecutive eigenmodes of the membrane having the shape of a stadium defined in Fig. 1. The eigen-wave numbers of the six modes are, respectively, $k_M = 10.458$; 10.734; 10.792; 10.847; 10.924; 10.924 in the units where the radius of the circular cap of the stadium is one. Note the expected localization on a circle of radius k_M and the large intensity fluctuations from point to point.

very large fluctuations from one region to another, even within a single radiation cone. These fluctuations are much larger than those present in the amplitude of vibration of the membrane, which is more or less uniform,[16] except for ''bouncing ball'' eigenmodes [see Fig. 3(a)].

It is possible in certain cases to understand the origin of this additional localization or special directivity. This is illustrated in Fig. 4. The first one on the left is the so-called ''bouncing ball'' mode characterized by a localization of the vibration amplitude in the rectangular portion of the stadium.[4,15] The Fourier transform of the vibration amplitude of this mode (and thus the radiation diagram) possesses a strong peak in the direction perpendicular to the long axis of the stadium. In this case, the radiation is almost unidirectional. In fact, this is not very surprising since this eigenmode essentially corresponds to a standing plane wave in the $0y$ direction, and therefore leads to dominant radiation in the same direction. In ''quantum chaos'' language, this mode is scarred by the ''bouncing ball'' periodic orbit, bouncing back and forth between the two parallel linear boundaries of the stadium. In Fourier space, this orbit is associated to two points ($k_{Mx} = 0$, $k_{My} = \pm \omega/c_M$): the Fourier transform of the eigenmode, scarred by the periodic bouncing ball orbit, is thus localized in the vicinity of these two points. This extreme localization in the Fourier space is in contrast with the relatively weaker localization of the amplitude of vibration within the membrane in the vicinity of the degenerate family of bouncing ball orbits. In other words, the classical ray dynamics is much simpler in Fourier space and the effect of localization by local resonances on special periodic orbits (so-called ''scars'' [12]) is much stronger. In Fig. 4 we show two other eigenmodes presenting ''scars'' due to special periodic orbits and their corresponding radiation diagram exhibiting again a very strong directivity, i.e., a strong localization in Fourier space. In addition to the ''bouncing ball'' mode, a mode scarred by the periodic orbit localized on the diameter of the stadium is represented. The third mode on the right is scarred by an orbit having four rebounds on the walls of the stadium (note that two such orbits are represented that are obtained one from the other by reflection symmetry with respect to the long diameter axis). In each

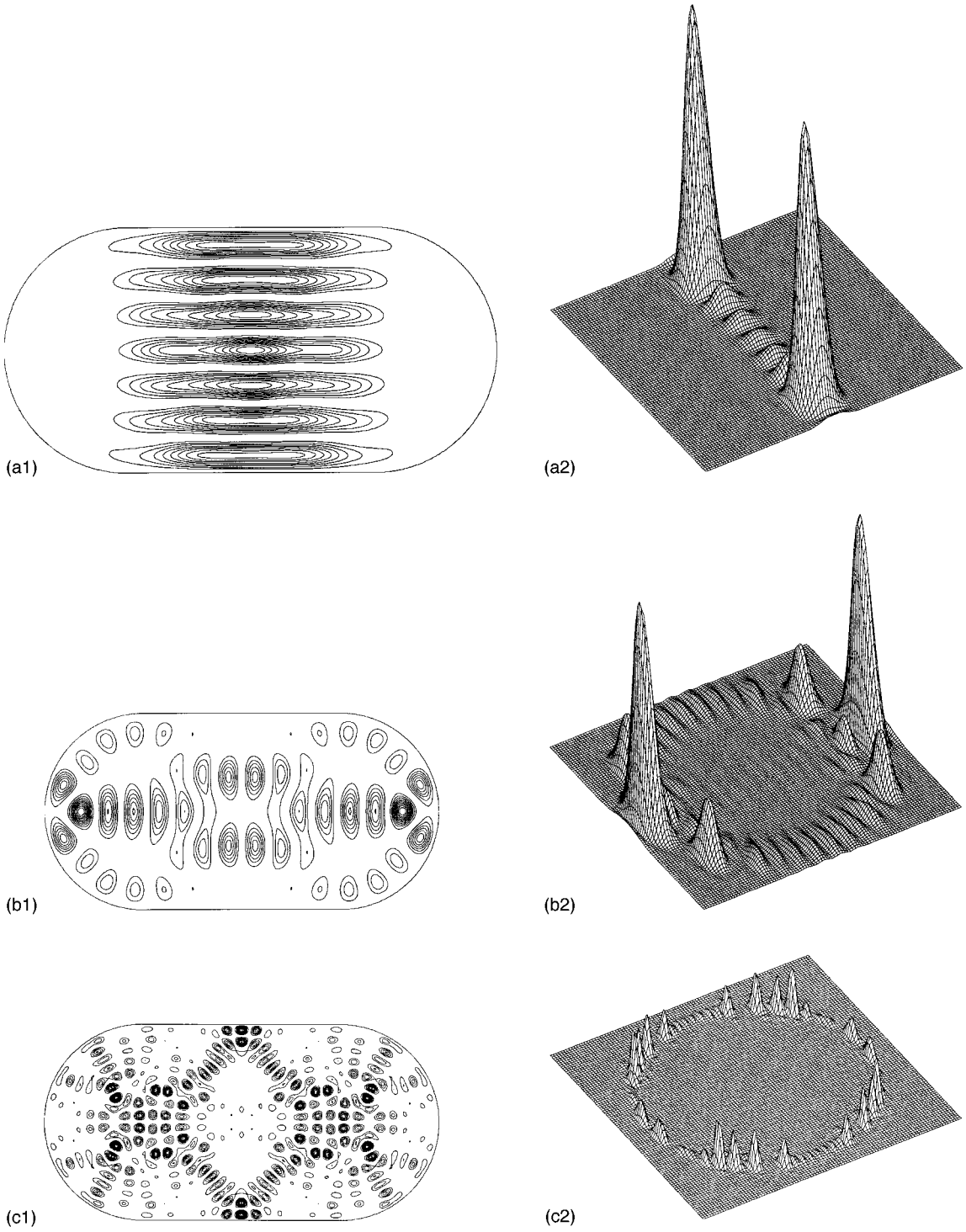

FIG. 4. Three eigenmodes presenting ''scars'' by periodic ray orbits and their corresponding radiation diagrams showing the large directivity in the direction of the periodic orbits. (a) $k=11.053$; (b) $k=12.918$; (c) $k=32.980$.

case, we note that the effect of localization is much more pronounced in the radiation diagram than in the amplitude of vibration. Typically, a local fluctuation of 50% of the amplitude of vibration in the vicinity of a periodic orbit of a given eigenmode induces a corresponding fluctuation of the radiation power by a factor of 3–10. ''Scars'' which have been initially discovered in configuration space,[12] i.e., in the amplitude of vibration of eigenmodes, are much more important in the radiation diagrams.

Reciprocally, we can make use of the much larger visibility of ''scars'' in the radiation diagrams to identify them in the amplitude of vibration, when they have been missed by a first direct inspection. Two such examples are shown in Fig. 5. Note that due to the stadium symmetries with respect to the $0x$ and $0y$ axis, it is necessary in a given ''scar'' to take into account all orbits deduced from a given one by the symmetries with respect to these two axis (see for instance Fig. 4, third mode on the right, and Fig. 5, second mode on

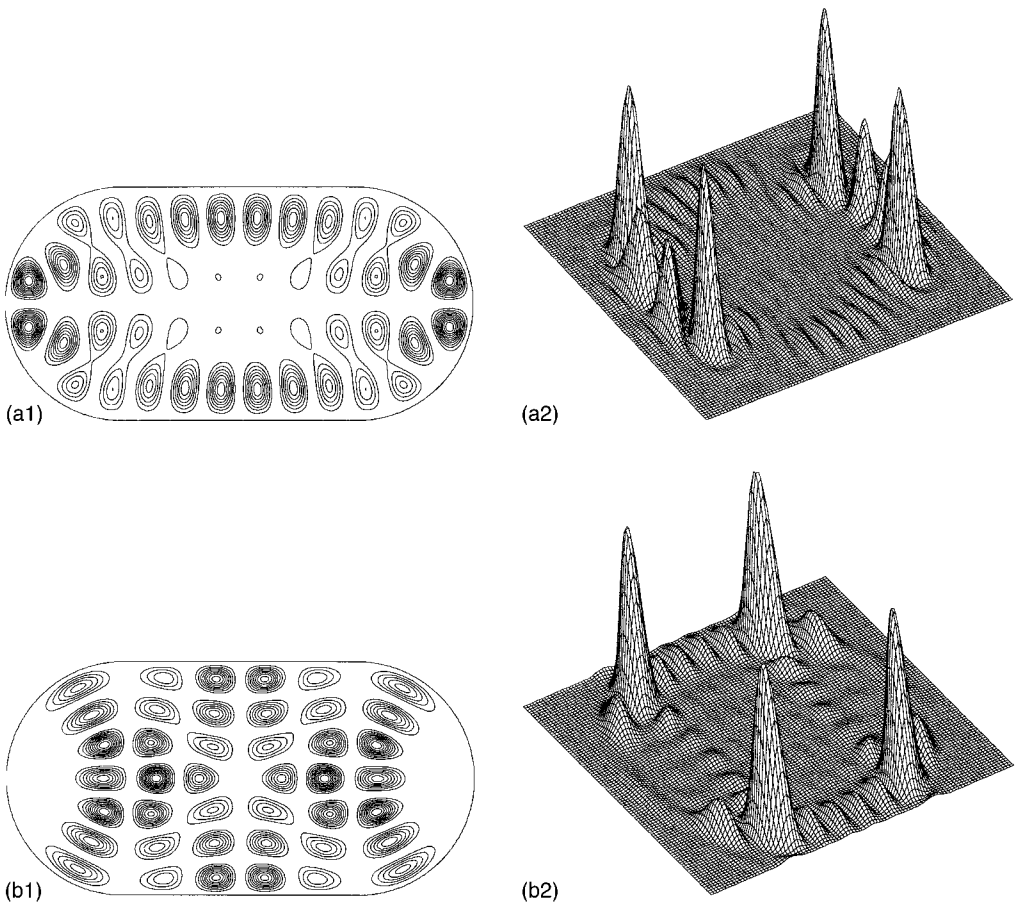

FIG. 5. Two eigenmodes presenting a ''scar'' of a periodic ray orbit which could be missed on the amplitude of vibration but which is clearly visible in the radiation diagram. (a) $k=11.598$; (b) $k=12.789$.

the right). Interference phenomena between their different symmetry replicas complicate the interpretation of the results. In the radiation diagram, the different contributions are well separated and this complication does not arise.

There are some cases where localization of both the vibration amplitude and the radiation diagram is not straightforwardly associated with a periodic orbit resonance. This is probably due to the interference between several periodic orbits.[3,4] Such an example is shown in Fig. 6.

B. Total radiated power

The total power radiated by a single eigenmode in the whole space is given by Eqs. (7) and (10). The important parameter is the dimensionless number σ, called the radiation efficiency, which depends in the membrane case on the single parameter $k=(k_M c_M)/c$. For a high-frequency mode, we have shown that the Fourier transform of the vibration amplitude is localized in the vicinity of the circle of radius k. Here again, the radiation efficiency is essentially controlled by the ratio c_M/c:

(i) For $c_M/c<1$, the integral in the numerator of σ does not contain the circle of radius k, which implies that it has a small value. This is the weak radiation regime for which $\sigma \ll 1$. The precise value of σ depends sensitively on the given eigenmode considered, and in particular on the spatial coherences between the amplitudes and phases of the vibrations of different points of the membrane.

(ii) For $c_M/c>1$, the integral in the numerator contains the circle of radius k which includes all the domains in which the Fourier transform of the vibration amplitude is large. The radiation efficiency is then close to unity. In the limit $c_M \gg c$, the two integrals of the numerator and of the denominator take the same value, implying that:[15]

$$\sigma \to 1 \quad \text{when} \quad \frac{c_M}{c} \to \infty. \tag{14}$$

In this regime, the radiation efficiency is universal and equal to 1 for all eigenmodes. According to Eq. (12), this means that all eigenmodes present the same frequency broadening due to radiation attenuation. Physically, this regime corresponds to the case where the acoustic radiation of different points of the membrane is spatially incoherent, thus leading to an average behavior which is universal. It is even possible to give an asymptotic expression of σ by remarking that the Fourier transform $\hat{w}$ takes a large value only in the neighborhood of k_M. This suggests that the square root in the integral in the numerator of Eq. (10) be removed to obtain

$$\sigma = \frac{1}{\sqrt{1-(c/c_M)^2}} \quad \text{for} \quad \frac{c_M}{c} > 1. \tag{15}$$

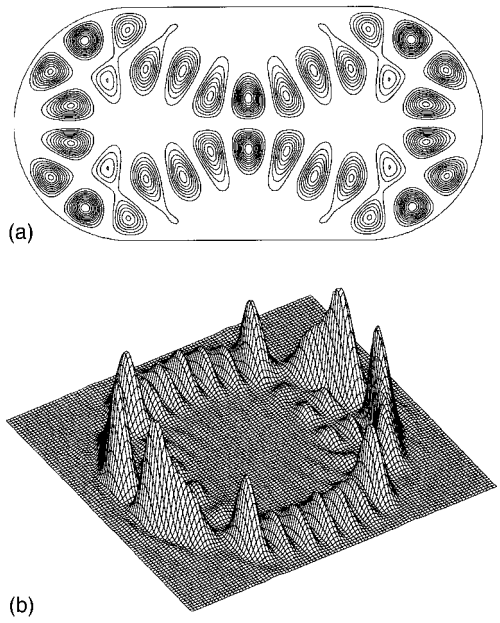

FIG. 6. Eigenmode whose structure cannot be put in correspondence with a ''scar'' of a periodic ray orbit: we do observe a localization of the amplitude of vibration but it does not correspond to any resonance on a single periodic orbit of the stadium. In this case, the single periodic orbit analysis reaches its limit: the localization of the vibration amplitude observed here probably results from the contribution of many periodic orbits. No theory exists in this case to describe the corresponding multiple ''scars.'' (a) and (b) $k=11.543$.

This law is well verified in our data.

(iii) For c_M/c close to 1, the integral in the numerator of Eq. (10) can take very large values, since $\hat{w}$ has a large value when the square root term diverges. The radiation efficiency σ can thus be larger than 1; the eigenmode radiates very efficiently mainly tangentially to the membrane (see our discussion above in Sec. II A).

These different regimes are illustrated in Fig. 7, which presents the radiation efficiency σ for six consecutive modes shown in Fig. 3 as a function of the parameter c_M/c. The behavior is as expected: (1) small σ for $c_M/c \ll 1$ with large fluctuations from mode-to-mode which are made more visible in the log–log representation; (2) a peak larger than 1 for c_M of the order of c; and (3) the universal regime where σ approaches 1 when $c_M/c \gg 1$ according to law (15). Note that the height and width of the peak for $c_M \approx c$ depend on the eigenmode. They are directly related to the localization of the Fourier transform $\hat{w}$ in the vicinity of the circle of radius k_M. The larger the eigenfrequency, the better the localization. As a first approximation, this localization effect is essentially limited by the finite size of the membrane. We thus expect asymptotically for large frequencies ($k_M \gg 1$):

$$\sigma_{\max} \approx \sqrt{k_M} \quad \text{and peak width} \approx \frac{1}{k_M}. \tag{16}$$

Equation (16) is only an order of magnitude and one observes in practice large fluctuations from mode-to-mode (of order a little less than a factor 2). We have found that the peak higher and more peaked, the more ''scarred'' the eigenmode is along the long diameter of the stadium. As the effect is inversed (lower and wider), the more ''scarred'' by the bouncing ball orbit is the eigenmode.

In the nonuniversal regime c_M/c, the most remarkable feature is the very rapid decay of the radiation efficiency and thus of the radiated acoustic power by the membrane. For eigenmodes around the 80th excited mode of the stadium (see Fig. 7), σ is no more than 0.1 at $c_M/c=0.8$ and less than 0.01 at $c_M/c=0.2$. When going to higher frequencies, this effect is all the more important. Another remarkable feature of this regime is the existence of very large fluctuations. For instance, at $c_M/c=0.1$, the radiation efficiency can vary by two orders of magnitude depending on the given eigenmode (typically between 10^{-5} and 5×10^{-3}).

In the regime $c_M/c \ll 1$, the radiation efficiency also depends on the symmetry properties of the eigenmodes with respect to the $0x$ and $0y$ axis. Indeed, for $c_M/c \ll 1$, the radiated power is essentially controlled by the monopolar moment $\hat{w}(0,0)$ of the mode. Due to symmetry, it is vanishing except for eigenmodes of even–even symmetry. This implies that the more efficient modes with respect to radiation are those of the even–even symmetry. The second efficient modes are of the odd–even and even–odd symmetries (but σ is in general 100 times smaller than for even–even modes). The less radiating modes are the odd–odd ones. In Sec. IV, we provide an explanation for the fluctuation of the radiation efficiency from mode to mode, in terms of an analogy with the so-called Porter–Thomas fluctuations.

III. RADIATION BY A MEMBRANE EXCITED OVER A FINITE BANDWIDTH

Using our previous results, we can now address the case of a membrane excited simultaneously over several eigenmodes, instead of a single one as has been studied above. We still consider the free radiation regime. The importance of this section is to show that the strong fluctuations in the radiation directivity survive under moderate bandwidth excitation. The ''scarred'' versus ''anti-scarred'' interpretation developed below is very important to understand our results.

This situation arises, for instance, when an external noise excites the membrane. We will restrict our study to the case of an incoherent excitation of the different eigenmodes. We assume that the noise frequency spectrum is a Gaussian centered on an average frequency f and with a specified width. Note that this hypothesis is not restrictive since arbitrary spectra can be used which give similar results as those presented below, as long as they have a finite width. The acoustic radiation is then the incoherent superposition of the individual contributions of each single eigenmode, i.e., we thus add the powers radiated by each single mode [see Eqs. (2) and (4)]. We will consider the case where a relatively large number of modes are excited, typically a few tens.

As for the single mode radiation problem, the controlling parameter is the ratio c_M/c. If it is small, the total radiation is weak. We have verified that if individual modes are nonisotropic, the sum over the modes introduces a kind of averaging and leads to an isotropic radiation diagram as soon as a few modes are notably excited.

The interesting regime is when c_M/c is larger than 1. In this case, we have shown that the total radiated power per

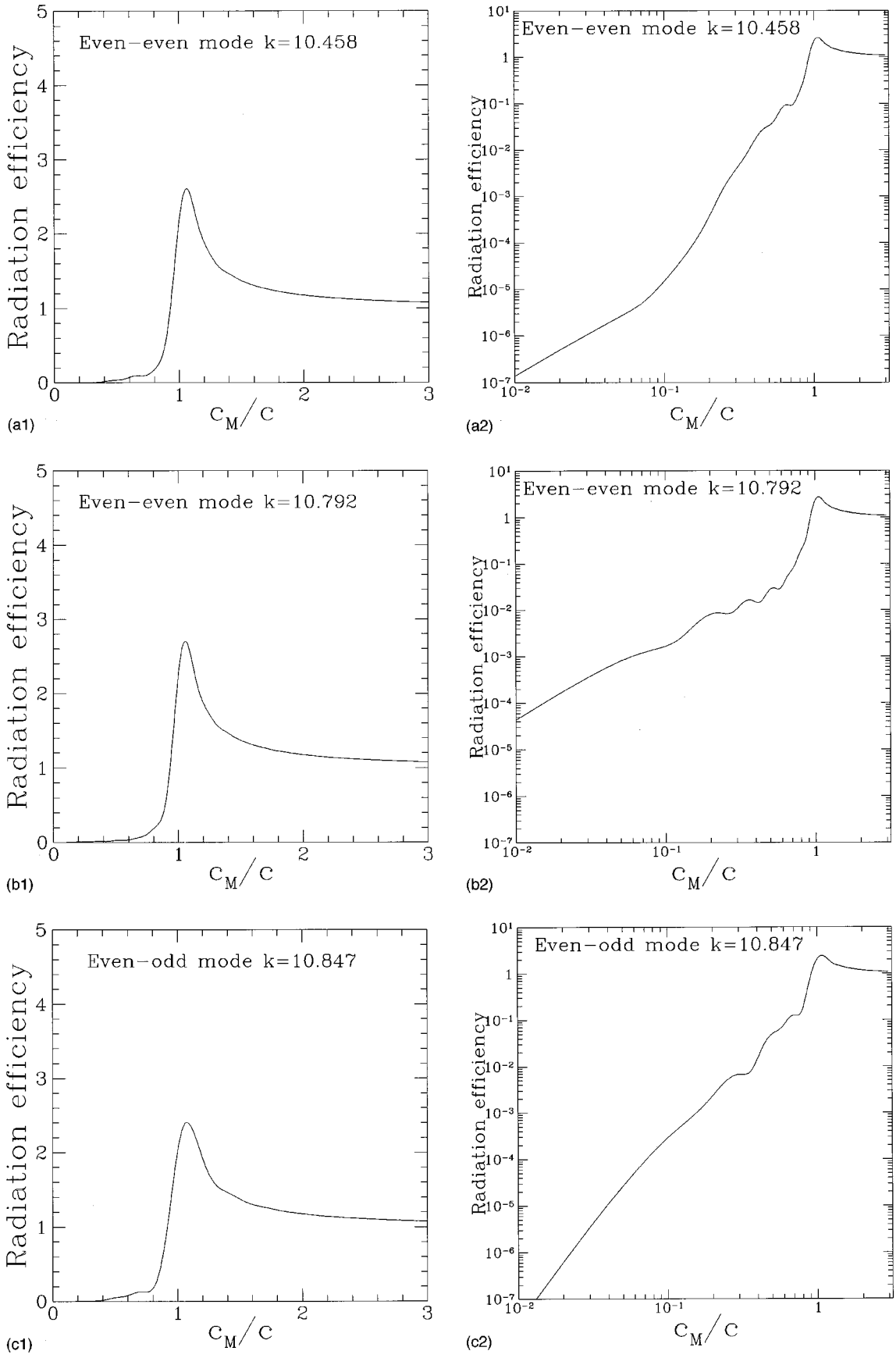

FIG. 7. Radiation efficiency σ for the six consecutive modes shown in Fig. 3. One can observe the universal behavior for $c_M/c>1$ (radiating regime), a peak close to $c_M/c=1$ (hyper-radiating regime), and the nonuniversal weakly radiating regime with large fluctuations from mode-to-mode for $c_M/c<1$. In each case, we present the function σ as a function of c_M/c in linear and in log–log scale in order to better appreciate the fluctuations in the $c_M/c\ll 1$ regime.

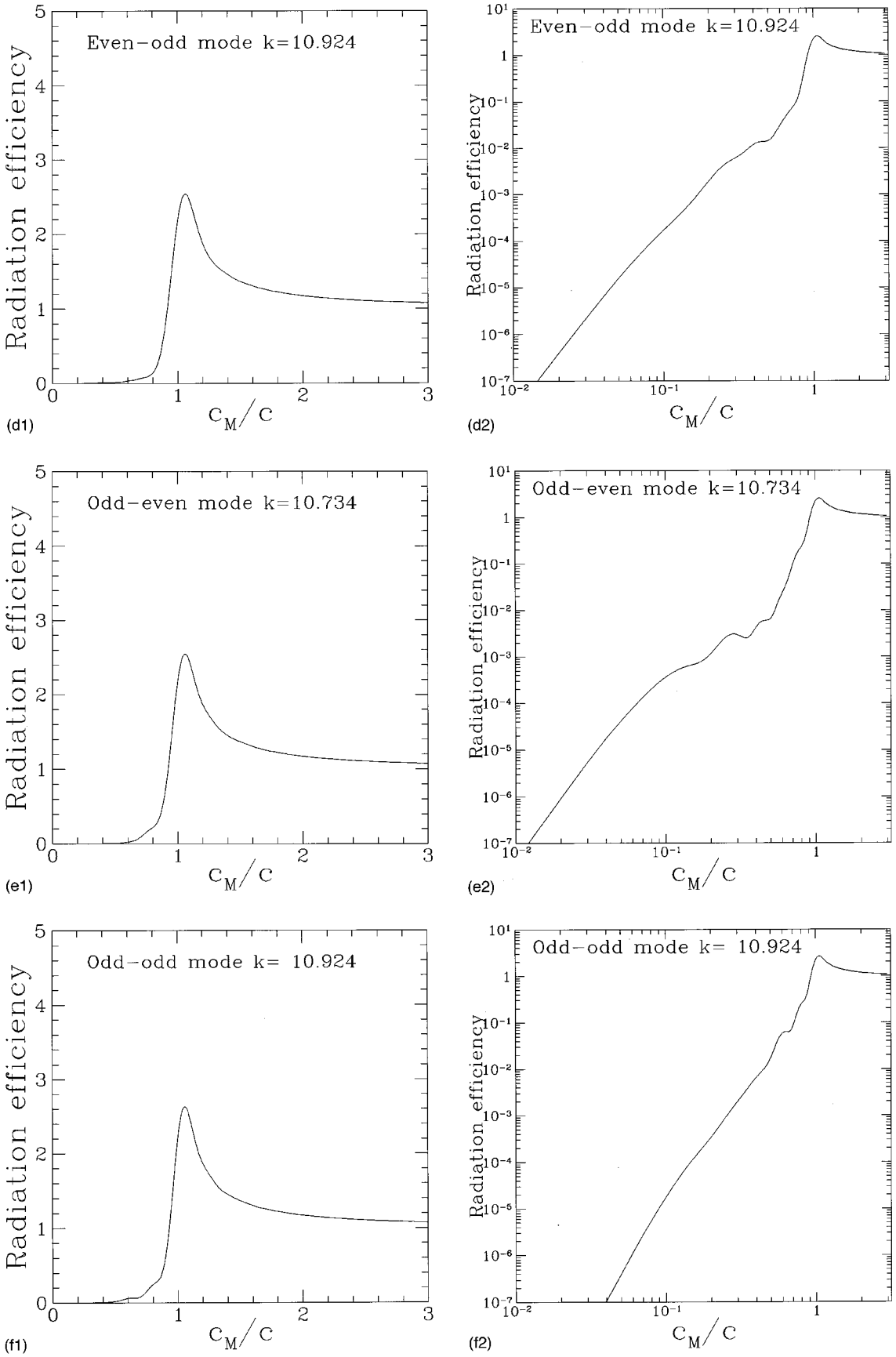

FIG. 7. *(Continued.)*

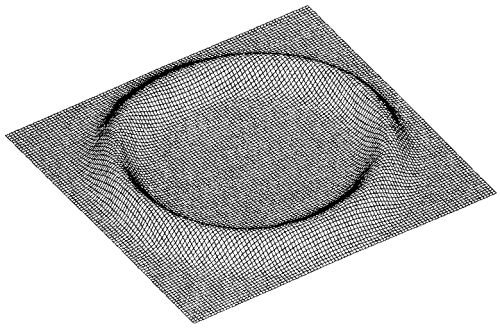

FIG. 8. Radiation diagram in the case of an excitation with a large bandwidth. The radiation is localized on the cone but with no prefered directions. $k=11.7\pm1.2$.

mode is the same for all modes (see Sec. II). This universal behavior is, of course, recovered for the total power radiated by a set of modes and one can use the formula (7) with $\sigma=1$.

The most interesting effects can be observed on the radiation diagram. As for the single mode problem, it is obtained from the sum of the square of the Fourier transform of the vibration amplitudes of the various excited eigenmodes. Since each mode radiates essentially on a cone whose half-opening angle is given by Eq. (13), the same effect is recovered for a set of modes around an average frequency. As with respect to ''scars,'' [12] resulting from amplitude localization in the neighborhood of periodic orbits, their visibility in the case of a finite bandwidth excitation crucially depends on the the frequency width of the excitation spectrum. Figure 8 shows the radiation diagram in the case of a large bandwidth such that all ''scars'' are averaged out and no preferential directions of radiation exists on the cone. Figure 9(a) shows the case of an excitation with a relatively small bandwidth (relative width around 5%). The maximum of radiation clearly corresponds to the ''bouncing ball'' directions $\pm k_M$. Comparing the distribution of vibration amplitude and the corresponding radiation diagram, the ''scar'' effect is much more apparent in the latter (intensity maximum of the order of 2–3 times the background) than in the former (relative intensity fluctuations of less than 20%).

The condition that must be met in order to observe a maximum in the direction of the periodic orbit is the so-called condition of quantization of ''scars.'' [12] It is simply a resonance criterion given by

$$\frac{k_M L}{2\pi}\approx n, \tag{17}$$

where L is the length of the periodic orbit, k_M is the wave number associated to the central frequency of the incoherent excitation, and n is a positive integer. For the case of Fig. 9(a), the ratio $k_M L/2\pi$ is equal to 7.07 which is close to 7. On the contrary, when this ratio is close to a half-integer, one observes an ''anti-scar,'' i.e., a minimum of the radiation in the direction of the periodic orbit, as shown in Fig. 9(b). Note that scars due to other periodic orbits can be observed on these radiation diagrams. They could also be observed for the case of single eigenmode excitations, but their intensity is smaller in the former case, of the order of a few tens of per cent. In addition to the scars, intensity fluctuations of order

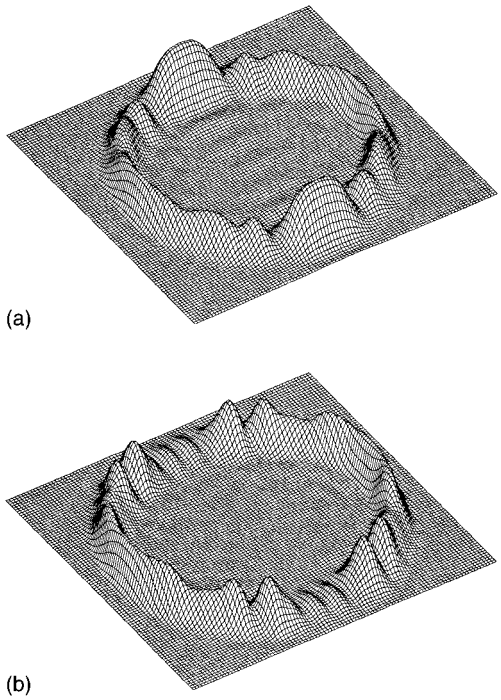

FIG. 9. Radiation diagram in the case of an excitation with a relatively small bandwidth. One can observe the localization of the radiation in two directions $\pm k_M$ corresponding to a resonance (''scar'') on a bouncing ball periodic orbit. It is noteworthy that the effect is clearly apparent in the radiation diagram but essentially absent in the spatial distribution of vibration amplitudes. Depending upon the central frequency of the excitation, the ''bouncing ball'' direction $\pm k_M$ can be favored or on the contrary left over with respect to the other directions on the cone. This comes from subtle interference effects. Figure 9(b) shows an ''anti-scar,'' i.e., a minimum of the radiation in the direction of the periodic orbit (see text for explanation). (a) $k=11.7\pm0.3$; (b) $k=12.0\pm0.3$.

20%–50% are present in the case of an excitation with a relatively small bandwidth, whose origin remains unclear.

When the bandwidth of the excitation is too large, both scarred and anti-scarred modes are simultaneously excited, and an isotropic radiation is obtained (see Fig. 8). This roughly corresponds to a change of unity in Eq. (17). A simple criterion to observe anisotropic acoustic radiation by a membrane excited by a noise of width $\Delta\omega$ is thus

$$\Delta\omega<\frac{2\pi}{c_M L}, \tag{18}$$

where L is the length of the shortest closed ray trajectory.

The ''bouncing ball'' scars exhibit some pecularities. One can observe in Fig. 10 that the directions of maximum radiation tend to go away from $k_y=\pm k_M$ as the central frequency increases. There is a kind of splitting to form pairs of secondary maxima on both sides of $k_y=\pm k_M$. We have verified that the position of their peaks is well-described by a wave vector ''quantization'' along the $0y$ axis given by

$$\frac{k_{My}L}{2\pi}=\frac{k_M \sin\varphi L}{2\pi}\approx n. \tag{19}$$

We do not understand the precise origin of these secondary peaks, which are not directly linked to periodic orbits.

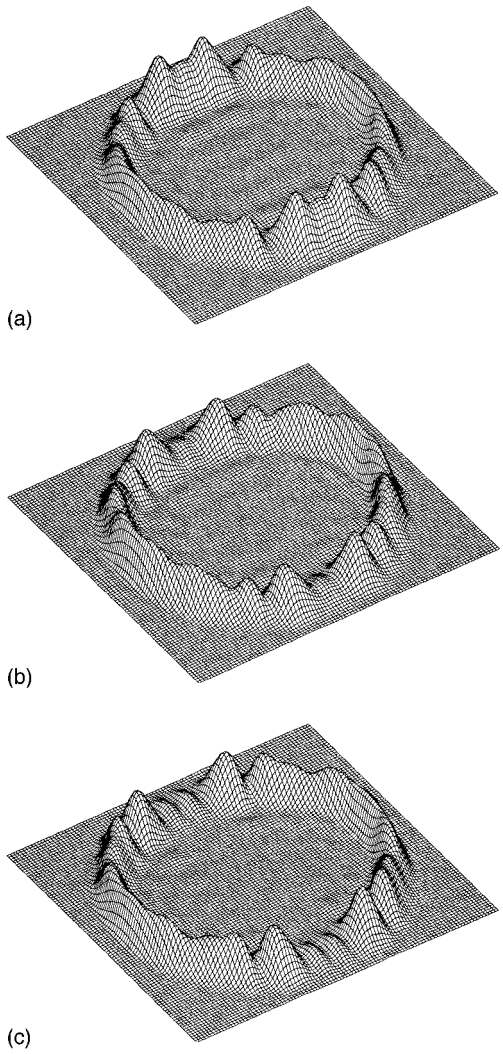

FIG. 10. Three other cases showing the radiation diagram for an excitation with a relatively small bandwidth. Depending on the central frequency, secondary peaks appear around the $0y$ axis (see text for an explanation). (a) $k=11.3\pm0.3$; (b) $k=11.6\pm0.3$; (c) $k=11.9\pm0.3$.

IV. DISSIPATION AND FLUCTUATIONS

Our previous results show the ubiquitous presence of fluctuations in the radiation of a vibrating membrane. In fact, such fluctuations are not restricted to radiation phenomena, but are more generally associated to dissipative phenomena in wave problems. There are a number of cases studied in the field of ''quantum chaos'' in which these fluctuation phenomena associated to dissipation are well understood and precise quantitative predictions exist. In more complex cases, these simplified models (to be described below) are still useful in order to identify the relevant parameters and the physical mechanisms. We now adapt these developments to the problem of membrane vibrations and illustrate them using simple examples.

These phenomena are dependent on two main physical parameters. The first one is the ratio $\Gamma/\Delta\omega$ of the dissipation rate Γ of the energy stored in the membrane [it is the inverse of the decay time given by Eq. (11)] to the mean frequency spacing $\Delta\omega$ between consecutive eigenfrequencies. The second feature is the coherent or incoherent nature of the dissipation phenomenon. More precisely, by coherency is meant the question of the number of channels which participate in the dissipation. If dissipation is restricted to a single channel, we deal with a ''coherent'' case. If there are many independent dissipation channels, the process is incoherent. Let us give a few examples in order to illustrate the point. If a small source is placed on a well-defined position of the vibrating membrane, the dissipation process due to the membrane-source coupling acts through a single mechanism in a localized spatial domain. It essentially depends on the square of the amplitude of vibration at this position. This corresponds to a coherent dissipation. Similarly, a loose screw at the border of a plate may induce some dissipation due to friction processes, which also constitutes a coherent dissipation in the previous sense. On the contrary, the dissipation associated to the radiation and viscous processes of a vibrating membrane in an heavy fluid occurs incoherently since vibrations in various regions of the membrane are uncorrelated. In the cases of the source or the screw, the relevant parameter quantifying the degree of coherence of the dissipation phenomenon is given by the ratio of the size of the source to the wavelength in the membrane. If it is smaller than one, dissipation is coherent, and incoherent in the other limit. Another example has been discussed previously in Secs. I–III with respect to acoustic radiation. When the membrane wave velocity c_M is much smaller than the sound speed in the fluid, the membrane acts as a single degree of freedom system and the dissipation due to radiation goes essentially through one channel, i.e., the monopolar moment of the mode of vibration. The dissipation is then coherent and is characterized by a single quantity. In this case, radiation is isotropic. In the other limit where c_M is larger than c, the membrane radiates in several independent directions. There are several channels (monopolar, dipolar, etc...) of dissipation which means that it is incoherent. There exists of course intermediate regimes with small but larger than unity number of channels. In the following, we will consider the extreme regimes: one channel (coherent case) and a large number of channels (incoherent case).

Once the coherent or incoherent nature of the dissipation is known, the dissipation rate Γ must be compared to the frequency spacing $\Delta\omega$ between neighboring eigenmodes. If $\Gamma\ll\Delta\omega$, there is essentially no coupling between modes. This is the regime which has been studied in the previous sections. In the opposite case $\Gamma>\Delta\omega$, modes are coupled and the concept of an isolated mode coupled coherently to a single dissipation channel has no meaning. Therefore, the regime $\Gamma\gg\Delta\omega$ with a coherent dissipation is not realistic and will not be considered. The regime $\Gamma\gg\Delta\omega$ with an incoherent dissipation has been discussed first by Ericson[17] in nuclear physics, by Main and Wunner[18] in atomic physics, and by Schröeder and others[19] in acoustics. It will not be addressed here.

Our approach here is somewhat reminiscent of the statistical energy analysis (SEA), which examines the ensemble average vibrational behavior of complex structures. It is true that the two approaches have in common the consideration that a given measurement can be seen as a specific realization within an ensemble of equivalent realizations. However,

SEA looks for an average response while we have described the full structure of the distribution around this average. In other words, our emphasis is on the fluctuations from mode-to-mode. We now show that this distribution retains important information on the system.

A. Coherent single dissipation channel (with $\Gamma \ll \Delta\omega$)

The description of this regime relies on the theory of random matrices[9] developed in the field of ''quantum chaos.'' It is now well established that this theory quantitatively accounts for the statistical properties of high-frequency vibrations of membranes, plates, and even bulk elasto-dynamics.[4,6–8] This model also allows us to predict the amplitude of the wave which controls a given dissipation phenomenon using a single channel. This amplitude is a random variable (hence the fluctuations) with a Gaussian distribution:

$$P(x) = \frac{1}{\sqrt{2\pi}\gamma} \exp\left(-\frac{x^2}{2\gamma^2} \right), \tag{20}$$

where γ represents the variance of this amplitude. It depends on the specific dissipation phenomenon. In the membrane problem treated above, the random variable x represents the amplitude of the membrane vibration at a given point. The Gaussian distribution (20) has been checked numerically in a variety of contexts and specifically for the membrane vibration problem.[16–20]

In general, the energy dissipation rate in a given channel is proportional to the square of the amplitude of the wave. This implies that the distribution of the dissipation rate Γ in a single channel is given that the distribution of the variable x^2, leading to

$$P(\Gamma) = \frac{1}{\sqrt{2\pi\Gamma\Gamma_0}} \exp\left(-\frac{\Gamma}{2\Gamma_0} \right), \tag{21}$$

where Γ_0 is the average of the dissipation rate Γ. This distribution (21) is called the Porter–Thomas distribution.[21] It has been observed experimentally for the first time in the dissociation rate of highly excited heavy nuclei, in the case when only a single channel of dissociation is allowed. Since then, it has also been observed in chaotic quantum systems in atomic physics.[22] Note that distribution (21) presents a large maximum (in fact a divergence) for $\Gamma \to 0$: since the dissipation phenomenon is a function of an amplitude which is distributed according to a Gaussian centered around zero, the most probable realization is to observe a small amplitude and thus an even smaller dissipation rate (due to the square). Quantitatively, the probability to observe a dissipation rate smaller than 0.01 is around 20%!

These properties directly apply to the radiation problem studied above in the regime $c_M \ll c$. In this case, the monopolar moment constitutes the main channel of dissipation. We have checked that its distribution is correctly described by a Gaussian law, taking into account the symmetry properties which consider only the even–even eigenmodes. This rationalizes the very large fluctuations from mode-to-mode obtained by our numerical computations of the radiation efficiency in the regime $c_M \ll c$. In particular, a large fraction of the eigenmodes must present a very weak radiation efficiency.

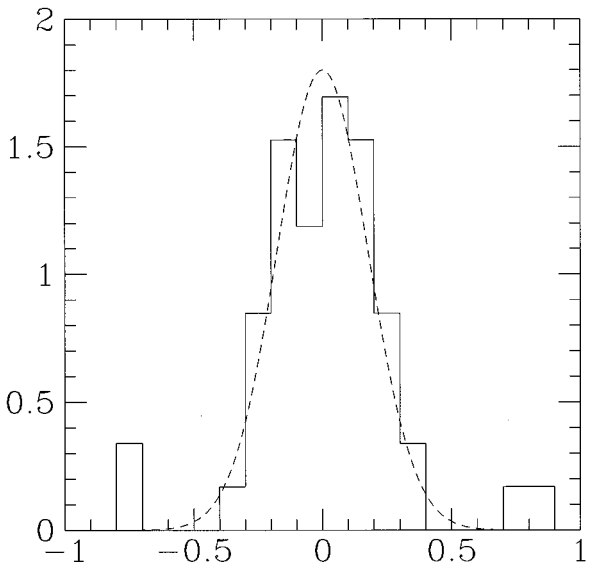

FIG. 11. Histogram of the gradients of the membrane vibration amplitude at point ($x=0.5$; $y=1$) on its border for 59 consecutive eigenmodes in the wave number interval $9.4<k_M<13$ (in units where the radius of the circular caps of the stadium is unity). The dashed line is the theoretical Gaussian distribution predicted from the theory of random matrices.

Let us discuss another example. Let us assume that a screw that holds a portion of the membrane border is slightly loose. The vibration amplitude of the membrane is zero on the screw, but the dissipation energy is proportional to the square of the gradient of the amplitude of vibration in the vicinity of the screw. Figure 11 shows the histogram of the gradient of the amplitude of vibration of a membrane having the shape of a stadium at point ($x=0.5$; $y=1$) on its border for 59 consecutive eigenmodes. The numerically determined distribution is in good agreement with the Gaussian prediction of the theory of random matrices[9] given by Eq. (20). The distribution of the dissipation rate is thus described by the Porter–Thomas distribution. Another case in which the Porter–Thomas distribution should be relevant is the description of the coupling between several elements (membranes, plates, etc...) by a joint whose transverse dimension are small compared to the wavelength.

B. Case of several incoherent dissipative channels (with $\Gamma \ll \Delta\omega$)

Due to the incoherence, the dissipation rates (one for each single channel) sum up to give the total dissipation rate. It is determined once the statistical distribution of the sum of squares of independent random variables is known, each of them distributed according to a Gaussian distribution. It is possible to establish general results, but the formulas are complicated and difficult to use.[21] In the particular case where all channels have the same average dissipation rate, the resulting distribution of the total dissipation rate is a simple χ^2 law with N degrees of freedom.[21] In general, when the number N of degrees of freedom goes to infinity, the

individual fluctuations of each channel average out and all the dissipation rates tend to be distributed according to a Gaussian law of nonzero average and whose width decreases as $N \to +\infty$. If the mean dissipation rate is less than the average frequency spacing between consecutive eigenfrequencies, inter-modal coupling can be neglected and all modes dissipate roughly identically without interacting. This is exactly the situation described above in Sec. II for the acoustic radiation problem in the limit $c_M \gg c$, for which the radiation efficiency of all eigenmodes is universal and goes to 1 for $c_M/c \to +\infty$. This regime also applies to the incoherent excitation case of several eigenmodes discussed in Sec. III. In summary, a uniform value of all dissipation rates is the generic situation for a weak incoherent dissipation.

V. CONCLUSIONS

We have presented an efficient and reliable numerical scheme to compute the radiation directivity and the total power radiated by isolated eigenmodes and by finite bandwidth excitations of a membrane of arbitray shape over the whole frequency domain. The calculations have been carried out in the free radiation regime and we have neglected the additional radiation mechanisms arising on the forced case.

We have recovered all well-known results on the different wave speed regimes, the radiation directivity controlled by the spatial coherence of the eigenmodes, the differing efficiency of modes depending on their parities being even or odd, etc. However, our emphasis has been to point out and quantify the large fluctuations on the directivity due to scars produced by underlying periodic ray orbits on the eigenmodes. We have also found extremely large variations in the radiation efficiency in the subsonic regime. Our results have been illustrated on the case of a membrane having the shape of a stadium, this shape having been studied intensively in the literature concerned with the correspondence between classical geometrical ray trajectories and high-frequency vibrations, the so-called ''quantum chaos'' problem. Our results have been made possible by the introduction of a trick, described in the Appendix, which allows us to compute with excellent precision a large number of eigenfrequencies and eigenmodes and their radiation. We have addressed in detail the properties of the fluctuations of the total radiated power, and more generally of any dissipation mechanism, as a function of frequency. We have shown that, for a single eigenmode radiation, one must distinguish between the case of a single dissipation channel and several incoherent dissipative channels. The theory of random matrices has allowed us to predict the distribution of power radiation from modes to modes. In the first case, this distribution is peaked at zero dissipation (or radiation) while we recover a nonzero centered Gaussian distribution in the second case. All of these results are in excellent agreement with our direct radiation calculations.

In conclusion, we hope to have shown that fluctuations can be predicted with good accuracy and reflect a very important part of the physics of structure vibrations. We could summarize our results by stressing that fluctuations are not noise, but, on the contrary, are genuine fingerprints of the underlying structure. We expect that useful information and quantification will be carried on in the future to characterize more complex structure vibrations and their radiations using the properties exhibited by the fluctuations.

APPENDIX: NUMERICAL CALCULATION OF ACOUSTIC RADIATION BY A VIBRATING MEMBRANE

In principle, Eqs. (2) and (4) enable one to calculate the power radiated by a vibrating membrane in a given direction of space. In practice, the Fourier transform of the membrane vibration amplitude must be evaluated. One thus needs to first compute the eigenfrequencies and eigenfunctions of the Helmholtz equation with Dirichlet boundary conditions in a membrane having the shape of a stadium. Toward this goal, we have developed efficient numerical schemes which allow to compute a large number of eigenfrequencies and eigenmodes. The basic method is an extended collocation technique: the solution is decomposed on the basis of plane waves (normal Bessel functions of the first kind can also be used). It thus automatically obeys the Helmholtz equation. The eigenfrequencies are then determined by imposing the Dirichlet boundary condition. A good stability is obtained by expanding the solution along the membrane border on the set of Fourier components as a function of the boundary curvilinear abscissa. A determinent of a matrix must vanish in order for a frequency to qualify as an eigenfrequency. We have carefully checked the stability of the algorithm as a function of the number of partial waves entering the decomposition of the full solution and as a function of the boundary curvilinear decomposition. These methods allow the determination of several thousand eigenmodes with a precision better than the 1/100th of the mean frequency spacing of consecutive eigenfrequencies.[3,4d,4e,9]

Once the eigenfrequencies and the eigenfunctions are known, the most natural method is to estimate the Fourier transform numerically. This turns out to be quite inefficient since the Fourier transform is very sensitive to long-range spatial correlations between different points of the membrane. The stabilized collocation method, using an expansion of the vibration amplitude on a discrete basis, gives a good description of the general aspects of the vibration amplitude. However, its precision is not good enough to describe the long-range spatial correlation, thus leading to a poor estimation of the Fourier transform.

In order to provide a remedy to this problem, we have developed a direct method of computation of the Fourier transform. In the collocation method,[4] the vibration amplitude is expanded in the following sum:

$$w(x,y) = \sum_{\theta_n} a_n(\theta_n) \exp(-jk_M(\cos\theta_n \; x + \sin\theta_n \; y)), \tag{A1}$$

where the sum is carried over all different possible directions of plane waves of amplitude a_n. Plugging expression (A1) in Eq. (2) shows that the Fourier transform that must be calculated can be expressed in terms of the Fourier transform of the indicator function of the membrane (which is equal to 1 on all points of the membrane and zero elsewhere):

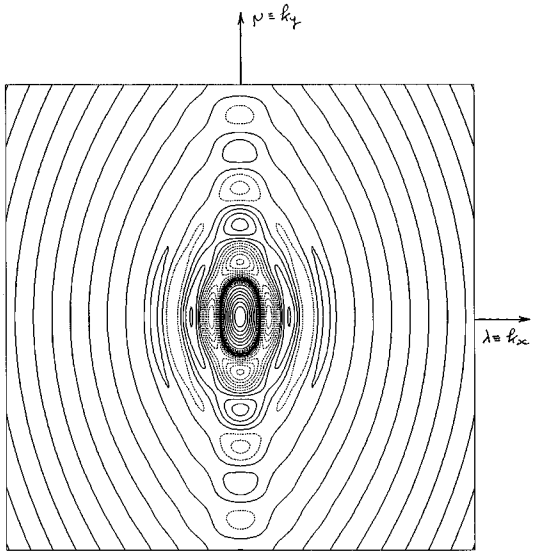

FIG. A1. Fourier transform of the indicator function of the membrane having the shape of a stadium (which is equal to 1 on all points of the membrane and zero elsewhere) given by Eq. (A2). It is centered on zero with an anisotropic shape reflecting that of the stadium.

$$H(\lambda,\mu)=\int_{\text{surface of the membrane}} \exp(\mathbf{j}(\lambda x+\mu y))dx\ dy. \tag{A2}$$

In the case of a membrane symmetric under $x\rightarrow -x$ and $y\rightarrow -y$, H is a real function. We thus obtain:

$$\hat{w}(\lambda,\mu)=\frac{1}{2\pi}\sum_n a_n(\theta_n) \times H(\lambda-k_M\cos\theta_n,\ \mu-k_M\sin\theta_n). \tag{A3}$$

Coefficients a_n are directly given by the collocation method.[4] We thus need to calculate only once for all the function H in order to compute all the needed Fourier transforms of all eigenmodes. Figure A1 shows the function H for the membrane having the shape of a stadium. It is centered on zero with an anisotropic shape. It is clear from Eq. (A3) that the Fourier transform of an eigenmode in the high-frequency regime is significant only when the argument of the function H is small, i.e., in the neighborhood of the circle of radius k_M. This property explains the preferential radiation on a cone.

It is also necessary to normalize the eigenmodes. The total integral over the whole membrane surface of the square of the vibration amplitude must be evaluated. In fact, it is easier to normalize the Fourier transform of the eigenmodes. Using Eq. (A2), this is carried over using only the function H, tabulated once and for all at the beginning of the calculation. We note that, since H decreases slowly at large distances due to the compact support of the membrane, extreme care must be exercised in the calculation of the normalization. In the same vain, one must be very careful in carrying the calculation of the oscillatory integrals in Eq. (10) giving the total radiated power, in order to avoid numerical errors especially at high frequencies.

[1] R. J. Bernhard and R. F. Keltie, Eds., ''Numerical techniques in acoustic radiation,'' presented at the Winter Annual Meeting of the ASME, San Francisco, 10–15 Dec. 1989, NCA, Vol. 6 (ASME, New York, 1989).

[2] Proceedings of the conference ''Prediction of the noise emitted by vibrating structures,'' CETIM Senlis, 26–28 March 1991, Revue Française de Mécanique, numéro spécial 1991.

[3] M.-J. Giannoni, A. Voros, and J. Zinn-Justin, *Chaos and quantum physics*, Les Houches 1989, Session LII (North-Holland, Amsterdam, 1991).

[4] (a) O. Legrand and D. Sornette, X-RS, ''Vibrations hautes fréquences et Chaos quantique,'' Report DRET 88/347, unpublished (1989); (b) D. Sornette, ''Vibrations de plaques et chaos quantique,'' in Ref. 2, pp. 364–381; ''Vibrations hautes fréquences des structures,'' Aux Frontières du Domaine, *Acoustique et Vibrations*, Science et Défense 92 (Dunod, Paris, 1992), pp. 185–205; (c) F. Mortessagne, O. Legrand, and D. Sornette, ''Sabine' reverberation law in chaotic rooms: Geometrical and wave theory,'' J. Acoust. Soc. Am. **93**, 2343(A) (1993); (d) D. Delande, O. Legrand, C. Schmit, and D. Sornette, X-RS, ''Vibrations de plaques et chaos quantique,'' Report DRET 89/543, unpublished (1991); (e) D. Delande, O. Legrand, F. Mortessagne, C. Schmit, and D. Sornette, X-RS, ''Couplage, rayonnement et chaos quantique,'' Report DRET 91, unpublished (1993); (f) O. Legrand and D. Sornette, *Quantum Chaos and Classical Waves*, in Lecture Notes in Physics Vol. 392 (Springer-Verlag, Berlin, 1991).

[5] R. Blümel, I. H. Davidson, W. P. Reinhardt, H. Lin, and M. Sharnoff, Phys. Rev. A **45**, 2641 (1992); F. Haake, G. Lenz, P. Seba, J. Stein, H.-J. Stöckmann, and K. Zyczkowski, Phys. Rev. A **44**, R6161 (1991); H.-J. Stöckmann and J. Stein, Phys. Rev. Lett. **64**, 2215 (1990); S. Sridhar, Phys. Rev. Lett. **67**, 785 (1991).

[6] (a) R. L. Weaver, J. Acoust. Soc. Am. **85**, 1001 (1989); (b) O. Bohigas, O. Legrand, C. Schmit, and D. Sornette, J. Acoust. Soc. Am. **89**, 1456 (1991); (c) D. Delande, D. Sornette, and R. Weaver, J. Acoust. Soc. Am. **96**, 1873–1880 (1994).

[7] O. Legrand, C. Schmit, and D. Sornette, Europhys. Lett. **18**, 101 (1992).

[8] (a) R. H. Bolt, J. Acoust. Soc. Am. **19**, 79 (1947); (b) V. M. Schröder, Acustica **4**, 456 (1954); (c) I. Dyer, Sci. Technol. 35 (August 1963); (d) see C. E. Porter, *Fluctuations and Quantum Spectra* (Academic, New York, 1965), p. 50 and footnote 25 in p. 50.

[9] (a) O. Bohigas, M. J. Giannoni, and C. Schmit, ''Spectral fluctuations of classically chaotic quantum systems,'' in *Quantum Chaos and Statistical Nuclear Physics*, edited by T. H. Seligman and H. Nishioka (Springer-Verlag, New York, 1986); (b) C. E. Porter (Ed.), *Statistical Theories of Spectra: Fluctuations* (Academic, New York, 1965); (c) M. L. Mehta, *Random Matrices and the Statistical Theory of Energy Levels* (Academic, New York, 1967); (d) O. Bohigas, M. J. Giannoni, and C. Schmit, Phys. Rev. Lett. **52**, 1 (1984).

[10] M. Gutzwiller, J. Math. Phys. (N.Y.) **12**, 343 (1971).

[11] D. Delande, in Ref. 3; D. Delande, Phys. Scrip. **T34**, 52 (1991).

[12] (a) E. J. Heller, Phys. Rev. Lett. **53**, 1515 (1984); in Ref. 3, p. 547; (b) E. B. Bogomolny, Physica D **31**, 169 (1988); (c) G. Tanner, P. Scherer, E. B. Bogomolny, B. Eckhardt, and D. Wintger, Phys. Rev. Lett. **67**, 2410 (1991).

[13] L. A. Bunimovich, Funct. Anal. Appl. **8**, 254 (1974); L. A. Bunimovich, Commun. Math. Phys. **65**, 295 (1979).

[14] P. M. Morse and K. U. Ingard, *Theoretical Acoustics* (Princeton U. P., Princeton, NJ, 1968).

[15] J. L. Guyader, Rev. Acoust. **79**, 26 (1986); A. Berry, J. L. Guyader, and J. Nicolas, J. Acoust. Soc. Am. **88**, 2792 (1990).

[16] S. W. McDonald and A. N. Kaufman, Phys. Rev. A **37**, 3067 (1988).

[17] T. Ericson, Phys. Rev. Lett. **5**, 430 (1960); Ann. Phys. (N.Y.) **23**, 390 (1963).

[18] J. Main and G. Wunner, Phys. Rev. Lett. **69**, 586 (1992).

[19] M. R. Schröeder, J. Acoust. Soc. Am. **34**, 1819 (1962); M. R. Schröeder and K. H. Kuttruff, J. Acoust. Soc. Am. **34**, 76 (1962); J. L. Davy, J. Sound Vib. **77**, 455 (1981); R. L. Weaver, J. Sound Vib. **130**, 487 (1989).

[20] M. Rollwage, K. J. Ebeling, and D. Guicking, Acustica **58**, 149 (1985).

[21] T. A. Brody, J. Flores, J. B. French, P. A. Mello, A. Pandey, and S. S. M. Wong, Rev. Mod. Phys. **53**, 385 (1981).

[22] B. Grémaud, D. Delande, and J. C. Gay, Phys. Rev. Lett. **70**, 615 (1993).

Transient acoustic wave fields in continuously layered media with depth-dependent attenuation: An analysis based on higher-order asymptotics

Martin D. Verweij[a)]
Laboratory of Electromagnetic Research, Department of Electrical Engineering, Centre for Technical Geoscience, Delft University of Technology, P.O. Box 5031, 2600 GA Delft, The Netherlands

(Received 11 September 1995; accepted for publication 15 October 1996)

A method is presented for the analysis of the space-time domain acoustic wave field in a continuously layered, lossy, isotropic fluid or equivalent fluid. Application of vertically varying compliance and inertia memory functions enables the modeling of a large class of depth-dependent loss properties. The method is based on integral transformations and consists of three steps. First, a temporal Laplace transformation with a real and positive transform parameter is applied, which is followed by horizontal spatial Fourier transformations. Second, higher-order, WKBJ-like asymptotic representations are derived that form approximate solutions of the resulting transform domain problem. With the chosen forward transformation process, problems caused by a zero vertical slowness are avoided, and the need for more intricate types of asymptotics is absent. Third, the Cagniard–De Hoop method is employed for the transformation back to the space-time domain. The form of the transform domain expressions allows for a very efficient use of the inversion process, while many steps of the inverse transformation may be performed analytically. Since the method does not impose a numerical limit on the bandwidth of the result, it may also be employed to generate a Green's function. Numerical results are presented for reflections from half-spaces filled with a continuously layered, equivalent fluid with depth-dependent losses. At each level these losses show an almost ''constant-*Q*'' behavior in the frequency domain. The results show that there is an interval, beginning with the arrival time, on which the improvement due to the use of higher-order asymptotics is significant. [S0001-4966(97)00304-4]

PACS numbers: 43.20.Bi, 43.20.Fn, 43.20.Hq [JEG]

INTRODUCTION

There are a number of areas where continuously layered fluids, fluids with medium properties that change in a continuous way in the vertical direction, may be applied for modeling purposes. For ocean acoustics and underwater acoustics, their usefulness is easily recognized. In seismics, continuously layered fluid models may be of benefit in cases where only the slow vertical changes of the medium properties of the Earth are relevant, e.g., in computational backgrounds. By using a continuously layered equivalent fluid instead of a continuously layered solid, the difficult task of determining the compressional wave field in the solid is replaced by the much easier task of finding the equivalent acoustic wave field in the fluid.

Unlike most fluids, the internal losses in many solids are significant. The loss of mechanical energy of a propagating wave field gives rise to attenuation and dispersion. For seismic applications it is therefore important that the loss behavior of a viscoelastic solid is carried over to its equivalent fluid representation. The following representations of the losses in a solid may serve as candidates for the representation of the losses in a fluid: the quality factor Q specifying the amount of loss in a solid (Ben-Menahem and Singh,[1] Johnston and Toksöz,[2] Aki and Richards[3]), a network model describing a constitutive differential equation between a stress and a strain (Kolsky,[4] Bland,[5] Ben-Menahem and Singh[1]), and a compliance memory function indicating how the stress at a particular moment depends on the strain at that moment and all previous moments (Boltzmann,[6,7] Kolsky,[4] Ben-Menahem and Singh[1]). We prefer to use the memory function representation because it can be directly incorporated in the basic acoustic equations.

In contrast to its vertical dependence, a continuously layered fluid shows shift invariance with respect to both horizontal directions. And as long as the memory functions of a lossy fluid are not parametrically affected, it is time invariant. There exist methods for the analysis of the acoustic wave field that exploit these invariances. For lossless, continuously layered media, the integral transformation-type methods are good examples. Based on the specific type of forward transformation, solution method in the transform domain, and inverse transformation, various integral transformation-type methods can be distinguished (Chapman,[8,9] Chapman and Orcutt,[10] Kennett[11]). One of these methods, consisting of the temporal Laplace transformation and horizontal spatial Fourier transformations, higher-order WKBJ (Wentzel–Kramers–Brillouin–Jeffreys; ''phase integral'') asymptotics, and the Cagniard–De Hoop method, is related to the present method (Verweij[12,13]). On the other hand, for homogeneous but lossy fluid media, the integral transformation approach applies as well. An example of this forms the method that has been based on the temporal Laplace transformation and horizontal spatial Fou-

a)Electronic mail: M.D.Verweij@ET.TUDELFT.NL

rier transformations, the Neumann series solution, and the Cagniard–De Hoop method (Verweij[14]). When the space-time domain wave field in an inhomogeneous and/or anisotropic, lossless medium is already known, the similarity principle may be employed to find the wave field in a corresponding lossy medium (Chao and Achenbach,[15] De Hoop[16,17]). A restriction of the latter approach is that the spatial and temporal behavior of the basic memory functions must be separable.

In this paper we will develop an integral transformation-type method that is primarily intended for the determination of the space-time domain acoustic wave field in a continuously layered, lossy, isotropic fluid. We assume that the properties of the fluid are represented by memory functions that may possess an intricate time behavior. Further, these memory functions may change in a continuous way in the vertical direction. Besides memory effects in the compliance behavior, for completeness of the theory we will include memory effects in the inertia behavior—friction—as well (cf. De Hoop[16]). The ingredients of our method are: the temporal Laplace transformation—with a real and positive transform parameter—combined with horizontal spatial Fourier transformations, higher-order WKBJ-like asymptotic representations of the transform domain solution for large values of the Laplace transform parameter (Verweij[12,13]), and the Cagniard–De Hoop method of inverse transformation (De Hoop[18]). Lerch's theorem for the Laplace transformation (Widder[19]) forms the basis of our choice. This theorem states that the time-domain counterpart of a Laplace-domain function is unique and causal if the latter is bounded for an infinite number of equidistant, positive real, and sufficiently large values of the transform parameter. Obviously, it is sufficient if an inverse Laplace transformation process only employs positive real values of the transform parameter. This is the case for the Cagniard–De Hoop method: no such thing as a complex Bromwich contour is involved in it. Subsequently, in our analysis a positive real transform parameter leads in all relevant cases to a nonzero vertical propagation coefficient or vertical slowness. Thus, due to the Laplace transformation, we do not have to worry about turning points or the Stokes phenomenon (Wasow[20]) when using asymptotics. Since in the transform domain we employ asymptotic representations for large values of the Laplace transform parameter, in the space-time domain we will obtain approximations of the wave field that are most accurate near the arrival time.

At forehand we can indicate several favorable characteristics of the proposed method. The occurrence of the same exponential function in the terms of the WKBJ-like asymptotic representations will enable us to organize the inverse transformation in a very efficient way. Moreover, by using the Cagniard–De Hoop method we may perform most steps of the inversion process analytically. Another point is that the Cagniard–De Hoop method gives us the possibility to deal with results that have an infinite bandwidth, e.g., Green's functions. By applying higher-order asymptotics our method will often yield more accurate results, especially somewhat away from the arrival time, than with the more common zero-order or first-order asymptotic methods. As always, there will also be another side of the coin. Due to the nature of the applied asymptotics, for finite values of the Laplace transform parameter there may exist a certain order beyond which the accuracy of the transform domain asymptotic representations will no longer improve (Erdélyi[21]). In the space-time domain this may lead to divergence of the higher-order approximations after a configuration-dependent time instant, i.e., the method may loose its significance for later time instants. When the first arrival at the point of observation is associated with a turning ray, it will not be accounted for by the exponential function in the WKBJ-like asymptotics, and the method cannot be applied.

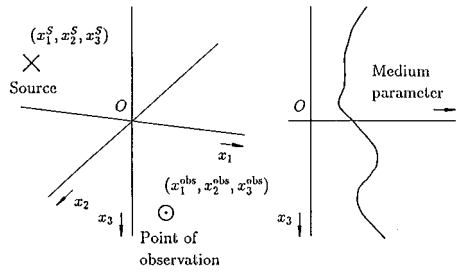

FIG. 1. The configuration with the spatial reference frame.

The theoretical description of our method starts in Sec. I with the presentation of the configuration and the introduction of the space-time domain basic acoustic equations. In Sec. II we will subject the latter to the one-sided Laplace transformation with respect to time and to two-sided Fourier transformations with respect to both horizontal spatial directions. The resulting transform domain ordinary differential equations will be recast into equivalent integral equations in Sec. III. In this section we also introduce higher-order WKBJ-like asymptotic representations of the solution of these integral equations. Subsequently, in Sec. IV we will derive a recurrence scheme for the coefficients of these asymptotic representations. The application of the Cagniard–De Hoop method for the transformation of the asymptotic representations back to the space-time forms the subject of Sec. V. In Sec. VI the numerical performance of our method is addressed. We will present results for equivalent fluids with an almost constant-Q loss behavior in the frequency domain, as possessed by most types of rock. In our examples, the losses, as well as the parameters that are associated with the instantaneous behavior of the medium, are depth dependent. Finally, we will give some conclusions with regard to the presented method in Sec. VII.

I. CONFIGURATION AND BASIC ACOUSTIC EQUATIONS

In this paper we will determine, for a known point source in a known continuously layered, lossy fluid, the acoustic wave field that is present at a point of observation. Figure 1 gives a schematical overview of the configuration. The indicated right-handed, orthonormal, Cartesian reference frame fixes the spatial coordinates $\{x_1, x_2, x_3\}$ of each point, and a standard clock provides the value of the time coordinate t at each instant. The fluid is isotropic, linear, locally reacting, and time invariant. We assume that the space-time

domain acoustic wave field in this fluid is described sufficiently accurate by the linearized basic acoustic equations

$$\partial_k v_k(x_i,t)+\partial_t[\chi(x_3,t)*p(x_i,t)]=q(x_i,t), \tag{1}$$

$$\partial_k p(x_i,t)+\partial_t[\mu(x_3,t)*v_k(x_i,t)]=f_k(x_i,t). \tag{2}$$

Here we have introduced the subscript notation and the summation convention, where the lowercase Latin subscripts (except the reserved symbol t denoting time) range from 1 to 3. The state quantities of the acoustic wave field are the particle velocity v_k and the acoustic pressure p. The symbols ∂_k and ∂_t denote a differentiation with respect to the spatial coordinate x_k and the time coordinate t, respectively. An asterisk indicates a temporal convolution. The action of the point source is contained in the volume density of volume injection rate q and the volume density of volume force f_k. Due to the horizontal and temporal shift invariance of the medium, without loss of generality we may assume that the point source is located on the vertical axis of the reference frame and that it starts to act at $t=0$, i.e.,

$$q(x_i,t)=Q^S(t)\,\delta(x_1,x_2,x_3-x_3^S), \tag{3}$$

$$f_k(x_i,t)=F_k^S(t)\,\delta(x_1,x_2,x_3-x_3^S), \tag{4}$$

with $Q^S(t)=0$ and $F_k^S(t)=0$ for $t<0$. In the basic acoustic equations, the behavior of the vertically dependent, lossy fluid is described by the compliance memory function $\chi(x_3,t)$ and the inertia memory function $\mu(x_3,t)$. These memory functions can be separated into

$$\chi(x_3,t)=\kappa(x_3)\,\delta(t)+k(x_3,t), \tag{5}$$

$$\mu(x_3,t)=\rho(x_3)\,\delta(t)+r(x_3,t). \tag{6}$$

The terms with the compressibility $\kappa(x_3)$ and the mass density $\rho(x_3)$ represent the instantaneous reaction of the medium. The bulk viscosity memory function $k(x_3,t)$ and friction memory function $r(x_3,t)$ represent the noninstantaneous reaction of the medium, i.e., the losses. If we use Eqs. (5) and (6) in Eqs. (1) and (2), we obtain the alternative basic acoustic equations

$$\partial_k v_k(x_i,t)+\kappa(x_3)\partial_t p(x_i,t)+a(x_3,t)*p(x_i,t)=q(x_i,t), \tag{7}$$

$$\partial_k p(x_i,t)+\rho(x_3)\partial_t v_k(x_i,t)+b(x_3,t)*v_k(x_i,t)=f_k(x_i,t), \tag{8}$$

where

$$a(x_3,t)=\partial_t k(x_3,t)=\partial_t^2\phi(x_3,t), \tag{9}$$

$$b(x_3,t)=\partial_t r(x_3,t). \tag{10}$$

The functions $a(x_3,t)$ and $b(x_3,t)$ have at most a delta-pulse behavior in time. The function $\phi(x_3,t)$ is known in the literature as the reduced creep function (Ben-Menahem and Singh[1]). Although $b(x_3,t)$ is virtually always taken equal to zero in the literature, for completeness we retain this memory function in our theoretical analysis. Regarding the dependence of the medium on the vertical coordinate, in this paper two canonical cases will be considered. In the first one we assume that an inhomogeneous fluid fills the entire space, and that $\kappa(x_3)$, $\rho(x_3)$, $a(x_3,t)$, and $b(x_3,t)$ are continuous functions of x_3 that are as often differentiable as required by our analysis. In the other case we assume that there is a homogeneous, lossless fluid with $\kappa(x_3)=\kappa^{\mathrm{hom}}$, $\rho(x_3)=\rho^{\mathrm{hom}}$, $a(x_3,t)=0$, and $b(x_3,t)=0$ above a level $x_3=x_3^{\mathrm{int}}$, and that an inhomogeneous, lossy fluid is present below this level. We demand that $\kappa(x_3)$ and $\rho(x_3)$ are continuous across the interface $x_3=x_3^{\mathrm{int}}$, while $a(x_3,t)$, $b(x_3,t)$ and the derivatives $\partial_3\kappa(x_3)$, $\partial_3\rho(x_3)$ are allowed to show a jump discontinuity here. This case is important when in marine seismics the effect of the sea surface is removed in order get a clearer view on the reflections from the geology (Fokkema and Van den Berg[22]).

II. FORWARD TRANSFORMATION

We exploit the time invariance of the fluid by subjecting the space-time domain basic acoustic equations to a one-sided, temporal Laplace transformation. This transformation replaces, for example, the space-time domain acoustic pressure $p(x_i,t)$ by its Laplace-transformed counterpart

$$\hat{p}(x_i,s)=\int_{0^-}^{\infty}p(x_i,t)\exp(-st)dt. \tag{11}$$

Reversely, an inverse Laplace transformation in fact performs the solution of Eq. (11) considered as an integral equation with a known function $\hat{p}(x_3,s)$ (Carson[23]). According to Lerch's theorem (Widder[19]), the solution $p(x_i,t)$ of this integral equation is unique and causal if $\hat{p}(x_i,s)$ is bounded for the infinite sequence $\{s_n\}$, where $s_n=s_0+nl$ with s_0 real, positive, and sufficiently large, $n=0,1,2,...$, and l positive and real. The theorem implies that in principle it is possible to perform an inverse Laplace transformation without the need to consider complex values of s (e.g., on a Bromwich contour). This fact is used in our analysis, in which we always keep s real and positive (cf. Cagniard[24]).

Subsequently, we employ the horizontal shift invariance of the fluid by performing a two-dimensional, two-sided, spatial Fourier transformation with respect to x_1 and x_2. Through this transformation, the Laplace-transformed function $\hat{p}(x_i,t)$ is replaced by its transformed counterpart

$$\tilde{p}(\alpha_1,\alpha_2,x_3,s)=\int_{-\infty}^{\infty}\int_{-\infty}^{\infty}\hat{p}(x_i,s)\times\exp[is(\alpha_1x_1+\alpha_2x_2)]dx_1\,dx_2. \tag{12}$$

The inverse Fourier transformation is

$$\hat{p}(x_i,s)=\left(\frac{s}{2\pi}\right)^2\int_{-\infty}^{\infty}\int_{-\infty}^{\infty}\tilde{p}(\alpha_1,\alpha_2,x_3,s)\times\exp[-is(\alpha_1x_1+\alpha_2x_2)]d\alpha_1\,d\alpha_2. \tag{13}$$

For later convenience we have chosen $s\alpha_1$ and $s\alpha_2$ as the Fourier transform parameters.

Application of the forward transformations to Eqs. (7) and (8), followed by the elimination of $\tilde{v}_1$ and $\tilde{v}_2$, results in the transform domain ordinary differential equations

$$\partial_3\tilde{v}_3+s\rho^{-1}(x_3)[\rho(x_3)\kappa(x_3)+\alpha_1^2+\alpha_2^2]\tilde{p}=\tilde{m}(x_3,s)\tilde{p}-\hat{a}(x_3,s)\tilde{p}+\hat{n}(x_3,s)(\alpha_1\tilde{f}_1+\alpha_2\tilde{f}_2)+\tilde{q}, \tag{14}$$

$$\partial_3\tilde{p}+s\rho(x_3)\tilde{v}_3=-\hat{b}(x_3,s)\tilde{v}_3+\tilde{f}_3, \tag{15}$$

where

$$\tilde{m}(x_3,s)=\frac{s\hat{b}(x_3,s)(\alpha_1^2+\alpha_2^2)}{\rho(x_3)[s\rho(x_3)+\hat{b}(x_3,s)]}, \tag{16}$$

$$\hat{n}(x_3,s)=\frac{is}{s\rho(x_3)+\hat{b}(x_3,s)}. \tag{17}$$

If no confusion can occur, some or all of the arguments of the functions are omitted for brevity. Equations (14) and (15) are expressed simultaneously by the state vector differential equation

$$\partial_3\tilde{b}_I+sA_{IJ}(x_3)\tilde{b}_J=K_{IJ}(x_3,s)\tilde{b}_J+\tilde{u}_I, \tag{18}$$

in which we have employed the subscript notation and the summation convention with uppercase Latin subscripts ranging from 1 to 2. The state vector

$$\tilde{b}_I=\begin{pmatrix}\tilde{v}_3\\ \tilde{p}\end{pmatrix} \tag{19}$$

contains the remaining transform domain state quantities of the acoustic wave field. The source is now represented by the notional source vector

$$\tilde{u}_I=\delta(x_3-x_3^S)\begin{pmatrix}\tilde{Q}^N\\ \tilde{F}^N\end{pmatrix}, \tag{20}$$

in which

$$\begin{pmatrix}\tilde{Q}^N\\ \tilde{F}^N\end{pmatrix}=\begin{pmatrix}\hat{Q}^S(s)+\hat{n}(x_3,s)[\alpha_1\hat{F}_1^S(s)+\alpha_2\hat{F}_2^S(s)]\\ \hat{F}_3^S(s)\end{pmatrix}. \tag{21}$$

Further, in Eq. (18) the system matrix

$$A_{IJ}(x_3)=\begin{pmatrix}0 & \gamma(x_3)Y(x_3)\\ \gamma(x_3)/Y(x_3) & 0\end{pmatrix} \tag{22}$$

has been introduced, which has been expressed here in terms of the vertical slowness

$$\gamma(x_3)=[c(x_3)^{-2}+\alpha_1^2+\alpha_2^2]^{1/2}, \tag{23}$$

and the vertical acoustic wave admittance

$$Y(x_3)=\gamma(x_3)/\rho(x_3). \tag{24}$$

In Eq. (23), the acoustic wave speed

$$c(x_3)=[\rho(x_3)\kappa(x_3)]^{-1/2} \tag{25}$$

shows up. For the remainder of this paper it is important that in our case $\gamma(x_3)$ is real and greater than zero for any of the values of α_1 and α_2 that occur in the inverse Fourier transformation in Eq. (13). Our memory matrix

$$K_{IJ}(x_3,s)=\begin{pmatrix}0 & \tilde{m}(x_3,s)-\hat{a}(x_3,s)\\ -\hat{b}(x_3,s) & 0\end{pmatrix}, \tag{26}$$

represents the loss properties of the fluid. We have put the term with this matrix at the right-hand side of Eq. (18) in preparation of the method that will be employed in the next section for finding approximations of the state vector.

III. WKBJ-LIKE ASYMPTOTIC REPRESENTATIONS OF THE TRANSFORM DOMAIN SOLUTION

As the first step in finding approximate solutions of the state vector differential equation, we introduce the wave vector $\tilde{w}_I$ through the linear transformation

$$\tilde{b}_I=N_{IJ}(x_3)\tilde{w}_J. \tag{27}$$

The matrix

$$N_{IJ}(x_3)=\frac{1}{2}\sqrt{2}\begin{pmatrix}Y^{1/2}(x_3) & -Y^{1/2}(x_3)\\ Y^{-1/2}(x_3) & Y^{-1/2}(x_3)\end{pmatrix} \tag{28}$$

consists of columns that are normalized eigenvectors of the system matrix $A_{IJ}(x_3)$. The wave vector components $\tilde{w}_1$ and $\tilde{w}_2$ represent waves that travel in the positive and the negative x_3 direction, respectively. Substitution of the so-called composition relation (27) in Eq. (18) yields the wave vector differential equation

$$\partial_3\tilde{w}_I+s\Lambda_{IJ}(x_3)\tilde{w}_J=\Theta_{IJ}(x_3,s)\tilde{w}_J+N_{IJ}^{-1}(x_3^S)\tilde{u}_J. \tag{29}$$

In this equation there appear the eigenvalue matrix

$$\Lambda_{IJ}(x_3)=\begin{pmatrix}\gamma(x_3) & 0\\ 0 & -\gamma(x_3)\end{pmatrix} \tag{30}$$

of $A_{IJ}(x_3)$, and the coupling matrix

$$\Theta_{IJ}(x_3,s)=\frac{1}{2}Y^{-1}(x_3)[\tilde{m}(x_3,s)-\hat{a}(x_3,s)]\begin{pmatrix}1 & 1\\ -1 & -1\end{pmatrix}+\frac{1}{2}Y(x_3)\hat{b}(x_3,s)\begin{pmatrix}-1 & 1\\ -1 & 1\end{pmatrix}+\Gamma(x_3)\begin{pmatrix}0 & 1\\ 1 & 0\end{pmatrix}, \tag{31}$$

in which

$$\Gamma(x_3)=\frac{\partial_3Y(x_3)}{2Y(x_3)}. \tag{32}$$

The matrix $\Theta_{IJ}(x_3,s)$ depends both on the losses of the medium [the terms with $\tilde{m}(x_3,s)$, $\hat{a}(x_3,s)$, and $\hat{b}(x_3,s)$], and on the inhomogeneity of the medium with regard to its instantaneous behavior [the term with $\Gamma(x_3)$]. Through this matrix, the equations for $\tilde{w}_1$ and $\tilde{w}_2$ become coupled.

Next, we recast the wave vector differential equation into a wave vector integral equation. We begin this process by writing Eq. (29) as two separate equations, and replacing their original right-hand sides by the shifted delta pulse $\delta(x_3-x_3')$. The causal solutions of these new equations, indicated by $\tilde{g}_1$ and $\tilde{g}_2$, are

$$\tilde{g}_1(x_3,x_3')=H(x_3-x_3')\exp\left[-s\int_{x_3'}^{x_3}\gamma(\zeta)d\zeta\right], \tag{33}$$

$$\tilde{g}_2(x_3,x_3')=-H(x_3'-x_3)\exp\left[-s\int_{x_3}^{x_3'}\gamma(\zeta)d\zeta\right]. \tag{34}$$

We then take the original right-hand sides, and consider these as continuous summations of shifted delta pulses. Application of the superposition principle now gives us the wave vector components $\tilde{w}_1$ and $\tilde{w}_2$ as continuous summations of the functions $\tilde{g}_1$ and $\tilde{g}_2$, respectively. In this way we

arrive at an implicit expression for the wave vector in the form of the integral equation

$$\tilde{w}_I = \mathsf{L}_{IJ}\tilde{w}_J + \tilde{h}_I. \tag{35}$$

The term

$$\mathsf{L}_{IJ}\tilde{w}_J = \begin{pmatrix} \int_{-\infty}^{x_3} [\Theta_{11}(x_3',s)\tilde{w}_1(x_3') + \Theta_{12}(x_3',s)\tilde{w}_2(x_3')] \exp\left(-s\int_{x_3}^{x_3'} \gamma\, d\zeta \right) dx_3' \\ -\int_{x_3}^{\infty} [\Theta_{21}(x_3',s)\tilde{w}_1(x_3') + \Theta_{22}(x_3',s)\tilde{w}_2(x_3')] \exp\left(-s\int_{x_3'}^{x_3} \gamma\, d\zeta \right) dx_3' \end{pmatrix} \tag{36}$$

stems from the losses and the inhomogeneity of the medium, and the term

$$\tilde{h}_I = \begin{pmatrix} \frac{1}{2}\sqrt{2}\tilde{a}_1 H(x_3 - x_3^S) \exp\left(-s\int_{x_3}^{x_3^S} \gamma\, d\zeta \right) \\ -\frac{1}{2}\sqrt{2}\tilde{a}_2 H(x_3^S - x_3) \exp\left(-s\int_{x_3^S}^{x_3} \gamma\, d\zeta \right) \end{pmatrix}, \tag{37}$$

with

$$\tilde{a}_1 = \tilde{F}^N Y^{1/2}(x_3^S) + \tilde{Q}^N Y^{-1/2}(x_3^S), \tag{38}$$

$$\tilde{a}_2 = \tilde{F}^N Y^{1/2}(x_3^S) - \tilde{Q}^N Y^{-1/2}(x_3^S), \tag{39}$$

originates from the source.

Subsequently, we have to solve the wave vector integral equation. Repeated substitution of Eq. (35) into itself yields, under very general conditions, a convergent Neumann series solution (cf. De Hoop[25]). As opposed to the homogeneous case, for a general inhomogeneous, lossy medium, the analytical evaluation of the higher-order terms of this series will be virtually impossible, and their numerical determination will require much computational effort, especially in combination with the inverse transformation. Therefore, in the present paper we take another approach. Knowing that $a(x_3,t)$ and $b(x_3,t)$ behave at most as a delta pulse in time, and taking into account Eqs. (16), (31), and (32), we conclude that the functions $\Theta_{IJ}(x_3,s)$ are at most of order zero in s. As a consequence, repeated integration by parts of the terms of the Neumann series solution will lead to a WKBJ-like asymptotic expansion of the wave vector in inverse powers of s (cf. Young[26]). This leads us to the idea of approximating the wave vector by higher-order WKBJ-like asymptotic representations. In Secs. III A and III B, the two cases that have been described in Sec. I will be considered.

A. Entirely inhomogeneous fluid

When an inhomogeneous fluid fills the entire space, we approximate the wave vector by

$$\tilde{w}_I \sim \exp\left(-s\int_{x_3^S}^{x_3} \gamma\, d\zeta \right) \sum_{n=0}^{N} s^{-n} P_I^{(n)}(x_3,s) \quad (x_3 > x_3^S), \tag{40}$$

$$\tilde{w}_I \sim \exp\left(-s\int_{x_3}^{x_3^S} \gamma\, d\zeta \right) \sum_{n=0}^{N} s^{-n} Q_I^{(n)}(x_3,s) \quad (x_3 < x_3^S). \tag{41}$$

These are Nth-order WKBJ-like asymptotic representations of the wave vector for large values of s. The exponential parts are supposed to give the propagation of the wavefront from the source to the point of observation, and the summation parts describe the behavior of the wave field at the point of observation after the arrival of the wavefront. The evaluation of the components of $P_I^{(n)}$ and $Q_I^{(n)}$ forms the subject of Sec. IV A.

B. Homogeneous fluid above and inhomogeneous fluid below

When the space is subdivided in an upper half-space that is homogeneous and lossless, and a lower half-space that is the inhomogeneous and lossy, then different situations arise, depending on the relative vertical positions of the source, the point of observation, and the interface in between the half-spaces. In this paper, two of these situations will be investigated in detail.

In the first situation we assume that the source is located in the homogeneous half-space and the point of observation lies in the inhomogeneous, lossy half-space ($x_3^S < x_3^{\mathrm{int}} < x_3$). In this situation, the asymptotic representation of Eq. (40) is maintained as an approximation of the wave vector. The corresponding components of $P_I^{(n)}$ will be evaluated in Sec. IV B.

In the second situation we consider a source and a point of observation that are both located in the upper homogeneous half-space ($x_3^S < x_3^{\mathrm{int}} \wedge x_3 < x_3^{\mathrm{int}}$). Now it follows from Eqs. (35)–(37) that

$$\tilde{w}_1 = \tfrac{1}{2}\sqrt{2}\tilde{a}_1 H(x_3 - x_3^S) \exp[-s\gamma(x_3^S - x_3)], \tag{42}$$

$$\tilde{w}_2 = -\tfrac{1}{2}\sqrt{2}\tilde{a}_2 H(x_3^S - x_3) \exp[-s\gamma(x_3 - x_3^S)] - \exp[-s\gamma(x_3^{\mathrm{int}} - x_3)]\tilde{w}_2(x_3^{\mathrm{int}} + 0), \tag{43}$$

where $\gamma = [(c^{\mathrm{hom}})^{-2} + \alpha_1^2 + \alpha_2^2]^{1/2}$, and where the argument $x_3^{\mathrm{int}} + 0$ indicates that the limit $x_3 \downarrow x_3^{\mathrm{int}}$ must be taken. The situation $x_3^S < x_3^{\mathrm{int}} < x_3$ provides us with appropriate approximations for $\tilde{w}_2(x_3^{\mathrm{int}} + 0)$. Using these in the present situation, we get

$$\tilde{w}_2 \sim -\tfrac{1}{2}\sqrt{2}\tilde{a}_2 H(x_3^S - x_3) \exp[-s\gamma(x_3 - x_3^S)] - \exp\{-s\gamma[(x_3^{\mathrm{int}} - x_3) + (x_3^{\mathrm{int}} - x_3^S)]\} \times \sum_{n=0}^{N} s^{-n} P_2^{(n)}(x_3^{\mathrm{int}} + 0, s). \tag{44}$$

The second terms on the right-hand sides of Eqs. (43) and (44) represent the reflection from the inhomogeneous half-space. The other terms in Eqs. (42)–(44) represent the direct wave from the source. The determination of the coefficients $P_2^{(n)}(x_3^{\rm int}+0,s)$ will be addressed in Sec. IV B. In Sec. VI the choice of an appropriate value of N will be discussed.

IV. RECURRENCE SCHEME FOR THE COEFFICIENTS OF THE ASYMPTOTIC REPRESENTATIONS

In Secs. IV A and IV B we will explain how the coefficients of the asymptotic representations are found.

A. Entirely inhomogeneous fluid

Substitution of Eqs. (40) and (41) into Eq. (35), followed by differentiation of the equations for $\tilde{w}_2$ with respect to x_3 and collection of the terms with equal powers of s, results in an *implicit* (i.e., with the unknown quantities being defined in terms of themselves) recurrence scheme for the components of $P_I^{(n)}$ and $Q_I^{(n)}$. We find for $n=0$

$$P_1^{(0)}=\tfrac{1}{2}\sqrt{2}\tilde{a}_1+\int_{x_3^S}^{x_3}\Theta_{11}P_1^{(0)}dx_3', \tag{45}$$

$$P_2^{(0)}=0, \tag{46}$$

$$Q_1^{(0)}=0, \tag{47}$$

$$Q_2^{(0)}=-\tfrac{1}{2}\sqrt{2}\tilde{a}_2-\int_{x_3}^{x_3^S}\Theta_{22}Q_2^{(0)}dx_3', \tag{48}$$

and for $n\geqslant 1$

$$P_1^{(n)}=\int_{x_3^S}^{x_3}[\Theta_{11}P_1^{(n)}+\Theta_{12}P_2^{(n)}]dx_3'+Q_1^{(n)}(x_3^S), \tag{49}$$

$$P_2^{(n)}=\frac{-1}{2\gamma}[\Theta_{21}P_1^{(n-1)}+\Theta_{22}P_2^{(n-1)}-\partial_3P_2^{(n-1)}], \tag{50}$$

$$Q_1^{(n)}=\frac{1}{2\gamma}[\Theta_{11}Q_1^{(n-1)}+\Theta_{12}Q_2^{(n-1)}-\partial_3Q_1^{(n-1)}], \tag{51}$$

$$Q_2^{(n)}=\int_{x_3}^{x_3^S}[\Theta_{21}Q_1^{(n)}+\Theta_{22}Q_2^{(n)}]dx_3'+P_2^{(n)}(x_3^S). \tag{52}$$

We have maintained the exact functions $\Theta_{IJ}(x_3,s)$ in this scheme because in our case it will be difficult to obtain accurate approximations of the functions $\Theta_{IJ}(x_3,s)$ in inverse powers of s within a reasonably low number of terms. This will be the case since we will employ memory functions with characteristic times that are small on the time scale that will be used for the wave field quantities. Since therefore the summation parts of the asymptotic representations will not only contain inverse powers of s, as with WKBJ asymptotics, but also the functions $\hat{a}(x_3,s)$, $\hat{b}(x_3,s)$, and $\tilde{m}(x_3,s)$, and/or their derivatives $\partial_3^k\hat{a}(x_3,s)$, $\partial_3^k\hat{b}(x_3,s)$, and $\partial_3^k\tilde{m}(x_3,s)$, we have adopted the notion WKBJ-*like* asymptotics in this paper.

To evaluate the recurrence scheme, we assume that on the closed interval between x_3^S (source level) and $x_3^{\rm obs}$ (observation level) the functions $\Theta_{IJ}(x_3,s)$, $1/2\gamma(x_3)$, and $\Theta_{IJ}(x_3,s)/2\gamma(x_3)$ may be approximated by the following Taylor polynomials

$$\Theta_{IJ}(x_3,s)\approx\sum_{m=0}^{M}\Theta_{IJ}^{(m)}(s)(x_3-x_3^S)^m, \tag{53}$$

$$\frac{1}{2\gamma(x_3)}\approx\sum_{m=0}^{M}\gamma^{(m)}(x_3-x_3^S)^m, \tag{54}$$

$$\frac{\Theta_{IJ}(x_3,s)}{2\gamma(x_3)}\approx\sum_{m=0}^{M}D_{IJ}^{(m)}(s)(x_3-x_3^S)^m. \tag{55}$$

The last equation is most easily obtained by multiplying the first two equations and omitting the terms of orders larger than M. Now our goal is to find approximate expressions for $P_I^{(n)}$ and $Q_I^{(n)}$ in the form of Taylor polynomials like

$$P_I^{(n)}(x_3,s)=\sum_{l=0}^{L}P_I^{(n,l)}(s)(x_3-x_3^S)^l. \tag{56}$$

Substitution of Eqs. (53)–(56) into Eqs. (45)–(52) and collection of the terms with equal powers of $(x_3-x_3^S)$ leads to an *explicit* (i.e., with the unknown quantities being defined only in terms of known quantities) recurrence scheme for the coefficients $P_1^{(n,l)}$, $P_2^{(n,l)}$, $Q_1^{(n,l)}$, and $Q_2^{(n,l)}$. For $n=0$ we obtain

$$P_1^{(0,l)}=\begin{cases}\tfrac{1}{2}\sqrt{2}\widetilde{a_1} & (l=0)\\ \dfrac{1}{l}\displaystyle\sum_{m=0}^{l-1}\Theta_{11}^{(m)}P_1^{(0,l-m-1)} & (l\geqslant 1),\end{cases} \tag{57}$$

$$P_2^{(0,l)}=0 \quad (l\geqslant 0), \tag{58}$$

$$Q_1^{(0,l)}=0 \quad (l\geqslant 0), \tag{59}$$

$$Q_2^{(0,l)}=\begin{cases}-\tfrac{1}{2}\sqrt{2}\tilde{a}_2 & (l=0)\\ \dfrac{-1}{l}\displaystyle\sum_{m=0}^{l-1}\Theta_{22}^{(m)}Q_2^{(0,l-m-1)} & (l\geqslant 1),\end{cases} \tag{60}$$

and for $n\geqslant 1$ we get

$$P_1^{(n,l)}=\begin{cases}Q_1^{(n,0)} & (l=0)\\ \dfrac{1}{l}\displaystyle\sum_{m=0}^{l-1}\Theta_{11}^{(m)}P_1^{(n,l-m-1)}\\ \qquad+\Theta_{12}^{(m)}P_2^{(n,l-m-1)} & (l\geqslant 1),\end{cases} \tag{61}$$

$$P_2^{(n,l)}=\sum_{m=0}^{l}[-D_{21}^{(m)}P_1^{(n-1,l-m)}-D_{22}^{(m)}P_2^{(n-1,l-m)}+(l-m+1)\gamma^{(m)}P_2^{(n-1,l-m+1)}] \quad (l\geqslant 0), \tag{62}$$

$$Q_1^{(n,l)}=\sum_{m=0}^{l}[D_{11}^{(m)}Q_1^{(n-1,l-m)}+D_{12}^{(m)}Q_2^{(n-1,l-m)}-(l-m+1)\gamma^{(m)}Q_1^{(n-1,l-m+1)}] \quad (l\geqslant 0), \tag{63}$$

$$Q_2^{(n,l)}=\begin{cases} P_2^{(n,0)} & (l=0) \\ \dfrac{-1}{l}\displaystyle\sum_{m=0}^{l-1}\Theta_{21}^{(m)}Q_1^{(n,l-m-1)} & \\ \quad+\Theta_{22}^{(m)}Q_2^{(n,l-m-1)} & (l\geqslant 1). \end{cases} \tag{64}$$

Investigation of the recurrence scheme reveals that the first l terms of the components of $P_1^{(n)}$, $P_2^{(n)}$, $Q_1^{(n)}$, and $Q_2^{(n)}$ are fully determined by the terms of order $m\leqslant l+n-1$ in Eqs. (53)–(55). Therefore, it suffices if for given L and N we take $M=L+N-1$. The recurrence scheme allows for a straightforward implementation in a symbolic manipulation program.

B. Homogeneous fluid above and inhomogeneous fluid below

An implicit recurrence scheme for the components of $P_1^{(n)}$ in the situation $x_3^S<x_3^{\rm int}<x_3$ is obtained in the same way as for an entirely inhomogeneous fluid, except that now care must be taken of the fact that $\Theta_{IJ}(x_3,s)=0$ for $x_3<x_3^{\rm int}$. We find for $n=0$

$$P_1^{(0)}=\tfrac{1}{2}\sqrt{2}\tilde{a}_1+\int_{x_3^{\rm int}}^{x_3}\Theta_{11}P_1^{(0)}dx_3', \tag{65}$$

$$P_2^{(0)}=0, \tag{66}$$

and for $n\geqslant 1$

$$P_1^{(n)}=\int_{x_3^{\rm int}}^{x_3}[\Theta_{11}P_1^{(n)}+\Theta_{12}P_2^{(n)}]dx_3', \tag{67}$$

$$P_2^{(n)}=\frac{-1}{2\gamma}[\Theta_{21}P_1^{(n-1)}+\Theta_{22}P_2^{(n-1)}-\partial_3 P_2^{(n-1)}]. \tag{68}$$

Now we assume that on $[x_3^{\rm int};\, x_3^{\rm obs}]$ the approximations

$$\Theta_{IJ}(x_3,s)\approx\sum_{m=0}^{M}\theta_{IJ}^{(m)}(s)(x_3-x_3^{\rm int})^m, \tag{69}$$

$$\frac{1}{2\gamma(x_3)}\approx\sum_{m=0}^{M}\gamma^{(m)}(x_3-x_3^{\rm int})^m, \tag{70}$$

$$\frac{\Theta_{IJ}(x_3,s)}{2\gamma(x_3)}\approx\sum_{m=0}^{M}D_{IJ}^{(m)}(s)(x_3-x_3^{\rm int})^m, \tag{71}$$

may be employed. Our aim is to find approximate expressions for $P_I^{(n)}$ in the form of the Taylor polynomials

$$P_I^{(n)}(x_3,s)=\sum_{l=0}^{L}P_I^{(n,l)}(s)(x_3-x_3^{\rm int})^l. \tag{72}$$

If we substitute Eqs. (69)–(72) into Eqs. (65)–(68) and collect the terms with equal powers of $(x_3-x_3^{\rm int})$, an explicit recurrence scheme for the coefficients $P_1^{(n,l)}$ and $P_2^{(n,l)}$ is obtained. For $n=0$ we get

$$P_1^{(0,L)}=\begin{cases} \tfrac{1}{2}\sqrt{2}\tilde{a}_1 & (l=0) \\ \dfrac{1}{l}\displaystyle\sum_{m=0}^{l-1}\Theta_{11}^{(m)}P_1^{(0,l-m-1)} & (l\geqslant 1) \end{cases}, \tag{73}$$

$$P_2^{(0,l)}=0 \quad (l\geqslant 0). \tag{74}$$

and for $n\geqslant 1$ we find

$$P_1^{(n,l)}=\begin{cases} 0 & (l=0) \\ \dfrac{1}{l}\displaystyle\sum_{m=0}^{l-1}\Theta_{11}^{(m)}P_1^{(n,l-m-1)} & \\ \quad+\Theta_{12}^{(m)}P_2^{(n,l-m-1)} & (l\geqslant 1), \end{cases} \tag{75}$$

$$P_2^{(n,l)}=\sum_{m=0}^{l}[-D_{21}^{(m)}P_1^{(n-1,l-m)}-D_{22}^{(m)}P_2^{(n-1,l-m)} \\ +(l-m+1)\gamma^{(m)}P_2^{(n-1,l-m+1)}] \quad (l\geqslant 0). \tag{76}$$

Again it is sufficient if $M=L+N-1$ is taken for given L and N. If $x_3^S<x_3^{\rm int}\wedge x_3<x_3^{\rm int}$, only $P_2^{(n)}(x_3^{\rm int}+0,s)$ plays a role [see Eq. (44)], and solely the zeroth-order terms in the Taylor polynomial of $P_2^{(n)}(x_3)$ are important. Consequently, we may set $L=0$ in this situation, and for $n\leqslant N$ the exact $P_2^{(n)}(x_3^{\rm int}+0,s)$ are obtained if we take $M=N-1$. The recurrence scheme may easily be implemented in a symbolic manipulation program.

V. INVERSE TRANSFORMATION

Once an asymptotic representation of the wave vector has been found, Eq. (27) may be used to obtain the associated state vector. The following stage is the transformation of the components of this state vector back to the space-time domain. This will be performed with the aid of the Cagniard–De Hoop method (Cagniard,[24] De Hoop[18,27]). To explain the inversion process, we employ as an example the acoustic pressure wave that is due to a source of volume injection in a homogeneous, lossless half-space that is located above an inhomogeneous, lossy half-space ($x_3^S<x_3^{\rm int}$). Before the Cagniard–De Hoop method will be invoked, we will first investigate the structure of the transform domain expressions for this acoustic pressure.

A. The structure of the transform domain expression

To avoid the loose occurrence of $\alpha_1^2+\alpha_2^2$ in the expression for $\tilde{m}(x_3,s)$, Eq. (16) is rewritten as

$$\tilde{m}(x_3,s)=\hat{M}(x_3,s)[\gamma^2(x_3)-c^{-2}(x_3)], \tag{77}$$

in which

$$\hat{M}(x_3,s)=\frac{s\hat{b}(x_3,s)}{\rho(x_3)[s\rho(x_3)+\hat{b}(x_3,s)]} \tag{78}$$

is a new memory function. From Eqs. (23), (24), (31), (32), and (77) it can be deduced that the coefficients $\Theta_{IJ}^{(m)}$, $\gamma^{(m)}$, and $D_{IJ}^{(m)}$ in Eqs. (69)–(71) consist of terms that contain integer powers of $\gamma(x_3^{\rm int}+0)=\gamma(x_3^S)$. In many of these terms the memory functions $\hat{a}(x_3^{\rm int}+0,s)$, $\hat{b}(x_3^{\rm int}+0,s)$, $\hat{M}(x_3^{\rm int}+0,s)$, and/or several of their derivatives $\partial_3^k\hat{a}(x_3^{\rm int}+0,s)$, $\partial_3^k\hat{b}(x_3^{\rm int}+0,s)$, $\partial_3^k\hat{M}(x_3^{\rm int}+0,s)$, occur as well. On the other hand, Eqs. (21), (38), and (39) show that in the present case

$$\tilde{a}_1=-\tilde{a}_2=Y^{-1/2}(x_3^S)\hat{Q}^S. \tag{79}$$

Combining the preceding facts with Eqs. (73)–(76), it becomes clear that $P_1^{(n,l)}$ and $P_2^{(n,l)}$ are composed of terms of the form

$$C_1\hat{Q}^S\hat{\Pi}(s)Y^{-1/2}(x_3^S)\gamma^{-\eta}(x_3^S). \tag{80}$$

In this expression, C_1 indicates a real constant. The function $\hat{\Pi}(s)$ stands for a certain product of the recently mentioned memory functions and/or several of their derivatives. The parameter η is an integer that is either positive, zero, or negative. With the aid of Eqs. (27), (40), (42), (44), and (72), we find that the transform domain acoustic pressure $\tilde{p}$ consists of terms of the form

$$C_2\hat{Q}^S(x_3^{\rm obs}-x_3^{\rm int})^l s^{-n}\hat{\Pi}(s)\tfrac{1}{2}Y^{-1/2}(x_3^S)Y^{-1/2}(x_3^{\rm obs})\gamma^{-\eta}(x_3^S)$$
$$\times\exp\left(-s\int\gamma\,d\zeta\right), \tag{81}$$

in which C_2 is a real constant and l and n are non-negative integers. In view of the further analysis it is convenient to write

$$\tilde{p}=s^2\hat{Q}^S\tilde{G}. \tag{82}$$

Here the Green's function $\tilde{G}$ has been introduced as the acoustic pressure that is generated by a source of volume injection rate with a unit ramp source signature Q^S (see Verweij,[14] Appendix C). This Green's function, in turn, is composed of a number of terms of the form

$$C_3 s^{-n}\hat{\Pi}(s)\tilde{\Upsilon}(\eta), \tag{83}$$

with

$$\tilde{\Upsilon}(\eta)=\tfrac{1}{2}s^{-2}Y^{-1/2}(x_3^S)Y^{-1/2}(x_3^{\rm obs})\gamma^{-\eta}(x_3^S)$$
$$\times\exp\left(-s\int\gamma\,d\zeta\right). \tag{84}$$

The constant C_3 is real: it is obtained by summing the products $C_2(x_3^{\rm obs}-x_3^{\rm int})^l$ of all the terms of the form (81) with corresponding n, $\hat{\Pi}(s)$, and η. When higher-order asymptotic representations are involved, the task of finding out which functions $\hat{\Pi}(s)$ show up in $\tilde{G}$ is almost impossible to carry out by hand, but forms no problem for a symbolic manipulation program (we have written a simple routine which employs the commands *Collect*, *Exponent*, and *Coefficient* of Mathematica[28,29]). The same is true for the determination of the constants C_3 belonging to each of the particular combinations of n, $\hat{\Pi}(s)$, and η.

The function $\tilde{\Upsilon}(\eta)$ that shows up in each term of the form (83) is the only part that depends on s as well as on α_1 and α_2, and only for the inversion of this part the Cagniard–De Hoop method needs to be employed. For the case $x_3^S<x_3^{\rm int}<x_3^{\rm obs}$, the space-time domain function $\Upsilon(\eta)$ will be presented in Sec. V B, while the case $x_3^S<x_3^{\rm int}\wedge x_3^{\rm obs}<x_3^{\rm int}$ will be addressed in Sec. V C. The other parts in (83) solely depend on s and only have to undergo a transformation from the Laplace domain back to the time domain. The inversion of s^{-n} is obtained by inspection. In the same way, the time domain function $\Pi(t)$ is recognized as the convolution of the relevant time domain memory functions $a(x_3^{\rm int}+0,t)$, $b(x_3^{\rm int}+0,t)$, $M(x_3^{\rm int}+0,t)$, and/or their derivatives $\partial_3^k a(x_3^{\rm int}+0,t)$, $\partial_3^k b(x_3^{\rm int}+0,t)$, $\partial_3^k M(x_3^{\rm int}+0,t)$. These constituents of $\Pi(t)$ are either known from the start (a, b and their derivatives), or are assumed to be obtainable by inspection (M and its derivatives). Convolution of the space-time domain counterparts of the functions in (83) yields the corresponding contribution to the space-time domain Green's function G. Once this function has been found, the space-time domain acoustic pressure follows from the time-domain version of Eq. (82), which is

$$p=\partial_t^2[Q^S*G]. \tag{85}$$

Since we have employed asymptotic representations to approximate the exact transform domain wave vector, the space-time domain functions p and G that have been derived in this section are approximations of the exact space-time domain acoustic pressure and the associated Green's function. This will become evident in Sec. VI.

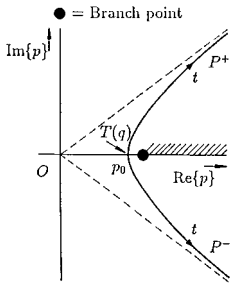

FIG. 2. Example of a Cagniard contour.

B. The case $x_3^S<x_3^{\rm int}<x_3^{\rm obs}$

When $x_3^S<x_3^{\rm int}<x_3^{\rm obs}$ (source above the interface and observation point below the interface), the vertical slowness $\gamma(x_3)$ that occurs in the integral in Eq. (84) may not be considered a constant function of x_3, and the inverse transformation of $\tilde{\Upsilon}(\eta)$ must be performed with the aid of the Cagniard–De Hoop method for continuously layered configurations (Verweij and De Hoop[30]). In all cases in which our WKBJ-like asymptotics are useful, the result of this process is

$$\Upsilon(\eta)=\frac{1}{2\pi^2}H(t-T_{\rm arr})\int_0^{Q(t)}{\rm Im}\{\overline{Y}^{-1/2}(x_3^S)\overline{Y}^{-1/2}(x_3^{\rm obs})$$
$$\times\overline{\gamma}^{-\eta}(x_3^S)\partial_t p\}dq, \tag{86}$$

In this equation, p is a (complex) horizontal slowness that satisfies

$$t=pr+\int_{x_3^S}^{x_3^{\rm obs}}\overline{\gamma(\zeta)}\,d\zeta={\rm real}. \tag{87}$$

In both foregoing equations the bar indicates that the vertical slowness has been changed into

$$\overline{\gamma(x_3)}=[c^{-2}(x_3)-p^2+q^2]^{1/2}. \tag{88}$$

The points p that satisfy Eq. (87) and that are relevant in view of the Cagniard–De Hoop method form a so-called Cagniard contour in the complex p plane. An example of a Cagniard contour is depicted in Fig. 2. Each Cagniard contour is dependent on the parameter q and is parameterized by the real variable t. The value of t associated with the point where a Cagniard contour crosses the real p axis is indicated by $T(q)$, the unique inverse of which is denoted by $Q(t)$ [not

to be confused with the source signature $Q^S(t)$]. The quantity $T_{\mathrm{arr}}=T(0)$ is the arrival time of the wavefront. In general, the evaluation of the expression for $\Upsilon(\eta)$ [i.e., finding $Q(t)$, performing the integration with respect to q, and obtaining the value of the integrand by finding the relevant root of Eq. (87) and substituting this in the expression of the integrand] must be performed numerically.

C. The case $x_3^S<x_3^{\mathrm{int}}\wedge x_3^{\mathrm{obs}}<x_3^{\mathrm{int}}$

When $x_3^S<x_3^{\mathrm{int}}\wedge x_3^{\mathrm{obs}}<x_3^{\mathrm{int}}$ (source and observation point above the interface), everywhere in Eq. (84) the same vertical slowness $\gamma=[(c^{\mathrm{hom}})^{-2}+\alpha_1^2+\alpha_2^2]^{1/2}$ shows up. As a consequence, $\tilde{\Upsilon}(\eta)$ may be written as

$$\tilde{\Upsilon}(\eta)=\tfrac{1}{2}\,s^{-2}\rho\,\gamma^{-(\eta+1)}\exp[-s\,\gamma z], \tag{89}$$

where $\rho=\rho^{\mathrm{hom}}$, and z is the relevant vertical length of the path between the source and the point of observation. Now the Cagniard–De Hoop method enables us to find the space-time domain counterpart of the function $\tilde{\Upsilon}(\eta)$ in a completely analytical way (Verweij[12,14]).

After defining the horizontal offset r and the total source–receiver distance R as

$$r=[(x_1^{\mathrm{obs}})^2+(x_2^{\mathrm{obs}})^2]^{1/2}, \tag{90}$$

$$R=(r^2+z^2)^{1/2}, \tag{91}$$

the space-time domain function $\Upsilon(\eta)$ may be written as

$$\Upsilon(\eta)=\frac{\rho}{2\pi^2R}\,H(t-T_{\mathrm{arr}})\int_0^{\pi/2}\mathrm{Re}\{\overline{\gamma^{-}}^{\eta}\}\,d\psi. \tag{92}$$

In this equation, the arrival time

$$T_{\mathrm{arr}}=R/c, \tag{93}$$

and the vertical slowness

$$\overline{\gamma}=\epsilon-i\sigma\,\cos\,\psi, \tag{94}$$

show up, in which

$$\epsilon=\frac{zt}{R^2}, \tag{95}$$

$$\sigma=\frac{r}{R^2}\left(t^2-\frac{R^2}{c^2}\right)^{1/2}. \tag{96}$$

For $\eta=0$, Eq. (92) gives

$$\Upsilon(0)=\frac{\rho}{4\pi R}\,H(t-T_{\mathrm{arr}}). \tag{97}$$

For $\eta=1$, we find that

$$\Upsilon(1)=\frac{\rho}{2\pi^2R}\,H(t-T_{\mathrm{arr}})\int_0^{\pi/2}\mathrm{Re}\left\{\frac{1}{\epsilon-i\sigma\,\cos\,\psi}\right\}d\psi$$

$$=\frac{\rho}{4\pi R}\,H(t-T_{\mathrm{arr}})(\epsilon^2+\sigma^2)^{-1/2}. \tag{98}$$

Substitution of Eqs. (95) and (96) then yields

$$\Upsilon(1)=\frac{\rho}{4\pi}\,H(t-T_{\mathrm{arr}})\left(t^2-\frac{r^2}{c^2}\right)^{-1/2}. \tag{99}$$

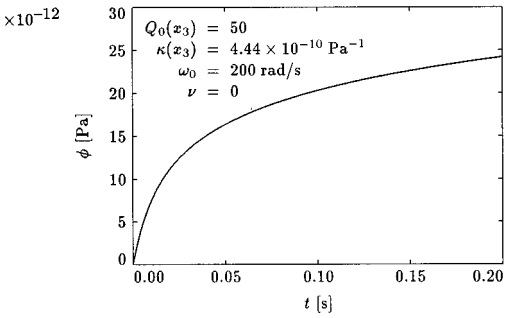

FIG. 3. The creep function ϕ versus time for $Q_0(x_3)=50$ and $\kappa(x_3)=4.44\times10^{-10}$ Pa^{-1}.

For $\eta\geqslant 2$, we find the function $\Upsilon(\eta)$ by differentiating the right-hand side of Eq. (98) $(\eta-1)$ times with respect to ϵ, followed by substituting Eqs. (95) and (96) into the resulting expression. For $\eta\leqslant 0$, we obtain $\Upsilon(\eta)$ through substitution of Eq. (94) into Eq. (92), evaluation of the resulting integral, and substitution of Eqs. (95) and (96) into the resulting expression. Symbolic manipulation enables us to generate the analytical results for all relevant $\Upsilon(\eta)$ in an easy manner.

VI. NUMERICAL RESULTS

In this section we will illustrate the numerical capabilities of our method by presenting results for the space-time domain acoustic wave field in several simplified versions of marine seismic configurations. This implies that the quantity of interest is the acoustic pressure, and that the point source is of the volume injection type. All configurations consist of a homogeneous, lossless upper half-space (water; the effects of the surface are discarded) and an inhomogeneous and/or lossy lower half-space (subsurface geology). The interface in between these half-spaces is located at $x_3^{\mathrm{int}}=100$ m, the point source is placed at the level $x_3^S=50$ m, and the point of observation is given the vertical position $x_3^{\mathrm{obs}}=0$ m, i.e., the source and the point of observation are situated in the upper half-space and Secs. III B, IV B, and V C apply. In this case it is interesting to look at the reflection coming from the lower half-space. This reflection is represented by the second term of $\tilde{w}_2$ in Eq. (44). The contribution of the direct wave, which is represented by $\tilde{w}_1$ in Eq. (42), is in the present case trivial and will not be taken into account. To describe the losses of the equivalent fluid in the lower half-space, we introduce specific creep functions $\phi(x_3,t)$, which in turn define memory functions $a(x_3,t)=\partial_t^2\phi(x_3,t)$. Further we follow the literature and take $b(x_3,t)=0$ everywhere in the lower half-space. Our creep functions are of the form

$$\phi(x_3,t)=\begin{cases}\dfrac{\kappa(x_3)\Delta(x_3)}{\nu}\,[{}_1F_1(-\nu,1;-\omega_0t)-1]H(t)\\ \quad(-1\leqslant\nu\leqslant1;\nu\neq0)\\ \kappa(x_3)\Delta(x_3)[\,\gamma_{\mathrm{euler}}+E_1(\omega_0t)+\ln(\omega_0t)]H(t)\\ \quad(\nu=0),\end{cases} \tag{100}$$

where $\kappa(x_3)$ is the compressibility, and

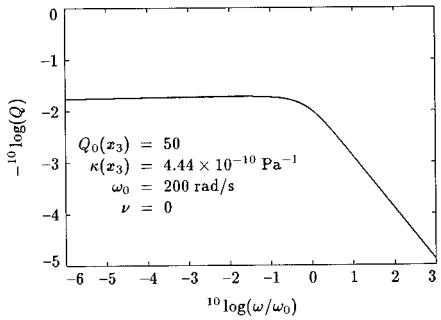

FIG. 4. The quality factor Q versus angular frequency for a medium with the creep function of Fig. 3.

$$\Delta(x_3) = \frac{2}{\pi Q_0(x_3)}. \tag{101}$$

The symbols ${}_1F_1$ and E_1 denote the confluent hypergeometric function and the exponential integral, respectively. This causal creep function is a depth-dependent version of the function that has been derived by Strick[31] for modeling the viscoelastic behavior of a large class of materials. The parameter ν determines the type of loss behavior of the equivalent fluid. It ranges from $\nu=-1$ (three element model), via $\nu=0$ (''constant-Q'' model; Becker creep), to $\nu=1$ (Maxwell model). The amount of loss at a certain level x_3 is inversely proportional to the value of the depth-dependent parameter $Q_0(x_3)$. The parameter ω_0 indicates the angular frequency beyond which the spectral plot of the quality factor Q of the medium increases monotonically for any value of ν. The behavior of Q for angular frequencies lower than ω_0 depends on the value of ν: for ν sufficiently greater than zero it increases with increasing frequency, for ν in the vicinity of zero it approximates a constant function of frequency with the value $Q_0(x_3)$, and for ν sufficiently smaller than zero it decreases with increasing frequency. In all the examples we take $\nu=0$, since this gives our equivalent fluid the ''constant-Q'' behavior that is shown by many practical solids, among which many types of rock. Further, in all our examples a source signature is applied for which it suffices to take $\omega_0=200$ rad/s. A plot of the thus defined creep function versus time for $Q_0(x_3)=50$ and $\kappa(x_3)=4.44\times10^{-10}$ Pa^{-1} is given in Fig. 3. In Fig. 4 the corresponding behavior of Q versus angular frequency is presented.

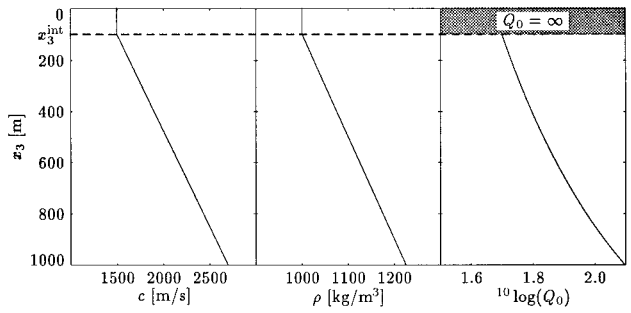

FIG. 5. The depth dependence of the wave speed c, the mass density ρ, and the parameter Q_0, for medium No. 1.

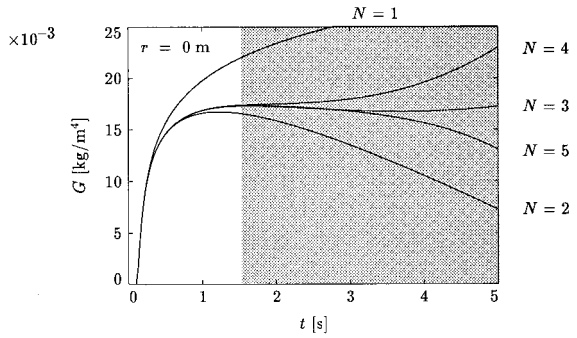

FIG. 6. Several approximate Green's functions G for medium No. 1 and a horizontal offset $r=0$ m. For $t\leqslant1.5$ s the differences between the subsequent higher-order approximations decrease (unshaded region), while for $t>1.5$ s the subsequent approximations diverge (shaded region).

Our first set of numerical results has been generated for an acoustic wave that reflects from the lower part of medium No. 1 given in Fig. 5. The creep function and quality factor in Fig. 3 and Fig. 4, respectively, refer to the loss behavior of this medium just below $x_3=x_3^{\rm int}$. Several approximate Green's functions for medium No. 1 and a horizontal offset $r=0$ m are depicted in Fig. 6. The value of N indicates the order of the asymptotic representation. We see that before approximately $t=1.5$ s (unshaded region) the differences between the subsequent higher-order approximations decrease: the approximations of order $N\geqslant3$ are even visibly indistinguishable. We assume that as soon as the latter is the case, the exact Green's function is arrived at. However, beyond approximately $t=1.5$ s (shaded region) the subsequent approximations diverge. The fact that useful results are generated only up until a specific time instant is a consequence of the application of WKBJ-like asymptotics and determines the applicability of the method in each specific case. A good strategy to find an appropriate value of N is to start with a low value and to increment it until the subsequent approximations clearly begin to coincide on a certain interval beginning with the arrival time. Obviously, in the present case this interval ranges from the arrival time to about $t=1.5$ s, and on this interval it suffices to take $N=3$.

In Fig. 7, the Green's function is shown for the case $r=300$ m. This graph, as well as any other graph of a Green's function that follows, actually depicts the lowest-

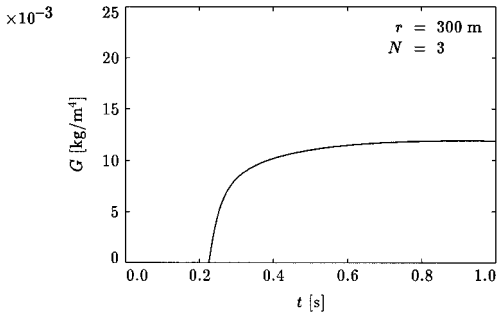

FIG. 7. The Green's function G for medium No. 1 and a horizontal offset $r=300$ m.

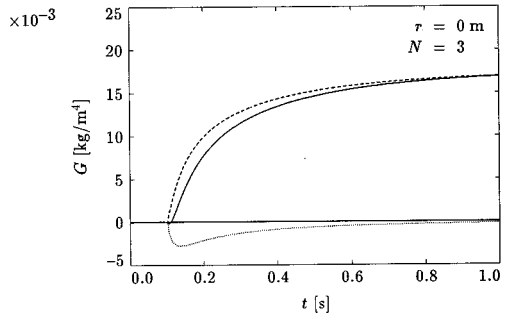

FIG. 8. The Green's functions G for medium No. 1 (solid line), a medium with the same wave speed and mass density as medium No. 1 but without losses (dashed line), and a medium with the same losses as medium No. 1 but with the constant wave speed $c=1500$ m/s and the constant mass density $\rho=1000$ kg/m^3 (dotted line). All three graphs apply to a horizontal offset $r=0$ m.

order member of the approximations that are visibly indistinguishable on the indicated time interval. If the horizontal offset is increased, the time interval on which the higher-order approximations overlay each other will in general shorten. From some value of the horizontal offset onwards, the approximations will diverge at any time instant, even at the arrival time. To understand why in this case the method is unable to deal with very high horizontal offsets, we turn our attention to the generalized rays that may be distinguished in the Neumann series solution (De Hoop,[25] Verweij and De Hoop,[30] Verweij[13]). Let us consider the path of a ray that originates at the source, reflects somewhere in the lower half-space, and arrives at the point of observation. For low values of the horizontal offset, the rays that reflect at the interface $x_3=x_3^{\text{int}}$ form the fastest path from the source, via the interface, to the receiver, and the arrival time corresponds to the time delay given by the exponential function in the second term of Eq. (44). The maximum value of the horizontal offset for which this is the case is for the present configuration at least $r=573.6$ m. For lower values of the horizontal offset there are no turning rays below the interface, so no rays will arrive earlier than the rays reflecting at the interface. For values higher than $r=573.6$ m there exist turning rays below the interface. These may arrive earlier than the

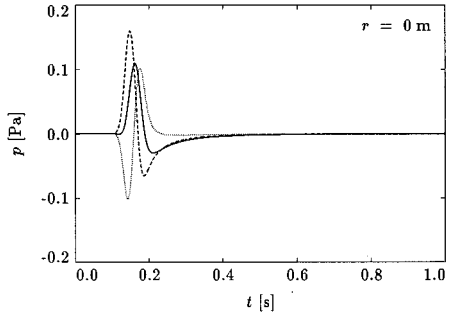

FIG. 9. The acoustic pressures p for medium No. 1 (solid line), a medium with the same wave speed and mass density as medium No. 1 but without losses (dashed line), and a medium with the same losses as medium No. 1 but with the constant wave speed $c=1500$ m/s and the constant mass density $\rho=1000$ kg/m^3 (dotted line). All three graphs apply to a horizontal offset $r=0$ m.

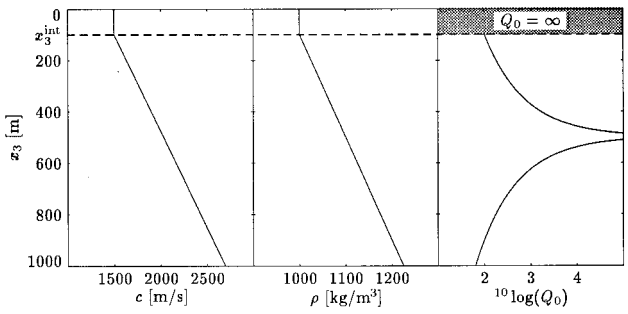

FIG. 10. The depth dependence of the wave speed c, the mass density ρ, and the parameter Q_0, for medium No. 2.

rays reflecting at the interface. If this occurs, the first arrival time will not be accounted for by the exponential function in the asymptotic representations. The method can never correct for this, and divergence occurs for any time instant.

Using medium No. 1, we can define two other media by either assuming the losses to be absent in the lower half-space ($Q_0=\infty$), or by taking the values of the wave speed and the mass density in the lower half-space equal to those of the upper half-space. The Green's functions for the media thus defined are given in Fig. 8 for the case $r=0$ m. In this figure we observe that it is possible that the effect due to the inhomogeneity of the wave speed and mass density is opposite to the effect due to the losses. In a medium in which both effects play a role, this may result in a Green's function that is approximately zero for some time after the arrival time. If this is the case in a practical, noisy situation, the danger of measuring an arrival time that is too large exists. This may also be concluded from Fig. 9, which shows the reflected acoustic pressures in the three media for a source with a four-point optimum Blackmann signature of 0.1 s duration and unit amplitude. We have obtained the acoustic pressures from the source signature and the Green's functions in Fig. 8 by performing the operations in Eq. (85).

We have determined a second set of numerical results for reflections from the lower part of medium No. 2 given in Fig. 10. At $x_3=500$ m, this medium is lossless. In Fig. 11, the Green's functions for medium No. 2 and a corresponding lossless medium are presented for a horizontal offset $r=0$ m.

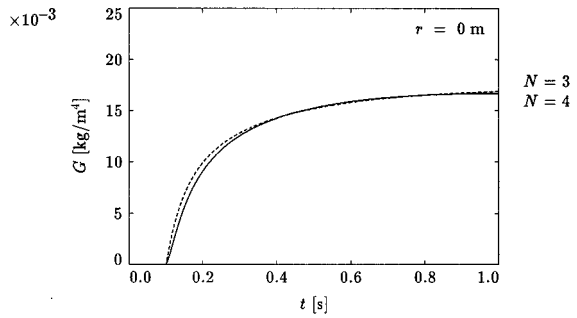

FIG. 11. The Green's functions G for medium No. 2 (solid line), and a medium with the same wave speed and mass density as medium No. 2 but without losses (dashed line). Both graphs apply to a horizontal offset $r=0$ m.

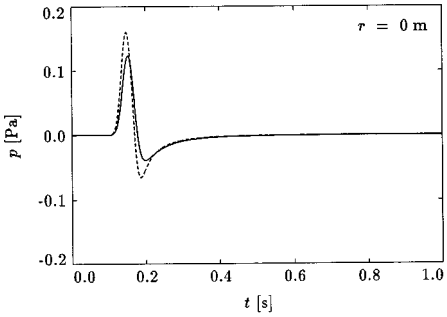

FIG. 12. The acoustic pressure p for medium No. 2 (solid line), and a medium with the same wave speed and mass density as medium No. 2 but without losses (dashed line). Both graphs apply to a horizontal offset $r=0$ m.

Between 0.4 and 0.8 s, both Green's functions have almost equal values; the time instants in this interval correspond with the times that are required to travel from the source, via a level in between approximately 400 and 700 m (where the medium is almost lossless) to the receiver. For a source with a four-point optimum Blackmann signature of 0.1 s duration and unit amplitude, the associated acoustic pressures are depicted in Fig. 12.

VII. CONCLUSIONS

In this paper we have derived a method for the determination of the space-time domain acoustic wave field, and the corresponding Green's function, in a continuously layered, lossy, isotropic fluid or equivalent fluid. To describe the medium properties, we have introduced a depth-dependent compliance memory function and a depth-dependent inertia memory function. Our method consists of three basic steps: forward transformation using a temporal Laplace transformation plus horizontal spatial Fourier transformations, approximation of the transform domain solution by higher-order WKBJ-like asymptotic representations, and inverse transformation with the aid of the Cagniard–De Hoop method. The form of the WKBJ-like asymptotic representations has enabled us to employ the Cagniard–De Hoop method in a very efficient way. Moreover, we have performed most steps of the inversion process analytically. Especially for the generation of Green's functions it is important that our method generates time-domain results without imposing a numerical limit on their bandwidth. We have tackled the problem of performing tasks that are almost impossible to carry out by hand, like the evaluation of the recurrence scheme for the coefficients of the asymptotic representations, by invoking a symbolic manipulation program. In our method causality has automatically been taken into account.

Numerical results have been generated for acoustic wave fields that are reflected by half-spaces filled with continuously layered, equivalent fluids with depth-dependent losses that at each level show an almost ''constant-Q'' behavior in the frequency domain. We have modeled these media by means of depth-dependent compliance memory functions. For low horizontal offsets we have observed that there is an interval, beginning with the arrival time, on which the differences between the approximate Green's functions with increasing orders become invisibly small. In general, for later time instants the subsequent approximations diverge. The method is applicable in case of nonzero horizontal offsets, but it becomes invalid when the first arrival at the point of observation is associated with a turning ray. We have shown numerically that near the arrival time the effect of the losses can counteract the effect of the inhomogeneity of the wave speed and mass density.

ACKNOWLEDGMENTS

The research of the author has been made possible by a fellowship of the Royal Netherlands Academy of Arts and Sciences. The research reported in this paper has been financially supported through research grants from the Stichting Fund for Science, Technology and Research (a companion organization to the Schlumberger Foundation in the USA).

[1] A. Ben-Menahem and S. J. Singh, *Seismic Waves and Sources* (Springer-Verlag, New York, 1981).
[2] D. H. Johnston and M. N. Toksöz, ''Definitions and terminology,'' in *Seismic Wave Attenuation*, edited by M. N. Toksöz and D. H. Johnston (Society of Exploration Geophysicists, Tulsa, 1981).
[3] K. Aki and P. G. Richards, *Quantitative Seismology: Theory and Methods* (Freeman, San Francisco, 1980), Vol. I.
[4] H. Kolsky, *Stress Waves in Solids* (Clarendon, Oxford, 1953).
[5] D. R. Bland, *The Theory of Linear Viscoelasticity* (Pergamon, Oxford, 1960).
[6] L. Boltzmann, ''Zur Theorie der elastischen Nachwirkung,'' Sitzungsber. K. Akad. Wiss. Wien, Math. Naturw. Kl. **70**, Sec. II, 275–306 (1874).
[7] L. Boltzmann, ''Zur Theorie der elastischen Nachwirkung,'' Ann. Phys. Chem. (Poggendorf), Ergänzungsband **7**, 624–654 (1876).
[8] C. H. Chapman, ''A new method for computing synthetic seismograms,'' Geophys. J. R. Astron. Soc. **54**, 481–518 (1978).
[9] C. H. Chapman, ''Long-period corrections to body waves: theory,'' Geophys. J. R. Astron. Soc. **64**, 321–372 (1981).
[10] C. H. Chapman and J. A. Orcutt, ''The computation of body wave synthetic seismograms in laterally homogeneous media,'' Rev. Geophys. **23**(2), 105–163 (1985).
[11] B. L. N. Kennett, *Seismic Wave Propagation in Stratified Media* (Cambridge U.P., Cambridge, England, 1983).
[12] M. D. Verweij, ''Transient acoustic wave modeling: Higher-order Wentzel-Kramers-Brillouin-Jeffreys asymptotics and symbolic manipulation,'' J. Acoust. Soc. Am. **92**, 2223–2238 (1992).
[13] M. D. Verweij, *Transient Acoustic Waves in Continuously Layered Media* (Delft U. P., Delft, The Netherlands, 1992).
[14] M. D. Verweij, ''Modeling space-time domain acoustic wave fields in media with attenuation: The symbolic manipulation approach,'' J. Acoust. Soc. Am. **97**, 831–843 (1995).
[15] C. -C. Chao and J. D. Achenbach, ''A simple viscoelastic analogy for stress waves,'' in *Stress Waves in Anelastic Solids*, edited by H. Kolsky and W. Prager (Springer-Verlag, Berlin, 1964).
[16] A. T. de Hoop, ''Similarity in wave propagation under a global relaxation law,'' in *Second International Conference on Mathematical and Numerical Aspects of Wave Propagation*, edited by R. Kleinman *et al.* (Society for Industrial and Applied Mathematics, Philadelphia, 1993).
[17] A. T. de Hoop, ''Similarity analysis for the elastic wave motion in a dissipative solid under a global relaxation law,'' in *IUTAM Symposium-Nonlinear Waves in Solids*, edited by J. L. Wegener and F. R. Norwood (American Society of Mechanical Engineers, Fairfield, NJ, 1995).
[18] A. T. de Hoop, ''A modification of Cagniard's method for solving seismic pulse problems,'' Appl. Sci. Res. Sec. B **8**, 349–356 (1960).
[19] D. V. Widder, *The Laplace Transform* (Princeton U.P., Princeton, 1946).
[20] W. Wasow, *Asymptotic Expansions for Ordinary Differential Equations* (Dover, New York, 1965).
[21] A. Erdélyi, *Asymptotic Expansions* (Dover, New York, 1956).
[22] J. T. Fokkema and P. M. van den Berg, *Seismic Applications of Acoustic Reciprocity* (Elsevier, Amsterdam, 1993).

[23] J. R. Carson, *Electric Circuit Theory and the Operational Calculus* (McGraw-Hill, New York, 1926).
[24] L. Cagniard, *Réflection et Réfraction des ondes Seismiques Progressives* (Gauthier-Villars, Paris, 1939) [in French; translated and revised version: E. A. Flinn and C. H. Dix, *Reflection and Refraction of Progressive Seismic Waves* (McGraw-Hill, New York, 1962)].
[25] A. T. de Hoop, ''Acoustic radiation from an impulsive point source in a continuously layered fluid—An analysis based on the Cagniard method,'' J. Acoust. Soc. Am. **88**, 2376–2388 (1990).
[26] R. M. Young, ''Formal power series and iterative methods for wave vectors,'' Geophys. J. R. Astron. Soc. **77**, 531–547 (1984).
[27] A. T. de Hoop, ''Theoretical determination of the surface motion of a uniform elastic halfspace produced by a dilatational, impulsive, point source,'' Proceedings Colloque International du C.N.R.S. No. 111, Marseille, 1961, pp. 21–31 (Centre National de La Recherche Scientifique, Paris, 1962).
[28] Mathematica is a registered trademark of Wolfram Research, Inc.
[29] S. Wolfram, *Mathematica-A System for doing Mathematics by Computer* (Addison-Wesley, New York, 1991).
[30] M. D. Verweij and A. T. de Hoop, ''Determination of seismic wavefields in arbitrarily continuously layered media using the modified Cagniard method,'' Geophys. J. Int. **108**, 731–754 (1990).
[31] E. Strick, ''Applications of linear viscoelasticity to seismic wave propagation,'' in *Wave Propagation in Viscoelastic Media*, edited by F. Mainardi (Pitman, London, 1982).

The complete extension of the Biot–Tolstoy solution to the density contrast wedge with sample calculations

Anthony M. J. Davis[a)]
Mathematics Department, University of Alabama, Tuscaloosa, Alabama 35487-0350

Robert W. Scharstein
Electrical Engineering Department, University of Alabama, Tuscaloosa, Alabama 35487-0286

(Received 11 April 1996; accepted for publication 16 December 1996)

The Biot–Tolstoy exact time-domain solution for the three-dimensional impulse response of an impenetrable wedge is extended to accommodate the isovelocity or density-contrast wedge. Fourier transformation of the time and axial variables, along with a Kantorovich–Lebedev transform applied to the cylindrical radial coordinate, leads to a solution in terms of residue series. When the wedge angle is a rational fraction of π, the residue series can be reduced to a finite sum which is evaluated for some special cases. The total pressure field consists of geometrical acoustics contributions, as predicted by Snell's laws, plus a modified version of the Biot–Tolstoy diffraction field. © *1997 Acoustical Society of America.* [S0001-4966(97)07004-5]

PACS numbers: 43.20.Fn, 43.20.Px [ANN]

INTRODUCTION

The three-dimensional problem of Fig. 1 is the scattering of the acoustic field radiated by an impulsive point source in the presence of a penetrable wedge having the same sound velocity as the external medium. The exact solution to this canonical boundary value problem is a first step toward extending some widely used techniques, notably the wedge-assemblage method[1] for rough surface scattering and the related variants of the geometrical theory of diffraction, to model scattering by penetrable surfaces. In underwater acoustics, the ratio of wave speeds in sea water (external medium) and in the ocean floor (internal medium) is often close to unity, i.e., $0.9<c_i/c_e<1.2$ for a variety of ocean floor sediments. This is the primary motivation for the present density-contrast solution.

Chu[2] suggested how the Biot–Tolstoy solution[3] might be extended to include the phenomenon of penetration when only a density contrast exists between the interior and exterior media but gave an incomplete presentation. He was unable to relate his coefficients to the source strength and considered only the known limiting cases. The following work first constructs the time-domain solution for an arbitrary wedge angle by the use of appropriate integral transforms and representations. This calculation differs principally from the impenetrable case in the nonavailability of the closed-form residue sum expression that subsequently yields a solution in the form of an eigenfunction expansion. The physical features of the pressure field are common to all wedge angles 2α ($<\pi$), but are most easily identified by considering rational fractions of π, as in other problems involving the wedge geometry, e.g., gravity waves on a sloping beach.

Fourier transformation of the time t and axial coordinate z in Sec. I, together with the Kantorovich–Lebedev transformation of the cylindrical radial coordinate r in Sec. II, results in a pair of ordinary differential equations in the azimuthal coordinate ϕ, subject to continuity conditions. The solution for the acoustic pressure field is split into its symmetric and antisymmetric parts with respect to the wedge bisector; this economization is employed throughout. Inversion of the multiple integral transforms yields expressions for the total field in the form of two types of residue series, corresponding to a geometrical acoustics field and the diffracted field. The summation of these time-domain series in closed form is the major difficulty of this work and is presently unavailable for arbitrary wedge angle 2α. The geometrical acoustics field is expected to reduce to a finite set of delayed and scaled Dirac-delta functions, in agreement with the results of a direct application of the localized interpretation of Snell's laws. Similarly, the turn-on time and strength of the diffracted field must originate from the critical point on the wedge apex, to be consistent with the generalized Fermat's principle. Agreement with the known Biot–Tolstoy solution for the impenetrable hard and soft cases is verified in the applicable limits because then the major difficulties due to penetration are eliminated.

The residue series require explicit knowledge of eigenvalues in the radial transform variable, which depend on both the density contrast, via the reflection coefficient Γ, and the wedge angle 2α. When α is a rational multiple of π, the eigenvalues are neatly ordered, as described in Sec. III, in a periodic form that ultimately allows each series to be reduced to a finite number of terms. This is accomplished by writing the wedge angle in the special form $1-2\alpha/\pi=N/M$. The ensuing analysis takes full advantage of symmetries in the eigenvalue equation for the required poles, and hence considers two separate classes of wedge angles: The case having M and N both odd in Sec. IV and the case of either M or N even in Sec. V. The explicit total field is presented in Sec. VI for the example cases $\alpha=\pi/3$, $2\pi/5$, $\pi/4$, and $\pi/6$. The results of Sec. VI clearly show the expected, but nontrivial, modifications to the geometrical

[a)]Electronic mail: adavis@ua1vm.ua.edu

 0001-4966/97/101(4)/1821/15/$10.00

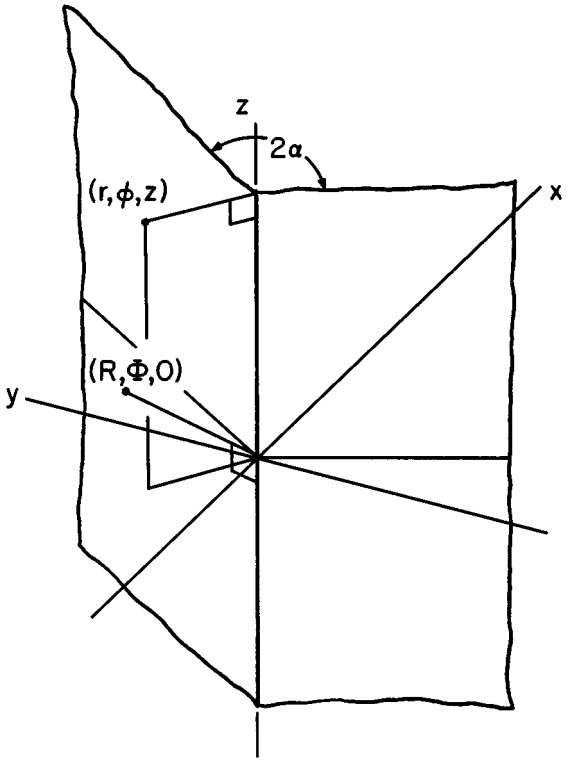

FIG. 1. Axonometric view of wedge geometry.

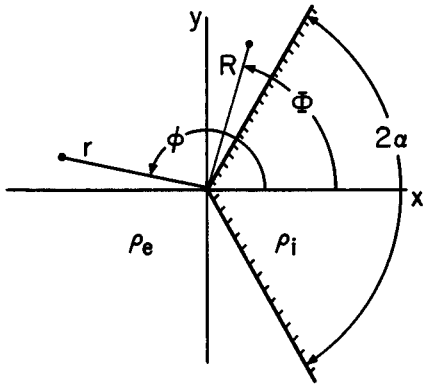

FIG. 2. Transverse sectional view of wedge geometry.

acoustics part of the total field due to penetration. Sec. VII is a detailed compilation and study of the diffraction field as the reflection coefficient Γ is varied from -1 (the perfectly soft, impenetrable case) to the other extreme of $+1$ (the perfectly hard, impenetrable case).

The dominant effects of a small velocity contrast can now be included, in principle, by a perturbative adjustment to this zero-order or isovelocity solution. Continuing progress based on the results presented here is planned via the adaptation of an iterative scheme by Rawlins,[4] valid for refractive indices in the range 1 to $\sqrt{2}$. Exploitation of the similar wave speeds circumvents the great difficulties inherent in an infinite boundary between arbitrarily different media.[5,6] The scattered waveforms resulting from more complicated source distributions, in both space and time, are obtained immediately by an appropriate spatial and/or temporal convolution between the source function and the resultant impulse response or Green's function of this paper.

I. PENETRATION PROBLEM WITH IMPULSIVE POINT SOURCE

The scalar pressure field $p(r,\phi,z,t)$ due to an impulsive source at $(R,\Phi,0,0)$ external to a wedge of angle 2α having the same wave speed c as the surrounding medium (Figs. 1 and 2) is the solution to

$$\begin{aligned}
&\left(\nabla^2-\frac{1}{c^2}\frac{\partial^2}{\partial t^2}\right)p^{(e)}(r,\phi,z,t)\\
&\quad=\frac{\delta(r-R)}{R}\,\delta(\phi-\Phi)\,\delta(z)\,\delta(t)\\
&\qquad(\alpha<\Phi<\pi,\alpha<\phi<2\pi-\alpha),\\
&\left(\nabla^2-\frac{1}{c^2}\frac{\partial^2}{\partial t^2}\right)p^{(i)}(r,\phi,z,t)=0\quad(-\alpha<\phi<\alpha),
\end{aligned}\tag{1}$$

subject to the boundary conditions

$$p^{(e)}=p^{(i)}\quad\text{and}\quad\rho\,\frac{\partial p^{(e)}}{\partial\phi}=\frac{\partial p^{(i)}}{\partial\phi}\quad\text{at}\quad\phi=\pm\alpha,\tag{2}$$

where the density ratio is $\rho=\rho_i/\rho_e$. Fourier transformation in both t and z, according to

$$\hat{p}(r,\phi,l,\omega)=2\int_{-\infty}^{\infty}e^{-i\omega t}\int_0^{\infty}p(r,\phi,z,t)\cos lz\;dz\;dt\tag{3}$$

and the definitions $k=\omega/c$, $\kappa=\sqrt{k^2-l^2}$, result in

$$\begin{aligned}
&\left[\frac{1}{r}\frac{\partial}{\partial r}\left(r\,\frac{\partial}{\partial r}\right)+\frac{1}{r^2}\frac{\partial^2}{\partial\phi^2}+\kappa^2\right]\hat{p}^{(e)}(r,\phi,l,\omega)\\
&\quad=\frac{\delta(r-R)}{R}\,\delta(\phi-\Phi),\\
&\left[\frac{1}{r}\frac{\partial}{\partial r}\left(r\,\frac{\partial}{\partial r}\right)+\frac{1}{r^2}\frac{\partial^2}{\partial\phi^2}+\kappa^2\right]\hat{p}^{(i)}(r,\phi,l,\omega)=0.
\end{aligned}\tag{4}$$

Before proceeding further, it is appropriate to emphasize the difficulties due to penetration by noting that in the hard ($\rho=\infty$) or soft ($\rho=0$) case, only the external problem is relevant and can be solved by introducing image singularities. The periodic delta function, defined by

$$\mathring{\delta}(\theta)=\sum_{n=-\infty}^{\infty}\delta(\theta-2n\pi)=\frac{1}{\pi}\left[\frac{1}{2}+\sum_{m=1}^{\infty}\cos m\theta\right],\tag{5}$$

enables this to be achieved by replacing $\delta(\phi-\Phi)$ in (4) by

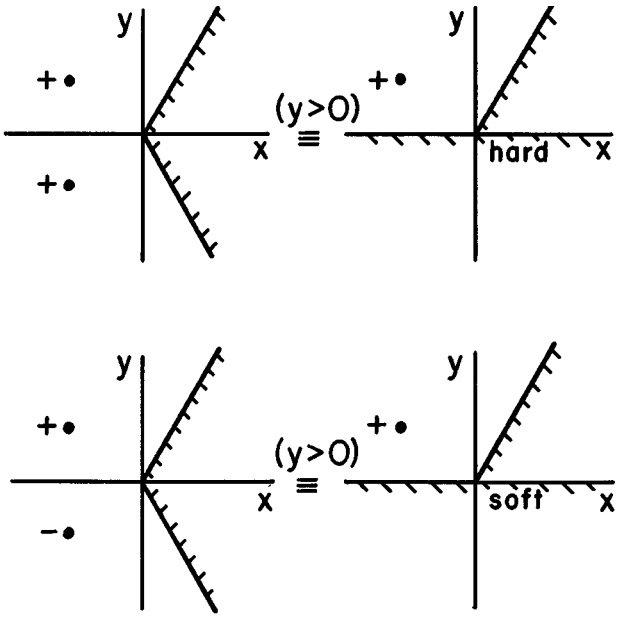

FIG. 3. Symmetric and antisymmetric source configurations.

$$\frac{\pi}{2(\pi-\alpha)}\left\{\mathring{\delta}\left[\frac{\pi}{2(\pi-\alpha)}(\phi-\Phi)\right]\right.$$
$$\left.\pm\mathring{\delta}\left[\frac{\pi}{2(\pi-\alpha)}(\phi+\Phi-2\alpha)\right]\right\}$$
$$=\frac{1}{\pi-\alpha}\left\{\begin{pmatrix}1/2\\0\end{pmatrix}\right.$$
$$\left.+\sum_{m=1}^{\infty}\begin{matrix}\cos\\\sin\end{matrix}\left(\frac{m\pi(\phi-\alpha)}{2(\pi-\alpha)}\right)\begin{matrix}\cos\\\sin\end{matrix}\left(\frac{m\pi(\Phi-\alpha)}{2(\pi-\alpha)}\right)\right\}. \tag{6}$$

Thus, for $\omega>0$,

$$\hat{p}^{(e)}(r,\phi,l,\omega)=\frac{\pi i}{2(\pi-\alpha)}\left\{\begin{pmatrix}1/2\\0\end{pmatrix}H_0^{(2)}(\kappa r_>)J_0(\kappa r_<)\right.$$
$$+\sum_{m=1}^{\infty}H_{\nu_m}^{(2)}(\kappa r_>)J_{\nu_m}(\kappa r_<)$$
$$\left.\times\begin{matrix}\cos\\\sin\end{matrix}[\nu_m(\phi-\alpha)]\begin{matrix}\cos\\\sin\end{matrix}[\nu_m(\Phi-\alpha)]\right)\Bigg\}, \tag{7}$$

where

$$\nu_m=\frac{m\pi}{2(\pi-\alpha)}\quad\text{and}\quad\begin{pmatrix}r_>\\r_<\end{pmatrix}=\begin{matrix}\max\\\min\end{matrix}(r,R). \tag{8}$$

The complex conjugate eigenfunction expansion is used for $\omega<0$. However, this method is unavailable for the density contrast ($0<\rho<\infty$) considered here, and an appropriate integral transform is needed to determine $\hat{p}^{(e)}$. In anticipation of this calculation, it is advantageous to work with the symmetric p_s and antisymmetric p_a parts of the pressure p in order to restrict the field to $0<\phi<\alpha$ and $\alpha<\phi<\pi$ in the interior and exterior regions, respectively.

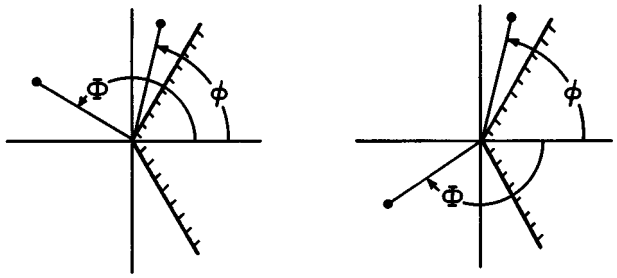

FIG. 4. Sum and difference of symmetric and antisymmetric cases.

II. SYMMETRIC AND ANTISYMMETRIC PARTS OF THE SOLUTION

Consider pairs of in-phase or out-of-phase singularities of half-strength, arranged symmetrically about the wedge bisector (Fig. 3). The source plus positive image is equivalent (in the upper half-space) to the source above a hard bisecting plane, while the antisymmetric arrangement of source plus negative image satisfies the soft boundary condition on the $y=0$ plane. Upon solving for the symmetric and antisymmetric fields, the sum p_s+p_a is the solution of the wedge problem at a point on the same side of the centerline as the source. Meanwhile, the difference p_s-p_a gives the solution of the wedge problem at a point on the opposite side of the centerline from the source (Fig. 4).

Fourier transforms $\hat{p}_s$ and $\hat{p}_a$, defined by (3), satisfy according to (4), the wave equations

$$\left[\frac{1}{r}\frac{\partial}{\partial r}\left(r\frac{\partial}{\partial r}\right)+\frac{1}{r^2}\frac{\partial^2}{\partial\phi^2}+\kappa^2\right]\hat{p}_{s,a}^{(e)}(r,\phi,l,\omega)$$
$$=\frac{\delta(r-R)}{2R}\,\delta(\phi-\Phi),$$
$$\left[\frac{1}{r}\frac{\partial}{\partial r}\left(r\frac{\partial}{\partial r}\right)+\frac{1}{r^2}\frac{\partial^2}{\partial\phi^2}+\kappa^2\right]\hat{p}_{s,a}^{(i)}(r,\phi,l,\omega)=0. \tag{9}$$

The Kantorovich–Lebedev transform[7]

$$P_{s,a}(\nu,\phi,\kappa)=\int_0^{\infty}\hat{p}_{s,a}(r,\phi,\kappa)r^{-1}H_\nu^{(2)}(\kappa r)\,dr \tag{10}$$

renders the pair of ordinary differential equations

$$\left(\frac{d^2}{d\phi^2}+\nu^2\right)P_{s,a}^{(e)}(\nu,\phi,\kappa)=\frac{1}{2}H_\nu^{(2)}(\kappa R)\,\delta(\phi-\Phi)$$
$$(\alpha<\phi<\pi),$$
$$\left(\frac{d^2}{d\phi^2}+\nu^2\right)P_{s,a}^{(i)}(\nu,\phi,\kappa)=0\quad(0<\phi<\alpha), \tag{11}$$

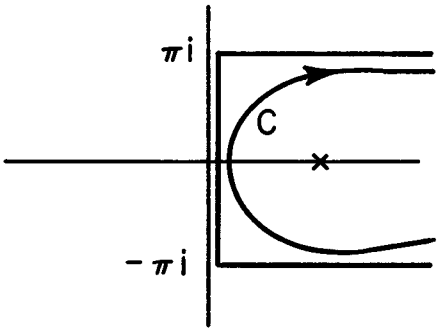

FIG. 5. Contour C in the complex w plane passes to the left of the point $w=\cosh^{-1}[(r^2+R^2+z^2)/2rR]$.

subject to continuity boundary conditions at the media interface

$$P_{s,a}^{(e)}=P_{s,a}^{(i)} \quad \text{and} \quad \rho\,\frac{dP_{s,a}^{(e)}}{d\phi}=\frac{dP_{s,a}^{(i)}}{d\phi} \quad \text{at} \quad \phi=\alpha \tag{12}$$

and appropriate Neumann or Dirichlet conditions on the geometrical plane of symmetry

$$\frac{dP_s}{d\phi}=0 \quad \text{or} \quad P_a=0 \quad \text{at} \quad \phi=0,\ \pi. \tag{13}$$

Boundary conditions at $\phi=0,\ \pi$ are satisfied by

$$\begin{aligned}&\frac{2\nu}{H_\nu^{(2)}(\kappa R)}\,P_{s,a}^{(i)}=A\,\underset{\sin}{\cos}\,\nu\phi \quad (0<\phi<\alpha)\\ &\frac{2\nu}{H_\nu^{(2)}(\kappa R)}\,P_{s,a}^{(e)}=B\,\underset{\sin}{\cos}\,\nu(\pi-\phi)+H(\Phi-\phi)\\ &\qquad\qquad \times\sin\,\nu(\Phi-\phi) \quad (\alpha<\phi<\pi),\end{aligned} \tag{14}$$

where H denotes the Heaviside unit function. Conditions (12) at $\phi=\alpha$ then yield

$$A=\frac{(1+\Gamma)\,\underset{-\sin}{\cos}\,\nu(\pi-\Phi)}{\sin\,\nu\pi\pm\Gamma\,\sin\,\nu(\pi-2\alpha)}$$

and

$$B=\frac{\underset{-\sin}{\cos}\,\nu\Phi+\Gamma\,\underset{\sin}{\cos}\,\nu(\Phi-2\alpha)}{\sin\,\nu\pi\pm\Gamma\,\sin\,\nu(\pi-2\alpha)}, \tag{15}$$

where the reflection coefficient is

$$\Gamma=\frac{\rho-1}{\rho+1} \quad (|\Gamma|\leqslant 1). \tag{16}$$

In the two limiting cases

$$\begin{aligned}&B=-\frac{\sin\,\nu(\Phi-\alpha)}{\underset{\sin}{\cos}\,\nu(\pi-\alpha)} \quad (\rho=0,\ \Gamma=-1),\\ &B=\frac{\cos\,\nu(\Phi-\alpha)}{\underset{-\cos}{\sin}\,\nu(\pi-\alpha)} \quad (\rho\to\infty,\ \Gamma=1),\end{aligned} \tag{17}$$

for which the eigenvalues are determined by (8). Even/odd values of m correspond to symmetric/antisymmetric solutions in the hard case but vice versa in the soft case. The $\alpha\to 0$ limits of the symmetric hard case and antisymmetric soft cases must be identical to the symmetric and antisymmetric solutions at $\Gamma=0$ ($\rho=1$).

With the function f defined by

$$f(\nu,\phi)=\frac{2\nu}{H_\nu^{(2)}(\kappa R)}\,P(\nu,\phi,\kappa), \tag{18}$$

inversion of the Kantorovich–Lebedev transform proceeds, for $r<R$, as

$$\begin{aligned}\hat{p}(r,\phi,\kappa)&=\lim_{\epsilon\to 0}-\frac{1}{4}\int_{-i\infty}^{i\infty}\exp(\epsilon\nu^2)J_\nu(\kappa r)H_\nu^{(2)}(\kappa R)f(\nu,\phi)\,d\nu\\ &=\lim_{\epsilon\to 0}\frac{1}{4\pi i}\int_{-i\infty}^{i\infty}\exp(\epsilon\nu^2)f(\nu,\phi)\int_0^{\gamma-i\infty}\exp\left[\frac{1}{2}\left(s-\frac{R^2+r^2}{s}\,\kappa^2\right)\right]I_\nu\left(\frac{\kappa^2 rR}{s}\right)\frac{ds}{s}\,d\nu\\ &=-\lim_{\epsilon\to 0}\frac{1}{8\pi i}\int_{-i\infty}^{i\infty}\exp(\epsilon\nu^2)f(\nu,\phi)\int_{\infty-\pi i}^{\infty+\pi i}e^{-\nu w}H_0^{(2)}[\kappa(r^2+R^2-2rR\,\cosh\,w)^{1/2}]dw\,d\nu\\ &=\frac{1}{4}\int_{\infty-\pi i}^{\infty+\pi i}H_0^{(2)}[\kappa(r^2+R^2-2rR\,\cosh\,w)^{1/2}]\sum_{n=0}^{\infty}{}'\,[\text{residues of } e^{-\nu w}f(\nu,\phi) \quad \text{at} \quad \nu=\nu_n]dw.\end{aligned} \tag{19}$$

The w integration is along the contour C of Fig. 5, $\nu_0=0$, $\nu_n>\nu_{n-1}$ $(n\geqslant 1)$, and the prime on the summation denotes that a 1/2 factor multiplies the residue at the origin, if it exists. The result, symmetric in r,R, is also valid for $r>R$ and the details are briefly described by Jones,[7] after correcting some misprints. Inversion of the z and t transforms then yields

$$p(r,\phi,z,t)=\frac{i}{4\pi}\int_{\infty-\pi i}^{\infty+\pi i}\frac{\delta[t-(1/c)(r^2+R^2-2rR\cosh\,w+z^2)^{1/2}]}{(r^2+R^2-2rR\,\cosh\,w+z^2)^{1/2}}\cdot\sum_{n=0}^{\infty}{}'\,[\text{residues of } e^{-\nu w}f(\nu,\phi) \quad \text{at} \quad \nu=\nu_n]dw \tag{20}$$

and subsequent deformation of the contour shows that

$$p(r,\phi,z,t)=-\frac{1}{2\pi}\frac{c}{rR\,\sin\,\eta}\sum_{n=0}^{\infty}{}'[\text{residues of } \cos\,\nu\eta\;\; f(\nu,\phi) \text{ at } \nu=\nu_n]$$

$$+\frac{1}{2\pi}\frac{c}{rR\,\sinh\,\xi}\sum_{n=1}^{\infty}[\text{residues of } e^{-\nu\xi}\sin\,\nu\pi\;\; f(\nu,\phi) \text{ at } \nu=\nu_n], \tag{21}$$

where the time and space dependence is folded into

$$\cos\,\eta=\frac{R^2+r^2+z^2-c^2t^2}{2Rr}\qquad(\sqrt{(R-r)^2+z^2}<ct<\sqrt{(R+r)^2+z^2}),$$

$$\cosh\,\xi=\frac{c^2t^2-R^2-r^2-z^2}{2Rr}\qquad(ct>\sqrt{(R+r)^2+z^2}), \tag{22}$$

with $0<\eta<\pi$ and contributions occurring in relevant time intervals.

It is instructive at this stage to illustrate how the subsequent calculation might proceed by considering one of the simple impenetrable cases. In the soft case ($\Gamma=-1$) the transform is, from (14) with (e) now disposable,

$$f_{s,a}(\nu,\phi)=-\frac{\sin\,\nu(\Phi-\alpha)}{\frac{\cos}{\sin}\,\nu(\pi-\alpha)}\frac{\cos}{\sin}\,\nu(\pi-\phi)\qquad(\phi>\Phi), \tag{23}$$

with Φ and ϕ interchanged if $\phi<\Phi$. Poles for the symmetric and antisymmetric fields are

$$\nu^s=\frac{(m+1/2)\pi}{\pi-\alpha}\quad(m\geqslant 0)\quad\text{and}\quad\nu^a=\frac{m\pi}{\pi-\alpha}\quad(m\geqslant 0). \tag{24}$$

The first residue sum above for the total pressure p is now

$$\sum_{n=0}^{\infty}{}'[\text{residues of } \cos\,\nu\eta\;\; f(\nu,\phi) \text{ at } \nu=\nu_n]$$

$$=\frac{1}{\pi-\alpha}\sum_{n=0}^{\infty}{}'\sin\frac{n\pi}{2(\pi-\alpha)}(\Phi-\alpha)\,\sin\,\frac{n\pi}{2(\pi-\alpha)}(\phi-\alpha)\,\cos\frac{n\pi\eta}{2(\pi-\alpha)}$$

$$=\frac{\pi}{4(\pi-\alpha)}\left\{\mathring{\delta}\left[\frac{\pi}{2(\pi-\alpha)}(\Phi-\phi+\eta)\right]+\mathring{\delta}\left[\frac{\pi}{2(\pi-\alpha)}(\Phi-\phi-\eta)\right]\right.$$

$$\left.-\mathring{\delta}\left[\frac{\pi}{2(\pi-\alpha)}(\Phi+\phi-2\alpha+\eta)\right]-\mathring{\delta}\left[\frac{\pi}{2(\pi-\alpha)}(\Phi+\phi-2\alpha-\eta)\right]\right\} \tag{25}$$

which, for $\alpha<\phi$, $\Phi<\pi$, and $0<\eta<\pi$, reduces to the geometrical acoustics field

$$\tfrac{1}{2}\,[\,\delta(\eta-|\Phi-\phi|)-\delta(\eta+2\alpha-\Phi-\phi)]. \tag{26}$$

The diffracted portion of the total field derives from the second residue sum of (21):

$$\sum_{n=1}^{\infty}[\text{residues of } e^{-\nu\xi}\sin\,\nu\pi\;\; f(\nu,\phi) \text{ at } \nu=\nu_n]$$

$$=\frac{1}{2(\pi-\alpha)}\sum_{n=1}^{\infty}\left[\cos\frac{n\pi}{2(\pi-\alpha)}(\Phi-\phi)-\cos\frac{n\pi}{2(\pi-\alpha)}(\Phi+\phi-2\alpha)\right]\sin\frac{n\pi^2}{2(\pi-\alpha)}\exp\frac{-n\pi\xi}{2(\pi-\alpha)} \tag{27}$$

which can be simplified by using

$$\sum_{n=1}^{\infty}e^{-n\beta}\sin\,n\gamma=\frac{\sin\,\gamma}{2(\cosh\,\beta-\cos\,\gamma)}. \tag{28}$$

Substitution of (26), (27) in (21) then shows that the total field is given by

$$p=\frac{-c}{4\pi rR}\Bigg\{\frac{1}{\sin\ \eta}[\,\delta(\eta-|\Phi-\phi|)-\delta(\eta+2\alpha-\Phi-\phi)]$$
$$-\frac{1}{4(\pi-\alpha)\ \sinh\ \xi}\Bigg[\frac{\sin\,[\pi(\pi+\phi-\Phi)/2(\pi-\alpha)]}{\cosh\,[\pi\xi/2(\pi-\alpha)]-\cos\,[\pi(\pi+\phi-\Phi)/2(\pi-\alpha)]}$$
$$+\frac{\sin\,[\pi(\pi-\phi+\Phi)/2(\pi-\alpha)]}{\cosh\,[\pi\xi/2(\pi-\alpha)]-\cos\,[\pi(\pi-\phi+\Phi)/2(\pi-\alpha)]}-\frac{\sin\,[\pi(\pi+\phi+\Phi-2\alpha)/2(\pi-\alpha)]}{\cosh\,[\pi\xi/2(\pi-\alpha)]-\cos\,[\pi(\pi+\phi+\Phi-2\alpha)/2(\pi-\alpha)]}$$
$$-\frac{\sin\,[\pi(\pi-\phi-\Phi+2\alpha)/2(\pi-\alpha)]}{\cosh\,[\pi\xi/2(\pi-\alpha)]-\cos\,[\pi(\pi-\phi-\Phi+2\alpha)/2(\pi-\alpha)]}\Bigg]\Bigg\} \tag{29}$$

which is equivalent to the form given by Biot and Tolstoy[3] and displays the features outlined in the introduction because of the time delay, given by (22), before the ξ variable becomes operative. This derivation of (29) is more efficient than that given by the original authors. Note the sign of the forcing term in (1).

However, the corresponding calculation in the penetrable case is substantially more difficult, if not impossible. For $0<\rho<\infty$, the ϕ-independent factor B of (15) is rewritten as

$$B=\frac{\sin}{-\cos}\ \nu(\pi-\Phi)$$
$$+\frac{\cos\ \nu\pi\pm\Gamma\ \cos\ \nu(\pi-2\alpha)}{\sin\ \nu\pi\pm\Gamma\ \sin\ \nu(\pi-2\alpha)}\frac{\cos}{\sin}\ \nu(\pi-\Phi), \tag{30}$$

which allows the exterior version of (18) to be expressed

$$f_{s,a}^{(e)}=\frac{\cos\ \nu\pi\pm\Gamma\ \cos\ \nu(\pi-2\alpha)}{\sin\ \nu\pi\pm\Gamma\ \sin\ \nu(\pi-2\alpha)}\frac{\cos}{\sin}\ \nu(\pi-\Phi)$$
$$\times\frac{\cos}{\sin}\ \nu(\pi-\phi)+\frac{\sin}{-\cos}\ \nu(\pi-\phi_<)\ \frac{\cos}{\sin}\ \nu(\pi-\phi_>) \tag{31}$$

with

$$\begin{pmatrix}\phi_>\\ \phi_<\end{pmatrix}=\frac{\max}{\min}(\phi,\Phi). \tag{32}$$

Similarly, the interior transform function is

$$f_{s,a}^{(i)}=(1+\Gamma)\ \frac{\frac{\cos}{-\sin}\ \nu(\pi-\Phi)\ \frac{\cos}{\sin}\ \nu\phi}{\sin\ \nu\pi\pm\Gamma\ \sin\ \nu(\pi-2\alpha)}. \tag{33}$$

According to (31), the symmetric and antisymmetric exterior fields are simply related by a change in sign of Γ and in terms that involve the sum $\Phi+\phi$.

Since $|\Gamma|<1$, the poles of (31) and (33) are such that

$$\nu_n=n+\gamma_n,\quad |\gamma_n|<\frac{1}{\pi}\ \text{arcsin}|\Gamma|\quad (n\geqslant 1). \tag{34}$$

If the wedge angle α is a rational multiple of π, the sequence γ_n becomes periodic and the residue series can be arranged as a finite number of summable series.

III. WEDGE ANGLE A RATIONAL MULTIPLE OF π

When the wedge angle 2α is a rational multiple of π, the poles of the above transforms, that is the roots of the denominator function

$$\sin\ \nu\pi\pm\Gamma\ \sin\ \nu(\pi-2\alpha)=0, \tag{35}$$

are explicitly procurable in terms of the zeros of a polynomial. The normalized supplementary angle

$$\frac{\pi-2\alpha}{\pi}=\frac{N}{M} \tag{36}$$

is now expressed in terms of integers such that $M>N$. With $\theta=\nu\pi/M$ the desired roots satisfy

$$\sin\ M\theta=\mp\Gamma\ \sin\ N\theta. \tag{37}$$

Thus, either $\sin\ \theta=0$ or, with the introduction of $x=\cos\ \theta$,

$$U_{M-1}(x)=\mp\Gamma U_{N-1}(x) \tag{38}$$

in terms of Chebyshev polynomials of the second kind. The first class of roots from $\theta=k\pi$ are designated

$$\nu_{kM}=kM\begin{cases}(k\geqslant 0) & \text{symmetric}\\ (k\geqslant 1) & \text{antisymmetric}\end{cases} \tag{39}$$

and the second class of $M-1$ roots x_i^s or x_i^a of (38), labeled in ascending order $(i=1,2,\ldots,M-1)$, translate to θ values

$$\theta=\underbrace{[k-\tfrac{1}{2}+\tfrac{1}{2}(-1)^k]}_{\text{even}}\pi-(-1)^k\ \cos^{-1}\ x_i$$
$$(k\geqslant 1,\ 1\leqslant i\leqslant M-1). \tag{40}$$

In the required transform variable ν, these roots are denoted

$$\nu_{(k-1)M+i}=(k-\tfrac{1}{2})M+(-1)^k(M/\pi)\ \sin^{-1}\ x_i$$
$$(k\geqslant 1,\ 1\leqslant i\leqslant M-1). \tag{41}$$

The fraction N/M is in its lowest form; if either M or N is even, then the antisymmetric x values are the negatives of the symmetric x values, i.e., $x_i^a=-x_{M-i}^s$ $(1\leqslant i\leqslant M-1)$. If M and N are both odd, then (38) is a polynomial of degree $(M-1)/2$ in x^2, i.e., $x_i^s=-x_{M-i}^s$ and $x_i^a=-x_{M-i}^a$ $[1\leqslant i\leqslant(M-1)/2]$. So the number of independent x_i values required for both symmetric and antisymmetric solutions is always $(M-1)$.

The residue of the pertinent first term of (31) at $\nu_{kM} = kM$ is

$$\frac{(-1)^{k(M-N)} \pm \Gamma}{\pi[(-1)^{k(M-N)} \pm N\Gamma/M]} \begin{matrix}\cos \\ \sin\end{matrix} kM(\pi - \Phi) \begin{matrix}\cos \\ \sin\end{matrix} kM(\pi - \phi), \tag{42}$$

while that at $\nu_{(k-1)M+i}$, defined by (41), is given in terms of Chebyshev polynomials of the first kind by

$$\frac{T_M(x_i) \pm \Gamma T_N(x_i)}{\pi[T_M(x_i) \pm N\Gamma T_N(x_i)/M]} \begin{matrix}\cos \\ \sin\end{matrix} [\nu_{(k-1)M+i}(\pi - \Phi)] \begin{matrix}\cos \\ \sin\end{matrix} [\nu_{(k-1)M+i}(\pi - \phi)]. \tag{43}$$

The Chebyshev recursion relation

$$T_M(x) = U_M(x) - xU_{M-1}(x) = xU_{M-1}(x) - U_{M-2}(x) \quad (M \geqslant 2) \tag{44}$$

is also true for $M=1$ by interpreting $U_{-1}(x)$ as zero, which is consistent with $U_{M-1}(x) = \sin M\theta / \sin \theta$. Subject to (38), the degree of the rational coefficient in (43) is therefore lowered by two in the identity

$$\frac{T_M(x_i) \pm \Gamma T_N(x_i)}{T_M(x_i) \pm N\Gamma T_N(x_i)/M} = \frac{U_{M-2}(x_i) \pm \Gamma U_{N-2}(x_i)}{U_{M-2}(x_i) \pm (N/M)\Gamma U_{N-2}(x_i) \pm (1-(N/M))\Gamma x_i U_{N-1}(x_i)}. \tag{45}$$

IV. *M* AND *N* BOTH ODD

When $M = 2m + 1, N = 2q + 1\ (0 \leqslant q < m)$, the symmetric and antisymmetric residues can be treated separately and a reduction in the algebra is achieved. In either case, the eigenvalue equation (38) becomes a polynomial of degree m in x^2 whose roots are structured

$$\begin{aligned} &x_1^s = -\beta_m, \quad x_2^s = -\beta_{m-1}, \ldots, \quad x_m^s = -\beta_1, \\ &x_{m+1}^s = \beta_1, \ldots, \quad x_{2m}^s = \beta_m, \end{aligned} \tag{46}$$

i.e., $x_{m+1-i} = -\beta_i, x_{m+i} = \beta_i (1 \leqslant i \leqslant m)$. The obvious pairings of residues can be exploited by defining $y = \cos 2\theta = 2x^2 - 1$, whence the eigenvalue equation can be rewritten as

$$U_m(y) + U_{m-1}(y) = \mp \Gamma [U_q(y) + U_{q-1}(y)], \tag{47}$$

where $U_{-1} = 0$, $U_0 = 1$, $U_1 = 2y$, etc. The eigenvalues are now $y_i = 2\beta_i^2 - 1$, i.e.,

$$\sin^{-1} \beta_i = \tfrac{1}{2} \cos^{-1}[1 - 2\beta_i^2] = \tfrac{1}{2} \cos^{-1}(-y_i). \tag{48}$$

Evidently, for any angle ψ, (48) and the definition (41) permit the economical summation of the pair of terms

$$\begin{aligned} &\sum_{k=1}^{\infty} \{\cos[\nu_{kM-m-i}\psi] + \cos[\nu_{(k-1)M+m+i}\psi]\} \\ &= 2 \cos\left[\frac{M\psi}{\pi} \sin^{-1} \beta_i\right] \sum_{k=1}^{\infty} \cos\left[\left(k - \frac{1}{2}\right) M\psi\right] \\ &= \pi \cos\left[\frac{M\psi}{\pi} \sin^{-1} \beta_i\right] \sum_{n=-\infty}^{\infty} (-1)^n \delta(M\psi/2 - n\pi) \\ &= \frac{2\pi}{M} \sum_{n=-\infty}^{\infty} \delta(\psi - 2n\pi/M) T_n(y_i). \end{aligned} \tag{49}$$

When the contributions of type (42) are included, the sum of all the symmetric/antisymmetric residues of $\cos \nu\eta\, f^{(e)}$ is

$$\begin{aligned} &\frac{1}{2} \sum_{n=-\infty}^{\infty} [\delta(\eta + |\Phi - \phi| - 2n\pi/M) + \delta(\eta - |\Phi - \phi| \\ &\quad - 2n\pi/M) \pm \delta(\eta + 2\pi - \Phi - \phi - 2n\pi/M) \\ &\quad \pm \delta(\eta - 2\pi + \Phi + \phi - 2n\pi/M)] \left[\frac{1 \pm \Gamma}{2(M \pm N\Gamma)}\right. \\ &\quad \left. + \sum_{i=1}^{m} \frac{T_M(\beta_i) \pm \Gamma T_N(\beta_i)}{MT_M(\beta_i) \pm N\Gamma T_N(\beta_i)} T_n(y_i)\right], \end{aligned} \tag{50}$$

in which the coefficients in the i summation can be simplified according to (45). Evidently this summation depends on n, which is restricted to values, dependent on N,M, that allow the vanishing arguments of the four delta functions in (50) to produce field contributions for $0 < \eta < \pi$ and the actual range of field and source angles

$$(m-q)\pi/M < \phi, \ \Phi < \pi \Rightarrow \begin{cases} 0 < |\Phi - \phi| < (m+1+q)\pi/M \\ 2(m-q)\pi/M < \phi + \Phi < 2\pi \end{cases}. \tag{51}$$

Thus the ranges of integer values of n for each delta function argument are:

$$\begin{aligned} &\eta + |\Phi - \phi| = 2n\pi/M \quad [1 \leqslant n \leqslant (m+q+M)/2], \\ &\eta - |\Phi - \phi| = 2n\pi/M \quad [-(m+q)/2 \leqslant n \leqslant m], \\ &\eta + 2\pi - \Phi - \phi = 2n\pi/M \quad (1 \leqslant n \leqslant M+q), \\ &\eta - 2\pi + \Phi + \phi = 2n\pi/M \quad [-(m+q) \leqslant n \leqslant m]. \end{aligned} \tag{52}$$

The sum of the symmetric/antisymmetric residues of $e^{-\nu\xi} \sin \nu\pi f^{(e)}$ can be similarly expressed, after the introduction of

$$\begin{aligned} &\psi_1 = \pi + \Phi - \phi, \quad \psi_2 = \pi - \Phi + \phi, \quad \psi_3 = 3\pi - \Phi - \phi, \\ &\psi_4 = \Phi + \phi - \pi, \quad \chi_i = \cos^{-1}(-y_i), \end{aligned} \tag{53}$$

as

$$\frac{1}{4\pi}\sum_{j=1}^{4}\frac{1}{\cosh M\xi-\cos M\psi_j}\times\sum_{i=1}^{m}\frac{T_M(\beta_i)\pm\Gamma T_N(\beta_i)}{T_M(\beta_i)\pm N\Gamma T_N(\beta_i)/M}\times\{\cosh[\tfrac{1}{2}M(1+\chi_i/\pi)\xi]\sin[\tfrac{1}{2}M(1-\chi_i/\pi)\psi_j]+\cosh[\tfrac{1}{2}M(1-\chi_i/\pi)\xi]\sin[\tfrac{1}{2}M(1+\chi_i/\pi)\psi_j]\} \tag{54}$$

in which, since M is odd,

$$\cos M\psi_1=\cos M\psi_2=-\cos M(\Phi-\phi),\qquad \cos M\psi_3=\cos M\psi_4=-\cos M(\Phi+\phi). \tag{55}$$

V. EITHER *M* OR *N* EVEN

In this case, it is advantageous to consider the sum and difference of the symmetric and antisymmetric residues. This is because the coefficient in (42) now depends on k and the property $x^a_{M-i}=-x^s_i\ (1\leqslant i\leqslant M-1)$ implies that the coefficients in (43) for x^a_{M-i} and x^s_i are identical. The sum of the symmetric and antisymmetric residues of $\cos\nu\eta\ f^{(e)}$ at ν_{kM} is

$$\frac{1}{2\pi}{\sum_{k=0}^{\infty}}'\frac{(-1)^k+\Gamma}{(-1)^k+N\Gamma/M}[\cos kM(\Phi-\phi)+\cos kM(2\pi-\Phi-\phi)]\cos kM\eta$$
$$+\frac{1}{2\pi}\sum_{k=1}^{\infty}\frac{(-1)^k-\Gamma}{(-1)^k-N\Gamma/M}[\cos kM(\Phi-\phi)-\cos kM(2\pi-\Phi-\phi)]\cos kM\eta$$
$$=\frac{1}{2\pi}\left(\frac{1-N\Gamma^2/M}{1-N^2\Gamma^2/M^2}\right){\sum_{k=0}^{\infty}}'[\cos kM(\Phi-\phi+\eta)+\cos kM(\Phi-\phi-\eta)]$$
$$+\frac{1}{2\pi}\left(\frac{(1-N/M)\Gamma}{1-N^2\Gamma^2/M^2}\right){\sum_{k=0}^{\infty}}'(-1)^k[\cos kM(2\pi-\Phi-\phi+\eta)+\cos kM(2\pi-\Phi-\phi-\eta)]$$
$$=\frac{1}{2M}\left(\frac{1-N\Gamma^2/M}{1-N^2\Gamma^2/M^2}\right)\sum_{n=-\infty}^{\infty}[\delta(\eta+|\Phi-\phi|-2n\pi/M)+\delta(\eta-|\Phi-\phi|-2n\pi/M)]$$
$$+\frac{1}{2M}\frac{(1-N/M)\Gamma}{(1-N^2\Gamma^2/M^2)}\sum_{n=-\infty}^{\infty}\left[\delta\left(\eta+2\pi-\Phi-\phi-\frac{2n-1}{M}\pi\right)+\delta\left(\eta-2\pi+\Phi+\phi-\frac{2n-1}{M}\pi\right)\right]. \tag{56}$$

For the difference, that is the symmetric minus the antisymmetric residues, interchange the coefficients of these two series. The sum of the symmetric and antisymmetric residues of $\cos\nu\eta\ f^{(e)}$ at $\nu^{s,a}_{(k-1)M+i}$ is

$$\frac{1}{\pi}\sum_{k=1}^{\infty}\sum_{i=1}^{M-1}\left\{\frac{T_M(x^s_i)+\Gamma T_N(x^s_i)}{T_M(x^s_i)+N\Gamma T_N(x^s_i)/M}\cos[\nu^s_{(k-1)M+i}(\pi-\Phi)]\cos[\nu^s_{(k-1)M+i}(\pi-\phi)]\cos[\nu^s_{(k-1)M+i}\eta]\right.$$
$$\left.+\frac{T_M(x^a_i)-\Gamma T_N(x^a_i)}{T_M(x^a_i)-N\Gamma T_N(x^a_i)/M}\sin[\nu^a_{(k-1)M+i}(\pi-\Phi)]\sin[\nu^a_{(k-1)M+i}(\pi-\phi)]\cos[\nu^a_{(k-1)M+i}\eta]\right\}, \tag{57}$$

which, in view of the relationships

$$x^a_i=-x^s_{M-i}\quad(1\leqslant i\leqslant M-1),\qquad \nu^a_{(k-1)M+i}=(k-\tfrac{1}{2})M-(-1)^k(M/\pi)\sin^{-1}x^s_{M-i}, \tag{58}$$

reduces to

$$\frac{1}{2M}\sum_{i=1}^{M-1}\frac{T_M(x^s_i)+\Gamma T_N(x^s_i)}{T_M(x^s_i)+N\Gamma T_N(x^s_i)/M}\sum_{n=-\infty}^{\infty}\left\{\left[\delta\left(\eta+|\Phi-\phi|-\frac{2n\pi}{M}\right)+\delta\left(\eta-|\Phi-\phi|-\frac{2n\pi}{M}\right)\right]T_{2n}(x^s_i)\right.$$
$$\left.+\left[\delta\left(\eta+2\pi-\Phi-\phi-\frac{2n-1}{M}\pi\right)-\delta\left(\eta-2\pi+\Phi+\phi-\frac{2n-1}{M}\pi\right)\right]T_{2n-1}(x^s_i)\right\}. \tag{59}$$

Hence the sum of all the symmetric plus antisymmetric residues of $\cos\nu\eta\ f^{(e)}$ is

$$\frac{1}{2M}\sum_{n=-\infty}^{\infty}\left\{\left[\delta\left(\eta+|\Phi-\phi|-\frac{2n}{M}\,\pi\right)+\delta\left(\eta-|\Phi-\phi|-\frac{2n}{M}\,\pi\right)\right]\left[\frac{1-N\Gamma^2/M}{1-N^2\Gamma^2/M^2}+\sum_{i=1}^{M-1}\frac{T_M(x_i^s)+\Gamma T_N(x_i^s)}{T_M(x_i^s)+N\Gamma T_N(x_i^s)/M}\,T_{2n}(x_i^s)\right]\right.$$
$$+\left[\delta\left(\eta+2\pi-\Phi-\phi-\frac{2n-1}{M}\,\pi\right)+\delta\left(\eta-2\pi+\Phi+\phi-\frac{2n-1}{M}\,\pi\right)\right]$$
$$\left.\times\left[\frac{(1-N/M)\Gamma}{1-N^2\Gamma^2/M^2}+\sum_{i=1}^{M-1}\frac{T_M(x_i^s)+\Gamma T_N(x_i^s)}{T_M(x_i^s)+N\Gamma T_N(x_i^s)/M}\,T_{2n-1}(x_i^s)\right]\right\}. \tag{60}$$

For the difference of all symmetric minus antisymmetric residues, interchange the angles $|\Phi-\phi|$ and $2\pi-\Phi-\phi$. The restrictions on the values of n are similar to (52).

The sum of symmetric plus antisymmetric residues of $e^{-\nu\xi}\sin\nu\pi f^{(e)}$ is

$$\frac{1}{4\pi}\sum_{k=1}^{\infty}\sum_{i=1}^{M-1}\frac{T_M(x_i^s)+\Gamma T_N(x_i^s)}{T_M(x_i^s)+N\Gamma T_N(x_i^s)/M}e^{-(k-1/2)M\xi}$$
$$\times\left\{e^{-(-1)^k(M\xi/\pi)\,\sin^{-1}x_i^s}\left[\sin\left\{\left[\left(k-\frac{1}{2}\right)M+(-1)^k\,\frac{M}{\pi}\,\sin^{-1}x_i^s\right](\pi+|\Phi-\phi|)\right\}\right.\right.$$
$$+\sin\left\{\left[\left(k-\frac{1}{2}\right)M+(-1)^k\,\frac{M}{\pi}\,\sin^{-1}\,x_i^s\right](\pi-|\Phi-\phi|)\right\}+2\ \text{similar terms with}\ 2\pi-\Phi-\phi\ \text{instead of}\ |\Phi-\phi|\Big]$$
$$+e^{(-1)^k(M\xi/\pi)\,\sin^{-1}x_i^s}\left[\sin\left\{\left[\left(k-\frac{1}{2}\right)M-(-1)^k\,\frac{M}{\pi}\,\sin^{-1}\,x_i^s\right](\pi+|\Phi-\phi|)\right\}\right.$$
$$\left.\left.+\sin\left\{\left[\left(k-\frac{1}{2}\right)M-(-1)^k\,\frac{M}{\pi}\,\sin^{-1}\,x_i^s\right](\pi-|\Phi-\phi|)\right\}\right.\right.$$
$$\left.\left.-2\ \text{similar terms with}\ 2\pi-\Phi-\phi\ \text{instead of}\ |\Phi-\phi|\right]\right\}. \tag{61}$$

For any angle ψ and $|\gamma|\leqslant 1/2$, the infinite series above are summable as

$$\sum_{k=1}^{\infty}\left[\sin\{[(k-\tfrac{1}{2})+(-1)^k\gamma]M\psi\}\exp\{-[k-\tfrac{1}{2}+(-1)^k\gamma]M\xi\}\pm\sin\{[(k-\tfrac{1}{2})-(-1)^k\gamma]M\psi\}\exp\{-[k-\tfrac{1}{2}-(-1)^k\gamma]M\xi\}\right]$$
$$=2\ \mathrm{Im}\sum_{k=1}^{\infty}e^{-[k-(1/2)]M(\xi-i\psi)}{}_{(-1)^{k-1}}\!\sinh^{\cosh}[\gamma M(\xi-i\psi)]$$
$$=\mathrm{Im}\,\frac{\sinh^{\cosh}[\gamma M(\xi-i\psi)]}{\cosh^{\sinh}[M/2(\xi-i\psi)]}$$
$$=\frac{\cosh[M\xi(1/2+\gamma)]\sin[M\psi(1/2-\gamma)]\pm\cosh[M\xi(1/2-\gamma)]\sin[M\psi(1/2+\gamma)]}{\cosh M\xi\mp\cos M\psi}, \tag{62}$$

and so the sum of the symmetric plus antisymmetric residues of $e^{-\nu\xi}\sin\nu\pi f^{(e)}$ is the finite sum

$$\frac{1}{4\pi}\sum_{i=1}^{M-1}\frac{T_M(x_i^s)+\Gamma T_N(x_i^s)}{T_M(x_i^s)+N\Gamma T_N(x_i^s)/M}\left\{\sum_{j=1}^{2}\frac{\cosh[M\xi(1/2+\lambda_i)[M\psi_j(1/2-\lambda_i)]+\cosh[M\xi(1/2-\lambda_i)]\sin[M\psi_j(1/2+\lambda_i)]}{\cosh M\xi-\cos M\psi_j}\right.$$
$$\left.+\sum_{j=3}^{4}\frac{\cosh[M\xi(1/2+\lambda_i)]\sin[M\psi_j(1/2-\lambda_i)]-\cosh[M\xi(1/2-\lambda_i)]\sin[M\psi_j(1/2+\lambda_i)]}{\cosh M\xi+\cos M\psi_j}\right\}, \tag{63}$$

with ψ_j ($j=1,2,3,4$) defined by (53) and $\lambda_i=(1/\pi)\sin^{-1}x_i^s$. An interchange of the j values yields the difference of the symmetric minus the antisymmetric residues.

VI. THE TOTAL FIELD AND SOME SPECIAL CASES

The results (50), (54), (60), (63) now enable the total field to be recovered by substituting these residue sums into (21), bearing in mind that, as stated in Sec. II, $p_s + p_a$ is the solution when the source angle Φ and the observation angle ϕ are both on the same side of the wedge bisector, while $p_s - p_a$ applies when Φ and ϕ are separated by the symmetry plane. The possible occurrence of delta functions of the general form $\delta(\eta-\psi)$ where η is defined in (22), is at the time instant

$$t_0=\frac{1}{c}\,(r^2+R^2+z^2-2rR\,\cos\,\psi)^{1/2}. \tag{64}$$

The scaling relation

$$\delta(\eta-\psi)d\eta=\delta(t-t_0)dt \tag{65}$$

allows these delta functions to be written in the expected form

$$\frac{c}{rR\,\sin\,\eta}\,\delta(\eta-\psi) = \frac{\delta[t-(1/c)(r^2+R^2+z^2-2rR\cos\,\psi)^{1/2}]}{(r^2+R^2+z^2-2rR\,\cos\,\psi)^{1/2}}. \tag{66}$$

Before proceeding to the special cases, note first that if $N=1$, the coefficient in (45) reduces to

$$\frac{U_{M-2}(x_i)}{U_{M-2}(x_i)\pm\left(1-\frac{1}{M}\right)\Gamma x_i} \tag{67}$$

which in turn, if $M=2m+1$, can be written as

$$\frac{U_{m-1}(y_i)}{U_{m-1}(y_i)\pm m\Gamma/M}. \tag{68}$$

A. Case $\alpha=\pi/3$

In this case $M=3$, $N=1$ and only the values of $\pm\,n$ up to 3 are relevant in (50). The eigenvalue equation (38) has the single solution

$$y_1=-\tfrac{1}{2}(1\pm\Gamma) \tag{69}$$

and the coefficient in (50) is now

$$\frac{1\pm\Gamma}{2(3\pm\Gamma)}+\frac{U_0(y_1)}{3U_0(y_1)\pm\Gamma}\,T_n(y_1) = \frac{1}{3\pm\Gamma}\left[\frac{1\pm\Gamma}{2}+T_n\left(-\frac{1\pm\Gamma}{2}\right)\right]. \tag{70}$$

This is simplified by the observation that $T_n(-x)+x$ has the factor $1+x$ to yield, for $n=0,1,2,3$, respectively:

$$1/2,\quad 0,\quad \pm\Gamma/2,\quad \text{and}\quad (1-\Gamma^2)/2. \tag{71}$$

The diffracted field expression (54) is simplified with

$$\chi=\cos^{-1}[\tfrac{1}{2}(1\pm\Gamma)]\quad (0<\chi<\pi/2),\quad \text{i.e.,}$$
$$\sin\,\tfrac{3}{2}(\pi\mp\chi)=-\cos(\tfrac{3}{2}\,\chi) =-\cos(\tfrac{1}{2}\chi)[2\cos\,\chi-1]=\mp\tfrac{1}{2}\Gamma\sqrt{3\pm\Gamma} \tag{72}$$

and substitution in (21) yields

$$p^{(e)}=\frac{-c}{8\pi rR\,\sin\,\eta}\,[\,\delta(\eta-|\Phi-\phi|)+\delta(\eta-2\pi+\Phi+\phi)\pm\Gamma\,\delta(\eta-4\pi/3+|\Phi-\phi|)$$
$$\pm\Gamma\,\delta(\eta+2\pi/3-\Phi-\phi)+(1-\Gamma^2)\,\delta(\eta-\Phi-\phi)\,]+\frac{\mp 3c\Gamma}{8\pi^2(3\pm\Gamma)^{1/2}rR\,\sinh\,\xi}\left[\frac{1}{\cosh 3\xi+\cos 3(\Phi-\phi)}\right.$$
$$\times\{\cosh[\tfrac{3}{2}\,(1+\chi/\pi)\xi]\cos[\tfrac{3}{2}\,(1-\chi/\pi)(\Phi-\phi)]+\cosh[\tfrac{3}{2}\,(1-\chi/\pi)\xi]\cos[\tfrac{3}{2}\,(1+\chi/\pi)(\Phi-\phi)]\}$$
$$\pm\frac{1}{\cosh 3\xi+\cos 3(\Phi+\phi)}\,\{\cosh[\tfrac{3}{2}\,(1+\chi/\pi)\xi]\cos[\tfrac{3}{2}\,(1-\chi/\pi)(2\pi-\Phi-\phi)]$$
$$\left.+\cosh[\tfrac{3}{2}\,(1-\chi/\pi)\xi]\cos[\tfrac{3}{2}\,(1+\chi/\pi)(2\pi-\Phi-\phi)]\}\right]. \tag{73}$$

The δ functions have range restrictions and, after using (52), the geometrical acoustics field (delta function contributions) caused by a point source on the same side of the symmetry plane ($p_s^{(e)}+p_a^{(e)}$) is therefore

$$p_g^{(e)}=-\frac{1}{4\pi}\left[\frac{\delta\{t-(1/c)[r^2+R^2+z^2-2rR\,\cos(\phi-\Phi)]^{1/2}\}}{[r^2+R^2+z^2-2rR\,\cos(\phi-\Phi)]^{1/2}}\right.$$
$$\left.+\Gamma\,\frac{\delta\{t-(1/c)[r^2+R^2+z^2-2rR\,\cos(\phi+\Phi-2\pi/3)]^{1/2}\}}{[r^2+R^2+z^2-2rR\,\cos(\phi+\Phi-2\pi/3)]^{1/2}}\,H(5\pi/3-\phi-\Phi)\right], \tag{74}$$

while, if the source angle Φ is measured in the opposite sense as the field angle ϕ (Fig. 4), then $(p_s^{(e)}-p_a^{(e)})$ leaves

$$p_g^{(e)}=-\frac{1}{4\pi}\left[\frac{\delta\{t-(1/c)[r^2+R^2+z^2-2rR\,\cos(2\pi-\phi-\Phi)]^{1/2}\}}{[r^2+R^2+z^2-2rR\,\cos(2\pi-\phi-\Phi)]^{1/2}}H(\phi+\Phi-\pi)\right.$$
$$+\Gamma\,\frac{\delta\{t-(1/c)[r^2+R^2+z^2-2rR\,\cos(4\pi/3-|\Phi-\phi|)]^{1/2}\}}{[r^2+R^2+z^2-2rR\,\cos(4\pi/3-|\Phi-\phi|)]^{1/2}}H(|\Phi-\phi|-\pi/3)$$
$$\left.+(1-\Gamma^2)\,\frac{\delta\{t-(1/c)[r^2+R^2+z^2-2rR\,\cos(\phi+\Phi)]^{1/2}\}}{[r^2+R^2+z^2-2rR\,\cos(\phi+\Phi)]^{1/2}}H(\pi-\phi-\Phi)\right]. \tag{75}$$

The first term in each of (74) and (75) is the direct ensonification from the point source, while the second terms are reflections from either wedge face. Penetration through the wedge is responsible for the last term of (75), where the total transmission coefficient is $(1+\Gamma)(1-\Gamma)$.

B. Case $\alpha=2\pi/5$

With $M=5$, $N=1$, the applicable range of $\pm\ n$ is 0–5 and the eigenvalue equation (47) is

$$U_1(y)+U_2(y)=2y+4y^2-1=\mp\Gamma, \tag{76}$$

i.e.,

$$y_1+y_2=-\tfrac{1}{2},\quad y_1y_2=-\tfrac{1}{4}(1\mp\Gamma),$$
$$y_2-y_1=\tfrac{1}{2}\sqrt{5\mp4\Gamma}. \tag{77}$$

The coefficient in (50) is thus

$$\frac{1\pm\Gamma}{2(5\pm\Gamma)}+\sum_{i=1}^{2}\frac{U_1(y_i)}{5U_1(y_i)\pm2\Gamma}\,T_n(y_i)$$
$$=\frac{1}{5\pm\Gamma}\left[\frac{1\pm\Gamma}{2}+T_n(y_2)+T_n(y_1)\right.$$
$$\left.\mp\frac{\Gamma}{2}\,\frac{T_n(y_2)-T_n(y_1)}{y_2-y_1}\right], \tag{78}$$

which produces, for $n=0,1,\ldots,5$, respectively,

$$1/2,\quad 0,\quad 0,\quad \pm\Gamma/2,\quad 0,\quad (1-\Gamma^2)/2. \tag{79}$$

Similarly, for the diffracted field, with $y_i=-\cos\chi_i$ as in (53)

$$\sum_{i=1}^{2}\frac{y_i}{y_i\pm\Gamma/5}\cosh\frac{5\chi_i}{2\pi}(\xi-i\psi)$$
$$=\frac{2}{1\pm\Gamma/5}\left\{\cosh\left[\frac{5(\chi_1+\chi_2)}{2\pi}(\xi-i\psi)\right]\cosh\left[\frac{5(\chi_1-\chi_2)}{2\pi}\right.\right.$$
$$\left.\times(\xi-i\psi)\right]\mp\frac{\Gamma}{\sqrt{5\mp4\Gamma}}\sinh\left[\frac{5(\chi_1+\chi_2)}{2\pi}\right.$$
$$\left.\left.\times(\xi-i\psi)\right]\sinh\left[\frac{5(\chi_1-\chi_2)}{2\pi}(\xi-i\psi)\right]\right\}. \tag{80}$$

But, if $\cos\chi_i\,(i=1,2)$ satisfy $\cos^2\chi-2b\,\cos\chi+c=0$, it may be shown, by observing that $\sin\chi_i=Ab\mp A^{-1}\sqrt{b^2-c}$ for some constant A, that

$$\sin\chi_1\,\sin\chi_2=\sqrt{(1+c)^2-4b^2}$$

i.e.,

$$\cos(\chi_1\pm\chi_2)=c\mp\sqrt{(1+c)^2-4b^2}. \tag{81}$$

Substitution of (79), (80) into (50), (54) and then (21) now shows that the symmetric field is given by

$$p_s^{(e)}=\frac{-c}{8\pi rR\,\sin\eta}\left[\delta(\eta-|\Phi-\phi|)+\delta(\eta-2\pi+\Phi+\phi)+\Gamma\,\delta(\eta-6\pi/5+|\Phi-\phi|)+\Gamma\,\delta(\eta+4\pi/5-\Phi-\phi)\right.$$
$$\left.+(1-\Gamma^2)\,\delta(\eta-\Phi-\phi)\right]+\frac{5c}{2\pi^2(5+\Gamma)rR\,\sinh\xi}\left[\frac{1}{\cosh5\xi+\cos5(\Phi-\phi)}\,\mathrm{Re}\left(\cosh\frac{5}{2}[\xi+i(\Phi-\phi)]\right.\right.$$
$$\times\left\{\cosh\left[\frac{5(\chi_2+\chi_1)}{2\pi}[\xi-i(\pi+\Phi-\phi)]\right]\cosh\left[\frac{5(\chi_2-\chi_1)}{2\pi}[\xi-i(\pi+\Phi-\phi)]\right]\right.$$
$$\left.\left.-\frac{\Gamma}{\sqrt{5-4\Gamma}}\sinh\left[\frac{5(\chi_2+\chi_1)}{2\pi}[\xi-i(\pi+\Phi-\phi)]\right]\sinh\left[\frac{5(\chi_2-\chi_1)}{2\pi}[\xi-i(\pi+\Phi-\phi)]\right]\right)\right\}$$
$$\left.+\text{three sets of similar terms with }\left\{\begin{matrix}\phi-\Phi\\2\pi-\Phi-\phi\\\Phi+\phi-2\pi\end{matrix}\right\}\text{ instead of }\Phi-\phi\right], \tag{82}$$

where, from (76) and (81)

$$\chi_1 \pm \chi_2 = \cos^{-1}\{-\tfrac{1}{4}[1+\Gamma \pm \sqrt{(5+\Gamma)(1+\Gamma)}]\}. \tag{83}$$

Results corresponding to (74) and (75) can readily be deduced for the antisymmetric field by changing the sign of Γ and the sign of terms involving the sum $\Phi+\phi$ in this symmetric field expression.

C. Case $\alpha=\pi/4$

In this case of the right-angled wedge, $N/M = 1/2$ and the eigenvalue equations (39), (41) reduce to

$$\nu_{2k} = 2k, \quad \nu^{s,a}_{2k-1} = (2k-1) \mp (-1)^k (2/\pi)\, \sin^{-1}(\Gamma/2). \tag{84}$$

The residue sum (60) reduces to

$$\frac{1}{4-\Gamma^2} \sum_{n=-\infty}^{\infty} \Bigg\{ [\delta(\eta + |\Phi-\phi| - n\pi) + \delta(\eta - |\Phi-\phi| - n\pi)][T_{2n}(\Gamma/2) - T_2(\Gamma/2)] + \left[\delta\left(\eta + 2\pi - \Phi - \phi - \frac{2n-1}{2}\,\pi\right) + \delta\left(\eta - 2\pi + \Phi + \phi - \frac{2n-1}{2}\,\pi\right)\right][\Gamma/2 - T_{2n-1}(\Gamma/2)] \Bigg\} \tag{85}$$

in which the relevant values of n are (1), (0), (1,2), (0,1) in the respective delta functions above. Since the only nonzero contributions arise from

$$T_0(\Gamma/2) - T_2(\Gamma/2) = \tfrac{1}{2}(4-\Gamma^2), \quad \Gamma/2 - T_3(\Gamma/2) = \tfrac{1}{2}\Gamma(4-\Gamma^2) \tag{86}$$

the total sum reduces to

$$\tfrac{1}{2}[\delta(\eta - |\Phi-\phi|) + \Gamma\,\delta(\eta + \pi/2 - \Phi - \phi)]. \tag{87}$$

After substituting (63) and (87) into (21), the field due to a point source on the same side of the symmetry plane is therefore

$$\begin{aligned} p_s^{(e)} + p_a^{(e)} = {} & \frac{-c}{4\pi r R\, \sin\,\eta}\,[\delta(\eta - |\Phi-\phi|) + \Gamma\,\delta(\eta + \pi/2 - \Phi - \phi)] \\ & + \frac{c\Gamma}{2\pi^2 r R\, \sinh\,\xi (4-\Gamma^2)^{1/2}} \Bigg[\frac{1}{\cosh 2\xi - \cos 2(\Phi-\phi)} \Bigg\{ \cosh\left[\left(1 + \frac{2}{\pi}\sin^{-1}(\Gamma/2)\right)\xi\right] \cos\left[\left(1 - \frac{2}{\pi}\sin^{-1}(\Gamma/2)\right) \\ & \times (\Phi-\phi)\right] - \cosh\left[\left(1 - \frac{2}{\pi}\sin^{-1}(\Gamma/2)\right)\xi\right] \cos\left[\left(1 + \frac{2}{\pi}\sin^{-1}(\Gamma/2)\right)(\Phi-\phi)\right]\Bigg\} - \frac{1}{\cosh 2\xi + \cos 2(\Phi+\phi)} \\ & \times \Bigg\{ \cosh\left[\left(1 + \frac{2}{\pi}\sin^{-1}(\Gamma/2)\right)\xi\right] \cos\left[\left(1 - \frac{2}{\pi}\sin^{-1}(\Gamma/2)\right)(2\pi - \Phi - \phi)\right] \\ & + \cosh\left[\left(1 - \frac{2}{\pi}\sin^{-1}(\Gamma/2)\right)\xi\right] \cos\left[\left(1 + \frac{2}{\pi}\sin^{-1}(\Gamma/2)\right)(2\pi - \Phi - \phi)\right]\Bigg\}\Bigg]. \end{aligned} \tag{88}$$

By a similar sequence of arguments, the field due to a point source on the opposite side of the symmetry plane is

$$\begin{aligned} p_s^{(e)} - p_a^{(e)} = {} & \frac{-c}{4\pi r R\, \sin\,\eta}\,[\delta(\eta - 2\pi + \Phi + \phi) + \Gamma\,\delta(\eta + |\Phi-\phi| - 3\pi/2) + (1-\Gamma^2)\,\delta(\eta - \Phi - \phi)] \\ & + \frac{c\Gamma}{2\pi^2 r R\, \sinh\,\xi (4-\Gamma^2)^{1/2}} \Bigg[\frac{1}{\cosh 2\xi - \cos 2(\Phi+\phi)} \Bigg\{ \cosh\left[\left(1 + \frac{2}{\pi}\sin^{-1}(\Gamma/2)\right)\xi\right] \cos\left[\left(1 - \frac{2}{\pi}\sin^{-1}(\Gamma/2)\right) \\ & \times (2\pi - \Phi - \phi)\right] - \cosh\left[\left(1 - \frac{2}{\pi}\sin^{-1}(\Gamma/2)\right)\xi\right] \cos\left[\left(1 + \frac{2}{\pi}\sin^{-1}(\Gamma/2)\right)(2\pi - \Phi - \phi)\right]\Bigg\} \\ & - \frac{1}{\cosh 2\xi + \cos 2(\Phi-\phi)} \Bigg\{ \cosh\left[\left(1 + \frac{2}{\pi}\sin^{-1}(\Gamma/2)\right)\xi\right] \cos\left[\left(1 - \frac{2}{\pi}\sin^{-1}(\Gamma/2)\right)(\Phi-\phi)\right] \\ & + \cosh\left[\left(1 - \frac{2}{\pi}\sin^{-1}(\Gamma/2)\right)\xi\right] \cos\left[\left(1 + \frac{2}{\pi}\sin^{-1}(\Gamma/2)\right)(\Phi-\phi)\right]\Bigg\}\Bigg]. \end{aligned} \tag{89}$$

D. Case $\alpha=\pi/6$

When $N/M = 2/3$ the eigenvalue equation (38) yields

$$\left.\begin{aligned} x_1^s &= -\tfrac{1}{4}\Gamma - \tfrac{1}{2}(1+\tfrac{1}{4}\Gamma^2)^{1/2} < 0; \quad x_2^s = -\tfrac{1}{4}\Gamma + \tfrac{1}{2}(1+\tfrac{1}{4}\Gamma^2)^{1/2} > 0 \\ x_1^a &= \tfrac{1}{4}\Gamma - \tfrac{1}{2}(1+\tfrac{1}{4}\Gamma^2)^{1/2} < 0; \quad x_2^a = \tfrac{1}{4}\Gamma + \tfrac{1}{2}(1+\tfrac{1}{4}\Gamma^2)^{1/2} > 0 \end{aligned}\right\} \begin{aligned} x_1^a &= -x_2^s \\ x_1^s &= -x_2^a \end{aligned} \tag{90}$$

i.e., from (41),

$$\left.\begin{matrix} \nu_{3k-2}^a \\ \nu_{3k-1}^s \end{matrix}\right\} = 3\left(k-\frac{1}{2}\right) \mp (-1)^k \frac{3}{\pi} \sin^{-1} x_2^s, \quad \left.\begin{matrix} \nu_{3k-2}^s \\ \nu_{3k-1}^a \end{matrix}\right\} = 3\left(k-\frac{1}{2}\right) \mp (-1)^k \frac{3}{\pi} \sin^{-1} x_2^a. \tag{91}$$

The coefficient in (57) can, by use of (90), be simplified to

$$\frac{T_3(x_i^s)+\Gamma T_2(x_i^s)}{T_3(x_i^s)+2\Gamma T_2(x_i^s)/3} = \frac{3}{9-4\Gamma^2}\left[3-\Gamma^2 \mp \frac{\Gamma(1-\Gamma^2)}{(4+\Gamma)^{1/2}}\right]; \quad i = \begin{cases} 1 \\ 2 \end{cases}. \tag{92}$$

The residue sum (60) can therefore be written

$$\begin{aligned} &\frac{1}{2}\sum_{n=-\infty}^{\infty} [\delta(\eta-|\Phi-\phi|-2n\pi/3)+\delta(\eta+|\Phi-\phi|-2n\pi/3)]\left\{\frac{3-2\Gamma^2}{9-4\Gamma^2}+\frac{3-\Gamma^2}{9-4\Gamma^2}[T_{2n}(x_2^s)+T_{2n}(x_1^s)]\right. \\ &\left.+\frac{\Gamma(1-\Gamma^2)[T_{2n}(x_2^s)-T_{2n}(x_1^s)]}{(9-4\Gamma^2)(4+\Gamma^2)^{1/2}}\right\}+\frac{1}{2}\sum_{n=-\infty}^{\infty}\left[\delta\left(\eta+2\pi-\Phi-\phi-\frac{2n-1}{3}\pi\right)+\delta\left(\eta-2\pi+\Phi+\phi-\frac{2n-1}{3}\pi\right)\right] \\ &\times\left\{\frac{\Gamma}{9-4\Gamma^2}+\frac{3-\Gamma^2}{9-4\Gamma^2}[T_{2n-1}(x_2^s)+T_{2n-1}(x_1^s)]+\frac{\Gamma(1-\Gamma^2)[T_{2n-1}(x_2^s)-T_{2n-1}(x_1^s)]}{(9-4\Gamma^2)(4+\Gamma^2)^{1/2}}\right\} \\ &=\tfrac{1}{2}[\delta(\eta-|\Phi-\phi|)+\Gamma\delta(\eta+\pi/3-\Phi-\phi)H(3\pi-10\alpha-\phi-\Phi)-\Gamma(1-\Gamma^2)\delta(\eta-\pi/3-\Phi-\phi) \\ &\quad\times H(3\pi-14\alpha-\phi-\Phi)], \end{aligned} \tag{93}$$

after retaining only the relevant values of n and simplifying the polynomial combinations according to

$$x_2^s+x_1^s = -\Gamma/2, \quad x_2^s-x_1^s = (1+\Gamma^2/4)^{1/2}. \tag{94}$$

This calculation is aided by defining

$$G_m = T_m(x_2^s)+T_m(x_1^s), \quad H_m = \frac{T_m(x_2^s)-T_m(x_1^s)}{x_2^s-x_1^s} \tag{95}$$

so that

$$G_0 = 2, \quad G_1 = -\Gamma/2, \quad H_0 = 0, \quad H_1 = 1 \tag{96}$$

and the remainder are determined by the difference equations

$$\begin{aligned} G_m &= -\Gamma G_{m-1}/2+(1+\Gamma^2/4)H_{m-1}-G_{m-2} \quad (m\geqslant 2), \\ H_m &= G_{m-1}-\Gamma H_{m-1}/2-H_{m-2} \quad (m\geqslant 2). \end{aligned} \tag{97}$$

Similarly, upon identifying the relevant values of n for the difference (symm−antisymm) residues, and noting that the only alteration is the interchange of $|\Phi-\phi|$ and $(2\pi-\Phi-\phi)$, the expression corresponding to (93) follows:

$$\begin{aligned} &\tfrac{1}{2}[\delta(\eta-2\pi+\Phi+\phi)H(\phi+\Phi-\pi) \\ &+\Gamma\delta(\eta+|\Phi-\phi|-5\pi/3)H(|\Phi-\phi|-2\pi/3) \\ &+(1-\Gamma^2)\delta(\eta-\Phi-\phi)H(\pi-\phi-\Phi)]. \end{aligned} \tag{98}$$

The diffraction field is similar in structure to the previously considered cases.

VII. SAMPLE RESULTS FOR THE DIFFRACTION FIELD

Temporal and spatial behavior of the diffraction field is succinctly displayed as a function of the single metric variable ξ of Eq. (22). The dominant factor $\sinh\xi$ in the denominator of the second term of Eq. (21) produces a first-order singularity at the onset ($\xi=0$) and exponential decay (for large ξ), characteristic of the ''afterglow'' of a time-domain field whose equivalent source is the infinitely long wedge apex. The suppression of this known factor greatly reduces the dynamic range required of linear scale graphs. Therefore, the variation of the diffracted field $p_d^{(e)}$ with source location (R,Φ), observation point (r,ϕ,z), and density contrast (in terms of Γ) is simplified by examining the scaled diffraction field $p_d^{(e)}(\xi) \times rR \sinh\xi/c|\Gamma|$ vs ξ. The additional factor rR/c is obvious from Eq. (21), while the normalizing factor $|\Gamma|$ lowers the sensitivity of the resultant graphs to Γ. Adoption of this scaled diffraction field eliminates any need to consider individual numerical values for the distances R, r, and z, as well as the time t. However, the inherent angular dependence of the solution requires the examination of a range of observation angles ϕ for a fixed source coordinate Φ.

All of the calculations reveal that the diffraction from a penetrable wedge ($-1<\Gamma<+1$) is simply related to that of the corresponding hard or soft wedge ($\Gamma=\pm 1$). Based on the sample wedges considered here, it is apparent that this basic relationship persists over a range of wedge angles. Therefore,

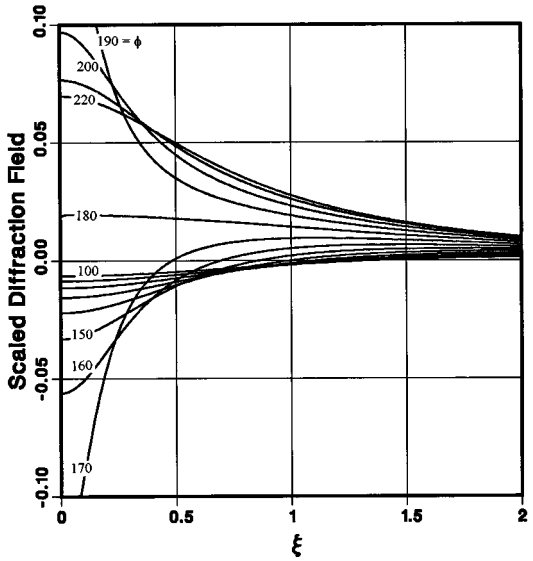

FIG. 6. Scaled diffraction field $p_d^{(e)} \times rR \sinh \xi/c|\Gamma|$ as a function of the metric variable ξ. Case: $\Gamma=-1$, $\alpha=\pi/4$, $\Phi=\pi/2$, $100° \leqslant \phi \leqslant 220°$.

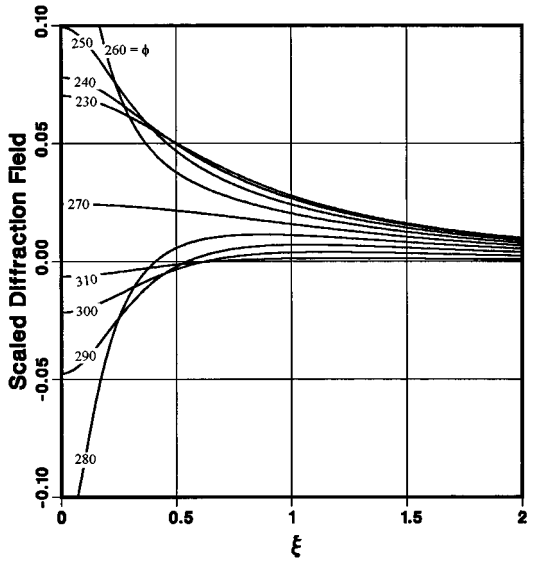

FIG. 8. Scaled diffraction field $p_d^{(e)} \times rR \sinh \xi/c|\Gamma|$ as a function of the metric variable ξ. Case: $\Gamma=-1$, $\alpha=\pi/4$, $\Phi=\pi/2$, $230° \leqslant \phi \leqslant 310°$.

the purposes of the present study are adequately served by graphing, in Figs. 6–10, the parametrized results for one typical case, the corner wedge ($\alpha=\pi/4$). With $\alpha=\pi/4$ and $\Phi=\pi/2$, the geometrical acoustics field suffers discontinuities at $\phi=\pi$ (the reflection boundary) and at $\phi=3\pi/2$ (the shadow boundary). The diffraction field is most important in the vicinity of these ray boundaries, where its primary role is to smooth-out the step discontinuities in the geometrical acoustics field. The second terms of Eqs. (88) and (89) reveal that this discontinuity at the reflection boundary is proportional to Γ, while the discontinuity at the shadow boundary is proportional to Γ^2, as indicated by the third term of Eq. (89).

The variation of the scaled diffraction field with ξ is graphed in Fig. 6 for the subject soft wedge ($\Gamma=-1$) at 13 observation angles ($100° \leqslant \phi \leqslant 220°$) that border the reflection boundary at $\phi=180°$. Note the change of sign and the higher initial bang ($\xi \to 0$) as the reflection boundary is crossed. When the reflection coefficient is changed to $\Gamma=-0.1$, the curves of Fig. 7 apply. Recall the use of Γ as a scaling factor. The qualitative similarity of the curves in Figs. 6 and 7 suggests that the presence of penetration does not dramatically alter the general nature of the external diffraction. As Γ varies from -1 to -0.1, the corresponding curves vary smoothly between those of Figs. 6 and 7. Also, positive Γ from $+0.1$ to $+1$ (hard wedge) yields similar results.

The shadow boundary at 270° is the subject of Figs. 8 and 9, where the observation angle is varied from 230° to 310° for $\Gamma=-1$ and -0.5, respectively. The diffraction fields of Fig. 9 are lower in magnitude, as anticipated from the weaker discontinuity in the geometrical acoustics field.

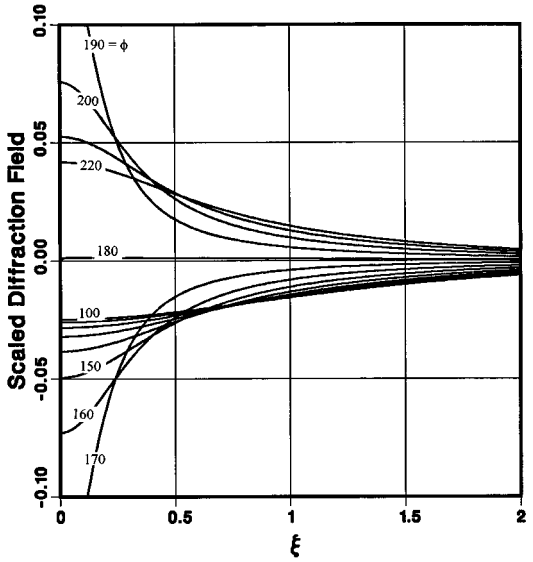

FIG. 7. Scaled diffraction field $p_d^{(e)} \times rR \sinh \xi/c|\Gamma|$ as a function of the metric variable ξ. Case: $\Gamma=-0.1$, $\alpha=\pi/4$, $\Phi=\pi/2$, $100° \leqslant \phi \leqslant 220°$.

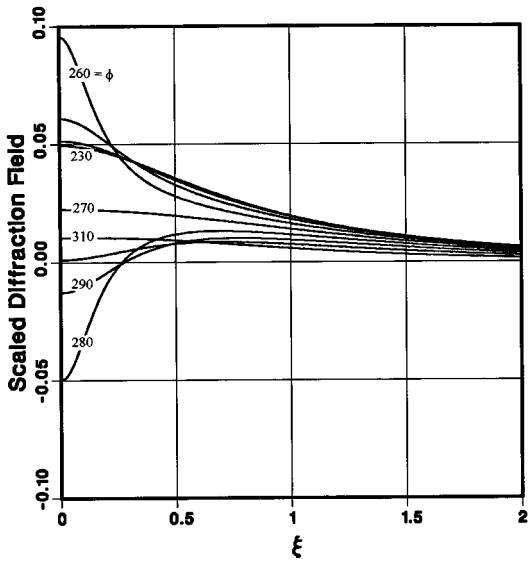

FIG. 9. Scaled diffraction field $p_d^{(e)} \times rR \sinh \xi/c|\Gamma|$ as a function of the metric variable ξ. Case: $\Gamma=-0.5$, $\alpha=\pi/4$, $\Phi=\pi/2$, $230° \leqslant \phi \leqslant 310°$.

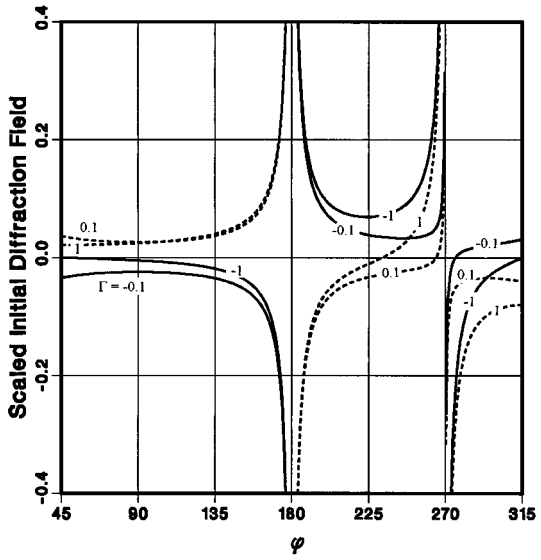

FIG. 10. Scaled initial diffraction field $\lim_{\xi\to 0} p_d^{(e)}(\xi)\times rR \sinh \xi/c|\Gamma|$ as a function of observation angle ϕ. Case: $\alpha=\pi/4$, $\Phi=\pi/2$, $\Gamma=-1$, -0.1, $+0.1$, $+1$.

Furthermore, this trend persists as the density contrast is varied over the entire range $-1\leqslant\Gamma\leqslant+1$.

Another view of the diffraction mechanism is provided by Fig. 10, which illustrates the initial bang of the scaled diffraction field

$$\lim_{\xi\to 0} p_d^{(e)}(\xi)\times rR \sinh \xi/c|\Gamma|$$

as a function of the observation angle for the complete exterior domain $45°\leqslant\phi\leqslant315°$. Only extreme values of the reflection coefficient are used, in particular $\Gamma=-1$, -0.1, $+0.1$, $+1$. The graphs for intermediate values of Γ all fall continuously between the selected curves. Again, note the change in sign at each ray boundary discontinuity and the shift in zero crossings.

VIII. CONCLUSIONS

Closed-form expressions for the complete pressure field caused by an impulsive point source in the region exterior to a density-contrast wedge are obtained for several specific wedges. The geometrical acoustics terms are consistent with the appropriate Snell's law ansatz, including reflection and shadow boundaries, multiple reflections, and the usual Fresnel reflection and transmission coefficients. In the presence of penetration, the diffracted field is structurally similar to the Biot–Tolstoy results, with the primary difference being a lower amplitude attributable to Γ or Γ^2. The persistent qualitative behavior is the initial singularity at the arrival time in accordance with the generalized Fermat's principle, followed by the exponential tail or ''afterglow'' of a time-domain field whose equivalent source is the infinitely long wedge apex.

[1] R. S. Keiffer and J. C. Novarini, ''A Wedge Assemblage Method for 3-D Acoustic Scattering from Sea Surfaces: Comparison with a Helmholtz-Kirchhoff Method,'' Computational Acoustics—Vol. 1, edited by D. Lee, A. Cakmak, and R. Vichnevetsky (Elsevier, Amsterdam, 1990), pp. 67–81.

[2] D. Chu, ''Impulse response of density-contrast wedge using normal coordinates,'' J. Acoust. Soc. Am. **86**, 1883–1896 (1989).

[3] M. A. Biot and I. Tolstoy, ''Formulation of wave propagation in infinite media by normal coordinates with an application to diffraction,'' J. Acoust. Soc. Am. **29**, 381–391 (1957).

[4] A. D. Rawlins, ''Diffraction by a Dielectric Wedge,'' J. Inst. Math Appl. **19**, 261–279 (1977).

[5] A. M. J. Davis, ''Two-dimensional acoustical diffraction by a penetrable wedge,'' J. Acoust. Soc. Am. **100**, 1316–1324 (1996).

[6] E. Marx, ''Electromagnetic Scattering from a Dielectric Wedge and the Single Hypersingular Integral Equation,'' IEEE Trans. Antennas Propag. **41**, 1001–1008 (1993).

[7] D. S. Jones, *Acoustic and Electromagnetic Waves* (Clarendon, Oxford, 1986), pp. 585–590.

Acousto-elastic multiple scattering: A comparison of ultrasonic experiments with multiple multipole expansions

Matthias G. Imhof and M. Nafi Toksöz
Earth Resources Laboratory, Department of Earth, Atmospheric, and Planetary Sciences, Massachusetts Institute of Technology, 42 Carleton Street, Cambridge, Massachusetts 02142-1324

(Received 10 June 1996; accepted for publication 17 December 1996)

Solid rods are submerged in a water tank and illuminated by an ultrasonic source transducer. Along the water surface, transducers are used to measure the propagating wave fields. Even for only three rods, the scattered wave field is very complex. Although the major events can be readily interpreted as direct reflections, the remaining wave field consists of complicated interactions of the wave fields with the scatterers and the water surface. To aid the interpretation, the experiment is modeled numerically using the multiple multipoles method which decomposes the wave fields by their respective origins. Hence, particular events can be correlated with particular scatterers as well as with particular paths of propagation. The numerical method has already been used as a versatile tool to model acoustic or elastic multiple-scattering problems where homogeneous scatterers were embedded in a homogeneous full space. In the present paper, the scheme is expanded to multiple scattering between solids submerged in a fluid. For each scatterer, the waves induced in the fluid are expressed by sets of multipole solutions with different origins. Thus by construction, the scattered wave fields are decomposed by scatterer. The numerical solutions match the ultrasonic experiments very well. Furthermore, the different events can be identified as reflections, internal multiples, or diffractions through the solid rods.
[S0001-4966(97)06604-6]

PACS numbers: 43.20.Fn, 43.30.Gv [ANN]

INTRODUCTION

The scattering of acoustic waves from solids submerged in a fluid has received well-deserved attention for a long time.[1,2] But the effects of multiple elastic scatterers have not been addressed very often. Even for simple cases, the scattered wave fields become very complex. For example, in the case of several submerged solid objects, the major events can readily be interpreted as direct reflections. However, the remaining wave field consists of complicated interactions of the wave fields with the scatterers and domain boundaries such as the water surface. Applications of scattering between multiple solids submerged in water can be found in physical, structural, or underwater acoustics, acoustical oceanography, medical imaging, or fluid-structure interactions. Extrapolating to solid backgrounds or void scatterers, similar problems arise in nondestructive testing or geophysics, e.g., the scattering from buried structures such as tunnels.

Forward modeling of the situation is a valuable aid to understand these interacting events better. Various methods have been applied. For a few simple geometries, analytic solutions are available, e.g., cylindrical objects.[3] For more complicated geometries, other methods have been used: integral equations,[4] the T matrix,[5] perturbation schemes,[6] boundary element methods[7] which might be coupled to finite elements,[8] or the finite difference method.[9]

Multiple multipole expansions (MMP) have already been shown to be a versatile tool to solve scattering problems in fluids[10] or solids.[11] In either case, homogeneous scatterers were embedded in a homogeneous full space. In the present paper, a combination of the acoustic with the elastic scheme is introduced as an interpretative aid to multiple scattering between solids submerged in a fluid. There are various reasons to use MMP expansions. First, they have been shown to converge faster than more traditional methods.[10,11] The resulting scheme is very naturally applied to situations of multiple-scattering objects. Most important, the scattered fields are by construction decomposed by scatterer. Thus the MMP method allows to identify which scatterer emanates a particular event. Although we will not exploit it, the wave field in each solid scatterer is also decomposed into P and S body waves.

The paper is structured as follows. In an ultrasonic water tank, we measure the scattering between three rods of lucite and the water surface. Even though the situation is rather simple, we find the scattered field to contain complex interactions between the rods and the surface. To aid the interpretation, we derive the acousto-elastic MMP scheme which we use to model the two ultrasonic experiments. A comparison of the experimental and numerical data not only validates the acousto-elastic scheme but also explains various events as reflections, internal multiples in the rods, or reverberations between the scatterers and the water surface. The numerical data also identifies some events as reflections being diffracted by the other scatterers.

I. ULTRASONIC EXPERIMENTS

A simple fluid-solid scattering experiment is performed in an ultrasonic water tank. Three rods of lucite are submerged in the tank. Two different geometries are used. The first one, shown in Fig. 1, is named ''down'' for obvious reasons. Accordingly, the second geometry (Fig. 2) is named ''up'' because it is the opposite of the first model. These

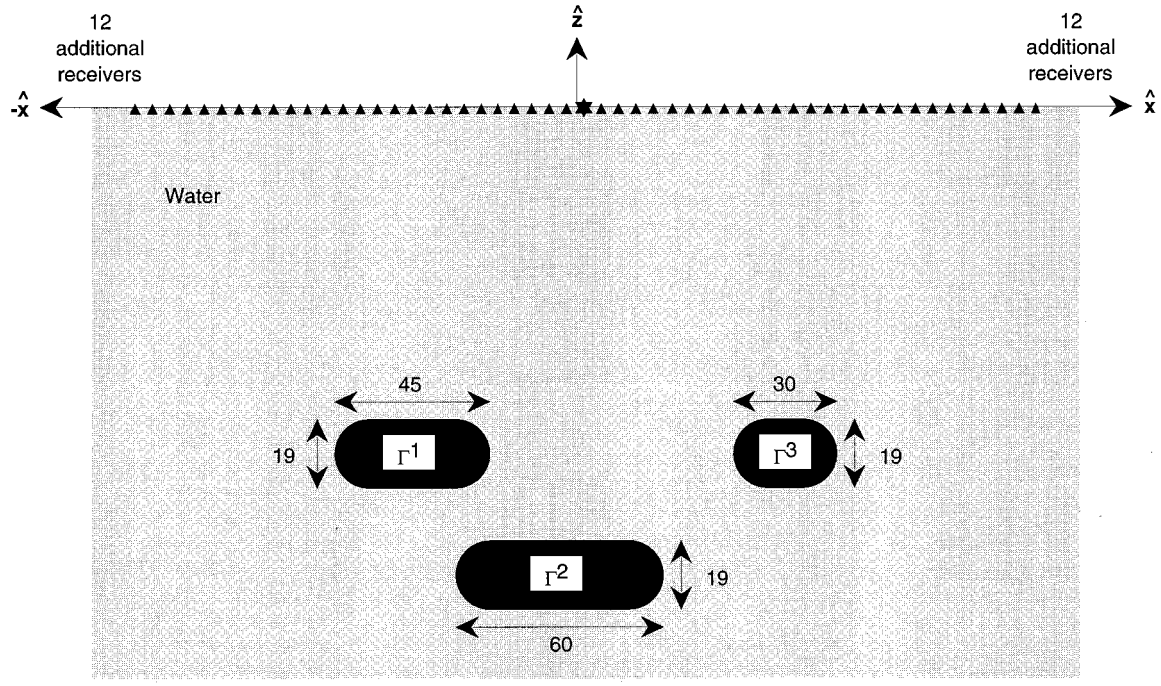

FIG. 1. ''Down'' model: Three oval rods of lucite are submerged in water. The source-transducer (star) generates a pressure wave which scatters between the rods and the water surface until it is picked up by the 75 receivers (triangles). All dimensions are in millimeters. The respective centers of the scatterers Γ^1, Γ^2, and Γ^3 are located at $(-42.5, -99)$, $(0, -136)$, and $(65, -98)$. Both the source and receiver 38 are positioned at (8,0). The spacing between the receivers is 5 mm.

geometries were chosen because they yield complexly scattered fields despite their apparently simple arrangements.

For both geometries, an acoustic source is placed above the rods. Receivers placed along a line perpendicular to the rods measure the signals reflected from the rods. Although the ultrasonic tank is of finite dimensions ($100\times60\times50$ cm), the experiment is designed that reflections from the sides and the bottom of the tank are outside the time window of interest. The tank is equipped with a PC-based control and data acquisition system. A schematic thereof is presented in Fig.

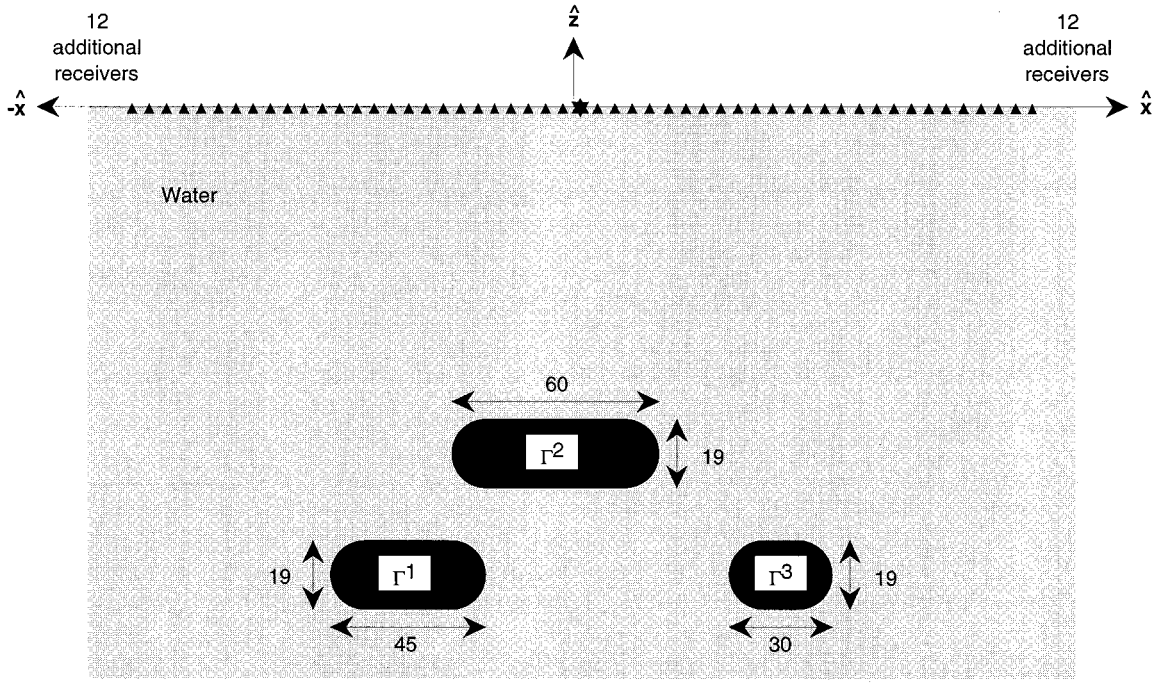

FIG. 2. ''Up'' model where the star denotes the source and the triangles symbolize the receivers. All dimensions are in millimeters. The respective centers of the oval scatterers Γ^1, Γ^2, and Γ^3 are located at $(-42.5, -135)$, $(0, -99)$, and $(65, -138)$. Both the source and receiver 38 are positioned at (8,0). The spacing between the receivers is 5 mm.

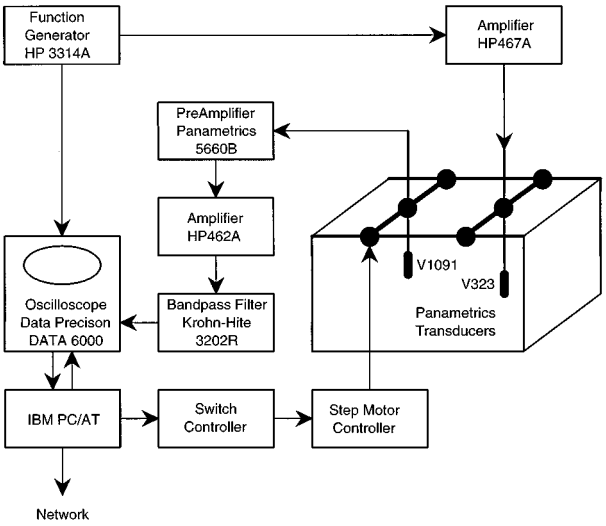

FIG. 3. Block diagram of the computer-based ultrasonic data-acquisition system.

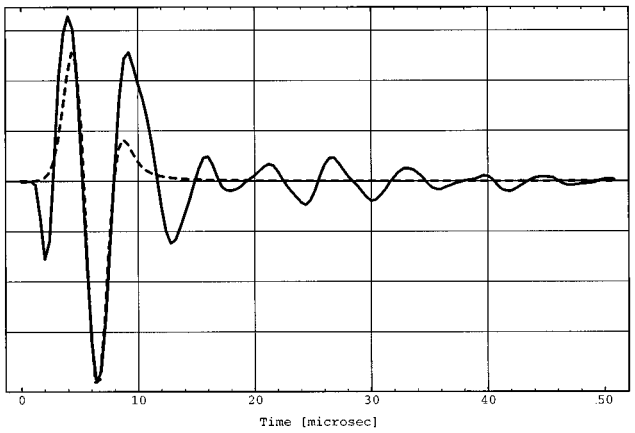

FIG. 4. Wavelets after propagating 30 wavelengths: measured in ultrasonic water tank (solid), Ricker wavelet used for numerical models (dashed).

3. Computer-controlled holders allow movement of a source and a receiver along a prescribed path within the tank. For a fixed source—scatterer—receiver geometry, the computer-controlled acquisition system allows to perform the same experiment a number of times to improve the signal-to-noise ratio. Without waveform averaging, the smaller events would vanish in the ambient noise which reaches the same amplitude level as the reflections.

Piezoelectric transducers act as source and receiver. The source (Panametrix V323) has a strong nonuniform vertical radiation pattern, as most of its energy is pointed vertically downward as expected from a vertical point force.[12] The receiver (Panametrix V1091) has a receiver pattern very similar to the source radiation pattern. This source-receiver combination tends to emphasize waves propagating in the vertical direction and to suppress waves propagating in the horizontal direction. The transducers are placed just beneath the water surface to suppress the source and receiver ghosts.

The rods have a P-wave velocity $\alpha=2570$ m/s, an S-wave velocity $\beta=1200$ m/s, and a density ρ_s of 1180 kg/m^3. The P-wave velocity γ in the water is 1460 m/s, the density ρ_f is 1000 kg/m^3. The width of the first scatterer is 45 mm, the second 60 mm, and the third 30 mm. All scatterers are 19 mm thick. Exciting the source transducer with a sharp pulse, the transducer emits a wavelet of approximately 190-kHz center frequency shown in Fig. 4. In the water, the resulting dominant wavelength is 7.7 mm. Thus, the scatterers are 4–8 times larger and 2.5 times thicker than the propagating pulse which allows to discriminate between reflections from the top or bottom of the scatterers. The sampling interval is chosen to be 400 ns which yields a corresponding Nyquist frequency of 1.25 MHz. The cutoff frequencies of the bandpass filter are set to 5 kHz and 300 kHz, respectively. For each trace, 512 samples are recorded. The recording is delayed by 120 μs to mute the direct arrivals and to maximize the time window of interest. The traces are averaged over 2048 sweeps to reduce the noise amplitudes. The receiver transducer is placed at 75 different positions along a line perpendicular to the rods. The spacing between the receiver points is 5 mm. The source transducer is located in the center of the receiver spread at position 38.

Figure 5 shows the measured record for the ''down'' model defined in Fig. 1. As expected, we obtain the bow tie pattern and triplicated raypaths which are typical for reflections from a focus such as a syncline, a valley, or another concave shape [Fig. 6(a)]. Figure 7 shows the measured record for the ''up'' model defined in Fig. 2. Similar to a convex geometry such as an anticline or a hill, this geometry contains multiple foci [Fig. 6(b)] generating multiple arrivals. For both geometries, the major events can readily be interpreted as direct reflections. But the remaining wave fields consist of complicated interactions of the wave fields

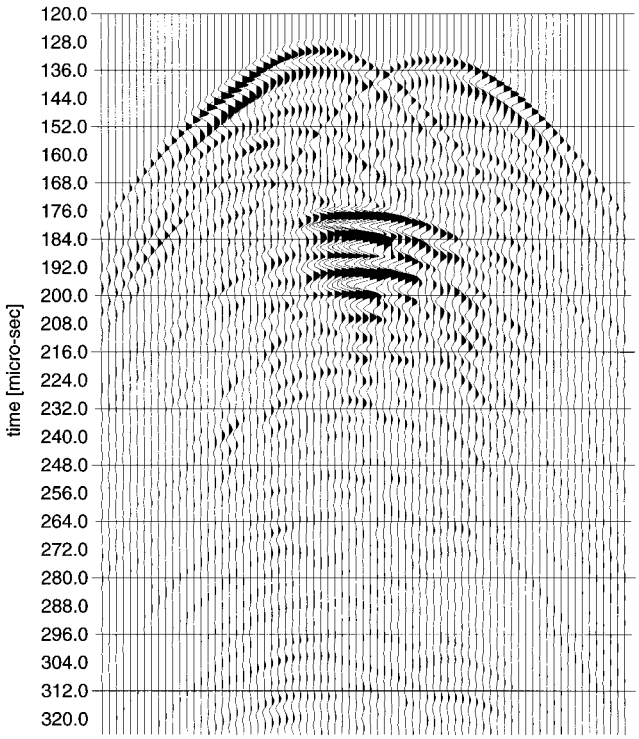

FIG. 5. The seismogram for the ''down'' model defined in Fig. 1 as measured in the ultrasonic water tank.

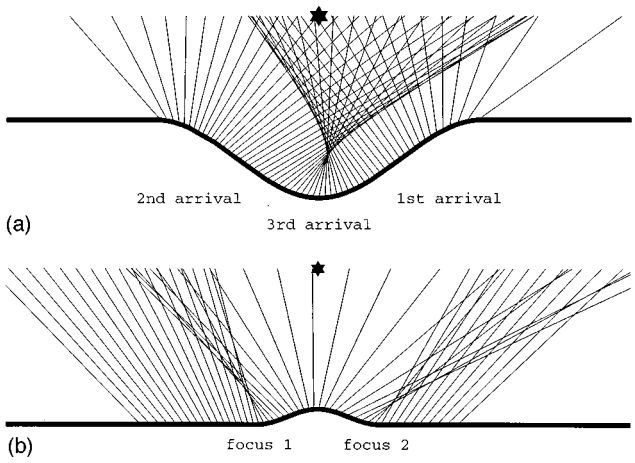

FIG. 6. (a) The reflected raypaths due to a concave geometry (e.g., Fig. 1, model ''down'') where the star denotes the source location and the downgoing rays are omitted for clarity. The focus causes three reflection contributions, first arrival from the right-hand side, second arrival from the left-hand side, and the retrograde rays reflected from the bottom (3rd arrival). (b) The reflected raypaths due to a convex geometry (e.g., Fig. 2, model ''up''). For some receivers, the two foci lead to multiple arrivals.

with the scatterers and the water surface. Despite the simple geometries, it is not obvious how to interpret the different events. As a consequence, we resort to forward-modeling as an interpretative aid.

II. THEORETICAL BACKGROUND

We need to model how the acoustic pulse described by the displacement $\mathbf{u}^{\mathrm{inc}}(\mathbf{x},\omega)e^{i\omega t}$ propagating in the water scatters from submerged solids. For the sake of simplicity, we will suppress the common time factor $e^{i\omega t}$ in all following expressions. To distinguish the different regions, we will use the symbol Γ^d. The fluid domain is denoted by Γ^0. The three solid scatterers are denoted by Γ^1, Γ^2, and Γ^3. The boundary between the fluid Γ^0 and, e.g., the solid Γ^1 is denoted by $\partial\Gamma_{01}$. We presume that waves propagate in two dimensions only. Furthermore, each region Γ^d is assumed to be homogeneous.

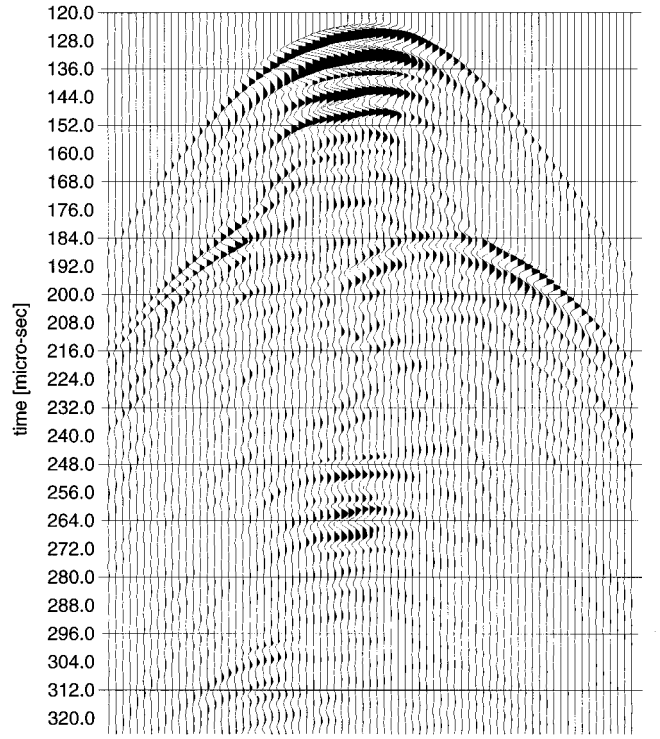

FIG. 7. The seismogram for the ''up'' model defined in Fig. 2 as measured in the ultrasonic water tank.

The interaction of the incident wave $\mathbf{u}^{\mathrm{inc}}(\mathbf{x},\omega)$ with the scatterers Γ^d $(d \neq 0)$ generates a scattered wave field $\mathbf{u}^f$ in the fluid Γ^0. In the frequency domain, the displacement $\mathbf{u}^f$ of the scattered field in Γ^0 is described by

$$\frac{1}{k_f^2}\,\boldsymbol{\nabla}\boldsymbol{\nabla}\cdot\mathbf{u}^f+\mathbf{u}^f=0, \tag{1a}$$

where we defined the wave number $k_f = \omega/\gamma$ for a particular frequency ω and the propagation velocity γ. The fluid velocity can also be written as $\gamma = (\kappa_f\rho_f)^{-1/2}$, where κ_f and ρ_f denote compressibility and density of the fluid.

In each solid Γ^d where $d \neq 0$, the incident wave field $\mathbf{u}^{\mathrm{inc}}(\mathbf{x},\omega)$ induces an elastic P-SV wave $\mathbf{u}_d^s$ which is described by

$$\frac{1}{k_s^2}\,\boldsymbol{\nabla}\boldsymbol{\nabla}\cdot\mathbf{u}_d^s-\frac{1}{l_s^2}\,\boldsymbol{\nabla}\times\boldsymbol{\nabla}\times\mathbf{u}_d^s+\mathbf{u}_d^s=0, \tag{1b}$$

where we defined the wave numbers $k_s=\omega/\alpha$ and $l_s=\omega/\beta$ for a particular frequency ω and the propagation velocities $\alpha=\sqrt{\lambda_s+2\mu_s/\rho_s}$ and $\beta=\sqrt{\mu_s/\rho_s}$. The parameter ρ_s, λ_s, and μ_s denote the density and the Lamé parameters of the medium.

Instead of working with the vector forms (1) of the wave equations, we will use the displacement potentials $\Theta(\mathbf{x},\omega)$, $\Phi_d(\mathbf{x},\omega)$, and $\Psi_d(\mathbf{x},\omega)$ which relate to the displacements $\mathbf{u}^f$ and $\mathbf{u}_d^s$ by

$$\mathbf{u}^f(\mathbf{x},\omega)=\mathbf{u}^{\Theta}(\mathbf{x},\omega)=\boldsymbol{\nabla}\Theta(\mathbf{x},\omega), \tag{2a}$$

$$\begin{aligned}\mathbf{u}_d^s(\mathbf{x},\omega)&=\mathbf{u}_d^{\Phi}(\mathbf{x},\omega)+\mathbf{u}_d^{\Psi}(\mathbf{x},\omega)\\&=\boldsymbol{\nabla}\Phi_d(\mathbf{x},\omega)+\boldsymbol{\nabla}\times\{\Psi_d(\mathbf{x},\omega)\hat{\mathbf{y}}\},\end{aligned} \tag{2b}$$

where the direction $\hat{\mathbf{y}}$ is perpendicular to the plane of propagation (x,z). Each scalar potential itself satisfies a scalar wave equation:

$$\nabla^2\Theta(\mathbf{x},\omega)+k_f^2\Theta(\mathbf{x},\omega)=0, \tag{3a}$$

$$\nabla^2\Phi_d(\mathbf{x},\omega)+k_s^2\Phi_d(\mathbf{x},\omega)=0, \tag{3b}$$

$$\nabla^2\Psi_d(\mathbf{x},\omega)+l_s^2\Psi_d(\mathbf{x},\omega)=0. \tag{3c}$$

Similar to the purely acoustic or elastic cases,[10,11] we expand the potential fields due to the elastic scatterers as

$$\Theta(\mathbf{x},\omega)=\sum_{d=1}^{D}\sum_{p=1}^{P_d^{\Theta}}\sum_{n=-N_{pd}^{\Theta}}^{N_{pd}^{\Theta}} a_{pnd}\cdot\vartheta_{pnd}(\mathbf{x},\mathbf{x}_{pd}^{\Theta},k_f)+e^{\Theta}, \tag{4a}$$

$$\Phi_d(\mathbf{x},\omega)=\sum_{p=1}^{P_d^{\Phi}}\sum_{n=-N_{pd}^{\Phi}}^{N_{pd}^{\Phi}} b_{pnd}\cdot\phi_{pnd}(\mathbf{x},\mathbf{x}_{pd}^{\Phi},k_s)+e_d^{\Phi}, \tag{4b}$$

$$\Psi_d(\mathbf{x},\omega)=\sum_{p=1}^{P_d^\Psi}\sum_{n=-N_{pd}^\Psi}^{N_{pd}^\Psi} c_{pnd}\cdot\psi_{pnd}(\mathbf{x},\mathbf{x}_{pd}^\Psi,l_s)+e_d^\Psi, \quad (4c)$$

where the subscript $d\leqslant D=3$ denotes the index of the scatterer. The expansions $\vartheta_{pnd}(\mathbf{x},\mathbf{x}_{pd}^\theta,\ k_f)$, $\phi_{pnd}(\mathbf{x},\mathbf{x}_{pd}^\Phi,\ k_s)$, and $\psi_{pnd}(\mathbf{x},\mathbf{x}_{pd}^\Psi,\ l_s)$ are all solutions to their respective Helmholtz equations (3). For each expansion, e.g., Φ_d, we choose a set of P_d^Φ expansion centers located at $\mathbf{x}_{pd}^\Phi$. At each expansion center $\mathbf{x}_{pd}^\Phi$, we place a multipole $\Sigma_n\phi_{pnd}(\mathbf{x},\ \mathbf{x}_{pd}^\Phi,\ k_s)$ of order $-N_{pd}^\Phi\leqslant n\leqslant N_{pd}^\Phi$. Because the maximal orders of the multipoles are finite and the resulting expansion is nonorthogonal, we also need to include an error term e_d^Φ. The remaining potential fields Θ and Ψ_d are defined in exactly the same way. This form of the expansion allows to choose different numbers and locations of the expansion centers for each scatterer and each field Θ, Φ_d, and Ψ_d. Also, the maximal orders for the different multipoles can be chosen independently.

An expansion of the form (4) is known as multiple multipole (MMP) expansion because we have in fact a summation over, e.g., P_d^Φ multipoles located at $\mathbf{x}_{pd}^\Phi$. In the fluid, we choose the propagatory solutions $H_{|n|}^{(1)}(k_fr)e^{in\varphi}$ to the Helmholtz equation (3a):

$$\vartheta_{pnd}(\mathbf{x},\mathbf{x}_{pd}^\Theta,k_f)=H_{|n|}^{(1)}(k_f|\mathbf{x}-\mathbf{x}_{pd}^\Theta|)e^{in\varphi_{pd}^\Theta} \quad \text{with } \mathbf{x}_{pd}^\Theta \text{ inside scatterer } d, \quad (5a)$$

where φ_{pd}^Θ is the angle $\sphericalangle(\hat{\mathbf{x}},\ \mathbf{x}-\mathbf{x}_{pd}^\Theta)$ with respect to the unit vector $\hat{\mathbf{x}}$ in the x direction. Foreseeing the need of a free surface in the fluid phase, we directly add the stationary phase contribution of the field reflected at the surface[10,13] to the expansion function (5a):

$$\vartheta_{pnd}(\mathbf{x},\mathbf{x}_{pd}^\Theta,k_f)=H_{|n|}^{(1)}(k_f|\mathbf{x}-\mathbf{x}_{pd}^\Theta|)e^{in\varphi_{pd}^\Theta}-H_{|n|}^{(1)}(k_f|\mathbf{x}-\tilde{\mathbf{x}}_{pd}^\Theta|)e^{-in\tilde{\varphi}_{pd}^\Theta}, \quad (5b)$$

where $\tilde{\varphi}_{pd}^\Theta=\sphericalangle(\hat{\mathbf{x}},\ \mathbf{x}-\tilde{\mathbf{x}}_{pd}^\Theta)$. The location $\tilde{\mathbf{x}}_{pd}^\Theta$ is the corresponding mirror source obtained by reflection of the expansion center $\mathbf{x}_{pd}^\Theta$ across the free surface.

In the solids, we can choose between two different sets of expansion functions for ϕ_{pnd} and ψ_{pnd}. Either we use the propagatory solutions $H_{|n|}^{(1)}(k_sr)e^{in\varphi}$ and $H_{|n|}^{(1)}(l_sr)e^{in\varphi}$, or we choose the standing wave solutions $J_{|n|}(k_sr)e^{in\varphi}$ and $J_{|n|}(l_sr)e^{in\varphi}$:

$$\phi_{pnd}(\mathbf{x},\mathbf{x}_{pd}^\Phi,k_s)=\begin{cases}J_{|n|}(k_s|\mathbf{x}-\mathbf{x}_{pd}^\Phi|)e^{in\varphi_{pd}^\Phi} & \text{if } \mathbf{x}_{pd}^\Phi \text{ is inside scatterer } d \quad (6a)\\ H_{|n|}^{(1)}(k_s|\mathbf{x}-\mathbf{x}_{pd}^\Phi|)e^{in\varphi_{pd}^\Phi} & \text{if } \mathbf{x}_{pd}^\Phi \text{ is outside scatterer } d. \quad (6b)\end{cases}$$

Similarly, we have:

$$\psi_{pnd}(\mathbf{x},\mathbf{x}_{pd}^\Psi,l_s)=\begin{cases}J_{|n|}(l_s|\mathbf{x}-\mathbf{x}_{pd}^\Psi|)e^{in\varphi_{pd}^\Psi} & \text{if } \mathbf{x}_{pd}^\Psi \text{ is inside scatterer } d \quad (7a)\\ H_{|n|}^{(1)}(l_s|\mathbf{x}-\mathbf{x}_{pd}^\Psi|)e^{in\varphi_{pd}^\Psi} & \text{if } \mathbf{x}_{pd}^\Psi \text{ is outside scatterer } d. \quad (7b)\end{cases}$$

The three different wave fields are coupled by the boundary conditions along the interface of the fluid and the solids. The boundary conditions require continuity of the normal displacement $\hat{\mathbf{n}}\cdot\mathbf{u}$, continuity of normal traction $\hat{\mathbf{n}}\cdot\boldsymbol{\sigma}\cdot\hat{\mathbf{n}}$, and vanishing tangential traction $\hat{\mathbf{t}}\cdot\boldsymbol{\sigma}\cdot\hat{\mathbf{n}}$. For a point $\mathbf{x}$ on the interface $\partial\Gamma_{0d}$ $(d\neq 0)$ with the unit normal $\hat{\mathbf{n}}$ and the unit tangential direction $\hat{\mathbf{t}}$, we have

$$\hat{\mathbf{n}}\cdot[\mathbf{u}^{\text{inc}}(\mathbf{x},\omega)+\mathbf{u}^\Theta(\mathbf{x},\omega)]=\hat{\mathbf{n}}\cdot[\mathbf{u}_d^\Phi(\mathbf{x},\omega)+\mathbf{u}_d^\Psi(\mathbf{x},\omega)], \quad (8a)$$

$$\hat{\mathbf{n}}\cdot[\boldsymbol{\sigma}^{\text{inc}}(\mathbf{x},\omega)+\boldsymbol{\sigma}^\Theta(\mathbf{x},\omega)]\cdot\hat{\mathbf{n}}=\hat{\mathbf{n}}\cdot[\boldsymbol{\sigma}_d^\Phi(\mathbf{x},\omega)+\boldsymbol{\sigma}_d^\Psi(\mathbf{x},\omega)]\cdot\hat{\mathbf{n}}, \quad (8b)$$

$$0=\hat{\mathbf{t}}\cdot[\boldsymbol{\sigma}_d^\Phi(\mathbf{x},\omega)+\boldsymbol{\sigma}_d^\Psi(\mathbf{x},\omega)]\cdot\hat{\mathbf{n}}; \quad (8c)$$

where the displacements are defined in (2). The stress tensor of the scattered field in the fluid is given by $\boldsymbol{\sigma}^\Theta(\mathbf{x},\omega)=-\mathbf{I}p(\mathbf{x},\omega)=-\mathbf{I}k_f^2\kappa_f^{-1}\Theta(\mathbf{x},\omega)$ which also defines the pressure $p(\mathbf{x},\omega)$. The stress tensors $\boldsymbol{\sigma}_d^\Phi(\mathbf{x},\omega)$ and $\boldsymbol{\sigma}_d^\Psi(\mathbf{x},\omega)$ are defined in a local coordinate system (r,y,φ) centered at the expansion center of the multipole.

$$\begin{aligned}
&\sigma_{d,rr}^\Phi=-\lambda_sk_s^2\Phi_d+2\mu\frac{\partial^2\Phi_d}{\partial r^2},\quad \sigma_{d,rr}^\Psi=2\mu\frac{\partial}{\partial r}\left(\frac{1}{r}\frac{\partial\Psi_d}{\partial\varphi}\right),\\
&\sigma_{d,\varphi\varphi}^\Phi=-\lambda_sk_s^2\Phi_d+2\mu\frac{1}{r}\left(\frac{\partial\Phi_d}{\partial r}+\frac{1}{r}\frac{\partial^2\Phi_d}{\partial\varphi^2}\right),\quad \sigma_{d,\varphi\varphi}^\Psi=2\mu\left[\frac{1}{r}\left(\frac{1}{r}\frac{\partial\Psi_d}{\partial\varphi}-\frac{\partial^2\Psi_d}{\partial r\,\partial\varphi}\right)\right],\\
&\sigma_{d,r\varphi}^\Phi=2\mu\left[\frac{1}{r}\frac{\partial^2\Phi_d}{\partial r\,\partial\varphi}-\frac{1}{r^2}\frac{\partial\Phi_d}{\partial\varphi}\right],\quad \sigma_{d,r\varphi}^\Psi=2\mu\left[\frac{1}{2r^2}\frac{\partial^2\Psi_d}{\partial\varphi^2}-\frac{r}{2}\frac{\partial}{\partial r}\left(\frac{1}{r}\frac{\partial\Psi_d}{\partial r}\right)\right].
\end{aligned} \quad (9)$$

Note that the components of displacements and of the stress tensors have to be transformed or rotated into the global coordinate frame (x,y,z) in which the unit normal $\hat{\mathbf{n}}$ and the unit tangential direction $\hat{\mathbf{t}}$ are defined.[11]

We solve for the unknown coefficients a_{pnd}, b_{pnd}, and c_{pnd} by enforcing the boundary conditions (8) on discrete matching points $\mathbf{x}_m$ along the boundaries of the scatterers. We obtain a linear system of equations

$$
\begin{pmatrix}
-\mathbf{A}_{11}^{\hat{n}} & -\mathbf{A}_{12}^{\hat{n}} & -\mathbf{A}_{13}^{\hat{n}} & \mathbf{P}_{11}^{\hat{n}} & \mathbf{S}_{11}^{\hat{n}} & \mathbf{0} & \mathbf{0} & \mathbf{0} & \mathbf{0} \\
-\mathbf{A}_{11}^{\hat{n}\hat{n}} & -\mathbf{A}_{12}^{\hat{n}\hat{n}} & -\mathbf{A}_{13}^{\hat{n}\hat{n}} & \mathbf{P}_{11}^{\hat{n}\hat{n}} & \mathbf{S}_{11}^{\hat{n}\hat{n}} & \mathbf{0} & \mathbf{0} & \mathbf{0} & \mathbf{0} \\
\mathbf{0} & \mathbf{0} & \mathbf{0} & \mathbf{P}_{11}^{\hat{n}\hat{t}} & \mathbf{S}_{11}^{\hat{n}\hat{t}} & \mathbf{0} & \mathbf{0} & \mathbf{0} & \mathbf{0} \\
-\mathbf{A}_{21}^{\hat{n}} & -\mathbf{A}_{22}^{\hat{n}} & -\mathbf{A}_{23}^{\hat{n}} & \mathbf{0} & \mathbf{0} & \mathbf{P}_{22}^{\hat{n}} & \mathbf{S}_{22}^{\hat{n}} & \mathbf{0} & \mathbf{0} \\
-\mathbf{A}_{21}^{\hat{n}\hat{n}} & -\mathbf{A}_{22}^{\hat{n}\hat{n}} & -\mathbf{A}_{23}^{\hat{n}\hat{n}} & \mathbf{0} & \mathbf{0} & \mathbf{P}_{22}^{\hat{n}\hat{n}} & \mathbf{S}_{22}^{\hat{n}\hat{n}} & \mathbf{0} & \mathbf{0} \\
\mathbf{0} & \mathbf{0} & \mathbf{0} & \mathbf{0} & \mathbf{0} & \mathbf{P}_{22}^{\hat{n}\hat{t}} & \mathbf{S}_{22}^{\hat{n}\hat{t}} & \mathbf{0} & \mathbf{0} \\
-\mathbf{A}_{31}^{\hat{n}} & -\mathbf{A}_{32}^{\hat{n}} & -\mathbf{A}_{33}^{\hat{n}} & \mathbf{0} & \mathbf{0} & \mathbf{0} & \mathbf{0} & \mathbf{P}_{33}^{\hat{n}} & \mathbf{S}_{33}^{\hat{n}} \\
-A_{31}^{\hat{n}\hat{n}} & -\mathbf{A}_{32}^{\hat{n}\hat{n}} & -\mathbf{A}_{33}^{\hat{n}\hat{n}} & \mathbf{0} & \mathbf{0} & \mathbf{0} & \mathbf{0} & \mathbf{P}_{33}^{\hat{n}\hat{n}} & \mathbf{S}_{33}^{\hat{n}\hat{n}} \\
\mathbf{0} & \mathbf{0} & \mathbf{0} & \mathbf{0} & \mathbf{0} & \mathbf{0} & \mathbf{0} & \mathbf{P}_{33}^{\hat{n}\hat{t}} & \mathbf{S}_{33}^{\hat{n}\hat{t}}
\end{pmatrix}
\cdot
\begin{pmatrix}
\mathbf{a}_1 \\ \mathbf{a}_2 \\ \mathbf{a}_3 \\ \mathbf{b}_1 \\ \mathbf{c}_1 \\ \mathbf{b}_2 \\ \mathbf{c}_2 \\ \mathbf{b}_3 \\ \mathbf{c}_3
\end{pmatrix}
\approx
\begin{pmatrix}
\mathbf{u}_1^{\hat{n}} \\ \boldsymbol{\sigma}_1^{\hat{n}\hat{n}} \\ \mathbf{0} \\ \mathbf{u}_2^{\hat{n}} \\ \boldsymbol{\sigma}_2^{\hat{n}\hat{n}} \\ \mathbf{0} \\ \mathbf{u}_3^{\hat{n}} \\ \boldsymbol{\sigma}_3^{\hat{n}\hat{n}} \\ \mathbf{0}
\end{pmatrix}, \tag{10}
$$

where we use the submatrices $\mathbf{A}_{sd}^{\hat{n}}$, $\mathbf{P}_{sd}^{\hat{n}}$, and $\mathbf{S}_{sd}^{\hat{n}}$ to denote the normal displacements $\hat{\mathbf{n}}\cdot\mathbf{u}$ at the matching points along the scatterer $s\in\{1,2,3\}$ due to ϑ_{pnd}, ϕ_{pnd}, and ψ_{pnd}. The submatrices $\mathbf{A}_{sd}^{\hat{n}\hat{n}}$, $\mathbf{P}_{sd}^{\hat{n}\hat{n}}$, and $\mathbf{S}_{sd}^{\hat{n}\hat{n}}$ are the same but for the normal stress $\hat{\mathbf{n}}\cdot\boldsymbol{\sigma}\cdot\hat{\mathbf{n}}$. The submatrices $\mathbf{P}_{sd}^{\hat{n}\hat{t}}$ and $\mathbf{S}_{sd}^{\hat{n}\hat{t}}$ contain the tangential stresses $\hat{\mathbf{t}}\cdot\boldsymbol{\sigma}\cdot\hat{\mathbf{n}}$. For the sake of clarity, the index d is used to indicate which scatterer induces the field. The index s indicates along which scatterer the boundary conditions are evaluated and thus on which boundary the matching points $\mathbf{x}_m$ lie. All three scatterers contribute to the scattered field $\Theta(\mathbf{x},\omega)$ in the fluid. Therefore, we have submatrices $\mathbf{A}_{sd}$ for each scatterer d and each boundary s. All multiple scattering between the scatterers is automatically accounted for by the boundary conditions. The boundary conditions along, e.g., $\partial\Gamma_{01}$ are established by $\Phi_1(\mathbf{x},\omega)$, $\Psi_1(\mathbf{x},\omega)$, and $\Theta_1(\mathbf{x},\omega)$, $\Theta_2(\mathbf{x},\omega)$, $\Theta_3(\mathbf{x},\omega)$. They are independent of $\Phi_2(\mathbf{x},\omega)$, $\Psi_2(\mathbf{x},\omega)$, $\Phi_3(\mathbf{x},\omega)$, and $\Psi_3(\mathbf{x},\omega)$. The individual scatterers interact only trough the scattered fields $\Theta_1(\mathbf{x},\omega)$, $\Theta_2(\mathbf{x},\omega)$, and $\Theta_3(\mathbf{x},\omega)$ propagating in the fluid. Thus for $s\neq d$, the submatrices $\mathbf{P}_{sd}$ and $\mathbf{S}_{sd}$ vanish. The only contribution for the fields within, e.g., scatterer Γ^1 are due to the (self) interactions of $\Phi_1(\mathbf{x}_m,\omega)$ and $\Psi_1(\mathbf{x}_m,\omega)$. Defining the matching points by their location $\mathbf{x}_{ms}$ along the boundary of scatterer s, we can write the submatrices as

$$
\begin{aligned}
&\mathbf{A}_{sd}^{\hat{n}}=[u_{\hat{n}}(\vartheta_{pnd}(\mathbf{x}_{ms},\omega))],\quad \mathbf{A}_{sd}^{\hat{n}\hat{n}}=[\sigma_{\hat{n}\hat{n}}(\vartheta_{pnd}(\mathbf{x}_{ms},\omega))],\\
&\mathbf{P}_{sd}^{\hat{n}}=[u_{\hat{n}}(\phi_{pnd}(\mathbf{x}_{ms},\omega))],\\
&\mathbf{P}_{sd}^{\hat{n}\hat{n}}=[\sigma_{\hat{n}\hat{n}}(\phi_{pnd}(\mathbf{x}_{ms},\omega))],\\
&\mathbf{P}_{sd}^{\hat{n}\hat{t}}=[\sigma_{\hat{n}\hat{t}}(\phi_{pnd}(\mathbf{x}_{ms},\omega))],\\
&\mathbf{S}_{sd}^{\hat{n}}=[u_{\hat{n}}(\psi_{pnd}(\mathbf{x}_{ms},\omega))],\\
&\mathbf{S}_{sd}^{\hat{n}\hat{n}}=[\sigma_{\hat{n}\hat{n}}(\psi_{pnd}(\mathbf{x}_{ms},\omega))],\\
&\mathbf{S}_{sd}^{\hat{n}\hat{t}}=[\sigma_{\hat{n}\hat{t}}(\psi_{pnd}(\mathbf{x}_{ms},\omega))].
\end{aligned} \tag{11}
$$

Similarly, the vectors $\mathbf{u}_s^{\hat{n}}$ and $\boldsymbol{\sigma}_s^{\hat{n}\hat{n}}$ on the right-hand side of (10) represent the incident wave field in the fluid evaluated at the matching points $\mathbf{x}_{ms}$:

$$
\mathbf{u}_s^{\hat{n}}=[u_n^{\mathrm{inc}}(\mathbf{x}_{ms},\omega)],\quad \boldsymbol{\sigma}_s^{\hat{n}\hat{n}}=[\sigma_{\hat{n}\hat{n}}^{\mathrm{inc}}(\mathbf{x}_{ms},\omega)]. \tag{12}
$$

Finally, the vectors $\mathbf{a}_d$, $\mathbf{b}_d$, and $\mathbf{c}_d$ contain the unknown coefficients a_{pnd}, b_{pnd}, and c_{pnd}. Because the MMP expansions (4) are commonly nonorthogonal, the system (10) is made overdetermined by choosing more matching points than needed. It is then solved in the least-squares sense by QR decomposition using Givens updating.[14]

III. NUMERICAL MODELING

To interpret the ultrasonic results, we model the scattering problems depicted in Figs. 1 and 2. We assume that the source is a vertical dipole exciting an acoustic wave which propagates downwards and interacts with the elastic scatterers. The source pulse is modulated by a Ricker wavelet[15] of 200 kHz. The resulting scattered fields are measured at 75 locations along the surface. Source, scatterers, and receivers are separated by at least 30 dominant wavelengths of 7.7 mm. Due to the resulting long propagation times, many frequencies are needed to calculate the traces. For a sampling interval of 400 ns, we will use 512 frequencies.

To damp resonances, we account for the intrinsic attenuation in the scatterers by making the wave number complex, e.g.,

$$
k=k_r+ia, \tag{13}
$$

where a is the attenuation coefficient. Alternatively, we use the quality factor Q_c which relates to the attenuation coefficient a by

$$
Q_c=\frac{\omega}{2ac}, \tag{14}
$$

where the velocity c is either α or β. Both quality factors Q_α and Q_β are assumed to be 100.

The scattered wave field in the fluid is expanded as (4a) where we choose $D=3$, $P_1^\Theta=4$, $P_2^\Theta=5$, and $P_3^\Theta=3$. For each of these multipoles, we choose $N_{pd}^\Theta=6$. As expansion function, we use (5b) which includes the reflections from the free surface. Figure 8 defines the exact locations of the expansion centers for the ''down'' model (Fig. 1). For the ''up'' model, the same locations relative to the solids are used for the expansion centers.

The wave fields in the solid scatterers are expanded as (4b) and (4c) for the P and the S wave. For scatterer Γ^1, we choose $P_1^\Phi=P_1^\Psi=12$. For scatterer Γ^2, we use $P_2^\Phi=P_2^\Psi=14$. Finally, for the third scatterer Γ^3 we employ $P_3^\Phi=P_3^\Psi=10$ expansion centers. At each expansion center, we use only the orders between -3 and 3. Thus, $N_{pd}^\Phi=N_{pd}^\Psi=3$. Because we placed the expansion centers for the wave fields in the solids outside the scatterers (Fig. 8), we have to use (6b) and (7b) to describe the P and the S waves. For

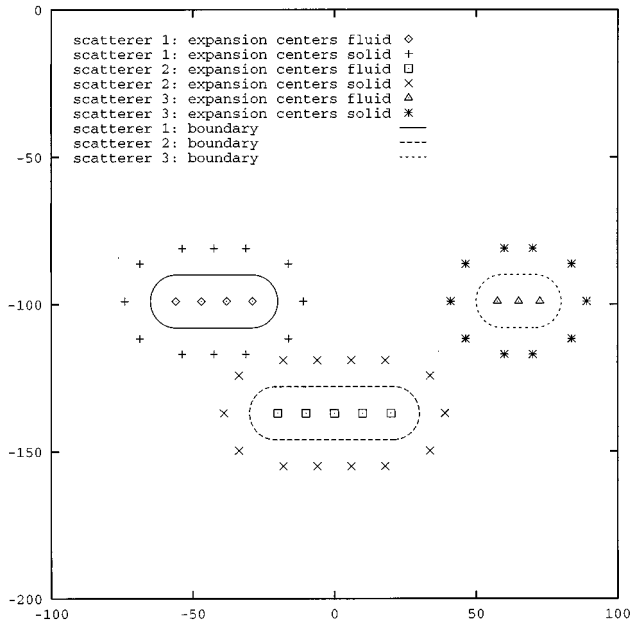

FIG. 8. MMP discretization for the ''down'' model. Shown are the locations of the expansion centers for the multipoles. The multipoles inside the scatterers govern the wave field in the fluid. Multipoles are placed all around the scatterers to model the *P* and *S* waves on the inside. The discretization for the ''up'' model is the same but upside down.

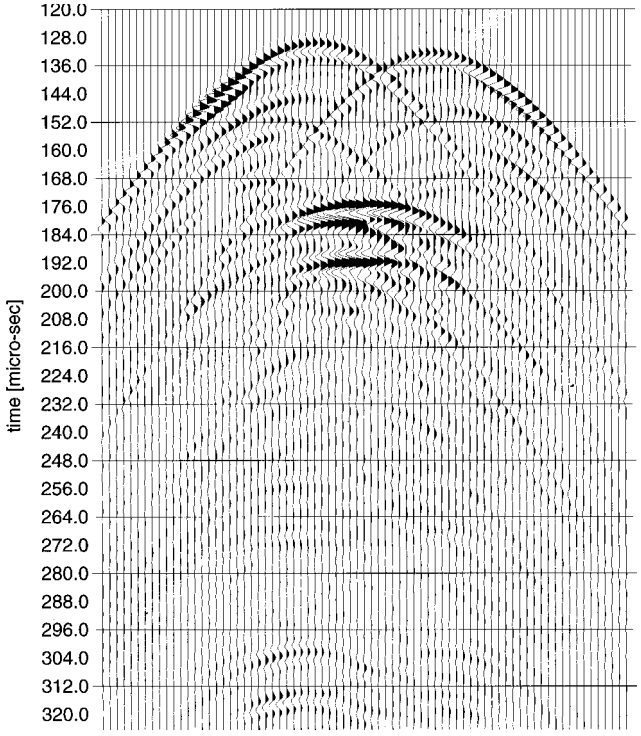

FIG. 9. The seismogram for the ''down'' model (Fig. 1) calculated by the MMP method.

resonating geometries such as the posed problem, the propagatory solutions (6b) and (7b) are superior to the standing wave solutions (6a) and (7a).[11] First, their amplitudes decay faster.[16] But they also force us to illuminate the scatterers from all sides which decouples the multipoles and the interfaces because each multipole illuminates mainly the region of the interface closest to its expansion center. This effect lowers the condition number and thus enhances the stability of the numerical matrix inversion. For both models, 660 expansion functions and 444 matching points (=1332 equations) are used.

Figures 9 and 15 show the synthetic seismograms as calculated by the MMP expansions for the ''down'' and the ''up'' model. The first 120 μs are suppressed since they only contain the direct arrival.

IV. COMPARISON OF THE TANK DATA WITH THE MMP SOLUTIONS

The advantage of the MMP solution over the ultrasonic water tank data is that, by construction, the wave fields are decomposed by scatterer. Once the overall equation system (10) is solved for a particular model, we can fix the summation index d to 1, 2, or 3 in expression (4a) when evaluating the seismograms. Remember that the index d denotes the scatterer which emits a particular field. For each of the three scatterers, we can plot the scattered wave fields independently which simplifies the seismograms and allows the correlation of events with scatterers. For example, fixing the index d to 2 allows to plot all events which were last reflected or diffracted by scatterer Γ^2 before being recorded.

In the ultrasonic experiment, we use a point source and a point receiver. The models contain no variation perpendicular to the source-receiver plane. Hence, the experiments are in fact $2\frac{1}{2}$-D experiments. However, the numerical MMP scheme is derived and applied in 2-D only. Comparing the experimental results to the numerical ones might be problematic. But Esmersoy[17] and Lo[18] showed that the differences between 2-D and $2\frac{1}{2}$-D are negligible as long as the scatterers are in the far field with respect to both the source and the receivers. At the center frequency of 190 kHz, the scatterers are at least 15 wavelengths away from either source or receivers for both geometries. Clearly, the far-field condition is satisfied.

A. ''Down'' model

A comparison between the ultrasonic record (Fig. 5) and the MMP solution (Fig. 9) shows that the arrival times and amplitudes for different events match very well. The main difference between Figs. 5 and 9, the real and the synthetic data, are the strong, repetitive events in the central part of the real seismogram. The cause is the signature of the source transducer (Fig. 4) which rings more than a Ricker wavelet.

The bow tie pattern typical for concaves can easily be seen.[19] As expected, each scatterer reflects twice with opposing polarity corresponding to reflections from the top and from the bottom. The two events are typically 14 μs separated. Toward the end of the traces at 300 μs, reverberations of the reflection from scatterer Γ^2 can be found which bounced between the surface and the scatterers Γ^1 and Γ^3. These effects can be seen more clearly in the MMP solution decomposed by scatterer shown in Figs. 10–12. All synthetic

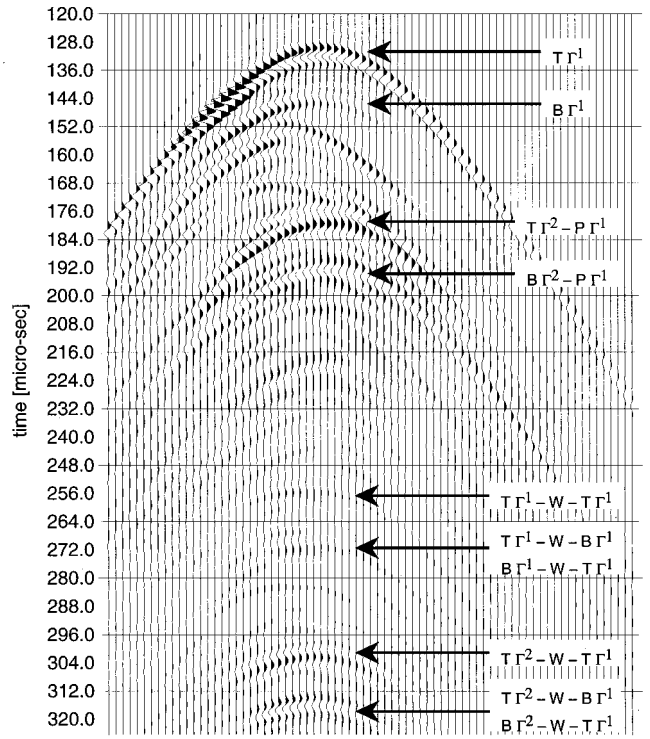

FIG. 10. ''Down'' model: The scattered field emanated by Γ^1. The events around 180 μs are reflections originating at scatterer Γ^2 but passing through scatterer Γ^1. The events at 300 μs are reflections from Γ^2 bouncing between the surface and Γ^1. The notation used to label different events is defined in Fig. 13.

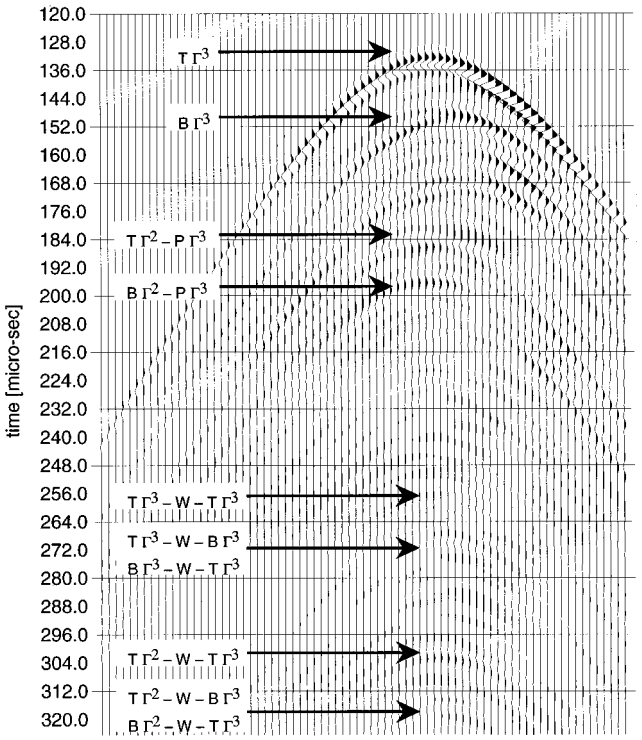

FIG. 12. ''Down'' model: The scattered field emanated by Γ^3. The events around 180 μs are reflections from scatterer Γ^2 passing through scatterer Γ^3. The events at 260 μs are reflections from Γ^3 bouncing between the water surface and scatterer Γ^3. The events at 300 μs are reflections from scatterer Γ^2 bouncing between the surface and scatterer Γ^3.

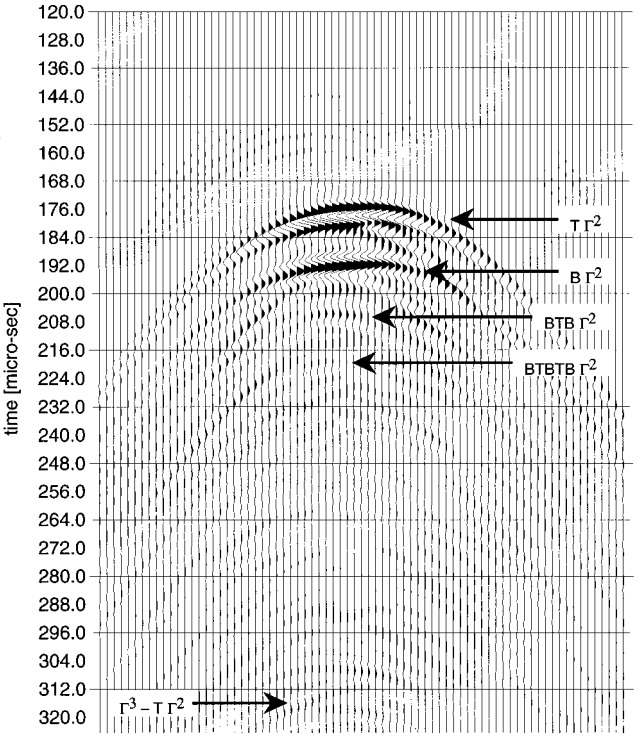

FIG. 11. ''Down'' model: The scattered field emanated by Γ^2 into the fluid.

seismograms are scaled similarly which allows to compare the amplitudes between the different figures. The notation used to label the events is defined in Fig. 13.

The decomposed MMP solution in Figs. 10–12 shows that the event around 180 μs in the tank data (Fig. 5) is in reality composed of different events. First, there is the direct reflection from scatterer Γ^2. But this reflection was also diffracted through the scatterers Γ^1 and Γ^3 as the seismograms 10 and 12 show. Also, the first multiple reflections from inside Γ^1 and Γ^3 appear nearly at that time. Another interesting set of events appears at 256 μs and 270 μs. Figure 10 correlates these two events with scatterer Γ^1. The travel times prove them to be reflections from Γ^1 bouncing between the water surface and Γ^1. The prior one reflected twice from the top of Γ^1. The latter one reflected once from the top, once from the bottom. Thus, one would expect another event about 14 μs later corresponding to a wave bouncing between the bottom of Γ^1 and the water surface. Indeed, a very weak event appears at the expected time in the tank data (Fig. 5) and the MMP solutions (Figs. 9 and 10). A final subtlety are the multiples arriving around 300 μs which justify the stationary phase reflections into the MMP expansion functions (5b). The scattered fields in Figs. 10–12 show very nicely that these events are a combination of different waves. First, there are waves reflected from Γ^2, then bounced off the water surface and finally rebounded from either Γ^1 or Γ^3. But we also encounter the opposite: waves reflecting from Γ^1 or Γ^3, bouncing off the water surface and finally rebounding from Γ^2. To demonstrate the effect of the multiple

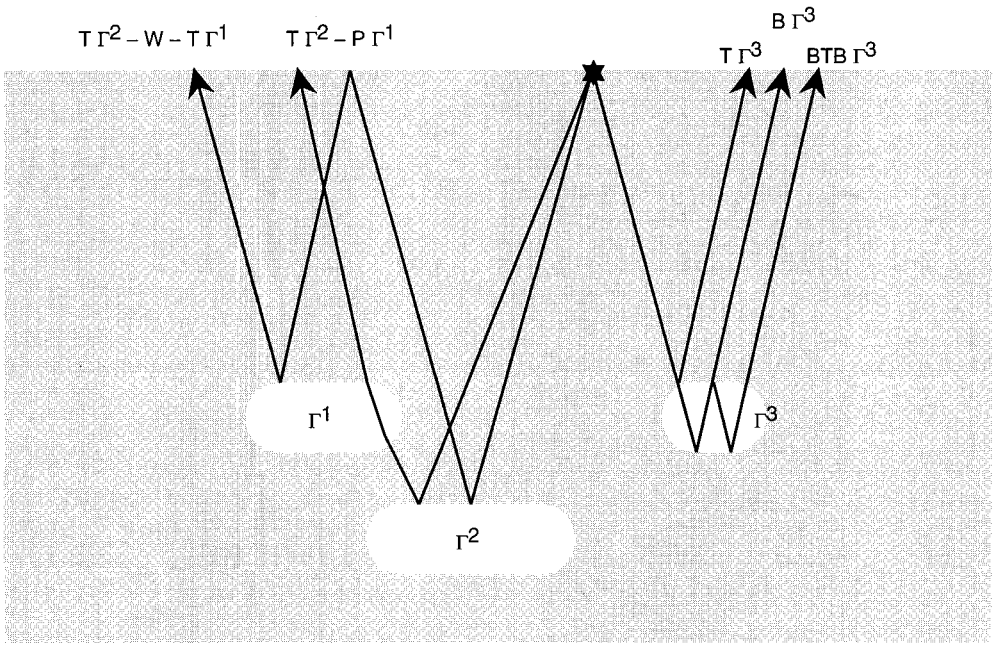

FIG. 13. Notation used to label different events. The symbol ''*T*'' denotes a reflection from the top of a scatterer, ''*B*'' a reflection from the bottom, ''*W*'' a reflection from the water surface, and ''*P*'' a diffraction caused by the scatterer. Again, the star denotes the source.

scattering, we calculate the acousto-elastic response for each scatterer separately and subtract them from the complete MMP solution (Fig. 9). The residual wave field is shown in Fig. 14. The amplitudes in both figures are scaled by the same amount to ease a direct comparison of single scattering versus multiple scattering. Clearly, the two scatterers Γ^1 and Γ^3 speed up the reflection from Γ^2. The remaining events are waves bouncing between the three scatterers and the water surface as well as internal multiples sped up passing through Γ^1 and Γ^3.

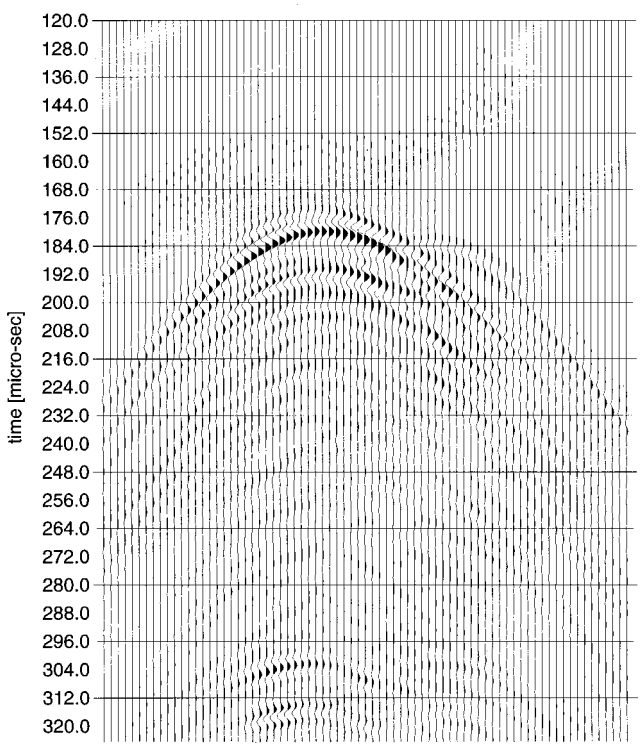

FIG. 14. ''Down'' model: The residual field between the complete MMP solution (Fig. 9) and the three scattered wave fields calculated for each rod separately.

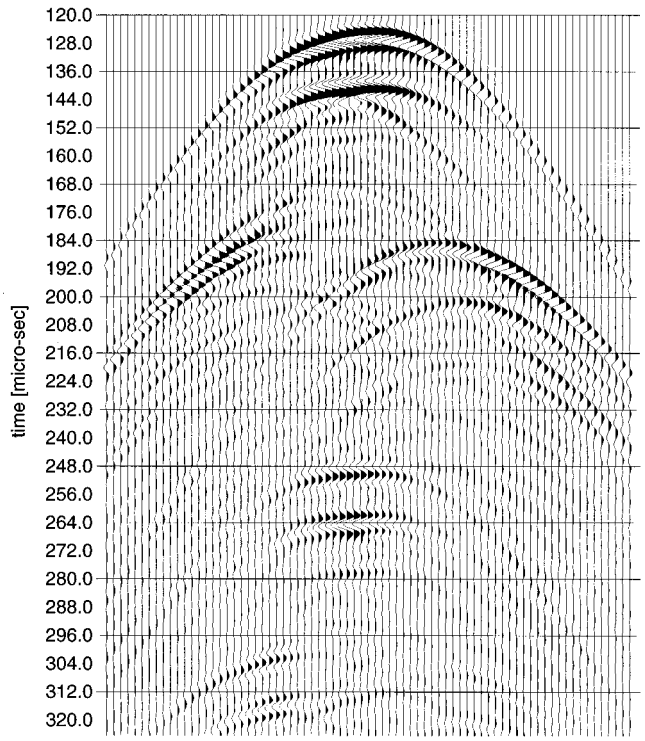

FIG. 15. The seismogram for the ''up'' model defined in Fig. 2 as calculated by the MMP method.

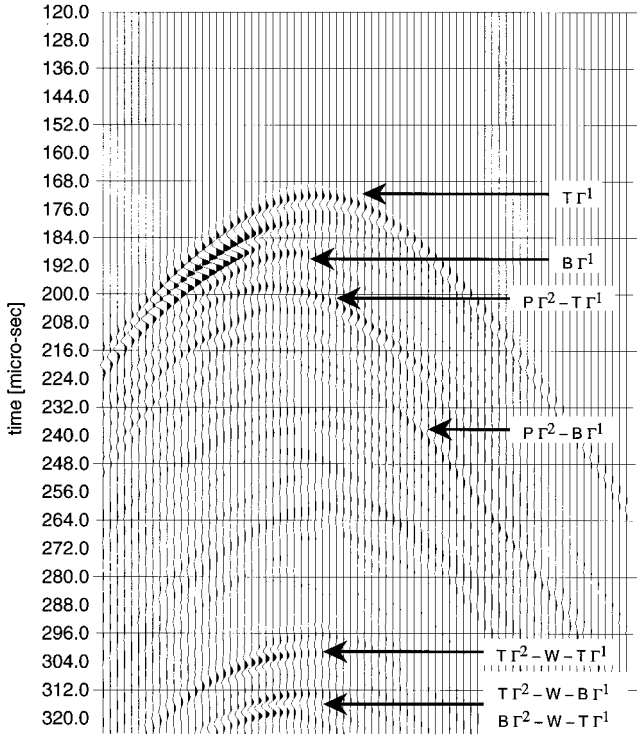

FIG. 16. ''Up'' model: The scattered field emanated by Γ^1. The events at 300 μs are reflections from Γ^2 bouncing between the surface and scatterer Γ^1. The notation used to label different events is defined in Fig. 13.

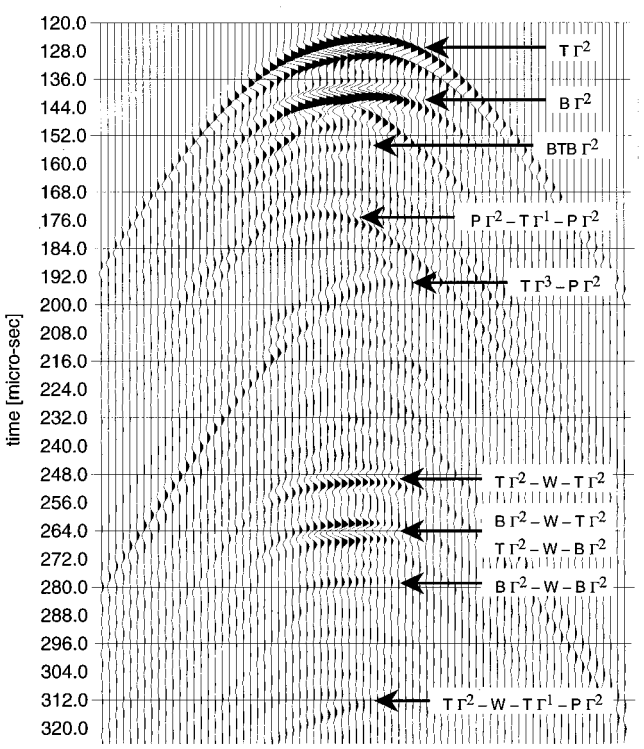

FIG. 17. ''Up'' model: The scattered field emanated by Γ^2 into the fluid. The events at 170 μs and 190 μs are the reflections from Γ^1, respectively, Γ^3, being transmitted through Γ^2.

B. ''Up'' model

Both the ultrasonic record (Fig. 7) and the MMP solution (Fig. 15) clearly show the reflections from the top and the bottom of each scatterer. Not surprisingly, scatterer Γ^2 shadows Γ^1 as the rather abrupt change in the reflection-amplitude around 170 μs demonstrates. To identify a few other events, we decompose the MMP solution by scatterer. The decomposed seismograms are shown in Figs. 16–18.

For example, Fig. 17 shows that part of the ringing main reflection around 130 μs is caused by multiple scattering inside Γ^2. The bottom reflection even splits into 2 events forming a bow tie pattern which repeats every 14 μs. At 170 μs, the main reflection from scatterer Γ^1 appears in the scattered field of Γ^2. This event can be interpreted as reflection from Γ^1 but propagating through Γ^2. Similarly at 190 μs, Fig. 17 shows the reflection of Γ^3 being diffracted through Γ^2. After both events, internal multiples from Γ^1 and Γ^3 show up in the fields scattered from Γ^1 and Γ^3, respectively. Diffractions of these multiples passing through Γ^2 are again present in Fig. 17.

To demonstrate the effect of the multiple scattering, we calculate the response of each scatterer alone and subtract it from the complete MMP solution (Fig. 15). The residual wave field is shown in Fig. 19. The amplitudes in both figures are scaled by the same amount to allow a direct comparison of single scattering versus multiple scattering. For the first 170 μs, the events emanated by scatterer Γ^2 are the same for single or multiple scattering. Clearly, the reflection from scatterer Γ^1 separates into two events in the residual seismogram shown in Fig. 19. Scatterer Γ^2 not only shadows

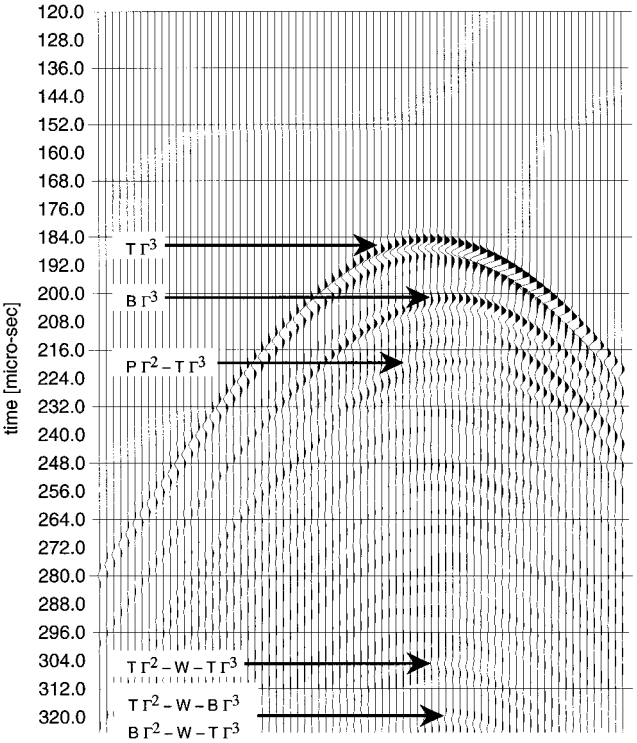

FIG. 18. ''Up'' model: The scattered field emanated by Γ^3. The events at 300 μs are reflections from scatterer Γ^2 bouncing between the surface and scatterer Γ^3.

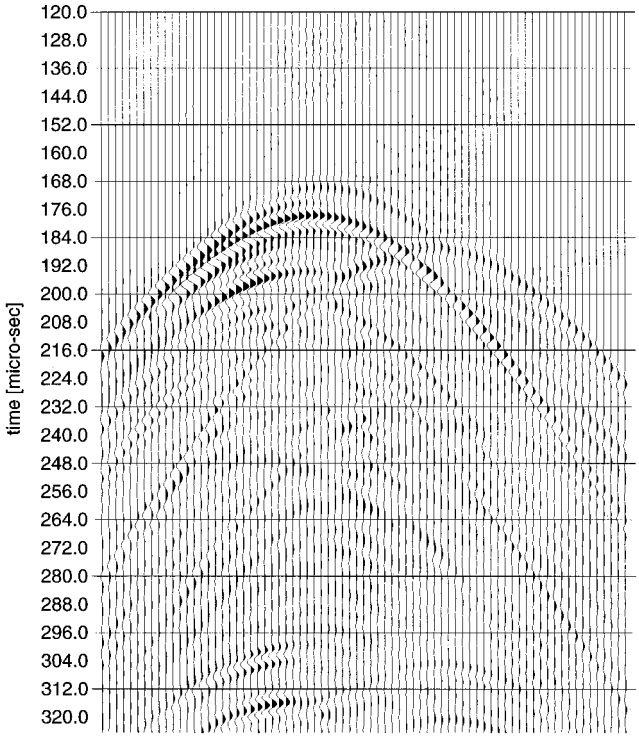

FIG. 19. ''Up'' model: The residual field between the complete MMP solution (Fig. 15) and the three scattered wave fields calculated for each rod separately.

Γ^1 but also speeds up the arrival time of the reflection passing through the fast solid. The same holds for some of the later events in Fig. 19 corresponding to internal multiples. The remaining events are generated by waves bouncing between the three scatterers and the water surface. For example, the reflections around 300 μs are caused by multiple scattering between Γ^2, the water surface, and either of Γ^1 or Γ^3.

V. SUMMARY

The wave field scattered from solids submerged in water can be rather complex even for simple geometries. Furthermore, the scattered wave field becomes even more complicated if the water surface interacts with the scatterers. The ''down'' experiment, where three lucite rods were submerged in an ultrasonic water tank, demonstrates this point especially well. Although the main reflections are simple to identify, the remaining events are very hard to interpret.

To aid the interpretation, we forward-modeled the situations numerically using the multiple multipole method (MMP). For each submerged solid, the scattered wave field induced in the fluid is expanded into a MMP expansion.[10] Similarly, in each solid two MMP expansions are used to describe the *P* and *S* components of the elastic wave fields.[11] The advantage of the MMP scheme is that the scattered wave fields are, by construction, decomposed by scatterer as well as by mode of propagation. Hence, the wave fields scattered from each solid can be plotted independently which facilitates the correlation of particular events with individual scatterers. Curiously, this allows to distinguish direct reflections from reflections diffracted by another scatterer along their path of propagation.

In conclusion, we found that acousto-elastic multiple multipole expansions are a versatile tool either to directly solve scattering problems or to aid in their interpretation. This work should find uses in a variety of fields, notable in geophysics and oil exploration, as well as in naval underwater applications.

ACKNOWLEDGMENTS

This work was supported by the Air Force Office of Scientific Research under Grant No. F49620-94-1-0282 and the Air Force Technical Applications Center/Phillips Laboratory under Contract No. F19628-95-C-0091. Also, the author was supported by the nCUBE fellowship.

[1] M. C. Junger and D. Feit, *Sound, Structures, and their Interaction* (MIT, Cambridge, MA, 1986), 2nd ed.
[2] G. Gaunaurd, ''Elastic and acoustic resonance wave scattering,'' Appl. Mech. Rev. **42**, 143–192 (1989).
[3] Y. H. Pao and C. C. Mow, *Diffraction of Elastic Waves and Dynamic Stress Concentrations* (Crane Russak, New York, 1973).
[4] C. J. Luke and P. A. Martin, ''Fluid-solid interaction: acoustic scattering by a smooth elastic obstacle,'' SIAM J. Appl. Math. **55**, 904 (1995).
[5] A. Boström, ''Scattering of stationary acoustic waves by an elastic obstacle immersed in a fluid,'' J. Acoust. Soc. Am. **67**, 390–398 (1980).
[6] A. N. Norris, ''Resonant acoustic scattering from solid targets,'' J. Acoust. Soc. Am. **88**, 505–514 (1990).
[7] F. B. Jensen, W. A. Kuperman, M. B. Porter, and H. Schmidt, *Computational Ocean Acoustics* (AIP, Woodbury, NY, 1994).
[8] G. C. Everstine and F. M. Henderson, ''Coupled finite element/boundary element approach for fluid-structure interaction,'' J. Acoust. Soc. Am. **87**, 1938–1947 (1990).
[9] J. R. Fricke, ''Acoustic scattering from elemental Artic ice features: Numerical modeling results,'' J. Acoust. Soc. Am. **93**, 1784–1796 (1993).
[10] M. G. Imhof, ''Multiple multipole expansions for acoustic scattering,'' J. Acoust. Soc. Am. **97**, 754–763 (1995).
[11] M. G. Imhof, ''Multiple multipole expansions for elastic scattering,'' J. Acoust. Soc. Am. **100**, 2969–2979 (1996).
[12] C. A. Schultz and M. N. Toksöz, ''Reflections from a randomly grooved interface: ultrasonic modelling and finite-difference calculations,'' Geophys. Prospecting **43**, 581–594 (1995).
[13] W. C. Chew, ''A quick way to approximate a Sommerfeld-Weyl-type integral,'' IEEE Trans. Antennas Propag. **36**, 1654–1657 (1988).
[14] H. R. Schwarz, *Numerical Analysis* (Wiley, New York, 1989).
[15] *Transient Waves in Visco-Elastic Media*, edited by N. H. Ricker (Elsevier Amsterdam, 1977).
[16] C. Hafner, *The Generalized Multipole Technique for Computational Electromagnetics* (Artech House, Boston, 1990).
[17] C. Esmersoy and M. Oristaglio, ''Reverse-time wave-field extrapolation, imaging and inversion,'' Geophysics **53**, 920–931 (1988).
[18] T. W. Lo, M. N. Toksöz, S. H. Xu, and R. S. Wu, ''Ultrasonic laboratory tests of geophysical tomographic reconstruction,'' Geophysics **53**, 947–956 (1988).
[19] M. W. Haartsen, M. Bouchon, and M. N. Toksöz, ''A study of seismic acoustic wave propagation through a laterally varying medium using the boundary-integral-equation-discrete-wave-number method,'' J. Acoust. Soc. Am. **96**, 3010–3021 (1994).

Speckle coherence and implications for adaptive imaging

William F. Walker and Gregg E. Trahey
Department of Biomedical Engineering, Duke University, Durham, North Carolina 27708

(Received 12 October 1995; accepted for publication 10 December 1996)

Tissue speed of sound inhomogeneities cause significant degradation of medical ultrasound images. In certain cases these inhomogeneities can be modeled as a thin, spatially varying time delay screen located at the face of the transducer. Correction of such aberrators requires the addition of compensating time delays to the normal system focusing delays. These compensating delays are estimated from the arrival time differences between echoes received on different array elements. The accuracy with which these arrival time differences can be estimated is limited by the level of correlation between received speckle signals. This paper derives analytical expressions predicting the correlation between speckle signals acquired by a pulse echo system with either point or larger receive elements in the presence of near-field phase aberrations. Simulations are presented which are in good agreement with theoretical predictions. Similarities between the derived expressions and the Van Cittert–Zernike Theorem are discussed. These results indicate that near-field phase aberration correction may be far more difficult than previous analyses suggest because of the low correlation between echoes received by adjacent elements in elevation in 1.5-D arrays. Transmit aperture amplitude apodization and a new translating aperture technique are presented as methods for improving speckle correlation. © *1997 Acoustical Society of America.* [S0001-4966(97)05304-6]

PACS numbers: 43.20.Fn, 43.80.Vj, 43.60.Lq [ANN]

INTRODUCTION

Medical ultrasonic imaging systems utilize electronically steered and focused arrays of piezoelectric elements to transmit short duration, focused ultrasonic pulses into the body. As these pulses propagate a fraction of their energy is reflected at acoustic impedance mismatches, generating echoes. The piezoelectric array is electronically steered and focused to acquire these echoes and an image is formed depicting echo magnitude and echo source location.

In current ultrasonic imaging systems electronic focusing delays are calculated to compensate for path length differences between array elements and the focal point by assuming a constant acoustic velocity of 1540 m/s. However, the speed of sound in soft tissues is known to vary from approximately 1470 m/s in fat to over 1600 m/s in muscle[1] and since soft tissues are geometrically complex, the speed of sound throughout a given image region may vary considerably. Such variations degrade focusing during both transmission and reception. This degradation typically takes the form of increased main lobe width and increased side lobe levels in the system point spread function. In severe cases the main lobe may even become split, generating multiple images of the same target. All of the noted changes reduce image quality and limit diagnostic utility.[2–4]

In certain areas, speed of sound inhomogeneities may be localized near the body's surface. In the abdomen, for example, a rippled layer of fat lying just under the skin may represent the most significant local speed of sound inhomogeneity. Aberrations in the abdomen have been measured and many studies indicate that the aberration can be modeled as a thin delay screen located near the surface of the body.[5–7]

In areas where acoustic velocity inhomogeneities can be modeled as a near-field thin time delay screen, their effect is conceptually equivalent to the addition of aberrating time delays to the normal system focusing delays. As such, the effect of these aberrations can be eliminated by adding appropriate compensating delays to the system focusing delays. Unfortunately, accurate estimation of the compensating delays is nontrivial. Although a number of algorithms have been proposed, all estimate compensating delays from arrival time differences between signals received from different array elements. In rare cases these differences can be estimated using echoes received from point targets. Point target echoes are attractive because they maintain a high level of coherence across the array, increasing the accuracy of arrival time difference estimates. More often, however, a point target is not available and arrival time differences are estimated using echoes acquired from diffuse scatterers. These speckle signals exhibit limited spatial coherence, and thus arrival time differences estimated from them exhibit reduced accuracy.[8] Errors in arrival time estimation degrade correction performance and reduce corrected image quality.

The spatial coherence of ultrasonic speckle in the absence of aberration has previously been described using the Van Cittert–Zernike Theorem (VCZT).[9] More recent work has utilized the VCZT to describe phase correction performance in terms of spatial coherence.[10] This paper presents a new version of the VCZT describing the effects of near-field thin screen aberrators on the spatial coherence of echoes received by pointlike as well as large array elements.

I. POINT RECEIVERS

Medical ultrasonic imaging systems utilize short time duration, broadband acoustic pulses. While time-domain analysis of such systems is intuitively pleasing, analytical results are difficult or impossible to derive. Instead it is easier to decompose the pulse into its constituent frequencies and perform continuous-wave analysis for each. This method

 0001-4966/97/101(4)/1847/12/$10.00

of analysis is typically applied to wave propagation through homogeneous, linear elastic media, however, it can be used to analyze the effect of speed of sound inhomogeneities by assuming that the velocity inhomogeneities consist of a thin spatially varying time delay screen at the face of the transducer. Following this approach, the inhomogeneities are represented as a distortion of the aperture, not an inhomogeneity in the medium. At a single frequency, f, the one-way sensitivity pattern $P(X_i,z,f)$ of a complex aperture $A(X_a, f)$ located at $z=0$, is given by the Rayleigh–Sommerfeld diffraction formula:[11]

$$P(X_i,z,f)=\frac{1}{j\lambda}\int_{-\infty}^{\infty}A(X_a,f)\,\frac{e^{jkr_{ai}}}{r_{ai}}\cos(\overline{n,r_{ai}})\,dX_a, \tag{1}$$

where $X_a'=(x_a\ y_a)$ (x and y coordinates in the aperture plane), $X_i'=(x_i\ y_i)$ (x and y coordinates in the image plane), λ is the wavelength, k is the wave number ($k=2\pi/\lambda$), z is the range of the image plane, r_{ai} is the length of the vector $\overline{r_{ai}}$ which points from $(x_a,y_a,0)$ to (x_i,y_i,z), and $\overline{n}$ is the unit vector normal to the aperture plane. It should be noted that the complex aperture function includes both the transducer geometry and weighting and the thin delay screen aberrator. If the area of interest in the image plane subtends a small angle in azimuth and elevation and the image plane is at the focus of the aperture or is in the far field of an unfocused aperture, Eq. (1) can be simplified to yield the Fraunhofer Approximation:[11]

$$P(X_i,z,f)=\frac{e^{jkz}e^{j(k/2z)(X_i'X_i)}}{j\lambda z}\times\int_{-\infty}^{\infty}A(X_a,f)e^{-j(2\pi/\lambda z)(X_i'X_a)}\,dX_a. \tag{2}$$

This expression indicates that (neglecting the multiplicative phase term outside the integral) the spatial response of an imaging system is the Fourier transform of the aperture with $f_X=X_i/\lambda z$. Medical ultrasonic imaging systems generally operate in pulse-echo mode for which the sensitivity pattern can be calculated by taking the product of the transmit and receive sensitivity patterns:

$$P_{\mathrm{TR}}(X_i,z,f)=P_T(X_i,z,f)P_R(X_i,z,f), \tag{3}$$

where $P_{\mathrm{TR}}(X_i,z,f)$ is the transmit-receive system response, $P_T(X_i,z,f)$ is the transmit system response, and $P_R(X_i, z,f)$ is the receive system response. Equations (2) and (3) can be combined to yield the two-way sensitivity pattern as a function of space and frequency, although for broadband systems the sensitivity also changes as a function of time. As the transmitted pulse propagates away from the transducer the sensitivity pattern narrows and then broadens as the pulse approaches and then passes the focal point. Also, scatterers located at increasing ranges are interrogated at later times as the transmitted pulse propagates away from the transducer. In this paper received signals are calculated considering only contributions from targets located at a specific range. Following this approach the estimated signal corresponds to the signal that would be received at the instant when the received echo originated from the range for which the calculation was performed. A more thorough motivation for this approach has been presented by Mallart.[9] Including the contributions from only a single range, the transmit-receive output $s_{\mathrm{TR}}(f)$ for a target distribution $t(X_i,z,f)$ is given by

$$s_{\mathrm{TR}}(f)=\int_{-\infty}^{\infty}P_T(X_i,z,f)P_R(X_i,z,f)t(X_i,z,f)\,dX_i. \tag{4}$$

This expression provides a method for calculating the received signal from arbitrary scatterer distributions using arbitrary apertures and arbitrary near-field aberrators. It assumes that data is acquired from either the far field or the focus of the transducer. In medical ultrasound both targets and aberrators may be spatially random processes. Thus, the correlation between two received signals can be calculated using:

$$\rho(f)=\frac{[\langle s_{T_0R_0}(f)s_{T_1R_1}^*(f)\rangle]}{\sqrt{[\langle s_{T_0R_0}(f)s_{T_0R_0}^*(f)\rangle][\langle s_{T_1R_1}(f)s_{T_1R_1}^*(f)\rangle]}}, \tag{5}$$

where $s_{T_0R_0}(f)$ is the signal received by transmit-receive system 0, $s_{T_1R_1}(f)$ is the signal received by transmit-receive system 1, the asterisk indicates the complex conjugate operation, [ ] indicates the expected value taken over an ensemble of aberrators, and $\langle\ \rangle$ indicates the expected value taken over an ensemble of scattering functions. Note that this expression allows both the transmit and receive aperture functions to vary between signal acquisitions and is thus more general than previous derivations.[9] Substituting Eq. (4) into the numerator of Eq. (5), rearranging the order of terms, rearranging the order of integration, and bringing the expectation over the scattering function inside the integrals yields:

$$\rho_n(f)=\left[\int_{-\infty}^{\infty}\int_{-\infty}^{\infty}P_{T_0}(X_{i_0},f)P_{R_0}(X_{i_0},f)P_{T_1}^*(X_{i_1},f)\times P_{R_1}^*(X_{i_1},f)\langle t(X_{i_0},f)t^*(X_{i_1},f)\rangle\times dX_{i_0}\,dX_{i_1}\right], \tag{6}$$

where $\rho_n(f)$ represents the numerator of Eq. (5). In this expression and the derivation that follows explicit reference to the range z has been removed to simplify notation. Assuming that the scattering function is a spatial white-noise process (speckle generating target) with uniform reflectivity as a function of frequency, the expected value of the product of the scattering functions is a spatial delta function located at $X_{i_0}-X_{i_1}=0$. Substituting the delta function into Eq. (6) and integrating eliminates one of the spatial variables. The resultant expression can be further simplified by applying the Fourier transform relationship of Eq. (2) to produce:

$$\rho_n(f)=\left[\int_{-\infty}^{\infty}\frac{1}{\lambda}\Phi(X_i,f)F\{A_{T_0}(X_i,f)\}\,\frac{1}{\lambda}\Phi(X_i,f)\times F\{A_{R_0}(X_i,f)\}\,\frac{1}{\lambda}\Phi^*(X_i,f)F^*\{A_{T_1}(X_i,f)\}\times\frac{1}{\lambda}\Phi^*(X_i,f)F^*\{A_{R_1}(X_i,f)\}\,dX_i\right], \tag{7}$$

where $\Phi(X_i,f)=-je^{jkz}e^{j(k/2z)(X_i'X_i)}$ and $F\{\}$ is the Fourier transform taken with $f_X=X_i/\lambda z$. Application of the Fourier transform assumes that the region of interest lies at the focal point of both imaging systems or is in the far field of unfocused systems which are steered to the same point. The $\Phi(X_i,f)$ terms all have unity magnitude, so conjugate pairs cancel. Application of the Power Theorem of Fourier Transforms[12] to this result yields:

$$\rho_n(f)=\frac{1}{\lambda^4}\left[\int_{-\infty}^{\infty}(A_{T_0}^*(X_a,f)\star A_{T_1}(X_a,f))\times(A_{R_1}(X_a,f)\star A_{R_0}^*(X_a,f))\,dX_a\right], \tag{8}$$

where the star represents the non-normalized cross-correlation function carried out in the X_a dimension. The complex conjugate operation is performed on one term in the cross correlation because the aperture definitions may be complex.[12] For arrays with extremely small receivers (two-dimensional arrays or one-dimensional arrays with small elevation dimension) the receivers may be modeled as delta functions. Substituting delta functions into Eq. (8), carrying out the cross correlation on the delta functions and integrating yields:

$$\rho_n(f)=\frac{1}{\lambda^4}\left[\int_{-\infty}^{\infty}A_{T_0}^*(X_a,f)A_{T_1}(X_a-\Delta X,f)\,dX_a\right], \tag{9}$$

where ΔX is the separation between the receivers ($\Delta X=X_{R_0}-X_{R_1}$). Expanding the transmit aperture functions $A_{T_0}(X_a,f)$ and $A_{T_1}(X_a,f)$ to indicate transducer geometry, weighting, and phase aberration produces:

$$A_{T_0}(X_a,f)=T_0(X_a)e^{-j2\pi f\tau(X_a)}, \tag{10}$$

$$A_{T_1}(X_a,f)=T_1(X_a)e^{-j2\pi f\tau(X_a)}, \tag{11}$$

where $T_0(X_a)$ and $T_1(X_a)$ reflect the transmit transducer geometry and weighting for the first and second signal acquisitions respectively, and $\tau(X_a)$ is the time delay aberration in seconds. The aberration is defined as a time delay screen to account for speed of sound inhomogeneities near the transducer. The constant time delay with frequency results in a linearly varying phase delay with frequency. Substituting these expressions into Eq. (9) reordering terms, combining complex exponentials, and bringing the expectation inside the integral yields:

$$\rho_n(f)=\frac{1}{\lambda^4}\int_{-\infty}^{\infty}T_0^*(X_a)T_1(X_a-\Delta X)\times[e^{j2\pi f(\tau(X_a)-\tau(X_a-\Delta X))}]\,dX_a. \tag{12}$$

The expected value within Eq. (12) can be simplified by performing a substitution of variables to yield:

$$[e^{j2\pi f(\tau(X_a)-\tau(X_a-\Delta X))}]=[e^{j2\pi f\zeta}], \tag{13}$$

where $\zeta=\tau(X_a)-\tau(X_a-\Delta X)$. The right-hand expression is equivalent to the characteristic function for the random variable ζ. Assuming that $\tau(X_a)$ and therefore ζ are Gaussian distributed random variables, the characteristic function of ζ is also a Gaussian. Following Papoulis[13] Eq. (13) can be rewritten:

$$[e^{-j2\pi f\zeta}]=e^{-(1/2)(2\pi f)^2[\zeta^2]}. \tag{14}$$

Substituting for ζ, expanding terms, and assuming that $\tau(X_a)$ is stationary yields:

$$\begin{aligned}e^{-(1/2)(2\pi f)^2[\zeta^2]}&=e^{-(1/2)(2\pi f)^2[\tau^2(X_a)+\tau^2(X_a-\Delta X)-2\tau(X_a)\tau(X_a-\Delta X)]}\\&=e^{-(2\pi f)^2(R_{\tau\tau}(0)-R_{\tau\tau}(\Delta X))},\end{aligned} \tag{15}$$

where $R_{\tau\tau}(X)$ is the spatial autocorrelation function of the aberrator. Substituting Eq. (15) into Eq. (12) yields:

$$\rho_n(f)=\frac{1}{\lambda^4}\int_{-\infty}^{\infty}T_0(X_a)T_1^*(X_a-\Delta X)\times e^{-(2\pi f)^2(R_{\tau\tau}(0)-R_{\tau\tau}(\Delta X))}\,dX_a. \tag{16}$$

A similar set of operations can be performed on the denominator of Eq. (5). Combining the numerator and the denominator yields:

$$\rho(f)=\frac{\int_{-\infty}^{\infty}T_0(X_a)T_1^*(X_a-\Delta X)\,dX_a}{\sqrt{\int_{-\infty}^{\infty}T_0(X_a)T_0^*(X_a)dX_a\int_{-\infty}^{\infty}T_1(X_a)T_1^*(X_a)\,dX_a}}\times e^{-(2\pi f)^2(R_{\tau\tau}(0)-R_{\tau\tau}(\Delta X))}. \tag{17}$$

This expression describes the decorrelation between speckle signals received by point receivers in different transmit-receive imaging systems in the presence of a near-field thin time delay screen aberration. For focused systems it assumes that both imaging systems are focused at the same point in space. For unfocused systems the expression assumes that the target is in the far field of both systems and that both are steered to the target. The first portion of the right-hand side of Eq. (21) represents the speckle decorrelation due to path length differences. When $T_0(X_a)=T_1(X_a)$ the geometric decorrelation term agrees exactly with the Van Cittert–Zernike Theorem as derived by Mallart.[9] The second portion of the right-hand side represents speckle decorrelation caused by phase aberration in the transmit aperture. Note that this aberrator induced decorrelation exhibits a Gaussian frequency dependence.

II. LARGE RECEIVERS

Equation (17) provides insight to the sources and magnitude of echo decorrelation in the presence of near-field phase aberration, however, this expression was derived assuming pointlike receive elements. Modern ultrasonic imaging systems utilize linear arrays (1-D arrays) which have elements which are narrow in azimuth but large in elevation. A number of groups have also developed 1.5-D arrays which consist of multiple rows of elements which are narrow in azimuth but have dimensions in elevation which are midway between those of 1-D and 2-D arrays.[14,15] In this section the previous analysis is expanded to consider more common array geometries with large receive elements. The numerator

of the correlation coefficient can be derived by substituting transmit and receive aperture functions into Eq. (9). The transmit aperture functions include both transmit transducer geometry and weighting as well as the near-field time delay aberration. These functions are given by Eqs. (10) and (11). Receive aperture functions also include element geometry, element weighting, and time delay aberration, however, the receive elements should also include a time delay correction so that the correlation coefficient is calculated at the peak correlation. Expanding the receive aperture functions yields:

$$A_{R_0}(X_a,f)=R_0(X_a)\exp\left(-j2\pi f\left(\tau(X_a)-(1/c_{R_0})\int_{-\infty}^{\infty}R_0(X)\tau(X)\,dX\right)\right), \tag{18}$$

$$A_{R_1}(X_a,f)=R_1(X_a)\exp\left(-j2\pi f\left(\tau(X_a)-(1/c_{R_1})\int_{-\infty}^{\infty}R_1(X)\tau(X)\,dX\right)\right), \tag{19}$$

where $c_{R_0}=\int_{-\infty}^{\infty}R_0(X)dX$ and $c_{R_1}=\int_{-\infty}^{\infty}R_1(X)dX$. Note that net time delay across each receive element is zero, to determine the peak correlation between signals. Substituting Eqs. (10), (11), (18), and (19) into Eq. (8) yields:

$$\rho_n(f)=\frac{1}{\lambda^4}\left[\int_{-\infty}^{\infty}((T_0^*(X_a)e^{j2\pi f\tau(X_a)})\star(T_1(X_a)e^{-j2\pi f\tau(X_a)}))\left(\left(R_1(X_a)\exp\left(-j2\pi f\left(\tau(X_a)-(1/c_{R_1})\int_{-\infty}^{\infty}R_1(X)\tau(X)\,dX\right)\right)\right)\star\left(R_0^*(X_a)\exp\left(j2\pi f\left(\tau(X_a)-(1/c_{R_0})\int_{-\infty}^{\infty}R_0(X)\tau(X)dX\right)\right)\right)\right)dX_a\right]. \tag{20}$$

Rewriting the cross-correlation functions in integral notation, rearranging the order of terms, grouping exponentials, and bringing the expected value inside the integral yields:

$$\rho_n(f)=\frac{1}{\lambda^4}\int_{-\infty}^{\infty}\int_{\infty}^{\infty}\int_{-\infty}^{\infty}T_0^*(X_0)T_1(X_0+X_a)R_1(X_1)R_0^*(X_1+X_a)\left[\exp\left(-j2\pi f\left(\tau(X_0)-\tau(X_0+X_a)-\tau(X_1)+(1/c_{R_1})\int_{-\infty}^{\infty}R_1(X)\tau(X)dX+\tau(X_1+X_a)-(1/c_{R_0})\int_{-\infty}^{\infty}R_0(X)\tau(X)\,dX\right)\right)\right]dX_0\,dX_1\,dX_a. \tag{21}$$

As with the previous derivation the expected value within Eq. (21) is further simplified by performing a substitution of variables and calculating a characteristic function to yield:

$$\left[\exp\left(-j2\pi f\left(\tau(X_0)-\tau(X_0+X_a)-\tau(X_1)+(1/c_{R_1})\int_{-\infty}^{\infty}R_1(X)\tau(X)dX+\tau(X_1+X_a)-(1/c_{R_0})\int_{-\infty}^{\infty}R_0(X)\tau(X)\,dX\right)\right)\right]=e^{-(1/2)(2\pi f)^2[\zeta^2]}, \tag{22}$$

where $\zeta=\tau(X_0)-\tau(X_0+X_a)-\tau(X_1)+(1/c_{R_1})\int_{-\infty}^{\infty}R_1(X)\tau(X)\,dX+\tau(X_1+X_a)-(1/c_{R_0})\int_{-\infty}^{\infty}R_0(X)\tau(X)\,dX$. Expanding terms in the expected value in the right-hand side of Eq. (22) and assuming that the aberrator is stationary yields:

$$\begin{aligned}[\zeta^2]=&4R_{\tau\tau}(0)-4R_{\tau\tau}(X_a)-4R_{\tau\tau}(X_0-X_1)+2R_{\tau\tau}(X_0-X_1-X_a)+2R_{\tau\tau}(X_0-X_1+X_a)\\&+\frac{1}{c_{R_0}^2}\int_{-\infty}^{\infty}[R_0(\Psi)\star R_0(\Psi)]R_{\tau\tau}(\Psi)d\Psi+\frac{1}{c_{R_1}^2}\int_{-\infty}^{\infty}[R_1(\Psi)\star R_1(\Psi)]R_{\tau\tau}(\Psi)d\Psi\\&-\frac{2}{c_{R_0}c_{R_1}}\int_{-\infty}^{\infty}[R_0(\Psi)\star R_1(\Psi)]R_{\tau\tau}(\Psi)d\Psi+\frac{2}{c_{R_1}}R_{\tau\tau}(X_0)\star R_1(X_0)-\frac{2}{c_{R_0}}R_{\tau\tau}(X_0)\star R_0(X_0)\\&-\frac{2}{c_{R_1}}R_{\tau\tau}(X_0+X_a)\star R_1(X_0+X_a)+\frac{2}{c_{R_0}}R_{\tau\tau}(X_0+X_a)\star R_0(X_0+X_a)-\frac{2}{c_{R_1}}R_{\tau\tau}(X_1)\star R_1(X_1)\\&+\frac{2}{c_{R_0}}R_{\tau\tau}(X_1)\star R_0(X_1)+\frac{2}{c_{R_1}}R_{\tau\tau}(X_1+X_a)\star R_1(X_1+X_a)-\frac{2}{c_{R_0}}R_{\tau\tau}(X_1+X_a)\star R_0(X_1+X_a).\end{aligned} \tag{23}$$

Using this result Eq. (21) can be rewritten to yield:

$$\rho_n(f)=\frac{1}{\lambda^4}\int_{-\infty}^{\infty}\int_{-\infty}^{\infty}\int_{-\infty}^{\infty}T_0(X_0)T_1^*(X_0+X_a)R_1(X_1)R_0^*(X_1+X_a)e^{-1/2(2\pi f)^2[\zeta^2]}dX_0\,dX_1\,dX_a, \tag{24}$$

where $[\xi^2]$ is defined by Eq. (23). Note that the exponential remains inside the integrals because of its dependence upon X_0, X_1, and X_a. A similar set of operations can be performed to compute the denominator of the of the correlation coefficient. Combining expressions for the numerator and denominator yields:

$$\rho(f)=\frac{\int_{-\infty}^{\infty}\int_{-\infty}^{\infty}\int_{-\infty}^{\infty}T_0(X_0)T_1^*(X_0+X_a)R_1(X_1)R_0^*(X_1+X_a)e^{-(1/2)(2\pi f)^2[\xi^2]}dX_0\ dX_1\ dX_a}{\sqrt{C_0C_1}} \tag{25}$$

where

$$C_0=\int_{-\infty}^{\infty}\int_{-\infty}^{\infty}\int_{-\infty}^{\infty}T_0(X_0)T_0^*(X_0+X_a)R_0(X_1)R_0^*(X_1+X_a)\times e^{-(1/2)(2\pi f)^2[\xi^2]}dX_0\ dX_1\ dX_a,$$

$$C_1=\int_{-\infty}^{\infty}\int_{-\infty}^{\infty}\int_{-\infty}^{\infty}T_1(X_0)T_1^*(X_0+X_a)R_1(X_1)R_1^*(X_1+X_a)\times e^{-(1/2)(2\pi f)^2[\xi^2]}dX_0\ dX_1\ dX_a,$$

and

$$[\xi^2]=4R_{\tau\tau}(0)-4R_{\tau\tau}(X_a)-4R_{\tau\tau}(X_0-X_1)+2R_{\tau\tau}(X_0-X_1-X_a)+2R_{\tau\tau}(X_0-X_1+X_a).$$

Equation (25) predicts the frequency-dependent decorrelation between speckle signals received by different transmit-receive imaging systems utilizing large receive elements. For focused systems it is valid at the focal plane if both systems are focused at the same point. For unfocused systems it is valid in the far field if both systems are steered to the same point at the range of interest. Although Eq. (25) provides limited analytical insight, it can be integrated numerically to explore the effects of phase aberrations on a broad range of realistic imaging systems. If phase aberration effects are neglected this expression agrees with those derived to predict echo decorrelation for spatial compounding.[16,17]

III. APODIZATION

Equation (17) predicts the spatial coherence of speckle signals acquired by pointlike receivers with arbitrary transmit aperture geometries. For many phase aberration correction algorithms echoes are acquired from a single transmitted pulse. In these cases $T_0(X)=T_1(X)$ and substitution into Eq. (17) yields:

$$\rho_n(f)=\frac{\int_{-\infty}^{\infty}T(X_a)T^*(X_a-\Delta X)\ dX_a}{\int_{-\infty}^{\infty}T(X_a)T^*(X_a)\ dX_a}\times e^{-(2\pi f)^2(R_{\tau\tau}(0)-R_{\tau\tau}(\Delta X))}, \tag{26}$$

where subscripts for the transmit aperture have been eliminated to simplify notation. This expression indicates that the spatial coherence function for speckle echoes received from a single transmitted pulse by pointlike receivers can be expressed as the product of the normalized autocorrelation of the transmit aperture and a term representing aberrator induced decorrelation.

For a rectangularly weighted transmit aperture the autocorrelation function is a triangle. Because the triangle function falls relatively rapidly from its peak, signals from nearby elements exhibit rapid spatial decorrelation. We hypothesize that transmit aperture apodization or weighting may be applied to smooth the aperture autocorrelation function near its peak and thus increase the coherence between echoes acquired by closely spaced elements. Although many types of apodization are possible, a Gaussian apodization curve is one simple example which should have the desired effect.

IV. TRANSLATING TRANSMIT APERTURES

Most currently proposed phase aberration correction algorithms acquire and align data acquired from a single transmit pulse. However, in situations where tissue motion is minimal or can be estimated, it is possible to perform phase correction using echo data acquired from successive transmitted pulses. In these cases echo spatial coherence is appropriately described by Eq. (17). If the aperture used for the second pulse transmission is simply a shifted version of the aperture used for the first transmission $[T_1(X)=T_0(X-\Delta X_T)]$ then Eq. (17) can be simplified to yield:

$$\rho_n(f)=\frac{\int_{-\infty}^{\infty}T(X_a)T^*(X_a-\Delta X-\Delta X_T)\ dX_a}{\int_{-\infty}^{\infty}T(X_a)T^*(X_a)\ dX_a}\times e^{-(2\pi f)^2(R_{\tau\tau}(0)-R_{\tau\tau}(\Delta X))}, \tag{27}$$

where ΔX_T represents the shift of the transmit aperture between the first and second transmission, ΔX is the shift between receivers and subscripts for the transmit apertures have been removed to simplify notation. Inspection of this expression indicates that if the transmit aperture shift is equal and opposite to the receiver separation then the decorrelation due to geometry is eliminated and Eq. (27) reduces to

$$\rho_n(f)=e^{-(2\pi f)^2(R_{\tau\tau}(0)-R_{\tau\tau}(\Delta X))}. \tag{28}$$

This expression assumes that both transmissions are focused at the same point and is only valid when $\Delta X_T=-\Delta X$. Equation (28) indicates that translation of transmit apertures between data acquisitions can be used to increase the spatial coherence of received echoes so that phase aberration is the only source of spatial echo decorrelation. We refer to this technique as the translating transmit apertures algorithm.[18,19]

V. SIMULATIONS

Simulations were performed to test the validity of Eqs. (26) and (28) for predicting speckle coherence using standard scanning methods and the translating transmit apertures algorithm both with and without phase aberration. For each of the four conditions examined 32 data sets consisting of 5.0

μs of received speckle data were generated using the FIELD simulation program.[20] This program uses Stepanishen's method of spatial impulse responses to determine the contribution from each scatterer in the field without assuming shift invariance of the imaging system.[21] Each data set consisted of radio frequency (rf) data acquired from each receive element in a 64-element array centered at the origin with $\lambda/2$ (at 5.0 MHz) square elements with element centers spaced by $\lambda/2$ (at 5.0 MHz). Standard simulations used the same geometry for transmit and receive apertures. Translating transmit aperture simulations used a transmit array identical to the receive array except for the translation applied to increase echo correlation. All translating transmit aperture transmit arrays were generated by selecting sets of 64 adjacent elements from a 128-element array containing the receive aperture as its central 64 elements. Data acquired for receive channel one was generated by transmitting elements 65–128 of the large transmit array, data for receive channel two was acquired by transmitting elements 64–127 and so on. All arrays were focused at a range of 40 mm directly in front of the center of the receive aperture. Simulations were performed with a field of 67 790 scatterers with a zero mean Gaussian amplitude distribution and a uniform random spatial distribution within a plane extending from 15.5 to 44.5 mm in range and from -30 to 30 mm laterally. This distribution provides a scatterer density of 15 scatterers per resolution volume. The large scattering region was used to ensure that contributions from the tails of the point spread function, which lag the main lobe in time, would be included in the simulations. Examination of the unaberrated point spread function for a 64 element transmit aperture and a single receive element indicated that the point spread function reached a point 40 dB down from its peak within the region of scatterers. Each set of speckle data was envelope detected and mean over standard deviation (μ/σ) was calculated for all data sets and found to average 1.84, in good agreement with theoretically predicted value of 1.91. All simulations utilized a Gaussian-enveloped sinusoidal transmit pulse with a 5.0 MHz center frequency and an 80% full width at half maximum (FWHM) bandwidth. Attenuation was not included in the simulations. rf data was generated with a 100-MHz sampling rate and then decimated to 50 MHz for processing.

Transmit phase aberrations were applied in a subset of the simulations by adding a zero mean, 100-ns root-mean-square (rms) aberrating time delay profile to the normal transmit focusing delays. Aberrating profiles were generated to exhibit a 5-mm FWHM Gaussian-shaped autocorrelation function and a Gaussian distribution of delays. These aberration characteristics were based on published aberration measurements.[2,22–24] Both rms levels and aberrator autocorrelation FWHM were increased over published values to correct for the arbitrary removal of linear or polynomial aberration components in these experiments. In standard simulations the applied aberrator was unchanged throughout the acquisition of each data set. For translating transmit aperture simulations the aberrator was held constant for the large 128-element transmit aperture within each data set, so each translating transmit aperture imaged through a different portion of the aberrator. Thirty-two aberrators were utilized with each standard simulation and each translating transmit aperture simulation utilizing a different aberrator from other simulations of the same type. Aberrating profiles were generated as described in the Appendix.

Simulated rf data sets were centered temporally about the focus, however, to increase the useful length of data continuous dynamic receive focusing was applied. Data sampled at 20 ns was interpolated using a cubic spline interpolation and resampled in a nonuniform manner to receive focus all samples.

After dynamic receive focusing, each 5.0-μs set of rf data was subdivided into five nonoverlapping 1.0-μs sets, yielding a total of 160 data sets for each trial condition. Complex Fourier coefficients for each 1.0-μs window of data were calculated at 3, 4, 5, 6, and 7 MHz to examine the frequency dependence of speckle coherence:

$$S(f,i)=\sum_{k=1}^{N} s(k,i)e^{-j2\pi fkT}, \tag{29}$$

where $s(k,i)$ is the sampled signal on element i, T is the sampling interval, and $S(f,i)$ is the complex Fourier coefficient of the signal received by element i at the frequency f. The 160 sets of Fourier coefficients were subdivided into eight groups of 20 data sets with data acquired from different ranges being uniformly distributed among groups. The correlation coefficient within each group was estimated for each receiver separation distance and frequency using:

$$\rho(f,\Delta i,l)$$

$$=\mathrm{Real}\left[\frac{(1/(20(64-\Delta i))\Sigma_{k=1}^{20}\Sigma_{i=1}^{64-\Delta i}S(f,i,k,l)S^{*}(f,i+\Delta i,k,l)}{((1/(20(64-\Delta i))\Sigma_{k=1}^{20}\Sigma_{i=1}^{64-\Delta i}S(f,i,k,l)S^{*}(f,i,k,l))(1/(20(64-\Delta i))\Sigma_{k=1}^{20}\Sigma_{i=\Delta i}^{64}S(f,i+\Delta i,k,l)S^{*}(f,i+\Delta i,k,l))^{1/2}}\right], \tag{30}$$

where $S(f,i,k,l)$ is the complex Fourier coefficient at frequency f for the signal from element i within data set k of group l. Mean values of the correlation coefficient were estimated by computing the average of the eight correlation coefficients (one from each group) calculated for each set of conditions. Standard error of the mean was also calculated to determine the statistical reliability of reported results.

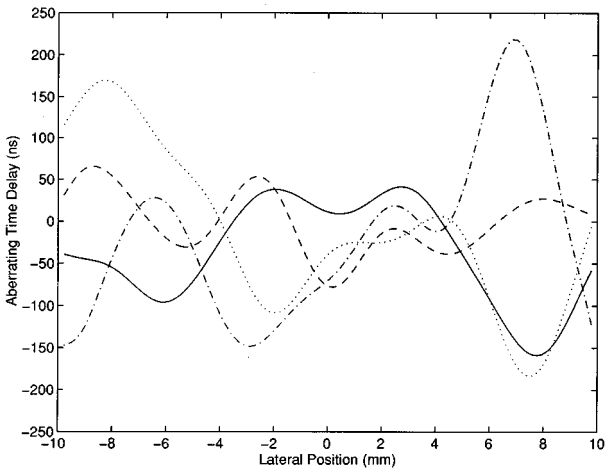

FIG. 1. Typical time delay aberrations used in simulations. All aberrations are 100-ns root-mean-squared with a 5-mm FWHM Gaussian autocorrelation function.

VI. RESULTS

Figure 1 depicts four sample aberrator functions, each indicated by a different line pattern. All aberrators have a 5-mm FWHM Gaussian autocorrelation function with 100-ns rms aberration and a Gaussian amplitude delay distribution.

Figure 2 depicts theoretical predictions and simulation results for decorrelation as a function of receive element separation for standard data acquisition using an unapodized 64 element array at 5.0 MHz both with and without aberration. Theoretical decorrelation calculated using Eq. (26) is shown by a solid line for the unaberrated case and a dashed line for the aberrated case. Mean correlation values determined by simulation are indicated by circles for the unaberrated case and X's for the aberrated case. Error bars indicate the standard error of the mean calculated using eight groups of data. Simulation results are in good agreement with theoretical predictions.

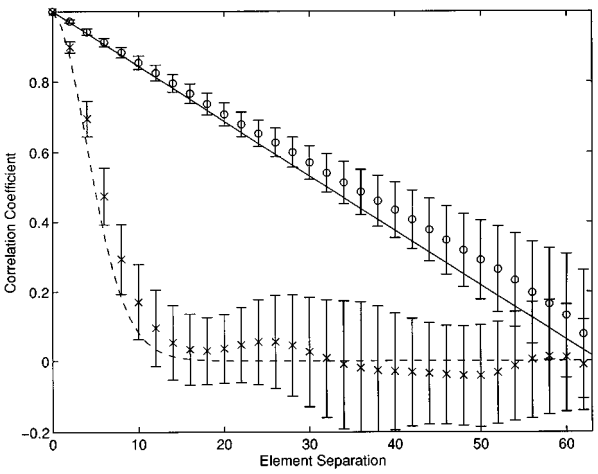

FIG. 2. Spatial coherence of echoes acquired at 5.0 MHz using standard data acquisition with a 64-element array of 0.154-mm square elements. Solid and dashed lines indicate theoretical coherence with and without aberration, respectively. Circles and X's indicate coherence estimated by simulation with and without aberration. Error bars indicate the standard error of the mean.

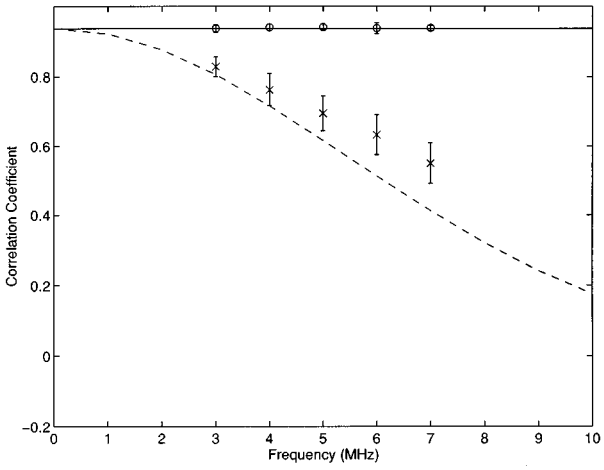

FIG. 3. Frequency dependence of coherence between echoes received by elements separated by 0.612 mm using standard data acquisition. Results are indicated in the same manner as in Fig. 2.

Figure 3 depicts received echo decorrelation as a function of frequency for a receiver separation of four elements or 0.616 mm. As with Fig. 2, theoretical decorrelation calculated using Eq. (26) is shown by a solid line for the unaberrated case and a dashed line for the aberrated case. Mean correlation values determined by simulation are indicated by circles for the unaberrated case and X's for the aberrated case. Simulation results and theoretical predictions are in good agreement.

Figure 4 indicates theoretical coherence predictions as a function of frequency for signals received by adjacent 3.33 mm elements in a three element 10-mm array. This array geometry was selected to mimic the relationship between adjacent elements in elevation in a typical 1.5-D array. Theoretical values were obtained by numerically integrating Eq. (25) using Simpson's rule with samples separated by 0.25 mm. As with previous figures the solid line indicates theoretical predictions for the unaberrated case and the dashed line indicates theoretical predictions for the aberrated case.

The effect of transmit aperture apodization on spatial

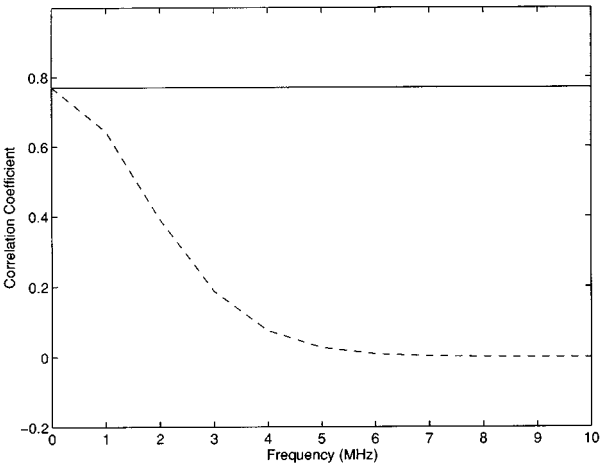

FIG. 4. Frequency dependence of coherence between echoes received by adjacent 3.33-mm elements in a 10-mm three element array. Solid and dashed lines indicate unaberrated and aberrated theory, respectively.

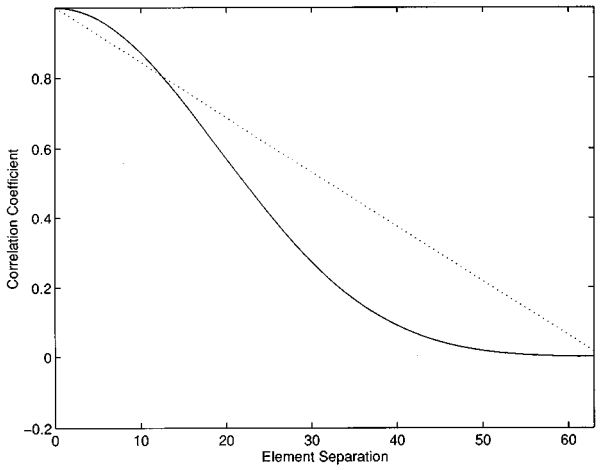

FIG. 5. Spatial coherence with (solid line) and without (dotted line) 32-element FWHM Gaussian transmit aperture apodization.

coherence is depicted in Fig. 5. The solid line indicates the spatial coherence of echoes received from a speckle target insonified by a 64-element array with 32-element FWHM Gaussian apodization. The dotted line indicates theoretical spatial coherence of echoes generated using the same 64-element array without apodization. As hypothesized, Gaussian transmit aperture apodization improved the correlation between signals received by closely spaced elements. For example, the correlation of echoes received by adjacent elements rose from 0.984 to 0.998 with the use of apodization.

Figure 6 depicts theoretical predictions and simulation results for decorrelation as a function of receive element separation for translating transmit apertures data acquisition using an unapodized 64-element array at 5.0 MHz both with and without aberration. The theoretical correlation calculated using Eq. (28) is equal to 1.0 for the unaberrated case and is indicated by a dashed line for the aberrated case. Mean correlation values determined by simulation are indicated by circles for the unaberrated case and X's for the aberrated

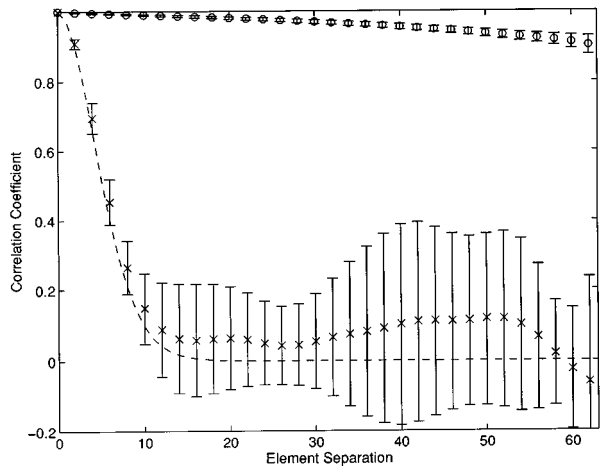

FIG. 6. Spatial coherence of echoes acquired at 5.0 MHz using the translating transmit apertures algorithm with a 64-element array of 0.154-mm square elements. Solid and dashed lines indicate theoretical coherence with and without aberration, respectively. Circles and X's indicate coherence estimated by simulation with and without aberration. Error bars indicate the standard error of the mean.

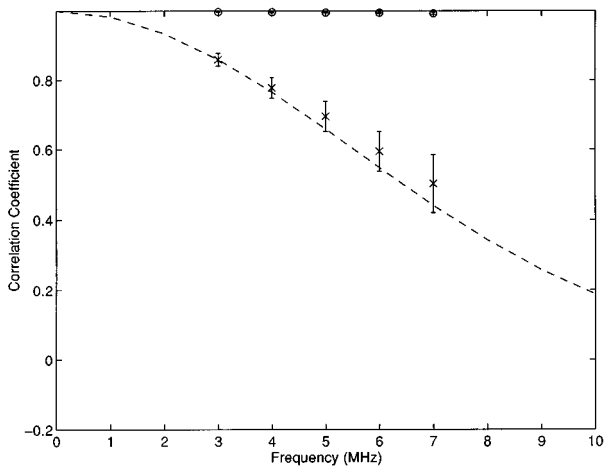

FIG. 7. Frequency dependence of coherence between echoes received by elements separated by 0.616 mm using the translating transmit apertures algorithm. Results are indicated in the same manner as in Fig. 6.

case. Error bars indicate the standard error of the mean calculated using eight groups of data. Simulation results are in good agreement with theoretical predictions.

Figure 7 depicts received echo decorrelation as a function of frequency for a receiver separation of four elements or 0.616 mm with data acquired using the translating transmit apertures algorithm. As with Fig. 6, theoretical decorrelation calculated using Eq. (28) is shown by a solid line for the unaberrated case and a dashed line for the aberrated case. Mean correlation values determined by simulation are indicated by circles for the unaberrated case and X's for the aberrated case. Simulation results and theoretical predictions are in good agreement.

VII. DISCUSSION

The accuracy of adaptive imaging algorithms is intimately tied to the correlation between received signals used in the necessary time delay estimates.[9,25] The theoretical and simulation results presented in this paper describe received echo coherence in the presence of near-field phase aberration for speckle generating targets. These results can be used to predict the performance of various adaptive imaging algorithms.

Simulation results shown in Fig. 2 indicate that the derived spatial coherence functions are valid for standard data acquisition. The unaberrated spatial coherence function is in excellent agreement with the triangular decorrelation seen in theory, simulations, and experiments published by Mallart[9] and Ng.[25] Reduced coherence between received signals is a direct result of differences in the transmit-receive point spread functions (PSF's) used to acquired those signals. For standard data acquisition without apodization the transmit-receive PSF is a $\sin(2\pi x)/\pi x$ function with zero phase (transmit contribution) multiplied by a spatial linear phase tilt with a slope proportional to the receiver's distance from the transmit array center (receiver contribution). As the receiver separation increases the differences in the linear phase tilts of the PSF's also increases causing their correlation to fall and the correlation between received echoes to fall as

well. The energy in the tails of the PSF tend to contribute more to decorrelation because the linear phase tilt produces a greater total phase change at these extremes.

Results in the presence of aberration show much more rapid decorrelation than in the unaberrated case. Phase aberration increases the energy in the sidelobes and tails of the transmit PSF and broadens the mainlobe so that the linear phase tilt caused by receiver displacement causes a change in a greater fraction of the energy of the PSF. Altering the phase of a greater fraction of PSF energy causes a more rapid reduction in echo spatial coherence. Simulation results for aberrated standard data acquisition are slightly higher than theoretical predictions for small element separations. This difference may result from the use of a finite region of scatterers which eliminates contributions from the extreme tails of the PSF which would otherwise contribute to spatial decorrelation.

Figure 4 depicts the predicted decorrelation between adjacent 3.33-mm elements in a three-element 10-mm array both with and without aberration. These conditions were chosen to mimic the coherence which can be expected between adjacent elements in elevation in a $3\times N$ element 1.5-D array. The unaberrated coherence is well above the 0.667 predicted by the point receiver theory. This result can be explained by considering that the average distance between points in the large array elements is less than the distance between the centers of the elements. Since shorter distances translate into higher coherence, the echoes received by large elements exhibit higher coherence than would be predicted by point receiver theory. In the presence of aberration, however, the coherence is lower because the PSF is broadened by the aberration and different large receive elements subtend different aberrations. Aberration correction using a $3\times N$ array appears impractical in cases where the aberration is close to the model presented because the correlation between echoes received by adjacent elements in elevation is effectively zero for useful imaging frequencies. Even if the mean aberrating delay across the element could be corrected, significant aberration would remain because the aberration varies considerably over the region subtended by a single large element. These results suggest that currently proposed 1.5-D arrays may not be adequate for near-field aberration correction. This result is in contradiction with previous, more optimistic work by Ng.[20] Discrepancies may result from Ng's use of an assumed echo coherence profile and aberration profiles which did not vary over individual array elements. Both assumptions would underestimate the reduction in signal coherence associated with the presence of aberration, leading to overly optimistic estimates of correction performance.

Figures 5 and 6 show the potential of Gaussian transmit apodization and the translating transmit apertures algorithm to increase echo spatial coherence and thus improve adaptive imaging performance. Gaussian apodization increases coherence at small element separations by decreasing sidelobes and PSF tails. The translating transmit apertures algorithm improves echo coherence by attempting to generate transmit-receive PSFs with a zero phase tilt at all receiver positions. By moving the transmit aperture and receive element equal distances in opposite directions transmit and receive PSFs are generated with opposite phase slopes. Thus, the transmit-receive PSF, which is the product of the transmit and receive PSFs, has a net phase tilt of zero regardless of the receiver position.

The simulation results presented in Fig. 6 are in good agreement with theoretical predictions for the translating transmit apertures algorithm. Simulation results for the unaberrated case are slightly below the theoretically predicted coherence of 1.0. This reduced coherence can be explained in part because the transmit beams from different transmit aperture locations do not perfectly overlap except at the focus. This hypotheses was confirmed after simulation results were examined and higher coherence was found for data closer to the focus. Coherence may also be reduced from the ideal by changes in the curvature of the isochronous volume, especially in the tails of the PSF, which result from increased separation between the transmit aperture center and receive element. We hypothesize that transmit apodization would reduce energy in the tails of the PSF and further improve spatial coherence. Aberrated simulation results are in excellent agreement with theoretical prediction. The translating transmit apertures algorithm offers only a slight increase in coherence over standard data acquisition for the severe aberrators examined. This is because the aberration-induced decorrelation is much greater than the geometry-induced decorrelation for the severe aberrators examined. In cases of less severe aberration the translating transmit apertures algorithm should produce a more significant increase in coherence, approaching the results of the upper curve of Fig. 6 as the aberration becomes progressively smaller. Since increased coherence results in reduced time delay estimation error, the translating transmit apertures algorithm offers the potential of improved phase aberration correction performance. Furthermore, iterative correction on the same array will reduce the decorrelation due to phase aberration, allowing the correlation coefficient to approach 1.0 and the correction algorithm to converge to the correct compensating profile. With standard data acquisition the correlation between signals does not approach 1.0 with repeated correction, thus phase aberration correction would not converge to the correct compensating profile.

The proposed translating transmit apertures technique is in some ways similar to data acquisition methods contained in phase aberration correction algorithms previously proposed by Rachlin[26] and Li.[27] All three techniques acquire data from multiple pulse transmissions with transmitters and receivers displaced by equal and opposite amounts between successive transmissions. However, both Rachlin's and Li's techniques use only a single array element for transmission, while the translating transmit apertures algorithm uses a large focused aperture. The use of only a single array element for transmission will limit acoustic power output, effectively decreasing electronic signal-to-noise ratio (SNR) and degrading aberration correction performance. Assuming that the power transmitted from each element in a phased

TABLE I. Theoretical time delay estimation errors.

Data acquisition method	SNR	Aberration	Correlation	Time delay estimation error
Standard	30 dB	No	0.9922	1.49 ns
Gaussian apodization	30 dB	No	0.9996	0.59 ns
Translating apertures	30 dB	No	1.0000	0.50 ns
Standard	50 dB	No	0.9922	1.41 ns
Gaussian apodization	50 dB	No	0.9996	0.32 ns
Translating apertures	50 dB	No	1.0000	0.05 ns
Standard	30 dB	5.0-mm FWHM, 100-ns rms	$0.9922\times e^{-f^2\times 1.0370\times 10^{-15}}$	3.03 ns
Gaussian apodization	30 dB	5.0-mm FWHM, 100-ns rms	$0.9996\times e^{-f^2\times 1.0370\times 10^{-15}}$	2.67 ns
Translating apertures	30 dB	5.0-mm FWHM, 100-ns rms	$1.0000\times e^{-f^2\times 1.0370\times 10^{-15}}$	2.65 ns
Standard	50 dB	7.5-mm FWHM, 75-ns rms	$0.9922\times e^{-f^2\times 2.5944\times 10^{-16}}$	1.92 ns
Gaussian apodization	50 dB	7.5-mm FWHM, 75-ns rms	$0.9996\times e^{-f^2\times 2.5944\times 10^{-16}}$	1.33 ns
Translating apertures	50 dB	7.5-mm FWHM, 75-ns rms	$1.0000\times e^{-f^2\times 2.5944\times 10^{-16}}$	1.29 ns

array is the maximum which can be practically realized and that only two transmissions are used by each algorithm, data acquired using the translating transmit apertures algorithm would exhibit an SNR as much as 42 dB higher (for a 128 element array) than data acquired using the other techniques. Conversely, data acquired using the translating transmit apertures algorithm will exhibit some signal decorrelation due to the changing aberration profile as the transmitting aperture is translated. The use of single elements for transmission in the other algorithms should eliminate this source of decorrelation. This decorrelation associated with the translating transmit apertures algorithms should have a lesser effect on phase aberration correction performance than the loss of SNR seen with the other techniques.

To determine the significance of changes in echo coherence induced by apodization, the translating transmit apertures algorithm, and aberration, we use the theoretically predicted coherence for point receivers to predict the time delay estimation error which can be expected when aligning echoes received by adjacent array elements. Equation (17) of Ref. 8 can be expressed without the assumption of constant decorrelation with frequency to yield:

$$\sigma(\Delta t-\Delta\hat{t})\geqslant \sqrt{\frac{1}{T\int_{-\infty}^{\infty}(2\pi f)^2\,\dfrac{\dfrac{\rho^2(f)\sigma_{s_1}^2\sigma_{s_2}^2G_{ss}^2(f)}{(\sigma_{s_1}^2G_{ss}(f)+\sigma_{n_1}^2G_{nn}(f))(\sigma_{s_2}^2G_{ss}(f)+\sigma_{n_2}^2G_{nn}(f))}}{1-\dfrac{\rho^2(f)\sigma_{s_1}^2\sigma_{s_2}^2G_{ss}^2(f)}{(\sigma_{s_1}^2G_{ss}(f)+\sigma_{n_1}^2G_{nn}(f))(\sigma_{s_2}^2G_{ss}(f)+\sigma_{n_2}^2G_{nn}(f))}}\,df}}, \tag{31}$$

where $\sigma(\Delta t-\Delta\hat{t})$ is the standard deviation of time delay estimation error, T is the window length, f is the frequency, $G_{ss}(f)$ is the signal power spectra normalized to have an integral of one, and $G_{nn}(f)$ is the noise power spectra normalized to have an integral of one. Table I indicates the predicted time delay estimation error incurred when attempting to align echoes from adjacent elements in a 128-element array, with 0.154-mm element spacing. When utilized, apodization consisted of a Gaussian apodization curve with 64-element FWHM. The standard deviation of time delay estimation errors were estimated assuming flat signal and noise spectra between 4.0 and 6.0 MHz, and a window length of 2.0 μs. Two aberrator models and signal-to-noise ratios were examined to explore the range of situations which might be encountered clinically.

Table I indicates that both Gaussian transmit apodization and the translating transmit apertures algorithm offer potential for improved phase aberration correction performance. For the severe aberrator, time delay estimation error was reduced by roughly 13% through application of the translating transmit apertures algorithm or Gaussian apodization. In the case with less severe aberration the improvement was even greater, at close to 33%. By reducing time delay estimation error the translating transmit apertures algorithm and transmit apodization should result in more accurate phase aberration correction, more rapid convergence of iterative algorithms, and more stable correction.

The results presented in Table I, for cases without aberration, indicate the potential of the translating transmit apertures algorithm or apodization to improve performance near phase correction convergence. For high SNR's the translating transmit apertures algorithm reduced time delay estimation errors by roughly 28 times. This improvement should make phase aberration correction algorithms more stable as they approach convergence and the aberration magnitude is reduced. Care should be taken in applying the results of

TABLE II. Theoretical residual aberration.

Data acquisition method	SNR	Aberration	Elevational error	Azimuthal error	Residual aberration
Standard	30 dB	5.0-mm FWHM, 100-ns rms	26.59 ns	3.03 ns	29.79 ns
Translating apertures	30 dB	5.0-mm FWHM, 100-ns rms	26.14 ns	2.65 ns	27.56 ns
Standard	50 dB	7.5-mm FWHM, 75-ns rms	11.25 ns	1.92 ns	16.32 ns
Translating apertures	50 dB	7.5-mm FWHM, 75-ns rms	10.20 ns	1.29 ns	12.13 ns

Table I to current imaging systems as the pointlike receive elements analyzed do not necessarily correspond to the linear array elements used by current systems.

The results in Table I imply that the gains achieved by apodization are nearly as great as those achieved by the translating transmit apertures algorithm at small element separations. However, as receiver separation increases the gains of apodization are reduced and eventually apodized data is less coherent than standard data. High-speed correction of coarsely structured aberrators may require time delay estimation using echoes acquired by widely separated elements. In these cases the translating transmit apertures algorithm should be used because its gains remain high even for large element separations.

The results in Table I indicate the potential of the translating transmit apertures algorithm, however, phase aberration correction algorithms generate a correction profile by combining many individual time delay estimates. Thus final judgment regarding performance should depend upon the accuracy of the correction profile. Expressions have been derived which predict the accumulation of time delay estimation errors in the formation of correction profiles.[29] Table II depicts the rms accumulated error for phase aberration correction using a slightly modified version of the Flax–O'Donnell phase aberration correction algorithm. These results are for a 1.5-D array with 128 elements in azimuth and 10 elements in elevation. Each element was 1.0 mm in elevation and 0.154 mm in azimuth. When applied, the translating transmit apertures algorithm was applied in both azimuth and elevation. The correlation between signals received by adjacent elements in azimuth was predicted using the point received theory of Eq. (26). Correlation between signals from adjacent elements in elevation was predicted using the large receiver theory of Eq. (25). Time delay estimation errors were predicted using Eq. (31) and errors were accumulated using Eq. (14) of Ref. 29. Both time delay estimation errors and residual aberration are presented in Table II as standard deviation.

The results of Table II clearly indicate that residual rms aberration remaining after a single step of phase correction is significant when compared to the normal system delay quantization error of roughly 3 ns. For severe aberrations the translating transmit apertures algorithm offered little benefit because aberration-induced decorrelation in elevation is the overwhelming source of error. However, in the case with less severe aberration the translating transmit apertures algorithm improved performance by 25%. Such improvement is significant and should lead to greater accuracy and more rapid convergence of phase aberration correction algorithms.

Time delay estimation error is not the only factor limiting phase aberration correction performance. Because elements may be large in at least one dimension with regards to aberrator variations, it is impossible for any phase aberration correction algorithm to completely eliminate phase aberrations across the array. The aberration remaining due only to aberrator variations across the element face, aberrator integration error, has been analyzed elsewhere.[30] While aberrator integration error increases the residual error in phase aberration correction, it does not eliminate the performance increases predicted for the translating transmit apertures algorithm or transmit apodization.

VIII. CONCLUSION

The spatial coherence of echoes from speckle generating targets is limited by transmit aperture geometry and phase aberration. Decorrelation due to geometry is frequency independent and can be reduced by transmit aperture apodization and the translating transmit apertures algorithm. Decorrelation due to aberration exhibits a Gaussian frequency dependence with higher frequencies exhibiting lower coherence. Aberration induced decorrelation can only be reduced by correction of the aberration. Both transmit aperture apodization and the translating transmit apertures algorithm show potential for improving phase aberration correction performance. The low correlation between echoes received by adjacent, aberrated 1.5-D array elements indicates that significant challenges remain for near-field phase aberration correction.

ACKNOWLEDGMENT

This work was supported by NIH Grant No. R01-43334.

APPENDIX: GENERATION OF SYNTHETIC ABERRATORS

Aberrating delay profiles were generated by summing weighted Gaussian random variables to generate a coarsely sampled random process and then performing cubic spline interpolation of the coarsely sampled process to yield the final smooth aberrator. A 32 sample coarse aberrator was generated using:

$$ab_i = 100 \times 10^{-9} \sum_{k=1}^{i} W_{k,i} g_i, \tag{A1}$$

where ab_i is the ith sample of the aberrator in seconds, g_k is the kth zero mean, variance 1.0 Gaussian random variable and $W_{k,i}$ is the element in the kth row and the ith column of a weighting matrix determined by taking the Cholesky factorization of the desired aberrator covariance matrix:[28]

$$WW^t = R_{\tau\tau}, \tag{A2}$$

where $R_{\tau\tau}$ is the desired normalized aberrator covariance matrix. Coarsely sampled aberrators were interpolated by a factor of 4 using cubic spline interpolation to yield 128 sample aberrators. Standard simulations used only the central 64 samples of these aberrators while translating aperture simulations utilized the entire 128 samples.

[1] P. N. T. Wells, *Biomedical Ultrasonics* (Academic, London, 1977).
[2] P. D. Freiburger, D. C. Sullivan, B. H. LeBlanc, S. W. Smith, and G. E. Trahey, ''Two-dimensional ultrasonic beam distortion in the breast: in vivo measurements and effects,'' Ultrason. Imaging **14**, 398–414 (1992).
[3] M. O'Donnell and S. W. Flax, ''Phase aberration correction using signals from point reflectors and diffuse scatters: measurements,'' IEEE Trans. Ultrason. Ferroelectr. Freq. Control **35**, 768–774 (1988).
[4] Q. Zhu and B. D. Steinberg, ''Large-transducer measurements of wavefront distortion in the female breast,'' Ultrason. Imaging **14**, 276–299 (1992).
[5] G. E. Trahey, D. Zhao, P. D. Freiburger, and B. A. Carroll, ''A Real-Time Adaptive Ultrasonic Imaging System,'' Invest. Radiol. **25**, 1029–1033 (1990).
[6] D. A. Carpenter, D. E. Robinson, P. L. Ho, D. C. C. Martin, and P. Issacs, ''Body wall aberration correction in medical ultrasonic images using synthetic aperture data,'' *IEEE Ultrasonics Symposium, Baltimore, MD* (IEEE, New York, 1993), pp. 1131–1134.
[7] H. W. Durgin, P. D. Freiburger, G. E. Trahey, and D. C. Sullivan, ''Large aperture phase error measurement and effects,'' *IEEE Ultrasonics Symposium, Tucson, AZ* (IEEE, New York, 1992), Vol. 1, pp. 623–627.
[8] W. F. Walker and G. E. Trahey, ''A Fundamental Limit on Delay Estimation Using Partially Correlated Speckle Signals,'' IEEE Trans. Ultrason. Ferroelectr. Freq. Control **42**, 301–308 (1995).
[9] R. Mallart and M. Fink, ''The Van Cittert-Zernike Theorem in pulse echo measurements,'' J. Acoust. Soc. Am. **90**, 2718–2727 (1991).
[10] R. Mallart and M. Fink, ''Adaptive Focusing in Scattering Media Through Sound-Speed Inhomogeneities: The Van Cittert Zernike Approach and Focusing Criterion,'' J. Acoust. Soc. Am. **96**, 3721–3732 (1994).
[11] W. Goodman, *Introduction to Fourier Optics* (McGraw-Hill, San Francisco, 1986).
[12] R. N. Bracewell, *The Fourier Transform and Its Applications* (McGraw-Hill, New York, 1986).
[13] A. Papoulis, *Probability Random Variables and Stochastic Processes* (McGraw-Hill, New York, 1984).
[14] R. L. Goldberg, *Multi-layer Piezoelectric Ceramics for Medical Ultrasound Transducers* (Duke, Durham, NC, 1994).
[15] C.-M. W. Daft *et al.*, ''A 1.5D Transducer for Medical Ultrasound,'' *IEEE Ultrasonics Symposium, Cannes, France* (IEEE, New York, 1994).
[16] C.-B. Burckhardt, ''Speckle in ultrasound B-mode scans,'' IEEE Trans. Sonics Ultrason. **SU-25**, 1–6 (1978).
[17] G. E. Trahey, J. W. Allison, S. W. Smith, and O. T. von Ramm, ''A quantitative approach to speckle reduction via frequency compounding,'' Ultrason. Imaging **8**, 151–164 (1986).
[18] W. F. Walker and G. E. Trahey, ''Fundamental Limits on the Correction of Near Field Phase Aberrations,'' Ultrason. Imaging **17**, 63 (1995).
[19] P. D. Freiburger, G. C. Ng, G. E. Trahey, and W. F. Walker, A Method for Aberration Correction in the Presence of a Distributed Aberrator (patent pending).
[20] J. A. Jensen and N. B. Svendsen, ''Calculation of Pressure Fields from Arbitrarily Shaped, Apodized, and Excited Ultrasound Transducers,'' IEEE Trans. Ultrason. Ferroelectr. Freq. Control **39**, 262–267 (1992).
[21] P. R. Stepanishen, ''The time-dependent force and radiation impedence on a piston in a rigid infinite planar baffle,'' J. Acoust. Soc. Am. **49**, 841–849 (1971).
[22] B. S. Robinson, A. Shmulewitz, and T. M. Burke, ''Waveform Aberrations in an Animal Model,'' *IEEE Ultrasonic Symposium, Cannes, France* (IEEE, New York, 1994), Vol. 3, pp. 1619–1624.
[23] L. M. Hinkelman, D. L. Liu, and R. C. Waag, ''Measurement and Correction of Ultrasonic Pulse Distortion Produced by the Human Breast,'' J. Acoust. Soc. Am. **97**, 1958–1969 (1995).
[24] L. M. Hinkelman, D. L. Liu, L. A. Metlay, and R. C. Waag, ''Measurements of ultrasonic pulse arrival time and energy level variations produced by propagation through abdominal wall,'' J. Acoust. Soc. Am. **95**, 530–541 (1994).
[25] G. C. Ng, S. S. Worrell, P. D. Freiburger, and G. E. Trahey, ''A comparative evaluation of several algorithms for phase aberration correction,'' IEEE Trans. Ultrason. Ferroelectr. Freq. Control **41**, 631–643 (1994).
[26] D. Rachlin, ''Direct estimation of aberrating delays in pulse-echo imaging systems,'' J. Acoust. Soc. Am. **88**, 191–198 (1990).
[27] Y. Li, ''Phase aberration Correction Algorithm Using Near-Field Signal Redundancy Method: Algorithm,'' Ultrason. Imaging **17**, 63 (1995).
[28] R. S. Walker, D. V. Crowe, and W. R. Mayo, ''Synthetic Multichannel Time Series for Simulating Underwater Acoustic Noise,'' *IEEE International Conference on Acoustics, Speech and Signal Processing, Atlanta, GA* (IEEE, New York, 1981), pp. 1042–1045.
[29] W. F. Walker and G. E. Trahey, ''Limits on the Performance of Near Field Phase Aberration Correction,'' *IEEE Ultrasonics Symposium, Seattle, WA* (IEEE, New York, 1995), pp. 1461–1465.
[30] W. F. Walker, *Adaptive Ultrasonic Imaging Performance for Near-Field Aberrating Layers* (Duke, Durham, NC, 1995).

Radiation from finite phased and focused linear array including interaction[a)]

Jamal Assaad and Christian Bruneel
Institut d'Electronique et de Microelectronique du Nord (IEMN), UMR CNRS 9929, OAE Department, Université de Valenciennes et du Hainaut Cambrésis, le Mont Houy, BP 311, 59304-Valenciennes Cedex, France

(Received 1 May 1996; revised 16 October 1996; accepted 27 October 1996)

Resultant pressure of linear arrays, consisting of N elementary transducers, are in general computed with the help of simplified assumptions for the displacement field of the transducer radiating surface. Moreover, interactions between neighboring elements are not included in most of the numerical approaches. In this paper, a new calculation scheme is proposed to compute the resultant pressure of such arrays, including interactions. For this purpose, using the finite element method (FEM), the far-field directivity pattern of a part of the array is computed using dipolar dampers and a previously described extrapolation algorithm [J. Assaad *et al.*, J. Acoust. Soc. Am. **94**, 562–573 (1993)]. This part is constituted of an active elementary transducer (electrically driven) mounted between $2Q$ passives (electrically grounded) neighboring transducers. Then, the resultant pressure of a finite phased and focused array can be obtained by summing up the far-field directivity patterns of the $2Q + 1$ transducers sets weighted by the classical term which takes into account the geometrical and electrical phase shifts. This new calculation scheme is then used to compute the resultant pressure of a lithium niobate linear array. It will be shown that mechanical interaction must be taken into account for high frequency arrays. © *1997 Acoustical Society of America.* [S0001-4966(97)02904-4]

PACS numbers: 43.20.Tb, 43.20.Rz, 43.38.Hz [JEG]

INTRODUCTION

In acoustic imaging and nondestructive testing applications, the resultant pressure of an array (Fig. 1) is very important and has to be determined by taking into account the ''true'' displacement profile of the radiating surface of the transducers. In fact, the knowledge of this resultant pressure allows us to obtain the characteristics of ultrasonic images. Measurement of such pressure is in most cases very difficult. Therefore, the ability to compute it is important in ultrasonic imaging research. Generally, to compute the resultant pressure of the array the piston mode is assumed for elementary transducer. In this condition, and if interactions are omitted, the far-field resultant pressure can be obtained using the diffraction theory and is then given by the product of the far-field directivity pattern of an elementary transducer and of the array phase factor. This method gives important results concerning grating lobes.[1] For example, all grating lobes can be avoided if $a<\lambda/2$, where a is the spacing between transducers and λ is the wavelength in the propagating medium. Also, it has been shown that the performance of ultrasonic phased arrays depend mainly on the far-field directivity pattern of the individual array element.[1,2]

At high frequencies (e.g., medical ultrasonic), in order to describe the behavior of the array including interaction, the following points must be kept in mind. First, when the electronic focusing is used the observed targets are in the near field of the array. Second, it is very important to take the ''true'' displacement profile of the transducer surface into account. In fact, experimental results concerning elementary transducer do not always agree with those obtained numerically using classical integrals[3,4] because the piston mode is generally assumed. Third, two kinds of interactions occur: mechanical interaction between the elementary transducers and acoustic interaction between the solid and the fluid media. In the following, it will be shown that acoustic interaction can be omitted. In addition, mutual impedance cannot be computed to describe interaction in such arrays. In fact, in

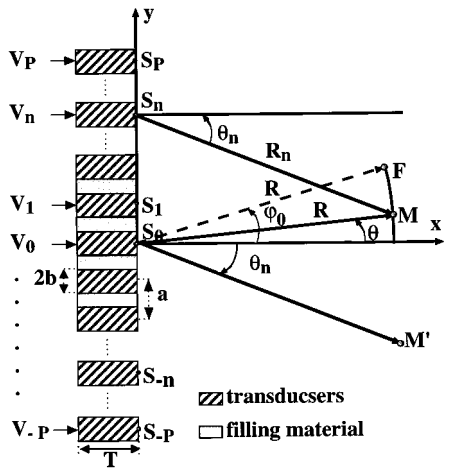

FIG. 1. Schematic description of the cross section of a high-frequency array that consists of N ($N=2P+1$, P is an integer) parallel, identical, and equidistant transducer bars, W/T is the width to thickness ratio ($W=2b$) of each transducer bar and F is the focal point. $R_n=S_nM$ (S_n being the middle of the nth transducer) and $R_0=R=S_0M$.

[a)]Presented in part at the 130th meeting of the Acoustical Society of America, St. Louis, MO, 27 Nov.–1 Dec 1995 [J. Acoust. Soc. Am. **98**, 2876(A) (1995)].

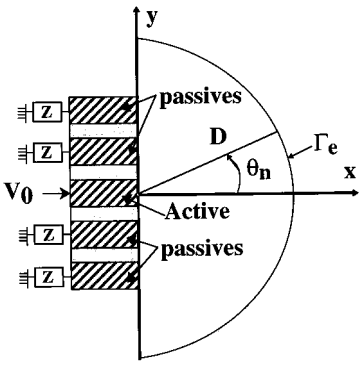

FIG. 2. A set of five transducers with only the middle active (electrically driven) and the others passive (electrically grounded or terminated by a chosen impedance Z).

some cases (e.g., in sonar field), mutual impedance can be computed for particular geometries with simplified hypotheses. Thus, there is no complete theoretical solution that will predict the behavior of high frequency arrays. Then the aim of this paper is to propose a new calculation scheme to compute the resultant pressure of such arrays including interactions.

The finite element method (FEM) is widely used and generally only the elementary transducer bar has been studied and results concerning width to thickness ratio (W/T) have been obtained.[4–7] However, it is very difficult to model a phased and focused array, completely and directly, by the FEM because the domain to be modeled is very large. In fact, the array contains a great number of elementary backed and matched transducers ($N=2P+1$ transducers), and the fluid medium is too large to be meshed.

To obtain the resultant pressure of the array, it is necessary to compute the far-field directivity pattern of an elementary transducer. This resultant pressure can be obtained by summing up the far-field directivity patterns of each elementary transducer weighted by the classical term which takes into account the geometrical and electrical phase shifts [see Eq. (4)]. In order to take interaction into account the far-field directivity pattern of a set of $2Q+1$ elementary transducers (Fig. 2), where only the middle one is active and the others are passive, is considered as the far-field directivity patterns of an elementary transducer. In fact, the driven transducer generates a parasitic displacement field at the radiated surface of the neighboring transducers.[6,8] The far-field directivity pattern of the set of $2Q+1$ transducers can be computed

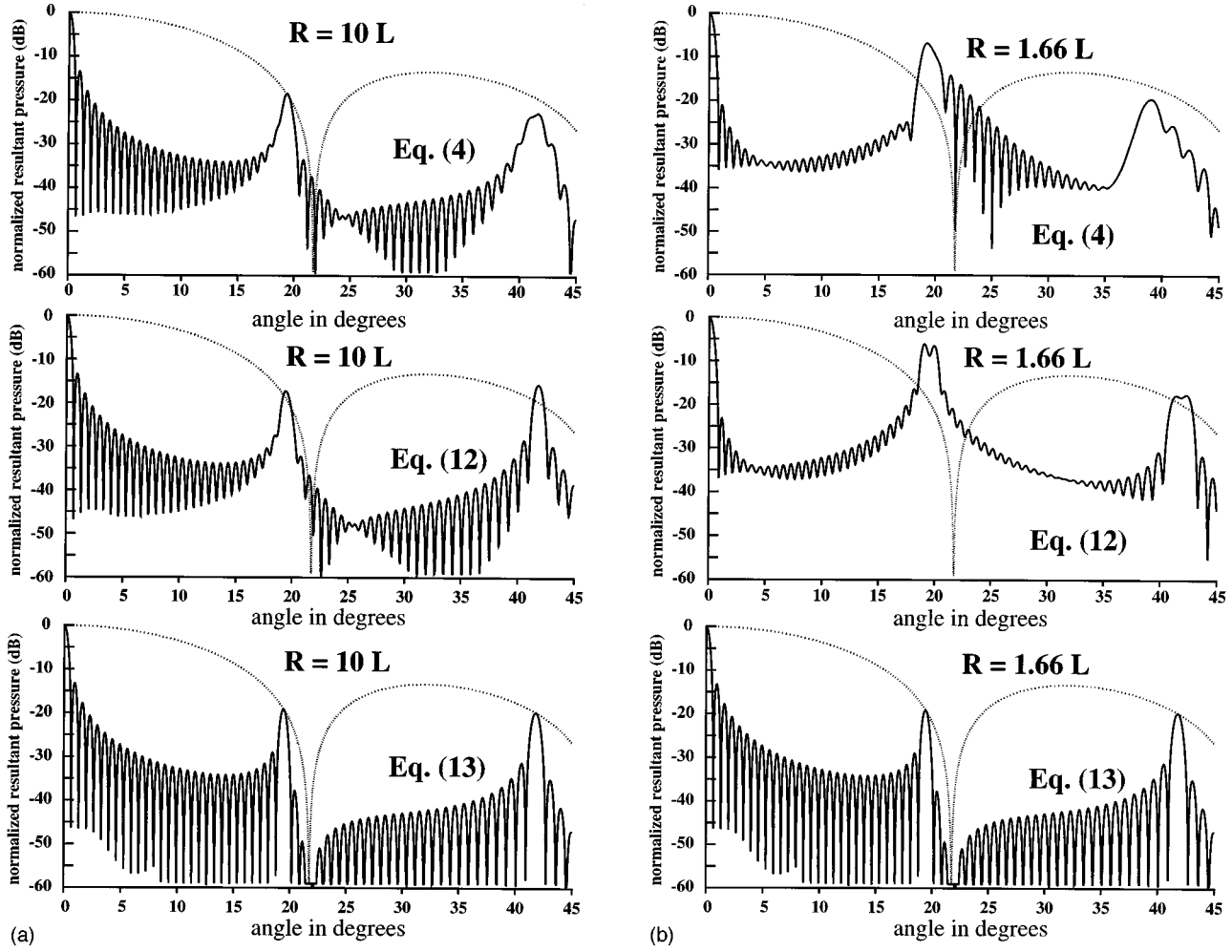

FIG. 3. Relative resultant pressures of an array consisting of 29 ($N=29$) transducer elements with $\varphi_0=0°$ and $R=10L$ (thick lines). Dotted lines represent the far-field directivity $f_0(\theta)$ that has been used in Eqs. (4), (12), and (13). (b) Same as (a) except that R is taken equal to $1.66L$. (c) Same as (a) except that R is taken equal to L.

numerically using the FEM. For this purpose, the fluid mesh (Fig. 2) is terminated by a nonreflecting surface Γ_e made up of dipolar elements that absorb the outgoing acoustic wave almost completely.[9–11] Then the displacement field of the radiating transducers surfaces and the near-field pressure, inside and on the reflecting surface (Fig. 2), can be computed numerically. Moreover, the far-field directivity pattern of the $2Q+1$ elementary transducers can be obtained by extrapolation[11] from the near-field pressure. Finally, the resultant pressure of the array, including interactions (mechanical and acoustical interactions), can be numerically obtained as will be shown in this paper.

I. RESULTANT PRESSURE OF AN ARRAY

Figure 1 describes the section of linear array that consist of N $(2P+1)$ parallel, identical and equidistant, long transducer bars. The width and the thickness of each transducer are respectively noted $W=2b$ and T. Usually, W is equal to one (or a few) acoustic wavelength(s). The transducer length (in the z direction) is always quite larger than the two other dimensions. Therefore, for the purpose of transducer analysis, this length can be considered as infinite, and the plane strain approximation, in the xy plane, is assumed (for more details see Ref. 7). Material used to fill the spacing between elementary transducer will be named filling material. In the realistic case elementary transducers must be matched and backed. In order to present the approach and to study the interaction of neighboring transducers due to the filling material and the fluid–solid interaction, the backing and the matching layer will be omitted in the following. The influence of the backing and matching layers can be found in many works.[6–8,12] Moreover, it is possible to model a set of $2Q+1$ backed and matched transducers by considering a small part of the backing and by scaling losses in the backing material [or scaled tan δ, where δ is the loss angle (see Ref. 13)]. In addition, due to the backing, no changes were observed in the matched resonator frequencies and relative displacement profiles of the transducer.[13]

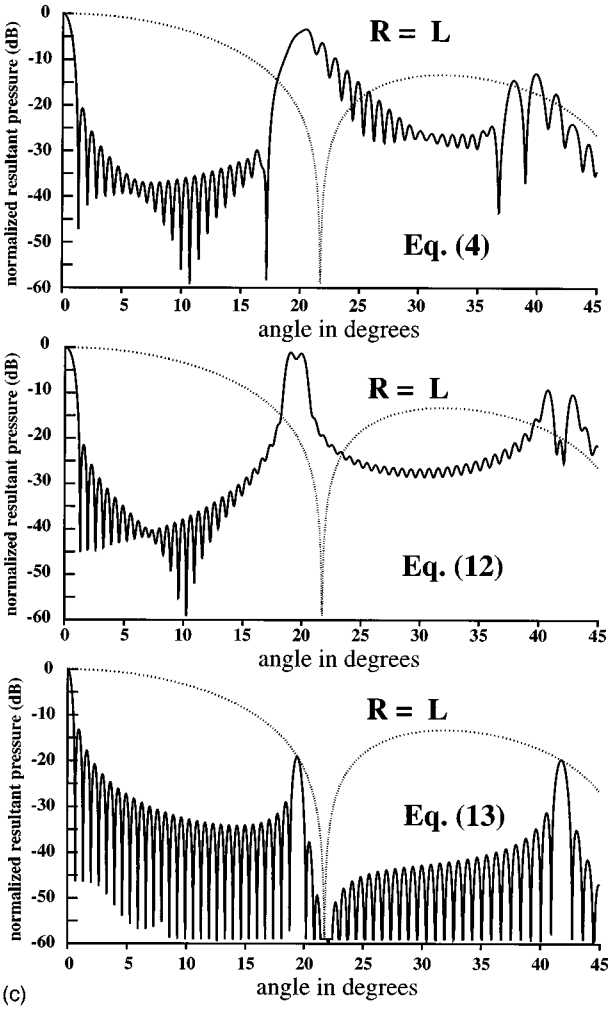

FIG. 3. (*Continued.*)

A. Theoretical approach

Consider a linear array with N $(N=2P+1)$ transducers as shown in Fig. 1. Using Rayleigh's formula and assuming nonmechanical and acoustical interaction between elementary transducers, the radiation field pressure p_n, at the field point M, produced by the nth transducer can be expressed as[11]

$$p_n=\beta V_n \exp(j\phi_n)\int_{na-b}^{na+b} u_n(y) \times\frac{\exp(-jk|SM|)}{\sqrt{k|SM|}}\,dy \quad \text{with} \quad \beta=e^{j\pi/4}\rho\omega^2/(2\pi), \tag{1}$$

where M and S are the running points on Γ_e (circle of radius R) and on the nth radiating transducer surface, respectively. In fact, $SM^2=y^2-2Ry\sin\theta+R^2$ with $na-b\leqslant y\leqslant na+b$. Here $u_n(y)$ is the normal displacement field, per volt unity, of the nth radiating transducer surface; ρ is the fluid density; k is the wave number equal to $2\pi/\lambda$ (λ being the acoustic wavelength in water); and θ_n is the angle between the normal of the nth transducer and $R_n=S_nM$ (S_n is the middle and gives the position of the nth transducer, see Fig. 1). The phase ϕ_n of the applied potential $V_n\exp(j\phi_n)$ of the nth transducer is defined with respect to the one at the origin. It is used for steering and focusing the beam in the azimuth direction (along the y axis) and can be obtained using a set of time delays applied to the array. The amplitude V_n of the applied voltage is the taper function or a window and then can be variable. Harmonic state $[\exp(j\omega t)]$ is considered, omitted, and retained as the phase reference. Finally, the position M is assumed to be in the far field with respect to the nth transducer. With this assumption p_n is given by[11]

$$p_n=V_n\exp(j\phi_n)\tilde{H}_0(kR_n)f_0(\theta_n) \tag{2}$$

with

$$\tilde{H}_0(kR_n)=\sqrt{\frac{2}{\pi kR_n}}\exp[j(kR_n-\pi/4)], \tag{3a}$$

where $f_0(\theta_n)$ is the far-field directivity pattern of the nth transducer and can be expressed in terms of its Fourier coefficients up to the order l_0-1 following the relation

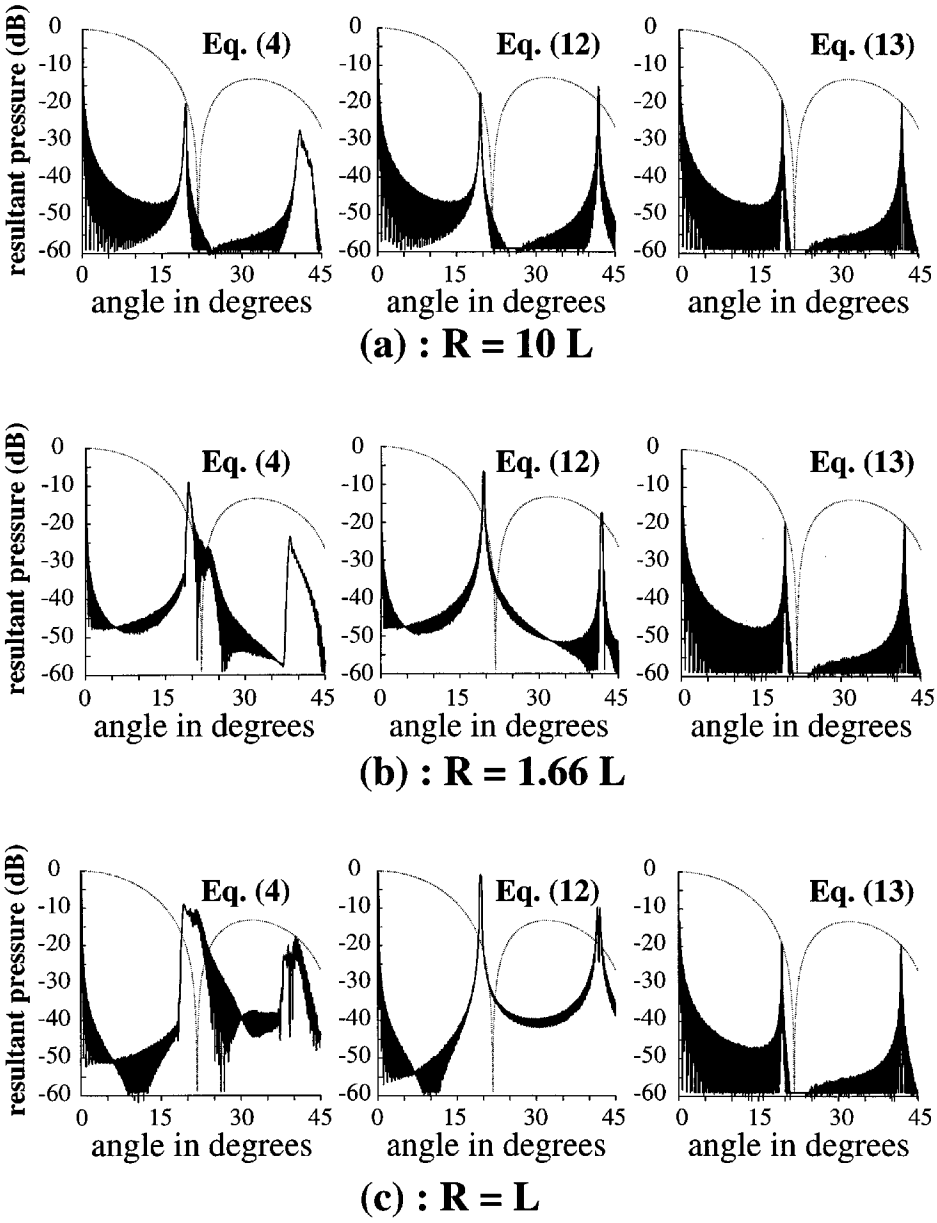

FIG. 4. Same as Fig. 3 except that N is taken equal to 129.

$$f_0(\theta_n)=\sum_{l=0}^{l_0-1}\ [a_l\cos(l\theta_n)+b_l\sin(l\theta_n)]. \tag{3b}$$

This directivity is obtained assuming that the applied potential is equal to 1 V (i.e., it does not depend upon the phase of the applied potential) and can be obtained numerically using the FEM.[11] Consequently, $f_0(\theta_n)$ can be considered as the far-field directivity pattern of any elementary transducer, in particular to that placed at S_0 (middle transducer). In fact, the radiation field at M of the nth transducer is equal to the radiation field at M' of the middle transducer (see Fig. 1). Moreover, $\widetilde{H}_0(kR_n)$ is proportional to the difference of phase between the pressure (at M) given by the nth transducer and to that given by the middle one. Linear superposition[14] of the sound from all the elements leads to the resultant pressure function:

$$p(R,\theta)=\sum_{n=-P}^{n=P} V_n\exp(j\phi_n)\widetilde{H}_0(kR_n)f_0(\theta_n), \tag{4}$$

where $R=R_0$ and $\theta=\theta_0$. The following equations,

$$R_n=[R^2-2naR\sin\theta+(na)^2]^{1/2} \tag{5}$$

and

$$\theta_n=\arcsin\left(\frac{-na+R\sin\theta}{R_n}\right), \tag{6}$$

can be easily obtained by the inspection of Fig. 1. For steering and focusing the beam at point F on the circle of radius R, ϕ_n must be equal to

$$\phi_n=-k(S_nF-R) \tag{7}$$

with

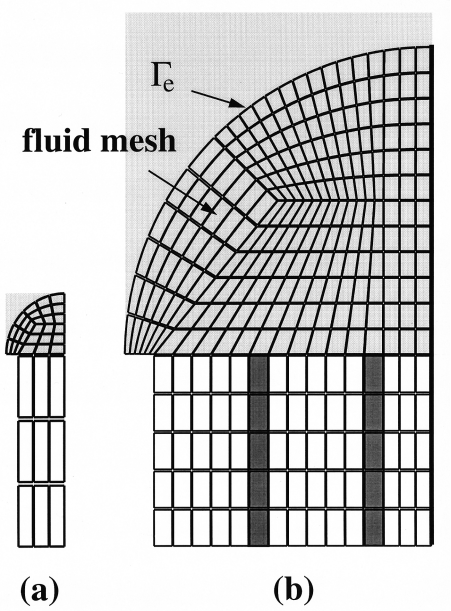

FIG. 5. Finite element mesh (a) for a single element and (b) for a set of five transducers.

$$S_nF=[R^2-2naR\ \sin\ \varphi_0+(na)^2]^{1/2}. \tag{8}$$

It is interesting to note that the resultant radiation, as given by Eq. (4), mainly depends on far-field directivity pattern of the individual array elements. The power radiation Π (Ref. 14) of the array can be also found by integrating the intensity $I(R,\theta)$ over a circular arc of radius R, i.e.,

$$\Pi=\int_{\theta=-\pi/2}^{\theta=\pi/2} I(R,\theta)R\ d\theta=\alpha\int_{\theta=-\pi/2}^{\theta=\pi/2}|p(R,\theta)|^2R\ d\theta, \tag{9}$$

where α is a constant taking into account the acoustic impedance of the fluid medium and the length of the elementary transducer.

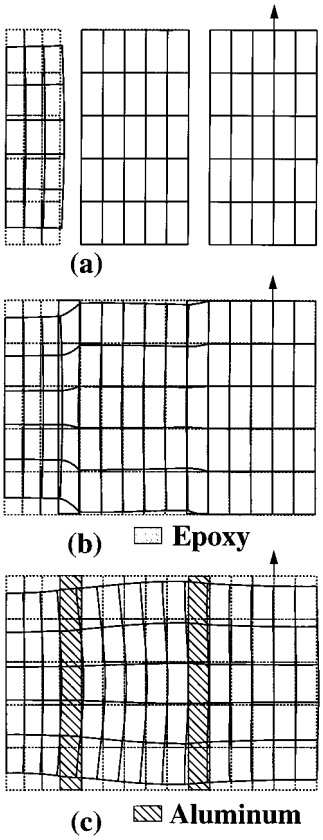

FIG. 6. The displacement field of the set of five transducers with only the middle active at resonance frequency in three cases: (a) no filling material, (b) when compliant material (for example epoxy) is used to fill the array and, (c) when stiff material (for example aluminum) is used to fill the array.

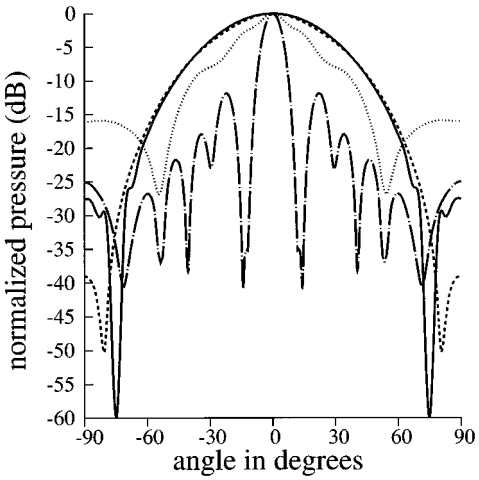

FIG. 7. The far-field directivity pattern of a single element (thick line) and of the set of five transducers with only the middle active. Dashed line: no filling material, dotted line: compliant material is used to fill the array, dashed-dotted line: stiff material is used to fill the array.

B. Far-field resultant pressure

Assuming that $Pa/R<1$ (but M is not in the far-field of the array), R_n and S_nF, as given by Eqs. (5) and (8), can be approximated by

$$R_n\approx R-na\ \sin\ \theta+\frac{(na)^2}{2R} \tag{10}$$

and

$$S_nF\approx R-na\ \sin\ \varphi_0+\frac{(na)^2}{2R}. \tag{11}$$

Then the resultant radiation [Eq. (4)] can be rewritten as

$$p(R,\theta)=p'\sum_{n=-P}^{n=P}\frac{f_0(\theta_n)}{\sqrt{kR_n}}\exp[-jnka(\sin\ \theta-\sin\ \theta_0)]\ \text{ with }\ p'=V_0\sqrt{\frac{2}{\pi}}\,e^{j(kR-\pi/4)}. \tag{12}$$

In the above equation V_n is taken equal to V_0. Two cases can be considered here.

1. Case 1: $Pa/R\ll 1$

Assuming that M is at distance such that $Pa/R\ll 1$ (i.e., M is in the far field of the array), then θ_n can be approximated by θ and R_n by R. In this case, it can be shown that $p(R,\theta)$ is given by

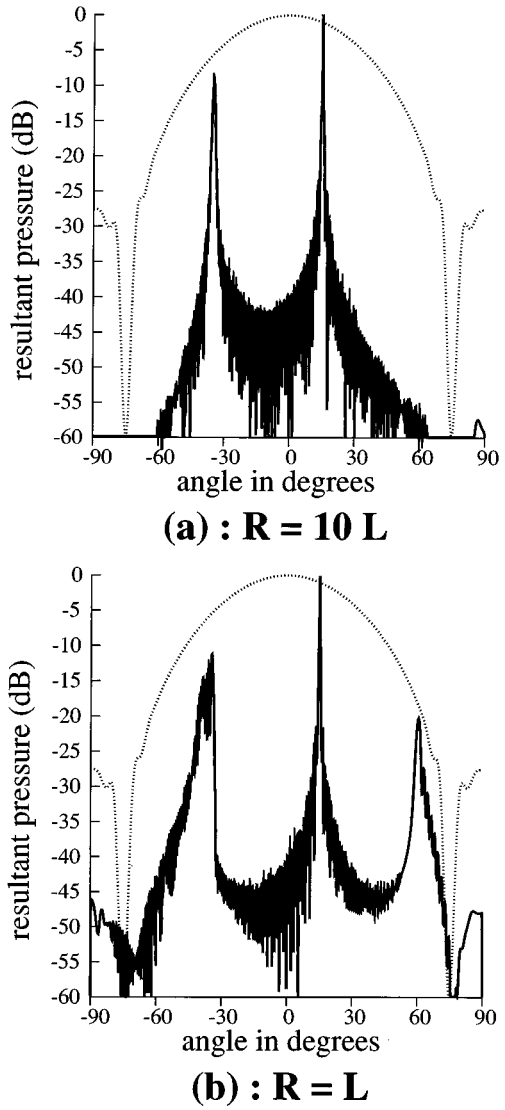

FIG. 8. Resultant pressures of an array (thick lines), as given by Eq. (4), without interaction for two values of R [(a) $R=10L$, (b) $R=L$]. Dotted lines represent the far-field directivity of a single element that has been used to compute the resultant pressures.

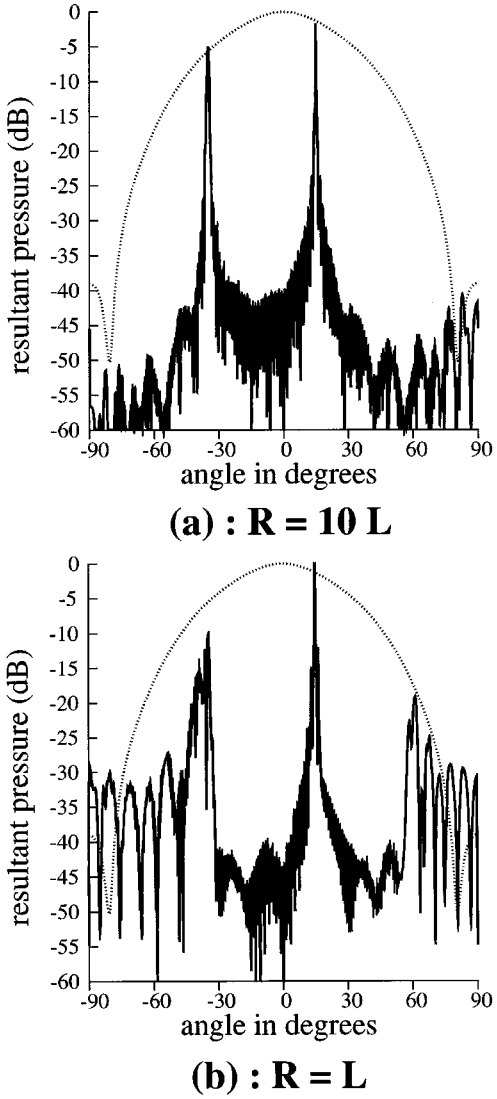

FIG. 9. Resultant pressures of an array (thick lines), as given by Eq. (4), without filling material for two values of R [(a) $R=10L$, (b) $R=L$]. Dotted lines represent the far-field directivity of the set of five transducers that has been used to compute the resultant pressures.

$$p(R,\theta)=\left(p' N \frac{f_0(\theta)}{\sqrt{kR}}\right) \times\left(\frac{\sin\left[\frac{Nka}{2}(\sin\theta-\sin\varphi_0)\right]}{N\sin\left[\frac{ka}{2}(\sin\theta-\sin\varphi_0)\right]}\right). \quad (13)$$

Using the above equation, the direction φ_m of lobes can be found:[1,2]

$$\sin\varphi_m=\sin\varphi_0\pm m\frac{\lambda}{a} \quad \text{with} \quad m=0,\pm1,\pm2,\ldots . \quad (14)$$

Here φ_0 is the direction of the main lobe while φ_m, for m different from zero, gives the direction of grating lobes. In Eq. (12), the first term is proportional to the far-field directivity pattern of an elementary transducer placed at the origin and the second is known as the array phase factor. The result presented by Eq. (13) is well known,[1,2] but the big problem here is that, in the far field, the focalization cannot be realized due to the diffraction phenomena.

2. Case 2: $Pa/R<1$

Assuming now that M is at distance such that $Pa/R<1$ (but M is not in the far field of the array) and that the width of the elementary transducer is very large compared to the acoustic wavelength (i.e., $2b/\lambda<1$), then $f_0(\theta_n)/\sqrt{kR_n}$ can be assumed to vary slowly and can be replaced by $f_0(\theta)/\sqrt{kR}$ near the axis of the array (x axis in Fig. 1). In these conditions Eq. (13) stays valid. In fact, if a piston mode is assumed ($u_n=u_0=$cons), then $f_0(\theta_n)$ is proportional to $\sin(kb\sin\theta_n)/(kb\sin\theta_n)$. In addition, if $2b/\lambda<1$, then the directivity $f_0(\theta_n)$ varies slowly near the x axis.

C. Resultant pressure including interaction

To take interaction into account between elementary transducers, the radiation field of the nth transducer includ-

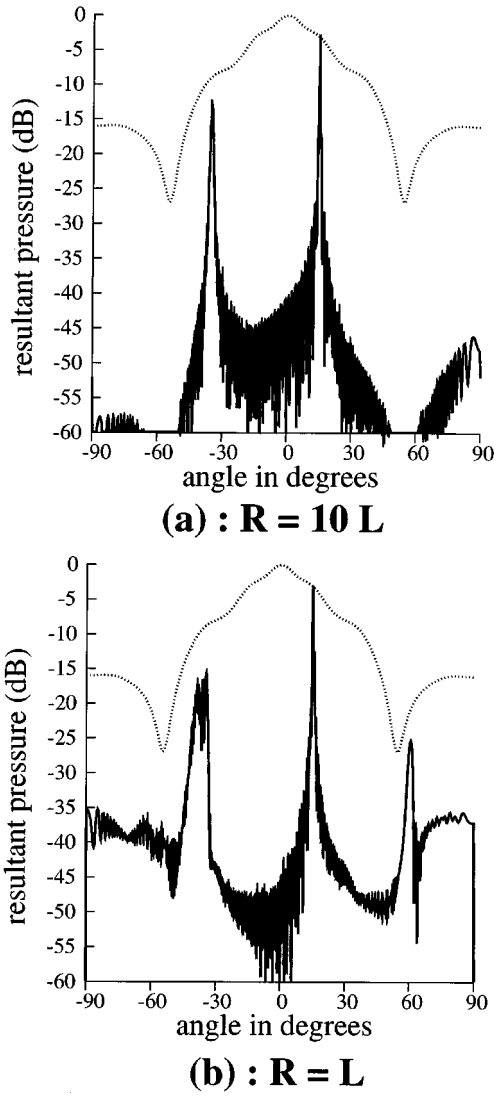

FIG. 10. Same as Fig. 8 but when compliant material is used to fill the array.

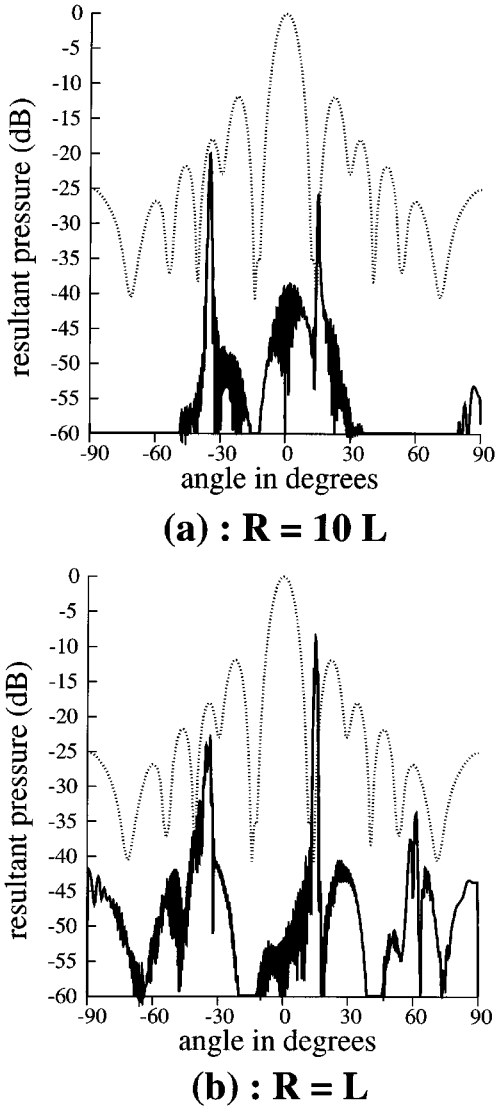

FIG. 11. Same as Fig. 8 but when stiff material is used to fill the array.

ing interaction can be considered as the radiation of a set of $2Q+1$ ($Q=1,2,...$) transducers. The middle one is active and the others are passive (Fig. 2). Then the radiation field of the nth transducer including interaction, at a field point M (Fig. 1), is given by

$$p_n=\beta V_0 \exp(j\phi_n)\int_{na-Qa-b}^{na+Qa+b} u_n(y)\,\frac{\exp(-jkSM)}{\sqrt{kSM}}\,dy, \tag{15}$$

where $u_n(y)$ is the displacement field of the radiating surface of the set of $2Q+1$ transducers. In fact, the driven or active transducer generates a parasitic displacement field at the radiated surface of the neighboring transducers.[7,8] Using the FEM, and supposing that M is in the far field of the set, Eq. (15) can be computed and expressed by a relation as given by Eq. (2) where $f_0(\theta_n)$ is the far-field directivity pattern of the set of $2Q+1$ transducers (Fig. 2). Then the resultant pressure of the array can be computed using Eq. (4).

II. NUMERICAL SIMULATIONS

A. Numerical simulations without interaction

To compare Eqs. (4), (12), and (13), supposing interaction is negligible and the displacement field of the nth elementary transducer is constant [piston mode: $u_n(y)=u_0$], then the far-field directivity pattern is given by[1]

$$f_0(\theta)=\gamma\,\frac{\sin(kb\,\sin\,\theta)}{kb\,\sin\,\theta} \quad \text{with} \quad \gamma=-j\rho\omega^2 u_0 b. \tag{16}$$

In this section (II A) the focal point F is supposed on the x axis ($\varphi_0=0$), $a=3\lambda$, and $2b/a=0.9$. In fact, it has been demonstrated that for $\varphi_0=0$ the relative level of the grating lobes are weak if $2b/a$ is near unity.[15] As a first example, the number of elementary transducers is taken equal to 29, i.e., $N=29$. Denoting by L the length of the array ($L=Na$), Fig. 3 shows the relative resultant pressures, as given by Eqs. (4), (12), and (13), for several values of R and L. In the same figure, and to help interpretation, the far-field directivity pattern $f_0(\theta)$ is represented using dotted lines. For $R=10L$ [Fig. 3(a)] and for $\theta<40°$, the three formulas give, practically, the

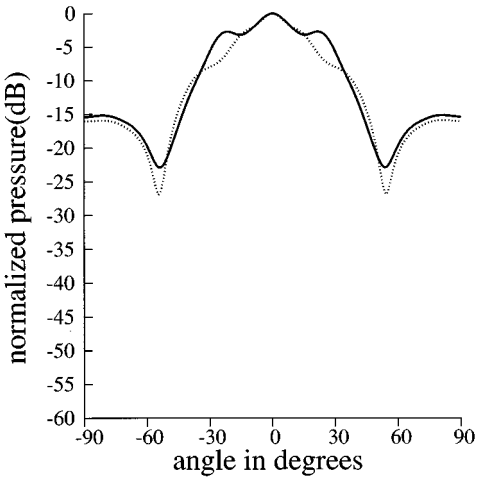

FIG. 12. The far-field directivity pattern $f_0(\theta)$ of the set of five transducers with only the middle active (Fig. 2). Thick line: $Z=50\ \Omega$, dotted line: $Z=0\ \Omega$.

same resultant pressure and the directions φ_m of the grating lobes are approximately equal to 19° ($m=1$) and to 42° ($m=2$) and practically equal to that given by Eq. (14). For $R=1.66L$ [Fig. 3(b)] the resultant pressure given by Eq. (13) is different from that given by Eq. (4) or (12). In fact, in this case $2b/\lambda=1.8$ and $L/(2R)$ is not very small compared to unity. For $R=L$ [Fig. 3(c)], Eqs. (12) and (13) are not available for $\theta>15°$ because the field point M is in the near field of the array. It has been demonstrated, numerically, that when $L/(2R)<1$ and when the product $L/(2R)\times 2b/\lambda<0.4$, Eq. (12) can be approximated by Eq. (13). It is interesting to note that the full widths at half-maximum (FWHM) of the grating lobes are greater than that obtained by Eqs. (12) and (13). Finally, it has been demonstrated (numerically) that when $2b/\lambda<1$ and when the field point (M) is near the axis of the array (x axis), Eqs. (4), (12), and (13) give practically the same resultant pressure.

Figure 4 shows the relative resultant pressures for conditions similar to Fig. 3 except that the number of elementary transducers is taken equal to 129 ($N=129$). By the inspection of Figs. 3 and 4, it is clear that the above comments on Eqs. (4), (12), and (13) hold also for great values of N, and therefore do not depend on N.

B. Numerical simulations with interaction

An array with N piezoelectrical transducer bars with $a=1.21\lambda$ and $2b/a=0.83$ will be considered. In order to show the directivity modifications due to interaction, the width to thickness ratio ($W/T=2b/T$) has been taken equal to 0.5.[4,5,7] In fact, for $W/T\sim 0.5$ a dominate thickness mode can be obtained. Lithium niobate bars [$(YZw)36°$ cut] have been chosen in the following. In fact, lithium niobate can be used in high-frequency applications. For example, for $T=0.1$ mm, the resonance frequency of the thickness mode is equal to 30 MHz.[4] To fill the array, two kinds of materials have been used: compliant (for example, epoxy) and stiff (for example, aluminium) materials. The mechanical impedances of lithium niobate, epoxy, and aluminium are respectively equal to 34.8×10^6 kg/s m^2, 2.5×10^6 kg/s m^2, and 16.7×10^6 kg/s m^2.[16] Numerical results that will be shown in the following stay valid if other equivalent materials have to be used. For example, instead of lithium niobate, PZT can be considered. In fact, for $W/T<0.6$, a thickness mode has been observed for the PZT.[5]

To compute the resultant pressure including interaction, a set of five elementary transducers with only the middle active (Fig. 2) has been modeled by FEM. Figure 5 shows the finite element mesh that have been used to compute the far-field directivity pattern for a single element [Fig. 5(a)] and for the set of five elements [Fig. 5(b)]. In the last case the radius of the circular boundary Γ_e has been taken equal to 3.3λ (for more details see Refs. 4 and 11 about the criteria of the finite element mesh). Only one-half of the domain is meshed for the sake of symmetry. Finally, the chosen impedance Z (Fig. 2) is taken equal to zero. Figure 6 displays the imaginary part of displacement field at the resonance frequency (thickness mode) for the set of five transducers with and without the filling material (stiff and compliant). The radiated surface, in contact with water, is always shown by an arrow. When there is no filling material, the displacement fields show that there are very few interactions between elementary transducers [Fig. 6(a)]. In fact, when there is no filling material, the interaction between the fluid and the passive transducers (acoustical interaction) can be omitted. Moreover, the displacement field of the active transducer [Fig. 6(a)] is practically the same as that obtained when only the active transducer has been modeled [Fig. 5(a)]. For this reason the displacement field of that transducer is not given. Interaction is important when the filling material is compliant [see Fig. 6(b)], but when stiff material is used for filling the array, interaction is very important [Fig. 6(c)]. When filling material is stiff, it is interesting to note that the displacement field presents harmonic oscillations [Fig. 6(c)] and a Lamb wave will be generated at the radiated surface of the array. In this last case, to take interaction into account, the whole array must be modeled with only the middle one active. Finally, it has been demonstrated that, when compliant material is used for filling the array, it is sufficient to consider four neighboring grounded transducers. This result has been also evidenced[17] when interactions are weak.

In Fig. 7, the far-field directivity patterns $f_0(\theta)$ at resonance for the set of five transducer bars (Fig. 2) are presented, for different filling materials, and compared to the far-field directivity pattern of a single element (thick line, $Q=0$). When there is no filling material, interaction can be considered as negligible (dashed line). When filling material is compliant (dotted line) there is little difference between the far-field directivity pattern of the set and that given by a single element. However, when stiff material is used (dashed dotted line), the difference is important between the far-field directivity pattern of the set and that given by a single element.

The above directivity patterns [$f_0(\theta)$] have been used to compute the resultant pressure with the help of Eq. (4) in the far field ($R=10L$) and in the near field ($R=L$) of the array. Figures 8–11 show the resultant pressures [Eq. (4)] of an array consisting of 129 elements ($L=Na$) and steering at 15° ($\varphi_0=15°$) in four different cases. In the same figures,

dotted lines represent the far-field directivity pattern $[f_0(\theta)]$ that has been used to compute the resultant pressure. In the first case (Fig. 8) interactions are omitted, i.e., the far-field directivity pattern that have been used to compute the resultant pressure has been obtained by modeling a single element. For the next three cases the resultant pressures are obtained using Eq. (4) together with the far-field directivity pattern of the set of five transducers $[f_0(\theta)]$ with only the middle active (Fig. 2). Figure 9 is obtained by omitting the filling material. Figure 10 is obtained when compliant material is used to fill the array. Finally, Fig. 11 is obtained when stiff material is used to fill the array. In the two cases ($R=L$ or $R=10L$) the maximum value (p_0) of the resultant pressure has been obtained, when interactions are omitted (Fig. 8), at $\theta \approx 15°$. Then the resultant pressures shown in Figs. 8–11 have been normalized with respect to this value. When there is no filling material, acoustical interactions can be omitted because the results shown by Figs. 8 and 9 are similar [see also the displacement field in Fig. 5(a)]. Generally, in the near field of the array the FWHM of the grating lobes increase and other grating lobes are observed at $\theta \approx 42°$. The level of the main lobe ($\varphi_0=15°$) decreases due to interactions. When interactions are important [Fig. 11(a)], it should be noted that the main-lobe ($\varphi_0=15$) array response is down 24 dB, approximately the same as the far-field directivity pattern [$\theta=15$, see also dotted lines in Fig. 11(a)] of the set of five transducers. It has been demonstrated that the backing cannot influence the relative directivity pattern of an array,[8] but can influence the radiated acoustic power in the fluid medium.

The above example has been reconsidered but for an impedance Z (Fig. 2) equal to 50 Ω. Figure 12 shows the far-field directivity pattern $f_0(\theta)$ for the set of five transducers (Fig. 2) when compliant material is used to fill the array. In the same figure the far-field directivity pattern $f_0(\theta)$ obtained when considering $Z=0$ (Fig. 7, dotted line) is also presented. There is little difference between these two directivities. The resultant pressures that have been obtained using these two directivities are practically the same.

Finally, the above conclusions concerning the interactions do not change if the value of N and φ_0 change. In fact, different computations have been realized and the corresponding results are not given in order to reduce considerably the number of figures.

III. CONCLUSION

This study has demonstrated that the finite element method can be used to compute the resultant pressure, including interactions, of a phased and focused array. It has been shown that the resultant pressure mainly depends upon the far-field pattern of a set of $2Q+1$ transducers where only the middle one is active. Our proposed calculation scheme has been used to compute the resultant pressure of different high-frequency linear arrays. Only results concerning a lithium niobate array have been given. It has been shown that mechanical interaction between elementary transducers plays a major role on the response of these linear arrays. Moreover, the interaction between the fluid medium and the passives transducers (acoustic interaction) can be omitted. Finally, work is now under progress to model a backed and matched high frequency array.

ACKNOWLEDGMENTS

Authors wish to thank Professor J-M. Rouvaen, Professor J-N. Decarpigny, and Dr. B. Dubus from IEMN for helpful discussions.

[1] B. D. Steingberg, *Principles of Aperture and Arrays System Design* (Wiley, New York, 1976).
[2] D. H. Turnbull and F. S. Foster, ''Beam steering with pulsed two-dimensional transducer arrays,'' IEEE Trans. Ultrason. Ferroelectr. Freq. Control **UFFC-38**, 320–333 (1991).
[3] B. Delannoy, C. Bruneel, F. Haine, and R. Torguet, ''Anomalous behavior in the radiation pattern of piezoelectric transducers induced by parasitic Lamb wave generation,'' J. Appl. Phys. **51**, 3942–3948 (1980).
[4] J. Assaad, C. Bruneel, J.-N. Decarpigny, and B. Nongaillard, ''Electromechanical coupling coefficients and farfield radiation patterns of Lithium Niobate bars (Y-cut) used in high frequency acoustical imaging and non destructive testing,'' J. Acoust. Soc. Am. **94**, 2969–2978 (1993).
[5] J. Sato, M. Kawabuchi, and A. Fukumoto, ''Dependance of electromechanical coupling coefficient on the width-to-thickness ratio of plank-shaped piezoelectric transducers used for electronically scanned ultrasound diagnostic systems,'' J. Acoust. Soc. Am. **66**, 1609–1611 (1979).
[6] W. Friedrich, H. Kaarmann, and R. Lerch, ''Finite element modeling of acoustic radiation from piezoelectric phased array antenna,'' IEEE Ultrason. Symp. Proc., 763–767 (1990).
[7] R. Lerch, ''Simulation of piezoelectrical devices by two- and three-dimensional finite elements,'' IEEE Trans. Ultrason. Ferroelectr. Freq. Control **UFFC-37**, 233–245 (1990).
[8] R. L. Jungerman, P. Bennett, A. R. Selfridge, B. T. Khuri-Yakup, and G. S. Kino, ''Measurement of normal surface displacements for the characterization of rectangular acoustic array elements,'' J. Acoust. Soc. Am. **76**, 516–524 (1984).
[9] A. Bayliss, M. Gunzburger, and E. Turkel, ''Boundary conditions for the numerical solution of elliptic equations in exterior regions,'' ICASE Report No. 80/1, NASA Langley (1980).
[10] P. M. Pinsky, L. L. Thompson, and N. N. Abboud, ''Local high-order radiation boundary conditions for the two-dimensional time-dependent structural acoustics problem,'' J. Acoust. Soc. Am. **91**, 1320–1335 (1992).
[11] J. Assaad J.-N. Decarpigny, C. Bruneel, R. Bossut, and B. Hamonic, ''Application of the finite element method to two-dimensional radiation problems,'' J. Acoust. Soc. Am. **94**, 562–573 (1993).
[12] J. W. Hunt, M. Arditi, and F. S. Foster, ''Ultrasound transducers for pulse-echo medical imaging,'' IEEE Trans. Biomed. Eng. **BME-30**, 453–481 (1983).
[13] J. Assaad, M. Ravez, and C. Bruneel, ''Application of the finite element method to modelling backed transducer,'' J. Acoust. Soc. Am. **100**, 3098–3103 (1996).
[14] A. Akay, ''Radiation from a finite array sources,'' J. Acoust. Soc. Am. **87**, 1449–1454 (1990).
[15] J. Assaad, ''Modélisation des transducteurs haute frequence à l'aide de la méthode des éléments finis,'' Thèse de Doctorat, Université de Valenciennes et du Hainaut-Cambrésis, France, 1992.
[16] A. W. Warner, M. Onoe, and G. A. Coquin, ''Determination of elastic and piezoelectric constants for crystals in class (3m),'' J. Acoust. Soc. Am. **42**, 1223–1231 (1967).
[17] See experimental results presented by Jungerman *et al.*[8] or numerical results presented by Friedrich *et al.*[6]

Acoustic wave propagation in two-phase viscoelastic fluids: The case of polymer emulsions

Claude Verdier and Monique Piau
Laboratoire de Rhéologie,[a] B.P. 53, Domaine Universitaire, 38041 Grenoble Cedex 09, France

(Received 13 February 1995; accepted for publication 14 October 1996)

Wave propagation in two-phase viscoelastic fluid media is studied. A theory based on previous ones for liquid–liquid or liquid–solid mixtures is developed. Acoustical parameters, i.e., velocity of propagation and attenuation, are related to the morphological properties (concentration and size of inclusions) through the thermal and viscoelastic effects. This general theory includes the Newtonian and elastic behaviors as limiting cases. In the case of molten polymer blends, viscoelastic effects may be dominant, unlike most of the Newtonian emulsions studied previously, where thermal effects usually prevail. Moreover, by taking into account the viscoelastic character of the fluids, important changes are obtained not only for the absorption due to the individual components, but also for the excess attenuation in the emulsion. © *1997 Acoustical Society of America.* [S0001-4966(97)00404-9]

PACS numbers: 43.20.Hq, 43.20.Bi, 43.35.Mr [JEG]

INTRODUCTION

Wave propagation in heterogeneous systems has been a source of great interest during the last forty years. Indeed the measurable wave parameters, velocity, and attenuation, provide a means of investigation of these systems. A description of the process for systems containing fluid particles suspended in a fluid medium was given in 1951 by Epstein and Carhart,[1] using some limiting assumptions. It was extended in 1972 by Allegra and Hawley,[2] to the case of liquid-liquid, as well as liquid–solid systems, using a different model for each case. Many of the authors who tried to model ultrasonic wave propagation in suspensions or emulsions have used approaches based on these works.

The varieties of theoretical formulations used to describe wave propagation in suspensions of particles in fluids was reviewed in 1988 by Harker and Temple.[3] They concluded that either formula leads to the same values of velocities, especially when inclusions are rather similar to the continuous fluid, in other words when they have close acoustic impedances.

Viscous and thermal processes occurring at the interfaces between the matrix and the inclusions are responsible for scattering mechanisms involving changes in wave velocity and attenuation. Usually, these effects can be separated, but only at low concentrations. Still an explicit expression cannot be obtained for the velocity of propagation and excess attenuation as a function of the volume fraction and the size of the particles. The system of equations describing the scattering processes has to be solved numerically.

Allegra and Hawley[2] found thermal transport process to be the major factor in the attenuation for the emulsions they studied (for example 20% toluene in water, 2–5 MHz). Similar results were found by McClements and Povey,[4] Schröder and Raphaël[5] for oil in water emulsions using longitudinal waves in the MHz range. The authors related their results to a theory including viscoinertial and thermal scattering mechanisms. In these cases a satisfactory relationship was found between long wavelength theories and experimental data.

In extending the formalism to multiple scattering effects in suspensions or emulsions, the value of the scattered amplitude as a function of the scattering angle has to be averaged over the particle mass centers distribution before relating it to the bulk values of ultrasonic velocity and attenuation (Lloyd and Berry[6]). This adds a correction term in the usual formulas for the velocity and attenuation.

Models developed for comparison with experimental data usually include the viscosity of the fluid components. Some authors (Meeten and Sherman[7]) have tried to combine the viscous and elastic effects in suspensions. They used a model with explicit formulas and were able to fit them with the experimental velocity and attenuation data using shear dependent viscosity estimations.

However, there is still a need for a complete theory describing these phenomena in the case of viscoelastic fluids, which would also be able to cover the limiting cases. This is what is done in the present paper. The theory uses a linear viscoelastic model, based on the one studied by Charlier and Crowet,[8] with a thermal coupling added through the energy equation. A new family of parameters is introduced, related to shear and compressional complex viscosities, and the wave propagation equations are obtained in Sec. I.

The general case of viscoelastic emulsions is examined in Sec. II. Following the method used by Epstein and Carhart[1] or Allegra and Hawley,[2] we write the boundary conditions at the interface between the phases, and obtain a modified system of equations. The limiting cases of a solid or liquid inclusion are verified. The system is solved numerically to obtain the parameters required for the computation of the velocity of propagation and attenuation of waves.

Effective calculations are deduced from our extended theory and are reported in Sec. III, for viscous and viscoelas-

[a]Université Joseph Fourier and INPG, associated with the Centre National de la Recherche Scientifique (U.M.R. 5520).

 0001-4966/97/101(4)/1868/9/$10.00

tic fluids tested in the ultrasonic range, with a special emphasis on viscoelastic emulsions, in particular polymer blends.

The main advantages of our model are underlined in the conclusion.

I. WAVE PROPAGATION IN VISCOELASTIC FLUIDS

A. Governing equations and linearization

We will use the following notations: $\rho=1/v$ is the density, reciprocal of the specific volume v, $\mathbf{v}$ is the eulerian velocity, $\boldsymbol{\Sigma}$ is the stress tensor, $\mathbf{D}$ is the symmetrical part of the velocity gradient tensor, τ is the thermal conductivity (assumed to be constant), T is the temperature, and u is the internal energy of the medium. The set of equations to be written for a continuous medium are the mass, momentum, and energy conservation equations:

$$\frac{\partial \rho}{\partial t}+\boldsymbol{\nabla}\cdot(\rho\mathbf{v})=0, \tag{1a}$$

$$\rho\left(\frac{\partial \mathbf{v}}{\partial t}+\mathbf{v}\cdot\boldsymbol{\nabla}\mathbf{v}\right)=\operatorname{div}\boldsymbol{\Sigma}, \tag{1b}$$

$$\rho\left(\frac{\partial u}{\partial t}+\mathbf{v}\cdot\boldsymbol{\nabla}u\right)=\operatorname{Tr}(\boldsymbol{\Sigma}\cdot\mathbf{D})+\tau\nabla^2 T. \tag{1c}$$

In addition to this, we need a constitutive equation for a viscoelastic fluid, to relate current stresses to the history of deformation.[8] Memory effects are taken into account for instance with the following viscoelastic constitutive equation of integral type.

$$\boldsymbol{\Sigma}=-p\mathbb{I}+\int_{-\infty}^{t}\left\{\widetilde{K}(t-t')-\frac{2}{3}G(t-t')\right\}\operatorname{Tr}\mathbf{D}(t')\mathbf{I}\,dt' +2\int_{-\infty}^{t}G(t-t')\mathbf{D}(t')dt', \tag{1d}$$

which is a linear approximation of the general form of a phenomenological constitutive equation for a compressible fluid.[9] The introduction of $\widetilde{K}(t)$ and $G(t)$ takes into account possible relaxation phenomena, due to the presence of long macromolecules for example, as in a polymeric material. This model works well in the case of small deformations, such as acoustical ones. It is more general than models often used which specify relaxation times. In Eq. (1d), p is the thermodynamic pressure, given by the equation of state (see Sec. I B), so that the mean principal stress $\overline{p}$ is given by:

$$\overline{p}=-\frac{1}{3}\operatorname{Tr}\boldsymbol{\Sigma}=p-\int_{-\infty}^{t}\widetilde{K}(t-t')\operatorname{Tr}\mathbf{D}(t')dt'.$$

The main principal stress $\overline{p}$ differs from the thermodynamic pressure because of relaxational compression effects. For materials of solid-type behavior, p is to be neglected with respect to the elastic moduli. For materials of fluid-type behavior, $\widetilde{K}$ does not include the usual K_0 term (reciprocal of the adiabatic compressibility), which will come out through the pressure p. Models for the linear elastic solid and the Newtonian fluid are obtained as limiting cases.

(a) The *perfectly elastic solid* is recovered by choosing:

$$\widetilde{K}(s)=(\lambda+\tfrac{2}{3}\mu)h(s),\quad G(s)=\mu h(s),\quad p\ll\lambda|\epsilon_{ij}|,\mu|\epsilon_{ij}|,\quad \text{for } i,j=1,2,3, \tag{2a}$$

where $h(s)$ is a step function (Heavyside). Thus, $\boldsymbol{\Sigma}=\lambda\times(\operatorname{Tr}\boldsymbol{\epsilon})\mathbf{I}+2\,\mu\boldsymbol{\epsilon}$, where $\boldsymbol{\epsilon}$ is the linearized deformation tensor, and λ and μ are the Lamé coefficients.

(b) On the other hand, the *Newtonian case* is obtained when

$$\widetilde{K}(s)=\eta_v\delta(s),\quad G(s)=\eta_s\delta(s),\quad \mathbf{D}(s)\approx\dot{\boldsymbol{\epsilon}}(s)\ \text{(small deformations)} \tag{2b}$$

in which $\delta(s)$ is the so-called Dirac ''function.''

This leads to: $\boldsymbol{\Sigma}=-p\mathbf{I}+(\eta_v-\frac{2}{3}\eta_s)\ (\operatorname{Tr}\mathbf{D})\mathbf{I}+2\eta_s\mathbf{D}$. η_v and η_s are, respectively, the volume and shear viscosities.

Let us look at the general case now. Using Eq. (1d) in Eq. (1b) and Eq. (1c), we obtain first:

$$\frac{\partial \rho}{\partial t}+\boldsymbol{\nabla}\cdot(\rho\mathbf{v})=0, \tag{3a}$$

$$\rho\left(\frac{\partial \mathbf{v}}{\partial t}+\mathbf{v}\cdot\boldsymbol{\nabla}\mathbf{v}\right) =-\boldsymbol{\nabla}p+\int_{-\infty}^{t}\left\{\widetilde{K}(t-t')+\frac{4}{3}G(t-t')\right\}\boldsymbol{\nabla}[\boldsymbol{\nabla}\cdot\mathbf{v}(t')]dt' -\int_{-\infty}^{t}G(t-t')\boldsymbol{\nabla}\times[\boldsymbol{\nabla}\times\mathbf{v}(t')]dt', \tag{3b}$$

$$\rho\left(\frac{\partial u}{\partial t}+\mathbf{v}\cdot\boldsymbol{\nabla}u\right)+p\boldsymbol{\nabla}\cdot\mathbf{v} =\operatorname{Tr}\left\{\mathbf{D}\cdot\left(\int_{-\infty}^{t}\left\{\widetilde{K}(t-t')+\frac{2}{3}G(t-t')\right\}\boldsymbol{\nabla}\cdot\mathbf{v}(t')dt'\mathbf{I} +2\int_{-\infty}^{t}G(t-t')\mathbf{D}(t')dt'\right)\right\}+\tau\nabla^2 T. \tag{3c}$$

We will now make use of the thermodynamic equations to obtain the pressure-coupling effects.

B. Thermodynamical relations

Starting with the equations of state $p=p(\rho,T)$ and $u=u(\rho,T)$, for an adiabatically isolated system, the spatial and time derivatives of p and u may be related to velocity and temperature variations, using thermodynamic relations. We introduce quantities such as the fluid isothermal compressibility $\kappa\ [\kappa=-1/v(\partial v/\partial p)_T]$, associated with the equation of state for the pressure p, the specific heat at constant volume C_v, and at constant pressure C_p, the specific heat ratio $\gamma=C_p/C_v$, the thermal dilatation β, as well as the adiabatic velocity of sound q such that $q^2=\gamma(\kappa\rho)^{-1}=K\rho^{-1}$.

The symbol of derivative with respect to time $\partial/\partial t$ will be replaced by a dot ($\dot{u}=\partial u/\partial t$). Then

$$\dot{u}=\left(\frac{\partial u}{\partial \rho}\right)_T\dot{\rho}+C_v\dot{T}, \tag{4}$$

$$\nabla p = \frac{q^2}{\gamma}\nabla\rho + \left(\frac{\partial p}{\partial T}\right)_\rho \nabla T. \tag{5}$$

Coefficients $(\partial p/\partial T)_\rho$ and $(\partial u/\partial\rho)_T$ can also be derived, so that:

$$\dot{u} = \left\{\frac{p}{\rho^2} - \frac{(\gamma-1)C_v}{\rho\beta}\right\}\dot{\rho} + C_v\dot{T}, \tag{6}$$

$$\nabla p = \frac{q^2}{\gamma}\nabla\rho + \frac{\rho q^2\beta}{\gamma}\nabla T. \tag{7}$$

We are now ready to derive the acoustical field equations.

C. The acoustical field equations

We will study the propagation of infinitesimal disturbances superimposed to the current state of deformation. Linearizing Eqs. (3) around the homogeneous state characterized by the values $p=p_0$, $T=T_0$, $\rho=\rho_0$, $u=u_0$, $\mathbf{v}=\mathbf{0}$. In Eqs. (8) and throughout the following discussion, ρ, p, $\mathbf{v}$, T,u will denote small deviations of the corresponding variables due to the acoustical field, whereas the index zero refers to the undisturbed solution.

$$\frac{\partial\rho}{\partial t} + \rho_0\nabla\cdot\mathbf{v} = 0, \tag{8a}$$

$$\rho_0\frac{\partial\mathbf{v}}{\partial t} + \nabla p - \int_{-\infty}^{t}\left\{\widetilde{K}(t-t') + \frac{4}{3}G(t-t')\right\}\nabla[\nabla\cdot\mathbf{v}(t')]dt' + \int_{-\infty}^{t}G(t-t')\nabla\times[\nabla\times\mathbf{v}(t')]dt' = \mathbf{0}, \tag{8b}$$

$$\rho_0\frac{\partial u}{\partial t} + p_0\nabla\cdot\mathbf{v} - \tau\nabla^2 T = 0. \tag{8c}$$

Thermodynamic relations are also linearized, after replacing $\dot{\rho}$ using Eq. (8a). In particular the pressure variation due to the acoustical field may be written:

$$\dot{p} = -\frac{\rho_0 q^2}{\gamma}\nabla\cdot\mathbf{v} + \frac{\rho_0 q^2\beta}{\gamma}\dot{T}. \tag{9}$$

The field equations for $\mathbf{v}$ and T will be obtained by eliminating the derivatives of p and u from the system (8), after differentiating Eq. (8b) and the linearized Eq. (7) with respect to time. We will use the fact that:

$$\frac{\partial}{\partial t}\int_{-\infty}^{t}a(t-t')b(t')dt' \overset{\text{Change of variables}}{=} \frac{\partial}{\partial t}\int_0^\infty a(s)b(t-s)ds \overset{\text{derivation}}{=} \int_0^\infty a(s)\dot{b}(t-s)ds \overset{\text{change of variables}}{=} \int_{-\infty}^{t}a(t-t')\dot{b}(t')dt'.$$

Finally, we are left with:

$$\frac{\partial^2\mathbf{v}}{\partial t^2} - \frac{q^2}{\gamma}\nabla(\nabla\cdot\mathbf{v}) - \frac{1}{\rho_0}\int_{-\infty}^{t}\left\{\widetilde{K}(t-t') + \frac{4}{3}G(t-t')\right\}\nabla[\nabla\cdot\dot{\mathbf{v}}(t')]dt' + \frac{1}{\rho_0}\int_{-\infty}^{t}G(t-t')\nabla\times[\nabla\times\dot{\mathbf{v}}(t')]dt' = -\frac{q^2\beta}{\gamma}\nabla\dot{T}, \tag{10a}$$

$$\frac{\gamma-1}{\beta}\nabla\cdot\mathbf{v} = \gamma\sigma\nabla^2 T - \dot{T}, \tag{10b}$$

where the thermal diffusivity $\sigma=\tau/\rho_0 C_p$ has been introduced. The system (10) gives four equations for the three components of the velocity field $\mathbf{v}$ and the temperature T.

We will now study the propagation of harmonic waves such that any quantity $T(\mathbf{x}, t)$ to be determined has a time dependence of the form: $T(\mathbf{x}, t)=T(\mathbf{x})e^{-i\omega t}$. The partial differentiation with respect to time gives rise to a multiplication by $-i\omega$: $\dot{T}(\mathbf{x}, t)=-i\omega T(\mathbf{x}, t)$. Under this hypothesis, it is convenient to introduce a dynamic shear viscosity $\eta_s{}^*(\omega)$ as a complex function of the frequency, associated with the complex shear modulus $G^*(\omega)=G'+iG''$. Similarly a complex compressional viscosity $\eta_v{}^*(\omega)$ associated with the complex modulus $\widetilde{K}^*(\omega)=\widetilde{K}'+i\widetilde{K}''$ will be used:

$$\eta_s{}^*(\omega) = \eta^r{}_s(\omega) - i\,\eta^i{}_s(\omega) = \int_0^\infty G(s)e^{-i\omega s}ds = \frac{G^*}{i\omega}, \tag{11a}$$

$$\eta_v{}^*(\omega) = \eta^r{}_v(\omega) - i\,\eta^i{}_v(\omega) = \int_0^\infty \widetilde{K}(s)e^{-i\omega s}ds = \frac{\widetilde{K}^*}{i\omega}. \tag{11b}$$

A change of variable from $(t-t')$ into s gives, for example:

$$\int_{-\infty}^{t}G(t-t')e^{-i\omega t'}dt' = e^{-i\omega t}\int_0^\infty G(s)e^{i\omega s}ds = e^{-i\omega t}\frac{i}{\omega}\overline{G^*} = e^{-i\omega t}\overline{\eta_s{}^*(\omega)},$$

where $\overline{a}$ designates the conjugate of the complex a. The field equations are then reduced to

$$\omega^2\mathbf{v} + \left\{\frac{q^2}{\gamma} + \frac{\overline{\widetilde{K}^*} + 4/3\,\overline{G^*}}{\rho_0}\right\}\nabla(\nabla\cdot\mathbf{v}) - \frac{1}{\rho_0}\nabla\times(\nabla\times\mathbf{v})\overline{G^*} = -i\omega\frac{q^2\beta}{\gamma}\nabla T, \tag{12a}$$

$$\frac{\gamma-1}{\beta}\nabla\cdot\mathbf{v} = \gamma\sigma\nabla^2 T + i\omega T. \tag{12b}$$

The velocity vector may be represented in terms of a scalar potential ϕ and a vector potential $\mathbf{A}$ associated with transverse displacements such that $\nabla\cdot\mathbf{A}=0$:

$$\mathbf{v} = -\nabla\overline{\phi} + \nabla\times\mathbf{A}. \tag{13}$$

Using Eq. (13) and the relation $\nabla\times(\nabla\times\mathbf{A}) = \nabla(\nabla\cdot\mathbf{A}) - \nabla^2\mathbf{A} = -\nabla^2\mathbf{A}$, Eqs. (12a) and (12b) become:

$$\nabla\left(\omega^2\overline{\phi}+\left\{\frac{q^2}{\gamma}+\frac{\overline{\widetilde{K}^*}+4/3\,\overline{G^*}}{\rho_0}\right\}\nabla^2\overline{\phi}-\frac{i\omega q^2\beta}{\gamma}\,T\right)$$
$$=\nabla\times\left(\omega^2\mathbf{A}+\frac{\overline{G^*}}{\rho_0}\,\nabla^2\mathbf{A}\right), \tag{14a}$$

$$\gamma\sigma\nabla^2T+i\omega T+\frac{\gamma-1}{\beta}\nabla^2\overline{\phi}=0. \tag{14b}$$

From Eq. (14a), keeping in mind that $\nabla\cdot\mathbf{A}=0$, we obtain the following two equations:

$$\omega^2\mathbf{A}+\frac{\overline{G^*}}{\rho_0}\,\nabla^2\mathbf{A}=0, \tag{15a}$$

$$\omega^2\overline{\phi}+\left\{\frac{q^2}{\gamma}+\frac{\overline{\widetilde{K}^*}+4/3\,\overline{G^*}}{\rho_0}\right\}\nabla^2\overline{\phi}-\frac{i\omega q^2\beta}{\gamma}\,T=0. \tag{15b}$$

Equation (15a) is a wave equation for $\mathbf{A}$ since it may be written in the form

$$\nabla^2\mathbf{A}+\kappa^2\mathbf{A}=\mathbf{0}\quad\text{with}\quad\kappa=\omega\sqrt{\rho_0/\overline{G^*}}. \tag{16}$$

The transverse wave associated with the vector potential $\mathbf{A}$ is a *viscoelastic shear wave* of complex number κ, independent of the thermal coefficients. In purely Newtonian media, the conjugate shear modulus $\overline{G^*}=G'-iG''$ simply reduces to $\overline{G^*}\approx-iG''=-i\omega\eta_s$, giving rise to the classical result: $\kappa=(1+i)\sqrt{\omega\rho_0/2\eta_s}$. The transverse wave is a damped viscous wave.

Equation (14b) is combined with Eq. (15b) to give an equation of the biharmonic type for ϕ:

$$\frac{\sigma\omega}{i}\left\{q^2+\frac{\gamma(\overline{\widetilde{K}^*}+4/3\,\overline{G^*})}{\rho_0}\right\}\nabla^4\overline{\phi}$$
$$+\omega^2\left(q^2+\frac{\overline{\widetilde{K}^*}+4/3\,\overline{G^*}}{\rho_0}+\frac{\gamma\sigma\omega}{i}\right)\nabla^2\overline{\phi}+\omega^4\overline{\phi}=0. \tag{17}$$

In contrast with Eq. (15a), terms with coefficients of thermal and viscoelastic origin coexist in Eq. (15b). The final result will strongly depend on the relative magnitude of these coefficients. Therefore, to compare the viscoelastic and thermal diffusivity effects with respect to the pressure effects, we let:

$$E=\frac{(\overline{\widetilde{K}^*}+4/3\,\overline{G^*})i}{\rho_0q^2}=\omega\left\{\frac{\overline{\eta_v^*(\omega)}+4/3\,\overline{\eta_s^*(\omega)}}{\rho_0q^2}\right\}, \tag{18}$$

$$F=\frac{\sigma\omega}{q^2}. \tag{19}$$

Using Eqs. (18) and (19) in Eq. (17), we obtain:

$$\{\nabla^2+k^2\}\{\nabla^2+K_T^2\}\overline{\phi}=0 \tag{20}$$

where k and K_T, corresponding to the harmonic solutions $\phi_0e^{\mathbf{ik}\cdot\mathbf{x}}$ of Eq. (17), are given by:

$$\frac{1}{k^2}\ \text{or}\ \frac{1}{K_T^2}=\frac{q^2}{2\omega^2}\{1-i(E+\gamma F)$$
$$\pm\sqrt{1-2iE-2iF(\gamma-2)-(E-\gamma F)^2}\}. \tag{21}$$

Finally, we use $\overline{\phi}=\phi+\Phi$, with ϕ and Φ solutions of the two harmonic equations:

$$\nabla^2\phi+k^2\phi=0,\quad\nabla^2\Phi+K_T^2\Phi=0, \tag{22}$$

k corresponds to an adiabatic longitudinal wave, and K_T to a thermal wave. When F *is small*, we find, to first order in F:

$$\frac{1}{k^2}\approx\frac{q^2}{\omega^2}\{1-iE-(\gamma-1)iF\}$$

and (23)

$$\frac{1}{K_T^2}\approx-\frac{q^2}{\omega^2}\,iF\,\frac{1-i\gamma E}{1-iE}.$$

Hence we find two wave numbers:

The first one is a *longitudinal complex wave number*. It should lead to the usual cases, as in Newtonian fluids or perfectly elastic solids.

1. The perfectly elastic solid

We can assume $E\gg1$ (pressure effects neglected) and $F\ll1$. Then

$$\frac{1}{k^2}\approx-\frac{q^2}{\omega^2}\,iE=\frac{\overline{\widetilde{K}^*}+4/3\,\overline{G^*}}{\rho_0\omega^2}.$$

In addition, from Eqs. (2a), $\overline{\widetilde{K}^*}=\lambda+2/3\mu$, $\overline{G^*}=\mu$, so to a good approximation

$$v^2=\frac{\lambda+2/3\mu}{\rho_0}+\frac{4/3\mu}{\rho_0}=\frac{\lambda+2\mu}{\rho_0},$$

which is the general formula for the velocity of propagation of longitudinal waves, and the attenuation is small in this case.

2. The Newtonian fluid

Let us determine the complex velocity of propagation v^*, defined by

$$\frac{k}{\omega}=\frac{1}{v^*}=\frac{1}{v}+\frac{i\alpha}{\omega}.$$

We use the fact that $q^2=K_0/\rho_0$; also from Eqs. (2b) $\overline{G^*}=-i\omega\eta_s$, $\overline{\widetilde{K}^*}=-i\omega\eta_v$, so that we obtain for the complex velocity of propagation v^*:

$$v^{*2}=q^2-i\omega\,\frac{(\eta_v+4/3\eta_s)}{\rho_0}-i\omega(\gamma-1)\sigma.$$

After considering that $\alpha/\omega\ll v^{-1}$, we come to the well-known result:

$$v = q = \sqrt{\frac{K_0}{\rho_0}}$$

and

$$\frac{\alpha}{\omega} = \frac{\omega}{2\rho_0 v^3}\left\{(\eta_v + 4/3\,\eta_s) + \frac{\tau(\gamma-1)}{C_p}\right\}.$$

The second term (thermal effects) in the expression for the attenuation can be neglected in usual liquids.

Finally we look at the second wave number [Eqs. (23), under the assumption $\gamma \approx 1$]: $K_T = (1+i)\sqrt{\omega/2\sigma}$. It represents a *damped thermal wave*, with a skin depth $\delta_T = \sqrt{2\sigma/\omega}$ (corresponding to a damping of $1/e$ of the wave after traveling a distance equal to δ_T). From Eqs. (16) and (23) we conclude that three waves are identified for $F \ll 1$:

(1) a longitudinal adiabatic wave (corresponding to ϕ);
(2) a damped thermal wave (corresponding to Φ);
(3) a damped shear wave (corresponding to **A**).

In our applications, F remains small ($F \approx 10^{-6}$), and the assumption $F \ll 1$, will be made throughout the following discussion.

D. The case of polymeric liquids

In polymeric fluids, viscosities and moduli are frequency dependent, so formulas for k and K_T will become, using the approximation $F \ll 1$:

$$\frac{1}{k^2} \approx \frac{q^2}{\omega^2}(1 - iE) = \frac{1}{\omega^2 \rho_0}\left(K_0 + \widetilde{\overline{K^*}} + \frac{4}{3}\,\overline{G^*}\right), \tag{24}$$

$$\frac{1}{K_T^2} \approx -\frac{q^2}{\omega^2}\, iF\, \frac{1 - i\gamma E}{1 - iE}. \tag{25}$$

We now look for the complex velocity $v^* = \omega/k$, and let $\overline{K^*} = K_0 + \widetilde{\overline{K^*}}$. This gives the well-known result: $\rho_0 v^{*2} = \overline{M^*} = K_0 + \widetilde{\overline{K^*}} + \frac{4}{3}\overline{G^*} = \overline{K^*} + \frac{4}{3}\overline{G^*}$. We introduce the real and imaginary parts of the complex modulus M^*, as well as the velocity of longitudinal waves and their attenuation. We plug this into Eq. (24)

$$\rho_0 v^{*2} = \rho_0\left(\frac{1}{v} + \frac{i\alpha}{\omega}\right)^{-2} = \frac{(R + iX)^2}{\rho_0} = M' - iM'', \tag{26}$$

which is solved to give:

$$R = \sqrt{\frac{\rho_0(|M^*| + M')}{2}}, \tag{27}$$

$$X = -\sqrt{\frac{\rho_0(|M^*| - M')}{2}}, \tag{28}$$

where $|M^*| = \sqrt{M'^2 + M''^2}$ is the complex modulus of M^*. The minus sign for X corresponds to the fact that positive attenuation α is required.

We relate X and R to v and α/ω, thus

$$v = |M^*| \sqrt{\frac{2}{\rho_0(|M^*| + M')}}, \tag{29}$$

$$\frac{\alpha}{\omega} = \frac{1}{|M^*|}\sqrt{\frac{\rho_0(|M^*| - M')}{2}}. \tag{30}$$

This result corresponds to the formulas of Piccirelli and Litovitz.[10] In usual cases dealing with polymeric fluids,[11] the loss moduli are such that $M'' \ll M'$ and we deduce: $|M^*| \approx M' = K' + \frac{4}{3}G' \approx K'$, therefore:

$$v = \sqrt{\frac{K'}{\rho_0}}, \tag{31}$$

$$\frac{\alpha}{\omega} = \frac{1}{2}\sqrt{\frac{\rho_0}{M'}}\,\frac{M''}{M'} \approx \frac{1}{2\rho_0 v^3}\left(K'' + \frac{4}{3}\,G''\right). \tag{32}$$

We note that Eqs. (29) and (30) are also valid for the case of the damped shear wave corresponding to the potential vector **A**, when replacing M^* by G^*. Finally, assuming $\gamma \approx 1$, which is usually verified, the wave number K_T associated with the thermal wave becomes:

$$\frac{1}{K_T^2} \approx -\frac{\sigma}{\omega}\, i. \tag{33}$$

Therefore our approach presented in this section may be used for any viscoelastic fluid ranging from a Newtonian behavior to the quasisolid state, as well as in the rubber to glass transition zone.

II. APPLICATION TO A TWO-PHASE MEDIUM

We study the propagation of waves in a medium containing inclusions, and we use the potential Eqs. (16) and (22), (23) with boundary conditions to be written at the interfaces between the fluid matrix and the inclusions.

Domains corresponding to the inclusions are supposed to be spherical of radius R. When an incident wave propagates into the matrix, its potential can be expressed by:

$$\phi_0(r,\theta) = e^{ikr\cos\theta} = \sum_{n=0}^{\infty} i^n(2n+1) j_n(kr) P_n(\cos\theta). \tag{34}$$

It meets an inclusion at the interface $r = R$, and three waves are generated (one longitudinal, one shear, and one thermal wave) on either side of the interface. In the matrix, the corresponding potentials may be written:

$$\phi(r,\theta) = \sum_{n=0}^{\infty} i^n(2n+1) A_n h_n(kr) P_n(\cos\theta), \tag{35a}$$

$$\Phi(r,\theta) = \sum_{n=0}^{\infty} i^n(2n+1) B_n h_n(K_T r) P_n(\cos\theta), \tag{35b}$$

$$A(r,\theta) = \sum_{n=0}^{\infty} i^n(2n+1) C_n h_n(\kappa r) P_n{}^1(\cos\theta), \tag{35c}$$

where, for a spherical wave: $\mathbf{A} = A(r,\theta)\mathbf{e}_\phi$. j_n and h_n are Bessel and Hankel functions, whereas P_n and $P_n{}^1$ are Legendre polynomials. Inside the inclusion, the coefficients will bear a prime, to give similarly:

$$\phi'(r,\theta) = \sum_{n=0}^{\infty} i^n(2n+1) A'_n j_n(k'r) P_n(\cos\theta), \tag{36a}$$

$$\Phi'(r,\theta)=\sum_{n=0}^{\infty} i^n(2n+1)B'_n j_n(K_T' r)P_n(\cos\ \theta), \tag{36b}$$

$$A'(r,\theta)=\sum_{n=0}^{\infty} i^n(2n+1)C'_n j_n(\kappa' r)P_n{}^1(\cos\ \theta). \tag{36c}$$

At $r=R$, the following boundary conditions (continuity of velocities, temperature, heat flux, and stresses) must be satisfied:

$$v_r=v'_r, \quad v_\theta=v'_\theta, \quad T=T',$$
$$\tau\frac{\partial T}{\partial r}=\tau'\frac{\partial T'}{\partial r}, \quad \sigma_{r\theta}=\sigma'_{r\theta}, \quad \sigma_{rr}=\sigma'_{rr}. \tag{37}$$

Thermal coupling will enter through these boundary conditions. Formulas giving v_r and v_θ can be found in Ref. 1. T is given by $T=g\phi+G\Phi$, where

$$g=-\frac{i\omega\gamma}{\beta q^2}+\frac{k^2}{\beta\omega}(i+\gamma E), \tag{38a}$$

$$G=-\frac{i\omega\gamma}{\beta q^2}+\frac{K_{T^2}}{\beta\omega}(i+\gamma E) \tag{38b}$$

with E defined by Eq. (18). $\sigma_{r\theta}$ and σ_{rr} are given by:

$$\sigma_{r\theta}=e^{-i\omega t}\overline{\eta_s^*(\omega)}\left\{-2\frac{\partial}{\partial\theta}\left(\frac{1}{r}\frac{\partial\overline{\phi}}{\partial r}-\frac{\overline{\phi}}{r^2}\right)-\left(\frac{\partial^2 A}{\partial r^2}-2\frac{A}{r^2}\right)+\frac{1}{r^2}\frac{\partial}{\partial\theta}\left\{\frac{1}{\sin\ \theta}\frac{\partial}{\partial\theta}(A\ \sin\ \theta)\right\}\right\}, \tag{39a}$$

$$\sigma_{rr}=e^{-i\omega t}\overline{\eta_s^*(\omega)}\left((\kappa^2-2k^2)\phi+(\kappa^2-2K_T^2)\Phi+2\times\left\{-\frac{\partial^2\overline{\phi}}{\partial r^2}+\frac{1}{\sin\ \theta}\frac{\partial}{\partial\theta}\left[\sin\ \theta\left(-\frac{A}{r^2}+\frac{1}{r}\frac{\partial A}{\partial r}\right)\right]\right\}\right). \tag{39b}$$

In these formulas, terms k^2 have been kept, although they might be small compared to κ^2. Moreover, we have $\phi=\phi_0+\phi+\Phi$ outside the sphere (matrix), and $\phi'=\phi'+\Phi'$ inside (inclusion). We introduce the adimensional numbers a, b, c, a', b', and c':

$$a=kR, \quad b=K_TR, \quad c=\kappa R,$$
$$a'=k'R, \quad b'=K_T'R, \quad c'=\kappa'R. \tag{40}$$

The six boundary conditions give rise, for each positive value of n, to the following system (41) similar to the system (8) in Ref. 2, in the fluid case, except that η_s must be replaced by a complex viscosity $\overline{\eta_s^*(\omega)}$. In addition, parameters k, K_T, κ, k', K_T', and κ' describing the different waves (longitudinal, thermal, and shear), have been computed using Eqs. (16) and (23). Equations (38a) and (38b) for g and G have also been used. The system is the following:

$$aj'_n(a)+A_n ah'_n(a)+B_n bh'_n(b)-C_n n(n+1)h_n(c)=A'_n a'j'_n(a')+B'_n b'j'_n(b')-C'_n n(n+1)j_n(c'), \tag{41a}$$

$$j_n(a)+A_n h_n(a)+B_n h_n(b)-C_n[h_n(c)+ch'_n(c)]=A'_n j_n(a')+B'_n j_n(b')-C'_n[j_n(c')+c'j'_n(c')], \tag{41b}$$

$$g[j_n(a)+A_n h_n(a)]+GB_n h_n(b)=g'A'_n j_n(a')+G'B'_n j_n(b'), \tag{41c}$$

$$\tau\{g[aj'_n(a)+A_n ah'_n(a)]+GB_n bh'_n(b)\}=\tau'\{g'A'_n a'j'_n(a')+G'B'_n b'j'_n(b')\}, \tag{41d}$$

$$\overline{\eta_s^*(\omega)}\{aj'_n(a)-j_n(a)+A_n[ah'_n(a)-h_n(a)]+B_n[bh'_n(b)-h_n(b)]-\tfrac{1}{2}C_n[c^2h''_n(c)+(n^2+n-2)h_n(c)]\}$$
$$=\overline{\eta'_s{}^*(\omega)}\{A'_n[a'j'_n(a')-j_n(a')]+B'_n[b'j'_n(b')-j_n(b')]-\tfrac{1}{2}C'_n[c'^2j''_n(c')+(n^2+n-2)j_n(c')]\}, \tag{41e}$$

$$\overline{\eta_s^*(\omega)}\{(c^2-2a^2)j_n(a)-2a^2j''_n(a)+A_n[(c^2-2a^2)h_n(a)-2a^2h''_n(a)]+B_n[(c^2-2b^2)h_n(b)-2b^2h''_n(b)]$$
$$+2n(n+1)C_n[ch'_n(c)-h_n(c)]\}$$
$$=\overline{\eta'_s{}^*(\omega)}\{A'_n[(c'^2-2a'^2)j_n(a')-2a'^2j''_n(a')]+B'_n[(c'^2-2b'^2)j_n(b')-2b'^2j''_n(b')]$$
$$+2n(n+1)C'_n[c'j'_n(c')-j_n(c')]\}. \tag{41f}$$

For $n=0$, the system (41) reduces to a system of four equations for four unknowns, because the two equations for v_θ and $\sigma_{r\theta}$ are satisfied automatically.

The method used to estimate the global attenuation of the two-phase medium, as well as the wave velocity, is:

(1) first solve the system (41) in the general case to obtain the coefficients A_n, B_n,...;
(2) take into account all the inclusions of concentration ϵ (volumic) by integrating over the various surface integrals;
(3) consider the incoming and outgoing waves at infinity to deduce the global attenuation and velocity of propagation.

We define the complex wave number $B=\omega/v_t+i\alpha_t$, and the

resulting attenuation α_t is (for small ϵ and neglecting multiple scattering effects):

$$\alpha_t = \alpha - \frac{3\epsilon v^2}{2\omega^2 R^3} \sum_{n=0}^{\infty} (2n+1)\mathrm{Re}(A_n), \tag{42}$$

where the host fluid (i.e., the continuous phase) is characterized by the wave number $k=\omega/v+i\alpha$. We would like to insist here on the fact that the total attenuation includes the α term, for this is not stated clearly in a few papers. The excess attenuation represents the difference between the total attenuation and the one due to the absorption of the two phases:

$$\alpha_{\mathrm{ex}} = \alpha_t - [(1-\epsilon)\alpha + \epsilon\alpha']. \tag{43}$$

Thus, one recovers the case of the host fluid, as $\epsilon \to 0$. Indeed, for this limiting case, $\alpha_t \to \alpha$, and $(1-\epsilon)\alpha+\epsilon\alpha' \to \alpha$, so that $\alpha_{ex} \to 0$.

Usually, the first two terms in the series expansion (42) are sufficient, in the long wavelength limit.

$$\alpha_t \approx \alpha - \frac{3\epsilon v^2}{2\omega^2 R^3}\,\mathrm{Re}(A_0+3A_1). \tag{44}$$

The velocity in the two-phase medium may be normalized with respect to v according to:

$$\frac{v_t}{v} \approx 1 - \frac{3\epsilon v^3}{2\omega^3 R^3}\,\mathrm{Im}(A_0+3A_1). \tag{45}$$

Lloyd and Berry[5] showed how to take into account multiple scattering effects by adding supplementary terms as corrections, the results are as follows:

$$\left(\frac{B}{k}\right)^2 = 1 - \frac{3i\epsilon}{k^3R^3}(A_0+3A_1) - \frac{27\epsilon^2}{k^6R^6}(A_0A_1+2A_1{}^2). \tag{46}$$

Taking real and imaginary parts of B leads to the determination of the velocity and the attenuation. The Lloyd and Berry correction is usually required when the volumic concentration is larger than 10%.

III. APPLICATION TO VISCOUS AND VISCOELASTIC FLUIDS

A. Preliminary test: Liquid–liquid emulsion

To validate our approach, the boundary condition system (41) is solved first in the particular case of an oil in water emulsion. McClements and Povey[4] studied sunflower oil in water emulsion and used a Newtonian model for the fluids. With the thermophysical parameters given in Ref. 4, we solve directly the system, then use the values obtained for A_0 and A_1 in Eqs. (44) and (45) to calculate the variation of excess attenuation and the normalized velocity. Results are plotted against $R\sqrt{f}$ (Figs. 1 and 2). This combination of variables arises in the system of boundary conditions. It allows to draw thermal and viscous contributions to the total attenuation on the same diagram. In this case, the thermal contribution to the attenuation prevails over the viscous one. Note that the authors have plotted their results using as a reference the average velocity, defined by:

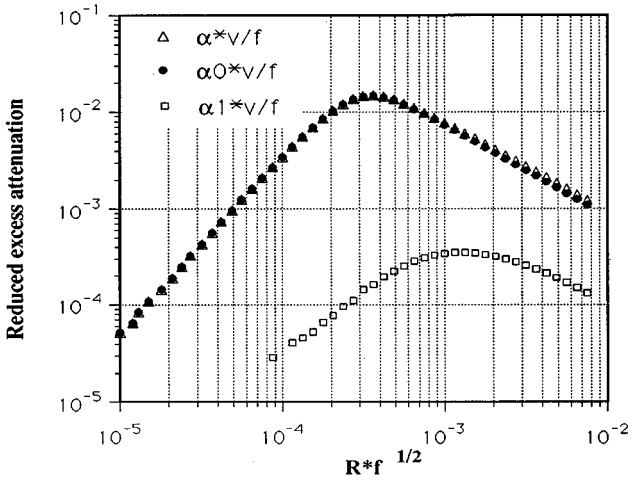

FIG. 1. Reduced excess attenuation (Neper) for an oil in water emulsion (10% volume) (α_0=thermal, α_1=viscous, α=total).

$$v_{\mathrm{av}}{}^2 = \frac{1}{\mathscr{K}_{\mathrm{av}}\rho_{\mathrm{av}}},$$

$$\mathscr{K}_{\mathrm{av}} = \mathscr{K}(1-\epsilon) + \mathscr{K}'\epsilon,$$

$$\rho_{\mathrm{av}} = \rho(1-\epsilon) + \rho'\epsilon. \tag{47}$$

Our results are similar to those of Ref. 4 where $\mathscr{K}=1/K$. The maxima of the attenuation curves are the same. The same limiting values are found for the low-frequency velocity ($\approx$0.992) and the high-frequency limit [=1, for in this case (47) is recovered].

A multiple scattering correction (Lloyd and Berry[5]) has been used but only gave a slight variation of the curves, as it could be anticipated from the rather low value of the concentration (ϵ=0.1).

Care must be taken because the system of equations includes Bessel functions with small arguments, so that the calculations can give rise to numerical instabilities and a good precision is needed to calculate α at low frequency (or small radii).

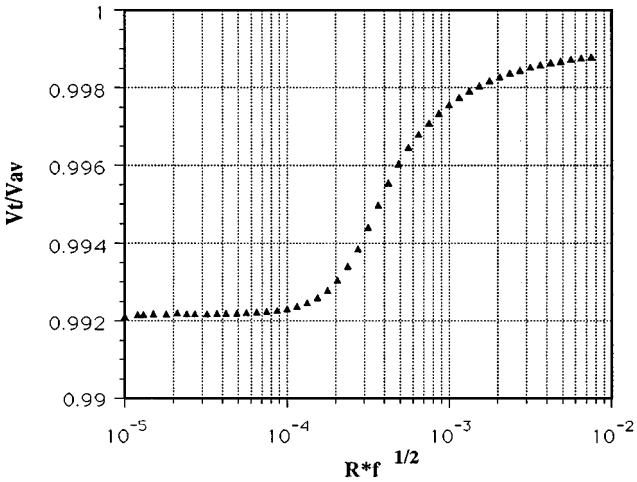

FIG. 2. Normalized velocity for an oil in water emulsion (10% volume).

TABLE I. Viscoelastic and thermophysical properties of the fluids (5 MHz, 230 °C).

Fluid	PA6	PP
α(dB/cm)	2.9	4.5
v (m/s)	1374	911
K' (Pa)	1.812×10^{9}	0.624×10^{9}
$K''+4/3G''$ (Pa)	5.293×10^{6}	1.875×10^{6}
G''(Pa)	1.481×10^{6}	0.469×10^{6}
η^{r}_{s} (Pa s)	0.0316	0.0112
τ(J/m/s/K)	0.14	0.15
C_p (J/kg/K)	3015	2822
ρ_0 (kg/m^3)	960	752
β (K^{-1})	5.4×10^{-4}	5.3×10^{-4}

We emphasized the fact that the same results are obtained by choosing R and letting f vary, or the other way.

B. Study of a PA6/PP polymer blend

Moving on to the viscoelastic case, we have applied the method to a polymer blend containing a matrix of polyamide (PA6) with inclusions of polypropylene (PP). Rheometrical measurements show that the viscoelastic effects can become very important in this case.

Table I gives measured or estimated values of the parameters to be used in the system of equations for the two viscoelastic fluids considered.

We have determined experimentally the values of v and α, allowing us to calculate the values of the combinations of the moduli $K'+4/3G'$ and $K''+4/3G''$. Densities were determined experimentally. Thermodynamic parameters are taken from Van Krevelen.[12]

Very few parameters are available in the literature at this frequency, so we assumed that G' and G'' are of the same order in the frequency range considered, which gives $\eta^{i}_{s}\approx\eta^{r}_{s}$. Table I uses also a relation proposed by Hunter *et al.*:[13] $\eta^{r}_{v}+4/3\,\eta^{r}_{s}\approx4(4/3\,\eta^{r}_{s})$ which is generally satisfied. In addition, rheometry curves (up to 10^4 rad/s) were extrapolated and the same order of magnitude of the shear viscosity was obtained at 5 MHz.

A calculation of the total excess attenuation as well as the individual contributions of the thermal and viscous parts is carried out using Eqs. (18) and (21) from Ref. 2 with real viscosities. The results are drawn in Fig. 3 and show some differences with the case of Fig. 1. At low frequency, the thermal part predominates as it was observed previously, but at higher frequencies, viscous attenuation prevails. This result is related to the fact that higher values of the viscosity are involved in the problem studied. Also the thermophysical parameters of the components of the blend are not very different, which leads to a smaller thermal attenuation.

This gives us a first indication of the different orders of magnitude of the attenuations in our melt.

Next, we carry out a calculation using the theory presented in Sec. II. For this calculation, the modified expressions for k, K_T, κ, g, and G are used and the viscosity η_s is changed into $\eta_s{}^{*}(\omega)$.

An example of the modifications induced by our theory is given in Fig. 4, where different curves are drawn, corresponding to various methods of calculating $\alpha v/f$. (a) is obtained using the explicit formulas of Ref. 2 and real viscosities, (b) is a curve corresponding to the resolution of the complete system, using real viscosities, (c) uses the general theory we derived in Sec. II with complex viscosities. The frequency interval (more precisely the $R\sqrt{f}$ interval) of Fig. 4 is selected for application purposes, corresponding to the size of domains studied (usually the domain sizes are of the order of the μm, and f is in the MHz range). Furthermore, in this interval, the hypotheses required by the theory and our rheological assumptions hold.

An extended description of these results as well as a comparison with experimental data is available.[14]

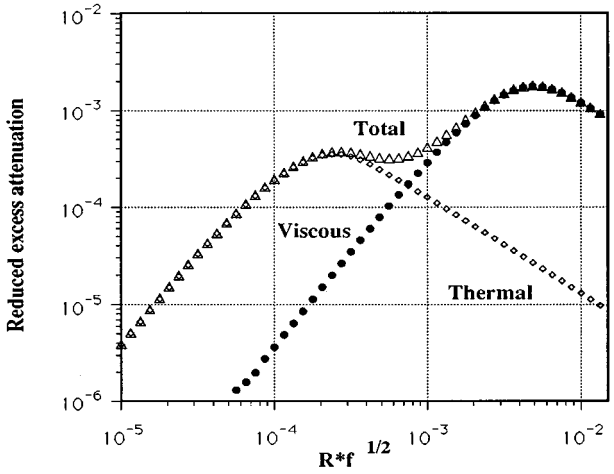

FIG. 3. Reduced excess attenuation (thermal, viscous and total) $\alpha(v/f)$ for a PA6/PP blend (ϵ=4.5%).

IV. CONCLUSION

The theory presented in this paper gives a rather complete description of the study of wave propagation in generalized emulsions or suspensions. It includes the previous models, valid for emulsions or suspensions involving New-

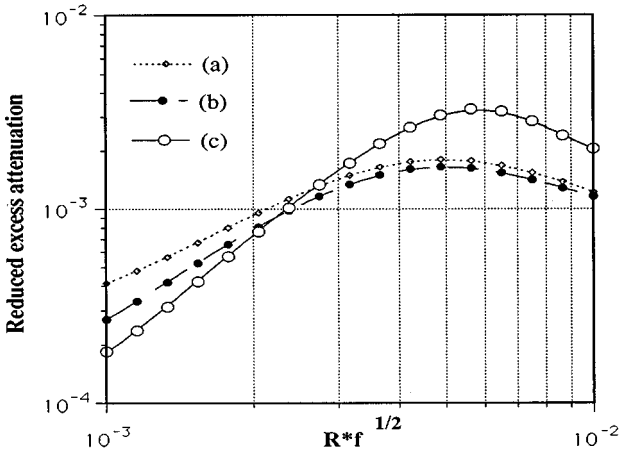

FIG. 4. Reduced excess attenuation $\alpha v/f$ for a PA6/PP blend (4.5% volumic concentration).

tonian fluids, and allows to treat the case of viscoelastic emulsions. Thermal, as well as viscoelastic effects are included.

Velocities of propagation as well as the attenuation mostly depend on the viscoelastic properties of the fluids considered and thermal coupling is weak. However, when two-phase media are considered, interfacial conditions play an important role, thus resulting in a combination of thermal and viscoelastic dissipations, especially in the expression for the attenuation, which depends on the concentration and the size of the inclusions.

We have shown that this theory is particularly relevant in the case of polymer blends. It could give a means to characterize their morphology.

[1] P. S. Epstein and R. R. Carhart, J. Acoust. Soc. Am. **25**, 553–565 (1953).
[2] J. R. Allegra and S. A. Hawley, J. Acoust. Soc. Am. **51**, 1545–1564 (1972).
[3] A. H. Harker and J. A. G. Temple, J. Phys. D: Appl. Phys. **21**, 1576–1588 (1988).
[4] D. J. McClements and M. J. W. Povey, J. Phys. D: Appl. Phys. **22**, 38–47 (1989).
[5] A. Schröder and E. Raphaël, Europhys. Lett. **17**(6), 565–570 (1992).
[6] P. Lloyd and M. V. Berry, Proc. Phys. Soc. London **91**, 678–688 (1967).
[7] G. H. Meeten and N. E. Sherman, Ultrasonics **31**(3), 193–199 (1993).
[8] J. P. Charlier and F. Crowet, J. Acoust. Soc. Am. **79**, 895–900 (1986).
[9] N. W. Tschoegl, *The Phenomenological Theory of Linear Viscoelastic Behaviour, an Introduction* (Springer-Verlag, Berlin, 1989), Chap. 11.
[10] R. Piccirelli and T. A. Litovitz, J. Acoust. Soc. Am. **29**(9), 1009–1020 (1957).
[11] M. Piau and C. Verdier, Ultrasonics International 93 Conference Proceedings, Vienne, pp. 423–426.
Case of a PDMS (47VT60000, Rhône-Poulenc) at 1 MHz: Here, v is usually around 1000 m/s which allows us to write (using $\rho \approx 1000$ kg/m^3)

$$\rho v^2 \approx 10^9 \ \text{Pa} = 2((M'^2+M''^2)/M''^2)(\sqrt{M'^2+M''^2}-M'). \quad \text{(a)}$$

At a frequency of 1 MHz, α equals 1 dB/cm$\approx$11.5 Neper/m, we have

$$1/\rho(\alpha/\omega)^2 \approx 3.4\times 10^{-15} \ \text{Pa}^{-1} = \tfrac{1}{2}(1/(M'^2+M''^2))(\sqrt{M'^2+M''^2}-M'). \quad \text{(b)}$$

We let $x=M''/M'$ and combine Eqs. (a) and (b), thus the equation $(\sqrt{1+x^2}-1)^2 = 3.4\times 10^{-6}\, x^2$ is obtained. The solution is $x \approx 3.7\times 10^{-3}$, $M' \approx \rho v^2 \approx 10^9$ Pa, et $M''=xM' \approx 3.7\times 10^6$ Pa. In this range of frequency, one can show that $G' \approx G''$ using rheological measurements. So we have $M' \approx K'$ and $M''=K''+4/3\, G''$.
[12] D. W. Van Krevelen, *Properties of Polymers* (Elsevier, New York, 1990), 3rd ed.
[13] J. L. Hunter, C. J. Montrose, and J. H. Shively, J. Acoust. Soc. Am. **36**, 953–960 (1964).
[14] C. Verdier and M. Piau, J. Phys. D: Appl. Phys. **29**, 1454–1461 (1996).

Transient vibratory response of fluid-loaded shells using convolution integral equations

Peter R. Stepanishen
Department of Ocean Engineering, University of Rhode Island, Narragansett, Rhode Island 02882

(Received 18 October 1995; accepted for publication 26 September 1996)

A general time-domain approach is presented to address the transient vibratory response of fluid-loaded shells of arbitrary shape when subjected to specified mechanical and/or acoustical excitations. The approach is based on utilizing an *in vacuo* eigenvector expansion with time-dependent coefficients to describe the velocity field of the shell. Fluid loading on the shells is described via the use of convolution integrals involving the modal velocity coefficients and mode-dependent acoustic radiation impulse responses. Time domain methods are used to develop a set of universal coupled convolution integral equations for the time-dependent modal velocity coefficients of the shell. Special cases which include a finite plate and an arbitrary shell of revolution are then addressed using the general approach. A reduced set of the coupled convolution integral equations for the time-dependent modal velocity coefficients is obtained for the plate and sets of similar equations are also obtained for the shell. © *1997 Acoustical Society of America.* [S0001-4966(97)05103-5]

PACS numbers: 43.20.Tb, 43.20.Rz, 43.40.Rj [JEG]

INTRODUCTION

The vibratory response of fluid-loaded plates and shells when subjected to either transient mechanical or acoustical excitations is an important subject of interest in underwater acoustics. Numerous combined finite and boundary element methods are presently available for addressing the analogous harmonic problem; however, relatively little effort has been devoted to the more general transient problem. Although the solution of the time-dependent problem can in principle be obtained from the solution of the corresponding harmonic problem using Fourier synthesis methods, an alternative time-domain method is presented here to address the general time-dependent fluid–solid interaction problem.

Much of the early work on the transient response of fluid-loaded elastic shells was motivated by attempts to understand the shock response of submerged structures. Numerous investigators addressed the two-dimensional acoustic scattering problem of a planar shock pulse impinging onto a fluid-loaded cylindrical shell. As a result of the separability of the acoustic wave equation in cylindrical coordinates and the periodicity of the displacement field of the shell in the circumferential direction, modal solutions using trigonometric expansions are readily used to address the problem. Among the earliest studies are the work of Carrier,[1] and Mindlin and Bleich.[2] Later work by Huang[3] and Geers[4] also addressed the two-dimensional acoustic scattering problem.

Since the acoustic-wave equation is separable in spherical coordinates, the transient response of fluid-loaded spherical shells is also a tractable problem. As a result of its relative simplicity, the transient axisymmetric response of fluid-loaded spherical shells has thus been the focus of numerous past studies. Huang used a Laplace transform method to obtain a formally exact solution to the scattering problem by transform inversion for the case of a single shell[5] and two concentric shells.[6] Menton and Magrab[7] also used a Laplace transform method to address the acoustic radiation problem from a concentric source within the spherical shell. Most recently, Chen and Stepanishen[8] addressed the axisymmetric response of arbitrary shells of revolution, including the spherical shell as a special case, using a time-dependent eigenvector expansion method.

Considerable effort has also been devoted to the planar problem in which the planar structure of interest is set in an infinite planar rigid baffle. As a result of the assumed baffle conditions the Green's function for the acoustic Neumann boundary value problem is known, thus leading to a simplification in the resulting analysis. Craggs[9] presented an analysis of a coupled plate-acoustic system using acoustic and plate finite elements. Stepanishen[10] and co-workers[11] used time-dependent eigenfunction expansion methods to address the transient vibratory response of fluid-loaded elastic planar structures to both specified mechanical and/or acoustical excitations.

As a result of the additional complexity, the transient vibratory response of fluid-loaded elastic shells of arbitrary shape, including curved panels and closed shells, has received considerably less attention. Various doubly asymptotic approximations (DAA) for the fluid loading on shells have been developed by Geers and co-workers[12,13] and are presently being widely used in practice.[14] Since the approximations are strictly valid only in the high-frequency region, where plane-wave relationships apply, and in the low-frequency region, where virtual mass approximations are applicable, the use of such approximations can lead to significant errors even for simple problems.

In the present paper a new approach is presented to evaluate the time-dependent vibratory response of fluid-loaded shells of arbitrary shape which are excited by time-dependent mechanical forces and/or incident acoustic fields. The approach is based on our earlier work[8] in which the axisymmetric velocity field of a fluid-loaded shell of revolution was expressed as an *in vacuo* eigenvector expansion with time-dependent coefficients. Fluid loading on the shell

 0001-4966/97/101(4)/1877/8/$10.00

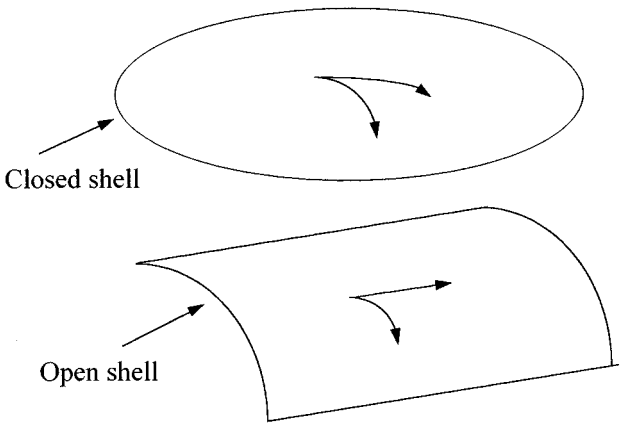

FIG. 1. Closed and open shell or curved panel.

is described[15,8] via the use of convolution integrals involving the modal velocity coefficients and mode-dependent acoustic radiation impulse responses. Time-domain methods are then used to develop a set of universal coupled convolution integral equations for the time-dependent modal velocity coefficients of the shell. Special cases which include a finite plate and an arbitrarily shaped shell of revolution are then addressed using the general approach.

I. THEORY

Consider an elastic shell of arbitrary shape which may be open or closed and is immersed in a fluid as indicated in Fig. 1. The basic problem of interest here is to determine the in-fluid vibratory response of the shell which results from a specified time-dependent mechanical excitation and/or an incident acoustic excitation on the shell. All acoustical and mechanical field variables are normalized in the manner indicated in Table I and the shell is assumed to be thin for all time and length scales of interest.

The normalized equations of motion for the shell when immersed in fluid can be expressed as follows:[16]

$$\begin{bmatrix} L_{11} & L_{12} & L_{13} \\ L_{21} & L_{22} & L_{23} \\ L_{13} & L_{32} & L_{33} \end{bmatrix} \begin{bmatrix} u(x,\tau) \\ v(x,\tau) \\ w(x,\tau) \end{bmatrix} + h \frac{\partial^2}{\partial \tau^2} \begin{bmatrix} u(x,\tau) \\ v(x,\tau) \\ w(x,\tau) \end{bmatrix} = \begin{bmatrix} f^u(x,\tau) \\ f^v(x,\tau) \\ f^w(x,\tau) - p^b(x,\tau) \end{bmatrix} - \begin{bmatrix} 0 \\ 0 \\ p(x,\tau) \end{bmatrix}, \tag{1}$$

where $x = x(\alpha_1, \alpha_2)$ denotes a position vector to a point on the shell and α_1 and α_2 are curvilinear surface coordinates.

TABLE I. Normalization factors for the variables.

Variable	Normalization factor
length	L (characteristic length)
velocity	c_s (plate wave velocity)
time	L/c_s
density	ρ_s (structural density)
frequency	c_s/L
pressure	$\rho_s c_s^2$

The L_{ij} represent partial differential operators in the curvilinear space-time coordinates, h is a normalized shell thickness, the $u(x,\tau)$ and $v(x,\tau)$ represent the orthogonal in-plane displacements, and $w(x,\tau)$ represents the normal displacement of the neutral or middle surface of the shell. The corresponding force density terms $f(x,\tau)$ in Eq. (1) represent the specified mechanical excitations on the shell whereas $p^b(x,\tau)$ represents the blocked pressure across the shell due to the incident acoustic excitation, i.e., the total pressure differential on the shell with zero normal velocity. Finally, $p(x,\tau)$ represents the acoustic pressure differential which acts on the shell as result of the nonzero normal velocity of the shell.

It is well known that the acoustic pressure field in the fluid external to the shell can be expressed as the following retarded potential or Kirchhoff surface integral solution:

$$\begin{aligned} p^t(y,\tau) = {} & p^i(y,\tau) \\ & + \frac{1}{4\pi} \int\int \frac{\rho_0}{\rho_s} \frac{\partial^2}{\partial \tau^2} \frac{w(x_s, \tau - (c_s/c_0)R)}{R}\, dS \\ & + \frac{1}{4\pi} \int\int \hat{e}_R \cdot \hat{n}_s \left(\frac{\partial}{\partial \tau} + \frac{c_s}{c_0} \frac{1}{R} \right) \\ & \times \frac{p^t(x_s, \tau - (c_s/c_0)R)}{R}\, dS, \end{aligned} \tag{2}$$

where $p^i(y,\tau)$ is the incident pressure field, $p^t(x_s,\tau)$ is the total surface pressure field, $R = |y - x_s|$, $\hat{e}_R = (y - x_s)/R$, and $\hat{n}_s$ is the unit normal vector into the fluid. The occurrence of c_s/c_0, where c_0 is the acoustic wave speed in the fluid, is the result of selecting the characteristic time in Table I to be based on c_s the plate velocity for the shell material. The difficulty of addressing the fully coupled fluid–solid interaction problem is obvious: in order to determine the external pressure field from Eq. (2) the normal displacement or velocity of the shell is required along with the surface pressure; however, the normal velocity is a function of the surface pressure on the shell as shown in Eq. (1).

It is useful to express the total surface pressure field as a sum of two components:

$$p^t(x,\tau) = p^i(x,\tau) + p^s(x,\tau), \tag{3}$$

where $p^s(x,\tau)$ is the total scattered surface pressure. The scattered surface pressure field can, however, also be decomposed as follows:

$$p^s(x,\tau) = p^0(x,\tau) + p(x,\tau), \tag{4}$$

where $p^{0(x,\tau)}$ is the scattered surface pressure from the shell, assuming it to be rigid, and $p(x,\tau)$ is the surface pressure field resulting from the normal velocity of the shell. Each of the latter components can be expressed as the solution of a Neumann boundary value problem.

For field points on the surface of the shell the integral solution in Eq. (2) yields the following integral equations for $p^0(x,\tau)$ and $p(x,\tau)$:

$$\alpha p^0(x,\tau)=p^i(x,\tau)+\frac{1}{4\pi}\int\int\left[\hat{e}_R\cdot\hat{n}_s\left(\frac{\partial}{\partial\tau}+\frac{c_s}{c_0}\frac{1}{R}\right)\times\frac{p^0(x_s,\tau-(c_s/c_0)R)}{R}\right]dS \tag{5}$$

and

$$\alpha p(x,\tau)=\frac{1}{4\pi}\int\int\left[\frac{\rho_0}{\rho_s}\frac{\partial^2}{\partial\tau^2}\frac{w(x_s,\tau-(c_s/c_0)R)}{R}+\hat{e}_R\cdot\hat{n}_s\left(\frac{\partial}{\partial\tau}+\frac{c_s}{c_0}\frac{1}{R}\right)\frac{p(x_s,\tau-(c_s/c_0)R)}{R}\right]dS, \tag{6}$$

where α is a geometric coefficient ($\alpha=1/2$ for a smooth surface with a continuous normal vector) and $w(x_s,\tau)$ is presumed known for the moment.

Since the *in vacuo* eigenvectors of the shell form a complete set of functions for the displacement field of the shell, the displacement or velocity field of the fluid-loaded shell subjected to the known mechanical and/or acoustical excitations of interest can be represented as an expansion of such eigenvectors. By their definition the *in vacuo* eigenvectors of the shell must satisfy the following homogeneous equation:

$$\begin{bmatrix}L_{11}&L_{12}&L_{13}\\L_{21}&L_{22}&L_{23}\\L_{13}&L_{32}&L_{33}\end{bmatrix}\begin{bmatrix}\phi^u_{lmn}(x)\\\phi^v_{lmn}(x)\\\phi^w_{lmn}(x)\end{bmatrix}-\Omega^2_{lmn}h\begin{bmatrix}\phi^u_{lmn}(x)\\\phi^v_{lmn}(x)\\\phi^w_{lmn}(x)\end{bmatrix}=\begin{bmatrix}0\\0\\0\end{bmatrix}, \tag{7}$$

which, for reasons of brevity, is now expressed as follows:

$$[L]\boldsymbol{\phi}_{lmn}-\Omega^2_{lmn}h\boldsymbol{\phi}_{lmn}=0, \tag{8}$$

where $[L]$ is the normalized matrix of partial differential operators L_{ij} in Eq. (1), $\boldsymbol{\phi}_{lmn}=\boldsymbol{\phi}_{lmn}(x)$ is the lmnth *in vacuo* eigenvector of the shell and Ω_{lmn} is the associated natural frequency. The orthogonality property of the *in vacuo* eigenvectors for a shell of constant density and thickness is noted as follows:

$$\int\int\boldsymbol{\phi}^T_{lmn}\boldsymbol{\phi}_{rst}\,dS=\begin{cases}0, & lmn=rst,\\ N_{lmn}, & lmn\neq rst.\end{cases} \tag{9}$$

Since the *in vacuo* eigenvectors of the shell form a complete set of functions over the surface of the shell, the displacement field of the shell may be expressed as the following *in vacuo* time-dependent eigenvector expansion:

$$\mathbf{d}(x,\tau)=\begin{bmatrix}u(x,\tau)\\v(x,\tau)\\w(x,\tau)\end{bmatrix}=\sum_l\sum_m\sum_n d_{lmn}(\tau)\boldsymbol{\phi}_{lmn}(x). \tag{10}$$

Similarly, the fluid-loading vector in Eq. (1) can be expressed as follows:

$$\mathbf{p}(x,\tau)=\begin{bmatrix}0\\0\\p(x,\tau)\end{bmatrix}=\sum_l\sum_m\sum_n p_{lmn}(\tau)\boldsymbol{\phi}_{lmn}(x). \tag{11}$$

Equation (1) can now be expressed as follows:

$$[L]\mathbf{d}+h\frac{\partial^2}{\partial\tau^2}\mathbf{d}=\mathbf{f}-\mathbf{p}, \tag{12}$$

where $\mathbf{f}$ is expressed as follows:

$$\mathbf{f}=\begin{bmatrix}f^u\\f^v\\f^w-p^b\end{bmatrix} \tag{13}$$

and $p^b=p^i+p^0$.

In order to determine the modal displacements and velocities of the shell, standard eigenfunction methods may now be employed. After substituting Eqs. (10), (11), and (13) into Eq. (12) it is readily shown that:

$$M_{lmn}\frac{d^2}{d\tau^2}d_{lmn}(\tau)+K_{lmn}d_{lmn}(\tau)=f_{lmn}(\tau)-f^a_{lmn}(\tau), \tag{14}$$

where

$$M_{lmn}=hN_{lmn}, \tag{15}$$

and

$$K_{lmn}=M_{lmn}\Omega^2_{lmn}, \tag{16}$$

$$f_{lmn}(\tau)=\int\int\mathbf{f}^T(x,\tau)\boldsymbol{\phi}_{lmn}(x)dS, \tag{17}$$

and

$$f^a_{lmn}(\tau)=\int\int\mathbf{p}^T(x,\tau)\boldsymbol{\phi}_{lmn}(x)dS. \tag{18}$$

Clearly, M_{lmn} and K_{lmn} are the usual modal mass and stiffness for the *in vacuo* shell and $f_{lmn}(\tau)$ is the modal excitation force due to the blocked mechanical and acoustical excitations. The remaining acoustical modal force $f^a_{lmn}(\tau)$ is clearly associated with the fluid loading on the shell and can also be expressed as

$$f^a_{lmn}(\tau)=\int\int p(x,\tau)\phi^w_{lmn}(x)dS, \tag{19}$$

where $p(x,\tau)$ is the surface pressure on the shell.

It is well known that the pressure field exterior to the shell can be related to the normal velocity of the shell $v(x,\tau)=\partial w(x,\tau)/\partial\tau$ via a standard time-dependent Green's function development which for the present case leads to

$$p(x,\tau)=\frac{\rho_0}{\rho_s}\frac{\partial}{\partial\tau}\sum_r\sum_s\sum_t\int\int G(x|\tau;x_0|\tau_0)\times v_{rst}(\tau)\phi^w_{rst}(x_0)dS_0, \tag{20}$$

where $G(x|\tau;x_0|\tau_0)$ is the Green's function for the exterior Neumann boundary value problem associated with the surface of the shell and ρ_0/ρ_s is the normalized density of the fluid. The acoustical modal force $f^a_{lmn}(\tau)$ can then be related to the modal velocity components $v_{rst}(\tau)$ as follows:

$$f^a_{lmn}(\tau)=\sum_r\sum_s\sum_t z_{lmn,rst}(\tau)\otimes v_{rst}(\tau), \tag{21}$$

where $\otimes$ denotes the convolution operator and the normalized acoustic radiation modal impulse response $z_{lmn,rst}(\tau)$ is expressed as

$$z_{lmn,rst}(\tau)=\frac{\rho_0}{\rho_s}\frac{\partial}{\partial\tau}\int\int\int\int G(x,\tau|x_0,\tau_0)\phi^w_{lmn}(x)\times\phi^w_{rst}(x_0)dS\ dS_0. \tag{22}$$

The $z_{lmn,rst}(\tau)$ can also be expressed in the following form[15] which is most useful for the present development:

$$z_{lmn,rst}(\tau)=R[N^w_{lmn,rst}\delta(\tau)+g_{lmn,rst}(\tau)], \tag{23}$$

where $R=\rho_0c_0/\rho_sc_s$ and $N^w_{lmn,rst}$ is defined as

$$N^w_{lmn,rst}=\int\int\phi^w_{lmn}(x)\phi^w_{rst}(x)dS.$$

It is noted that $N^w_{lmn,rst}$ is a measure of the similarity of the radial components of the lmnth and the rstth modes. The Dirac delta function which is present in the normalized acoustic self-radiation modal impulse response $z_{lmn,lmn}(\tau)$ accounts for the familiar high-frequency behavior in which the lmnth modal force and velocity are scaled replicas of one another; however, the Dirac delta function may also be present in the normalized acoustic mutual radiation modal impulse response $z_{lmn,rst}(\tau)$ when $N^w_{lmn,rst}\neq 0$. In general, for such cases the lmnth modal force and the rstth modal velocity are linearly related in the high-frequency regime. The $g_{lmn,rst}\ (\tau)$ account for the memory effect of the fluid and are low pass functions, i.e., functions whose spectral content is primarily low frequency in nature. These latter modal impulse responses are responsible for the large-time inter-modal coupling between the *in vacuo* eigenvectors when the shell is in contact with a fluid.

A more useful form of the modal equations in Eq. (14) can now be obtained. After substituting Eq. (23) into Eq. (21) the following set of coupled differential-integral equations for the modal displacements is obtained from Eq. (14):

$$M_{lmn}\frac{d^2}{d\tau^2}d_{lmn}(\tau)+R_{lmn}\frac{d}{d\tau}d_{lmn}(\tau)+K_{lmn}d_{lmn}(\tau)$$
$$=f_{lmn}(\tau)-R\sum_{r\neq l}\sum_{s\neq m}\sum_{t\neq n}N^w_{lmn,rst}v_{rst}(\tau)$$
$$-R\sum_r\sum_s\sum_t g_{lmn,rst}(\tau)\otimes v_{rst}(\tau), \tag{24}$$

where $R_{lmn}=RN^w_{lmn}$. The above equations are then simply expressed in terms of the modal velocities as follows:

$$L_{lmn}v_{lmn}(\tau)=f_{lmn}(\tau)-R\sum_{r\neq l}\sum_{s\neq m}\sum_{t\neq n}N^w_{lmn,rst}v_{rst}(\tau)$$
$$-R\sum_r\sum_s\sum_t g_{lmn,rst}(\tau)\otimes v_{rst}(\tau), \tag{25}$$

where the operator L_{lmn} is defined as follows:

$$L_{lmn}=M_{lmn}\frac{d}{d\tau}+R_{lmn}+K_{lmn}\int^\tau d\tau'. \tag{26}$$

The modal admittance impulse response $y_{lmn}(\tau)$ is now introduced such that

$$L_{lmn}y_{lmn}(\tau)=\delta(\tau) \tag{27}$$

and

$$y_{lmn}(\tau)=L^{-1}_{lmn}\delta(\tau). \tag{28}$$

It is noted that $y_{lmn}(\tau)$ corresponds to the impulse response of a simple second-order linear system and is thus known in closed form. In general the impulse response depends on the quality factor of the modal admittance Q_{lmn} where

$$Q_{lmn}=\frac{\Omega_{lmn}M_{lmn}}{R}=\frac{\sqrt{M_{lmn}K_{lmn}}}{R}. \tag{29}$$

As an example the modal admittance impulse response $y_{lmn}(\tau)$ for the underdamped case where $Q_{lmn}>\frac{1}{2}$ can be simply expressed as

$$y_{lmn}(\tau)=\frac{1}{M_{lmn}\sqrt{1-(1/2Q_{lmn})^2}}e^{-\Omega_{lmn}\tau/2Q_{lmn}}\times\cos\left(\Omega_{lmn}\sqrt{1-\left(\frac{1}{2Q_{lmn}}\right)^2}\tau+\eta_{lmn}\right),\quad \tau\geqslant 0, \tag{30}$$

where

$$\eta_{lmn}=\tan^{-1}\left(\frac{(1/2\Omega_{lmn})}{\sqrt{1-(1/2Q_{lmn})^2}}\right). \tag{31}$$

For the *in vacuo* case it is noted that $Q_{lmn}=\infty$ and

$$y_{lmn}(\tau)=\frac{1}{M_{lmn}}\cos(\Omega_{lmn}\tau),\quad \tau\geqslant 0. \tag{32}$$

Since the sifting property of the Dirac delta function leads to

$$f_{lmn}(\tau)-R\sum_{r\neq l}\sum_{s\neq m}\sum_{t\neq n}N^w_{lmn,rst}v_{rst}(\tau)$$
$$-R\sum_r\sum_s\sum_t g_{lmn,rst}(\tau)\otimes v_{rst}(\tau)$$
$$=\delta(\tau)\otimes\left[f_{lmn}(\tau)-R\sum_{r\neq l}\sum_{s\neq m}\sum_{t\neq n}N^w_{lmn,rst}v_{rst}(\tau)-R\sum_r\sum_s\sum_t g_{lmn,rst}(\tau)\otimes v_{rst}(\tau)\right], \tag{33}$$

the following set of coupled convolution integral equations for the modal velocities is then readily obtained:

$$v_{lmn}(\tau)=y_{lmn}(\tau)\otimes f_{lmn}(\tau)-Ry_{lmn}(\tau)\otimes\sum_{r\neq l}\sum_{s\neq m}\sum_{t\neq n}N^w_{lmn,rst}v_{rst}(\tau)$$
$$-Ry_{lmn}(\tau)\otimes\sum_r\sum_s\sum_t g_{lmn,rst}(\tau)\otimes v_{rst}(\tau). \tag{34}$$

Alternately, the above set of coupled convolution integral equations for the modal velocities can be expressed as

$$v_{lmn}(\tau)=y_{lmn}(\tau)\otimes f_{lmn}(\tau)-Ry_{lmn}(\tau)\otimes\sum_{r\neq l}\sum_{s\neq m}\sum_{t\neq n}N^{w}_{lmn,rst}v_{rst}(\tau)-R\sum_{r}\sum_{s}\sum_{t}j_{lmn,rst}(\tau)\otimes v_{rst}(\tau), \tag{35}$$

where

$$j_{lmn,rst}(\tau)=y_{lmn}(\tau)\otimes g_{lmn,rst}(\tau). \tag{36}$$

Several approximate expressions for the modal velocities are apparent from the set of coupled convolution integral equations in Eq. (35). The *in vacuo* case is simply obtained by taking the limit as $R\rightarrow 0$ to obtain the following result:

$$v_{lmn}(\tau)=\frac{1}{M_{lmn}}\cos(\Omega_{lmn}\tau)\otimes f_{lmn}(\tau). \tag{37}$$

For the fluid-loaded case it is noted that at early times where $\tau<<<1$ the latter terms in Eq. (35), which account for the large time modal velocity coupling, may be ignored thus leading to the following approximation:

$$v_{lmn}(\tau)=y_{lmn}(\tau)\otimes f_{lmn}(\tau)-Ry_{lmn}(\tau)\otimes\sum_{r\neq l}\sum_{s\neq m}\sum_{t\neq n}N^{w}_{lmn,rst}v_{rst}(\tau). \tag{38}$$

This latter result is equivalent to the solution which would be obtained more directly via the use of the plane-wave approximation used by numerous earlier authors in addressing specific problems.

In order to evaluate the modal velocities using Eq. (35) it is now noted the modal forces $f_{lmn}(\tau)$ are first required. From Eq. (18) it is obvious that

$$f_{lmn}(\tau)=\int\int[f^{u}(x,\tau)\phi^{u}_{lmn}(x)+f^{u}(x,\tau)\phi^{u}_{lmn}(x)+f^{u}(x,\tau)\phi^{u}_{lmn}(x)]dS+f^{b}_{lmn}(\tau), \tag{39}$$

where the acoustical blocked force component is defined as

$$f^{b}_{lmn}(\tau)=-\int\int p^{b}(x,\tau)\phi^{u}_{lmn}(x)dS \tag{40}$$

and

$$p^{b}(x,\tau)=p^{i}(x,\tau)+p^{0}(x,\tau). \tag{41}$$

To determine $p^{0}(x,\tau)$ it is first noted that the blocked boundary condition can be expressed as

$$\hat{n}\cdot[\mathbf{v}^{i}(x,\tau)+\mathbf{v}^{0}(x,\tau)]=0. \tag{42}$$

It then follows that $p^{0}(x,\tau)$ can be interpreted as resulting from a specified normal velocity field of the shell, i.e., $-\hat{n}\cdot[\mathbf{v}^{i}(x,\tau)]$, where $\mathbf{v}^{i}(x,\tau)$ can be expressed as

$$\mathbf{v}^{i}(x,\tau)=\sum_{l}\sum_{m}\sum_{n}v^{i}_{lmn}(\tau)\boldsymbol{\phi}_{lmn}(x), \tag{43a}$$

where the modal components of the incident velocity field $v^{i}_{lmn}(\tau)$ are simply expressed as

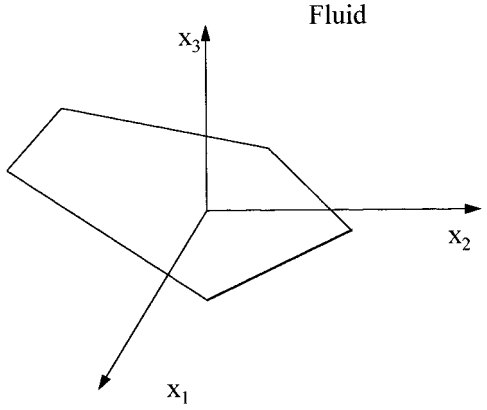

FIG. 2. A finite plate of arbitrary shape.

$$v^{i}_{lmn}(\tau)=\frac{1}{N_{lmn}}\int\int[\mathbf{v}^{i}(x,\tau)]^{T}\boldsymbol{\phi}_{lmn}(x)dS. \tag{43b}$$

Finally, from Eq. (21) it then follows that the modal force components of the associated blocked scattered surface pressure can be expressed as:

$$f^{0}_{lmn}(\tau)=-\sum_{l}\sum_{m}\sum_{n}\sum_{r}\sum_{s}\sum_{t}z_{lmn,rst}(\tau)\otimes v^{i}_{rst}(\tau). \tag{44}$$

The acoustical blocked force component can then be viewed as a sum of two terms: the first of which is simply related to a modal decomposition of the incident pressure field and the second of which is related to the incident velocity field.

II. SPECIAL CASES

The development in the preceding section is applicable to thin structures of arbitrary shape. As special geometries of interest the case of finite fluid-loaded plates and fluid-loaded shells of revolution are now addressed. Both of these cases are important and of practical interest.

A. Finite plates

Consider now the case of a finite plate of arbitrary shape and constant thickness as illustrated in Fig. 2. The normalized equations of motion for the plate in-fluid can be expressed as follows:

$$\begin{bmatrix}L_{11}&L_{12}&0\\L_{21}&L_{22}&0\\0&0&L_{33}\end{bmatrix}\begin{bmatrix}u(x,\tau)\\v(x,\tau)\\w(x,\tau)\end{bmatrix}+h\frac{\partial^{2}}{\partial\tau^{2}}\begin{bmatrix}u(x,\tau)\\v(x,\tau)\\w(x,\tau)\end{bmatrix}=\begin{bmatrix}f^{u}(x,\tau)\\f^{v}(x,\tau)\\f^{w}(x,\tau)-p^{b}(x,\tau)\end{bmatrix}-\begin{bmatrix}0\\0\\p(x,\tau)\end{bmatrix}, \tag{45}$$

where $L_{11}=L_{22}$ for isotropic plates and the form of the L_{33} depends on the particular plate theory. Once again the u and v represent the in-plane displacements whereas w represents the normal displacement of the plate. The corresponding f terms in Eq. (45) again represent the blocked excitations which are due to the specified mechanical excitations on the

shell whereas p^b represents the blocked pressure due to the incident acoustic excitation and p represents the acoustic pressure which acts on the shell as result of the nonzero normal velocity of the plate.

It is obvious from Eq. (45) that the in-plane displacements are decoupled from the normal displacement of the plate. Since the pressure $p(x,\tau)$ is dependent on $w(x,\tau)$ as noted earlier, the structural equation of interest reduces to the single equation:

$$L_{33}w(x,\tau)+h\,\frac{\partial^2}{\partial\tau^2}\,w(x,\tau)=f^w(x,\tau)-p^b(x,\tau)-p(x,\tau). \tag{46}$$

The normal velocity of the plate can now be expressed as an eigenfunction expansion, i.e.,

$$\frac{\partial}{\partial\tau}\,w(x,\tau)=\sum_l\,\sum_m\,v_{lm}(\tau)\,\phi^w_{lm}(x), \tag{47}$$

where the $\phi^w_{lm}(x)$ are the scalar eigenfunctions of the homogeneous plate equation of motion in Eq. (46) which form a complete set of functions for the normal displacement of the plate and are also orthogonal, i.e.,

$$\int\int\,\phi^w_{lm}\phi^w_{rs}\,dS=\begin{cases}0, & lm\neq rs,\\ N_{lm}, & lm=rs.\end{cases} \tag{48}$$

Standard modal analysis methods again lead to the following equations for the modal velocities:

$$M_{lm}\,\frac{d^2}{d\tau^2}\,d_{lm}(\tau)+K_{lm}d_{lm}(\tau)=f_{lm}(\tau)-f^a_{lm}(\tau), \tag{49}$$

where $f_{lm}(\tau)$ and $f^a_{lm}(\tau)$ are now defined as follows:

$$f_{lm}(\tau)=\int\int\,[f^w(x,\tau)-p^b(x,\tau)]\phi^w_{lm}(x)dS \tag{50}$$

and

$$f^a_{lm}(\tau)=\sum_r\,\sum_s\,z_{lm,rs}(\tau)\otimes v_{rs}(\tau) \tag{51a}$$

with

$$z_{lm,rs}(\tau)=R[N_{lm}\delta(\tau)\,\delta_{lr}\,\delta_{ms}+g_{lm,rs}(\tau)], \tag{51b}$$

where $g_{lm,rs}(\tau)$ accounts for the memory effect of the fluid. Then, following the same procedure as presented in the preceding section the following set of coupled convolution equations are obtained for the modal velocity coefficients:

$$v_{lm}(\tau)=y_{lm}(\tau)\otimes f_{lm}(\tau)-R\sum_r\,\sum_s\,j_{lm,rs}(\tau)\otimes v_{rs}(\tau), \tag{52}$$

where $y_{lm}(\tau)$ is the modal admittance impulse response of the lmth mode and

$$j_{lm,rs}(\tau)=y_{lm}(\tau)\otimes g_{lm,rs}(\tau). \tag{53}$$

B. Shells of revolution

Consider now the case of a closed shell of revolution of arbitrary shape and constant thickness as illustrated in Fig. 3. With little loss in generality the mechanical and/or acoustical excitations of the shell are considered here to be even functions of the circumferential coordinate. The displacement field of the shell may then be expressed as the following *in vacuo* time-dependent eigenvector expansion:

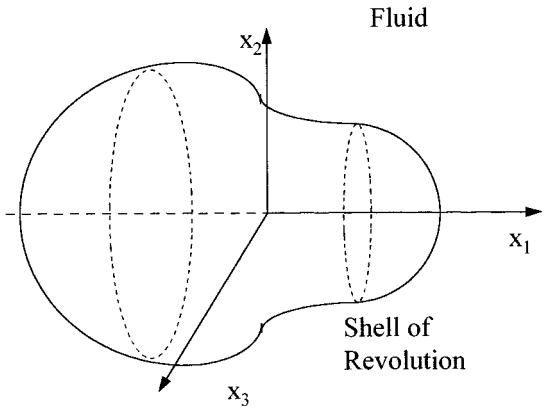

FIG. 3. A closed shell of revolution.

$$\mathbf{d}(x,\tau)=\begin{bmatrix}u(x,\tau)\\ v(x,\tau)\\ w(x,\tau)\end{bmatrix}=\sum_l\,\sum_m\,\sum_n\,d_{lmn}(\tau)\,\boldsymbol{\phi}_{lmn}(x) \tag{54}$$

where $\boldsymbol{\phi}_{lmn}(x)$ can now be expressed as

$$\boldsymbol{\phi}_{lmn}(x)=\begin{bmatrix}\cos(l\alpha_1)\,\phi^u_{mn}(\alpha_2)\\ \sin(l\alpha_1)\,\phi^v_{mn}(\alpha_2)\\ \cos(l\alpha_1)\,\phi^w_{mn}(\alpha_2)\end{bmatrix}, \tag{55}$$

where $x=(\alpha_1,\,\alpha_2)$ are the two-dimensional orthogonal curvilinear coordinates of the neutral surface and l now denotes the circumferential order of interest. Similarly, the fluid-loading vector in the shell equations can again be expressed as follows:

$$\mathbf{p}(x,\tau)=\begin{bmatrix}0\\ 0\\ p(x,\tau)\end{bmatrix}=\sum_l\,\sum_m\,\sum_n\,p_{lmn}(\tau)\,\boldsymbol{\phi}_{lmn}(x) \tag{56}$$

and thus the surface pressure on the shell $p(x,\tau)$ can be expressed as

$$p(x,\tau)=\sum_l\,\sum_m\,\sum_n\,p_{lmn}(\tau)\cos(l\alpha_1)\,\phi^w_{mn}(\alpha_2). \tag{57}$$

In contrast to the indices l and m which range over all positive integers including zero, the range of the index n is from 1 to 3 which corresponds to the three branches of the frequency spectrum for the shell.

From the general development in the preceding section, standard eigenfunction methods again lead to

$$M_{lmn}\,\frac{d^2}{d\tau^2}\,d_{lmn}(\tau)+K_{lmn}d_{lmn}(\tau)=f_{lmn}(\tau)-f^a_{lmn}(\tau), \tag{58}$$

where M_{lmn} and K_{lmn} are the previously defined modal mass and stiffness for the *in vacuo* shell. Since the incremental surface area on the shell can be expressed as $dS=A_1A_2\,d\alpha_1\,d\alpha_2$ where A_1 and A_2 are the fundamental form parameters for the neutral surface, then

$$f_{lmn}(\tau)=\int\int \mathbf{f}^T(x,\tau)\boldsymbol{\phi}_{lmn}(x)A_1A_2\ d\alpha_1\ d\alpha_2 \tag{59}$$

and

$$f^a_{lmn}(\tau)=\int\int p(x,\tau)\phi^w_{lmn}(x)A_1A_2\ d\alpha_1\ d\alpha_2, \tag{60}$$

where $p(x,\tau)$ is the surface pressure on the shell. After noting that $A_1=\beta(\alpha_2)$ and $A_2=1$, where $\beta(\alpha_2)$ is the radius of curvature in the circumferential direction then the modal coupling force $f^a_{lmn}(\tau)$ can be expressed as

$$\begin{aligned} f^a_{lmn}(\tau)&=\sum_r\sum_s\sum_t\int\int p_{rst}(\tau)\cos(r\alpha_1)\phi^w_{st}(\alpha_2)\\ &\quad\times\cos(l\alpha_1)\phi^w_{mn}(\alpha_2)\beta(\alpha_2)d\alpha_1\ d\alpha_2\\ &=\sum_s\sum_t\int\int p_{lst}(\tau)\cos(l\alpha_1)\\ &\quad\times\phi^w_{st}(\alpha_2)\cos(l\alpha_1)\phi^w_{mn}(\alpha_2)\beta(\alpha_2)d\alpha_1\ d\alpha_2. \end{aligned} \tag{61}$$

Equation (61) simply expresses the obvious result that modal forces with different circumferential orders are uncoupled. The acoustical modal force $f^a_{lmn}(\tau)$ for the shell of revolution can then be related to the modal velocity components $v_{lst}(\tau)$ as follows:

$$f^a_{lmn}(\tau)=\sum_s\sum_t z_{lmn,lst}(\tau)\otimes v_{lst}(\tau), \tag{62}$$

where the normalized acoustic radiation impulse response $z_{lmn,lst}(\tau)$ is expressed as

$$\begin{aligned} z_{lmn,lst}(\tau)&=\frac{\rho_0}{\rho_s}\frac{\partial}{\partial\tau}\int\int\int\int G(x,\tau|x_0,\tau_0)\\ &\quad\times\phi^w_{lmn}(x)\phi^w_{lst}(x_0)dS\ dS_0. \end{aligned} \tag{63}$$

Again using the results of the general analysis it is apparent that $z_{lmn,rst}(\tau)$ can now be expressed as

$$z_{lmn,rst}(\tau)=R[N^w_{lmn,lst}\delta(\tau)+g_{lmn,rst}(\tau)]\delta_{lr}. \tag{64}$$

In light of Eq. (64) it then follows from Eq. (58) that the modal equations for each circumferential order l can be expressed in terms of the modal velocities as follows:

$$\begin{aligned} L_{lmn}v_{lmn}(\tau)&=f_{lmn}(\tau)-R\sum_{s\neq m}\sum_{t\neq n}N^w_{lmn,lst}v_{lst}(\tau)\\ &\quad-R\sum_s\sum_t g_{lmn,lst}(\tau)\otimes v_{lst}(\tau). \end{aligned} \tag{65}$$

The following set of coupled convolution integral equations for the modal velocities is then simply obtained:

$$\begin{aligned} v_{lmn}(\tau)&=y_{lmn}(\tau)\otimes f_{lmn}(\tau)-Ry_{lmn}(\tau)\\ &\quad\otimes\sum_{s\neq m}\sum_{t\neq n}N^w_{lmn,lst}v_{lst}(\tau)-Ry_{lmn}(\tau)\\ &\quad\otimes\sum_s\sum_t g_{lmn,lst}(\tau)\otimes v_{lst}(\gamma). \end{aligned} \tag{66}$$

Finally, the above set of coupled convolution integral equations for the modal velocities for each circumferential order l can be expressed as

$$\begin{aligned} v_{lmn}(\tau)&=y_{lmn}(\tau)\otimes f_{lmn}(\tau)-Ry_{lmn}(\tau)\\ &\quad\otimes\sum_{s\neq m}\sum_{t\neq n}N^w_{lmn,lst}v_{lst}(\tau)\\ &\quad-R\sum_s\sum_t j_{lmn,lst}(\tau)\otimes v_{lst}(\tau), \end{aligned} \tag{67}$$

where

$$j_{lmn,lst}(\tau)=y_{lmn}(\tau)\otimes g_{lmn,lst}(\tau). \tag{68}$$

In contrast to the set of fully coupled convolution integral equations for the case of a shell of arbitrary shape, the present analysis for the special case of shells of revolution leads to a series of reduced sets of convolution integral equations for the modal velocities corresponding to each circumferential order 1. It is noted that the set of coupled convolution integral equations corresponding to each circumferential order for the special case of shells of revolution is similar in form to the set of coupled convolution integtral equations for the plate noted earlier.

III. SUMMARY AND CONCLUSIONS

A general time-domain approach has been presented to evaluate the transient vibratory response of fluid-loaded shells of arbitrary shape when subjected to specified space and time-dependent force excitations. The shells of interest include both closed and open shells or plates as a limiting case. Although the excitations of interest in the paper are specified mechanical and/or acoustical excitations, the approach is equally applicable to problems involving hydroacoustic or shock excitations providing the structural response levels are such that a linear structural analysis suffices.

The present approach is based on utilizing an *in vacuo* eigenvector expansion with time-dependent coefficients to describe the velocity field of the fluid-loaded shell. Since the *in vacuo* eigenvectors form a complete and orthogonal set of functions for the displacement or velocity field of the structure under any loading condition within the linear regime of the shell, the response of the fluid-loaded shell can be evaluated using such an expansion. However, in contrast to the *in vacuo* case, fluid loading on the shell will in general couple all time-dependent coefficients of the eigenvectors.

A key feature of the present approach is that fluid loading on the shell is described via the use of convolution integrals involving the modal velocity coefficients and mode-dependent acoustic radiation impulse responses. The basic idea behind the use of such an approach goes back to our earlier work on the time-dependent radiation and scattering from fluid-loaded baffled plates and membranes and more recently for the axisymmetric response of shells. The self-radiation impulse responses, i.e., $z_{lmn,lmn}(\tau)$, provide a direct time-domain measure of the reaction effect of the fluid on a mode of vibration, whereas the mutual radiation impulse responses $z_{lmn,rst}(\tau)$ provide a direct time-domain measure of the fluid-induced coupling between two modes of

vibration. In addition, the impulse responses are also used to evaluate the time-dependent blocked surface pressure resulting from an incident pressure field.

Time-domain methods are used to develop a set of universal coupled convolution integral equations for the time-dependent modal velocity coefficients of the fluid-loaded shell. Modal impulse responses $y_{lmn}(\tau)$ of the $\rho_0 c_0$ damped modal admittances of the shell enter into the equations and are expressed in closed form involving modal masses and stiffnesses. Additional velocity impulse responses $j_{lmn,rst}(\tau)$ also enter into the convolution integral equations. These latter impulse responses provide a direct measure of the fluid-induced coupling between the lmn^{th} and the rst^{th} modal velocities. It is noted that the *in vacuo* result in which the modal velocity coefficients are uncoupled is simply obtained from the universal equations and, for this case, each coefficient is simply expressed as a convolution integral.

Special cases which include a finite plate and an arbitrarily shaped shell of revolution are addressed using the general approach. In contrast to the general case of a closed shell or curved panel a reduced form of the coupled convolution integral equations for the time-dependent modal velocity coefficients is obtained for the plate. The reduction is the direct result of the usual thin plate assumption that in-plane and normal displacements are independent of one another. As a result of the periodicity of the velocity field of a closed shell of revolution in the circumferential direction, the modal velocities of the same circumferential order are shown to satisfy a reduced form of the coupled convolution integral equations similar to those of the plate. Uncoupled sets of coupled convolution integral equations for the time-dependent modal velocity coefficients are thus obtained.

In concluding, it is noted that the universal coupled convolution integral equations are readily discretized and solved in a recursive manner as noted in earlier work. Prior to solving the equations the *in vacuo* eigenvectors, modal masses and stiffnesses of the particular shell of interest must be determined. Mature finite element or other numerical methods are, however, readily available to address the task. In contrast to the *in vacuo* structural analysis, the evaluation of the mode-dependent acoustic radiation impulse responses is a more formidable task. One obvious approach is to utilize time-dependent boundary element methods, e.g., the Kirchhoff retarded potential approach. An alternative generalized internal source density method is also being presently investigated and the results will be reported at a later time.

[1] G. F. Carrier, ''The interaction of an acoustic wave and an elastic cylindrical shell,'' Brown University Technical report, 1951.

[2] R. D. Mindlin and H. H. Bleich, ''Response of an elastic cylindrical shell to a transverse step shock wave,'' Trans. ASME **20**, 189–195 (1953).

[3] H. Huang, ''An exact analysis of the transient interaction of acoustic plane waves with a cylindrical shell,'' ASME J. Appl. Mech. **36**, 1091–1099 (1970).

[4] T. L. Geers, ''Excitation of an elastic cylindrical shell by a transient acoustic wave,'' ASME J. Appl. Mech. **35**, 459–469 (1969).

[5] H. Huang, ''Transient interaction of plane acoustic waves with a spherical elastic shell,'' J. Acoust. Soc. Am. **45**, 661–668 (1969).

[6] H. Huang, ''Transient response of two fluid-coupled spherical elastic shells to an incident pressure pulse,'' J. Acoust. Soc. Am. **65**, 881–887 (1979).

[7] R. T. Menton and E. B. Magrab, ''Farfield radiation of internally generated transient acoustic pulses transmitted through a spherical shell,'' J. Acoust. Soc. Am. **55**, 237–246 (1974).

[8] H. W. Chen and P. R. Stepanishen, ''Acoustic transient radiation from fluid loaded shells of revolution using time-dependent *in-vacuo* eigenvector expansions,'' J. Acoust. Soc. Am. **95**, 601–616 (1995).

[9] A. Craggs, ''The transient response of a coupled plate-acoustic system using plate and acoustic finite elements,'' J. Acoust. Soc. Am. **15**, 509–528 (1971).

[10] P. R. Stepanishen and D. D. Ebenezer, ''An *in-vacuo* modal expansion to determine the transient response of fluid loaded planar vibrators,'' J. Acoust. Soc. Am. **153**, 453–472 (1992).

[11] D. D. Ebenezer and P. R. Stepanishen, ''Transient response of fluid loaded plates via an impulse response method,'' J. Acoust. Soc. Am. **82**, 659–666 (1987).

[12] T. L. Geers, ''Residual potential and approximate methods for three dimensional fluid–structure interaction problems,'' J. Acoust. Soc. Am. **49**, 1505–1510 (1971).

[13] T. L. Geers, ''Doubly asymptotic approximations for transient motions of submerged structures,'' J. Acoust. Soc. Am. **64**, 1500–1508 (1978).

[14] J. A. DeRuntz, T. L. Geers, and C. A. Felippa, ''The underwater shock analysis(usa) code, a reference manual,'' Defense Nuclear Agency Report No. 4524F, 1978.

[15] P. R. Stepanishen and H. W. Chen, ''Acoustic time-dependent loading on elastic shells of revolution using the internal source density and svd method,'' J. Acoust. Soc. Am. **99**, 1913–1923 (1996).

[16] A. Leissa, *Vibration of Shells* (Acoustical Society of America, New York, 1973), reprint ed.

On the quasi-analytic treatment of hysteretic nonlinear response in elastic wave propagation

Koen E-A Van Den Abeele,[a] Paul A. Johnson,[b] Robert A. Guyer,[c] and Katherine R. McCall[d]
EES-4, MS D443, and IGPP, Los Alamos National Laboratory, Los Alamos, New Mexico 87545

(Received 10 May 1996; revised 11 November 1996; accepted 14 November 1996)

Microscopic features and their hysteretic behavior can be used to predict the macroscopic response of materials in dynamic experiments. Preisach modeling of hysteresis provides a refined procedure to obtain the stress–strain relation under arbitrary conditions, depending on the pressure history of the material. For hysteretic materials, the modulus is discontinuous at each stress–strain reversal which leads to difficulties in obtaining an analytic solution to the wave equation. Numerical implementation of the integral Preisach formulation is complicated as well. Under certain conditions an analytic expression of the modulus can be deduced from the Preisach model and an elementary description of elastic wave propagation in the presence of hysteresis can be obtained. This approach results in a second-order partial differential equation with discontinuous coefficients. Classical nonlinear representations used in acoustics can be found as limiting cases. The differential equation is solved in the frequency domain by application of Green's function theory and perturbation methods. Limitations of this quasi-analytic approach are discussed in detail. Model examples are provided illustrating the influence of hysteresis on wave propagation and are compared to simulations derived from classical nonlinear theory. Special attention is given to the role of hysteresis in nonlinear attenuation. In addition guidance is provided for inverting a set of experimental data that fall within the validity region of this theory. This work will lead to a new type of NDT characterization of materials using their nonlinear response. [S0001-4966(97)01304-0]

PACS numbers: 43.25.Dc [MAB]

INTRODUCTION

Nature accommodates some bizarre and unique elastic systems. Static stress–strain tests on rocks, for instance, illustrate their extremely nonlinear response, including both hysteresis and end point memory.[1–8] The principal theoretical component in static and dynamic studies is the equation of state (EOS), which relates stress to strain. In the case of rocks (and some other materials, such as shape memory alloys,[9] PZTs,[10,11] etc.), the deformation is a complex multi valued function of the external stress (hysteresis) and of the history of its changes (memory): in fact, rocks can be considered as systems having an infinite number of state relations. It is the EOS that we must understand in order to describe the dynamic response of rock.

Initially, nonlinear elasticity models were based on theory derived from the domain of nonlinear fluid acoustics.[12,13] A first-order perturbation expansion of the modulus or velocity in terms of the strain is incorporated into the wave equation to describe nonlinear effects such as wave distortion and the corresponding generation of harmonics. With the modulus depending on the excited strain levels, the stress–strain relation becomes nonlinear, too. It is important to note that this model has worked very well for ordinary materials that exhibit small nonlinear response.[14] It is not appropriate for most rocks, however. In a number of papers by our group at Los Alamos, we generalized the stress–strain relation to include higher-order anharmonicity and applied the results to rock dynamics. Both wave propagation and resonance experiments under different conditions have been evaluated using the generalized expansion theory.[8,15–20] From the standpoint of an overview of numerous experiments on rock over a broad frequency and strain interval,[21] we conclude that classical perturbation theory is incorrect or at least incomplete. Coefficients of nonlinearity deduced from dynamic studies do not agree with static predictions, and display amplitude dependence in simulations of a set of experimental wave propagation data.[18] In resonance experiments on rock, classical perturbation theory of a ''Duffing-type'' resonating particle predicts an incorrect dependence of the frequency shift on the measured acceleration.[8,20] The reason for these discrepancies is that the traditional theory makes no attempt to describe experiments that show hysteresis. With rocks, a rather complex picture emerges. Experimental evidence suggests that hysteresis and end point memory are omnipresent even at dynamic levels, calling for a discontinuous model of the equation of state as an alternative and more physically realistic approach. It is the microscopic structure (cracks, grain-to-grain boundaries, etc.) of

[a]Also Post-Doctoral Research Fellow of the Belgian Foundation for Scientific Research, Catholic University Leuven Campus Kortrijk (Interdisciplinary Research Center), Kortrijk, Belgium, and presently at Los Alamos National Laboratory on a NATO Advanced Fellowship.
[b]Also at Université Pierre et Marie Curie, Laboratoire d'Acoustique Physique, Paris, France.
[c]Also at Department of Physics and Astronomy, University of Massachusetts, Amherst, MA.
[d]Also at Department of Physics, University of Nevada, Reno, NV.

the elastic features and their hysteretic behavior that determines the macroscale nonlinear response.

McCall and Guyer have introduced a new model of rock elasticity and developed this model in a series of papers.[7,8,22,23] As McCall and Guyer noted, the basic idea behind the model is presented in earlier work of Walsh[24] and Holcomb.[1] This approach takes the elastic properties of a macroscopic sample of material to result from the workings of a large number of mesoscopic elastic elements (on the order of 10^{12} in a cubic centimeter). These elastic elements can individually have complex hysteretic behavior. The most important portion of the theory is the Preisach–Mayergoyz (P–M) space, which provides an infinite number of state relations by tracking the behavior of the individual elastic elements depending on the excitation and the pressure history. The theory reduces to the traditional theory in the limit of no hysteresis and no discrete memory, and—as a consequence of its greater generality—is more difficult to apply. We refer the reader to Refs. 7 and 22 for a full description of the P–M model for rocks.

In this paper we focus on a (quasi-)analytic approach of the P–M space in connection to the wave propagation equation. Our goal is to achieve a *dynamic* calculation for application to wave propagation in rocks using input data from a P–M space density found empirically from *static* tension-compression measurements. The major difficulty in obtaining an analytic solution is in addressing discontinuities in the modulus–strain relation (see details later). Simple approximations will be made concerning the P–M space in order to treat the problem quasi-analytically. Doing so, the modified nonlinear wave equation, which includes hysteresis and discrete memory in the equation of state, translates into a differential equation with discontinuous coefficients. To a certain extent the solution can be obtained by avoiding the discontinuity and interpreting the problem in the Fourier domain. This problem has been briefly illustrated by McCall and Guyer[23] and will be elaborated on in this paper. Examples will be provided showing the effects of hysteresis and discrete memory on the dynamic wave propagation behavior in combination with traditional nonlinearity. We carefully study the influence of hysteresis on the waveform and its harmonic spectra, on attenuation properties, and on the functional distance, source amplitude, and frequency dependencies of harmonics. We conclude by discussing the limits of the analytic treatment and address the complexity of numerical modeling involving the integral P–M space.

I. THEORY AND LIMITATIONS

In this section we start with the classical nonlinear wave equation from acoustics. This is followed by incorporating an analytic formulation of hysteresis resulting from P–M space considerations. We will show that, to first order, hysteresis introduces a discontinuous term in the wave equation. The solution for this equation can be obtained by application of Green's function and perturbation methods. We explicitly derive the solution for a continuous source signal with an arbitrary (discrete) frequency spectrum. Finally, we indicate the limitations of this quasi-analytic approach in connection to the Fourier transformation of the discontinuous term.

Because our laboratory bench top experiments involving wave propagation are usually performed in small diameter cylindrical bars by exciting the lowest-order Pochammer mode (or Young's mode),[15] we can simplify the problem to a one-dimensional description using a wave equation of the following type:

$$\rho_0 \frac{\partial^2 u}{\partial t^2} = M_2(1+\kappa(x,t)) \frac{\partial^2 u}{\partial x^2} + S(x,t). \tag{1}$$

Here S is the source function, u is the particle displacement at Lagrangian position x and time t, ρ_0 is the unstrained density of the medium, M_2 is the linear Young's modulus (a combination of second order elastic constants equal to $\rho_0 c_0^2$ where c_0 is the linear velocity), and $\kappa(x,t)$ is the ratio of the nonlinear to linear contributions to the modulus.

Traditional theoretical models simply make use of a series expansion expression of $\kappa(x,t)$ in terms of the strain $\varepsilon = \partial u/\partial x$, introducing nonlinear coefficients in the equation of state. In this case,

$$\kappa(x,t) = \beta \frac{\partial u}{\partial x} + \delta \left(\frac{\partial u}{\partial x} \right)^2 + \cdots , \tag{2}$$

where $\beta = M_3/M_2$ and $\delta = M_4/M_2$. Here, M_3 and M_4 are, respectively, linear combinations of second- and third-order elastic constants, and second-, third-, and fourth-order constants, in the direction of propagation.

Classical nonlinear theory generally does a poor job in predicting behavior in rock. As shown and discussed in one of our previous papers,[18] the application of the traditional nonlinear model including cubic anharmonicity to experimental data results in nonlinearity parameters with magnitudes that are difficult to justify when compared to static stress–strain test predictions. In particular, the cubic anharmonicity term, which arises from nonzero fourth-order elastic constants, is two to three orders of magnitude larger than its estimation based on static measurements. Also, we noticed a systematic amplitude dependence of the nonlinearity coefficients indicating that the assumptions of the model are incorrect and that the theory is at the very least incomplete. Finally, classical nonlinear models do not display the multivalued state relations as predicted by comprehensive static stress–strain test, i.e., excursions up and down in pressure.

Convinced by the large number of experimental observations illustrating the presence of hysteresis and discrete memory in rocks over a broad interval in frequency and strain,[1–6] McCall and Guyer developed a new theoretical paradigm for the description of the elastic behavior of rocks.[7,22,23] This alternative model is based on the Preisach model for hysteresis[25] and uses Mayergoyz' ideas[26] to translate the properties of the microscopic structure, i.e., the nature of the compliant portion of the material (grain to grain contacts, cracks, contained fluids, etc.), into the macroscopic behavior of the rock using effective medium theory. In the model, the fundamental building blocks are the individual hysteretic mesoscopic elastic units [HMEU, Fig. 1(a)] assembled into the Preisach–Mayergoyz (or P–M) space which represents the density of individual HMEU's [Fig. 1(b)]. The P–M space is a pressure–pressure space (P_c, P_0). As illustrated in Fig. 1(a), the closing pressure P_c corre-

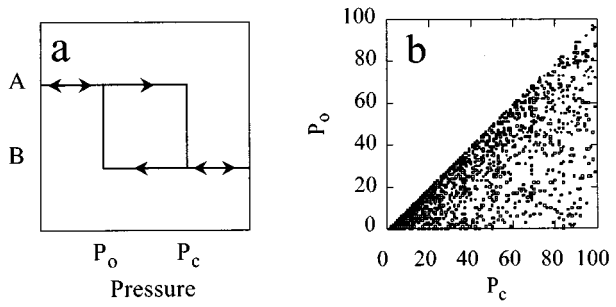

FIG. 1. (a) Representation of a hysteretic mesoscopic elastic unit (HMEU). (b) Typical P–M space representing the density of HMEU's in a sample.

sponds to the pressure at which a HMEU changes from state A to state B while increasing the pressure. The opening pressure P_0 then represents the pressure at which the same feature changes from state B back to its initial state A while decreasing the pressure. A large number of the HMEU's with differing P_c, P_0 comprise a model of the compliant features of a sample material. The P–M space is constructed by plotting the characteristic (P_c, P_0) pressures for the individual HMEU's and filling the lower triangular half-space $(P_c \geqslant P_0)$ as seen in Fig. 1(b). Nonhysteretic units (i.e., $P_c = P_0$) are on the diagonal, and hysteretic units fall in the bottom triangle in P—M space. The more hysteretic a HMEU is, the farther from the diagonal it resides. Using statistics, a density of compliant features can be associated to each point of the P–M space, given by $\rho(P_c, P_0)$. It is beyond the scope of this paper to review this model in more detail. We refer the reader to the extensive work of our colleagues.[7,22,23]

The P–M space representation with its associated density can be used to construct realistic stress–strain curves that include hysteresis and discrete memory and that model static observations very well. Static pressure excursions sample different volumes of HMEU's for increasing or decreasing pressure. This results in typical hysteresis loops showing discontinuities and discrete memory in the equation of state depending on the pressure path. Based on laboratory observations it is reasonable to assume that dynamic excursions also display hysteresis and discrete memory. In the following we will describe how $\kappa(x,t)$, the ratio of nonlinear to linear moduli in Eq. (1), can be obtained for dynamic experiments using very simple assumptions about the P–M space density in the region of interest. This will provide us the tools to correctly model dynamic observations.

Suppose we simulate a wave propagation experiment in which the source is a sequence of sinusoidal oscillations, or identically pressure excursions of amplitude ΔP, centered at average pressure P. Because ΔP in dynamic excursions is very small, two assumptions can be made: (1) The P–M density of the nonhysteretic elastic features on the diagonal of Fig. 1(b) (which corresponds to the major percentage of the P–M density) can be expanded in the pressure deviation p around P, where $p = P - P$, and $-\Delta P \leqslant p \leqslant \Delta P$. (The presupposition of a series expansion will enable us to easily obtain analytic solutions and to retrieve the classical nonlinear theory formalism as a special case.) (2) The P–M density of the hysteretic elastic units off the diagonal $(P_c < P_0)$ is considered constant (uniform background) near the diagonal. This yields the following approximate expression for the P–M density $\rho(P_c, P_0)$ in the case of a dynamic wave experiment:

$$\rho(P_c, P_0) = [a_0 + a_1 p + a_2 p^2 + \cdots] \cdot \hat{\delta}(P_0 - P_c) + \hat{\rho}_B, \tag{3}$$

where $\hat{\rho}_B$ is the constant P–M space density off the diagonal in the pressure region of interest, and $\hat{\delta}(\bullet)$ is the delta distribution function. The P–M space density given in Eq. (3) is expressed in units of P^{-2}. Therefore, $\hat{\rho}_B$ also has units of P^{-2}, and because a delta function has units inversely proportional to its argument, a_0 must be expressed in units of P^{-1}, a_1 in units of P^{-2}, and a_2 in units of P^{-3}.

Following equations 28–32 in McCall and Guyer's derivation of the modulus from the P–M space density,[22] the inverse elastic modulus then corresponds to

$$\frac{1}{M} = \xi_0 [a_0 + a_1 p + a_2 p^2 + \cdots + \hat{\rho}_B (\Delta P \pm p)], \tag{4}$$

where the plus sign corresponds to the (inverse) modulus for increasing pressure and the minus sign for decreasing pressure. Here ξ_0 is a dimensionless constant that can be found from experiment. Assuming p and ΔP are small, Eq. (4) can be inverted to find the following first-order expression for the modulus. Identifying the constant pressure independent contribution with the ''linear'' dynamic modulus M_2 gives

$$M = [M_2 + b_1 p + b_2 p^2 - \rho_B (\Delta P \pm p) + \cdots] \tag{5}$$

(b_1, b_2, and ρ_B can be calculated from the inversion using a Taylor series expansion). The last step consists of the substitution of the relationship between pressure and strain to first order in Eq. (5) (Hooke's law $p = -M_2\, \varepsilon = -M_2\, \partial u/\partial x$, and $\Delta P = M_2\, \Delta\varepsilon = M_2 \Delta\, \partial u/\partial x$ with $\Delta\varepsilon$ or $\Delta\, \partial u/\partial x$ being the maximum strain excursion), which results in

$$M = M_2 \left[1 + \beta \frac{\partial u}{\partial x} + \delta \left(\frac{\partial u}{\partial x} \right)^2 - \rho_B \left(\Delta \frac{\partial u}{\partial x} \pm \frac{\partial u}{\partial x} \right) + \cdots \right] \tag{6}$$

with $\beta = -b_1$ and $\delta = b_2 M_2$. Here, β, δ, and ρ_B are dimensionless parameters. The plus sign corresponds to the modulus for increasing strain and the minus sign for decreasing strain. It must be noted that this substitution is only correct under the assumption that dissipation does not contribute to the forces to first order. We will return later to the subject of attenuation.

Equation (6) gives the formulation of the dynamic modulus resulting from rudimentary P–M space considerations. In view of Eq. (1), we can identify the ratio of the nonlinear to linear contributions to the modulus, $\kappa(x,t)$, as

$$\kappa(x,t) = \beta \frac{\partial u}{\partial x} + \delta \left(\frac{\partial u}{\partial x} \right)^2 - \rho_B \left(\Delta \frac{\partial u}{\partial x} \pm \frac{\partial u}{\partial x} \right) + \cdots . \tag{7}$$

It is clear that the elastic modulus is hysteretic for $\rho_B \neq 0$. For $\rho_B = 0$, the modulus is a power series in the strain and does not differ for increasing or decreasing strain. In this case the model reverts to the traditional theory corresponding to Eq. (2).

As a first approximation, the P–M paradigm for rocks accounts for hysteresis and end point memory by introducing a discontinuous term in the dynamic modulus. The elastic modulus depends not only on the instantaneous value of the strain but also on its amplitude and the reversal points at each extremum. This complicates the manipulation of the wave equation significantly. The problem becomes a differential equation with discontinuous coefficients that are functions of the dependent variable by its derivatives and their amplitude. A quasi-analytic solution can be obtained using a Green's function formalism in combination with perturbation theory.[16,17,23] We illustrate this in the following.

We write the solution to the nonlinear wave equation as the sum of the zeroth-order ''linear'' displacement $[u^{(0)}(x,t)]$ and a nonlinear contribution $[u^{(1)}(x,t)]$, and we assume that every nonlinear term in $\kappa(x,t)$ [Eq. (7)] contributes as a first-order perturbation to the linear solution. In a previous paper we proved that higher-order terms can be accounted for by performing small iteration steps in distance, i.e., using a variant of the finite difference procedure.[17] Using Green's function theory, the Fourier transformation of the linear displacement component satisfies

$$\begin{aligned}\tilde{u}^{(0)}(x,\omega) &= \int_{-\infty}^{+\infty} dt\; u^{(0)}(x,t)e^{i\omega t} \\ &= \int_{-\infty}^{+\infty} dx'\; \frac{e^{i(\omega/c_0)cq(\omega)|x-x'|}}{-2i(\omega/c_0)cq(\omega)} \cdot \frac{\tilde{S}(x',\omega)}{M_2},\end{aligned} \tag{8}$$

where $c_0 = \sqrt{M_2/\rho_0}$ is the linear velocity, and $\tilde{S}(x,\omega)$ is the Fourier transformation of the source function. The factor $cq(\omega)$ equals $(1+i\,\mathrm{sign}(\omega)/2Q)$, and is an *ad hoc* manner in which we introduce intrinsic attenuation, linear with frequency, for a given quality factor Q.

Our primary interest in this paper lays in the investigation of nonlinear distortion of propagating pulsed waves. Therefore we can specify $\tilde{S}(x,\omega)$ by its discrete Fourier spectrum. Assuming a ''breathing'' mode source where the source expands symmetrically about its vertical axis [i.e., $u(-x,t) = -u(x,t)$],

$$\begin{aligned}\tilde{S}(x,\omega) &= \int_{-\infty}^{+\infty} dt\; S(x,t)e^{i\omega t} \\ &= -2M_2 \frac{\partial[\hat{\delta}(x)]}{\partial x} \cdot 2\pi \sum_{n=-\infty}^{+\infty} U_n \hat{\delta}(\omega - n\omega_0)\end{aligned} \tag{9}$$

in which ω_0 is the fundamental source frequency, and $U_n = [U_{-n}]^*$ is a complex number describing the amplitude A_n and phase ϕ_n of the nth harmonic displacement component at $x=0$, i.e., $U_n = -(i/2)A_n e^{i\phi_n}$, and again, $\hat{\delta}(\bullet)$ is the delta distribution function. In this case $\tilde{u}^{(0)}(x,\omega)$ becomes

$$\tilde{u}^{(0)}(x,\omega) = 2\pi \frac{x}{|x|} \sum_{n=-\infty}^{+\infty} U_n \hat{\delta}(\omega - n\omega_0) e^{i(\omega/c_0)cq(\omega)|x|}. \tag{10}$$

The first-order perturbation contribution to the solution satisfies the following linear differential equation:

$$\begin{aligned}&\left[\frac{\partial^2}{\partial x^2} + \frac{\omega^2}{c_0^2}\right]\tilde{u}^{(1)}(x,\omega) \\ &\quad = -\beta \int_{-\infty}^{+\infty} \frac{\partial u^{(0)}}{\partial x}(x,t) \cdot \frac{\partial^2 u^{(0)}}{\partial x^2}(x,t) e^{i\omega t}\, dt \\ &\quad - \delta \int_{-\infty}^{+\infty} \left[\frac{\partial u^{(0)}}{\partial x}(x,t)\right]^2 \cdot \frac{\partial^2 u^{(0)}}{\partial x^2}(x,t) e^{i\omega t}\, dt \\ &\quad + \rho_B \int_{-\infty}^{+\infty} \left[\Delta\left(\frac{\partial u^{(0)}}{\partial x}\right) \pm \frac{\partial u^{(0)}}{\partial x}(x,t)\right] \\ &\qquad \cdot \frac{\partial^2 u^{(0)}}{\partial x^2}(x,t) e^{i\omega t}\, dt.\end{aligned} \tag{11}$$

As seen from this equation, the source for $u^{(1)}(x,t)$ is composed of three nonlinear contributions in $u^{(0)}(x,t)$ and its derivatives which identify the nonconstant distribution of HMEU's on the diagonal in P–M space and the nonzero background value off the diagonal. The third term on the right-hand side of Eq. (11) contains the discontinuity introduced by hysteresis considerations. The switching between plus and minus occurs at each strain reversal in time. Obtaining an analytic solution to Eq. (11) is problematic because of this discontinuity. One can sidestep this difficulty by approximating the function $[\Delta(\partial u^{(0)}/\partial x) \pm \partial u^{(0)}/\partial x](x,t)$ [which we rename $H_0(x,t)$ in the following] using its discrete Fourier series expansion. Suppose $\{h_m\}$ are the complex Fourier coefficients of this function. Then

$$\begin{aligned}H_0(x,t) &= \left[\Delta\left(\frac{\partial u(0)}{\partial x}\right) \pm \frac{\partial u^{(0)}}{\partial x}\right](x,t) \\ &= \sum_{m=-\infty}^{+\infty} h_m e^{im(\omega_0/c_0)cq(\omega)|x| - im\omega_0 t}\end{aligned} \tag{12}$$

from which

$$\tilde{H}_0(x,\omega) = 2\pi \sum_{m=-\infty}^{+\infty} h_m e^{i(\omega/c_0)cq(\omega)|x|} \hat{\delta}(\omega - m\omega_0). \tag{13}$$

Rearranging integrands in Eq. (11) by use of the convolution rule for Fourier transformations and subsequent application of the Green's function theory yields the following general solution for $\tilde{u}^{(1)}(x,\omega)$:

$$\tilde{u}^{(1)}(x,\omega)=\frac{\beta}{2\pi}\int_{-\infty}^{+\infty}dx'\,\frac{e^{i(\omega/c_0)cq(\omega)|x-x'|}}{-2i(\omega/c_0)cq(\omega)}\cdot\int_{-\infty}^{+\infty}\frac{\partial\tilde{u}^{(0)}}{\partial x'}(x',\omega')\cdot\frac{\partial^2\tilde{u}^{(0)}}{\partial x'^2}(x',\omega-\omega')\,d\omega'$$
$$+\frac{\delta}{(2\pi)^2}\int_{-\infty}^{+\infty}dx'\,\frac{e^{i(\omega/c_0)cq(\omega)|x-x'|}}{-2i(\omega/c_0)cq(\omega)}\cdot\int_{-\infty}^{+\infty}\int_{-\infty}^{+\infty}\frac{\partial\tilde{u}^{(0)}}{\partial x'}(x',\omega')\cdot\frac{\partial\tilde{u}^{(0)}}{\partial x'}(x',\omega'')$$
$$\cdot\frac{\partial^2\tilde{u}^{(0)}}{\partial x'^2}(x',\omega-\omega'-\omega'')\,d\omega'\,d\omega''$$
$$-\frac{\rho_B}{2\pi}\int_{-\infty}^{+\infty}dx'\,\frac{e^{i(\omega/c_0)cq(\omega)|x-x'|}}{-2i(\omega/c_0)cq(\omega)}\cdot\int_{-\infty}^{+\infty}\tilde{H}_0(x',\omega')\cdot\frac{\partial^2\tilde{u}^{(0)}}{\partial x'^2}(x',\omega-\omega')\,d\omega'. \tag{14}$$

Substituting the expression for $\tilde{u}^{(0)}(x,\omega)$ [Eq. (10)] and the Fourier transformation of $H_0(x,t)$ [Eq. (13)] in Eq. (14) and working through the immense job of analytically calculating the integrals we obtain a general expression describing the harmonic distortion of a pulsed signal propagated over a distance x in an elastically nonlinear and hysteretic medium. However, because this expression is obtained using perturbation theory, it is restricted in its analytic form to small distances x from the source. For large distances L, the distortion must be calculated by a finite difference or iterative procedure.[17,27,28] Therefore we divide the total distance L into N intervals, each of length $\Delta x=L/N$. The calculated signal at the beginning of each interval is used as the source for the computation of the waveform and spectrum propagating over the next interval L/N. As illustrated in our previous papers, frequency-dependent attenuation can be accounted for at each step in the iteration. In terms of the strain components

$$\varepsilon_n(x)=i\,\frac{n\omega_0}{c_0}\,cq(n\omega_0)U_n(x)$$
$$=n\,\frac{\omega_0}{2c_0}\,cq(n\omega_0)A_n(x)\exp[i\phi_n(x)], \tag{15}$$

the perturbation solution at $x_0+\Delta x$, based on the virtual ''source'' at x_0, for each frequency component is given by

$$\varepsilon_n(x_0+\Delta x)=\varepsilon_n(x_0)\exp\left[i\,\frac{n\omega_0}{c_0}\,cq(n\omega_0)|\Delta x|\right]$$
$$+i\,\frac{\Delta x}{|\Delta x|}\,\frac{\omega_0}{2c_0}\sum_{m=-\infty}^{+\infty}(n-m)\cdot cq((n-m)\omega_0)$$
$$\cdot\varepsilon_{n-m}(x_0)\cdot\mathrm{Int}(n,m,n-m,0)\cdot[-\beta\varepsilon_m(x_0)$$
$$+\rho_B h_m(x_0)]-i\delta\,\frac{\Delta x}{|\Delta x|}\,\frac{\omega_0}{2c_0}\sum_{m,l=-\infty}^{+\infty}l$$
$$\cdot cq(l\omega_0)\cdot\varepsilon_{n-m-l}(x_0)\cdot\varepsilon_m(x_0)\cdot\varepsilon_l(x_0)$$
$$\cdot\mathrm{Int}(n,n-m-l,m,l). \tag{16}$$

where

$$\mathrm{Int}(n_1,n_2,n_3,n_4)=2k_1\,\frac{e^{ik_1|\Delta x|}-e^{ik_{234}|\Delta x|}}{i(k_1^2-k_{234}^2)}$$

with

$$k_1=\frac{n_1\omega_0}{c_0}\,cq(n_1\omega_0)$$

and

$$k_{234}=\frac{n_2\omega_0}{c_0}\,cq(n_2\omega_0)+\frac{n_3\omega_0}{c_0}\,cq(n_3\omega_0)$$
$$+\frac{n_4\omega_0}{c_0}\,cq(n_4\omega_0). \tag{17}$$

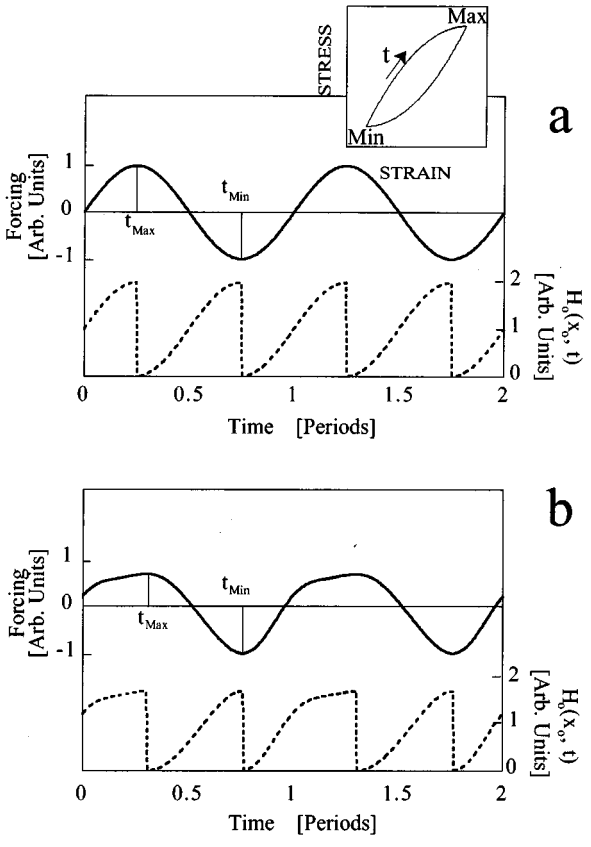

FIG. 2. Examples of the function $H_0(x,t)$ (the discontinuous portion of the nonlinear modulus) for a pure monofrequency (a) and a moderately distorted (b) sinusoidal ''simplex'' wave forcing function representative for an equation of state with one major stress–strain hysteresis loop (see inset).

The discontinuous function $H_0(x,t)$ and its Fourier transformation $\tilde{H}_0(x,\omega)$ pose rather severe restraints as to the extent on which this problem can be solved analytically (or better quasi-analytically). In the case of a periodic monofrequency sinusoidal time history for the strain, McCall and Guyer,[23] proved that only even Fourier coefficients in Eqs. (12) and (13) are nonzero, resulting eventually in the creation of odd harmonics in the distorted spectrum along the propagation path. However, the analytic representation of the nonlinear part of the modulus given by McCall and Guyer is only valid for a pure single frequency sinusoidal forcing function. As the propagation path increases, the local strain becomes progressively distorted, its maximum and minimum change (not necessarily symmetrically) and are shifted in time (not necessarily separated by half a period). Multiple maxima and minima may be observed during one period. In these cases the analytic expressions for the Fourier coefficients of $H_0(x,t)$ generally become far more elaborate. As long as the strain has a periodic time history with only one maximum and one minimum per period, which we will define as ''simplex wave'' henceforth, one can proceed with the following algebraic formulas:

$$H_0(x,t)=\begin{cases}\dfrac{\partial u^{(0)}}{\partial x}(x,t)-\left(\dfrac{\partial u^{(0)}}{\partial x}\right)_{\mathrm{Min}} & \text{if } \dfrac{\partial^2 u^{(0)}}{\partial t\,\partial x}(x,t)\geqslant 0,\\ \left(\dfrac{\partial u^{(0)}}{\partial x}\right)_{\mathrm{Max}}-\dfrac{\partial u^{(0)}}{\partial x}(x,t) & \text{if } \dfrac{\partial^2 u^{(0)}}{\partial t\,\partial x}(x,t)<0.\end{cases} \tag{18}$$

Examples of the discontinuous function $H_0(x,t)$ for a pure monofrequency and a moderately distorted sinusoidal ''simplex'' wave forcing function are illustrated in Fig. 2.

Suppose the zeroth-order approximation of the local strain near x_0, i.e.,

$$\frac{\partial u^{(0)}}{\partial x}(x_0+x,t)=\sum_{n=-\infty}^{+\infty}\varepsilon_n(x_0)e^{in(\omega_0/c_0)cq(n\omega_0)|x|-in\omega_0 t},$$

has a maximum $\varepsilon_{\mathrm{Max}}$ at t_{Max} and a minimum $\varepsilon_{\mathrm{Min}}$ at t_{Min} for $x=\Delta x$. Then

$$\begin{aligned}h_n=&\overline{\delta_{n,0}}[\varepsilon_{\mathrm{Min}}+\varepsilon_{\mathrm{Max}}](t_{\mathrm{Min}}-t_{\mathrm{Max}})-\overline{\delta_{n,0}}\varepsilon_{\mathrm{Min}}\frac{2\pi}{\omega_0}-2\varepsilon_n\left(t_{\mathrm{Min}}-t_{\mathrm{Max}}-\frac{\pi}{\omega_0}\right)\\&+(1-\overline{\delta_{n,0}})[\varepsilon_{\mathrm{Min}}+\varepsilon_{\mathrm{Max}}]e^{-in(\omega_0/c_0)cq(n\omega_0)|\Delta x|}\cdot\frac{e^{in\omega_0 t_{\mathrm{Min}}}-e^{in\omega_0 t_{\mathrm{Max}}}}{in\omega_0}\\&-2\sum_{m=-\infty}^{+\infty}(1-\overline{\delta_{n,m}})\varepsilon_m e^{-i(\omega_0/c_0)(n\cdot cq(n\omega_0)-m\cdot cq(m\omega_0))|\Delta x|}\cdot\frac{e^{i(n-m)\omega_0 t_{\mathrm{Min}}}-e^{i(n-m)\omega_0 t_{\mathrm{Max}}}}{i(n-m)\omega_0}\end{aligned} \tag{19}$$

with $\overline{\delta_{ij}}=0$ if $i\neq j$ and $\overline{\delta_{i,j}}=1$ if $i=j$.

One easily recovers McCall and Guyer's expressions when $\varepsilon_m=0$ for $|m|\neq 1$, $\varepsilon_{\mathrm{Max}}=-\varepsilon_{\mathrm{Min}}$, $t_{\mathrm{Min}}-t_{\mathrm{Max}}=\pi/\omega_0$, and when no attenuation is taken into account. Equation (19), however, can be used in the iteration to calculate the distortion due to hysteresis at any distance as long as the wave satisfies the criteria of a simplex wave at that distance (i.e., being periodical with only one maximum and one minimum in one period of the strain).

When more than one maximum and minimum occur during a period (we refer to this as a ''complex'' wave), it means that the stress–strain relation experiences internal hysteresis loops within a larger loop. Figure 3 shows an example where two inner loops are formed on the descending stress–strain branch corresponding to two additional maxima and minima in the history of the forcing function. In order to find the hysteretic term in the modulus, one must keep track of all reversal points $\{t_m\}$ and of the end points of each inner loop $\{t'_m\}$ as shown in Fig. 3. The discontinuous function $H_0(x,t)$, which now also takes into account the additional local maxima and minima, becomes quite complicated to describe analytically. Perhaps Fourier analysis could still work in the most simple cases; however, once more and more extrema are formed the set of time reversal points and respective maxima and minima is difficult to keep track of analytically. Approximating a function $H_0(x,t)$ such as the one illustrated in Fig. 3 requires the computation of a large number of Fourier coefficients. Even if one is capable of doing so, it remains a question as to whether it would be a worthwhile endeavor. Recall that we introduced the function

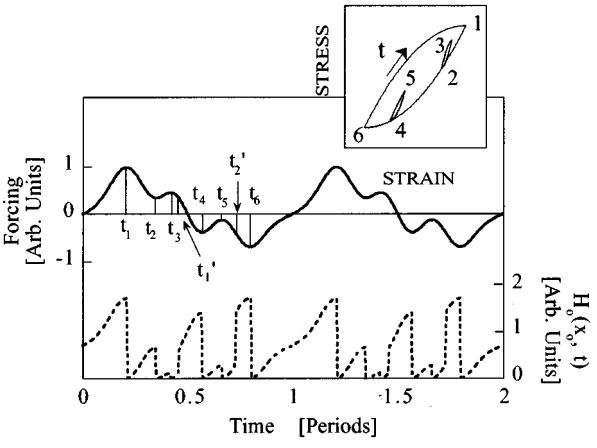

FIG. 3. Example of the function $H_0(x,t)$ for a highly distorted sinusoidal ''complex'' wave forcing function representative for an equation of state with internal stress–strain hysteresis loops (see inset). Here, $\{t_m\}$ and $\{t'_m\}$ are reversal and inner loop end points corresponding to discontinuities in the stress–strain relation.

$H_0(x,t)$ as an ''analytic'' approximation to the exact process given by P–M space. For complicated forcing functions the latter approximation may very well introduce a far larger error than a Fourier analysis representation. In this case we gain nothing by solving the problem in the Fourier domain because the function we started from does not describe the physics well. One alternative (and frankly it seems to be the only possibility) is to leave the analytic treatment and switch to a numerical approach that solves the differential equation in the time domain while linking to a numerical (tabulated) representation of the appropriate P–M space. This work is currently in progress.

II. EXAMPLES WITHIN THE LIMITATION OF SIMPLEX WAVES

In this section we illustrate some effects of hysteresis on the time waveform and frequency spectrum for conditions in which the above analytic treatment (within its limitations of simplex waves) can be applied. We begin this section with some examples of classical nonlinear theory using a Taylor series expansion of the stress–strain relation. Subsequently we illustrate the effects of introducing hysteresis. For clarity we will refer henceforth to the first-order (one parameter) Taylor series expansion as the β model [i.e., δ and ρ_B are both zero in Eqs. (6) and (7)], and to the extended second-order expansion as the β, δ model (i.e., ρ_B is zero). When hysteresis is taken into account in the model, we will use the term β, ρ_B model (δ will always be assumed zero in the β, ρ_B model examples). The nonlinearity parameters used in the model simulations will be indicated by the triplet $[\beta,\delta,\rho_B]$. In all of the examples the source function is a monofrequency continuous pressure wave of frequency f and displacement amplitude A. The propagation distance is 1 m except where noted otherwise. The linear sound velocity in the model is fixed at 2500 m/s and the linear attenuation corresponds to a quality factor (Q) of 50 except where noted. The number of distance iteration steps or finite difference back substitutions was set to 100, resulting in an acceptable calculation step size of 1 cm.

A. Classical nonlinear theory results

Figures 4–6 summarize results obtained from the classical nonlinear models. In Fig. 4(a) time waveforms are shown using the β model ($[\beta,\delta,\rho_B]=[-1000, 0, 0]$) for a single-frequency 10-kHz sinusoidal source at progressively larger amplitude levels. One observes an increased asymmetry with drive level and a correspondingly larger distribution of energy into harmonics as illustrated in Fig. 4(b). The harmonic energy in the spectral components tends to fall off rapidly (nearly exponentially) as a function of frequency. The nonlinear effect in this case is essentially frequency mixing between two spectral components: the double-frequency component is generated by a mixing of the fundamental with itself; the third harmonic arises by interaction of the second harmonic and the fundamental, etc. Figure 5, on the other hand, illustrates a threefold spectral component frequency mixing, resulting from the classical β, δ model with β equal to zero. The top figure shows the waveform calculations for a positive and negative value of the second nonlinearity parameter ($[\beta,\delta,\rho_B]=[0, \pm 10^8, 0]$). In both cases, the distortion from a sinusoidal waveform is readily visible. The amplitude spectrum [Fig. 5(b)] is composed of odd harmonics only. This is the result of three-component mixing starting from a single-frequency source spectrum. That is, three fundamental frequencies can mix energy to form the third harmonic and corrections to the fundamental component. The third harmonic mixes with two fundamental components to form the fifth harmonic and so on. It is interesting that the frequency amplitude spectrum is identical for positive and negative δ values. The phase spectrum is different, however: the $(2m+1)$th spectral component for negative δ differs in phase from the $(2m+1)$th spectral component for positive δ by $m\pi$. This results in the mirror effect in the time history of the signal observed from Fig. 5(a). Figure 6 illustrates the result of combining the first and second nonlinearity parameter effects by fixing β and progressively increasing δ. The bold line in Fig. 6(a) shows the effect when $\delta=0$. As in Fig. 5(a), positive δ values force the peak in the strain history to shift to earlier times, whereas negative values contribute to a shift to later times. Typically, absolute values for δ of one to two orders of magnitude larger than β^2 are required to notice differences in the distorted wavefrom. Characteristic spectra corresponding to a combination of first and second nonlinearity parameters are shown in Fig. 6(b). Due to the simul-

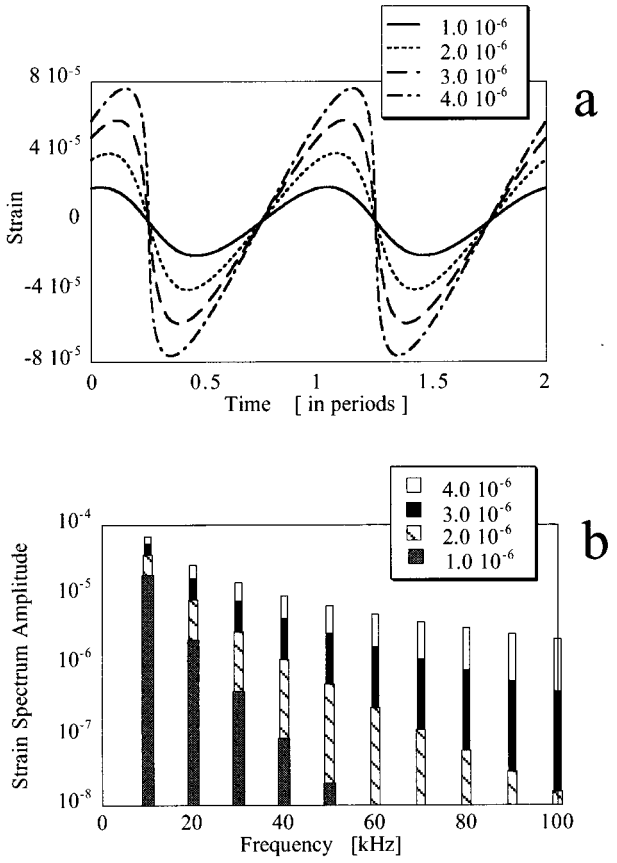

FIG. 4. (a) Strain waveforms from a sinusoidal monofrequency 10-kHz source signal after propagation of 1 m for different source displacement amplitudes (10^{-6} to 4.0×10^{-6} m, corresponding to strains of 2.5×10^{-5} to 10^{-4}). Model parameters: $[\beta,\delta,\rho_B]=[-1000, 0, 0]$. (b) Amplitude spectra for the waveforms shown in (a).

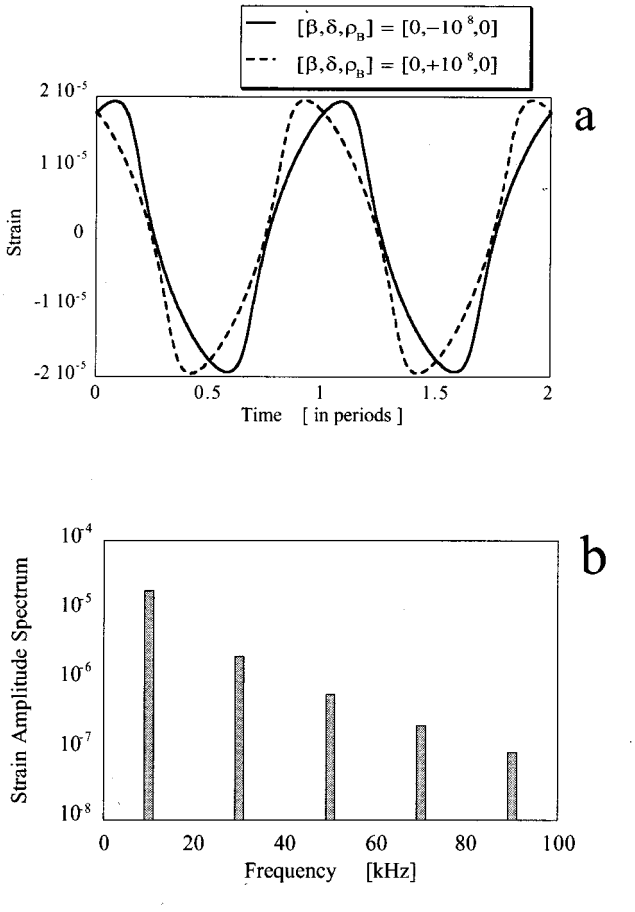

FIG. 5. (a) Strain waveforms from a sinusoidal monofrequency 10-kHz source signal with source displacement amplitude of 10^{-6} m after propagation of 1 m. Model parameters: solid line: $[\beta,\delta,\rho_B]=[-1000,\ -10^8,\ 0]$; dashed line: $[\beta,\delta,\rho_B]=[-1000,\ +10^8,\ 0]$. (b) Amplitude spectra for the waveforms shown in (a). The amplitude spectra are not influenced by the sign of δ.

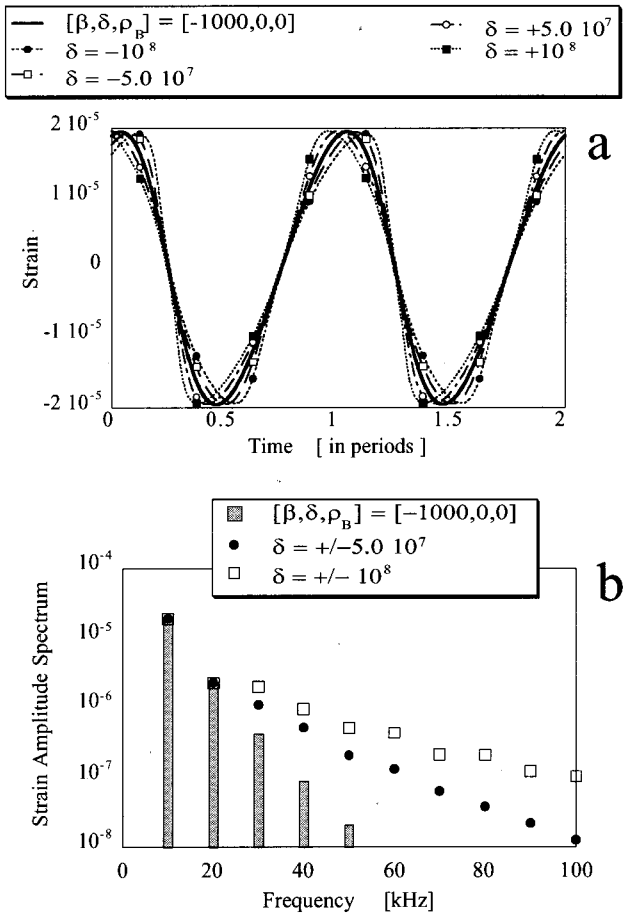

FIG. 6. (a) Strain waveforms from a sinusoidal monofrequency 10-kHz source signal with source displacement amplitude of 10^{-6} m after propagation of 1 m. Model parameters: bold line: $[\beta,\delta,\rho_B]=[-1000,\ 0,\ 0]$, others: $[\beta,\delta,\rho_B]=[-1000,\ -10^8,\ 0]$, $[-1000,\ -5\cdot10^7,\ 0]$,$[-1000,\ +5\cdot10^7,\ 0]$, $[-1000,\ +10^8,\ 0]$. (b) Amplitude spectra for the waveforms shown in (a). The amplitude spectra are not influenced by the sign of δ.

taneous presence of two- and three-fold frequency interactions, one observes a richer spectrum with both even and odd harmonics present (as opposed to the case when $\beta=0$). Compared to the spectrum for $\delta=0$ [bars in Fig. 6(b)], we also note that more energy is pumped into the higher harmonics, increasing the higher frequency portion of the spectrum markedly. Because much energy can be transferred to odd harmonics by threefold frequency mixing δ contributions, a subsequent twofold mixing between an odd harmonic and the fundamental adds considerably to the energy content of its neighboring even components. In extreme cases this can lead to spectra which show a predilection for odd harmonics. We refer, for instance, to our previous papers for such observations and an attempt to model them using the classical nonlinear β, δ approach.[15,18]

B. Quasi-analytic hysteretic approach

Figures 7 and 8 depict results from the quasi-analytic approach of the β, ρ_B model. We first illustrate the nonlinear effects introduced by the hysteretic coefficient without taking into account the nonlinearity parameter β. The waveform represented by the dashed line in Fig. 7(a) is a typical result of a purely hysteretic model. Because it is nearly triangular, it consists of only odd harmonics [Fig. 7(b)]. The transformation of a smooth wave into a sawtooth form in hysteretic materials has also been noticed by Nazarov,[29] independently of our research. Mathematically one can explain this result as the twofold mixing between the fundamental source amplitude and a discontinuous function composed of only even harmonics which results from the analytic P–M space function $H_0(x,t)$ described in the above theory section. [The discontinuous function is composed of only even harmonics because it is periodic over half a source period as is illustrated in Fig. 2(a).] Compared to the linearly attenuated signal propagated over the same distance, one notes the strong generation of harmonics and a supplemental loss of energy due to hysteresis. We will return to the latter subject later. Figure 8 illustrates the combination of the first-order classical nonlinear theory with the hysteretic model for three different ρ_B values at fixed β ($[\beta,\delta,\rho_B]=[-1000,\ 0,\ 0]$, $[-1000,\ 0,\ 2000]$, $[-1000,\ 0,\ 4000]$). The waveforms become more and more symmetric (triangular) as ρ_B increases, diminishing the shock wave tendency effect imposed by the first nonlinearity parameter β. In addition, the strain amplitude becomes progressively reduced when compared to the classical result over the same propagation distance. Again, the combination

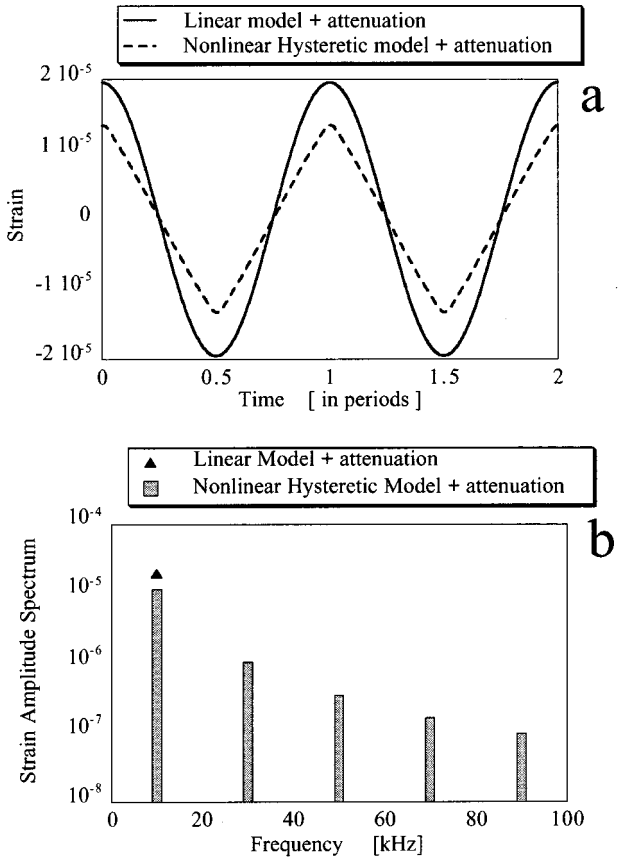

FIG. 7. (a) Strain waveform from a sinusoidal monofrequency 10-kHz source signal with source displacement amplitude of 10^{-6} m after propagation of 1 m (dashed line) and comparison with a purely linear signal with *ad hoc* attenuation. Model parameters for dashed waveform: $[\beta,\delta,\rho_B]=[0,0,4000]$. (b) Amplitude spectra for the linear and nonlinear waveforms shown in (a).

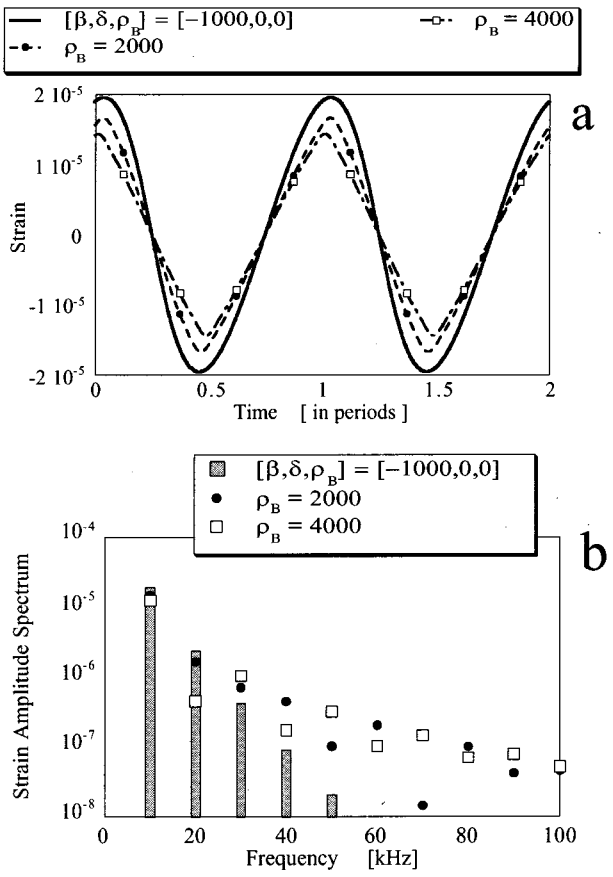

FIG. 8. (a) Strain waveforms from a sinusoidal monofrequency 10-kHz source signal with source displacement amplitude of 10^{-6} m after propagation of 1 m. Model parameters: bold line: $[\beta,\delta,\rho_B]=[-1000, 0, 0]$, others: $[\beta,\delta,\rho_B]=[-1000, 0, 2000]$, $[-1000, 0, 4000]$. (b) Amplitude spectra for the waveform shown in (a).

of twofold odd harmonic generation due to hysteresis and the classical twofold frequency mixing leads to rich spectra with a predilection for odd harmonics as illustrated in Fig. 8(b).

C. Local dynamic modulus

Using Eq. (6) one can calculate the local dynamic modulus at any distance from the source as a function of time or strain. Figure 9 shows the normalized local modulus after a propagation distance of 1 m as a function of time [Fig. 9(a)] and strain history at that same position [Fig. 9(b)] for examples of the three models considered. The normalization is performed with respect to the linear modulus, i.e., with respect to the modulus in the absence of any form of nonlinearity. Because the term $\delta(\partial u/\partial x)^2$ is either positive or negative depending on the sign of δ, its contribution causes an offset in the modulus–time and modulus–strain relation. The same is true for the hysteretic contribution which is always definite negative. Both classical models (β and β, δ approach) display a continuous variation of the modulus with time. The extended classical model shows more variation which is related to the richer frequency content at that distance. As a function of strain, the simple β model delineates a linear dependence with no discontinuities. The second-order β, δ model accounts for some curvature in the modulus–strain relation, but even in this case the modulus is continuous and single valued at every strain level. As explained in the theory section, hysteresis introduces a discontinuous term in the modulus which shows up in both its time and strain dependence. As a function of strain, the β, ρ_B model results in a multivalued modulus–strain relationship with a typical bow tie behavior. The modulus becomes discontinuous at peaks in the strain history, and differs for increasing or decreasing strain values. This type of discontinuous relationship is also a common observation in static experiments on rocks.[4–6,22,23]

D. Hysteresis induced nonlinear attenuation

In Figs. 7 and 8 we noted that hysteresis contributes substantially to the nonlinear attenuation of a propagating wave. Given the same propagation distance, source frequency, and source amplitude, we plotted the maximum strain excursion (peak to peak) as a function of the hysteresis strength given by the parameter ρ_B in Fig. 10. The classical nonlinearity parameters β and δ are set equal to zero in order to emphasize on the contribution due to hysteresis only. The value at $\rho_B=0$ corresponds to the linearly attenuated signal amplitude (i.e., $Q=50$ and $[\beta,\delta,\rho_B]=[0,0,0]$), which is about 78% of the source amplitude measured peak to peak at 1 m

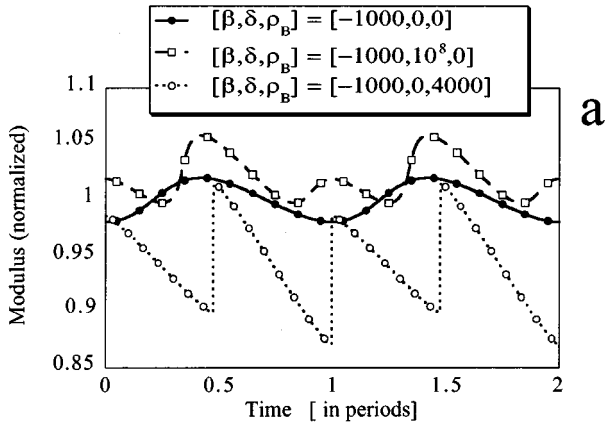

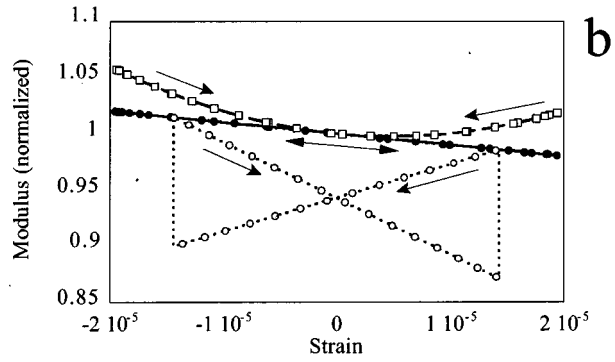

FIG. 9. Typical local dynamic (normalized) modulus–time (a) and modulus–strain (b) behavior for the three models. Normalization is with respect to the linear modulus (i.e., with respect to the modulus in the absence of any form of nonlinearity).

distance. For nonzero values of hysteretic strength, the amplitude monotonically decreases with increasing hysteresis. For instance, there is an additional 30% attenuation due to hysteresis for the model parameters $[\beta,\delta,\rho_B]=[0,0,5000]$, increasing the total attenuation to about 48% of the source signal.

Figure 11 illustrates the hysteretic damping characteristic in a somewhat different way. In a previous paper on the

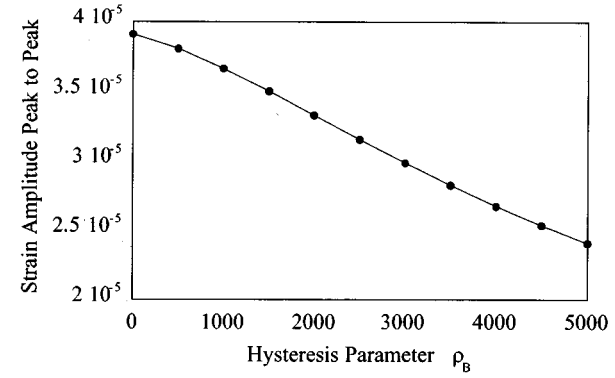

FIG. 10. Dependence of the peak-to-peak strain amplitude on the hysteresis strength for a sinusoidal monofrequency 10-kHz source signal with source displacement amplitude of 10^{-6} m after 1-m propagation distance (peak-to-peak strain at source $\approx 5\times 10^{-5}$).

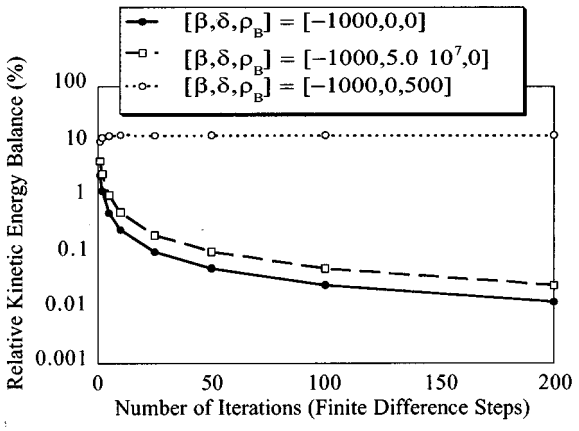

FIG. 11. Percentage of the relative kinetic energy balance [Eq. (20)] at 1-m propagation distance in the absence of attenuation (Q=infinity) as a function of number of iteration (finite difference steps) for the three models. Note that the relative kinetic energy balance is expressed in percentage.

discussion of the classical nonlinear theory[17] we proved that the finite difference procedure provides a means of accounting for energy conservation in the absence of attenuation. To show this, we plotted the relative kinetic energy balance at distance L,

$$\left|\frac{E_L-E_0}{E_0}\right| \cong \left|\frac{\Sigma_{n=-\infty}^{+\infty}|V_n(L)|^2-\Sigma_{n=-\infty}^{+\infty}|V_n(0)|^2}{\Sigma_{n=-\infty}^{+\infty}|V_n(0)|^2}\right|, \qquad (20)$$

as a function of the number of steps taken during the calculation. Here, E_0 and E_L are the kinetic energy at the source and at distance L, and $V_n=-in\omega_0 U_n$ are the spectral components of the velocity. The relative kinetic energy balance is a measure for energy loss integrated over the complete amplitude spectrum. Its value (zero or nonzero) determines whether energy is conserved or not. This should not be confused with the apparent losses in the fundamental due to harmonic generation. For the classical models (where $\rho_B\equiv 0$) and in the absence of linear attenuation, the theoretical value of the relative kinetic energy balance always corresponds to an energy excess ($E_L>E_0$), meaning that more energy is being transferred to harmonics than is being corrected for in the fundamental frequency. The relative error, however, decreases monotonically to acceptable values as the number of iterations is increased (solid circles and open squares in Fig. 11). The smaller the finite difference step, the more accurately energy conservation is satisfied in the model calculations. The results for the extended β,δ model decrease less rapidly than the simple β-approach due to the more pronounced higher harmonic generation. Classical nonlinear theory, in the absence of attenuation, thus preserves the total energy in the amplitude spectrum as a whole, even though losses can be noted in the amplitude of the fundamental due to nonlinear frequency mixing. Introducing hysteresis in the model reduces the kinetic energy at distance L significantly, resulting in an energy deficiency ($E_L<E_0$). In this case, the absolute value of the kinetic energy balance (open circles) asymptotically approaches a fixed nonzero value as the step-size decreases (13% for the model parameters chosen in this example). This is a clear indication that there is no energy

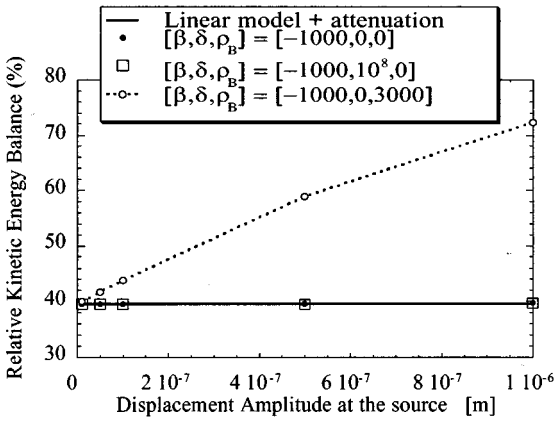

FIG. 12. Relative kinetic energy balance (in percentage) at 1-m propagation distance as a function of source displacement amplitude at 10 kHz for the linear and the three nonlinear models ($Q=50$).

conservation when hysteresis is present. Because classical nonlinearity does not cause energy reduction, we can state that hysteresis is responsible for all the ''nonlinear energy loss'' in a wave propagation experiment. Again, we emphasize that this loss should not be confused with the apparent nonlinear loss in the fundamental due to harmonic generation.

Analyzing the kinetic energy loss may thus be a simple manner by which to verify whether or not hysteresis is present in a material. We can illustrate this with one more figure. Given a quality factor $Q=50$, Fig. 12 shows the relative kinetic energy balance [Eq. (20)] for the classical models and the quasi-analytic hysteretic approach as a function of the displacement amplitude at the source. Both classical models do not significantly alter the kinetic energy balance as a function of amplitude. The only loss of energy in these cases is due to the linear attenuation. (The linear model and both classical models predict the same energy loss.) In the hysteresis model simulation, however, a clear linear dependence of kinetic energy loss with amplitude can be noted. The numerical calculations presented here are consistent with the analytic calculations by McCall and Guyer.[23] Thus, experimental verification of this observation somehow characterizes the role of hysteresis in the dynamic behavior of the sample. It simply requires the integration of the power spectrum of the velocity for different initial amplitudes at the source and at some propagation distance L. One can do this without any knowledge of the linear attenuation.

The order of magnitude of nonlinear attenuation and the manner in which it scales with ρ_B and strain amplitude can be understood from the following argument. A pressure cycle of amplitude ΔP carries a point in the material through a strain cycle of amplitude $\Delta\varepsilon$. From the expression of the inverse modulus [Eq. (4)], the associated strain hysteresis (e.g., measured at the midpoint of the pressure cycle) is

$$\partial\varepsilon \approx \left(\frac{1}{M_{(p:-\Delta P\rightarrow\Delta P)}}-\frac{1}{M_{(p:\Delta P\rightarrow-\Delta P)}}\right)\Delta P = 2(\xi_0\hat{\rho}_B\Delta P)\Delta P. \tag{21}$$

Note that there is no influence of the classical nonlinearity parameters. The associated irreversible energy loss is

$$\partial E \approx \partial\varepsilon\,\Delta P. \tag{22}$$

Since the energy ''stored'' in a pressure cycle, E_0, is of order $\Delta\varepsilon\Delta P$, we have

$$\frac{1}{Q_{\text{Hyst}}}\approx\frac{\partial E}{E_0}\approx\frac{\partial\varepsilon}{\Delta\varepsilon}\approx 2\rho_B\Delta\varepsilon. \tag{23}$$

Here Q^{-1}_{Hyst} denotes the attenuation due to hysteresis effects. In arriving at the right-hand side we have used $M_2^2\xi_0\hat{\rho}_B=\rho_B$ and $\Delta P\approx M_2\Delta\varepsilon$.

In Eq. (23) we see that the nonlinear attenuation is proportional to ρ_B and to $\Delta\varepsilon$. The proportionality of Q^{-1}_{Hyst} to ρ_B is demonstrated in Fig. 10; the proportionality of Q^{-1}_{Hyst} to $\Delta\varepsilon$ is demonstrated in Fig. 12.

Let us compare calculated strain levels in Fig. 10 with the levels deduced from the analysis of the amplitude reduction using Eq. (23). We focus on $\rho_B=5000$. The calculated strain amplitude (one-half peak-to-peak) at this value of hysteretic strength ($\Delta\varepsilon_{5000}$) is 1.2×10^{-5}. Also in Fig. 10 we see that the amplitude decreases (compared to the linear attenuated strain level $\Delta\varepsilon_0$) by an amount of order one, $(\Delta\varepsilon_0-\Delta\varepsilon_{5000})/\Delta\varepsilon_0\approx0.4$, in traveling 1.0 m or 4 wavelengths. Using Eq. (23) we estimate the contribution to the nonlinear attenuation over that distance

$$\frac{1}{Q_{\text{Hyst}}}=\frac{\partial\varepsilon}{\Delta\varepsilon_0}\approx\frac{\Delta\varepsilon_0-\Delta\varepsilon_{5000}}{\Delta\varepsilon_0}\approx4\cdot(2\rho_B\Delta\varepsilon_{\text{estim}})\approx0.4,$$

or $\Delta\varepsilon_{\text{estim}}\approx1.0\times10^{-5}$, a strain in good agreement with the calculated value of 1.2×10^{-5}. Thus we find that Eq. (23) is qualitatively and quantitatively (order of magnitude) correct.

The results confirmed in this discussion suggest that the nonlinear attenuation can be regarded as a direct probe of ρ_B.

An important implication of energy loss due to hysteresis is that materials exhibiting hysteretic behavior such as certain rock and shape memory alloys could be used in building construction as supplementary damping layers for seismic activity.[30,31] In the same context, it is also widely known that soils counteract soft surface layer resonance due to hysteresis induced energy losses.[32] This becomes more and more important in site response studies for weak and strong motion in regions with conceivable damaging earthquake activity.

E. Dependence relations as guidance for inversion methods

Models can be very informative when used in a forward direction. However, a more interesting goal is to achieve a means of inverting the outcome of an experiment (or set of experiments) and to quantify the nonlinearity for characterization of the material. In the following we indicate some criteria that may help in the inversion process within the validity of simplex waves.

Assume three ''virtual'' materials, each of which satisfies the simulation by one of the three models considered in this paper: the simple β model, the extended classical β, δ approach, and the new β,ρ_B model. For simplicity we sup-

pose that the linear sound speed, linear attenuation, and the first nonlinearity parameter are the same for all three materials: $c_0=2500$ m/s, $Q=50$, and $\beta=-1000$.

First of all, we have shown in the above discussion of Figs. 10 and 12 that analyzing the kinetic energy loss may be a simple manner by which to verify whether or not hysteresis is present in a material.

In addition, an analysis of the time waveform and its frequency spectrum at a fixed propagation distance can provide a qualitative measure of the importance of the second nonlinearity parameter and of the hysteresis strength. Figures 4, 6, and 8 illustrate this for $[\beta,\delta,\rho_B]=[-1000,\ 0,\ 0]$, $[-1000,\ 10^8,\ 0]$, and $[-1000,\ 0,\ 4000]$, respectively. The presence of higher harmonics is an indication that some form of additional higher nonlinearity is necessary to describe the material's dynamic behavior. Furthermore, if the strain history takes on a typical triangular wave shape there is strong evidence that hysteresis is present.

Another way of obtaining information about the dominant nonlinear process (classical or hysteretic) is by looking at the individual spectral components and their dependence on distance, source frequency, and source amplitude. Recalling theoretical calculations by McCall,[16] Van Den Abeele,[17] and McCall and Guyer[23] for the propagation of a continuous monofrequency source signal in a nonlinear medium, we can summarize these elementary relationships for the second and third harmonic as follows:

(i) simple classical β models;

$$U_2 \propto \beta x f^2 U^2, \quad U_3 \propto \beta^2 x^2 f^4 U^3,$$

(ii) extended classical β, δ model:

$$U_2 \propto \beta x f^2 U^2,$$

$$U_3 \propto \beta^2 x^2 f^4 U^3 \quad \text{if } \frac{\beta^2 x f}{c_0} >>> |\delta| \text{ or}$$

$$U_3 \propto \delta x f^3 U^3 \quad \text{if } \frac{\beta^2 x f}{c_0} <<< |\delta|;$$

(iii) hysteresis β, ρ_B model:

$$U_2 \propto \beta x f^2 U^2,$$

$$U_3 \propto \beta^2 x^2 f^4 U^3 \quad \text{if } \frac{\beta^2 x f^2 U}{c_0^2} >>> \rho_B \text{ or}$$

$$U_3 \propto \rho_B x f^2 U^2 \quad \text{if } \frac{\beta^2 x f^2 U}{c_0^2} <<< \rho_B$$

(x is the distance to the source, f is the source frequency, U is the source displacement amplitude, and U_2, U_3 are the displacement amplitudes for the second and third harmonics at distance x).

These relationships are deduced in the absence of attenuation and apply for small propagation distances only. They also appear as the asymptotic behavior of our numerical calculation scheme using Eq. (16). In Figs. 13–15 we visualize these dependence relations for the second and third harmonic using the numerical simulations of the three model materials (under the conditions $\beta^2 x f <<< c_0|\delta|$ and $\beta^2 x f^2 U <<< c_0^2 \rho_B$). (Note, however, that we plotted strain amplitudes instead of displacement, which means that the power law dependence for frequency increases by 1 because $\varepsilon_n \propto n f U_n$.) The behavior of the second harmonic as a function of distance, frequency, and amplitude does not provide comprehensible differentiation in the form of higher nonlinearity. Even in the presence of higher-order nonlinearity or hysteresis the classical dependence relations remain valid: the second harmonic is linearly dependent on the propagation distance, quadratic in source amplitude and source frequency, and the proportionality coefficient is a measure of the first nonlinearity parameter β. There is only a small difference when hysteresis is involved due to nonlinear attenuation. Study of the third harmonic, however, indicates significantly different behavior in the three model materials. A square law dependence for the distance (Fig. 13) of the third harmonic indicates that first-order nonlinearity dominates the dynamic behavior at this source frequency and amplitude. The observation of a linear dependence on distance indicates that either higher-order nonlinearity or hysteresis must be taken into account. Figure 14 tells us that the frequency dependence relation for the strain amplitude of third harmonic differs in all three models. Note, however, that this is only the case if the source displacement is kept constant at all frequencies. When strain amplitude is kept constant at the source, ε_3 is square law dependent on frequency in the β model and linearly proportional to frequency in the extended classical and hysteretic model. Figure 15 illustrates the

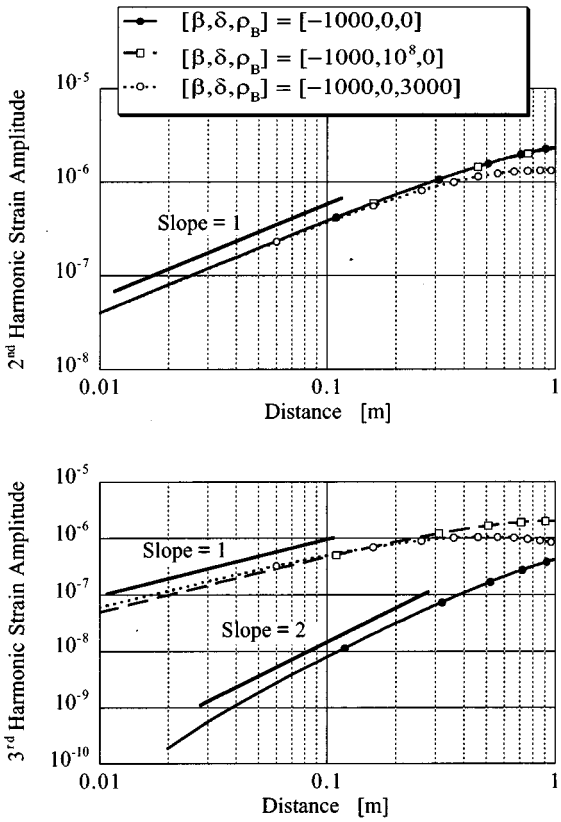

FIG. 13. Distance dependence of the second and third harmonic strain amplitudes for a sinusoidal monofrequency 10-kHz source signal with fixed source displacement amplitude of 10^{-6} m. Theoretical results for the three model materials.

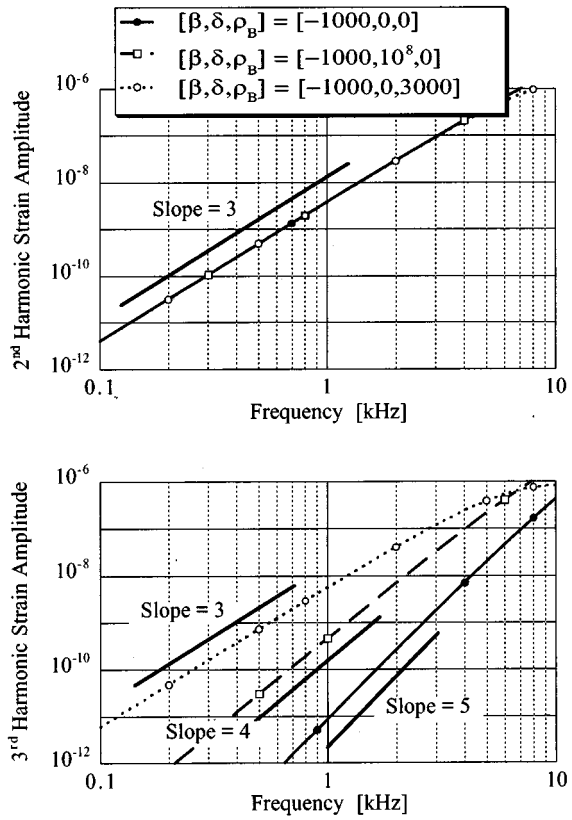

FIG. 14. Source frequency dependence of the second and third harmonic strain amplitudes for a sinusoidal monofrequency source signal with fixed source displacement amplitude of 10^{-6} m at 1-m propagation distance. Theoretical results for the three model materials.

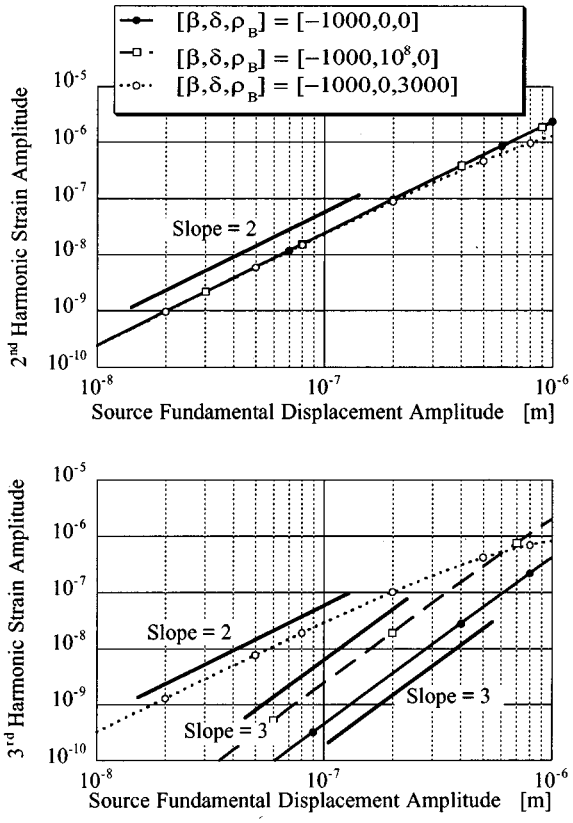

FIG. 15. Source amplitude dependence of the second and third harmonic strain amplitude for a sinusoidal monofrequency 10-kHz source signal after 1-m propagation distance. Theoretical results for the three model materials.

source amplitude dependence (in displacement) for fixed frequency and propagation distance. The third harmonic strain amplitude satisfies a dependence on the source amplitude to the third power except when hysteresis is dominant in which case a square law relation applies.

In summary we can state that an analysis of the second harmonic is always restricted to information about the first-order nonlinear coefficient only. An evaluation of the third harmonic provides more insight into the dominant nonlinear characteristics. Given its dependence relations, third harmonic measurements can provide the clue as to whether the simple classical theory is sufficient, or if higher nonlinear constants or hysteresis must be considered.

We have only supplied some extreme characteristics. Real materials will usually have a nonlinear behavior that fall in between the theoretical bounds illustrated in this paper. Most certainly noninteger power law dependencies will be observed for real data, indicating that a combination of higher-order nonlinearity and hysteresis is present in the material. This is unquestionably the case for most rock for instance. That is why a large number of ''basic'' experimental data in the three-dimensional space of distance, frequency, and amplitude is necessary to perform a unique inversion within the limitations of this theory. In this context we also want to point out some experimental difficulties that are involved in obtaining such an extensive data set. Site response generally complicates corrections on distance measurements; the transfer function of the source transducer and receivers requires comprehensive deconvolution while stepping in frequency; and the generation of harmonics at the source with increasing drive level is a critical problem for the source amplitude dependence measurements.

Another important remark is that the theoretical model presented here is only a first-order approximation of the complex modeling that is involved based on the integral P–M space. The inversion for the triplet β, δ, and ρ_B only makes sense in the framework of this quasi-analytic treatment. These parameters are local and may depend strongly on the average pressure condition under which the experiment has been performed. Ultimately, we would like to arrive at a general description of the forward and backward models in terms of the global P–M space density $\rho(P_c, P_0)$. The local parameters β, δ, and ρ_B can then be readily obtained from this global density distribution.

III. CONCLUSION

A first-order approximation of the complex manifestation of hysteresis has been presented for the description of dynamic wave propagation in hysteretic materials by using an analytic expression for the modulus derived from P–M space modeling. The model is limited in validity to simplex waves, i.e., periodic waves with only one maximum and one minimum in one period of the strain. Within this limitation, the model illustrates that hysteretic effects can be identified

through a variety of experimental observations: triangular shaped waveform, predilection for odd harmonics, kinetic energy loss as a result of nonlinear attenuation, and particular source frequency and amplitude dependence relations for the third harmonic. Because hysteresis adds considerably to the attenuation of propagating waves, hysteretic materials can be used in basement constructions for large structures as additional effective damping layers counteracting seismic waves of large amplitude.

Even though this analytic description may only be a crude approximation of the complexity contained in the P–M space model of hysteresis, its simple implementation can be helpful in evaluating the applicability of classical nonlinear theory and in determining the strength of hysteresis in the material. The model will eventually be applied for inversion of experimental data sets to qualify and quantify the nonlinearity of the material in view of a new NDT characterization method.

ACKNOWLEDGMENTS

The authors thank J. A. Ten Cate, T. J. Shankland, A. Kadish, P. Rasolofosaon, and B. Zinszner for helpful discussions and valuable comments. This research is supported by NATO Scientific and Environmental Affairs (Advanced Fellowship for Koen Van Den Abeele), the Office of Basic Energy Science, Engineering and Geoscience under Contract No. W7405-ENG-36 with Los Alamos National Laboratory, by internal funds from Institutional Support, and the Institute of Geophysics and Planetary Physics.

[1] D. J. Holcomb, ''Memory, relaxation and microfracturing in dilatant rock,'' J. Geophys. Res. **86**, 6235–6248 (1981).
[2] C. H. Scholz and S. H. Hickman, ''Hysteresis in the closure of nominally flat joints,'' J. Geophys. Res. **88**, 6501–6504 (1983).
[3] V. E. Nazarov, L. A. Ostrovsky, I. A. Soustova, and A. M. Sutin, ''Nonlinear acoustics of micro-inhomogeneous media,'' Phys. Earth Planet. Interiors **50**, 65–73 (1988).
[4] G. N. Boitnott, ''Fundamental observations concerning hysteresis in the deformation of intact and jointed rock with applications to nonlinear attenuation in the near source region,'' in *Proceedings of the Numerical Modeling of Underground Nuclear Test Monitoring Symposium*, Durango, CO, 1993, edited by S. R. Taylor and J. R. Kamm, Los Alamos National Laboratory Report (LA-UR-93-3839), 1993.
[5] G. A. Gist, ''Fluid effects on velocity and attenuation in sandstones,'' J. Acoust. Soc. Am. **96**, 1158–1173 (1994).
[6] L. B. Hilbert, Jr., T. K. Hwong, N. G. W. Cook, K. T. Nihei, and L. R. Myer, ''Effects of strain amplitude on the static and dynamic nonlinear deformation of Berea sandstone,'' in *Rock Mechanics Models and Measurements: Challenges From Industry*, edited by P. P. Nelson and S. E. Laubach (Balkema, Rotterdam, 1994), pp. 497–504.
[7] R. A. Guyer, K. R. McCall, and G. N. Boitnott, ''Hysteresis, discrete memory and nonlinear wave propagation in rock: a new paradigm,'' Phys. Rev. Lett. **74**, 3491–3494 (1994).
[8] R. A. Guyer, K. R. McCall, P. A. Johnson, P. N. J. Rasolofosaon, and B. Zinszner, ''Equation of state hysteresis and resonant bar measurements on rock,'' in *1995 International Symposium on Rock Mechanics*, edited by J. J. K. Daemon and R. A. Schultz (Balkema, Rotterdam, 1995), pp. 177–181.
[9] J. Ortin, ''Preisach modeling of hysteresis for a pseudoelastic Cu–Zn–Al single crystal,'' J. Acoust. Soc. Am. **71**, 1454–1461 (1992).
[10] H. H. Law, P. L. Rossiter, G. P. Simon, and J. Unsworth, ''A model for the structural hysteresis in poling and thermal depoling of PZT ceramics,'' J. Mater. Sci. **30**, 4901–4905 (1995).
[11] S. A. Mansour, G. L. Liedl, and R. W. Vest, ''Microstructural developments and dielectric properties of rapid thermally processed PZT thin-films derived by metalloorganic decomposition,'' J. Am. Ceram. Soc. **78**, 1617–1623 (1995).
[12] F. D. Murnaghan, *Deformation of an Elastic Solid* (Wiley, New York, 1951).
[13] L. D. Landau and E. M. Lifshitz, *Theory of Elasticity* (Pergamon, Oxford, 1959).
[14] L. K. Zarembo and V. A. Krasil'nikov, ''Nonlinear phenomena in the propagation of elastic waves in solids,'' Sov. Phys. Usp. **13**, 778–797 (1971) (in English).
[15] G. D. Meegan, P. A. Johnson, R. A. Guyer, and K. R. McCall, ''Observations of nonlinear elastic wave behavior in sandstone,'' J. Acoust. Soc. Am. **94**, 3387–3391 (1993).
[16] K. R. McCall ''Theoretical study of nonlinear elastic wave propagation,'' J. Geophys. Res. **99**, 2591–2600 (1994).
[17] K. E. Van Den Abeele, ''Elastic pulsed wave propagation in media with second or higher order nonlinearity. Part I. Theoretical framework,'' J. Acoust. Soc. Am. **99**, 3334–3345 (1996).
[18] K. E. Van Den Abeele and P. A. Johnson, ''Elastic pulsed wave propagation in media with second or higher order nonlinearity. Part II. Simulation of experimental measurements on Berea sandstone,'' J. Acoust. Soc. Am. **99**, 3346–3352 (1996).
[19] J. A. Ten Cate, K. Van Den Abeele, T. J. Shankland, and P. A. Johnson, ''Laboratory study of linear and nonlinear elastic pulse propagation in sandstone,'' J. Acoust. Soc. Am. **100**, 1383–1391 (1996).
[20] P. A. Johnson, B. Zinszner, and P. N. J. Rasolofosaon, ''Resonance and nonlinear elastic phenomena in rock,'' J. Geophys. Res. **101**(B5), 11 553–11 564 (1996).
[21] P. A. Johnson and P. N. J. Rasolofosaon, ''Manifestation of nonlinear elasticity in rock: convincing evidence over large frequency and strain intervals from laboratory studies,'' Nonlinear Proc. Geophys. **3**, 77–88 (1996).
[22] K. R. McCall and R. A. Guyer, ''Hysteresis, discrete memory and nonlinear elastic wave propagation in rock: a new theoretical paradigm,'' Nonlinear Proc. Geophys. **3**, 89–101 (1996).
[23] K. R. McCall and R. A. Guyer, ''Equation of State and wave propagation in hysteretic nonlinear elastic materials,'' J. Geophys. Res. **99**, 23 887–23 897 (1994).
[24] J. B. Walsh, ''The effect of cracks on the compressibility of rocks,'' J. Geophys. Res. **70**, 381–389 (1965); ''The effect of cracks on the uniaxial elastic compression of rocks,'' J. Geophys. Res. **70**, 399–411 (1965).
[25] F. Preisach, ''Über die Magnetische Nachwirkung,'' Z. Phys. **94**, 277–302 (1935).
[26] J. D. Mayergoyz, ''Hysteresis models from the mathematical and control theory points of view,'' J. Appl. Phys. **57**, 3803–3805 (1985).
[27] F. M. Pestorius and D. T. Blackstock, ''Propagation of finite amplitude noise,'' in *Finite amplitude wave effects in fluids, Proceedings of the 1973 Symposium*, edited by L. Bjorno (Copenhagen, DK, 1973) (IPC Science and Technology Press Ltd., Westbury House, Guildford, England, 1973), pp. 24–29.
[28] M. E. Haran and B. D. Cook, ''Distortion of finite amplitude ultrasound in lossy media,'' J. Acoust. Soc. Am. **73**, 774–779 (1983).
[29] V. Nazarov, ''Propagation of a unipolar impulse in a medium with hysteretic nonlinearity,'' preprint IAP n.383, N. Novgorod, 1995, (in Russian), submitted to Akust. Zh.
[30] J. M. Kelly, ''Application of shape memory materials for reduction of structural response to earthquake ground motion,'' Proceedings of the Workshop on Smart and High Performance materials and structures, Tskuba, Japan (May 1993).
[31] P. W. Clark, I. D. Aiken, J. M. Kelly, M. Higashino, and R. Krumme, ''Experimental and analytical studies of shape memory alloys dampers for structural control,'' in *Smart Structures and Materials 1995: Industrial and commercial applications of smart structures technologies*, 2–3 March 1995, San Diego, CA, edited by C. R. Crowe (Bellingham, WA, 1995).
[32] I. A. Beresnev and K.-L. Wen, ''Nonlinear soil response—A reality?,'' Bull. Seis. Soc. Am. **86**(6), 1964–1978 (1996).

Streaming generated by a bubble in an ultrasound field

Junru Wu
Department of Physics, University of Vermont, Burlington, Vermont 05405

Gonghuan Du
Institute of Acoustics, Nanjing University, Nanjing, The People's Republic of China

(Received 4 March 1996; accepted for publication 18 December 1996)

A theory has been developed to calculate microstreaming velocity inside and outside an isolated air bubble in a liquid produced by a bubble-scattered sound field, taking account of two predominant modes of the bubble's motion: a monopole (pulsation), and a dipole (translational harmonic vibrations). It has been demonstrated that the streaming velocity inside a bubble is much greater than that outside the bubble. It has also been shown that the microstreaming is most pronounced for a bubble undergoing volume resonance, which is in agreement with Elder's experimental observations. If the viscosity of the gas medium in a bubble is neglected in theory, the results obtained agree qualitatively with Davidson and Riley's. © *1997 Acoustical Society of America.* [S0001-4966(97)06404-7]

PACS numbers: 43.25.Nm, 43.25.Yw [MAB]

INTRODUCTION

The variety of chemical and biological effects of ultrasound have been reported and utilized in many applications.[1] Very recently, ultrasound has been shown to enhance the permeability of human skin to many drugs. This effect may provide a possibility to use ultrasound as a noninvasive substitute for traditional methods of drug delivery.[2] The mechanisms involved could be quite complex, however, it is believed that acoustic cavitation played an important role. The underlying mechanisms of the effect are far from fully understood.

It is well-known that the propagation of sound waves in a fluid may lead to a bulk nonperiodic motions of the fluid; it is called the acoustic streaming.[3] Acoustic streaming is a nonlinear phenomenon which is directly related to the second-order terms of the sound field. Acoustic streaming related to bubbles' activities in a sound field has been a topic of research for many years. In the past, attention was focused on small-scale acoustic streaming (microstreaming) in a liquid (outside a bubble) generated by bubble-scattered sound waves.[4–8] In particular, Davidson and Riley[7] considered microstreaming in a liquid outside an isolated bubble induced by the translational harmonic oscillation of the bubble by assuming viscosity of the gas medium in the bubble to be zero. Recently, acoustic streaming within a bubble started to attract peoples' attention. Nyborg[9] has shown that significant streaming can take place in a gas medium generated by surface waves at a liquid-gas interface by assuming the interface is a plane.

In this paper, we develop a theory to calculate streaming velocity inside and outside an air bubble produced by a bubble-scattered sound field, primarily taking account of two predominant modes of the bubble's motion: a monopole (pulsation), and a dipole (translational harmonic vibrations). We demonstrate that the streaming velocity inside a bubble is much greater than that outside the bubble. We also show that the microstreaming is most pronounced for a bubble undergoing volume resonance (monopole motion), which is in agreement with Elder's experimental observations.[5] The streaming due to a monopole motion of a bubble has not been studied in the past. If the viscosity of the gas medium in a bubble is neglected in our theory, our results agree qualitatively with Davidson and Riley's. Our results further indicate that microstreaming velocity due to a monopole becomes zero and microstreaming velocity due to a dipole decreases significantly if the viscosity of the gas medium in a bubble is neglected.

It is our belief that streaming, both inside and outside a bubble, generated by a bubble-scattered sound field, may enhance the transporting mechanism in a fluid, which often plays an essential role in many effects related to ultrasound.

I. THEORY

The configuration of the system to be studied is as follows: an isolated air bubble of radius r_0 is situated at the origin of spherical coordinates (r,θ,ϕ) if there is no external sound field. A plane acoustic wave propagates along the positive z direction; its wave number k is such that $kr_0 \ll 1$. Under the influence of the sound wave, among other things, the bubble can pulsate as a monopole (the $n=0$ mode), and oscillate like a dipole (the $n=1$ mode). Streaming in a liquid (outside the bubble) or in air (inside the bubble) generated by the bubble is primarily a result of the presence of a boundary layer at the liquid-gas interface of the bubble.[10]

Due to viscosity, a thin boundary layer is formed at the liquid–gas interface. The boundary layer actually consists of two parts; the inner one is more like air and the outer one is more like a liquid (for example, water) (Fig. 1). The thicknesses of the two parts are, respectively, of the orders of β_i^{-1} and β_o^{-1} (henceforth the subscripts i and o denote inside and outside the bubble, respectively), where $\beta_i=\sqrt{\omega/2\nu_i}$, $\beta_o=\sqrt{\omega/2\nu_o}$, $\nu_i=\mu_i/\rho_{0i}$, $\nu_o=\mu_o/\rho_{0o}$, μ_i and μ_o are the shear viscosity coefficients of air and water, respectively, ρ_{0i} and ρ_{0o} are densities of air and water, respectively, and ω is the angular frequency. Plugging the parameters of air and

 0001-4966/97/101(4)/1899/9/$10.00

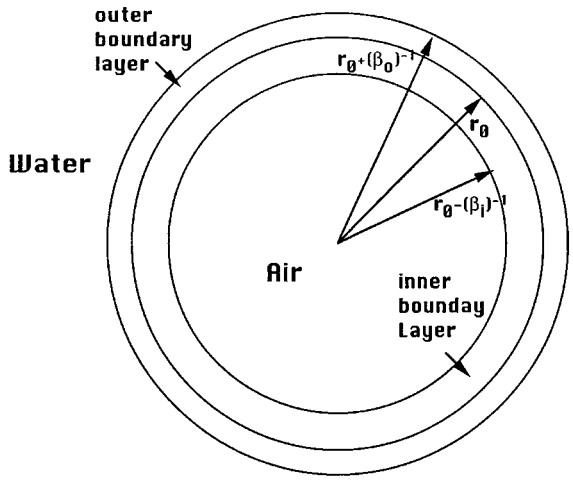

FIG. 1. Illustration of an air bubble and its boundary layer. The thickness of the inner boundary layer is $1/\beta_i$ and that of the outer boundary layer is $1/\beta_o$.

water at a room temperature of 20 °C and the atmospheric pressure:

$$\mu_0 = 0.001 \text{ kg/(m s)}, \quad \mu_i = 1.84\times 10^{-5} \text{ kg/(m s)},$$
$$\rho_{0o} = 1000 \text{ kg/m}^3, \quad \rho_{0i} = 1.21 \text{ kg/m}^3,$$

we obtain $\beta_i^{-1} = 0.002\,20/\sqrt{f}$ m, $\beta_o^{-1} = 0.000\,564/\sqrt{f}$ m, where f is frequency. Thus, the outer part of the boundary layer is much thinner than the inner part.

The theory, that is to be discussed, is based on two conditions: (1) The radius of the bubble r_0 is much greater than the boundary layer thickness, i.e., $r_0 \gg \beta_i^{-1}$, $r_0 \gg \beta_o^{-1}$; (2) $k_i r_0 \ll 1$ and $k_o r_0 \ll 1$, where k_i and k_o are, respectively, the wave number in air and in water and they are, respectively, equal to ω/c_i and ω/c_o (c_i and c_o are the speeds of sound in air and in water, respectively).

A. The first-order flow velocity

The presence of a boundary layer significantly changes the fluid dynamics within the layer. Beyond the boundary layer, the fluid can still be considered to be inviscid. For an inviscid fluid, we have

$$(\nabla^2 + k^2)\varphi_1 = 0, \tag{1}$$

where $k = \omega/c$, ω is the angular frequency, c is the speed of sound, and φ_1 is called the velocity potential, which is related to the first-order flow velocity $\mathbf{u}_1$ as $\mathbf{u}_1 = -\nabla\varphi_1$. The governing equation for the first-order oscillatory flow in a viscous medium, however, is given by[10]

$$(\nabla^2 + h^2)\mathbf{u}_1 = (1 - h^2 k^{-2})\nabla\nabla\cdot\mathbf{u}_1, \tag{2}$$

where $h = (1+j)\beta$, $\beta = \sqrt{\omega\rho_0/2\mu}$, $j^2 = -1$, μ and ρ_0 are, respectively, the viscosity and density of a fluid. Equation (2) is satisfied by any vector function $\mathbf{u}_1$ for which either the following Eq. (3) or Eq. (4) are true,

$$\nabla\times\mathbf{u}_1 = 0, \quad (\nabla^2 + k^2)\mathbf{u}_1 = 0 \tag{3}$$

and

$$\nabla\cdot\mathbf{u}_1 = 0, \quad (\nabla^2 + h^2)\mathbf{u}_1 = 0. \tag{4}$$

The vector function $\mathbf{u}_1$, which satisfies Eq. (3), can be defined as $\mathbf{u}_1 = -\nabla\varphi_1$. Thus, from Eq. (3) we obtain

$$(\nabla^2 + k^2)\varphi_1 = 0. \tag{5}$$

Therefore, within the boundary layer, there are two possible types of solutions of $\mathbf{u}_1$, i.e., $\mathbf{u}_1 = \mathbf{u}_a + \mathbf{u}_b$. Here, $\mathbf{u}_a$, are solutions of Eq. (3) or Eq. (1), and $\mathbf{u}_b$ are solutions of Eq. (4). Equation (4) is called the vector Helmholtz equation; in spherical coordinates, both the r component and θ component or $\mathbf{u}_b$ should satisfy the equation.

The solutions by omitting the time factor (up to the first-order) of Eq. (1) under the condition that $k_i r_0 \ll 1$ and $k_o r_0 \ll 1$, are (see Appendix A)

$$\begin{aligned} u_{ari} &= \frac{-ju_0 A_0 \chi k_i r}{3\lambda\sigma} + 3ju_0 A_1 \cos\theta, \\ u_{a\theta i} &= -3ju_0 A_1 \sin\theta, \\ u_{aro} &= \frac{-ju_0 A_0 \chi k_o r}{3\lambda\sigma^2} + 3ju_0 A_1 \cos\theta, \\ u_{a\theta o} &= -3ju_0 \lambda A_1 \sin\theta, \end{aligned} \tag{6}$$

where u_{ari}, $u_{a\theta i}$, u_{aro}, $u_{a\theta o}$ are, respectively, the r component and θ component of the first-order velocity in air and in water, $\chi = 1/\sqrt{(1-\Omega^2)^2 + \Omega^2\delta^2}$, δ is the damping coefficient for the bubble $\Omega = \omega/\omega_0 = f/f_0$, $\lambda = \rho_{0i}/\rho_{0o}$, $\sigma = k_o/k_i$, $\omega_0 = 2\pi f_0$, $\omega = 2\pi f$, f_0 is the resonance frequency of a bubble, $A_0 = 1$ and $A_1 = -j$ for a plane wave (Appendix A).

As far as Eq. (4) is concerned, let us concentrate on the r component first. If we use u_{bri}, u_{bro}, respectively, to represent the r components of the relevant first-order velocity inside and outside the bubble, their solutions should be of the forms of $u_{bri} \propto h_n^{(2)}(h_i r) P_n(\cos\theta)$, $u_{bro} \propto h_n^{(1)}(h_o r) \times P_n(\cos\theta)$, where $h_n^{(1)}$, $h_n^{(2)}$ are, respectively, Hankel functions of the first kind and the second kind, $h_i = (1+j)\beta_i$, and $h_o = (1+j)\beta_o$. Noting in general the magnitudes of h_i and h_o have dimensions of 1/length, $h_i r$ and $h_o r$ are dimensionless and their magnitudes are much greater than unity within a boundary layer. Using asymptotic forms of Hankel functions, i.e., as $|hr| \gg 1$, $h_n^{(1)}(hr) \to (-j)^{n+1} e^{jhr}/hr$, $h_n^{(2)}(hr) \to (j)^{n+1} e^{-jhr}/hr$, up to the first order, we obtain

$$\begin{aligned} u_{bri} &\approx D_{0i}\frac{e^{-jh_i r}}{h_i r} + D_{1i}\frac{e^{-jh_i r}}{h_i r}\cos\theta, \\ u_{bro} &\approx D_{0o}\frac{e^{jh_o r}}{h_o r} + D_{1o}\frac{e^{jh_o r}}{h_o r}\cos\theta, \end{aligned} \tag{7}$$

where D_{0i}, D_{0o}, D_{1i}, and D_{1o} are constants to be determined. It should be emphasized that Eqs. (7) are valid only inside or in the neighborhood of the boundary layer. The corresponding θ components inside and outside the bubble, $u_{b\theta i}$ and $u_{b\theta o}$ can be found by using the relationship $\nabla\cdot\mathbf{u}_b = 0$ in spherical coordinates and satisfying the condition that they should be finite for any θ in the range of 0 to π. The consequent results are $D_{0i} = D_{0o} = 0$, and

$$u_{b\theta i}=\frac{D_{1i}j}{2}e^{-jh_i r}\sin\theta,$$
$$u_{b\theta o}=\frac{-D_{1o}j}{2}e^{jh_o r}\sin\theta. \tag{8}$$

Therefore, combining the viscous and nonviscous contributions, the r component and θ component of $\mathbf{u}_1$ within or near the boundary layer inside and outside the bubble are, respectively, given by

$$u_{1ri}=u_{ari}+u_{bri}=\frac{-ju_0A_0\chi k_i r}{3\lambda\sigma}+3ju_0A_1\cos\theta + D_{1i}\frac{e^{-jh_i r}}{h_i r}\cos\theta,$$
$$u_{1\theta i}=u_{a\theta i}+u_{b\theta i}=-3ju_0A_1\sin\theta+\frac{D_{1i}j}{2}e^{-jh_i r}\sin\theta,$$
$$u_{1ro}=u_{aro}+u_{bro}=\frac{-ju_0A_0\chi k_o r}{3\lambda\sigma^2}+3ju_0A_1\cos\theta + D_{1o}\frac{e^{jh_o r}}{h_o r}\cos\theta, \tag{9}$$
$$u_{1\theta o}=u_{a\theta o}+u_{b\theta o}=-3ju_0\lambda A_1\sin\theta-\frac{D_{1o}j}{2}e^{jh_o r}\sin\theta,$$

where u_{1ri}, $u_{1\theta i}$, u_{1ro}, and $u_{1\theta o}$ are, respectively, the r-component and θ-component flow velocity inside and outside the bubble, respectively.

It is often advantageous to rewrite Eqs. (9) in another form in terms of parameters g_i and g_o, which will be defined, instead of D_{1i} and D_{1o}. At the boundary ($r=r_0$), we introduce a quantity u_0^0, such that we may rewrite $u_{1\theta i}=[-3ju_0A_1+(D_{1i}j/2)e^{-jh_i r_0}]\sin\theta=-3ju_0^0A_1\sin\theta$. Letting $g_i=1-(u_0^0/u_0)$, thus $D_{1i}=6u_0A_1g_ie^{jh_i r_o}$. If there is no viscosity or viscous boundary layer, it is required that $u_0=u_0^0$, thus $g_i=0$. Similarly, we have $u_{1\theta o}=-3ju_0A_1\lambda\sin\theta-(D_{1o}j/2)e^{jh_o r}\sin\theta=-3ju_0'^0A_1\lambda\sin\theta$. Thus $D_{1o}\approx-6u_0A_1g_oe^{-jh_o r_o}$, where $g_o=\lambda(1-u_0'^0/u_0)$. If there is no viscosity g_o is also required to be zero.

Now Eqs. (9) can be expressed in terms of parameters g_i and g_o, instead of D_{1i} and D_{1o}, as

$$u_{1ri}=-ju_0A_0\frac{\chi k_i r}{3\lambda\sigma}+3ju_0A_1\cos\theta + 6u_0A_1g_i\frac{e^{-jh_i(r-r_0)}}{h_i r}\cos\theta,$$
$$u_{1\theta i}=-3ju_0A_1\sin\theta+3u_0A_1g_ije^{-jh_i(r-r_0)}\sin\theta,$$
$$u_{1ro}=-ju_0\frac{A_0\chi k_o r}{3\sigma^2\lambda}+j3u_0A_1\cos\theta - 6u_0g_oA_1\frac{e^{jh_o(r-r_0)}}{h_o r}\cos\theta, \tag{10}$$
$$u_{1\theta o}=-3ju_0A_1\lambda\sin\theta+3ju_0A_1g_oe^{jh_o(r-r_0)}\sin\theta.$$

Like D_{1i} and D_{1o}, g_i and g_o are to be determined by the following boundary conditions when viscosity is included: At $r=r_0$, shear velocity and shear stress are continuous, i.e.,

$$u_{1\theta i}=u_{1\theta o},\quad \sigma_{1r\theta i}=\sigma_{1r\theta o}, \tag{11}$$

where

$$\sigma_{1r\theta i}=\mu_i\left(\frac{1}{r}\frac{\partial u_{1ri}}{\partial\theta}+\frac{\partial u_{1\theta i}}{\partial r}-\frac{u_{1\theta i}}{r}\right),$$
$$\sigma_{1r\theta o}=\mu_o\left(\frac{1}{r}\frac{\partial u_{1ro}}{\partial\theta}+\frac{\partial u_{1\theta o}}{\partial r}-\frac{u_{1\theta o}}{r}\right). \tag{12}$$

Substituting Eqs. (10) into Eqs. (11), we can calculate

$$g_i=\frac{\alpha(1-\lambda)}{1+\alpha}\approx 0.994,$$
$$g_o=\frac{\lambda-1}{1+\alpha}\approx -0.004\,69, \tag{13}$$

where $\alpha=\beta_o\mu_o/\beta_i\mu_i$. The physical meaning of g_i and g_o now becomes clear. If there were no viscosity, $g_i=g_o=0$, and From Eqs. (10), $u_{1\theta o}/u_{1\theta i}=\lambda=1.21\times10^{-3}$. In other words, compared with the shear flow within the bubble, the shear flow outside the bubble is negligible. This is the so-called free-slip condition. Because of the presence of the viscous boundary layer, g_i and g_o are given by Eqs. (13) and the shear flow velocities are continuous across the boundary; it is now called the nonslip condition.

B. Acoustic streaming

After obtaining the solutions of the first-order flow velocity, now we are going to find the streaming velocity which is the second-order time-independent term, $\mathbf{u}_2$. Nyborg[3] obtained an equation governing streaming which is accurate up to the second order. Noting that $\nabla\cdot\mathbf{u}_2\approx0$,[11] the results may be written as

$$\langle\mathbf{F}\rangle=\nabla\langle p_2\rangle-\mu\nabla^2\mathbf{u}_2, \tag{14}$$

where p_2 is pressure, the symbol $\langle x\rangle$ denotes the time average of x at a fixed point of space, and $\mathbf{F}$ is the source force of the streaming and here it is related to the first-order flow velocity $\mathbf{u}_1$ as

$$\langle\mathbf{F}\rangle=-\rho_0\langle\mathbf{u}_1\cdot\nabla\mathbf{u}_1+\mathbf{u}_1\nabla\cdot\mathbf{u}_1\rangle. \tag{15}$$

As discussed earlier, $\mathbf{u}_1$ in general consists of two parts, i.e.,

$$\mathbf{u}_1=\mathbf{u}_a+\mathbf{u}_b, \tag{16}$$

where $\mathbf{u}_a$ and $\mathbf{u}_b$, respectively, satisfy Eqs. (3) and (4). Substituting Eq. (16) into Eq. (15) and noting $\nabla\cdot\mathbf{u}_b=0$, and the fact that the term of $\langle\mathbf{u}_a\cdot\nabla\mathbf{u}_a+\mathbf{u}_a\nabla\cdot\mathbf{u}_a\rangle$ has no contribution to streaming and only leads to a static pressure distribution which is balanced by $\nabla\langle p_2\rangle$ according to Bernoulli's principle,[10,11] we obtain from Eq. (14)

$$\langle\mathbf{F}\rangle=-\mu\nabla^2\mathbf{u}_2, \tag{17}$$

where

$$\langle\mathbf{F}\rangle=-\rho_0\langle\mathbf{u}_a\cdot\nabla\mathbf{u}_b+\mathbf{u}_b\cdot\nabla\mathbf{u}_b+\mathbf{u}_b\cdot\nabla\mathbf{u}_a+\mathbf{u}_b\nabla\cdot\mathbf{u}_a\rangle. \tag{18}$$

Substituting Eqs. (10) into Eqs. (17) and (18), inside the bubble we obtain approximately

$$\frac{\partial^2u_{2\theta i}}{\partial r^2}+\frac{2}{r}\frac{\partial u_{2\theta i}}{\partial r}\approx f_{\theta i}(r,\theta), \tag{19}$$

where

$$f_{\theta i}(r,\theta)\approx\left\langle u_{ar}\frac{\partial u_{b\theta}}{\partial r}\right\rangle = f_{\theta i0}+f_{\theta i1},$$

$$f_{\theta i0}=\frac{\chi u_0^2 k_i r g_i \beta_i e^{-\beta_i(r_0-r)}}{2\nu_i\sigma\lambda}[\cos\beta_i(r_0-r) - \sin\beta_i(r_0-r)]\sin\theta, \tag{20}$$

$$f_{\theta i1}=\frac{9u_0^2 g_i\beta_i e^{-\beta_i(r_0-r)}}{2\nu_i}[\cos\beta_i(r_0-r) + \sin\beta_i(r_0-r)]\cos\theta\sin\theta.$$

Here $f_{\theta i0}$ and $f_{\theta i1}$ are, respectively, due to the contributions of the $n=0$ and $n=1$ modes of the bubble's motion. It should be noted that here we neglected the terms which are related to $\partial u_{2\theta i}/\partial\theta$ and $\partial^2 u_{2\theta i}/\partial\theta^2$, because $r_0\gg 1/\beta_i$.[10] Similarly, outside the bubble we have

$$\frac{\partial^2 u_{2\theta o}}{\partial r^2}+\frac{2}{r}\frac{\partial u_{2\theta o}}{\partial r}\approx f_{\theta o}(r,\theta), \tag{21}$$

where

$$f_{\theta o}(r,\theta)=f_{\theta o0}+f_{\theta o1},$$

$$f_{\theta o0}=\frac{-\chi u_0^2 g_o\beta_o k_o r e^{-\beta_o(r-r_0)}}{2\lambda\sigma^2\nu_o}[\cos\beta_i(r-r_0) - \sin\beta_i(r-r_0)]\sin\theta$$

for the $n=0$ mode, and

$$f_{\theta o1}=\frac{-9u_0^2 g_o\beta_o e^{-\beta_{oi}(r-r_0)}}{2\nu_o}[\cos\beta_i(r-r_0) + \sin\beta_i(r-r_0)]\cos\theta\sin\theta \tag{22}$$

for the $n=1$ mode.

Equations (19) and (21) can be solved (Appendix B) to satisfy the following boundary conditions: at $r=r_0$, shear streaming velocity and shear stress due to streaming are continuous, i.e.,

$$u_{2\theta i}=u_{2\theta o},\quad \sigma_{2r\theta i}=\sigma_{2r\theta o}, \tag{23}$$

where

$$\sigma_{2r\theta i}=\mu_i\left(\frac{1}{r}\frac{\partial u_{2ri}}{\partial\theta}+\frac{\partial u_{2\theta i}}{\partial r}-\frac{u_{2\theta i}}{r}\right),$$

$$\sigma_{2r\theta o}=\mu_o\left(\frac{1}{r}\frac{\partial u_{2ro}}{\partial\theta}+\frac{\partial u_{2\theta o}}{\partial r}-\frac{u_{2\theta o}}{r}\right). \tag{24}$$

The final results are

$$u_{2\theta i}=u_{2\theta i0}+u_{2\theta i1}, \tag{25}$$

where

$$u_{2\theta i0}=\frac{-u_0^2\chi k_i}{4\lambda\sigma}\left[\frac{r g_i e^{-\beta_i(r_0-r)}}{\beta_i\nu_i}\{\cos[\beta_i(r_0-r)] + \sin[\beta_i(r_0-r)]\}-r_0\left(\frac{g_i}{\nu_i\beta_i}-\frac{g_o}{\nu_o\beta_o}\right)\right]\sin\theta$$

for the $n=0$ mode,

$$u_{2\theta i1}=\frac{9u_0^2}{4}\left\{\frac{g_i e^{-\beta_i(r_0-r)}}{\beta_i\nu_i}\{\cos[\beta_i(r_0-r)] - \sin[\beta_i(r_0-r)]\}-\left[\left(\frac{g_i}{\nu_i\beta_i}-\frac{g_o}{\nu_o\beta_o}\right) + r_0\left(\frac{g_i\rho_{oi}}{\mu_o}+\frac{g_o}{\nu_o}\right)\right]\right\}\cos\theta\sin\theta$$

for the $n=1$ mode, and

$$u_{2\theta o}=u_{2\theta o0}+u_{2\theta o1}, \tag{26}$$

where

$$u_{2\theta o0}=\frac{-u_0^2\chi k_o r}{4\lambda\sigma}\frac{g_o e^{-\beta_o(r-r_0)}}{\beta_o\nu_o}\{\cos[\beta_o(r-r_0)] + \sin[\beta_{oi}(r-r_0)]\}\sin\theta$$

for the $n=0$ mode,

$$u_{2\theta o1}=\frac{9u_0^2}{4}\left[\frac{g_o e^{-\beta_o(r-r_0)}}{\beta_o\nu_o}\{\cos[\beta_o(r-r_0)]-\sin[\beta_o(r-r_0)]\}-\left(\frac{g_i\rho_{0i}}{\mu_o}+\frac{g_o}{\nu_o}\right)\frac{r_0^2}{r}\right]\cos\theta\sin\theta$$

for the $n=1$ mode.

The streaming velocity r component inside and outside the bubble, u_{2ri}, and u_{2ro}, can be evaluated by using $\nabla\cdot\mathbf{u}_2=0$ and satisfying $u_{2ri}=u_{2ro}=0$ at $r=r_0$ (otherwise the bubble will not be stable). They are given by

$$u_{2ri}=u_{2ri0}+u_{2ri1}, \tag{27}$$

where

$$u_{2ri0}=\frac{u_0^2 k_i r_0^2\chi\cos\theta}{2r^2\sigma\lambda}\left[\frac{g_i}{\nu_i\beta_i^2}[1-e^{-\beta_i(r_0-r)}\times\cos\beta_i(r_0-r)]+\frac{r_0}{2}\left(1-\frac{r^2}{r_0^2}\right)\left(\frac{g_i}{\nu_i\beta_i}-\frac{g_0}{\nu_o\beta_o}\right)\right]$$

for the $n=0$ mode,

$$u_{2ri1}=\frac{9u_0^2}{2r^2}\left\{\frac{g_i r_0}{\nu_i\beta_i^2}e^{-\beta_i(r_0-r)}\sin\beta_i(r_0-r)-2(r_0^2-r^2)\times\left[\left(\frac{g_i}{\nu_i\beta_i}-\frac{g_0}{\nu_o\beta_o}\right)+\left(\frac{g_i r_0\rho_{0i}}{\mu_o}+\frac{g_o r_0}{\nu_o}\right)\right]\right\}\times P_2(\cos\theta)$$

for the $n=1$ mode, and

$$u_{2ro}=u_{2ro0}+u_{2ro1}, \tag{28}$$

where

$$u_{2ro0}=\frac{u_0^2 k_i r_0^2 g_o\cos\theta}{2r^2\beta_0^2\nu_o}\frac{\chi}{\lambda\sigma}(e^{-\beta_o(r-r_0)}\times\cos\beta_o(r-r_0)-1)$$

for the $n=0$ mode,

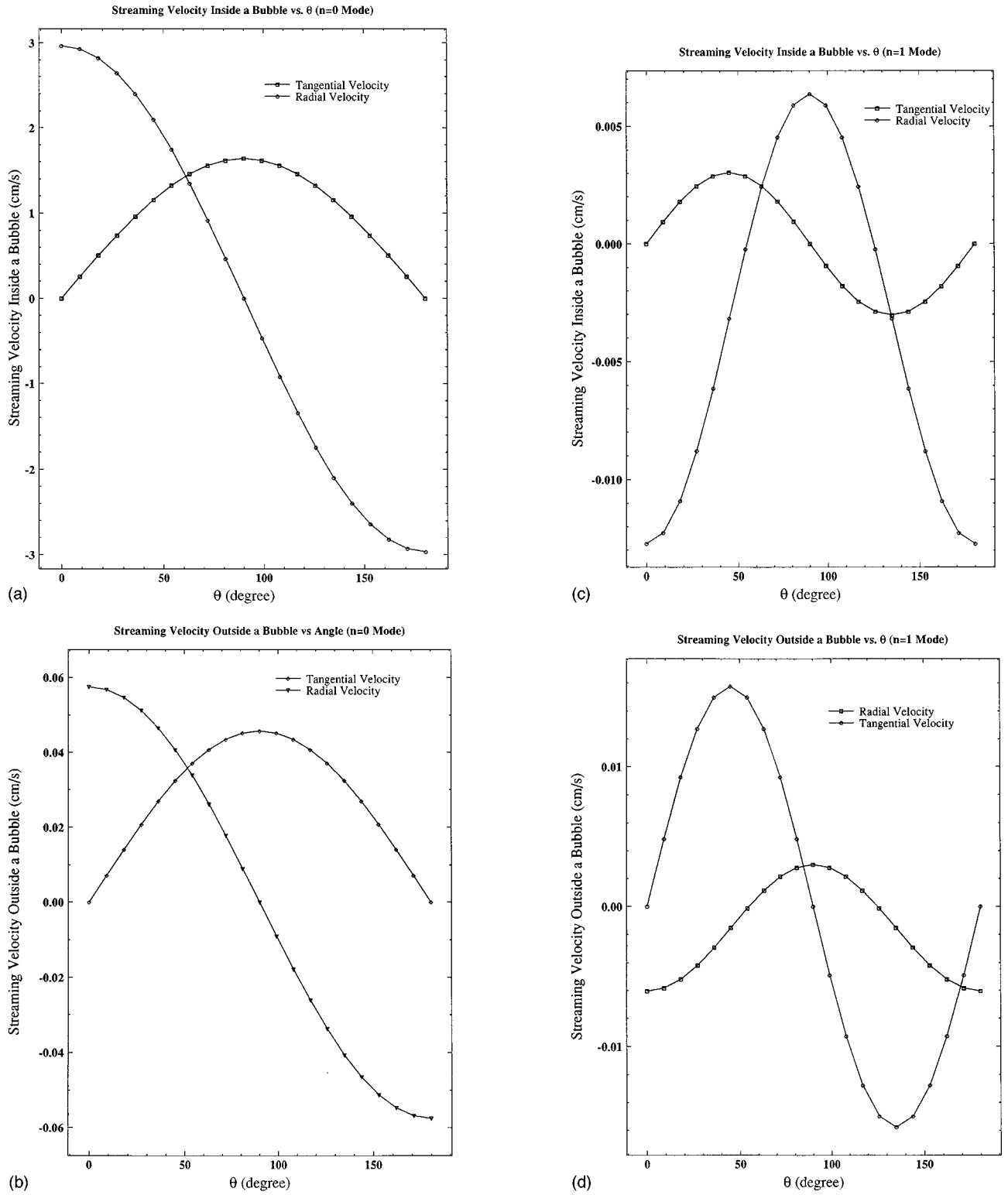

FIG. 2. Streaming velocity versus θ. The size of the bubble is 33 μm and the frequency of the incident sound wave is 100 000 Hz which is equal to the resonance frequency of the bubble. The sound intensity is 1000 W/m^2. (a) Streaming velocity inside the bubble due to the $n=0$ mode, $r=r_0-0.1/\beta_i$. (b) Streaming velocity outside a bubble due to the $n=0$ mode, $r=r_0+2/\beta_o$. (c) Streaming velocity inside the bubble due to the $n=1$ mode, $r=r_0-0.1/\beta_i$. (d) Streaming velocity outside the bubble due to the $n=1$ mode, $r=r_0+2/\beta_o$.

$$u_{2ro1}=\frac{-9u_0^2r_0}{2r^2}\left(\frac{g_o}{\beta_o^2\nu_o}e^{-\beta_o(r-r_0)}\sin\beta_o(r-r_0)+\left(\frac{g_i\rho_{0i}r_0}{\mu_o}+\frac{g_or_0}{\nu_o}\right)(r_0-r)\right]P_2(\cos\theta)$$

for the $n=1$ mode.

II. NUMERICAL RESULTS

Based on Eqs. (25)–(28), we can calculate the streaming velocity inside and outside a bubble. As an example, we consider a case when $f=f_0=100$ kHz and $r_0=33$ μm. The damping coefficient $\delta=0.1$ was used. Thus $\chi=10$. In other words, since the bubble is under the resonance condition, the

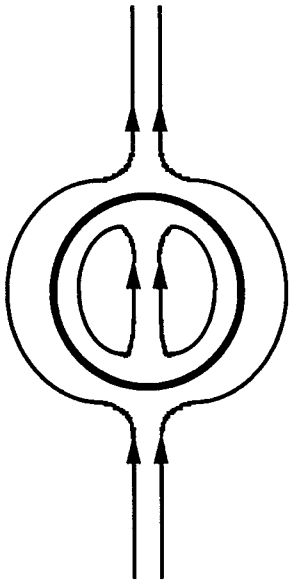

FIG. 3. Illustration of streamlines generated by the $n=0$ mode. The direction of the arrow is that of the sound propagation.

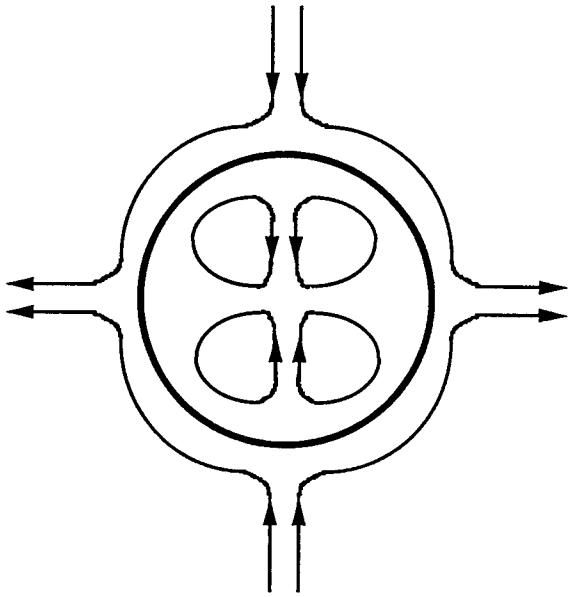

FIG. 4. Illustration of streamlines generated by the $n=1$ mode. The incoming sound wave propagates from bottom to top.

contribution due to the $n=0$ mode is amplified by approximately a factor of 10. Therefore, it dominates. Figure 2(a)–(d) are plots of tangential streaming velocity and radial streaming velocity versus θ due to the $n=0$ and $n=1$ modes, respectively. For streaming velocities inside the bubble, $r=r_0-0.1/\beta_i$ was used; for streaming velocities outside the bubble, $r=r_0+2/\beta_o$ was used. The following observations can easily be reached: (1) Tangential and radial streaming velocities are always out of phase for each mode; wherever the magnitude of tangential streaming velocity reaches the maximum, that of radial streaming velocity reaches minimum (zero). (2) In a period of π, streaming velocity due to the $n=0$ mode changes sign once, while that due to the $n=1$ mode changes sign twice. To illustrate the features mentioned above, streamlines due to the $n=0$ mode and $n=1$ mode are qualitatively plotted in Figs. 3 and 4.

Figure 5(a)–(d) are plots for $u_{2\theta}$ (tangential streaming velocity) and u_{2r} (radial streaming velocity) versus r due to the $n=0$ and $n=1$ modes, respectively. The angle θ in each plot was chosen in such a way that tangential or radial velocity reaches the local maximum. Thus, for tangential velocities $\theta=90°$ in Fig. 5(a) and $\theta=45°$ for Fig. 5(c), for radial velocities $\theta=0°$ in Fig. 5(b) and (d), the range of r is between (r_0-2/β_i) to (r_0+3/β_o) for all the plots. For easy comparison, the same, although arbitrary, vertical scale was used for all four plots. It is quite evident that we can achieve the following observations: (1) The contribution from the $n=0$ mode is much greater than that from the $n=1$ mode for both tangential and radial streaming velocities. It is especially true for streaming velocities inside the bubble due to the resonance condition. (2) Both tangential and radial streaming velocities are much higher inside the bubble than outside the bubble. To show how streaming velocities outside the bubble vary with r, each plot includes an insertion for its outside streaming velocity using much smaller vertical scale. (3) Both tangential and radial streaming velocities are continuous at $r=r_0$; the radial streaming velocities are all equal to zero at $r=r_0$ (it is required for the size stability of a bubble). It should be noted that since the theory works better inside and near the boundary layer, the farther from the boundary, inside or outside the bubble, the greater the error it introduces.

III. DISCUSSION

In general, streaming velocities inside and outside a bubble should be the sum of the contributions from the $n=0$ and $n=1$ modes. As shown above, at resonance, the contribution due to the $n=0$ mode dominates. The contributions of the two modes near the boundary layer, however, should be comparable off resonance.

The results that streaming velocity inside a bubble is much greater than that outside a bubble imply that convection in a gas state may be significantly enhanced by acoustic streaming. It also suggests that acoustic streaming inside a bubble may play an important role in the enhancement of chemical rate processes when ultrasound is applied to chemical applications.

To see the effects of neglecting viscosity for air in our theory, we can let $\mu_i=0$. That is equivalent to saying there is no boundary layer inside a bubble, therefore no streaming within the bubble. Streaming velocity outside a bubble can be calculated as follows. Since $\mu_i=0$, $\alpha=\beta_o\mu_o/\beta_i\mu_i\to\infty$. Thus, according to Eq. (13), $g_i=1$, $g_o=0$. Equation (26) becomes

$$u_{2\theta o0}=0, \quad \text{for the } n=0 \text{ mode},$$
$$u_{2\theta o1}=\frac{-9u_0^2}{4}\frac{\rho_{0i}}{\mu_o}\frac{r_0^2}{r}\cos\theta\sin\theta \quad \text{for the } n=1 \text{ mode}, \tag{26′}$$

and Eq. (28) becomes

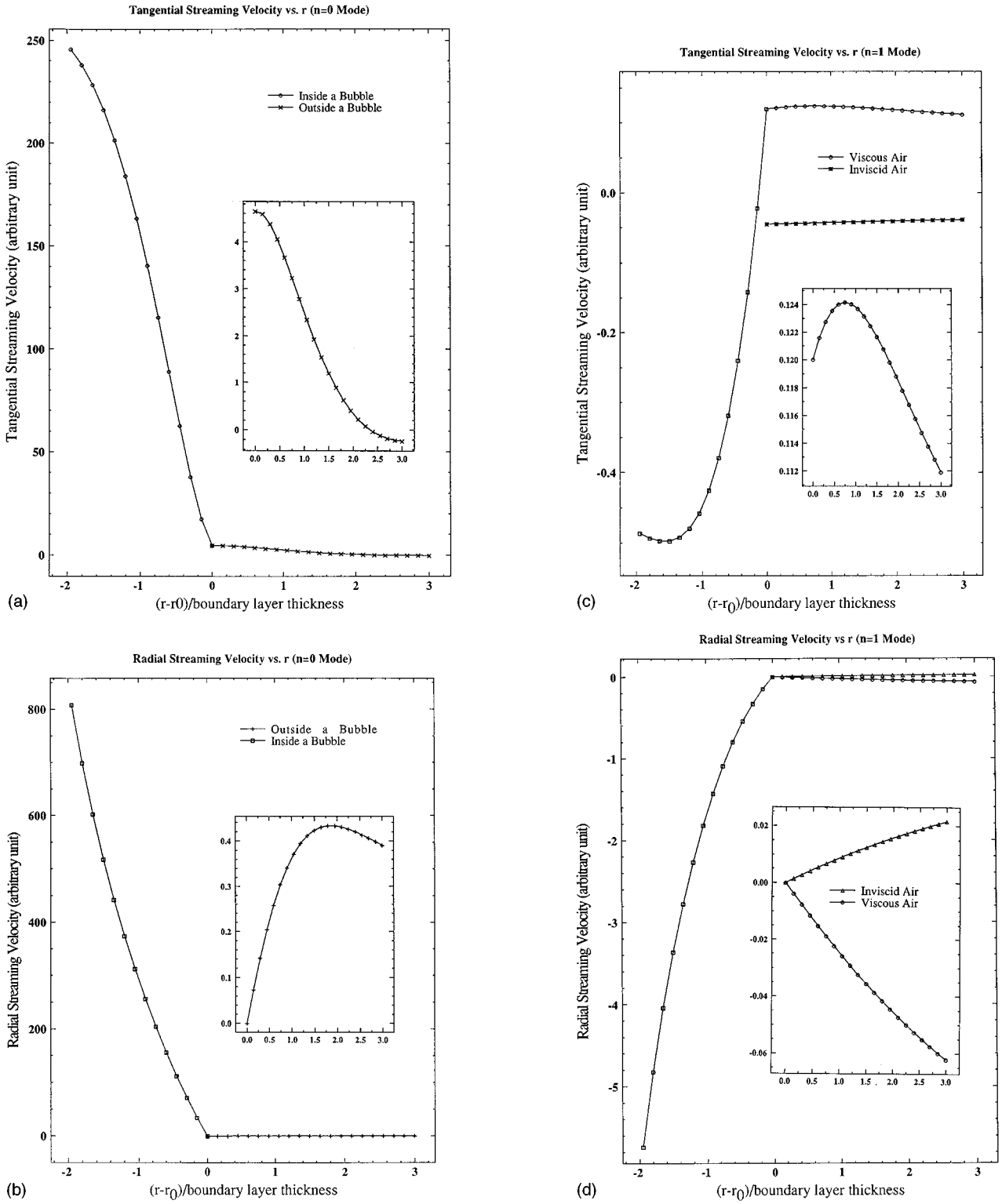

FIG. 5. Streaming velocity versus r. The size of the bubble is 33 μm and the frequency of the incident sound wave is 100 000 Hz which is equal to the resonance frequency of the bubble. The angle θ in each plot was chosen in such a way that tangential or radial velocity reaches the local maximum. (a) Tangential streaming velocity due to the $n=0$ mode. (b) Radial streaming velocity due to the $n=0$ mode. (c) Tangential streaming velocity due to the $n=1$ mode. (d) Radial streaming velocity due to the $n=1$ mode.

$$u_{2ro0}=0 \quad \text{for the } n=0 \text{ mode,}$$

$$u_{2ro1}=\frac{-9u_0^2 r_0}{2r^2}\frac{\rho_{0i} r_0}{\mu_o}(r_0-r)P_2(\cos\theta) \quad \text{for the } n=1 \text{ mode.} \tag{28}$$

The above results suggests that if $\mu_i=0$, the streaming outside a bubble is due to the $n=1$ mode, which agrees with Davidson and Riley's results. Since their results are qualita-

tive in nature, direct comparison was not possible. However, qualitatively, θ dependent and r dependent of streaming velocities given by Eqs. (26′) and (28′) are the same as those given by their results. In Fig. 5(c) and (d) we include streaming velocities outside the bubble when air was treated as an inviscid fluid. Now, tangential streaming velocity is no longer continuous and the magnitude of both tangential and radial velocity are only about 1/3 of their viscous air counterparts. Additionally, the signs of both tangential and radial velocity also change.

In the above discussion, the streaming velocity $\mathbf{u}_2$ was defined as the time average of the second-order velocity term. When we took the time average of velocity, it was done at a fixed point in space. It is called the Eulerian average. Thus, the streaming velocity calculated above is the Eulerian streaming velocity. Another type of time average is done on the velocity of a particle during a short time interval immediately after passing a point in space. It is called the Lagrangian average. The corresponding streaming velocity is called the Lagrangian streaming velocity $\mathbf{U}_L$. They are related by[12]

$$\mathbf{U}_L=\mathbf{u}_2+\langle\mathbf{I}\rangle/(\rho_0 c_0^2), \tag{29}$$

where $\mathbf{I}$ is the acoustic intensity. Experimentally, the Eulerian streaming velocity can be measured by, for example, a hotwire and the Lagrangian streaming velocity can be measured by small particle tracers. In many cases, the difference is small. The streaming velocity discussed in this paper is the former.

ACKNOWLEDGMENT

The authors wish to thank Dr. Wesley L. Nyborg for his insightful comments.

APPENDIX A

To solve Eq. (5) for φ_a, i.e., $(\nabla^2+k^2)\varphi_a=0$ for a scattering problem of a bubble under the conditions $k_i r_0 \ll 1$ and $k_o r_0 \ll 1$, we assume that the incoming symmetrical sound field propagates along the z axis. Thus, its velocity potential can be written as

$$\phi_{ao1}=\sum_{n=0} A_n \gamma_n j_n(k_o r) P_n(\cos\,\theta), \tag{A1}$$

where $\gamma_n=-j(2n+1)(u_0/k_o)$, u_0 is the velocity amplitude of a sound source, $j_n(k_o r)$ and $P_n(\cos\theta)$ are the spherical Bessel function and Legendre polynomial. The scattered field outside of the bubble can be written as

$$\phi_{ao2}=\sum_{n=0} B_n \gamma_n h_n^{(2)}(k_o r) P_n(\cos\,\theta). \tag{A2}$$

Thus, the total field outside the bubble is

$$\phi_{ao}=\phi_{ao1}+\phi_{ao2}. \tag{A3}$$

The sound field within the bubble can be written as

$$\phi_{ai}=\sum_{n=0} C_n \gamma_n j_n(k_i r) P_n(\cos\,\theta). \tag{A4}$$

To satisfy the boundary conditions: (1) $\rho_{0i}\phi_{ai}=\rho_{0o}\phi_{ao}$, (2) $\partial\phi_{ai}/\partial r=\partial\phi_{ao}/\partial r$, we obtain

$$\begin{aligned} B_n&=A_n\frac{\lambda\sigma j_n(k_i r_0)j_n'(k_o r_0)-j_n'(k_i r_0)j_n(k_o r_o)}{j_n'(k_i r_0)h_n^{(2)}(k_o r_0)-\lambda\sigma j_n(k_i r_0)h_n^{(2)\prime}(k_o r_0)},\\ C_n&=A_n\frac{\sigma j}{k_o^2 r_0^2}[-\lambda\sigma j_n(k_i r_0)h_n^{(2)\prime}(k_o r_0)\\ &\quad+h_n^{(2)}(k_o r_0)j_n'(k_i r_0)]^{-1}. \end{aligned} \tag{A5}$$

For a plane wave, $A_n=(-j)^n$. Under the conditions: $k_i r_0 \ll 1$ and $k_o r_0 \ll 1$, we obtain

$$\begin{aligned} B_0&=\frac{jA_0\chi(k_o r_0)^3}{3\lambda\sigma^2}(1-\lambda\sigma^2),\\ B_1&=\frac{-jA_1(1-\lambda)(k_o r_0)^3}{3(1+2\lambda)},\\ C_0&=\frac{A_0\chi}{\lambda},\quad C_1=\frac{3\sigma A_1}{1+2\lambda}. \end{aligned} \tag{A6}$$

Thus the velocities inside and outside the bubble can be calculated. It should be mentioned that the derivation introduced here is for a bubble without any damping. Therefore, $\chi=1/(1-\Omega^2)$. Considering damping, $\chi=1/\sqrt{(1-\Omega^2)^2+\Omega^2\delta^2}$.

APPENDIX B

Equations (19) and (21) belong to the differential equations of $d^2y/dx^2+a(x)(dy/dx)=f(x)$ type provided that x corresponds to r, y corresponds to $u_{2\theta i}$ or $u_{2\theta o}$, and $f(x)$ is given by Eq. (20) or (22). The general solutions of this type of equation can be found as $y=c_1(x)y_1+c_2(x)y_2$, where y_1 and y_2 are solutions of its corresponding homogeneous equation, i.e.,

$$\frac{d^2y}{dx^2}+a(x)\frac{dy}{dx}=\frac{d^2y}{dx^2}+\frac{2}{x}\frac{dy}{dx}=0, \tag{B1}$$

and $c_1(x)$ and $c_2(x)$ can be determined as follows:

$$c_1(x)=\int\frac{-f(x)y_2}{q}dx,\quad c_2(x)=\int\frac{f(x)y_1}{q}dx, \tag{B2}$$

where

$$q=y_1\frac{dy_2}{dx}-y_2\frac{dy_1}{dx}.$$

Noting that $y_1=1$ and $y_2=1/x$ are solutions for Eq. (B1), thus, $q=-1/x^2$. Therefore, $c_1(x)$ and $c_2(x)$ can be calculated. After satisfying the boundary conditions of Eq. (23), the final results can be obtained as described by Eqs. (25) and (26).

[1] *Ultrasound, Its Chemical, Physical, and Biological Effects*, edited by K. S. Suslick (VCH, Verlagsgesellschaft, Berlin, 1988).

[2] S. M. Mitragotri, D. Blankschtein, and R. Langer, Science **269**, 850–853 (1995).

[3] W. L. Nyborg, ''Acoustic Streaming,'' in *Physical Acoustics*, edited by W. Mason (Academic, New York, 1965), Vol. IIB, pp. 266–331.

[4] S. A. Elder, J. Kolb, and W. L. Nyborg, J. Acoust. Soc. Am. **26**, 933(A) (1954).

[5] S. A. Elder, J. Acoust. Soc. Am. **31**, 54–64 (1959).

[6] Yu. G. Statnikov, Sov. Phys. Acoust. **13**, 398–399 (1968).
[7] B. J. Davidson and N. Riley, J. Sound Vib. **15**, 217–233 (1971).
[8] R. K. Gould, J. Acoust. Soc. Am. **56**, 1740–1746 (1974).
[9] W. L. Nyborg, J. Acoust. Soc. Am. **96**, 3279 (1994).
[10] W. L. Nyborg, J. Acoust. Soc. Am. **30**, 329–339 (1958).
[11] C. P. Lee and T. G. Wang, ''Outer acoustic streaming,'' J. Acoust. Soc. Am. **88**, 2367–2375 (1990).
[12] J. Lighthill, ''Acoustic Streaming,'' J. Sound Vib. **61**, 391–418 (1978).

A spark-generated bubble model with semi-empirical mass transport

Jeffrey A. Cook, Austin M. Gleeson, and Randy M. Roberts
Department of Physics and Applied Research Laboratories, The University of Texas at Austin, P.O. Box 8029, Austin, Texas 78713-8029

Robert L. Rogers
Applied Research Laboratories, The University of Texas at Austin, P.O. Box 8029, Austin, Texas 78713-8029

(Received 22 November 1994; revised 10 December 1996; accepted 10 December 1996)

This paper describes the time evolution of bubbles generated by underwater electrical discharges. The oscillations of these high-temperature vapor and plasma bubbles generate acoustic signatures similar to the signatures generated by air guns, underwater explosions, and combustible sources. A set of model equations is developed that allows the time evolution of the bubble generated by a spark discharge to be calculated numerically from a given power input. The acoustic signatures produced by the model were compared to previously recorded experimental data, and the model was found to agree over wide ranges of energy and ambient pressure on several characteristic values of the acoustic signatures. The bubble period in particular matched very well between model and experiment, indicating that the total energy losses predicted by the model over the oscillation of the bubble were approximately correct, although no reliable information was gained about the relative magnitudes of the individual energy loss mechanisms examined. The bubble period and the minimum rarefaction pressure were found to depend on depth, while the peak pressures in the expansion and collapse pulses and the acoustic energy in the expansion pulse were not found to depend on depth over the parameter ranges investigated. [S0001-4966(97)06904-X]

PACS numbers: 43.25.Yw, 43.30.Zk, 43.38.Yn [MAB]

INTRODUCTION

The underwater spark discharge creates a high-pressure plasma/vapor bubble in water, and the expansion and collapse of this bubble generate an acoustic signature similar to the signatures generated by air guns, underwater explosions, and combustible sources.[1–3] These hydrodynamic sources (including the spark discharge) radiate sound by creating a bubble in a body of water. Underwater spark discharges have been used as active sources in such roles as sub-bottom profiling, performing many of the same tasks as the other hydrodynamic sources.[4–7] A set of model equations that describes the time evolution of the bubble generated by a spark discharge is given in this paper. Although this model was developed specifically for spark discharge bubbles, the time evolution of any of the hydrodynamic sources could be investigated using this model with appropriate choices of parameters, as the model is essentially a thermal impulse model.

A very simple diagram of a typical spark discharge system is shown in Fig. 1. A high voltage source is used to charge a capacitor that is isolated from the electrodes. After the capacitor is charged, a switch (ignitron tube) is closed and the voltage appears across the electrode gap underwater. The dielectric in this gap (water) breaks down after a period of time referred to as the breakdown time, and an arc is formed. The measured electrical characteristics (voltage and current) of a typical small discharge are shown in Fig. 2. Photographs in the literature show that plasma fills the bubble in the early stages, then retreats to the center of the bubble as the bubble expands and cools.[8]

I. ACOUSTIC SIGNATURE OF A SPARK-GENERATED BUBBLE

The acoustic signature produced by the electrical discharge shown in Fig. 2 is plotted in Fig. 3, and a modeled bubble radius is overlaid with the acoustic signature. Several parts of the acoustic signature are labeled in Fig. 3. The expansion pulse is a positive pressure pulse radiated as the bubble expands and cools. The radiated acoustic energy in this first pulse was found to be a useful descriptive quantity for spark-generated bubbles. The acoustic energy radiated can be calculated from the pressure signature and the particle velocity.[9] For a spherically spreading wave, the particle velocity is not generally in phase with the pressure. If kr is large, however, the acoustic energy (E_{acoustic}) is given approximately by

$$E_{\text{acoustic}} = \frac{4\pi r^2}{\rho_\infty c_\infty} \int [p(r,t) - p_\infty]^2 dt, \tag{1}$$

where p_∞, ρ_∞, and c_∞ are the ambient pressure, density, and speed of sound, and $p(r,t)$ is the liquid pressure. The rarefaction pulse is the negative overpressure part of the signature radiated while the bubble is large. It is responsible for the low-frequency acoustic radiation from the bubble. The pressure inside the bubble at its maximum radius is small compared to the ambient static pressure and the bubble is

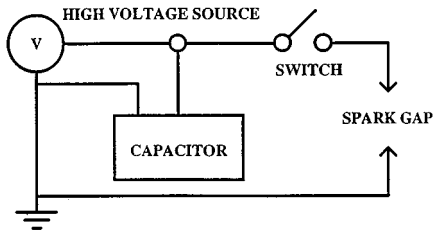

FIG. 1. Typical spark discharge system.

similar to an empty cavity. At a bubble radius (R) given by $R = R_{\max}$, the kinetic energy vanishes, and the potential energy of the cavity is given by

$$E = \tfrac{4}{3}\pi R_{\max}^3 p_\infty . \tag{2}$$

This energy is the total energy for the empty cavity. If the cavity was created by an electrical discharge, the energy delivered by that discharge ($E_{\text{discharge}}$) is related to the energy in the cavity by the hydraulic efficiency (ϵ_{hyd}) of the discharge:[10]

$$\epsilon_{\text{hyd}} = E/E_{\text{discharge}} . \tag{3}$$

The bubble collapses, and the pressure inside the bubble increases until the pressure inside the bubble becomes sufficiently high to arrest the collapse. High-speed photographs show that this process is often very violent and unstable. The positive pressure pulse radiated at this time is referred to as the collapse pulse. Because of the violent nature of the collapse, multiple peaks near the time of the collapse are not unusual in the measured signatures. The time between the collapse pulse and expansion pulse pressure peaks defines the bubble period. This period can be used to estimate the total energy in the bubble. The collapse time (τ_{collapse}) of an empty cavity of radius $R_{\max}$ in an infinite liquid was calculated by Lord Rayleigh as[8,11,12]

$$\tau_{\text{collapse}} = 0.915 R_{\max} (\rho_\infty / p_\infty)^{1/2}. \tag{4}$$

Assuming that for spark-generated bubbles the expansion phase is the mirror image of the collapse phase, the total period of oscillation (τ, the bubble period) is given by

$$\tau = 2 \cdot \tau_{\text{collapse}} = 1.83 R_{\max} (\rho_\infty / p_\infty)^{1/2}. \tag{5}$$

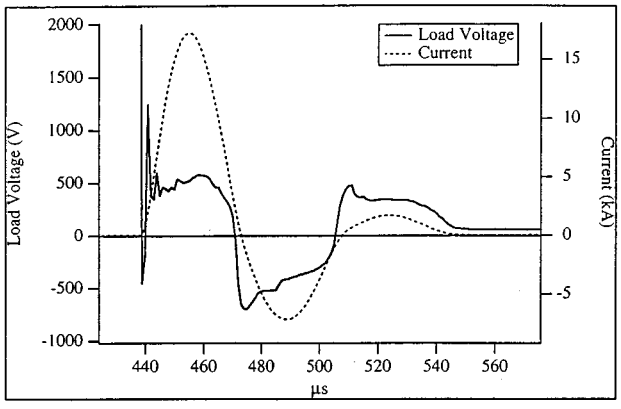

FIG. 2. Typical measured electrical data.

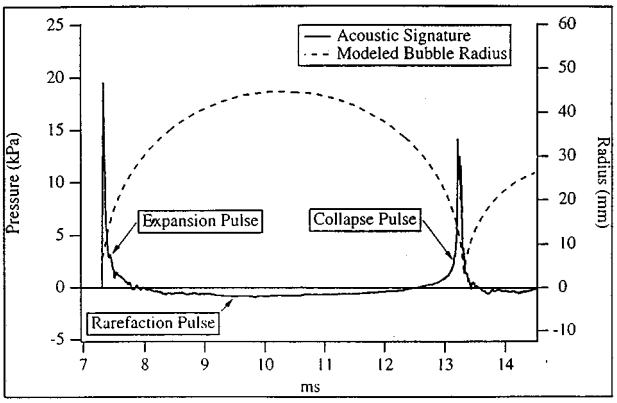

FIG. 3. Typical measured acoustic signature.

This equation for the bubble period can be written in terms of the total energy in the bubble. Using Eqs. (2) and (3), Eq. (5) can be written as

$$\tau = 1.83 \left(\frac{3}{4\pi}\right)^{1/3} \frac{\rho_\infty^{1/2} (\epsilon_{\text{hyd}} E_{\text{discharge}})^{1/3}}{p_\infty^{5/6}}. \tag{6}$$

This expression for the bubble period is useful for gauging the behavior of spark bubbles. Although this expression was derived for an empty cavity, it also approximates the bubble period for a bubble filled with water vapor. A calculation has been done[13] for a gas-filled bubble, and the result is that

$$\tau \cong (1 + P_0 / p_\infty) \cdot \tau_{\text{collapse}} , \tag{7}$$

where P_0 is the initial pressure in the gas and τ_{collapse} is given by Eq. (4). This expression probably overestimates the correction because some of the vapor will condense against the bubble wall. Because the vapor pressure is typically only about 1% of the ambient pressure in the experiments performed, the bubble period shift from this effect is expected to be about 1%. The standard deviation on the bubble periods in the experiments performed was about 3%. In this case, it does not appear that a correction to the bubble period calculated from the Rayleigh calculation is necessary, except that the discharge energy should be multiplied by an efficiency (ϵ_{hyd}) that is dependent on the electrical discharge system. The data taken in previous experiments with spark-generated bubbles tend to confirm this choice,[14,15] although it has been reported[16] that spark-generated bubbles do not obey Eq. (6).

II. MODEL OVERVIEW

A robust model that described the behavior (especially the acoustic signature) of a single isolated spark-generated bubble was desired. For this application, the match between the experimental and model signatures was most important, and an *ab initio* calculation of all aspects of the model was not necessary. Data from previous single spark discharge experiments conducted at Applied Research Laboratories, The University of Texas at Austin (ARL:UT), were available and allowed the development of a comprehensive model. This model describes the large amplitude radial oscillations of an isolated spherical bubble containing water vapor and plasma. The dynamical equations describing the oscillations are second-order nonlinear differential equations, so a closed-

form solution of the equations was not possible. Instead, the equations governing the dynamics of the bubble were numerically integrated, using a published fourth-order Runge–Kutta routine.[17]

The bubbles created by spark discharges share many characteristics with cavitation bubbles, because they are essentially vapor bubbles, without any noncondensable gas inside. Many papers have been published describing the dynamics of single isolated gas bubbles and cavitation bubbles in a compressible liquid. The papers of Herring[18] and Trilling[19] discuss gas bubbles in a compressible liquid, as do those of Gilmore[20] and Flynn.[21] An interesting discussion was published by Lastman and Wentzell,[22] comparing five of the available models. The recent work by Fujikawa and Akamatsu[23] and Shima and Tomita[24] add a number of terms that greatly complicate the equations. The model developed by Keller and Miksis[25] is made more rigorous by Prosperetti[26,27] and Lezzi.[28] The equations developed for this last model are the ones used here in this paper.

It was assumed that the contents of the spark-generated bubble were homogeneous and in thermodynamic equilibrium. It was also assumed that the contents obeyed the ideal gas law, with modifications to allow for changes in the equation of state as the water vapor inside the bubble became dissociated. These modifications were necessary because of the high temperatures reached inside the bubble during the spark discharge.[29–32] These temperatures indicated that thermal radiation might play an important role in the energy transport out of the bubble. The emissivity of the bubble contents was determined approximately by using a frequency-averaged mean-free path inside the bubble. The attenuation properties of water as a function of wavelength were used to determine an approximate radiative transfer from the bubble. Besides providing for a heat loss, electromagnetic radiation deposited near the bubble wall was assumed to bring mass into the bubble. Mass flow from evaporation and condensation is modeled according to the kinetic theory equation for mass flow developed by Schrage[33] in 1953. Indications in the literature[23,34–37] were that the finite rate of condensation and evaporation affects the dynamics of cavitation vapor bubbles, so a nonequilibrium model describing the exchange of mass between the bubble and surrounding liquid was included. One effect not included was the thermal conductivity of heat into the liquid. For transient vapor bubbles such as the ones examined here, thermal conductivity is not generally an important effect.[18,34]

III. BUBBLE DYNAMICS

The equations of bubble dynamics used for the modeling were the set of equations developed by Lezzi and Prosperetti in 1986 and 1987.[27,28] These equations were developed as perturbation solutions of the partial differential equations governing motion in a compressible liquid. This approach was a more rigorous extension of the mathematical formulation proposed and developed by Keller and several others.[2,25,38] The two papers by Lezzi and Prosperetti developed approximate equations of motion for the bubble radius to first and second order in the bubble wall mach number. In their paper, they also gave an interesting discussion regarding the equivalence of the large number of bubble dynamics equation available in the literature. In particular, the equations developed were not unique. Instead, a one-parameter family of equations of motion for the bubble wall was found to exist at first order, and a two-parameter family was found at second order. An important part of developing an equation of bubble dynamics was determining the parameters in these equations. This was accomplished by comparing the solutions of the equations to the numerical results obtained by solving the complete partial differential equations by the method of characteristics. Forms of the first- and second-order equations that agreed most closely with this exact solution were given in the conclusion of the second paper by Lezzi and Prosperetti. The first-order equation given was very similar to the equation given by Keller and Miksis, which was in turn a further development of the equation given by Keller and Kolodner:

$$\left(1-\frac{\dot{R}}{c_\infty}\right)R\ddot{R}+\frac{3}{2}\left(1-\frac{\dot{R}}{3c_\infty}\right)\dot{R}^2 = \left(1+\frac{\dot{R}}{c_\infty}+\frac{R}{c_\infty}\frac{d}{dt}\right)\left(h_B-\frac{p_v(t)}{\rho_\infty}\right). \tag{8}$$

The overdots denote derivatives with respect to time, and h_B is the specific enthalpy at the bubble wall. The term $p_v(\overline{x_i},t)$ was introduced to represent the variable part of the liquid pressure at the center of the bubble in the absence of the bubble, and this term vanishes for an isolated bubble. This first-order equation was determined by Lezzi and Prosperetti to be valid up to bubble wall Mach numbers of about 0.5. Unless the Mach number exceeds this value, or the pressure inside the bubble exceeds about 5000 times the undisturbed value in the liquid, it should give good results. This equation is written explicitly in terms of the specific enthalpy (h), which is defined as[20]

$$h=\int_{p_\infty}^{p}\frac{dp}{\rho}. \tag{9}$$

This expression actually gives the enthalpy difference between the liquid at pressure p and the liquid at pressure p_∞, and is consistent with an assumption of isentropic motion in the liquid.[26] The sound speed is then defined as

$$\frac{dp}{d\rho}=c^2. \tag{10}$$

With this definition and the one given for the liquid enthalpy, a Taylor series expansion of the liquid enthalpy around ρ_∞ and c_∞ can be performed:

$$\begin{aligned} h&=\int_{p_\infty}^{p}\frac{dp}{\rho}\\ &=\int_{p_\infty}^{p}\frac{dp}{\rho_\infty}\left(1-\frac{p-p_\infty}{\rho_\infty c_\infty^2}+\cdots\right)\\ &=\frac{p-p_\infty}{\rho_\infty}-\frac{1}{2c_\infty^2}\left(\frac{p-p_\infty}{\rho_\infty}\right)^2+\cdots. \end{aligned} \tag{11}$$

This equation is integrated simultaneously with the equations describing the interior of the bubble (derived in the next section) to find the time evolution of the bubble radius and the bubble wall velocity.

The liquid equation of state is taken to be a pressure–density relationship of the modified Tait form[39]

$$\frac{p+B}{p_\infty+B}=\left(\frac{\rho}{\rho_\infty}\right)^n, \quad n=7.15, \quad B=304.913 \text{ MPa}. \tag{12}$$

From the previous equation for sound speed [Eq. (10)] and this equation of state

$$c^2=\frac{n(p+B)}{\rho}=c_\infty^2+(n-1)h, \tag{13}$$

where the sound speed in the undisturbed liquid (c_∞^2) can now be given by

$$c_\infty^2=\frac{n(p_\infty+B)}{\rho_\infty}. \tag{14}$$

The specific enthalpy in the liquid is given by

$$h=\frac{c^2-c_\infty^2}{n-1}=\frac{c_\infty^2}{n-1}\left[\left(\frac{p+B}{p_\infty+B}\right)^{(n-1)/n}-1\right], \tag{15}$$

and the liquid pressure at the bubble wall is given by

$$p_B(t)=P-(1/R)(2\sigma+4\mu\dot{R}), \tag{16}$$

where the surface tension (σ) and viscosity (μ) terms have been retained. These terms were dropped in the equation of bubble dynamics. This is because the equation of dynamics is dominated by times when either the bubble is large or the pressure is large and these terms are always negligible. In the liquid pressure equation these terms may not be negligible for small bubbles.[26] The specific enthalpy at the bubble wall (h_B) is found by evaluating the specific enthalpy at the bubble wall liquid pressure:

$$h_B=\frac{c_\infty^2}{n-1}\left[\left(\frac{p_B+B}{p_\infty+B}\right)^{(n-1)/n}-1\right]. \tag{17}$$

The equation for the specific enthalpy at the bubble wall can be used to find an expression for $\dot{h}_B$ in terms of the other variables:

$$\dot{h}_B\equiv\frac{d}{dt}h_B=\frac{\dot{p}_B}{p_B+B}\left[\frac{n-1}{n}h_B+\frac{c_\infty^2}{n}\right]. \tag{18}$$

The expression for $\dot{p}_B$ is found by taking the time derivative of Eq. (16):

$$\dot{p}_B=\dot{P}-\frac{4\mu}{R}\ddot{R}+\frac{\dot{R}}{R^2}(2\sigma+4\mu\dot{R}). \tag{19}$$

The dynamical equations were examined to determine what modifications might be made to the movement of the bubble wall as a result of the movement of the bubble boundary due to mass flow. A comparison of the terms in these equations was made to determine whether or not the additional complications in the dynamical equations were warranted for the regimes examined. It was determined that the additional terms due to mass flow were of lower magnitude than the errors in the estimates that were made in other parts of the model, and they were neglected. These terms were included in a bubble collapse study performed by Fujikawa and Akamatsu.[23]

IV. THERMAL RADIATION

The radiation from low-pressure gas discharges generally consists of spectral lines from atomic electronic transitions, bremsstrahlung, and continuous recombination radiation. As the pressure increases, the spectral lines broaden and the portion of the radiation due to recombination increases so that the radiation becomes continuous. Based on the experimental evidence,[29,30] the spark-generated bubble might be expected to radiate with the spectra distribution of a blackbody, if the internal pressure is greater than about 20 MPa. If a thermal distribution is to be established, the contents of the bubble must be in equilibrium, and the photon mean free path must be small compared to the size of the bubble.

If the bubble is assumed to radiate as a homogeneous spherical radiator, then the thermal radiation from the bubble (F_T) is given as a function of temperature (T), bubble radius (R), and emissivity (ϵ) by the Stefan–Boltzmann law in terms of the spectral flux [$\Phi(\lambda,T)$], where λ is the wavelength, and $\sigma_{\rm BB}$ is the Stefan–Boltzmann constant:[40]

$$F_T=4\pi R^2\epsilon f_{\rm BB}, \tag{20}$$

$$f(T)\equiv\int_0^\infty\Phi(\lambda,T)d\lambda=\sigma_{\rm BB}T^4, \tag{21}$$

$$f_{\rm BB}=f(T)-f(T_\infty)=\sigma_{\rm BB}(T^4-T_\infty^4), \tag{22}$$

$$\epsilon^{-1}=\epsilon_{\rm water}^{-1}+\epsilon_{\rm sphere}^{-1}-1, \quad \overline{\epsilon_{\rm water}}\cong 0.65. \tag{23}$$

In this equation, the factors $\epsilon_{\rm water}$ and $\epsilon_{\rm sphere}$ are the emissivities of the water and the spherical bubble, while ϵ is the total emissivity, $f_{\rm BB}$ is the specific blackbody radiation, and T_∞ is the ambient temperature in the undisturbed liquid. The absorption (and therefore the emissivity) has been calculated[41] for a spherical radiator of radius R and is given as

$$\epsilon_{\rm sphere}=1-\frac{1}{2}\left(\frac{l(\nu)}{R}\right)^2\left[1-\left(1+\frac{2R}{l(\nu)}\right)\exp\left(\frac{-2R}{l(\nu)}\right)\right], \tag{24}$$

where $l(\nu)$ is the frequency-dependent photon mean free path, and R is the radius of the sphere. Using the emissivity in this form requires an integration over frequency at each time step. Instead of performing this integration, the frequency-dependent photon mean free path was replaced by a frequency-averaged mean free path. A frequency-dependent weighting was chosen to calculate the average mean free path. An analysis was performed on the output from the model before the thermal radiation part of the model was implemented to determine what effects the radiation might have in the model, and what portions of the acoustic signature it might affect. Equations are available in the literature to calculate the mean free path as a function of the thermodynamic variables in the bubble. When the mean free path is very small compared to the size of the bubble, the bubble is considered optically thick, and when the mean

free path is very large compared to the size of the bubble, the bubble is considered optically thin.[42] An inspection of the mean-free path at several points in the bubble evolution indicated that it varied over several orders of magnitude. The bubble was found to be optically thick when the bubble radius was small and the temperature high. Because of the strong temperature dependence in the Stefan–Boltzmann law, almost all of the thermal radiation is radiated at these same times. The restrictions outlined above also require an optically thick body for the assumption of a blackbody radiation spectrum to be valid. This preliminary analysis indicated that a frequency weighting assuming an optically thick body would be appropriate. The Rosseland weighting assumes an optically thick body, and gives the following average photon mean free path (l_R):

$$l_R = C\frac{T^2 m_w}{\rho}\exp\left(\frac{I}{k_B T}\right), \tag{25}$$

$$m_w = 3\times 10^{-26}\ \text{kg}, \quad C = 9\times 10^{10}\ (\text{m °K})^{-2}, \tag{26}$$

$$I = 13.6\ \text{eV}, \quad k_B = 1.380\,66\times 10^{-23}\ \text{J/°K}, \tag{27}$$

where m_w is the mass of a water molecule, I is the first ionization energy of each of the atomic species, C is a constant, and k_B is Boltzmann's constant. The emissivity of a spherical radiator is then given approximately by

$$\epsilon_{\text{sphere}} \approx 1 - \frac{1}{2}\left(\frac{l_R}{R}\right)^2\left[1-\left(1+2\frac{R}{l_R}\right)\exp\left(\frac{-2R}{l_R}\right)\right]. \tag{28}$$

V. MASS FLOW

The mass flow into the bubble is composed of two portions, which are assumed to operate independently and simultaneously. There is a mass influx from the heating of the water outside the bubble wall by the absorption of the thermal radiation ($\dot{m}_T$), and there is a mass exchange from molecules of water vapor colliding with the bubble wall and condensing ($\dot{m}_C$). The total specific mass flow ($\dot{m}$) is the sum of these two mass flows:

$$\dot{m} = \dot{m}_T + \dot{m}_C. \tag{29}$$

It is related to the total mass flow ($\dot{M}$) by the relation:

$$\dot{M} = 4\pi R^2 \dot{m}. \tag{30}$$

It is assumed that thermal radiation will bring mass into the bubble by depositing a portion of the total radiated power near the bubble wall. This radiation will heat the surrounding water, changing it to water vapor that will find its way into the bubble. This vapor is assumed to come into the bubble at the evaporation temperature. The amount of mass brought into the bubble depends on how much heat is deposited in the water near the bubble. Energy deposited far from the bubble will probably not contribute significantly to bringing mass into the bubble. To capture this feature, a fixed dissipation length was chosen for the radiation. Energy deposited beyond a given dissipation length was assumed lost to the surrounding water by the bubble contents in the energy balance equations. The proportion of the radiation dissipated is a complicated function (Π) of the layer thickness (x) and bubble temperature (T). An exact determination of $\Pi(x,T)$ requires a consideration of the absorption coefficient, which varies over many orders of magnitude over the frequency range of interest.[43] Rather than trying to determine the exact proportion of the radiation dissipated, an approximate method was used to compile a table from which estimated values of this function could be interpolated. The table was constructed for temperatures (T) ranging from 100 to 100 000 °K, and for dissipation lengths (x) ranging from 1 to 100 000 Å. The details of the method are described elsewhere,[44] and the results for $\Pi(x,T)$ are shown in Fig. 4. Experimental work performed by Robinson[32] indicated that about 30% of the radiation would be trapped near the surface of the bubble, based on the portion of the radiation in the ultraviolet band.

The mass flow into the bubble as a result of thermal radiation is determined by assuming that the radiation heats water through the phase transition to water vapor, requiring a total specific energy

$$E_{\text{Thermal}} = c_{pw}(T_E - T_\infty) + L, \tag{31}$$

where c_{pw} is the specific heat capacity for water, T_E is the evaporation temperature, T_∞ is the ambient temperature, and L is the mean heat of evaporation. Because the absorption and emissivity of the water vapor is very low when the vapor is cold, it is unlikely that the radiation contributes strongly to heating the vapor. The expression for the specific mass flow from evaporation by heating via thermal radiation is then given as

$$\dot{m}_T = \frac{\Pi(x,T)\epsilon f_{\text{BB}}}{E_{\text{Thermal}}}, \tag{32}$$

where the emissivity (ϵ) and specific blackbody radiation (f_{BB}) are as defined in Sec. IV. The evaporation temperature, T_E, is calculated from the following:

$$T_E = \frac{L}{g(\alpha).\mathscr{R}\ln(p_0/p_\infty)}, \tag{33}$$

where $g(\alpha)$ is a function describing the effects of dissociation, and is described more fully in Sec. VI. $\mathscr{R}$ is the ratio of specific heats, p_0 is a constant associated with the equilibrium vapor pressure, and p_∞ is the ambient liquid pressure. The factor $\Pi(x,T)$ given in Eq. (32) gives the percentage of the total power radiated that brings mass into the bubble. The rest of the radiation is presumed to be radiated far away from the bubble. The heat loss from the bubble as a result of thermal radiation (q_T) is therefore

$$q_T = (1-\Pi)\epsilon f_{\text{BB}}. \tag{34}$$

The portion of the thermal radiation that brings mass back into the bubble is not actually lost, since the mass that comes into the bubble has been heated from the ambient temperature up through the phase change. The energy required for this heating is returned to the bubble when the mass enters the bubble.

The specific mass flow as a result of condensation is given by the kinetic theory equation for mass flow:[33]

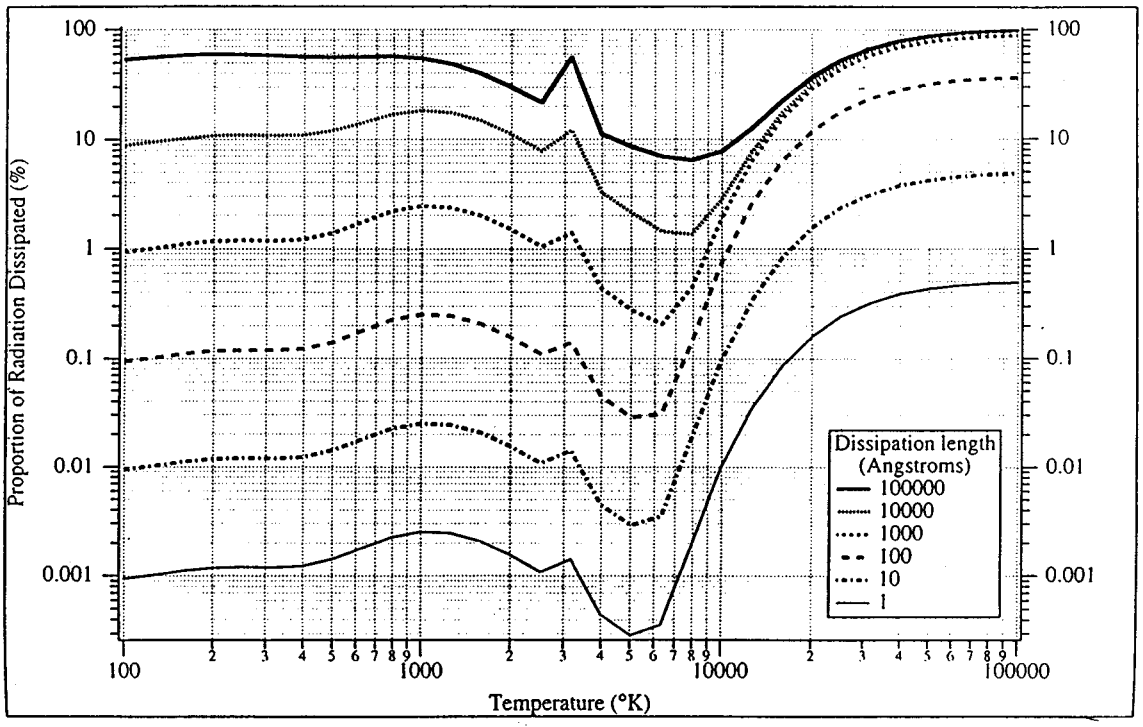

FIG. 4. Proportion of radiation dissipated.

$$\dot{m}_C = \frac{\alpha_M}{\sqrt{2\pi\mathscr{R}}}\left[\frac{p^*}{\sqrt{T_\infty}} - \Gamma\frac{P}{\sqrt{T}}\right]. \tag{35}$$

The equilibrium vapor pressure (p^*) is calculated from

$$p^* = p_0 \exp\left(\frac{-L}{\mathscr{R}T_\infty}\right). \tag{36}$$

The accommodation coefficient (α_M) will be discussed in Sec. VI. It can take on values ranging from zero to unity.

Γ is a correction factor which compensates for the net mass flow toward or away from the phase change interface, when the departure from equilibrium is assumed small. It describes the deviation of the velocity distribution from a Maxwellian distribution, and is equal to unity for equilibrium conditions. Equation (35) accounts for both evaporation and condensation, but the simulations indicate that for spark-generated bubbles condensation dominates over evaporation because of the high pressures, and the mass flow is predominantly out of the bubble. It reaches its most negative values when the bubble is small and pressures are high. This is also when the incoming mass flow from thermal radiation reaches its largest values, and it offsets much of the mass flow due to condensation. The mass flow from thermal radiation therefore negates much of the mass migration toward the boundary, and Γ was fixed at a value of unity in this study.

These expressions were developed for conditions near equilibrium, and the conditions in the bubble created by the spark discharge should be examined to determine if these equations will be strictly applicable. The contents of a vapor or gas bubble are generally considered to be in equilibrium if the bubble wall velocity is less than the speed of sound in the gas.[23] This corresponds to a bubble wall Mach number of about 0.3, assuming internal temperatures on the order of the ambient temperature. In fact, the internal temperatures are somewhat higher, which leads to a higher speed of sound in the gas. The bubble also contains some plasma, at least in the early stages of the bubble expansion. An analysis by Naugol'nykh and Roi[8] indicates that the bubble contents are very likely to be in equilibrium for this regime also. This study has assumed that the bubble contents are in equilibrium, and these two referenced works tend to support that assumption.

The bubble contents are assumed to supply the heat to bring water from the ambient temperature through the phase transition and up to the temperature of the bubble. The heat removed from the bubble to heat this incoming mass serves to quench the high temperatures inside the bubble. The heat flow required for the total mass flow quench (q_M) is given by the sum of two terms, one that describes the heating of the incoming water up through the phase change at the evaporation temperature (q_{Evap}), and one that describes the heating of the incoming vapor at constant pressure up to the temperature of the internal contents of the bubble (q_p):

$$q_M = q_{\text{Evap}} + q_p\,. \tag{37}$$

This first term (q_{Evap}) is given by the product of the mass flow into the bubble ($\dot{m}_{\text{in}}$), and the specific thermal energy (E_{Thermal}), defined in Eq. (31):

$$q_{\text{Evap}} = \dot{m}_{\text{in}} E_{\text{Thermal}},$$

$$\dot{m}_{\text{in}} = \dot{m}_T + \dot{m}_C \Theta(\dot{m}_C), \tag{38}$$

$$\Theta(\dot{m}_C) \equiv \begin{cases} 1, & \dot{m}_C \geqslant 0, \\ 0, & \dot{m}_C < 0. \end{cases}$$

Here Θ is a unit step function utilized because heat is removed from the bubble when mass comes into the bubble, but is not added to the bubble when mass condenses on the bubble wall. This is because the heat in each case will flow to the coolest reservoir. The current model assumes that the thermal conductivity of the water is sufficiently large that the temperature does not increase near the bubble wall as a result of the condensation. In fact, the amount of mass flow out of the bubble predicted by the model indicates that this may be a poor approximation, and the temperature near the bubble wall probably does increase somewhat. The added heat would bring mass back into the bubble, either directly, as thermal radiation does, or through a modification to the equilibrium pressure and the liquid temperature in the mass flow equation. These assumptions should be considered when the results are compared to the experimental data available. The quench due to the heating and phase change of the water is given by

$$q_{\text{Evap}}=(\dot{m}_{\text{BB}}+\dot{m}_E\Theta(\dot{m}_E))\cdot E_{\text{Thermal}}. \tag{39}$$

The quench due to the heating of the vapor is given by

$$q_p=(\dot{m}_{\text{BB}}+\dot{m}_E\Theta(\dot{m}_E))\int_{T_E}^{T} c_p(T')dT'. \tag{40}$$

The specific heat capacity (c_p) written in Eq. (40) is generally a function of temperature.

VI. CONSERVATION OF ENERGY

The contents of the spark-generated bubble have been assumed to be described by the pressure (P) and temperature (T). The goal of this section is to develop equations for $\dot{P}$ and $\dot{T}$ that will be integrated simultaneously with the equation of bubble dynamics. To understand the relation between pressure, temperature, mass flow, and heat flow, some simplifying assumptions will be made for the internal contents of the bubble. These assumptions are the following:

(1) The pressure and temperature inside the bubble are uniform.
(2) The bubble contents obey some form of the ideal gas law.
(3) The bubble is filled with water vapor only, which may be dissociated.
(4) A single average $\alpha(P,T)$ gives the degree of dissociation.

The function $\alpha(P,T)$ will range from 0 (no dissociation) to 1 (full dissociation), and the number of molecules from a single water molecule will range from 1 to 3. The ideal gas law for water vapor then takes the form

$$PV=Mg\mathscr{R}T, \quad g(\alpha)=1+2\alpha. \tag{41}$$

This bulk-properties form of the ideal gas law, in terms of the gas pressure (P), volume (V), mass (M), and temperature (T), describes the varying constituents of the bubble, but still assumes the particles inside the bubble do not interact. The function $g(\alpha)$ describes the number of molecules in the bubble per original water molecule, and serves here to account for the increase in pressure associated with dissociation. The energy of an ideal gas (U), allowing dissociation but neglecting ionization, is given by[8,45]

$$U=M\mathscr{R}\left[3T\left(1+\frac{\alpha}{2}\right)+\alpha\frac{L_{\text{dis}}}{\mathscr{R}}\right], \tag{42}$$

where L_{dis} is the mean heat of dissociation. It is obvious from the above that $U=U(M,T,\alpha)$, but the independent variables in this equation can also be chosen so that $U=U(T,V,M)$. Both of these formulations are useful here. The time derivative of this latter form of the ideal gas energy gives an energy balance equation:

$$\dot{U}=\left(\frac{\partial U}{\partial T}\right)_{V,M}\dot{T}+\left(\frac{\partial U}{\partial V}\right)_{T,M}\dot{V}+\left(\frac{\partial U}{\partial M}\right)_{T,V}\dot{M}. \tag{43}$$

Using the formulation of $U=U(M,T,\alpha)$ given above [Eq. (42)], expressions can be found for each of these differentials. Taking the time derivative of Eq. (42),

$$\dot{U}=\left(\frac{\partial U}{\partial T}\right)_{\alpha,M}\dot{T}+\left(\frac{\partial U}{\partial \alpha}\right)_{T,M}\dot{\alpha}+\left(\frac{\partial U}{\partial M}\right)_{T,\alpha}\dot{M}. \tag{44}$$

Given $\alpha=\alpha(P,T)$,

$$\dot{\alpha}=\left(\frac{\partial \alpha}{\partial P}\right)_{T}\dot{P}+\left(\frac{\partial \alpha}{\partial T}\right)_{P}\dot{T}. \tag{45}$$

Taking the time derivative of the ideal gas law,

$$\dot{P}=\frac{P}{g}\frac{\partial g}{\partial \alpha}\dot{\alpha}+P\left[\frac{\dot{T}}{T}+\frac{\dot{M}}{M}-\frac{\dot{V}}{V}\right]. \tag{46}$$

Equations (45) and (46) can be used to find an explicit expression for $\dot{\alpha}$:

$$\dot{\alpha}=\eta\left\{\left(\frac{\partial \alpha}{\partial P}\right)_{T}\left[\frac{P}{T}\dot{T}+\frac{g\mathscr{R}T}{V}\dot{M}-\frac{P}{V}\dot{V}\right]\dot{P}+\left(\frac{\partial \alpha}{\partial T}\right)_{P}\dot{T}\right\}, \tag{47}$$

$$\eta=\left[1-\frac{P}{g}\frac{\partial g}{\partial \alpha}\left(\frac{\partial \alpha}{\partial P}\right)_{T}\right]^{-1}. \tag{48}$$

The function η is introduced to make Eq. (47) more tractable. Substituting Eqs. (46) and (47) into Eq. (44), collecting like terms, and using Eq. (43) to identify the differentials:

$$\left(\frac{\partial U}{\partial T}\right)_{V,M}\equiv C_v=Mc_v$$
$$=\left(\frac{\partial U}{\partial T}\right)_{\alpha,M}+\left(\frac{\partial U}{\partial \alpha}\right)_{T,M}\eta\left[\left(\frac{\partial \alpha}{\partial P}\right)_{T}\frac{P}{T}+\left(\frac{\partial \alpha}{\partial T}\right)_{P}\right], \tag{49}$$

$$\left(\frac{\partial U}{\partial V}\right)_{T,M}=-\frac{P\eta}{V}\left(\frac{\partial U}{\partial \alpha}\right)_{T,M}\left(\frac{\partial \alpha}{\partial P}\right)_{T}, \tag{50}$$

$$\left(\frac{\partial U}{\partial M}\right)_{T,V}=\left(\frac{\partial U}{\partial M}\right)_{T,\alpha}+\frac{g\mathscr{R}T\eta}{V}\left(\frac{\partial U}{\partial \alpha}\right)_{T,M}\left(\frac{\partial \alpha}{\partial P}\right)_{T}. \tag{51}$$

The first law of thermodynamics for an open system gives another expression for the energy balance that describes the heat flow:

$$\dot{U}=\left(\frac{\Omega U}{\partial M}\right)_{T,V}\dot{M}-\dot{W}+Q. \tag{52}$$

The mechanical power ($\dot{W}$) is given by

$$\dot{W}=P\dot{V}. \tag{53}$$

The heat added to the spark-generated bubble system will be assumed to take the following form:

$$Q=4\pi R^2 q=4\pi R^2(\Omega-q_{\mathrm{BB}}-q_M). \tag{54}$$

The function Ω is the external delivered power per unit area, and will be discussed more in Sec. VII. The terms q_{BB} and q_M were defined in Eqs. (34) and (37). From Eqs. (43) and (52), an expression for the conservation of energy can be written:

$$Mc_v\dot{T}+\left(\frac{\partial U}{\partial V}\right)_{T,M}\dot{V}=Q-P\dot{V}. \tag{55}$$

This equation may be solved for $\dot{T}$, with c_v given by Eq. (49):

$$\dot{T}=\left[Q-\left(\left(\frac{\partial U}{\partial V}\right)_{T,M}+P\right)\dot{V}\right]\frac{g\mathscr{R}T}{c_v PV}. \tag{56}$$

We may use Eqs. (46) and (47) to determine the equation for $\dot{P}$:

$$\dot{P}=\eta P\left[\left(\frac{\partial g}{\partial\alpha}\frac{1}{g}\left(\frac{\partial\alpha}{\partial T}\right)_P+\frac{1}{T}\right)\dot{T}+\frac{g\mathscr{R}T}{PV}\dot{M}-\frac{1}{V}\dot{V}\right]. \tag{57}$$

With the volume and its derivatives written in terms of the radius, these equations take the final form:

$$\dot{T}=\frac{3g\mathscr{R}T}{c_v PR}\left[q-\dot{R}\left(\left(\frac{\partial U}{\partial V}\right)_{T,M}+P\right)\right], \tag{58}$$

$$\dot{P}=\eta P\left[\left(\frac{\partial g}{\partial\alpha}\frac{1}{g}\left(\frac{\partial\alpha}{\partial T}\right)_P+\frac{1}{T}\right)\dot{T}+\frac{3g\mathscr{R}T}{PR}\dot{m}_T-\frac{3\dot{R}}{R}\right]. \tag{59}$$

These equations are the ones which are integrated simultaneously with the equation of bubble dynamics to give the time evolution of the spark-generated bubble.

Values for α and the specific heat at constant pressure have been calculated numerically for the water vapor system over wide ranges of pressure and temperature, and the results were used to fit the following empirical functions to the calculated values:[41]

$$\alpha=\frac{1}{2}\left[\tanh\left(\frac{T-T_0}{\tau}-\chi\right)+1\right], \tag{60}$$

$$\overline{c_p(T)}=\frac{1}{T-T_0}\int_{T_0}^{T}c_p(T')dT'$$

$$=c_{p,0}+\left(c_{p,1}-c_{p,0}+\frac{L_{\mathrm{dis}}}{T-T_0}\right)\alpha(P,T), \tag{61}$$

$$\tau=\tau_0(P/\mathrm{Pa})^{\tau_2}+\tau_1\ \ ^\circ\mathrm{K},\quad \chi=\chi_0\ \ln(P/\mathrm{Pa})+\chi_1. \tag{62}$$

See Table I for the constants used in these equations and throughout this paper. These functions are shown in Figs. 5 and 6 over typical ranges of pressure and temperature. Equation (61) for the average specific heat is then used in Eq. (40). With the form given for the dissociation [Eq. (60)], expressions for the necessary differentials can be found:

TABLE I. Constants.

$T_0=100\ \ ^\circ\mathrm{K}$	$\mathscr{R}=461.522\ \mathrm{J/kg}\ ^\circ\mathrm{K}$	$L_{\mathrm{dis}}=50\,950\,000\ \mathrm{J/kg}$
$\tau_0=12.2384\ ^\circ\mathrm{K/Pa}$	$\tau_1=261.336\ ^\circ\mathrm{K}$	$\tau_2=0.253\,283$
$\chi_0=-0.507\,92$	$\chi_1=13.017$	$p_0\equiv 4.8\cdot 10^{10}\ \mathrm{Pa}$
$c_{p,0}=1846.10\ \mathrm{J/kg}\ ^\circ\mathrm{K}$	$c_{p,1}=3461.43\ \mathrm{J/kg}\ ^\circ\mathrm{K}$	

$$\left(\frac{\partial\alpha}{\partial T}\right)_P=\frac{1}{2\tau}\mathrm{sech}^2\left(\frac{T-T_0}{\tau}-\chi\right), \tag{63}$$

$$\left(\frac{\partial\alpha}{\partial P}\right)_T=\frac{-1}{2P}\left[(T-T_0)(\tau-\tau_1)\frac{\tau_2}{\tau^2}+\chi_0\right]\times\mathrm{sech}^2\left(\frac{T-T_0}{\tau}-\chi\right), \tag{64}$$

$$\left(\frac{\partial U}{\partial V}\right)_{T,M}=\frac{-\eta P^2}{g}\left(\frac{3}{2}+\frac{L_{\mathrm{dis}}}{T\mathscr{R}}\right)\left(\frac{\partial\alpha}{\partial P}\right)_T, \tag{65}$$

$$c_v=\mathscr{R}\left[\frac{3}{2}\alpha+3+\eta\left(\frac{3}{2}+\frac{L_{\mathrm{dis}}}{T\mathscr{R}}\right)\left[P\left(\frac{\partial\alpha}{\partial P}\right)_T+T\left(\frac{\partial\alpha}{\partial T}\right)_P\right]\right]. \tag{66}$$

VII. DISCHARGE PARAMETERS

Some parameters are needed to describe the energy and power delivered during the discharge. The energy delivered by the spark discharge was previously identified in Sec. I as $E_{\mathrm{discharge}}$. The power delivery as a function of time is determined by the circuit and the water/vapor environment of the developing bubble. A detailed study of the evolution of this complex system is beyond the scope of this paper. Instead, the actual power delivery curves will be approximated by functions that match the observed power delivery characteristics. The discharges in the sea tests[14] were nearly critically damped, and were approximated by the following function $\Omega(t)$, first introduced in Eq. (54), with $k=0.6$:

$$4\pi R^2\Omega(t)=P_0(1-kt_*^2)\sin(\pi t_*). \tag{67}$$

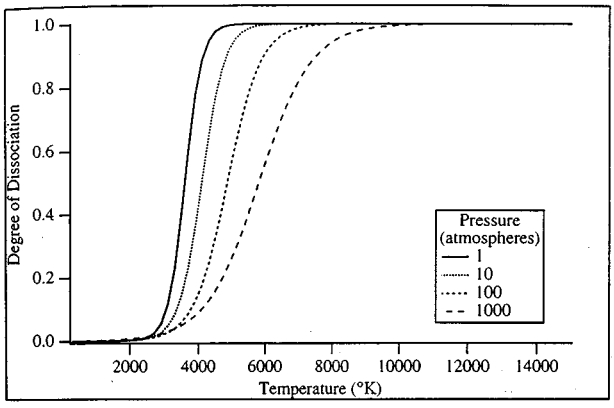

FIG. 5. Degree of dissociation.

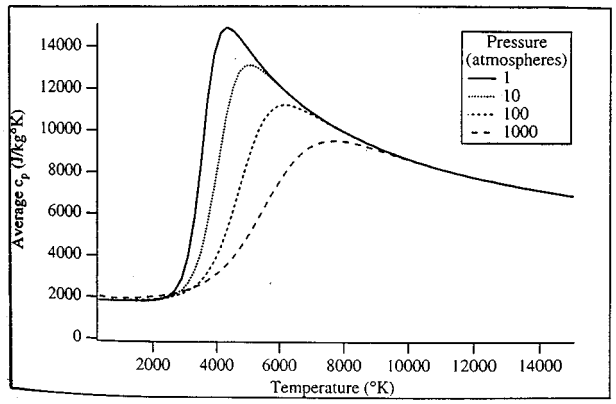

FIG. 6. Average constant pressure specific heat capacity.

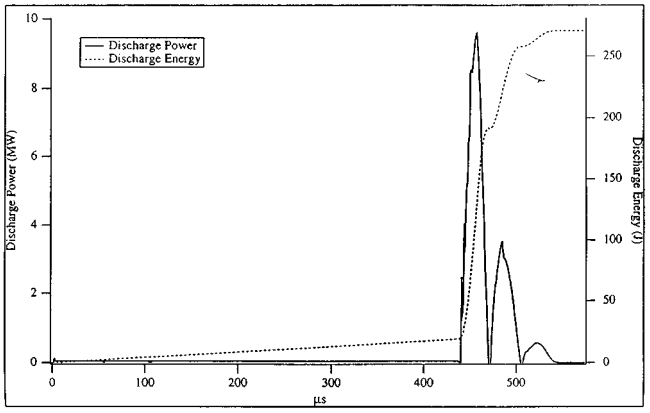

FIG. 7. Typical discharge power and energy.

The function t_* is the nondimensional discharge time:

$$t_* = \frac{t - t_{\text{breakdown}}}{\tau_{\text{discharge}}}. \tag{68}$$

A finite period of time will pass before the gap ''breaks down'' and the main discharge begins. This time is referred to as the breakdown time ($t_{\text{breakdown}}$), and typically ranges from about 50 to 500 ms. The total discharge time is identified as $\tau_{\text{discharge}}$.

The constant P_0 in Eq. (67) is approximately the power amplitude, and is used as a fitting parameter for the discharge. Integration of Eq. (67) yields the following expression for the total energy delivered during the discharge:

$$\begin{aligned} E_{\text{discharge}} &= \int_0^1 4\pi R^2 \Omega(t)\, dt_* \\ &= \frac{4k + (2-k)\pi^2}{\pi^3} \tau_{\text{discharge}} P_0 \\ &\approx 0.523 \tau_{\text{discharge}} P_0. \end{aligned} \tag{69}$$

VIII. INITIAL CONDITIONS

Initial conditions had to be chosen for the variables to be integrated in the model equations. Logical choices for the initial pressure (P_{init}) and temperature (T_{init}) are the following:

$$P_{\text{init}} = P_\infty, \quad T_{\text{init}} = T_E, \tag{70}$$

where T_E was previously given by Eq. (33). The initial volume is somewhat arbitrary, but some insight as to a reasonable choice can be gained by examining the discharge energy in Fig. 7. It can be seen on the plot of discharge energy that a small portion of the energy is delivered to the cavity before the main discharge actually starts. This ''predischarge'' energy is typically only a small fraction of the total energy delivered to the bubble. Part of this predischarge energy will probably be lost, but part of it may also be responsible for initiating a small cavity. Even if a cavity is not actually create by this portion of the discharge, the liquid in the vicinity of the electrodes may be ''prepared'' for the main discharge. Regardless of the physical mechanism, a reasonable choice for the initial conditions is that the initial potential energy of the cavity is proportional to this predischarge energy. Further examination of the energy delivery characteristics of a number of shots over a range of energy shows that the fraction of the total energy delivered in this predischarge stage is roughly constant. This would mean that the initial potential energy of the cavity might then be proportional to the discharge energy:

$$P_{\text{init}} V_{\text{init}} = \eta_{\text{init}} E_{\text{discharge}}. \tag{71}$$

The proportion of the discharge energy in the initial cavity potential energy is given by η_{init}. This choice gives good results in matching the data. Values tested for η_{init} ranged from about 0.05% to 0.3%.

IX. MODEL PARAMETERS

The preceding discussion outlines the model equations that will be integrated to determine the time evolution of spark-generated bubbles. Three fitting parameters were introduced and discussed.

(1) α_M: The accommodation coefficient affects the mass flow resulting from collision and sticking in the model. This parameter describes the condition of the interface. A ''dirty'' interface interferes with mass transfer across the bubble boundary, and will result in a lower coefficient.

(2) x: The dissipation length is used in the radiation model to balance the mass flow as a result of heating from blackbody radiation against the radiation losses. A larger value of x will result in a larger portion of the radiation contributing to the mass flow, while a smaller value allows more radiation to escape from the bubble.

(3) η_{init}: The proportion of the discharge energy in the initial cavity potential energy was discussed in Sec. III immediately preceding this one. It is used in Eq. (71) to determine the initial radius.

Model simulations were conducted using the equations developed for several values of three parameters identified, and the best values found are given below. In determining these parameters, characteristics of the model acoustic signatures were compared to characteristics of the measured acoustic signatures over the full ranges of energy and depth for which data were taken in the referenced paper. Characteristics examined for the purpose of determining the model parameters were the following:

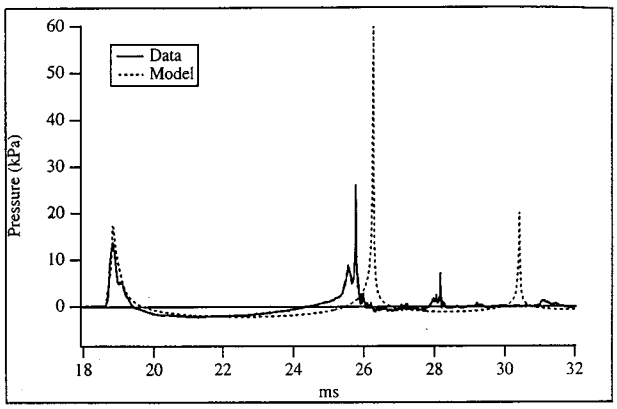

FIG. 8. The 9.5-kJ acoustic signature; depth: 55 m.

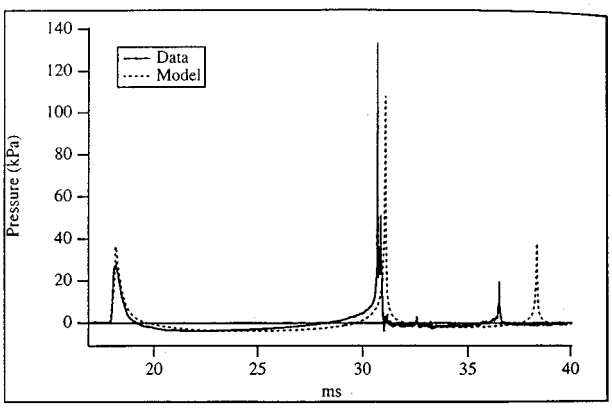

FIG. 10. The 49-kJ acoustic signature; depth: 55 m.

(1) Bubble period:
(2) Radiated acoustic energy in the expansion pulse; and
(3) Minimum rarefaction pressure.

These characteristics were identified in Fig. 3, and were discussed in the Introduction. The complete parameter adjustment procedure has been given previously.[44] The following set of values resulted in a reasonable match between model and experiment:

$$\alpha_M = 0.005, \quad x = 20\ \text{Å}, \quad \eta_{\text{init}} = 0.001. \tag{72}$$

X. RESULTS

The acoustic signatures produced by the model were compared to experimental data previously recorded in the Gulf of Mexico by Rogers in 1990.[14] The energy of the spark discharges ranged from about 4.5 to 68 kJ, and data were taken at electrode depths of 30.5, 55, and 74.5 m, ±1 m. This is the most comprehensive set of data on spark bubbles known to be available over these ranges of energy and depth.

The model equations were integrated for each of the energies and depths at which data were taken. The output signatures were then compared to the data. Several of the experimental acoustic signatures representative of the data are plotted in Figs. 8, 9, 10, and 11, with the model acoustic signatures overlaid. The agreement between the model and experiment is reasonable over the ranges of energy and depth examined, although the experimental acoustic signatures are asymmetric in the negative part of the overpressure, while the model signatures are symmetric. The single bubble signatures recorded in lower-energy tests are symmetric, so it is possible that this asymmetry is an artifact of the measurement method.

A plot of the bubble period as a function of energy and depth is shown in Fig. 12. The dependence of the model on depth and discharge energy is very similar to the dependence in the data. In particular, the hydraulic efficiency did increase slightly with depth, from about 29% at 30.5 m to about 32% at 74.5 m. This efficiency appeared to depend weakly on the discharge parameters. For example, a few of the data points in Fig. 12 were taken at similar energies but with different discharge times (identified in Fig. 12 as open symbols). The simple model Rogers used to examine the data failed to pick up the dependence of the bubble period on discharge time. Unfortunately, this model seems to do little better, despite its matching the bubble period dependence on depth and discharge energy, predicting only about a 1% decrease in the hydraulic efficiency, while the data show a decrease in efficiency of about 3%–7%.

The results found here are not universally accepted. The technical report written by Gibson[16] indicated that the pulsation time of spark-generated bubbles did not obey the energy scaling given by Eq. (6). This study considered spark discharge bubbles in water of varying temperatures, and found that for all temperatures, and especially for water near the

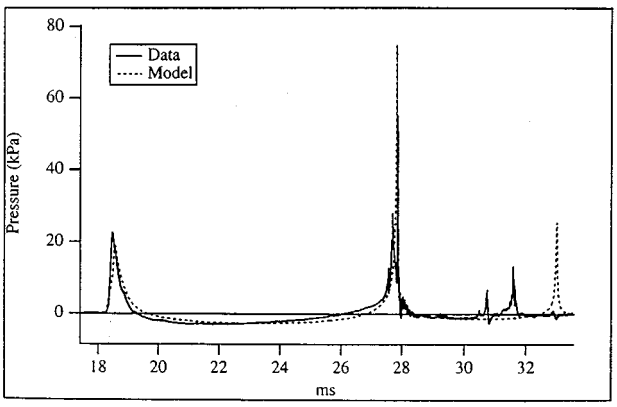

FIG. 9. The 19-kJ acoustic signature; depth: 55 m.

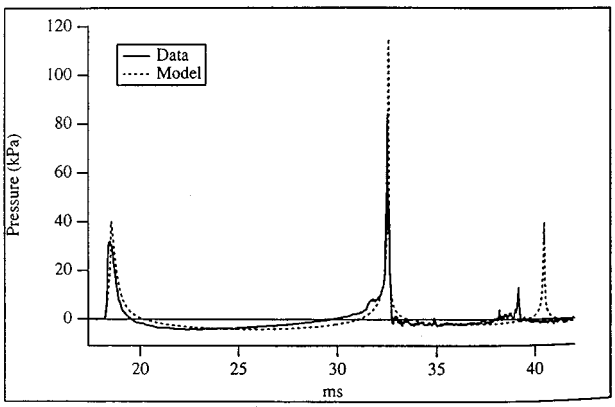

FIG. 11. The 62.5-kJ acoustic signature; depth: 55 m.

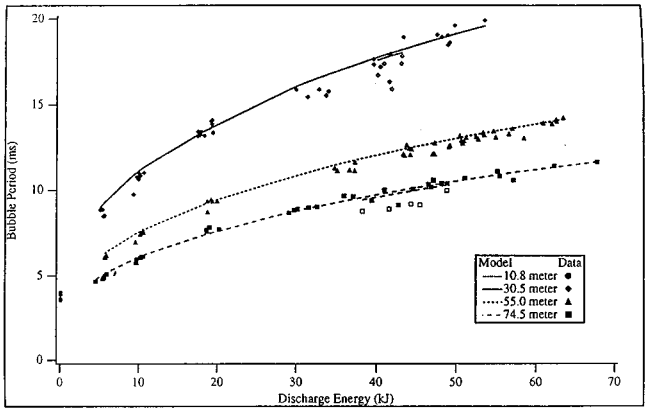

FIG. 12. Bubble period versus energy and depth.

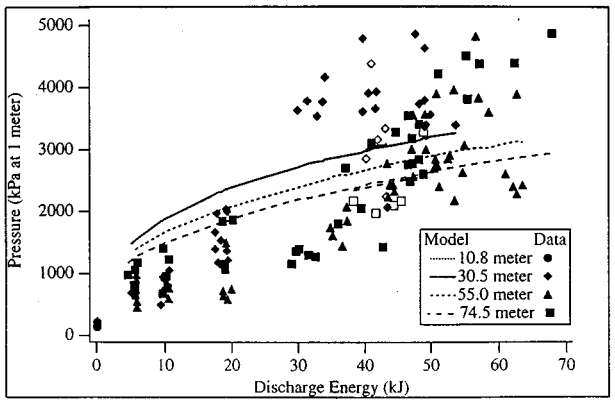

FIG. 14. Peak collapse pulse pressure.

boiling point, the scaling in Eq. (6) predicted a change in the bubble period as a function of energy that was too large. Those studies were based on the energy stored in the capacitor, and made no attempt to find the actual energy delivered to the cavity, but assumed that the energy delivered would be some fraction of the stored energy. Most discharge systems, however, deliver energy most efficiently in a narrow regime of discharge parameters, and the ratio of energy delivered to energy stored is rarely constant over a wide range of energy. The study by Rogers measured the energy delivered to the spark cavity at the discharge, removing any effect of the electrical discharge system on the energy measurements. This technique allows the electrical discharge characteristics and the production of a bubble by a given electrical discharge to be considered independently.

Plots of the peak pressures in the expansion and collapse pulses are shown in Figs. 13 and 14, respectively. The data in these plots are somewhat more stochastic than the bubble periods, and exhibit no strong dependence on depth. The agreement between experiment and model is good for the initial peak, while the agreement is not as good for the collapse peak. A possible explanation for the poorer agreement on the collapse is the more violent nature of the collapse, during which the bubble often breaks apart before reaching the minimum radius. The minimum rarefaction pressure is plotted in Fig. 15. The experimental and model data show a similar dependence on depth, although the values do not match exactly. The acoustic energy in the expansion pulse is plotted in Fig. 16. As with the peak pressures, the acoustic energy does not exhibit a strong depth dependence, and the agreement is good between model and experiment.

Of the characteristics examined above, the bubble period and minimum negative pressure exhibited a measurable depth dependence, while the peak pressures and acoustic energy in the initial peak do not. The explanation for this is that the internal pressures in the bubble at the time of the initial expansion and at the collapse are 100–1000 times the ambient pressure, while the internal pressure at the time of the minimum negative pressure is only about 10% of the ambient pressure. The depth dependence of the bubble period is essentially the dependence predicted by Eq. (6), with the slight increase in the hydraulic efficiency mentioned above.

XI. CONCLUSIONS

The bubble period in particular matched very well between model and experiment, indicating that the total energy losses predicted by the model over the oscillation of the bubble were approximately correct, although no information is gained about the relative magnitudes of the individual energy loss mechanisms examined. The bubble period and the minimum rarefaction pressure are found to depend on depth, while the peak pressures in the expansion and collapse pulses and the acoustic energy in the expansion pulse are not found to depend on depth.

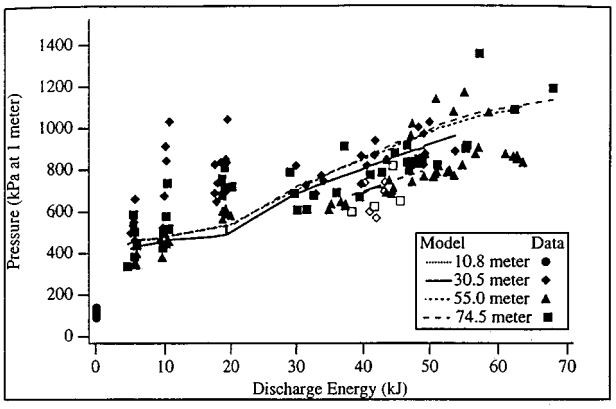

FIG. 13. Peak expansion pulse pressure.

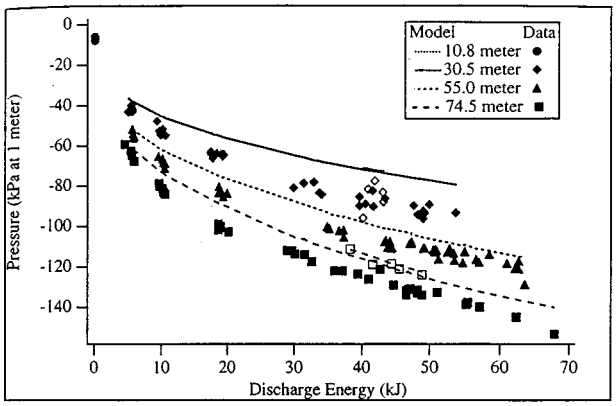

FIG. 15. Minimum rarefaction pressure.

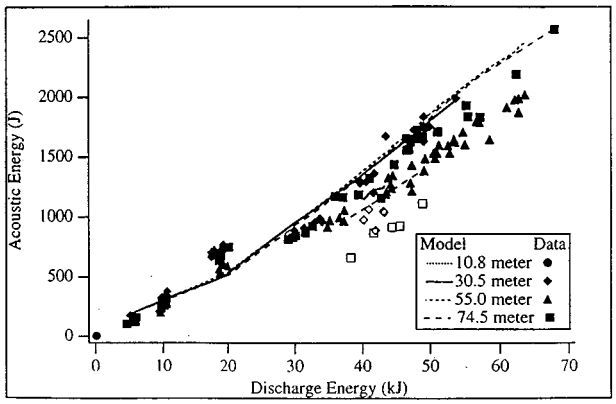

FIG. 16. Acoustic energy in expansion pulse.

The model developed in this paper provides a good description of several important features of spark-generated bubbles. The parameters determined allowed the model to predict the time evolution of the bubbles from a given class of similar discharges. The model did not, however, capture all of the subtleties of the internal dynamics, because it did not correctly calculate the acoustic signatures from the discharges with longer discharge times, despite picking up the shift in hydraulic efficiency with depth. Part of the problem may lie in the use of the parameterized discharges, and the use of sampled data for all of the discharges may have resulted in a better match. Further study is needed to determine how crucial the exact discharge characteristics are for the model. The predictions by the model of the other characteristics of the acoustic signature indicated that the model equations were a reasonable approximation to the gross features of the internal dynamics, and the model was useful in calculating these characteristics from a given discharge. Unfortunately, the ability of the model to significantly enhance the bubble period information available from Eq. (6) is somewhat questionable, because the scaling of the bubble period with energy is given very closely by that equation.

The data presented in this paper support statements characterizing single spark-generated bubbles, and describe the nature of the interaction between multiple elements. The model developed is found to predict for a single spark-generated bubble a time evolution in good agreement with the experimentally measured signatures. The single spark-generated bubbles were found to have a bubble period consistent with accepted laws for cavitation bubbles, when an allowance was made for some energy loss between the electrical discharge energy and the total energy of the bubble. The model failed to capture the subtle differences between discharges of similar energies but different discharge times. Both experimental and model data on the characteristics of the discharge were found to agree with theoretical studies of single spark-generated bubbles in the literature. Predictions by the model of temperatures reached during the discharge were in reasonable agreement with measurements made of the temperatures of bubbles created under similar experimental conditions.

ACKNOWLEDGMENTS

This research was supported primarily by the Office of Naval Research. The authors thank T. A. Griffy for several helpful discussions and contributions and the reviewer for many good comments.

[1] L. Bjorno, ''A comparison between measure pressure waves in water arising from electrical discharges and detonation of small amounts of chemical explosives,'' Trans. ASME, J. Eng. Ind., Paper No. 69-Unt-1, 1-8 (1969).
[2] J. B. Keller and I. I. Kolodner, ''Damping of underwater explosion bubble oscillations,''J. Appl. Phys. **27**, 1152–1161 (1956).
[3] I. Z. Okun', ''Generation of compression waves by a pulsed discharge in water,''Zh. Tekh. Fiz. **41**, 292–301 (1971) [English transl: Sov. Phys. Tech. Phys. **16**, 219–226 (1971)].
[4] W. C. Beckmann, A. C. Roberts, and B. Luskin, ''Sub-bottom depth recorder,''Geophysics **24**, 749–760 (1959).
[5] D. D. Caulfield, ''Predicting sonic pulse shapes of underwater spark discharges,'' Deep-Sea Res. **9**, 339–348 (1962).
[6] H. Edelmann, ''An underwater sound source with higher seismic efficiency,'' Geophys. Prospecting **16**, 474–490 (1968).
[7] S. Gardner, ''Electro-acoustic properties of the underwater spark discharge'' (Edo Corporation, College Point, NY, 1961), Report 5480.
[8] K. A. Naugol'nykh and N. A. Roi, Elecktricheskie Razrjady v vode (Nauka, Moskva, 1971) [English transl.: *Spark Discharges in Water* (Applied Research Laboratories, Austin, TX, 1987), Internal Report].
[9] L. E. Kinsler, A. R. Frey, A. B. Coppens, and J. V. Sanders, *Fundamentals of Acoustics* (Wiley, New York, 1982), 3rd ed.
[10] A. G. Ryabinin and G. A. Ryabinin, ''Gas-bubble energy in an underwater electrical discharge,''Zh. Tekh. Fiz. **46**, 881–884 (1976) [English transl.: Sov. Phys. Tech. Phys. **21**, 512–514 (1976)].
[11] F. R. Young, *Cavitation* (McGraw-Hill, London, 1989), Chap. 2, pp. 8–37.
[12] E. A. Neppiras, ''Acoustic cavitation,''Phys. Rep. **61**, 159–251 (1980).
[13] G. A. Khoroshev, ''Collapse of vapor-air cavitation bubbles,''Akust. Zh. **9**, 340–346 (1963) [English transl.: Sov. Phys. Acoust. **9**, 275–279 (1964)].
[14] R. L. Rogers, ''Intermediate energy tests and analysis of a plasma sound source'' (Applied Research Laboratories, University of Texas at Austin, Austin, TX, 1992), Report ARL-TR-92-15.
[15] R. H. Mellen, ''An experimental study of the collapse of a spherical cavity in water,'' U.S. Navy Underwater Sound Laboratory, New London, CT, 1955, Research Report 279.
[16] D. C. Gibson, ''The pulsation time of spark induced vapor bubbles,'' Trans. ASME, J. Basic Eng. **94**, 248–249 (1972).
[17] W. H. Press, B. P. Flannery, S. A. Teukolsky, and W. T. Vetterling, *Numerical Recipes in Pascal* (Cambridge U.P., Cambridge, 1989), Chap. 15, pp. 599–632.
[18] C. Herring, *Theory of the Pulsations of the Gas Bubble Produced by an Underwater Explosion* (Columbia University, New London, CT, 1941), NDRC Report No. C4-sr20-010.
[19] L. Trilling, ''The collapse and rebound of a gas bubble,''J. Appl. Phys. **23**, 14–17 (1952).
[20] F. R. Gilmore, ''The growth or collapse of a spherical bubble in a viscous compressible liquid,'' California Institute of Technology Hydrodynamics Laboratory, Pasadena, CA, 1952, Rep. 26-4.
[21] H. G. Flynn, ''Cavitation dynamics. 1. A mathematical formulation,''J. Acoust. Soc. Am. **57**, Pt. 1, 1379–1396 (1975).
[22] G. J. Lastman and R. A. Wentzell, ''Comparison of five models of spherical bubble response in an inviscid compressible liquid,''J. Acoust. Soc. Am. **69**, 638–642 (1981).
[23] S. Fujikawa and T. Akamatsu, ''Effects of the non-equilibrium condensation of vapor on the pressure wave produced by the collapse of a bubble in a liquid,''J. Fluid Mech. **97**, 481–512 (1980).
[24] A. Shima and Y. Tomita, ''Some numerical aspects of cavitation bubble collapse,'' in *Annual Review of Numerical Fluid Mechanics and Heat Transfer*, edited by L. A. Dziobek and B. Brienza (Hemisphere, Washington, DC, 1989), Vol. 2, Chap. 5, pp. 198–226.
[25] J. B. Keller and M. Miksis, ''Bubble oscillations of large amplitude,''J. Acoust. Soc. Am. **68**, 628–633 (1980).
[26] A. Prosperetti, ''Bubble phenomena in sound fields: Part one,''Ultrasonics **22**, 69–77 (1984).

[27] A. Prosperetti and A. Lezzi, ''Bubble dynamics in a compressible liquid. Part 1. First-order theory,''J. Fluid Mech. **168**, 457–478 (1986).
[28] A. Lezzi and A. Prosperetti, ''Bubble dynamics in a compressible liquid. Part 2. Second-order theory,''J. Fluid Mech. **185**, 289–321 (1987).
[29] E. A. Martin, ''The underwater spark: An example of gaseous conduction at about 10 000 atmospheres,'' Ph.D. dissertation (University of Michigan, Ann Arbor, 1956).
[30] E. A. Martin, ''Experimental investigation of a high-energy density, high-pressure arc plasma,''J. Appl. Phys. **31**, 255–267 (1960).
[31] A. I. Ioffe, ''Theory of the initial stage of an electrical discharge in water,'' J. Appl. Mech. Tech. Phys. (PMTF) **7**, 69–72 (1966).
[32] J. W. Robinson, M. Ham, and A. N. Balaster, ''Ultraviolet radiation from electrical discharges in water,''J. Appl. Phys. **44**, 72–75 (1973).
[33] R. W. Schrage, *A Theoretical Study of Interphase Mass Transfer* (Columbia U.P., New York, 1953).
[34] M. S. Plesset and A. Prosperetti, ''Bubble dynamics and cavitation,''Annu. Rev. Fluid Mech. **9**, 145–185 (1977).
[35] W. J. Bornhorst and G. N. Hatsopoulos, ''Analysis of a liquid vapor phase change by the methods of irreversible thermodynamics,'' J. Appl. Mech. **34**, 840–846 (1967).
[36] W. J. Bornhorst and G. N. Hatsopoulos, ''Bubble-growth calculation without neglect of interfacial discontinuities,'' J. Appl. Mech. **34**, 847–853 (1967).
[37] T. Mitchell and F. G. Hammitt, ''On the effects of heat transfer upon collapsing bubbles,''Nucl. Sci. Eng. **53**, 263–276 (1974).
[38] D. Epstein and J. B. Keller, ''Expansion and contraction of planar, cylindrical, and spherical underwater gas bubbles,''J. Acoust. Soc. Am. **52**, Pt. 2, 975–980 (1972).
[39] R. H. Cole, *Underwater Explosions* (Princeton U.P., Princeton, NJ, 1948).
[40] *A Physicist's Desk Reference*, edited by H. L. Anderson (American Institute of Physics, New York, 1989), 2nd ed. of *Physics Vade Mecum*, pp. 267–268.
[41] R. M. Roberts, ''The energy partition of underwater sparks,'' Ph.D. dissertation, University of Texas at Austin, Austin, TX (to be published).
[42] Y. B. Zel'dovich and Y. P. Raizer, *Physics of Shock Waves and High-Temperature Hydrodynamic Phenomena*, edited by W. D. Hayes and R. F. Probstein (Academic, New York, 1966), Vol. I, Chap. 6, pp. 269–276.
[43] J. D. Jackson, *Classical Electrodynamics* (Wiley, New York, 1975), 2nd ed., pp. 290–292.
[44] J. A. Cook, ''Interaction of multiple spark-generated bubbles,'' Applied Research Laboratories, University of Texas at Austin, Austin, TX, 1993, Report ARL-TR-93-10.
[45] D. C. Kelly, *Thermodynamics and Statistical Physics* (Academic, New York, 1973).

Analysis and model/data comparison of broadband acoustic propagation at the Atlantic Generating Station (AGS) site

M. Badiey
Ocean Acoustics Laboratory, Graduate College of Marine Studies, University of Delaware, Newark, Delaware 19716

K. P. Bongiovanni[a] and W. L. Siegmann
Department of Mathematical Sciences, Rensselaer Polytechnic Institute, Troy, New York 12180

(Received 28 September 1995; accepted for publication 4 November 1996)

An investigation of broadband acoustic propagation in a shallow-water environment is performed by comparing experimental acoustic data [Badiey *et al.*, J. Acoust. Soc. Am. **96**, 3593–3604 (1994)] with results from a frequency-domain, high-order parabolic equation technique. The principal quantity examined, transmission loss versus frequency, is determined for fixed source/receiver positions over short ranges (≈0.5 km) corresponding to experimental configurations. High-resolution geoacoustic data from extensive coring of the site, along with CTD and detailed bathymetric data, are used to construct accurate range-dependent input for PE simulations and range-varying wave number spectra calculations. Generally very good agreement between the PE results and data are observed. Range-dependent mechanisms are seen to have a strong azimuthal dependence in both TL and wave number results for this site. Shear losses are considered by exploiting equivalent fluid relationships. The effects of sediment dispersion through frequency dependent sound speed are also examined. © *1997 Acoustical Society of America.* [S0001-4966(97)00103-3]

PACS numbers: 43.30.Bp, 43.30.Ft, 43.30.Ma [MBP]

INTRODUCTION

Understanding broadband acoustic propagation in shallow-water ocean environments presents a host of challenges for the underwater acoustics community. Insufficient environmental and experimental data make quantitative assessments of predictive models very difficult. The models themselves must account for the complications of energy propagating within the sediment. In essence the problem is an initial-boundary value problem, the solution of which requires accurate initial, boundary, and medium information; it cannot be constructed with any accuracy unless the required physical properties of the environment are known.

Most existing seafloor data in shallow regions have been or are being collected with the aim of understanding the geological origin and formation process of the underlying sediments.[1] Due to the substantial cost incurred in obtaining the ground truth data, this information is usually limited to a single or at most very few cores in a given area. On the other hand, seismic data sets cover large areas, but are primarily focused on the larger and deeper scale features. It is most desirable in shallow-water acoustic studies to test the agreement between predictive models and collected acoustic data in an area in which high-resolution geologic and oceanographic parameters are known in three dimensions and time. In fact, the creation of a natural ocean laboratory in shallow waters where relatively inexpensive, repeated, and calibrated experiments can be conducted to study the fundamentals of frequency-dependent propagation is necessary. For acoustic applications, geological data need to be converted to a set of geoacoustic parameters such as compressional and shear wave speeds, their attenuations, and the bulk density of the sediment. Both range and depth information would be needed, with accuracy depending on acoustic frequency, so as to assess completely the solutions to shallow-water propagation problems.

In the last four decades, much has been done with narrow-band and single-frequency acoustic signals in shallow water.[2–10] The first work on broadband acoustic propagation by Pekeris proposed a simple model to analyze the experimental results of explosive charges in shallow-water regions.[2] This work was later extended by Tolstoy[3] who obtained a solution using a fluid bottom first[11] and later for elastic media with attenuation.[12] More recently, many researchers have presented excellent results which indicate the high degree of complexity encountered in understanding shallow-water acoustics. Among these, the works of Jensen[7] and Kuperman,[8] Lynch and co-workers,[13] and others[9,10,14] should be mentioned. However, a common conclusion in all these papers is that a greater understanding of shallow-water acoustics will follow from more complete and realistic environmental data incorporation.[15–17] In this paper we provide such a data set, along with experimental and simulated acoustic results.

In the 1970s an intensive geological survey, employing borehole techniques, was conducted in a shallow region five miles off the southern New Jersey coast, resulting in a uniquely comprehensive data set for the seabed.[18] This area has been the focus of our experimental work for the past few years. Throughout this work we have directed our attention to the frequency domain and the interference patterns of the transmission loss (TL) versus frequency.[19–21] It is believed

[a]Current address: Ocean Acoustics Laboratory, Graduate College of Marine Studies, University of Delaware, Newark, DE 19716.

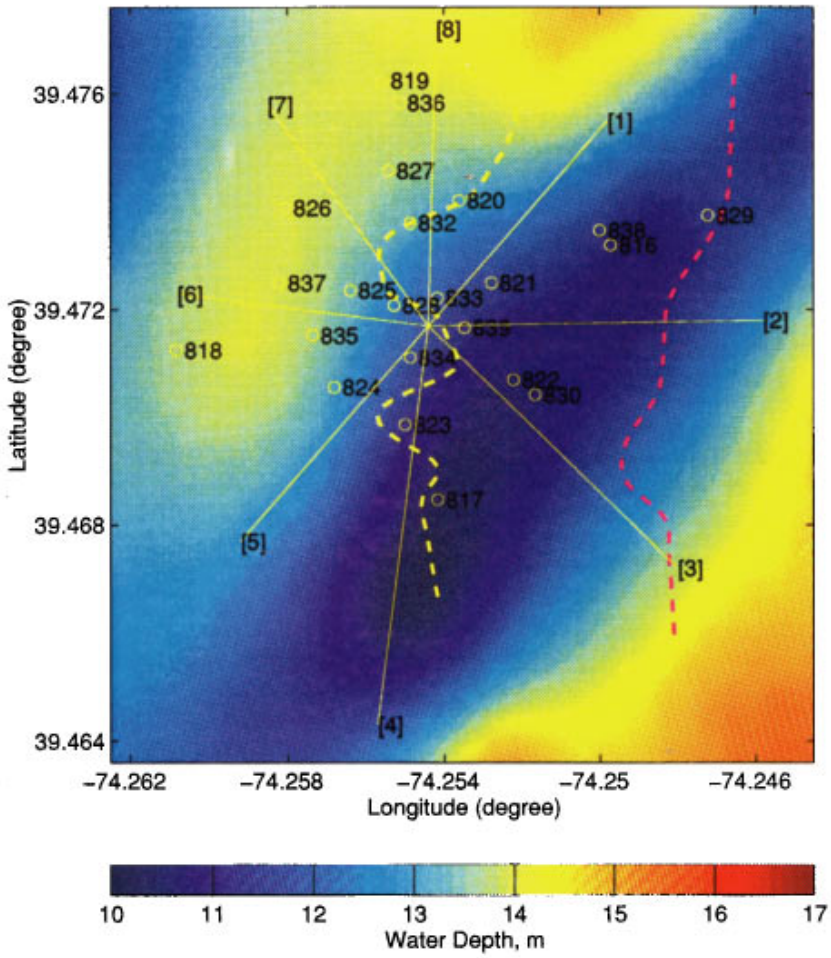

FIG. 1. Measured bottom topography at the Atlantic Generating Station (AGS) site. Core positions along with the eight source–receiver tracks are shown. The receiver is located at the center and subsurface channel boundaries are shown with dashed lines.

that a detailed understanding of the signal characteristics in this well-known environment may provide a new treatment for inverse problems in the frequency domain.[22] An extensive parameter study showing the effects of range dependence on acoustic wave propagation at the AGS site concluded that inhomogeneities in depth as well as in range are both important.[23] It was shown that bathymetric effects and sediment compressional sound-speed range variability have considerable effects over short ranges. However, only cw cases for a fluid bottom was assumed. In another study we showed that the layering structure of the seafloor and the statistical distribution of the geoacoustic parameters in depth can cause a frequency-dependent effect on the reflection coefficient.[24]

The purpose of this paper is to continue our research in developing a better understanding of the physics of pulse propagation in an environmentally complex region of the AGS site. We wish to classify the important relationship between the geoacoustic data and the water-borne acoustic signals. Consequently, a thorough comparison using a PE model between TL versus frequency calculations and our 1992 experimental results is undertaken here. In addition, we present an investigation of the wave number spectra with respect to both frequency and range in order to show the relationship between geoacoustic properties and frequency-dependent acoustic signals. It is shown that the acoustic wave attenuation in sediments and modal dispersion are very important factors to consider in the shallow water acoustics. We include an equivalent fluid representation of the sediment geoacoustic structure in the modeling of the test site and also consider intrinsic sediment dispersive effects. It is noted in this study that azimuthal variations can cause significant effects on the propagation results.

In Sec. I, we describe the AGS environment and how it is represented in this study. A brief overview of the data and its processing from our 1992 at-sea experiment[19,20] is given. We present the propagation model used here and discuss the influences of range dependence in the sediment geoacoustic properties on the interference patterns of transmission loss versus frequency in Sec. II. We also examine the evolution of wave number spectra in range and discuss effects of sediment attenuation due to the seafloor properties. In Sec. III, we compare frequency-response curves of the transmission loss between the field data and the simulated results. In addition, we discuss the absorption of broadband acoustic sig-

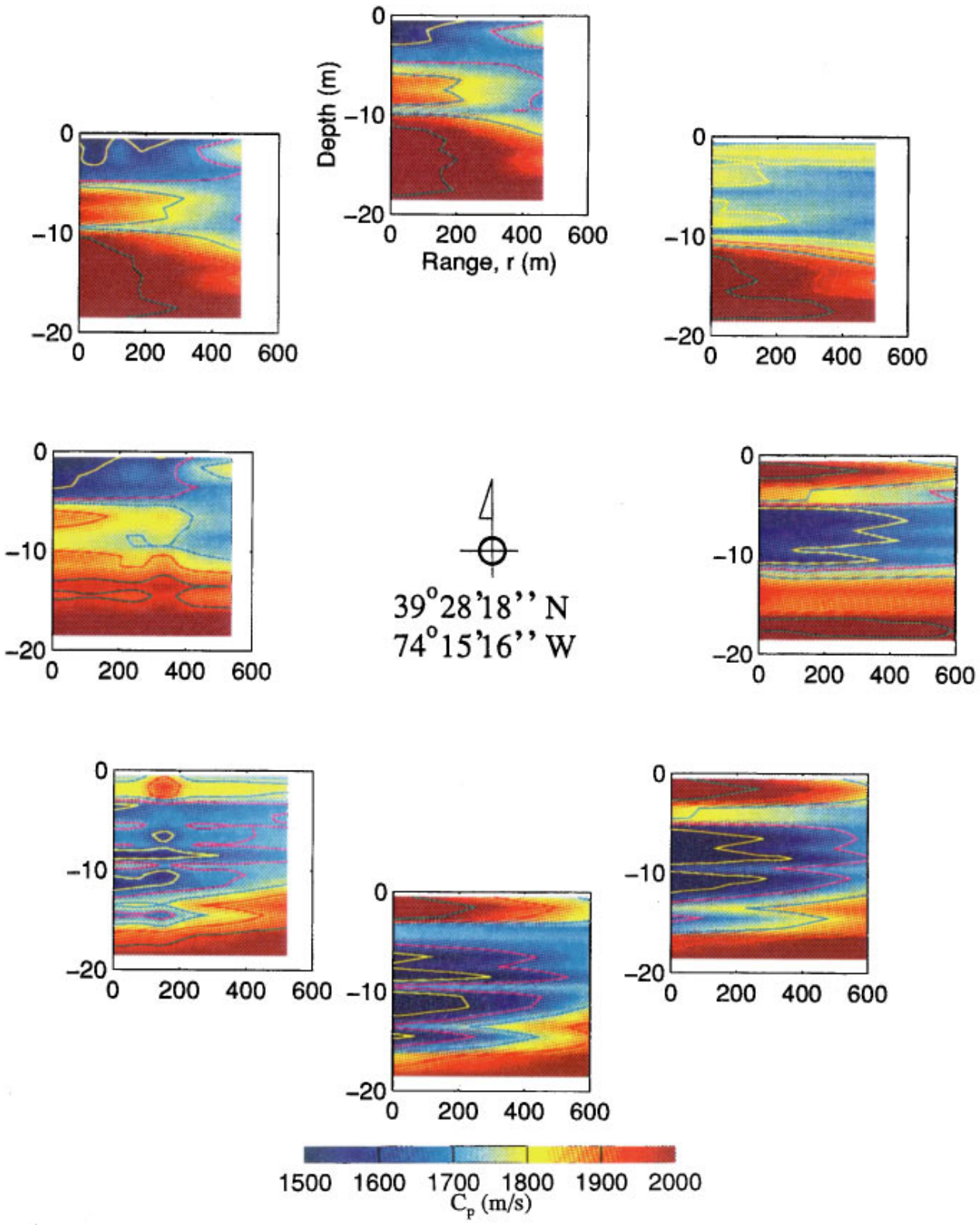

FIG. 2. Compressional wave speed versus sediment depth and range for each of the eight propagation track [1] to [8], arranged in the same positions as Figs. 1 and 3.

nals interacting with the seafloor. In Sec. IV, a discussion of the effects that range-dependent geoacoustic properties of the AGS site have on the acoustic response is given. Finally, in Sec. V, we present the summary of this work and state the conclusions.

I. FIELD OBSERVATIONS

Very little data exist for both range- and depth-dependent geoacoustic properties of surfacial sediments in coastal regions. Where data are available, it is either limited

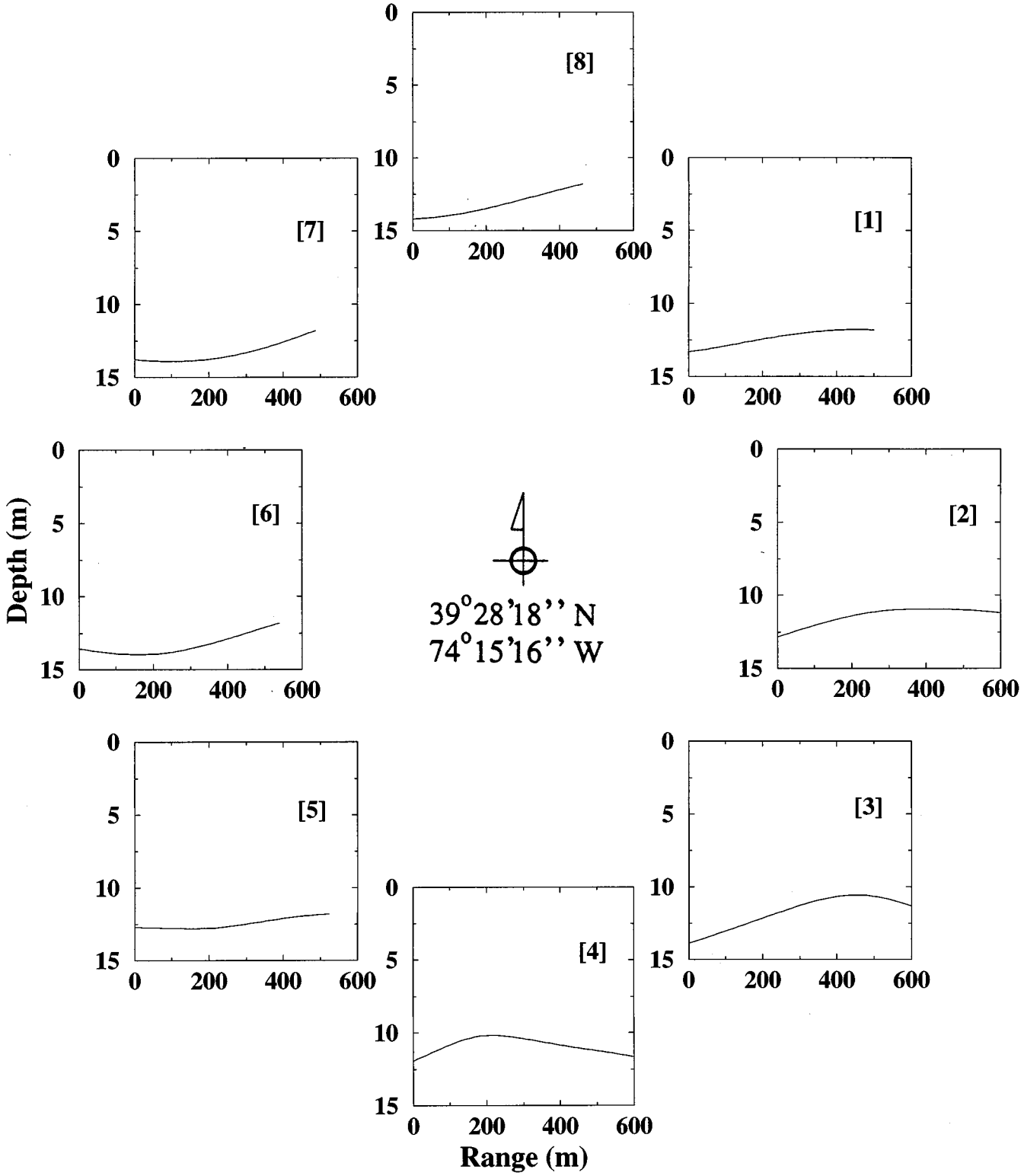

FIG. 3. Mean water depth versus range (from source to receiver) along the eight propagation tracks. The receiver position is shown (center) and the tracks are numbered clockwise from [1] to [8].

to a single core or to sparse boreholes in a large region. Many studies in recent years have shown that shallow-water sediment stratigraphy develops under a variety of processes which make their physical properties vary in range and depth.[25,26] This section summarizes the AGS geological data from which we have a unique geoacoustic data set and outlines a series of acoustic experiments conducted there in 1992.

A. Environmental data at the AGS site

The AGS site is located in very shallow water from 8.5 to 14 m deep overlying a sandy ridge-and-swale topography.[18,19] Figure 1 details the bathymetry (contours), core positions (circles), and eight tracks along which the acoustic experiments and simulations were performed (solid lines). A principal geological feature of this region is a north–south subsurface channel, consisting of thicker sediment layering structure than elsewhere, and is demarked by the dotted lines.

For the investigation in Ref. 23, geoacoustic profiles were obtained from the processed core data[19] directly, with no effort to interpolate between core locations. In order to construct good estimates for profiles at arbitrary points, a kriging technique is employed.[27] This is a weighted least-squares fitting approach which lays the core data on a three-dimensional grid and provides vertical slices corresponding to the eight tracks. Other interpolation schemes such as Akima splines[28] and nearest-neighbor techniques are also being examined for this site. In Fig. 2 the sediment compressional sound-speed (c_P) contours versus range and depth from the kriging fits are shown for the eight tracks. The strong variability within each track, as well as from track to track, is easily seen. The influence of the subsurface channel is seen as the high c_P values occurring in the top 3 m of tracks 2, 3, and 4, which correspond to the fine sand deposit. Other geoacoustic parameters such as shear speed, density, compressional and shear attenuations were obtained in the same manner. Cross sections of the bathymetry along the eight tracks are given in Fig. 3. Note that all the curves begin and end at the source and receiver positions, respectively.

Oceanographic data used in this study came from a set of eight CTD measurements[19] which show a downward sloping sound-speed profile. Also, a series of oceanographic measurements has been collected in recent years indicating the seasonal variability of the temperature and salinity in this region[29] (the AGS site is referred to as the LEO-15 site in Ref. 29). The influence of the downward-refracting character of the water profiles for this site has been examined.[23] Because an isospeed approximation to the mean profile was insufficiently accurate for propagation simulations, we use the mean water profile for modeling in this paper.

B. Acoustic experiments and data processing

During the 1992 and subsequent experiments, an airgun source was towed to various positions around a fixed receiving array and series of shots were performed.[19,30] The receiving array consisted of ten hydrophones mounted vertically in 1-m intervals, thereby extending over the entire water column (Fig. 4). Fortunately, near ideal weather conditions and calm seas prevailed throughout the experiment, resulting in little or no array drifting and high signal-to-noise ratios. Table I provides information about the distribution of ranges for shots within each group. Generally, the ranges are slightly more than half a kilometer.

Since the source and receiver positions were fixed and the airgun provides a broadband signal, it is natural to examine the spectral characteristics of the recorded signals. One possible measure for transients is the energy spectral density level (ESD) given by[31]

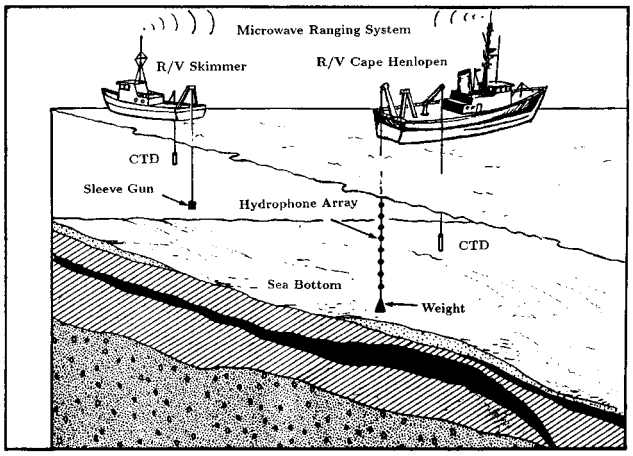

FIG. 4. Schematic of configuration for the 1992 acoustic experiments.

$$\mathrm{ESD}(f) = 10 \log_{10} \frac{|P(f)|^2}{(1\,\mu\mathrm{Pa\ s})^2} \quad [\mathrm{dB}\ re:\ \mu\mathrm{Pa}^2\,\mathrm{s/Hz}\ @1\ \mathrm{m}], \tag{1}$$

where $P(f)$ is the Fourier transform of the pressure time series in μPa. In order to compare data with simulations we can consider the ESD differences between source and receiver, that is, an ESD loss defined as

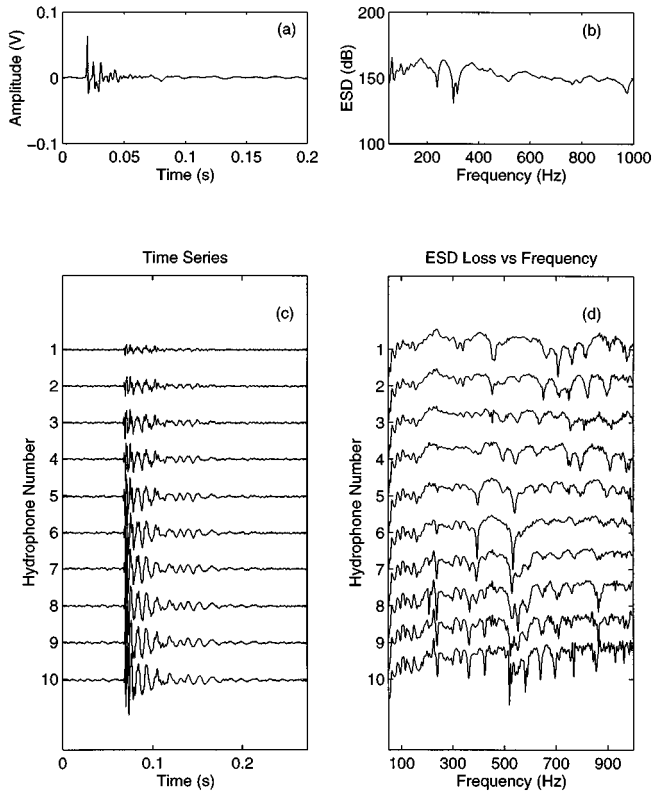

FIG. 5. A sample airgun shot (No. 65) signature and received vertical hydrophone measurements during the 1992 AGS experiment: (a) source signature, (b) source energy spectral density level, (c) received signals by hydrophones spaced 1 m apart in depth, (d) processed energy spectral density versus frequency at each hydrophone.

TABLE I. Experimental shot data, range statistics, and level bias for each track.

Track No.	Mean water depth (m)	Shots	Group symbol	Range (m)			Bias (dB)
				$R_{\min}$	$R_{\max}$	R	
1	12.3	64–67	▶	621	631	627	10
2	11.4	68–71	▲	720	727	724	12
3	11.7	72–75	*	635	658	645	12
4	10.9	76–80	+	700	724	712	12
5	12.4	46–49	■	474	562	529	5
6	13.3	51–55	♦	593	638	619	5
7	13.3	56–59	◀	668	712	685	5
8	13.2	60–63	▼	707	737	721	5

$$\mathrm{ESDL}(f) \equiv \mathrm{ESD}_R(f) - \mathrm{ESD}_S(f) \quad [\mathrm{dB}\ re:\ \mu\mathrm{Pa}^2\,\mathrm{s/Hz}\ @1\ \mathrm{m}], \tag{2}$$

where the subscripts R and S denote receiver and source, respectively.

For the experiments considered here, *in situ* source signatures were not collected, so care has been taken to obtain an appropriate substitute. Fortunately, a large number of reference signals were collected during the subsequent 1994 experiment[30] at various positions throughout the AGS site. By selectively averaging groups of shots, in order to avoid potential shot-to-shot variabilities, a representative spectrum was calculated for each of the eight source positions (Fig. 1). Furthermore, to overcome uncertainties that may occur in the levels, a level bias is introduced only for comparisons to be made with modeling results subsequently. This is justifiable since our primary concern will be to compare level variations and interference structure as opposed to absolute levels.

Figure 5 shows a sample of the acoustic data and the processed signals. In Fig. 5(a) the measured source signature, sampled at 5 kHz, is displayed beside its spectrum in Fig. 5(b). We mention that the energy is sufficiently spread such that for the ranges and frequency band (<1 kHz) considered here, received signal levels lie well above the ambient noise level. In Fig. 5(c), the corresponding received signals, sampled at 7.5 kHz, for the ten hydrophones are displayed, and finally each signal is converted to ESDL in Fig. 5(d). All the spectra were calculated using an FFT on the detrended time series.

II. PROPAGATION MODELING

A. Frequency-dependent ESD loss calculations

Simulations of ESDL are constructed in order to compare with broadband data of the type illustrated in Fig. 5(d). A propagation model is used for a series of single-frequency loss calculations over a band comparable to the data spectrum. For time-domain modeling of broadband sources this is known as the Fourier synthesis technique when the results are summed appropriately.[32]

The individual simulations are executed using a finite element PE (FEPE) developed by Collins.[33] Various approximations to the PE operator have led to different methods, with improvements being developed[34] for such features as very wide-angle capabilities, strong range and depth variability, and poro-elastic bottoms among others.[35] The high-order, energy-conserving FEPE model is obtained by approximating the pseudo-differential operator with Padé rational functions. It has been shown to model propagation in complicated environments such as the AGS site quite well (in particular, see Fig. 15 in Ref. 23).

The complex pressure $u(r,z)$ output for a given frequency band can be used to synthesis the time-dependent pressure field. Conversely, the PE solutions represent Fourier transform components of the time-harmonic wave equation, with the usual definition for transmission loss for a *fixed* frequency

$$\mathrm{TL} = -20\log|u(r,z)| + 10\log r \quad [\mathrm{dB}\ re:\ \mu\mathrm{Pa}^2\,\mathrm{s/Hz}\ @1\ \mathrm{m}]. \tag{3}$$

The reference pressure P_{ref} is defined as having an intensity corresponding to a plane wave with rms amplitude of 1 μPa @1 m from the source. Consequently, by taking the P_{ref} for the ESDL calculations to have a 1-Hz reference band and an rms amplitude of 1 μPa when referenced at 1 m, we obtain the relation $\mathrm{TL}(f) = \mathrm{ESDL}(f)$.

Computational parameters for ESDL versus frequency runs are shown in Table II. PE simulations start at a minimum frequency $f_{\min}$ and proceed to a maximum frequency $f_{\max}$ by steps of Δf. Different frequency steps Δf were tested, and the selected value was found to provide sufficient resolution for the comparisons in this paper. For each run Δr and Δz are the range and depth steps, z_{MAX} is the maximum depth of the computational grid, c_0 is the reference sound speed, and *nPadé* is the number of terms used in the Padé series. For all simulations a wide-angle PE starter[36] is used, along with source depth z_S of 5 m, and a pressure-release boundary condition at the surface $z=0$. Many receiver depths z_R were used, but for convenience only those at 5 and 10 m will be shown here.

B. Range-dependent influence of geoacoustic parameters on interference patterns

Because shallow-water regions are typically range dependent, this feature must be taken into account through the input parameters for accurate predictive modeling. Previously we examined range-dependent effects on TL as a function of range.[23] Here we provide a representative illustration of range-dependent input parameter effects on TL (or ESDL)

TABLE II. Computational parameters for representative FEPE-synthesis calculations.

$f_{\min}$ (Hz)	$f_{\max}$ (Hz)	Δf (Hz)	Δr (m)	Δz (m)
50	1000	5	1.0	0.2
z_{MAX} (m)	z_S (m)	z_R (m)	c_0 (m/s)	*nPadé*
100	5	1–10	1500	3

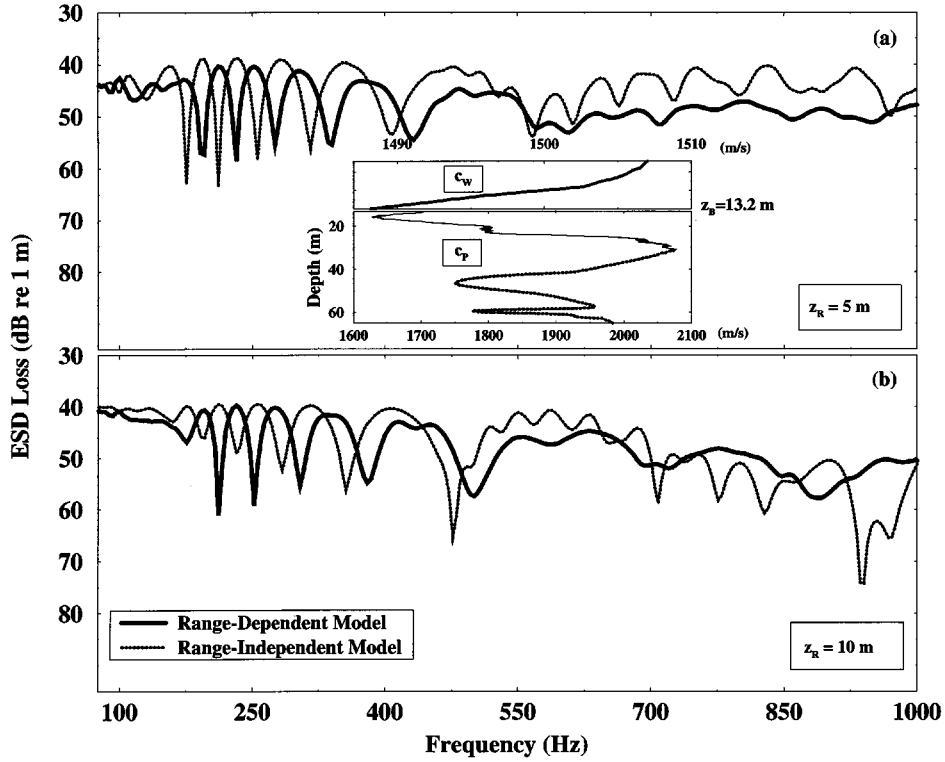

FIG. 6. Comparison of ESD loss versus frequency for range-independent and range-dependent environments along track 8. Source depth z_S=5 m, receiver depth z_R (a)=5 m, and (b)=10 m. Inset shows range-independent mean water and sediment compressional sound speed for track 8.

as a function of frequency. These effects can be observed in variations of the frequency response pattern from those corresponding to range-independent environments.

Range-dependent environments are constructed from the kriged data of bathymetry, sediment sound-speed c_P, density ρ, and attenuation α_P as indicated in Sec. I. For appropriate range-independent input streams, preliminary modeling is needed. Density and attenuation profiles are averaged over depth and range, leading to constant representative regional values (ρ=2.0 g/cc and α_P=0.2 dB/λ). Averaging along the bathymetry of any given track yields a mean depth (see Table I). Finding an appropriate profile for c_P is important because this parameter plays a dominant role in propagation. Vertical profiles are first merged into a single set which is used to generate a mean profile by taking a sliding window average over depth.[23] For cases considered here, the window width was selected between 1 and 2 m, depending on the point density. Since the kriged data extended only 18 m into the sediment, c_P was extrapolated by averaging the (deeper) core data values.

The inset in Fig. 6 shows the sound-speed structure for the range-independent environment appropriate for track 8 (Fig. 1) with mean depth 13.2 m. The dotted portion appended to the mean c_P (solid) curve indicates the extrapolation into the deeper sediment. Since no interfacial data were obtained, a gap of 0.5 m exists at the water-sediment interface. This value can be determined using Hamilton's results.[37] The range-independent track 8 profile has a typical two-layer structure with a low-speed layer ($c_p \approx$1600 m/s) overlying a high-speed layer ($c_p \approx$2000 m/s). Referring to Fig. 2, the sound-speed cross-section structure is quite different since this track straddles the subsurface channel.

Figure 6 shows ESDL versus frequency curves for track 8 at two different receiver depths for the range-independent (dotted) and range-dependent (solid) FEPE simulations. For this track, in addition to loss differences of about 10 dB for some frequencies, there is a phase shift in the ESDL patterns. Also above 550 Hz the range-independent case produces a two-mode pattern, while the range-dependent case is dominated by a single mode. The relatively strong range-dependent effects in the ESDL curve are consistent with the variations in the sediment c_P field along this track. Differences in ESDL curves between range-dependent and range-independent models are smaller for other tracks with less environmental variation (such as track 3). Nonetheless, it is important to see from Fig. 6 the significant ESDL differences that are possible over a very short transmission range and, moreover, why coherent loss calculations may not be very useful in regions where bottom properties are poorly known.

C. Wave number spectra

A useful tool for investigating acoustic propagation at range-dependent sites is the horizontal wave number spectrum versus range. This quantity, the spatial analog of the Fourier transform, can be obtained from the full-field output of range-dependent PE propagation models, and we employ the technique of Ref. 38 as detailed in Refs. 16 and 23. This approach allows examination of how the depth-averaged mode amplitudes evolve with range. In this section we describe the mode evolution along a single track for several different frequencies to illustrate some key features and to

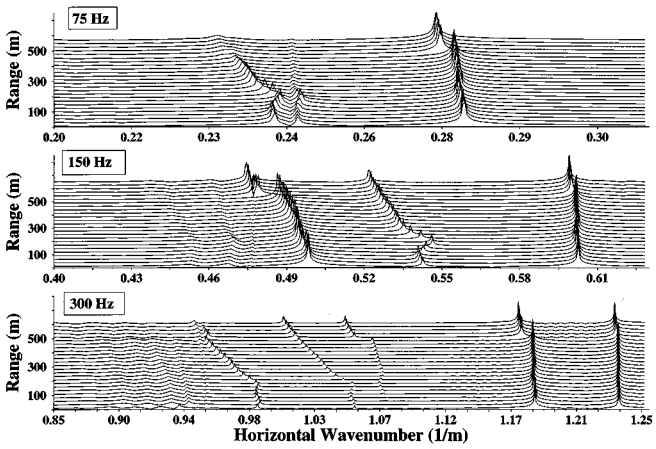

FIG. 7. Horizontal wave number spectra versus range for track 5 at (a) 75 Hz, (b) 150 Hz, and (c) 300 Hz.

motivate the more comprehensive examination in Sec. IV. Track 5 is chosen for this example, and the range evolution of the spectra is shown for 75, 150, and 300 Hz in Fig. 7.

Several modes can be seen at all three frequencies. At 75 Hz only three modes are present, with mode 1 near 0.285 m^{-1}, and modes 2 and 3 near 0.24 m^{-1}. As can be seen clearly, the first-mode variations in range correlate with bathymetric variations (see Fig. 3), as would be expected by plane-wave propagation in a channel with rigid boundaries.[39] On the other hand, the second and third modes show the effect of subsurface features seen in the geoacoustic data (Fig. 2). In particular, at a range of about 200 m, the modes undergo significant changes that reflect substantial variations in the seabed properties at depths of 5 m$<h<$10 m (where h is the depth into the seabed). Other changes at range near 420 m are correlated with variations for $h>$12 m. The upsloping bathymetry between 300 and 500 m also influences the higher modes.

At 150 Hz, three modes occur with the first around 0.6 m^{-1}, the second between 0.52 and 0.55 m^{-1}, and the third between 0.47 and 0.5 m^{-1}, with higher modes having much smaller amplitudes. The first and third modes are seen to follow the bathymetry, with larger variation occurring for the higher mode. The second mode has a striking variation around a range of about 200 m which corresponds to the presence of a sediment sound-speed anomaly around the same range, as seen in Fig. 2 for $0<h<3$ m.

The last case of 300 Hz shows a predominantly five-mode pattern with two dominant lower modes and three smaller amplitude higher ones. The variations with range of these modes show an increasing shift with mode number. The first mode remains near 1.23 m^{-1} with a slight decrease after about 450 m, and the same behavior is observed in the second mode but with an exaggerated variation. The higher modes again clearly show the acoustic influence of subsurface features.

D. Geoacoustic influence on acoustic propagation

Shallow water propagation can be characterized by the increasing number of bottom interactions. When sound waves interact with the seabed, energy loss arises from several mechanisms. The total loss, also referred to as effective attenuation, is the sum of (a) intrinsic attenuation due to material properties, (b) inhomogeneous layering which can cause sound scattering, (c) porosity of the seafloor and the associated fluid–solid interactions, and (d) gas bubbles acting as strong reflectors and scatterers.[26,40] These may not be the only sources of attenuation. Other factors such as conversion from compressional to shear wave and multiple reflections in different sediment layers may also involved.[26] This complicates the isolation of a single mechanism.[41] Moreover, for broadband signals, intrinsic as well as geometric dispersion characteristics may influence the propagation.[40,42]

The typically low rigidity seabed at the AGS site (shear speeds on the order of 250 m/s) suggests a fluid approximation might suffice for bottom modeling, yet the very shallow nature should warrant, to some degree, the inclusion of elastic effects. Since we are only interested in water-born acoustic measurements and want a straightforward incorporation of elastic effects for range-dependent sediments, we exploit the recent equivalent fluid developments of Tindle and Zhang.[43,44] In particular, for relatively low grazing angles, the shear loss can be approximated by replacing density and attenuation with ''equivalent fluid'' density ρ_P' and attenuation α_P' values as given by Eqs. (12) and (13) in Ref. 43, respectively.

A consequence of the requirement of causality is that the phase velocity c_P must be frequency dependent.[41,45] Generally, for low rigidity sediments the effect of this frequency-dependent dispersion factor can be small, and to verify this a correction to c_P as given by Eq. (57) of Ref. 46 was incorporated into the FEPE simulations. Sound-speed differences on the order of 10 m/s are seen, but generally are much less, and the overall structure of the profile is maintained. The corresponding effects on ESDL are to weaken the interference patterns slightly, and so this mechanism is neglected here.

III. MODEL-DATA COMPARISONS

We now construct range-dependent model environments for each of the eight tracks, as described in Sec. II, and compare results of FEPE simulations with the 1992 experimental data.[19] Preliminary comparisons of the overall levels led to different bias values applied to the raw experimental data for each group of shots. The last column of Table I shows the biases used. Again we emphasize that here we are only interested in comparing level variations and interference patterns without regard to absolute level.

Figures 8–15 depict ESDL curves for shot data (light solid) and simulations (thick solid) for the mean shot range (Table I). The frequency interval examined, from 50 Hz to 1 kHz, is chosen as representative of low- to high-frequency propagation, since low end roll-off is around 50 Hz and the signal-to-noise ratio drops quickly after 1 kHz. Also for brevity, we show only signals received at hydrophones 5 and 10 which lie at 5 and 10 m depth, respectively. Insets showing the track positions relative to the core locations are included. A certain amount of variability will be seen between

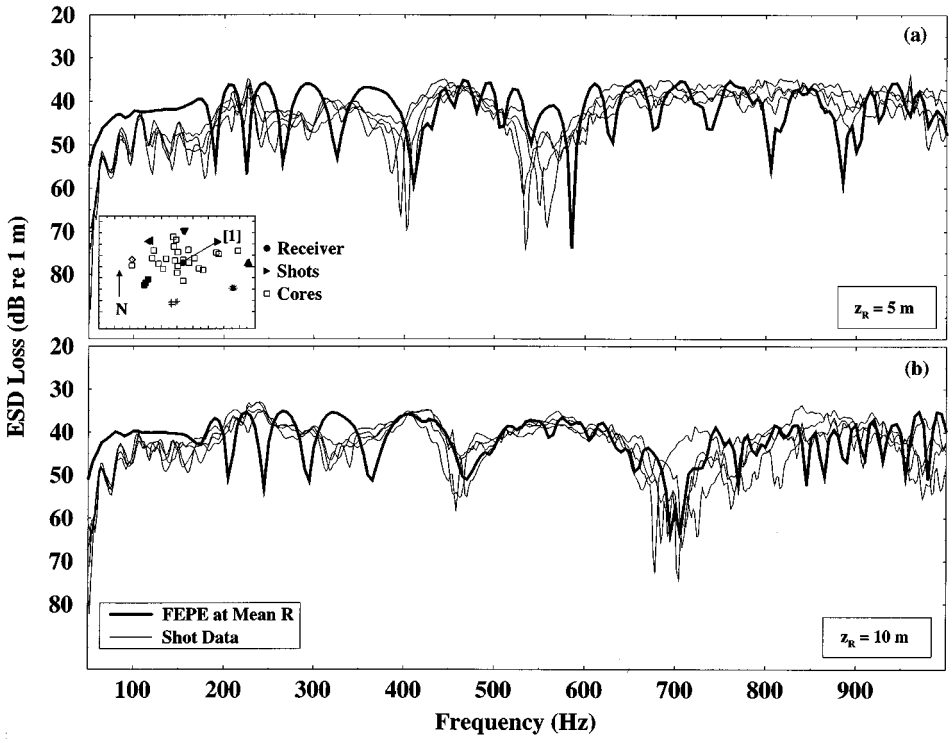

FIG. 8. Comparison of ESD loss versus frequency along track 1 for experimental data (thin solid lines) and FEPE simulation at mean shot range. (a) z_S=5 m, z_R=5 m; (b) z_S=5 m, z_R=10 m. Inset shows AGS site with track 1.

the various shots in a given group. This results from drift in the source ship position as the experiment was being conducted, as suggested by the ''Range'' columns in Table I. Note that other reasonable causes for the variability, such as water profile variability or source spectrum changes, can be eliminated.

The first track lies to the northeast of the receiver and remains over the subsurface channel (Fig. 1). In Fig. 8 very

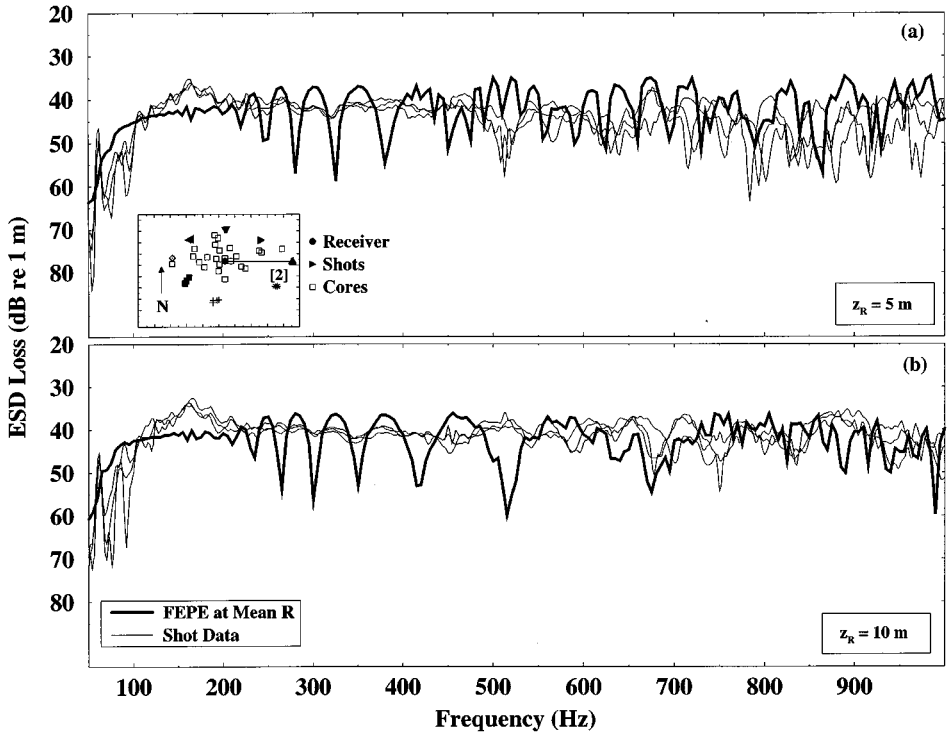

FIG. 9. Comparison of ESD loss versus frequency along track 2 for experimental data (thin solid lines) and FEPE simulation at mean shot range. (a) z_S=5 m, z_R=5 m; (b) z_S=5 m, z_R=10 m. Inset shows AGS site with track 2.

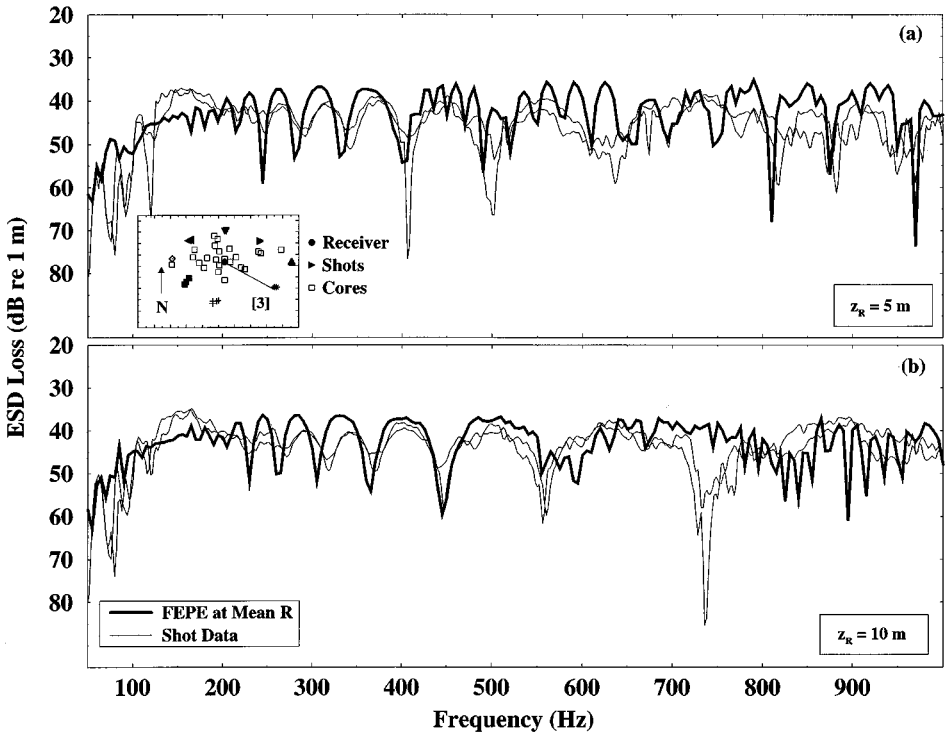

FIG. 10. Comparison of ESD loss versus frequency along track 3 for experimental data (thin solid lines) and FEPE simulation at mean shot range. (a) z_S=5 m, z_R=5 m; (b) z_S=5 m, z_R=10 m. Inset shows AGS site with track 3.

good agreement is seen in the trend over all frequencies between the simulations and shot data. Particularly striking is the strong correspondence in interference patterns from about 400 to 700 Hz for both hydrophones. Both data and simulations show a widening of the interference pattern with increasing frequency. Another interesting feature of the data is the shot-to-shot correlation with frequency; for low frequencies the pattern is relatively tight, and it becomes less coherent with increasing frequency. This phenomenon, indicative of frequency-dependent sensitivity to spatial varia-

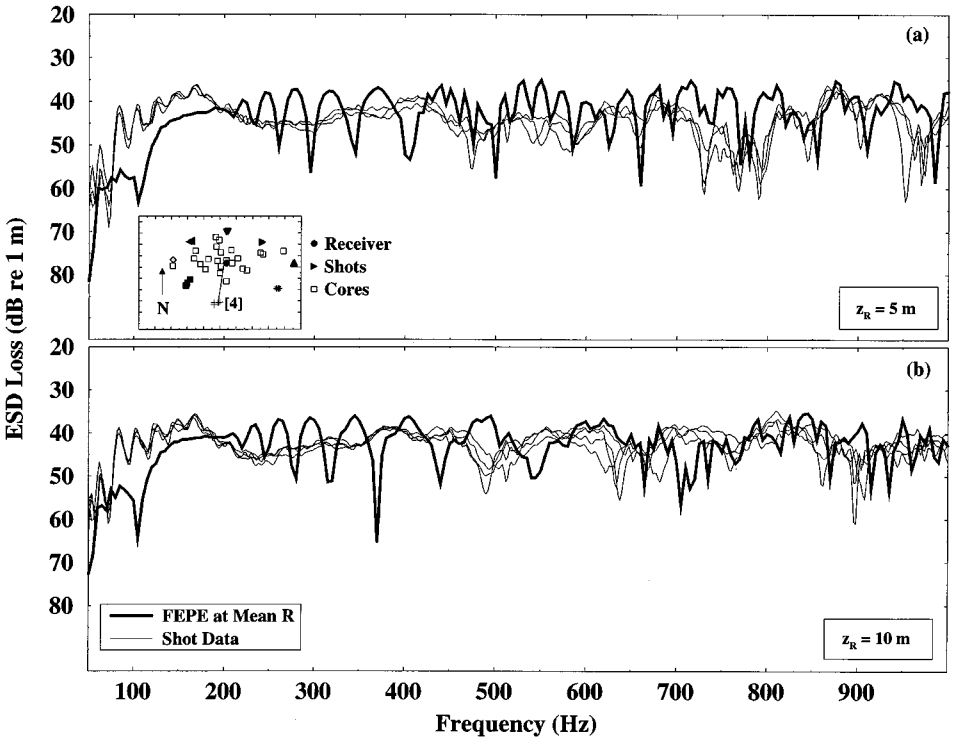

FIG. 11. Comparison of ESD loss versus frequency along track 4 for experimental data (thin solid lines) and FEPE simulation at mean shot range. (a) z_S=5 m, z_R=5 m; (b) z_S=5 m, z_R=10 m. Inset shows AGS site with track 4.

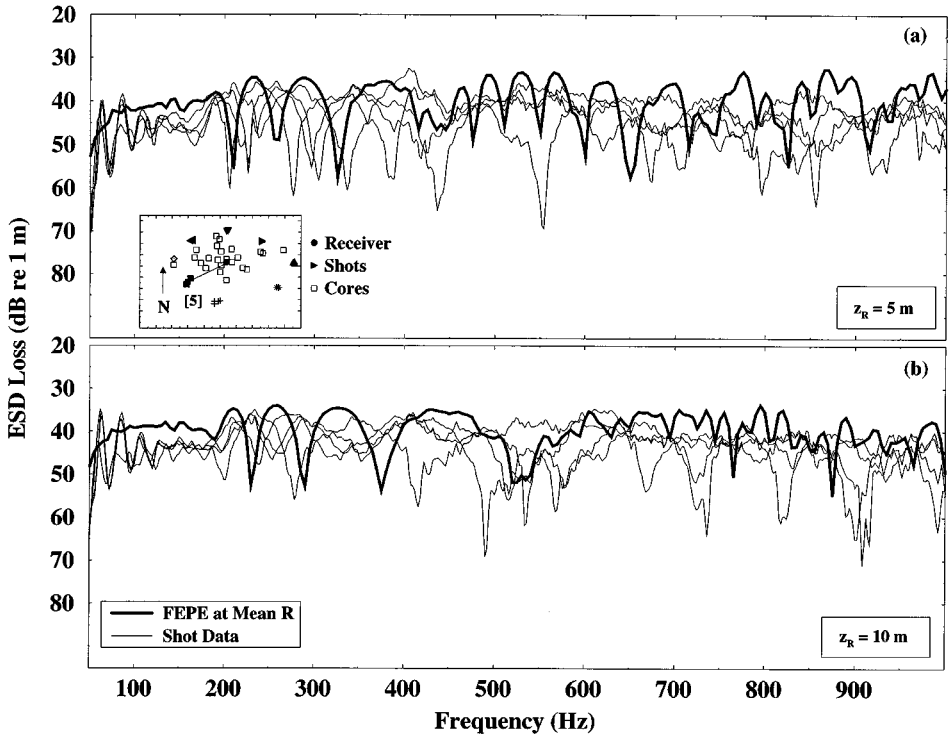

FIG. 12. Comparison of ESD loss versus frequency along track 5 for experimental data (thin solid lines) and FEPE simulation at mean shot range. (a) z_S=5 m, z_R=5 m; (b) z_S=5 m, z_R=10 m. Inset shows AGS site with track 5.

tions of the water volume, can be observed to vary for different propagation paths.

The next track lying due east of the receiver shows a distinct difference in ESDL from track 1 results (Fig. 9), especially for the higher frequencies. The mid- to high-frequency nulls in the shot data are less pronounced for this case. This is unsurprising because the geoacoustic properties over the two tracks are considerably different (Fig. 2). The FEPE results have a good match in overall level variation, but a stronger interference pattern than the data, except pos-

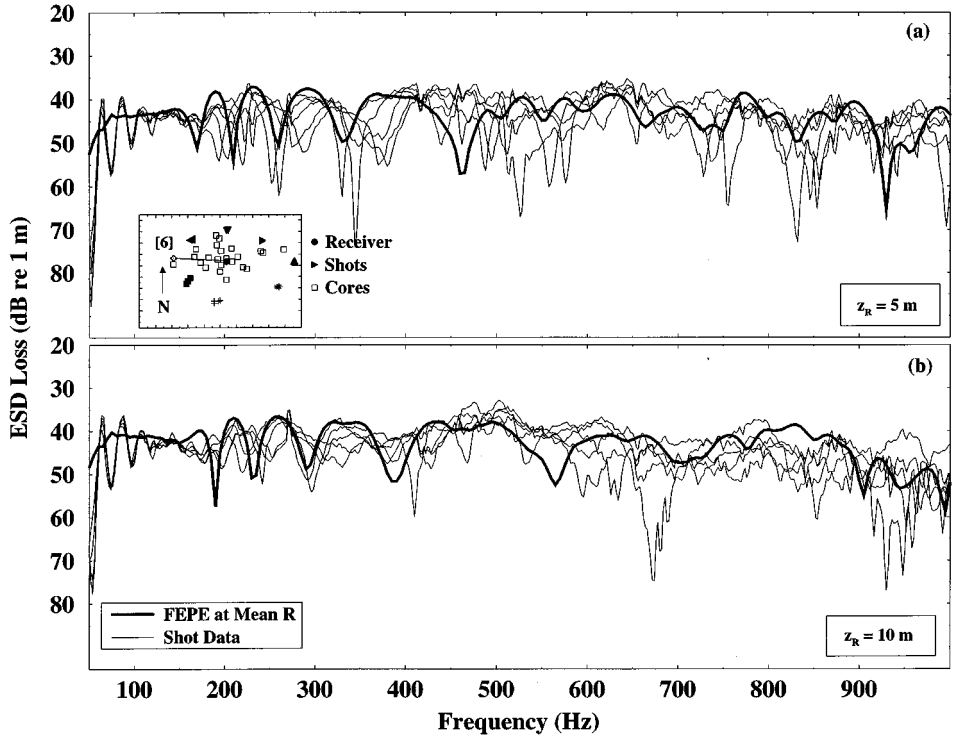

FIG. 13. Comparison of ESD loss versus frequency along track 6 for experimental data (thin solid lines) and FEPE simulation at mean shot range. (a) z_S=5 m, z_R=5 m; (b) z_S=5 m, z_R=10 m. Inset shows AGS site with track 6.

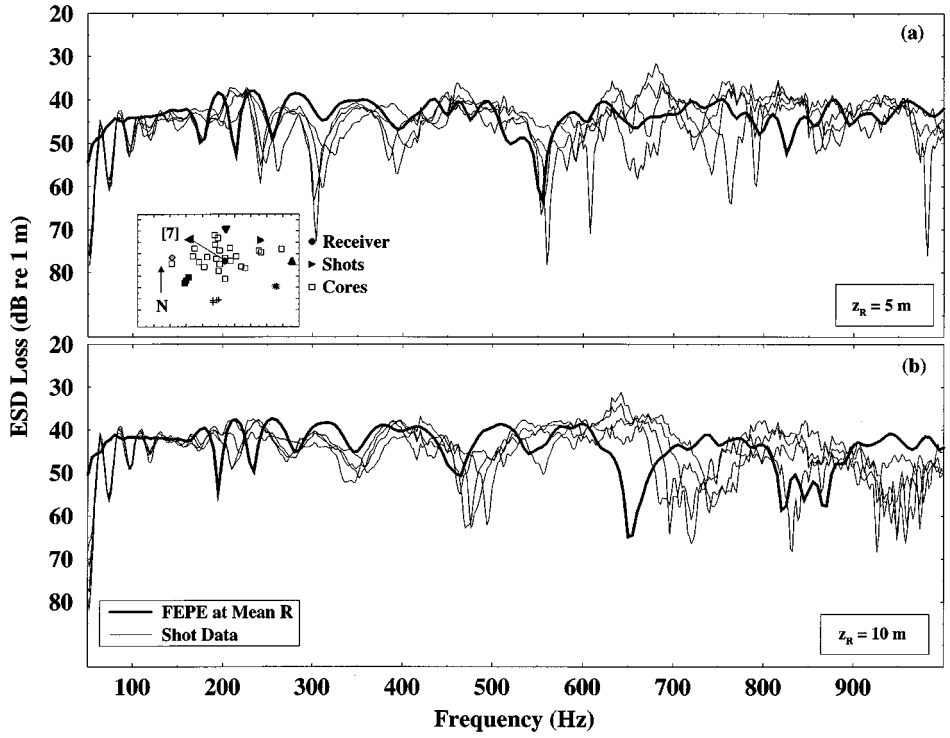

FIG. 14. Comparison of ESD loss versus frequency along track 7 for experimental data (thin solid lines) and FEPE simulation at mean shot range. (a) z_S=5 m, z_R=5 m; (b) z_S=5 m, z_R=10 m. Inset shows AGS site with track 7.

sibly at the higher frequencies where comparable structure is clearly observable.

Still within the subsurface channel, southeast of the receiver, track 3 results (Fig. 10) show a strong correspondence between both data and model interference patterns. Note at mid-frequencies, higher modes predicted by the simulations are apparent in the experimental data but are significantly more damped. This could be indicative of a deficiency within the geoacoustic data set or of an attenuation mechanism not properly accounted for in the model. How-

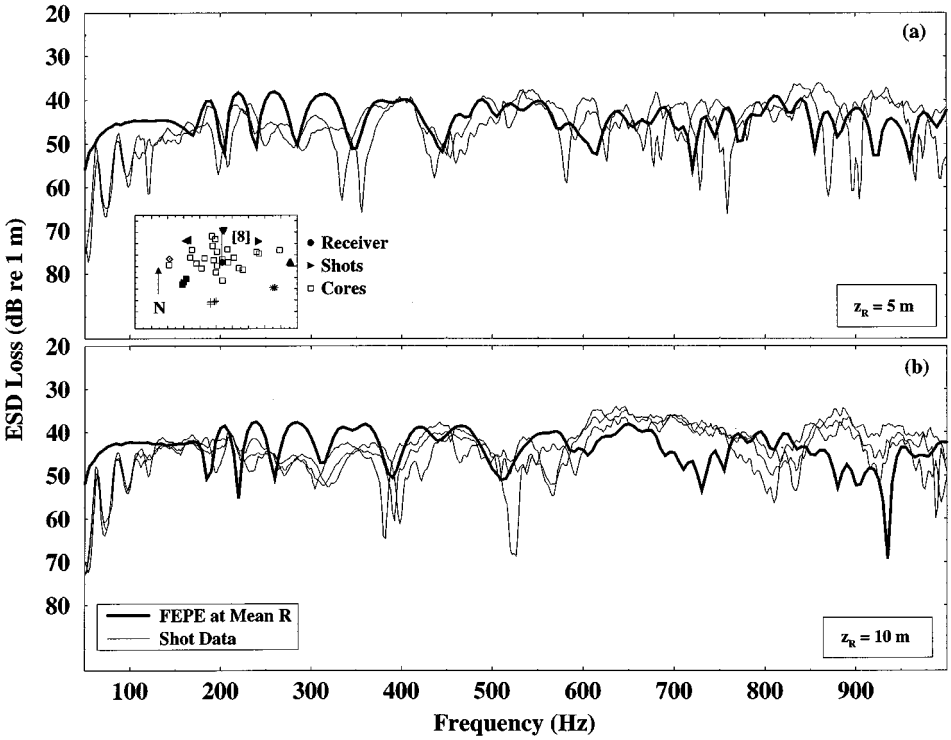

FIG. 15. Comparison of ESD loss versus frequency along track 8 for experimental data (thin solid lines) and FEPE simulation at mean shot range. (a) z_S=5 m, z_R=5 m; (b) z_S=5 m, z_R=10 m. Inset shows AGS site with track 8.

ever, in the 200–500 Hz band for both receiver depths the striking bimodal nature of the pattern is clearly captured in the simulations.

Track 4 lies along the channel boundary south of the receiving array. The kriged subsurface c_P field is similar to track 3 (Fig. 2), and the similarity of the FEPE curves is apparent. It is interesting to note that significant differences are present in Fig. 11 between hydrophones 5 and 10 at frequencies above 600 Hz for both the model and data. This can also be observed to some extent for all the tracks, indicating the potential usefulness of a modal decomposition in depth.[19] The interference patterns correlate well, aside from a noticeable phase shift, with the simulations giving more exaggerated peak-null trails. Note that the low end roll-off is not as severe as for the previous tracks, since the subbottom effects of a highly attenuating silty-clay layer are no longer present, yet due to the nature of the kriging algorithm this boundary is ''smeared,'' as seen by the higher simulation losses.

The next group of shots, collected along track 5, lie southwest of the receiving array and is outside the buried channel (along with tracks 6 and 7). Notice that this group of shots has the largest amount of variability between the source and receiving array (see Table I). Consequently, it is difficult to correlate the behavior between the model and data (Fig. 12), but the trends and the overall level variations generally agree. It is apparent that a source/receiver ranging error could possibly explain the phase shift between the data and simulation, as the ship drift can be correlated with the observed null drift.

With a few exceptions, track 6 results (Fig. 13) are very similar to track 7 (Fig. 14) for both data and simulations. The simulations for these tracks provide very good agreement in level variations and match the peak-null patterns generally over the entire spectra. As seen in both figures, the shot-to-shot variability increases considerably with frequency for both tracks.

Finally, track 8 (Fig. 15) lies along the channel boundary to the north of the receiving array. Level variations between the data and simulations correlate very well except at roll off (for the same reasons as track 4) and higher frequencies for hydrophone 10. The interference pattern is captured well by the model over low to mid frequencies. One difficulty with the correspondence at higher frequencies may be due to small variations in the sediment properties close to the water-sediment interface, precisely where data are lacking (the first data value lies 0.5 m into the seabed[19,23]).

IV. DISCUSSION

Thus far we have presented a comparison between experimental acoustic data and PE simulations based on geoacoustic data. To investigate the physical mechanisms operating in this environment, we begin by reexamining the ESDL results of the previous section. By comparing features observed in both experimental and simulated results, the ESDL curves can be grouped into three distinct categories: group I, which consists of tracks 2, 3, and 4; group II, tracks 6, 7, and 8; and group III, the ''anomalous'' tracks 1 and 5. Group I features are characterized by sharp ESDL structures

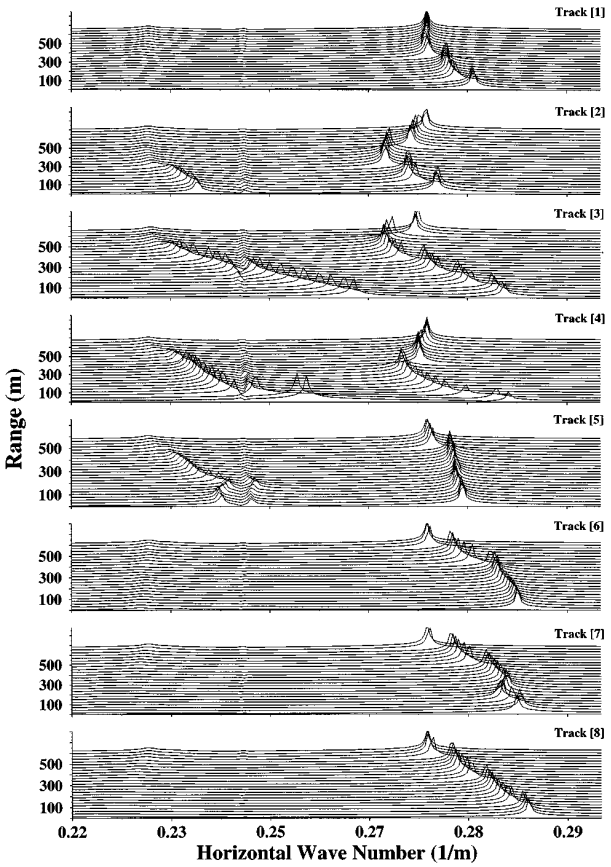

FIG. 16. Range-dependent simulations of horizontal wave number versus range for all eight tracks at 75 Hz.

and interference patterns, while group II results show smoother interference patterns, especially for mid to higher frequencies. Tracks 1 and 5 show different patterns that have characteristics of both groups. We notice also that the wavelength of interference patterns vary from track to track.

To examine these features in more detail, we turn attention to Figs. 2 and 3. Notice first the bathymetry of the group I tracks are concave up, group II concave down, while tracks 1 and 5 remain relatively flat. The general similarities in ESDL patterns suggest bathymetry as a dominant mechanism for this region.[13,16] The layering structure of the sediments as shown in Fig. 2 vary considerably within the groups, suggesting the lesser importance of this mechanism. However, we know also from ESDL and wave number simulations that compressional sound-speed effects are non-negligible in many parts of the AGS region. Note that the cross section of compressional speed versus depth for group I tracks 2, 3, and 4 are different than those of group II tracks 6, 7, and 8. Again, tracks 1 and 5 are different than results in either groups. The correlation between bathymetry and sediment layering in the groups makes it difficult to isolate which of them is the dominant physical process in ESDL data.

To examine these mechanisms from another perspective, we show the horizontal wave number versus range for all eight tracks calculated using the kriged input data. Figures 16 and 17 show these results for 75 Hz and 300 Hz, respectively. At 75 Hz, a dominant first mode is shown in all tracks, whereas only tracks 2, 3, 4, and 5 support higher-

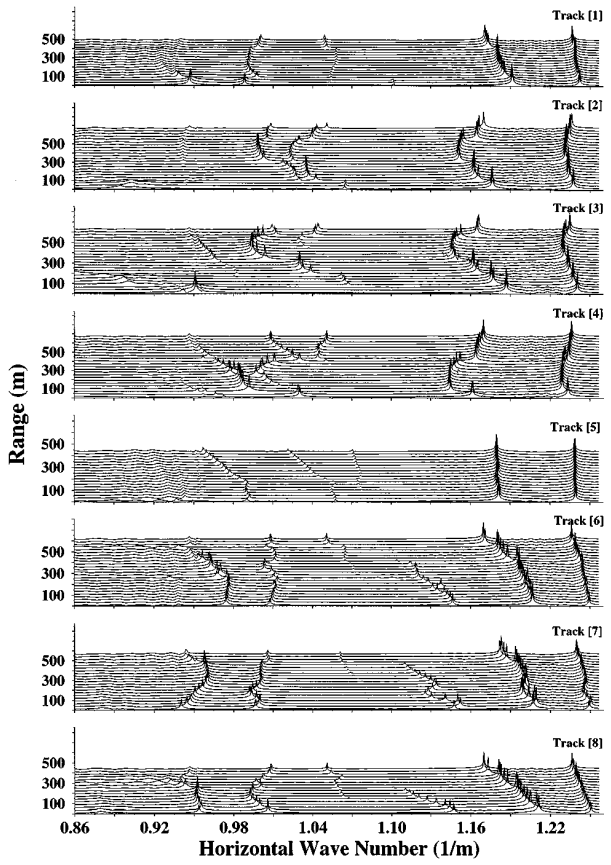

FIG. 17. Range-dependent simulations of horizontal wave number versus range for all eight tracks at 300 Hz.

order modes. Note that track 5 shows two distinct higher-order modes, while in the others they are not as clearly separated from each other. At 300 Hz the two dominant modes exist in all tracks, with higher-order modes being a complicated function of range and azimuth. A splitting of higher modes is seen between tracks 4 and 5, and this new pattern persists for tracks 6–8. It is evident from these calculations that in a realistic environment where both range and depth dependence in sediment properties exist, the modal evolution offers a way to quantify the propagation characteristics. Lacking sufficient sediment data, acoustic predictions from simulations can be biased and unreliable. Note that at both 75 and 300 Hz, certain modes split in range (for examples, mode 2 in track 3 at 75 Hz and higher modes in track 4 at 300 Hz). Frisk *et al.*[47] showed that the splitting of modal spectral peaks suggests the presence of two different seabed parameters over a range. This observation, which led to the study of Ohta,[48] suggests that the information contained in the range-dependent evolution of local modes can provide a clue to resolving the spatial variability of the bottom environment in a continuous manner. This idea may result in improved inverse techniques in the future.[22]

V. SUMMARY AND CONCLUSIONS

The existence of high-resolution geoacoustic data from an extensive geological survey at the AGS site has presented a unique opportunity to investigate the influence of seabed characteristics on shallow-water broadband propagation. We have exploited this knowledge by conducting a series of acoustic experiments throughout this region.[19,30] A broadband source was placed in a number of configurations about a fixed receiving array which extended over the entire water column. In particular, eight groups of shots were performed in a circular pattern ranging from 500 to 700 m from the array.

A parameter study was conducted previously to show the importance of range dependence.[23] Using a high-order PE model (FEPE), range-dependent calculations for the AGS environment were generated here to compare with the acoustic data. A geostatistical technique provided data between core positions.[24] Using fits for sediment sound-speed, density, and attenuation, representative range- and depth-dependent input streams were constructed. Since the acoustic data were collected at fixed ranges, transmission (or equivalently energy spectral density) loss as a function of frequency provides a natural representation for comparing the broadband data with frequency-domain simulations. Synthesis of FEPE simulations were performed along the eight tracks. The comparisons show that the geoacoustic model provides a generally accurate representation of the dominant mechanisms influencing the propagation. Equivalent fluid bottom representation show that shear effects do not provide a major loss mechanism and can be safely ignored at even very shallow sites as long as the rigidity of the seabed is relatively low. Additionally, intrinsic attenuation is considered through sediment dispersion which did not provided sufficient influence on the modeling to justify its importance for broadband propagation in the examples considered. Another technique for investigating seabed influences on propagation is the evolution of the horizontal wave number spectra over range. Simulations for the eight tracks are performed using a known technique.[38] It is seen that the lowest modes correlate directly with the bottom bathymetry, while higher modes are influenced by variations in the seabed structure and composition. The splitting behavior of higher modes can distinguish between the two distinct environments over which the tracks lie.

We have observed competing mechanisms that strongly influence broadband propagation in this shallow-water environment. An important factor is seabed bathymetry, the influence of which is observed in the range evolution of the lowest modes. Changes in the characteristics of the ESDL curves, primarily in the interference patterns, suggest the importance of this mechanism. Since some of the tracks have similar bathymetries, differences in the modal structure and TL patterns indicate substantial effects caused by inhomogeneities within the seabed.

ACKNOWLEDGMENTS

We wish to thank Dr. Michael Collins for providing us with the FEPE-synthesis code and for very insightful discussions. We also wish to thank Dr. Jim Lynch whose very helpful and continued discussions have improved our understanding of shallow-water acoustics. Special thanks to the anonymous reviewers who provided many helpful insights that greatly improved the original manuscript. Finally, we thank the many other individuals who have contributed to

both the AGS experiment and the data processing, including I. Jaya, M. Pulaski, A. Sundberg, and the crew of the R/V Cape Henlopen. This work was supported by the Office of Naval Research.

[1] R. L. Nitrouer and J. H. Kravitz, ''Integrated continental margin research to benefit ocean and earth sciences,'' EOS Trans. Am. Geophys. Union **76**, 121–126 (1995).
[2] C. L. Pekeris, ''Theory of propagation of explosive sound in shallow water,'' Geol. Soc. Am. Mem. **27**, 1–117 (1948).
[3] I. Tolstoy, ''Resonant frequencies and high modes in a layered wave guide,'' J. Acoust. Soc. Am. **28**, 1182–1192 (1956).
[4] C. S. Clay, ''Coherence of waveguide propagation,'' J. Acoust. Soc. Am. **36**, 833–837 (1964).
[5] F. Ingenito, ''Measurements of mode attenuation coefficients in shallow water,'' J. Acoust. Soc. Am. **53**, 858–863 (1973).
[6] F. B. Jensen and W. A. Kuperman, ''Experimental acoustic modeling at SACLANT-CEN,'' Rep. SR-34, SACLANT ASW Research Centre, La Spezia, Italy (1979).
[7] F. B. Jensen, ''Sound propagation in shallow water: A detailed description of the acoustic field close to the surface and bottom,'' J. Acoust. Soc. Am. **70**, 1397–1406 (1981).
[8] F. B. Jensen and W. A. Kuperman, ''Optimum frequency of propagation in shallow water environments,'' J. Acoust. Soc. Am. **73**, 813–818 (1983).
[9] G. V. Frisk and J. F. Lynch, ''Shallow water waveguide characterization using the Hankel transform,'' J. Acoust. Soc. Am. **76**, 205–216 (1984).
[10] J. X. Zhou, X. Z. Zhang, and P. H. Rogers, ''Effect of frequency dependence of sea-bottom attenuation on the optimum frequency for acoustic propagation in shallow water,'' J. Acoust. Soc. Am. **82**, 287–292 (1987).
[11] I. Tolstoy, ''Shallow water test of the theory of layered wave guides,'' J. Acoust. Soc. Am. **30**, 348–361 (1958).
[12] I. Tolstoy, ''Guided waves in a fluid with continuously variable velocity overlaying an elastic solid: Theory and experiment,'' J. Acoust. Soc. Am. **32**, 81–87 (1960).
[13] J. F. Lynch, S. D. Rajan, and G. V. Frisk, ''A comparison of broadband and narrow-band modal inversions for bottom geoacoustic properties at a site near Corpus Christi, Texas,'' J. Acoust. Soc. Am. **89**, 648–665 (1991).
[14] J. X. Zhou, X. Z. Zhang, P. H. Rogers, and J. Jarzynski, ''Geoacoustic parameters in a stratified sea bottom from shallow water acoustic propagation,'' J. Acoust. Soc. Am. **82**, 2068–2074 (1987).
[15] R. J. Cederberg, W. L. Siegmann, M. J. Jacobson, and W. M. Carey, ''Predictability of acoustic intensity in shallow water at low frequencies using the parabolic approximation,'' J. Acoust. Soc. Am. **89**, 89–96 (1991).
[16] R. J. Cederberg, W. L. Siegmann, and W. M. Carey, ''Influence of geoacoustic modeling on predictability of low frequency propagation in range dependent, shallow water environments,'' J. Acoust. Soc. Am. **97**, 2754–2766 (1995).
[17] R. L. Field and J. H. Leclere, ''Measurements of bottom-limited ocean impulse responses and comparisons with the time-domain parabolic equation,'' J. Acoust. Soc. Am. **93**, 2599–2615 (1993).
[18] L. Stahl, J. Koczan, and D. Swift, ''Anatomy of a shoreface-connected sand ridge on the New Jersey Shelf: Implications for the genesis of the shelf surfacial sand sheet,'' Geology **2**, 117–120 (1974).
[19] M. Badiey, I. Jaya, and A. H.-D. Cheng, ''Shallow water acoustic/geoacoustic experiments near the New Jersey Atlantic Generating Station site,'' J. Acoust. Soc. Am. **96**, 3593–3604 (1994).
[20] M. Badiey, ''Influences of sediment variability on broadband acoustic wave propagation in shallow water,'' in *Full Field Inversion Methods in Ocean and Seismic Acoustics*, edited by O. Diachok, A. Caiti, P. Gerstoft, and H. Schmidt (Kluwer Academic, Dordrecht, 1995), pp. 365–370.
[21] M. Badiey, K. P. Bongiovanni, and W. L. Siegmann, ''Interpretation of frequency-dependent transmission loss interference patterns,'' J. Ocean Eng. (in press).
[22] J. Lynch, private communication, 1995.
[23] K. P. Bongiovanni, M. Badiey, and W. L. Siegmann, ''Shallow water sediment layer structure and composition effects on range-dependent acoustic propagation at the Atlantic Generating Station site,'' J. Acoust. Soc. Am. **98**, 2249–2261 (1995).
[24] M. Badiey, A. H.-D. Cheng, and I. Jaya, ''Deterministic and stochastic analysis of acoustic plane wave reflection from inhomogeneous porous seafloor,'' J. Acoust. Soc. Am. **99**, 903–913 (1996).
[25] J. Ewing, J. A. Carter, G. H. Sutton, and N. Barstow, ''Shallow water sediment properties derived from high frequency shear and interface waves,'' Geophys. Res. **92**, 4739–4762 (1992).
[26] R. D. Stoll, *Sediment Acoustics* (Springer-Verlag, New York, 1989).
[27] J. C. Davis, *Statistics and Data Analysis in Geology* (Wiley, New York, 1986).
[28] M. Badiey, W. L. Siegmann, G. Botseas, and D. Lee, ''Three-dimensional acoustic/geoacoustic modeling of the New Jersey Atlantic Generating Station site,'' J. Acoust. Soc. Am. **97**, 3316 (A) (1995).
[29] S. Glenn and M. Crowley, ''Coastal upwelling and its relation to hypoxia in New York bight,'' Am. Geophys. Union S183 (1995).
[30] M. Pulaski, M. Badiey, S. Forsythe, I. Jaya, S. Shaw, and K. Bongiovanni, ''Cruise report: Phase II of the shallow water acoustic experiments at the Atlantic Generating Station (AGS) Site,'' Tech. Report, College of Marine Studies, University of Delaware, Newark, DE (1994).
[31] W. J. Marshall, ''Descriptors of impulsive signal levels commonly used in underwater acoustics,'' IEEE J. Ocean Eng. **21**, 108–110 (1996).
[32] F. B. Jensen, W. A. Kuperman, M. B. Porter, and H. Schmidt, *Computational Ocean Acoustics* (AIP, New York, 1994).
[33] M. D. Collins and E. K. Westwood, ''A higher-order energy-conserving parabolic equation for range-dependent ocean depth, sound speed, and density,'' J. Acoust. Soc. Am. **89**, 1068–1075 (1991).
[34] *PE WORKSHOP II, Proceedings of the Second Parabolic Workshop*, edited by S. A. Chin-Bing, D. B. King, J. A. Davis, and R. B. Evans (Naval Research Laboratory, Stennis Space Center, 1993).
[35] M. D. Collins, W. A. Kuperman, and W. L. Siegmann, ''A parabolic equation for poro-elastic media,'' J. Acoust. Soc. Am. **98**, 1645–1656 (1995).
[36] R. R. Greene, ''The rational approximation to the acoustic wave equation with bottom interaction,'' J. Acoust. Soc. Am. **76**, 1764–1773 (1984).
[37] E. L. Hamilton, ''Geoacoustic modeling of the seafloor,'' J. Acoust. Soc. Am. **68**, 1313–1340 (1980).
[38] D. J. Thomson, ''Modal decomposition of PE fields in a range-dependent environment.'' Defence Research Establishment Pacific, Canada, Preprint 90-08, 1990.
[39] L. M. Brekhovskikh and Y. P. Lysanov, *Fundamentals of Ocean Acoustics* (Springer-Verlag, Berlin, 1982).
[40] A. C. Kibblewhite, ''Attenuation of sound in marine sediments: A review with emphasis on new low frequency data,'' J. Acoust. Soc. Am. **86**, 716–738 (1989).
[41] P. C. Wuenschel, ''Dispersive body waves—An experimental study,'' Geophysics **30**, 539–551 (1965).
[42] D. J. Wingham, ''The dispersion of sound in sediment,'' J. Acoust. Soc. Am. **78**, 1757–1760 (1985).
[43] C. T. Tindle and Z. Y. Zhang, ''An equivalent fluid approximation for a low shear speed ocean bottom,'' J. Acoust. Soc. Am. **91**, 3284–3256 (1992).
[44] Z. Y. Zhang and C. T. Tindle, ''Improved equivalent fluid approximations for a low shear speed ocean bottom,'' J. Acoust. Soc. Am. **98**, 3391–3396 (1995).
[45] W. I. Futterman, ''Dispersive body waves,'' Geophys. Res. **67**, 5279–5291 (1962).
[46] M. D. Collins, ''The time-domain solution of the wide-angle parabolic equation including the effects of sediment dispersion,'' J. Acoust. Soc. Am. **67**, 2114–2125 (1988).
[47] G. V. Frisk, J. F. Lynch, and S. D. Rajan, ''Determination of compressional wave speed profiles using modal inverse techniques in a range-dependent environment in Nantucket Sound,'' J. Acoust. Soc. Am. **86**, 1928–1939 (1989).
[48] K. Ohta, ''Analysis of Modal Evolution Caused by a Weakly Range-Dependent Seabed in Shallow Water and its Application to Inversion for Geoacoustic Properties,'' Ph.D. thesis, MIT/WHOI Woods Hole Report, WHOI-93-35 (1993).

Acoustic propagation through a low Mach number, stratified flow

Pierre Elisseeff and Henrik Schmidt
Department of Ocean Engineering, Massachusetts Institute of Technology, Cambridge, Massachusetts 02139

(Received 11 March 1996; accepted for publication 20 August 1996)

Propagation of sound in an oceanic waveguide in the presence of a low Mach number, stratified flow is investigated. Equations for the wave-number integration (WI) and normal-mode (NM) approaches are simultaneously derived in a consistent formulation. At low Mach numbers acoustic azimuthal coupling is negligible and the effect of current can be accounted for by a simple modification of existing WI and NM, codes. Numerical results for low- and high-frequency sources in a simple waveguide show a high degree of agreement between modified versions of OASES and KRAKEN, and confirm previous theoretical results. An approximate modal closed-form solution based on the medium-at-rest mode set is then derived assuming adiabatic propagation (no current-induced mode coupling). Comparison with the modified versions of KRAKEN and OASES shows this assumption breaks down if there is bottom penetration or if the current profile exhibits somewhat sharp variations with respect to depth. An application to matched-field current tomography is eventually presented. Assuming accurate knowledge of the acoustic waveguide, a current velocity of 1.5 m/s can be measured at a range of 2 km with a resolution of 0.2 m/s using a multitone cw signal spanning 200–250 Hz. © *1997 Acoustical Society of America.* [S0001-4966(97)01204-6]

PACS numbers: 43.30.−k, 43.20.Mv [JHM]

INTRODUCTION

Ray-based ocean acoustic tomography has received much attention over the past two decades.[1,2] Experimental current tomography in particular became the focus of several research efforts in the eighties. Mesoscale current profiles were measured by Howe *et al.* in deep ocean over a distance of 300 km west of Bermuda.[3] Ray paths were found to be nearly reciprocal. No significant range dependence of the current was observed. Depth-averaged currents in the Florida Straits were measured by DeFerrari and Nguyen over a distance of 25 to 45 km (Ref. 4) in a 500-m-deep bottom-limited environment. Using the same data set, Ko *et al.* subsequently computed estimates of the current vorticity in this region.[5] Similar measurements were made by Dushaw *et al.* in the North Pacific Ocean in 1987 over a distance of 1000 km.[6]

While ray-based tomography has demonstrated its feasibility in deep ocean, its applicability to shallow-water waveguides remains problematic. High-frequency transmissions become less deterministic due to the small scale variability of coastal regions. Ray tracing is then highly sensitive to initial conditions. Low-frequency transmissions, on the other hand, are known to yield robust results in shallow-water environments. But the full wave field must be modeled as diffraction effects become non-negligible. After decades of ray-based modeling of propagation through a moving medium,[7–11] parabolic equation (PE) methods have become increasingly popular. A variety of schemes has been developed,[12–14] confirming that small currents and current shears can have a significant impact on shallow-water propagation. Although the PE method yields a full field solution, it does so at the expense of not comprehending the mechanism of propagation analytically, depriving us of a powerful interpretative tool.

The modal approach, on the other hand, seems extremely promising in spite of its difficulty. If valid assumptions can be made in the case of ocean acoustics, the modal formalism will lead to a deeper understanding of sound advection by currents and thus to more efficient inversion algorithms. In this context an extensive theoretical framework was recently developed by Godin.[15,16] Several mistakes were found in previous derivations of modal expressions.[17–19] The eigenvalue problem was shown to reduce to that of a medium at rest by using an equivalent density and an equivalent sound speed. Prior to this a numerical scheme for solving the modified Sturm–Liouville problem involved in moving medium propagation was developed by Porter[20] as an extension of his previous work.[21] Although match-field processing (MFP) is an obvious candidate for full field current inversions, it has not yet been exploited to its full potential in this context.

A shallow-water high-frequency tomography experiment was conducted in Haro Strait (British Columbia, Canada)[22] in June 1996. Its goal was to demonstrate the feasibility of real-time acoustic imaging of a tidal front, for which salinity and temperature effects are of the same order of magnitude as current effects. A numerically accurate forward model is then required in order to develop any realistic inversion scheme. The purpose of this paper is to generalize the existing medium-at-rest wave number integration and normal-mode approaches[23] to the case of a low Mach number, stratified flow within a single formulation directly related to measurable or computable quantities. This leads to a modified eigenvalue problem which can be solved numerically by a simple modification of the code KRAKEN.[21] The

modified wave-number integration scheme amounts to an equally simple modification of SAFARI/OASES.[24] A modal closed-form solution based on the medium-at-rest mode set is then derived assuming adiabatic propagation (no current-induced mode coupling). These results are subsequently applied to simple scenarios for low- and high-frequency sources. Acoustic fields computed by KRAKEN and OASES are compared to one another. Their agreement with the closed-form solution is then discussed. Finally, assuming full knowledge of the acoustic waveguide, the feasibility of a matched-field current tomographic inversion for a realistic environment is investigated.

I. ANALYSIS

A. The wave equation

The wave equation for a point source in a stationary layered medium can be expressed, using classical tensor notation, as[16]

$$\rho \frac{\partial}{\partial x_j}\left(\frac{1}{\rho}\frac{\partial p(\mathbf{x},t)}{\partial x_j}\right)-\frac{1}{c^2}\left(\frac{\partial}{\partial t}+U_j\frac{\partial}{\partial x_j}\right)^2 p(\mathbf{x},t) + 2\rho\frac{dU_j}{dz}\frac{\partial u_z}{\partial x_j}=-S(t)\delta(\mathbf{x}-\mathbf{x}_s), \tag{1}$$

where U and u are the local hydrodynamic and acoustic flow velocities. Environmental range dependence is implicitly neglected throughout this paper unless otherwise stated. The hydrodynamic flow is assumed to be incompressible ($\nabla\cdot\mathbf{U}=0$), stratified ($\mathbf{U}\cdot\hat{\mathbf{z}}=0$) and depends on depth only. Current shear may be arbitrarily large. Taking the Fourier transform of (1) with respect to time then leads to the modified Helmholtz equation:

$$\left[\rho\frac{\partial}{\partial x_j}\left(\frac{1}{\rho}\frac{\partial}{\partial x_j}\right)+k^2+2ik\mathscr{M}_j\frac{\partial}{\partial x_j} -2i\frac{\partial}{\partial x_j}\left(\frac{\mathscr{M}_l}{k}\right)\frac{\partial^2}{\partial x_l\partial x_j}\right]p(\mathbf{x},\omega) =-S(\omega)\delta(\mathbf{x}-\mathbf{x}_s), \tag{2}$$

where the Mach number $\mathscr{M}=U/c$ is assumed to be small and terms of order $\mathscr{M}^2$ and higher are neglected. The acoustic velocity was expressed to a first order approximation as a function of ∇p. The term in $\mathscr{M}\cdot\nabla$ represents convective transport of the acoustic wave and usually is the dominant flow-related term. The second term in $\mathscr{M}$ becomes significant at low frequencies when the current profile exhibits sharp variations over distances of the order of a wavelength.

The terms in $\mathscr{M}$ in (2) can equally be thought of as source terms. In this case, assuming the pressure field is the sum of a perturbation and a mean field, the solution to (2) could be written as the three-dimensional convolution of a Green's function with the three source terms expressed using the mean field.[25] This approach is however limited by the fact that, as range increases, so does the pressure perturbation and one can then expect the small perturbation assumption to break down for $kr\mathscr{M}>1$.

Transforming (2) into cylindrical coordinates (r,θ,z), the derivatives with respect to θ account for azimuthal coupling. These terms are, however, of order at least $1/kr$ compared to other flow-related terms and were shown to be negligible in the far field in the absence of strong horizontal sound-speed gradients.[26–28] Consequently, (2) can be rewritten for a given azimuth as

$$\left[\frac{1}{r}\frac{\partial}{\partial r}\left(r\frac{\partial}{\partial r}\right)+\rho\frac{\partial}{\partial z}\left(\frac{1}{\rho}\frac{\partial}{\partial z}\right)+k^2+2ik\mathscr{M}\frac{\partial}{\partial r} -2i\frac{d}{dz}\left(\frac{\mathscr{M}}{k}\right)\frac{\partial^2}{\partial r\partial z}\right]p(r,z,\omega)=-S(\omega)\delta(\mathbf{x}-\mathbf{x}_s), \tag{3}$$

where $\mathscr{M}$ is from now on the projected Mach number $U\cos\theta/c$. Thus the inherently 3-D problem of acoustic propagation through a moving medium can be reduced to a series of 2-D problems corresponding to different azimuths for low Mach number, stratified flows.

B. Wave-number integration representation

Azimuthal coupling being neglected, the 2-D propagation problem can be interpreted as that of acoustic propagation through a perfectly symmetric waveguide. The total acoustic field can then be decomposed into a sum conical waves using the Hankel transform defined as

$$p(k_r,z,\omega)=\int_0^\infty p(r,z,\omega)J_0(k_r r)r\,dr. \tag{4}$$

Combining (3) and (4) yields the following modified depth-separated wave equation:

$$\left[\rho\frac{d}{dz}\left(\frac{1}{\rho}\frac{d}{dz}\right)+k^2-k_r^2-2k_r k\mathscr{M}+2k_r\frac{d}{dz}\left(\frac{\mathscr{M}}{k}\right)\frac{d}{dz}\right] \times p(k_r,z,\omega)=-S(\omega)\delta(z-z_s). \tag{5}$$

The first term in $\mathscr{M}$ accounts for current-induced refraction. The second term represents the effect of shear stress or equivalently vorticity. While the former is almost always the dominant flow-related term, the latter may under certain circumstances become non-negligible. The ratio of shear over current can be represented by the shear number ζ:[29]

$$\zeta=\frac{1}{k}\max\left(\frac{1}{U}\frac{dU}{dz}\right)=\frac{1}{kL}. \tag{6}$$

For deep water, the length scale L is typically 100 m.[30] This means the shear term can be neglected above 20 Hz. For shallow water L may be as small as 10 m,[29] making the shear term negligible above 200 Hz. Below this limit, shear may be neglected for long range propagation insofar as the vertical wave number is small, i.e., for low grazing angles. The limit frequency is then given by $c\sin\theta_c/L$, where θ_c is the grazing angle of interest.

Assuming the current profile $\mathscr{M}(z)$ is piecewise constant with respect to z, the derivative of $\mathscr{M}$ with respect to z vanishes almost everywhere. Equation (5) therefore becomes identical to the classical depth-separated equation[23] provided the sound-speed profile is replaced by the following wave-number-dependent equivalent sound-speed profile:

$$\tilde{c}(z)=\frac{c(z)}{1-(k_r/k(z))\mathscr{M}(z)}. \tag{7}$$

In contrast to previous expressions for an effective sound speed,[29,31] we here take into account the anisotropic nature of propagation, do not require that any derivative of the current profile be known and do not require any current-dependent mapping of the depth variable. Singularities arising between constant current layers are handled through the boundary condition, i.e., by imposing continuity of pressure and continuity of the modified particle displacement:[20,31]

$$\tilde{w}(z)=\frac{w(z)}{[1-(k_r/k(z))\mathscr{M}(z)]^2}. \tag{8}$$

The presence of current shear can therefore be taken into account by discretizing the waveguide into isocurrent layers whose thickness is small compared to the acoustic wavelength. The current discontinuity arising between layers is known to introduce additional poles in the complex k_r plane[32] at the approximate location $(1\pm i)k/\mathscr{M}$ (for small $\mathscr{M}$). Its effect on acoustic reciprocity is briefly discussed in section I D. When the traditional integration contour is considered (upper half-plane), the presence of these poles makes the resulting acoustic field noncausal. This lack of causality can be seen as the effect of having a pole above the real axis. In the case of a Pekeris waveguide, for instance, poles corresponding to leaky modes are displaced slightly above the real axis, breaking in a much more dramatic fashion the causality of the field. This effect is important for receivers located in the near field (for a discussion of attenuation effects on causality, see Refs. 33 and 34). In the far field, however, this lack of causality has no visible effect on the modeled signal. It will thus be ignored in the rest of this paper. The approach presented here is numerically convenient as its implementation requires a very simple modification of a wave-number-integration code such as OASES.

C. Normal mode representation

Ignoring the branch line contribution the pressure field can be decomposed as the following sum of normal modes (in matrix notation):[23]

$$p(r,z,w)=\boldsymbol{\psi}^T(z)\mathbf{h}(r), \tag{9}$$

where $\mathbf{h}$ is the projection of p on $\boldsymbol{\psi}(z)$, and $\boldsymbol{\psi}(z)$ is the medium-at-rest mode set associated with the eigenvalue problem:

$$\left[\rho\frac{d}{dz}\left(\frac{1}{\rho}\frac{d}{dz}\right)+k^2\right]\boldsymbol{\psi}=\Lambda\boldsymbol{\psi}$$

with the normalization condition

$$\int_0^D\frac{1}{\rho}\boldsymbol{\psi}(z)\boldsymbol{\psi}^T(z)dz=\mathbf{I},$$

where $\mathbf{I}$ is the identity matrix. Λ is a diagonal matrix whose elements are the modal eigenvalues k_{rn}^2. Equations (3) and (9) can then be recombined as (see Appendix)

$$\left[\frac{1}{r}\frac{d}{dr}\left(r\frac{d}{dr}\right)+2i\mathbf{K}\frac{d}{dr}+\Lambda\right]\mathbf{h}(r)=-\frac{S(\omega)\delta(\mathbf{r})}{\rho(z_s)}\boldsymbol{\psi}(z_s), \tag{10}$$

where the current coupling matrix $\mathbf{K}$ is defined as

$$\mathbf{K}=[\kappa_{mn}]=\int_0^D\frac{1}{\rho}k\mathscr{M}\boldsymbol{\psi}\boldsymbol{\psi}^T dz-\int_0^D\frac{1}{\rho}\frac{d}{dz}\left(\frac{\mathscr{M}}{k}\right)\frac{d\boldsymbol{\psi}}{dz}\boldsymbol{\psi}^T dz.$$

Equation (10) is similar in many respects to that recently derived by Collins.[14] The first term in $\mathbf{K}$ is Hermitian and accounts for current-induced refraction. The second term explicitly accounts for the presence of shear in the flow. Their relative importance is characterized by the shear number ζ. In some cases the current profile is smooth enough and $\mathbf{K}$ can be considered diagonal. Propagation is then adiabatic and a closed-form solution for p can be derived as shown in the next section. In general, however, off-diagonal elements of $\mathbf{K}$ do not vanish. This mode coupling can be induced by either current-based refraction (first term in $\mathbf{K}$) or shear stress (second term). Equation (10) in this case is a set of fully coupled equations. In order to decouple them, one could try to diagonalize $\mathbf{K}$ and reformulate (10) in the eigenbasis of $\mathbf{K}$. This would, however, introduce coupling in Λ, which unfortunately has a different set of eigenvectors.

Assuming shear stress is negligible, i.e., for small shear numbers, the difficulty outlined above can be circumvented by using a modified mode set. Current-induced refraction is then taken into account in the mode set by solving the following eigenvalue problem:

$$\left[\rho\frac{d}{dz}\left(\frac{1}{\rho}\frac{d}{dz}\right)+k^2\right]\boldsymbol{\psi}=(\Lambda+2k\mathscr{M}\Lambda^{1/2})\boldsymbol{\psi}. \tag{11}$$

The normalization condition becomes

$$\int_0^D\frac{1}{\rho}\boldsymbol{\psi}(z)\boldsymbol{\psi}^T(z)dz=\mathbf{J},$$

$$[J]_{mn}=\begin{cases}1, & \text{if } m=n,\\ -2\displaystyle\int_0^D\frac{1}{\rho}\frac{k\mathscr{M}}{k_{rn}+k_{rm}}\psi_n\psi_m\,dz, & \text{if } m\neq n.\end{cases} \tag{12}$$

Thus the modified mode set is no longer orthogonal. As shown below this, however, has a limited impact on the approximate representation of the field. The main features of the effect of current are captured by the modified set of eigenvalues for small Mach numbers. Combining (11) with (3) and (9) then leads to the following modified modal equation:

$$\left[\mathbf{J}\frac{1}{r}\frac{d}{dr}\left(r\frac{d}{dr}\right)+2i\mathbf{K}\frac{d}{dr}+2\Lambda^{1/2}\mathbf{K}+\Lambda\mathbf{J}\right]\mathbf{h}(r)=-\frac{S(\omega)\delta(\mathbf{r})}{\rho(z_s)}\boldsymbol{\psi}(z_s), \tag{13}$$

where **K** accounts for refraction only and is thus Hermitian. This equation is satisfied in the far field by the medium-at-rest solution:

$$h_n(r) \simeq \sqrt{\frac{2}{\pi}}\, e^{-i\pi/4} S(\omega)\, \frac{\psi_n(z_s)}{\rho(z_s)}\, \frac{e^{ik_{rn}r}}{\sqrt{k_{rn}r}}, \tag{14}$$

where ψ_n and k_{rn} are solution to the eigenvalue problem (11). The accuracy of (14) is of order $\mathscr{M}/kr$. The contribution of off-diagonal terms in **J** is of order $\mathscr{M}/(kr)^2$. The eigenvalue problem stated in (11) can be numerically solved by a code such as KRAKEN, simply by replacing k_r^2 in the code by $k_r^2 + 2k_r k\mathscr{M}$ and by using the modified boundary condition stated in Sec. I B. The pressure field is then obtained by summing up modes as one would do for a medium at rest. This solution is compared to the wave number integration approach in Sec. II.

D. Adiabatic mode solution

Equation (10) can be conveniently reformulated in the wave number domain as

$$(k_r^2\mathbf{I} + 2k_r\mathbf{K} - \Lambda)\mathbf{h}(k_r) = \frac{S(\omega)}{\rho(z_s)}\, \boldsymbol{\psi}(z_s), \tag{15}$$

where $\mathbf{h}(k_r)$ is the transform of $\mathbf{h}(r)$. The current coupling matrix **K** includes again both the effect of current refraction and current shear. The solution to this equation is

$$\mathbf{h}(k_r) = \frac{S(\omega)}{\rho(z_s)}\, (k_r^2\mathbf{I} + 2k_r\mathbf{K} - \Lambda)^{-1}\boldsymbol{\psi}(z_s). \tag{16}$$

The matrix inversion can be performed analytically if terms of order $\mathbf{K}^2$ and higher are negligible, i.e., for low Mach numbers and low to moderate shear ($\zeta \leqslant 1$). A first-order coupled-mode expression for p can then be derived. However, this procedure appears to be numerically unstable and remains a topic of current research. In some cases the current profile is smooth enough with respect to depth so that mode-coupling can be neglected (adiabatic propagation) and **K** becomes diagonal. The wave number domain pressure $\mathbf{h}(k_r)$ can then be simplified and its components become

$$h_n(k_r) = \frac{S(\omega)}{\rho(z_s)}\, \frac{\psi_n(z_s)\psi_n(z)}{(k_r + \kappa_{nn})^2 - k_{rn}^2}. \tag{17}$$

The effect of current is to shift poles of the Green's function by κ_{nn} in the complex k_r plane. This pole translation is a fundamental property of moving waveguides which does not depend on adiabaticity. In the adiabatic case the translation is parallel to the real axis and can be characterized by a simple expression. This shift is the very reason acoustic reciprocity is broken, as poles are no longer symmetric with respect to the imaginary axis. When current discontinuities are present additional poles appear on the right half-plane as pointed out in Sec. I B, making the asymmetry even stronger. Substituting the inverse Hankel transform of (16) in (9) leads to

$$p(r,z,\omega) = \frac{iS(\omega)}{4\rho(z_s)} \sum_n \psi_n(z_s)\psi_n(z) H_0^{(1)}((k_{rn} - \kappa_{nn})^r). \tag{18}$$

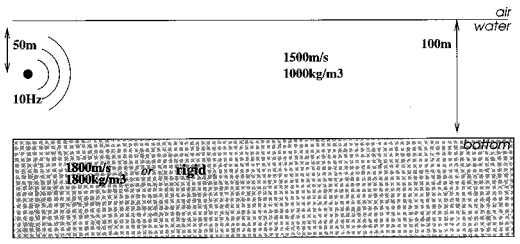

FIG. 1. Shallow-water waveguide with a uniform current of 100 m/s in the water column. Two kinds of bottoms were considered: rigid and fluid.

If $\mathscr{M}$ is constant, this expression becomes identical to that derived by Schmidt and Kuperman for a source and receiver moving at the same speed in a medium at rest.[35]

Bearing in mind that mode coupling is neglected, the previous result can be generalized to the case of weakly range-dependent flows $\mathscr{M}(r,z)$:

$$p(r,z,\omega) = \frac{iS(\omega)}{4\rho(z_s)} \sum_n \psi_n(z_s)\psi_n(z) \times H_0^{(1)}\left(k_{rn}r - \int_0^r \kappa_{nn}(r')\,dr' \right). \tag{19}$$

The notion of weak range dependence is voluntarily left undefined as a precise validity statement for the heuristic expression above lies beyond the scope of this paper.

Hence in the case where mode-coupling can be neglected, the effect of an arbitrary range-independent stratified current profile is modeled by a simple modal wave-number shift. Having computed the normal modes $\{\psi_n\}$ with a code such as KRAKEN[21] the coefficients $\{\kappa_{nn}\}$ can be straightforwardly evaluated and included in sum (18), yielding an adiabatic estimate of the acoustic pressure field in the presence of a stratified flow. However, as shown in the next section, this result is limited to smooth current profiles and no bottom penetration.

II. NUMERICAL RESULTS

Practical applications of the wave number and normal mode representations are presented below for two simple isovelocity waveguides. Versions of KRAKEN and OASES modified as indicated in the previous section are compared for a low-frequency scenario. A high-frequency source for a similar environment is subsequently considered. In both cases the validity of the closed-form solution outlined in Sec. I D is discussed. A simple application to matched-field current tomography is then presented.

A. Low-frequency case

1. Rigid bottom

The case of a 10-Hz omnidirectional source in a rigid bottom waveguide with a uniform current in the water column is considered here (see Fig. 1). An unrealistic current speed of 100 m/s is chosen here in order to emphasize the qualitative features of the acoustic field. A single mode is propagating in the water column. As no energy is exchanged with the bottom, this is somewhat akin to a cylindrical wave propagating in free space. As shown in Fig. 2 the current-

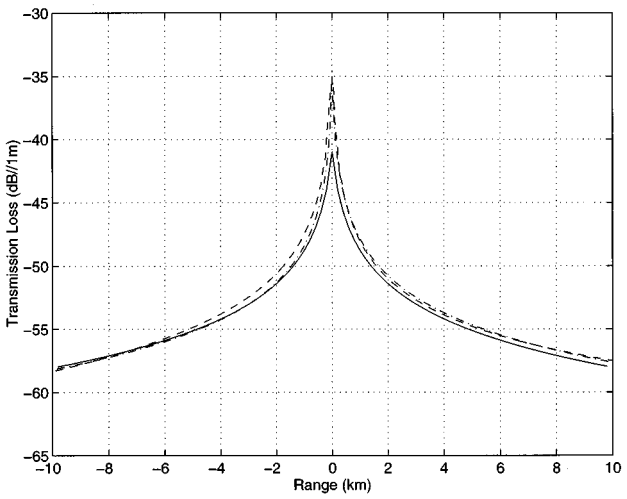

FIG. 2. Transmission loss versus range for a 10-Hz source in a free/rigid waveguide with a uniform current (100 m/s) flowing towards positive ranges. Solid line: KRAKEN. Dashed line: OASES. Dash-dotted line: closed-form solution.

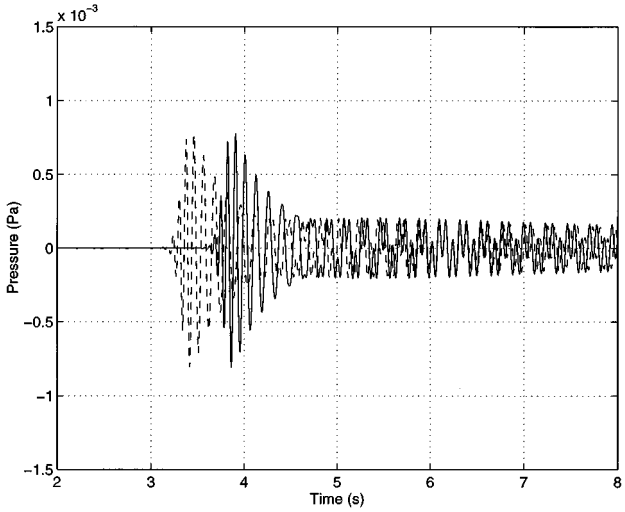

FIG. 4. Received signal for a source signal of bandwidth 20 Hz and center frequency 10 Hz in a free/rigid waveguide with a uniform current (100 m/s). Receiver depth: 50 m. Receiver range: 5 km. Solid line: receiver is upstream. Dotted line: receiver is downstream.

modified versions of KRAKEN and OASES as well as the modal closed-form solution agree to within 1 dB beyond 1 km in range both upstream and downstream. The acoustic field is, for all practical purposes, axisymmetric as shown in Fig. 3. This is in agreement with Godin's result for a spherical wave in free space.[16]

Signals received 5 km upstream and downstream at the same depth (50 m) were computed using OASES and are shown in Fig. 4. The difference in arrival times matches the theoretical value of 0.4 s. Amplitudes are identical, as expected from Fig. 3.

2. Fluid bottom

The same source is now placed in a waveguide of identical dimensions with a fluid bottom (see Fig. 1). The outputs of KRAKEN and OASES are compared in Fig. 5 and show very good agreement with each other, whereas a large discrepancy with the closed-form solution can be noted. Although no azimuthal coupling was taken into account, the nature of the bottom has a clear impact on the azimuthal dependence of the acoustic field. In particular the bottom reflection coefficient is going to be lower downstream due to a decreased equivalent sound-speed contrast at the interface, resulting in a higher level of energy transmitted in the bottom and a larger transmission loss in the water column. The transmission loss pattern in the horizontal plane is dictated by this mechanism (see Fig. 6). This furthermore provides an interpretation of the failure of the closed-form solution to match KRAKEN and OASES's result: based on the medium-at-rest mode set, this solution merely shifts modal wave numbers by a certain amount and does not take into account changes in the bottom reflection coefficient.

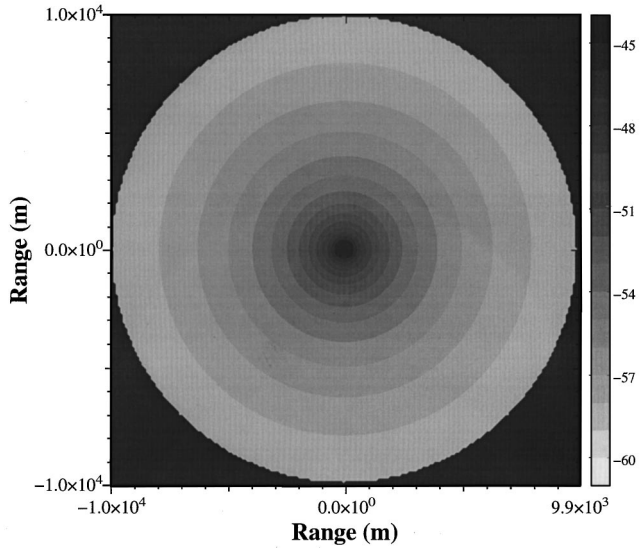

FIG. 3. Transmission loss versus azimuth for a 10-Hz source in a free/rigid waveguide with a uniform current (100 m/s) flowing eastward. Receiver depth: 50 m.

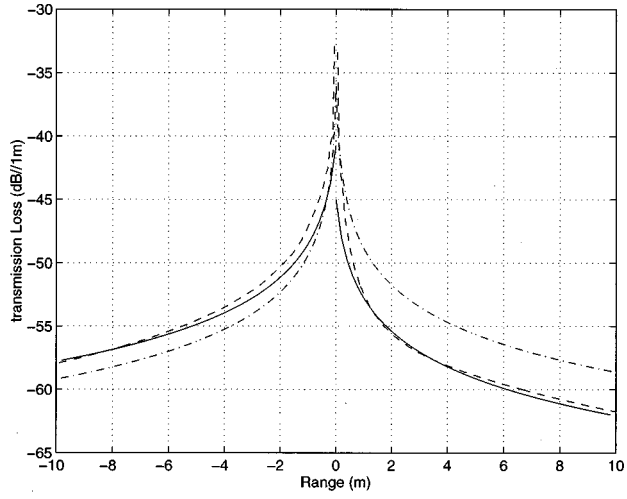

FIG. 5. Transmission loss versus range for a 10-Hz source in a free/fluid waveguide with a uniform current (100 m/s) flowing toward positive ranges. Full line: KRAKEN. Dashed line: OASES. Dash-dotted line: closed-form solution.

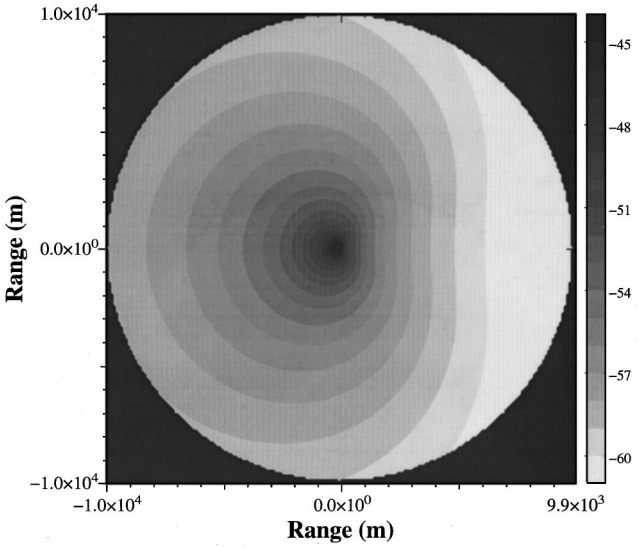

FIG. 6. Transmission loss versus azimuth for a 10-Hz source in a free/fluid waveguide with a uniform current (100 m/s) flowing eastward. Receiver depth: 50 m.

Similarly to the rigid bottom case, time arrivals are shifted by roughly half a second (see Fig. 7). As expected from Fig. 6 the upstream signal is stronger. It is preceded by a head wave, which reaches the receiver at the same time regardless of the direction of propagation since the bottom is azimuthally symmetric.

B. High-frequency case

The high-frequency shallow-water environment considered in this section is shown in Fig. 8. Its features are very similar to that of the Haro Strait tomography experiment (British Columbia, Canada).[22] Upwelling, however, is explicitly neglected. The current magnitude is chosen ten times larger than its actual value in order to emphasize qualitative features of the acoustic field. The time-domain output of a

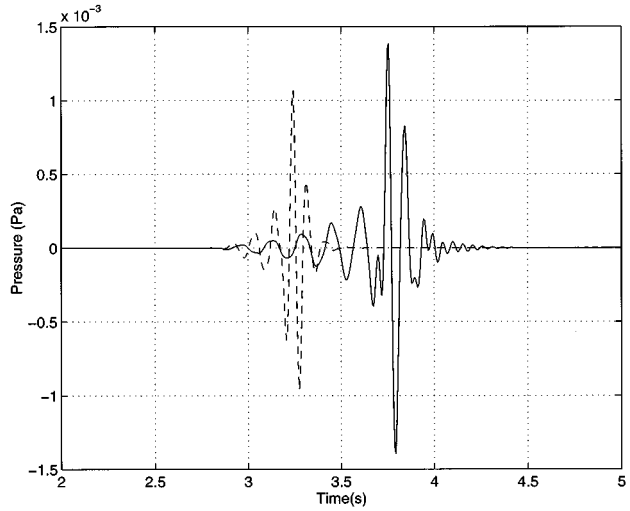

FIG. 7. Received signal for a source signal of bandwidth 20 Hz and center frequency 10 Hz in a free/fluid waveguide with a uniform current (100 m/s). Receiver depth: 50 m. Receiver range: 5 km. Solid line: receiver is upstream. Dotted line: receiver is downstream.

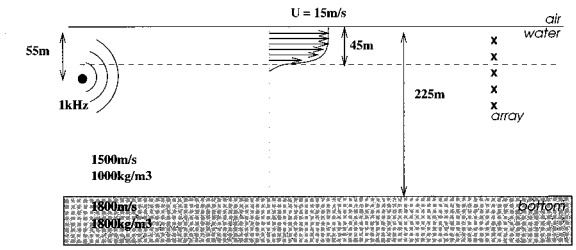

FIG. 8. High-frequency shallow water waveguide with a uniform current (15 m/s) in the upper 45 m. The transition zone is 10 m deep (40 to 50 m).

vertical line array spanning the entire water column was computed separately by KRAKEN and OASES. The corresponding synthetic I/Q demodulated time series shown in Figs. 9 and 10 exhibit a remarkable agreement. The array range is 2 km. The bottom is at a depth of 225 m. The different types of wave predicted by Jones and Morgan[32] are present as outlined in Fig. 9: a primary wave in the nonmoving layer (45 to 225 m), various specularly reflected waves, a transmitted wave in the moving layer (0 to 45 m) and a head wave linking the transmitted and direct waves. The gray scale is in Pascals. No unstable interface wave is present since we did not impose any causality constraint. Numerical noise caused by wrap-around is absent of the OASES output as a complex frequency was used in the Fourier synthesis.[23]

The modal closed-form solution output is plotted in Fig. 11 and shows a strong discrepancy with the previous numerical solutions. The transmitted wave and the head wave have vanished. In addition the whole primary wavefront is shifted slightly towards earlier arrivals. This stems from the fact that the wave number shift κ_{nn} is proportional to the current velocity integrated over the entire water column. The current profile being sharp enough to break the orthogonality of the medium-at-rest mode set, the current coupling matrix **K** in Eq. (8) can no longer be considered diagonal. It is worth noticing that this coupling depends on the current profile and not its magnitude, which can be factored out. In other words the pertinent variable from an acoustic perspective is not the

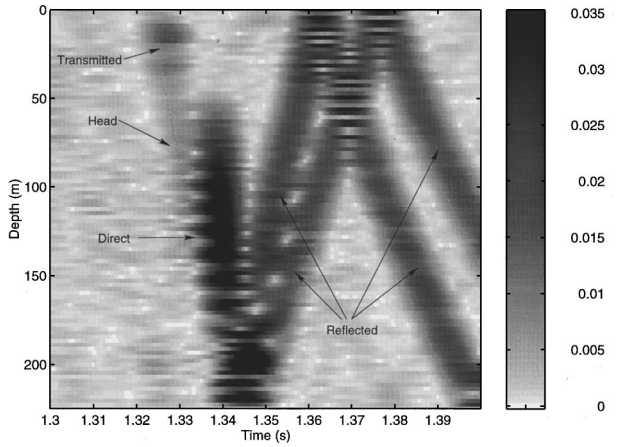

FIG. 9. KRAKEN synthetic data: signal received at 2 km for a 1-kHz source of bandwidth 200 Hz in a free/fluid waveguide with a uniform current (15 m/s) in the upper 45 m. The transition zone is 10 m deep (40 to 50 cm).

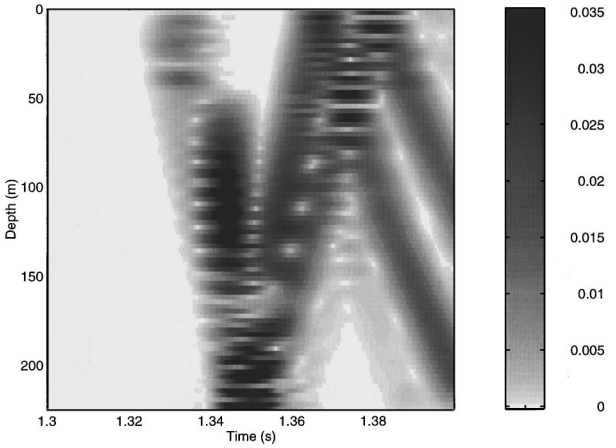

FIG. 10. OASES synthetic data: signal received at 2 km for a 1-kHz source of bandwidth 200 Hz in a free/fluid waveguide with a uniform current (15 m/s) in the upper 45 m. The transition zone is 10 m deep (40 to 50 m).

current magnitude but its length scale L as defined in Sec. I B. More generally, current effects are averaged over the entire water column in the adiabatic approach and mode shapes remain those of the medium at rest. It is then impossible to observe any transmitted or head wave regardless of the current magnitude, because the adiabatic representation is fundamentally unsuited to describe the relevant propagation mechanisms.

An important consequence of this result is that if the medium-at-rest mode set is to be used, e.g., for tomographic purposes, the propagation cannot be considered adiabatic. Modes are then inherently coupled through **K** and expression (16) must be used. In terms of computational efficiency this makes the forward as well as the inverse problem at least one order of magnitude more intensive.

C. Matched-field current tomography

Reciprocal matched-field current tomography can be simulated as described in Ref. 23 using the model developed in this paper. Two vertical receiver arrays are moored 2 km apart and consist of 32 elements equally spaced along a cable spanning the upper 100 m of the water column (similar to the high-frequency scenario, see Fig. 8). A 55-m-deep source on each array transmits a CW signal at 8 different frequencies equally spaced from 200 to 250 Hz. The source level is 120 dB $re{:}1\mu$Pa. Both sources transmit alternatively so that reciprocal transmissions are available for the eight frequency bins. Replicas of the channel response function are generated by KRAKEN for various current velocities and various current layer depths. Each replica is then subtracted from its reciprocal counterpart, so that the quantity matched is the coherent difference in acoustic pressure between upstream and downstream propagation.

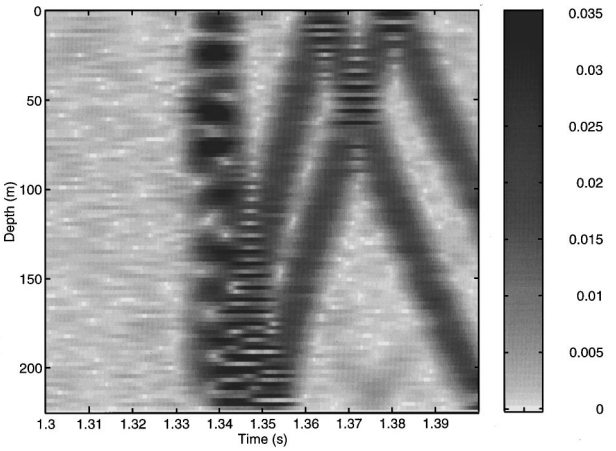

FIG. 11. Closed-form solution synthetic data: signal received at 2 km for a 1-kHz source of bandwidth 200 Hz in a free/fluid waveguide with a uniform current (15 m/s) in the upper 45 m. The transition zone is 10 m deep (40 to 50 m).

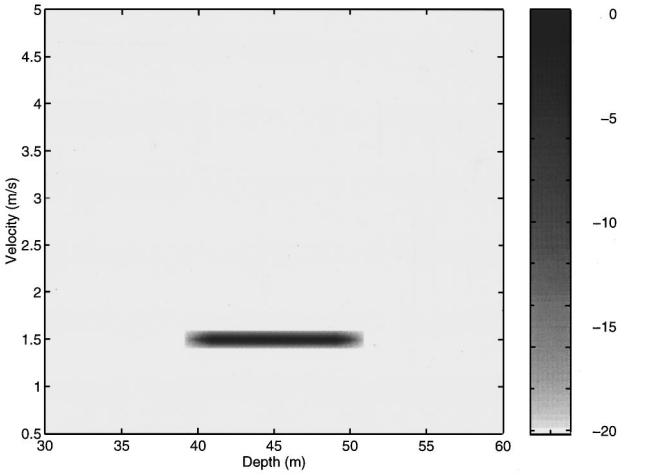

FIG. 12. Ambiguity surface for a vertical 32-element receiver array (dB scale). Receiver range: 2 km. Source frequency: 200–250 kHz. Current velocity: 1.5 m/s. Current layer depth: 45 m. MLM beamformer. White noise level: −50 dB.

The true current layer extends from 0 to 45 m. The actual transition zone goes from 40 to 50 m. Current shear can then be neglected as argued in Sec. I B. The true current magnitude is 1.5 m/s and the true current depth is 45 m for MFP purposes. The corresponding broadband ambiguity surface, generated using a minimum-variance beamformer, is the frequency average of the output in decibels of an MLM beamformer[36] (see Fig. 12). The true current velocity and current layer depth can be resolved with an accuracy of respectively ± 0.1 m/s and ± 5 m. The depth resolution is limited by the smooth transition zone from 40 to 50 m where the true current goes from 1.5 m/s to 0 m/s. The width of the main lobe is extremely narrow considering that the Mach number is very small (0.001).

Environmental mismatches are known to dramatically decrease the performance of MLM beamformers.[37] This is due to the fact that the MLM main lobe is extremely narrow at high signal-to-noise ratios, making this beamformer highly sensitive to any parameter offset. Bartlett beamformers, on the other hand, have a good mismatch tolerance at the expense of an increase in main lobe width. In the case of current tomography, the Bartlett main lobe is so wide that no current inversion is possible. Since the MLM beamformer degenerates into a Bartlett beamformer at low signal-to-noise ratios, artificially increasing the level of noise in the data

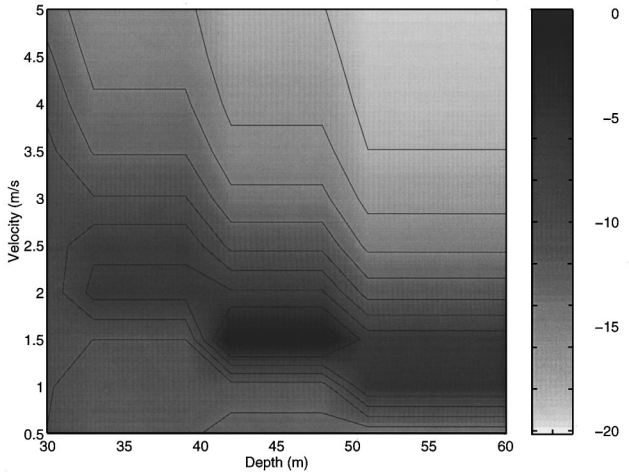

FIG. 13. Ambiguity surface for a vertical 32-element receiver array (dB scale). Receiver range: 2 km. Source frequency: 200–250 kHz. Current velocity: 1.5 m/s. Current layer depth: 45 m. MLM beamformer. White noise level: +40 dB. Contour lines are 2 dB apart. Main lobe level: 0 dB.

provides the means of controlling the MLM mainlobe width. By increasing the noise level we are effectively destroying information, degrading the array gain but also decreasing the sensitivity to mismatch while achieving a controllable main lobe width. The ambiguity surface for a white noise level of 40 dB is shown in Fig. 13. The velocity resolution is expectedly somewhat lower than that of the no noise case (about ± 0.2 m/s). The depth resolution remains unchanged. The same ambiguity surface is shown in Fig. 14 in the case of a range mismatch of 2 m and a bottom mismatch of 25 m/s. The range mismatch corresponds to an error of 1.3 ms in travel time assuming a high-frequency range positioning device is available. The main lobe level is 5 dB lower than in the no mismatch case, and the -8-dB ambiguity ridge is only 3 dB below, making the inversion less accurate. Adding more noise to the data would broaden the main lobe, making it even less distinguishable from the -8-dB ridge. Less noise, on the other hand, would lower the main lobe further below.

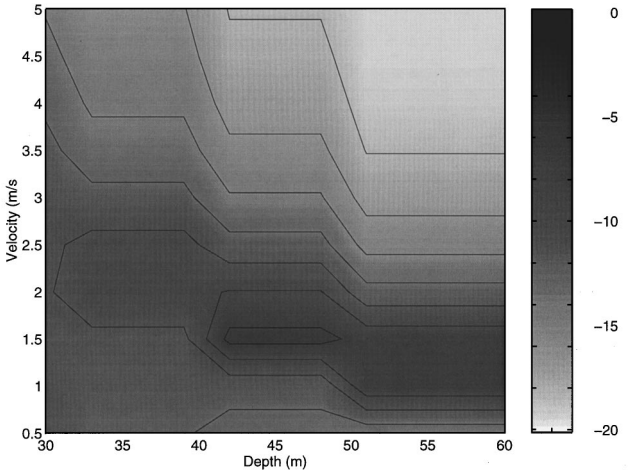

FIG. 14. Ambiguity surface for a vertical 32-element receiver array (dB scale). Receiver range: 2 km. Source frequency: 200–250 kHz. Current velocity: 1.5 m/s. Current layer depth: 45 m. Range mismatch: 2 m. Bottom sound-speed mismatch: 25 m/s. MLM beamformer. White noise level: +40 dB. Contour lines are 2 dB apart. Main lobe level: -5 dB.

Shallow-water current tomography appears to be an achievable goal provided accurate information about the medium is available. This result is at variance with Godin's result for the deep ocean case.[38] Godin considered a 50-Hz cw signal with a range mismatch close to one wavelength and showed that reciprocal matched-field tomography was not feasible if mismatches were present. The present paper, however, assumes the source is broadband (200–250 Hz) and the range mismatch is only one third of a wavelength. Furthermore we use an MLM beamformer where Godin simply looked at the normalized difference between the actual and the synthetic field.

III. CONCLUSION

The classical depth-separated and modal equations have been modified to account for the effect of a low Mach number, horizontal, depth varying current profile. It has been demonstrated that these equations can be solved by making minor modifications of existing wave-number integration and normal-mode codes. Numerical results for low- and high-frequency sources in a simple waveguide show a high degree of agreement between the two solutions, and confirm previous theoretical results.[16,32,35] An analytical solution was also derived based on the mode set of the medium at rest. In doing so, the waveguide propagation was, however, assumed to occur adiabatically. Comparison with the numerical model presented in this paper shows this assumption breaks down if there is bottom penetration or if the current profile exhibits sharp variations with respect to depth. The theoretical feasibility of reciprocal matched-field current tomography is then demonstrated. Assuming accurate knowledge of the acoustic waveguide, a current velocity of 1.5 m/s can be measured at a range of 2 km with a resolution of 0.2 m/s using a multitone cw signal spanning 200-250 Hz.

ACKNOWLEDGMENT

Funding was provided by the Office of Naval Research through Grant No. N00014-95-1-0495.

APPENDIX: DERIVATION OF THE MODAL EQUATION

Substituting (9) and (3) leads to

$$\boldsymbol{\psi}^T \frac{1}{r}\frac{d}{dr}\left(r\frac{d\mathbf{h}}{dr}\right)+\rho\frac{d}{dz}\left(\frac{1}{\rho}\frac{d\boldsymbol{\psi}^T}{dz}\right)\mathbf{h}+k^2\boldsymbol{\psi}^T\mathbf{h}+2ik\mathscr{M}\boldsymbol{\psi}^T\frac{d\mathbf{h}}{dr}$$
$$-2i\frac{d}{dz}\left(\frac{\mathscr{M}}{k}\right)\frac{d\boldsymbol{\psi}^T}{dz}\frac{d\mathbf{h}}{dr}$$
$$=-S(\omega)\delta(\mathbf{r})\delta(z-z_s). \tag{20}$$

Using the eigenvalue properties of ψ, its second derivative can be replaced by $(\mathbf{\Lambda}-k^2\mathbf{I})\psi$. Equation (20) can then be rewritten as

$$\boldsymbol{\psi}^T \frac{1}{r}\frac{d}{dr}\left(r\,\frac{d\mathbf{h}}{dr}\right)+\boldsymbol{\Lambda}\boldsymbol{\psi}^T\mathbf{h}+2ik\mathscr{M}\boldsymbol{\psi}^T\frac{d\mathbf{h}}{dr}$$
$$-2i\,\frac{d}{dz}\left(\frac{\mathscr{M}}{k}\right)\frac{d\boldsymbol{\psi}^T}{dz}\frac{d\mathbf{h}}{dr}=-S(\omega)\,\delta(\mathbf{r})\,\delta(z-z_s). \qquad (21)$$

Projecting this equation on $\boldsymbol{\psi}$ then leads to (10) in Sec. I C.

[1] W. Munk and C. Wunsch, ''Ocean acoustic tomography: a scheme for large scale monitoring,'' Deep Sea Res. A **26**, 123-161 (1979).
[2] W. Munk, P. Worcester, and C. Wunsch, *Ocean Acoustic Tomography* (Cambridge U. P., Cambridge, 1995).
[3] B. M. Howe, P. F. Worcester, and R. C. Spindel, ''Ocean acoustic tomography: mesoscale velocity,'' J. Geophys. Res. **92**(C4), 3785–3805 (1987).
[4] H. A. DeFerrari and H. B. Nguyen, ''Acoustic reciprocal transmission experiments, Florida Straits,'' J. Acoust. Soc. Am. **79**, 299–315 (1986).
[5] D. S. Ko, H. A. DeFerrari, and P. Malanotte-Rizolli, ''Acoustic tomography in the Florida Strait: temperature, current and vorticity measurements,'' J. Geophys. Res. **94**, 6197–6211 (1989).
[6] B. D. Dushaw, P. F. Worcester, B. D. Cornuelle, and B. M. Howe, ''Barotropic currents and vorticity in the central north Pacific Ocean during summer 1987 determined from long-range reciprocal acoustic transmission,'' J. Geophys. Res. **99**, 3263–3272 (1994).
[7] D. I. Blokhintsev, ''The propagation of sound in an inhomogeneous and moving medium,'' J. Acoust. Soc. Am. **18**, 322–328 (1946).
[8] E. T. Kornhauser, ''Ray theory for moving fluids,'' J. Acoust. Soc. Am. **25**, 945–949 (1953).
[9] P. Ugincius, ''Acoustic ray equations for a moving, inhomogeneous medium,'' J. Acoust. Soc. Am. **37**, 476–479 (1965).
[10] L. A. Stallworth and M. J. Jacobson, ''Acoustic propagation in an isospeed channel with uniform tidal current and depth change,'' J. Acoust. Soc. Am. **48**, 382–391 (1970).
[11] E. R. Franchi and M. J. Jacobson, ''Ray propagation in a channel with depth-variable sound speed and current,'' J. Acoust. Soc. Am. **52**, 316–331 (1972).
[12] J. S. Robertson, W. L. Siegmann, and M. J. Jacobson, ''Current and current shear effects in the parabolic approximation for underwater sound channels,'' J. Acoust. Soc. Am. **77**, 1768–1780 (1985).
[13] N. P. Lan and F. D. Tappert, ''Parabolic equation modeling of the effects of ocean currents on sound transmission and reciprocity in the time domain,'' J. Acoust. Soc. Am. **78**, 642–648 (1985).
[14] M. D. Collins, B. E. McDonald, W. A. Kuperman, and W. L. Siegmann, ''Jovian acoustics and comet Shoemaker-Levy 9,'' J. Acoust. Soc. Am. **97**, 2147–2158 (1995).
[15] O. A. Godin, ''Discrete spectrum of a sound field in a moving medium,'' Sov. Phys. Acoust. **36**(4), 355–359 (1990).
[16] L. M. Brekhovskikh and O. A. Godin, *Acoustics of Layered Media II* (Springer-Verlag, New York, 1992).
[17] I. P. Chunchuzov, ''Field of a low-frequency point source of sound in an atmosphere with a nonuniform wind-height distribution,'' Sov. Phys. Acoust. **30**(4), 323–326 (1984).
[18] V. E. Ostashev, ''Discrete spectrum of the sound field of a point source in a stratified moving medium,'' Sov. Phys. Acoust. **32**(4), 303–306 (1986).
[19] N. S. Grigor'eva and M. I. Yavor, ''Influence on the sound field in the ocean of a large-scale ocean current that qualitatively alters the nature of guided-wave sound propagation,'' Sov. Phys. Acoust. **32**(6), 482–485 (1986).
[20] M. B. Porter and E. L. Reiss, ''Numerical method for acoustic normal modes for shear flows,'' J. Sound Vib. **100**(1), 91–105 (1985).
[21] M. B. Porter and E. L. Reiss, ''A numerical method for ocean acoustic normal modes,'' J. Acoust. Soc. Am. **76**, 244–252 (1984).
[22] H. Schmidt, J. G. Bellingham, M. Johnson, D. Herold, D. Farmer, and R. Pawlowicz, ''Real-time frontal mapping with AUVs in a coastal environment,'' in *IEEE Proceedings Oceans 96*, 1094–1098, 1996.
[23] F. B. Jensen, W. A. Kuperman, M. B. Porter, and H. Schmidt, *Computational Ocean Acoustics* (AIP, New York, 1994).
[24] H. Schmidt, *SAFARI: Seismo-acoustic fast field algorithm for range independent environments. User's Guide* (SACLANT Undersea Research Centre, La Spezia, Italy, 1988).
[25] P. M. Morse and K. U. Ingard, *Theoretical Acoustics* (Princeton U. P., Princeton, NJ, 1986).
[26] E. R. Franchi and M. J. Jacobson, ''Effect of hydrodynamic variations on sound transmission across a geostrophic flow,'' J. Acoust. Soc. Am. **54**, 1302–1311 (1973).
[27] J. S. Robertson, W. L. Siegmann, and M. J. Jacobson, ''A treatment of three-dimensional underwater propagation through a steady shear flow,'' J. Acoust. Soc. Am. **86**, 1484–1489 (1989).
[28] Y. L. Li, M. J. White, and S. J. Franke, ''New fast field programs for anisotropic sound propagation through an atmosphere with a wind velocity profile,'' J. Acoust. Soc. Am. **95**, 718–726 (1994).
[29] J. S. Robertson, W. L. Siegmann, and M. J. Jacobson, ''Acoustical effects of ocean current shear structures in the parabolic approximation,'' J. Acoust. Soc. Am. **82**, 559–573 (1987).
[30] T. B. Sanford, ''Observation of strong current shears in the deep ocean and some implications on sound rays,'' J. Acoust. Soc. Am. **56**, 1118–1121 (1974).
[31] L. M. Brekhovskikh and O. A. Godin, *Acoustics of Layered Media I* (Springer-Verlag, New York, 1990).
[32] D. S. Jones and J. D. Morgan, ''The instability of a vortex sheet on a subsonic stream under acoustic radiation,'' Proc. Cambr. Philos. Soc. **72**, 465–488 (1972).
[33] J. E. White, *Underground Sound—Application of Seismic Waves* (Elsevier, Amsterdam, 1983).
[34] W. I. Futterman, ''Dispersive body waves,'' in *Seismic Wave Attenuation*, edited by D. H. Johnston and M. N. Toksoz, Society of Exploration Geophysicists, (Tulsa, 1981), Geophysics reprint series No. 2.
[35] H. Schmidt and W. A. Kuperman, ''Spectral and modal representation of the Doppler-shifted field in ocean waveguides,'' J. Acoust. Soc. Am. **96**, 386–395 (1994).
[36] A. B. Baggeroer, W. A. Kuperman, and H. Schmidt, ''Matched field processing: Source localization in correlated noise as an optimum parameter estimation problem,'' J. Acoust. Soc. Am. **83**, 571–587 (1988).
[37] R. M. Hamson and R. M. Heitmeyer, ''Environmental and system effects on source localization in shallow water by the matched-field processing of a vertical array,'' J. Acoust. Soc. Am. **86**, 1950–1959 (1989).
[38] O. A. Godin, Y. U. Mikhin, and A. V. Mokhov, ''A full field inversion method for acoustic tomography of ocean currents,'' in *Full Field Inversion Methods in Ocean and Seismo-acoustics*, edited by O. Diachok, A. Caiti, P. Gerstoft, and H. Schmidt (Kluwer, Dordrecht, 1995), pp. 261–266.

Low-frequency acoustic scattering by gas-filled prolate spheroids in liquids

Zhen Ye[a)]
Institute of Ocean Sciences, Sidney, British Columbia V8L 4B2, Canada

(Received 29 February 1996; revised 1 July 1996; accepted 21 August 1996)

This paper presents an analytic method for studying scattering of acoustic waves by gas-filled prolate spheroids at low frequencies. The method is based on the Kirchhoff integral theorem and Strasberg's finding that the surface acoustic field and the velocity normal to the surface are mathematically equivalent to electrostatic potential and charge density on a perfect conductor having the same shape [M. Strasberg, J. Acoust. Soc. Am. **25**, 536–537 (1953)]. The boundary-value problem is solved with aid from a thermodynamic relation. An analytic formula for the sound scattering function is derived, and is compared to the results obtained using the deformed cylinder method and that obtained by the *T*-matrix numerical method. It is shown that the results compare favorably with that from the *T*-matrix method, but differ from that obtained by the deformed cylinder approach, with respect to the dependence of the peak scattering value on the aspect ratio of prolate spheroids. However, away from the resonance region, the results from the deformed cylinder method seem to approach to the present results. The results show that both the present method and the *T*-matrix approach yield nearly the same resonance frequency and the quality *Q* factor, while the deformed cylinder method predicts lower values in the resonance scattering regime. However, there exist some differences between the present results and that from the *T*-matrix method as the aspect ratio increases. Possible criteria for the present approach to be valid are also discussed. © *1997 Acoustical Society of America.* [S0001-4966(97)01104-1]

PACS numbers: 43.30.Gv, 43.30.Dr, 43.20.Fn [JHM]

INTRODUCTION

The analysis of the sound scattering by spheroids has been a classical subject for several decades.[1–9] It is well known that the problem can be solved exactly by separating variables in spheroidal coordinates and the solution obtained can be written in terms of an infinite series of spheroidal wave functions.[1] Unfortunately, computation of these spheroidal wave functions is by no means an easy task. Therefore most previous works based on the exact solution were limited to approximations for special cases such as low-frequency scattering from soft or penetrable spheroids,[6,8] rigid body scattering,[4] scattering from weak scatterers or spheroidal voids,[9] or scattering from rigid prolate spheroid of large aspect ratio (length-to-diameter) at high frequencies.[10] These approximate results are useful in lending physical insights to more complicated problems, and providing verification for alternative numerical methods.

Relatively little attention has been paid to sound scattering from gas-filled spheroids. Although scattering from such spheroids can be regarded as a special case of the scattering from penetrable spheroids,[7,8] practical computation of the scattering function of gas-filled spheroids for a wide range of frequency is problematic. The main difficulty arises from the slow convergence of series for spheroidal wave functions (Furusawa, personal communication). Research has been mainly restricted to low-frequency cases, in which the acoustic wavelength is much larger than the size of spheroids. Low-frequency scattering from gas-filled objects is of particular interest, since resonance behaviors appear, which have potentially useful applications in fish stock quantification[11] and upper-ocean bubble population estimates.[12,13]

Strasberg[3] was able to obtain the exact resonance frequency of a gas-filled spheroid at low frequencies by converting the problem to the determination of the capacitance of a perfect conductor having the same shape. However, Strasberg's approach does not allow derivation of the scattering amplitude and the quality factor *Q* characterizing the resonant scattering. Later, the exact spheroidal wave function series solution was used by Burke to obtain low-frequency approximations in ascending powers of wave number $k=2\pi/\lambda$ to sound scattering from fluid spheroids.[8] However, Burke's results were presented in such complicated form that an extension to the scattering by gas-filled spheroids appears difficult, and to our knowledge, such an extension has not been achieved. Due to computational difficulties associated with the exact solution, approximate methods have been developed to study low-frequency scattering by gas-filled spheroids, the deformed cylinder method,[14] the numerical *T*-matrix method[15] originated by Waterman,[16] and the surface average method.[17] The former two methods are powerful but numerical, and do not provide solutions in closed form. The surface average method, on the other hand, does yield a simple analytic representation of the resonant scattering of spheroidal gas bubbles, but lack of rigor in the treatment of the boundary conditions is discomforting.[17]

The present paper presents a rigorous approach to acoustic scattering by gas-filled prolate spheroids at low frequen-

[a)]Current address: Department of Physics, National Central University, Chung-Li, Taiwan 320, ROC.

 0001-4966/97/101(4)/1945/8/$10.00

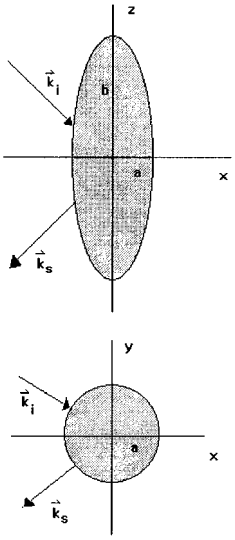

FIG. 1. A sketch of a prolate spheroid scatterer in rectangular coordinates.

cies, i.e., the resonant scattering, based on the Kirchhoff integral theorem[16] and the finding of Strasberg that the surface acoustic field and the velocity normal to the surface are mathematically equivalent to the electrostatic potential and charge density on a perfect conductor having the same shape.[3] The scattering wave of prolate spheroidal gas bubbles will be derived in a closed form. Particular attention will be paid to the far-field scattering function. Features of the scattering function will be examined by considering several examples, and comparisons with other numerical results will be made. For simplicity, the viscosity and heat conduction effects are ignored.

It is hoped that the present work will provide a justification to various numerical methods for sound scattering from spheroidal bubbles. Since the present results are only valid for low-frequency scattering by gas-filled spheroids, it is thus also hoped that this work can stimulate further investigations of sound scattering from all types of spheroids for a wider range of frequency.

I. SOUND SCATTERING FROM GAS-FILLED PROLATE SPHEROIDS

A. General

Consider a plane wave incident on a gas-filled prolate spheroid located at the origin (Fig. 1). The surface of the spheroid is represented by the equation

$$\frac{x^2}{a^2}+\frac{y^2}{a^2}+\frac{z^2}{b^2}=1, \tag{1}$$

where a and b are the minor and major radii, respectively, with $b>a$ and the aspect ratio is given by b/a.

The pressure wave equation in the surrounding liquid can be written as

$$(\nabla^2+k^2)p=0. \tag{2}$$

The plane wave can be expressed as $p_i=\exp(i\mathbf{k}_i\cdot\mathbf{r})$ with suppressed time dependence $\exp(-i\omega t)$. Here ω is the angular acoustic frequency, $\mathbf{k}_i$ is the wave vector and its magnitude equals ω/c with c being the sound speed in the surrounding liquid.

According to the Kirchhoff integral theorem, the total pressure wave satisfying Eq. (2) can be written as[16]

$$\left.\begin{matrix}p(\mathbf{r}')\\0\end{matrix}\right\}=p_i(\mathbf{r}')+\frac{1}{4\pi}\int_S ds[p_+\mathbf{n}\cdot\nabla g(k|\mathbf{r}-\mathbf{r}'|) - i\omega\rho_l u_n g(k|\mathbf{r}-\mathbf{r}'|)] \quad \text{for } \mathbf{r}'\begin{cases}\text{outside the spheroid,}\\ \text{inside the spheroid,}\end{cases} \tag{3}$$

where the integration is performed over the surface of the object, p_+ and u_n are the total field and the normal velocity at the surface, approached from the outside, $\mathbf{n}$ is a unit outward normal vector to the surface, g is the known free space Green's function $(1/R)\exp(ikR)$, and ρ_l is the density of the surrounding liquid. The second term in Eq. (3) represents the scattered wave.

It is well known that when $r'\gg r$, the scattering wave can be written as an outward going form (Sommerfeld radiation condition),

$$p_s(\mathbf{r}')\to f(\mathbf{k}_i,\mathbf{k}_s)\,\frac{\exp(ikr')}{r'}, \tag{4}$$

where $\mathbf{k}_i$, $\mathbf{k}_s$ are the incidence and scattered wave vectors, respectively. The scattering amplitude in the above equation $f(\mathbf{k}_i,\mathbf{k}_s)$ can be derived as [refer to Eq. (9.125) in Ref. 18]

$$f(\mathbf{k}_i,\mathbf{k}_s)=-\frac{1}{4\pi}\int_S ds\,\exp(-i\mathbf{k}_s\cdot\mathbf{r})[i\mathbf{k}_s\cdot\mathbf{n}p_+ + i\omega\rho_l u_n]. \tag{5}$$

From Eqs. (3) and (5), it is clear that the scattering wave and scattering amplitude can be determined by the respective integrals once the surface values are obtained. Therefore the rest of the task is to solve for u_n and p_+.

Boundary conditions require that the pressure p, and the normal component of particle velocity u_n, be continuous across the interface, giving, respectively,[16]

$$p_g=p_+, \quad u_{g,n}=u_n. \tag{6}$$

The index ''g'' refers to the quantities inside the gas spheroid. From the discussion in Ref. 3, the pressure inside the bubble can be approximated as constant if the wavelength of the sound is much larger than the bubble dimensions. Indeed, at low frequencies, only the volume pulsation needs to be considered.

A useful relation can be deduced as follows. For the gas inside the prolate spheroid, the following thermodynamics relation, an equation of state for gases, may be used [e.g., Eq. (A6.1.11) in Ref. 19],

$$PV^{\gamma}=\text{constant}, \tag{7}$$

where γ is the gas polytropic exponent. For an ideal diatomic gas in the thermal adiabatic process, the polytropic exponent γ can be taken approximately as 1.4. When the viscosity and heat conduction are considered, γ should be regarded as a complex constant (Appendix 6 in Ref. 19). Differentiating

Eq. (7) with respect to time, we obtain [(A6.1.11)–(A6.1.13) in Ref. 19]

$$\frac{dV}{dt}=\frac{i\omega V}{\gamma P_0}\,p_g, \tag{8}$$

which can be rewritten as

$$\frac{1}{S}\int_S ds\; u_n=\frac{i\omega}{\gamma P_0}\,\frac{V}{S}\,p_g, \tag{9}$$

since $dV/dt=\int_S ds\; u_n$. Here V and S are the volume and surface area of the prolate spheroid, respectively, and P_0 is the hydrostatic pressure. In deriving Eq. (9), the boundary conditions Eq. (6) have been used. Here V and S can be calculated as in standard mathematical handbooks:

$$V=(4\pi a^2 b)/3,\quad S=4\pi ab(e/2+\sin^{-1}\,\epsilon/2\epsilon),$$

where we define

$$e\equiv a/b\quad\text{and}\quad \epsilon\equiv\sqrt{1-e^2}. \tag{10}$$

To solve for u_n and p_+ (or p_g), an additional equation is needed. This equation can be obtained by setting $\mathbf{r}'$ to be inside the prolate spheroid in Eq. (3), which gives

$$0=p_i(\mathbf{r}')+\frac{1}{4\pi}\int_S ds[p_+\mathbf{n}\cdot\boldsymbol{\nabla}g(k|\mathbf{r}-\mathbf{r}'|) - i\omega\rho_l u_n g(k|\mathbf{r}-\mathbf{r}'|)]. \tag{11}$$

For convenience, set $\mathbf{r}'=0$. Using $p_i(0)=1$ and

$$\boldsymbol{\nabla}g(k|\mathbf{R}|)=\left(-\frac{1}{R}+ik\right)\frac{\exp(ikR)}{R}\,\frac{\mathbf{R}}{R}$$

with $\mathbf{R}=\mathbf{r}-\mathbf{r}'$, we obtain the low-frequency result from Eq. (11),

$$\frac{i\omega\rho_l}{4\pi}\int_S ds\,\frac{u_n}{r}\,(1+ikr)+\frac{p_g}{4\pi}\int_S ds\,\frac{\mathbf{n}\cdot\mathbf{r}}{r}\left(\frac{1}{r^2}-\frac{ik}{r}\right)\times(1+ikr)=1, \tag{12}$$

in which $\mathbf{r}=(x,y,z)$ and x, y, z are the rectangular coordinates for the points on the surface. Note that the right-hand side of the above equation bears usual unit for the pressure. Here the Taylor expansion, $\exp(ikr)\approx 1+ikr$, has been used. A more general solution can be found in the Appendix.

According to Strasberg,[3] u_n is mathematically equivalent to the surface charge density of a perfect conductor having the same shape, for which the solution has been well known.[20] Accordingly, the normal velocity at surface is of the following form [e.g., pp. 207–209 in Ref. 20].

$$u_n=\frac{A}{\sqrt{x^2/a^4+y^2/a^4+z^2/b^4}}, \tag{13}$$

where A is a constant to be determined. In the earlier paper, u_n is approximated as the average value,[17]

$$\langle u_n\rangle=\frac{1}{S}\int_S ds\; u_n=\frac{i\omega}{\gamma P_0}\,\frac{V}{S}\,p_g.$$

Solving A and p_g from Eqs. (9), (12), and (13), we obtain

$$A=\frac{i\omega}{3\gamma P_0 B-\omega^2\rho_l a^2(\{\ln[(1+\epsilon)/e]/\epsilon\}+ikb)}, \tag{14}$$

and

$$p_g=\frac{3\gamma P_0}{3\gamma P_0 B-\omega^2\rho_l a^2(\{\ln[(1+\epsilon)/e]/\epsilon\}+ikb)}. \tag{15}$$

In these two equations, the parameter B is defined as

$$B\equiv\frac{1}{4\pi}\int_S ds\,\frac{\mathbf{n}\cdot\mathbf{r}}{r}\left(\frac{1}{r^2}-\frac{ik}{r}\right)(1+ikr). \tag{16}$$

Using the Green's theorem, B can be further simplified as

$$B=1+(ka)^2\,\frac{1}{\epsilon}\sinh^{-1}(\epsilon/e) =1+(ka_e)^2e^{2/3}\,\frac{1}{\epsilon}\sinh^{-1}(\epsilon/e). \tag{17}$$

The factor $(e^{2/3}/\epsilon)\sinh^{-1}(\epsilon/e)$ is a slowly varying function of the aspect ratio $1/e$. The second term in B can thus be neglected when $ka_e\ll 1$. Ignoring this high-order term, we get

$$B\approx 1. \tag{18}$$

A few notes about the derivations of Eqs. (14) and (15) may be helpful to the reader. First, substituting Eq. (13) into Eq. (9) and performing appropriate integration would yield an equation relating A and p_g. Second, taking Eq. (13) into Eq. (12) would lead to another equation for A and p_g. Then the two unknown quantities A and p_g can be solved from these two equations. In the procedure, the following relations are useful (Chapter 3 in Ref. 20):

$$\int_S ds\,\frac{1}{\sqrt{x^2/a^4+y^2/a^4+z^2/b^4}}=4\pi a^2 b \tag{19}$$

and

$$\int_S ds\,\frac{1}{\sqrt{x^2/a^4+y^2/a^4+z^2/b^4}}\,\frac{1}{\sqrt{x^2+y^2+z^2}} =\frac{4\pi a^2}{\epsilon}\ln\left(\frac{1+\epsilon}{e}\right). \tag{20}$$

With aid of the boundary conditions, we can obtain an expression for the scattered wave by substituting the results in Eqs. (14) and (15) to Eq. (3):

$$p_s(\mathbf{r}')=\frac{1}{4\pi}\int_S ds[p_g\mathbf{n}\cdot\boldsymbol{\nabla}g(k|\mathbf{r}-\mathbf{r}'|) - i\omega\rho_l u_n g(k|\mathbf{r}-\mathbf{r}'|)], \tag{21}$$

where p_g is given by Eq. (15) and u_n is given by Eqs. (13) and (14).

Substituting Eqs. (13)–(15) into Eq. (5), we obtain an explicit expression for the scattering amplitude:

$$f(\mathbf{k}_i,\mathbf{k}_s)=\frac{U_1-U_2}{(\omega_0^2/\omega^2)-1-ikb\{\ln[(1+\epsilon)/e]/\epsilon\}^{-1}}, \tag{22}$$

where

$$\omega_0^2=\frac{3\gamma P_0}{a^2\rho_l\{\ln[(1+\epsilon)/e]/\epsilon\}}, \tag{23}$$

$$U_1=\frac{1}{4\pi a^2\{\ln[(1+\epsilon)/e]/\epsilon\}}\int_S ds\ \exp(-i\mathbf{k}_s\cdot\mathbf{r}) \times\frac{1}{\sqrt{x^2/a^4+y^2/a^4+z^2/b^4}}. \tag{24}$$

$$U_2=\frac{\omega_0^2}{\omega^2}\frac{1}{4\pi}\int_S ds\ \exp(-i\mathbf{k}_s\cdot\mathbf{r})(i\mathbf{k}_s\cdot\mathbf{n}). \tag{25}$$

In the long wavelength approximation, the quantities U_1 and U_2 can be simplified as

$$U_1=\frac{b}{\{\ln[(1+\epsilon)/e]/\epsilon\}}, \tag{26}$$

$$U_2=\frac{\omega_0^2}{\omega^2}\left[\frac{i}{4\pi}\int_S ds(\mathbf{k}_s\cdot\mathbf{n})(1-i\mathbf{k}_s\cdot\mathbf{r})\right]. \tag{27}$$

The scattering function in Eq. (22), similar to Eq. (18) in Ref. 17, clearly shows the resonance feature. The resonance frequency is ω_0:

$$\omega_0^2=\frac{3\gamma P_0}{a^2\rho_l\{\ln[(1+\epsilon)/e]/\epsilon\}}. \tag{28}$$

In Eq. (22), the term $kb\{\ln[(1+\epsilon)/e]\epsilon\}^{-1}$ is identified as the damping factor due to acoustic radiation. Consider an equivalent spherical bubble, i.e., the spherical bubble having the same volume as the prolate spheroid bubble under consideration. The radius and resonance frequency of the equivalent spherical bubble are readily calculated as

$$a_e=ae^{-1/3},\quad \omega_e=\frac{1}{a_e}\sqrt{\frac{3\gamma P_0}{\rho_l}}. \tag{29}$$

Therefore the resonance frequency increase ω_0/ω_e for the prolate spheroid bubble is calculated as

$$\frac{\omega_0}{\omega_e}=e^{-1/3}(1-e^2)^{1/4}\left[\ln\left(\frac{1+\sqrt{1-e^2}}{e}\right)\right]^{-1/2}, \tag{30}$$

or

$$\frac{\omega_0}{\omega_e}=2^{1/2}e^{-1/3}(1-e^2)^{1/4}\left[\ln\left(\frac{1+\sqrt{1-e^2}}{1-\sqrt{1-e^2}}\right)\right]^{-1/2}. \tag{31}$$

This is exactly what has been derived in the past.[21,22] Note that there is a typographical error in Weston's result,[21] which has been corrected in Ref. 22. The original Wenston's formula reads

$$\frac{\omega_0}{\omega_e}=2^{1/2}e^{-1/3}(1-e^2)^{1/4}\left(\frac{\ln[1+\sqrt{1-e^2}]}{1-\sqrt{1-e^2}}\right)^{-1/2}.$$

From Eq. (22), we see that in the low-frequency approximation, e.g., $kb\ll 1$, the scattering function seems independent of the wave incidence direction; this differs from the results obtained by the T-matrix numerical computation;[15] however, the scattering function is a function of scattering direction through the term involving U_2. But the dependence on scattering direction is very weak at low frequencies. The reason is as follows. From Eq. (27), one can show that U_2 is of the order of $(k_0b)^2b$, with $k_0=\omega_0/c$. Using

$$\frac{1}{4\pi}\int_S ds(\mathbf{k}_s\cdot\mathbf{n})=0$$

and

$$\frac{1}{4\pi}\int_S ds(\mathbf{k}_s\cdot\mathbf{n})(\mathbf{k}_s\cdot\mathbf{r})\leqslant k^2b^3,$$

we obtain

$$|U_2|\leqslant\frac{\omega_0^2}{\omega^2}k^2b^3=(k_0b)^2b. \tag{32}$$

Therefore $U_2/b\sim O((k_0b)^2)$. It will become clear later that the term involving U_2 is indeed negligible, since we will be mainly concerned with cases in which $kb<0.35$ and in such cases the U_2 term can at most change the result by about 12% at the largest possible kb.

We finally get a simple isotropic scattering function

$$f=\frac{\epsilon b\Big/\left(\ln\dfrac{1+\epsilon}{e}\right)}{(\omega_0^2/\omega^2)-1-ikb\{\ln[(1+\epsilon)/e]/\epsilon\}^{-1}}, \tag{33}$$

from which the quality factor Q at resonance is calculated as

$$Q^{-1}=k_0b\{\ln[(1+\epsilon)/e]/\epsilon\}^{-1}, \tag{34}$$

where $k_0=\omega_0/c$ with ω_0 given by Eq. (28). It is clear that $kb\{[\ln(1+\epsilon)/e]/\epsilon\}^{-1}$ is the radiation damping factor. In the later calculation we shall ignore U_2, since we mainly work with low-frequency cases. For a general solution, the reader may refer to the Appendix.

B. Special cases

First consider a spherical gas bubble. When $a=b$, the radius of the spherical bubble is a. Equation (33) then reduces to the well-known result in the literature [see, e.g., Eq. (A6.1.20) in Ref. 19 and Ref. 23]:

$$f=\frac{a}{(\omega_s^2/\omega^2)-1-ika}, \tag{35}$$

in which

$$\omega_s=\frac{1}{a}\sqrt{\frac{3\gamma P_0}{\rho_l}}. \tag{36}$$

Here ω_s is the resonance frequency of the spherical bubble.

When $\omega\ll\omega_0$, the scattering function can be simplified as

$$f=be^{2/3}\frac{\omega^2}{\omega_e^2} \tag{37}$$

or

$$f=\left(\frac{3V}{4\pi}\right)^{1/3}\frac{\omega^2}{\omega_e^2}=\frac{V}{4\pi}\frac{\rho_l}{\gamma P_0}\omega^2, \tag{38}$$

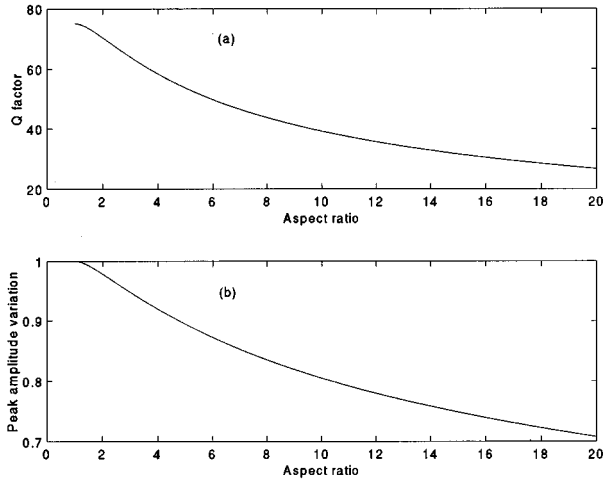

FIG. 2. (a) The quality factor Q as a function of the aspect ratio. (b) The scaled peak scattering amplitude as a function of the aspect ratio.

following the Rayleigh volume scattering. Therefore at very low frequencies, the scattering will be independent of the aspect ratio of spheroids.

II. NUMERICAL EXAMPLES

A. Examples

In all the cases considered below the bubble consists of air entrained in water. The following parameters will be used in the numerical calculation: $c=1500$ m/s, $\rho_l=1000$ kg/m^3, $\rho_g=1.29$ kg/m^3, $\gamma=1.4$, and $P_0=10^5$ kg/m^2. From these parameters, the sound speed in the air inside the bubble is calculated as

$$c_g=\sqrt{\frac{\gamma P_0}{\rho_g}}\approx 329 \text{ m/s},$$

which is almost the same as used in, for example, Ref. 15. In addition we assume that the prolate spheroids are at a constant volume and the radius of the equivalent sphere is 0.01 m.

We will compare the backscattering results from the present approach to that obtained from the deformed cylinder method, following the line of Clay,[24] and also with the results in Ref. 15 obtained by the T-matrix method. As usual, the target strength is defined as

$$\text{TS}=10\log_{10}|f|^2.$$

Since the deformed cylinder method is developed based on the broadside scattering assumption, we will only consider the broadside incidence when using the deformed cylinder method.

First we plot the quality factor as a function of the aspect ratio in Fig. 2(a). Here it shows that the quality factor decreases significantly as the aspect ratio increases. In Fig. 2(b), we plot the resonance peak value as a function of the aspect ratio. Note the amplitude is scaled against the value for the equivalent sphere.

Figure 3 shows the target strength as a function of ka_e for three aspect ratios 1, 10, and 20, where a_e is the radius of the equivalent sphere. In the three cases, kb at the resonance equals 0.0136, 0.0789, and 0.129. The results in Fig. 3(a) are from the present approach [Eq. (33)], while the curves in Fig. 3(b) are from the deformed cylinder method.[14] Figure 3(c) is the comparison between the deformed cylinder method and the present method for aspect ratio 20. The results shown in

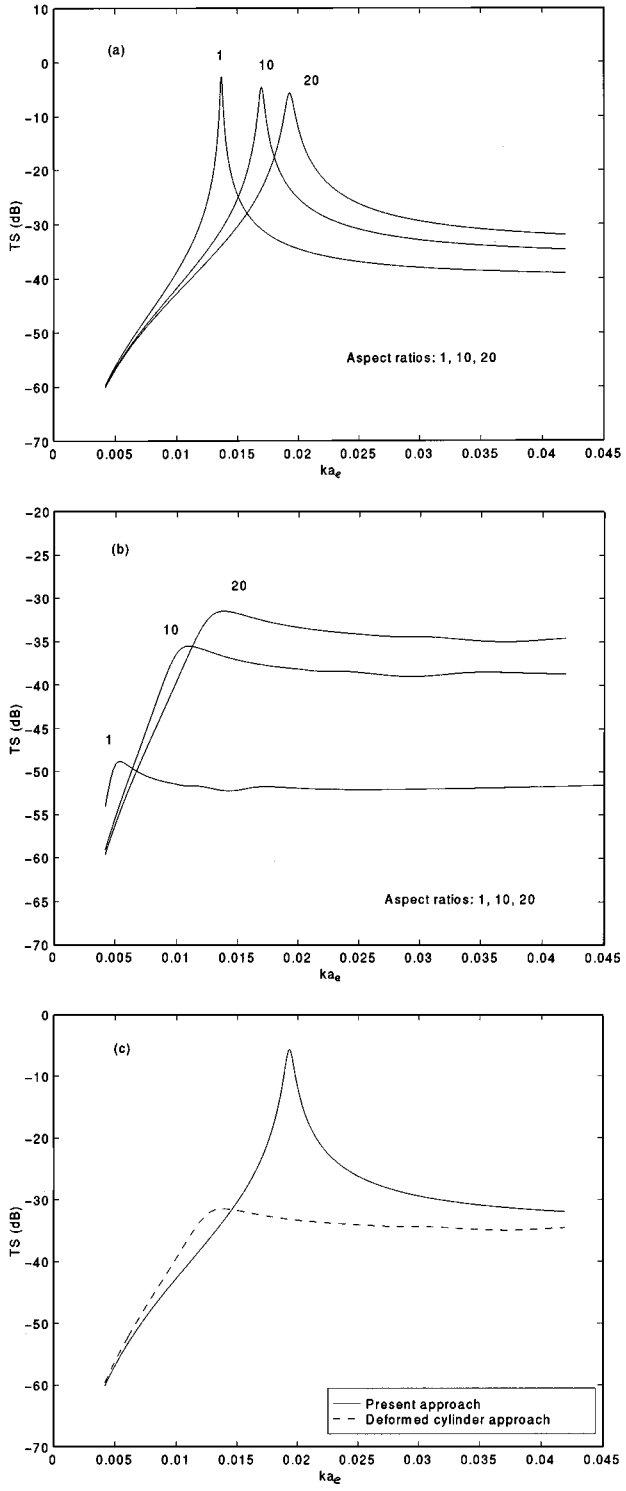

FIG. 3. Target strength as a function of ka for three aspect ratios: 1, 10, 20. The results from the present approach are presented in (a), and (b) is for the results from the deformed cylinder method. The plot in (c) is the comparison between the deformed cylinder method and the present method for aspect ratio 20.

TABLE I. Variation of peak frequency, amplitude, and Q for prolate spheroid gas bubbles obtained from the present approach and the T-matrix method. The peak frequency and amplitude value are scaled against the values for the equivalent spherical bubble.

Aspect ratio	Frequency	Peak	Q	Frequency[a]	Peak[a,b]	Peak[a,c]	Q[a]
1	1	1	75.11	1	1	1	75.11
1.414	1.0054	0.9946	73.91	1.0057	0.9979	0.9926	74.48
2	1.0217	0.9788	70.43	1.0218	0.9837	0.9721	68.53
3	1.0548	0.9481	64.01	1.0550	0.9568	0.9351	63.13
4	1.0874	0.9196	58.41	1.0875	0.9316	0.9002	57.89
8	1.1973	0.8352	43.77	1.1968	0.8621	0.7882	43.15
10	1.2421	0.8051	39.19	1.2412	0.8399	0.7428	38.75
16	1.3524	0.7394	30.36	1.3495	0.8011	0.6287	30.09
20	1.4125	0.7080	26.65	1.4079	0.7894	0.5639	26.51

[a]Results obtained by the T-matrix method from Ref. 15.
[b]Broadside incidence.
[c]Endfire incidence.

(b) are consistent with that shown in Fig. 5 of Ref. 5. Here we see that (1) the scattering amplitude at resonance decreases with aspect ratio in the present approach, in agreement with the results in Ref. 17, while the deformed cylinder approach predicts the opposite; (2) in the present approach, the broadening of the resonance peak increases with aspect ratio, similar to the results from the deformed cylinder method; (3) the deformed cylinder approach predicts much smaller resonance peaks and lower resonance frequencies; (4) both approaches show that the resonance frequency increases with aspect ratio; (5) the scattering function becomes independent of the aspect ratio for very low frequencies; (6) the target strength predicted by the deformed cylinder method is always smaller than that from the present approach for the low frequencies considered here; however, (7) away from the resonance region, the results from the deformed cylinder method seem to approach the results from the present method [Fig. 3(c)].

The above findings can be compared to the results by the T-matrix method shown in Ref. 15. In general, the resonance frequencies predicted by the T-matrix method match those predicted by Eq. (28), and the order of magnitude of the scattering is of the same order as the present approach. Note that the Q factor in Fig. 2(a) and the peak variation in Fig. 2(b) compare favorably to the results from the T-matrix method.[15] In particular, in Table I results from the present method are compared to the results from the T-matrix method.

From Table I, it is clear that both the present method and the T-matrix method predict almost the identical Q factor and resonance frequency. The peak amplitudes from the two methods also compare favorably. The results are also in good agreement with that from the surface average method.[17] However, there are a few differences between the two results. (1) In the present approach, the scattering resonance peak decreases slightly more rapidly as the aspect ratio increases than the broadside scattering peak amplitude predicted by the T-matrix method. (2) When compared to the endfire scattering peak amplitude from the T-matrix method, the present scattering peak amplitude seems to decrease slower as the aspect ratio increases. (3) The T-matrix method shows that the scattering shows noticeable angular dependence even at low frequencies, while the present theory predicts a nearly omnidirectional scattering. A possible implication of the discrepancies will be addressed later.

B. Discussion

To provide a check on the deformed cylinder method and the present method, we may compare the results for the spherical bubble from the two methods with that obtained by an exact solution.[26]

First consider backward scattering. Figure 4 plots the target strength as a function of ka: (a) for small ka, i.e., at low frequencies and (b) for larger ka, or high-frequency limit. In the plots, the solid lines are from the exact solution,[26] the dotted-broken lines are from the deformed cylinder method, and the dashed lines [hardly seen in (a)] are from Eq. (33). Here we see that (1) the target strength predicted by the deformed cylinder method differs quite significantly from both the exact approach and the present approach at low frequencies; (2) the present approach agrees with the exact approach for ka up to about 0.35, after which the result from the present approach is higher than the exact result until $ka>1.5$; (3) when $ka>1$, the result from the deformed cylinder method approaches that from the exact approach, and both approach the result from the Kirchhoff approximation at the optical limit, i.e., $10\log_{10}(a^2/4)=-46$ dB; this has been shown to be true also for a prolate spheroid;[27] (4) at the optical limit, the result from the present method decreases with ka, showing the present method is not valid for large ka. In general, these results show that for backscattering in the spherical case, the present approach is valid for ka up to about 0.35 for the spherical case, while the deformed cylinder method is a better approximate approach for $ka>1$ (use 1 dB difference as the criterion).

Earlier it is argued that for low frequencies, the scattering by gas bubbles may be approximated as omnidirectional. We now examine the validity of this assumption using the spherical bubble example, by comparing two extreme cases: backward scattering and forward scattering. For this comparison, the exact solution is used. Figure 4(c) and (d) show the target strength in the two scattering directions as a function of ka. The solid and dashed lines are for the backscattering and forward scattering, respectively. The results show

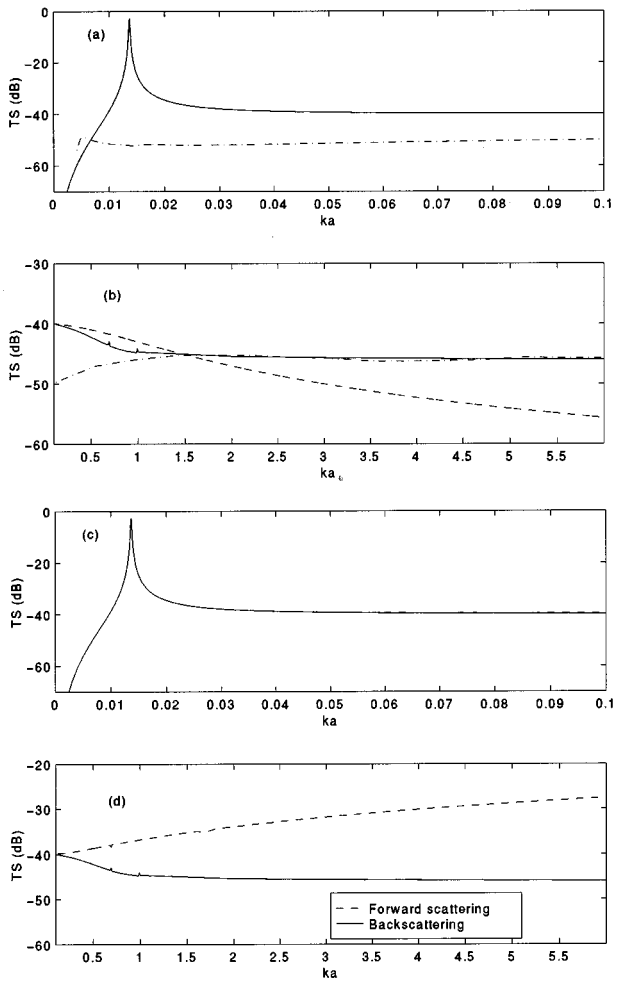

FIG. 4. (a) and (b) Target strength as a function of ka for a gas-filled spherical bubble: the solid lines are from the exact approach,[26] the dotted-broken lines are from the deformed cylinder method,[14] and the dashed lines are from the present approach. (c) and (d) Target strength as a function of ka for a gas-filled spherical bubble for backward and forward scattering from the exact solution: the solid and dashed lines are for the backscattering and the forward scattering, respectively.

that the assumption of omnidirectional scattering may be valid for $ka<0.3$.

Returning to the scattering from the prolate spheroid gas bubbles, we investigate the range of validity of the present approach. One must stress that Eq. (33) is expected to be valid only for $ka<kb\ll 1$. As shown above, the spherical case is valid when $ka=kb<0.35$ for backscattering and $ka=kb<0.3$ for the forward scattering. Although the exact upper limit of kb for a prolate spheroid gas bubble is unclear, a general valid range may be estimated as follows. Since b can be regarded as the radius of the circumscribing sphere and the long wavelength approximation is expected to be valid within the sphere, it therefore may be reasonable to assume that the present approach is valid for $kb<0.35$ for backscattering and $kb<0.3$ for forward scattering, where b is the major radius of the prolate spheroid (Fig. 1). When these criteria hold, the valid range for ka_e is $ka_e<0.35e^{2/3}$ for backscattering and $ka_e<0.3e^{2/3}$ for forward scattering, since $b=a_e(1/e)^{2/3}$. Therefore, increasing the aspect ratio reduces the valid range for the present method. Here, note again that a_e is the radius of the equivalent sphere. For aspect ratios of 10 and 20, and considering backscattering we have $ka_e<0.0754$ and 0.0475. Therefore, the range for the results in Fig. 3(a) satisfies these criteria. One must be aware that the criteria $kb<0.35$ for backscattering and $kb<0.3$ for forward scattering are by no means rigorous. The differences between the present approach and the T-matrix, as shown earlier, could imply stricter conditions for the present method. Research along this line is ongoing. Nevertheless, our approach is generally expected to be valid for prolate spheroids with small aspect ratios at low frequencies.

III. SUMMARY

In this paper, we proposed an approach to estimate sound scattering from prolate spheroid gas bubbles at low frequencies. This approach is based on the Kirchhoff integral theorem and the finding of Strasberg.[3] The sound field values at the scattering surface were solved with aid from a thermodynamic relation. Then the scattering function is obtained by integrating the Kirchhoff surface integral. It was shown that at low frequencies, the scattering function can be written in a simple form.

The features of the scattering function were examined with comparison to that obtained from two previous approaches, namely, the deformed cylinder method and the T-matrix method. It was shown that the present results are in good agreement with that obtained by the T-matrix method and the surface average method.[17] However, the agreements degrade as the aspect ratio increases. The comparison between the deformed cylinder method and the present approach showed significant differences between the two methods. However, the deformed cylinder method can be a good approximation for high frequencies. The valid range for the present approach has also been discussed.

ACKNOWLEDGMENTS

The author sincerely thanks Enyu Wang, Kelin Wang, and David Farmer for valuable discussions. C. S. Clay (Wisconsin-Madison), T. K. Stanton, and D. Chu (WHOI), and C. Feuillade (Mississippi) are thanked for comments and suggestions. The detailed comments and corrections from D. V. Holliday (Tracor) and D. E. Weston (UK) are greatly appreciated. The three anonymous referees are thanked for valuable comments and helpful English corrections. The work received support from a National Program for Fisheries Acoustics, Department of Fisheries and Oceans, Canada.

APPENDIX

In solving Eq. (11), we have made use of the Taylor expansion in Eq. (12): $\exp(ikr)\approx 1+ikr$. In this Appendix we show a general solution to Eq. (11) when $\mathbf{r}'=0$.

At $\mathbf{r}'=0$, Eq. (11) becomes

$$\frac{i\omega\rho_l}{4\pi}\int_S ds\,\frac{u_n}{r}\exp(ikr)+\frac{p_g}{4\pi}\int_S ds\,\frac{\mathbf{n}\cdot\mathbf{r}}{r}\left(\frac{1}{r^2}-\frac{ik}{r}\right)\times\exp(ikr)=1. \tag{A1}$$

We define

$$C_1+iC_2$$

$$\equiv \frac{1}{4\pi a^2}\int_S ds\ \frac{\exp(ikr)}{\sqrt{x^2+y^2+z^2}\sqrt{x^2/a^4+y^2/a^4+z^2/b^4}}, \tag{A2}$$

and

$$B_1-iB_2\equiv \frac{1}{4\pi}\int_S ds\ \frac{\mathbf{n}\cdot\mathbf{r}}{r}\left(\frac{1}{r^2}-\frac{ik}{r}\right)\exp(ikr), \tag{A3}$$

where $C_{1,2}$ and $B_{1,2}$ are real variables. Substituting these into Eq. (A1), we can solve for A and p_g with help from Eq. (9), which can be shown to be

$$A=\frac{i\omega}{3\gamma P_0}\,p_g\,. \tag{A4}$$

We write out the solutions as

$$A=\frac{i\omega}{3\gamma P_0 B_1(1-iB_2)-\omega^2 a^2\rho_l C_1(1+iC_2/C_1)}, \tag{A5}$$

$$p_g=\frac{3\gamma P_0}{3\gamma P_0 B_1(1-iB_2)-\omega^2 a^2\rho_l C_1(1+iC_2/C_1)}. \tag{A6}$$

Taking these solutions into Eq. (5), we obtain the scattering function

$$f(\mathbf{k}_i,\mathbf{k}_s)$$

$$=\frac{U_1-U_2}{(\omega_0^2/\omega^2)-1-i[C_2/C_1+(B_2/B_1)\ (\omega_0^2/\omega^2)]}, \tag{A7}$$

where

$$\omega_0^2=\frac{3\gamma P_0 B_1}{a^2\rho_l C_1},$$

$$U_1=\frac{1}{4\pi a^2 C_1}\int_S ds\ \frac{\exp(-i\mathbf{k}_s\cdot\mathbf{r})}{\sqrt{x^2/a^4+y^2/a^4+z^2/b^4}},$$

and

$$U_2=\frac{\omega_0^2}{\omega^2}\frac{1}{4\pi B_1}\int_S ds\ \exp(-i\mathbf{k}_s\cdot\mathbf{r})(i\mathbf{k}_s\cdot\mathbf{n}).$$

From Eq. (A7), we see that the resonance frequency is ω_0 and the damping factor is given by $C_2/C_1+(B_2/B_1)\omega_0^2/\omega^2$. When ignoring high-order terms involving k^2, Eq. (A7) reduces to Eq. (33).

[1] P. M. Morse and H. Feshbach, *Method of Theoretical Physics* (McGraw-Hill, New York, 1946), pp. 1503–1511.
[2] R. D. Spence and S. Granger, ''The scattering of sound from a prolate spheroid,'' J. Acoust. Soc. Am. **23**, 701–706 (1951).
[3] M. Strasberg, ''The pulsation frequency of nonspherical gas bubbles in liquids,'' J. Acoust. Soc. Am. **25**, 536–537 (1953).
[4] T. B. A. Senior, ''Scalar diffraction by a prolate spheroid at low frequencies,'' Can. J. Phys. **38**, 1632–1641 (1960).
[5] A. Silbiger, ''Scattering of sound by an elastic prolate spheroid,'' J. Acoust. Soc. Am. **35**, 564–570 (1963).
[6] J. E. Burke, ''Low-frequency scattering by soft spheroids,'' J. Acoust. Soc. Am. **39**, 826–831 (1966).
[7] C. Yeh, ''Scattering of acoustic waves by a penetrable prolate spheroid. I. Liquid prolate spheroid,'' J. Acoust. Soc. Am. **42**, 518–521 (1967).
[8] J. E. Burke, ''Scattering by penetrable spheroids,'' J. Acoust. Soc. Am. **43**, 871–875 (1968).
[9] M. Furusawa, ''Prolate spheroidal models for predicting general trends of fish target strength,'' J. Acoust. Soc. Jpn. (E) **9**, 13–24 (1988).
[10] G. C. Lauchle, ''Short-wavelength acoustic backscattering by a prolate spheroid,'' J. Acoust. Soc. Am. **58**, 576–580 (1975).
[11] For example, D. V. Holliday, ''Resonance structure in echoes from schooled pelagic fish,'' J. Acoust. Soc. Am. **51**, 1322–1332 (1972).
[12] D. M. Farmer and S. Vagle, ''Waveguide propagation of ambient sound in the ocean-surface bubble layer,'' J. Acoust. Soc. Am. **86**, 1897–1908 (1989).
[13] Z. Ye, ''On acoustic propagation in exponential ocean surface waveguides,'' J. Appl. Phys. **78**, 6389–6396 (1995).
[14] T. K. Stanton, ''Sound scattering by cylinders of finite length. III. Deformed cylinders,'' J. Acoust. Soc. Am. **86**, 691–705 (1989).
[15] C. Feuillade and M. F. Werby, ''Resonances of deformed gas bubbles in liquids,'' J. Acoust. Soc. Am. **96**, 3684–3692 (1994).
[16] P. C. Waterman, ''New formulation of acoustic scattering,'' J. Acoust. Soc. Am. **45**, 1417–1429 (1969).
[17] Z. Ye, ''Acoustic scattering from fish swimbladders,'' J. Acoust. Soc. Am. **99**, 785–792 (1996).
[18] J. D. Jackson, *Classical Electrodynamics* (Wiley, New York, 1975).
[19] C. S. Clay and H. Medwin, *Acoustic Oceanography* (Wiley, New York, 1977).
[20] J. A. Stratton, *Electromagnetic Theory* (McGraw-Hill, New York, 1941).
[21] D. E. Weston, ''Sound propagation in the presence of bladder fish,'' *Underwater Acoustics*, edited by V. M. Albers (Plenum, New York, 1967).
[22] R. H. Love, ''Resonant acoustic scattering by swimbladder-bearing fish,'' J. Acoust. Soc. Am. **64**, 571–580 (1978).
[23] C. Devin, ''Survey of thermal, radiation, and viscous damping of pulsating air bubbles in water,'' J. Acoust. Soc. Am. **31**, 1654–1667 (1959).
[24] C. S. Clay, ''Low-resolution acoustic scattering models. Fluid-filled cylinders and fish with swim bladders,'' J. Acoust. Soc. Am. **89**, 2168–2179 (1991).
[25] T. K. Stanton, ''Sound scattering by spherical and elongated shelled bodies,'' J. Acoust. Soc. Am. **88**, 1619–1633 (1990).
[26] V. C. Anderson, ''Sound scattering from a fluid sphere,'' J. Acoust. Soc. Am. **22**, 426–431 (1950).
[27] Z. Ye and M. Furusawa, ''Modeling of target strength of swimbladder fish at high frequencies,'' J. Acoust. Soc. Jpn. (E) **16**, 371–379 (1995).

Bottom reflection coefficient measurement and geoacoustic inversion at the continental margin near Vancouver Island with the aid of spiking filters

Garry J. Heard[a)]
Defence Research Establishment Pacific, FMO Esquimalt, British Columbia V0S 1B0, Canada

(Received 16 September 1994; revised 16 July 1996; accepted 11 November 1996)

This paper presents the results of an experiment to measure the reflection coefficient versus grazing angle at the continental margin west of Vancouver Island. The measured reflection coefficients are inverted and estimates of the surficial sediment geoacoustic properties obtained. The receiver used in this experiment was a long towed array with the source in aft-endfire aspect. The acoustic sources for this experiment were explosives that produced direct-path arrivals approximately 0.1 s in length. Bottom and sub-bottom arrivals continued for several seconds duration. Explosives were detonated at intervals such that bottom reflected energy received at the array sampled grazing angles in the interval 10°–80°. Source–receiver ranges were computed by measuring arrival time differences at each of the array elements, comparing these time differences with those computed using a ray-tracing propagation model, and globally minimizing the accumulated squared time difference residuals. To aid in the measurement of arrival times, spiking filters were employed to produce a *deconvolution-like* output that separates arrivals overlapped in the original time series. The reflection coefficient estimates were determined from the linear spiking filter outputs by forming the ratio of the direct-path and bottom-reflected arrival amplitudes. This technique is efficient and provides estimates of the surficial sediment reflection coefficient by excluding energy returned from sub-bottom layers. [S0001-4966(97)01004-7]

PACS numbers: 43.30.Pc, 43.30.Ma [JHM]

INTRODUCTION

The WEDGEX field trial was carried out using the Canadian oceanographic acoustic measurement system (COAMS)[1] off the west coast of Vancouver Island to investigate low-frequency propagation for upslope and downslope geometries. In order to interpret the propagation loss[2] it was necessary to estimate the geoacoustic bottom parameters in a region where the sea floor sloped almost uniformly along the track up the slope at the edge of the continental margin.

Signal underwater sound (SUS) charge explosives were used as the acoustic sources in this experiment. The explosion signals were received on a 32-element sub-array of the 128-channel COAMS array. The array was oriented in aft-endfire aspect to the source location such that each detonation provided data that could be used to estimate the reflection coefficient at 32 different grazing angles. In total, 11 source detonations occurred and the first eight of these were employed in this study providing 256 measurements of reflection loss versus grazing angle over a range of 10°–80°.

Acoustic arrival timing information was used to determine the source–receiver range. Direct measurement of the acoustic arrival times in the recorded data was made difficult by the overlap of the arrivals in the raw data. This was further complicated by the inclusion of a prewhitening filter in the array system that tended to destroy the impulsive nature of the explosion signals. These difficulties were overcome by employing a linear filter commonly known as a ''spiking'' filter. The spiking filter was developed using a standard technique and employed a sampled waveform as the ''input'' that was to be converted to a short duration triangular spike of unit amplitude. The result of spiking the raw data was to produce a time series in which acoustic arrivals appear as triangular-shaped pulses in a background of noise. The result is an approximation of the desired deconvolution of the raw data. Timing information was obtained by determining the sample that corresponded with the leading edge of each triangular spike.

Time differences between acoustic arrivals were compared with time differences calculated using a ray-tracing propagation model. The array position was determined by globally minimizing the accumulated squared residuals of the difference between measured and modeled time differences.[3] The resulting array positions were considered to be accurate to approximately 10 m.

Inspection of the spiked data records showed that sub-bottom arrivals were separable from the bottom-reflected arrivals over a large range of grazing angles. Similarly, the direct-path and surface-reflected arrivals were also separable over a large spread of source–receiver ranges. This separation of secondary arrivals implied that the amplitudes of the spikes would be a good estimate of the wavelet amplitudes by nature of the linear character of the spiking filters.[4] This fact suggested that an estimate of the reflection coefficients could be obtained by adjusting the spiked arrival amplitudes by a factor related to the time of flight (spherical spreading) and forming the ratio of the adjusted bottom-reflected spike amplitude to the adjusted direct-path spike amplitude. The final requirement was to relate each reflection coefficient es-

[a)]Now at: Defence Research Establishment Atlantic, P.O. Box 1012, Dartmouth, Nova Scotia B2Y 3Z7, Canada.

timate to the appropriate grazing angle. This task was easily accomplished using the same ray-tracing model used earlier.

Once the reflection coefficient-versus-grazing angle estimate has been made, an estimate of the surficial sediment geoacoustic properties can be obtained by inversion. In this paper, the geoacoustic properties of the sediment have been inverted using two different techniques: the first, a brute force search over allowable parameter ranges described by Chapman *et al.*,[5] and the second, a simulated annealing search due to Hannay and Chapman.[6] The inversion process is somewhat similar to that which arises in matched field processing, however, the dimensionality of the inversion space is generally smaller and the forward modeling much simpler and faster in this problem than in many matched field inversion problems. Rather than trying to match field values at various receivers, which requires the use of a computationally intensive propagation model, we simply fit a reflection coefficient curve to the measured reflection curve for a simple layered bottom. Using this technique we can obtain inversion results for the surficial sediments very rapidly even on a small computer. In addition, this method is relatively insensitive to the receiving array position uncertainty that would otherwise require the use of focalization techniques[7] and an increase in the computation time. It may be that some individuals would use our technique to provide initial estimates and bounds for the surficial sediment properties to be used in a more elaborate matched field inversion scheme where *a priori* information might otherwise be minimal.

In the next section, the WEDGEX experiment and the methods that were employed to develop a suitable spiking filter for the analysis are described. Section II describes the technique used to measure the arrival times and estimate the reflection coefficient. Section III presents the geoacoustic inversion results obtained with the two techniques previously mentioned. Finally, Sec. IV presents conclusions and briefly summarizes the results.

In Appendix A spiking filters are described in more detail following the approach described in Robinson and Trietel.[8] Appendix B summarizes the results of a heuristic study of the uncertainties in the timing and amplitude measurements for simulated conditions similar to those encountered with the WEDGEX data set.

I. WEDGEX TRIAL AND SPIKING FILTER DESIGN

A. WEDGEX field trial

In 1987, the WEDGEX field trial was conducted at a location off the west coast of Vancouver Island. Figure 1 shows the source location, the track of the COAMS receiver, and the bathymetry.

During the trial 11 signal underwater sound (SUS) charges were dropped at roughly 10-min intervals from a stationary source ship at the location indicated, while the COAMS array was towed directly away from the source ship location up the slope of the continental margin. The SUS charges detonated at approximately 183 m and produced a broadband signal with a 6-dB bandwidth of approximately 120 Hz and a maximum source level at 50 Hz.[9,10]

The COAMS array was towed at a nearly constant speed

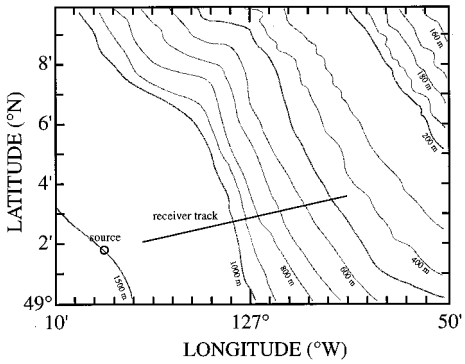

FIG. 1. The source location, receiver track, and bathymetry at the experiment site.

of 4 kn, at a mean depth of 221 m. The tow direction was almost directly up the slope toward the shallow water with the array in aft-endfire aspect to the source. The towed-array system provided data on a 32-element subarray with a sampling rate of 699.05 Hz. The inter-element spacing within the array was 38.1 m providing a total aperture of 1181.1 m.

The bathymetry in the area was almost uniformly shelving from a depth of 1500 to 450 m along the 15-km track, except in the region between the source and the early portion of the receiver track. In this particular area, a shallow canyon exists that runs parallel to the 1500-m depth contour.

The sound speed profiles were measured before, during, and after the experiment with the aid of expendable sound velocity probes (XSV). A mean sound-speed profile was adopted for use with the ray-tracing model that was employed to determine the grazing angles and source–receiver ranges.

The model employed was a simple implementation of the constant-gradient ray-tracing method with the ability to handle a range-dependent bottom. The model breaks the environment into a number of layers in which the sound-speed can be approximated by a linear profile. Relatively simple numerical integrations are then performed to calculate the time-of-flight and end-point location of the acoustic ray. A binary search is performed to find the eigenray that connects the source and receiver given a desired number of surface and bottom interactions. Corrections to the bottom interaction angles are made by looking at bottom-slope data obtained from an echo-sounder record made simultaneously with the reflection loss experiment.

B. Spiking filter design for the estimation of ocean bottom reflection coefficients

Spiking filters are well-known amongst the geophysical community, but they are rarely used in underwater acoustics. The spiking filter used in this application is developed using fairly standard techniques as described by Robinson and Treitel.[8] A summary description of the technique for creating spiking filters is given in Appendix A.

For the current application of estimating ocean bottom reflection coefficients it is assumed that the acoustic energy is composed of a sum of delayed, amplitude reduced, and phase-shifted replicas of an input wavelet corresponding to

the initial shock and subsequent bubble pulses of the explosive source modified by the prewhitening filter of the receiving array system. When a properly designed spiking filter is applied to such a signal, the resulting output is a sequence of spikes (of the desired shape) that appear at times corresponding to the arrivals of the source wavelet after transmission along various isolated propagation paths. The amplitudes of the spikes are a measure of the amplitudes of the wavelet arrivals after having suffered spreading and reflection/transmission losses in the media and at boundaries. The relationship between the wavelet amplitudes and those of the resulting spikes is guaranteed by the linear nature of the spiking filters, which are implemented as simple finite impulse response (FIR) filters. The major factors that effect the performance of the spiking filter are dispersion, and the degree of wavelet overlap in the received time series.

Geometrical dispersion is not a problem in the current work because the data are modeled as a sum of delayed, scaled multipath arrivals and we limit the application of the filter to situations where the filter is able to separate the bottom and sub-bottom arrivals. This separation of sub-bottom energy allows us to treat the bottom as a simple half-space and allows the direct determination of the surficial sediment properties independent of frequency. Intrinsic dispersion can be ignored because absorption in the water is extremely small at the frequencies of interest (i.e., 25–145 Hz). The major difficulty arises when the spiking filter is unable to resolve highly overlapped arrivals. In the current situation, this effect was observed on occasion and resulted in anomalous values of the reflection coefficient (i.e., responsible for some scatter in the reflection coefficient). Fortunately, the technique was applicable to the majority of the data (the first 8 of the 11 shots) and the critical angles were observable in the applicable data. The method might not have been applicable had the critical angles been smaller than they were or if strong sub-bottom returns were observed to merge with the bottom reflected signal sooner than they did due to a thinner layer of sediment being present. Appendix B summarizes the results of a heuristic study that was conducted to estimate the timing and amplitude measurement accuracy of the filter used in this study.

In the current application, the input waveform used was an isolated direct-path arrival observed in the data for shot number 1 on the hydrophone at the shortest range. It was assumed that each shot will produce a similar waveform, so that a single spiking filter would suffice for all of the recorded data. The input wavelet is denoted by x_t and the spiking filter must reshape this wavelet into a short duration spike. Figure 2 shows the wavelet used as the input x_t in this analysis. The selected waveform was obtained from the hydrophone closest to the detonation and is 69 samples in length.

The choice of the desired output waveform z is somewhat arbitrary in this case. Various candidates included a narrow square-topped pulse, a Gaussian-shaped pulse, and a triangular pulse. All of these were tried with various durations. Since accurate timing measurements were required, the duration of the pulse had to be small and contain a recognizable feature in the output shape that would serve as a reference point in the timing measurements. A subjective choice was made that the triangular pulse with a duration of four samples (1, 0.75, 0.5, 0.25) provided the best combination of a high-P value (performance measure, cf. Appendix A), a short duration, and a clearly recognizable feature (i.e., the apex between the vertical leading edge and the linearly decreasing tail).

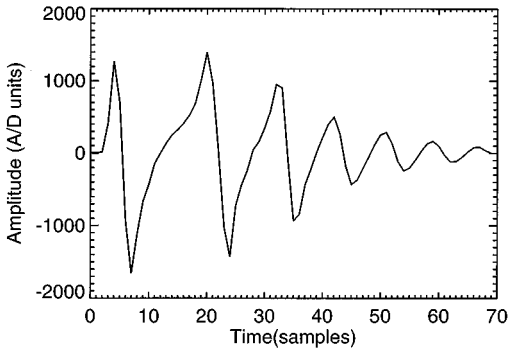

FIG. 2. Resolved direct-path arrival obtained from first shot detonation. This waveform was used as the input waveform x in the spiking filter normal equations.

In practice, a number of zeroes are added to either end of the pulse z to make the total waveform length, $m+1$, the same length as the input x_t. The delay of the pulse z refers to the numbers of zeroes prefixed to the z waveform. Searching for the best spiking filter with the triangular pulse shape amounts to computing P for various combinations of delay and total length of the filter, and then finding the length-delay combination that results in the highest P value. In the present case, a search of the parameter space over the region where the Toeplitz matrix was nonsingular determined that P was optimized for a filter length of 76 points and a delay of 51 samples.

Figure 3 shows the 76-point filter generated for the input waveform x and the output waveform z with a delay of 51 samples. The filter performance factor for this example is $P=0.916$. Application of this filter to recorded shot data should result in an output time series composed of recognizable triangular-shaped pulses superimposed on a noise background. Figure 4 shows a close-up of the result of applying the filter to the direct and surface-reflected arrivals from two different shots. Note that the origins of the time series in this

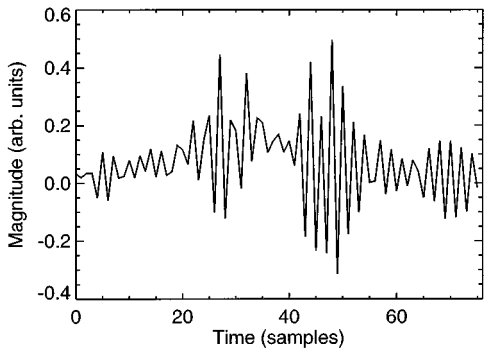

FIG. 3. A near optimal spiking filter for the isolated direct-path arrival of the SUS energy. For this filter $P=0.916$, the length is 76 points, and the output delay is 51 samples.

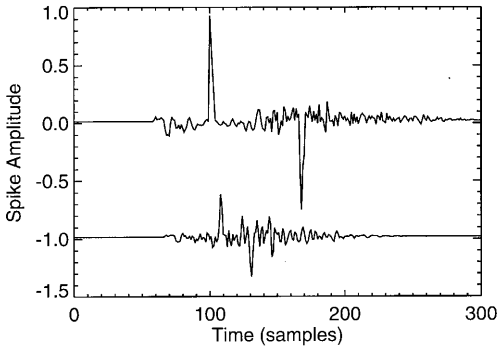

FIG. 4. The result of applying the filter in Fig. 3 to the direct and surface-reflected path arrivals from two different shot records. The lower curve has been offset by -1.

plot are arbitrarily chosen for display purposes and that the samples correspond to intervals equal to 1/699.05 s. The upper curve of the figure shows the spiked output obtained by applying the optimal spiking filter to the data record, as seen by the hydrophone closest to the detonation, for shot number 1. The positive going spike corresponds to the arrival of the direct path signal, while the negative going spike corresponds to the arrival of the surface-reflected path signal. Note that the peak amplitude of the first spike is approximately 0.9 in good agreement with the value of P for this filter. The lower curve is the result of applying the optimal spiking filter to the data record for shot number 2 (note that the curve has been offset by -1 for clarity). The resulting spiked signals are of lower amplitude for the second shot since the receiving array has moved approximately 1.2 km further away from the source position than it was for the first shot. Note that for this second shot the filter output contains a higher noise level than for the first shot; however, the timing and amplitudes of the real arrivals are accurately measured. As the signals become weaker for successive shot detonations (recall that the ship is continuously moving away from the source), the triangular shape of the spike is harder to recognize and spurious spikes can approach amplitudes similar to that of the desired signals. In practice, stacking the spiked time series for each hydrophone group in the array aids in the recognition of *real* arrivals and noise spikes.

II. REFLECTION COEFFICIENT ESTIMATION

The method for estimating the reflection coefficient is based on the measurement of the amplitudes and the time differences between arrivals associated with the direct path, surface-reflected path, and bottom-bounce paths. The time differences were determined by counting the number of samples between the peak values at the onset of the spiked arrivals. The triangular shape of the spike was clearly recognizable in many, but not all of the processed data. In those records where the spike shape was not easily distinguished, it was usually possible to recognize a local maximum near the expected arrival time, and the peak instant was recorded. In addition, the relative amplitudes of the arrivals were determined by measuring the peak spike amplitudes.

For each shot, measured time differences between the direct and surface-reflected arrivals were used to determine

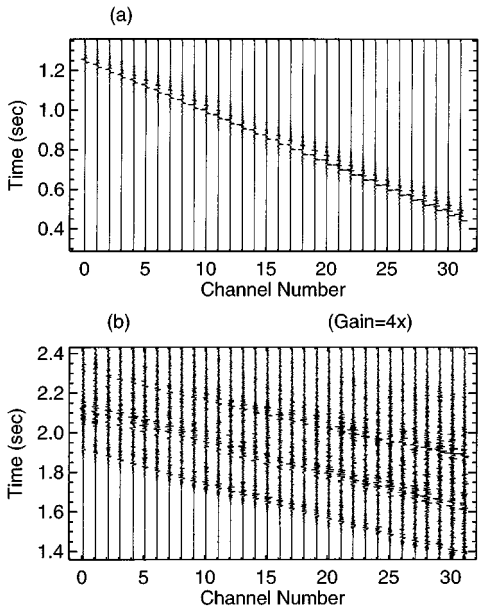

FIG. 5. The result of applying the filter in Fig. 3 to the data obtained from shot number 2. Each trace corresponds to one of 32 hydrophones in the receiving array. (a) The direct and surface-reflected arrivals and (b) first bottom-bounce arrivals.

the source range by globally minimizing the sum of the squared difference between a modeled and measured arrival time difference on each array element.[3] The source range was then used to provide spherical spreading corrections that were applied to both the measured direct and bottom-reflected arrival amplitudes. The ratio of the corrected bottom reflection spike amplitude to the corrected direct path arrival amplitude was formed to provide an estimate of the reflection coefficient versus range. The ray-trace model was then used to convert the coefficient estimates at given ranges to reflection coefficient versus grazing angle. The reflection coefficient versus grazing angle information was then inverted to obtain the geoacoustic parameters.[5,6]

III. RESULTS FROM WEDGEX DATA

This section presents some selected results of the application of spiking filters to the WEDGEX[2] field data, shows and describes the reflection coefficient versus grazing angle data, and presents the results from inverting the reflection coefficient data.

Figure 5 shows the results obtained from the application of the spiking filter to the second shot in the data set. In Fig. 5(a), the direct and surface-reflected arrivals are shown. Channel 31 corresponds to the hydrophone closest to the detonation and shows the earliest arrivals. Note that the direct path corresponds to the peak in the trace pointing to the right, while the opposite polarity surface-reflected arrival corresponds to the second peak in the trace and points to the left. The hydrophone corresponding to channel 0 is approximately 1200 m further from the detonation than the hydrophone corresponding to channel 31. Note the reduction in the relative amplitude of the spikes and the decreasing time separation between the arrivals. Figure 5(b) shows the spiked primary bottom-bounce return. The traces in this figure have

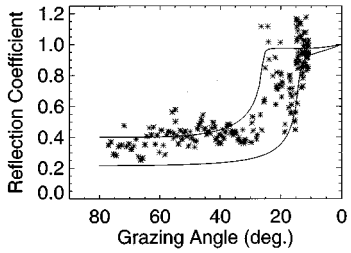

FIG. 6. Seafloor reflection coefficient estimates obtained from the ratio of the direct and bottom-reflected spiked arrival amplitudes. Solid curves represent the computed reflection coefficients using the geoacoustic parameters obtained by inversion.

been given a gain of 4 relative to the traces shown in part (a). The four main ray arrivals can be identified in this figure, but the surface-bottom and bottom-surface reflected paths are difficult to untangle from each other. In this work, the main interest is on the bottom-reflected path. This arrival is easily identified as the positive spike in the time period 1.4–1.9 s. The amplitude of this bottom-reflected arrival is much smaller than the arrivals shown in part (a) of the figure, but it was possible to identify the arrival on almost all of the hydrophones for each of the precritical reflections.

Figure 6 shows the estimated seafloor reflection coefficient obtained by forming the ratio of the spiked amplitudes of the bottom-bounce and direct arrivals corrected for spherical spreading loss. For the larger grazing angles a reasonably accurate reflection coefficient estimate is anticipated because the first bottom-bounce return is well separated from other arrivals. As the grazing angle is reduced, a loss of accuracy can be expected due to the decreasing separation of bottom-bounce and sub-bottom arrivals.

In this particular application the direct and bottom-bounce arrivals were always well separated; unfortunately, multiple returns occur in the bottom interacting signals that are not always well separated from the primary bottom-reflected arrival. The interfering returns are primarily caused by reflections from a subsurface layer varying in depth from 40–15 m as the point of observation moves up-slope. Figure 7 is a sketch of the bottom and subsurface reflector. The

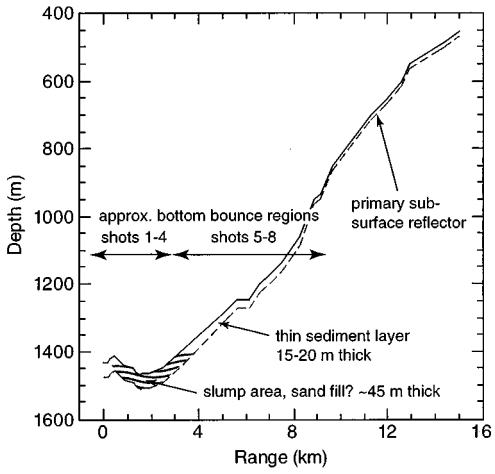

FIG. 7. Sketch of the bathymetry (dark line), primary sub-bottom reflector (dashed line), slump area, and reflection regions.

sub-bottom returns influence the estimation of the reflection coefficient by causing errors in the measurement of the primary bottom-reflected signal amplitude. Fortunately, over most of the sampled grazing angles the sub-bottom returns are quite weak and have only minimal and sporadic effects resulting in some scatter in the reflection coefficient. As the grazing angle is reduced, some dominant sub-bottom returns are noted and these returns are responsible for many of the anomalously large reflection coefficient values (i.e., those greater than unity). This mostly occurs for the data from shot number 8, which was the shot at greatest range from the receivers and, hence, supplied the smallest grazing angle data.

Care was taken to exclude those arrivals where sub-bottom returns greatly influenced the results. One can generally tell when this is happening by observing two consistent spikes in the data approaching one another and merging as the range to the source increases for successive hydrophones in the array. It was fortunate that the current problem allowed the critical angle to be clearly delineated. Had the surficial sediment layer been thinner, the arrivals from sub-bottom reflections might have obscured the critical angle of the surficial sediments. This problem with separating arrivals will limit the applicability of this reflection coefficient estimation technique in some cases, but the use of spiking filters to aid in preliminary interpretation is still recommended due to the relative ease and simplicity of their use and the resolution benefits that are realized. It should be noted that the scatter in the reflection coefficients obtained in the current analysis with this technique is comparable to the scatter that results when other techniques are used.

The reflection coefficient data have been interpreted as being the result of energy returns from a region of the seafloor with changing properties.[3,2] Figure 7 shows the bathymetry of the bottom, the probable extent of a sand-filled slump area, and the regions of the bottom where primary reflections occur. Using a ray-trace model it was determined that the first four shots lead to bottom interactions not far from the 1500-m depth contour. The sudden increase in the reflection coefficient near 25° is interpreted as the result of having reached the critical angle for the seafloor material in the slump region. Shots 5–8 result in bottom interactions further up the slope away from the slump area. The increase in the reflection coefficient below 20° is interpreted as being due to reaching the critical angle for the slope material. The timing of the returns from the primary subsurface reflector indicates that the thickness of the sediment layer above is reducing as the observation point moves toward the shallower water.

Using two different inversion schemes,[5,6] the reflection loss data were used to provide estimates of the geoacoustic parameters of the material in the canyon area and on the slope. The results from these two different inversion schemes were quite similar; however, there were some differences observed in the estimated shear speeds. In general, the shear wave velocity estimates are very uncertain and tend to be coupled with the attenuation values which we have taken to be 0.5 dB/λ (Ref. 2) as the precritical reflection data are insensitive to attenuation. Data from shots 1–4 were used to

estimate the geoacoustic properties of the deep water region where the grazing angles were larger, while data from shots 5–8 were used to estimate the geoacoustic properties for the slope region. The results are that in the canyon the compressional speed is approximately 1650 m/s with a density $\rho \approx 2.1$ g/cm^3 and shear speed less than 300 m/s. On the slope, the compressional speed is 1530 m/s and the shear speed is (very approximate) 80 m/s. Estimating the density on the slope is more difficult than in the canyon, but it appears that a density of 1.5 g/cm^3 would fit well with the observed data and agrees with the density found by other researchers[11] working nearby.

The solid curves in Fig. 6 represent the reflection coefficient versus grazing angle computed using a fluid-solid interface calculation.[12] The upper curve was calculated using the values determined from shots 1–4 (i.e., a water speed of 1485 m/s, a sediment compressional speed of 1650 m/s, a density of 2.1 g/cm^3 and a compressional attenuation of 0.5 dB/λ). The lower curve was calculated using the values determined from shots 5–8 (i.e., a sediment compressional speed of 1530 m/s and a density of 1.5 g/cm^3). The upper curve fits the observed data at steep grazing angles reasonably well, while the lower curve fits the data well at the shallow grazing angles.

Both inversion schemes are particularly sensitive to the rapid increase in the reflection coefficient estimates near the critical angle. It is obvious that one should attempt to measure the reflection coefficient at angles close to the critical angle to obtain minimum uncertainty in the inversion results.

IV. CONCLUSIONS

With the aid of spiking filters the reflection coefficient versus grazing angle has been measured at a location near the continental margin off the west coast of Vancouver Island. An interpretation of the acoustic data from the WEDGEX trial has previously determined that the geoacoustic properties of the seafloor are changing along the tow path.[2,3] The reflection coefficient data has been interpreted as being due to reflections from two different regions of the seafloor. The reflection coefficients were separated according to the bottom regions where the reflections occurred and inverted. The results are that in the slump region (see Fig. 7) the sediments have properties similar to sand, while on the slope region the sediment is very similar to that found further out to sea.[11]

An introduction to the technique for computing spiking filters has been presented in Appendix A and the accuracy of the spiking filter method for estimating the bottom loss has been investigated in a heuristic study of timing and amplitude measurement accuracy summarized in Appendix B. The accuracy study indicates that potential problems do exist for this method of determining the bottom-loss. In particular, the existence of secondary arrivals that are highly overlapped with the primary arrival can produce erroneous results. This fact may limit the applicability of the technique in thin sediment regions. However, spiking filters provide a very convenient way of reducing the confusion resulting from moderately overlapped arrivals in the data record, and provide a means for making accurate estimates of arrival times and amplitudes in many situations of interest in underwater acoustics.

APPENDIX A: SPIKING FILTERS

Spiking filters are a class of least-squares shaping filters that convert a given waveform of specific functional shape to a new waveform of shorter duration and generally with a different functional description. These filters are well-known to the seismic community, but they are not in widespread use in underwater acoustics. This section provides a brief description of spiking filters, but does not provide a complete background. Interested readers are referred to Robinson and Treitel[8] for a more comprehensive introduction to the topic.

The spiking filters are designed by minimizing the expected value of the squared error, J, determined from the input waveform x_t (with $t=1\cdots n$) and the desired output waveform z_t,

$$J=\sum_{t=1}^{n}\left\{\left(z_t-\sum_{t=0}^{m} f_i x_{t-i}\right)^2\right\}, \tag{A1}$$

with respect to the $m+1$ spiking filter coefficients f_i. The minimization of J leads to the normal equations[8]

$$\sum_{i=0}^{m} f_i \phi_{xx}(k-i)=\phi_{zx}(k), \tag{A2}$$

for $k=0,1,2,\ldots,m$, where ϕ_{xx} is the Toeplitz autocorrelation matrix of the input waveform x, and ϕ_{zx} is the cross-correlation vector of z and x. The solution of the normal equations gives the filter coefficients.

The squared error J is also used to assess the performance of the filter. Robinson and Treitel[8] define the *normalized mean-square error* as

$$E=1-\sum_{i=0}^{m} f_i \frac{\phi_{zx}(i)}{\phi_{zz}(0)}. \tag{A3}$$

The normalized error is then complemented to give $P=1-E$. This performance measure runs from zero to one, with a value of 0 indicating poor performance and a value of 1 indicating good performance. The problem of finding the optimum spiking filter involves searching for the filter that results in the maximum value of P. In general, the longer the filter the better the result, but a practical upper limit to the filter length occurs when the Toeplitz matrix ϕ_{xx} becomes ill-conditioned. Another factor affecting the value of P is the delay of the desired output pulse relative to the start of the input waveform. Qualitatively, the best filter performance is obtained when the delay of the output spike best matches the delay of energy delivery in the input waveform. For example, poor performances will result if the user attempts to create an output spike near the beginning of the output waveform when the input waveform is a maximum-delay waveform.

In spiking filter applications the specification of the desired output waveform shape may be explicitly defined by the case at hand or it may be somewhat arbitrary. If the user is seeking accurate timing measurements, then the desired output pulse will necessarily be of short duration and will

need to possess a clearly recognizable feature that can be used as a reference point for the timing measurement. Robinson and Treitel[8] give examples of a step function with a linearly decaying trailing edge (called here for convenience, a triangular pulse), a narrow square-topped pulse, a broader square-topped pulse, and a Gaussian-shaped pulse. Guidelines on how to choose the nature of the output pulse are limited, but Robinson and Treitel[8] suggest that, intuitively, output pulses with spectra similar to that of the input waveform may perform best.

APPENDIX B: ACCURACY OF TIMING AND REFLECTION COEFFICIENT AMPLITUDE

This paper has shown the result of applying a spiking filter to the WEDGEX data and using the amplitudes of the spikes to estimate the seafloor reflection coefficient. The question now arises as to how accurate are the estimates that have been obtained using the spiking filter method? In order to answer this question in at least a heuristic manner, a study using simulated waveforms with varying arrival separations, signal-to-noise ratios, bandwidths, and filter characteristics was carried out.[4] Results of this study are summarized here, to provide an indication of the accuracy of the results that have been obtained.

The accuracy of the spiking filter approach to range and bottom parameter estimation was investigated by generating realistic simulated data with known arrival time separations and amounts of added noise. The direct-path waveform shown in Fig. 2 was used as a model, $a(t)$, of a realistic acoustic arrival and the received time series were assumed to consist of delayed, scaled replicas of this model waveform. The simulated time series, $s(t)$, were given by

$$s(t)=a(t)-b\cdot a(t-\tau)+c\cdot n(t), \tag{B1}$$

where b is a constant (usually equal to 1) that controls the amplitude of a second arrival, τ is the delay of the second arrival relative to the primary arrival a, and $n(t)$ is a sampled, zero mean, unity variance, Gaussian-noise time series whose amplitude is controlled by the constant c. The second arrival is multiplied by a negative value to simulate the phase change that occurs on reflection at the surface of the sea. Simulated data were generated for arrival separations of 5–100 samples (i.e., waveforms overlapping by as much as 93%, to being completely separated by a time interval of almost half of the waveform length), for signal-to-noise ratios of 3.5–13.2 dB, for $P=0.67-0.92$, and for nominal bandwidths $\Delta f=200$, 140, and 90 Hz.

To summarize the results of the simulation study it was found that timing measurements were relatively insensitive to changes in the signal-to-noise ratio, the P value, and the bandwidth (at least for the bandwidths that were considered, using a greatly reduced bandwidth might have produced more effect). In general, timing estimates were accurate to within one sampling period, although at low signal-to-noise (3.5 dB) and for signals overlapped more than 60% of their length, a decreased accuracy was noted (error of up to 4 time samples). These results imply that for the shorter range shots that give rise to well-separated direct and surface-reflected arrivals, the source-receiver distance should be very accurately determined. As the propagation distance becomes greater, the separation of the arrivals will be decreased and the resulting range estimates should become less accurate. Fortunately, some increase in the absolute range error can usually be tolerated at the larger ranges as the relative error remains small.

The measured amplitudes were found to be more sensitive to degraded conditions than the timing measurements were. In general, for separations exceeding 43% of the length of waveform a [i.e., $\tau \geqslant 0.43$ length(a)], the measured amplitude was proportional to the value of P and degraded with decreasing signal-to-noise ratio. When the input signal amplitude was 5 or more times the noise amplitude, then performance was basically equivalent to the noise-free performance. For separations of less than 25% of the input waveform length ($\approx$25 ms), the amplitude measurement was significantly in error.

In the WEDGEX experiment the direct path arrival and the bottom-reflected arrivals were always well separated; however, sub-bottom arrivals were not always well separated from the primary bottom-bounce arrival, and the surface-reflected arrival was not always well separated from the direct path arrival. The interference of additional arrivals can have significant impact on the measured amplitude of the primary arrival. These effects are believed to be the cause of the scatter in the reflection coefficient measurements shown in Fig. 6 and also the primary cause of the anomalous values greater than unity. In fact, the potential exists for creating the appearance of a false critical angle due to the effect of highly overlapped arrivals. However, in the present case, care was taken to exclude situations where sub-bottom arrivals were not separable from the primary bottom-reflection and the existence of two critical angle regions is believed to represent the actual bottom conditions based on the good agreement with the results of others[11] found for the slope material parameters and knowledge of the bottom materials obtained from Bornhold and Barrie,[13] and Bornhold.[14]

The heuristic analysis of the spiking filter accuracy has indicated that applications involving timing measurements only are robust, and likely to produce accurate results when the degree of signal overlap is less than 60% of the input waveform length. On the other hand, caution must be applied to applications that require the measurement of spike amplitudes. When the signal-to-noise ratio is greater than 10 dB and the overlap of the arrival waveforms is less than 57%, then the amplitude measurements can be confidently accepted. These conditions were met for the majority of the data obtained from the first 8 of the 11 shots in the WEDGEX data set. Shot number 8 presented the majority of the difficulties in the data used in this paper due to the presence of a sub-bottom reflection that became inseparable from the bottom-bounce reflection.

[1] D. W. Craig and L. McKee, ''High Performance Shipboard Acoustics Data Acquisition, Imaging,'' Sea Technol. **31**, 51–53 (1990).
[2] G. J. Heard, D. J. Thomson, and G. H. Brooke, ''Two-way *PE* versus upslope propagation,'' *Ocean Reverberation*, edited by D. D. Ellis, J. R. Preston, and H. G. Urban (Kluwer, Dordrecht, 1993), pp. 247–252.
[3] G. J. Heard, ''Array positioning, bathymetry, and geoacoustic parameter estimation in a wedge-shaped ocean environment,'' in *Proceedings of*

Oceans'93, Victoria, BC, Canada (IEEE and Oceanic Engineering Society, New York, 1993), Vol. I, pp. 427–432.
[4] G. J. Heard, ''Application of spiking filters to arrival time and amplitude measurement of underwater acoustic signals,'' Defence Research Establishment Pacific Report No. DREP TM94-112, 1994.
[5] N. R. Chapman, K. Stinson, S. Levy, J. Cabrera, and D. W. Oldenburg, ''Estimation of the Elastic Properties of Seafloor Sediments by Inversion of Precritical Reflection Data,'' IEEE J. Oceanic Eng. **13**(4), 215–221 (1988).
[6] D. E. Hannay and N. R. Chapman, ''Inversion of geoacoustic profiles in thin-sediment environments from ocean bottom reflection loss data,'' in *Proceedings of Oceans'93*, Victoria, BC, Canada (IEEE and Oceanic Engineering Society, New York, 1993), Vol. III, pp. 381–386.
[7] M. D. Collins and W. A. Kuperman, ''Focalization: environmental focusing and source localization,'' J. Acoust. Soc. Am. **90**, 1410–1422 (1991).
[8] E. A. Robinson and S. Treitel, *Geophysical Signal Analysis* (Prentice-Hall, Englewood Cliffs, NJ, 1980), pp. 140–212.
[9] N. R. Chapman, ''Source levels of shallow explosive charges,'' J. Acoust. Soc. Am. **84**, 697–702 (1988).
[10] D. E. Hannay, ''Estimation of geoacoustic parameters of the ocean bottom by inversion of reflection loss data,'' Master's thesis, Department of Physics and Astronomy, University of Victoria, Victoria, BC, Canada, 1995.
[11] M. K. Sen, L. N. Frazer, S. Mallick, and N. R. Chapman, ''Analysis of multipath sound propagation in the ocean near 49° N, 128° W,'' J. Acoust. Soc. Am. **83**, 588–597 (1988).
[12] L. M. Brekhovskikh, *Waves in Layered Media* (Academic, New York, 1960).
[13] B. D. Bornhold and J. V. Barrie, ''Surficial sediments on the western Canadian continental shelf,'' Continental Shelf Res. **11**(8–10), 685–699 (1991).
[14] B. D. Bornhold (private communication).

Active, wideband detection and localization in an uncertain multipath environment

M. Wazenski
Digital System Resources, 12450 Fair Lakes Circle, Suite 500, Fairfax, Virginia 22033

D. Alexandrou
SACLANT Undersea Research Centre, Viale San Bartolomeo, 400, 19138 La Spezia, Italy

(Received 19 January 1996; accepted for publication 21 October 1996)

Active, wideband detection and localization of targets in a dense multipath environment is approached via optimal detection and estimation theory in conjunction with a received signal model described by weighted, delayed, and phase-shifted replicas of the transmitted signal. These multipath signal parameters are known to vary with acoustic medium properties including sound-speed profile, bottom composition and topography, and sea surface state. The optimum receiver is a time domain processor based on the statistical properties of the multipath parameters. An acoustic propagation model drives the optimum receiver by mapping acoustic medium parameters to multipath signal parameters through Monte Carlo simulation. The generic sonar model (GSM) software package provides the required simulation environment. Illustrative detection and localization examples are presented in the form of receiver operator characteristics (ROC) and localization ROCs, respectively. Results demonstrate significant improvement in detection and localization over standard matched filtering, even with uncertainty of the physical environment and random effects of boundary scattering. © *1997 Acoustical Society of America.*
[S0001-4966(97)01403-3]

PACS numbers: 43.30.Vh, 43.30.Wi [MBP]

INTRODUCTION

Traditionally, detection and localization of targets via active sonar has been approached through matched filtering. In dense multipath environments (e.g., shallow water), this approach produces a multitude of temporally smeared correlation peaks, making detection and localization difficult. In this paper, we approach this problem through application of optimum physics-based signal processing which merges statistical physical modeling of the propagation medium and stochastic descriptions of environmental uncertainty within a Bayesian decision-theoretic framework. This approach produces a robust matched field method of detection and is additionally capable of localizing the target.

The sensitivity of traditional matched field processing (MFP) to environmental mismatch is well documented.[1,2] Our approach provides an explicit means of expressing uncertainty regarding the acoustic environment, resulting in the best possible processor given the extent of knowledge of propagation conditions. Previous applications of optimum physics-based signal processing include robust passive source localization by Richardson and Nolte with the optimal uncertain field processor (OUFP).[3] Application of the OUFP in a random scattering environment has been presented by Haralabus *et al.*[4] and Premus *et al.*[5] The present work extends application to active wideband scenarios.

Our approach amounts to a time domain matched field technique in that we endeavor to describe the target echo through acoustic modeling. Utilizing all available *a priori* information regarding the environment, we build a probabilistic description of the acoustic medium. The acoustic model converts this acoustic medium information to a description of the target echo waveform at the receiver. A detection decision is based on the resulting stochastic description of the received target echo.

A key consideration in the present development is the representation of the target echo at the receiver. Here we employ a signal model described by weighted, delayed, and phase-shifted replicas of the transmitted signal. This model provides an efficient parametric method for representing the target echo waveform using information inherently known in an active sonar application, namely the type of signal and time of transmission. Successful application of time domain matched field to real data has been reported by Michalopoulou *et al.*[6] for broadband source localization.

Detection techniques which employ a multipath signal model for the received target echo have been reported by Lourtie and Carter for both *ad hoc*[7] and optimal[8] approaches. While these works integrate *a priori* descriptions of multipath propagation into the detector, no means of obtaining such prior information is provided. As an alternative to comprehensive signal modeling, Giannakis and Tsatsanis developed a general detection method for random non-Gaussian signals in additive Gaussian noise using third-order cumulant sums.[9] Techniques which attempt to acquire an understanding of multipath propagation include neural nets trained with *in situ* data,[10] and adaptive algorithms such as blind deconvolution.[11] For the present approach, we obtain descriptions of the physical environment, utilizing current *in situ* measurements as well as relevant historical data. Through acoustic modeling, these prior physical descriptions are converted to a probabilistic description of multipath parameters.

The paper is organized as follows. In Sec. I, a discussion

and supportive reasoning for choosing the signal model is presented. Section II presents a theoretical development and functional description of the detector. In Sec. III, we discuss the simulation environment and associated implementation issues. Results of simulation are reported in Sec. III C.

I. SIGNAL MODELING

The signal model employed assumes the received pressure field can be adequately described as the sum of complex weighted and delayed replicas of the transmitted signal.[12,8,13] The complex baseband signal is expressed as

$$r(n)=\sum_{i=0}^{M-1} \alpha_i s(n-\tau_i)e^{-j\theta_i}, \tag{1}$$

where s is the complex baseband transmit signal and α, τ, and θ, are the amplitudes, delays, and phase shifts over M multipaths, respectively. The signal model makes no assumption as to the nature of the transmit signal. Thus, constant wave (CW), FM, pulse trains, and other signals with unique range/Doppler properties can be accommodated.

The primary value of this signal model is that it provides an efficient means of characterizing the acoustic channel independent of the frequency regime employed. Moreover, this model provides a physically meaningful method of translating uncertain physical descriptions of the ocean to a stochastic representation of the acoustic signal.

The assumed signal model has restricted application in certain ocean scenarios with large bandwidth signals. In particular, this signal model does not account for dispersive effects in the ocean. Generally, there are two sources of dispersion in an ocean waveguide. Intrinsic dispersion, a relatively minor effect, results from frequency-dependent attenuation in the medium.[12] The more significant source of dispersion is geometrical dispersion. In situations where the ocean depth is on the order of an acoustic wavelength, group velocity is strongly frequency dependent.[14] Thus, the model is most accurately employed in situations where the acoustic wavelength is at least an order of magnitude smaller that the ocean waveguide depth. If, for a particular application, dispersive effects are significant, such effects, which are generally deterministic, can be accounted for by adjusting the signal, s, in the signal model.

Another potential limitation of the signal model concerns boundary scattering. In the general situation, a number of multipaths propagate via surface and/or bottom interaction. Generally, boundary scattering is frequency dependent due to multiscale roughness features that may exist. Since the signal model assumes frequency-independent scattering, application is limited to environments exhibiting small scale roughness, where the frequency dependence of scattering is minimal.

II. DETECTOR DEVELOPMENT

For an arbitrary array of elements, the observation vector $\mathbf{x}$ is defined as the set of complex pressure signals, basebanded from some center frequency f_0 and comprised of N discrete time samples over K different receiver elements. The vector $\mathbf{x}_k$ represents the received waveform at the k^{th} element, and thus,

$$\mathbf{x}=[\mathbf{x}_1^T \vdots \mathbf{x}_2^T \vdots \ldots \vdots \mathbf{x}_K^T]^T \tag{2}$$

is the column vector containing NK complex signal samples.

The detection problem begins with the standard two hypothesis approach,

$$H_0: \quad \mathbf{x}=\mathbf{n}(\boldsymbol{\Psi}), \tag{3}$$

$$H_1: \quad \mathbf{x}=\mathbf{r}(\boldsymbol{\Phi})+\mathbf{n}(\boldsymbol{\Psi}), \tag{4}$$

in which the observation vector $\mathbf{x}$ falls under either hypothesis H_1 in which both signal and noise are present or hypothesis H_0 in which noise alone is observed. The observed noise $\mathbf{n}$ is expressed as a function of physical environment param-

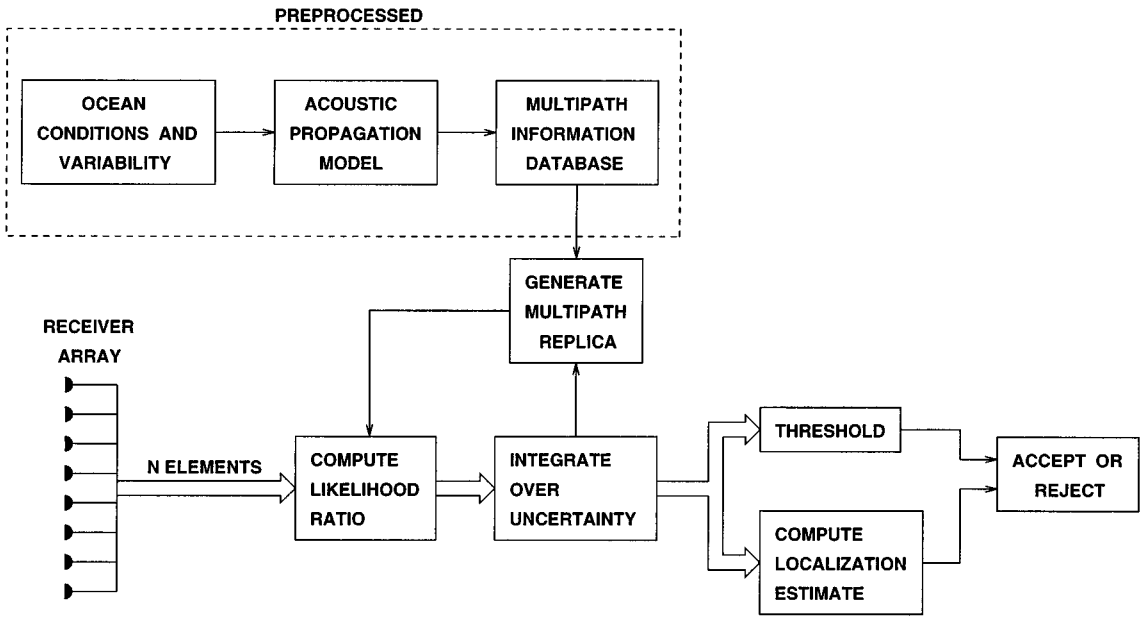

FIG. 1. Functional diagram of the optimal multipath detector showing a preprocessed multipath database and iterative integration.

eters, $\boldsymbol{\Psi}$. The signal vector $\mathbf{r}$ is expressed as a function of acoustic channel parameters, $\boldsymbol{\Phi}$. In our case, $\boldsymbol{\Phi}$ is defined as the set of multipath amplitudes $\boldsymbol{\alpha}$, delays $\boldsymbol{\tau}$, and phases $\boldsymbol{\theta}$ for each receiver element. Although not explicitly stated, it should be noted that the set of $\boldsymbol{\alpha}$, $\boldsymbol{\tau}$, and $\boldsymbol{\theta}$ vary as a function of the physical environment and the target location, denoted by the set parameters $\boldsymbol{\Psi}$ and $\boldsymbol{\Xi}$, respectively.

$\boldsymbol{\Psi}$ represents measurable and meaningful ocean properties affecting acoustic propagation. Such properties include a description of the sound-speed profile, surface roughness, and bottom composition and roughness. In the general case, $\boldsymbol{\Psi}$ affects the propagation of noise through the ocean, ultimately affecting the statistical properties of the received noise. Indirectly, $\boldsymbol{\Psi}$ also affects the received multipath signal since $\boldsymbol{\alpha}$, $\boldsymbol{\tau}$, and $\boldsymbol{\theta}$ are determined by the physical environment. This indirect influence on the received multipath signal holds for $\boldsymbol{\Xi}$ as well.

The optimal detector for any reasonable cost function is the likelihood ratio[15]

$$\lambda(\mathbf{x}) \equiv \frac{p(\mathbf{x}|H_1)}{p(\mathbf{x}|H_0)}. \tag{5}$$

For signal or noise parameters which are uncertain, the optimal receiver requires integration over the unknowns and their associated *a priori* distributions,[16] yielding

$$\lambda(\mathbf{x}) = \frac{\int_{\boldsymbol{\Xi}}\int_{\boldsymbol{\Psi}}\int_{\boldsymbol{\Phi}} p(\mathbf{x}|\boldsymbol{\Phi},\boldsymbol{\Psi},\boldsymbol{\Xi},H_1)p(\boldsymbol{\Phi},\boldsymbol{\Psi},\boldsymbol{\Xi}|H_1)}{\int_{\boldsymbol{\Psi}} p(\mathbf{x}|\boldsymbol{\Psi},H_0)p(\boldsymbol{\Psi}|H_0)}. \tag{6}$$

Since the observed noise varies as a function of the physical ocean environment, our detector is a doubly composite hypothesis problem, requiring integration over the noise environment separately under each hypothesis.

By definition under the H_1 hypothesis, $\mathbf{x}$ depends on $\boldsymbol{\Phi}$ and $\boldsymbol{\Psi}$ only. Thus, the above conditional pdf simplifies to,

$$p(\mathbf{x}|\boldsymbol{\Phi},\boldsymbol{\Psi},\boldsymbol{\Xi},H_1) = p(\mathbf{x}|\boldsymbol{\Phi},\boldsymbol{\Psi},H_1). \tag{7}$$

Through the definition of conditional probability, we separate $\boldsymbol{\Phi}$ from $\boldsymbol{\Psi}$ and $\boldsymbol{\Xi}$. Thus, we have,

$$p(\boldsymbol{\Phi},\boldsymbol{\Psi},\boldsymbol{\Xi}|H_1) = p(\boldsymbol{\Phi}|\boldsymbol{\Psi},\boldsymbol{\Xi},H_1)p(\boldsymbol{\Psi},\boldsymbol{\Xi}|H_1). \tag{8}$$

Using the above expressions, Eq. (6) can be rewritten as

$$\lambda(\mathbf{x}) = \frac{\int_{\boldsymbol{\Xi}}\int_{\boldsymbol{\Psi}}\int_{\boldsymbol{\Phi}} p(\mathbf{x}|\boldsymbol{\Phi},\boldsymbol{\Psi},H_1)p(\boldsymbol{\Phi}|\boldsymbol{\Psi},\boldsymbol{\Xi},H_1)p(\boldsymbol{\Psi},\boldsymbol{\Xi}|H_1)}{\int_{\boldsymbol{\Psi}} p(\mathbf{x}|\boldsymbol{\Psi},H_0)p(\boldsymbol{\Psi}|H_0)}. \tag{9}$$

Finally, substituting for $\boldsymbol{\Phi}$ the set of multipath parameters, $\boldsymbol{\alpha}$, $\boldsymbol{\tau}$, and $\boldsymbol{\theta}$, the expression for our detector becomes

$$\lambda(\mathbf{x}) = \frac{\int_{\boldsymbol{\Xi}}\int_{\boldsymbol{\Psi}}\int_{\boldsymbol{\alpha}}\int_{\boldsymbol{\tau}}\int_{\boldsymbol{\theta}} p(\mathbf{x}|\boldsymbol{\alpha},\boldsymbol{\tau},\boldsymbol{\theta},\boldsymbol{\Psi},H_1)p(\boldsymbol{\alpha},\boldsymbol{\tau},\boldsymbol{\theta}|\boldsymbol{\Psi},\boldsymbol{\Xi},H_1)p(\boldsymbol{\Psi},\boldsymbol{\Xi}|H_1)}{\int_{\boldsymbol{\Psi}} p(\mathbf{x}|\boldsymbol{\Psi},H_0)p(\boldsymbol{\Psi}|H_0)}. \tag{10}$$

In addition, we assume that the noise process is Gaussian. Thus, the conditional probabilities are given by

$$p(\mathbf{x}|\boldsymbol{\alpha},\boldsymbol{\tau},\boldsymbol{\theta},\boldsymbol{\Psi},H_1) = \frac{1}{(2\pi)^{N/2}|\boldsymbol{\Lambda}(\boldsymbol{\Psi})|^{1/2}} \times \exp[-\tfrac{1}{2}(\mathbf{x}-\mathbf{r}(\boldsymbol{\alpha},\boldsymbol{\tau},\boldsymbol{\theta}))^H \boldsymbol{\Lambda}(\boldsymbol{\Psi})^{-1}(\mathbf{x}-\mathbf{r}(\boldsymbol{\alpha},\boldsymbol{\tau},\boldsymbol{\theta}))] \tag{11}$$

and

$$p(\mathbf{x}|\boldsymbol{\Psi},H_0) = \frac{1}{(2\pi)^{N/2}|\boldsymbol{\Lambda}(\boldsymbol{\Psi})|^{1/2}} \exp\left(-\frac{1}{2}\mathbf{x}^H \boldsymbol{\Lambda}(\boldsymbol{\Psi})^{-1}\mathbf{x}\right), \tag{12}$$

where $\boldsymbol{\Lambda}$ is the complex covariance matrix of the noise process.

Equations (10)–(12) define the optimum uncertain multipath receiver (OUMR). Note that the replica signal $\mathbf{r}$ is specified by the multipath signal parameters. Also, the noise covariance depends on the acoustic environment.

For the purposes of this paper, we focus on propagation effects on the target signal and treat the noise environment as white both spatially and temporally. Thus, we eliminate dependence of the conditional pdf's for both hypotheses on $\boldsymbol{\Psi}$ and simplify Eq. (10) to

$$\lambda(\mathbf{x}) = \int_{\boldsymbol{\Xi}}\int_{\boldsymbol{\Psi}}\int_{\boldsymbol{\alpha}}\int_{\boldsymbol{\tau}}\int_{\boldsymbol{\theta}} \frac{p(\mathbf{x}|\boldsymbol{\alpha},\boldsymbol{\tau},\boldsymbol{\theta},H_1)}{p(\mathbf{x}|H_0)} \times p(\boldsymbol{\alpha},\boldsymbol{\tau},\boldsymbol{\theta}|\boldsymbol{\Psi},\boldsymbol{\Xi},H_1)p(\boldsymbol{\Psi},\boldsymbol{\Xi}|H_1). \tag{13}$$

Recognizing the definition of the likelihood ratio, we simplify our detector as

$$\lambda(\mathbf{x}) = \int_{\boldsymbol{\Xi}}\int_{\boldsymbol{\Psi}}\int_{\boldsymbol{\alpha}}\int_{\boldsymbol{\tau}}\int_{\boldsymbol{\theta}} \lambda(\mathbf{x}|\boldsymbol{\alpha},\boldsymbol{\tau},\boldsymbol{\theta}) \times p(\boldsymbol{\alpha},\boldsymbol{\tau},\boldsymbol{\theta}|\boldsymbol{\Psi},\boldsymbol{\Xi},H_1)p(\boldsymbol{\Psi},\boldsymbol{\Xi}|H_1). \tag{14}$$

The conditional likelihood ratio in Eq. (14) is simply the likelihood function of a signal known exactly (SKE).[16] Thus,

$$\lambda(\mathbf{x}|\boldsymbol{\alpha},\boldsymbol{\tau},\boldsymbol{\theta}) = \exp\left[\frac{1}{\sigma_n^2}\,\mathrm{Re}(\mathbf{x}^H\mathbf{r}(\boldsymbol{\alpha},\boldsymbol{\tau},\boldsymbol{\theta})) - \frac{1}{2\sigma_n^2}(\mathbf{r}(\boldsymbol{\alpha},\boldsymbol{\tau},\boldsymbol{\theta})^H\mathbf{r}(\boldsymbol{\alpha},\boldsymbol{\tau},\boldsymbol{\theta}))\right], \tag{15}$$

where σ_n^2 is the variance of the noise for all receivers.

Accurate prior distributions of multipath parameters are critical for effective operation of our detector. Previous works assume these distributions are either known *a priori*[7,8] or completely unknown, requiring either *in situ*

measurements,[10] or adaptive estimation.[11] Our approach, instead, takes advantage of information available about the physical environment, however uncertain or incomplete. Through acoustic modeling, we convert this information to a probabilistic description of multipath parameters.

The mechanism that allows the acoustic model to drive the OUMR is the conditional pdf, $p(\boldsymbol{\alpha},\boldsymbol{\tau},\boldsymbol{\phi}|\boldsymbol{\Psi},\boldsymbol{\Xi},H_1)$. This function maps specifications of target location, $\boldsymbol{\Xi}$, and environment parameters, $\boldsymbol{\Psi}$, to probabilistic descriptions of signal parameters, $\boldsymbol{\alpha}$, $\boldsymbol{\tau}$, and $\boldsymbol{\theta}$. A key consideration here is the treatment of acoustic propagation as a random process. This allows a proper treatment for such effects as boundary scattering and internal waves. In addition, this treatment accommodates the type and scope of physical parameters used to describe the environment. By and large, one can only make general descriptions of physical properties, supportable by historical databases and sparse *in situ* measurements. These descriptions give rise to an ensemble of possible ocean realizations. For example, it is reasonable to assume a general seasonal SSP description, which supports an entire family of sound-speed profiles. Thus, $\boldsymbol{\Psi}$ contains the set of physical parameters describing an ensemble of possible oceans, leading to a statistical description of multipath parameters.

A distinction should be made between the conditional pdf given above and the prior pdf, $p(\boldsymbol{\Psi},\boldsymbol{\Xi}|H_1)$. This function describes the uncertainty of the physical parameters themselves; the conditional pdf describes the uncertainty of the multipath parameters given a deterministic set of physical parameters. Thus, two layers of uncertainty are treated within the OUMR. We refer to the uncertainty of the physical parameters as the outer layer, and the uncertainty of the multipath parameters as the inner layer.

A functional description of the detector is shown in Fig. 1. Information about the acoustic environment is used to produce realizations of the propagation medium. Through an acoustic propagation model, descriptions of the multipath's amplitude, delay, and phase can be obtained and stored in a database. From the multipath database, a multipath replica is generated and correlated with the received array signals. This process is repeated in order to properly integrate over the uncertain and random ocean conditions. Once integration is completed, a detection decision is made based on a chosen threshold.

Since the target's location is an additional uncertainty, we integrate over potential target locations for optimal detection. As is typical with matched field methods, the received multipath signal is highly dependent on target location, and hence, offers the opportunity to accurately estimate a target's location. In our approach, such an estimate is obtained directly from the detector without additional processing. This benefit is explored through simulation in the next section.

III. SIMULATION

Simulations of the optimal detector were performed in a relatively shallow water environment where moderately dense multipath conditions were expected. For the purposes of simulation, we limited ourselves to an azimuthally homogeneous, range independent environment. It is important to note that our approach is valid for the general situation where the ocean environment changes as a function of azimuth and range. This, however, requires a more comprehensive propagation model.

We considered a moderately shallow water waveguide of 300-m depth. A vertical array of five elements operating at a center frequency of 250 Hz served as both the transmitter and receiver platform. The array spanned 50–130 m in depth with 20-m spacing between elements. A single target was placed at 2000 m in range and 150 m in depth.

The sound-speed profile (SSP) was considered uncertain in our simulation. We operated under the assumption that a mean summer Mediterranean profile was valid but a degree of uncertainty existed due to dynamic ocean processes. These effects were modeled by adding Gaussian noise to the mean sound-speed profile, the variance of which decreased from 2.5 m/s at the surface to 0.05 m/s at the bottom. In order to produce a realistic SSP, a correlation coefficient of 0.5 was introduced between successive points along the profile. The summer Mediterranean profile was characterized by strong thermal gradient near the surface, a sound channel axis at about 100 m, and a pressure gradient below the sound channel axis.

Boundary interaction was considered as a random process in our simulation. The surface model employed was derived from a 2D scattering simulation reported by Haralabus *et al.*[4] which uses the Kirchoff approximation to the Helmholtz integral equation as developed by Thorsos.[17] The rms wave height was 0.56 m corresponding to a sea state of two. Figure 2 shows histograms for the specular reflection coefficient in amplitude and phase. The bottom was similarly modeled but made slightly smoother and lossy. Figure 3 shows histograms for the bottom. Notice that phase perturbations are smaller indicating a smoother bottom. The reflection coefficient magnitude is also smaller, indicating greater loss.

A. Acoustic propagation modeling

The acoustic propagation software selected for simulation was the generic sonar model (GSM) which utilizes ray theory. Ray methods are ideal because they work in synergy with the signal model in providing the necessary multipath parameters. Frequency domain propagation models such as normal mode, parabolic equation, or fast-field program (FFP) are applicable; however, acquiring the necessary multipath parameters is less efficient with these methods since they require a Fourier synthesis. Alternative time domain propagation models, including time-marched FFP[18] and time domain parabolic equation,[12] offer similar benefits to ray methods.

In order to confirm the applicability of ray theory to the selected simulation scenario, an initial comparison between ray theory (GSM) and normal mode propagation, using SNAP[19] was performed. A test simulation was carried out using a 1-s linear FM signal centered at 250 Hz and sweeping ± 64 Hz. The selected SSP was that of a mean summer Mediterranean profile, and the boundaries were specified as smooth with the bottom composed of gravel.[12] This promoted moderate multipath propagation. Figure 4 shows the one-way transfer function for both models at 70-m depth for

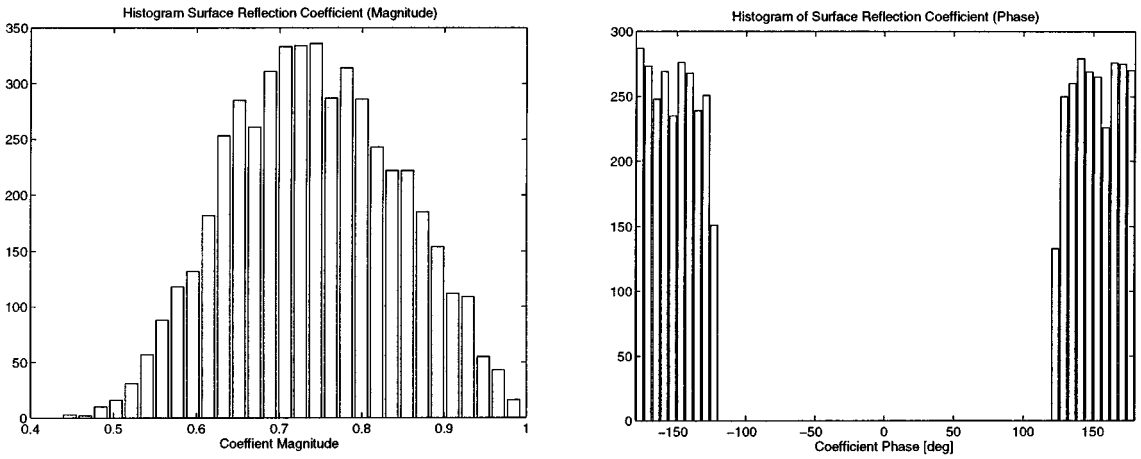

FIG. 2. Histograms of amplitude and phase variations in the surface reflection coefficient in the forward scattering direction.

an active source located 2000-m away and 150-m deep. Good agreement between GSM and SNAP was observed. Differences in amplitude were the primary source of disagreement, which is ray theory's main deficiency. Figure 5 shows the corresponding received signal. A correlation coefficient of 0.85 was observed between the two waveforms. Further simulations were performed for both a softer bottom (silty sand) and harder bottom (basalt). The softer bottom demonstrated less multipath propagation due to higher bottom loss. A correlation coefficient of 0.93 was observed in this case. Conversely, the harder bottom demonstrated significantly more multipath propagation. A correlation coefficient of 0.61 was observed. These results suggest that amplitude prediction differences become more significant with denser multipath environments. That withstanding, the agreement observed is supportive of the use of ray methods for propagation modeling.

Active propagation for the main simulation was performed in two steps. Rays were first traced from the source to the target and then from the target to the receiver. The overall source-target-receiver transfer function was obtained through convolution of the two one-way propagation paths. The target was modeled as a point scatterer of arbitrary scattering strength.

B. Monte Carlo integration

Integration over the uncertain environment parameters is generally very costly computationally. Monte Carlo integration techniques provide a powerful tool for approximating integrals. Generally, computations can be reduced by orders of magnitudes. Such techniques have been applied previously by Shorey and Nolte,[20] Haralabus *et al.*,[4] and Premus *et al.*[5]

The application of Monte Carlo integration generally requires summation of the integrand for randomly selected values of the integral. As the number of random computations increases, the variance of the error approaches zero in a $1/\sqrt{n}$ fashion.[21] The number of iterations required depends on the sensitivity of the integrand to the variable and generally cannot be determined analytically. In practice, one investigates the change in the solution as iterations increase. As an example, Fig. 6 shows ROC performance as a function of the number of Monte Carlo trials. The figure illustrates

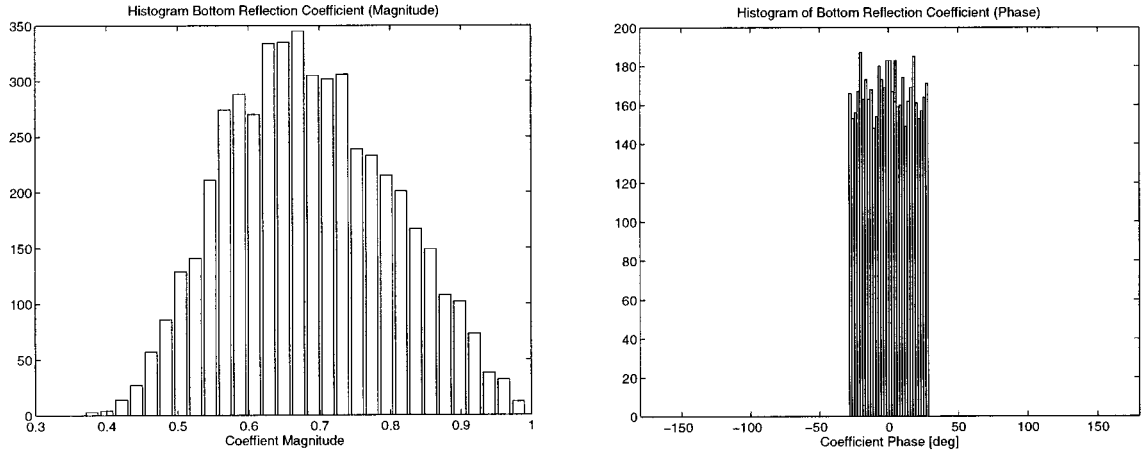

FIG. 3. Histograms of amplitude and phase variations in the bottom reflection coefficient in the forward scattering direction.

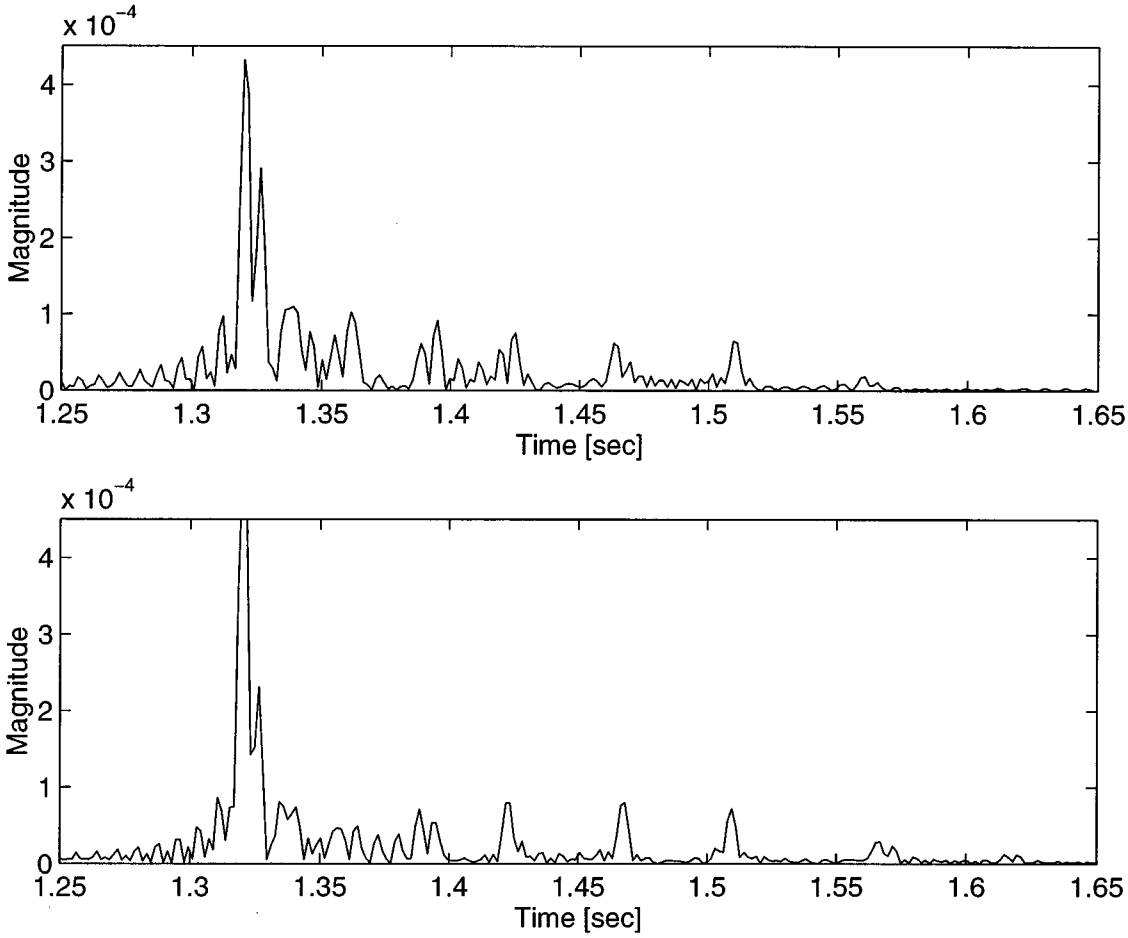

FIG. 4. Comparison of transfer functions using SNAP (upper graph) with GSM (lower graph).

that suitable convergence is achieved after 300 trials. For the simulation results reported here, 1000 trials were used to ensure adequate convergence.

C. Detection results

Detection results from our multipath detector are summarized in the form of receiver operator characteristics (ROC). To facilitate a direct comparison with standard replica correlation (matched filtering with the transmit waveform), we consider a target of known location.

The first ROC results were generated using a 1-s CW pulse at 250 Hz. Additive white Gaussian was included to produce a signal-to-noise ratio (SNR) of 11.0 dB. Figure 7 shows a set of typical ocean transfer functions for the array of elements, obtained through GSM simulation. By convolving these functions with the transmit waveform, a set of received basebanded signals is shown in Fig. 8.

Figure 9 shows the ROC results for optimal, ideal, mismatched, and matched filter processors. The ideal processor is one which operates without uncertainty regarding acoustic propagation. It essentially match filters the received signal with the complete multipath waveform and serves as the absolute upper bound for our problem. Differences in performance between the ideal and optimal processors are due to the uncertainty in prior knowledge and random behavior of acoustic propagation. The mismatched result is derived from a processor which accounts only for the mean acoustic propagation, ignoring the statistical effects of boundary interaction. In situations where the actual propagation conditions closely approximate the mean conditions, the mismatched result will approximate the ideal; however, in the general situation, where actual propagations conditions deviate from the mean, the mismatched performance is poor. This processor demonstrates the classic sensitivity issue regarding MFP techniques and demonstrates the importance of treating acoustic propagation as a random phenomena. The matched filter result, a replica correlator using the transmit waveform as the replica, is also shown.

In the narrow-band case above, the small time–bandwidth product of the transmit signal correlates satisfactory with the multipath signal. Thus the performance difference between optimal detection and replica correlation is not too significant—about 2.5 dB. Repeating the above simulation with a 1-s linear FM signal of 100-Hz sweep, a set of received basebanded signals shown in Fig. 10. ROC performance for this wideband signal is shown in Fig. 11 for an SNR of 11.0 dB. In this wideband case, substantial improvement in detectability by about 25 dB is demonstrated over replica correlation. For a probability of false alarm at 10^{-3}, the probability of detection rises from about 1% to nearly 80%. Moreover, the optimal result demonstrates robust performance when compared to the mismatched result.

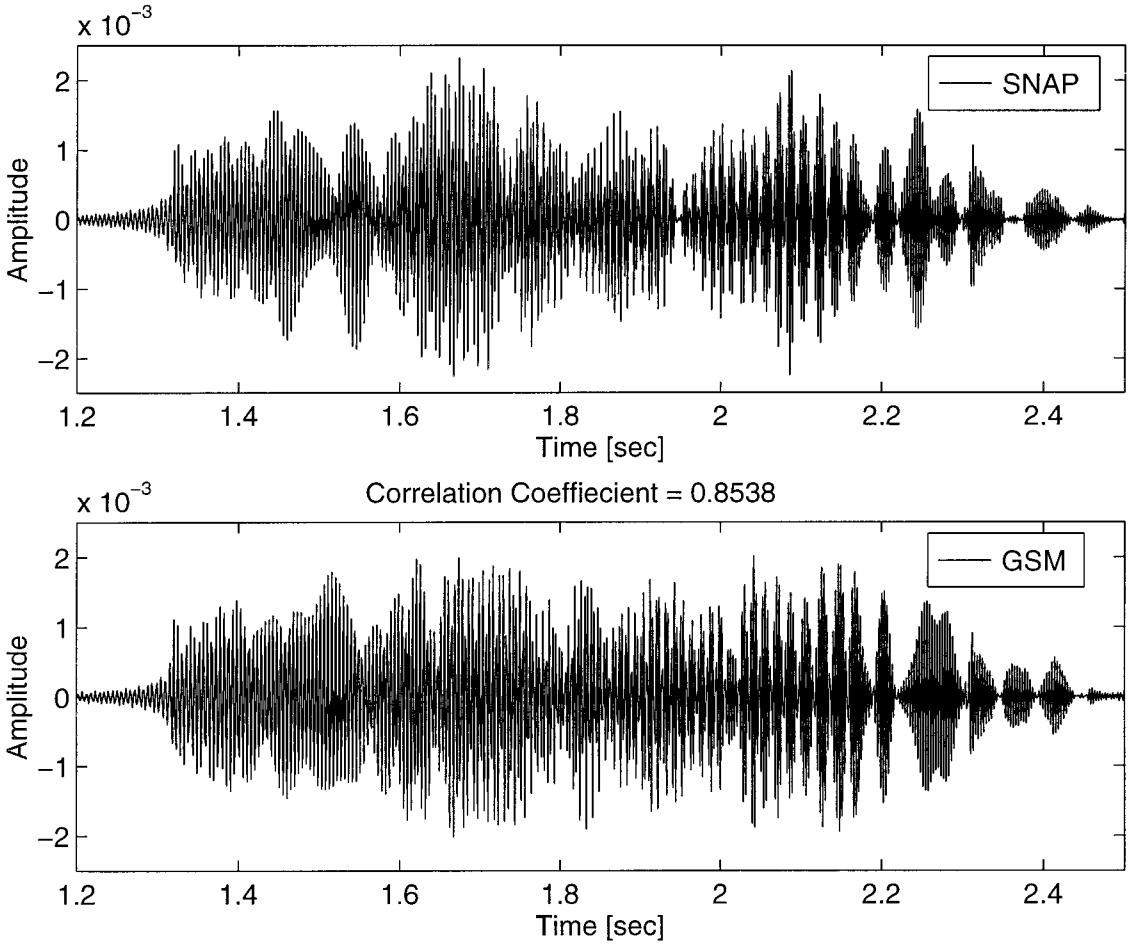

FIG. 5. Comparison of received multipath waveforms using SNAP (upper graph) with GSM (lower graph). A correlation coefficient of 0.85 was observed between these waveforms.

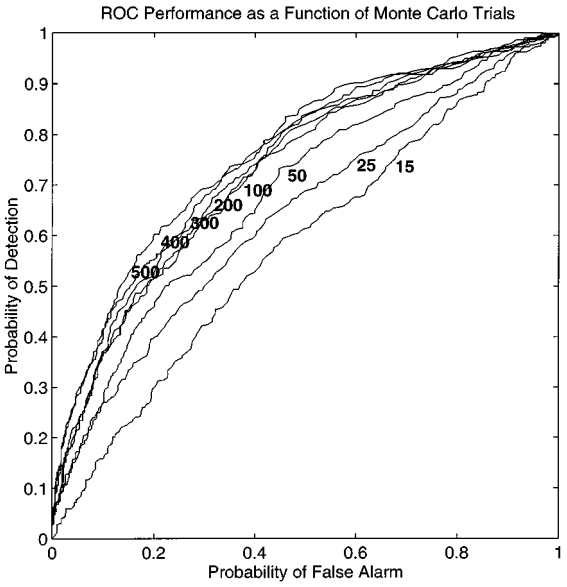

FIG. 6. ROC performance given as a function of Monte Carlo trials. Convergence is demonstrated when increased trials incrementally improve performance.

D. Localization results

In normal situations, target location is uncertain. Thus, operation of the optimal detector requires integration over potential target locations. When a detection decision in the

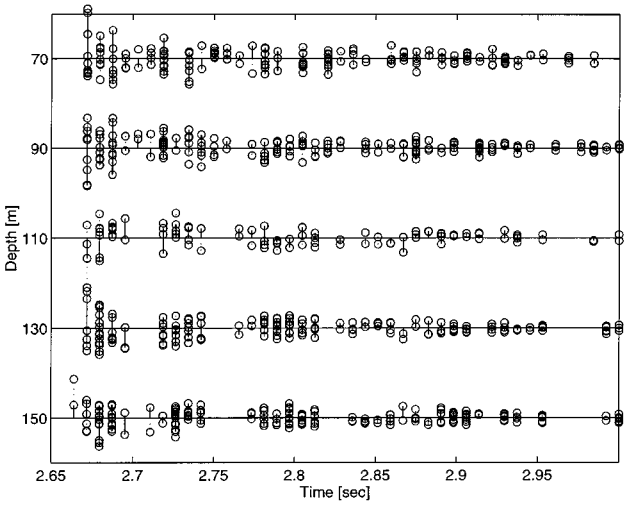

FIG. 7. Impulse response (two-way) of the simulation ocean environment. Solid lines denote in-phase, dotted lines denotes quadrature.

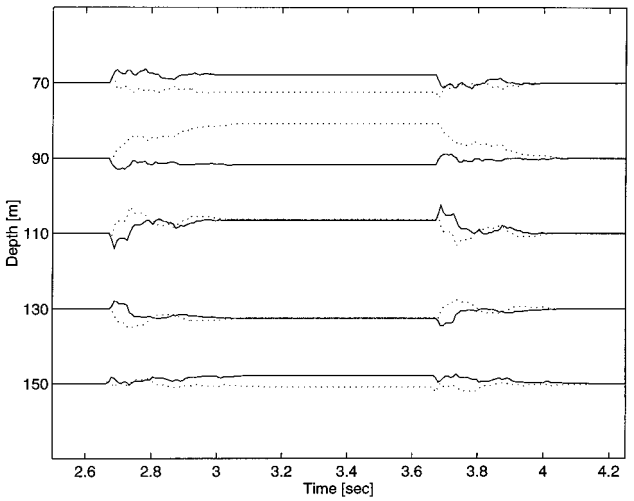

FIG. 8. Array of received signals in the absence of noise using a CW transmit waveform. Solid lines denote in-phase, dotted lines denotes quadrature.

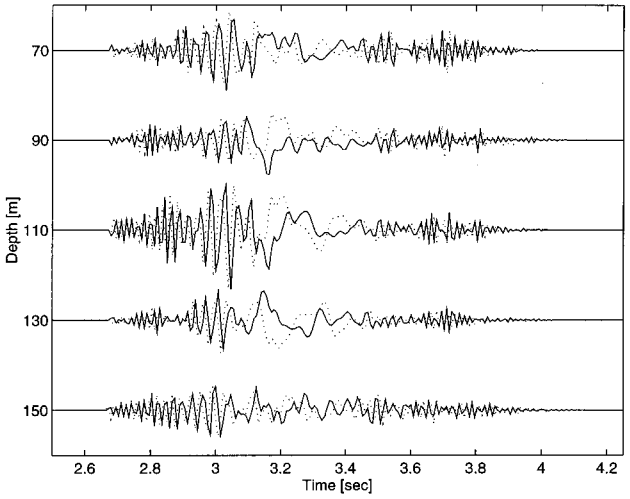

FIG. 10. Array of received signals in the absence of noise using an FM transmit waveform. Solid lines denote in-phase, dotted lines denotes quadrature.

affirmative is made, the range/depth cell that maximizes the integrand can be used as a maximum likelihood estimate of the target's position.[22] As an example, Fig. 12 shows the log-likelihood ratio as a function of target range and depth. The peak near the center represents the true target location—this for a nearly noise free situation.

In order to gauge the localization performance in typical noise situations, trials were iterated to produce localization ROCs or LROCs.[23] Figure 13 shows the localization performance using the linear FM signal for an SNR of 11 dB. The maximum probability in correctly localizing the target is about 92% for the ideal case in which the environment is known exactly and about 80% for the optimal processor which accounts for the uncertain knowledge of the ocean. Repeating LROC analysis for various detection indices, the probability of correct localization (PCL) can be plotted as a function of SNR PCL curves for this simulation is shown in Fig. 14. In this simulation, 90% probability of correct localization of the target was observed for an SNR of 12 dB.

IV. CONCLUSION

Temporal smearing of match filter output associated with traditional active detection systems inhibits the detection of low SNR targets and reduces the accuracy of range estimation in dense multipath environments. In this paper, we have applied optimum physics-based signal processing in an effort to improve detection performance and extend localization capability under these conditions. We have shown through simulation that an optimal approach using acoustic propagation modeling can improve active detection in a dense multipath environment and offer localization in both range and depth in a manner similar to matched field meth-

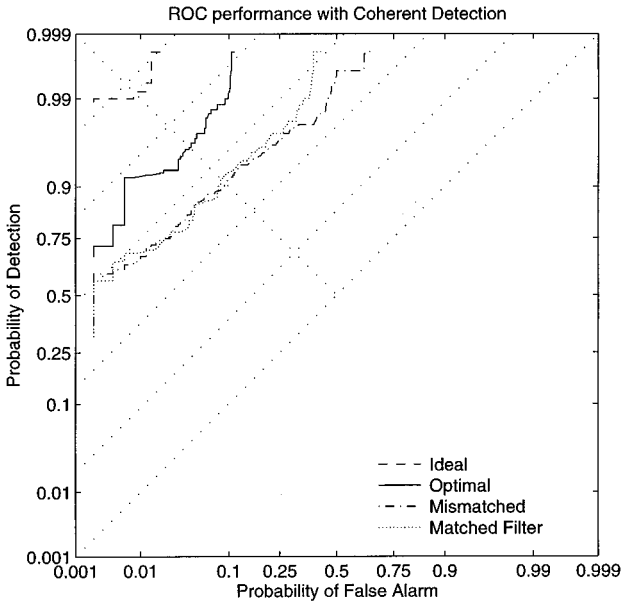

FIG. 9. ROC performance using a CW signal.

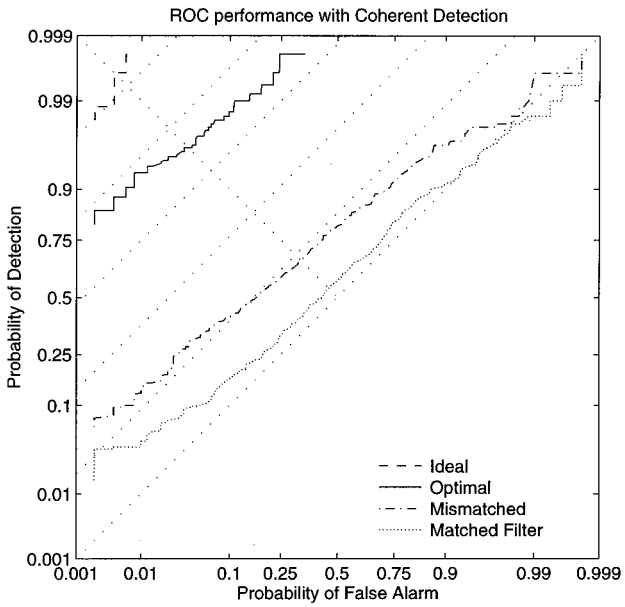

FIG. 11. ROC performance using an FM signal.

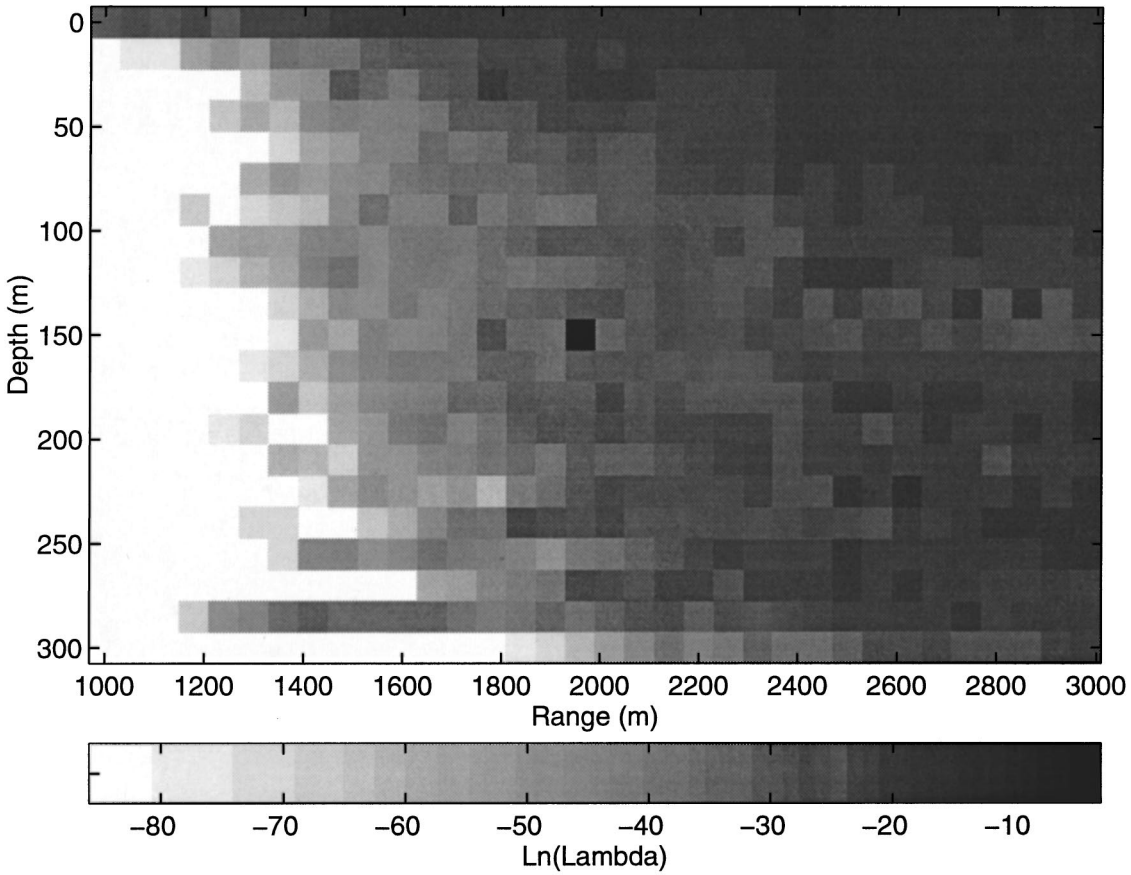

FIG. 12. Plot of the log-likelihood ratio, $\ln(\lambda(x))$, as a function of target range and depth. The peak is shown at the correct location (150 m, 2000 m).

ods. Furthermore, the approach demonstrates robust performance with respect to uncertainty surrounding the true acoustic environment.

Efficient implementation of optimal methods was of foremost importance in our approach. The selected time domain signal model provides a reasonably accurate and efficient means of describing the acoustic return from a target in all but significantly dispersive environments. When combined with ray models and Monte Carlo integration techniques, the OUMR demonstrated improved detection and localization performance with moderate computational requirements.

The development of the detection/localization algorithm yielded two layers of stochastic processing—an outer layer and an inner layer. The outer layer expresses the uncertainty in knowledge of the true physical environment. As demonstrated by simulation (i.e., ideal versus optimal), system performance correlates with the certainty in environmental

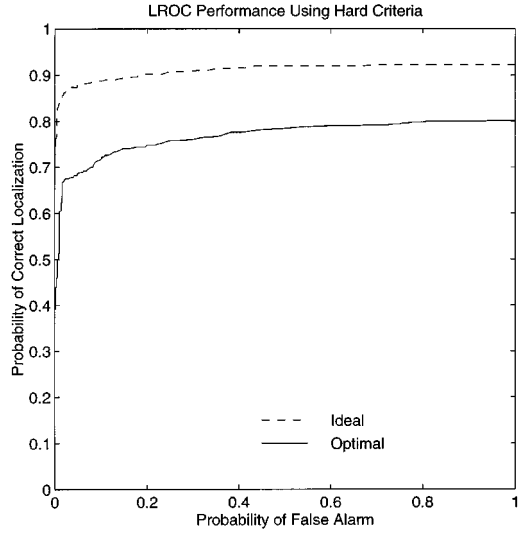

FIG. 13. LROC performance for an SNR of 11 dB.

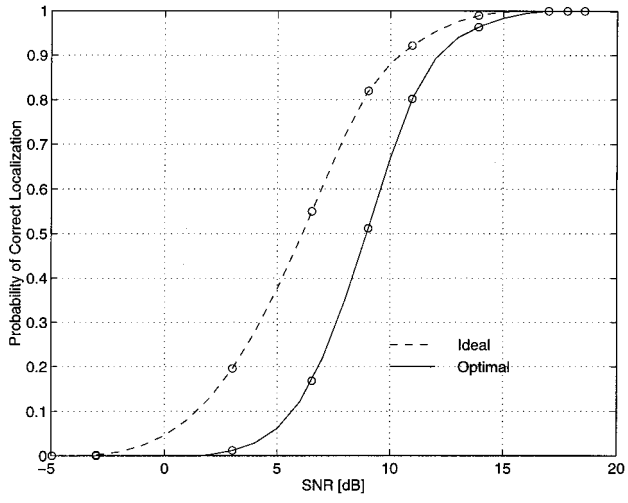

FIG. 14. Localization performance given as a function of overall SNR.

knowledge. Thus, efforts to refine prior distributions will result in better system performance. Future work should look at models and methods for obtaining and updating prior distributions using estimates of the physical environment from system output and external sources of information. This would provide an avenue for the development adaptive matched field processors.

The inner layer expresses the stochastic nature of acoustic propagation. This is where the acoustic propagation model serves as the engine for the detection/localization system by converting deterministic descriptions of the environment to stochastic descriptions of the multipath signal. As demonstrated by simulation, the mismatched processor (which did not account for stochastic effects of propagation) performed unreliably. It is thus concluded that deterministic MFP will, in general, perform unreliably even with exact knowledge of the physical environment. A notable lack of stochastic propagation models has impeded the development of stochastic MFP methods.

A simulation of a typical summer Mediterranean environment at a sea state of two was performed. Results demonstrated that that a significant improvement in detection is achievable with wideband signals over standard matched filtering. Furthermore, localization capability was extended to include both range and depth. The margin of improvement with simulations is significant enough to justify further work and analysis with real data.

[1] A. Tolstoy, ''Sensitivity of matched-field processing to sound-speed profile mismatch for vertical arrays in a deep-water pacific environment,'' J. Acoust. Soc. Am. **85**, 2394–2404 (1989).

[2] D. F. Gingras, ''Methods of predicting sensitivity of matched-field processors to mismatch,'' J. Acoust. Soc. Am. **86**, 1940–1949 (1989).

[3] A. M. Richardson and L. W. Nolte, ''*A posteriori* probability source localization in an uncertain sound speed, deep ocean environment,'' J. Acoust. Soc. Am. **89**, 2280–2284 (1991).

[4] G. Haralabus, V. Premus, and D. Alexandrou, ''Source localization in an uncertain acoustic scattering environment,'' J. Acoust. Soc. Am. **94**, 3379–3386 (1993).

[5] V. Premus, D. Alexandrou, and L. W. Nolte, ''Full-field optimum detection in an uncertain, anisotropic random wave scattering environment,'' J. Acoust. Soc. Am. **98**, 1097–1110 (1995).

[6] Z.-H. Michalopoulou, M. B. Porter, and J. P. Ianniello, ''Broadband source location in the Gulf of Mexico,'' J. Comput. Acoust. **4**(4), 361–370 (1996).

[7] I. M. G. Lourtie and G. C. Carter, ''Signal detection in the presence of inaccurate multipath time delay modeling,'' J. Acoust. Soc. Am. **88**, 2692–2694 (1990).

[8] I. M. G. Lourtie and G. C. Carter, ''Signal detectors for random ocean media,'' J. Acoust. Soc. Am. **92**, 1420–1427 (1992).

[9] G. B. Giannakis and M. K. Tsatsanis, ''Signal detection and classification using matched filtering and higher order statistics,'' IEEE Trans. Signal Process **38**, 1284–1296 (1990).

[10] C. W. Victory and R. Trueblood, ''The use of multilayer perceptron for adaptive correlation active sonar in an acoustically complex environment'' (unpublished).

[11] S. Haykin, *Adaptive Filter Theory*, 2nd ed. (Prentice-Hall, Englewood Cliffs, NJ, 1996).

[12] F. B. Jensen, W. A. Kuperman, M. B. Porter, and H. Schmidt, *Computational Ocean Acoustics* (AIP Press, New York, 1993).

[13] M.-A. Jourdain and G. Jourdain, ''Active high resolution time delay estimation for large BT signals,''IEEE Trans. Signal Process. **39**, 781–788 (1991).

[14] L. Brekhovskikh and Yu. Lysanov, *Fundamentals of Ocean Acoustics* (Springer-Verlag, New York, 1982).

[15] W. W. Peterson, T. G. Birdsall, and W. C. Fox, ''The theory of signal detectability,'' IRE Trans. **PGIT-4**, 171–212 (1954).

[16] A. D. Whalen, *Detection of Signals in Noise* (Academic New York, 1971).

[17] E. I. Thorsos, ''The validity of the Kirchoff approximation for rough surface scattering using a Gaussian roughness spectrum,'' J. Acoust. Soc. Am. **83**, 78–92 (1988).

[18] M. B. Porter, ''The time-marched fast-field program (ffp) for modeling acoustic pulse propagation,'' J. Acoust. Soc. Am. **87**, 2013–2023 (1989).

[19] C. M. Ferla, M. B. Porter, and F. B. Jensen, ''C-SNAP: Coupled SACLANTCEN normal propagation loss model,'' Saclant Undersea Research Centre, December 1993. SM-274.

[20] J. A. Shorey, L. W. Nolte, and J. L. Krolik, ''Computationally efficient Monte Carlo estimation algorithms for matched field processing in uncertain ocean environments,''J. Comput. Acoust. **2**, 285–314 (1994).

[21] J. M. Hammersley and D. C. Handscomb, *Monte Carlo Methods* (Methuen, London, 1964).

[22] D. Middleton and R. Esposito, ''Simultaneous optimum detection and estimation of signals in noise,'' IEEE Trans. Inf. Theory **14**, 434–444 (1968).

[23] D. Jalihal and L. W. Nolte, ''A note on the localization receiver operating characteristic (LROC) for optimal classification,'' internal memorandum.

Analytic investigation of chaos in a class of parabolic ray systems

Zhong-Yue Jiang, Todd A. Pitts, and James F. Greenleaf
Department of Physiology and Biophysics, Mayo Clinic and Foundation, Rochester, Minnesota 55905

(Received 23 January 1996; accepted for publication 30 October 1996)

It has been shown that acoustic ray paths in range-dependent ocean models exhibit chaotic behavior. Most of the investigations into the ray chaos phenomenon have been primarily numerical in nature. Analytical derivation of *sufficient* conditions for chaos in acoustic systems has been restricted to inherently discrete problems. This article reports a theoretical study of the existence of ray chaos in a class of continuous parabolic ray systems. This class of ray systems is indexed by a family of analytically prescribed double-channel sound-speed profiles perturbed by periodic range-dependent disturbances. The perturbed Hamiltonian ray systems are studied analytically via the Melnikov method. It is shown that, under certain conditions, ray trajectories of the systems are equivalent to trajectories of a classic chaotic system known as the horseshoe map when the perturbation is periodic and small. These conditions are sufficient for ray chaos and easily satisfied, thus explaining why double-channel propagation is very likely to exhibit chaotic behavior. © *1997 Acoustical Society of America.* [S0001-4966(97)00503-1]

PACS numbers: 43.30.Cq, 43.25.Rq, 43.25.Ts [MBP]

INTRODUCTION

When sound speed varies as a function of depth and range, the acoustic wave equation can be studied by a variety of methods. When the index of refraction changes slowly with respect to the wavelength of the field, the Helmholtz equation may be reduced to a ray acoustic model.[1,2] Such a model provides a computationally efficient and intuitive means of analysis.

Typical high-frequency approximations to the Helmholtz equation give the standard (two-way) elliptic ray equations. The assumption that rays travel only in the direction of increasing range coordinate yields the one-way elliptic ray equations. Requiring ray angles with respect to the range axis to be small yields the parabolic ray equations. All three sets of ray equations have been shown to be integrable when the sound speed is independent of range.[2] The integrability of ray systems guarantees regular ray motion, i.e., neighboring ray trajectories diverge and converge at a polynomial rate. It should be clear that when we speak of two rays converging we mean that all components (i.e., position and angle) of the ray vector become arbitrarily close. In the generic range-dependent problem, however, the ray equations are not integrable and some systems may be chaotic. A chaotic system possesses at least some trajectories which are extremely sensitive to initial conditions. Such chaotic trajectories converge and diverge in an apparently random fashion. Locally, these orbits may diverge/converge at an exponential rate.

The study of ray chaos in underwater acoustics involves the application of results from the study of nonintegrable Hamiltonian systems. This topic has been reviewed and discussed by many authors. Palmer *et al.*[3] showed numerically that acoustic ray paths in a weakly range-dependent deterministic ocean model exhibit chaotic behavior. Tappert *et al.*[4] and Brown *et al.*[5] investigated sound ray propagation in the ocean modeled by an area preserving mapping. Smith *et al.*[2] numerically investigated ray chaos in a more realistic range-dependent ocean model, taking into account internal waves and mesoscale structure.

The aforementioned studies demonstrate that sound ray trajectories in range-dependent ocean models exhibit chaotic behavior. While these studies are insightful, they are primarily numerical in nature and do not provide strict proof that the observed complex behaviors are in fact chaotic. The objective of this paper is to study theoretically the existence of ray chaos in a class of parabolic ray systems. This class of ray systems is indexed by a family of analytically prescribed double-channel sound-speed profiles perturbed by weak periodic range-dependent disturbances.

We begin this study by modeling the acoustic system via the parabolic ray equations. After specifying the description of the sound-speed profiles the *ordinary* differential nature of the ray equations and the *periodic* character of the perturbation are exploited to define a mapping relating the transverse coordinates (depth and angle) of a ray on successive planes orthogonal to the range coordinate. These planes are separated by a single period of the weak range-dependent sound-speed perturbation. We note that such mappings may be defined for both the perturbed and unperturbed systems (in each case the successive planes are separated by a distance equal to a single period of the disturbance in the *perturbed* system).

Examining the mapping for the unperturbed system we observe the presence of a saddle point. Physically, a saddle point represents simultaneously two phenomena. First, a ray with initial conditions of depth and angle corresponding to the saddle-point coordinates will be observed with the same depth and angle after propagating a distance equal to that separating mapping planes. An infinitesimal perturbation of such a ray will generally cause it to leave this saddle point and approach an unstable trajectory. Second, there exists a trajectory describing rays whose transverse coordinates as-

ymptotically approach those of the saddle point (as the range-coordinate approaches infinity). If the stable and unstable trajectories[6] are concurrent on some segment, introduction of the small periodic disturbance into this system may cause such an orbit to separate into two trajectories intersecting nontangentially at some points. This indicates the presence of chaos in the perturbed system. The Melnikov method applied in this paper is a means of obtaining conditions under which this separation and transverse intersection *must* occur. Thus we demonstrate *theoretically* the presence of chaos in a class of *continuous* systems. It is important to note that the congruence of stable and unstable trajectories may occur in sound speed profiles that are not double-channel in nature. Of equal significance is the fact that many ocean waveguides do not possess this phenomenon rendering the Melnikov method inapplicable.

The paper is organized as follows: In Sec. I the relationship between the three sets of ray models (two-way elliptic, one-way elliptic, and parabolic) is presented. Next, a class of ocean models is introduced. Analytic expressions are given for both the background and perturbed sound-speed fields. In Sec. II the relationship between the continuous dynamic system (parabolic ray system) and a mathematical abstraction referred to as a symbolic dynamic system is investigated theoretically via the Melnikov method.[7] This relationship permits the analytic study of chaotic ray motion in our ocean models. Numerical application of our theoretical results to a subclass of parabolic ray systems based on a fourth order polynomial sound speed model is found in Sec. III. Summary and discussion are given in Sec. IV.

I. THE RAY EQUATIONS AND THE OCEAN MODEL

Following the discussion of Smith *et al.*,[8] we first review the three sets of ray equations and the relationships among them. After showing the parabolic ray model to be sufficient for the study of ray chaos in underwater acoustics, a class of sound speed profiles and periodic perturbations are defined analytically. The parabolic ray approximation together with the description of refractive index comprise the ocean model under investigation.

A. The ray equations

The acoustic ray equations following from the elliptic (Helmholtz) wave equation in two-dimensional space are[1,2]

$$\frac{dz}{dt}=\frac{\partial\omega}{\partial k_z}, \tag{1}$$

$$\frac{dk_z}{dt}=-\frac{\partial\omega}{\partial z}, \tag{2}$$

$$\frac{dr}{dt}=\frac{\partial\omega}{\partial k_r}, \tag{3}$$

$$\frac{dk_r}{dt}=-\frac{\partial\omega}{\partial r}, \tag{4}$$

where $\omega=\omega(z,r,k_z,k_r)=c\sqrt{k_z^2+k_r^2}$, is the angular frequency of the wave, $c=c(z,r)$ the sound speed, $k=(k_z,k_r)$, the wave number vector with magnitude $|k|=\sqrt{k_z^2+k_r^2}=k$, and t is time. Depth and range are denoted by z and r, respectively.

The acoustic ray model in Eqs. (1)–(4) can be reduced to a system of one-way elliptic ray equations, if range r increases monotonically along all ray trajectories of interest, i.e., $dr/dt>0$. The resultant one-way ray equations can be written as

$$\frac{dz}{dr}=\frac{\partial H}{\partial k_z}, \tag{5}$$

$$\frac{dk_z}{dr}=-\frac{\partial H}{\partial z}, \tag{6}$$

where $H(z,k_z,r)=-k_r=-\sqrt{w^2/c^2(z,r)-k_z^2}$.

If we introduce the parabolic approximation, which is valid when ray angles with respect to the horizontal are very small, the one-way ray system yields the parabolic ray equations

$$\frac{dz}{dr}=\frac{\partial H}{\partial p}, \tag{7}$$

$$\frac{dp}{dr}=-\frac{\partial H}{\partial z}, \tag{8}$$

where $p=k_z/k_0$, and

$$H(z,p,r)=p^2/2+[c(z,r)-c_0]/c_0. \tag{9}$$

Notice that Eqs. (7)–(9) define a Hamiltonian system with z, p, and r as ''position,'' ''momentum,'' and ''time'' variables, respectively.

When sound speed, c, is range independent, the elliptic ray system [Eqs. (1)–(4)] defines an autonomous Hamiltonian system with two degrees of freedom. This system possesses two independent constants of motion (ω and k_r) which are in involution, and is therefore integrable.[2] Range independence of the sound speed implies that the one-way [Eqs. (5) and (6)] and parabolic ray systems [Eqs. (7)–(9)] are both autonomous Hamiltonian systems with one degree of freedom and are thus integrable. When a Hamiltonian system is integrable, its trajectories are regular.

In the general range-dependent problem, however, the ray equations are generically nonintegrable.[9] While it is easy to see that nonintegrability of a Hamiltonian system provides a necessary condition for chaotic trajectories, it is usually very difficult to find a sufficient condition for the existence of such trajectories in a nonintegrable system. It is the main purpose of this paper to obtain a sufficient condition for ray chaos in a class of parabolic ray systems.

B. The ocean model

In the remainder of this paper, we restrict our attention to the parabolic ray system [Eqs. (7)–(9)], in which the sound speed is modeled as

$$c(z,r)=f(z)+\epsilon g(z,r), \tag{10}$$

where ϵ is the perturbation coefficient. The parabolic ray system is simple but nevertheless exhibits the complex chaotic behavior we wish to study. Numerical studies also indicate that this idealized approximation possesses dynamic be-

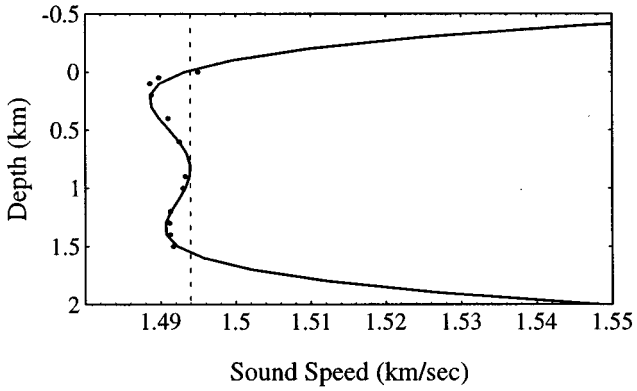

FIG. 1. Double-channel sound-speed profile. The points represent the data in Boyles (Ref. 9). The solid line is the profile calculated by fitting the data [the lowest data point in Boyles (Ref. 9) has been omitted to simplify the study in this paper]. The vertical dashed line intersects the solid line at three different depths: b_1, r_1, and b_2.

havior similar to that of the more realistic one-way elliptic model.[2]

The sound-speed profile studied in this paper is obtained by fitting a portion of the data from measurements made on a North Atlantic double-channel system.[10] Note that the data in Boyles[10] indicate a near linear increase in sound speed with depth past 1.5 km and that this has been ignored in our model. Figure 1 shows both the measured data (from the ocean surface down to 1.5 km) and the fitted profile. We may generalize this profile to a class of double-channel sound-speed profiles, $f(z)$ defined by

$$f(z)=a_0+a_1z+a_2z^2+a_3z^3+a_4z^4, \tag{11}$$

where $f(z)$ has three extremes and $a_4>0$. The reasons for studying this kind of profile will be clear in Sec. II C.

The perturbation model used in this study is the same as that of Palmer *et al.*,[3] i.e.,

$$g(z,r)=\sqrt{2}\ \exp(-1.5z/B)\sin(2\pi r/R), \tag{12}$$

where R is the perturbation period, and the depth scale B is typically 1 km. This perturbation could be interpreted as a highly idealized internal wave or as a single baroclinic mode representing mesoscale structure.[3,8] The exponential dependence on depth in Eq. (12) was derived from the Brunt–Väisälä frequency.[8] The sinusoidal formulation is similar to what many authors employ in their papers to investigate the effects of internal waves on sound in the ocean.[2,11–13] While the exponential dependence of the amplitude is not vital for our study, the periodic range dependence of the model is very important. The periodicity in r of this model allows application of a powerful tool known as the Poincaré section to our problem (see Sec. II A).

In summary, the dynamic system we are going to study is described by Eqs. (7) and (8). Related functions are defined in Eqs. (9)–(12). With the help of these functions, the dynamic system can be rewritten as

$$\frac{d\mathbf{x}}{dr}=\begin{pmatrix} p \\ h_1(z)\end{pmatrix}+\epsilon\begin{pmatrix} 0 \\ h_2(z,r)\end{pmatrix}, \quad \mathbf{x}=(z,p)^T, \tag{13}$$

where

$$h_1(z)=-(a_1+2a_2z+3a_3z^2+4a_4z^3)/c_0,$$
$$h_2(z,r)=\frac{3}{2Bc_0}\sqrt{2}\ \exp\left(-\frac{1.5z}{B}\right)\sin\left(\frac{2\pi r}{R}\right). \tag{14}$$

II. THEORETICAL ANALYSIS OF RAY CHAOS

In this section, we briefly review some basic concepts and methods in the analysis of complicated behavior in dynamic systems. We then apply the Melnikov method to the parabolic ray system.

A. Nonlinear dynamics and chaos

The word *chaos* appeared as a scientific term more than one hundred years ago. It was used to denote disorder caused by or closely related to stochastic processes.[14] Modern usage of the word for intrinsic complicated behavior in deterministic systems seem to begin with Li and York's 1975 paper.[15] To the best of the authors' knowledge, there is still no generally accepted definition of chaos. However, one of the most important and ubiquitous characteristics of chaotic motion is its sensitivity to initial conditions. A useful model for describing this behavior is the symbolic dynamic system. It can be shown that the complicated behavior described by these discrete systems is chaotic by almost every definition.[7,16,17] An example of a symbolic dynamic system is the Smale horseshoe.[18] Below we review briefly some of the concepts in modern chaos theory central to the demonstration in this article. For a more complete exposition of these ideas we refer the reader to Ref. 19.

Consider the system described by Eqs. (13) and (14). A set of initial conditions on ray depth and angle specifies a unique solution to this system. Such a solution represents a ray (a path along which energy is transported in the physical system). (Examples of ray paths are given in Fig. 5.) We may also consider the phase space representation of this problem. A path in phase space is a trajectory in all the problem coordinates (depth, angle, and range). The family of all such paths (or *orbits* as they are often called) leads us to the concept of topological orbital equivalence (TOE). We may compare the *qualitative* behavior of two different dynamical systems by comparing the surfaces described by their phase space paths. If two systems have similar phase space portraits then they exhibit the same dynamic behaviors. We use *topological* comparisons because we wish to capture the qualitative similarities between systems.[20] Quite amazingly, many realistic dynamic systems exhibit TOE with a variety of symbolic dynamic systems.[6,8] As mentioned above, symbolic dynamic systems possess prototypical chaotic behavior. Thus, if a system has TOE with a symbolic dynamic system it must be chaotic. TOE between a continuous system and a dynamic symbolic system may be established by defining a map for the system under study and examining its properties. In this paper we define a map for our class of ray systems and study it analytically via the Melnikov method.

The *periodic* nature of the perturbation provides the means of establishing the aforementioned map. Essentially, we may use a *circular* (as opposed to an infinite) range co-

ordinate. The trajectory in phase space begins at a point representing a set of initial conditions (depth and angle) on some plane transverse to the range coordinate (in this paper the r coordinate represents range). It then moves a distance in the r-coordinate direction equal to a single period of the disturbance and delivers a *new* set of initial conditions. The periodic nature of the perturbation allows us to imagine the continuation of the trajectory as originating on the same plane as the first set of initial conditions. In fact, we may reduce our consideration to a mapping between successive sets of initial conditions. Such a mapping is referred to as a *Poincaré* map. The plane on which the mapping takes place is called the *Poincaré surface of section.*

The use of the Poincaré map and section simplify the description of the system dynamics, reduce the order of the model by one, and at the same time retain a qualitative description of the essential features of the motion. For example, a simple periodic orbit would become a single fixed point of the Poincaré map, a quasiperiodic trajectory would draw a closed curve in the Poincaré section, a chaotic motion would produce erratically scattered points.

Even with the help of the Poincaré map and other techniques, the study of chaotic behaviors of a realistic dynamic system is still very difficult. As we see above, it usually requires the investigation of the TOE relation between the system under study and some known chaotic dynamic system. These difficulties explain why very few realistic chaotic systems yield to analytical investigation. A method for studying a subclass of these systems is described in the next section.

B. The Melnikov method and the horseshoe map

The class of near-integrable. Hamiltonian systems may be studied via a global perturbation technique known as the Melnikov method. More specifically, consider an integrable Hamiltonian system with one degree of freedom perturbed by a weak disturbance. If the disturbance in the near-integrable system is periodic, one can define a Poincaré map and section for the system. Furthermore, if there exists a *homoclinic* orbit (a special trajectory which approaches a particular phase space saddle point as $t\to\infty$) in the unperturbed system, some properties of the Poincaré map can be studied analytically. Such a trajectory actually represents a congruence of the stable and unstable manifolds of the saddle point. If the system is perturbed the stable and unstable manifolds may separate and even intersect transversely (i.e., nontangentially). Such a point of intersection is referred to as a *transversal homoclinic point*. The existence of a transversal homoclinic point in the Poincaré map of the perturbed system can be determined via the Melnikov method.[7]

Smale succeeded in establishing the TOE relationship between a class of discrete dynamic systems possessing a transversal homoclinic point and subshifts of finite type (a generalization of symbolic dynamic systems).[22] In this paper the application of the Melnikov method delivers conditions for the existence of a transversal homoclinic point in the Poincaré map used to study the ray systems. If these conditions are satisfied, Smale's result guarantees TOE between the Poincaré map and the famous horseshoe map (a classic system exhibiting chaotic behavior). Notice that a trajectory of a Poincaré map of a continuous dynamic system is merely a discretized representation (determined by the selection of a Poincaré surface of section) of the related smooth orbit in the continuous system. Thus, the class of near-integrable Hamiltonian systems possesses the complex dynamic behavior characteristic of chaotic systems.

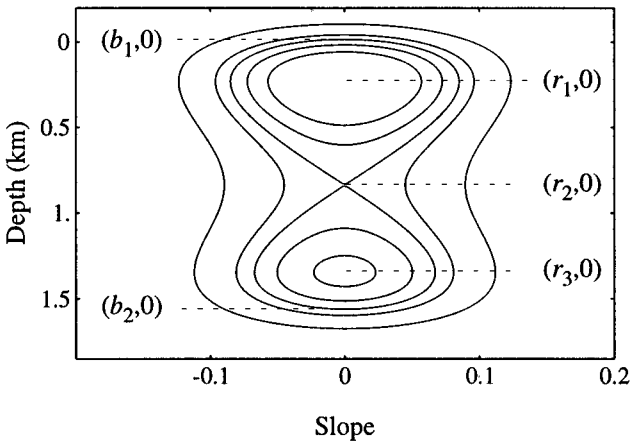

FIG. 2. Phase portrait of a typical unperturbed system defined by Eq. (15) with $a_4>0$. Two homoclinic orbits passing through points $(b_1,0)$ and $(b_2,0)$ respectively are labeled.

C. Analysis of unperturbed systems

The Melnikov method for the prediction of chaos has been applied to many different dynamic systems.[7,23] In the next two subsections, we apply the Melnikov method step by step to the study of ray chaos in parabolic ray systems.

Consider system (13) when $\epsilon=0$, i.e., the unperturbed system

$$\frac{dz}{dr}=p, \quad \frac{dp}{dr}=h_1(z). \tag{15}$$

The double-channel sound-speed profile implies $h_1(z)$ has three distinct zeros. More specifically, there exist three real numbers $r_3>r_2>r_1$ such that

$$h_1(z)=-4a_4(z-r_1)(z-r_2)(z-r_3)/c_0. \tag{16}$$

By conducting straight forward local linear analysis,[19] one can easily check that the differential system in (15) has three singular points: $(r_1,0)$, $(r_2,0)$, $(r_3,0)$. If $a_4<0$, they are, respectively, saddle, center, and saddle points. While $a_4>0$ implies center, saddle, and center points, respectively. The phase portrait of the unperturbed system with $a_4>0$ is shown in Fig. 2.

In order to provide a realistic double-channel model we restrict the singular points to lie beneath the ocean surface (i.e., r_1, r_2, $r_3>0$) and require that $a_4>0$. Unlike the requirement that $h_1(z)$ has three distinct zeros it should be noted that these conditions are not mathematically necessary. For the remainder of this paper ray systems are assumed to satisfy the above conditions.

The Hamiltonian of the unperturbed system is

$$H(z,p,r)=[a_0+a_1z+a_2z^2+a_3z^3+a_4z^4-c_0]/c_0 + p^2/2. \tag{17}$$

The Hamiltonian is always a constant of the system motion allowing Eq. (15) to be rewritten as follows:

$$[a_0+a_1z+a_2z^2+a_3z^3+a_4z^4-c_0]/c_0+p^2/2=C,$$
$$p=\frac{dz}{dr}, \tag{18}$$

where C is the constant associated with a specific trajectory.

For proper choice of the constant C, the homoclinic orbits of the system can be obtained as follows. Let $(b_1,0)$, and $(b_2,0)$ denote the points at which the two homoclinic orbits intersect the z axis as shown in Fig. 2. Both orbits approach the saddle point $(r_2,0)$ when $t\to\pm\infty$. From this and Eq. (18) we may deduce that following equations for the homoclinic orbits:

$$a_4(z-r_2)^2(z-b_1)(z-b_2)/c_0+p^2/2=0,$$
$$p=\frac{dz}{dr}. \tag{19}$$

Some algebraic manipulation yields

$$b_1+b_2=\tfrac{4}{3}r_1-\tfrac{2}{3}r_2+\tfrac{4}{3}r_3,$$
$$b_1b_2=-\tfrac{2}{3}r_1r_2+2r_1r_3+\tfrac{1}{3}r_2^2-\tfrac{2}{3}r_2r_3. \tag{20}$$

Therefore, b_1 and b_2 are determined by a second-order algebraic equation with discriminant $\Delta=b^2-4ac=8[2(r_3-r_1)^2+(r_3-r_2)(r_2-r_1)]/9$. As the discriminant is always greater than zero for our systems, b_1 and b_2 are always distinct real numbers. Without loss of generality, we assume $b_1<r_2<b_2$.

Solving Eq. (19), we obtain the following description of the *lower* homoclinic orbit [passing through point $(b_2,0)$]:

$$z_h=r_2+e_1/[\cosh(e_2r)+e_3]$$
$$p_h=-e_1e_2\ \sinh(e_2r)/[\cosh(e_2r)+e_3]^2, \tag{21}$$

where

$$e_1=2(r_2-b_1)(r_2-b_2)/(b_1-b_2)>0,$$
$$e_2=\sqrt{-2a_4(r_2-b_1)(r_2-b_2)/c_0}, \tag{22}$$
$$e_3=(b_1+b_2-2r_2)/(b_1-b_2),\quad |e_3|<1.$$

The *upper* homoclinic orbit (passing through point $(b_1,0)$ can be obtained in the same way.

In some ocean models the upper homoclinic orbit may intersect the ocean surface. The effect of the ocean surface typically provides difficulty for an analytical study. Fortunately, the high-frequency assumption that yields the ray equations implies that surface boundary effects are important only for trajectories actually intersecting the ocean surface. The results of our study may therefore be applied to such models if attention is restricted to those trajectories confined in the lower channel (or to nearby regions). Proof that there exist trajectories of interest (i.e., chaotic trajectories) that do not intersect the ocean surface is given at the end of this section.

D. Analysis of perturbed systems

Now we turn to system (13), which satisfies the conditions stated in the previous subsection. We first define a Poincaré section and map for the system as follows. Note that system (13) is periodic in range r. This periodicity allows us to view propagation in the system as repeated application of an operator. This operator propagates a ray through the medium in the range direction a distance R. Both the domain and range of the operator is a plane indexed by depth and angle pairs. This plane defines a Poincaré section. Note that this Poincaré section manifests itself in the system's three-dimensional phase space as an infinite number of planes normal to the range axis separated by a distance R. The operator is, in fact, the associated Poincaré map. The Poincaré section and map are denoted symbolically by Σ^{r_0} and $P_\epsilon^{r_0}:\Sigma^{r_0}\to\Sigma^{r_0}$, respectively, where the perturbation phase term r_0 is the distance (in the positive range direction) between the Poincaré section and the plane over which the perturbation is zero.

System (13) satisfies all necessary conditions required by the Melnikov method, i.e., (a) the unperturbed system is Hamiltonian and possesses at least one homoclinic orbit passing through saddle point $p_0(r_2,0)$; (b) the perturbation term $\epsilon h_2(z,r)$ is a periodic function of the ''time'' r. Therefore, according to a Lemma found in Guckenheimer *et al.*[7] system (13) possesses a unique hyperbolic periodic trajectory, and the corresponding Poincaré map $P_\epsilon^{r_0}$ has a unique hyperbolic saddle point close to p_0.

The Melnikov method predicts analytically the presence of a transversal homoclinic point of the Poincaré map. The method involves the calculation of the Melnikov function (which depends explicitly on the phase term r_0)

$$M(r_0;h_1,h_2)=\int_{-\infty}^{\infty}\begin{pmatrix}p_h\\ h_1(z_h)\end{pmatrix}\wedge\begin{pmatrix}0\\ h_2(z_h,r+r_0)\end{pmatrix}dr, \tag{23}$$

where the operator $\wedge$ is defined as

$$a\wedge b=a_1b_2-a_2b_1,\quad a=(a_1,a_2)^T,\quad b=(b_1,b_2)^T. \tag{24}$$

After some tedious calculation, one obtains the following analytic expression for the Melnikov function (see the Appendix):

$$M(r_0;h_1,h_2)=\frac{9\pi}{c_0}\sqrt{\frac{3\pi}{2BR}}\sqrt{\frac{c_0}{2a_4}} \times\exp\left(-\frac{1.5r_2}{B}\right)\cos\left(\frac{2\pi r_0}{R}\right) \times\left[\frac{J_1\left(\sqrt{\frac{3\pi}{2BR}}\sqrt{\frac{c_0}{2a_4}}\right)}{(1-e^{-4\pi^2/\mathrm{Re}_2})e^{2\pi\alpha/\mathrm{Re}_2}} -i\frac{J_1\left(i\sqrt{\frac{3\pi}{2BR}}\sqrt{\frac{c_0}{2a_4}}\right)}{(1-e^{4\pi^2/\mathrm{Re}_2})e^{-2\pi\alpha/\mathrm{Re}_2}}\right], \tag{25}$$

where

$$\alpha = \arccos(-e_3). \tag{26}$$

Notice that if

$$M' = e^{4\pi^2/\mathrm{Re}_2} J_1\left(\sqrt{\frac{3\pi}{2BR}}\sqrt{\frac{c_0}{2a_4}}\right) + ie^{4\pi\alpha/\mathrm{Re}_2} J_1\left(i\sqrt{\frac{3\pi}{2BR}}\sqrt{\frac{c_0}{2a_4}}\right) \neq 0, \tag{27}$$

the Melnikov function has simple zeros independent of ϵ. Therefore for sufficiently small ϵ there exists a transversal homoclinic point of the Poincaré map of system (13), $P_\epsilon^{r_0}$.[7] According to the Homoclinic Theorem in dynamic system theory, the existence of a transversal homoclinic point together with the fact that our system is of order 2 implies a TOE relation between the Smale horseshoe and $P_\epsilon^{r_0}$ on some invariant set Λ.[7,22] Combining the above with the fact that the Smale horseshoe is chaotic,[21,24] we have

Proposition: If Eq. (27) holds, system (13) possesses a transversal homoclinic point. Therefore there exists an invariant set Λ; on which the Poincaré map of the system, $P_\epsilon^{r_0}$, is topologically equivalent to the Smale horseshoe, and thus, the map $P_\epsilon^{r_0}$ and the system itself are chaotic.

We have shown that if Eq. (27) is satisfied then the trajectories of a Poincaré map of system (13) on some invariant set exhibit complicated behavior. Note that any dynamic system is chaotic if its dynamic behavior on the chaotic invariant set is the same as that of a chaotic system. System (13) has a chaotic invariant set contained in the lower channel (According to Smale's proof of the Homoclinic Theorem, there exists such an invariant set near the related homoclinic orbit. This fact also implies there exists a chaotic invariant set in the upper channel); therefore it is clear that system (13) is chaotic even if the ocean surface intersects with the upper channel of the system (i.e., does not pass through any part of the lower homoclinic orbit). It should be noted that a chaotic system may also have regular trajectories. In fact, the celebrated KAM theorem guarantees the coexistence of regular and chaotic trajectories in near-integrable Hamiltonian systems.[2] We have demonstrated the existence of chaotic behavior in a class of ray systems under the assumption of sufficiently small periodic perturbation. Although, the intuitive assumption that a larger perturbation would be more likely to result in chaotic behavior is supported by numerical studies, it is typically very difficult to confirm such observations analytically.

III. NUMERICAL STUDIES AND APPLICATIONS

In this section we present a graphical representation of the sufficient condition [see Eq. (27)] for chaotic behavior in our class of ray systems and investigate numerically a specific system satisfying this criterion.

A. Method

The family of parabolic ray systems in Eq. (13) with double-channel sound-speed profile as defined in Eq. (11) has been investigated in the previous section. The proposition provides a theoretical criterion for determining whether a particular member of this class is chaotic. In this section we apply this criterion to a subset of the class. Next, a specific member of this subset is investigated numerically.

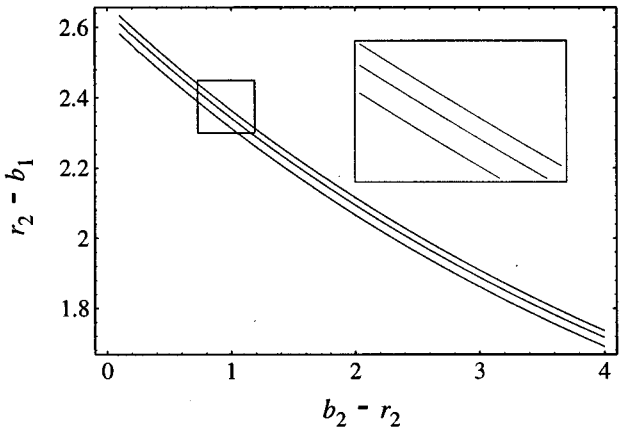

FIG. 3. Plot showing curves along which the coefficient of the Melnikov function M' is zero for system (13) with various values of a_4. From top to bottom the values of a_4 are 10, 0.045, and 0.02, respectively.

To study the sufficient conditions for chaotic behavior we fix B and R leaving the coefficient of the Melnikov function in Eq. (27) with three independent parameters. The mathematical fact that α and e_2 can be expressed in terms of e_4 and the channel widths $r_2 - b_1$ and $b_2 - r_2$ is consistent with the physical intuition that translations of the sound speed profile in the range and depth coordinates yield systems which have identical acoustic behaviors. Eliminating these two degrees of freedom from the fourth-order polynomial sound-speed profile leaves us with a ray system whose basic behavior is determined by three independent variables. Furthermore, fixing e_4 allows us to investigate the coefficient of the Melnikov function in a two-dimensional parameter space.

To provide a concrete example of double-channel sound-speed systems we will use a profile derived from data taken in the North Atlantic Ocean (see Fig. 1). Note again that our model is a simple fourth-order polynomial and does not imply linear sound-speed variation below 1.5 km. The sound speed for this model is described with[10]

$$f(z) = 1.493\,23 - 0.047\,00z + 0.147\,14z^2 - 0.145\,17z^3 + 0.045\,11z^4. \tag{28}$$

In all numerical studies we use $c_0 = 1.5$ km/s, $B = 1.0$ km, $\epsilon = 0.0025$, and $R = 50$ km.

B. Results

Shown in Fig. 3 is a representation of the coefficient of the Melnikov function. Here we have overlaid three plots obtained by using three different values of e_4 as indicated in the figure caption. In each plot there is a single curve on which the value of M' as a function of $r_2 - b_1$ and $b_2 - r_2$ is identically zero. The proposition does not tell us anything about systems represented by points on the curves. In each plot all points not on the curve correspond to chaotic systems for the specified a_4. The low dimensionality of the manifold defined by $M' = 0$ in each plot implies that the ray system

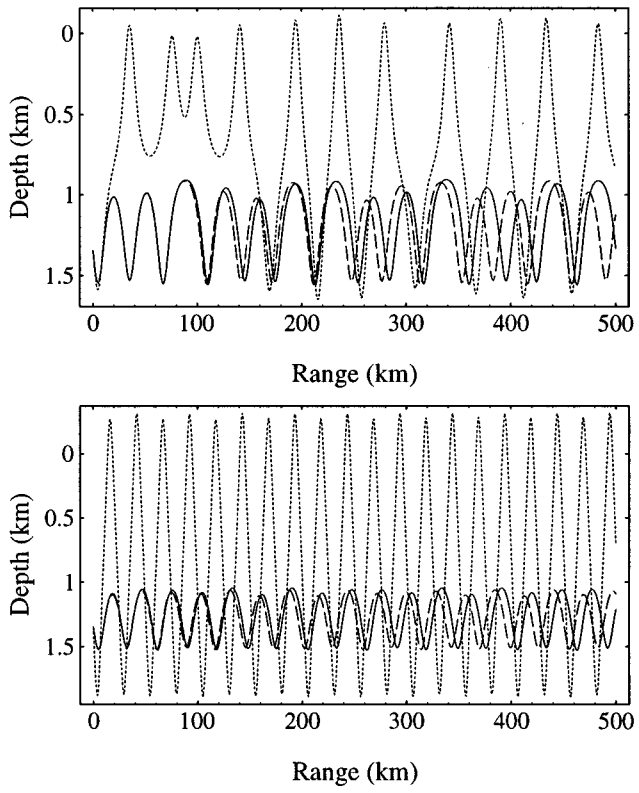

FIG. 4. Four typical types of ray trajectories in the two-dimensional (z,r) space, each having initial depth of 1.345 km. (a) Chaotic ray trajectory with initial angle 4.5° hopping between upper and lower channels (dotted). Two chaotic ray trajectories with initial angles 3.6° and 3.61°, respectively which appear to be confined in the lower channel (dashed and solid). (b) A regular trajectory starting with angle 12.0° traveling in the large waveguide (dotted). Two regular trajectories having initial angles 3.0° and 3.1°, respectively trapped in the lower channel (dashed and solid).

(13) with the investigated values of a_4 are generically chaotic. The wide range of a_4 strongly suggests that the entire class of systems under study is generically chaotic.

In Fig. 4 we see examples of four different types of ray trajectories in the particular ray system defined by Eq. (28). In part (a) we see a trajectory (dotted line) which jumps between the upper and lower channels in a pseudo-random fashion. The pair of trajectories (dashed and solid lines) confined to the lower channel have nearly identical initial conditions. Comparison of the depth of these two rays at various range values reveals an irregular pattern of convergence and divergence. In part (b) of Fig. 4 we see a set of periodic orbits. The ray path with the largest amplitude (dotted line) effectively sees only a single, large waveguide. The pair of rays (dashed and solid lines) remaining in the lower channel diverge slowly and regularly. The effect of the ocean surface was not considered in these calculations for simplicity.

After computing a number of ray trajectories (such as those in Fig. 4) we may construct a Poincaré section as shown in Fig. 5. The randomly distributed points represent the ray chaos or chaotic trajectories. Those points lying on well defined curves correspond to regular or periodic orbits. The periodic trajectories or orbits found between $z=0.9$ and $z=1.6$ correspond to rays confined to the lower waveguide. A periodic trajectory can also be found in the upper channel. Some small islands of periodic behavior are seen outside the chaotic region. It is interesting to note that all of these *islands* are generated by a single ray path in our plot.

All of the numerical studies in this paper were done using an adaptive Runge–Kutta method available in the Mathematica™ software package.

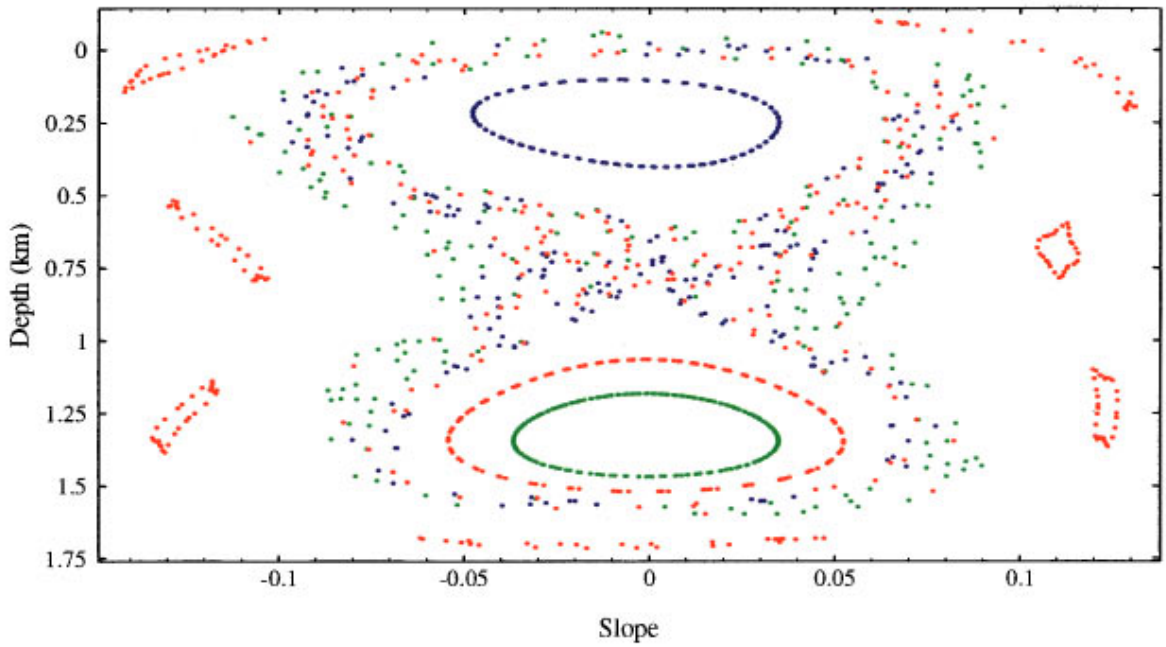

FIG. 5. Poincaré section for sound rays in the double channel. Sources are placed near the lower channel axis at $z=1.345$ km or the upper channel axis at $z=0.25$ km. Clearly visible are two regular trajectories confined in the lower channel (green and red dots correspond to initial angles 2.0° and 3.0°, respectively) and a single regular trajectory outside the chaotic region.

IV. SUMMARY AND DISCUSSION

We have derived sufficient conditions [Eq. (27) for sufficiently small perturbation coefficient ϵ] for chaotic behavior in a general class of parabolic ray systems. A number of numerical studies demonstrating such behavior are presented. Also, an investigation of conditions under which chaotic behavior is to be expected is discussed. These results strongly suggest that the ray systems under consideration are generically chaotic. They also lend support to the intuitive notion (suggested by numerical studies[2]) that systems with large periodic perturbations also possess chaotic trajectories.

As implied in the previous section, chaotic behavior precludes long distance prediction of ray trajectories. It may even be impossible to tell which channel a particular ray will be in after an arbitrarily large distance. Furthermore, in practice, it is extremely difficult to determine the entire set of initial conditions leading to chaotic orbits. For the ray systems considered, it is shown that there exists a chaotic region near the lower homoclinic orbit. If the perturbation is larger, the extent and shape of the chaotic region may become complex. This places severe restrictions on predictions made with a chaotic ray model.

The problem treated in this paper is, of course, an ideal one, in which the parabolic ray model is assumed to be exact, the sound-speed profile a fourth-order polynomial, and the perturbation periodic. Parabolic ray systems are viewed as reasonable approximations of realistic ray models due to the similarity of their dynamic behavior to that found in one-way elliptic ray systems (see Smith *et al.*[2]). More importantly, the systems are used for the simplicity they lend to theoretical analysis. The fourth-order polynomial sound-speed profile considered in this paper is a generalization of the North Atlantic profile based on actual measured data. As such, it provides a reasonable approximation of some realistic sound speed profiles. It should be noted that the North Atlantic profile can not be fit with great precision by a single fourth-order polynomial sound-speed profile. It may be possible to apply an analysis similar to that presented here to a more realistic sound speed model.

ACKNOWLEDGMENTS

The authors thank Elaine C. Quarve for her secretarial assistance. This work was supported in part by Grant No. CA 43920 from the National Institutes of Health.

APPENDIX: CALCULATION OF THE MELNIKOV FUNCTION

In this Appendix, Eq. (25) is derived.

Inserting Eqs. (14), (21), and (24) into Eq. (23), and noticing symmetry present in the integrands, we have

$$
\begin{aligned}
M(r_0;h_1,h_2) &= \int_{-\infty}^{\infty} \frac{3\sqrt{2}}{2Bc_0}\, p_h \exp\left(\frac{-1.5z_h}{B}\right)\sin\left(\frac{2\pi(r+r)}{R}\right)dr \\
&= \int_{-\infty}^{\infty} \frac{3\sqrt{2}}{2Bc_0}\, p_h \exp\left(\frac{-1.5z_h}{B}\right)\sin\left(\frac{2\pi r}{R}\right)\cos\left(\frac{2\pi r_0}{R}\right)dr \\
&= \frac{3\sqrt{2}}{2Bc_0}\, p_h \cos\left(\frac{2\pi r_0}{R}\right)\int_0^{\infty} p_h \exp\left(\frac{-1.5z_h}{B}\right)\sin\left(\frac{2\pi r}{R}\right)dr \\
&= -\frac{3\sqrt{2}e_1}{2Bc_0}\exp\left(\frac{-1.5r_2}{B}\right)\cos\left(\frac{2\pi r_0}{R}\right)\int_{1+e_3}^{\infty}\frac{1}{u^2}\exp\left(\frac{-1.5e_1}{Bu}\right)\sin\left[\frac{2\pi}{\mathrm{Re}_2}\,\mathrm{Arch}(u-e_3)\right]du,
\end{aligned}
$$

where $u=\cosh(e_2 r)+e_s$ and $\mathrm{Arch}(x)$ is the inverse hyperbolic cosine.

To calculate the last integral in the above equation, residue theory is used to evaluate the following two integrals;

$$
\begin{aligned}
I_1 &= \int_{1+e_3}^{\infty}\frac{1}{u^2}\exp\left(\frac{-1.5e_1}{Bu}\right) \\
&\quad\times\exp\left[\, i\,\frac{2\pi}{\mathrm{Re}_2}\,\mathrm{Arch}(u-e_3)\right]du, \\
I_1 &= \int_{1+e_3}^{\infty}\frac{1}{u^2}\exp\left(\frac{-1.5e_1}{Bu}\right) \\
&\quad\times\exp\left[-i\,\frac{2\pi}{\mathrm{Re}_2}\,\mathrm{Arch}(u-e_3)\right]du.
\end{aligned}
\tag{A1}
$$

The Melnikov function can be written in terms of I_1 and I_2 as

$$
M(r_0;h_1,h_2) = -\frac{3\sqrt{2}e_1}{2Bc_0}\exp\left(\frac{-1.5r_2}{B}\right)\times\cos\left(\frac{2\pi r_0}{R}\right)\frac{I_1-I_2}{2i}. \tag{A2}
$$

Consider the following complex functions:

$$
\begin{aligned}
f_1(z) &= \frac{1}{z^2}\exp\left(\frac{-1.5e_1}{Bz}\right)\exp\left[\, i\,\frac{2\pi}{\mathrm{Re}_2}\,\mathrm{Arch}(z-e_3)\right], \\
f_2(z) &= \frac{1}{z^2}\exp\left(\frac{-1.5e_1}{Bz}\right)\exp\left[-i\,\frac{2\pi}{\mathrm{Re}_2}\,\mathrm{Arch}(z-e_3)\right].
\end{aligned}
\tag{A3}
$$

Here z is not the depth but a complex number. We are required to find

$$I_1=\lim_{\rho\to\infty,e=1+e_3}\int_e^{\rho} f_1(z)dz \tag{A4}$$

and

$$I_2=\lim_{\rho\to\infty,e=1+e_3}\int_e^{\rho} f_2(z)dz. \tag{A5}$$

For this purpose we form a closed contour containing the segment $[e,\rho]$ (see Fig. A1), where $e=1+e_3$ is always positive and ρ is large enough so that the only singularity of both $f_1(z)$ and $f_2(z)$ (i.e., an essential singularity at the origin) lies inside the contour. In addition, according to convention, we define the multiple-valued function $f_1(z)$ as follows:[25]

$$f_1(z)=\begin{cases}\dfrac{1}{z^2}\exp\left(\dfrac{-1.5e_1}{Bz}\right)\exp\left[i\,\dfrac{2\pi}{\mathrm{Re}_2}\,\mathrm{Arch}(z-e_3)\right] \\ \quad \text{on}\ \ \gamma_1,\Gamma_e,C_\rho, \\ \dfrac{1}{z^2}\exp\left(\dfrac{-1.5e_1}{Bz}\right)\exp\left[i\,\dfrac{2\pi}{\mathrm{Re}_2}\,\mathrm{Arch}(z-e_3)+2\pi i\right] \\ \quad \text{on}\ \ \gamma_2.\end{cases} \tag{A6}$$

We define $f_2(z)$ similarly.

There is no singularity between the two circles. Thus, by the residue theorem, we have[25]

$$\left(\int_{\Gamma_e}+\int_{C_\rho}+\int_{\gamma_1}+\int_{\gamma_2}\right)f_{1,2}(z)=0. \tag{A7}$$

Making use of Eq. (25), one has

$$\left(\int_{\gamma_1}+\int_{\gamma_2}\right)f_1(z)dz=\left[1-\exp\left(-\frac{4\pi^2}{\mathrm{Re}_2}\right)\right]\int_{\gamma_1}f_1(z). \tag{A8}$$

The essential singularity at the origin inside Γ_e implies that

$$\int_{\Gamma_e}f_1(z)dz=-2\pi i\ \mathrm{Res}(f_1;0), \tag{A9}$$

where $\mathrm{Res}(f;z_0)$ denotes the residue of f at z_0.

Furthermore, on the circle of radius ρ, we have

$$|f_1(z)|\leqslant\frac{1}{|z^2|}\left|\exp\left(\frac{-1.5e_1}{Bz}\right)\right|\left|\exp\left(\frac{4\pi^2}{\mathrm{Re}_2}\right)\right|\leqslant\frac{C_1}{\rho^2}, \tag{A10}$$

where C_1 is a bounded read number. The above estimation yields

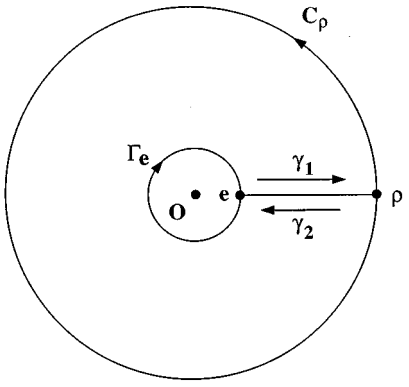

FIG. A1. The closed contour used to calculate I_1 and I_2.

$$\left|\int_{C_\rho}f_1(z)dz\right|\leqslant\frac{C_1}{\rho^2}\times 2\pi\rho=\frac{2\pi C_1}{\rho}. \tag{A11}$$

Consequently, the integral over C_ρ tends to zero as $\rho\to\infty$.

Taking the limit as $\rho\to\infty$ and $e=1+e_3$ in Eq. (A7), we obtain

$$-2\pi i\ \mathrm{Res}(f_1;0)+0+\left[1-\exp\left(-\frac{4\pi^2}{\mathrm{Re}_2}\right)\right]I_1=0. \tag{A12}$$

Similarly, for integral I_2, one has

$$-2\pi i\ \mathrm{Res}(f_2;0)+0+\left[1-\exp\left(-\frac{4\pi^2}{\mathrm{Re}_2}\right)\right]I_2=0. \tag{A13}$$

It is sufficient to evaluate the residues of functions f_1 and f_2 at their singularity (the origin). Again, residue theory yields

$$\begin{aligned}2\pi i\ \mathrm{Res}(f_1;0)&=\int_{C_1}f_1(z)dz,\\ 2\pi i\ \mathrm{Res}(f_2;0)&=\int_{C_1}f_2(z)dz,\end{aligned} \tag{A14}$$

where C_ρ is a positively oriented circle with ρ sufficiently small.

Using a known formula,[26] residues in Eq. (A14) can be calculated as follows:

$$\begin{aligned}2\pi i\ \mathrm{Res}(f_1;0)&=\lim_{\rho\to0}\int_{z=\rho e^{i\theta}}\frac{1}{z^2}\exp\left(\frac{-1.5e_1}{Bz}\right)\\ &\quad\times\exp\left[i\,\frac{2\pi}{\mathrm{Re}_2}\,\mathrm{Arch}(z-e_3)\right]dz,\\ &=\lim_{\rho\to0}\,i\int_0^{2\pi}\frac{e^{-i\theta}}{\rho}\exp\left(\frac{-1.5e_1}{B\rho e^{i\theta}}\right)\\ &\quad\times\exp\left[i\,\frac{2\pi}{\mathrm{Re}_2}\right.\\ &\quad\left.\times\left(i\alpha+\frac{\rho(\sin\theta-i\cos\theta)}{\sqrt{1-e_3^2}}\right)\right]d\theta,\\ &=\lim_{\rho\to0}\,ie^{-(2\pi\alpha/\mathrm{Re}_2)}\int_0^{2\pi}\frac{1}{\rho}\,e^{\beta_1\cos\theta}\\ &\quad\times e^{i\beta_2\sin\theta}d\theta,\end{aligned}$$

where

$$\beta_1=\frac{2\pi\rho}{\mathrm{Re}_2\sqrt{1-e_3^2}}-\frac{1.5e_1}{B\rho},$$

$$\beta_2=\frac{2\pi\rho}{\mathrm{Re}_2\sqrt{1-e_3^2}}+\frac{1.5e_1}{B\rho}.$$

Evaluating the limit and integral yields

$$2\pi i\ \mathrm{Res}(f_1;0) = -e^{-(2\pi\alpha/\mathrm{Re}_2)}\ \frac{3\pi Bi}{e_1}\ \sqrt{\frac{3\pi e_1}{B\ \mathrm{Re}_2\sqrt{1-e_3^2}}} \times J_1\left(\ \sqrt{\frac{12\pi e_1}{B\ \mathrm{Re}_2\sqrt{1-e_3^2}}}\right),$$

$$= -e^{-(2\pi\alpha/\mathrm{Re}_2)}\ \frac{3\pi Bi}{e_1}\ \sqrt{\frac{3\pi}{BR}}\ \sqrt{\frac{c_0}{2a_4}} \times J_1\left(\ \sqrt{\frac{3\pi}{BR}}\ \sqrt{\frac{c_0}{2a_4}}\right), \tag{A15}$$

where the last equality is obtained with the help of Eq. (22). $J_1(\cdot)$ is the Bessel function of the first kind and first order, and

$$\alpha = \arccos(-e_3). \tag{A16}$$

Similarly,

$$2\pi i\ \mathrm{Res}(f_1;0) = \lim_{\rho\to 0}\int_{z=\rho e^{i\theta}} \frac{1}{z^2}\exp\left(\frac{-1.5e_1}{Bz}\right) \times\exp\left[-i\ \frac{2\pi}{\mathrm{Re}_2}\ \mathrm{Arch}(z-e_3)\right]dz$$

$$= e^{(2\pi\alpha/\mathrm{Re}_2)}\ \frac{3\pi Bi}{e_1}\ \sqrt{\frac{3\pi}{BR}}\ \sqrt{\frac{c_0}{2a_4}} \times\ J_1\left(\ i\sqrt{\frac{3\pi}{BR}}\ \sqrt{\frac{c_0}{2a_4}}\right). \tag{A17}$$

Inserting results in Eqs. (A12), (A13), (A15), and (A17) into Eq. (A2), we finally obtain Eq. (25).

[1] L. Landau and E. Lifshitz, *Fluid Mechanics* (Pergamon, New York, 1959).
[2] K. Smith, M. Brown, and F. Tappert, J. Acoust. Soc. Am. **19**, 1939–1949 (1992).
[3] D. Palmer, M. Brown, F. Tappert, and H. Bezdek, Geophys. Res. Lett. **BME-30**, 569–572 (1988).
[4] F. Tappert, M. Brown, and G. G̃oni, Phys. Lett. A **153**, 181–185 (1991).
[5] M. Brown, F. Tappert, and G. G̃oni, Wave Motion **14**, 93–99 (1991).
[6] Strictly speaking we should speak of stable and unstable *manifolds*.
[7] J. Guckenheimer and P. Holmes, *Nonlinear Oscillation, Dynamical Systems, and Bifurcations of Vector Fields* (Springer-Verlag, New York, 1986), 2nd ed.
[8] K. Smith, M. Brown, and F. Tappert, J. Acoust. Soc. Am. **91**, 1950–1959 (1992).
[9] L. Marcus and K. Meyer, Mem. Am. Math. Soc. (1974).
[10] C. Boyles, *Acoustic Waveguides, Application to Ocean Science* (Wiley, New York, 1984).
[11] J. Yan, J. Acoust. Soc. Am. **94**, 2739–2745 (1993).
[12] O. Lee, J. Acoust. Soc. Am. **33**, 677–681 (1961).
[13] L. Baxter and M. Orr, J. Acoust. Soc. Am. **71**, 61–65 (1982).
[14] B.-L. Hao, *Elementary Symbolic Dynamics and Chaos in Dissipative Systems* (World Scientific, Singapore, 1989).
[15] T. Li and J. York, Am. Math. Monthly **82**, 995 (1975).
[16] S. Wiggins, *Dynamical Systems and Chaos* (Springer-Verlag, New York, 1990).
[17] Z. Jiang, J. Fa, Y. Zheng, and S. He, in *12th World Congress of the International Federation of Automation Control* (Sydney, Australia, 1993), Vol. 3, pp. 481–484.
[18] Consider a two-dimensional phase space. Stretch the space along one coordinate axis and bend it into a *u*-shape (hence the name *horseshoe map* or *Smale horseshoe* after the mathematician who first conceived it). Points that were in the ''upper half'' of the space have now moved down and to one side. Upon continued iteration of these steps we see that points starting arbitrarily close to one another may soon be arbitrarily far apart. For a more detailed discussion of such maps see Jackson.[19]
[19] E. Jackson, *Perspectives of Nonlinear Dynamics* (Cambridge U.P., New York, 1989).
[20] For example, A damped pendulum will produce a spiral shape in its phase space shrinking to a point after an infinite amount of time. Different amounts of damping will change the rapidity of spiral but not the essential features of the motion.
[21] Z. Jiang, in *12th World Congress of the International Federation of Automation Control* (Sydney, Australia, 1993), Vol. 3, pp. 477–480.
[22] S. Smale, Bull. Am. Math. Soc. **73**, 747–817 (1967).
[23] Z. Jiang and R. Jiang, J. Hunan Univ. **19**, 1–6 (1992).
[24] D. Holm and G. Kovacic, Physica D **51**, 177–188 (1991).
[25] E. Saff and A. Snider, *Fundamentals of Complex Analysis (For Mathematics, Science and Engineering)* (Prentice-Hall, Englewood Cliffs, NJ, 1976).
[26] I. Gradshteyn and I. Ryzhik, *Table of Integrals, Series, and Products*, 5th ed. (Academic, New York, 1994).

The use of a combination frequency technique to measure the surf zone bubble population

Andy D. Phelps,[a] David G. Ramble, and Timothy G. Leighton
Institute of Sound and Vibration Research, University of Southampton, Southampton SO17 1BJ, United Kingdom

(Received 1 July 1996; accepted for publication 16 October 1996)

There are great benefits to sizing bubbles using a two frequency technique, which examines the appearance of sum-and-difference signals generated by the interaction between a resonant bubble pulsation and a much higher frequency imaging beam. This paper presents the results from using the technique to size bubbles in the ocean surf zone, and details the pulsation model used to calibrate the returned data such that the height of the bubble scattered signal can be related to the number of resonant bubbles of that size. It also shows how ambiguities and inaccuracies (brought on through turbulence and the substantial off-resonance nature of the signal) which affected earlier oceanic tests using the same method can be identified in the returned signal or removed from the estimate during the data processing. © *1997 Acoustical Society of America.* [S0001-4966(97)00604-8]

PACS numbers: 43.30.Pc, 43.30.Lz, 43.25.Yw [JHM]

INTRODUCTION

There are many practical applications where a knowledge of the size and distribution of a bubble population would be of benefit,[1–3] and the strong backscattering properties due to the impedance mismatch at the bubble surface makes acoustic measurements particularly amenable to the task. When excited by sound, bubbles pulsate volumetrically as a single degree of freedom system, where the inertia arises from fluid around the bubble, the stiffness through gas compression inside the bubble, and the damping is brought on through viscous losses at the wall, thermal dissipation into the fluid, and acoustic radiation. These volumetric pulsations have a well-defined acoustic resonance frequency, given by[4]

$$\omega_0 \approx \frac{1}{R_0\sqrt{\rho}}\sqrt{3\kappa\left(p_0+\frac{2\sigma}{R_0}\right)-\frac{2\sigma}{R_0}-\frac{4\mu^2}{\rho R_0^2}}, \tag{1}$$

where ω_0 is the resonant frequency in rad/s, R_0 is the equilibrium bubble radius, ρ is the density of the surrounding fluid (assumed to be incompressible), κ is the polytropic index of the gas compression, p_0 is the hydrostatic pressure at the bubble wall, σ is the surface tension of the gas/liquid interface, and μ is the shear viscosity coefficient of the liquid.

It is possible to measure the resonance frequencies of a bubble population through observing the strength of a backscattered acoustic signal,[5] which is assumed to be a maximum when the driving signal frequency, here called the ''pump'' frequency ω_p, is coincident with a bubble resonance. However, such estimates have poor spatial resolution, since at resonance the radii of bubbles are orders of magnitude smaller than the wavelength of the sound field, and provide ambiguous results, in that a bubble much larger than resonance may scatter more sound than a smaller resonant bubble.[4] This ambiguity may by reduced by monitoring the nonlinear behavior of a bubble, because at large pulsation amplitude (typically taken to be an indicator of resonance) the bubble motion becomes increasingly asymmetric: As an obvious example, a bubble can theoretically expand without limit but only contract to zero radius. This results in integer related harmonics of the driving signal frequency at $2\omega_p$, $3\omega_p$, etc. It has been demonstrated,[6] however, that exploitation of these particular nonlinear effects suffers in that the signals are difficult to distinguish from other harmonic distortion in the measuring equipment, and also fail to address the problem of poor spatial resolution. Other noninteger harmonics of the sound field, typically a subharmonic at $\omega_p/2$ and ultraharmonics at $3\omega_p/2$, $5\omega_p/2$, etc., are also stimulated near resonance. These have been shown to be unambiguous indicators of a resonant bubble and provide greater accuracy in determining its resonance frequency owing to the much reduced off-resonance signal contribution.[7] However, these signals are impractical for a generalized bubble sizer when stimulated at resonance as they are parametric in nature, and arise from surface effects which do not propagate into the medium. Specifically, the subharmonic at $\omega_p/2$ arises through Faraday waves set up on the bubble surface,[7] which do not bring about a volumetric change in the bubble and therefore do not emit as monopoles.

Many of these limitations have been overcome through use of a two frequency technique, where a bubble population is simultaneously insonified with a high-frequency fixed signal ω_i (the ''imaging'' signal) as well as the lower frequency signal ω_p intended to drive the population at their resonant frequencies.[8] When this low-frequency sound field is coincident with a bubble resonance and the wall pulsations are large, the high-frequency sound scattered from the bubble is amplitude modulated at this frequency, and this gives rise to sum-and-difference components in the returned signal at $\omega_i \pm \omega_p$. Therefore the technique allows the exploitation of the basic resonant behavior of a bubble, but without the potential ambiguity caused when a large bubble is mistaken for a small resonant bubble. Additionally, the use of combination frequency measurements allows very specific spatial lo-

[a]Electronic mail: ap@isvr.soton.ac.uk

calization, and the signal-to-noise ratio is greatly improved as the process translates only bubble-mediated information from the noisy frequency window around their resonance up to the comparatively quieter frequency window around the imaging signal.

This particular method of sizing bubbles has been investigated by earlier workers for laboratory populations employing increasingly more sophisticated signal processing techniques,[8–10] and once on an oceanic population.[11] The oceanic data was taken using a chirped signal between 2.5 and 6 kHz, with an imaging frequency of 450 kHz, but in the tests no distinction was made between bubble-mediated coupling and that caused by turbulence, or compensation for the significant off-resonance contribution which is characteristic of the $\omega_i \pm \omega_p$ signal, and the pump transducer frequency response. This paper describes the results of work undertaken to build a more robust and accurate bubble population estimator, and describes results collected in oceanic surf zone measurements, taken at four spot frequencies of 28, 50, 60, and 88 kHz. The choice of three of these frequencies allows comparison of the returned data with earlier oceanic bubble population estimates taken exploiting the resonant backscatter effect.[5] The paper shows how turbulent effects are differentiated from the bubble signals, and demonstrates how the off-resonant contribution to the $\omega_i \pm \omega_p$ signal can find compensation in the calibration of the equipment. As individual tones were employed, the variable frequency response of the source transducer could be removed, and constant and clearly defined bubble insonification conditions could be chosen. The paper first describes the theoretical model used in the estimation of the strength of the signal coupling, then proceeds to describe the calibration of the equipment. The experimental oceanic setup is discussed, with the results collected on site presented, analyzed, and compared with historical data.

I. BUBBLE RESPONSE TO TWO FREQUENCY INSONIFICATION

There are a number of different bubble models currently available which can be used to calculate radius-time curves for pulsating bubbles, and which differ from each other in complexity and in the range of insonification amplitudes and bubble size over which they are applicable. One of the best known and simplest of these models is the Rayleigh–Plesset equation, which considers the volumetric pulsations of an assumed spherical bubble existing in a infinite and incompressible medium.[12] Although this model is nonlinear and can only be solved numerically, there are certain simplifying assumptions which can be made to allow an analytical solution. This was the subject of the analysis performed by Zabolotskaya and Soluyan[13] and Newhouse and Shankar,[8] who derived expressions for the pressure amplitudes at the various frequency locations through consideration of a small volumetric or radial perturbation. However, their analyses did not account fully for the various damping mechanisms that affect the radial pulsations of a bubble, and which are of considerable importance when estimating its resonant behavior.

There are three damping mechanisms which have been identified and theoretically considered, and they must all be included in any full consideration of the resonant properties of a pulsating bubble. These are losses through viscous action at the bubble wall, thermal conduction between gas and liquid, and energy dissipation through acoustic radiation. Of these, only viscous losses were included in the original theory:[8] the gas was considered to behave adiabatically and no account was taken of the energy radiation into the fluid brought about through the passage of the sound through a compressible medium. However, over the range of bubble sizes which were examined in the earlier work,[8] and are examined in this paper, viscous losses are orders of magnitude smaller than the other two damping mechanisms, and thus using the expression to calculate the expected amplitudes of the various signals at resonance will yield erroneous results. It should be noted that Newhouse and Shankar[8] identified this potential for error, and in comparing measured results to their theory they left the total damping coefficient δ as a variable which was then altered to provide a least squares fit to their data.

For the theory applied in calibrating the oceanic sizer, the work of Newhouse and Shankar is extended to include explicitly for these extra damping mechanisms. A corrected form of the Rayleigh–Plesset equation is used as a starting expression, which includes an extra term which has been shown to give a reliable measure of the dissipative effects of sound radiation through a compressible medium.[14] Additionally, the thermal conduction into the fluid is included in an approximate manner by assuming that the pulsations behave polytropically, with an index κ calculated theoretically using the expressions of Eller.[15] The modified form of the Rayleigh–Plesset differential equation is

$$\rho R\ddot{R} + \frac{3}{2}\rho\dot{R}^2 = p_B(t) - p_0 - P(t) + \frac{R}{c}\left(1 - \frac{\dot{R}}{c}\right)\frac{dp_B}{dt}, \tag{2}$$

where R is the instantaneous bubble radius, c is the speed of sound in the liquid, and $P(t)$ is the acoustic driving term. The remaining term $p_B(t)$ is a measure of the pressure immediately outside the bubble wall, and represents the forcing term on the liquid due to the bubble which the acoustic pressure has to overcome. It is given by

$$p_B(t) = \left(p_0 + \frac{2\sigma}{R_0}\right)\left(\frac{R_0}{R}\right)^{3\kappa} - \frac{2\sigma}{R} - \frac{4\mu\dot{R}}{R}. \tag{3}$$

Following the earlier methodology, an approximate solution to this expression is sought by considering a small radial perturbation, where the variable R can be rewritten in terms of a displacement variable x as

$$R = R_0(1+x) \quad \text{with} \quad x \ll 1. \tag{4}$$

Using this substitution, and neglecting all terms beyond those in x^2, Eq. (2) can be rewritten as:

$$\rho R_0^2(1+x)\ddot{x}+\frac{3}{2}\rho R_0^2\dot{x}^2=\left(p_0+\frac{2\sigma}{R_0}\right)\left[1-3\kappa x+\frac{3}{2}\kappa(3\kappa+1)x^2\right]-\left[p_0+\left(\frac{2\sigma}{R_0}\right)(1+x+x^2)\right]$$
$$-4\mu(\dot{x}-x\dot{x})+p_1\cos\omega_1 t+p_2\cos\omega_2 t+\frac{R_0}{c}\left\{3\kappa\dot{x}\left(p_0+\frac{2\sigma}{R_0}\right)\left(3\kappa x+\frac{R_0}{c}\dot{x}-1\right)\right.$$
$$\left.+4\mu\left(\dot{x}^2-\ddot{x}+\frac{R_0}{c}\dot{x}\ddot{x}\right)+2\sigma\dot{x}\left(\frac{1}{R_0}-\frac{x}{R_0}-\frac{\dot{x}}{c}\right)\right\}, \tag{5}$$

where ω_1 and ω_2 are the two angular frequencies of the sinusoidal driving sound fields and p_1 and p_2 are their corresponding pressure amplitudes. If the acoustic radiation terms (shown grouped in curly brackets) are removed by considering the incompressible case of $c\to\infty$, this equation becomes Eq. (5) from Newhouse and Shankar's paper.[8] The subsequent analysis follows the method in their paper of writing a solution to the displacement variable x in terms of the sum of radial excursions at ω_1, ω_2, $2\omega_1$, $2\omega_2$, $\omega_1+\omega_2$, and $\omega_1-\omega_2$, substituting this into the modified Rayleigh–Plesset equation, and then equating the terms at the various different frequencies. The analytical solution is readily obtained (but cannot be simplified to obtain a transparent expression of the form obtained by Newhouse and Shankar,[8] and is therefore not presented here), and its use is described in the next section. It is the case, however, that the results for the radiated pressures at the sum-and-difference frequency locations are numerically equal to those obtained by augmenting the damping term given in Newhouse and Shankar's Eq. (8) with the expression for the nondimensional radiated damping coefficient presented by Eller.[15] If the more general off-resonance form for the viscous damping is employed, then their variable δ can be replaced with the general damping parameter d_{tot} given by

$$d_{\text{tot}}=\frac{4\omega_2\mu}{3\kappa p_0}+\frac{\rho}{3\kappa p_0}\frac{(R_0\omega_2)^3}{c}, \tag{6}$$

where ω_2 is considered to be the angular frequency of the pump sound field.

II. EQUIPMENT AND APPARATUS

A. Laboratory calibration

The calibration of the apparatus was performed both to test that the pulsation model described above presented correct predictions for the relative heights of the different frequencies in the returned signal, and to enable the absolute height of the signals in the oceanic tests to be related to the signal strength associated with one resonant bubble. This was achieved by repeatedly insonifying a steady bubble stream of known resonant frequency, and examining the form of the returned signal. The laboratory tests were performed in a 1.8-m×1.2-m×1.2-m-deep glass reinforced plastic tank which is vibration isolated from the floor, and is filled with tap water to 1-m depth. The equipment schematic is shown in Fig. 1, and a detail of the transducer arrangement is included in Fig. 2. This is the same transducer head which was later used in the oceanic tests, and it will be demonstrated that fixing the geometry in this way allows certain parameters in the pulsation model to be poorly defined without any loss of accuracy.

The pump frequency signal generation was achieved using a Tektronix 2005 arbitrary waveform generator controlled via a GPIB cable connected to a PC, which was passed into a Bruel & Kjaer 2713A power amplifier. The pump transducer comprised a 104-mm-i.d. piezoceramic ring transducer which was set into a polyurethane foam and encased in a nylon housing. The imaging signal was generated by a 1-MHz crystal oscillator amplified with an ENI 240L rf power amplifier, and this was passed to the imaging signal transducer—the head of a Therasonic 1030 ultrasonic therapy unit as manufactured by Electro Medical Supplies,

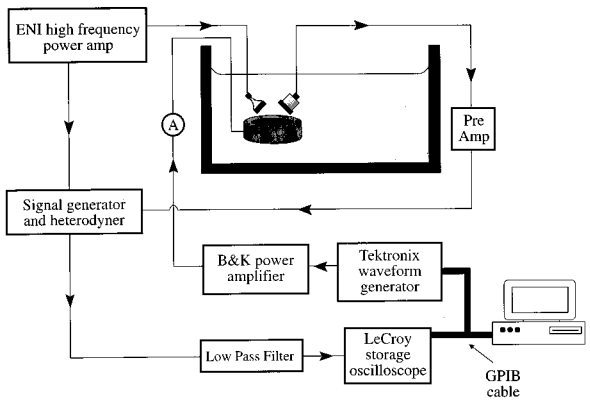

FIG. 1. Schematic of the equipment used in the laboratory tests.

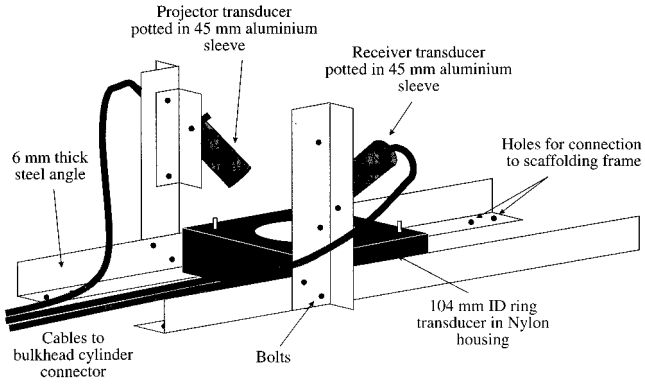

FIG. 2. Close up of the transducer arrangement used in both the laboratory tests and the oceanic measurements.

and which was potted inside a 45-mm-diam aluminum cylinder to protect it when used in the open sea. The imaging signal amplitude at the focus of the two transducers was measured as 30 kPa using a calibrated needle hydrophone (active element diameter=0.5 mm) with a HP1 submersible preamplifier, as manufactured by Precision Acoustics Ltd.

The returned signal from the bubble was monitored using a Panametrics V302 piezoceramic transducer, similarly potted in a 45-mm-diam sleeve, and conditioned using a Panametrics 5670 preamplifier. The preamplified signal was then heterodyned with a dummy signal from the crystal oscillator: this results in the useful information contained just above and below the imaging frequency being reproduced at just above dc, enabling much lower sampling rates and data storage. The low-frequency information was filtered to prevent aliasing using a Barr and Stroud EF5-02 46 dB/octave filter and acquired on a LeCroy 9314L storage oscilloscope. For the laboratory tests the data were sampled at 50 kHz and 10 000 points taken. The beam patterns of the two high-frequency transducers were modeled by performing a Rayleigh integral over their surfaces. When these patterns were overlapped in a similar layout to the transducer arrangement, they allowed the insonification volume to be estimated. This gave an insonification volume, defined by where the sensitivity fell off to 3 dB of its peak value, of 0.2 cm^3, demonstrating the potential of the technique to achieve high spatial resolution. Because of this, it should be noted that the equipment cannot provide depth profiles of the bubble population, although it is conceivable that a vertically mounted array of the sensors could be used to obtain depth-dependent measures of the local population.

The bubble stream was generated by passing compressed air through a Hamilton 701RN laboratory syringe, which was additionally constricted at its base to provide the high-pressure drop necessary to give a repeatable size.[16] This resulted in a bubble stream of resonant frequency 4300 Hz, which was then allowed to rise through the transducer focus where it was insonified at a pump signal amplitude of 200 Pa. The power spectral density of the signal scattered by the bubbles was then calculated, and the total energy contribution for each peak was estimated. The heights of the heterodyned imaging peak and the $\omega_i+\omega_p$ signals were measured over ten different sweeps and averaged, and were found to be repeatable to within $\pm 3\%$ and $\pm 5\%$, respectively.

Typical results for the laboratory measurements are shown in Fig. 3(a) and (b). Here the bubble stream was insonified between 3800- and 4800 Hz pump frequency in 25 Hz steps, such that the bubbles passed through the transducer focus at a depth of 29 cm. Figure 3(a) shows a mesh of the matrix formed by stacking the frequency responses of the heterodyned returned signals from adjacent pump frequencies together, and the locations of the ω_i, $\omega_i+\omega_p$, and $\omega_i-\omega_p$ signals are labeled. Clearly evident is the heterodyned Doppler shifted imaging signal which plots as a continuous ridge to the left of the plot; this is constant over the 41 different pump frequencies. To the right of this are two broken ridges which rise up to a maximum value at 4300 Hz and then fall off again. These are the two combination frequency signals at $\omega_i+\omega_p$ and $\omega_i-\omega_p$. Peaks separation is

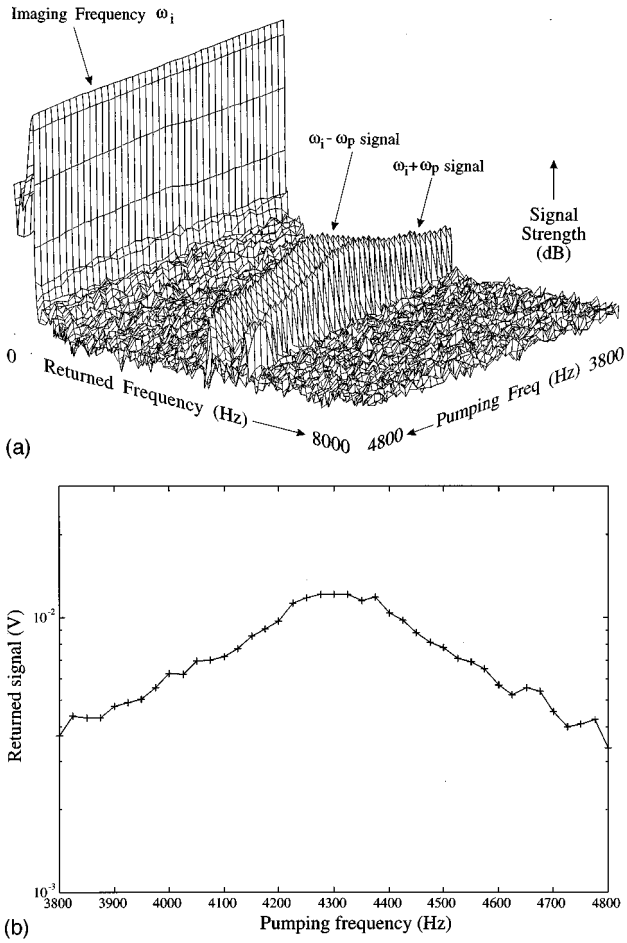

FIG. 3. (a) Typical results from the laboratory measurements on a rising bubble stream, with all the bubbles resonant at 4300 Hz. The bubbles were insonified at 200-Pa amplitude between 3800 and 4800 Hz in 25-Hz steps. (b) Height of the $\omega_i+\omega_p$ signal taken from the data in (a).

due to the Doppler shift on the scattered signal, which when heterodyned with the original imaging signal causes the 500-Hz frequency offset. The amplitude of the $\omega_i+\omega_p$ signal is also shown in Fig. 3(b) over the pumping frequency range considered. These plots demonstrate an important property of the $\omega_i\pm\omega_p$ signal, the substantial off-resonant behavior of the signal. In order to calculate the number of bubbles at a specific radius per micrometer radial increment, which is the historical method of representing the data, this off-resonance effect must be removed. This is achieved by calculating the heights of the response of the bubbles whose radii lie on either side of the resonant bubble radius, and looking for the width of the radius spread before the signal strength falls off by 3 dB. The effect of off-resonant bubbles contributing to the output signal can then be removed by dividing the measured bubble sound pressure levels by the 3-dB widths corresponding to that particular bubble radius.

The second stage of the calibration involved modeling the bubble-mediated sound pressure at the receiver transducer due to the two insonifying sound fields. The same bubble size and insonification conditions as employed in the laboratory experiments were used, such that a comparison of the results of the simulation with the experimentally estimated values would allow the validity of the model to be

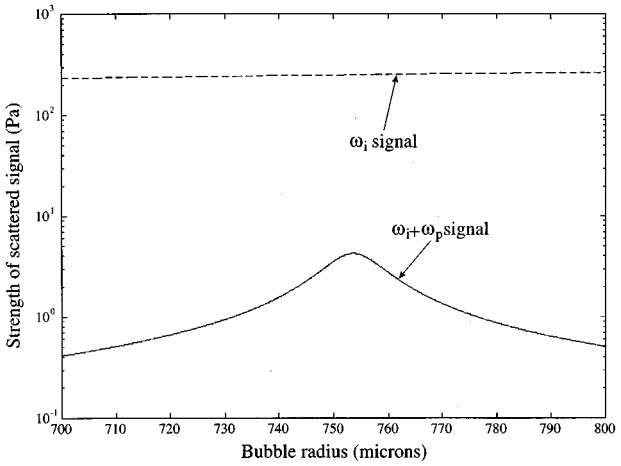

FIG. 4. Theoretically estimated amplitudes of the imaging signal and the $\omega_i+\omega_p$ signal for an insonifying sound field of frequency 4300 Hz and amplitude 200 Pa, over a radius range of 700–800 μm.

examined and the sensitivity of the receiver transducer to be evaluated. The results from estimating the height of the $\omega_i+\omega_p$ and the imaging signal using the extended Rayleigh Plesset model are shown in Fig. 4. This is done for a range of bubble sizes from 700 to 800 μm insonified by a 200 Pa amplitude sine wave of frequency 4300 Hz. It is clear from the figure that the strength of the backscattered $\omega_i+\omega_p$ signal reaches a maximum of 4.3 Pa at a bubble radius of 754 μm, and at this point the height of the scattered imaging signal is 251 Pa. This can now be compared with the measurement of the scattered signal from the 4300-Hz bubble stream, which showed an average height of the imaging signal of 1.27 ± 0.04 V and an $\omega_i+\omega_p$ signal height of 17.3 ±0.9 mV. Comparison of the heights of the two imaging signal strengths, and consideration of the frequency responses of the preamplifier and heterodyner, allow the sensitivity of the high-frequency transducer to be estimated at 13.4 μV/Pa. As a method of testing the validity of the model, the difference in the strengths of the imaging signal and $\omega_i+\omega_p$ were also calculated. The ratio of the two signal components is 35.3 dB in the theoretical predictions, compared with 37.3 dB in the laboratory measurements, a 2-dB discrepancy which is equivalent to a 20% error in the $\omega_i+\omega_p$ pressure. If the damping was taken to comprise viscous losses alone, the ratio of the two signal heights would be less than 1 dB, which is equivalent to a discrepancy of $>$36 dB. The contribution of the 2-dB error to the final bubble number estimates will be discussed later.

Having verified the performance of the pulsation model, the sensitivity of the high-frequency receiver transducer can be estimated. Following this, the behavior of resonant bubbles at the four pump frequencies used in the oceanic tests of 28, 50, 60, and 88 kHz were modeled (using parameters applicable to sea water rather than those of fresh water used in modeling the lab tests). With application of the same sensitivity adjustment and the relevant preamplifier/heterodyner corrections, this provided an estimate of the signal levels expected from the different bubbles resonant at the four frequencies. This estimate relies on the sensitivity of the receiver transducer being flat over the frequency range 1–1.1 MHz (as verified by the manufacturers data), and on the theory maintaining its validity over the greatly extrapolated frequency range considered.

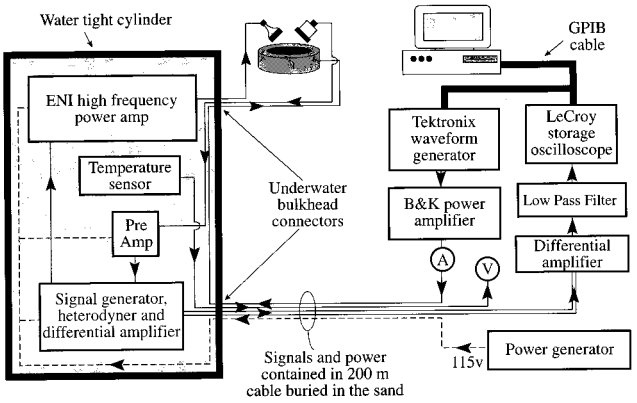

FIG. 5. Schematic of the apparatus used in the oceanic measurements.

B. Oceanic data collection

The equipment used in the sea trials was largely similar to that used in the laboratory experiments, and the schematic is shown in Fig. 5. The most important difference in the layout of the oceanic equipment is the provision of a remote equipment canister, which was set up in the sea and attached to the land-based equipment via an underwater bulkhead connector and 200 m of waterproof cable, as manufactured by PDM Group. The canister comprised a 1000-mm-long $\times$355-mm-diam watertight aluminum alloy cylinder, which was painted to minimize corrosion, and clamped to a rigid scaffold structure as shown in Fig. 6. This canister contained the high-frequency power amplifier, the crystal oscillator and heterodyner equipment, the returned signal rf preamplifier, and a temperature sensor to monitor the effects that the enclosed space had on the potential of the equipment to overheat. Additionally, a differential amplifier pair was added to the returned signal circuit to ensure that no signal corruption occurred when passed down the 200-m cable: this additional step was analyzed in the laboratory and its frequency response quantified. Because of the higher-pump frequencies involved, the data were sampled at 500 kHz, and 50 000

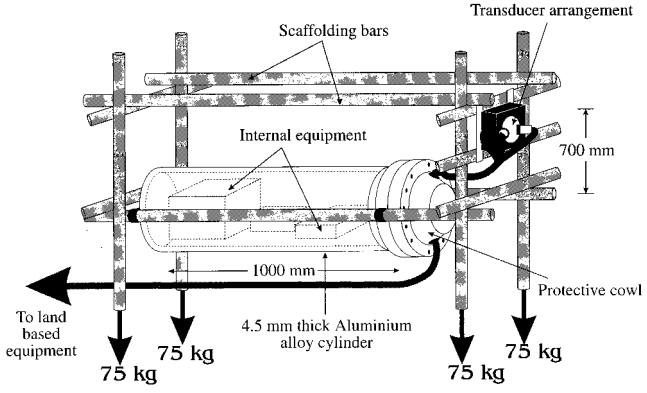

FIG. 6. Deployment details of the watertight canister and scaffolding.

points were taken. To speed up the data collection and storage, the Tektronix output waveform comprised all four frequencies in one signal, and the LeCroy oscilloscope sampling the data was triggered by markers from the signal generator to allow the individual sections to be identified in the returned waveform.

Preliminary calibration tests to prepare the apparatus were carried out in an underground experimental tank, which measures 8 m×8 m×5 m deep. The equipment was lowered into the tank such that the transducer focus was 1.5 m underwater, the same depth as anticipated in the sea trials, and the pump signal amplitude measured with a constant input signal level at each of the four frequencies using a Bruel & Kjaer 8103 hydrophone conditioned with a 2635 charge amplifier. This allowed the frequency response of the pump transducer to be inverted, and a constant and known pump signal amplitude to be employed.

The oceanic tests were performed in the North Sea between the 26th and 30th of November 1995, on a beach in Tunstall, East Yorkshire, and were carried out in tandem with a group from the Southampton Oceanography Centre. The beach was chosen due to its slight gradient, which allowed the equipment to be set up at low tide and anchored to the beach, such that as the tide came in it would eventually cover the rig to enable measurements to be taken. The rig was weighed down with 75-kg metal weights at each corner which were buried in the sand. The data collection used a 3000-Pa pump signal amplitude, and 25 four-frequency samples were taken over a 3.5-min period every half hour while the transducers were immersed. As the signals were broadcast consecutively with no gap, each measurement lasted only 0.4 s.

Every attempt was made to ensure that the scaffolding and canister created as little disturbance to the flow of water and bubble generation mechanisms as possible, by setting the transducers remote from the body of the canister and angling the ring transducer to the expected direction of the flow. The results presented in this text were taken at high tide when the transducers were 1.5-m underwater, so even though the equipment setup had to be of robust construction due to the inhospitable nature of the local sea dynamics, the measurements should represent a reasonable sample of the bubble population there.

III. RESULTS AND DISCUSSION

A typical spectrum from the sea trials is presented in Fig. 7, taken from a 28-kHz insonification. The particular data were collected at high tide (22.30) on the 29th of November 1995, when the wind speed at 10 m above sea level was 11 m/s, and the transducers were immersed at a depth of approximately 1.5 m in water approximately 3-m deep. The data show the heterodyned signal from the high-frequency receiver, in which the imaging signal is visible at 1.5 kHz (not at dc due to the Doppler shift from the moving bubble targets). The sum frequency spectral information contained just above the imaging signal is also shown, at approximately 29.5 kHz, and the difference data shown at 26.5 kHz. These signals would overlap were the measured bubbles stationary. Between the two combination frequency peaks is a

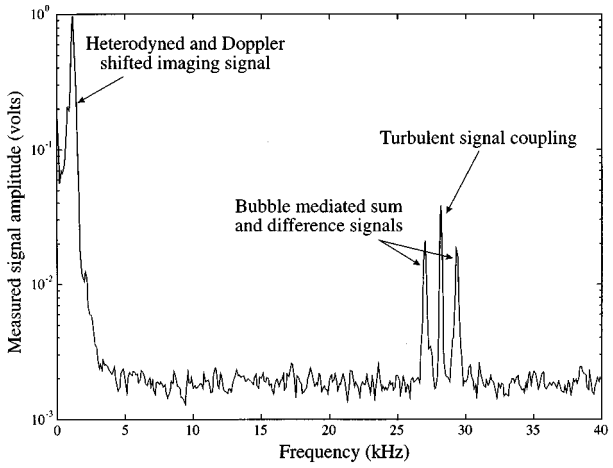

FIG. 7. Typical results from the oceanic measurements, showing the heterodyned frequency content. The particular data were collected at 28-kHz pump frequency and an amplitude of 3000 Pa. Clearly visible are the Doppler shifted imaging signal, the two combination frequency bubble indicators, and a single peak caused by turbulent coupling which is easily differentiated from the bubble-mediated peaks.

single spike at 28 kHz. This is caused by the nonlinear combination of the pump and imaging signals by turbulence in the detection zone, and can be therefore distinguished from the actual bubble-mediated information.

The data collected in each of the 25 time intervals were broken into 10 adjacent sections and the averaged power spectral density determined. These were then analyzed individually to get the energy contained in each of the heterodyned sum signals, and the result converted back to volts. Following that, the 25 samples were averaged to allow comparisons with existing time-averaged bubble data. This averaged measured voltage level was then corrected with the estimate for the sensitivity of the receiver transducer and the measured frequency responses of the preamplifier and heterodyner to give a measured bubble sound pressure level. This was converted into the number of bubbles per micrometer radius range by dividing the estimate with the theoretical 3-dB spread of the $\omega_i + \omega_p$ signal, and scaled to give the number per unit volume by dividing by the estimated insonification volume. This was repeated at each of the four frequencies.

The data are shown in Fig. 8 compared with historical data, taken from Farmer and Vagle,[5] Breitz and Medwin,[17] and Johnson and Cooke[18] who have all previously applied different bubble estimators to oceanic distributions. The plot shows the three sets of data superposed with the time-averaged population measured using the two-frequency technique. The results show that the bubble population measured using the two-frequency technique considerably exceeds the other estimates over the whole radius range. This is to be expected as the data were collected in the surf zone where because of the continual wave action a high concentration of bubbles is created. Farmer and Vagle collected their data from bubble scatter in a 4-km-deep channel using upwards facing sonar designed to listen for the linear backscatter from the bubble population. The data presented were taken in a 12–14 m/s wind speed. Johnson and Cooke used photo-

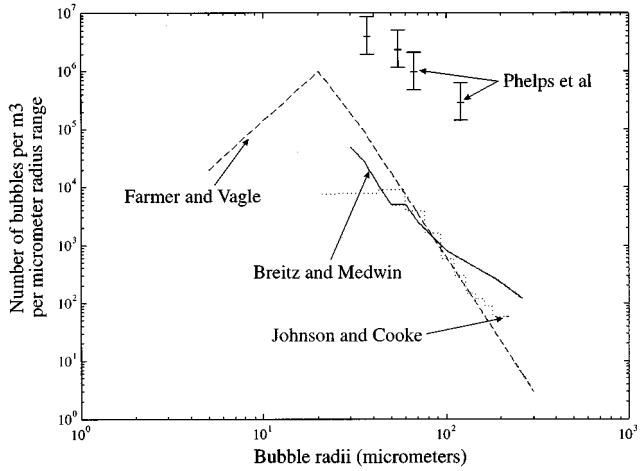

FIG. 8. Comparison of time-averaged data measured in the oceanic surf zone with historical estimates, taken from Farmer and Vagle,[5] Breitz and Medwin,[17] and Johnson and Cooke.[18] The error bars on the surf zone measurements mostly reflect an uncertainty in the measurement volume. The bubble population is expressed as the number of bubbles of a specific radius over a 1-μm range, per unit volume.

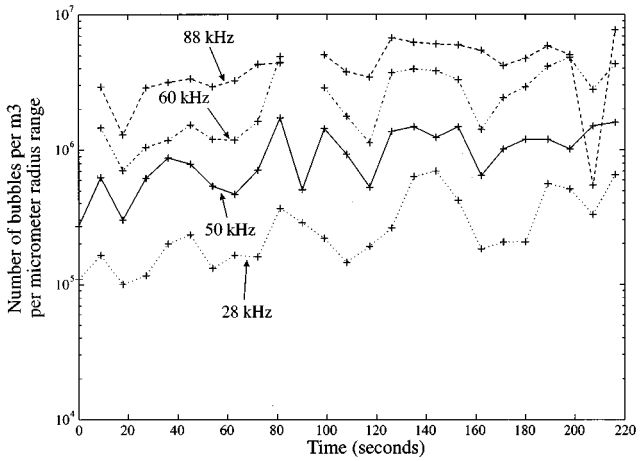

FIG. 9. Time-variant information at the four frequencies used, which represents resonant bubbles of radii 120, 66, 55, and 37 μm. This is the same data as were averaged to produce Fig. 8, and therefore have the same error margins as the data on that plot.

graphic estimates in 20–30-m-deep water, of which the population estimate at 0.7-m depth and 11–13 m/s wind speed is included. Breitz and Medwin collected their oceanic data with a flat plate resonator, which again exploits the linear resonance of bubbles. They measured in water 120-m deep in 12–15 m/s wind speeds and at a depth of 25 cm. Thus, although the environmental measurement conditions were similar over the four sets of collected data, the local sea dynamics were very different for the Tunstall measurements owing to the presence of surging breakers. The heights of the error bars on the data points will be discussed in the next section.

A further advantage of the method employed here is the speed of the data collection. The data are collected in a series of 0.4-s ''snapshots,'' being the time required to output the pump signal at all four frequencies and collect the heterodyned data onto the storage oscilloscope. This therefore allows the time variant nature of the bubble population to be investigated, rather than the technique requiring the time averaging inherent in earlier studies. Although the actual data acquisition is very fast, there is a longer delay caused by the transfer of the oscilloscope files onto the PC, of around 4 s. For the data collected in the oceanic tests an additional 5-s delay was added between successive snapshots to enable a longer and therefore more representative section of time to be taken (of around $3\frac{1}{2}$ min), as this study was primarily concerned with measuring time-averaged data for comparison with earlier oceanic measurements. All the processing of the raw data was performed later. The time variant nature of the measurements is demonstrated in Fig. 9. The four different frequencies all show peaks in the signal at around 40 s and again at 140 s, and all demonstrate a dip in the signal at 110 s and again at 160 s. It should be noted that on occasions during the analysis the signal height peaked below the noise floor, and in these cases the particular readings have been left as gaps.

IV. POSSIBLE SOURCES OF ERROR

The data collection technique was employed to measure a real bubble population in the sea, and as a preliminary data collection exercise the bubble measurement apparatus was incorporated into a surf zone monitoring program which was being conducted by the Southampton Oceanographic Centre. Thus the field data were necessarily collected in a dense bubble population. To prevent the bubble signals being screened by nearby bubbles in this dense environment, the high-frequency transducers had to be located close to the intended measurement area, and eventually a distance of 90 mm from the faces of both the transmitter and receiver transducers was chosen. However, as the high-frequency crystals are 31- and 28-mm-diam, respectively, this measurement volume is in the near field of both. This represents a trade-off in the measurement procedure, as although the bubble sizer gave the required high-spatial resolution and signal strength, the actual determination of the insonification volume is considerably harder to estimate, and the experimental insonification conditions are less well-defined. This gives an error associated with the data collection which is larger than that which would be achieved in more typical measurement conditions, where the risk of signal corruption and screening is less, allowing the transducers to be set to insonify a volume of fluid which is in the far field of each. The analytical estimate of the insonification volume of 0.2 cm^3 is taken to be where the combined sensitivity of the two transducers falls to 3 dB of the maximum level, and it is considered that the volume estimate is only accurate to $+200\%$ and -50%, which is reflected in the height of the error-bars in Fig. 8.

A further systematic error is included in the calibration of the hydrophone sensitivity using the comparison of the theoretical model and the laboratory measured data. The predicted height of the $\omega_i + \omega_p$ signal is 20% higher than the measured data, suggesting either that even with the revised model the damping is still not perfectly represented or that the laboratory insonification conditions were imperfectly known. Harder to evaluate is the effect of this discrepancy as

the bubble sizes get smaller. For the high-resonance frequency bubbles, the primary source of the damping is thermal losses, which is the least well-defined of the three mechanisms. As an indication, the assumed value for κ for the 88-kHz bubbles (estimated using Eller's theory) is 1.23, but using the analysis presented by Prosperetti[19] in his reworking of the thermal effects in a forced bubble, it is 1.25. It would appear that at the low driving amplitudes employed, this is not sufficiently different to contribute an error of the same order as the volume estimate, although the systematic error of 20% has been included in the error spread calculations over the entire frequency range.

Also as the bubble radii become smaller, the effects of surface tension become much larger, and the model becomes more dependant on a less clearly defined parameter. Thorpe[20] supposes that over the course of a few tens of seconds ''clean'' bubbles of small radius in the sea become ''dirty,'' that is coated in surfactant, and gives an estimate for the surface tension parameter σ of 0.036 N/m for these dirty bubbles, and 0.072 N/m for the clean bubbles. He estimates that the lifetimes of bubbles are considerably longer than the time it takes to become dirty, and therefore treats all bubbles as such, but it is evident that under a breaking wave such as experienced in these experimental conditions, the surfactant coating of the measured bubbles is harder to determine. However, this will not contribute significantly to the measurement error, as the smallest bubble size considered in the tests is still large enough not to be affected overly by this. For example, for those bubbles resonant at 88 kHz, the Laplace pressure inside a motionless clean bubble due to the surface tension is $\sim$4000 Pa, i.e., approximately 4% of the total internal pressure. As the bubbles in the ocean will fall between the two surface conditions, the surface tension should only account for between 2% and 4% of the internal pressure even for these smallest bubbles.

Though measured in our experiment, it is apparent that certain insonification parameters need not be well-defined, as the same transducer arrangement is used in both the laboratory calibration and the actual sea trials. An example is the absolute amplitude of the imaging signal at 30 kPa, as the theory indicates that the height of the $\omega_i + \omega_p$ signal scales linearly with this parameter. Thus an error in the estimate of the amplitude will affect the calculated sensitivity of the high-frequency transducer, but this effect will be removed when the sensitivity correction is applied to the oceanic bubbles. Another parameter which will be insensitive to poor definition in the model is the distance of the bubbles from the measurement transducer, although this will affect the calculation of the insonification volume.

V. CONCLUSIONS

The paper has described the design and implementation of an oceanic bubble measurement device capable of sampling a small volume, and presented the results taken from initial studies in the shallow and high bubble density surf zone. Unlike previous oceanic measurements, the technique employed here provides an unambiguous and potentially more accurate estimate of the local bubble population. Additionally, as the device collects data over a period of only 0.4 s for all four frequencies, the results can be used to investigate the temporal changes in the bubble distribution. To our knowledge, these are the first measurements of the bubble spectral density in the shallow surf zone, and it is planned to mount the equipment from a buoy in the deeper ocean where historical studies have been made, which will enable comparative data to be collected. The main source of error in the estimates of the population arises through an imperfect knowledge of the insonification volume, as the high bubble densities measured required the employment of a very small insonification volume. This was necessarily located in the near field of both high-frequency transducers. However, this limitation will be removed for the planned lower density studies by the use of a larger measurement volume.

ACKNOWLEDGMENTS

The authors wish to extend their thanks to David Baldwin, Alan Hall, and Professor Steve Thorpe from the Southampton Oceanography Centre for their assistance with the beach tests, and to Rob Stansbridge, Daniel Russell, John Taylor, Mike Bartlett, Dave Edwards, John Hawkes, and the Southampton University Physics Technical Workshop for their help with the design and manufacture of the oceanic rig. Thanks also are extended to Dr. Ulrich Pollmann for helpful discussion. The work was funded using a NERC award (ref. GR3 09992), and Mr. Ramble was funded by EPSRC (ref. GR/H 79815).

[1] D. K. Woolf, ''Bubbles and the air-sea transfer velocity of gases,'' Atmosphere-Ocean **31**, 451–474 (1993).
[2] T. J. Lin and H. G. Donnelly, ''Gas bubble entrainment by plunging laminar liquid jets, '' AIChE. J. **12**, 563–571 (1966).
[3] E. O. Belcher, ''Quantification of bubbles formed in animals and man during decompression,'' IEEE Trans. Biomed. Eng. **27**, 330–338 (1980).
[4] T. G. Leighton, *The Acoustic Bubble* (Academic, London, 1994).
[5] D. M. Farmer and S. Vagle, ''Waveguide propagation of ambient sound in the ocean-surface bubble layer,'' J. Acoust. Soc. Am. **86**, 1897–1908 (1989).
[6] T. G. Leighton, D. G. Ramble, and A. D. Phelps, ''The detection of tethered and rising bubbles using multiple acoustic techniques,'' J. Acoust. Soc. Am. (in press).
[7] A. D. Phelps and T. G. Leighton, ''High resolution bubble sizing through detection of the subharmonic response with a two frequency excitation technique,'' J. Acoust. Soc. Am. **99**, 1985–1992 (1996).
[8] V. L. Newhouse and P. M. Shankar, ''Bubble sizing using the nonlinear mixing of two frequencies,'' J. Acoust. Soc. Am. **75**, 1473–1477 (1984).
[9] J. Y. Chapelon, P. M. Shankar, and V. L. Newhouse, ''Ultrasonic measurement of bubble cloud size profiles,'' J. Acoust. Soc. Am. **78**, 196–201 (1985).
[10] P. M. Shankar, J. Y. Chapelon, and V. L. Newhouse, ''Fluid pressure measurement using bubbles insonified by two frequencies,'' Ultrasonics **24**, 333–336 (1986).
[11] D. Koller, Y. Li, P. M. Shankar, and V. L. Newhouse, ''High speed bubble sizing using the double frequency technique for oceanographic applications,'' IEEE J. Oceanic Eng. **17**, 288–291 (1992).
[12] B. E. Noltingk and E. A. Neppiras, ''Cavitation produced by ultrasonics,'' Proc. Phys. Soc. London, Ser. B **63**, 674–685 (1950).
[13] E. A. Zabolotskaya and S. I. Soluyan, ''Emission of harmonic and combination-frequency waves by air bubbles,'' Sov. Phys. Acoust. **18**, 396–398 (1973).
[14] E. A. Neppiras, ''Acoustic cavitation,'' Phys. Rep. **61**, 159–251 (1980).
[15] A. I. Eller, ''Damping constants of pulsating bubbles,'' J. Acoust. Soc. Am. **47**, 1469–1470 (1970).
[16] R. Clift, J. R. Grace, and M. E. Weber, *Bubbles, Drops and Particles* (Academic, New York, 1978).

[17] N. Breitz and H. Medwin, ''Instrumentation for in situ acoustical measurements of bubble spectra under breaking waves,'' J. Acoust. Soc. Am. **86**, 739–743 (1989).
[18] B. D. Johnson and R. C. Cooke, ''Bubble populations and spectra in coastal waters; a photographic approach,'' J. Geophys. Res. **84**, 3761–3766 (1979).
[19] A. Prosperetti, ''Thermal effects and damping mechanisms in the forced radial oscillations of gas bubbles in liquids,'' J. Acoust. Soc. Am. **61**, 17–27 (1977).
[20] S. A. Thorpe, ''On the clouds of bubbles formed by breaking wind-waves in deep water, and their role in air–sea gas transfer,'' Philos. Trans. R. Soc. London, Ser. A **304**, 155–210 (1982).

Elastic characterization of isotropic materials by a single test based on the experimental determination of natural frequencies using laser interferometry

A. Bayón and A. Varadé
Departamento de Fisica Aplicada a los Recursos Naturales, ETSI Minas, Universidad Politécnica de Madrid, Rios Rosas 21, 28003 Madrid, Spain

F. Gascón
Departamento de Física Aplicada, ETS Arquitectura, Universidad de Sevilla, Avd. Reina Mercedes 2, 41012 Sevilla, Spain

(Received 5 August 1996; accepted for publication 11 November 1996)

An experimental method is proposed for the elastic characterization of an isotropic material based upon the vibration natural frequencies recorded by means of a single assembly and experiment. Speckle heterodyne optic interferometry is applied to detect the tangential component of the vibration at a point. The sample is a slender rod excited through a broad-spectrum percussion, where the vibration recorded is a superposition of the transverse and torsional natural modes. Spectral analysis of the vibration allows the identification of the transverse and torsional natural frequencies. This is followed by calculation of the elastic moduli. © *1997 Acoustical Society of America.* [S0001-4966(97)03204-9]

PACS numbers: 43.35.Cg, 43.35.Yb [HEB]

INTRODUCTION

In recent years laser technology has been increasingly applied to the elastic characterization of materials through nondestructive dynamic tests.[1–5] By means of these methods the elastic constants are preferentially determined from the measurement of ultrasonic velocities. Lasers are usually used to generate and detect ultrasound at a distance, in the absence of contact with the sample. This has made it possible to determine the elastic constants of different materials both at room and at elevated temperatures. These methods have thus contributed to improve understanding of the elastic characteristics of new materials required in modern technological designs.

Another nondestructive dynamic method used to determine elastic constants is based upon measurements of the natural frequencies of samples of known geometry. In this method, at least two different experiments are required to characterize an isotropic material: one to measure the longitudinal or flexional natural frequencies, and the other to establish the corresponding torsional natural frequencies. Laser techniques have also been applied to the study of vibration frequencies,[6,7] and to the elastic characterization of isotropic materials.[8]

The present study applies the above-mentioned technique,[8] with the aim of determining the elastic constants of an isotropic material by means of a single experimental measurement. The methodology employed is based upon the vibrations analysis of a rod using laser interferometry.

I. METHOD

The study of the natural vibration modes of slender rods is well established.[9,10] In this context, our interest is centered on the transverse and torsional frequencies, for the reasons outlined below. The elementary analysis of transverse vibrations in slender rods yields a fourth-degree differential equation, where phase velocity is dependent upon frequency. The natural frequencies are obtained taking into account the conditions associated to the free ends. Finally, the following expression may be obtained, in which the Young's modulus E is related to the transverse natural frequencies $\nu_{T,n}$, corresponding to vibration mode number n,

$$E=\frac{64\rho L^4}{\pi^2 k'^2}\left(\frac{\nu_{T,n}}{m_n^2}\right)^2, \quad m_n=3.0112,5,7,9,\ldots, \tag{1}$$

where ρ is the density, L is the length of the rod, and k' is the radius of gyration. The latter is a function of the polar moment of inertia I and of the rod sectional area S, $k'^2=I/S$.

The analysis of the above equation shows that for a given slender rod of a certain material and geometry, the quotient $\nu_{T,n}/m_n^2$ is a constant. In consequence, if the spectrum associated to the vibration of the sample is known, it is possible to establish the values of the frequencies associated to the transverse modes, taking into account that the quotient given above must be verified for these modes. The interpretation of the results is made easier by increasing the number of modes excited and detected. Finally, the Young's modulus may be calculated by applying Eq. (1).

In order to characterize an isotropic material, its shear modulus G must also be determined. This modulus may be calculated from the torsional modes. The phase velocity of the torsional waves is $v_\tau=(G/\rho)^{1/2}$. By imposing the conditions of free ends, we obtain the frequencies $\nu_{\tau,n}$ related to the different natural vibration modes n. The shear modulus may be expressed in terms of these frequencies as follows:

$$G=4\rho L^2(\nu_{\tau,n}/n)^2, \quad n=1,2,3,\ldots, \tag{2}$$

where $\nu_{\tau,n}/n$ is a new characterizing constant.

 0001-4966/97/101(4)/1990/4/$10.00

Our aim is to excite simultaneously transverse and torsional modes in a single experiment, to obtain all the information needed to establish the elastic characteristics of the isotropic medium.

In the experimental assembly the sample used is a slender cylindrical rod, positioned horizontally, and supported at its center on a rubber. A small steel sphere is used to deliver a very brief impact to the rod, thus initiating its vibration. This form of excitation allows the rod to vibrate freely at its natural frequencies, for once the percussion has terminated no further forces act upon the sample. In addition, excitation has a broadband spectrum. In order to secure the simultaneous excitation of the transverse and torsional modes, a grazing horizontal impact is delivered perpendicular to the axis of the rod, at a point on the lateral surface close to one end. The percussion is the equivalent of an equipollent percussion applied to the center of the base plus a couple with a moment in the direction of the axis of the rod. Both transverse and torsional modes are simultaneously excited in consequence. The resulting vibration is detected at the opposite base in our experiments. The displacement component of interest is contained in the plane of the base, and the direction of the displacement to be detected is horizontal. In addition, detection should preferably be carried out at a point far from the axis, to maximize the couple-generated amplitude of motion.

In order to detect the sample vibration at a given point, a speckle heterodyne optic interferometer (OP-35-I/O from Ultra-Optec Inc.)[11,12] is employed. This system incorporates a 5-mW He–Ne laser, and its operating principle is based on the speckle phenomenon,[13,14] and on the phase shift of the light associated to the variation in optic trajectories produced by the vibration of the sample. This interferometer allows us to measure both displacement components at the same detection point, i.e., that contained in the plane of the sample (in-plane) and in the direction perpendicular to it (out-of-plane)—though not at the same instant. The bandwidth is from 1 kHz to 35 MHz, the illuminated zone has a diameter of approximately 20 μm, and the smallest detectable displacement is about 1 nm. Due to the operating principle of the system, the sample must possess a scattering surface.

In both operation modes, two beams interfere and the resulting beam is directed towards a photodiode to obtain an output signal with a carrier frequency of 40 MHz, which is phase modulated by the displacement of the study object. This signal is then processed by a demodulating unit to yield a final signal proportional to the investigated displacement component of the point on the sample surface.

The signal obtained is digitized by a 400-MHz HP54504A oscilloscope and processed with a PC microcomputer to calculate its fast Fourier transform (FFT). The natural vibration frequencies may be obtained from the spectral analysis, as they coincide with the values corresponding to the peak amplitudes. In the experiments carried out, $N=2048$ samples were obtained, and the sampling frequency was selected according to the resolution requirements and frequency interval investigated.

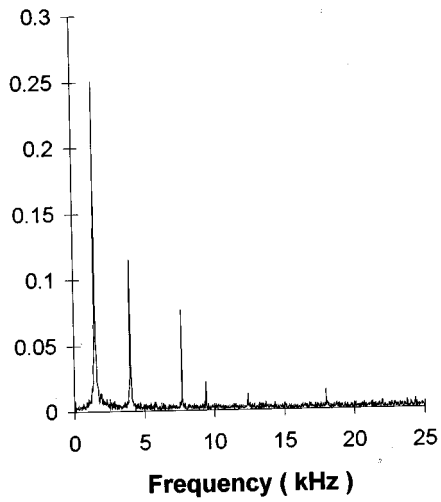

FIG. 1. Amplitude spectrum of the transverse vibration natural frequencies and the first torsional natural frequency of the rod.

II. EXPERIMENTAL RESULTS

A slender aluminum rod was used, measuring 9.00 mm in diameter and 164 mm in length. The density of the sample is 2808 kg/m^3. The base where the vibrations were detected was adequately scratched so as to secure a maximum intensity of light diffracted in the plane associated to the optic components of the interferometer. The sample was positioned horizontally, with a base parallel to the frontal panel of the interferometer, and was supported at the center point on a small rubber block so movement was hardly restrained. The center of the rod is a nodal position not only of the first torsional mode but also of the second and forth transverse modes.

The above-described method was used with the aim of allowing the rod to vibrate freely in the transverse and torsional modes. Thus, the rod was struck by a steel sphere with a diameter of about 1.5 mm, an approximate speed of 100 cm/s, and a kinetic energy of 19 mJ. The percussion applied was horizontal and perpendicular to the axis, and acted at a point of maximum height of the lateral surface, near to the base. The in-plane component of the displacements was detected at a point of the opposite base close to the lateral surface. The sampling rate used in digitizing the signal was $f_s=50$ ks/s. The FFT of this signal was then calculated, the corresponding systematic uncertainty being $f_s/N\approx 25$ Hz. The resulting spectrum is shown in Fig. 1, where the peak amplitudes correspond to the natural vibration frequencies associated to the rod and to the excitation applied. These frequencies were $\nu_1=1489$ Hz, $\nu_2=4003$ Hz, $\nu_3=7666$ Hz, $\nu_4=9375$ Hz, $\nu_5=12\,377$ Hz, and $\nu_6=17\,968$ Hz.

Based on Eqs. (1) and (2), the following expression is obtained, which corresponds to the quotient of the frequencies of the first torsion maximum and first transverse vibration maximum

$$\frac{\nu_{\tau,1}}{\nu_{T,1}}\approx 0.28\left(\frac{G}{E}\right)^{1/2}\frac{L}{R}. \tag{3}$$

Taking into account that the Poisson's ratio of materials

$\mu=(E/2G)-1$ ranges between 0 and 0.5, the Young's modulus will be between $2G$ and $3G$; this implies that, depending on the characteristics of the material, the proportion $\nu_{\tau,1}/\nu_{T,1}$ for the first mode is comprised within the interval $0.16L/R<\nu_{\tau,1}/\nu_{T,1}<0.20L/R$. In consequence, and independently of the material employed, $\nu_{\tau,1}$ will be greater than $\nu_{T,1}$ if $0.16L/R>1$, i.e., if $R/L<0.16$. This condition must always be met in the case of slender rods for which Eqs. (1) and (2) are applicable. Specifically, in the case of the rod investigated in the present study, $R/L=0.027$.

The above analysis indicates that the first harmonic detected experimentally, $\nu_{T,1}=1489$ Hz, in being the lowest, corresponds to the first transverse mode. Taking into account Eq. (1), it is deduced that $\nu_{T,n}/m_n^2=$const and since $\nu_{T,1}=1489$ Hz, it is possible to determine the expected theoretical values for the higher-order transverse modes. Specifically, the theoretical values obtained were 4105, 8046, 13 301, 19 870, 27 752 Hz,..., for the second, third, etc., modes, respectively. On comparing these theoretical values with those obtained experimentally and shown in Fig. 1, it is deduced that the second harmonic detected corresponds to the second transverse mode $\nu_{T,2}=4003$ Hz, the third to $\nu_{T,3}=7666$ Hz, the fifth to $\nu_{T,4}=12\,377$ Hz, and the sixth to $\nu_{T,5}=17\,968$ Hz. The variations with respect to the expected values are 2%, 4.7%, 6.9%, and 9.6%, respectively.

According to the previously derived theoretical values, the fourth frequency detected experimentally does not correspond to any transverse mode. Taking into account the type of excitation applied, if not transverse, this fourth experimental frequency will represent the first torsional frequency, i.e., $\nu_{\tau,1}=9375$ Hz. It is of interest to point out that the interval in which the first torsional frequency is to be found may be predicted if the first transverse natural frequency is previously known, for according to the above reasoning $0.16\nu_{T,1}L/R<\nu_{\tau,1}<0.20\nu_{T,1}L/R$. In the case studied, 8682 Hz$<\nu_{\tau,1}<$10853 Hz—a result that agrees with the value obtained.

We propose another method to determine whether the natural vibration frequencies found correspond to one or another vibration mode. The technique proposed is based in part upon Eq. (1), i.e., to the degree in which the equation is applicable to a given rod, the expression $\nu_{T,n}/m_n^2=k$ is verified—k being a constant independent of the frequency $\nu_{T,n}$. We now suppose that the six natural frequencies recorded, ν_i, correspond to transverse modes. However, we do not know the mode number corresponding to each ν_i. Then a table is prepared where the quotients ν_i/m_n^2 for all the possible values of m_n (at least for the first 6) are determined

Figure 2 in turn presents the frequencies ν_i plotted along the abscissas axis, and the quotients ν_i/m_n^2 on the ordinates axis. A logarithmic scale was chosen for the vertical axis to allow a sufficiently spaced representation of all the values in the table. At first glance, Fig. 2 shows that only five points possess the same ordinate value, i.e., only five points verify Eq. (1). Therefore, the only transverse vibration frequencies are ν_1, ν_2, ν_3, ν_5, and ν_6.

The above reasoning is also applicable to the torsional oscillations. In effect, Eq. (2) shows that whenever it is applicable, and for a given rod, the quotient $\nu_{\tau,n}/n$ must be

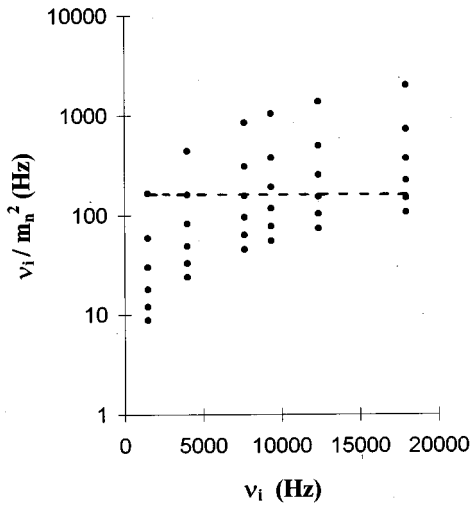

FIG. 2. The natural vibration frequencies ν_i detected are represented on the abscissas axis, with the ν_i/m_n^2 values corresponding to the different transverse modes plotted on the ordinates axis. The scale of the vertical axis is logarithmic.

constant, regardless of the frequency. If a second table is prepared representing ν_i/n as a function of ν_i, followed by the corresponding graphic representation, a first inspection quickly shows that no single pair of points is situated at the same height. In consequence, of the six frequencies detected, no more than one corresponds to a torsional mode vibration.

The aforementioned differences 2%,...,9.6%, between our experimental values and the theoretical ones, may be due to the elementary theory applied. When the ratio R/L or the frequency increase, the elementary theory fails.[15]

A second experiment was carried out with the aim of providing further data to confirm the frequency selection made. In the new assembly, only the excitation and detection plane were varied. The aim was to excite only the transverse modes; in consequence, the impact was applied to a point on the lateral surface close to one end and contained in the horizontal plane passing through the axis. The direction of impact was horizontal and perpendicular to the axis, and the tangential component of displacement was detected at a point of the opposite base in proximity to the center. The spectrum obtained corresponding to the detected signal is shown in Fig. 3. According to the excitation applied, the amplitude peaks are associated to the transverse vibration natural frequencies. The values obtained were $\nu_{T,1}=1489$ Hz, $\nu_{T,2}=4003$ Hz, $\nu_{T,3}=7666$ Hz, $\nu_{T,4}=12\,353$ Hz, $\nu_{T,5}=17\,968$ Hz, and $\nu_{T,6}=24\,316$ Hz, which correspond to the transverse modes. As seen on comparing Figs. 1 and 3, the transverse frequencies are accurately coincident, though a higher order transverse mode is also observed in Fig. 3. A characteristic frequency is seen in Fig. 1 that distinguishes it from Fig. 3, i.e., the torsional frequency $\nu_{\tau,1}=9375$ Hz.

Lastly, we determined the elastic characteristics of the material. The data used were obtained from Fig. 1, i.e., the frequency of the first transverse mode and of the first torsional mode. On applying Eqs. (1) and (2), values of $E=70\,164$ MPa and $G=26\,551$ MPa were obtained.

As a final verification, we determined the natural fre-

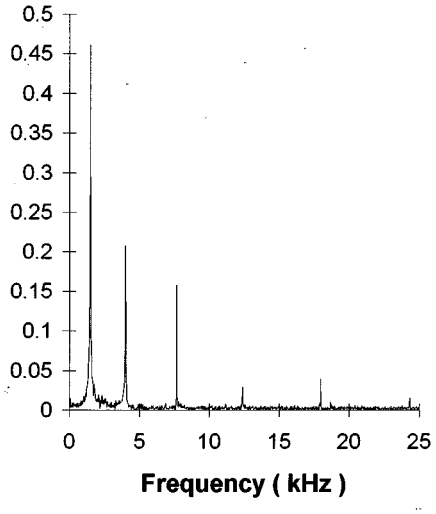

FIG. 3. Amplitude spectrum of the transverse vibration natural frequencies, showing the first six harmonics.

quencies corresponding to the longitudinal modes. The methodology described in Sec. I was adopted. A perpendicular percussion was applied at the center of one base. The out-of-plane component of the displacements was detected at a point of the opposite base. The frequency obtained for the first longitudinal mode was 15 332 Hz. Taking into account that the longitudinal frequencies are related to E,[9] a value $E=71\,013$ MPa was obtained by applying the elemental slender rod theory. This value differs 1.2% with respect to the value obtained previously from the transverse frequencies. *The Metals Handbook*[16] provides for aluminum a static modulus of $E=62$ GPa and a value of $G=25$ GPa. These values show that the static moduli are smaller than the dynamic ones, like it is known. Nevertheless, the values that are cited in the bibliography are in a wide range,[16,17] among other reasons, due to the different composition of the samples.

III. CONCLUSIONS

The present study demonstrates how the elastic properties of an isotropic material may be determined from the data obtained by a single experimental assembly and experiment. The method proposed is based on speckle interferometry, which allows detection of the in-plane vibration component at a given point. If the study sample is conveniently excited, the tangential component is related to the displacement associated to the vibration corresponding to the superposition of the transverse and torsional modes. Spectral analysis of the displacement recorded at a given point in turn allows us to identify the frequencies associated to the different modes, and to derive the information required to establish the corresponding Young's modulus and Poisson's ratio.

Unlike the traditional techniques in which at least two different assemblies are needed to determine the elastic characteristics from resonance frequencies, the proposed procedure requires only one experimental assembly with a single experiment, and the methodology employed is both simple and direct. Moreover, it offers the well-established advantages of laser interferometry, where detection is carried out at a point, without contact, and a broadband frequency response is achieved, which makes possible to simultaneously register various vibration modes.

The procedure is highly reproducible, for we have found that for different percussion intensities the displacement recordings and corresponding spectra differ in the amplitudes of the modes detected, but not in the values of the natural frequencies. By obtaining several frequencies simultaneously, complementary information is obtained that in turn allows us to precisely characterize the study material.

This method represents an experimental step forward, for it considerably reduces the time required to characterize materials. Once the system is prepared, the time required for characterization is only dictated by computer processing of the data—which at present may be regarded as almost instantaneous.

[1] J. F. Chain and T. T. Wu, ''Determination of anisotropic elastic constants using laser-generated surface waves,'' J. Acoust. Soc. Am. **95**, 3232–3241 (1994).
[2] C. A. Calder, E. C. Draney, and W. W. Wilcox, ''Noncontact measurement of the elastic constants of plutonium at elevated temperature,'' J. Nucl. Mater. **97**, 126–136 (1981).
[3] B. Catagnede, K. Yul Kim, W. Sachse, and M. O. Thompson, ''Determination of the elastic constants of anisotropic materials using laser-generated ultrasonic signals,'' J. Appl. Phys. **70**, 150–157 (1991).
[4] J. D. Aussel and J. P. Monchalin, ''Precision laser-ultrasonic velocity measurement and elastic constant determination,'' Ultrasonics **27**, 165–177 (1989).
[5] A. Varadé, A. Bayón, P. N. J. Rasolofosaon, and F. Gascón, ''Experimental results on bulk waves and Rayleigh waves in slate,'' J. Acoust. Soc. Am. **99**, 292–298 (1996).
[6] A. Bayón, F. Gascón, and A. Varadé, ''Measurement of the longitudinal and transverse vibration frequencies of a rod by speckle interferometry,'' IEEE Trans. Ultrason. Ferroelectr. **40**, 265–269 (1993).
[7] M. L. Lyamshev, J. Stanullo, and G. Busse, ''Thermo Acoustic Vibrometry,'' Mater. Prüfung (Mater. Test.) **37**, 22–24 (1995).
[8] A. Bayón, A. Varadé, and F. Gascón, ''Determination of the elastic constants of isotropic solids by optical heterodyne interferometry,'' J. Acoust. Soc. Am. **96**, 2589–2592 (1994).
[9] L. E. Kinsler, A. R. Frey, A. B. Coppens, and J. V. Sanders, *Fundamentals of Acoustics* (Wiley, New York, 1982), Chap. 3, pp. 70–75.
[10] K. F. Graff, *Wave Motion in Elastic Solids* (Dover, New York, 1975), pp. 125–127, 140–209.
[11] J. P. Monchalin, ''Optical detection of ultrasound,'' IEEE Trans. Ultrason. Ferroelectr. **33**, 485–499 (1986).
[12] J. P. Monchalin, J. D. Aussel, R. Heon, C. K. Jen, A. Boundreault, and R. Bernier, ''Measurement of in-plane and out-of-plane ultrasonic displacements by optical heterodyne interferometry,'' J. Nondestruct. Eval. **8**, 121–132 (1989).
[13] J. W. Goodman, ''Statistical properties of laser speckle patterns'' in *Laser Speckle and Related Phenomena*, edited by J. C. Dainty (Springer-Verlag, Berlin, 1984), Chap. 2, pp. 9–75.
[14] A. E. Ennos, ''Speckle interferometry,'' in *Laser Speckle and Related Phenomena*, edited by J. C. Dainty (Springer-Verlag, Berlin, 1984), Chap. 6, pp. 203–253.
[15] A. W. Leissa and J. So, ''Comparisons of vibration frequencies for rods and beams from one-dimensional and three-dimensional analyses,'' J. Acoust. Soc. Am. **98**, 2122–2135 (1995).
[16] *Metals Handbook* (American Society for Materials, Metals Park, OH, 1990), 10th ed., Vol. 2, p. 1100.
[17] J. A. Pero-Sanz, *Ciencia e Ingeniería de Materiales* (Dossat 2000, Madrid, 1996), p. 577.

Optical pulse width measurements of sonoluminescence in cavitation-bubble fields

Thomas J. Matula, Ronald A. Roy,[a] and Pierre D. Mourad
Applied Physics Laboratory, University of Washington, 1013 NE 40th Street, Seattle, Washington 98105

(Received 31 July 1996; accepted for publication 8 November 1996)

Optical pulse width measurements of sonoluminescence from cavitation-bubble fields have been obtained for two well-defined cavitation zones in an aqueous solution of Glycerin using a fast (650 ps rise-time) PMT and a fast (10 GS/S) digitizer. One zone corresponds to cavitation produced from an ultrasonic homogenizer. A lens was used to focus on a particular region of ''streaming'' sonoluminescence. A second, more localized cavitation zone was produced using a 2-in-diam PZT driving crystal in a rectangular fluid-filled container. Single-bubble sonoluminescence was used to characterize the response of the PMT to low-level light input. The measured rise-time and pulse width for sonoluminescence from cavitation fields is indicative of the response of the PMT and suggests that the pulse width of cavitation-field sonoluminescence is much less than 1.1 ns. © *1997 Acoustical Society of America.* [S0001-4966(97)03004-X]

PACS numbers: 43.35.Ei, 43.35.Sx [HEB]

INTRODUCTION

Sonoluminescence (SL) refers to the phenomenon of light emission during acoustic irradiation of a liquid and is associated with cavitation bubbles present in the liquid. Sonoluminescence can be subdivided into at least two regimes that depend on the relative density of bubbles present, SBSL and CFSL. Single-bubble sonoluminescence (SBSL) refers to sonoluminescence from a single bubble in a degased (usually aqueous) liquid.[1] The bubble is acoustically levitated in a standing wave field by means of the primary Bjerknes force.[2,3] At driving pressures near 1 bar the bubble oscillates in a highly nonlinear fashion, emitting a short flash of light at or near the minimum bubble radius.[4] The bubble does not appear to disintegrate and coalesce during each acoustic cycle, but rather appears to remain intact throughout the cycle, repeating its behavior during subsequent cycles in a synchronous fashion.[5]

In addition to the highly regular dynamics associated with SBSL, the light emission from SBSL also has unique properties. Its spectrum appears to be continuous, with no molecular or atomic emission bands.[6,7] Also, and of special interest here, is that the optical pulse duration of SBSL is extremely short, apparently less than 12 ps in duration.[8]

The amazing properties of SBSL have led to equally amazing theoretical models to explain the observed behavior. The absence of emission bands together with the extreme brevity of the flash implies that SBSL is not due to an adiabatic collapse of the bubble. Such a collapse would most certainly require that the bubble stays hot for an extended period of time. One popular theory that appears to explain some of the observed results involves the geometrical convergence of shock waves.[9,10] Another theory holds that a microplasma is generated inside the bubble, resulting in an electrical discharge.[11] Still other theories involving molecular collisions[12] or dynamical Casimir energies[13] have been introduced to explain the observations of SBSL.

In trying to explain the physics behind SBSL, one should keep in mind that SL from cavitation-bubble fields has been observed and studied for many years.[14,15] This form of sonoluminescence is CFSL, or cavitation-field sonoluminescence, and refers to sonoluminescence from multi-bubble acoustic cavitation fields—a complex distribution of gas and vapor-filled bubbles of various equilibrium sizes that pulsate at various phases relative to the driving acoustic field. During the negative portion of the applied sound field, some of the bubbles may grow dramatically, followed by a Rayleigh-like collapse (either immediately or after several cycles of prolonged growth) that results in the emission of light. Unlike the behavior of single bubbles in SBSL, these bubbles presumably disintegrate into micro-bubbles that then coalesce during subsequent acoustic cycles to repeat the process.

The CFSL is readily generated using an ultrasonic horn (homogenizer) immersed in the fluid. The resulting pressure field within the cell is extremely complex. Standing wave regions may exist, though this is not required for CFSL (SL from the tip of the horn is common). Peak pressures within the cell may be 10 bar or higher. Unlike SBSL, CFSL is easily generated in nonaqueous solutions. The associated spectra show molecular and atomic emission bands influenced by the fluid.[14,16] The intensity and width of the emission spectrum can be used to infer the approximate temperature and pressure of the emission zone provided one has sufficient knowledge of the system to model the emission process. Using synthetic spectra, Flint and Suslick inferred a temperature of approximately 5000 K for CFSL from silicon oil.[17]

Theoretical models that describe MSBL fall into two main categories, thermal and electrical. The most common model involves the near-adiabatic collapse of bubbles and the subsequent emission of light due to radical recombination,[18] although shock wave formation has also been mentioned as a mechanism for CFSL.[19] Electrical theo-

[a]Current address: Boston University, Dept. of Aerospace and Mechanical Engineering, 110 Cummington Street, Boston, MA 02215.

ries (such as Kurochkin *et al.*[20]) have typically been discounted due to observations that seem to indicate a thermal origin to CFSL.[21]

The theoretical description of the dynamics of the individual bubbles is made difficult due to the presence of other bubbles, boundaries, a complicated pressure field within the fluid, and, in general, the statistical nature of cavitation fields. Descriptions of the effects of sonication usually rely on chemical kinetics equations. Inferences are then made to describe the conditions within the bubble necessary for the observed kinetics. A recent model for the dynamical behavior of bubbles suggests that temperatures within a 26-μm equilibrium size bubble driven at 20 kHz can remain ''hot'' for tens of nanoseconds.[18] It is important to note that this calculation does not match the actual conditions of our experiment and is only mentioned here to illustrate the possible difference between pulse widths from SBSL bubbles and bubbles in cavitation fields. It should also be noted that a simple adiabatic model would predict high temperatures on the order of a nanosecond only, though such a model is invalid under the conditions of sonoluminescence.

On the surface it appears that CFSL and SBSL are completely different processes. It is also apparent that the commonality of cause (acoustic cavitation) and effect (light emission) for both types of SL suggests some association of the underlying physics. Indeed, there is a resemblance of the continuum structure in the spectra for both CFSL and SBSL as evidenced by a recent experiment involving the comparison of SBSL and CFSL spectra from aqueous solutions.[7] The near-adiabatic collapse theory for CFSL provides another opportunity for comparisons between SBSL and CFSL. The SBSL flashes are extremely short and a major difference in the pulse widths between CFSL and SBSL may provide clues into the mechanism for SL in general. Measurements of CFSL flash widths have been previously reported to be less than 12 ns.[20,22,23] Using more contemporary instrumentation, we believed that a more well-defined pulse width, or range of pulse widths, could be made. Thus, we have attempted to measure the temporal flash duration of CFSL in order to make more quantitative comparisons with SBSL pulse durations.

I. EXPERIMENT

The CFSL experiments were carried out in a solution of 80% glycerin in air-saturated, filtered water, within a light-tight enclosure. Air was used to keep from having to provide a gas-tight enclosure. To offset the decrease in expected SL intensity by using air, instead of say, argon, glycerin was added to the solution. Furthermore, the temperature of the solution was brought to approximately 10 °C to aid in providing brighter sonoluminescence. No other additives, such as wavelength shifters, were used. We note that the glycerin solution will modify the bubble dynamics somewhat compared to the use of water alone. These changes obviously affect the light intensity. It is unknown if pulse durations are also affected, though, in separate preliminary tests in water alone, the pulse durations in water also appear similar to those in the glycerin solution.

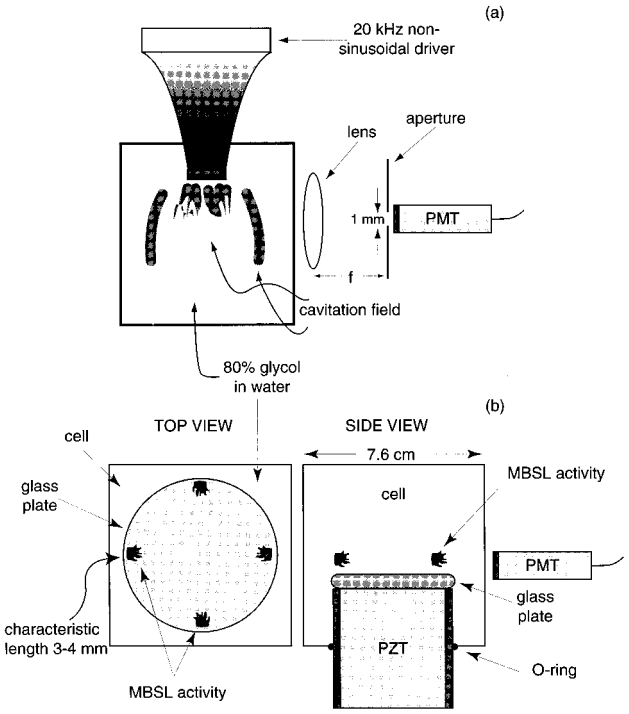

FIG. 1. (a) The tip of the homogenizer is placed approximately 1 cm below the fluid level, centered within the cell. Sonoluminescence is observed both at the tip of the horn and in the bulk fluid. A 50-mm focal length lens is used to focus on the region of interest, either at the tip or at some location within the bulk. An aperture is used to image only a small area. The imaging region is chosen visually. (b) A PZT attached to the bottom of the cell and driven at 27.9 kHz was used to generate CFSL within the solution. The SL activity was observed in four regions near the bottom of the cell. The PMT was positioned near one of these regions. The phase of SL activity in adjacent regions occurred in quadrature.

A. CFSL acoustical systems

Two separate acoustical systems were used to generate cavitation fields in the glycerin solution, both incorporating a 7.6 cm by 7.6 cm cross section levitation cell[24] (used in some SBSL studies, as well) filled with the glycerin solution to a height of 4.5 cm. Figure 1 illustrates the two different setups. The first system employed an ultrasonic homogenizer (BraunSonic 1000 L with a 1.9-cm-diam tip), operated at full power (200 W), generating a 20-kHz nonsinusoidal signal, with the tip of the homogenizer immersed approximately 1 cm into the liquid. Sonication with the homogenizer resulted in sonoluminescence that extended throughout a relatively large volume of the fluid. That is, sonoluminescence could be seen both at the tip of the homogenizer and in the bulk fluid, several centimeters from the tip. Measuring the pressure field produced by the homogenizer is difficult, but an order-of-magnitude calculation suggests that the pressure near the horn tip is $p \approx 9.2 \pm 2.8$ bar. (This was determined by taking the mean of two calculation methods. In one case we assumed a 100% efficiency in converting electrical power into acoustical power. In the other case we measured the temperature increase in the liquid and assumed all the power input was used to increase the liquid temperature.[25])

In addition to using the homogenizer, a second system was employed to produce CFSL [Fig. 1(b)]. For this system, a piezoelectric (PZT) cylindrical crystal is used to generate

cavitation. A 6.35-mm-thick glass plate attached to the driving PZT separates the fluid from the acoustic source. Driven at 27.9 kHz, four distinct cavitation regions could be seen near the bottom of the cell, just above the glass plate. These same regions corresponded to zones of SL activity, as confirmed by switching the room lights off. The SL activity in each region extended upwards nearly 5 mm, and appeared to occupy a volume of approximately 50 mm^3. The linear separation between adjacent SL activity was at least 50 mm.

The peak acoustic pressure obtained from this PZT cylinder system was estimated using a calibrated Dapco Needle hydrophone to quantify the response of the system at subcavitation drive levels. Linear extrapolation to the higher applied voltages used in generating CFSL corresponded to peak pressure amplitudes of approximately 5 bar. Cavitation and nonlinearities associated with the mechanical system at the higher applied voltages will affect the actual pressure profile, so this technique is not accurate; however, it does give some indication of the magnitude of the applied pressure.

The PZT cylinder system provided several advantages for measuring CFSL pulse widths from cavitation fields. First, it provided a means to measure CFSL pulse widths without the influence of an immersed metallic horn. Second, the distinct and well-separated regions enabled a simpler means of viewing singular CFSL pulses (the amount of cavitation in this system was noticeably smaller though no quantitative measure of bubble population densities were made). Finally, the temperature of this system changed little over the duration of the experiment relative to the homogenizer system. A constant temperature bath could not prevent rapid heating of the solution when using the homogenizer, and thus for this system, it was necessary to stop data collection intermittently and allow the solution to cool again.

With the homogenizer system, it can be difficult observing individual flashes associated with individual bubbles without some sort of filter. We overcame this problem by using a lens and focused on a relatively small region of sonoluminescent activity, as illustrated in Fig. 1(a). In the actual experiment we placed the lens so that the focal region was approximately 2 cm below and to the side of the homogenizer. This region appeared as a ''streaming'' region of CFSL. We also employed a 1-mm-diam aperture to keep the observed region as small as possible. This procedure worked to some degree, since by changing the power settings on the homogenizer, we could still observe SL activity in general. However, the locations of this activity changed, resulting in a substantial decrease in the recorded PMT output.

As explained later, we chose to measure the impulse response of our detection system using SBSL, since SBSL represents a delta-function input to our PMT. Our SBSL apparatus is explained elsewhere.[7] The SBSL pulses were collected by placing the PMT such that it looked into the cell through a glass plate. The distance between the bubble and the PMT was approximately 7 cm.

II. TECHNICAL CONSIDERATIONS

The fluctuating nature of the CFSL process precludes the use of a very-high-speed coherent data acquisition technique such as the sampling oscilloscope; rather, we opt for single-shot waveform acquisition techniques. Individual CFSL pulses are collected with a photomultiplier tube (PMT), digitized, and then downloaded to a computer for later analysis. This analysis includes pulse width distributions and rise-time distributions.

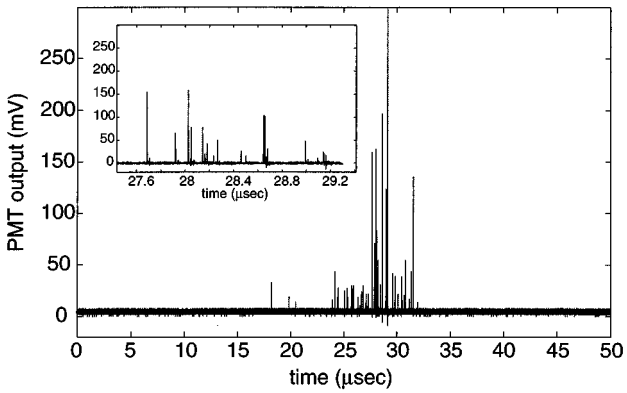

FIG. 2. Sonoluminescence activity in the 80% glycerin solution over an acoustic cycle using the homogenizer. The vertical scale represents the (inverted) voltage output from the PMT. Note that most MBSL activity is concentrated within a small portion of an acoustic cycle. A blowup of a section of MBSL activity is shown in the inset. The small amplitude pulses of ≈20 mV are single photoelectron peaks. The actual pulse amplitudes may be higher than recorded here, due to the relatively slow digitizer used for this particular data set.

Figure 2 shows a typical distribution of CFSL pulses collected over an acoustic cycle, using the homogenizer. This data set was collected by directly placing a PMT approximately 1 cm from the cell, without the use of a lens or aperture (the PMT window itself is approximately 1.9 cm in diameter). The discrete, sporatic temporal distribution of CFSL activity from this figure is attributed to both the complex nature of the pressure field within the cell and to the distribution in bubble sizes. That is to say, the collapse phase of a bubble (which gives rise to SL) depends on the pressure *at* the location of the bubble as well as the equilibrium size of the bubble.

Though Fig. 2 illustrates the basic technique used to collect CFSL pulses (using a PMT and digitizer in single-shot acquisition mode), this data set was collected with a PMT having a relatively slow response time, and acquired on a relatively slow digitizer. Actual data sets used in the experiments were collected with a much faster system, usually capturing a single pulse in any given acoustic cycle (described below). However, Fig. 2 does illustrate the technical issues that must be considered for interpreting the results. These include accounting for the influences of the limiting resolution of the data acquisition system, signal-to-noise, and the statistical nature of the efficiency of the PMT.

A. Limiting resolution of the data acquisition system

The data acquisition system included a Hamamatsu R5600U-3 PMT having a rated 650-ps rise-time,[26] a LeCroy 9362 digital oscilloscope with a 10-GS/S sampling rate (and 1.5-GHz analog bandwidth) in single-shot mode,[27] and a 50-Ω, 11-GHz bandwidth coaxial cable for delivering the PMT signal to the scope. Assuming statistical independence

of the components, and a Gaussian response, the total response of our system is given by the convolution of the responses of the individual components. For a delta function input the response for this system is $\tau_{sys}=\sqrt{\tau_{pmt}^2+\tau_{cab}^2+\tau_{scp}^2}$, where τ_{pmt}, τ_{cab}, and τ_{scp} are the rise-times associated with the PMT, cable, and scope, respectively; τ_{sys} is the rise-time associated with the combined system. [Also, given the bandwidth (f_c, at the 3-dB point) of an instrument, the rise-time can be computed from $f_c\tau=0.35$.[28]] From the information above, the response of the system is calculated to be $\tau_{sys}\approx 740$ ps. The corresponding pulse width [measured as the full width of the signal at half the maximum amplitude (FWHM)] is FWHM$\approx 1.4\tau\approx 1$ ns.[29] This provides the limiting resolution for our data acquisition system. Experimental verification of this limitation is given later. Although this is too slow to resolve the pulse duration of SBSL, we believed that such speed would permit resolution of the CFSL flash duration.

B. Signal-to-noise issues

A PMT can generate a signal even in total darkness.[30] This constitutes a source of noise. Light leaks also contribute to unwanted noise pulses. It is important to try to minimize the number of noise pulses received during the experiment. For these reasons care was taken in order to maximize the potential for collecting a signal directly due to CFSL, and not from any other source. For example, from Fig. 2 one can see that the optimal time during an acoustic cycle for collecting data is during the time period of most observed CFSL activity. With proper gating of the detection system, we could lower the rate of background noise collection dramatically, down to approximately 0.3 counts per minute.

In order to time-gate the digitizer system, we had to measure the phase of CFSL relative to the driving frequency. A trigger pulse occurring at a fixed time in the acoustic cycle is sent to an SRS DG535 pulse/delay generator. The output of the pulse generator is 500 ns long and delayed relative to the trigger by a known amount. An HP5335A gated frequency counter is used to count the number of pulses it receives from the PMT during the 500-ns gate time from the pulse generator. The average number of pulses received per gate cycle (averaged over 100 acoustic cycles) is then downloaded to a computer, which then increments the delay on the pulse generator by 250 ns. The counting procedure then repeats for the new delay time. Note that no amplitude information is contained and all pulses equal to or above the minimum trigger level (set equal to half the single photoelectron pulse height of the PMT, 20 mV) were counted with equal weight. In this way, a statistical measure of the phase of SL activity over an acoustic cycle was made. Note that the variable delay is incremented in such a way that there is overlap between two successive count measurements. Also note that the 500-ns gate time implies that for a 20-kHz frequency (with period 50 μs), the precision in a phase measurement is only 1% of an acoustic cycle. This was sufficient for our purposes.

A typical (and repeatable) CFSL count versus phase is shown in Fig. 3 for the homogenizer acoustic system. Note

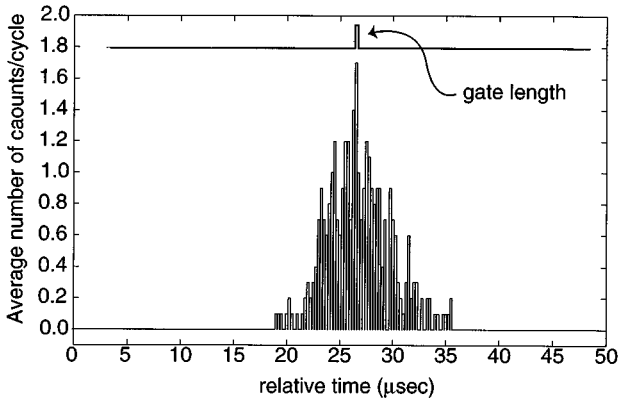

FIG. 3. The number of counts per cycle (averaged over 100 cycles) generated by the homogenizer, using the lens and aperture system illustrated in Fig. 1. The low number of counts, even during the maximum of SL activity, indicates only a few bubbles are generating SL in the region of observation, during the gate time. Also shown is a representative gate to illustrate the gate time relative to an acoustic cycle. When collecting pulses, the gate is positioned as shown, during the time of most observed SL activity.

that the low average number of counts per cycle, even at the maximum, indicates that only a few bubbles are generating sonoluminescence in the specific areas that are being observed (using the lens and aperture), during the 500-ns gate period. Using the phase information it was possible to ''look'' for individual pulses from CFSL at a particular phase of the acoustic cycle. A gate of 500 ns, centered in time over the phase of maximum SL activity, was used in combination with the smart trigger capability of the oscilloscope so that the scope only accepted PMT pulses during this gate time, in effect, discriminating against signals generated at other times during the cycle.

Acquiring and downloading individual waveforms takes approximately 250 ms; therefore pulses from successive acoustic cycles could not be collected owing to a dead time of approximately 8000 acoustic cycles. A typical pulse is shown in Fig. 4. For pulse parameter statistics, the pulse height is measured by taking the maximum data point in the signal, while the pulse width is measured as the full width at half-maximum (FWHM).

C. PMT issues

A PMT converts a photon incident on the photocathode into a photoelectron, which then passes through gain stages (dynodes) and finally becomes a current pulse at the anode. For low-level light emissions such as CFSL, it is important to consider the quantum efficiency of the PMT and the response of the PMT to multi-photon events. In general, PMT's do not have a 100% efficiency for conversion of photons into photoelectrons that results in an observable pulse at the anode. The probability for photoelectron emission p as a function of the number of incident photons m is[30]

$$p_r(\varepsilon)=\varepsilon^r(1-\varepsilon)^{m-r}\,\frac{m!}{r!(m-r)!}. \tag{1}$$

Here, ε is the quantum efficiency of the PMT ($=0.15$ at 440 nm for our case) and r is the number of photoelectrons emitted from the photocathode.

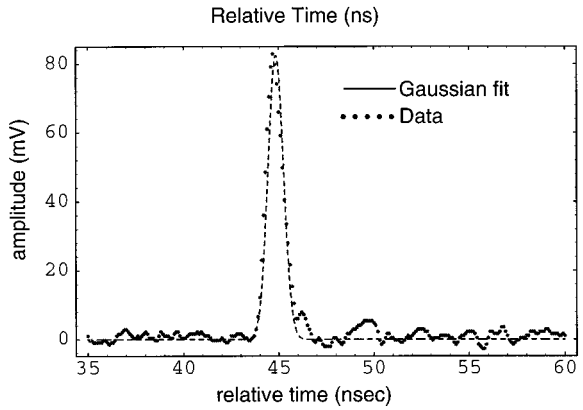

FIG. 4. A typical pulse observed from CFSL using the 650-ps rise-time PMT. The signal has been inverted so that references to its amplitude would be clear. This particular representative pulse comes from CFSL generated using the homogenizer. The pulse height of approximately 80 mV is within the linear operating region of the PMT (the single photoelectron pulse height is near 20 mV). The slight ringing at the end of the pulse is typical of fast PMT's and is due to the external circuitry. The pulse width of this particular signal at FWHM is about 1.1 ns. A Gaussian function (dashed line) is overlayed. The signal has a measured rise-time of 618 ps and a FWHM of 1.07 ns. A Gaussian fit with σ=0.949 ns, and with an amplitude factor of 0.9, is overlayed on the data. Note that the signal has a slightly faster rise and slightly slower decay than the amplitude-modified Gaussian.

A signal corresponding to a single photoelectron may actually be from a multi-photon incident pulse. Regardless, the response of the PMT to a single photoelectron will always correspond to the impulse response of the PMT. Hence it is important not to include such pulses in measured CFSL pulse width distributions. Therefore, all pulses with amplitudes less than 35 mV were discarded (the single photoelectron pulse height for the conditions of our experiment was $\approx$20 mV).

A second important consideration with the PMT involves its response to multi-photon inputs generating multi-photoelectron events. The greater the number of charges built up at the anode of the PMT, the larger the anode pulse height. The repulsive nature of the charges spreads out the pulse, so that the larger number of initial photoelectrons, the greater the pulse width seen at the anode. Therefore, a higher intensity delta-function light source should have a slightly longer response than a low level delta-function light source. This is important since even though CFSL is a low-level light source, it usually generates multi-photoelectron events.

From the above argument, the impulse response of the PMT depends somewhat on the amplitude of the pulse at the anode of the PMT. For example, Fig. 5(a) gives the pulse width distribution for essentially noise level pulses. Here, a small light leak was allowed in order to collect single photoelectron pulses. Note that the distribution is centered at approximately 1.0 ns. This experimental measurement of the impulse response of our system is in agreement with the calculated response, given earlier. The spread in the distribution is mostly due to the transit time spread (TTS) of electrons within the PMT (the rated TTS of the PMT is 280 ps at FWHM). The TTS is mainly due to the spread of velocities and directions of electrons emitted from the photocathode of the PMT.

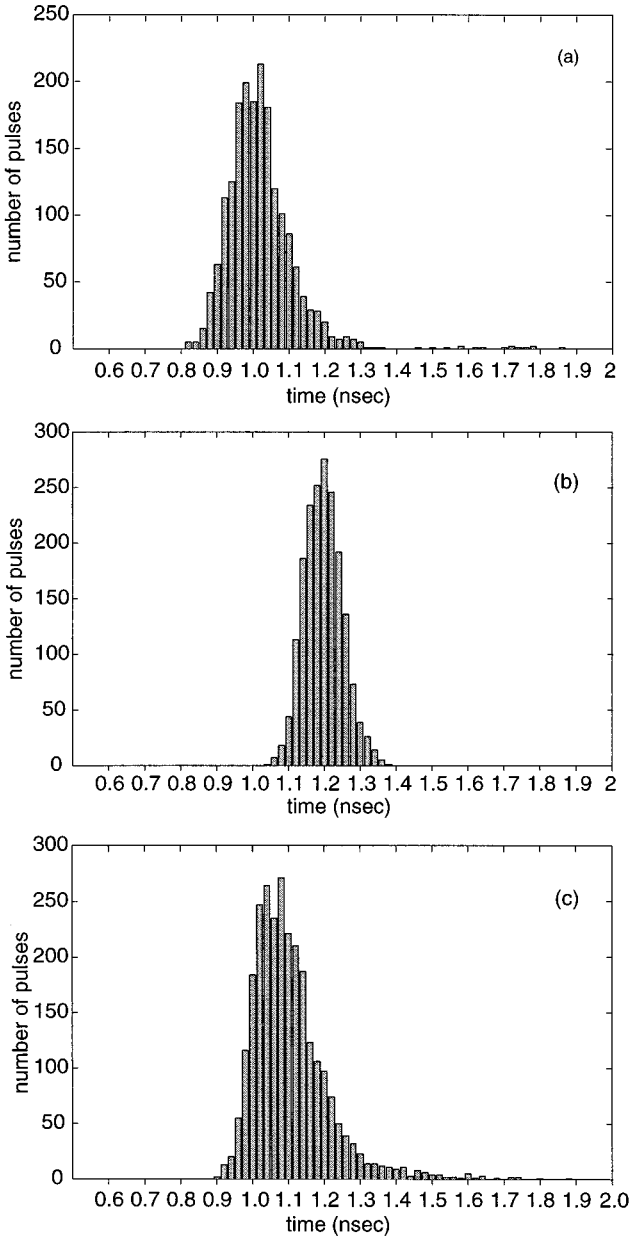

FIG. 5. Pulse width distribution for (a) noise level pulses, (b) a bright, stable bubble undergoing SBSL, and (c) a SBSL bubble driven at a lower pressure amplitude and slightly detuned from the mechanical resonance of the system. The peaks in the distribution are centered near 1.0, 1.2, and 1.1 ns, respectively. The multiple peaks in the distribution [seen at 1.02 and 1.08 ns in (c), for instance] are most likely the result of the statistical process. The transit time spread (TTS) of electrons within the PMT results in a spread in the distribution. Note that the known upper limit for pulse widths of SBSL ($<$12 ps) implies that (b) and (c) correspond to the impulse response of the 5600U-3 PMT under slightly different conditions. In (b) the light emission is relatively bright and stable, while in (c) the emission is dimmer and slightly unstable.

In order to determine the experimental impulse response for our system under the conditions of CFSL (which has higher intensities than the noise pulses), it is necessary to obtain a light source that is a delta-function input for our system, *and* with an intensity similar to CFSL. We have chosen to use single-bubble sonoluminescence as such a source (recall that the pulse width of SBSL is less than 12 ps). This appears to be the first utilization of SBSL for research applications.

Figure 5(b) and (c) gives the pulse width distribution of SBSL for two different conditions. In both cases, SBSL was obtained in an air/water system. In Fig. 5(b), a bright, stable SBSL bubble gives a pulse width centered near 1.20 ns. For this data set, digitized PMT signal amplitudes ranged from approximately 500 mV to above 1000 mV. This is within the linear operating region of the PMT. Note that the center of the distribution occurs at a slightly longer pulse width. As argued above, this slightly longer pulse width is expected due to the increased intensity of the source, relative to noise pulses. In Fig. 5(c), the SBSL apparatus is driven at a lower amplitude and slightly detuned, in order to decrease the intensity and make it more variable, to better match the conditions of CFSL. In this case, the central region of the pulse width distribution is slightly less, near 1.1 ns. The spread in the distribution is greater than in Fig. 5(b) and more closely matches that of the noise pulses. We believe this is mostly due to the lowered intensity. The TTS is expected to increase with a decrease in converted photoelectrons. This is because the initial spread in velocities and directions of the photoelectrons is more important when only a few photoelectrons are generated. An increase in the variability of the pulse amplitudes is also expected to play a role in increasing the TTS, as outlined above.

Though somewhat complicated, the SBSL system does give the experimental impulse response of our system under the needed conditions; that is, for low, but above noise level amplitudes. This allows for a better characterization of the PMT response.

III. RESULTS

As discussed in the last section, it was necessary to discriminate against single photoelectron pulses since these pulses constitute delta-function sources. All other pulse heights were included in the distributions. The actual measured amplitudes of the signals ranged from ≈40 mV to greater than 500 mV.

Typical pulse width distributions for a CFSL experiment with the rectangular cell and homogenizer are shown in Fig. 6. The peaks in the distributions (corresponding to the most common pulse width) are centered around 1.1 ns in each case [recall that Fig. 6(b) is due to CFSL at a distance of about 2 cm below and to the side of the tip of the homogenizer]. Due to the rapid temperature change (over tens of seconds) associated with generating CFSL using the homogenizer, and the associated decrease in light intensity, obtaining pulse statistics was difficult. As shown in Fig. 6(b), there are fewer pulses used in the distribution (though not shown, pulse width distributions for CFSL at the tip of the homogenizer showed similar results in the pulse width distributions).

In addition to pulse width distributions, rise-time distributions were measured for both CFSL (using the rectangular cell) and SBSL, and are shown in Fig. 7. Rise-times were measured as the time for the signal to rise from 10% to 90% of its maximum amplitude. The peak in each distribution is slightly less than the rated rise-time of the PMT. This is partially due to having an applied voltage to the PMT of −850 Vdc instead of −800 Vdc, the latter being used for rating the PMT. The higher applied voltage gives an improved response time. Though not shown, the rise-time distribution from CFSL using the homogenizer system closely matched that of the rectangular cell system.

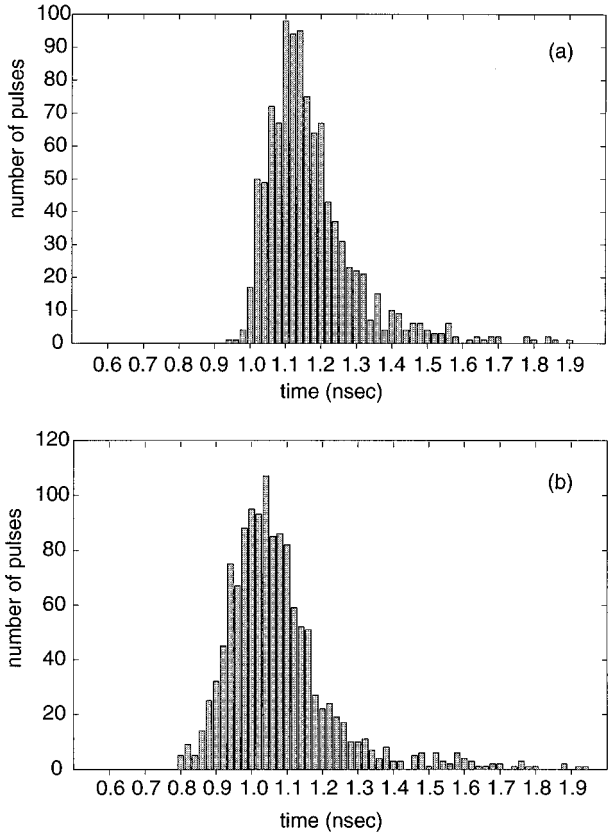

FIG. 6. The distribution of pulse widths (at FWHM) for CFSL in the 80% glycerin solution from the rectangular cell (a) and the homogenizer (b). The bin size for the distribution is 20 ps. Note that the pulses have widths near 1.1 ns long, with a spread of about 250 ps at FWHM. The TTS of the PMT is rated at 280 ps, FWHM.

IV. DISCUSSION

The results have been tabularized in Table I for ease of reference. Note that the pulse width measured for CFSL has a similar distribution to that obtained with SBSL [Fig. 5(c)], and appears to be representative of the impulse response of the PMT. This would suggest that the actual pulse width of CFSL is much shorter than what we measured, 1.1 ns. In addition, the signal rise-time for CFSL is very similar to that of SBSL, under the limitations of our system.

One difficulty in interpreting the measurements is the possibility that the actual pulse width is longer than observed, and that due to the limited number of incident photons, the possible longer pulse width manifests itself as a series of smaller, seemingly independent pulses. This was of great concern, and special efforts were made to explore this possibility. However, it was found that individual pulses (of all amplitudes) were usually separated by more than 100 ns, ensuring that consecutive pulses did not represent a single long (yet dim) pulse. It could be said that the observed pulse width is due to the inefficiency of the PMT to convert photons into photoelectrons, and that higher light intensities might result in longer pulse durations; however, even the

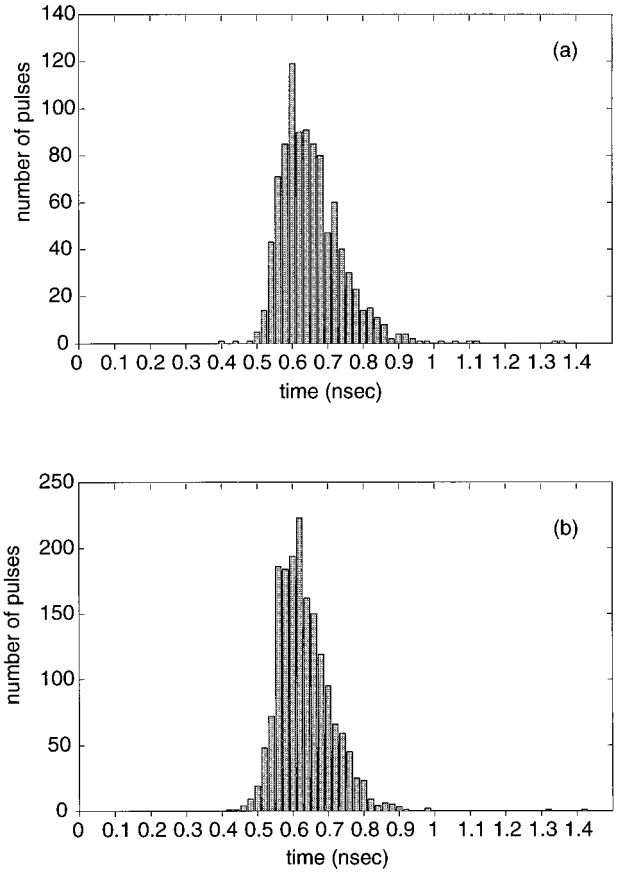

FIG. 7. The rise-time distribution for (a) CFSL, and (b) SBSL. The rise-time is a measure of the time it takes for a signal to rise from 10% to 90% of its maximum height. The bin size for the distribution is 20 ps. The rated rise-time of the PMT is 650 ps.

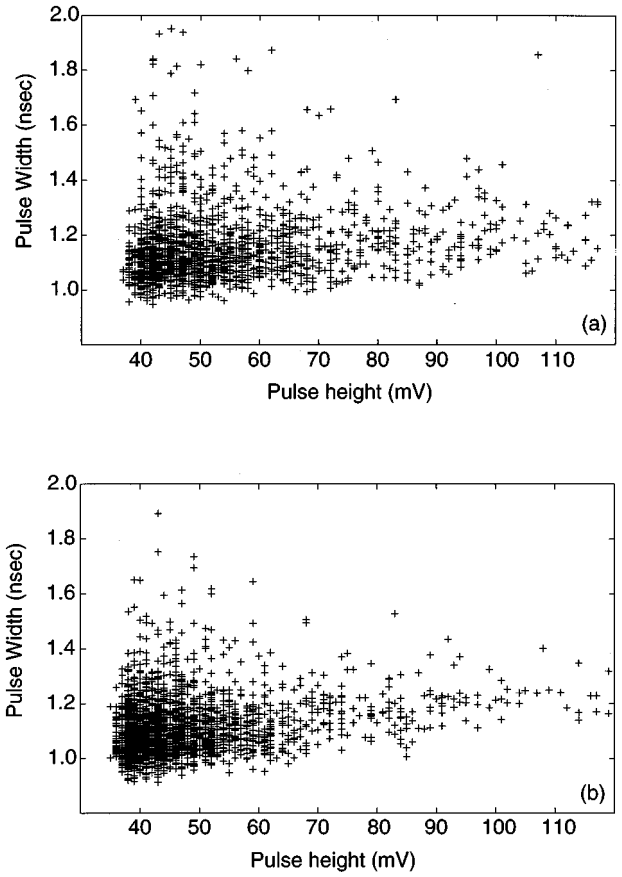

FIG. 8. The pulse width of individual pulses is plotted here as a function of their corresponding pulse amplitudes: (a) corresponds to CFSL from the rectangular cell system, having a pulse width distribution shown in Fig. 6(a), while (b) corresponds to SBSL having a pulse width distribution shown in Fig. 5(c). In both cases, there appears to be a slight increase in the minimum of the pulse width at higher pulse amplitudes. Also note the lack of large-amplitude pulses with corresponding large pulse widths.

fewer, but larger amplitude pulses showed pulse widths and rise-times corresponding to the center regions of the distributions. Figure 8 plots the pulse widths of individual pulses (at FWHM) against their corresponding pulse amplitude, for both CFSL (using the rectangular cell system) and SBSL. The data shown in Fig. 8(a) corresponds to the pulse width distribution shown in Fig. 6(a), while the data of Fig. 8(b) corresponds to the pulse width distribution shown in Fig. 5(c). By plotting the data in this fashion we can see an apparent increase in the *minimum* pulse width with increasing pulse height. Also apparent is a lack of large amplitude pulses with large pulse widths, alleviating our concern that larger amplitude pulses would give longer pulse widths.

Since the signal is digitized (and if the signal is short in duration), there will be a slight error in measuring the maximum of the signal. The largest error occurs when the true maximum is at the midpoint between consecutive data points. We can estimate the true maximum amplitude of the signal by assuming the pulse has a Gaussian profile. This assumption is not, strictly speaking, correct since the PMT responds as a discharge through a capacitor. Figure 4 shows that the PMT response has a sharper rise-time than a Gaussian (with identical FWHM), while the decay of the PMT output is slightly slower than for the Gaussian function. Nevertheless, the PMT signal appears very similar to the Gaussian function and we believe justifies our use of a Gaussian function to use as a model for delta-function input pulses.

TABLE I. The measured (center) pulse width and risetimes for various PMT signals.

Data set	Pulse width peak (ns)	Rise-time peak (ps)
Single photoelectron pulses	1.0	570
SBSL-bright and stable	1.2	600
SBSL-dim and unstable	1.1	630
CFSL-rectangular cell	1.1	650
CFSL-homogenizer	1.1	600

In addition, we tested the response of the PMT to longer-lasting pulses from a low-level light emitter, in this case, a LED. Figure 9 shows the PMT response from a 10-ns-long pulse from a LED with an amplitude near that of the present series of experiments. The variation in signal amplitude is at least partially due to the quantum efficiency of the PMT. Note that the observed width of the pulse from the LED is indicative of the current pulse through the LED. No such pulse lengths were found in the CFSL experiments.

Another concern in the interpretation of the measurements is the possibility that the pulses are the result of radiative recombination of excited hydroxyl radicals, which may

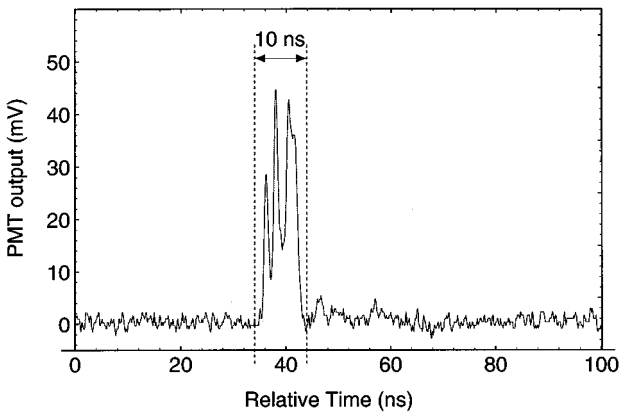

FIG. 9. The PMT output from a 10-ns current pulse is applied to a red LED. Note the length of the pulse is near 10 ns. The fluctuation in the intensity is due in part to the photon-to-photoelectron conversion efficiency of the PMT. The current to the LED is determined by the pulse generator (the LED has a rated rise-time of 150 ns).

also manifest itself as a series of pulses. Here, the bubble remains ''hot'' for an extended period of time, during which time several ''generations'' of radiative recombinations can occur. It is difficult to examine this with our experimental configuration. The extended spatial region seen by the PMT makes it difficult to estimate the influence that radiative recombination has on the results. However, again, pulses are normally separated in time by hundreds of nanoseconds, and, in addition, there are usually much less than 100 pulses (with magnitude equal to or greater than the single photoelectron pulse height) occurring during any single acoustic cycle in the spatial regions that we focused on. One might expect that a bubble undergoing repeated radiative recombination might result in a greater number of observed pulses. It should be noted that a PMT with greater sensitivity might be able to observe more pulses. Parenthetically, though no quantitative measure of the bubble population was made, from the number of CFSL pulses observed, it appeared that only a few of the cavitation bubbles actually produced CFSL during any given acoustic cycle.

It is interesting to note that our results deviate from that predicted by Kamath and Prosperetti,[18] a state-of-the-art model incorporating well-accepted theories for bubble dynamics in the absence of shock wave formation. Though the model assumes low applied pressures, relative to the conditions of our experiment, we would expect that under higher applied pressures, the temperature profile in the model would change such that the peak temperature would increase, and the ''width'' of the profile would, at the very least, not decrease. Since our observations indicate a much shorter pulse width than predicted in the model, this suggests that a fundamental physical mechanism occuring within sonoluminescing bubbles is not accounted for in present models that incorporate Rayleigh–Plesset-type bubble dynamics, and this mechanism is the dominant mechanism for the observed light emission. Even so, this model should still apply to some degree, and, if so, there may be some ''residual'' light emission that has yet to be observed. Such residual emission would be much less intense than the main flash, so dynamical range would be a problem in trying to detect this emission.

Our results suggest that sonoluminescence from cavitation fields is similar to that from single bubbles, in the sense that both types of SL have extremely short pulse durations. There appears to be a commonality of SL from single bubbles and cavitation fields, even with the apparent differences outlined in the introduction. It would be interesting to determine whether the pulse width of CFSL is actually as short as SBSL. A measurement of the flash width from CFSL with a 50-ps resolution should limit the number of models currently used for predicting sonoluminescence behavior. In our work, an upper limit for the pulse width from CFSL of 1.1 ns has been observed. Since this corresponds to the impulse response of the PMT, the actual pulse width of CFSL may be much shorter. In fact, we can make a crude estimate of the maximum pulse width from CFSL assuming a Gaussian structure, and assuming a Gaussian response for our system. Using the experimentally determined response of our system for single photon pulses ($\approx$1.0 ns), and the measured width of the signal ($\approx$1.1 ns), the maximum FWHM of the actual pulse width from CFSL is calculated to be 460 ps (using the sum-of-squares rule). The actual width of CFSL is probably less than this calculated value, since the system response to multi-photoelectrons increases slightly.

ACKNOWLEDGMENTS

We wish to thank L. A. Crum for valuable insights, and Todd Brooks for his assistance in the laboratory. This research is supported by ONR and NSF.

[1] D. Felipe Gaitan, L. A. Crum, C. C. Church, and R. A. Roy, ''Sonoluminescence and bubble dynamics for a single, stable, cavitation bubble,'' J. Acoust. Soc. Am. **91**, 3166–3183 (1992).
[2] A. I. Eller, ''Force on a bubble in a standing acoustic wave,'' J. Acoust. Soc. Am. **43**, 170–171 (1968).
[3] L. A. Crum, ''Bjerknes forces on bubbles in a stationary sound field,'' J. Acoust. Soc. Am. **57**, 1363–1370 (1975).
[4] B. P. Barber and S. J. Putterman, ''Light scattering measurements of the repetitive supersonic implosion of a sonoluminescing bubble,'' Phys. Rev. Lett. A **69**, 3839–3842 (1992).
[5] B. P. Barber, R. Hiller, K. Arisaka, H. Fetterman, and S. Putterman, ''Resolving the picosecond characteristics of synchronous sonoluminescence,'' J. Acoust. Soc. Am. **91**, 3061–3063 (1992).
[6] R. Hiller *et al.*, ''Effect of noble gas doping in single bubble sonoluminescence,'' Science **445**, 248–250 (1994).
[7] T. J. Matula *et al.*, ''Comparison of multibubble and single-bubble sonoluminescence spectra,'' Phys. Rev. Lett. **76**, 2602–2606 (1995).
[8] M. J. Moran *et al.*, ''Direct observations of single sonoluminescence pulses,'' NIM B **96**, 651–656 (1995).
[9] C. C. Wu and P. H. Roberts, ''A model of sonoluminescence,'' Proc. R. Soc. London, Ser. A **445**, 323–349 (1994).
[10] W. C. Moss *et al.*, ''Hydrodynamic simulations of bubble collapse and picosecond sonoluminescence,'' Phys. Fluids **6**, 2979–2985 (1994).
[11] T. Lepoint, N. Voglet, L. Faille, and F. Mullie, ''Bubble Dynamics and Interface Phenomena,'' in *Proceedings of an IUTAM Symposium*, edited by J. R. Blake, J. M. Boulton-Stone, and N. H. Thomas (Kluwer, Boston, 1993), pp. 321–333; F. Mullie and D. De Pauw and T. Lepoint, ''Nature of the 'extreme conditions' in single sonoluminescing bubbles,'' submitted to J. Phys. Chem.
[12] L. Frommhold and A. A. Atchley, ''Is sonoluminescence due to collision-induced emission?,'' Phys. Rev. Lett. **73**, 2883–2886 (1994).
[13] J. Schwinger, ''Casimir energy for dielectrics: Spherical geometry,'' Proc. Natl. Acad. Sci. USA **89**, 11 118–11 120 (1992).
[14] For a review of sonoluminescence, see, e.g., A. J. Walton and G. T. Reynolds, ''Sonoluminescence,'' Adv. Phys. **33**, 595–660 (1984).

[15] K. S. Suslick, ''Sonochemistry,'' Science **247**, 1439–1445 (1990).
[16] K. S. Suslic and E. B. Flint, ''Sonoluminescence of alkali metal salts,'' J. Phys. C **95**, 1484–1488 (1991).
[17] E. B. Flint and K. S. Suslick, ''The Temperature of Cavitation,'' Science **253**, 1397–1399 (1991).
[18] V. Kamath, A. Prosperetti, and F. N. Egolfopoulos, ''A theoretical study of sonoluminescence,'' J. Acoust. Soc. Am. **94**, 248–260 (1993).
[19] P. W. Vaughan and S. Leeman, ''Some comments on mechanisms of sonoluminescence,'' Acustica **59**, 279–281 (1986).
[20] A. K. Kurochkin *et al.*, ''Study of the mechanism of sonoluminescence. II. Form of the light pulse in sonoluminescence,'' Russ. J. Phys. Chem. **60**, 731–734 (1986).
[21] F. R. Young, ''Sonoluminescence from water containing dissolved gases,'' J. Acoust. Soc. Am. **57**, 100–104 (1976).
[22] C. D. West and R. Howlett, ''Timing of sonoluminescence flash,'' Nature **215**, 727 (1967).
[23] G. Gimenez, ''The simultaneous study of light emissions and shock waves produced by cavitation bubbles,'' J. Acoust. Soc. Am. **71**, 839–846 (1982).
[24] T. J. Asaki and P. L. Marston, ''Shape oscillations of bubbles in water driven by modulated ultrasonic radiation pressure: Observations and detection with scattered laser light,'' J. Acoust. Soc. Am. **93**, 706–713 (1993).
[25] T. J. Mason, J. P. Lorimer, and D. M. Bates, ''Quantifying sonochemistry: casting some light on a 'black art','' Ultrasonics **30**, 40–42 (1992).
[26] The rise-time is defined as the time it takes for a signal to rise from 10% to 90% of its maximum value. The rated 650-ps rise-time of the PMT is for an applied voltage of −800 Vdc. For these experiments, we applied −850 Vdc, which gives a slight improvement in the response time. Other properties of the R5600U-3 include a spectral response from 185–650 nm and a gain of 3×10^5 for an applied voltage of −800 Vdc.
[27] The analog bandwidth refers to the input amplifiers of the scope, and is the limiting factor in the speed of this 9362. The sampling rate of 10 GHz refers to the digitizing rate only.
[28] This relation assumes a single-pole, or lag network with a bandwidth of $f_c=1/(2\pi RC)$. The rise-time of a lag network is $\tau\approx2.2RC$. Substituting for RC gives $f_c\tau=0.35$. See, e.g., A. P. Malvino, *Electronic Principles* (McGraw-Hill, New York, 1984), pp. 426–428.
[29] The relationship between the FWHM and rise-time of a Gaussian signal can easily be determined by applying the equation for a Gaussian to the FWHM and rise-time, respectively. The common parameter of the Gaussian width can then be used to relate the FWHM and rise-time.
[30] R. W. Engstrom, *Photomultiplier Handbook* (RCA, Lancaster, PA, 1980).

A new mechanism for sonoluminescence

A. Prosperetti[a)]
Department of Mechanical Engineering, The Johns Hopkins University, Baltimore, Maryland 21218

(Received 12 June 1996; accepted for publication 11 November 1996)

It is argued that a pulsating acoustically levitated bubble cannot possibly maintain a spherical shape. A jet forms during compression, and the sound amplitude such that the jet first strikes the other side of the bubble with sufficient energy is hypothesized to be the threshold for sonoluminescence. It is proposed that the connection between jet impact and light emission is a fracturing of the liquid that cannot flow during the extremely short time scale over which pressure is applied. With this hypothesis, sonoluminescence would therefore be a manifestation of the non-Newtonian nature of water and other simple liquids when stressed with sufficient intensity and rapidity. © *1997 Acoustical Society of America.* [S0001-4966(97)03104-4]

PACS numbers: 43.35.Ei, 78.60.Mq [HEB]

After its original discovery by Gaitan and Crum,[1] the fascinating phenomenon of stable, single-bubble sonoluminescence has attracted considerable attention for its unexpected and unique features.[2–11] Currently, the accepted working hypothesis as to its origin is the generation of a shock wave in the gas, its focusing at the center of the bubble, and the consequent formation of a plasma.[12] In my view this hypothesis faces serious difficulties both on a theoretical and an experimental level. The purpose of this note is to substantiate this statement and to suggest a possible alternative explanation of the phenomenon.

Most of the work carried out to date assumes that the bubble maintains a more or less spherical shape in the course of the oscillations.[13] A consideration of the mechanism responsible for the trapping of the bubble in the sound field uncovers some problems with this picture. Since bubbles tend to move in the direction opposite to the local pressure gradient $\nabla P(\mathbf{x},t)$, in a sound field a bubble drifts toward the pressure minimum (i.e., the antinode) when the pressure falls and toward the pressure node when it rises. If the bubble is driven below resonance, its volume v expands when the pressure falls so that the force $-v\nabla P$ is greater in magnitude during the expansion than during the contraction phase. Thus, the bubble executes a periodic translational motion in which the upward displacement in the compressed state, under the action of gravity and of the acoustic pressure gradient, is exactly equal to the pressure-gradient-induced downward displacement in the expanded state against gravity.

Observation as well as computation and a simple ''thought experiment'' all show that translation causes the formation inside the bubble of a jet oriented in the direction in which the bubble moves during the compression half-cycle. Consider a spherical bubble with negligible internal pressure that is released with a certain initial translational velocity. The bubble will start collapsing and its translational velocity U to increase due to the conservation of the liquid impulse $\frac{1}{2}v\rho U$, where ρ is the liquid density. It was pointed out a long time ago by Benjamin and Ellis[14] that, if the bubble were to collapse spherically and (in the idealized case of an empty bubble) reduce to a vanishing point, the impulse of the system could not be conserved. Instead a jet forms, directed in the same direction as the translational velocity, that will ultimately span the bubble and give rise to a toroidal vortex that conserves the total impulse. The first photographic evidence was provided by Benjamin and Ellis in Fig. 2 of their paper. A numerical simulation, generated by a standard boundary integral method documented elsewhere (see, e.g., Ref. 15), is shown in Fig. 1. Results of this type have been available in the literature for many years (see, e.g., Ref. 16 and references therein).

The point of this argument is to demonstrate that, during the collapse of a translating bubble, fluid dynamic conditions must prevail that tend to promote the formation of a jet. In a sound field, whether this jet traverses the entire bubble or has time only to develop to the embryonic stage of a dimple depends on the amplitudes of the volume pulsation and of the translational motion, i.e., ultimately, on the sound level.

Figure 2 shows a sequence of bubble shapes (computed by the same method used for the previous figure) in which the effects of surface tension, gravity, and spatial variation of the acoustic field are included. The latter is specified to be $P(z,t) = P_\infty + P_a \sin(\omega t)\cos(\omega z/c+\phi)$, with $P_\infty = 1$ bar, $P_a = 1.35$ bar, $\omega/2\pi = 26.5$ kHz, $c = 1{,}500$ m/s, $\phi = 0.58$ rad, and the time unit is 1.1 μs. Gravity acts downward along the z axis, the liquid is water, and the gas behaves isothermally. Initially the bubble is at rest with its center at $z = 0$ and an equilibrium radius of 4.5 μm. A similar calculation, but extending over more than one cycle and demonstrating the stabilizing effect of surface stretching during the expansion phase, may be found in Ref. 17. Although none of these examples exactly simulates the situation prevailing during sonoluminescence (the motion is neither steady nor periodic, viscous effects are ignored, the bubble internal pressure is calculated crudely, etc.), the point here is to substantiate the preceding conclusion that a jet forms in the direction of the bubble translational velocity during the compression phase. Another aspect worthy of notice in Fig. 2 (especially in connection with results recently published in Ref. 18) is the nearly perfect spherical shape of the bubble until less than 10 ns before the jet strikes the other side.[19]

[a)]Electronic mail: prosper@titan.me.jhu.edu

 0001-4966/97/101(4)/2003/5/$10.00

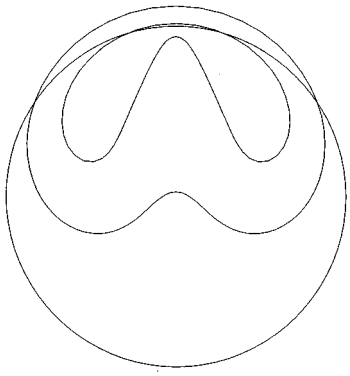

FIG. 1. Successive shapes of an axisymmetric translating and collapsing bubble in an unbounded, inviscid, incompressible liquid. The initial upward velocity of translation equals $0.6\times\sqrt{\Delta P/\rho}$, where ΔP is the difference (assumed constant) between the internal and external pressures and ρ is the liquid density. The successive shapes shown are at times 0, 0.6, and 0.86 in units of $R_0\sqrt{\rho/\Delta P}$. For $\Delta P=1$ bar and the density of water, with $R_0=10$ μm, this equals 1 μs. Surface tension is neglected. Note the jet directed in the same direction as the translational velocity. The jet becomes thinner with increasing translational velocity.

If one accepts then that, in the conditions prevailing during sonoluminescence, a bubble translates up and down with a jet that forms during collapse and disappears during expansion due to the stretching of the interface, and that the jet extends more and more into the bubble as the translation and pulsation amplitudes increase, it is then obvious that there must be a threshold value of the sound pressure (depending on bubble radius and other parameters) such that the jet just makes it across the bubble. I propose that this is the threshold at which sonoluminescence first sets in (provided the impact velocity is sufficiently large).

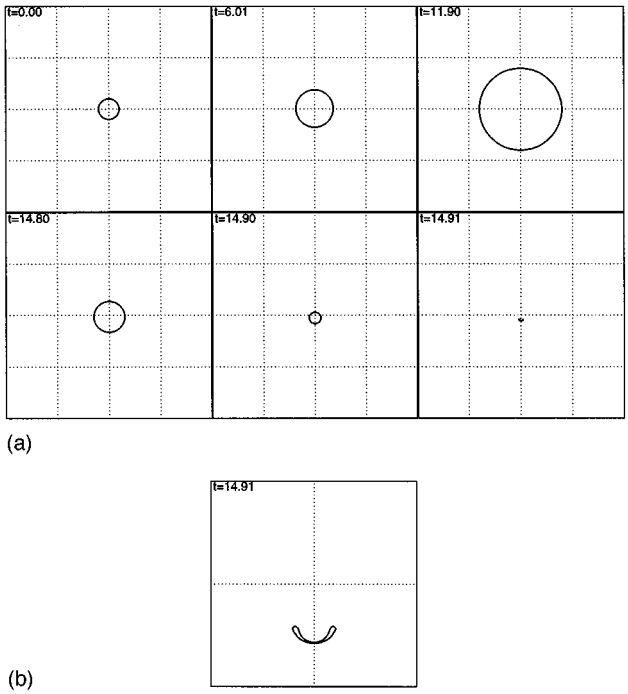

FIG. 2. Successive shapes of a 4.5-μm radius bubble in water placed in a pressure gradient in an unbounded liquid and subject to a pressure field oscillating at 26.5 kHz. The flow is assumed to be axisymmetric, irrotational, and incompressible, and the bubble initial velocity vanishes. Surface tension effects are accounted for. Times are in units of 1.1 μs. Figure (b) is an enlargement of the last frame of (a).

Before discussing the point further, let me address what in my view is a serious weakness of the shock wave hypothesis, namely that ''it explains too much.'' For clarity, let us separate two aspects of the experimental evidence. On the one hand there is the fact that light is emitted at all. On the other is the issue of stability and repeatability. The key to the second aspect has been correctly identified, I believe, in the balance that must prevail among the processes responsible for acquisition and loss of dissolved gas by the bubble.[9] But if shock waves are the light-emission mechanism, then why is luminescence (but not, necessarily, stability) not observed more commonly than it actually is? In other words, with a shock wave mechanism, one would expect to see quite easily light on and off for one or a few cycles as bubbles translate and evolve in a sound field under a variety of conditions, pressure amplitudes, etc. Yet this does not seem to happen in a normal cavitation field at weak to moderate amplitudes, but only at the very elevated amplitudes characteristic of the earlier work on sonoluminescence (see, e.g., Ref. 20). In the framework of the shock wave model, this lack of emission is explained with the hypothesis that translating bubbles distort too much to provide the necessary focusing. Yet, some bubbles ''can be seen to emit light as they rise from the nichrome wire,''[9] which seems to be in contrast with this explanation. As pointed out in Ref. 11, the shock wave hypothesis has another weakness, namely that it has difficulties accounting for the extreme sensitivity of the phenomenon to temperature, the nature of the liquid, and that of the gas. This argument may be countered by pointing out that changing conditions changes the nature of the gas in the bubble, a point that could be settled by experiments on the effect of similar changes on shock wave luminescence in standard shock-tube experiments. A further difficulty with the shock wave hypothesis is the recently reported observation of sonoluminescence with gases, such as ethane, having an adiabatic index close to 1.[8,9]

The argument often heard to oppose the notion that jets straddle the bubble is the observation that the bubble maintains its integrity for a very long time. Yet, there are at least two pieces of experimental evidence showing that jets do not necessarily destroy the bubble. The first one is the observation by Crum of a large bubble pulsating near a wall on a vibrating table.[21] At every cycle a jet forms that bridges the bubble during compression and is torn apart during expansion. While the parameter values for this experiment were vastly different from those prevailing during sonoluminescence, the fact remains that there is no necessary connection between jet formation and bubble disintegration. A more cogent observation was reported over 20 years ago by Lauterborn and Bolle, who produced a bubble near a solid wall with a focused laser flash and filmed the event at 75 000 frames per second.[22] In their beautiful Fig. 2 the bubble is observed to grow first and then collapse. After undergoing a strong distortion near the point of minimum volume, it rebounds (due to inflow of dissolved gas during the previous expansion), maintaining its integrity and a very nearly

spherical shape, except for a curious ''stem'' on the side near the wall. This feature is produced by the impact of a microjet that has traversed the bubble and that is visible in its interior while being stretched by the rebound.

Most interestingly, the stem of the bubble in Lauterborn and Bolle's sequence is eventually seen to undergo a separate collapse, leaving behind a number of minute microbubbles. This observation is of particular relevance to the present discussion because it offers a likely explanation of the observed decrease of the equilibrium size of the bubble corresponding to the onset of sonoluminescence, and it also explains the gas loss of about 0.01% per cycle that is estimated from diffusion theory.[9] In the words of the authors of Ref. 9, ''the process that leads to this [gas] ejection is the key to SL in a single bubble.'' The hypothesis of a connection between this ''anomalous'' mass loss and the stem collapse is obvious. The shedding of microbubbles has also been offered as an explanation for ''phase glitches'' observed with argon bubbles.[8] Another piece of evidence in favor of the above scenario is that, contrary to the nonluminescing case, a luminescing bubble is observed to bounce around its minimum radius less than a nonluminescing one.[9] This behavior may be due to the fact that the jet threading the bubble represents a significant energy loss that inhibits the bouncing.[23]

In summary, my hypothesis so far is the following: *The sonoluminescence lower threshold coincides with the pressure amplitude at which the jet developing during the collapse phase impacts (with sufficient energy) the opposite side of the bubble.* The upper threshold is due to the total disruption of the integrity of the bubble when the impact becomes too violent.

If one rejects the shock wave mechanism, what is the origin of the light emission? How is it connected with the jet striking the opposite side of the bubble? At this point I must leave what I believe are rather solid grounds and venture into speculation. The mechanism I propose is *fracto-luminescence,* the emission of light associated with the ''fracture'' of the liquid.[24]

It is a documented fact that, when some solid materials (including ice and Wint-O-Green Lifesavers® candy) fracture, light emission is observed (see, e.g., Refs. 25–30). This effect can be due to several factors, the relative importance of which has not been entirely sorted out. It is possible that the material behind the crack tip is left in a highly excited state due to nonadiabatic processes associated with bond breaking,[29,30] or, stated differently, that plastic deformation produces a strong thermal excitation. Other possibilities are defect production and electron capture, electron bombardment of the freshly created surface, and charge separation during crack growth followed by microdischarge.[29] The last mechanism is supported by the presence of spectral lines of the ambient gas in some (but definitely not all) experiments.[25,26] Interestingly, the spectra observed by Chapman and Walton[25] and others during the fracture of quartz were continuous, with no spectral lines, and resembled a blackbody spectrum, qualitatively very similar to single-bubble sonoluminescence spectra.[6]

While there is no actual proof that something resembling fracture does indeed occur in sonoluminescence, a series of considerations may make it at least plausible.

The first question is whether the very process of fracture, as opposed to flow, is actually possible. The following quotation from a section entitled ''The rigidity of liquids'' in Ref. 31 is relevant here: ''If the rate of shear is sufficiently great there may not be time for the [liquid] molecules to advance to a neighbouring site. In this case the liquid will not show viscous flow, but will show a finite elastic rigidity.'' An example is silicone putty, which fractures in a brittle fashion under rapid stretching, but flows in a viscous manner at low rates. Continuing with the quotation ''For simple liquids the rates of shear for this [i.e., rigidity] to occur are enormous...'' but not infinite. In other words, any liquid will exhibit a non-Newtonian behavior over sufficiently short time scales. Water is particularly likely to exhibit such ''rigidity'' due to the strong hydrogen bonding that confers to the liquid a structure bearing unusual similarities to the crystalline state. If stresses are applied too fast for relaxation, i.e., flow, to take place, the hydrogen bonds remain ''frozen.'' This peculiarity of water (together with another one mentioned below) may explain why ''water is by far the most friendly fluid for SL.''[8] An estimate of the necessary rate may be found if one assumes that the relevant time scale cannot be shorter than the inverse of the vibrational frequency of water molecules, which is of the order of 10^{13} Hz. If the microjet hits the other side of the bubble with a velocity U, the rise time of the overpressure can be assumed to be a mean intermolecular distance d divided by U. This estimate assumes that the most superficial layer of molecules is instantaneously accelerated to the velocity U and has to travel a distance d to compress the next layer. Assuming $d \sim 1$ Å, we have $d/U \sim 10^{-13}$ s for $U \sim 1{,}000$ m/s which is of the order of the speed of sound in the liquid (as expected), and of the estimated radial bubble velocity and therefore of the jet's velocity as well.

The duration of the tremendous overpressure due to the jet impact must be of the order of the time taken by a pressure wave to traverse the jet in the transverse direction. If, on the basis of published computational results, the jet radius r is estimated to be about 10% of the minimum bubble radius, ~ 1 μm or less, and the pressure wave speed $c \sim 2{,}000$ m/s, we have $r/c \sim 50$ ps or less.

Just as it is difficult to nucleate a bubble in a pure liquid, so it is to initiate a crack in a perfect crystal. In the usual fracture processes, cracks initiate at defects or other ''weak spots'' in the solid. As a matter of fact, fracto-luminescence in some solids has been reported to increase many times after exposure to x-irradiation that produces a large number of defects.[27] The observed strong sensitivity of sonoluminescence to small amounts of dissolved noble gases[7] may perhaps be explained on similar grounds. Since all the multipole moments of a noble gas atom vanish, at most only very weak bonds with the surrounding water molecules are possible. An argon atom could therefore function as a weak spot favorable for crack initiation. The xenon atom is larger than the argon one, the spot weaker, and crack formation easier. Conversely, helium is smaller and the tendency to crack formation inhibited. Nitrogen and oxygen molecules have a nonzero quadrupole moment, the binding with water is therefore

stronger, the weak spot not as weak, and cracking not as likely. The implications of these considerations for the intensity of luminescence are borne out by experiment.[7] If too many weak spots are present (high noble gas concentration), the material becomes friable and the process of crack opening may not be as energetic and disruptive of the liquid structure. This consideration might explain the luminescence intensity reduction in going from 1% to 100% argon concentration.[7] Another factor to keep in mind in this connection is of course that the bubble dynamics is strongly affected by the large difference in the value of the specific heat ratio between monatomic and diatomic gases.

It may also be relevant here to recall the existence of *clathrates*, compounds formed by the inclusion of molecules in cells that are present in some crystal lattices due to the particular geometry of the molecular structure.[32–34] Interestingly, although other types exist, the ability to form clathrates is a peculiarly characteristic property of water, and the xenon hydrate is one of the easiest-to-prepare and most widely investigated clathrates.[32] It will be recalled that xenon is also the ''best'' gas for sonoluminescence.[7] Although clathrates occur in the solid phase, it would seem quite reasonable that clathrate-like structures continually form and disintegrate in liquid water due to molecular agitation. Furthermore, some clathrates are stabilized by pressure, and, up to a point, high pressures promote the formation of clathrates even in some systems that show no clathrate formation at normal pressure.[34]

In conclusion I add a few considerations that reasons of space prevent me from developing more fully:

(1) Cooling the liquid has the effect of increasing the number of hydrogen bonds, or increasing the relaxation time for flow. Cracking is therefore more likely, and light intensity should increase in agreement with observation.[5] Since deuterium confers to heavy water more structural order than normal water (see, e.g., Ref. 35), one would expect differences between the two liquids. Unfortunately, current data are inconclusive, although they show the dramatic effects of minute impurities that would affect the liquid far more than the vapor.[36]

(2) Since 1-butanol is known to be surface active,[37] and therefore to adsorb at the bubble surface, the initiation of sonoluminescence at the surface, rather than in the bulk, might explain why the addition of as little as 40 ppm of this alcohol in water reduces the light intensity by a factor of nearly 25.[10] It may also explain the observed increase in jitter and rise time associated with aging of the water.[4]

(3) Field and co-workers have published high-speed photographs of the shock-wave-induced collapse of cylindrical cavities.[38–40] Some of these photos show an intense luminescence around the point of jet impact and the surrounding gas areas, the latter of which persist over two consecutive frames, i.e., for times in excess of hundreds of nanoseconds. The most probable cause of this effect is compressional heating of the gas, a mechanism proposed a long time ago[41] to explain sonoluminescence effects and substantiated by theory.[42] The effect is evidently different from that responsible for single-bubble sonoluminescence, as pointed out by Crum.[2] In addition to compressional heating, jet impacts of the type hypothesized here are also likely to occur in multiple-bubble sonoluminescence, which might therefore be a combination of both mechanisms. Interestingly, the photos of Ref. 40 also show (unfocused) shock waves harmlessly rattling around the bubble.

(4) Luminescence can be observed without difficulty in shock-tube experiments when the shock intensity is sufficiently strong. Its duration is far too long to account for the observed brevity of single-bubble sonoluminescence.[43]

Several aspects of the mechanism hypothesized here can be checked experimentally. In the first place, since the jet is predicted to be directed vertically, one would expect a variation of the light intensity along ''meridians'' in a vertical plane. Preliminary results on this aspect of the phenomenon have recently been reported.[44] Second, since jet formation depends on translational velocity, which is increased by buoyancy, sonoluminescence intensity is expected to increase in an artificially increased gravitational field. Third, a considerable amount of information on the effects of various types of dissolved molecules on the structure of liquids is available.[45] For example, water/methane solutions are expected to be very different from carbon tetrachloride/methane solutions. Similarly, water/ammonia, water/carbon dioxide, and water/dimethyl sulfate should have very different properties. Experiments of the type reported in Ref. 39 in which high-velocity liquid jets are made to impinge on liquid surfaces could also be revealing under the proper experimental conditions. Finally, it is obvious that fracture and light emission should also occur in the hypervelocity impact of solid bodies on liquid surfaces, although direct observation of the phenomenon may be difficult.

If the present hypothesis is correct, the implications on the mechanisms underlying sonochemical effects can be quite far reaching and a host of new techniques (and possibly technologies) can be developed to exploit microjet effects advantageously.

ACKNOWLEDGMENTS

Many of the ideas described before were prompted by conversations with N. Bourne, J. Field, W. Proud, A. Walton, and S. Putterman. The author also gratefully acknowledges discussions with R. Hickling, K. Stebe, L. Hargrove, L. Crum, R. Roy, R. Apfel, M. Longuet-Higgins, J. R. Blake, M. Paulaitis, and G. Astarita. Special thanks are due to J. Zheng and H. Oğuz for their help in generating Figs. 1 and 2. This study has been supported by the Office of Naval Research.

[1] D. F. Gaitan and L. A. Crum, in *Frontiers in Nonlinear Acoustics*, edited by M. Hamilton and D. T. Blackstock (Elsevier, New York, 1990), pp. 459–463; D. F. Gaitan, L. A. Crum, C. C. Church, and R. A. Roy, J. Acoust. Soc. Am. **91**, 3166–3183 (1992).

[2] L. A. Crum, J. Acoust. Soc. Am. **95**, 559–562 (1994); see also Phys. Today **47**(9), 22–29 (1994).

[3] B. P. Barber and S. J. Putterman, Nature **352**, 318–320 (1991); Phys. Rev. Lett. **69**, 3839–3842 (1992).
[4] B. P. Barber, R. A. Hiller, K. Arisaka, H. Fetterman, and S. J. Putterman, J. Acoust. Soc. Am. **91**, 3061–3063 (1992).
[5] B. P. Barber, K. K. Wu, R. Löfstedt, P. H. Roberts, and S. J. Putterman, Phys. Rev. Lett. **72**, 1380–1383 (1994).
[6] R. A. Hiller, S. J. Putterman, and B. P. Barber, Phys. Rev. Lett. **69**, 1182–1184 (1992).
[7] R. A. Hiller, K. Weninger, S. J. Putterman, and B. P. Barber, Science **265**, 248–250 (1994).
[8] B. P. Barber, K. Weninger, R. Löfstedt, and S. J. Putterman, ''Pressures,'' Phys. Rev. Lett. **74**, 5276–5279 (1995).
[9] R. Löfstedt, K. Weninger, S. J. Putterman, and B. P. Barber, Phys. Rev. E **51**, 4400–4410 (1995).
[10] K. Weninger, R. A. Hiller, B. P. Barber, D. Lacoste, and S. J. Putterman, J. Phys. Chem. **99**, 14 195–14 197 (1995).
[11] B. P. Barber, K. Weninger, and S. J. Putterman. Trans. Soc. Ser. A (in press).
[12] H. P. Greenspan and A. Nadim, Phys. Fluids A **5**, 1065–1067 (1993); C. C. Wu and P. H. Roberts, Phys. Rev. Lett. **70**, 3424–3427 (1993); W. C. Moss, D. B. Clarke, J. W. White, and D. A. Young, Phys. Fluids **6**, 2979–2985 (1994).
[13] A notable exception is the work of Lepoint and co-authors, e.g., T. Lepoint, N. Voglet, L. Faille, and F. Mullie, in *Bubble Dynamics and Interface Phenomena*, edited by J. R. Blake, J. M. Boulton-Stone, and N. H. Thomas (Kluwer, Dordrecht, 1994), pp. 321–333; also T. Lepoint, D. De Pauw, F. Lepoint-Mullie, M. Goldman, and A. Goldman, submitted to J. Acoust. Soc. Am.
[14] T. B. Benjamin and A. T. Ellis, Philos. Trans. R. Soc. London, Ser. A **260**, 221–240 (1966).
[15] H. N. Oğuz and A. Prosperetti, J. Fluid Mech. **219**, 143–179 (1990).
[16] Several examples can be found in papers by J. R. Blake and co-workers, e.g., J. P. Best and J. R. Blake, J. Fluid Mech. **261**, 75–93 (1994); J. P. Best and A. Kucera, J. Fluid Mech. **245**, 137–154 (1992); J. P. Best, J. Fluid Mech. **251**, 79–107 (1993); J. R. Blake, M. C. Hooton, P. B. Robinson, and R. P. Tong, Philos. Trans. R. Soc. Lond., to appear, December 1996.
[17] A. Prosperetti, in *Bubble Dynamics and Interface Phenomena*, edited by J. R. Blake, J. M. Boulton-Stone, and N. H. Thomas (Kluwer, Dordrecht, 1994), pp. – .
[18] Y. Tian, J. A. Ketterling, and R. E. Apfel, J. Acoust. Soc. Am. **100**, 3976–3978 (1996).
[19] It goes without saying that the *systematic* phenomenon that drives the jet may be compounded with the *random* and well-known instabilities of the spherical shape so that more than one jet may be present. The fact that the sonoluminescence region of parameter space is often next to one of jittering translations may be relevant here (see Refs. 6 and 10).
[20] R. E. Verrall and C. M. Sehgal, in *Ultrasound: its Chemical, Physical, and Biological Effects*, edited by K. S. Suslick (VCH, New York, 1988), pp. 227–286.
[21] L. A. Crum, J. Phys. (France) **40**, C8.285–C8.288 (1979); reproduced in Ref. 2.
[22] W. Lauterborn and H. Bolle, J. Fluid Mech. **72**, 391–399 (1975). Figure 2 of this paper is reproduced as Fig. 7 in W. Lauterborn and A. Vogel, Annu. Rev. Fluid Mech. **16**, 223–244 (1984).
[23] Another factor to keep in mind is that, at this stage, most likely the bubble is highly distorted and the algorithm used to deduce the radius from light scattering might fail as it is predicated on the assumption of sphericity.
[24] This notion bears some similarity with a proposal of Hickling, R. Hickling, Phys. Rev. Lett. **73**, 2853–2856 (1994); R. Hickling and I. M. Svishchev (preprint) according to which the high pressure inside a spherical bubble promotes solidification of the liquid at the bubble surface. It is clear, however, that the details of the two postulated mechanisms are quite different.
[25] G. N. Chapman and A. J. Walton, J. Appl. Phys. **54**, 5961–5965 (1983).
[26] J. Wollbrandt, U. Bruckner, and E. Linke, Phys. Status Solidi A **77**, 545–552 (1983); D. Hanemann, N. S. McAlpine, E. Busch, and C. Kaalund, Appl. Surf. Sci. **92**, 484–490 (1996).
[27] W. Strube and E. Linke, Cryst. Res. Technol. **19**, 965–972 (1984).
[28] M. Zhenyi, S. C. Langford, J. T. Dickinson, M. H. Engelhard, and D. R. Baer, J. Mater. Res. **6**, 183–195 (1991).
[29] S. C. Langford, J. T. Dickinson, and L. C. Jensen, J. Appl. Phys. **62**, 1437–1449 (1987); K. A. Zimmerman, S. C. Langford, J. T. Dickinson, and P. Dion, J. Polym. Sci. B **31**, 1229–1243 (1993).
[30] J. T. Dickinson, S. C. Langford, L. C. Jensen, G. L. McVay, J. F. Kelso, and C. G. Pantano, J. Vac. Sci. Technol. A **6**, 1084–1089 (1988).
[31] D. Tabor, *Gases, liquids, and solids* (Cambridge U.P., Cambridge, 1991), p. 310.
[32] L. Pauling, *The Nature of the Chemical Bond* (Cornell U.P., Ithaca, 1960), 3rd ed.; J. A. Ripmeester and C. I. Ratcliffe, in *Inclusion Compounds*, edited by J. L. Atwood, J. E. D. Davies, and D. D. MacNicol (Oxford U.P., Oxford, 1991), Vol. 5, pp. 37–89.
[33] G. A. Jeffrey, in *Inclusion Compounds*, edited by J. L. Atwood, J. E. D. Davies, and D. D. MacNicol (Academic, New York, 1984), Vol. 1, pp. 135–190.
[34] Y. A. Dyadin, I. V. Bondaryuk, and F. V. Zhurko, in *Inclusion Compounds*, edited by J. L. Atwood, J. E. D. Davies, and D. D. MacNicol (Oxford U.P., Oxford, 1991), Vol. 5, pp. 213–275.
[35] S. R. Billeter, P. M. King, and W. F. van Gunsteren, J. Chem. Phys. **100**, 6692–6699 (1994).
[36] R. A. Hiller and S. J. Putterman, Phys. Rev. Lett. **75**, 3549–3551 (1995); addendum *ibid.* **77**, 2345 (1996).
[37] K. Stebe, personal communication.
[38] J. P. Dear, J. E. Field, and A. J. Watson, Nature **332**, 505–508 (1988); N. K. Bourne and J. E. Field, J. Fluid Mech. **244**, 225–240 (1992).
[39] N. K. Bourne, T. Obara, and J. E. Field, Philos. Trans. R. Soc. Lond. to appear December 1996.
[40] J. E. Field, in *Bubble Dynamics and Interface Phenomena*, edited by J. R. Blake, J. M. Boulton-Stone, and N. H. Thomas (Kluwer, Dordrecht, 1994), pp. 17–31.
[41] P. Jarman, J. Acoust. Soc. Am. **32**, 1459–1462 (1960); K. S. Suslick, Science **247**, 1439–1445 (1990).
[42] R. Hickling, J. Acoust. Soc. Am. **35**, 967–974 (1963); V. Kamath, A. Prosperetti, and F. Egolfopoulos, J. Acoust. Soc. Am. **93**, 248–260 (1993).
[43] N. K. Bourne, W. G. Proud, and J. E. Field, J. Acoust. Soc. Am. **100**, 2716 (1996).
[44] K. Weninger, S. J. Putterman, and B. P. Barber, Phys. Rev. E **54**, R2205–R2208 (1996).
[45] See, e.g., T. Lazaridis and M. E. Paulaitis, J. Phys. Chem. **96**, 3847–3855 (1992); A. Luzar and D. Chandler, Phys. Rev. Lett. **76**, 928–931 (1996); Nature **379**, 55–56 (1996).

Sound absorption height and width limits for polymer relaxations[a)]

Bruce Hartmann, Gilbert F. Lee, John D. Lee, and Jeffry J. Fedderly
Polymer Science Group, Naval Surface Warfare Center, 9500 MacArthur Boulevard, West Bethesda, Maryland 20817-5700

(Received 3 May 1996; accepted for publication 21 October 1996)

An analysis was performed to relate the height and width of the peak in shear sound absorption per wavelength as a function of frequency for the glass transition of a polymer. For the single relaxation time model, the width is 1.14 decades only at small values of the ratio of relaxed to unrelaxed sound speed. For the larger values of sound-speed ratio observed in polymer glass transitions, the width increases as the height increases. For the Havriliak–Negami model, the width increases as the height decreases in a manner similar to that for the complex modulus, though in this case there is a cutoff below the absolute maximum. The curve can be described by the relation that height times width is 1.5 decades of frequency. These predictions are in good agreement with experimental data for 21 polyurethanes. [S0001-4966(97)02804-X]

PACS numbers: 43.35.Fj [HEB]

INTRODUCTION

The purpose of this work is to establish the relation between the height and width of the peak in sound absorption per wavelength as a function of frequency for the glass transition in polymers. A similar program was followed in our earlier paper[1] for the height and width of the complex modulus loss factor peak. In the present work, the analysis is extended to shear sound absorption per wavelength. Calculations are done for both the single relaxation time model and the Havriliak–Negami[2] (HN) model. The results are compared and contrasted with the earlier study of the height and width of the loss factor peak.

The analysis begins with the relation between complex modulus and sound speed,[3]

$$G^*=\frac{\rho C^2}{(1-iR)^2}, \tag{1}$$

where $G^*=G'+iG''$ is complex shear modulus, ρ is density, C is shear sound speed, and R is defined as

$$R=\frac{\alpha C}{\omega}=\frac{\alpha\lambda}{2\pi}, \tag{2}$$

where α is shear absorption, $\omega=2\pi f$ is circular frequency, and λ is shear wavelength. The quantity $\alpha\lambda$ is the shear absorption per wavelength and R will be referred to as the normalized absorption per wavelength.

Separating G^* into real and imaginary parts yields

$$G'=\frac{\rho C^2(1-R^2)}{(1+R^2)^2}, \tag{3}$$

$$G''=\frac{2\rho C^2 R}{(1+R^2)^2}, \tag{4}$$

$$\tan\delta=\frac{G''}{G'}=\frac{2R}{1-R^2}, \tag{5}$$

where δ is the phase angle by which the shear strain lags the shear stress. In the complex modulus description, absorption is quantified by $\tan\delta$. For a material with no shear absorption, $\delta=0$ and $\tan\delta=0$. For a material that absorbs all shear waves (a typical liquid), $\delta=\pi/2$ and $\tan\delta$ is infinite.

Solving Eq. (5) for R yields

$$R=\frac{-1+\sqrt{1-\tan^2\delta}}{\tan\delta}, \tag{6}$$

where the positive root of the quadratic formula is chosen so that R will be a positive quantity. For small $\tan\delta$,

$$R\approx\tfrac{1}{2}\tan\delta, \quad \tan\delta\ll 1, \tag{7}$$

so that if $\tan\delta=0$, then $R=0$. For large $\tan\delta$,

$$R\approx 1-\cot\delta, \quad \tan\delta\gg 1, \tag{8}$$

so that if $\tan\delta$ is infinite, then $R=1$. Thus, as $\tan\delta$ varies between zero and infinity, R varies from zero to one, justifying calling this quantity the normalized absorption.

Sound speed can be calculated from Eq. (3) to yield

$$C^2=\frac{G'(1+R^2)^2}{\rho(1-R^2)}. \tag{9}$$

The high- and low-frequency behavior of C can be determined in the following manner. Qualitatively, $\tan\delta$ has a peak in the glass transition region and approaches zero above and below the peak.[1] From Eq. (6), it follows that as $\tan\delta$ approaches zero, R also approaches zero. Thus at high frequency (relative to the glass transition frequency), $R\to 0$ and $G'\to G_\infty$, the unrelaxed modulus, so that

$$C_\infty=\sqrt{G_\infty/\rho}, \tag{10}$$

where C_∞ is the limiting sound speed at high frequency or unrelaxed sound speed. At low frequency (relative to the

[a)]A preliminary version of this paper was published in the Proceedings of the 15th International Congress on Acoustics, Trondheim, Norway, June, 1995.

glass transition frequency), once again $R \to 0$ and $G' \to G_0$, the relaxed modulus, so that

$$C_\infty = \sqrt{G_0/\rho}, \tag{11}$$

where C_0 is the limiting sound speed at low frequency or relaxed sound speed. The ratio of Eq. (11) to Eq. (10) yields the useful relation

$$C_0^2/C_\infty^2 = G_0/G_\infty. \tag{12}$$

The basic equation being examined here is Eq. (6). By choosing a model for the frequency dependence of tan δ, the frequency dependence of R can be determined. The particular interest here is the glass transition relaxation in polymers, for which tan δ versus frequency has a peak of a certain height and width. The normalized absorption per wavelength will likewise have a peak and the relation between the height and width of this peak is desired. In the earlier paper,[1] these relations were determined for tan δ.

I. SINGLE RELAXATION TIME MODEL

Before considering the general dispersion relation for a polymer relaxation, it is instructive to look at the simple case of a single relaxation time (SRT) model. For the SRT model,[1]

$$\tan\,\delta = \frac{(1-G_0/G_\infty)\omega\tau}{G_0/G_\infty + \omega^2\tau^2} = \frac{(1-C_0^2/C_\infty^2)\omega\tau}{C_0^2/C_\infty^2 + \omega^2\tau^2}, \tag{13}$$

where τ is the relaxation time and Eq. (12) has been used. Using this particular dispersion relation in the general expression in Eq. (6) yields

$$R = \frac{-(C_0^2/C_\infty^2 + \omega^2\tau^2) + \sqrt{(C_0^2/C_\infty^2 + \omega^2\tau^2)^2 + (1-C_0^2/C_\infty^2)^2\omega^2\tau^2}}{(1-C_0^2/C_\infty^2)\omega\tau}. \tag{14}$$

A plot of R versus log-reduced frequency, $\omega\tau$, is shown as the solid line in Fig. 1 for $C_0/C_\infty = 0.055$, a typical value for the glass transition.

The high- and low-frequency limits of Eq. (14) are given by

$$R \approx \frac{1}{2\omega\tau}, \quad \omega\tau \gg 1 \tag{15}$$

and

$$R \approx \frac{\omega\tau}{2C_0^2/C_\infty^2}, \quad \omega\tau \ll 1. \tag{16}$$

Here R reaches its maximum value at the same frequency that tan δ reaches its maximum, which has already been shown[1] to be

$$\omega_{\max}\tau = \sqrt{G_0/G_\infty} = C_0/C_\infty. \tag{17}$$

From Eq. (13), at this frequency

$$\tan\,\delta_{\max} = \frac{(1-C_0^2/C_\infty^2)}{2C_0/C_\infty}. \tag{18}$$

Substituting this result into Eq. (6) yields

$$R_{\max} = \frac{1-C_0/C_\infty}{1+C_0/C_\infty}. \tag{19}$$

As noted before, tan $\delta_{\max}$ diverges as $C_0 \to 0$ (a typical liquid). On the other hand, $R_{\max} \to 1$ as $C_0 \to 0$. The quantity $R_{\max}$ will be referred to as the height H.

The next step is to determine the full width at half-height of the peak in R, defined as the log frequency range over which R drops to $H/2$. This quantity also depends only on the sound-speed ratio. Standard texts[4,5] quote a width of 1.14 decades for the SRT model, but this is an approximation valid only for $C_0/C_\infty \geqslant 0.6$. By numerical evaluation, we find the plot shown in Fig. 2, which shows that the width is not constant but has the unusual behavior of increasing without limit as the sound-speed ratio approaches zero.

The results of Fig. 2 can be thought of representing three different physical processes. The small sound-speed ratio region corresponds to liquidlike behavior. Here the height is nearly one and the width extremely broad, given by the equation

$$W = -2\log(C_0/C_\infty) - 0.25, \quad C_0/C_\infty \leqslant 0.001. \tag{20}$$

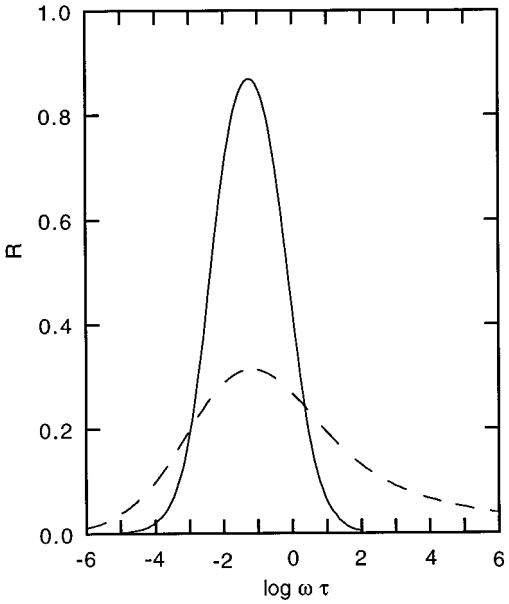

FIG. 1. Normalized absorption per wavelength versus reduced frequency for the single relaxation time model (solid line, $C_0/C_\infty = 0.055$, $\alpha = 1$, $\beta = 1$) and for the Havriliak–Negami model (dashed line, $C_0/C_\infty = 0.055$, $\alpha = 0.5$, $\beta = 0.1$).

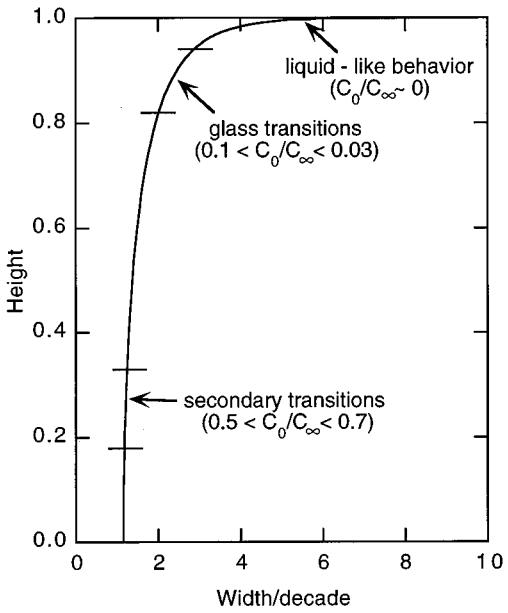

FIG. 2. Normalized absorption per wavelength peak height versus width for the single relaxation time model ($0.0024<C_0/C_\infty<1$, $\alpha=1$, $\beta=1$).

In other words, a typical liquid absorbs most of the shear energy for almost all frequencies. Somewhat larger sound-speed ratios, from about 0.1 to 0.03, are observed in polymer glass transitions. In this region, the width increases from about two to three decades as the height increases from 0.82 to 0.94. Finally, secondary transitions in polymers (such as crankshaft rotation[6]) correspond to higher sound-speed ratios, from about 0.5 to 0.7, where the width is essentially constant at 1.14 decades while the height varies from about 0.18 to 0.33. This is the region more familiar to those dealing with relaxations in simple liquids and gases.

II. HAVRILIAK–NEGAMI MODEL

The most successful model for the frequency dependence of the complex modulus in the glass transition relaxation for polymers is that of Havriliak and Negami.[2] This model describes all the important features of the relaxation: a peak in tan δ that is broad and asymmetric. The model is given by

$$\frac{G^*-G_\infty}{G_0-G_\infty}=\frac{1}{[1+(i\omega\tau)^\alpha]^\beta}, \tag{21}$$

where α is a dimensionless parameter with magnitude between zero and one that governs the width of the relaxation and β is another dimensionless parameter, also with magnitude between zero and one, that governs the asymmetry of the relaxation. Note that when $\alpha=\beta=1$, the HN model reduces to the SRT model.

Using this model for the dispersion relation, the height and width of the peak in R can be calculated numerically. As with the SRT model, the height and width are independent of τ. For the SRT model, height and width depend only on the sound-speed ratio, C_0/C_∞. In the HN model, height and width depend on α and β as well as the sound-speed ratio. A plot of R versus log-reduced frequency for typical glass transition values of $\alpha=0.5$, $\beta=0.1$, and $C_0/C_\infty=0.055$ is shown in Fig. 1. In comparison to the result for the SRT model with the same sound-speed ratio, also shown in Fig. 1, the absorption peak for the HN model is lower, broader, and less symmetrical.

In the general case, all three parameters (α, β, and C_0/C_∞) vary arbitrarily in the calculation of height and width. This produces a complicated multidimensional function. However, when specifically considering the glass transition, the range of the parameters is limited and some simplification results. The parameter range is based on experimental measurements, previously reported and summarized in our earlier paper on complex modulus. A brief description of the experimental data is in order before further analysis of the HN equation.

All of the experimental data were obtained in our laboratory using a resonance apparatus. Data are taken over a frequency range of about 2 decades around 1 kHz and a temperature range from −60 °C to 70 °C. The data is then shifted using the time–temperature superposition principle to obtain a master curve of shear modulus and loss factor over a very wide frequency range at a constant reference temperature (25 °C). This data is fitted to Eq. (21) using nonlinear regression. The five HN parameters are then used to describe each polymer. This procedure was used for a variety of polyurethanes synthesized in this laboratory, and the HN parameters were published in various places. The polymers vary in molecular weight, hard segment concentration, polyol type, isocyanate type, and chain extender type. Data for 21 polyurethanes was presented in our earlier study.[1] It is not expected that there is anything special about the polyurethanes, they are merely a convenient class of polymers to obtain a wide range of properties, from soft to hard.

The height and width of the normalized absorption per wavelength was calculated for each of these 21 polymers. The following ranges were observed: $0.2<\alpha<0.8$, $0.02<\beta<0.50$, and $0.03<C_0/C_\infty<0.10$. Calculations done in the observed parameter space demonstrate that α is the key parameter governing the height–width relation. It is sufficient to pick a typical value for β and the sound-speed ratio and allow α to vary over its allowable range to obtain a description of the behavior of polymers. The representative values of $\beta=0.1$ and $C_0/C_\infty=0.055$ were chosen here.

Taking $\beta=0.1$, $C_0/C_\infty=0.055$, and $0.2<\alpha\leqslant1$, numerical calculation yields the solid line in Fig. 3 along with the experimental data discussed above. The agreement between the calculated curve and the experimental data is considered satisfactory to confirm the relation between absorption height and width.

Note that the point of maximum height (0.773), calculated numerically as described above, on the solid line of Fig. 3 corresponds to $\alpha=1$ and is the theoretically maximum height that can be achieved for any polyurethane. This is a difference with the loss factor height–width relation, for which there is no theoretical upper limit.

It has sometimes been suggested that the area under the glass transition absorption peak is a constant. Crudely, this would imply that the product of height times width is a constant. Fitting this relation to the predicted curve in Fig. 3, we

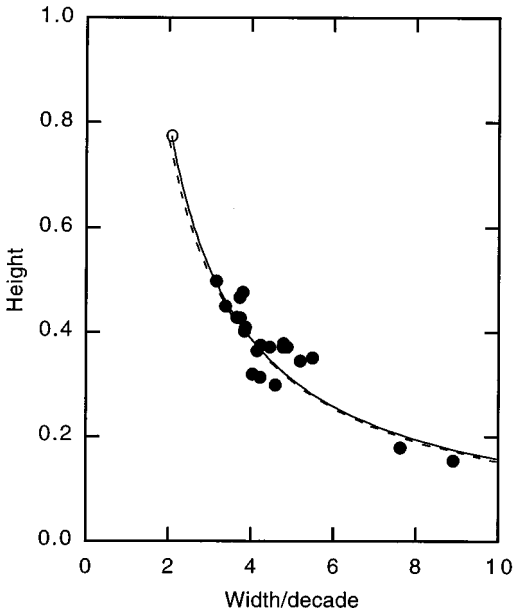

FIG. 3. Normalized absorption per wavelength peak height versus width for the Havriliak–Negami model with $0.2<\alpha<1$, $C_0/C_\infty=0.055$, and $\beta=0.1$ (solid line) compared with experimental data (solid circles) and with the approximation $HW=1.5$ decades (dashed line). The open circle is the maximum allowable height.

find $HW=1.5$ decades. This reciprocal curve is also shown in Fig. 3 as the dashed line. Since the agreement between the two curves is well within the scatter of the data, $HW=1.5$ decades is a useful summary of the results obtained here. This result was obtained using the height times width as an approximation to the area under the absorption curve. An exact evaluation of the area was also determined by numerical integration using $\beta=0.1$, $C_0/C_\infty=0.055$, and $0.2<\alpha\leqslant 1$. In this case, the product of height times width varied from 1.8 to 2.1 decades. Thus, the area under the curve is very nearly a constant and that constant is close to the value obtained by approximating the area as height times width.

III. CONCLUSIONS

Like the loss factor, the minimum absorption per wavelength width at half-height is 1.14 decades. Unlike the loss factor, the width has the unusual behavior of increasing without limit as the sound-speed ratio decreases. Polymer glass transitions are in the intermediate region of this behavior.

Like the loss factor, the predicted height versus width curve for polymer glass transitions has a reciprocal shape, showing that high peaks are necessarily narrow and broad peaks are necessarily low. Unlike the loss factor, there is an upper bound on the sound absorption per wavelength which is less than the maximum theoretical value of unity.

Specifically, the highest value that can be obtained is 0.773 and has a width of about 2 decades. For a width of 10 decades, the height is no more than about 0.2. As a useful summary of the results, the product of the height and width is 1.5 decades.

ACKNOWLEDGMENT

This project was supported by the Carderock Division of the Naval Surface Warfare Center's In-house Laboratory Independent Research Program sponsored by the Office of Naval Research.

[1] B. Hartmann, G. F. Lee, and J. D. Lee, ''Loss factor height and width limits for polymer relaxations,'' J. Acoust. Soc. Am. **95**, 226–233 (1994).
[2] S. Havriliak and S. Negami, ''A Complex Plane Representation of Dielectric and Mechanical Relaxation Processes in Some Polymers,'' Polymer **8**, 161–210 (1967).
[3] R. S. Marvin and J. E. McKinney, ''Volume Relaxations in Amorphous Polymers,'' in *Physical Acoustics*, edited by W. P. Mason (Academic, New York, 1965), Vol. IIB, Chap. 9, pp. 165–229.
[4] K. F. Herzfeld and T. A. Litovitz, *Absorption and Dispersion of Ultrasonic Waves* (Academic, New York, 1959).
[5] H.-J. Bauer, ''Phenomenological Theory of the Relaxation Phenomena in Gases,'' in *Physical Acoustics*, edited by W. P. Mason (Academic, New York, 1965), Vol. IIA, Chap. 2, pp. 48–131.
[6] N. G. McCrum, B. E. Read, and G. Williams, *Anelastic and Dielectric Effects in Polymeric Solids* (Wiley, New York, 1967).

Sonoluminescence: An alternative "electrohydrodynamic" hypothesis

Thierry Lepoint,[a] Damien De Pauw, and Françoise Lepoint-Mullie
Laboratoire de Sonochimie et d'Etude de la Cavitation, Institut Meurice-CERIA 1, Avenue E. Gryson, 1070 Brussels, Belgium

Max Goldman and Alice Goldman
Laboratoire de Physique des Décharges, Ecole Supérieure d'Electricité, Plateau de Moulon, 91192 Gif-sur-Yvette Cedex, France

(Received 4 April 1996; accepted for publication 24 September 1996)

A mechanism is proposed for the sonoluminescence (SL) arising from a single bubble maintained in levitation by an acoustic field. This proposal follows from a plasma diagnostic analysis which reveals that a single Ar bubble is characterized by a sparklike plasma (electron temperature and density: 20 000 K and 10^{25} m^{-3}, respectively). The theoretical scenario (based on four hypotheses) is as follows. During its expansion and the major part of its collapse, a levitating bubble is governed by Rayleigh–Plesset dynamics. Several ns before maximum collapse the bubble interface becomes unstable and needlelike jets (the number of which is thought to be about 10) invade the bubble more or less symmetrically. Each jet (radius≈65 nm) reaches a distance equal to half of the radius of the bubble and releases a droplet (radius≈150 nm), so that an intracavity spray is released about 3 ns (perhaps less) before the time of collapse. It is implicitly proposed that the acoustic pressure at which inward jets (likely to disintegrate) may form constitutes the sonoluminescence threshold. Because of the serious distortion of the electrical double layer surrounding the bubble, both jets and droplets are electrically (but oppositely) charged. The electrical field is so high that electron emission occurs to such an extent that within 16 fs an enormous amount of energy (Joule effect) is released in the jet volume (4×10^{11} J m^{-3}). The jets are ablated and a microplasma highly charged with energy (electronic temperature ⩾30 000 K; electronic density: 10^{26} m^{-3}; lifetime <10 ps) expands at a velocity higher than 60 000 m s^{-1} so that a diverging shock wave is generated. An overpressure (higher than 1000 atm) accompanies the microplasma formation and is believed to induce strong deceleration in the bubble wall. The mechanism proposed is showed to apply to the case of bubbles in nonaqueous solvents, too. Some open questions are reported. Amongst them, (1) the possible role of the overpressure on Rayleigh–Plesset dynamics (particularly in the collapse zone) and on the aborted growth of the intracavity protuberances which might result from an incomplete ablation of the jets during the microplasma formation, (2) the effects of dissolved gases (air versus H_2 or D_2), (3) the effect of the liquid temperature, and (4) the role of small amounts of organic substances on SL intensity. Some experiments are suggested that may be capable of checking and distinguishing the present hypothesis from others. [S0001-4966(97)04704-8]

PACS numbers: 43.35.Ud, 78.60.Mq [HEB]

LIST OF SYMBOLS

a	acceleration of the bubble wall at the instant of SL flash emission
c	sound velocity
d	length of a gap where a discharge is triggered off
$D_{\text{H-O}}$	dissociation energy of the hydroxyl radical (kJ mole^{-1})
$D_{\text{H-OH}}$	dissociation energy of water (kJ mole^{-1})
E	electrical field
E^+	electrical field between a droplet and a jet (in the case of a positively charged droplet)
E^-	electrical field between a droplet and a jet (in the case of a negatively charged droplet)
E_R	residual energy distributed on the translational degrees of freedom of ions and electrons
$E(t=0)$	initial electrical field
$E(t)$	instantaneous value of E
h	Planck constant
I	charging electrical current
I_s	electrical current in the case of a spark triggered off in air
J	electric current density
$J(t)$	instantaneous value of J
J_{FN}	electric current density associated with the Fowler–Nordheim (tunnel) effect
J_{RD}	electric current density associated with thermoelectronic emission (Richardson–Dushman)
J_{tot}	sum of J_{FN} and J_{RD}
k	Boltzmann constant
l_n	length of a neck between a filament of liquid and a droplet in formation

[a]Electronic mail: tlepoint@resulb.ulb.ac.be

 0001-4966/97/101(4)/2012/19/$10.00

L	length of an intracavity jet
m	electron mass
n	multiplying factor in an avalanche process
n_e	number of electrons resulting from the ionization of atoms constituting the matter of a jet
n_{ion}	number of ions resulting from the ionization of atoms constituting the matter of a jet
n_j	number of intracavity jets
n_0	number of ions (at the vicinity of an interface) per volume unit
N_{col}	mean number of ionizing collision
N_e	electron density in a plasma (cm^{-3})
$N_{e,\text{th}}$	theoretical electron density in a plasma
N_g	gas density (number of molecules per unit volume)
P_a	acoustic pressure
P_a'	maximum amplitude of the acoustic pressure
ΔP_d	pressure required to generate a droplet from a jet in collapse
$P_{\text{exp }d}$	pressure required to induce the flow of liquid in order to create a droplet from a jet
$P_{\text{exp jet}}$	pressure required to induce the flow of liquid in order to create an intracavity jet
P_g	gas pressure inside a cavity
ΔP_{jet}	pressure required to generate an intracavity jet from a collapsing cavity
ΔP_m	overpressure associated with the formation of the microplasma
P_0	equilibrium pressure inside a cavity
q	electron charge
Q^+	total positive charge acquired by a droplet or a jet
Q^-	total negative charge acquired by a droplet or a jet
r_{jet}	radius of an intracavity jet
r_n	radius of a neck between a filament of liquid and a droplet in formation
r_s	radius of a spark channel
R	bubble radius at any given moment
R_0	initial radius of a bubble
R_{co}	radius of a bubble at maximum compression (determined by the Rayleigh–Plesset equation)
R_d	droplet radius
R_{max}	radius of a bubble at maximum expansion
$\dot{R}$	bubble wall velocity
$\ddot{R}$	bubble wall acceleration
t	time
Δt	time during which electron emission occurs ($=\Sigma \Delta t_n$)
t_m	lifetime of the microplasma
Δt_n	time interval used in an iterative procedure for the determination of $J(t)$ and $E(t)$
t_s	time of expansion for a plasma to reach an envelop of radius r_S
T	temperature (absolute)
T_e	electronic temperature in a plasma
T_{ion}	ionic temperature in a plasma
v_g	gas velocity in the vicinity of a liquid jet
v_{jet}	velocity of a liquid jet
v_m	expansion velocity of the microplasma
v_x	velocity of the flow of liquid rushing through a neck between a filament and a droplet in formation (along the x axis)
α	radius of the van der Waals hard core
β	neutralization efficiency
γ	ratio of the specific heats of the intracavity gas (c_p/c_v)
ϵ	product of the relative permittivity of a given medium and vacuum permittivity
ϵ_g	gas permittivity (relative value)
ϵ_0	vacuum permittivity
ϕ	work function (eV)
ϕ_w	work function of water (eV)
λ_e	mean free path of electrons
ζ	electrokinetic potential
η	dynamic viscosity
θ	relaxation time of the electrical double layer
ν	kinematic viscosity
ρ	density of a liquid
ρ_{ch}	electrical charge density
ρ_g	density of the intracavity gas
ρ_s	initial density of air in which a spark is triggered off
σ	surface tension
τ	total shear stress
τ_{jet}	shear stress associated with jet formation
τ_d	shear stress associated with droplet formation
χ_{H}	first ionization potential of H
χ_{O}	first ionization potential of O
ψ	electrical potential at any point of the electrical double layer
ψ_0	electrical potential at the gas-liquid interface
ψ_δ	electrical potential at the slipping plane separating the fixed layer and the diffuse layer constituting the electrical double layer
ω_a	acoustic pulsation

INTRODUCTION

This paper deals with the ''extreme conditions'' at the origin of sonoluminescence (SL), i.e., the weak emission of light observed when cavitation bubbles collapse under the influence of an acoustic field passing through a liquid. More particularly, we focus our attention on the luminescence arising from a single bubble maintained in levitation by an acoustic field (single-bubble sonoluminescence, SBSL). We report on the outlines of an original proposal presented orally at the 128th meeting of the Acoustical Society of America (Lepoint *et al.*, 1994).

In 1933, Marinesco and Trillat (1933) discovered that photographic plates could be darkened when submerged in ultrasonically irradiated water. One year later, Zimakov (1934) and Frenzel and Schultes (1934) attributed this result to the luminescence from the sound field. Later, Levshin and

Rzheykin (1937) provided proof that SL arises from the gaseous phase of cavities.

Such results triggered off the search for a correlation between bubble behavior (i.e., bubble dynamics) and SL emission. For a long time, the determination of the parameters relevant to SL (bubble radii, SL flash duration and phase, etc.) was difficult and limited in accuracy. In fact, SL was almost exclusively generated in inertial cavitation—a regime under which bubbles undergo fragmentation after violent collapse—and in a multibubble field—a system in which bubbles of various sizes are loosely coupled and in which growth and collapse are rather random (multibubbles sonoluminescence in inertial cavitation, MBSL-IC). However, according to Matula and Roy (1995), MBSL-IC flash duration does not exceed 1 ns in the case of low frequencies (20 kHz). For the frequency range from 20 to 400 kHz, it has also been established that SL is produced during the compression phase of the sound field (Günther *et al.*, 1959; Jarman, 1960; Macleay and Holroyd, 1961; Neghisi, 1961; Kuttruff, 1962). These results have been corroborated in the case of multibubble sonoluminescence in stable cavitation (MBSL-SC), a regime under which bubbles oscillate for long periods around their equilibrium radius. Crum and Gaitan (1989) showed that near the cavitation threshold, SL emission only occurs at a fixed phase of the acoustic cycle compression.

Substantial progress was made more recently when Gaitan *et al.* (1992) showed that a single bubble of air could be trapped in a standing acoustic setup in a water-filled container. In a typical experiment, the nonlinear pulsations of the cavity displayed an abrupt transition as the intensity of the sound wave was increased, and light was then emitted from the gaseous phase of the bubble. This observation opened the way to striking new experimental results very recently reported by the Putterman (Löfstedt *et al.*, 1995) and Atchley (1993) groups.

A single levitating bubble shows a great ability to focus the low-energy density of a sound field, typically by a factor of 10^{12} (Barber and Putterman, 1991). The main characteristics of the SBSL are: (1) the duration of each pulse of light emitted measured as less than 50 ps (Barber *et al.*, 1991); (2) synchronous emission, with one burst per cycle with a ''jitter'' phase of less than 40–50 ps (Barber *et al.*, 1991); and (3) the spectral distribution of light characterized by broad continua extending from 800 nm to probably much less than 200 nm whatever the nature of the gas dissolved (air, He, Ar, Xe, N_2 and their mixtures) (Hiller *et al.*, 1992; Carlson *et al.*, 1993; Hiller *et al.*, 1994). More recently, SBSL spectra were reported which concern (i) water or heavy water in the presence of H_2 or D_2 [Hiller and Putterman (1995)] and (ii) organic solvents (Weninger *et al.*, 1995). The temporal localization of the SBSL flash is still a matter of discussion. Indeed, to begin with, Barber and Putterman (1992) reported that SBSL emission occurs 5–10 ns before maximum collapse. More recently, however, Putterman (1994) suggested that the flash could occur less than 5 ns before maximum compression, and perhaps at the same time as this maximum.

A great deal of theoretical effort has been devoted to explaining these facts and, indeed, still is. The first analysis exploited the hot-spot theory, based on the Rayleigh–Plesset equation, which describes the local heating of the intracavity gaseous phase through adiabatic compression (or more sophisticated descriptions) (Gaitan *et al.*, 1992; Kamath *et al.*, 1993; Yasui, 1995). In this theory, the SL is considered to be the emission of excited species superimposed on the radiative recombination of radicals (chemiluminescence) generated during the ultraflash pyrolysis of the intracavity content. However, if this model can predict intracavity temperatures of several thousand kelvins and pressures of several hundred atmospheres, it fails to explain the extremely short duration of the flashes of light. Indeed, some calculations have shown that in typical SBSL conditions, the intracavity temperatures due to compression could be more than 2000 K for about 20 ns (Kamath *et al.*, 1993). This has led to the question: How can the bubble content remain compressed for so long without radiating?

Concluding that the assumption of adiabaticity (or any improvements integrated under the label of the hot-spot theory) cannot account for the experimental results, Barber and Putterman (1992) and Löfstedt *et al.* (1993) were the first to rehabilitate the hypothesis of an imploding shock wave launched from the cavity walls which are assumed to reach supersonic speeds toward the end of the bubble compression. This proposal stimulated numerical calculations based on the coupling of the Rayleigh–Plesset and Euler equations (Wu and Roberts, 1993, 1994; Moss *et al.*, 1994). These computations predict that the gaseous nucleus at the very center of the bubble could be energized by a shock wave so that thermodynamic temperatures between 10^5 and 10^6 K could be reached. In this context, light emission would result from bremsstrahlung. Clearly, this model is closely associated with the hypothesis according to which the shock-wave front remains stable during its progression. Otherwise, the internal temperature could decrease dramatically because of the front instability associated with the launch from a rough bubble interface, or because of the amplification of instability during the shock-wave progression. Other calculations providing more modest heating (7000 to 44 000 K) have recently been reported (Kwak and Yang, 1995).

A complement to this initial approach (based on relatively more modest heating) was recently introduced by Frommhold and Atchley (1994), who show that the collision-induced emission of atom-atom or atom-molecule pairs excited by a shock wave is an attractive alternative to bremsstrahlung.

In an alternative model, Schwinger (1993) suggests that the filling of a dielectric hole (a bubble) by a liquid with a different permittivity can be associated with the release of Casimir energy. In this way, the focusing of acoustic stress is transduced directly into quantum excitation through the change in the zero point energy as the hole is filled. The simplified theory yields a calculated spectrum which is steeper than those obtained experimentally.

In an independent approach, Eberlein (1996) proposes that sonoluminescence is explained in terms of quantum ra-

diation by moving interfaces between media of different polarizability.

Bernstein and Zakin (1995) suggested that SL emission arises from electrons confined to voids in the hot, dense fluid formed during the final stages of bubble collapse, with the electrons produced by high temperatures of bubble constituants (ionization degree $\leqslant 10^{-2}$).

Besides, Hickling (1994) proposed that sonoluminescence could arise from the cracking of an ice shell formed in the close vicinity of the bubble-liquid interface while the bubble was near maximum compression (the solidification would be forced because of the high pressure inside the cavity).

Basing himself on the theoretical description that an inward microjet may form during compression (Longuet-Higgins and Oguz, 1995), Prosperetti (1996) recently suggested that light emission could be due to a fracturing of the liquid caused by the rapid impact of the jet on the other side of the bubble.

The absence of any consensus on the nature and magnitude of the ''extreme conditions'' occurring in a collapsing cavity has led us to carry out an analysis based on plasma diagnostic techniques (Lepoint-Mullie *et al.*, 1996). Via this independent analysis (summarized in Sec. I), we arrived at the conclusion that the intracavity medium of a single sonoluminescing argon bubble is a hot and dense plasma with an electronic temperature of about 20 000 K (perhaps more) and an electron density of about 10^{25} m^{-3}. Such a plasma is compatible with a sparklike process. It may also be noticed that SBSL spectra strikingly ressemble the high-pressures sparks which were studied in the past as possible calibration sources in emission spectroscopy (Lochte-Holtgreven and Richter, 1968). We thus formulate a few hypotheses (Sec. II) in order to establish a reasonable link between bubble dynamics and the possible formation of a microplasma presenting the characteristics matching the properties of SBSL. The development of the proposed mechanism is reported in Secs. III and IV. Before the Conclusion, Sec. V contains (i) a ''triangular'' comparison between the plasma characteristics obtained in the field of the ''electrohydrodynamic hypothesis,'' those obtained from SBSL spectral density, and exogeneous results (capillary sparks), (ii) suggested experiments which could (in)validate the mechanism proposed, and (iii) a discussion.

I. NATURE OF THE EXTREME CONDITIONS AT THE ROOT OF SBSL

Amongst results of the numerous experiments on SBSL several optical spectra have been reported which correspond to broad continua extending from 600 nm to below 200 nm (except in the case of Xe bubbles in water or D_2 (or H_2) bubbles in D_2O, for which the intensity of the continua strongly decreases in the near UV region). The question to be answered is why only continua were measured and not the discrete spectra of OH, C_2, O, N, He, Ar, and Xe. In a recent analysis, Lepoint-Mullie *et al.* (1996) arrive at the conclusion that the radiative recombinations of electrons and excited states (ions or atoms) may reveal an answer to this question. This analysis is based on plasma diagnostic techniques. Considering the spectrum emitted by a single Ar bubble such as studied by Hiller *et al.* (1994) and assuming that the bubble is mainly filled with Ar atoms, it was deduced (i) that the plasma is optically thin, (ii) that the excitation temperature of the intracavity medium was about 20 000 K, perhaps more, (iii) that at such temperatures the radiative recombinations of electrons and excited states of ions and atoms (free-bound transitions) largely dominates bremmstrahlung (free-free transitions), (iv) that the electron density (N_e) is about 10^{25} m^{-3}. Temperature was obtained under the assumption that the plasma is in local thermodynamic equilibrium (equivalence of the different temperatures at least ''locally,'' this assumption is verified via the Griem criterion). Based on Saha–Eggert equations, a calculation gives the degree of ionization as being 50%, approximately. By spotting the couple $\{N_e\,;\,T_e\}$ on a plasma states diagram (Venugopalan, 1971), it has been deduced that the intracavity medium developed by a single sonoluminescing Ar bubble corresponds to a high-energy process as a spark. By taking into account the high temperatures associated with the intracavity plasma, the conclusion emerges that it is not expected to observe the emission lines associated with the presence of nonvolatile substances even if they penetrate into a single-collapsing bubble. One of the reason for this is that in the case of high temperatures, the excited level(s) of a neutral species is/are depopulated in aid of ionization. The higher the temperature (and the lower the ionization potential of the species considered), the higher the degree of ionization.

How can a link be established between the observation that a sparklike plasma state is generated inside a collapsing bubble and single-bubble behavior, i.e., collapse?

II. HYPOTHESES

A link could be established if a few hypotheses were formulated which concern both bubble dynamics and the role of the microstructured bubble-liquid interface.

The first hypothesis consists of acknowledging that the bubble liquid interface may be subjected to nonradial distortions coming from (i) light departures from sphericity which lead to inward critical microjets, such as described by Longuet-Higgins and Oguz (1995), or (ii) the Rayleigh–Taylor (RT) instability so that towards the end of bubble implosion, the bubble-liquid interface is unstable and liquid jets can partially penetrate the cavity.

While it is of major interest, the description of critical microjets is not yet sufficiently developed in the case of a gas bubble pulsating nonlinearly in an acoustic field. Taking this observation into consideration, we will focus our attention to the case of RT instability. Our hypothesis results from an extrapolation of what is known in the case of inertial cavitation (Leighton, 1994; see pp. 335–341). On the one hand, it has been reported that the range of acoustic pressures needed to make a single bubble luminescent is just below the inertial cavitation threshold (Gaitan *et al.*, 1992). On the other hand, since the work of Plesset and Mitchell (1956) [which constitutes an extension of a previous study by Taylor (1950), extended in the case of Plesset and Mitchell to spherical interfaces], it has been accepted that bubble interfaces are

unstable on collapse when the acceleration is directed from liquid to gas (see also Birkhoff, 1954, 1956). A recent analysis of the nonradial distortions of bubbles during their collapse has been reported in the case of a single bubble in water (Brenner *et al.*, 1995). In Sec. V, we propose a possible mechanism for damping the growth of RT instability which, in the absence of this mechanism, could amplify until bubble demise.

The second hypothesis is to assume that liquid jets can fragment so that a spray of tiny electrified droplets is shed inside the bubble. The hypothesis of electrification is based on work on atmospheric (static) electrification which helps to explain the origin of thunderstorms (Magono, 1980; Wahlin, 1986). More particularly, we will focus on the work by Iribarne (1972), who studied the electrification of spray droplets attributed to the shearing of the Stern–Helmoltz electrical layer at gas-liquid interfaces, and who also pointed out that this type of mechanism is present in most liquid-disrupting processes, particularly in the case of water (bubble-bursting, splashing, the break up of large drops in falls, etc.).

The third hypothesis is related to the calculated values of the electrical field between the jets and the droplets projected inside the cavity ($E \approx 10^9$ to 10^{10} V m^{-1}, see Sec. III). Given the emission of electrons from both metals and dielectric materials when submitted to high electrical fields (von Engel, 1983) (even in the case of more modest values of E than those reported above), we assume that liquids behave analogously. Though most organic liquids are known to be electrified through spraying process, which leads to burning or explosions in the case of organic liquids (Schaeffer, 1958), we will consider the particular case of water because of the numerous data associated with it.

The fourth hypothesis is to consider by analogy what occurs in the case of metals submitted to electrical fields to the extent that matter is ablated as a result of an extremely brief but violent release of energy induced by the high values of the electric current density associated with high electrical fields. We consequently assume that microplasma will result from this local ''overheating'' of the liquid constituting the droplets and jets, and that this microplasma will be at the root of sonoluminescence. The theoretical scenario is given in the abstract.

This reasoning is based on the well-established fact that the rupture of liquids may cause microsparks that sometimes lead to gas explosions (Loeb, 1958). By way of an example, the luminescence of waterfalls or tanker explosions (during washing operation or due to splashing in partially filled tanks in heavy seas) was finally traced back to electrostatic charges on droplets and in mist (von Engel, 1983). In such case, the microspark is not actuated by an applied voltage between electrodes, but by electric charges carried by small drops.

It shall be noted that in this work, we do not deal with *ad hoc* hypotheses (in the sense that these latter have not been selected with the specific intention to obtain the most coherent results) but that we consider *ab initio* hypotheses associated with the different fields concerned (via strict applications or extrapolations of existing knowledges).

In the text below, we use parameter values both arbitrarily chosen and taken from the literature in order to accede to the calculations. Our intention is to determine whether SL can be explained in terms of the hypothesis cited above with reasonable parameters values. For reasons of clarity the present analysis is restricted to this approach. Of course, we are concerned about the sensitivity of the proposed model and other choices of parameter values are possible. Both the great number of parameters and the fact that a given parameter can be found in different stages of the model with contradictory effects (and often in nonlinear equations) lead us to confine the present report to a possible scenario for explaining SL from bubble collapse. However, it should be noted that the model presents a certain robustness. For example we propose (1) an analysis of the variation of the electric charges and field with respect to droplets and jets radius (Sec. III C 3) and (2) an analysis (based on a review of the literature) which reveals that not only water but organic solvants too, can be involved in electrification and explosions (Sec. IV A).

III. FROM BUBBLE-LIQUID INSTABILITY TO THE ELECTRIFICATION OF INTRACAVITY DROPLETS

A. Bubble distortion-temporal localization

The interface between two superimposed immiscible fluids can undergo instability, a case of which, the so-called Kelvin–Helmoltz instability, describes the disturbances at the interface of a stratified heterogeneous fluid in relative horizontal motion.

When two immiscible fluids are accelerated one relative to the other, this can produce Rayleigh–Taylor instability. Two case are envisageable: (1) the case of a plane interface, for which Taylor (1950) showed that the interface is stable when the acceleration is directed from a denser toward a lighter fluid, and unstable when it goes in the opposite direction, (2) the case of a spherical interface, for which Plesset (1954) shows that the stability conditions derived by Taylor for plane interfaces do not apply without significant modifications.

Indeed in the case of an expanding bubble, for example, there is a balance between two antagonistic effects, i.e., the stabilizing effect of the diverging streamlines and the destabilizing influence associated with the acceleration of the intracavity gas towards the liquid. On the other hand, in the case of a collapsing bubble, the stabilizing effect associated with the acceleration of the liquid towards the gas can be thwarted by the destabilizing influence of the converging streamlines. The (in)stability characteristics of a spherical interface are not only related to the acceleration of this latter (such as in the case of RT instability for plane interfaces) but also depend on the velocity of the interface. In several usual analysis, the specification of the bubble shape involves the use of an expansion in terms of spherical harmonics for which the amplitude of the spherical harmonic components have to be determined. To this end several authors have obtained more or less complex equations. Plesset (1954) solved the equation of motion of an incompressible, inviscid, unbounded fluid in the case of the small-amplitude approximation. Birkoff (1954, see also 1956) analyzed the role of sur-

face tension. A summary is given by Plesset and Prosperetti (1977).

The quantitative investigation of the stability of an expanding or collapsing cavitation bubble has been carried out by Plesset and Mitchell (1956), who obtained solutions of the equation allowing the determination of the amplitude of the spherical harmonic components. Plesset and Mitchell showed that, although on the basis of the plane RT case it would be expected that the growth phase would be accompanied by surface instability, no significant deviations from spherical shape occur. The explanation is that though the acceleration is large, its destabilizing influence is of short duration and therefore very effectively counterbalanced by the stretching of the bubble surface (divergent streamlines). It must be emphasized that this is not always the case. For example, the growth of underwater-explosion bubbles is often accompanied by RT instability because large accelerations occur over a sufficiently long duration (Plesset and Prosperetti, 1977).

In the case of a collapsing bubble, Plesset and Mitchell found that the amplitude of the spherical harmonic components increases proportionally to $R^{-1/4}$ and oscillates with increasing frequency as R tends towards zero. This is a situation for which the sinklike nature of the flow gets the better of stabilization due to the acceleration. This case is at the root of our first hypothesis.

Moreover, the analysis by Brenner *et al.* (1995) of the nonradial distortions that a single bubble can undergo shows that a bubble with $R_0=4.5$ μm submitted to an acoustic pressure between 1.1 and 1.4 atm [typical conditions of SBSL (Barber and Putterman, 1992; Barber *et al.*, 1994)] belongs to a region of the phase diagram which corresponds to moderate RT instability.

A possible explanation of the fact that light scattering measurements do not reveal strong surface oscillations [though a ''rattling'' in the first part of the first rebound is observed (Barber and Putterman, 1992)] could be that the length of the distortions is smaller than the wavelength of the laser used for the light scattering measurements. In the case of single bubbles remoted from boundaries (such as laser-generated cavities, Lauterborn, 1974; Vogel *et al.*, 1989) it is extremely difficult, from the experimental point of view, to detect nonradial oscillations able to occur near maximum collapse (blurred images, due to ''long'' exposure time, of both bubble contour, and the possible diverging shock wave in the liquid near the bubble-liquid interface, and also to the optical resolution, etc.). However, it must be pointed out that using extremely fast picture repetition rates (900 000 pictures/s), Lauterborn (1974) studied the final stage of single bubbles in water and remoted from boundaries. This author reported very nice photographs showing that (i) in the last stage of collapse a bubble is nonspherical, (ii) the jet formation is quite pronounced, and (iii) the bubble maintains its integrity [see particularly Figs. 3 and 6, Sec. 5, paragraphs 5.1 and 5.2 of Lauterborn (1974)].

In our hypothesis, SL emissions require the formation of a spray caused by nonradial bubble oscillations. Consequently, if the SL flash occurs at maximum collapse or a few ns before the time at which the collapse radius is reached (R_{co} is predicted theoretically by the Rayleigh–Plesset model), intracavity jet formation and the oscillations causing them must occur at least a few ns before R_{co} is attained.

In order to localize the time at which interfacial disturbances can occur, the radius (or the radii range) associated with these disturbances, must be known. Furthermore, this radius will be reported on the R-t curve, which describes the temporal evolution of the bubble radius. This means that we consider that the first part of the bubble dynamics (expansion and part of the collapse) may be described as a case of Rayleigh-like dynamics until some important nonradial distortions occur.

With respect to our first hypothesis (Sec. II) and also taking into account the fact that jets are initially caused by small distortions which intensify, we suggest using the results obtained by Plesset and Mitchell (1956) who, by means of a linearized perturbation theory, describe interface distortions as a sum of spherical harmonics. These authors found that any perturbations of a spherical surface remain small for $0.2 \leqslant R/R_{\max} < 1$ and that instability becomes violent for $R/R_{\max} \leqslant 0.1$, i.e., before the effects of viscosity, surface tension, and liquid compressibility become considerable. To obtain R we must know the value of $R_{\max}$, which can be determined by solving the equation giving the dynamic development of the bubble radius.

Assuming an initially spherical bubble, the idealized temporal development of the bubble radius can be determined by using the Rayleigh–Plesset equation (1):

$$R\ddot{R}+\frac{3}{2}\dot{R}^2=\frac{1}{\rho}[P_g-P_a-P_0]+\frac{R}{\rho c}\frac{d[P_g-P_a]}{dt}-\frac{4\nu\dot{R}}{R}. \tag{1}$$

To determine P_g we used the van der Waals adiabatic equation of state (2):

$$P_g=\frac{P_0R_0^{3\gamma}}{[R^3-\alpha^3]^{\gamma}}. \tag{2}$$

This set of equations was chosen in order to remain close of the previous work by Barber and Putterman (1992) (see also Löfstedt *et al.*, 1993) and, in the same vein, we used similar parameters values: $R_0=4.5\times10^{-6}$ m; $\nu=7\times10^{-6}$ m^2 s^{-1}; $\rho=10^3$ kg m^{-3}; $c=1481$ m s^{-1}; $P_0=1.01\times10^5$ Pa (1 atm); $P_a'=1.39\times10^5$ Pa (1.375 atm); $\omega_a=26\,500\times2\pi$; $\gamma=1.4$ (air bubble); $\alpha=R_0/8.5$. Figure 1 gives the typical behavior of a Rayleigh-like cavity in the case of such conditions. Figure 2 is a blowup of the collapse zone. Taking the Plesset–Mitchell theory as our basis we deduced that, since the bubble expands up to 45 μm, the upper value of the radius at which violent instabilities occur is approximately 4.5 μm (situation corresponding to $R/R_{\max} \leqslant 0.1$, see above). When this R value is applied to the R-t curve, it appears that the time at which nascent nonradial distortions occur is approximately 7 ns before the theoretical maximum of collapse. Considering the hypotheses, this value agrees relatively well with the experimental constraints.

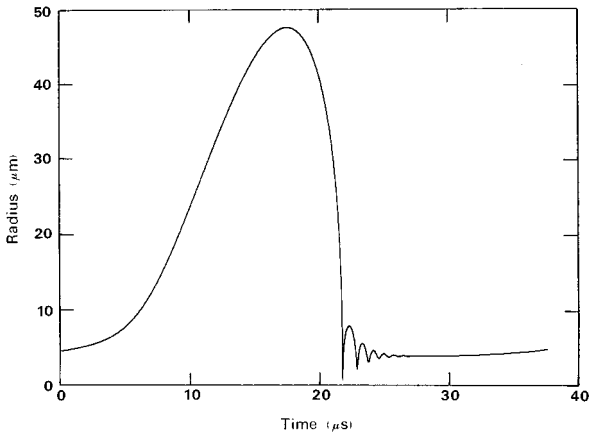

FIG. 1. Theoretical ''radius-time'' curve calculated using the Rayleigh–Plesset equation (1) for water ($\rho=10^3$ kg m^{-3}; $\nu=7\times10^{-6}$ m^2 s^{-1}; $c=1481$ m s^{-1}) for an air bubble ($\gamma=1.4$; $R_0=4.5$ μm) driven by an acoustic field ($P'_a=1.375$ atm; $\omega_a=2\pi$ 26 500) under ambient pressure ($P_0=1$ atm). The time scale starts with an acoustic cycle (depression followed by compression) of a duration of 37.736 μs.

B. Formation of an intracavity spray

With respect to our second hypothesis, the intracavity jets break up to give rise to tiny droplets inside the cavity. What can be done to describe the properties of such a possible ''spraying'' process, i.e., mainly droplet size and the spraying period, in order to further quantify the electrification of the droplets (Sec. III C)?

1. Statement of the problem

We must bear in mind that in Sec. III A the use of the Plesset–Mitchell theory is associated with nascent surface oscillations and their growth to moderate amplitudes. As Plesset and Mitchell emphasize, with such a linearized perturbation theory one cannot hope to describe the amplification of surface oscillations into needlelike irregularities until the breakup of the latter. Such a description would imply other methods such as those proposed by Hsieh (1974) in terms of variational methods (this author evokes the breakup process) or, more recently, by Longuet–Higgins and Oguz (1995), who describe the formation of critical microjets inside collapsing cavities. However, at the present time, at least as far as we are concerned, we do not know of any full description of the breakup of liquid jets as the result of their penetration into a collapsing cavity.

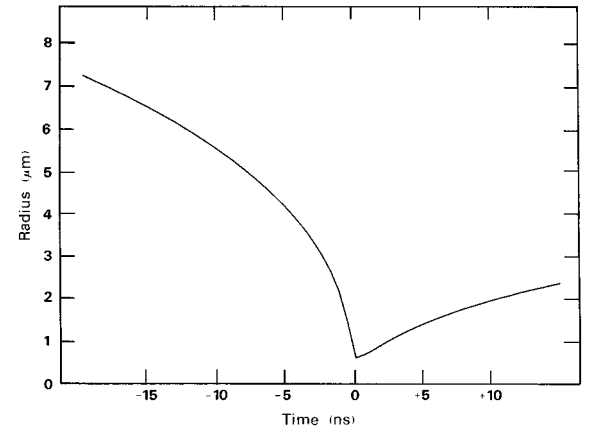

FIG. 2. Blowup of the ''radius-time'' curve calculated using the Rayleigh–Plesset equation (1) for water ($\rho=10^3$ kg m^{-3}; $\nu=7\times10^{-6}$ m^2 s^{-1}; $c=1481$ m s^{-1}) for an air bubble ($\gamma=1.4$; $R_0=4.5$ μm) driven by an acoustic field ($P'_a=1.375$ atm; $\omega_a=2\pi$ 26 500) under conditions of ambient pressure ($P_0=1$ atm). The time scale is rearranged so that the radius minimum (maximum collapse) corresponds to zero time (relative scale of time).

TABLE I. Characteristics of droplet emission in the case of high-flow velocity (atomization and long distortion waves) and low viscosity liquid.

Parameters	Short distortion wave (atomization)	Long distortion wave
Time of spraying	$\left(\frac{\rho}{\rho_g}\right)^{1/2}\frac{r_{\text{jet}}}{v_g}$	$\left(\frac{\rho}{\rho_g}\right)^{1/2}\frac{r_{\text{jet}}}{v_g}$
Droplet radius	$\frac{1}{2}\frac{\sigma}{\rho_g v_g^2}$	$\frac{0.75}{r_{\text{jet}}}$ (cgs unit)
Length of jet without distortion	$30\ r_{\text{jet}}$	$\left(\frac{\rho}{\rho_g}\right)^{1/2} r_{\text{jet}}$

However, the description of capillary hydrodynamics [a synthesis of which has been reported by Levich (1962)] could be exploited with a view to obtaining an order of magnitude for the characteristics of the droplet release process.

From a general point of view, the rupture of jets under the influence of capillary distortion waves may occur under the following conditions: (i) jets at low-flow velocities, (ii) jets at high-flow velocities with short distortion waves (atomization process), or (iii) jets at high-flow velocities with long distortion waves (large droplets emission) (Levich, 1962).

We thus need to determine the jet velocities and, in the case of high-flow velocities, whether jet rupture occurs in the form of atomization or breakup as the result of long distortion waves.

2. Rupture modes

We do not possess any *a priori* data on the velocity of jets able to be formed slightly before maximum collapse. However, in order to determine an order of magnitude in the jet velocities we can use (i) experimental data relating to a single sonoluminescing bubble or (ii) the theoretical velocity reached by the bubble wall approximately 7 ns before maximum collapse (this time value has been chosen in order to remain consistent with the calculation described in Sec. III A). By means of a light scattering technique Löfstedt *et al.* (1993) obtained some experimental data on the dynamics of a single bubble in water. We deduce from this work that the maximum experimental velocity of the bubble wall is about 250 m s^{-1} [on the basis of Fig. 3(a) by Löfstedt *et al.* (1993)]. This value is relatively close of the bubble-wall velocity (i.e., 300 m s^{-1} corresponding to a time of 7 ns before maximum collapse) obtained via the integration of the Rayleigh–Plesset equation, Sec. III A. If jets penetrate into the bubble, jet velocities higher than bubble-wall velocities must be expected. Such values correspond to high-flow velocities, and we arbitrarily chose $v_{\text{jet}}=400$ m s^{-1} as a typical value.

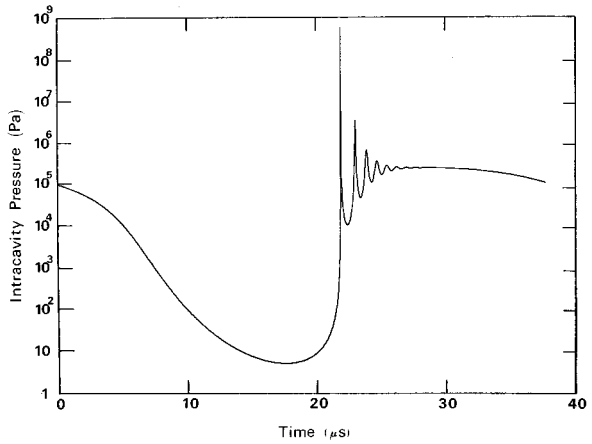

FIG. 3. Theoretical ''intracavity pressure-time'' curve (semilogarithmic representation) calculated for the same conditions as described in Fig. 1, on the basis of Eq. (2) with $\alpha = R_0/8.5$.

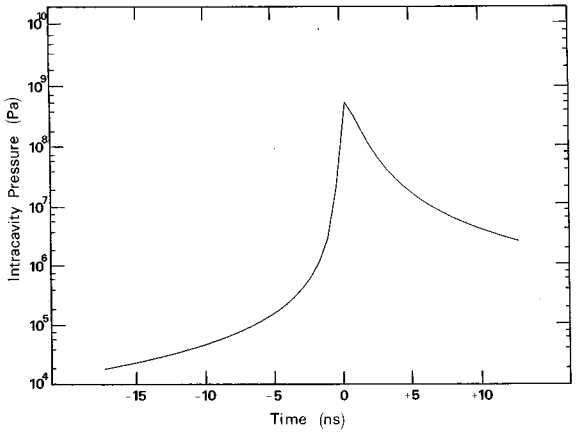

FIG. 4. Blowup of the theoretical ''intracavity pressure-time'' curve (semilogarithmic representation) in the region of collapse in the case of a bubble submitted to the conditions reported in Fig. 3. The time scale is rearranged so that the maximum of intracavity pressure (maximum collapse) corresponds to zero time (relative scale of time).

We must now discover what kind of jet rupture we are confronted with (atomization or the emission of large droplets) in order to use the formulas summarized in Table I. These formulas will help us to determine the droplet radius, the period of breakup, and the length of the jet before distortion and rupture (Levich, 1962).

According to Levich, the ambiguity between these two processes may be eliminated on the basis of condition (3):

$$(\eta/\sigma)(\rho_g/\rho)^{1/2} v_g \ll 1. \tag{3}$$

If condition (3) is fulfilled, atomization is a possibility. Otherwise (because of overhigh jet velocities, or overhigh density of the gas in which the jet moves, or overhigh viscosity of the liquid), the rupture of the jets undergoing long wave distortion, and thus large droplet emission, must be considered.

The evaluation of (3) requires a knowledge of v_g and ρ_g.

The value of v_g depends directly on v_{jet} since one of the boundary conditions on the jet surface implies $v_g = v_{\text{jet}}$.

The value of ρ_g depends on the time at which the jets penetrate the bubble or, in other words, on the intracavity pressure. For the sake of simplicity, we will consider only the situation associated with the R-t curve computed above (see Fig. 1). The intracavity pressure versus the time curve is given in Fig. 3. Figure 4 is a blowup of Fig. 3 in the region of collapse.

The range of times at which surface distortion (and the jets) is developed corresponds to a range of intracavity pressures, the order of magnitude of which is one atmosphere. In our future estimations we will adopt $P_g = 0.14$ MPa (≈ 1.4 atm) as obtained in Fig. 4. Condition (3) will thus be realized for $v_g \ll 2200$ m s^{-1} (approximately).

Taking into account the jet velocity values that we had previously estimated approximately, the condition (3) indicates that jet breakup could be assimilated to atomization.

3. Droplet size and breakup period

According to Table I, the radius of the droplets (R_d) could be ≈ 160 nm (order of magnitude) in the case where $v_g = v_{\text{jet}} \approx 400$ m s^{-1} and $\rho_g \approx 1.4$ kg m^{-3} (corresponding to $P_g \approx 0.14$ MPa). This situation is related to an instantaneous penetration and breakup of the jets. Actually, the penetration and breakup of the intracavity jets require a finite time that we estimate to be the few ns (see below) during which the bubble collapse continues, so leading to a non-negligible increase in intracavity pressure. The droplet radius will therefore be less than 160 nm. Moreover, since atomization is a random process, it concerns more or less extended sizes distributions. We will consider this aspect when we determine the electrification process.

If we use Fig. 2, the bubble is characterized by a radius $R \approx 4$ μm when it is invaded by the jets. By ascertaining that the rupture of the jets occurs when their tips reach distances of about $R/2$, we can deduce that $r_{\text{jet}} = 65$ nm. In the case of these needlelike jets penetrating the collapsing cavity, the complete period of atomization can be estimated as being of the order of a few nanoseconds (≈ 4 ns, under the conditions taken into consideration, Table I). Here again, these values agree relatively well with the experimental constraints.

C. Electrification of the intracavity spray

The picture so obtained is therefore as follows. During the first part of its cycle (expansion and collapse up to the generation of needlelike jets), a bubble conforms to the Rayleigh–Plesset dynamics. Some 10 ns before the theoretical time of collapse, as predicted if the bubble were spherical and its interface perfectly smooth (Rayleigh–Plesset dynamics), surface oscillations are triggered off and amplified so that needlelike jets penetrate into the cavity. In a period of a few ns some droplets, the size of which could be around 150 nm, are released from the thin jets, the radius of which is approximately 70 nm.

It should be remembered that the formation of microjets in collapsing cavities has been studied recently by Longuet-Higgins and Oguz (1995).

Moreover, it should be noted that the scenario according to which droplet release could happen in a collapsing bubble has been evoked recently by Prosperetti and Oguz (1992),

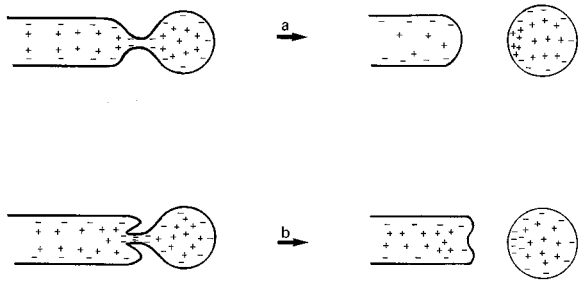

FIG. 5. Schematic representation of the two models of jet breakup: (a) breakup associated with the positive mode of charging [''positive'' curvature of the neck according to the nomenclature by Iribarne and Klemes (1974)]; (b) negative mode of charging.

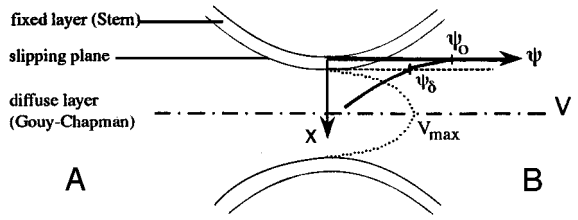

FIG. 6. Representation of both the velocity profile of the liquid through the neck and the spatial distribution of the electrical potentials. Ψ_0 represents the interfacial potential. Ψ_δ is the potential value actually experienced by the ions of the diffuse layer (Ψ_δ is a theoretical parameter at which the ζ potential, an experimental parameter, is assimilated in first approximation). Below the slipping surface ($x<\delta$), the ions and dipoles have a velocity equal to zero.

but in a completely different connexion. These authors were investigating a possible mechanism for the rapid damping of SL pulses that they assumed to be generated through violent heating caused by rapid compression.

If liquid disruption occurs, droplets (and jets) may acquire an electrical charge, as is generally the case during atomization, splashing, the disintegration of large drops, and the bubbling of liquids (Pierce, 1970; Iribarne, 1972; Bailey, 1988). During such processes, the random charging of tiny droplets, i.e., the formation of positively and negatively charged entities, results because of the statistical fluctuations in the concentration of positive and negative ions present in the liquid bulk. Since the pioneer experiments by Sir J. J. Thomson (1894), a lot of work has been devoted to understanding the mechanisms responsible for the droplet charging that results from the breakup of small jets, threads, or filaments of liquids.

In this paper, we modify Iribarne and Kleme's (1974) ''theory of electrification associated with droplet production from liquid jets,'' in order to adapt it to the case of a spray assumed to invade a collapsing bubble a few nanoseconds before the end of its compression.

As in the study by Iribarne and Klemes (1974), we expect to obtain an order-of-magnitude approximation of the charge acquired by the intracavity droplets. In this way we will estimate (Sec. IV) whether a process analogous to a spark could be triggered off inside the collapsing cavity.

In the case of liquid filament rupture, Iribarne and Klemes (1974) show that two modes of breakup can exist which depend on the curvature of the collapsing neck linking the filaments in the process of breaking up and the droplets in the process of formation. In the case of the intracavity spray which we envisage, we admit that both modes could also occur and lead to positive and negative charging as is showed qualitatively in Fig. 5. As in the analysis by Iribarne and Klemes (1974), the case of the simplest curvature, i.e., the positive mode of electrical charging, is only considered in order to establish a simplified calculation.

However, we bear in mind that Iribarne and Klemes (1974) showed experimentally that the negative mode of charging gives electrical charges one order of magnitude higher than the positive mode. And we repeat the same line of reasoning.

1. Qualitative aspect of the charging process

The electrification process can be qualitatively summarized as follows. Like any other interface, the bubble-liquid interface is characterized by the formation of a fixed dense layer of ions and dipoles (even present as traces, as in the case of nonpolar media). The origin of this dense layer [the so-called Stern–Helmoltz layer (Stern, 1924)] is that some dipoles (for example, water) have a nonrandom orientation in the vicinity of the interface. Consequently, the interface preferentially ''attracts'' ions of a given sign. A diffuse layer is formed far from the interface, a process that is initially described by Gouy (1910) and Chapman (1913). This layer is made up of moving ions in a statistical distribution. Since the liquid is electrically neutral, the diffuse layer is enriched with ions of the sign opposite to those mostly found in the vicinity of the interface. The structure of this electrical double layer explains why bubbles carry an electrical charge (electrophoresis experiments).

Let us now envisage the process of charge separation associated with the rupture of liquid filaments. The blowup of the zone linking the filament and the droplet must now be considered (Fig. 6). During the constriction of a filament, some liquid rushes through the neck from part A (the filament) towards part B (the droplet). This liquid flow carries electrical charges, but selectively, according to their signs. Let us consider water in order to illustrate this idea. In this case, some nonrandomly orientated water dipoles and some ions are fixed near the interface, and these are characterized by a preferentially negative sign (this has been shown through electrophoresis experiments; indeed, gas bubbles in water carry a negative charge). Because of the electrical neutrality of the liquid, the liquid bulk is characterized by an excess of positive charges. When the liquid rushes through the neck it is largely positive while the negative layer remains fixed at the interface. The outcome in the case of water is that after rupture, the filament is low on positive charges while the droplet is enriched in positive ones.

The migration of charges associated with both the flow of liquid and the existence of an electrical double layer is at the basis of the charge separation induced by jet rupture.

When the liquid flows through the neck, it induces a charging current. Because of the generation of a charge concentration gradient, a back current develops which tends to neutralize the charge separation. The back current is a diffu-

sional process which thus depends in particular on the cross section of the neck. Consequently, the balance between the two antagonistic currents only becomes favorable to the charging current at the end of the collapse of the neck (as shown by Iribarne and Klemes). Moreover, if the flow of liquid is very rapid, the back current can be considered as negligible with respect to the charging current.

2. Quantitative aspect (theoretical equation of the charge)

In this paragraph we reproduce the analysis by Iribarne and Klemes (1974) up to the point where we adapt it to the situation in hand. We will note precisely when our analysis moves away from Iribarne's and Klemes'.

According to the qualitative description reported above, the charging current (I) is proportional to the charge flow velocity and the charge density of the liquid:

$$I=\int\int \rho_{\mathrm{ch}} v_x \, dx \, dy. \tag{4}$$

The charge density is determined by Poisson's equation ($\Delta\psi=-4\pi\rho_{\mathrm{ch}}/\epsilon$). Poisson's equation can be simplified when one considers that the charge displacement occurs along one axis (x):

$$\rho_{\mathrm{ch}}=-(\epsilon/4\pi)d^2\psi/dx^2. \tag{5}$$

In a first approximation, the dependence of the liquid velocity in relation to the shearing stress (τ) may be represented as in a Poiseuille flow, i.e., in the form of $dv_x/dx=\tau/\eta=$const. If this expression is integrated with τ considered as constant in the liquid bulk, one obtains:

$$v_x=x\cdot\tau/\eta. \tag{6}$$

If (6) and (5) are substituted into (4), the charging current (I) appears as:

$$I=-(\tau\epsilon/4\pi\eta)\int\int x(d^2\psi/dx^2)dx \, dy. \tag{7}$$

In order to simplify this expression, it is possible to consider the integration along the x axis alone. To this end ψ_δ must be expressed as is associating with the slipping plane circumscribed by circumference C surrounding the neck section (perpendicular to the x axis). This can be formulated as $\int dy=\int dC=2\pi r_n$.

Integral $\int x(d^2\psi/dx^2)dx$ represents the potential at the slipping plane noted as ψ_δ (a theoretical parameter) usually approximated as ζ (the electrokinetic potential, an experimental parameter) (see Fig. 6 for the definition of terms).

The value of the charging current is thus given as

$$I=-(\tau\epsilon/2\eta)r_n\zeta. \tag{8}$$

At this point, we must modify Iribarne's model to state that on the one hand the shearing stress describes the penetration of the jet (idealized as a cylinder) from the interface of the bubble and, on the other, the formation of the droplet (idealized as a sphere) through the neck:

$$\tau=\tau_{\mathrm{jet}}+\tau_d. \tag{9}$$

The penetration of the cylindrical jet from the bubble interface requires that the pressure (ΔP_{jet}) applied to a surface corresponding to the base of the cylinder is counterbalanced by the shearing stress along the surface of the cylinder:

$$2\pi r_{\mathrm{jet}} L\tau_{\mathrm{jet}}=\Delta P_{\mathrm{jet}}\pi r_{\mathrm{jet}}^2. \tag{10}$$

By analogy, the formation of a droplet occurs under the effect of pressure ΔP_d through the formation of neck in length (l_n):

$$2\pi r_n l_n\tau_d=\Delta P_d\pi r_n^2. \tag{11}$$

The term ΔP_{jet} contains the Laplace pressure for the cylinder (σ/r_{jet}) and the pressure needed to expel the jet of liquid of density ρ inside the cavity ($P_{\exp\,\mathrm{jet}}$). This pressure is given in (12). In this equation, the acceleration is estimated on the basis of the work by Lentz *et al.* (1993) concerning a single sonoluminescing bubble ($a\sim10^9$ m s^{-2}).

$$P_{\exp\,\mathrm{jet}}=(\rho\pi r_{\mathrm{jet}}^2 L)a/\pi r_{\mathrm{jet}}^2. \tag{12}$$

The value of ΔP_{jet} is given by

$$\Delta P_{\mathrm{jet}}=(\sigma/r_{\mathrm{jet}})+(\rho La). \tag{13}$$

In the case of the formation of a droplet we can neglect the contributions associated with a radius higher than r_n in the Laplace term, which thus reduces to σ/r_n. This term must be added to $P_{\exp\,d}$, which represents the pressure necessary to induce the flow of liquid in order to create a droplet with a radius of R_d:

$$P_{\exp\,d}=4/3\pi R_d^3\rho a/\pi r_n^2. \tag{14}$$

The total contribution to the formation of a droplet is thus:

$$\Delta P_d=(\sigma/r_n)+(4R_d^3\rho a/3r_n^2). \tag{15}$$

Consequently, the shear stress can be obtain by the association of (9), (10), (11), (13), and (15) as

$$\tau=\frac{1}{2}\left[\left(\frac{\sigma}{L}+r_{\mathrm{jet}}\rho a\right)+\left(\frac{\sigma}{l_n}+\frac{4}{3}\frac{R_d^3\rho a}{r_n l_n}\right)\right]. \tag{16}$$

When (16) is introduced into (8), since $L>l_n$ (thus σ/L negligible with respect to σ/l_n) we obtain after simplification the equation of the charging current:

$$I=-\frac{\epsilon\zeta}{4\eta}r_n\left[\frac{\sigma}{l_n}+\left(r_{\mathrm{jet}}+\frac{4}{3}\frac{R_d^3}{r_n l_n}\right)\rho a\right]. \tag{17}$$

Considering the time scale of jet rupture, the back current can be considered as negligible. We can deduce the charge acquired in the positive mode (Q^+) by integrating the expression $dQ^+=I\,dt$. The value of Q^+ thus represents the total charge acquired by a droplet:

$$Q^+=-\frac{\epsilon\zeta}{4\eta}r_n\left[\frac{\sigma}{l_n}+\left(r_{\mathrm{jet}}+\frac{4}{3}\frac{R_d^3}{r_n l_n}\right)\rho a\right]t. \tag{18}$$

3. The theoretical estimation of the droplet charges (Q^+,Q^-) and of the electrical fields between jets and droplets (E^+,E^-)

In order to solve (18) which gives positive charge (Q^+), we consider the case of an air bubble in water as in

the picosecond SL experiments: $\eta = 9 \times 10^{-4}$ kg m^{-1} s^{-1}, $\sigma = 0.073$ N m^{-1}, $\epsilon = \epsilon_0 \times \epsilon_r = 80 \times 8.8 \times 10^{-12}$ C V^{-1} m^{-1}, $a = 10^9$ m s^{-2}. The time of charging can be assimilated to the period of jet rupture, i.e., of the order of 4 ns. We also adopt $l_n = 2r_n$ with $r_n = 0.1R_d$, as Iribarne and Klemes (1974) consider in their calculation.

Let us consider the value of electrokinetic potential (ζ). Usually, ζ is determined in the case of nonpulsating gas bubbles in a given liquid and equilibrium situation. In the case of a pulsating bubble in the expansion phases, the interface area grows so that the electrical double layer rebuilds by attracting ions from the solution in order to reach the equilibrium condition. In the collapse, the reverse phenomenon occurs via the desorption of ions from the interface. The process of equilibration is characterized by relaxation time (θ), the typical value of which has been estimated as being $\approx 5 \times 10^{-5}$ s in the case of gas bubbles in water (Iribarne and Mason, 1967). This means that, in the case of a bubble driven at about 25 kHz, the electrokinetic potential reaches its equilibrium value in a few acoustic cycles. However, the collapse corresponds to a situation far removed from equilibrium. Indeed, if the data in the literature concerning a single sonoluminescing bubble are taken into consideration, it will be noted that the period of collapse does not exceed a few μs (see also Fig. 1). Such periods of time are much lower than the relaxation time in the case of water. Consequently, we must expect that the elementary charges accumulated during bubble expansion do not have sufficient time to desorb from the interface during the collapse and that in this phase the charge density considerably increases, so inducing a modification to ζ.

A reevaluation of ζ can be carried out as follows. In the case of a gas bubble in water containing very low concentration of ions, the value of $|\zeta|$ may reach 0.025 V (typical mean value for water). As reported by Iribarne and Mason (1967) in a first approximation, the interfacial potential (ψ_0) may reach $\sim 2\zeta$. If we consider that the value of the charge density ($\rho_{ch} = 2.64 \times 10^{-6}$ C m^{-2}) as measured by Whybrew *et al.* (1952) is associated with $\zeta = 0.025$ V, it is possible to employ Gouy and Chapman's simplified formula (19) with T the liquid temperature = 300 K in order to determine the numbers of ions fixed at the interface (n_0).

$$\rho_{ch} = -\sqrt{\frac{\epsilon n_0 kT}{2\pi}} \left[e^{-(q\Psi_0/2kT)} - e^{q\Psi_0/2kT} \right]. \tag{19}$$

We thus deduce that $n_0 = 3 \times 10^{18}$ m^{-3}.

Using the charge density obtained by Whybrew *et al.* (1952), we deduce that the equilibrium value of the charge in the case of a bubble expanding at a radius of ~ 40 μm is 5.3×10^{-14} C. If no (or at least negligible) ion desorption occurs, this charge value will also be the charge associated with the collapse and more particularly with the radius of ~ 4 μm, at which jets penetrate the cavity. The charge density is now 2.64×10^{-4} C m^{-2}. Once again using (19), we find that ψ_0 out-of-equilibrium (end of collapse) tends towards 0.28 V and ζ (out-of-equilibrium) towards 0.14 V.

If we consider the droplet radii centered around the value of the radius determined previously in Sec. III B 3 and, as Iribarne and Klemes (1974) do, the fact that the negative mode of charging leads to $Q^+ < Q \leqslant 10Q^+$, we will obtain a dependence of Q^- or Q^+ as a function of R_d as is shown in Fig. 7.

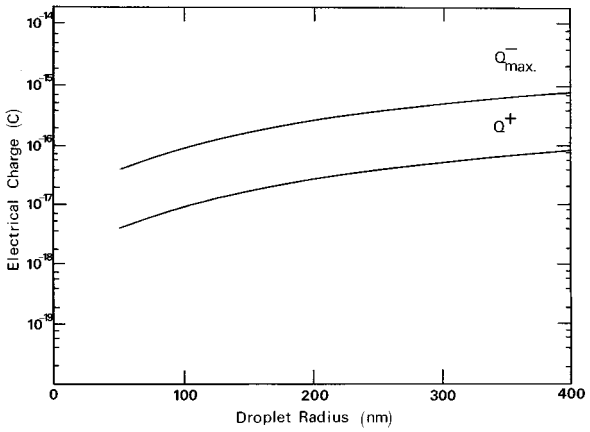

FIG. 7. Dependence of the total electrical charge as a function of the droplets radius, in the case of positive mode of charging (Q^+) and in the case of negative mode of charging [Q^-; the maximum value of $Q^- = 10Q^+$ is reported; see Iribarne *et al.* (1974) and text].

We can also calculate the electrical field between a jet and a droplet separated by a distance corresponding to the length of the now destroyed ($l_n = 2r_n$) neck. The link between the electrical field and the charge is

$$E = \frac{Q}{\pi \epsilon_g \epsilon_0 (2r_n)^2}, \tag{20}$$

where ϵ_g is the permittivity of the gas in which the electrical field is applied. The dependence of E^- and E^+ as a function of the droplet radius is shown in Fig. 8.

IV. FROM THE ELECTRIFICATION OF INTRACAVITY DROPLETS TO THE DEVELOPMENT OF A SPARKLIKE MICROPLASMA

A. Electrification and sparking process: A brief review of the literature

The possible release of an electrified spray in a collapsing bubble is a situation reminiscent of the electrification of natural and man-made sprays (Magono, 1980; Wahlin, 1986).

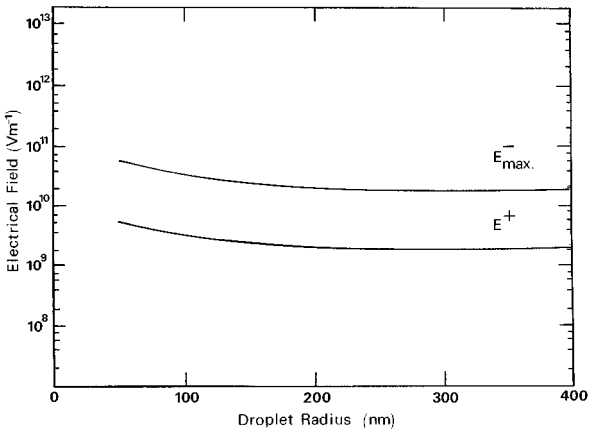

FIG. 8. Dependence of the electrical fields (E^+ and E^-_{max}) associated with the charges as calculated in Fig. 7 (Q^+ and $Q^-_{max} = 10Q^+$).

Such processes are now considered as a contribution to the charging of clouds in relation to thunderstorms, or to radio-frequency emissions from electrically charged clouds. In the case of water, the electrification associated with the disruption of jets has been shown to be at the origin of waterfall luminescence as Lenard (1892) and Pierce and Whitson (1965) report. Electrostatic hazards in the oil industry, such as oil cargo and supertanker explosions during washing operation by water spraying are now well understood (Bustin and Dukek, 1983).

However, water is not the only liquid to be electrified when disrupted. Watanabe *et al.* (1981) show clearly that jet rupture in the case of aliphatic alcohols leads to the electrification of the alcohol droplets. Hydrocarbons, which constitute a class of nonpolar compounds, present an electrokinetic potential, the mean value of which (0.02 V; Felici *et al.*, 1981) is close to the electrokinetic potential of water.

Such nonpolar liquids acquire electrification through the breakup of jets, a process which is even responsible for incendiary sparking during filling of road and rail tankers for example. Direct observations of the sparks at a filling pipe outlet were carried out using image intensifiers (Strawson and Lyle, 1975).

In the same family of organic compounds, oils present some hazards associated with the formation of droplets. In 1958, while studying the behavior of a large oil fog generator which he had developed in 1941 in association with Langmuir to produce an artificial oil-based fog. Schaeffer observed that the low-vapor oil-fog that he produced ignited spontaneously. Langmuir suggested that the fog was ignited by an electrical discharge associated with the electrification accompanying the formation of small oil droplets. Schaeffer said: ''It was also possible that a similar phenomenon caused the disastrous explosions [...] following the rupture of high pressure hydraulic systems associated with plane catapults on several U.S. aircraft carriers. The dense cloud of oil smoke formed by the pipe breakage might have been ignited by a spark discharge generated by a charging mechanism similar to that observed with our oil fog generator.''

Considering the first stage in the development of a spark from electrified droplets and jets, it is often acknowledged that this preliminary stage corresponds to a corona discharge or an avalanche process connected with electron emission from either droplets or jets (Barreto, 1979; Magono, 1980; Elghazaly and Castle, 1987).

Can such a mechanism be involved in the mechanism that we suggest for sonoluminescence?

B. A return to sonoluminescence

To begin with, in the following paragraphs, we will consider the possible mechanism(s) involving a single ''droplet/jet'' couple. However, we will indicate when we are dealing with series of ''droplet/jet'' couples, particularly in the determination of the pressure and electron density of the microplasma. For a quantitative evaluation, we will focus on the case of a negatively charged jet and a positive droplet.

Faced with the high fields calculated above and reported in Fig. 8 and also with the high temperatures deduced from the plasma diagnostic analysis on a single Ar bubble ($T_e \approx 20\,000$ K, perhaps more) (Sec. I) that led to the conclusion that SBSL could be analogous with a sparklike process, we arrive at the questions: how could a sparklike process initiate and develop in a collapsing cavity? Is the situation of ''atmospheric sparking'' transposable as such to the case of SL?

C. Can an intracavity gas discharge develop by gas ionization processes?

The development of such discharges, through gas ionization, implies electron avalanche processes, i.e., one seed electron for one avalanche and electrical fields high enough to obtain large cross sections for the electron-molecule ionizing collisions. As is shown macroscopically by the Paschen law (von Engel, 1983), the ignition of a gas discharge strongly depends on product $N_g \cdot d$, which defines the average number of possible ionization collisions in a gap of length d. As the gas pressure in the collapsing cavity at the end of the spraying process is calculated as being a very few atmospheres (Fig. 4, $P_g \approx 1.4$ atm for a time of ≈ 3 ns before maximum theoretical collapse), the mean-free path of an electron between two successive collisions can be taken as $\lambda_e = 2\ \mu$m. Consequently, the mean number of ionizing collisions to be expected in an intracavity gap of a maximum length equal to the bubble radius at the end of the spraying process (i.e., about 3–4 μm) can be expressed by $N_{\mathrm{col}} = d/\lambda_e$, i.e., $N_{\mathrm{col}} = 1.5$–2. As the development of an electron avalanche can be described by the elementary relation $N_{\mathrm{col}} = 2^n$ (Raether, 1964), this gives a multiplication factor which can be estimated as $n \leqslant 1$ for an avalanche bridging the gap from the droplet tip to the opposite wall of the cavity. Such a value of n invalidates the hypothesis of gas discharges as the main process in order to explain the electrical and light emission phenomena observed in SBSL.

In fact, since recent studies (Dejean *et al.*, 1992; Morshuis, 1993), scientists familiar with partial discharges (i.e., arc discharges developing in gaseous voids inside insulating materials) known that (i) in the case of microvoids characterized by diameters of one to ten microns or less, the ''discharges'' exhibit much shorter current and light pulses than larger discharges and (ii) that the theories established for large voids are invalid for small gaps.

D. Field emission hypothesis

1. Comment

As a matter of fact, it may be noticed that there is a great similarity between the situation with which we are dealing (i.e., SBSL) and the situation encountered in electrical discharges in ''vacuum.'' In both cases, the collision rates of electrons with molecules are low in ''vacuum'' because of the low pressure and, in the case of SBSL, because of the small gaps involved.

This led us to the question: Under the influence of high electric fields such as those calculated above, should a discharge be initiated by field emission from the front of the jets?

At the present time our knowledge of the subject does not provide a direct answer because field emission processes

are almost only known in the case of metal surfaces, for which high-level field emission currents can be expected according to the Fowler–Nordheim equation (21) as soon as the electric field exceeds some 10^9 V m^{-1} (Fowler and Nordheim, 1928; Nordheim, 1928).

Concerning the field emission from nonmetallic surfaces, though our knowledge at the present time is very poor, it is, however, sufficient to support the idea of applying field emission theories and to correlate these latter with the liquid jets injected inside the collapsing bubbles. In order to justify this assertion, it should be noted that even if higher values are generally advanced for the work function of insulating materials than for the work function of metallic surfaces, experimental data available from the literature show (i) that impurities in insulating materials can increase the field emission efficiency (Bayliss and Latham, 1986) and (ii) that electron emission relations commonly used for metallic surfaces can be used satisfactorily in the case of insulating surfaces (Laube, 1992; Fitaire, 1995). This gives support on application of Eq. (21) to the liquid droplet involved in this study.

$$J_{\mathrm{FN}}=1.54\times10^{-6}E^2\ \exp\left\{\frac{14.56}{\phi^{1/2}}-\frac{6.83\phi^{3/2}}{E}-\frac{1.79\times10^{-4}E^{1/2}}{\phi^{3/2}}\right\}. \tag{21}$$

However, before doing so, it should be noted that in order to proceed, field emission requires the rapid replacement of any electron leaving the surface. This replacement is necessary in order to neutralize the remaining positive charges. In the case of low-conductivity-emitting materials, this can constitute a problem as it has been demonstrated via photoemission experiments carried out on polymers by the authors. These experiments showed that the charge neutralization necessary for a durable emission had to tolerate the presence of a given amount of water in the atmosphere, and this also means on the surface.

Concerning SBSL experiments, the problem of charge neutralization is automatically solved with water as the solvent. It should be noted that the situation is not so different in the case of nonaqueous and nonpolar solvents. Indeed, the emission of electrons from electrified droplets of nonpolar solvents which leads to the sparking process (Schaeffer, 1958; Strawson and Lyle, 1975) provides an answer, based on experiments, to the problem posed. Moreover, it must be noted that in the particular case of pulsating bubbles, the interfacial density of charges increases dramatically because of the rapid collapse which prevents the charge desorption (Sec. III C 3). Consequently, we can expect a relatively good aptitude on the part of nonpolar liquids surrounding a bubble for participating to the neutralization process, at least in the limits of their electrical conductibilities at the vicinity of the gas-liquid interface.

2. Description of the process of field emission in the case of a water jet

When electrons are extracted from a given material under the influence of a strong electric field, the electric current density [J_{FN}; Eq. (21)] associated with their motion leads to a release of energy in the material, which usually occurs as heating (Joule effect). In turn, this energy release, if significant, may lead electrons to leave the surface of the material, so giving rise to thermoelectronic emission.

In the case of a jet (Sec. IV B), the determination of the energy released in the volume of water constituting the jet may be carried out under the assumption of adiabaticity (fast process) by a knowledge of J, E, and Δt which represents the time during which energy is released. Any realistic description must involve both field and thermoelectronic emissions so that $J_{\mathrm{tot}}=J_{\mathrm{FN}}+J_{\mathrm{RD}}$ where J_{RD} is the current density associated with thermoelectronic emission described by the Richardson–Dushman equation (22) (Nottingham, 1956).

$$J_{\mathrm{RD}}=\frac{4\pi mqk^2}{h^3}\ T^2\ \exp-\left\{\frac{\phi}{kT}\right\}. \tag{22}$$

However, two problems arise concerning the determination of the energy density (i.e., the amount of energy with which the jet is endowed): (1) J_{tot} and E are time dependent because of the neutralization of the droplet which uptakes the electric charges emitted by the jet, (2) electron emission is not exclusively directed towards the droplet but instead is spread out over a part of the hemisphere in front of the jet.

We can analyze this last aspect by defining the neutralization efficiency (β) as the ratio of two surfaces. The first is the cross section of a droplet. The second corresponds to the base of a right circular cone with the tip coinciding with the extremity of the jet and the base intersecting the plane defining the cross section of the droplet. In our calculation we adopt $\beta=1\%$. By this way, though the choice of 1% is arbitrary, we describe the fact that the electron emission is not directional, at least in the first instant after that electrons leave from the jets.

We will now consider the calculation procedure in order to evaluate the total energy density while taking into account the temporal evolution of $J(t)$ and $E(t)$. This iterative procedure is carried out with a time interval Δt_n. Knowing the initial value of the electric field [$E(t=0)$ as determined by Eq. (20)], we deduce the total current density ($J_{\mathrm{tot}}=J_{\mathrm{FN}}+J_{\mathrm{RD}}$) from Eqs. (21) and (22). With this value of J_{tot} we use Eq. (23) to deduce the electrical field at the end of the time lapse for a given neutralization efficiency.

$$E(t=n)=E(t=n-1)-\frac{J_{\mathrm{tot}}\beta\Delta t_n}{\epsilon_0}. \tag{23}$$

This procedure is performed until $E(t)$ reaches a minimum critical value, below which negligible amounts of energy are produced. We calculate that this lower boundary of $E(t)$ is 7.5×10^9 V m^{-1}.

If the emission process occurs when the jets are negatively charged (Sec. IV B), the case to be analyzed will be the same as for $E^-\approx3\times10^{10}$ V m^{-1} (corresponding to the most probable droplet radius, Sec. III B 3). In order to apply Eq. (21), we have to introduce the work function for water droplet (ϕ_w) as measured by Kovalchuk and Shchekatolina (1983) who reported that the experimental value of ϕ_w decreases (i) as the droplet radius decreases and (ii) as the concentration of anions increases. In the case of water contaminated by a very small amount of a very usual anion,

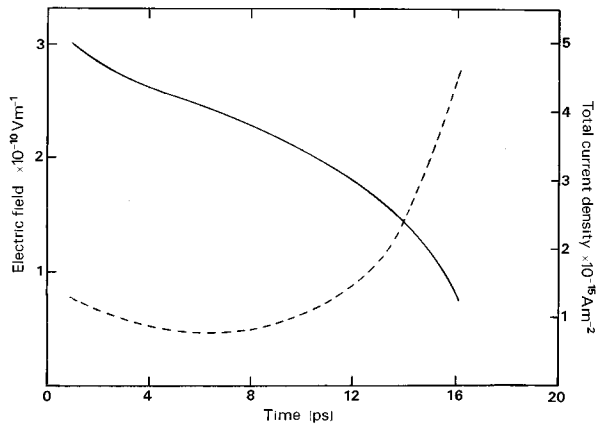

FIG. 9. Temporal evolution of $E(t)$ (left vertical axis; continuous curve) and $J(t)$ (right vertical axis; dashed line).

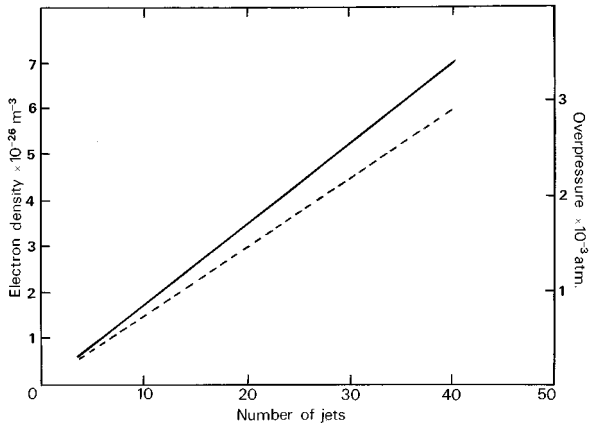

FIG. 10. Dependence of the theoretical electron density ($N_{e,\mathrm{th}}$) (continuous line) and overpressure generated by the microplasma (ΔP_m) (dashed line) with the number of intracavity jets (n_j).

namely Cl^-, $\phi_w=4.6$ eV. Applying the procedure with $\Delta t_n=1$ fs, $\beta=0.01$, and $E(t=0)=3\times10^{10}$ V m^{-1}, we find that during a period of 16 fs ($=\Delta t=\Sigma\Delta t_n$, after which $E<7.5\times10^9$ V m^{-1} so that the heating is negligible), a maximum energy of 7.8×10^{-9} J is released in a jet volume of 2×10^{-20} m^3 (corresponding to $L=1.5$ μm and $r_{\mathrm{jet}}=65$ nm, Sec. III B 3). The temporal evolution of $J(t)$ and $E(t)$ is reported in Fig. 9. This brief and violent release of energy is thought to ablate the matter constituting the jet, as is the case when a metal needle explodes when submitted to high electrical fields (Chatterton, 1966). This is the basis of our fourth hypothesis. Consequently, we expect that this ablation will be accompanied by the formation and rapid expansion of microplasma.

Considering the total energy released to the water of a jet, what can be done to characterize the microplasma (i.e., the electronic temperature and density, the overpressure associated with the burst of matter from the jets, the lifetime)?

3. Estimation of the electronic temperature of the microplasma

The total amount of energy (7.8×10^{-9} J) with which the jet volume (2×10^{-20} m^3) is endowed will serve to evaporate water, dissociate water molecules or hydroxyl radicals, and ionize H and O atoms. The residual energy (E_R) will be distributed between the translation degree of freedom of the ions and the electrons spread out in the microplasma.

Considering (1) a complete dissociation and a monoionization applying to any atom belonging to the water constituting the jet under consideration, (2) the dissociation energy of water ($D_{\mathrm{H\text{-}OH}}=489$ kJ mol^{-1}), of OH ($D_{\mathrm{H\text{-}O}}=428$ kJ mol^{-1}), the ionization potential of H ($\chi_{\mathrm{H}}=1313$ kJ mol^{-1}), of O ($\chi_{\mathrm{O}}=1313$ kJ mol^{-1}) and (3) the vaporization enthalpy (44.3 kJ mol^{-1}) as negligible for these values, we estimate $E_R=2.5\times10^{-9}$ J. Assuming that the plasma is in local thermodynamic equilibrium [all the temperatures equal and in particular the electronic and the ionic temperatures (T_e and T_{ion})], E_R will be distributed equally in the translational degrees of freedom of the ions and electron as in (24).

$$E_R=3/2k[T_e n_e+T_{\mathrm{ion}}n_{\mathrm{ion}}]. \tag{24}$$

In the case of a monoionization of all the H and O atoms involved in a jet of volume equal to 2×10^{-20} m^3 (i.e., $n_e=n_{\mathrm{ion}}=2\times10^9$), we deduce that $T_e\approx30\,000$ K (considering this temperature, monoionization must be accompanied by some di-ionization that we neglected in order to simplify the calculation, however). This value is relatively close to the electronic temperature obtained by plasma diagnostic analysis (Sec. I).

4. Dependence of the electronic density and overpressure with the number of intracavity jets

If the electronic temperature depends on the energy density and the rates of dissociation and ionization alone, the access to $N_{e,\mathrm{th}}$ requires a knowledge of the overall number of electrons released in the cavity volume and thus the number of jets (n_j). Since no such information is available at the present time (to our knowledge at least), we propose to establish the dependence of $N_{e,\mathrm{th}}$ and the overpressure (ΔP_m) generated inside the bubble by the microplasma. Considering a bubble with a radius $R\simeq3$ μm at the time of light emission (the case associated with the initial values of R_0, P_A, and frequency as described in Sec. III A), we obtain a dependence of $N_{e,\mathrm{th}}$ as shown in Fig. 10. As can be seen in comparison with the value of N_e as obtained via plasma diagnostic analysis (Sec. I), we arrive at an overestimation by one order of magnitude of $N_{e,\mathrm{th}}$. Concerning the value of $N_{e,\mathrm{th}}$ itself, this result is relatively satisfactory if the different hypotheses are taken into consideration, and the difference of situation compared (theoretical analysis related to an air bubble in water; plasma diagnostic analysis on a single Ar bubble in water). It should be noted that is it not out of order to have determined N_e on the basis of Ar as the main gas involved in the plasma while the calculation reported above involves water. First, the only expression of the structure of Ar is the quantum defect, the value of which only appears in the formula linking the electronic density to the volumic radiant flux associated with recombination. A modification of the value of the quantum defect to take the structure of O atoms into consideration will have a negligible effect on the

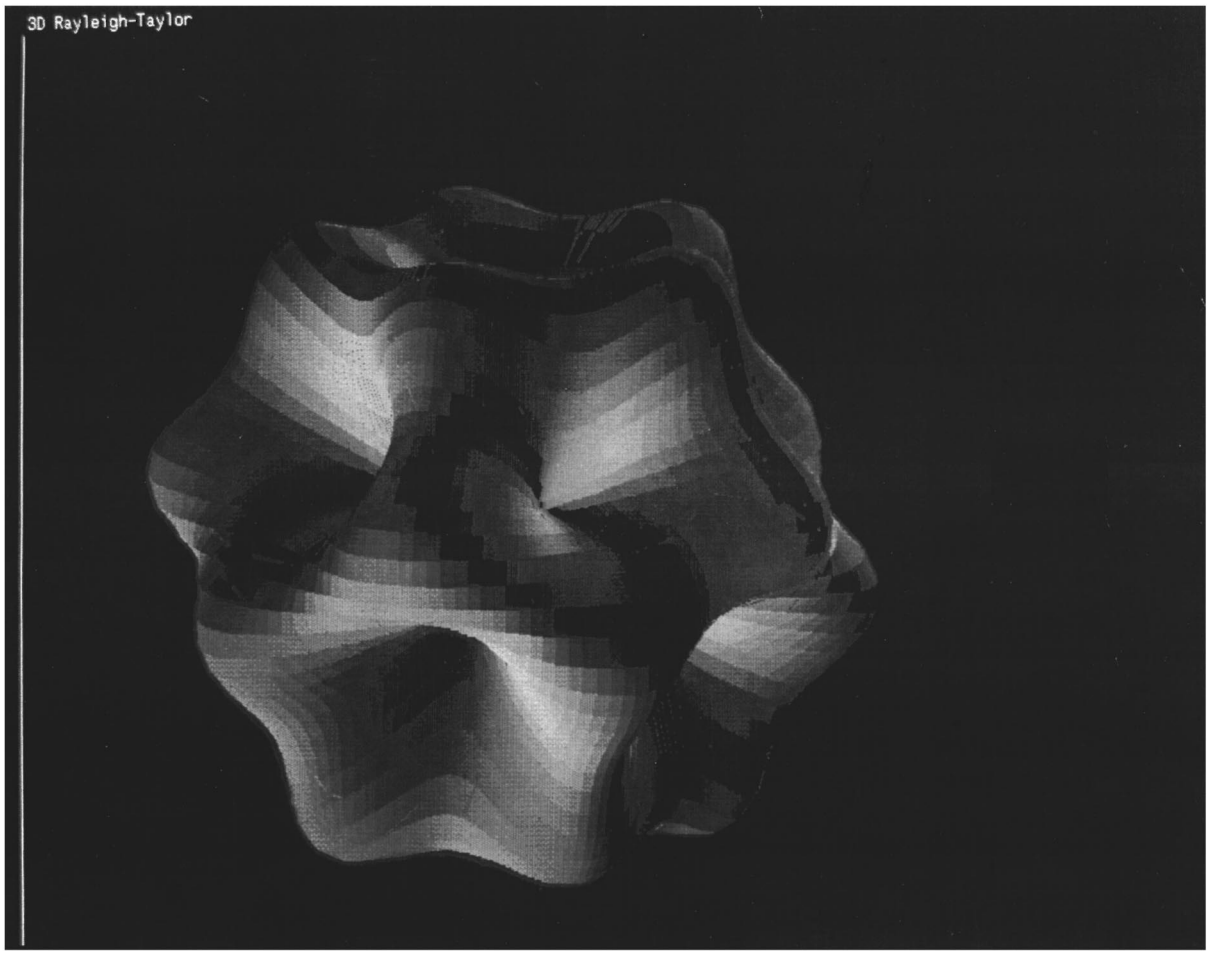

FIG. 11. Illustration concerning a gaseous ''pellet'' (inertial confinement) undergoing Rayleigh–Taylor instability (theoretical simulation; reprinted by permission of R. A. Bell, Imperial College, London).

determination of the order of magnitude of N_e. Second, at the present time, we have greatly simplified the process of energy distribution. The atoms of the gas phase are involved in the expansion of the microplasma.

It is difficult to estimate the number of jets in the absence of a complete simulation describing the collapse of a bubble undergoing Rayleigh–Taylor instability. However, the range of n_j values (about 10) found to correspond to a value of $N_{e,\mathrm{th}}$ which is only one order of magnitude above N_e ($\sim 10^{25}$ m^{-3} via plasma diagnostic analysis) is reminiscent of a situation encountered during a simulation carried out by Bell, who studied the collapse of a gaseous pellet (like those used in inertial confinement in order to trigger off nuclear fusion) undergoing R–T instability (Fig. 11). Though care is advised (the jets that we considered are thinner than those associated with picture in Fig. 11 and the process at which Bell refers is not exactly the process with which we are concerned), the result that we obtained does not seem to be unrealistic.

Taking into account the ablation of the matter constituting the jets, it must be expected that almost immediately after its formation, the plasma is characterized by very high internal pressure. By analogy with what occurs in the generation of sparks, the plasma is expected to expand so that (1) it acts as a ''piston'' able to induce the formation of a diverging shock wave and (2) it relaxes in order to cool. The consequence is that the microplasma generates an overpressure ΔP_m in the cavity. The dependance of ΔP_m with n_j (Fig. 10) leads to the determination of $\Delta P_m \sim 1000$ to 1500 atm.

5. Lifetime of the microplasma

The situation with which we are dealing is reminiscent of the violent release of energy occurring in the formation of brightly luminescent sparks such those experimentally studied by Mandel'shtam and Sukhodrev (1952) and Demidov *et al.* (1961), for example, or theoretically by Drabkhina (1951) and Braginskii (1958). Theoretical work is confined to the description of a spark channel with cylindrical symmetry, while we are concerned with a microplasma expanding rather spherically. In order to avoid theoretical complications, we propose to use the experimental data so that the expansion velocity (v_m) can be estimated.

Considering that the bubble radius at the instant of microplasma formation is ~ 3 μm, we will assume that the microplasma will cool and stop luminescing when it reaches the bubble wall. This is a maximalist hypothesis because the sudden burst of pressure could favor a rapid recombination

of atomic debris. In this context, the extinction of the microplasma will occur before the complete expansion inside the bubble occurs. The expansion velocity has to be determined. As reported via experimental methods in the case of actual sparks (Demidov *et al.*, 1961), the expansion velocity strongly depends on the initial current derivative which is related to the characteristics of the electric circuit. With rate of rise of the current at about 3×10^{12} A s^{-1}, Demidov *et al.* measured expansion velocities as high as 6×10^{4} m s^{-1}. In our estimation of the current density, we arrived at $J_{\text{tot}}=4.5\times10^{15}$ A m^{-2} for an electron emission cross section of 13×10^{-15} m^2 (πr_{jet}^2 with $r_{\text{jet}}=65$ nm, see Sec. III B 3). This gives an equivalent current derivative of 60 A/16 fs, i.e., 3×10^{15} A s^{-1}. This value is much higher than the current derivative obtained experimentally by Demidov *et al.* The expansion velocity can thus be expected to be such that the lifetime of the microplasma $t_m<50$ ps, which is in good agreement with the experimental data.

It is possible to ascertain a maximum boundary for the intracavity plasma lifetime. The procedure consists of transposing the theoretical description of the radial (2D) expansion of a filamentary spark to the radial (3D) expansion of the intracavity plasma. Considering the case of a cylindrical spark expanding radially in air, Braginskii (1958) provided the relationship between the expansion time (t_s) required for such a plasma to reach an envelop of radius r_s [Eq. (25), with ρ_s as the air density just before the spark is triggered off and I_s as the electrical current].

$$t_s=11.6r_s^2\rho_s^{1/3}I_s^{-2/3}. \tag{25}$$

Considering that $I_s=60$ A (see above), $r_s=3\times10^{-6}$ m (radius of the bubble at the time flash, the value has been chosen to remain consistent with the description above) and an initial air density $\rho_s=1.4$ kg m^{-3} [associated with an intracavity pressure of about 1.4 atm, i.e., just before the intracavity plasma is released (see Sec. III A)], it appears that the intracavity microplasma would reach the bubble wall and stop luminescing within about 8 ps.

V. SUMMARY

A. Experimental and theoretical (i.e., present model) plasma analysis: Exogeneous confirmation

A significant ''clue'' able to support (but not to demonstrate definitively) the consistency of the present hypothesis would be to find an experimental spectrum associated with a ''certified'' plasma, the spectral distribution of which matched the SBSL one. Moreover, it would be necessary to have at one's disposal a diagnostic analysis of this plasma that revealed a similar (if not the same) couple $\{N_e;T_e\}$ to the one obtained for SBSL. Moreover, if the implementation of the diagnostic analysis was different from the one used by Lepoint-Mullie *et al.* (1996) (in the case of SBSL), the triangular comparison ''results from the electrohydrodynamic hypothesis/SBSL diagnostics/diagnostics of a certified plasma'' would gain in value and contribute to highlighting the consistency of the present model.

It must be noted that SL plasma diagnostic analysis was carried out on the SBSL spectrum of an Ar bubble in water

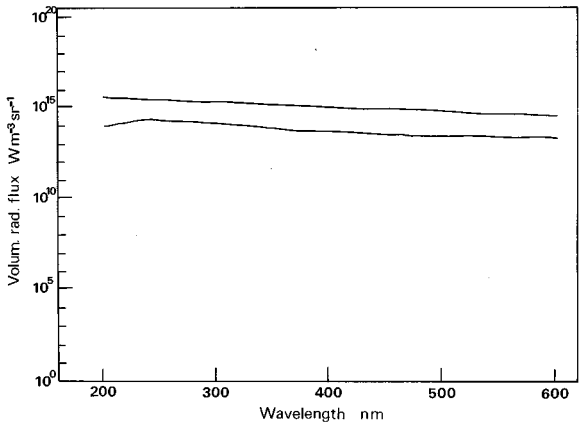

FIG. 12. Comparison between the spectrum of a capillary spark in air ($N_e=3\times10^{25}$ m^{-3}; $T_e=19\,000$ K; after Lochte-Holtgreven and Richter, 1968) (upper curve) and the SBSL spectrum (air bubble, Hiller *et al.*, 1992) (lower curve). In the case of the SBSL spectrum, the spectral irradiance [in W/nm, as obtained by Hiller *et al.* (1992)] is converted into volumic radiant flux (W m^{-3} s^{-1}) assuming that the radius of the bubble at the time of emission is 2 μm and the duration of emission is 50 ps (see Lepoint-Mullie *et al.*, 1996). The emission time is taken from Barber *et al.* (1991). The value of the bubble radius is taken from Barber and Putterman (1992). Discussion in Sec. V A.

(Sec. I). We thus tried to find the experimental spectrum of a capillary spark triggered off in Ar (type of plasma with a short electrical current pulse, a short lifetime, high internal pressure, and the smallness of the development zone). Our search was unsuccessful. However, the spectrum of a capillary spark in air has been reported (Lochte-Holtgreven and Richter, 1968). Whereas the spectral distributions in the case of single Ar or air bubbles are close (Hiller *et al.*, 1992, 1994; in the wavelength range for which no disturbances due to setup could occur, i.e., below 220 nm), we can consider that (i) the electronic temperatures are close enough and (ii) electronic densities for single sonoluminescing air and Ar bubbles are in the same order of magnitude. We therefore suggest comparing (i) the spectra of SBSL (air bubble) and air capillary sparks and (ii) diagnostics data (i.e., N_e and T_e).

The plasma diagnostic analysis of the air capillary spark revealed $N_e=3\times10^{25}$ m^{-3} and $T_e=19\,000$ K. Since the volumic radiant flux (W m^{-3} sr^{-1}) essentially depends on N_e^2 (free-bound and free-free transitions), it must be expected that the volumic radiant flux of the capillary spark is 10 times more intense than the SL one of a single air bubble (with approximately N_e: 10^{25} m^{-3} and T_e: 20 000 K). Figure 12 illustrates this prediction.

B. Suggested experiments

In order to check and distinguish the present model of SL from others, three further studies can be mentioned which appear feasible in view of up-to-date technology and knowledge. The first proposal consists of submitting a single levitating bubble either to an electrical or a magnetic field. A plasma diagnostic analysis associated with these situations should reveal that either the electronic temperature or the density (perhaps both) is (are) affected (the ''pinch'' effect). Moreover, this analysis should highlight the consistency of

the results obtained in the undisturbed (Lepoint-Mullie *et al.*, 1996) and disturbed cases. In principle, this double analysis should not be ambigous and should enable a distinction to be made between the different theories since the physical basis associated with the latter are different. It must be noted that a similar proposal (''magnetic-field diagnostic for sonoluminescence'') has recently been formulated to check the shock wave model (Chou and Blackman, 1996).

Secondly, as can be deduced from Sec. IV D 4, the higher the number of intracavity jets, the higher the electronic density and the SBSL intensity. One should expect that any mechanical process increasing the bubble asymmetry (such as translational acceleration) enhances the light intensity. This proposal is based on calculations showing that gravity may facilitate the formation of inward jets in collapsing bubbles (preprint of a paper by Longuet–Higgins and Oguz, to be published in Proc. R. Soc., London, 1997). Again, in this field it may be expected that our model is distinguished from others. For example, the higher the symmetry of the bubble (in the shock-wave model), the higher the SBSL intensity (and the temperature) while it should be the opposite according to the electrohydrodynamic hypothesis. Moreover, in this latter hypothesis it is not particularly expected that the radiation should be anisotropic. While Eberlein (1996) states in the field of the theory of quantum radiation, i.e., ''dynamic Casimir light,'' that ''...if the bubble is spheroidal rather than spherical during the radiation process, one expects anisotropy.''

The third proposal is based on work by Butterworth (1979) who showed experimentally that the analysis of the radio wave emission from an electrostatic spark may yield information about the nature of the discharge itself. If the problem of the smallness of the zone of emission in the case of SBSL is circumvented (Atchley, 1996), it might be possible to distinguish the electrohydrodynamic from the shock-wave hypothesis.

C. Discussion and further studies

By dealing with the processes able to occur only in the interior and the vicinity of a collapsing bubble, the modeling proposed in Secs. III and IV constitutes (in the best case) part of a vaster description of the ''bubble/liquid/acoustic field'' ensemble. With only this modeling as a tool, it would be inappropriate to want to ''solve'' in a definitive way the questions asked by Crum (1994), Crum and Roy (1994), or Weninger *et al.* (1995). At the present time, our objective is not to afford *direct* answers to all the questions asked, but, to open a discussion on the consequences related to such a model and its connections with experiments.

The first example is related to experiments carried out by Sir J. J. Thomson (1894) on the electricity of water drops formed by splashing. Thomson said: ''The first variation that I tried was to make the drops fall through water vapor instead of air [...]. In this case no electrical separation whatever was observed, though when air was blown into the vessel the normal effect at once reappeared.'' We can now return to the case of a collapsing bubble. If an intracavity spray is formed, it may be thought, by analogy, that the higher the intracavity vapor content is (due to any increase in the temperature of the host-liquid), the less marked the electrification and smaller the energy will be that is released to form the microplasma. This means that this latter will be less luminescent and less hot. Is the observation, according to which SL intensity decreases when liquid temperature increases (Hiller *et al.*, 1992; with a shift toward higher wavelength), linked to Thomson's work?

The second item also concerns the work by Thomson (1894) [and also Lenard (1915)], who found that electrification in the presence of H_2 decreases strongly. Is this observation related with the work by Hiller and Putterman (1995) according to which SL intensity of a hydrogen bubble in water (even near the freezing point of water) is less by a factor of 10 than in the case of an air bubble in water (at 20 °C; Hiller *et al.*, 1992)?

Again, the third item deals with the work on electrification of drops (Thomson, 1894) in which it has been shown that a small amount of organic acids induces a strong decrease of the charge acquired by droplets during splashing experiments. Thomson also noted that very concentrated solutions of organic acids give more electrification than diluted ones, though the former never reach the electrification obtained with water itself. Unfortunately, as far as we are concerned we do not possess any data on the effect of aliphatic alcohols. Is the fact related to these observations, according to which the addition of tiny amounts of alcohols (i.e., 1-butanol) (Weninger *et al.*, 1995) to water rapidly degrade the SL to a level lower by at least a factor of 10 from what can be seen in ''pure'' alcohol? In the same vein, are the Thomson's observations extendable to the case of water/glycerol mixtures, for which it is known that the higher the glycerol concentration is, the cooler the interior of single bubbles is (Carlson *et al.*, 1993)? Is the presence of small amounts of alcohols (acting as surface-active agents) able to damp capillary waves (Levich, 1962) and consequently inward jets so decreasing SL intensity?

Concerning bubble dynamics, the model could perhaps be helpful to account for experimental observations. One cannot help noting the remarkable synchronism of SL flashes. It is possible that the small jitter ($<$50 ps, Barber and Putterman, 1992) is associated with the dissipation of small amount of energy induced by the occurrence of inward jets (Longuet-Higgins, 1995). The ablation of the jets in the process of microplasma formation may explain the stability of a bubble which otherwise could be destroyed because of the exponential growth of the jets. The overpressure associated with the formation of the microplasma may contribute to damping the growth of the residual inward protuberances of the liquid by inducing a sufficiently strong deceleration of the bubble wall. This overpressure could slow down the implosion, so preventing the bubble from reaching its minimum theoretical radius of collapse. The overpressure which exists during the time required for recombination of the radicals (i.e., several ns) could be able to favor the outward nondiffusive mass transfer, and this could explain that a single bubble seems to be in a regime of ''controlled'' rectified diffusion.

VI. CONCLUSION

How can we approach the apparent complexity of the phenomenon of sonoluminescence, for which each new experimental result seems to take us further away from an elementary solution? Two kinds of behavior may be encountered in relation to this fundamental question. The first possible thing is to think that SL can be described by means of a ''simple'' model, i.e., a model involving only one field (hydrodynamics, for example). This is the case of the converging shock-wave model, for which it can be expected that it contains all the information required to account for the different aspects of SBSL. Is it actually the case?

Another type of behavior is to think that the complexity of the phenomenon is the image of a string of events appealing to a multidisciplinary description. This is the approach used in this paper. Of course, the hypothetical character of this approach and the considerations developed above need no emphasizing. However, a possible way to (in)validate the model proposed is to analyze in more detail the items discussed in Sec. V which show the possible intrinsic wealth of the ''electrohydrodynamical'' model. Work is in progress in this direction, and in the analysis of the sensitivity of the modeling to parametric variation.

ACKNOWLEDGMENTS

The authors wish to acknowledge many helpful discussions with Professor M. S. Longuet-Higgins and Professor R. A. Roy. They wish to express their thanks to the Fonds National de la Recherche Scientifique (Belgium) and Electricité de France for financial support.

Atchley, A. A. (**1993**). ''Review of recent advances in synchronous picosecond sonoluminescence,'' in *Non Linear Acoustics*, 13th ISNA, Bergen, Norway, edited by H. Hobaek (World Scientific, London), pp. 36–42.

Atchley, A. A. (**1996**). (Personal communication.)

Bailey, A. G. (**1988**). *Electrostatic Spraying of Liquids* (Wiley, New York).

Barber, B. P., Hiller, R., Arisaka, K. , Fetterman, H. , and Putterman, S. (**1991**). ''Resolving the picosecond characteristics of synchronous sonoluminescence,'' J. Acoust. Soc. Am. **91,** 3061–3063.

Barber, B. P., and Putterman, S. (**1991**). ''Observation of synchronous picosecond sonoluminescence,'' Nature (London) **352,** 318–320.

Barber, P. B., and Putterman, S. (**1992**). ''Light scattering measurements of the repetitive supersonic implosion of a sonoluminescing bubble,'' Phys. Rev. Lett. **69,** 3839–3842.

Barber, P. B., Wu, C. C., Löfstedt, P. H., and Putterman, S. J. (**1994**). ''Sensitivity of sonoluminescence to experimental parameters,'' Phys. Rev. Lett. **72,** 1380–1383.

Barreto, E. (**1979**). ''Ignition by electric sparks,'' Inst. Phys. Conf. Ser. **48,** 135–144.

Bayliss, K. H., and Latham, R. V. (**1986**). ''An analysis of field-induced hot-electron emission from metal-insulator microstructures on broad-area high-voltage electrodes,'' Proc. R. Soc. London, Ser. A **403,** 285–311.

Bernstein, L. S., and Zakin, M. R. (**1995**). ''Confined electron model for single-bubble sonoluminescence,'' J. Phys. Chem. **99,** 14619–14627.

Birkhoff, G. (**1954**). ''Note on Taylor instability,'' Q. Appl. Math. **12,** 306–309.

Birkhoff, G. (**1956**). ''Stability of spherical bubbles,'' Q. Appl. Math. **13,** 451–453.

Braginskii, S. I. (**1958**). ''Theory of the development of a spark channel,'' J. Exp. Theor. Phys. **34**, 1068–1074.

Brenner, M. P., Lohse, D., and Dupont, T. F. (**1995**). ''Bubble shape oscillations and the onset of sonoluminescence,'' Phys. Rev. Lett. **75,** 954–957.

Bustin, W. M., and Dukek, W. G. (**1983**). *Electrostatic Hazards in Petroleum Industry* (Research Studies, Lechtworth, UK).

Butterworth, G. J. (**1979**). ''The detection and characterisation of electrostatic sparks by radio methods,'' Inst. Phys. Conf. Ser. **48,** 161–169.

Carlson, J. T., Lewia, S. D., Atchley, A. A., Gaitan, D. F., Maruyama, X. K., Lowry, M. E., Moran, M. J., and Sweider, D. R. (**1993**). ''Spectra of picosecond sonoluminescence,'' in *Non Linear Acoustics*, 13th ISNA, Bergen, Norway, edited by H. Hobaek (World Scientific, London), pp. 406–411.

Chapman, D. L. (**1913**). ''A contribution to the theory of electrocapillarity,'' Philos. Mag. **25,** 475–481.

Chatterton, P. A. (**1966**). ''A theoretical study of field emission initiated vacuum breakdown,'' Proc. R. Soc. London **88,** 231–245.

Chou, T., and Blackman, E. G. (**1996**). ''Magnetic field diagnostic for sonoluminescence,'' Phys. Rev. Lett. **76,** 1549–1552.

Crum, L. A., and Gaitan, D. F. (**1989**). ''Sonoluminescence and its application to medical ultrasound risk assessment,'' SPIE New Methods in Microscopy and Low Light Imaging. **1161**, 125–135.

Crum, L. A., and Roy, R. A. (**1994**). ''Sonoluminescence,'' Science **226,** 233–234.

Crum, L. A. (**1994**). ''Sonoluminescence, sonochemistry, and sonophysics,'' J. Acoust. Soc. Am. **95,** 559–562.

Dejean, P., Berg, G., Goldman, M., Sigmond, R. S., and Dejean, H. (**1992**). ''Ageing kinetics of solid insulating materials submitted to partial discharges,'' in *Proceedings of the 4th International Conference on Conduction and Breakdown in Solid Dielectrics*, Sestri Levante, Italy (IEEE Dielectrics and Electrical Insulation Society, New York), pp. 200–204.

Demidov, B. A., Skachkov, Y. F., and Fanchenko, S. D. (**1961**). ''Channel expansion in small intense sparks,'' J. Exp. Theor. Phys. **13**, 263–267.

Drabkina, S. I. (**1951**). ''Theory of the development of a gas discharge,'' J. Exp. Theor. Phys. **21**, 473–483.

Eberlein, C. (**1996**). ''Theory of quantum radiation observed as sonoluminescence,'' Phys. Rev. E **53,** 2772–2787.

Elghazaly, H. A., and Castle, G. S. P. (**1987**). ''The charge limit of liquid droplets due to electron avalanches and surface disruption,'' Inst. Phys. Conf. Ser. (IOP, Bristol), pp. 121–126.

Felici, N. J., Gosse, J. P., and Solufamboahangy, A. (**1981**). ''Liquid flow electrification and zeta potential in hydrocrabons,'' in Proceedings of the 7th Conference on Conduction and Breakdown in Dielectric Liquids, Berlin-West, Germany, edited by W. F. Schmidt (IEE Electrical Insulation Society, Piscataway, NJ), pp. 284–288.

Fitaire, M. (**1995**). (Private communication.)

Frenzel, H., and Schultes, H. (**1934**). ''Lumineszenz in Ultraschallbeschickten Wasser,'' Z. Phys. Chem. Abt. B **27,** 421–424.

Frommhold, L., and Atchley, A. A. (**1994**). ''Is sonoluminescence due to collision-induced emission?,'' Phys. Rev. Lett. **73,** 2883–2886.

Fowler, R. H., and Nordheim, L. W. (**1928**). ''Electron emission in intense electric fields,'' Proc. R. Soc., London Ser. A **119,** 173–181.

Gaitan, D. F., Crum, L. A., Church, C. C., and Roy, R. A. (**1992**). ''Sonoluminescence and bubble dynamics for a single, stable, cavitation bubble,'' J. Acoust. Soc. Am. **91,** 3166–3183.

Gouy, G. (**1910**). ''Sur la constitution de la charge électrique à la surface d'un électrolyte,'' J. Phys. Théor. Appl. **9**, 457–468.

Günther, P., Heim, E., and Eichkorn, G. (**1959**). ''Phasen-Korrelation Schallwechseldruck und Sonolumineszenz,'' Z. Angew. Phys. **11,** 274–277.

Hickling, R. (**1994**). ''Transient high-pressure solidification associated with cavitation in water,'' Phys. Rev. Lett. **73,** 2853–2856.

Hiller, R., Putterman, S., and Barber, B. P. (**1992**). ''Spectrum of synchronous sonoluminescence,'' Phys. Rev. Lett. **69,** 1182–1184.

Hiller, R., Weninger, K., Putterman, S. J., and Barber, B. P. (**1994**). ''Effect of noble gas doping in single-bubble sonoluminescence,'' Science **266,** 248–250.

Hiller, R., and Putterman, S. J. (**1995**). ''Observations of isotope effect in sonoluminescence,'' Phys. Rev. Lett. **75,** 3549–3551.

Hsieh, D. Y. (**1974**). ''On the thresholds for surface waves and subharmonics of an oscillating bubble,'' J. Acoust. Soc. Am. **56,** 392–393.

Iribarne J. V. (**1972**). ''The electrical double layer and electrification associated with water disruption processes,'' J. de Recherches Atmos. **6**, 265–281.

Iribarne, J. V., and Klemes, M. (**1974**). ''Electrification associated with droplet production from liquid jets,'' J. Chem. Soc. Faraday Trans. **70,** 1219–1227.

Iribarne, J. V., and Mason, B. J. (**1967**). ''Electrification accompanying the bursting of bubbles in water and dilute aqueous solutions,'' Trans. Faraday Soc. **63,** 2234–2245.

Jarman, P. (**1960**). ''Sonoluminescence: a discussion,'' J. Acoust. Soc. Am. **32,** 1459–1462.
Kamath, V., Prosperetti, A., and Egolfopoulos, F. N. (**1993**). ''A theoretical study of sonoluminescence,'' J. Acoust. Soc. Am. **94**, 248–260.
Kovalchuk, E. Y., and Shchekatolina, S. A. (**1983**). ''Determination of the effort of electron emission from a polar liquid in the gas phase,'' Fiz. Aerodispersnykh Sist. **23**, 32–33.
Kuttruff, H. (**1962**). ''Uber den Zusammenhang Zwischen der Sonoluminezenz und der Schwingungskavitation in Flussigkeiten,'' Acustica **12**, 230–254.
Kwak, H.-Y., and Yang, H. (**1995**). ''An aspect of sonoluminescence from hydrodynamic theory,'' J. Phys. Soc. Jpn. **64,** 1980–1992.
Laube, S. (**1992**). ''Exoélectrons et amorçage de décharges électriques,'' Ph.D. thesis, Université Paris-Sud, France.
Lauterborn, W. (**1974**). ''General and basic aspects of cavitation,'' in *Finite-Amplitude Wave Effects in Fluids*, edited by L. Bjorno (IPC Sci. Technol., Guilford), pp. 195–202.
Leighton, T. G. (**1994**). *The Acoustic Bubble* (Academic, London).
Lenard, P. (**1892**). ''Ueber die Elektrizität der Wasserfalle,'' Wiedermann's Ann. **46**, 584.
Lenard, P. (**1915**). ''Uber Wasserfällelektrizitaet und über die Oberflächenbeschaffenheit der Flüssigkeiten,'' Ann. d. Phys. **47**, 463–524.
Lentz, W. J., Atchley, A. A., Gaitan, F. D., and Maruyama, X. K. (**1993**). ''Mie scattering from a sonoluminescing bubble,'' in *Non Linear Acoustics*, 13th ISNA, Bergen, Norway, edited by H. Hobaek (World Scientific, London), pp. 400–405.
Lepoint, T., Mullie, F., Lambillotte, Y., Goldman, M., Goldman, A., and Tardiveau, P. (**1994**). ''Picosecond sonoluminescence from macroscopic to microscopic models,'' J. Acoust. Soc. Am. **96**, 3239–3240 (A).
Lepoint-Mullie, F., De Pauw, D., Lepoint, T., Supiot, P., and Avni, R. (**1996**). ''Nature of the ''extreme conditions'' in single sonoluminescing bubbles,'' J. Phys. Chem. **100,** 12138–12141.
Levich, V. G. (**1962**). *Physicochemical Hydrodynamics* (Prentice-Hall, Englewood Cliffs, NJ), pp. 591–668.
Levshin, V. L., and Rzheykin, S. N. (**1937**). ''On the mechanism of luminescence in liquids under ultrasonic treatment,'' C. R. Acad. Sci. URSS **16**, 399–407.
Lochte-Holtgreven, W., and Richter, J. (**1968**). ''Quantitative spectroscopy and spectral photometry,'' in *Plasma Diagnostics*, edited by Lochte-Holtgreven (North-Holland, Amsterdam), pp. 250–346.
Loeb, L. B. (**1958**). *Static Electrification* (Springer-Verlag, Berlin).
Löfstedt, R., Barber, B. P., and Putterman, S. J. (**1993**). ''Toward a hydrodynamic theory of sonoluminescence,'' Phys. Fluids A **5,** 2911–2928.
Löfstedt, R., Weninger, K., Putterman, S., and Barber, B. P. (**1995**). ''Sonoluminescing bubbles and mass diffusion,'' Phys. Rev. E **51,** 4400–4410.
Longuet-Higgins, M. S. (**1995**). (Private communication.)
Longuet-Higgins, M. S., and Oguz, H. (**1995**). ''Critical microjet in collapsing cavity,'' J. Fluid Mech. **290,** 183–201; (**1997**) (preprint). ''Critical jets in surface waves and collapsing cavities,'' to be published in Philos. Trans. R. Soc. London, Ser. A.
Macleay, R. Q., and Holroyd, L. F. (**1961**). ''Space time analysis of the sonoluminescence emitted by cavitated water,'' J. Appl. Phys. **32,** 449–453.
Magono, C. (**1980**). *Thunderstorms* (Elsevier, Amsterdam), pp. 77–134.
Mandel'shtam, S. L., and Suhkodrev, N. K. (**1953**). ''Elementary processes in the spark-discharge channel,'' Zh. Eksp. Teor. Fiz. **24,** 701–707.
Marinesco, M., and Trillat, J. J. (**1933**). ''Action des ultrasons sur les plaques photographiques,'' C. R. Acad. Sci. **196,** 858–860.
Matula, T. J., and Roy, R. A. (**1995**). (Private communication.)
Morshuis, P. H. F. (**1993**). ''Time resolved discharge measurements,'' in Proceedings of the IEE International Conference on Partial Discharge, Canterbury, United Kingdom (IEE Electrical Insulation Society, Piscataway, NJ), pp. 43–46.
Moss, W. C., Clarke, D. B., White, J. W., and Young, D. A. (**1994**). ''Hydrodynamic simulations of bubble collapse and picosecond sonoluminescence,'' Phys. Fluids **6,** 2979–2985.
Negishi, K. (**1961**). ''Experimental studies on sonoluminescence and ultrasonic cavitation,'' J. Phys. Soc. Jpn. **16,** 1450–1465.
Nordheim, L. W. (**1928**). ''The effect of the image force on the emission and reflexion of electrons by metals,'' Proc. R. Soc. London, Ser. A **121,** 626–639.
Nottingham, W. B. (**1956**). ''Thermoionic emission,'' in *Encyclopedia of Physics*, edited by S. Flügge (Springer-Verlag, Berlin), Vol. XXI, pp. 1–175.
Pierce, E. T. (**1970**). ''Waterfalls, bathrooms, and perhaps supertanker explosions,'' Proceedings of the 1970 Lightning and Static Electricity Conference, pp. 89–96.
Pierce, E. T., and Whitson, A. L. (**1965**). ''Atmospheric electricity and the waterfalls of Yosemite Valley,'' J. Atmos. Sci. **22,** 314–319.
Plesset, M. S., and Mitchell, T. P. (**1956**). ''On the stability of the spherical shape of a vapor cavity in a liquid,'' Q. Appl. Math. **13,** 419–430.
Plesset, M. S., (**1954**). ''On the stability of fluid flows with spherical symmetry,'' J. Appl. Phys. **25,** 96–98.
Plesset, M. S., and Prosperetti, A. (**1977**). ''Bubble dynamics and cavitation,'' Annu. Rev. Fluid Mech. **9**, 145–185
Prosperetti, A., and Oguz, H. (**1992**). ''A mechanism for the rapid quenching of sonoluminescent pulses,'' J. Acoust. Soc. Am. **91**, Pt. 2, 2331. (Abstract of the 123th Meeting of the Acoustical Society of America.)
Prosperetti, A. (**1996**). (Personal communication; paper submitted.)
Putterman, S. J. (**1994**). (Personal communication.)
Raether, H. (**1964**). *Electron Avalanches and Breakdown in Gases* (Butterworths, London).
Schaeffer, V. J. (**1958**). ''The electrification of oil and water clouds,'' in *Recents Advances in Atmospheric Electricity*, Proceedings of the Second Conference on Atmospheric Electricity, Portsmouth, New Hampshire, edited by L. G. Smith (Pergamon, New York), pp. 431–434.
Schwinger, J. (**1993**). ''Casimir light: the source,'' Proc. Natl. Acad. Sci. USA **90,** 2105–2106.
Stern, O. (**1924**). ''Zür Theorie der Elektrolytischen Doppelschicht,'' Z. Elektrochem. **30,** 508–516.
Strawson, H., and Lyle, A. R. (**1975**). ''Safe charge densities for road and rail tank car filling,'' in *Static Electrification*, 4th Conference on Static Electrification, CEGB Headquarters, London, UK, edited by A. R. Blythe (IEE Electrical Insulation Society, Piscataway, NJ), pp. 276–289.
Taylor, G. (**1950**). ''The instability of liquid surfaces when accelerated in a direction perpendicular to their planes. I,'' Proc. R. Soc. London, Ser. A **201,** 192–196.
Thomson, J. J. (**1894**). ''On the electricity of drops,'' Philos. Mag. **37,** 341–358.
Venugopalan, M. (**1971**). *Reactions under Plasma Conditions* (Wiley, New York), p. 8.
Vogel, A., Lauterborn, W., and Timm, R. (**1989**). ''Optical and acoustic investigations of the dynamics of laser-produced cavitation bubbles near a solid boundary,'' J. Fluid Mech. **206,** 299–338.
von Engel, A. (**1983**). *Electric Plasmas: Their Nature and Uses* (Taylor and Francis, London), p. 165.
Wahlin, L. (**1986**). *Atmospheric Electrostatic* (Wiley, New York).
Watanabe, S., Ohashi, A., and Ito, M. (**1981**). ''Charging tendency of aliphatic alcohols,'' in *Proceedings of the 7th Conference on Conduction and Breakdown in Dielectric Liquids*, Berlin-West, Germany, edited by W. F. Schmidt (IEE Electrical Insulation Society, Piscataway, NJ), pp. 328–332.
Weninger, K., Hiller, R., Barber, B. P., Lacoste, D., and Putterman, S. J. (**1995**). ''Sonoluminescence from single bubble in non-aqueous liquids: new parameter space for sonochemistry,'' J. Phys. Chem. **99,** 14195–14197.
Whybrew, W. E., Kinzer, G. D., and Gunn, R. (**1952**). ''Electrification of small air bubbles in water,'' J. Geophys. Res. **57,** 459–471.
Wu, C. C., and Roberts, P. H. (**1993**). ''Shock-wave propagation in a sonoluminescing gas bubble,'' Phys. Rev. Lett. **70,** 3424–3427.
Wu, C. C., and Roberts, P. H. (**1994**). ''A model of sonoluminescence,'' Proc. R. Soc. London, Ser. A **445,** 323–349.
Yasui, K. (**1995**). ''Effects of thermal conduction on bubble dynamics near the sonoluminescence threshold,'' J. Acoust. Soc. Am. **98,** 2772–2782.
Zimakov, P. V. (**1934**). ''Uber Das Verhalten der Einigen Wässerigen Lössungen in Eihem Hochfrequenten Elektrishen Felde,'' C. R. Acad. Sci. USSR **3**, 452–455.

Analysis of different boundary condition models for study of wave scattering from fiber–matrix interphases

W. Huang,[a] S. I. Rokhlin, and Y. J. Wang[b]
The Ohio State University, Nondestructive Evaluation Program, Department of Industrial, Welding, and Systems Engineering, 190 West 19th Avenue, Columbus, Ohio 43210

(Received 21 August 1995; accepted for publication 2 October 1996)

In this paper different approximate boundary conditions (BC) describing a thin fiber–matrix interphase are used to study ultrasonic wave scattering from a multiphase fiber embedded in a solid matrix. To facilitate the analysis of scattering from a multilayered fiber, a matrix differential equation is derived for elastic fields in a cylindrical medium with radially-dependent properties. From this equation the transfer matrix for each intermediate layer between the fiber core and matrix, relating the stress and displacement fields on the inner and outer boundaries of the layer, is obtained. To describe the effect of the interphase the first- and second-order asymptotic and the spring boundary conditions are derived using an asymptotic expansion of the transfer matrix for a thin fiber–matrix interphase. Analysis performed for different models of spring boundary conditions shows the advantage of preserving the interphase gap connected by springs versus the spring BC defined on an infinitely thin interface, after eliminating the interphase layer and filling the remaining gap by matrix or fiber material. In the last two cases the geometry of the system changes due to change of the scattering surface radius, leading to error in the scattering amplitude. Numerical examples are given for scattering cross sections of longitudinal and shear waves from a multiphase SiC fiber in titanium. It is shown that the spring BC can be used to represent a thin interphase layer with elastic moduli smaller than those of the fiber. [S0001-4966(97)05403-9]

PACS numbers: 43.35.Zc [HEB]

INTRODUCTION

Specially designed fiber–matrix interphases are used in modern composites to improve fracture toughness, chemical compatibility, and matching of thermal expansion coefficients between composite constituents. They are usually designed and manufactured in the form of thin layers. For example, in metal and intermetallic matrix composites special interfacial reaction barrier coatings[1] are introduced to improve chemical and thermal compatibility. In ceramic matrix composites, interphases in the form of compliant coatings are added to provide frictional sliding contact between fiber and matrix to prevent fiber fracture triggered by matrix cracking.[2,3] For polymer matrix composites various forms of interphases are also widely applied to improve composite performance, such as in carbon/epoxy composites.[4,5]

Since the interphase transfers the load between fibers and matrix, the interphase properties and the quality of bonding with the surrounding fiber and matrix are essential in determining composite mechanical performance. Ultrasonic waves can be a useful nondestructive tool to sense these interphase characteristics since wave scattering from fibers is strongly affected by both the interphase's elastic properties and its mechanical contact with the neighboring matrix and fiber. Due to manufacturing processes and in-service conditions, interphase properties such as thickness and elastic moduli are often difficult to measure and define. To simplify interphase description one can introduce approximate boundary conditions (BC) to relate elastic fields across the interphase for modeling of composite properties and wave scattering from fibers. In this paper we will address this problem with emphasis on the asymptotic BC and spring boundary models to describe a thin fiber-matrix interphase.

Although much work has been done for elastic wave scattering from a cylindrical inclusion in a solid[6–11] (for a comprehensive list of early publications, see Ref. 11), most previous studies address scattering of an elastic wave on a solid cylinder perfectly bonded to the solid matrix. In our own work[12–14,27] a scattering model for multilayered fibers has been developed which allows treatment of the fiber–matrix interphase effect. A spring BC model for the fiber–matrix interphase was used[12,13] to simplify the study of the interphase effect on wave scattering, where the springs were defined on an infinitely thin interface after eliminating the interphase layer and filling the remaining gap by fiber material. Later a transfer matrix method was developed in Ref. 14 to simplify calculation of wave scattering from a multiphase SiC fiber.

In this paper a more general and elegant transfer matrix method will be introduced for 2-D and 3-D scattering cases by solving a matrix differential equation for the elastic field in a cylindrical medium with radially dependent properties. The solution obtained makes it possible to derive different BC models by expanding in series the transfer matrix for a

[a]Now with Digital Wave Corporation, 14 Inverness Drive East B-120, Englewood, CO 80112.
[b]Permanent address: Institute of Acoustics, Nanjing University, Nanjing 210093, People's Republic of China.

thin fiber–matrix interphasial layer. This treatment is similar to that used for plane interphases.[15,16] Numerical examples will be given to compare different approximate BC models with the exact solution. A detailed analysis will be done on the application of different spring BC. We will demonstrate the advantage of the spring BC applied across the interphase gap when springs are used to substitute for the interphase layer thus preserving the system geometry.

I. EXPONENTIAL TRANSFER MATRIX DESCRIPTION OF ELASTIC FIELD FOR A MULTILAYERED FIBER IN SOLID

A. Problem statement

The treatment of wave phenomena in multilayered cylinders is important for ultrasonic characterization of modern high-temperature composites where both the fibers and the fiber–matrix interphases can have multilayered structures due to design and to the manufacturing process. In a recent paper[13] wave scattering from a three-phase fiber in a solid matrix was obtained by solving a 12×12 system of boundary equations. If one need consider more layers the analysis and computations become tedious. More recently the analysis was extended to multilayered fibers with an arbitrary number of phases using a transfer matrix approach based on multiplication of matrices built on wave solutions.[14] There is an alternate way to derive the transfer matrix by solving a matrix differential equation for elastic fields in a cylindrical medium with radially dependent properties. The latter approach is more convenient for discussion of different BC models derived by different approximations to the transfer matrix, since the transfer matrix is in an elegant exponential form. Both approaches for derivation of the transfer matrix have been widely used for multilayered isotropic and anisotropic plane layered systems[17–23] and for multilayered solids with spherical interfaces.[24,25]

B. Matrix differential equation

1. 2-D case

In a cylindrical system (r,θ,z), the elastic field can be described by a scalar potential φ and the z component of the vector potential ψ_z if it is independent of z. One example is scattering of a normally incident longitudinal or transverse wave by a fiber as shown in Fig. 1. The two elastic potentials have the following well-known expansion in Bessel series

$$\varphi=\sum_{n=-\infty}^{\infty}[A_nJ_n(k_lr)+C_nN_n(k_lr)]\exp(in\theta), \tag{1}$$

$$\psi_z=\sum_{n=-\infty}^{\infty}[B_nJ_n(k_tr)+D_nN_n(k_tr)]\exp(in\theta), \tag{2}$$

where k_l and k_t are the wave numbers of the longitudinal and transverse modes, respectively; $J_n(\cdot)$ is the nth-order Bessel function of the first kind, and $N_n(\cdot)$ is the nth-order Neumann function. The time-dependent factor $e^{-i\omega t}$ is omitted throughout.

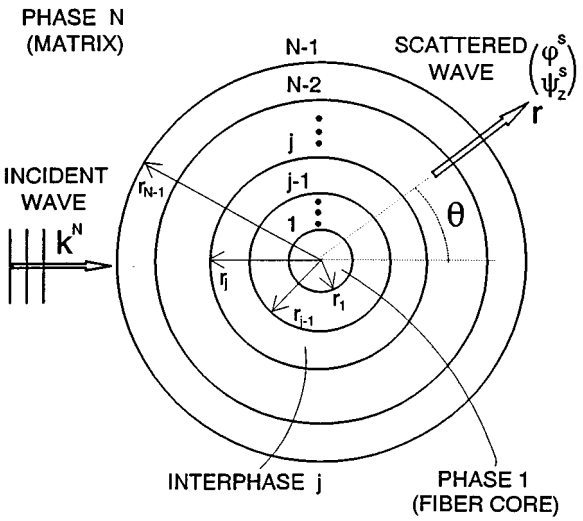

FIG. 1. Scattering from an $N-1$-phase multilayered cylinder in a solid matrix. k^N is the incident wave number in the matrix material (phase N).

The displacements and stresses can be found from the elastic potentials through the following relations:

$$u_r=\frac{\partial\varphi}{\partial r}+\frac{1}{r}\frac{\partial\psi_z}{\partial\theta}, \tag{3}$$

$$u_\theta=\frac{1}{r}\frac{\partial\varphi}{\partial\theta}-\frac{\partial\psi_z}{\partial r}, \tag{4}$$

$$\sigma_{rr}=\lambda\Delta^2\varphi+2\mu\left[\frac{\partial^2\varphi}{\partial r^2}+\frac{\partial}{\partial r}\left(\frac{1}{r}\frac{\partial\psi_z}{\partial\theta}\right)\right], \tag{5}$$

$$\sigma_{r\theta}=2\mu\left(\frac{1}{r}\frac{\partial^2\varphi}{\partial r\partial\theta}-\frac{1}{r^2}\frac{\partial\varphi}{\partial\theta}\right)+\mu\left[\frac{1}{r^2}\frac{\partial^2\psi_z}{\partial\theta^2}-r\frac{\partial}{\partial r}\left(\frac{1}{r}\frac{\partial\psi_z}{\partial r}\right)\right], \tag{6}$$

where λ and μ are the Lamé constants.

For a cylindrical system with nonhomogeneous properties in the radial direction one can obtain a governing matrix differential equation for the elastic field by combining Hooke's law, the equation of equilibrium, the wave equation for the elastic potentials, the wave solutions (1), and the displacement, stress-potential relations (3)–(6)

$$\frac{\partial}{\partial r}\begin{pmatrix} u_r \\ u_\theta \\ \sigma_{rr} \\ \sigma_{r\theta} \end{pmatrix}_n = \begin{pmatrix} -\frac{\lambda}{r(\lambda+2\mu)} & -\frac{in\lambda}{r(\lambda+2\mu)} & \frac{1}{\lambda+2\mu} & 0 \\ -\frac{in}{r} & \frac{1}{r} & 0 & \mu \\ \frac{4\mu(\lambda+\mu)}{r^2(\lambda+2\mu)}-\rho\omega^2 & \frac{4in\mu(\lambda+\mu)}{r^2(\lambda+2\mu)} & -\frac{2\mu}{r(\lambda+2\mu)} & -\frac{in}{r} \\ -\frac{4in\mu(\lambda+\mu)}{r^2(\lambda+2\mu)} & \frac{4n^2\mu(\lambda+\mu)}{r^2(\lambda+2\mu)}-\rho\omega^2 & -\frac{in\lambda}{r(\lambda+2\mu)} & -\frac{2}{r} \end{pmatrix} \begin{pmatrix} u_r \\ u_\theta \\ \sigma_{rr} \\ \sigma_{r\theta} \end{pmatrix}_n, \tag{7}$$

or

$$\frac{\partial \mathbf{U}_n(r)}{\partial r} = \mathbf{t_n}(r)\mathbf{U}_n(r), \tag{8}$$

where λ, μ, and ρ are functions of the radius r, $\mathbf{U}_n(r)$ denotes the displacement and stress vector $(u_r, u_\theta, \sigma_{rr}, \sigma_{r\theta})_n^T$, $\mathbf{t_n}(r)$ is the characteristic matrix of the elastic field at r, and n is the order of the Bessel series for representation of the elastic field.

2. 3-D case

A 3-D solution for oblique scattering by a cylinder can be described by three scalar elastic potentials φ, ψ_{t1}, and ψ_{t2},[27] which are solutions of the Helmholtz equations. Their expansions in Bessel series are

$$\varphi = \exp(ik_z z)\sum_{n=-\infty}^{\infty}[A_n J_n(k_{lr}r) + D_n N_n(k_{lr}r)]\exp(in\theta) = \sum_{n=-\infty}^{\infty}\varphi_n,$$

$$\psi_{t1} = \exp(ik_z z)\sum_{n=-\infty}^{\infty}[B_n J_n(k_{tr}r) + E_n N_n(k_{tr}r)]\exp(in\theta) = \sum_{n=-\infty}^{\infty}\psi_{t1n}, \tag{9}$$

$$\psi_{t2} = \exp(ik_z z)\sum_{n=-\infty}^{\infty}[C_n J_n(k_{tr}r) + F_n N_n(k_{tr}r)]\exp(in\theta) = \sum_{n=-\infty}^{\infty}\psi_{t2n}.$$

Here k_z is the z component of the wave number (due to Snell's law it is independent of radius) and k_{lr} and k_{tr} are the radial components of the longitudinal and transverse wave numbers, respectively.

As in the 2-D case one can obtain the matrix differential equation for the elastic field as

$$\frac{\partial}{\partial r}\begin{pmatrix} u_r \\ u_\theta \\ u_z \\ \sigma_{rr} \\ \sigma_{r\theta} \\ \sigma_{rz} \end{pmatrix}_n = \mathbf{t_n}\begin{pmatrix} u_r \\ u_\theta \\ u_z \\ \sigma_{rr} \\ \sigma_{r\theta} \\ \sigma_{rz} \end{pmatrix}_n, \tag{10}$$

where $\mathbf{t_n}$ is

$$\begin{pmatrix} -\frac{\lambda}{r(\lambda+2\mu)} & -\frac{in\lambda}{r(\lambda+2\mu)} & -\frac{i\lambda}{(\lambda+2\mu)}k_z & \frac{1}{\lambda+2\mu} & 0 & 0 \\ -\frac{in}{r} & \frac{1}{r} & 0 & 0 & \frac{1}{\mu} & 0 \\ -ik_z & 0 & 0 & 0 & 0 & \frac{1}{\mu} \\ \frac{4\mu(\lambda+\mu)}{r^2(\lambda+2\mu)}-\rho\omega^2 & \frac{4in\mu(\lambda+\mu)}{r^2(\lambda+2\mu)} & \frac{i\lambda}{r}k_z & -\frac{2\mu}{r(\lambda+2\mu)} & -\frac{in}{r} & -ik_z \\ -\frac{4in\mu(\lambda+\mu)}{r^2(\lambda+2\mu)} & \frac{4n^2\mu(\lambda+\mu)}{r^2(\lambda+2\mu)}+\mu k_z^2-\rho\omega^2 & \frac{n(3\lambda\mu+2\mu^2)}{r(\lambda+2\mu)}k_z & -\frac{in\lambda}{r(\lambda+2\mu)} & -\frac{2}{r} & 0 \\ \frac{i\ 2\mu\lambda}{r\lambda+2\mu}k_z & \frac{n(3\mu\lambda+2\mu^2)}{r(\lambda+2\mu)}k_z & \frac{n^2}{r^2}\ \mu+\frac{\lambda^2+3\lambda\mu+\mu^2}{\lambda+2\mu}k_z^2-\rho\omega^2 & -\frac{i\lambda}{\lambda+2\mu}k_z & 0 & -\frac{1}{r} \end{pmatrix}. \tag{11}$$

C. The transfer matrix solution

The matrix differential equations (8) and (10) have a well-known exponential solution:

$$\mathbf{U}_n(r+\delta r)=\exp\left\{\int_r^{r+\delta r}\mathbf{t_n}(r)dr\right\}\mathbf{U}_n(r). \tag{12}$$

The exponential matrix function can be represented by series[26] and the transfer matrix for an intermediate layer $(r_{J-1}\leqslant r\leqslant r_j)$ can be found as

$$\begin{aligned}\mathbf{T_n^j}&=\exp\left\{\int_{r_{J-1}}^{r_J}\mathbf{t_n^j}(\mathrm{r})dr\right\}\\&=\mathrm{I}+\int_{r_{j-1}}^{r_J}\mathbf{t_n^j}(\mathrm{r})dr+\int_{r_{j-1}}^{r_J}\mathbf{t_n^j}(\mathrm{r})dr\int_{r_{j-1}}^{r}\mathbf{t_n^j}(\tau)d\tau+\cdots.\end{aligned} \tag{13}$$

The transfer matrix $\mathbf{T_n^j}$ is a function of the material properties and geometry of the jth cylindrical layer, and it relates the elastic fields on both sides of this layer. The representation of the transfer matrix in the series form (13) is convenient for deriving asymptotic BC models which we will address in the following section.

A similar of the transfer matrix (13) has been obtained using wave solutions in the Bessel function form[14] for the 2-D case, and in[27] for the 3-D case. Here for comparison purpose we rewrite the transfer matrix solution for the 2-D case in the form of[14]

$$\mathbf{T_n^j}=\mathbf{K_n^j}|_{r=r_j}(\mathbf{K_n^j}|_{r=r_{j-1}})^{-1}, \tag{14}$$

where

$$\mathbf{K_n^j}=\begin{pmatrix} i\frac{n}{r}J_n(k_l^jr) & -k_tJ_n(k_t^Jr) & i\frac{n}{r}N_n(k_l^Jr) & -k_tN_n(k_t^jr)\\ k_l^jJ_n'(k_l^jr) & i\frac{n}{r}J_n(k_t^jr) & k_l^jN_n'(k_l^jr) & i\frac{n}{r}N_n(k_t^jr)\\ 2i\mu^J\frac{n}{r^2}[k_l^jrJ_n'(k_l^jr)-J_n(k_l^jr)] & -\mu^j(k_t^j)^2[2J_n''(k_t^jr)+J_n(k_t^jr)] & 2i\mu^j\frac{n}{r^2}[k_l^jrN_n'(k_l^jr)-N_n(k_l^jr)] & -\mu^j(k_t^j)^2[2N_n''(k_t^jr)+N_n(k_t^jr)]\\ (k_l^j)^2\left[2\mu^JJ_n''(k_l^jr)-\lambda^JJ_n\left(k\int_l^j r\right)\right] & 2i\frac{n\mu^j}{r^2}[k_t^jrJ_n'(k_t^jr)-J_n(k_t^jr)] & (k_l^j)^2[2\mu^jN_n''(k_l^jr)-\lambda^jN_n(k_l^jr)] & 2i\frac{n\mu^j}{r^2}[k_t^jrN_n'(k_t^jr)-N_n(k_t^jr)]\end{pmatrix}. \tag{15}$$

Here λ^j,μ^j are the Lamé constants, and k_l^j,k_t^J are the wave numbers of the jth intermediate layer. Representation in the form of series (13) is advantageous in considering the asymptotic approximation given below.

II. APPROXIMATE BC MODELS FOR A THIN FIBER–MATRIX INTERPHASE

A. Transfer matrix approximations

To derive approximate BC models we will use here a similar approach to that recently proposed for a thin anisotropic plane interphase.[15,16] We will develop the first- and second-order asymptotic and the spring BC to model a thin cylindrical fiber–matrix interphase.

Let us as an example consider the SiC/Ti model system. The SiC fiber is SCS-6 as shown in Fig. 2(a); it consists of a carbon core, a SiC shell, and a 3-μm carbon-rich interphase coating. The actual microstructure is more complicated, however, the schematic in Fig. 2(a) provides adequate approximation for analysis of wave phenomena in this material.[28] As shown previously we can apply the transfer matrix $\mathbf{T_n^i}$ to represent the effect of the actual fiber–matrix interphase as shown in Fig. 2(b),

$$\mathbf{U}_n|_{r=r_i}=\mathbf{T_n^i}\mathbf{U}_n|_{r=r_f}, \tag{16}$$

where $\mathbf{T_n^i}$ can be represented as

$$\mathbf{T_n^i}=\exp\left\{\int_{r_f}^{r_i}\mathbf{t_n^i}(r)dr\right\}. \tag{17}$$

Here r_f and r_i are the radii of the interphase inner and outer boundary.

When the fiber–matrix interphase is thin, i.e., $h=(r_i-r_f)\ll r_f$ (e.g., the SCS-6 fiber: $h/r_f=3/68$) and $k_{l,t}h\ll 1$, one can simplify the transfer matrix $\mathbf{T_n^i}$ by an asymptotic expansion in h. From Eq. (17), one has

$$\mathbf{T_n^i}\approx\mathrm{I}+h\mathbf{t_n^i}(r_f). \tag{18}$$

Now we write the BC (16) across the interphase gap $(r_f\leqslant r\leqslant r_i)$ as:

$$\mathbf{U}_n|_{r=r_i}\approx[\mathrm{I}+h\mathbf{t_n^i}(r_f)]\mathbf{U}_n|_{r=r_f}. \tag{19}$$

We call (19) the first-order asymptotic BC and $\mathbf{T_n^i}$ (18) the first-order asymptotic transfer matrix.

For the 2-D case the first-order asymptotic BC for a thin fiber–matrix interphase $r_i>r>r_f$ can be written as:

$$[(u_r,u_\theta,\sigma_{rr},\theta_{r\theta})_n^{r=ri}]^T=\mathbf{T_n^i}[(u_r,u_\theta,\sigma_{rr},\sigma_{r\theta})_n^{r=rf}]^T, \tag{20}$$

where $[(\cdot)]^T$ denotes the transpose of that function, and

$$\mathbf{T}_\mathbf{n}^\mathbf{i}=\begin{pmatrix} 1-\dfrac{h\lambda}{r_f(\lambda+2\mu)} & -\dfrac{inh\lambda}{r_f(\lambda+2\mu)} & \dfrac{h}{\lambda+2\mu} & 0 \\ -\dfrac{inh}{r_f} & 1+\dfrac{h}{r_f} & 0 & \dfrac{h}{\mu} \\ \dfrac{4h\mu(\lambda+\mu)}{r_f^2(\lambda+2\mu)}-\omega^2\rho h & \dfrac{4inh\mu(\lambda+\mu)}{r_f^2(\lambda+2\mu)} & 1-\dfrac{2h\mu}{r_f(\lambda+2\mu)} & -\dfrac{inh}{r_f} \\ -\dfrac{4inh\mu^i(\lambda+\mu)}{r_f^2(\lambda+2\mu)} & \dfrac{4n^2h\mu(\lambda+\mu)}{r_f^2(\lambda+2\mu)}-\omega^2\rho h & -\dfrac{inh\lambda}{r_f(\lambda+2\mu)} & 1-\dfrac{2h}{r_f} \end{pmatrix}^i. \tag{21}$$

In Eq. (21), the superscript $\imath$ denotes that λ, μ, ρ, and h in the matrix are interphase properties and i in the matrix elements stands for the unit imaginary number. One sees that for each Bessel order n there exists a unique transfer matrix $\mathbf{T}_\mathbf{n}^\mathbf{i}$-associated with the elastic fields of that order. A similar transfer matrix $\mathbf{T}_\mathbf{n}^\mathbf{i}$ for the 3-D case can be found from the 3-D expression for matrix $\mathbf{t}_\mathbf{n}$ (11).

Note that the same first-order transfer matrix (21) can be derived from the representation of $\mathbf{T}_\mathbf{n}^\mathbf{i}$ in the form of (14), i.e., from

$$\mathbf{T}_\mathbf{n}^\mathbf{i}=\mathbf{K}_\mathbf{n}^\mathbf{i}|_{r=r_i}(\mathbf{K}_\mathbf{n}^\mathbf{i}|_{r=r_f})^{-1}. \tag{22}$$

Approximating each elements in matrix $\mathbf{K}_\mathbf{n}^\mathbf{i}|_{r=r_i}$ by

$$\begin{aligned} J_n(kr_i)&\approx J_n(kr_f)+(kh)J_n'(kr_f);\\ N_n(kr_i)&\approx N_n(kr_f)+(kh)N_n'(kr_f), \end{aligned} \tag{23}$$

one can reduce the transfer matrix (22) to the first-order transfer matrix (21) through a rather tedious procedure. The same procedure applies to the 3-D case. From the approximate equations (23) one sees that the conditions for a valid approximation (21) are $h\ll r_f$ and $k_{l,t}h\ll 1$.

It is interesting to consider several limiting cases. First let $r_f\to\infty$, thus physically reducing the cylindrical interphase to a plane interphase. In this case the first-order transfer matrix (21) becomes

$$\mathbf{T}^\mathbf{i}=\begin{pmatrix} 1 & 0 & \dfrac{h}{\lambda+2\mu} & 0 \\ 0 & 1 & 0 & \dfrac{h}{\mu} \\ -\omega^2\rho h & 0 & 1 & 0 \\ 0 & -\omega^2\rho h & 0 & 1 \end{pmatrix}, \tag{24}$$

which is identical to the first-order transfer matrix for a wave normally incident on a plane thin layer with thickness h.[20] Further if one replaces the fraction n/r_f by k in (21) where k is the projection of the wave number on the interphase, and after that takes the limit $r_j\to$infinity one obtains the first-order transfer matrix derived in[20] for a wave obliquely incident on a plane interphase with thickness h.

Next consider the static case when the frequency approaches zero ($\omega=0$, $n=0$). The first-order transfer matrix (21) reduces to

$$\mathbf{T}^\mathbf{i}\approx\begin{pmatrix} 1-\dfrac{h\lambda}{r_f(\lambda+2\mu)} & 0 & \dfrac{h}{\lambda+2\mu} & 0 \\ 0 & 1+\dfrac{h}{r_f} & 0 & \dfrac{h}{\mu} \\ \dfrac{4h\mu(\lambda+\mu)}{r_f^2(\lambda+2\mu)} & 0 & 1-\dfrac{2h\mu}{r_f(\lambda+2\mu)} & 0 \\ 0 & 0 & 0 & 1-\dfrac{2h}{r_f} \end{pmatrix}^i, \tag{25}$$

which equals the first-order transfer matrix derived for a thin

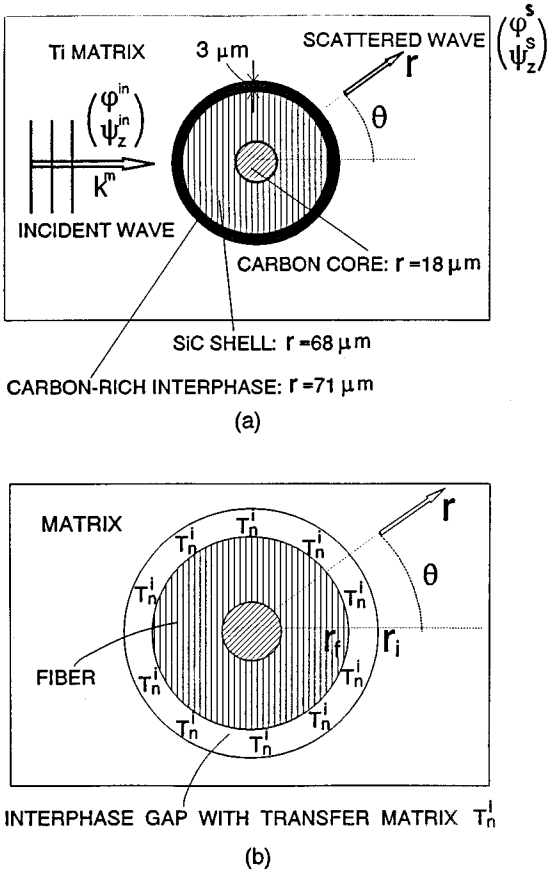

FIG. 2. (a) Scattering from an SCS-6 fiber in a titanium matrix. (b) Replacement of the fiber-matrix interphase by an interphase gap with transfer matrix $\mathbf{T}_\mathbf{n}^\mathbf{i}$, r_f and r_i are the radius of fiber and interphase, respectively.

TABLE I. Properties of each phase of the SCS-6 fiber and titanium alloy matrix, where E is Young's modulus, ν is Poisson's ratio, λ and μ are the Lamé constants, ρ is the density, and r the radius of the boundary of that phase.

Phase	E (GPa)	ν	λ (GPa)	G (GPa)	ρ (g/cc)	r (μm)
Core (carbon)	41.0	0.25	16.4	16.4	1.7	18
Shell (SiC)	415.0	0.17	91.36	177.35	3.205	68
Interphase (carbon coating)	41.0	0.25	16.4	16.4	1.7	71
Matrix (Ti)	121.6	0.348	103.26	45.1	5.4	

interphase from static transverse elastic field solutions,[29,30] where the analysis is focused on the transverse elastic properties of composites reinforced with multilayered fibers.

One may also define the second-order asymptotic BC for a plane interphase[15,16] by applying the finite difference approximation to the matrix differential equations (8)

$$\frac{\mathbf{U}_n(r=r_i)-\mathbf{U}_n(r=r_f)}{h} = \mathbf{t_n}(r=\overline{r})\,\frac{\mathbf{U}_n(r=r_i)+\mathbf{U}_n(r=r_f)}{2}, \qquad \overline{r}=\frac{r_f+r_i}{2}, \tag{26}$$

where on the left side of the equation a finite difference approximation is used in (8) to replace the derivative $\partial \mathbf{U}_n(r)/\partial r$, while on the right side the averaged elastic field is used to replace the radially-dependent function $\mathbf{U}_n(r)$. The second-order BC can be rewritten in the transfer matrix format as:

$$\mathbf{U}_n(r=r_i)=\left[\mathbf{I}-\frac{h}{2}\,\mathbf{t_n^i}(\overline{\mathbf{r}})\right]^{-1}\left[\mathbf{I}+\frac{h}{2}\,\mathbf{t_n^i}(\overline{\mathbf{r}})\right]\mathbf{U}_n(r=r_f). \tag{27}$$

The advantage of the first- and second-order BC models is that Bessel functions are not involved in the calculation of fields in the thin interphasial layer.

For further approximation it is reasonable to approximate the interphase by springs. This model has been used to describe the static elastic field on the fiber–matrix interphase in composites by Aboudi[31] and Hashin[32] and to describe the interphase scattering in[13] where an imperfect infinitely thin interface with the spring BC is used to replace a fiber–matrix interphase. As we will see below it is advantageous to preserve the system geometry by applying the spring BC across the interphase gap instead of filling the gap by fiber or matrix materials. If one keeps in the first-order BC model (20), (21) only the spring stiffnesses terms, one obtains the spring BC as

$$\begin{pmatrix} u_r \\ u_\theta \\ \sigma_{rr} \\ \sigma_{r\theta} \end{pmatrix}_n^{r=r_i} = \begin{pmatrix} 1 & 0 & \dfrac{h}{\lambda+2\mu} & 0 \\ 0 & 1 & 0 & \dfrac{h}{\mu} \\ 0 & 0 & 1 & 0 \\ 0 & 0 & 0 & 1 \end{pmatrix}^i \begin{pmatrix} u_r \\ u_\theta \\ \sigma_{rr} \\ \sigma_{r\theta} \end{pmatrix}_n^{r=r_f}, \tag{28}$$

i.e.,

$$\sigma_{rrn}^{r=r_i}=\sigma_{rrn}^{r=r_f}=K_n(u_{rn}^{r=r_i}-u_{rn}^{r=r_f}), \qquad \sigma_{r\theta n}^{r=r_i}=\sigma_{r\theta n}^{r=r_f}=K_t(u_{\theta n}^{r=r_i}-u_{\theta n}^{r=r_f}), \tag{29}$$

where the normal and shear spring stiffnesses are $K_n=(\lambda^i+2\mu^i)/h$ and $K_t=\mu^i/h$. This time the spring BC do not depend on the order of Bessel series for the wave solutions. Note the same spring BC (28) can be obtained directly by preserving in $\mathbf{t_n^i}$ (7) only two terms related to the spring stiffnesses: $1/(\lambda^i+2\mu^i)$ and $1/\mu^i$; then the transfer matrix $\mathbf{T_n^i}$ (13) reduces exactly to the same form as (28) since the higher-order terms vanish ($\mathbf{t_n^i t_n^i}=0$).

The 3-D version of the spring BC can be obtained by using a similar simplification in Eq. (10) as:

$$\begin{pmatrix} u_r \\ u_\theta \\ u_z \\ \sigma_{rr} \\ \sigma_{r\theta} \\ \sigma_{rz} \end{pmatrix}_n^{r=r_i} = \begin{pmatrix} 1 & 0 & 0 & \dfrac{h}{\lambda+2\mu} & 0 & 0 \\ 0 & 1 & 0 & 0 & \dfrac{h}{\mu} & 0 \\ 0 & 0 & 1 & 0 & 0 & \dfrac{h}{\mu} \\ 0 & 0 & 0 & 1 & 0 & 0 \\ 0 & 0 & 0 & 0 & 1 & 0 \\ 0 & 0 & 0 & 0 & 0 & 1 \end{pmatrix}^i \begin{pmatrix} u_r \\ u_\theta \\ u_z \\ \sigma_{rr} \\ \sigma_{r\theta} \\ \sigma_{rz} \end{pmatrix}_n^{r=r_f}. \tag{30}$$

B. Analysis of approximations. Numerical examples

Next we give numerical examples for scattering of normally incident longitudinal and transverse waves on an SCS-6 fiber in titanium alloy to demonstrate the applicability of different approximate BC models. The properties of each phase in the multiphase SCS-6 fiber are listed in Table I. The elastic properties of the carbon-rich interphase are equal to those of the carbon core; the interphase thickness is 3 μm. The unit scalar φ^{in} and vector ψ_z^{in} potentials for the incident longitudinal and transverse waves [see Fig. 2(a)] are expanded in Bessel series

$$\begin{pmatrix} \varphi^{\text{in}} \\ \psi_z^{\text{in}} \end{pmatrix} = \sum_{n=-\infty}^{\infty} (i)^n J_n\begin{pmatrix} k_l^m \\ k_t^m \end{pmatrix} r\, e^{\text{in}\theta}, \tag{31}$$

where k_l^m and k_t^m are the wave numbers of the longitudinal and transverse modes in the matrix material, respectively. The scattered waves in the matrix are represented as outgoing waves:

$$\varphi^s = \sum_{n=-\infty}^{\infty} A_n H_n(k_l^m r)\exp(in\theta),$$
$$\psi_z^s = \sum_{n=-\infty}^{\infty} B_n H_n(k_t^m r)\exp(in\theta), \tag{32}$$

where $H_n(x)=J_n(x)+iN_n(x)$ is the nth-order Hankel function of the first kind. The procedure to find the scattering coefficients A_n and B_n for a multiphase fiber in a solid using the transfer matrix formalism has been described in Ref. 14 for the 2-D case, and in Ref. 27 for the 3-D case.

Once the scattering coefficients A_n and B_n for the longitudinal and transverse waves are found, the scattered fields can be calculated using (32). The far-field scattering angle dependence can be obtained using the asymptotic expressions for Hankel functions of large argument

$$H_n(kr)\approx \sqrt{\frac{2}{\pi kr}}\exp\left\{i\left[kr-\left(n+\frac{1}{2}\right)\frac{\pi}{2}\right]\right\}$$
$$\text{for } kr\to\infty \tag{33}$$

and the scattering cross section, which is defined as the total power scattered per unit length divided by the incident wave intensity (power per unit area), is found to be[8]

$$Q_l=\frac{1}{k_{(l,t)}^m r_i}\sum_{n=-\infty}^{\infty}|A_n|^2, \quad Q_t=\frac{1}{k_{(l,t)}^m r_i}\sum_{n=-\infty}^{\infty}|B_n|^2. \tag{34}$$

The scattering cross sections Q_l and Q_t in the equations are normalized by the geometric limit $4r_i$ ($r_i=r_{N-1}$ the fiber radius including the outermost interphase). Note that for transverse isotropy, one need only replace λ and μ in Eqs. (3)–(6) by $C_{rr}-2G_t$ and G_t, respectively, where C_{rr} is the radial modulus and G_t is the transverse shear modulus. To determine the truncation number $n=M$ in the Bessel series summation of the scattering cross sections the following inequalities are used:

$$\frac{|A_{M+1}^N|^2}{\Sigma_{n=-M}^{M}|A_n^N|^2}<10^{-8} \quad \text{and} \quad \frac{|B_{M+1}^N|^2}{\Sigma_{n=-M}^{M}|B_n^M|^2}<10^{-8}. \tag{35}$$

When (35) is satisfied the significance of the newly added $(M+1)$th term on the scattering cross sections Q_l and Q_t is negligible. Generally M increases for greater kr values. Typical values for M are: 4 for $kr=0.1$, 7 for $kr=1$, and 25 for $kr=10$.

The scattering cross section as a function of frequency calculated using different approximate BC models are shown in Fig. 3 for both longitudinal (a) and shear (b) wave incidence. In the figure the top axis is frequency in MHz and the bottom axis is the nondimensional wave number $k^m r_i$ where k^m is the wave number in the matrix and $r_i=71$ μm is the outer radius of the interphase. One sees from the figure that the second-order solutions (coarse dashed lines) are almost indistinguishable from the exact (solid lines). The spring

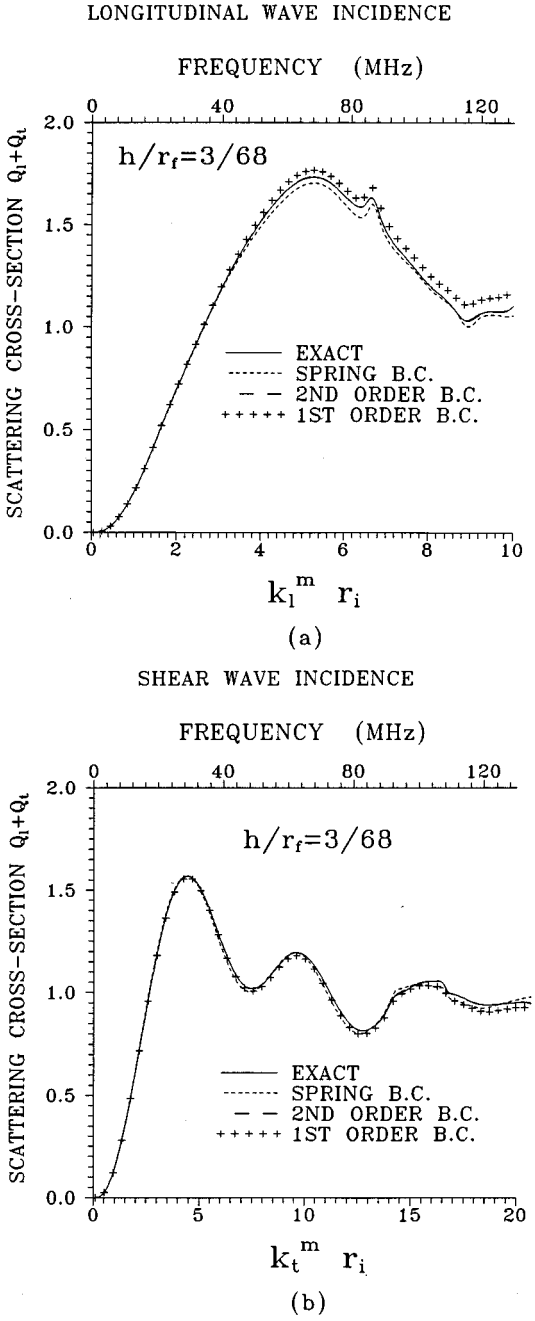

FIG. 3. Total scattering cross sections versus frequency and nondimensional wave number calculated using different BC models at interphase Young's modulus $E^i=41$ GPa. (a) Results for longitudinal-wave incidence. (b) Results for shear-wave incidence.

(fine dashed lines) and first-order (crosses) BC models also give good predictions at this interphase thickness and stiffness for low frequencies, especially for $k_{l,t}^m r_i<4$ or $k_{l,t}^i h<0.2$.

The difference between different approximations is more pronounced with the increase of the interphase thickness to fiber radius ratio h/r_f. Figure 4(a) shows the calculated scattering cross sections versus h/r_f for shear-wave incidence using different approximate BC models at frequency=13 MHz ($k_t^i h=0.08$). The fiber radius $r_f=68$ μm is kept constant. The legends in this figure are the same as in Fig. 3. One sees from the figure that all the BC models give

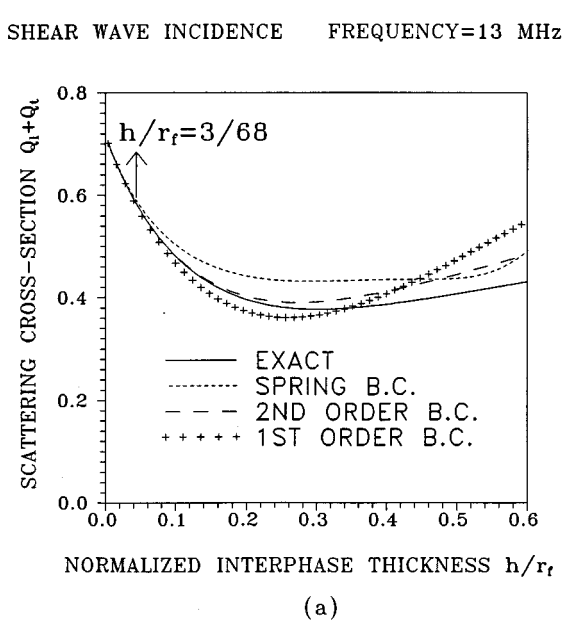

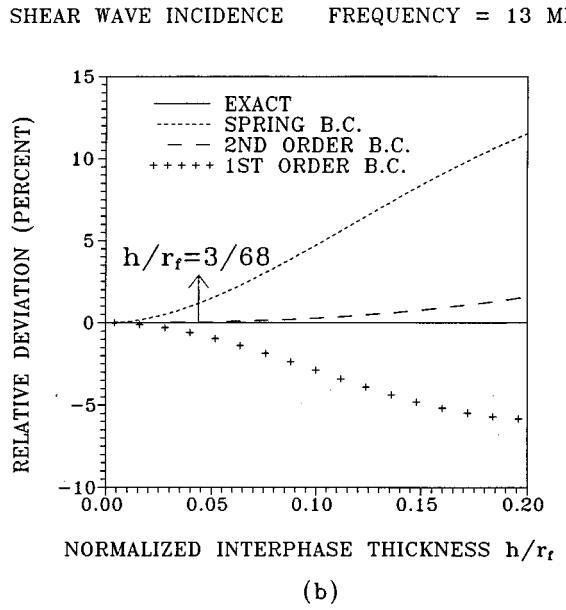

FIG. 4. (a) Total scattering cross sections versus interphase thickness parameter h/r_f calculated using different BC models at interphase Young's modulus $E^i=41$ GPa. The results are given for an incident shear wave at frequency=13 MHz. (b) The relative percentage deviations from the exact for the approximate BC models shown in Fig. 4(a).

good results for $h/r_f<0.05$. For greater interphase thickness, the second-order BC is satisfactory until $h/r_f=0.2$, while the spring and first-order BC models begin to deviate significantly from the exact results. To illustrate this more clearly, we present in Fig. 4(b) the relative deviation in percentage between the exact and the approximate solutions versus h/r_f. One sees that the second-order BC give the best results, while the spring and first-order BC models are sufficient for $h/r_f<0.05$.

To check further the applicability of the spring BC model let us compare the spring stiffness values to those calculated directly from the stress-displacement-difference ratios across the interphase gap. Specifically, from (29) one

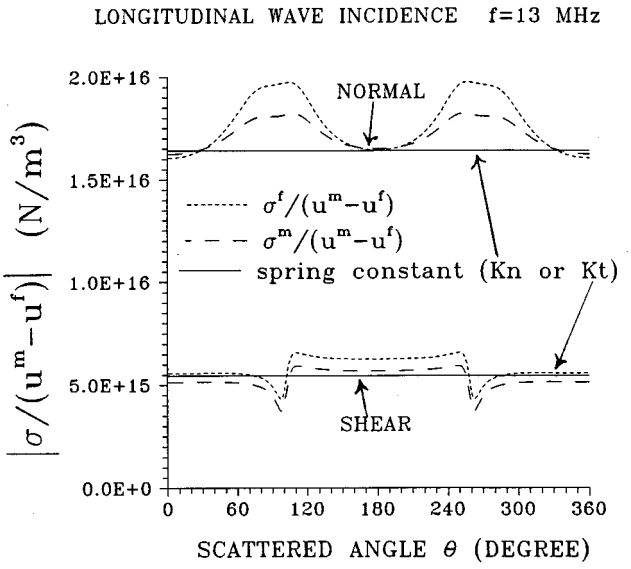

FIG. 5. Comparison of stiffnesses calculated using $\sigma/(u^m-u^f)$ with $K_n=(\lambda^i+2\mu^i)/h$ and $K_t=\mu^i/h$. Assume a longitudinal-wave incident at frequency=13 MHz.

can find alternative definitions for K_n and K_t as

$$K_n=\sigma^m_{rr}/(u^m_r-u^f_r), \quad K_t=\sigma^m_{r\theta}/(u^m_\theta-u^f_\theta) \tag{36}$$

or

$$K_n=\sigma^f_{rr}/(u^m_r-u^f_r), \quad K_t=\sigma^f_{r\theta}/(u^m_\theta-u^f_\theta), \tag{37}$$

where quantities with superscript m are the fields defined on the matrix side of interphase gap, while quantities with superscript f are the fields defined on the fiber side. We have calculated these stress-displacement-difference ratios as functions of the scattered angle θ using the exact interphase layer model, and compared them with K_n and K_t values defined as $K_n=(\lambda^i+2\mu^i)/h$ and $K_t=\mu^i/h$. The results are shown in Fig. 5 for longitudinal wave incidence at frequency=13 MHz ($k^i_t h=0.08$, $k^l_t h=0.04$), thus the interphase can be considered very thin. The solid lines in the figure are $K_n=(\lambda^i+2\mu^i)/h$ and $K_t=\mu^i/h$. The coarse dashed lines are ratios calculated using (36) and the fine dashed lines are those calculated using (37). One sees from the figure that there exists good agreement between the stress-displacement-difference ratios (dashed lines) and the K_n and K_t values (solid lines). However, these ratios depend on the scattered angle θ thus the assumption of homogeneously distributed springs with constant stiffness constants is only approximately true.

To demonstrate applicability of different BC approximations to interphase layers with different stiffnesses we calculated the scattering cross section versus interphase stiffnesses. In the calculations the interphase Young's modulus is varied while the interphase thickness, density, and Poisson's ratio are kept constant. The results are shown in Fig. 6 for incident longitudinal (a) and shear (b) wave at frequency $f=13$ MHz and interphase thickness $h=3$ μm. In the figure, all legends are the same as in Fig. 3, the horizontal axis is the interphase Young's modulus in log scale, and $E^m=122$ GPa and $E^f=415$ Gpa are the Young's moduli for the matrix and

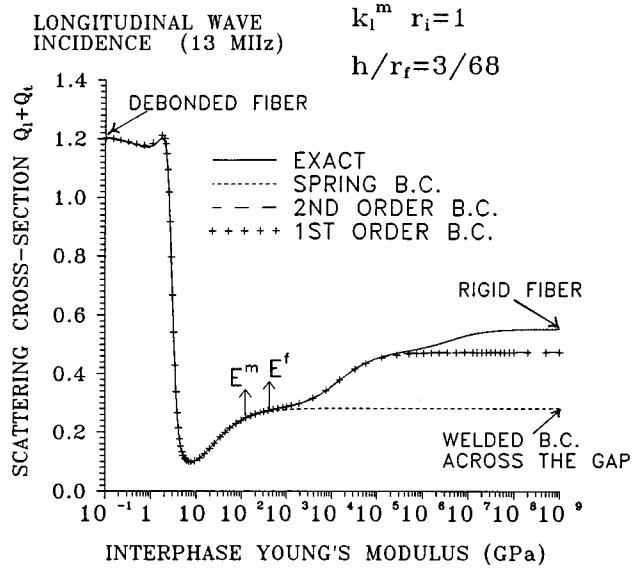

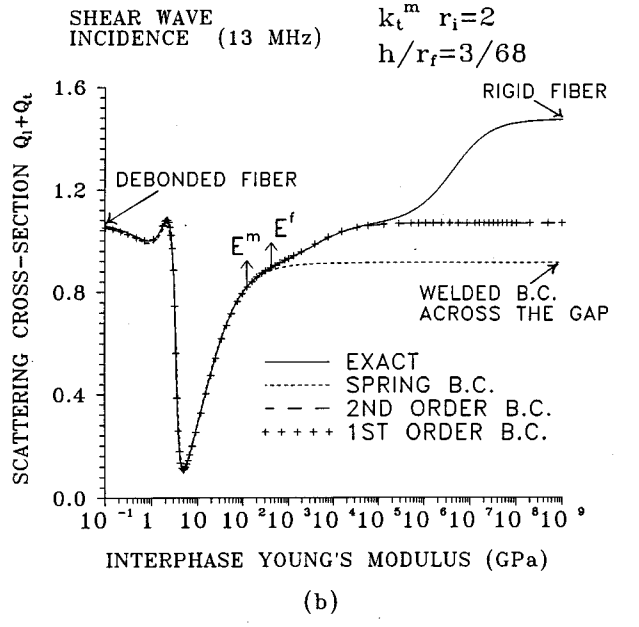

FIG. 6. Total scattering cross sections versus interphase stiffnesses calculated using different BC models for an SCS-6 fiber in titanium matrix. (a) Results for longitudinal-wave incidence. (b) Results for shear-wave incidence.

fiber, respectively. One sees from the figure that the spring BC model gives good predictions up to interphase stiffness equaling that of the fiber, while the first- and second-order asymptotic BC continue to give good results for much stiffer interphases.

It is interesting to discuss the limiting cases presented in Fig. 6. When the interphase Young's modulus is extremely small, the fiber with the interphase acts like a debonded fiber or a cylindrical cavity with radius that of the outer interphase boundary r_i. All the approximate BC models give the correct limit. For example, for the spring BC model, since K_n and K_t approach zero in this case, the spring BC (29) simplifies to

$$\sigma_{rr}^{r=r_i}=\sigma_{r\theta}^{r=r_i}=0, \tag{38}$$

which is the free-stress condition for a cylindrical cavity with radius r_i.

On the other hand, when the interphase Young's modulus is extremely high, the fiber with the interphase acts like a rigid cylinder with radius r_i, i.e., the BC should be

$$u_{r|r=r_i}=u_{\theta|r=r_i}=0. \tag{39}$$

However, neither of the approximate BC models gives the correct limit. For the spring BC model, K_n and K_t approach infinity, the spring BC (29) simplifies to

$$\begin{aligned} &u_r^{r=r_i}=u_r^{r=r_f}, \quad u_\theta^{r=r_i}=u_\theta^{r=r_f}, \\ &\sigma_{rr}^{r=r_i}=\sigma_{rr}^{r=r_f}, \quad \sigma_{r\theta}^{r=r_i}=\sigma_{r\theta}^{r=r_f}, \end{aligned} \tag{40}$$

i.e., the spring BC reduce to welded BC across the interphase gap. The discrepancy between the resulting BC for the rigid interphase (39) and rigid springs (40) explains the large deviation of the spring approximation for very high interphase stiffness as shown in Fig. 6. In summary the spring BC model is sufficient for a thin fiber–matrix interphase ($h/r_f<0.05$, $k_{l,t}^i \ll 1$) whose stiffness is less than that of the fiber.

Another interesting phenomenon observable from Fig. 6 is that there exists a scattering cross-section minimum. The minimum is explained by matching of impedances between matrix and the effective fiber formed by the actual fiber and the interphase. The decrease of the effective fiber impedance to a value lower than that of the matrix results in a sharp increase in the scattering cross section, reaching in the limit the scattering level from a cylindrical cavity for zero interphase moduli (disbond). Detailed analyses of this phenomenon were given in.[13,14]

III. DISCUSSION OF SPRING BC MODEL: SPRINGS ON INTERPHASE GAP VERSUS THOSE ON INTERFACE BOUNDARY WITH GAP FILLED BY EITHER MATRIX OR FIBER

Applying the approximate BC across an interphase gap rather than on an interface boundary, we have maintained the scattering fiber geometry. Another approach would be to fill the interphase gap with either fiber or matrix material and apply BC on the interface. This point is illustrated in Fig. 7 which shows three different ways of applying the spring BC model to replace a thin fiber–matrix interphase. The first is to remove the interphase layer as shown by Fig. 7(b) and to apply the spring BC across the gap as given by (29):

$$\begin{aligned} &\sigma_{rr}^m|_{r=r_i}=\sigma_{rr}^f|_{r=r_f}=K_n(u_r^m|_{r=r_i}-u_r^f|_{r=r_f}), \\ &\sigma_{r\theta}^m|_{r=r_i}=\sigma_{r\theta}^f|_{r=r_f}=K_t(u_\theta^m|_{r=r_i}-u_\theta^f|_{r=r_f}), \end{aligned} \tag{41}$$

where quantities with superscript m are fields defined on the matrix side of the gap, while quantities with superscript f are fields defined on the fiber side. One sees from Eq. (41) that the displacements jump across the interphase gap from r_f to r_i, while the stresses on both sides of the gap are continuous.

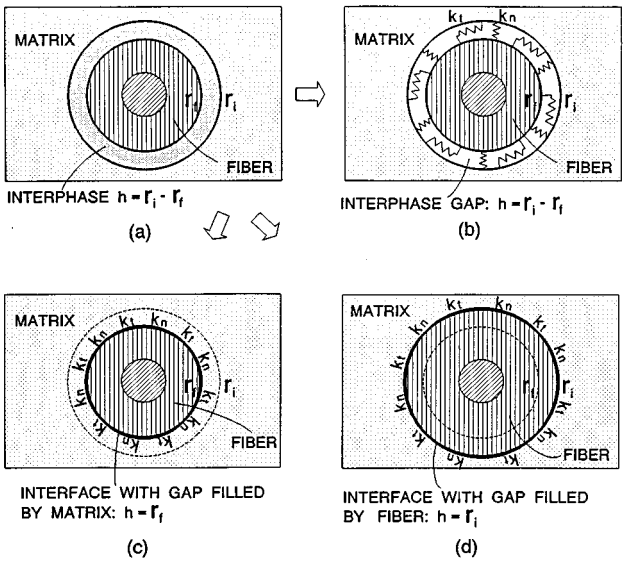

FIG. 7. The exact interphase layer model (a) and different spring BC models for a thin fiber-matrix interphase. (b) is for the spring BC model with the interphase gap connected by springs, (c) for that with the gap filled by matrix, and (d) for that with the gap filled by fiber.

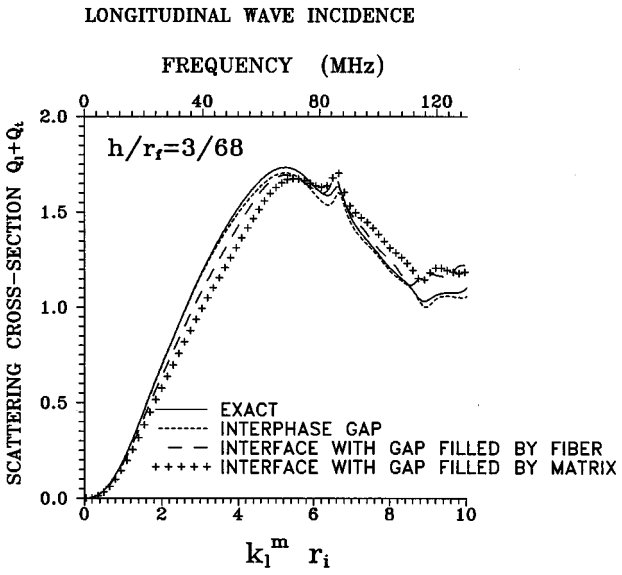

FIG. 8. Total scattering cross sections versus frequency and nondimensional wave number calculated using different spring BC models for longitudinal-wave incidence.

The other two ways involve applying the spring BC to an interface with the gap filled by either matrix or fiber materials. In this case the spring BC on an interface with radius R are:

$$\sigma_{rr}^{m}|_{r=R}=\sigma_{rr}^{f}|_{r=R}=K_n(u_r^m|_{r=R}-u_r^f|_{r=R}),$$
$$\sigma_{r\theta}^{m}|_{r=R}=\sigma_{r\theta}^{f}|_{r=R}=K_t(u_\theta^m|_{r=R}-u_\theta^f|_{r=R}). \tag{42}$$

Physically, $R=r_f$ implies that the interphase gap is filled by matrix as shown by Fig. 7(c), while $R=r_i$ corresponds to the case when the gap is filled by fiber as shown by Fig. 7(d). One sees from Eqs. (42) that the displacements jump occurs on the interface boundary $r=R$, while the stresses on this interface boundary are continuous.

After composite manufacture due to chemical reactions at the interphase the interphase thickness may not be known exactly. In this case there is an advantage in using the spring BC on the boundary between matrix and fiber eliminating the gap and filling it with matrix material (usually the fiber diameter is known). Thus to describe the mechanical contact across the interphase one can use just two parameters K_n and K_t. Of course additional error may be introduced in this simplification as we will see below. To compare these different cases we carried out a numerical analysis similar to that in the previous section for the three types of the spring BC. The calculations of the scattering cross section similar to those given in Fig. 6 show that the spring BC model with interphase gap gives a good approximation for interphase stiffness to that of the fiber. The spring BC model with gap filled by fiber or matrix material gives acceptable results for much less stiff interphases and the spring BC model with gap filled by matrix diverges from the exact results for interphase modulus above 10 GPa.

It is interesting to examine the limits for very compliant and stiff interphases. First for an extremely compliant interphase the spring BC models with gap and with gap filled by fiber material yield the same free stress BC (38) (they provide the correct radius of the cylindrical cavity). However, the spring BC model with gap filled by matrix reduces to a cylindrical cavity with radius equal to the interphase inner boundary r_f:

$$\sigma_{rr}|_{r=r_f}=\sigma_{r\theta}|_{r=r_f}=0. \tag{43}$$

When the interphase Young's modulus is extremely high, none of the spring BC models give the rigid BC on the outer boundary of the interphase; instead they give welded BC in different forms. The two spring BC models without gap give welded BC on an interface with the radius of the fiber R:

$$u_r|_{r=R}=u_r|_{r=R}, \quad u_\theta|_{r=R}=u_\theta|_{r=R},$$
$$\sigma_{rr}|_{r=R}=\sigma_{rr}|_{r=R}, \quad \sigma_{r\theta}|_{r=R}=\sigma_{r\theta}|_{r=R}, \tag{44}$$

where $R=r_f$ is for the spring BC model with gap filled by matrix material and $R=r_i$ is for that with gap filled by fiber material. The spring BC with gap give the welded BC across the interphase gap as given by (40). So all three spring BC models give different limits for infinitely high interphase stiffnesses.

Next the effect of other parameters, such as frequency and interphasial layer thickness, on the approximation of spring BC models are studied. The scattering cross sections for incident longitudinal wave versus the nondimensional wave number calculated exactly and using different spring BC models are shown in Fig. 8. The parameters are the same as in Fig. 3 (interphase thickness $h=3$ μm). One sees from the figure that the spring BC model (41) with interphase gap (the fine dashed line) gives the best results, while those (42) with gap filled by either matrix (crosses) or fiber (coarse dashed lines) material may deviate considerably from the exact even at low frequencies. It also shows that the spring BC model with gap filled by fiber gives better results than the model with gap filled by matrix.

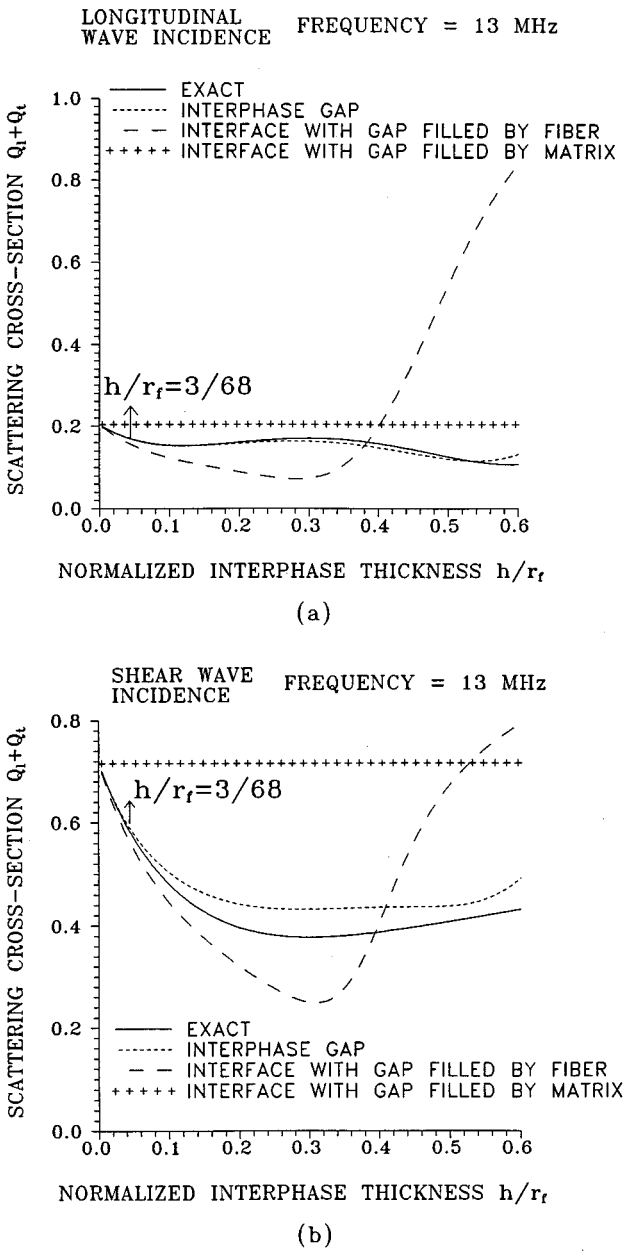

FIG. 9. Total scattering cross sections versus interphase thickness calculated using different spring BC models at frequency=13 MHz. (a) Results for longitudinal-wave incidence. (b) Results for shear-wave incidence.

Figure 9(a) shows the longitudinal and shear-wave scattering cross sections versus interphase thickness to fiber radius ratio h/r_f at frequency=13 MHz. The fiber radius r_f=68 μm is kept constant. All other parameters are the same as in Fig. 4. One sees from the figure that the spring BC model with interphase gap consistently gives very good approximation especially for longitudinal wave incidence. The spring BC model with gap filled by fiber material gives better results than the model with gap filled by matrix material. Note that the latter model predicts a constant cross section as interphase thickness increases since the fiber radius is constant.

IV. CONCLUSIONS

In this paper we have demonstrated a transfer matrix approach for analysis of wave scattering from a multilayered cylinder in a solid. The transfer matrix is obtained by solving a matrix differential equation for the elastic field in a cylindrical medium with radially dependent properties. The advantage of the transfer matrix formulation lies in its natural application for multilayered fibers and interphases. The first- and second-order asymptotic BC models are derived to replace a thin fiber–matrix interphase by asymptotically expanding the transfer matrix for the interphase layer. The spring BC model is investigated as an effective replacement of a thin fiber–matrix interphase. Different forms of spring BC models with interphase gap and with gap filled by matrix or fiber material are studied. Numerical analysis shows that although the second-order asymptotic BC give the best overall results, the spring approximation with springs connecting the interphase gap is sufficient for a thin ($h/r_f<0.05$, $k^i_{l,t}h\ll 1$) interphase which is softer than the fiber. For even thinner and softer interphases the spring BC model with gap filled with fiber material may also be used.

[1] A. K. Misra, ''Interfacial Reaction Barriers between NiAl and Nb_2Be_{17} and Compliant Layers for the Ti_3Al/SiC Composite System,'' in HITEMP REVIEW-1991, NASA CP-10082, 15-1 to 15-15 (1991).

[2] A. G. Evans and D. B. Marshall, ''The Mechanical Properties of Fiber Reinforced Ceramic Matrix Composites,'' Mater. Res. Soc. Symp. Proc. **120**, 213–246 (1988).

[3] K. M. Prewo, ''Glass and Ceramic Matrix Composites Present and Future,'' Mater. Res. Soc. Symp. Proc. **120**, 145–156 (1988).

[4] W. W. Wright, ''The Carbon Fibre/Epoxy Resin Interphase—A Review—Part II,'' Compos. Polym. **3**, 360 (1990).

[5] J. D. H. Hughes, ''The Carbon Fiber/Epoxy Interface—A Review,'' Compos. Sci. Technol. **41**, 13 (1991).

[6] R. M. White, ''Elastic Wave Scattering at a Cylindrical Discontinuity in a Solid,'' J. Acoust. Soc. Am. **30**, 771–785 (1958).

[7] V. V. Tyutekin, ''Scattering of Plane Waves by a Cylindrical Cavity in an Isotropic Elastic Medium,'' J. Sov. Phys. Acoust. **5**, 105–109 (1959).

[8] Y. H. Pao and C. C. Mow, *Diffraction of Elastic Waves and Dynamic Stress Concentrations* (Crane, Russack, New York, 1973).

[9] D. J. Jain and R. P. Kanwal, ''Scattering of Elastic Waves by Circular Cylindrical Flaws and Inclusions,'' J. Appl. Phys. **50**, 4067–4109 (1979).

[10] P. Beattie, R. C. Chivers, and L. W. Anson, ''Ultrasonic Backscattering from Cylindrical Inclusions in Solid Elastic Matrices: A Comparison of Theory and Experiment,'' J. Acoust. Soc. Am. **94**, 3421–3427 (1993).

[11] A. N. Sinclair and R. C. Addison, Jr., ''Acoustic Diffraction Spectrum of a SiC fiber in a Solid Elastic Medium,'' J. Acoust. Soc. Am. **94**, 1126–1135 (1993).

[12] W. Huang, S. Brisuda, and S. I. Rokhlin, ''Fiber-Matrix Interface Characterization by Ultrasonic Wave Scattering,'' in *Review of Progress in QNDE*, edited by D. O. Thompson and D. E. Chimenti (Plenum, New York, 1994), Vol. 13, pp. 1367–1374.

[13] W. Huang, S. Brisuda, and S. I. Rokhlin, ''Ultrasonic Wave Scattering from Fiber-Matrix Interphases,'' J. Acoust. Soc. Am. **97**, 807–817 (1995).

[14] W. Huang, S. I. Rokhlin, and Y. J. Wang, ''Effect of Fiber-Matrix Interphase on Wave Propagation along and Scattering from Multilayered Fibers in Composites. Transfer Matrix Approach,'' Ultrasonics **33**, 365–375 (1995).

[15] S. I. Rokhlin and W. Huang, ''Ultrasonic Wave Interaction with a Thin Anisotropic Interfacial Layer between Two Anisotropic Solids. II: Second Order Asymptotic Boundary Conditions,'' J. Acoust. Soc. Am. **94**, 3405–3420 (1993).

[16] W. Huang and S. I. Rokhlin, ''Elastic Wave Scattering and Stoneley Wave Localization by Anisotropic Imperfect Interfaces between Solids,'' Geophys. J. Int. **118** (Stoneley Centenary Issue), 285–304 (1994).

[17] W. T. Thomson, ''Transmission of Elastic Waves through a Stratified Solid Material,'' J. Appl. Phys. **21**, 89 (1950).

[18] N. A. Haskell, ''Dispersion of Surface Waves on Multilayered Media,'' Bull. Seism. Soc. Am. **43**, 17 (1953).

[19] L. M. Brekhovskikh, *Waves in Layered Media*, 2nd ed. (Academic, New York, 1980).

[20] S. I. Rokhlin and Y. J. Wang, ''Analysis of Boundary Conditions for

Elastic Wave Interaction with an Interface between Two Solids,'' J. Acoust. Soc. Am. **89**, 503–513 (1991).
[21] A. H. Fahmy and E. L. Adler, ''Propagation of Acoustic Waves in Multilayers: A Matrix Description,'' Appl. Phys. Lett. **20**, 495–497 (1973).
[22] S. I. Rokhlin and Y. J. Wang, ''Equivalent Boundary Conditions for Thin Orthotropic Layer Between Two Solids. Reflection, Refraction, and Interface Waves,'' J. Acoust. Soc. Am. **91**, 1875–1887 (1992).
[23] S. I. Rokhlin and W. Huang, ''Ultrasonic Wave Interaction with a Thin Anisotropic Interfacial Layer between Two Anisotropic Solids: Exact and Asymptotic-Boundary-Condition Methods,'' J. Acoust. Soc. Am. **92**, 1729–1742 (1992).
[24] K. Aki and P. G. Richards, *Quantitative Seismology. Theory and Methods* (Freeman, San Francisco, 1980), Vol. I.
[25] H. Schmidt, ''Numerically Stable Global Matrix Approach to Radiation and Scattering from Spherically Stratified Shells,'' J. Acoust. Soc. Am. **94**, 2420–2430 (1993).
[26] F. R. Gantmacher, *The Theory of Matrices* (Chelsea, New York, 1959), Vol. II, Chap. 14.
[27] W. Huang, Y. J. Wang, and S. I. Rokhlin, ''Oblique Scattering of an Elastic Wave from a Multilayered Cylinder in a Solid. Transfer Matrix Approach,'' J. Acoust. Soc. Am. **99**, 2742–2754 (1996).
[28] Y. C. Chu and S. I. Rokhlin, ''Effective Elastic Moduli of Fiber-Matrix Interphase in High-Temperature Composites,'' Metall. Mater. Trans. A **27**, 165–182 (1995).
[29] Y. C. Chu and S. I. Rokhlin, ''Determination of Fiber-Matrix Interphase Moduli from Experimental Moduli of Composites with Multi-Layered Fibers,'' Mech. Mater. **21**, 191–215 (1995).
[30] W. Huang and S. I. Rokhlin, ''Generalized Self Consistent Model for Composites with Functionally Graded and Multilayered Interphases,'' Mech. Mater. **22**, 219–247 (1996).
[31] J. Aboudi, ''Damage in Composites—Modeling of Imperfect Bonding,'' Compos. Sci. Technol. **28**, 102–128 (1987).
[32] Z. Hashin, ''Thermoelastic Properties of Fiber Composites with Imperfect Interface,'' Mech. Mater. **8**, 333–348 (1990).

Lateral resonances in 1–3 piezoelectric periodic composite: Modeling and experimental results

Dominique Certon, Frédéric Patat, Franck Levassort, Guy Feuillard, and Brynjar Karlsson
G.I.P. ULTRASONS, Jeune Equipe 409, Faculté de Médecine, 2 bis boulevard Tonnellé BP 3223, 37032 Tours cedex, France

(Received 5 January 1996; accepted for publication 22 November 1996)

The objective of this work is to provide an accurate model of the lateral resonance modes in 1–3 piezoelectric composite materials. These materials are widely used in ultrasonic transducers and the lowest lateral mode frequency gives the upper limit for the usable transducer bandwidth. Considering the propagation of purely transverse waves in a 2-D periodic medium of infinite thickness, two different approaches for obtaining the solutions are presented and compared. The first approach is based on the use of the Bloch waves theory. The second is a straightforward method (a so-called membrane method) which consists in numerically solving the propagation equation in the two-phase medium while taking into account the periodic boundary conditions. Methods based on both models are described that allow the calculation of the dispersion curves and the stop band limits, as well as the frequencies and the displacement fields of the lateral modes. A test case is used to compare and discuss the theoretical predictions provided by each model. The calculations of the first lateral mode frequency are compared with experimental values obtained for samples with different ceramic volume fractions. The conclusion reached indicates that the infinite thickness assumption is valid for plates of practical interest and that the membrane model enables the prediction of lateral mode frequency with low computation effort and an accuracy better than 5%.
 [S0001-4966(97)01404-5]

PACS numbers: 43.38.Ar, 43.38.Fx, 43.40.At, 43.20.Ks [SLE]

INTRODUCTION

Recently, 1–3 connectivity piezoelectric composites[1,2] have become widely used in medical ultrasonic transducers. They offer a high thickness coupling coefficient (>0.6), a tuneable acoustic impedance ($10<Z<20$ MPa·s/m) and can be shaped easily to make focused transducers.

The 1–3 composites consist of piezoelectric ceramic rods or fibers embedded in an epoxy matrix with regular arrangement (Fig. 1). A popular technique for manufacturing 1–3 piezoelectric composites is the dice-and-fill process proposed by Savakus[3] in 1981, which provides a homogeneous matrix with a periodic arrangement of rods with operating frequencies up to 10 MHz. In periodic microstructures, Bragg diffraction can occur and lead to lateral resonances (so-called spurious modes). In 1985 Gururaja *et al.*[5] studied resonances of 1–3 composites and identified the two lowest frequency lateral modes. He showed that lateral oscillations are due to the Bragg diffraction of z-polarized waves (transverse waves), propagating along a plane parallel to the surface of the sample. The first lateral vibration mode appears when constructive reflections of transverse waves occur from vertical planes of ceramic rods. For the second lateral mode, constructive reflections occur from planes of rods aligned along directions at 45° to the axes Ox and Oy (Fig. 1). When the working frequency increases, these lateral resonances become critical to the efficiency of the transducer due to their coupling with the fundamental thickness mode[6] which is used to transmit and receive ultrasonic waves in medical imaging transducers. Thus, for successfully designing ultrasonic composite transducers, simple and accurate models predicting lateral mode frequencies are required. The Bragg diffraction theory may be used to predict the position of vibration nodes and antinodes of lateral resonances. However, prediction of lateral mode frequencies using this model is erroneous because the ceramic rods are assumed to be simple masses and their geometry is not taken into account.

This paper presents theoretical approaches for predicting the frequency and the vertical displacement field of the two first lateral resonances. In Sec. I, a theoretical formulation of the modeling of these resonances is presented. When considering the propagation of a transverse wave in a 2-D periodic medium with infinite thickness, two approaches can be adopted. The first one consists in determining an analytical solution which applies to both polymer and ceramic. The Bloch waves theory implemented by Wang and Auld[7] in the case of a 1-D periodic structure is used and extended to a 2-D periodic structure. In the second approach, the propagation equation of a transverse wave (a so-called membrane model) is solved in each phase with appropriate interfacial boundary conditions (continuity of stress and displacement). In the case of 1-D composite, this method allows the determination of analytical solutions of transverse waves[8,9] as well as the dispersion relation. This particular case is known as the Kronig–Penney model[10] and was experimentally verified by C. G. Oakley.[11,12] Here, the case of 2-D periodic medium is studied using a finite difference technique which allows the prediction of the lateral mode frequencies and displacement fields.

In Sec. II, theoretical dispersion curves for a test case are calculated and discussed. Both methods are used to calculate the displacement field and frequency of the first two lateral modes, allowing the comparison of the two models.

 0001-4966/97/101(4)/2043/9/$10.00

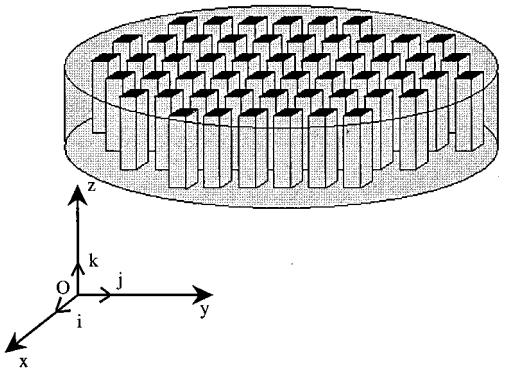

FIG. 1. Schematic diagram of 1–3 piezocomposite.

Then, the variations of the phase velocity of the first lateral resonance as a function of the ceramic rod width to pitch ratio are studied and compared to experimental measurements.

I. THEORETICAL APPROACHES

A. Bloch waves theory

The Bloch waves theory was first developed in the area of solid state physics to calculate the energy bands in a crystal lattice. This approach has been described by Auld and Wang[13–15] in general terms for elastic propagation in a 3-D periodic medium and they have applied it to the particular case of a 1-D periodic structure. We shall develop the calculations for the case of a 2-D periodic structure.

In an elastic medium, the propagation of acoustic plane waves is governed, at frequency ω, by the general motion equation, written according to Auld's notation[16]

$$\nabla_{iI} C_{IJ} \nabla_{Jj} u_j = -\rho\omega^2 u_i, \qquad I,J=1,\ldots,6, \quad i,j=x,y,z, \tag{1}$$

where C_{IJ} is the stiffness tensor, ρ is the density, and ∇_{iI} and ∇_{Jj} are respectively the divergence and gradient matrix operators.

For the propagation medium defined in Fig. 2, the stiffness tensor of the piezoelectric phase is marked with a superscript ''p'' (C_{IJ}^p) and the stiffness tensor of the resin is marked with a superscript ''r'' (C_{IJ}^r). In the same manner, the density of the ceramic and of the polymer are respectively referred to as ρ^p and ρ^r. The elastic stiffnesses of the piezoelectric medium are the open circuit values (at constant electric displacement) which afterwards will make it possible to determine the antiresonance frequencies of the piezoelectric composite plate.

We define $\overline{C_{IJ}}$ and $\overline{\rho}$, the spatial averages of the stiffness tensor $C_{IJ}(x,y)$ and of the density $\rho(x,y)$. The mean value of the functions $C_{IJ}(x,y)$ and $\rho(x,y)$ is calculated using the definition of the mean value of a periodic function, which gives

$$\overline{C_{IJ}} = \frac{\int_{-d/2}^{+d/2}\int_{-d/2}^{+d/2} C_{IJ}(x,y)\, dx\, dy}{\int_{-d/2}^{+d/2}\int_{-d/2}^{+d/2} dx\, dy}$$

and

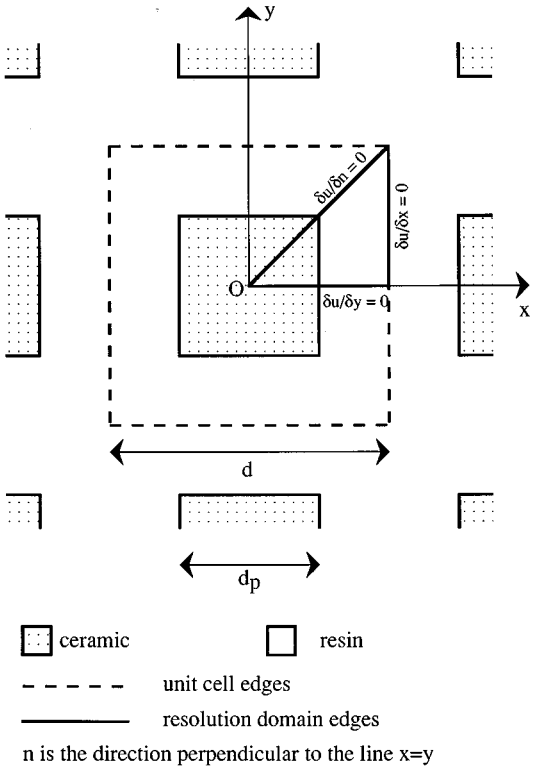

FIG. 2. Geometry of 2-D periodic medium. d_p is the ceramic rod width and d is the pitch.

$$\overline{\rho} = \frac{\int_{-d/2}^{+d/2}\int_{-d/2}^{+d/2} \rho(x,y)\, dx\, dy}{\int_{-d/2}^{+d/2}\int_{-d/2}^{+d/2} dx\, dy}.$$

The integration of $C_{IJ}(x,y)$ and $\rho(x,y)$ over the elementary cell gives the following expression for C_{IJ} and $\overline{\rho}$:

$$\overline{C_{IJ}} = \left(\frac{d_p}{d}\right)^2 C_{IJ}^p + \left(1-\frac{d_p}{d}\right)^2 C_{IJ}^r$$

and

$$\overline{\rho} = \left(\frac{d_p}{d}\right)^2 \rho^p + \left(1-\frac{d_p}{d}\right)^2 \rho^r.$$

Here d_p is the ceramic rod width and d the pitch of the structure, as defined in Fig. 2. We then express $C_{IJ}(x,y)$ and $\rho(x,y)$ as

$$\begin{aligned} C_{IJ}(x,y) &= \overline{C_{IJ}} + \delta C_{IJ}(x,y), \\ \rho(x,y) &= \overline{\rho} + \delta\rho(x,y), \end{aligned} \tag{2}$$

where $\delta C_{IJ}(x,y)$ and $\delta\rho(x,y)$ represent the spatial variations of the stiffness tensor and of the density around their mean value.

For a z-polarized wave, propagating in the xy plane, Eq. (1) reduces to

$$\frac{\partial}{\partial x}\left(C_{44}\frac{\partial u_z}{\partial x}\right) + \frac{\partial}{\partial y}\left(C_{44}\frac{\partial u_z}{\partial y}\right) = -\rho\omega^2 u_z, \tag{3}$$

where C_{44} is the shear stiffness of the composite material which exhibits an (x,y) dependence:

$$C_{44}=\overline{C_{44}}+\delta C_{44}(x,y). \tag{4}$$

Using relations (2) and (4) in Eq. (3) we obtain

$$\overline{C_{44}}\Delta u_z+\overline{\rho}\omega^2 u_z=-[\delta C_{44}\Delta u_z+\delta\rho\omega^2 u_z] - \left[\frac{\partial \delta C_{44}}{\partial x}\cdot\frac{\partial u_z}{\partial x}-\frac{\partial \delta C_{44}}{\partial y}\cdot\frac{\partial u_z}{\partial y}\right]. \tag{5}$$

Due to the periodicity of the medium, the solution for the displacement $u_z(x,y)$ must verify the Bloch periodicity condition:[10]

$$u_z(\mathbf{r}+\mathbf{T}_{m,n})=u_z(\mathbf{r})\mathbf{e}^{\mathbf{j}\mathbf{k}_0\cdot\mathbf{T}_{m,n}} \tag{6a}$$

with $\mathbf{r}=x\mathbf{i}+y\mathbf{j}\mathbf{k}_0$ is the wave vector of the shear plane wave and $\mathbf{T}_{mn}=md\mathbf{i}+nd\mathbf{j}$ (m and n are integers) are the translation vectors of the lattice.

Between two points separated by a vector $\mathbf{T}_{mn}$, the phase difference $\mathbf{k}_0\cdot\mathbf{T}_{m,n}$ is linked to the time delay of the wave, and the solutions for $u_z(x,y)$ satisfying the (6a) condition are necessarily Bloch wave functions,[10]

$$u_z(x,y)=F(\mathbf{r})e^{j(\omega t-\mathbf{k}_0\cdot\mathbf{r})}, \tag{6b}$$

where $F(\mathbf{r})$ is a scalar periodic function of the space. It can therefore be expressed as a double Fourier series in the harmonic space which is called the reciprocal lattice:

$$F(\mathbf{r})=\sum_{m,n=-\infty}^{m,n=+\infty} a_{mn}e^{-j(\mathbf{K}_{mn}\cdot\mathbf{r})} \tag{6c}$$

with $\mathbf{K}_{mn}=(2\pi/d)m\mathbf{i}+(2\pi/d)n\mathbf{j}$.

The expression of the solutions $u_z(x,y)$ becomes

$$u_z(x,y)=\left[\sum_{m,n=-\infty}^{m,n=+\infty} a_{mn}e^{-j(\mathbf{k}_{mn}\cdot\mathbf{r})}\right]e^{j\omega t} \tag{7}$$

with $\mathbf{k}_{mn}=\mathbf{K}_{mn}+\mathbf{k}_0$.

The determination of the solutions $u_z(x,y)$ requires, for a given wave vector $\mathbf{k}_0$, the calculation of the coefficients a_{mn}. For this, $u_z(x,y)$ in the relation (3) is substituted by the expression (7). Then, we follow calculation procedures described by Wang in Ref. 13 to express Eq. (3) in terms of an infinite set of linear equations which has the coefficients a_{mn} as unknowns:

$$\overline{\rho}(\omega^2-\omega_{mn}^2)a_{mn}=-\sum_{p,q} K_{mnpq}a_{pq}, \qquad m,n\rightarrow-\infty \text{ to } +\infty. \tag{8}$$

Here ω_{mn} is the eigenfrequency associated with the shear plane wave propagating in the medium of characteristics $\overline{\rho}$ and $\overline{C_{44}}$ with the wave vector $\mathbf{k}_{mn}$. We have $\omega_{mn}=\sqrt{\overline{C_{44}}/\overline{\rho}}|\mathbf{k}_{mn}|$. The coefficients K_{mnpq} are called the space harmonic coupling coefficients[13] and have the following explicit form:

$$K_{mnpq}=\frac{1}{d^2}\int_{-d/2}^{+d/2}\int_{-d/2}^{+d/2}[\delta\rho(x,y)\omega^2 - \delta C_{44}(x,y)k_{pq}^2]e^{j(\mathbf{k}_{mn}-\mathbf{k}_{pq})\cdot\mathbf{r}}\,dx\,dy + \frac{1}{d^2}\int_{-d/2}^{+d/2}\int_{-d/2}^{+d/2}-j\left[k_{pq,x}\frac{\partial\delta C_{44}}{\partial x} + k_{pq,y}\frac{\partial\delta C_{44}}{\partial y}\right]e^{j(\mathbf{k}_{mn}-\mathbf{k}_{pq})\cdot\mathbf{r}}\,dx\,dy, \tag{9}$$

where $\mathbf{k}_{pq}=k_{pq,x}\mathbf{i}+k_{pq,y}\mathbf{j}$.

Further details concerning the calculation of the coefficients K_{mnpq} are reported in Ref. 17. This calculation leads to the following result:
If $m\neq p$ or $n\neq q$,

$$K_{mnpq}=(\Delta\rho\omega^2-\Delta C_{44}\mathbf{k}_{mn}\cdot\mathbf{k}_{pq})\frac{d_p^2}{d^2} \times\operatorname{sinc}\left(\frac{\pi(n-q)d_p}{d}\right)\operatorname{sinc}\left(\frac{\pi(m-p)d_p}{d}\right). \tag{10}$$

If $m=p$ and $n=q$,

$$K_{mnpq}=0$$

with

$$\Delta C_{44}=C_{44}^p-C_{44}^r, \quad \Delta\rho=\rho^p-\rho^r.$$

Using Eq. (8), a numerical approximation of the functions $u_z(x,y)$ is calculated by truncating the number of spatial harmonics to the first N. Then a set of $N*N$ linear equations is obtained in a matrix form:

$$\begin{pmatrix} \overline{\rho}(\omega^2-\omega_{-N-N}^2) & -K_{-N-N-N-(N-1)} & \cdots & -K_{-N-NNN} \\ -K_{-N-(N-1)-N-N} & \overline{\rho}(\omega^2-\omega_{-N-(N-1)}^2) & \cdots & -K_{-N-(N-1)N(N-1)} \\ -K_{NN-N-N} & -K_{NN-N-(N-1)} & \cdots & \overline{\rho}(\omega^2-\omega_{NN}^2) \end{pmatrix}\cdot\begin{pmatrix} a_{-N-N} \\ a_{-N-(N-1)} \\ \cdots \\ a_{NN} \end{pmatrix}=0. \tag{11}$$

The solutions of the matrix equation (11) are nontrivial if the determinant of the matrix is equal to zero. This additional condition enables the determination of the frequency ω associated with the wave vector $\mathbf{k}_0$, providing the dispersion relationships. The calculation procedure of the frequency ω can be simplified by rearranging the factors K_{mnpq} as

$$K_{mnpq}=\omega^2\alpha_{mnpq}+\beta_{mnpq}, \tag{12a}$$

where

$$\alpha_{mnpq}=\frac{d_p^2}{d^2}\,\Delta\rho\,\operatorname{sinc}\left(\frac{\pi(n-q)d_p}{d}\right)\operatorname{sinc}\left(\frac{\pi(m-p)d_p}{d}\right) \tag{12b}$$

for $m\neq p$ or $n\neq q$,

$$\alpha_{mnpq}=\overline{\rho} \tag{12c}$$

for $m=p$ and $n=q$,

$$\beta_{mnpq}=\frac{d_p^2}{d^2}\,\Delta C_{44}\mathbf{k}_{mn}\cdot\mathbf{k}_{pq}\times\operatorname{sinc}\left(\frac{\pi(n-q)d_p}{d}\right)\operatorname{sinc}\left(\frac{\pi(m-p)d_p}{d}\right) \tag{12d}$$

for $m\neq p$ or $n\neq q$, and

$$\beta_{mnpq}=\overline{C_{44}}k_{mn}^2 \tag{12e}$$

for $m=p$ and $n=q$.

Using the set of equations (12a)–(12e), the matrix in Eq. (11) becomes the sum of two matrices A and B, respectively, constructed from the coefficients α_{mnpq} and β_{mnpq}:

$$[B+\omega^2A]\cdot\begin{pmatrix} a_{-N-N} \\ a_{-N-(N-1)} \\ \cdots \\ a_{NN}\end{pmatrix}=0 \tag{13}$$

with

$$A=\begin{pmatrix} \overline{\rho} & -\alpha_{-N-N-N-(N-1)} & \cdots & -\alpha_{-N-NNN} \\ -\alpha_{-N-(N-1)-N-N} & \overline{\rho} & \cdots & -\alpha_{-N-(N-1)N(N-1)} \\ \cdots & \cdots & \cdots & \cdots \\ -\alpha_{NN-N-N} & -\alpha_{NN-N-(N-1)} & \cdots & \overline{\rho}\end{pmatrix}$$

and

$$B=\begin{pmatrix} \overline{C_{44}}k_{-N-N}^2 & -\beta_{-N-N-N-(N-1)} & \cdots & -\beta_{-N-NNN} \\ -\beta_{-N-(N-1)-N-N} & \overline{C_{44}}k_{-N-(N-1)}^2 & \cdots & -\beta_{-N-(N-1)N(N-1)} \\ \cdots & \cdots & \cdots & \cdots \\ -\beta_{NN-N-N} & -\beta_{NN-N-(N-1)} & \cdots & \overline{C_{44}}k_{NN}^2\end{pmatrix}.$$

The coefficients a_{mn} and the frequency ω of each solution $u_z(x,y)$ are obtained from the eigenvalues and eigenvectors of the matrix $[A^{-1}B]$. From Eq. (13), the dispersion curves can be calculated by fixing the direction of propagation and the modulus of the wave vector $\mathbf{k}_0$.

B. Membrane model

In this section, the problem will not be considered in the Fourier space of the displacement field. The propagation equation will be solved in the (O,x,y) real space by a numerical finite difference method.

Considering the propagation equation (3) for each of the media, it splits into

$$C_{44}^p\Delta u_z^p(x,y)=-\rho^p\omega^2u_z^p(x,y), \tag{14a}$$

$$C_{44}^r\Delta u_z^r(x,y)=-\rho^r\omega^2u_z^r(x,y). \tag{14b}$$

Due to the similarity between these equations and the wave equation of a rectangular membrane, we called this second theoretical approach the ''membrane model.''

The solutions of Eqs. (14a) and (14b) must respect the interfacial boundary conditions between the ceramic and the polymer (Fig. 2); continuity of the displacement and the stress

$$[u_z^p]_{x=d_p/2,0\leqslant y\leqslant d_p/2}=[u_z^r]_{x=d_p/2,0\leqslant y\leqslant d_p/2}, \tag{15a}$$

$$\left[C_{44}^p\,\frac{\partial u_z^p}{\partial x}\right]_{x=d_p/2,0\leqslant y\leqslant d_p/2}=\left[C_{44}^r\,\frac{\partial u_z^r}{\partial x}\right]_{x=d_p/2,0\leqslant y\leqslant d_p/2}. \tag{15b}$$

Taking into account the periodicity of the medium, (14a) and (14b) can be solved for a unit cell (Fig. 2). However, the boundary conditions over its edges must be chosen with great care depending on the kind of problem that is to be solved.

For the most general problem, where all solutions associated with any wave vectors $\mathbf{k}_0$ are needed, the Bloch relations provide boundary conditions of the form

$$u_z(\mathbf{r}+\mathbf{T}_{m,n})=u_z(\mathbf{r})\cdot e^{j\mathbf{k}_0\cdot\mathbf{T}_{m,n}}$$

with m, $n=0$ or 1.

TABLE I. Acoustical parameters used for simulating 1–3 piezoelectric composite behavior.

	C_{44} (10^{10} Pa)	ρ (kg/m^3)
Ceramic	4.2	7500
Resin	0.17	1150

Then, for each $\mathbf{k}_0$, the problems (14) and (15) have nontrivial solutions for a finite number of values of ω. This enables the dispersion curves to be drawn. However, in designing piezoelectric composite materials, the important features are the values of the lateral resonance frequencies. Generally, resonance conditions are expressed by the Bragg relationship:[10]

$$2\mathbf{k}_0.\mathbf{K}_{mn}=|\mathbf{K}_{mn}|^2.$$

However, in our case, one can be more restrictive by using the following simple arguments. As the piezocomposite plate has electrodes on both faces, all the ceramic rods have the same electric potential. They then must vibrate in phase and the term $e^{j\mathbf{k}_0.\mathbf{T}_{mn}}$ in (5a) is equal to 1 for any $\mathbf{T}_{mn}$. This means that the values for the solution $u_z(x,y)$ are equal for the lower and upper limits. The same applies for the two lateral edges. Solutions will then be symmetrical or antisymmetrical along O_x, O_y, and the bisecting lines. We are only looking for piezoelectrically coupled modes and this excludes any antisymmetry since that would lead to a total charge over a unit cell equal to zero. We are then left with symmetric solutions which must be symmetric along O_x, O_y, and the diagonals. Calculations can then be simplified and the resolution domain reduced to one-eighth of the unit cell (Fig. 2) where Neumann boundary conditions are applied:

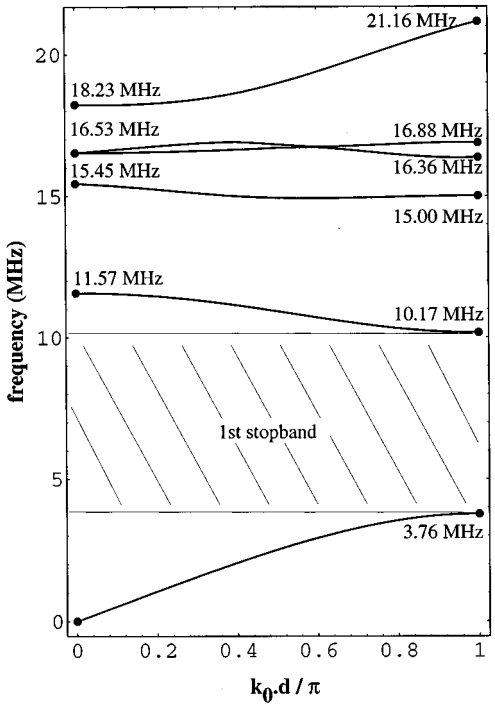

FIG. 3. Dispersion curve of shear wave propagating along the O_x axis.

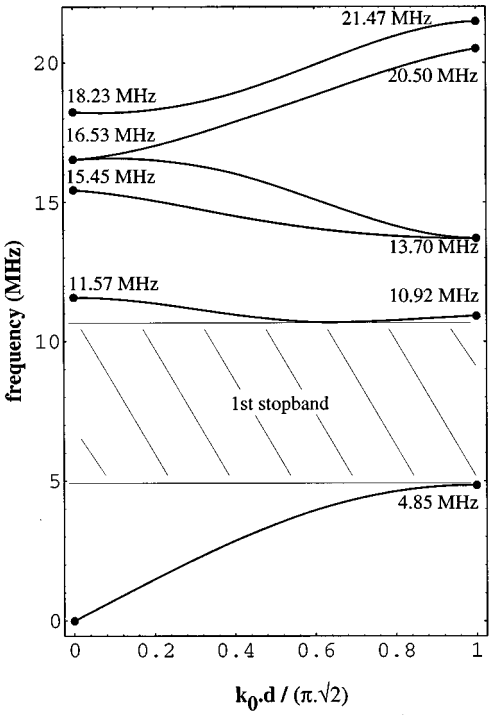

FIG. 4. Dispersion curve of shear wave propagating along the line $x=y$.

$$\frac{\partial u_z}{\partial n}=0,$$

where n is the direction perpendicular to the sides of the triangle.

Due to the rectangular geometry of the structure, no analytical solutions can be obtained for Eqs. (14) and (15). We chose to solve these equations numerically using a finite difference method. The domain is meshed and Eqs. (14a) and (14b) are discretized. Calculations of the lateral mode frequencies and displacement fields are then a problem similar to the kettledrum equation except that the Dirichlet condition ($u_z=0$) has been replaced with a Neumann condition. We finally obtain a classical eigenvalue problem

$$[K-M\omega^2]X=0,$$

where vector X corresponds to the nodal values of the displacement, K is the elastic stiffness matrix, and M is the mass matrix.

Eigenvalues and eigenvectors of the matrix $[K.M^{-1}]$ respectively give the resonance frequencies and displacement fields associated with the lateral modes.

II. RESULTS AND DISCUSSION

A 1–3 piezoelectric composite (Fig. 2) with the characteristics presented in Table I was modeled with the two approaches presented above. The ceramic rod width is 50 μm and the width-to-pitch ratio is 0.5.

A. Dispersion curves

The Bloch waves theory provides the dispersion curves. We have chosen to use the reduced diagram[10] to draw the dispersion curves where the variations of ω as a function of

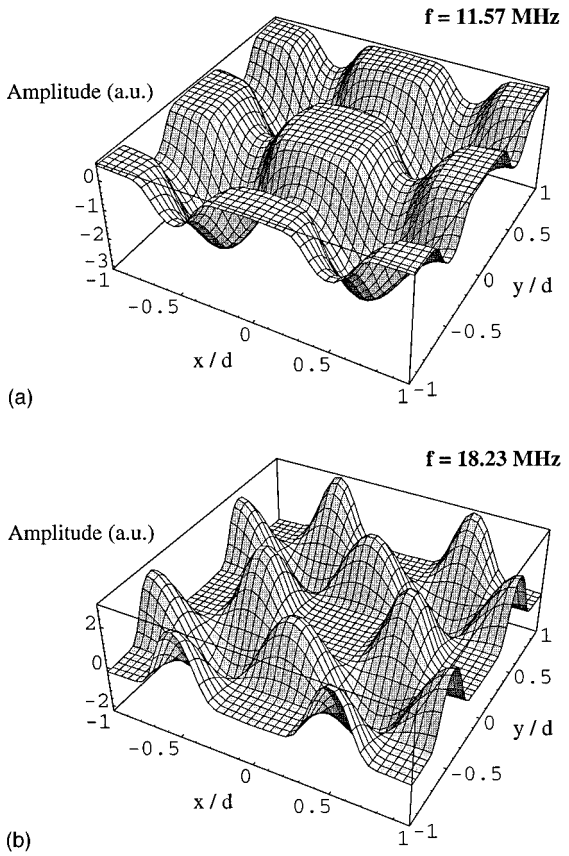

FIG. 5. Vertical displacement field of the first (a) and the second (b) lateral resonance predicted by the Bloch waves theory. Amplitude of the displacements is expressed with arbitrary units (a.u.).

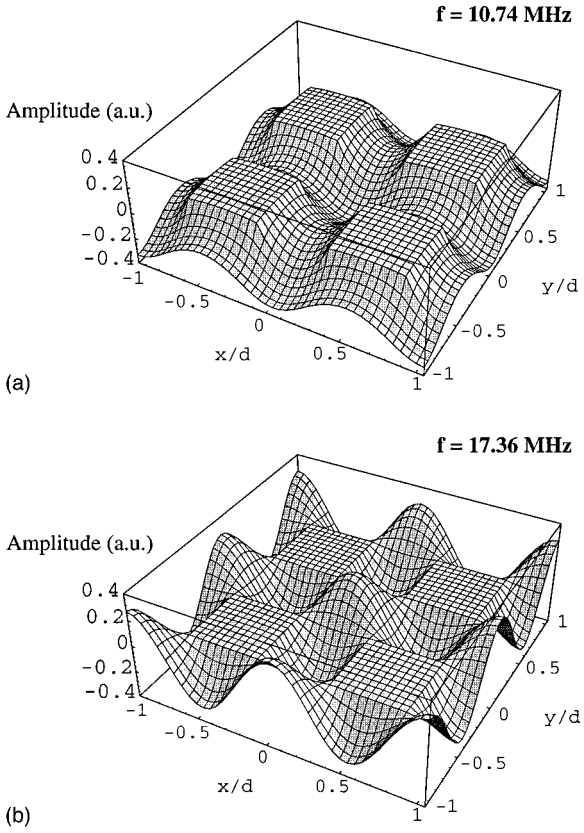

FIG. 6. Vertical displacement field of the first (a) and the second (b) lateral resonance predicted by the membrane model. Amplitude of the displacements is expressed with arbitrary units (a.u.).

$|\mathbf{k}_0|$ are brought back to the first Brillouin zone. Gururaja[4] has shown that the two interesting directions of propagation for the calculation of the first two lateral modes are in the direction of the vectors **i** and (**i**+**j**). Thus, the solutions have been respectively calculated between $|\mathbf{k}_0|=0$ and $|\mathbf{k}_0|=\pi/d$ and between $|\mathbf{k}_0|=0$ and $|\mathbf{k}_0|=\pi\sqrt{2}/d$. Figures 3 and 4 show the normalized dispersion curves for these two directions.

For $k_0 d/\pi$ or $k_0 d/\pi\sqrt{2}$ equal to 0 or 1, the incident wave vector $\mathbf{k}_0$ is at the edge of a Brillouin zone where the Bragg diffraction condition is satisfied and corresponds to resonant standing waves.

For resonances where $k_0 d/\pi$ or $k_0 d/\pi\sqrt{2}$ equals 1, the adjacent ceramic rods are separated by an odd number of half-wavelengths, so their vibrations are 180° out of phase. These resonances are not electrically coupled. On the other hand, when $k_0 d/\pi$ or $k_0 d/\pi\sqrt{2}$ is equal to 0, all the rods vibrate in phase. These displacement fields are either symmetrical or antisymmetrical, but, due to the transduction effect, only the former are piezoelectrically coupled. For instance 11.57 and 18.23 MHz are the first and second lateral modes. Figure 5 shows the associated displacement field. Dispersion curves display frequency bands where no propagation can occur, which are known as stop bands, for example between 3.76 and 10.17 MHz for Fig. 3.

B. Lateral resonance behavior

In order to compare the two theoretical approaches, the same composite has been modelled using the membrane model. Theoretical displacement fields of the first and second lateral modes calculated by the membrane model are shown in Fig. 6.

The two calculated displacement fields are qualitatively similar, but the use of the Bloch wave theory does not show the discontinuity of the strain at the ceramic/resin boundary. This is not surprising since the numerical computation truncates the summation over the space harmonics. Increasing this number improves the result, but at a rather high computing cost, since the convergence is slow. On the other hand, the membrane model naturally takes into account the material discontinuity and gives accurate results provided that the space sampling is fine enough; 20 samples per period in our case. This also explains the discrepancy between the calculated values of the lateral mode frequencies which are overestimated by the use of the Bloch wave theory (11.57–10.74 MHz and 18.23–17.36 MHz).

It is interesting to compare the theoretical fields of Figs. 5 and 6 to the results given by the Brillouin zone theory similar to those predicted by the Bragg diffraction theory. This approach, as specified in the Introduction, does not include the geometry of the structure since ceramic rods are reduced to nodes of the lattice associated with the periodic structure. Figure 7 shows the picture of the positive and negative maxima of displacement for the first and second lateral resonances. More details about the process used to obtain these results are available.[17]

Concerning the first lateral oscillation, the three theoreti-

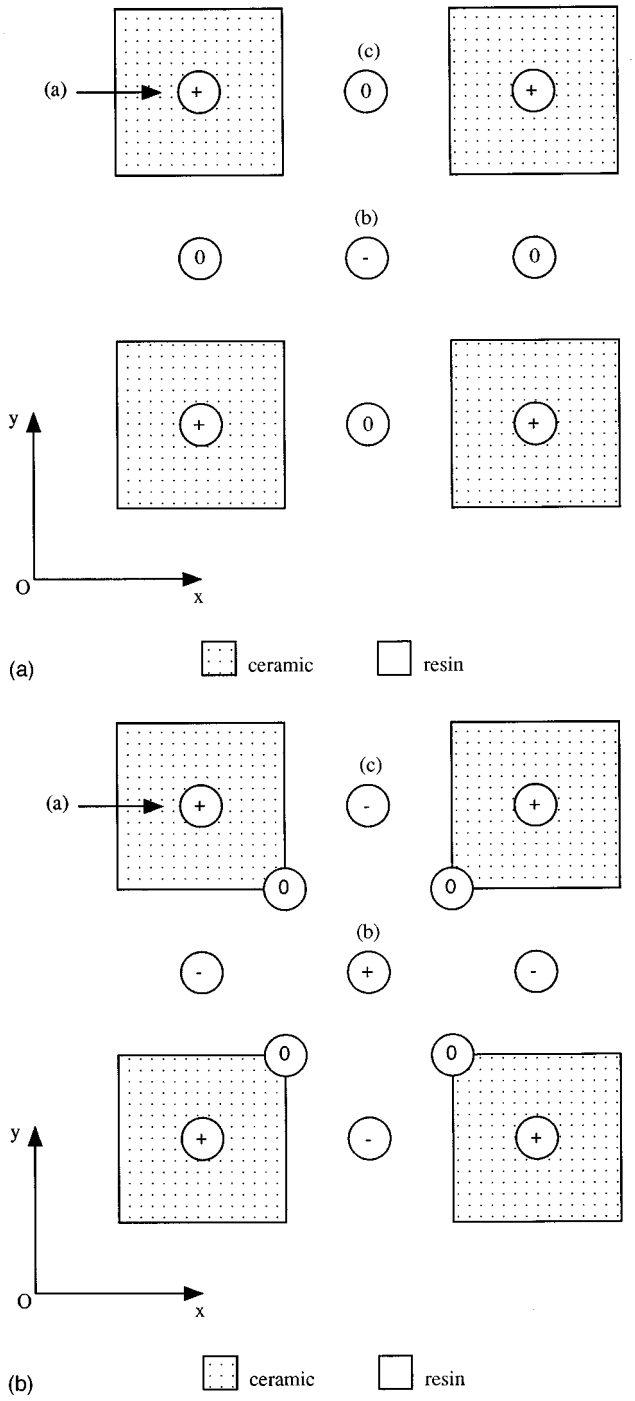

FIG. 7. Cartography of the maximum positive vertical displacements (+), maximum negative vertical displacements (−), and null vertical displacements (0) for the first (a) and second (b) lateral mode.

cal results predict positive and negative displacement maximum at positions (a) and (b) [Fig. 7(a)]. However, at the position (c), the approach using the Bragg diffraction seems to be deficient. We observe no displacement for the Bragg diffraction while the two other models predict that at (c), the polymer moves with a higher amplitude than the ceramic. Moreover, due to the big difference of stiffness between the two phases, the resin and ceramic vibrate with a strong difference in amplitude, as seen in Figs. 5(a) and 6(a). Indeed, this situation is not suitable for an efficient transducer which

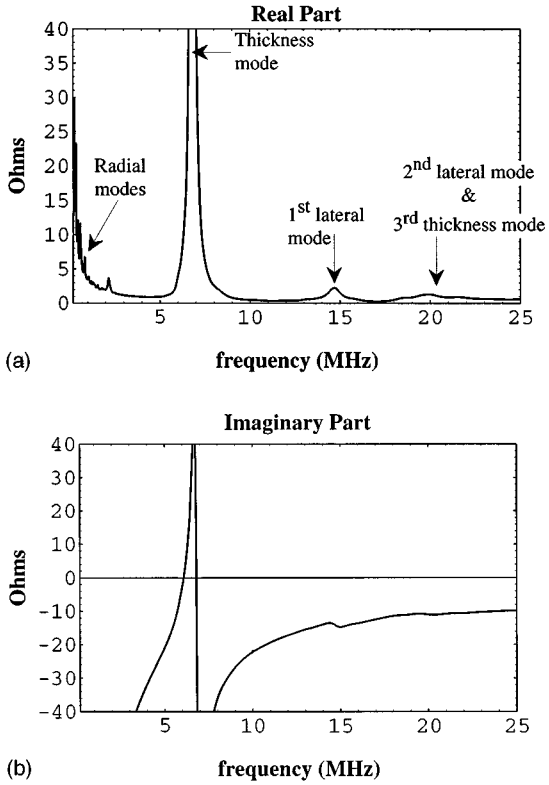

FIG. 8. Real part (a) and imaginary part (b) of the electrical impedance spectrum of a 1–3 piezo-electric composite.

requires that all its parts move in phase with similar amplitude. As for the second lateral resonance, similar observations can be made. It can be observed that a part of the polymer moves in phase with the ceramic rods [point (b)] while another part, situated at position (c), is 180° out of phase with the ceramic.

C. Experimental results

The measurements made to validate our approach were made on samples using a network/spectrum analyzer. The measurement of the electric impedance allows the resonance and antiresonance frequencies of each composite sample to be obtained. The real and imaginary parts of the electric impedance of one of the samples are represented in Fig. 8. For low frequencies, we observe the radial modes, the third and fifth harmonics of the thickness mode, and the two first lateral modes. With the determination of the antiresonance frequencies of each lateral mode, the phase velocity associated with the shear plane wave is obtained. For the first lateral mode, the value of the wavelength is d, the pitch of the structure. For the second lateral mode, the wavelength is $d/\sqrt{2}$.

Seven composite samples with different volume fractions of ceramic have been manufactured with an epoxy resin and a lead zirconate titanate (PZT) ceramic. The thickness of the samples was chosen to have the frequency of the first lateral mode approximately two times greater than the frequency of the fundamental thickness mode. In this configuration, the coupling between the first and third harmonics of the thickness mode and the first lateral mode is minimal and

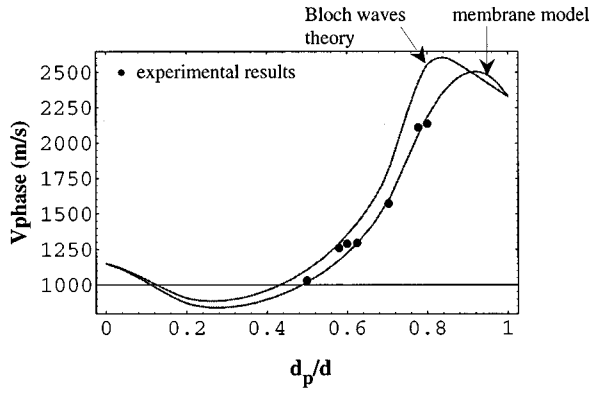

FIG. 9. Variations of the phase velocity as a function of the ceramic rod width to pitch ratio for PZT/epoxy composite.

the measurement of the first lateral mode frequency is not disturbed. For the second lateral mode, accurate measurements were impossible, its coupling with the third and fifth harmonics of the thickness mode being too high. Figure 9 shows the theoretical and experimental variations of the shear phase velocity for the first lateral mode as a function of the ceramic rod width-to-pitch ratio. The elastic characteristics of the polymer used to realize the simulations were obtained experimentally by measuring the shear velocity in the resin. For the ceramic, the characteristics provided by the manufacturer were used.

In order to complete the comparison between theory and experiment, the two models were compared with the experimental results obtained by C. G. Oakley[11,12] with a set of 1–3 piezoelectric composite samples. The phase velocity variations are presented in Fig. 9. The polymer used is an epoxy resin and the PZT ceramic is not the same as the previous one.

The theoretical curves in Figs. 9 and 10 show the same aspect and are consistent with experimental results. We observe that the Bloch wave model overestimates the lateral mode frequencies and that the precision of the membrane model results is better than 5%. The aspect of the variations of the phase velocity as a function of the ceramic rod-width-to-pitch ratio is similar to the variations of the effective elastic properties of a loaded resin matrix (0–3 connectivity) as a

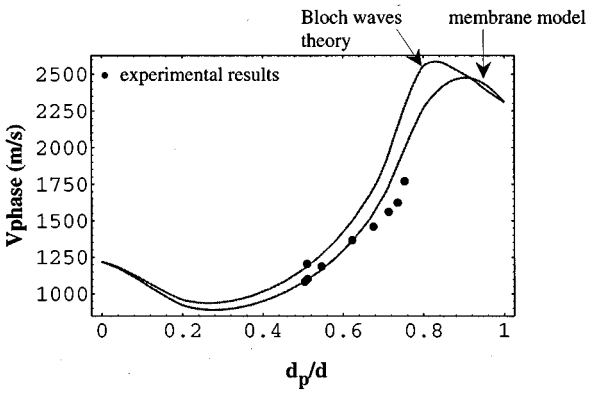

FIG. 10. Variations of the phase velocity as a function of the ceramic rod width to pitch ratio for composite samples measured by C. G. Oakley.[11,12]

function of the load volume fraction. For a low ceramic volume fraction, the phase velocity decreases due to the mass loading effect of PZT rods. The use of low density ceramics closer to that of the polymer should increase the phase velocity and therefore the lateral mode frequency. For d_p/d values higher than 0.5, the ceramic predominates and the stiffness of the matrix increases. This leads to an increase of the phase velocity up to d_p/d values equal to 0.85, where a maximum is reached. Next, the curve descends to reach the value of the shear velocity in the ceramic. To explain this maximum, the variations of the effective stiffness and the density of the composite must be compared simultaneously. These two parameters are always lower than the value of the ceramic but they progress differently. When the relative variations of the stiffness are greater than the relative variations of the density, their ratio (and therefore the transverse velocity) can surpass the shear velocity in the ceramic. The position of the maximum changes as a function of the elastic characteristics of each phase. In particular, the choice of a ceramic transversely stiffer and with a density lower than the PZT permits an increase in the value of this maximum (for example, lead titanate ceramics). This alternative may be used to increase the lateral mode frequencies.

Between $d_p/d=0.5$ and $d_p/d=0.8$, the phase velocity variations are particularly sensitive to the ceramic volume fraction variations. Then, the accuracy of the theoretical predictions is strongly dependent on the measurement accuracy of the piezocomposite geometry. This probably explains the slight differences observed in Fig. 10 between the membrane model and the experimental results from $d_p/d=0.7$ and $d_p/d=0.8$.

The sensitivity of the phase velocity to the volume fraction can generate some problems of reproducibility for the manufacture of 1–3 composites. For example, considering a set of 1–3 piezoelectric composite samples in which the volume fraction can vary up to 5%, the variations of the frequency of the first lateral mode can reach 10%. Consequently, the electrical and acoustical performances of each composite will probably be different depending on the importance of the coupling between lateral and thickness modes.

To design a transducer, for a fixed pitch structure, the volume fraction of ceramic can be chosen to be placed near the maximum of the phase velocity. For this geometrical configuration, the frequency of the first lateral mode is maximum and a larger range to increase the working frequency of the transducer is available. However, for a high volume fraction of ceramic (>75%), the specific acoustic impedance of the composite is near that of the ceramic and the performance of the transducer decreases (bandwidth and sensitivity). A tradeoff must be made between the frequency of the first lateral mode and the acoustic impedance of the material.

III. CONCLUSION

Theoretical investigation of the first and second lateral modes in 1–3 piezoelectric composite has been conducted. Analysis has been made without taking into account the coupling with the fundamental thickness mode of the plate. This leads us to study the propagation of a transverse wave in an

infinite thickness composite. We have shown that this fundamental assumption is realistic and consistent with experimental results.

Two approaches have been compared. The first, the Bloch wave theory, requires long computing times and, due to the truncation process of the harmonic number, its level of precision is low. The second method, more straightforward, consists in solving the equation of propagation of transverse waves in each phase and to include the interfacial boundary conditions. Simple symmetric conditions have been deduced from the electric boundary conditions and the transduction effect. These conditions simplify the determination of the piezoelectrically coupled lateral modes.

These models provide the important physical parameters which govern the lateral mode frequencies. For a given structure, the interesting characteristic which determines the frequency is the phase velocity of the transverse waves. This parameter allows one to compare the performance of a 2-D periodic medium with different geometries. The variations of the phase velocity for the first lateral mode with the ceramic-rod-width-to-pitch ratio reveals a tradeoff between the specific acoustic impedance of the composite and the first lateral mode frequency. Moreover, the models show that in the useful frequency range of piezoelectric composites, the first lateral mode frequency is particularly sensitive to the variations of the ceramic rod width to pitch ratio.

The membrane model can be used to define guidelines for transducer design. More complex structures can be analyzed further such as pseudo-periodic media. In particular, the effects of the pseudo-periodicity on the stop band width and the resonance frequencies can be analyzed.

ACKNOWLEDGMENTS

The authors wish to thank the Vermon Company (ultrasound transducers manufacturer in Tours, France) for their warm support in the course of this study.

[1] R. E. Newnham, D. P. Skinner, and L. E. Cross, ''Connectivity and piezoelectric-pyroelectric composites,'' Mater. Res. Bull. **13**, 525–536 (1978).

[2] W. A. Smith, ''New opportunities in ultrasonic transducers emerging from innovations in piezoelectric materials,'' Proc. SPIE **1733**, 3–26 (1992).

[3] H. P. Savakus, K. A. Klicker, and R. E. Newham, ''PZT-Epoxy Piezoelectric Transducers: A Simplified Fabrication Procedure,'' Mater. Res. Bull. **16**, 677–680 (1981).

[4] T. R. Gururaja, W. A. Schulze, L. E. Cross, R. E. Newham, B. A. Auld, and Y. J. Wang, ''Piezoelectric composites materials for ultrasonic transducer applications. Part I: Resonant modes of vibration of PZT rod-polymer composites,'' IEEE Trans. Ultrason. Ferroelectr. Freq. Control **SU-32**, 481–498 (1985).

[5] T. R. Gururaja, W. A. Schulze, L. E. Cross, and R. E. Newham, ''Piezoelectric composites materials for ultrasonic transducer applications. Part II: Evaluation of ultrasonic medical applications,'' IEEE Trans. Ultrason. Ferroelectr. Freq. Control **SU-32**, 499–513 (1985).

[6] W. A. Smith and B. A. Auld, ''Modeling 1–3 Composite Piezoelectrics: Thickness-Mode Oscillations,'' IEEE Trans. Ultrason. Ferroelectr. Freq. Control **SU-38**, 40–47 (1991).

[7] Y. Wang and B. A. Auld, ''Numerical analysis of Bloch theory for acoustic wave propagation in one dimensional periodic composites,'' *in Proceedings of the 1986 IEEE International Symposium on Applications of Ferroelectrics*, 261–264 (1986).

[8] F. Craciun, L. Sorba, E. Molinari, and M. Pappalardo, ''A coupled-Mode theory for periodic piezoelectric composites,'' IEEE Trans. Ultrason. Ferroelectr. Freq. Control **SU-36**, 50–56 (1989).

[9] A. Alippi, ''Propagation of elastic waves in one-dimensional composites,'' Mater. Res. Bull. **122**, 71–75 (1989).

[10] C. Kittel, *Introduction to Solid State Physics* (Wiley, New York, 1976), 5th ed., Chap. 2.

[11] C. G. Oakley, ''Analysis and development of piezoelectric composites for medical ultrasound transducer applications,'' Ph.D. thesis, The Pennsylvania State University, 1991.

[12] C. G. Oakley, ''Geometric effects on the stop-band structures of 2–2 piezoelectric composite plates,'' in *Proceedings of the 1991 IEEE Ultrasonics Symposium* (1991), pp. 657–660.

[13] Y. Wang, ''Waves and vibrations in elastic superlattice composites,'' Ph.D. thesis, Standford University, 1986.

[14] B. A. Auld, Y. A. Shui, and Y. Wang, ''Elastic wave propagation in three-dimensional periodic composite materials,'' J. Phys. **45**, 159–163 (1984).

[15] B. A. Auld and Y. Wang, ''Waves and vibrations in periodic composite plates,'' in Proceedings of the 1984 IEEE Ultrasonics Symposium (1984), pp. 528–532.

[16] B. A. Auld, *Acoustic Fields and Waves in Solids* (Krieger, Melbourne, FL, 1990), 2nd ed., Vol. 1.

[17] D. Certon, ''Propagation acoustique dans les matériaux piezo-composites périodiques de connectivité 1–3 appliqués aux transducteurs ultrasonores,'' Ph.D. Thesis, Université François Rabelais de Tours, France, 1994.

Spectral Green's function for wave excitation and propagation in a piezoelectric, continuously twisted, structurally chiral medium

Akhlesh Lakhtakia
CATMAS-Computational and Theoretical Materials Sciences Group, Department of Engineering Science and Mechanics, The Pennsylvania State University, University Park, Pennsylvania 16802-1401

Kevin Robbie and Michael J. Brett
Alberta Microelectronic Centre and Department of Electrical Engineering, University of Alberta, Edmonton, Alberta T6G 2G7, Canada

(Received 25 April 1996; accepted for publication 9 December 1996)

A continuously twisted, structurally chiral medium (CTSCM) is a reciprocal medium whose constitutive properties vary helicoidally along its axis of spirality (say, the z axis), and the corresponding piezoelectric medium is abbreviatedly called the PCTSCM. Very recent progress in thin-film research is presented here to show that technologically significant CTSCM's and PCTSCM's are waiting in the wings and calling for theoretical advances in the understanding of wave excitation and propagation in these novel materials. A spectral Green's function is obtained as a bilinear composition of two matrices, after implementing a spatial Fourier transform in the xy plane as well as the Oseen transformation. As a result, multilayered media problems as well as grating problems utilizing CTSCM's and PCTSCM's become accessible to theoretical exploration leading to novel transducers, sensors, and other devices. © *1997 Acoustical Society of America.* [S0001-4966(97)04904-7]

PACS numbers: 43.38.Fx, 43.20.Bi [CBB]

INTRODUCTION

When the continuously twisted, structurally chiral medium (CTSCM) was introduced, a model of wave propagation based on the pile-of-plates realization of a structurally chiral medium (SCM) was described in this journal.[1] This model essentially replicates the microstructure of a cholesteric liquid crystal[2] as a stack of uniaxial plates of identical constitution and thickness. Each plate can be made by embedding parallel fibers lying normally to the thickness (i.e., the z) direction. Fibers in a given plate are offset by a fixed small angle in the xy plane with respect to the fibers—emulating the arrangement of aciculate molecules in a cholesteric liquid crystal—in the plate just below it, the fiber direction thus varying stepwise helicoidally along the z axis, which is the axis of spirality; see Fig. 1. At sufficiently low frequencies, the stepwise variation will appear to be continuous;[3] and the SCM can then be thought of as a smoothly nonhomogeneous continuum with helicoidally varying properties. Further generalization is also possible; thus a CTSCM can be conceived from anisotropic plates with other than uniaxial *reference symmetries*,[4] as also are piezoelectric CTSCM'sS (i.e., PCTSCM's).[5] The characteristics of axial propagation modes (i.e., $\partial/\partial x=0$ and $\partial/\partial y=0$) in CTSCM's and PCTSCM's with reference hexagonal 6mm crystal symmetry have been theoretically analyzed in the last two years.[6–8]

Early on, hope was held out[1] for a thick-film realization of CTSCM's and PCTSCM's, based on some experimental work of Motohiro and Taga[9] on thin films with oblique columnar fine structure. This proposal was examined further for helicoidal bianisotropic mediums (HBM's),[4] which are the electromagnetic/optical analogs of CTSCM's. The first thin-film HBM's were realized last year at the Alberta Microelectronic Centre.[10] These can be thought of as assemblies of almost identical ''bedsprings'' made of a ''wire'' with a diameter on the order of 5 nm and whose pitch is fabricated to be in the 50–500-nm range. The realization of thin-film HBM's initiated the concept of sculptured thin films (STF's) for optical, chemical, and biological applications described elsewhere.[11]

Thin-film techniques are generally unsuitable, but not always, for growing thick films. This is because films are systems far from equilibrium. As a result, internal stresses build up as a film grows, causing the film to break up or delaminate if it is allowed to become too thick. However, the bedspring morphology of thin-film HBM's prevents the buildup of internal stresses. This is because thin-film HBM's are highly porous, each bedspring being completely separated from its neighbors by void regions. Therefore, we have very recently been able to grow thin-film HBM's with up to 2000-nm pitches. Shown, for example, in Figs. 2 and 3 are scanning electron micrographs of MgF_2 sculptured thin films grown on silicon substrates at the Alberta Microelectronic Centre. Figure 2(a) and (b) shows a film composed of parallel one-turn bedsprings of pitch $\sim$1.2 μm. The two micrographs show two different views, of the same film, 90° apart from each other around a corner of the cleaved substrate. Figure 3(a) and (b) shows a three-turn sculptured thin film with a pitch $\sim$700 nm.

Experimental effort continues to produce thin-film HBM's of larger pitches, possibly $\sim$20 μm. Of course, the bedsprings in these large-pitch films shall then have wire

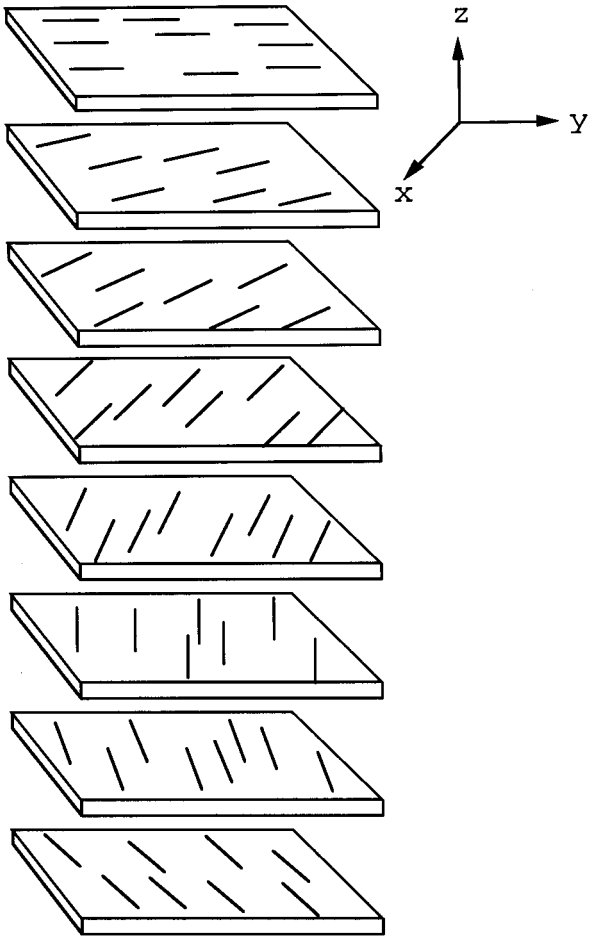

FIG. 1. To explain the conception of a particular structurally chiral medium (SCM). Identical fiber-reinforced composite plates with parallel fibers are transversely welded. Fiber directions in adjacent plates rotate in the transverse plane helicoidally. When the plate thickness is considerably less than the principal wavelengths, the SCM can be considered to be continuously twisted.

diameters ~100 nm. Let us hypothesize that a certain thin-film HBM is a continuum and suppose that a representative acoustic phase velocity in the film is ~500 m/s, close to that of air because of the film's high porosity. Let the film be acoustically excited at 50-MHz frequency. Then, a representative acoustic wavelength in the film is ~10 μm. As this wavelength is much larger than the bedspring wire diameter, our hypothesis of the film being a continuum is upheld. But this continuum is not homogeneous; instead it is a helicoidally nonhomogeneous medium, a CTSCM, in other words. Let us also note here that the void regions can be filled with some polymer or fluid to alter the film's acoustic response.

As we stated earlier, our experimental efforts to make large-pitch films continue, and we imagine that the fabrication of technologically significant CTSCM's and PCTSCM's is imminent. Theoretical progress is necessary to keep in step with materials technology. Therefore, our aim here is to construct a spectral Green's function for a PCTSCM, the corresponding result for any CTSCM being a subset thereof. Free wave propagation as well as source-excited time-harmonic fields in a PCTSCM are being handled here.

The plan of this paper is as follows: After assuming that $\partial/\partial x = i\kappa \cos\psi$, $\partial/\partial y = i\kappa \sin\psi$ and $\partial/\partial t = -i\omega$, in Sec. I, the elastodynamic and the electromagnetic field equations in a PCTSCM are converted into a set of field equations depending on z alone. The constitutive equations of the PCTSCM are also described in that section, and a transformation we have named after Oseen[12] is implemented on all relevant equations. A 10×10 matrix ordinary differential equation with nonconstant coefficients is formulated in Sec. II. Similar differential equations had been derived earlier for axial modes ($\kappa=0$),[5] and more recently for $\psi=0$,[13] when neither electric nor elastodynamic sources are present. An auxiliary differential equation is solved in terms of a uniformly convergent matrix polynomial in Sec. III. The solution of the auxiliary differential equation is used in Sec. IV to construct a Green's function in matrix form. This is a spectral Green's function as it depends on both κ and ψ, and is useful for both wave excitation and propagation problems. Its bilinear form definitely gives it a certain attraction for solving multilayered problems. With the formulation of the spectral Green's function, many problems can be attempted, with particular relevance to the technological exploitation of CTSCM's and PCTSCM's.

I. FIELD EQUATIONS AND CONSTITUTIVE EQUATIONS

Four differential equations crucially govern wave excitation and propagation in a piezoelectric medium. With an $\exp(-i\omega t)$ time dependence, and therefore in the frequency domain, these four equations may be stated as

$$\nabla\times\mathbf{E}(\mathbf{r}) = i\omega\mu_0\mathbf{H}(\mathbf{r}), \tag{1a}$$

$$\nabla\times\mathbf{H}(\mathbf{r}) = -i\omega\mathbf{D}(\mathbf{r}) + \mathbf{J}(\mathbf{r}), \tag{1b}$$

$$\nabla\cdot\mathsf{T}(\mathbf{r}) = -\rho\omega^2\mathbf{u}(\mathbf{r}) - \mathbf{F}(\mathbf{r}), \tag{1c}$$

$$\mathsf{S}(\mathbf{r}) = \tfrac{1}{2}[\nabla\mathbf{u}(\mathbf{r}) + \{\nabla\mathbf{u}(\mathbf{r})\}^t], \tag{1d}$$

where $\mathsf{T}(\mathbf{r})$ and $\mathsf{S}(\mathbf{r})$ are the stress and the strain tensors, respectively, at position $\mathbf{r}$; $\mathbf{u}(\mathbf{r})$ is the particle displacement vector and $\mathbf{F}(\mathbf{r})$ is the force vector; $\mathbf{E}(\mathbf{r})$, $\mathbf{D}(\mathbf{r})$, and $\mathbf{H}(\mathbf{r})$ are the electric field, the electric displacement, and the magnetic field vectors, respectively; $\mathbf{J}(\mathbf{r})$ is the electric current density vector; $\mu_0 = 4\pi\times10^{-7}$ H/m is the permeability of free space or vacuum and ρ is the mass density of the medium; while the superscript t denotes the transpose. Whereas $\mathbf{F}(\mathbf{r})$ is the elastodynamic source, $\mathbf{J}(\mathbf{r})$ is the electric source of time-harmonic waves.

Equations (1a)–(1d) are converted into matrix equations in the three steps outlined as follows: First, as our interest lies in oblique propagation with respect to the z axis, we can take the Fourier transforms of all tensors and vectors in Eqs. (1a)–(1d) with respect to x and y. Therefore, let us set

$$\mathsf{T}(\mathbf{r}) = e^{i\kappa_x x}e^{i\kappa_y y}\mathsf{T}(z), \tag{2a}$$

$$\mathbf{u}(\mathbf{r}) = e^{i\kappa_x x}e^{i\kappa_y y}\mathbf{u}(z), \tag{2b}$$

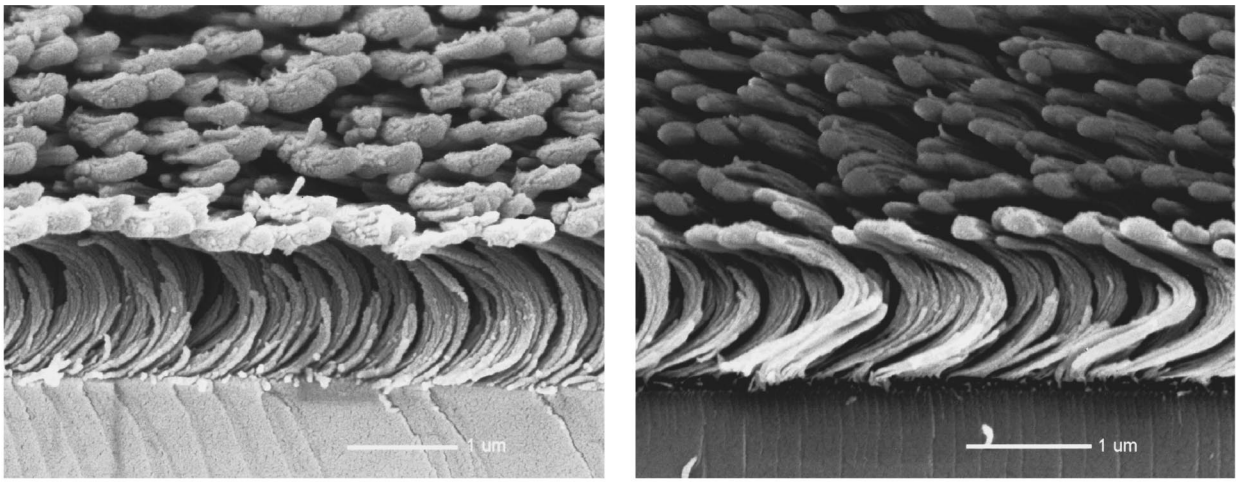

(a) (b)

FIG. 2. Scanning electron micrographs of a MgF_2 sculptured thin film on a silicon substrate. The film is made of 1-turn helices of pitch ~ 1.2 μm. The two views (a) and (b) are 90° apart from each other around a corner of the cleaved substrate.

etc., in Eqs. (1a)–(1d), $\kappa_x = \kappa \cos\psi$ and $\kappa_y = \kappa \sin\psi$ being the transversal wave numbers.

Second, employing the Kelvin notation as elaborated by Auld,[14] let us represent the two tensors by column six-vectors as follows:

$$[\mathbf{T}(z)] = [T_{xx}(z); T_{yy}(z); T_{zz}(z); T_{yz}(z); T_{xz}(z); T_{xy}(z)]^t, \tag{3a}$$

$$[\mathbf{S}(z)] = [S_{xx}(z); S_{yy}(z); S_{zz}(z); 2S_{yz}(z); 2S_{xz}(z); 2S_{xy}(z)]^t. \tag{3b}$$

The remaining field quantities are written as column three-vectors, e.g.,

$$[\mathbf{u}(z)] = [u_x(z); u_y(z); u_z(z)]^t. \tag{3c}$$

Third and finally, let us effect a transformation inspired by Oseen's visualization[12] of electromagnetic fields in a cholesteric liquid crystal: thus,[13]

$$[\mathbf{T}'(z)] = [\mathbf{R}(-z)][\mathbf{T}(z)], \tag{4a}$$

$$[\mathbf{S}'(z)] = [\mathbf{R}(z)]^t[\mathbf{S}(z)], \tag{4b}$$

for the stress and the strain column six-vectors, respectively, and[13]

$$[\mathbf{u}'(z)] = [\mathbf{A}(z)]^t[\mathbf{u}(z)], \tag{4c}$$

etc., for all column three-vectors. Here,

$$[\mathbf{A}(z)] = \begin{pmatrix} \cos\dfrac{\pi z}{\Omega} & -\sin\dfrac{\pi z}{\Omega} & 0 \\ \sin\dfrac{\pi z}{\Omega} & \cos\dfrac{\pi z}{\Omega} & 0 \\ 0 & 0 & 1 \end{pmatrix} \tag{5a}$$

is a rotation matrix and

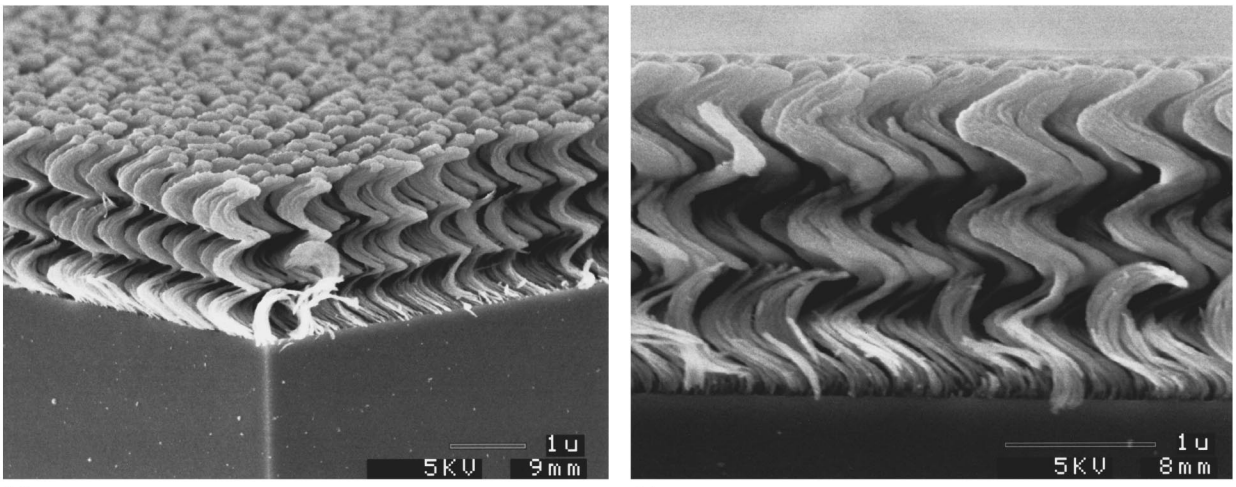

(a) (b)

FIG. 3. Scanning electron micrographs of a MgF_2 sculptured thin film on a silicon substrate. This film has 3 helical turns of pitch ~ 700 nm.

$$[\mathbf{R}(z)]=\begin{pmatrix} \cos^2\frac{\pi z}{\Omega} & \sin^2\frac{\pi z}{\Omega} & 0 & 0 & 0 & -\sin\frac{2\pi z}{\Omega} \\ \sin^2\frac{\pi z}{\Omega} & \cos^2\frac{\pi z}{\Omega} & 0 & 0 & 0 & \sin\frac{2\pi z}{\Omega} \\ 0 & 0 & 1 & 0 & 0 & 0 \\ 0 & 0 & 0 & \cos\frac{\pi z}{\Omega} & \sin\frac{\pi z}{\Omega} & 0 \\ 0 & 0 & 0 & -\sin\frac{\pi z}{\Omega} & \cos\frac{\pi z}{\Omega} & 0 \\ \frac{1}{2}\sin\frac{2\pi z}{\Omega} & -\frac{1}{2}\sin\frac{2\pi z}{\Omega} & 0 & 0 & 0 & \cos\frac{2\pi z}{\Omega} \end{pmatrix}. \tag{5b}$$

is the corresponding Bond matrix.[14] This step is necessary to accommodate the helicoidally varying constitutive properties of a PCTSCM shown later as Eqs. (8a) and (8b).

In consequence, Eqs. (1a)–(1d) may be rewritten in matrix-vector notation as

$$[\mathbf{\Sigma}_z]\frac{d}{dz}[\mathbf{E}'(z)]=\frac{\pi}{\Omega}[\mathbf{\Pi}][\mathbf{E}'(z)]-i\kappa[\mathbf{\Theta}(z)][\mathbf{E}'(z)]+i\omega\mu_0[\mathbf{H}'(z)], \tag{6a}$$

$$[\mathbf{\Sigma}_z]\frac{d}{dz}[\mathbf{H}'(z)]=\frac{\pi}{\Omega}[\mathbf{\Pi}][\mathbf{H}'(z)]-i\kappa[\mathbf{\Theta}(z)][\mathbf{H}'(z)]-i\omega[\mathbf{D}'(z)]+[\mathbf{J}'(z)], \tag{6b}$$

$$[\mathbf{\Lambda}_z]\frac{d}{dz}[\mathbf{T}'(z)]=\frac{\pi}{\Omega}[\mathbf{\Gamma}][\mathbf{T}'(z)]-i\kappa[\mathbf{\Phi}(z)][\mathbf{T}'(z)]-\rho\omega^2[\mathbf{u}'(z)]-[\mathbf{F}'(z)], \tag{6c}$$

$$[\mathbf{S}'(z)]=\frac{\pi}{\Omega}[\mathbf{\Gamma}]^t[\mathbf{u}'(z)]+i\kappa[\mathbf{\Phi}(z)]^t[\mathbf{u}'(z)]+[\mathbf{\Lambda}_z]^t\frac{d}{dz}[\mathbf{u}'(z)]. \tag{6d}$$

The following six matrices help keep the notation compact:

$$[\mathbf{\Lambda}_z]=\begin{pmatrix} 0 & 0 & 0 & 0 & 1 & 0 \\ 0 & 0 & 0 & 1 & 0 & 0 \\ 0 & 0 & 1 & 0 & 0 & 0 \end{pmatrix}, \tag{7a}$$

$$[\mathbf{\Sigma}_z]=\begin{pmatrix} 0 & -1 & 0 \\ 1 & 0 & 0 \\ 0 & 0 & 0 \end{pmatrix}, \tag{7b}$$

$$[\mathbf{\Gamma}]=\begin{pmatrix} 0 & 0 & 0 & 1 & 0 & 0 \\ 0 & 0 & 0 & 0 & -1 & 0 \\ 0 & 0 & 0 & 0 & 0 & 0 \end{pmatrix}, \tag{7c}$$

$$(\mathbf{\Pi})=\begin{pmatrix} 1 & 0 & 0 \\ 0 & 1 & 0 \\ 0 & 0 & 0 \end{pmatrix}, \tag{7d}$$

$$[\mathbf{\Phi}(z)]=\begin{pmatrix} \cos\left(\frac{\pi z}{\Omega}-\psi\right) & 0 & 0 & 0 & 0 & -\sin\left(\frac{\pi z}{\Omega}-\psi\right) \\ 0 & -\sin\left(\frac{\pi z}{\Omega}-\psi\right) & 0 & 0 & 0 & \cos\left(\frac{\pi z}{\Omega}-\psi\right) \\ 0 & 0 & 0 & -\sin\left(\frac{\pi z}{\Omega}-\psi\right) & \cos\left(\frac{\pi z}{\Omega}-\psi\right) & 0 \end{pmatrix}, \tag{7e}$$

$$[\mathbf{\Theta}(z)]=\begin{pmatrix} 0 & 0 & -\sin\left(\frac{\pi z}{\Omega}-\psi\right) \\ 0 & 0 & -\cos\left(\frac{\pi z}{\Omega}-\psi\right) \\ \sin\left(\frac{\pi z}{\Omega}-\psi\right) & \cos\left(\frac{\pi z}{\Omega}-\psi\right) & 0 \end{pmatrix}. \tag{7f}$$

The frequency-domain constitutive equations of a PCTSCM may be stated in matrix-vector notation as

$$[\mathbf{D}(z)]=[\mathbf{A}(z)][\boldsymbol{\epsilon}'][\mathbf{A}(z)]^t[\mathbf{E}(z)] + [\mathbf{A}(z)][\mathbf{e}'][\mathbf{R}(z)]^t[\mathbf{S}(z)], \tag{8a}$$

$$[\mathbf{T}(z)]=-[\mathbf{R}(z)][\mathbf{e}']^t[\mathbf{A}(z)]^t[\mathbf{E}(z)] + [\mathbf{R}(z)][\mathbf{c}'][\mathbf{R}(z)]^t[\mathbf{S}(z)], \tag{8b}$$

where the 3×3 *reference permittivity* matrix $[\boldsymbol{\epsilon}']$, the 6×6 *reference stiffness* matrix $[\mathbf{c}']$, and the 3×6 *reference piezoelectric stress* matrix $[\mathbf{e}']$ denote the constitutive properties of the PCTSCM in the reference plane $z=0$. The helicoidal variation of the constitutive properties along the z axis is captured by the matrices $[\mathbf{A}(z)]$ and $[\mathbf{R}(z)]$ in Eqs. (8a) and (8b). On implementing the Oseen transformation described by Eqs. (4a)–(4c), we obtain

$$[\mathbf{D}'(z)]=[\boldsymbol{\epsilon}'][\mathbf{E}'(z)]+[\mathbf{e}'][\mathbf{S}'(z)], \tag{9a}$$

$$[\mathbf{T}'(z)]=-[\mathbf{e}']^t[\mathbf{E}'(z)]+[\mathbf{c}'][\mathbf{S}'(z)], \tag{9b}$$

from Eqs. (8a) and (8b).

II. MATRIX DIFFERENTIAL EQUATION

The next step in our analysis is to eliminate $[\mathbf{D}'(z)]$ and $[\mathbf{S}'(z)]$ from Eqs. (6a)–(6d), (9a), and (9b). Implementing that step, we obtain the four matrix equations,

$$[\boldsymbol{\Sigma}_z]\frac{d}{dz}[\mathbf{E}'(z)]=\frac{\pi}{\Omega}[\boldsymbol{\Pi}][\mathbf{E}'(z)]-i\kappa[\boldsymbol{\Theta}(z)][\mathbf{E}'(z)] + i\omega\mu_0[\mathbf{H}'(z)], \tag{10a}$$

$$[\boldsymbol{\Sigma}_z]\frac{d}{dz}[\mathbf{H}'(z)]=\frac{\pi}{\Omega}[\boldsymbol{\Pi}][\mathbf{H}'(z)]-i\kappa[\boldsymbol{\Theta}(z)][\mathbf{H}'(z)] - i\omega[\tilde{\boldsymbol{\epsilon}}'][\mathbf{E}'(z)]-i\omega[\mathbf{d}'][\mathbf{T}'(z)] + [\mathbf{J}'(z)], \tag{10b}$$

$$[\boldsymbol{\Lambda}_z]\frac{d}{dz}[\mathbf{T}'(z)]=\frac{\pi}{\Omega}[\boldsymbol{\Gamma}][\mathbf{T}'(z)]-i\kappa[\boldsymbol{\Phi}(z)][\mathbf{T}'(z)] - \rho\omega^2[\mathbf{u}'(z)]-[\mathbf{F}'(z)], \tag{10c}$$

$$[\boldsymbol{\Lambda}_z]^t\frac{d}{dz}[\mathbf{u}'(z)]=-\frac{\pi}{\Omega}[\boldsymbol{\Gamma}]^t[\mathbf{u}'(z)] - i\kappa[\boldsymbol{\Phi}(z)]^t[\mathbf{u}'(z)]+[\mathbf{s}'][\mathbf{T}'(z)] + [\mathbf{d}']^t[\mathbf{E}'(z)], \tag{10d}$$

whose left sides alone contain the derivatives with respect to z. Here, the auxiliary constitutive matrices,

$$[\tilde{\boldsymbol{\epsilon}}']=[\boldsymbol{\epsilon}']+[\mathbf{e}'][\mathbf{c}']^{-1}[\mathbf{e}']^t, \tag{11a}$$

$$[\mathbf{s}']=[\mathbf{c}']^{-1}, \tag{11b}$$

$$[\mathbf{d}']=[\mathbf{e}'][\mathbf{c}']^{-1}, \tag{11c}$$

have been defined for simplicity and we have used the fact that $[\mathbf{c}']$ is symmetric.

Equations (10a)–(10d) together amount to a system of ten ordinary differential equations and five purely algebraic equations. Each one of the Oseen-transformed source components $F'_x(z)$, $F'_y(z)$, $F'_z(z)$, $J'_x(z)$, and $J'_y(z)$ appears in a differential equation; $J'_z(z)$ appears in an algebraic equation; while five differential equations and four algebraic equations are sourceless. The ten differential equations are distinguished by their involvement of the first derivatives of $E'_x(z)$, $E'_y(z)$, $H'_x(z)$, $H'_y(z)$, $u'_x(z)$, $u'_y(z)$, $u'_z(z)$, $T'_{xz}(z)$, $T'_{yz}(z)$, and $T'_{zz}(z)$ with respect to z. The five algebraic equations may be used to eliminate $E'_z(z)$, $H'_z(z)$, $T'_{xx}(z)$, $T'_{xy}(z)$, and $T'_{yy}(z)$ from the differential equations. This elimination may be carried out provided the algebraic system is nonsingular. As no specific crystallographic symmetries have been assumed for $[\boldsymbol{\epsilon}']$, $[\mathbf{c}']$, and $[\mathbf{e}']$, the general condition for nonsingularity is too cumbersome for reproduction here.

After stipulating that the five algebraic equations are linearly independent, the ten differential equations may be written compactly as the 10×10 matrix differential equation

$$\frac{d}{dz}[\mathbf{f}(z)]=i[\mathbf{Q}'(z)][\mathbf{f}'(z)]+[\mathbf{L}'(z)][\mathbf{g}'(z)], \tag{12}$$

where the column ten-vector $[\mathbf{f}'(z)]$ is given by

$$[\mathbf{f}'(z)]=[E'_x(z);E'_y(z);H'_x(z);H'_y(z);u'_x(z);u'_y(z); u'_z(z);T'_{xz}(z),T'_{yz}(z);T'_{zz}(z)]^t, \tag{13a}$$

and the column six-vector $[\mathbf{g}'(z)]$ contains the sources:

$$[\mathbf{g}'(z)]=[F'_x(z);F'_y(z);F'_z(z);J'_x(z);J'_y(z);J'_z(z)]^t. \tag{13b}$$

The 10×10 matrix $[\mathbf{Q}'(z)]$ and the 10×6 matrix $[\mathbf{L}'(z)]$ are far too huge for reproduction here but were ascertained using MATHEMATICA™, and can be easily obtained by interested reader using commonplace symbolic manipulation programs. More importantly, MATHEMATICA™ helped establish the structure of $[\mathbf{Q}'(z)]$ as

$$[\mathbf{Q}'(z)]=[\mathbf{P}]+\kappa(e^{i\xi}[\mathbf{W}_1]+e^{-i\xi}[\mathbf{W}_2])+\kappa^2([\mathbf{W}_3] + e^{i2\xi}[\mathbf{W}_4]+e^{-i2\xi}[\mathbf{W}_5]) \tag{14}$$

for any PCTSCM, where all six 10×10 matrices $[\mathbf{P}]$ and $[\mathbf{W}_l]$ $(1\leqslant l\leqslant5)$, are independent of z, κ, and ψ, but not necessarily of Ω; while

$$\xi=\frac{\pi z}{\Omega}-\psi. \tag{15}$$

Our interest now is in finding the solution $[\mathbf{f}'(z)]$ of Eq. (12) when $[\mathbf{g}'(z)]$ is prescribed.

III. AUXILIARY DIFFERENTIAL EQUATION

Let us commence on the solution of Eq. (12) by determining a nonsingular matrix $[\mathbf{M}'(z)]$ that satisfies the auxiliary matrix differential equation

$$(d/dz)[\mathbf{M}'(z)]=i[\mathbf{Q}'(z)][\mathbf{M}'(z)], \tag{16}$$

subject to the boundary condition $[\mathbf{M}'(0)]=[\mathbf{I}]$, where $[\mathbf{I}]$ is the 10×10 identity matrix.

The matrix $[\mathbf{Q}'(z)]$ is holomorphic in z. In fact, if we rewrite Eq. (14) as the polynomial expansion

$$[\mathbf{Q}'(z)]=\sum_{m=0}^{\infty}[\mathbf{Q}'_m]z^m, \tag{17}$$

the right side of Eq. (17) is uniformly convergent for all z. The constant matrices used in this expansion are the following ones:

$$[\mathbf{Q}'_0]=[\mathbf{P}]+\kappa(e^{-i\psi}[\mathbf{W}_1]+e^{i\psi}[\mathbf{W}_2])+\kappa^2([\mathbf{W}_3]+e^{-i2\psi}[\mathbf{W}_4]+e^{i2\psi}[\mathbf{W}_5]), \tag{18a}$$

$$[\mathbf{Q}'_{2m+1}]=\frac{(i\pi/\Omega)^{2m+1}}{(2m+1)!}[\kappa(e^{-i\psi}[\mathbf{W}_1]-e^{i\psi}[\mathbf{W}_2])+2^{2m+1}\kappa^2(e^{-i2\psi}[\mathbf{W}_4]-e^{i2\psi}[\mathbf{W}_5])]\quad(m=0,1,2,3,\ldots), \tag{18b}$$

$$[\mathbf{Q}'_{2m}]=\frac{(i\pi/\Omega)^{2m}}{(2m)!}[\kappa(e^{-i\psi}[\mathbf{W}_1]+e^{i\psi}[\mathbf{W}_2])+2^{2m}\kappa^2(e^{-i2\psi}[\mathbf{W}_4]+e^{i2\psi}[\mathbf{W}_5])]\quad(m=1,2,3,\ldots). \tag{18c}$$

The solution of Eq. (16) is the polynomial expansion[15]

$$[\mathbf{M}'(z)]=\sum_{m=0}^{\infty}[\mathbf{R}_m]z^m, \tag{19}$$

which is also convergent for all z. The matrices $[\mathbf{R}_m]$ have to be calculated from the recurrence relation[15]

$$(m+1)[\mathbf{R}_{m+1}]=i\sum_{n=0}^{m}[\mathbf{Q}'_{m-n}][\mathbf{R}_n]\quad(m=0,1,2,3,\ldots), \tag{20}$$

beginning with $[\mathbf{R}_0]=[\mathbf{M}'(0)]=[\mathbf{I}]$. In practice, the infinite summation on the right side of Eq. (17) would have to be suitably truncated. However, $[\mathbf{M}'(z)]$ can be computed to an arbitrary degree of precession because the right side of Eq. (19) is uniformly convergent for all z. In addition, the normalization of z with respect to the magnitude of the largest-in-magnitude eigenvalue of $[\mathbf{P}]$ shall assist in stabilizing the computation of $[\mathbf{R}_m]$ as m increases in Eq. (20). Efficient computation would also entail the use of convergence acceleration techniques of the kind discussed by Brezinski and Redivo Zaglia,[16] and shall be addressed in future publications.

IV. SPECTRAL GREEN'S FUNCTION

We are now ready to solve Eq. (12) in order to determine $[\mathbf{f}(z)]$ due to a given $[\mathbf{g}'(z)]$. The solution will naturally yield a spectral Green's function in bilinear form.

After assuming that $[\mathbf{M}'(z)]$ is nonsingular and using $[\mathbf{M}'(z)]^{-1}[\mathbf{M}'(z)]=[\mathbf{I}]$, the adjoint of Eq. (16) can be stated as follows:

$$\frac{d}{dz}[\mathbf{M}'(z)]^{-1}=-i[\mathbf{M}'(z)]^{-1}[\mathbf{Q}'(z)]. \tag{21}$$

Now

$$\frac{d}{dz}\{[\mathbf{M}'(z)]^{-1}[\mathbf{f}'(z)]\}=\left\{\frac{d}{dz}[\mathbf{M}'(z)]^{-1}\right\}[\mathbf{f}'(z)]+[\mathbf{M}'(z)]^{-1}\left\{\frac{d}{dz}[\mathbf{f}'(z)]\right\}, \tag{22}$$

which simplifies to

$$\frac{d}{dz}\{[\mathbf{M}'(z)]^{-1}[\mathbf{f}'(z)]\}=[\mathbf{M}'(z)]^{-1}[\mathbf{L}'(z)][\mathbf{g}'(z)], \tag{23}$$

on using Eqs. (12) and (21).

Equation (23) is a simple first-order matrix differential equation with a known right side. Its solution may be stated as

$$[\mathbf{M}'(z)]^{-1}[\mathbf{f}'(z)]=[\mathbf{M}'(0)]^{-1}[\mathbf{f}'(0)]+\int_0^z[\mathbf{M}'(\zeta)]^{-1}[\mathbf{L}'(\zeta)][\mathbf{g}'(\zeta)]d\zeta, \tag{24}$$

where $[\mathbf{f}'(0)]$ is the boundary value. Furthermore, as $[\mathbf{M}'(0)]=[\mathbf{I}]$, we obtain the solution of Eq. (12) as follows:

$$[\mathbf{f}'(z)]=[\mathbf{M}'(z)][\mathbf{f}'(0)]+[\mathbf{M}'(z)]\int_0^z[\mathbf{M}'(\zeta)]^{-1}[\mathbf{L}'(\zeta)][\mathbf{g}'(\zeta)]d\zeta. \tag{25}$$

The first term on the right side of Eq. (25) is the standard complementary function, while the second term is the particular integral. Once the right side of Eq. (25) becomes available, we can recover $E'_z(z)$, $H'_z(z)$, $T'_{xx}(z)$, $T'_{xy}(z)$, and $T'_{yy}(z)$ from the five algebraic equations that are represent in Eqs. (10a)–(10d). Inverting the Oseen transformation, we can then get $[\mathbf{T}(z)]$, $[\mathbf{u}(z)]$, etc.

The variable z in Eq. (25) can be negative, zero, or positive, while the plane $z=0$ can be positioned as desired. Therefore, we are able to define a *spectral Green's function* in the form of a matrix as

$$[\mathbf{G}'(z,\zeta)]=[\mathbf{M}'(z)][\mathbf{M}'(\zeta)]^{-1}, \tag{26}$$

and compactly state the complete solution of Eq. (12) as

$$[\mathbf{f}'(z)]=[\mathbf{G}'(z,0)][\mathbf{f}'(0)]+\int_0^z[\mathbf{G}'(z,\zeta)][\mathbf{L}'(\zeta)]\times[\mathbf{g}'(\zeta)]d\zeta. \tag{27}$$

The first term on the right side of (27) is appropriate for propagation problems, the second for excitation problems.

V. CONCLUDING REMARKS

A square matrix can always be interpreted as a dyadic.[17] as $[\mathbf{G}'(z,\zeta)]$ is a composition of two square matrices, it can therefore be interpreted as a tetradic.[17] Very significantly, this tetradic has a bilinear form, with one matrix dependent on the field point z and the other on the source point ζ. This

bilinear form is very attractive for solving multilayered media and grating problems.[18–20] Multilayered transducer geometries can now be explored, particularly for sensing elastodynamic waves incident obliquely on a transducer face. Very significantly, the concept of sculptured thin films, that originated in optics, can now be extended to elastodynamics and acousto-optics.

[1] A. Lakhtakia, ''Elastodynamic wave propagation in a continuously twisted structurally chiral medium along the axis of spirality,'' J. Acoust. Soc. Am. **95**, 597–600 (1994); erratum: **95**, 3669 (1994).

[2] P. G. de Gennes and J. Prost, *The Physics of Liquid Crystals* (Clarendon, Oxford, 1993).

[3] W. S. Weiglhofer and A. Lakhtakia, ''Electromagnetic wave propagation in super-cholesteric materials parallel to the helical axis,'' J. Phys. D: Appl. Phys. **26**, 2117–2122 (1993).

[4] A. Lakhtakia and W. S. Weiglhofer, ''On light propagation in helicoidal bianisotropic mediums,'' Proc. R. Soc. London, Ser. A **438**, 419–437 (1995).

[5] A. Lakhtakia, ''Wave propagation in a piezoelectric, continuously twisted, structurally chiral medium along the axis of spirality,'' Appl. Acoust. **44**, 25–37 (1995); errata: **44**, 385 (1995).

[6] S. F. Nagle, A. Lakhtakia, and W. Thompson, Jr., ''Modal structures for axial wave propagation in a continuously twisted structurally chiral medium (CTSCM),'' J. Acoust. Soc. Am. **97**, 42–50 (1995).

[7] S. F. Nagle and A. Lakhtakia, ''Shear axial modes in a PCTSCM. Part I: piezoelectric stiffening and selective attenuation,'' Sensors and Actuators A: Physical **49**, 195–201 (1995); errata: **55**, 229 (1996).

[8] S. F. Nagle and A. Lakhtakia, ''Shear axial modes in a PCTSCM. Part II: towards transduction applications,'' Sensors and Actuators A: Physical **55**, 139–147 (1996).

[9] T. Motohiro and Y. Taga, ''Thin film retardation plate by oblique deposition,'' Appl. Opt. **28**, 2466–2482 (1989).

[10] K. Robbie, M. J. Brett, and A. Lakhtakia, ''First thin film realization of a helicoidal bianisotropic medium,'' J. Vac. Sci. Technol. A **13**, 2991–2993 (1995).

[11] A. Lakhtakia, R. Messier, M. J. Brett, and K. Robbie, ''Sculptured thin films (STFs) for optical, chemical and biological applications,'' Innov. Mater. Res. **1**, 165–176 (1996).

[12] C. W. Oseen, ''The theory of liquid crystals,'' J. Chem. Soc. Faraday Trans. II **29**, 883–899 (1933).

[13] A. Lakhtakia, ''Exact analytic solution for oblique propagation in a piezoelectric, continuously twisted, structurally chiral medium,'' Appl. Acoust. **49**, 225–236 (1996).

[14] B. A. Auld, *Acoustic Fields and Waves in Solids* (Krieger, Malabar, FL, 1990), Vol. I.

[15] H. Hochstadt, *Differential Equations—A Modern Approach* (Dover, New York, 1975).

[16] C. Brezinski and M. Redivo Zaglia, *Extrapolation Methods: Theory and Practice* (North-Holland, Amsterdam, 1991).

[17] P. M. Morse and H. Feshbach, *Methods of Theoretical Physics* (McGraw-Hill, New York, 1953), Vol. I.

[18] V. K. Varadan, A. Lakhtakia, V. V. Varadan, and C. A. Langston, ''Radiation characteristics of elastodynamic line sources buried in layered media with periodic interfaces. I. SH-wave analysis,'' Bull. Seismol. Soc. Am. **77**, 2181–2191 (1987).

[19] V. K. Varadan, A. Lakhtakia, V. V. Varadan, and C. A. Langston, ''Radiation characteristics of elastodynamic line sources buried in layered media with periodic interfaces. II. *P*- and *SV*-wave analysis,'' Bull. Seismol. Soc. Am. **77**, 2192–2211 (1987).

[20] A. Lakhtakia, V. K. Varadan, and V. V. Varadan, ''Excitation of layered media having rough interfaces by line sources,'' IEEE Trans. Antennas Propag. **35**, 462–466 (1987).

Vibratory power flow through a nonlinear path into a resonant receiver

T. J. Royston[a)]
Vibrations and Acoustics Laboratory, Department of Mechanical Engineering, The University of Illinois at Chicago, Chicago, Illinois 60607-7022

R. Singh
Acoustics and Dynamics Laboratory, Department of Mechanical Engineering, The Ohio State University, Columbus, Ohio 43210-1107

(Received 20 June 1996; accepted for publication 2 December 1996)

Vibratory power flow through a nonlinear path into a resonant receiver is considered via a specific vibration isolation example case, the automotive hydraulic engine mount. System equations for the source—nonlinear path—receiver system are developed based on prior experimental and analytical studies. For periodic excitation, an efficient solution method is formulated for the calculation of the steady-state stable response using a multi-term harmonic balance approach with condensation and continuation. In this computational study it is shown that, while modeling the isolation path with a ''softened'' nonlinear expression may only moderately alter the predicted system behavior at the excitation harmonic, it can significantly alter it at higher harmonics. Computational studies of multi-harmonic motion and power transmission show that audible structure-borne noise may be generated from subaudio frequency excitations due to path nonlinearities. It is also observed that support base (receiver) resonances can significantly affect the overall dynamic behavior. For instance, with a multi-degree-of-freedom base model, significant levels of vibratory energy at higher harmonics of the excitation are transmitted through the path, especially when these harmonics coincide with the natural frequencies of the receiver. [S0001-4966(97)04504-9]

PACS numbers: 43.40.At, 43.25.Ts, 43.40.Tm [CBB]

INTRODUCTION

Fundamental studies of vibration isolation in *linear* systems have shown that compliant support structure dynamics can significantly affect the performance.[1–7] For example, it has been observed that the vibratory power flow into the support base is directly related to its mobility[1–5] and the mobilities of the source and path, as well.[2,3] It has also been determined that power flow for the general isolator configuration is multi-dimensional including translational force and rotational moment coupling paths.[1,4–6] In fact, coupling mobility functions between these paths play a significant role in overall isolator performance.[5] Some investigators have shown that spectrally averaged behavior can be approximated for finite beam and platelike structures by replacing them with mobility expressions of corresponding infinite structures.[1–5] However, unique behavior at resonant conditions is then missed, especially near the first few system natural frequencies where peak power flow occurs.[3–6] Also, if active vibration isolation were to be attempted, lightly damped support base resonances with minimal modal overlap could have a detrimental effect on the stability of feedback control schemes.[7]

In compliant base (receiver) problems, the most appropriate measure with which to define isolation from a source to the receiver is vibratory power flow which accounts for both force and motion characteristics.[1–6] However, the problem of determining vibratory power flow through a *nonlinear* isolator path to a compliant, linear receiver is more complex. Here, the relationship between path and receiver mobilities can be excitation amplitude dependent and the dynamic response may have a wide spectral content, even for harmonic excitation.[8] Consequently, significant vibratory energy transmission may occur in a critical audio frequency range, even if the excitation source contains only lower-frequency components. Additionally, it is computationally difficult to analyze the complete system including the nonlinear path and compliant support base, especially when the base model is of high dimension. Traditionally, investigators have either focused on the localized nonlinear path while ignoring receiver dynamics or have resorted to a linear analysis of the complete system.

Compliant receiver problems commonly occur in vehicle applications where weight reduction for fuel efficiency consideration results in relatively flexible supporting frames.[9–11] It is also common to find that the isolation path between the excitation source and the compliant receiver contains significant, physically localized nonlinear elements.[12–14] As a practical illustration, consider the automotive hydraulic engine mount system of Fig. 1 which will serve as the primary example case in this article. A detailed cut-away of the mount is shown in Fig. 2. Construction details and other features may be found in the Ref. 13. Here, only vertical translational motion is being considered but the concepts introduced can easily be extended to the multi-

[a)]Corresponding Author Tel: (312) 413-7951, Fax: (312) 413-0447; Electronic mail: troyston@uic.edu

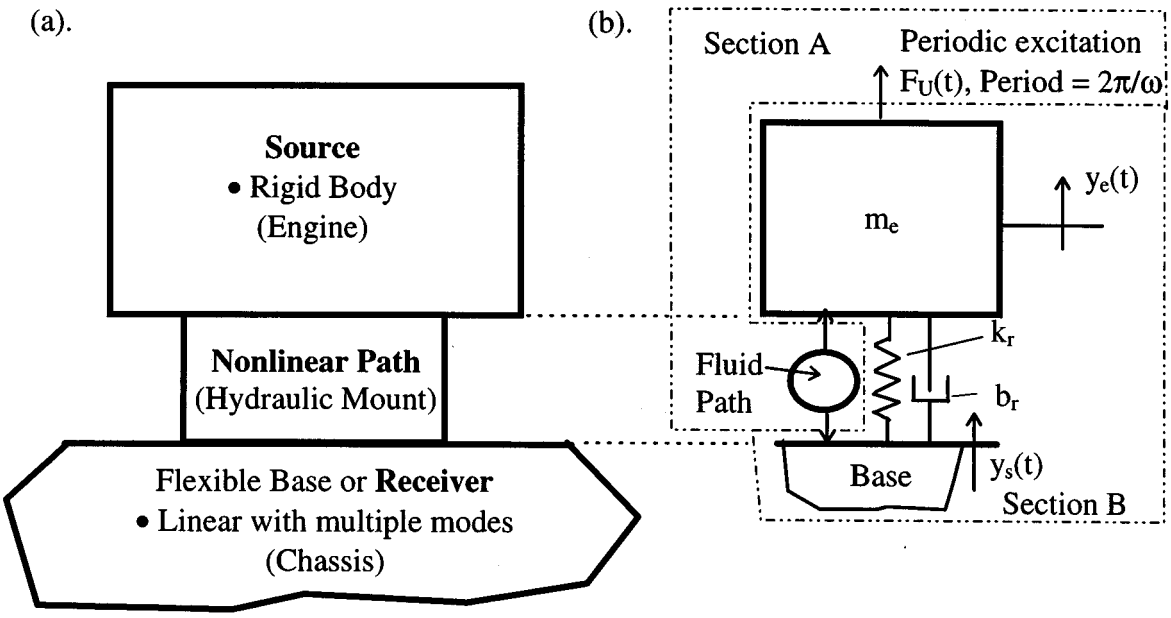

FIG. 1. Engine mount system.

dimensional case. The engine is assumed to be driven by a periodic vertical excitation force $F_U(t)$ of fundamental frequency ω, say representing imbalance forces. (Use of this simplistic model for unbalance force does have repercussions which will be discussed.) The engine is modeled as a rigid body and at the connection point to the mount, vertical motion is given by y_e. The vehicle chassis or support base is modeled using a linear multi-degree-of-freedom (MDOF) formulation and vertical displacement at the connection point to the mount is denoted as y_s.

Robustly modeling the hydraulic mount for a wide range of operating conditions requires a nonlinear description for several of its dynamic characteristics.[12] Recent studies by Kim and Singh[13] and Colgate *et al.*[14] have specifically focused on the strong nonlinearities associated with the decoupler. Such studies have employed the direct time domain numerical integration method which obviously is time consuming and may not lead to much physical insight. Additionally, if one also wishes to understand the coupled interaction of the engine mount with a compliant receiver, one has the increasingly difficult task of simultaneously integrating numerous coupled differential equations.

A common method of experimentally assessing the mount's isolation performance has been via dynamic stiffness in the frequency domain.[12,14] Some articles, in the context of a simplified vehicle model, have also used accelerance, chassis acceleration, force transmissibility and other motion and force related frequency response criteria.[12,13] All of these descriptors essentially assume the system is linear and they intentionally ignore response at frequencies other than the primary excitation frequency based on the ''low-pass filter'' argument. If the nonlinearity is very localized in the isolation path and there is sufficient damping in the system, then other frequency components of its response, assumed to be at higher harmonics, could be attenuated by the inherent low-pass filtering effect of inertial systems. This implies that subharmonic behavior is not present.

It is clear that a more fundamental study of vibratory power flow through a nonlinear path into a resonant receiver is needed. The hydraulic engine mounting system is an appropriate and practical example of such a situation. In a recent article by the authors,[15] a computational strategy based on the Galerkin method was proposed for an efficient analysis of complex mechanical systems with local nonlinearities. In the present article, this approach is extended to the rigid body source—nonlinear isolation path—compliant receiver

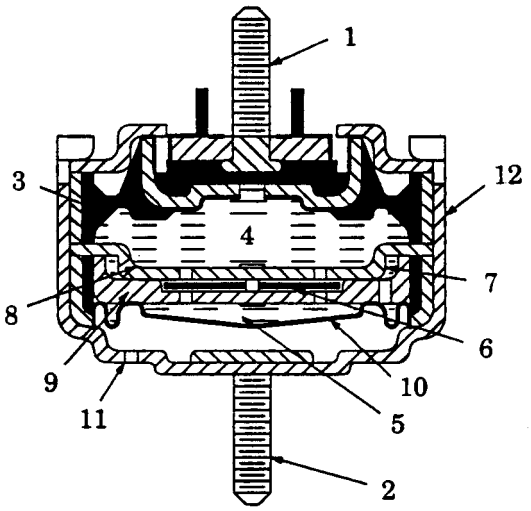

FIG. 2. Engine mount components. (1) and (2) mounting studs; (3) rubber which supports engine weight; (4) upper and (5) lower chambers filled with glycol fluid mixture; (6) decoupler; (7) inertia track; (8) upper and (9) lower plates which define decoupler gap; (10) lower chamber thin rubber bellow; (11) air breather; and (12) canister. See Kim and Singh (Ref. 13) for a more complete description.

TABLE I. Parameter values for engine mounting system.

$A_1=A_2=0.2726$ cm^2	$k_s=2\times10^4$ N/m	$p_{\text{atm}}=101.232$ kPa
$A_d=2.3\times10^{-3}$ m^2	$l_1=16.1$ cm, $l_2=5$ cm	$\rho_g=1.059\times10^{-3}$ kg/cm^3
$A_p=5.027\times10^{-3}$ m^2	$\eta_1=1.9\times10^{-3}$ kPa s^2/cm^3	$\overline{V_1}=0.715$ cm^3
$b_r=1000$ N s/m	$\eta_2=3.4\times10^{-3}$ kPa s^2/cm^3	$\overline{V_2}=28.251$ cm^3
$b_s=1400$ N s/m	$m_s=270$ kg	$\overline{V_{\text{air}}}=4$ cm^3
$C_{de}=0.65$	$m_e=122.7$ kg	$\omega_s=\sqrt{k_s/m_s}$
$k_r=2.7\times10^5$ N/m	$\overline{p}=116.4$ kPa	$\zeta_s=b_s/2\sqrt{k_s m_s}$

problem. The impact of ''softening'' the nonlinearity on predicted system response is investigated and isolation performance is assessed via calculation of total (multi-harmonic) vibratory power flow for harmonic excitation conditions. While the hydraulic engine mounting system serves as the primary example, the results should be conceptually applicable to many practical situations. Nonetheless, one must recognize that specific nonlinear path(s) must be carefully considered within the context of a system problem as illustrated in this article.

I. SYSTEM EQUATIONS

The physical system and theoretical model described below are based on papers co-authored by Kim and Singh[12,13] covering theoretical and experimental studies of production-grade hydraulic mounts. For periodic excitation at frequency ω, system response is assumed to be periodic with superharmonic content up to the N_pth order and subharmonic content up to the N_bth order. Kim and Singh's model was only experimentally validated for excitation frequencies below 50 Hz and this limitation is obeyed here. Equations are written as a function of the nondimensional time variable $\tau=\omega t/N_b$ or in terms of their frequency response at $\omega_n'=n\omega/N_b$, $n=1,\ldots,N_bN_p$. Governing equations are defined around static equilibria; hence, the static (gravitational) force is not present in the following formulation. Stiffness and damping elements, k_r and b_r, respectively, account for the rubber portion of the mount. They are shown schematically in Fig. 1. They are moderately nonlinear and are typically given as frequency-dependent parameters. Nominal values are provided in Table I. Since their amplitude dependence is minimal, the force associated with the mount rubber at a particular response frequency ω_n' can be expressed as follows where $j=\sqrt{-1}$:

$$F_r(\omega_n')=\left[\, j\,\frac{\omega_n'}{N_b}\, b_r(\omega_n')+k_r(\omega_n')\right][y_e(\omega_n')-y_s(\omega_n')]. \tag{1}$$

The fluid portion of the mount consists of upper and lower liquid-filled chambers connected via a large decoupler orifice and an inertia track. The inertia track refers to two relatively long and narrow fluid paths with significant inertial and damping properties. The inertia track acts as a vibration absorber tuned to the fundamental engine mounting resonance, providing inertia-augmented damping. For small amplitude excitation, the decoupler orifice is always open and essentially ''short circuits'' the inertia track. For larger amplitude motion, a plate in the decoupler orifice bottoms out and restricts flow for portions of the vibratory cycle, forcing fluid to flow through the inertia track.

The force from the fluid components acting on the engine and chassis is given by the following expression where A_p refers to the mount's equivalent fluid piston area, p_1 denotes its upper chamber fluid pressure, and $\overline{p}$ is the static equilibrium pressure in the fluid chambers:

$$F_f(\tau)=A_p[p_1(\tau)-\overline{p}]. \tag{2}$$

Newton's law applied to the engine mass, m_e, leads to the following:

$$\frac{\omega^2}{N_b^2}\, m_e\ddot{y}_e(\tau)=F_u(\tau)+F_f(\tau)-F_r(\tau). \tag{3}$$

First-order nonlinear differential equations describe the relationship between the pressure differential between the lower (2) and upper (1) fluid chambers and the resulting flow q_i through each inertia path, $i=1,2$:

$$\frac{N_b}{\omega I_i}\,[p_2(\tau)-p_1(\tau)]-\frac{\eta_i N_b}{I_i\omega}\, q_i(\tau)^2\ \text{sign}[q_i(\tau)]-\dot{q}_i(\tau) =0. \tag{4}$$

Here, $\dot{}$ denotes $d/d\tau$, $I_i=\rho_g l_i/A_i$ is the effective fluid inertia, and η_i is an experimentally measured fluid resistance parameter. Also, ρ_g refers to the mount fluid density, l_i denotes the ith inertia track length, and A_i is ith inertia track cross-sectional area. Flow through the decoupler orifice q_d is given by a similar nonlinear first-order differential equation:

$$\frac{N_b}{\omega I_d}\,[p_2(\tau)-p_1(\tau)]-\frac{\eta_d(\tau)N_b}{\omega I_d}\, q_d(\tau)^2\ \text{sign}[q_d(\tau)] -\dot{q}_d(\tau)=0, \tag{5}$$

where the expression for η_d is based on a turbulent flow assumption:

$$\eta_d(\tau)=\left(\frac{1}{C_{de}A_{de}(\tau)}\right)^2\frac{\rho_g}{2}, \tag{6}$$

with C_{de} denoting the discharge coefficient and $A_{de}(\tau)$ denoting the effective decoupler area. A kinematic model of the decoupler behavior is as follows. In the decoupled state, $A_{de}(\tau)=A_d$, and in the coupled state, $A_{de}(\tau)=0$, i.e., $q_d(\tau)=0$. The total volume flow through the decoupler orifice is denoted as v_d. Thus, we have $\dot{v}_d(\tau)=q_d(\tau)$. The decoupler free volume gap is given by $V_{\text{gap}}=A_d\Delta_d$, where Δ_d is the decoupler path length. At static equilibrium, the decoupler plate floats in the center. Hence, for $|v_d|\leqslant V_{\text{gap}}/2$ the decoupler plate does not block flow and $A_{de}(\tau)=A_d$. Under cyclic loading, starting from the equilibrium position, a positive pressure differential $[p_2(\tau)-p_1(\tau)]>0$ will result in an increase in $v_d(\tau)$. When $v_d(\tau)=V_{\text{gap}}/2$, $A_{de}(\tau)=0$ and hence v_d will not exceed $V_{\text{gap}}/2$. When the direction of flow reverses and $[p_1(\tau)-p_2(\tau)]<0$, the decoupler plate becomes unseated and again $A_{de}(\tau)=A_d$ until $v_d(\tau)=-V_{\text{gap}}/2$, at which time $A_{de}(\tau)=0$. As the flow reverses again, the process repeats itself. The effective orifice area can be expressed logically as follows: $A_{de}(\tau)=A_d$ if $|v_d|\leqslant V_{\text{gap}}/2$ or $v_d[p_1-p_2]>0$. Otherwise, $A_{de}(\tau)=0$. The

total flow between the two fluid chambers is given by the following first-order linear differential equation:

$$\frac{N_b}{\omega}(q_1(\tau)+q_2(\tau)+q_d(\tau))-\dot{v}(\tau)=0, \tag{7}$$

where v represents increments in the upper and lower chamber volumes from the $p_1=p_2=\overline{p}$ condition. The remaining equations relating pressure and volume in this lumped parameter fluid model are given below[12]

$$p_2(\tau)=5.26\times10^{-3}V_2(\tau)^{2.5}-8.9\times10^{-8}V_2(\tau)^6 + 1.41\times10^{-8}V_2(\tau)^{6.5}+p_{\text{atm}}, \tag{8a}$$

$$p_1(\tau) = \begin{cases} -6.4\overline{V_1}(\tau)+29.2V_1(\tau)^{7/6}+p_{\text{atm}}, & V_1(\tau)\geqslant 0, \quad (8b)\\ p_{\text{atm}}\overline{V}_{\text{air}}/(\overline{V}_{\text{air}}+|V_1(\tau)|), & V_1(\tau)<0, \quad (8c)\end{cases}$$

$$V_1(\tau)=\overline{V_1}+v(\tau)-A_p[y_e(\tau)-y_s(\tau)],$$
$$V_2(\tau)=\overline{V_2}-v(\tau). \tag{8d}$$

Here, V_1 and V_2 denote the hydraulic engine mount upper and lower fluid chamber volumes, respectively, p_{atm} denotes atmospheric pressure, and V_{air} is the air volume trapped in the upper fluid chamber.

For the engine and chassis, regardless of the number of degrees of freedom used to model them, the relationship between the force and motion at the interface to the fluid components of the mount can always be expressed as a transfer function in the frequency domain. The mount rubber dynamics can also be expressed this way. Consider harmonic motion of frequency ω_n'. Then, we will have harmonic displacement and force response at these connection points of the following form where $\sim$ denotes a complex-valued amplitude:

$$y_e(\tau)=\tilde{y}_e e^{j\omega_n'\tau}, \tag{9a}$$

$$y_s(\tau)=\tilde{y}_s e^{j\omega_n'\tau}, \tag{9b}$$

$$F_e(\tau)=\tilde{F}_e e^{j\omega_n'\tau}, \tag{9c}$$

$$F_s(\tau)=\tilde{F}_s e^{j\omega_n'\tau}. \tag{9d}$$

Consequently, a transfer function in the frequency domain between displacement and force at the connection points to section (A) of Fig. 1(b) can be written as such.

$$\tilde{\mathbf{T}}(\omega_n')=\begin{bmatrix} \dfrac{\tilde{y}_e}{\tilde{F}_e} & \dfrac{\tilde{y}_e}{\tilde{F}_s} \\ \dfrac{\tilde{y}_s}{\tilde{F}_e} & \dfrac{\tilde{y}_s}{\tilde{F}_s} \end{bmatrix}. \tag{10}$$

For the simplest case, where the engine mass is assumed to be rigid and the chassis is modeled as a single-degree-of-freedom (SDOF) linear system, we have the following expression, where m_s, b_s, and k_s denote the mass, linear viscous damping coefficient, and stiffness coefficient of the chassis:

$$\tilde{\mathbf{T}}(\omega_n')=\begin{bmatrix} k_r(\omega_n')-\omega_n'^2 m_e+j\omega_n' b_r(\omega_n') & -k_r(\omega_n')-j\omega_n' b_r(\omega_n') \\ -k_r(\omega_n')-j\omega_n' b_r(\omega_n') & k_r(\omega_n')+k_s-\omega_n'^2 m_s+j\omega'[b_r(\omega_n')+b_s] \end{bmatrix}. \tag{11}$$

II. MODELING AND COMPUTATIONAL STRATEGIES

A. Modeling issues

If the single-degree-of-freedom receiver model is used, it is fairly straightforward to analyze the system response using the direct time numerical integration technique. The system is composed of four first-order and two second-order differential equations. Of course, the mount rubber nonlinearity, which is defined in the frequency domain, must be approximated; but this is one of the weaker nonlinearities. For more complex support structure models where many degrees of freedom are considered, numerical integration will become very complex and inefficient. In a previous article, a solution method for complex systems with local nonlinearities was developed.[15] The method is based on the Galerkin procedure and employs order reduction to reduce the number of degrees of freedom to be solved using an iterative strategy, and continuation to aid in parametric studies. The advantage of the method is that complex linear receiver models of many degrees of freedom, either based on theory or experimental transfer function data, are easily incorporated with minimal additional cost in solution time.

Several difficulties are encountered when trying to solve the decoupler-equipped, multi-path inertia track equations using the Galerkin procedure. Explicit differentiable analytical expressions are needed. An approximation for the logic-based decoupler equations is proposed here based on physical reasoning. If there is any compliance in the decoupler orifice plate or the mechanical stops, one should approximate its force versus position relationship as a spring with a backlash or deadspace regime and stiffness k_d. In general, piecewise discontinuity in the Galerkin code is tolerable. But if the degree of nonlinearity is very high, many frequency components are needed in the periodic solution. A further approximation using a polynomial stiffness expression can be more easily handled and is given as follows where γ refers to the order of the polynomial:

$$F_d=k_d(2v_d/A_d\Delta_d)^{\gamma}. \tag{12}$$

Urabe and Reiter[16] formulated the Galerkin procedure for either first- or second-order differential equations. The

hydraulic mounting system model, excluding base dynamics, consists of four first-order differential equations for the fluid processes and one second-order differential equation for the mount rubber/engine mass degree of freedom. While, both first- and second-order differential equations can be simultaneously handled using the procedure, some modifications are proposed for the sake of computational efficiency. Additionally, direct calculation of v_d is needed to implement Eq. (12).

Two first-order differential equations representing the volume of fluid flow through a single inertia track may be cascaded to obtain one second-order differential equation. This reduces the complexity of the Galerkin implementation since the order of the problem (in terms of the sizes of arrays that must be handled) is the same for each additional first- or second-order equation. However, representing the total fluid volume flow through each path with a second-order differential equation results in an unrestrained degree of freedom. While the ''spring'' force of the decoupler acts to restore the total flow through it to zero, no such force is applied on either inertia path. Consequently, total volume flow through either inertia path is unrestrained, which allows a nonzero mean circulating fluid flow. While this condition has little consequence in the physical system dynamics, it is a source of numerical instability in the Galerkin method. To remedy this difficulty, it is proposed to approximate the two in-parallel inertia paths ($i=1,2$) with one equivalent path (e) using the following dynamic relationships:

$$\eta_e = \frac{\eta_1 \eta_2}{(\sqrt{\eta_1}+\sqrt{\eta_2})^2}, \tag{13a}$$

$$I_e = \rho_g l_e / A_e, \tag{13b}$$

$$l_e = l_1 l_2 / (l_1 + l_2), \tag{13c}$$

$$A_e = A_1 = A_2. \tag{13d}$$

This further reduces the equations for the fluid processes to only two degrees of freedom with nonlinearities defined in the time domain which are given as follows:

$$\frac{N_b^2}{\omega^2 I_e}[p_2(\tau)-p_1(\tau)] - \frac{\eta_e}{I_e}\dot{v}_e(\tau)^2 \operatorname{sign}[\dot{v}_e(\tau)] - \ddot{v}_e(\tau) = 0, \tag{14a}$$

$$\frac{N_b^2}{\omega^2 I_d}[p_2(\tau)-p_1(\tau)] - \frac{\eta_d}{I_d}\dot{v}_d(\tau)^2 \operatorname{sign}[\dot{v}_d(\tau)] - \frac{N_b^2}{\omega^2 I_d}F_d(\tau) - \ddot{v}_d(\tau) = 0. \tag{14b}$$

B. Computational method

With the above modifications, application of the Galerkin strategy is briefly reviewed. As indicated in Fig. 1(b), the system can be divided into two sections, (A) and (B). Section (A), comprising the fluid components of the mount, contains the $N_v=2$ second-order differential equations (14a) and (14b) with nonlinearities defined in the time domain. These two expressions are the determining equations, $\mathbf{d}^v(\tau)$, for the Galerkin method. Section (B), the engine, chassis and rubber components of the mount, consists of N_w linear differential equations as well as equations with nonlinearities defined in the frequency domain. These N_w equations will be dependent on the displacement vector $\mathbf{w}$ or state variables in section (B). This section can be analyzed completely in the frequency domain using linear algebraic methods. The connection between section (B) and section (A), as indicated above, is described by the vector $\mathbf{y}(\tau) \equiv [y_e(\tau) y_s(\tau)]^T$ which is a linear mapping of $\mathbf{w}(\tau)$. Here, superscript T denotes the transpose. Likewise, the force vector at this connection is described by an $N_y=2$ dimensional vector $\mathbf{F}_y(\tau) \equiv [F_e(\tau) F_s(\tau)]^T$. Hence, for section (B), a frequency-dependent transfer function may be defined as follows:

$$\tilde{\mathbf{T}}_{\mathbf{y}}(\omega') \equiv \frac{\tilde{\mathbf{y}}}{\tilde{\mathbf{F}}_{\mathbf{y}}}(\omega'). \tag{15}$$

Now, the $N_b N_p$th approximate solution to the problem will have the following form:

$$\mathbf{v}(\tau) = \mathbf{a}_0^v + \sum_{n=1}^{N_b N_p} \mathbf{a}_{2n-1}^v \sin(n\tau) + \mathbf{a}_{2n}^v \cos(n\tau),$$

$$\mathbf{v} \equiv [v_e, v_d]^T, \quad \mathbf{a}_n^v \equiv [a_n^{v_e}, a_n^{v_d}]^T, \tag{16a}$$

$$\mathbf{y}(\tau) = \mathbf{a}_0^y + \sum_{n=1}^{N_b N_p} \mathbf{a}_{2n-1}^y \sin(n\tau) + \mathbf{a}_{2n}^y \cos(n\tau),$$

$$\mathbf{y} \equiv [y_e, y_s]^T, \quad \mathbf{a}_n^y \equiv [a_n^{y_e}, a_n^{y_s}]^T. \tag{16b}$$

By substituting expressions (16a) and (16b) into Eqs. (14a) and (14b) and numerically calculating the Fourier coefficients of $\mathbf{d}^{\mathbf{v}}(\tau)$, we obtain the following $(4N_b N_p+1)\times(N_v)$ nonlinear algebraic determining equations for finding the values of the coefficients

$$\boldsymbol{\alpha}^v \equiv [\mathbf{a}_0^v \ \ \mathbf{a}_1^v \ \cdots \ \mathbf{a}_{4N_b N_p}^v]$$

and

$$\boldsymbol{\alpha}^y \equiv [\mathbf{a}_0^y \ \ \mathbf{a}_1^y \ \cdots \ \mathbf{a}_{4N_b N_p}^y]:$$

$$\mathbf{D}_i^v(\boldsymbol{\alpha}) \equiv \mathscr{F}_i[\mathbf{d}^v(\tau)] = \mathbf{0}, \quad i = 0, \ \ldots, 4N_b N_p,$$

where

$$\boldsymbol{\alpha} \equiv [\boldsymbol{\alpha}^v \ \ \boldsymbol{\alpha}^y]^T, \quad \mathscr{F}_0[d(\tau)] \equiv \frac{1}{2N_f}\sum_{n_f=1}^{2N_f} d(\tau_{n_f}),$$

$$\mathscr{F}_{2n-1}[d(\tau)] \equiv \frac{1}{N_f}\sum_{n_f=1}^{2N_f} d(\tau_{n_f})\sin(n\tau_{n_f}),$$

$$\mathscr{F}_{2n}[d(\tau)] \equiv \frac{1}{N_f}\sum_{n_f=1}^{2N_f} d(\tau_{n_f})\cos(n\tau_{n_f}),$$

$$n = 1, \ \ldots, 2N_b N_p,$$

and

$$\tau_{n_f} = \frac{2n_f - 1}{2N_f}\pi \ \text{ with } \ N_f \geqslant 2N_b N_p, \ n_f = 1, \ \ldots, N_f. \tag{17}$$

The remaining $(4N_b N_p+1)\times(N_y)$ determining equations which are needed take the following form. Here, Re and Im

refer to the real and imaginary parts, respectively:

$$D_0^{y_r}(\boldsymbol{\alpha}) \equiv \sum_{z=1}^{N_y} \{\mathrm{Re}[\tilde{T}_y^{r,z}(0)] a_0^{F_z}\} - a_0^{y_r} = 0, \tag{18a}$$

$$D_{2n-1}^{y_r}(\boldsymbol{\alpha}) \equiv \sum_{z=1}^{N_y} \left\{ \mathrm{Re}\left[\tilde{T}_y^{r,z}\left(\frac{n\omega}{N_b}\right)\right] a_{2n-1}^{F_z} + \mathrm{Im}\left[\tilde{T}_y^{r,z}\left(\frac{n\omega}{N_b}\right)\right] a_{2n}^{F_z} \right\} - a_{2n-1}^{y_r} = 0, \tag{18b}$$

$$D_{2n}^{y_r}(\boldsymbol{\alpha}) \equiv \sum_{z=1}^{N_y} \left\{ \mathrm{Re}\left[\tilde{T}_y^{r,z}\left(\frac{n\omega}{N_b}\right)\right] a_{2n}^{F_z} - \mathrm{Im}\left[\tilde{T}_y^{r,z}\left(\frac{n\omega}{N_b}\right)\right] a_{2n-1}^{F_z} \right\} - a_{2n}^{y_r} = 0, \tag{18c}$$

where $r=1,\ldots,N_y$, $n=1,\ldots,2N_bN_p$ and

$$a_i^{F_z} \equiv \mathscr{F}_i[F_z(\tau)], \quad i=0,\ldots,4N_bN_p.$$

Consequently, using this order reduction technique, the number of coupled nonlinear algebraic equations to be iteratively solved remains fixed at $N=(N_y+N_v)\times(4N_bN_p+1)$ regardless of the number of equations N_w describing motion in section (B). Once the nonlinear solution is obtained, the response of any variable in section (B) is quickly found by simple linear algebraic calculations.

The Galerkin method employs an iterative method to solve the coupled nonlinear algebraic equations, minimizing the sum of the squares of the determining equations in the frequency domain (a least squares approach). Further details of the method can be found in Refs. 15 and 16.

C. Power flow computation

Assuming a periodic response with fundamental frequency ω/N_b, the spectral content of vibratory power flow throughout the system may be calculated from the Galerkin procedure results. For a given dynamic displacement variable $z(\tau)$, there is an associated constraint force variable $F_z(\tau)$, both of which can be expressed in the following series forms:

$$z(\tau) = a_0^z + \sum_{n=1}^{N_bN_p} a_{2n-1}^z \sin(n\tau) + a_{2n}^z \cos(n\tau), \tag{19a}$$

$$F_z(\tau) = a_0^{F_z} + \sum_{n=1}^{N_bN_p} a_{2n-1}^{F_z} \sin(n\tau) + a_{2n}^{F_z} \cos(n\tau). \tag{19b}$$

The associated vibratory power flow can then be formulated from the inner product of the force and velocity by summing respective harmonic contributions:

$$P(\omega) = \sum_{n=1}^{N_bN_p} \frac{n\omega}{2N_b} [-a_{2n-1}^{F_z} a_{2n}^z + a_{2n}^{F_z} a_{2n-1}^z]. \tag{20}$$

For example, vibratory power flow through the mount into the automotive chassis will be given by Eqs. (19) and (20) where

$$F_z(\tau) = F_r(\tau) - F_f(\tau), \quad a_i^{F_z} \equiv \mathscr{F}_i[F_z(\tau)],$$

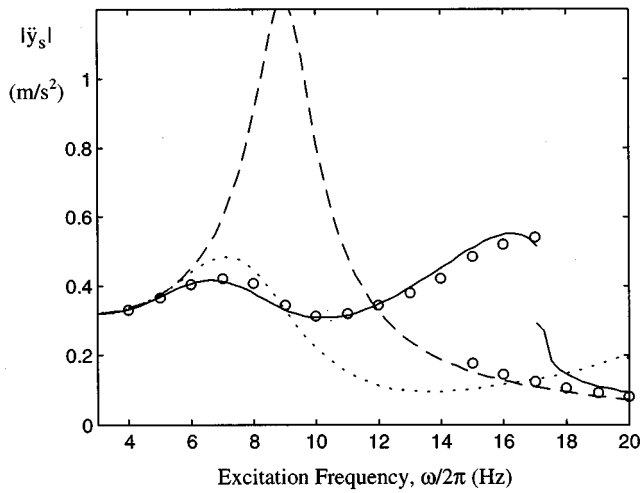

FIG. 3. Mounting system frequency response. Base acceleration at the excitation frequency, $\ddot{y}_s(\omega)$, for, $F_u(t)=100\sin(\omega t)N$. Key: – – – rubber mount (modal method), - - - - inertia mount with no decoupler, $\Delta_d=0$ mm (Galerkin solution and numerical integration), ∘∘∘ kinematic decoupler model, $\Delta_d=0.7$ mm (numerical integration), — polynomial-stiffness decoupler model with $\gamma=3$, $\Delta_d=0.7$ mm (Galerkin solution and numerical integration).

and (21)

$$a_i^z = a_i^{y_s}.$$

Vibratory power flow through the rubber component or the fluid component of the mount may be considered separately by using $F_z(\tau)=F_r(\tau)$ or $F_z(\tau)=-F_f(\tau)$, respectively.

III. RESULTS AND DISCUSSION

A. Improvement in mount models

In the previous section, modifications to the vibration mount model were proposed to make the problem tractable using the Galerkin method. The impact of these changes is assessed via comparison of the modified case to the exact kinematic case for harmonic excitation using the SDOF base model. System parameter values used in this study are provided in Table I. These values are based on experimental studies of a typical commercially used engine mount system. In Fig. 3, base acceleration $\ddot{y}_s$ at the fundamental harmonic of the excitation force $F_U(t)=100\sin(\omega t)N$ for $3<\omega/2\pi<20$ Hz is shown for the kinematic and polynomial-stiffness decoupler models. This range of excitation values represents realistic conditions. Also shown is the system response using the rubber mount alone (excluding fluid elements) and using the inertia track mount which does not possess a decoupler, i.e., $\Delta_d=0$. Results of Fig. 3 bear much similarity to comparable cases reported in Fig. 9a of Kim and Singh[13] supporting the validity of the equivalent inertia track formulation. The superiority of the highly nonlinear decoupler-equipped mount is evident from the fact that it allows the inertia track to act like a tuned absorber at the engine mounting resonance, attenuating the otherwise large peak near $\omega/2\pi=10$ Hz, but then it decouples the track as the frequency is increased for reduced motion transmissibility.

The two decoupler models agree fairly well over this frequency range. A hardening stiffness effect associated with

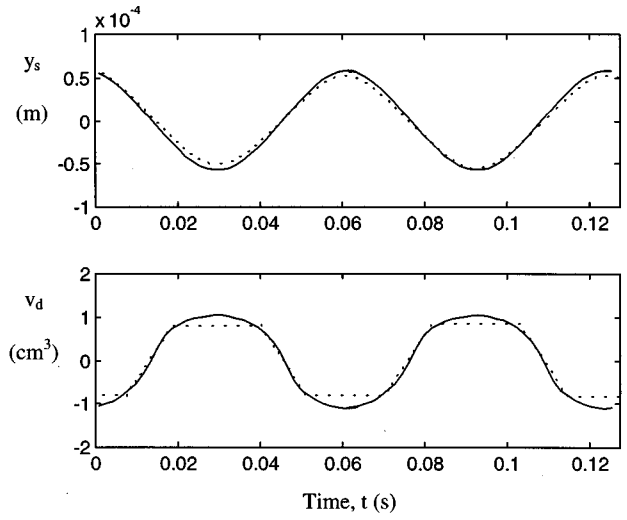

FIG. 4. Mounting system time response. Base motion, $y_s(t)$, and the total volume flow through the decoupler orifice, $v_d(t)$, for $\Delta_d=0.7$ mm and $F_u(t)=100\sin(15.86\times 2\pi t)N$ (large amplitude solution). Key - - - - kinematic decoupler model (numerical integration), — polynomial-stiffness decoupler model with $\gamma=3$ (Galerkin solution and numerical integration).

the decoupler is evident in both cases as the system resonance has the characteristic upward bend in frequency.[17] For the kinematic model with the stronger nonlinearity, a jump phenomenon is also observed with multiple solution regimes. The weaker polynomial-stiffness model did not predict a strong jump phenomenon, but did have a region of numerical difficulty where a solution, either stable or unstable, could not be found with the Galerkin method. Hence, there is a break in the solution path.

In Fig. 4, selected time domain plots of the decoupler total volume displacement v_d and the base motion y_s are provided to illustrate the following points. First, the ''low-pass filter effect'' is evident as high-frequency motion of the base is significantly curtailed. In other words, the sharp discontinuities in v_d are not evident in y_s. Second, it is clear that ''softening'' the decoupler model, i.e., weakening the path nonlinearity, also lowers the high-frequency response of the system. The solid line in Fig. 4b, based on the ''softened'' model, is smoother. In Fig. 5, this same trend is observed where fundamental and higher harmonic responses to harmonic excitation are shown for the kinematic and polynomial-stiffness decoupler models. Neither model predicted any significant subharmonic response. Results shown here also raise questions with respect to how nonlinear isolation performance should be assessed. Clearly, it seems that ignoring the system response at frequencies other than the excitation frequency may be inappropriate. This issue is addressed in the next section.

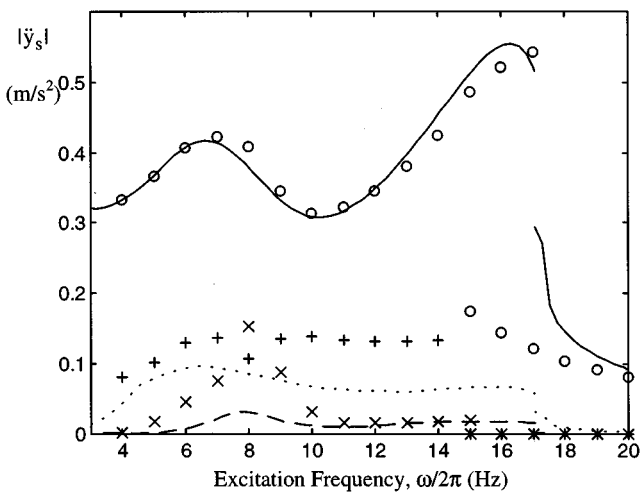

FIG. 5. Mounting system frequency response. Base acceleration at the excitation frequency and its first two harmonics, $\ddot{y}_s$, for $\Delta_d=0.7$ mm and $F_u(t)=100\sin(\omega t)N$. Key: Kinematic decoupler model, ∘∘∘ 1st, ××× 2nd, +++ 3rd harmonics (numerical integration), polynomial-stiffness decoupler model with $\gamma=3$, — 1st, – – 2nd, - - - - 3rd harmonics (Galerkin solution and numerical integration).

B. Vibratory power flow

Using Eqs. (19)–(21), several vibratory power flow variables are calculated and graphed in Fig. 6 for the different

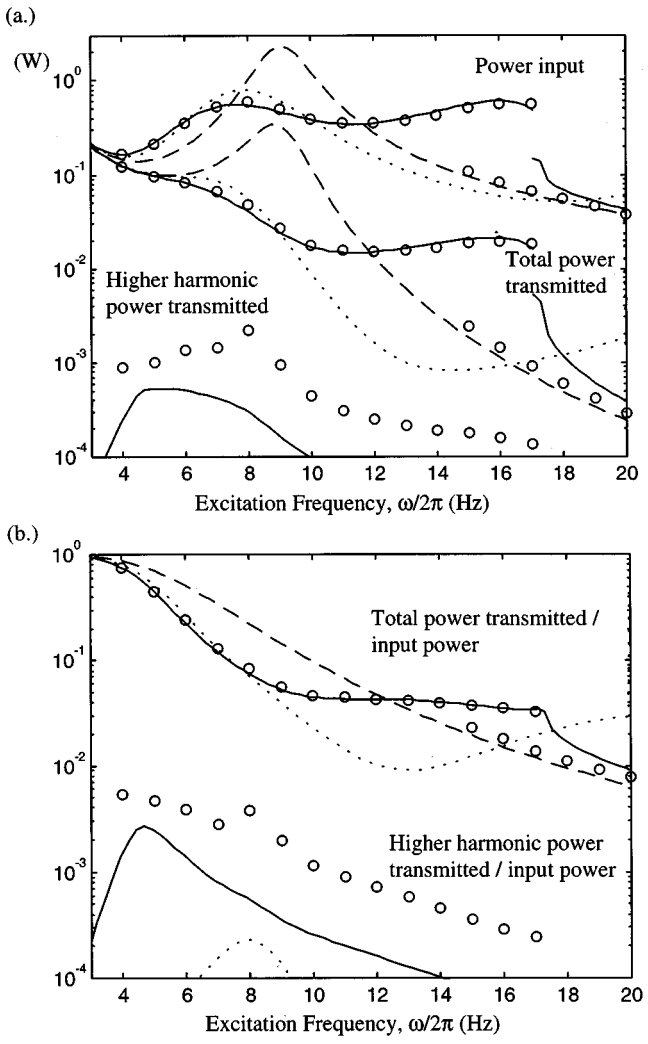

FIG. 6. Mounting system frequency response. Vibratory power flow for different mount models. (a) Power input, total and higher harmonic power transmission into support base. (b) Ratio of total and higher harmonic power transmission to power input. Here, $F_u(t)=100\sin(\omega t)N$. Key: – – – rubber mount (modal method), - - - - inertia mount with no decoupler, $\Delta_d=0$ mm (Galerkin solution and numerical integration), ∘∘∘∘ kinematic decoupler model $\Delta_d=0.7$ mm (numerical integration), — polynomial-stiffness decoupler model with $\gamma=3$, $\Delta_d=0.7$ mm, (Galerkin solution and numerical integration).

decoupler configurations and models. Power related quantities are also provided in Table II. Directions of positive vibratory power flow in Fig. 7 show that the fluid component of the engine mount absorbs vibratory energy at the excitation frequency coming from both the engine (source) and the chassis (receiver). However, it also acts as a source of vibratory energy at higher frequencies which is then transmitted and dissipated throughout the rest of the system. Vibratory power results support the conclusion based on motion descriptor analysis that the ''softened'' nonlinear decoupler model does predict less vibration transmission at higher frequencies than is predicted by the kinematic decoupler model.

Results also show that, on a quantitative basis, the contribution to the total vibratory energy transmission of the higher harmonic components is negligible with respect to the primary harmonic, supporting performance assessment methods based on the ''low-pass filter'' assumption in this particular case. This fact must however, be qualified by two remarks. First, the frequency of transmission in addition to its level is of interest. Results reported here indicate that, even for source excitation below 20 Hz, structure-borne noise is transmitted through the mount in the audible frequency range. Even if the relative energy is low, its perceived level in terms of radiated sound in, for example, the passenger compartment may still be significant. Second, in this example case, the base is a simplistic, SDOF model, with a 40 dB/decade attenuation in the mobility spectrum above its resonance frequency near 1.36 Hz. Other base models with reduced frequency attenuation or high-frequency resonant conditions may lead to different conclusions. This is discussed in the next section.

C. MDOF resonant receivers

Due to computational difficulty, most prior studies of isolation systems with localized mount nonlinearities have typically either focused on the mount alone and ignored complex support base dynamics or have resorted to a linear analysis of the complete system. Here, using the Galerkin-based computational strategy, both path nonlinearities and more realistic, MDOF receiver dynamics are considered. Several generic receiver models are considered for evaluation of their impact on system performance. They include the

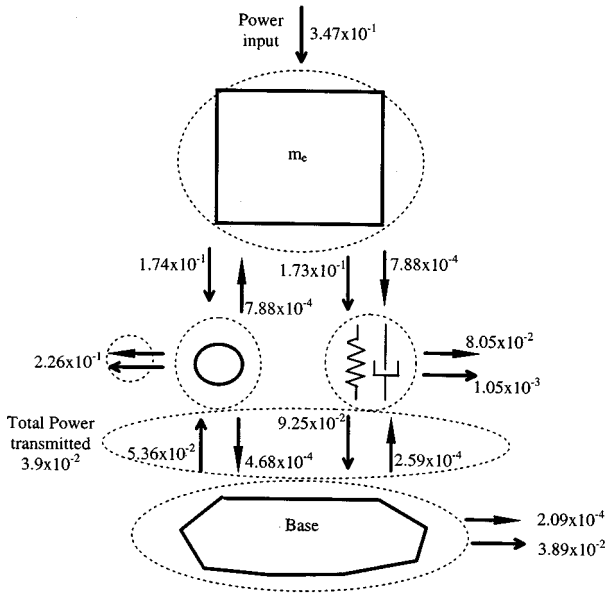

FIG. 7. Mounting system schematic showing directions of positive vibratory power flow for the SDOF base model and the polynomial-stiffness decoupler model with $\gamma=3$. Key: → primary harmonic, → higher harmonics.

SDOF base used in the previous sections, a purely viscous damper base, a MDOF base with heavy modal damping comparable to that of the SDOF base, and a more lightly damped MDOF base. Mobilities for each of these bases are given by the following equations:

SDOF base:

$$\frac{\tilde{y}_s}{\tilde{F}_s}(\omega_n')=\frac{1}{k_s}\frac{j\omega_n'}{(1-(\omega_n'/\omega_s)^2)+j(2\varsigma_s\omega_n'/\omega_s)}. \tag{22}$$

Pure viscous damper base:

$$\frac{\tilde{y}}{\tilde{F}_s}(\omega_n')=\frac{1}{b_s}. \tag{23}$$

MDOF heavily damped base:

TABLE II. Vibratory power flow for different mount models. Given SDOF base of Eq. (22).

Power quantity[a] (Watts)	Rubber mount (linear system)	Inertia track without decoupler	With inertia track and decoupler $\Delta_d=0.7$ mm	
			Kinematic model	Poly-stiffness model, $\gamma=3$
Power input				
primary harmonic only	0.398	0.244	0.341	0.347
Power transmitted to Base				
primary harmonic	8.60×10^{-2}	3.55×10^{-2}	4.01×10^{-2}	3.89×10^{-2}
(% of TOTAL)	(100)	(99.9)	(98.5)	(99.5)
superharmonics	0	2.65×10^{-5}	5.93×10^{-4}	2.08×10^{-4}
(% of TOTAL)	(0)	(0.1)	(1.5)	(0.5)
TOTAL	8.60×10^{-2}	3.55×10^{-2}	4.07×10^{-2}	3.91×10^{-2}
(% of power input)	(21.6)	(14.5)	(11.9)	(11.3)

[a]Averaged over $3<\omega/2\pi<20$ Hz.

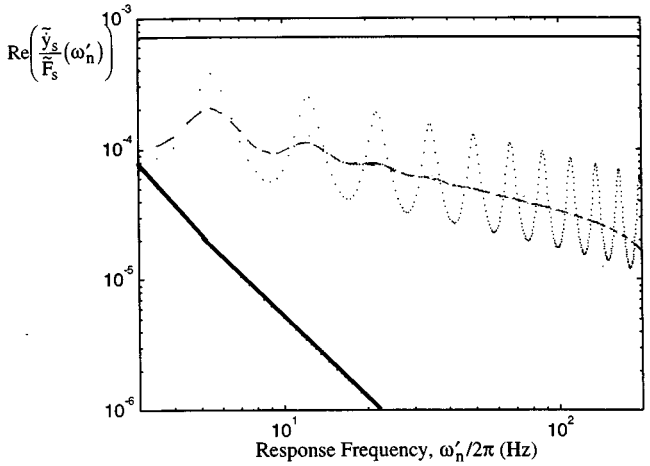

FIG. 8. Mobility of base models. Key: — SDOF base, Eq. (22), — viscous damper base, Eq. (23), – – MDOF heavily damped base, Eq. (24), ···· MDOF lightly damped base; Eq. (25).

$$\frac{\tilde{\ddot{y}}_s}{\tilde{F}_s}(\omega_n')=\sum_{i=1}^{12}\frac{1}{i^4 k_s}\frac{j\omega_n'}{(1-(\omega_n'/i^2\omega_s)^2)+j(2\varsigma_s\omega_n'/i^2\omega_s)}. \tag{24}$$

MDOF lightly damped base:

$$\frac{\tilde{\ddot{y}}}{\tilde{F}_s}(\omega_n')=\sum_{i=1}^{12}\frac{1}{i^4 k_s}\frac{j\omega_n'}{(1-(\omega_n'/i^2\omega_s)^2)+j(2\varsigma_s\omega_n'/i^3\omega_s)}. \tag{25}$$

The real part of their mobilities is shown in Fig. 8 since it is proportional to the level of vibratory power transmission from a force applied directly to the support base point, y_s.[1] As seen in the log–log plot, the SDOF base has a mobility that is attenuated at a rate of 40 dB/decade above its resonance frequency. Thus, it is operated almost entirely in the inertia-driven regime. The mobility of a pure viscous damper is constant with respect to frequency. The mobilities of the MDOF bases are more complex, particularly for the lightly damped base, but follow a mean attenuation trend with frequency that lies somewhere in-between the SDOF and the viscous damper cases.

Vibratory power flow through the mount into the SDOF support base is shown in Fig. 9. Vibratory power flow for the cases of the pure viscous damper base, MDOF heavily damped base, and MDOF lightly damped base are shown in Figs. 10, 11, and 12, respectively. Some numerical values are also given in Table III. Several observations can be made. First, with the SDOF base, the highest levels of power dissipation in the mount are obtained. This is because excitation is well above the base natural frequency which acts as a mass barrier with a high impedance, or equivalently a low mobility, for power transmission.

Second, for the viscous damper, a greater ratio of power flow to input power occurs due to the relative higher mobility, i.e., lower impedance, of the base as frequency increases. Increasing the level of damping in the base, i.e., lowering the mobility, does decrease the level of transmission. Note also that, for the viscous damper base, the level of vibratory input has been significantly decreased. Changing the mobility of

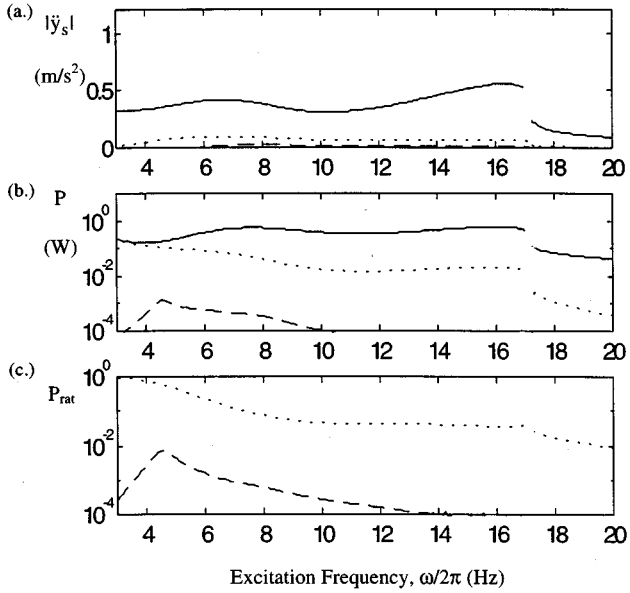

FIG. 9. Mounting system frequency response. Vibratory power flow into the SDOF support base (Polynomial-stiffness decoupler model with $\gamma=3$, Galerkin solution). Here, $F_u(t)=100\sin(\omega t)N$ and $\Delta_d=0.7$ mm. (a) Base vertical acceleration, $\ddot{y}_s$, — 1st harmonic, – – 2nd harmonic, - - - - 3rd harmonic. (b) Power transmission, — Power input, - - - - Total power transmitted, – – Power transmitted at higher harmonics. (c) Power transmission ratios, - - - - Total power transmitted/Power input, – – Power transmitted at higher harmonics/ Power input.

the base also changes the mobility at the excitation drive point. This brings up the point that a force input alone is often not a true representation of dynamic engine imbalance or other practical sources of vibration excitation. Other in-

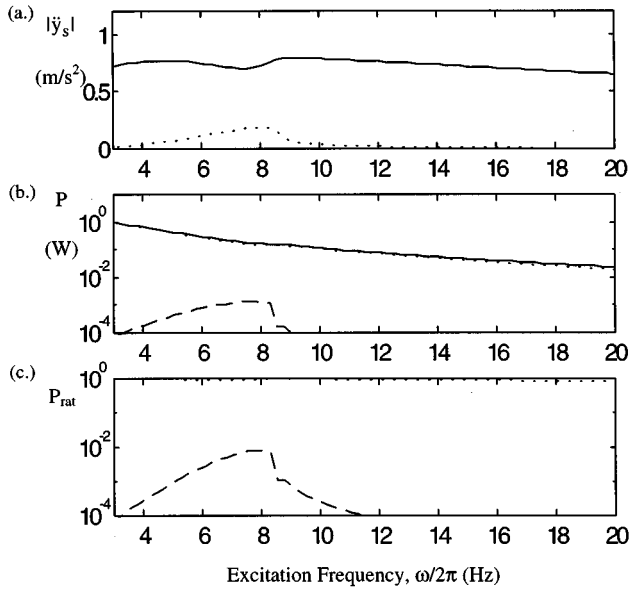

FIG. 10. Mounting system response. Vibratory power flow into the pure viscous damper base (Polynomial-stiffness decoupler model with $\gamma=3$, Galerkin solution). Here, $F_u(t)=100\sin(\omega t)N$ and $\Delta_d=0.7$ mm. (a) Base vertical acceleration, $\ddot{y}_s$, — 1st harmonic, – – 2nd harmonic, - - - - 3rd harmonic. (b) Power transmission, — Power input, - - - - Total power transmitted, – – Power transmitted at higher harmonics. (c) Power transmission ratios, - - - - Total power transmitted/Power input, – – Power transmitted at higher harmonics/Power input.

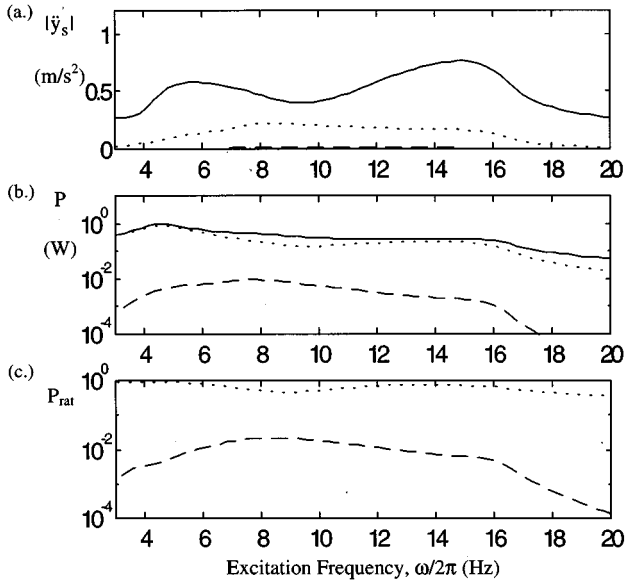

FIG. 11. Mounting system response. Vibratory power flow into the MDOF heavily damped support base (Polynomial-stiffness decoupler model with $\gamma=3$, Galerkin solution). Here, $F_u(t)=100\sin(\omega t)N$ and $\Delta_d=0.7$ mm. (a) Base vertical acceleration, $\ddot{y}_s$, — 1st harmonic, – – 2nd harmonic, - - - - 3rd harmonic. (b) Power transmission, — Power input, - - - - Total power transmitted, – – Power transmitted at higher harmonics. (c) Power transmission ratios, - - - - Total power transmitted/Power input, – – Power transmitted at higher harmonics/Power input.

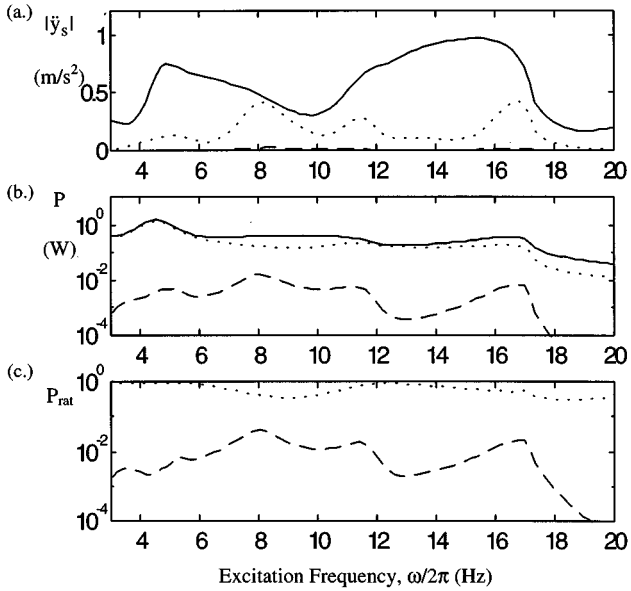

FIG. 12. Mounting system response. Vibratory power flow into the MDOF lightly damped support base (Polynomial-stiffness decoupler model with $\gamma=3$, Galerkin solution). Here, $F_u(t)=100\sin(\omega t)N$ and $\Delta_d=0.7$ mm. (a) Base vertical acceleration, $\ddot{y}_s$, — 1st harmonic, – – 2nd harmonic, - - - - 3rd harmonic. (b) Power transmission, — Power input, - - - - Total power transmitted, — — Power transmitted at higher harmonics. (c) Power transmission ratios, - - - - Total power transmitted/Power input, – – Power transmitted at higher harmonics/Power input.

puts, such as velocity or more complex ones which are dependent on the system response may be more suitable for a given application. In fact, it has been shown in previous linear system isolation studies on resonant support structures that force inputs will favor power transmission at resonances.[2,3] Since there are no such resonances for the viscous damper case in the frequency range of interest, power input is reduced.

Third, for the MDOF bases considered, regardless of the level of damping, a greater amount of vibratory power flows to the base than in the SDOF case since the mobility is significantly higher. Note also, that a greater percentage of the power transmission occurs at higher harmonics of the excitation frequency. For the lightly damped MDOF base, isolation performance is more frequency dependent. But, for both MDOF cases, even when the level of modal damping in the base is increased, while vibratory power transmission at specific frequencies may be attenuated, the overall level of transmission for wideband excitation is virtually unchanged. This has important practical implications, as it shows that added base damping (with more weight, of course) may not offer substantial gains in performance depending on the excitation conditions.

Finally, in Table III it is interesting to note that trends in the percentage of higher harmonic power flow do not match trends in the overall power flow which were easily related to trends in support base mobility. This is due to the mechanism of generating higher harmonics which is related to the mount nonlinearity and is highly amplitude dependent. Even though the pure viscous damper has a higher mobility, it does not produce large amplitude motion across the mount. Thus, while the percentage level of overall power flow may be well correlated with the level of base mobility, the generation and

TABLE III. Vibratory power flow for different base models ($\Delta_d=0.7$ mm, polynomial decoupler model with $k_d=10$ KPa and $\gamma=3$).

Power quantity[a] (Watts)	SDOF Eq. (22)	Viscous Eq. (23)	MDOF heavily damped. Eq. (24)	MDOF lightly damped. Eq. (25)
Power input				
primary harmonic only	0.347	0.176	0.349	0.360
Power transmitted to Chassis				
primary harmonic	3.89×10^{-2}	1.66×10^{-1}	2.45×10^{-1}	2.42×10^{-1}
(% of TOTAL)	(99.5)	(99.9)	(98.6)	(98.5)
superharmonics	2.08×10^{-4}	2.14×10^{-4}	3.53×10^{-3}	3.63×10^{-3}
(% of TOTAL)	(0.5)	(0.1)	(1.4)	(1.5)
TOTAL	3.91×10^{-2}	1.67×10^{-1}	2.49×10^{-1}	2.46×10^{-1}
(% of power input)	(11.3)	(94.9)	(70.2)	(68.7)

[a]Averaged over $3<\omega/2\pi<20$ Hz.

transmission of higher harmonic vibratory energy is dependent in a more complex way on the interactions between the support base dynamics and the mount dynamics.

IV. CONCLUSION

This study has made a number of contributions to the general understanding of vibratory power flow through a nonlinear isolator path into a resonant receiver with some particular insights into the hydraulic engine mounting system. An enhanced Galerkin method, a multi-term harmonic balance strategy, was used to solve for the steady-state periodic response and isolation performance was assessed in terms of total (multi-harmonic) vibratory power flow under harmonic excitation conditions.

Several key findings are reported, including the following. While modeling the isolation path with a ''softened'' nonlinear expression may only moderately alter the fundamental harmonic response, it can significantly alter higher harmonic responses. In some cases, these higher harmonic responses represent structure-borne noise which has been generated by subaudio frequency excitations. It has also been shown that compliant base (receiver) dynamics can significantly affect isolation performance. Use of a SDOF support structure produces superior performance relative to a MDOF base since the base mobility is less for the SDOF case. Also, for a MDOF base, significant levels of vibratory power flow may be transmitted at higher harmonics of the excitation frequency for a wide range of base damping levels. For spectrally averaged analysis, it is the mean level of mobility that is important at higher frequencies. This is somewhat independent of the modal damping level but dependent on the number of degrees of freedom. Finally, it has been shown that while overall levels of vibratory power flow are well correlated with support base mobility, the generation and transmission of higher harmonic power flow are more dependent on the coupled source—nonlinear path—receiver dynamics.

The study of nonlinear paths is a fertile ground for future research. For instance, issues which still need to be addressed include a careful consideration of vibratory power flow under multi-harmonic and other nonperiodic excitation conditions coming from both force and motion-type sources applied through multi-dimensional path configurations. Unlike linear systems, nonlinear system responses due to different excitation frequencies are not independent. Additionally, other MDOF receiver models representing typical applications, including those with structural damping as opposed to viscous damping, should be considered. These situations are currently being investigated by the authors.

[1] H. G. D. Goyder and R. G. White, ''Vibrational power flow from machines into built-up structures, Part I: Introduction and approximate analyses of beam and plate-like foundations,'' J. Sound Vib. **68**, 59–75 (1980).
[2] H. G. D. Goyder and R. G. White, ''Vibrational power flow from machines into built-up structures, Part III: Power flow through isolation systems,'' J. Sound Vib. **68**, 97–117 (1980).
[3] R. J. Pinnington and R. G. White, ''Power flow through machine isolators to resonant and non-resonant beams,'' J. Sound Vib. **75**, 179–197 (1981).
[4] Y. K. Koh and R. G. White, ''Analysis and control of vibrational power transmission to machinery supporting structures subjected to a multi-excitation system, Part I: Driving point mobility matrix of beam and rectangular plates,'' J. Sound Vib. **196**, 469–493 (1996).
[5] Y. K. Koh and R. G. White, ''Analysis and control of vibrational power transmission to machinery supporting structures subjected to a multi-excitation system, Part II: Vibrational power analysis and control schemes,'' J. Sound Vib. **196**, 495–508 (1996).
[6] J. Pan, J. Pan, and C. H. Hansen, ''Total power flow from a vibrating rigid body to a thin panel through multiple elastic mounts,'' J. Acoust. Soc. Am. **92**, 895–907 (1992).
[7] K. B. Scribner, L. A. Sievers, and A. H. von Flotow, ''Active narrowband vibration isolation of machinery noise from resonant substructures,'' J. Sound Vib. **167**, 17–40 (1993).
[8] T. J. Royston and R. Singh, ''Optimization of passive and active nonlinear vibration mounting systems based on vibratory power tranmission,'' J. Sound Vib. **194**, 295–316 (1996).
[9] T. D. Gillespie, *Fundamentals of Vehicle Dynamics* (Society of Automotive Engineers, Warrendale, PA, 1992).
[10] T. C. Lim, ''Case history: Finite element and experimental modeling approaches for automotive noise control problems,'' Noise Control Eng. J. **44**, 245–248 (1996).
[11] D. A. Swanson, L. R. Miller, and M. A. Norris, ''Multidimensional mount effectiveness for vibration isolation,'' J. Aircraft **31**, 188–96 (1994).
[12] G. Kim and R. Singh, ''Nonlinear analysis of automotive hydraulic engine mount,'' Trans. ASME, J. Dyn. Syst. Meas. **115**, 482–487 (1993).
[13] G. Kim and R. Singh, ''A study of passive and adaptive hydraulic engine mount systems with emphasis on nonlinear characteristics,'' J. Sound Vib. **179**, 427–53 (1995).
[14] J. E. Colgate, C.-T. Chang, Y.-C. Chiou, W. K. Liu, and L. M. Keer, ''Modeling of a hydraulic engine mount focusing on response to sinusoidal and composite excitations,'' J. Sound Vib. **184**, 503–28 (1995).
[15] T. J. Royston and R. Singh, ''Periodic response of mechanical systems with local nonlinearities using an enhanced Galerkin technique,'' J. Sound Vib. **194**, 243–263 (1996).
[16] M. Urabe and A. Reiter, ''Numerical computation of nonlinear forced oscillations by Galerkins's procedure,'' J. Math. Anal. Appl. **14**, 107–140 (1966).
[17] T. J. Royston and R. Singh, ''Experimental study of mechanical systems with mean-loaded localized continuous stiffness nonlinearities,'' J. Sound Vib. **198**, 279–298 (1996).

Response of a two-layer compliant slab to inviscid incompressible fluid flow

Cahit A. Evrensel, Li Zhou, and Md. Raquib U. Khan
Department of Mechanical Engineering, University of Nevada, Reno, Nevada 89557-0154

(Received 14 July 1993; revised 5 February 1996; accepted 20 August 1996)

In this study, the dynamics of two-dimensional wave trains at the interface between a two-layer viscoelastic coating and flow of an inviscid fluid is examined theoretically. The objective is to understand the interaction mechanism between the two media better, and to explore the effects of different geometric and material properties on this mechanism. Each layer of coating is treated as an infinite, elastic, or viscoelastic solid of finite thickness, bonded to each other. The flow is modeled by the potential theory. The two media, two-layer slab and the fluid, are coupled through stress and velocity, normal to the surface of the slab. Two layers of the slab are assumed to be bonded to each other. The proposed mathematical model is used to predict the appearance of unstable surface waves of the coating. A few dimensionless parameters are identified. The model predicts that the instabilities initiate in the form of *standing waves* for the viscoelastic coating while the speed of the unstable waves at the interface of the elastic coating and the fluid is relatively high. © *1997 Acoustical Society of America.* [S0001-4966(97)04612-2]

PACS numbers: 43.40.Dx [PJR]

INTRODUCTION

Theoretical and experimental studies have shown that the interaction of fluid flow with a compliant layer results in either propagating or standing waves at the interface of two media.[1,2] These suddenly appearing wavelike folds have been a growing interest for scientists due to the new possibilities in engineering applications, such as skin friction drag reduction on moving vehicles, sound absorption, vibration reduction, and noise shielding.[2]

The design of a compliant coating to achieve a particular objective requires a thorough understanding of the interaction mechanism between the two media. This interaction mechanism has been explored experimentally by many investigators.[3–8] Their results have shown that water flow can set a compliant slab, bonded to a rigid base, in motion. In particular, for a slab with high viscosity, waves that propagate slowly in the direction of water flow are observed on the surface of the slab, the propagation speed being a few percent of the flow velocity. Boggs and Hahn[3] were the first to point out the existence of these waves that have a spanwise straight-crested form with amplitudes of the order of the slab thickness. In another series of experiments by Gad-el-Hak,[8] for a slab with very low viscosity, the appearance of waves with smaller amplitudes but much higher velocities was reported. A comprehensive review of the boundary layer interactions with compliant coating is given by Gad-el-Hak,[2] Riley *et al.*,[9] and Carpenter.[10]

In experiments presented in Refs. 4, 5, 7, and 8 for turbulent flow over a compliant coating, the waves are observed to appear only after a certain magnitude of flow velocity is reached; i.e., there exists a clearly observable onset flow velocity. This fact suggests that the waves are produced by the instability of the coupled fluid–solid system, rather than by the direct application of the pressure fluctuations on the surface of the compliant layers. The arguments in support of this claim can be found in a number of papers, such as, for example, in the papers by Evrensel an Kalnins.[11,12]

The stability problem associated with the interaction of compliant layers with the flow of viscous fluids has been studied by using several approaches. One approach simplified the solid region of the problem by studying either the boundary layer flow over moving wavy walls or by approximating the slab as a membrane.[13–15] Another approach has modeled the fluid region as an inviscid flow and modified the surface pressure by introducing experimentally determinable parameters.[16]

Benjamin[13,17] studied the theoretical problem of shearing flows bounded by a moving or stationary wavy surface. He developed a theory on the basis of a model of laminar boundary layer flow. He also discussed the different types of system instabilities that occur when a flexible surface is coupled with a flowing fluid.[18] Landahl[14] considered the stability of small two-dimensional traveling-wave disturbances in an incompressible laminar boundary layer over a flexible surface. Kaplan[15] has explored the interaction of boundary layer flow with a spring-backed membrane. The aim of these studies was to investigate the effect of a compliant wall on the stability of laminar flow.

The first theoretical study of an inviscid compressible fluid flow past an elastic slab was done by Pierucci.[19] He described the basic features of the coupled inviscid fluid–solid stability problem. By assuming the fluid to be incompressible, this model was further investigated by Duncan *et al.*,[16] with the objective of applying the results to a turbulent boundary layer flow. By introducing two experimentally determinable parameters, they were able to predict, for large slab thicknesses, the onset velocities that were reported in the experiments of Gad-el-Hak *et al.*[7] The values of the parameters were taken from the experimental results of Kendall.[20] Evrensel and Kalnins[11] reconsidered an inviscid, incompressible fluid model and noted discrepancies between

 0001-4966/97/101(4)/2070/5/$10.00

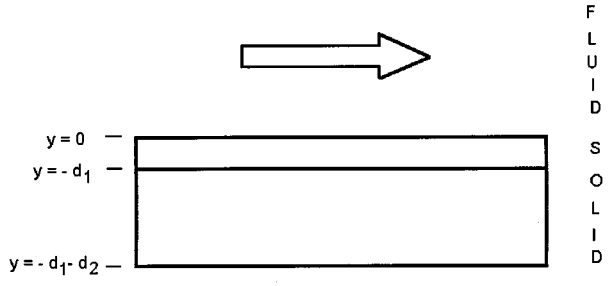

FIG. 1. Geometry of the problem.

the results of this model and the experimental results. They also explored the interaction of viscoelastic slab with boundary layer flows.[12] The key features of their model are that the two media are fully coupled through stresses and velocities in both tangential and normal directions, and boundary conditions are satisfied at the deformed surface of the slab. This model is able to explain most of the experimental observations of Gad-el-Hak,[7,8] both qualitatively and quantitatively.

Lucey and Carpenter[21] numerically simulated the hydroelastic behavior of a one-layer compliant wall of finite dimensions. Using an unsteady potential flow model and a specially developed boundary-element method, they calculated the perturbation pressures which arise from wall disturbances of arbitrary form. They showed that above a critical flow speed and once sufficient time has passed, the compliant wall adopts the particular profile of an unstable mode.

I. STATEMENT OF THE PROBLEM

In this paper, the interaction of a fluid flow with a compliant coating is studied theoretically (Fig. 1). The coating is treated as a two-layer elastic or viscoelastic solid of finite thickness, bonded to a rigid half-space. The fluid is modeled by the potential theory and slip is allowed at the fluid–solid interface. The objective is to examine the behavior of the two-layer slab with increasing flow speed and to determine the effect of different material and geometric parameters on the onset flow velocity, phase speed, and wavelength for unstable surface waves.

II. FORMULATION OF THE PROBLEM

A. Fluid

A propagating sinusoidal wave on the solid boundary can be expressed as

$$\eta = \hat{\eta} e^{i\alpha(x-ct)}, \tag{1}$$

where $\hat{\eta}$ is the wave amplitude (assumed to be small), α is the wave number, c is the wave speed, x is the horizontal axis, and t is time. A surface deformation given in this form generates a change in the fluid pressure that can be derived as[11]

$$\Delta p = p - p_0 = -[\rho_f (U_0 - c)^2 \alpha + g]\eta, \tag{2}$$

where p is the surface pressure, p_0 is the pressure at the undeformed surface at $\eta = 0$, ρ_f is the fluid density, and g is the acceleration of gravity. This expression gives the relation between the surface deformation and the pressure in an inviscid fluid with uniform velocity U_0.

B. Solid

The solution for a two-dimensional elastic slab in a form needed in this paper was derived and it is included in a paper by Evrensel and Kalnins.[11] By using this solution, the stress-displacement relations for each slab can be written as follows:

$$\{S_1\} = [K1]\{u_1\}, \quad \{S_2\} = [K2]\{u_2\},$$

where $\{S\},\{u\}$ are the stresses and displacements on the boundaries of a slab, subscripts 1 and 2 denote the variables for the slabs 1 and 2, respectively, and they are given as

$$\begin{aligned}
\{S_1\} &= \{\sigma_{yy1}(x,0,t) \;\; \tau_{xy1}(x,0,t) \;\; \sigma_{yy1}(x,-d_1,t) \\
&\qquad \tau_{xy1}(x,-d_1,t)\}^T, \\
\{S_2\} &= \{\sigma_{yy2}(x,-d_1,t) \;\; \tau_{xy2}(x,-d_1,t) \\
&\qquad \sigma_{yy2}(x,-d_2,t) \;\; \tau_{xy2}(x,-d_2,t)\}^T, \\
\{u_1\} &= \{u_{y1}(x,0,t) \;\; u_{x1}(x,0,t) \;\; u_{y1}(x,-d_1,t) \\
&\qquad u_{x1}(x,-d_1,t)\}^T, \\
\{u_2\} &= \{u_{y2}(x,-d_1,t) \;\; u_{x2}(x,-d_1,t) \\
&\qquad u_{y2}(x,-d_2,t) \;\; u_{x2}(x,-d_2,t)\}^T.
\end{aligned}$$

$[K1]$ and $[K2]$ are stiffness matrices for slabs 1 and 2, respectively, and they can be written in partitioned form as

$$\begin{aligned}
[K1] &= \begin{bmatrix} K1_1 & K1_2 \\ K1_3 & K1_4 \end{bmatrix}, \\
[K2] &= \begin{bmatrix} K2_1 & K2_2 \\ K2_3 & K2_4 \end{bmatrix}.
\end{aligned} \tag{3}$$

Stiffness matrix for an elastic slab of constant thickness is given by Evrensel and Kalnins.[11] By knowing that the stresses and displacements should be continuous at $y = -d_1$ and the displacements are zero at $y = -(d_1 + d_2)$, one can derive the relation between stresses and displacements at $y = 0$ as

$$\{S_b\} = [K]\{u_b\}, \tag{4}$$

where

$$\begin{aligned}
[K] &= [K1_1] + [K1_2]\{[K2_1] - [K1_4]\}^{-1}[K1_3], \\
\{S_b\} &= \{\sigma_{yy1}(x,0,t) \;\; \tau_{xy1}(x,0,t)\}^T, \\
\{u_b\} &= \{u_{y1}(x,0,t) \;\; u_{x1}(x,0,t)\}^T.
\end{aligned}$$

C. Coupled problem

By considering fluid to be inviscid, the boundary conditions at $y = 0$ can be written as

$$\begin{aligned}
\sigma_{yy1}(x,0,t) &= \Delta p = -\rho_f[(U_0 - c)^2 \alpha + g]\eta, \\
\tau_{xy1}(x,0,t) &= 0,
\end{aligned} \tag{5}$$

where $\eta = u_{y1}(x,0,t)$. Equation (4) and boundary conditions given in Eqs. (5) represents an eigenvalue problem with ei-

genvalues wave speed c, wave number α, and eigenfunctions $\{\sigma_{yy}(x,y,t)\ \tau_{xy}(x,y,t)\ u_y(x,y,t)\ u_x(x,y,t)\}$. Substituting Eqs. (5) into Eq. (4), including the gravity, the dispersion relation is obtained as

$$[K_{11}-K_{12}(K_{21}/K_{22})]-\rho_f[(U_0-c)^2\alpha]+(\rho_f-\rho_s)g=0, \quad (6)$$

where K_{ij}'s are the elements of the $[K]$ matrix, which is defined by Eq. (4). In general K_{ij}'s are complex, and the solutions, both eigenvalues and eigenfunctions, are expected to be complex, and either α or c, or both can be chosen as complex parameters. This study assumes c, wave speed, to be the complex eigenvalue for a given real α, wave number, and U_0, fluid velocity. In other words, temporal instability is sought.

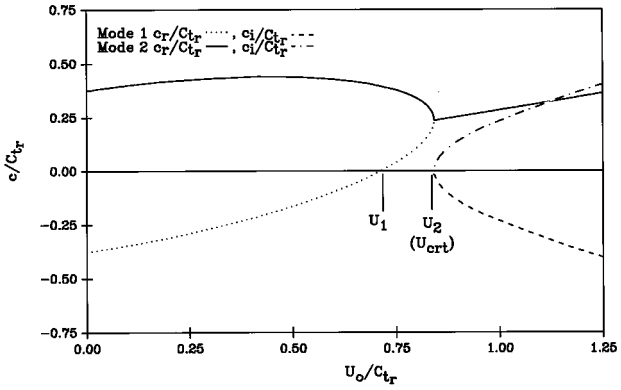

FIG. 2. Phase speed versus flow velocity for $\alpha(d_1+d_2)=1.5$, elastic slab.

III. RESULTS

All results given in this section are for shear modulus ratio $G_{1_r}/G_{2_r}=13$, Poisson's ratio of 0.49 (nearly incompressible material), and slabs and fluid (water) have equal densities, $\rho_{s_1}=\rho_{s_2}=\rho_s$, $\rho_s/\rho_f=1$ and $\alpha(d_1+d_2)=1.5$, $d_2/d_1=5$, unless otherwise stated. G_{j_r} is the real part of the complex shear modulus of the jth viscoelastic slab which is defined as (for Kelvin–Voigt model)

$$G^*=G_r+G_i=G_r(1-i\delta\omega),$$

where ω is the radian frequency and δ is zero for an elastic slab. G_r and G_i are referred to as the storage (represents elasticity) and loss (represents viscosity) moduli, respectively. It should also be noted that since $\rho_s=\rho_f$ gravity term in Eq. (6) vanishes.

For each value of U_0 and a given α, there exists an infinite number of solutions, each with a different wave speed and a different distribution of stresses, displacements, velocity, and pressure throughout the slab and the fluid. Knowing that the higher modes correspond to higher frequencies, which damp out faster in the presence of viscosity, only the lowest two modes are considered in this paper. Results are given in dimensionless forms U_0/C_{t_r}, c/C_{t_r} and $\alpha(d_1+d_2)$, where C_{t_r} is the shear wave speed for the upper slab and it is defined as

$$C_{t_r}=(G_{1_r}/\rho_{s_1})^{1/2}.$$

Here, G_1 is the shear modulus of the upper slab and subscript r stands for the real part of a complex number.

A. Elastic slab

Dimensionless wave speed versus dimensionless flow velocity, for inviscid, incompressible fluid flow over a two-layer elastic slab is given in Fig. 2. The mode with downstream running waves (positive phase speed, real part of c) is named mode 2 and the one with upstream running waves at lower flow speeds and downstream running waves for higher flow speeds is referred to as mode 1. These modes are ''slab modes'' which are modified due to the presence of fluid (a discussion on the distinction between the ''solid'' and ''fluid'' modes is given in Ref. 12). For this case, the dimensionless wave number, $\alpha(d_1+d_2)$ is 1.5, subscript r stands for the real part of the complex wave speed, and i represents the imaginary part. Three different regions can be identified. For a flow velocity less than U_1, where the wave speed for the mode 1 changes sign, both modes have real wave speed with positive or negative magnitudes. This means that the perturbation waves, depending on the initial conditions, can propagate in the positive or negative x direction. Since the wave speeds are real, the waves will propagate forever without any change in amplitudes for $U_0/C_{t_r}<U_1$. If the dimensionless flow velocity is increased to U_1, mode 1 predicts that wave speed is zero (standing wave). At $U_0/C_{t_r}=U_{\rm crt}=0.85$ two modes merge together, and for higher U_0/C_{t_r} values the imaginary part of the wave speed is no longer zero, and the amplitudes will not stay constant, but will grow or decay exponentially with time, depending on the sign of the imaginary part of c (positive imaginary part indicates growth or instability). The value of U_0/C_{t_r} at $U_{\rm crt}$ is called the critical flow velocity, because this is the flow velocity where the coupled system becomes unstable for the given value of the dimensionless wave number $\alpha(d_1+d_2)$. The phase speed, the real part of c, at the critical flow velocity $U_{\rm crt}$ is about half the flow velocity. In other words, inviscid theory predicts that instability originates in the form of a propagating wave form, with phase speed 50% of the flow velocity, as experimentally observed.[8]

$U_{\rm crt}=C_{t_r}$ decreases with increasing $\alpha(d_1+d_2)$ for a given d_1+d_2 up to a critical value and increases beyond that, i.e., there is a minimum value of the critical speed which is the onset flow speed. This onset flow speed as a function of slab thickness is discussed in the next section.

Figure 3 gives the eigenfunctions u_y and u_x, both real and imaginary parts, as a function of y. In this figure, subscript r stands for the real part and subscript i designates the imaginary part. It is clear that this is the solution for the lowest mode. Also, note that the displacement is continuous at $y=-d_1$, as required by the continuity, but the slope is not. This is due to different material properties for each layer, which causes the strains to be discontinuous at the interface.

B. Viscoelastic slab

Figure 4 shows the dispersion relation for a viscoelastic slab with $\delta=0.002$ for both layers. For this case wave speed

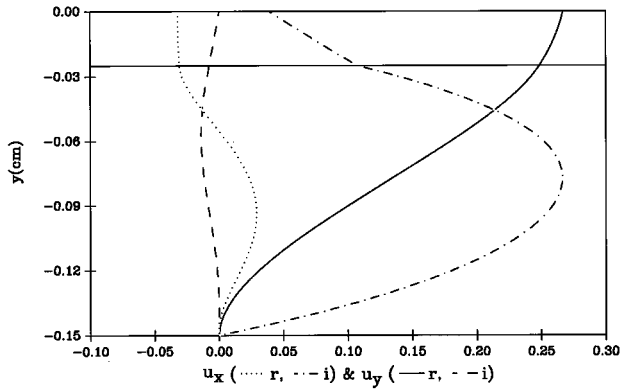

FIG. 3. Eigenfunctions u_y and u_x for $U_0/C_{t_r}=1.16$, $c/C_{t_r}=0.33-0.35i$, and $\alpha(d_1+d_2)=1.5$, elastic slab.

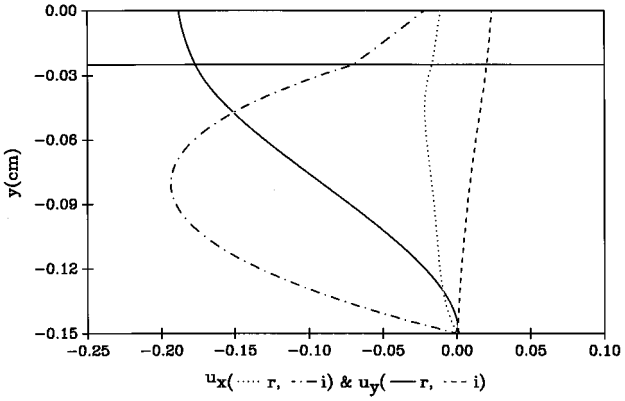

FIG. 5. Eigenfunctions u_y and u_x for $U_0/C_{t_r}=1.04$, $c/C_{t_r}=0.34-0.23i$, and $\alpha(d_1+d_2)=1.5$, viscoelastic slab with $\delta_1=\delta_2=0.002$.

is no longer real for $U_0/C_{t_r} < U_1$, but it has negative imaginary part for both modes. If the flow velocity is increased to U_1, both real and imaginary parts of the wave speed for the mode 1 become positive, indicating initiation of instability. This flow velocity is called U_{crt}/C_{t_r} which changes with wave number. If Figs. 2 and 4 are compared, it can be seen that mode 1 is stable between U_1 and U_2 for an elastic slab, but it is unstable for a viscoelastic slab. In other words, positive portion of the mode 1 is destabilized by the solid ''viscosity.'' Note that for inviscid flow over a viscoelastic slab, instability originates in the form of a *static* wave form, instead of a *propagating* wave. If the ''viscosity'' term, δ, for both slabs is increased, the magnitude of the imaginary part of c increases but the critical flow speed for which the instability initiates remains the same. In other words, according to the model, although growth rate, αc_i, increases with the ''viscosity'' of the slab, the critical velocity is not sensitive to it, if both layers of the slab are viscoelastic. Eigenfunctions for a two-layer viscoelastic slab shown in Fig. 5 have the same general behavior as the eigenfunctions of an elastic slab (Fig. 3). The difference in magnitudes and signs of eigenfunctions is immaterial.

Figure 6 shows the case where the upper layer is elastic and the lower layer is viscoelastic. Although the general behavior of the curves remain unchanged, critical flow speed, $U_{\text{crt}}/C_{t_r}=0.8$, is higher than the case where both layers are viscoelastic, $U_{\text{crt}}/C_{t_r}=0.7$, but lower than the case where both layers are elastic, $U_{\text{crt}}/C_{t_r}=0.85$. U_{crt}/C_{t_r} for the viscoelastic upper layer and elastic lower layer is comparable to the case with elastic upper layer and viscoelastic lower layer, although c_i is smaller in magnitude for all U_0/C_{t_r} values. This is expected since the upper layer is thinner and its ''viscosity'' will have a less overall effect on the ''viscosity'' of the two-layer slab.

Onset flow velocity, defined as the minimum U_{crt}/C_{t_r}, is sensitive to the total slab thickness, d_1+d_2 for a ''thin'' slab and approaches to an asymptotic value for a ''thick'' slab as shown in Figs. 7 and 8. In these figures, two cases are shown: either the d_2/d_1 (Fig. 7) ratio or d_1 (Fig. 8) kept constant. For the case where d_2/d_1 is kept constant (Fig. 7) the onset flow velocity increases with increasing slab thickness. This can be explained by the increased ''bending stiffness'' of the two-layer slab due to increased thickness of the upper slab, which is much stiffer than the lower one. On the other hand, if d_1 is kept constant, as shown in Fig. 8, the thickness of the ''softer'' slab is increased only and the overall stiffness of the slab decreases, and this results in decreased onset speed. Also, as discussed earlier, onset velocity for the viscoelastic slab is lower than the one for elastic slab.

IV. CONCLUSIONS

The model discussed in this paper assumes the flow of an inviscid, incompressible fluid over a two-layer slab

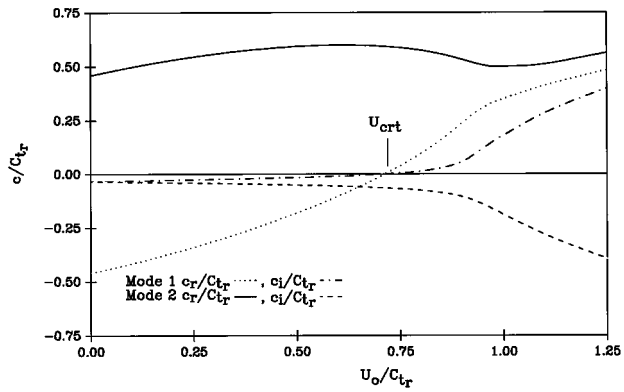

FIG. 4. Phase speed versus flow velocity, viscoelastic slab, $\delta_1=\delta_2=0.002$.

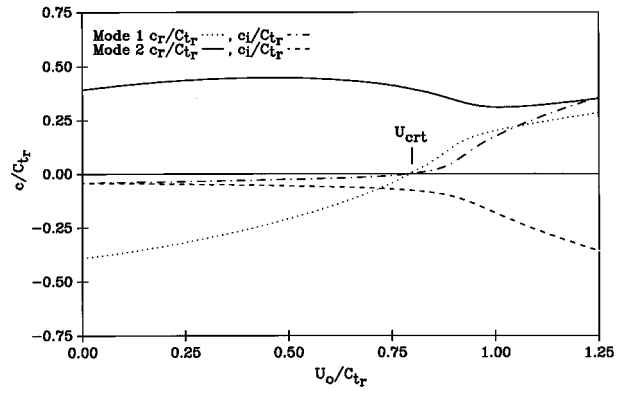

FIG. 6. Phase speed versus flow velocity, viscoelastic slab, $\delta_1=0.00$, $\delta_2=0.002$.

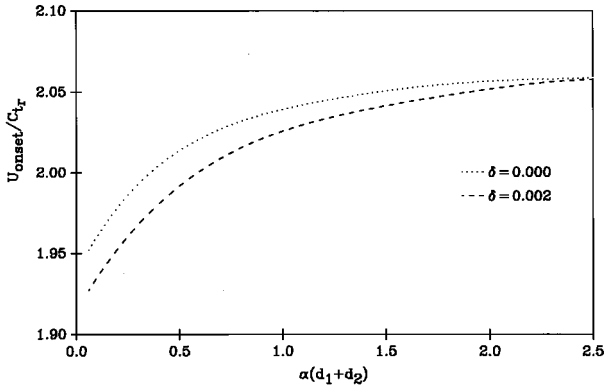

FIG. 7. Onset velocity versus slab thickness, viscoelastic slab, $d_2/d_1=5$.

bonded to a rigid base. It can explain most of the qualitative characteristics of the compliant-layer: fluid interaction, such as initiation of instability in the form of propagating waves for an elastic slab and standing waves for a viscoelastic slab, change in onset flow velocity with total slab thickness, etc. A quantitative agreement between the experimental results and the predictions of this model should not be expected because of the absence of fluid viscosity and the resulting boundary layer.

Some of the predictions of the model can be summarized as:

(1) Unstable surface waves at the interface of inviscid flow and two-layer elastic slab (both layers are elastic) have phase speeds of about 50% of the flow velocity.
(2) Instabilities of a two-layer viscoelastic slab (at least one layer is viscoelastic) originate in the form of standing waves.

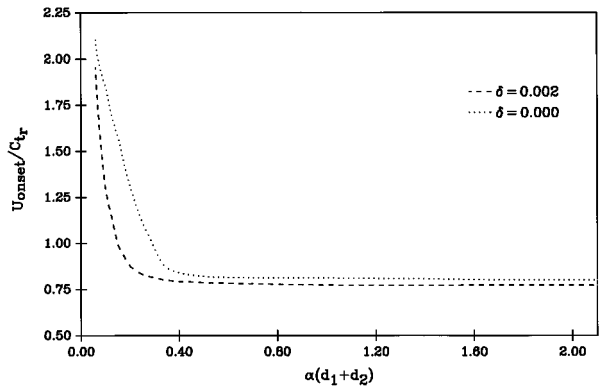

FIG. 8. Onset velocity versus slab thickness, viscoelastic slab, $d_1=0.15$ cm.

(3) The onset flow speed decreases with the addition of ''viscosity'' to one of the layers, and it is minimum if both layers are viscoelastic.
(4) The onset flow speed is sensitive to total slab thickness as well as the thickness ratio of layers.

[1] A. Kalnins and C. A. Evrensel, ''Simple low-frequency model for response of compliant coatings,'' J. Acoust. Soc. Am. Suppl. 1 **77**, S24 (1985).
[2] M. Gad-el-Hak, ''Boundary layer interactions with compliant coatings: An overview,'' Appl. Mech. Rev. **39**, 511–523 (1986).
[3] F. W. Boggs and E. R. Hahn, ''Performance of compliant skins in contact with high velocity flow in water,'' in *Proceedings of the 7th Joint Army–Navy–Air Force Conference on Elastomer Research and Development* (U.S. Office of Naval Research, Washington, DC, 1962), pp. 443–464.
[4] R. J. Hansen and D. L. Hunston, ''An experimental study of turbulent flows over compliant surfaces,'' J. Sound Vib. **34**, 297–308 (1974).
[5] R. J. Hansen, D. L. Hunston, C. C. Ni, and N. M. Reischman, ''An experimental study of flow-generated waves on a flexible surface,'' J. Sound Vib. **68**, 317–334 (1980).
[6] R. J. Hansen and D. L. Hunston, ''Fluid property effects on flow-generated waves on a compliant surface,'' J. Fluid Mech. **133**, 161–177 (1983).
[7] M. Gad-el-Hak, R. F. Blackwelder, and J. J. Riley, ''On the interaction of compliant coatings with boundary layer flows,'' J. Fluid Mech. **140**, 257–280 (1984).
[8] M. Gad-el-Hak, ''The response of elastic and viscoelastic surfaces to a turbulent boundary layer,'' J. Appl. Mech. **53**, 206–212 (1986).
[9] J. R. Riley, M. Gad-el-Hak, and R. W. Metcalfe, ''Compliant coatings,'' Ann. Rev. Fluid Mech. **20**, 393–420 (1988).
[10] P. W. Carpenter, ''Status of transition delay using compliant walls'', in *Viscous Drag Reduction in Boundary Layers*, edited by D. M. Bushnell and J. M. Hefner (AIAA, Washington, DC, 1990), pp. 79–113.
[11] C. A. Evrensel and A. Kalnins, ''Response of a compliant slab to inviscid incompressible fluid flow,'' J. Acoust. Soc. Am. **78**, 2034–2041 (1985).
[12] C. A. Evrensel and A. Kalnins, ''Response of a compliant slab to viscous incompressible fluid flow,'' J. Appl. Mech. **55**, 660–666 (1988).
[13] T. B. Benjamin, ''Shearing flow over a wavy boundary,'' J. Fluid Mech. **6**, 161–205 (1959).
[14] M. T. Landahl, ''On the stability of a laminar incompressible boundary layer over a flexible surface,'' J. Fluid Mech. **13**, 609–632 (1962).
[15] R. E. Kaplan, ''The stability of laminar incompressible boundary layers in the presence of compliant boundaries,'' ScD thesis, MIT, 1964.
[16] J. H. Duncan, A. M. Waxman, and M. P. Tulin, ''The dynamics of waves at the interface between a viscoelastic coating and a fluid flow,'' J. Fluid Mech. **158**, 177–197 (1985).
[17] T. B. Benjamin, ''Effects of a flexible boundary on hydrodynamic stability,'' J. Fluid Mech. **9**, 513–532 (1960).
[18] T. B. Benjamin, ''The threefold classification of unstable disturbances in flexible surfaces bounding inviscid flows,'' J. Fluid Mech. **16**, 436–450 (1963).
[19] M. Pierucci, ''Surface waves of an elastic medium in the presence of an inviscid flow field,'' J. Acoust. Soc. Am. **61**, 965–971 (1977).
[20] J. M. Kendall, ''The turbulent boundary layer flow over a wall with progressive waves,'' J. Fluid Mech. **41**, 259–281 (1970).
[21] A. D. Lucey and P. W. Carpenter, ''A numerical simulation of the interaction of a compliant wall and inviscid flow,'' J. Fluid Mech. **234**, 121–146 (1992).

Placing constrained layer damping patches using reactive shearing structural intensity measurements

Daniel H. Kruger, J. Adin Mann III, and Ted Wiegandt
Department of Aerospace Engineering and Engineering Mechanics, 2019 Black Engineering Building, Iowa State University, Ames, Iowa 50011

(Received 15 May 1996; accepted for publication 22 October 1996)

The use of reactive shearing structural intensity to place small patches of constrained layer damping material in order to achieve the largest reduction in the radiated sound power of a cubic structure is described. The normal surface velocity of a square plate was measured using a laser vibrometer. The plate was measured with no damping and with various damping configurations. Reactive structural intensity was calculated for the undamped plate for velocity distributions at resonance frequencies of the first and third modes of the plate. A cube was simulated by placing various measured plate velocity distributions at these same two frequencies on one side of the cube while leaving the remaining five sides rigid. The sound power radiated by the cubic structure as a function of normal surface velocity was written using the boundary element method. Experimental results indicated that patches of constrained layer damping material placed over areas of high reactive structural intensity reduced the radiated sound power significantly more than patches of the same area placed over areas of low reactive structural intensity. Reductions as high as 10.25 dB were achieved for patches comprising only 6.4% of the area of one side of the cube by varying the number, size, shape, and placement of constrained layer damping patches to correspond to areas where the reactive shearing structural intensity magnitude was high. [S0001-4966(97)02503-4]

PACS numbers: 43.40.Dx, 43.40.Rj, 43.20.Ye [CBB]

INTRODUCTION

Reducing the sound radiated by structures with outer surfaces consisting mainly of thin metal sheets or plates is of great interest to many working in structural acoustics. Examples of such structures are washing machines, refrigerators, or even a car body. Typically, the existing structure has been designed for performance specifications other than low noise levels and cannot be dramatically redesigned. Active control solutions are often costly and hard to incorporate into the manufacturing process of existing designs. A passive solution that could be added to existing structures, either before or after manufacture, is extremely desirable.

While it is common to cover as much of a structure as possible with vibration damping material, in order to reduce material and manufacturing costs the use of small damping patches is desirable. Applying small patches of constrained layer damping material to an existing structure, placed using reactive shearing structural intensity, can significantly alter the vibration of that structure. Specifically, Spalding and Mann[1] showed that reactive shearing structural intensity could be used to place constrained layer damping patches in order to achieve global or local changes in the normal surface velocity of a plate. It is the main goal of this research to show that the ideas of Spalding and Mann concerning reactive shearing structural intensity can be extended to place constrained layer damping patches on a plate in such a way as to significantly reduce the radiated sound power from a vibrating structure.

This paper begins with a brief summary of the methods used to calculate reactive shearing structural intensity. Then the experimental procedure for measuring normal surface velocity of a plate with clamped boundary conditions using a laser velocimeter is presented. Next, four experiments involving various configurations of constrained layer damping patches placed on the plate and measured using the experimental procedure presented are described. A velocity pattern for a cube is constructed by placing the plate velocity on one side of the cube and a velocity of zero on the other five sides.

The sound power radiated by the cubic structure is calculated as a quadratic function of the normal surface velocity assembled from the plate velocity using the boundary element method (BEM).[2] The cube was chosen because the boundary element code that was used to calculate the radiated sound power was a three-dimensional code. Results of the four experiments are used to explore the reductions in calculated radiated sound power for a cube. Finally, conclusions describing the reactive shearing structural intensity as an effective tool for placing small patches of constrained layer damping material are made.

I. STRUCTURAL INTENSITY

The equations for structural intensity and their development are well documented in the literature.[3,4] So are the methods for signal processing and filtering required to effectively implement the structural intensity equations on the computer.[1,5–7] In this research, Pavic's equations were used.[4,7] For a plate lying in the xy plane, the structural intensity in the x direction is written as

$$I_x = \frac{D}{2}\left[-\left(\frac{\partial^2 w}{\partial x^2} + \nu \frac{\partial^2 w}{\partial y^2}\right)\left(\frac{\partial}{\partial x}\dot{w}^*\right) - (1-\nu) \times \frac{\partial^2 w}{\partial x\,\partial y}\left(\frac{\partial}{\partial y}\dot{w}^*\right) + \left(\frac{\partial^3 w}{\partial x^3} + \frac{\partial^3 w}{\partial x\,\partial y^2}\right)\dot{w}^*\right]. \quad (1)$$

The structural intensity in the y direction is written as

$$I_y = \frac{D}{2}\left[-\left(\frac{\partial^2 w}{\partial y^2} + \nu \frac{\partial^2 w}{\partial x^2}\right)\left(\frac{\partial}{\partial y}\dot{w}^*\right) - (1-\nu) \times \frac{\partial^2 w}{\partial x\,\partial y}\left(\frac{\partial}{\partial x}\dot{w}^*\right) + \left(\frac{\partial^3 w}{\partial y^3} + \frac{\partial^3 w}{\partial x^2\,\partial y}\right)\dot{w}^*\right], \quad (2)$$

where * denotes complex conjugate, w is the normal displacement of the plate surface, ν is Poisson's ratio for the plate, $\cdot$ denotes a time derivative, and $D = Eh^3/12(1-\nu^2)$, where h is the plate thickness and E is Young's modulus.

Structural intensity in either direction can be split into three parts, bending, twisting, and shearing, each corresponding to a wave type propagating through the plate.[5] For example, structural intensity in the y direction, shown in Eq. (2), can be split into these three parts as

$$I_{y,\text{bending}} = -\frac{D}{2}\left(\frac{\partial^2 w}{\partial y^2} + \nu \frac{\partial^2 w}{\partial x^2}\right)\left(\frac{\partial}{\partial y}\dot{w}^*\right), \quad (3)$$

$$I_{y,\text{twisting}} = -\frac{D}{2}(1-\nu)\frac{\partial^2 w}{\partial x\,\partial y}\left(\frac{\partial}{\partial x}\dot{w}^*\right), \quad (4)$$

$$I_{y,\text{bending}} = +\frac{D}{2}\left(\frac{\partial^3 w}{\partial y^3} + \frac{\partial^3 w}{\partial x^2\,\partial y}\right)\dot{w}^*. \quad (5)$$

In all five equations, the structural intensity is written as a complex quantity. The real part of intensity is called the active intensity and corresponds directly to power flow through the plate. The imaginary part is called the reactive intensity, and does not in general have a direct physical counterpart like the active intensity. However, the reactive intensity can be shown in special cases to relate to some simple physical ideas.[8] Based on the work by Zhang[6,7] and Spalding and Mann,[1] reactive shearing structural intensity will be used as a tool to place small patches of constrained layer damping material to achieve large reductions in radiated sound power.

II. EXPERIMENTAL PROCEDURE

The normal velocity of a thin square aluminum plate with clamped boundary conditions on all four sides was measured using a laser velocimeter. Clamped boundary conditions were enforced by a steel frame with 2.54 cm by 5.08-cm-thick rectangular bars on either side of the plate around all of the edges of the plate. All experiments were performed without altering the frame. The square plate measured 60.96 cm on a side inside the edges of the frame, and was 3.175 mm thick. A total of 1024 evenly spaced measurement points on a 32×32-point grid were used to sample the undamped plate for the purpose of calculating the reactive shearing structural intensity. For the purpose of calculating the radiated sound power for the cube, the undamped plate was measured again for a grid of 225 evenly spaced points. This grid

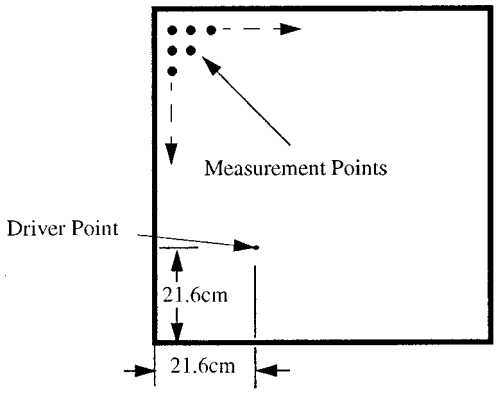

FIG. 1. Experimental setup, shaker location, and measurement grid for the square plate.

was chosen so that measurement points corresponded to node points for a cube discretized into 294 boundary elements. The 225-point measurement grid was also used to sample damped plates with the laser velocimeter.

The plate was point driven by a shaker in the lower left-hand corner of the plate, as shown in Fig. 1. All constrained layer damping patches consisted of 3M Scotchdamp viscoelastic damping material number SJ 2015 type 1205 constrained by a 0.3-mm-thick aluminum layer. Patches were applied to the back side of the plate. Patches were varied in number, size, and shape.

The normal surface velocity was measured with a Polytec OFV 1102 laser vibrometer. The plate was excited by a B&K 4809 shaker attached to the plate with a 5-cm-long stinger attached to a PCB 208 A02 force transducer. The signals from the force transducer and the laser vibrometer were amplified by an Ithaco 453 amplifier and filtered by Krohn–Hite model 30 low-pass elliptical filters with roll offs of 148 dB per octave. Each signal was amplified 20 dB and low-pass filtered with a 500-Hz cutoff frequency. The signals were sampled at 2048 Hz by a Concurrent computer. The Fourier transform of each signal was calculated and the frequency response function was calculated at each frequency. Thus the final data that was obtained was the velocity per unit input force at each measurement location.

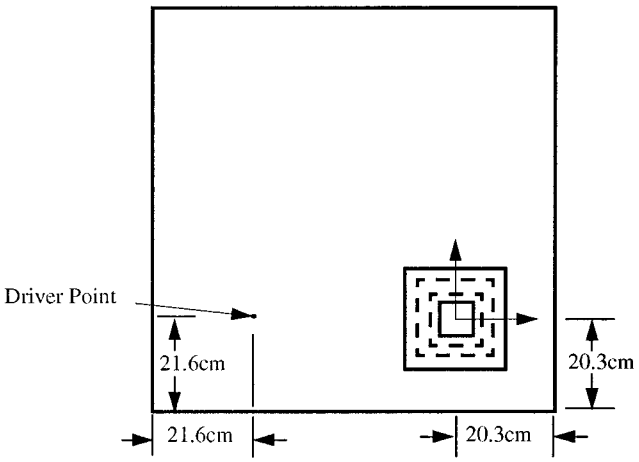

FIG. 2. Measurement situation for the square damping patches.

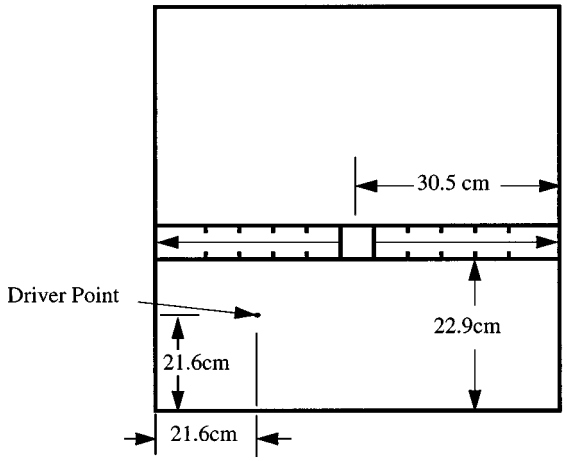

FIG. 3. Measurement situation for the rectangular damping patches.

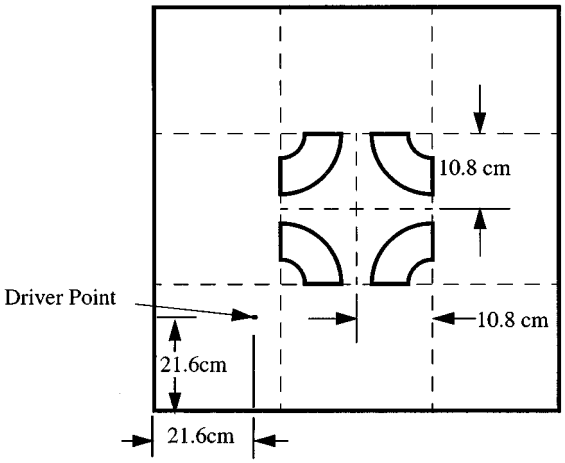

FIG. 5. Measurement situation for the second configuration of four circular arcs.

A total of four experiments were performed using the measurement procedures previously described. The undamped plate was measured first in each of the four experiments. Also, the same plate was used for all four experiments. Existing damping patches were easily removed by first pulling off the constraining layer, and then soaking the viscoelastic material with acetone. After about a half-hour of soaking, the material could be easily wiped off the plate with a cloth soaked with acetone. The positioning of the patches will be described in the remainder of this section. The reasoning behind this positioning will be described in Sec. III.

The first experiment involved a series of eight square constrained layer damping patches. The size of the first patch was 5.08 cm by 5.08 cm, about 0.69% of the total plate area. For the other seven measurements, the size of the damping patch was uniformly increased by 0.69% of the total plate area while keeping the patch square, until a maximum of 5.56% of the total plate area was reached for measurement 8. Figure 2 shows the position of the patches in this experiment.

The second experiment involved a series of 23 rectangular patches of constrained layer damping material. Again, the first patch was 5.08 cm by 5.08 cm but was positioned differently, as shown in Fig. 3. The length of each successive patch was increased by 2.54 cm. The largest patch of the 23 measured was 5.08 cm by 60.96 cm, or 8.3% of the total plate area.

In the third experiment, only two constrained layer damping patch configurations were measured in addition to the bare plate. The first configuration is shown in Fig. 4. In this configuration, four identical arcs with inner radii of 3.8 cm and outer radii of 9.5 cm were applied in a circular arrangement centered on the plate. The second configuration consisted of four arcs identical to those in Fig. 4, only this time they were placed with the smaller radii facing the corners of the plate instead of the centers. The patches were placed symmetrically with the center of the inner radii 10.8 cm away from the center of the plate in each direction in the plane of the plate. This arrangement can be seen in Fig. 5. The arcs covered 6.4% of total plate area in both experiments.

The fourth and final experiment consisted of four identical constrained layer damping patches arranged in two different, symmetrical configurations, shown in Figs. 6 and 7. In the first configuration, four square patches measuring 5.08 cm by 5.08 cm were applied to the plate symmetrically.

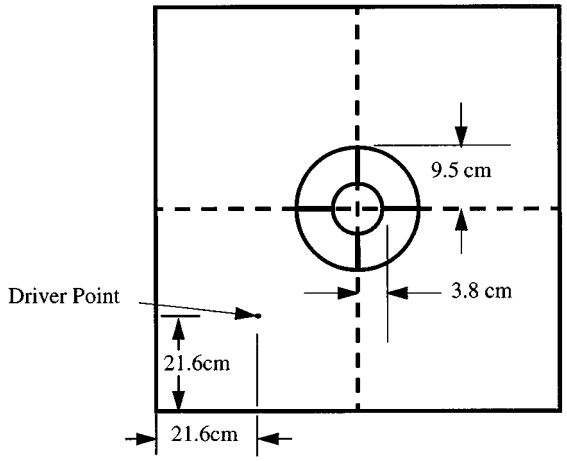

FIG. 4. Measurement situation for the first configuration of four circular arcs.

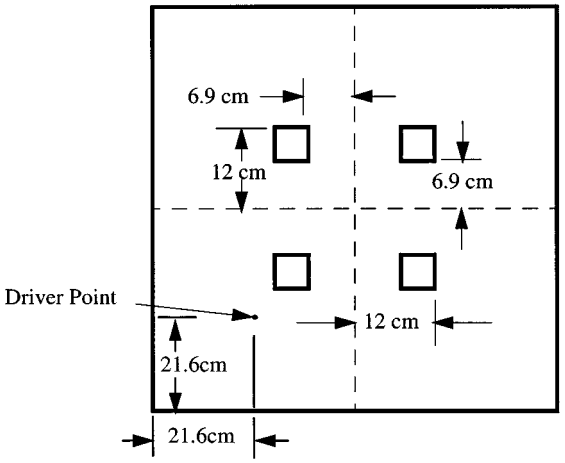

FIG. 6. Measurement situation for the first configuration of four square patches.

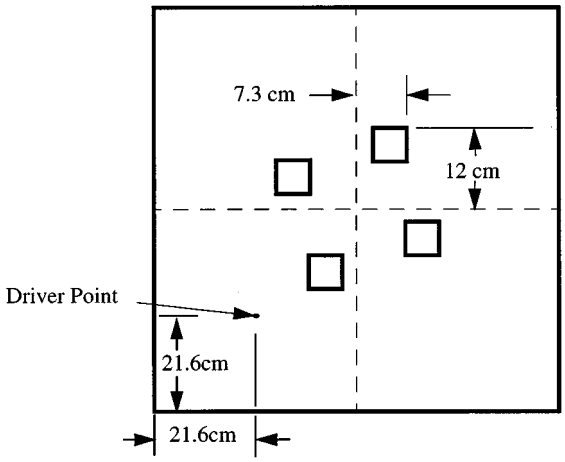

FIG. 7. Measurement situation for the first configuration of four square patches.

These patches were placed with the edges 6.9 cm from the center lines of the plate and covered 2.8% of the total plate area, as shown in Fig. 6. The outer edges were 12 cm from the center line in each direction. For the second configuration, the patches were moved symmetrically closer to the center line of the plate in one direction, as in Fig. 7. The resulting distances to the outer edges from the center lines of the plate were 7.3 and 12 cm. Five additional measurements were made for patches arranged as in the second configuration uniformly increased in size until a maximum patch size of 8.3 cm by 8.3 cm was reached.

III. RESULTS AND DISCUSSION

In all four studies, the velocity patterns for a cubic structure were constructed by placing the velocity distributions from the square plate measurements on one side of the cube while leaving the other five sides rigid, as shown in Fig. 8. This allows the cube to have any one of the damped square plate velocity distributions on the top side of the cube. A rigid velocity pattern was zero velocity at every node on a side of the cube. The radiated sound power was then calculated for the cube using the BEM formulation developed by Cunefare and Koopman.[2]

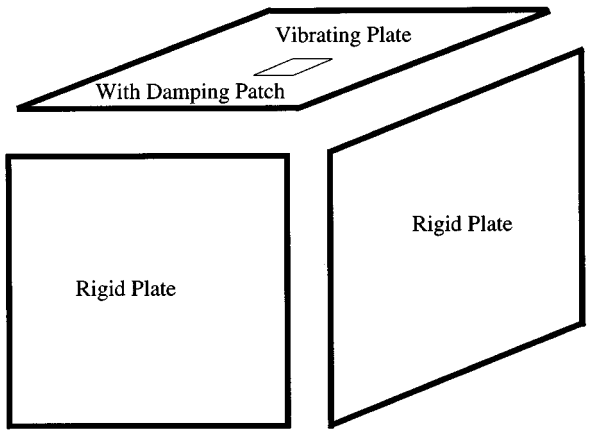

FIG. 8. A cube assembled from one vibrating plate with various damping patches and five rigid plates.

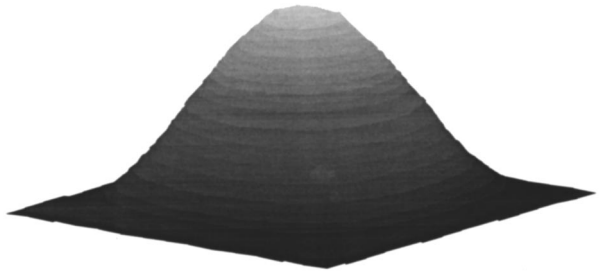

FIG. 9. Measured normal velocity magnitude of the first mode of the clamped plate.

The velocity patterns at the frequency of resonance of the first and third modes of the plate were targeted for reduction in this research. The magnitude of the velocity of these modes for the undamped plate are shown in Figs. 9 and 10. The natural frequency of the first mode was 70.0 Hz and 217 Hz for the third mode. This gave values for the nondimensional wave number ka of 0.4 and 1.2, where k is the acoustic wave number and a is one-half the length of a side of the plate. The radiated sound power was calculated at these single frequencies for each mode shape.

In the first experiment, described in the previous section, the damping patches were placed over areas of high vibration in hopes of achieving reduction in radiated sound power. For the first mode, reductions were less than 0.1 dB until the three largest square patches were applied to the plate. The maximum reduction was 1.6 dB and occurred for the largest patch size. Thus, significant reductions in sound power only occurred for the three largest patches, even though all of the patches were over areas of large vibration.

For the third mode, Fig. 11, reductions of about 2 dB were achieved for the small patch sizes. The reduction jumped suddenly to 7.2 dB for a patch that was 11.4 cm by 11.4 cm, or 129 square cm. However, reductions only increased to 8.7 dB when the patch size was increased to 14.4 cm by 14.4 cm, or 206 cm^2. As with mode 1, significant reduction occurred only after a certain size patch was applied to the plate. After that, reduction only increased by about 1.0 dB when patch area was increased by 60%, even though all patches were over areas of large vibration.

Since placing damping patches over areas of large vibration did not necessarily correspond to significant reductions in radiated sound power, it was concluded that the two vi-

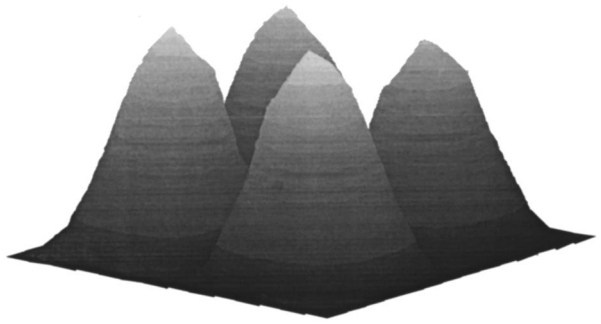

FIG. 10. Measured normal velocity magnitude of the third mode of the clamped plate.

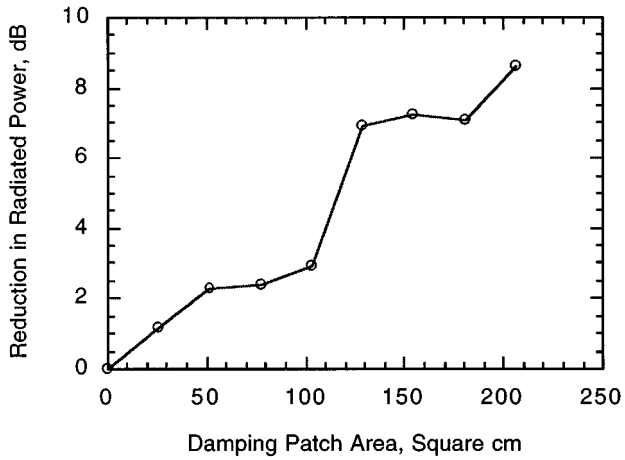

FIG. 11. Reduction in radiated sound power of mode 3 as a function of square damping patch size.

bration modes must have something else in common besides areas of high vibration. The literature indicated the strong relationship between reactive structural shearing intensity and alterations in plate vibration.[1] Reactive structural shearing intensity was calculated for modes 1 and 3 of the undamped plate. The magnitude of intensity is shown in Figs. 12 and 13, respectively. In the figures, white indicates areas of the plate where reactive structural shearing intensity is high, and black indicating areas where it is low. Note that the areas of highest intensity for mode 1 occur in an annulus centered on the plate. On the other hand, reactive shearing intensity is highest in four arcs near the center of the plate for mode 3. The first mode also has some fairly large areas of reactive structural intensity near these arcs.

The relationship between reactive structural shearing intensity becomes apparent when the areas of the damping patches applied to the plate are compared to the intensity plots. For the first mode, Fig. 14, only the three largest patches cover significant areas of the plate where reactive structural shearing intensity is large. These three patches produced reductions in sound power of 0.6, 0.9, and 1.6 dB, respectively, for a cube with a mode 1 velocity pattern on its top side.

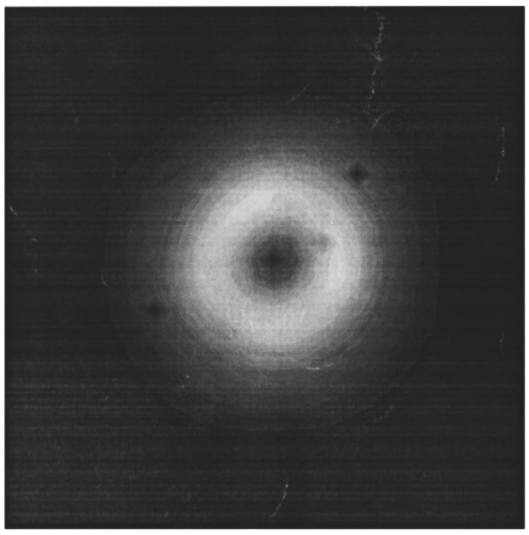

FIG. 12. Reactive shearing structural intensity for the first normal velocity mode of the plate vibration with no damping.

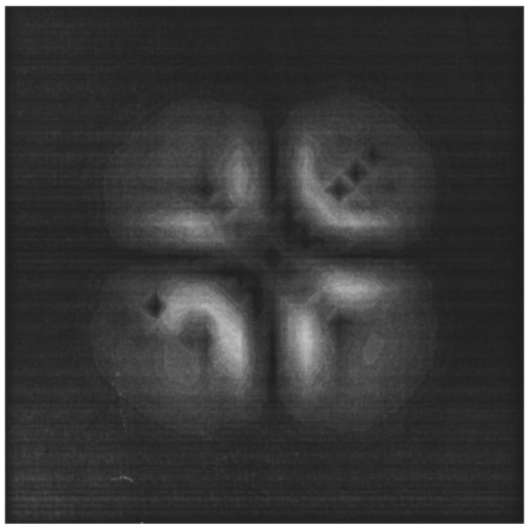

FIG. 13. Reactive shearing structural intensity for the third normal velocity mode of the plate with no damping.

For mode 3 in Fig. 15, the reductions in power are small, less than 2 dB, until the patches are large enough to cover areas that had a high reactive structural shearing intensity when the plate was undamped. Then, reductions suddenly increased to 7.2 dB for the fifth largest patch size. This patch is represented by the dashed line in Fig. 15. Careful observation of Fig. 15 shows that the increased area covered by patches 6, 7, and 8 mostly includes areas of relatively lower reactive structural intensity. This increased area covered directly corresponded to a further reduction in radiated sound power of only 1.5 dB.

Thus, after the first experiment, it was concluded that a strong link between areas of large reactive structural shearing

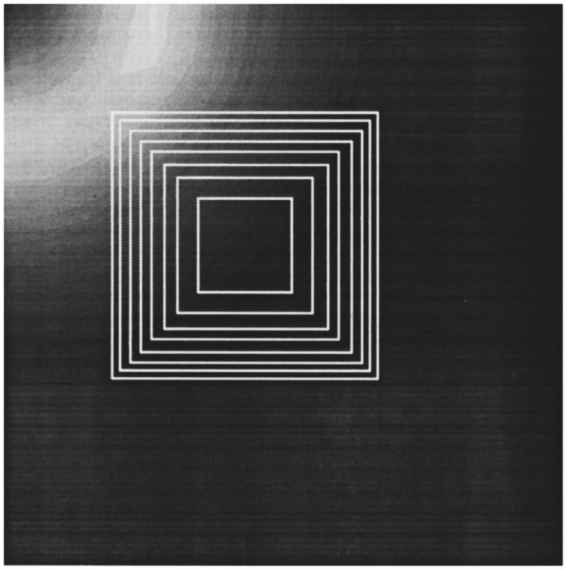

FIG. 14. The undamped reactive shearing structural intensity of mode 1 superimposed with the square damping patches used in experiment 1. Only part of the plate is shown.

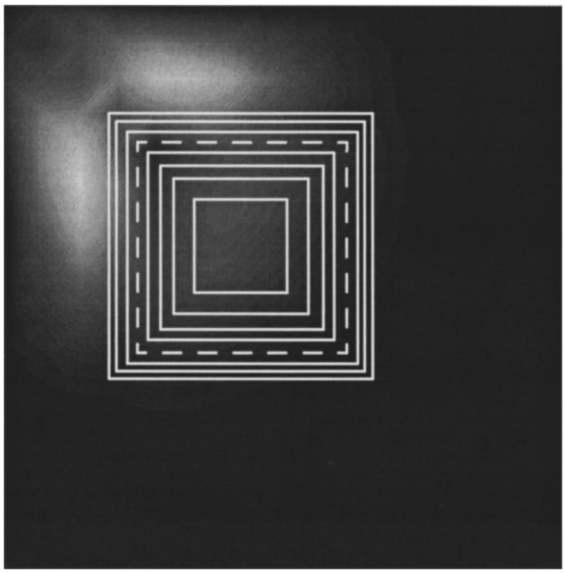

FIG. 15. The undamped reactive shearing structural intensity of mode 3 superimposed with the square damping patches used in experiment 1. Only part of the plate is shown.

intensity and areas of the plate which resulted in large reductions in radiated sound power when covered by patches of constrained layer damping material.

In experiment 2, damping patches were placed as described in the previous section to see if this apparent correlation could be used to more effectively reduce the sound power radiated by mode 1.

Figure 16 shows a comparison between the damping patches used in experiment 2 and the reactive shearing structural intensity of mode 1 for the undamped plate and Fig. 17 shows the corresponding reduction in radiated sound power. This time, as the patch size increased in length until it reached the limit of where intensity values were high, power reductions increased to 2.44 dB. After that, reductions decreased slightly, which is a topic to be discussed in another paper.[9] The solid vertical white lines in Fig. 16 show the length of the damping patch that obtained 2.44 dB reduction in sound power radiated by the cube, indicated by the vertical line in Fig. 17.

Comparing experiment 1 to experiment 2 for mode 1, reduction in radiated sound power reached a maximum of 1.6 dB for a square patch of constrained layer damping material that was 206 cm^2 in experiment 1, and reached a maximum of 2.44 dB for a rectangular patch that was 5.1 cm by 30.5 cm and covered 155.6 cm^2 in experiment 2. Once again in experiment 2, reductions in power ceased to increase when additional area covered by larger patches no longer corresponded to areas where undamped reactive shearing structural intensity was large.

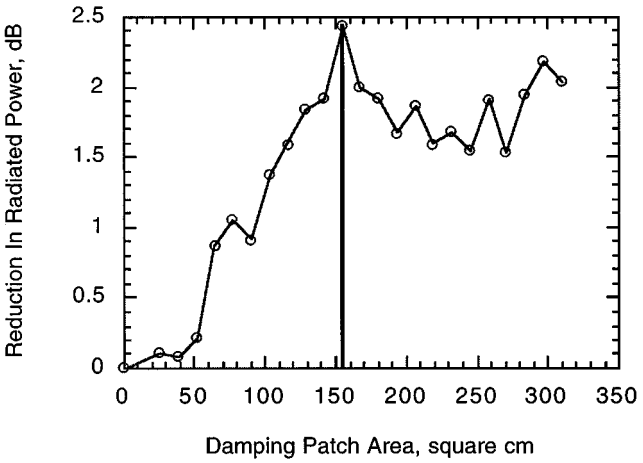

FIG. 17. Reduction in radiated sound power of mode one as a function of rectangular damping patch size.

The two damping configurations used in experiment 3, and described in the previous section, were designed to more closely test the correlation between areas of the plate with high reactive shearing intensity and those which result in the highest reductions in the radiated sound power when covered by constrained layer damping material. As shown in Fig. 18, configuration 1 was designed to cover as much of the highest areas of reactive shearing for mode 1. The damping material consisted of four identical arcs so that four additional identical patches could be used to cover the areas of high reactive shearing intensity for mode three in the second configuration, Fig. 19. The two configurations covered identical 239-cm^2 areas. The hypothesis in experiment 3 is that for indentical

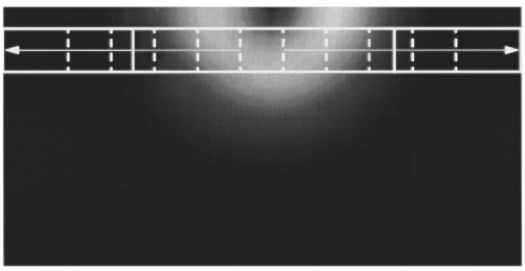

FIG. 16. The undamped reactive shearing structural intensity of mode 1 superimposed with the rectangular damping patches used in experiment 2. Only part of the plate is shown.

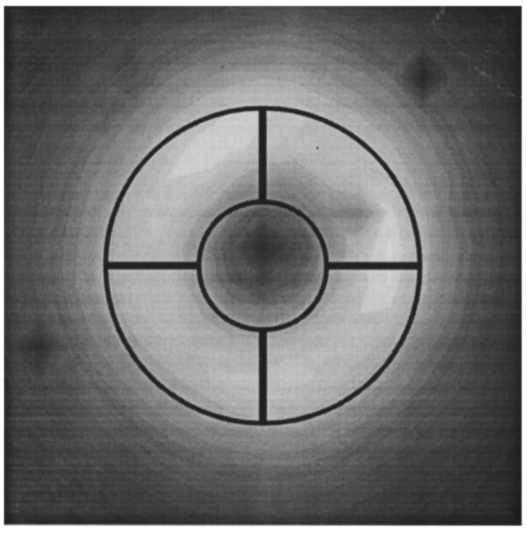

FIG. 18. The undamped reactive shearing structural intensity of mode 1 superimposed with the circular are damping patches used in experiment 3 configuration 1.

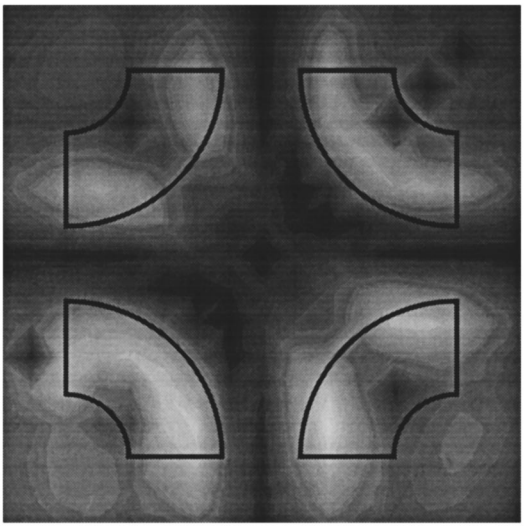

FIG. 19. Comparison of the reactive shearing structural intensity of mode three with the circular arc damping patches used in experiment 3, configuration 2.

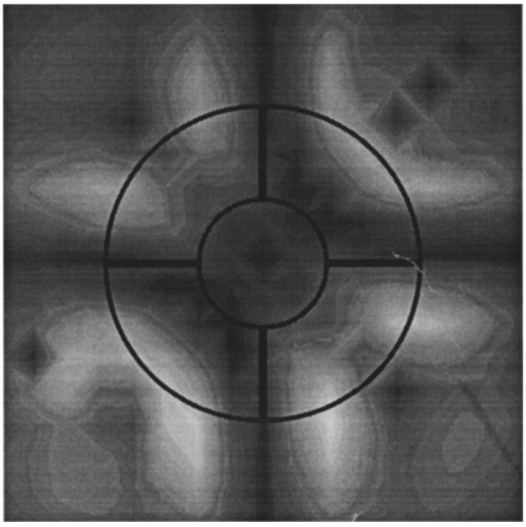

FIG. 21. The undamped reactive shearing structural intensity of mode 3 superimposed with circular arc damping patches used in experiment 3, configuration 1.

patches, configuration 1 will result in more reduction in sound power than configuration 2 for mode 1. At the same time, configuration 2 will result in more reduction in sound power than configuration 1 for mode 3. A third part of the hypothesis is that configuration 1 will reduce power radiated for mode 1 and configuration 2 will reduce power radiated for mode 3 more than any patch in experiments 1 and 2.

Configuration 1 reduced the radiated sound power by 4.47 dB for mode 1, while configuration two resulted in a reduction of 4.17 dB. For mode 3, configuration 2 resulted in a 10.25-dB reduction in the radiated sound power, while configuration 1 achieved a reduction of 9.02 dB. The 10.25-dB reduction was 2.05 dB more than that achieved by experiment 1. Thus all parts of the hypothesis were proven. Further, these large reductions were achieved by covering just 6.4% of the cube's top surface area.

An unexpected result is that though reductions corresponded to the three-part hypothesis, the difference in the reduction for each patch placement was not as large as might have been expected. For instance, configuration 1 only exceeded configuration 2 by 0.3 dB for mode 1. Configuration 2 exceeded configuration 1 by a wider margin of 1.23 dB for mode 3, but was still not as large a difference as might have been expected.

Figures 20 and 21 help explain this result. Figure 20 shows damping configuration 2 superimposed on the undamped reactive shearing intensity. The figure shows that configuration 2 also covers a large portion of the areas where reactive shearing intensity is large for mode 1, although not as much as configuration 1. Figure 21 shows damping configuration 1 superimposed on the undamped reactive shearing intensity for mode 3. Configuration 1 also covers a large portion of the areas where reactive shearing intensity for mode 3 is high. After considering these two figures, it was

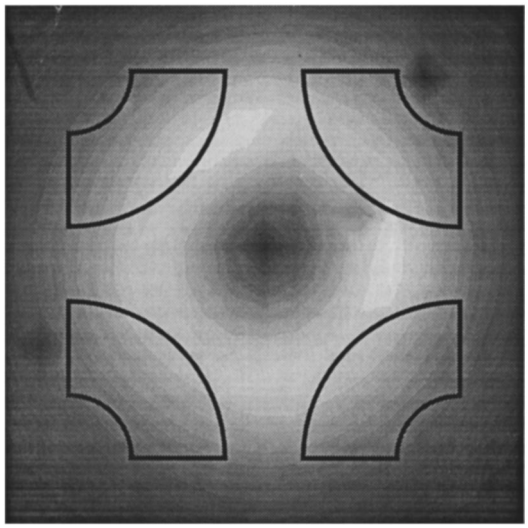

FIG. 20. The undamped reactive shearing structural intensity of mode 1 superimposed with circular arc damping patches used in experiment 3, configuration 2.

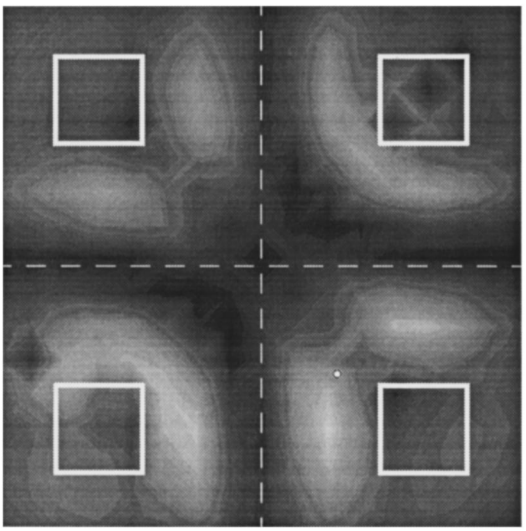

FIG. 22. The undamped reactive shearing structural intensity of mode 3 superimposed with the square damping patches used in experiment 4, configuration 1.

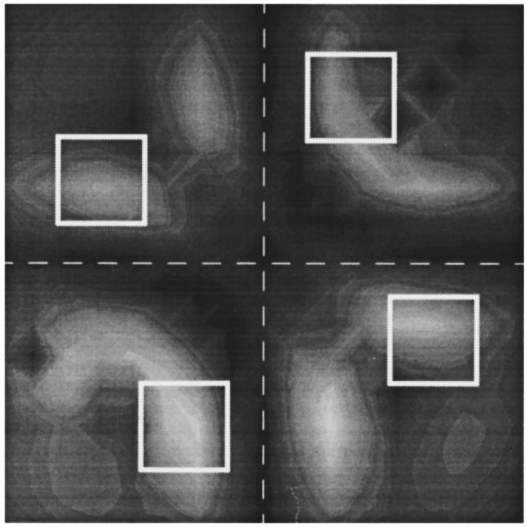

FIG. 23. The undamped reactive shearing structural intensity of mode 3 superimposed with the square damping patches used in experiment 4, configuration 2.

apparent that the unintended high correlation between areas with large reactive shearing intensity and areas covered by damping resulted in reductions nearly as large as those where damping patches corresponded to configurations intended to correlate highly with structural reactive shearing intensity.

The fourth and final experiment was designed to target mode 3 only. The first configuration, Fig. 22, was designed to cover areas of the reactive shearing intensity of mode 3 which were close to, but relatively lower in value than, areas where intensity was the highest. The second configuration, Fig. 23, was designed to cover areas of mode 3 with the highest structural reactive shearing intensity. Both configurations were symmetric, and covered just 103 cm^2, or 2.8% of the cube's top surface area. The hypothesis was that, based on the respective correlations of configuration 1 and configuration 2 to the undamped structural reactive shearing intensity of mode 3, the power radiated by the cube with the damped velocity produced by the configuration in Fig. 23 on one side would be reduced more than a cube with the configuration in Fig. 22. Also, it was hoped that, even though the total area was less than half of that used in experiment 3, the difference in reduction would be greater than that for mode three achieved in experiment 2.

Configuration 1 produced a reduction in radiated sound power of 4.49 dB while configuration 2 achieved a 5.82-dB decrease. The difference in radiated power of the two configurations was 1.33 dB. Thus both parts of the hypothesis of experiment 4 were fulfilled. However, the 1.33-dB difference in reduction only exceeded the 1.23-dB difference in reduction of experiment 3 by 0.1 dB. The 0.1-dB increase in performance of experiment 4 was achieved with only 103 cm^2 of constrained layer damping material while experiment 3 used 239 cm^2. This is a reduction in the area covered by constrained layer damping patches of 56.9% from experiment 3 to experiment 4. Thus, if placed properly, the small damping patches can exceed the performance of large damping patches.

IV. CONCLUSIONS

Two important and useful conclusions were reached. First, it was shown that it is possible to achieve large reductions in the radiated sound power for a cubic structure while modifying only a small percentage of the total surface area of the structure with constrained layer damping material. In fact, a reduction of 5.82 dB in the radiated sound power of a cube with a velocity pattern consisting of a measured plate velocity on one side and the other five sides held rigid was achieved by damping just 2.8% of the total surface area. A reduction of 10.25 dB was reached by damping 6.4% of the cube's top surface area.

Second, the reactive shearing structural intensity is an effective tool for choosing the shape, position, and number of patches of constrained layer damping material in order to effectively reduce the radiated sound power of a structure. The size, shape, and number of patches should be chosen so that they cover areas of the highest structural reactive shearing intensity calculated for the undamped mode of interest.

No general conclusions were made concerning the size of patches to be used in order to maximize the reduction of the radiated sound power for a given damping consideration. Further work is currently being done to resolve this issue.

ACKNOWLEDGMENTS

This research was funded by the National Science Foundation under contract number MSS9103377. 3M Corporation provided the viscoelastic material used.

[1] A. B. Spalding and J. A. Mann III, ''Placing small constrained layer damping patches on a plate to attain global or local velocity changes,'' J. Acoust. Soc. Am. **97**, 3617–3624 (1995).
[2] K. A. Cunefare and G. H. Koopman, ''A boundary element approach to optimization of active noise control sources on three-dimensional structures,'' J. Vib. Acoust. **113**, 387–394 (1991).
[3] D. E. Noiseux, ''Measurement of power flow in uniform beams and plates,'' J. Acoust. Soc. Am. **47**, 238–247 (1970).
[4] G. Pavic, ''Measurement of power flow in uniform beams and plates,'' J. Sound Vib. **49**, 221–230 (1976).
[5] E. Williams, ''Structural intensity in thin cylindrical shells,'' J. Acoust. Soc. Am. **89**, 1615–1622 (1991).
[6] Y. Zhang, ''Examples of using structural intensity and the force distribution to study vibrating plates,'' J. Acoust. Soc. Am. **99**, 354–361 (1996).
[7] Y. Zhang and J. A. Mann III, ''Measuring the structural intensity and force distribution in plates,'' J. Acoust. Soc. Am. **99**, 345–353 (1996).
[8] Y. Zhang, ''An experimental method for structural intensity and source location,'' Ph.D. dissertation, Iowa State University, 1993.
[9] D. H. Kruger, ''Minimizing the radiated sound power with minimal structural modification,'' Ph.D. dissertation, Iowa State University, 1995.

Theory of the background amplitudes in acoustic resonance scattering

Myoung-Seon Choi and Young-Sang Joo
Nondestructive Evaluation Team, Korea Atomic Energy Research Institute, P.O. Box 105, Yusong, Taejon 305-600, Korea

(Received 27 August 1996; accepted for publication 8 December 1996)

For problems of resonance scattering of acoustic waves from penetrable targets of canonical geometry, a general approach which yields an exact and simple expression, named the *inherent* background coefficient, for the acoustical background is proposed. By analyzing the effect of the structural damping of targets, it is found that, within each modal surface admittance of targets, including a negligible effect of the structural damping, there are two interacting contributions: a constant contribution and a resonant contribution. The constant contribution, which corresponds to the inherent background coefficient, can be obtained from the zero-frequency limit of an equivalent fluid target. For targets including a significant effect of the structural damping, the inherent background depends on the damping effect. The inherent background coefficients for empty, elastic, spherical shells not including the structural damping effect are shown explicitly. The coefficients are described by a generalization of the fluid-loading parameter. Also, it is analytically and numerically shown that the inherent background undergoes a transition to the rigid or soft background in the appropriate limit, and correctly describes the acoustical background for any shell over all frequencies. © *1997 Acoustical Society of America.* [S0001-4966(97)04804-2]

PACS numbers: 43.40.Ey, 43.30.Gv, 43.20.Fn [CBB]

INTRODUCTION

In the physical world, the importance of wave scattering phenomena cannot be emphasized too much. This is obvious from the fact that many theories and techniques have been developed over the years to study the general interaction of waves and targets. One of the important and fundamental problems is to model the scattering of a monochromatic, continuous, plane wave by a single target of canonical geometry.[1] The Rayleigh normal mode (also called ''partial wave'') series, which is the classical solution for the plane-wave scattering problem, is useful particularly for low frequencies. The convergence of the series solution slows with increasing frequency. This limitation can be improved considerably by high-frequency approaches such as Watson–Sommerfeld and Keller methods.[2,3] For the mid-frequency region (i.e., resonance region), where target size and wavelength are of comparable dimensions, the scattered field is so complicated that other approaches such as the resonance scattering theory (RST) and the singularity expansion method[4] are required. This is particularly true when the targets are penetrable and admit interior fields, since the size of the resonance region for penetrable targets is considerably larger than that for impenetrable targets.

The RST, established originally for nuclear scattering and applied to acoustic, elastic, and electromagnetic scattering,[5–9] postulates that there are two interacting contributions within each partial wave: a nonresonant background term, which is a smooth function of frequency, and a resonance term, which is significant at and near resonance and is small off resonance. The former is mainly due to reflection and diffraction from the target surface and the latter is due to transmission and reradiation into the target. In order to obtain the resonance features of the target, the background has to be subtracted numerically from each partial wave. Unfortunately, until now, the background is unknown *a priori*. Further, it varies with each scattering problem.

In air acoustics or in electromagnetism, the impedance mismatch between target materials (metals) and surrounding medium (air) is so large that unless the target is coated with soft (rubber or dielectric) layers, the field scattered from an impenetrable target with a Neumann boundary (perfectly rigid body in acoustics or perfect conductor in electromagnetism) can be used as a proper model for the background (the so-called rigid background). Similarly, in acoustic or elastic wave scattering problems dealing with cavities within solids or liquids, the scattered field from a perfectly soft body with a Dirichlet boundary can be used as a proper model (the so-called soft background). For solid or liquid targets within solid or liquid media, the situation is not so simple. If the target is a shell, it is more complicated. For a thick or very thin elastic shell submerged in a fluid, the rigid or soft background may still be used as the proper one. For shells of intermediate thickness, however, it has been proven that the acoustical backgrounds exhibit a transition from the soft background at low frequencies to the rigid one at higher frequencies. Further, a number of models for the intermediate or transitional backgrounds have been suggested with some success when applied in limited ranges of shell thicknesses, geometry, and frequency. They involve the intermediate background by Murphy *et al.*,[10,11] the midway background by Ayres and Gaunaurd,[12] the liquid-shell background by Veksler,[13] the hybrid background by Werby and Gaunaurd,[14,15] and the matched asymptotic background by Norris and Vasudevan.[16] However, an exact expression of the acoustical background for any penetrable target has been elusive over the years.

In this paper, it is reported for the first time that the acoustical background for any penetrable target of canonical geometry can be determined *a priori* by a general approach which yields an exact and simple expression for the background, named the ''*inherent* background coefficient.'' This approach is based on the consideration that the background coefficient is present just in the scattering coefficient. It starts from the idea that after removing all resonances from the scattering coefficient, the remainder can be used as the background coefficient. The complex wave numbers, whose imaginary parts are the attenuation coefficients of bulk waves in the target, are introduced to damp out the resonances. The approach may be applicable to any target of canonical geometry. Because the mathematical formalism is different for each geometry, however, it is impossible to deal with all geometries at once. Thus we deal only with an empty spherical shell submerged in a fluid which has received much attention over the past two decades. However, we use a methodology easily applicable to other geometries. It is shown analytically that the inherent background coefficient undergoes a transition to the rigid or soft background coefficient in the appropriate limit. Also, it is shown numerically that the inherent background coefficient describes correctly the background for shells of arbitrary thickness and material over all frequencies.

I. SCATTERING COEFFICIENT AND SURFACE ADMITTANCE

When a plane acoustic wave of unit amplitude $e^{i(k_1 r\cos\theta-\omega t)}$ is incident normally on an empty spherical shell of outer radius a and inner radius b (thus, thickness $d=a-b$), the scattered pressure at an observation point (r,θ) located outside the shell is given by the Rayleigh normal mode series.

$$p_{\rm sc}(r,\theta,t)=e^{-i\omega t}\sum_{n=0}^{\infty} i^n(2n+1)R_n h_n(k_1 r)P_n(\cos\theta), \tag{1}$$

where R_n is a coefficient from the five boundary conditions (three at the outer surface and two at the inner surface of the shell) and P_n is a Legendre polynomial.[17] The scattering coefficient R_n is expressed as a ratio of 5×5 determinants: $R_n=B_n/D_n$. The elements of these determinants, listed in Ref. 17, contain the spherical Bessel and outgoing Hankel functions (j_n, y_n, and h_n) and their derivatives (j_n', y_n', and h_n') with regard to the argument $x_i(\equiv k_i a,\ i=1,L,T)$, or $y_i(\equiv k_i b,\ i=L,T)$ where k_1 is a wave number of the incident wave in the outer fluid and $k_{L,T}$ are those of longitudinal and transverse bulk waves in the shell. The dimensionless frequencies of the elastic waves are linearly related to that of the incident wave by

$$x_{L,T}=x_1(C_1/C_{L,T}) \tag{2a}$$

and

$$y_{L,T}=x_{L,T}(1-h), \tag{2b}$$

where C_1 and $C_{L,T}$ are the velocities of the incident wave and the elastic waves, and h is the ratio of thickness to outer radius of the shell, i.e., $h=d/a$. In the far field (i.e., $r\to\infty$) region, the outgoing spherical Hankel function is replaced by its asymptotic representation:

$$h_n(k_1 r)\approx\frac{1}{k_1 r}(-i)^{n+1}e^{ik_1 r}, \tag{3}$$

and the scattered pressure field becomes

$$p_{\rm sc}(r,\theta,t)\approx\frac{a}{2r}e^{i(k_1 r-\omega t)}f(\theta,x_1), \tag{4}$$

where the function $f(\theta,x_1)$, called the scattering form function, is given by

$$f(\theta,x_1)=\sum_{n=0}^{\infty} f_n(\theta,x_1)$$

$$=\sum_{n=0}^{\infty}\frac{2}{ix_1}(2n+1)R_n P_n(\cos\theta). \tag{5}$$

By expanding the secular determinants, B_n and D_n, with regard to their first column, the scattering coefficient is expressed as

$$R_n=-\frac{x_1 j_n'(x_1)-F_n j_n(x_1)}{x_1 h_n'(x_1)-F_n h_n(x_1)}, \tag{6}$$

where $F_n=-(\rho_1/\rho_2)x_T^2 D_n^{11}/D_n^{21}$. ρ_1 and ρ_2 are the material densities of the outer fluid and the shell, respectively. D_n^{11} and D_n^{21} are the 4×4 minor determinants of the nonvanishing first two elements in the first column of D_n. The function F_n, called the surface admittance,[18] depends on the density ratio explicitly, and the propagation characteristics of the elastic bulk waves in the shell and the relative shell thickness h implicitly. It had been shown by Murphy *et al.*[10,11] that the function F_n in Eq. (6) changes with x_1 rather slowly, with the exception of the resonance regions around the frequencies at which D_n^{21} passes through zero. This slowly varying ''plateau'' corresponds to the intermediate background model. However, it is practically difficult to utilize this model for isolating the resonances because the magnitude of the plateau should be chosen individually for each normal mode and resonance type, and furthermore, the choice is not unique.

By taking advantage of the fluid-loading parameter, $\Omega\equiv(\rho_1/\rho_2)/h$,[16,19] the following function G_n is defined:

$$G_n\equiv F_n/\Omega=-hx_T^2 D_n^{11}/D_n^{21}. \tag{7}$$

This function G_n no longer depends on the density ratio. The fluid-loading parameter Ω, also called the null frequency, provides a rough separation for thin shells between the low-frequency, heavy fluid-loading regime in which the shells act more like a pressure release surface, and higher frequencies where the fluid loading is weak, and the shells are more like a rigid target.

II. EFFECT OF STRUCTURAL DAMPING ON SURFACE ADMITTANCE

This section discusses a way of looking at the remainder within the function G_n of Eq. (7) after damping out all the

resonances for a given shell of relative thickness h. In order to diminish the resonances, we now introduce the complex wave numbers

$$\tilde{k}_{L,T}=k_{L,T}+i\alpha_{L,T}, \tag{8}$$

where $\alpha_{L,T}$ are the attenuation coefficients of longitudinal and transverse bulk waves in the shell. The attenuation coefficients are usually dependent on frequency but, when the internal friction of the shell is great enough, they are independent of frequency.[20] Then, the dimensionless frequencies of Eq. (2) are rewritten by

$$\tilde{x}_{L,T}=x_1(C_1/C_{L,T})+i\beta_{L,T}/h \tag{9a}$$

and

$$\tilde{y}_{L,T}=\tilde{x}_{L,T}(1-h), \tag{9b}$$

where $\beta_{L,T}=\alpha_{L,T}d$. In this case, the function G_n has complex values. This means that the incident sound energy is absorbed as well as scattered. The dimensionless physical parameters $\beta_{L,T}$ denote the attenuation values (in Nepers) for the elastic bulk waves propagating through the shell thickness. In previous works on acoustic wave scattering from absorptive targets,[12,21–23] it has been shown that the structural damping effect is very important in the vicinity of the resonance frequencies. What is interesting is that the decrease in resonant amplitude is apparent due to the damping effect. The amount it decreases depends on the width of each resonance. The wider the resonance width, the smaller is the decrease in amplitude.

In order to damp out all the resonances, values of $\beta_{L,T}$ larger than unity must be used. Then, it can be assumed that the damping factors $\beta_{L,T}$ are independent of frequencies, i.e., they are constants. In general, $\beta_T>\beta_L$ and in acoustic wave scattering, the resonances due to shear waves have narrower widths than those due to longitudinal waves. Thus, when $\beta_{L,T}$ are large, the shear waves may be neglected and an elastic shell will act like a liquid shell.

For sound wave scattering from a liquid shell,[13] there are only three boundary conditions and the relevant secular determinants are third order. Then, the surface admittance of a liquid shell is given as $F_n^{(L)}=\Omega G_n^{(L)}$, where

$$G_n^{(L)}=h\tilde{x}_L\,\frac{j_n(\tilde{y}_L)y_n'(\tilde{x}_L)-j_n'(\tilde{x}_L)y_n(\tilde{y}_L)}{j_n(\tilde{y}_L)y_n(\tilde{x}_L)-j_n(\tilde{x}_L)y_n(\tilde{y}_L)}. \tag{10}$$

Recently, without any consideration of the structural damping, it has been shown by Veksler[13] that the field scattered from a liquid shell can be used as a model of the background for an elastic shell. However, this model has a limitation in applicable frequency range because the resonances due to longitudinal waves still remain in a liquid shell. For example, Fig. 1(a) shows the function $G_n^{(L)}$ of the lowest order ($n=0$) partial wave for the liquid shells ($h=0.5$ and $C_L=6380$ m s^{-1}) in water ($C_1=1480$ m s^{-1}). Three resonances are shown at an equal interval, $\Delta x_1=\pi(C_L/C_1)/h\approx 27.1$, which is easily obtained from the thickness resonance condition that longitudinal wavelength in the liquid shell must be equal to two times the shell thickness. As the relative thickness h increases or the relative velocity C_L/C_1 decreases, the resonance interval becomes narrower and the applicability of the liquid-shell background is greatly limited. Figure 1(b) illustrates the real parts of the function $G_n^{(L)}$ for various β_L in comparison with Fig. 1(a). The resonances become weak apparently as β_L increases. For $\beta_L\geqslant 3$, all the resonances disappear and only the plateau remains. The magnitude of the plateau increases with β_L.

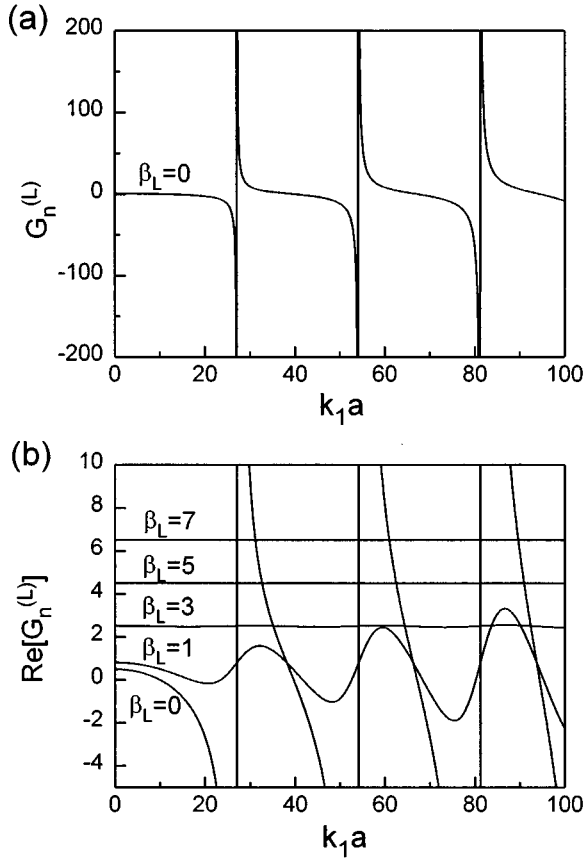

FIG. 1. (a) The surface admittance (divided by the fluid-loading parameter) $G_n^{(L)}$ for the vanishing structural damping factor ($\beta_L=0$) and (b) the real parts of the admittance for various structural damping factors β_L, of the lowest order ($n=0$) partial wave for the liquid shell ($h=0.5$ and $C_L=6380$ m s^{-1}) in water ($C_1=1480$ m s^{-1}).

When β_L is large enough, the longitudinal waves barely reach the inner surface of a liquid shell and the function $G_n^{(L)}$ can be approximated with a liquid sphere:[7,15]

$$G_n^{(L\,\mathrm{sphere})}=h\tilde{x}_L j_n'(\tilde{x}_L)/j_n(\tilde{x}_L). \tag{11}$$

For a large β_L, the ratio of Bessel functions in Eq. (11) reduces to $-i$ and then the real part of the function $G_n^{(L\,\mathrm{sphere})}$ is equal to β_L. This is in good agreement with the value of $G_n^{(L)}$ for $\beta_L\geqslant 3$ shown in Fig. 1(b). Here, it should be noted that the plateau is independent of frequency; in other words, it is a constant. For $\beta_L\leqslant 1$ in Fig. 1(b), the plateau and the resonances appear mixed. The changes of the resonances are apparent but the changes of the plateau are few. It is thought that the plateau is inherently constant, but it is distorted apparently due to an interaction with the resonances.

III. INHERENT BACKGROUND COEFFICIENT

From the observations in the above section, it can be inferred that for the vanishing $\beta_{L,T}$, the function F_n in Eq. (6) consists of two components: a constant component and a resonance component. The constant component corresponds to the inherent background. But it seldom manifests itself because of an interaction with the resonance component. In fact, when the structural damping factors are small, the function F_n of an elastic shell can no longer be approximated by the function $F_n^{(L)}$ of the equivalent liquid shell. This is true in the vicinity of resonances, particularly resonances due to shear waves. However, as implied from the liquid-shell background by Veksler,[13] it is thought that a constant component of F_n will still be equal to that of $F_n^{(L)}$. If so, the constant component can be determined from its value near zero frequency, $F_n^{(L)}(0^+)$, since, for the liquid shell, even the fundamental resonance is so far away from zero frequency that the interaction with the resonance is negligible. By replacing the function F_n in Eq. (6) with its constant component $F_n^{(L)}(0^+)$, therefore, the inherent background coefficient of Eq. (12) is obtained:

$$R_n^{(b)} = -\frac{x_1 j_n'(x_1) - F_n^{(L)}(0^+) j_n(x_1)}{x_1 h_n'(x_1) - F_n^{(L)}(0^+) h_n(x_1)}, \tag{12}$$

where $F_n^{(L)}(0^+) = \Omega G_n^{(L)}(0^+)$. By substituting the approximate expressions of the Bessel functions for $x(=x_L$ or $y_L) \ll 1$,

$$j_n(x) \approx 2^n n! x^n/(2n+1)! \tag{13a}$$

and

$$y_n(x) \approx -(2n)! x^{-(n+1)}/(2^n n!), \tag{13b}$$

into Eq. (10), the zero-frequency limit of the function $G_n^{(L)}$ is given as

$$G_n^{(L)}(0^+) = h\,\frac{n+(n+1)(1-h)^{2n+1}}{1-(1-h)^{2n+1}}. \tag{14}$$

Figure 2 shows the graphical plots of $G_n^{(L)}(0^+)$ for the lowest six ($n=0$–5) partial waves as a function of h. For thin shells with $h \ll 1$, $G_n^{(L)}(0^+) \approx 1$ and then $F_n^{(L)}(0^+)$ leads to the fluid-loading parameter, Ω. Therefore, it can be said that $G_n^{(L)}(0^+)$ of Eq. (14) plays the role of a correction factor for a thick shell which indicates a deviation from the fluid-loading parameter. This implies that $F_n^{(L)}(0^+)$ can be defined as the generalized fluid-loading parameter. For spheres with $h \approx 1$, $G_n^{(L)}(0^+) \approx n$, and, from Eq. (12), it is easily shown that the inherent background, which is determined uniquely by the generalized fluid-loading parameter, leads to the soft background in the low-frequency regime of $x_1 \ll F_n^{(L)}(0^+)$ and to the rigid background in the high-frequency regime of $x_1 \gg F_n^{(L)}(0^+)$.

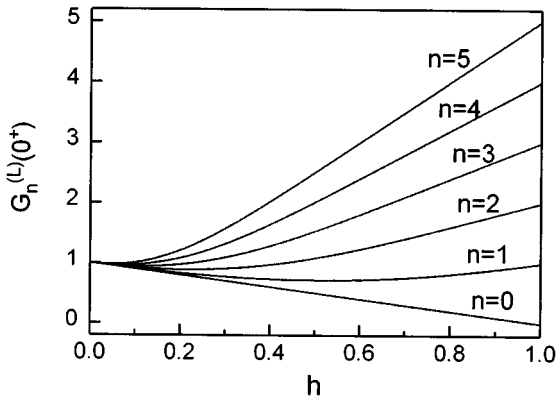

FIG. 2. $G_n^{(L)}(0^+)$ of the first six ($n=0$–5) partial waves plotted as a function of relative shell thickness.

In order for the inherent background coefficient $R_n^{(b)}$ to be utilized as an exact expression for the acoustical background for a shell, it should be verified that the background coefficient coincides with the scattering coefficient R_n excluding the domain where resonances take place, and all the resonances are isolated cleanly by subtracting the inherent background coefficient from the scattering coefficient. These requirements were checked for each partial wave up to $n=60$

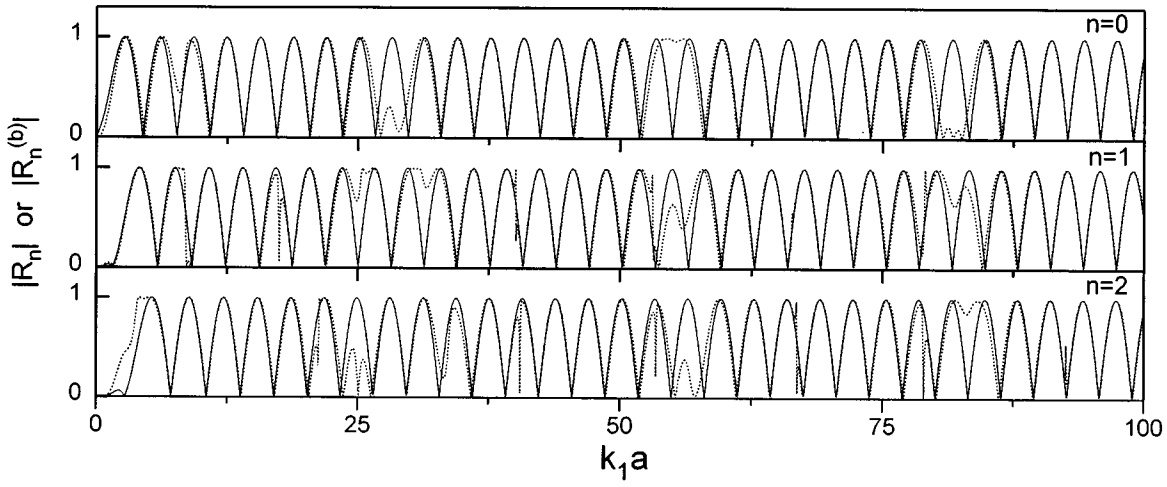

FIG. 3. Comparison of moduli of the inherent background coefficient and the scattering coefficient, $|R_n^{(b)}|$ (solid line) and $|R_n|$ (dotted line), of the first three ($n=0$–2) partial waves for a 50% thick, empty, spherical, aluminum shell in water.

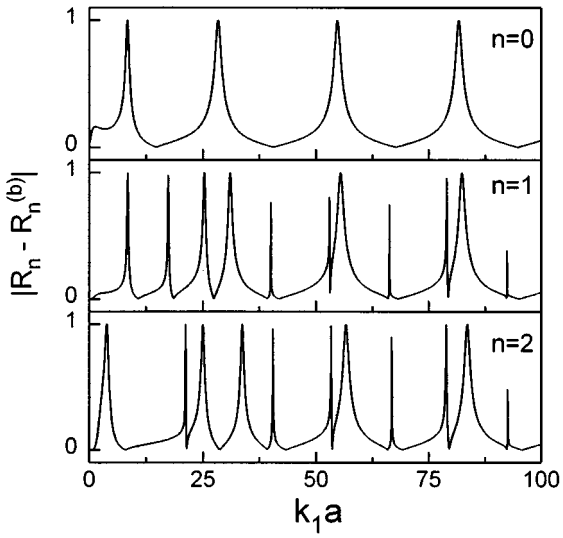

FIG. 4. Moduli of the residual coefficients $|R_n - R_n^{(b)}|$ of the first three ($n=0$–2) partial waves for a 50% thick, empty, spherical, aluminum shell in water.

for aluminum, stainless steel, and tungsten carbide shells of $h=0.02$, 0.50, and 0.99. As a result, we were convinced that the inherent background coefficients describe the backgrounds of the shells correctly over the entire frequency region, regardless of shell thickness and material. For example, Figs. 3 and 4 show a comparison of moduli of the scattering coefficient and the inherent background coefficient, and the isolated resonances of the first three ($n=0$–2) partial waves for a 50% thick, empty, aluminum shell in water. The calculation step size of $\Delta x_1=0.05$ was used. The material properties of the pertinent substances were as follows: $\rho_1=1.0$ g cm^{-3}, $\rho_2=2.79$ g cm^{-3}, $C_1=1480$ m s^{-1}, $C_L=6380$ m s^{-1}, and $C_T=3100$ m s^{-1}.

IV. CONCLUSIONS

It has been found that within each modal surface admittance of elastic shells including a negligible effect of the structural damping, there are two interacting components: a constant component and a resonant component. The constant component, which corresponds to the inherent background, can be determined from the zero-frequency limit of an equivalent fluid shell. For shells including a significant effect of the structural damping, the inherent background depends on the damping effect.

The approach to the inherent background coefficient of Eqs. (12) and (14) from the scattering coefficient of Eq. (6) brings about a more profound understanding of resonance scattering phenomena because it emerges from a physical concept. It seems to be applicable for shells of arbitrary thickness and material makeup, and over all frequencies and mode numbers. A cylindrical version of the inherent background coefficients will be presented in the near future. Also, future works will show that the approach is applicable to more complicated targets, such as concentric layered shells.

[1] J. Bowman, T. Senior, and P. Uslenghi, *Electromagnetic and Acoustic Scattering by Simple Shapes* (Wiley Interscience, New York, 1969).

[2] G. N. Watson, ''The diffraction of elastic waves by the earth,'' Proc. R. Soc. London, Ser. A **95**, 83–99 (1918); A. Sommerfeld, *Partial Differential Equations in Physics* (Academic, New York, 1949).

[3] J. B. Keller, ''Geometrical theory of diffraction,'' J. Opt. Soc. Am. **52**, 116–130 (1962).

[4] H. Überall, P. P. Delsanto, J. D. Alemar, E. Rosario, and A. Nagl, ''Application of the singularity expansion method to elastic wave scattering,'' Appl. Mech. Rev. **43**, 235–249 (1990).

[5] H. Feshbach, D. C. Peaslee, and V. F. Weisskopf, ''On the scattering and absorption of particles by atomic nuclei,'' Phys. Rev. **71**, 145–158 (1947).

[6] L. Flax, L. R. Dragonette, and H. Überall, ''Theory of elastic resonance excitation by sound scattering,'' J. Acoust. Soc. Am. **63**, 723–731 (1978).

[7] D. Brill and G. Gaunaurd, ''Resonance theory of elastic wave ultrasonically scattered from an elastic sphere,'' J. Acoust. Soc. Am. **81**, 1–21 (1987).

[8] G. C. Gaunaurd and M. F. Werby, ''Acoustic resonance scattering by submerged elastic shells,'' Appl. Mech. Rev. **43**, 171–208 (1990); and also, G. C. Gaunaurd, ''Elastic and acoustic resonance wave scattering,'' *ibid.* **42**, 143–193 (1989).

[9] H. Überall, P. J. Moser, J. P. Murphy, A. Nagl, G. Igiri, J. V. Subrahmanyam, G. Gaunaurd, D. Brill, P. P. Delsanto, J. D. Alemar, and E. Rosario, ''Electromagnetic and acoustic resonance scattering theory,'' Wave Motion **5**, 307–329 (1983).

[10] J. D. Murphy, E. D. Breitenbach, and H. Überall, ''Resonance scattering of acoustic waves from cylindrical shells,'' J. Acoust. Soc. Am. **64**, 677–683 (1978).

[11] J. D. Murphy, J. George, A. Nagl, and H. Überall, ''Isolation of the resonant component in acoustic scattering from fluid-loaded elastic spherical shells,'' J. Acoust. Soc. Am. **65**, 368–373 (1979).

[12] V. M. Ayres and G. C. Gaunaurd, ''Acoustic resonance scattering by viscoelastic objects,'' J. Acoust. Soc. Am. **81**, 301–311 (1987).

[13] D. N. Veksler, ''Intermediate background in problems of sound waves scattering by elastic shells,'' Acustica **76**, 1–9 (1992).

[14] M. F. Werby, ''The acoustical background for a submerged elastic shell,'' J. Acoust. Soc. Am. **90**, 3279–3287 (1991).

[15] G. C. Gaunaurd, ''Hybrid background coefficients to isolate the resonance spectrogram of submerged shells,'' J. Acoust. Soc. Am. **92**, 1981–1984 (1992).

[16] A. N. Norris and N. Vasudevan, ''Acoustic wave scattering from thin shell structures,'' J. Acoust. Soc. Am. **92**, 3320–3336 (1992).

[17] G. C. Gaunaurd and M. F. Werby, ''Lamb and creeping waves around submerged spherical shells resonantly excited by sound scattering,'' J. Acoust. Soc. Am. **82**, 2021–2033 (1987); and also, ''Sound scattering by resonantly excited, fluid-loaded, elastic spherical shell,'' J. Acoust. Soc. Am. **90**, 2536–2550 (1991).

[18] P. M. Morse and K. U. Ingard, *Theoretical Acoustics* (McGraw-Hill, New York, 1968), pp. 425–426.

[19] D. G. Crighton, A. D. Dowling, J. E. Ffowcs Williams, M. Heckl, and F. G. Leppington, *Modern Methods in Analytical Acoustics: Lecture Notes* (Springer-Verlag, New York, 1992), p. 510.

[20] P. M. Morse and H. Feshbach, *Methods of Theoretical Physics* (McGraw-Hill, New York, 1953), p. 137.

[21] X. Y. Huang, ''Energy dissipation in sound scattering by a submerged cylindrical shell,'' Acustica **77**, 221–231 (1992).

[22] L. W. Anson and R. C. Chivers, ''Ultrasonic scattering from spherical shell including viscous and thermal effects,'' J. Acoust. Soc. Am. **93**, 1687–1699 (1993).

[23] J.-P. Lee, J.-H. Song, and M.-S. Choi, ''The effects of material attenuation on acoustic resonance scattering from cylindrical tubes,'' Ultrasonics **34**, 737–745 (1996).

Design of active structural acoustic control systems using a nonvolumetric eigenproperty assignment approach

Z. Li, C. Guigou, C. R. Fuller, and R. A. Burdisso
Vibration and Acoustic Laboratories, Mechanical Engineering Department, Virginia Polytechnic Institute and State University, Blacksburg, Virginia 24061-0238

(Received 5 March 1996; accepted for publication 11 October 1996)

Sound radiation of planar radiators such as beams and plates is known to be directly related to the velocity distribution over the structural surface at low frequencies. For example, nonvolumetric modes correspond to poor sound radiators for small k_0a. In this work, to achieve significant sound attenuation in the low-frequency range, the SISO eigenassignment technique is used to modify the eigenproperties of a planar structure using structural actuators and sensors so that all the modes of the controlled structure are nonvolumetric. The main advantage of such an approach is that the design is independent of the disturbance characteristics (i.e., type, position, and frequency content) and does not require sensors in the radiation field. The design procedure for the control system in the modal domain is presented. The formulation is applied to a simply supported beam with SISO feedforward control. Radiation efficiency, far-field sound radiated power and mean-square surface velocity are extensively studied. The results show that the control scheme proposed here is very efficient in reducing sound radiation at low frequencies. © *1997 Acoustical Society of America.* [S0001-4966(97)03604-7]

PACS numbers: 43.40.Vn, 43.50.Ki [PJR]

INTRODUCTION

The attenuation of sound radiation from vibrating structures is an important issue in practical engineering. Passive noise control approaches are inefficient at low frequencies and difficult to implement. In recent years, active control of sound radiation has emerged as a very promising method to reduce noise, especially at low frequencies. Extensive research has been conducted in developing efficient control strategies. One such strategy is active structural acoustic control (ASAC) proposed by Fuller.[1] In this approach, control inputs are applied directly to the vibrating structures (which is responsible for the sound radiation) while minimizing sound pressure or other related quantities. It is shown that, in general, this strategy requires a small number of control inputs for a global sound reduction in acoustic field. The efficiency of this approach in conjunction with adaptive feedforward control is now widely recognized.

The traditional design approach in adaptive feedforward control is to select the error sensors and actuators based on some physical understanding of the dynamical characteristics of the uncontrolled system or use standard optimization techniques.[1,2] In their recent work,[3–5] Burdisso and Fuller extensively studied the dynamics of the adaptive feedforward controlled system and revealed that the adaptive feedforward control, similar to feedback control, will alter the eigenproperties of the controlled system. They further developed a design methodology, the eigenassignment design technique, based on their findings for single-input, single-output systems. In this work, the eigenassignment method is adopted to design a system whose vibration modes under control are nonvolumetric and thus radiate sound weakly at low frequencies.

Efficient control methods are usually based on a full understanding of the physics involved in sound radiation. Low-frequency sound radiation of planar radiators such as beams and plates is known to be directly related to velocity distribution over the structural surface. In recent publications,[6,7] the radiated acoustic power has been expressed in terms of the contributions from a number of independently radiating surface velocity distributions. It is shown that velocity distributions corresponding to vibration modes of the system will in general be coupled in the acoustic field. The ''radiation modes'' are surface velocity distributions that radiate sound power independently in the acoustic far field. It can be shown that, in the low-frequency range, i.e., for dimensionless frequency $k_0a \ll 1$ (where k_0 is the wave number in the air and a is the characteristic dimension of the structure), the shape of radiation modes is reasonably independent of frequency and only the first radiation mode is significant in terms of sound radiation.[8] The first radiation mode is the piston-type mode, which represents the monopole behavior of the structure and whose amplitude corresponds to the net volume velocity of the structure. It can then be further deduced that the first radiation mode is a combination of structural modes associated with a volumetric component (i.e., structural modes corresponding to a nonzero net volume velocity). These ''volumetric modes'' radiate sound efficiently at low frequencies (small k_0a), since they behave as monopole radiators.[9–12] On the other hand, ''nonvolumetric modes'' (i.e., structural modes corresponding to a zero net volume velocity), radiate poorly in the low-frequency region where their directivity patterns resemble dipoles, quadrapoles, or higher-order patterns. This observation provides the physical background for the current work.

In this work, the overall goal is to design a control system with structural actuators and sensors so as to markedly reduce the low-frequency sound radiation efficiency. To achieve this, a SISO feedforward control is used to modify

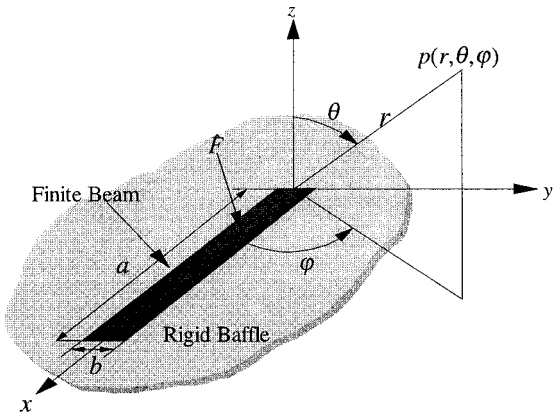

FIG. 1. Schematic of beam system and coordinate system.

the eigenproperties of a planar beam structure so that the vibration modes of the controlled system are nonvolumetric and radiate sound weakly. The complete design procedure consists of two parts: first, the design of global control system parameters in the modal domain by eigenassignment is carried out; second, the design of physical system (realistic structural error sensors and actuators) to implement the control strategy is performed.[5] In this paper, only the first stage is presented; a companion paper will discuss the experimental implementation of the proposed design. The main advantage of the method presented here is that the design is independent of the characteristics of the disturbance applied to the system (i.e., independent of form, location, and frequency content). A simply supported beam is studied to demonstrate the efficiency of the described design. However, the approach can be easily extended to more complicated boundary conditions and structures as the proposed design only requires knowledge of the system eigenproperties (which could be experimentally obtained by modal analysis for example). The radiation efficiency, far-field radiated power and mean-square velocity are extensively studied to understand the controlled system acoustic and structural behavior. The results of the proposed control approach are also compared with that obtained using a similar control approach except that a volume velocity sensor, as described in Ref. 10, and an accelerometer at the beam center are implemented as error sensors. These comparisons are used to evaluate the relative efficiency of the approach proposed here.

I. THEORETICAL ANALYSIS

A. System response

The studied system is presented in Fig. 1 and consists of a baffled finite beam of length a and width b. Simply supported boundary conditions are applied at $x=0$ and $x=a$. The beam is assumed to be excited by a harmonic point force disturbance input $\hat{F}e^{j\omega t}$ located at $x=x_d$. The analysis is carried out in frequency domain. The cross-sectional dimensions of the beam are considered small compared with its length and the frequency of vibration to be low so that both the shear and rotatory inertia effects can be neglected. The equation of motion of the beam can then be written as

$$\frac{\partial^2}{\partial x^2}\left[EI(x)\,\frac{\partial^2 w(x,t)}{\partial x^2}\right]+m(x)\,\frac{\partial^2 w(x,t)}{\partial t^2}=\hat{F}e^{j\omega t}. \tag{1}$$

In the frequency domain, the response of the beam can be generally described as

$$w(x,\omega)=\sum_{n=1}^{N} q_n(\omega)\phi_n(x), \tag{2}$$

where $w(x,\omega)$, is the displacement distribution, and $\phi_n(x)$ is the nth eigenfunction depending on the beam boundary conditions. The eigenfunctions are assumed to be normalized with respect to mass distribution. The generalized coordinates in the frequency domain, $q_n(\omega)$, can be expressed as

$$q_n(\omega)=[f_n\hat{F}(\omega)+u_nU(\omega)]H_n(\omega), \tag{3}$$

where $U(\omega)$ is the magnitude of control input, and f_n and u_n are the unit modal disturbance and unit modal control input, respectively.[3] The nth modal frequency response function is represented by $H_n(\omega)=(\omega_n^2-\omega^2+2j\zeta_n\omega_n^2)^{-1}$, where ζ_n and ω_n are the nth modal damping ratio and natural frequency, respectively. The optimal control input can be obtained by minimizing the square of an error sensor output $e(\omega)$, represented as the sum of a linear contribution of each mode, i.e.,

$$e(\omega)=\sum_{n=1}^{N} q_n(\omega)\xi_n, \tag{4}$$

where ξ_n is the nth modal error sensor component and is a function of the characteristics of the error sensor.[3] Minimizing Eq. (4) leads to the control input magnitude expressed as[3]

$$U(\omega)=-G(\omega)\hat{F}(\omega)=-\frac{\Sigma_{n=1}^{N}\xi_n f_n H_n(\omega)}{\Sigma_{n=1}^{N}\xi_n u_n H_n(\omega)}\,\hat{F}(\omega). \tag{5}$$

B. Radiation in acoustic far field

The sound pressure in the far field for a planar radiator can be written as[13]

$$p(r,\theta,\varphi)=-\omega^2\,\frac{\rho_0 e^{-jk_0 r}}{2\pi r}\times W(k_0\sin\theta\cos\varphi, k_0\sin\theta\sin\varphi), \tag{6}$$

where $k_0=\omega/c_0$ is the acoustic wave number in the acoustic medium, ρ_0 and c_0 are the density of the acoustic medium (air in this case) and sound velocity, respectively; $W(k_x,k_y)$ is the displacement wave number spectrum defined as the double spatial Fourier transform of the displacement distribution over the surface of the structure, i.e.,

$$W(k_x,k_y)=\int_{-\infty}^{+\infty}\int_{-\infty}^{+\infty} w(x,y)e^{jk_x x}e^{jk_y y}\,dx\,dy. \tag{7}$$

For the baffled beam, the system out-of-plane displacement depends only on the x coordinate and is constant along the beam width. The spatial displacement distribution can then be rewritten as

$$w(x,y)=\begin{cases} w(x), & \text{for } 0\leqslant x\leqslant a,\ -b/2\leqslant y\leqslant b/2 \\ 0, & \text{otherwise.}\end{cases} \tag{8}$$

The total acoustic power radiated by the structure is the integral over a hemisphere of the far-field acoustic intensity, i.e.,

$$\Pi(\omega)=\int_0^{2\pi}\int_0^{\pi/2}\frac{|p(r,\theta,\varphi)|^2}{2\rho_0 c}\,r^2\,\sin\,\theta\,d\theta\,d\varphi. \tag{9}$$

The radiation efficiency of a vibrating structure is defined as[12]

$$\sigma=\frac{\Pi(\omega)}{\rho_0 c_0 ab\overline{\langle \dot{w}^2(x)\rangle}}, \tag{10}$$

where $\overline{\langle \dot{w}^2(x)\rangle}$ is the spatial average mean square velocity defined as[10,12]

$$\overline{\langle \dot{w}^2(x)\rangle}=\frac{\omega^2}{2a}\int_0^a |w(x)|^2 dx. \tag{11}$$

C. Controlled system eigenproperties

Feedforward control has been successfully applied in the active control of sound and vibration. In their recent study, Burdisso and Fuller[3] revealed that the feedforward control, similar to feedback control, will generally alter the eigenproperties of the controlled structure. It is shown that the feedforward-controlled system effectively responds with a new set of eigenfunctions and eigenvalues to the disturbance input. Based on this observation, they further developed an eigenassignment design technique.[4,5] This technique is outlined in this section.

The eigenproperties of the feedforward-controlled structure are governed by the characteristics of the controller defined by $G(\omega)$ [see Eq. (5)]. The controlled eigenvalues λ_l are the roots of the following characteristic equation of the controlled system[5]

$$\prod_{n=1}^{N}\xi_n u_n\prod_{\substack{m=1\\ m\neq n}}^{N}(\mu_m-\lambda_1)=0,\quad \text{for}\quad l=1,2,\ldots,N-1, \tag{12}$$

where $\mu_m=\omega_m^2$ is the mth eigenvalue of the uncontrolled system. The controlled eigenvalues λ_l are therefore only a function of the unit modal control input, modal error sensor components, and eigenproperties of the uncontrolled structure and are independent of the disturbance loading, i.e., type, location, and frequency content. It is also important to note that the applied control input reduces the dynamic degrees of freedom of the structure by one due to the constraint imposed by driving the response of error sensor to zero.[3] The corresponding eigenfunctions of the controlled system $\phi_l^c(x)$ are linear combinations of those of the uncontrolled system expressed as[3]

$$\phi_l^c(x)=\sum_{n=1}^{N}G_{ln}\phi_n(x),\quad \text{for}\quad l=1,2,\ldots,N-1, \tag{13}$$

where the expansion coefficients G_{ln} for $n=1,2,\ldots,N$ and $l=1,2,\ldots,N-1$ are defined as[3]

$$G_{ln}=\begin{cases}\dfrac{u_n}{\lambda_l-\mu_n}\left\{\displaystyle\sum_{n=1}^{N}[u_n/(\lambda_l-\mu_n)]^2\right\}^{-1/2}, & \text{for}\quad \lambda_l\neq\mu_n\\ \delta_{ln}, & \text{for}\quad \lambda_l=\mu_n.\end{cases} \tag{14}$$

For $\lambda_l=\mu_n$, the lth controlled eigenfunction is identical to the corresponding nth uncontrolled one (i.e., $G_{ln}=\delta_{ln}$), regardless of the unit modal control input u_n. Therefore, once the control actuator and error sensor are selected, the eigenstructure of the controlled system is then completely determined by Eqs. (12)–(14), independent of the nature of disturbance loading including frequency content, location, and distribution. On the other hand, if the controlled system eigenstructure is specified, then the unit modal control input and modal error sensor components can be determined such that the controlled system dynamics have these characteristics. This aspect is discussed further in the following section.

D. Proposed control scheme

As discussed previously, some vibration modes are more efficient sound radiators at low frequencies ($k_0 a\ll 1$) than others. ''Nonvolumetric modes'' are defined as modes with a zero integral of the normal velocity distribution over the surface of the planar structure. These modes radiate poorly at low frequencies where their directivity patterns resemble dipoles, quadrapoles, or higher-order patterns. On the other hand, volumetric modes, corresponding to monopole radiators, are responsible for most sound radiation at low frequencies ($k_0 a\ll 1$). Therefore, the basic concept of this approach is to achieve a controlled structure that responds only with nonvolumetric modes so as to attenuate the radiated sound power. Thus, the structural eigenproperties have to be altered in such a way that the controlled eigenfunctions are all nonvolumetric and preferably orthogonal. To allow flexibility in the design process, it was chosen to construct the pth controlled eigenfunction as a linear combination of the first ($p+1$) uncontrolled eigenfunctions, i.e.,

$$\phi_p^c(x)=\sum_{k=1}^{p+1}\overline{G_{pk}}\phi_k(x),\quad \text{for}\quad p=1,2,\ldots,N-1, \tag{15}$$

where the coefficients $\overline{G_{pk}}$ are derived by imposing the nonvolumetric and the orthogonality conditions, as well as normalizing the new eigenfunction to unity, i.e.,

$$\int_0^a \phi_p^c(x)\,dx=0\quad \text{(nonvolumetric condition)} \tag{16a}$$

$$\int_0^a \phi_p^c(x)\,\phi_{p'}^c(x)\,dx=\delta_{pp'},\quad \text{for}\quad p'\leqslant p\ \text{(orthonormal condition)}, \tag{16b}$$

where $\delta_{pp'}$ represents the Kronecker delta function (i.e., $\delta_{pp'}=1$ for $p=p'$ and $\delta_{pp'}=0$ for $p\neq p'$). Thus, it can be noticed from Eqs. (15) and (16) that the first controlled eigenfunction is constructed from a linear combination of the first and second uncontrolled eigenfunctions. In general, the pth controlled eigenfunction is a linear combination of the

first $(p+1)$ uncontrolled eigenfunctions. If the number of uncontrolled modes (to be taken into account in the frequency range of concern) has to be increased, new controlled eigenfunctions are added without changing the lower order ones. By placing Eq. (15) into Eqs. (16a) and (16b), it is easily shown that the coefficients G_{pk} can be expressed as

$$G_{pk}=\begin{cases}\gamma_k\gamma_{p+1}\left[\sum_{j=1}^{p}\gamma_j^2\sum_{i=1}^{p+1}\gamma_i^2\right]^{-1/2}, & \text{for } 1<k\leqslant p\\ \left(\sum_{j=1}^{p}\gamma_j^2\right)\left[\sum_{j=1}^{p}\gamma_j^2\sum_{i=1}^{p+1}\gamma_i^2\right]^{-1/2}, & \text{for } k=p+1\\ 0, \text{ for } p+1<k\leqslant N,\end{cases} \tag{17}$$

where γ_n is defined as

$$\gamma_n=\int_0^a \phi_n(x)\,dx. \tag{18}$$

If γ_n is zero, the nth mode then obeys the nonvolumetric condition [Eq. (16a)]. Equation (17) shows that the $p+1$ uncontrolled mode is the most significant contributor to the pth controlled mode and that the contribution of the kth uncontrolled mode $(1\leqslant k\leqslant p)$ to the controlled mode decreases as the controlled mode order is increased. This is also related to the fact that controlled eigenfunctions become more complex (i.e., with increasing number of nodes) as the mode order p increases. The expansion coefficients G_{ln} are also defined by Eq. (14) as functions of the unit modal control inputs u_n, and the uncontrolled and controlled system eigenvalues μ_n and λ_l, respectively. Thus, the objective is to find the N unit modal control inputs u_n and the $N-1$ controlled system eigenvalues λ_l, that yield the desired expansion coefficients as defined in Eq. (17). Since there are $(N-1)\times N$ expansion coefficients to match and only $N+(N-1)$ unknown, a solution can only be accomplished in some least-square sense. The controlled eigenvalues λ_l and unit modal control inputs u_n can then be obtained by solving a constrained least-square minimization problem,[5] where the objective function to be minimized is

$$F(u_n,\lambda_l)=\sum_{l=1}^{N-1}\sum_{n=1}^{N}[\overline{G_{ln}}-G_{ln}]^2 \tag{19}$$

subject to

$$\begin{cases}\sum_{n=1}^{N}u_n^2=1\\ (\lambda_l)_{\text{lower}}\leqslant\lambda_l\leqslant(\lambda_l)_{\text{upper}}\\ 0\leqslant\lambda_1\leqslant\lambda_2\leqslant\cdots\leqslant\lambda_{N-1}\end{cases}, \tag{20}$$

where the equality constraint represents the normalization of modal control input (since the relative controllability of the modes is the only relevant information), and $(\lambda_l)_{\text{lower}}$ and $(\lambda_l)_{\text{upper}}$ are the lower and upper bounds for the lth controlled eigenvalue. These lower and upper bounds for the lth controlled eigenvalues, i.e., $(\lambda_l)_{\text{lower}}$ and $(\lambda_l)_{\text{upper}}$ are selected to ensure that the optimal expansion coefficients G_{ln} be as close as possible to the desired expansion coefficients G_{ln}, and such that the following equation is satisfied:

$$\mu_1\leqslant\lambda_1\leqslant\mu_2\leqslant\lambda_2\leqslant\mu_3\leqslant\cdots\mu_{N-1}\leqslant\lambda_{N-1}\leqslant\mu_N. \tag{21}$$

If, for example, the excitation consists of multiple harmonics, the controlled eigenvalues can also be selected (by properly choosing the upper and lower bounds) such that they do not coincide with any of these harmonics. The above nonlinear optimization problem can be carried out by using any of several standard routines. In this work, it was solved by using the program CONSTR in MATLAB optimization toolbox.[14]

Once the optimal unit modal control input u_n and the controlled system eigenvalues λ_l are determined, the modal error sensor components ξ_n can be obtained by solving a linear system of equations given by Eq. (12). Assuming that the Nth mode is fully observable, and setting $\xi_n=1$, the error sensor modal components are obtained by solving the following linear system[4]

$$\begin{bmatrix}\eta_{11} & \eta_{12} & \cdots & \eta_{1N-1}\\ \eta_{21} & \eta_{22} & \cdots & \eta_{2N-1}\\ \vdots & \vdots & \vdots & \vdots\\ \eta_{N-1,1} & \eta_{N-1,2} & \cdots & \eta_{N-1,N-1}\end{bmatrix}\begin{Bmatrix}\xi_1\\ \xi_2\\ \vdots\\ \xi_{N-1}\end{Bmatrix}=\begin{Bmatrix}\eta_{1,N}\\ \eta_{2,N}\\ \vdots\\ \eta_{N-1,N}\end{Bmatrix}, \tag{22}$$

where

$$\eta_{ln}=u_n\prod_{\substack{m=1\\ m\neq n}}^{N}(\mu_m-\lambda_l). \tag{23}$$

The determination of optimal modal error sensor components ξ_n and the unit modal control input u_n completely defines the control system configuration in the modal domain. The performance of the controlled system can then be investigated. The physical implementation of the control system, i.e., the design of structural error sensors and actuators, is not be presented in this paper. However, it can be obtained following the steps as described in Ref. 5.

II. NUMERICAL SIMULATIONS, RESULTS AND DISCUSSION

In this section numerical simulations for a vibrating simply supported finite beam are presented to demonstrate the design methodology and the effectiveness of the method. The beam is constructed from steel (i.e., density $\rho=7860$ kg/m^3 and Young modulus $E=200$ Gpa) with a length $a=0.38$ m, a width $b=0.038$ m, and a thickness $h=0.0048$ m. The beam is assumed to have a damping factor of $\zeta_n=1\%$ for all modes, and $N=7$ modes are included in the analysis to describe the response of the system. The first seven natural frequencies for the simply supported beam are listed in Table I. The beam is assumed to be driven by harmonic disturbance point force of $1N$ amplitude located at $x_d=0.1$ m. The excitation frequency is varied in the frequency band 10–3000 Hz.

A. Implementation for simply supported beam

This section presents some simplifications of the previously developed general formulation for the case of a lightly

TABLE I. Simply supported beam natural frequencies.

Mode	Uncontrolled (Hz)	Controlled (Hz)
1	76.03	304.13
2	304.13	653.12
3	684.30	1216.52
4	1216.53	1876.79
5	1900.82	2737.19
6	2737.18	3677.88
7	3725.61	

damped, simply supported beam. For simply supported boundary conditions, the nth eigenfunction is

$$\phi_n(x) = \sqrt{\frac{2}{\rho S a}} \sin(k_n x), \tag{24}$$

where $k_n = n\pi/a$ is the nth structural wave number and the nth associated eigenvalue is $\mu_n = \omega_n^2 = k_n^4 EI/\rho S$ (EI is the beam bending stiffness, ρ the density, and S the cross-section area). From Eq. (24), it can easily be noticed that the even-order modes of the beam are nonvolumetric, i.e., the parameter γ_n in Eq. (18) becomes

$$\gamma_n = \sqrt{\frac{2}{\rho S a}} \left(\frac{1-(-1)^n}{k_n} \right), \quad n = 1,2, \ldots, N. \tag{25}$$

Thus, the even-order uncontrolled modes do not need to be changed by the control as they already satisfy the nonvolumetric condition. From Eq. (25) and Eq. (17), it can be found that the controlled eigenfunctions can be expressed as

$$\phi_{2n-1}^c(x) = \phi_{2n}(x), \tag{26a}$$

$$\phi_{2n}^c(x) = \sum_{j=1}^{n+1} G_{2n,2j-1} \phi_{2j-1}(x), \tag{26b}$$

where the coefficients $G_{2n,2j-1}$ are defined by Eq. (17), and $n = 1,2, \ldots$. Equations (26) state that the controlled eigenfunctions with odd order are identical to the uncontrolled ones with even order: for example the first controlled mode is $\phi_1^c(x) = \phi_2(x)$. On the other hand, the controlled eigenfunctions with even order are only a linear combination of the uncontrolled eigenfunctions with odd order: for example the second controlled mode is $\phi_2^c(x) = G_{1,1}\phi_1(x) + G_{1,3}\phi_3(x)$.

Having obtained the expansion coefficients and the controlled eigenfunctions for the finite beam considered in this example; the constrained least-square minimization problem [as expressed in Eqs. (19) and (20)] is solved for the controlled eigenvalues λ_l and the unit modal control input u_n. The modal error sensor components ξ_n are then found using Eqs. (22) and (23). Once these components are found correctly, the controlled system will respond with the desired nonvolumetric eigenfunctions or modes.

B. Optimal controller in the modal domain

The controlled nonvolumetric modes [see Eq. (17)] are given by

$$\phi_1^c(x) = \phi_2(x),$$

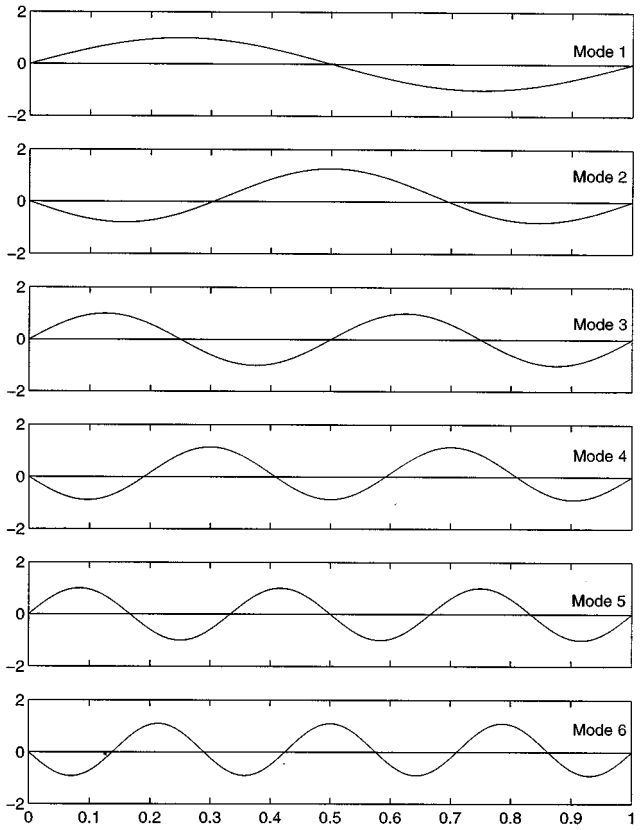

FIG. 2. Optimal controlled mode shapes of simply supported beam.

$$\begin{aligned}
\phi_2^c(x) &= 0.3162\phi_1(x) - 0.9487\phi_3(x),\\
\phi_3^c(x) &= \phi_4(x),\\
\phi_4^c(x) &= 0.1768\phi_1(x) + 0.0589\phi_3(x) - 0.9487\phi_5(x),\\
\phi_5^c(x) &= \phi_6(x),\\
\phi_6^c(x) &= 0.123\phi_1(x) + 0.041\phi_3(x) + 0.0246\phi_5(x)\\
&\quad - 0.9913\phi_7(x),
\end{aligned} \tag{27}$$

and the associated mode shapes are shown in Fig. 2. As mentioned previously, the odd-order controlled modes correspond to the even-order uncontrolled ones (i.e., the first controlled mode is the second mode of the uncontrolled system). On the other hand, the controlled modes with even order only depend on the uncontrolled ones with odd order (i.e., the second controlled mode is a combination of mode 1 and 3 of the uncontrolled system). It can also be noticed in Eqs. (27) that the largest expansion coefficient for controlled modes corresponds to the highest order uncontrolled mode in the decomposition. This can be associated with the fact that the mode shape becomes more complex (increasing number of nodes) with increasing mode order as seen in Fig. 2. Then, the $N-1$ controlled system eigenvalues λ_l and the N unit modal control inputs u_n are obtained by solving the optimization problem [Eqs. (19) and (20)] and are used to solve for the modal error sensor components defined by Eq. (22).

The eigenfrequencies of the controlled system are given in Table I. As expected, the resonant frequency of the odd-

TABLE II. Optimal modal control input and error sensor modal components.

Mode	Modal control components u_n	Modal error sensor components ξ_n
1	0.931	0.925
2	0.000	0.013
3	0.277	0.306
4	0.000	0.010
5	0.135	0.182
6	0.000	−0.006
7	0.195	0.132

order controlled modes are identical to those of the even-order uncontrolled modes (as their associated eigenfunctions are the same). The modal parameters for the control input and the error sensor, presented in Table II, completely define the controlled system in the modal domain. As discussed previously, the optimization process is independent of the type, location and frequency content of the disturbance acting on the beam. The design process is different from that presented in Ref. 5 where the eigenfunctions are found to minimize the radiation efficiency at one particular frequency. The eigenstructure of the system has been changed in such a way that all the controlled modes are nonvolumetric, which radiate poorly in the low-frequency region.

After carrying out the above steps the eigenassignment has been completed and the controlled eigenstructure is fixed. The performance of the design is then examined by studying the acoustic and vibrational responses of the uncontrolled and controlled systems when the excitation frequency is varied from 10 to 3000 Hz ($0.069<k_0a<20.76$).

C. Control design performance

As expected, the controlled modes radiate less efficiently than the uncontrolled modes. Figure 3 shows the radiation efficiencies of modes 1–4 for both the uncontrolled and controlled systems. At low frequencies, the radiation efficiencies of controlled modes decrease compared to those of the uncontrolled modes corresponding to monopole radiators. This decrease implies that the controlled modes are weaker radiators than the uncontrolled ones. It is also interesting to note that the radiation efficiency is even lower for the second controlled mode, which is a linear combination of the first and third uncontrolled modes (monopole radiators), than for the second uncontrolled mode (dipole radiator). This is probably because the second controlled mode has one more degree of freedom than the second uncontrolled mode. Similar observations hold true for other even-order controlled modes.

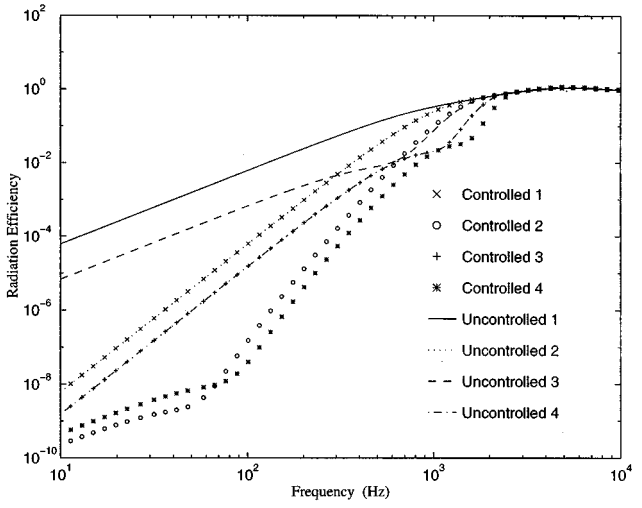

FIG. 3. Modal radiation efficiencies of modes 1–4 of a simply supported beam.

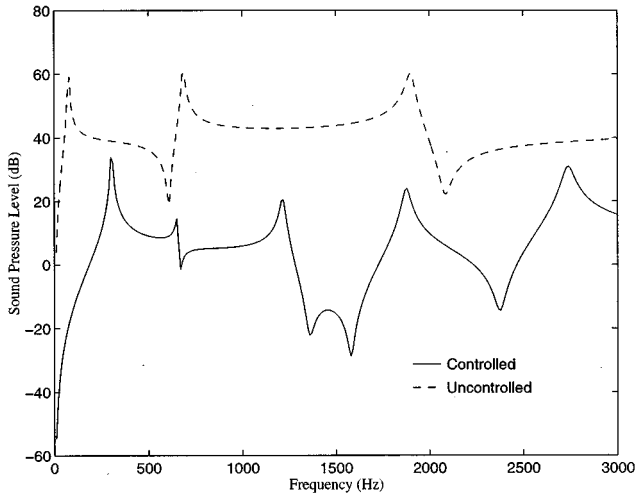

FIG. 4. Far-field radiated pressure in a direction perpendicular to the beam ($\theta=0°$).

To illustrate the effectiveness of the control strategy, the far-field sound-pressure levels (in dB, *re:* 20 μPa) before and after control at $\tilde{r}(5\times a,\ \theta=0,\ \varphi=0)$, i.e., in the direction perpendicular to the center of the finite beam, are shown in Fig. 4. The sound-pressure level is significantly reduced over a wide frequency range (10–3000 Hz). This reduction is mainly due to the fact that the nonvolumetric controlled modes are associated with a dipole radiation pattern in the far field, and therefore have a minimum radiation in the direction perpendicular to the vibrating structure. The far-field pressure directivity in the $x-z$ plane is shown in Figs. 5 and 6 for frequencies of 76 and 200 Hz, respectively, where negative value of θ corresponds to $\phi=0$ in the positive x

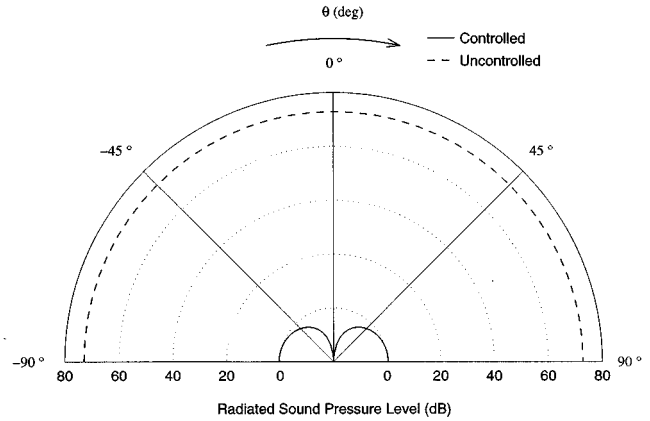

FIG. 5. Radiation directivity at 76 Hz (first uncontrolled resonance).

plane. The sound-pressure levels are calculated at a radius $r=5\times a$. For an excitation frequency of 76 Hz, corresponding to the first resonant frequency of the uncontrolled system, significant global sound attenuation has been achieved. Similar results can be observed when the system is driven at other uncontrolled resonant frequencies. At 200 Hz, i.e., an off-resonant frequency of the uncontrolled and controlled system, excellent global sound attenuation is also obtained as seen in Fig. 6. However, the global sound attenuation decreases as the frequency increases. The results show that the controlled system behaves very much like a dipole type radiator.

Sound radiation at the controlled resonant frequencies is also studied. Figure 7 shows the far-field pressure directivity at 653.1 Hz, corresponding to the second controlled resonant frequency. The sound radiation decreases near $\theta=0$ but increases elsewhere. However, the global radiation level does not increase significantly. Similar conclusion holds for other controlled resonant frequencies.

To evaluate the overall performance of the controlled systems obtained, the total radiated sound power (in dB *re*: 10^{-12} W) and radiation efficiency for both the uncontrolled and controlled systems are shown in Figs. 8 and 9, respectively. Figure 8 shows excellent sound power attenuation below the first controlled (or second uncontrolled) natural frequency. The radiation efficiency plot (see Fig. 9) shows that the controlled system efficiency is decreased when the frequency is below the second controlled (or third uncontrolled) natural frequency. In general, the controlled system corresponds to an inefficient radiator for frequencies below the first controlled resonant frequency. Figure 8 also shows good sound power attenuation for off-resonance frequencies, in contrast to the work described in Ref. 10. To further understand the underlying mechanism for the controlled system, the spatial average mean-square velocity before and after control [see Eq. (11)] is presented in Fig. 10. It can seen that the controlled vibrational levels are in general reduced in the studied frequency range. This fact suggests that the ''modal reduction''[15] is an important mechanism in the proposed control process. On the other hand, the controlled modes are a linear combination of the uncontrolled modes and the controller is designed to make all the controlled modes nonvolumetric. This fact implies that ''modal-restructuring''[15] is also

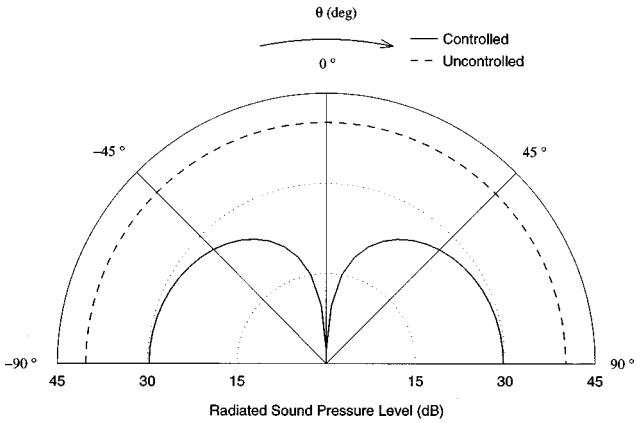

FIG. 6. Radiation directivity at 200 Hz (off resonance).

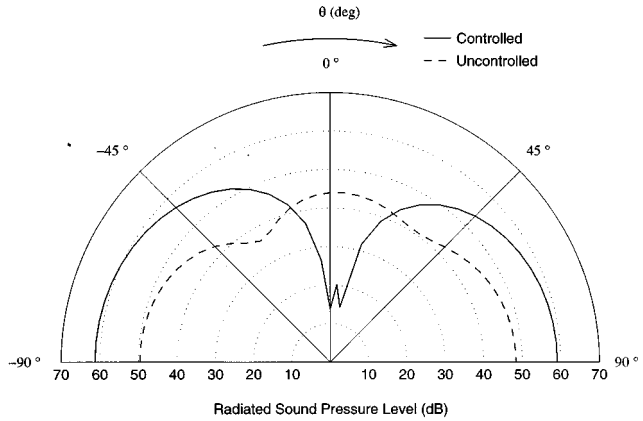

FIG. 7. Radiation directivity at 653.1 Hz (second controlled resonance).

an important mechanism in the control behavior. In general, the overall performance of the controlled system is limited by the first natural frequency of the controlled system. To overcome this limit, one may want to increase this first controlled resonant frequency. However, as expressed in Eq. (21), the upper bound for the first controlled natural frequency is given by the second uncontrolled resonant frequency. Thus, for the present design, the control efficiency is restricted in frequency by the constraint on the controlled resonant frequencies. This limitation could be overcome by adopting a similar control design using a MIMO feedforward controller and a recursive formulation as proposed in Ref. 16.

D. Control performance comparison

In this section, different control methods are compared for the previous system of the simply supported beam. The ''nonvolumetric design'' corresponds to the approach proposed in this paper (results from the previous section). The ''volume velocity sensing design'' considers the use a volume velocity sensor on the simply supported beam as described in Ref. 10. The ''accelerometer sensing design'' uses an accelerometer located at the center of the beam as error

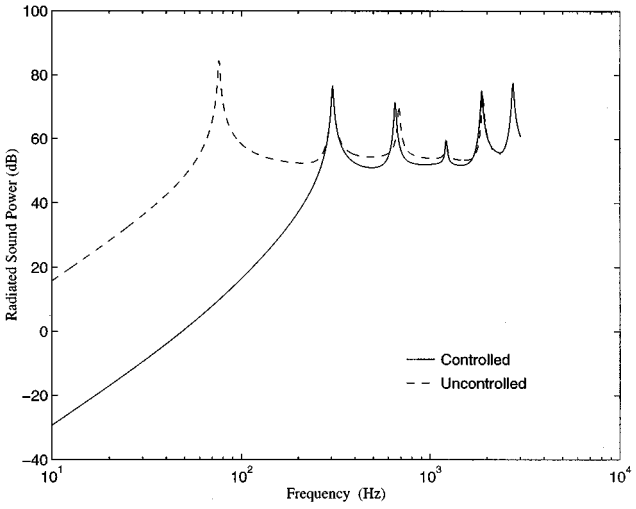

FIG. 8. Total radiated sound power.

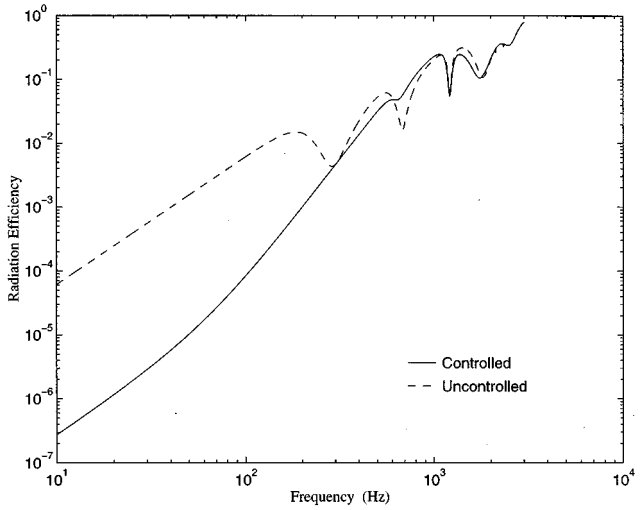

FIG. 9. Radiation efficiency.

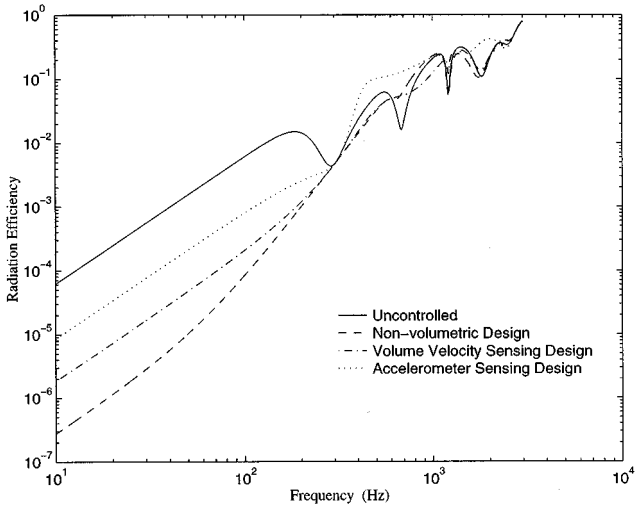

FIG. 11. Comparison of radiation efficiency for different control methods.

sensor. All other system parameters are identical. For the latter two approaches, the error sensor detects only odd-order modes as they are the only ones that are nonvolumetric. The control input in these two cases is assumed to be a control force located at the middle of the beam. This location was selected to avoid the control force coupling into the even-order modes that are already nonvolumetric sources and thus radiate weakly. The last two methods do not include design of the actuator load; indeed, they are purely based upon a sensing strategy and the control load is only chosen based upon physical insight.

The radiation efficiency of the three different controlled systems is shown in Fig. 11. All methods provide a large decrease of the radiation efficiency in the low-frequency domain. However, the use of the accelerometer as an error sensor leads the poorest results (an increase of the radiation efficiency can be noticed at high frequencies) as its signal is not directly related to sound radiation. The method proposed in this paper gives better results at low frequencies than volume velocity sensing design as it provides the modal characteristics of both the sensor and the actuator simultaneously. At higher frequencies, both nonvolumetric design and the volume velocity sensing design give similar results. The associated controlled radiated sound power and mean-square velocity are shown in Figs. 12 and 13, respectively. The nonvolumetric design is the most efficient in the low-frequency region (up to 10 dB improvement) in terms of controlling sound radiation. It is also apparent from Fig. 12 that the nonvolumetric design (the procedure of this paper) does not lead to a large increase of radiated sound and vibrational levels at off-resonance excitation of the uncontrolled system while the other two methods do. For the volume velocity sensing design, the sound radiation is increased significantly around 1 kHz because of a large increase of the displacement in the same frequency range (see Fig. 13). It can be noticed in Fig. 13 that the volume velocity sensing design and the accelerometer sensing design are associated with very large increase of vibrational levels in the higher-frequency region. Thus, it appears that the method developed

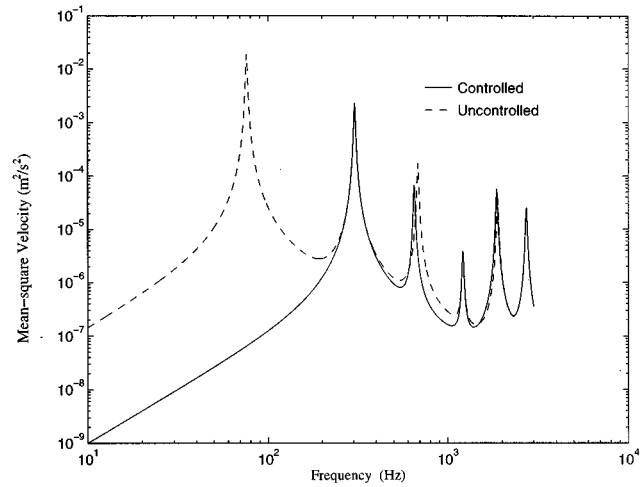

FIG. 10. Mean-square velocity.

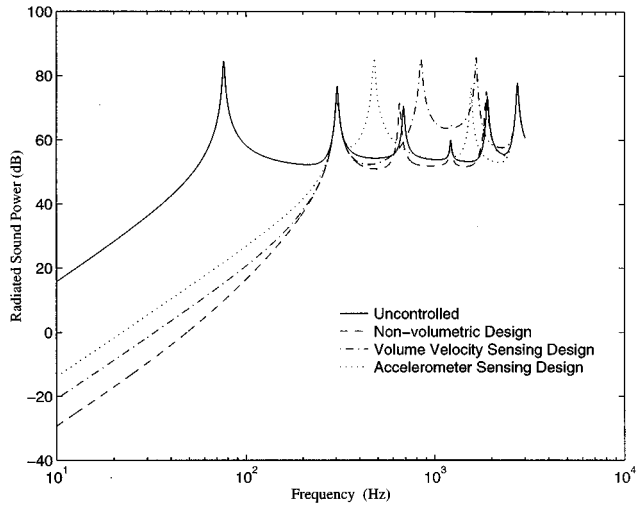

FIG. 12. Comparison of total radiated power for different control methods.

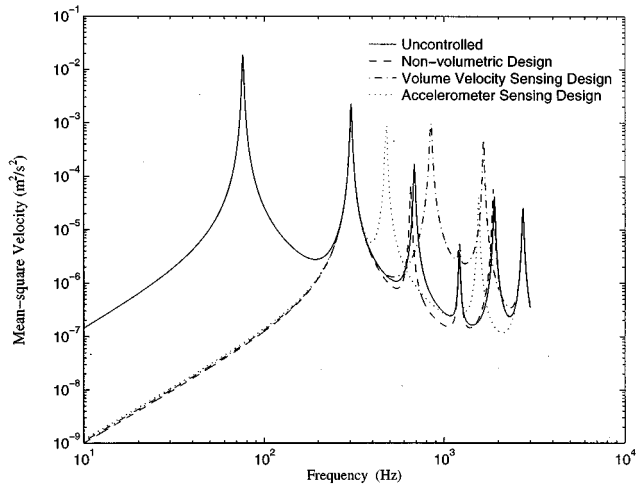

FIG. 13. Comparison of mean-square velocity for different control methods.

in this paper provides a better controlled system as the vibrational and acoustic levels are generally not increased for off-resonance of the uncontrolled and controlled system while the low-frequency performance is significantly improved. This improvement is due to the fact that the sensor and the control input are optimized at the same time regardless of frequency and excitation characteristics, thus limiting control spillover effects.

III. CONCLUSIONS

In this paper a new formulation for the design of ASAC systems is proposed. The design methodology proposed here is based on the fact that elemental radiators with zero integrals of normal velocity over their surface (i.e., nonvolumetric) are inefficient radiators of sound at low frequencies. A SISO eigenassignment method is thus developed in order to modify the system eigenstructure so that all controlled modes are nonvolumetric, therefore leading to an overall sound attenuation in the far field. Although the design procedure is carried out in the modal domain for a simple one-dimensional structure located in rigid baffle, it is readily extensible to more general planar structures since it is based upon a normal mode analysis. One main advantage of this method is that the design does not depend on the characteristics of the external disturbance, such as the form, location, and frequency contents. The design is only based on the modal behavior of the structure. The effectiveness of this formulation is demonstrated through numerical simulation for control of radiation from a simply supported beam. Significant sound power attenuation is achieved in the low frequencies, up to the first controlled resonant frequency. The present approach is also compared to other approaches employing a volume velocity sensor or an accelerometer as a sensor at the center of the beam. The control method discussed in this paper provides larger attenuation of both sound radiation and vibrational levels than the two latter cases. This increased control performance is associated with the fact that the proposed method optimizes both the error sensor and control input simultaneously.

ACKNOWLEDGMENT

The authors gratefully acknowledge the support of this work by the Office of Naval Research under Grant No. ONR N00014-92-J-470, Dr. Kam Ng, Technical Monitor.

[1] C. R. Fuller, ''Active control of sound transmission/radiation from elastic plates by vibrational inputs: I. Analysis,''J. Sound Vib. **136**, 1–15 (1990).
[2] B. T. Wang, R. A. Burdisso, and C. R. Fuller, ''Optimal placement of piezoelectric actuators for active control of sound radiation from elastic plates,'' Proc. Noise-Conf. **91**, 267–275 (1991).
[3] R. A. Burdisso and C. R. Fuller, ''Theory of feedforward controlled system eigenproperties,'' J. Sound Vib. **153**, 437–452 (1992).
[4] R. A. Burdisso and C. R. Fuller, ''Feedforward controller design by eigenvalue assignment,'' AIAA J. Guidance Control **17**, 466–472 1994.
[5] R. A. Burdisso and C. R. Fuller, ''Design of active structural acoustic control systems by eigenproperty assignment,'' J. Acoust. Soc. Am. **96**, 1582–1591 (1994).
[6] K. A. Cunefare, ''The minimum multimodal radiation efficiency of baffled finite beams,'' J. Acoust. Soc. Am. **90**, 2521–2529 (1991).
[7] R. F. Keltie and H. Peng, ''The effects of modal coupling on the acoustic power radiation from panels,'' Trans. ASME J. Vib. Acoust. Stress Reliability Design **109**, 48–54 (1987).
[8] S. J. Elliott and M. E. Johnson, ''Radiation modes and the active control of sound power,'' J. Acoust. Soc. Am. **94**, 2194–2204 (1993).
[9] R. L. Clark and C. R. Fuller, ''Modal sensing of efficient acoustic radiators with PVDF distributed sensors in active structural acoustic control approaches,'' J. Acoust. Soc. Am. **91**, 3321–3329 (1992).
[10] C. Guigou, F. Charette, and A. Berry, ''Active control of sound by minimization of volume velocity on finite beam,'' Proceedings of 3rd International congress on Air- and Structure-Borne Sound and Vibration, Montreal, Canada, May 1994, 169–174.
[11] M. E. Johnson and S. J. Elliott, ''Volume velocity sensors for active control,'' Proc. Inst. Acoust. **15**, 411–420 (1993).
[12] F. Fahy, *Sound and Structural Vibration/Radiation, Transmission and Response* (Academic, London, 1985), pp. 64–77.
[13] M. C. Junger and D. Feit, *Sound, Structures, and Their Interaction* (MIT, Cambridge, 1986), 2nd. ed.
[14] *Matlab Optimization Toolbox* (The MathWorks, Inc., South Natick, MA, 1992).
[15] J. Pan, S. D. Snyder, C. H. Hansen, and C. R. Fuller, ''Active control of far-field sound radiated by a rectangular panel—A general analysis,'' J. Acoust. Soc. Am. **91**, 2056–2066 (1992).
[16] R. A. Burdisso, C. R. Fuller, and Z. Li, ''Eigenproperties of MIMO feedforward controlled flexible systems'' (unpublished).

Adaptive IIR filtered-v algorithms for active noise control

David H. Crawford[a] and Robert W. Stewart
Signal Processing Division, Department of Electronic and Electrical Engineering, University of Strathclyde, Glasgow G1 1XW, United Kingdom

(Received 26 January 1996; revised 17 September 1996; accepted 13 December 1996)

This paper reports on the development of ''full-gradient'' and ''simplified-gradient'' versions of the filtered-u algorithm for active noise control. After discussing the general principles of active noise control, the paper presents full mathematical derivations of the full-gradient, simplified-gradient, and Feintuch-based versions of the filtered-u algorithm, clearly showing the various levels of simplifying assumptions that are made along the way. Finally, some illustrative simulation results are presented. © *1997 Acoustical Society of America.* [S0001-4966(97)03404-8]

PACS numbers: 43.50.Ki [GAD]

INTRODUCTION

Active noise control (ANC) is based on the simple physics of destructive interference of propagating acoustic waves. In the 1930s a U.S. patent was taken out by Lueg for an analog ANC system.[1] However, success with early analog controllers was very limited and it is only in recent years that powerful digital signal processing (DSP) devices have made possible the development of real-time digital ANC systems, with applications including air conditioning ducts,[2] aircraft,[3] cars,[4] and magnetic resonance imaging (MRI) systems.[5] Analog controllers have also been further developed and many of the ANC headsets now available use analog ''error feedback'' techniques.[6]

Many digital ANC systems use adaptive filtering techniques, often based on the ''filtered-x'' [6] or ''filtered-u'' [7] algorithms for finite impulse response (FIR) and infinite impulse response (IIR) filters, respectively. The filtered-u algorithm is an extension of Feintuch's IIR-LMS algorithm,[8] which involves a considerable degree of approximation. While Feintuch's IIR-LMS algorithm performs well in many situations, it has been shown that in terms of minimizing the mean squared error (MSE), it is theoretically incorrect.[9,10] The ''full-gradient'' and ''simplified-gradient'' IIR-LMS algorithms,[11] however, are more rigorous in terms of minimizing the MSE, although these, too, are based on several approximations.

In the following sections, full-gradient and simplified-gradient versions of the filtered-u algorithm are derived, clearly showing the various levels of simplifying assumptions that are made. Because of the basic differences in the adaptive architecture, these algorithms will be called ''full-gradient filtered-v'' and ''simplified-gradient filtered-v'' algorithms in this paper.

I. PRINCIPLES OF ACTIVE NOISE CANCELLATION

Figure 1(a) shows the generic single-channel noise canceller, and Fig. 1(b) the corresponding system block diagram. In order to analyze this system, all signals are assumed to be discrete-time sequences and all transfer functions are given in the z domain. A number of acoustic paths can be identified from Fig. 1:

- $H_e(z)$ the acoustic path from secondary source to error microphone;
- $H_r(z)$ the acoustic feedback path from secondary source to reference microphone;
- $G_r(z)$ the acoustic path from noise source to reference microphone;
- $G_e(z)$ the acoustic path from noise source to error microphone.

There are two paths through which the noise signal, $n(k)$, travels to reach the error microphone: the *primary* path $G_e(z)$ and the *secondary* path comprising $G_r(z)$, $W(z)$, $H_r(z)$, and $H_e(z)$, as illustrated in Fig. 1(b). For *perfect* cancellation to occur at the error microphone, it is necessary to have

$$y_e(k) = -d(k), \tag{1}$$

and, therefore, from Fig. 1, the transfer function of the secondary path must be made equal to the negative of the transfer function of the primary path. The required controller transfer function is therefore

$$W_{\text{reqd}}(z) = \frac{-G_e(z)}{G_r(z)H_e(z) - G_e(z)H_r(z)}. \tag{2}$$

Note that even if the transfer functions of all the acoustic paths can be considered as having no poles, it can be seen from the denominator of Eq. (2) that $W_{\text{reqd}}(z)$ will, in general, have poles. Therefore, in theory $W_{\text{reqd}}(z)$ is best implemented using an IIR filter.

II. ADAPTIVE CONTROL OF $W(z)$

Direct calculation of Eq. (2) is generally not feasible, and in fact $W_{\text{reqd}}(z)$ will generally be noncausal. In order to find an optimum causal control filter, adaptive techniques are usually employed. The problem can be expressed in the context of system identification, in which the unknown system to be modeled by the adaptive filter is $W_{\text{reqd}}(z)$. It can be seen from Fig. 1(b), however, that the existence of the transfer functions $H_e(z)$ and $H_r(z)$ makes the problem slightly different from that of standard system identification (shown

[a]Electronic mail: david@spd.eee.strath.ac.uk

 0001-4966/97/101(4)/2097/7/$10.00

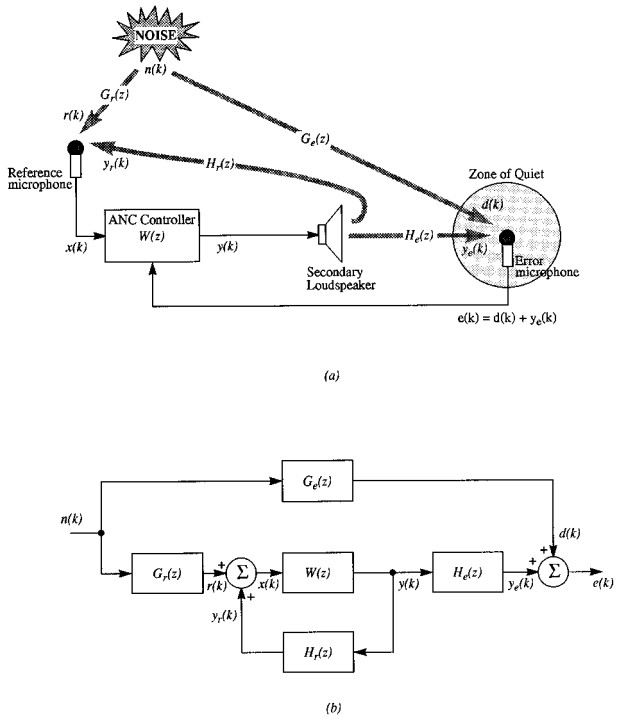

FIG. 1. (a) General ANC system setup. (b) Equivalent system block diagram.

in Fig. 2), in which $H_e(z)=1$ and $H_r(z)=0$. The algorithm used to train the adaptive filter must take account of these transfer functions. For the time being, all acoustic paths will be assumed time invariant, and the primary noise signal will be assumed wide-sense stationary and ergodic. This then means that *all* the signals can be assumed wide-sense stationary and ergodic.

The general aim of system identification is to find a filter weight vector which can subsequently be used as a reliable model of the unknown system. In order to calculate this *optimum* weight vector, a known noise sequence, $x(k)$, is fed to both the unknown system and the modeling filter, and the output signals, $d(k)$ and $y(k)$, are measured. The error signal, $e(k)$, then represents the difference between the output of the unknown system and that of the modeling filter, and the aim is to find the weight vector for which the average magnitude of $e(k)$ is as small as possible.

Many adaptive control algorithms use a gradient descent technique to iteratively search for the minimum of the mean squared error performance surface.[12] The filter's weight vector is adjusted by a small amount in the direction of steepest descent, and after several iterations it will, it is hoped, be close to the optimum weight vector.

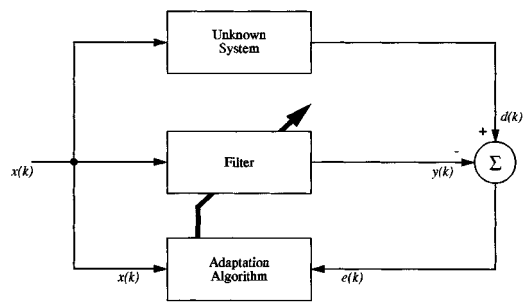

FIG. 2. Generic system identification setup.

In the *least-mean-squares* (LMS) family of adaptation algorithms, an estimate of the direction of steepest descent is used, rather than the actual direction of steepest descent. This results in significant computational savings, and the weight vector at time $k+1$ is calculated as

$$\mathbf{w}(k+1)=\mathbf{w}(k)+\mu(-\hat{\nabla}(k)), \tag{3}$$

where $\hat{\nabla}(k)$ is the estimate of the gradient vector corresponding to the weight vector at time k, and μ is used to control convergence and stability of the algorithm.

An important point worth noting is that the suitability of a particular weight vector as a possible model should be assessed as though that weight vector had been the time-invariant model for all time. This is not merely a simplifying assumption, but is in fact an implicit aim of system identification: since the model obtained will subsequently be used as a time-invariant model of the unknown system, any potential candidate should be assessed as though it were time invariant.

A. The full-gradient filtered-v algorithm

Referring to Fig. 1, the error signal is

$$e(k)=d(k)+y_e(k)=d(k)+\sum_{n=0}^{\infty} h_e(n)y(k-n). \tag{4}$$

The output, $y(k)$, of the IIR filter is

$$y(k)=\sum_{i=0}^{N-1} a_i(k)x(k-i)+\sum_{j=1}^{M} b_j(k)y(k-j)$$

$$=\mathbf{a}^T(k)\mathbf{x}(k)+\mathbf{b}^T(k)\mathbf{y}(k-1), \tag{5}$$

where $\mathbf{x}(k)$ and $\mathbf{y}(k-1)$ are vectors of past input and output samples defined as

$$\mathbf{x}(k)=[x(k)x(k-1)\cdots x(k-N+1)]^T, \tag{6a}$$

$$\mathbf{y}(k-1)=[y(k-1)y(k-2)\cdots y(k-M)]^T, \tag{6b}$$

and $\mathbf{a}(k)$ and $\mathbf{b}(k)$ are the feedforward and feedback weight vectors at time index k:

$$\mathbf{a}(k)=[a_0(k)a_1(k)\cdots a_{N-1}(k)]^T, \tag{7a}$$

$$\mathbf{b}(k)=[b_1(k)b_2(k)\cdots b_M(k)]^T. \tag{7b}$$

Note that Eq. (5) can also be expressed as

$$y(k)=\mathbf{w}^T(k)\mathbf{u}(k), \tag{8}$$

where

$$\mathbf{w}(k)=\begin{bmatrix}\mathbf{a}(k)\\ \mathbf{b}(k)\end{bmatrix} \quad \text{and} \quad \mathbf{u}(k)=\begin{bmatrix}\mathbf{x}(k)\\ \mathbf{y}(k-1)\end{bmatrix}. \tag{9}$$

The mean squared error resulting from using the weight vector at time k as the model is

$$J(k)=E[e^2(k)|_{\mathbf{w}(k)}], \tag{10}$$

where the subscript "$\mathbf{w}(k)$" is used to explicitly indicate that the error values are to be calculated using $\mathbf{w}(k)$ as

though it had been the filter's weight vector for all time.[13] The aim is to adjust the weight vector according to Eq. (3), in the hope that $\mathbf{w}(k+1)$ will be closer to the optimum weight vector than $\mathbf{w}(k)$ is.

The estimated gradient vector corresponding to $\mathbf{w}(k)$ is

$$\hat{\boldsymbol{\nabla}}(k)=\frac{\partial}{\partial \mathbf{w}(k)}\{e^2(k)|_{\mathbf{w}(k)}\}$$
$$=2e(k)|_{\mathbf{w}(k)}\sum_{n=0}^{\infty} h_e(n)\frac{\partial}{\partial \mathbf{w}(k)}\{y(k-n)|_{\mathbf{w}(k)}\}. \tag{11}$$

Using Eq. (5), $[\partial/\partial \mathbf{w}(k)]\{y(k)|_{\mathbf{w}(k)}\}$ can be expressed as

$$\frac{\partial}{\partial \mathbf{w}(k)}\{y(k)|_{\mathbf{w}(k)}\}$$
$$=\mathbf{u}(k)|_{\mathbf{w}(k)}+\sum_{i=0}^{N-1} a_i(k)\frac{\partial}{\partial \mathbf{w}(k)}\{x(k-i)|_{\mathbf{w}(k)}\}$$
$$+\sum_{j=1}^{M} b_j(k)\frac{\partial}{\partial \mathbf{w}(k)}\{y(k-j)|_{\mathbf{w}(k)}\}. \tag{12}$$

If the acoustic feedback is ignored [i.e., $H_r(z)=0$ in Fig. 1], the summation term over i in Eq. (12) will be zero, since $x(k)=r(k)$, which is independent of $\mathbf{w}(k)$, resulting in the derivative of $x(k)$ with respect to $\mathbf{w}(k)$ being zero. In the general case, however, acoustic feedback *will* exist $[H_r(z)\neq 0]$, and $x(k)$ *will* be dependent on the filter weights. Specifically,

$$x(k)=r(k)+\sum_{m=0}^{\infty} h_r(m)y(k-m). \tag{13}$$

Substituting Eq. (13) into Eq. (12) gives

$$\frac{\partial}{\partial \mathbf{w}(k)}\{y(k)|_{\mathbf{w}(k)}\}$$
$$=\mathbf{u}(k)|_{\mathbf{w}(k)}+\sum_{i=0}^{N-1} a_i(k)$$
$$\times\sum_{m=0}^{\infty} h_r(m)\frac{\partial}{\partial \mathbf{w}(k)}\{y(k-i-m)|_{\mathbf{w}(k)}\}$$
$$+\sum_{j=1}^{M} b_j(k)\frac{\partial}{\partial \mathbf{w}(k)}\{y(k-j)|_{\mathbf{w}(k)}\}. \tag{14}$$

Equation (14) involves considerable computational effort, since all past values of y and their derivatives have to be calculated using the current weight vector, $\mathbf{w}(k)$, as though it were the time-invariant model.[14] However, if the filter weights are made to adapt slowly enough with time such that all previous weight vectors which significantly influence $e(k)$ are approximately equal to $\mathbf{w}(k)$, then $y(k)|_{\mathbf{w}(k)}\approx y(k)$, $\mathbf{u}(k)|_{\mathbf{w}(k)}\approx u(k)$, $e(k)|_{\mathbf{w}(k)}\approx e(k)$, and

$$\frac{\partial}{\partial \mathbf{w}(k)}\{y(k-j)|_{\mathbf{w}(k)}\}\approx\frac{\partial}{\partial \mathbf{w}(k-j)}\{y(k-j)|_{\mathbf{w}(k-j)}\}. \tag{15}$$

These approximations allow Eq. (14) to be written as

$$\mathbf{v}(k)\approx\mathbf{u}(k)+\sum_{i=0}^{N-1} a_i(k)\sum_{m=0}^{\infty} h_r(m)\mathbf{v}(k-i-m)$$
$$+\sum_{j=1}^{M} b_j(k)\mathbf{v}(k-j), \tag{16}$$

where, for convenience, the vector $\mathbf{v}(k)$ has been defined as

$$\mathbf{v}(k)\triangleq\frac{\partial}{\partial \mathbf{w}(k)}\{y(k)|_{\mathbf{w}(k)}\}, \tag{17}$$

i.e.,

$$\mathbf{v}(k)=[\alpha_0(k)\alpha_1(k)\cdots\alpha_{N-1}(k)\beta_1(k)\beta_2(k)\cdots\beta_M(k)]^T, \tag{18}$$

where

$$\alpha_p(k)=\frac{\partial}{\partial a_p(k)}\{y(k)|_{\mathbf{w}(k)}\},\quad 0\leqslant p<N, \tag{19a}$$

$$\beta_p(k)=\frac{\partial}{\partial b_p(k)}\{y(k)|_{\mathbf{w}(k)}\},\quad 0<p\leqslant M. \tag{19b}$$

Note that Eq. (16) has straightforward recursion, i.e., $\mathbf{v}(k)$ is calculated using past values, $\mathbf{v}(k-j)$, which have been previously calculated. This was not the case in Eq. (14), where $[\partial/\partial \mathbf{w}(k)]\{y(k)|_{\mathbf{w}(k)}\}$ is calculated using values of $[\partial/\partial \mathbf{w}(k)]\{y(k-j)|_{\mathbf{w}(k)}\}$, which are calculated using $\mathbf{w}(k)$. Equation (16) is therefore computationally simpler than Eq. (14).

Having calculated $\mathbf{v}(k)$ using Eq. (16), Eq. (11) approximates to

$$\hat{\boldsymbol{\nabla}}(k)\approx 2e(k)\sum_{n=0}^{\infty} h_e(n)\mathbf{v}(k-n). \tag{20}$$

Defining a *filtered-v* vector as

$$\mathbf{v_f}(k)=\sum_{n=0}^{\infty} h_e(n)\mathbf{v}(k-n) \tag{21}$$

allows Eq. (20) to be written as

$$\hat{\boldsymbol{\nabla}}(k)\approx 2e(k)\mathbf{v_f}(k). \tag{22}$$

Note that $\mathbf{v_f}(k)$ may also be expressed as

$$\mathbf{v_f}(k)=[f_0(k)f_1(k)\cdots f_{N-1}(k)g_1(k)g_2(k)\ldots g_M(k)]^T, \tag{23}$$

where

$$f_p(k)=\sum_{n=0}^{\infty} h_e(n)\alpha_p(k-n),\quad 0\leqslant p<N, \tag{24a}$$

$$g_p(k)=\sum_{n=0}^{\infty} h_e(n)\beta_p(k-n),\quad 0<p\leqslant M. \tag{24b}$$

Equations (3), (16), (21), and (22) form what could be called the *full-gradient filtered-v* algorithm, since the vector $\mathbf{v}(k)$ is filtered by $H_e(z)$ to form $\mathbf{v_f}(k)$. Table I summarizes the algorithm, and Fig. 3 shows the block diagram. Note that the impulse responses of $H_r(z)$ and $H_e(z)$ must be known; these can be obtained *a priori* using the system identification setup of Fig. 2. The unknown system comprises the loudspeaker, acoustic path, and microphone, as well as all amplifiers and filters in the signal path, and the standard LMS algorithm is used to update the adaptive filter. Once adapted,

TABLE I. Summary of the full-gradient filtered-v adaptation algorithm.

Initialization: $\mathbf{v}(0)=\mathbf{0}$

$$y(k)=\mathbf{w}^T(k)\mathbf{u}(k)$$

$$\mathbf{v}(k)=\mathbf{u}(k)+\sum_{i=0}^{N-1} a_i(k)\sum_{m=0}^{L_r}\hat{h}_r(m)\mathbf{v}(k-i-m)+\sum_{j=1}^{M} b_j(k)\mathbf{v}(k-j)$$

$$\mathbf{v_f}(k)=\sum_{n=0}^{L_e}\hat{h}_e(n)\mathbf{v}(k-n)$$

$$\mathbf{w}(k+1)=\mathbf{w}(k)-2\mu e(k)\mathbf{v_f}(k)$$

the coefficients are used as a model of the acoustic path in question. The number of coefficients in the reference and error path models, $\hat{h}_r(k)$ and $\hat{h}_e(k)$, are denoted as L_r and L_e, respectively. Note that if $H_r(z)=0$ and $H_e(z)=1$, the algorithm reduces to the full-gradient IIR-LMS algorithm.[11] Note also that, since Eq. (16) is recursive, an initial vector must be chosen for $\mathbf{v}(0)$, a common initial condition being $\mathbf{v}(0)=\mathbf{0}$. It should be emphasized that, despite the term *full-gradient*, the algorithm relies on the assumption that the weight vector is made to adapt slowly with time, and therefore it is not an exact stochastic gradient algorithm.

B. The simplified-gradient filtered-v algorithm

In a manner similar to that used for the simplified gradient IIR-LMS algorithm,[11] the fact that the weights are made to adapt slowly can be further used to simplify the calculation of $\mathbf{v_f}(k)$, such that only $f_0(k)$ and $g_1(k)$ need to be calculated at time index k. The other elements of $\mathbf{v_f}(k)$, namely $f_1(k),\ldots,f_{N-1}(k),g_2(k),\ldots,g_M(k)$, are approximated as delayed values of $f_0(k)$ and $g_1(k)$. In other words, having calculated $f_0(k)$ and $g_1(k)$, the other elements of $\mathbf{v_f}(k)$ are obtained as follows:

$$\mathbf{v_f}(k)=[f_0(k)f_0(k-1)\cdots f_0(k-N+1)g_1(k)\; g_1(k-1)\cdots g_1(k-M+1)]^T. \quad (25)$$

This results in the *simplified-gradient filtered-v* algorithm, which is summarized in Table II, and a block diagram of which is shown in Fig. 4. As can be seen from the figure, the simplified-gradient filtered-v algorithm requires considerably less computational effort than the full-gradient filtered-v algorithm requires.

Note that if the adaptive filter is FIR, Fig. 4 will become the simplified-gradient filtered-x algorithm. If $H_r(z)=0$, this

TABLE II. Summary of the simplified-gradient filtered-v adaptation algorithm.

Initialization: $\alpha_0(0)=\beta_1(0)=0$

$$y(k)=\mathbf{w}^T(k)\mathbf{u}(k)$$

$$\alpha_0(k)=x(k)+\sum_{i=0}^{N-1} a_i(k)\sum_{m=0}^{L_r}\hat{h}_r(m)\alpha_0(k-i-m)+\sum_{j=1}^{M} b_j(k)\alpha_0(k-j)$$

$$\beta_1(k)=y(k-1)+\sum_{i=0}^{N-1} a_i(k)\sum_{m=0}^{L_r}\hat{h}_r(m)\beta_1(k-i-m)+\sum_{j=1}^{M} b_j(k)\beta_1(k-j)$$

$$f_0(k)=\sum_{n=0}^{L_e}\hat{h}_e(n)\alpha_0(k-n)$$

$$g_1(k)=\sum_{n=0}^{L_e}\hat{h}_e(n)\beta_1(k-n)$$

$$\mathbf{v_f}(k)=[f_0(k)f_0(k-1)\cdots f_0(k-N+1)g_1(k)g_1(k-1)\cdots g_1(k-M+1)]^T$$

$$\mathbf{w}(k+1)=\mathbf{w}(k)-2\mu e=(k)\mathbf{v_f}(k)$$

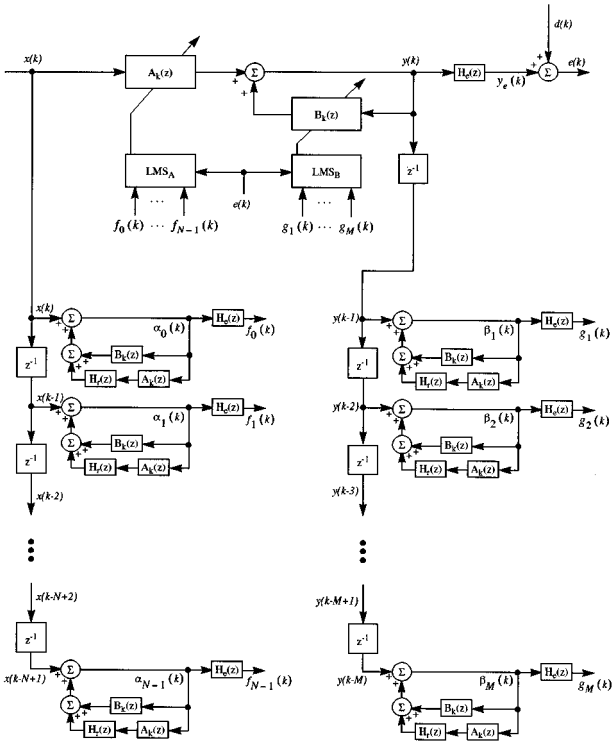

FIG. 3. Block diagram of the full-gradient filtered-v algorithm.

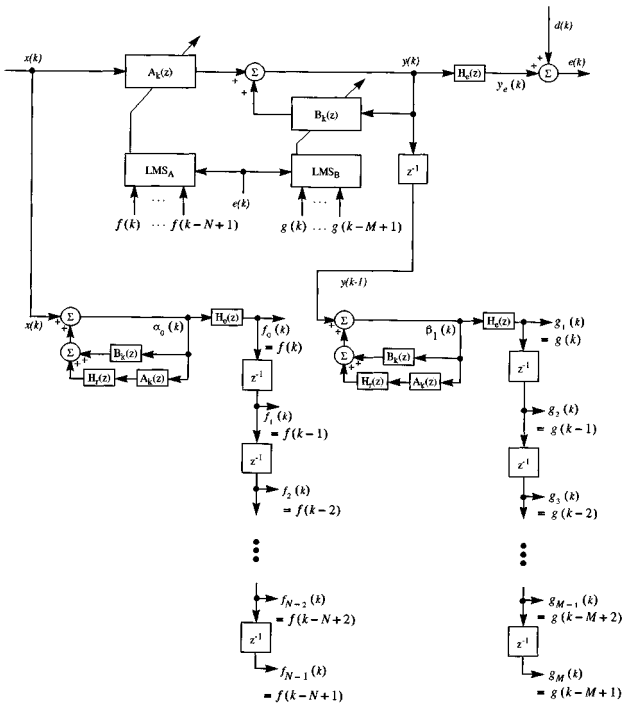

FIG. 4. Block diagram of the simplified-gradient filtered-v algorithm.

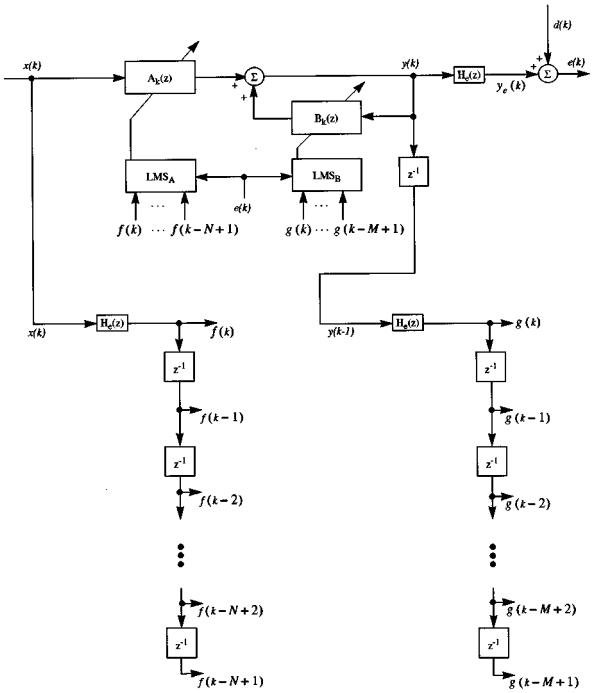

FIG. 5. Block diagram of the filtered-u algorithm.

will be identical to the well-known filtered-x algorithm.[6] However, if $H_r(z)\neq 0$, the recursive filtering of $\alpha_0(k)$ through $A_k(z)H_r(z)$ should, in theory, be performed; the simplified-gradient filtered-x algorithm does this, while the filtered-x algorithm does not.

C. The filtered-u algorithm

Yet another simplification can be applied, in which the summation terms in Eq. (16) are omitted, giving

$$\mathbf{v}(k)\approx\mathbf{u}(k). \tag{26}$$

This allows Eq. (21) to be expressed as

$$\mathbf{v_f}(k)=\sum_{n=0}^{\infty} h_e(n)\mathbf{u}(k-n). \tag{27}$$

Since $\mathbf{v_f}(k)$ is now calculated simply by filtering $\mathbf{u}(k)$ by $H_e(z)$, it is usually referred to as the *filtered-u* vector, and the resulting weight update algorithm is known as the *filtered-u* algorithm.[7] (In the context of this paper, it might also be called the *Feintuch-based filtered-v algorithm*, but the name ''filtered-u'' is well established and it describes the algorithm more concisely.) Figure 5 shows a block diagram of the filtered-u algorithm, in which the recursive filters involving $B_k(z)$ and $H_r(z)A_k(z)$ have been removed, and Table III summarizes the algorithm. This approach was proposed by Feintuch,[8] in the context of adaptive IIR filters [i.e., with $H_e(z)=1$ and $H_r(z)=0$], and is based on Feintuch's assumption that the derivatives of past output values with respect to the current weight vector are zero. While it is correct that any change in the current weight vector cannot affect past output values, $y(k-1),y(k-2)$, etc., it must be remembered that we require the change in past values of y as they *would* have been if $\mathbf{w}(k)$ had *always* been the (time-invariant) weight vector, and these values *will* be affected by a change in $\mathbf{w}(k)$. However, although the omission of the summation terms in Eq. (16) is not mathematically justified in the specific context of minimizing the cost function given by Eq. (10), the algorithm does perform well in many situations, and has the advantage of being computationally simple.[9] It also has an inherent tendency to maintain a stable IIR filter.[10]

TABLE III. Summary of the filtered-u adaptation algorithm.

$$y(k)=\mathbf{w}^T(k)\mathbf{u}(k)$$
$$\mathbf{v_f}(k)=\sum_{n=0}^{L_e}\hat{h}_e(n)\mathbf{u}(k-n)$$
$$\mathbf{w}(k+1)=\mathbf{w}(k)-2\mu e(k)\mathbf{v_f}(k)$$

Furthermore, it can be intuitively seen that if the feedback weights, $\mathbf{b}(k)$, happen to be small, which may be the case in many situations, then the summation terms are likely to be small relative to $\mathbf{u}(k)$, in which case Feintuch's approximation in Eq. (26) becomes valid.

Note that, unlike the full-gradient and simplified-gradient filtered-v algorithms described previously, the filtered-u algorithm does not require any knowledge of the acoustic feedback path, $H_r(z)$, since the summation terms involving $H_r(z)$ have been omitted. However, a model of the error path, $H_e(z)$, is still required.

Note also that if the adaptive filter is FIR, the filtered-u algorithm becomes the filtered-x algorithm. It has already been mentioned that when acoustic feedback exists, the filtered-x and simplified-gradient filtered-x algorithms differ from each other. More specifically, when $H_r(z)\neq 0$, the filtered-x algorithm is ''Feintuch-like,'' while the simplified-gradient filtered-x algorithm is not.

III. SIMULATION RESULTS

In this section, some illustrative results of comparisons between the simplified-gradient filtered-v algorithm and the filtered-u algorithm are presented. Three examples are given:

(1) ANC using an adaptive IIR filter [with $H_r(z)=0$];
(2) ANC using an adaptive IIR filter [with $H_r(z)\neq 0$];
(3) ANC using an adaptive FIR filter [with $H_r(z)\neq 0$].

In each case, the noise source was stationary white noise, and the results were obtained from an ensemble of 20 trials.

Case 1: The acoustic paths were chosen as

$$G_e(z)=0.05-0.001z^{-1}+0.001z^{-2}+0.8z^{-3}+0.6z^{-4}-0.2z^{-5}-0.5z^{-6}-0.1z^{-7}+0.4z^{-8}-0.05z^{-9};$$

$$G_r(z)=-0.02+0.4z^{-1}-0.1z^{-2};$$

$$H_e(z)=0.005-0.01z^{-1}+0.95z^{-2}+0.01z^{-3}-0.9z^{-4};$$

$$H_r(z)=0.$$

The order of the adaptive filter was 7/3 (i.e., 7 feedforward coefficients and 3 feedback coefficients).

From the results shown in Fig. 6, it can be seen that the convergence of the simplified-gradient filtered-v algorithm is

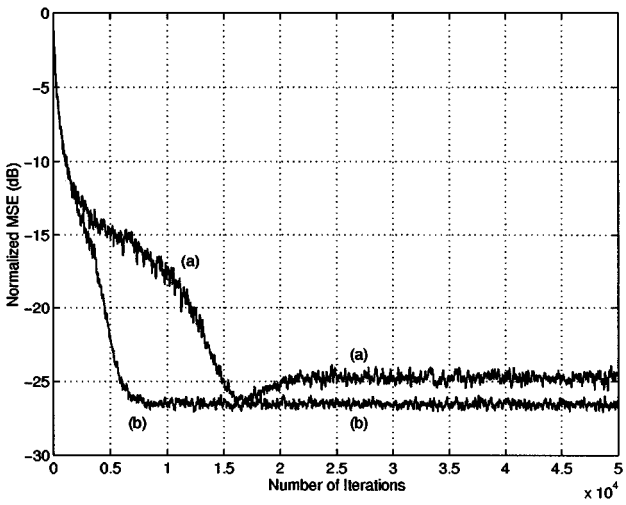

FIG. 6. Active noise cancellation using (a) the filtered-u algorithm, and (b) the simplified-gradient filtered-v algorithm, with no acoustic feedback. In each case, the order of the adaptive filter was 7/3 (i.e., 7 feedforward coefficients and 3 feedback coefficients).

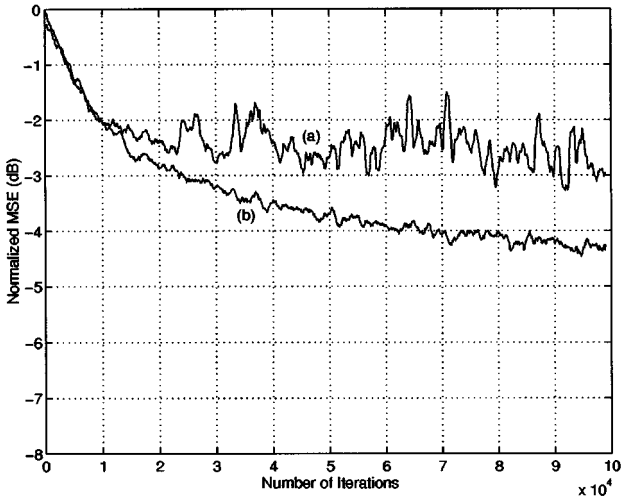

FIG. 8. Active noise cancellation using (a) the filtered-x algorithm, and (b) the simplified-gradient filtered-x algorithm, with acoustic feedback. In each case, the order of the adaptive filter was 50/0 (i.e., 50-tap FIR).

superior to that of the filtered-u algorithm. Note that the filtered-u algorithm does converge briefly to the same level of MSE as the simplified-gradient algorithm, but it then diverges, settling on a level approximately 2 dB above that of the simplified-gradient filtered-v algorithm. A 20-tap FIR filter updated using the filtered-x algorithm converged to -18.34 dB.

Case 2: The acoustic paths were the same as those in Case 1, except $H_r(z)=0.6z^{-1}$. The order of the filter in each case was again 7/3, and Fig. 7 shows the resulting MSE. Both plots were still slowly converging after 50 000 iterations. (In fact, they were found to be still slowly converging even after 200 000 iterations, and any attempt to speed this up by increasing μ_a or μ_b resulted in instability.) A 20-tap FIR filter updated using the filtered-x algorithm converged to -6.20 dB.

Case 3: In this case, the acoustic paths were $G_e(z)=0.5z^{-12}$; $G_r(z)=0.9z^{-4}$; $H_e(z)=0.95z^{-2}$; and $H_r(z)=0.9z^{-3}$. The order of the adaptive filter was 50/0 (i.e., 50-tap FIR), and Fig. 8 shows that in this case, the convergence of the simplified-gradient filtered-x algorithm is superior to that of the filtered-x algorithm.

The adaptation characteristics of the ''filtered'' algorithms described above will depend on the accuracy of the acoustic models. For the filtered-u algorithm, only $\hat{h}_e(k)$ is of concern, since $\hat{h}_r(k)$ is not used in the weight update equation. For the simplified-gradient filtered-v algorithm, however, both $\hat{h}_e(k)$ and $\hat{h}_r(k)$ are used, and both will affect the convergence of the algorithm. In Ref. 15, an analysis of the effects of plant modelling inaccuracies is presented for the filtered-x algorithm.

For errors in $\hat{h}_e(k)$, the converged MSE of both the filtered-u and the simplified-gradient filtered-v algorithms is affected by a similar amount; however, the simplified-gradient filtered-u algorithm must be made to converge more slowly than the filtered-u algorithm when the acoustic path error is large, otherwise it tends to become unstable. Errors in $\hat{h}_r(k)$ also affect the simplified-gradient filtered-v algorithm, although they tend to be less significant than errors in $\hat{h}_e(k)$. Of course, errors in $\hat{h}_r(k)$ have no effect on the filtered-u algorithm.

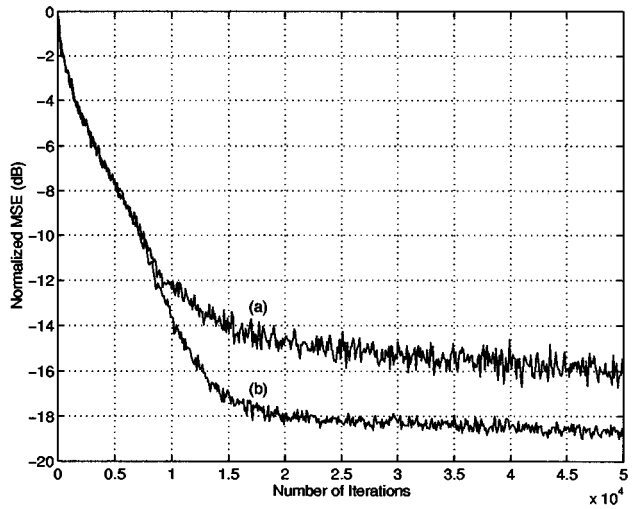

FIG. 7. Active noise cancellation using (a) the filtered-u algorithm, and (b) the simplified-gradient filtered-v algorithm, with acoustic feedback. The order of the adaptive filter was 7/3 in each case.

IV. CONCLUSIONS

In this paper, we have mathematically derived the full-gradient, simplified-gradient, and Feintuch-based versions of the filtered-u algorithm, specifically noting the various stages of simplifying assumptions that are required at each stage. Some simulation results have been presented, showing cases in which the simplified-gradient filtered-v algorithm performs better than the filtered-u algorithm. This improvement in performance can be understood in terms of the Feintuch-

based approximations made in the derivation of the filtered-u algorithm. It should be pointed out that in our experience with real-time ANC, the filtered-u algorithm performs as well as the simplified-gradient filtered-v algorithm in most practical situations. Nevertheless, the full-gradient and simplified-gradient algorithms are important in order to present a full picture of the underlying theory of adaptive IIR filtering for ANC.

Our current work is focusing on an investigation into alternative forms of adaptive IIR filter structures and adaptation algorithms that may give improved performance for active noise control applications.[16,17]

ACKNOWLEDGMENTS

This work was funded by the U.K. Engineering and Physical Sciences Research Council (EPSRC) under CASE Award (Motorola) 94564410.

[1] P. Lueg, ''Process of Silencing Sound Oscillations,'' U.S. Patent 2,043,416 (1936).
[2] M. C. Allie, C. D. Bremigan, L. J. Eriksson, and R. A. Greiner, ''Hardware and Software Considerations for Active Noise Control,'' in *Proceedings of the IEEE International Conference on Acoustics, Speech, and Signal Processing*, New York, USA, April 1988 (IEEE, New York, 1988), Vol. 5, pp. 2598–2601.
[3] S. J. Elliott, P. A. Nelson, and I. M. Stothers, ''In-Flight Experiments on the Active Control of Propeller-Induced Cabin Noise,'' J. Sound Vib. **140**(2), 219–238 (1990).
[4] S. Hasegawa, T. Tabata, A. Kinoshita, and H. Hyodo, ''The Development of an Active Noise Control System for Automobiles,'' in *Proceedings of the Worldwide Passenger Car Conference and Exposition*, Dearborn, Michigan, September/October 1992 (SAE International, Warrendale, PA, 1993).
[5] A. M. Goldman, W. E. Gossman, and P. C. Friedlander, ''Reduction of Sound Level with Antinoise in MR Imaging,'' Radiology **41**(4), 549–550 (1989).
[6] S. J. Elliott and P. A. Nelson, ''Active Noise Control,'' IEEE Signal Process. Mag. **10**(4), 12–35 (1993).
[7] L. J. Eriksson, ''Development of the Filtered-U Algorithm for Active Noise Control,'' J. Acoust. Soc. Am. **89**, 257–265 (1991).
[8] P. L. Feintuch, ''An Adaptive Recursive LMS Filter,'' Proc. IEEE **64**(11), 1622–1624 (1976).
[9] C. R. Johnson, Jr. and M. G. Larimore, ''Comments on and Additions to 'An Adaptive Recursive LMS Filter','' Proc. IEEE **65**(9), 1399–1402 (1977).
[10] B. Widrow and J. M. McCool, ''Comments on 'An Adaptive Recursive LMS Filter','' Proc. IEEE **65**(9), 1402–1404 (1977).
[11] J. J. Shynk, ''Adaptive IIR Filtering,'' IEEE ASSP Mag. **6**(2), 4–21 (1989).
[12] B. Widrow and S. D. Stearns, *Adaptive Signal Processing* (Prentice–Hall, Englewood Cliffs, NJ, 1985).
[13] O. Macchi, *Adaptive Processing: The Least Mean Squares Approach with Applications in Transmission* (Wiley, New York, 1996).
[14] C. R. Johnson, Jr., ''Adaptive IIR Filtering: Current Results and Open Issues,'' IEEE Trans. Inf. Theory **IT-30**(2), 237–250 (1984).
[15] E. Bjarnason, ''Analysis of the Filtered-X Algorithm,'' IEEE Trans. Speech Audio Process. **3**(6), 504–514 (1995).
[16] D. H. Crawford, R. W. Stewart, and E. Toma, ''An Alternative and Effective Adaptive IIR Filter Structure,'' IEE Electron. Lett. **31**(22), 1906–1907 (1995).
[17] D. H. Crawford, R. W. Stewart, and E. Toma, ''A Novel Adaptive IIR Filter for Active Noise Control,'' in *Proceedings of the IEEE International Conference on Acoustics, Speech, and Signal Processing*, Atlanta, May 1996 (IEEE, New York), Vol. III, pp. 1629–1632.

Characterization of the natural ambient sound environment: Measurements in open agricultural grassland

Hielke Freerk Boersma[a)]
Natuurkundewinkel, University of Groningen, Nijenborgh 4, NL-9747 AG Groningen, The Netherlands and Wetenschapswinkel Natuurkunde, University of Utrecht, P. O. Box 80170, NL-3508 TD Utrecht, The Netherlands

(Received 13 July 1995; revised 4 June 1996; accepted 15 November 1996)

The audibility of manmade sound in a natural environment is affected because of masking by ambient sound. In this report results are presented of measurements of the level and spectral composition of natural ambient sound. The statistical L_{95} level was determined, i.e., the sound pressure level which is exceeded for 95% of the time, at various wind velocities in open agricultural grassland. The total L_{95} is described by $L_{95}=37.9\ \log(v)+42.5$, where v is the wind velocity. The standard deviation with respect to the data points is 2.4 dB. For the A-weighted L_{95} we found a similar relation $[L_{A95}=22.6\ \log(v)+22.7]$. The relation between wind speed and natural ambient sound level for each $\frac{1}{3}$-oct band was also determined with nominal midband frequencies ranging from 6.3 Hz to 20 kHz separately. The frequency spectrum of ambient sound shows at low frequencies a behavior typical for turbulent processes. The $\frac{1}{3}$-oct band intensity of sound at these frequencies is found to be proportional to f^{-2}. Dimensionless spectra obtained for low frequencies at wind speeds exceeding 2 m/s collapse into a line almost identical to results of low-turbulence measurements performed by Strasberg. [S0001-4966(97)01504-X]

PACS numbers: 43.50.Qp, 43.28.Hr [GAD]

INTRODUCTION

As the number of environmentally protected areas is steadily growing, methods for judging effects of human activities in such areas are needed. In silent areas, defined here as areas of at least a few square kilometers where noise levels due to human activities are negligible, a judging method should take into account the ambient sound level. In the densely populated Netherlands where some silent areas have been given a legal status, there is at present no method for assessing acoustical disturbances. Therefore, the primary goal of the present work is to contribute to the development of a proper judging method.

The audibility of exogenous sound in natural areas is determined by the ratio of the signal to noise intensities. Exogenous sound is the signal, ambient sound the noise. If this ratio is of the order of one or more, acoustical disturbances may be heard. If the ratio is less than one, the exogenous source will generally be masked.

To gain more insight into the masking effect of ambient sound a study of both level and spectral composition of natural ambient sound is required. These properties will depend on the origin(s) of the sound. The sources may differ in different areas (e.g., open grassland, sea, or forest). Each type of area should therefore be characterized separately. Furthermore diurnal, seasonal, and meteorological variations will play an important role. The final goal of this line of research would be to give empirical relations which present a reliable estimate of the ambient sound level under various conditions.

Little is known about this topic sofar. In 1978 Miller[1] reported on a study of sound levels of wind in trees. Fifteen years later, the indigenous sound environment of coniferous forests in the United States was the main objective of studies of Sneddon *et al.*[2,3] Meanwhile Jakobsen and Andersen[4] presented data on wind noise generated not only by vegetation but also by the microphone system. Mechanisms of low-frequency wind noise generation are the main topic of a study of Morgan and Raspet.[5] In various other studies, some attention is paid to the generation of natural ambient sound, too. Yamada *et al.*[6] investigated the noise-screening effect of vegetation and reported on the masking effect of rustling leaves on traffic noise. Part of the work of Larsson, Israelsson, and Hallberg,[7,8] devoted to the influence of meteorological parameters on sound propagation and the audibility of noise from transmission lines, deals with wind noise due to the microphone system. Finally, the masking effect of wind noise is an important topic in a study on noise by windmills by Jakobsen and Pedersen.[9] For recent results on background wind noise in relation to wind turbine noise we refer to Refs. 10–12.

In open areas, i.e., areas with little vegetation, wind noise caused by the microphone system can certainly not be neglected. In contrast to wind noise induced by vegetation, this microphone noise can also be studied in laboratory experiments. In the work of Hosier and Donavan,[13] Strasberg,[14] and Brüel and Kjær laboratories,[15] various aspects of this wind-generated noise, such as frequency distribution and dependence on wind speed, are treated.

In the present work, we have for practical reasons focused on one specific type of area (open agricultural grassland) in the summertime. Keeping the results of a preliminary investigation by the Natuurkundewinkel (Science Shop

[a)]Present address: Arbo-en Milieudienst, University of Groningen, Visserstraat 47, NL-9712 CT Groningen, The Netherlands.

Physics) in mind,[16] we expected simple relations between the ambient sound level and the wind speed on one hand and the $\frac{1}{3}$-oct band level and the frequency on the other.

This paper is constructed as follows. In the next section we give a description of our definition of natural ambient sound and by which quantity it can be characterized. Section II is devoted to the description of the method used for determining the ambient sound level. In Sec. III results of our measurements are presented. This paper is concluded with discussion (Sec. IV), and conclusions and outlook (Sec. V).

I. DEFINITION OF NATURAL AMBIENT SOUND

In this work we define natural ambient sound as the sound produced by natural sources as well as noise caused by human activities, which cannot be identified. This definition is not generally applied. Some authors (see, e.g., Ref. 17) do not take into account clearly identifiable sources of natural origin like bird-singing, rustling of leaves, etc. However, as these sources are not removable, they should, in our opinion, be included in the definition of natural ambient sound. Note that indigenous human sources (e.g., due to agricultural activities) are not included in our definition.

In this study we have focused on the level and spectral distribution of ambient sound. The level of ambient sound is determined by the sound pressure level which is exceeded for most of the time. In the Netherlands it is customary to use the statistical A-weighted L_{95} (L_{A95}) as a measure for the ambient sound level. The L_{95} represents the sound pressure level which is exceeded for 95% of the time. Disturbances with short duration do not affect results like the L_{95} significantly.

Physically, sound is an adiabatic pressure wave propagating in a medium like air. However, microphones do not only detect sound pressure variations. Turbulent air movements also cause detectable pressure variations, usually referred to as wind-generated noise. In fact, wind-generated noise originates from three sources:[18] (1) hydrodynamic pressure fluctuations occurring in the wake of the flow around a microphone (self-noise or windscreen noise), (2) hydrodynamic pressure fluctuations inherent in a turbulent flow, and (3) noise (i.e., physical sound) radiated by turbulent flow over structures like buildings and trees. Notwithstanding the fact that turbulence produces hydrodynamic pressure fluctuations which do not represent radiated sound, we will denote it as such for convenience. More information on these sources of aerodynamically generated noise can be found in Refs. 13, 14, 19, and 20.

Morgan and Raspet[5] noted that the outdoor ambient sound pressure variations are the result of the intrinsic turbulence of the air flow (type 2) instead of turbulence due to the microphone (type 1). This is in contrast to low-turbulence conditions where self-noise due to the microphone does play an important role.[5,13] As we did not perform our measurements in low-turbulence conditions, we expected our measured ambient sound levels to consist of wind-generated noise of types 2 and 3, and other sounds produced by the natural environment.

II. METHOD

In this section we discuss the equipment used for measuring sound levels in open grassland, the choice of suitable locations for measurements, and the determination of meteorological variables.

All sound levels have been determined with a Larson–Davis sound analyzer model 2800 (LD2800), determining the sound pressure level and performing real-time frequency analysis simultaneously. We have focused on the L_{95} in $\frac{1}{3}$-oct bands with nominal midband frequencies ranging from 6.3 Hz to 20 kHz. These L_{95} were determined from a series of sound level measurements sampled every 0.1 s, over a total measurement time of 5 min and using an exponential time weighting constant $\tau=125$ ms. In the next paragraph we will show that the choice for a measurement duration of 5 min is not arbitrary. We also measured the total A-weighted L_{95} using the LD2800 (with rms ''slow'' as time constant: $\tau=1$ s). The microphone used was a $\frac{1}{2}''$-microphone, type B&K 4165, covered with a 90-mm foam windscreen, type B&K UA0237. The microphone was placed on a tripod, about 1.5 m above ground level. The axis of the microphone was directed at (i.e., diaphragm perpendicular to) the wind.

In the test series, we used measurement times ranging from 15–3600 s. It turns out that standard deviations of the L_{95} do not change significantly for measurement times longer than about 2 min.[21] This is not surprising as high-frequency variations in the wind velocity occur at frequencies around 1 per minute.[22] Variations with frequencies of about 0.1 per minute are practically absent. From our tests we conclude that a total measurement time of 5 min is satisfactory.

The most important meteorological parameter, the wind speed, was determined with a simple Deuta wind speed indicator ''Anemo'' at the location of measurement. This was done about 15 times for each measurement. From these data the average wind speed and its standard deviation were calculated. The wind velocity was taken about 2 m above ground level.

A number of measurement locations were chosen in the northern part of the Netherlands according to two criteria. First of all, the noise level due to human activities should be as low as possible. This was achieved using criteria developed by the province of Drenthe to determine silent areas.[23] These criteria effectively boil down to determining zones within which the L_{Aeq} due to human activities like traffic, industry, and recreation is expected to be less than 30 dB(A). Second, the area should be agricultural open grassland. The nearest obstacle in the wind direction (for example, a number of trees or a house) should be located at a distance of at least a few hundred meters from the measuring device. If this is the case, influence of the obstacle on the ambient sound level is practically excluded.[24]

III. RESULTS

During the summer of 1994 we performed a total of 39 measurements suitable for analysis. A number of measurements were excluded, primarily due to significant disturbances (e.g., overflying aircraft). Disturbances should not ap-

TABLE I. Time, location, and wind speed data of measurements. The first four measurements originate from locations in the province of Drenthe (location I: N. lat. 53°02.4′, E. long. 6°39.0′; location II: N. lat. 53°05.8′, E. long. 6°28.9′). The remaining measurements were taken in the province of Groningen (location III: N. lat. 53°17.2′, E. long. 6°27.9′; location IV: N. lat. 53°18.0′, E. long. 6°28.0′; location V: N. lat. 53°16.9′, E. long. 6°29.8′). Other meteorological data can be found in Ref. 21.

Date	Time (GMT)	Location	v (m/s)	σ_v (m/s)	Date	Time (GMT)	Location	v (m/s)	σ_v (m/s)
110794	13:00	I	1.9	0.7	100894	07:29	V	7.1	1.3
150794	10:25	II	2.0	0.7	100894	07:34	V	6.1	0.9
150794	10:34	II	0.9	0.9	160894	02:56	V	1.0	$\ll$1.0
150794	10:43	II	2.0	1.1	160894	03:03	V	1.0	$\ll$1.0
020894	08:17	III	5.2	0.5	160894	03:14	V	1.0	$\ll$1.0
020894	08:23	III	4.6	1.0	180894	07:39	IV	5.3	0.7
020894	08:33	III	5.0	0.6	180894	07:45	IV	5.5	0.9
020894	10:05	V	5.7	0.9	180894	12:45	IV	7.6	1.5
020894	10:10	V	5.7	1.2	180894	12:51	IV	7.9	1.9
020894	10:16	V	6.6	1.0	180894	12:57	IV	9.5	1.6
030894	09:08	V	1.0	0.7	240894	09:07	V	5.5	0.9
030894	09:23	V	1.4	0.7	240894	09:13	V	5.7	1.3
090894	08:18	V	3.4	0.7	240894	09:20	V	4.6	0.9
090894	08.25	V	3.3	0.5	240894	09:51	III	4.6	0.9
090894	08.38	V	3.0	1.0	240894	09:57	III	4.1	0.7
090894	15:03	V	6.3	1.3	240894	10:09	III	4.9	1.1
090894	15:09	V	4.9	1.2	240894	10:47	III	4.1	0.8
090894	15:15	V	5.3	0.8	240894	10:55	III	4.8	0.9
090894	15:45	V	5.4	1.0	240894	11:02	III	3.8	1.0
100894	07:23	V	7.0	0.8					

pear for more than 20% of the measurement time. If they occur during 20% of the time, the determined L_{95} in fact represents the L_{94} which is being considered allowable [keep in mind that the most silent period (5%) of the total time length then originates from 80% of this time length, i.e., from the silent period; this is slightly more than 6% of the undisturbed period]. About 90% of the measurements were performed on locations about 10 km northwest of the city of Groningen; the remaining measurements were carried out in the province of Drenthe. All locations are situated in areas with a flat terrain. The pasture land was primarily covered with grass of approximately 10-cm height. In some situations, there was a ditch close to the measurement location surrounded by vegetation with an approximate height of 50 cm. In Table I we have given time, location, and wind speed data of our measurements.

In Fig. 1 we have plotted both the unweighted and A-weighted L_{95} as a function of the logarithm of the wind speed. The choice for the logarithm of the wind speed is a natural one, as it shows immediately whether the sound pressure p or sound intensity I is proportional to a power of the wind speed. The unweighted data are obtained by logarithmic summation of the $\frac{1}{3}$-oct band results. The A-weighted data directly originate from the measuring device. Using a least-squares routine we determined the following relations:

$$L_{95}=37.9\ \log(v)+42.5, \tag{1}$$

$$L_{A95}=22.6\ \log(v)+22.7, \tag{2}$$

for the unweighted and A-weighted sound pressure levels, respectively. The standard deviations with respect to the data points are 2.4 and 2.0 dB. The respective correlation coefficients are 0.97 and 0.95. We have chosen to calculate the line of regression for $\log(v)$ vs L_{95}, using L_{95} as the independent variable, since the statistical error of the average value of $\log(v)$ significantly exceeds the error in the L_{95}.

In the same way we have determined linear relations between the L_{95} per $\frac{1}{3}$-oct band and the logarithm of the wind speed. In Table II we summarize our results. With parameters a and b defined according to

$$L_{95}=a\ \log(v)+b, \tag{3}$$

Table II shows that a decreases with frequency from 43 dB to a minimum of 20.5 dB at 1 kHz, then increases again. Over the entire frequency range b is shown to decrease with frequency. We furthermore listed the standard deviations

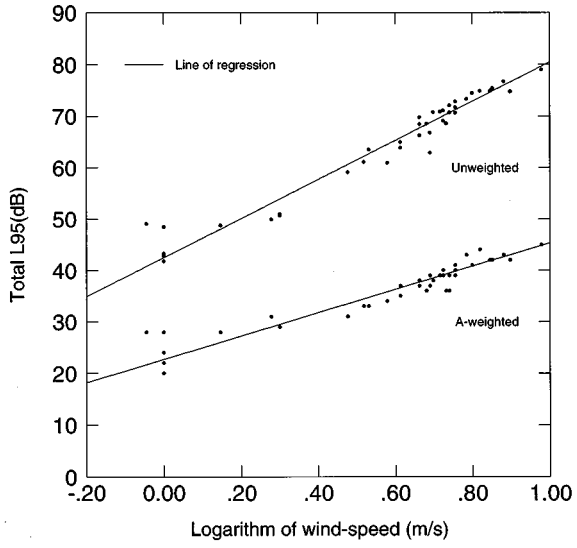

FIG. 1. The total unweighted and A-weighted L_{95} as a function of the logarithm of the wind speed.

TABLE II. Relation between L_{95} per $\frac{1}{3}$-oct. band and wind speed according to $L_{95}=a\ \log(v)+b$.

f_i (Hz)	a (dB)	b (dB)	σ_{L95} (dB)	C	N	f_i (Hz)	a (dB)	b (dB)	σ_{L95} (dB)	C	N
6	43.0	33.3	2.2	0.98	39	400	24.5	9.0	3.5	0.91	20
8	43.4	31.8	2.3	0.98	39	500	22.9	9.6	2.8	0.93	23
10	41.2	32.0	2.3	0.98	39	630	22.9	9.3	2.4	0.95	24
12	39.8	31.3	2.5	0.98	39	800	23.3	8.9	2.6	0.94	22
16	37.5	31.5	2.7	0.97	39	1000	20.5	11.1	2.8	0.91	19
20	37.7	29.8	2.6	0.97	39	1250	23.2	8.9	2.9	0.93	19
25	33.0	31.4	2.8	0.96	39	1600	26.0	6.6	2.3	0.96	21
31	33.5	29.9	3.7	0.92	39	2000	26.1	6.5	2.3	0.96	21
40	32.9	28.2	4.2	0.89	39	2500	24.9	7.8	2.3	0.95	23
50	34.1	25.1	4.8	0.87	39	3150	30.0	4.9	1.6	0.99	19
63	33.4	23.1	5.3	0.83	39	4000	28.5	5.8	2.0	0.97	18
80	27.3	24.6	4.2	0.84	39	5000	30.1	4.7	1.4	0.99	14
100	31.1	18.3	5.1	0.82	39	6300	29.8	4.7	1.4	0.99	14
125	30.5	15.2	4.7	0.84	38	8000	30.3	4.3	1.4	0.99	12
160	27.7	14.2	4.2	0.85	37	10000	29.3	4.3	1.5	0.99	11
200	28.3	11.3	4.2	0.88	30	12500	29.2	3.9	0.8	1.00	8
250	24.0	12.4	4.2	0.85	25	16000	30.0	3.2	1.0	1.00	4
315	25.4	09.9	3.7	0.90	24	20000					1

σ_{L95} of the line of regression with respect to the data points, the correlation coefficients C, and the number of data points N involved in the analysis. N can be less than the number of measurements, i.e., 39. This can be understood as follows. For each measurement the sound level in each $\frac{1}{3}$-oct band is determined about 3000 times. If about 1% of these values are below the detection level of the sound level meter, the L_{95} of the remaining measurements in the corresponding $\frac{1}{3}$-oct band in fact represents the L_{94} of the total time length. This is considered allowable (in agreement with the earlier requirement). If in contrast more than 1% of the values are below the detection level, the associated L_{95} is omitted.

Using the parameters listed in Table II, we determined the spectral distribution of the L_{95} for various wind speeds ranging from 1–8 m/s. Both the unweighted and A-weighted frequency spectra have been plotted (Figs. 2 and 3). The unweighted spectrum is dominated by frequencies below 100 Hz. Furthermore it can roughly be divided into three parts. For wind speeds exceeding 3 m/s we find in the low-frequency range ($f_i<100$ Hz)

$$L_{95}\approx -20\log f_i + c(v), \tag{4}$$

where f_i is the midband frequency of $\frac{1}{3}$-oct band i and c is a constant which only depends on the wind speed. For wind speeds above 3 m/s, L_{95} is approximately constant in the high-frequency range ($f_i>1$ kHz). The intermediate frequency range represents a transitional area. If L_{95} and L_{eq} only differ by a constant, we can easily derive from Eq. (4) that the (time-)averaged sound intensity $I_{1/3}(f_i)$ of band i is proportional to f_i^{-2}. As we derived[21]

$$L_{95}\approx 0.86L_{50}-1.3, \tag{5}$$

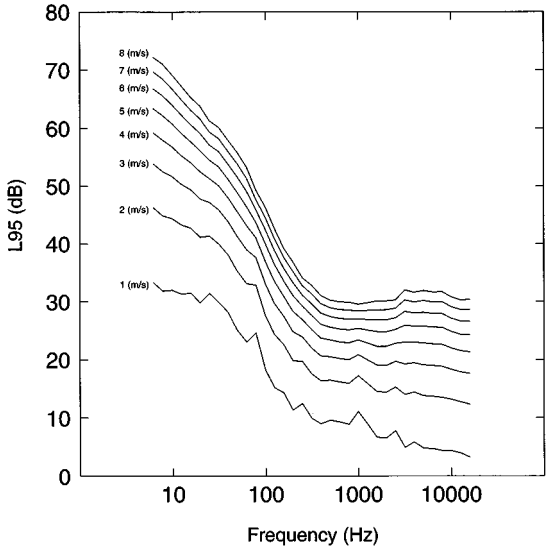

FIG. 2. One-third-octave band spectrum of the L_{95} for wind speeds ranging from 1–8 m/s.

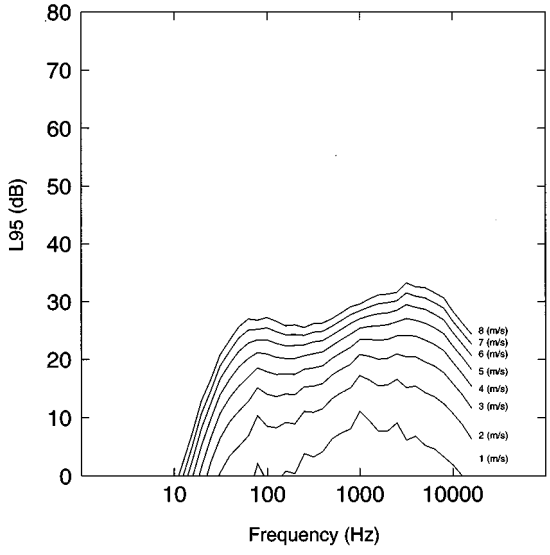

FIG. 3. One-third-octave band spectrum of the L_{A95} for wind speeds ranging from 1–8 m/s.

and Larsson *et al.*[8] showed that $L_{\mathrm{Aeq}} \approx L_{\mathrm{A50}}$, the above assumption, $L_{95} \approx L_{\mathrm{eq}} -$ constant, is reasonable. The A-weighted frequency spectrum is primarily dominated by the frequency range from 500 Hz to 10 kHz, which more or less coincides with audible sound in open grassland (due to waving grass, rustling reed, etc.).

IV. DISCUSSION

For various reasons the range of validity of Eqs. (1) and (2) is restricted. First of all, only one measurement was done at a wind speed over 8 m/s. The same holds for wind speeds below 1 m/s. One should therefore be cautious when applying these results at high or very low wind speeds. Second, as the experiments were performed in July and August, the obtained relations might not be applicable in other seasons. We finally note that the results were obtained in open agricultural grassland and will therefore in general not be valid in areas with different ground cover or profile. These restrictions of course also apply to the parameter values in Table II.

Apart from these considerations, the parameters given in Table II for the high-frequency range (especially frequencies exceeding 10 kHz) are derived from a limited number of data and should therefore be handled with care.

As indicated before, the unweighted frequency distribution has a distinct behavior in both the high- and the low-frequency range. The very high levels at low frequencies are due to air turbulences (i.e., wind-generated noise of types 2 and 3), while the audible sound caused by other environmental factors (and possibly wind-generated noise of type 3) occur at high frequencies. A simple linear relationship between (the logarithm of the) frequency and L_{95} can therefore not be given.

Our results indicate that, for wind speeds exceeding 3 m/s and frequencies below 100 Hz, the $\frac{1}{3}$-oct band intensity $I_{1/3}(f_i)$ is approximately proportional to f_i^{-2}. This is in good agreement with the result of Morgan and Raspet,[5] obtained under similar conditions using an 18-cm-diam windscreen. Hydrodynamic pressure fluctuations in the frequency range from 1–20 Hz are approximately proportional to $f_i^{-0.7}$,[25] and thus show a different type of spectral distribution (of band intensity spectra). Sutherland[18] claims that the results of Morgan and Raspet[5] are in very good agreement with this prediction at very low frequencies. Although the slope of the spectral distribution of L_{95} tends to decrease when going to the lowest frequencies (Fig. 2), our lower band limit does not allow us to confirm this claim. The fact that in our results the slope in the frequency range from 10–100 Hz corresponds to f_i^{-2} instead of $f_i^{-0.7}$ might reflect the increasing effect of the windscreen at these frequencies.

Measurements carried out by Jakobsen and Pedersen[9] also show good agreement with our results as far as the frequency distribution in the range from 125 Hz to 5 kHz is concerned (see Fig. 3.7 of Ref. 9). Note that Jakobsen *et al.* used the wind velocities at 10-m height. In the same frequency range, they obtain linear relations between L_{95} and wind speed for each $\frac{1}{3}$-oct band. The slope of the regression lines turned out to be rather independent of the center frequency of the $\frac{1}{3}$-oct band. It ranges from 1.9–2.5 m^{-1} s. In the wind speed range from 2–8 m/s these results can easily be transferred to a linear relationship between the L_{95} and $\log(v)$, yielding a constant of proportionality of 20 to 25. This is close to the parameters reported in Table II. We note that in contrast to this, earlier work by Jakobsen and Andersen reveals steeper slopes (see, e.g., Fig. 5.2 of Ref. 4).

The fact that in the frequency range from 30 Hz to about 1 kHz the correlation coefficient as listed in Table II is significantly smaller than outside this range can be understood as follows. In this frequency range, we observed that at low wind speed the $\frac{1}{3}$-oct band L_{95} is practically constant.[21] It is therefore concluded that at low wind speed air turbulence is less important in this frequency range. At increasing wind speed turbulence starts to dominate the sound level: as a consequence a kink in the relation between the logarithm of the wind speed and L_{95} seems more appropriate for the frequency range from 30 Hz to 1 kHz. The limited number of data points, however, made us stick to the present approach, giving rise to relatively small correlation coefficients. For frequencies below 30 Hz turbulence is dominant for all wind velocities and therefore the kink as seen for higher frequencies is absent, yielding correlation coefficients close to one.

A division of the total L_{95} into a high- and low-wind-speed component does not seem to be necessary (see Fig. 1): low frequencies dominate the spectrum. The total L_{95} as given in Eq. (1) should therefore be attributed to wind-generated noise. Due to the A-weighting the high levels at low frequencies almost completely disappear (Fig. 3). Therefore the L_{A95} in Eq. (2) gives a reasonable representation of audible natural ambient sound.

Assuming that the L_{95} only differs by a constant from the L_{eq}, it can easily be seen from Eq. (1) that the average sound intensity varies approximately as v^4. From Table II it is clear that the same dependence holds for the average $\frac{1}{3}$-oct band levels at low frequencies. It is known from literature that aerodynamically generated noise shows dependences varying from about $v^{4.8}$ to $v^{6.3}$ (see, e.g., Ref. 18 and references therein). Recent unpublished measurements by Chanaud[26] in barren areas in Utah, focusing on the sound level as a function of the maximum hourly wind speed, suggest a v^6 dependence. This observation is consistent with the theoretical expectation that air flowing around an object acts as a dipole source, for which the noise level varies as v^6. In the present outdoor measurements it is likely that the natural ambient sound level results from many different noise sources of both aerodynamic and nonaerodynamic origin and of different characteristic dimensions. A v^4 dependence should therefore not surprise the reader too much.

By plotting the dimensionless $\frac{1}{3}$-oct band pressure level $\log(p_{1/3}/\rho v^2)$ versus the logarithm of the Strouhal number $\log(f_i D/v)$ it is possible to shed some more light on the problem of identifying the source of ambient sound. Here ρ is the ambient density of air and D is the windscreen diameter, 9 cm in the present work. Strasberg[14] showed that this scaling collapses data from a large number of flow noise measurements under low-turbulence conditions into a line satisfying

$$20 \log(p_{1/3}/\rho v^2) = -81 - 23 \log(f_i D/v). \tag{6}$$

Application of this method to our measurements, using the L_{95} data for the separate $\frac{1}{3}$-oct bands, does not reveal a clear

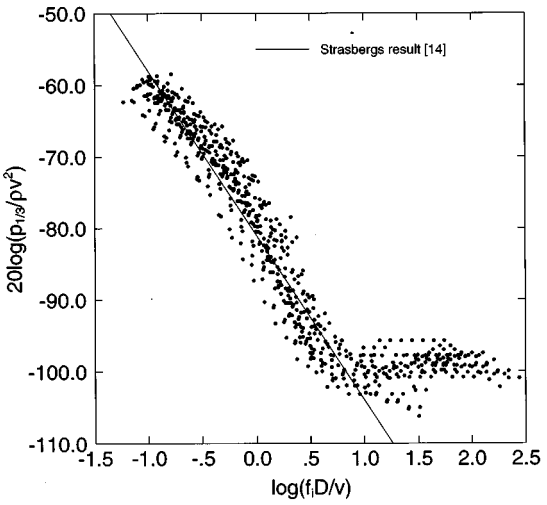

FIG. 4. Dimensionless sound pressure level versus logarithm of the Strouhal number for wind speeds exceeding 2 m/s. The line results from the Strasberg equation [Eq. (6)].

picture. However, as shown in Fig. 4, this situation changes dramatically if data obtained at wind velocities of 2 m/s and below are eliminated from the analysis. For comparison we have also drawn the result of Strasberg in Fig. 4. Notwithstanding the fact that our results were obtained outdoors, i.e., in a turbulent environment, the data in the low-frequency region almost coincide with Strasbergs results. This seems to be in contradiction with the work of Morgan and Raspet.[5] It is not clear whether this result should be interpreted as self-noise (wind-generated noise of type 1) being the dominant noise source at low frequencies and wind speeds exceeding 2 m/s. For completeness we note that Eq. (6) corresponds to a $v^{6.3}$ dependence of the sound pressure level.

In the high-frequency range the dimensionless sound pressure level is more or less constant. This range is probably the part of the spectrum that is dominated by audible natural sound. Furthermore, it was noted before that in the frequency range from 30–1000 Hz turbulence does not dominate the ambient sound level at low wind speeds either. It is therefore not surprising to observe that scaled low wind speed data do not fit into Eq. (6). We thus conclude once more that the v^4 dependence we found for the total natural ambient sound level is indeed the result of different noise sources.

The total L_{A95} in Eq. (2) is in agreement with results obtained by Kerkers,[10] who determined wind noise at a farm close to a potential windfarm. However, it is not known what the effect of the nearby farm and trees on the detected sound level was. Similar qualitative agreement is observed with the work of Hayes[11] and Legerton[12] who present the total L_{A90} of background noise. Here, too, the effect of nearby obstacles is unknown; the same holds for the terrain profile which might differ from the situation at our measurement sites. Finally, it is not yet understood why extensive results of Larsson *et al.*[7,8] show a much steeper behavior between the wind noise (L_{A95}) and wind speed. Their results suggest that $L_{A95} \propto 80 \log(v)$.

In Refs. 5, 13, and 14 the effect of windscreens on the sound level is subject of research. We have not studied this effect in great detail. However, a few data were obtained without using a windscreen.[21] The sound intensity still seems to vary approximately as $40 \log(v)$, although the absolute level generally is 5–10 dB higher. However, for wind speeds over 4 m/s, the L_{A95} increases by up to 20 dB, in agreement with Ref. 7.

V. CONCLUSIONS AND OUTLOOK

This work confirms the existence of a linear relationship between the natural ambient sound level and the logarithm of the wind speed [Eqs. (1) and (2)]. The overall sound intensity and low-frequency $\frac{1}{3}$-oct band intensities were found to vary approximately as v^4, which is somewhat lower than expectations for aerodynamic noise sources. Relations similar to Eq. (1) were derived for each $\frac{1}{3}$-oct band separately.

At frequencies below 100 Hz, the frequency distribution of natural ambient sound shows a behavior which is typical for turbulent processes. In this frequency range the $\frac{1}{3}$-oct band intensity of ambient sound is approximately proportional to f^{-2}. At high frequencies ($f_i > 1$ kHz) the frequency spectrum is almost flat. The A-weighted spectrum is dominated by this high-frequency range, which probably represents audible sound of nonaerodynamic origin (like rustling grass and reed).

Calculation of dimensionless spectra shows that at wind speeds exceeding 2 m/s outdoor sound levels in the low-frequency domain collapse into a line coinciding with results from low-turbulence measurements by Strasberg.[14]

Recently results of extensive measurements in deciduous forest were reported.[27,28] In the future this work will be continued to determine natural ambient sound in other environments and other seasons. A more detailed study of the effect of the present screening of the microphone (or alternatives) is desirable. Furthermore the influence of ground absorption and meteorological parameters like the gradient of wind velocity and temperature should be studied. Apart from experimental data there is also a need for theoretical models describing natural ambient sound, which is not aerodynamically generated. Exploratory models for ambient sound produced in a forest have been proposed.[21,27]

ACKNOWLEDGMENTS

The author would like to thank Frits van den Berg for many useful discussions and critical reading of the manuscript. Furthermore, information provided by L. C. Sutherland, J. Jakobsen, C. Larsson, and R. Chanaud is gratefully acknowledged.

[1] L. N. Miller, ''Sound Levels of Rain and of Wind in the Trees,'' Noise Control Eng. J. **11**, 101–115 (1978).
[2] M. Sneddon, L. Silvati, K. S. Pearsons, and S. Fidell, ''Measurements and analyses of the indigenous sound environment of coniferous forests,'' BBN Report No. 7210 (NPOA Report No. 91-1) (1994).
[3] S. Fidell, M. Sneddon, and L. Silvati, ''Predicting sound levels from wind speed in a coniferous forest,'' J. Acoust. Soc. Am. **88**, S74 (1990).
[4] J. Jakobsen and B. Andersen, ''Wind Noise. Measurements of Wind-Generated Noise from Vegetation and Microphone System,'' Danish Acoustical Institute Report No. 108 (Lyngby, 1983).
[5] S. Morgan and R. Raspet, ''Investigation of the mechanisms of low-

frequency wind noise generation outdoors,'' J. Acoust. Soc. Am. **92**, 1180–1183 (1992).
[6] S. Yamada *et al.*, ''Noise Reduction by Vegetation,'' in *Proceedings of Internoise 1977* (Zürich, 1977), p. B599–B603.
[7] C. Larsson and S. Israelsson, ''The Effects of Meteorological Parameters on Sound Propagation from a Point Source,'' Meteorologiska Institutionen Report No. 67 (Kungliga Universitetet Uppsala, Uppsala, 1982).
[8] C. Larsson, B. Hallberg, and S. Israelsson, ''Long-term audible noise from an operating 400-kV transmission line,'' Meteorologiska Institutionen Report No. 82 (Kungliga Universitetet Uppsala, Uppsala, 1985).
[9] J. Jakobsen and T. H. Pedersen, ''Noise by Windmills and the Masking Effect of Wind Noise,'' Lydteknisk Institut Report No. 141 (Lyngby, 1989) (in Danish).
[10] A. J. Kerkers, ''Noise of wind and windturbines,'' Acustica **82**, S81 (1996).
[11] M. D. Hayes, ''The measurement of noise from wind farms and background noise levels,'' in *Proceedings Internoise 1996* (Liverpool, 1996), p. 471–478.
[12] M. L. Legerton, ''Recommendations of the working group on wind turbine noise,'' in *Proceedings of Internoise 1996* (Liverpool, 1996), p. 2547–2552.
[13] R. N. Hosier and P. R. Donavan, ''Microphone Windscreen Performance,'' National Bureau of Standards, Acoustical Engineering Division, Report No. NBSIR 79-1599 (1979).
[14] M. Strasberg, ''Dimensional analysis and windscreen noise,'' J. Acoust. Soc. Am. **83**, 544–548 (1988).
[15] Brüel and Kjær, *Condensor Microphones and Microphone Preamplifiers for Acoustic Measurements* (Brüel and Kjær Laboratories, Nærum, 1982).
[16] S. van Beveren, *Ambient Noise and Wind Speed* (Natuurkundewinkel, Groningen, 1993), internal report (in Dutch).
[17] B. van Steenbruggen and W. C. Verboom, *Guidelines for characterizing and measuring ambient noise*, TPD-TNO Report 007.726 (TPD-TNO, Delft, 1980) (in Dutch).
[18] L. C. Sutherland, ''Wind-generated background noise in long range sound propagation measurements,'' in *Proceedings of the Fifth International Symposium on Long Range Sound Propagation* (Milton Keynes, 1992), p. 372.
[19] M. S. Howe, ''On the generation of sound by turbulent boundary layer flow over a rough wall,'' Proc. R. Soc. London, Ser. A **395**, 247–263 (1984).
[20] H. H. Hubbard (ed.), ''Aeroacoustics of Flight Vehicles: Theory and Practice,'' NASA Ref. Publ. 1258, WADC Tech Rep. 90-3052, **1** (1991).
[21] H. F. Boersma, ''Characterization of the Natural Ambient Sound Environment—Measurements in Open Grassland,'' Natuurkundewinkel Report No. NWU-63 (Natuurkundewinkel, Groningen, 1995) (in Dutch, with English summary).
[22] A. Moerkerken, ''Meteorological factors affecting the transmission of sound,'' TPD-TNO Report No. VL-DR-21-03 (TPD-TNO, Delft, 1975) (in Dutch, with English summary).
[23] Intentionprogram 'Silent areas' Drenthe (concept) (Province of Drenthe, Assen, 1986) (in Dutch).
[24] B. Kruijt, ''Turbulence over forest downwind of an edge,'' Ph.D. thesis, Groningen, 1994, unpublished; W. Klaassen and B. Kruijt, private communication.
[25] H. A. Panofsky and J. A. Dutton, *Atmospheric Turbulence* (Wiley, New York, 1984).
[26] R. Chanaud (private communication).
[27] R. S. Etienne, *Characterization of the Natural Ambient Sound Environment—Measurements in Deciduous Forest* (Wetenschapswinkel Natuurkunde, Utrecht, 1996) (in Dutch, with English summary).
[28] H. F. Boersma and R. S. Etienne, ''The natural ambient sound environment,'' in *Proceedings of Internoise 1996* (Liverpool, 1996), p. 2465–2468.

Determination of the higher-order elastic compliance constants of metals from measurements of the dependence of ultrasound velocity on stress

Masaru Kato, Takuso Sato, and Kazutaka Ando
Interdisciplinary Graduate School of Science and Engineering, Tokyo Institute of Technology, 4259 Nagatsuta, Midori-ku, Yokohama, 226 Japan

(Received 19 May 1995; revised 8 July 1996; accepted 14 November 1996)

A new approach to describe the dependence of ultrasound velocity on stress in metals is presented to analyze the relation between acoustoelasticity which shows that the change of the ultrasound velocity depends on the stress in metals and the macroscopic characteristics of metals. It uses the effective higher-order elastic compliance constants which are determined from measurements of the ultrasound velocity in a metal. First, the nonlinear relation between stress and strain is described in terms of the second-, third-, and fourth-order elastic constants. Then, for the quasilongitudinal and quasitransverse waves which propagate in the symmetry planes of the metal, the ultrasound velocities in the statically stressed metals are presented by using these constants. They are explicitly derived as a function of the applied stress. The measurements of the dependence of ultrasound velocity on the applied stress due to the uniaxial compression in an aluminum alloy are performed and their results show the nonlinear dependence on the applied compressive stress. Finally, on the basis of the dependence, the effective elastic and elastic–plastic constants are determined by means of the least-squares method and the nonlinear acoustoelastic contribution to the deformation in the metal is discussed through the determined effective constants. [S0001-4966(97)00804-7]

PACS numbers: 43.58.Dj, 43.20.Ye, 43.35.Zc [SLE]

INTRODUCTION

The higher-order elastic constants which are mostly defined as elastic stiffness are of considerable interest to the quantitative evaluation of the properties of metals. They have much information on the nonlinear properties of metals. Especially, the elastic–plastic condition of metals which can be specified by the stress state in the vicinity of the elastic limit should be analyzed because it sometimes leads to the processes such as fracture and destruction. Elastic constants can be determined from measurements of the velocity of the small amplitude ultrasonic waves in the statically stressed metals.[1–3] Hence, it is important to obtain the explicit description of the ultrasound velocity in the stressed metals.

A new approach to derive the formula for the dependence of ultrasound velocity on stress is proposed to evaluate the stressed state in metals. The representation of the macroscopic material properties mostly employs elastic stiffness constants. In this case, the derived formula of the ultrasound velocity becomes a function of strain. The acoustoelastic effect shows the phenomenon that the ultrasound velocity is changed by the stresses in a metal and therefore it is useful to express the velocity as a function of stress. This effect can be used as one of the powerful means to measure the internal stress in metals.[4] Utrata *et al.* applied the linear dependence of ultrasonic velocity as a function of stress to stress measurement in railroad rail.[5] For the propagation of a Rayleigh surface wave in the multilayered plates, displacements and stresses can be determined as functions of position within the plate.[6] In this paper, we consider the longitudinal and transverse waves propagating in a metal. The velocities are expressed as functions of stress and elastic compliance constants are employed instead of elastic stiffness constants, but they also have much information on the nonlinear properties of metals. In order to evaluate their changes in the elastic–plastic stress condition on the basis of the nonlinear dependence of ultrasonic velocity on stress, the velocity change can be characterized in terms of higher-order elastic constants. To get the information on the elastic–plastic stress condition through the change in the constants to specify the nonlinear properties, our derived formulas can express this nonlinear dependence, especially, the ultrasound velocity change in the vicinity of the elastic limit. This point is a key difference from other approaches to describe the velocity of ultrasonic waves propagating in the stressed metals.[7–11]

In order to describe the velocity of ultrasonic waves propagating in the stressed metals, three configurations should be considered, which include a stressless original body, a stressed and deformed body, and a body when a ultrasonic wave motion is superposed on the deformation in the stressed body.[12,13] They are called the free state, the initial state, and the final state, respectively. Here, an assumption has been made that the initial state experiences the finite deformation and the ultrasonic wave motion in the final state generates the infinitesimal deformation.

The constants determined from measurements of the ultrasonic velocity in metal alloys can be regarded as the effective elastic constants which show the material properties through the ultrasonic probing. In this paper, experimental analysis focuses on observing the changes of the effective constants in the elastic–plastic region. The changes might help the evaluation of the stress condition in the vicinity of

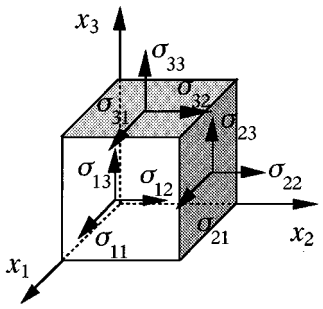

FIG. 1. Notation for stress components in an infinitesimal material body with Cartesian coordinate system.

the elastic limit in metals. Generally, the constants estimated in the plastic region include the work-hardening effect.[7] Hence, since they should not be called elastic constants, in order to deal with the change of the effective coefficients due to the addition of the plastic properties to the elastic ones, they are defined as the effective elastic–plastic constants to be unspecified functions of the work-hardening parameter.

The stress–strain relation in terms of the second- and third-order constants leads to the linear velocity change of the ultrasonic waves in metals.[7] On the other hand, considering up to the fourth-order constants, the nonlinear properties on the ultrasonic velocity change can be expressed.

First, the nonlinear relation between stress and strain is defined in terms of the higher-order elastic compliance constants and then the velocities of quasilongitudinal and quasitransverse waves propagating in the planes of the statically stressed metals are formulated by solutions to the equation of motion which are combined with the nonlinear relation between stress and strain.

Section I is devoted to the formulation of the velocities of the ultrasonic waves in the statically stressed metals. In Sec. II, the measurements of the dependence of ultrasound velocity on the applied stress due to the uniaxial compression in a aluminum alloy are performed and the nonlinear dependence of ultrasound velocity on stress are shown. The determination of the effective elastic and elastic–plastic compliance constants from this result is made by means of the least-squares method in Sec. III. The acoustoelastic contribution of the determined effective constants to the deformation in the metal is also discussed.

I. THE FORMULATION FOR DEPENDENCE OF ULTRASOUND VELOCITY ON STRESS IN METALS

In order to derive the formula of the velocity of ultrasonic waves propagating in the statically stressed metals, it is convenient to consider the three configurations (free state, initial state, and final state) in an infinitesimal material body as shown in Fig. 1. First, the relation between stress and strain is defined in terms of the higher-order elastic compliance constants:

$$\epsilon_{ij}=f_{ijkl}\sigma_{kl}+g_{ijklmn}\sigma_{kl}\sigma_{mn}+h_{ijklmnop}\sigma_{kl}\sigma_{mn}\sigma_{op}, \quad (1)$$

where ϵ_{ij} $(i,j=1,\ldots,3)$ are the components of the Lagrangian strain tensor, σ_{kl} $(k,l=1,\ldots,3)$ are the components of the second Piola–Kirchhoff stress tensor, and f_{ijkl}, g_{ijklmn}, and $h_{ijklmnop}$ are the second-, third-, and fourth-order elastic compliance constants, respectively. Here, ϵ_{ij} and σ_{kl} are the symmetric tensors: $\epsilon_{ij}=\epsilon_{ji}$, $\sigma_{kl}=\sigma_{lk}$. These relations make it possible to diminish the number of distinct elastic constants in Eq. (1). A pair of subscripts are replaced by a new subscript. Thus, Eq. (1) is rewritten as

$$\epsilon_I=f_{IJ}\sigma_J+g_{IJK}\sigma_J\sigma_K+h_{IJKL}\sigma_J\sigma_K\sigma_L, \quad (2)$$

where ϵ_I $(I=1,\ldots,6)$ and σ_J $(J=1,\ldots,6)$ are the rewritten components of the Lagrangian strain tensor and the second Piola–Kirchhoff stress tensor, and f_{IJ}, g_{IJK}, and h_{IJKL} are the second-, third-, and fourth-order elastic compliance constants, respectively. Here, the subscripts for the stress and the strain tensors are replaced according to the scheme of $\sigma_1=\sigma_{11}$, $\sigma_2=\sigma_{22}$, $\sigma_3=\sigma_{33}$, $\sigma_4=2\sigma_{23}=2\sigma_{32}$, $\sigma_5=2\sigma_{13}=2\sigma_{31}$, $\sigma_6=2\sigma_{12}=2\sigma_{21}$, $\epsilon_1=\epsilon_{11}$, $\epsilon_2=\epsilon_{22}$, $\epsilon_3=\epsilon_{33}$, $\epsilon_4=\epsilon_{23}=\epsilon_{32}$, $\epsilon_5=\epsilon_{13}=\epsilon_{31}$, and $\epsilon_6=\epsilon_{12}=\epsilon_{21}$.

Let the coordinates a_i, x_i, and $x_i'(i=1,2,3)$ denote the position of a material point in the free state with the mass density of the material body ϱ_0, the initial state with the density ϱ, and the final state with the density ϱ', respectively. At the initial state previous to the propagation of ultrasonic waves, the statically applied stress σ_{ij} must satisfy the equation of equilibrium,

$$\frac{\partial\sigma_{ij}}{\partial x_j}=0. \quad (3)$$

The mass densities in the free and initial states are related by

$$\frac{\varrho_0}{\varrho}=\det\left(\frac{\partial x_i}{\partial a_j}\right). \quad (4)$$

At the final state, the components of the displacement vector due to the ultrasonic wave motion are denoted by $\xi_i=x_i'-x_i$. The Lagrangian strain for the infinitesimal deformation due to the propagation of the ultrasonic wave is given by

$$\epsilon_{ij}=\frac{1}{2}\left(\frac{\partial\xi_i}{\partial x_j}+\frac{\partial\xi_j}{\partial x_i}\right). \quad (5)$$

The equation of motion due to the propagation of the ultrasonic wave is given by

$$\varrho'\,\frac{\partial^2\xi_i}{\partial t^2}=\frac{\partial\sigma_{ij}'}{\partial x_j'}, \quad (6)$$

where σ_{ij}' is the Cauchy stress tensor at the final state, which is related with the second Piola–Kirchhoff stress tensor P_{kl}' at the final state as

$$\sigma_{ij}'=\frac{\varrho'}{\varrho}\cdot\frac{\partial x_i'}{\partial x_k}\cdot\frac{\partial x_j'}{\partial x_l}\cdot P_{kl}', \quad (7)$$

with

$$\frac{\partial x_i'}{\partial x_k}=\frac{\partial\xi_i}{\partial x_k}+\frac{\partial x_i}{\partial x_k}=\delta_{im}\left(\frac{\partial\xi_m}{\partial x_k}+\delta_{mk}\right), \quad (8)$$

where δ_{ij} is the Kronecker's delta. Substituting Eqs. (7) and (8) into Eq. (6), the equation of motion in the initial coordinate is obtained as

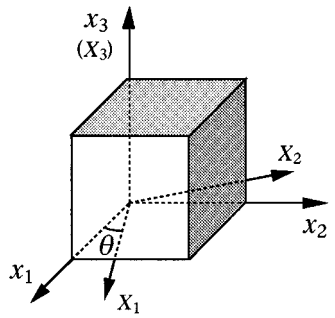

FIG. 2. Wave propagation direction in the symmetry plane with coordinate X_i $(i=1,2,3)$.

$$\varrho\,\frac{\partial^2 \xi_i}{\partial t^2}=\frac{\partial}{\partial x_l}\left\{P'_{il}+\frac{\partial \xi_i}{\partial x_k}\,P'_{kl}\right\}. \tag{9}$$

The stress P'_{kl} at the final state is given by a sum of the static stress at the initial state σ_{il}, and the dynamic stress due to the propagation of the ultrasonic wave, $\Delta P'_{il}$. Thus,

$$P'_{il}=\Delta P'_{il}+\sigma_{il}, \tag{10}$$

where it is assumed that the dynamic stress is small: $\sigma_{il} \gg \Delta P'_{il}$. By using Eq. (3), substitution of Eq. (10) into Eq. (9) leads to the final equation of motion:

$$\varrho\,\frac{\partial^2 \xi_i}{\partial t^2}=\frac{\partial \Delta P'_{il}}{\partial x_l}+(\Delta P'_{kl}+\sigma_{kl})\cdot\frac{\partial^2 \xi_i}{\partial x_l\,\partial x_k}. \tag{11}$$

Now, let us consider the quasilongitudinal ultrasonic wave propagating in the x_2-x_3 symmetry plane at an angle θ with respect to x_2 axis as shown in Fig. 2. The coordinate X_i $(i=1,2,3)$ with the stress components σ''_{ij} $(i,\,j=1,\ldots,3)$ and the strain components ϵ''_{kl} $(k,\,l=1,\ldots,3)$ are introduced so that X_2 axis coincides with the propagation direction of the ultrasonic wave. Using the abbreviated subscript introduced in Eq. (2), the stress components σ_{ij} and σ''_{ij} are related by

$$\begin{pmatrix}\sigma''_1\\ \sigma''_2\\ \sigma''_3\\ \sigma''_4\\ \sigma''_5\\ \sigma''_6\end{pmatrix}=\begin{pmatrix}\sigma_1\\ \sigma_2\cos^2\theta+\sigma_3\sin^2\theta+\sigma_4\sin 2\theta\\ \sigma_2\sin^2\theta+\sigma_3\cos^2\theta-\sigma_4\sin 2\theta\\ (\sigma_3-\sigma_2)\sin\theta\cos\theta+\sigma_4\cos 2\theta\\ \sigma_5\cos\theta-\sigma_6\sin\theta\\ \sigma_5\sin\theta+\sigma_6\cos\theta\end{pmatrix}, \tag{12}$$

and the strain components ϵ_{kl} and ϵ''_{kl} are related by

$$\begin{pmatrix}\epsilon''_1\\ \epsilon''_2\\ \epsilon''_3\\ \epsilon''_4\\ \epsilon''_5\\ \epsilon''_6\end{pmatrix}=\begin{pmatrix}\epsilon_1\\ \epsilon_2\cos^2\theta+\epsilon_3\sin^2\theta+\epsilon_4\sin 2\theta\\ \epsilon_2\sin^2\theta+\epsilon_3\cos^2\theta-\epsilon_4\sin 2\theta\\ (\epsilon_3-\epsilon_2)\sin\theta\cos\theta+\epsilon_4\cos 2\theta\\ \epsilon_5\cos\theta-\epsilon_6\sin\theta\\ \epsilon_5\sin\theta+\epsilon_6\cos\theta\end{pmatrix}. \tag{13}$$

The dynamic stress $\Delta P''_2$ due to the propagation of the ultrasonic wave gives the stress perturbation $\Delta\sigma_I$ superposed in the stress components σ_I:

$$\begin{pmatrix}\Delta\sigma_1\\ \Delta\sigma_2\\ \Delta\sigma_3\\ \Delta\sigma_4\\ \Delta\sigma_5\\ \Delta\sigma_6\end{pmatrix}=\begin{pmatrix}0\\ \Delta P''_2\cos^2\theta\\ \Delta P''_2\sin^2\theta\\ \Delta P''_2\sin\theta\cos\theta\\ 0\\ 0\end{pmatrix}. \tag{14}$$

In the same way as the derivation of Eq. (11), the final equation of motion in the coordinate system X_i is obtained as

$$\varrho\,\frac{\partial^2 \xi''_i}{\partial t^2}=\frac{\partial \Delta P''_{il}}{\partial X_l}+(\Delta P''_{kl}+\sigma''_{kl})\cdot\frac{\partial^2 \xi''_i}{\partial X_l\,\partial X_k}, \tag{15}$$

where ξ''_i $(i=1,2,3)$ are the components of the displacement vector. For the propagation of the ultrasonic wave along X_2 axis, the subscripts of Eq. (15), i, k, and l, have only to be 2. Thus, using the stress components with abbreviated description,

$$\varrho\,\frac{\partial^2 \xi''_2}{\partial t^2}=\frac{\partial \Delta P''_2}{\partial X_2}+\sigma''_2\cdot\frac{\partial^2 \xi''_2}{\partial X_2^2}, \tag{16}$$

and the dynamic stress due to the propagation of the ultrasonic wave is defined as

$$\Delta P''_2=A\,\cos(\omega t-kX_2). \tag{17}$$

Substituting Eq. (17) into Eq. (16), the displacement due to the propagation of the ultrasonic wave is obtained by

$$\xi''_2=\frac{kA}{\sigma''_2k^2-\varrho\,\omega^2}\sin(\omega t-kX_2). \tag{18}$$

Thus, from Eqs. (5) and (18), the strain at the final state is derived as

$$\epsilon''_2=\epsilon''_{22}=\frac{\partial \xi''_2}{\partial X_2}=-\frac{k^2A}{\sigma''_2k^2-\varrho\,\omega^2}\cos(\omega t-kX_2). \tag{19}$$

In view of the stress perturbation of the wave which causes the infinitesimal dynamic strain, using Eq. (14), the dynamic strain component defined in Eq. (2) is derived as

$$\begin{aligned}\epsilon_2^{\mathrm{dyn}}=\{&f_{22}\cos^2\theta+f_{23}\sin^2\theta+f_{24}\sin\theta\cos\theta\\ &+g_{212}\sigma_1\cos^2\theta+g_{213}\sigma_1\sin^2\theta\\ &+g_{214}\sigma_1\sin\theta\cos\theta+g_{221}\sigma_1\cos^2\theta\\ &+2g_{222}\sigma_2\cos^2\theta+g_{223}(\sigma_2\sin^2\theta+\sigma_3\cos^2\theta)\\ &+\cdots+h_{2662}\sigma_6^2\cos^2\theta+h_{2663}\sigma_6^2\sin^2\theta\\ &+h_{2664}\sigma_6^2\sin\theta\cos\theta\}\Delta P''_2.\end{aligned} \tag{20}$$

In Eq. (20), there is no way to distinguish experimentally between g_{IJK} and g_{IKJ}. The same is true of h_{IJKL}. These arguments show that

$$\begin{aligned}&g_{IJK}=g_{IKJ},\\ &h_{IJKL}=h_{IJLK}=h_{IKJL}=h_{IKLJ}=h_{ILJK}=h_{ILKJ}.\end{aligned} \tag{21}$$

The dynamic strain components $\epsilon_3^{\mathrm{dyn}}$ and $\epsilon_4^{\mathrm{dyn}}$ are also obtained in the same way as the derivation of Eq. (20). Substituting the dynamic strain components into Eq. (13) and using the property of Eq. (21), the dynamic strain $\epsilon_2''^{\mathrm{dyn}}$ due to the propagation of the ultrasonic wave with a fundamental frequency is obtained as

$$\begin{aligned}\epsilon_2''^{\mathrm{dyn}}=\{&f_{22}\cos^4\theta+f_{23}\sin^2\theta\cos^2\theta+f_{24}\sin\theta\cos^3\theta+f_{32}\sin^2\theta\cos^2\theta+f_{33}\sin^4\theta+f_{34}\sin^3\theta\cos\theta\\&+f_{42}\sin\theta\cos^3\theta+f_{43}\sin^3\theta\cos\theta+f_{44}\sin^2\theta\cos^2\theta+2g_{221}\sigma_1\cos^4\theta+2g_{231}\sigma_1\sin^2\theta\cos^2\theta\\&+2g_{241}\sigma_1\sin\theta\cos^3\theta+2g_{321}\sigma_1\sin^2\theta\cos^2\theta+2g_{331}\sigma_1\sin^4\theta+2g_{341}\sigma_1\sin^3\theta\cos\theta+2g_{421}\sigma_1\sin\theta\cos^3\theta\\&+2g_{431}\sigma_1\sin^3\theta\cos\theta+2g_{441}\sigma_1\sin^2\theta\cos^2\theta+\cdots+2g_{244}\sigma_4\sin\theta\cos^3\theta+2g_{245}\sigma_5\sin\theta\cos^3\theta\\&+2g_{246}\sigma_6\sin\theta\cos^3\theta+2g_{344}\sigma_4\sin^3\theta\cos\theta+2g_{345}\sigma_5\sin^3\theta\cos\theta+2g_{346}\sigma_6\sin^3\theta\cos\theta\\&+2g_{444}\sigma_4\sin^2\theta\cos^2\theta+2g_{445}\sigma_5\sin^2\theta\cos^2\theta+2g_{446}\sigma_6\sin^2\theta\cos^2\theta+3h_{2112}\sigma_1^2\cos^4\theta\\&+3h_{2113}\sigma_1^2\sin^2\theta\cos^2\theta+3h_{2114}\sigma_1^2\sin\theta\cos^3\theta+3h_{3112}\sigma_1^2\sin^2\theta\cos^2\theta+3h_{3113}\sigma_1^2\sin^4\theta\\&+3h_{3114}\sigma_1^2\sin^3\theta\cos\theta+3h_{4112}\sigma_1^2\sin\theta\cos^3\theta+3h_{4113}\sigma_1^2\sin^3\theta\cos\theta+3h_{4114}\sigma_1^2\sin^2\theta\cos^2\theta+\cdots\\&+3h_{2455}\sigma_5^2\sin\theta\cos^3\theta+6h_{2456}\sigma_5\sigma_6\sin\theta\cos^3\theta+3h_{2466}\sigma_6^2\sin\theta\cos^3\theta+3h_{3455}\sigma_5^2\sin^3\theta\cos\theta\\&+6h_{3456}\sigma_5\sigma_6\sin^3\theta\cos\theta+3h_{3466}\sigma_6^2\sin^3\theta\cos\theta+3h_{4455}\sigma_5^2\sin^2\theta\cos^2\theta+6h_{4456}\sigma_5\sigma_6\sin^2\theta\cos^2\theta\\&+3h_{4466}\sigma_6^2\sin^2\theta\cos^2\theta\}\Delta P_2''\equiv P_2(\sigma_I,\theta)\cdot\Delta P_2'' \quad (I=1,\ldots,6).\end{aligned} \tag{22}$$

From Eqs. (17), (19), and (22), the quasilongitudinal wave velocity in the stressed body is obtained by

$$V_2^{\mathrm{long}}(\sigma_I,\theta)=\frac{\omega}{k}=\left\{\frac{\sigma_2''}{\varrho}+\frac{1}{\varrho P_2(\sigma_I,\theta)}\right\}^{1/2}. \tag{23}$$

Using Eq. (12), Eq. (23) is rewritten as

$$V_2^{\mathrm{long}}(\sigma_I,\theta)=\left\{\frac{\sigma_2\cos^2\theta+\sigma_3\sin^2\theta+\sigma_4\sin 2\theta}{\varrho}+\frac{1}{\varrho P_2(\sigma_I,\theta)}\right\}^{1/2}. \tag{24}$$

Let us consider a slightly orthotropic material with the shear stress components being zero, whose symmetry axes coincide with the principal stress axes. Taking the symmetry of the elastic constants into account, Eq. (24) becomes

$$V_2^{\mathrm{long}}(\sigma_I,\theta)=\left\{\frac{\sigma_2\cos^2\theta+\sigma_3\sin^2\theta}{\varrho}+\frac{1}{\varrho P_2(\sigma_I,\theta)}\right\}^{1/2} \quad (I=1,\ldots,3), \tag{25}$$

where

$$\begin{aligned}P_2(\sigma_I,\theta)=&f_{22}\cos^4\theta+(2f_{23}+f_{44})\sin^2\theta\cos^2\theta+f_{33}\sin^4\theta+2g_{221}\sigma_1\cos^4\theta+2(2g_{231}+g_{441})\sigma_1\sin^2\theta\cos^2\theta\\&+2g_{331}\sigma_1\sin^4\theta+2g_{222}\sigma_2\cos^4\theta+2(2g_{232}+g_{442})\sigma_2\sin^2\theta\cos^2\theta+2g_{332}\sigma_2\sin^4\theta+2g_{223}\sigma_3\cos^4\theta\\&+2(2g_{233}+g_{443})\sigma_3\sin^2\theta\cos^2\theta+2g_{333}\sigma_3\sin^4\theta+3h_{2211}\sigma_1^2\cos^4\theta+3(2h_{2311}+h_{4411})\sigma_1^2\sin^2\theta\cos^2\theta\\&+3h_{3311}\sigma_1^2\sin^4\theta+6h_{2212}\sigma_1\sigma_2\cos^4\theta+6(2h_{2312}+h_{4412})\sigma_1\sigma_2\sin^2\theta\cos^2\theta+6h_{3312}\sigma_1\sigma_2\sin^4\theta\\&+6h_{2213}\sigma_1\sigma_3\cos^4\theta+6(2h_{2313}+h_{4413})\sigma_1\sigma_3\sin^2\theta\cos^2\theta+6h_{3313}\sigma_1\sigma_3\sin^4\theta+3h_{2222}\sigma_2^2\cos^4\theta\\&+3(2h_{2322}+h_{4422})\sigma_2^2\sin^2\theta\cos^2\theta+3h_{3322}\sigma_2^2\sin^4\theta+6h_{2223}\sigma_2\sigma_3\cos^4\theta\\&+6(2h_{2323}+h_{4423})\sigma_2\sigma_3\sin^2\theta\cos^2\theta+6h_{3323}\sigma_2\sigma_3\sin^4\theta+3h_{2233}\sigma_3^2\cos^4\theta\\&+3(2h_{2333}+h_{4433})\sigma_3^2\sin^2\theta\cos^2\theta+3h_{3333}\sigma_3^2\sin^4\theta.\end{aligned}$$

For the quasitransverse ultrasonic wave which is polarized in the x_2-x_3 plane and whose propagation direction lies in the x_2-x_3 symmetry plane at an angle θ with respect to x_2 axis, using the stress components with abbreviated description, the final equation of motion in the coordinate system X_i is obtained as

$$\varrho\,\frac{\partial^2 \xi_3''}{\partial t^2}=\frac{\partial \Delta P_4''}{\partial X_2}+\sigma_2''\cdot\frac{\partial^2 \xi_3''}{\partial X_2^2}, \tag{26}$$

where $\Delta P_4''$ is the dynamic stress due to the propagation of the quasitransverse ultrasonic wave and defined as

$$\Delta P_4''=B\,\cos(\omega t-kX_2). \tag{27}$$

A solution of Eq. (26) leads to the strain component due to the wave propagation:

$$\epsilon_4''=-\frac{k^2 B}{\sigma_2'' k^2-\varrho\,\omega^2}\cos(\omega t-kX_2). \tag{28}$$

The dynamic stress $\Delta P_4''$ due to the wave propagation gives the stress perturbation $\Delta\sigma_I$ superposed in the stress components σ_I:

$$\begin{pmatrix}\Delta\sigma_1\\ \Delta\sigma_2\\ \Delta\sigma_3\\ \Delta\sigma_4\\ \Delta\sigma_5\\ \Delta\sigma_6\end{pmatrix}=\begin{pmatrix}0\\ -\Delta P_4''\sin 2\theta\\ \Delta P_4''\sin 2\theta\\ \Delta P_4''\cos 2\theta\\ 0\\ 0\end{pmatrix}. \tag{29}$$

Using Eqs. (13), (21), and (29), the infinitesimal dynamic strain components $\epsilon_2^{\rm dyn}$, $\epsilon_3^{\rm dyn}$, and $\epsilon_4^{\rm dyn}$ caused by the stress perturbation of the quasitransverse wave, which are defined in Eq. (2), lead to the dynamic strain $\epsilon_4''^{\rm dyn}$ due to the propagation of the ultrasonic wave with a fundamental frequency:

$$\begin{aligned}\epsilon_4''^{\rm dyn}=\{&f_{22}\sin^2 2\theta-f_{23}\sin^2 2\theta-f_{24}\sin 2\theta\cos 2\theta-f_{32}\sin^2 2\theta+f_{33}\sin^2 2\theta+f_{34}\sin 2\theta\cos 2\theta-f_{42}\sin 2\theta\cos 2\theta\\
&+f_{43}\sin 2\theta\cos 2\theta+f_{44}\cos^2 2\theta+2g_{221}\sigma_1\sin^2 2\theta-2g_{231}\sigma_1\sin^2 2\theta-2g_{241}\sigma_1\sin 2\theta\cos 2\theta-2g_{321}\sigma_1\sin^2 2\theta\\
&+2g_{331}\sigma_1\sin^2 2\theta+2g_{341}\sigma_1\sin 2\theta\cos 2\theta-2g_{421}\sigma_1\sin 2\theta\cos 2\theta+2g_{431}\sigma_1\sin 2\theta\cos 2\theta+2g_{441}\sigma_1\cos^2 2\theta\\
&+\cdots-2g_{244}\sigma_4\sin 2\theta\cos 2\theta-2g_{245}\sigma_5\sin 2\theta\cos 2\theta-2g_{246}\sigma_6\sin 2\theta\cos 2\theta+2g_{344}\sigma_4\sin 2\theta\cos 2\theta\\
&+2g_{345}\sigma_5\sin 2\theta\cos 2\theta+2g_{346}\sigma_6\sin 2\theta\cos 2\theta+2g_{444}\sigma_4\cos^2 2\theta+2g_{445}\sigma_5\cos^2 2\theta+2g_{446}\sigma_6\cos^2 2\theta\\
&+3h_{2112}\sigma_1^2\sin^2 2\theta-3h_{2113}\sigma_1^2\sin^2 2\theta-3h_{2114}\sigma_1^2\sin 2\theta\cos 2\theta-3h_{3112}\sigma_1^2\sin^2 2\theta+3h_{3113}\sigma_1^2\sin^2 2\theta\\
&+3h_{3114}\sigma_1^2\sin 2\theta\cos 2\theta-3h_{4112}\sigma_1^2\sin 2\theta\cos 2\theta+3h_{4113}\sigma_1^2\sin 2\theta\cos 2\theta+3h_{4114}\sigma_1^2\cos^2 2\theta+\cdots\\
&-3h_{2455}\sigma_5^2\sin 2\theta\cos 2\theta-6h_{2456}\sigma_5\sigma_6\sin 2\theta\cos 2\theta-3h_{2466}\sigma_6^2\sin 2\theta\cos 2\theta+3h_{3455}\sigma_5^2\sin 2\theta\cos 2\theta\\
&+6h_{3456}\sigma_5\sigma_6\sin 2\theta\cos 2\theta+3h_{3466}\sigma_6^2\sin 2\theta\cos 2\theta+3h_{4455}\sigma_5^2\cos^2 2\theta+6h_{4456}\sigma_5\sigma_6\cos^2 2\theta\\
&+3h_{4466}\sigma_6^2\cos^2 2\theta\}\Delta P_4''\equiv Q_2(\sigma_I,\theta)\cdot\Delta P_4''\quad (I=1,\ldots,6).\end{aligned} \tag{30}$$

From Eqs. (28) and (30), the quasitransverse wave velocity in the stressed body is obtained by

$$V_2^{\rm trans}(\sigma_I,\theta)=\frac{\omega}{k}=\left\{\frac{\sigma_2\cos^2\theta+\sigma_3\sin^2\theta+\sigma_4\sin 2\theta}{\varrho}+\frac{1}{\varrho\,Q_2(\sigma_I,\theta)}\right\}^{1/2}. \tag{31}$$

When a material body has the slightly orthotropic property whose symmetry axes coincide with the principal stress axes and the shear stress components in the material are zero, taking the symmetry of the elastic constants into account, Eq. (31) becomes

$$V_2^{\rm trans}(\sigma_I,\theta)=\left\{\frac{\sigma_2\cos^2\theta+\sigma_3\sin^2\theta}{\varrho}+\frac{1}{\varrho\,Q_2(\sigma_I,\theta)}\right\}^{1/2}\quad (I=1,\ldots,3), \tag{32}$$

where

$$\begin{aligned}Q_2(\sigma_I,\theta)=&(f_{22}+f_{33}-2f_{23})\sin^2 2\theta+f_{44}\cos^2 2\theta+2(g_{221}+g_{331}-2g_{231})\sigma_1\sin^2 2\theta+2g_{441}\sigma_1\cos^2 2\theta\\
&+2(g_{222}+g_{332}-2g_{232})\sigma_2\sin^2 2\theta+2g_{442}\sigma_2\cos^2 2\theta+2(g_{223}+g_{333}-2g_{233})\sigma_3\sin^2 2\theta+2g_{443}\sigma_3\cos^2 2\theta\\
&+3(h_{2211}+h_{3311}-2h_{2311})\sigma_1^2\sin^2 2\theta+3h_{4411}\sigma_1^2\cos^2 2\theta+6(h_{2212}+h_{3312}-2h_{2312})\sigma_1\sigma_2\sin^2 2\theta\\
&+6h_{4412}\sigma_1\sigma_2\cos^2 2\theta+6(h_{2213}+h_{3313}-2h_{2313})\sigma_1\sigma_3\sin^2 2\theta+6h_{4413}\sigma_1\sigma_3\cos^2 2\theta\\
&+3(h_{2222}+h_{3322}-2h_{2322})\sigma_2^2\sin^2 2\theta+3h_{4422}\sigma_2^2\cos^2 2\theta+6(h_{2223}+h_{3323}-2h_{2323})\sigma_2\sigma_3\sin^2 2\theta\\
&+6h_{4423}\sigma_2\sigma_3\cos^2 2\theta+3(h_{2233}+h_{3333}-2h_{2333})\sigma_3^2\sin^2 2\theta+3h_{4433}\sigma_3^2\cos^2 2\theta.\end{aligned}$$

Equations (25) and (32) are functions of stress and describe the dependence of ultrasound velocity on stress in metals. From Eqs. (4) and (5), the density ϱ can be expressed by using the density at the free state:

$$\varrho = \frac{\varrho_0}{(1+\epsilon_1)(1+\epsilon_2)(1+\epsilon_3)} \approx \varrho_0(1+\epsilon_1+\epsilon_2+\epsilon_3)^{-1}. \tag{33}$$

The formulas of the quasilongitudinal and quasitransverse wave velocities in the other two planes are given in Appendix A.

An uniaxial stress loading helps the evaluation in the applied stress direction.[14] When the longitudinal wave propagates at angle $\theta=0$ in the material to which the uniaxial stress is applied, Eq. (25) gives the wave velocities as follows:

(i) The propagation of an ultrasonic wave whose direction is parallel to the applied uniaxial stress σ_2,

$$V_2^{\text{long}}(\sigma_2,0) = \left\{ \frac{\sigma_2}{\varrho} + \frac{1}{\varrho(f_{22}+2g_{222}\sigma_2+3h_{2222}\sigma_2^2)} \right\}^{1/2}; \tag{34}$$

(ii) The propagation of an ultrasonic wave whose direction is perpendicular to the applied uniaxial stress σ_3,

$$V_2^{\text{long}}(\sigma_3,0) = \left\{ \frac{1}{\varrho(f_{22}+2g_{223}\sigma_3+3h_{2233}\sigma_3^2)} \right\}^{1/2}. \tag{35}$$

Though the goal of this paper is not the determination of all constants in the derived formulas, it is easily understood that all constants can be obtained from measurements of the propagation velocities of the ultrasonic waves at some different angles with the applied uniaxial stress or the applied plane stress. The relations between compliance constants and stiffness constants are obtained in Appendix B.

II. MEASUREMENT OF THE ULTRASOUND VELOCITY IN A STRESSED METAL

As for the conventional methods to measure the ultrasound velocity in the stressed metals, sing-around method,[15] pulse-echo-overlap method,[16] and pulse superposition method[17] are well-known. The ultrasound velocity in the stressed metals can also be measured by detecting the phase change of the ultrasonic wave propagating in the stressed metals.[18] The schematic construction of a measuring system is shown in Fig. 3.

An aluminum alloy (A5052) was used as a metal sample with the cubic shape. A 50-MHz longitudinal ultrasonic probing wave passed through the center of the metal sample at room temperature. The external compression by a hydraulic pressure pump which can generate up to 20-ton force generates the uniaxial compressive stress in the sample and it was uniformly applied from the upper and lower surfaces of the sample. When the propagation direction of the probing wave coincides with the direction of the applied stress, the specific adapters which can inset the ultrasonic probing wave transmitter/receiver are inserted between the sample and the cylinder of the pressure pump.

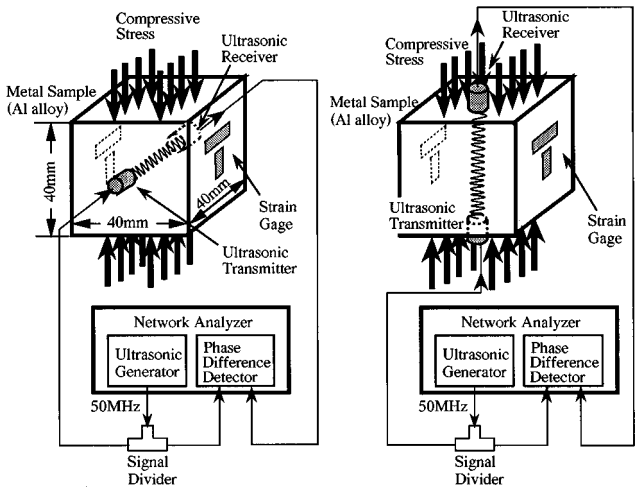

FIG. 3. Schematic construction of a measuring system of the dependence of ultrasound velocity on the stress in a metal. The ultrasonic wave propagates at the center of the metal sample with cubic shape.

The change in the ultrasound velocity due to the applied stress is measured as the phase difference between the reference wave and the wave passing through the metal sample. Since the measured phase difference includes the change due to the strain in the propagation direction of the probing wave, the strain in this direction was measured and was used for compensation. The strain in the direction perpendicular to the direction of the applied stress was also measured to compensate for the density of the sample by using Eq. (33).

The phase difference $\Delta\varphi$ between the reference wave and the wave passing through the sample is given by

$$\Delta\varphi = 2\pi f\left(\frac{(1+\epsilon)l_0}{V_0+\Delta V} - \frac{l_0}{V_0} \right), \tag{36}$$

where V_0 is the ultrasound velocity at the free state, l_0 is the propagation length of the ultrasonic probing wave, f is the frequency of the probing wave, ϵ is the strain in the direction of the propagation of the probing wave, and ΔV is the change in the ultrasound velocity due to the applied stress.

From Eq. (36), the ultrasound velocity in a stressed state is derived as

$$V = V_0 + \Delta V = \frac{1+\epsilon}{\Delta\varphi/2\pi f l_0 + 1/V_0}. \tag{37}$$

The transducers for transmitting and receiving the probing wave were 6 mm in diameter. For the measurement of the phase difference, a network analyzer (Hewlett–Packard 4195A) was used and the strain was measured by the strain gage which was adhered to the surface close to the propagation path of the probing beam. As given in Eq. (34) when the stress is zero, the initial velocity is determined by the density of the sample and the second-order elastic compliance constant near the stressless condition. The density of the sample was measured with a caliper and an electronic balance before ultrasonic measurements, whose value was 2.69×10^3 kg/m^3. The elastic compliance constant is obtained by the measured stress-strain data and the value was 9.95×10^{-12} Pa^{-1}. The measured phase difference data have the probable errors less

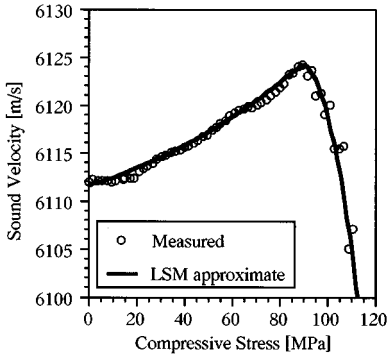

FIG. 4. The dependence of the ultrasound velocity on the stress in an aluminum alloy (A5052). The propagation direction of the wave is in the direction of the applied uniaxial stress.

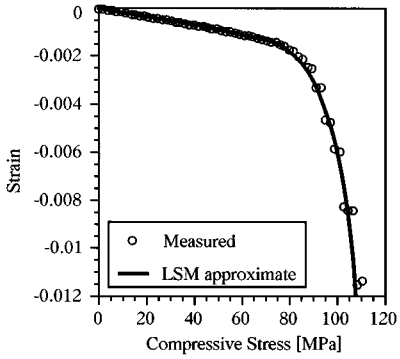

FIG. 6. Measured stress–strain curve for an aluminum alloy (A5052). The strain in the direction of the applied stress is measured and used for compensation of the measured phase difference to obtain Fig. 4.

than 5%. Using these measured data, Eq. (37) gives the ultrasound velocity data. In the constructed setup, using the metal sample whose length is 40.0 mm, the velocity change can be detected with the accuracy of 2.97×10^{-4}.

For the ultrasonic probing beam propagating in the direction of the applied stress, a typical experimental result of the ultrasound velocity in an aluminum alloy sample is shown in Fig. 4. It shows a nonlinear relation between the ultrasound velocity and the stress in the metal sample. That is, with the increase of the compressive stress, first, the ultrasound velocity increases monotonically where the rate of the increase is almost linear, and then the curve shows a peak value at approximately 90 MPa. Then the sign of the derivative of ultrasound velocity with respect to stress is reversed and the ultrasound velocity decreases monotonically at a high rate.

For the ultrasonic probing beam propagating in the direction perpendicular to the direction of the applied stress, a typical experimental result of the ultrasound velocity in an aluminum alloy sample is shown in Fig. 5. It also shows a nonlinear dependence of the ultrasound velocity on the stress in the metal sample. With the increase of the compressive stress, first, the ultrasound velocity decreases monotonically at a lower rate of change as compared with Fig. 4. Then the rate of the decrease is reduced and the curve becomes flat at approximately 80 MPa. Further, the sign of the derivative of ultrasound velocity with respect to stress is reversed and the ultrasound velocity increases monotonically at a high rate. Thus, the effect of the stress in the metal on the velocities of ultrasonic waves propagating in the different directions has been shown. According to law of propagation of errors, the obtained velocity data have the probable errors less than 0.04%.

Experimental results of the relation between compressive stress and strain are shown in Figs. 6 and 7. These results have the probable errors less than 9% and are used for compensation of the ultrasound velocity data. Figure 6 shows that the strain in the propagation direction of the ultrasonic wave decreases with the increase of the compressive stress. Figure 7 shows that the strain in the direction perpendicular to the direction of the applied stress increases with the increase of the compressive stress. From these results, elastic deformation limit which is defined as the stress which yields a plastic strain of 2.0×10^{-4} can be determined. Hence, the elastic deformation limit of this metal sample should be at approximately 86 MPa in the applied stress direction and at approximately 76 MPa in the direction perpendicular to the applied stress.

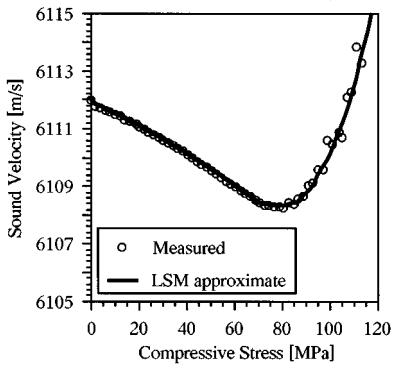

FIG. 5. The dependence of the ultrasound velocity on the stress in an aluminum alloy (A5052). The wave propagates in the direction perpendicular to the direction of the applied uniaxial stress.

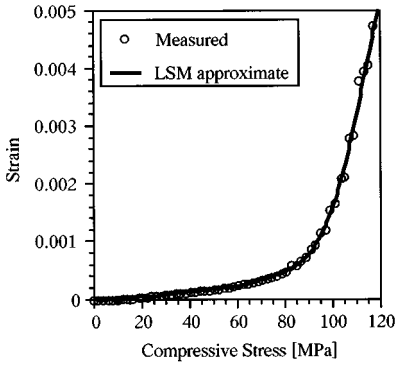

FIG. 7. Measured stress–strain curve for an aluminum alloy(A5052). The strain is in the direction perpendicular to the direction of the applied stress. It is used for compensation of the measured phase difference to obtain Fig. 5.

TABLE I. The determined effective elastic and elastic–plastic compliance constants from the measurement of the ultrasound velocity in an aluminum alloy (A5052). The ultrasonic wave propagates in the direction of the applied uniaxial stress. The fourth-order constants have the difference between two regions in the observing stress range.

Effective elastic/elastic-plastic compliance constants	Elastic region [<86 MPa]	Plastic region [>86 MPa]
f_{22} [$\times 10^{-6}$ Pa^{-1}]	9.95×10^{-6} $\pm4.08\times10^{-10}$	9.95×10^{-6} $\pm5.23\times10^{-8}$
g_{222} [$\times 10^{-12}$ Pa^{-2}]	1.71×10^{-10} $\pm1.58\times10^{-11}$	1.71×10^{-10} $\pm9.04\times10^{-11}$
h_{2222} [$\times 10^{-18}$ Pa^{-3}]	-1.16×10^{-12} $\pm1.54\times10^{-13}$	5.56×10^{-11} $\pm3.54\times10^{-11}$

III. DETERMINATION OF THE EFFECTIVE COMPLIANCE CONSTANTS FROM THE MEASURED ULTRASOUND VELOCITY

The least-squares method is one of the conventional methods to analyze the measured data.[10] This is mainly applied to the measured data to find the optimum fitting curve profile which is usually described by a polynomial expression. For the measured ultrasound velocity data, the optimum fitting curve profile obtained by the least-squares method (Deming's method[19]) determines the higher-order effective elastic and elastic-plastic compliance constants. Using Eq. (34), the determined constants for the ultrasonic probing beam propagating in the direction of the applied stress are shown in Table I. It is clear that the second-order constant from ultrasonic measurements coincides with the second-order compliance constants obtained by the measured stress–strain relation. The stress range is separated into two regions with the boundary of the elastic deformation limit. Here, the properties of the metal in the applied stress direction have been of interest and uniaxial compression was performed. Thus, the effective elastic and elastic–plastic constants for the ultrasonic probing beam only in the direction of the applied stress should be determined. The validity of these determined constants is confirmed by the procedures as shown in Fig. 8. The calculated velocity change cannot be larger than the detectable value in the constructed setup. If the velocity data have lower noises, they generally satisfy this condition. The drastic change in the vicinity of the elastic limit may be the key to evaluate the stress condition in metals. Although the second- and third-order effective compliance constants in the regions have the same value, the fourth-order effective compliance constants are different. The second-order constants are related to the velocity in the stressless condition and the third-order constants are related to the linear velocity change in the elastic region. In the vicinity of elastic limit, though the plastic properties are added to the elastic properties, the elastic properties are preserved in the plastic region.

Using the determined constants, the relation between stress and strain is obtained as shown in Fig. 9. In the plastic region, the difference between the measured strain and the calculated strain by using the determined effective compliance constants becomes larger with the increase of the compressive stress. It is likely that this may be caused by the slip

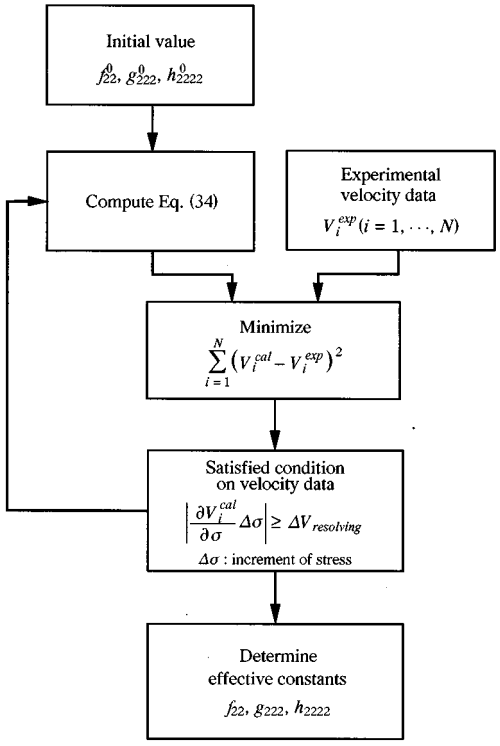

FIG. 8. The procedure of determination of the effective constants from ultrasound velocity data. For the wave propagation in the other plane, the same procedure can also be employed.

deformation which is a kind of the plastic deformation. With the increase of the compressive stress, the slip deformation in a microscopic part of metals should grow to be reflected in macroscopic deformation. The deformation in the plastic region can be effectively characterized by the determined constants as well as by the work-hardening parameter. From an acoustoelastic point of view, this result means that the slip deformation in the plastic region grows with keeping the fourth-order effective compliance constant. In other words, the slip deformation which has completely been grown makes little contribution to the determination of the fourth-order effective constants from measurements of the change

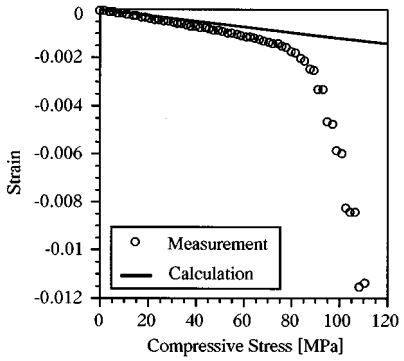

FIG. 9. The stress–strain curve determined by the effective elastic and elastic–plastic compliance constants which makes the difference from the measured stress–strain curve of Fig. 6. In the plastic region, especially, it can be seen the remarkable difference which is considered to be caused by the slip deformation.

in the ultrasound velocity depending on the stress in the metal.

IV. CONCLUSION

For the quasilongitudinal and quasitransverse waves which propagate in the symmetry planes of a metal, the formulation for the dependence of ultrasound velocity on the stress in the metal was completed with the expression in terms of the elastic compliance constants and the derived formulas are explicitly expressed as a function of stress. The ultrasound velocity was measured through the detection of the phase change of the ultrasonic probing wave propagating in the stressed metal. On the basis of the measured ultrasound velocity, the effective elastic and elastic–plastic compliance constants were determined by means of the least-squares method. The determined fourth-order effective compliance constants have the remarkable difference in the plastic region with the boundary of the elastic deformation limit. From an acoustoelastic point of view, it became clear that in the observing stress range the slip deformation in the plastic region grows with keeping the fourth-order effective compliance constant.

APPENDIX A: THE FORMULAS OF ULTRASONIC WAVE VELOCITIES

In the same way as the derivation of the ultrasound velocities in the x_2-x_3 symmetry plane, the formulas of the wave velocities in the x_1-x_2 and x_1-x_3 planes can be derived. The case of a slightly orthotropic material with the shear stress being zero, whose symmetry axes coincide with the principal stress axes, will be examined. In any planes, the transverse wave is polarized in the plane in which the propagation direction lies.

When the waves propagate in the x_1-x_2 plane at angle ϕ with respect to x_1 axis, the velocities of the quasilongitudinal and quasitransverse waves are obtained by

$$V_1^{\mathrm{long}}(\sigma_I,\phi)=\left\{\frac{\sigma_1\cos^2\phi+\sigma_2\sin^2\phi}{\varrho}+\frac{1}{\varrho P_1(\sigma_I,\phi)}\right\}^{1/2}\quad (I=1,\ldots,3), \tag{A1}$$

$$V_1^{\mathrm{trans}}(\sigma_I,\phi)=\left\{\frac{\sigma_1\cos^2\phi+\sigma_2\sin^2\phi}{\varrho}+\frac{1}{\varrho Q_1(\sigma_I,\phi)}\right\}^{1/2}\quad (I=1,\ldots,3), \tag{A2}$$

where

$$\begin{aligned}P_1(\sigma_I,\phi)=&f_{11}\cos^4\phi+(2f_{12}+f_{66})\sin^2\phi\cos^2\phi+f_{22}\sin^4\phi+2g_{111}\sigma_1\cos^4\phi+2(2g_{121}+g_{661})\sigma_1\sin^2\phi\cos^2\phi\\&+2g_{221}\sigma_1\sin^4\phi+2g_{112}\sigma_2\cos^4\phi+2(2g_{122}+g_{662})\sigma_2\sin^2\phi\cos^2\phi+2g_{222}\sigma_2\sin^4\phi+2g_{113}\sigma_3\cos^4\phi\\&+2(2g_{123}+g_{663})\sigma_3\sin^2\phi\cos^2\phi+2g_{223}\sigma_3\sin^4\phi+3h_{1111}\sigma_1^2\cos^4\phi+3(2h_{1211}\\&+h_{6611})\sigma_1^2\sin^2\phi\cos^2\phi+3h_{2211}\sigma_1^2\sin^4\phi+6h_{1112}\sigma_1\sigma_2\cos^4\phi+6(2h_{1212}+h_{6612})\sigma_1\sigma_2\sin^2\phi\cos^2\phi\\&+6h_{2212}\sigma_1\sigma_2\sin^4\phi+6h_{1113}\sigma_1\sigma_3\cos^4\phi+6(2h_{1213}+h_{6613})\sigma_1\sigma_3\sin^2\phi\cos^2\phi+6h_{2213}\sigma_1\sigma_3\sin^4\phi\\&+3h_{1122}\sigma_2^2\cos^4\phi+3(2h_{1222}+h_{6622})\sigma_2^2\sin^2\phi\cos^2\phi+3h_{2222}\sigma_2^2\sin^4\phi+6h_{1123}\sigma_2\sigma_3\cos^4\phi\\&+6(2h_{1223}+h_{6623})\sigma_2\sigma_3\sin^2\phi\cos^2\phi+6h_{2223}\sigma_2\sigma_3\sin^4\phi+3h_{1133}\sigma_3^2\cos^4\phi\\&+3(2h_{1233}+h_{6633})\sigma_3^2\sin^2\phi\cos^2\phi+3h_{2233}\sigma_3^2\sin^4\phi,\end{aligned}$$

$$\begin{aligned}Q_1(\sigma_I,\phi)=&(f_{11}+f_{22}-2f_{12})\sin^2 2\phi+f_{66}\cos^2 2\phi+2(g_{111}+g_{221}-2g_{121})\sigma_1\sin^2 2\phi+2g_{661}\sigma_1\cos^2 2\phi\\&+2(g_{112}+g_{222}-2g_{122})\sigma_2\sin^2 2\phi+2g_{662}\sigma_2\cos^2 2\phi+2(g_{113}+g_{223}-2g_{123})\sigma_3\sin^2 2\phi+2g_{663}\sigma_3\cos^2 2\phi\\&+3(h_{1111}+h_{2211}-2h_{1211})\sigma_1^2\sin^2 2\phi+3h_{6611}\sigma_1^2\cos^2 2\phi+6(h_{1112}+h_{2212}-2h_{1212})\sigma_1\sigma_2\sin^2 2\phi\\&+6h_{6612}\sigma_1\sigma_2\cos^2 2\phi+6(h_{1113}+h_{2213}-2h_{1213})\sigma_1\sigma_3\sin^2 2\phi+6h_{6613}\sigma_1\sigma_3\cos^2 2\phi\\&+3(h_{1122}+h_{2222}-2h_{1222})\sigma_2^2\sin^2 2\phi+3h_{6622}\sigma_2^2\cos^2 2\phi+6(h_{1123}+h_{2223}-2h_{1223})\sigma_2\sigma_3\sin^2 2\phi\\&+6h_{6623}\sigma_2\sigma_3\cos^2 2\phi+3(h_{1133}+h_{2233}-2h_{1233})\sigma_3^2\sin^2 2\phi+3h_{6633}\sigma_3^2\cos^2 2\phi.\end{aligned}$$

For the propagation of the quasilongitudinal and quasitransverse waves in the x_1-x_3 plane at angle φ with respect to x_3 axis, the velocities are obtained by

$$V_3^{\mathrm{long}}(\sigma_I,\varphi)=\left\{\frac{\sigma_3\cos^2\varphi+\sigma_1\sin^2\varphi}{\varrho}+\frac{1}{\varrho P_3(\sigma_I,\varphi)}\right\}^{1/2}\quad (I=1,\ldots,3), \tag{A3}$$

$$V_3^{\mathrm{trans}}(\sigma_I,\varphi)=\left\{\frac{\sigma_3\cos^2\varphi+\sigma_1\sin^2\varphi}{\varrho}+\frac{1}{\varrho Q_3(\sigma_I,\varphi)}\right\}^{1/2}\quad(I=1,\ldots,3),\tag{A4}$$

where

$$\begin{aligned}P_3(\sigma_I,\varphi)=&f_{33}\cos^4\varphi+(2f_{13}+f_{55})\sin^2\varphi\cos^2\varphi+f_{11}\sin^4\varphi+2g_{331}\sigma_1\cos^4\varphi+2(2g_{131}+g_{551})\sigma_1\sin^2\varphi\cos^2\varphi\\&+2g_{111}\sigma_1\sin^4\varphi+2g_{332}\sigma_2\cos^4\varphi+2(2g_{132}+g_{552})\sigma_2\sin^2\varphi\cos^2\varphi+2g_{112}\sigma_2\sin^4\varphi+2g_{333}\sigma_3\cos^4\varphi\\&+2(2g_{133}+g_{553})\sigma_3\sin^2\varphi\cos^2\varphi+2g_{113}\sigma_3\sin^4\varphi+3h_{3311}\sigma_1^2\cos^4\varphi+3(2h_{1311}+h_{5511})\sigma_1^2\sin^2\varphi\cos^2\varphi\\&+3h_{1111}\sigma_1^2\sin^4\varphi+6h_{3312}\sigma_1\sigma_2\cos^4\varphi+6(2h_{1312}+h_{5512})\sigma_1\sigma_2\sin^2\varphi\cos^2\varphi+6h_{1112}\sigma_1\sigma_2\sin^4\varphi\\&+6h_{3313}\sigma_1\sigma_3\cos^4\varphi+6(2h_{1313}+h_{5513})\sigma_1\sigma_3\sin^2\varphi\cos^2\varphi+6h_{1113}\sigma_1\sigma_3\sin^4\varphi+3h_{3322}\sigma_2^2\cos^4\varphi\\&+3(2h_{1322}+h_{5522})\sigma_2^2\sin^2\varphi\cos^2\varphi+3h_{1122}\sigma_2^2\sin^4\varphi+6h_{3323}\sigma_2\sigma_3\cos^4\varphi\\&+6(2h_{1323}+h_{5523})\sigma_2\sigma_3\sin^2\varphi\cos^2\varphi+6h_{1123}\sigma_2\sigma_3\sin^4\varphi+3h_{3333}\sigma_3^2\cos^4\varphi\\&+3(2h_{1333}+h_{5533})\sigma_3^2\sin^2\varphi\cos^2\varphi+3h_{1133}\sigma_3^2\sin^4\varphi,\\Q_3(\sigma_I,\varphi)=&(f_{11}+f_{33}-2f_{13})\sin^2 2\varphi+f_{55}\cos^2 2\varphi+2(g_{111}+g_{331}-2g_{131})\sigma_1\sin^2 2\varphi+2g_{551}\sigma_1\cos^2 2\varphi\\&+2(g_{112}+g_{332}-2g_{132})\sigma_2\sin^2 2\varphi+2g_{552}\sigma_2\cos^2 2\varphi+2(g_{113}+g_{333}-2g_{133})\sigma_3\sin^2 2\varphi+2g_{553}\sigma_3\cos^2 2\varphi\\&+3(h_{1111}+h_{3311}-2h_{1311})\sigma_1^2\sin^2 2\varphi+3h_{5511}\sigma_1^2\cos^2 2\varphi+6(h_{1112}+h_{3312}-2h_{1312})\sigma_1\sigma_2\sin^2 2\varphi\\&+6h_{5512}\sigma_1\sigma_2\cos^2 2\varphi+6(h_{1113}+h_{3313}-2h_{1313})\sigma_1\sigma_3\sin^2 2\varphi+6h_{5513}\sigma_1\sigma_3\cos^2 2\varphi\\&+3(h_{1122}+h_{3322}-2h_{1322})\sigma_2^2\sin^2 2\varphi+3h_{5522}\sigma_2^2\cos^2 2\varphi+6(h_{1123}+h_{3323}-2h_{1323})\sigma_2\sigma_3\sin^2 2\varphi\\&+6h_{5523}\sigma_2\sigma_3\cos^2 2\varphi+3(h_{1133}+h_{3333}-2h_{1333})\sigma_3^2\sin^2 2\varphi+3h_{5533}\sigma_3^2\cos^2 2\varphi.\end{aligned}$$

APPENDIX B: THE RELATIONS BETWEEN COMPLIANCE CONSTANTS AND STIFFNESS CONSTANTS

Using the higher-order stiffness constants, the relation between stress and strain is obtained by

$$\sigma_I=C_{IJ}\epsilon_J+C_{IJK}\epsilon_J\epsilon_K+C_{IJKL}\epsilon_J\epsilon_K\epsilon_L,\tag{B1}$$

where C_{IJ}, C_{IJK}, and C_{IJKL} are the second-, third-, and fourth-order elastic stiffness constants. Substitution of Eq. (2) into Eq. (B1) leads to the relations between the stiffness constants and the compliance constants:

$$f_{IJ}C_{JK}=\delta_{IK},\tag{B2}$$

$$C_{IJ}g_{JXY}+C_{IJK}f_{JX}f_{KY}=0,\tag{B3}$$

$$C_{IJ}h_{JXYZ}+C_{IJK}f_{JX}g_{KYZ}+C_{IJK}g_{JXY}f_{KZ}+C_{IJKL}f_{JX}f_{KY}f_{LZ}=0,\tag{B4}$$

where X, Y, and Z are free indices. In order to obtain the stiffness constants, all of the compliance constants which are not zero must be determined.

[1] D. S. Hughes and J. L. Kelly, ''Second-Order Elastic Deformation of Solids,'' Phys. Rev. **92**, 1145–1149 (1953).

[2] Y. C. Chu, A. D. Degtyar, and S. I. Rokhlin, ''On determination of orthotropic material moduli from ultrasonic velocity data in nonsymmetry planes,'' J. Acoust. Soc. Am. **95**, 3191–3203 (1994).

[3] R. T. Smith, R. Stern, and R. W. B. Stephens, ''Third-Order Elastic Moduli of Polycrystalline Metals from Ultrasonic Velocity Measurements,'' J. Acoust. Soc. Am. **40**, 1002–1008 (1966).

[4] ''Looking for stress? New ultrasound mapping does,'' J. Res. Natl. Inst. Stand. Technol. **100**, 260–265 (1995).

[5] D. Utrata, A. Storm, and M. Negley, ''Stress Measurement in Railroad Rail using Ultrasonic and Magnetic Techniques,'' in *Review of Progress in QNDE*, edited by D. O. Thompson and D. E. Chimenti (Plenum, New York, 1995), Vol. 14B, pp. 1683–1691.

[6] A. H. Nayfeh and T. W. Taylor, ''Dynamic Distribution of Displacement and Stress Considerations in the Ultrasonic Immersion Nondestructive Evaluation of Multilayered Plates,'' Trans. ASME J. Eng. Mater. Technol. **112**(3), 260–265 (1990).

[7] George C. Johnson, ''Acoustoelastic theory for elastic–plastic materials,'' J. Acoust. Soc. Am. **70**, 591–595 (1981).

[8] Y. H. Pao, W. Sachse, and H. Fukuoka, ''Acoustoelasticity and Ultrasonic Measurements of Residual Stresses,'' in *Physical Acoustics*, edited by W. P. Mason and R. N. Thurston (Academic, New York, 1984), Vol. XVII.

[9] R. N. Thurston and K. Brugger, ''Third-order Elastic Constants and the Velocity of small Amplitude Elastic Waves in Homogeneously Stressed Media,'' Phys. Rev. A **133**(6), 1604–1610 (1964).

[10] A. D. Degtyar and S. I. Rokhlin, ''Absolute stress determination in orthotropic materials from angular dependences of ultrasonic velocities,'' J. Appl. Phys. **78**(3), 1547–1556 (1995).

[11] C.-S. Man, W.-y. Lu, Q. Gu, and W. Tang, ''Ultrasound measurement of stress in weakly anisotropic thin sheets,'' J. Acoust. Soc. Am. **91**, 2643–2653 (1992).

[12] R. A. Toupin and B. Bernstein, ''Sound Waves in Deformed Perfectly Elastic Materials Acoustoelastic Effect,'' J. Acoust. Soc. Am. **33**, 216–225 (1961).

[13] R. N. Thurston, ''Wave Propagation in Fluids and Normal Solids,'' in *Physical Acoustics*, edited by W. P. Mason (Academic, New York, 1964), Vol. I, Part A.

[14] M. Boukhny, G. L. Bullock, B. S. Shivaram, and D. G. Hinks, ''Ultrasound study of the superconducting phases of UPt_3 under uniaxial stress,'' Physica B **199**&**200**, 132–134 (1994).

[15] N. P. Cedrone and D. R. Curran, ''Electronic Pulse Method for Measuring the Velocity of Sound in Liquids and Solids,'' J. Acoust. Soc. Am. **26**, 963–966 (1954).

[16] E. P. Papadakis, ''Ultrasonic Phase Velocity by the Pulse-Echo-Overlap

Method Incorporating Diffraction Phase Corrections,'' J. Acoust. Soc. Am. **42**, 1045–1051 (1967).
[17] H. J. McSkimin, ''Pulse Superposition Method for Measuring Ultrasonic Wave Velocities in Solids,'' J. Acoust. Soc. Am. **33**, 12–16 (1961).
[18] T. Sato, W. Ma, H. Ninoyu, K. Y. Jhang, and Y. Kosugi, ''Estimation of the stress state inside metals using stress perturbing waves and probe waves,'' NDT&E Int. **26**(3), 119–126 (1993).
[19] W. E. Deming, *Statistical adjustment of data* (Wiley, New York, 1948).

Electroacoustical measurements of silicon microphones on wafer scale

Michael Pedersen, Ralf Schellin, Wouter Olthuis, and Piet Bergveld
MESA Research Institute, University of Twente, P.O. Box 217, NL-7500 AE Enschede, The Netherlands

(Received 4 December 1995; accepted for publication 15 November 1996)

A new method for the electroacoustic characterization of small-sized silicon microphones is described. Using closed-field acoustical measurements, it is demonstrated how a precise device characterization can be carried out directly on wafer-scale, thereby eliminating the need to separate and mount each microphone. The performance of the setup is illustrated by measurements on piezoelectric and condenser microphones. Accurate measurements of the frequency response can be performed between 100 Hz and 15 kHz. The determination of the total harmonic distortion of the condenser microphones has been done for SPL (SPL=sound pressure level) from 95 to 125 dB and of the piezoelectric microphones for SPL from 110 to 127 dB, respectively. Furthermore, the A-weighted noise voltage of the microphones can be measured easily. Regarding size, 2- to 4-in. wafers may be used and the minimum measurable chip area is about 1.5 mm^2. An almost complete characterization of a microphone, including the different measurements mentioned above, can be carried out within a few minutes. By measuring several microphones on several wafers, important information, such as yield and reproducibility, can be obtained. Additionally, statistical calculations on sensitivity, equivalent noise level, etc. can be performed. © *1997 Acoustical Society of America.* [S0001-4966(97)00904-1]

PACS numbers: 43.58.Vb, 43.38.Kb [SLE]

INTRODUCTION

Recently, several micromachined microphones, using capacitive,[1–8] field-effect transistor (FET),[9,10] piezoelectric,[11–14] piezoresistive,[15,16] and optical[17,18] detection principles have been developed. Common to all these acoustical sensors for airborne sound is the use of microelectronical and micromechanical batch fabrication techniques. Typical dimensions of the microphones are in the order of $3\times3\times0.3$ mm^3 with membrane areas of about 1–9 mm^2. Usually, 2-, 3-, or 4-in. wafers are used, where one wafer contains several hundreds of microphones. Potential applications of such microphones may be in high volume markets such as telephones, camcorders, etc. and, to some smaller extent in other areas, like hearing aids, etc.

Generally, the electroacoustic properties (sensitivity, frequency response, equivalent noise level, distortion, etc.) of these devices are measured by dicing the wafer into chips, each containing one microphone. Subsequently, the sensors are mounted onto a special substrate carrier, bonded and connected to a low-noise preamplifier. Then, standard measurement techniques, e.g., self-reciprocity method for free-field calibration, auxiliary-transducer method for free-field calibration, auxiliary-transducer method for pressure calibration, etc. are applied (the forementioned methods are briefly described, for instance, in Ref. 19).

In order to reduce development time and costs, quick and accurate measurement techniques are required. Properly performed, the measurements mentioned above are accurate but the described mounting procedure is rather time consuming. To reduce the measurement time significantly, a special setup has been developed, which allows electroacoustical measurements directly on wafer scale. This greatly improves the turnover time, since a precise acoustical measurement can be done without having to separate and mount the microphones. The procedure is analogous to the wafer-scale testing of integrated circuits in the microelectronics industry, before dicing and encapsulation of the chips.

I. THE ELECTROACOUSTIC MEASUREMENT SETUP

A. Description of the setup

The acoustical setup, shown in Fig. 1, basically consists of a loudspeaker (Brüel & Kjær acoustical voice 4219) and a reference microphone (Brüel & Kjær 4136). The volume inside the sealed acoustic chamber is very small, thereby allowing closed field measurements. The chamber is filled with a foam material, in order to avoid any standing waves induced by the sidewalls, which may produce undesired resonances within the measurement range. In the top of the chamber a small opening is made, over which the wafer containing the microphone under test (MUT) can be placed. In order to avoid any phase shift between the reference microphone and the MUT, the distance between the two has been reduced as much as possible. The electrical connections to the device are made with standard probe needles. During the measurements a metal cover is placed over the needles, thereby creating a Faraday cage which removes the influence of any outside electrical noise (e.g., 50 Hz). Furthermore, since the output impedance of the microphones is extremely high, a small battery-powered preamplifier, consisting of a JFET source follower, is placed inside the Faraday cage to eliminate the electrical loading of the BNC connections and the probe needles. The setup is controlled by a Hewlett–Packard 35670A dynamical signal analyzer, which drives the

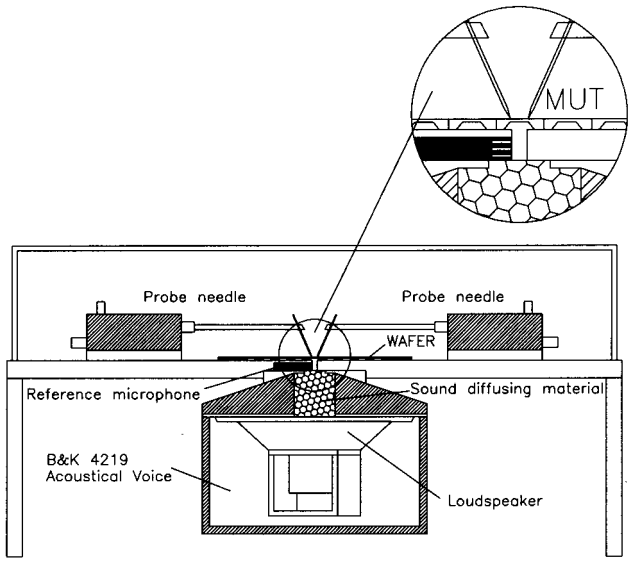

FIG. 1. Setup for on-wafer electroacoustical measurements (MUT =microphone under test).

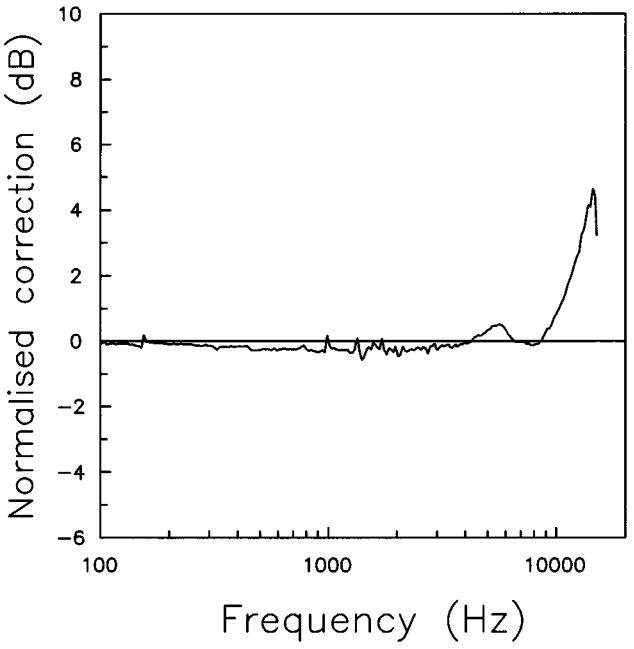

FIG. 3. Normalized correction function of the acoustical setup.

loudspeaker and measures the output of the reference microphone and the MUT. The signal from the reference microphone is obtained with a Brüel & Kjær preamplifier placed in the acoustical voice and a Brüel & Kjær 2610 measurement amplifier. The sensitivity of the reference microphone is 1.4 mV/Pa for a polarization voltage of 200 V.

B. Performing measurements with the setup

For the measurements of the acoustical frequency response (Fig. 2), the swept sine option with auto leveling is used on the HP analyzer. In this mode the analyzer performs individual measurements at a number of frequencies within the specified frequency range, and uses the signal from the reference microphone in a feedback loop to adjust the output of the loudspeaker to the specified sound pressure. The advantage of this method over measurements with random noise or bursts is that the frequency characteristic of the loudspeaker can be compensated for, thereby ensuring the best signal-to-noise ratio in the specified frequency range. The frequency range of the setup is currently 100 Hz to 15 kHz, which is mainly limited by very steep cutoffs in the characteristic of the loudspeaker. The sound pressure mostly used in the measurements was 2 Pa (SPL=100 dB). The setup has been calibrated by determining the acoustical response of the setup itself. This was done by placing a 1/8 in. Brüel & Kjær reference microphone (4138) over the small opening. The recorded normalized correction function is shown in Fig. 3. As it may be seen, the setup itself produces a considerable resonance of about 5 dB around 14 kHz.

Furthermore, due to the high-output impedance of the MUT, the electrical loading of the electrical connection through the probe needle to the preamplifier, and the preamplifier itself, has to be determined. By correcting the acoustical measurements for this loading, it is possible to calculate the open-circuit response, which is an independent universal parameter. The electrical load may be determined with a gain-phase measurement as shown in Fig. 4.

Noise measurements can also be performed with the analyzer, whereby the noise spectrum, with or without A-weighting, can be obtained. Alternatively, the noise can be measured with the Brüel & Kjær 2610 measurement ampli-

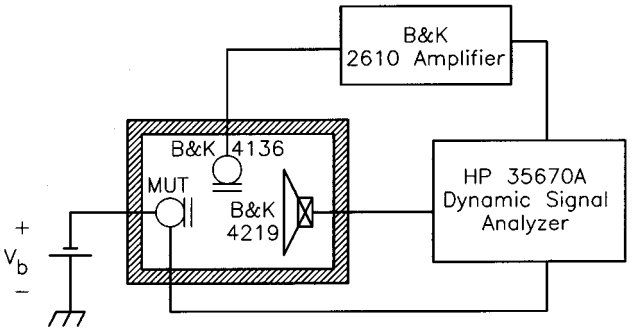

FIG. 2. Measurement of acoustical response ($V_b=0$ for piezoelectric microphones).

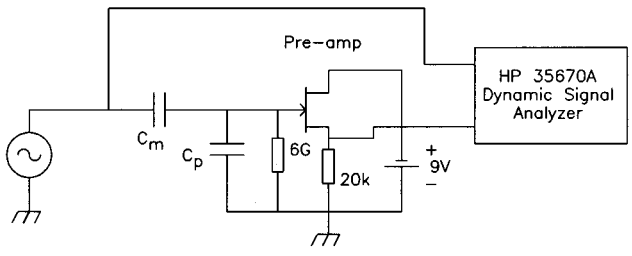

FIG. 4. Measurement of electrical loading of the microphone by the setup (C_m is the capacitance of the microphone, C_p are the parasitic capacitances in the setup and the microphone itself).

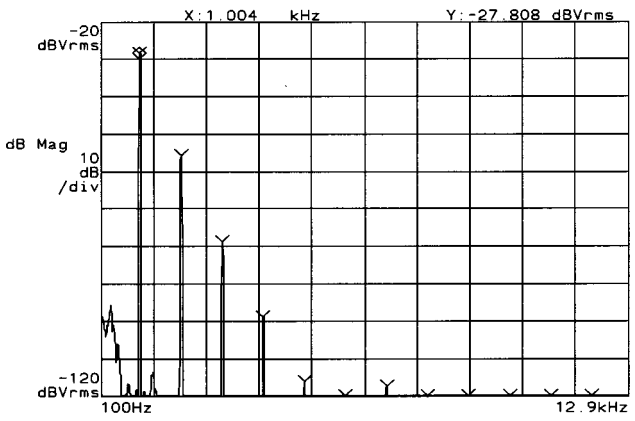

FIG. 5. Measurement of the harmonic distortion.

fier. In general, it should be noted that the noise level of the considered silicon microphones is very low, meaning that the noise generated in the preamplifier is dominating.

Another important issue in silicon microphones is the total harmonic distortion (THD). This distortion, which is normally caused by nonlinear effects in the transducer, may be easily measured by using a built-in function in the analyzer. In the same configuration as in Fig. 2, the analyzer excites the loudspeaker with a 1.004-kHz signal. By using the reference microphone as a monitor, a specific sound pressure level (SPL *re*: to 20 μPa) can be generated. If the signal produced by the microphone is analyzed with FFT, a spectrum of the type shown in Fig. 5 is obtained. Clearly visible is the response at the fundamental frequency (1.004 kHz), but also higher harmonics are generated. By weighting the magnitude of these higher harmonics against that of the fundamental frequency, the THD may be calculated. In the particular measurement in Fig. 5, the result was 4.1%. It should be noted that the lowest measurable distortion is determined by the signal-to-noise ratio of the MUT or the reference microphone inside the chamber.

II. MEASUREMENTS ON PIEZOELECTRIC SILICON MICROPHONES

Since a more detailed description of the piezoelectric microphone has been given in Ref. 14, only the most important features of the microphone are presented. A schematic view of the piezoelectric microphone is shown in Fig. 6 (cut and top view). The sensor consists of an aluminized silicon nitride membrane (the metallization acts as one single bottom electrode), covered with a thin polymer layer of P(VDF/TrFE) and a top electrode split into two separate parts. In case of a deflection of the membrane an electrical voltage between the top and the bottom electrode is generated due to the transversal piezoelectric effect of the corona poled polymer. The voltages, which are generated at the inner and outer part of the top electrode, are connected in series by the bottom electrode, increasing the sensitivity of the microphone. The area of the membrane is about 1 mm^2 and the source impedance amounts to 10–20 pF, depending on the thickness of the polymer layer.

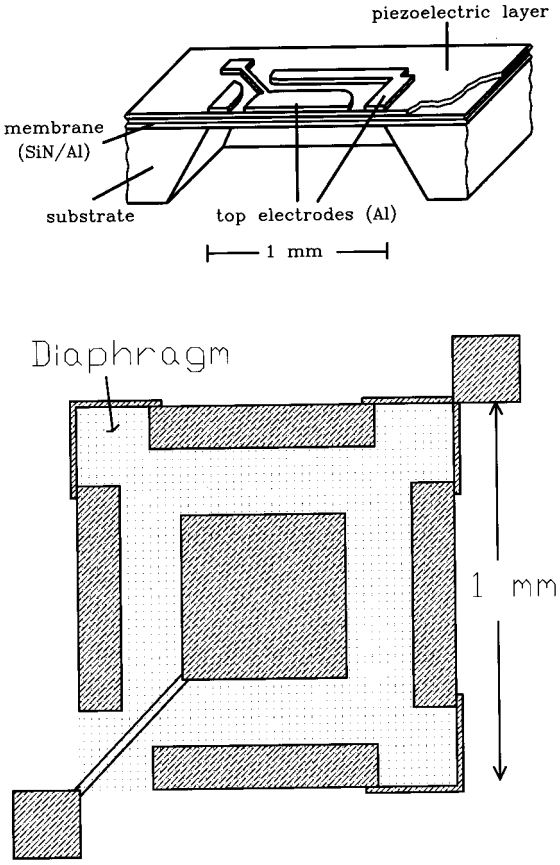

FIG. 6. Cut and top view of a silicon microphone with a piezoelectric polymer layer.

A. Frequency response and sensitivity

The electroacoustic properties have been determined as described in Sec. I of this paper. A measured open-circuit frequency response of a piezoelectric microphone (polymer thickness: 4.3 μm, membrane thickness: approximately 300 nm, polarization field about 1.5 MV/cm), is shown in Fig. 7. The measured frequency response is flat within ± 1 dB between 100 Hz and 10 kHz with a slight increase of 3 dB between 10 and 15 kHz. This increase may be due to a reso-

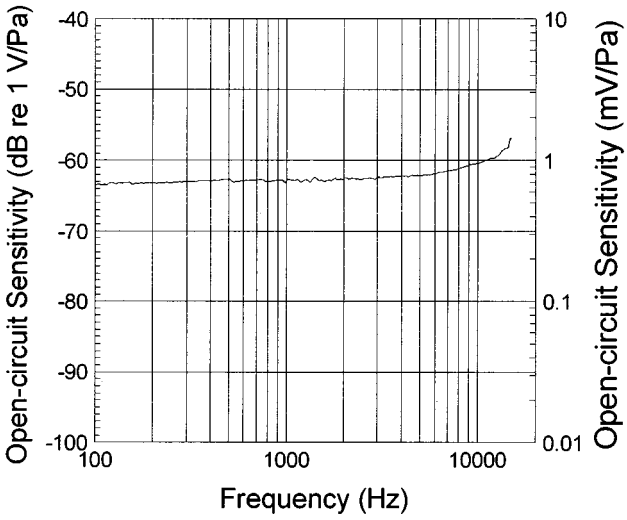

FIG. 7. Measured open-circuit frequency response of a piezoelectric microphone (membrane area: 1 mm^2).

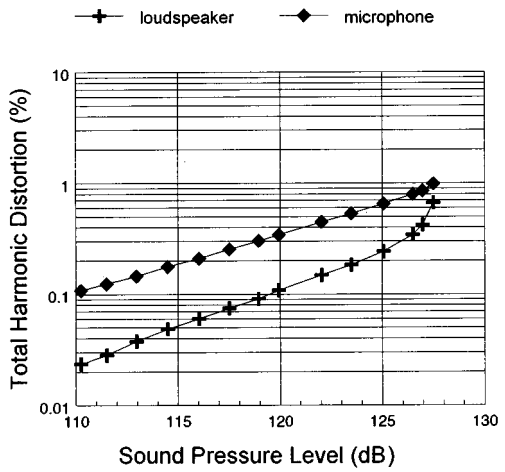

FIG. 8. Total harmonic distortion versus sound pressure level of a piezoelectric microphone and the loudspeaker.

nance of the microphone above 20 kHz. The measured sensitivity to airborne sound at 1 kHz is 0.21 mV/Pa (−73.6 dB *re*: 1 V/Pa) and the loading amounts to −11 dB. Using these two values, an open-circuit sensitivity of 0.74 mV/Pa (−62.6 dB *re*: 1 V/Pa) is achieved.

B. Equivalent noise level

The measured A-weighted noise voltage is 2.25 μV, leading (for a sensitivity of 0.21 mV/Pa) to a signal-to-noise ratio of 93.33, and to an A-weighted equivalent noise level (ENL) of 54.6 dB. Thus, a minimum detectable sound pressure (A-weighted) of about 10 mPa can be calculated. Taking the loading of −11 dB into account, a theoretical A-weighted ENL of 43.6 dB may be expected. The forementioned ENL is the maximum attainable with any preamplifier, and is sufficient for the detection of normal speech, the average value of which has an SPL between 60 and 70 dB. Nevertheless, the signal-to-noise ratio still can be improved by optimizing the electrode shapes of the microphone structure (see, e.g., Ref. 20).

C. Total harmonic distortion

The measured THD of a piezoelectric microphone as a function of the applied sound pressure is shown in Fig. 8. Furthermore, the measured THD of the loudspeaker is included. One can conclude that the distortion of the loudspeaker may be neglected. Obviously, the distortion of the piezoelectric microphone is strongly dependent on the SPL. The shown relationship, which is following a power law, is in good agreement to measurements on nonsilicon microphones (see, e.g., Ref. 21). The distortion at the highest SPL (127 dB) is still lower than 1%, which is sufficient for most of the applications mentioned in the introduction. As already remarked in Sec. I, the lowest measurable distortion (at an SPL of 110 dB) is determined by the signal-to-noise ratio of the microphone.

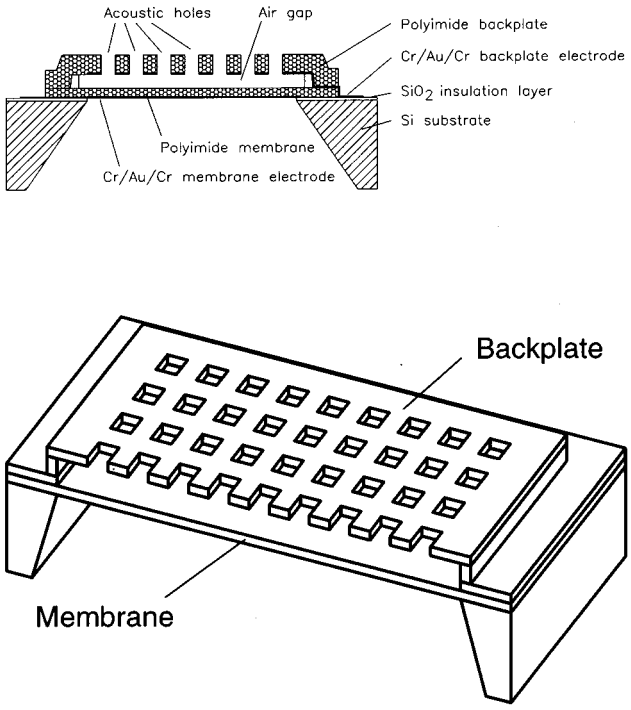

FIG. 9. A silicon condenser microphone with polyimide membrane and backplate.[7]

III. MEASUREMENTS ON SILICON CONDENSER MICROPHONES

The measurement setup has also been used for the characterization of silicon condenser microphones. The condenser microphone, shown in Fig. 9, consists of a polyimide membrane sensitive to airborne sound and a polyimide back plate, which is transparent to sound in the audio frequency range. When the membrane moves according to the sound pressure, a change of capacitance between the electrodes attached to the membrane and backplate may be detected. The microphones can be fabricated with a complementary metal-oxide-semiconductor (CMOS) compatible process, thereby making them suited for monolithic integration with a preamplifier. An elaborate description of the fabrication process has been given in Ref. 7.

Microphones with membrane sizes of 1.6×1.6 mm^2 and 2.1×2.1 mm^2 have been fabricated. The air gap, which was realized with an Al sacrificial layer technique, was 1.5 μm. The thickness of the membrane and the backplate was 0.9 and 17 μm, respectively.

A. Frequency response and noise level

The recorded frequency response of two different polyimide condenser microphones (A=1.6×1.6 mm^2, B=2.1×2.1 mm^2) is shown in Fig. 10. From the figure it may be seen that both responses are flat within ±2 dB in the frequency range between 100 Hz and 15 kHz. The sensitivities measured with the setup, were −56.6 dB *re*: 1 V/Pa for A and −51.6 dB *re*: 1 V/Pa for B with an external dc bias voltage of 15 V. Furthermore, the electrical loading of the microphone was determined according to Fig. 4, and the measured amplifications were −10.8 dB for (A) and −9.8

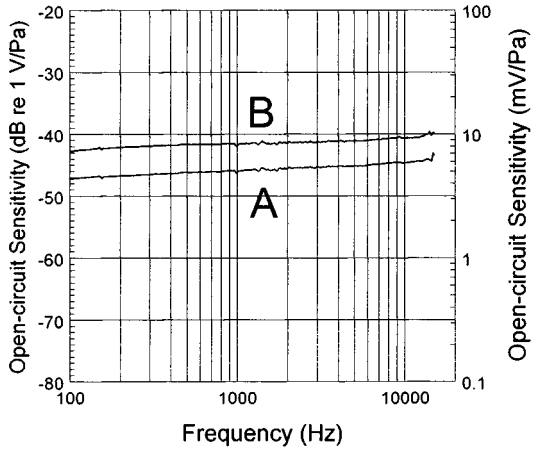

FIG. 10. Measured frequency response of two polyimide microphones (A $=1.6\times1.6$ mm^2, B$=2.1\times2.1$ mm^2).

dB for (B). The open-circuit sensitivities were therefore calculated (at 1 kHz) to be -45.8 dB *re*: 1 V/Pa (5.1 mV/Pa) for A and -41.8 dB *re*: 1 V/Pa (8.1 mV/Pa) for B. The source capacitance of the microphones were determined to be $\approx$16 pF for A and $\approx$20 pF for B, using an Hewlett–Packard 4194A impedance analyzer.

The A-weighted noise with no bias voltage was measured to be 2.5 μV for both microphones. This yields an A-weighted equivalent noise level of 38.5 dB for A and 33.1 dB for B. It should be noted that acoustical noise is not considered, since the setup is currently placed in a relatively noisy environment (A-weighted SPL $\approx$47 dB). Furthermore, since the equivalent noise levels were measured with the preamplifier in the measurement setup, it should be kept in mind that the noise level of a packaged microphone and amplifier will be lower, since the parasitic input capacitance of the preamplifier in the setup is still considerable ($\approx$40 pF).

B. Sensitivity versus dc bias voltage

Using the same setup, the microphone sensitivity was recorded as a function of the dc bias voltage. In Fig. 11, measurements on the two microphones A and B are shown.

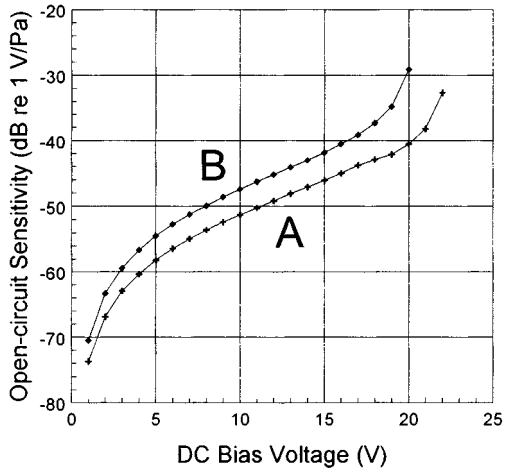

FIG. 11. Measured open-circuit sensitivity versus dc bias voltage for microphones A and B.

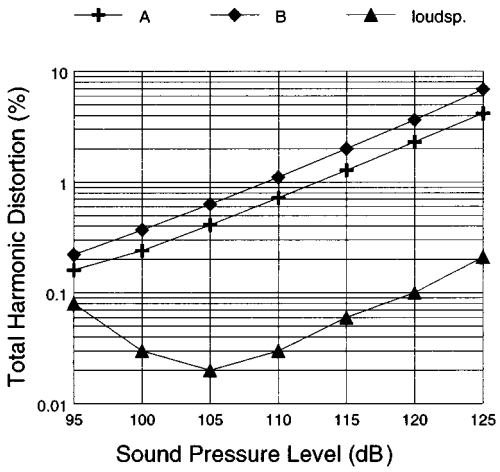

FIG. 12. Total harmonic distortion versus sound pressure level of two polyimide condenser microphones (dc bias voltage$=$15 V).

As it can be seen from the figure, both microphones show a relation between bias voltage and sensitivity, which is characteristic for condenser microphones. For small bias voltages, the sensitivities show a linear relation, since the electrostatic forces are very small compared with the sound pressure. Therefore, only the linear increase of the electrical field between the two electrodes have an effect. In the midrange of the bias voltage, the electrostatic forces begin to play a more significant role, thereby causing an exponential relation to the sensitivity. For bias voltages close to the collapse of the microphone, the electrostatic forces are dominating and the sensitivity shows a stronger than exponential dependence on the bias voltage. The collapse voltages were determined to be $\approx$22 V for A and $\approx$21 V for B. It should be mentioned that these microphones present no problems regarding sticking. This means that they can recover from a collapse, simply by removing the bias voltage. Furthermore, since the electrodes remain insulated during a collapse, problems with large voltages on the input of the preamplifier are avoided.

C. Total harmonic distortion

The distortion of the two microphones was determined with the method according to Fig. 5. In Fig. 12, the recorded distortion is shown as a function of the applied sound pressure. Also shown in the figure is the distortion from the reference microphone. Since the distortion of the reference microphone itself at these relatively low sound pressures is neglectable, the measured distortion is therefore produced by the loudspeaker. The dip in the measured distortion of the loudspeaker is caused by the relatively bad signal-to-noise ratio of the reference microphone at low sound pressures. As it may be seen, the distortion of the two polyimide microphones has the well-known double-logarithmic dependence on the sound pressure.[21] The total harmonic distortion at an SPL of 120 dB and with a bias voltage of 15 V was 2.3% and 3.6% for A and B, respectively. The bias voltage also influences the distortion, because the electrostatic forces them-

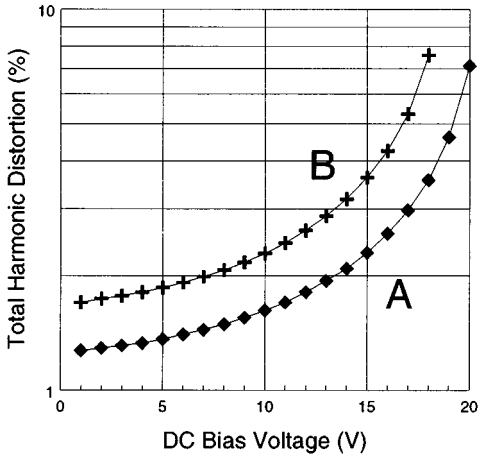

FIG. 13. Total harmonic distortion versus bias voltage for two polyimide condenser microphones.

selves are nonlinear, and since the static deflection induced by the forces decrease the air gap, thereby further contributing to the nonlinearity of the microphone. The relation between the total harmonic distortion and the bias voltage is shown in Fig. 13. As can be seen from both these figures, the qualitative expectation that the distortion increases for increasing membrane area is confirmed. A more detailed analysis of distortion measurements on silicon condenser microphones is given elsewhere.[22]

IV. CONCLUSIONS AND REMARKS

A new method has been presented, providing the possibility of an on-wafer characterization of the electroacoustic properties of silicon microphones. This method is quick and flexible and highly accurate in a measurement range between 100 Hz and 15 kHz.

Using a microscope, which is also part of the setup, the placement of the wafers and thus the adjustment of the chips across the pressure outlet is uncritical. A good reproducibility of the measurements has been achieved, whereby small and unavoidable misalignments of the membrane with respect to the opening lead to uncertainties of the measured sensitivities of less than 0.5 dB. Furthermore, since the chips are slightly pressed against the wafer holder, just by using the measurement needles, the leakage between the holder and the chip could be minimized. In addition, no fixation of the wafer by using a special vacuum chuck is necessary and the externally induced stresses are kept low.

Measurements of the total harmonic distortion have been carried out from 95 to 126 dB SPL. These values are mainly determined by the quality and thus by the electroacoustic properties of the loudspeaker. For frequencies outside the range mentioned above, the SPL, which can be generated by the loudspeaker, is either too small or the signal is highly distorted. Furthermore, the lowest SPL where the total harmonic distortion can be determined is influenced by the signal-to-noise ratio of the microphones, the higher the signal-to-noise ratio, the lower the SPL can be used to measure the total harmonic distortion.

To increase the measurable frequency range down to 20 Hz and up to 50 kHz another loudspeaker should be used, since it is restricting the measurable frequency and SPL ranges. Furthermore, by placing the whole setup inside a special acoustical chamber, better shielding against acoustical and vibrational noise pickup from the outside can be achieved, thereby allowing measurements at lower acoustic noise levels. However, it should be noted that the equivalent noise levels measured with the built-in preamplifier of the setup only provide information about the microphone performance in this particular configuration with this particular amplifier, and that the noise level of a packaged device is likely to be lower due to reduction of the parasitic load.

The setup may be used for the determination of the electroacoustic properties of other silicon microphones, e.g., piezoresistive sensors, as well by using another preamplifier.

ACKNOWLEDGMENTS

The authors are indebted to the Dutch Technical Foundation STW for supporting the project on capacitive microphones and to the European Union, which is funding the project on piezoelectric acoustical sensors for airborne sound within the ''Human Capital and Mobility'' program.

[1] D. Hohm and G. Hess, ''A subminiature condenser microphone with silicon nitride membrane and silicon back plate,'' J. Acoust. Soc. Am. **85**, 476–480 (1989).
[2] A. J. Sprenkels, ''A Silicon Subminiature Electret Microphone,'' Ph.D. thesis, University of Twente, Enschede, The Netherlands, 1988.
[3] W. Kuehnel and G. Hess, ''A silicon condenser microphone with structured back plate and silicon nitride membrane,'' Sens. Actuators A **30**, 251–258 (1992).
[4] J. Bergqvist and F. Rudolf, ''A silicon condenser microphone using bond and etch-back technology,'' Sens. Actuators A **45**, 115 (1994).
[5] P. R. Scheeper, A. G. H. van der Donk, W. Olthuis, and P. Bergveld, ''Fabrication of Silicon Condenser Microphones using Single Wafer Technology,'' IEEE J. Microelectromechanical Syst. **1**, 147 (1992).
[6] J. J. Bernstein, ''A silicon micromachined condenser microphone/hydrophone,'' J. Acoust. Soc. Am. **92**, 2355(A) (1992).
[7] M. Pedersen, P. Bergveld, and W. Olthuis, ''A silicon condenser microphone with polyimide diaphragm and backplate'' (unpublished).
[8] Y. B. Ning, A. W. Mitchell, and R. N. Tait, ''Fabrication of a silicon micromachined capacitive microphone using a dry-etch process,'' Sens. Actuators A **53**, 237 (1996).
[9] W. Kuehnel, ''Silicon Condenser Microphone with Integrated Field Effect Transistor,'' 13th International Congress on Acoustics, Yugoslavia **3**, 487 (1989).
[10] E. Graf, W. Kronast, S. Duehring, B. Mueller, and A. Stoffel, ''Silicon membrane condenser microphone with integrated field-effect transistor,'' Sens. Actuators A **37-38**, 708–711 (1993).
[11] M. Royer, J. O. Holmen, M. A. Wurm, and O. S. Aadland, ''ZnO on Si Integrated Acoustic Sensor,'' Sens. Actuators A **4**, 357–362 (1983).
[12] J. Franz, ''Piezoelektrische Sensoren auf Siliziumbasis fuer akustische Anwendungen,'' VDI—Verlag; Reihe 10: Informatik/Kommunikationstechnik, Nr. 87; Fortschrittberichte; VDI; dissertation, 1988.
[13] R. P. Ried, E. S. Kim, D. M. Hong, and R. S. Muller, ''Piezoelectric Microphone with On-Chip CMOS Circuits,'' IEEE J. Microelectromechanical Syst. **2**, 111–120 (1993).
[14] R. Schellin, G. Hess, R. Kressmann, and P. Wassmuth, ''Corona poled piezoelectric polymer layers of P(VDF/TrFE) for micromachined silicon microphones,'' Workshop Digest, MME '94, Pisa, Italy, 48 (1994).
[15] R. Schellin and G. Hess, ''A Silicon Subminiature Microphone Based on

Piezoresistive Polysilicon Strain Gauges,'' Sens. Actuators A **32**, 555 (1992).
[16] R. Schellin, M. Strecker, U. Nothelfer, and G. Schuster, ''Piezoresistive Subminiature Microphones with Electrochemically Etched Silicon Diaphragms'' (unpublished).
[17] W. Lukosz and P. Pliska, ''Integrated optical nanomechanical light modulators and microphones,'' Sens. Mater. **3**(5), 261 (1992).
[18] U. Schneider and R. Schellin, ''A phase-modulating microphone utilizing integrated optics and micromachining in silicon,'' Sens. Actuators A **41-42**, 695 (1994).
[19] L. L. Beranek, *Acoustics* (Acoustical Society of America, Woodbury, NY, 1993).
[20] R. Schellin, P. Bergveld, W. Olthuis, R. Kressmann, and B. Wagner, ''Optimization of the electrode shapes of micromachined piezoelectric microphones to minimise the influence of in-plane stress on the S/N-ratio,'' in *Simulation and Design of Microsystems and Microstructures*, edited by R. A. Adey, A. Lahrmann, and C. Lessmoellmann (Computational Mechanics, Southampton, UK, 1995), p. 235.
[21] Data Handbook, ''Condenser microphones and microphone preamplifiers for acoustic measurements,'' Revision Sept. 1982, Brüel & Kjær.
[22] M. Pedersen, W. Olthuis, and P. Bergveld, ''Harmonic distortion in silicon condenser microphones'' (unpublished).

A theoretical basis for the high-frequency performance of the outer hair cell's receptor potential

El-S. Hassan
Arbeitsgruppe III (Biophysik), Institut für Zoologie, Johannes-Gutenberg-Universität, Saarstrasse 21, 55099 Mainz, Germany

(Received 28 March 1996; revised 16 October 1996; accepted 24 October 1996)

The frequency response of the outer hair cell (OHC) was studied theoretically. An electrical model of the OHC was analyzed mathematically, taking into account the effect of its inherent voltage-dependent capacitance. It was found that the variations of the capacitance dependent on the membrane potential could enhance the high-frequency response of the OHC, so that its cutoff frequency could be extended into the audio range. It was found further that the enhancement of the frequency response of the OHC was strongly dependent on its resting potential and on the ratio of the maximum voltage-dependent capacitance to the membrane linear capacitance. © *1997 Acoustical Society of America.* [S0001-4966(97)02803-8]

PACS numbers: 43.64.Bt, 43.64.Ld, 43.64.Nf [RDF]

INTRODUCTION

The outer hair cell (OHC) is considered to play an essential role in the enhancement of the sensitivity and frequency selectivity of the mammalian cochlea (Brownell *et al.*, 1985; Zenner *et al.*, 1988; Patuzzi *et al.*, 1989; Patuzzi and Rajan, 1990; see also for review Dallos, 1988; Ashmore, 1994). Due to its voltage-dependent mechanical activity (Brownell *et al.*, 1985; Hallworth *et al.*, 1993; Evans and Dallos, 1993), the OHC is thought to feed mechanical energy back to the basilar membrane (BM) thus amplifying its vibrational movements (Mountain, 1980; Siegel and Kim, 1982; Mammano and Ashmore, 1993). The term cochlear amplifier (CA) has become established for this mechanism (Davis, 1983). The CA has been shown to operate at high speed, up to 30 kHz in the cat and the guinea pig (Cooper and Rhode, 1992). It was also shown that the OHC in the guinea pig can vibrate at such a high frequency (Gitter and Zenner, 1995). The high speed motility of the OHC is thought to be essential for the operation of the CA, as it is believed that the OHC must act thereby on the BM on a cycle-by-cycle basis (Dallos and Evans, 1995).

The electromotility of the OHC has been shown to be associated with the magnitude of the transmembrane potential (Santos-Sacchi and Dilger, 1988; Dallos *et al.*, 1991). At high frequencies, however, the transmembrane potential would be attenuated due to the filtering effect of the membrane capacitance and resistance, which would limit the high frequency response of the OHC. Measurements of the membrane time constant of the OHC in the guinea pig have shown a variation in its value from 3 to 0.2 ms from the apex to the base of the cochlea (Housley and Ashmore, 1992), which correspond to a cutoff frequency of about 50 to 800 Hz, respectively. This fact led to the question of how the CA can operate at frequencies of the audio range, which can be as high as 100 kHz in bat (Reuter *et al.*, 1994), despite the large time constant of the OHC's membrane (Dallos and Evans, 1995; Kolston, 1995).

Recently, the nonlinear charge movement of the OHC, which is equivalent to a voltage-dependent capacitance, was investigated (Ashmore, 1989, 1992; Santos-Sacchi, 1991, 1993; Dallos *et al.*, 1991; Iwasa, 1993; Gale and Ashmore, 1994; Huang and Santos-Sacchi, 1993, 1994; Kakehata and Santos-Sacchi, 1995). It was found that the voltage-dependent capacitance increases with depolarization when the OHC contracts, and decreases with hyperpolarization when the OHC elongates. The increase of the capacitance with the depolarization, however, attains a certain maximum value ($C_{\max}$) at a certain membrane potential and thereafter decreases with further depolarization. It was also supposed that the nonlinear capacitance would dynamically influence the time constant of the OHC (Santos-Sacchi, 1991).

In this paper the effect of the nonlinear capacitance on the frequency response of the OHC was studied. An electrical model of the OHC incorporating a voltage-dependent capacitance as a component was analyzed mathematically. The calculations showed that for a certain ratio of the nonlinear to the linear capacitance, and at a certain resting potential value, the high-frequency response of the OHC could become unlimited.

I. MODEL FORMULATION

The OHCs are embedded in the organ of Corti with their apex facing the endolymph of the scala media and their basolateral membrane facing the perilymph within the organ of Corti. This partition of the OHC was taken into account in the electrical model given in Fig. 1. The apical part of the OHC in the model has a constant conductance g_c, a linear capacitance C_c, and a parallel shunting conductance g_s representing the mechanically activated transducer conductance. The constant conductance g_c together with the basolateral membrane conductance g_m give rise to a standing current maintained by the positive polarized potential of the endolymph (V_e) and by the negative potassium potential (V_k). The standing current is modified when the conductance g_s is modulated according to the mechanical stimulus acting on the OHC. The endolymph potential arises due to the activity of the stria vascularis, which has been shown to function as a constant current source (Zidanic and Brownell, 1990). This

 0001-4966/97/101(4)/2129/6/$10.00

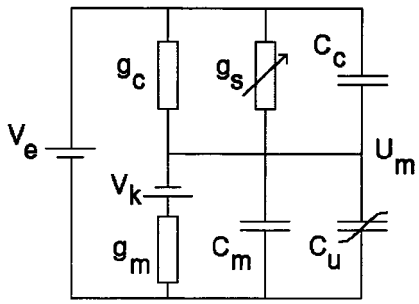

FIG. 1. OHC model used to determine the membrane potential. The model consists of an apical conductance of the OHC at rest g_c, an apical capacitance C_c, and a parallel shunting conductance g_s, whose value is proportional to the stimulus. The basolateral part of the OHC is modeled as a conductance g_m and a capacitance composed of a linear part C_m and a voltage-dependent part C_u, whose value is dependent on the membrane potential U_m. The voltage sources V_e and V_k represent the endocochlear potential and the potassium potential, respectively.

strial current is divided between the receptor cell pathway and a leakage pathway. For an individual OHC, the strial constant current source is shunted with the conductance of the leakage pathway as well as with the conductance of the rest of the receptor cell pathway, and the sum of these two conductances is much higher than that of an individual OHC. On the other hand, a constant voltage source with a small series resistance may substitute a constant current source shunted with a high conductance. Thus in the model a constant voltage source with a strength equal to the endolymph potential (the small series resistance omitted for simplification) substitutes the action of the stria vascularis. The basolateral membrane capacitance in the model has a linear part C_m, for the linear capacitance of the membrane, and a voltage-dependent part C_u, equivalent to the nonlinear gating charge movement of the OHC, whose value is dependent on the membrane potential U_m (see Santos-Sacchi, 1993).

A. Mathematical description

Assuming that g_s varies sinusoidally with the radian frequency ω, $g_s=|g_s|\cos(\omega t)$, and equating the currents through the apical and basolateral parts of the OHC yields

$$(V_e-U_m)(g_c+|g_s|\cos(\omega t))-C_c\frac{dU_m}{dt}$$
$$=(U_m-V_k)g_m+C_m\frac{dU_m}{dt}+\frac{d(C_uU_m)}{dt}. \quad (1)$$

Consider in the last term of the equation the coefficient C_u representing the voltage-dependent capacitance. The expression for the dependence of C_u on the membrane potential as given by Santos-Sacchi (1993) is rewritten here in another equivalent form:

$$C_u=\frac{2C_{\max}}{[1+\cosh(\alpha(U_m-V_p))]}, \quad (2)$$

where $C_{\max}=((\alpha/4)q_{\max})$, $\alpha=(ze/kT)$, $q_{\max}$ is the maximum nonlinear charge moved, V_p is voltage at peak capacitance, z is valence, e is the elementary charge, k is Boltzmann's constant, and T is the absolute temperature. For small variations of the membrane potential around its resting value U_r, the expression of C_u can be approximated with the first two terms of its Taylor expansion to

$$C_u\approx 2C_{\max}\left[\frac{1}{D}-\frac{1}{D^2}\sinh(\alpha(U_r-V_p))\alpha(U_m-U_r)\right]$$
$$=\left[2C_{\max}\left(\frac{1}{D}+\frac{1}{D^2}\sinh(\alpha(U_r-V_p))\alpha U_r\right)\right]$$
$$-\left[2C_{\max}\frac{1}{D^2}\sinh(\alpha(U_r-V_p))\right]\alpha U_m$$
$$=C_o-C_s\alpha U_m, \quad (3)$$

where $D=1+\cosh(\alpha(U_r-V_p))$.

Multiplying both sides of Eq. (1) with α, and substituting for C_u the approximated expression yields after some simplifications

$$V_e^*g_c(1+\beta\cos(\omega t))+V_k^*g_m$$
$$=U_m^*[g_m+g_c(1+\beta\cos(\omega t))]$$
$$+sC_h(1-\varepsilon U_m^*)\frac{dU_m^*}{dt}, \quad (4)$$

where $\beta=|g_s|/g_c$, $C_h=C_c+C_m$, $s=1+C_o/C_h$, and $\varepsilon=2C_s/(C_h+C_o)$.

The symbol (*) marking the voltage and potential variables in this equation means that these variables are multiplied with the constant α. This convention will be followed in the rest of the paper. As the dimension of α is V^{-1} the new variables are then dimensionless and the solution of the equations will be independent of a specific value of α.

B. Solutions

Consider the factor β in Eq. (4), which represents the ratio of the conductance proportional to the stimulus to the constant apical conductance of the OHC. For low stimulus magnitudes, where the feedback effect of the OHC motility is presumed to be important, the value of β will be of the order of 0.1 (Santos-Sacchi, 1993). This allows us to solve Eq. (4) using the perturbation theory with β as the perturbation quantity. In this way, the membrane potential U_m^* can be represented as an infinite asymptotic power series:

$$U_m^*=\sum_{n=0}^{\infty}\beta^nU_n^*. \quad (5)$$

Substituting this expression for U_m^* in Eq. (4) and equating terms with like powers of β yields

$$U_0^*+s\tau_h(1-\varepsilon U_0^*)\frac{dU_0^*}{dt}=\frac{V_e^*g_c+V_k^*g_m}{g_m+g_c},$$

$$U_1^*+s\tau_h\left[(1-\varepsilon U_0^*)\frac{dU_1^*}{dt}-\varepsilon U_1^*\frac{dU_0^*}{dt}\right]$$
$$=\frac{(V_e^*-U_0^*)g_c}{g_m+g_c}\cos(\omega t),$$

and for $n>1$,

$$U_n^* + s\tau_h\left[\frac{dU_n^*}{dt} - \varepsilon\sum_{j=0}^{n}\left(U_{(n-j)}^*\frac{dU_j^*}{dt}\right)\right]$$

$$+\frac{g_c}{g_c+g_m}U_{(n-1)}^*\cos(\omega t) = 0, \tag{6}$$

with $\tau_h = C_h/(g_m+g_c)$.

As can be seen from this system of equations, the terms of the U_m^* series can be determined recursively. Here, the first two terms, U_0^* and U_1^*, will be determined. We seek the steady-response-solution of the equations. The solution of the first equation for $n=0$ is then simply the resting potential of the OHC U_r^*:

$$U_0^* = U_r^* = \frac{V_e^* g_c + V_k^* g_m}{g_c+g_m}. \tag{7}$$

As U_0^* is constant, the terms including the derivative of $U_0{}^*$ with respect to time in the subsequent equations, for $n>0$, will disappear. Consequently, the steady-response-solution of the second equation for $n=1$ is

$$U_1^* = \frac{g_c}{g_m+g_c}(V_e^* - U_r^*)\frac{\cos(\omega t) + sp\tau_h\omega\ \sin(\omega t)}{1+s^2p^2\tau_h^2\omega^2}, \tag{8}$$

with $p = 1-\varepsilon U_r^*$.

The term U_1^* then represents an alternating component with the frequency ω, the same as that of the stimulus. Even, higher-order terms will involve components with even, multiple frequencies as well as dc components. So, U_0^* represents the dc component of the membrane potential with a remainder of order β^2. Likewise, odd, higher-order terms will involve components with the same frequency as the stimulus as well as components with odd, multiple frequencies. So, the second term of the U_m^* series, βU_1^*, represents the ac component of the membrane potential with the same frequency as the stimulus with a remainder of order β^3.

II. ANALYZING THE MODEL

The expression of U_1^* as given in Eq. (8) possesses low-pass characteristic with the cutoff frequency

$$\omega_c = \frac{1}{sp\tau_h} = \frac{1}{sp}\omega_h, \tag{9}$$

with $\omega_h = 1/\tau_h$.

In this equation ω_c and ω_h are the cutoff frequencies of the OHC with and without nonlinear capacitance, respectively. The ratio of ω_c to ω_h, which will be called the cutoff-frequency extension factor (K), is then

$$K = \frac{\omega_c}{\omega_h} = \frac{1}{sp}. \tag{10}$$

Consider now the factor P in this equation. This factor, which is given in Eq. (8), becomes diminished when the quantity εU_r^* approaches 1. When the factor P diminishes, however, the cutoff frequency extension factor K becomes higher and will be infinite when P is exactly equal to zero. In this special case the cutoff frequency is extended to infinity. To explore this case for infinite cutoff frequency, the relation between the nonlinear and the linear capacitance for $P=0$ was determined. Substituting the expressions for C_o and C_s from Eq. (3) in the expression of the factor ε as defined in Eq. (4) and using the result in the equation $P=0$ yields an expression for the capacitance ratio (μ) of $C_{\max}$ to C_h, which depends on the resting potential U_r^* and the voltage at peak capacitance V_p^* as follows:

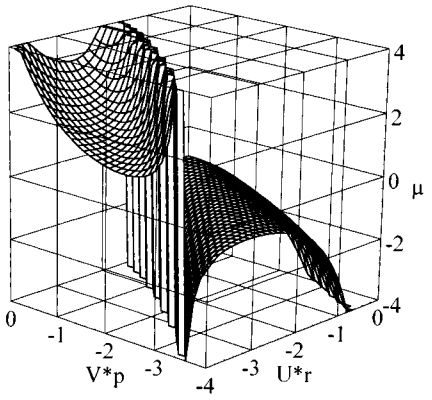

FIG. 2. A three-dimensional plot representing the capacitance ratio μ for $P=0$ in dependance on the resting potential U_r^* and the voltage at peak capacitance V_p^*.

$$\mu = \frac{C_{\max}}{C_h}$$

$$= -\left(\frac{1}{2}\right)\frac{[1+\cosh(V_p^*-U_r^*)]^2}{1+\cosh(V_p^*-U_r^*)+U_r^*\ \sinh(V_p^*-U_r^*)}. \tag{11}$$

A three-dimensional plot of this relation, representing the capacitance ratio μ for $P=0$ in dependence on U_r^* and V_p^*, is depicted in Fig. 2. The highest absolute value represented for μ is limited to 4 in this plot. As can be seen from this plot, there are two different regions; in one of which the capacitance ratio μ is negative and positive in the other. Consider the region in which μ is positive, which corresponds to the actual case. This region extends diagonally with a base at V_p^* equal to zero and between U_r^* equal to -2 and -4, and terminates at the point -3.5 and -4 for V_p^* and U_r^*, respectively. The actual values of the resting potential of the OHC, U_r, and the voltage at peak capacitance, V_p, of about -70 and -30 mV, respectively, were found to lie within the described positive region when their values are multiplied by a value for α equal to that given in the literature of about 0.038 mV^{-1} (Santos-Sacchi, 1993). For the rest of the paper, this specific value of α will be kept and all considerations will deal with voltages and potentials rather than with the dimensionless variables marked with (*).

Figure 3(a) and (b) show two cross sections in the three-dimensional plot of μ through the point $U_o^* = -2.66$ and $V_p^* = -1.14$, which correspond to $U_r = -70$ mV and $V_p = -30$ mV. The cross section in (a) represents μ in dependence on the resting potential when the voltage at peak capacitance is held constant at -30 mV, and the cross section in (b) represents μ in dependence on the voltage at peak capacitance when the resting potential is held constant at -70 mV. The highest absolute value represented for μ in these plots is limited to 10. As can be seen from the plot in

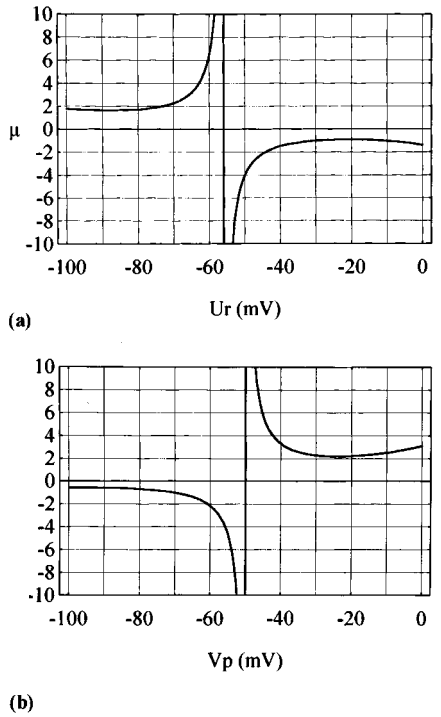

FIG. 3. A plot of the capacitance ratio, μ, for $P=0$, (a) in dependence on the resting potential U_r with the voltage at peak capacitance $V_p=-30$ mV and (b) in dependence on the voltage at peak capacitance V_p with $U_r=-70$ mV.

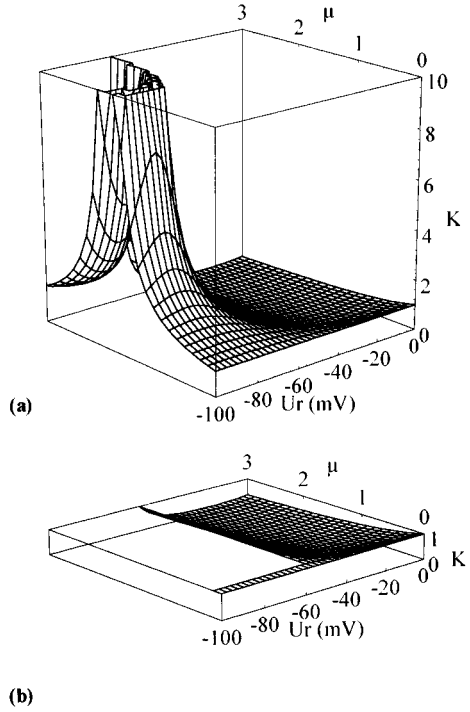

FIG. 4. (a) Three-dimensional plots of the absolute value of the cutoff frequency extension factor K, the ratio of the cutoff frequency of the OHC with and without nonlinear capacitance, in dependence on the capacitance ratio (μ) and the resting potential U_r. The highest value represented for K in this plot is limited to 10. (b) The region in which K values are equal to or less than 1.

(a), the capacitance ratio μ for $P=0$ has a singularity at a resting potential value of about -56 mV, and is negative at the right side and positive at the left side of this singularity. On the left side, the capacitance ratio decreases rapidly at first to values of 6.44 and 2.28 at -60 and -70 mV, respectively, and then slowly at more negative resting potential to a value of about 1.65 at -90 mV. So, it seems to be of interest to study the effect of the voltage-dependent capacitance for capacitance ratio values around 2. From the plot in (b) it can be seen that the capacitance ratio is positive for V_p values less negative than -50 mV and remains nearly constant between -20 mV and -30 mV, attaining about the same value of 2.2 as determined above for the resting potential at -70 mV. For more negative values of V_p the capacitance ratio increases rapidly and then becomes negative for values higher than -50 mV. A value of -30 mV will be taken for V_p for the rest of the paper.

A. OHC cutoff-frequency

Figure 4(a) shows a three-dimensional plot of the absolute value of the frequency extension factor K in dependence on the capacitance ratio (μ) (between 0 and 3) and on the resting potential U_r (between 0 and -100 mV). The highest value represented for K in this plot is limited to 10. Figure 4(b) gives the region in which K-values are equal to or less than 1 separately. As can be seen from the plot in (b), the factor K is smaller than 1 in a certain region of resting potential values, which were found to be less negative than -56 mV. So, in this region of the resting potential between 0 and -56 mV, there is no enhancement, but, on the contrary, a deterioration of the frequency response of the OHC. However, as can be seen in Fig. 4(a), the factor K is larger than 1 for potentials more negative than -56 mV, and it increases in a certain way to become infinite at certain values of the capacitance ratio μ and the resting potential U_r, which correspond to the values given in the plot in Fig. 3(a), when the factor p is equal to zero. Figure 5 shows some cross sections in the three-dimensional plot of the cutoff frequency extension factor K at certain values of μ (1, 1.5, 1.75, 2, and 2.25) in dependance on U_r (between -55 and -90 mV). Here, the highest value for K is limited to 50. As can be seen in this figure, the factor K has a value of about 1 at -55 mV for all values of μ. For $\mu=1$, K increases slowly

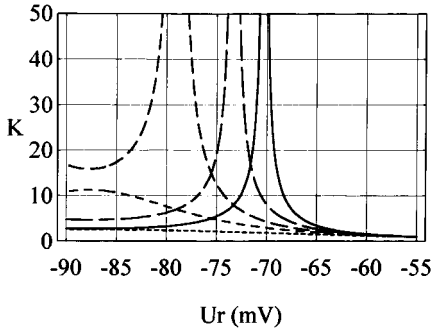

FIG. 5. Some cross sections in the three-dimensional plot of the cutoff frequency extension factor K at certain values of μ in dependence on U_r (between -55 and -90 mV). Beginning from the fine dashed curve to the solid line the values of μ are as follows: 1, 1.5, 1.75, 2, and 2.25. The highest value represented for K is limited to 50.

when the resting potential becomes more negative and it attains a value of about 3 at -90 mV. A similar increase in K, but more rapid, is to be seen for $\mu=1.5$, where in this case the factor K attains a value of about 10 at -85 mV. For $\mu=1.75$, however, the increase in K becomes steeper and a value of 50 is already attained at about -78 mV. The calculated value of the resting potential, at which K becomes infinite for this value of μ, is -79 mV. At more negative resting potential, K decreases again to attain a value in the order of 15 at -90 mV. Curves for K similar to the former one are to be seen for $\mu=2.0$ and 2.25. However, as μ values becomes higher, the curves shift more to the right at less negative resting potentials and they become narrower. An infinite K-value is attained for these values of μ at U_r equal to -73 and -70.25 mV, respectively. The interval in which K attains values higher than 10, which will be called the enhancement interval, amounts to about 6 mV for μ equal to 2.0 and it decreases to about 4 mV for μ equal to 2.25.

III. DISCUSSION

These results indicate that the nonlinear voltage-dependent capacitance can theoretically enhance the performance of the OHC to sustain membrane potential at high frequencies. The enhancement effect occurs for resting potential values more negative than -56 mV. It depends strongly on the value of the resting potential and on the ratio of the nonlinear to the linear capacitance of the OHC. For a given value of this capacitance ratio there is a certain value of the resting potential, at which the cutoff frequency of the OHC response is extended to infinity. This occurs at a resting potential of -90 mV when the capacitance ratio amounts to about 1.65 and at -70 mV when the capacitance ratio is increased to about 2.28. With higher capacitance ratio values, however, the enhancement interval becomes narrower and amounts to about 4 mV for a capacitance ratio of 2.28.

It is of interest to note here that the enhancement effect of the nonlinear capacitance is restricted to a region of resting potential more negative than -56 mV. The actual resting potential of the OHC was found to be in this region, with values equal to or more negative than -70 mV (Dallos *et al.*, 1982; Russell and Sellick, 1983; Cody and Russell, 1987). The OHC differs in this respect from the inner hair cell (IHC), whose resting potential amounts to about -40 mV. So, the high negative resting potential of the OHC correlates well with the conditions under which the enhancement effect of the nonlinear capacitance could be well developed. The enhancement effect, however, was shown above to be dependent on the ratio of the nonlinear to the linear capacitance. Actual values of the capacitance ratio have been found to be in the order of 1 for OHCs from the apical turns of the organ of Corti in the guinea pig (Santos-Sacchi, 1991). This value corresponds to the theoretically determined value at which the enhancement effect is relatively small. However, as the best frequencies of the OHCs at the apical turns are relatively low, it might be expected that the enhancement of the OHC's frequency response in this region would also be small. At the basal turns, however, where the OHCs possess higher frequencies, the ratio of the nonlinear to the linear capacitance has recently been shown to increase as OHC length decreases (Santos-Sacchi and Kakehata, 1996), reaching values above 2 (Santos-Sacchi, personal communication). This is in the range of the theoretical values where the enhancement effect becomes large at a resting potential of -70 mV (see Fig. 5). It must be noted here that the necessary capacitance ratio for a certain defined extension of the cutoff frequency, when the resting potential of the OHC is held constant at a certain value, is smaller than that necessary for an infinite extension. This can be seen in Fig. 4, where an extension factor of 4 or 8 is attained for a resting potential of -70 mV when the capacitance ratio amounts to 1.75 or 2.0, respectively. On the other hand, it was reported that the lateral wall of OHCs possesses a mechano-sensitivity which appears to complement that of the stereocilia (Iwasa *et al.*, 1991). Stretching of the membrane was shown to activate potassium channels and to generate a hyperpolarization in the order of 10 mV. This sensitivity was suggested to be responsible for the production of a hyperpolarizing response to sound stimuli observed in the OHC. A hyperpolarizing response, however, would shift the resting potential of the OHC, as the theoretical findings have shown, to the region in which lower capacitance ratios are necessary to extend the frequency response of the OHC. For example, as can be seen in Fig. 4, when the resting potential of the OHC is at -70 mV and the cell possesses a capacitance ratio of 2.0, a hyperpolarizing response of the OHC to sound stimuli of about 3 mV will extend its cutoff frequency from a value of 8 to infinity. OHCs with higher hyperpolarizing responses or with more negative resting potentials would attain the same effect with lower capacitance ratios. So, it can be concluded that a value less than 2 would be a value for the capacitance ratio of the OHC suitable to extend its frequency response in the audio-range. In this context, it must be noted here that the value of the capacitance ratio and that of the voltage at peak capacitance were shown to be dependent on the OHC turgor pressure (Kakehata and Santos-Sacchi, 1995). Reducing the turgor pressure increases the value of the capacitance ratio and shifts the voltage at peak capacitance to more negative values. It is to be expected then that modulation of turgor pressure would have an effect on the frequency response of the OHC, and, as has been stated in the above cited article, ''may provide a unique mechanism for gain control of the cochlear amplifier.''

The obtained theoretical findings permit some predictions that correlate well with the operating features of the OHC. For example, it was shown that the enhancement effect of the nonlinear capacitance is well developed at more negative resting potential. In other words, functioning of the CA would be dependent on the OHC resting potential. Acoustic overstimulation experiments in the guinea pig have indicated such a dependency, as the recovery of the sensitivity of the IHCs was correlated with the repolarization of the OHCs (Cody and Russell, 1985). Also it has been shown that K^+ intoxication of the basolateral OHC's surface, which inhibits the repolarizing K^+ efflux and induces depolarization of the cell, resulted in loss of the OHC motility (Zenner *et al.*, 1994). Another feature of the OHC, which might be well correlated with the theoretical finding, is that its receptor potential has a relatively small dc component, which can

also be negative as described above, when compared with the receptor potential of the IHC (Dallos *et al.*, 1982; Russell and Sellick, 1983; Cody and Russell, 1987). As the dc component shifts the dc membrane potential, a large dc component may shift the operating point of the OHC outside the enhancement interval, which has been shown to be narrow, amounting to few mV. This would be avoided when a small dc component is generated, which is the actual case in the OHCs. On the other hand, the CA is thought to be effective for low stimulus magnitudes, where the dc component is small. It can be speculated then that with high stimulus magnitudes, the dc component would become larger, and the operating point of the OHC would be shifted out of the enhancement interval so that the CA would not function properly at high stimulus magnitudes.

IV. CONCLUSION

The theoretical findings allow the hypothesis that the nonlinear voltage-dependent capacitance can enhance the high-frequency performance of the OHC, and that the enhancement is dependent on the resting potential of the OHC and on the ratio of its nonlinear to its linear capacitance.

ACKNOWLEDGMENTS

I would like to thank Prof. C. v. Campenhausen and Dr. K. Behrend for critically reading the manuscript. I am also very grateful for the valuable recommendations of the reviewers. Further, I wish to thank Neil Beckhaus for improving the English as well as Ms. Grosz for the technical assistance.

Ashmore, J. F. (**1989**). ''Transducer motor coupling in cochlear outer hair cells,'' in *Mechanics of Hearing*, edited by D. Kemp and J. P. Wilson (Plenum, New York), pp. 107–113.

Ashmore, J. F. (**1992**). ''Mammalian hearing and the cellular mechanisms of the cochlear amplifier,'' in *Sensory Transduction*, edited by D. P. Corey and S. D. Roper (Rockefeller U.P., New York), pp. 395–412.

Ashmore, J. F. (**1994**). ''The G. L. Brown prize lecture. The cellular machinary of the cochlea,'' Exp. Physiol. **79**, 113–134.

Brownell, W. E., Bader, C. R., Bertrand, D., and De Ribaupierre, Y. (**1995**). ''Evoked mechanical responses of isolated chochlear hair cells,'' Science **227,** 194–196.

Cody, A. R., and Russell, I. J. (**1985**). ''Outer hair cells in the mammalian cochlea and noise-induced hearing loss,'' Nature (London) **315,** 662–665.

Cody, A. R., and Russell, I. J. (**1987**). ''The responses of hair cells in the basal turn of the guinea-pig cochlea to tones,'' J. Physiol. (London) **383,** 551–569.

Cooper, N. P., and Rhode, W. S. (**1992**). ''Basilar membrane mechanics in the hook region of cat and guinea-pig cochlea: Sharp tuning and nonlinearity in the absence of baseline position shifts,'' Hear. Res. **63,** 163–190.

Dallos, P. (**1988**). ''Cochlear Neurobiology: Some key experiments and concepts of the past two decades,'' in *Auditory functions. Neurobiological basis of hearing*, edited by G. M. Edelman, W. E. Gall, and W. M. Cowan (Wiley, New York), pp. 153–188.

Dallos, P., and Evans, B. N. (**1995**). ''High-frequency motility of outer hair cells and cochlear amplifier,'' Science **267,** 2006–2009.

Dallos, P., Evans, B. N., and Hallworth, R. (**1991**). ''Nature of the motor element in electrokinetic shape changes of cochlear outer hair cells,'' Nature (London) **350,** 155–157.

Dallos, P., Santos-Sacchi, J., and Flock, A. (**1982**). ''Intracellular recording from cochlear outer hair cells,'' Science **218,** 582–584.

Davis, H. (**1983**). ''An active process in cochlear mechanics,'' Hear. Res. **9,** 79–90.

Evans, B. N., and Dallos, P. (**1993**). ''Stereocilia displacement induced somatic motility of cochlear outer hair cells,'' Proc. Natl. Acad. Sci. USA **90,** 8347–8351.

Gale, J. E., and Ashmore, J. F. (**1994**). ''Charge displacement induced by rapid stretch in the basolateral membrane of the guinea-pig outer hair cell,'' Proc. R. Soc. London, Ser. B **255,** 243–249.

Gitter, A. H., and Zenner, H. P. (**1995**). ''Electromotile responses and frequency tuning of isolated outer hair cells of the guinea-pig cochlea,'' Eur. Arch. Otorhinolaryngol. **252**(1), 15–19.

Hallworth, R., Evans, B. N., and Dallos, P. (**1993**). ''The location and mechanism of electromotility in guinea pig outer hair cells,'' J. Neurophysiol. **70**(2), 549–558.

Housley, G. D., and Ashmore, J. F. (**1992**). ''Ionic currents of outer hair cells isolated from the guinea-pig cochlea,'' J. Physiol. (London) **448,** 73–98.

Huang, G., and Santos-Sacchi, J. (**1993**). ''Mapping the distribution of the outer hair cell motility voltage sensor by electrical amptuation,'' Biophys. J. **65,** 2228–2236.

Huang, G., and Santos-Sacchi, J. (**1994**). ''Motility voltage sensor of the outer hair cell resides within the lateral plasma membrane'' Proc. Natl. Acad. Sci. USA **91,** 12 268–12 272.

Iwasa, K. H. (**1993**). ''Effect of stress on the membrane capacitance of the auditory outer hair cell,'' Biophys. J. **65,** 492–498.

Iwasa, K. H., Li, M. X., Jia, M., and Kachar, B. (**1991**). ''Stretch sensitivity of the lateral wall of the auditory outer hair cell from the guinea pig,'' Neurosci. Lett. **133**(2), 171–174.

Kakehata, S., and Santos-Sacchi, J. (**1995**). ''Membrane tension directly shifts voltage dependence of outer hair cell motility and associated gating charge,'' Biophys. J. **68,** 2190–2197.

Kolston, P. J. (**1995**). ''A faster transduction mechanism for the cochlear amplifier,'' TINS **18**(10), 427–429.

Mammano, F., and Ashmore, J. F. (**1993**). ''Reverse transduction measured in the isolated cochlea by laser Michelson interferometry,'' Nature (London) **365,** 838–841.

Mountain, D. C. (**1980**). ''Changes in endolymphatic potential and crossed olivocochlear bundle stimulation alter cochlear mechanics,'' Science **210,** 71–72.

Patuzzi, R., and Rajan, R. (**1990**). ''Does electrical stimulation of the crossed olivo-cochlear bundle produce movement of the organ of Corti?,'' Hear. Res. **45,** 15–32.

Patuzzi, R. B., Yates, G. K., and Johnstone, B. M. (**1989**). ''Outer hair cell receptor current and sensorineural hearing loss,'' Hear Res. **42,** 47–72.

Reuter, G., Kössl, M., Hemmert, W., Preyer, S., Zimmermann, U., and Zenner, H. P. (**1994**). ''Electromotility of outer hair cells from the cochlea of the echolocating bat, Carollia perspicillata,'' J. Comp. Physiol. A **175**, 449–455.

Russell, I. J., and Sellick, P. M. (**1983**). ''Low-frequency characteristics of intracellularly recorded receptor potentials in guinea-pig cochlear hair cells,'' J. Physiol. (London) **338,** 179–206.

Santos-Sacchi, J. (**1991**). ''Reversible inhibition of voltage-dependent outer hair cell motility and capacitance,'' J. Neurosci. **11,** 3096–3110.

Santos-Sacchi, J. (**1993**). ''Harmonics of outer hair cell motility,'' Biophys. J. **65,** 2217–2227.

Santos-Sacchi, J., and Dilger, J. P. (**1988**). ''Whole cell currents and mechanical responses of isolated outer hair cells,'' Hear. Res. **35,** 143–150.

Santos-Sacchi, J., and Kakehata, S. (**1996**). ''Nonlinear capacitance of the outer hair cell is inversely related to linear capacitance,'' 40th annual Biophysical Society Meeting, February 17–21, Baltimore, Biophys. J. **70,** Tu-Pos481.

Siegel, J. H., and Kim, D. O. (**1982**). ''Efferent neural control of cochlear mechanics? Olivocochlear bundle stimulation affects cochlear biomechanical nonlinearity,'' Hear. Res. **6,** 171–182.

Zenner, H. P., Zimmermann, R., and Gitter, A. H. (**1988**). ''Active movements of the cuticular plate induce sensory hair motion in mammalian outer hair cells,'' Hear. Res. **34**(3), 233–239.

Zenner, H. P., Reuter, G., Zimmermann, U., Gitter, A. H., Fermin, C., and LePage, E. L. (**1994**). ''Transitory endolymph leakage induced hearing loss and tinnitus: depolarization, biphasic shortening and loss of electromotility of outer hair cells,'' Eur. Arch. Otorhinolaryngol. **251**(3), 143–153.

Zidanic, M., and Brownell, W. E. (**1990**). ''Fine structure of the intracochlear potential field. I. The silent current,'' Biophys. J. **57,** 1253–1268.

Sound-power collection by the auditory periphery of the Mongolian gerbil *Meriones unguiculatus*: III. Effect of variations in middle-ear volume

Michael E. Ravicz
The Eaton–Peabody Laboratory of Auditory Physiology, Massachusetts Eye and Ear Infirmary, 243 Charles Street, Boston, Massachusetts 02114 and The Research Laboratory of Electronics, Massachusetts Institute of Technology, 77 Massachusetts Avenue, Cambridge, Massachusetts 02139

John J. Rosowski
The Department of Otology and Laryngology, Harvard Medical School, and The Eaton–Peabody Laboratory of Auditory Physiology, Massachusetts Eye and Ear Infirmary, 243 Charles Street, Boston, Massachusetts 02114 and The Research Laboratory of Electronics, Massachusetts Institute of Technology, 77 Massachusetts Avenue, Cambridge, Massachusetts 02139

(Received 7 June 1996; accepted for publication 13 August 1996)

The effects of variations in middle-ear cavity size on hearing sensitivity in the Mongolian gerbil are predicted by computing the effect on acoustic power input to the middle ear. Acoustic power collection from a diffuse sound field was computed from measurements of the middle-ear input impedance and external-ear radiation impedance and mathematical models of the middle and external ear presented in the first two papers of this series [J. Acoust. Soc. Am. **92**, 157–177 (1992); J. Acoust. Soc. Am. **99**, 3044–3063 (1996)]. A reduction in middle-ear cavity volume to $\frac{1}{4}$ its normal value is predicted to cause a frequency-selective elevation in auditory threshold of as much as 12 dB, with the largest elevation occuring in the 1–2 kHz range. Greater reductions produce larger threshold elevations. Increases in cavity volume cause decreases in the predicted threshold of at most 12 dB. Threshold predictions for volumes equal to those of the smaller hamster and the larger kangaroo-rat middle-ear cavity volumes resemble threshold functions measured in those animals. Results are consistent with the idea that large middle-ear cavities evolved in gerbil to improve hearing sensitivity below 3 kHz and thereby improve the animal's chances for survival. © *1997 Acoustical Society of America.* [S0001-4966(97)00903-X]

PACS numbers: 43.64.Ha, 43.64.Tk, 43.64.Yp, 43.80.Lb [RDF]

INTRODUCTION

The increased sensitivity of some desert rodents to sounds at frequencies below a few kilohertz, relative to other rodents of similar body size, has been associated with the *relatively* large middle-ear structures found in those rodents relative to other rodents of comparable body size (Webster, 1962; Webster and Webster, 1972, 1975, 1984; Lay, 1972, 1974; Plassmann and Brändle, 1992). The mechanisms that provide this increased sensitivity are not clear. In general, larger mammals are sensitive to low-frequency sounds, while the auditory sensitivity of small mammals is limited to high-frequency sounds (Heffner and Masterton, 1980; Rosowski and Graybeal, 1991). The auditory thresholds of Mongolian gerbil (*Meriones unguiculatus*, a gerbilline) and kangaroo rat (*Dipodomys merriami*, a heteromyid) below 2 kHz are 15–30 dB lower than the auditory threshold of hamster, a rodent of similar body size and weight but much smaller middle-ear volume; see Fig. 1 (see also Table I). The tympanic membrane area A_{TM} and middle-ear cavity volume V_{MEC} in gerbil and kangaroo rat are generally $2\times$–$5\times$ the size of A_{TM} and V_{MEC} in most other small rodents (Legouix and Wisner, 1955; Webster, 1961; Webster and Webster, 1975; Lay, 1972). Kangaroo rats and gerbils also have a more mobile ossicular structure than most other small rodents (Fleischer, 1973), and their cochleae show low-frequency specializations as well (Webster, 1961; Webster and Webster, 1975, 1977; Plassmann *et al.*, 1987).

More direct evidence for a connection between middle-ear volume and low-frequency hearing in small rodents is provided by Webster and Webster (1971, 1972), who reduced the middle-ear volume in kangaroo rats and observed a reduction in the cochlear microphonic (Webster, 1961) and an elevation of the behavioral hearing threshold (Webster and Webster, 1972). On average, at least 10-dB threshold elevation was observed below 2 kHz when middle-ear volume was reduced by 75%. In addition, animals whose middle-ear volumes were reduced were increasingly susceptible to predation, especially during the dark phase of the moon when vision was less useful (Webster and Webster, 1971). Such observations of the effect of reducing middle-ear cavity volume on hearing in one species provide insight on the benefit provided by large middle-ear cavities (without modification to other middle-ear structures). What is less clear is whether large middle-ear cavities explain *all* of the difference in threshold seen in species with large middle-ear cavities compared to species with more conventional middle ears.

What are the physical mechanisms which might relate large middle-ear air volumes to improved low-frequency hearing capabilities? Investigators from several disciplines, including comparative anatomy and animal psychophysics as

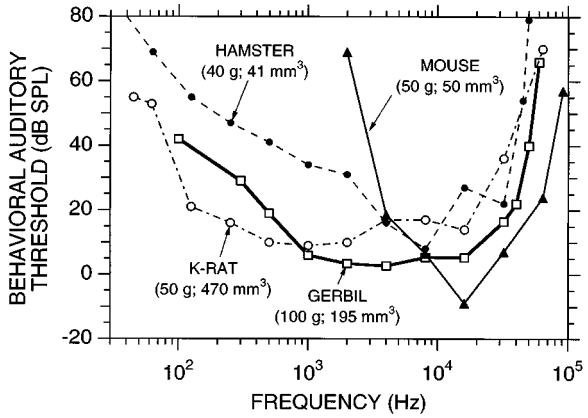

FIG. 1. Audiograms of four small rodents of comparable body size: the Mongolian gerbil *Meriones unguiculatus*, the kangaroo rat *Dipodymus merriami*, the golden hamster *Mesocricetus auritus*, and the mouse *Mus musculus*. The body weight in grams and the middle-ear volume in mm^3 are shown for each species. The ossicular structures of gerbil, kangaroo rat, and hamster are similar, while the ossicular structure of mouse is more typical of small rodents (Fleischer, 1973). Audiograms of kangaroo rat and gerbil, two species with large middle-ear volumes, have a different shape and show better low-frequency hearing than hamster or mouse. Audiograms: gerbil—Ryan (1976); kangaroo rat—Webster and Webster (1972), 125 Hz–8 kHz; Heffner and Masterton (1980), <125 Hz, >8 kHz; hamster—Heffner *et al.* (1994); mouse—Heffner and Masterton (1980). Middle-ear volume data: gerbil—Ravicz *et al.* (1992); kangaroo rat—Webster and Webster (1975); hamster—Zwillenberg *et al.* (1981); mouse—Rosowski (1994).

well as physiological acoustics, have postulated that the range of frequencies audible to humans and other animals is shaped by the properties and capabilities of the auditory periphery (e.g., Henson, 1961, 1974; Dallos, 1973; Fleischer, 1973, 1978; Zwislocki, 1975; Pye and Hinchcliffe, 1976; Hunt and Korth, 1980). We have shown in the first paper of this series (Ravicz *et al.*, 1992) that the magnitude of the middle-ear input impedance $\mathbf{Z_T}$ is smaller in gerbil than in hamster, another rodent of similar body size but smaller middle-ear volume. The lower impedance implies that a given pressure in the ear canal produces a larger volume velocity at the tympanic membrane in gerbil, and therefore probably a larger volume-velocity input to the cochlea, than in animals with a higher middle-ear impedance. However, the functional relationship between the size of the gerbil middle ear and low-frequency sensitivity is not clear, especially since the absolute gerbil middle-ear areas and volumes are small compared to the middle-ear areas and volumes in larger mammals (Rosowski, 1994). Furthermore, the middle-ear air space of the gerbil is not so large that it has no effect on the impedance; in fact, the stiffness of the air in the gerbil middle ear accounts for about 75% of the total stiffness of the middle-ear input impedance at low frequencies (Ravicz *et al.*, 1992).

The second paper of this series laid out a framework for computing sound power transmission from an external sound field to the middle ear (Ravicz *et al.*, 1996). A relationship between external sound pressure and power entering the middle ear was computed from measurements of $\mathbf{Z_T}$ and the external-ear radiation impedance $\mathbf{Z_E}$ and models of the external ear developed from those measurements. The results suggest that, at each frequency, the hearing threshold in gerbil corresponds to the diffuse-field sound pressure required to deliver 5×10^{-17} W of sound power to the middle ear.

In the present paper we use the previously reported $\mathbf{Z_E}$ measurements and $\mathbf{Z_T}$ model to predict the effect of a reduction in middle-ear volume on the amount of power transmitted to the middle ear and, by extension, on the auditory threshold. In the $\mathbf{Z_T}$ model, the middle-ear volume can be varied mathematically (Ravicz *et al.*, 1992). We compare the predicted changes in middle-ear power input to changes in hearing threshold observed behaviorally in the kangaroo rat by Webster and Webster (1972). We also compare predictions of the hearing threshold in gerbil after manipulations of the middle-ear cavity volume to the behavioral thresholds of hearing in kangaroo rat and hamster, two animals of similar body size and ossicular structure but greatly different middle-ear air volumes (Rosowski, 1994).

I. METHODS

A. Threshold of hearing, power collection, and effective area of the external and middle ear

The previous paper in this series showed that the auditory threshold of the gerbil between 100 Hz and 18 kHz was well predicted by the sound pressure in an external diffuse sound field required to deliver 5×10^{-17} W of acoustic power to the middle ear (Ravicz *et al.*, 1996). As pointed out by Shaw (1976, 1979, 1988), the average power entering the middle ear Π_T is related to the sound pressure in the diffuse field[1] P_{DF} by the diffuse-field effective area of the external ear at the tympanic membrane $EA_{\mathrm{TM}}^{\mathrm{DF}}$. If $EA_{\mathrm{TM}}^{\mathrm{DF}}$ is known, the diffuse-field sound pressure necessary to produce a given value of Π_T is

$$P_{\mathrm{DF}}=\left(\frac{\rho_0 c\Pi_T}{EA_{\mathrm{TM}}^{\mathrm{DF}}}\right)^{1/2}, \tag{1}$$

where ρ_0 is the density of air and c is the sound speed.[2] The effective area $EA_{\mathrm{TM}}^{\mathrm{DF}}$, which quantifies the power-collecting abilities of the external ear, has units of area and is generally dependent on frequency (e.g., Rosowski, 1991a,b; Keefe *et al.*, 1994).

The effective area depends on three factors: (1) a geometric constant $\lambda^2/4\pi$, which varies as the square of the wavelength of sound λ and hence inversely as the square of frequency f; (2) the radiation efficiency η_R, a measure of power dissipation within the external ear; and (3) the power utilization ratio PUR, a measure of power transmission between the external ear and the middle ear at the tympanic membrane:

$$EA_{\mathrm{TM}}^{\mathrm{DF}}=\frac{\lambda^2}{4\pi}\,\eta_R\mathrm{PUR}. \tag{2}$$

The radiation efficiency η_R (Keefe *et al.*, 1994; Ravicz *et al.*, 1996) was estimated from a mathematical model of the gerbil external ear (see $\tilde{\eta}_R$ in Fig. 16 of Ravicz *et al.*, 1996). The PUR is the ratio of the average power absorbed at the TM to the power available there (Rosowski *et al.*, 1986; Rosowski, 1991a, b). The PUR in the gerbil has been computed from measurements of $\mathbf{Z_T}$ (Ravicz *et al.*, 1992) and the radiation impedance looking out through the external ear

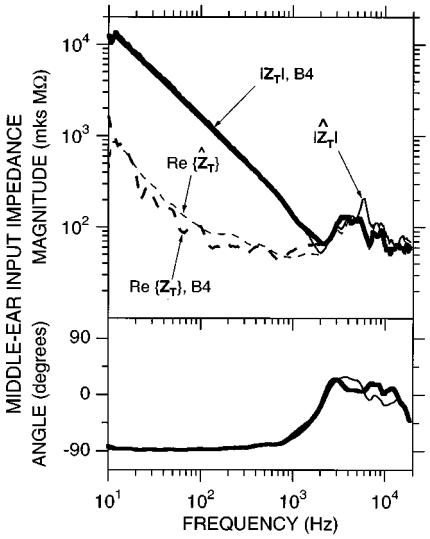

FIG. 2. Middle-ear input impedance $\mathbf{Z_T}$ measured in the left ear of animal B4 (thick lines) and the model middle-ear impedance $\hat{\mathbf{Z}}_\mathbf{T}$ (thin lines). $\hat{\mathbf{Z}}_\mathbf{T}$ was computed from the measured impedance of the tympanic membrane, ossicles, and cochlea $\mathbf{Z_{TOC}}$ and the theoretical impedance of a sphere $\hat{\mathbf{Z}}_\mathbf{MEC}$ of volume equal to the middle-ear cavities $V_{\mathrm{MEC}}=195$ mm^3 (see Ravicz *et al.*, 1992, Figs. 11 and 14). Impedance magnitudes and angles are shown as solid lines; real parts are shown as dashed lines.

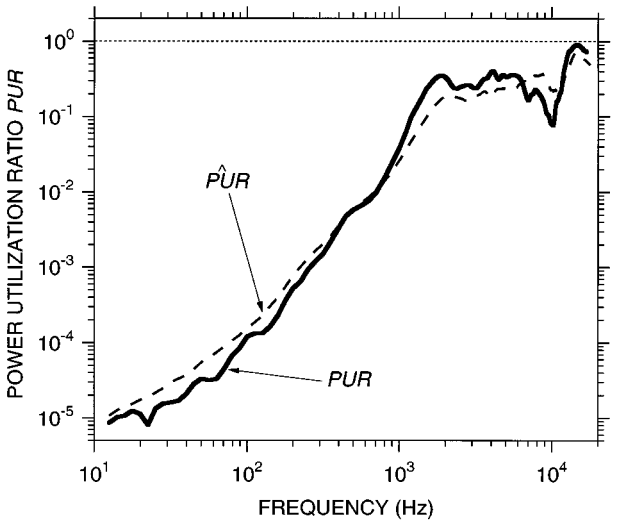

FIG. 3. Comparison of the power utilization ratio PUR computed from $\mathbf{Z_T}$ measured in animal B4 (solid line) to P$\hat{\mathrm{U}}$R from the model $\hat{\mathbf{Z}}_\mathbf{T}$ (dashed line). Both PUR computations used the external-ear radiation impedance $\mathbf{Z_E}$ measured in animal B4. Both PUR curves show that power transmission to the middle ear is small below 1.5 kHz and is still only about 40% of the ideal (dotted line at PUR=1) at higher frequencies. Differences between PUR computed from the measured or model $\mathbf{Z_T}$ are small.

from the tympanic ring $\mathbf{Z_E}$ (Ravicz *et al.*, 1996) by

$$\mathrm{PUR}=\frac{4\,\mathrm{Re}\{\mathbf{Z_E}\}\mathrm{Re}\{\mathbf{Z_T}\}}{|\mathbf{Z_E}+\mathbf{Z_T}|^2}. \tag{3}$$

Equations (2) and (3) point out that power collection by the auditory periphery depends on the impedances of both the external and middle ear. $\mathbf{Z_E}$ and η_R are determined by the size and shape of the external ear, while $\mathbf{Z_T}$ depends on the tympanic membrane, ossicles, cochlea, and middle-ear air spaces (Zwislocki, 1962; Ravicz *et al.*, 1992). The segregation of middle-ear effects into a single term enables a *model* of the middle-ear impedance $\hat{\mathbf{Z}}_\mathbf{T}$ to be used with empirically derived values of $\mathbf{Z_E}$ and η_R to quantify the effect of varying middle-ear volume on power collection by the external and middle ear.[3]

B. The middle-ear cavity model

The effects of altering middle-ear cavity volume V_{MEC} on $\mathbf{Z_T}$ have been explored via a mathematical model of the middle ear (Ravicz *et al.*, 1992) that will be summarized here. The model middle-ear input impedance $\hat{\mathbf{Z}}_\mathbf{T}$ is the sum of two components: the measured impedance of the tympanic membrane, middle-ear ossicles, and cochlea $\mathbf{Z_{TOC}}$, and the impedance predicted for the middle-ear cavities $\hat{\mathbf{Z}}_\mathbf{MEC}$ (Ravicz *et al.*, 1992):

$$\hat{\mathbf{Z}}_\mathbf{T}=\mathbf{Z_{TOC}}+\hat{\mathbf{Z}}_\mathbf{MEC}. \tag{4}$$

Here, $\mathbf{Z_{TOC}}$ is the impedance measured in a representative ear (the left ear of gerbil B4) when the bulla was opened as widely as possible to remove the effect of the middle-ear air space. The model $\hat{\mathbf{Z}}_\mathbf{MEC}$ is the impedance of a sphere[4] of 195 mm^3 volume, the mean volume of the middle-ear air space V_{MEC} in five ears.

Figure 2 illustrates that, with $V_{\mathrm{MEC}}=195$ mm^3, $\hat{\mathbf{Z}}_\mathbf{T}$ is a good match to $\mathbf{Z_T}$ measured in the same ear used for modeling. The small discrepancy between $\hat{\mathbf{Z}}_\mathbf{T}$ and $\mathbf{Z_T}$ near 6 kHz is believed to be due to a resonance between the middle-ear volume and the acoustic mass associated with the bulla opening used for measuring $\mathbf{Z_{TOC}}$ when the middle-ear cavity was opened (Ravicz *et al.*, 1992). The real part of $\hat{\mathbf{Z}}_\mathbf{T}$ also matches Re$\{\mathbf{Z_T}\}$ well.

Figure 3 compares the power utilization ratio P$\hat{\mathrm{U}}$R computed by Eq. (3) from measurements of $\mathbf{Z_E}$ in our representative animal (B4) and the model $\hat{\mathbf{Z}}_\mathbf{T}$ (Fig. 2) to the PUR in animal B4 computed from $\mathbf{Z_E}$ and measurements of $\mathbf{Z_T}$ (Ravicz *et al.*, 1996, Fig. 13). Both PUR curves show the same features: PUR is small at low frequencies ($<10^{-4}$ below 100 Hz), increases rapidly with frequency to about 0.3 at 2 kHz, and varies between 0.09 and 0.9 at higher frequencies. The differences between PUR and P$\hat{\mathrm{U}}$R are less than a factor of 2 at any frequency (except at 10 kHz). A corner frequency f_c at 1.5 kHz in both curves is defined as the frequency where PUR is 3 dB down from its mean value between 2 and 5 kHz. Both PUR curves show that less than 5% of the available power in the ear canal enters the middle ear at frequencies below 1 kHz (as little as 0.01% at 100 Hz) and that only about 40% of the available power is absorbed between 1 and 10 kHz.

C. Effect of cavity size on the model Z_T

Variations in the middle-ear volume V_{MEC} are predicted to have significant effects on the middle-ear input impedance $\hat{\mathbf{Z}}_\mathbf{T}$ [Ravicz *et al.*, 1992, Figs. 18, 19(a)].[5] Figure 4(a) shows $\hat{\mathbf{Z}}_\mathbf{T}$ computed from Eq. (4) with V_{MEC} varying from $\frac{1}{16}$ to 8× the normal middle-ear cavity volume of 195 mm^3. Also shown is $\hat{\mathbf{Z}}_\mathbf{T}$ with the middle-ear cavity open. As noted previously, decreasing V_{MEC} produces nearly proportionate *in-*

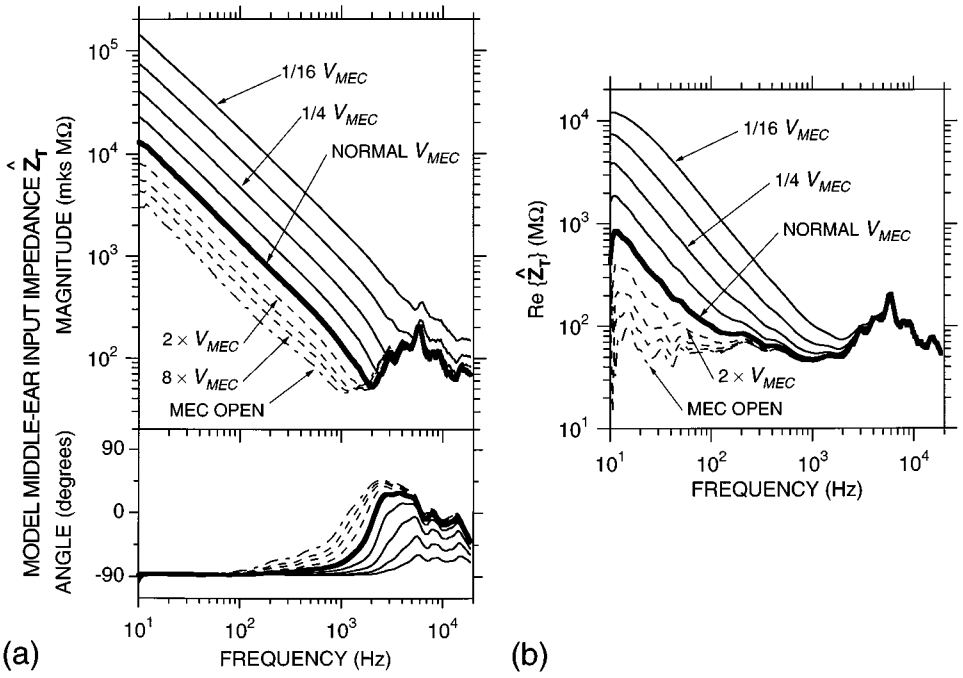

FIG. 4. Effect of variations in middle-ear cavity volume V_{MEC} on the middle-ear input impedance $\hat{\mathbf{Z}}_{\mathbf{T}}$. (a) Values of $\hat{\mathbf{Z}}_{\mathbf{T}}$ predicted for $V_{\mathrm{MEC}}=\frac{1}{2}$, $\frac{1}{4}$, $\frac{1}{8}$, and $\frac{1}{16}$ its normal value of 195 mm^3 are shown by the thin solid lines; values of $\hat{\mathbf{Z}}_{\mathbf{T}}$ predicted for $V_{\mathrm{MEC}}=2$, 4, and 8× its normal value are shown by the dashed lines; and $\hat{\mathbf{Z}}_{\mathbf{T}}$ with the middle-ear cavity open is shown by the dot–dashed line (from Ravicz *et al.*, 1992, Fig. 18, corrected for a middle-ear vent). (b) Real parts of the various $\hat{\mathbf{Z}}_{\mathbf{T}}$s in (a). Effects of different values of V_{MEC} on Re$\{\hat{\mathbf{Z}}_{\mathbf{T}}\}$ are generally restricted to low frequencies.

creases in $|\hat{\mathbf{Z}}_{\mathbf{T}}|$, while increasing V_{MEC} produces less than proportionate *decreases* in $|\hat{\mathbf{Z}}_{\mathbf{T}}|$. Changes in $|\hat{\mathbf{Z}}_{\mathbf{T}}|$ are generally limited to frequencies below 4 kHz. The relative effects of changes in V_{MEC} reflect the contributions of $\mathbf{Z_{TOC}}$ and $\hat{\mathbf{Z}}_{\mathbf{MEC}}$ to the total impedance [Eq. (4)]. When the middle-ear air spaces are made smaller, $|\hat{\mathbf{Z}}_{\mathbf{MEC}}|$ increases and eventually dominates $\hat{\mathbf{Z}}_{\mathbf{T}}$. On the other hand, *increases* in middle-ear volume lead to smaller and smaller contributions of $\hat{\mathbf{Z}}_{\mathbf{MEC}}$ to $\hat{\mathbf{Z}}_{\mathbf{T}}$. When V_{MEC} becomes sufficiently large ($V_{\mathrm{MEC}}\geqslant 1560$ mm^3), $\hat{\mathbf{Z}}_{\mathbf{T}}\approx\mathbf{Z_{TOC}}$, and further increases in volume have no significant effect. Variations in V_{MEC} have a less pronounced effect on the real part of $\hat{\mathbf{Z}}_{\mathbf{T}}$, and these effects are confined to lower frequencies, as shown in Fig. 4(b). There is no significant increase in Re$\{\hat{\mathbf{Z}}_{\mathbf{T}}\}$ above 2 kHz when V_{MEC} is reduced to as small as 12 mm^3, $\frac{1}{16}$ its normal value.

II. RESULTS

A. Effect of variations in middle-ear cavity volume on power entering the middle ear

Measurements of $\mathbf{Z_E}$, estimates of η_R, and model predictions of the effect of variations in V_{MEC} on $\hat{\mathbf{Z}}_{\mathbf{T}}$ were used to predict the relationship between middle-ear volume and power flow into the middle ear (Fig. 5). The effects of variations in V_{MEC} on (a) $\hat{\mathrm{PUR}}$, (b) $\hat{E}A_{\mathrm{TM}}^{\mathrm{DF}}$, and (c) the diffuse-field sound pressure $\hat{P}_{\mathrm{DF}}^{\mathrm{TH}}$ required to deliver 5×10^{-17} W to the middle ear were computed by Eqs. (3), (2), and (1), respectively, using $\mathbf{Z_E}$ measured in animal B4 and $\hat{\mathbf{Z}}_{\mathbf{T}}$ computed by Eq. (4) for various middle-ear cavity volumes (Fig. 4).

The effects of varying the middle-ear volume occur mostly below 4 kHz. As V_{MEC} is reduced (thin solid lines), the corner frequency f_c between the frequency-dependent and frequency-independent parts of the $\hat{\mathrm{PUR}}$ curve [see Fig. 4(a)] shifts upward [panel (a)]. The upward shift in f_c is also seen in $\hat{E}A_{\mathrm{TM}}^{\mathrm{DF}}$ [panel (b)] and $\hat{P}_{\mathrm{DF}}^{\mathrm{TH}}$ [panel (c)]. Below f_c, reducing middle-ear volume (a) reduces power transfer at the tympanic membrane, (b) reduces the effective area of the external ear, and (c) increases the diffuse-field sound pressure required to deliver a given sound power to the middle ear; hence, reducing V_{MEC} is predicted to raise the auditory threshold at low frequencies. The change in $\hat{\mathrm{PUR}}$ produced by reductions in cavity volume is most dramatic between 1–2 kHz, where reducing V_{MEC} by factors of 2, 4, and 8 causes a reduction in power transmission by factors of 3, 10, and 30, respectively. At still lower frequencies, the effect of reducing V_{MEC} diminishes: at 100 Hz, reducing V_{MEC} by factors of 2, 4, and 8 decreases $\hat{\mathrm{PUR}}$ by factors of 2, 3, and 6. The reduction in $\hat{\mathrm{PUR}}$ extends to 3 kHz when V_{MEC} is reduced to $\frac{1}{4}$ its normal value and to 5 kHz when V_{MEC} is reduced to $\frac{1}{16}$. Reducing V_{MEC} *increases* power transfer into the middle ear somewhat between f_c and about 7 kHz, but this effect is not as large as the low-frequency decrease in power transfer (approximately a factor of 2). Above 7 kHz, power transfer is decreased by a smaller amount.

The changes in $\hat{\mathrm{PUR}}$ produced by reducing middle-ear volume can be explained in terms of Eq. (3), which shows that $\hat{\mathrm{PUR}}$ is proportional to Re$\{\hat{\mathbf{Z}}_{\mathbf{T}}\}$ and $|\hat{\mathbf{Z}}_{\mathbf{T}}+\mathbf{Z_E}|^{-2}$. Above the corner frequency f_c [Fig. 5(a)], reductions in V_{MEC} have little effect on either the magnitude or the real part of $\hat{\mathbf{Z}}_{\mathbf{T}}$ (Fig. 4). Below f_c, reductions in V_{MEC} lead to roughly proportionate increases in $|\hat{\mathbf{Z}}_{\mathbf{T}}|$ and lesser increases in Re$\{\hat{\mathbf{Z}}_{\mathbf{T}}\}$. Between 0.5 and 2 kHz, Re$\{\hat{\mathbf{Z}}_{\mathbf{T}}\}$ does not vary much with changes in middle-ear volume [Fig. 4(b)], and $|\hat{\mathbf{Z}}_{\mathbf{T}}+\mathbf{Z_E}|^{-2}$

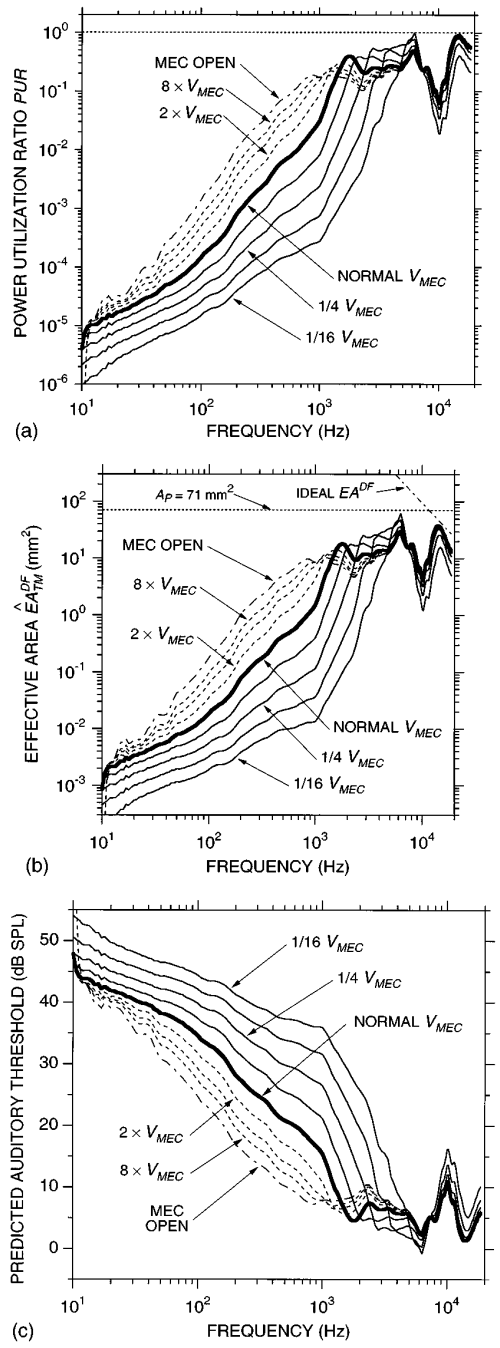

FIG. 5. Effect of variations in middle-ear cavity volume V_{MEC} on several measures of the acoustic performance of the auditory periphery. In all panels the thick solid curve denotes quantities computed from $\hat{\mathbf{Z}}_{\mathbf{T}}$ with a normal $V_{\mathrm{MEC}}=195\ \mathrm{mm}^3$; the thin solid lines show quantities computed with $\hat{\mathbf{Z}}_{\mathbf{T}}$ with a middle-ear volume $\frac{1}{2}$, $\frac{1}{4}$, $\frac{1}{8}$, and $\frac{1}{16}$ the anatomical middle-ear volume; the thin dashed lines show quantities calculated with $\hat{\mathbf{Z}}_{\mathbf{T}}$ with a middle-ear volume 2, 4, and $8\times V_{\mathrm{MEC}}$; and the dot–dashed line shows quantities computed from $\hat{\mathbf{Z}}_{\mathbf{T}}$ with an infinitely large V_{MEC} (see Fig. 4). (a) Effects of variations in V_{MEC} on the power utilization ratio PUR. An ideal PUR=1 is shown by the dotted horizontal line at the top of the figure. (b) Effects of variations in V_{MEC} on the effective area at the tympanic membrane $\hat{E}A_{\mathrm{TM}}^{\mathrm{DF}}$. The thick curve shows $\hat{E}A_{\mathrm{TM}}^{\mathrm{DF}}$ computed from an estimate of the radiation efficiency ($\tilde{\eta}_R$, Ravicz *et al.*, 1996, Fig. 16) and the ''NORMAL'' PUR in panel (a). The dot–dashed line in the upper right-hand corner is the ideal EA^{DF} computed for PUR$=\eta_R=1$ and is equal to $\lambda^2/4\pi$; the dotted horizontal line denotes the anatomical pinna area $A_P=71\ \mathrm{mm}^2$. (c) Effect of variations in V_{MEC} on the predicted auditory threshold, computed from the effective areas $\hat{E}A_{\mathrm{TM}}^{\mathrm{DF}}$ shown in panel (b). Each curve represents the diffuse-field sound pressure $\hat{P}_{\mathrm{DF}}^{\mathrm{TH}}$ necessary to provide a power input Π_T of 5×10^{-17} watts to the middle ear.

$\approx|\hat{\mathbf{Z}}_{\mathbf{T}}|^{-2}$ (Ravicz *et al.*, 1996); consequently, PÛR varies approximately with the square of V_{MEC}. This effect is readily apparent in Fig. 5(a) where, at 1.5 kHz, the factor of 8 decrease in V_{MEC} between $\frac{1}{2}$ and $\frac{1}{16}$ normal volume produces a factor of 60 reduction in PÛR. At lower frequencies, decreases in V_{MEC} lead to larger increases in $\mathrm{Re}\{\hat{\mathbf{Z}}_{\mathbf{T}}\}$ that reduce the change in PÛR produced by the increases in $|\hat{\mathbf{Z}}_{\mathbf{T}}|$. Below 0.5 kHz, decreases in V_{MEC} lead to proportionate increases in both $\mathrm{Re}\{\hat{\mathbf{Z}}_{\mathbf{T}}\}$ and $|\hat{\mathbf{Z}}_{\mathbf{T}}|$ such that PÛR varies with V_{MEC}.

The effect of decreasing V_{MEC} can be reasonably approximated by shifting the PÛR curve up in frequency. Hence, the effect of the gerbil's hypertrophied bulla can be assessed by comparing the PÛR computed for the normal gerbil middle ear with the PÛR computed for a hamster-size middle ear [41 mm^3 (Zwillenberg *et al.*, 1981)$\approx\frac{1}{4}$ V_{MEC}]. The greatest increase in PÛR between the $\frac{1}{4}$ V_{MEC} and NORMAL V_{MEC} curves occurs between 1 and 3 kHz, the frequency range over which f_c is shifted. By this reasoning, the net effect of the hypertrophied bulla in the gerbil is to enhance power transfer from the external ear into the middle ear at frequencies below 3 kHz.

The effects of reductions in V_{MEC} on PÛR are also evident in the effective area $EA_{\mathrm{TM}}^{\mathrm{DF}}$ and the predicted auditory threshold $\hat{P}_{\mathrm{DF}}^{\mathrm{TH}}$. Panel (b) of Fig. 5 shows the diffuse-field effective area of the external ear at the tympanic membrane $\hat{E}A_{\mathrm{TM}}^{\mathrm{DF}}$ computed from the PÛR and the radiation efficiency ($\tilde{\eta}_R$, Ravicz *et al.*, 1996, Fig. 16) by Eq. (2). The area of the pinna opening $A_P=71\ \mathrm{mm}^2$ is shown as the dotted horizontal line, and the geometric limit $\lambda^2/4\pi$ is shown as the short dot–dashed line (IDEAL EA^{DF}) at the upper right-hand corner of the figure. The estimate of $\hat{E}A_{\mathrm{TM}}^{\mathrm{DF}}$ for the normal ear shown here approaches A_P and the geometrical limit only above 6 kHz and is approximately 10 mm^2 at frequencies above the normal corner frequency f_c of 1.5 kHz. Reductions in V_{MEC} cause f_c to increase and $\hat{E}A_{\mathrm{TM}}^{\mathrm{DF}}$ to decrease at frequencies below f_c, similar to the effect on PÛR [see panel (a)]. When V_{MEC} is reduced to $\frac{1}{4}$ its normal value, f_c increases to 3 kHz, and $\hat{E}A_{\mathrm{TM}}^{\mathrm{DF}}$ is reduced by as much as a factor of 16 between 1 and 1.5 kHz.

Panel (c) of Fig. 5 shows that, as V_{MEC} is reduced from its normal value, $\hat{P}_{\mathrm{DF}}^{\mathrm{TH}}$ increases. The frequency range over which $\hat{P}_{\mathrm{DF}}^{\mathrm{TH}}$ is fairly constant with frequency is also reduced: with the normal V_{MEC}, $\hat{P}_{\mathrm{DF}}^{\mathrm{TH}}$ increases sharply below the corner frequency at about 1.5 kHz; when V_{MEC} is reduced by a factor of 4, f_c increases to about 3 kHz. Each halving of V_{MEC} causes an elevation in $\hat{P}_{\mathrm{DF}}^{\mathrm{TH}}$ of about 5 dB between 1 and 2 kHz, with somewhat smaller effects at lower frequencies. It can be clearly seen, then, that reducing V_{MEC} by a factor of 4 has a detrimental effect on power delivery to the middle ear below 3 kHz, which implies that the hypertrophy of the gerbil middle ear over that of similar animals serves to improve hearing below 3 kHz.

Increasing the middle-ear volume V_{MEC} has a smaller effect on $\hat{\mathbf{Z}}_{\mathbf{T}}$ and a lesser effect on PÛR and power flow into the middle ear. Increasing V_{MEC} (dashed curves in Fig. 5) increases PÛR below 1.5 kHz and moves the corner frequency f_c down [panel (a)]; however, these changes are smaller than those produced by decreases in V_{MEC}. Doubling

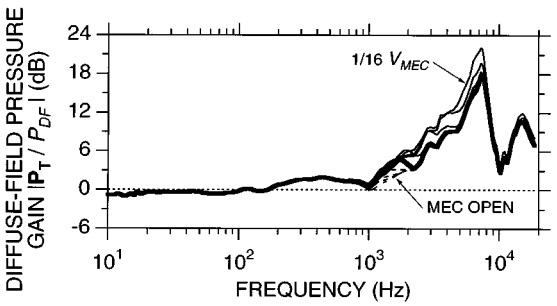

FIG. 6. Effects of variations in middle-ear cavity volume V_{MEC} on the predicted pressure gain from a diffuse field to the tympanic membrane $|\mathbf{P_T}/P_{\mathrm{DF}}|$. The gain predicted for $V_{\mathrm{MEC}}=195\ \mathrm{mm}^3$ is shown as the thick solid line; gains predicted for reductions or increases in V_{MEC} are shown by the thin solid or dashed lines, respectively.

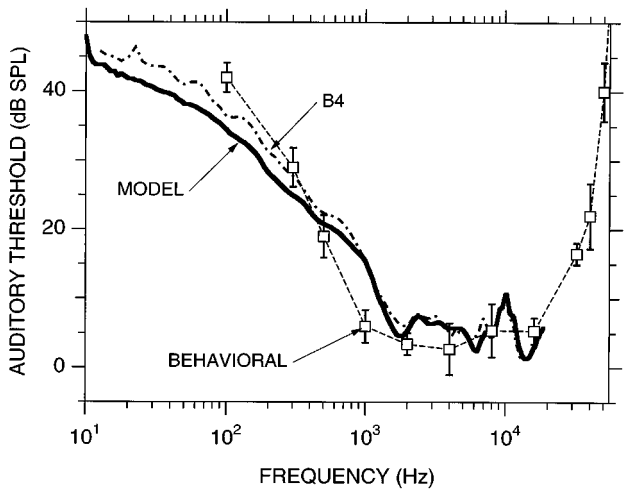

FIG. 7. Comparison of threshold estimates from $\mathbf{Z_T}$ measurements and models to the behavioral auditory threshold (dashed line, open squares, error bars; Ryan, 1976). The dot–dashed line is the predicted threshold $P_{\mathrm{DF}}^{\mathrm{TH}}$ computed from PUR in animal B4, and the thick solid line is the predicted threshold $\hat{P}_{\mathrm{DF}}^{\mathrm{TH}}$ computed from the model [thick solid line in Fig. 5(c)]. Both threshold predictions show the diffuse-field sound pressure necessary to deliver $\Pi_T=5\times10^{-17}$ W of sound power to the middle ear.

V_{MEC} increases PÛR by only a factor of 2.3 between 200 Hz and 1 kHz, and opening the middle-ear cavities (to simulate an infinite V_{MEC}—dot–dashed line) increases PÛR by at most a factor of 12 from 100–800 Hz.[6] A larger V_{MEC} has no effect on PÛR above 2 kHz. Similarly, increasing V_{MEC} has a much lesser effect on $\hat{E}A_{\mathrm{TM}}^{\mathrm{DF}}$ [panel (b)]: doubling V_{MEC} increases $\hat{E}A_{\mathrm{TM}}^{\mathrm{DF}}$ by just over a factor of 2. Even with a very large V_{MEC}, the corner frequency decreases to only 1 kHz, and $\hat{E}A_{\mathrm{TM}}^{\mathrm{DF}}$ is increased below that by at most a factor of 12. Above f_c, variations in V_{MEC} have no significant effect on $\hat{E}A_{\mathrm{TM}}^{\mathrm{DF}}$. Increases in V_{MEC} have diminishing effects on $\hat{P}_{\mathrm{DF}}^{\mathrm{TH}}$ [panel (c)], and the effects occur at lower frequencies than the effects of reducing V_{MEC}. Doubling V_{MEC} leads to a decrease in threshold of about 3 dB and a shift in f_c to about 1 kHz; but even opening the ME cavities improves power flow into the middle ear by only about 10 dB at the most and only below 1.5 kHz. Increasing V_{MEC} has no significant effect on $\hat{P}_{\mathrm{DF}}^{\mathrm{TH}}$ above 3 kHz.

B. Effect of variations in middle-ear cavity volume on pressure gain

What is the effect of a smaller or larger middle-ear cavity on the sound pressure at the tympanic membrane? The diffuse-field pressure gain, defined as the ratio of the sound pressure at the tympanic membrane $\mathbf{P_T}$ to the sound pressure in an external diffuse field P_{DF}, was computed from η_R, $\mathbf{Z_E}$, and $\hat{\mathbf{Z}}_{\mathbf{T}}$ for various values of V_{MEC} (see Fig. 4) by

$$\left|\frac{\mathbf{P_T}}{P_{\mathrm{DF}}}\right|=\left|\frac{\hat{\mathbf{Z}}_{\mathbf{T}}}{\hat{\mathbf{Z}}_{\mathbf{T}}+\mathbf{Z_E}}\right|\left(\eta_R\,\frac{c\ \mathrm{Re}\{\mathbf{Z_E}\}}{\pi\rho_0 f^2}\right)^{1/2} \tag{5}$$

(Shaw, 1976, 1988; Rosowski *et al.*, 1988; Ravicz *et al.*, 1996).[7] Figure 6 shows $|\mathbf{P_T}/P_{\mathrm{DF}}|$ for the normal V_{MEC} as well as for values of V_{MEC} larger and smaller than normal. Neither decreasing nor increasing V_{MEC} has any large effect on $|\mathbf{P_T}/P_{\mathrm{DF}}|$ over the frequency range shown. Reducing V_{MEC} increases $|\mathbf{P_T}/P_{\mathrm{DF}}|$ by as much as 3 dB between 2 and 8 kHz; increasing V_{MEC} decreases $|\mathbf{P_T}/P_{\mathrm{DF}}|$ by only 2 dB between 1 and 2 kHz.

III. DISCUSSION

A. Measured threshold versus predictions

How well does the diffuse-field pressure at auditory threshold predicted by impedance measurements and models match the behavioral threshold? Figure 7 compares two estimates of the diffuse-field sound pressure $P_{\mathrm{DF}}^{\mathrm{TH}}$ necessary to deliver $\Pi_T=5\times10^{-17}$ W to the middle ear with the behavioral auditory threshold (audiogram—open squares and thin dashed line). The dot–dashed line is $P_{\mathrm{DF}}^{\mathrm{TH}}$ predicted from $\mathbf{Z_E}$ and $\mathbf{Z_T}$ in animal B4, and the thick solid line is $\hat{P}_{\mathrm{DF}}^{\mathrm{TH}}$ predicted from $\mathbf{Z_E}$ in animal B4 and $\hat{\mathbf{Z}}_{\mathbf{T}}$ [thick solid line in Fig. 5(c)]. (Recall that the value of Π_T used in $P_{\mathrm{DF}}^{\mathrm{TH}}$ calculations was chosen for the best match of $P_{\mathrm{DF}}^{\mathrm{TH}}$ computed from mean $\mathbf{Z_E}$ and $\mathbf{Z_T}$ measurements to the audiogram, so the vertical position of $P_{\mathrm{DF}}^{\mathrm{TH}}$ curves can be varied.) Both estimates of $P_{\mathrm{DF}}^{\mathrm{TH}}$ are similar, and both tend to underestimate the audiogram below 200 Hz and overestimate it at 1 kHz. The rms error between $\hat{P}_{\mathrm{DF}}^{\mathrm{TH}}$ and the audiogram between 125 Hz and 16 kHz is approximately 2 dB.

What could explain the difference between threshold predictions and the behavioral data? The use of the power entering the middle ear Π_T as a predictor of the behavioral threshold relies on two assumptions: (1) at all frequencies, the auditory threshold corresponds to the stimulus pressure necessary to produce some constant power level in the cochlea; and (2) the percentage of power lost in transmission through the middle ear [the middle-ear efficiency—Rosowski (1991a, b)] is similar at all frequencies. Deviations of the predicted threshold from the behavioral data at low frequencies could be explained by losses within the middle-ear mechanism that are greater at 100 Hz than above 1 kHz or so, e.g., the action of the gerbil *pars flaccida* (Teoh *et al.*, in press). Another possibility is that the cochlea itself may be less sensitive to sound below a few hundred hertz, where the peak of the cochlear traveling wave is near the helicotrema,

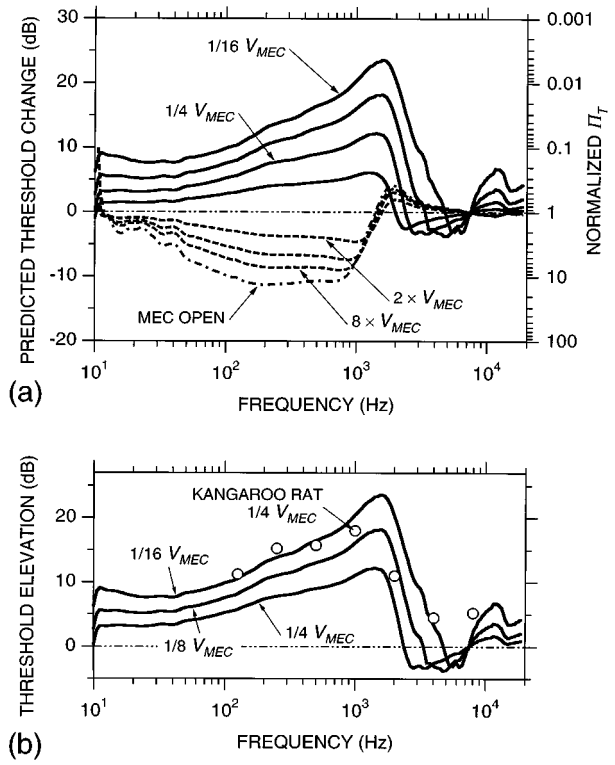

FIG. 8. (a) Changes in diffuse-field hearing threshold $\hat{P}_{\mathrm{DF}}^{\mathrm{TH}}$ (left axis) and middle-ear input power Π_T (right axis) predicted from decreases or increases in V_{MEC}. Curves show $\hat{P}_{\mathrm{DF}}^{\mathrm{TH}}$ and Π_T for decreases (solid lines) or increases (dashed lines) in middle-ear volume, normalized by $\hat{P}_{\mathrm{DF}}^{\mathrm{TH}}$ or Π_T, respectively, for a normal V_{MEC}. Note that, since Π_T is inversely proportional to the square of $\hat{P}_{\mathrm{DF}}^{\mathrm{TH}}$ [Eq. (1)], the right axis is reversed. (b) The increase in $\hat{P}_{\mathrm{DF}}^{\mathrm{TH}}$ (solid lines) predicted for reductions in gerbil middle-ear volume V_{MEC} to $\frac{1}{4}$, $\frac{1}{8}$, and $\frac{1}{16}$ its normal value, compared with threshold elevations observed in kangaroo rat when V_{MEC} was reduced by approximately 75% (open circles—Webster and Webster, 1972).

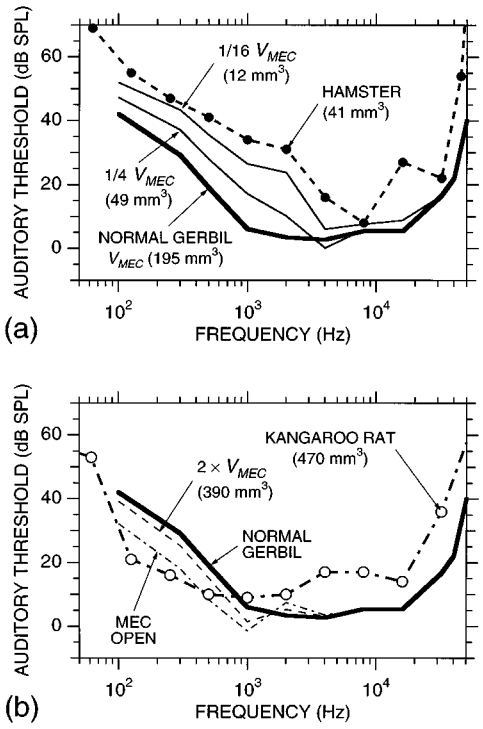

FIG. 9. (a) Comparison of gerbil thresholds predicted from reductions in middle-ear volume V_{MEC} to the hamster audiogram (dashed line and filled circles—Heffner *et al.*, 1994). Gerbil thresholds were computed by multiplying the gerbil audiogram (thick line—Ryan, 1976) by the changes in predicted threshold shown in Fig. 8(b). The thin solid lines are thresholds predicted for $V_{\mathrm{MEC}}=\frac{1}{4}$ and $\frac{1}{16}$ its normal value of 195 mm^3. Though the hamster V_{MEC} is approximately $\frac{1}{4}$ that of gerbil, the threshold is matched better by the threshold predicted for $V_{\mathrm{MEC}}=\frac{1}{16}$ normal. (b) Comparison of gerbil thresholds predicted from increases in V_{MEC} to the kangaroo rat audiogram (dot–dashed line and open circles—Webster and Webster, 1972; Heffner and Masterton, 1980). The thick solid line is the gerbil audiogram as above, the thin dashed line is the threshold predicted for $V_{\mathrm{MEC}}=2\times$ its normal value of 195 mm^3, and the dot–dashed line is the threshold predicted for the middle-ear cavities open. As V_{MEC} is increased, the modified threshold approaches the kangaroo rat threshold.

than at higher frequencies. This decrease in sensitivity would violate the assumption of constant cochlear sensitivity to power made earlier; it seems reasonable, though, that the assumption is less likely to hold near the extremes of the range of hearing.

B. Comparison with effect of middle-ear cavity volume reduction in kangaroo rat

The predicted changes in auditory threshold resulting from changes in V_{MEC} are shown in Fig. 8(a). Shown are the thresholds predicted for reductions (solid lines) or increases (dashed line) in middle-ear volume [from Fig. 5(c)], normalized by $\hat{P}_{\mathrm{DF}}^{\mathrm{TH}}$ with a normal V_{MEC}. The right-hand axis shows the change in middle-ear power input Π_T resulting from changes in V_{MEC}, normalized by Π_T for a normal V_{MEC}. An elevation in threshold means that the sound power Π_T entering the middle ear for a given external sound pressure is reduced; so the scale for Π_T is inverted. Note that the effects of reductions in V_{MEC} on the predicted threshold and power are much smaller below 100 Hz than at higher frequencies; in contrast, the effects of reducing the middle-ear volume on $|\hat{\mathbf{Z}}_{\mathbf{T}}|$ are virtually invariant with frequency below 1.5 kHz (Fig. 4).

When Webster and Webster (1972) reduced the middle-ear volume of kangaroo rats by ''approximately 75%'' of its normal volume of 470 mm^3, they observed that the threshold of hearing was elevated at low frequencies. Figure 8(b) compares the mean elevation in kangaroo rat behavioral threshold to the predicted threshold elevation in gerbil resulting from reductions in middle-ear volume V_{MEC} to $\frac{1}{4}$, $\frac{1}{8}$, and $\frac{1}{16}$ its normal volume of 195 mm^3. The thick solid lines show the predicted threshold changes from panel (a). Though the kangaroo rat threshold is elevated by a greater amount for a given percentage reduction in volume than the gerbil threshold at almost all frequencies, the frequency dependence of the change in behavioral threshold in kangaroo rat is similar to the predicted changes in Π_T. The similarity in the frequency dependence of the measured and predicted effects, which occurs in spite of differences in the structures of the TM, ossicles, and cochlea between the two species (Webster and Plassmann, 1992), suggests that changes in behavioral threshold caused by modifying the middle-ear cavities can be predicted by considering the effect of such modifications on power flow into the middle ear. This is not to say that the other middle-ear structures do not contribute to the sensitiv-

ity of the ear to low-frequency sound; however, the similarity of the gerbil model predictions to the measured effect in kangaroo rat supports the idea that the role of the cavity is similar in these two species that appear specialized for sensitive low-frequency hearing.

C. Threshold predictions for interspecies comparison

Are the predicted volume-induced changes in gerbil thresholds comparable to measured auditory thresholds in other rodents? Figure 9(a) compares predictions of gerbil auditory threshold with reduced V_{MEC} to the hamster audiogram. The gerbil threshold predictions are produced by multiplying the gerbil audiogram (thick solid line) by the threshold changes shown in Fig. 8(b). The hamster auditory threshold is higher than the predicted gerbil threshold for $\frac{1}{4}$ V_{MEC} (comparable to the hamster middle-ear volume of 41 mm^3). Even when the gerbil V_{MEC} is reduced to $\frac{1}{16}$ its normal value (12 vs 195 mm^3), the predicted threshold underestimates the audiogram at all frequencies below 8 kHz. However, the spectral shape of the predicted gerbil audiogram with $V_{\mathrm{MEC}}=12$ mm^3 more closely resembles the hamster audiogram. Similarly, Fig. 9(b) shows that the decreased gerbil auditory thresholds predicted from an increase in power flow resulting from enlarging V_{MEC} (dashed lines) begin to approximate the kangaroo rat auditory threshold. Clearly, variations in the gerbil middle-ear volume produce changes in middle-ear power flow that result in predicted audiograms that *can* approximate other rodents with smaller and larger middle-ear volumes. Therefore, at least some of the differences in auditory threshold between species can be explained by differences in power flow into the middle ear resulting from differences in middle-ear volume.

While the overall similarity of the predicted and measured thresholds demonstrated above establishes that middle-ear air volume can have a profound effect on middle-ear function, the smaller but persistent differences between the predictions and the measured thresholds of the different species indicate that other features contribute to audiometric shape. These other contributors might include differences in the sensitivity of the inner ear to sound, differences in other middle ear features (including the tympanic membrane and ossicles), as well as differences in the external ear. Several demonstrated differences exist among the middle ears of hamster, gerbil, and kangaroo rat. These species have different tympanic membrane areas and stiffnesses (Ravicz *et al.*, 1992), and Webster and Webster (1977) and Plassman *et al.* (1987) have demonstrated that the inner ears of kangaroo rat and gerbil are specialized for the reception of low-frequency sound.

D. Audiometric measures of effect of middle-ear cavity volume

1. Middle-ear air volume and behavioral audiometry

We have predicted that the shape of the gerbil audiogram is altered by changes in the volume of the middle-ear cavities, where increased cavity volume results in improved low-frequency hearing; and we have shown that the predicted gerbil audiograms are similar to audiograms of hamster or kangaroo rat when the middle-ear volume is changed to match V_{MEC} in these species. Is there a general relationship between the shape of the audiogram and middle-ear air volume that holds across mammalian species? Table I is a compilation of estimates of middle-ear air volumes, descriptors of behavioral audiograms, and estimates of the TM–ossicular stiffness and total middle-ear stiffness in ten mammalian species. Middle-ear volumes among this sample population range from 41 mm^3 in hamster (Ma) to 6500 mm^3 in human (Hs). Audiometric descriptors include: (a) the ''best frequency'' BF, the frequency of best hearing (lowest threshold); (b) the ''best'' or lowest threshold BT; (c) the low- and high-frequency limits of hearing f_L and f_H, where the threshold is 30 dB above BT; and (d) the ''auditory bandwidth'' $\mathrm{BW}=\log_{10}(f_H/f_L)$. The middle-ear stiffness K_T was computed from $\mathbf{Z_T}$ near 300 Hz by $K_T=-2\pi f\ \mathrm{Im}\{\mathbf{Z_T}\}$. The combined stiffness of the TM, ossicles, and cochlea K_{TOC} was computed similarly from measurements and estimates of $\mathbf{Z_{TOC}}=\mathbf{Z_T}-\mathbf{Z_{MEC}}$ (Ravicz *et al.*, 1992, Table III).

We investigated the possible relationships among the different Table I data groups by fitting power functions $y=ax^b$ between all possible data pairs using least-squares linear regression. The significance of the computed fits was estimated by computing the probability p that the power-function exponent (the slope of the log-transformed variables) equals zero (an exponent of zero indicates the two variables are unrelated). The smaller the value of p, the more significant the fit. The more significant relationships are listed in Table II and illustrated in Fig. 10. No significant relationship was found between best threshold or best frequency and middle-ear volume ($p>50\%$ in each case).

Both the high- and low-frequency limits of the audiogram appear significantly and inversely related to middle-ear volume ($p<2\%$ and $p<1\%$, respectively, Table II). There is a direct but less significant relationship between auditory bandwidth and volume ($p<10\%$, Table II). The relationships between the frequency limits and volume are illustrated in Fig. 10 (solid lines) along with the 95% confidence limits of predictions based on the power-function fits (dashed lines). The kangaroo rat Dm and the house mouse Mm are outliers in the low-frequency limit relationship, with the kangaroo rat having a lower f_L than predicted by the fit and the mouse having a higher f_L than predicted. The f_L for gerbil Mu is just outside the lower 95% confidence limit. Despite these outliers, there is a clear association of larger middle-ear volumes with lower limits of hearing. There is also a clear association of larger middle-ear volumes and lower high-frequency hearing limits (although the log-log slope of the relationship is less steep than that for f_L vs V_{MEC}). The one species that falls outside the 95% confidence interval of the f_H vs V_{MEC} fit is the cat Fc. This species is unusual in that it has two anatomically separated middle-ear air spaces connected by a narrow foramen which has a significant impedance at auditory frequencies. The tympanic cavity behind the tympanic membrane is about 200 mm^3 in volume (Lynch, 1981; Huang *et al.*, 1997). The bullar cavity (volume of about 600 mm^3) is connected to the tympanic cavity via a narrow tubelike foramen. The acoustic impedance of

TABLE I. Dimensions of anatomical features and audiometric descriptors for seven rodents and three other species for which data exist. The ''middle-ear type'' refers to Fleischer's (1973) classification of ossicular chains: ''Microtype'' (M), in which the malleus has a substantial long anterior process which is rigidly attached to the tympanic ring; ''Freely mobile'' (F), in which the malleus has no long anterior process; and ''Intermediate'' (I), in which the anterior process appears vestigial or is not rigidly attached to the tympanic ring. Classification of middle-ear types by Fleischer (1973), except hamster, classified by us based on anatomy presented in Stephens (1972) and gerbil (Teoh *et al.*, 1997). Audiometric descriptors: The ''best frequency'' is defined as the frequency with the lowest threshold of hearing; the ''low-'' and ''high-frequency limits'' denote the limits of the ''range of best hearing'' or ''bandwidth'' within which the hearing threshold is within 30 dB of the threshold at the best frequency (see Masterton *et al.*, 1969; Dooling, 1980). The bandwidth is the ratio of the high- to the low-frequency limit, expressed in decades. Compiled by Rosowski and Graybeal (1991) and Rosowski (1994); see also Rosowski (1992). References listed under ''Best threshold'' are for the entire audiogram except as noted.

		Mean anatomical measurements			Audiometric descriptors					Acoustic stiffness	
Species	Common name	Middle-ear type	Body weight W (g)	Middle-ear cavity volume V_{MEC} (mm^3)	Best threshold (dB SPL)	Best frequency f_B (kHz)	Low-frequency limit f_L (kHz)	High-frequency limit f_H (kHz)	Bandwidth BW (decades)	K_T (Pa/mm^3)	K_{TOC} (Pa/mm^3)
Meriones unguiculatus	gerbil	I[†]	100[i]	195[q]	3[s]	4	0.21	46	2.3	1000	360
Dipodomys merriami	kangaroo rat	F	50[x]	470[x]	9[w]	1	0.1[e]	34[e]	2.5	1400	1100
Mesocricetus auratus	hamster	F	40[v]	41[z]	8[c]	8	0.75	38	1.7	3800	400
Mus musculus	mouse	M	50[t]	50[r]	−9[f]	16	3.9	62	1.2	85 000	82 000
Rattus norvegicus	rat	M	200[b]	82[p]	0[g]	8	0.9	55	1.8	3800	2000
Cavia procellus	guinea pig	F	400[o]	250[k]	−9[e]	8	0.55	35	1.8	680	120
Chinchilla laniger	chinchilla	F	800[a]	2200[a]	0[l]	3	0.09	29	2.5	58	8
Oryctolagus cuniculus	rabbit	F	1800[h]	130[m]	5[f]	2	0.33	38	2.1	1600	500
Felis catus	cat	I	2500[b]	892[j]	−3[d]	8	0.2	59	2.5	410	250
Homo sapiens	human	F	75 000[y]	6500[n]	−4[u]	4	0.15	14	2.0	190	170

[a]Drescher and Eldredge, 1974.
[b]Fleischer, 1973.
[c]Heffner *et al.*, 1994.
[d]Heffner and Heffner, 1985.
[e]Heffner *et al.*, 1971.
[f]Heffner and Masterton, 1980.
[g]Kelly and Masterton, 1977.
[h]Kirikae, 1960.
[i]Lay, 1972.
[j]Lynch *et al.*, 1994.
[k]Mean of Mundie, 1963; Teas and Nielson, 1975; and Wilson and Johnstone, 1975.
[l]Miller, 1970.
[m]Møller, 1965.
[n]Molvær *et al.*, 1978.
[o]Mundie, 1963.
[p]Ravicz *et al.*, 1990.
[q]Ravicz *et al.*, 1992.
[r]Rosowski, 1994.
[s]Ryan, 1976.
[t]Saunders and Garfinkle, 1983.
[u]Sivian and White, 1933.
[v]Stephens, 1972.
[†]Teoh *et al.*, 1997.
[w]Webster and Webster, 1972.
[x]Webster and Webster, 1975.
[y]Wever and Lawrence, 1954.
[z]Zwillenberg *et al.*, 1981.

the foramen is thought to increase with frequency, such that the foramen effectively closes off the bullar cavity at frequencies above 4–5 kHz (Møller, 1965; Guinan and Peake, 1967). Therefore, at frequencies above 5 kHz, the effective volume of the cat middle-ear air cavity is reduced to the volume of the tympanic cavity alone (200 mm^3; the * in the upper part of Fig. 10). With the reduced V_{MEC} at high frequencies, f_H in cat is within the 95% confidence interval.[8] The cat is an unusual animal with exceptional low- and high-frequency hearing. Henson (1974) has suggested that the frequency-dependent functional middle-ear volume in the cat is a special adaptation in that the large volume at low frequencies is necessary for improved low-frequency hearing, while the small functional volume at high frequencies is necessary for improved high-frequency hearing. The significant power-function fits described in Table II and Fig. 10, together with the f_H predicted for the cat with only the tympanic cavity functional, are consistent with Henson's suggestion.

2. Middle-ear stiffness and behavioral audiometry

Measurements of the effect of variations in middle-ear cavity configuration on middle-ear input impedance (Møller, 1965; Lynch, 1981; Zwillenberg *et al.*, 1981; Ravicz *et al.*, 1992; Lynch *et al.*, 1994) demonstrate that the stiffness of the middle ear K_T depends on both the acoustic stiffness of the middle-ear air K_{MEC} and the stiffness contributed by the tympanic membrane, ossicles, and cochlea K_{TOC}. Both K_T and K_{TOC} are known to vary widely across mammalian species (Table I; see also Rosowski, 1992, 1994). Power functions representing least-square fits to the relationships between audiometric variables and K_T or K_{TOC} are shown in panels (a) and (b), respectively, of Fig. 11 (see also Table II).

TABLE II. Coefficients of power-function fits (via least-squares regression) to audiometric descriptors, middle-ear volume, and acoustic variables. Independent variables are the middle-ear air volume V_{MEC}, the total middle-ear stiffness K_T, and the stiffness of the tympanic membrane, ossicles, and cochlea K_{TOC}. Dependent variables are the low-frequency limit f_L, high-frequency limit f_H, and bandwidth BW of behavioral audiograms, estimated at 30 dB above best threshold (Fay, 1988; Heffner *et al.*, 1994; see Rosowski and Graybeal, 1991 for a description of the determination of the limits). Auditory bandwidth is defined as $BW=\log_{10}(f_H/f_L)$. The significance of the correlation is related to the probability p that the exponent in the fitted power-function relation equals zero; lower p values are more significant. The data from the ten species used in the regression analysis are listed in Table I. Similar analyses with best threshold and best frequency as dependent variables have $p>50\%$.

Independent variable	Dependent variable	Power function fit	Probability p that exponent $=0$
V_{MEC} (mm^3)	f_L (kHz)	$f_L=7.8V_{MEC}^{-0.54}$	$<1\%$
	f_H (kHz)	$f_H=110V_{MEC}^{-0.19}$	$<2\%$
	BW (decades)	$BW=4.2+0.36\log_{10}(V_{MEC})$	$<10\%$
K_T (Pa/mm^3)	f_L (kHz)	$f_L=0.0087K_T^{0.52}$	$<0.1\%$
	f_H (kHz)	$f_H=15K_T^{0.13}$	$<10\%$
	BW (decades)	$BW=6.2-0.38\log_{10}(K_T)$	$<1\%$
K_{TOC} (Pa/mm^3)	f_L (kHz)	$f_L=0.033K_{TOC}^{0.38}$	$<1\%$
	f_H (kHz)	$f_H=21K_{TOC}^{0.10}$	$<20\%$
	BW (decades)	$BW=5.8-0.28\log_{10}(K_{TOC})$	$<5\%$

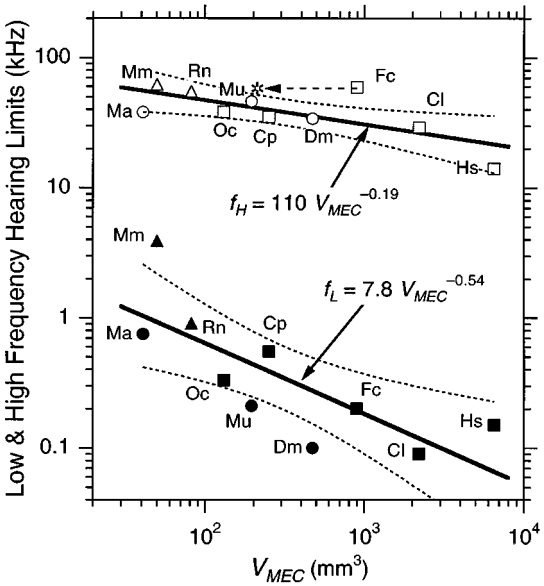

FIG. 10. Power–function relationship between low- and high-frequency limits of the behavioral audiogram f_L and f_H and middle-ear volume V_{MEC} for the ten species listed in Table I. Data are separated into classifications as follows: three small rodent species with freely mobile or intermediate-type ossicular chains (Fleischer, 1973)—gerbil, kangaroo rat, and hamster (circles); two rodent species with microtype ossicular chains—mouse and rat (triangles); the other species with freely mobile or intermediate-type ossicular chains (squares). Filled symbols represent low-frequency limits; open symbols represent high-frequency limits. Labels are the abbreviation of the genus and species names from Table I: *Cl*=chinchilla, *Cp*=guinea pig, *Dm*=kangaroo rat, *Fc*=cat, *Hs*=human, *Ma*=hamster, *Mm*=mouse, *Mu*=gerbil, *Oc*=rabbit, and *Rn*=rat. The solid lines represent least-square fit power functions described by the equations. (The power–function parameters are listed in Table II.) The thin dashed lines are the 95% confidence limits of predictions based on the least-squares analysis. The * and the dashed arrow show the cat high-frequency limit with tympanic cavity volume alone.

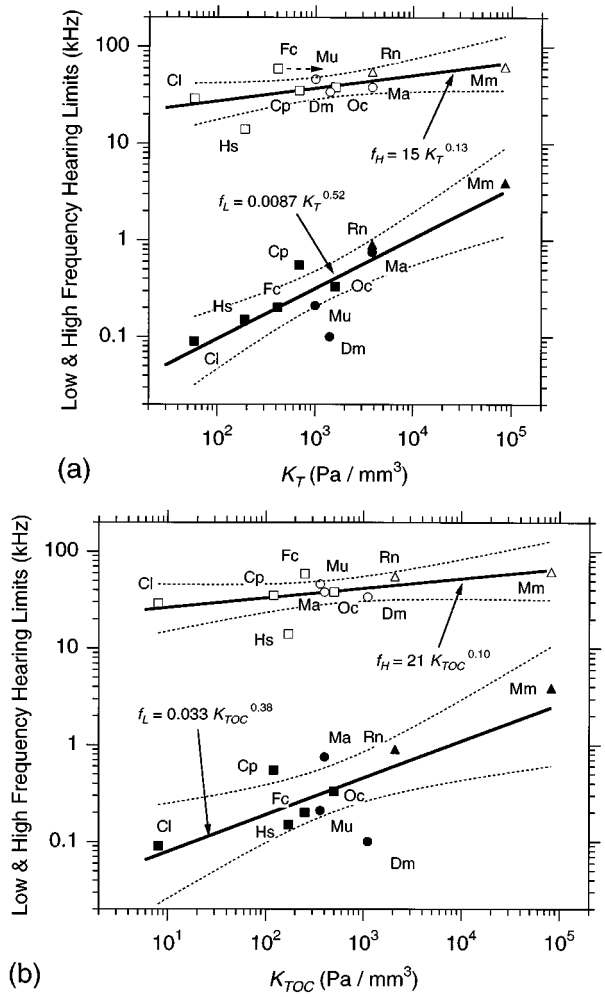

FIG. 11. Power–function relationships between the low- and high-frequency limits of hearing f_L and f_H and the acoustic stiffnesses of (a) the entire middle ear K_T or (b) the stiffness of the tympanic membrane, ossicles, and cochlea alone K_{TOC}. The data are listed in Table I; the power–function fits to the data are described in Table II. Relationships between variables for all species are shown by a thick solid line; thin dashed lines are 95% confidence intervals. Symbols as defined in Fig. 10.

Not surprisingly, there are strong relationships between f_L and both K_T and K_{TOC}: the log of the low-frequency limit varies regularly with the log of either stiffness with an exponent between 0.3 and 0.5 ($p<1\%$ in both cases). Such a relationship is expected, since there is a strong inverse correlation between middle-ear volume and both K_T and K_{TOC} (Ravicz *et al.*, 1992; Rosowski, 1994).

No strong relationship was found between the high-frequency limit of hearing and either K_T or K_{TOC}. The f_H data generally fall within the 95% confidence intervals of the predictions (top of panels), but the log–log slopes are small and not significantly different from zero ($p\geqslant 10\%$). However, moderately significant inverse relationships ($p<2\%$ for K_T; $p<5\%$ for K_{TOC}) were found between the stiffnesses and the bandwidth of the behavioral audiograms. Figures 10 and 11 demonstrate some difference between stiffness and volume, in that middle-ear volume can be related to both high- and low-frequency hearing limits, while the middle-ear stiffnesses [which vary regularly with middle-ear volume

TABLE III. Effects of variations in middle-ear cavity volume on features of the predicted gerbil auditory threshold, shown in Fig. 9. Audiometric descriptors as defined in Table I. Low- and high-frequency limits f_L and f_H and bandwidth BW computed 30 dB above best threshold.

		Characteristic of hearing abilities				
Change in middle-ear cavity volume	Middle-ear cavity volume V_{MEC} (mm^3)	Best frequency BF (kHz)	Best threshold BT (dB SPL)	Low-frequency limit f_L (kHz)	High-frequency limit f_H (kHz)	Bandwidth BW (decades)
$\frac{1}{16}$ normal	12	4	6	0.5	48	2.0
$\frac{1}{8}$ normal	25	4	0	0.6	44	1.9
$\frac{1}{4}$ normal	49	4	0	0.4	44	2.0
$\frac{1}{2}$ normal	98	4	2	0.3	45	2.1
Normal	195	4	3	0.2	46	2.3
2×normal	390	1	1	0.2	45	2.4
4×normal	780	1	−1	0.2	44	2.4
8×normal	1560	1	−2	0.2	43	2.4
MEC open	infinite	1	−2	0.1	43	2.5
Hamster	41	8	8	0.75	38	1.7
Kangaroo rat	470	2	9	0.1	34	2.5

(Rosowski, 1994)] are strongly associated with low-frequency hearing limits only. The implication is that the relationship between volume and stiffness is affected by frequency.

The observed correlations between the low-frequency limit and bandwidth of behavioral audiograms and the middle-ear stiffness are consistent with several views of the evolution of mammalian hearing. Masterton *et al.* (1969) and Heffner and Masterton (1980) suggest that primitive animals had a narrow hearing range restricted to high frequencies. As mammals evolved, the structure of the ear changed to increase sensitivity to low frequencies without sacrificing high-frequency sensitivity, thereby increasing auditory bandwidth. Structural analysis suggests that the middle ears of primitive mammals were acoustically stiff (Rosowski and Graybeal, 1991; Rosowski, 1992) and that decreased middle-ear stiffness was an acquired trait. There then appears to be a temporal parallel between the development of decreased middle-ear stiffness and the achievement of low-frequency hearing sensitivity and increased auditory bandwidth.

3. Threshold description—modifications to middle-ear volume

Effects of variations in the predicted gerbil auditory threshold when the middle-ear volume V_{MEC} is varied, shown in Fig. 5(c), are summarized in Table III. The low- and high-frequency limits are taken at the points where the threshold is 30 dB above the best threshold (as in Table I) to compare the predicted effects of variations in V_{MEC} on the threshold and range of hearing with the hearing abilities of different species described in Table I. The effect of reducing V_{MEC} is to move the low-frequency limit up in frequency and reduce the bandwidth, though the best frequency remains unchanged. When V_{MEC} is reduced by a factor of 8 or 16, the low-frequency limit f_L and bandwidth BW approach that seen for hamster. The low-frequency limit is raised from 210 to 600 Hz, and the bandwidth is reduced from 2.3 to 1.9 decades, values closer to $f_L = 750$ Hz and BW = 1.7 decades seen in hamster. Similarly, the low-frequency limit decreases and the bandwidth increases when V_{MEC} is doubled to approach the kangaroo rat middle-ear volume, though f_L and BW are approximated better by using larger values of V_{MEC}.

E. Possible evolutionary pressures for middle-ear hypertrophy

It has been argued (Webster and Webster, 1971) that a sensitivity to sounds of 1–2 kHz is of vital importance in the desert rodent's daily life. Kangaroo rats and gerbils are primarily nocturnal animals that rest in burrows in the desert during the day and forage for seeds at night. Their primary predators are snakes and owls. Experiments with kangaroo rats and their predators in a large cage have shown that kangaroo rats avoid predation by evading the strike of a snake or owl with a quick vertical or sideward jump at the last instant. Kangaroo rats rely primarily on vision to detect the strike, but hearing is also important, especially in circumstances when vision is compromised (Webster, 1962; Webster and Webster, 1971). Though the flight of owls is virtually silent, the owl's wing motion as it brakes to strike generates sound with a spectral peak near 1.2 kHz. Snakes also move quietly but generate noise at frequencies below 2 kHz when they strike (Webster, 1962). Kangaroo rats whose thresholds of hearing had been elevated at low frequencies by reducing the middle-ear volume were more susceptible to predation than those whose middle ears were not modified, both in a cage and in the wild, under circumstances where hearing was critical to avoid predators, e.g., during the dark phase of the moon (Webster and Webster, 1971, 1984). The social and feeding habits of gerbils are similar to those of kangaroo rats, and the primary predators of gerbils are owls and snakes as well (Lay, 1972, 1974). Young gerbils whose middle-ear volumes are smaller than those of adult gerbils are more subject to predation by owls than older gerbils (Lay, 1974). Presumably the large middle-ear air spaces evolved in gerbil in response to the same environmental pressures experienced by kangaroo rats (Webster and Webster, 1984; Webster and Plassmann, 1992). We have shown that they could provide similar benefits.

IV. SUMMARY AND CONCLUSIONS

Model predictions of the middle-ear input impedance $\hat{\mathbf{Z}}_{\mathbf{T}}$ (Ravicz *et al.*, 1992) and measurements of the external-ear radiation impedance $\mathbf{Z}_{\mathbf{E}}$ (Ravicz *et al.*, 1996) were used to investigate the effect of variations in middle-ear volume V_{MEC} on sound power collection from a diffuse sound field and delivery to the middle ear. Acoustic power entering the middle ear Π_T has been shown to be a good predictor of auditory threshold in gerbil (Ravicz *et al.*, 1996) and other animals (Rosowski *et al.*, 1986; Rosowski, 1991a, b). Reducing V_{MEC}, which increases $|\hat{\mathbf{Z}}_{\mathbf{T}}|$ at low frequencies, predicts a decrease in power transmission from the external to the middle ear, as evidenced by a decrease in the predicted power utilization ratio $\hat{\mathrm{PUR}}$. This predicted decrease in power transmission is also evident as a decrease in the effective area of power collection $\hat{E}A_{\mathrm{TM}}^{\mathrm{DF}}$ and an elevation of the predicted auditory threshold $\hat{P}_{\mathrm{DF}}^{\mathrm{TH}}$ below a few kilohertz. Increasing V_{MEC} predicts a lesser increase in power transmission. The predicted threshold elevation due to V_{MEC} reduction is similar to the behavioral threshold elevation measured in kangaroo rats by Webster and Webster (1972) when the middle-ear volume was reduced. Behavioral auditory thresholds in hamster and kangaroo rat can be predicted by the gerbil threshold computed for reductions or increases in middle-ear volume. Among ten species, three audiogram descriptors, the low- and high-frequency limits of good hearing f_L and f_H and the bandwidth BW, vary significantly with V_{MEC}; but the best threshold and the frequency of best thresholds are not correlated with V_{MEC}. f_L appears to be proportional to the square root of the middle-ear stiffness K_T and approximately proportional to the square root of the stiffness of the TM and ossicular chain K_{TOC}, but BW is only moderately correlated to K_T or K_{TOC}. There is no significant correlation between f_H and either K_T or K_{TOC}. The predicted reduction in gerbil auditory threshold due to the large middle-ear cavity volume occurs at frequencies important for the animal's survival.

ACKNOWLEDGMENTS

The authors wish to thank W. T. Peake, Sunil Puria, Christopher Shera, and Su Wooi Teoh for their comments on earlier versions of this manuscript, and Helen Peake for her translation of Legouix and Wisner (1955) from the French. Portions of this work were presented at the 17th Midwinter Meeting of the Association for Research in Otolaryngology (Ravicz and Rosowski, 1994). This work was supported by NIH Grant No. R01 DC00194.

[1]The time-averaged sound power impinging on an object immersed in a diffuse sound field is the same from all directions. Properties developed for a diffuse field, such as the pressure gain from a diffuse field to the tympanic membrane, are equivalent to the spatial average of such properties determined from all directions. It has been shown that diffuse-field properties are similar to properties from preferred directions (Rosowski, 1991a, b). We use a diffuse field for simplicity and because the variation in external-ear power collection properties with direction in the gerbil is unknown (Ravicz *et al.*, 1996).

[2]The time-averaged sound power that enters the middle ear Π_T is related to the rms sound pressure at the tympanic membrane $\mathbf{P}_{\mathbf{T}}$ and the middle-ear input impedance $\mathbf{Z}_{\mathbf{T}}$ by

$$\Pi_T = \left|\frac{\mathbf{P_T}}{\mathbf{Z_T}}\right|^2 \mathrm{Re}\{\mathbf{Z_T}\}.$$

($\mathbf{Z}_{\mathbf{T}}$ relates $\mathbf{P}_{\mathbf{T}}$ and the rms volume velocity of the tympanic membrane $\mathbf{U}_{\mathbf{T}}$ by $\mathbf{Z_T}=\mathbf{P_T}/\mathbf{U_T}$.)

[3]Variables set in bold type, e.g., $\mathbf{Z}_{\mathbf{T}}$, denote complex quantities that have a magnitude $|\mathbf{Z}_{\mathbf{T}}|$ and a phase angle $\angle\mathbf{Z}_{\mathbf{T}}$. Variables with a circumflex, e.g., $\hat{\mathbf{Z}}_{\mathbf{T}}$, denote model estimates.

[4]Viscous and thermal losses are included in $\hat{\mathbf{Z}}_{\mathbf{MEC}}$ (Daniels, 1947). The losses are significant at frequencies below 100 Hz. At higher frequencies the impedance of the sphere is approximately equal to $\hat{\mathbf{Z}}_{\mathbf{MEC}} \approx \rho_0 c^2 / j\omega V_{\mathrm{MEC}}$ (Beranek, 1986).

[5]The $\hat{\mathbf{Z}}_{\mathbf{T}}$ curves shown in Fig. 18 of Ravicz *et al.* (1992) include the impedance of a middle-ear vent. Model $\hat{\mathbf{Z}}_{\mathbf{T}}$ predictions without the vent are shown here. The effect of the vent is to increase Re $\{\hat{\mathbf{Z}}_{\mathbf{T}}\}$ below 100 Hz.

[6]Of course, if the middle-ear cavities were open, TM motion would be disrupted by sound entering the middle-ear cavities through the opening.

[7]$|\mathbf{P}_{\mathbf{T}}/P_{DF}|$ computed for a single animal is larger between 3 and 8 kHz than $|\mathbf{P}_{\mathbf{T}}/P_{DF}|$ computed from mean $\mathbf{Z}_{\mathbf{E}}$ and $\mathbf{Z}_{\mathbf{T}}$ measurements (Ravicz *et al.*, 1996, Fig. 17).

[8]There are similar changes in effective middle-ear volume that occur in other species at high frequencies. The human, chinchilla, and gerbil middle-ear air spaces are made up of compartments connected by foramena. The human tympanic cavity has a volume of about 1000 mm^3, while the chinchilla and gerbil tympanic cavity volumes are on the order of 500 and 150 mm^3, respectively.

Beranek, L. L. (**1986**). *Acoustics* (American Institute of Physics, New York).

Daniels, F. B. (**1947**). ''Acoustical impedance of enclosures,'' J. Acoust. Soc. Am. **19,** 569–571.

Dallos, P. (**1973**). *The Auditory Periphery* (Academic, New York).

Dooling, R. J. (**1980**). ''Behavior and psychophysics of hearing in birds,'' in *Comparative Studies of Hearing in Vertebrates*, edited by A. N. Popper and R. R. Fay (Springer-Verlag, New York), pp. 261–288.

Drescher, D. G., and Eldredge, D. H. (**1974**). ''Species differences in cochlear fatigue related to acoustics of outer and middle ears of guinea pig and chinchilla,'' J. Acoust. Soc. Am. **56,** 929–934.

Fay, R. R. (**1988**). *Hearing in Vertebrates: A Psychophysics Databook* (Hill-Fay, Winnetka, IL).

Fleischer, G. (**1973**). ''Studien am Skelett des Gehörorgans der Säugetiere, einschliesslich des Menschen,'' Säugetierkundl. Mitteilungen (München) **21**, 131–239.

Fleischer, G. (**1978**). ''Evolutionary principles of the mammalian middle ear,'' Adv. Anat. Embryol. Cell Biol. **55**, 3–69.

Guinan, J. J., and Peake, W. T. (**1967**). ''Middle-ear characteristics of anesthetized cats,'' J. Acoust. Soc. Am. **41,** 1237–1261.

Heffner, R. S., and Heffner, H. E. (**1985**). ''Hearing range of the domestic cat,'' Hear. Res. **19**, 85–88.

Heffner, H. E., and Masterton, R. B. (**1980**). ''Hearing in *Glires*: Domestic rabbit, cotton rat, feral, house mouse and kangaroo rat,'' J. Acoust. Soc. Am. **68,** 1584–1599.

Heffner, R. S., Heffner, H. E., and Masterton, R. B. (**1971**). ''Behavioral measurement of absolute and frequency-difference thresholds in guinea pig,'' J. Acoust. Soc. Am. **49,** 1888–1895.

Heffner, R. S., Koay, G., Gandy, R., Heffner, H. E., and Wollberg, Z. (**1994**). ''Role of vision in development of spatial acuity in hamsters,'' Abstracts of the 17th Midwinter Meeting of the Association for Research in Otolaryngology (Des Moines, IA), p. 25.

Henson, O. W., Jr. (**1961**). ''Some morphological and functional aspects of certain structures of the middle ear in bats and insectivores,'' Univ. Kansas Sci. Bull. **42**, 151–255.

Henson, O. W., Jr. (**1974**). ''Comparative anatomy of the middle ear,'' in *The Handbook of Sensory Physiology: The Auditory System, Vol. 1,* edited by W. D. Keidel and W. D. Neff (Springer-Verlag, New York), pp. 39–110.

Huang, G. T., Rosowski, J. J., Flandermeyer, D. T., and Peake, W. T. (**1996**). ''Middle ear of a lion: Comparison of structure and function to domestic cat,'' J. Acoust. Soc. Am. **99,** 2562.

Huang, G. T., Rosowski, J. J., Flandermeyer, D. T., Lynch, T. J., III, and Peake, W. T. (**1997**). ''The middle ear of a lion: Comparison of structure and function to domestic cat,'' J. Acoust. Soc. Am. **101**, 1532–1549.

Hunt, Jr., R. M., and Korth, W. W. (**1980**). ''The auditory region of *Dermoptera*: Morphology and function relative to other living mammals,'' J. Morphol. **164,** 167–211.
Keefe, D. H., Bulen, J. C., Campbell, S. L., and Burns, E. M. (**1994**). ''Pressure transfer function and absorption cross-section from the diffuse field to the human infant ear canal,'' J. Acoust. Soc. Am. **95,** 355–372.
Kelly, J. B., and Masterton, R. B. (**1977**). ''Auditory sensitivity of the albino rat,'' J. Comp. Physiol. Psychol. **91**, 930–936.
Kirikae, I. (**1960**). *The Structure and Function of the Middle Ear* (Univ. of Tokyo, Tokyo).
Lay, D. M. (**1972**). ''The anatomy, physiology, functional significance and evolution of specialized hearing organs of gerbilline rodents,'' J. Morphol. **138,** 41–120.
Lay, D. M. (**1974**). ''Differential predation on gerbils (Meriones) by the little owl, *Athene brahma*,'' J. Mammal. **55**, 608–613.
Legouix, J. P., and Wisner, A. (**1955**). ''Role fonctionnel des bulles tympaniques géantes de certains rongeurs (*Meriones*),'' Acustica **5,** 208–216.
Lynch, T. J., III (**1981**). ''Signal processing by the cat middle ear: Admittance and transmission, measurements and models,'' Sc.D. thesis, Massachusetts Institute of Technology, Cambridge, MA.
Lynch, T. J., III, Peake, W. T., and Rosowski, J. J. (**1994**). ''Measurements of the acoustic input-impedance of cat ears: 10 Hz to 20 kHz,'' J. Acoust. Soc. Am. **96,** 2184–2209.
Masterton, B., Heffner, H., and Ravizza, R. (**1969**). ''The evolution of human hearing,'' J. Acoust. Soc. Am. **45,** 966–985.
Miller, J. D. (**1970**). ''Audibility curve of the chinchilla,'' J. Acoust. Soc. Am. **48,** 513–523.
Møller, A. R. (**1965**). ''Experimental study of the acoustic impedance of the middle ear and its transmission properties,'' Acta Otolaryngol. **60**, 129–149.
Molvær, O., Vallersnes, F. M., and Kringlebotn, M. (**1978**). ''The size of the middle ear and the mastoid air cell,'' Acta Otolaryngol. **85**, 24–32.
Mundie, J. R. (**1963**). ''The impedance of the ear—a variable quantity,'' in *Proceedings of the Middle-Ear Function Seminar*, edited by J. L. Fletcher (U.S. Army Medical Res. Lab., Ft. Knox, KY), Report 576, pp. 63–85.
Plassmann, W., and Brändle, K. (**1992**). ''A functional model of the auditory system in mammals and its evolutionary implications,'' in *The Evolutionary Biology of Hearing*, edited by D. B. Webster, R. R. Fay, and A. N. Popper (Springer-Verlag, New York), pp. 637–653.
Plassmann, W., Peetz, W., and Schmidt, M. (**1987**). ''The cochlea in gerbilline rodents,'' Brain Behav. Evol. **30**, 82–101.
Pye, A., and Hinchcliffe, R. (**1976**). ''The comparative anatomy of the ear,'' in *Scientific Foundations of Otolaryngology*, edited by R. Hinchcliffe and D. Harrison (William Heineman, London), pp. 184–202.
Ravicz, M. E., and Rosowski, J. J. (**1994**). ''The effect of middle-ear cavity size on acoustic power flow in the ear of the Mongolian gerbil,'' Abstracts of the 17th Midwinter Meeting of the Association for Research in Otolaryngology (Des Moines, IA), p. 145.
Ravicz, M. E., Rosowski, J. J., and Hall, R. D. (**1990**). Unpublished observations.
Ravicz, M. E., Rosowski, J. J., and Voigt, H. F. (**1992**). ''Sound power collection by the auditory periphery of the Mongolian gerbil *Meriones unguiculatus:* I. Middle-ear input impedance,'' J. Acoust. Soc. Am. **92,** 157–177.
Ravicz, M. E., Rosowski, J. J., and Voigt, H. F. (**1996**). ''Sound power collection by the auditory periphery of the Mongolian gerbil *Meriones unguiculatus:* II. External-ear radiation impedance and power collection,'' J. Acoust. Soc. Am. **99,** 3044–3063.
Rosowski, J. J. (**1991a**). ''The effects of external- and middle-ear filtering on auditory threshold and noise-induced hearing loss,'' J. Acoust. Soc. Am. **90,** 124–135.
Rosowski, J. J. (**1991b**). ''Erratum: The effects of external- and middle-ear filtering on auditory threshold and noise-induced hearing loss,'' J. Acoust. Soc. Am. **90,** 3373.
Rosowski, J. J. (**1992**). ''Hearing in transitional mammals: Predictions from the middle-ear anatomy and hearing capabilities of extant mammals,'' in *The Evolutionary Biology of Hearing*, edited by D. B. Webster, R. R. Fay, and A. N. Popper (Springer-Verlag, New York), pp. 615–631.
Rosowski, J. J. (**1994**). ''Outer and middle ear,'' in *The Springer Series in Auditory Research, Volume IV: Comparative Mammalian Hearing* (Springer-Verlag, New York), pp. 172–247.
Rosowski, J. J., and Graybeal, A. (**1991**). ''What did *Morganucodon* hear?'' Zool. J. Linnean Soc. **101**, 131–168.
Rosowski, J. J., Carney, L. H., and Peake, W. T. (**1988**). ''The radiation impedance of the external ear of cat: Measurements and applications,'' J. Acoust. Soc. Am. **84,** 1695–1708.
Rosowski, J. J., Carney, L. H., Lynch, T. J., III, and Peake, W. T. (**1986**). ''The Effectiveness of External and Middle Ears in Coupling Acoustic Power into the Cochlea,'' in *Peripheral Auditory Mechanisms*, edited by J. B. Allen, J. L. Hall, A. Hubbard, S. T. Neely, and A. Tubis (Springer-Verlag, New York), pp. 3–12.
Ryan, A. (**1976**). ''Hearing sensitivity of the Mongolian gerbil, *Meriones unguiculatis*,'' J. Acoust. Soc. Am. **54,** 1222–1226.
Saunders, J. C., and Garfinkle, T. J. (**1983**). ''Peripheral anatomy and physiology,'' in *Auditory Psychobiology of the Mouse*, edited by J. F. Willot (Thomas, Springfield, IL), pp. 131–168.
Shaw, E. A. G. (**1976**). ''Diffuse-field sensitivity of external ear based on reciprocity principle,'' J. Acoust. Soc. Am. Suppl. 1 **60,** S102.
Shaw, E. A. G. (**1979**). ''Performance of the external ear as a sound collector,'' J. Acoust. Soc. Am. Suppl. 1 **65,** S9.
Shaw, E. A. G. (**1988**). ''Diffuse field response, receiver impedance, and the acoustic reciprocity principle,'' J. Acoust. Soc. Am. **84**, 2284–2287.
Sivian, L. J., and White, S. D. (**1933**). ''On minimum audible fields,'' J. Acoust. Soc. Am. **4,** 288–321.
Stephens, C. B. (**1972**). ''Development of the middle and inner ear in the golden hamster (*Mesocricetus auratus*): A detailed description to establish a norm for physiological study of congenital deafness,'' Acta Otolaryngol. Suppl. **296**, 1–51.
Teas, D. C., and Nielsen, D. W. (**1975**). ''Interaural attenuation versus frequency for guinea pig and chinchilla CM response,'' J. Acoust. Soc. Am. **58,** 1066–1072.
Teoh, S. W., Flandermeyer, D. T., and Rosowski, J. J. (**1997**). ''Effects of *pars flaccida* on sound conduction in ears of Mongolian gerbil: Acoustic and anatomic measurements,'' Hear. Res. (in press).
Webster, D. B. (**1961**). ''The ear apparatus of the kangaroo rat, *Dipodomys*,'' Am. J. Anat. **108**, 123–147.
Webster, D. B. (**1962**). ''A function of the enlarged middle-ear cavities of the kangaroo rat, *Dipodomys*,'' Physiol. Zool. **35**, 248–255.
Webster, D. B., and Plassmann, W. (**1992**). ''Parallel evolution of low frequency sensitivity in Old World and New World desert rodents,'' in *The Evolutionary Biology of Hearing*, edited by D. B. Webster, R. R. Fay, and A. N. Popper (Springer-Verlag, New York), pp. 633–636.
Webster, D. B., and Webster, M. (**1971**). ''Adaptive value of hearing and vision in kangaroo rat predator avoidance,'' Brain Behav. Evol. **4**, 310–322.
Webster, D. B., and Webster, M. (**1972**). ''Kangaroo rat auditory thresholds before and after middle ear reduction,'' Brain Behav. Evol. **5**, 41–53.
Webster, D. B., and Webster, M. (**1975**). ''Auditory systems of Heteromyidae: Functional morphology and evolution of the middle ear,'' J. Morphol. **146,** 343–376.
Webster, D. B., and Webster, M. (**1977**). ''Auditory systems of Heteromyidae: Cochlear diversity,'' J. Morphol. **152,** 153–170.
Webster, D. B., and Webster, M. (**1984**). ''The specialized auditory system of kangaroo rats,'' in *Contributions to Sensory Physiology, Vol. 8* (Academic, New York), pp. 161–196.
Wever, E. G., and Lawrence, M. (**1954**). *Physiological Acoustics* (Princeton U.P., Princeton, NJ).
Wilson, J. P., and Johnstone, J. R. (**1975**). ''Basilar membrane and middle-ear vibration in guinea pig measured by capacitive probe,'' J. Acoust. Soc. Am. **57,** 705–723.
Zwillenberg, D., Konkle, D. F., and Saunders, J. C. (**1981**). ''Measures of middle ear admittance during experimentally induced changes in middle ear volume in the hamster,'' Otolaryngol. Head Neck Surg. **89**, 856–860.
Zwislocki, J. (**1962**). ''Analysis of the middle-ear function. Part I: Input impedance,'' J. Acoust. Soc. Am. **34,** 1514–1523.
Zwislocki, J. J. (**1975**). ''The role of the external and middle ear in sound transmission,'' in *The Nervous System, Vol. 3: Human Communication and its Disorders*, edited by D. B. Tower (Raven, New York), pp. 45–55.

Classical and non-classical models of the cochlea

Egbert de Boer[a)]
Room D2-226, Academic Medical Center, Meibergdreef 9, 1105 AZ Amsterdam, The Netherlands

(Received 15 April 1996; revised 10 June 1996; accepted 30 September 1996)

In a ''classical'' model of the cochlea the response is controlled by a local parameter function, for instance, the BM impedance. In a non-classical model, the response is controlled by parameters that are distributed over space. In this note it is shown to which extent classical and non-classical models are equivalent. To each non-classical model there exists one classical model that yields the same response. However, the BM impedance of that classical model does not necessarily obey the requirements of a driving-point impedance. © *1997 Acoustical Society of America.*
[S0001-4966(97)02604-1]

PACS numbers: 43.64.Kc, 43.64.Bt [RDF]

INTRODUCTION

In a ''classical'' macromechanical model of the cochlea (Viergever, 1986) the dynamics of the cochlear partition (CP) at a certain location x is described by a *local* parameter, i.e., by a parameter that depends only on one location, x. In the case of a linear model, that parameter is usually referred to as the BM impedance, written as $Z_{BM}(x,\omega)$ (cf. Viergever, 1978). Of late, ''non-classical'' models are beginning to appear in which the dynamics of the CP is not determined by a local parameter. For instance, Hubbard (1993) described a model based on two interacting wave-propagating structures. In the model proposed by Steele *et al.* (1993) the response-enhancing outer hair cells (OHCs) receive their input from another location than where they deliver their ''load,'' i.e., the pressure or force they generate. In a more detailed form, this idea has been worked out by Geisler and Sang (1995) who achieved model responses with quite remarkable properties. These non-classical models—note that all are *linear* models—form a welcome extension of the class of models considered earlier. This note describes the connection between classical and non-classical models. The basis of the derivation lies in the hydrodynamics of the fluid, which is, for simplicity, assumed to be ideal (i.e., incompressible, inviscid and linear). It will be shown that, once the *effective BM impedance* of a non-classical model has been determined, a classical model with the same function inserted as its BM impedance will have the same response. Some implications of this property are obvious. A short concluding section is devoted to a few less obvious corollaries.

I. DERIVATION

We will consider a linear three-dimensional model of the cochlea that is described in a Cartesian coordinate system x-y-z. When the fluid is linear, all parameters and variables can be considered as functions of the radian frequency ω. In such a model the fluid pressure at the level of the BM can generally be expressed as an integral of the BM acceleration over the length of the model. In terms of BM velocity $v_{\mathrm{BM}}(x,\omega)$ and channel pressure $p(x,\omega)$ (both taken at the center of the BM), this property reads:

$$p(x,\omega)=2i\omega\rho\int_0^L g(x,x')v_{BM}(x',\omega)dx' + i\omega\rho(L-x)v_{\mathrm{stapes}}(\omega). \quad (1)$$

Here, L is the length of the model, $v_{\mathrm{stapes}}(\omega)$ the velocity of the stapes (assumed constant over the area of the stapes), and $g(x,x')$ is the *Green's function* associated with the geometry of the fluid channels. See for the derivation in a two-dimensional model Allen (1977), Equations (3) and (12). Models with different dimensionality differ in their $g(x,x')$ functions. See, for instance, Mammano and Nobili (1993). In simple structures with a completely regular geometry, $g(x,x')$ depends only on $(x-x')$ (cf. Sondhi, 1978). *Equation (1) is valid for classical as well as non-classical models because it expresses only a property of the fluid.*

It is stressed at this point that Eq. (1) does not include any specification of the organ of Corti or any steps taken in the actual solution of the model equations. The equation represents—by way of the functional form of the function $g(x,x')$—the type of longitudinal coupling that is purely due to the fluid, irrespective of any assumptions about the mechanics of the organ of Corti. In the case of a two-dimensional model the equation takes into account that the fluid is moving uniformly over the width of the partition. In the case of a three-dimensional model a specific pattern of movement over the width is assumed, namely, that the BM is moving as a (co)sine function over its width (cf. de Boer, 1981). Pressure and BM velocity are then taken at the center of the BM.

Consider a *non*-classical model of the cochlea, and let it be linear in all variables. Assume that BM velocity $v_{\mathrm{BM}}(x,\omega)$ and channel pressure $p(x,\omega)$ have been solved as functions of x. The quotient of $p(x,\omega)$ and $v_{\mathrm{BM}}(x,\omega)$ produces the *effective BM impedance* $Z_{\mathrm{BM}}^{(\mathrm{eff})}(x,\omega)$. According to Eq. (1) there is only one function $p(x,\omega)$ associated with the 'given' $v_{\mathrm{BM}}(x,\omega)$ function, and thus there is only *one* effective BM impedance $Z_{\mathrm{BM}}^{(\mathrm{eff})}(x,\omega)$ associated with this solution. This fact solely relates to the fluid. The computed imped-

a)Electronic mail: e.deboer@amc.uva.nl

ance, however, includes all details about the dynamics of the cochlear partition that have been used in the formulation of the model.

Consider now a *classical* model, also linear, with exactly the same geometry, insert the effective impedance $Z_{\mathrm{BM}}^{(\mathrm{eff})}(x,\omega)$ as its BM impedance $Z_{\mathrm{BM}}(x,\omega)$ and use the same boundary conditions at the stapes and helicotrema ends. Next, solve the equations for that model. Let the solutions for BM velocity and pressure be $w_{\mathrm{BM}}(x,\omega)$ and $q(x,\omega)$, respectively. According to Eq. (1), the two solution functions $w_{\mathrm{BM}}(x,\omega)$ and $q(x,\omega)$ are related in the same way as $v_{\mathrm{BM}}(x,\omega)$ and $p(x,\omega)$. They are also related because they have the same ratio, namely, the function $Z_{\mathrm{BM}}^{(\mathrm{eff})}(x,\omega)$. In the Appendix it is shown that there exists only one set of functions having both these properties. Therefore, $w_{\mathrm{BM}}(x,\omega)$ is identical to $v_{\mathrm{BM}}(x,\omega)$, and $q(x,\omega)$ is identical to $p(x,\omega)$.

In general terms, *the response of a classical model which has the effective BM impedance* $Z_{\mathrm{BM}}^{(\mathrm{eff})}(x,\omega)$ *of the non-classical model as its BM impedance, is equal to the response of that non-classical model*. The two models must have the same structure and geometry, and the solutions must obey the same boundary conditions at the two ends of the models. This property is valid for long-wave, two- and three-dimensional models.

II. COROLLARIES

The first consequence of the property derived in the preceding section is that *a non-classical model always shows a response that could also have been obtained in a classical model*. In this respect there seems to be no difference between these two classes of models. The major point is, however, that a non-classical model *allows for a far greater freedom in the functional form of the effective BM impedance* $Z_{\mathrm{BM}}^{(\mathrm{eff})}(x,\omega)$. Indeed, we have to remember that $Z_{\mathrm{BM}}^{(\mathrm{eff})}(x,\omega)$ is a *derived* parameter: it can only be found *after* pressure and BM velocity in the nonclassical model have been solved. Therefore, the function $Z_{\mathrm{BM}}^{(\mathrm{eff})}(x,\omega)$ depends on the character of the solution and the form of the model, and it cannot be chosen beforehand or independently (as in a classical model). An additional, not too obvious, factor involved is the following. In a classical model the BM impedance $Z_{\mathrm{BM}}(x,\omega)$ must be a *causal* function, which means that it must correspond to a causal impulse response. The same applies to the admittance function $1/Z_{\mathrm{BM}}(x,\omega)$. This restriction does not apply to the non-classical model because $Z_{\mathrm{BM}}^{(\mathrm{eff})}(x,\omega)$ is derived from two functions $p(x,\omega)$ and $v_{\mathrm{BM}}(x,\omega)$, each of which can be seen as the response of a model to excitation at the stapes, and is therefore causal. However, their quotient does not need to be causal: the denominator $v_{\mathrm{BM}}(x,\omega)$ in $Z_{\mathrm{BM}}^{(\mathrm{eff})}(x,\omega)$ may well have zeros in the right-half of the complex s-plane that are not offset by corresponding zeros in the numerator $p(x,\omega)$. Hence $Z_{\mathrm{BM}}^{(\mathrm{eff})}(x,\omega)$ may well be non-causal.[1] In general, in a non-classical model, the relation of the local pressure $p_{\mathrm{OHC}}(x,\omega)$ generated by, for instance, outer hair cells (OHCs) to the distribution of BM velocity $v_{\mathrm{BM}}(x,\omega)$ over x may well be non-local; in that case the OHC pressure $p_{\mathrm{OHC}}(x,\omega)$ is a functional of $v_{\mathrm{BM}}(x,\omega)$ defined over a certain domain of x. Furthermore, the pressure $p_{\mathrm{OHC}}(x,\omega)$ does not necessarily contribute to the channel pressure $p(x,\omega)$ at the *same* place x. For all these reasons, the impedance function $Z_{\mathrm{BM}}^{(\mathrm{eff})}(x,\omega)$ cannot always be realized as a driving-point impedance and the resulting response cannot be obtained in a classical model with a realizable BM impedance. In this respect, the class of non-classical models is definitely wider than that of classical models (see also Geisler and Sang, 1995).

A principal point in the use of classical models has always been that longitudinal stiffness in the BM had to be neglected. In fact, it has invariably been found that very small amounts of longitudinal coupling destroyed the main character of the model response (Allen and Sondhi, 1979). At present it is possible to explore this limitation to a far greater degree of accuracy, and to study the influence of mechanical and constructual constraints based on material properties on the performance of the model. The property derived here may well be of use in this field.

In the field of cochlear nonlinearity, the equivalence between classical and non-classical models may be exploited, too. It has been shown by Kanis and de Boer (1993) that, in view of the small degree of nonlinearity that the cochlea exhibits in most stimulation conditions, non-linear effects may be treated as perturbations. That is, concepts of linear-system theory like impedance, amplitude and phase angle, can be retained and used to full advantage. It remains to be studied whether the Kanis–de Boer method is equally useful in non-classical as in classical models. If this proves to be correct, non-classical nonlinear models can be studied in the same way as nonlinear classical models via the quasi-linear approximation.

ACKNOWLEDGMENTS

The author is indebted to Dan Geisler (Madison WI), Fred Nuttall (Portland, OR) and Arnold Tubis (Purdue U., West Lafayette IN) for their participation in discussions on the relative merits of classical and non-classical models.

APPENDIX

In this Appendix we prove that there is only one pair of functions $p(x)$ and $v_{\mathrm{BM}}(x,\omega)$ that have a given impedance function $Z_{\mathrm{BM}}^{(\mathrm{eff})}(x,\omega)$ as their quotient, *and* are related to each other as dictated by the geometry of the fluid channels and the properties of the fluid. Divide the x axis into N discrete points x_{i} and rewrite Eq. (1) in a more universal form as a matrix equation:

$$\mathbf{p}=\mathbf{G}\mathbf{v}-\mathbf{s}. \tag{A1}$$

Here $\mathbf{p}$ and $\mathbf{v}$ are column vectors representing the pressure $p(x)$ and the BM velocity $v_{\mathrm{BM}}(x,\omega)$, respectively, at the points x_i $(i=1,\ldots,N)$ and $\mathbf{s}$ is a column vector which represents the way the stapes boundary condition expresses itself in the pressure $p(x)$; see, e.g., the term $i\omega\rho(L-x)v_{\mathrm{stapes}}(\omega)$ in Eq. (1). The matrix $\mathbf{G}$ (size $N\times N$) represents the fluid coupling — the function $2i\omega\rho g(x,x')$ in Eq. (1). Assume that pressure and velocity are solutions of

the model equation for the non-classical model and that their ratio is $Z_{\mathrm{BM}}^{(\mathrm{eff})}(x,\omega)$. Rewrite this condition as

$$\mathbf{p}=\mathbf{Z}\mathbf{v}, \tag{A2}$$

where $\mathbf{Z}$ is an $N\times N$ matrix which has $Z_{\mathrm{BM}}^{(\mathrm{eff})}(x_i,\omega)$ $(i=1,...,N)$ in its main diagonal and zeros everywhere else. Substitute Eq. (A2) in Eq. (A1):

$$(\mathbf{G}-\mathbf{Z})\mathbf{v}=\mathbf{s}. \tag{A3}$$

This matrix equation has to be obeyed by the solution to the non-classical model. It is, however, exactly the same matrix equation that *produces* the solution to a classical model with the same $\mathbf{Z}$. Equation (A3) has, in general, a unique solution. This, then, must be the same for the classical and the non-classical model. Therefore, there exists only one velocity vector $\mathbf{v}$ which has the property that its associated pressure vector $\mathbf{p}$ is related to it by Eq. (A1) as well as Eq. (A2) (with $\mathbf{Z}$ given). In other words, for a model with given geometry there is only one solution for which pressure and velocity have the quotient $Z_{\mathrm{BM}}^{(\mathrm{eff})}(x,\omega)$.

[1]In less abstract terms: assume that the model studied is a simple non-dispersive transmission line and that the input to OHCs at location x is taken from a more basalward location $x-\Delta x$; in this case $Z_{\mathrm{BM}}^{(\mathrm{eff})}(x,\omega)$ contains a component that is a pure predictor.

Allen, J. B. (**1977**). ''Two-dimensional cochlear fluid model: New Results,'' J. Acoust. Soc. Am. **61,** 110–119.

Allen, J. B., and Sondi, M. M. (**1979**). ''Cochler macromechanics-time domain solutions,'' J. Acoust. Soc. Am. **66,** 123–132.

de Boer, E. (**1981**). ''Short waves in three-dimensional cochlea models: Solution for a 'block' model,'' Hear. Res. **4**, 53–77.

Geisler, C. D., and Sang, C. (**1995**). ''A cochlear model using feed-forward outer-hair-cell forces,'' Hear. Res. **86**, 132–146.

Hubbard, A. E. (**1993**). ''A traveling wave-amplifier model of the cochlea,'' Science **259,** 68–71.

Kanis, L. J., and de Boer, E. (**1993**). ''Self-suppression in a locally active nonlinear model of the cochlea: A quasi-linear approach,'' J. Acoust. Soc. Am. **94,** 3199–3206.

Mammano, F., and Nobili, R. (**1993**). ''Biophysics of the cochlea: Linear approximation,'' J. Acoust. Soc. Am. **93,** 3320–332.

Sondhi, M. M. (**1978**). ''Method for computing motion in a two-dimensional cochlear model,'' J. Acoust. Soc. Am. **63,** 1468–1477.

Steele, C. R., Baker, G., Tolomeo, Jr., and Zetes, D. (**1993**). ''Electromechanical models of the outer hair cell,'' in *Biophysics of Hair-Cell Sensory Systems*, edited by H. Duifhuis, J. W. Horst, P. van Dijk, and S. M. van Netten (World Scientific, Singapore), pp. 207–214.

Viegever, M. A. (**1978**). ''On the physical background of the point-impedance characterization of the basilar membrane in cochlear mechanics,'' Acustica **39,** 292–297.

Viergever, M. A. (**1986**). ''Cochlear macromechanics-a review,'' in *Peripheral Auditory Mechanisms*, edited by J. B. Allen, J. L. Hall, A. Hubbard, S. T. Neely, and A. Tubis (Springer-Verlag, Berlin), pp. 63–72.

Basilar-membrane responses to tones at the base of the chinchilla cochlea

Mario A. Ruggero
The Hugh Knowles Center (Dept. of Communication Sciences and Disorders), and Institute for Neuroscience, Northwestern University, 2299 North Campus Drive, Evanston, Illinois 60208-3550

Nola C. Rich
1193 Liberty Church Road, Mocksville, North Carolina 27028

Alberto Recio and S. Shyamla Narayan
The Hugh Knowles Center (Dept. of Communication Sciences and Disorders), Northwestern University, Evanston, Illinois 60208-3550

Luis Robles
Departamento de Fisiología y Biofísica, Facultad de Medicina, Universidad de Chile, Santiago, Chile

(Received 24 June 1996; accepted for publication 13 September 1996)

Basilar-membrane responses to single tones were measured, using laser velocimetry, at a site of the chinchilla cochlea located 3.5 mm from its basal end. Responses to low-level (<10–20 dB SPL) characteristic-frequency (CF) tones (9–10 kHz) grow linearly with stimulus intensity and exhibit gains of 66–76 dB relative to stapes motion. At higher levels, CF responses grow monotonically at compressive rates, with input–output slopes as low as 0.2 dB/dB in the intensity range 40–80 dB. Compressive growth, which is significantly correlated with response sensitivity, is evident even at stimulus levels higher than 100 dB. Responses become rapidly linear as stimulus frequency departs from CF. As a result, at stimulus levels >80 dB the largest responses are elicited by tones with frequency about 0.4–0.5 octave below CF. For stimulus frequencies well above CF, responses stop decreasing with increasing frequency: A plateau is reached. The compressive growth of responses to tones with frequency near CF is accompanied by intensity-dependent phase shifts. Death abolishes all nonlinearities, reduces sensitivity at CF by as much as 60–81 dB, and causes a relative phase lead at CF. © *1997 Acoustical Society of America.* [S0001-4966(97)05104-7]

PACS numbers: 43.64.Kc, 43.64.Jb, 43.64.Ld, 43.64.Pg [RDF]

INTRODUCTION

Perhaps the most influential event in mammalian cochlear physiology during the last quarter century was Rhode's discovery of a basilar-membrane nonlinearity (Rhode, 1971). Rhode showed that, in relatively healthy cochleae, basilar-membrane responses to characteristic-frequency (CF) tones grow at compressive rates (less than 1 dB/dB) at moderate-to-intense stimulus levels. This discovery met with much initial skepticism, but the central findings have been subsequently replicated and refined in several laboratories (Sellick *et al.*, 1982; Robles *et al.*, 1986; Cooper and Rhode, 1992; Nuttall and Dolan, 1993; Murugasu and Russell, 1995). Nevertheless, there are many aspects of basilar-membrane responses to tones which, although already addressed by previous studies, could be usefully documented with greater quantitative detail in healthy cochleae. Among the issues that merit further investigation are (1) What is the magnitude of basilar-membrane vibration at neural-threshold levels?; (2) Do basilar-membrane responses to CF tones grow linearly at these threshold levels?; (3) How do the compressive rates of growth vary with stimulus intensity?; (4) Does the compressive rate of growth persist at intense stimulus levels?; (5) How does the compressive rate vary as a function of frequency?; (6) Is there a high-frequency magnitude plateau?; (7) Is there a phase plateau?

Rhode's finding of a basilar-membrane nonlinearity and its initial confirmations and extensions were obtained using the Mössbauer technique (Rhode, 1971, 1978; Sellick *et al.*, 1982; Robles *et al.*, 1986), which is time consuming, highly nonlinear, and probably deleterious to cochlear health (Kliauga and Khanna, 1983) and thus severely limits the extent and quality of the attainable data. More recently, most laboratories performing basilar-membrane measurements have adopted some form of laser interferometry. Application of this technique, which is essentially linear and offers other advantages over the Mössbauer technique (see Ruggero and Rich, 1991a), has permitted a detailed description of basilar-membrane responses to tones at the 18-kHz site of the healthy guinea pig cochlea (Nuttall and Dolan, 1996). The present account provides a comparable description for the 9–10 kHz basilar-membrane site of the chinchilla cochlea, updating a report that was based on the Mössbauer technique (Robles *et al.*, 1986) and addressing the questions posed above. A summary of the main results has been published in abstract form (Ruggero *et al.*, 1996c).

I. METHODS

A. Animal preparation

Basilar-membrane responses to tones were measured, using laser velocimetry, at a site of the chinchilla cochlea located 3.5 mm from the oval window. Chinchillas, anesthetized with sodium pentobarbital (initial dose: 65 mg/kg; injected intraperitoneally), were tracheotomized and intubated,

but forced respiration was usually not used. Normal body temperature was maintained by means of a heating pad servocontrolled by a rectal probe but no other precaution (e.g., heating of the headholder) was taken to maintain cochlear temperature. The left pinna was resected, the bulla was widely opened, and the tensor tympani muscle was cut. In many experiments, the stapedius muscle was detached from its anchoring. A silver-wire electrode was placed on the round window to record compound action potentials evoked by tone bursts (fundamental frequency: 500 Hz to 16 kHz, in 1/2 octave steps). Compound action potential (CAP) thresholds (sound-pressure levels—SPLs—required to elicit 10-μV $N1$ responses) served to monitor the physiological state of the cochlea. A small hole made in the basal turn of the otic capsule allowed direct visualization of the basilar membrane and placement on it of a few glass microbeads (diameter: 10–30 μm), which served as reflecting targets for the light beam of the laser velocimeter. In some experiments, basilar-membrane vibrations were measured after covering the hole in the otic capsule with a small window fashioned from slide coverslip glass.

B. Acoustic stimulation

Acoustic stimuli were produced under computer control by either a custom-built arbitrary waveform generator (Ruggero and Rich, 1983) or by a Tucker–Davis system, and were delivered through a Beyer DT-48 earphone. This was mounted on the back of a plastic speculum sealed to the bony ear canal by means of ear-impression compound. A Knowles (1842 or 1785) miniature microphone equipped with a probe tube was used to measure the sound pressure within 2 mm of the tympanic membrane. Single-tone stimuli were gated tones modulated at onset and offset by 1/2 period of a raised cosine waveform (1.16-ms rise/fall time). The tone bursts had durations of 5, 10, 25, or, exceptionally, 3 ms, and repetition periods of 25, 50, 100, or 15 ms, respectively. The use of large off-time/on-time ratios prevented the induction of threshold shifts by the repeated presentation of intense stimuli (see Fig. 16 and corresponding text). Tone stimuli were typically presented in steps of 1 kHz and 10 dB.

C. Laser velocimetry

Laser velocimetry measures the velocity of a vibrating object by detecting the Doppler frequency shift of light reflected from it. In our application of this method, the laser beam is reflected from glass microbeads placed on the basilar membrane. The velocimeter used in these experiments consisted of a 20-mW He–Ne laser (Spectra Physics 106-1), a Dantec 41X60 fiber vibrometer, and a Dantec 55N20 Doppler frequency tracker. The velocimeter head was coupled to a compound microscope (Olympus BHMJ) equipped with 5X and 20X ultralong working-distance objectives (Mitutoyo Plan Apo 5X, N. A. 0.14, and 20X, N.A. 0.42). The electrical output of the Doppler frequency tracker, a voltage (1–10 V) proportional to velocity, was frequency filtered with a pass band of 1–15 000 Hz (1–20 000 Hz exceptionally) before analog-to-digital conversion under computer control (typical sampling rate: 40 kHz; exceptionally: 100 or 166.6 kHz). Responses were usually averaged over 512 or 1024 stimulus repetitions (exceptionally: 64 repetitions) and velocity spectra were computed off-line by Fourier transformation. Response magnitudes are given throughout the paper as the peak amplitudes of velocity waveforms. For more details on the application of laser velocimetry to the measurement of basilar-membrane vibration in the chinchilla, see Ruggero and Rich (1991a).

II. RESULTS

The initial preparations for basilar-membrane recordings were performed in 129 chinchillas but useful data were obtained in only 43. Judging from elevations in compound action potential (CAP) thresholds at near-CF frequencies, all experimental cochleae were damaged to some extent by the surgical procedures involved in opening the otic capsule. The present paper is largely based on the analysis of data from the six cochleae that yielded the most sensitive basilar-membrane responses to CF tones. Two of these cochleae, which yielded an extensive sampling of basilar-membrane responses to tones as a function of stimulus frequency and intensity, are highlighted throughout the paper. These responses were selected for presentation because: (1) they were exceptionally stable (remaining invariant over several hours of recording); (2) they were collected in near-normal cochleae (surgically induced CAP threshold elevations at CF of 6–12 dB); and (3) they were especially sensitive.

All the recordings were obtained at a region of the basilar membrane located about 3.5 mm from the oval window (Robles *et al.*, 1986). At the beginning of the recording sessions (and usually also at later times throughout the sessions) basilar-membrane responses to clicks were measured at several intensities. Responses to low-intensity clicks provided for rapid estimation of CF and basilar-membrane sensitivity. Responses to tones were then measured as a function of intensity and frequency, typically in 10-dB and 1-kHz steps. CFs were always in the range 8–11 kHz, most often 9 or 10 kHz.

A. Waveshape and spectrum of responses to tones

Figure 1 illustrates basilar-membrane velocity recordings from a cochlea in which the preparatory surgery caused only small (6 dB) elevations of the CAP thresholds for stimulus frequencies (8 and 11.3 kHz) closely flanking the CF (10 kHz) of the recording site. The traces show the averaged responses to 10-kHz tone bursts presented at 30–70 dB SPL. The responses to the lower-level stimuli resemble the stimulus waveforms, which have symmetric envelopes. At higher stimulus levels, the response offsets are longer than the onsets and the traces exhibit ''ringing'' that persists well after the end of the stimulus. At even higher stimulus intensities (not shown), response asymmetry is often accompanied by overshoot-like irregularities with instantaneous frequency equal to CF regardless of the stimulus frequency. Asymmetry and ''overshoots'' are usually present in the responses of sensitive cochleae to intense tones with frequency near to or higher than CF, but are absent from responses to tones with frequency well below CF or, at any frequency, in insensitive cochleae.

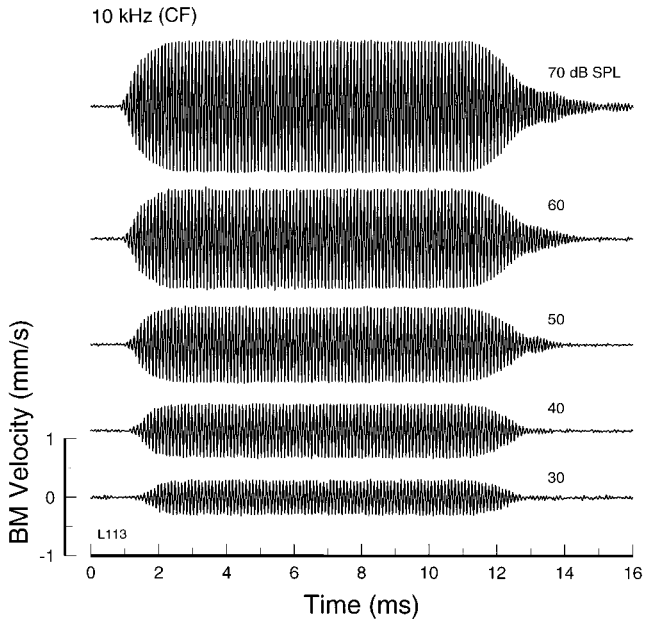

FIG. 1. Basilar-membrane velocity responses to 10-kHz (=CF) tones. Each waveform represents the average of 512 responses. Stimulus intensity is indicated at right. Zero time corresponds to the onset of the electrical input to the earphone. Data recorded in cochlea L113.

Although the waveforms of Fig. 1 are not visibly distorted, their Fourier transforms (not shown) do contain even-order harmonics. In general, responses to tones, regardless of frequency, are symmetric (i.e., they are devoid of dc components) and exhibit very low levels of harmonic distortion. Second-harmonic components occasionally reach levels as high as −20 to −30 dB relative to the fundamental. Such distortion, which is generally accompanied by a small dc shift, appears to arise as an artifact in the velocimeter system. The presence of even-order distortion is typically associated with poor recording conditions (when little light is reflected from the target) and/or with a large fundamental signal and high-sensitivity settings of the Doppler-frequency tracker. Under such circumstances, decreasing the sensitivity setting dramatically reduces the magnitudes of both the second harmonic and the dc shift.

B. Magnitude of responses to CF tones as a function of intensity

The steady-state amplitudes of velocity traces such as those of Fig. 1 were measured by means of Fourier transformation. Figure 2 displays velocity-intensity functions for basilar-membrane responses to CF tones in six sensitive cochleae. The CFs (determined to the nearest kHz) are: 8 kHz (L126), 9 kHz (L13 and L125), or 10 kHz (L57, L113, and L110). Response amplitudes generally grow monotonically with stimulus intensity, with remarkably little variation among different cochleae in the intensity range 20–70 dB SPL. To a first approximation, in the 20–70 dB range all the velocity-intensity curves lie close to a single straight line in log–log coordinates, defining velocity as a simple power function of stimulus pressure. However, all curves grow more steeply at the lowest stimulus intensities (<20 dB) than

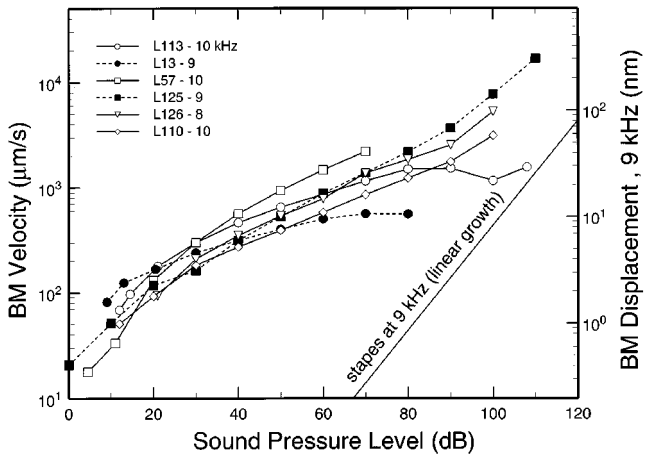

FIG. 2. Velocity-intensity functions for basilar-membrane responses to CF tones. The steady-state peak velocities of waveforms such as those of Fig. 1 are plotted for six relatively healthy cochleae against stimulus intensity. The straight line at right indicates the average motion of the stapes in response to 9-kHz tones (measured by Ruggero *et al.*, 1990). The right ordinate indicates basilar-membrane displacement. This scale is exact for responses to 9-kHz tones but approximate for responses to 8 or 10 kHz.

at moderate intensities (40–80 dB). At the highest stimulus intensities (>80 dB), the curves tend to diverge. Two velocity-intensity functions (L13 and L113) reach asymptotic velocities of 0.6 and 1.6 mm/s (10 and 25 nm), but three curves show increased rates of growth between 90 and 110 dB, reaching velocities of 3–8 mm/s (60–140 nm) at 100 dB SPL.

Figure 3 displays the slopes of the input–output functions of Fig. 2. Growth rates are highest, approaching linearity, at intensities lower than 20 dB SPL. Growth rate is compressive (<1 dB/dB) at all intensities higher than 20 dB. In the range 40–90 dB, rates are relatively stable for any single cochlea but vary across cochleae between 0.2 and 0.5 dB/dB. Probably not coincidentally, the lowest rates of growth (<0.3 dB/dB) in the mid-intensity range belong to cochleae (L13 and L113) that produced the largest responses at low stimulus levels (Fig. 2).

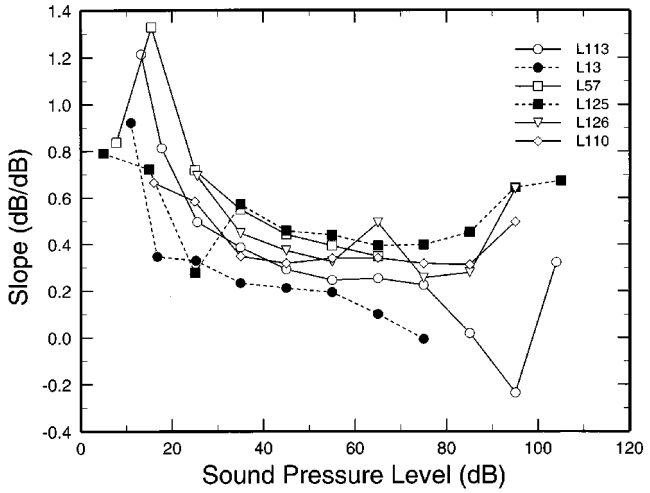

FIG. 3. Slopes of basilar-membrane responses to CF tones, plotted against stimulus intensity. The slopes of the CF input–output functions of Fig. 2 are expressed in units of dB (velocity)/dB (pressure).

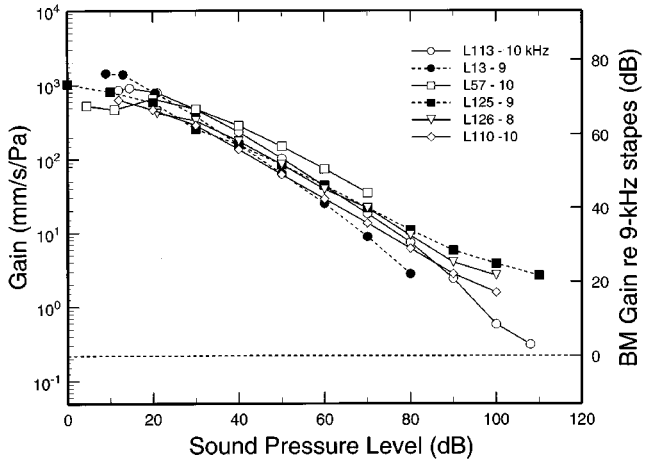

FIG. 4. Gain of basilar-membrane responses to CF tones, plotted against stimulus intensity. Basilar-membrane gains were computed by dividing the peak response velocities shown in Fig. 2 by the corresponding stimulus pressures (left scale). The right scale indicates the gain (in decibels) of basilar membrane motion relative to stapes motion (horizontal dash line, Ruggero *et al.*, 1990). This scale is exact for responses to 9-kHz tones but approximate for responses to 8 or 10 kHz.

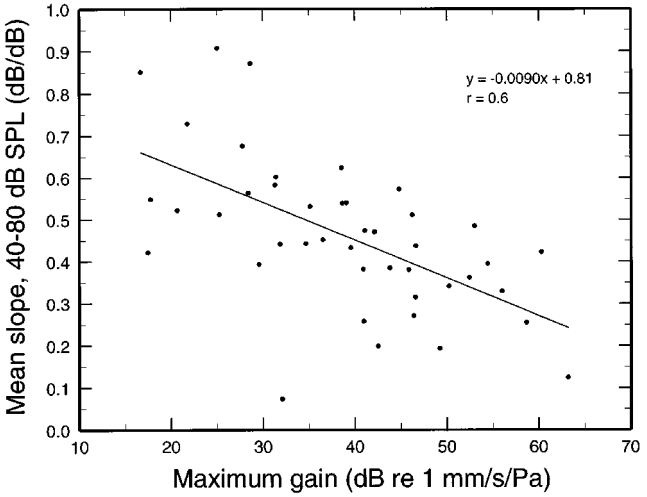

FIG. 5. Relationship between the sensitivity and the nonlinear growth of basilar-membrane responses to CF tones. The scatter diagram plots, for each of 43 cochleae, the maximal gain of basilar-membrane vibration (e.g., Fig. 4) against the average slope of the velocity-intensity function (e.g., Fig. 3) measured between 40 and 80 dB SPL.

In all cochleae represented in Fig. 3, the nonlinear growth of basilar-membrane motion persists even at the highest of physiologically relevant stimulus intensities. In the two most sensitive cochleae (L13 and L113), the rates of growth dip down to zero or negative values at the highest stimulus intensities. In other cochleae, growth rates climb to values of 0.5–0.7 dB/dB at intensities higher than 90 dB. In even less sensitive cochleae (not shown) that nevertheless retain some degree of nonlinearity, responses to intense CF tones can reach nearly linear growth rates (0.8–0.9 dB/dB). This suggests that the increase in the slope of response growth at high stimulus levels varies directly with the extent of surgically induced cochlear damage and may be smaller (or even absent) in completely normal cochleae.

Figure 4 illustrates the systematic decrease in gain (i.e., velocity per unit pressure) that basilar-membrane responses to CF tones undergo with increasing stimulus intensity. At 100–110 dB SPL, basilar-membrane gain can be as much as 69 dB lower than at intensities <20 dB. The right scale (the magnitude of basilar-membrane motion relative to stapes motion; Ruggero *et al.*, 1990), indicates that at low stimulus levels basilar-membrane vibrations are enormously larger than stapes motion, amounting to gains of 66–76 dB. Basilar-membrane vibration exceeds stapes motion even at stimulus levels as high as 110 dB SPL.

It was noted above that, among the cochleae represented in Figs. 2–4, the two with the most compressive rates of response growth (Fig. 3) were also among the most sensitive ones (Figs. 2 and 4). We explored the relationship between sensitivity and nonlinear growth in a sample of 43 cochleae (Fig. 5) by correlating the maximal gains (Fig. 4) with the average slopes of velocity-intensity functions in the range 40–80 dB SPL (Fig. 3). These quantities (gain: dB *re*: 1 mm/s/Pa; slope: dB/dB) were significantly and negatively correlated, with $r=-0.60$, slope of -0.0090 (dB/dB)/(dB *re*: 1 mm/s/Pa) and y intercept of 0.81 dB/dB. Applying the regression-line equation to the measured maximal gains at CF in cochleae L13 and L113 (63 and 59 dB *re*: 1 mm/s/Pa) yields slopes of 0.24 and 0.28 dB/dB, respectively. If one takes into account sensitivity losses due to surgery (12 and 6 dB, respectively, in cochleae L13 and L113) the predicted slopes (based on corrected maximal gains of 75 and 65 dB *re*: 1 mm/s/Pa) are 0.14 and 0.23 dB/dB. Thus, one expects that velocity-intensity functions for CF tones in entirely normal cochleae have slopes of approximately 0.2 dB/dB in the 40–80 dB intensity range.

C. Variation of velocity-intensity functions with stimulus frequency

Figure 6 presents a family of velocity-intensity functions for responses of a single basilar-membrane site to tones with frequency equal to and higher than CF (10 kHz). Responses to 11-kHz tones grew at rates slightly more compressive than

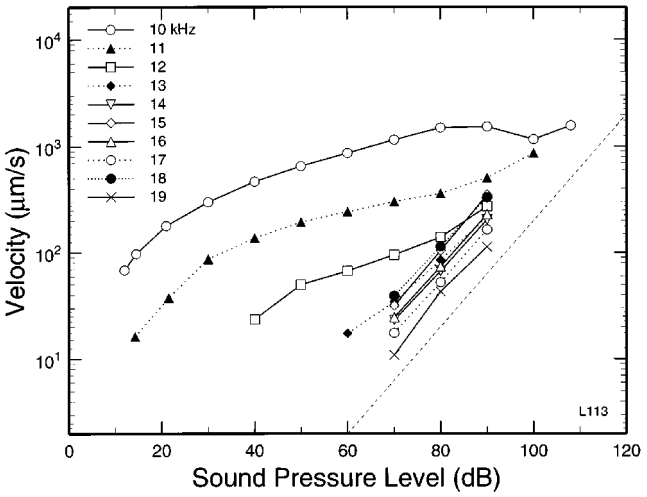

FIG. 6. Velocity-intensity functions of basilar-membrane responses to tones with frequency equal to and higher than CF (10 kHz). The straight dashed line at right has a linear slope (1 dB/dB). The data were recorded in cochlea L113.

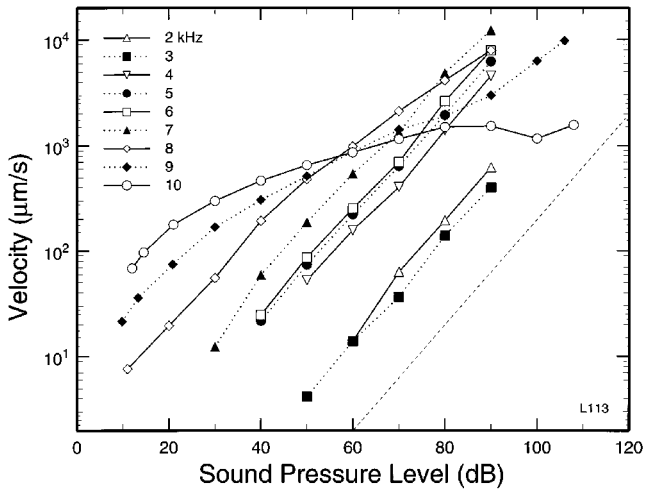

FIG. 7. Velocity-intensity functions of basilar-membrane responses to tones with frequency equal to and lower than CF (10 kHz). The straight dashed line at right has a linear slope (1 dB/dB). The data were recorded in the same cochlea (L113) represented in Fig. 6.

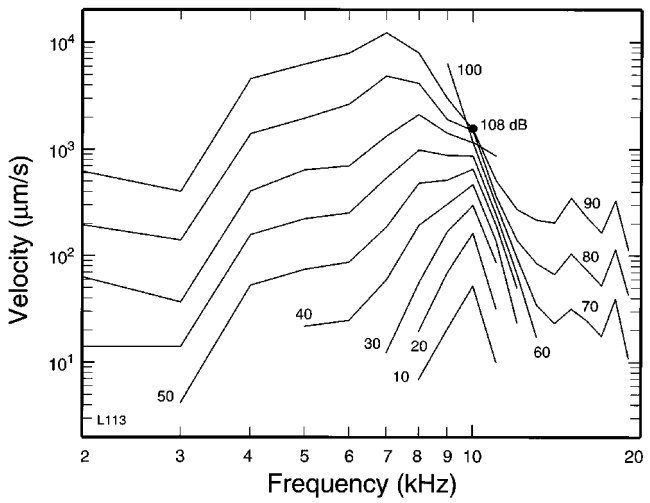

FIG. 8. A family of isointensity curves representing the velocity of basilar-membrane responses to tone pips as a function of frequency (abscissa) and intensity (parameter, in dB SPL). The isointensity curves represent the same data of Figs. 6 and 7.

responses to CF tones at intensities of 40–80 dB but grew at higher rates (closer to linear) at intensities lower than 30 dB SPL and higher than 80 dB. Responses to 12-kHz tones also displayed a central compressive region flanked by less nonlinear regions at lower and higher intensities. In this case, however, the highly compressive region was restricted to a narrower range, 50–80 dB. Responses to tones with frequency higher than 13 kHz were linear.

Figure 7 shows velocity-intensity functions at the same cochlear site for tones with frequency of 10 kHz (=CF) and lower. Responses to 9-kHz tones grew nonlinearly but at rates higher than responses to CF. Thus, although 9-kHz responses were some 7.3 dB smaller than at CF for 10-dB stimuli, they surpassed CF responses at 60 dB SPL and were some 6 dB larger at 90 dB. Responses to 8-kHz tones grew linearly between 10 and 50 dB, displayed a mildly nonlinear rate of growth between 50 and 90 dB, and exceeded CF responses by some 14 dB at 90 dB. Responses to tones with frequencies lower than 7 kHz were linear and, in the range 4–7 kHz, larger than responses to CF tones at 90 dB. For frequencies near CF, the slopes of the velocity-intensity functions varied systematically with frequency (not shown explicitly). For example, in the 40–80 dB range the slopes for tones with frequency of 6, 7, 8, 9, 10, 11, and 12 kHz were 0.99, 0.94, 0.66, 0.41, 0.25, 0.21, and 0.37 dB/dB, respectively.

D. Variation of isointensity functions with stimulus intensity

The variation of response velocity as a function of stimulus frequency and intensity can be viewed comprehensively by recasting the data of Figs. 6 and 7 into a family of isointensity functions (Fig. 8). For tones with frequency well below CF, isointensity curves for stimuli 10 dB apart are separated by velocities that differ by a ratio of 3.1 (i.e., 10 dB), indicating linear growth. Response growth became increasingly compressive as stimulus frequency approached CF. Responses to CF tones (10 kHz) grew linearly between 10 and 20 dB SPL but grew at highly compressive rates at higher intensities. (The 10-dB curve in Fig. 8 has been extrapolated linearly from responses to stimuli presented at slightly higher levels; see Figs. 6 and 7.) The most nonlinear growth rates were those for tones with frequency (11 kHz) just above CF. At stimulus frequencies of 14 kHz and higher, responses grew linearly and reached a plateau.

The frequency-specific compressive nonlinearity caused a systematic reduction of the most effective stimulus frequency as a function of increasing stimulus intensity. At intensities equal to or lower than 50 dB SPL, the peak responses occurred at 10 kHz; at 60 and 70 dB the largest responses were elicited by 8-kHz tones; at 80 and 90 dB SPL, the peak response shifted to 7 kHz, equivalent to a frequency decrease of 0.51 octave relative to CF. Peak re-

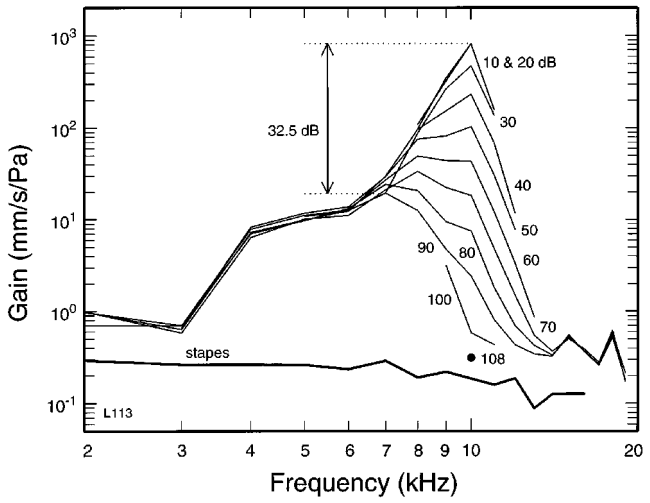

FIG. 9. A family of isointensity curves representing the gain (velocity divided by stimulus pressure) of basilar-membrane responses to tone pips as a function of frequency (abscissa) and intensity (parameter, in dB SPL). The isointensity curves represent the same data of Figs. 6–8, recorded in cochlea L113. The thick line at bottom indicates the average motion of the stapes (Ruggero *et al.*, 1990).

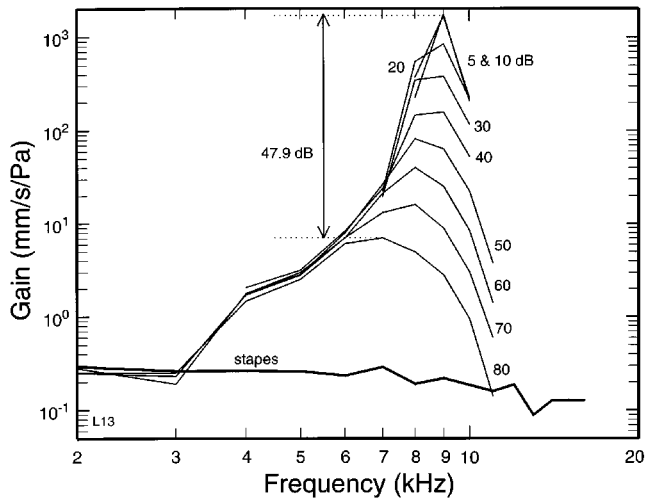

FIG. 10. A family of isointensity curves representing the gain (velocity divided by stimulus pressure) of basilar-membrane responses to tone pips as a function of frequency (abscissa) and intensity (parameter, in dB SPL). The thick line at bottom indicates the average motion of the stapes (Ruggero *et al.*, 1990). Data recorded in cochlea L13.

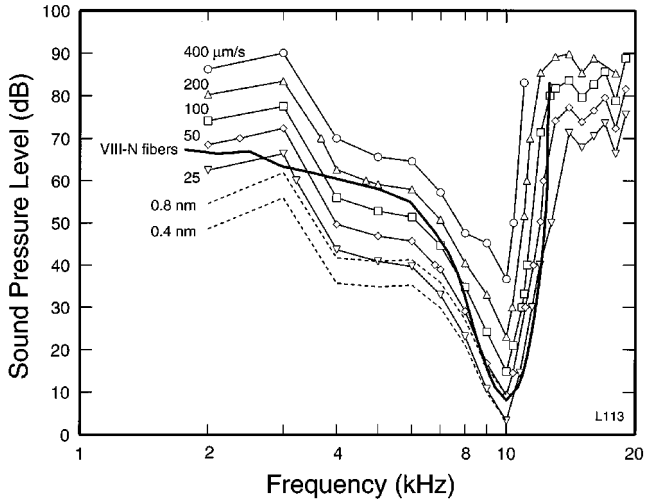

FIG. 11. Basilar-membrane and auditory-nerve tuning curves. The data of Figs. 6–9 are presented as isovelocity contours for responses of 25, 50, 100, 200, and 400 μm/s (thin solid lines) and isodisplacement (0.4 and 0.8 nm) contours (dashed lines). The thick solid line is an average frequency-threshold tuning curve computed from the rate thresholds of 50–274 chinchilla auditory-nerve fibers with CFs of 8–12 kHz and high spontaneous activity.

sponses in another sensitive cochlea (L13; see Fig. 10) changed from 9 kHz (CF) at low stimulus levels to 7 kHz at 80 dB, amounting to a decrease of 0.36 octave relative to CF. Another trend of the variation of isointensity functions with stimulus intensity consists of a systematic broadening of the response bandwidth: Whereas for 20-dB stimuli the 10-dB bandwidth in this cochlea is 2.5 kHz, at 90 dB the 10-dB bandwidth is 5 kHz.

The data of Fig. 8 are replotted in Fig. 9 after normalization to stimulus intensity, thus yielding gains (velocity per unit stimulus pressure). Had responses grown linearly with stimulus intensity, the isointensity gain curves would superimpose. In fact, the curves superimpose only at frequencies removed from CF, i.e., below 7 kHz and above 13 kHz. At near-CF frequencies, gain grows systematically larger as a function of decreasing stimulus level, except between 10 and 20 dB, in which range responses grow linearly and gains attain a maximal (asymptotic) value. The change in gain associated with nonlinear growth at CF cannot be expressed as a single value because compressive growth prevails even at levels higher than 100 dB (compare 10-kHz gains at 100 and 108 dB SPL). Thus, it is only possible to specify a *minimum* change in gain (e.g., 69 dB in cochlea L113, measured between 20 and 108 dB SPL; see also Fig. 4). However, it is possible to specify a single value for the difference between the maximal sensitivity at CF and the peak sensitivity for responses that grow linearly or nearly so (i.e., at 7 kHz). In cochlea L113, this difference between the peak gain at low (10–20 dB) and high (90 dB) stimulus levels amounts to 32.5 dB (Fig. 9). Taking into account that cochlea L113 had experienced a 6-dB sensitivity loss at CF during the preliminary surgery (as judged by CAP threshold elevations at 8 and 11.3 kHz), one can estimate that the difference in the intact cochlea would have amounted to 38.5 dB.

Figure 10 presents another family of isointensity functions normalized to stimulus intensity. The basilar-membrane responses in cochlea L13 resembled those of L113 but were more sensitive at low stimulus levels. CF responses grew linearly between 5 and 10 dB SPL but exhibited strongly compressive growth between 10 and 80 dB. The change of response gain at CF as a function of stimulus level was 55.6 dB (measured between 10 and 80 dB SPL). As previously noted in the case of L113, the change of response gain would presumably have been even larger had responses been available for higher stimulus intensities. The difference between the peak gains for low-level (5 or 10 dB) and intense (80-dB) stimuli was 47.9 dB. Corrected for the surgically induced deterioration of the preparation (12 dB, estimated from CAP threshold elevations at 8 and 11.3 kHz), the corresponding value is 59.9 dB.

E. Tuning curves

For comparison with responses to sound at more central stages of cochlear processing (e.g., hair cells, auditory-nerve fibers), it is convenient to present basilar-membrane magnitude data in the form of isoresponse contours (i.e., ''tuning curves''). Figure 11 shows tuning curves for velocities of 25, 50, 100, 200, and 400 μm/s (thin solid lines), derived by interpolation from the velocity-intensity curves for a single cochlea (L113: Figs. 6 and 7), and isodisplacement tuning curves (dashed lines) for displacement values of 0.4 and 0.8 nm (derived from the isovelocity curves at 25 and 50 μm/s, respectively). On the high-frequency side, isovelocity tuning curves have slopes averaging 260 dB/octave between 40 and 70 dB SPL. On the lower-frequency side, the slopes are much lower, in the order of -52 dB/octave. Q_{10} values (CF divided by 10-dB bandwidth) for the 25-, 50-, 100-, 200-, and 400-μm/s curves are 5.3, 5.6, 6.1, 7.1, and 5.2, respectively. Q_{20} values (CF divided by 20-dB bandwidth) are 3.2, 3.3, 3.3, 3.4, and 2.9, respectively.

In addition to basilar-membrane tuning curves, Fig. 11 depicts an average frequency-threshold tuning curve com-

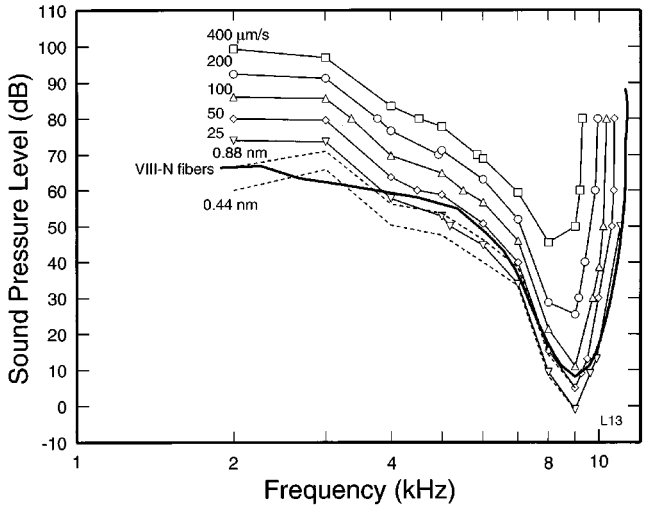

FIG. 12. Basilar-membrane and auditory-nerve tuning curves. The data of Fig. 10 are presented as isovelocity contours for responses of 25, 50, 100, 200, and 400 μm/s (thin solid lines) and isodisplacement (0.44 and 0.88 nm) contours (dashed lines). The thick solid line is an average frequency-threshold tuning curve computed from the rate thresholds of 50–274 auditory-nerve fibers with CFs of 8–12 kHz and high spontaneous activity.

puted from the rate responses of chinchilla auditory-nerve fibers with CFs in the range of 8–12 kHz and spontaneous activity higher than 18 spikes/s. The tuning curve is a detailed composite of the features of 58–274 fibers (depending on frequency) in 86 animals (Temchin *et al.*, 1997). For frequencies near CF, the averaged features were the frequencies corresponding to stimulus intensities sampled in 3–5 dB steps between CF threshold and 70–80 dB SPL. For ''tail'' frequencies, the averaged features were the SPLs corresponding to frequencies sampled in 0.25 octave steps (relative to CF). The average frequency-threshold curve has a CF threshold of 8 dB SPL, which corresponds to a velocity of 39 μm/s or a displacement of 0.62 nm in cochlea L113. The neural tuning curve has high- and low-frequency slopes of 318 and −117 dB/oct, respectively, and its Q_{10} is 4.6. The

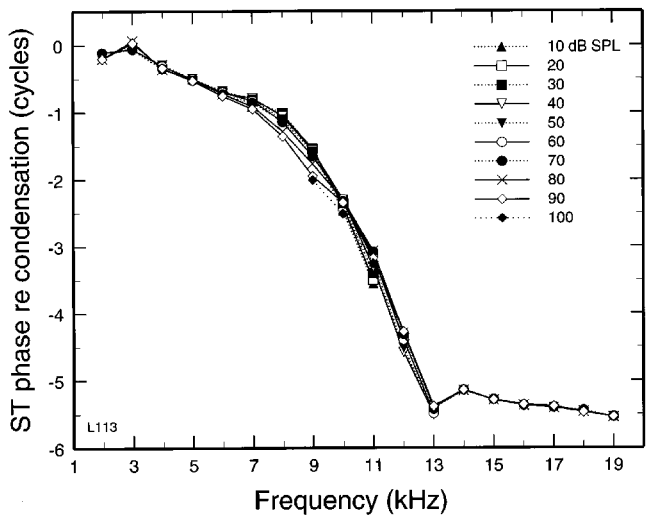

FIG. 13. The variation of basilar-membrane response phases as a function of frequency. Phases—displacement toward scala tympani relative to condensation at the eardrum—were computed from the responses of cochlea L113, whose magnitudes are represented in Figs. 6–9 and 11. Each curve represents data for a single stimulus intensity (legend).

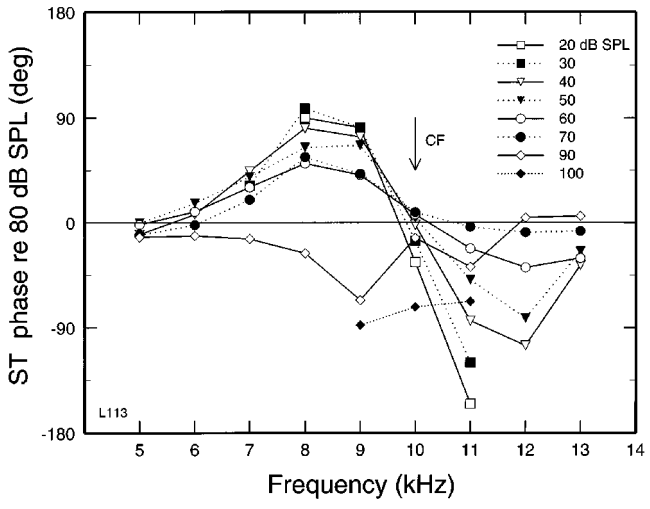

FIG. 14. Intensity dependence of basilar-membrane response phases. The phases represented in Fig. 13 have been normalized to those at 80 dB SPL. Positive phases indicate leads relative to responses at 80 dB.

neural and mechanical tuning curves resemble each other closely at near-CF frequencies but the resemblance is weaker at frequencies well below CF. In the range 2–10 kHz, the neural curve most closely approximates the 50-μm/s isovelocity curve.

Figure 12 shows isovelocity and isodisplacement tuning curves for another cochlea (L13). For the 50–200 μm/s isovelocity curves, high- and low-frequency slopes average 589 and −125 dB/oct, respectively. For the same curves, Q_{10} values average 6.0. The CF threshold from the average auditory-nerve frequency-threshold curve (8 dB SPL) corresponds in cochlea L13 to a basilar-membrane velocity of 73 μm/s or a displacement of 1.3 nm. In this case, one isodisplacement curve (0.88 nm) provides a better match to the neural tuning curve than the isovelocity curves.

F. Variation of response phases as a function of stimulus frequency and intensity

Figure 13 shows the phases of responses in cochlea L113, corresponding to the magnitudes of Figs. 6–9. Each phase curve, which indicates displacement toward scala tympani relative to condensation at the eardrum, represents one stimulus intensity. The curves show phase lags that increase monotonically as a function of increasing frequency. In order to resolve 360-deg ambiguities in unfolding the phases, we have taken advantage of recordings of responses to clicks (not shown), whose spectral phases match fairly closely those of responses to tones (Ruggero *et al.*, 1992a). The slopes of the curves become steeper as CF is approached. For stimulus frequencies 4–7 kHz, for which response magnitudes grow linearly or nearly so (Figs. 7–9), the slope varies little with stimulus intensity, averaging −1.15 rad/kHz, equivalent to a group delay of 183 μs. Near CF, the slopes vary systematically with stimulus intensity: Group delays range from 0.99 ms for 10-dB tones to 0.61 ms for 90-dB tones. The phase slope is steepest at frequencies just higher than CF. Measured between 10 kHz (CF) and 12 kHz, the group delays are 1.1–1.3 ms. The rapid increase of phase lag

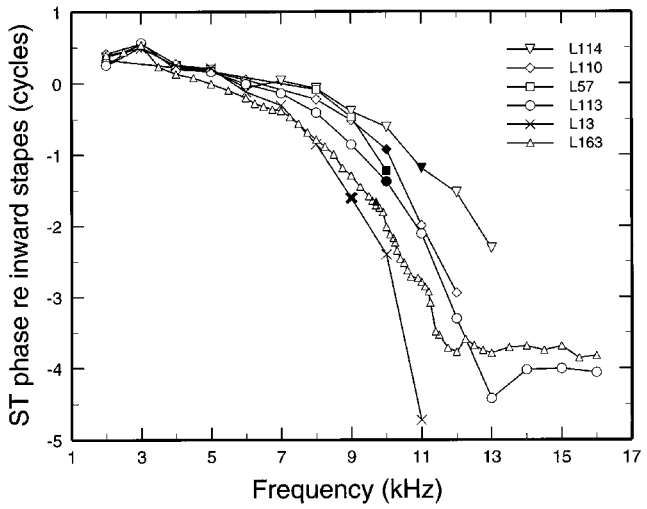

FIG. 15. Phase-versus-frequency curves, relative to stapes motion, of basilar-membrane responses to 70- or 80-dB tones in several cochleae. The filled symbols indicate phases at the CF frequencies.

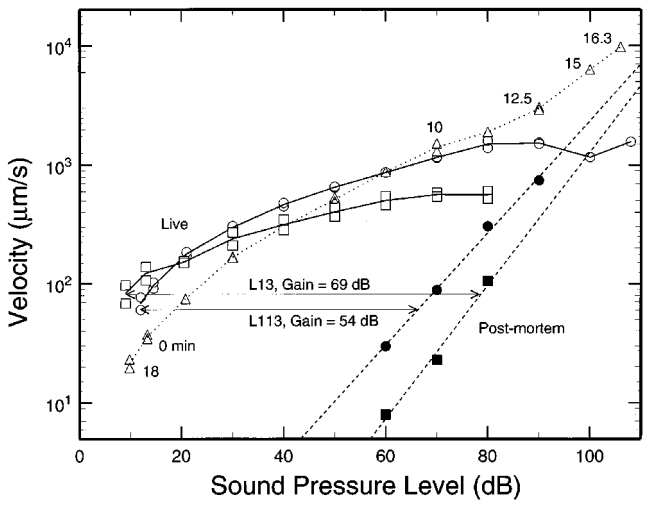

FIG. 16. Stability and vulnerability of responses to CF and near-CF tones. The open symbols depict the peak velocities of responses to CF tones (L13: squares; L113: circles) and 9-kHz tones (L113: triangles) recorded in the sensitive cochleae of two live chinchillas. The filled symbols represent the CF responses recorded immediately after (within minutes of) death. Responses to CF tones in both cochleae (and also responses to 9 kHz in cochlea L113) were measured both early in the experiment and 160–240 min later. The numbers next to the 9-kHz data points indicate the relative times (in min) of the early recordings.

with stimulus frequency is interrupted at frequencies higher than 12 kHz, at which the phase lags essentially reach a plateau.

At near-CF stimulus frequencies, where response magnitudes grow nonlinearly, response phases vary with stimulus intensity. The phases are displayed in Fig. 14 after normalization to the responses to 80-dB tones. In the intensity range 30–80 dB, responses to CF tones (arrow) change little with stimulus intensity. In the same intensity range, response phases for frequencies lower than CF systematically lag phases for lower-intensity stimuli. The lags are largest (>100 deg between 30 and 80 dB) for responses to 8 kHz and diminish at lower frequencies, becoming insignificant below 6 kHz. Response phases for tones with frequency just higher than CF systematically lead the phases for lower-intensity stimuli. For any given intensity, the largest leads (exceeding 90 deg) occur for tones with frequency of 11–12 kHz. The systematic leads do not persist at levels of 90 and 100 dB. At these intensities, regardless of stimulus frequency, response phases lag responses to lower-level stimuli. Thus, for frequencies lower than CF, responses to intense tones can be nearly antiphase relative to responses to low-level tones (e.g., 9 kHz). A dependence of response phase on stimulus intensity similar to that depicted in Fig. 14 also characterized the near-CF basilar-membrane responses in other sensitive cochleae, including L13 (see Figs. 10 and 12). The phase effects appeared to be extremely dependent on the state of the cochlea, since only small phase shifts could be demonstrated in many less-sensitive cochleae that nevertheless retained substantial nonlinearity.

Phase-versus-frequency curves for basilar-membrane responses to 70- or 80-dB tones in several cochleae are plotted in Fig. 15 after normalization to stapes displacement. The curve for L163 was normalized using stapes data collected in the same animal. The other curves were normalized using average stapes data (''open'' curve in Fig. 11 of Ruggero *et al.*, 1990). All the phase curves contain a low-frequency segment, with relatively shallow slope, and a near-CF segment, with steep slope. The phase lags at CF amount to 0.9–1.6 cycles. The transition frequency between the two segments seems to increase as a function of increasing CF. The low-frequency segments of the phase-versus-frequency curves have similar group delays (i.e., slopes), averaging 144 μs. The segments with frequency just higher than CF have group delays that may grow larger with decreasing CF (e.g., 1.6, 1.0, and 0.56 ms for L13, L113, and L114, with CFs of 9, 10, and 11 kHz, respectively).

Two of the phase curves of Fig. 15 exhibit plateaus at frequencies higher than CF. One curve (L163) was obtained with small frequency steps and therefore it was not subject to phase ambiguities. In the case of the other curve (L113), a 2π phase ambiguity at frequencies of 12 kHz and higher was resolved using phase-versus-frequency curves computed from responses to clicks in the same cochlea. [The phase-versus-frequency curves for responses to clicks closely resemble those of responses to tones (Ruggero *et al.*, 1992a).] In both cochleae, the plateaus hovered around phase lags of 3.7–4.1 cycles relative to inward stapes displacement.

G. Response stability and the effects of death

Basilar-membrane responses to near-CF tones often deteriorated with the passage of time, becoming less sensitive and more linear. However, responses in several cochleae retained their initial sensitivity and nonlinearity over several hours. Figure 16 shows two velocity-intensity functions (open circles) for the responses of cochlea L113 to 10-kHz (CF) tones, one recorded early in the experiment and the other about 4 h later, after recording the responses depicted in Figs. 6–9, 11, 13, and 14. The two velocity-intensity functions were very similar. The responses of another cochlea, L13, to CF tones (open squares) were measured some 2 h and 40 min apart, before and after the recordings illustrated

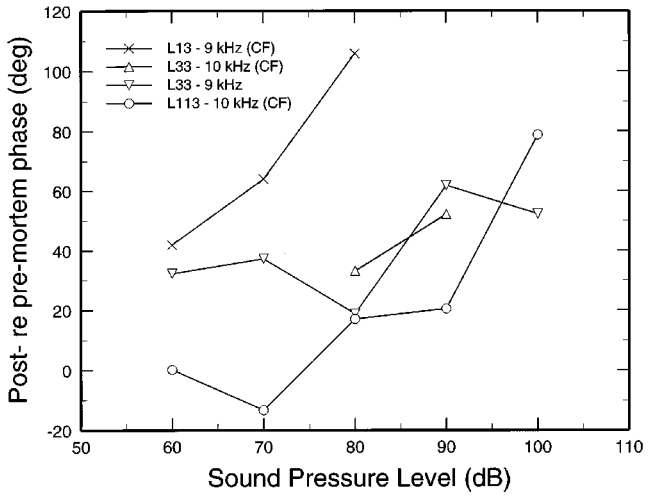

FIG. 17. The effects of death on the phases of responses to near-CF tones, plotted as a function of stimulus intensity. The phases for the responses to CF tones in live animals (open circles and squares in Fig. 16) were subtracted from the post-mortem response phases (filled symbols). Thus, positive phase values indicate relative phase leads of the post-mortem responses. Also shown are the net post-mortem phase changes for 10-kHz (CF) and 9-kHz tones in another cochlea.

in Figs. 10 and 12. As in the case of L113, the responses remained quite stable. The stability of the responses to CF tones in these two cochleae convincingly demonstrates that the frequency specificity of the magnitude and phase nonlinearities illustrated in Figs. 6–14 is not an artifact of recordings obtained under dissimilar physiological conditions (see Khanna, 1984, p. 216).

Also shown in Fig. 16 are responses to 9-kHz tones (open triangles) in cochlea L113 that demonstrate that the repeated presentation of intense near-CF stimuli did not lead to changes in response sensitivity (such as noted in some Mössbauer studies: Sellick *et al.*, 1982; Patuzzi *et al.*, 1984). Two velocity-intensity functions were recorded, one early in the experiment and the other nearly 4 h later. At each stimulus intensity, 512 repetitions of 10-ms tone bursts were presented every 50 ms. Responses for the curve obtained earlier were measured with tones presented at systematically increasing intensity, from 13 to 106 dB SPL, followed immediately by a presentation at 10 dB. Comparison of the response magnitudes at the latter intensity shows that they are nearly identical, thus demonstrating that the repeated presentation of 106-dB tone bursts did not alter the sensitivity of responses to low-level stimuli. Presumably the threshold shifts reported in some Mössbauer studies (Sellick *et al.*, 1982; Patuzzi *et al.*, 1984) resulted from the presentation of long-duration tones.

Figure 16 allows a comparison of velocity-intensity functions for CF tones in cochleae L13 and L113 before (open circles and squares) and after death (solid symbols). Death produced large decreases in the sensitivity and nonlinearity of responses. For low-level CF stimuli, death diminished sensitivity by 54 (L113) or 69 dB (L13). Taking into account that the pre-mortem responses were measured in cochleae that had suffered (surgically induced) sensitivity losses of 6–12 dB, it is likely that the net effect of death in intact cochleae would have amounted to 60 dB in L113 and 81 dB in L13.

Whereas the slopes of the intensity functions at moderate stimulus levels were originally lower than 0.3 dB/dB (see Fig. 3), the post-mortem curves had essentially linear slopes (dashed lines; L13: 1.12 dB/dB; L113: 0.95 dB/dB). Although no post-mortem responses are available for intensities higher than 80 or 90 dB, linear extrapolation suggests that the latter became larger than pre-mortem responses at stimulus levels higher than 100 dB SPL in both cochleae.

The post-mortem reductions in the magnitude of responses to CF tones were accompanied by relative phase leads (Fig. 17). The phase leads were small at stimulus intensities <70 dB but tended to grow with intensity. For the two cochleae illustrated in Fig. 16, the phase leads amounted to 79–105 deg at stimulus intensities of 80–100 dB. Post-mortem phase changes for responses to 10-kHz (CF) and 9-kHz tones were similar but somewhat smaller in another, less-sensitive, cochlea (L33; see Ruggero *et al.*, 1992a and Ruggero, 1994).

III. DISCUSSION

A. Evaluation of laser-velocimetry recordings: Contamination by a fluid-depth artifact

Cooper and Rhode (1992) have described an artifact that must be taken into account in interpreting basilar-membrane recordings obtained using laser velocimetry. These authors noted that a laser velocimeter cannot distinguish Doppler shifts caused by motion of the laser-beam target (the beads on the basilar membrane) from frequency shifts caused by changes of the path length of the laser beam due to alterations in the depth of the fluid in scala tympani. The latter are certain to exist as result of stapes vibration. When the stapes is pushed inward, the fluid meniscus overlying the recording site must bulge out of the otic capsule, causing an increased beam path length. When the stapes is pulled outward, the path length must be shorter. Thus, when basilar-membrane motion is small in comparison with the variation in fluid depth, the velocimeter output should grow in proportion to stapes velocity rather than in proportion to basilar-membrane velocity.

The effect of fluid-meniscus motion is most conspicuous for low stimulus frequencies, which elicit the largest middle-ear responses and the smallest basilar-membrane vibrations (e.g., Ruggero *et al.*, 1990; Cooper and Rhode, 1992). Indeed, we have strong evidence that responses to tones with frequencies lower than 2–3 kHz actually reflect stapes motion. At such frequencies, stapes and ''basilar-membrane'' motion can have comparable magnitudes (Figs. 9 and 10; see also Fig. 19 of Ruggero *et al.*, 1990) and the response phase (out-of-phase with stapes inward displacement) differ from those previously recorded with the Mössbauer technique (Ruggero *et al.*, 1986) but are consistent with those expected from the artifact (Cooper and Rhode, 1992; p. 176). Most convincingly, when measurements at the chinchilla cochlea are performed after covering the hole in the otic capsule with a glass window, responses for low stimulus frequencies are selectively reduced relative to those recorded without the

window (Recio *et al.*, 1997). Therefore, in this paper we have not presented data for stimulus frequencies lower than 2 kHz and view responses to 2–3 kHz tones with caution.

Fluid-meniscus motion could conceivably also contaminate responses to near-CF stimuli at sufficiently high levels, when the linear growth of the artifact might overtake the slower (compressive) growth of basilar-membrane responses. In such a case, responses should grow linearly and their gain should be comparable to that of stapes motion. In fact, responses to CF tones had magnitudes that exceeded stapes vibration even at intensities of 100 dB or higher (Fig. 2) and their growth remained substantially nonlinear even at intensities of 100–110 dB (Fig. 3). Perhaps most telling, the magnitude of basilar-membrane responses to CF tones exceeded stapes vibration even in cochleae that yielded insensitive and nearly linear responses (not shown) as a result of surgical damage.

Finally, it is worth considering whether the high-frequency magnitude plateau (Figs. 8 and 9) reflects the fluid-depth artifact. Although this hypothesis seems to be supported by the linearity and the insensitivity of responses at the plateau, we tend to discount it because a plateau with identical characteristics has also been demonstrated at the same site of the chinchilla cochlea using the Mössbauer technique (Robles *et al.*, 1986). Gamma rays are far more penetrating than visible-light photons and thus are minimally refracted at the air-perilymph interface. Therefore, changes in perilymph depth should translate into insignificant changes in effective path length.

B. Waveshape and spectrum of basilar-membrane responses to tones

Because of the inherent severe nonlinearity of the Lorentzian function that relates gamma-ray counts to velocity (Rhode, 1971; Ruggero and Rich, 1991a), studies that used the Mössbauer method (e.g., Sellick *et al.*, 1982, 1983b; Robles *et al.*, 1986; Ruggero *et al.*, 1986) could not address effectively the question of whether basilar-membrane responses to tones contain harmonic distortion. The present chinchilla data concur with laser velocimetry recordings in guinea pig (see Fig. 20 of Cooper and Rhode, 1992) in showing that basilar-membrane responses to tones, regardless of CF, are largely free of harmonic distortion, even though their rate of growth with intensity may be highly compressive.

C. Magnitude and rate of growth of basilar-membrane responses to near-threshold CF tones

Mössbauer measurements of basilar-membrane vibrations at the 3.5-mm site of the chinchilla cochlea suggested, but could not establish unequivocally, that CF input–output functions grow linearly at low stimulus intensities (Robles *et al.*, 1986). Describing responses in one sensitive cochlea, Robles *et al.* stated that, for the CF velocity-intensity function expressed in logarithmic coordinates, ''slope is less than unity even at the lowest velocities we were able to measure with our system.'' Subsequent recalibration of the acoustic-stimulus system has revealed that such apparent compressive growth at low stimulus levels was an artifact caused by incomplete correction of attenuation errors at large nominal attenuations (Pfeiffer, 1974). After fully correcting for this ''feed-through'' artifact, we are now convinced that, at the 8–10 kHz site of the chinchilla cochlea, basilar-membrane responses to CF tones grow linearly at stimulus levels <20 dB SPL (Figs. 2 and 3).

The intensity of CF tones at the transition between linear and compressive basilar-membrane growth (Figs. 2 and 3) nearly coincides with the threshold of chinchilla auditory-nerve fibers (Figs. 11 and 12). Our present estimate of maximal basilar-membrane gain at the 3.5-mm site of the healthy chinchilla cochlea is similar to a previous one that was based on Mössbauer data (Robles *et al.*, 1986). This similarity suggests that the two sets of measurements were carried out in cochleae that were in similar (i.e., near-normal) physiological state, and that the basilar-membrane recording sites were also comparable. [Radial position, which was not measured in these experiments, could cause variations in vibration magnitude as large as 20 dB, depending on distance from the spiral lamina or the spiral ligament (Cooper and Rhode, 1992).] The newly estimated average neural threshold (8 dB SPL), based exclusively on fibers with high-spontaneous activity, differs from a previous value (16 dB) which was based on a different population of auditory-nerve fibers, averaged without regard to spontaneous activity. Thus, our revised estimate of the magnitude of basilar-membrane vibration at neural threshold (39–73 μm/s or 0.62–1.3 nm) is slightly lower than the previous estimate of 100 μm/s or 2 nm (Robles *et al.*, 1986). At the guinea pig basilar-membrane site with CF 18–20 kHz, the transition between linear and nonlinear growth also occurs at intensities close to neural threshold (0–10 dB; Nuttall and Dolan, 1996). However, another study in guinea pig found nearly linear growth for responses to CF (15 kHz) tones at levels as high as 50 dB SPL (Murugasu and Russell, 1995). There is no obvious explanation for the discordant ranges of linear response growth found in these two studies.

D. Nonlinear growth of basilar-membrane responses to supra-threshold CF tones

Mössbauer experiments showed that basilar-membrane responses to CF tones in healthy chinchilla cochleae grow at rates as low as 0.3 dB/dB (Robles *et al.*, 1986) but provided little detail on the range over which such compressive growth occurred. In particular, due to the limited dynamic range of the Lorentzian function, and because of the need to limit the duration of cochlear exposure to intense tones, almost no Mössbauer data were obtained at the chinchilla basilar membrane for responses larger than 1 mm/s or CF tone intensities higher than 90 dB SPL. Taking advantage of the greater linearity and speed of laser velocimetry, the present experiments were able to collect data at more intense stimulus levels, using large off/on time ratios to prevent acoustic trauma (see Sellick *et al.*, 1982 and Patuzzi *et al.*, 1984). It is now clear that basilar-membrane responses to CF tones in normal chinchilla cochleae grow at rates as low as 0.2 dB/dB, and that these highly compressive growth rates may be maintained over a 40–60 dB range of stimulus intensity (Fig.

3), from 40 dB SPL or lower intensities to 90 dB or even higher intensities.

Some of our laboratory's publications noted in passing that velocity-intensity functions of chinchilla basilar-membrane responses to CF tones could approach linearity at high stimulus intensities (Ruggero and Rich, 1991b; Ruggero *et al.*, 1992b; Ruggero *et al.*, 1993). Such tendency toward linearization was rarely observed in Mössbauer experiments in normal cochleae (Sellick *et al.*, 1982; Robles *et al.*, 1986), but some authors argued for its existence on the basis of the effects of acoustic trauma (Patuzzi *et al.*, 1984) and from theoretical considerations (Johnstone *et al.*, 1986; Patuzzi *et al.*, 1989; Yates, 1990; Goldstein, 1995; Nobili and Mammano, 1996). The present investigation shows that within the range of intensities that are physiologically relevant (e.g., up to 100–110 dB) complete linearization does not occur in healthy cochleae. The rate of growth in some sensitive cochleae does become less compressive at the highest intensities than in the mid-intensity range, but it never surpasses 0.7 dB/dB (Fig. 3). On the other hand, responses to high-intensity CF tones do reach growth rates of 0.8–0.9 dB/dB in many insensitive cochleae that nevertheless retain some nonlinearity (not shown), suggesting that the less compressive growth rates at high intensities reflect cochlear damage. Our conclusion is that if responses to CF tones in normal chinchilla cochleae become linear at high stimulus intensities, they must do so at levels higher than 110 dB SPL. In fact, it is possible that in completely normal cochleae responses may approach saturation (i.e., undergo little growth) at levels higher than 70–80 dB SPL (e.g., cochlea L113 in Figs. 2 and 3).

The growth of responses to CF tones at basal sites of the guinea pig basilar membrane is at least as compressive as in chinchilla. Nuttall and Dolan (1996; Table AI) have shown a velocity-intensity function for CF (18-kHz) tones with an average slope of 0.23 dB/dB between 20 and 80 dB and Murugasu and Russell (1995) have measured slopes that average 0.12 dB/dB for CF (16-kHz) tones at stimulus intensities between 50 and 100 dB. Minimal response growth, approaching saturation, has also been deduced from responses of high-CF auditory-nerve fibers in guinea pig (Cooper and Yates, 1994). Similarly, in the hook region of the cat cochlea responses to tones with frequency slightly higher than CF grow at rates as low as 0.3 dB/dB between 65 and 100 dB SPL (Cooper and Rhode, 1992).

E. Nonlinear growth of basilar-membrane responses at frequencies other than CF

Basilar-membrane responses to tones with frequencies somewhat higher than CF grow at highly compressive growth rates (guinea pig: Sellick *et al.*, 1982; Murugasu and Russell, 1995, and Nuttall and Dolan, 1996; cat: Cooper and Rhode, 1992; chinchilla: Robles *et al.*, 1986). At the chinchilla cochlea, for CFs of 9 or 10 kHz, growth rates for tones with frequency 1 kHz higher than CF are at least as compressive as at CF (Figs. 5 and 7). The nonlinearity disappears abruptly at higher frequencies: Growth rates become essentially linear at a frequency about 1/3 octave higher than CF, coinciding with the onset of a magnitude plateau (discussed below; Figs. 8, 9, and 11).

Nonlinear growth disappears progressively at frequencies lower than CF so that, for CFs of 9–10 kHz, responses are linear at all stimulus frequencies lower than 0.4–0.5 octave below CF. At these frequencies, responses are larger than at CF or at any other stimulus frequency at intensities higher than 80–90 dB. The intensity-dependent shift of the response peak toward lower frequencies probably accounts adequately both for equivalent shifts in responses to tones of high-CF auditory-nerve fibers (Geisler *et al.*, 1974; Sachs and Abbas, 1974) and for the fact that temporary threshold shifts induced by intense tones are maximal at frequencies about 0.5 octave higher than the stimulus frequency (Davis *et al.*, 1950; Hood, 1950; Hubbard and Geisler, 1972; Lonsbury-Martin and Meikle, 1978; Cody and Johnstone, 1981).

F. The gain of the ''cochlear amplifier''

There is widespread belief that something akin to an amplifier (Davis, 1983; Dallos, 1988, 1992), active in healthy cochleae and presumably residing in the organ of Corti, is responsible for boosting the otherwise insensitive basilar-membrane responses of ''passive'' cochleae. One proposed method for measuring the gain of the cochlear amplifier is based on the presumption that responses to CF tones grow linearly at both low and high levels of stimulation (e.g., Johnstone *et al.*, 1986; Patuzzi *et al.*, 1989; Yates, 1990; Goldstein, 1995). The gain is defined as the difference between the sensitivities of responses to high- and low-level CF tones. However, this method is impractical because basilar-membrane responses to CF tones grow compressively even at the highest of physiologically relevant stimulus intensities (Figs. 2–4, 9). Assuming that linear growth would occur for sufficiently intense stimulation, the data for cochleae L113 and L13 indicate that the amplifier gain must be larger than 69 or 56 dB, respectively (Figs. 4, 9, and 10).

A second definition states that the gain of the amplifier corresponds to the difference between the sensitivity of responses to low-level CF tones in healthy cochleae and in freshly dead cochleae (Nuttall and Dolan, 1996). According to this definition, at the base of the chinchilla cochlea the gain amounts to 60–81 dB (taking into account pre-existing cochlear damage; Fig. 16). At the 18-kHz site of the guinea pig basilar-membrane, the corresponding gain amounts to 65–78 dB (as measured, respectively, by Nuttall and Dolan, 1996 and Sellick *et al.*, 1982, Fig. 15B). All of these values should be viewed with some caution because of the possibility that even the acute effects of death may alter not only ''active'' processes (i.e., requiring expenditure of metabolic energy) but also passive mechanics (e.g., the elasticity of the basilar membrane).

Yet a third definition is possible: The gain of the amplifier corresponds to the difference between the gains of responses to low-level CF tones and of the peak responses to high-intensity tones. According to this definition, the gain of the amplifier at the base of the chinchilla cochlea amounts to 39–60 dB (taking into account surgically induced trauma; Figs. 9 and 10).

G. The variation of response phases with stimulus frequency and intensity

An intensity dependence of near-CF response phases was first described for auditory-nerve fibers (Anderson *et al.*, 1971) and subsequently demonstrated at high-CF basilar-membrane sites in several species (Rhode and Robles, 1974; Geisler and Rhode, 1982; Sellick *et al.*, 1982; Cooper and Rhode, 1992; Ruggero *et al.*, 1992a; Nuttall and Dolan, 1993, 1996). At the chinchilla basilar membrane (Fig. 14), the pattern of the variation of phase with increasing intensity—phase lags for frequencies lower than CF, phase leads for frequencies higher than CF, and little phase variation at CF—strongly resembles that for low-CF auditory-nerve fibers. In the chinchilla, the largest phase leads for frequencies higher than CF are comparable to those measured in basal regions of the cat and guinea pig cochleae (140–230 deg: Cooper and Rhode, 1992; Nuttall and Dolan, 1993, 1996) but the phase lags for frequencies lower than CF (e.g., 100 deg for 8 kHz in the 30–80 dB interval) are larger than those measured in other studies.

The frequency range over which phases are intensity dependent, from about 1/2 octave below CF to 1/3 octave above CF, is similar to the frequency range over which compressive growth occurs at the chinchilla basilar membrane (compare Figs. 9 and 14). Further, the changes of phase are qualitatively appropriate for the concomitant changes of tuning: As intensity increases, the sharpness of tuning decreases (Fig. 9) and group delay (i.e., minus the slope of the phase-versus-frequency curve) also decreases (Fig. 13). It is puzzling that such coupling of tuning and group delays at the basilar membrane, whose responses are nonlinear and non-minimum phase (Recio *et al.*, 1996a, 1996b), are those predictable, at least qualitatively, for linear minimum-phase systems (Geisler and Rhode, 1982).

Most previous investigations of the effects of cochlear insults (such as acoustic trauma or ototoxic drugs) on basilar-membrane responses to sound have found relative phase lags at near-CF frequencies (Cooper and Rhode, 1992; Recio and Ruggero, 1995; Ruggero and Rich, 1991b; Ruggero *et al.*, 1993, 1996a, 1996b; however, see also Patuzzi *et al.*, 1984). The phase effects of death are more controversial. In his pioneering study in squirrel monkey, Rhode (1973) showed post-mortem phase lags at CF, whereas Nuttall and Dolan (1996) found large (270 deg) post-mortem phase leads in guinea pig. Our chinchilla data (Fig. 17; see also Fig. 2 in Ruggero, 1994) also show post-mortem phase leads at frequencies near CF, albeit smaller than in the guinea pig study. The discordance between the phase effects of death and those of other cochlear insults suggests that the former are more complex, probably affecting several sites and processes in a time-varying manner (e.g., the stria vascularis, causing changes of the endocochlear potential, or the concentration of endolymphatic calcium, resulting in mechanical alterations of the tectorial membrane).

H. High-frequency plateau

A high-frequency plateau (a frequency region above CF where response magnitude varies little with stimulus frequency) was first described by Rhode (1971) at the basilar membrane of squirrel monkey cochleae that responded nonlinearly to near-CF tones. Magnitude plateaus were also found at the basilar membrane of cat and guinea pig cochleae (Wilson and Johnstone, 1975; Wilson and Evans, 1983) that responded linearly, presumably as the result of surgically induced damage. The existence of a magnitude plateau in normal cochleae was questioned by Gummer and Johnstone (1984) who, on the bases of the experiments by Sellick *et al.* (1982, 1983b), suggested that the plateau resulted from cochlear damage, including acoustic trauma incurred while testing for the presence of the plateau. Robles *et al.* (1986), however, presented evidence that the plateau is demonstrable in normal chinchilla cochleae using test stimuli that do not impair normal sensitivity (see their Fig. 10). The present results (and those of other investigations using laser interferometry: Cooper and Rhode, 1992, and Nuttall and Dolan, 1996) support the existence of the plateau.

However, we still entertain serious doubts regarding the existence of the plateau, in part because of the possibility that laser velocimetry recordings are contaminated by the aforementioned fluid-depth artifact (Cooper and Rhode, 1992, 1996). Although fluid-meniscus motion probably cannot account for the presence of the plateau in recordings using the Mössbauer method (see Sec. III A), it is possible that the plateau is associated with opening of the otic capsule (Cooper and Rhode, 1996). Furthermore, it is disturbing that recordings from auditory-nerve fibers have never revealed a counterpart of the mechanical plateau, which should appear as a prominent inflection of the frequency-threshold tuning curve (Fig. 11).

ACKNOWLEDGMENTS

We thank Andrei Temchin for processing the neural tuning-curve data. We also thank Mary Ann Cheatham, Laura Dreisbach, John Guinan, and two anonymous reviewers for reading and commenting on previous versions of the manuscript. We were supported by Grants No. 5-P01-DC-00110-21 and 5-R01-DC-00419-09 from the National Institute on Deafness and Other Communication Disorders. L.R. was partially supported by FONDECYT (Chile) Grant No. 92-0976 and DTI, Universidad de Chile Grant No. B-2895.

Anderson, D. J., Rose, J. E., Hind, J. E., and Brugge, J. F. (**1971**). ''Temporal position of discharges in single auditory nerve fibers within the cycle of a sine-wave stimulus: frequency and intensity effects,'' J. Acoust. Soc. Am. **49,** 1131–1139.

Cody, A. R., and Johnstone, B. M. (**1981**). ''Acoustic trauma: Single neuron basis for the 'half-octave' shift,'' J. Acoust. Soc. Am. **70,** 707–711.

Cooper, N. P., and Rhode, W. S. (**1992**). ''Basilar membrane mechanics in the hook region of cat and guinea-pig cochleae: Sharp tuning and nonlinearity in the absence of baseline position shifts,'' Hear. Res. **63,** 163–190.

Cooper, N. P., and Rhode, W. S. (**1996**). ''Fast traveling waves, slow traveling waves, and their interactions in experimental studies of apical cochlear mechanics,'' Aud. Neurosci. **2**, 289–299.

Cooper, N. P., and Yates, G. K. (**1994**). ''Nonlinear input–output functions derived from the responses of guinea-pig cochlear nerve fibres: Variations with characteristic frequency,'' Hear. Res. **78,** 221–234.

Dallos, P. (**1988**). ''Cochlear neurobiology: Some key experiments and concepts of the past two decades,'' in *Auditory Function-Neurobiological Bases of Hearing*, edited by G. M. Edelman, W. E. Gall, and W. M. Cowan (Wiley, New York), pp. 153–188.

Dallos, P. (**1992**). ''The active cochlea,'' J. Neurosci. **12,** 4575–4585.
Davis, H. (**1983**). ''An active process in cochlear mechanics,'' Hear. Res. **9,** 79–90.
Davis, H., Morgan, C. T., Hawkins, Jr., J. E., Galambos, R., and Smith, F. W. (**1950**). ''Temporary deafness following exposure to loud tones and noise,'' Acta Oto-Laryngol. Suppl. **88,** 1–56.
Geisler, C. D., and Rhode, W. S. (**1982**). ''The phases of basilar-membrane vibrations,'' J. Acoust. Soc. Am. **71,** 1201–1203.
Geisler, C. D., Rhode, W. S., and Kennedy, D. T. (**1974**). ''Responses to tonal stimuli of single auditory nerve fibers and their relationship to basilar membrane motion in the squirrel monkey,'' J. Neurophysiol. **37,** 1156–1172.
Goldstein, J. L. (**1995**). ''Relations among compression, suppression, and combination tones in mechanical responses of the basilar membrane: Data and MBPNL model,'' Hear. Res. **89,** 52–68.
Gummer, A. W., and Johnstone, B. M. (**1984**). ''Group delay measurements from spiral ganglion cells in the basal turn of the guinea pig cochlea,'' J. Acoust. Soc. Am. **76,** 1388–1400.
Hood, J. D. (**1950**). ''Studies in auditory fatigue and adaptation,'' Acta Oto-Laryngol. **92,** 1–57.
Hubbard, A. E., and Geisler, C. D. (**1972**). ''A hybrid-computer model of the cochlear partition,'' J. Acoust. Soc. Am. **51,** 1895–1903.
Johnstone, B. M., Patuzzi, R., and Yates, G. (**1986**). ''Basilar membrane measurements and the travelling wave,'' Hear. Res. **22,** 147–154.
Khanna, S. M. (**1984**). ''Inner ear function based on the mechanical tuning of the hair cells,'' in *Hearing Science: Recent Advances*, edited by C. I. Berlin (College Hill Press, San Diego), pp. 213–240.
Kliauga, P., and Khanna, S. M. (**1983**). ''Dose rate to the inner ear during Mössbauer experiments,'' Phys. Med. Biol. **28,** 359–366.
Lonsbury-Martin, B. L., and Meikle, M. B. (**1978**). ''Neural correlates of auditory fatigue: Frequency-dependent changes in activity of single cochlear nerve fibers,'' J. Neurophysiol. **41,** 987–1006.
Murugasu, E., and Russell, I. J. (**1995**). ''Salicylate ototoxicity: The effects on basilar membrane displacement, cochlear microphonics, and neural responses in the basal turn of the guinea pig cochlea,'' Aud. Neurosci. **1**, 139–150.
Nobili, R., and Mammano, F. (**1996**). ''Biophysics of the cochlea. II: Stationary nonlinear phenomenology,'' J. Acoust. Soc. Am. **99,** 2244–2255.
Nuttall, A. L., and Dolan, D. F. (**1993**). ''Two-tone suppression of inner hair cell and basilar membrane responses in the guinea pig,'' J. Acoust. Soc. Am. **93,** 390–400.
Nuttall, A. L., and Dolan, D. F. (**1996**). ''Steady-state sinusoidal velocity responses of the basilar membrane in guinea pig,'' J. Acoust. Soc. Am. **99,** 1556–1565.
Patuzzi, R., Johnstone, B. M., and Sellick, P. M. (**1984**). ''The alteration of the vibration of the basilar membrane produced by loud sound,'' Hear. Res. **13,** 99–100.
Patuzzi, R. B., Yates, G. K., and Johnstone, B. M. (**1989**). ''Outer hair cell receptor current and sensorineural hearing loss,'' Hear. Res. **42,** 47–72.
Pfeiffer, R. R. (**1974**). ''Consideration of the acoustic stimulus,'' in *Handbook of Sensory Physiology, Vol. V/1: Auditory System*, edited by W. Keidel and W. Neff (Springer-Verlag, Berlin), pp. 9–38.
Recio, A., Narayan, S. S., and Ruggero, M. A. (**1996a**). ''Wiener-kernel analysis of basilar-membrane responses to white noise,'' Assoc. Res. Otolaryngol., Midwinter Meet., Abstracts, 19, 55.
Recio, A., Narayan, S. S., and Ruggero, M. A. (**1996b**). ''Wiener-kernel analysis of basilar-membrane responses to white noise,'' in *Diversity in Auditory Mechanics*, edited by E. R. Lewis, G. R. Long, P. A. Leake, P. M. Narins, and C. R. Steele (World Scientific Publishing, Singapore) (in press).
Recio, A., Rich, N. C., Narayan, S. S., and Ruggero, M. A. (**1997**). ''Basilar-membrane responses to clicks at the base of the chinchilla cochlea'' (submitted).
Recio, A., and Ruggero, M. A. (**1995**). ''Effects of quinine on basilar-membrane responses to sound,'' Assoc. Res. Otolaryngol., Midwinter Meet., Abstracts, 18, 200.
Rhode, W. S. (**1971**). ''Observations of the vibration of the basilar membrane in squirrel monkeys using the Mössbauer technique,'' J. Acoust. Soc. Am. **49,** 1218–1231.
Rhode, W. S. (**1973**). ''An investigation of post-mortem cochlear mechanics,'' in *Basic Mechanisms in Hearing*, edited by A. R. Møller (Academic, New York), pp. 49–63.
Rhode, W. S. (**1978**). ''Some observations on cochlear mechanics,'' J. Acoust. Soc. Am. **64,** 158–176.
Rhode, W. S., and Cooper, N. P. (**1993**). ''Two-tone suppression and distortion production on the basilar membrane in the hook region of cat and guinea pig cochleae,'' Hear. Res. **66,** 31–45.
Rhode, W. S., and Robles, L. (**1974**). ''Evidence from Mössbauer experiments for nonlinear vibration in the cochlea,'' J. Acoust. Soc. Am. **55,** 588–596.
Robles, L., Ruggero, M. A., and Rich, N. C. (**1986**). ''Basilar membrane mechanics at the base of the chinchilla cochlea. I. Input–output functions, tuning curves, and response phases,'' J. Acoust. Soc. Am. **80,** 1364–1374.
Ruggero, M. A. (**1994**) ''Cochlear delays and traveling waves: comments on 'Experimental look at cochlear mechanics' [A. Dancer, Audiology **31**, 301–312 (1992)],'' Audiology **33**, 131–142.
Ruggero, M. A., and Rich, N. C. (**1983**). ''Chinchilla auditory nerve responses to low-frequency tones,'' J. Acoust. Soc. Am. **73,** 2096–2108.
Ruggero, M. A., and Rich, N. C. (**1991a**). ''Application of a commercially manufactured Doppler-shift laser velocimeter to the measurement of basilar-membrane vibrations,'' Hear. Res. **51,** 215–230.
Ruggero, M. A., and Rich, N. C. (**1991b**). ''Furosemide alters organ of Corti mechanics: Evidence for feedback of outer hair cells upon the basilar membrane,'' J. Neurosci. **11,** 1057–1067.
Ruggero, M. A., Robles, L., and Rich, N. C. (**1986**). ''Basilar membrane mechanics at the base of the chinchilla cochlea. II. Responses to low-frequency tones and relationship to microphonics and spike initiation in the VIII-Nerve,'' J. Acoust. Soc. Am. **80,** 1375–1383.
Ruggero, M. A., Rich, N. C., Robles, L., and Shivapuja, B. G. (**1990**). ''Middle ear response in the chinchilla and its relationship to mechanics at the base of the cochlea,'' J. Acoust. Soc. Am. **87,** 1612–1629.
Ruggero, M. A., Rich, N. C., and Recio, A. (**1992a**). ''Basilar membrane responses to clicks,'' in *Auditory Physiology and Perception*, edited by Y. Cazals, L. Demany, and K. Horner (Pergamon, London), pp. 85–91.
Ruggero, M. A., Robles, L., and Rich, N. C. (**1992b**). ''Two-tone suppression in the basilar membrane of the cochlea: Mechanical basis of auditory-nerve rate suppression,'' J. Neurophysiol. **68,** 1087–1099.
Ruggero, M. A., Rich, N. C., and Recio, A. (**1993**). ''Alteration of basilar membrane responses to sound by acoustic overstimulation,'' in *Biophysics of Hair Cell Sensory Systems*, edited by H. Duifhuis, J. W. Horst, P. van Dijk, and S. M. van Netten (World Scientific Publishing, Singapore), pp. 258–264.
Ruggero, M. A., Rich, N. C., and Recio, A. (**1996a**). ''The effect of intense acoustic stimulation on basilar-membrane vibrations,'' Aud. Neurosci. **2**, 329–345.
Ruggero, M. A., Rich, N. C., Robles, L., and Recio, A. (**1996b**). ''The effects of acoustic trauma, other cochlear injury, and death on basilar-membrane responses to sound,'' in *Scientific Basis of Noise-Induced Hearing Loss*, edited by A. Axelsson, H. Borchgrevink, R. P. Hamernik, P.-A. Hellstrom, D. Henderson, and R. Salvi (Thieme Medical Publishers, New York), pp. 23–35.
Ruggero, M. A., Rich, N. C., Robles, L., Recio, A., and Narayan, S. S. (**1996c**). ''Laser velocimetry measurements of basilar-membrane responses to tones at the base of the chinchilla cochlea,'' Assoc. Res. Otolaryngol., Midwinter Meet., Abstracts, 19, 101.
Sachs, M. B., and Abbas, P. J. (**1974**). ''Rate versus level functions for auditory-nerve fibers in cats: Tone-burst stimuli,'' J. Acoust. Soc. Am. **56,** 1835–1847.
Sellick, P. M., Patuzzi, R., and Johnstone, B. M. (**1982**). ''Measurement of basilar membrane motion in the guinea pig using the Mössbauer technique,'' J. Acoust. Soc. Am. **72,** 131–141.
Sellick, P. M., Patuzzi, R., and Johnstone, B. M. (**1983b**). ''The influence of Mössbauer source size and position on phase and amplitude measurements of the guinea pig basilar membrane,'' Hear. Res. **10,** 101–108.
Temchin, A. N., Rich, N. C., and Ruggero, M. A. (**1997**). ''Frequency-threshold curves of chinchilla auditory-nerve fibers,'' Assoc. Res. Otolaryngol., Midwinter Meet., Abstracts, 20, 152.
Wilson, J. P., and Evans, E. F. (**1983**). ''Some observations on the 'passive' mechanics of the cat basilar membrane,'' in *Mechanisms of Hearing*, edited by W. R. Webster and L. M. Aitkin (Monash University Press, Clayton, Victoria, Australia), pp. 30–35.
Wilson, J. P., and Johnstone, J. R. (**1975**). ''Basilar membrane and middle-ear vibration in guinea pig measured by capacitive probe,'' J. Acoust. Soc. Am. **57,** 705–723.
Yates, G. K. (**1990**). ''The basilar membrane nonlinear input–output function,'' in *The Mechanics and Biophysics of Hearing*, edited by P. Dallos, C. D. Geisler, J. W. Matthews, M. A. Ruggero, and C. R. Steele (Springer-Verlag, Berlin), pp. 106–113.

The effect of the evanescent wave upon acoustic measurements in the human ear canal

David Brass and Antony Locke
Institute of Laryngology and Otology, London WC1X 8EE, England

(Received 19 June 1995; accepted for publication 22 October 1996)

When making acoustic measurements in a human ear canal, it is often necessary to monitor the output of a sound source with a microphone positioned within a few millimeters of that sound source. This microphone will not only measure the pressure due to the propagated acoustic wave, which we wish to measure, but also the pressure due to the evanescent wave. The pressure due to the evanescent wave can be viewed as a source of error in the measurement of the propagating acoustic wave. This paper attempts to quantify the magnitude of this error. Theoretical predictions are made of the relative level of the evanescent sound pressure in a number of source and microphone arrangements applicable to ear canal measurements. It is shown that these theoretical predictions represent an upper limit of evanescent sound pressure that can be measured experimentally. The maximum measurement error due to the presence of the evanescent wave in human ear canals below 10 kHz is predicted to be 3 dB in adults and 1.3 dB in 1 month old infants, when the loudspeaker and microphone ports are spaced more than 2 mm apart. [S0001-4966(97)05004-2]

PACS numbers: 43.64.Yp, 43.64.Ha, 43.58.Bh, 43.20.Mv [RDF]

INTRODUCTION

A. The nature of the evanescent wave

An acoustic source (such as a moving object or the end of a tube connected to a loudspeaker) produces an acoustic pressure field that can be thought of as consisting of two parts[1] (Rayleigh, 1937; Ingard, 1948):

(1) The medium immediately around the source moves in sympathy with the displacement of the source. This is the evanescent wave. The evanescent wave is always in phase with the displacement of the source, and hence in quadrature to its velocity. As we move away from the source the amplitude of the evanescent wave decreases rapidly.

(2) A propagating acoustic wave is generated. The propagating acoustic wave differs from the evanescent wave in that it propagates with a finite velocity away from the source. Hence, its phase, relative to the source, decreases at a rate defined as the wave number k as we move away from the source.

Figure 1 shows the propagating and evanescent waves that are present when a large diameter circular tube is driven by a sound emanating from a much smaller diameter tube. We shall consider the ''source'' to be at $x=0$, where the end of the small tube interfaces with the larger tube. This situation is closely analogous to an ear canal driven by an ''acoustic probe'' containing a loudspeaker connected to a length of small diameter tubing.[2]

Figure 1(a) shows the propagating acoustic wave. This wave is exactly the same as the pressure field that would be generated if the source was replaced by a vibrating flat piston of the same cross-sectional area as the tube. The propagating wave varies only in phase as we move in a longitudinal direction away from the source—it is a ''plane wave.''

Figure 1(b) shows the evanescent wave. The evanescent wave is concentrated around the source, rapidly becoming smaller in amplitude as we move away from the source in either a longitudinal or a radial direction.

Figure 1(c) shows the total sound field in tube, due to both the evanescent and propagating waves. It can be seen that the sound field at $x=L$, several wavelengths away from the source, is almost exactly the same as the propagating wave alone, because the evanescent wave amplitude has become close to zero at this point. However, close to $x=0$, near the source, the total sound field is quite different to the propagating wave alone, due to the effect of the evanescent wave.

The evanescent wave in this situation can be considered as the ''spreading'' of the acoustic field from the small source into the larger tube. This effect can be seen in Fig. 1(c) with the ''curved'' wave close to the source becoming planer as we move down the tube, away from the source.

B. The evanescent wave and ear canal measurements

When we make measurements in a human ear canal, such as impedance or otoacoustic emission measurements, we generally use an ''acoustic probe.'' This acoustic probe consists of an acoustic source, such as a loudspeaker, and a microphone, mounted together so that they are both acoustically coupled to the ear canal. In most ear canal acoustic measurements we wish to generate a stimulus using the loudspeaker and monitor the level of stimulus using the microphone. The microphone will measure the pressure due to both the propagating acoustic and evanescent waves.

Ideally we would wish to measure only the propagating acoustic wave for three main reasons: (1) The tympanum is sufficiently far down the ear canal that it is not affected by the evanescent wave, therefore the evanescent wave has no effect upon the middle or inner ears and hence upon the phenomena we wish to measure. (2) When the ear is driven

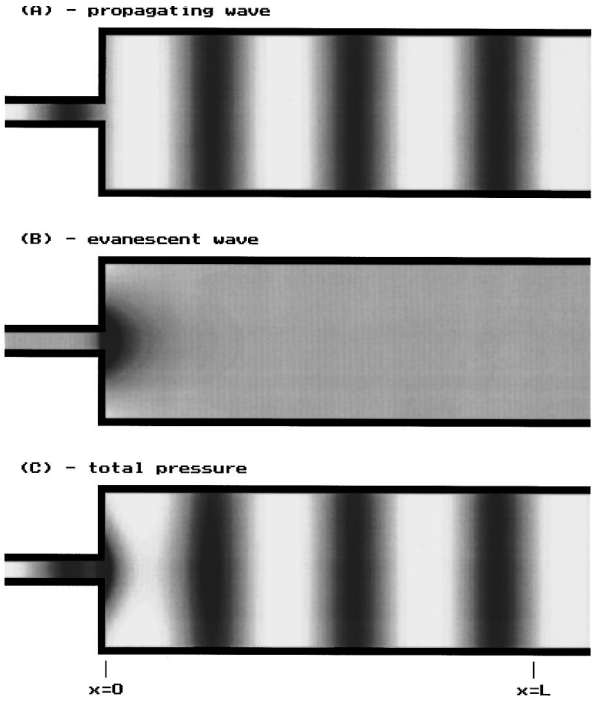

FIG. 1. Diagrammatic view of (a) the propagating acoustic wave, (b) the evanescent wave, and (c) the total pressure due to both waves when a larger diameter duct is driven with sound delivered via a much smaller duct. The end of the smaller duct (at $x=0$) is viewed as the source of sound in the larger duct. The figure shows the instantaneous pressure (with higher pressure shown darker) at a moment of maximum particle displacement at the source. The pressure variation of the source is sinusoidal.

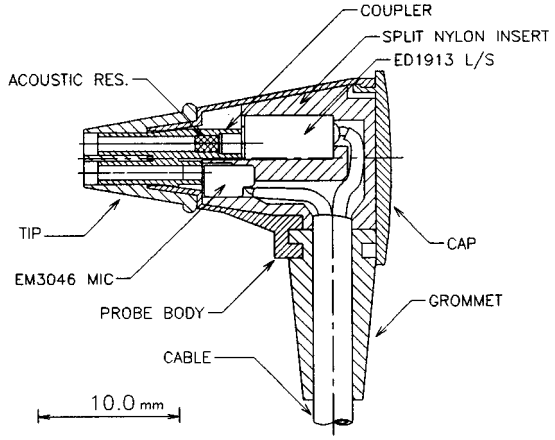

FIG. 2. Cross section of a typical probe used for making acoustic measurements in a human ear canal. The miniature loudspeaker (L/S) and microphone (MIC.) are mounted in the probe body. The transducers and the acoustic resistor (ACOUSTIC RES.) are Knowles types (Knowles Electronics Inc., Itasca, IL). The transducers are acoustically coupled to the ear canal by small tubes. The effective sound generation and measurement sites are thus the small loudspeaker and microphone ''ports,'' at the open ends of the tubes. The figure shows an acoustic probe designed for use in a neonatal ear canal. A typical acoustic probe for use in adult ear canal would be similar, but with correspondingly larger external dimensions. Drawing courtesy of Otodynamics (Otodynamics Ltd., Hatfield, Herts, U.K.).

by its normal stimulus (i.e., an external sound field incident upon the head) there is no evanescent wave at the position of the probe in the ear canal. (3) The size and shape of the evanescent wave is dependant on the design of the acoustic probe and must be discounted if we wish to compare measurements made using different probes.

For these reasons the pressure due to the evanescent wave can be considered to be an error in the measurement of the propagating wave. A sensible design of an acoustic probe must try to reduce this error to a manageable level.

One definition of an error is as follows: The difference between a measurement and the actual value of a quantity being measured. In this sense the pressure due to the evanescent field is not an error, since the evanescent pressure is physically present and the measurement is a reflection of this. However, if we define an error as the difference between the measurement that we are attempting to make (of the plane wave only) and the results of the measurement (necessarily including the evanescent wave), then we can view the pressure due to the evanescent wave as an error.

One design of acoustic probe, used in many commercial instruments, consists of one or more miniature (hearing aid type) loudspeakers and a microphone mounted in a small plastic enclosure. Figure 2 shows a typical design. The loudspeaker(s) and microphone are coupled to the ear canal by means of short lengths of small diameter tubing. This allows the probe to present a small overall diameter that fits in the ear canal. This inevitably means that the microphone is close to the acoustic source, with the possibility of the amplitude of the evanescent wave becoming significant and affecting the measurement of the propagating acoustic wave generated by the source.

Acoustically, the ear canal can be thought of as a short length of duct terminated by a lumped element representing the impedance of the middle and inner ear systems. The diameter of the duct does not exceed about 9 mm (Egolf *et al.*, 1993).[3] Hence, the duct can be considered as a one-dimensional acoustic system for frequencies up to about 10 kHz (Keefe and Benade, 1981). In such a system, in general, the amplitude of the evanescent wave will decay faster than the propagating acoustic wave with distance from the source. Thus, we can minimize the contribution of the evanescent wave by placing the microphone port a small distance from the loudspeaker port.

C. How far apart can we space the loudspeaker and microphone ports?—Practical considerations

We can increase the distance between the source and microphone by: spacing the microphone and loudspeaker ports across the width of the ear canal; spacing the ports along the length of the ear canal by extending one of the ports with extra tubing; or, using both of these strategies.

Spacing the ports across the width of the ear canal is limited by the width of the ear canal itself. Furthermore, for many measurements, it is advantageous to provide an acoustic seal around the acoustic probe in order to exclude external noise, and in the case of tympanometry to allow the ear canal to be pressurized. This sealing requires a few millimeters of some soft material around the end of the acoustic probe in order to fit any irregularities in the ear canal shape. This limits the spacing of the ports across the width of the ear canal to about 4 mm for adults and about 2 mm for infants.

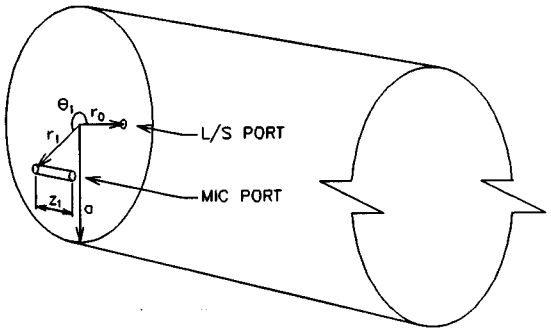

FIG. 3. The coordinate system used throughout this paper. The acoustic probe is assumed to be driving into a cylindrical duct of radius a. One end of the duct is terminated by a rigid surface at $z=0$. The loudspeaker port is positioned flush with the rigid surface at $(r_0,0,0)$. The microphone port is positioned at (r_1,θ_1,z_1). All positions are given in cylindrical coordinates with the origin at the center of the duct at the rigid surface.

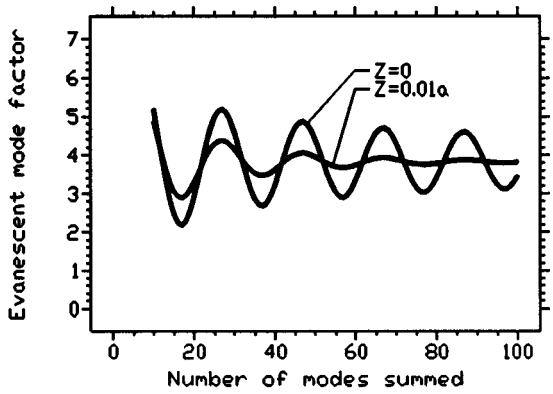

FIG. 4. The effect of truncating the series in Eq. (4) upon the estimate of evanescent mode factor. Equation (4) is evaluated with the loudspeaker port mounted in the center of the duct at $(r_0=0,0,0)$ and the microphone port at $(r_1=0.1a,\ \theta_1=0,\ z_1)$. $z_1=0$ and $0.01a$ as marked.

At first sight it would appear that there is much more latitude for spacing the ports along the length of the ear canal, since, in general, the length of the ear canal is greater than its width. However, there is a practical problem with this strategy. If we extend, say, the microphone tubing a few millimeters beyond the rest of the end of the probe, it will achieve our aim of spacing out the ports. This would result in a probe with a small, thin projection from its end. Using such a probe for routine or clinical work would be impractical since the projecting tube could come into contact with the ear canal wall during fitting. This could result in both damage to the ear canal, and the tube becoming more easily blocked with debris from the ear canal wall. In the case of neonatal measurements, the projecting tube could even be pushed right up against the tympanum, since neonatal ear canals are very short.

Thus, practical considerations of acoustic probe design limit the spacing of the microphone and loudspeaker ports to a few millimeters. When probes are used for routine clinical use, it is also advantageous to mount the microphone and loudspeaker ports on the same plane perpendicular to the long axis of the ear canal, so that there are no projecting tubes.

I. THE SCOPE OF THIS PAPER

The question arises: Is the spacing of the microphone and loudspeaker ports on a practical acoustic probe sufficient to reduce the error in stimulus measurements due to the evanescent wave to a negligible level in the human ear canal? Furthermore, is it possible to design a probe with no projecting tubes that can satisfy the requirement of a negligible error due to the evanescent wave? In this paper we shall attempt to answer these questions.

II. THEORY

In this paper we shall make theoretical predictions of the effects of the evanescent wave by using the method outlined by Keefe and Benade (1981) and described in detail by Morse and Ingard (1968). In order to use this analysis we have to make some assumptions about the system we are modeling: (1) The system can be viewed as an acoustic transmission line in which there is only one mode of propagating acoustic wave (the size of duct is sufficiently small that all the other modes are evanescent). (2) The part of the system where the evanescent modes are significant is a hard walled circular duct of constant radius. (3) The acoustic transmission line is long enough that there is no significant reflection of any of the evanescent modes. (4) There is insignificant dissipation of the evanescent modes, either at the duct walls or in the acoustic medium. (5) The microphone is ''perfect''—its introduction into the acoustic system does not affect the acoustic field.

The amplitude of the pressure, P, measured at some position (r,θ,z) in the duct due to a source, situated at $z=0$ and generating volume velocity, $U_s\cdot e^{j\omega t}$, can be written as

$$P=U_sR_0\cdot\frac{(e^{-jkz}+\Re e^{jkz})}{(e^{-jkz}-\Re e^{jkz})}+jU_sR_0ka\,\epsilon[r/a,\theta,z/a,\omega], \tag{1}$$

where r, θ, and z are the position of the microphone in cylindrical coordinates, with the z axis running down the center of the duct (the coordinate system is illustrated in Fig. 3); $\omega=2\pi f$, where f is the input frequency; k is the propagating mode wave number (given by ω/c, where c is the speed of sound in free space); a is the radius of the circular duct; ϵ is the ''evanescent mode factor,'' given below; $j=(-1)^{1/2}$; and $\Re$ and R_0 are the reflection coefficient and characteristic impedance of the acoustic transmission line, as defined below.

The first term of Eq. (1) represents the acoustic wave which propagates along the length of the duct. This propagating acoustic wave will be reflected back from the termination of the transmission line. The ratio of amplitudes of the reflected to the incident wave is given by $\Re$, which can be expressed as

$$\Re=\frac{(Z_{\text{in}}/R_0-1)}{(Z_{\text{in}}/R_0+1)}, \tag{2}$$

where Z_{in} is the acoustic input impedance of the duct measured at $z=0$ (the position of the source); and R_0 is the characteristic impedance of the duct (given by $\rho c/\pi a^2$ for a

nondissipative circular duct, where ρ is the density of the acoustic medium).

The second term of Eq. (1) represents the contribution to the total pressure from the evanescent wave. The evanescent mode factor, ϵ, is strongly dependent upon the configuration of the source and measuring microphone.

Consider the situation illustrated in Fig. 3. Sound is generated by an insignificantly small source situated at ($r=r_0$, $\theta=0$, $z=0$). Pressure is measured by an ''ideal microphone'' (i.e., capable of measuring the pressure at a single point in a sound field without affecting the sound field) situated at ($r=r_1$, $\theta=\theta_1$, $z=z_1$). For this arrangement of source and microphone, the evanescent mode factor, ϵ, in a hard walled lossless circular duct can be shown to be (Keefe and Benade, 1981):

$$\epsilon[r_0/a, r_1/a, \theta_1, z_1/a] = \sum_{n=1}^{\infty} \frac{J_0[\mu_{0n} r_1/a] J_0[\mu_{0n} r_0/a] \cdot \exp[-(\mu_{0n} z_1/a)\cdot(1-(ka/\mu_{0n})^2)^{1/2}]}{\mu_{0n} \cdot J_0[\mu_{0n}]^2 \cdot (1-(ka/\mu_{0n})^2)^{1/2}} + \sum_{m=1}^{\infty} 2\cos[m\theta_1] \sum_{n=0}^{\infty} \frac{J_m[\mu_{mn} r_1/a] \cdot J_m[\mu_{mn} r_0/a] \cdot \exp[(\mu_{mn} z_1/a)\cdot(1-(ka/\mu_{mn})^2)^{1/2}]}{\mu_{mn} \cdot J_m[\mu_{mn}]^2 \cdot (1-(m/\mu_{mn})^2) \cdot (1-(ka/\mu_{mn})^2)^{1/2}}, \tag{3}$$

where $\exp[x]=e^x$; $J_m[x]$ is the mth Bessel function evaluated at x; and μ_{mn} is the $(n+1)$th zero of $dJ_m[x]/dx$ (the so-called ''Bessel prime zeros'').

Expression (3) expresses the evanescent mode factor as the addition of two sums of terms: a sum of ''$m=0$'' terms that are radially symmetrical, and a double summation of ''$m>0$'' terms that are not radially symmetrical. Note that because of the appearance of the wave number (k) in expression (3), the evanescent mode factor is dependent on the frequency of the source. As the driving frequency increases, k also increases. This has two effects upon the evanescent mode factor: (1) The distance over which each evanescent mode factor decays (the ''$1/e$'' distance) increases; and (2) at $z=0$ the evanescent mode factor decreases. Hence, as frequency increases, the pressure field due to the evanescent wave is smaller at the source end of the tube but stretches further down the tube away from the source.

If the frequency of the source is low enough that the condition $(ka/\mu_{mn})^2 \ll 1$ holds true, then $(1-(ka/\mu_{mn})^2)^{1/2} \approx 1$. Under these conditions, ϵ is nearly independent of frequency (Keefe and Benade, 1981). For such ''low frequencies'' (up to about 10 kHz in an adult ear canal) the evanescent mode factor is approximately given by

$$\epsilon(r_0/a, r_1/a, \theta_1, z_1/a) \approx \sum_{n=1}^{\infty} \frac{J_0[\mu_{0n} r_1/a] \cdot J_0[\mu_{0n} r_0/a] \cdot e^{(-\mu_{0n} z_1/a)}}{\mu_{0n} \cdot J_0[\mu_{0n}]^2} + 2\sum_{m=1}^{\infty} \cos[m\theta_1] \times \sum_{n=0}^{\infty} \frac{J_m[\mu_{mn} r_1/a] \cdot J_m[\mu_{mn} r_0/a] \cdot e^{(-\mu_{mn} z_1/a)}}{\mu_{mn} \cdot J_m[\mu_{mn}]^2 \cdot (1-(m/\mu_{mn})^2)}. \tag{4}$$

Let us assume that the maximum radius of the adult ear canal is 4.5 mm. The smallest Bessel prime zero involved in expression (4) is $\mu_{01} \approx 1.84$. The maximum error in the evanescent mode factor at $z=0$ caused by using the low-frequency approximation in Eq. (4) is given by $1-(1-(ka/1.84)^2)^{1/2}$. At 10 kHz the error is -11%. For lower frequencies the magnitude of the error drops rapidly. At 5 kHz the error reduces to -2.5%, and at 2 kHz it is -0.5%.

It can be seen that expression (4) giving the evanescent mode factor consists of the sum of an infinite series of terms. With the exception of a few trivial situations, this sum must be evaluated numerically in order to find the approximate evanescent mode factor. This is not a trivial matter, often requiring 10 000 terms, each involving the evaluation of three Bessel functions, to be summed before the result is accurate to within a few percent. For each term the ''Bessel prime zero,'' μ_{mn}, must also be found numerically using a root finding procedure.

The evanescent mode factor was evaluated numerically for a variety of source and microphone arrangements relevant to those used in probe designs for ear canal measurements. The results are given in the following two sections.

A. Predicted evanescent mode factor for a source at the center of the duct

Consider the situation in which a point source is situated at the center of the end of a cylindrical duct ($r_0=0$) and the sound pressure is measured using a negligibly small microphone situated at (r_1, θ_1, z_1). By the principle of reciprocity, the results of this section apply equally to a situation in which the source is situated at (r_1, θ_1, z_1) and the microphone was mounted at the center of the end of the duct. Because of the rotational symmetry of the source and duct, we would expect the microphone pressure to be independent of θ_1. This is the case with all the terms of the second sum in Eq. (4) being equal to zero. In other words, only the rotationally symmetrical ''$m=0$'' modes are excited.

It can be demonstrated using D'Alembert's ratio test that the summations in Eq. (4) converge for $z_1>0$. However, we do not know how fast the series converges; in other words, how many terms do we have to calculate and sum in order to obtain a reasonable estimate of the value of Eq. (4)? [By number of terms we mean the value of the upper limit on the summations in Eq. (4), i.e., using ten terms means estimating

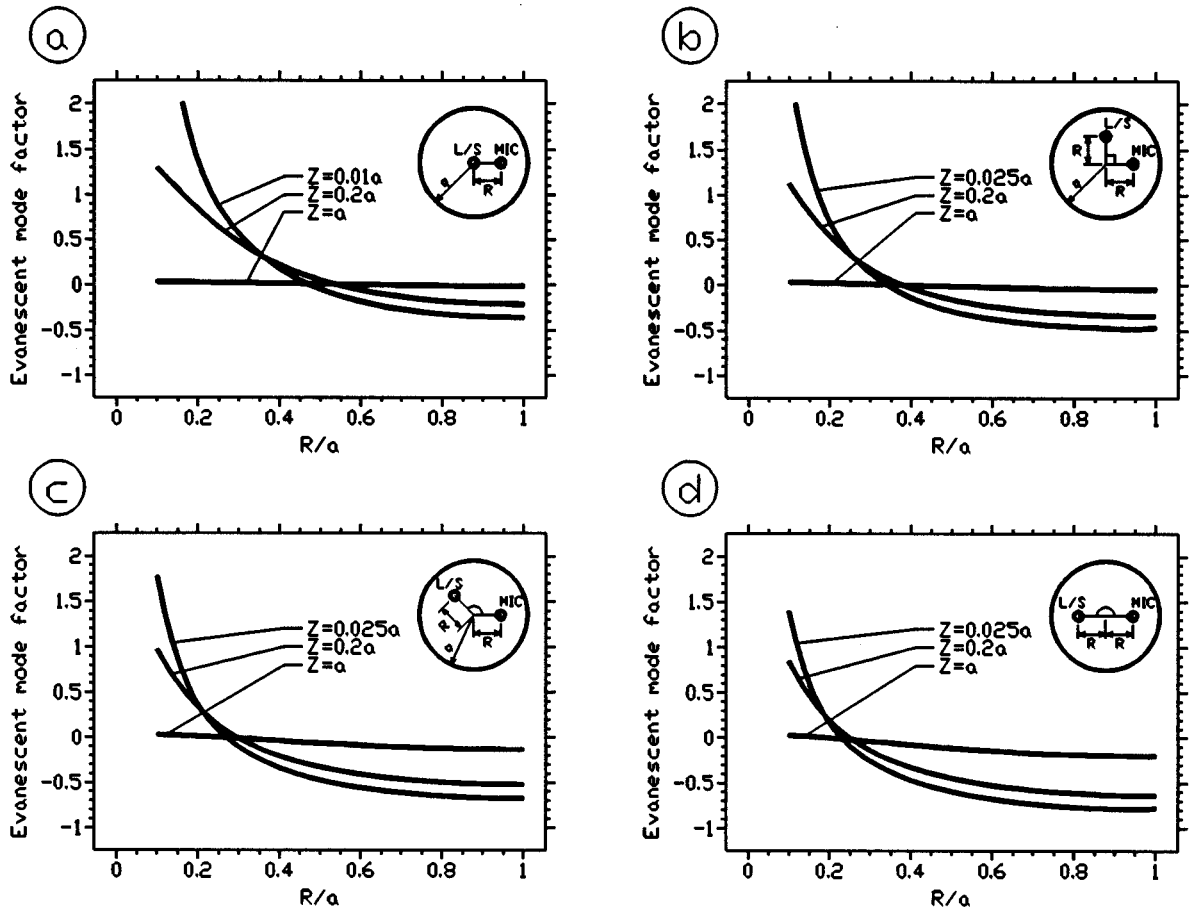

FIG. 5. Levels of evanescent mode factor predicted by Eq. (4) for different arrangements of loudspeaker and microphone ports. (a) The loudspeaker port is mounted at the center of the duct at (r_0=0,0,0), and the microphone port is mounted at ($r_1=R$, $\theta_1=0$, $z_1=Z$). Note that the result would be identical for any value of θ_1, since only rotationally symmetrical modes are excited with the loudspeaker port in this position. (b) The loudspeaker port is mounted at ($r_0=R$,0,0), and the microphone port is mounted at ($r_1=R$, $\theta_1=\pi/2$, $z_1=Z$). (c) The loudspeaker port is mounted at ($r_0=R$,0,0), and the microphone port is mounted at ($r_1=R$, $\theta_1=2\pi/3$, $z_1=Z$). (d) The loudspeaker port is mounted at ($r_0=R$,0,0), and the microphone port is mounted at ($r_1=R$, $\theta_1=\pi$, $z_1=Z$). All angles are given in radians.

Eq. (4) using summations with limiting values of n and m of up to 10.]

Figure 4 shows estimates of Eq. (4) made with series of from 10 to 100 terms, for the situation where $r_1/a=0.1$ and $z_1/a=0$ and 0.01. It can be seen that when $z_1/a=0.01$ and 100 terms are used the evanescent mode factor has ''settled'' to within a few percent of its final value. When $z_1/a=0$ the evanescent mode factor is still oscillating by $\pm 20\%$ or so of its final value even when 100 terms are used. However, the evanescent mode factor given when $z_1/a=0.01$ is a good estimate of that given when $z_1/a=0$, so there is no need to calculate the evanescent mode factor at $z_1/a=0$. In other words, if we estimate the value of the evanescent mode factor when $z_1/a=0$ using many thousands of terms (when the value has converged to a few percent of its final value) then it is very close (within 1%) of the evanescent mode factor found for $z_1/a=0.01$. Other values of r_1/a and z_1/a used in this study converge faster than $r_1/a=0.1$ and $z_1/a=0.01$. Hence, we can make a reasonable estimate of the value of Eq. (4) using 100 terms.

Figure 5(a) shows the evanescent mode factor predicted by Eq. (4) in the situation outlined above. The variables r_1 and z_1 are expressed as the nondimensional ratios r_1/a and z_1/a, where a is the radius of the duct.

B. Predicted evanescent mode factor for a source and microphone equal distances from the center of the duct

Another common arrangement of the source and microphone in ear canal measurement probes is one in which the ports are spaced around a pitch circle (i.e., laying upon a circle with its center at the center of the duct cross section). This is the case with the probe design shown in Fig. 2. We shall consider the situation when such a probe is mounted in a cylindrical duct. In this situation $r_0=r_1$.

This arrangement of source and duct is not rotationally symmetrical, and we would expect the pressure measured by the microphone to depend on θ_1. This is the case and, in general, we have to consider both the symmetrical ($m=0$) and the asymmetrical ($m>0$) summations in Eq. (4).

The $m>0$ terms involve a double summation of both n and m. For this reason many more terms have to be calcu-

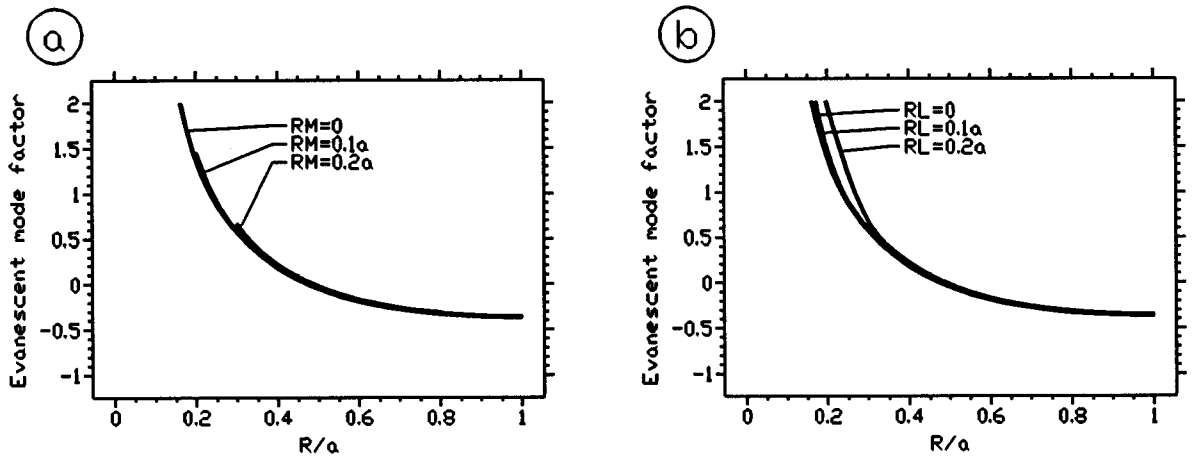

FIG. 6. The effect of finite sized ports on the predicted level of the evanescent mode factor. The arrangement of loudspeaker and microphone ports is identical to that used in Fig. 5(a). $z_1=0.01$ for all the results shown in this figure. (a) The effect of a finite sized microphone port. Predicted evanescent mode factors are given by Eq. (5). Results are shown for ports of radius $r_{\text{mic}}=RM=0$, $0.1a$ and $0.2a$. (b) The effect of a finite sized loudspeaker port. Predicted evanescent mode factors are given by Eq. (6). Results are shown for ports of radius $r_s=RL=0$, $0.1a$ and $0.2a$.

lated for this arrangement than for the situation with the source at the center of the duct. For instance, if an upper limit of 100 is set for both n and m in the summations, 10 000 terms have to be calculated when the source is not at the center of the duct, as opposed to 100 when the source is at the center of the duct.

A study of series truncation effects, similar to that illustrated in Fig. 4, was carried out for the transducer arrangements considered in this section. It was found that setting an upper limit of 100, on both n and m, in Eq. (4) gave estimates of the evanescent mode factor accurate to a few percent for: $0.025 \leqslant z_1/a \leqslant 1$ and $0.1 \leqslant r_1/a \leqslant 1$. Figures 5(b), (c), and (d) shows the predicted evanescent mode factors when θ_1 was set to 90, 120, and 180 deg, respectively.

C. The effect of using a finite sized microphone or source

So far we have only considered situations in which both the source and microphone are negligibly small and can thus be considered to be point sources. Real acoustic probes have ports with radii of the order of a millimeter. This is of considerable size compared with the radius of the ear canal. The question arises: Does this finite port size have a large effect on the evanescent mode factor?

First, let us consider a finite sized microphone port. An estimate of the pressure ''seen'' by the finite sized port can be made by simply finding the average pressure over the whole port. The equivalent evanescent mode factor for a circular microphone is then given by

$$\epsilon_{\text{mic}}=1/(\pi r_{\text{mic}}^2)\int\int_{\text{mic}}\epsilon(r_0/a,r_1/a,\theta_1,z_1/a)\times d\theta_1 r_1\, dr_1, \tag{5}$$

where $\int\int_{\text{mic}}[\cdot\cdot]d\theta_1 r_1\, dr_1$ represents an integration over the area of the microphone; $\epsilon(r_0/a,r_1/a,\theta_1,z_1/a)$ is given by Eq. (4); and r_{mic} is the radius of the microphone.

Figure 6(a) shows the equivalent evanescent mode factor for a finite sized microphone, with $r_{\text{mic}}/a=0.2$, compared with that for a negligibly small microphone. The negligibly small source was positioned at the center of the duct ($r_0=0$) and $z_1/a=0.01$. This situation models a microphone port of 1.8 mm diameter in a 9 mm diameter ear canal. It can be seen that the equivalent evanescent mode factor does not differ from that of the negligibly small microphone by more than a few percent, except where the edges of the ports are closer than $0.1a$.

Second, we consider a finite sized source. We shall consider the loudspeaker (or source) port to be a circular rigid piston of radius r_s. The piston is mounted at the center of one end of a circular duct of radius a. We set the velocity of the surface of the piston to $U_s/(\pi r_s^2)$, so that the total volume velocity across the surface of the piston is constant when r_s is varied. Following the analysis of Keefe and Benade (1981), we obtain the following evanescent mode factor for a microphone at (r_1,θ_1,z_1):

$$\epsilon_s(r_s/a,r_1/a,\theta_1,z_1/a)\approx 1/(\pi r_s^2)\sum_{n=1}^{\infty}\frac{J_0(\mu_{0n}r_1/a)\cdot e^{(-\mu_{0n}z/a)}\cdot\int_0^{r_s}\int_0^{2\pi}[J_0(\mu_{0n}r_0/a)]d\theta_0 r_0\, dr_0}{\mu_{0n}\cdot J_0(\mu_{0n})^2}. \tag{6}$$

Figure 6(b) shows the predicted evanescent mode factors for finite sized sources with $r_s/a=0.1$ and 0.2 compared with a negligibly sized source, measured with a microphone at $z_1/a=0.01$. The effect of increasing the source size on the evanescent mode factor is no more than a few percent providing that the microphone is no closer than $0.1a$ to the edge of the source.

III. EXAMPLE: A HARD WALLED TUBE

In order to provide an example of the effects of the evanescent wave on acoustic probe measurements, the pressure in a hard walled tube was measured at various positions close to a small source. The tube used was a rigidly terminated 100 mm long cylindrical duct of 9 mm diameter. These measurements will also allow us to check the accuracy of the predictions of evanescent mode factor given above.

A. Theory

The acoustic input impedance of a rigidly terminated hard walled cylindrical duct, including visco-thermal losses, is given by

$$Z_{in}=-j\cdot R_t\cot[k_t\cdot l], \tag{7}$$

where l is the length of the duct; and R_t and k_t are the complex characteristic impedance and wave number allowing for dissipation at the duct walls (see Kirchhoff, 1868, and Keefe, 1984).

The sound-pressure level at a point (r_1,θ_1,z_1) in a rigidly terminated cylindrical duct driven by a volume velocity source situated at $(r_0,0,0)$ is given by

$$P(r_0,r_1,\theta_1,z_1)=U_s(-j\cdot R_t\cos[k_t(l-z_1)]/\sin[k_t l] + jR_0ka\epsilon(r_0/a,r_1/a,\theta_1,z_1/a)), \tag{8}$$

where U_s is the volume velocity produced by the source.

The magnitude of the acoustic input impedance of the duct exhibits a series of maxima and minima. As Keefe and Benade (1981) pointed out, the evanescent wave will have maximum effect at an impedance minimum. If we drive the tube with a high impedance (or volume velocity) source, then Eq. (1) shows that the magnitude of the propagating acoustic wave is directly proportional to the input impedance of the duct, whereas the magnitude of the evanescent wave is independent of the input impedance. The ratio of evanescent wave to propagating acoustic wave magnitude, and hence the effect of the evanescent wave, is greatest at an input impedance minimum.

The most easily measurable effect of the evanescent wave is a shift in the frequency of the sound-pressure level minima. This can be interpreted in terms of the evanescent wave, adding a small mass (positive or negative) to the effective acoustic input impedance of the duct. The sound-pressure minima is located at the frequency where the imaginary part of the effective input impedance of the duct [given by $P(r_0,r_1,\theta_1,z_1)/U_s$] passes through zero. Examination of Eq. (8) shows that the effect of the evanescent wave is to add a small imaginary part to the effective input impedance. This ''shift'' in the imaginary part of the effective input impedance causes the zero crossing point, and hence the minima, to also shift frequency.

This shift in the frequency of the pressure minima is independent of the value of U_s, providing that U_s varies slowly with frequency. We can ensure this by using a ''well behaved'' high output impedance source. By ''well behaved'' we mean that there are no lightly damped resonances in the source output impedance at around the measurement frequencies. We use a high output impedance source so that the volume velocity produced by the source for a given input is nearly constant irrespective of the load impedance. A source such as a loudspeaker driving via a length of small diameter tubing will provide a nearly constant volume velocity because of its high output impedance and will be ''well behaved'' because of its high damping.

Figure 7(a) illustrates the frequency shift of the sound-pressure minima. The figure shows the sound-pressure level predicted by Eq. (8) for a small frequency sweep at around the frequency of the first input impedance minima, when the duct is driven by a high impedance source. Curves are shown for evanescent mode factors of 0 (no evanescent wave), 1, and -1. The main effect of the change in evanescent mode factor is a change in the frequency of the sound-pressure level minima.

Figure 7(b) shows the first predicted frequency minima at distance z_1 from the source along a rigidly terminated cylindrical duct of diameter 9 mm and length 100 mm. Curves are shown for different levels of evanescent mode factor. It can be seen how the frequency of the frequency minima can be related to the evanescent mode factor.

We can use this frequency shift as the basis of a method to check our predictions of the evanescent mode factor. We can calculate the predicted frequencies of the sound-pressure minima in a particular duct with only propagating acoustic waves, and with both propagating waves and evanescent waves for a particular arrangement of source and microphone. We can also make a measurement of the frequency minima in a real duct. By comparing the predicted and measured minima frequencies, we can then check our predictions.

B. Measurements

Figure 8 illustrates the apparatus used to make measurements of the acoustic field in the vicinity of a acoustic source driving a rigidly terminated tube. This apparatus consists of a 100-mm long, 9-mm internal diameter rigidly terminated duct, a source consisting of a miniature loudspeaker driving via an acoustic resistor and a length of small diameter tubing, mounted at the center of one end of the duct, and a probe microphone mounted at a fixed r_1 with z_1 adjustable using a ''micrometer'' type mechanism.

The acoustic source has a much higher acoustic impedance than the acoustic input impedance of the duct at around an impedance minimum. Figure 7(a) shows that the magnitude of the acoustic input impedance of the duct is of the order of 2×10^5 MKS acoustic ohms, at frequencies around the frequency minima. The input impedance at a frequency minima for this arrangement of a duct is R_0/Q. The 3-dB

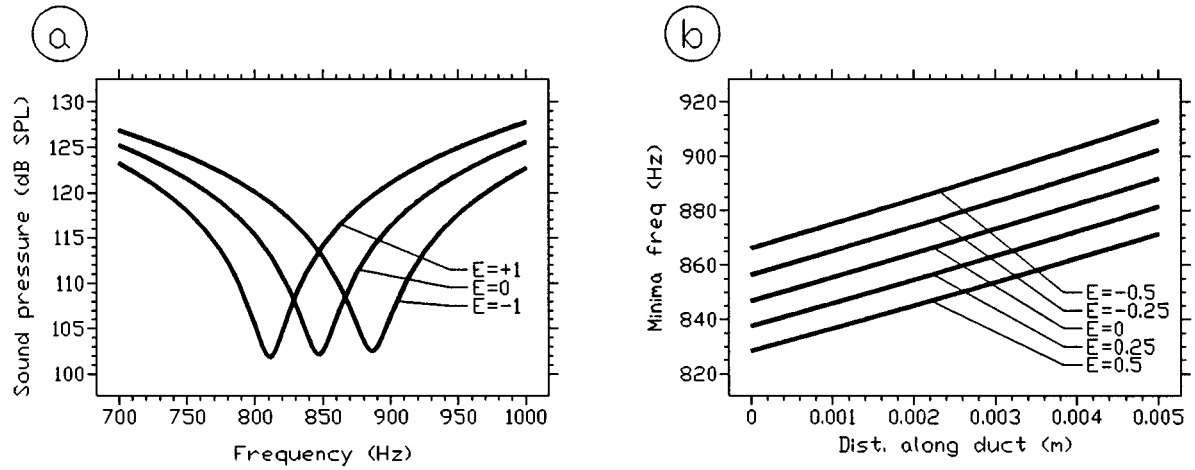

FIG. 7. The effect of the evanescent wave on the frequency of the sound-pressure level minimum. All results are for a high output impedance source driving a rigidly terminated cylindrical duct of length 100 mm and radius 4.5 mm. The source is mounted flush with one end of the duct, at $z_0=0$. (a) The predicted sound-pressure level amplitude at frequencies around the first frequency minima produced by a volume velocity source of amplitude 2×10^{-5} m^3/s (the sound-pressure amplitude, dB relative to 2×10^{-5} Pa, is numerically equal to the acoustic input impedance of the duct, in dB relative to 1 MKS ohm, when driven by this source). Sound pressure is measured at $z_1=0$. Frequency sweeps are shown in the presence of evanescent waves with evanescent mode factors ($\epsilon=E$) of -1, 0 and $+1$. (b) The predicted frequencies of the first sound-pressure level minimum at different distances along the duct, from the source, and different evanescent mode factors.

bandwidth of the system shown in Fig. 7(a) is about 25 Hz, giving a Q of about 35. The minimum input impedance is $R_0/Q\approx2\times10^5$ MKS acoustic ohms.

A minimum value of the magnitude of the acoustic output impedance of the source can be predicted by considering the source to be a 25 mm×1 mm length of tubing terminated by a 2.2×10^8 MKS acoustic ohms resistor, plus an unknown impedance with a positive acoustic resistance. Using the equations for the characteristic impedance and wave number for a duct from Kirchhoff (1898), it can be shown that the output impedance at the end of the tube is greater than 5×10^7 MKS acoustic ohms at all frequencies considered in these measurements (830–2700 Hz). Hence, the acoustic source can be considered to be a high impedance or volume velocity source.

The miniature loudspeaker was driven using a broadband electrical signal. The spectrum of the output of the probe microphone was displayed using a Brüel and Kjær 2035 spectrum analyzer. From this spectrum it was possible to measure the frequencies of the sound-pressure minima at various positions around the source. The frequencies of these sound-pressure minima can be related to the evanescent mode factor using the method outlined above.

Figure 9 shows measurements of the frequency of the first and second sound-pressure minima at various positions in the apparatus illustrated in Fig. 8. Measurements were made at z_1 distances (parallel to the axis of the tube) of 0–5 mm in 0.5-mm steps with r_1 set to 1.5, 3, and 4.5 mm. Figure 9 also shows the frequency of the sound-pressure minima predicted using Eq. (8).

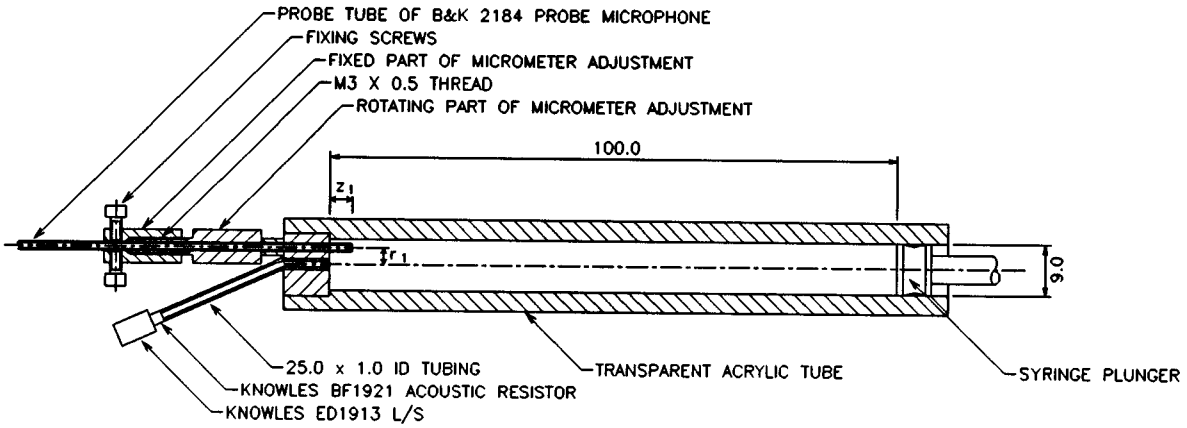

FIG. 8. Apparatus used for making measurements of the sound field immediately around a small acoustic source in a rigidly terminated cylindrical duct. The duct is formed from a 100 mm length of transparent acrylic tubing with an internal diameter of 9 mm, terminated by a syringe plunger. The acoustic source drives the duct at ($r_0=0$, $\theta_0=0$, $z_0=0$). It consists of a Knowles ED1912 miniature loudspeaker driving via a 2.2×10^8 MKS acoustic ohm resistor and a length of small diameter tubing. The sound field is measured using a Brüel and Kjær 2184 probe microphone. The probe microphone is inserted through one of several holes drilled in the duct end, determining r_1. A ''micrometer adjustment'' allows z_1 to be set to an accuracy of better than 0.1 mm.

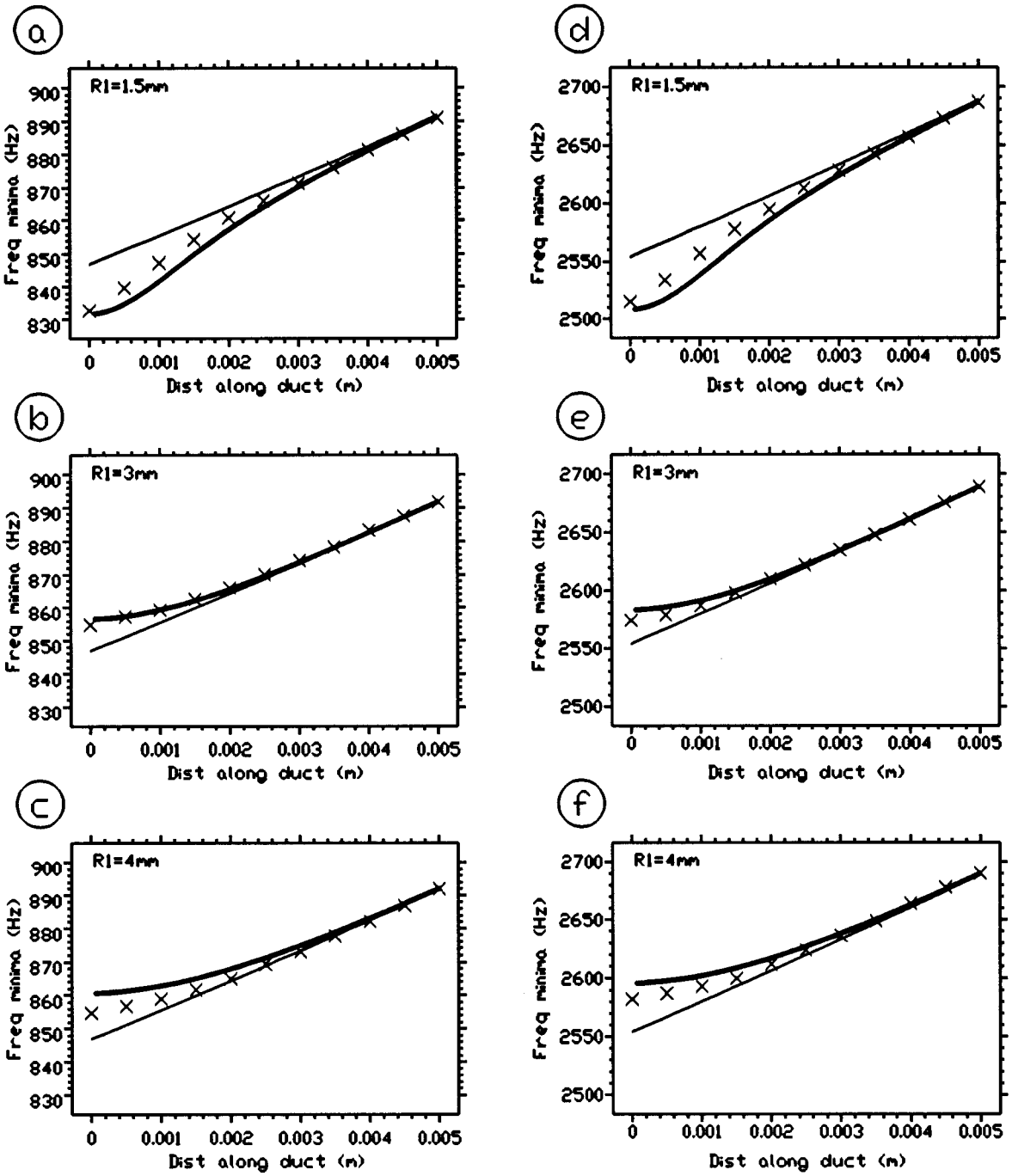

FIG. 9. Predicted and measured sound-pressure level minima frequencies at various positions in a rigidly terminated cylindrical duct. All predictions are made using Eq. (8) for the apparatus shown in Fig. 8. The thin lines show the predicted minima frequencies if the effect of the evanescent wave is not included (ϵ is set to zero). The thick lines show the predicted minima frequencies when the effect of the evanescent wave is included [ϵ is set to the value given by Eq. (4)]. The crosses show actual measurements of minima frequencies made using the apparatus illustrated in Fig. 8. (a), (b), and (c) show predictions and measurements of the first minima frequency, when z_1 ($z_1 = Z1$) is varied and r_1 ($r_1 = R1$) is set to 1.5, 3, and 4 mm, respectively. (d), (e), and (f) show the predictions and measurements of the second minima frequency.

Errors will occur in the measurements shown in Fig. 9 due to factors such as acoustic noise, inaccurate setting of distance, and inaccuracies in the estimation of the minima frequencies. It is necessary to make an estimate of the confidence interval for the measurement of minima frequency in order to show that the apparent deviation of the results from the predicted values were not due to these errors.

The 95% confidence interval of the measurements shown in Fig. 9 was estimated in the following way: The measured values of minima frequency for a given mode and r_1 (i.e., the crosses from one of the graphs shown in Fig. 9) were fitted to a third-order polynomial; the variance was estimated as the sum of the squares of differences between the measured values and the fitted curve divided by the number of degrees of freedom of the fit; the 95% confidence interval was estimated as twice the square root of the estimated variance. The method assumes that the actual function is smooth

and can be accurately represented as a third-order polynomial.

The average estimated 95% confidence interval for the measurements made around the first and second frequency minima were ± 1.06 Hz and ± 3.78 Hz, respectively. This level of random error is not enough to account for the discrepancies between the predicted values and the measurements.

As well as random measurement errors there could also be systematic errors present in the data in Fig. 9. One likely cause of systematic errors is the sound source not maintaining constant volume velocity across different frequencies. For instance if the source volume velocity showed a ''low-pass'' function, with less output at higher frequencies, then the minima will shift to a higher frequency than its true value. However, it is unlikely that the results shown in Fig. 9 could arise from such a source. For instance, Fig. 9(a) shows minima frequencies higher than their predicted values and Fig. 9(c) shows minima frequencies lower than their predicted values. Both situations could not be caused by a frequency dependence of the source volume velocity.

C. Comparison of predicted and measured values of evanescent mode factor

It can be seen from Fig. 9 that the measured minima frequencies are, allowing for the errors, between the values predicted by Eq. (8) and the minima frequencies predicted when the effects of the evanescent wave are not included. [The measured points (crosses) lie between the two lines in the figure.] This means that the real evanescent mode factor magnitude is always less than or equal to the value predicted in Eq. (4). Hence, the value given by Eq. (4) represents the upper limit of measured evanescent mode factor magnitude.

The reason that the magnitude of the evanescent mode factor in the measurements lies below that predicted by the theory must be that some of the assumptions made in formulating the model were incorrect. In particular, assumptions (4) and (5) (that the boundaries of the duct are lossless and that the presence of the microphone does not affect the sound field) are probably in error.

The largest deviations of the measured value of the evanescent mode factor from its predicted value occur close to the duct boundaries. Both in the measurements made at $r_1=4$ mm (when the microphone was only 0.5 mm from the duct wall) and in the measurements when z_1 was small (and the microphone was close to the rigid termination at $z=0$), there were significant deviations. These differences between measurements and theory were probably due to frictional losses close to the duct walls.

The thickness of the ''boundary layer,'' beyond which frictional losses become unimportant, is of the order of 0.1 mm, at the frequencies used in the measurements (Lighthill, 1978). The probe microphone used in these measurements is of the order of 1 mm diameter at the tip and the duct has a radius of 4.5 mm. Therefore, the edge of the probe microphone is in contact with the duct wall when measurements are made at $r_1=4$ mm and part of the measurement orifice of the probe microphone is within the boundary layer. Hence, any values of evanescent mode factor derived from measurements made at $r_1=4$ mm will not be accurately predicted by the above lossless theory.

The measurements made at $r_1=1.5$ mm also show large deviations from the predicted values, even when measurements were made well away from the duct walls. These deviations are probably due to the presence of the probe microphone close to the source.

Acoustically, the probe microphone is a hard walled cylinder (with its associated boundary layer) with an opening on the end with an acoustic impedance equivalent to that of a cavity of a few mm^3. The presence of such an object close to a high impedance source will affect the sound field from that source. Moving the acoustic load at the end of the microphone close to the source will change the nature of the evanescent field since each evanescent mode has a different ''$(1/e)$ decay length'' (Keefe and Benade, 1981). When the end of the microphone is close to the source, it will load the rapidly decaying evanescent modes far more than when it is distant from the source.

Another way of stating how the presence of the probe microphone effects the evanescent pressure field is this: The presence of the probe microphone, both its hard walled tube and the effect of the impedance at its open end, make the eigenfunctions used in the derivation of Eq. (3) invalid. The transverse eigenfunctions given in Eq. (1) of Keefe and Benade (1981) assume a lossless circular tube filled completely with a uniform acoustic medium. The presence of the probe microphone obviously makes this assumption invalid, and therefore these eigenfunctions do not accurately describe the system.

If we wished to devise a model that accurately predicted the evanescent mode factor in a long cylindrical duct, then we would have to include the effects of frictional dissipation at the duct walls [a model including this effect is outlined in Morse and Ingard (1968) and further developed and tested in Hudde (1988)], frictional dissipation at the rigid termination at $z=0$, the effect of the microphone tube on the sound field [this factor was studied by Rabbitt and Friedrich (1991)], and the effect of the acoustic load presented by the microphone port.

Fortunately, a model that predicts an upper limit of the evanescent mode factor is adequate for our purposes. This upper limit allows us to predict the maximum effect of the evanescent wave upon our measurements. If this maximum effect is negligible then we can safely ignore the effects of the evanescent wave. Therefore, in the following sections we shall use the model outlined above to examine the effect of the evanescent wave on various measurements.

IV. THE EFFECT OF THE EVANESCENT WAVE ON ADULT HUMAN EAR CANAL MEASUREMENTS

Figure 5 shows that the magnitude of the evanescent mode factor is always less than 1 if the loudspeaker and microphone ports are spaced by more than $0.4a$. This is so for any value of z_1, down to zero, and for any of the four

arrangements of transducers shown in the figure. If an adult human ear canal has a maximum radius of 5 mm, then this represents a loudspeaker and microphone port spacing of 2 mm. This spacing is quite easy to realise in a practical probe design. The question arises: What would be the effect of this evanescent mode factor on measurements of the acoustic wave generated by the loudspeaker in an adult human ear canal?

Equation (1) shows that, for unit volume velocity from the source, the propagating acoustic wave sound pressure is equal to the acoustic input impedance of the ear canal (Z_{ec}). For unit volume velocity the evanescent wave sound pressure is equal to $jR_0ka\epsilon$. Hence, the percentage change of the magnitude of the pressure in the ear canal due to the evanescent wave is given by

$$\% \text{ change in } |P_t| = [(|Z_{ec} + jR_0ka\epsilon|/|Z_{ec}|) - 1] \times 100, \quad (9)$$

where P_t is the total pressure in the ear canal, and $|P|$ is the magnitude of P.

In the adult human ear canal the effect of the evanescent wave reaches its maximum when the magnitude of Z_{ec} is at its minimum. According to the measurements of Keefe *et al.* (1993), for frequencies of below 10 kHz this is at around 6 kHz, when $|Z_{ec}|$ falls to about 3×10^6 MKS acoustic ohms.

If ϵ is a maximum of 1, then $R_0ka\epsilon$ is maximally 3.22×10^6 MKS acoustic ohms, if the radius of the ear canal is 4.5 mm. Hence, at the microphone port the magnitude of the pressure due the evanescent wave is maximally about the same as that due to the propagating acoustic wave. Z_{ec} is totally real at the minimum of its magnitude (Keefe *et al.*, 1993). Thus, the evanescent and acoustic sound pressures will be 90 degrees out of phase.

With $|Z_{ec}|$ at its minimum and $\epsilon=1$, $|Z_{ec}+jR_0ka\epsilon| \approx 2^{1/2}|Z_{ec}|$, because Z_{ec} and $jR_0ka\epsilon$ are 90 deg out of phase and $|Z_{ec}| \approx |jR_0ka\epsilon|$. Therefore, the maximum change in $|P_t|$ due to the evanescent wave is approximately 41%, or 3 dB. The maximum increase in sound pressure due to the presence of the evanescent wave in an adult human ear canal is about 3 dB, when the microphone and loudspeaker are spaced by 2 mm. Below 4 kHz the maximum increase in sound pressure due to the evanescent wave is reduced to below 0.5 dB. It would be easy to engineer a probe in which the arrangement of loudspeaker and microphone ports gave an evanescent mode factor of below 0.5. This would result in a maximum increase in sound pressure due to the evanescent wave of about 1 dB at 6 kHz.

One factor affecting the accuracy to which it is reasonable to make acoustic measurements in the ear canal is the variation of level along the ear canal due to standing waves. Siegel (1994) showed that, due to a quarter wavelength resonance, the sound-pressure level wave generated by an acoustic probe can vary by up to 20 dB along the ear canal at frequencies around 6 kHz. In particular, the sound-pressure level at the ear drum is up to 20 dB larger than that measured at the probe. Furthermore, this ''ear canal gain'' varies with the position of the probe along the ear canal. In view of these variations, the 3-dB variation due to the evanescent wave is probably insignificant.

V. THE EFFECT OF THE EVANESCENT WAVE ON ONE MONTH OLD HUMAN EAR CANAL MEASUREMENTS

Keefe *et al.* (1993) present measurements of the input impedances of the ear canals of human infants of various ages down to one month. The ear canal input impedance of the 1 month old human infant is very different to that of the adult. There is a difference of input impedance magnitude of up to 15 dB, presumably reflecting the anatomical changes that occur in the auditory system between 1 month and full maturity.

Keefe *et al.* (1993) made measurements of the mean acoustic input impedance in 1 month old infants at frequencies from 125 Hz to 10 kHz. The minimum acoustic input impedance magnitude that they measured was about 1.5×10^7 MKS ohms at 10 kHz. The phase of the input impedance is close to 90 deg at this frequency. Keefe *et al.* (1993) estimate the mean ear canal radius of 1 month old human infants to be 2.2 mm. If we allow a minimum of 1 mm between the loudspeaker and microphone ports, then Fig. 5 shows that for all four port arrangements the maximum evanescent mode factor magnitude is 0.8. With a source frequency of 10 kHz, $R_0ka\epsilon \approx 8.8\times10^6$ MKS acoustic ohms.

With $|Z_{ec}|$ at its minimum and $\epsilon=0.8$, $|Z_{ec}+jR_0ka\epsilon| \approx 1.16\times|Z_{ec}|$, because Z_{ec} and $jR_0ka\epsilon$ are 90 deg out of phase and $|Z_{ec}| \approx 1.7\times|jR_0ka\epsilon|$. Therefore the maximum change in $|P_1|$ due to the evanescent wave is approximately 16%, or 1.3 dB. This means that the maximum error in measuring the acoustic field due to the presence of the evanescent wave is about 1.3 dB. At frequencies below 4 kHz the error is reduced to below 0.8 dB.

VI. SUMMARY

(1) A method of predicting the amplitude of the evanescent wave relative to that of the propagating acoustic wave in cylindrical ducts was presented.

(2) This method was used to predict the relative amplitude of the pressure due to the evanescent wave in a variety of sound source and microphone configurations relevant to the design of acoustic probes for ear canal measurements.

(3) The magnitude of the relative pressure due to the evanescent wave in a duct of adult human ear canal sized cross-sectional area was measured. The relative magnitude of the pressure of the evanescent wave in the measurements was always less than or equal to that predicted by theory.

(4) The effect of the evanescent wave on measurements of sound pressure generated and measured by an acoustic probe in a human ear canal was shown to be small. For frequencies below 10 kHz the maximum effect is 3 dB in an adult human and 1.3 dB in a 1 month old infant's ear canal, if the loudspeaker and microphone ports are separated by more than 2 mm. At frequencies below 4 kHz, the maximum effect is below 0.5 dB and 0.8 dB for the adult and 1 month old infant ear canals, respectively. These errors are probably acceptable for most ear canal measurements in view of the

much larger variations due to standing waves. If these errors are acceptable, then it is unnecessary to further reduce the effect of the evanescent wave by extending one of the transducer port tubes down the ear canal.

[1]In the following discussion, the acoustic medium is assumed to be nondissipative, and the boundaries of the acoustic medium are assumed to be perfectly rigid and nondissipative. If the effects of dissipation or nonrigid boundaries are not neglected, the situation becomes more complex, with additional phase and amplitude changes in both the evanescent and propagating acoustic waves (Morse and Ingard, 1968).

[2]The situation illustrated in Fig. 1 is only valid for a tube of sufficiently small diameter where only one propagating mode is present and of sufficient length that no reflections of the propagating wave occur. The first of these conditions is met in the human ear canal for frequencies up to about 10 kHz. The second of these conditions is not met in the ear canal and the resulting standing waves cause a more complicated pressure field than that illustrated in Fig. 1. However, the effect of the evanescent waves will be qualitatively similar to that shown in Fig. 1.

[3]The cross-sectional area of the adult ear canal does not exceed 70 mm^2, from 5 mm, from the concha to the apex (Egolf *et al.*, 1993). The maximum diameter of about 9 mm assumes that the ear canal is circular.

Egolf, D. P., Nelson, D. K., Howel III, H. C., and Larson, V. D. (**1993**). ''Quantifying ear canal geometry with multiple computer assisted tomographic scans,'' J. Acoust. Soc. Am. **93,** 2809–2819.

Hudde, H. (**1988**). ''The propagation constant in lossy circular tubes near the cutoff frequencies of higher-order modes,'' J. Acoust. Soc. Am. **83,** 1311–1318.

Ingard, U. (**1948**). ''On the radiation of sound into a circular tube, with an application to resonators,'' J. Acoust. Soc. Am. **20,** 665–683.

Keefe, D. H. (**1984**). ''Acoustical wave propagation in cylindrical ducts: Transmission line parameter approximations for isothermal and nonisothermal boundary conditions,'' J. Acoust. Soc. Am. **75,** 58–62.

Keefe, D. H., and Benade, A. H. (**1981**). ''Impedance measurement source and microphone proximity effects,'' J. Acoust. Soc. Am. **69,** 1489–1495.

Keefe, D. H., Bulen, J. C., Arehart, K. H., and Burns, E. M. (**1993**). ''Ear-canal impedance and reflection coefficient in human infants and adults,'' J. Acoust. Soc. Am. **94,** 2617–2638.

Kirchhoff, G. (**1868**). ''On the influence of heat conduction in a gas on sound propagation,'' Ann. Phys. Chem. **134**, 177–193.

Lighthill, J. (**1978**). *Waves in Fluids* (Cambridge U. P., Cambridge), p. 136.

Morse, P., and Ingard, U. (**1968**). *Theoretical Acoustics* (McGraw-Hill, New York), pp. 492–511.

Rabbitt, R. D., and Friedrich, M. T. (**1991**). ''Ear canal cross sectional pressure distributions: Mathematical analysis and computation,'' J. Acoust. Soc. Am. **89,** 2379–2390.

Rayleigh, Lord (**1937**). *Theory of Sound* (MacMillan, London), 2nd ed., Vol. II, p. 297.

Siegel, J. H. (**1994**). ''Ear-canal standing waves and high-frequency sound calibration using otoacoustic emission probes,'' J. Acoust. Soc. Am. **95,** 2589–2597.

Loudness adaptation and excitation patterns: Effects of frequency and level

Rhona Hellman
Auditory Perception Laboratory, Northeastern University, Boston, Massachusetts 02115

Andrzej Miśkiewicz
Chopin Academy of Music, Warsaw, Poland

Bertram Scharf
Auditory Perception Laboratory, Northeastern University, Boston, Massachusetts 02115

(Received 6 March 1996; revised 24 September 1996; accepted 13 December 1996)

Simple loudness adaptation for pure tones was measured at frequencies from 0.125 to 16 kHz and at sensation levels from 5 to 60 dB. Sixteen young listeners with normal hearing participated in four experiments. Most of the loudness measurements were obtained by the method of successive magnitude estimation; some were also obtained by loudness matching. The two indices of loudness adaptation gave similar results. At all frequencies, loudness adaptation increased as sensation level decreased. After 6 min, average loudness declined at most frequencies by about 20% at 40-dB sensation level (SL) and by between 70% and almost 100% at 5-dB SL. Adaptation also increased with increasing frequency, and was especially marked at 16 kHz, where loudness declined more than 60% at a sensation level as high as 40 dB. Most of the adaptation occurred usually within the first 3 min of exposure, but loudness continued to diminish at a slower rate up to around 6 min. The dependence of loudness adaptation on frequency and level can be largely accounted for by the restricted-excitation-pattern hypothesis. Adaptation is assumed to take place when excitation is restricted to a narrow region of the cochlea. This hypothesis is supported by a quantitative analysis based on excitation patterns derived from measurements of masking. [S0001-4966(97)05604-X]

PACS numbers: 43.66.Ba, 43.66.Cb [WJ]

INTRODUCTION

Simple loudness adaptation occurs primarily at low sensation levels (SL).[1] Earlier results suggested that, at most frequencies, loudness declines little over time unless the tone is within about 30 dB of threshold. Those results were based mainly on exposure periods of 3 min or less (e.g., Scharf, 1983). Extending the exposure period to 6 min Miśkiewicz *et al.* (1993) found that loudness continues to adapt at levels above 30-dB SL becoming most pronounced at very high frequencies. The strong adaptation obtained at very high frequencies at levels well above 30 dB was ascribed to the restricted spread of excitation that is the consequence of the upper limit of human hearing. Thus, the excitation evoked by a 16-kHz tone has little room to spread because auditory sensitivity in humans does not generally extend beyond 18 or 20 kHz. Preliminary calculations of excitation patterns, based on Zwicker's model (Zwicker, 1958; Zwicker and Fastl, 1990), supported this conjecture (Miśkiewicz *et al.*, 1993).

Of special relevance to these issues is a comprehensive study of long-term adaptation from 38 eighth-nerve fibers in cats (Javel, 1996). Both the amount and time course of the neural adaptation measured by Javel resemble those of our loudness-adaptation functions (Miśkiewicz *et al.*, 1993). Adaptation in the auditory nerve diminishes most rapidly within approximately 1 min of signal onset and then continues to diminish at a slower rate up to at least 5 min. Moreover, Javel found that the degree of adaptation varies considerably from fiber to fiber, even among those within the same ear at the same characteristic frerquency (CF). Fibers with low spontaneous rates (SR) adapt more markedly than medium- and high-SR fibers. Since responses from the cochlear base, where high frequencies are transduced, are mediated by neurons that behave like the strongly adapting low-SR fibers, this may be part of the reason that loudness adaptation is greatest at high frequencies. However, a striking difference between the two sets of data is that the adaptation of single neurons increases with sensation level whereas loudness adaptation decreases with sensation level. The effects of restricted excitation patterns on loudness adaptation suggest a likely basis for this difference. Specifically, we hypothesize that one requirement for loudness to adapt is that neural excitation be limited to a narrow region of the cochlea, as is true for pure tones at low stimulus levels.

The present study provides a further test of our restricted excitation-pattern hypothesis. The results buttress the posited relation between excitation patterns, which vary with frequency and level, and loudness adaptation. Four new experiments extend our previous findings to many more frequencies and levels. The first is the main experiment that defines the existence region for loudness adaptation over 6 min of exposure to a continuous tone. Experiment 2 repeats some of the main measurements using a different psychoacoustical method to ensure the generality and reproducibility of the main results. Experiments 3 and 4 clarify some empirical ambiguities and expand on the results of experiment 1. A

detailed evaluation of our restricted-excitation-pattern hypothesis is presented in the General Discussion and Conclusions.

I. EXPERIMENT 1: EFFECT OF FREQUENCY AND SENSATION LEVEL ON SIMPLE LOUDNESS ADAPTATION

Loudness adaptation for pure tones was measured over a 6-min exposure duration at eight frequencies and five sensation levels.

A. Method

1. Stimuli and apparatus

All stimuli were pure tones presented in quiet to the right ear. A PDP-11/73 minicomputer controlled the stimulus presentation and also recorded and stored the listener's responses which were made on a microterminal (Burr-Brown CTM-250). The tones were generated by a programmable oscillator (Krohn-Hite 4180), gated by an electronic switch (Wilsonics BSIT), led through an attenuator (Wilsonics PATT), and then amplified (Crown D-75). Listening was in a double-walled sound-insulated booth via a single Yamaha YH-1 earphone. In accord with the equivalent free-field sound-pressure levels reported for the Yamaha earphone (Buus *et al.*, 1986a), we used a calibration value of 92-dB sound-pressure level (SPL) for a 1-V input at all frequencies.

2. Procedure

Sensation levels were based on individual thresholds measured at the appropriate exposure frequency in each session, prior to the adaptation measurements. Thresholds were determined in the right ear by an adaptive, two-interval, two-alternative forced choice procedure (2IFC) with feedback. Duration of the test tone was 350 ms, with a 10-ms, cosine-shaped rise and fall. The signal level was varied according to a five-down/one-up decision rule that provides an estimate of the 87% correct point on the psychometric function (e.g., Green, 1990). The initial step size of 5 dB was reduced to 2 dB after the second reversal. The last four of six reversals were averaged to yield an estimated threshold for the run. The mean of two such estimates was taken as the threshold unless the two estimates differed by more than 1.5 dB, in which case a third estimate was obtained and included in the overall mean. Based on the assumption that performance in a detection task changes at the rate of 5% per dB (Buus *et al.*, 1986b), 3 dB was subtracted from each mean threshold to approximate the signal level necessary to yield approximately 72% correct responses. This level was used as the reference for setting the sensation level of the tone because it is close to the 71% correct response level usually taken as threshold.

Following the threshold determinations, loudness adaptation was measured by the method of successive magnitude estimation (Scharf, 1983). At regular intervals, the listener judged the loudness of a continuous tone, as perceived at the moment the judgment was called for by a visual signal. Listeners were instructed to assign a number to the loudness of the tone so that the perceived magnitudes of the two continua, loudness and assigned number, were subjectively equal. [For a more detailed discussion of this magnitude-scaling procedure, see Zwislocki and Goodman (1980).] The judgments were made without any designated standard or modulus. Instead, listeners were free to use any positive number, including decimals, regardless of the number they assigned to the previous stimulus. The only restriction was that the assigned number match the loudness of the tone at the given moment. Zero meant that the tone was inaudible.

Before the onset of the continuous tone, the listener judged the loudness of two 500-ms tone bursts. The bursts acquainted the listener with the test-tone frequency and helped to focus attention on it. After 10 s, the continuous tone at the same frequency and level as the bursts came on for 367 s. At 2 s after the tone's onset and every 20 s thereafter, the listener judged loudness for a total of 19 judgments at a given frequency and level.

Adaptation was measured for eight frequencies at 0.125, 0.4, 1, 2, 4, 8, 12, and 16 kHz and five sensation levels set at 5, 10, 20, 30, and 40 dB, giving a total of 40 frequency-level combinations. The combinations were presented in random order, except that two combinations with the same frequency were not run in succession. This constraint prevented residual adaptation effects. For the same reason, the minimum pause between frequencies was 8 min. The pause comprised a 2-min break plus the time required to measure the threshold for the next exposure frequency. Miśkiewicz *et al.* (1995) found residual effects mainly when an exposure tone was presented twice in a row at the same frequency after a pause of less than approximately 6 min.

Typically, four combinations chosen randomly were run during each 1-h session. To avoid any changes in sensation level that might be caused by a change in earphone placement, especially at high frequencies, listeners were instructed not to move their heads nor to remove or reposition the earphones during a run.

3. Listeners

Eight paid listeners, three men and five women, from 18 to 23 years old were tested on all combinations. Their thresholds were initially measured by a fixed frequency Békésy tracking procedure to ensure normal hearing levels at all exposure frequencies as well as thresholds below 50-dB SPL at 16 kHz. We chose the 50-dB criterion to (1) avoid exposing listeners for many minutes to high-frequency sounds at 40-dB SL that would exceed an SPL of 90 dB, and (2) ensure that excitation patterns at high frequencies were not unduly restricted by less acute hearing at the upper boundary of hearing (cf. Miśkiewicz *et al.*, 1993). Sensation levels in the main part of the experiment were based on thresholds measured by the adaptive 2IFC procedure. Table I presents the mean 2IFC thresholds for group 1 and their associated standard deviations at the eight test frequencies. Each mean is based on 40 threshold determinations (for the eight listeners, five repetitions at each frequency corresponding to the five combinations of sensation level and frequency). Thresholds are given as the free-field equivalent SPL; they are close to the 10th percentile threshold contour reported by Zwicker and Fastl (1990) for over 100 listeners under 25 years of age.

TABLE I. Group mean thresholds and standard deviations (s.d.).

Frequency (kHz)	0.125	0.4	1	2	4	8	12	16
Group 1								
Threshold (dB SPL)	16.7	0.3	−5.3	−1.8	−5.4	9.9	15.6	25.9
s.d. (dB)	1.6	3.1	2.0	4.8	3.3	6.6	8.0	7.2
Group 2								
Threshold (dB SPL)	18.8	4.1	⋯	−8.1	−4.6	⋯	16.2	⋯
s.d. (dB)	4.1	5.3	⋯	2.0	4.4	⋯	6.7	⋯

In accord with earlier reports, the standard deviations tend to increase above 8 kHz (e.g., Green *et al.*, 1987; Schecter *et al.*, 1986). The intrasubject standard deviations exhibit a similar pattern ranging from 1 to 3 dB at 0.125 kHz, from 1.5 to 8 dB at 12 kHz, and from 2 to 9 dB at 16 kHz.

B. Results and discussion

As a measure of the amount of change in loudness over time, loudness estimates were transformed for each listener to the percentage of loudness decline by the following equation:

$$\text{Percentage decline} = 100(E_i - E_t)/E_g,$$

where E_i is the initial loudness estimate 2 s after onset of the continuous tone, E_t is the loudness estimate at time, t, after tonal onset, and E_g is the greater of the two. A value of 100% means that the tone became inaudible ($E_t = 0$); a negative value means that the loudness increased.[2]

Figure 1 shows the percentage of loudness decline as a function of exposure duration at the eight exposure frequencies. Within each panel, the parameter is the sensation level of the tone at onset. Plotted are the group means and associated standard-error bars. At all frequencies loudness declines most steeply at the lowest sensation levels, usually during the first 3 min or so. With increasing sensation level, adaptation becomes weaker. After 6 min of exposure, adaptation at 5-dB SL is greater than 70% at nearly all frequencies; it is almost 100% at 16 kHz. At 40 dB, the highest sensation level tested, adaptation is between 10% and 30%, except at 16 kHz where it exceeds 60%. The dependence of loudness adaptation on sensation level is shown more directly in Fig. 2. The group means for five frequencies, from 0.125 to 16 kHz, are taken from Fig. 1. Except at 16 kHz (filled circles), adaptation decreases markedly as the tone's sensation level increases.

The overall picture from experiment 1 is clear. Loudness declines over 6 min at all frequencies from 0.125 to 16 kHz, more so at low sensation levels than at higher ones (30- and 40-dB SL). Moreover, adaptation is greater at 8 kHz and above than at lower frequencies, especially at 5- and 10-dB SL and at 16 kHz.

II. EXPERIMENT 2: LOUDNESS ADAPTATION MEASURED BY LOUDNESS MATCHING

The mass of data gathered in experiment 1 required only approximately ten 1-h sessions. This efficiency was made possible by the method of successive magnitude estimation, which permits the rapid assessment of loudness by the frequent assignment of numbers to the magnitude of perceived loudness. However, the successive matching of numbers to loudness may involve biases that could lead to spurious results and false conclusions. Therefore, to obtain an independent measure of adaptation, instead of having listeners match numbers to loudness, we had them match the loudness of one sound to another. When loudness matching is performed, it is necessary to avoid interactions between the comparison and the exposure sounds, because a comparison sound presented at the same time as the exposure sound may induce adaptation, whether the comparison is presented to the same ear as the exposure sound (Canévet *et al.*, 1983), or to the other ear (Petty *et al.*, 1970; Scharf, 1983). (See footnote 1.) To prevent both intra-aural and interaural interactions between such simultaneous sound presentations, the comparison sound must be presented after the exposure sound has ended, preferably to the contralateral, unexposed ear. Experiment 2 fulfilled these requirements by having the listener adjust the level of a brief, intermittent comparison tone so that it was as loud as a continuous 6-min tone just before its termination. To assess possible distortions in the interaural matching to a remembered sound, two control conditions preceded the main experimental condition.

A. Method

1. Stimulus and apparatus

The apparatus for stimulus generation and data storage was the same as in experiment 1, except that a sone potentiometer (60-dB range) and a manual attenuator (Hewlett–Packard 350D) were added to the circuit. The attenuator was used to control the input sound-pressure levels to the potentiometer to ensure that the listener's settings remained within the middle of the potentiometer's range. It enabled signal levels to be adjusted from well below threshold to as high as 110-dB SPL.

2. Procedure

The loudness-matching data were obtained by the method of adjustment in two 1-h sessions. Prior to the matches, thresholds at the chosen stimulus frequency were measured in both the left and right ears by the adaptive 2IFC procedure described in experiment 1. The eight listeners who took part in experiment 1 also participated in experiment 2.

The first control condition assessed possible interaural loudness differences and biases in interaural loudness matching. A 1-s tone burst at 1 kHz alternated between the left and right ears, with an interburst interval of 0.5 s. In each of two runs, eight loudness matches were made with a standard tone set at one of four levels, 10-, 20-, 30-, or 40-dB SL. In the first run, four of the eight listeners adjusted the loudness of the tone in the right ear to match the loudness of the standard tone in the left ear. In the second run, they adjusted the loudness of the tone in the left ear. The other four listeners adjusted first the loudness of the tone in the left ear to match the loudness of the standard tone in the right ear, and in a second run, they adjusted the loudness of the tone in the right ear. Two matches were made in each run at each standard level. The tones continued to alternate between ears while the listener adjusted the comparison tone by bracketing, that

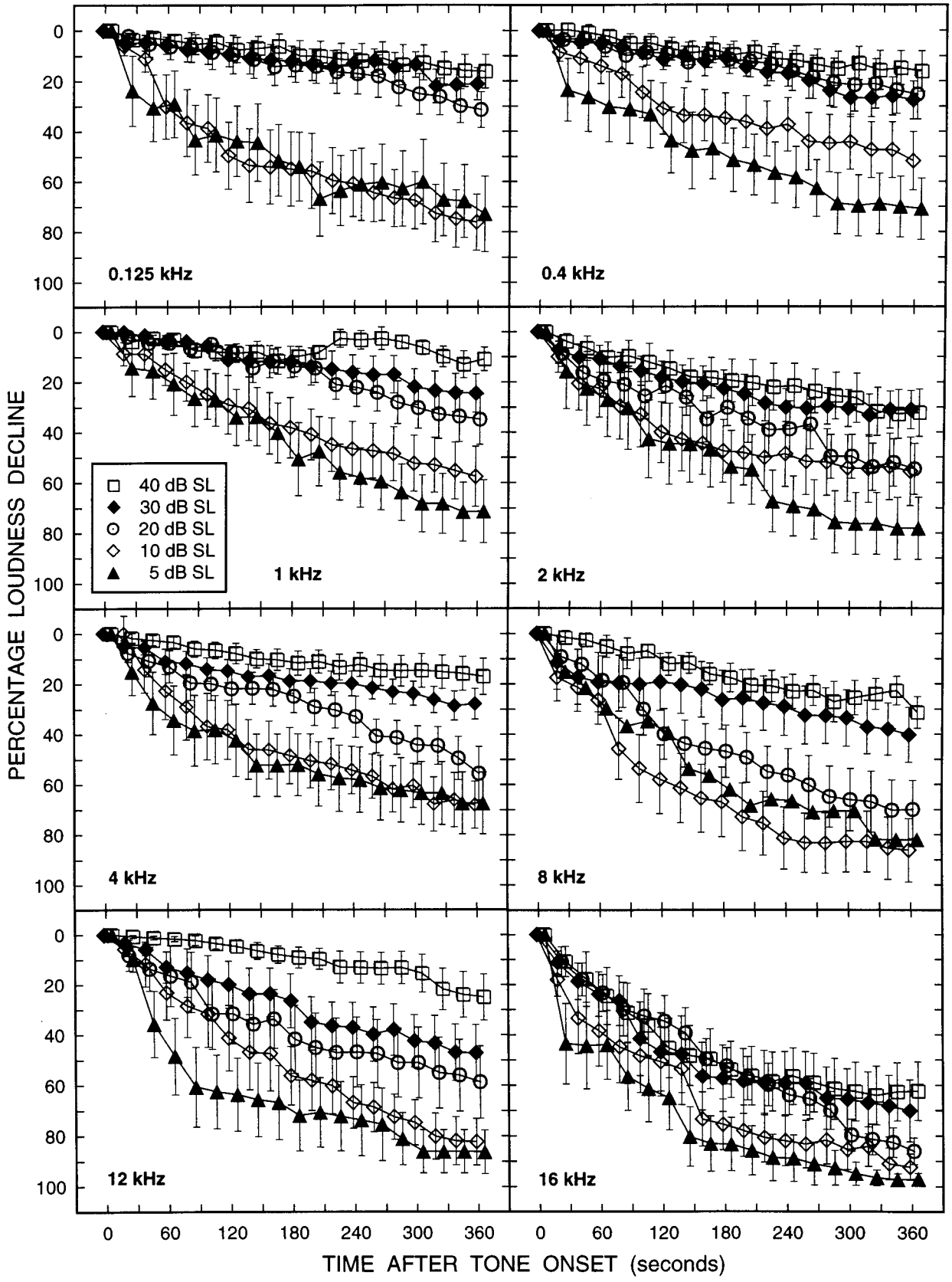

FIG. 1. Mean percentage of loudness decline for eight listeners as a function of time in seconds after the onset of a continuous tone. The frequency of the tone is given in eight separate panels. Within a panel, each of the five sensation levels is indicated by a different symbol as shown in the legend. For clarity, the symbols at 5- and 40-dB SL are shifted 4 s to the right, and those at 10- and 30-dB SL are shifted 4 s to the left. The vertical bars indicate ±1 standard error around the means.

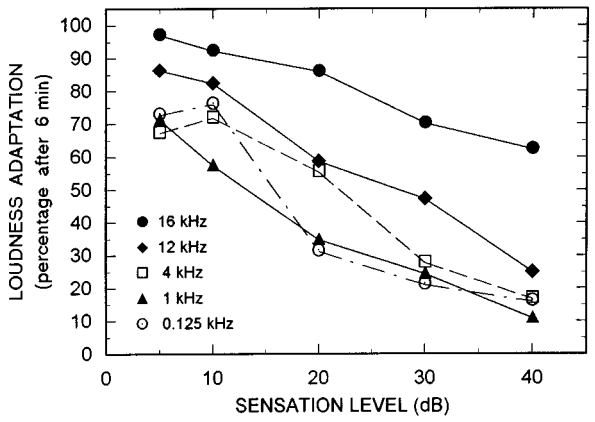

FIG. 2. Loudness adaptation as a function of sensation level at five frequencies which span the range of frequencies tested. The group means, taken from Fig. 1, are the percentage decline in loudness after 6 min of exposure.

is, by setting the loudness of the comparison tone first clearly louder, then clearly softer, next a bit louder, then a bit softer, and so on until the loudness of the standard and comparison tones seemed equal. The adjustments were made by turning an unmarked knob attached to the sone potentiometer. When the listener reached a decision, the tones were turned off and the adjusted level was recorded. The listener was given as much time as needed to make the match, typically about 1 min.

The second control condition assessed the precision of loudness matches between a current sound and the memory of a past sound. A 1-kHz tone to the right ear came on once only, for 1 s; its level was fixed at 10-, 20-, 30-, or 40-dB SL as in the first condition. Half a second later, a 1-kHz tone came on in the left ear, also for 1 s but it was repeated over and over again every 1.5 s. The listener was instructed to adjust the loudness of the ongoing intermittent tone in the left ear to match the loudness of the standard right-ear tone, which had been presented just once. Two such matches were made at each of the four standard sensation levels. The listener had as much time as needed to make the match which was readily made in about 1 min. Hence, a loudness match was obtained between an ongoing, intermittent sound and the memory of a past sound.

The main experimental condition compared directly loudness adaptation measured by delayed interaural loudness matching to adaptation measured by successive magnitude estimation. The experiment consisted of two parts. In part one, following threshold measurements in each ear by the adaptive 2IFC procedure, simple adaptation in the right ear was measured over a 6-min exposure period by the method of successive magnitude estimation as described in experiment 1. Immediately after the continuous tone in the right ear ended, a 1-s tone burst was presented intermittently to the left ear every 1.5 s as in control condition two. The listeners made a loudness match by adjusting the loudness of the intermittent tone to the memory of the loudness of the continuous tone heard just before it ended. One such match followed a single series of loudness judgments obtained by magnitude estimation for each of five stimulus combinations: a 1-kHz continuous tone set to 10- or 40-dB SL and a 4-kHz tone set to 10-, 20-, or 40-dB SL. As in the two control conditions, each listener was given as much time as needed to make the match.

B. Results and discussion

In the first control condition with the 1-s tones alternating between the left and right ears, the eight listeners overestimated the loudness of the standard sound at all four sensation levels by an average of 0.9 dB; they set the tone—whether to the left ear or to the right ear—they were adjusting 0.9 dB higher than the standard. This adjustment error, which has been reported before (e.g., Stevens, 1956; Zwicker *et al.*, 1957), was approximately symmetrical. Based on an average of the two sets of data (left ear standard and right ear standard), the 1-kHz tone was equally loud in the two ears when at the same sound-pressure level in accord with an earlier study (Hellman and Zwislocki, 1964). In the second control condition, on the average, listeners set the ongoing left-ear tone to the same level to which they had set it in the first control condition, even though the standard right-ear tone in the second condition was now presented only once for 1 s. Over all four sensation levels and eight listeners the differences between the adjusted settings made in the first and second conditions ranged from -4 to $+4$ dB with a mean of 0 dB. This result shows that listeners are able to adjust the loudness of an ongoing comparison tone to the remembered loudness of a standard tone.

The results of the main condition are given in Fig. 3. The unfilled symbols give the percentage loudness decline derived from the magnitude-estimation judgments as a function of time after tone onset. The filled symbols give the percentage decline based on loudness matching, measured at one point in time, after a 6-min exposure. Group means obtained at 1 kHz are shown in the upper panel and those at 4 kHz are in the lower panel. The vertical bars show ± 1 SE around the means obtained for each procedure after 6 min. As in Fig. 1, within each panel the parameter is the sensation level of the tone at onset. Whereas the percentage decline in loudness was obtained directly from the magnitude-estimation data as described for experiment 1, in order to compare the original loudness-matching data in decibels to the magnitude-estimation data several transformations were needed. First, to take into account the adjustment error noted in control condition one, the mean decibel settings (sensation levels) were reduced by 0.9 dB. Next, the adjusted sensation levels were changed to their corresponding monaural sone values (Hellman and Zwislocki, 1963), which were then used to calculate the percentage loudness decline.

Figure 3 shows that the two very different procedures for measuring adaptation yield similar data. However, the results of loudness matching are more variable than those of magnitude estimation, possibly due, at least in part, to the increased difficulty of producing loudness matches to the memory of a past sound. At 1 kHz, the mean difference between these two adaptation measures was 2% at 10-dB SL and 17% at 40-dB SL; at 4 kHz, the mean difference was 11% both at 10- and 40-dB SL and 6% at 20 dB. Converted to absolute loudness values in sones and then to decibels, the mean percentage difference ranges from the equivalent of a

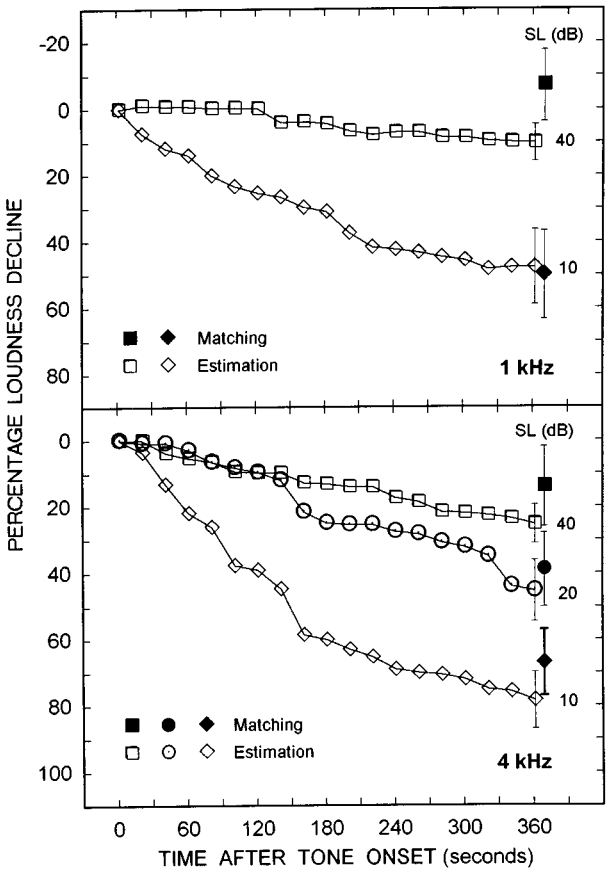

FIG. 3. Percentage of loudness decline as a function of time after tone onset. Each point is the mean from eight listeners. The unfilled symbols were obtained by the method of successive magnitude estimation; the filled symbols were obtained by delayed loudness matching (after a 6-min exposure). The vertical bars indicate ±1 standard error around the means obtained at the end of 6 min. The upper panel gives the results at an exposure frequency of 1 kHz, and the lower panel gives those at 4 kHz. The parameter in both panels is the sensation level of the tone at onset.

level change of nearly 0 dB (2% for a 1-kHz tone at 10-dB SL) to 3 dB (17% for a 1-kHz tone at 40-dB SL).

On the whole then, these findings lend added confidence to the conclusions drawn in experiment 1 on the basis of successive magnitude estimation alone. Both magnitude estimation and loudness matching show that loudness adaptation decreases with increases in level. Based on the data from the two stimulus frequencies, the correlation coefficient between the two indices of adaptation, one derived from numerical estimations and the other, from an adjustment procedure, is 0.975. Moreover, the percentages of loudness decline closely agree with those for the same frequencies in Fig. 1, although the decline by loudness matching is somewhat smaller than that measured by magnitude estimation. Schlauch (1992) reported a similar but much larger difference in the degree of adaptation when he used magnitude estimation and delayed loudness matching to measure the terminal loudness of a sound that physically declined in level over an exposure period of 3 min. However, there were many differences between the two experiments. One big difference is that Schlauch required his listeners to make a match within 10 s, whereas in the current study the listeners were given as much time as needed to bracket the loudness until a match was obtained.

To summarize, the overall internal consistency of the results indicates that any biases in successive magnitude estimation are either minimal, or are also inherent in loudness matching, since the two procedures yield such similar measurements of adaptation. The results also make it clear that the efficiency of successive magnitude estimation is dramatically greater. In a single run lasting 6 min, the whole time course of loudness adaptation can be measured, whereas loudness matching provided a value at only one point in time.

III. EXPERIMENT 3: LOUDNESS ADAPTATION AT 60-dB SL

From earlier measurements over exposure durations not exceeding 2 or 3 min, it seemed that above 30-dB SL loudness adaptation is essentially absent (e.g., Canévet *et al.*, 1989). Indeed, Fig. 1 shows that at the end of 3 min, at 40-dB SL, the loudness of most tones declines by about 10% for exposure frequencies below 8 kHz. After 3 min, however, loudness continues to decline and adaptation often reaches 20% and beyond after 6 min. The question arises as to how much adaptation takes place at still higher levels when the exposure duration exceeds 3 min.

A. Method

The apparatus and procedure were the same as in experiment 1. Stimuli were pure tones at 2, 4, and 12 kHz presented at 40- and 60-dB SL. Adaptation in the right ear was measured by the method of successive magnitude estimation after the threshold for the exposure frequency had been measured by the adaptive 2IFC method described in experiment 1.

Eight new listeners, three men and five women, 18–22 years old, took part in this experiment; they were paid for their participation. These listeners met the same threshold criteria for normal hearing as did those in experiment 1. Table I gives the mean thresholds for group 2, each based on eight measurements. The means are similar to those for group 1, except at 2 kHz where thresholds for group 2 were more than 6 dB lower.

B. Results and discussion

Figure 4 plots the mean percentage loudness decline as a function of exposure duration. Each panel is for a different stimulus frequency with sensation level of the tone at onset as the parameter. At all three frequencies, adaptation is greater at 40-dB SL than at 60-dB SL. Consistent with earlier data (Miśkiewicz *et al.*, 1993) and with the results in Fig. 1, loudness declines over time beyond 3 min of exposure. After 6 min, adaptation at 60-dB SL ranges from 16% to 26%, and at 40-dB SL, it ranges from 25% to 35%.

The results of experiment 3 show that loudness adaptation continues to diminish as sensation level increases above 40 dB, but it is still evident at 60-dB SL. From earlier results

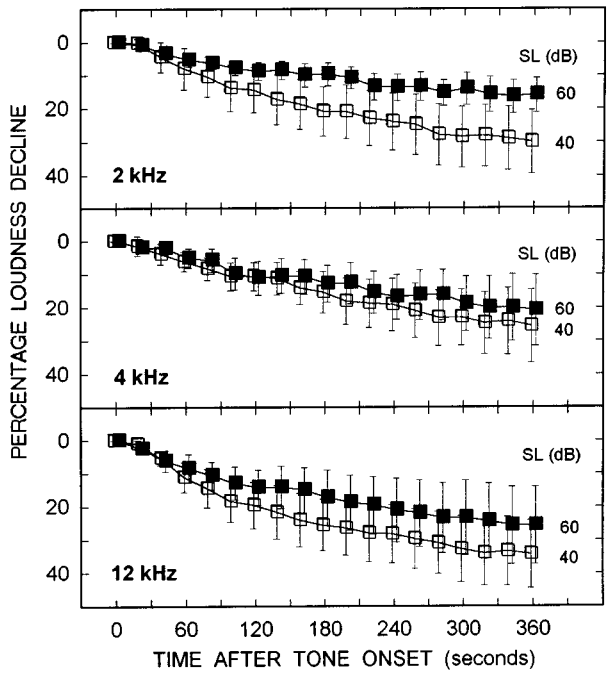

FIG. 4. Percentage decline in loudness at 40-dB SL (unfilled squares) and 60-dB SL (filled squares) for eight listeners as a function of time after tone onset. Group means are shown in separate panels for tones at 2, 4, and 12 kHz. For clarity, the symbols are shifted slightly along the abscissa. The vertical bars indicate ±1 standard error around the means.

(e.g., Scharf, 1983), we should expect adaptation to diminish still further at higher levels. Once again, adaptation is greatest at the highest frequency, here 12 kHz.

IV. EXPERIMENT 4: LOUDNESS ADAPTATION AT LOW FREQUENCIES

Experiment 4 addresses certain anomalies in the results of experiment 1 at 0.125 and 0.4 kHz. Specifically, in experiment 1 loudness adaptation for tones at 0.125 and 0.4 kHz did not exhibit a progressive increase with decreasing sensation level below 30 dB as it did for tones at higher frequencies.

A. Method

The apparatus and procedure were the same as in experiment 1. Simple adaptation was measured by the method of successive magnitude estimation for 0.125- and 0.4-kHz tones at 5-, 10-, 15-, and 20-dB SL. All eight listeners in experiment 3 also took part in experiment 4. Their mean thresholds at 0.125 and 0.4 kHz, measured in the right ear by the adaptive 2IFC procedure, are shown under group 2 in Table I.

B. Results and discussion

The group means are presented in the two panels in Fig. 5. Within each panel, the parameter is the sensation level of the tone at onset. Figure 5 shows that at both 0.125 and 0.4 kHz loudness adaptation diminishes monotonically as sensation level increases. After 6 min of exposure, the loudness of a 0.125-kHz tone adapts by 80% at 5-dB SL and by 40% at 20-dB SL. Likewise, after 6 min a 0.4-kHz tone adapts by close to 80% at 5-dB SL and by less than 35% at 20-dB SL. At most levels loudness declines more rapidly during the first 2 or 3 min of exposure and more gradually during the next 3 min, approaching what may be an asymptote at 6 min.

At both frequencies, adaptation is distinctly greater at 20-dB SL than it was at 20-dB SL in experiment 1. Moreover, at 0.125 kHz adaptation is now greater at 5 dB than at 10-dB SL, which was not so in experiment 1. These relatively minor discrepancies between experiments 1 and 4 may stem from individual differences and from the very different context of the much shorter experiment 4. Figure 5 does reveal at both 0.125 and 0.4 kHz a clear monotonicity in the dependence of loudness adaptation on sensation level between 5 and 20 dB. Accordingly, we conclude that with re-

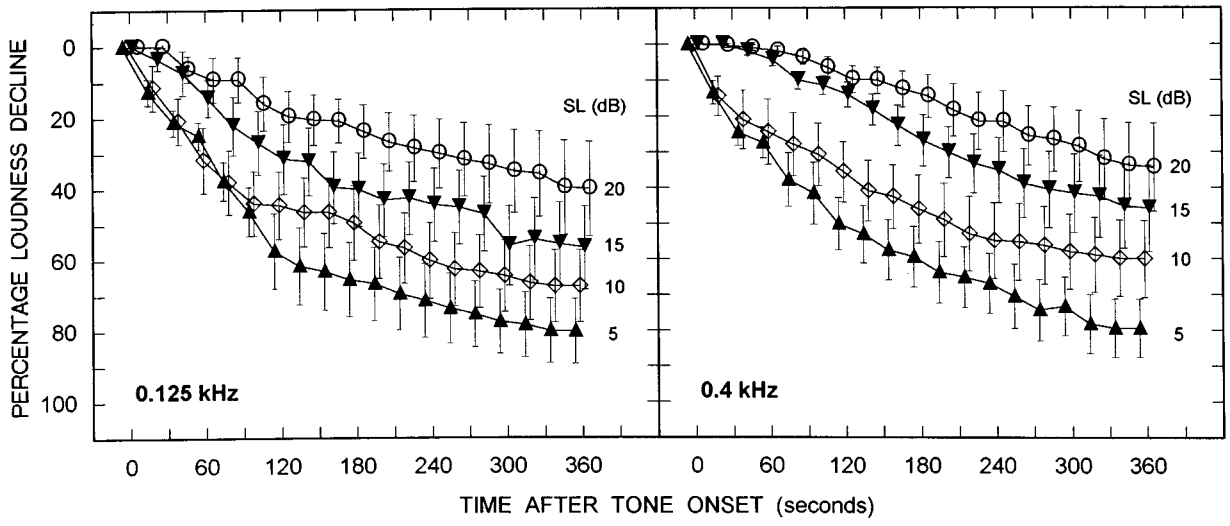

FIG. 5. Percentage decline in loudness for eight listeners as a function of time in seconds after tone onset. Group means at 0.125 and 0.4 kHz are shown in separate panels. The four sensation levels are represented by different symbols as indicated. As in Fig. 4, the symbols are shifted slightly along the abscissa. The vertical bars represent ±1 standard error around the means.

spect to its dependence on level, loudness adaptation is similar at low and high frequencies. The exception is at 16 kHz where adaptation is pronounced at all sensation levels (see Fig. 1).

V. GENERAL DISCUSSION AND CONCLUSIONS

Combining data from experiments 1, 3, and 4 we can draw some overall conclusions about how loudness adaptation for pure tones depends on frequency and level. Adaptation is generally greater at the higher frequencies than at the lower frequencies, increasing gradually with frequency until at 16 kHz, after 6 min of exposure, loudness declines by more than 60% even at a level as high as 40-dB SL. At all frequencies, the degree of adaptation decreases as sensation level increases. Although it is also true that adaptation slows as a function of exposure duration beyond about 3 min at most sensation levels and frequencies, adaptation almost always continues up to 6 min and possibly beyond. Both the amount and time course of loudness adaptation resemble, especially at high frequencies, those of long-term neural adaptation in single eighth-nerve fibers, but the neural adaptation is usually more rapid during the first minute (Javel, 1996). It is important to note that these results apply only to pure tones. Noise, whether broadband or narrow band, and multitone complexes adapt much less than tones under most stimulus conditions (Scharf, 1983), but just how or whether the adaptation of such sounds depends on frequency and level has not been determined.

The close agreement in experiment 2 between the results of magnitude estimation—on which the foregoing generalizations are based—and those of loudness matching suggests that the dependence of loudness adaptation on frequency, sensation level, and exposure duration reflects primarily sensory effects rather than judgmental biases. However, because magnitude estimation is so rapid and efficient, it is better suited than a comparison procedure for tracking the temporal course of loudness adaptation.

The question remains as to why at most frequencies loudness adapts so little, except at low levels whereas adaptation in other sensory systems usually is strong and increases with level. From a functional point of view, we have argued that, if loudness adapted strongly at high levels, then exposed organisms would be less likely to leave or avoid noisy environments (e.g., Canévet *et al.*, 1989). Our reasoning is that intense noise is aversive mainly because it is so loud; the louder a noise, the more aversive it is. Thus, adaptation to intense sounds would mean reduced loudness and reduced aversiveness resulting in greater hearing loss from longer exposures to loud sounds.

Whether accurate or not, the functional point of view does not tell us about the neurophysiological mechanism underlying loudness adaptation. Scharf (1983) suggested that loudness adaptation required that the excitation evoked by a sound be restricted to a relatively narrow region of the basilar membrane, as is true for tones near threshold. He assumed that with increasing spread of excitation at higher stimulus levels, more neurons would be excited intermittently, just as if the stimulus itself were intermittent. In taste and vision as well as in hearing, intermittent stimulation reduces or eliminates sensory adaptation, perhaps because intermittency leads to more on-responses in individual neurons. Intermittency may be inherent in either the stimulus (e.g., a tone modulated in amplitude, a noise with its internal amplitude fluctuations) or the sensory system (e.g., ocular nystagmus or fluctuations associated with a wide-spread excitation pattern). Near threshold, where the excitation pattern for pure tones is restricted, presumably the neural activity evoked in the few active fibers fluctuates so little as to permit strong loudness adaptation to occur.

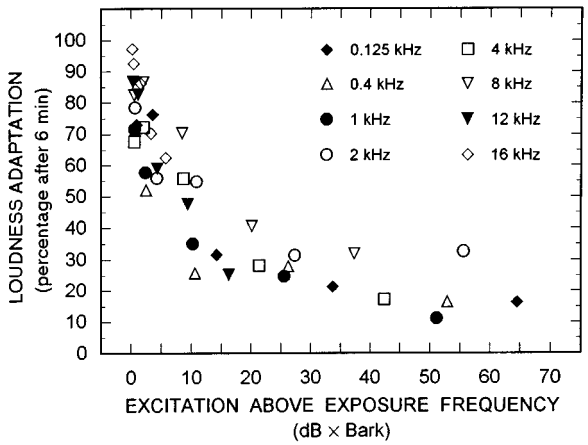

FIG. 6. Loudness adaptation (percentage loudness decline after 6 min) as a function of the amount of excitation in dB times Bark above the exposure frequency. Excitation patterns were derived at each of the eight frequencies and four sensation levels from Zwicker's model (Zwicker and Fastl, 1990).

Scharf (1983) provided tentative support for the restricted-excitation-pattern hypothesis by showing that in the presence of a high-pass noise, the loudness of a tone adapts even at high sound levels, levels at which relatively little adaptation is observed in the quiet. However, the noise not only restricted the spread of excitation but also raised the threshold for the tone, thereby reducing its sensation level and making it more prone to adaptation. Better support for the restricted-excitation-pattern hypothesis came from our finding that loudness adaptation is much greater at 16 kHz than at lower frequencies (Miśkiewicz *et al.*, 1993), a finding that the present data confirm and extend. The excitation pattern evoked by a 16-kHz tone would be restricted at all stimulus levels by the upper frequency boundary of hearing. Consequently, the degree of adaptation should be directly related to the spread of excitation toward that part of the basilar membrane that mediates the higher frequencies; the greater the spread, the less the adaptation. To test this prediction, we calculated the amount of excitation above the exposure frequency on the basis of masking patterns used by Zwicker in his model of loudness summation (Zwicker and Fastl, 1990). In Zwicker's model, the amount of excitation corresponds to the area between the absolute and masked threshold curves. This area is plotted on a critical-band-rate or Bark scale. The derived unit is dB times Bark.

Calculations of the amount of excitation were made for each of the 40 combinations of frequency and sensation level from experiment 1 (see Fig. 1). The Appendix gives details about how the calculations were obtained. Figure 6 shows

the results. Plotted in Fig. 6 is the measured loudness adaptation (taken as the percentage decline in loudness after a 6-min exposure) as a function of the area under the excitation pattern lying at frequencies above that of the exposure tone. As predicted, the greater the spread of excitation, which is indexed on the abscissa, the less loudness adapts. Particularly revealing are the unfilled diamonds, representing the 16-kHz tone. Even at 40-dB SL (the unfilled diamond furthest to the right), excitation is so highly restricted, amounting to only 5.6 dB× Bark, that adaptation exceeds 60%. In contrast, at 40-dB SL the excitation evoked by a 0.4-kHz tone (the unfilled triangle furthest to the right) is greater than 50 dB×Bark and adaptation is reduced to 16%.

The results in Fig. 6 are based only on the spread of excitation toward frequencies above that of the tonal stimulus. A similar analysis that takes into account also the spread of excitation toward lower frequencies led to poorer correlations between the degree of adaptation and the spread of excitation. This was found whether the spread of excitation was indexed by the total excitation or the percentage of excitation outside the critical band surrounding the frequency of the tonal stimulus. Although the downward spread of excitation may also play a role in reducing loudness adaptation, the high-frequency part of the excitation pattern appears to be the main contributor to the suppression of loudness adaptation, just as Hellman (1978) has shown it to be the main contributor to the growth of loudness. Consistent with this assumption, our calculations show that for a 40-dB SL tone at 16 kHz loudness adaptation is very pronounced despite much excitation at lower frequencies and little at higher frequencies. Why the spread of excitation in one direction appears to inhibit adaptation so much more than in the other is unclear.

In summary, Fig. 6 provides additional support for the restricted-excitation-pattern hypothesis and, consequently, for the notion that loudness adaptation is a peripheral phenomenon (Javel, 1996; Scharf, 1983). Thus, loudness adaptation, like loudness, is dependent on neural activity generated by basilar membrane stimulation within and across frequency-selective channels. Nonetheless, despite the clear association between the spread of excitation and the degree of loudness adaptation, the discrepancy between loudness adaptation, which decreases with increasing stimulus level, and long-term neural adaptation, which increases with level (Javel, 1996; Young and Sachs, 1973) remains unresolved.

One possible explanation for this discrepancy may be related to the slope of the loudness function. In a log–log plot loudness changes more rapidly with level between threshold and 30-dB SL than at higher levels (e.g., Hellman and Zwislocki, 1961). Thus, although the driven neural firing rate decreases relatively less over time at low levels than at higher levels, this smaller decrease may well correspond to a greater percentage decline in loudness than does a larger decrease in firing rate at higher levels. Such an effect may result from the steepening of the loudness function as threshold is approached. For example, at 5-dB SL, a 2-dB decrease in level corresponds to a 35% decline in loudness but at 40-dB SL, the same 2-dB decrease corresponds to a 12% decline in loudness, and a 4-dB decrease corresponds to a 24% decline [based on the monaural loudness function at 1 kHz in Hellman and Zwislocki (1963)]. Thus at higher levels, where the loudness function becomes more shallow, a given percentage decrease over time in neural firing rate would yield a smaller percentage decline in loudness than at low levels.

The relation between the amount of loudness adaptation and the slope of the loudness function is not sufficient to account for the strong adaptation observed at very high frequencies. In addition to the severely restricted excitation patterns which surely play an important role, Javel's (1996) physiological measurements point to still another basis. He found that long-term adaptation of single eighth-nerve fibers of the cat is more pronounced in low-SR fibers, which mediate the high frequencies, than in high-SR fibers. Although the responses of fibers at the very highest CFs in the cat were not measured, the results at lower CFs led Javel (1996, p. 1048) to cautiously suggest that ''fibers with very high CFs tend to exhibit... a higher percentage of long-term adaptation than... fibers with lower CFs.'' Hence, it appears likely that the strongly adapting low-SR high-threshold fibers combined with the effects of a restricted high-frequency excitation pattern, would both also contribute to the marked loudness adaptation at very high frequencies found even at the higher sensation levels.

ACKNOWLEDGMENTS

We thank Eric Javel for making available to us his article on long-term neural adaptation prior to publication, and Malvin Teich and Laurel Carney for fruitful discussions. We also thank Carol Meiselman for her help with data collection in experiment 2. Martha Teghtsoonian and an anonymous reviewer also provided many helpful suggestions for improving the manuscript.

This research was supported in part by Grant No. RO 1 DC00084 from NIH to Bertram Scharf.

APPENDIX: CALCULATION OF THE AMOUNT OF EXCITATION ABOVE EXPOSURE FREQUENCY

Figure 6 gives the amount of excitation above the exposure frequency calculated from excitation patterns used by Zwicker in his model of loudness summation (Zwicker, 1958; Zwicker and Fastl, 1990). Zwicker derived these patterns from psychoacoustical measurements of the masking of pure tones by narrow bands of noise (Zwicker and Scharf, 1965). The model assumes that a sound's masking pattern reflects the spectral spread of excitation evoked by the sound in the auditory system. Thus, masking patterns are essentially excitation patterns with excitation level plotted as a function of the critical-band rate in Barks. Excitation level, L_E, in decibels, is defined as

$$L_E = 10 \log(E/E_0). \tag{A1}$$

where E is the excitation falling in a critical band centered at a given frequency, and E_0 is the excitation at threshold in the same critical band. Excitation within the critical band in which the tone frequency falls is called the *main excitation*, and excitation above and below the critical band is called the

slope excitation. The excitation pattern is represented by a triangular-like shape; the peak indicates the maximum excitation elicited within the critical band at the tone's frequency, the two limbs indicate the low- and high-frequency skirts, and the base is the segment of the absolute threshold curve spanning the involved frequency range.

The threshold curve used to obtain excitation patterns in Zwicker's model can be approximated by the following equation

$$L_{\mathrm{HS}}=\{3.64f^{-0.8}-6.5^{*}\ \exp[-0.6(f-3.3)^2]+10^{-3}f^4\}, \tag{A2}$$

where L_{HS} is the absolute threshold in dB SPL, and f is the tone frequency in kHz (Terhardt, 1979). Frequency is transformed into the critical-band rate by the general equation given by Zwicker and Terhardt (1980)

$$z_c=13^{*}\ \arctan(0.76f\ )+3.5\ \arctan(f/7.5)^2, \tag{A3}$$

where z_c is the critical-band rate in Barks, and f is the frequency in kHz. Within the model it is assumed that the excitation pattern has a constant slope of 27 dB/Bark on the low-frequency side, independent of the tone's level and frequency (Zwicker and Fastl, 1990). On the high-frequency side, the slope of the excitation pattern becomes shallower as the tone's level increases. This slope can be expressed in the form

$$S=24+0.23/f-0.2L, \tag{A4}$$

where S is the slope in dB/Bark, f is the frequency in kHz, and L is the sound-pressure level in dB (Terhardt, 1979).

Typically, the main excitation level in Zwicker's model is based on the sound-pressure level in the critical band surrounding the stimulus tone. We used sensation level instead of sound-pressure level for two reasons: (1) in our experiments, the exposure tones were set at given sensation levels, and (2) sensation levels are unaffected by absolute threshold values. Thus, although our measured thresholds were lower than those obtained by Eq. (A2), the relation between excitation levels and thresholds remains the same.

The total amount of excitation is the area under the excitation pattern. To obtain the relation between loudness adaptation and excitation above the exposure frequency, just the area under the excitation pattern at frequencies above the exposure tone was determined for each of the 40 stimulus combinations used in experiment 1. Because the critical-band rate on the abscissa is expressed in Barks and the excitation level on the ordinate is in decibels, the unit for the amount of excitation determined from Zwicker's model becomes dB*Bark (decibels times Bark).

[1]Simple loudness adaptation refers to the time-dependent decline in the loudness of a continuous sound presented by itself. A different kind of adaptation can be induced either by presenting an intermittent sound to the contralateral ear simultaneously with a continuous sound or by incrementing a continuous sound in one ear at regular intervals by at least 5 dB without any contralateral sound. A discussion of simple adaptation, contralaterally induced adaptation, and ipsilaterally induced adaptation can be found in Canévet *et al.* (1989).

[2]The percentage decline in loudness provides a more accurate index of loudness adaptation than the decibel. Decibel values do not reflect the fact that loudness changes more rapidly with level below 30-dB SL than at higher levels. As we illustrate in the General Discussion and Conclusions, decibel values could actually be misleading because small decibel changes may correspond to considerably more adaptation near threshold than at higher levels. Moreover, a conversion from the measured loudness values to decibels would require assumptions about how loudness depends on level at frequencies above 3 kHz where direct loudness measurements are not available.

Buus, S., Florentine, M., and Mason, C. (**1986a**). ''Tuning curves at high frequencies and their relation to the absolute threshold curve,'' in *Auditory Frequency Selectivity*, edited by B. C. J. Moore and R. D. Patterson (Plenum, New York), pp. 341–350.

Buus, S., Schorer, E., Florentine, M., and Zwicker, E. (**1986b**). ''Decision rules in detection of simple and complex tones,'' J. Acoust. Soc. Am. **80,** 1646–1657.

Canévet, G., Scharf, B., and Botte, M.-C. (**1983**). ''Loudness adaptation, when induced, is real,'' Brit. J. Audiol. **17,** 49–57.

Canévet, G., Scharf, B., and Botte, M.-C. (**1989**). ''Loudness adaptation: When and why it occurs,'' in *Proceedings of the 13th International Congress on Acoustics*, Vol. 1, edited by P. Pravica and G. Drakulic (Dragan Srnic, Belgrade), pp. 381–384.

Green, D. M. (**1990**). ''Stimulus selection in adaptive psychophysical procedures,'' J. Acoust. Soc. Am. **87,** 2662–2674.

Green, D. M., Kidd, G., and Stevens, K. N. (**1987**). ''High-frequency audiometric assessment of a young adult population,'' J. Acoust. Soc. Am. **81,** 485–494.

Hellman, R. P. (**1978**). ''Dependence of loudness growth on skirts of excitation patterns,'' J. Acoust. Soc. Am. **63,** 1114–1119.

Hellman, R. P., and Zwislocki, J. J. (**1961**). ''Some factors affecting the estimation of loudness,'' J. Acoust. Soc. Am. **33,** 687–694.

Hellman, R. P., and Zwislocki, J. J. (**1963**). ''Monaural loudness function at 1000 cps and interaural summation,'' J. Acoust. Soc. Am. **35,** 856–865.

Hellman, R. P., and Zwislocki, J. J. (**1964**). ''Loudness function of a 1000 cps tone in the presence of a masking noise,'' J. Acoust. Soc. Am. **36,** 1618–1627.

Javel, E. (**1996**). ''Long-term adaptation in cat auditory nerve fiber responses,'' J. Acoust. Soc. Am. **99,** 1040–1052.

Miśkiewicz, A., Hellman, R., and Scharf, B. (**1995**). ''Frequency and temporal effects in loudness adaptation,'' in *Proceedings of the 15th International Congress on Acoustics*, Vol. II, edited by M. Newman (Trondheim, Norway), pp. 203–206.

Miśkiewicz, A., Scharf, B., Hellman, R., and Meiselman, C. (**1993**). ''Loudness adaptation at high frequencies,'' J. Acoust. Soc. Am. **94,** 1281–1286.

Petty, J. W., Fraser, W. D., and Elliot, D. N. (**1970**). ''Adaptation and loudness decrement: A reconsideration,'' J. Acoust. Soc. Am. **47,** 1074–1082.

Scharf, B. (**1983**). ''Loudness adaptation,'' in *Hearing Research and Theory*, edited by J. V. Tobias and E. D. Schubert (Academic, New York), Vol. 2, pp. 1–56.

Schechter, M. A., Fausti, S. A., Rappaport, B. Z., and Frey, R. H. (**1986**). ''Age categorization of high-frequency auditory threshold data,'' J. Acoust. Soc. Am. **79,** 767–771.

Schlauch, R. S. (**1992**). ''A cognitive influence on the loudness of tones that change continuously in level,'' J. Acoust. Soc. Am. **92,** 758–765.

Stevens, S. S. (**1956**). ''Calculation of the loudness of complex noise,'' J. Acoust. Soc. Am. **28,** 807–832.

Terhardt, E. (**1979**). ''Calculating virtual pitch,'' Hearing Res. **1,** 155–172.

Young, E., and Sachs, M. B. (**1973**). ''Recovery from sound exposure in auditory-nerve fibers,'' J. Acoust. Soc. Am. **54,** 1535–1543.

Zwicker, E. (**1958**). ''Ueber psychologische und methodische Grundlagen der Lautheit,'' Acustica **8**, 237–258.

Zwicker, E., and Fast, H. (**1990**). *Psychoacoustics: Facts and Models* (Springer-Verlag, Berlin).

Zwicker, E., Flottorp, G., and Stevens, S. S. (**1957**). ''Critical bandwidth in loudness summation,'' J. Acoust. Soc. Am. **29,** 548–557.

Zwicker, E., and Scharf, B. (**1965**). ''A model of loudness summation,'' Psychol. Rev. **72,** 3–26.

Zwicker, E., and Terhardt, E. (**1980**). ''Analytical expressions for critical-band rate and critical bandwidth as a function of frequency,'' J. Acoust. Soc. Am. **68,** 1523–1525.

Zwislocki, J. J., and Goodman, D. A. (**1980**). ''Absolute scaling of sensory magnitudes: A validation,'' Percept. Psychophys. **28,** 28–38.

Linearized response growth inferred from growth-of-masking slopes in ears with cochlear hearing loss

David A. Nelson and Anna C. Schroder
Clinical Psychoacoustics Laboratory, Department of Otolaryngology, and Department of Communication Disorders, University of Minnesota, Minneapolis, Minnesota 55455

(Received 5 July 1996; revised 24 September 1996; accepted 2 December 1996)

Growth of masking for OFF-frequency conditions (probe frequency above the masker spectrum) and ON-frequency conditions (probe within the masker spectrum) was investigated using simultaneous masking in three subjects with normal hearing and nine subjects with high-frequency sensorineural hearing loss. Growth-of-masking functions (probe thresholds as a function of masker intensity) for OFF-frequency conditions were obtained for probe tones placed at six frequencies above a 200-Hz-wide masker with an upper edge at 520 Hz. Growth-of-masking functions for ON-frequency conditions were obtained for probe tones placed within the 200-Hz-wide masker and for probe tones placed within 400-Hz-wide maskers with upper edges at 1040, 1300, 1627, and 2040 Hz (probe tones placed 20 Hz below the upper edge frequency). Growth-of-masking functions were fit with a power function of masker intensity added to an internal noise with intensity equal to the absolute threshold for the probe, and were well described by two free parameters and a threshold constant: the growth-of-masking slope (β), a masking sensitivity constant (κ) that indicated the minimum effective masker level at which masking began, and the intensity of the probe at absolute threshold (I_T). For OFF-frequency masking conditions, growth-of-masking slopes (β) decreased by a factor of 0.8 for every 10 dB of hearing loss. Comparisons with data from previous studies of upward spread of masking, and assumptions about underlying physiological mechanisms, led to the conclusion that more gradual than normal growth-of-masking slopes reflect larger (steeper) growth-of-response slopes at the probe frequency in regions of hearing loss. Derived response-growth exponents increased by a factor of 1.2 for every 10 dB of hearing loss (HL), from an exponent around 0.25 at 0 dB HL to an exponent around 1.0 at 75 dB HL (linear response growth). Masking sensitivity constants (κ), the minimum effective masker levels, indicated that masking began at slightly higher masker levels in subjects with sensorineural hearing loss than in subjects with normal hearing. It was concluded that higher masked thresholds in regions of hearing loss were due primarily to a loss of active gain at the probe frequency and were not due to an excessive response at the probe frequency to the lower-frequency masker. For ON-frequency masking conditions, growth-of-masking slopes were not different from normal in hearing-impaired subjects. ON-frequency masking began when the effective power within an auditory filter at the probe frequency reached elevated absolute threshold at the probe frequency. Critical ratios were normal except for one subject with the most hearing loss. © *1997 Acoustical Society of America.* [S0001-4966(97)04304-X]

PACS numbers: 43.66.Ba, 43.66.Dc, 43.66.Mk, 43.66.Sr [WJ]

INTRODUCTION

Masking produced by low-frequency sounds at higher frequency regions, often referred to as *upward spread of masking*, has been thoroughly investigated since Wegel and Lane (1924) demonstrated that masking spreads more toward higher frequencies than lower frequencies. In listeners with high-frequency sensorineural hearing loss, upward spread of masking is typically considered to be ''excessive'' because higher masked thresholds are seen in regions of hearing loss than observed in normal-hearing listeners for the same low-frequency masker (Jerger *et al.*, 1960; Harbert and Young, 1965; Martin and Pickett, 1970; Florentine, 1978; Florentine *et al.*, 1980; Smits and Duifhuis, 1982; Gagne, 1983; Hannley and Dorman, 1983; Picard and Couture-Metz, 1985; Trees and Turner, 1986; Buus and Florentine, 1988, 1989; Klein *et al.*, 1990; Dubno and Schaefer, 1991; Murnane and Turner, 1991; Klein and Dubno, 1993; Dubno and Ahlstrom, 1995a,b; Dubno and Schaefer, 1995). This means that a listener with a high-frequency hearing loss may not hear certain higher-frequency sounds in the presence of a low-frequency masker, even though those sounds may be more intense than the elevated high-frequency threshold, a situation that may be particularly relevant to the problem of listening to speech in background noise.

If the amount of masking in the region of hearing loss is considered, i.e., the amount of threshold shift, then it is typical to observe *less* masking in regions of high-frequency hearing loss than observed in normal-hearing listeners (Martin and Pickett, 1970; Nelson and Bilger, 1974; Smits and Duifhuis, 1982; Gagne, 1983; Trees and Turner, 1986; Klein *et al.*, 1990; Dubno and Schaefer, 1992). Furthermore, in normal-hearing listeners, upward spread of masking is generally characterized by nonlinear growth of masking with

masker intensity (Wegel and Lane, 1924; Zwicker, 1970), i.e., for every 1-dB increase in masker intensity the signal must be increased by more than 1 dB. By contrast, in listeners with sensorineural hearing loss, the rate at which masking grows with masker intensity (the growth-of-masking slope) is more gradual than it is in normal-hearing listeners (Nelson and Bilger, 1974; Smits and Duifhuis, 1982; Stelmachowicz *et al.*, 1987; Buus and Florentine, 1989; Murnane and Turner, 1991). Thus, we are faced with a situation in which masked thresholds for low-frequency maskers are higher in regions of high-frequency hearing loss, but the amount of masking is usually less and the rate at which masking grows with masker intensity is more gradual.

The physiological mechanisms underlying these results are not clear. One interpretation is that the higher-than-normal masked thresholds are due to excessive upward spread of excitation into higher frequency regions, where auditory fibers tuned to those higher-frequency regions are responding excessively to the low-frequency masker (Trees and Turner, 1986) due to hypersensitive neural tuning-curve tails, as is sometimes seen in cases of acoustic trauma (Salvi *et al.*, 1977; Cody and Johnstone, 1980; Liberman and Dodds, 1984). Another interpretation is that sensitivity to excitation is reduced by damage to cochlear amplifiers in the hearing-loss region, thereby elevating absolute threshold at those frequencies. In addition, the response growth in those regions, once signals are intense enough to overcome the sensitivity loss, is steeper than normal, thereby reducing the rate at which masked threshold grows with masker intensity. This latter interpretation, which is consistent with changes in basilar membrane (BM) transfer characteristics associated with cochlear damage (Ruggero and Rich, 1990, 1991; Ruggero *et al.*, 1993, 1996), was recently proposed by Nelson and Schroder (1996), as a *linearized response growth* (LRG) model of upward spread of masking. The model accounts for reduced release from masking in regions of high-frequency hearing loss for maskers with fluctuating envelopes (Buus, 1985; Moore and Glasberg, 1987), and is consistent with interpretations of reduced additivity of masking in hearing-impaired ears (Oxenham and Moore, 1995). Nelson and Schroder derived growth-of-masking slope-reduction factors that would be needed to account for reduced masking release in regions of hearing loss and found that those slope-reduction factors were consistent with more gradual growth-of-masking slopes in regions of hearing loss reported by previous investigators (Murnane and Turner, 1991). Their slope-reduction factors were interpreted as normalized growth-of-masking slopes that followed the form

$$\beta_{\mathrm{hls}} = \alpha^{*} \beta_{\mathrm{nrm}}, \tag{1}$$

where β_{nrm} is the growth-of-masking slope at a particular frequency in the normal ear, α is the derived reduction factor for a hearing-impaired ear, and β_{hls} is the growth-of-masking slope in a hearing-impaired ear. The derived slope reduction factor α was a function of the amount of hearing loss as in

$$\alpha = -0.0125(\mathrm{dB\ HL}) + 0.93, \tag{2}$$

which implies that the slope of the growth of masking in a region of hearing loss (β_{hls}) decreases proportionately with amount of hearing loss.

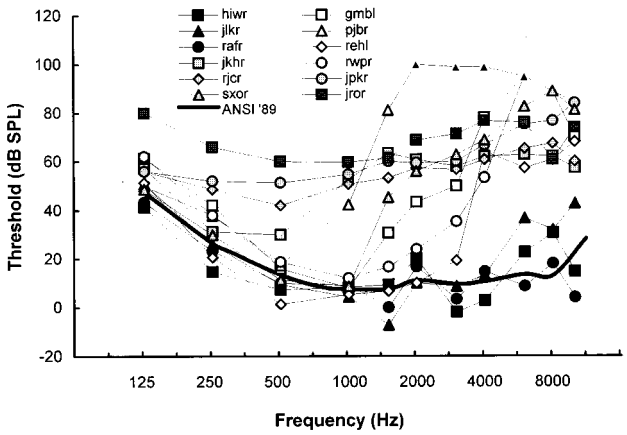

FIG. 1. Absolute thresholds from normal-hearing (dark filled symbols) and hearing-impaired listeners for 200-ms duration tone bursts, measured with a 3AFC adaptive threshold procedure, are shown as a function of the frequency of the test signal. The wide shaded curve shows average normal-hearing thresholds as a function of frequency as defined by ANSI (1989) norms. Small dark triangles indicate intensity limits of the instrumentation (e.g., *pjbr* at 2000 Hz and above).

The purpose of the present investigation was to examine characteristics of upward spread of masking in regions of cochlear hearing loss, *once signals are made sufficiently intense to overcome the hearing loss*. In many patients with cochlear hearing loss, current hearing-aid technology can selectively amplify signals to make them audible at hearing-loss frequencies to overcome frequency-dependent sensitivity losses. What is not well defined is how susceptible those amplified signals might be to masking from unamplified lower-frequency sounds. Specifically, we wished to determine whether slopes of the growth of masking in regions of hearing loss decrease proportionately with hearing loss, as implied by the reduction factor α derived by Nelson and Schroder (1996), and to examine upward-spread-of-masking in terms of the LRG model of masking that associates steeper response growth with cochlear hearing loss. To that end, the growth of upward spread of masking with masker intensity was measured in listeners with cochlear hearing losses, growth-of-masking slopes and masking sensitivity constants (the masker level at which masking begins) were examined as a function of the amount of hearing loss, and the results were compared with data from previous investigations.

I. METHODS

A. Subjects

Three normal-hearing listeners and nine listeners with bilateral sensorineural hearing loss served as subjects. Their absolute thresholds are shown in Fig. 1. Five of the listeners with hearing loss exhibited normal absolute thresholds at the 500-Hz masker frequency and below, with cochlear hearing loss at higher frequencies. Four listeners exhibited mild or moderate hearing losses at the masker frequency as well as significant hearing losses at higher frequencies. Their ages and etiologies are given in Table I.

TABLE I. Demographics of subjects with sensorineural hearing loss.

HF HI subjects	Age	Sex	Etiology
gmbl	62	Female	Hereditary/presbycusis
pjbr	37	Female	Ototoxicity
rehl	56	Male	Unknown/presbycusis?
rwpr	66	Male	Presbycusis
jkhr	47	Female	Hereditary
rjcr	25	Male	Hereditary
sxor	44	Female	Unknown
jpkr	53	Male	Barotrauma
jror	65	Male	Unknown

B. Stimuli

Masked thresholds as a function of masker level, or growth-of-masking functions, were obtained for narrowband (NB) noise maskers with bandwidths of 200 or 400 Hz. The 200-Hz-wide NB noise was centered at 420 Hz, with an upper edge at 520 Hz. It was constructed by multiplying a 100-Hz low-pass noise (135 dB/oct slope) with a pure tone at 420 Hz. The 400-Hz wide NB noises were centered at 840, 1100, 1427, or 1840 Hz. They were constructed by multiplying a 200-Hz low-pass noise with pure tones at the appropriate center frequencies. The mean number of envelope peaks per second in the maskers was about 0.64 of the bandwidth of the low-pass noises (Rice, 1954), or about 64 and 128 Hz for the 200- and 400-Hz NB noises, which were constructed from 100- and 200-Hz low-pass noise, respectively.

Masker and probe (signal) frequencies were chosen so that growth of masking could be examined for six OFF-frequency and six ON-frequency masking conditions. For the OFF-frequency conditions the probe frequency was higher than the passband of the masker, i.e., in the ''upper accessory region'' of the masker (Zwicker, 1970). The 200-Hz NB noise with an upper edge at 520 Hz was used as a masker, with probe frequencies at 650, 814, 1020, 1280, 1607, and 2020 Hz. At 650 Hz, masker energy was attenuated by 43 dB; at the five test frequencies from 814 to 2020 Hz, masker energy was attenuated by more than 87 dB. Thus, at these six frequencies the probe tones were effectively above the passband of the masker, representing OFF-frequency masking conditions. For the ON-frequency conditions, the probe frequencies were within the passband of the masker, i.e., within the ''main excitation region'' of a masker (Zwicker, 1970). Two of the ON-frequency conditions were within the spectrum of the 200-Hz NB noise at probe frequencies of 500 and 520 Hz. The four remaining ON-frequency conditions utilized probe frequencies at four of the same frequencies tested for OFF-frequency masking (1020, 1280, 1607, and 2020 Hz), but the maskers were 400-Hz NB noises with upper edges at 1040, 1300, 1627, and 2040. Thus, in all cases except 520 Hz, the probe frequency was 20 Hz below the upper edge of the masker passband, representing ON-frequency masking conditions.

Maskers and signals were gated with 10-ms cosine-squared rise/decay ramps. The duration of the maskers and signals at peak amplitude were 500 and 250 ms, respectively. The signals were temporally centered within the maskers. Pure tones for signals and for constructing the NB noise maskers were produced by frequency synthesizers (Rockland). The signals and maskers were routed separately through programmable attenuators, added together in a resistive mixer and presented monaurally through a UTC L-33 transformer and a TDH-49 earphone mounted in an MX/AR-1 cushion. Subjects were seated in a double-walled sound-treated booth and conveyed their responses to the computer by pressing buttons on a custom response panel.

C. Psychophysical procedures

Thresholds were determined with a three-alternative forced-choice adaptive procedure. A trial consisted of a 500-ms warning interval followed by three 520-ms observation intervals, each separated by a 250-ms silent interval. Maskers occurred in all three intervals. The signal was presented with the masker in one of the three intervals, chosen randomly from trial to trial. Correct-answer feedback was provided following each trial.

Growth-of-masking functions were collected with two different adaptive procedures: a fixed probe level procedure and a fixed masker level procedure. For the fixed probe procedure, probe level was held constant and masker level was adjusted to reach masked threshold. Probe levels were tested in 5-dB steps beginning at probe levels 5 dB or more above absolute threshold (averaged over multiple test sessions). At probe frequencies where large amounts of hearing loss existed, probe levels were sometimes tested in 3-dB steps (e.g., subject *pjbr* at 1280 and 1607 Hz in Fig. 2). For the fixed masker procedure, masker level was held constant and probe level was adjusted to reach masked threshold. Masker levels were tested in 5-dB steps, beginning with maskers more than 10 dB below the point where any masking began. At probe frequencies where large amounts of hearing loss existed, masker levels were sometimes tested in 3-dB steps (*jror* at 1607 Hz). The fixed-masker procedure was implemented with five of the hearing-impaired listeners (*jkhr*, *rjcr*, *sxor*, *jpkr* and *jror*) to examine more closely the transition region on the masking curve where masking begins. The adaptive procedures estimated the 71% correct threshold with a two-down/one-up (fixed masker) or two-up/one-down (fixed probe) tracking procedure that averaged the last 6 out of 12 reversals, during which the level varied in 2-dB steps for the fixed-masker-level procedure and 1-dB steps for the fixed-probe-level procedure. The first six reversals were used to move quickly into the range of threshold. For the fixed-masker-level procedure, an 8-dB step size existed for the first four reversals and a 2-dB step size existed for the next two reversals, both with a one-down/one-up stepping rule. For the fixed-probe-level procedure, a 4-dB step size existed for the first four reversals and a 1-dB step size existed for the next two reversals, both with a one-up/one-down stepping rule. Each data point represents the mean of at least three threshold estimates.

D. Fitting procedure for growth-of-masking functions

Growth-of-masking curves were specified in terms of probe intensity at masked threshold as a function of masker intensity, in order to simplify comparisons with previous

studies of the slopes of the growth of masking in hearing-impaired listeners (Smits and Duifhuis, 1982; Stelmachowicz *et al.*, 1987; Murnane and Turner, 1991). Growth-of-masking curves were fitted with least-squares regressions between probe intensity at masked threshold (I_P) and masker intensity (I_M) to derive the fitting parameters k and β, using probe thresholds 5 dB or more above absolute threshold. Then the intensity at absolute threshold (I_T) was added to represent an internal noise, as in

$$I_P = kI_M^{\beta} + I_T,, \tag{3}$$

with the slope of the growth of masking given by β. All intensity units (I) are expressed here as power ratios between the measured quantity (dB SPL) and the reference intensity at 0 dB SPL (10^{-12} W/cm^2), e.g., $I_M = 10^{(0.1*\mathrm{Lm})}$, where Lm is the masker level in dB SPL. Equation (3) implies that the intensity of the probe at masked threshold, I_P, is equal to the sum of the internal representation of the masker, kI_M^{β}, and an internal noise that determines absolute threshold, I_T. Typically, as was done in the present study, growth-of-masking parameters are derived by fitting masked thresholds (in dB SPL) as a function of masker level (in dB SPL) with a linear least-squares regression, using only those masked thresholds for which masking is greater than about 5 dB. This avoids the curvilinear portion of the masking function where masked thresholds are close to absolute threshold. Equation (3) is one way to represent masked thresholds close to absolute threshold, where the internal representation of the masker and the internal noise appear to sum together to produce a curvilinear masking function.

From Eq. (3), sensitivity to masking can be specified as the intensity of the masker where the internal representation of the masker, kI_M^{β}, is equal to absolute threshold I_T, as in

$$I_M = (I_T/k)^{1/\beta}, \tag{4a}$$

or in decibels as

$$\kappa = 10 \log\{(I_T/k)^{1/\beta}\}. \tag{4b}$$

The value of κ is the masker level (in dB SPL) where linear extrapolation of the masking curve intersects with absolute threshold, which has been referred to as the Minimum Effective Masker Level (MEML) by Buus and Florentine (1988), and is one convenient and objective way of specifying the masker level at which masking begins for comparisons between normal-hearing and hearing-impaired data. In the present context, as with psychophysical tuning curves, sensitivity to masking is inversely proportional to κ (or MEML), in that a larger κ means that the masker level required to just begin masking has to be increased, therefore, sensitivity to masking is less (in the same sense that an elevated absolute threshold, I_T, indicates a loss of sensitivity).

This reasoning assumes that an elevated absolute threshold at the probe frequency, I_T, reflects changes in cochlear sensitivity for neural fibers with a characteristic frequency (CF) near the probe frequency. That is, neural excitation by a probe tone begins when its intensity reaches absolute threshold at the probe frequency. It is further assumed that sensitivity of the same fibers to a low-frequency masker, at a frequency well below CF, can be inferred from the level of the low-frequency masker at which the CF threshold begins to be masked, which is specified by κ. This inference requires some knowledge about the masker/probe intensity ratio needed to reach masked threshold, which can be estimated from conditions in which both masker and probe stimuli are at the same frequency region.

In tuning-curve terms, a larger κ for a low-frequency masker indicates (for example) an elevated tail to the tuning curve, which indicates less sensitivity to masking by the low-frequency stimulus. The inverse, a smaller κ, indicates more sensitivity to masking, a situation referred to as hypersensitive tuning-curve tails (Salvi *et al.*, 1977; Cody and Johnstone, 1980; Liberman and Dodds, 1984). The most common results observed in physiological experiments involving moderate cochlear damage (Salvi *et al.*, 1977; Cody and Johnstone, 1980; Schmiedt and Zwislocki, 1980; Schmiedt *et al.*, 1980; Liberman, 1984; Liberman and Dodds, 1984) have been elevated tuning-curve tips and normal tail levels. The elevated thresholds at tuning-curves tips indicates a loss of sensitivity for CF tones, which should be reflected psychophysically by an elevated I_T. The demonstration of threshold levels at tail frequencies that were the same as in normal cochleas indicates normal sensitivity for tail-frequency tones, which should be reflected psychophysically by normal κ values for low-frequency maskers.

Because we wished to make comparisons of sensitivity to masking for ON-frequency conditions at different probe frequencies, it was necessary to adjust values of κ for equivalent effective power within an auditory-filter bandwidth at each probe frequency, as in

$$\kappa_{\mathrm{ERB}} = \kappa + 10 \log\{((\mathrm{ERB}/2) + 20)/\mathrm{BW}\}, \tag{5}$$

where ERB is the equivalent rectangular bandwidth of an auditory filter centered at the probe frequency (Glasberg and Moore, 1990), and BW is the masker bandwidth. This was done by assuming that the auditory filter was centered at the probe frequency, that the critical masking band extended to the upper edge of the masking band (20 Hz above the probe except at a probe frequency of 520 Hz), and that it extended to one-half an ERB below the probe. For the present purposes, ERB calculations in subjects with hearing loss were the same as those for normal-hearing subjects.

II. RESULTS

A. Typical growth-of-masking functions

To illustrate the adequacy of Eq. (3) for representing masked thresholds as a function of masker level, both for ON-frequency and OFF-frequency conditions, Fig. 2 shows typical growth-of-masking functions obtained from one normal-hearing listener (*hiwr*) and two hearing-impaired listeners (*jkhr* and *pjbr*). The fits to individual growth-of-masking functions using Eq. (3) are shown by the solid curves in each panel. Those curves represent the individual masked thresholds with considerable accuracy over the range of masker levels tested, which indicates that the parameters k, β, and I_T can accurately specify changes in individual masking curves from both normal-hearing and hearing-impaired listeners, including masked thresholds near abso-

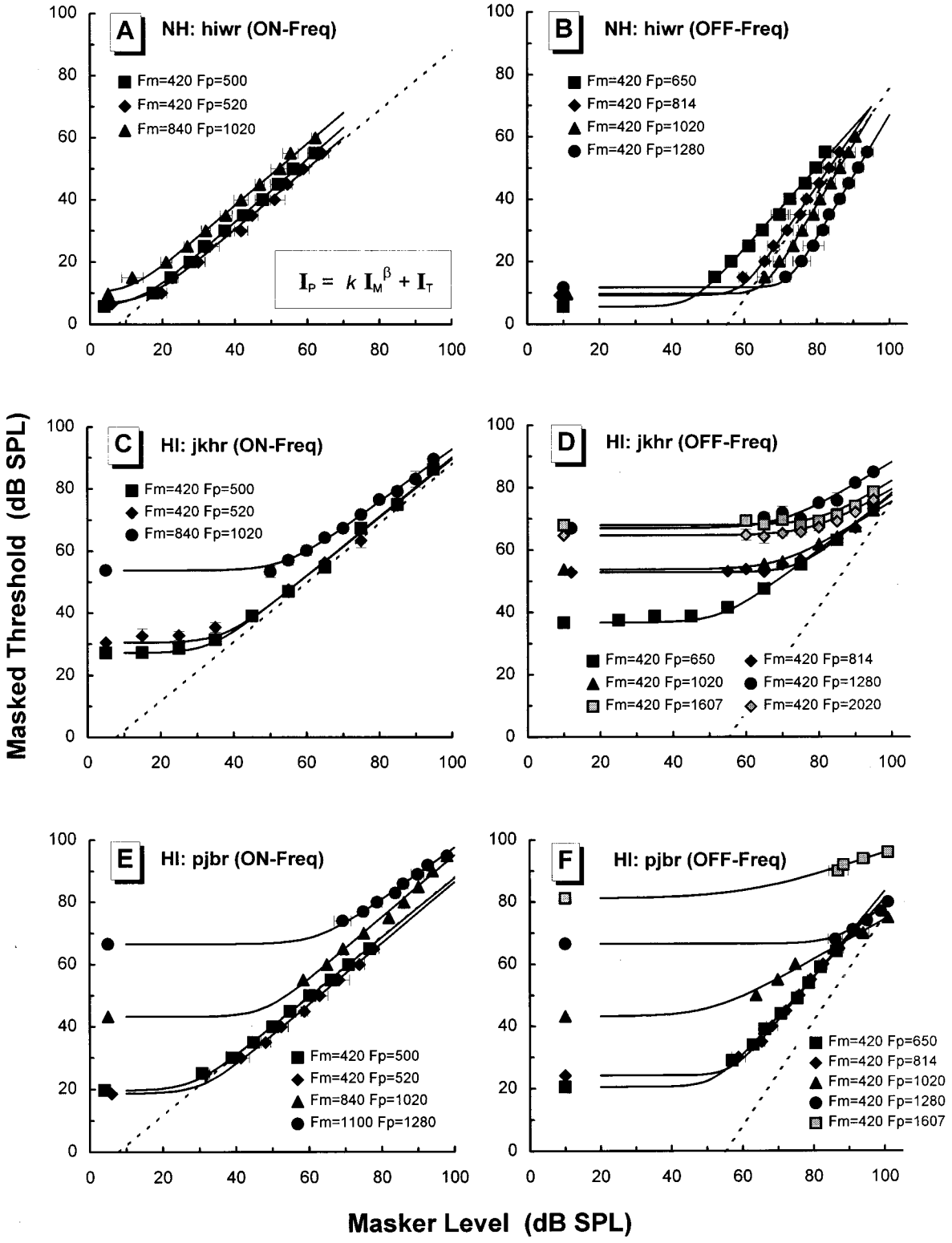

FIG. 2. Representative growth-of-masking functions for normal-hearing listeners (NH) and listeners with high-frequency sensorineural hearing loss (HI). Left panels: Growth-of-masking functions for ON-frequency masking conditions. Probe frequencies (Fp) and masker center frequencies (Fm) are labeled within each panel. Dashed lines show the average normal growth-of-masking slope of 0.96 dB/dB. Right panels: Growth-of-masking functions for OFF-frequency masking conditions. Dashed lines show the average normal growth-of-masking slope at 1280 and 1607 Hz of 1.67 dB/dB. Panels a and b show growth-of-masking functions from a listener with normal hearing (*hiwr*). Panels c and d, and panels e and f, show growth-of-masking functions from two listeners with sensorineural hearing loss (*jkhr* and *pjbr*, respectively). Solid curves in each panel are least-squares fits to the equation shown within panel a. The points to the left of each curve are the absolute thresholds at the probe frequency. Error bars indicate ± one standard deviation from the mean threshold.

lute probe threshold. The three normal-hearing listeners and four of the hearing-impaired listeners (*gmbl*, *pjbr*, *rehl*, *rwpr*) were tested with the fixed-probe-level procedure. The average standard deviation across repeated threshold estimates for both groups was 1.5 dB, with 95% of the standard deviations less than 2.6 dB. The remaining four hearing-impaired listeners were tested with the fixed-masker-level procedure. The average standard deviation across repeated threshold estimates for this group was 1.3 dB, with 95% of the standard deviations less than 2.4 dB. One standard deviation above and below each average masked-threshold estimate can be seen, for some of the functions in Fig. 2, as the horizontal (for fixed-probe-level data) or vertical (for fixed-masker-level data) error bars.

Figure 2 also illustrates the principal differences between growth-of-masking functions in normal-hearing and hearing-impaired listeners, which have been reported in the literature (Nelson and Bilger, 1974; Smits and Duifhuis, 1982; Stelmachowicz *et al.*, 1987; Murnane and Turner, 1991) and are the focus of a more detailed examination here. Slopes of the growth of masking for OFF-frequency conditions are more gradual in hearing-impaired listeners than in normal-hearing listeners. This can be seen by comparing the masking curves for a normal-hearing ear in Fig. 2(b) with the masking curves for hearing-impaired ears in Fig. 2(d) and (e). To facilitate comparisons, the average normal masking slope of 1.67 at 1280 and 1607 Hz (from Table III) is shown by the dashed line in each panel. Notice that masking curves from the two hearing-impaired ears in Fig. 2(d) and (e), at frequencies where absolute threshold is elevated, have dramatically shallower slopes than those from the normal-hearing ear in Fig. 2(b). By way of contrast, slopes of the growth of masking for ON-frequency conditions are essentially the same in hearing-impaired listeners and normal-hearing listeners. This is illustrated by comparing the masking curves for a normal-hearing ear in Fig. 2(a) with the masking curves for hearing-impaired ears in Fig. 2(c) and (e). For comparison, the average normal masking slope of 0.96 (from Table III) is shown by the dashed line in each panel. All masking curves are parallel to one another, except in a few cases where large amounts of hearing loss existed at the probe frequency [e.g., Fm=1100, Fp=1280 for *pjbr* in Fig. 2(e)].

B. ON-frequency growth-of-masking parameters

Since growth-of-masking parameters for ON-frequency conditions were not markedly different in hearing-impaired and normal-hearing ears, they will be examined briefly before OFF-frequency results are considered. Table II contains the fitting parameters β and κ_{ERB} for the ON-frequency masking conditions. For normal-hearing ears, average growth-of-masking slopes (β) varied between 0.93 and 0.99 across probe frequencies, but no significant trend across probe frequency was observed. The average slope across test frequency was 0.96. Similarly, the average masking sensitivity constant, specified by κ_{ERB}, which ranged between 6 and 13.8 dB SPL and averaged 8.7 dB, did not exhibit a significant trend across probe frequency. In both cases a single factor ANOVA failed to yield a significant effect of probe frequency ($p>0.19$).

TABLE II. Growth-of-masking parameters for ON-frequency conditions (signal within masker spectrum) from normal-hearing subjects (bold) and subjects with sensorineural hearing loss (italics). **Fm**=masker center frequency (200-Hz bandwidth for 420 Hz; 400-Hz bandwidth for others). **Fp**=probe frequency. β=growth-of-masking slope. $\kappa_{\mathbf{ERB}}$=level of masker (Lm) at probe threshold (Tp) where masking begins (in dB SPL), corrected for equivalent rectangular bandwidth (ERB).

ON-frequency conditions (signal within masker spectrum)						
Fm=	420 Hz	420 Hz	840 Hz	1100 Hz	1427 Hz	1840 Hz
Fp=	500 Hz	520 Hz	1020 Hz	1280 Hz	1607 Hz	2020 Hz
Subject	β	β	β	β	β	β
hiwr	101	0.98	1.00	0.88	0.96	0.98
jlkr	0.87	0.99	1.07	1.05	0.99	0.96
rafr	0.94	0.93	0.90	0.91	0.95	0.87
NH Ave	**0.94**	**0.97**	**0.99**	**0.95**	**0.97**	**0.93**
gmbl	1.00	0.97	0.99	1.09	1.00	1.05
pjbr	0.95	0.98	1.00	0.83	…	…
rehl	0.95	0.94	0.98	0.91	0.95	1.07
rwpr	0.93	0.92	0.97	0.94	1.02	1.00
jkhr	0.95	0.94	0.84	0.95	0.72	0.95
rjcr	0.90	0.90	1.01	0.98	0.87	0.93
sxor	…	0.96	0.97	1.01	0.95	0.93
jpkr	0.96	0.98	1.00	0.99	0.94	1.00
jror	0.97	1.04	0.81	0.89	0.91	0.72
Subject	κ_{ERB}	κ_{ERB}	κ_{ERB}	κ_{ERB}	κ_{ERB}	κ_{ERB}
hiwr	7.5	8.0	4.1	9.2	16.9	16.1
jlkr	3.3	9.2	11.8	8.0	3.9	10.6
rafr	7.1	8.6	5.9	4.9	8.5	14.7
NH Ave	**6.0**	**8.6**	**7.1**	**7.3**	**9.7**	**13.8**
gmbl	13.9	17.4	9.6	22.1	32.6	46.9
pjbr	22.7	23.2	40.7	56.3	…	…
rehl	2.0	4.6	4.5	3.8	11.3	15.7
rwpr	16.7	19.5	12.3	12.2	26.1	28.9
jkhr	28.1	29.5	46.6	57.8	53.8	55.8
rjcr	44.6	40.9	56.3	56.3	59.2	58.8
sxor	…	13.0	10.1	24.8	44.3	53.2
jpkr	52.1	52.4	58.4	62.2	62.8	68.2
jror	55.0	56.9	54.1	58.9	61.3	57.3

Growth-of-masking slopes (β) for ON-frequency conditions were generally not different in hearing-impaired ears compared to those in normal-hearing ears. This is evident in Fig. 3(a), which shows slopes normalized to the average slope from normal-hearing ears at each probe frequency (β'), along with the 95% confidence limits expressed as ± 2.1 standard deviations ($N=18$) from the average slope across probe frequency (0.96). Normalized slopes are plotted as a function of probe threshold. Although most of the slopes were within the normal range, even when thresholds exceeded 60 dB SPL, some of the subjects with higher absolute thresholds at the probe frequency (>50 dB SPL) exhibited slopes that were at or below the lower limit of normal (-2.1 sd), e.g., see the masking curve for subject *pjbr* at Fm =1100, Fp=1280 in Fig. 2(e). These latter data points were largely responsible for the significant linear regression between normalized slopes and probe threshold [see inset, Fig. 3(a)].

The masker level at which masking begins in the hearing-impaired ear for ON-frequency conditions, expressed as the effective power within a normal auditory-filter

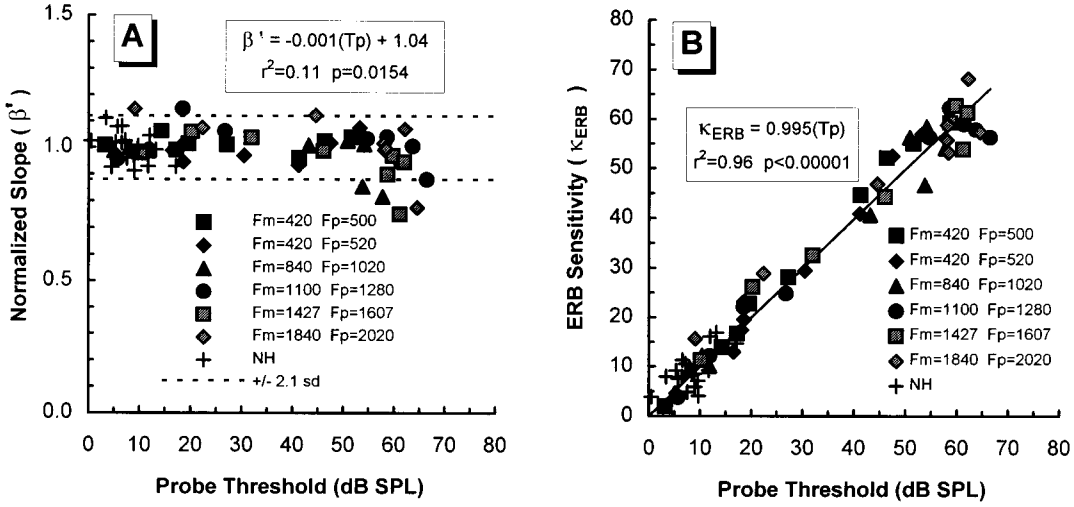

FIG. 3. Fitting parameters for growth-of-masking functions from normal-hearing and hearing-impaired listeners for ON-frequency masking conditions. Fm=center frequency of the masker. Fp=probe frequency. Data for normal-hearing (NH) subjects are shown by plus symbols. Data for hearing-impaired subjects are shown by filled symbols, coded by probe frequency. Panel a: Normalized slope (β') is the slope of the growth of masking normalized to the average slope obtained from normal-hearing ears at each probe frequency. Normalized slopes are plotted as a function of probe threshold. Results of a linear regression between normalized slope (β') and probe threshold (Tp) are given within the panel. Panel b: ERB sensitivity (κ_{ERB}), or masking sensitivity (κ) adjusted for equal power within an auditory-filter bandwidth at each probe frequency, is plotted as a function of probe threshold. ERB=equivalent rectangular-bandwidth (Moore and Glasberg, 1983). Results of a linear regression between ERB sensitivity (κ_{ERB}) and probe threshold (Tp), with the intercept forced through zero, are given within the panel. The dark solid line shows the linear regression with a slope of 0.995.

bandwidth, increased with increasing absolute threshold at the probe frequency. This is shown in Fig. 3(b) by the strong correlation ($r=0.98$) between the sensitivity constant κ_{ERB} and probe threshold. The fact that κ_{ERB} is a direct function of absolute probe threshold indicates that, in a hearing-impaired ear, masking begins when masker level is sufficient to elevate probe threshold in a normal ear to a level equal to the elevated absolute threshold in the hearing-impaired ear. The slope of this relation (0.995) is close to the average growth-of-masking slope in normal ears (0.96). This suggests that sensitivity to ON-frequency masking was not abnormal in these hearing-impaired listeners at the frequency regions where OFF-frequency masking was measured, i.e., critical ratios were within normal limits.

C. OFF-frequency growth-of-masking parameters

Growth-of-masking parameters for OFF-frequency conditions were noticeably different in hearing-impaired and normal-hearing ears. Table III contains the fitting parameters β and κ for the OFF-frequency masking conditions. In normal-hearing ears, average growth-of-masking slopes (β) varied with probe frequency from 1.32 at 650 Hz to 1.65 at 1020 Hz, remained relatively constant up to 1607 Hz, and then decreased to 1.28 at 2020 Hz. The largest growth-of-masking slope of 1.96 was exhibited by subject *hiwr* at a probe frequency of 1280 Hz. Masking sensitivity constants, κ, increased with probe frequency, which indicated that sensitivity to masking decreased with probe frequency, i.e., larger κ values indicated reduced sensitivity to masking. For OFF-frequency masking, the intercept k in Eq. (3) can be interpreted as the amount of reduction in masker intensity provided by the auditory filter at the probe frequency, and κ is inversely related to k by Eq. (4); therefore, the masking

TABLE III. Growth-of-masking parameters for OFF-frequency conditions (signal within masker spectrum) from normal-hearing subjects (bold) and subjects with sensorineural hearing loss (italics). **Fm**=masker center frequency (200-Hz bandwidth). **Fp**=probe frequency. β=growth-of-masking slope. κ=level of masker (Lm) at probe threshold (Tp) where masking begins (in dB SPL).

OFF-frequency conditions (signal above masker spectrum)						
Fm=	420 Hz	420 Hz	420 Hz	420 Hz	420 Hz	420 Hz
Fp=	650 Hz	814 Hz	1020 Hz	1280 Hz	1607 Hz	2020 Hz
Subject	β	β	β	β	β	β
hiwr	1.30	1.68	1.92	1.96	1.75	1.28
jlkr	1.20	1.31	1.34	1.31	1.51	1.11
rafr	1.46	1.52	1.68	1.73	1.76	1.46
NH Ave	**1.32**	**1.50**	**1.65**	**1.67**	**1.67**	**1.28**
gmbl	1.51	1.93	1.87	1.53	1.60	0.76
pjbr	1.27	1.39	0.64	0.97	0.39	…
rehl	1.48	1.88	1.94	1.92	1.83	1.55
rwpr	1.49	1.41	1.91	1.74	1.42	1.05
jkhr	0.87	1.01	0.72	0.70	0.74	0.69
rjcr	0.94	0.97	0.56	0.56	0.58	0.45
sxor	…	…	1.56	1.41	0.82	0.77
jpkr	0.82	0.75	0.94	0.58	0.56	0.44
jror	0.84	0.76	0.65	0.66	0.94	0.57
Subject	κ	κ	κ	κ	κ	κ
hiwr	45.7	59.2	65.2	71.9	75.6	68.1
jlkr	44.9	53.7	57.5	61.3	67.5	60.3
rafr	51.4	56.8	69.2	72.6	76.9	78.2
NH Ave	**47.3**	**56.6**	**63.9**	**68.6**	**73.3**	**68.9**
gmbl	64.3	70.7	69.0	72.7	84.1	83.2
pjbr	52.1	57.2	51.5	87.6	62.5	…
rehl	47.5	58.5	61.7	65.6	68.1	68.8
rwpr	61.8	67.6	74.3	76.7	81.2	72.0
jkhr	53.2	74.9	69.7	69.9	81.1	78.8
rjcr	66.9	78.5	75.6	74.0	81.1	76.5
sxor	…	…	60.5	65.9	76.6	68.3
jpkr	65.0	72.7	79.5	78.2	82.6	79.3
jror	67.5	71.5	69.1	76.7	84.9	84.3

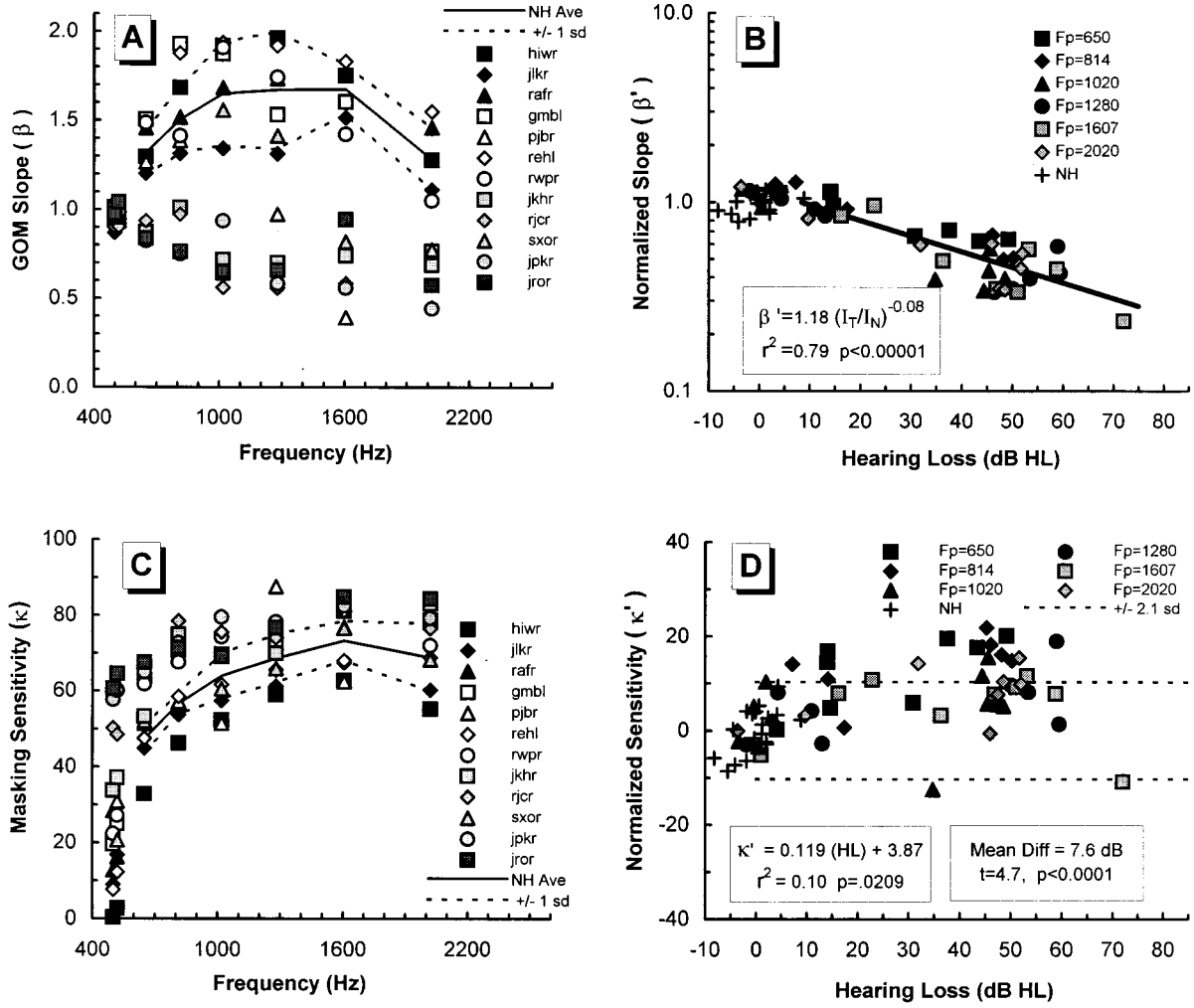

FIG. 4. Fitting parameters for growth-of-masking functions from normal-hearing and hearing-impaired listeners for OFF-frequency masking conditions. The masker was a 200-Hz-wide noise band with an upper edge at 520 Hz. Panel a: Growth-of-masking (GOM) slopes (β) as a function of probe frequency. Data for normal-hearing subjects are shown by dark filled symbols, with the average (NHave) shown by the solid line. Data for hearing-impaired subjects are shown by open and shaded symbols coded by subject. Data derived from ON-frequency masking (Fp=500 and 520 Hz) are also shown for comparison. Panel b: Normalized slopes (β'), which are GOM slopes (β) relative to the average normal-hearing slopes at each probe frequency, are plotted as a function of amount of hearing loss. Data for normal-hearing (NH) subjects are shown by plus symbols and data for hearing-impaired subjects are shown by filled symbols coded by probe frequency. The straight line is the best-fitting least-squares regression to the data, the results of which are included within the inset. Panel c: Masking sensitivity (κ) plotted as a function of probe frequency. Data derived from ON-frequency masking (Fp=500 and 520 Hz) are also shown for comparison. Panel d: Normalized sensitivity (κ'), the difference between κ and the average κ from normal-hearing ears at each probe frequency, as a function of the amount of hearing loss. Statistics of the regression and of the group differences are shown within the insets. Dashed lines indicate 95% confidence limits ($\pm$2.1 sd).

sensitivity constant κ can be thought of, at least in part (ignoring signal-to-noise ratio at masked threshold), as the attenuation (in decibels) of masker effectiveness by the auditory filter at the probe frequency. Larger values of κ indicate more attenuation by the auditory filter and, consequently, *less sensitivity* to OFF-frequency masking. Thus, as probe frequency increased above the edge of the masker, attenuation in masker intensity provided by the auditory filter increased from 47 dB at 650 Hz to 69 dB at 2020 Hz, which would be expected for increased frequency distance between masker and probe given a fixed set of filter characteristics.

Growth-of-masking slopes (β) from hearing-impaired listeners for OFF-frequency conditions were sometimes more gradual (shallower) than in normal-hearing ears at the same probe frequencies. Figure 4(a) shows growth-of-masking slopes as a function of probe frequency. Six of the hearing-impaired listeners (*pjbr*, *jkhr*, *rjcr*, *sxor*, *jpkr*, and *jror*) exhibited growth-of-masking slopes more gradual than normal at most of the probe frequencies. These subjects had substantial hearing losses at those probe frequencies. The other three hearing-impaired listeners (*gmbl*, *rehl*, and *rwpr*), who had normal-hearing or mild hearing losses at the probe frequencies, exhibited growth-of-masking slopes well within or above the range of normal (except for *gmbl* at 2020 Hz). Steep growth-of-masking slopes were exhibited in these subjects, despite the fact that they had substantial hearing losses at higher frequencies. This suggests that hearing loss above the probe frequency does not reduce growth-of-masking slopes at the probe frequency; if anything, it may increase them, as will become apparent later.

Figure 4(b) shows normalized growth-of-masking slopes (β') as a function of the amount of hearing loss at the probe frequency. Slopes for individual ears were expressed relative to the average slope in normal-hearing ears at each probe

frequency, thereby removing the confounding effects of slope changes with probe frequency seen in Fig. 4(a). Those normalized slopes were then fit to a power function of probe threshold intensity (I_T) relative to average normal threshold intensity (I_N) as in

$$\beta' = \mathbf{m}(I_T/I_N)^{\mathbf{n}}, \tag{6}$$

where **m** and **n** are fitting constants. Figure 4(b) shows that growth-of-masking slopes decreased in an orderly fashion as hearing loss increased. A least-squares regression indicated that a significant inverse relation ($p<0.00001$) existed between growth-of-masking slope and hearing loss [see inset in Fig. 4(b)]. Growth-of-masking slopes decreased by a factor of 0.83 ($10^{\mathbf{n}=-0.08}$) for every 10-dB increase in amount of hearing loss. For a hearing loss of 8.4 dB the normalized slope predicted by Eq. (6) was 1.0; for a hearing loss of 75 dB the normalized slope was 0.3. These results indicate that hearing loss at the probe frequency reduced the slope of the growth of masking in a predictable way. Given an elevated probe threshold, reduced growth-of-masking slopes can be predicted by Eq. (6) with some degree of accuracy, irrespective of probe frequency.

Notice also in Fig. 4(b) that data from hearing-impaired ears who had normal-hearing or mild hearing losses at probe frequencies below 1500 Hz (*gmbl*, *rehl*, and *rwpr*) exhibited growth-of-masking slopes that tended to be slightly larger (steeper), at probe frequencies of 814, 1020, and 1280 Hz, than those from normal-hearing ears (see Table III). This is reflected by $\mathbf{m}=1.18$ from the regression between β' and I_T/I_N [see inset in Fig. 4(b)], and could have been largely due to the data from only one subject, *rehl*, who exhibited absolute thresholds better than 10 dB HL at all the probe frequencies below 3 kHz and sizable hearing losses above 3 kHz. However, an additional regression between β' and I_T/I_N, without subject *rehl*, yielded essentially the same regression parameters. This suggests that, for OFF-frequency conditions, growth-of-masking slopes in regions of normal hearing may tend to be slightly steeper when hearing loss exists at higher frequency regions. This finding should be considered with some caution, however, because only three normal-hearing ears were tested. Had more been tested, perhaps some of them would have exhibited slopes as large as, or larger than, subject *hiwr*.

Sensitivity to OFF-frequency masking was slightly reduced in hearing-impaired listeners. Figure 4(c) shows the sensitivity constant, κ, as a function of probe frequency. The average values of κ in normal-hearing ears, along with the 95% confidence limits specified by ± 2.1 standard deviations, are shown in the figure for comparison. Values of κ for listeners with hearing loss tended to be slightly larger than for listeners with normal hearing, particularly at probe frequencies of 650 and 814 Hz, which indicates reduced sensitivity to masking at those probe frequencies (larger κ values reflect poorer sensitivity to OFF-frequency masking).

Figure 4(d) shows normalized masking sensitivity constants (κ') as a function of probe threshold for normal-hearing and hearing-impaired ears. Sensitivity constants (κ) for individual ears are expressed relative to the average in normal-hearing ears at each probe frequency, thereby removing the confounding effects of changes with probe frequency seen in Fig. 4(c). Figure 4(d) shows that normalized sensitivity constants increased moderately with increased hearing loss. A linear least-squares regression indicated a significant relation ($p=0.02$) existed between normalized sensitivity and probe threshold [see inset in Fig. 4(d)]. As a group, sensitivity constants exhibited by listeners with hearing loss were significantly larger than normal ($t=4.7$, $p<0.0001$). On average, listeners with hearing loss exhibited sensitivity constants that were 7.6 dB larger than normal, which indicates that sensitivity to masking at frequency regions above the masker is slightly *reduced* compared to listeners with normal hearing, i.e., masker levels required to produce elevated probe thresholds were, on average, about 7 dB greater than those required in normal-hearing ears.

III. DISCUSSION

A. Growth of masking for OFF-frequency masking conditions

1. More gradual growth-of-masking slopes in the presence of hearing loss

The principal finding of the present study is that, once signals are amplified to overcome the sensitivity loss associated with a cochlear hearing loss, growth-of-masking slopes for upward spread of masking decrease with hearing loss in a predictable way. Three previous studies reported growth-of-masking slopes from listeners with sensorineural hearing loss in sufficient detail to allow accurate comparisons with the present results. Figure 5 shows the growth-of-masking slopes obtained in those studies. They are replotted here in the same form as the present data [Fig. 4(a)], except that slopes are plotted as a function of frequency ratio between probe and masker because the three studies used different maskers. Figure 5(a) shows results from Smits and Duifhuis (1982), who reported growth-of-masking functions from three listeners with sensorineural hearing loss, along with average growth-of-masking functions from two normal-hearing listeners. They used a 50-Hz-wide noise band centered at 1 kHz as a masker. Growth-of-masking functions from their figure 4 were digitized and fit to Eq. (3) to derive growth-of-masking parameters. Figure 5(b) shows results from Stelmachowicz *et al.* (1987), who reported growth-of-masking slopes from five hearing-impaired ears along with the average slopes from five normal-hearing ears. They used 100-Hz-wide noise bands as maskers and a probe tone at 2000 Hz. Figure 5(c) shows results from Murnane and Turner (1991), who obtained growth-of-masking functions from nine listeners with sensorineural hearing loss and three normal-hearing listeners, using a $\frac{1}{3}$-oct band of noise centered at 1 kHz as a masker. They fitted their growth-of-masking functions using only those masked thresholds greater than 5 dB above absolute probe threshold, and reported the growth-of-masking slopes they obtained from each listener.

From Fig. 5, it is apparent that the overall pattern of results is similar across these three studies employing different masker frequencies and masker bandwidths, and it is similar to that seen in the present study [see Fig. 4(a)]. For comparison purposes, slopes from normal-hearing ears in the present study are plotted in each panel (shaded squares). In

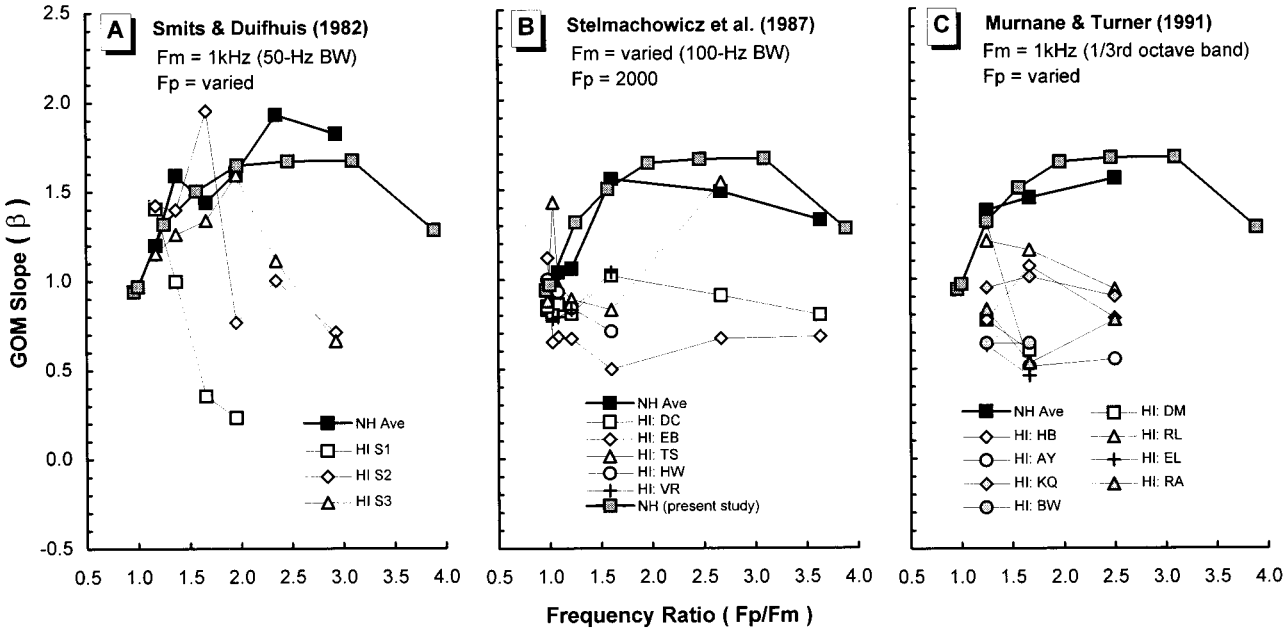

FIG. 5. Growth-of-masking slopes from three previous studies of upward spread of masking, plotted as a function of the frequency ratio between probe frequency and the upper-edge frequency of the masking band. Dark filled squares are the average slopes obtained from normal-hearing listeners in each study (NH Ave). Shaded squares are the average slopes obtained from normal-hearing listeners in the present study. Other unfilled and shaded symbols are for hearing-impaired listeners from each study coded by subject. Fp=frequency of the probe. Fm=center frequency of the masker (bandwidth in parentheses).

normal-hearing ears, growth-of-masking slopes are near 1.0 where probe and masker spectra overlap. Growth-of-masking slopes increase as the probe/masker frequency ratio increases, until, at a frequency ratio of 2.0 and above the average slope reaches asymptote around a slope of about 1.67. In hearing-impaired ears, growth-of-masking slopes tend to cluster around a slope of 1.0 where probe and masker spectra overlap, and as probe/masker frequency ratio increases the slopes tend to remain near unity or become more gradual. Considerable variability exists between individual hearing-impaired listeners, which reflects the degree of hearing loss at the probe frequency, as shown below.

Figure 6(a) shows normalized slopes (β') as a function of amount of hearing loss, calculated for data from two of the previous studies and the present study. Notice that normalized slopes from the previous studies essentially overlay

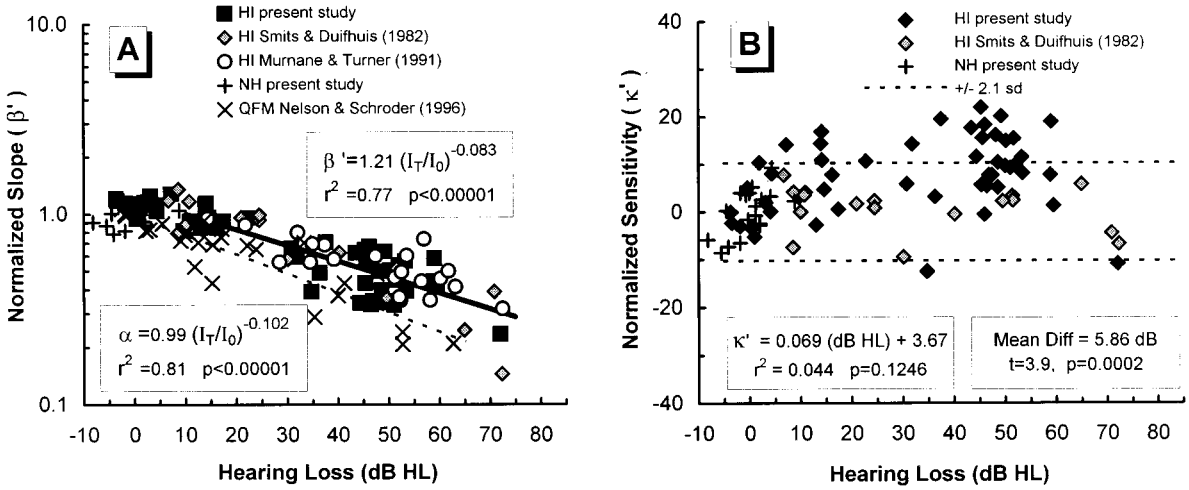

FIG. 6. Growth-of-masking fitting parameters from the present study and two previous studies of upward spread of masking. Dark symbols=data for hearing-impaired subjects from the present study. Shaded symbols=data for hearing-impaired subjects from Smits and Duifhuis (1982). Open symbols=data for hearing-impaired subjects from Murnane and Turner (1991). + symbols=data for normal-hearing subjects from the present study. Panel a: Normalized growth-of-masking slopes (β') plotted as a function of amount of hearing loss (dB HL). The least-squares regression line is shown for the combined subjects (solid line), with the regression results included in the upper inset. × symbols=slope-reduction factors (α) from Nelson and Schroder (1996). Dashed line=regression line for α, with regression parameters given within the lower inset. Panel b: Normalized sensitivity constant (κ') plotted as a function of amount of hearing loss (dB HL), where $\kappa'=\kappa_{HI}-\kappa_{NH}$ (average κ for normal-hearing ears subtracted from κ for an individual hearing-impaired ear, at the same probe frequency). Statistics of the regression and of the group differences in κ' are shown within the insets. Thin dashed lines indicate 95% confidence limits (±2.1 sd).

the normalized slopes obtained in the present study. The parameters defining changes in normalized slope as a function of hearing loss for the previous studies essentially fell on either side of the parameters for the present data. Least-squares regressions between β' and hearing loss, Eq. (6), yielded values of **m** of 1.42 and 1.15 for the Smits and Duifhuis (1982) and the Murnane and Turner (1991) data, respectively, compared to 1.18 for data from the present study and values of **n** of -0.10 and -0.07, respectively, compared with -0.08 for the present data. Thus, there is remarkably good agreement between the results of three separate investigations of the growth of masking for upward spread of masking, despite nearly an octave difference in the frequency region over which measurements were made (520-Hz upper edge in the present study and 1-kHz center frequencies for the other two studies). As indicated within the upper inset of Fig. 6(a), a least-squares regression of the combined data using Eq. (6) yields the fitting constants: $\mathbf{m}=1.21$ and $\mathbf{n}=-0.083$. This indicates that normalized slopes decrease by a factor of 0.83 ($10^{\mathbf{n}}$) for every 10 dB of hearing loss. With a 10-dB hearing loss at the probe frequency, but hearing loss at higher frequencies, the predicted normalized slope is 1.0. For a hearing loss of 75 dB, the predicted normalized slope is 0.3.

Such good agreement among studies with different maskers suggests that the parameters derived from growth-of-masking slopes in the present study should allow accurate predictions of upward spread of masking in persons with sensorineural hearing loss to be made from measurements of upward spread of masking slope in normal-hearing ears using a wide range of maskers. Given the growth of masking slope in normal-hearing ears, for a specific low-frequency masker and a higher-frequency probe, the predicted slope can be obtained from Eq. (6) using the values of $\mathbf{m}=1.21$ and $\mathbf{n}=-0.083$ and the amount of hearing loss at the probe frequency. Further research is needed to test this possibility.

These results support the inferences about growth-of-masking slopes made by Nelson and Schroder (1996), who determined that reduced masking release by envelope fluctuations in listeners with hearing loss could be accounted for by a presumed reduction in the slope of the growth of masking. Although they did not measure growth-of-masking slopes, the slope-reduction factors they derived to fit their data implied that growth-of-masking slopes should be inversely proportional to the amount of hearing loss. The slope-reduction factors (α) they derived to fit their QFM-masker data are replotted in Fig. 6(a) ($\times$ symbols) for comparison with the normalized growth-of-masking slopes (β') obtained in the present study. As indicated within the lower inset of Fig. 6(a), a least-squares regression for α using Eq. (6) yields the fitting constants: $\mathbf{m}=0.99$ and $\mathbf{n}=-0.102$. This indicates that growth-of-masking slopes implied by α decreased by a factor of 0.79 for every 10 dB of hearing loss. The actual reduction in growth-of-masking slopes combined across the three studies evaluated here was slightly less, at 0.83 for every 10 dB of hearing loss. When fit with the linear equation used previously by Nelson and Schroder (1996), the fitting parameters compare favorably with the parameters shown in Eq. (2): $\beta'=-0.129(\mathrm{HL})+1.13$. The change in growth-of-masking slopes with hearing loss observed in the present study is essentially the same as that predicted by Nelson and Schroder to account for reduced masking release in regions of hearing loss. They suggested that masking release was reduced in hearing-impaired ears because growth-of-masking slopes decrease with amount of hearing loss, which implies an increase in response growth with amount of hearing loss. Thus, the ''linearized response growth'' explanation for reduced masking release offered by Nelson and Schroder would appear to be reasonable.

2. Steeper slopes at normal-hearing frequencies with hearing loss at higher frequencies

A value of $\mathbf{m}=1.21$ for the combined data implies that growth-of-masking slopes at probe frequencies with normal hearing (0 dB HL) are larger (steeper) than normal when hearing loss exists at higher frequencies. This implies that high-frequency hearing loss may affect slopes in regions of normal hearing at lower frequencies. One explanation for this may be that normal-hearing growth-of-masking slopes are limited by tails of excitation patterns at higher probe levels. At higher probe levels, growth of response at the peak of the probe excitation pattern may be limited by compression, while growth of response at the high-frequency tail of the probe excitation pattern may be more linear because of the lower excitation levels on the tail of the excitation pattern. Steeper probe response growth should result in more gradual growth of masking. Thus, the slope of the growth of masking might be reduced by the steeper response growth at higher frequency regions. The tendency toward steeper slopes from hearing-impaired ears, with near normal probe thresholds but considerable hearing loss at higher frequencies, may reflect the reduced extent of excitation-pattern tails in regions of high-frequency hearing loss (Schroder *et al.*, 1994). Further research with high-pass noise to mask excitation pattern tails in normal-hearing ears might provide some insight into this phenomenon.

3. Reduced masking sensitivity in ears with hearing loss

Another finding of the present study was that the sensitivity constant (κ), was slightly larger in ears with hearing loss than observed in ears with normal hearing. This suggests that sensitivity to upward spread of masking is slightly *reduced* from what is observed in ears with normal hearing (a larger κ value indicates less sensitivity to masking). Figure 6(b) shows normalized sensitivity ($\kappa'=\kappa_{\mathrm{HI}}-\kappa_{\mathrm{NH}}$) from the present study compared with the same parameters from the growth-of-masking functions obtained by Smits and Duifhuis (1982). Masking sensitivity in their hearing-impaired subjects did not differ significantly from masking sensitivity exhibited by their average normal curve. However, even when their data are combined with ours the mean difference in masking sensitivity of 5.86 dB, between normal-hearing and hearing-impaired data, reaches statistical significance ($t=3.9$, $p=0.0002$).

The slightly larger κ values from subjects with hearing loss could be interpreted as indicating they required a larger signal-to-noise ratio at masked threshold than did the

normal-hearing subjects. However, the earlier analysis of ON-frequency sensitivity constants showed that critical ratios were essentially normal. This reduced masking sensitivity (larger κ values) could also be interpreted as sharper filtering by the auditory filter at these probe frequencies, which is contrary to expectations of reduced auditory filtering in the presence of a hearing loss. However, the fact that larger κ values than normal tend to occur at 650 and 814 Hz [Fig. 4(c)], and the fact that they occur for subjects with the highest probe thresholds at those frequencies (*rjcr* and *jkhr*), suggests an alternative interpretation. If masking at 650 and 814 Hz involved spread of physical energy to those frequency regions, as is the case for ON-frequency masking, then one would expect elevated κ values based on the results presented earlier for ON-frequency masking, which indicated that ON-frequency masking does not begin until the masker level is equal to probe absolute threshold [Fig. 3(b)].

It should also be noted that the present method of estimating κ, which involves extrapolation to probe threshold, can be problematic when the slopes of the growth-of-masking vary across subjects. However, in the present case, slopes of the growth-of-masking in hearing-impaired ears were more gradual, which would tend to lower estimates of κ, not elevate them.

Nevertheless, these results demonstrate that upward of spread of masking in the hearing-impaired ear begins at slightly higher masker levels than in the normal-hearing ear. This *does not* support the idea that listeners with hearing loss are more susceptible to upward spread of masking (threshold shift), or that they are hypersensitive to excitation by maskers on the tails of tuning curves, or that a low-frequency masker actually produces more excitation at higher frequencies in an ear with hearing loss. The higher masked thresholds observed in regions of hearing loss, which have been interpreted as excessive upward spread of masking, are primarily due to an elevated absolute threshold at the probe frequency, I_T in Eq. (3), which is associated with a loss of sensitivity (cochlear gain) at the probe frequency only. Sensitivity to masking by low-frequency sounds is not dramatically affected, or, if it is, there is a slight decrease in sensitivity (slightly higher masker levels are needed).

4. Estimating response-growth exponents in hearing-impaired ears

Recently, animal studies have revealed changes in the basilar membrane (BM) transfer function associated with cochlear damage, which are consistent with the more gradual growth-of-masking slopes observed here in regions of hearing loss. Both BM studies (Yates *et al.*, 1990; Ruggero and Rich, 1991; Ruggero *et al.*, 1993, 1996) and neurophysiological studies (Sachs and Abbas, 1974; Harrison, 1981; Gorga and Abbas, 1981a, 1981b) report results consistent with the concept that, in normal-hearing ears, excitation by a tone at its characteristic frequency (CF) involves a relatively *nonlinear* (compressed) BM transfer characteristic (exponent <1), whereas excitation by a tone much lower in frequency (below CF) involves a more *linear* basilar membrane transfer characteristic (exponent $\cong 1$). In ears with cochlear damage, threshold is elevated and the BM transfer characteristic is ''linearized'' (Ruggero and Rich, 1991; Ruggero *et al.*, 1993, 1996), presumably because the active gain mechanism is disrupted. This suggests that excitation by a probe tone in a region of hearing loss is subject to a more *linear* BM transfer characteristic than in a region of normal hearing (Stelmachowicz *et al.*, 1987; Oxenham and Moore, 1995; Moore, 1996; Oxenham and Moore, 1996). This ''linearized response growth'' (LRG) associated with cochlear damage should lead to steeper than normal response growth (sensory excitation) to a probe tone in the region of hearing loss, which, according to the following reasoning, would translate to a more gradual slope to the growth of upward spread of masking.

If it is assumed that masked threshold for a probe tone is reached when the response to the probe tone (R_p) exceeds the response to the masker (R_M) by some critical ratio (k), as in

$$k = R_P / R_M, \tag{7}$$

then it can be shown that the growth-of-masking slope, (β) reflects the LRG characteristic of cochlear damage. Response growth to a probe tone or a masker can be represented as a power function of stimulus intensity relative to absolute threshold at the probe frequency (I_T), as in

$$R_P = (1 + I_P / I_T)^{\mathbf{p}} \quad \text{and} \quad R_M = (1 + I_M / I_T)^{\mathbf{q}}, \tag{8}$$

with **p** and **q** reflecting exponents for BM transfer characteristics for the probe and masker, respectively. Given these relations, one can then solve for the intensity of a probe at masked threshold as in

$$I_P = ((k(1 + I_M / I_T)^q)^{1/p} - 1) * I_T, \quad \text{or} \tag{9a}$$

$$I_p = (k^{1/p}(1 + I_M / I_T)^{\beta} - 1) * I_T, \quad \text{with} \ \beta = \mathbf{q}/\mathbf{p}. \tag{9b}$$

Since the BM transfer function for a low-frequency masker at a higher-frequency place is assumed to be relatively linear, one can set $\mathbf{q} \cong 1$. Then **p** becomes proportional to $1/\beta$. In a normal ear, the nonlinear BM transfer function for a probe tone at some frequency above the masker would lead to a value of $\mathbf{p} < 1$; therefore, the slope of the growth of masking β_{NRM}, would be greater than 1. In an ear with sufficient hearing loss to affect the active gain process, the BM transfer function is linearized, which would lead to a value of $\mathbf{p} \cong 1$; therefore, the slope of the growth of masking, β_{HLS}, would be more gradual than in a normal ear ($\cong 1$). Thus, it appears that the LRG associated with cochlear hearing loss may increase the response growth exponent for the probe tone (**p**) but not for the masker (**q**); consequently, the slope of the growth of masking (β_{HLS}) is reduced from what it is in the normal-hearing ear.

Unfortunately, response growth to a probe tone (**p**) in a hearing-impaired ear cannot be directly estimated by $1/\beta$ values for all of the probe frequencies tested in the present study, because the probe/masker frequency ratios used here varied from 1.25 up to 3.88, and $\mathbf{q} = 1$ can only be assumed for large probe/masker frequency ratios, perhaps ratios of 2.0 or greater. However, one can estimate response growth for probe and masker in a normal ear at each probe frequency, and then specify response growth in the impaired ear from the change in growth-of-masking slopes relative to normal at

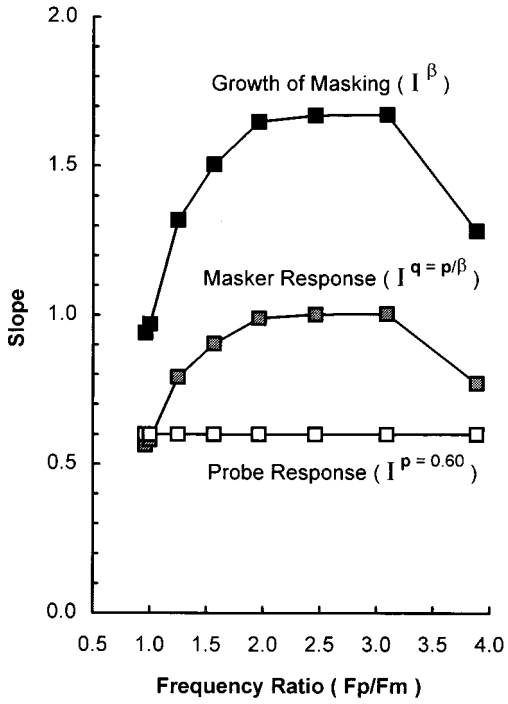

FIG. 7. An illustration of how slopes for probe response growth (**p**) and masker response growth (**q**) were inferred from growth-of-masking slopes (β) in normal-hearing ears. From Eqs. (7)–(9) growth-of-masking slopes were shown to be related to slopes of masker and probe response growth by $\beta=\mathbf{q}/\mathbf{p}$. Based on reports of basilar membrane measurements in the literature, probe response growth (**p**) was calculated by assuming $\mathbf{q}=1$ (linear masker response growth) for large frequency ratios between probe and masker, then **p** became $1/\beta$ and masker response growth became $\mathbf{q}=\mathbf{p}/\beta$.

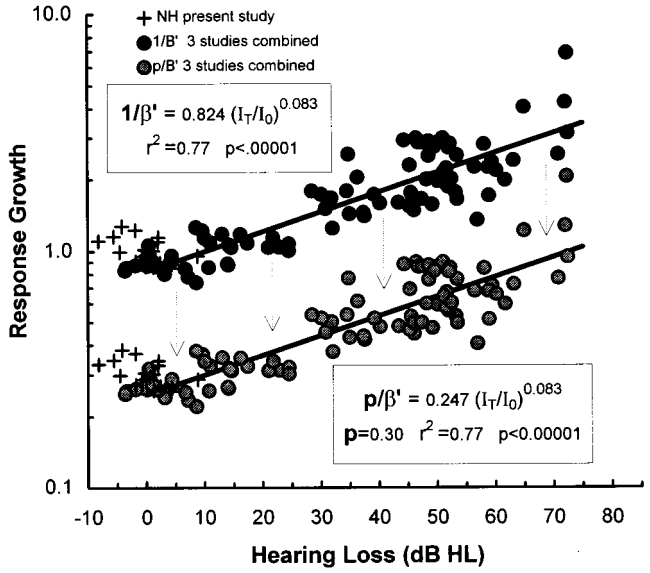

FIG. 8. Response growth normalized to average response growth from normal-hearing listeners at each test frequency ($\mathbf{1}/\beta'$) is shown for the normal-hearing listeners in the present study (+ symbols) and for the hearing-impaired listeners combined from three studies (dark filled circles). If normal-hearing response growth at the probe frequency is *assumed* to have a slope of $\mathbf{p}=0.30$, then response growth ($\mathbf{p}/\beta'$) in ears with hearing loss (shaded symbols) varied from 0.25 at 0 dB HL (normal compression) to 1.0 at 75 dB HL (linear response growth). Regression statistics are shown within the insets.

each probe frequency. In this way one obtains an estimate of normalized response growth, which can be examined independent of probe frequency.

Estimation of probe and masker response growth from growth-of-masking slopes in the normal-hearing ear is illustrated in Fig. 7. The upper curve shows growth-of-masking slopes from the average normal-hearing ear as a function of frequency ratio between probe and masker. For frequency ratios of 2.0 and larger, the average growth-of-masking slope is around 1.67. At these large probe/masker frequency ratios, the assumption of $\mathbf{q}=1$ is reasonable, thus the growth of response to the probe tone (**p**) becomes $1/\beta$, or $\mathbf{p}\cong 0.60$. As indicated by the bottom curve, it is also reasonable to assume that response growth for a probe tone is the same ($\mathbf{p}\cong 0.60$) at all probe frequencies over this limited range of probe frequencies, even though compression varies with level, because the probe levels at masked threshold are all roughly within the same range for all probe frequencies. Then, from Eq. (9), response growth for the masker (**q**) at different probe/masker frequency ratios becomes $\mathbf{p}/\beta$. The middle curve in Fig. 7 shows that response growth to the masker increases from just below 0.60 where probe and masker spectra overlap to 1.0 for large frequency ratios. When the masker and probe are close together they are both subjected to the same compressive nonlinearity given by the 0.60 exponent. Since the slope of the growth of masking (β) is given by $\mathbf{q}/\mathbf{p}$, the growth-of-masking slope is near 1.0. As the masker is moved farther from the probe, toward lower frequencies, it is subjected to less nonlinearity and its response growth approaches linearity. Thus, at large probe/masker frequency ratios, the growth-of-masking slope becomes 1.0/0.60, or 1.67.

At the largest frequency ratio (3.88) where the probe frequency is at 2020 Hz, the average growth-of-masking slope decreased to 1.28. The masker levels are about the same as those required for the next lower probe frequency (1607 Hz), as indicated by the values of κ in Fig. 4(c), the probe levels at masked threshold are within the same range, and the growth-of-masking functions were as well fit by Eq. (3) as at the lower probe frequencies, yet growth-of-masking slopes were reduced. We can find no adequate explanation for this result, except that the acoustic reflex may have attenuated the low-frequency masker more than the higher-frequency probes. If that were so, one might expect to see some roll-over in the individual masking functions at higher masker levels where the acoustic reflex might begin to play a role. That, however, was not the case for any of the individual masking functions at 2020 Hz. Of the four studies examined here, only the Stelmachowicz *et al.* (1987) study examined frequency ratios as large [Fig. 5(b)]. Their slopes also showed a tendency to be reduced slightly at large frequency ratios. Further research is needed to explain the reduction in masking slope at very large probe/masker frequency ratios.

Relative response growth at the probe frequency in hearing-impaired ears can be estimated from the change in observed masking slopes relative to the slopes obtained from normal-hearing ears. Response growth relative to normal hearing is illustrated in Fig. 8. The upper set of data points in Fig. 8 (solid circles) shows relative response-growth expo-

nents ($1/\beta'$) calculated from the normalized growth-of-masking slopes (β') combined from three studies and shown in Fig. 6(a). It can be seen that relative response-growth exponents increase as a power function of threshold intensity relative to normal threshold intensity (see upper inset). Relative response-growth exponents vary from near normal at 0 dB HL to more than three times normal at 70 dB HL. This reasoning suggests that response growth increases by a factor of about 1.2 for every 10 dB of hearing loss ($10^{0.083}$).

Values of $\mathbf{p}/\beta'$ can provide estimates of absolute response-growth exponents in hearing-impaired ears, if one assumes an average value for the response growth exponent ($\mathbf{p}$) in normal-hearing ears. In Fig. 7 a value of $\mathbf{p}=0.60$ was derived for normal probe response growth by assuming $\mathbf{q}=1$ for large probe/masker frequency ratios. This value of $\mathbf{p}$ yields estimates of absolute response-growth exponents in hearing-impaired ears from around 0.60 at 0 dB HL to around 2.0 at 75 dB HL. A response-growth exponent of 2.0 for a hearing loss of 75 dB is inconsistent with BM measurements that suggest the system is linear ($\mathbf{p}=1.0$) in the presence of cochlear damage (Ruggero and Rich, 1990, 1991; Ruggero *et al.*, 1993, 1996). Thus it appears that our response growth estimates are in error by about a factor of 2. If our estimate of normal-hearing $\mathbf{p}$ is reduced by a factor of 2 (to $\mathbf{p}=0.30$), then absolute response growth estimates in hearing-impaired ears become consistent with BM transfer characteristics. This is shown by the bottom set of data points in Fig. 8, which show $\mathbf{p}/\beta'$ calculations as a function of amount of hearing loss, with $\mathbf{p}=0.30$. With a factor of 2 adjustment to the exponent for normal response growth, response-growth exponents in hearing-impaired ears vary from around 0.25 at 0 dB HL to around 1.0 at 75 dB HL. Now response growth is linear for a large sensorineural hearing loss, which is consistent with BM transfer characteristics in the presence of cochlear damage. Furthermore, normal response growth at the probe frequency is more consistent with BM transfer characteristics found in undamaged cochleas ($\mathbf{p}=0.20$) and it is also consistent with exponents for the growth of loudness in normal-hearing ears ($\mathbf{p}=0.30$).

One possible complicating factor might be our failure to take suppression mechanisms into account (Javel *et al.*, 1983; Delgutte, 1990). The BM transfer characteristics were measured with single tones that would not reflect suppression. The simultaneous-masking measures made here from normal-hearing ears most certainly involved suppression by the masker at the probe frequency, in addition to swamping of neural response at the probe frequency due to excitation by the masker. Therefore, accurate estimates of probe response growth from simultaneous growth-of-masking data should probably include a slope adjustment for the effects of suppression, such as $\mathbf{p}=1/\beta-\mathbf{s}$, where $\mathbf{s}$ is the exponent defining the growth of suppression with intensity, which, from our factor of 2 error, might be around $\log(2)=0.30$. However, the situation is likely to be much more complex because suppression varies with frequency ratio between probe and masker. Further research is needed to clarify this issue. An obvious approach would be to obtain growth-of-masking slopes under nonsimultaneous masking conditions where suppression effects will not occur. Recently, a response growth exponent of 0.16 was derived for moderate signal levels with a 6-kHz probe tone and a 3-kHz nonsimultaneous masker by Oxenham and Plack (1996, 1997), which is more in line with what one might expect at moderate probe levels, and is consistent with the interpretation here that suppression may reduce growth-of-masking slopes and elevate estimates of response growth.

B. Growth of masking for ON-frequency masking conditions

Results of the present study indicated that, for hearing-impaired subjects, growth-of-masking slopes for ON-frequency conditions were not markedly different from normal. Slopes did not change with probe frequency or with probe threshold. These are conditions where the spectrum of the masker and the probe are the same and subject to the same BM transfer function and the same cochlear nonlinearities. In this situation, detection threshold may involve the physical addition of stimulus power from masker and probe before exciting the auditory system, as compared to the OFF-frequency case where the combined sensory response to stimuli at different frequencies very likely involves different BM transfer functions and cochlear nonlinearities for masker and probe.

For ON-frequency conditions, masking began when the power within an auditory-filter bandwidth was approximately equal to absolute threshold at the probe frequency. Examination of individual data in Fig. 3(b) indicates that masking sensitivity seemed to be slightly greater (sensitivity constants κ were smaller) in some of subjects with larger hearing losses, which could mean that critical masking bands in those subjects might have been wider. This interpretation is consistent with results reported by Nelson (1991), where markedly abnormal tuning was only seen when absolute thresholds exceeded 60 dB SPL. That abnormal tuning was exhibited by abnormal downward spread of masking, not abnormal upward spread of masking, i.e., only the high-frequency sides of forward-masking psychophysical tuning curves were flatter than normal. However, that explanation is problematic because the masking bands were not more than 2.5 ERBs wide, which should only lead to a 4-dB reduction in κ. An alternative explanation might be that those subjects with larger hearing losses exhibited smaller sensitivity constants κ because their internal noise effectively had a larger variance requiring a larger signal-to-noise ratio to reach detection threshold.

IV. CONCLUSIONS

(1) OFF-frequency growth-of-masking slopes decrease with amount of sensorineural hearing loss in a predictable fashion. An analysis of results from four studies of upward spread of masking that employed different types of low-frequency maskers indicates that growth-of-masking slopes decrease as a power function of threshold stimulus intensity relative to normal threshold intensity, i.e., growth-of-masking slopes decrease by a factor of about 0.8 for every 10 dB of hearing loss. The parameters derived from growth-of-masking slopes in the present

study should allow accurate predictions of upward spread of masking in persons with sensorineural hearing loss to be made from measurements of upward spread of masking in normal-hearing ears.

(2) More gradual OFF-frequency growth-of-masking slopes from ears with hearing loss reflect steeper-than-normal response growth slopes at the probe frequency. Assumptions about underlying physiological mechanisms lead to the conclusion that probe-tone response-growth exponents vary from around 0.3 at 0 dB HL to near 1.0 at 75 dB HL.

(3) Subjects with normal hearing at the probe frequency, but significant hearing loss at higher frequency regions, may exhibit larger (steeper) than normal growth-of-masking slopes in regions of normal hearing. This could reflect a reduction in excitation pattern tails associated with high-frequency hearing losses.

(4) Sensitivity to OFF-frequency masking is slightly *reduced* in regions of hearing loss, i.e., upward spread of masking begins at slightly higher masker levels in persons with hearing loss than in persons with normal hearing. Persons with sensorineural hearing loss exhibit higher masked thresholds primarily because they have elevated absolute thresholds at the probe frequency, which is due to a loss of active gain at that frequency, they do not demonstrate an excessive response to lower-frequency maskers (excessive upward spread of excitation).

(5) ON-frequency growth-of-masking slopes are approximately the same in normal-hearing and hearing-impaired ears, although more gradual slopes in some subjects at frequencies with larger hearing losses suggest additional research is needed with subjects who have large amounts of hearing loss.

(6) ON-frequency masking begins when effective masker power within the auditory-filter bandwidth at the probe frequency reaches elevated absolute threshold at the probe frequency.

(7) Growth-of-masking functions are well fit as a power function of masker intensity. Curvilinear masking function, observed for masked probe thresholds near absolute probe threshold (small amounts of masking), are well fit by assuming a power summation at the probe frequency between an internal representation of masker intensity and an internal noise at absolute threshold intensity.

ACKNOWLEDGMENTS

This work was supported largely by grants DC00149 and DC00110 from NIDCD. This research was also supported in part by the Lion's 5M International Hearing Foundation. We wish to thank Gail Donaldson for her valuable suggestions to previous versions of this manuscript as well as Søren Buus and Brian Moore for their helpful reviews.

ANSI **(1989)**. *S3.6–1989, Specification for Audiometers* (American National Standards Institute, New York).

Buus, S. (**1985**). ''Release from masking caused by envelope fluctuations,'' J. Acoust. Soc. Am. **78,** 1958–1965.

Buus, S., and Florentine, M. (**1988**). ''Growth of masking in listeners with cochlear impairments and impairments simulated by masking'' J. Acoust. Soc. Am. **83,** S76.

Buus, S., and Florentine, M. **(1989)**. ''Simulated hearing loss as a baseline for the assessment of auditory function in cochlearly impaired listeners,'' in *Proceedings of the Fifteenth Annual Bioengineering Conference*, edited by S. Buus (IEEE, Piscataway, NJ).

Cody, A. R., and Johnstone, B. M. (**1980**). ''Single auditory neuron responses during acute acoustic trauma,'' Hearing Res. **3**, 3–16.

Delgutte, B. (**1990**). ''Physiological mechanisms of psychophysical masking: Observations from auditory-nerve fibers,'' J. Acoust. Soc. Am. **87,** 791–809.

Dubno, J. R., and Ahlstrom, J. B. (**1995a**). ''Masked thresholds and consonant recognition in low-pass maskers for hearing-impaired and normal-hearing listeners,'' J. Acoust. Soc. Am. **97**, 2030–2041.

Dubno, J. R., and Ahlstrom, J. B. (**1995b**). ''Growth of low-pass masking of pure tones and speech for hearing-impaired and normal-hearing listeners,'' J. Acoust. Soc. Am. **98,** 3113–3124.

Dubno, J. R., and Schaefer, A. B. **(1991)**. ''Frequency selectivity for hearing-impaired and broadband-noise-masked normal listeners,'' Q. J. Exp. Psychol. Special Issue on Hearing and Speech **43A**, 543–564.

Dubno, J. R., and Schaefer, A. B. (**1992**). ''Comparison of frequency selectivity and consonant recognition among hearing-impaired and masked normal-hearing listeners,'' J. Acoust. Soc. Am. **91,** 2110–2121.

Dubno, J. R., and Schaefer, A. B. (**1995**). ''Frequency selectivity and consonant recognition for hearing-impaired and normal-hearing listeners with equivalent masked thresholds,'' J. Acoust. Soc. Am. **97,** 1165–1174.

Florentine, M. **(1978)**. ''Frequency selectivity in normal-hearing and hearing-impaired observers,'' Doctoral Dissertation Thesis, Northeastern University.

Florentine, M., Buus, S., Scharf, B., and Zwicker, E. **(1980)**. ''Frequency selectivity in normally-hearing and hearing-impaired observers,'' J. Speech Hear. Res. **23**, 646–669.

Gagne, J. P. (**1983**). ''Excess masking among listeners with high-frequency sensorineural hearing loss,'' Ph.D. Thesis, Washington University.

Glasberg, B. R., and Moore, B. C. J. (**1990**). ''Derivation of auditory filter shapes from notched-noise data,'' Hearing Res. **47,** 103–138.

Gorga, M. P., and Abbas, P. J. (**1981a**). ''AP measurement of short-term adaptation in normal and in acoustically traumatized ears,'' J. Acoust. Soc. Am. **70,** 1310–1321.

Gorga, M. P., and Abbas, P. J. (**1981b**). ''Forward-masking AP tuning curves in normal and in acoustically traumatized ears,'' J. Acoust. Soc. Am. **70,** 1322–1330.

Hannley, M., and Dorman, M. F. (**1983**). ''Susceptibility to intraspeech spread of masking in listeners with sensorineural hearing loss,'' J. Acoust. Soc. Am. **74,** 40–51.

Harbert, F., and Young, I. M. (**1965**). ''Spread of masking in ears showing abnormal adaptation and conductive deafness,'' Acta Otolaryngol. **60**, 49–58.

Harrison, R. V. (**1981**). ''Rate-versus-intensity functions and related AP responses in normal and pathological guinea pig and human cochleas,'' J. Acoust. Soc. Am. **70,** 1036–1044.

Javel, E., McGee, J., Walsh, E. J., Farley, G. R., and Gorga, M. P. (**1983**). ''Suppression of auditory-nerve responses. II. Suppression threshold and growth, isosuppression contours,'' J. Acoust. Soc. Am. **74,** 801–813.

Jerger, J. F., Tillman, T. W., and Peterson, J. L. (**1960**). ''Masking by octave bands of noise in normal and impaired ears,'' J. Acoust. Soc. Am. **32,** 385–390.

Klein, A. J., and Dubno, J. R. (**1993**). ''Minimal upward spread of masking: Correlations with speech and auditory brainstem response masked thresholds,'' J. Acoust. Soc. Am. **93,** 3422–3430.

Klein, A. J., Mills, J. H., and Adkins, W. Y. (**1990**). ''Upward spread of masking, hearing loss, and speech recognition in young and elderly listeners,'' J. Acoust. Soc. Am. **87,** 1266–1271.

Liberman, M. C. (**1984**). ''Single-neuron labeling and chronic cochlear pathology. I. Threshold shift and characteristic-frequency shift,'' Hearing Res. **16**, 33–41.

Liberman, M. C., and Dodds, L. W. (**1984**). ''Single-neuron labeling and chronic cochlear pathology. III. Stereocilia damage and alterations of the threshold tuning curves,'' Hearing Res. **16**, 55–74.

Martin, E. S., and Pickett, J. M. (**1970**). ''Sensorineural hearing loss and upward spread of masking,'' J. Speech Hear. Res. **13**, 426–437.

Moore, B. C. J. (**1996**). ''Perceptual consequences of cochlear hearing loss

and their implications for the design of hearing aids,'' Ear Hear. **17**, 133–161.
Moore, B. C. J., and Glasberg, B. R. (**1983**). ''Suggested formulae for calculating auditory-filter bandwidths and excitation patterns,'' J. Acoust. Soc. Am. **74,** 750–753.
Moore, B. C. J., and Glasberg, B. R. (**1987**). ''Factors affecting thresholds for sinusoidal signals in narrow-band maskers with fluctuating envelopes,'' J. Acoust. Soc. Am. **82,** 69–79.
Murnane, O., and Turner, C. W. (**1991**). ''Growth of masking in sensorineural hearing loss,'' Audiology **30**, 275–285.
Nelson, D. A. (**1991**). ''High-level psychophysical tuning curves: Forward masking in normal-hearing and hearing-impaired listeners,'' J. Speech Hear. Res. **34**, 1233–1249.
Nelson, D. A., and Bilger, R. C. (**1974**). ''Pure-tone octave masking in listeners with sensorineural hearing loss,'' J. Speech Hear. Res. **17**, 252–269.
Nelson, D. A., and Schroder, A. C. (**1996**). ''Release from upward spread of masking in regions of high-frequency hearing loss,'' J. Acoust. Soc. Am. **100**, 2266–2277.
Oxenham, A. J., and Moore, B. C. J. (**1995**). ''Additivity of masking in normally hearing and hearing-impaired subjects,'' J. Acoust. Soc. Am. **98,** 1921–1934.
Oxenham, A. J., and Moore, B. C. J. (**1996**). ''Modeling the effects of peripheral nonlinearity in normal and impaired hearing,'' in *Modeling Sensorineural Hearing Loss*, edited by W. Jesteadt (Erlbaum, Hillsdale, NJ).
Oxenham, A. J., and Plack, C. J. (**1996**). ''Peripheral origins of the upward spread of masking,'' J. Acoust. Soc. Am. **99,** 2542 (A).
Oxenham, A. J., and Plack, C. J. (**1997**). ''A behavioral measure of cochlear function in normally hearing and hearing-impaired listeners,'' J. Acoust. Soc. Am. (in press).
Picard, M., and Couture-Metz, F. (**1985**). ''Debordement de masquage normal et anormal sur les aigus (Upward spread of masking in normal and impaired ears),'' Audiology **24**, 81–91.
Rice, S. O. (**1954**). ''Mathematical analysis of random noise,'' in *Noise and Stochastic Properties*, edited by N. Wax (Dover, New York).
Ruggero, M. A., and Rich, N. C. (**1990**). ''Systemic injection of furosemide alters the mechanical response to sound of the basilar membrane,'' in *The Mechanics and Biophysics of Hearing*, edited by P. Dallos, C. D. Geisler, J. W. Matthews, M. A. Ruggero, and C. R. Steele (Springer Verlag, Berlin), pp. 314–321.
Ruggero, M. A., and Rich, N. C. (**1991**). ''Furosemide alters organ of Corti mechanics: evidence for feedback of outer hair cells upon the basilar membrane,'' J. Neurosci. **11,** 1057–1067.
Ruggero, M. A., Rich, N. C., and Recio, A. (**1993**). ''Alteration of basilar membrane responses to sound by acoustic overstimulation,'' in *Biophysics of Hair Cell Systems*, edited by H. Duifhuis, J. W. Horst, P. van Dijk, and S. M. van Netten (World Scientific, Singapore), pp. 258–264.
Ruggero, M. A., Rich, N. C., Robles, L., and Recio, A. (**1996**). ''The effects of acoustic trauma, other cochlear injury and death on basilar-membrane responses to sound,'' in *Proceedings of the Vth International Symposium on the Effects of Noise on Hearing*, edited by A. Axelsson, H. Borchgrevink, D. Henderson, R. P. Hamernik, and R. Salvi (Thieme Medical, Stuttgart), pp. 258–264.
Sachs, M. B., and Abbas, P. J. (**1974**). ''Rate versus level functions for auditory-nerve fibers in cats: tone-burst stimuli,'' J. Acoust. Soc. Am. **56,** 1835–1847.
Salvi, R. J., Henderson, D., and Hamernik, R. D. (**1977**). ''Auditory nerve fiber activity, behavioral thresholds and cochlear histology following noise-induced asymptotic threshold shift,'' J. Acoust. Soc. Am. **62,** S35.
Schmiedt, R. A., and Zwislocki, J. J. (**1980**). ''Effects of hair cell lesions on responses of cochlear nerve fibers. II. Single- and two-tone intensity functions in relation to tuning curves,'' J. Neurophysiol. **43,** 1390–1405.
Schmiedt, R. A., Zwislocki, J. J., and Hamernik, R. P. (**1980**). ''Effects of hair cell lesions on responses of cochlear nerve fibers. I: Lesions, tuning curves, two-tone inhibition, and responses to trapezoidal-wave patterns,'' J. Neurophysiol. **43,** 1367–1389.
Schroder, A. C., Viemeister, N. F., and Nelson, D. A. (**1994**). ''Pure-tone intensity discrimination in normal-hearing and hearing-impaired listeners,'' J. Acoust. Soc. Am. **96,** 2683–2693.
Smits, J. T. S., and Duifhuis, H. (**1982**). ''Masking and partial masking in listeners with a high frequency hearing loss,'' Audiology **21**, 310–324.
Stelmachowicz, P., Lewis, D. E., Larson, L., and Jesteadt, W. (**1987**). ''Growth of masking as a measure of response growth in hearing-impaired listeners,'' J. Acoust. Soc. Am. **81,** 1881–1887.
Trees, D. E., and Turner, C. W. (**1986**). ''Spread of masking in normal subjects and in subjects with high frequency hearing loss,'' Audiology **24**, 678–693.
Wegel, R. L., and Lane, C. E. (**1924**). ''The auditory masking of one pure tone by another and its probable relation to the dynamics of the inner ear,'' Phys. Rev. **23,** 266–285.
Yates, G. K., Winter, I. M., and Robertson, D. (**1990**). ''Basilar membrane nonlinearity determines auditory nerve rate-intensity functions and cochlear dynamic range,'' Hearing Res. 45, 203–220.
Zwicker, E. (**1970**). ''Masking and psychological excitation as consequences of the ear's frequency analysis,'' in *Frequency Analysis and Periodicity Detection in Hearing*, edited by R. Plomp and G. F. Smoorenburg (Sijthoff, Leiden, The Netherlands), pp. 376–394.

Psychoacoustical evaluation of the pitch-synchronous overlap-and-add speech-waveform manipulation technique using single-formant stimuli

Reinier W. L. Kortekaas and Armin Kohlrausch
Institute for Perception Research/IPO, P.O. Box 513, 5600 MB Eindhoven, The Netherlands

(Received 8 July 1996; revised 14 October 1996; accepted 1 November 1996)

This article presents two experiments dealing with a psychoacoustical evaluation of the pitch-synchronous overlap-and-add (PSOLA) technique. This technique has been developed for modification of duration and fundamental frequency of speech and is based on simple waveform manipulations. Both experiments were aimed at deriving the sensitivity of the auditory system to the basic distortions introduced by PSOLA. In experiment I, manipulation of fundamental frequency was applied to synthetic single-formant stimuli under minimal stimulus uncertainty, level roving, and formant-frequency roving. In experiment II, the influence of the positioning of the so-called ''pitch markers'' was studied. Depending on the formant and fundamental frequency, experimental data could be described reasonably well by either a spectral intensity-discrimination model or a temporal model based on detecting changes in modulation of the output of a single auditory filter. Generally, the results were in line with psychoacoustical theory on the auditory processing of resolved and unresolved harmonics.
[S0001-4966(97)03903-9]

PACS numbers: 43.66.Fe, 43.66.Ba, 43.72.Ja [WJ]

INTRODUCTION

Over the past few decades, considerable research activities have concentrated on instrumental modification of the fundamental frequency and duration of natural speech. These types of modification enable the manipulation of speech prosody: modification of duration typically alters speech rhythm and tempo, whereas modification of fundamental frequency changes intonation. Characteristics not strictly pertaining to prosody, such as phonemic content and voice quality, ideally remain unaffected by these modifications. Numerous techniques have been proposed with the general aim of both maximizing intelligibility and perceived synthesis quality and minimizing computational complexity. A class of digital-signal-processing techniques with generally low complexity is the so-called overlap and add (OLA) framework (Rabiner and Schafer, 1978). For instance, time-domain OLA, where all operations are performed on the waveform itself, has been successfully applied not only in speech manipulation (e.g., Roucos and Wilgus, 1985) but also in other fields such as music synthesis (e.g., Roads, 1988).

This article will focus on pitch-synchronous overlap-and-add (PSOLA: Moulines and Charpentier, 1990; Moulines and Laroche, 1995), which is a variant of time-domain OLA.[1] The main feature of PSOLA is that the OLA operations are aligned to the (quasi)-periodicity of the input speech signal. PSOLA has found widespread application, e.g., in modules for text-to-speech synthesis and as a tool for fundamental speech-perception research (Moulines and Laroche, 1995). PSOLA-manipulated natural speech is generally characterized not only by high intelligibility but also by high synthesis quality. This finding is remarkable given the fact that, as will be described in the following section, the technique is based on rather rough signal operations.

Despite the generally satisfactory synthesis quality of PSOLA, annoying artefacts are sometimes introduced. Although a strict categorization is difficult, these artefacts can often be described as hoarseness and roughness of the synthesized signal. In addition, artefacts similar to comb filtering are observed in practice. As far as we know, the occurrence of these artefacts cannot be predicted beforehand. This unpredictability is, in our opinion, caused to a great extent by the lack of knowledge of the perceptual effects of the (PS)OLA operations, a view that was also expressed by Moulines and Laroche (1995).

Even if PSOLA manipulation of a speech signal does not lead to the perception of either of the artefacts mentioned above, the manipulation does affect its spectral content. To explain the success of PSOLA manipulation, one may hypothesize that these spectral changes are either perceptually subliminal or, within the context of speech perception, phonetically less relevant (cf. Klatt, 1982). This paper addresses the first hypothesis by determining the detectability of the spectral changes and by deriving the auditory cues involved in this detection process. Such a psychoacoustical basis is probably important for the long-term aim of increasing the predictability of audible (and annoying) artefacts. In addition, psychophysical evaluation may also increase knowledge about the auditory processing of speech.

In the experiments, synthetic single-formant signals (Klatt, 1980) were PSOLA manipulated. Apart from their application in speech synthesizers, single- or multiple-formant signals have been used to determine, e.g., jnd's in formant frequency (for a recent overview, see Lyzenga and Horst, 1995) and in fundamental frequency (Flanagan and Saslow, 1958; Klatt, 1973). Single-formant signals are used here to derive the sensitivity of the auditory system to the

''basic distortions'' introduced by the PSOLA operations. To establish the link to ''classical'' psychoacoustics, the Appendix presents experimental results concerning the auditory sensitivity to basic distortions when manipulating pure tones.

In experiment I, the perceptual effects of fundamental frequency ($F0$) manipulation for three levels of stimulus uncertainty, mimicking particular aspects of natural speech, are investigated. In experiment II, the perceptual effects of the ''pitch-marker'' location are studied (see Sec. I). Both experiments focus on $F0$ modification only because, in practice, this type of manipulation is more likely to result in annoying artefacts than the manipulation of duration. In addition, the experimental data are compared with predictions of two model simulations: a model based on detecting intensity differences between excitation patterns (Durlach *et al.*, 1986; Gagné and Zurek, 1988) and a model based on the discrimination of modulation depth within a single auditory filter.

I. GENERAL METHODS

A. The PSOLA technique

The PSOLA technique is a time-domain variant of the so-called overlap–add (OLA) technique for analysis–synthesis (Rabiner and Schafer, 1978; Allen and Rabiner, 1977). OLA generally consists of three steps: (1) decomposition of a signal into separate, but often overlapping, segments; (2) optional modification of these segments; and (3) recombination of the segments by means of overlap–adding. PSOLA consists only of steps (1) and (3). A short introduction to PSOLA will be presented here; for further details the reader is referred to Moulines and Charpentier (1990) and Moulines and Laroche (1995).

Figure 1(a) shows the waveform of a synthetic single-formant signal as used in both experiments. This signal is decomposed into separate segments in analysis step (1) by windowing it at particular time instances. These instances, represented by vertical lines in Fig. 1(a), are positioned *pitch synchronously* and are called ''pitch markers.'' Pitch markers are determined either manually by inspection of the speech waveform or automatically by means of some local $F0$ estimation (e.g., Ma *et al.*, 1994; Smits and Yegnanarayana, 1995). Figure 1(b) shows two segments extracted from the input signal. The maxima of the Hanning (raised-cosine) windows coincide with the pitch markers. The window duration depends on the temporal spacing between pitch markers; consecutive windows have 50% overlap. Because adjacent windows samplewise add up to one, the input signal can be restored perfectly. Note that in natural speech windows will typically be asymmetrical due to variation in $F0$.

Segment recombination in synthesis step (3) is performed after *defining* a new pitch-marker sequence. In Fig. 1(c), the new sequence is represented by vertical lines. An output signal is synthesized by first assigning a decomposed segment to each of the new pitch markers and then performing the samplewise overlap–add operation. Manipulation of fundamental frequency is achieved by changing the time intervals between pitch markers. In Fig. 1(c), for instance, these intervals are increased, leading to the percept of a lower pitch. Modification of duration, on the other hand, is achieved by either repeating or omitting segments. Note that, in principle, modification of fundamental frequency also implies a modification of duration.

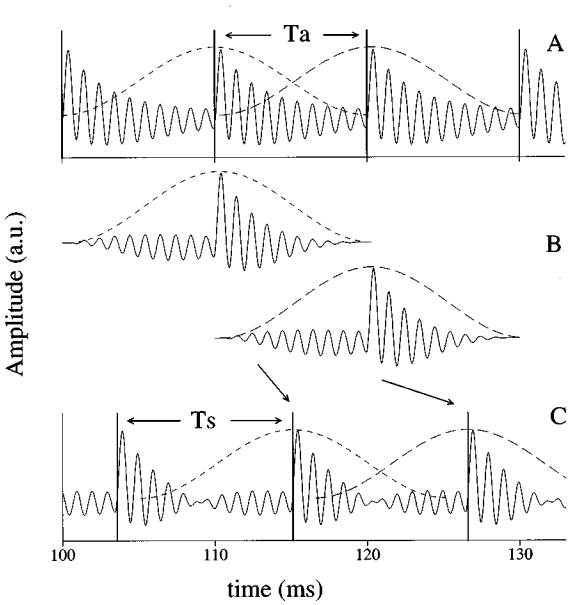

FIG. 1. Illustration of the PSOLA technique: Panel (a) shows the waveform of a synthetic 1000-Hz single-formant signal with a fundamental of 100 Hz. At the pitch-marker locations, indicated by thick vertical lines, the signal is decomposed by means of Hanning windowing. The interval between two pitch markers is indicated by T_a. Two segments are shown in panel (b). These segments are recombined by means of overlap-adding at the new pitch-marker positions indicated by thick vertical lines in panel (c). These pitch markers are regularly spaced at 11.5 ms, indicated by T_s, which gives a fundamental frequency of 87 Hz.

B. Terminology

In the experiments manipulation was investigated for signals having a constant $F0$. This means that the pitch markers in the decomposition and synthesis phase are positioned at regular intervals. These intervals will be denoted by T_a and T_s, respectively. Analogous with the fundamental frequency, we introduce the ''window rates'' $F_{wa} = 1/T_a$ and $F_{ws} = 1/T_s$. In the experiments the analysis window rate F_{wa} was fixed and F_{ws} was the experimental parameter. In what follows, experimental results will be presented as a function of ΔF given by

$$\Delta F = \frac{F_{ws} - F_{wa}}{F_{wa}} \times 100\%.$$

For positive and negative values of ΔF, the symbols ΔF^+ and ΔF^- will be used.

Under some experimental conditions the perceptual effects of pitch-marker location were investigated. The pitch-marker location will be denoted by the parameter ΔP. As will be described in Sec. II A 1, the single-formant signals are generated by exciting a formant filter with a regular pulse train. The parameter ΔP indicates the shift of the pitch markers relative to the excitatory pulses. This shift will be given as a percentage of T_a. In Fig. 1(a), for instance, the pitch markers coincide with the formant-filter excitations so that

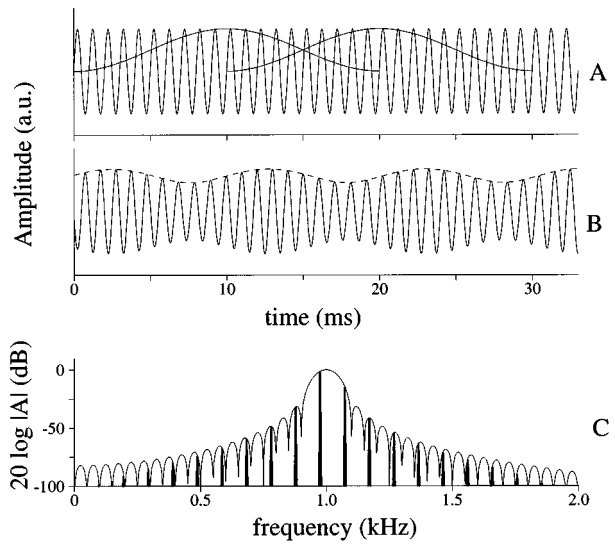

FIG. 2. A pure-tone signal of $f_c=1000$ Hz, shown in panel (a), is decomposed into segments by windowing the signal at a rate of $F_{wa}=100$ Hz. These segments are recombined at a rate of $F_{ws}=97.56$ Hz to synthesize the signal in panel (b). The dashed line represents the Hilbert envelope of the synthesized signal. Panel (c) shows the log-amplitude spectra of a single segment (thin solid line) and the synthesized signal (thick vertical lines).

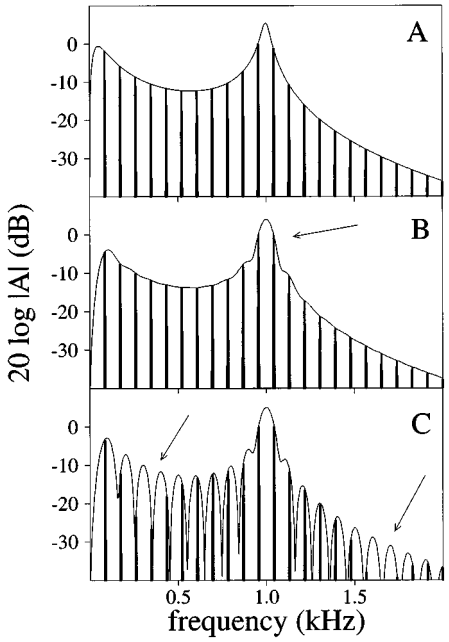

FIG. 3. Panel (a) shows the log-amplitude spectrum of a 1000-Hz single-formant signal with a fundamental of 87 Hz. The thin line represents the amplitude transfer function of the formant filter including pre-emphasis. Panel (b) shows the log-amplitude spectrum for a PSOLA-manipulated single-formant signal, shifted in fundamental frequency from 100 to 87 Hz. Parameter ΔP was set to 0%. The thin solid line now represents the log-amplitude spectrum of a single segment decomposed from the input signal. Arrows indicate frequency regions of maximal difference between the spectra in panels (a) and (b). Panel (c) shows the spectrum of a PSOLA-manipulated signal but now with ΔP set to 50%. Arrows indicate notches introduced in the log-amplitude spectrum.

$\Delta P=0\%$. Because the formant filter is minimum phase, the amplitude maxima of the signal in Fig. 1(a) are only slightly delayed relative to the maxima of the Hanning window. On the other hand, if $\Delta P=50\%$ the pitch markers are located *between* excitations of the formant filter. In that case maxima of the input signal and the Hanning windows are maximally misaligned.

C. Distortions in pure tones

First, we consider PSOLA manipulation of a single pure tone which is thought of as a component of a harmonic spectrum. Figure 2(a) depicts a pure tone of carrier frequency $f_c=1000$ Hz, assumed to be the tenth harmonic of a 100-Hz fundamental. After decomposition at intervals of $T_a=10$ ms and overlap–adding, the signal shown in Fig. 2(b) is synthesized where $\Delta F=-2.44\%$ ($F_{ws}=97.56$ Hz, $T_s=10.25$ ms). In contrast to the original pure tone, this signal shows amplitude modulation (AM) in its envelope and frequency modulation (FM) in its fine structure. For a sinusoidal input signal these two changes are the basic distortions introduced by PSOLA. Experimental results relating to the auditory sensitivity to these distortions will be presented in the Appendix. The AM of the envelope is partly caused by the fact that adjacent Hanning windows do not sum up to one if $T_a\neq T_s$. This can be compensated for by using a ''synthesis window.'' The perceptual relevance of using such a window will be discussed in Sec. III.

Alternatively, we can describe the distortions in the spectral domain. Time-domain multiplication (windowing) results in frequency-domain convolution of the spectra of the Hanning window and the pure tone (e.g., Rabiner and Schafer, 1978). The thin solid line in Fig. 2(c) depicts the log-amplitude spectrum of a single segment decomposed from the original pure tone of Fig. 2(a). The overlap–adding operation in synthesis, which extends the signal periodically in the time domain, is equivalent to *resampling* the (complex) spectrum of a single segment (Moulines and Laroche, 1995). The log-amplitude spectrum of the synthesized signal in Fig. 2(b) is shown by the line spectrum in Fig. 2(c). The spectral lines are harmonics of $F_{ws}=97.56$ Hz. For example, the strongest harmonic has a frequency of $10\times F_{ws}=975.6$ Hz. In other words, the introduction of AM and FM has a spectral counterpart in terms of the interaction of introduced components (Goldman, 1948).[2]

D. Distortions in single-formant signals

The experiments deal with the discrimination of PSOLA-manipulated and -unmanipulated single-formant signals. Such signals intrinsically have a harmonic structure so that the introduction of side components *per se* cannot be a cue for discrimination. In fact, cues may be changes in both spectral envelope and phase relations between harmonics. These changes will be illustrated below.

Figure 3(a) shows the log-amplitude spectrum of an unmanipulated single-formant signal with an $F0$ of 87 Hz, a formant frequency of 1000 Hz, and a formant bandwidth of 50 Hz. This spectrum also shows the effects of pre-emphasis applied to the formant signal (see Sec. II A 1). The corresponding phase spectrum (not shown here) is approximately linear except for a phase jump of π rad around the formant frequency.

Figure 3(b) shows the log-amplitude spectrum of a PSOLA-manipulated signal obtained by generating a 1000-Hz formant signal with an $F0$ of 100 Hz, decomposing it at $F_{wa}=100$ Hz, and resynthesizing it at $F_{ws}=87$ Hz. Here, ΔP is set to 0%. The Hanning-windowing operation has ''smeared out'' the spectral envelope: the bandwidth of the pronounced formant is increased to approximately F_{wa} Hz. The spectral slope, however, remains almost unaffected. Changes to the phase spectrum (not shown) are a phase shift of approximately $\pi/4$ rad for the two harmonics around the formant frequency. Figure 3(c) shows the spectrum of a signal synthesized with ΔP set to 50%. Its spectral envelope is clearly discontinuous which introduces pronounced notches in spectral envelope after resampling. The notch depth depends monotonically on ΔP. The corresponding phase spectrum (not shown) is discontinuous as well.

II. EXPERIMENTS

The main questions in these experiments are: (1) What are the thresholds for the discrimination of PSOLA-manipulated and -unmanipulated single-formant signals; (2) what is the influence of pitch-marker location on discrimination performance; and (3) how do the discrimination results relate to psychoacoustical models.

A. Method

1. Stimuli

For generation of the single-formant signals, a second-order digital resonator was implemented as proposed by Klatt (1980).[3] This filter was excited by a pulse train with an $F0$ of 100 or 250 Hz. The window rate F_{wa} was accordingly set to these values. Low-pass characteristics of natural voicing and high-pass radiation at the mouth opening, as described in Klatt (1980), were included as pre-emphasis. Formant frequencies f_r were 500, 1000, and 2000 Hz with -3-dB bandwidths of 50, 50, and 100 Hz, respectively.

As a baseline experiment, a minimal stimulus-uncertainty condition was investigated in which f_r was fixed and the overall level L was set to 70 dB SPL. To increase stimulus uncertainty, level roving between intervals was applied in the second condition. The level rove was uniformly distributed in the range ± 5 dB. As a third condition, the overall level L was fixed but the formant frequency f_r was roved uniformly over a range of $\pm 2\,\Delta f_r$. Here, Δf_r denotes one jnd in formant frequency for which Gagné and Zurek (1988) reported the following relation: $\Delta f_r = 0.079 f_r/\sqrt{Q}$, where Q is the Q factor of the formant filter. The range of f_r roving was within the range measured in a study by Pisoni (1980) in which subjects were instructed to ''reproduce'' steady-state synthetic vowels.

To investigate the perceptual effects of pitch-marker positioning, ΔP was set to 0% and 50% in experiment I. In experiment II, psychometric functions for ΔP were determined for two particular values of ΔF.

Stimuli were software generated on a Silicon Graphics Indigo workstation. The sampling frequency was 32 kHz. Apart from the built-in filters of the workstation, no additional anti-aliasing filtering was applied. Because the amplitude spectrum of the single-formant signals monotonically falls off to approximately -80 dB (relative to the formant peak) at the Nyquist frequency, no aliasing is to expected. After DA conversion signal levels were adjusted by means of analog attenuation. Stimuli were presented to the subject, seated in a soundproof booth, over Beyer DT 990 headphones. Subjects responded via a keyboard and received immediate feedback. Stimulus duration was 300 ms, the first and last 25 ms were ramped using a Hanning window. The interval separation was 200 ms.

2. Procedure

Psychometric functions were measured using a 3I3AFC odd-ball procedure with fixed levels of ΔF in each run. The odd-ball interval contained the PSOLA-manipulated single-formant signal. This signal was obtained by (1) generating a formant signal with an $F0$ of F_{wa} Hz; (2) decomposing this signal at a window rate of F_{wa} Hz; and (3) resynthesizing it at a rate of F_{ws} Hz. The reference intervals contained a single-formant signal generated directly with an $F0$ of F_{ws} Hz. For determination of the psychometric function, F_{ws} was varied according to

$$F_{ws}=\frac{1}{T_a+(n/4)}[\text{Hz}], \tag{1}$$

where $n = \pm 1$ ms, ± 2 ms, ± 3 ms, ...

Each run consisted of 15 trials. For each condition, i.e., a combination of ΔF, F_{wa}, and f_r, a total of five runs were performed of which the first run was omitted from the analysis. Each data point thus represents 60 trials. All conditions were measured once before the next set of runs was initiated. Mean values and standard deviations of the four runs are shown in the figures below. Instead of plotting percentage correct as a function of ΔF, the Pc values were converted to d' using a conversion table (MacMillan and Creelman, 1991).

3. Subjects

Three subjects (aged 25, 27, and 35) participated in the experiments. All subjects had normal pure-tone thresholds in quiet for the frequencies 500, 1000, and 2000 Hz. Unlike subject RK (the first author), subjects MB and KM had no or little experience in psychoacoustic listening experiments. All subjects performed experiments I and II for $f_r=1000$ Hz. Subjects KM and RK performed experiment I for $f_r=2000$ Hz. Results for $f_r=500$ Hz (experiment I) were obtained only for subject RK.

B. Experiment I: Influence of ΔF

1. Minimal stimulus uncertainty

Psychometric functions for minimal stimulus uncertainty are shown in the left-hand panels of Figs. 4–6. Figure 4 presents the data for $F_{wa}=100$ Hz and $f_r=1000$ Hz. Data points for $\Delta P=50\%$, indicated by filled squares, are generally far above the threshold $d'=1$ for all subjects. For $\Delta P=0\%$, however, the psychometric functions show a non-monotonic behavior. For all three subjects, subthreshold discrimination performance is found for $\Delta F=-16.66\%$,

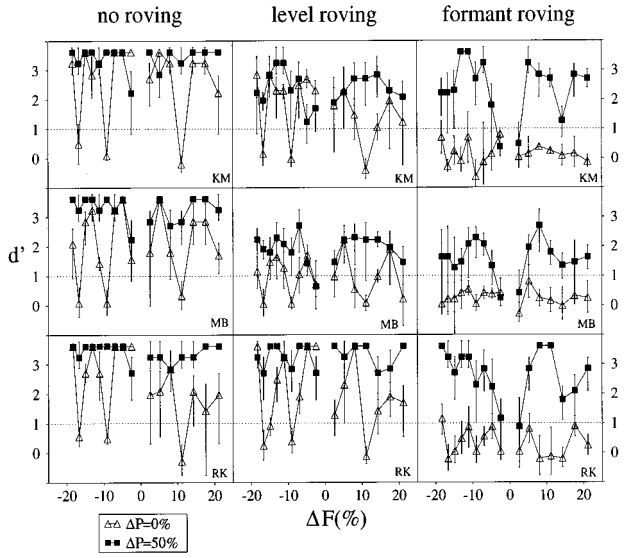

FIG. 4. Psychometric functions for discrimination of PSOLA-manipulated and unmanipulated single-formant signals with formant frequency $f_r=1000$ Hz and $F_{wa}=100$ Hz. Mean data for $\Delta P=0\%$ are shown by triangles, those for $\Delta P=50\%$ by filled squares. Standard deviations are indicated by vertical lines. Left-hand panels show results for the minimal-stimulus-uncertainty condition. Center panels show psychometric functions for the level-roving condition, and the right-hand panels data for roving of f_r.

-9.09%, and $+11.11\%$. These values correspond to values for T_s of 12, 11, and 9 ms, respectively, while T_a equals 10 ms. Because the 50-Hz formant bandwidth is rather small, it can be stated that each decomposed segment contains 20 periods of a 1000-Hz carrier (cf. Fig. 1). Setting T_s to an integer multiple of 1 ms, which is the period of the 1000-Hz carrier, thus results in an *in-phase* addition of the fine structure of adjacent windows. This results in minimal distortion of the temporal envelope of the signal. In spectral terms, setting T_s to an integer multiple of the carrier period results in a harmonic coinciding with the formant frequency, due to the resampling property of PSOLA.

Using the same line of reasoning for the case of

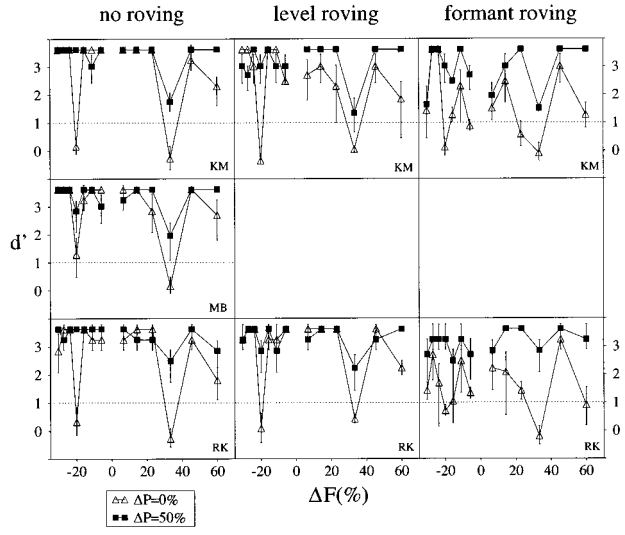

FIG. 5. Psychometric functions as in Fig. 4 but now for $f_r=1000$ Hz and $F_{wa}=250$ Hz.

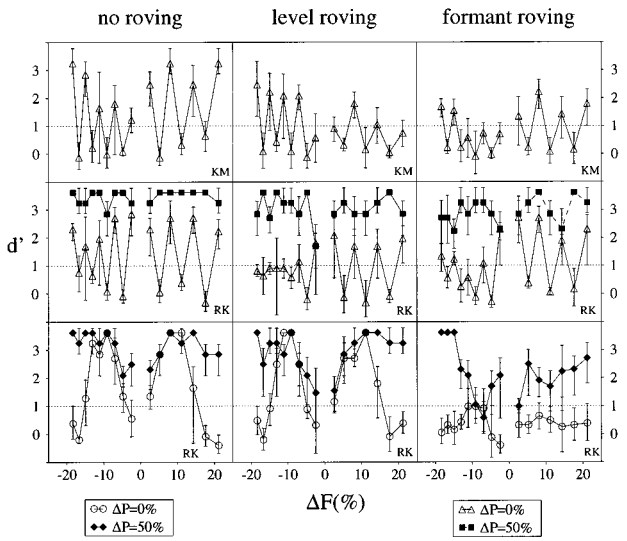

FIG. 6. Psychometric functions as in Figs. 4 and 5. Top and middle panels: psychometric functions for $f_r=2000$ Hz and $F_{wa}=100$ Hz. Bottom panels: psychometric function for $f_r=500$ Hz. Circles here are data for $\Delta P=0\%$, filled diamonds data for $\Delta P=50\%$.

$f_r=1000$ Hz and $F_{wa}=250$ Hz, subthreshold discrimination performance is predicted for $\Delta F=-20\%$ and $+33.33\%$. This is confirmed by the psychometric functions shown in the left-hand panels in Fig. 5. Note also that the data for other ΔF values show ceiling effects to even greater extent than the data in Fig. 4.

Data for the minimal stimulus-uncertainty conditions for $f_r=500$ and 2000 Hz are shown in the left-hand panels of Fig. 6 (subjects KM and RK only). The argumentation presented above also holds for these two formant frequencies. For $f_r=2000$ Hz, the general shapes of the psychometric functions are similar for both subjects, although the subjects are seen to have unequal difficulty in discrimination for ΔF^-.

2. Level roving

The center panels of Figs. 4–6 show psychometric functions for level roving. Starting with Fig. 4, i.e., $f_r=1000$ Hz and $F_{wa}=100$ Hz, it can be observed that discrimination performance is generally deteriorated relative to the minimal stimulus-uncertainty condition. Nevertheless, the general pattern of discrimination behavior is almost unaffected: The psychometric function for $\Delta P=50\%$ (squares) is almost always considerably above threshold. Moreover, the subthreshold data points for $\Delta P=0\%$ occur for the same ΔF values. Of all subjects, the performance of subject MB is seen to be affected most.

Level roving does not have a great influence on discrimination performance for $F_{wa}=250$ Hz and $f_r=1000$ Hz, as shown in Fig. 5. The middle panels of Fig. 6 show the psychometric functions for $f_r=2000$ and 500 Hz ($F_{wa}=100$ Hz). For $f_r=2000$ Hz, discrimination performance is reasonably affected, especially for ΔF^- for subject RK. On the other hand, performance for $f_r=500$ Hz is as good with level roving applied as without level roving.

3. Formant-frequency roving

The right-hand panels in Fig. 4 show that, for $f_r=1000$ Hz with $F_{wa}=100$ Hz and $\Delta P=0\%$, discrimination performance under f_r roving drops below $d'=1$ for *all* ΔF shifts. For $\Delta P=50\%$, performance is generally only moderately affected. A similar trend is observed for $f_r=500$ Hz (Fig. 6) but, here, performance is also deteriorated for $\Delta P=50\%$ for some values of ΔF. For $f_r=2000$ Hz, the alternating pattern is still observable for ΔF^+ if $\Delta P=0\%$. For ΔF^-, however, discrimination performance drops below threshold for almost all values. As is shown in the right panels of Fig. 5, roving of f_r has a moderate influence on performance for $F_{wa}=250$ Hz.

4. Discussion

The psychometric functions show a clear interaction between f_r, F_{wa}, and F_{ws}. The pattern of these functions is not greatly influenced by roving of overall level which also occurs in natural speech. Roving of formant frequency, on the other hand, can drastically affect performance in the sense that the distortions introduced by PSOLA apparently are no longer usable cues for discrimination. This suggests that the non-steady-state nature of natural speech may explain part of the success of PSOLA. Because setting ΔP to 50% provides strong and stable discrimination cues, the next experiment aims at determining discriminability as a function of ΔP.

C. Experiment II: Variation of the pitch-marker position

Psychometric functions as a function of ΔP were measured for $f_r=1000$ Hz and $F_{wa}=100$ Hz. Two values of the $F0$ shift were selected for which results for $\Delta P=0\%$ were below threshold: $\Delta F=-9.09\%$ and $+11.11\%$ (cf. Fig. 4). The parameter ΔP was varied in equal steps between -50% and 50% (note that these two values are identical for strictly periodic signals). Psychometric functions were obtained for the minimal stimulus-uncertainty conditions (all subjects) and for both roving conditions ($\Delta F=-9.09\%$, and subjects KM and RK only).

Figure 7 shows the data for $\Delta F=-9.09\%$ (squares) and $+11.11\%$ (circles) for the three stimulus-uncertainty conditions. The data in Fig. 7 do not show systematic differences for the two ΔF values. Also, the psychometric functions are seen to be symmetric around $\Delta P=0\%$. Thresholds are approximately reached at $|\Delta P|=25\%$, which means that pitch markers do not necessarily have to coincide exactly with either the filter excitation or the signal energy maximum. Moreover, these thresholds are reasonably stable under level and formant-frequency roving. The psychometric functions for subject KM become shallower with increasing stimulus uncertainty.

D. Model predictions

1. Intensity discrimination

Gagné and Zurek (1988) used an intensity-discrimination model (Florentine and Buus, 1981) to account for jnds in the resonance frequency of a single resonator. A

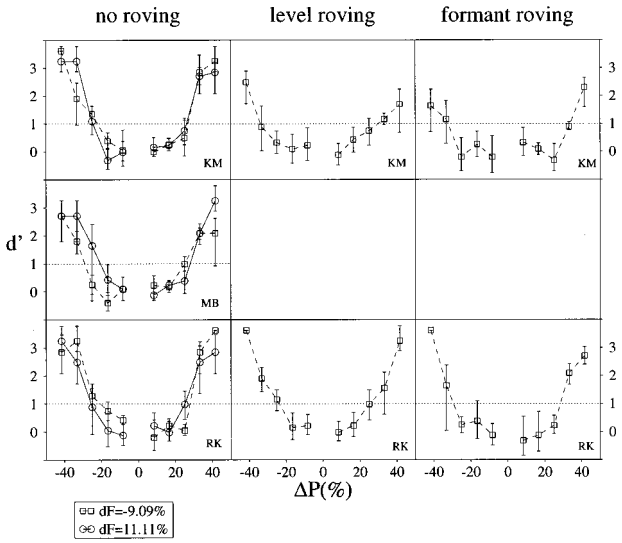

FIG. 7. Psychometric functions for $F_{wa}=100$ Hz and $f_r=1000$ Hz with ΔP as experimental parameter. Squares are data for $\Delta F=-9.09\%$, circles data for $\Delta F=+11.11\%$. Data for $\Delta P=0\%$ and $\pm 50\%$ have already been shown in Fig. 4.

model of this kind takes only spectral cues into account. The model is based on a channelwise determination of level differences between the excitation patterns of a reference and a signal. Channels here refer to critical bands. The model assumes that the partial sensitivity d'_i in channel i is proportional to the level difference $\Delta L_{E,i}$ between the two excitation patterns: $d'_i=k\cdot\Delta L_{E,i}$, where k is a constant which is the same for all channels. The overall sensitivity d' is derived from the partial sensitivities. In the single-band version of the model overall sensitivity d' is equal to the maximum of the partial sensitivities:

$$d'=\max_{i=1,N}(d'_i)=k\cdot D_{\max}, \tag{2}$$

where N is the number of channels. In the multiband version partial sensitivities are optimally combined (Durlach *et al.*, 1986):

$$d'=\left(\sum_{i=1}^{N} d'^{2}_i\right)^{1/2}=k\cdot D_{\text{sum}}. \tag{3}$$

Gagné and Zurek found that resonance-frequency jnds could be best described by the single-band version of the model. In the present study both the single- and the multi-band model were implemented as a Gammatone filterbank (Patterson *et al.*, 1987). Simulation of absolute hearing threshold was included by adding an ''internal noise'' value to the power estimate at the output of each filter (cf. Moore and Glasberg, 1987).

According to formulas 2 and 3, d' is linearly related to $D_{\max}$ or D_{sum}. The predictive power of the models can thus be investigated by performing a linear regression on the experimental d' data in dependence on either $D_{\max}$ or D_{sum}. The regression equations were forced to intersect with the origin. As a measure of goodness of fit, the amount of explained variance, as expressed by the square of the correlation coefficient r, will be used.

TABLE I. For both intensity-discrimination models, the square of the correlation coefficient of the linear regression, r^2, is tabulated for each of the subjects. Here, the ΔP experimental data for the minimal stimulus-uncertainty condition are used.

	Single band	Multiband
KM	0.77	0.84
MB	0.78	0.82
RK	0.74	0.81

First, the data of ΔP experiment II were used for finding the slopes k of the linear regression equations, for each subject individually. The minimal stimulus-uncertainty data from Fig. 7 for both values of ΔF were used for this regression. Data points were discarded if $d' \geqslant 3.62$, i.e., $Pc \geqslant 99\%$. The linear regression results, in terms of r^2, are presented in Table I. For all subjects, the multi-band model yields the highest value of r^2. Differences between the two models are, however, small. All regression slopes are significantly different from zero at the $p<0.0001$ level. The slopes k for the multi-band model are: 0.18, 0.15, and 0.17 for subjects KM, MB, and RK, respectively. The threshold value for D_{sum}, yielding $d'=1$, is thus approximately equal to 6 dB. This value is a factor 2.5 higher than the value reported in Gagné and Zurek (1988). For the single-band model, the slopes k are 0.31, 0.24, and 0.28, respectively. At threshold $D_{\text{max}} \simeq 3.5$ dB, which is also a factor 2.5 higher than the value reported by Gagné and Zurek.

Second, the data of ΔF experiment I were used for linear regression for D_{sum}. Here again, only the data for the minimal stimulus-uncertainty conditions (left-hand panels in Figs. 4–6) were used, with $\Delta P=0\%$. The results are listed in Table II. For $F_{wa}=100$ Hz, r^2 is in the range 0.4–0.6. The slopes k are similar across subjects and are approximately 1, 0.8, and 1.4 for $f_r=500$, 1000, and 2000 Hz, respectively. The threshold value for D_{sum} yielding $d'=1$ is thus approximately 1 dB, which is clearly at variance with the results for the ΔP experiment. For $F_{wa}=250$ Hz, however, k is approximately equal to 0.16, which is in good agreement with the slope found for the ΔP experiment. The high p levels, $p>0.1$, for subjects KM and MB are probably due to the small number of data points resulting from ceiling effects in the ΔF experiment. As nearly all data points were far above threshold for $\Delta P=50\%$, the corresponding r^2 values did not exceed 0.3 (not listed in Table II).

2. Modulation discrimination

This model is based on the discrimination of amplitude-modulation depth in the envelope of a single auditory-filter output. The auditory filter was simulated by a single Gammatone filter having a bandwidth of 1 ERB. The center frequency f_{cf} was varied over the range $[f_r - F_{WA}, f_r + F_{WA}]$, simulating off-frequency listening, in order to find the maximum difference between reference and signal. The maximum distances were mainly observed for filters centered at the boundaries of the f_{cf} range. The modulation indices M_{ref} and M_{sig} were calculated at the output of the filter.[4] The model is based on the assumption that sensitivity d' is governed by

$$d' = k \cdot |M_{\text{ref}}^2 - M_{\text{sig}}^2| = k \cdot D_{\text{mod}}, \tag{4}$$

where k is some constant. Moore and Sek (1992) found that, for low modulation rates (below 10 Hz), *detection* sensitivity was linearly related to the square of the modulation index. Wakefield and Viemeister (1990) used sinusoidally amplitude-modulated (SAM) noise and found almost linear relations between d' and $M_{\text{ref}}^2 - M_{\text{sig}}^2$. Because M_{ref}^2 may be smaller than M_{sig}^2 for the present signals, the absolute value of the difference was taken.

TABLE III. Values of r^2 for linear regression on the d' data of the ΔF experiment using the modulation-discrimination model. Only data for $F_{wa}=100$ Hz are shown. Significance levels p are indicated as in Table II.

f_r (Hz)	500	1000	2000
KM		0.52**	0.69***
MB		0.35*	
RK	0.33*	0.59**	0.92***

Table III shows the r^2 values for linear regression of D_{mod} on the experimental d' data of the ΔF experiment ($F_{wa}=100$ Hz and $\Delta P=0\%$ only). For $f_r=1000$ Hz and $\Delta P=0\%$, the slope k is found to be approximately 7 for all subjects. This corresponds to a modulation-discrimination threshold of 0.14 for D_{mod}. The explained variance for subject MB, however, is rather low. For $f_r=2000$ Hz, slope k is about 4 so that the threshold would be at $D_{\text{mod}}=0.25$. These D_{mod} values are in reasonable agreement with the data reported in Wakefield and Viemeister (1990) for SAM noise, provided M_{ref} is large, i.e., $10 \log (M_{\text{ref}}^2) \geqslant -5$ dB. For the present signals, M_{ref} is indeed in this range.

III. DISCUSSION

Although not explicitly verified experimentally, $|\Delta F|$ shifts as small as approximately 2% may lead to detectable distortions, as can be inferred from the region around $\Delta F=0\%$ in the psychometric functions in Figs. 4, 5, and 6. This finding agrees with the results presented in the Appendix for manipulation of pure tones. Remarkably, the psychometric functions for minimal stimulus uncertainty and level roving,

TABLE II. Values of r^2 for linear regression on the d' data of the ΔF experiment using the multiband intensity-discrimination model. Significance levels p, indicating the probability that the slope of the linear regression equation is equal to zero, are indicated as follows: $*p<0.05$, $**p<0.01$, $***p<0.001$.

f_r (Hz)	500	1000	2000	1000 ($F_{wa}=250$ Hz)
KM		0.48*	0.45**	0.54
MB		0.56**		0.55
RK	0.61**	0.54**	0.40**	0.79**

provided $\Delta P = 0\%$, were nonmonotonic, revealing a clear interaction between f_r, F_{wa}, and F_{ws}. This finding is not in agreement with the intuitive expectation that distortions are more easily detectable for larger shifts in $F0$. We will try to explain the discrimination results in terms of spectral and temporal cues by first comparing the present results with data from the literature and then discussing our modeling results.

A. Comparison with the literature

As a result of PSOLA manipulation with $\Delta P = 0\%$, changes in the intensity of spectral components, in combination with phase shifts, occur in the spectral region of f_r, as was illustrated in Fig. 3. Changes in component intensities also occur due to changes in formant frequency. A number of studies (e.g., Gagné and Zurek, 1988; Kewley-Port and Watson, 1994; Lyzenga and Horst, 1995; Sommers and Kewley-Port, 1996) have explained formant-frequency jnd's in terms of profile analysis, i.e., in terms of discrimination of spectral shape (Richards *et al.*, 1989; Zera *et al.*, 1993). With minimal stimulus uncertainty and for $F_{wa} = 100$ Hz in the present study (absolute), component-level differences between signal and reference maximally amount to 2.5, 2.5, and 1.5 dB for $f_r = 500$, 1000, and 2000 Hz, respectively. These values are valid for the range of ΔF investigated in the experiments. The lower value for $f_r = 2000$ Hz is a consequence of the larger formant bandwidth of 100 Hz.

Thresholds for the detection of level increments of single components of a complex tone of equal-amplitude harmonics were reported by Zera *et al.* (1993). For complex tones consisting of 60 harmonics of 100 Hz, level-increment thresholds for harmonics at 500, 1000, and 2000 Hz were found to be approximately 2, 2.5, and 4 dB, respectively. This means that for $f_r = 500$ and 1000 Hz, the level changes of individual harmonics due to PSOLA manipulation would be near detection threshold. For $f_r = 2000$ Hz, level changes would be below threshold. The psychometric functions in Figs. 4 and 6, however, showed that discrimination sensitivity generally was above $d' = 2$. For the fifth harmonic of 200 Hz, on the other hand, Henn and Turner (1990) and Zera *et al.* (1993) reported level-increment thresholds of 2 dB. For $F_{wa} = 250$ Hz and $f_r = 1000$ Hz, spectral-envelope level differences are maximally 10 dB so that level differences of single components were potential cues for discrimination.

Instead of just a single harmonic, however, the intensities of a number of harmonics are changed both as a result of PSOLA manipulation and by changing the formant frequency. Sommers and Kewley-Port (1996) found that salient cues for formant-frequency jnds were mediated by the level changes of the three harmonics closest to the formant frequency. Using an excitation pattern model (Moore and Glasberg, 1987), they also found that formant-frequency jnds under different conditions resulted in more or less constant level differences between excitation patterns. Sommers and Kewley-Port (1996) only investigated formants at 500 and 1350 Hz with an $F0$ of 200 Hz, so that harmonics around the formant frequencies were likely to be resolved. Particularly for $f_r = 2000$ Hz and $F_{wa} = 100$ Hz in the present study, harmonics are unresolved so that temporal cues may have been used for discrimination. Lyzenga and Horst (1995), who used formantlike signals around 2000 Hz with an $F0$ of 200 Hz, also proposed a temporal mechanism, at least for part of their jnd data.

Roving of the *overall* stimulus level affected discrimination performance only to a small degree. This finding is in agreement with results presented by Farrar *et al.* (1987) on formant-frequency discrimination using noise sources as input to the Klatt synthesizer. Because the overall level of the intervals was normalized in the minimal stimulus condition, differences in loudness between signal and reference may have been a cue (cf. Lyzenga and Horst, 1995). Taking into account the rather small spectral-envelope differences mentioned above, however, it is more likely that discrimination performance under level roving is affected by the increase in distracting stimulus uncertainty.

The present results show that f_r roving can affect discrimination performance considerably. Roving of f_r results in spectral-envelope level differences near f_r, not only between signal and references, but also between references. The distribution of level differences has a standard deviation of approximately 4 dB for all f_r values and bandwidths under consideration. This value is of the same order of magnitude as the spectral-envelope differences introduced by PSOLA for $F_{wa} = 100$ Hz (see above). This means that if the harmonics around f_r are resolved, excitation-pattern differences between the two references are comparable to the differences between signal and references due to PSOLA. Discrimination performance can then be expected to drop below $d' = 1$, as observed for $f_r = 500$ and 1000 Hz. For $F_{wa} = 250$ Hz, level differences due to PSOLA can exceed those due to f_r roving (see above) so that discrimination is expected to be, at most, moderately influenced, which is in agreement with the experimental data. If, on the other hand, components are unresolved, as for $f_r = 2000$ Hz and $F_{wa} = 100$ Hz, the differences in the phase spectra between signal and references may become a cue. In other words, the effect of (in)coherent addition of subsequent segments is preserved in peripheral filtering. For ΔF^+, roving of f_r did indeed not deteriorate discrimination performance. It is not clear, however, why performance dropped below $d' = 1$ for ΔF^-.

In an additional, informal experiment, the phases of the components of the single-formant signal were randomized. For $f_r = 500$ Hz, phase randomization had only a small effect on discrimination performance. This was also observed for $f_r = 1000$ Hz with $F_{wa} = 250$ Hz. For $f_r = 1000$ and 2000 Hz ($F_{wa} = 100$ Hz), however, discrimination performance was below $d' = 1$. This provides additional evidence for the hypothesis that, for the latter two conditions, temporal cues played a dominant role.

In experiment II, the detection threshold was found to be $|\Delta P| \simeq 25\%$. The spectral ''notch depth'' at this value of $|\Delta P|$ is approximately 3 dB. Turner and Van Tasell (1984) found comparable thresholds for a notch with linear flanks on a dB scale, centered at 2120 Hz within the spectrum of a synthetic vowel with 120-Hz fundamental. If intensity discrimination determines detectability, however, then lower ΔP thresholds are to be expected if the components in the notches are resolved. The results of informal tests for $F_{wa} = 250$ Hz confirmed this expectation: with minimal

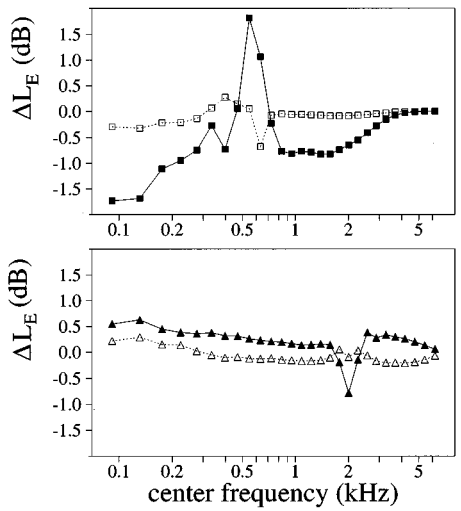

FIG. 8. Illustration of excitation-pattern level differences between unmanipulated and PSOLA-manipulated single-formant signals. The top panel shows the level differences $\Delta L_{E,i}$ for $f_r=500$ Hz. Filled squares indicate level differences for $\Delta F=-11.1\%$, open squares for $\Delta F=-2.4\%$. The corresponding values of D_{sum} are 1.9 and 0.5 dB, respectively. The bottom panel shows level differences for $f_r=2000$ Hz, where the filled and open triangles indicate differences for $\Delta F=8.1\%$ and 11.1%, respectively. For these ΔF values, D_{sum} is 0.8 and 0.5 dB, respectively.

stimulus uncertainty, ΔP thresholds were considerably smaller than 25%.

B. Models

In contrast to the findings of Gagné and Zurek (1988), the best results for the intensity-discrimination model were obtained here for the multiband version, although the differences between the single- and multiband model were small. The multiband model could describe the data for the ΔP experiment reasonably well, which suggests that discrimination was based on profile analysis. In the case of the ΔF experiment, the descriptive power of this model depended on whether harmonics around f_r were resolved by peripheral filtering. For both conditions in which harmonics were resolved, i.e., $f_r=500$ Hz ($F_{wa}=100$ Hz) and $f_r=1000$ Hz ($F_{wa}=250$ Hz), reasonable r^2 values were obtained. For the latter condition, the regression slopes for the ΔP and ΔF data were almost identical. For $f_r=1000$ Hz and $F_{wa}=100$ Hz, where harmonics 9–11 around f_r are only just resolved, the r^2 values were reasonable but the regression slope was much smaller than for the ΔP data. For $f_r=2000$ Hz and $F_{wa}=100$ Hz, where harmonics 19–21 are unresolved, r^2 values were lowest.

Figure 8 illustrates excitation-pattern differences between a PSOLA-manipulated signal and the unmanipulated reference for $f_r=500$ (top panel) and 2000 Hz (bottom panel). For both formant frequencies, ΔF conditions for which performance was above or below $d'=1$ are indicated by the filled and open symbols, respectively. As the data in Fig. 8 suggest, excitation-pattern differences for above-threshold stimuli are larger if the harmonics around f_r are resolved (top) than for unresolved harmonics (bottom).

For the modulation-discrimination model, r^2 values were highest for $f_r=2000$ Hz and lowest for $f_r=500$ Hz, as

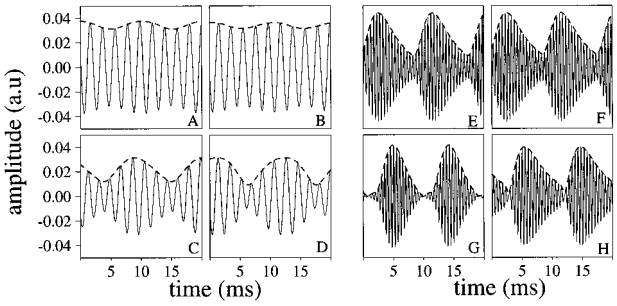

FIG. 9. Illustration of AM differences in the output of Gammatone filters. Panels A–D show portions of the output waveforms of a filter centered at 500 Hz ($f_r=500$ Hz): panel A shows the waveform for $\Delta F=-2.4\%$ for the PSOLA-manipulated signal, panel B for the unmanipulated reference. The modulation-depth measure D_{mod} is equal to 0.003. Panels C and D show the corresponding output waveforms for $\Delta F=-11.1\%$ ($D_{\text{mod}}=0.04$). Panels E–H show output waveforms of a filter centered at 2000 Hz ($f_r=2000$ Hz); $\Delta F=11.1\%$ in panels E and F ($D_{\text{mod}}=0.05$) and $\Delta F=8.1\%$ in panels G and H ($D_{\text{mod}}=0.7$).

would be expected on the basis of unresolved and resolved harmonics, respectively. Figure 9 illustrates this expectation by showing, for the same ΔF values as in Fig. 8, the output of Gammatone filters centered at the formant frequencies 500 and 2000 Hz. In the experiments the ΔF value of the top panels resulted in performance below $d'=1$. Accordingly, for both formants the difference in modulation depth is small. The ΔF value of the bottom panels resulted in above-threshold performance. Only for $f_r=2000$ Hz, however, a substantial difference in modulation depth can be observed.

As the r^2 values were moderate for both models for $f_r=1000$ Hz and $F_{wa}=100$ Hz, a multicue model might be reasonable. This was not verified, however, because we judged the amount of experimental data insufficient for performing multiple regressions reliably.

C. Synthesis window

Some of the effects of envelope modulation introduced by PSOLA (cf. Fig. 2) can be canceled by applying a so-called ''synthesis window.'' Such a window corrects for the fact that adjacent Hanning windows do not add up to one if $T_s \neq T_a$. A simple realization of such a window is to calculate the temporal envelope of the adjacent Hanning windows, spaced at intervals of T_s ms. By taking the reciprocal of this envelope and multiplying it with the PSOLA-manipulated (speech) signal, the degree of AM of the latter signal is reduced. Such an operation, however, does not correct for the AM introduced by out-of-phase addition of the fine structures of adjacent segments.

Experimental results for $f_r=1000$ and 2000 Hz, obtained by including the synthesis window as described above, are shown in Fig. 10 by the open symbols ($F_{wa}=100$ Hz with level roving, subject RK only). The filled symbols indicate corresponding data from experiment I. The synthesis window seems to cancel the ceiling effects for $f_r=1000$ Hz, although the fact that performance is still above $d'=2$ suggests that this effect is perceptually less relevant. Even in the case of $f_r=2000$ Hz, a condition for which temporal cues

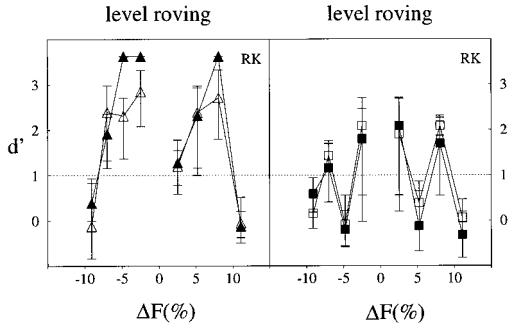

FIG. 10. Psychometric functions obtained by including a synthesis window (open symbols) and by the standard PSOLA operations (filled symbols, data already shown in Figs. 4 and 6). Data for f_r=1000 Hz are shown in the left-hand panel, data for f_r=2000 Hz in the right-hand panel. In both cases, level roving was applied.

presumably dominate detection performance, the two psychometric functions are basically identical.

D. Natural speech

In order to understand the perceptual effects of PSOLA manipulation of natural speech, the following aspects should, in our view, be additionally investigated. First of all, natural speech is generally characterized by the presence of at least 2 to 3 formants, at least in vowels. The use of multiple-formant signals may inform about the way in which cues occurring in several frequency regions are combined. Second, it should be investigated to what extent the detectability of distortions is influenced by fluctuations in both spectral content and $F0$. These fluctuations can be either of a random nature (e.g., jitter) or more deterministic (e.g., formant and $F0$ trajectories). In addition, the perceptual consequences of errors in $F0$ estimation in natural speech, leading to incorrect pitch-marker positioning, should be investigated. Third, the present experiments were performed under well-controlled acoustical conditions. The amplitude and phase transfer characteristics of (normal) playback rooms, however, will in their turn affect stimulus characteristics. It is conceivable that, under such listening conditions, the perceptual tolerance for the distortions introduced by PSOLA is actually increased.

IV. CONCLUSIONS

(1) Discrimination thresholds as a function of ΔF (the shift in fundamental frequency) for PSOLA-manipulated and -unmanipulated single-formant signals are found to be low: $|\Delta F| \leqslant 2\%$. Moreover, the psychometric functions reported here typically show an interaction between the formant and fundamental frequency.

(2) Roving of overall level does not seem to greatly affect discrimination performance as a function of ΔF. Roving of the formant frequency does impair performance: for formants at 500 and 1000 Hz (100-Hz fundamental), performance drops below $d'=1$ for all ΔF values tested. For a fundamental of 250 Hz, performance seems to be only moderately influenced by formant roving.

(3) Discrimination thresholds as a function of ΔP (the pitch-marker location) reported here are approximately a quarter of the fundamental period. The discrimination cues that occur due to incorrect positioning of the pitch markers seem to be robust under level and formant frequency roving. These findings apply to signals with a fundamental of 100 Hz; ΔP thresholds for higher $F0$ values are expected to be lower.

(4) The discrimination data as a function of ΔP can be described well with an intensity-discrimination model. This model can also account moderately well for the experimental data as a function of ΔF, in the case of resolved harmonics around the formant frequency (e.g., a formant at 1000 Hz with a 250-Hz fundamental). The modeled discrimination sensitivities, however, generally differ across the ΔP and ΔF conditions. For unresolved harmonics, such as for a 2000-Hz formant and a 100-Hz fundamental, the modulation-discrimination model matches the experimental data reasonably well. These findings are in agreement with the psychoacoustical notion of different modes of processing for resolved and unresolved harmonics.

(5) As for natural speech, distortions introduced to signals with higher fundamental frequencies are expected to be more easily detectable [see conclusions (2) and (3)]. In the case of low fundamental frequencies, the occurring phase cues are often subtle and may not be stable under different playback conditions.

ACKNOWLEDGMENTS

The authors thank Dik Hermes, Adrian Houtsma, Andrew Oxenham, Steven van de Par, Raymond Veldhuis, Rob Maher, and an anonymous reviewer for critically reading earlier versions of this article and for providing useful suggestions for improvement.

APPENDIX: PURE TONES

The main question of this baseline experiment was to what extent the basic distortions described in Sec. I C are detectable by the human auditory system. Pure tones with carrier frequencies f_c=500, 1000, and 2000 Hz were PSOLA manipulated. The carriers were thought of as harmonics of a fundamental of 100 or 250 Hz. In order to determine the detectability of the introduced side components, the references were unmanipulated pure tones having the same frequency as the strongest component in the manipulated-tone spectrum [cf. Fig. 2(c)]. Instead of taking all side component into account, the results presented below were obtained for signals consisting of the three strongest spectral components only. These results were compared with results for ''real'' PSOLA-manipulated tones and did not differ considerably. Three overall levels L were used: 45, 60, and 75 dB SPL in combination with a level rove uniformly distributed between -5 and $+5$ dB. Stimulus characteristics such as duration and stimulus generation were the same as described in Sec. II A 1.

A two-down, one-up 3IFC adaptive procedure was used in which ΔF was varied adaptively for the determination of discrimination thresholds. After a learning phase, three measurements for each condition were collected whose mean and

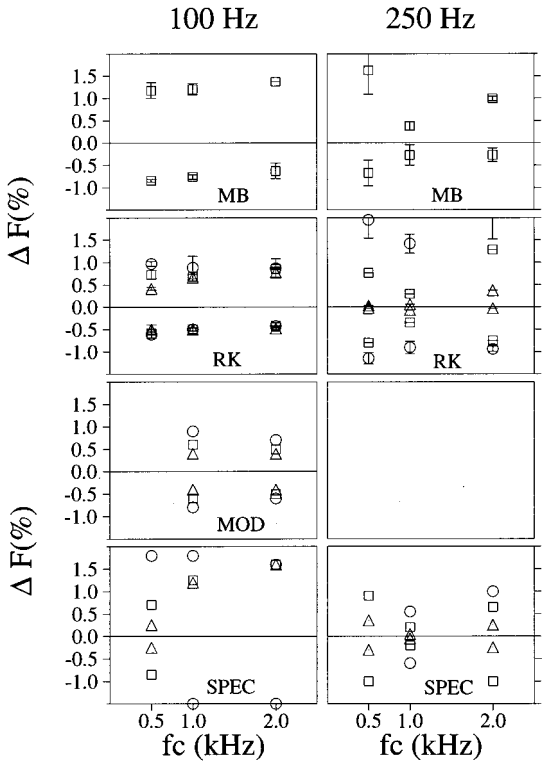

FIG. A1. Detection thresholds for subjects MB and RK for ΔF^+ and ΔF^- for the manipulation of pure tones. Left-hand panels give the data for $F_{wa}=100$ Hz, right-hand panels those for 250 Hz. Data for $L=45$ dB SPL are shown by circles, those for 60 dB SPL by squares, and those for 75 dB SPL by triangles. Standard deviations are indicated by vertical lines. Threshold predictions on the basis of a modulation-detection model are denoted by MOD. Predicted thresholds using a spectral masking model are marked SPEC.

standard deviation will be presented below. Two subjects (MB and RK) participated in this experiment.

Figure A1 presents both the ΔF thresholds for subjects MB and RK and predictions from two models (the models are different from the models of experiments I and II, see below). Squares indicate data for $L=60$ dB SPL (both subjects) and circles and triangles for $L=45$ and 75 dB SPL, respectively (subject RK only). Generally, thresholds for both subjects are low: $|\Delta F| \leqslant 2\%$. Thresholds for ΔF^- tend to be lower than for ΔF^+. Carrier frequency does not greatly influence thresholds for $F_{wa}=100$ Hz but does have an effect for $F_{wa}=250$ Hz. Likewise, level does affect thresholds for $F_{wa}=100$ Hz, except for $f_c=500$ Hz, but influences thresholds for $F_{wa}=250$ Hz.

In the spectral masking model (SPEC), the detection of the side components is determined by their masked threshold in the presence of the much stronger center component [cf. the ''No Summation Model'' of Hartmann and Hnath (1982)]. The masked thresholds were estimated using the data in Schöne (1979).[5] The modulation-detection model (MOD) is based on determining[6] the AM and FM indices of the PSOLA-manipulated pure tone as a function of ΔF. As in Zwicker (1952), threshold predictions were only derived for $F_{wa}=100$ Hz, with $f_c=1000$ or 2000 Hz (where the ''Phasengrenzfrequenz'' is approximately 80 and 140 Hz, respectively). Although the signals used actually had mixed modulation (Hartmann and Hnath, 1982; Moore and Sek, 1992), the lowest prediction based on detection of either AM or FM was taken.

In the case of resolved harmonics, i.e., for $f_c=1000$ and 2000 Hz with $F_{wa}=100$ Hz (harmonics 9–11 and 19–21, respectively), the predictions based on modulation detection are in reasonable agreement with the experimental data. The predictions based on the spectral masking model are less accurate, especially for ΔF^-, with the possible exception of $f_c=500$ Hz. For conditions with resolved harmonics (i.e., $f_c=500$, 1000, and 2000 Hz with $F_{wa}=250$ Hz, and $f_c=500$ Hz with $F_{wa}=100$ Hz), the spectral-masking model predictions are qualitatively similar to the experimental data, also showing level dependency. The actual predicted thresholds, however, do not exactly match the experimental data, especially for $L=45$ dB SPL.

[1]Although a frequency-domain (FD-PSOLA) variant has also been proposed, the time-domain version (TD-PSOLA) has been commonly preferred due to its computational efficiency.

[2]Strictly speaking, this only applies if the pure tone is a harmonic of F_{wa}.

[3]The implementation described in Klatt (1980) is based on a sample rate of 10 kHz. Cox *et al.* (1989) address the issue of using other sample rates, such as 32 kHz used here, which leads to differences in spectral envelope. They propose to introduce additional poles in the resonance-filter transfer function to compensate for the high-frequency attenuation. In the present study no compensation is taken into account because just a single formant is simulated (the high-frequency mismatch is more severe for multiple formants). Nevertheless, the spectral difference at 5 kHz between a signal generated at 10 kHz and at 32 kHz amounts to 10 dB. Around the formant frequency, differences are within 0.5 dB.

[4]Because the AM in the auditory filter output generally was not sinusoidal, the modulation index M was calculated:

$$M=\frac{\sqrt{2}\sigma_e}{m_e},$$

where σ_e and m_e are the standard deviation and average of the envelope of the output, respectively. The envelope is obtained by calculating a discrete Hilbert Transform. For an unmanipulated sinusoid of amplitude 1, $m_e=1$ but $\sigma_e=0$, so that $M=0$. For a 100% amplitude-modulated sinusoid of amplitude 1, $\sigma_e=1/\sqrt{2}$ and $m_e=1$, so that $M=1$, as expected.

[5]Predictions for spectral masking are based on Fig. 3 in Schöne (1979).

[6]Visual inspection showed that, for the range of ΔF used here, both the envelope and the instantaneous frequency were modulated in a sinusoidal fashion. The AM index m and FM index $\Delta f/f_{\text{mod}}$ were therefore calculated using their definition in Zwicker (1952).

Allen, J. B., and Rabiner, L. R. (**1977**). ''A unified approach to short-time Fourier analysis and synthesis,'' Proc. IEEE **65,** 1558–1564.

Cox, N. B. , Ito, M. R., and Morrison, M. D. (**1989**). ''Technical considerations in computation of spectral harmonics-to-noise ratios for sustained vowels,'' J. Speech Hear. Res. **32**, 203–218.

Durlach, N. I., Braida, L. D., and Ito, Y. (**1986**). ''Towards a model for discrimination of broadband sounds,'' J. Acoust. Soc. Am. **80,** 63–72.

Farrar, C. L., Reed, C. M., Ito, Y., Durlach, N. I., Delhorne, L. A., Zurek, P. M., and Braida, L. D. (**1987**). ''Spectral-shape discrimination. I. Results from normal hearing listeners for stationary broadband noises,'' J. Acoust. Soc. Am. **81,** 1085–1092.

Flanagan, J. L. and Saslow, M. G. (**1958**). ''Pitch-discrimination for synthetic vowels,'' J. Acoust. Soc. Am. **30,** 435–442.

Florentine, M., and Buus, S. (**1981**). ''An excitation-pattern model for intensity discrimination,'' J. Acoust. Soc. Am. **70,** 1646–1654.

Gagné, J., and Zurek, P. M. (**1988**). ''Resonance-frequency discrimination,'' J. Acoust. Soc. Am. **83,** 2293–2299.

Goldman, S. (**1948**). *Frequency Analysis, Modulation and Noise* (McGraw-Hill, New York).

Hartmann, W. M., and Hnath, G. M. (**1982**). ''Detection of mixed modulation,'' Acustica **50,** 297–312.

Henn, C. C., and Turner, C. W. (**1990**). ''Pure-tone increment detection in harmonic and inharmonic backgrounds,'' J. Acoust. Soc. Am. **88,** 126–131.
Kewley-Port, D., and Watson, C. S. (**1994**). ''Formant-frequency discrimination for isolated English vowels,'' J. Acoust. Soc. Am. **95,** 485–496.
Klatt, D. H. (**1973**). ''Discrimination of fundamental frequency contours in synthetic speech: Implications for models of pitch perception,'' J. Acoust. Soc. Am. **53,** 8–16.
Klatt, D. H. (**1980**). ''Software for a cascade/parallel formant synthesizer,'' J. Acoust. Soc. Am. **67,** 971–995.
Klatt, D. H. (**1982**). ''Predictions of perceived phonetic distance from critical-band spectra: A first step,'' in *Proc. IEEE International Conference on Acoustics, Speech, and Signal Processing*, Paris (IEEE, New York), Vol. 2, pp. 1278–1281.
Lyzenga, J., and Horst, J. W. (**1995**). ''Frequency discrimination of bandlimited harmonic complexes related to vowel formants,'' J. Acoust. Soc. Am. **98,** 1943–1955.
Ma, C., Kamp, Y., and Willems, L. F. (**1994**). ''A Frobenius norm approach to glottal closure detection from the speech signal,''IEEE Trans. Speech Audio Process. **2**, 258–265.
MacMillan, N. A., and Creelman, C. D. (**1991**). *Detection Theory: A Users Guide* (Cambridge U.P., New York).
Moore, B., and Glasberg, B. (**1987**). ''Formulae describing frequency selectivity as a function of frequency and level, and their use in calculating excitation patterns,'' Hearing Res. **28**, 209–225.
Moore, B. C. J., and Sek, A. (**1992**). ''Detection of combined frequency and amplitude modulation,'' J. Acoust. Soc. Am. **92,** 3119–3131.
Moulines, E., and Charpentier, F. (**1990**). ''Pitch-synchronous waveform processing techniques for text-to-speech synthesis using diphones,'' Speech Commun. **9**, 453–467.
Moulines, E., and Laroche, J. (**1995**). ''Non-parametric techniques for pitch-scale and time-scale modification of speech,'' Speech Commun. **16**, 175–205.
Patterson, R. D., Nimmo-Smith, I., Holdsworth, J., and Rice, P. (**1987**). ''An efficient auditory filterbank based on the gammatone function,'' in *Appendix B of SVOS Final Report: The Auditory Filterbank*, APU report 2341.
Pisoni, D. B. (**1980**). ''Variability of vowel formant frequencies and the quantal theory of speech: A first report,'' Phonetica **37**, 285–305.
Rabiner, L. R., and Schafer, R. W. (**1978**). *Digital Processing of Speech Signals* (Prentice-Hall, Englewood Cliffs, NJ).
Richards, V. M., Onsan, Z. A., and Green, D. M. (**1989**). ''Auditory profile analysis: Potential pitch cues,'' Hearing Res. **39**, 27–36.
Roads, C. (**1988**). ''Introduction to granular synthesis,'' Comput. Music. J. **12**, 11–13.
Roucos, S., and Wilgus, A. (**1985**). ''High quality time-scale modification for speech,'' in *IEEE ICASSP-85*, Vol. 2, pp. 493–496.
Schöne, P. (**1979**). ''Mithörschwellen–Tonheitsmuster maskierender Sinustöne,'' Acustica **43,** 197–204.
Smits, R., and Yegnanarayana, B. (**1995**). ''Determination of instants of significant excitation in speech using group delay function,'' IEEE Trans. Speech Audio Process. **3**, 325–333.
Sommers, M. S., and Kewley-Port, D. (**1996**). ''Modeling formant frequency discrimination of female vowels,'' J. Acoust. Soc. Am. **99,** 3770–3781.
Turner, C. W., and Van Tasell, D. J. (**1984**). ''Sensorineural hearing loss and the discrimination of vowel-like stimuli,'' J. Acoust. Soc. Am. **75,** 562–565.
Wakefield, G. H., and Viemeister, N. F. (**1990**). ''Discrimination of modulation depth of sinusoidal amplitude modulation (SAM) noise,'' J. Acoust. Soc. Am. **88,** 1367–1373.
Zera, J., Onsan, Z. A., Nguyen, Q. T., and Green, D. M. (**1993**). ''Auditory profile analysis of harmonic signals,'' J. Acoust. Soc. Am. **93,** 3431–3441.
Zwicker, E. (**1952**). ''Die Grenzen der Hörbarkeit der Amplitudenmodulation und der Frequenzmodulation eines Tones,'' Acustica **2**, Akustische Beihefte AB125–AB133.

Age-related changes in temporal gap detection

Karen B. Snell
Department of Audiology, Rochester Institute of Technology, 52 Lomb Memorial Drive, Rochester, New York 14623-5604

(Received 8 July 1996; accepted for publication 6 December 1996)

The purpose of this study was to clarify and extend the results of earlier studies of age-related effects on temporal resolution by precisely matching young and old subjects with normal hearing and measuring gap thresholds in a variety of listening conditions. Younger subjects were between 17 and 40 years of age, older subjects between 64 and 77 years. Signals were noisebursts which varied in upper-cutoff frequency, overall level, and sinusoidal-amplitude-modulation depth. Signals were presented in quiet, in a noise floor, and with a gated-high-frequency masker in a noise floor. Significant main effects were found for signal frequency, intensity, modulation, age, and background condition. Mean gap thresholds ranged between 2.1 and 10.1 ms and were larger for the older subjects in all 24 conditions. In some conditions, introduction of a noise floor increased the gap thresholds of the older subjects relative to those of the younger. Analyses of individual data support the conclusion that the mean differences between groups reflect shifts in the distributions of gap thresholds of the older subjects towards poorer temporal resolution. © *1997 Acoustical Society of America.* [S0001-4966(97)05204-1]

PACS numbers: 43.66.Mk, 43.66.Sr, 43.66.Dc [JWH]

INTRODUCTION

A general decline in the speed of behavior is one of the most ubiquitous and significant characteristics of mature organisms (Birren and Fisher, 1995). Age-related slowing has been observed in mammals other than humans (Salthouse, 1982) and shown to be mediated primarily by the central nervous system rather than peripheral factors (Salthouse, 1991). In the past, declines in processing speed have been demonstrated primarily in verbal or visual tasks but there is no reason to suspect that the auditory system is immune from similar age-related slowing in processing. By examining temporal acuity in a simple paradigm such as an auditory gap-detection task, we can explore declines in processing rate on a more elemental level (Wingfield, 1996). Age-related changes in the speed of auditory processing are also of great importance because they have been linked to age-related changes in processing of speech, especially in acoustically complex conditions (van Rooij and Plomp, 1992).

Since gap resolution has been demonstrated to be strongly dependent on the audibility of high-frequency energy in a test signal (Buus and Florentine, 1985) and generally gap thresholds in people with cochlear hearing loss are reported to be higher (Moore and Glasberg, 1988), the need to measure temporal acuity in older adults without hearing loss is clear. Other investigators who have explored temporal resolution in older subjects using a gap-detection paradigm (e.g., Moore *et al.*, 1992; Schneider *et al.*, 1994) have noted the importance of not confounding age and hearing loss. Nevertheless, the absolute thresholds of the older subjects in previous studies were less acute than those of the young subjects to whom they were compared. Thus, it remains unclear whether the decreased temporal acuity reported for the older subjects reflects age-related changes alone or interactions between age and hearing loss.

Also, previous studies of gap detection and aging have used sinusoidal signals (Moore *et al.*, 1992 with 400-ms sinusoids; Schneider *et al.*, 1994 with tone pips). While frequency specificity is often desirable, age-related changes in temporal resolution measured in tasks other than gap detection have been reported to increase with the complexity of the stimulus condition (Fitzgibbons and Gordon-Salant, 1995). This finding is consistent with other studies which indicate the magnitude of the age-related slowing is proportional to task complexity (Sliwinski *et al.*, 1994). The use of more complex sets of conditions in studying gap detection in aging adults may increase the likelihood of detecting age-related differences. Of practical consequence, results with acoustically complex signals in complex background may be more directly relevant to understanding the speech perception problems of older adults (CHABA, 1988). The purpose of this study is to clarify and extend our understanding of age-related changes in temporal resolution by matching pairs of young and old subjects for absolute sensitivity across a wider range of frequencies than in previous studies and measuring temporal resolution in conditions varying in stimulus and background complexity. If previously reported age-related differences reflected primarily differences in absolute sensitivity or its interactions with age, groups matched audiometrically should have comparable gap thresholds in all conditions. On the other hand, comparable gap detection in quiet but group differences in complex backgrounds would be consistent with reports of relatively greater difficulty understanding speech in noisy or complex listening environments which cannot be explained by audiometric thresholds alone. Finally, differences between groups in all conditions would support the hypothesis that a more generalized age-related change occurs in the speed of auditory processing.

TABLE I. Mean audiometric thresholds (dB HL) and standard deviations (dB) for the young and old groups of subjects.

	Mean absolute threshold (dB HL) Frequency (kHz)						
	0.25	0.5	1	2	4	6	8
	Young subjects ($N=20$)						
Mean	7.0	6.8	6.2	6.0	9.0	8.9	6.0
s.d.	(5.0)	(4.7)	(5.1)	(4.2)	(6.2)	(8.2)	(8.0)
	Old subjects ($N=20$)						
Mean	7.2	6.5	7.2	6.5	12.5	16.4	17.8
s.d.	(4.7)	(6.7)	(5.0)	(6.4)	(5.7)	(4.3)	(7.5)

I. METHOD

A. Subjects

Twenty young and 20 old adults served as subjects. Young subjects were between 17 and 40 years of age (mean age of 25.6 years); old subjects were between 64 and 77 years (mean age of 69.6 years). Each young subject was matched with an old subject of the same gender by a sliding window algorithm based on audiometric thresholds between 0.25 and 6 kHz. As shown in Table I, this method resulted in a mean between-group difference in threshold at octave frequencies between 0.25 and 4 kHz of 1.1 dB. Audiometric thresholds at octave frequencies between 0.25 and 4 kHz in all test ears were 20-dB HL or less (ANSI S3.6-1989). At 6 and 8 kHz, close matching could not be achieved despite extensive audiometric screening of potential subjects. The effect of the relatively small differences in high-frequency absolute sensitivity (7.5 and 11.8 dB at 6 and 8 kHz, respectively) was estimated by introducing a gated, high-frequency, bandpass masker in some conditions. If younger listeners make use of their more sensitive high-frequency hearing to detect gaps, then the high-frequency masker should have a more deleterious effect on their performance. All subjects were recruited from local university communities and were paid for their participation.

Subject selection may pose the greatest problem in design of gerontological research (Hertzog, 1996). We chose to emphasize obtaining maximally comparable samples of young and old subjects rather than samples that were fully representative of their age cohort. In particular, older subjects with more acute absolute sensitivity than the population that they represented were selected so that age-related changes in temporal resolution could be directly examined. Younger subjects with excellent high-frequency absolute sensitivity were eliminated during screening because of the unlikelihood of finding a comparable older match. Achieving comparable groups required extensive screening and many potential subjects were excluded from the study because an adequate match in the other age group could not be identified. This contrasts with previous studies in which high-frequency absolute thresholds were not included in the criteria for selection of older subjects with normal hearing. For example, in the study by Moore *et al.* (1992) only audiometric frequencies of 2 kHz and below were used to select ''elderly normal'' subjects; half of the older subjects showed 8-kHz absolute thresholds of 60-dB HL or higher. In the study by Schneider *et al.* (1994) mean thresholds between 0.25 and 3 kHz fell within the normal audiometric range but those of the older group exceeded those of the younger by roughly 5 to 15 dB; at 6 and 8 kHz the mean thresholds of the older group were greater by 20 dB.

Our age groups were unusually comparable in other respects. Subjects were matched on the bases of gender and ear because age-related changes in absolute sensitivity differ for women and men as well as left and right ears (Pearson *et al.*, 1995). Subjects were screened not only for significant otological history but for mental status. Compared to previous studies, our younger group was more heterogeneous than the typical group of undergraduate subjects but more comparable in life experience to our older group. Many older subjects were part-time students in a university-based adult education program, some were staff or faculty, and others were retired faculty. Most younger subjects were undergraduate students, but many were younger staff or faculty.

B. Stimuli

The stimuli were low-pass noisebursts, digitized with cutoff frequencies of 1 or 6 kHz, and randomly generated for each presentation by a signal-processing board [Tucker Davis Technologies (TDT) Array Processor 2]. For simplicity's sake, these signals will be referred to as the 1- and 6-kHz signals throughout the remainder of the paper. In half the experimental conditions, the random noisebursts were digitally modulated in amplitude with 20-Hz sinusoids at a fixed 0° phase angle to achieve a 12.6% modulation depth. The noisebursts were transduced by a 16-bit D/A converter (TDT DA Converter 1) and attenuated (TDT PA 4) to an overall level of 70- or 80-dB sound-pressure level (SPL). The noisebursts were routed through a signal mixer (TDT SM3) to a headphone buffer (TDT HB5), and then led to an earphone (Beyer DT48) in a circumaural cushion. These earphones have an extended high-frequency response, the circumaural cushion minimizes the possibility of ear-canal collapse, and the additional padding of the headset increased the comfort of some of the older subjects.

The overall duration of the noisebursts was held constant at 150 ms and the waveforms were digitally shaped at onset and offset with 10-ms cosine-squared envelopes. Gaps were shaped with 1-ms cosine-squared rise–fall envelopes and placed in the signal noisebursts 100 ms after signal onset rather than at the stimulus midpoint to facilitate comparisons with animal studies in progress (see Walton *et al.*, in press). An identical 1-ms cosine-squared rise–fall envelope at 100 ms after stimulus onset was placed in the standard (no-gap) stimulus to minimize the spectral differences between the gap and the no-gap stimuli and therefore the likelihood that subjects would perform the detection task based on energy at off- or remote frequencies. Signal durations and gap size were defined as the intervals between the half amplitude points on the stimulus waveforms. A pilot study indicated a relatively long interstimulus interval of 600 ms was preferred by the older subjects and thus was used in this study with both groups of subjects.

In the first set of conditions, no background noise was present. In the noise-floor conditions, continuous white noise was digitally generated (TDT WG 1), attenuated (TDT PA 4) to an overall level of 45-dB SPL (N_0=4 dB), and then mixed with the gated noisebursts. This level was sufficient to shift absolute thresholds of the signal noisebursts by at least 10 dB as well as mask any spectral splatter (Moore *et al.*, 1992). In the third set of conditions, a high-frequency bandpass masker was present in addition to the noise floor. The spectrum level of the high-frequency noiseburst was fixed at 20 dB below that of the signal and had cutoff frequencies of 6 and 12 kHz. The high-frequency masker was gated on and off with the signal noiseburst but it did not contain a gap at 100 ms after onset. The purpose of this high-frequency masker was to minimize the potential contribution of auditory fibers tuned to high frequencies where our subject groups were not as well matched, i.e., at 6 kHz and above. If the younger listeners displayed smaller gap thresholds without the high-frequency masker because of their better high-frequency hearing, then the addition of the high-frequency masker should degrade their performance more so than the performance of the older listeners with poorer high-frequency hearing. Thus, in the noise floor and high-frequency masker condition the gap was partially filled by the high-frequency masker as well as by the noise floor.

In summary, gap thresholds were obtained for two intensities (overall levels of 70- and 80-dB SPL), two levels of modulation (0% and 12.6%), two cutoff frequencies (low-passed at 1 and 6 kHz), and three background conditions (quiet, noise floor, noise floor and high-frequency masker) for a total of 24 conditions.

C. Procedure

The subjects sat in a double-walled sound booth (Acoustic Systems RE243), faced a monitor which provided visual feedback, and entered responses with a keyboard. Gap thresholds were estimated in an adaptive two-interval, forced-choice (2IFC) procedure. A 2IFC rather than a 3IFC procedure was used because it increased the physical comfort of older subjects who found it easier to key in a response with two alternatives. Before each experimental run, the subject was familiarized with samples of the stimuli used in the run. During each run consisting of 99 trials, gap duration was decreased after three correct responses, and increased after one incorrect response to estimate the 79.4% point on the psychometric function (Levitt, 1971). Step size was logarithmically varied to minimize the standard error of the threshold estimate. Gap thresholds were estimated from the average of the last even number of reversals excluding the first three reversals. During each run, the intensity, bandwidth, modulation depth, and background condition were held constant. Two runs were completed for each condition by each subject. The order of conditions was randomized across sessions and subjects. Absolute and masked thresholds were also obtained for the experimental stimuli by the subjects. All subjects practiced for the same amount of time (one and one-half hours) prior to data collection to minimize variability associated with practice effects (Snell and Hu, 1995). No subject was eliminated from the study because of an inability to perform the gap-detection task. Subjects listened in six to eight sessions, each one to one and one-half hours in length, for a total of 8 to 10 h.

II. RESULTS AND DISCUSSION

The mean gap thresholds are shown in Fig. 1. The data in the middle and upper panels represent the overall 70- and 80-dB SPL signal conditions, respectively. The data in the left and right panels represent the unmodulated (0% modulation depth) and modulated (12.6% modulation depth) signal conditions, respectively. The bottom panel on the left contains mean data that has been averaged across intensity and modulation. The background conditions in which the gap thresholds were obtained are indicated by the symbols: circles, squares, and triangles represent quiet, noise floor, and noise floor plus gated high-frequency masker conditions, respectively. Closed symbols represent older subjects, open symbols, younger subjects. The upper-cutoff frequency in kHz of the signal is shown on the abscissa. Gap thresholds in ms are plotted on the ordinate. Vertical bars indicating plus and minus one standard error of the mean (SEM) are smaller than the symbols in the top four plots and therefore not visible. The symbol size was reduced in the bottom left panel so that error bars could be seen. Symbols are offset to improve readability.

As shown in Fig. 1, gap detection appears to be influenced most strongly by signal frequency and age, i.e., gap thresholds are smaller for the 6- than for the 1-kHz signals and mean thresholds of the younger subjects are smaller than those of older subjects in all conditions. Mean gap thresholds appear to be larger in conditions in which the signal noiseburst is modulated or in which a high-frequency masker is present. The effect of intensity appears to be small and varies with signal frequency. The mean thresholds of the older subjects appear larger for all conditions, but, in general, the patterns for the older and younger subjects appear similar.

Analyses of variance (ANOVA's) were carried out using a logarithmic transformation to stabilize the variance at the two signal frequencies (Winer, 1971). A repeated measures design (SYSTAT, 1992) with one between factor (two age groups) and four within factors (two intensity levels, two modulation depths, two cutoff frequencies, and three background conditions) was used for the initial analysis. The results of the overall ANOVA of these data were significant for the main effects: signal frequency [$F(1,38)=1214.96$, $p<0.001$], intensity [$F(1,38)=17.62$, $p<0.001$], depth of modulation [$F(1,38)=68.31$, $p<0.001$], group [$F(1,38)=12.10$, $p<0.001$], and background condition [$F(1,38)=15.013$, $p<0.001$]. One first-order interaction: intensity $\times$frequency [$F(1,38)=44.08$, $p<0.001$] and one-higher order interaction: group$\times$frequency$\times$background [$F(2,76)=3.37$, $p=0.039$] were significant. Significant interactions were examined in subsequent ANOVA's and pairwise comparisons.

A. Signal intensity and frequency

The most robust effect in this study was cutoff frequency. Gap sensitivity increased with an increase in upper-cutoff frequency, with the mean threshold decreasing from

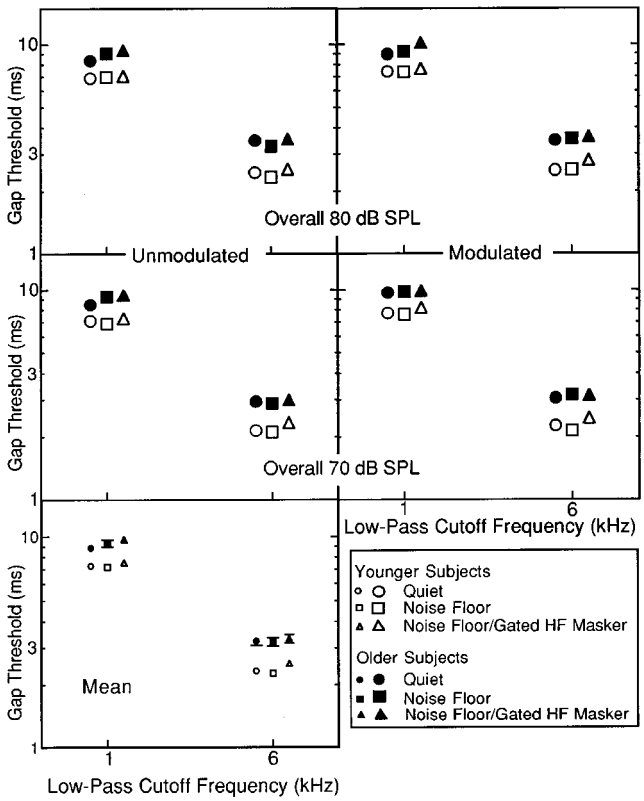

FIG. 1. Gap thresholds in ms are plotted on the ordinate and upper-cutoff frequency in kHz is shown on the abscissa. Vertical bars indicate plus and minus one standard error of the mean (SEM) and are visible only in the bottom-left panel where the symbol size is reduced. Upper and middle panels represent overall signal levels of 70- and 80-dB SPL, respectively. The left and right panels represent unmodulated and modulated signals; the bottom panel on the left represents overall mean thresholds. The background condition is indicated by the symbol: circles, squares, and triangles represent the quiet, noise floor, and noise floor plus high-frequency masker conditions, respectively. The closed and open symbols represent older and younger subjects, respectively.

8.3 ms for the 1-kHz signal to 2.8 ms for the 6-kHz signal. These results are in good agreement with previous studies (e.g., Formby and Muir, 1988; Snell *et al.*, 1994).

Because the intensity×frequency interaction was significant in the initial ANOVA, subsequent analyses examined the effects of intensity for the 1- and 6-kHz signals separately. Mean gap thresholds for the 70-dB SPL and 80-dB SPL 1-kHz signals were 8.4 and 8.2 ms, respectively. This difference [$F(1,38)=3.774$, $p>0.05$] was not significant. In contrast, gap thresholds for the 70-dB SPL and 80-dB SPL 6-kHz signals were 2.6 and 3.0 ms, respectively, a significant increase at the higher level [$F(1,38)=38.76$, $p<0.001$].

These results are consistent with previous reports that gap thresholds for noisebursts increase at high intensity levels (e.g., Buus and Florentine, 1985). Similarly, Moore *et al.* (1992) in a study using sinusoids to study age-related effects noted that the gap thresholds of a few subjects increased as the level was raised to 85-dB SPL. Finally, a signal level of 85-dB SPL may have contributed to the relatively large mean thresholds (13–14 ms) reported in an earlier study of age-related effects on gap detection (Lutman, 1991).

B. The effect of signal modulation

Gap sensitivity decreased significantly when the signal noisebursts were modulated. The mean gap thresholds were about 7% larger for the modulated than for the unmodulated signals. The nonsignificant effect of 20% modulation reported in a previous study (Snell, 1995) probably resulted from jittering of the signal intensity level. While jittering was necessary in that study to minimize the use of intensity cues at higher depths of modulation, that technique may have obscured the effects of modulation at the lower depths.

C. Age-related effects

Mean gap thresholds were significantly greater for the older group in all 24 conditions. The robustness of the effect given the variety of signals and listening conditions is striking. The mean gap thresholds of the older subjects were about 27% and 37% larger with the 1- and 6-kHz signals, respectively, than those of the younger subjects. These results are important for several reasons. First, the differences cannot be easily attributed to differences in absolute sensitivity as can the differences reported in previous studies. Half of the conditions used a noiseburst signal with an upper-cutoff frequency of 1 kHz and encompassed frequencies for which absolute sensitivity was the same in each group (see Table I). Second, the magnitude of the difference in gap thresholds is similar to age-related differences which have been recently reported in recordings from mice (Walton *et al.*, 1995). Third, regardless of the significant differences in method and subject selection, the magnitude of the differences between groups are consistent with those reported by Moore *et al.* (1992) and Schneider *et al.* (1994).

D. Interaction between age and background condition

To explore the significant interaction group×frequency ×background condition obtained in the initial ANOVA, two ANOVA's were performed, one at each signal frequency with group and background condition as factors. The interaction between group and background condition was significant at neither signal frequency: for the 1-kHz signal [$F(2,316)=1.859$, $p=0.158$], for the 6 kHz signal [$F(2,316)=1.392$, $p=0.25$], suggesting the effect of background condition differed at the two frequencies. Subsequent ANOVA's and pairwise comparisons were completed to further explore the group×background condition interaction at each frequency.

1. Gap thresholds for the 6-kHz signal

As shown in the bottom panel of Fig. 1, the background condition had little effect on mean gap thresholds for the low-passed noisebursts with a cutoff frequency of 6 kHz. The mean gap thresholds in quiet, with a noise floor, and with a noise floor and high-frequency masker were 2.8 ms, 2.7 ms, and 2.9 ms, respectively. Pairwise comparisons for the 6-kHz signal indicated the mean gap thresholds of neither group increased with the addition of a noise floor. Gap thresholds increased only when both a noise floor and a gated-high-frequency masker were present, and then only slightly (although significantly at $p<0.05$). Mean gap thresh-

olds of the young subjects in the three background conditions were 2.3 (quiet), 2.3 (noise floor), and 2.5 ms (noise floor and gated-high-frequency masker). The mean gap thresholds of the older subjects in the corresponding background conditions were 3.2, 3.2, and 3.3 ms, respectively.

The high-frequency masker conditions had been introduced to the design to provide a straightforward interpretation of between group differences in the noise floor conditions even if high-frequency absolute thresholds were not exactly matched. That is, the gap thresholds of the two groups were expected to be comparable in the quiet condition and increase in the noise floor conditions for the older group only. If the relatively better performance in the noise floor condition reflected the more sensitive high-frequency hearing of the young group, then addition of a high-frequency masker should have eliminated their relative advantage. As a result, group performance should have been equivalent in the noise floor plus high-frequency masker conditions. Contrary to expectations, the addition of the high-pass masker resulted in increases in mean gap thresholds for the 6-kHz signal in both groups of subjects. To estimate the contribution of high-frequency hearing, gap thresholds were correlated with absolute thresholds at 8 kHz. Correlations were insignificant, ranging from 0.010 to 0.143. Correlations with 6-kHz absolute thresholds were also calculated and were similarly small. While this probably reflects, in part, the narrow range of absolute thresholds at 6 and 8 kHz, the lack of significant correlations suggests that it is unlikely that the differences between age groups are primarily related to the very small differences in high-frequency sensitivity.

There are at least four possible reasons for the effect of the high-frequency masker. First, remote signal energy may have influenced gap detection in the quiet and noise floor only conditions but may have been masked by the high-frequency masker. This possibility seems unlikely since (a) the level of the noise floor in itself was sufficient to mask remote energy, (b) the remote spectral profiles were similar for gap and ''no-gap'' stimuli, and (c) correlations between absolute sensitivity in these remote regions and gap thresholds were insignificant. Second, detection thresholds reflected the response of auditory fibers with high characteristic frequencies which responded to on-frequency signal energy and influenced gap detection in the quiet and noise floor only conditions but were masked by the high-frequency masker. This also seems unlikely because correlations between absolute high-frequency sensitivity and gap thresholds in the quiet and noise floor conditions would have been robust instead of insignificant. A third possibility is that ultrahigh-frequency fibers contributed to detection. Although absolute thresholds between 10 and 14 kHz were not measured, it is possible that more acute absolute sensitivity in this region contributed to more acute gap thresholds for the younger subjects. However, if this were the case, neither the noise floor nor the high-frequency masker should have influenced the gap thresholds of the younger group. A fourth possibility is that detection thresholds may have increased because of the increased complexity of the stimulus configuration resulting from partial filling of the gap (Forrest and Green, 1987). Regardless of the mechanism, what is most significant is that the gap thresholds for both groups of subjects became longer when the high-frequency masker was added.

2. Gap thresholds for the 1-kHz signal

As shown in the bottom panel of Fig. 1 and by the results of pairwise comparisons ($p<0.05$), the mean gap thresholds of the older group were most acute in quiet but significantly increased in the presence of a noise floor both with and without the gated-high-frequency masker; mean gap detection thresholds for quiet, noise floor, and gated-high-frequency masker in noise floor conditions were 8.8, 9.3, and 9.7 ms, respectively. In contrast, the mean gap thresholds for the younger subjects were *smaller* (but nonsignificantly so) in the presence of a noise floor and significantly increased with the addition of the gated-high-frequency masker to the noise floor; mean gap detection thresholds for quiet, noise floor, and gated-high-frequency masker with noise floor conditions were 7.3, 7.2, and 7.5 ms, respectively.

To investigate whether the larger 1-kHz gap thresholds in the high-frequency masker conditions could be attributed to the masking of auditory-nerve fibers with high-characteristic frequencies, 8-kHz absolute thresholds (db HL) were correlated with gap thresholds for each subject. As before, it was hypothesized that if better absolute high-frequency sensitivity contributed to gap thresholds, correlations between the 8-kHz absolute thresholds and 1-kHz gap thresholds should be robust in the quiet and noise floor conditions but weaker with the addition of the high-frequency masker. Average correlations for the quiet, noise floor, and noise floor plus high-frequency masking conditions were 0.178, 0.238, and 0.154 and ranged between 0.115 and 0.286. It is intriguing that the correlations between high-frequency hearing and gap thresholds were largest in conditions where only the noise floor was present, conditions where contributions from high-frequency fibers have sometimes been thought to be important (Strickland *et al.*, 1994). However, less than 5% of the variance is explained by high-frequency sensitivity and none of the correlations reached significance. Correlations between gap thresholds and 6-kHz absolute thresholds (dB HL) were calculated and found to be similar or smaller. Although the small range of absolute thresholds at 6 and 8 kHz may have contributed to the small correlations, it seems unlikely that high-frequency sensitivity played a major role. Ultrahigh-frequency (10 to 14 kHz) absolute sensitivity was not measured in this study and contributions to gap detection from this frequency region need to be clarified in the future. Regardless, the increase in mean gap thresholds at 1 kHz in the noise floor condition for the older group cannot be attributed to differences in absolute sensitivity in the frequency regions studied thus far. Nor is the increase likely to reflect differences in the auditory filter widths and the resulting effective signal-to-noise floor ratios of the two groups (Patterson and Henning, 1977) since auditory filters are broader than normal only when absolute thresholds are elevated (Peters and Moore, 1992).

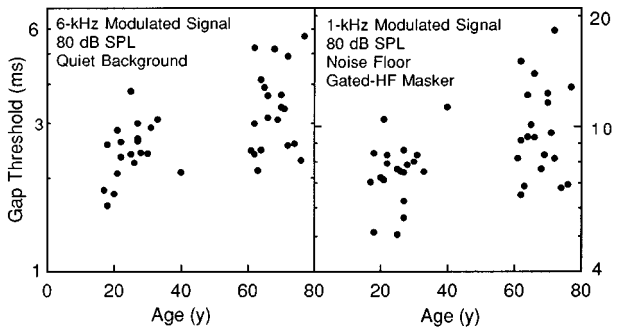

FIG. 2. Scatterplots with age shown on the abscissa and gap thresholds on the ordinate. Each data point represents the mean gap detection threshold of one subject. The panel on the left contains the individual data for a modulated noiseburst with an upper-cutoff frequency of 6 kHz, at an overall level of 80-dB SPL, presented in a quiet background. The panel on the right contains the individual data for a modulated noiseburst with an upper-cutoff frequency of 1 kHz, at an overall level of 80-dB SPL, presented with a noise floor and a high-frequency gated masker.

E. Individual differences

Individual data of the 40 subjects was examined in 24 scatterplots representing each of the experimental conditions. Two representative conditions are shown in Fig. 2. Subject age in years is plotted on the abscissa; gap thresholds in ms on the ordinate. Each data point represents the mean gap threshold of one subject. There are several aspects worth noting, which have been discussed in previous studies. First, there is considerable overlap between age groups in the distributions of gap thresholds. Second, the range of gap thresholds of the older group is broader than the range of thresholds for the younger group, although the variability is similar when examined on a log scale. Finally, several older subjects appear to have exceptionally poor temporal resolution in each condition.

One aspect of the data which has not been previously noted is shown in both panels of Fig. 2. Note that gap detection by several younger subjects appears exceptionally acute when compared to even the smallest gap thresholds of the older subjects. Young subjects with exceptionally small gap thresholds can also be identified in Table II (subjects MS, CC, and MG) of Schneider *et al.* (1994) and in Fig. 3 of Moore *et al.* (1992). Small (1–2 ms) neural correlates of gap thresholds measured in onset and primarylike neurons in the inferior colliculus of young mice have also been reported (Walton *et al.*, in press). These scatterplots illustrate that the age-related increase in mean gap thresholds reflects not just larger gap thresholds in a few older subjects but an overall shift in the distribution of gap thresholds with age. While there is considerable overlap between the two distributions, roughly a third of the gap thresholds of the older subjects fall well outside the range of the younger subjects and the gap thresholds of a few younger subjects are considerably smaller than the smallest gap thresholds of the older group.

While pairs of subjects had been matched for absolute sensitivity at audiometric frequencies, it was possible that age-related differences in absolute sensitivity to the wideband signals could have contributed to between-group differences in gap thresholds. To examine this possibility, individual absolute and masked thresholds obtained for sample signals in the three background conditions were examined using ANOVA and pairwise comparisons. The results of these analyses indicated that the mean masked thresholds did not significantly differ between groups and therefore could not have contributed to the between-group differences in the noise floor conditions. Also, the masked thresholds (dB SPL) for each subject were higher than the corresponding absolute thresholds, ensuring that the gap thresholds obtained in the noise floor condition were actually masked gap thresholds. Sensation levels for the unmasked signals were slightly higher for the younger subjects but exceeded 30-dB SL for all subjects.

III. SUMMARY

Our results indicate that age-related changes in temporal acuity occur across a range of stimulus characteristics and background conditions. Mean gap thresholds of older subjects were larger when compared to mean gap thresholds of younger subjects with matched audiograms for signals varying in spectra, intensity, and depth of modulation. Although the gap thresholds of younger and older subjects showed similar patterns in response to various signal manipulations, older subjects were more sensitive to background noise in some conditions. When a noise floor was added to a low-passed noiseburst signal with a cutoff frequency of 1 kHz, the gap thresholds of the older subjects increased, whereas the gap thresholds of the younger subjects did not. Mean thresholds of both groups increased slightly when a high-frequency masker was gated with the signal and allowed to partially fill the gap. Four possible explanations of the effect of the high-frequency masker were discussed. The most likely is that it is the increase in the complexity of the stimulus, i.e., the partial filling of the temporal gap with the gated masker, rather than a masking effect *per se* (Forrest and Green, 1987).

Examination of individual data in 24 scatterplots representing the experimental conditions suggested that the distributions of the young and old groups varied in several ways. The range of gap thresholds was greater in each condition for older subjects, although the variability was comparable when viewed on a log scale. Roughly one-third of the older subjects showed larger gap thresholds than the younger subjects and a few young subjects showed acuity more sensitive than any of the older subjects. Thus, although there was some overlap between the distributions, generally the differences between the means reflected not only poorer performance by a few older individuals but overall shifts in the distribution of gap thresholds with age.

ACKNOWLEDGMENTS

This research was supported by the Rochester International Center for Hearing and Speech Research and a grant from NIA (No. AG09524). I am grateful to Chris Turner for his help in designing the study, D. Robert Frisina for selecting and matching subjects, Donald Sims and Cindy Hogan for screening subjects, Ajit Janardan for assistance with data collection, and Mary Florentine and Mark Lutman for their perceptive and helpful comments.

ANSI (**1989**). ANSI S3.6-1989, ''Specifications for Audiometers'' (American National Standards Institute, New York).
Birren, J. E., and Fisher, L. M. (**1995**). ''Aging and speed of behavior: possible consequences for psychological functioning,'' Annu. Rev. Psychol. **46,** 329–353.
Buus, S., and Florentine, M. (**1985**). ''Gap detection in normal and impaired listeners: The effect of level and frequency,'' in *Time Resolution in Auditory Systems*, edited by A. Michelsen (Springer-Verlag, New York), pp. 159–179.
Committee on Hearing, Bioacoustics, and Biomechanics (CHABA): Working Group on Speech Understanding (**1988**). ''Speech understanding and aging,'' J. Acoust. Soc. Am. **83,** 859–895.
Fitzgibbons, P. J., and Gordon-Salant, S. (**1995**). ''Age effects on duration discrimination with simple and complex stimuli,'' J. Acoust. Soc. Am. **98,** 3140–3145.
Formby, C., and Muir, K. (**1988**). ''Modulation and gap detection for broadband and filtered noise signals,'' J. Acoust. Soc. Am. **84,** 545–550.
Forrest, T. G., and Green, D. M. (**1987**). ''Detection of partially filled gaps in noise and the temporal modulation transfer function,'' J. Acoust. Soc. Am. **82,** 1933–1943.
Hertzog, C. (**1996**). ''Research design in studies of aging and cognition'' in *Handbook of the Psychology of Aging*, 4th ed., edited by J. E. Birren and K. W. Schaie (Academic, San Diego, CA), pp. 24–37.
Levitt, H. (**1971**). ''Transformed up-down methods in psychoacoustics,'' J. Acoust. Soc. Am. **49,** 467–477.
Lutman, M. E. (**1991**). ''Degradations in frequency and temporal resolution with age and their impact on speech identification,'' Acta Otol. Suppl. **476**, 120–126.
Moore, B. C. J., and Glasberg, B. R. (**1988**). ''Gap detection with sinusoids and noise in normal, impaired and electrically stimulated ears,'' J. Acoust. Soc. Am. **83,** 1093–1101.
Moore, B. C. J., Peters, R. W., and Glasberg, B. R. (**1992**). ''Detection of temporal gaps in sinusoids by elderly subjects with and without hearing loss,'' J. Acoust. Soc. Am. **92,** 1923–1932.
Patterson, R. D., and Henning, G. B. (**1977**). ''Stimulus variability and auditory filter shape,'' J. Acoust. Soc. Am. **62,** 649–664.
Pearson, J. D., Morrell, C. H., Gordon-Salant, S., Brant, L. J., Metter, E. J., Klein, L. L., and Fozard, J. L. (**1995**). ''Gender differences in a longitudinal study of age-associated hearing loss,'' J. Acoust. Soc. Am. **97,** 1196–1205.
Peters, R. W., and Moore, B. C. G. (**1992**). ''Auditory filters and aging: filters when auditory thresholds are normal,'' in *Ninth International Symposium on Hearing: Auditory Physiology and Perception*, edited by Y. Cazals, L. Demany, and K. Horner (Pergamon, Oxford), pp. 179–188.
Salthouse, T. A. (**1982**). *Adult Cognition: An Experimental Psychology of Human Aging* (Springer-Verlag, New York).
Salthouse, T. A. (**1991**). *Theoretical Perspectives on Cognitive Aging* (Erlbaum, Hillsdale, NJ), pp. 77–83.
Schneider, B. A., Pichora-Fuller, M. K., Kowalchuk, D., and Lamb, M. (**1994**). ''Gap detection and the precedence effect in young and old adults,'' J. Acoust. Soc. Am. **95,** 980–991.
Sliwinski, M., Buschke, H., Kuslansky, G., Senior, G. and Scarisbrick, D. (**1994**). ''Proportional slowing and addition speed in old and young adults,'' Psychol. Aging **9**, 72–80.
Snell, K. B. (**1995**). ''The effects of sinusoidal amplitude modulation on gap detection in noise,'' J. Acoust. Soc. Am. **98,** 1799–1802.
Snell, K. B., and Hue, H.-L. (**1995**). ''The effect of temporal placement on gap detectability,'' J. Acoust. Soc. Am. **97,** 3330(A).
Snell, K. B., Ison, J. R., and Frisina, D. R. (**1994**). ''The effects of signal frequency and absolute bandwidth on gap detection in noise,'' J. Acoust. Soc. Am. **96,** 1458–1464.
Strickland, E. A., Viemeister, N. F., Van Tasell, D. J., and Preminger, J. E. (**1994**). ''Is useful speech information carried by fibers with high characteristic frequencies?'' J. Acoust. Soc. Am. **95,** 497–501.
SYSTAT for Windows: Statistics, Version 5 Edition, SYSTAT, Inc., Evanston, IL, 1992, 750 pp.
van Rooij, J. C. G. M., and Plomp, R. (**1992**). ''Auditive and cognitive factors in speech perception by elderly listeners. III. Additional data and final discussion,'' J. Acoust. Soc. Am. **91,** 1028–1033.
Walton, J. P., Frisina, R. D., Ison, J. E., and O'Neill, W. E. (**1997**). ''Neural correlates of behavioral gap detection in the inferior colliculus of the young CBA mouse,'' J. Comp. Physiol. (in press).
Walton, J. P., Wilson, W. W., Mees, A. J., O'Neill, W. E., Frisina, R. D. (**1995**). ''Age-related alteration in temporal processing of amplitude modulation and silent gaps in the inferior colliculus of the CBA mouse,'' Assoc. Res. Otolaryngol. Abstr. **18**, 71.
Winer, B. J. (**1971**). *Statistical Principles in Experimental Design* (McGraw-Hill, New York), p. 400.
Wingfield, A. (**1996**). ''Cognitive factors in auditory performance: context speed of processing, and constraints of memory,'' J. Am. Acad. Aud. **7**, 175–182.

Labiovelar compensation in back vowels

Kenneth J. de Jong
Department of Linguistics, 322 Memorial Hall, Indiana University, Bloomington, Indiana 47405

(Received 21 June 1995; accepted for publication 12 November 1996)

Various studies have revealed apparent motoric compensation between articulatory structures such as the jaw and lips which contribute to articulatory goals of vocal tract constriction. The present study, like Perkell *et al.* [J. Acoust. Soc. Am. **93**, 2948–2961 (1993)] and Savariaux *et al.* [J. Acoust. Soc. Am. **98**, 2428–2442 (1995)], investigates the possibility of compensation between labial protrusion and constriction and dorsovelar constriction—a relationship based on the similarity of the acoustic effects of such articulatory goals. The present study differs from these earlier studies in that it assumes an articulatory model of gestures, and it examines nonperipheral back vowels. X-ray microbeam records of American English speakers producing back vowels under various stress conditions were investigated. Results reveal systematic speaker differences in the direction of correlation between measures of labial and dorsal position. These results show that speakers differ as to whether they exhibit coupling between labial and dorsal activity in the lowering of back vowel timbre. © *1997 Acoustical Society of America.* [S0001-4966(97)00504-3]

PACS numbers: 43.70.Bk, 43.70.Gr [AL]

INTRODUCTION

The theory of task dynamics (Saltzman and Munhall, 1989) models speech production as the result of a combination of underlying abstract gestures. These gestures specify speech activity in terms of dynamic equations which describe attractor functions toward articulatory goals of vocal tract constriction. Thus, for example, the specification of an alveolar consonant would not be stated in terms of muscle activity patterns, such as the contraction of the genioglossus, nor in terms of actual articulator goals, such as advancing and raising the tongue away from the mandible, but rather in terms of motion toward the constriction of the oral cavity around the alveolar ridge. Gestures generally involve a complex of articulators which each can contribute to the motion toward the articulatory goal. Specifying gestures with abstract articulatory goals allows task dynamics to capture the results of studies which have shown compensatory behavior between jaw and tongue tip in the attainment of alveolar constrictions (Kelso *et al.*, 1984), between jaw and tongue body in the production of vocalic constrictions (Gay *et al.*, 1981), and jaw and lip in the attainment of labial closures (Folkins and Abbs, 1975; Abbs *et al.*, 1984; Shaiman, 1989). In each of these studies, perturbations of the position of one of the articulators (the jaw) was compensated for in the positioning of another articulator, which, provided the perturbation was not too large, allowed the speakers to attain the articulatory goal of vocal tract constriction.

In this gestural theory, the dynamics of speech are said to arise from the nature of phonetic primitives as gestures. Though the acoustic results of these motions most certainly play a role in the evolution of a language over time (as noted in Goldstein, 1983, 1989), and are important for acquisition, they are not needed in the specifications of a speaker's production system once the system has been acquired. To quote Browman and Goldstein (1989), ''...gestural descriptions are purely articulatory,'' and Browman and Goldstein (1990), ''[o]utput considerations do not... appear to constrain actively the processes of variation in speech production.'' Similarly, the synthesis technique outlined by Saltzman and Munhall (1989) makes no use of the acoustic signal, neither in the specification of gestural primitives nor in the process of sequencing and combining the actions of the various articulators. Acoustic transformation is the last step in the process and has no feedback into the production system. The most striking piece of evidence for this position is the existence of ''hidden'' gestures in casual speech, actions which correspond to expected linguistic specifications, but leave little or no mark on the acoustic output of the vocal tract. Such actions seem to occur without regard to the fact that they might be imperceptible to the listener.

This approach differs from that taken by other speech researchers. Perkell (1990) claims acoustic factors not only influence the choice of articulatory goals, but also the functioning of the system which is designed to attain the goals. He states,

> The programming of articulatory movements is a function of the sequence of articulatory goals, the moment-to-moment state of the vocal tract and the particular *acoustic requirements of the individual utterances* (p. 264, emphasis mine).

and later,

> ... our approach also claims that some aspects of speech kinematics have to be determined on the basis of the communicative (acoustic) requirements of the sound sequences. (p. 266)

In line with this view of the role of acoustics in articulatory control, Perkell *et al.* (1993) report an investigation of the relationship between tongue-dorsum position and lip positions in the production of /u/. While there is no direct biomechanical connection between the tongue body and the lips, there is an acoustic coupling. Acoustic models of the vocal tract show that dorsovelar and labial constrictions should have similar lowering effects on the second formant ($F2$)

(Chiba and Kajiyama, 1941; Stevens and House, 1953; Fant, 1960; Lindblom and Sundberg, 1971). If the phonetic goals are specifically acoustic in nature, one would expect the same kind of complementary synergistic relationship between lip and dorsum as is found between biomechanically connected articulators such as jaw and tongue tip. In the same way that both jaw and tongue tip positioning may contribute to the formation of an alveolar constriction (an articulatory goal), both lip protrusion and dorso-velar constriction may contribute to the lowering of $F2$ (an acoustic goal).

Perkell *et al.* (1993) used an electromagnetic midsagittal articulometer to track the position of flesh points on the tongue, the mandible incisor, and the upper and lower lip in the sagittal plane. Flesh point positions of the lips and tongue dorsum at vowel midpoint were first correlated with the $F2$ at that time and then correlated with one another. Results varied from speaker to speaker. Three of four speakers showed significant correlations between tongue-body raising and one or more labial dimensions, upper lip protrusion, lower lip protrusion, or upper lip raising. Correlations, though significant, were rather weak, Pearson r-squared values varying from 0.046 to 0.220. One of these three speakers also showed no significant correlation between the relevant articulatory dimensions and the height of $F2$. The authors conclude tentatively that labio-velar compensation does occur.

Savariaux *et al.* (1995) report an acoustic and articulatory study with a similar premise. They report an examination of sagittal x-ray scans of French speakers producing a sustained /u/ with and without a tube inserted between the speakers' lips. Seven of eleven speakers showed retraction of the dorsal constriction location in compensation for the artificially expanded lip aperture. The authors then conclude ''... that speaker behavior is basically directed toward an enhancement of the acoustic end product.'' In this case, the acoustic end product is appropriate formant frequencies for the vowel.

Surveying the evidence for labiovelar compensation presented in these two articles, however, reveals several potential weaknesses. The compensation study by Savariaux *et al.* (1995) studied multiple repetitions of sustained vowels. Thus, the compensation observed may not be indicative of an ability which speakers exhibit in naturally running speech. In addition, speakers were recorded making several successive attempts. This multiple-trial structure of their task insures that the compensation observed is not immediate, but could be mediated by acoustically-based error correction immediately after the time of utterance. Compensation among biomechanically linked structures found in dynamic perturbation studies (such as reported in Folkins and Abbs, 1975; Kelso *et al.*, 1984) occurs immediately, apparently before acoustic feedback is available.

Perkell *et al.* (1993), since they studied running speech, were faced with a decision about where to sample the time-varying speech signal. They chose to examine articulatory positions and acoustic output at the temporal midpoint of the vowel, as demarcated by onsets and offsets in voicing. This method is potentially problematic assuming a task dynamic approach. If, for example, the labial protrusion gesture and the dorsovelar constriction gesture are typically asynchronous, any variation in the timing of the sampled time slice with respect to these gestures will artifactually produce a negative correlation between labial protrusion and dorsal constriction. Time slices at the attainment of dorsal constriction will not be at the maximum labial protrusion; time slices at the attainment of labial protrusion will not be at the maximum dorsal constriction.

In view of the weakness of the correlations obtained by Perkell *et al.* (1993) and these potential problems in time-slice location, the present paper presents the results of a similar analysis of a corpus of x-ray microbeam trajectories. In the present study, articulatory positions were chosen which reasonably represented the time of maximum approximation to the relevant gestural goals. In order to examine the acoustic outcome of the gestures, a similar acoustic approach is taken. Minimum $F2$ values were calculated to give an indication as to how effective at lowering $F2$ the entire articulatory activity during the vowel was. Minimum $F2$'s were calculated, rather than $F2$'s at the time of the articulatory events, because dorsal retraction and lip protrusion are often asynchronous. de Jong (1993) and de Jong (1995a) report an analysis of part of the present corpus which indicates that the two events may occur as far as 100 ms apart. In addition, the minimum $F2$ in the vowel is sometimes more synchronous with the dorsal retraction event, and sometimes more synchronous with the labial protrusion event. These facts suggest that one effect of redundancy of lip rounding and dorsal constriction is to allow for one or the other action to create the acoustic effect of timbre lowering. If this is the case, the most appropriate measure of the acoustic effectiveness of the articulatory ensemble is an acoustically defined event, in this case, minimum $F2$.

It should be noted that using the minimum value of $F2$ is a large simplification in at least two ways. First, it assumes that $F2$ is an appropriate dimension to measure the acoustic contrasts represented by the back, rounded vowels studied. Thus, any potential effect of $F1$ and of $F3$ is ignored. Second and more important, minimum $F2$ is a static measure. It has been amply demonstrated that dynamic information is important in hearers' identification of the phonemic content of an utterance (Strange *et al.*, 1976; Strange *et al.*, 1983; Nearey and Assmann, 1986; Nearey, 1989). More perceptual work on the structure of vowel categories, as well as the structure of dynamic auditory information is needed to fully assess the effect of these simplifications on the results presented below. Any acoustic or perceptual model of articulatory goals must eventually address these issues.

A second motivation for the present study is to extend Perkell *et al.*'s (1993) results to other back vowels. The vowels in the present corpus were nonperipheral back vowels, /o/ and /U/, rather than /u/. Although there has been some work modeling the point vowel /u/, there is little or no work modeling nonperipheral back vowels. In addition, there are several potential oddities of the English /u/ category which make it useful to compare /u/ with other similar categories. Perkell *et al.* (1993) note that the vowel /u/, being a category on the extremity of the acoustic vowel space, might make relatively inflexible demands on both the lips and the dor-

sum, precluding speakers from adopting compensatory strategies. In supporting this conjecture, they show more and stronger correlations for portions of the data with higher $F2$—that is, acoustically more underarticulated renditions of /u/. Similar arguments from the opposite viewpoint might also be raised. Since the vowel category /u/ varies considerably in English, the acoustic demands might not be sufficient to induce speakers to adopt compensatory strategies. In addition, different dialects of American English vary remarkably as to the quality and production of the vowel /u/. Anglo dialects of southern California are commonly noted to have little or no rounding in /u/. A complementary situation occurs in various midstates dialects. X-ray microbeam records of a speaker native to St. Louis show tongue body positions in /u/ to be roughly equivalent to tongue body positions in /i/ (de Jong, 1995a). Thus, the inconsistency between speakers might also reflect dialectal or ideolectal variation in the /u/ category. Using other back rounded vowels in this study extends the observations of Perkell *et al.* (1993) to other phonemic categories.

Like Perkell *et al.* (1993), the present study also controls the factor of stress. In the model of linguistic stress presented in de Jong (1995b), stress enhances phonemic distinctions within the stressed syllable. This model leads to two expectations. First, the presence of accent should increase the magnitude of articulations leading to distinctions—in this case the dorsal constriction movement and the labial protrusion movement. Thus, across stress conditions one would expect a positive correlation between the amount of labial protrusion and the amount of dorsal raising. This positive correlation would obscure any compensatory (negative) relationship between the lips and the dorsum. Second, if one assumes that speech operates well within the range of human articulatory capabilities (as is claimed by Lindblom, 1990) and if less stressed items are hypoarticulate, one would expect the effects of energy cost reduction to be more apparent in less stressed syllables. This expectation is partially supported by Perkell *et al.*'s (1993) findings that compensatory correlations were stronger in tokens which were less distinctly /u/-like, that is, tokens with higher $F2$.

I. METHODS

A. Procedure

The Wisconsin x-ray microbeam system (Nadler *et al.*, 1987) was used to record the movement trajectories of gold pellets attached to the tongue, jaw, and lips of three American English speakers while producing monosyllabic words containing the vowels [U] and [ow]. Three 2.5-mm pellets were attached using a dental adhesive to the superior surface of the tongue at distances of 10, 30, and 50 mm from the tongue apex, as measured with the tongue extended. Two 3-mm pellets indexed jaw movement, one placed on a mandible molar, one placed at the base of the mandible incisors. Two 3-mm pellets indexed the movement of the upper and lower lip. Since a dental adhesive was used to fix the pellets to the articulators, the labial pellets could not be attached to the smooth inferior surface of the upper lip and superior surface of the lower lip; rather they were attached to the vermilion border of both lips. Since labial movements tend to be relatively small, and the mechanical connection between the various parts of the lips is quite complicated, this positioning of the pellets may not index the motion of the internal surfaces of the lips very well. Thus, the pellet motion is at best an indirect index of articulatory position as it affects the acoustic output of the vocal tract.

The tongue pellets and the lower lip pellets were sampled at 100 Hz, while the other, slower moving pellets were sampled at 50 Hz. After acquisition, the data were smoothed and oriented so that the x dimension is parallel to the occlusal plane. The method used on the present corpus differs from that described in Westbury (1991), in that there was no correction for yaw. Two pellets were temporarily attached to a maxillary incisor and molar to determine the occlusal plane. Two other reference pellets, one at the base of a maxillary incisor, and one on a pedestal on the bridge of the nose were tracked during acquisition. Previous to acquisition, the position of these reference pellets to the occlusal pellets was determined by means of a full sagittal scan. The distance between the pellets was also measured with calipers to check the calibration of the system. The two occlusal pellets were removed during acquisition, since they would likely interfere with articulation. After acquisition, head movement in the sagittal plane was subtracted out by means of the reference pellets. Thus, x-dimension data indicate position of the pellet in a dimension parallel to the occlusal plane, and y-dimension data indicate position in a perpendicular dimension. The origin of the space is an arbitrary point slightly posterior and below the typical dorsal pellet position. Positive indicates anterior and superior.

The subjects were three speakers of a northern, midwestern dialect of American English. All were undergraduate students at the University of Wisconsin who were paid for their participation in the experiment. Northern dialects typically have impressionistically rather back /o/, in opposition to more southern midwestern dialects. Two subjects were male, SD and MB; one was female, TG.

The words containing /o/ were all monosyllables beginning with /t/ and ending with zero to three alveolar consonants. Thus the words with /o/ were *toe*, *toes*, *toad*, *toads*, *tote*, *totes*, *toast*, and *toasts*, occurring in a frame sentence of the form, ''I said, 'Put the _____ on the table.' '' The vowels in the word *Put* were also examined.

The amount of stress placed on the target words was varied by giving the subjects miniature discourse settings in which they were to respond to an imaginary hearer who misheard part of the sentence. The speakers consistently responded with nuclear (sentence) accent on the misheard portion. There were three elicitation conditions, nuclear accent on the target word, nuclear accent on the following *on* (in which subjects consistently placed a prenuclear pitch accent on the target word), and nuclear accent on *put* (which precludes placement of an accent on the target word). For example, to obtain an utterance with the word *toad*, and nuclear accent on the preposition, *on*, the subjects were given the following cue:

Did you say, ''Put the toad under the table?''

I said, ''Put the toad ON the table.''

TABLE I. Number of utterances in each stress category.

Subject	MB	SD	TG
Unaccented	29	32	48
Prenuclear accented	32	30	47
Nuclear accented	29	31	47

The speakers then said the second line of the dialogue. They were given a chance to practice the sentences before the pellets were attached.

The stress pattern of each of the utterances was verified by an intonational analysis using the transcriptional system described in Pierrehumbert (1980) and further developed in Pierrehumbert and Beckman (1988). Pitch tracks were obtained for each utterance, and then analyzed for pitch accents by two transcribers. Pitch accents indicate the degree of stress on each item, either unaccented, prenuclear accented, or nuclear accented (bearing the sentence accent). For more details concerning this analysis, see de Jong (1995b). The words in these three elicitation conditions were repeated six times in a random order by TG, and four times by SD and MB. This yielded the eight target words by three levels of stress (nuclear accented, prenuclear accented, and unaccented), totaling 144 utterances for TG and 96 for the other two subjects. Due to various mechanical and software problems in recording and porting the data onto PC's a small number of the tokens for each subject were rendered unanalyzable. The total number of tokens in each stress condition which were analyzed are given in Table I. Since the word with /o/ varied from trial to trial, speakers were likely to have focused more attention on the part of the utterance with /o/ than on that with /U/.

B. Articulatory analyses

Articulatory analyses were performed using the XD program developed by Joan Miller implemented on a PC under MS-DOS. Time slices were determined using articulatory criteria. This method differed from that used in Perkell *et al.* (1993), who analyzed articulatory positions in the vowel midportion, where vowels were defined acoustically as the voiced portion of the signal. Using these acoustic criteria would not select the articulatory postures most indicative of the articulatory goal of the action. Tongue positions during /o/ showed a considerable amount of motion during the middle portion of the vowel, due to the fact that American English /o/ is diphthongized. /U/ created a different problem. The tongue dorsum typically reached a point of maximum retraction at a time very close to (and sometimes preceding) the onset of voicing for the vowel.

Measurements for tongue and lip positions were taken at time points chosen using criteria established after inspecting a large number of trajectories from each subject. The criteria were devised to select the position which seems most indicative of the goal of the underlying gesture, as modeled in the task dynamics of Saltzman and Munhall (1989). In this formulation of task dynamics, gestures are modeled using second-order dynamic equations which are over-damped. Such equations describe nonoscillating point attractors, functions which approach an asymptote without overshooting it. The actual motions expected in this model, however, are often complicated by the existence of multiple gestures influencing especially tongue movement at any given time.

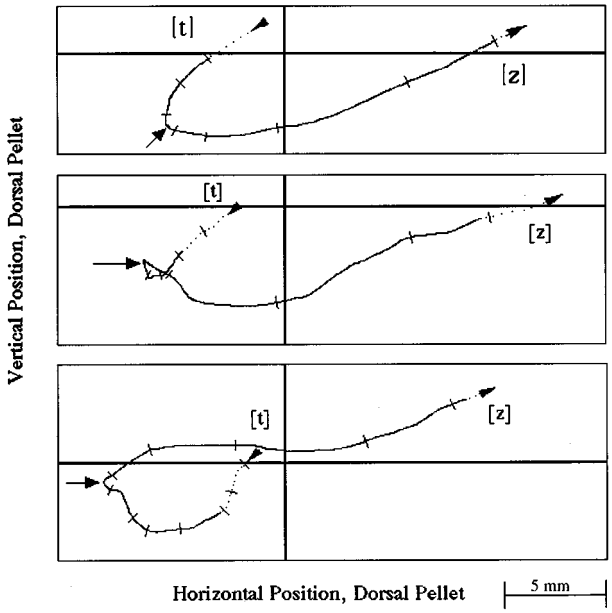

FIG. 1. Three dorsal pellet trajectories of speaker MB plotted in the sagittal plane. Each trajectory occurred during the production of the word *toes*. Trajectories begin at the release of the onset [t]. Tick marks perpendicular to the trajectory indicate 25-ms increments. Voiceless portions are indicated by dotted lines, voiced portions are indicated by solid lines. The frame extracted for the back vowel is indicated by an arrow in the left portion of each panel.

Two labial maxima were marked; one in the horizontal dimension of the upper lip pellet, and a second in the horizontal dimension of the lower lip pellet. Dorsal trajectories for [U] involved a posterior and anterior movement with a clear maximum in retraction. Measurements of dorsal position for [U] were taken at the most retracted dorsal location. Trajectories for /o/ showed a considerable amount of variation, due apparently to the interaction of the complex diphthongal nature of the vowel and the neighboring alveolar consonants. Figure 1 shows three illustrative trajectories. More stressed cases tended to exhibit two separate movements corresponding to the two parts of the diphthong (bottom of Fig. 1), while in less stressed cases, the two movements tended to coalesce into a single movement (top of Fig. 1). Measurements for /o/ were taken at the end of the second movement, the most retracted position, corresponding to the velar constriction for the diphthongal offglide. The velar offglide is examined because (1) the dorsal pellet position is likely to be closer to the maximum point of constriction for the [w] offglide than for the [o] nucleus, and (2) the offglide will correspond more closely to the maximum lowering of $F2$ in the acoustic output. In cases such as that in the top of Fig. 1 where there is one point of minimum speed, rather than two, a single point indicating the extremum in a posterior and inferior direction (a minimum in a dimension 45° anterior of vertical) corresponded closely to the point of minimum speed. This point was taken as the dorsal position for the [w] offglide. A small number of unstressed tokens did

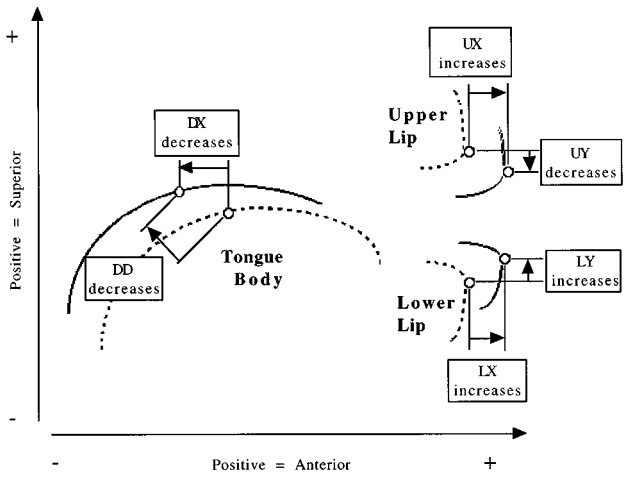

FIG. 2. A schematic illustration of the expected articulatory changes involved with lowering $F2$. Directions of correlation expected across stress conditions, and if speakers are compensating for less dorsal constriction with more labial constriction or protrusion are given in Table II.

not always have a downward movement out of the onset [t]. In such cases, the point of minimum speed during the vowel was taken as the measurement for the vowel.

C. Acoustic analyses

In addition to articulatory measurements, the time-aligned acoustic records were submitted to an acoustic analysis to obtain a measure of the amount of $F2$ lowering effected by the articulatory motions. Acoustic measurements were made using the Kay Elemetrics CSL on a PC under MS-DOS. The time of minimum $F2$ in the vowel was determined with a spectrographic display generated with a filter bandwidth of 300 Hz. $F2$ values at this time were obtained using a 12th-order LPC analysis.

It should be noted that these $F2$ minima were not always synchronous with the articulatory events noted above; indeed, the articulatory events were not entirely synchronous with one another. As would be expected given the measurement criteria, all of the events occurred well within 150 ms of one another. Labial events typically come later than the dorsal events in less stressed utterances. Minimum $F2$ values sometimes more closely corresponded in time to dorsal retraction events, and sometimes more closely to labial events. An analysis of some of these facts is presented in de Jong (1993, 1995a). The full analysis of the temporal relations between these events goes beyond the scope of the present paper, though timing must be carefully considered in determining how the present results are to be integrated into a complete model of speech production.

D. Hypotheses

Figure 2 illustrates changes in articulatory position expected to lower $F2$. Six articulatory dimensions were analyzed, the x position of the dorsal pellet (henceforward DX), the position of the dorsal pellet in a dimension 45° posterior of vertical (henceforward DD), and the x and y position of the upper and lower lip pellets (UX, UY, LX, and LY). Since DD behaved substantially similar to DX, only the results concerning DX will be presented here. If dorsovelar constriction, labial protrusion, and labial constriction all lower $F2$, we expect correlations of $F2$ and articulatory positions in each of these dimensions to have the signs given in Table II.

TABLE II. Expected correlations between variables with acoustically based compensation.

Variable	$F2$	Stress	DX/DD
DX	+	−	
UX	−	+	+
UY	+	−	−
LX	−	+	+
LY	−	+	+
Stress	−		

If the pellet dimensions do index $F2$-sensitive differences in the speakers' articulatory positioning, and the present speakers are employing compensatory strategies between the positioning of the tongue body and the positioning of the lips, one would expect correlations between the articulatory dimensions to have the signs indicated in the right column of Table II. For ease of reference, such correlations will be henceforward termed compensatory correlations. Correlations opposite in sign to these will be called anticompensatory correlations.

Regarding the results of controlling the amount of stress, one would expect positive correlations between dorsovelar constriction and labial protrusion across stress conditions, since stress should act to enhance activity associated with lowering $F2$ in back vowels. Correlations produced as an artifact of stress should be anticompensatory, and thus have the signs indicated in the middle column of Table II. Thus, within each stress condition compensatory correlations should be stronger than across stress conditions. Stronger correlations indicating compensation should be obtained in less stressed items.

II. RESULTS

Table III gives mean articulator positions and mean minimum $F2$ values for each speaker for each stress condition for each vowel. Stress effects on $F2$ are consistently in the expected direction, more stressed tokens have lower average $F2$. The pattern of differences in articulator position across the stress conditions is somewhat more complicated. In general, differences are in the expected directions, though SD often does not show lip position differences in the expected direction, and TG does not show a difference in lip approximation in the expected direction.

In order to simplify the presentation of the results, the signs of the articulatory dimensions will be reoriented such that positions expected to produce more distinctive output (lower $F2$) will be more positive. Lower $F2$'s will also be treated as more positive. Thus, expected correlations between the articulatory dimensions and $F2$ will all be positive. In addition, compensatory correlations will all be negative (less dorsal retraction correlated with more lip protrusion or compression).

Table IV summarizes the results of correlating $F2$ values with the two dorsal position variables and four lip posi-

TABLE III. Mean $F2$ (in Hz) and articulatory position (in mm) divided by stress condition.

	Unaccented		Accented		Nuclear		All data	
Vowel /o/	mean	st. dev.	mean	st. dev.	mean	st. dev.	mean	st. dev.
SD								
$F2$	1073	68	1070	61	1012	59	1052	68
DX	9.91	2.55	9.43	2.67	8.63	2.81	9.33	2.70
UX	46.80	0.18	46.62	0.25	47.05	0.22	46.82	0.28
UY	47.24	0.25	47.52	0.31	47.35	0.26	47.37	0.29
LX	44.98	0.18	44.95	0.26	45.05	0.30	45.00	0.25
LY	29.15	0.43	29.09	0.46	29.01	0.42	29.08	0.43
MB								
$F2$	1045	106	1016	79	919	90	993	105
DX	10.84	1.22	10.85	1.41	10.22	1.32	10.64	1.34
UX	46.65	0.22	46.69	0.27	46.92	0.15	46.75	0.25
UY	49.26	0.28	49.40	0.20	49.29	0.26	49.32	0.25
LX	46.58	0.75	46.60	0.75	46.82	0.43	46.66	0.66
LY	29.90	0.84	29.51	0.84	29.08	0.75	29.49	0.87
TG								
$F2$	1271	156	1196	157	1179	153	1216	159
DX	8.19	1.29	8.90	1.45	8.75	1.40	8.61	1.41
UX	45.36	2.01	45.36	0.23	45.40	0.25	45.37	0.23
UY	45.82	0.31	45.93	0.27	45.62	0.43	45.79	0.37
LX	43.04	0.35	43.43	0.49	43.47	0.48	43.31	0.48
LY	32.03	0.50	32.14	0.67	32.11	0.58	32.09	0.58
Vowel /ʊ/								
SD								
$F2$	1195	52			1100	42	1161	7
DX	9.09	0.80			6.93	0.85	8.30	1.33
UX	47.76	0.20			47.86	0.29	47.79	0.24
UY	47.30	0.27			47.36	0.33	47.33	0.29
LX	46.31	0.24			46.01	0.29	46.20	0.30
LY	29.04	0.30			28.55	0.27	28.86	0.37
MB								
$F2$	1267	46	1256	56	1130	49	1220	80
DX	10.76	0.74	10.88	0.81	10.01	0.89	10.54	0.88
UX	47.01	0.25	46.99	0.25	47.19	0.24	47.06	0.26
UY	49.15	0.25	49.11	0.18	48.85	0.35	49.04	0.30
LX	46.30	0.38	46.38	0.67	46.41	0.41	46.35	0.39
LY	29.72	0.49	29.92	0.45	29.03	0.56	29.54	0.62
TG								
$F2$	1720	119	1694	107	1612	94	1669	112
DX	10.65	1.10	9.99	0.91	8.93	0.88	9.71	1.10
UX	45.53	0.29	45.61	0.31	45.83	0.38	45.67	0.35
UY	44.59	0.32	44.71	0.50	44.64	0.41	44.67	0.45
LX	42.57	0.30	42.69	0.50	42.89	0.54	42.74	0.50
LY	31.49	0.57	31.60	0.58	31.33	0.64	31.50	0.61

tion variables. Correlations were calculated separately for the two vowels, since the positioning of the articulators is likely to be somewhat different, and hence the sensitivity of $F2$ to the indices of articulator position is also likely to be different. Correlations significant above the 0.008 level are in bold. This level was determined following Kirk (1982) by setting a family-wise error level for each block of six correlations of 0.05. Correlations in the expected direction are marked as (+). In general, $F2$ correlates more consistently with dorsal positions than with lip positions. All three subjects show significant correlations of $F2$ with measures of dorsovelar approximation. Correlations between $F2$ and labial position, however, are both speaker and vowel dependent. TG shows no significant correlations in the expected direction. MB shows significant correlations in the expected direction for the upper lip in /ʊ/, while SD shows significant correlations in the expected direction for the protrusion of both lips in /o/. All speakers show significant correlations of LY and $F2$, however, in the wrong direction. This reverse relationship is possibly due to an indirect effect of stress, which both increases dorsal retraction and lowers the jaw (see de Jong, 1995b, for a fuller description of these effects).

Table V summarizes regression analyses of $F2$ against binary effects-coding variables indicating levels of accenting. Stress level is coded by two variables, one indicating the presence of an accent, and the other indicating the presence of a tonic (nuclear) accent. Correlations are in the expected direction; MB shows the most consistent correlations.

With these acoustic sensitivities and stress effects in mind, we turn to the interarticulator correlations. Table VI

TABLE IV. Pearson r^2 values for $F2$ versus articulatory dimensions. Signs in parentheses indicate direction of correlation; positive indicates a correlation in the expected direction, as illustrated in Fig. 2. Boldface indicates effects significant at the 0.008 level.

/o/ Variable	SD	MB	TG
DX	**0.247** (+)	**0.191** (+)	**0.164** (+)
UY	0.002 (+)	0.044 (+)	0.005 (−)
UX	**0.248** (+)	0.032 (+)	0.002 (−)
LY	**0.184** (−)	**0.082** (−)	0.011 (−)
LX	**0.135** (+)	0.002 (−)	0.000 (−)
/U/ Variable	SD	MB	TG
DX	**0.559** (+)	**0.145** (+)	**0.196** (+)
UY	0.058 (−)	**0.218** (+)	0.017 (+)
UX	0.011 (+)	**0.106** (+)	0.023 (+)
LY	**0.231** (−)	**0.333** (−)	0.004 (−)
LX	**0.134** (−)	0.006 (+)	0.012 (+)

summarizes the results of correlating the four dimensions of lip pellet position with the horizontal position of tongue dorsum pellet. Effects significant at the 0.013 level (family-wise error for four correlations=0.05) are boldfaced. Compensatory effects are indicated with a (−). TG shows compensatory correlations for all of the labial variables in /o/, but none in /U/. SD shows compensatory correlations for LX and LY in /U/, and LY in /o/. MB shows compensatory correlations for LY in /U/ and UX, LX, and LY in /o/. Anticompensatory correlations are also obtained. TG shows such effects for UX in /U/, MB for UY in both vowels, and SD for UX and LX in /o/.

Some of the strongest compensatory correlations between lip and dorsum concern the variable LY. This variable, however, consistently has the opposite effect on $F2$ from that expected by labial constriction. Two types of explanations for the results concerning lip lowering come to mind. The first is that lip pellet lowering is actually an index of lip protrusion. The motion of the lips during protrusion is often a rotation outward and downward. This explanation fits with the results that lip lowering decreases $F2$, but fails to support the conjecture that dorsal retraction and lip lowering are mutually compensating. The second, and more likely, explanation for this relationship would see lip lowering as connected to a general opening of the oral cavity. Thus, the present results would indicate a parallel relationship between dorsovelar constriction and oral cavity opening. Tokens with more retraction tend to have more opening (and hence, less labial constriction). Both are plausible characteristics of hyperarticulation, one for lowering the vowel timbre, one for increasing the loudness of the acoustic output. This conjecture, like the first, does not support calling the relationship between dorsal retraction and lip lowering a compensatory relationship involving $F2$. With LY correlations eliminated, then, the strongest compensatory correlations obtained for each subject explain about 20% of the variance in labial position.

TABLE V. Pearson r^2 values for $F2$ versus accent conditions. Boldface indicates effects significant at the 0.025 level. All correlations are in the expected direction; greater stress correlates with lower $F2$ values.

/o/ Variable	SD	MB	TG
Accented	**0.050**	**0.112**	**0.061**
Nuclear	**0.168**	**0.245**	**0.026**
/U/ Variable	SD	MB	TG
Accented	**0.474**	**0.289**	**0.028**
Nuclear	**0.474**	**0.621**	**0.135**

TABLE VI. Pearson r^2 values: correlations between dorsal and labial dimensions. Signs in parentheses indicate direction of correlation; negative indicates a correlation in a compensatory direction. Boldface indicates effects significant at the 0.013 level.

DX versus...	Labial variable	SD	MB	TG
/o/	UX	**0.251** (+)	**0.072** (−)	**0.050** (−)
	UY	0.004 (−)	**0.062** (+)	**0.056** (−)
	LX	**0.385** (+)	**0.222** (−)	**0.181** (−)
	LY	**0.490** (−)	**0.266** (−)	**0.054** (−)
/U/	UX	0.041 (+)	**0.064** (+)	**0.058** (+)
	UY	0.063 (−)	**0.146** (+)	0.002 (+)
	LX	**0.202** (−)	0.049 (−)	0.004 (+)
	LY	**0.446** (−)	**0.255** (−)	0.000 (−)

Since stress differences are likely to obscure compensatory correlations, a stepwise regression was performed to factor out the effect of stress on the interarticulator correlations. Labial position measures were regressed against DX and the two binary effects-coding variables indicating stress. The stress variables were forced first, and DX regressed against the residual. If stress differences are weakening the strength of compensatory correlations, factoring out stress should strengthen the correlations. If stress differences are producing the anticompensatory correlations, factoring out stress should eliminate the correlations. Results of this analysis are summarized in Table VII. The pattern of results is very similar to those without stress factored out. Compensatory correlations of UX and LX appear for MB in /o/, UY and LX for TG in /o/, and UY for SD in /U/. Anticompensatory correlations generally do not disappear with stress factored out.

The correlations summarized here are illustrated in Figs. 3 and 4, which plot labial variables against DX. Considering the direction of the interarticulator relationships, we note a general difference between the speakers. While the correlations for MB tend to be in the direction expected of compensation, the correlations for SD are typically in the opposite direction. This is especially clear in the labial x dimensions for /o/, where some of the strongest correlations were obtained. In addition to this, Figs. 3 and 4 show regression lines for each of the stress conditions considered separately. No simple pattern of stress differences occurs across all of the speakers. If we consider the expected pattern for compensation to be as listed in Table II, MB does tend to show a general pattern of less stressed items showing regression slopes more in the direction appropriate for compensation. However, no pattern emerges for the other speakers.

TABLE VII. Summary of stepwise regression analyses with stress variables forced. Signs in parentheses indicate a compensatory (−) or anticompensatory (+) correlation. All correlations with stress are in the expected direction. Boldface indicates effects significant at the 0.013 level.

		SD		MD		TG	
/o/		r^2 stress	partial r (DX)	r^2 stress	partial r (DX)	r^2 stress	partial r (DX)
	UX	**0.389**	**−0.543** (+)	**0.225**	**0.429** (−)	0.008	0.221 (−)
	UY	**0.151**	−0.053 (−)	0.058	**0.241** (+)	**0.123**	**−0.261** (−)
	LX	0.027	**−0.615** (+)	0.027	**0.525** (−)	**0.170**	**0.381** (−)
	LY	0.016	**0.694** (−)	**0.143**	**0.495** (−)	0.006	0.223 (−)
/U/							
	UX	0.043	−0.066 (+)	**0.108**	−0.134 (+)	**0.109**	−0.077 (+)
	UY	0.009	**−0.286** (−)	**0.202**	**0.243** (+)	0.01	0.043 (+)
	LX	**0.244**	0.113 (−)	0.018	0.290 (−)	0.048	0.067 (−)
	LY	**0.408**	**0.347** (−)	**0.350**	**0.350** (−)	0.041	−0.111 (+)

Finally, in order to confirm whether the articulatory dimensions examined here contribute to $F2$ lowering in the expected fashion, one further stepwise regression was performed. $F2$ was regressed against DX; and the residual regressed against the labial variables which showed significant correlations with DX in the previous analysis. The results of these analyses are summarized in Table VIII. With the exception of LY for speaker MB, each of the labial dimensions have either no significant separable effect on $F2$, or an effect in the expected direction. One result is particularly striking in this analysis; for both SD and MB, UX has a negative correlation with $F2$, even though the relationship between UX and DX differed between the two speakers. Thus, the difference in direction of correlation between labial protrusion and dorsal retraction between these two speakers cannot be attributed to differences in how UX indexes $F2$-lowering labial articulation.

To summarize, considering only labial constriction and protrusion dimensions which lower $F2$, labial positions and dorsal positions are complementary to one another for two speaker's renditions of /o/. The strongest of these correlations has an r-squared value of 0.222. This study also finds a correlation between LY and dorsal retraction; the lower lip has a lower position in tokens with a more retracted dorsum. However, since lip raising is associated with higher $F2$ values, this relationship cannot be seen as indicative of a complementary relationship between lip and dorsum in lowering $F2$. Finally, however, noncomplementary relationships also appear for the upper lip for MB in /U/ and for upper lip protrusion for SD in /o/. R-squared values in one of these cases reached 0.251. In these cases, $F2$ lowering is adversely affected by the anticompensatory relationship.

III. DISCUSSION

Three aspects of the present results bear some comment. First, using articulatory criteria for extracting articulator positions did not eliminate compensatory correlations between lip and tongue positions. Thus, compensatory correlations are not an artifact of measurement technique.

Second, the general pattern of results obtained by Perkell *et al.* (1993) for /u/ generalize to the offglide of /o/, and to a lesser extent to /U/. The correlations found here are similar in magnitude to those found in this previous study. Thus, the presence of compensatory correlations is not due to any oddity in the /u/ category of English, nor due to the fact that /u/ occupies the edge of the vowel space. Rather, to the extent that labiodorsal compensation is apparent, it seems to occur with any of the nonlow back vowels—vowels which are characterized by lip rounding and lower than average $F2$. The present results also indicate that the results of Perkell *et al.* (1993) are not due to artifacts of the articulatory measurement system, since similar patterns are found here using a radically different data acquisition system.

Third, the present study has found two different and opposite relationships between labial and dorsal position. The present study has found some examples of compensatory relationships between dorsal activity and labial activity. It has also found some examples of anticompensatory relationships, relationships where lip and dorsum not only fail to compensate for underarticulation in the other articulator, but also underarticulate in the same fashion. Such correlations, if anything, are stronger than compensatory correlations. These anticompensatory relationships cannot be simply attributed to categorical differences in stress, since the different interarticulatory relationships generally hold within stress categories as well as across stress categories. The anticompensatory

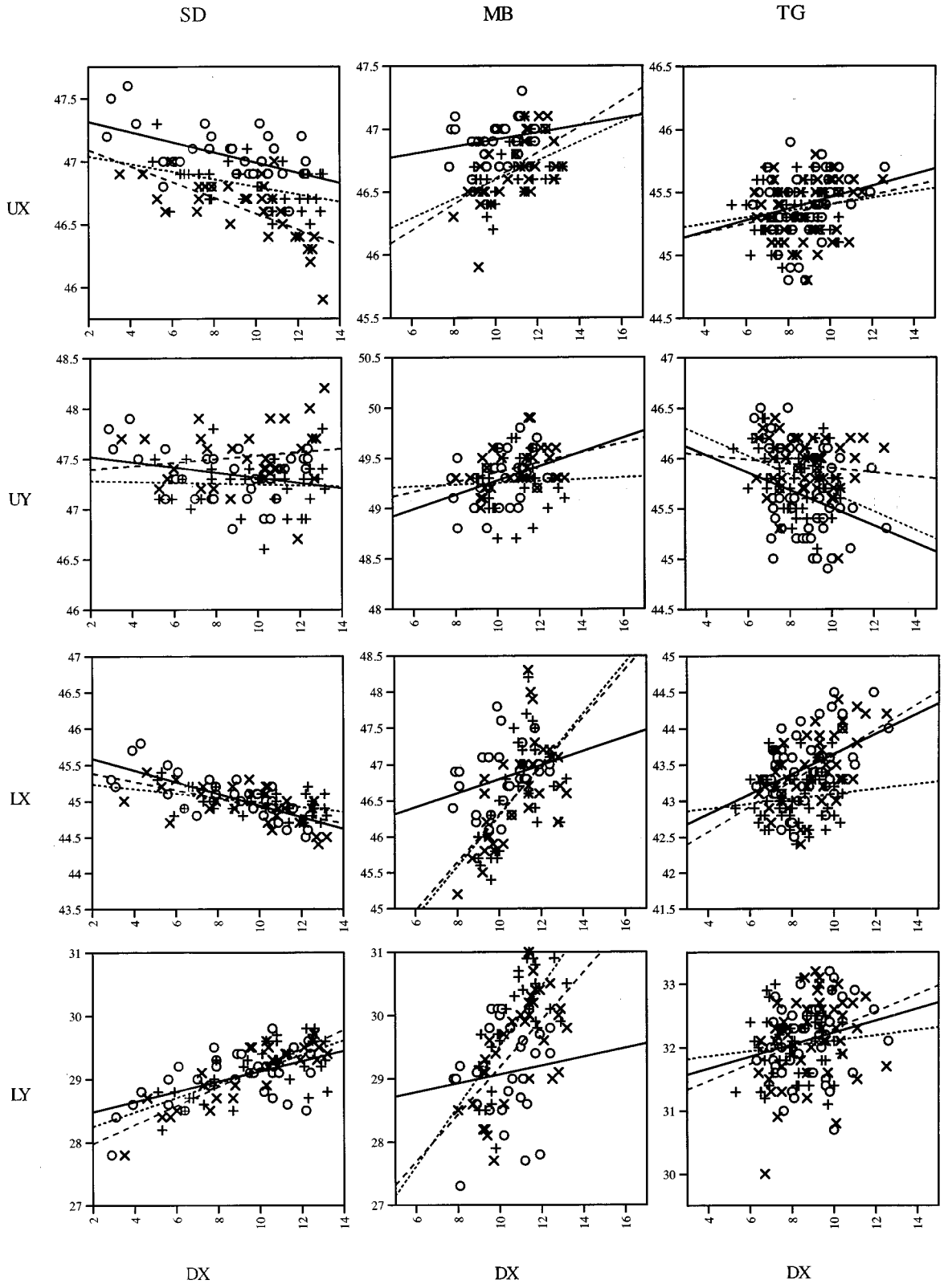

FIG. 3. *X*-dimension and *y*-dimension positions of the upper lip pellet (UX and UY, respectively), and lower lip pellet (LX and LY) plotted against the position of the tongue dorsum pellet (DX) extracted for the [w] offglide of the target words. As in Fig. 1, the *x* dimension is parallel to the occlusal plane. Values indicate distance from a point near the end of the condyle; positive values indicate a more superior or anterior position. Dorsolabial compensation should be manifested in a positive correlation between DX and UX (top row), LX and LY (bottom two rows), and a negative correlation between DX and UY (second row from top). Circles indicate nuclear accented tokens; ×'s indicate prenuclear accented tokens; and +'s indicate unaccented tokens. Regression lines indicate tokens divided by stress condition; nuclear accented, solid line; prenuclear accented, long-dashed line; unaccented, short-dashed line.

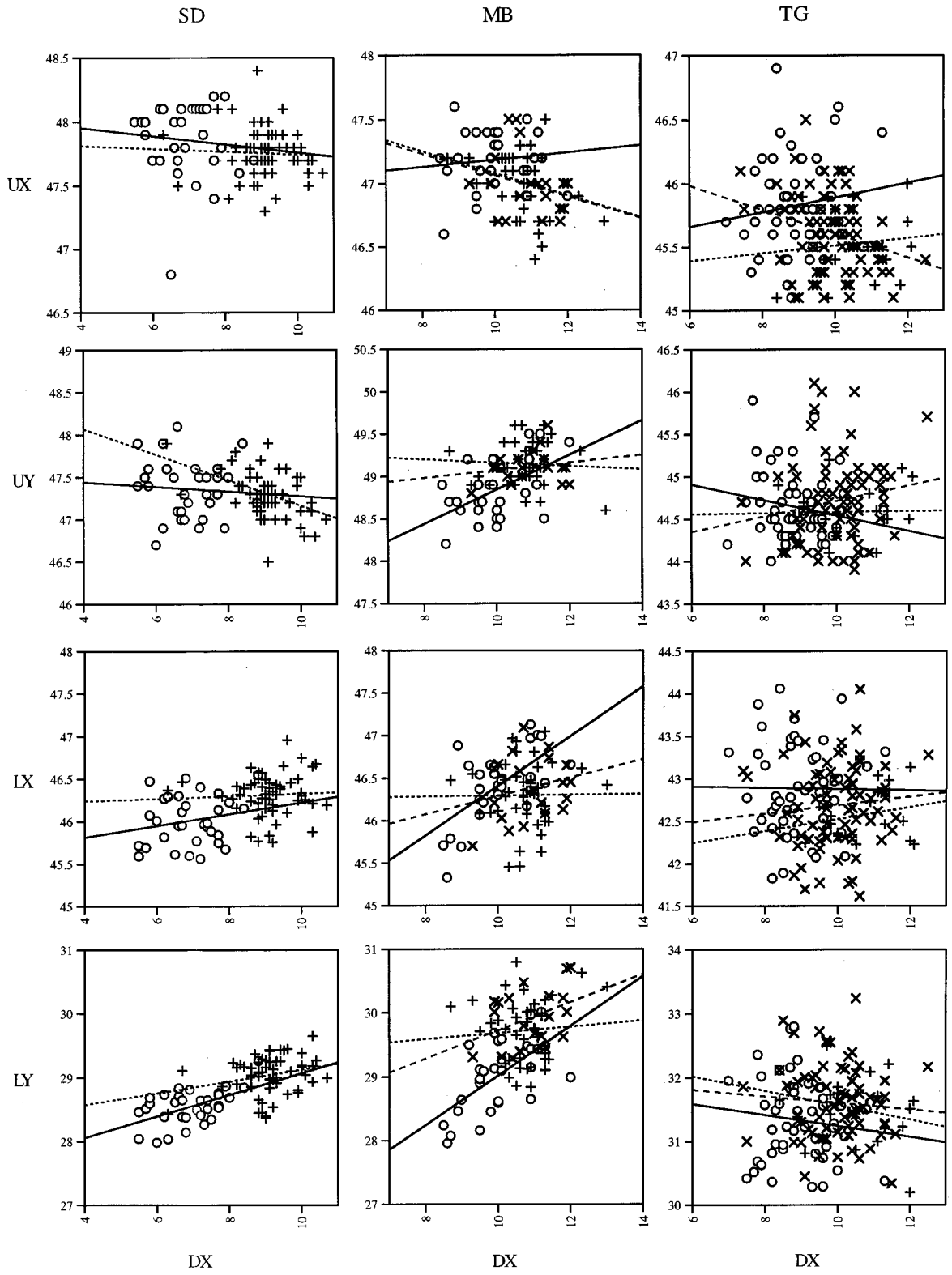

FIG. 4. Labial positions plotted against dorsal positions. Positions are extrema during the vowel /ʊ/. Symbols and regression lines are as in Fig. 3. Expected correlations are as listed in the caption to Fig. 3.

correlations can be explained as the results of a shift in degree of articulation, a dimension described by Lindblom (1990) as the $H+H$ dimension. A reduction in distance traveled by the articulators corresponding to an economization strategy will likely result in shifts in the position of one articulator away from a gestural goal being accompanied by parallel shifts in the other articulator away from its gestural goal. This effect, which one observes across stress conditions, is apparently observable within stress conditions as well.

Four factors could be considered in accounting for the differences in relationship. First, it is possible that the differ-

TABLE VIII. Partial regression coefficients of $F2$ regressed against labial variables after DX was forced. Signs in parentheses indicate whether correlations are in the expected direction (+), or unexpected direction (−). Boldface indicates effects significant at the 0.013 level.

		SD	MB	TG
/o/	UX	**−0.332(+)**	**−0.341(+)**	−0.052(+)
	UY		0.114(+)	0.032(+)
	LX	−0.086(+)	−0.198(+)	**−0.223(+)**
	LY	0.131(−)	0.081(−)	0.014(−)
/U/				
	UX	0.049(−)	**−0.256(+)**	−0.052(+)
	UY	−0.081(−)	**0.377(+)**	
	LX		−0.180(+)	
	LY	−0.026(+)	**0.482(−)**	

ences in results are simply due to methodological problems with the present study. For example, using asynchronous measures of $F2$ and the different articulators may have obscured some of the effects in some of the vowels for some of the speakers, but not others. In addition, the flesh points which were tracked were, at best, indirect indices of the gestures involved. This is especially true of the labial indices. While such factors are likely contributors to some of the irregularities of the present results, they do not seem to afford explanations for the clear differences in correlational patterning between, especially, the two male speakers.

Second, vowel categories may differ. However, one speaker shows anticompensatory relationships in /o/, while the other shows compensatory relationships in /o/. Both of these speakers arguably show no clear relationship in /U/. The third speaker exhibits both types of correlations for both vowels. Thus, vowel category does not seem to have a clear effect on the pattern of results.

Third, one might appeal to a general difference between hypo- and hyperarticulate speech (Lindblom, 1990). Perhaps, different types of relationships are apparent in hyperarticulate speech and hypoarticulate speech. One way to examine this possibility is to compare patterns obtained in the various stress conditions. For one speaker, there was a trend toward more compensatory correlations in less stressed tokens, a result which compares well with Perkell *et al.* (1993). This patterning suggests that compensatory behavior is indicative of cases of hypoarticulation. However, this pattern only appears in one of the three speakers.

Another way of evaluating this explanation is to compare vowel categories. One major difference between /o/ and /U/ in this experiment is that /o/ is clearly the experimental focus in the corpus. Speakers were much more likely to give attention to the item which changed from trial to trial. Thus, /o/ would be an example of more hyperarticulate speech. Pursuing this explanation, one sees that no particular correlational pattern is associated with hyperarticulate speech. Rather, the correlational patterns simply become more apparent for two of the present speakers. The patterns, however, are different, compensatory in one, anticompensatory in the other. Thus, the present data does not strongly indicate that a difference in level of hyperarticulation will explain the correlational differences. This potential relationship between direction of correlation and level of hyperarticulation is worth more systematic investigation.

Finally, the difference in patterning might be seen as indicative of speaker differences. Each speaker exhibits compensatory relationships between one or another labial dimension and dorsal retraction. However, for one speaker, SD, the relationships are rather weaker, and furthermore, none of the appropriate labial dimensions have a demonstrable effect on $F2$. It is also true that anticompensatory results are restricted to two of the three speakers; TG exhibits no anticompensatory relationships. However, although speaker differences do exist, it is not the case that there are compensatory and anticompensatory speakers. One speaker (MB) shows different correlational patterns with different articulatory dimensions.

The fact that one speaker exhibits two opposite correlational patterns for the two dimensions of upper lip positioning suggests that articulatory goals are more complicated than simply making a constriction, on the one hand, or lowering $F2$ on the other. In this case, it seems there are at least two partially antagonistic goals involved in rounded vowels, rounding/timbre lowering, and oral cavity opening. This is apparent also in the results obtained for lower lip position. The strongest and most consistent lip-to-dorsum correlations obtained here are between lower lip height and dorsal retraction. However, since the effect of lip height on $F2$ is opposite to that expected by the effect of labial constriction (lip raising is associated with higher $F2$), one cannot see this as an example of a compensatory relationship. Rather, lip lowering is associated with oral cavity opening. Thus, even if we considered this speaker as having acoustically focused vowel production goals, it is difficult to know which effect is best seen as compensation—that which lowers $F2$, or that which opens the oral cavity. More progress must be made in assessing what counts as an acoustic goal within the particular linguistic system the speaker is assuming before such questions can be fully addressed.

IV. CONCLUSION

The present study has found that speakers exhibit acoustically based compensation. One potential objection to this conclusion, however, is that the compensatory correlations tend to be rather weak, and are speaker dependent. However, considering the number of factors which might obscure such a relationship, and the good reasons to expect anticompensatory relationships, what is surprising is that compensatory correlations are detectable at all. Flesh-point choice, measurement error inherent in the articulatory tracking system, and time-slice choice each will likely weaken the correlations. Factors which reduce the extent of a tongue gesture, such as undershoot due to the conflicting demands of neighboring speech actions or a reduction in articulatory cost, will either reduce the lip and dorsum gestures in a parallel fashion or leave them unaffected. Since speech occurs in the background of a communicative system which embodies a tremendous amount of flexibility and redundancy, one can reasonably expect speakers to happily allow such parallel underarticulation to occur, yielding anticompensatory corre-

lations. Thus, it is significant that compensatory correlations are observable in the face of such obscuring and conflicting factors.

Johnson *et al.* (1993), finding speaker differences in amount and type of labial and velar articulation in back vowels, argued for a common, auditorily based target that all of the speakers were aiming at. This paper presents data which corroborates Perkell *et al.* (1993) and Savariaux *et al.* (1995) which suggest further that speakers not only differ as to their solutions to the problem of what articulatory configurations will produce socially acceptable acoustic output, but also in their use of the various articulatory techniques which can produce this output. Some speakers seem to utilize a linkage between the lips and tongue dorsum, and others do not. The present study shows this variation in ''on-line'' speech activity. Savariaux *et al.* (1995), since they report on an external perturbation study, show this variation is not just due to the obscuring effects of processes such as parallel underarticulation which occur in normal running speech.

The existence of such interspeaker variation is not surprising if we consider speech as simply analogous to other motor control problems. There is certainly anecdotal evidence concerning the variability in human abilities to perform all kinds of tasks. Some typists use both right and left index fingers to reach numerals in the middle of the key board. Some drivers will use both left and right foot for breaking. The present situation is similar in that there are two types of solutions for a particular task. Some speakers will rely on one, some another, and yet others will switch back and forth according to the exigencies of the moment. Previous studies such as Edwards (1992), Johnson *et al.* (1993), Lee (1994), and de Jong (1995b) all comment on this kind of variation in speakers' use of the jaw. The question at hand, however, is the definition of the task to be performed. In the case of such things as typing, the task is defined by making sufficient contact with the appropriate key; in stopping a car, the task is defined by exerting sufficient pressure on a break pedal. In each case, the mechanics of the goal and what constitutes an achievement are relatively easy to understand. In speech, however, the nature of the goal and what constitutes a successful performance of a task is inextricably tied to the complexities of the perceiver, including not just the abilities of the perceiver to overcome a large amount of ambiguity by drawing inferences, but also the sum total of the perceiver's experience with the linguistic system, both as a perceiver and a producer.

Thus, the general question addressed here is whether the task from the producer's standpoint is to be seen as an acoustic one or an articulatory one. The conclusion suggested by this and previous studies is that the answer depends, in part, on the individual. It is the sum total of the varied individuals acting both as perceivers and producers that constitutes a complete system in which communication takes place successfully.

ACKNOWLEDGMENTS

I thank the staff of the Wisconsin x-ray microbeam facility, in particular, Karl Johnson and Robert Nadler, for their work in the acquisition and processing of the data. I also thank Keith Johnson, Gary Weismer, and Anders Löfqvist for valuable commentary on earlier versions of this paper. Work supported by the NSF under Grant No. IRI-8617852 to Mary Beckman and NIDCD under Grant No. T32DC00029 to the UCLA Phonetics Laboratory.

Abbs, J. L., Gracco, V. L., and Cole, K. J. (**1984**). ''Control of multimovement coordination: Sensorimotor mechanisms in speech motor programming,'' J. Mot. Behav. **16**(2), 195–231.

Browman, C., and Goldstein, L. (**1989**). ''Tiers in articulatory phonology: Some implications for casual speech,'' in *Papers in Laboratory Phonology: Between the Grammar and the Physics of Speech*, edited by J. Kingston and M. E. Beckman (Cambridge U. P., Cambridge, England), pp. 341–376.

Browman, C., and Goldstein, L. (**1990**). ''Gestural specifications using dynamically-defined articulatory gestures,'' J. Phon. **18**, 299–320.

Chiba, T., and Kajiyama, M. (**1941**). *The Vowel: Its Nature and Structure* (Phonetic Society of Japan, Tokyo).

de Jong, K. (**1993**). ''Phonetic units and American English [ow],'' UCLA Working Papers in Phonetics **83**, 117–139.

de Jong, K. (**1995a**). ''On the status of redundant features: the case of backness and roundness in American English,'' in *Papers in Laboratory Phonology 4*, edited by B. Connell and A. Arvaniti (Cambridge U. P., Cambridge, England).

de Jong, K. (**1995b**). ''The supraglottal articulation of prominence in English: Linguistic stress as localized hyperarticulation,'' J. Acoust. Soc. Am. **97,** 491–504.

Edwards, J. (**1992**). ''Compensatory speech motor abilities in normal and phonologically disordered children,'' J. Phon. **20**, 189–207.

Fant, G. (**1960**). *The Acoustic Theory of Speech Production* (Mouton, The Hague).

Folkins, J. W., and Abbs, J. H. (**1975**). ''Lip and jaw motor control during speech: Responses to resistive loading of the jaw,'' J. Speech Hearing Res. **18**, 207–220.

Gay, T., Lindblom, B. E. F., and Lubker, J. (**1981**). ''Production of bite-block vowels: Acoustic equivalence by selective compensation,'' J. Acoust. Soc. Am. **69,** 802–810.

Goldstein, L. (**1983**). ''Vowel shifts and articulatory-acoustic relations,'' in *Abstracts of the Tenth International Congress of Phonetic Sciences, Utrecht, 1983*, edited by A. Cohen and M. P. V. van den Broeke (Foris, Dordrecht), pp. 267–273.

Goldstein, L. (**1989**). ''On the domain of quantal theory,'' J. Phonetics **17**, 91–97.

Johnson, K., Ladefoged, P., and Lindau, M. (**1992**). ''Individual differences in vowel production,'' J. Acoust. Soc. Am. **94,** 701–714.

Kelso, J. A. S., Tuller, B., Vatikiotis-Bateson, E., and Fowler, C. A. (**1984**). ''Functionally specific articulatory cooperation following perturbations during speech: Evidence for coordinative structures,'' J. Exp. Psychol. Hum. Percept. Perform. **10**(6), 812–832.

Kirk, R. E. (**1982**). *Experimental Design: Procedures for the Behavioral Sciences* (Brook/Cole, Monterey, CA), 2nd ed.

Lee, S. H. (**1994**). ''A Cross-linguistic Study of the Role of the Jaw in Consonant Articulation,'' Ph.D. dissertation, Ohio State University (unpublished).

Lindblom, B. (**1990**). ''Explaining phonetic variation: a sketch of the H&H theory,'' in *Speech Production and Speech Modeling, NATO ASI Series D: Behavioural and Social Sciences*, edited by H. J. Hardcastle and A. Marchal (Kluwer, Dordrecht), Vol. 55, pp. 403–439.

Lindblom, B., and Sundberg, J. (**1971**). ''Acoustical consequences of lip, tongue, and larynx movement,'' J. Acoust. Soc. Am. **50,** 1166–1179.

Nadler, R., Abbs, J. H., and Fujimura, O. (**1987**). ''Speech movement research using the new X-ray microbeam system,'' in *Proceedings of the 11th International Congress of Phonetic Sciences, Tallinn, 1987* (Academy of Sciences of the Estonian Soviet Socialist Republic, Tallinn), Vol. 1, pp. 221–224.

Nearey, T. M. (**1989**). ''Static, dynamic, and relational properties in vowel perception,'' J. Acoust. Soc. Am. **85,** 2088–2113.

Nearey, T. M., and Assmann, P. (**1986**). ''Modeling the role of inherent spectral change in vowel identification,'' J. Acoust. Soc. Am. **80,** 1297–1308.

Perkell, J. S. (**1990**). ''Testing theories of speech production: Implications of some detailed analyses of variable articulatory data,'' in *Speech Pro-*

duction and Speech Modeling, NATO ASI Series D: Behavioural and Social Sciences, edited by H. J. Hardcastle and A. Marchal (Kluwer, Dordrecht), Vol. 55, pp. 263–288.

Perkell, J. S., Matthies, M. L., Svirsky, M. A., and Jordan, M. I. (**1993**). ''Trading relations between tongue-body raising and lip rounding production in the vowel /u/: a pilot 'motor equivalence' study,'' J. Acoust. Soc. Am. **93,** 2948–2961.

Pierrehumbert, J. B. (**1980**). *The Phonology and Phonetics of English Intonation* (Indiana University Linguistics Club, Bloomington, IN).

Pierrehumbert, J. B., and Beckman, M. E. (**1988**). *Japanese Tone Structure*, *Linguistic Inquiry*, *Monograph* 15 (MIT, Cambridge, MA).

Saltzman, E. L., and Munhall, K. G. (**1989**). ''A dynamical approach to gestural patterning in speech production,'' Eco. Psychol. **1**, 333–382.

Savariaux, C., Perrier, P., and Orliaguet, P. P. (**1995**).''Compensation strategies for the perturbation of the rounded vowel [u] using a lip tube: A study of the control space in speech production,'' J. Acoust. Soc. Am. **98,** 2428–2442.

Shaiman, S. (**1989**). ''Kinematic and electromyographic responses to perturbation of the jaw,'' J. Acoust. Soc. Am. **86,** 78–88.

Stevens, K. N., and House, A. S. (**1953**). ''Development of a quantitative description of vowel articulation,'' J. Acoust. Soc. Am. **27,** 484–493.

Strange, W., Verbrugge, R., Shankweiler, D., and Edman, T. (**1976**). ''Consonant environment specifies vowel identity,'' J. Acoust. Soc. Am. **60,** 213–214.

Strange, W., Jenkins, J. J., and Johnson, T. L. (**1983**).''Dynamic specification of coarticulated vowels,'' J. Acoust. Soc. Am. **74,** 695–705.

Westbury, J. R. (**1991**). ''The significance and measurement of head position during speech production experiments using the x-ray microbeam system,'' J. Acoust. Soc. Am. **89,** 1782–1791.

Acoustic interactions of the voice source with the lower vocal tract

Ingo R. Titze and Brad H. Story
Department of Speech Pathology and Audiology and The National Center for Voice and Speech, The University of Iowa, Iowa City, Iowa 52242-1012

(Received 29 July 1996; revised 8 November 1996; accepted 25 November 1996)

The linear source-filter theory of speech production assumes that vocal fold vibration is independent of the vocal tract. The justification is that the glottis often behaves as a high-impedance (constant flow) source. Recent imaging of the vocal tract has demonstrated, however, that the epilarynx tube is quite narrow, making the input impedance to the vocal tract comparable to the glottal impedance. Strong interactions can exist, therefore. In particular, the inertance of the vocal tract facilitates vocal fold vibration by lowering the oscillation threshold pressure. This has a significant impact on singing. Not only does the epilarynx tube produce the desirable singer's formant (vocal ring), but it acts like the mouthpiece of a trumpet to shape the flow and influence the mode of vibration. Effects of the piriform sinuses, pharynx expansion, and nasal coupling are also discussed. © *1997 Acoustical Society of America.* [S0001-4966(97)01704-9]

PACS numbers: 43.70.Bk, 43.75.Rs [WJS]

INTRODUCTION

Adjustments in the lower vocal tract (the epilarynx tube, the piriform sinuses, the pharynx) and the nasal port seem to play an important role in regulating voice quality (Bartholomew, 1934; Laver, 1980; Estill, 1981). Fiberoptic observations of the supraglottal structures of voice impersonators (Feder, 1988) suggest that the epiglottis, the pharyngeal walls, the opening to the piriform sinuses, the false vocal folds, and the aryepiglottic folds can all be adjusted to create special vocal effects. Estill (1981) and Colton and Estill (1981) observed differences in these supralaryngeal configurations between normal *speech* quality, *opera* quality, *twang*, and *sob*. Later, Estill and co-workers added *belt*, which is a quality characteristic of modern musical theater singing (Yanagisawa *et al.*, 1989; Estill, 1995). *Twang* and *belt* qualities generally have both a narrow epilarynx tube and a narrow pharynx, whereas *sob* exhibits a widening of both structures. *Opera* quality demonstrates a relatively wide pharynx with a relatively narrow epilarynx tube. Part of this quality is vocal *ring*, the percept of a bell-like constant background tone, which spectrally shows up as a prominence of acoustic energy in the 2500–3500 Hz range, independent of vowel (Bartholomew, 1934; Helmholtz, 1954; Sundberg, 1974; Yanagisawa *et al.*, 1989).

Quantitative analysis of vocal *ring* was conducted by Sundberg (1974). By modeling the epilarynx tube as a separate small resonator inside and at the base of a larger tube representing the vocal tract, Sundberg was able to show that a large concentration of acoustic energy was produced around 3000 Hz. He called this the singer's formant because it spectrally appears like a new formant, although it is generally a clustering of the third, fourth, and fifth formant. The singer's formant was particularly prominent when the open end of the small tube (the aryepiglottic collar) expanded abruptly into the wider tube (the lower pharynx). An area expansion of 6:1 or greater produced large amounts of *ring*. In such a sudden expansion, the small resonator is relatively independent of the large resonator and has its own formant structure. In particular, for an approximate 3-cm length, the epilarynx tube is about $\frac{1}{6}$ the length of a typical 17.5-cm male vocal tract. Given the same boundary condition (open at the top and closed at the bottom), the first formant frequency should be six times higher than the 500-Hz first formant frequency of a uniform vocal tract, or about 3000 Hz.

Figures 1 and 2 show sagittal and anterio-lateral views, respectively, of a vocal tract airway as imaged by electron beam computed tomography (EBCT). The epilarynx tube is the narrow portion above the glottis in each figure. In Fig. 1, the epilarynx tube is slanted upward to the left and a little more of the tracheal airway is shown below the glottis than in Fig. 2. Note that at the top of the epilarynx tube, the airway widens and becomes complicated. The lower pharynx, near the vallecula, is seen as a sudden expansion and the two piriform sinuses protrude downward from this expansion. The piriform sinuses are acoustic side branches that can have a profound effect on the resonance of the entire system. Dang and Honda (1996), have recently studied this effect in detail. Using both a human subject and a physical model, they filled the piriform sinuses with water to eliminate the acoustic side branches. In each case, the epilarynx tube resonance was enhanced with the elimination of the side branches. Thus, the piriform sinuses acted as energy absorbers (spectral zeros). It would seem, then, that a vocalist intending to produce *ring* in the voice would find a strategy to block or reorient the side branches in a way that would minimize their absorption effect.

The current study is a theoretical investigation of how the entire back portion of the vocal tract can be adjusted geometrically to produce the most favorable conditions for vocal fold oscillation. The basic question is: As relative areas or lengths of the epilarynx, the pharynx, the piriform sinuses, and the nasal tract are varied, what is the effect of the spectral balance, the glottal waveform, and the phonation threshold pressure? The first step in the analysis is to compute the

 0001-4966/97/101(4)/2234/10/$10.00

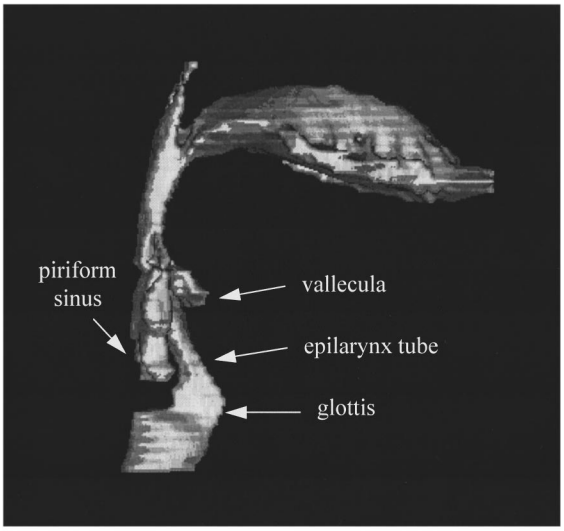

FIG. 1. Sagittal section of an electron beam CT scan of the vocal tract airway of a normal 30-year-old male subject phonating an /ə/ vowel (from Story *et al.*, 1996, by permission).

input impedance and transfer function of the vocal tract for a variety of geometries. This computation is in the form of a sensitivity analysis to determine the critical parameters. The second step is to simulate the glottal waveform and the oral radiated pressure interactively with the vocal tract for critical parameter changes.

I. VOCAL TRACT INPUT IMPEDANCE CALCULATION

To determine the relative importance of a variety of areas and lengths in the airway structures, it is instructive to begin with a sensitivity analysis of the input impedance and the transfer function of the vocal tract. The input impedance, defined as the ratio of supraglottal pressure to glottal flow (both as complex numbers), can have a profound effect on the conditions of the vocal fold oscillation, as will be seen later. The transfer function, defined as the ratio of oral radiated pressure to glottal flow (likewise as complex numbers), determines the output for a given input.

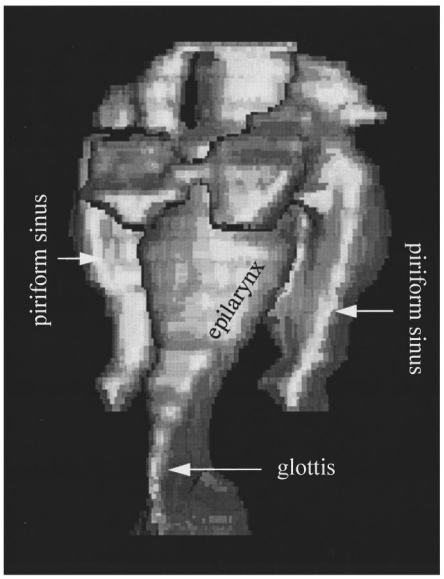

FIG. 2. Anterio-lateral view of an approximate 2:1 enlargement of the laryngeal-pharyngeal portion of Fig. 1 (from Story *et al.*, 1996, by permission).

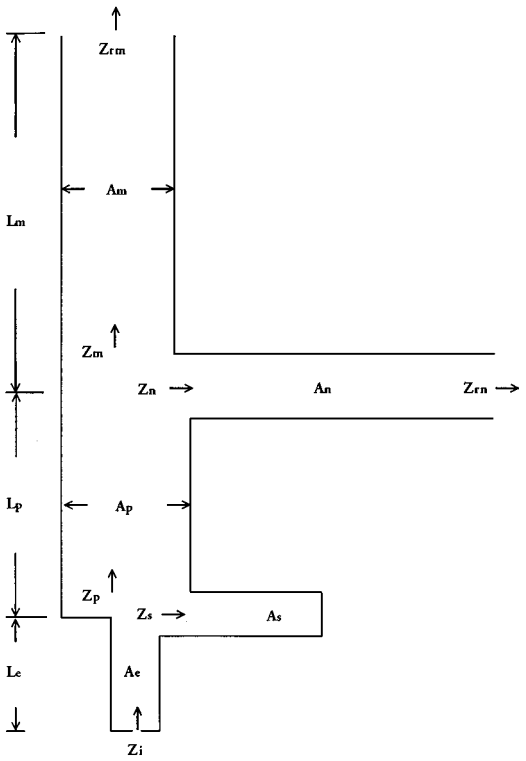

FIG. 3. Schematic diagram of an acoustic transmission line with a narrowed epilarynx at the bottom and two side branches.

Consider the vocal tract to be a transmission line with side branches as shown in Fig. 3. The following parameters are defined:

A_m, L_m = cross-sectional area and length of the mouth section;
A_n, L_n = cross-sectional area and length of the nasal section;
A_p, L_p = cross-sectional area and length of the pharynx section;
A_s, L_s = cross-sectional area and length of the piriform sinus section;
A_e, L_e = cross-sectional area and length of the epilarynx section.

The impedance and transfer function calculations follow the chain matrix approach used by Sondhi and Schroeter (1987). We will not restate all the mathematical steps in this calculation, but give an equivalent abbreviated derivation for the impedance only. The calculation begins by defining a frequency f and a corresponding wave number for one-dimensional wave propagation in a tube,

$$\beta = 2\pi f/c, \tag{1}$$

where c is the sound propagation velocity (350 m/s in a warm, humid vocal tract). Next, an attenuation factor α is defined (or more detailed frequency-dependent losses), which together with the wave number gives a complex propagation constant

$$\gamma = \alpha + j\beta, \tag{2}$$

where $j=(-1)^{1/2}$.

Using standard transmission line theory (see, for example Flanagan, 1972, p. 52, equation 3.53), the input impedance to the mouth section can be written as

$$Z_m=\frac{\rho c}{A_m}\frac{Z_{rm}\cosh\ \gamma L_m+(\rho c/A_m)\sinh\ \gamma L_m}{(\rho c/A_m)\cosh\ \gamma L_m+Z_{rm}\sinh\ \gamma L_m}, \tag{3}$$

where ρ is the density of air and Z_{rm} is the radiation impedance at the mouth end. The radiation impedance is also given by Flanagan:

$$Z_{rm}=\rho f[\beta+j\tfrac{16}{3}(\pi A_m)^{-1/2}]. \tag{4}$$

The input impedance to the nasal section can be written in an identical fashion, replacing the subscript m by n.

Continuing downward in the impedance calculation of Fig. 3, the impedance at the end of the pharynx section is now the parallel combination of the mouth and nose input impedance,

$$Z_{mn}=\frac{Z_mZ_n}{Z_m+Z_n}. \tag{5}$$

Using the transmission-line equation again, the input impedance to the pharynx is

$$Z_p=\frac{\rho c}{A_p}\frac{Z_{mn}\cosh\ \gamma L_p+(\rho c/A_p)\sinh\ \gamma L_p}{(\rho c/A_p)\cosh\ \gamma L_p+Z_{mn}\sinh\ \gamma L_p}. \tag{6}$$

The input impedance to the piriform sinuses is simpler because the termination impedance of the sinuses is infinite at the closed end. If we assume that the two sinuses are identical, then a single cross-sectional area A_s can represent the sum of the two cross-sectional areas, and

$$Z_s=\frac{\rho c}{A_s}\frac{\cosh\ \gamma L_s}{\sinh\ \gamma L_s}. \tag{7}$$

Once again, the parallel combination of Z_s and Z_p can be computed as in Eq. (5) to get Z_{ps}, and the final expression for the input impedance to the vocal tract becomes

$$Z_i=\frac{\rho c}{A_e}\frac{Z_{ps}\cosh\ \gamma L_e+(\rho c/A_e)\sinh\ \gamma L_e}{(\rho c/A_e)\cosh\ \gamma L_e+Z_{ps}\sinh\ \gamma L_e}. \tag{8}$$

We now choose a *nominal configuration* around which the parameter variation will be carried out:

$$\begin{aligned}
&A_e=0.5\ \text{cm}^2, \quad L_e=3.1744\ \text{cm},\\
&A_s=1.0\ \text{cm}^2, \quad L_s=2.3808\ \text{cm},\\
&A_p=3.0\ \text{cm}^2, \quad L_p=4.7616\ \text{cm},\\
&A_n=0.0\ \text{cm}^2, \quad L_n=11.1104\ \text{cm},\\
&A_m=3.0\ \text{cm}^2, \quad L_m=9.5232\ \text{cm}.
\end{aligned} \tag{9}$$

None of the areas are constant as a function of length in a human vocal tract (Story, 1995; Story *et al.*, 1996; Dang and Honda, 1996) but in the calculation they are chosen constant to limit the number of parameters. The lengths are chosen to correspond to integral numbers of discrete sections of the vocal tract to be discussed later. The nominal value for A_e may be a little large for speech quality (a value of 0.3 cm^2 is more typical in the data sets cited above), but given that other qualities such as *sob* are also of interest, it is a reasonable compromise. Note also that the nominal configuration has a closed nasal port, but the piriform sinuses are open. In various plots to follow, the *nominal configuration* will always be represented by *dashed lines*.

Figure 4 shows the magnitude of the transfer function (in dB) at the top left, the magnitude of the input impedance (in dB) at the top right, the real part of the input impedance (in dyn-s/cm^5) at the bottom left, and the imaginary part of the input impedance (in dyn-s/cm^5) at the bottom right. The solid curve on each plot illustrates the case *without* a narrowed epilarynx tube. Although this case is physiologically unrealistic, it is of theoretical interest because the uniform tube has been used extensively as the starting point for vocal tract modeling, without much consideration of the epilarynx tube. With this uniform tube ($A_e=A_p=3.0\ \text{cm}^2$), there are roughly equally spaced formant frequencies near $(2n-1)$ (501) Hz, the quarter-wave resonance frequencies for a 17.46-cm tube, but the formants are detuned slightly because of the radiation impedance and the piriform sinuses. This detuning will be discussed later. For the moment, the most important observation is that the reactance curve (bottom right) crosses the zero line at the formant frequencies, alternating between positive (inertive) reactance and negative (compliant) reactance. Also, both resistance and reactance are generally low.

With a narrowed epilarynx tube ($A_e=0.5\ \text{cm}^2$, dashed lines) the magnitudes of all the functions are generally higher throughout the frequency range, particularly in the 2500–3500 Hz region. The resistance (real part of input impedance) rises sharply for the third and fourth formant, while the reactance is generally more positive (inertive) below 2500 Hz and generally more negative above 2500 Hz. The increased inertive reactance below 2500 Hz is significant. Earlier analysis (Titze, 1988) has shown that inertive reactance effectively becomes negative resistance for small oscillation of glottal airflow and vocal fold tissue.

Figure 4 also shows that the first three formant frequencies for the narrowed epilarynx are raised in comparison to the uniform tract. However, the fourth and fifth formant frequencies are lowered. The narrowed epilarynx tube therefore ''attracts'' all formant frequencies toward the 2500–3000 Hz region. This attraction of all the formant frequencies toward a single frequency focus was noted by Sundberg (1974) in his analysis.

If we consider the epilarynx tube to be a separate quarter-wave resonator, its uncoupled formant frequencies are

$$F_{en}=(2n-1)\frac{c}{4L_e} \tag{10}$$

$$=(2n-1)\frac{35\,000\ \text{cm/s}}{(4)(3.1744)\ \text{cm}} \tag{11}$$

$$=(2n-1)2756\ \text{Hz}. \tag{12}$$

We can say, then, that the first five formant frequencies are attracted toward F_{e1} (2756 Hz, represented by the left-most vertical dotted line in Fig. 4). In the limit, as A_e becomes

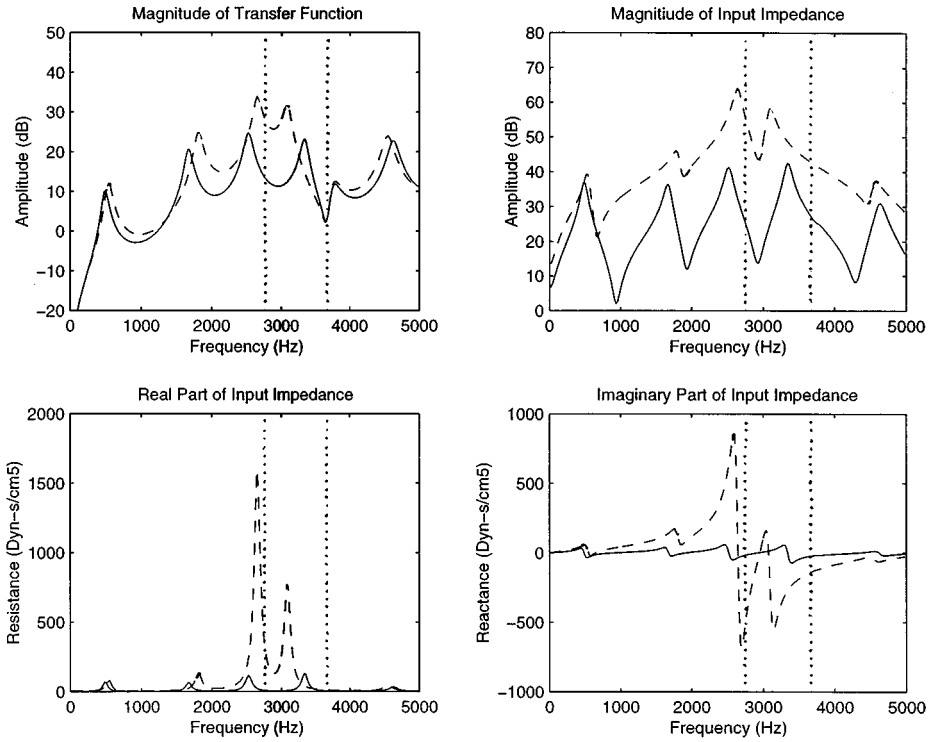

FIG. 4. Magnitude of the transfer function, magnitude of input impedance, resistance (real part), and reactance (imaginary part) of the input impedance for the idealized transmission system shown in Fig. 3. Solid lines are for $A_e=3.0$ cm^2 (a wide epilarynx tube) and dashed lines are for $A_e=0.5$ cm^2 (a narrow epilarynx tube).

very small, the epilarynx tube has its own series of formants as given in Eq. (12), with the formants of the larger tube (the vocal tract) becoming insignificant.

Another possibility is to consider the epilarynx tube as a Helmholtz resonator. One would have to identify a resonator neck and a resonator volume. If the volume is taken to be $L_eA_e=1.6$ cm^3, then the ratio of the neck area to the neck length would need to be 0.46 cm in order to get a 3000-Hz resonance frequency (see, for example, Kinsler and Frey, 1962, Chap. 8, for a discussion of the Helmholtz resonator). Assuming a neck area of 0.2 cm^2 at the aryepiglottic folds, the neck length would have to be 0.43 cm. Such a configuration is possible, but the frequency would be too critically dependent on the shape of the resonator neck. Given the constancy of the frequency and the variability of the neck region, it is our opinion that the quarter-wave resonance concept is more viable. Dang and Honda (1996) came to the same conclusion with regard to the piriform sinuses.

Note that the transfer function (upper left in Fig. 4) has a spectral zero at 3675 Hz, the resonance frequency of the piriform sinuses (second vertical dotted line). Using again the quarter-wave resonator formula, a collection of resonance frequencies is predicted at

$$F_{sn}=(2n-1)\,\frac{c}{4L_s}. \tag{13}$$

The first resonance frequency F_{s1} is at 3675 Hz when $L_s=2.3808$ cm, the nominal value selected above. At this piriform sinus frequency, there is a large energy exchange between the epilarynx tube and the sinuses, but little of this energy gets into the upper vocal tract and out of the mouth. The energy is dissipated within the vocal tract, as the transfer function shows. However, the input impedance is not affected by this energy exchange, showing nothing remarkable in the 3675-Hz region, neither in terms of resistance nor reactance.

Dang and Honda's spectral zero was slightly higher (about 4000–4200 Hz) because they measured a piriform sinus length of slightly less than 2.0 cm on a human subject. The length chosen here was dictated by a need for an even number of cylindrical sections of a wave reflection model (to be discussed later). The difference is not of fundamental importance, given the variability in laryngeal anatomy among humans.

An interesting situation arises when the length of the piriform sinuses is chosen to be the same as the length of the epilarynx tube. A resonance and an anti-resonance (a pole and a zero) are then juxtaposed. This situation is shown in Fig. 5 (solid lines). The arrow to the left shows the direction in which the zero has shifted. Note that the transfer function shows no effect of the zero anymore, but the input impedance rises to a maximum at the combined resonance frequency ($F_{e1}=F_{s1}=2756$ Hz), which is very close to F_3 of the vocal tract. The low-frequency region is basically unaffected, except for a small reduction in F_2. A complete juxtaposition of this type is unlikely in human phonation because an exact match in both length and cross-sectional area of the two resonators is difficult to achieve. However, the result is interesting because it shows a possible target strategy to counteract the effects of the piriform sinuses.

Total elimination of the piriform sinuses has a similar effect. As shown in Fig. 6 (solid lines), the zero is obviously

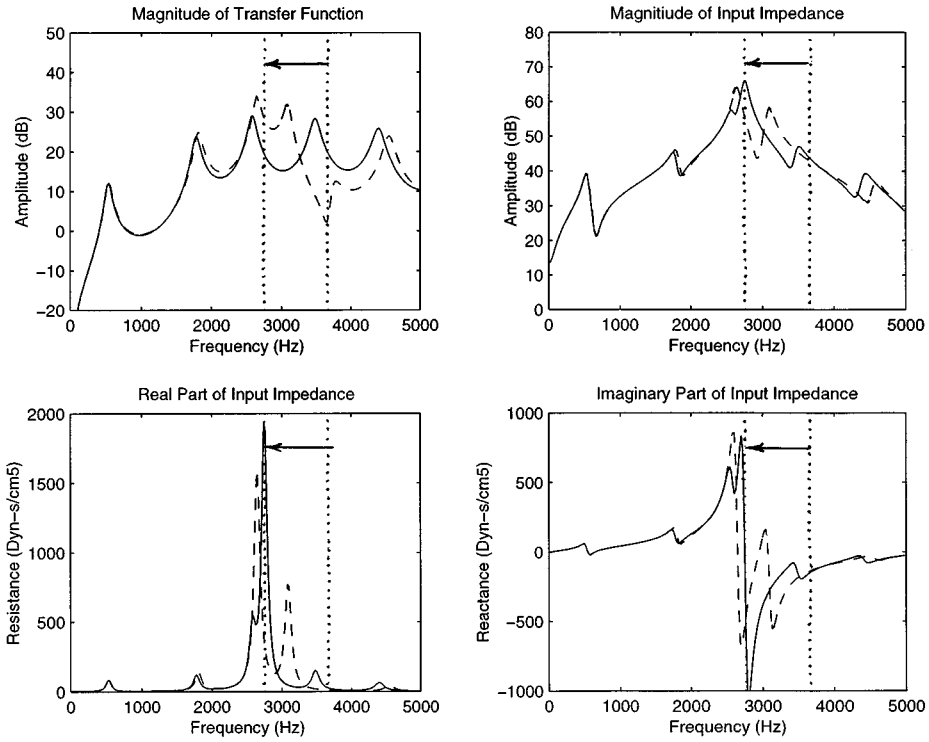

FIG. 5. Magnitude of the transfer function, magnitude of input impedance, resistance (real part), and reactance (imaginary part) of the input impedance for the idealized transmission system shown in Fig. 3. Solid lines are for $L_s = L_e$ (length of piriform sinuses equals length of epilarynx) and dashed lines are for the nominal configuration.

removed from the transfer function, and the input impedance is again raised slightly *vis a vis* the nominal configuration; another effect is that $F_2 - F_4$ are raised. On the other hand, F_5 is lowered. We conclude, therefore, that the piriform sinuses have the effect of ''repelling'' the formants on both sides of their resonance frequency. They push $F_1 - F_4$ lower and F_5 higher. F_3 is least affected by this push because it is highly ''attracted'' by the epilarynx resonance. Again, this

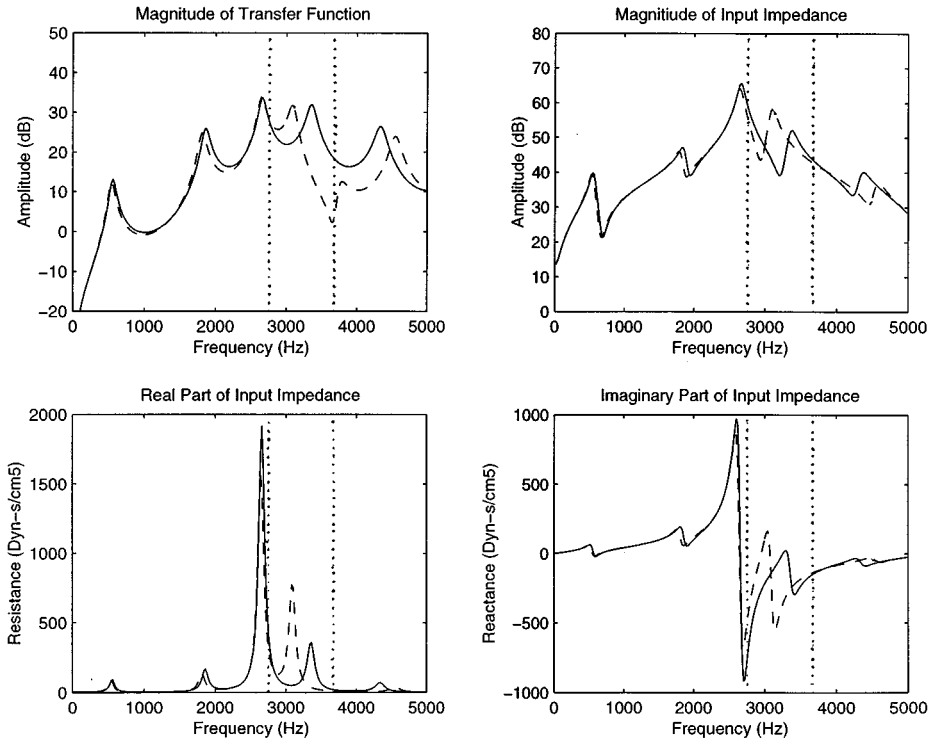

FIG. 6. Magnitude of the transfer function, magnitude of input impedance, resistance (real part), and reactance (imaginary part) of the input impedance for the idealized transmission system shown in Fig. 3. Solid lines are for no piriform sinuses and dashed lines are for the nominal configuration.

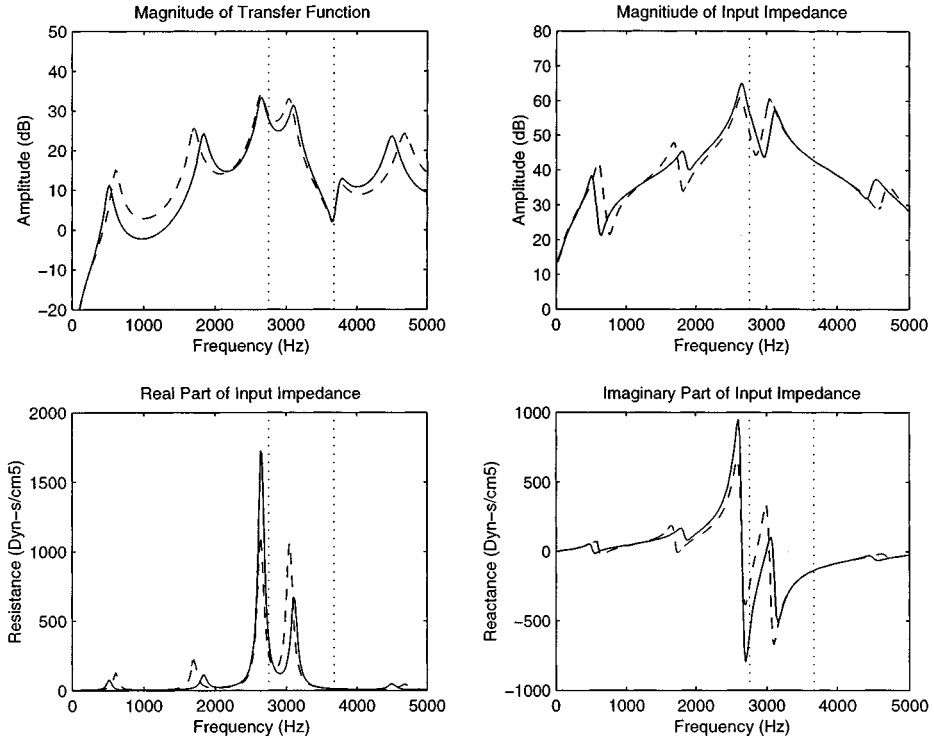

FIG. 7. Magnitude of the transfer function, magnitude of input impedance, resistance (real part), and reactance (imaginary part) of the input impedance for the idealized, transmission system shown in Fig. 3. Solid lines are for a widened pharynx (A_p=6.0 cm^2) and dashed lines are for the nominal configuration.

''elimination'' of the piriform sinuses is a theoretical exercise. It is not known whether a singer or speaker can actually utilize muscular control in the neck to effectively shut off the piriform sinuses. Perhaps a thick neck, with an abundance of soft tissue that can be pushed medially, could facilitate this shut-off, but this remains a research question.

Consider now a widened pharynx in addition to the epilarynx tube and the piriform sinuses, as in the *opera* quality. In Fig. 7 (solid lines), A_p was increased from 3 to 6 cm^2. Given that A_e was maintained at 0.5 cm^2, the A_p/A_e ratio was now 12 instead of 6. Note that this widened pharynx lowers F_1 and raises F_2. This is well known from basic acoustic theory of an /i/ vowel, which has a widened pharynx relative to the oral tract. A more interesting result is that the resistance is lowered at F_1 and F_2 but raised at F_3. Furthermore, the reactance curve is smoothed out (less ripple) in the F_1 and F_2 regions and also rises to a large peak at F_3 (near 2500 Hz). F_4, on the other hand, is reduced in both resistance and reactance. Thus, the combination of a narrow epilarynx tube and a wide pharynx is ideal for maintaining a positive and steadily rising inertive reactance from 0-F_{e1}, but at the expense of a more compliant reactance above F_{e1}. This is important for self-oscillation conditions. A positive reactance, combined with a low resistance in the low-frequency range, reduces the oscillation threshold pressure. This will be demonstrated in Sec. III.

If the pharynx is narrowed (to, say, 1.0 cm^2), the opposite effects occur. Low-frequency resistance increases, reactance is more fluctuating (even going negative), and F_3 exchanges its level of prominence with F_4. This is the condition for *belt* quality. The increased resistance probably accounts (at least in part) for the greater lung pressures that appear to be used in this vocal quality (informal observation).

As a final impedance calculation, consider the effect of the nasal tract. As shown in Fig. 8 (solid lines), opening the nasal port to 1.0 cm^2 and maintaining a uniform nasal tract at this value adds some predictable zeros to the transfer function. Since the tube is open at both ends, the resonance frequencies are at

$$nc/2L_n = n(1575) \quad \text{Hz}. \tag{14}$$

Note that the first three of these zeros are seen in Fig. 8 at 1575, 3150, and 4725 Hz.

The input impedance shows no profound changes with nasality, but there are a few minor observations. An extra ripple is seen in the F_2 region (both in resistance and reactance) because the nasal zero is close to F_2. Also, the zero at 3150 Hz pushes F_3 and F_4 downward a bit (recall that a zero repels a nearby formant). It must be stated, however, that this is not a thorough study of the effects of nasal coupling. In particular, a nonuniform nasal tract may give rather different pole-zero configurations, which might combine with the epilarynx tube and the piriform sinuses in interesting ways. This is also a topic for future research.

II. EFFECT OF VOCAL TRACT IMPEDANCE ON OSCILLATORY CONDITIONS

The effect of vocal tract impedance on vocal fold oscillation was discussed previously in analytical terms (Titze, 1988). The results are restated here to relate them to the new findings. Neglecting the subglottal system, the pressure-flow equation was written as

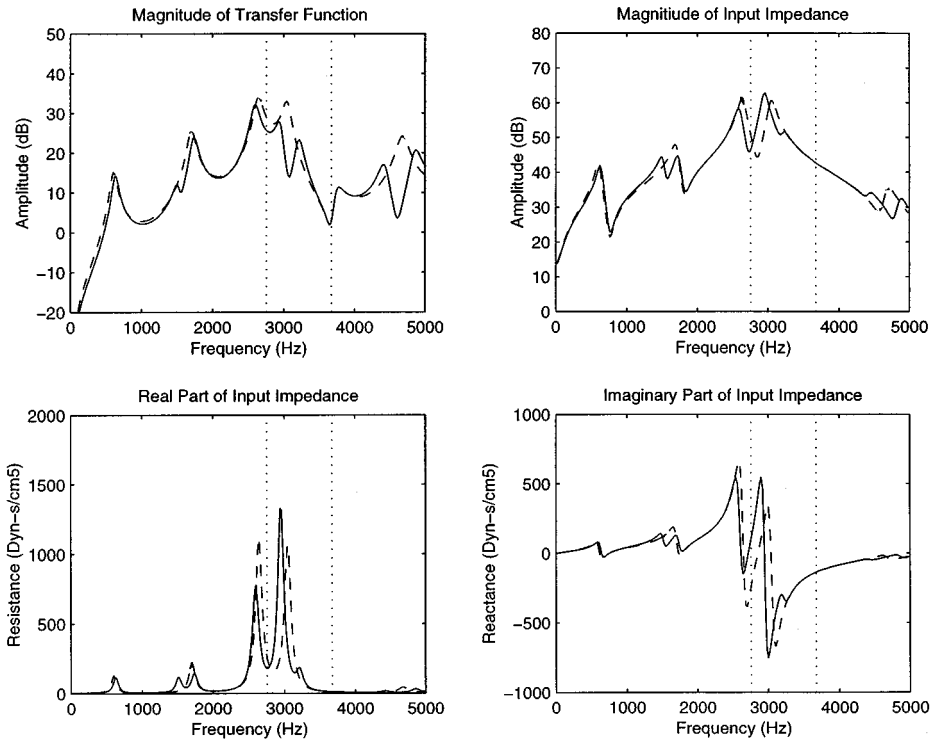

FIG. 8. Magnitude of the transfer function, magnitude of input impedance, resistance (real part), and reactance (imaginary part) of the input impedance for the idealized transmission system shown in Fig. 3. Solid lines are for an open nasal port (A_n=10 cm^2) and dashed lines are for the nominal configuration.

$$P_L=\tfrac{1}{2}k_t\rho|U|UA_g^2+RU+I\dot{U}, \tag{15}$$

where P_L is the lung pressure, k_t is a transglottal pressure coefficient (determined empirically to be about 1.1), A_g is the glottal area, U is the glottal flow, $\dot{U}$ is the flow derivative, and R and I are vocal tract input resistance and inertance, respectively. This equation is a nonlinear differential equation in U that can, under certain conditions, produce an oscillatory solution. By relating the glottal area A_g to vocal fold displacement, mass, stiffness, and damping of a simple one-mass oscillator, it was shown that the oscillation threshold pressure is

$$P_{\text{th}}=\frac{1}{2}\,k_t\rho\left(\frac{B}{2LI}\right)^2, \tag{16}$$

where B is the viscous damping coefficient of vocal fold tissue and L is the vocal fold length. The assumption was made in this derivation that vocal tract resistance R was small in comparison to vocal tract reactance $\omega_0 I$ at the fundamental frequency of oscillation ($\omega_0=2\pi F_0$).

This assumption of small resistance is valid only if the resonance qualities (Qs) of the formants (and epilaryngeal and piriform sinuses) are greater than about 10, which is evident from the impedance and transfer function curves in Figs. 4–8. (A resonance Q is defined as the ratio of the resonance frequency to the resonance bandwidth, ± 3 dB down from the peak.)

Consider now a low-frequency approximation to the input impedance Z_i as given in Eq. (8). If the epilarynx is narrow (0.5 cm^2 or less) and the expansion into the pharynx is wide (3.0 cm^2 or more), then $Z_{ps}\approx Z_p$ and the entire upper vocal tract impedance is negligible in relation to $\rho c/A_e$. Furthermore, for low frequencies, $\sinh(\gamma L_e)\approx\gamma L_e$, and Eq. (8) reduces

$$Z_i=\frac{\rho c}{A_e}\,\gamma L_e. \tag{17}$$

Substituting γ from Eq. (2) and β from Eq. (1), we get

$$Z_i=\frac{\rho c}{A_e}\left(\alpha+j\,\frac{\omega_0}{c}\right)L_e. \tag{18}$$

The resistance in this expression is

$$R=\rho c\,\alpha L_e/A_e, \tag{19}$$

and the inertance is

$$I=\rho L_e/A_e. \tag{20}$$

It is clear that the combined assumptions of low loss, low frequency, and narrow epilarynx are rather drastic, but they are interesting in that they reduce the vocal tract impedance to nothing but the epilarynx tube impedance. This is a bit like saying that the impedance of a trumpet is the same as the impedance of its mouthpiece. Although it cannot be justified in general, it helps to understand the nature of the source-resonator coupling when the entry to the resonator is narrow.

If we now substitute I from Eq. (20) into Eq. (16), the oscillation threshold pressure becomes

$$P_{th}=\frac{1}{8}\left(\frac{k_t}{\rho}\right)\left(\frac{BA_e}{LL_e}\right)^2. \tag{21}$$

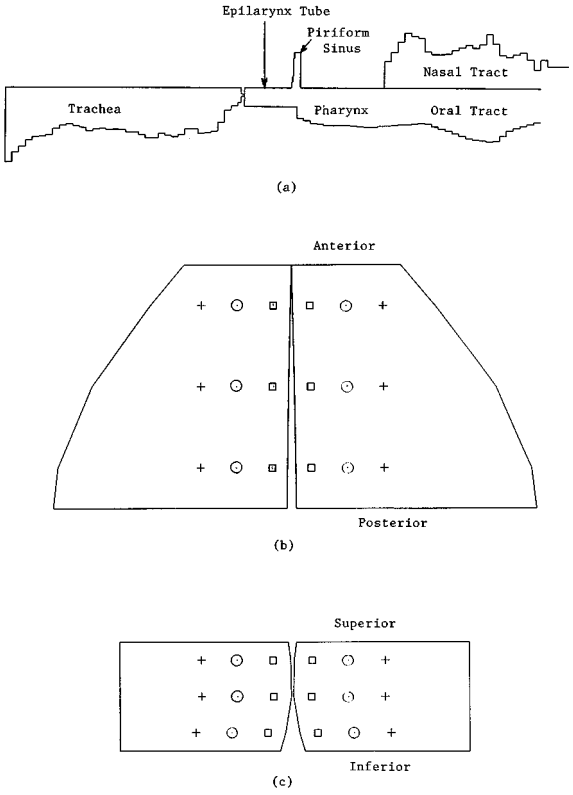

FIG. 9. Sketches illustrating the components of a simulation model. (a) Vocal tract outline with the bend removed, showing equivalent tube diameters of all sections, (b) top view of vocal folds, showing tissue-points of the cover (open squares), ligament (dots), and muscle (plus signs) to form a 3×3 matrix, and (c) coronal section through vocal folds, showing a similar matrix of tissue points.

Focusing on the A_e/L_e ratio in this expression, it is clear that a long, narrow epilarynx tube can have a substantial effect on lowering the oscillation threshold pressure. This will now be shown with a more sophisticated self-oscillating model.

III. SIMULATION OF GLOTTAL FLOW AND OUTPUT SPECTRA

Having discussed the input impedance to the vocal tract in detail, it is now appropriate to examine how this input impedance can affect self-sustained oscillations of the vocal folds. This is best done with numerical simulation. The vocal tract is spatially discretized into 44 cylindrical sections from the glottis to the lips [Fig. 9(a)] and represents the neutral vowel /ə/ of a 30-year-old male subject as measured with magnetic resonance imaging (MRI). A basic speech quality was used to obtain this scan. The length of each section is set to 3.968 mm, as dictated by a chosen sampling frequency of 44.1 kHz and a wave propagation velocity of 350 m/s. A 28-section nasal tract and an 8-section piriform sinus are included. (We are assuming that the two piriform sinuses are identical and that their combined effect can be modeled by a single sinus of twice the cross-sectional area.) A subglottal system is also included, which is 36 sections long from the glottis to the bronchial bifurcation.

One-dimensional acoustic wave propagation is simulated in all the tubes according to the algorithms described by Liljencrants (1985) and Story (1995). Basically, at each junction between two adjacent cylindrical sections, two reflected waves are computed from two incident waves known from the previous time step. The solution is synchronized in time with the wave velocity through the tubes. Due to the nature of the wave reflection algorithm, the vocal tract is effectively sampled at 88.2 kHz while the glottal source and the pressure output from the vocal tract are sampled at 44.1 kHz (Liljencrants, 1985).

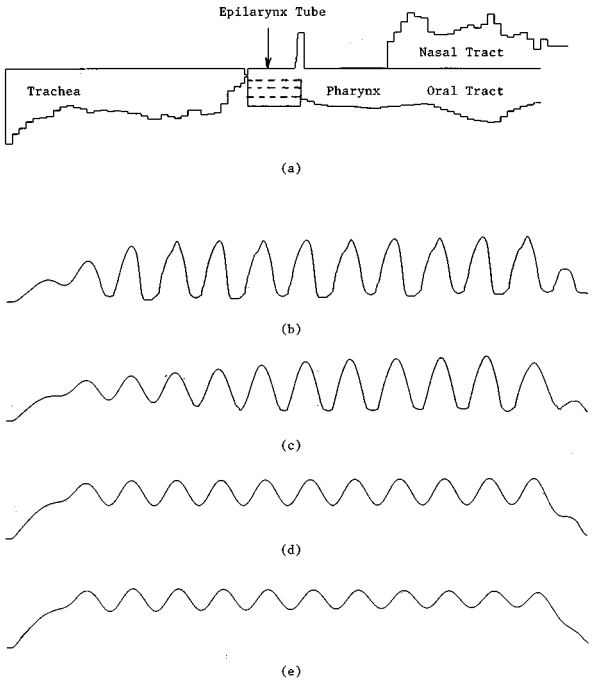

FIG. 10. The effect of a widening the epilarynx tube. Dashed lines in part (a) show the equivalent diameters for A_e=0.2, 0.5, 1.1, and 2.0 cm^2 and correspond to the glottal flow waveforms shown in (b)–(e). The waveform amplitudes are normalized to show the shape differences only. The pharynx areas vary around 2.0 cm^2 and the mouth area reaches a maximum of about 4.1 cm^2.

The vocal folds are represented by a three-dimensional array of point masses and their respective nearest-neighbor coupling springs. The array is 3×3×3, with three masses along the length of the folds, three masses in the vertical dimension, and three masses in the lateral dimension [Fig. 9(b) and (c)]. In the programming, which follows the multimass approach by Titze (1973, 1974), Wong *et al.* (1991), and Story and Titze (1995), the open squares, circles, and pluses represent the flesh points of the mucosa, the vocal ligament, and the thyroarytenoid muscle, respectively. The use of three masses in all directions approximates the low-order modes of the vocal fold tissues (Titze and Strong, 1975; Berry *et al.*, 1994). It should be kept in mind that increasing the number of masses in each direction not only increases the degrees of freedom of the tissue, but is also allows for a more accurate adjustment of the prephonatory glottis. In all simulations to follow, the prephonatory glottis was slightly open posteriorly (at the vocal process), closed anteriorly (at the anterior commissure), and curved in the coronal plane as shown in Fig. 9. Oscillations were then computed around this configuration.

Figure 10 shows the effect of widening the epilarynx tube. Part (a) shows the change in vocal tract configuration and parts (b) and (c) show the corresponding glottal flow

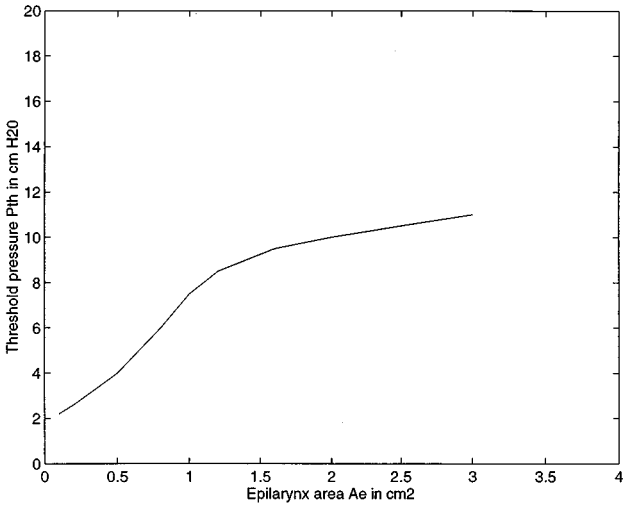

FIG. 11. Oscillation threshold pressure (P_{th}) as a function of epilarynx tube area A_e. The remainder of the vocal tract was held constant as shown at the top of Fig. 10.

waveforms. All parameters of the vocal fold model were kept identical; only A_e was systematically changed from 0.2 to 0.5 cm^2, then to 1.1 cm^2, and finally to 2.0 cm^2. The lung pressure was always maintained 8 cm H_2O (about 0.8 kPa). Note that this pressure is the oscillation threshold pressure for $A_e = 1.1$ cm^2 because the amplitude is neither growing nor decaying and vocal fold collision has not been reached.

The oscillation threshold pressure was probed for many values of A_e by moving gradually from damped oscillation to growing oscillation without collision. The results are shown in Fig. 11. Note the strong dependence of P_{th} on epilaryngeal tube area in the lower range of A_e. The curve appears to follow a parabolic path (up to about 1.0 cm^2) as predicted by Eq. (21). Above about 1.0 cm^2, however, the parabolic path is abandoned and the threshold pressure flattens out. This is because the resistive part of the vocal tract becomes more significant and the epilarynx tube merges with the vocal tract as a single tube of larger dimensions. The vocal folds then vibrate more independently of the vocal tract, their threshold pressure being determined by the tissue properties (Titze, 1988).

Of all the other parameters of the vocal tract probed, none had the dramatic effect on oscillation that A_e had. Figure 12 shows the effect of increasing and decreasing the pharyngeal area by a factor of 2. The narrowed pharynx (typical of *twang* and *belt* quality), produced some roughness in the waveform (a period-3 subharmonic). This is probably because the epilarynx tube is now acoustically coupled to the entire vocal tract. It no longer serves as an independent resonator, but mixes with all the formants of the vocal tract. Hence, the source–tract interactions are more complicated. Interestingly, Estill *et al.* (1996) reported subharmonic structure in the *sob* voice quality, associated with a tightening of the aryepiglottic sphincter at the top of the epilarynx tube.

IV. CONCLUSIONS

A number of interesting conclusions can be drawn from this study. First and foremost, a narrow epilarynx tube acts a bit like the mouthpiece of a brass instrument, matching the

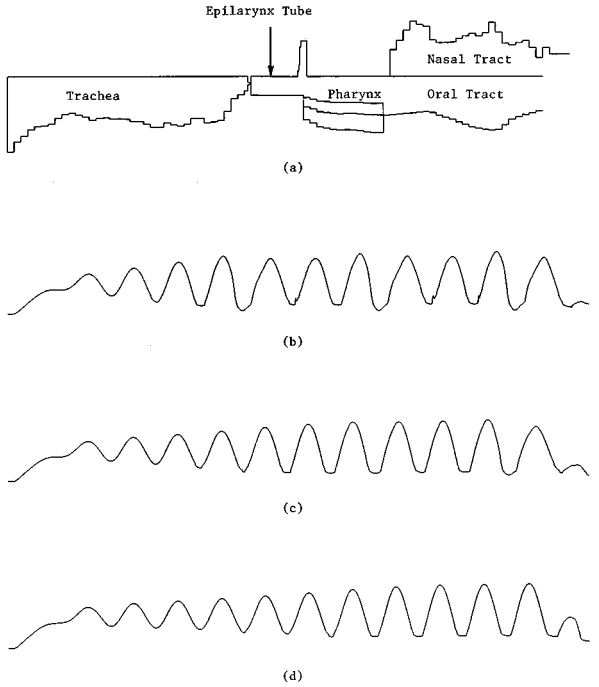

FIG. 12. The effect of increasing and decreasing the pharyngeal area by a factor of 2: (a) vocal tract outline, and (b)–(d), glottal flow.

high internal impedance of the glottis to the lower impedance of the vocal tract and free space. In terms of an impedance matching concept, the small-amplitude acoustic impedance of the glottis can be approximated as

$$Z_g = \frac{dP_g}{dU} = \frac{d}{dU}\left[\frac{1}{2}\,k_t \rho\, v^2\right] = k_t \rho\, v\,\frac{dv}{dU} = \frac{k_t \rho\, v}{A_g}, \tag{22}$$

where P_g is the pressure across the glottis and v is the glottal air particle velocity. Glottal inertance and several shape-dependent factors are neglected. This relationship was introduced earlier in Eq. (15), with U being the glottal flow, k_t being an empirical pressure coefficient (about 1.1), ρ being the air density, and A_g being the glottal area. Here Z_g is a time-varying impedance, of course, with both v and A_g changing throughout the glottal cycle. However, we are only interested in order-of-magnitude effects here.

If we compare this impedance with the intrinsic acoustic impedance of the epilarynx section of the vocal tract,

$$Z_e = \rho c / A_e, \tag{23}$$

which is also only a rough estimate because it neglects all the standing waves in the tract, there is a clear symmetry between *particle velocity* in the glottis and *wave velocity* in the vocal tract. Likewise, there is a symmetry between *glottal area* and *epilarynx tube area*. The ratios v/c and A_g/A_e are apparently significant in establishing general impedance matching conditions. Typically, v is on the order of 20–50 m/s during glottal opening and $c = 350$ m/s. Thus, the v/c ratio is on the order of 0.1. Also, A_g/A_e is typically on the order of 0.1 if the time-average glottal area is about 0.1 cm^2 (a 1-cm glottal length times a 1-mm glottal width) and A_e is on the order of 1.0 cm^2. To maintain similar impedance conditions across pitches and loudness, a vocalist may want to decrease the epilaryngeal area when the glottal area decreases. This may occur at high pitches, low intensities, or

pressed phonation. Also, the air particle velocity v can be adjusted by subglottal pressure to bring the v/c ratio in line.

It is not yet clear, however, whether the larynx works best as a constant flow source (with $Z_g \gg Z_e$) or under nearly matched conditions ($Z_g \approx Z_e$). In normal speech, and more so in the *sob* and *falsetto* quality, the epilarynx tube can be fairly wide. There appears to be no great difficulty in maintaining vocal fold oscillation in these cases. In high-pitched operatic singing, *belting*, and *twang* quality, on the other hand, the narrow epilarynx seems to be the configuration of choice. It may also be the preferred configuration in the so-called *resonant speaking voice* (Verdolini *et al.*, 1994). This configuration provides the desirable inertive reactance to facilitate vocal fold oscillation. When the narrowed epilarynx is combined with a wide pharynx, the reactance never goes negative below about 3000 Hz, which means that the acoustic load is inertive for all possible values of F_0.

Our findings confirm the earlier results of Sundberg (1974) that the epilarynx tube clusters the third, fourth, and fifth formants to generate the vocal *ring* (singer's formant). The focal point in the spectrum is the uncoupled (free) resonance frequency of the epilarynx tube, which can be computed simply on the basis of tube length. The epilarynx resonance frequency ''attracts'' all formant frequencies of the vocal tract. Generally, F_1 and F_2 are pulled upward, whereas F_4 and F_5 are pulled downward; F_3 is sometimes entrained by the epilarynx resonance, thereby not moving much. However, a short epilarynx tube can also entrain F_4, in which case F_3 will be pulled upwards toward it.

The piriform sinuses introduce a zero into the transfer function, but have no profound effect on the magnitude of the input impedance. The formant frequencies are shifted slightly, however. In contrast to the epilarynx tube, the piriform sinuses ''repel'' the formants, generally pushing F_1, F_2, F_3, and F_4 lower and pushing F_5 higher. If the lengths of the piriform sinuses were to be the same as the length of the epilarynx tube, the pole-zero pair would produce a complete cancellation in the transfer function, but the impedance would remain high.

An open nasal port introduces zeros into the spectrum (at the resonance frequencies of the nasal tract), but in this study it showed no measurable effect on oscillation threshold pressure or glottal flow. We suspect, therefore, that the highly touted benefit of nasalization in singing is less acoustic than biomechanical. As Estill (1995) has pointed out, the palatopharyngeal muscles probably help to stabilize the larynx to maintain a constant epilaryngeal configuration. This may open the nasal port or close it in the process. Acoustically, the opening may not matter much, but our investigation was not extensive enough throughout the F_0, vowel and intensity ranges to be draw firm conclusions. Further investigation of nasality as a pedagogical tool is therefore recommended.

ACKNOWLEDGMENT

This work was supported by a grant from the National Institute on Deafness and Other Communication Disorders, No. P60 DC00976.

Bartholomew, W. T. (**1934**). ''A physical definition of good 'voice-quality' in the male voice,'' J. Acoust. Soc. Am. **1,** 24–33.

Berry, D., Herzel, H., Titze, I. R., and Krischer, K. (**1994**). ''Interpretation of biomechanical simulations of normal and chaotic vocal fold oscillations with empirical eigenfunctions,'' J. Acoust. Soc. Am. **95,** 3595–3604.

Colton, R. H., and Estill, J. (**1981**). ''Elements of voice quality: Perceptual, acoustic and physiologic aspects,'' in *Speech and Language: Advances in Basic Research and Practice*, edited by N. J. Lass (Academic, New York), Vol. V, pp. 311–403.

Dang, J., and Honda, K. (**1995**). ''Local and global effects of the pyriform fossa on speech spectra,'' J. Acoust. Soc. Am. **98,** 2931(A).

Dang, J., and Honda, K. (**1996**). ''Acoustic characteristics of the piriform fossa in models and humans,'' J. Acoust. Soc. Am. **100,** 3374–3383.

Estill, J. (**1981**). ''An analysis of spectra of four voice qualities: Speech, sob, twang and opera,'' in *Transcripts of the Tenth Symposium, Care of the Professional Voice*, Juilliard School, edited by V. Lawrence (The Voice Foundation, Philadelphia).

Estill, J. (**1995**). *Voice Craft: Some Basic Voice Qualities* (Estill Voice Training Systems, Santa Rosa, CA).

Estill, J., Fujimura, O., Sawada, M., and Beechler, K. (**1996**). ''Temporal perturbation and voice qualities,'' in *Vocal Fold Physiology: Controlling Complexity and Chaos*, edited by P. Davis and N. Fletcher (Singular Publishing Group, San Diego), pp. 237–252.

Feder, F. (**1988**). Personal communication, based on videostroboscopic examination of professional voice impersonators.

Flanagan, J. L. (**1972**). *Speech Analysis: Synthesis and Perception* (Springer-Verlag, Berlin).

Helmholtz, H. L. F. (**1954**). *On the Sensation of Tone*, translated by H. Margenan (Dover, New York), p. 116.

Kinsler, L., and Frey, A. (**1962**). *Fundamentals of Acoustics* (Wiley, New York), 2nd ed.

Laver, J. (**1980**). *The Phonetic Description of Voice Quality* (Cambridge U. P., Cambridge).

Liljencrants, J. (**1985**). ''Dynamic line analogs for speech synthesis,'' in *Quarterly Progress and Status Report, STL-QPSR* 1/1985 [Speech Transmission Laboratory, Royal Institute of Technology (KTH), Stockholm, Sweden], pp. 1–14.

Sondhi, M., and Schroeter, J. (**1987**). ''A hybrid time-frequency domain articulatory speech synthesizer,'' IEEE Trans. Acoust. Speech Signal Process. **ASSP-35,** 7, 955–967.

Story, B. (**1995**). ''Physiologically-based Speech Simulation Using an Enhanced Wave-Reflection Model of the Vocal Tract,'' Doctoral dissertation, University of Iowa, Iowa City.

Story, B., and Titze, I. R. (**1995**). ''Voice simulation with a body cover model of the vocal folds,'' J. Acoust. Soc. Am. **97,** 1249–1260.

Story, B., Titze, I., and Hoffman, E. (**1996**). ''Vocal tract area functions from magnetic resonance imaging,'' J. Acoust. Soc. Am. **100,** 537–554.

Sundberg, J. (**1974**). ''Articulatory interpretation of the singing formants,'' J. Acoust. Soc. Am. **55,** 838–844.

Titze, I. R. (**1973**). ''The human vocal cords: A mathematical model. Part I,'' Phonetica **28**(3-4), 129–170.

Titze, I. R. (**1974**). ''The human vocal cords: A mathematical model. Part II,'' Phonetica **28**(3-4), 129–170.

Titze, I. R. (**1988**). ''The physics of small-amplitude oscillation of the vocal folds,'' J. Acoust. Soc. Am. **83**, 1536–1552.

Titze, I. R., and Strong, W. J. (**1975**). ''Normal modes in vocal cord tissues,'' J. Acoust. Soc. Am. **57,** 736–744.

Verdolini, K., Druker, D., Palmer, P., and Samawi, H. (**1994**). ''Psychological study of 'resonant voice,' '' *National Center for Voice and Speech Status and Progress Report*, Vol. 6, pp. 147–153.

Wong, D., Ito, M., Cox, N., and Titze, I. (**1991**). ''Observation of perturbations in a lumped-element model of the vocal folds with applications to some pathological cases,'' J. Acoust. Soc. Am. **89,** 383–394.

Yanagisawa, E., Estill, J., Kmucha, T., and Leder, S. B. (**1989**). ''The contribution of aryepiglottic constriction to ''ringing'' voice quality—A videolaryngoscopic study with acoustic analysis,'' J. Voice **3**, 342–350.

Changes in sound pressure and fundamental frequency contours following changes in hearing status

Harlan Lane,[a] Jane Wozniak, Melanie Matthies, Mario Svirsky, Joseph Perkell, Michael O'Connell, and Joyce Manzella

Massachusetts Institute of Technology, Research Laboratory of Electronics, Room 36-511, 50 Vassar Street, Cambridge, Massachusetts 02139

(Received 5 July 1995; accepted for publication 29 November 1996)

Sound-pressure level (SPL) and fundamental frequency ($F0$) contours were obtained from four postlingually deafened adults who received cochlear implants and from a subject with Neurofibromatosis-2 (NF2) who had her hearing severely reduced following surgery to remove an auditory-nerve tumor and to implant an auditory brainstem implant. SPL and $F0$ contours for each phrase in passages read before and after changes in hearing were averaged over repeated readings and then normalized with respect to the highest SPL or $F0$ value in the contour. The regularity of each average contour was measured by calculating differences between successive syllable means and averaging the absolute values of these differences. With auditory feedback made available, the cochlear implant user with the least contour variation preimplant showed no change but all of the remaining speakers produced less variable $F0$ contours and three also produced less variable SPL contours. In complementary fashion, when the NF2 speaker had her auditory feedback severely reduced, she produced *more* variable $F0$ and SPL contours. The results are interpreted as supporting a dual-process theory of the role of auditory feedback in speech production, according to which one role of self-hearing is to monitor transmission conditions, leading the speaker to make changes in speech postures aimed at maintaining intelligibility. [S0001-4966(97)03304-3]

PACS numbers: 43.70.Dn, 43.70.Bk, 43.70.Fq, 43.71.Ky [AL]

BACKGROUND

There is a body of evidence from postlingually deafened adults and from users of cochlear implants that implicates a role for hearing in regulating average parameter values of speech sound-pressure level (SPL) and fundamental frequency ($F0$). Leder *et al.* (1987b) reported that postlingually deafened men with profound bilateral sensorineural losses read at higher average SPL than did normally hearing males. Leder *et al.* (1987) reported that deafened men had a higher $F0$ when reading than normally hearing age-matched men (also see Binnie *et al.*, 1982; Leder and Spitzer, 1993; Plant, 1984).

When some hearing has been restored to deafened adults by means of a cochlear prosthesis, reductions in average SPL and $F0$ have been found. These parameters of the speech signal appear to be relatively well represented by the electrical stimulation delivered by the implant speech processor (cf. Shannon, 1993). Leder and Spitzer (1990) reported reduced speech amplitude, $F0$, and duration during readings of the Rainbow Passage by ten deafened adult males using single-channel implants. After only one day of prosthetic audition, their speakers reduced average $F0$ significantly while subsequent reductions were smaller and not reliable. This indicates a relatively rapid change in $F0$ with provision of auditory feedback. Oster (1987) also reported $F0$ reductions with cochlear prosthesis use in two postlingually deafened adults, one male and one female, and Lane *et al.* (1994) obtained a comparable result with two female implant users. However, Kirk and Edgerton (1983) found $F0$ higher when comparing speech in aided to unaided conditions with two female speakers who had been using their implants for two and eight years. Both of these implant users had a lower $F0$ unaided than the average of five hearing female control speakers, so the direction of change in this parameter with auditory feedback supplied appears to have been toward normal.

In a longitudinal study of vowel production by implant users, Perkell *et al.* (1992) also found reductions in SPL, $F0$, and duration of vowels following activation of the patients' implant speech processors. A companion study that introduced short-term changes in processor status obtained similar results (Svirsky *et al.*, 1992). In the longitudinal study, we observed informally that the reductions in average speech parameter values with auditory feedback available were accompanied by increases in the regularity of SPL and $F0$ contours obtained for one speaker who read sentences from the Rainbow Passage during the same elicitation sessions in which she read a vowel inventory. However, studies of changes in $F0$ contours with deafening and cochlear prosthesis have yielded apparently inconsistent results. Some studies report that the speech of postlingually deafened subjects is ''monotonous'' (Binnie *et al.*, 1982; Plant, 1983, 1984) and several have found restricted $F0$ range (Plant, 1983; Plant and Hammarberg, 1983; Ball and Ison, 1984; Plant and Oster, 1986; Ball and Faulkner, 1989). In a finding that may be related, Cowie and Douglas-Cowie (1992) reported too little pitch movement to and from prominent syllables in tone groups.

[a]Also at Northeastern University, Boston, MA.

On the other hand, the findings of several studies point to increased variation of $F0$ contours with deafening. Thus, Cowie and Douglas-Cowie (1983) found abrupt switches from low to high pitches in adjacent words or syllables uttered by postlingually deafened speakers and Lane and Webster (1991) found that such speakers produced the prominent syllable in each sentence with excessively high $F0$. Additionally, Leder *et al.* (1986) reported $F0$ measures for contrastive stress in noun/verb bisyllables spoken by a deafened adult cochlear implant user. After four months of implant use, the speaker had improved the contrast between the nouns and corresponding verbs, and had reduced the average $F0$ difference between the stressed and unstressed syllables within words.

The present study was aimed at clarifying the influence of auditory feedback on SPL and $F0$ contours. Those contours were obtained from five speakers who underwent changes in long-term hearing status. Four speakers were postlingually deafened adults who had some auditory feedback restored with a cochlear prosthesis. In a complementary situation, a fifth speaker, a patient with Neurofibromatosis-2 (NF2), had her hearing severely reduced following surgery to remove an auditory-nerve tumor and to implant an auditory brainstem implant.

We have presented a dual-process theory of the role of hearing in speech production, based in part on our prior studies of changes in speech production by cochlear implant users (Perkell *et al.*, 1992; Svirsky *et al.*, 1992; Lane *et al.*, 1994; Matthies *et al.* 1994; Lane *et al.*, 1995). Briefly, auditory feedback serves to validate articulatory/acoustic relations that underlie synergisms for phoneme production. (Investigators of deafened adult speech who have advanced some form of validation hypothesis include Gammon *et al.*, 1971; Sherrard, 1982; and Waldstein, 1990.) In order to maintain intelligibility, auditory feedback also serves to monitor transmission conditions, leading the speaker to respond adaptivity with changes in average SPL, $F0$, and syllable duration by implementing changes in underlying speech ''postures,'' such as the balance between expiratory and inspiratory forces associated with a subglottal pressure, average tension in and separation of the vocal folds, and speaking rate. We hypothesize that changes in the variability of SPL and $F0$ contours reflect that same role of self-hearing; exaggerated SPL and $F0$ inflections serve to enhance intelligibility under adverse transmission conditions. Therefore, we have compared each speaker's contours obtained with auditory feedback (implant users after activation of their speech processors and the NF2 patient before hearing loss) to those obtained without feedback (preactivation for implant users) or with severely reduced feedback (postsurgery for the NF2 patient). A finding that contours obtained with auditory feedback are less variable than those obtained under reduced or absent auditory feedback would be consistent with this hypothesis.

I. METHOD

A. Subjects

Four of the five speakers in this experiment used cochlear prostheses. Prior to implant, all four had three-frequency pure-tone average losses (at 0.5, 1, and 2 kHz) greater than 102 dB in each ear; therefore, we refer to their hearing status preintervention as without auditory feedback. Three of these four implant users were women (the same three women studied by Lane *et al.*, 1994).

The first subject with a cochlear implant, CFA,[1] had a monaural impairment in her left ear with onset at age 18. At age 33, she experienced a rapid hearing loss in her right ear and began wearing a hearing aid in her left ear. She discontinued hearing aid use at age 45, and was implanted at age 49.

Subject CFB had normal hearing until age 21 and bilateral progressive hearing loss. She used a hearing aid in her left ear from ages 23–40, whereupon that ear received a cochlear implant. She also wore a hearing aid in her right ear ages 31–39.

Subject CFC had a severe bilateral hearing loss with onset at age 2. She began using a hearing aid in her right ear at age 5 and in her left at age 29. She wore hearing aids until age 47, when she discontinued use because of dizziness. In the same year, she underwent implant surgery.

The one male implant subject, CMD, had a congenital binaural loss. He began wearing a hearing aid in his right ear at age 3 and in his left at age 11. He wore these aids until age 36, when he discontinued use because of dizziness. In the same year, he underwent implant surgery. He was always tested in this research without hearing aids.

Subject NFA was diagnosed with Neurofibromatosis-2 (NF2) at age 17. NF2 is a genetic disorder that causes bilateral acoustic neuromas. Patients with this disease are at high risk of losing their hearing, usually due to the surgical intervention necessary to remove the tumor before it impinges on life-sustaining brain functions. At age 17, NFA had a right acoustic neuroma surgically removed, and suffered complete loss of hearing on that side. Over the next few years, she experienced a gradual progressive hearing loss on the left side caused by the growth of another acoustic neuroma. By age 20, she had a mild-to-moderate, fairly flat, hearing loss. She began wearing a hearing aid at age 22. By age 26, the loss was moderate and continued to increase slowly. At the time of our first baseline recording of her speech production, at age 27, she had excellent aided speech discrimination scores (above 90%, NU-6; Tillman and Carhart, 1966). At age 27, NFA had surgery for both the removal of her left acoustic neuroma and implantation of an auditory brainstem implant (ABI). During surgery, the auditory nerve had to be severed and there was damage to the left facial nerve, which caused a readily apparent left facial palsy. Her glottal function was observed with endoscopy to be normal following the tumor removal and ABI implantation. In all the postintervention recordings, NFA's ABI was in operation. However, her speech discrimination scores with bilateral deafness and the ABI ranged from 0% to 4% correct between 3 and 15 months after surgery. Clearly, NFA's access to acoustic information was severely reduced after her surgery, despite use of the ABI.

B. Prostheses

The Ineraid cochlear implant (Richards Medical Co.) consists of an implanted electrode array, a percutaneous pedestal and connector, and an external sound processor. The sound processor has an ear level microphone, a wideband automatic gain control, and four overlapping bandpass filters with crossover frequencies of approximately 0.7, 1.4, and 2.3 kHz. The four analog filter outputs are delivered individually (via the percutaneous connector) to four monopolar intracochlear electrodes, with a common return electrode. The electrodes, spaced approximately 4 mm apart, were positioned successfully in all subjects by insertion into the scala tympani through the round window, with the first placed most apically, some 22 mm from the round window. Although the speech processing strategy was the same for all implant users, there were user adjustments for input sensitivity and volume, and channel specific gains set by the clinician for each subject. During voiced segments, $F0$ is represented in the sound pressure×time waveforms coming from several channels of the speech processor by the periodicity of the complex waveform. The SPL is represented by the amplitude of those waveforms.

Subject NFA was surgically implanted at the House Ear Institute (Los Angeles, CA) with a multichannel version of the auditory brainstem implant (Brackmann *et al.*, 1993). The implant consists of an eight-electrode array placed on the cochlear nucleus, a receiver/stimulator providing transcutaneous electromagnetic signal transmission and an external microphone and signal processor. Subject NFA was fitted with a processor programmed to stimulate seven electrodes referenced to an indifferent electrode on the receiver/stimulator case (monopolar mode). An $F0$ $F1$ $F2$ $F5$ feature-extraction encoder was used to provide spectral, amplitude, and temporal information. In this processing strategy, $F0$ is represented by the repetition rate of the pulse train applied to the stimulating electrodes which, in turn, are activated based upon the spectral characteristics of the input speech signal. The SPL is represented by the amplitude of these pulse trains.

C. Speech elicitation

Two baseline recordings of speech production were made prior to surgical intervention. Postintervention recordings were made repeatedly at variable intervals. The time elapsed between intervention and the two consecutive recordings analyzed for this study were, for both CFA and CFB, 1 and 2 yr; for CFC and CMD, 0.5 and 1 yr; and for NFA, 11 and 35 weeks.

The speech material consisted of readings of the Rainbow Passage (Fairbanks, 1960), read three times each for subjects CFA, CFB, and CFC, and five times each for subjects CMD and NFA. Other speech material was read for approximately 15 min between each reading of the passage.

D. Recording, calibration, and signal processing

The subject was seated in a chair in a sound-attenuating room. A small electret microphone was placed at a fixed distance of 20 cm in front of the subject's lips by attaching it to a flexible arm affixed to the back of the chair. Lung volume was measured using a Respitrace inductive plethysmograph (Ambulatory Monitoring, Inc.). The utterance materials were projected on a screen located several feet in front of the subject. For calibration of sound-pressure level, at the start of each hour-long recording session, a sound source (electrolarynx) was placed in front of the subject's lips, while an experimenter observed the sound level value on a SPL meter (C scale) held next to the microphone. The microphone signal was amplified, recorded, and later low-pass filtered at 4.8 kHz and digitized at 10 kHz. The Respitrace signal was digitized at 312.5 Hz. Digitization, signal processing, and interactive data extraction were performed with procedures written in the MITSYN languages (Henke, 1989; Perkell *et al.*, 1991) running on a Digital Equipment Corporation engineering workstation. The digitized signals were demultiplexed into two time-aligned signal files.

E. Data extraction

Respiratory patterns and phrase selection. In an attempt to control for the effect of breathing pauses on $F0$ and SPL contours, the breath groups in each repetition of the Rainbow Passage were determined from a display of the Respitrace signal. A breath group is defined as the segment of speech from the beginning of an expiratory limb to the start of the next inspiration. By viewing the Respitrace signal and listening to the time synchronized acoustic signal, an experimenter marked on a printed copy of the Rainbow Passage the location of the beginning of each breath group in a given speaker's reading. Next, that speaker's first breath group preintervention was compared with the first breath group postintervention and a match was counted if the same one or more phrases of the Rainbow Passage (see Appendix) were in that breath group pre and post. Then the second breath group was compared pre and post for a match, and so on through the passage. Only phrases in breath groups that matched pre- and postintervention were analyzed since the addition or omission of a breath pause after a phrase might be associated with a substantial change in the $F0$ and SPL contours of that phrase. The number of phrases that could be matched up in this way ranged, depending on the speaker, from the full 16 in the Rainbow Passage to only half that many. The number of repetitions of each phrase that could be matched up in this way also varied across speakers, with a maximum of 10 and a minimum (required for that phrase's inclusion in the data set) of 4.

Vowel acoustics. Algorithms implemented with a MITSYN command language script were developed to facilitate the acoustic data extraction. A spectrographic display was used to aid in determining vowel boundaries, and a time-aligned amplitude envelope was displayed along with the sound-pressure waveform and $F0$ contour. To calculate the SPL of each vowel, the rms of the recorded, digitized signal at the peak amplitude in each syllable nucleus was divided by the rms of the calibration tone and converted to dB. The mean $F0$ in each syllable nucleus was determined with an algorithm, supplied with the MITSYN languages, which tracked and displayed individual periods of the voice fundamental. The algorithm, called FPRD, uses heuristic proce-

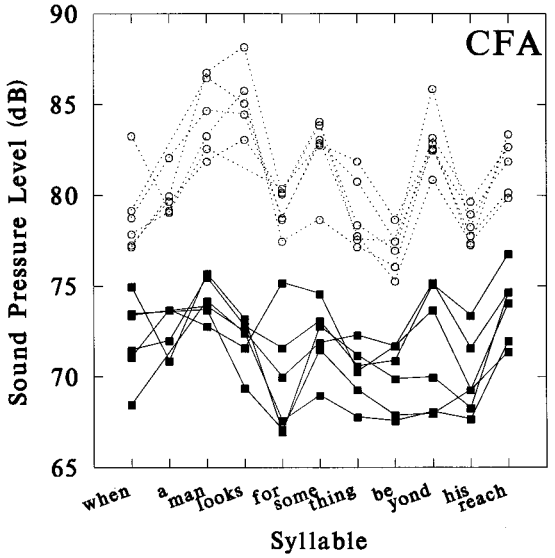

FIG. 1. Sound-pressure level maxima (SPL) for all of the syllable nuclei in the thirteenth phrase of the Rainbow Passage read by subject CFA in two baseline sessions (open circles) and in two recordings made more than a year following the activation of her cochlear implant speech processor (filled squares).

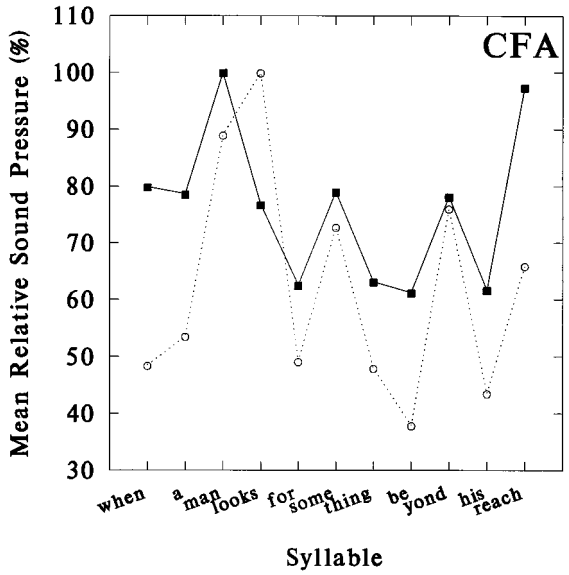

FIG. 2. The SPL contours in Fig. 1 averaged and then normalized. The mean parameter value of each syllable nucleus was divided, for the pre- and postintervention sets of contours separately, by the highest mean parameter value on the contour and the result expressed as a percent. Each point is based on between two and six observations.

dures to identify individual periods in the sound-pressure waveform (no published reference). The average value of $F0$ over the entire vowel duration was retained. Spurious $F0$ values due to transition effects, creak, etc., were not included in the calculation of average $F0$ for a given vowel.

II. DATA ANALYSIS

To illustrate the procedure followed for data analysis, Fig. 1 plots the SPL maximum of each syllable nucleus in each reading of the thirteenth phrase of the Rainbow Passage by subject CFA in two baseline sessions (open circles) and in the recordings 58 and 85 weeks following the activation of her cochlear implant speech processor (filled squares). (Data points are missing for some individual syllables whose parameter values could not be accurately determined.) The marked reduction in SPL postactivation of the implant user's speech processor hinders comparison of the shapes of contours pre- and postintervention.

Consequently, each of the two sets of contours was averaged and normalized as follows. First, corresponding syllable nuclei in each set of readings (pre- and postactivation) were matched up and their parameter values averaged across the set in arithmetic units (sound pressure in μbars or $F0$ in Hz) to yield an average contour for the set. Next, each value on the average contour was divided by the highest value on that contour and expressed as a percent; the result is shown in Fig. 2. The highest value on the average contour preactivation shown in Fig. 2 occurred during the word **looks**; postactivation, the highest value occurred during the word **man**.

Comparing the average normalized contour in Fig. 2 obtained without auditory feedback (open circles) to that, also shown, obtained with prosthetic hearing (filled squares), it is evident that SPL varies less on the average from syllable to syllable in the condition where auditory feedback was available (filled squares). One way of parametrizing the variation in the averaged SPL contour is to subtract the percent-of-maximum value of each syllable from that of the following syllable. These successive differences are positive where the contour is rising and negative where it is falling; the average of their absolute values is the mean successive difference (MSD). The MSD of the preimplant contour in Fig. 2 was 25.3%, that of the postimplant contour 16.3%, a reduction of 9.0% in the average variation of SPL from syllable to syllable following the provision of some auditory feedback. To evaluate the statistical significance of such changes, for each subject, clause, and parameter, corresponding absolute values of successive differences on the pre- and postintervention average contours were paired off. For example, there were 10 such values paired off in clause 13 (Fig. 2; the number of successive differences is one less than the number of syllables). Proceeding likewise for the other ten clauses retained for this speaker (since they were uttered on comparable breath groups pre- and postintervention), there were a total of 73 paired pre- and postintervention measures. The two grand means of the paired measures were entered in Table I, and the reliability of the difference between the means was tested with the t-test for matched pairs and 72 df.

Table I shows the result of comparing pre- and postintervention phrases with respect to MSD in their SPL and $F0$ contours for each of the speakers. It presents the value of the t-test for matched pairs of changes in relative syllable sound pressure or $F0$ (cols. 4 and 8) and the associated average MSD pooled over all phrases pre- and postimplant separately (cols. 2–3 and 6–7) for the four implant users, or pre- and post-hearing-loss for speaker NFA.

Some indication of the regularity of contours in a hearing subject can be had from the measures obtained with speaker NFA (row 5) before her surgery; although she had a total hearing loss in one ear and a moderate loss in the other, her speech discrimination was excellent, as reported above. However, MSD values in the ''Pre'' and ''Post'' columns of

TABLE I. Variation of SPL and $F0$ contours. Mean successive differences in normalized SPL and $F0$ contours as a function of auditory feedback conditions in four cochlear implant users and an NF2 patient. Preintervention recordings were made prior to activating speech processors in the implant users, and prior to surgery and severe hearing loss in the NF2 patient. The table presents the value of the t-test for matched pairs of phrases and the associated global averages of mean successive differences pre- and postimplant or pre- and post-hearing-loss for the NF2 speaker, NFA. Also shown are the values of MSD for a phrase read by all speakers preimplant (and pre-hearing loss for NFA) that allow between-speaker comparisons (* = $p < 0.05$; ** = $p < 0.01$, two-tailed test).

		Mean successive difference							
		Relative sound pressure (%)				Relative fundamental frequency (%)			
1		2	3	4	5	6	7	8	9
Subject		Pre	Post	t PRE vs POST	Common Phrase PRE	Pre	Post	t PRE vs POST	Common Phrase PRE
1	CMD	24.0	24.9	−0.6	34.0	9.1	7.2	3.2**	11.2
2	CFA	26.2	17.9	3.6**	42.8	8.8	6.9	2.7**	9.6
3	CFB	22.0	18.2	2.0*	49.9	5.5	4.4	2.0*	3.8
4	CFC	19.5	19.1	0.2	27.8	4.6	5.0	−0.7	2.4
5	NFA	15.4	21.4	−4.3**	25.8	5.4	6.8	−3.4**	8.4

Table I cannot be used for comparisons among speakers because MSD varies depending on which phrase is considered, and the phrases included in the analysis varied from one speaker to the next, depending on which phrases fell into breath groups that matched from pre- and postintervention in that speaker. In order to make between-subject comparisons of MSD, a phrase in the Rainbow Passage was identified that had been analyzed for all speakers in the preintervention sessions (labeled phrase 9 in the Appendix). The average values of MSD for the ''phrase in common'' appear in Table I (cols. 5 and 9, for SPL and $F0$ contours, respectively). They were obtained in the absence of hearing for the implant users and with hearing for speaker NFA.

III. RESULTS

A. SPL contours

On the phrase in common, the implant user with the highest measure of SPL contour fluctuation preimplant was CFB (MSD=49.9%, row 3, col. 5). This speaker significantly decreased the average variation of her SPL contours (from 22.0% to 18.2%) after extended prosthetic audition ($p<0.05$). Speaker CFA (common phrase MSD=42.8%) gave a comparable result ($p<0.01$). Consistent with those results, speaker NFA, prior to her severe hearing reduction, yielded the lowest value of sound pressure contour variation (25.8%) on the phrase read in common by all speakers. She increased the variation of her sound-pressure contours after her auditory capacity was severely reduced ($p<0.01$). Two implant users, CFC and CMD (rows 4 and 1), did not change SPL contour variation with some auditory feedback supplied, and these were the speakers who varied SPL least preimplant (as indexed by MSD on the phrase in common, col. 5). Implant user CFC had the lowest contour variation before processor activation. Although deaf, her MSD on the phrase in common was quite close to that of speaker NFA prior to her hearing loss. Not surprisingly, then, CFC did not reduce SPL contour variation further with the restoration of auditory feedback. CMD also did not reduce SPL contour fluctuation with implant use.

B. *F0* contours

Table I also shows average MSD for the $F0$ contours of the same phrases that were analyzed for SPL variation. All speakers who decreased SPL contour variation with feedback also decreased $F0$ contour variation in that condition; however, the converse is not true. To some extent the changes in $F0$ pre- and postintervention may reflect the operation of speech production mechanisms that also brought about the SPL changes (Titze, 1991). The product-moment correlations between SPL and $F0$ across all the syllable nuclei uttered by each speaker varied from a low of 0.3 ($p<0.01$) to a high of 0.68 ($p<0.01$). Lane (1962) found that speakers asked to make magnitude productions of vocal loudness increased $F0$ by about 25% for each 10-dB increase in SPL. Applying that estimate to the present study, where speakers on the average had a vocal level 4.34 dB greater without auditory feedback, yields a predicted associated increase in $F0$ of 10%; the observed average increase in $F0$ was greater, 16%.

Speaker CMD, whose $F0$ contour on the phrase in common yielded the highest MSD, reduced $F0$ contour variation after more than a year of processor use from MSD=9.1% to 7.2% (see Table I; $p<0.01$). Speaker CFA had an average MSD in her $F0$ contours preimplant of 8.8%. Following more than a year of implant use, her MSD had fallen to 6.9% ($p<0.01$). Likewise, speaker CFB showed a significant reduction in the variation of her $F0$ contours when auditory feedback was supplied ($p<0.05$), even though her MSD on the phrase in common was low to begin with. Speaker NFA yielded a MSD of 5.4% in her $F0$ contours while her hearing was still intact (monaurally); after her auditory capacity was severely reduced, MSD rose to 6.8% ($p<0.01$). The remaining speaker, CFC, had the lowest value of $F0$ contour variation on the phrase in common, and—as was the case with her sound-pressure contours—that measure did not change when auditory feedback was supplied.

It is noteworthy that the values of MSD measured on $F0$ contours produced by speakers CFA and CMD in the absence of self-hearing (9.6% and 11.2%, respectively, on the phrase in common) were higher (greater variation) than the

comparable normative value provided by speaker NFA before her binaural hearing loss (col. 9: 8.4%). As we have seen, those speakers significantly reduced inflection of their $F0$ contours with the restoration of some self hearing. Speaker CFC, who was the implant user with the lowest value of SPL variation without auditory feedback (col. 5: 27.8%), also had the least $F0$ contour variation (col. 9: 2.4%); her value for $F0$ variation on the phrase in common was indeed below the value obtained from NFA with auditory feedback (8.4%).

C. Scaled contours

We explored the contributions of three possible components of MSD to the differences observed with and without auditory feedback—namely, jitter, inflection (see Baken, 1987), and average level. (The measures of jitter and inflection, designed to index variation in successive glottal periods, were applied here to changes in the mean SPL or $F0$ of successive syllables.) With respect to SPL, three speakers significantly changed MSD and two did not; four of those five outcomes were concordant in the jitter measure (the exception: CFB significantly changed MSD but not jitter) and three out of five were concordant on the measure of inflection. With respect to $F0$, four speakers significantly changed MSD and one did not; all five of those outcomes were concordant in the jitter measure and four out of five in the inflection measure. Thus, speakers who reduced MSD, for example, were not solely inflecting each overall phrase less, nor were they solely reducing fluctuation from one syllable to the next within a phrase.

The subjects spoke with higher SPL and $F0$ in the absence of auditory feedback than in its presence (with one exception: CFC did not change average SPL pre- and postactivation). The contributions of average levels of SPL and $F0$ to measures of contour variation are reduced in computing MSD when SPL or $F0$ values on the average contour (pre- and postintervention) are normalized by the highest value on that contour. To explore another method of reducing the influence of average level, we ''scaled up'' with-feedback contours to the same average level as their counterpart without-feedback contours: we divided the mean value of each contour obtained with auditory feedback into the mean value of its associated contour obtained without auditory feedback, and then multiplied values on the former contour by this ratio. Finally, MSD was computed for the magnified with-feedback contour and for its no-feedback partner without, however, normalizing each contour by its maximum (since that would nullify the effect of the scale transformation). Scaling the with-feedback contour up toward its partner in this way increases its unnormalized MSD and reduces the difference in MSD between it and the no-feedback contour.

However, wherever the difference in unnormalized MSD was significant without the scaling it remained significant after the scaling: all speakers except CFC yielded significant changes in unnormalized MSD in both SPL and $F0$ (CFC did neither) both without the scaling and with it. Hence the differences in measurements of contour variation with and without auditory feedback cannot be attributed solely to associated differences in average SPL and $F0$.

IV. DISCUSSION

The findings for SPL and $F0$ contours of implant users and a NF2 patient summarized in Table I show that speakers without auditory feedback, in the former case, or severely reduced auditory feedback in the latter, read passages with more inflected SPL and $F0$ contours than in the presence of auditory feedback. An interpretation of these findings arises from our dual-process theory of the role of auditory feedback in speech production. The theory provides that one of the roles of self-hearing is to monitor transmission conditions, leading the speaker to make changes in speech postures that in turn maintain intelligibility. According to this view, exaggerated SPL and $F0$ inflections occur in the absence of auditory feedback since such changes may enhance intelligibility under adverse transmission conditions. This line of reasoning places speaking without auditory feedback in the class of speaking under adverse transmission conditions, and it postulates that increased SPL and $F0$ inflection enhance intelligibility under those conditions.

Table II assembles evidence from several studies to support the views that (1) speech prosody in the absence of auditory feedback has much in common with speech prosody under adverse transmission conditions (and under instructions to provide ''clear speech''); and (2) that the prosodic parameter values associated with speaking under these three conditions enhance the speaker's intelligibility.

SPL. Increases in average SPL (row 1) have been found in studies of clear speech, and of speaking in noise (the Lombard effect; see the review in Lane and Tranel, 1971). Lane *et al.* (1970) also found increases in speech SPL under reduced auditory feedback (first reported by Fletcher *et al.*, 1918) and suggest that a common variable controlling the speaker's increase of sound level in noise and increase of sound level with reduced auditory feedback is the perceived signal-to-noise ratio during speech communication. In postlingually deafened adults (col. 3), SPL was higher than normal prior to implantation, when the speakers received no auditory feedback, and fell following implant use.

F0. Table II also cites increases in average $F0$ (row 2) reported by one study of clear speech (and one of loud speech—Schulman, 1989; col. 1), by three studies of speech communication in noise (col. 2), and by several studies of the speech of postlingually deafened adults (col. 3), who speak at higher average $F0$ without auditory feedback (compared to hearing controls) and at lower average $F0$ than formerly when they are provided with cochlear prosthesis (studies labeled ''CI'').

Duration. Increases in the duration of words (row 3) have been reported under all three conditions and increases in systematic pausing at syntactic boundaries (row 4) have been found in studies of clear speech. In postlingually deafened adults, Plant (1983) found longer pause durations as well as segment durations, compared to speakers with normal hearing.

F0 inflection. Increased $F0$ inflection (row 6) was found in a study of clear speech. Picheny *et al.* (1986) asked speak-

TABLE II. Increases in parameters of speech prosody reported in the literature under three conditions. (1) Subjects are instructed to speak clearly. (2) Subjects are instructed to speak under adverse transmission conditions, such as masking noise. (3) Postlingually deafened adults are compared with hearing controls or with themselves after receiving a cochlear implant (CI). Also shown (row 7) are studies of the intelligibility of speech produced under these conditions.

1 Parameters that increase	2 Clear speech	3 Adverse transmission conditions	4 Postlingually deafened adults
(1) SPL	Picheny *et al.*, 1986	Bond *et al.*, 1989 Clark *et al.*, 1987 Dreher and O'Neil, 1958 Hanley and Steer, 1949 Lane *et al.*, 1970 Tartter *et al.*, 1993 Van Summers *et al.*, 1988 Webster and Klumpp, 1962	Lane *et al.*, 1995 (CI, NF2) Leder *et al.*, 1987b Leder and Spitzer, 1990, 1993 Perkell *et al.*, 1992 (CI) Svirsky *et al.*, 1992 (CI)
(2) *F*0	Picheny *et al.*, 1986 Schulman, 1989	Bond *et al.*, 1989 Clark *et al.*, 1987 Van Summers *et al.*, 1988	Binnie *et al.*, 1982 Lane *et al.*, 1995 (CI, NF2) Leder and Spitzer, 1993 Leder *et al.*, 1987 Oster, 1987 Perkell *et al.*, 1992 (CI) Plant, 1984 Svirsky *et al.*, 1992 (CI)
(3) Duration (word or segment)	Cutler and Butterfield, 1990, 1991 Lindblom, 1990 Moon and Lindblom, 1989 Picheny *et al.*, 1986 Schulman, 1989	Clark *et al.*, 1987 Dreher and O'Neil, 1958 Hanley and Steer, 1949 Tartter *et al.*, 1993 Van Summers *et al.*, 1988	Binnie *et al.*, 1982 Lane and Webster, 1991 Leder *et al.*, 1987a Leder and Spitzer, 1990, 1993 Perkell *et al.*, 1992 (CI) Plant, 1983, 1984 Waldstein, 1990
(4) Pausing	Cutler and Butterfield, 1990, 1991 Picheny *et al.*, 1986		Plant, 1983
(5) SPL inflection			Leder *et al.*, 1987b Present study
(6) *F*0 inflection	Cutler and Butterfield, 1991 Picheny *et al.*, 1986 Price *et al.*, 1991	Clark *et al.*, 1987	Lane and Webster, 1991 Leder *et al.*, 1986 (CI) Present study
(7) Intelligibility	Bond and Moore, 1994 Chen *et al.*, 1983 Larkey and Danly, 1983 Picheny *et al.*, 1985 Tolhurst, 1954, 1957	Dreher and O'Neil, 1958 Peters, 1955 Van Summers *et al.*, 1988	

ers to read sentences conversationally in one experimental condition and to read them clearly in another condition. They found increases in the range of *F*0 (as well as increases in average syllable duration, *F*0, and SPL) when speakers produced clear speech. Similarly, a study of radio news broadcasting style of speech found it to have ''more clearly and consistently marked prosodic cues than a non-professional speaking style'' (Price *et al.*, 1991, p. 2959); it is included in Table II under clear speech. Clark *et al.* (1987) found increased inflection within words when speaking in noise. Lane and Webster (1991) report this result in postlingually deafened adults and they also found, as mentioned earlier, that pitch prominence was exaggerated in these speakers. Waldstein (1990) found that some deafened adults spoke with greater *F*0 range but these subjects as a group could not be distinguished reliably on this measure from their hearing counterparts.

In the present study, we have found greater SPL inflection and *F*0 inflection in the absence of auditory feedback than in its presence. In addition, measures of vowel parameters in word lists read by four of these subjects during the same recording sessions showed higher average SPL and *F*0 in the absence of auditory feedback than in its presence (implant users: Lane *et al.*, 1995; NFA: Perkell *et al.*, 1995).

Intelligibility. The last row in Table II lists studies that have measured the change in intelligibility associated with these increases in the parameter values of speech prosody. Clear speech is more intelligible than conversational speech (Chen *et al.*, 1983; Picheny *et al.*, 1985). Bond and Moore (1994) report that talkers who were more intelligible had characteristics similar to those distinguishing deliberately clear speech. When transmission conditions are in fact impaired, speakers do speak more intelligibly. For example, Peters (1955) found that when speakers had their voices filtered electronically and fed back to them their subsequent utterances were more intelligible. The author suggests that

speakers articulated more clearly with filtered auditory feedback because they were trying to compensate for an apparent lack of precision in their speech. Larkey and Danly (1983) found that listener reaction times to inflected sentences were faster than their reaction times to the same sentences presented in a monotone. This result, like that of Picheny *et al.* (1985), who found enhanced intelligibility of recordings with enhanced $F0$ inflection, is consistent with our hypothesis that the increased $F0$ inflection of our speakers in the absence of auditory feedback is a response to adverse transmission conditions and aimed at enhancing intelligibility.

Prosodic parameters of speech under adverse conditions have been linked in prior studies to clear speech (Lindblom, 1990; Van Summers *et al.*, 1988), emphatic speech (Van Summers *et al.*, 1988), and heightened intelligibility (Lane and Tranel, 1971). We have reviewed some evidence suggesting that prosodic parameters of speech under adverse conditions, in clear speech, and in the speech of postlingually deafened adults may reflect a common underlying process, namely an adaptive response of the speaker to actual or perceived adverse transmission conditions. That response may be aimed at maintaining intelligibility. When speakers think they may not be understood, one of the things they may do is to exaggerate the changes in prosodic parameters that they would normally make. Such a strategy could lead to greater average values of SPL, $F0$, and word durations (Cooper *et al.*, 1985); it might also entail more inflected SPL and $F0$ contours. At the same time that some speech synergisms may gradually break down at the phonemic level without auditory validation, yielding a loss in intelligibility (Cowie and Douglas-Cowie, 1983), prosodic changes such as slowing of speech, increased level, and heightened inflection may offset that loss to some degree. It is possible, on the other hand, that any such postural compensation is a fortuitous by-product of the role of self-hearing in regulating prosody and not an adaptive response to apparently degraded transmission conditions. It remains to be determined whether the prosodic changes in postlingual deafness do indeed enhance intelligibility.

ACKNOWLEDGMENTS

Clay Mitchell assisted with data extraction. This work was supported by N.I.D.C.D. Grant No. DC 00361 to the Massachusetts Eye and Ear Infirmary, the Massachusetts Institute of Technology, and Northeastern University, Dr. Joseph B. Nadol and Dr. Donald Eddington, Co-Principal Investigators and by N. I. D. C. D. Grant No. DC03007 to the Massachusetts Institute of Technology and Northeastern University, Dr. Joseph Perkell, Principal Investigator. We acknowledge the helpful criticism of an earlier version of this article provided by Dr. Anders Löfqvist, Haskins Laboratories; Dr. Steven Otto, House Ear Institute; Dr. Emily A. Tobey, University of Texas; and two anonymous reviewers.

APPENDIX: RAINBOW PASSAGE PHRASES

Division of the Rainbow Passage into 16 phrases, which correspond to the breath groups produced by one or more speakers in this study:

1 When the sunlight strikes raindrops in the air,
2 they act like a prism and form a rainbow.
3 The rainbow is a division of white light
4 into many beautiful colors.
5 These take the shape of a long round arch,
6 with its path high above,
7 and its two ends apparently beyond the horizon.
8 There is,
9 according to legend,
10 a boiling pot of gold at one end
11 People look,
12 but no one even finds it.
13 When a man looks for something beyond his reach,
14 his friends say
15 he is looking for the pot of gold
16 at the end of the rainbow.

[1]To facilitate subject identification in this paper, subjects are labeled CFA, CFB, and CFC (for the three female) and CMD (for the male) cochlear implant users. In other publications from our laboratory that include findings from these subjects they are identified as, respectively, S09, S15, S23, and S27. Perkell *et al.* (1992) reported on changes in vowel production in four implanted speakers including CFA and CFB. Lane *et al.* (1995) reported on changes in plosive voicing and in postural variables in CFA, CFB, CFC, and CMD. The NF2 patient is designated NFA. The subject descriptions in this study are based on supplemental information and supersede those published in prior studies.

Baken, R. J. (**1987**). *Clinical Measurement of Speech and Voice* (College Hill, Boston).

Ball, G., and Faulkner, A. (**1989**). ''Speech production of postlingually deafened adults using electrical and acoustic speech pattern prostheses,'' Speech Hear. Lang. Works Prog. (UCLA) **3**, 13–32.

Ball, V., and Ison, K. T. (**1984**). ''Speech production with electrocochlear stimulation,'' Br. J. Audiol. **18**, 251.

Binnie, C. A., Daniloff, R. G., and Buckingham, H. (**1982**). ''Phonetic disintegration in a five-year-old following sudden hearing loss,'' J. Speech Hear. Disord. **47**, 181–189.

Bond, Z. S., and Moore, T. J. (**1994**). ''A note on the acoustic-phonetic characteristics of inadvertently clear speech,'' Speech Commun. **14**, 325–337.

Bond, Z. S., Moore, T. J., and Gable, B. (**1989**). ''Acoustic-phonetic characteristics of speech produced in noise and while wearing an oxygen mask,'' J. Acoust. Soc. Am. **85**, 907–912.

Brackmann, D. E., Hitselfberger, W. E., Nelson, R. A., Moore, J., Waring, M. D., Portillo, F., Shannon, R. V., and Telischi, F. F. (**1993**). ''Auditory brainstem implant: I. Issues in surgical implantation.'' Otolaryngol. Head Neck Surg. **108**, 624–633.

Chen, F. R., Zue, V. W., Picheny, M. A., Durlach, N. I., and Braida, L. D. (**1983**). ''Speaking clearly: Acoustic characteristics and intelligibility of stop consonants,'' Working Papers, Research Laboratory of Electronics, MIT, Vol. 2, pp. 1–8.

Clark, J. E., Lubker, J. F., and Hunnicutt, S. (**1987**). ''Some preliminary evidence for phonetic adjustment strategies in communication difficulty,'' in *Language Topics: Essays in Honour of Michael Halliday*, edited by R. Steele and T. Threadgold (Benjamins, Amsterdam), pp. 161–180.

Cooper, W. E., Eady, S. J., and Mueller, P. R. (**1985**). ''Acoustical aspects of contrastive stress in question-answer contexts,'' J. Acoust. Soc. Am. **77**, 2142–2156.

Cowie, R., and Douglas-Cowie, E. (**1983**). ''Speech production in profound post-lingual deafness,'' in *Hearing Science and Hearing Disorders*, edited by M. E. Lutman and M. P. Haggard (Academic, New York), pp. 183–231.

Cowie, R., and Douglas-Cowie, E. (**1992**). *Postlingually Acquired Deafness: Speech Deterioration and the Wider Linguistic Consequences* (Mouton De Gruyter, New York).

Cutler, A., and Butterfield, S. (**1990**). ''Durational cues to word boundaries in clear speech,'' Speech Commun. **9**(5-6), 485–495.

Cutler, A., and Butterfield, S. (**1991**). ''Word boundary cues in clear speech: A supplementary report,'' Speech Commun. **10**, 335–353.
Dreher, J. J., and O'Neill, J. J. (**1958**). ''Effects of ambient noise on speaker intelligibility of words and phrases,'' Laryngoscope **68**, 539–548.
Fairbanks, G. (**1960**). *Voice and Articulation Drill Book* (Holt, Rinehart, Winston, New York).
Fletcher, H., Raff, G. M., and Parmley, F. (**1918**). ''Study of effects of different amounts of sidetone in the telephone set,'' Western Electric Company Rep. No. 19412, Case No. 120622.
Gammon, S. A., Smith, P. J., Daniloff, R. G., and Kim, C. W. (**1971**). ''Articulation and stress/juncture production under oral anaesthetization and masking,'' J. Speech Hear. Res. **14**, 271–282.
Hanley, T. D., and Steer, M. (**1949**). ''Effect of level of distracting noise upon speaking rate, duration and intensity,'' J. Speech Hearing Disord. **14**, 363–368.
Henke, W. (**1989**). *MITSYN Languages, Language Reference Manual* (WMH, Belmont, MA).
Kirk, K. I., and Edgerton, B. J. (**1983**). ''Effects of cochlear implant use on voice parameters,'' Otolaryngol. Clin. North Am. **16**, 281–292.
Lane, H. (**1962**). ''Psychophysical parameters of vowel perception,'' Psychol. Monogr. **76**, 1–25.
Lane, H., and Tranel, B. (**1971**). ''The Lombard sign and the role of hearing in speech,'' J. Speech Hear. Res. **14**, 677–709.
Lane, H., and Webster, J. (**1991**). ''Speech deterioration in postlingually deafened adults,'' J. Acoust. Soc. Am. **89**, 859–866.
Lane, H., Tranel, B., and Sisson, C. (**1970**). ''Regulation of voice communication by sensory dynamics,'' J. Acoust. Soc. Am. **47**, 618–624.
Lane, H., Wozniak, J., and Perkell, J. (**1994**). ''Changes in voice-onset time in speakers with cochlear implants,'' J. Acoust. Soc. Am. **96**, 56–64.
Lane, H., Wozniak, J., Matthies, M., Perkell, J., and Svirsky, M. (**1995**). ''Phonemic resetting vs. postural adjustments in the speech of cochlear implant users: The case of voice-onset time,'' J. Acoust. Soc. Am. **98**, 3096–3106.
Larkey, L. S., and Danly, M. (**1983**). ''Fundamental frequency and the comprehension of simple and complex sentences,'' J. Acoust. Soc. Am. Suppl. 1 **74**, S67.
Leder, S., and Spitzer, J. B. (**1990**). ''Longitudinal effects of single-channel cochlear implantation on voice quality,'' Laryngoscope **100**, 395–398.
Leder, S., and Spitzer, J. B. (**1993**). ''Speaking fundamental frequency, intensity and rate of adventitiously profoundly hearing impaired adult women,'' J. Acoust. Soc. Am. **93**, 2146–2151.
Leder, S., Spitzer, J. B., and Kirchner, J. C. (**1987**). ''Speaking fundamental frequency of postlingually profoundly deaf adult men,'' Ann. Otol. Rhinol. Laryngol. **96**, 322–324.
Leder, S., Spitzer, J. B., Kirchner, J., Flevaris Philips, C., and Richardson, F. (**1987a**). ''Speaking rate of adventitiously deaf male cochlear implant candidates,'' J. Acoust. Soc. Am. **82**, 843–846.
Leder, S., Spitzer, J. B., Milner, P., Flevaris-Phillips, C., Kirchner, J. C., and Richardson, F. (**1987b**). ''Voice intensity of prospective cochlear-implant candidates and normal-hearing adult males,'' Laryngoscope **97**, 224–227.
Leder, S., Spitzer, J. B., Milner, P., Flevaris Philips, C., Richardson, F., and Kirchner, J. (**1986**). ''Reacquisition of contrastive stress in an adventitiously deaf speaker using a single-channel cochlear implant,'' J. Acoust. Soc. Am. **79**, 1967–1974.
Lindbolm, B. (**1990**). ''Explaining phonetic variation: A sketch of the H & H theory,'' in *Speech Production and Speech Modeling*, edited by W. J. Hardcastle and A. Marchal (Kluwer, Dordrecht), pp. 403–439.
Matthies, M., Svirsky, M., Lane, H., and Perkell, J. (**1994**). ''A preliminary study of the effects of cochlear implants on the production of sibilants,'' J. Acoust. Soc. Am. **96**, 1367–1373.
Moon, S. J., and Lindblom, B. (**1989**). ''Formant undershoot in clear and citation-form speech: A second progress report,'' Speech Transmission Laboratory, QPSR, 1-1989, pp. 121–123.
Oster, A. (**1987**). ''Some effects of cochlear implantation on speech production,'' Speech Transmission Laboratory, Quarterly Progress and Status Report, 1-1987, pp. 81–89.
Perkell, J., Holmberg, E., and Hillman, R. (**1991**). ''A system for signal processing and data extraction from aerodynamic, acoustic, and electroglottographic signals in the study of voice production,'' J. Acoust. Soc. Am. **89**, 1777–1781.
Perkell, L., Lane, H., Svirsky, M., and Webster, J. (**1992**). ''Speech of cochlear implant patients: A longitudinal study of vowel production,'' J. Acoust. Soc. Am. **91**, 2961–2978.
Perkell, J. Manzella, J., Wozniak, Matthies, M., Lane, H., Svirsky, M., Guiod, P., Delhorne, L., Short, P., MacCollin, M., and Mitchell, C. (**1995**). ''Changes in speech production following hearing loss due to bilateral acoustic neuromas,'' in *Proceedings of the XIII International Congress of Phonetic Sciences* (Royal Institute of Technology and Stockholm University, Stockholm, Sweden), Vol. 3, pp. 194–197.
Peters, R. W. (**1955**). ''The effect of filtering of sidetone upon speaker intelligibility,'' J. Speech Hear. Disord. **20**, 371–375.
Picheny, M. A., Durlach, N. I., and Braida, L. D. (**1985**). ''Speaking clearly for the hard of hearing I: Intelligibility differences between clear and conversational speech,'' J. Speech Hear. Res. **28**, 96–103.
Picheny, M. A., Durlach, N. I., and Braida, L. D. (**1986**). ''Speaking clearly for the hard-of-hearing II: Acoustic characteristics of clear and conversational speech,'' J. Speech Hear. Res. **29**, 434–446.
Plant, G. (**1983**). ''The effects of a long-term hearing loss on speech production,'' Speech Transmission Laboratory, Quarterly Status and Progress Reports (Stockholm), 1-1983, pp. 18–35.
Plant, G. (**1984**). ''The effects of an acquired profound hearing loss on speech production,'' Br. J. Audiol. **18**, 39–48.
Plant, G. L., and Hammarberg, B. (**1983**). ''Acoustic and perceptual analysis of the speech of the deafened,'' Speech Transmission Laboratory, Quarterly Progress and Status Report (Stockholm), 2-/3-1983, pp. 85–107.
Plant, G., and Oster, A. (**1986**). ''The effects of cochlear implantation on speech production. A case study,'' Speech Transmission Laboratory, Quarterly Progress and Status Report, 1-1986, pp. 65–84.
Price, P. J., Ostendorf, M., Shattuck-Hufnagel, S., Fong, C. (**1991**). ''The use of prosody in syntactic disambiguation,'' J. Acoust. Soc. Am. **90**, 2956–2970.
Schulman, R. (**1989**). ''Articulatory dynamics of loud and normal speech,'' J. Acoust. Soc. Am. **85**, 295–312.
Shannon, R. V. (**1993**). ''Psychophysics,'' in *Cochlear Implants: Audiologic Foundation*, edited by R. S. Tyler (Singular, San Diego, CA), pp. 357–368.
Sherrard, C. A. (**1982**). '' 'Auditory feedback' or 'sidetone'? The effects on speech production and intelligibility of auditory stimulation from the larynx,'' Lang. Speech **25**, 283–292.
Svirsky, M., Lane, H., Perkell, J., and Wozniak, J. (**1992**). ''Effects of short term auditory deprivation on speech production in adult cochlear implant users,'' J. Acoust. Soc. Am. **92**, 1284–1300.
Tartter, V. C., Gomes, H., and Litwin, E. (**1993**). ''Some acoustic effects of listening to noise on speech production,'' J. Acoust. Soc. Am. **94**, 2437–2440.
Tillman, T. W., and Carhart R. (**1966**). ''An expanded test for speech discrimination utilizing CNC monosyllable words,'' Northwestern University auditory test no. 6, Technical report SAM-TR-66-55. USAF School of Aerospace Medicine, Brooks Air Force Base.
Titze, I. R. (**1991**). ''Mechanisms underlying the control of fundamental frequency,'' in *Vocal Fold Physiology*, edited by J. Gauffin and B. Hammarberg (College-Hill, Boston).
Tolhurst, G. (**1954**). ''The effect on intelligibility scores of specific instructions regarding talking,'' Joint Project report No. 35, U.S. Naval School of Aviation Medicine, Pensacola, FL.
Tolhurst, G. (**1957**). ''Effects of duration and articulation changes on intelligibility, word reception, and listener preference,'' J. Speech Hear. Disord. **22**, 328–334.
Van Summers, W., Pisoni, D. B., Bernacki, R. H., Pedlow, R. I., and Stokes, M. A. (**1988**). ''Effect of noise on speech production: Acoustic and perceptual analyses,'' J. Acoust. Soc. Am. **84**, 917–928.
Waldstein, R. (**1990**). ''Effects of postlingual deafness on speech production: Implications for the role of auditory feedback,'' J. Acoust. Soc. Am. **88**, 2099–2114.
Webster, J. C., and Klumpp, R. G. (**1962**). ''Effects of ambient noise and nearby talkers on a face-to-face communication task,'' J. Acoust. Soc. Am. **34**, 936–941.

Predicting developmental shifts in perceptual weighting schemes

Susan Nittrouer and Marnie E. Miller
Boys Town National Research Hospital, 555 North 30th Street, Omaha, Nebraska 68131

(Received 17 March 1996; revised 28 September 1996; accepted 22 November 1996)

Recent models of developmental changes in speech perception suggest that the weights assigned to acoustic properties change as children gain experience with a native language. Empirical evidence supports this position, but few suggestions have been offered as to what guides this shift. These three experiments were designed to improve our ability to predict how perceptual weighting schemes change with development. The specific hypothesis explored was twofold: (1) the weight assigned by adults to any one acoustic property differs across phonetic environments according to how informative that property is in each environment; and (2) the weight assigned by children to any one acoustic property differs less across phonetic environments because children have not fully learned the patterns of covariation between phonetic informativeness and environment for each property. Experiment 1 replicated previous findings of age-related differences in the weights assigned to noise spectra and formant transitions in labeling of syllable-initial fricatives (/s/ or /ʃ/). In experiment 2 the variation in *F*3-onset frequency associated with place of fricative constriction was eliminated. This property differs more (i.e., is more informative) in /u/ than in /ɑ/. Accordingly adults' transition effect was reduced more for /u/ than for /ɑ/ from experiment 1. Children's transition effect was similarly reduced across vowel environments. In experiment 3, *F*3-onset frequency was appropriately manipulated for both vowels, and adults transition effect increased more for /u/ than for /ɑ/ from experiment 2. The increase in children's transition effect was more similar across vowels. We conclude that the children had not fully learned how information provided by *F*3 transitions varies across /ɑ/ and /u/ environments, and suggest that developmental weighting shifts may be guided by children learning the relation between phonetic informativeness and environment. © *1997 Acoustical Society of America.* [S0001-4966(97)03504-2]

PACS numbers: 43.71.An, 43.71.Ft [WS]

INTRODUCTION

Recent theories of speech perception propose that listeners derive phonetic structure from the acoustic speech signal by integrating multiple properties from across the temporal and spectral domains of that signal (e.g., Bailey and Summerfield, 1980; Best *et al.*, 1981; Fitch *et al.*, 1980; Kluender *et al.*, 1988; Oden and Massaro, 1978). Because several properties contribute to the perception of phonetic structure in these accounts, it is reasonable to assume that different perceptual weights may be assigned to these various properties. Accordingly we may ask what principle (or principles) determines the weight to be assigned to each property in each context. Dorman *et al.* (1977) suggested that, for adult listeners, the perceptual weight assigned to each acoustic property varies with the acoustic salience of that property in the specific phonetic environment in which it is perceived. Thus they found that the weights assigned to the burst spectrum and formant transitions at voicing onset in decisions of stop place varied across vowel contexts such that the precise weights correlated with differences in the acoustic salience of each property in each vowel environment. This proposal of Dorman *et al.* led to the hypothesis to be tested in these experiments, with one modification. The concept of ''acoustic salience'' used by them suggests an attribute that can be described in real physical terms. We know from cross-linguistic research (e.g., Best and Strange, 1992; Crowther and Mann, 1992, 1994; Flege *et al.*, 1996; MacKain *et al.*, 1984; Werker *et al.*, 1981) that a property can be physically distinctive, and yet some listeners (such as non-native listeners) nonetheless fail to use it in reaching phonetic decisions, presumably because that property conveys little or no phonetic information in their native language. Therefore, we substituted the term ''phonetic informativeness'' for ''acoustic salience'' in the Dorman *et al.* account. The findings of cross-linguistic research (that the weights assigned to specific acoustic properties vary across languages) suggest that some perceptual learning must be involved in acquiring the weighting schemes most useful to deriving phonetic structure from the acoustic speech signal. The specific hypothesis to be explored in this series of experiments is twofold: (1) the weight assigned by adults to any one acoustic property differs across phonetic environments, depending on how informative that property is in each environment; and (2) the weight assigned by children to any one acoustic property will vary less across phonetic environments because children have not fully learned how phonetic informativeness varies across environments for each property.

The concept that children weight the acoustic properties of speech differently from adults is not new. Greenlee (1980) investigated age-related differences in the labeling of syllable-final stops as voiced or voiceless, and concluded that ''...differences between children's and adults' identifications may reflect, not an absolute difference in whether or not multiple acoustic cues are used, but rather a difference in the

extent to which they are used by the two age groups'' (p. 467). Similarly, Wardrip-Fruin and Peach (1984), also studying the voicing of syllable-final stops, concluded that ''...spectral cues such as voicing during closure and final transitions were, in general, more influential in the voicing decision than were changes in [vocalic] duration. However, there were age differences in the weighting of the cues in the present study'' (p. 376). Thus, there have been reports over the past 15 years or so suggesting that the weights assigned to acoustic speech properties are modified through childhood, and it is these reports that led to a model termed the Developmental Weighting Shift (Nittrouer *et al.*, 1993). This model specifically suggests that children initially show a preferential weighting of dynamic, acoustic properties (i.e., those that change spectrally over time) because these properties help them recognize syllabic structure in the speech stream. With linguistic experience, children gradually decrease their attention to these dynamic properties, and increase their attention to the static properties (i.e., those that do not involve spectral change over time) that are particularly informative about phonetic structure in their native language. The experiments described here explored one hypothesis about what guides developmental changes in how acoustic properties are weighted in speech perception: that children's growing familiarity with the variability in amount of information conveyed by each property across phonetic environments guides this developmental shift.

To achieve our goal, this series of experiments exploited modified versions of some previously used stimuli: fricative-vowel syllables. The synthetic fricative noises form a continuum from ''s'' to ''sh,'' and the vocalic portions are /ɑ/ and /u/ with initial transitions appropriate for either a preceding /s/ or /ʃ/. We expected to replicate earlier findings for fricative-vowel syllables showing that children weight vocalic formant transitions more than adults in decisions of fricative identity (Nittrouer, 1992, 1996a; Nittrouer and Studdert-Kennedy, 1987), and attempted to do so in experiment 1. These results then served as a base against which to compare results from the next two experiments. As stated earlier, Dorman *et al.* (1977) showed that the weights assigned to burst spectrum and formant transitions at voicing onset differed depending on vowel environment. When these two properties were put into conflict with each other (such that one specified one place of closure and the other specified a different place of closure), response labels more strongly reflected the place of closure specified by the most salient (or informative) property. A stronger test of this hypothesis (that perceptual weights covary with phonetic informativeness) would be had if it could be shown that neutralizing a property (i.e., eliminating its phonetic informativeness) had a stronger effect in some phonetic environments than in others. Specifically, we would expect that neutralizing a property would have a more deleterious perceptual effect in the phonetic environments in which it is normally particularly informative than in environments in which it is normally not very informative. The effect of vocalic formant transitions on decisions of fricative identity in fricative-vowel (FV) syllables is generally attributed to both second and third formant ($F2$ and $F3$) transitions. $F2$ and $F3$ transitions in natural fricative-vowel syllables are inextricably linked because both vary with the place of fricative constriction. The perceptual consequences of neutralizing either one of these properties should be deleterious, but we chose to manipulate $F3$ in these experiments because $F3$ frequency at voicing onset varies more depending on whether the preceding fricative is /s/ or /ʃ/ for /u/ than for /ɑ/ (Mann and Repp, 1980; also see Table I). In other words, $F3$-onset frequency provides more information about the preceding fricative in the /u/ than in the /ɑ/ environment. Thus, adults should weight $F3$ onsets more for /u/ than for /ɑ/, and so /u/ stimuli should demonstrate a greater decrease than /ɑ/ stimuli in the magnitude of the transition effect (defined operationally as the separation in labeling functions depending on whether formant transitions at voicing onset are appropriate for a preceding /s/ or /ʃ/). If children need experience with a language to learn which properties are acoustically salient (or, using our terminology, which are phonetically informative) in specific environments, then the weight they assign to individual properties should not vary greatly across environments, and so the effect of neutralizing $F3$-onset frequency should be similar for /u/ and /ɑ/. To test these predictions, we neutralized $F3$-onset frequencies in the second experiment. In the third experiment, $F3$-onset frequencies varied as they would naturally depending on whether the initial fricative was an /s/ or /ʃ/, for both /u/ and /ɑ/. In this case, the transition effect for adults' responses should increase more for /u/ than for /ɑ/ over what was observed in experiment 2, whereas children's transition effect should increase similarly for the two vowels.

This series of experiments also allowed us to examine two concerns regarding earlier work. Our previous developmental studies of fricative labeling have commonly used synthetic noises and natural vocalic portions (Nittrouer, 1992, 1996a; Nittrouer and Studdert-Kennedy, 1987). Consequently it is possible that children show a greater weighting of vocalic formant transitions than adults, while demonstrating a lesser weighting of the fricative noise, because children fail to process synthetic speech components as they do natural speech. In experiments 1 and 3 of the present study, both $F2$ and $F3$ varied appropriately as a function of preceding fricative place, but vocalic signal portions were natural in experiment 1 and synthetic in experiment 3. Therefore, if we found similar age-related trends for experiments 1 and 3, it would refute the notion that previously observed differences in weighting schemes for children and adults were due to children failing to process synthetic signal components as they process natural speech.

We were also able to address the suggestion that children's speech perception strategies largely reflect constraints imposed by immature auditory capabilities (Elliott *et al.*, 1986; Elliott *et al.*, 1981; Sussman, 1993; Sussman and Carney, 1989). Regarding the fricative-vowel stimuli, the specific suggestion is that children's lesser weighting of the fricative noise, compared to that of adults, reflects children's limits in discriminating noise spectra (Allen and Wightman, 1989). Although we have investigated this possibility to some extent (Nittrouer, 1996a), we wished to investigate it further. Our reasoning here was that if children assigned more weight to the fricative noise when the amount of infor-

mation conveyed by the formant transitions was reduced then children's weighting of the noise in earlier experiments could not be strictly explained by auditory constraints.

Finally, we examined what has traditionally been labeled the ''vowel effect.'' Interest in how the rounding characteristic of the vowel influences perception of fricative noises actually preceded interest in how vocalic onset transitions influence that perception (Kunisaki and Fujisaki, 1977). The hypothesis was that noises ambiguous between an /ʃ/ and /s/ percept would more frequently be heard as /s/ when the following vowel was rounded (such as /u/) than when it was unrounded (such as /ɑ/), thus pushing phoneme boundaries between /ʃ/ and /s/ to lower frequencies. The basis for this suggestion was that anticipatory liprounding should lower the overall spectrum of the noise, a context effect with which listeners should be familiar and able to use in their phonetic decisions. Articulatory data has supported this suggestion by showing that listeners do round their lips before the start of rounded vowels (e.g., Daniloff and Moll, 1968; Bell-Berti and Harris, 1979), but support from acoustic analyses has been scant. From utterances produced by one male, Japanese speaker, Kunisaki and Fujisaki determined that the fricative first pole was generally higher when the fricative preceded an unrounded vowel, rather than a rounded vowel. However, the effect was neither consistent nor strong: there was no difference in the fricative first pole for /ɑsɑ/ compared to /ɑsu/, and the fricative first pole was actually a bit lower for /ɑʃɑ/ compared to /ɑʃu/. Nonetheless, the general finding was complementary to what Heinz and Stevens (1961) had reported: Measuring fricative pole frequencies for individual tokens from an English, male speaker [recorded by Hughes and Halle (1956)], they found that fricative first poles were higher for ''sect'' and ''salve'' than for ''soothe.'' However, they found that fricative second poles were a little lower in the unrounded vowel contexts. In a study with 40 speakers, Nittrouer (1995) showed that there were no systematic differences in first spectral moments for noises, depending on whether the following vowel was /ɑ/ or /u/, either for the fricatives /s/ and /ʃ/ or for the stops /t/ and /k/. In spite of this lack of evidence for the acoustic effect, several studies have shown the predicted perceptual effect: listeners labeled ambiguous noises ''s'' more frequently when /u/ followed than when /ɑ/ followed (Kunisaki and Fujisaki, 1977; Mann and Repp, 1980; Nittrouer, 1992; Whalen, 1981).

One study did not show this effect consistently. Nittrouer and Studdert-Kennedy (1987) found, for listeners of all ages, that the vowel effect was ''reversed'' from what was predicted for stimuli with formant transitions appropriate for a preceding /ʃ/: more ''s'' judgments were made for stimuli with the unrounded vowel /i/ than for those with the rounded vowel /u/. That result was interpreted as indicating an interaction between the vowel effect and transition effect: /ʃ/ transitions influenced listeners more against responding ''s'' than the /u/ vowel influenced listeners in favor of responding ''s.'' Nittrouer (1992) did not observe this reverse vowel effect for stimuli with the vowels /ɑ/ and /u/, but there was a trend toward smaller vowel effects for younger listeners. Thus, at the start of this study there were contradictory results concerning the vowel effect itself, and whether it varies with the age of the listener.

In summary, the primary goal of the experiments described here was to examine more closely developmental changes in the perceptual weighting of the acoustic properties relevant to fricative judgments. We wished to see if the transition effects of children and adults could be explained by how informative each transition is in the /u/ and /ɑ/ context, and how familiar listeners are with this vowel-specific information. The results should further our ability to predict how perceptual weighting schemes change with development. Secondary objectives of this work were (i) to determine if children's enhanced attention to vocalic formant transitions, compared to that of adults, is contingent on the use of hybrid stimuli (i.e., synthetic fricative noises and natural vocalic portions); (ii) to examine the possibility that developmental shifts in perceptual weighting of speech-relevant acoustic properties primarily reflect developmental changes in the auditory system; and (iii) to examine the vowel effect for children and adults.

I. EXPERIMENT 1: NATURAL VOCALIC PORTIONS

The primary goal of this experiment was to replicate earlier studies (Nittrouer, 1992, 1996a; Nittrouer and Studdert-Kennedy, 1987) with the equipment and procedures to be used in the next two experiments.

A. Method

1. Subjects

Twenty children of each of the ages of four and seven years and 20 adults between 20 and 40 years participated. The mean age of 4-year-olds was 4 years, 7 months (4;7), with a range from 4;1 to 5;3. The mean age of 7-year-olds was 7;2, with a range from 6;4 to 7;11. Three additional 4-year-olds and two additional 7-year-olds started the experiment, but were dismissed because they did not meet the criterion of getting at least 80% of the ''best exemplars'' correct during testing (see Sec. I A 4). All listeners passed a hearing screening, consisting of pure tones of 0.5, 1, 2, 4, and 6 kHz presented at 25 dB HL (ANSI, 1989). Children were given the Goldman-Fristoe Test of Articulation (Goldman and Fristoe, 1969), and were required to score at better than the 30th percentile for their age. In particular, all children produced perceptually acceptable versions of /s/ and /ʃ/. All children were free from significant histories of otitis media, defined as six or more episodes during the first two years of life. Adults were given the reading subtest of the Wide Range Achievement Test-Revised [WRAT-R (Jastak and Wilkinson, 1984)], and were required to demonstrate at least an 11th-grade reading level.

2. Equipment

All testing took place in a soundproof booth. Synthetic stimulus portions were generated using a Sensimetrics software synthesizer. Hearing was screened with a Maico MA41 audiometer using TDH-39 headphones. Recorded stories were presented via a Nakamichi MR-2 audiocassette player with AKG-K141 headphones. Synthetic versions of the sto-

TABLE I. Means across the five tokens for the phonetically relevant acoustic dimensions of the vocalic portions used in experiment 1: $f0$=fundamental frequency (Hz); dur=duration (ms); $F2$-onset=frequency of second formant at voicing onset (Hz); $F3$-onset=frequency of third formant at voicing onset (Hz).

Portion	$f0$	dur	$F2$-onset	$F3$-onset
(s)ɑ	93	333	1365	2457
(ʃ)ɑ	95	337	1532	2367
(s)u	99	347	1520	2496
(ʃ)u	97	348	1706	2288

ries were generated with DEC talk, a text-to-speech synthesizer. Presentation of stimuli and recording of responses was controlled by a computer. A Data Translation 2801A digital-to-analog converter, a Frequency Devices 901-F filter, a Crown D-75 amplifier, and AKG-K141 headphones were used for stimulus presentation. Cartoon drawings were shown on a color-graphics monitor.

3. Stimuli

The stimuli were similar to those of experiment 1 in Nittrouer (1992) and to the hybrid stimuli in Nittrouer (1996a). A 20-kHz sampling rate was used, with low-pass filtering below 9.8 kHz. The fricative noises were single-pole, synthetic noises, with the center frequency ranging from 2.2 to 3.8 kHz in nine 200-Hz steps. The vocalic portions in this experiment were natural, and were taken from a male speaker saying /su/, /sɑ/, /ʃu/, and /ʃɑ/. Five tokens of each syllable type were used, and Table I shows the means for the relevant acoustic parameters. For /u/, $F2$ fell in frequency through the entire portion to a mean ending frequency of 930 Hz. For /ɑ/, $F2$ fell in frequency over the first 60 to 90 ms to a mean steady-state frequency of 1309 Hz. For all stimuli, $F3$ fell in frequency over roughly the first 100 ms. For /u/ the mean steady-state $F3$ frequency was 2320 Hz; for /ɑ/, the mean steady-state $F3$ frequency was 2365 Hz. The vocalic portions were separated from the fricative noises using a waveform editor, and recombined with each of the synthetic noises, yielding 180 stimuli (9 noises $\times$ 4 syllable types $\times$ 5 tokens).

4. Procedures

The screening tasks were presented first, followed by the labeling task. Stimuli with each vowel were presented separately. Half of the subjects heard the /u/ stimuli first, and half heard the /ɑ/ stimuli first. For adults, stimuli in each vowel context were presented in a single session. For children, stimuli in each vowel context were presented on separate days, thus requiring two sessions.

Children were introduced to the response labels (''sa,'' ''sha,'' ''sue,'' or ''shoe'') with tape-recorded stories accompanied by pictures. Each story was presented twice: once with natural speech and once with synthetic speech. These stories served both to familiarize children with the response labels and to provide experience listening to synthetic speech. All subjects heard ten practice items (five each of /sV/ and /ʃV/) before testing, using the best exemplars of each category. For example, the best exemplar of ''sue'' was the 3.8-kHz noise paired with the /(s)u/ vocalic portions.[1] Each subject had to label nine of these ten best exemplars correctly to proceed to testing.

Each stimulus was presented twice across the test session, in randomized blocks of 18: each of the nine noises paired with a /(ʃ)V/ and a /(s)V/. Within each block, tokens of /(ʃ)V/ and /(s)V/ varied. Thus ten responses were obtained to each fricative noise paired with each vocalic portion [/(ʃ)ɑ/, /(s)ɑ/, /(ʃ)u/, and /(s)u/], and vocalic portions varied sufficiently across presentations so that results attributed to formant transitions could not reasonably be explained by any other acoustic parameter. Listeners indicated their responses by pointing to one of two pictures and saying the response label. The experimenter entered the responses into the computer. Cartoon drawings were shown to children at the end of each block, and they got to move a marker to the next number on a game board. For a subject's data to be included in the final analysis, at least 80% accurate responses had to be given to the best exemplars during testing, thereby insuring that data were included only from subjects who maintained attention to the task.

Labeling data for each vocalic context for each listener were transformed to probit scores. From each probit distribution, a mean (i.e., the point on the fricative-noise continuum at which 50% of responses were /ʃ/ and 50% were /s/) and a slope (change in probit units per kHz of change in fricative noise) were derived. In computing distribution means, the analysis will extrapolate beyond the limits of the physical continuum if the labeling function does not cross the 50% point within this range. Thus it was possible to have distribution means for stimuli with /s/ transitions that were lower than 2200 Hz (if a listener responded predominantly ''s'' to stimuli with /s/ transitions) and to have distribution means for stimuli with /ʃ/ transitions that were higher than 3800 Hz (if a listener responded predominantly ''sh'' to stimuli with /ʃ/ transitions). However, distribution means that were less than 1500 Hz or greater than 4500 Hz were set to 1500 Hz or 4500 Hz, respectively. This procedure kept distribution means within a reasonable range, but did not affect our analyses in any way that would invalidate our results. Past experiments have shown that younger children are most likely to demonstrate extreme distribution means, leading to greater transition effects for these children than for older children and adults. Consequently, truncating the range of possible distribution means mainly affects children's results, and so we only decrease the probability of finding significant age effects. Distribution means were considered to be phoneme boundaries.

The slope of the function is generally taken as an index of the weight assigned to the parameter represented on the abscissa, which in this case was the fricative-noise spectrum. The steeper the function, the more weight that was assigned to the fricative-noise spectrum. The separation in functions indexes the weight assigned to formant transitions [i.e., the transition effect: /(ʃ)u/ versus /(s)u/ or /(ʃ)ɑ/ versus /(s)ɑ/] and the weight assigned to vowel quality [i.e., the vowel effect: /(ʃ)ɑ/ versus /(ʃ)/u/ or /(s)ɑ/ versus /(s)u/].

Three-way analyses of variance (ANOVA's) were performed on phoneme boundaries and slopes, with age as a

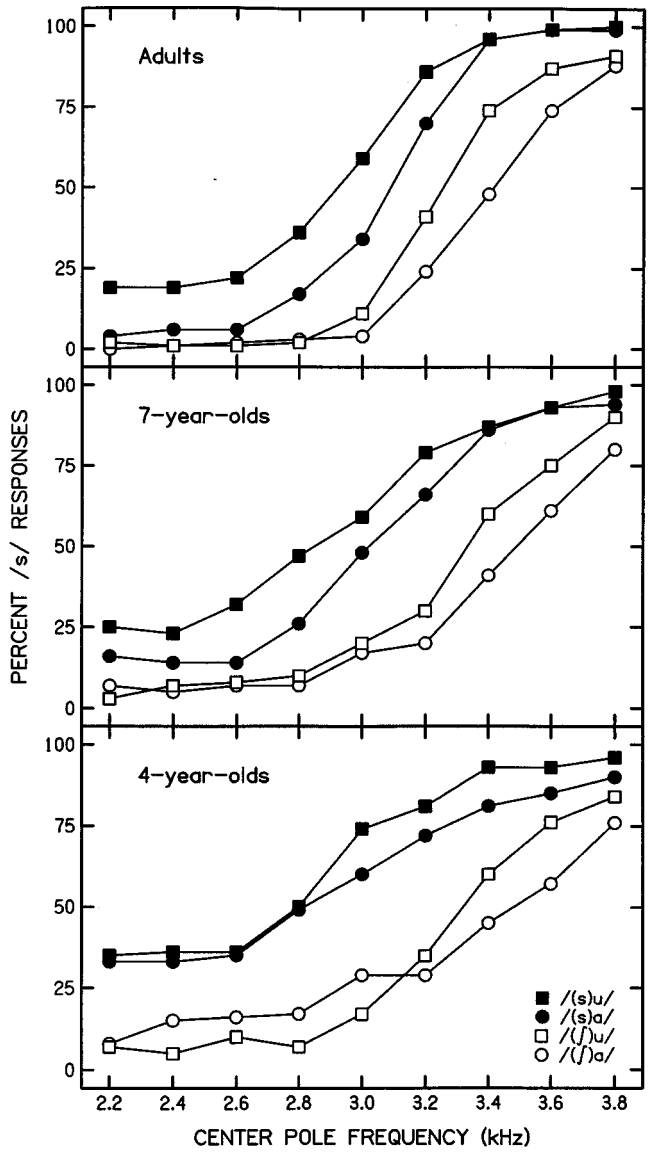

FIG. 1. Labeling functions for experiment 1 for adults (top), 7-year-olds (center), and 4-year-olds (bottom). Center frequencies of the synthetic fricative noises are shown on the abscissa, and percent ''s'' responses are shown on the ordinate. A separate function is plotted for each syllable type.

between-subjects factor, and vowel (/ɑ/ or /u/) and transition (appropriate for /s/ or /ʃ/) as within-subjects factors. To examine potential developmental changes more closely, two planned, orthogonal comparisons were performed: adults versus all children, and 7-year-olds versus 4-year-olds.

B. Results

1. Phoneme boundaries

Figure 1 displays labeling functions for adults, 7-year-olds, and 4-year-olds, and Table II shows mean phoneme boundaries. The transition effect (i.e., the separation in the open versus filled squares or circles) is clearly greater for children than for adults. The vowel effect (i.e., the separation in the circles versus squares, whether open or filled) is smaller for 4-year-olds than for older children and adults, but this trend is not as clear as the age difference for the transition effect.

TABLE II. Mean phoneme boundaries for experiment 1 in Hz (top). Mean differences in phoneme boundaries (in Hz) for the transition effect [/(ʃ)V/-/(s)V/] and for the vowel effect [/(F)ɑ/-/(F)u/] (bottom). Standard deviations are in parentheses.

	4-year-olds	7-year-olds	Adults
/(s)ɑ/	2685	2982	3033
	(366)	(186)	(158)
/(ʃ)ɑ/	3516	3546	3429
	(327)	(301)	(143)
/(s)u/	2550	2739	2794
	(444)	(319)	(263)
/(ʃ)u/	3355	3379	3286
	(215)	(273)	(188)
/(ʃ)ɑ/-/(s)ɑ/	832	564	396
	(300)	(358)	(152)
/(ʃ)u/-/(s)u/	805	640	492
	(427)	(391)	(252)
/(s)ɑ/-/(s)u/	134	242	238
	(444)	(256)	(211)
/(ʃ)ɑ/-/(ʃ)u/	162	167	143
	(347)	(362)	(215)

The overall effect of age was marginally significant [$F(2,57)=2.97$, $p=0.059$], and the planned comparison of 7-year-olds versus 4-year-olds was significant [$F(1,57)=5.28$, $p=0.025$]. This age effect reflects the asymmetric influences of /s/ and /ʃ/ transitions on responses of different-aged listeners. Phoneme boundaries are similar across age groups for stimuli with /ʃ/ transitions. However, /s/ transitions exerted a much greater influence on the responses of younger listeners than on those of older listeners, and so phoneme boundaries for stimuli with /s/ transitions are lower for younger listeners. Consequently, mean phoneme boundaries (across the four vocalic portions) were 3135 Hz for adults, 3161 Hz for 7-year-olds, and 3026 Hz for 4-year-olds. The other main effects were also significant: the transition effect [$F(2,57)=316.69$, $p<0.001$]; and the vowel effect [$F(2,57)=29.21$, $p<0.001$].

The only significant interaction was the age×transition interaction [$F(2,57)=9.66$, $p<0.001$]. Both planned comparisons for the transition effect were significant: adults versus all children [$F(1,57)=12.93$, $p<0.001$]; and 7-year-olds versus 4-year-olds [$F(1,57)=6.39$, $p=0.014$]. Thus there was a significant developmental decrease in the size of the transition effect, but no significant developmental trend for the vowel effect.

2. Slopes

From Fig. 1 it appears that adults' labeling functions were steeper than those of children, and that 7-year-olds' functions were steeper than those of 4-year-olds. These impressions are supported by Table III, which shows mean slope for each syllable type (top) and mean slope for each vowel across transition conditions (bottom).

The main effect of age was significant [$F(2,57)=27.10$, $p<0.001$], as were the planned comparisons of adults versus all children [$F(1,57)=48.66$, $p<0.001$], and of 7-year-olds versus 4-year-olds [$F(1,57)=5.55$, $p=0.022$]. There was also a significant age×vowel interaction

TABLE III. Mean slope for each syllable type for experiment 1, in probit units per kHz of fricative noise (top). Mean slope for each vowel across transition conditions (bottom). Standard deviations are in parentheses.

	4-year-olds	7-year-olds	Adults
/(s)ɑ/	1.57	2.62	4.44
	(0.71)	(1.51)	(1.43)
/(ʃ)ɑ/	1.64	2.43	3.82
	(1.10)	(1.27)	(1.04)
/(s)u/	1.83	2.49	3.21
	(0.81)	(1.41)	(1.42)
/(ʃ)u/	2.59	2.77	4.40
	(1.36)	(1.21)	(1.30)
/ɑ/ mean	1.60	2.52	4.13
	(0.79)	(1.29)	(1.05)
/u/ mean	2.21	2.63	3.80
	(0.99)	(1.15)	(1.00)

$[F(2,57)=3.62,\ p=0.033]$, as well as a significant vowel effect for the planned comparison of adults versus all children $[F(1,57)=5.18,\ p=0.027]$. This last effect, indicating that slope varied across the two vowels differently for children and adults, is probably attributable to the fact that adults showed steeper functions for /ɑ/ than for /u/, but children showed steeper functions for /u/.

C. Discussion

The goal of this experiment was met: The age-related differences found in earlier experiments were replicated. There was a developmental decrease in the separation between labeling functions depending on whether formant transitions were appropriate for /ʃ/ or /s/, and so we conclude that there was a developmental decrase in the perceptual weight assigned to formant transitions. There was also a developmental increase in the steepness of the functions, and so we conclude that there was a developmental increase in the perceptual weight assigned to the fricative-noise spectra.

The predicted vowel effect was observed for all listener groups. Although a significant age×vowel interaction was not observed for phoneme boundaries, there was nonetheless a trend toward an attenuated vowel effect for stimuli with /s/ transitions for 4-year-olds, compared to what was found for older children and adults.

II. EXPERIMENT 2: SYNTHETIC VOCALIC PORTIONS, *F*2 ONLY VARYING

The goals of this experiment were to test the predictions that eliminating the difference in $F3$-onset frequency associated with place of preceding fricative constriction would (1) decrease the transition effect more for /u/ than for /ɑ/ stimuli in adults' labeling responses; and (2) decrease the transition effect similarly for /u/ and /ɑ/ stimuli in children's labeling responses. The $F3$-onset frequency presumably provides more information about the preceding fricative in /u/ than in /ɑ/ because $F3$-onset frequency differs more depending on whether the preceding fricative was /s/ or /ʃ/ in fricative-/u/ syllables. If perceptual weight for a property is determined by the amount of phonetic information it conveys in a specific environment, and if children need to learn about these informational-environmental relations, then we would expect that the effects of neutralizing $F3$ would show stronger vowel specificity for adults' responses than for those of children.

A. Method

1. Subjects

Listeners were the same ages and met the same criteria as in experiment 1. Nineteen 4-year-olds participated, with a mean age of 4;7 (range from 4;3 to 4;11). Four additional 4-year-olds started in the study, but one did not meet our training criterion and three did not meet our testing criterion. Twenty-two 7-year-olds participated, with a mean age of 7;3 (range from 6;3 to 7;11). Twenty adults participated.

2. Stimuli and equipment

The same equipment was used for this experiment as for experiment 1. The stimuli had both synthetic fricative noises and synthetic vocalic portions. The noises were the same as those of experiment 1. Parameter settings for the vocalic portions were largely based on Whalen (1981), with some modification based on the acoustic analysis of the natural vocalic portions from experiment 1. Each portion was 270-ms long. For all stimuli, $F3$ started at 2400 Hz, and fell over the first 50 ms to a steady-state frequency of 2100 Hz. We used roughly the highest $F2$ onsets for /(ʃ)u/ and /(ʃ)ɑ/ found in the tokens from experiment 1, and roughly the lowest $F2$ onsets for /(s)u/ and /(s)ɑ/. These frequencies were adjusted only enough to keep the difference in $F2$ onsets between the /ʃ/ and the /s/ conditions the same for /u/ and /ɑ/ stimuli. We chose these extreme $F2$ onsets to make sure that $F2$ transitions were informative, as long as we were eliminating any information provided by $F3$ transitions. For the /u/ portions, $F2$ fell through the entire portion to an ending frequency of 850 Hz. $F2$ onset for /(ʃ)u/ was 1800 Hz, and $F2$ onset for /(s)u/ was 1480 Hz. Fundamental frequency ($f0$) fell through the entire /u/ portion from 120 to 100 Hz, and the first formant ($F1$) was constant at 250 Hz. For the /ɑ/ portions, $F2$ fell over the first 100 ms to a steady-state frequency of 1130 Hz. For /(ʃ)ɑ/, $F2$ onset was 1570 Hz; for /(s)ɑ/, $F2$ onset was 1250 Hz. The $f0$ fell through the entire /ɑ/ portion from 100 to 80 Hz. $F1$ started at 450 Hz, rose over the first 50 ms to 650 Hz, and remained there for the remainder of the vocalic portion. Each of these four vocalic portions was combined with each of the nine fricative noises, yielding 36 stimuli.

3. Procedures

The procedures were the same as those of experiment 1. Stimuli in this experiment were presented ten times each, in randomized blocks of 18, providing ten responses to each fricative noise with each vocalic portion. In addition to the statistical tests described under experiment 1, *t* tests comparing results from experiments 1 and 2 were done for each age group on the transition effect [/(ʃ)u/-/(s)u/ and /(ʃ)ɑ/-/(s)ɑ/], the vowel effect [/(ʃ)u/-/(ʃ)ɑ/ and /(s)u/-/(s)ɑ/], and mean slope for each vowel.

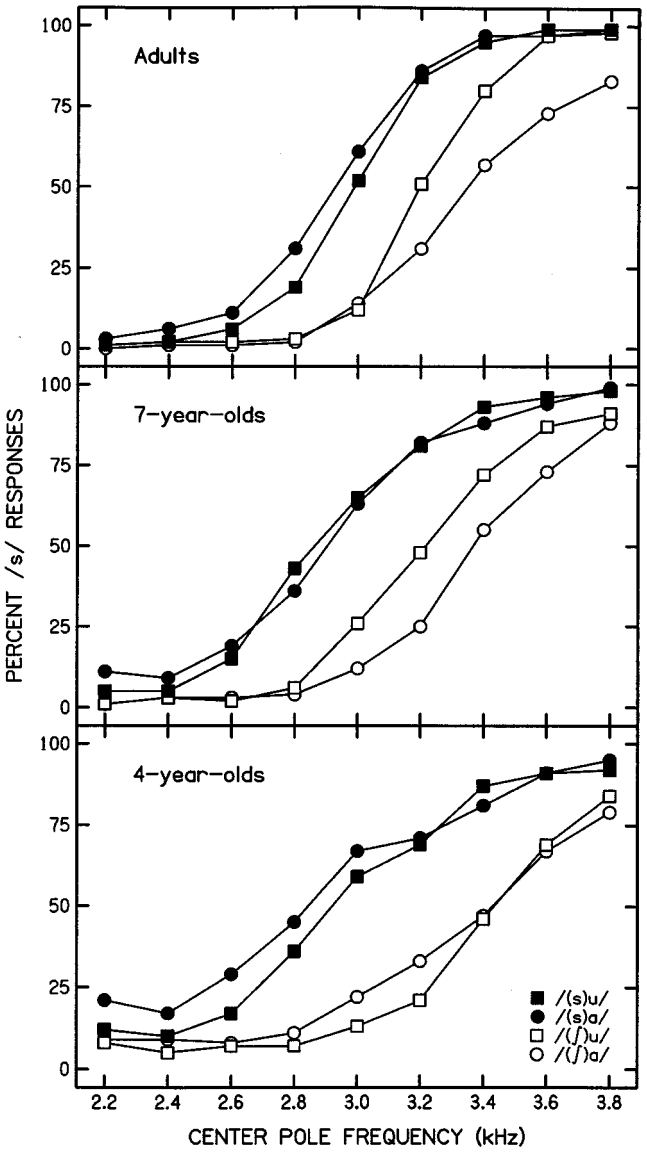

FIG. 2. Labeling functions for experiment 2 for adults (top), 7-year-olds (center), and 4-year-olds (bottom). See legend for Fig. 1 for more detail.

B. Results

1. Phoneme boundaries

Figure 2 displays labeling functions for adults, 7-year-olds, and 4-year-olds, and Table IV shows mean phoneme boundaries. Clearly there is a separation in functions depending on whether $F2$-onset frequency was appropriate for a preceding /s/ or /ʃ/, as indicated by a significant main effect of transition [$F(1,58)=311.19$, $p<0.001$]. This transition effect was greater for children than for adults. The age ×transition interaction was significant [$F(2,58)=3.30$, $p=0.044$], as was the planned comparison of adults versus all children [$F(1,58)=5.62$, $p=0.021$].

The separation in functions depending on vowel is present and in the predicted direction (i.e., more ''s'' responses for /u/ than for /ɑ/) for stimuli with /ʃ/ transitions. For stimuli with /s/ transitions, we see the reverse vowel effect (i.e., more ''s'' responses for /ɑ/ than for /u/). Because of this difference in vowel effects across transition conditions, the main effect of vowel was not significant. In fact, the only other significant result of this analysis was the vowel×transition interaction [$F(1,58)=33.32$, $p<0.001$]. Therefore, it may be concluded that there was a developmental decrease in the transition effect, and that the vowel effect was in the predicted direction for stimuli with /ʃ/ transitions, but in the opposite direction for stimuli with /s/ transitions. This difference in the direction of the vowel effect across transitions held for all three listener groups.

TABLE IV. Mean phoneme boundaries for experiment 2 in Hz (top). Mean differences in phoneme boundaries (in Hz) for the transition effect [/(ʃ)V/-/(s)V/] and for the vowel effect [/(F)ɑ/-/(F)u/] (bottom). Standard deviations are in parentheses.

	4-year-olds	7-year-olds	Adults
/(s)ɑ/	2857	2884	2870
	(251)	(185)	(238)
/(ʃ)ɑ/	3455	3428	3368
	(327)	(252)	(442)
/(s)u/	2956	2895	2988
	(203)	(150)	(132)
/(ʃ)u/	3381	3242	3198
	(244)	(142)	(124)
/(ʃ)ɑ/-/(s)ɑ/	598	543	497
	(174)	(259)	(405)
/(ʃ)u/-/(s)u/	425	348	210
	(227)	(136)	(157)
/(s)ɑ/-/(s)u/	−99	−10	−118
	(190)	(153)	(205)
/(ʃ)ɑ/-/(ʃ)u/	73	185	170
	(350)	(251)	(410)

Table IV provides other insights into age-related differences in perceptual strategies, especially when results for this experiment are compared to those from experiment 1. First, listeners in all groups showed transition effects for /u/ that were roughly half the size of those found in experiment 1: All t tests comparing the transition effect for /u/ stimuli for same-aged listeners across these two experiments were significant [adults' $t(38)=4.24$, $p<0.001$; 7-year-olds' $t(40)=3.30$, $p<0.001$; and 4-year-olds' $t(37)=3.44$, $p<0.001$]. For /ɑ/, only 4-year-olds showed a reduction in the size of the transition effect across experiments [$t(37)=2.99$, $p=0.005$]. Regarding the vowel effect, all listeners showed a reverse vowel effect for stimuli with transitions appropriate for /s/. In the first experiment, the vowel effect for stimuli with /s/ transitions was in the predicted direction, and so we find significant t tests when the vowel effect for these stimuli are compared within age groups across the two experiments [adults' $t(38)=5.41$, $p<0.001$; 7-year-olds' $t(40)=3.91$, $p<0.001$; and 4-year-olds' $t(37)=2.12$, $p=0.041$]. For stimuli with /ʃ/ transitions, the vowel effect is in the predicted direction for all listener groups, as it was in experiment 1.

2. Slopes

As with experiment 1, Fig. 2 and Table V (showing mean slopes) show that adults' labeling functions were steeper than those of children, and that 7-year-olds' functions were steeper than those of 4-year-olds. The main effect of

TABLE V. Mean slopes for each syllable type for experiment 2, in probit units per kHz of fricative noise (top). Mean slope for each vowel across transition conditions (bottom). Standard deviations are in parentheses.

	4-year-olds	7-year-olds	Adults
/(s)ɑ/	2.27	3.13	4.14
	(1.09)	(1.33)	(1.52)
/(ʃ)ɑ/	2.18	3.30	3.52
	(1.04)	(1.18)	(1.63)
/(s)u/	2.85	3.68	4.97
	(1.65)	(1.28)	(1.26)
/(ʃ)u/	2.73	3.64	4.67
	(1.26)	(1.52)	(1.28)
/ɑ/ mean	2.22	3.21	3.83
	(1.03)	(1.09)	(1.41)
/u/ mean	2.79	3.66	4.82
	(1.31)	(1.30)	(1.10)

age was significant [$F(2,58)=16.19$, $p<0.001$], as were the two planned comparisons: adults versus all children [$F(1,58)=24.74$, $p<0.001$]; and 7-year-olds versus 4-year-olds [$F(1,58)=8.83$, $p=0.004$]. There was also a significant main effect of vowel [$F(1,58)=14.13$, $p<0.001$], indicating that functions were steeper for /u/ than for /ɑ/ for all listener groups. Compared to the first experiment, the /u/ functions of all three groups appear steeper, as well as the /ɑ/ functions of both children's groups. However, only some *t* tests comparing slopes across experiments reached statistical significance: adults' /u/ [$t(38)=-3.06$, $p=0.004$], 7-year-olds' /u/ [$t(40)=-2.70$, $p=0.010$], and 4-year-olds' /ɑ/ [$t(37)=-2.12$, $p=0.041$].

C. Discussion

The general age-related trends in perceptual weighting of acoustic properties that were observed in earlier experiments, including experiment 1 of this study, were observed in this experiment. That is, there was a developmental decrease in the weight assigned to formant transitions, and a developmental increase in the weight assigned to the fricative-noise spectra. Although these general developmental trends were seen here, there were nonetheless differences in the perceptual weight assigned to each acoustic property by each age group between experiment 1 and this experiment. With the exception of adults' responses to /ɑ/ stimuli, there was a general increase in the weight assigned to the fricative-noise spectrum (as estimated from the increases in slopes) and a decrease in the weight assigned to the vocalic formant transitions (as estimated from the decreases in separation between /ʃ/ and /s/ functions). Consequently, one conclusion that may be drawn is that the perceptual weights assigned to various acoustic properties do not reflect differences in auditory capacities for adults and children. In particular, children appear to have weighted the fricative-noise spectra more in this experiment than in experiment 1, and so their auditory sensitivity to differences in noise spectra cannot explain their weak weighting of these spectra in earlier experiments. Whatever age-related differences may exist in auditory capacities, these differences cannot entirely explain age-related differences in speech perception. Most likely the parameter settings that define phonetic categories are well within the sensory limits of the auditory system for listeners of all ages.

Our predictions regarding the effects across age groups and across vowels of neutralizing $F3$ onsets were observed. Adults showed a larger decrease from the first experiment to this one in the transition effect for /u/ than for /ɑ/. We suggest that this vowel-specific result for adults is based on the fact that $F3$ onset differs more depending on the place of the preceding fricative for /u/ than for /ɑ/. When this $F3$ information is neutralized then, it decreases the transition effect more for /u/ than for /ɑ/. Four-year-olds, on the other hand, demonstrated a similar reduction in the transition effect from experiment 1 to this one for both vowels. We suggest that this age-related difference in perceptual effect indicates that young children have not yet learned to tune their perceptual attention to $F3$ more for /u/ than for /ɑ/.

Although not found to be statistically significant, it is worth noting that adults' responses indicate some changes in the weighting of fricative spectra and formant transitions for /ɑ/ stimuli. Adults' mean transition effect for /ɑ/ stimuli increased from the first experiment to this one, and mean slope decreased. We suggest that these vowel-specific effects may be due to the fact that the $F3$ transition is not normally very informative in fricative-/ɑ/ stimuli, and so any transition effect observed for /ɑ/ may be largely attributed to the $F2$ transition. Although $F3$-onset frequencies were neutralized in this experiment, $F2$-onset frequencies were enhanced due to our setting $F2$ onsets to the maximum differences observed for /(s)V/ and /(ʃ)V/ in experiment 1. Adults' slight increase in weighting of formant transitions and decrease in weighting of noise spectra may be due to this enhancement of the information provided by $F2$ onsets.

Neutralizing $F3$-onset frequencies influenced the vowel effect, as well as the transition effect. For stimuli with $F2$-onset frequencies appropriate for a preceding /s/, listeners in all groups demonstrated a decrease in the magnitude of the vowel effect. In fact, for these stimuli, all groups showed the reverse vowel effect. This finding is intriguing because it cannot be explained as was the reverse vowel effect observed for stimuli with /ʃ/ transitions by Nittrouer and Studdert-Kennedy (1987). In that study, we explained the effect as the interaction of the /ʃ/ transition (''pulling'' the /ʃu/ function to higher phoneme boundaries) and of the /u/ (''pulling'' the /ʃu/ function to lower phoneme boundaries). Simply put, it was suggested that the /ʃ/ transition exerted a bit more pull than the rounded vowel in that experiment. In this case, the /s/ transition and the /u/ should both be pulling the /(s)u/ function to lower phoneme boundaries, which should result in lower phoneme boundaries for /(s)u/ than for /(s)ɑ/. In fact, /(s)ɑ/ had lower phoneme boundaries than /(s)u/, for all listener groups.

III. EXPERIMENT 3: SYNTHETIC VOCALIC PORTIONS, *F2* AND *F3* VARYING

The goal of this experiment was to vary $F3$ onsets appropriately according to whether the preceding fricative was /s/ or /ʃ/ to test the prediction that the increase in the transition effect from experiment 2 would be greater for /u/ than

for /ɑ/ for adults' responses but similar across vowels for children's responses. This manipulation of varying $F2$ and $F3$ onsets appropriately for a preceding /s/ or /ʃ/ in synthetic vocalic portions also allowed us to evaluate the suggestion that previous findings of an enhanced transition effect for children compared to adults was due to difficulty on the part of children in processing synthetic speech components. If the age-related trend of decreasing transition effects with increasing age reported previously was found for these stimuli, we could allay concern that previous results were due simply to age-related differences in processing of synthetic speech components.

A. Method

1. Subjects

For this experiment, age groups were modified slightly. Instead of 7- and 4-year-olds, 7-, 5-, and 3-year-olds participated. This minor change was made simply to allow us to draw listeners from different pools of potential subjects. Twelve 7-year-olds participated, with a mean age of 7;0 (range from 6;9 to 7;4). Ten 5-year-olds participated, with a mean age of 5;0 (range from 4;10 to 5;4). Three additional 5-year-olds started the experiment, but one did not meet the training criterion and two did not meet the testing criterion. Fourteen 3-year-olds participated, with a mean age of 3;10 (range from 3;8 to 3;11). Seven additional 3-year-olds started the experiment, but four failed to meet the training criterion and three failed to meet the testing criterion. Ten adults participated.

2. Stimuli and equipment

The same equipment was used for this experiment as for the first two. The stimuli were identical to those of experiment 2, except that $F3$ transitions differed for each vocalic portion. These stimuli were generated at a 10-kHz sampling rate, with low-pass filtering below 4.9 kHz. This change was made simply to save disk space, but pilot work in our laboratory has failed to find differences in response patterns as a function of sampling rate. As with $F2$ settings in experiment 2, settings for $F3$ were based both on Whalen (1981) and on the natural vocalic portions of experiment 1. For the two /ɑ/ tokens, $F3$ fell over the first 100 ms to a steady-state frequency of 2300 Hz. For /(ʃ)ɑ/, $F3$ onset was 2300 Hz (i.e., the formant transition was 0 Hz), and for /(s)ɑ/, $F3$ onset was 2460 Hz. For the two /u/ portions, $F3$ fell over the first 130 ms to a steady-state frequency of 2100 Hz. For /(ʃ)u/, $F3$ onset was 2200 Hz, and for /(s)u/, $F3$ onset was 2520 Hz. These $F3$-onset frequencies maintained the relative differences between /(s)V/ and /(ʃ)V/ across vowels observed for natural portions in experiment 1: this transition-related difference is roughly twice as large for /u/ as for /ɑ/. These four vocalic portions were combined with each of the nine synthetic fricative noises, yielding 36 stimuli.

3. Procedures

The procedures for this experiment were the same as those in experiment 2. However, the planned comparisons were modified to reflect the change in age groups. For this experiment, the planned comparisons were: adults versus all children, 7-year-olds versus 5-year-olds, and 7- and 5-year-olds versus 3-year-olds. Within-group t tests comparing transition and vowel effects and slopes across experiments 2 and 3 were conducted. Data for the 3- and 5-year-olds in this experiment were combined and compared to data for 4-year-olds in experiment 2.

B. Results

1. Phoneme boundaries

Figure 3 displays labeling functions for adults, 7-year-olds, 5-year-olds, and 3-year-olds, and Table VI shows mean phoneme boundaries. Labeling functions are more separated depending on formant transitions than in the two earlier experiments, for all groups. However, there is a developmental decrease in the separation of functions depending on transition. The separation in functions depending on vowel is in the predicted direction for adults and 7-year-olds for both transitions, but reversed for 5- and 3-year-olds. Statistical analysis supports these observations. The overall age effect was significant [$F(3,42)=3.58$, $p=0.022$], as was the planned comparison of adults versus all children [$F(1,42)=8.53$, $p=0.006$]. This age effect reflects the same trend described for 4-year-olds in experiment 1: children responded with many more ''s'' responses than adults when the transition was appropriate for /s/, rather than responding with many more ''sh'' responses than adults when the transition was appropriate for /ʃ/. Consequently, if we compute a mean phoneme boundary for each age group across the four vocalic portions, we find that mean to be 3035 Hz for adults, 2825 Hz for 7-year-olds, 2819 Hz for 5-year-olds, and 2715 Hz for 3-year-olds. The main effect of transition was also significant [$F(1,42)=268.17$, $p<0.001$]. The age×transition interaction was significant [$F(3,42)=4.47$, $p=0.008$], as were two planned comparisons for the transition effect: adults versus all children [$F(1,42)=4.61$, $p=0.038$]; and 7- and 5-year-olds versus 3-year-olds [$F(1,42)=8.08$, $p=0.007$]. Thus, there was a developmental decrease in the size of the transition effect, with 3-year-olds showing a significantly larger effect than older children and adults but with all children showing a significantly larger effect than adults. The age×vowel interaction was significant [$F(3,42)=9.07$, $p<0.001$], as were two planned comparisons for the vowel effect: adults versus all children [$F(1,42)=11.81$, $p=0.001$]; and 7-year-olds versus 5-year-olds [$F(1,42)=13.36$, $p<0.001$]. Thus, there was a developmental increase in the size of the vowel effect. With this effect we find that 3- and 5-year-olds performed similarly, but 7-year-olds performed somewhat more as adults had. Finally, there was a significant transition×vowel interaction [$F(1,42)=6.73$, $p=0.013$], which indicates both that there was a difference in the size of the transition effect across vowels (larger for /u/ than for /ɑ/) and that there was a difference in the size of the vowel effect for transitions (larger for /s/ than for /ʃ/).

Comparing results for experiments 2 and 3, we find that there were significant increases in the transition effect for all groups for both /ɑ/ [adult's $t(28)=-2.47$, $p=0.020$; 7-year-

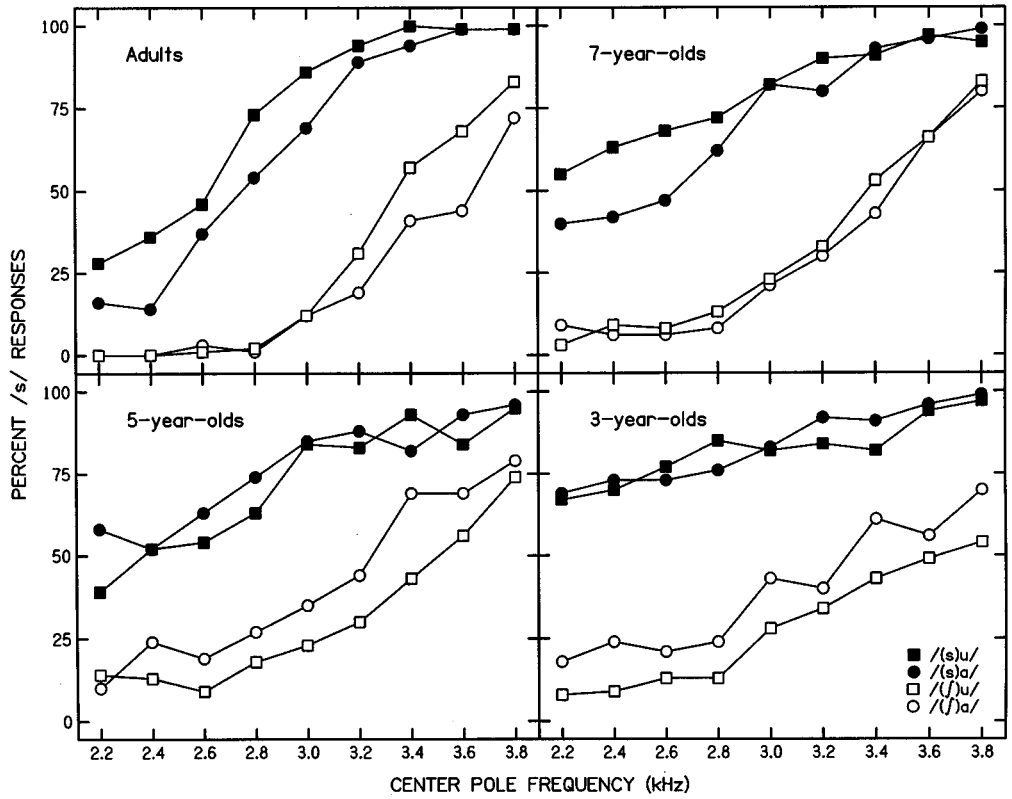

FIG. 3. Labeling functions for experiment 3 for (clockwise from upper, left) adults, 7-year-olds, 3-year-olds, and 5-year-olds. See legend for Fig. 1 for more detail.

olds' $t(32)=-3.60$, $p=0.001$; and younger children's $t(41)=-6.37$, $p<0.001$] and /u/ [adult's $t(28)=-5.67$, $p<0.001$; 7-year-olds' $t(32)=-6.94$, $p<0.001$; and younger children's $t(41)=-6.50$, $p<0.001$]. However, the statistics do not tell the complete story. For adults, the transition effect for /u/ increased by 500% from experiment 2 to this one, but for /ɑ/, the increase was only 175%. For 7-year-olds, the transition effect for /u/ increased by 400% while the effect for /ɑ/ increased by 200%. For the youngest children, the change in the transition effect was 375% and 225% for /u/ and /ɑ/, respectively. Thus, we find the vowel-related difference in the size of the change in transition effects across experiments to be greater for older listeners. This finding supports the conclusion of greater vowel specific effects for older listeners.

TABLE VI. Mean phoneme boundaries for experiment 3 in Hz (top). Mean differences in phoneme boundaries (in Hz) for the transition effect [/(ʃ)V/-/(s)V/] and for the vowel effect [/(F)ɑ/-/(F)u/] (bottom). Standard deviations are in parentheses.

	3-year-olds	5-year-olds	7-year-olds	Adults
/(s)ɑ/	1848	2109	2378	2738
	(288)	(449)	(494)	(271)
/(ʃ)ɑ/	3388	3234	3461	3613
	(421)	(423)	(183)	(277)
/(s)u/	1880	2339	2071	2366
	(422)	(416)	(444)	(493)
/(ʃ)u/	3742	3596	3390	3423
	(597)	(410)	(312)	(409)
/(ʃ)ɑ/-/(s)ɑ/	1540	1126	1083	874
	(499)	(353)	(617)	(371)
/(ʃ)u/-/(s)u/	1862	1257	1319	1057
	(793)	(592)	(638)	(641)
/(s)ɑ/-/(s)u/	−32	−230	307	373
	(358)	(489)	(280)	(441)
/(ʃ)ɑ/-/(ʃ)u/	−355	−362	71	190
	(480)	(533)	(308)	(438)

Regarding the vowel effect, adults and 7-year-olds showed a significant increase in the size of this effect for stimuli with /s/ transitions from the last experiment to this one, such that now the effect is in the predicted direction [adults' $t(28)=-4.19$, $p<0.001$; 7-year-olds' $t(32)=-4.30$, $p<0.001$]. These listeners show no change in this effect for stimuli with /ʃ/ transitions, which was in the predicted direction in experiment 2. For the younger children, on the other hand, there was a decrease in the size of the vowel effect for stimuli with /ʃ/ transitions such that this effect is now in the reverse direction [$t(41)=3.31$, $p=0.002$].

Finally, we investigated the suggestion that previously observed age effects were due to children having more difficulty than adults processing synthetic speech components by comparing the transition effect for the youngest children between the first experiment, using natural vocalic portions, and this one, using synthetic vocalic portions. $F2$ and $F3$ were manipulated appropriately depending on place of the preceding fricative in both experiments. Children demonstrated larger transition effects in this experiment than in the

TABLE VII. Mean slopes for each syllable type for experiment 3, in probit units per kHz of fricative noise (top). Mean slope for each vowel across transition conditions (bottom). Standard deviations are in parentheses.

	3-year-olds	5-year-olds	7-year-olds	Adults
/(s)ɑ/	1.17	1.11	1.84	3.54
	(0.63)	(0.57)	(0.99)	(1.08)
/(ʃ)ɑ/	1.16	1.53	1.86	3.30
	(0.43)	(0.83)	(0.69)	(1.10)
/(s)u/	1.01	1.34	1.27	2.46
	(0.70)	(0.79)	(1.13)	(1.29)
/(ʃ)u/	1.13	1.42	2.32	3.94
	(0.77)	(0.81)	(1.05)	(1.73)
/ɑ/ mean	1.16	1.32	1.85	3.42
	(0.45)	(0.65)	(0.78)	(1.00)
/u/ mean	1.07	1.38	1.79	3.20
	(0.60)	(0.72)	(0.96)	(1.04)

first for /u/ [$t(42)=-4.18$, $p<0.001$] and for /ɑ/ [$t(42)=-4.15$, $p<0.001$].

2. Slopes

As in the first two experiments, there was a developmental increase in the steepness of functions. Table VII shows mean slopes, and confirms this impression. The main effect of age was significant [$F(3,42)=23.19$, $p<0.001$], as were the planned comparisons of adults versus all children [$F(1,42)=61.14$, $p<0.001$], and 7- and 5-year-olds versus 3-year-olds [$F(1,42)=4.19$, $p=0.047$]. The main effect of transition was significant [$F(1,42)=11.31$, $p=0.002$], indicating that functions were, on the whole, steeper for stimuli with /ʃ/ transitions than for those with /s/ transitions. However, there were age- and vowel-related variations to this pattern. The two-way interaction of transition × vowel was significant [$F(1,42)=8.66$, $p=0.005$], indicating that /u/ functions were generally steeper for stimuli with /ʃ/ transitions than for those with /s/ transitions. The /ɑ/ functions were similar in steepness across the transition conditions for listeners of all ages.

Comparing slopes to those of experiment 2, we find that all groups showed a decrease in steepness for /u/ stimuli [adults' $t(28)=3.88$, $p<0.001$; 7-year-olds' $t(32)=4.36$, $p<0.001$; and younger children's $t(41)=5.20$, $p<0.001$]. Children showed a decrease for /ɑ/ stimuli as well [7-year-olds' $t(32)=3.80$, $p<0.001$; and younger children's $t(41)=4.10$, $p<0.001$].

C. Discussion

We find here the trends observed previously: There was a developmental decrease in the weight assigned to formant transitions, and a developmental increase in the weight assigned to fricative-noise spectra. Finding these trends for stimuli with synthetic vocalic portions shows that results of previous experiments were not simply due to age-related differences in biases against synthetic speech components. Moreover, finding that listeners of the same ages modified the weights assigned to these acoustic properties across experiments indicates that weighting schemes reflect more than the limits of the auditory system.

Turning our attention to changes in the transition effect from the last experiment to this one, we see more of a vowel-specific effect for adults than for children: the increase in transition effect was much greater for /u/ than for /ɑ/ in adults' responses, whereas these increases were more equivalent across vowels in children's responses. Thus, further support is garnered for the suggestion that adults are aware of how $F3$ transitions vary between the /s/ and /ʃ/ conditions across /u/ and /ɑ/, and so tune their attention to these transitions more when the vowel is /u/ than when it is /ɑ/. Children, on the other hand, have not completely learned this vowel-specific relation, and so do not tune their attention to $F3$ in /u/ much more than they do in /ɑ/.

Regarding the vowel effect, adults and 7-year-olds showed this effect in the predicted direction for stimuli with both /s/ and /ʃ/ transitions. Five- and 3-year-olds showed a reverse vowel effect for stimuli with both /s/ and /ʃ/ transitions.

IV. GENERAL DISCUSSION

This study supported the conclusions of earlier developmental studies using FV stimuli (Nittrouer, 1992, 1996a; Nittrouer and Studdert-Kennedy, 1987). Clearly the perceptual weights children assign to fricative-noise spectra and vocalic formant transitions differ from those of adults. The direction of the developmental weighting shift was similarly replicated: the weight assigned to fricative-noise spectra increased with age (and presumably, with linguistic experience), while the weight assigned to vocalic formant transitions decreased. Furthermore, this study helped demonstrate that observed age-related differences in perceptual weighting schemes are just that: differences in how adults and children direct their perceptual attention. These observed differences are not consequences of some other general (i.e., nonspeech) age-related difference or some aspect of experimental design. First, children's perceptual weighting schemes do not simply reflect a processing difficulty for synthetic speech components: children's weighting of formant transitions was actually greater in experiment 3, using synthetic vocalic portions, than in experiment 1, using natural portions. Second, children's perceptual weighting schemes do not merely reflect the limits of their auditory capacities: the weight assigned to the fricative-noise spectra varied across experiments, and so must be amenable to factors other than auditory sensitivity.

The primary goal of this study was to improve our ability to predict changes in perceptual weighting schemes as children gain experience with a native language by testing a two-part hypothesis: (1) the phonetic informativeness of a property in a specific environment determines its perceptual weighting in that environment for experienced language users; and (2) children need to learn these informational-environmental relations. Two sources of evidence supported the first part of the hypothesis. First, when $F3$-onset frequency was neutralized, adults' transition effect decreased for /u/ but not for /ɑ/. Second, when $F3$ was appropriately varied, there was a larger increase in the magnitude of adults' transition effect for /u/ than for /ɑ/. These findings support the first part of the hypothesis because $F3$ varies

more depending on preceding fricative identity for /u/ than for /ɑ/. Two kinds of evidence supported the second part of the hypothesis, as well. First, changes in children's transition effects for /u/ and for /ɑ/ when $F3$ was neutralized were similar. Second, the increase in the transition effect when $F3$ was appropriately varied was more similar across vowels for children than for adults. Thus, we conclude that children as old as seven years have not had sufficient experience with FV syllables to ascertain fully the differences in how formant transitions convey information about the preceding fricative in each vowel environment.

Additional support for the age-related differences described above is derived from slopes. Although not perfect, somewhat of a reciprocal relation is observed between the weight assigned to the fricative-noise spectrum and the weight assigned to formant transitions. Therefore, when the separation in functions based on formant transitions increases, slope should decrease, indicating a decrease in the weighting of the fricative noise. When the separation in functions based on formant transitions decreases, slope should increase. In particular, adults' slopes for /u/ stimuli increased from experiment 1 to 2, indicating that more weight was assigned to fricative-noise spectra. For these stimuli, the weight adults assigned to formant transitions decreased (i.e., the separation between /(ʃ)u/ and /(s)u/ decreased), with the neutralizing of $F3$-onset frequency. For both children's groups, there was a tendency for slope to increase from experiment 1 to 2 for both /u/ and /ɑ/, while the separation between /(ʃ)V/ and /(s)V/ generally decreased. For experiment 3, slope decreased for all listeners from experiment 2. This decrease in the weight assigned to noise spectra mirrors an increase in weight assigned to formant transitions with the incorporation of appropriate variation in $F3$-onset frequencies. In summary, several kinds of evidence indicate that the perceptual weights adults assign to acoustic properties are the result of learning how phonetic information conveyed by each property varies across environments, and children as old as seven years have not completely learned these informational-environmental relations.

Another goal of these experiments was to examine the vowel effect. We were specifically interested in why this effect has been observed when the acoustic and perceptual data supporting the prediction are inconsistent, at best. We also wished to see if there would be age-related differences in the magnitude of the effect. In this study, a vowel effect in the direction predicted was reliably observed for adults' responses when (and only when) $F3$ varied appropriately for a preceding /s/ or /ʃ/ (experiments 1 and 3, but not 2). This finding contradicts the usual explanation for the vowel effect, which suggests that mature listeners tacitly know that anticipatory liprounding can lower fricative spectra, and make use of this knowledge. According to this explanation, a vowel effect should be observed as long as vowel quality is preserved (which it was in all conditions in all experiments, including stimuli with /s/ transitions in experiment 2). Thus, it may be that rather than vowel quality providing indirect information about what the fricative-noise spectrum should be for /s/ or /ʃ/, formant transitions provide direct information about place of fricative constriction. Developing this idea further, we obtain a possible explanation for the commonly observed vowel effect, and for age-related differences in vowel effects, that does not involve listeners tacitly using phonetic knowledge.

The first few pitch periods of voicing provide information about both fricative and vowel gestures. The task facing the listener is to make a decision about fricative identity (because vowel quality is clear in these experiments). The listener can use two sources of information in making the fricative decision: the fricative-noise spectrum and the formant transitions. The probability of reaching a decision that the fricative heard was ''s'' can be represented by the following, simple equation:

$$p_s = p_s(\text{fricative noise}) + p_s(\text{formant transitions}),$$

where p_s is the probability of reaching an ''s'' decision; p_s(fricative noise) is the probability of the fricative noise having been generated by an ''s'' gesture, according to the listener's estimate; and p_s (formant transitions) is the probability of the formant transitions having been generated by an ''s'' gesture, according to the listener's estimate.

Nittrouer (1995) demonstrated that the fricative-noise spectrum for either /s/ or /ʃ/ does not vary depending on whether the following vowel is /ɑ/ or /u/, but Table I shows that formant frequencies at voicing onset vary for both /s/ and /ʃ/, depending on which of these vowels is produced. For example, $F2$-onset frequency for /sɑ/ is 1365 Hz; for /su/, it is 1520 Hz. Thus some portion of the formant-onset spectrum should be attributed to the vowel gesture. Fowler (1990) suggested that listeners routinely parse the signal according to the gestures that they interpret to be shaping the signal at any given point in time. We suggest that the results observed for adults' and children's fricative perception indicate that children attribute more of the formant-onset spectrum to fricative gestures than adults, and attribute less to vowel gestures.

To illustrate, let's say a listener hears a FV syllable for which there is a high $F2$-onset frequency (indicating a small cavity behind the constriction) and a low $F3$-onset frequency (indicating a large cavity in front of the constriction). The listener can attribute these onset frequencies mainly to the placement of the tongue body for fricative production, as we suggest children do. Then the probability of an ''s'' response is quite low: from this spectral pattern, a relatively back placement would be deduced (i.e., /ʃ/). On the other hand, the listener may attribute some part of these onset frequencies to the placement of the tongue body (and lips) for production of a back, rounded vowel, as we suggest adults do. Then the probability of an ''s'' response is higher: with some of the onset spectrum being attributed to the vowel gesture, a more forward place of constriction will be associated with the fricative gesture. Given a constant p_s(fricative noise), this increase in p_s(formant transitions) leads to more ''s'' responses than would occur if no part of the onset spectrum was attributed to vowel production. In general, if adults attribute some portion of the variation in $F2$- and $F3$-onset frequencies to the gestures associated with /u/ production in fricative-/u/ syllables, it would always increase p_s(formant transitions), and lead to more ''s'' responses for fricative-/u/.

In conclusion, this series of experiments has led to a hypothesis for predicting developmental shifts in perceptual weighting schemes. For any given acoustic property, it should be the case that children learn to increase the weight assigned to that property for environments in which it is particularly informative, and learn to decrease the weight assigned to the property for environments in which it is not particularly informative. Previously it was suggested that children may initially show a general weighting preference for dynamic properties that may be related to their initial attention to syllabic structure, rather than to segmental structure (e.g., Nittrouer, 1992, 1996b; Nittrouer and Studdert-Kennedy, 1987). This preference has been observed as a greater weighting of formant transitions by children, compared to adults, and as a reduced weighting of other, more detailed properties of the signal by children. Thus, for experiments using FV stimuli, it was observed that children generally weighted formant transitions more than adults, but weighted the fricative-noise spectrum less (e.g., Nittrouer, 1992, 1996a; Nittrouer and Studdert-Kennedy, 1987). The suggestion being made here does not contradict that interpretation; instead, it refines it. It should be the case for phonetic environments in which formant transitions are not particularly informative about segment identity (and, reciprocally, in which another property is especially informative) that the weight children assign to those transitions should decrease with language experience. However, for phonetic environments in which formant transitions are informative (and, reciprocally, in which other properties are not) the weight children assign to those transitions should continue to be substantial. Accordingly, the weight that children assign to vocalic formant transitions should decrease for FV syllables in which the fricative is /s/ or /ʃ/. This prediction follows from Harris (1958), who demonstrated that the noise is the primary property on which adults make this fricative decision (and so is presumably informative concerning fricative identity). Conversely, Harris showed that the noise is not weighted heavily by adults when the fricative is /f/ or /ɵ/ (and so is presumably not informative). Consequently, adults weight formant transitions strongly in fricative decisions of /f/ or /ɵ/. Children's weighting of formant transitions in this phonetic environment should remain unchanged through development. Future experiments will need to test this specific prediction. Of course, given that adults are former children, Harris already made one test of the prediction.

ACKNOWLEDGMENTS

This work was supported by research Grant No. 4R01 DC00633-09 from the National Institute on Deafness and Other Communication Disorders, National Institutes of Health. We thank Kris Kalil for help testing subjects, and Robert Fulkerson for programming help. The comments of Carol Fowler, Tom Carrell, Court Crowther, and Donna Neff improved this manuscript greatly.

[1]Throughout this paper, the symbol in parentheses will indicate the fricative for which the vocalic transitions were appropriate.

Allen, P., and Wightman, F. (**1989**). ''Spectral pattern discrimination in children,'' J. Acoust. Soc. Am. Suppl. 1 **85,** S37.

ANSI. (**1989**). ANSI S3.6-1989, ''Specifications for Audiometers'' (ANSI, New York).

Bailey, P., and Summerfield, Q. (**1980**). ''Information in speech: Observations on the perception of [s]-stop clusters,'' J. Exp. Psychol. Hum. Percept. Perform. **6,** 356–563.

Bell-Berti, F., and Harris, K. (**1979**). ''Anticipatory coarticulation: Some implications from a study of lip rounding,'' J. Acoust. Soc. Am. **65,** 1268–1270.

Best, C., and Strange, W. (**1992**). ''Effects of phonological and phonetic factors on cross-language perception of approximates,'' J. Phon. **20**, 305–330.

Best, C. T., Morrongiello, B. A., and Robson, R. C. (**1981**). ''Perceptual equivalence of acoustic cues in speech and nonspeech perception,'' Percept. Psychophys. **29,** 191–211.

Crowther, C. S., and Mann, V. A. (**1992**). ''Native language factors affecting use of vocalic cues to final consonant voicing in English,'' J. Acoust. Soc. Am. **92,** 711–722.

Crowther, C. S., and Mann, V. A. (**1994**). ''Use of vocalic cues to consonant voicing and native language background: The influence of experimental design,'' Percept. Psychophys. **55,** 513–525.

Daniloff, R., and Moll, K. (**1968**). ''Coarticulation of lip rounding,'' J. Speech Hear. Res. **11**, 707–721.

Dorman, M., Studdert-Kennedy, M., and Raphael, L. J. (**1977**). ''Stop-consonant recognition: Release bursts and formant transitions as functionally equivalent, context-dependent cues,'' Percept. Psychophys. **22,** 109–122.

Elliot, L. L., Longinotti, C., Meyer, D., Raz, I., and Zucker, K. (**1981**). ''Developmental differences in identifying and discriminating CV syllables,'' J. Acoust. Soc. Am. **78,** 669–677.

Elliot, L. L., Busse, L., Partridge, R., Rupert, J., and DeGraaff, R. (**1986**). ''Adult and child discrimination of CV syllables differing in voicing onset time,'' Child Development **57**, 628–635.

Fitch, H., Hawles, T., Erickson, D., and Liberman, A. M. (**1980**). ''Perceptual equivalence of two acoustic cues for stop-consonant manner,'' Percept. Psychophys. **27,** 343–350.

Flege, J. E., Takagi, N., and Mann, V. (**1996**). ''Lexical familiarity and English-language experience affect Japanese adults' perception of /r/ and /l/,'' J. Acoust. Soc. Am. **99,** 1161–1173.

Fowler, C. A. (**1990**). ''Listener-talker attunements in speech,'' Hask. Lab. Stat. Rep. Sp. Res. **SR-101/102**, 110–129.

Goldman, R., and Fristoe, M. (**1969**). *Goldman-Fristoe Test of Articulation* (American Guidance Service, Circle Pines, MN).

Greenlee, M. (**1980**). ''Learning the phonetic cues to the voiced-voiceless distinction: A comparison of child and adult speech perception,'' J. Child Lang. **7**, 459–468.

Harris, K. S. (**1958**). ''Cues for the discrimination of American English fricatives in spoken syllables,'' Lang. Speech. **1**, 1–7.

Heinz, J. M., and Stevens, K. N. (**1961**). ''On the properties of fricative consonants,'' J. Acoust. Soc. Am. **33,** 589–593.

Hughes, G. W., and Halle, M. (**1956**). ''Spectral properties of fricative consonants,'' J. Acoust. Soc. Am. **28,** 303–310.

Jastak, S., and Wilkinson, G. S. (**1984**). *The Wide Range Achievement Test-Revised* (Jastak Associates, Wilmington, DE).

Klatt, D. (**1980**). ''Software for a cascade/parallel formant synthesizer,'' J. Acoust. Soc. Am. **67,** 971–995.

Kluender, K., Diehl, R., and Wright, B. (**1988**). ''Vowel-length differences before voiced and voiceless consonants: An auditory explanation,'' J. Phon. **16**, 153–169.

Kunisaki, O., and Fujisaki, H. (**1977**). ''On the influence of context upon perception of voiceless fricative consonants,'' Ann. Bull. RILP **13**, 85–91.

MacKain, K. S., Best, C. T., and Strange, W. (**1981**). ''Categorical perception of English /r/ and /l/ by Japanese bilinguals,'' Appl. Psycholinguistics **2**, 369–390.

Mann, V. A., and Repp, B. H. (**1980**). ''Influence of vocalic context on perception of the [ʃ]-[s] distinction,'' Percept. Psychophys. **28,** 213–228.

Nittrouer, S. (**1992**). ''Age-related differences in perceptual effects of formant transitions within syllables and across syllable boundaries,'' J. Phon. **20**, 1–32.

Nittrouer, S. (**1995**). ''Children learn separate aspects of speech production at different rates: Evidence from spectral moments,'' J. Acoust. Soc. Am. **97,** 520–530.

Nittrouer, S. (**1996a**). ''Discriminability and perceptual weighting of some acoustic cues to speech perception by 3-year-olds,'' J. Speech Hear. Res. **39**, 278–297.

Nittrouer, S. (**1996b**). ''The relation between speech perception and phonemic awareness: Evidence from low-SES children and children with chronic OM,'' J. Speech Hear. Res. **39**, 1059–1070.

Nittrouer, S., Manning, C., and Meyer, G. (**1993**). ''The perceptual weighting of acoustic cues changes with linguistic experience,'' J. Acoust. Soc. Am. **94,** S1865.

Nittrouer, S., and Studdert-Kennedy, M. (**1987**). ''The role of coarticulatory effects in the perception of fricatives by children and adults,'' J. Speech Hear. Res. **30**, 319–329.

Oden, G. C., and Massaro, D. W. (**1978**). ''Integration of featural information in speech perception,'' Psychol. Rev. **85,** 172–191.

Sussman, J. E. (**1993**). ''Auditory processing in children's speech perception: Results of selective adaptation and discrimination tasks,'' J. Speech Hear. Res. **36**, 380–395.

Sussman, J. E., and Carney, A. E. (**1989**). ''Effects of transition length on the perception of stop consonants by children and adults,'' J. Speech Hear. Res. **32**, 151–160.

Wardrip-Fruin, C., and Peach, S. (**1984**). ''Developmental aspects of the perception of acoustic cues in determining the voicing feature of final stop consonants,'' Lang. Speech **27**, 367–379.

Werker, J. F., Gilbert, J. H. V., Humphrey, K., and Tees, R. C. (**1981**). ''Developmental aspects of cross-language speech perception,'' Child Development **52**, 349–355.

Whalen, D. H. (**1981**). ''Effects of vocalic transitions and vowel quality on the English /s/-/ʃ/ boundary,'' J. Acoust. Soc. Am. **69,** 275–282.

Fundamental frequency of phonation and perceived emotional stress

Athanassios Protopapas[a] and Philip Lieberman
Department of Cognitive and Linguistic Sciences, Brown University, Box 1978, Providence, Rhode Island 02912

(Received 27 December 1995; revised 18 November 1996; accepted 22 November 1996)

Nonlinguistic information about the speaker's emotional state is conveyed in spoken utterances by means of several acoustic characteristics and listeners can often reliably identify such information. In this study we investigated the effect of short- and long-term F_0 measures on perceived emotional stress using stimuli synthesized with the LPC coefficients of a steady vowel and varying F_0 tracks. The original F_0 tracks were taken from naturally occurring speech in highly stressful (contingent on terror) and nonstressful conditions. Stimuli with more jitter were rated as sounding more hoarse but not more stressed, i.e., a demonstrably perceptible amount of jitter did not seem to play a role in perceived emotional stress. Reversing the temporal pattern of F_0 did not affect the stress ratings, suggesting that the directionality of variations in F_0 does not convey emotional stress information. Mean and maximum F_0 within an utterance correlated highly with stress ratings, but the range of F_0 did not correlate significantly with the stress ratings, especially after the effect of maximum F_0 was removed in stepwise regression. It is concluded that the range of F_0 *per se* does not contribute to the perception of emotional stress, whereas maximum F_0 constitutes the primary indicator. The observed effects held across several voices that were found to sound natural (three male voices and one of two female ones). An effect of the formant frequencies was also observed in the stimuli with the lowest F_0; it is hypothesized that formant frequency structure dominated the F_0 effect in the one voice that gave discrepant results. [S0001-4966(97)02504-6]

PACS numbers: 43.71.Bp, 43.70.Gr, 43.66.Lj, 43.72.Ja [WS]

INTRODUCTION

It is well established that the speech signal carries, in addition to linguistic content, information about the speaker's intentions and emotional state, and that listeners are capable of perceiving this information. The nature of speech production and the human vocal apparatus allow for the encoding of emotional and other nonlinguistic information in several ways. The fundamental frequency of phonation (henceforth F_0) and its prosodic patterns, glottal source characteristics, as well as articulatory details may all be involved in conveying information about the emotional state of the speaker. In fact, previous studies have found correlations with speaker mood or style in all of these (see reviews in Murray and Arnott, 1993; Scherer, 1986). Scherer (1986), reviewing acoustic–phonetic findings on vocal affect, proposed a ''sequence theory of emotional differentiation,'' rooted in the physiology of speech production and taking into account the physiological effects of emotional status. According to Scherer's theory, stimuli are evaluated according to functionally defined criteria, such as ''novelty,'' ''need,'' ''coping potential,'' etc. The net result of the outcomes of all evaluation checks affects the nervous system and, in turn, the physiological consequences of the nervous system's response define the changes in voice characteristics that carry the emotional information. For example, unpleasant stimuli cause ''faucal and pharyngeal constriction and tensing as well as shortening of the vocal tract,'' leading to stronger high-frequency resonances, a rise in the first formant, a fall in the second formant, narrow formant bandwidths, etc. (Scherer, 1986, p. 152).

Beginning with the comprehensive study by Darwin (1872) that outlined the principles of emotional expression independently of will, several different speaker moods or emotions and their vocal consequences have been investigated, including workload (or task-induced) stress (Ruiz *et al.*, 1990; Hecker *et al.*, 1968; Streeter *et al.*, 1983), anxiety (Fuller *et al.*, 1992; Smith, 1977), and simulated emotions such as anger, fear, sorrow, happiness, etc. (Lieberman and Michaels, 1962; Williams and Stevens, 1972; Cummings and Clements, 1995). Extreme levels of stress, in particular those of pilots during (often fatal) inflight emergencies have also been examined, and several F_0-related parameters have been identified as good correlates of stress level (Williams and Stevens, 1969; Kuroda *et al.*, 1976). F_0-related parameters, including short-term perturbations, long-term variability, and mean value, are among the measures often reported to correlate with elevated levels of speaker emotional stress, either task-induced or in real-life emergencies. However, in all of the aforementioned studies it was evident that the acoustic correlates of emotions in the human voice are subject to large individual differences (i.e., among speakers). Streeter *et al.* (1983) concluded that there are no ''reliable and valid acoustic indicators of psychological stress'' (p. 1359).

[a]Present address: Scientific Learning Corp., 417 Montgomery St., Ste. 500, San Francisco, CA 94104; Electronic mail: protopap@scilearn.com

In contrast, there appears to be some regularity in the *perception* of the speakers' emotions based on acoustic parameters, such as F_0. In particular, studies have been conducted to assess the extent to which F_0 measures carry emotional information independently of the speaker's intentions and of the semantic content of an utterance. Lieberman and Michaels (1962) used a fixed-vowel synthesizer driven by natural and smoothed F_0 tracks to investigate identification of emotional content by pitch and amplitude information alone. The original amplitude and F_0 information were taken from utterances spoken in various simulated emotional modes. They found that intact F_0 information, including gross changes and fine temporal structure, was crucial for the correct identification of the original (simulated) emotion. The speech envelope amplitude was found to contribute less to the differentiation between emotional modes. Scherer (1977) used synthesized tone sequences with varying prosodic characteristics to investigate the predictive strength of single acoustic parameters and their interactions in emotional state attribution. He reported ''strong systematic effects of the manipulation of acoustic parameters'' supporting ''a linear model of the judges' response system'' (p. 341). More recently, Scherer *et al.* (1984) used speech degraded by filtering, splicing, or time-reversal and found that F_0 and voice quality ''can convey affective information independently of the verbal context.'' They recommended distinguishing ''linguistic'' and ''paralinguistic'' F_0 features by manipulating acoustic stimuli in a systematic way.

In the present study, we investigated the effects of F_0 measures on perceived emotional stress *in the absence* of verbal content. We employed a method similar to that of Lieberman and Michaels (1962) in that we synthesized fixed-vowel utterances with variations of the F_0 track, and asked listeners to rate their perceived level of stress. In contrast to the study of Lieberman and Michaels (1962), we used original speech taken from a real-life highly stressful situation (i.e., no simulated emotions), we used a single ''stress'' gradient as opposed to several ''emotional modes,'' and we employed more advanced methods for manipulating the F_0-related parameters and for resynthesizing the experimental stimuli, which allowed for better control over the acoustics and more natural-sounding speech. The acoustic parameters of interest were short-term F_0 fluctuations and gross F_0 measures, such as peak values, melodic shape, and range. We conducted experiments with speech synthesized using a constant set of LPC coefficients and varying F_0 tracks. The source and articulatory characteristics were thus kept constant and any perceptual effects could be attributed to the F_0 manipulations.

For our measurements and experiments we used natural speech from a male helicopter pilot. Some utterances were recorded during routine communication with a control tower (unstressful condition) and some were recorded shortly thereafter, when the pilot had lost control of the helicopter and was about to crash (highly stressful condition). The utterances were sampled at 20 kHz using 12-bit linear quantization and the waveform peaks that marked pitch periods were located via a semi-automatic procedure. Temporal resolution in the position of the peaks was increased by quadratic interpolation (as recommended by Titze *et al.*, 1987).

I. JITTER

Period-to-period fluctuations in F_0, known as jitter, are always found in natural speech (Lieberman, 1961), and are known to be more pronounced in cases of pathological conditions such as functional voice disorders (Klingholz and Martin, 1985) and growths on or inflammations of the vocal folds (Lieberman, 1963). The F_0 perturbations have been found to differ among ''emotional modes,'' such as anxiety, fear, anger, etc. (Lieberman and Michaels, 1962; Smith, 1977; Williams and Stevens, 1972), and were predicted to increase in such emotional conditions by Scherer's (1986) model of vocal affect. The empirical status of the reliability of jitter as an emotional indicator remains, however, unresolved. Fuller *et al.* (1992) found *increased* jitter to be an ''indicator of stressor-provoked anxiety [of] excellent validity and reliability'' that is not dependent on individual subjects' ''coping styles.'' They concluded that jitter may be a ''more clinically useful indicator of anxieties'' than other acoustic parameters that may vary with people's coping strategies. In stark contrast, Coster (1986) and Kagan *et al.* (1988) reported that vocal perturbations in children's speech *decreased* with increased stress, and that ''inhibited, compared to the uninhibited, children showed a significantly greater decrease.'' In all, the issues of interpersonal variability and emotional distinctions need to be addressed in more detail before the role of vocal jitter as an affective index can be conclusively established.

A. Jitter analysis

We analyzed unstressed and highly stressed segments of speech (as defined above) using the Average Perturbation Contour (APC) index (proposed by J. Mertus of Brown University) which, for a speech segment containing N pitch periods, is given by the formula

$$\mathrm{APC}_\alpha = \frac{1}{N}\sum_{i=1}^{N} \frac{1}{1+\dfrac{\alpha}{(p_i - m_i)^2}},$$

where p_i is the length of the ith pitch period, m_i is the corresponding ''mean'' period that is obtained by smoothing the pitch contour, and α is a weighting constant. This formula is an extension of the Pitch Perturbation Quotient of Davis (1976); the APC gives more weight to larger departures from the smooth contour, but is not thrown off by isolated extreme deviations, because the weighting curve gradually levels off, depending on α. For our measurements, we used α values of 0.10, 0.25, and 0.50. Smoothing was done first with a five-point median, and then using low-pass filtering with a triangular, Hamming, or Savitsky–Golay filter (known to preserve higher momentum; Press *et al.*, 1992, pp. 650ff). Analysis of unstressed and highly stressed speech segments in the same recordings (about 13 s of each) showed that their jitter ranges overlapped completely, the APC ranging between 0.00032 and 0.0057 for the unstressed segments and between 0.00042 and 0.0050 for the stressed segments (depending mostly on the shape and length of the smoothing

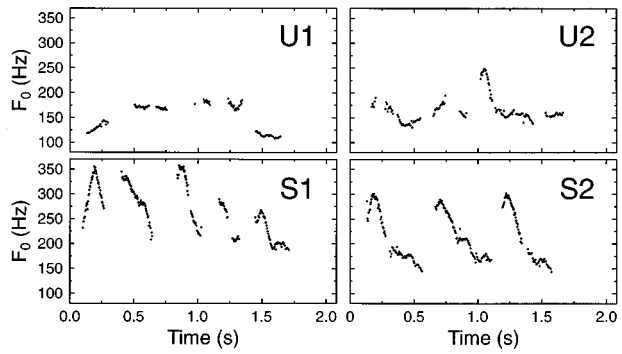

FIG. 1. The F_0 tracks of the four speech segments that were used to synthesize constant-vowel stimuli. U1, U2: unstressed; S1, S2: stressed.

window and on the value of α). Analyses of variance showed that the APC did not differ significantly between unstressed and highly stressed speech [$F(1,76)<1$] for any weighting parameter value of α and for any of the above contour-smoothing windows with lengths between 3 and 15. Identical results were obtained when the instantaneous frequency ($1/p_i$) was used instead of the period and when each period value (p_i) was normalized by the corresponding moving average value (m_i).

From the analysis it appears that, for this speaker, jitter was not an indicator of extreme stress (or terror). Still, it may be that jitter is an indicator of stress in most cases (or other speakers). If this is true, listeners may generally expect jitter to change between various states of stress and, consequently, interpret such changes in their evaluation of the speaker's emotional state. Because of the large individual differences found in vocal indicators of emotion, and because such indicators may result from common underlying sources, it is also possible that jitter may have a perceptual effect only in the context of other acoustic indicators of stress. To test these hypotheses, we presented subjects with F_0 tracks originating from speech produced under the two distinct emotional conditions, in which the jitter was systematically varied but everything else was kept constant.

B. Experiment 1: Perceived stress

The F_0 tracks of two unstressed (U1 and U2) and two stressed (S1 and S2) segments (ranging in length from 1.6 to 2.0 s) were used to synthesize stimuli with varying degrees of jitter. Figure 1 plots the four F_0 tracks that were used. Ten listeners were then asked to rate the stimuli according to the ''emotional stress of the speaker.'' We expected that, if speech with more jitter sounds more ''stressed,'' stimuli with higher degrees of jitter would get higher ratings. If jitter has an effect only in the context of additional acoustic indicators of stress, we should observe a perceptual effect of jitter in the ratings of S1 and S2 variants but not in those of U1 and U2.

1. Method

The four F_0 tracks were smoothed, first with five-point median smoothing and then linearly with a five-point triangular window. The differences, for each pitch period, between each smoothed track and the corresponding original track were then multiplied by 0.0, 0.5, 1.0, 1.5, and 2.0, to create five ''jitter-tracks,'' which were separately added to the smoothed track to create five new F_0 tracks. Thus the smoothed F_0 track plus the 0.0 jitter-track was identical to the smoothed F_0 track, the smoothed plus 1.0 was identical to the original F_0 track of the utterance, and the remaining combinations corresponded to lower (0.5) or higher (1.5, 2.0) degrees of jitter than in the original. Variation of jitter in this manner has the advantage that the spectral distribution of the F_0 perturbations remains constant (and therefore natural) across all degrees of jitter. Using the particular perturbation pattern of each utterance for synthesis also means that, if different ''kinds'' of jitter are somehow present under different emotional conditions, these distinctions are preserved in their acoustic context and will facilitate the desired perception (if jitter has the expected perceptual effect).

A 20-ms segment corresponding to the middle portion of the vowel [a] was excised from the word ''top'' spoken by a male native speaker of American English. The digitized waveform was upsampled to 200 kHz for increased temporal resolution (in particular, for precise control of jitter by means of fine resolution placement of the impulses prior to resynthesis) and analyzed using 200-pole LPC analysis. The analysis program used the autocorrelation method with Durbin's recursive algorithm for solving the LPC equations (Rabiner and Schafer, 1978, pp. 411–413). The resulting coefficients were combined with the jittered F_0 tracks using LPC synthesis to create five (constant–vowel) synthetic stimuli from each of the four original utterances. Synthesis was done by direct implementation of the recursive LPC filter, driven by constant-amplitude impulses. Finally, the stimuli were low-pass filtered with a 1001-tap FIR filter at 9.5 kHz and downsampled to 20 kHz. Calculation of the APC index of the synthesized stimuli indicated that jitter was indeed varying as intended.

In this and in all following experiments, subjects were recruited from the Brown University community (ten for each experiment, ranging in age between 18 and 40 years, mostly undergraduate students) through announcements at local bulletin boards and were paid for their participation. In this experiment, subjects were asked to listen to the synthetic stimuli and were told that ''an 'ah' sound had replaced all the words so [they] could concentrate on the voice and would not be influenced by what had been said.'' Their task was to rate each utterance according to the ''emotional stress'' of the speaker, from 1 (calm) to 7 (very stressed) by pressing the appropriate button on a seven-button response box. The direction of the rating scale, indicated by labels on the response box, was counterbalanced between subjects, and the order of the trials was randomized separately for each participant. Each subject rated each stimulus twice.

2. Results

Listeners did not find it difficult to imagine that real utterances, spoken in different situations of stress, had been ''masked'' with [a] for the purpose of the experiment. Figure 2 (top) shows the ratings for each utterance as a function of relative jitter. Each utterance received different ratings, in accord with its recording situation, but jitter differences did not seem to affect the stress judgments.

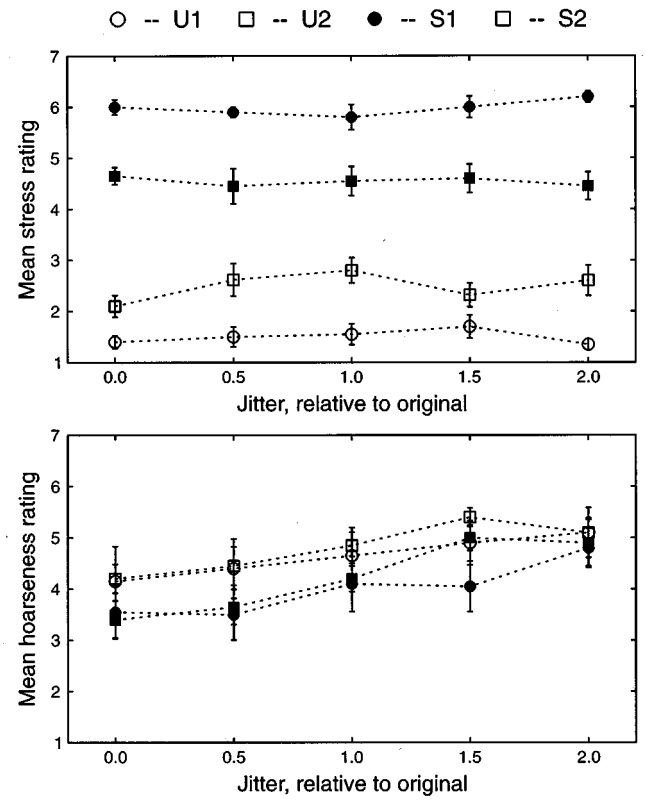

FIG. 2. Mean ratings of speaker's stress (top) and speaker's voice hoarseness (bottom), averaged across subjects, for the four utterances, as a function of relative amount of jitter. The rating scale was 1 to 7; error bars show standard error.

In a 4×5 two-way ANOVA (4 utterances × 5 jitter levels) there was a significant main effect of utterance [$F(3,27)=275.53$, $p<0.00005$], but neither a main effect of jitter [$F(4,36)<1$] nor an interaction between the two [$F(12,108)=1.15$, $p>0.25$]. Thus the four original F_0 tracks indeed reflected very different levels of speaker emotional stress, but the amount of jitter had no effect on the perceived stress level. The average ratings by utterance were (on a scale of 1 to 7) 1.5, 2.5, 6.0, and 4.5 for U1, U2, S1, and S2, respectively.

C. Experiment 2: Perceived hoarseness

In order to rule out the possibility that the null result of experiment 1 was due to a failure of the synthesis method or to other methodological reasons, it was necessary to verify that the jitter differences in the stimuli were perceptible as intended. Since voice hoarseness is known to be a perceptual correlate of jitter (Lieberman, 1963; Muta *et al.*, 1988); particularly in synthesized voices (Hillenbrand, 1988), we conducted an experiment identical to Experiment 1, in which the only difference was in the instructions to the participants: instead of the ''emotional stress of the speaker,'' listeners were now asked to judge the ''hoarseness of the speaker's voice.''

1. Method

The stimuli and procedure for this experiment were identical to those of experiment 1, with the exception of instructions, as described above. Ten subjects from the same population who had not participated in experiment 1 rated the synthesized stimuli for perceived voice hoarseness.

2. Results

Figure 2 (bottom) shows the mean hoarseness ratings, averaged across subjects, for the five levels of jitter. This time the ratings for the four utterances overlapped completely, indicating that the jitter levels were comparable among utterances, as intended, in that the hoarseness ratings were mainly affected by jitter level, equally so for all utterances. However, there is now a strong linear effect of jitter on hoarseness ratings, as expected, that is nearly identical in the four utterances.

Note that the range of hoarseness ratings is relatively small, most of the ratings being around the midpoint of the available scale. Presumably, it would take much more extreme levels of jitter to obtain a mean hoarseness rating closer to 6 or 7.[1] The ''zero jitter'' condition did not give rise, on average, to very low hoarseness ratings (1 or 2) because the ''smooth'' contour is a smoothed version of the original F_0 track and not a perfectly smooth artificial contour. In other words, there is no ''zero jitter'' condition, but only a ''minimal jitter'' condition, relative to the other conditions.

In a 4×5 ANOVA (4 utterances×5 jitter levels) there was no main effect of utterance [$F(3,27)<1$] but there was a significant main effect of jitter [$F(4,36)=11.88$, $p<0.00005$] which did not interact with utterance [$F(12,108)<1$]. Trend analysis of the data indicated that there was a significant linear trend [$F(1,9)=41.85$, $p=0.0001$] that did not interact with utterance ($F<1$), and that there was no quadratic trend ($F<1$). Therefore the jitter differences between the stimuli were perceptible, equally so in all four utterances. In particular, the synthesis method was appropriate in that increasing amounts of jitter led to monotonically increasing hoarseness ratings.

3. Discussion

Our findings indicate that jitter does not affect perceived emotional stress. Experiment 2 clearly showed that the intended jitter gradation was indeed present in our stimuli, so the interpretation of the results of experiment 1 is rather straightforward. However, it must be noted that the type of stress we examined and individual differences in the acoustic correlates of emotional stress may have played an important role. In particular, since jitter was not a factor, in this speaker's voice, that conveyed the emotional distinction under investigation, it is possible that the distribution or some other characteristic of the natural perturbations of his voice was not of the kind that can lead to perception of an utterance as stressed. Alternatively, jitter may be an indicator of other emotional distinctions, as previous studies have suggested, but perhaps not a consistent correlate of extreme stress or terror and thus our subjects ignored it in their interpretation of the stimuli. In particular, jitter may serve to distinguish between states of low level anxiety or task-induced stress, as previous findings have indicated (cf. Fuller *et al.*, 1992;

Coster, 1986). Both of these explanations are compatible with Scherer's (1986) model of vocal affect, since perturbation variations are optional for this emotional condition (''fear/terror,'' pp. 158, 161). On the other hand, our subjects were not instructed as to the kind of stress to pay attention to and had no reason to consider only terror as a stress condition. Nonetheless, it may still be the case that jitter conveys subtle distinctions that were washed out in the context of the extreme F_0 excursions that were present in the recordings from the highly stressed condition. Furthermore, due to the individual differences often found in vocal affect (Hecker *et al.*, 1968) and in vocal jitter measurements in particular (Coster, 1986; Nittrouer *et al.*, 1990), jitter may be too unreliable an indicator to be used by listeners in emotional assessments when the ''normal'' voice of a particular speaker is not known.

II. MELODIC CHARACTERISTICS

In addition to short-term F_0 variability, long-term F_0 measures have also been found to correlate with emotional stress. Scherer (1986) reported in his review that the mean F_0 and the variability of F_0 have been found to increase in situations of fear/terror; his model of vocal affect predicted such changes through the stimulus evaluation checks and their physiological consequences. However, the F_0-related parameters that have been investigated are highly interrelated in natural utterances, and it is not clear whether some of them convey the actual emotional information or whether the whole acoustic constellation is necessary for correct perceptual interpretation. For example, utterances with higher mean F_0 also have higher F_0 range. Does either the high F_0 or the wide range of its values signify a high degree of emotional stress, or is the whole F_0 pattern perceived as a holistic stress indicator?

A. Experiment 3: Perceived stress

In order to investigate the individual contributions of F_0 measures to perceived emotional stress, we examined several parameters. From the F_0 tracks of the original utterances we calculated the mean and maximum F_0, as well as the F_0 range, $\mathrm{Max}(F_0)-\mathrm{Min}(F_0)$, and what we call the ''geometric range,'' $\mathrm{Max}(F_0)/\mathrm{Min}(F_0)$. S1 and S2 gave higher values in all these measures than U1 and U2, as expected, but the small sample and the relations between these measures precludes conclusions about their relative importance in general. The perceptual effects of each of the F_0-related measures that were found to differ between stressed and unstressed utterances were examined in an experiment using stimuli, synthesized as before, whose F_0 tracks were manipulated to contrast mean, maximum, range, and geometric range of F_0.

1. Method

For each of the four utterances, four F_0 tracks were used: (a) the *original* F_0 track, as measured from the natural speech; (b) the *time-inverted* track, in which the order of pitch periods was the inverse of that in the original, but their length was unchanged; (c) the *scaled* track, in which each pitch period was multiplied by a constant; and (d) the *shifted* one, in which a constant was added to the inverse of each pitch period. Figure 3 illustrates the four manipulation conditions using the U1 utterance. In order to preserve the melodic shape and the duration of the utterance in the scaled and shifted versions, the actual pitch periods that were used in LPC synthesis were calculated by interpolation from the scaled or shifted values, respectively.

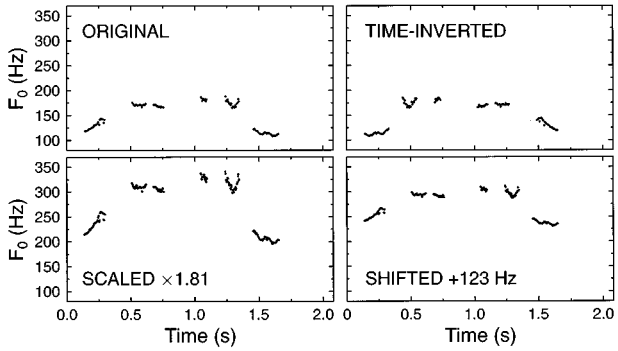

FIG. 3. The F_0 tracks of the four stimuli from experiment 3 that were based on utterance U1.

Each unstressed utterance was paired with a stressed one (U1 with S1 and U2 with S2). The shift and scale constants for each utterance were chosen so that the altered F_0 tracks of one member of each pair resulted in a mean F_0 approximately equal to that of the original F_0 track of the other member of the pair. For example, the pitch periods of U1 were scaled by 1.81 in the scaled condition and shifted by 123 Hz in the shifted condition, the resulting F_0 tracks having a mean F_0 approximately equal to that of S1 (277 Hz). Conversely, the pitch periods of S1 were scaled by 0.55 and shifted by -123 Hz, the resulting mean F_0 being approximately equal to that of U1. Table I shows the F_0 mean, maximum, range, and geometric range of each stimulus. The same LPC coefficients for a male [a] were used as in the previous experiments, and all stimuli were synthesized with jitter equal to that of the corresponding original utterances.

Because it is impossible to completely separate the parameters under investigation, multiple comparisons between the stimuli are necessary. For example, increasing the mean F_0 value to a given value by multiplication and by addition leads to stimuli with matched mean F_0 and different ranges and geometric ranges, respectively. The original and the scaled stimuli are matched in geometric range but differ in F_0 mean and range, whereas the original and the shifted ones are matched in range but differ in F_0 mean and geometric range. Examination of the pattern of results should thus indicate which parameters are most closely related to differences in perceptual judgements of stress.

Ten subjects from the same population who had not participated in the previous experiments rated each stimulus five times, in a procedure identical to that of Experiment 1 (including instructions).

2. Results

Figure 4 shows the ratings of the original and time-inverted stimuli for each utterance. The stress ratings of utterances with time-inverted F_0 tracks were not significantly different from the ratings of the original utterances [$F(1,9)$

TABLE I. The F_0 measurements of the stimuli used in experiment 3. Data for time-inverted stimuli are not shown, as they are identical to those of the original ones. Mean, maximum, and range of F_0 are in Hz, geometric range is a ratio (no units).

	F_0 measurements			
F_0 track	Mean	Maximum	Range	Geometric range
U1				
Original	151.2	188.4	80.0	1.739
Scaled	275.2	340.9	145.4	1.744
Shifted	273.1	311.4	80.4	1.348
U2:				
Original	169.4	248.5	117.6	1.899
Scaled	225.4	331.3	156.8	1.898
Shifted	224.2	303.8	117.4	1.630
S1:				
Original	276.8	355.1	167.6	1.894
Scaled	151.7	198.0	94.3	1.910
Shifted	160.6	232.7	166.8	3.530
S2:				
Original	222.6	302.0	156.7	2.078
Scaled	166.6	226.5	117.8	2.084
Shifted	170.8	247.0	156.9	2.742

<1], and there was no interaction between track-direction and utterance [$F(3,27)<1$]. Therefore, for the stimuli we used, the direction of the melodic patterns (rising versus falling, breath-group slope, etc.) did not affect the perception of stress. In the following analyses the ratings of the time-inverted stimuli were not used, because they were identical to those of the original F_0 tracks (as were also their F_0 measures) and, if used, they would effectively duplicate the corresponding points, thus artificially inflating correlation coefficients.

Figure 5 shows the mean ratings of the stimuli (excluding time-inverted stimuli) plotted against their (a) maximum F_0, (b) mean F_0, (c) range of F_0, and (d) geometric range of F_0. Mean and maximum F_0 correlated well with stress ratings (mean F_0: $r=0.82$, $p=0.001$; maximum F_0: $r=0.89$, $p=.0001$), but range and geometric range of F_0 did not (range: $r=0.51$, $p=0.09$; geom. range: $r=-0.29$, $p=0.37$). In stepwise regression analysis, F_0 range did not correlate significantly with stress ratings after the linear effect of maximum F_0 had been removed (partial $r=0.22$, $p>0.5$) but approached significance after the linear effect of mean F_0 had been removed (partial $r=0.56$, $p=0.056$). The multiple-r correlation coefficient using both mean and range was 0.89, equal to the correlation between ratings and maximum F_0 alone.

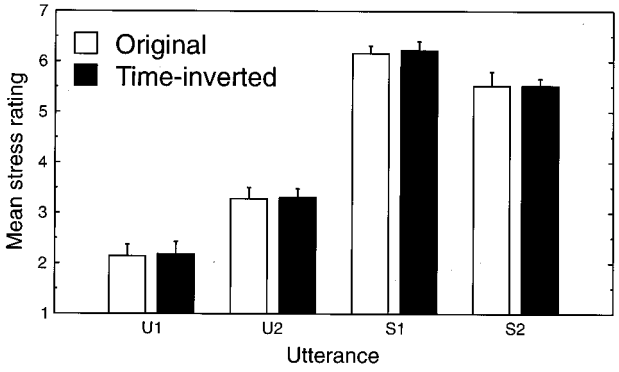

FIG. 4. Stress ratings of the original and time-inverted stimuli for each utterance. Error bars show standard error.

Variants of the stressed utterances received higher ratings than the corresponding (matched) variants of unstressed utterances. Although such differences were generally not quite significant (using Tukey's procedure for *post hoc* pairwise comparisons, as described in Maxwell and Delaney, 1990, pp. 181–184), some aspect of the melodic patterns of stress utterances seemed to have perceptual effects beyond gross statistical measures. For example, the original F_0 track from S2 was rated more stressed than the ''matched'' F_0 track of scaled U2 although the latter had the same mean and range of F_0, higher maximum F_0, and lower geometric range.

3. Discussion

The strong correlation between maximum (and mean) F_0 and the stress ratings comes as no surprise, given previous reports on speech production under various emotional conditions. The lack of a perceptual effect of range and directionality, however, stands in contrast to popular belief that increased F_0 range also conveys such information. Melodic directionality, as defined for our purposes by such parameters as rising versus falling melody and breath-group slope,[2] did not affect perceived emotional stress for any of the four utterances. However, other aspects of the melodic pattern seem to have some influence as mentioned above. Since the exact nature of the salient patterns is not known it is not possible at this stage to systematically vary them in order to investigate them in more detail.

Close inspection of Fig. 5, in conjunction with the results of the regression analysis, leads to the conclusion that mean and maximum F_0 are *the* salient F_0 measures that convey emotional information, at least for the extreme kind of emotional stress that was investigated in this study. Note that, in Fig. 5(a) and (b), ratings of variants of each utterance

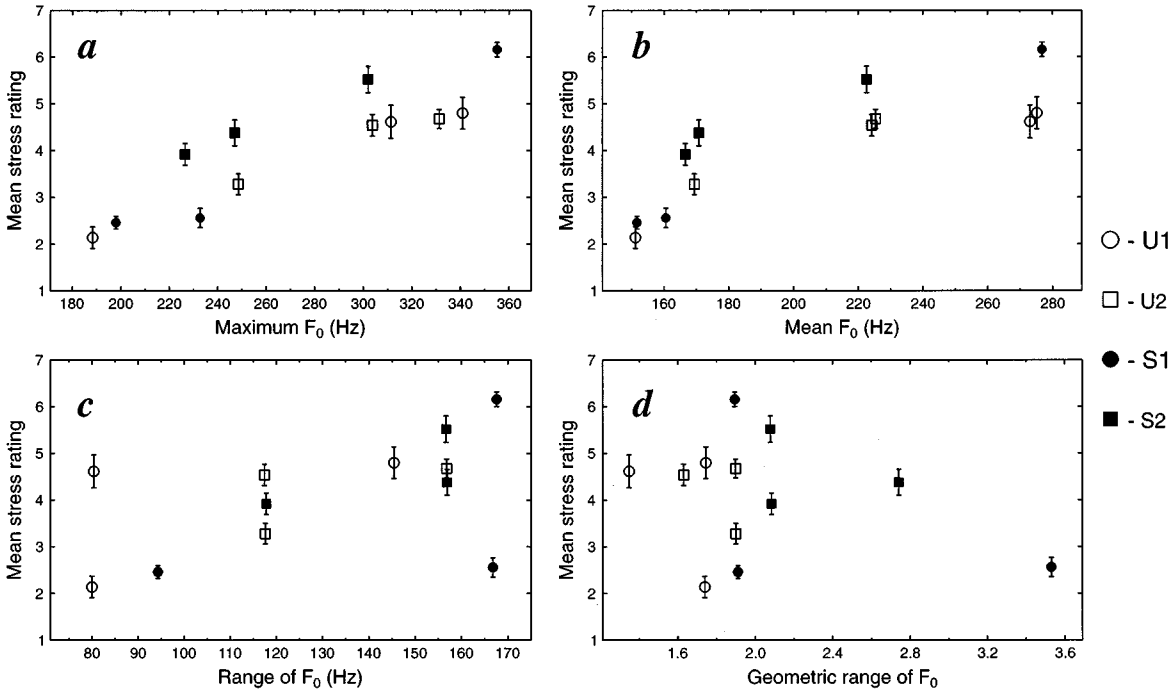

FIG. 5. Stress ratings to the resynthesized stimuli in experiment 3 as a function of (a) maximum F_0, (b) mean F_0, (c) range of F_0, and (d) geometric range of F_0 (excluding ratings to time-inverted stimuli). Refer to Table I for identification of individual stimuli on the basis of their F_0 measures. Error bars show standard error.

(represented by identical markers) lie approximately on straight lines parallel to each other, indicating the gradual, almost linear, effect of maximum and mean F_0 on perceived emotional stress. In contrast, in Fig. 5(c) and (d), ratings of variants of each utterance form right angles with one vertical and one horizontal side, one stimulus pair having almost identical range (or geometric range) but very different ratings, and the other pair having very different range (or geometric range) and almost identical ratings. The apparent weak correlation between F_0 range and the stress ratings is entirely due to the correlation between F_0 range and F_0 maximum (and mean). After removing the linear effect of maximum F_0, there is no other significant correlation. After removing the linear effect of mean F_0, the apparent correlation of the (normalized) stress ratings with F_0 range is an artifact that results from the unequal range of shift and scale of the two utterance pairs. As shown in Fig. 6, the points of each utterance still lie approximately on right angles with a vertical and a horizontal side (except S2), but the higher minimum range of S2 and U2 (compared to that of S1 and U1) combines with their higher ratings to produce a spurious correlation that approaches statistical significance when all points are considered together.

A consideration for the manipulation of F_0 range has been to implement both the arithmetic range, which is calculated by subtraction of the lowest from the highest value, and the geometric range, which is the result of the division of the highest by the lowest value. Although the arithmetic range is the parameter usually examined, the logarithmic nature of human frequency representation might lead one to expect that the geometric mean would correlate better with perceptual effects. Our use of both parameters effectively counters this possibility as it allows for control of each of the two using the other one. It should be clear that no range parameter affects perceived emotional stress, and this finding could be of use to speech synthesis systems, when a high level of stress needs to be conveyed. Apparently, the perceptual system evaluates the *effort* of the speaker, which is higher in order for higher F_0 to be produced (deriving from higher subglottal pressure and laryngeal muscle tension), to assess the degree of emotional stress the speaker is under. The relative importance of maximum F_0 is also evidenced by the fact that high-F_0 variants of unstressed utterances received higher ratings than low-F_0 variants of stressed utterances, i.e., F_0 information was enough to override all other prosodic cues that might have been present in the highly stressful recordings.

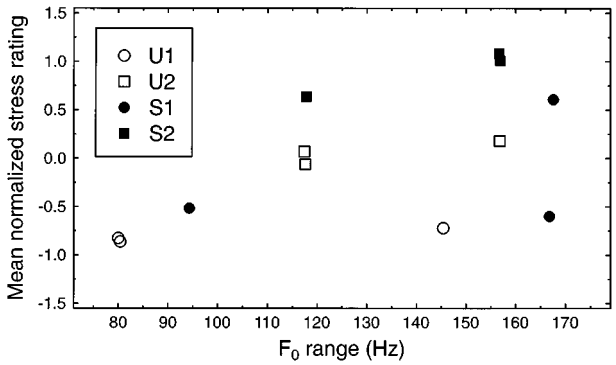

FIG. 6. Normalized stress ratings in experiment 3 as a function of F_0 range, after subtracting the linear effect of mean F_0. (Ratings to time-inverted stimuli are not included.)

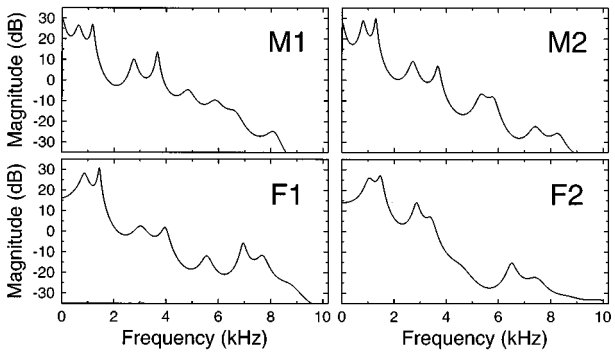

FIG. 7. All-pole power spectra calculated from the LPC coefficients of the four vowels that were used to synthesize the stimuli in experiment 4. M1, M2: male voices; F1, F2: female voices.

B. Experiment 4: Different voices

Given the findings of experiment 3, it was of interest to investigate whether the information conveyed by the F_0 measures we examined varies with voice quality or is speaker independent. Previous studies have identified ''voice quality'' (or timbre) as a primary acoustic carrier of emotional information (Scherer *et al.*, 1984; Scherer, 1986). In the context of the present study, the question is not so much that of distinguishing between different emotions as it is of assessing the degree of a particular emotional state given particular F_0 information. Therefore, it is not of primary importance to systematically examine the effects of acoustic energy distribution but, rather, to establish the F_0 effects in a wide range of voice qualities. To this end, we repeated experiment 3 using four different voices by recording the [a] vowel from four new speakers.

1. Method

Four speakers were recruited from the same population as the listeners, including one relatively large and one relatively small person of each sex (to cover a larger range of formant frequencies). Each was asked to say the word ''top'' and 20 ms of the vowel [a] were excised from its center portion (after digitizing at 20 kHz and upsampling to 200 kHz, as for experiment 3). The four vowels were subjected to 200-pole LPC analysis and each set of parameters that was generated was used in conjunction with the 12 F_0 tracks to synthesize a set of stimuli as in experiment 3 (excluding the time-inverted tracks, which showed no effect). Figure 7 shows the LPC spectra of the four vowels (for the frequencies 0–10 kHz only, since all stimuli were downsampled to 20 kHz after synthesis). For each of the 12 F_0 tracks there were now four versions, labeled M1, M2, F1, and F2, corresponding to the four speakers, bringing the total number of stimuli for this experiment to 48.

The testing procedure and instructions were identical to those for experiment 3. Ten new subjects were recruited from the same population and each one rated each stimulus three times (as opposed to five times in experiment 3, which had quite fewer stimuli) in different random orders. The mean of the three ratings was used for the analysis.

2. Results

With one exception, participants said that they did not find the voices particularly unnatural and that they could imagine utterances spoken with these intonations and voices in various stressful conditions. One listener reported that she found some of the stimuli very unnatural, sounding like a musical instrument. Most listeners correctly identified four distinct voices in the experiment, but three of them thought there were maybe ten or fifteen different voices. These concerns regarding stimulus naturalness will be further addressed below, in experiment 5.

Although the same F_0 tracks were used with all voices, there was a significant effect of voice [$F(3,27)=20.09$, $p<0.0005$], with M1 receiving the lowest ratings (mean 3.78), F2 the highest (mean 4.24), and M2 and F1 intermediate ratings (means 3.88 and 3.89, respectively). Note that this ordering pattern parallels that of the voices' first two formant frequencies (see Fig. 7), which are lowest for M1, highest for F2, and intermediate for M2 and F1. The mean rating for each voice was subtracted from the ratings to all utterances of the same voice, in order to make the correlations meaningful, independently of the voice effect.

Multiple regression analysis of the ratings onto the four predictor F_0 measures gave results similar to those of experiment 3: after subtracting the voice mean from each stimulus, the ratings correlated best with maximum F_0 (partial $r=0.69$, $p<0.00005$) and mean F_0 (partial $r=0.65$, $p<0.00005$), weakly with F_0 range (partial $r=0.37$, $p=0.01$), and not at all with geometric range (partial $r=-0.26$, $p=0.08$). Again, the correlation of the ratings with F_0 range was owed to the interrelation between maximum F_0 and range of F_0 and was not significant after the linear effect of maximum F_0 had been removed (partial $r=0.06$, $p=0.7$). It was, however, weak but still significant after the removal of the linear effect of mean F_0 only (partial $r=0.29$, $p=0.049$), as in experiment 3. The multiple-r correlation coefficient after inclusion of mean F_0 and F_0 range was 0.69, equal to the partial correlation of the normalized stress ratings with maximum F_0 alone. In all, the pattern of results is identical to that of experiment 3 and the same considerations lead us to conclude that F_0 range did not contribute to the perception of emotional stress whereas maximum F_0 is once again the critical parameter.

Additional correlational analyses were performed using the stimuli generated from each voice separately. Table II shows the partial correlation coefficients between the stress ratings of each utterance and the F_0 measures separately for each voice. Note that maximum F_0 correlated most strongly with stress ratings for M1 and M2, followed by mean F_0, whereas maximum F_0 correlated only slightly less strongly than mean F_0 with the stress ratings for F1. The correlation of the stress ratings with range of F_0 approached significance only for M1, and from the pattern of results from M1 we may safely attribute this to the correlation between F_0 maximum and F_0 range, as before. The geometric range of F_0 failed to correlate significantly with the stress ratings of any voice. Surprisingly, none of the F_0 measures correlated significantly with the stress ratings of the stimuli with the F2 voice (which received the highest overall ratings).

TABLE II. Correlation coefficients between the F_0 measures and the stress ratings of the utterances listed separately for each voice. F_0 maximum, mean, and range were measured in Hz, F_0 geometric range is a ratio (no units).

	F_0 measurements			
Voice	Maximum	Mean	Range	Geometric range
M1	0.845[a]	0.782[a]	0.561	0.177
M2	0.763[a]	0.741[b]	0.469	0.159
F1	0.632[c]	0.659[c]	0.109	0.449
F2	0.454	0.353	0.224	0.339

[a]$p<0.005$.
[b]$p<0.01$.
[c]$p<0.05$.

3. Discussion

The stress ratings of the utterances that were synthesized with LPC parameters derived from male voices corroborate the findings of experiment 3 (whose stimuli were also based on a male voice). In addition, there seems to be a correlation between formant frequencies and perceived stress, because stimuli with identical F_0 tracks but higher formants were judged to sound more stressed. The ratings of the female voice stimuli, however, correlate less strongly (F1) or not at all (F2) with F_0 mean and maximum. Possible explanations, other than women's vocal affect being unrelated to F_0, include precedence of voice-specific characteristics and stimulus quality considerations. In particular, it is possible that somehow the voice quality of F2 (and perhaps, to some extent, F1) is such that any utterance sounds equally stressed. If voice quality is a more salient cue for vocal affect, then it may override F_0 measures under certain unknown circumstances that were present in the case of F2. Alternatively, the speech synthesis method may have been inconsistent in that some LPC parameter sets may have led to higher quality (more natural sounding) speech stimuli than others, and this difference may have affected the stress ratings. Since the latter option is much easier to investigate than the former, we examined it in a subsequent experiment. Further discussion of the stress ratings across voices is deferred until the results of the study on the quality of the stimuli for each voice are presented.

C. Experiment 5: Naturalness of stimuli

One issue that needed to be investigated before firm conclusions could be drawn from the results of experiment 4 was whether the stimuli that were given different stress ratings sounded equally natural. It may be the case that more natural stimuli sounded more (or less) stressed than more synthetic-sounding ones, or that the gradual F_0 effects were an artifact of the synthetic character of the stimuli. In particular, we also needed to examine whether the lack of an F_0 effect for the F2 stimuli was a result of that group of stimuli sounding less natural than those of the other voices. The one subject's difficulty imagining real voices with some stimuli suggested that naturalness varied among the stimuli. We therefore conducted an experiment in which subjects were asked to rate the naturalness of the stimuli, and we looked for differences between naturalness ratings that would correlate with differences in F_0 effects on the stress ratings.

1. Method

All the stimuli from experiment 4 were used, along with an equal number of lower quality stimuli that were added in order to create a wider range of naturalness. The new stimuli were created in the exact same way as those for experiment 4, but using 50-pole LPC analysis and synthesis (as opposed to 200-pole LPC for the original ones). This had the effect of maintaining the intonation, intensity, and some of the vowel quality, but giving a clearly synthetic quality to the sound. Thus, subjects could get a better idea of what ''natural'' and ''synthetic'' meant for the purposes of this experiment. Given that even real voices would not be judged to be ''perfectly natural'' if they only said [a] with some intonation, we considered it necessary to make the distinction more salient. It should be noted that what was of interest is not whether our stimuli sounded perfectly natural (which they certainly did not, mainly because people don't generally say ''ah'' with sentential intonation) but, rather, whether there were any correlations between the degree of naturalness and the observed F_0 effects that might render the interpretation of the findings of experiment 4 less meaningful.

Ten new subjects were recruited (from the same population) for this experiment. They were seated in front of a seven-button response box, as before, with the endpoints labeled ''natural'' and ''synthetic.'' Half the participants had ''natural'' at the rightmost end and the other half at the leftmost end. The participants were instructed to rate each stimulus for naturalness on a scale from 1 (natural) to 7 (synthetic), based on whether ''a real person would sound like that if (s)he were to say 'ah' with the same intonation and intensity.'' The order of the stimuli was randomized separately for each participant. Each stimulus was rated twice by each participant in a single session that lasted about 15 min; the mean of the two ratings was used for the analysis.

2. Results

Stimuli synthesized using 50-pole LPC received a mean naturalness rating of 5.7, which was significantly different from the 3.2 mean rating of the stimuli that were synthesized using 200-pole LPC and were used in experiment 4 [$F(1,9)=142.65$, $p<0.0005$], as expected. The ratings to low-quality stimuli were not considered further in the analysis, as the sole purpose of those stimuli was to expand the naturalness range.

Mean naturalness by voice was 2.88, 2.80, 3.34, and 3.93 for M1, M2, F1, and F2, respectively. Mean naturalness by utterance ranged between 2.91 and 3.78. In a two-way analysis of variance (4 voices×12 utterances) there was a significant effect of voice on the naturalness ratings [$F(3,27)=14.21$, $p<0.0005$] but no significant effect of utterance [$F(11,99)=1.15$, $p=0.33$]. There was an interaction between voice and utterance [$F(33,297)=1.79$, $p=0.007$], indicating that the voice effect was different across utterances.

In particular, there was a significant effect of voice (after Bonferonni adjustment, described in Maxwell and Delaney, 1990, pp. 177–180) for the shifted and scaled S1 and S2. Voice pairwise comparisons (with Bonferonni adjustment) using the naturalness ratings of these four utterances only indicated that F2 was rated significantly less natural than either of the other three voices, F1 was judged significantly less natural than either male voice (and more natural than F2), and the two male voices did not differ significantly from each other in naturalness.

3. Discussion

The pattern of the naturalness ratings of the stimuli parallels the strength of the correlation between maximum (and mean) F_0 and the stress ratings: the two male voices sounded more natural and showed a strong linear relationship between maximum F_0 and perceived emotional stress, the F1 stimuli sounded somewhat less natural and their maximum F_0 correlated less well with their stress ratings, and the F2 stimuli sounded the most synthetic and their maximum and mean F_0 did not predict their stress ratings at all.

The synthetic quality of the F2 stimuli makes the evaluation of the results of experiment 4 regarding F2 more difficult. It is not possible to conclude that the observed correlation between maximum F_0 and perceived emotional stress does *not* hold for all voices, because it may well hold for all *natural* voices. The conclusion that this correlation holds for *any* voice is also unwarranted, because we cannot prove that it is the synthetic quality of the F2 stimuli that was responsible for the lack of correlation. However, since the strength of the correlation follows the same pattern as the degree of naturalness of the stimuli, we suspect that stimulus quality is probably the reason that differences in the correlations were found between voices. Because the F2 stimuli that were rated as sounding most unnatural were those with the lowest *minimum* F_0, we suggest that the low-F_0 stimuli were too low in F_0 for women's voices and were thus not perceived as intended. In particular, the low F_0 may have led subjects to interpret the problematic stimuli as male, but the high formants then imposed an interpretation of an abnormally small male or, most likely, a male with a vocal tract shortened by an expression of terror (tightened larynx, mouth wide open, and retracted lips). This may have served as an overriding cue to perceived emotional stress that countered the F_0 effect so that low-F_0 F2 stimuli were perceived as highly stressed, i.e., in the opposite direction from the expected correlation.

III. CONCLUSION

In agreement with previous findings by Scherer *et al.* (1984), we conclude that vocal F_0 carries emotional information independently of the verbal content of an utterance, in fact, even in the absence of verbal content. Lieberman and Michaels (1962) showed in a similar manner that amplitude and F_0 information alone can be utilized by listeners to distinguish between different emotional modes of the speaker, although they found that F_0 perturbations were important for the emotional distinctions and we found no evidence for such a role of jitter. Again, it should be emphasized that we were not concerned with the distinctions between various emotions but with the gradual perception of an undifferentiated ''emotional stress'' which, given the source of our F_0 tracks, was closer to terror than to task-induced anxiety. It is possible that vocal perturbations are a cue to low levels of stress. We believe that the great individual differences found between speakers in jitter studies make jitter an unlikely indicator of emotional state (or stress level), except in cases where a particular speaker's ''normal'' voice is well known, so that departures from it can be reliably evaluated. It appears more promising to concentrate on the diagnostic potential of perturbation measurements, given recent advances in our understanding of voice disorders and in automated voice-analysis systems (Laver *et al.*, 1992).

For all three male voices (one in experiment 3 and two in experiment 4) we found maximum F_0 to be the single best predictor of emotional stress ratings, independently of voice, melodic shape, F_0 range, and jitter. The F_0 range failed to correlate with emotional stress ratings, and it was shown that its often-reported correlation with speaker emotional stress owes to its correlation with maximum F_0. In order to be able to compare the effects of F_0 in different voices we used identical F_0 tracks with male and female voices, resulting, in some cases, in female-voice stimuli that sounded unnatural, possibly due to their very low minimum F_0. Because of the strong and robust correlations found with all male voices, we conclude that maximum F_0 is the most important F_0-related parameter in vocal affect for all voices, and we would expect to find the same pattern with female voices if more appropriate F_0 ranges were used. Although our stimuli were not designed to assess the effects of formant frequencies on perceived emotional stress, our findings indicate that voices with higher formants sound more stressed. The contribution of higher formants in the stress ratings may in fact be quite significant, if the alternative interpretation of the findings with the female voices, particularly F2, is correct. That is, if the formant structure dominated the F_0 effect and caused it to all but disappear.

The fact that high correlations are obtained between some acoustic parameters (here, maximum F_0) and stress ratings is in agreement with the claim of Streeter *et al.* (1983) that ''listeners view certain vocal behaviors as indicative of particular emotional states'' (p. 1359). Consequently, findings on the perceptual role of acoustic parameters in emotional vocalizations can be of practical use in speech synthesis programs, to increase the perceived naturalness, or to convey additional nonlinguistic (emotional) information. The present study clearly shows that the range of F_0, contrary to what is often taken for granted, does not contribute to perceived stress when decorrelated from mean and maximum F_0. This finding is less surprising when one considers the multitude of attention-driving uses of vocalizations with great F_0 excursions, notably including infant-directed speech.

Perhaps more surprising than the lack of an F_0-range effect, reversing the temporal structure of the entire F_0 track resulted in virtually identical ratings of perceived stress. This does not mean that the temporal structure of F_0 variations within an utterance plays no role in conveying emotional

information; such an extreme conclusion is unwarranted and probably wrong. It is likely that the speed of change, or other gross temporal characteristics of the F_0 track, affect the perceived emotional state of a speaker. After all, variants of stressed utterances were always rated more stressed (if only slightly) than matched variants of unstressed utterances, therefore something in the overall shape of the F_0 track carries perceptible emotional information. The null result of the time-reversal manipulation suggests that the *direction* of F_0 variations is insignificant with respect to the emotional information of the utterance, and this is a novel and important finding from the point of view of vocal affect research as well as for practical systems of recognition and synthesis of emotional speech.

Since F_0 is also used to convey linguistic (verbal) information, such as lexical stress and some syntactic properties, it is necessary to examine the role of F_0 in normal utterances. Although the present method cannot be dismissed for that purpose, it should be noted that LPC is an inadequate model of most speech sounds, and that it is unlikely to produce natural-sounding stimuli that contain phonemes other than vowels and glides. Consonants, with sound sources not at the glottis, and nasals, with the coupled resonators, are certain to cause problems for the researchers. However, in order to further our understanding of vocal affect, natural utterances with precisely controlled acoustics are necessary. Advanced speech synthesis technology must be used in order to investigate in detail the emotional information conveyed by speech.

ACKNOWLEDGMENTS

This work was supported in part by consortium agreement NCC2-5041 from NASA Ames Research Center to Brown University; portions of it were first reported at the ESCA/NATO Tutorial and Research Workshop on Speech Under Stress, Lisbon, Portugal, September 14–15, 1995. We thank the participants of the workshop, especially R. K. Moore, for their constructive criticism and comments. We also thank David Ascher, Peter Eimas, Laurie Heller, Emily Pickett, Jennifer Utman, and two anonymous reviewers for valuable comments on the manuscript.

[1]Such extreme levels of jitter were judged by the experimenters as sounding overly unnatural in the context of constant–vowel stimuli and were thus not employed in the present experiments.

[2]We did not specifically measure any parameters of directionality. Presumably, inverting the entire F_0 track effectively reversed all directional characteristics.

Coster, W. J. (**1986**). ''Aspects of voice and conversation in behaviorally inhibited and uninhibited children,'' unpublished Ph.D. dissertation, Harvard University.

Cummings, K. E., and Clements, M. A. (**1995**). ''Analysis of the glottal excitation of emotionally styled and stressed speech,'' J. Acoust. Soc. Am. **98,** 88–98.

Darwin, C. (**1872**). *The Expression of the Emotions in Man and Animals* (Appleton, London).

Davis, S. B. (**1976**). ''Computer evaluation of laryngeal pathology based on inverse filtering of speech,'' SCRL Monograph 13, Speech Communications Research Lab, Santa Barbara, CA.

Fuller, B. F., Horii, Y., and Conner, D. A. (**1992**). ''Validity and reliability of nonverbal voice measures as indicators of stressor-provoked anxiety,'' Res. Nurs. Health **15**, 379–389.

Hecker, M. H. L., Stevens, K. N., von Bismark, G., and Williams, C. E. (**1968**). ''Manifestations of task-induced stress in the acoustic speech signal,'' J. Acoust. Soc. Am. **44,** 993–1001.

Hillenbrand, J. (**1988**). ''Perception of aperiodicities in synthetically generated voices,'' J. Acoust. Soc. Am. **83,** 2361–2371.

Kagan, J., Reznick, J. S., and Snidman, N. (**1988**). ''Biological bases of childhood shyness,'' Science **240,** 167–171.

Klingholz, F., and Martin, F. (**1985**). ''Quantitative spectral evaluation of shimmer and jitter,'' J. Speech Hear. Res. **28**, 169–174.

Kuroda, I., Fujiwara, O., Okamura, N., and Utsuki, N. (**1976**). ''Method for determining pilot stress through analysis of voice communication,'' Aviat. Space Environ. Med. **47**, 528–533.

Laver, J., Hiller, S., and Mackenzie Beck, J. (**1992**). ''Acoustic waveform perturbation and voice disorders,'' J. Voice **6**, 115–125.

Lieberman, P. (**1961**). ''Perturbations in vocal pitch,'' J. Acoust. Soc. Am. **33,** 597–603.

Lieberman, P. (**1963**). ''Some acoustic measures of the fundamental periodicity of normal and pathologic larynges,'' J. Acoust. Soc. Am. **35,** 344–353.

Lieberman, P., and Michaels, S. B. (**1962**). ''Some aspects of fundamental frequency and envelope amplitude as related to the emotional content of speech,'' J. Acoust. Soc. Am. **32,** 922–927.

Maxwell, S. E., and Delaney, H. D. (**1990**). *Designing Experiments and Analyzing Data: A Model Comparison Perspective* (Wadsworth, Belmont, CA).

Murray, I. R., and Arnott, J. L. (**1993**). ''Toward the simulation of emotion in synthetic speech: A review of the literature on human vocal emotion,'' J. Acoust. Soc. Am. **93,** 1097–1108.

Muta, H., Baer, T., Wagatsuma, K., Muraoka, T., and Fukuda, H. (**1988**). ''A pitch-synchronous analysis of hoarseness in running speech,'' J. Acoust. Soc. Am. **84,** 1292–1301.

Nittrouer, S., McGowan, R. S., Milenkovic, P. H., and Beehler, D. (**1990**). ''Acoustic measurements of men's and women's voices: A study of context effects and covariation,'' J. Speech Hear. Res. **33**, 761–775.

Press, W. H., Teukolsky, S. A., Vetterling, W. T., and Flannery, B. P. (**1992**). *Numerical Recipes in C, The Art of Scientific Computing* (Cambridge U. P., Cambridge), 2nd ed., pp. 650–654.

Rabiner, L. R., and Schafer, R. W. (**1978**). *Digital Processing of Speech Signals*, Prentice–Hall signal processing series (Prentice–Hall, Englewood Cliffs, NJ).

Ruiz, R., Legros, C., and Guell, A. (**1990**). ''Voice analysis to predict the psychological or physical state of a speaker,'' Aviat. Space Environ. Med. **61**, 266–271.

Scherer, K. R. (**1977**). ''Cue utilization in emotional attribution from auditory stimuli,'' Motivat. Emot. **1**, 331–346.

Scherer, K. R. (**1986**). ''Vocal affect expression: a review and a model for future research,'' Psychol. Bull. **99,** 143–165.

Scherer, K. R., Ladd, D. R., and Silverman, K. A. (**1984**). ''Vocal cues to speaker affect: testing two models,'' J. Acoust. Soc. Am. **76,** 1346–1356.

Smith, G. A. (**1977**). ''Voice analysis for the measurement of anxiety,'' Br. J. Med. Psychol. **50**, 367–373.

Streeter, L. A., Macdonald, N. H., Apple, W., Krauss, R. M., and Galotti, K. M. (**1983**). ''Acoustic and perceptual indicators of emotional stress,'' J. Acoust. Soc. Am. **73,** 1354–1360.

Titze, I. R., Horii, Y., and Scherer, R. C. (**1987**). ''Some technical considerations in voice perturbation measurements,'' J. Speech Hear. Res. **30**, 252–260.

Williams, C. E., and Stevens, K. N. (**1969**). ''On determining the emotional state of pilots during flight: an exploratory study,'' Aerospace Med. **40**, 1369–1372.

Williams, C. E., and Stevens, K. N. (**1972**). ''Emotions and speech: some acoustical correlates,'' J. Acoust. Soc. Am. **52,** 1238–1250.

Stimulus variability and spoken word recognition. II. The effects of age and hearing impairment

Mitchell S. Sommers[a)]
Department of Psychology, Washington University, Campus Box 1125, St. Louis, Missouri 63130

(Received 19 January 1996; revised 20 November 1996; accepted 27 November 1996)

Three experiments were conducted to investigate the effects of variations in talker characteristics, speaking rate, and overall amplitude on perceptual identification in normal-hearing young (NHY), normal-hearing elderly (NHE), and hearing-impaired elderly (HIE) listeners. The three dimensions were selected because variations in voice characteristics and speaking rate affect features of speech signals that are important for word recognition while overall amplitude changes do not alter stimulus parameters that have direct effects on phonetic identification. Thus, the studies were designed to examine how variations in both phonetically relevant and irrelevant stimulus dimensions affect speech processing in a number of different populations. Age differences, as indicated by greater effects of variability for the NHE compared with the NHY listeners, were observed for mixed-talker and mixed-amplitude word lists. Effects of age-related hearing impairment, as indicated by reduced scores for the HIE compared with the NHE group, were observed for variations in speaking rate and talker characteristics. Considered together, the findings suggest that age-related changes in perceptual normalization and selective attention may contribute to the reduced speech understanding that is often reported for older adults.
[S0001-4966(97)04204-5]

PACS numbers: 43.71.Bp, 43.71.Es, 43.71.Ky, 43.71.Lz [WS]

INTRODUCTION

A principal challenge confronting listeners when they attempt to understand spoken language is that the relationship between speech waveforms and linguistic perceptions is not invariant. Changes in phonetic context (Liberman *et al.*, 1967), talker characteristics (Peterson and Barney, 1952), speaking rate (Miller and Liberman, 1979), as well as other factors, can all affect the acoustic realization of speech sounds. Consequently, a many-to-one mapping exists between acoustic signals and phonetic representations such that speech sounds with distinct physical properties can give rise to the same linguistic perception. Theories of speech perception have traditionally accounted for listeners' ability to maintain perceptual constancy, despite the extensive acoustic–phonetic variability present in spoken language, by positing a stage of perceptual normalization or compensation during which listeners derive standardized phonetic representations that can then be matched to canonical forms stored in long-term memory (Joos, 1948; Nearey, 1989; Johnson, 1990).

Perceptual normalization provides a highly effective mechanism for accommodating the variability present in speech signals. However, it does so at the cost of a significant amount of cognitive processing needed to continuously convert incoming speech waveforms into standardized phonetic representations. Consistent with this proposal, a number of recent investigations have reported that increased demands on the perceptual normalization system can significantly impair the speed and accuracy of identifying words and sentences (Mullennix *et al.*, 1989; Karl and Pisoni, 1994; Sommers *et al.*, 1994). Sommers *et al.* (1994) for example, demonstrated that lists of words spoken by multiple talkers or at different speaking rates were identified less accurately than the identical items produced by single talkers or at one articulation rate. To account for these findings, Sommers *et al.* (1994) suggested that compensating for the increased acoustic-phonetic variability in multiple-talker and multiple-rate lists required listeners to divert limited processing resources to mechanisms mediating perceptual normalization, leaving fewer available for identification.

An essential control condition included in the Sommers *et al.* (1994) investigation was to demonstrate that perceptual identification scores were not affected by variations in overall amplitude; items were recognized equally well whether they were produced in lists with constant or varying overall presentation levels. Thus it was not the case that *any* source of variability reduced spoken word recognition. Instead, Sommers *et al.* (1994) suggested that the effects of increased acoustic-phonetic variability will be observed only for factors that alter properties of the speech signal important for identification. Changing talker characteristics or speaking rate can affect spectral and temporal parameters, such as formant center frequencies and voice-onset-times (VOT's), that are known to influence phonetic perception. Therefore, perceptual compensation for such variations is mandatory to maintain accurate spoken word recognition (Miller, 1987). In contrast, overall amplitude changes do not affect stimulus features that have direct effects on spoken word recognition [however, see Dorman and Dougherty (1981) for a possible exception]. Consequently, few, if any, resources should be devoted to processing this dimension of the signal. Subjects in the Sommers *et al.* (1994) study therefore behaved as efficient processors of speech; they normalized for phoneti-

a)Electronic mail: MSommers@Artsci.wustl.edu

 0001-4966/97/101(4)/2278/11/$10.00

TABLE I. Subject characteristics for normal-hearing young (NHY), normal-hearing elderly (NHE) and hearing-impaired elderly (HIE) participants in experiment 1.

	Mean age (s.d.)	Range	Males	Females	Education (yrs.)
NHY	20.4 (2.1)	18–24	22	27	13.8
NHE	69.3 (6.8)	65–74	8	11	14.2
HIE	71.6 (8.2)	67–79	11	10	15.3

cally relevant sources of variability while simultaneously ignoring phonetically irrelevant ones.[1]

Although the findings from previous investigations provide compelling evidence that perceptual normalization can significantly affect spoken word recognition, the studies have been conducted primarily with normal-hearing young listeners [but see Kirk *et al.* (1995) for data from pediatric cochlear implant patients]. The purpose of the present series of experiments was to extend these earlier results by establishing how stimulus variability affects spoken word recognition in normal-hearing and hearing-impaired elderly listeners. Contrasting the ability of older and younger normal-hearing adults to compensate for acoustic–phonetic variability provides an indication of how age, independent of hearing loss, affects listeners' capacity to maintain perceptual constancy. Similarly, comparing normal-hearing and hearing-impaired older listeners can serve to specify how age-related hearing impairment affects perceptual normalization in older adults.

Consider first, how the effects of stimulus variability might differ as a function of age. Several studies (Kausler and Puckett, 1981; Jerger *et al.*, 1993; Naveh-Benjamin and Craik, 1995) have reported age-related differences in the encoding and retention of voice information. Jerger *et al.* (1993), for example, found that older listeners were less affected than young subjects by irrelevant talker variations in a speeded classification task (Garner, 1974). Jerger *et al.* (1993) suggested that one explanation for the reduced talker interference in older adults may be that they do not encode voice information as well as young adults. If contextual details, such as voice characteristics, are not as well represented or retained by older listeners, then they may be *less* affected by acoustic–phonetic variability than young subjects. Thus, in the present study, normal-hearing older adults might be expected to show less of a difference between single- and multiple-talker contexts than young subjects.

In contrast to this hypothesis, diminished-resource accounts of cognitive aging argue that age differences will be exaggerated on tasks that have greater cognitive demands. The results of several investigations indicate that identification of multiple-talker and multiple-rate word lists requires more processing resources than the corresponding single-dimension conditions (Martin *et al.*, 1989; Mullennix and Pisoni, 1990; Sommers *et al.*, 1994; Nygaard *et al.*, 1995). Thus, according to resource-based proposals, older adults would be expected to show *greater* effects of stimulus variability than young listeners. One purpose of the present study was to distinguish between the predictions made by diminished-resource theories (greater effects of stimulus variability) and those suggested by voice encoding deficits (decreased effects of stimulus variability).

In addition to examining possible age differences in the ability to compensate for phonetically relevant acoustic variations (e.g., those due to changing speaking rate or talker characteristics), the current experiments were also designed to investigate how trial-to-trial changes in phonetically irrelevant properties, such as overall amplitude variations, affect normal-hearing and hearing-impaired older listeners. Several recent studies (Hasher *et al.*, 1991; Balota *et al.*, 1992; Eberhard, 1994) have reported that older adults are less able than young subjects to inhibit or ignore irrelevant stimulus information. On the basis of these findings, we predicted that, in contrast to young adults (Sommers *et al.*, 1994), older listeners would exhibit reduced identification performance for multiple- compared with single-amplitude word lists.

Lastly, the investigations were designed to determine how age-related hearing impairment might modulate the effects of both phonetically relevant and irrelevant stimulus variability. Mullennix *et al.* (1989) reported a significant interaction between the effects of talker variability and signal-to-noise (S/N) ratio, such that differences between single- and multiple-talker lists were greater for lower S/N ratio values. Extending this finding to the current study, hearing-impaired older adults were expected to exhibit greater effects of stimulus variability than normal-hearing elderly listeners.

I. EXPERIMENT 1: TALKER VARIABILITY

A. Methods

1. Subjects

Thirty-nine normal-hearing young (NHY) adults were recruited from the Washington University student population and surrounding community through posted advertisements. Two groups of community-dwelling older adults, normal-hearing (19 subjects) and hearing-impaired (21 subjects), were recruited from the volunteer pool maintained by the Aging and Development Program at Washington University. All of the normal-hearing listeners (both young and old) had absolute thresholds less than 20 dB HL for octave frequencies from 250 to 4000 Hz. The 21 hearing-impaired elderly (HIE) participants all had thresholds exceeding 25 dB HL for at least two of the test frequencies. Table I lists age, gender, and education information for all participants. Table II displays the average thresholds and standard deviations for listeners in the three groups (NHY, NHE, and HIE). The number of HIE listeners with losses exceeding 25 dB HL is listed in brackets for each frequency. Note that all of the HIE listeners had losses exceeding 25 dB HL for 2000 and 4000 Hz and that a majority had thresholds above this criterion for 1000 Hz. Thus, on both an individual and group basis, these subjects demonstrated hearing losses that are typical of older

TABLE II. Thresholds (HL) (*re*: ANSI, 1989) and standard deviations (shown in parentheses) of NHY, NHE, and HIE listeners for octave frequencies from 250 to 4000 Hz. The bold numbers in brackets for the HIE group indicate the number of listeners (out of 21) whose thresholds exceeded 25 dB HL. Group names are the same as those in Table I.

	Frequency (Hz)				
	250	500	1000	2000	4000
NHY	7.5 (7.2)	11 (9.8)	12.8 (8.5)	14.4 (9.7)	13.3 (13.1)
NHE	15.3 (11.4)	10.1 (8.7)	16.3 (12.1)	15.9 (13.4)	18.6 (17.2)
HIE	14.2 (12.4)	11.4 (13.8)	26.3 (19.4)	35.4 (15.7)	40.1 (20.0)
	[**5**]	[**4**]	[**14**]	[**21**]	[**21**]

adults (CHABA, 1988). All subjects had normal middle-ear function (normal typanograms and presence of acoustic reflex for contralateral stimulation with a 1000-Hz pure tone at 100 dB HL) and were native speakers of English.

2. Stimulus materials

The stimuli for experiment 1 consisted of 150 highly familiar monosyllabic words. All items had a familiarity rating (Nusbaum *et al.*, 1984) of 6.2 or higher on a 7-point scale. The mean familiarity rating for all 150 items was 6.8.[2] Ten young talkers (five male and five female) between the ages of 18 and 24 produced all 150 items embedded in the carrier phrase ''please say the word _____ for me,'' where the blank corresponded to a particular monosyllabic target word. Eight of the talkers had a Midwest dialect (they had resided in the St. Louis area for their entire lives) and two spoke with an east-coast dialect (both were from the New York City area). Talkers were seated in a double-walled sound-attenuating booth (IAC model 1204A) and were asked to read the entire phrase from sheets placed in front of them at three different speaking rates (fast, medium, and slow). Prior to recording, the talkers were told that they would be asked to produce the items at three different speaking rates. However, other than indicating that the different speaking rates should be distinct, no additional instructions regarding articulation rate were given. The talkers were asked to vary their speaking rate as they would in normal conversations (no instructions to speak clearly or with added emphasis were given). All 150 productions at a given rate were recorded in a single block. The order in which talkers recorded the different rates and word order within each rate was determined randomly.

The productions were transduced using a microphone (Shure model BG 4.0), low-pass filtered at 8.5 kHz, and digitized on-line using a 16-bit A/D converter and a 20-kHz sampling rate. Target words were edited from the carrier phrase using a commercial waveform editor (Computerized Speech Research Environment, 4.2) and the rms amplitude level of all words was digitally equated. Average durations for the isolated words were 753 ms (range 625–942 ms), 420 ms (range 367–590 ms), and 303 ms (range 265–381 ms) for the slow, medium, and fast items, respectively. All productions were checked independently for misarticulations or mispronunciations by three listeners with phonetic training. Items identified as containing a production error by any of the judges were rerecorded. Approximately seven to ten words from each talker needed to be rerecorded.

3. Procedure

a. General identification paradigm. Experiment 1 measured identification performance for single- and multiple-talker word lists. Only the medium rate items were used in this study. Subjects were tested individually in the same double-walled sound attenuating booth used for stimulus recording. At the beginning of each trial, listeners heard a 500-Hz warning tone followed 500 ms later by presentation of a stimulus item. The digital files were converted to analog signals using a 16-bit D/A converter and a 20-kHz sampling rate. The stimuli were then low-pass filtered at 8.5 kHz and presented monaurally to the better ear of each subject over headphones (Sennheiser, HD 250) at approximately 80 dB sound-pressure level (SPL). Presentation levels refer to the sound-pressure level measured at the output of the transducer in a NBS-9A 6-cm^3 coupler with a Bruel & Kjaer sound-level meter (model 2204) set on the linear weighting scale. Listeners were asked to write down the word that they thought was presented on an answer form provided. Subjects were asked to make a response for each item. If they were unsure of the item presented, they were asked to make their best guess. When they were ready for the next item, subjects pressed a button on a keyboard and the warning tone was again presented after a 1-s interstimulus interval (ISI). Listeners received a five-item practice block at the beginning of the test session to familiarize them with the experimental procedures. If they had no questions about the procedures, the test items were presented in random order. Only exact phonetic matches to the stimulus item were counted as correct responses.

All of the items were presented in a background of white noise. The noise was generated using a noise generator (Grason Stadler, 901B) and was gated on and off coincident with stimulus presentation. The NHY, NHE, and HIE subjects were tested at signal-to-noise (S/N) ratios of +7, +10, and +12 dB, respectively. Background noise was used to avoid ceiling effects and pilot testing indicated that the specific S/N ratios selected produced approximately equal performance in the single-talker condition for the three subject groups.

b. Intelligibility measures. To determine whether productions by one or more of the talkers were significantly more difficult for any of our three subject groups to identify, twelve additional listeners from each group were recruited to obtain intelligibility measures for all ten talkers. For the normal-hearing groups (both young and elderly) these 12 new listeners had hearing thresholds less than 20 dB HL for octave frequencies from 250 to 4000 Hz. The 12 additional

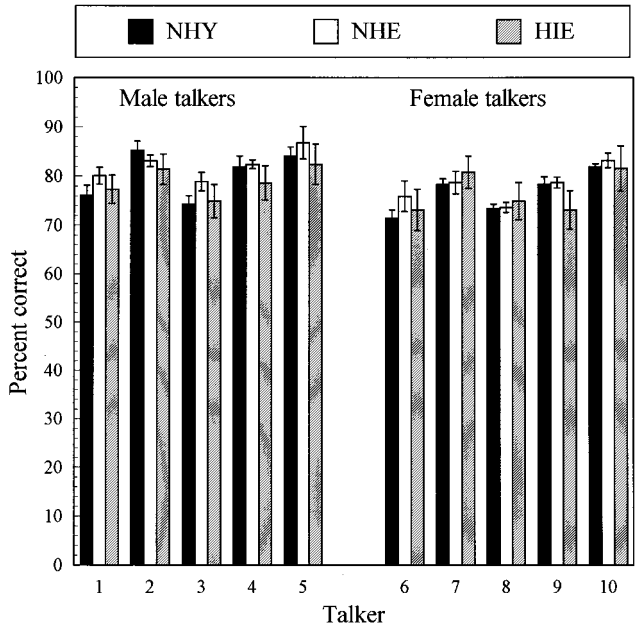

FIG. 1. Intelligibility scores for normal-hearing young (NHY), normal-hearing elderly (NHE) and hearing-impaired elderly (HIE) listeners for the individual talkers used in experiment 1. In this and all subsequent figures, error bars show standard deviations of the means.

hearing-impaired elderly listeners who participated in the intelligibility measures all had thresholds within 7 dB of the average for the HIE group used in the variability study at each of the frequencies tested. None of the listeners who participated in the intelligibility testing served as subjects in the variability studies.

The 12 subjects in each group participated in a total of three testing sessions. Signal-to-noise ratios for the intelligibility testing were the same as those used for the main experiment (+7, +10, and +12, for NHY, NHE, and HIE, listeners, respectively). During sessions 1 and 2 listeners heard all 150 medium-rate words produced by three of the ten talkers (450 stimuli during each session). In the final session, participants identified items from the remaining four talkers (600 items). Words from an individual talker were presented in a single block and block order was selected pseudorandomly for each listener. Although an independent measures design would have been preferable to avoid repeating items to a listener, it was not possible to obtain sufficient numbers of normal-hearing older listeners to have talker serve as a between-subjects factor. The principal goal of these measures, however, was to determine whether the intelligibility of productions by one or more of the ten talkers differed across the three subject groups. Using a different order of talkers for each subject should therefore have reduced the likelihood that systematic differences in intelligibility would be masked by repeated presentations of an item.

Figure 1 shows average intelligibility scores for each talker across the three groups. Of particular importance for the present experiment is that planned comparisons of recognition scores revealed no significant differences within a talker for the three subject groups. These findings suggest that any differences obtained between the groups are unlikely due to differential intelligibility of one or more of the talkers across the three groups of listeners.

c. Single versus multiple talkers. A two (single versus multiple talker)×three (subject group: NHY, NHE, HIE) mixed design was used to assess the effects of age and age-related hearing loss on identification scores for single- and multiple-talker word lists. Talker variability was manipulated as a within-subjects factor while subject group served as a between-subjects factor. The specific words selected for the single- and multiple-talker conditions were chosen pseudorandomly without replacement for each participant so that items were never repeated to a listener and the probability of a given item appearing in the single- or multiple-talker context was approximately equal. In the single-talker condition, listeners heard 75 words presented by the same talker. Each of the ten talkers served as the single talker for approximately the same number of listeners in each group.[3] In the multiple-talker condition, listeners heard a total of 75 words produced by all ten talkers. The specific talker presented on a given trial was selected randomly (with the exception that the same talker could not be presented on more than three consecutive trials). Five of the talkers contributed eight words each to the mixed-talker condition and five contributed seven items. The specific words selected from a given talker were chosen pseudorandomly for each subject. Approximately half of the participants in each group heard the single-talker condition first while the remainder heard the multiple-talker list first.

B. Results

Identification scores for all three groups are shown in Fig. 2. A three-way analysis of variance (ANOVA) with order (single-talker first versus multiple-talker first) and subject group (NHY, NHE, and HIE) as between-subjects variables and stimulus variability (single versus mixed talker) as a within-subjects variable was conducted on the data. In this and all subsequent analyses, no significant effects of order were observed ($p>0.5$ for all three experiments). Therefore, the data in all three studies have been collapsed across order. Significant main effects of subject group [$F(2,76)=15.4$, $p<0.001$] and variability [$F(1,76)=8.3$, $p<0.001$] were observed. However, Tukey HSD *post hoc* analyses indicated that performance in the single-talker condition did not differ significantly across the three subject groups [$p>0.2$ for NHY vs NHE; NHE vs HIE; and NHY vs HIE]. Thus the use of different S/N ratios was successful in generating approximately equivalent performance levels for the single-talker condition across the three subject groups.

A significant subject group×variability interaction was also observed [$F(2,76)=11.4$, $p<0.001$]. To further examine the source of this interaction and to investigate the effects of age *per se* (i.e., independent of hearing loss) on identification of words produced in single- and multiple-talker contexts, a separate two-way ANOVA with age as a between-subjects variable and stimulus variability as a within-subjects variable was performed on the data obtained from the normal-hearing listeners (i.e., for the NHY and NHE groups). As expected, a significant main effect of stimulus variability was observed [$F(1,56)=389.9$, $p<0.001$]; identification scores were sig-

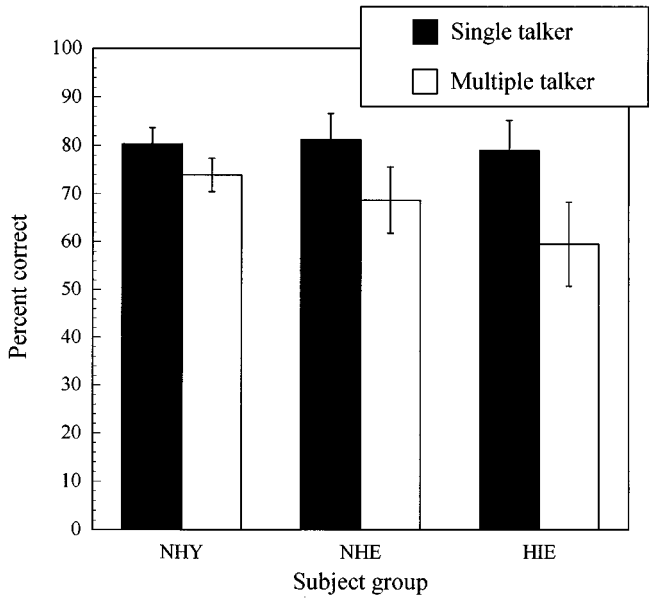

FIG. 2. Identification scores for NHY, NHE, and HIE listeners in single- (solid bars) and mixed-talker (open bars) contexts. The NHY, NHE, and HIE listeners were tested at signal-to-noise ratios of +7, +10, and +12, respectively.

nificantly reduced in the multiple- compared with the single-talker condition. Most important for purposes of the present study, however, was that a significant age×stimulus variability interaction was also obtained [$F(1,56)=49.5$, $p<0.001$]; although the NHY and NHE groups performed similarly in the single-talker condition, the elderly participants exhibited significantly poorer performance than the young adults when lists contained trial-to-trial talker variations ($p<0.01$).

To examine the effects of age-related hearing impairment on recognition scores for multiple-talker word lists, a two-way ANOVA was performed on the data from the older adults. Hearing impairment (normal-hearing versus hearing-impaired) was treated as a between-subjects variable and stimulus variability (single versus multiple talkers) as a within-subjects variable. Significant main effects of hearing impairment [$F(1,36)=8.8$, $p<0.05$] and stimulus variability [$F(1,36)=539.2$, $p<0.001$] were observed. In addition, the hearing impairment×stimulus variability interaction was also significant [$F(1,36)=17.1$, $p<0.001$]; performance in the multiple-talker context was significantly worse for the hearing-impaired, compared with the normal-hearing older adults. As noted, however, scores in the single-talker condition for these two groups did not differ. These findings suggest that hearing-impaired elderly participants were affected to a greater extent than their normal-hearing counterparts by trial-to-trial variations in talkers.

II. EXPERIMENT 2: SPEAKING RATE VARIABILITY

One question raised by the findings from experiment 1 is whether a similar pattern of results would be observed for other sources of variability known to alter phonetically relevant features of speech signals. Experiment 2 was therefore designed to examine the effects of age and age-related hearing impairment on the ability to accommodate trial-to-trial variations in speaking rate. Results comparable to those of experiment 1 would be consistent with the hypothesis that age and age-related sensory impairments both reduce perceptual normalization capacities. Differential findings between experiments 1 and 2, in contrast, would argue against any generalized age- or hearing-related declines in the ability to maintain perceptual constancy. Instead, such differences would support the proposal that distinct mechanisms are engaged to accommodate the different types of variability present in speech signals and that these mechanisms can differ in their vulnerability to age- and age-related hearing declines.

A. Procedure

1. Subjects

Normal-hearing young, normal-hearing elderly, and hearing-impaired elderly listeners were recruited from the same subject populations used in experiment 1. None of the participants in experiment 2 served as subjects in the first study. A total of 30 young and 26 elderly listeners were tested. The older adults consisted of 12 normal-hearing subjects (thresholds less than 20 dB HL for octave frequencies from 250 to 4000 Hz) and 14 hearing-impaired listeners. Means and standard deviations (shown in parentheses) of hearing loss for the HIE group were 19.1(12.1), 16.2(10.4), 38.3(13.9), 46.9(18.7), and 47.8(22.1) dB HL for octave frequencies from 250 to 4000 Hz. All of the hearing-impaired older listeners had losses exceeding 25 dB HL for frequencies of 1000, 2000, and 4000 Hz. Four had thresholds exceeding 25 dB HL at 250 Hz and five had greater than a 25-dB loss at 500 Hz. Overall, hearing loss for this group was somewhat greater than for the participants tested in the first study. Thresholds for the NHY and NHE groups were comparable to those of experiment 1. Age and education for the younger and older participants were also similar to those of the first study. All subjects had normal middle-ear function and were native speakers of English.

2. Stimulus materials

The stimuli for experiment 2 were the same 150 monosyllabic words used in experiment 1. However, in the present investigation, 50 words from each of the three speaking rates were selected pseudorandomly for presentation to the listeners. Twenty-five items from each speaking rate were selected for the three single-rate conditions (fast only, medium only, and slow only) and 25 at each rate were selected for the mixed-rate context. Approximately half of the subjects in each group heard items produced by a male talker and the remainder heard stimuli produced by a female talker. Average durations for words produced by the male talker were 780 ms (range 675–815 ms), 460 ms (range 427–501 ms), and 323 ms (range 285–351 ms) for the slow, medium, and fast items, respectively. The corresponding values for the female talker were 723 ms (range 655–770 ms), 420 ms (range 393–475 ms), and 289 ms (range 265–323 ms).

3. Rate judgments

To ensure that listeners perceived three distinct speaking rates for both the male and female talker, a procedure first

used by Sommers *et al.* (1994) was adopted to examine perceived speaking rate for all of the items used in experiment 2. A total of 12 additional subjects (6 young and 6 old) were recruited to judge the speaking rate of the 450 items (150 words×3 speaking rates) produced by one of the two talkers (three subjects from each age group heard the male talker and three heard the female talker). Three of the older adults were normal hearing and three had losses exceeding 25 dB HL at both 2000 and 4000 Hz. None of the listeners in this pilot study was used in the main part of experiment 2. Participants heard stimuli produced at approximately 80 dB SPL and were asked to judge whether the items were spoken at a fast, medium, or slow speaking rate. Correct rate categorizations (i.e., judgments matching the speaking rate designated during stimulus recording) did not differ significantly for the male and female talker. Average correct judgments combined across the two speakers were 92%, 78%, and 84% for the slow-, medium-, and fast-rate words, respectively. No significant age differences were observed in percentage of correct rate judgments. Considering that the listeners had no prior experience with the talkers' voices and heard only isolated words, these relatively high accuracy levels indicated that the three speaking rates used in the present study were quite distinct. Moreover, the absence of significant age differences in the accuracy of rate judgments indicated that the speaking rates were equally distinct for young and old listeners.

4. Procedure

The identification procedure, testing equipment, and presentation level were the same as those used in experiment 1. Speaking rate (fast, medium, slow) and stimulus variability (single versus multiple speaking rates) were manipulated as within-subjects variables while subject group (NHY, NHE, HIE) and speaker (male versus female talker) served as between-subjects factors. A total of four conditions were tested with each subject: (1) single rate, slow (2) single rate, medium (3) single rate, fast; and (4) mixed rate. Each of the first three conditions contained 25 stimuli and speaking rate remained constant for all items within the block. The final condition contained a total of 75 items (25 at each rate) and speaking rate was allowed to vary from trial to trial. The particular words assigned to a given speaking rate, order of presentation within a condition, and the order of conditions were selected randomly for each subject.

As in the first experiment, a primary concern was to reduce the possibility that any observed effects of age or hearing impairment were due to differences in overall task difficulty for the three groups. Therefore, several pilot experiments were conducted to determine signal-to-noise ratios that would yield approximately equal identification performance in the single-rate conditions for all three speaking rates. None of the subjects used in the pilot studies participated in the main experiment. Young subjects were always tested at a +5 S/N ratio. The older normal-hearing group was tested at an S/N ratio of +8 for the slow- and medium-rate items and at a +10 S/N ratio for the fast-rate words. The corresponding signal-to-noise ratios for the hearing-impaired older listeners were +12, +12, and +16 for the slow, medium, and fast rate items, respectively. These S/N ratios were used in both the single- and mixed-rate contexts. Thus, for example, when an individual from the NHE group heard a fast-rate item, it was always presented at a +10 S/N ratio.

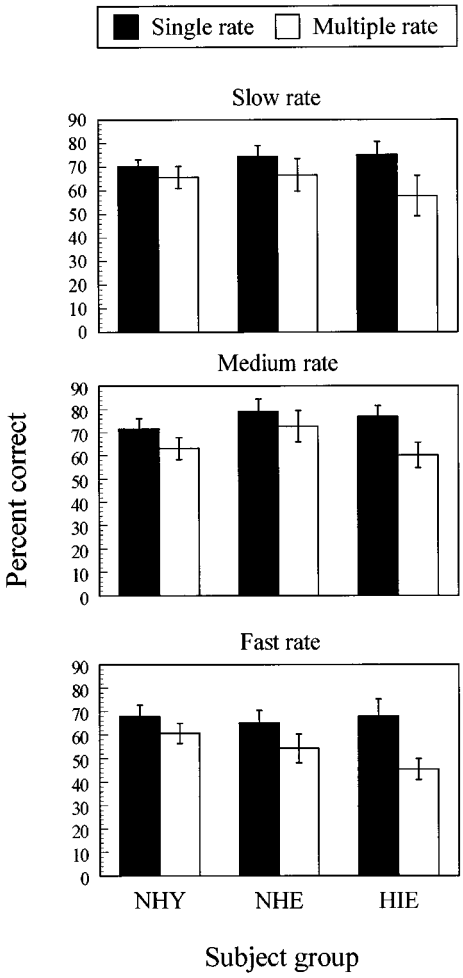

FIG. 3. Identification scores for NHY, NHE, and HIE listeners in single- and mixed-rate contexts. The top panel displays scores for slow-rate words presented in single- and mixed-rate contexts. The middle and bottom panels display the corresponding medium- and fast-rate scores. See text for signal-to-noise ratios.

B. Results

Figure 3 displays identification scores for the three subject groups at each speaking rate. A four-way ANOVA with talker (male versus female) and subject group (NHY, NHE, and HIE) as between-subjects factors and speaking rate (fast, medium, or slow) and stimulus variability (single versus multiple rates) as within-subjects factors, revealed no significant main effects or interactions with the talker variable. Therefore, in the remaining analyses the data have been combined for the male and female talker. The ANOVA revealed a significant main effect of rate [$F(2,106)=62.7$, $p<0.001$] as well as reliable rate×subject group [$F(2,53)=22.6$, $p<0.001$] and rate×variability [$F(4,106)=6.0$, $p<0.001$] interactions. The data in Fig. 3 are therefore presented sepa-

rately for each of the three speaking rates. The top panel, for example, compares identification performance for the 25 words presented in the slow-rate list with the 25 slow-rate words presented in the mixed-rate context. Tukey HSD post hoc analyses revealed that, within a given speaking rate, the only statistically reliable difference between groups in the single-rate conditions was that the NHE group had identification scores that were significantly better ($p<0.05$) than the NHY group for the medium rate words. Thus, in general, the use of different S/N ratios was successful in obtaining approximately equal single-rate performance within each speaking rate. The only other statistically reliable finding obtained in the overall ANOVA was a main effect of variability [$F(1,53)=59.8$, $p<0.001$] indicating that performance in the mixed-rate conditions was poorer than in the single-rate contexts.

To examine the effects of age, independent of hearing loss, on identification scores for single- and mixed-rate word lists, a three-way ANOVA with rate and variability as within-subjects variables and age as a between-subjects factor was conducted on the data from the NHY and NHE subject groups. A significant main effect of variability [$F(1,40)=61.3$, $p<0.001$)] was observed; identification performance was poorer for the mixed-, compared with the single-rate conditions. A significant main effect of speaking rate [$F(2,80)=54.6$, $p<0.001$] was also obtained. Tukey HSD post hoc analyses revealed that spoken word recognition was poorer for the fast speaking rate compared with either the slow or medium rate items. These last two conditions did not differ significantly. The only other significant effect was a reliable age×speaking rate interaction [$F(2,80)=12.2$, $p<0.01$]; as had been reported previously (Schmitt and Carroll, 1985; Schmitt and Moore, 1989; Tun *et al.*, 1992), older adults were affected to a greater extent by fast speaking rates. Most importantly for purposes of the present study, however, no significant age×variability interaction was observed [$F(1,40)=0.37$, $p>0.5$]. Thus age *per se* did not produce greater decrements in the ability to accommodate trial-to-trial variations in speaking rate.

To examine the effects of age-related hearing impairment on recognition performance for single- and mixed-speaking rates, a separate. ANOVA was conducted on the data from the older adults, with speaking rate and stimulus variability as within-subjects factors and hearing impairment as a between-subjects variable. Significant main effects of variability [$F(1,24)=62.8$, $p<0.001$] and speaking rate [$F(2,48)=30.6$, $p<0.001$] were obtained, spoken word recognition decreased as a function of both greater stimulus variability and faster speaking rates. However, a significant hearing-impairment×stimulus variability interaction was also observed [$F(1,24)=9.4$, $p<0.01$]; hearing-impaired older listeners exhibited significantly greater reductions in identification performance as a result of changing from single- to multiple-speaking rates than did normal-hearing elderly adults. None of the remaining effects reached statistical significance.

Experiments 1 and 2 demonstrated that both age and age-related hearing impairment can affect listeners' ability to compensate for acoustic-phonetic variations in phonetically relevant stimulus parameters. Recall, however, that Sommers *et al.* (1994) failed to find changes in spoken word recognition for young adults following the introduction of variations in another dimension, overall amplitude, that does not affect properties of the speech signal important for phonetic discrimination. Experiment 3 was designed to examine whether normal-hearing and hearing-impaired older adults would also demonstrate comparable identification performance for single- and multiple-amplitude word lists.

III. EXPERIMENT 3: AMPLITUDE VARIABILITY

A. Methods

1. Subjects

Twenty young adults and 27 older listeners were recruited from the same subject populations used in the first two studies. None of the subjects had participated in experiments 1 or 2 or in any of the pilot investigations. All of the young listeners and 13 of the older individuals were considered normal hearing, with thresholds less than 20 dB HL for octave frequencies from 250 to 4000 Hz. Average thresholds for the 14 hearing-impaired older listeners (with standard deviations shown in parentheses) were 27.3(18.1), 16.8(16.7), 18.2(8.4), 39.4(15.7), and 43.9(21.2) dB HL, respectively, for the five frequencies tested. All subjects in this group exhibited hearing losses greater than 25 dB HL for frequencies of 2000 and 4000 Hz. Eight of the 14 listeners had greater than a 25 dB loss at 250 Hz and 6 had losses exceeding 25 dB HL at 500 and 1000 Hz. Therefore, except for a somewhat greater low-frequency hearing loss, these individuals had absolute thresholds similar to the HIE groups of experiments 1 and 2. Means and standard deviations of age and education for the three groups tested in experiment 3 were also similar to those of the first two studies. All subjects had normal middle-ear function and were native speakers of English.

2. Stimulus materials

The stimuli for experiment 3 were generated by digitally manipulating the rms amplitude levels of the 150 medium-rate monosyllabic items used in experiments 1 and 2. The 150 words from each talker were digitized at three overall amplitudes and individual items were presented to listeners at approximately 65, 75, or 85 dB SPL. Stimuli from two talkers [one male (talker 3) and one female (talker 6)] were used in the experiment.

3. Loudness ratings

To determine if the amplitude manipulation produced three distinct loudness levels, an additional 10 young and 20 elderly listeners were recruited to categorize amplitude for the 450 items (150 words×3 levels) that were generated for one of the two talkers. All of the young and eight of the elderly listeners were normal hearing (thresholds less than 20 dB HL for octave frequencies from 250 to 4000 Hz). The remaining 12 elderly listeners all had thresholds that were within 7 dB of the average for the HIE group at the five frequencies tested. Mean percentage correct loudness categorizations (as specified by loudness ratings corresponding to

the rms amplitude level of the item) ranged between 77% and 91%. An ANOVA conducted on the loudness judgments failed to reveal a significant main effect or interaction with subject group. Thus the loudness recruitment that has been demonstrated in some older adults (Jerger, 1960) did not affect the elderly listeners' ability to perceive three distinct presentation levels.

4. Procedure

The same general identification paradigm used in experiments 1 and 2 was also used in the present study. A total of four experimental conditions were tested: (1) single amplitude, low (65 dB SPL); (2) single amplitude, medium (75 dB SPL); (3) single amplitude, high (85 dB SPL); and (4) mixed amplitude. Each of the first three conditions contained a total of 25 items. The mixed amplitude condition had a total of 75 items with 25 words presented at each of the three overall levels. The particular words presented in each of the four conditions as well as the order in which the conditions were presented were selected pseudorandomly for each subject.

Several pilot studies were conducted to determine signal-to-noise ratios that would yield approximately equivalent performance levels in the single-amplitude conditions across the three subject groups. On the basis of these pilot experiments, the following S/N ratios were used. All of the young normal-hearing listeners were tested at a +5 S/N ratio. All of the normal-hearing elderly participants were tested at a +8 S/N ratio. The hearing-impaired elderly were tested at S/N ratios of 14, 12, and 11 for the low-, medium-, and high-amplitude stimuli, respectively.

B. Results

Figure 4 displays results for all conditions tested in experiment 3. A four-way ANOVA with talker (male versus female) and subject group (NHY, NHE, HIE) as between-subjects factors and variability (single versus mixed amplitude) and amplitude (low, medium, or high) as within-subjects factors revealed no significant main effect or interactions with talker. Therefore, the data in Fig. 4 have been combined for the male and female talker. Significant main effects were observed for subject group [$F(2,44)=13.2$, $p<0.001$], variability [$F(1,44)=19.6$, $p<0.001$], and overall amplitude [$F(2,88)=11.6$, $p<0.001$]. In addition, significant subject group×variability [$F(2,44)=5.7$, $p<0.001$] and subject group × overall amplitude [$F(4,88)=4.0$, $p<0.001$] interactions were also observed. None of the remaining two- or three-way interactions reached statistical significance. Tukey HSD post hoc analysis revealed that, within each amplitude level, identification scores for the single-amplitude conditions were not significantly different across the three subject groups except for the difference between the NHY and HIE groups at high amplitudes which was marginally significant ($p<0.09$).

To further examine the interaction of age and overall amplitude variability, a separate ANOVA was conducted on the data only from the normal-hearing listeners (NHY and NHE groups). Main effects of age [$F(1,31)=7.6$, $p<0.01$], stimulus variability [$F(1,31)=4.5$, $p<0.05$] and overall amplitude [$F(2,62)=11.0$, $p<0.001$] were observed. Most important for purposes of the present study, however, was a significant age×variability interaction [$F(1,31)=8.9$, $p<0.005$]; older normal-hearing listeners exhibited significantly greater effects of amplitude variability than did the normal-hearing young adults. Tukey HSD post hoc analyses revealed that, for young listeners, differences between single- and multiple-amplitude conditions were not significant at any of the three overall levels tested ($p>0.7$ for all comparisons). In contrast, amplitude variability significantly reduced identification scores for older listeners at all three levels ($p<0.05$ for all comparisons). The only other effect that approached significance was the age×amplitude interaction [$F(2,62)=2.7$, $p<0.1$] indicating a trend for older listeners to be more affected than younger listeners by presentation level.

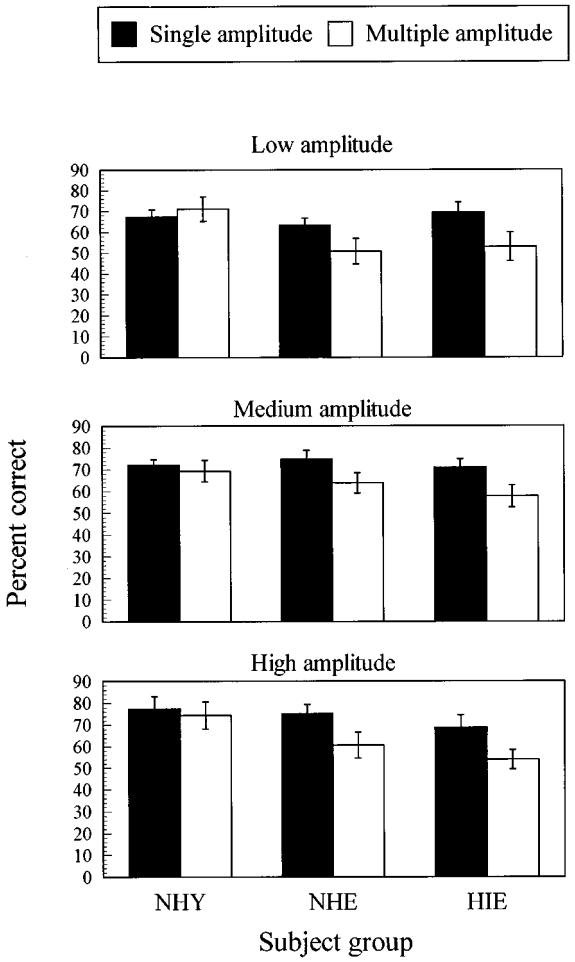

FIG. 4. Identification scores for NHY, NHE, and HIE listeners in single- and mixed-amplitude conditions. The top panel shows scores for words presented at a low (65 dB SPL) level in single and mixed amplitude conditions. The corresponding medium (75 dB SPL) and high (85 dB SPL) amplitude data are shown in the middle and bottom panels. See text for signal-to-noise ratios.

To examine the effects of age-related hearing impairment on identification scores for single- and mixed-amplitude word lists, a separate ANOVA was conducted on the data from older adults (NHE and HIE groups). Only the main effects of variability [$F(1,44)=23.2$, $p<0.001$] and overall amplitude [$F(2,88)=11.6$, $p<0.001$] reached statistical significance. The hearing impairment×stimulus variability interaction was not statistically significant ($p>0.4$) indi-

cating that hearing-impaired elderly listeners were not differentially affected by increased amplitude variability relative to their normal-hearing counterparts.

IV. GENERAL DISCUSSION

One of the principal objectives of the present experiments was to determine some of the factors that may affect spoken-word recognition in normal-hearing and hearing-impaired older listeners. The findings from experiment 1 demonstrated that both age and age-related hearing loss reduced the ability to compensate for acoustic–phonetic variations resulting from changes in talkers. In contrast, the results of experiment 2 indicated that the ability to accommodate variability from alterations in speaking rate does not decline with age but is affected by age-related hearing impairment. Finally, findings from the third study suggested that older adults are impaired by variations in a phonetically irrelevant stimulus dimension, overall amplitude, but that this impairment is not exaggerated by age-related hearing loss.

Before discussing possible explanations for the observed changes in the effects of stimulus variability, it is important to consider a number of limitations on the current study. First, although preliminary testing indicated that the talker, rate, and amplitude changes were all clearly perceptible to our listeners, differences in the saliency of each dimension, the range over which variations were introduced, and the number of stimulus properties affected all may have influenced how acoustic–phonetic variability affected the three subject groups. Future studies could therefore incorporate methodologies, such as multi-dimensional scaling, that are capable of assessing perceived similarity across a number of different stimulus dimensions (Goldinger, 1992; Lively, 1994). Second, the effects of hearing impairment were examined only in older adults. It remains unclear, therefore, whether the results would generalize to other types of hearing loss or to other populations of impaired listeners. Third, it is important to recognize that the present findings were obtained only for a restricted range of performance levels. Although this minimized differences in absolute recognition scores among the three groups, the magnitude of the effects may differ for other levels of performance. Mullennix *et al.* (1989), for example, reported that the effects of talker variability in young adults was inversely related to signal-to-noise ratio.

The findings from the present study must also be viewed with respect to other factors affecting speech perception in older adults. For example, several investigators have reported that, for items presented in background noise, differences in absolute sensitivity account for at least 50% of the variance in speech perception scores among older listeners (van Rooij and Plomp, 1992; Humes *et al.*, 1994). Although these findings suggest that changes in sensory abilities, not differences in perceptual normalization, are the principal reason that older adults have difficulty recognizing speech, the results of the present experiments expand on the previous investigations in several ways. First, the independent effects of age (i.e., differences between the NHY and NHE groups), on identification of word lists with multiple talkers and multiple amplitudes indicates that a reduced ability to accommodate at least two sources of stimulus variability may also contribute to age-related changes in spoken-word recognition. Second, the significant decrease in identification scores for the HIE group, relative to age-matched normal-hearing controls, in both the mixed-talker and mixed-rate conditions suggests that, in addition to its effects on audibility, age-related hearing loss may also impair other perceptual abilities that are necessary for accurate spoken-word recognition.

Theoretical accounts of speech perception should not only describe the perceptual abilities of the mature, optimally performing, listener but should also provide principled explanations of how and why these abilities are altered in different subject populations. In general, two theoretical frameworks have been used to account for age differences in perceptual and cognitive abilities such as spoken-word recognition (Salthouse, 1991). Information processing approaches have emphasized the importance of age-related declines (or lack thereof) in individual cognitive abilities. According to this proposal, the component operations required for speech perception may be differentially vulnerable to the effects of aging (Phillips and Bashore, 1995). In contrast, single-factor theories have attempted to isolate one factor (or a small subset of factors) responsible for age differences in cognitive processing. For example, general-slowing theories suggest that age-related declines in cognitive capacities occur primarily because older listeners take longer to complete each of the component cognitive operations necessary to perform a given task. Therefore, general slowing would predict that any source of variability requiring normalization would reduce performance in older listeners (although the absolute size of the effect may be domain specific).

The results of the current experiment are clearly more consistent with an information processing approach that emphasizes age changes in individual cognitive mechanisms. For instance, although changes in both talker characteristics and speaking rate alter phonetically relevant properties of speech signals, age-related reductions in identification performance were observed only for trial-to-trial variations in talkers. Nygaard *et al.* (1995) also found a divergent pattern of results for talker and rate variability in young adults using a serial recall paradigm. Taken together, the findings suggest that the mechanisms used to compensate for variations in talker differences and speaking rate are, at least in part, independent and that they exhibit differential susceptibility to the effects of aging.

Nygaard *et al.* (1995) suggested that the distinct effects of variability in speaking rate and talker characteristics are not unexpected given the nature of the two stimulus properties. Talker or voice characteristics are relatively permanent and are important for identifying age, race, and gender (Laver and Trudgill, 1979). Speaking rate, on the other hand, changes dramatically, even over short segments (Miller *et al.*, 1984), and therefore may be less permanent and informative than talker characteristics. Furthermore, talker normalization might include compensation for several kinds of acoustic variations, including dialect and vocal-tract differences, that result from changing speakers. It will be impor-

tant, therefore, for future investigations to determine whether these distinct types of talker effects also exhibit differences in their vulnerability to age-related declines.

In addition to age differences in the effects of talker variability, overall amplitude variations also reduced identification scores for NHE listeners. The pattern of age effects for variations in this dimension, however, was different from that observed with trial-to-trial changes in talkers. Young adults exhibited similar identification performance for single- and mixed-amplitude word lists while normal-hearing older listeners were significantly impaired when overall level variations were introduced. As noted, Sommers *et al.* (1994) suggested that the comparable performance of young adults in single- and multiple-amplitude conditions was due to their ability to either ignore overall level changes or to process them more automatically. A number of investigations examining age-related changes in selective attention and automatic processing have reported that older adults exhibit a reduced ability to ignore irrelevant stimulus attributes but that automatic processing capabilities remain relatively intact (Hasher and Zacks, 1984; Hasher *et al.*, 1991; Stern *et al.*, 1991; Balota *et al.*, 1992). Balota *et al.* (1992), for example, demonstrated that age-related reductions in the ability to inhibit irrelevant lexical information contributed to age differences in semantic priming. Stern *et al.* (1991), however, failed to find age differences in the processes mediating automatic lexical access. Considered together, the results of these investigations suggest that the effects of overall amplitude variations on older listeners are most likely due to age-related breakdowns in selective attention that reduce older adults' capacity to ignore variations in a phonetically irrelevant stimulus dimension.

The picture that begins to emerge when the results of the present investigations are considered with findings from other recent studies of auditory and cognitive factors affecting speech perception in older adults (Jerger *et al.*, 1989; Humes and Roberts, 1990; Humes, 1991; Tun *et al.*, 1991; Tun *et al.*, 1992; van Rooij and Plomp, 1992; Wingfield and Stine, 1992; Humes *et al.*, 1994; Sommers, 1996) is one in which sensory and cognitive factors have both independent and interactive effects on spoken word recognition in the elderly. One of the goals of future studies should be to elaborate on current findings by establishing how different age-related changes, both isolated and combined, contribute to the speech perception difficulties of older adults. This type of integrated approach, incorporating both cognitive and sensory factors is likely to be of greatest benefit to understanding the speech perception abilities of normal and impaired populations.

V. CONCLUSIONS

Three experiments were conducted to examine how age and age-related hearing impairment affect spoken-word recognition with several sources of stimulus variability. The results support the following conclusions.

(1) Age and age-related hearing loss both reduced listeners' ability to compensate for variations in the acoustic realization of speech sounds that result from changes in talker characteristics.

(2) Age-related hearing loss, but not age *per se*, impaired listeners' ability to accommodate acoustic–phonetic variations due to changes in speaking rate. This finding suggests that an interaction between peripheral auditory analysis and central cognitive functions is important for understanding spoken-word recognition in older adults.

(3) Age, but not age-related hearing loss, reduced listeners' capacity to selectively ignore or automatically process acoustic-phonetic variations due to overall level changes. Because altering overall amplitude does not affect properties of the speech signal that have direct effects on identification, the findings indicate that one factor contributing to poorer spoken-word recognition in older listener is that they may attend to phonetically irrelevant aspects of speech waveforms.

ACKNOWLEDGMENTS

This work was supported by the Brookdale Foundation. The author wishes to thank James Sawusch and an anonymous reviewer for their helpful comments.

APPENDIX: LIST OF MONOSYLLABIC WORDS USED IN EXPERIMENTS 1, 2, AND 3

bomb	gap	pace
bead	gave	pad
beak	gill	page
bean	give	pause
bike	goal	pawn
boat	goat	peace
boil	gone	pet
boon	gore	pull
boss	gut	pup
bout	hack	purse
bud	hag	rage
bug	hair	real
bull	heed	rhyme
bum	hick	ride
bush	hone	rim
cash	hoot	rob
chain	hum	rot
chase	jeer	route
chat	joke	rum
check	jot	rut
chore	juice	sauce
chute	kin	serve
coach	king	ship
cod	knob	shop
comb	lace	sill
con	lad	size
cot	last	soak
couch	laugh	soil
dame	league	suck
death	liar	tape
deck	live	thick
deep	long	thing
dice	loud	tire
din	love	toot
dirt	main	tot
dive	map	tough
does	mar	tub
doll	mat	vote
doom	merge	wade
down	mitt	was

dune	moan	wash
faith	mob	wean
fin	mole	wed
fish	mouse	week
five	move	wife
food	mutt	will
fool	neck	wipe
full	nerve	work
fuss	noise	wrong
gang	nurse	young

[1]Sommers *et al.* (1994) suggested that the absence of an effect of overall amplitude variations on perceptual identification does not necessarily indicate that listeners simply ignore absolute level differences. Instead, they proposed that overall amplitude changes may be accommodated more automatically, for example, by some type of automatic gain control, than variations in either talker characteristics or speaking rate.

[2]A list of stimulus items is provided in the Appendix.

[3]The number of listeners in the three groups was not evenly divisible by 10. Therefore, it was necessary to have slightly unequal numbers of subjects for some of the talkers.

ANSI (**1989**). ANSI S3.6, 1989, ''Specification for audiometers'' (American National Standards Institute, New York).

Balota, D. A., Black, S. R., and Cheney, M. (**1992**). ''Automatic and attentional priming in young and older adults: Reevaluation of the two-process model,'' J. Exp. Psychol. Hum. Percept. Perform. **18,** 485–502.

CHABA, Working Group on Speech Understanding and Aging. (**1988**). ''Speech understanding and aging,'' J. Acoust. Soc. Am. **83,** 859–895.

Dorman, M. F., and Dougherty, K. (**1981**). ''Shifts in phonetic identification with changes in signal presentation level,'' J. Acoust. Soc. Am. **69,** 1439–1440.

Eberhard, K. M. (**1994**). ''Phonological inhibition in auditory word recognition,'' in *Inhibitory Processes in Attention, Memory, and Language*, edited by D. Dagenbach and T. H. Carr (Academic, San Diego, CA).

Garner, W. (**1974**). *The Processing of Information and Structure* (Erlbaum, Hillsdale, NJ).

Goldinger, S. D. (**1992**). ''Words and voices: Implicit and explicit memory for spoken words,'' Res. Speech Percept. Tech. Rep. No. 7 (Indiana University, Bloomington, IN).

Hasher, L., Stoltzfus, E. R., Zacks, R. T., and Rypma, B. (**1991**). ''Age and inhibition,'' J. Exp. Psychol. Learn. Mem. Cog. **17**, 163–169.

Hasher, L., and Zacks, R. T. (**1984**). ''Automatic processing of fundamental information: The case of frequency of occurrence,'' Am. Psychol. **39**, 1372–1388.

Humes, L. E. (**1991**). ''Understanding the speech-understanding problems of the hearing impaired,'' J. Am. Acad. Aud. **2**, 59–69.

Humes, L. E., and Roberts, L. (**1990**). ''Speech-recognition difficulties of the hearing-impaired elderly: The contributions of audibility,'' J. Speech Hear. Res. **33**, 726–735.

Humes, L. E., Watson, B. U., Christopherson, L., Cokely, C. G., Halling, D. C., and Lee, L. (**1994**). ''Factors associated with individual differences in clinical measures of speech recognition among the elderly,'' J. Speech Hear. Res. **37**, 465–474.

Jerger, J. (**1960**). ''Bekesy audiometry in analysis of auditory disorders,'' J. Speech Hear. Res. **3**, 275–287.

Jerger, J., Jerger, S., Oliver, T., and Pirozzolo, F. (**1989**). ''Speech understanding in the elderly,'' Ear Hear. **10**, 79–89.

Jerger, S., Pirozzolo, F., Jerger, J., Elizondo, R., Desai, S., Wright, E., and Reynosa, R. (**1993**). ''Developmental trends in the interaction between auditory and linguistic processing,'' Percept. Psychophys. **54,** 310–320.

Johnson, K. (**1990**). ''The role of perceived speaker identity in *F*0 normalization of vowels,'' J. Acoust. Soc. Am. **88,** 642–654.

Joos, M. A. (**1948**). ''Acoustic phonetics,'' Language **24**, Suppl. 2, 1–136.

Karl, J., and Pisoni, D. B. (**1994**). ''The role of talker-specific information in memory for spoken sentences,'' Res. Speech Percept. Prog. Rep. No. 19 (Indiana University, Bloomington, IN), pp. 145–193.

Kausler, D. H., and Puckett, J. M. (**1981**). ''Adult age differences in memory for modality attributes,'' Exp. Aging Res. **7**, 117–125.

Kirk, K. I., Pisoni, D. B., and Osberger, M. J. (**1995**). ''Lexical effects on spoken word recognition by pediatric cochlear implant users,'' Ear Hear. **16**, 470–481.

Laver, J., and Trudgill, P. (**1979**). ''Phonetic and linguistic markers in speech,'' in *Social Markers in Speech*, edited by K. R. Scherer and H. Giles (Cambridge U. P., Cambridge, MA).

Liberman, A. M., Cooper, F. S., Shankweiler, D. P., and Studdert-Kennedy, M. (**1967**). ''Perception of the speech code,'' Psychol. Rev. **74,** 431–461.

Lively, S. E. (**1994**). ''Preserving the perceptual record: Retention of talker-specific information in long-term memory,'' Res. Speech Percept. Tech. Rep. No. 10 (Indiana University, Bloomington, IN).

Martin, C. S., Mullennix, J. W., Pisoni, D. B., and Summers, W. V. (**1989**). ''Effects of talker variability on recall of spoken word lists,'' J. Exp. Psych. Learn. Mem. Cog. **15**, 676–684.

Miller, J. L. (**1987**). ''Mandatory processing in speech perception: A case study,'' in *Modularity in Knowledge Representation and Natural Language Understanding*, edited by L. Garfield (MIT, Cambridge, MA).

Miller, J. L., and Liberman, A. M. (**1979**). ''Some effects of later-occurring information on the perception of stop consonant and semivowel,'' Percept. Psychophys. **25,** 457–465.

Miller, J. L., Grosjean, F., and Lomanto, C. (**1984**). ''Articulation rate and its variability in spontaneous speech: A reanalysis and some implications,'' Phonetica **41**, 215–225.

Mullennix, J. W., and Pisoni, D. B. (**1990**). ''Stimulus variability and processing dependencies in speech perception,'' Percept. Psychophys. **47,** 379–390.

Mullennix, J. W., Pisoni, D. B., and Martin, C. S. (**1989**). ''Some effects of talker variability on spoken word recognition,'' J. Acoust. Soc. Am. **85,** 365–378.

Naveh-Benjamin, M., and Craik, F. I. (**1995**). ''Memory for context and its use in item memory: Comparisons of younger and older persons,'' Psychol. Aging **10**, 284–293.

Nearey, T. M. (**1989**). ''Static, dynamic, and relational properties in vowel perception,'' J. Acoust. Soc. Am. **85,** 2088–2113.

Nusbaum, H. C., Pisoni, D. B., and Davis, C. K. (**1984**). ''Sizing up the Hoosier mental lexicon: Measuring the familiarity of 20,000 words,'' Res. Speech Percept. Prog. Rep. No. 10 (Indiana University, Bloomington, IN).

Nygaard, L. C., Sommers, M. S., and Pisoni, D. B. (**1995**). ''Effects of stimulus variability on perception and representation of spoken words in memory,'' Percept. Psychophys. **57,** 989–1001.

Peterson, G. E., and Barney, H. L. (**1952**). ''Control methods used in a study of the vowels,'' J. Acoust. Soc. Am. **24,** 175–184.

Phillips, A. A., and Bashore, T. R. (Eds.) (**1995**). *Age Differences in Word and Language Processing* (Amsterdam, Elsevier).

Salthouse, T. A. (**1991**). *Theoretical Perspectives on Cognitive Aging* (Erlbaum, Hillsdale, NJ).

Schmitt, J. F., and Carroll, M. R. (**1985**). ''Older listeners' ability to comprehend speaker-generated rate alteration of passages,'' J. Speech Hear. Res. **28**, 309–312.

Schmitt, J. F., and Moore, J. R. (**1989**). ''Natural alteration of speaking rate: the effect on passage comprehension by listeners over 75 years of age,'' J. Speech Hear. Res. **32**, 445–450.

Sommers, M. S., Nygaard, L. C., and Pisoni, D. B. (**1994**). ''Stimulus variability and spoken word recognition. I. Effects of variability in speaking rate and overall amplitude,'' J. Acoust. Soc. Am. **96,** 1314–1324.

Sommers, M. S. (**1996**). ''The structural organization of the mental lexicon and its contribution to age-related deficits in spoken word recognition,'' Psychol. Aging **11**, 333–341.

Stern, C., Prather, P., Swinney, D. and Zurif, E. (**1991**). ''The time course of automatic lexical access and aging,'' Brain Lang. **40**, 359–372.

Tun, P. A., Wingfield, A., and Stine, E. A. (**1991**). ''Speech-processing capacity in young and older adults: a dual-task study,'' Psychol. Aging **6**, 3–9.

Tun, P. A., Wingfield, A., and Stine, E. A., and Mecsas, C. (**1992**). ''Rapid speech processing and divided attention: Processing rate versus processing resources as an explanation of age effects,'' Psychol. Aging **7**, 546–550.

van Rooij, J. C., and Plomp, R. (**1992**). ''Auditive and cognitive factors in speech perception by elderly listeners. III. Additional data and final discussion'' J. Acoust. Soc. Am. **91,** 1028–1033.

Wingfield, A., and Stine, E. A. (**1992**). ''Age differences in perceptual processing and memory for spoken language,'' in *Everyday Memory and Aging: Current Research and Methodology*, edited by R. L. West and J. D. Sinnott (Springer-Verlag, New York).

A computerized adaptive testing system for speech discrimination measurement: The Speech Sound Pattern Discrimination Test

Joseph Bochner,[a] Wayne Garrison, Linda Palmer, Douglas MacKenzie, and Amy Braveman
National Technical Institute for the Deaf, Rochester Institute of Technology, P.O. Box 9887, Rochester, New York 14623

(Received 13 December 1995; revised 29 November 1996; accepted 12 December 1996)

A computerized, adaptive test-delivery system for the measurement of speech discrimination, the Speech Sound Pattern Discrimination Test, is described and evaluated. Using a modified discrimination task, the testing system draws on a pool of 130 items spanning a broad range of difficulty to estimate an examinee's location along an underlying continuum of speech processing ability, yet does not require the examinee to possess a high level of English language proficiency. The system is driven by a mathematical measurement model which selects only test items which are appropriate in difficulty level for a given examinee, thereby individualizing the testing experience. Test items were administered to a sample of young deaf adults, and the adaptive testing system evaluated in terms of respondents' sensory and perceptual capabilities, acoustic and phonetic dimensions of speech, and theories of speech perception. Data obtained in this study support the validity, reliability, and efficiency of this test as a measure of speech processing ability. © *1997 Acoustical Society of America.* [S0001-4966(97)06704-0]

PACS numbers: 43.71.Gv, 43.71.Ky, 43.66.Sr [WS]

INTRODUCTION

Conventional methods and materials used in the clinical assessment of speech processing may be traced to the development of articulation and intelligibility tests (Egan, 1948; Fletcher, 1929). Specifically, the work of Egan and his colleagues at the Harvard Psychoacoustics Laboratory in the 1940s led to the development of phonetically balanced monosyllabic word-recognition measures, such as the CID Auditory Test W-22 (Hirsch *et al.*, 1952). These so-called PB-50 tests historically have constituted the primary tools of speech audiometry. Other, more recent approaches to the assessment of speech perception, such as the SPIN test (Kalikow *et al.*, 1977) and the MAC battery (Owens *et al.*, 1985), have used different methods and materials designed to provide more useful information about individuals' speech processing ability.

In speech audiometry, tests have also been developed to assess listeners' ability to perceive phonetic segments and patterns. For example, tests of consonant perception in word and nonsense-syllable contexts have been developed (Dubno *et al.*, 1982; Owens and Schubert, 1977). These tests, however, have not seen widespread use in clinical or rehabilitative settings. Given the history and limitations of speech perception tests currently available, a need exists for the advent of new approaches to the measurement of speech processing abilities adapted to the characteristics of individuals receiving audiological services (Tyler, 1994).

At the heart of the adaptive testing procedure is the simple proposition that an examinee is measured most effectively when the test tasks are neither too difficult nor too easy. For speech discrimination measurement, this condition can occur when an examinee responds correctly to, say, a predetermined percentage of test items administered (e.g., 50%). Consequently, adaptive testing involves the selection of test items during the testing process which are appropriate in difficulty level for a given examinee. Adaptive tests are designed to provide successively refined estimates of an examinee's proficiency or capability, on the basis of his/her responses to items already administered. Using these successive approximations of, in the present discussion, sensory and perceptual capability, decisions are made about what (if any) test items are to be administered next. This iterative procedure generally continues until established criteria for test termination have been met. Because of their computational and branching requirements, adaptive tests most frequently are implemented using computer-interactive methods.

This paper describes the development of a computerized adaptive form of the Speech Sound Pattern Discrimination Test (SSPDT) developed by Bochner *et al.* (1986), and evaluates its reliability and validity from multiple perspectives. The rationale for developing this test was to construct a reliable, valid instrument for measuring speech processing ability that utilizes naturalistic sentence-length utterances and efficiently provides meaningful information about the perceptual capabilities of listeners with a wide range of hearing loss and English language proficiency. The initial version of the SSPDT was a prototype containing only 30 items. The current SSPDT item pool includes 130 items used in an adaptive testing format. The purpose of this study was to evaluate the hypothesis that a computerized adaptive form of the SSPDT can serve as a functional tool for speech discrimination measurement; hence, measurement reliability

[a]Electronic mail: JHBNCP@ritvax.isc.rit.edu

 0001-4966/97/101(4)/2289/10/$10.00

and validity have been approached from a variety of perspectives.

I. METHOD

A. A psychometric model for person measurement

Although it is possible to design and administer computerized adaptive tests without an explicit theory of item responses, psychometric models that represent the influence of specific person and item parameters on the outcome of the person-item interaction have proven useful. Item response theory models are mathematical abstractions based on suppositions or hypotheses about what happens when an examinee responds to a test item. The simplest of these models, and also the basis of the present work, is the generalized Rasch (1980) model for person measurement.

In the situation where examinees' responses to test items can be scored ''right/wrong,'' the Rasch model provides a means of predicting success or failure on specific test items in probabilistic terms. These probabilities reflect the difference between an examinee's position along a continuum of capability, and the difficulty of items scaled along the same continuum. Thus, the Rasch model conceptualizes the result of the person-item interaction in terms of a single person parameter (i.e., ability or capability, used interchangeably in the current discussion), and a single item parameter (i.e., difficulty). These parameters are expressed in a metric known as logits. A person's ability in logits is his/her natural log odds for succeeding on items with ''zero'' difficulty. The item difficulty scale is centered at zero. An item's difficulty is its natural log odds for eliciting failure from persons with ''zero'' ability (Wright and Stone, 1979). In the present study, the item difficulty parameter was decomposed further to investigate factors suspected of causing variation in the item difficulty values.

B. Item pool

The SSPDT is a flexible, broad-range test of speech discrimination ability. It is constructed on a respondent-by-respondent basis from a pool of 130 potential items. An item is a modified discrimination task in which listeners are required to make judgments on whether each of four sentences, presented in succession, is identical to a standard (target) sentence. Accordingly, the term *item*, as used in this paper, denotes a set of four trials. An orthographic representation of the target sentence appears on a computer monitor throughout the presentation of acoustic stimuli. The listener must indicate whether comparison sentences are either the same or different using designated response keys on the computer keyboard. A special keyboard template can be used to prevent access to all but appropriate response keys.

Examinees are instructed that any number of comparison stimuli may match the target, making it possible for 0–4 matches to occur for a given target. Matching stimuli are exact repetitions of the target utterances. Items are scored correct/incorrect as blocks, minimizing the influence of guessing on the estimation of ability. That is, items scored correct are those for which all four discrimination judgments are correct. An error on any one of the four comparison tasks within a block results in an item score corresponding to incorrect.

C. Instrumentation

The stimulus sentences were uttered by a male speaker with a General American dialect. The speech was digitized at 10 kHz for storage on computer disk using a 12-bit A/D module (AD12FA) interfaced to a Masscomp 5600 UNIX Workstation. Rockland antialiasing filters with a roll off of 48 dB/oct were set to 5 kHz. A body microphone (Electravoice RE51) was placed 1 in. from the speaker's mouth. A preamp (Shure M67) and compression limiter (dbx 161) were used to amplify the microphone signals. The speaker was instructed to utter each sentence in an item block with the same pace, clarity, and effort, changing only the portion containing lexical/phonetic contrasts. Each sentence was spoken three times. The best utterances were later selected and edited into individual sentence files. Recordings were made in a double-walled IAC sound booth. Signal levels were monitored on a VU meter throughout the recording to assure that the peaks were not clipped.

D. Adaptive testing procedure

The adaptive testing system elaborated herein operates from a calibrated item pool and, generally, comprises three components: (1) an item selection routine; (2) an ability estimation technique; and (3) rules for test termination. The calibrated item pool consists of SSPDT items and associated difficulty values. The item calibrations (i.e., difficulty values) were those obtained using the BISGSTEPS Rasch scaling program developed by Linacre and Wright (1994). Data for the estimation of difficulty values were the scored responses to items presented to listeners in this study.

Procedurally, the adaptive testing system operated in the following manner:

(1) The first SSPDT item administered to each examinee had a difficulty value closest to the central reference value of 0.00 logit.

(2) If an examinee responded correctly, an item of greater difficulty was administered next. If an examinee responded incorrectly, an item of lesser difficulty was administered. The difficulty increment (decrement) was set at 0.50 logit.

(3) When the response record contained at least one correct and one incorrect item score (1 and 0, respectively), a finite maximum likelihood estimate of ability, and its associated standard error, was obtained [the reader is referred to Wright and Stone (1979) for solution equations]. The numerical estimation method employed here has the property that an examinee's number right (raw) score is a sufficient statistic for estimation of the ability parameter.

(4) Using the estimate of ability just computed, test items in the pool which had not already been administered were evaluated for their potential to enhance information about the examinee's speech discrimination ability. Specifically, the next item to be administered in the testing sequence was that with difficulty closest to the ability estimate,

with the further provision that the difference between the ability estimate and the selected item's difficulty had to be less than the standard error associated with the ability estimate (i.e., difficulty in the range ±one standard error of the ability estimate). Otherwise, items remaining in the pool (not administered) were considered to be out-of-range, and testing was terminated.

(5) After each newly selected test item was presented and the examinee's response evaluated for correctness/incorrectness, the ability estimate was recomputed, making use of the additional information. The new ability estimate was compared, as before, with the difficulty values of items remaining in the pool. Items continued to be administered as long as the difference between their difficulty and each newly computed ability estimate remained within a (decreasing) standard error of measurement.

(6) Testing was terminated when items remaining in the pool were of inappropriate difficulty (i.e., outside the established range), or when a maximum number of items had been administered (25 items here).

E. Subjects and test administration

Seventy-three adults participated in the study. Seventy-two were students with sensorineural hearing losses enrolled in courses of study at the National Technical Institute for the Deaf and one was a normal-hearing undergraduate. Ages of the study participants ranged from 17 to 49 years, with a mean age of 22 years. Subjects were paid for their participation.

Twenty-eight subjects (sample A) were administered a common set of seventy items (fixed-item nonadaptive format) during the spring, 1993. Adaptive tests for sample A respondents were *simulated* from their responses to these 70 items. Data obtained from these participants were used primarily to estimate the difficulty values of these 70 items. The second purpose was to evaluate a simulated adaptive testing protocol.

Forty-five subjects (sample B) responded to a different, common set of sixty items (fixed-item nonadaptive format). These 60 items were intended to extend the range of difficulty upward from that realized from the sample A testing. Sample B respondents were also administered an *actual* adaptive test with an item pool composed of the 70 items calibrated from the sample A testing. Data obtained from sample B examinees were used primarily, then, to evaluate the adaptive testing system. Simultaneously, these data provided an empirical basis for the calibration of 60 new SSPDT items. Subjects in sample B were tested during the spring and fall of 1994.

Five subjects were common to samples A and B. Consequently, for correlational analyses to be reported later, the final sample size was reduced from 73 to 68 respondents (sample C). Sample C subjects had a mean pure-tone average (ANSI S3.6, 1989) in the better ear for 0.5, 1, and 2 kHz of 73.1 dB HL (s.d.=23.8). The range was 107 dB (minimum=0, maximum=107).

An effort was made to group subjects on the basis of their audiometric configuration using the criteria employed by Dubno *et al.* (1982). A group of 22 subjects was identified as having flat hearing losses. A group of 13 subjects had gradually sloping high-frequency hearing losses. A group of nine subjects had steeply sloping hearing losses. The remaining subjects were either not tested to 4000 Hz, or their audiograms could not be clearly placed into one of these three configuration classes.

All subjects were tested individually in a sound-treated room and received stimuli dichotically under earphones (TDH-39P) at a comfortable listening level using a clinical audiometer (Madsen OB 822). In order to establish a comfortable listening level for each subject, a sample stimulus was presented repeatedly and its level adjusted until the subject reported it to be most comfortable. For the nonadaptive testing component of this study involving subjects in sample A, the digitized stimulus sentences were converted to analog signals and recorded on a cassette tape recorder (Nakamichi 1000 II). The stimuli were played back to subjects in sample A on another tape recorder (Wollensak 2556 AV) routed through an amplifier (Crown model D 60). A warning light cued subjects to the onset of each stimulus, and the subjects used pen/pencil to indicate their responses (''S'' for same, ''D'' for different) on an answer sheet.

Subjects in sample B were seated in front of a VT100 computer terminal. The edited sentence files were played back directly from the computer, routed through a 12 bit D/A module (DA04H), and low-pass filtered at 5 kHz (48-dB/oct attenuation). The timing of the stimuli was controlled by a programmable clock module. A flash of light from a visual response box placed next to the terminal alerted subjects to the onset of a sentence, and number prompts displayed on the computer screen marked opportunities to respond ''S'' for same or ''D'' for different. Practice items were provided to all subjects to ensure that the task was understood. Each testing session took approximately 1 h. The time required for the administration of the adaptive test to subjects in sample B, however, was approximately 10 min.

II. RESULTS

A. Model/data conformity

The usefulness of any psychological testing device is gauged, in part, by its success in differentiating respondents. This amounts to asking the question, ''How well do test items separate the persons tested?'' In Rasch measurement practice, a person separation index has been developed (Wright and Stone, 1991). The person separation reliability (PSR) index, ranging in value from 0.00 to 1.00, provides insight into the extent to which the items comprising a test are members of the same conceptual domain. The reliability index for the 70 items calibrated from sample A examinees was found to be 0.95, indicating that these items separated the 28 respondents very well. We conclude from this finding that these 70 items define a single, dominant variable (i.e., the items are homogeneous and internally consistent).

In Rasch measurement practice, an item separation reliability (ISR) index has also been introduced by Wright and Stone (1991) to evaluate how well respondents differentiate items. This amounts to asking the question, ''How broad is the range of difficulty operationalized by an item set?'' The

ISR is algebraically similar to the PSR and ranges in value from 0.00 to 1.00. The ISR for the sample A data was found to be 0.90, indicating that the difficulty of these 70 items spread over a considerable range, giving breadth and meaning to the variable being assessed (i.e., speech discrimination). The mean difficulty value was 0.00 logit (s.d.=2.14), with item difficulties spanning a range of −4.61 to +5.00 logits. The distribution of item difficulty values was symmetrical and, essentially, normal.

PSR and ISR are gross statistical indicators, providing a general characterization of test qualities. To guide us in our understanding of more specific person and item attributes, two additional statistics have been introduced. These statistics, usually expressed as INFIT and OUTFIT, are discussed elsewhere at length by their developers (Wright and Linacre, 1991; Wright and Masters, 1982; Wright and Stone, 1979). In general, item fit values reflect the extent to which the observed responses to items (across persons) agree with those predicted by the Rasch measurement model. Examination of the fit statistics associated with the 70 items calibrated from sample A data indicated conformity between observation (data) and prediction (model). That is, there were no misfitting items.

When the INFIT and OUTFIT statistics are applied to persons, we are able to evaluate the extent to which individual examinees' responses to items are in accord with those predicted by the measurement model. One of the 28 individuals included in sample A had an INFIT statistic indicating misfit. Person misfit to the measurement model results when a respondent makes too many correct discriminations on items predicted to be much harder than the examinee is able or, conversely, when a respondent makes many errors on items predicted to be relatively easy. Aberrance within the response vector for this examinee was attributed to ''lapse of attention,'' noted during the testing session by the audiologist who was overseeing the test administrations.

The final analysis performed on the sample A data involved the simulation of adaptive test records for these 28 individuals. Using the adaptive testing procedure detailed earlier, the simulated test record represented scored responses to a *subset* of the 70 items. The first item in the simulated record was the same for all respondents. Thereafter, a variable branching scheme which involved person-ability/item-difficulty comparisons was used to construct the simulated test records, Ability estimates obtained from the adaptive test simulation were compared, then, to the ability estimates obtained in the situation where the same examinees responded to all 70 items.

The mean performance of the 28 subjects on the 70 items was 1.33 logits (s.d.=1.90) and the mean performance of the same individuals on the simulated tests was 1.43 logits (s.d.=2.12). For the group, the difference in performance between simulated and fixed-item conditions is not statistically significant.

When the data were subjected to casewise analysis, 27 of the 28 examinees obtained measures on the simulated tests that were statistically equivalent to the ability estimate computed from their responses to all 70 items. This result is reflected in a substantial correlation of +0.95 between the score pairs. The statistical test for the equivalence of two measures evaluates the magnitude of a difference in terms of the expected standard error of the difference.

The one individual for whom statistical equivalence of measures was not observed was the same individual suspected of ''attention lapses'' by the audiologist who supervised test administration. For all 70 items, this subject attained a measure of 2.06 logits. On the simulated test, the same individual attained a measure of 4.61 logits. The aberrance within the item response vector signaled by the magnitude of the person fit statistics in the first instance was not manifested in the latter (i.e., the person fit statistics in simulated test mode failed to reach significance level). Importantly, what we observe for this examinee is a deleterious effect of administering test items which, in the fixed-item format, are off-target (e.g., items which are too easy).

The average length of a simulated test was 14 items (s.d.=3.4). Thus, only 20% of the items in the pool were required to reproduce the ability measures implied by responses to all 70 items. The minimum number of items administered under the simulated condition was 10, the maximum was 23. The frequency distribution of number of items administered was positively skewed, with 75% of the persons tested responding to 15 or fewer items. Testing was terminated for all respondents due to insufficiency of items remaining in the pool which were appropriate in difficulty level.

With the goal of enlarging and extending the range of usefulness of the item bank, and to evaluate the adaptive testing system in an actual rather than simulated setting, additional data were obtained from 45 individuals (sample B). Specifically, individuals in sample B interacted with a computerized adaptive testing system limited to administration of the 70 SSPDT items discussed above. The same persons also responded to a fixed set of 60 new, experimental items (also computer administered, but in a nonadaptive format) which were evaluated for fit to the Rasch measurement model and, hence, addition to the item bank.

The person separation reliability for the 60 new SSPDT items, calibrated from the sample B data, was found to be 0.94, indicating that these items separated the 45 persons tested very well. Mean performance of the same individuals on the 60-item fixed form of the SSPDT was 1.12 logits (s.d.=1.79). The item separation reliability for the sample B data was found to be 0.91, indicating that the difficulties of the 60 new items spread out over a broad range.

Fifty-nine of the sixty new SSPDT items had fit statistics indicating model/data conformity. One item had associated INFIT and OUTFIT values indicating that it should be monitored (i.e., administered, but not scored) presently. Forty-four of the forty-five persons tested fit the Rasch measurement model. That is, in the evaluation of the regularity of individual response vectors, 44 persons responded to items consistent with model predictions; irregularity in the response pattern was observed for one examinee, reflecting too many errors on items predicted to be relatively easy for the respondent.

Mean performance of the 45 persons tested on the adap-

tive SSPDT format was 2.64 logits (s.d.=1.91). The measurements of these persons on the adaptive and fixed-item formats constitute the essential ''common person'' data for linking the 60 new items onto the reference scale defined by the 70 items calibrated with sample A data. Specifically, the difference in the two ability means [2.64−1.12=1.52 logits] corresponds to the translation constant necessary to bring the items calibrated with sample A and sample B data onto a common scale.

With this scaling adjustment, the 60 items calibrated using sample B data spanned a difficulty range of −1.19 to +5.00 logits. The intent to extend the range of difficulty of the items upward from that observed with the sample A data was not realized. Rather, the sample B data served to enlarge the item bank in regions defining moderate and very difficult speech discrimination tasks.

For the adaptive test format, the mean number of items administered to sample B respondents was 14 (s.d.=4.0). This is consistent with what was observed with simulated adaptive testing in sample A. All but one examinee exited the testing sequence due to insufficiency of items remaining in the pool with appropriate difficulty levels. One examinee (with normal hearing) attained a perfect score upon reaching the extreme level of item difficulty.

Just as the items were combined into a common bank, the persons tested were pooled into a common sample (sample C). For each individual in sample C, there were two estimates of speech discrimination ability. One estimate, and its associated standard error, was obtained using a common-item test format; the other estimate, and its associated standard error, was the result of adaptive test administration (simulated or real). Sixty-one of the sixty-eight persons in sample C attained statistically equivalent ability estimates. For these 68 individuals, the Pearson correlation between the ability estimates was +0.93. For sample B respondents only, the comparable correlation was +0.92. We conclude from analyses presented to this point that the test data are characterized rather well by the Rasch model for person measurement. Further, once we have estimated the item difficulties, we are able to tailor tests to test-takers in a manner which is both informative and efficient.

B. Item content analysis

The analysis of item content is concerned with the characterization of contrasts occurring within the block of trials comprising an item. The contrasts manifested in each block of trials were characterized according to categories of phonetic features and acoustic properties. In this analysis, consonant contrasts were, for the most part, classified according to phonetic features of place, manner, and voicing, while vowel contrasts were classified according to features of tongue position/advancement and tongue height. These phonetic features are associated with specific acoustic properties of speech, and their perception is known to vary as a function of the portion of the speech spectrum which is audible to listeners (e.g., Dubno and Levitt, 1981; Miller and Nicely, 1955; Pickett *et al.*, 1970). Trials involving replication of the target sentence (i.e., ''same'' trials) have not been included in this analysis because they do not involve a contrast (i.e., a difference) in item content and because previous reserach has shown that these trials are inherently easier than their counterparts (Bochner *et al.*, 1992). Four of the 130 SSPDT items had 4/4 trials which were replications of the target stimulus (i.e., comparisons were ALL ''same'').

Since an item is scored correct if and only if an examinee's response to each of the four trials is correct, we reasoned that the difficultly of an item would be determined by that of its most difficult trial. An analysis of examinees' responses supported this reasoning, indicating that trials which involved contrasts in the phonetic features and acoustic properties expected to be least audible consistently presented the greatest difficulty for listeners. Within each item, then, the trial involving the least audible contrast may be regarded as dominant because it determines the difficulty of the entire block of four trials comprising the item. In a few items, however, one trial could not be deemed more difficult than others. Such items are, therefore, regarded as having more than one dominant trial.

The test items were characterized in terms of four content categories. Three categories account for one or more segmental contrasts occurring within a single syllable, and characterize item difficulty in terms of differences in phonetic and acoustic content observed between the pair of utterances comprising the dominant trial. The fourth category accounts for gross contrasts extending across two or more syllables, and characterizes item difficulty without reference to phonetic features or the notion of a dominant trial. The four categories are ordered from most difficult (category Z) to least difficult (category W). Examples of items in each category are shown in Table I.

Category Z items are characterized by spectral cues contained in the vicinity of the second format, such as cues for place of articulation for consonants and tongue position/advancement for vowels. Contrasts among semivowels (e.g., ''led''—''wed''—''read'') are also included in category Z, as are certain contrasts involving sibilants. Some items classified in category Z contain more than one contrast within a single syllable. Such items may contain a contrast involving the semivowels /y,w,l,r/, an extra /s/ segment, and/or a contrast in place of articulation (e.g., ''trap''—''strap,'' ''stray''—''clay,'' and ''throat''—''float''). These contrasts are characterized by phonetic cues contained in the upper regions of the speech spectrum. Since their perception tends to be associated with acoustic cues in the vicinity of the second formant and above, and they occur within a single syllable, these contrasts conform to the criteria for classifying items in category Z.

Category Y items are characterized by spectral and temporal cues appearing in the vicinity of the first formant, such as cues for manner of articulation for consonants (with or without an accompanying place contrast) and tongue height for vowels. Contrasts involving the presence of an extra voiceless consonant (other than an extra /s/ segment as described above), and/or an extra semivowel within a consonant cluster are also included in category Y, as are some items containing more than one contrast within a single syllable (e.g., ''car''—''cart,'' ''tie''—''try,'' ''crime''—''time,'' and ''shoes''—''clues''). Category Y, therefore, in-

TABLE I. Sample SSPDT items. (Note: In the sample items [T] denotes target sentence, * denotes dominant trial.)

Category	Example
Z	My grandmother left her CAKE at the party. [T] My grandmother left her CANE at the party. My grandmother left her CAPE at the party. *
	We quickly had to brush off the SEAT. [T] We quickly had to brush off the SOOT. We quickly had to brush off the SUIT. *
Y	MAKE a dozen cookies for the party next week. [T] TAKE a dozen cookies for the party next week. BAKE a dozen cookies for the party next week. *
	The children dropped the PAN. [T] The children dropped the PEN.* The children dropped the PIN.
X	She felt like KILLING him when the dance was over. [T] She felt like KISSING him when the dance was over. * She felt like KICKING him when the dance was over.
	She wants to see the SHIP. [T] She wants to see the SHEEP. * She wants to see the SHAPE. She wants to see the SHOP.
W	Plants need RAIN. [T] Plants need WATER AND SOIL. Plants need SUNSHINE.
	The boys played IN THE STREET. [T] The boys played TENNIS. The boys played WITH MATCHES. The boys played BASEBALL. The boys played FOOTBALL.

cludes items with acoustic cues occurring within a single syllable which can be discerned in the central and lower regions of the speech spectrum.

Category X items are characterized by spectral and temporal cues available in the lower region of the first formant (i.e., below about 500 Hz), such as cues for consonant voicing (with or without an accompanying place and/or manner contrast) and vowel length/tenseness. Contrasts involving the presence of an extra voiced consonant (other than an extra semivowel as described above) and some items containing more than one contrast within a single syllable are also included in category X (e.g., ''rush''—''brush,'' ''rides''—''writes,'' ''food''—''wood,'' and ''sand''—''sun''). Category X, therefore, includes items with acoustic cues occurring within a single syllable which can be detected in the lower regions of the speech spectrum.

Category W items have multiple phonetic contrasts occurring across two or more syllables. These contrasts in frequency, intensity, and time are associated with changes in the shape of the speech waveform envelope. Contrasts of the sort included in category W items can be detected in the lowest regions of the speech spectrum.

Each test item was classified according to the category schema described above. The relationship between category membership and item difficulty was examined. Table II presents the mean difficulties (in logits) of items contained in each of the four categories, along with standard deviations, minimum and maximum difficulty values. Results of an analysis of variance indicated that the difficulty values of the items differ significantly across content categories ($F_{3,122}=123.2$, $p<0.001$). Pairwise comparisons between the means using Newman–Keuls range tests indicated that each of the item categories differs reliably from all others ($p<0.05$). For category Y and Z items, contrasts involving voiceless consonants were found to be more difficult than contrasts involving voiced consonants ($F_{1,45}=8.57$, $p<0.01$).

TABLE II. SSPDT item difficulty by content categories. (Note: Difficulty values are in logits.)

Category	Mean	S.D.	Min	Max
W (Multiple contrasts)	−2.91	1.15	−4.61	−0.73
X (Voicing)	0.22	1.09	−2.56	2.23
Y (Manner)	1.16	0.99	−1.19	3.06
Z (Place)	2.86	1.33	0.23	5.00

Finally, the test items vary somewhat with respect to the number of segmental contrasts occurring within a single syllable. That is, items contain contrasts in one, two, or three phonetic segments as described in the characterization of categories Z, Y, and X. Variation of this sort, however, is not associated with item difficulty. For each item, differences in the number of contrasting segments were quantified in terms of the minimum, maximum, and average number of contrasts occurring within a single syllable. Pearson correlation analysis indicated that, regardless how variation in the number of contrasts was quantified, this variable was not associated with item difficulty.

C. Multiple regression and correlation analyses

When a test is used to describe the extent to which a person manifests some trait or ability, construct validity is a relevant concern. Essentially, the construct validation process invites analyses of the meaning of test scores in terms of psychological constructs. Before concluding that the information provided by the SSPDT reflects the degree to which one can discriminate or process speech sound patterns, we sought to inquire further as to the functional relationships which might exist between this test and conventional measures of speech discrimination, as well as hearing loss for pure tones. The attempt here was to study the linkage between different, related constructs.

Pearson correlation between respondents' adaptive test scores on the SSPDT and scores on the CID Everyday Sentences Test (lists 2, 5, and 8: Davis and Silverman, 1978) yielded a coefficient of +0.82, indicating a respectable amount of shared variance. A subset of respondents in sample C also had data available on their performance on PB-50 word discrimination tests ($n=41$). These tests included CID Auditory Test W-22 (Hirsch *et al.*, 1952), the NU-6 (Tillman and Carhart, 1966), and PAL PB-50 (Egan, 1948). The correlation between SSPDT adaptive test scores and scores on the word lists for these 41 individuals was found to be +0.66. The correlation between adaptive test

TABLE III. Summary regression analysis. (**$p<0.01$.)

Variable		B	s_e	β	t
X_1	CID Everyday Sentences Test Score	4.06	0.57	0.59	7.14**
X_2	Pure Tone Threshold	−0.03	0.01	−0.35	−4.27**
	(Constant)	2.11	0.78		2.72**

scores on the SSPDT and hearing loss for pure tones was −0.74 for all respondents in sample C.

Table III presents the results of a stepwise multiple regression analysis performed on sample C data. In this analysis, the SSPDT adaptive test score served as a criterion variable, and score on the CID Everyday Sentences Test (X_1) and pure tone threshold (X_2) served as predictors. Both predictor variables met the minimal criteria for entry into the regression equation. Reported in the table are the raw score or unstandardized regression coefficients (B) and their standard errors (s_e), standardized regression coefficients (β) indicating the relative importance of X_1 and X_2 in predicting the SSPDT score, and t-statistics resulting from a test of the significance of each β against a reference value of zero.

In all, the predictor variables yielded a multiple R of +0.87, accounting for approximately 75% of the variation in examinees' scores on the SSPDT. There appears to be, then, something of a working equivalence between performance on the SSPDT and independent assessments of related sensory and perceptual capabilities, with 25% unexplained variation remaining. While the range of values which the predictor variables can assume in the regression equation is infinite, only values in the range 0.00–1.00 (proportions) for X_1,and 0–107 (dB) for X_2 are meaningful in the present discussion. These limits establish floor and ceiling values. The correlational findings presented above, as evidences of construct validity of the SSPDT, are discussed in detail in the following section.

Finally, differences among subjects based on the shape of their audiometric configuration (i.e., flat, gradually sloping, and steeply sloping hearing losses) were evaluated. An analysis of variance performed on their adaptive SSPDT scores revealed no statistically significant differences in performance based on the configuration of their hearing losses.

III. DISCUSSION

A. Adaptive testing with a Rasch measurement model

Reported in the previous section are the results of detailed analyses of the fit of individual test items to the Rasch model, as well as the fit of persons to the measurement model. The results of Rasch test analysis have been used to position items along a hypothetical continuum. The locations of the items along this continuum correspond to their relative difficulty. Estimates of person ability are used to position persons along the continuum, and represent the speech discrimination capability implied by their SSPDT scores. The outcome of the interaction that occurs when an examinee is presented with an item is governed by the difference between person ability and item difficulty.

Reliabilities of the SSPDT were studied from multiple perspectives. We evaluated the extent to which the SSPDT items, as a set, were internally consistent. We also studied the internal consistency of individual examinees' responses to test items. We asked what the items told us about the persons tested, and what the persons tested told us about the items. Correlational analyses were used to compare part- and whole-test scores for statistical equivalence in simulated and actual computerized testing situations. When the results of the individual analyses are considered collectively, we conclude that the data are well-characterized by the Rasch measurement model, leaving us with an item bank composed of 130 blocks of speech discrimination trials.

With the item difficulty and person abilities estimated from common-item test administrations, our attention turned to the evaluation of an adaptive testing system designed to reduce the imprecision inherent in conventional forms of speech discrimination measurement. The adaptive testing system sought to eliminate from the testing experience items which were inappropriate in difficulty for given examinees (i.e., items judged to be either too easy or too hard). The success of our efforts was measured by the ability of the adaptive test scores to predict performance on a lengthier common-item test form. From these analyses, we conclude that the adaptive testing system represents a reliable, efficient alternative to traditional methods of speech discrimination measurement. The adaptive test requires approximately 10 min to administer. A shorter administration time is desirable for use in clinical settings, and is achievable through modification of the testing protocol.

Among its positive qualities, the SSPDT uses items comprised of sentences which approximate natural, everyday speech. The testing system is driven by a mathematical measurement model which has been the subject of extensive, rigorous research. The adaptive testing procedure uses an objective ''up–down'' method of item selection designed to limit testing to maximally informative scorable units. The item bank is large enough that individual items do not have to be used repeatedly for a given examinee on multiple testing occasions.

The test is capable of effecting equiprecise measurement across a wide range of speech processing capability. It has diagnostic/analytic utility, providing immediate scoring and substantive feedback concerning the processing of acoustic and phonetic dimensions of speech. Evidences of test reliability are comparable to those reported for conventional forms of speech recognition measurement (cf. Thornton and Raffin, 1978).

B. Construct validity

The results of the correlation and multiple regression analyses provide evidence of the construct validity of the SSPDT. The correlation between adaptive test scores on the SSPDT and scores on the CID Everyday Sentences Test ($r = +0.82$) indicates that these tests measure a common construct. Furthermore, the magnitude of the correlation is what

one might expect given the measurement error associated with CID Everyday Sentences Test scores. Similar correlation have been obtained between scores on the CID Everyday Sentences Test and CID Auditory Test W-22 (Sims, 1975).

The correlation between adaptive test scores on the SSPDT and average hearing loss for pure tones ($r = -0.74$) is high in comparison to correlations obtained between pure tone thresholds and scores on conventional, monosyllabic word-recognition measures of speech discrimination. In a study of the relationship between measures of hearing loss for pure tones and scores on conventional speech discrimination tests, Elliott (1964) obtained moderate correlations ranging from approximately -0.50 to -0.70. In this context, the magnitude of the correlation observed in this study ($r = -0.74$) is quite reasonable.

The results of the multiple regression analysis indicate that CID Everyday Sentences Test scores and average hearing loss for pure tones collectively account for a large proportion (75%) of the variance in examinees' adaptive test scores on the SSPDT. This finding, in conjunction with the results of the correlational analyses above, demonstrates that the SSPDT is measuring sensory and perceptual capabilities associated with the processing of speech sound patterns. These data are evidences of construct validity of the SSPDT.

Similarities between the SSPDT listening task and models of the speech perception process provide additional evidence of the construct validity of the test. The listening task is not a simple discrimination task. In previous research (Bochner *et al.*, 1992), the task has been described as a modified discrimination task because each item consists of a block of discrimination trials in which a target sentence is ''paired'' with each of four comparison sentences. Describing the listening task in this way, however, does not capture the fundamental similarities it shares with the process of speech perception. Although the listening task performed by examinees responding to SSPDT items is not equivalent to the perception of fluent speech in communicative contexts, it nevertheless incorporates two components included in conventional models of speech perception, an auditory memory component and a comparison/matching component.

Various models of speech perception include an auditory memory component such as the precategorical acoustic storage described by Crowder and Morton (1969). A sensory register of this sort is incorporated in analysis-by-synthesis (Stevens, 1960; Stevens and Halle, 1967; Stevens and House, 1972), template-matching (Klatt, 1980; Oden and Massaro, 1978) and information-processing (Pisoni and Sawusch, 1975) models. The SSPDT listening task requires an auditory memory buffer to store each incoming comparison stimulus while it is being compared to the target sentence.

Analysis-by-synthesis and template-matching models also include components in which the identity of linguistic representations is determined by a matching procedure and/or verified by a comparison procedure. Matching and comparison are inherently similar activities; however, they can serve two distinct purposes. They can serve an identification function or a verification function. The identification function is associated with template-matching models The verification function, on the other hand, is associated with analysis-by-synthesis. Some models (e.g., Klatt, 1980) may even utilize comparison/matching routines for both identification and verification purposes.

The SSPDT listening task requires that a comparison be made to verify utterance content. The comparison routine involved in the SSPDT listening task is, therefore, similar to the comparison function depicted in the analysis-by-synthesis model. This routine, moreover, is similar to the process listeners use to verify the identity of linguistic representations in communication situations where contextual cues have been used to predict or anticipate the lexical content of a portion of an utterance (see Klatt, 1980; Stevens and House, 1972). Even though the primary purpose of the comparison/matching routine is verification, not identification, the SSPDT listening task still bears resemblance to template-matching procedures designed to ascertain the degree of similarity between perceptual prototypes of speech sounds and representations stored in auditory memory. This listening task also bears indirect resemblance to discovery procedures designed to detect the presence/absence of acoustic properties of speech in the information-processing model (Pisoni and Sawusch, 1975).

The SSPDT listening task is, in some respects, analogous to a closed response set (multiple-choice) procedure. Closed response set procedures involve the selection of one correct response from among a set of alternatives, and may be considered logically equivalent to a discrimination task in which the target utterance is paired with each response alternative. In other words a closed response set task can be reduced to a series of discrimination judgments involving paired comparisons between the utterance and each response alternative. While closed-set procedures permit one and only one response alternative to match the utterance, the SSPDT listening task allows for every possible combination of matches between the utterance and response alternatives (i.e., responses ranging from all ''same'' to all ''different'' to everything in between). As a result, this listening task is not strictly equivalent to a closed response set procedure because it permits a greater range of response variation. The SSPDT listening task, therefore, may be considered a variant of the closed response set procedure.

In summary, the construct validity of the SSPDT has been supported with reference to the results of correlation and multiple regression analyses and with reference to similarities between the listening task and models of the speech perception process. Taken together, these data and arguments provide strong evidences of the construct validity of the SSPDT.

C. Content validity

The results of the item content analysis provide evidence of the content validity of the SSPDT. The analysis of variance results indicate close correspondence between placement of items along the difficulty continuum and classification of items in terms of categories of acoustic and phonetic features. Data from studies conducted with degraded speech (Dubno and Levitt, 1981; Miller and Nicely, 1955) and studies conducted on hearing-impaired listeners (Dubno *et al.*,

1982; Owens *et al.*, 1972; Pickett *et al.*, 1970) have shown that phonetic features of place, manner, and voicing comprise a hierarchy of audibility for consonants. Within the categories used to characterize place and manner contrasts (i.e., categories Y and Z), a tendency was observed for items containing voiceless consonants to be more difficult than items containing voiced consonants. Dubno and her colleagues (1982) reported a similar finding for listeners with steeply sloping audiograms, as did Dubno and Levitt (1981) for normal-hearing subjects listening to degraded speech.

The acoustic correlates of tongue position/advancement and tongue height (Peterson and Barney, 1952) and of tenseness/length (Peterson and Lehiste, 1960) suggest a hierarchy of audibility for vowels similar to that for consonants (see Boothroyd, 1988; Pickett *et al.*, 1970). Acoustic and phonetic features used to characterize consonants and vowels, as well as distinctions pertaining to changes in the shape of the speech waveform envelope, are clearly associated with differences in item difficulty. Since item difficulty is related to acoustic and phonetic patterns, scores on the SSPDT can be interpreted in terms of a speech sound pattern audibility hierarchy and used for diagnostic/analytic purposes.

The categories used to characterize item contents (i.e., categories X, Y, and Z) permit more than one segmental contrast to occur within a single syllable. Since the results of previous reserach suggested that the quantity of segmental contrasts might influence item difficulty (Bochner *et al.*, 1992), it was thought that items containing two or three phonetic contrasts within a single syllable might be easier than items containing one such contrast. Analyses of data in this study, however, indicate that the quantity of contrasts within a single syllable does not influence item difficulty. Items containing two or three segmental contrasts within a single syllable are not inherently easier than items containing one such contrast. Therefore, the nature of phonetic contrasts occurring within a single syllable is the primary determinant of item difficulty.

Previous research has suggested that overall performance on consonant recognition tests is not strongly associated with specific patterns of perceptual confusion (Bilger and Wang, 1976; Dubno *et al.*, 1982), or with scores on conventional speech discrimination tests (Owens and Shubert, 1977). Bilger and Wang (1976) concluded that overall performance and patterns of perceptual confusion on a nonsense-syllable recognition task are relatively independent of one another, and Owens and Shubert (1977) reported a weak correlation ($r = +0.35$) between scores on the California Consonant Test and scores on CID Auditory Test W-22. Unlike the tests used in these studies, the SSPDT does not provide information about a listener's performance on individual sound segments. The SSPDT does, however, provide information of a more general sort pertaining to the processing of speech sound contrasts, perception of phonetic feature categories and recognition of acoustic patterns. In addition, the SSPDT provides information about a listener's overall speech discrimination ability.

Various studies (Bilger and Wang, 1976; Dubno *et al.*, 1982; Owens *et al.*, 1972) have reported relationships between certain confusions in consonant perception and audiometric configurations. In general, listeners with flat hearing losses tend to perform better than listeners with sloping high-frequency hearing losses on consonant recognition tasks. More specifically, it has been found that sibilant consonants, for example, tend to be recognized better by listeners with flat hearing losses.

Unlike the findings of Dubno *et al.* which showed effects of audiometric configuration on performance on a nonsense-syllable task, performance on the SSPDT was not influenced by audiometric configuration. Since it is reasonable to expect that listeners with flat hearing losses may have less difficulty with speech sounds characterized by high-frequency acoustic cues, such as sibilants, we conclude that the disparity in our respective findings may reflect differences in the magnitude of hearing loss of listeners who participated in the separate studies. Dubno *et al.* selected subjects broadly representative of listeners with mild to moderate sensorineural hearing loss, while our sample included a disproportionate number of listeners who were severely to profoundly deaf. This pattern of results combined with item-difficulty data suggests that the SSPDT, in its present form, may not be as useful for persons with mild to moderate hearing loss as it is for persons with severe to profound hearing loss.

Although item difficulty is determined primarily by phonetic and acoustic factors, other variables may influence listeners' performance. For example, reserach has shown that the location of a contrast within a syllable (Dubno *et al.*, 1982) and within a sentence (Bochner *et al.*, 1992) can affect listeners' performance. It is also possible that exchanging the target sentence with a comparison sentence may, under certain circumstances, influence the difficulty of an item (e.g., exchanging the target ''trap'' with the comparison ''strap'' may alter item difficulty). The identity of the talker might also affect performance on a listening task. That is, it is reasonable to expect that use of a female's voice might shift the item calibrations upward in the direction of greater difficulty. These possibilities should be investigated in future research. More importantly, they point out the need to emphasize that the SSPDT provides a general indication of listeners' ability to process categories of phonetic features, as opposed to detailed information about the processing of specific features.

The content validity of the SSPDT is enhanced by the fact that items are comprised of meaningful sentences having vocabulary and syntax generally appropriate for individuals with limited English language proficiency. Specifically, difficult vocabulary, subordinate clauses, and passive constructions have, for the most part, been avoided. Furthermore, listeners' responses are not influenced by their English language proficiency since they (the responses) are merely computer keystrokes corresponding to ''same'' and ''different.'' That is, the responses ''same'' and ''different'' do not involve linguistic competencies which underlie expressive language production. Viewed from a slightly different perspective, sentence-level stimuli have the advantage of more closely resembling actual listening activity in terms of acoustic and linguistic context than do word-level stimuli. It is possible, however, that similar results may be obtained with

word-level stimuli; but, this possibility will need to be investigated in future research.

In summary, scores on the SSPDT provide information pertaining to an examinee's ability to: (1) process speech in sentence contexts; and (2) discriminate acoustic and phonetic patterns in fluent speech. The data reported herein provide convincing evidence of the content validity of this test.

IV. CONCLUSIONS

The results of this investigation indicate that the SSPDT is a valid, reliable, efficient test of speech processing ability which measures sensory and perceptual capabilities used to process speech in sentence contexts. Test scores were found to be correlated with pure-tone thresholds and with scores on independent measures of speech discrimination. Moreover, scores on the SSPDT provide diagnostic/analytic information about examinees' ability to process acoustic and phonetic dimensions of speech in a highly reliable manner. These characteristics of the SSPDT make it a potentially attractive tool for the field of audiology (see Boothroyd, 1991; Tyler, 1994).

The computerized adaptive delivery system affords this test a number of advantages over conventional speech discrimination tests. Most importantly, the testing experience is individualized, with items being selected by an objective ''up–down'' method on the basis of their information value. The SSPDT also permits equally precise measurement across a wide range of speech processing ability. The pool of items is sufficiently large to enable an examinee to be tested on multiple occasions with no two occasions containing identical sets of items. These characteristics make the SSPDT a very efficient measurement tool.

ACKNOWLEDGMENT

This research was conducted in the course of an agreement between the Rochester Institute of Technology and the U.S. Department of Education.

ANSI. (**1989**). ANSI S3.6-1989, ''Specifications for audiometers'' (American National Standards Institute, New York).

Bilger, R. C., and Wang, M. D. (**1976**). ''Consonant confusions in patients with sensorineural hearing loss,'' J. Speech Hear. Res. **19,** 718–740.

Bochner, J., Garrison, W., and Palmer, L. (**1986**). ''A closed-set sentence protocol for assessing speech discrimination in deaf individuals: The Speech Sound Pattern Discrimination Test,'' Ear Hear. **7**, 370–376.

Bochner, J., Garrison, W., and Palmer, L. (**1992**). ''Simple discrimination isn't really simple: A confirmatory analysis of the Speech Sound Pattern Discrimination Test,'' Scand. Audiol. **21,** 37–49.

Boothroyd, A. (**1988**). ''Perception of speech pattern contrasts from auditory presentation of voice fundamental frequency,'' Ear Hear. **9**, 313–321.

Boothroyd, A. (**1991**). ''Assessment of speech perception capacity in profoundly deaf children,'' Am. J. Otology **12**, 67–72.

Crowder, R. G., and Morton, J. (**1969**). ''Pre-categorical acoustic storage (PAS),'' Percept. Psychophys. **5,** 365–373.

Davis, H., and Silverman, S. R. (**1978**). *Hearing and Deafness* (Holt, Reinholt & Winston, New York), 4th ed.

Dubno, J. R., and Levitt, H. (**1981**). ''Predicting consonant confusions from acoustic analysis,'' J. Acoust. Soc. Am. **69,** 249–261.

Dubno, J. R., Dirks, D. D., and Langhofer, L. R. (**1982**). ''Evaluation of hearing-impaired listeners using a nonsense syllable test. II. Syllable recognition and consonant confusion patterns,'' J. Speech Hear. Res. **25,** 141–148.

Egan, J. (**1948**). ''Articulation testing methods,'' Laryngoscope **58,** 955–991.

Elliott, L. L. (**1964**). ''Note on predicting speech discrimination scores,'' J. Acoust. Soc. Am. **36,** 1961–1962.

Fletcher, H. (**1929**). *Speech and Hearing* (Van Nostrand, New York).

Hirsch, I. J., Davis, H., Silverman, S. R., Reynolds, E. G., Eldert, E., and Benson, R. W. (**1952**). ''Development of materials for speech audiometry,'' J. Speech Hear. Disord. **17**, 321–337.

Kalikow, D. N., Stevens, K. M., and Elliott, L. L. (**1977**). ''Development of a test of speech intelligibility in noise using sentence materials with controlled word predictability,'' J. Acoust. Soc. Am. **61,** 1337–1351.

Klatt, D. H. (**1980**). ''Speech perception: A model of acoustic-phonetic analysis and lexical access,'' in *Perception and Production of Fluent Speech*, edited by R. A. Cole (Erlbaum, Hillsdale, NJ).

Linacre, J. M., and Wright, B. D. (**1994**). BIGSTEPS: *Rasch-model computer program*, version 2.52 (MESA Press, Chicago).

Miller, G. A., and Nicely, P. E. (**1955**). ''An analysis of perceptual confusions among some English consonants,'' J. Acoust. Soc. Am. **27,** 338–352.

Oden, G. C., and Massaro, D. W. (**1978**). ''Integration of featural information in speech perception,'' Psychol. Rev. **85,** 172–191.

Owens, E., and Schubert, E. D. (**1977**). ''Development of the California Consonant Test,'' J. Speech Hear. Res. **20,** 463–474.

Owens, E., Benedict, M., and Schubert, E. D. (**1972**). ''Consonant phonemic errors associated with pure tone configurations and certain kinds of hearing impairment,'' J. Speech Hear. Res. **15,** 308–322.

Owens, E., Kessler, D. K., Raggio, M. W., and Schubert, E. D. (**1985**). ''Analysis and revision of the Minimal Auditory Capabilities (MAC) battery,'' Ear Hear. **6**, 280–290.

Peterson, G. E., and Barney, H. L. (**1952**). ''Control methods used in a study of the vowels,'' J. Acoust. Soc. Am. **24,** 175–184.

Peterson, G. E., and Lehiste, I. (**1960**). ''Duration of syllable nuclei in English,'' J. Acoust. Soc. Am. **32,** 693–703.

Pickett, J. M., Martin, E. S., Johnson, D. D., Smith, S. B., Daniel, Z., Willis, D., and Otis, W. (**1970**). ''On patterns of speech feature reception by deaf listeners,'' in *Proceedings of the International Symposium on Speech Communication and Profound Deafness*, Stockholm, edited by G. Fant (A. G. Bell Association for the Deaf, Washington, DC), pp. 119–133.

Pisoni, D. B., and Sawusch, J. R. (**1975**). ''Some stages of processing in speech perception,'' in *Structure and process in speech perception*, edited by A. Cohen and S. G. Nooteboom (Springer-Verlag, New York).

Rasch, G. (**1980**). *Probabilistic Models for Some Intelligence and Attainment Tests* (University of Chicago Press, Chicago). (Originally published by Danmarks Paedagogiske Institut, Copenhagen, 1960.)

Sims, D. G. (**1975**). ''The validation of the CID everyday sentences test for use with the severely hearing impaired,'' J. Acad. Rehab. Audiol. **3**, 70–79.

Stevens, K. N. (**1960**). ''Toward a model for speech recognition,'' J. Acoust. Soc. Am. **32,** 47–55.

Stevens, K. N., and Halle, M. (**1967**). ''Remarks on analysis by synthesis and distinctive features,'' in *Models for the perception of speech and visual form*, edited by W. Wathen-Dunn (MIT, Cambridge).

Stevens, K. N., and House, A. S. (**1972**). ''Speech perception,'' in *Foundations of modern auditory theory: Volume II*, edited by J. Tobias (Academic, New York), pp. 1–62.

Thornton, A. R., and Raffin, M. J. M. (**1978**). ''Speech discrimination scores modeled as a binomial variable,'' J. Speech Hear. Res. **21,** 507–518.

Tillman, T. W., and Carhart, R. (**1966**). ''An expanded test for speech discrimination using CNC monosyllabic words; Northwestern University Auditory Test No. 6,'' USAF School of Aerospace Medicine, Technical Report No. SAM-TR-66-55 (Brooks Air Force Base, Texas).

Tyler, R. S. (**1994**). ''The use of speech-perception tests in audiological rehabilitation: Current and future research needs,'' in *Research in audiological rehabilitation: Current trends and future directions* (Monograph Supplement), edited by J. -P. Gagne and N. Tye-Murray, J. Acad. Rehab. Audiol. **27**, 47–66.

Wright, B. D., and Linacre, J. M. (**1991**). *Rasch-Model Computer Program*, version 2.0 (MESA Press, Chicago).

Wright, B. D., and Masters, G. N. (**1982**). *Rating Scale Analysis* (MESA, Chicago).

Wright, B. D., and Stone, M. H. (**1979**). *Best Test Design: Rasch Measurement* (MESA, Chicago).

Wright B., and Stone, M. (**1991**). *Separation Statistics*, Research Primer No. 1 (Jastak Associates, Wilmington, DE).

Training Japanese listeners to identify English /r/ and /l/: IV. Some effects of perceptual learning on speech production

Ann R. Bradlow and David B. Pisoni
Speech Research Laboratory, Department of Psychology, Indiana University, Bloomington, Indiana 47405-1301

Reiko Akahane-Yamada and Yoh'ichi Tohkura
ATR Human Information Processing Research Laboratories, 2-2 Hikaridai, Seika-cho Soraku-gun, Kyoto, 619-02 Japan

(Received 16 January 1996; revised 28 August 1996; accepted 22 November 1996)

This study investigated the effects of training in /r/–/l/ perceptual identification on /r/–/l/ production by adult Japanese speakers. Subjects were recorded producing English words that contrast /r/ and /l/ before and after participating in an extended period of /r/–/l/ identification training using a high-variability presentation format. All subjects showed significant perceptual learning as a result of the training program, and this perceptual learning generalized to novel items spoken by new talkers. Improvement in the Japanese trainees' /r/–/l/ spoken utterances as a consequence of perceptual training was evaluated using two separate tests with native English listeners. First, a direct comparison of the pretest and post-test tokens showed significant improvement in the perceived rating of /r/ and /l/ productions as a consequence of perceptual learning. Second, the post-test productions were more accurately identified by English listeners than the pretest productions in a two-alternative minimal-pair identification procedure. These results indicate that the knowledge gained during perceptual learning of /r/ and /l/ transferred to the production domain, and thus provides novel information regarding the relationship between speech perception and production. [S0001-4966(97)02404-1]

PACS numbers: 43.71.Hw, 43.71.An, 43.71.Es [WS]

INTRODUCTION

The relationship between speech perception and speech production has been a long-standing issue in speech science and experimental phonetics. Some researchers have proposed a direct link between perception and production. For example, motor theorists (e.g., Liberman *et al.*, 1967; Liberman and Mattingly, 1985; Liberman and Mattingly, 1989) claim that listeners perceive speech in terms of their own articulatory gestures that would produce the perceived sound. A central tenet of motor theory is that there is a specialized phonetic module that represents speech units in terms of articulatory gestures, and that this module mediates both speech perception and production. Thus, motor theory supposes a single, shared representation for speech perception and production. Other theorists have viewed the two processes of speech communication as much more autonomous. For example, proponents of acoustic-auditory theories of speech perception (e.g., Stevens and Blumstein, 1981; Diehl and Kluender, 1989) have argued that the processes of speech perception operate on the acoustic medium independently of the articulatory gestures that produced it. In other words, this approach takes the acoustic signal as the object of speech perception, and makes no explicit claims about the perception–production relationship. However, this approach does presuppose that speech perception and production are indirectly linked via common acoustically defined targets and auditory feedback mechanisms that operate during speech production. A third theoretical position, the direct-realist approach to speech perception (e.g., Fowler, 1986; Best, 1995), proposes that the listener directly perceives the articulatory gestures of the speaker in terms of the structure they impart to the acoustic medium. According to this view which is also known as event perception, the objects (events) of speech perception are the articulatory gestures, and speakers aim to achieve gesturally defined targets during speech production. Thus, the direct-realist approach proposes that speech perception and production are inextricably linked by virtue of their common communicative goal. In contrast to motor theory, however, the direct-realist approach does not propose a specialized phonetic module that mediates the direct perception–production link. Rather, direct-realism proposes that the direct speech perception–production link, which helps to ensure speaker–hearer parity, is a specific case of generally integrated event perception and action systems.

Also of long-standing interest is the acquisition of novel phonetic categories by non-native speakers. Previous research has shown that foreign accents persist even for highly proficient speakers of a non-native language (e.g., Tahta *et al.*, 1981; Flege and Hillenbrand, 1987), and that non-native speakers have extreme difficulty with both the perception and production of certain non-native phonetic contrasts (e.g., Flege, 1988; Goto, 1971). Second-language learners thus present cases where certain aspects of speaker–hearer parity break down; that is, where there is a mismatch between the phonetic system of the language-user and of the target language community. For this reason an investigation of speech perception and production by these subjects, and of the changes that occur as a result of second-language

training, can provide a behavioral window into the mental representation that underlies the perception–production link.

To this end, the present study builds on earlier research from our laboratories that has established an effective procedure for training Japanese listeners to identify the English /r/–/l/ contrast, which is neutralized in Japanese (Logan *et al.*, 1991; Lively *et al.*, 1993, 1994). We wanted to know how the acquisition of a non-native perceptual contrast would affect control over production of that contrast. Thus, by directly examining the effect of perceptual learning on speech production, this project attempted to provide novel information regarding the relationship between speech perception and production in general. To accomplish this, we examined the effectiveness of perceptual identification training procedures for the acquisition of a non-native phonetic contrast in both perception and production. Any transfer of learning in perception to the production domain would provide important new evidence for a direct perception–production link. Furthermore, this outcome would suggest that perceptual identification training can facilitate the acquisition of production categories for second-language learners, as well as for other ''special populations.''

Previous studies that have investigated the relationship between perception and production of non-native phonetic contrasts, have generally focused on the subjects' performance in perception and production at a single point in time. For example, studies by Goto (1971) and by Sheldon and Strange (1982) showed that some Japanese subjects were able to produce identifiable /r/ and /l/ tokens even though they were unable to reliably identify native English /r/ and /l/ tokens. This finding led these researchers to conclude that production can precede perception in the acquisition of a non-native contrast. Similarly, in a study of /r/, /l/, and /w/ productions by a large number of Japanese speakers with varying degrees of exposure to English, Yamada *et al.* (1994) found that for some of the subjects, production abilities exceeded perception abilities, but not vice versa. Although these studies are informative about the relationship between perception and production in adult second-language learners, they do not provide quantitative information about how the changes in one domain (i.e., perception) affect performance in the other domain (i.e., production). Whereas the information provided by the studies discussed above is correlational, the major goal of the present study was to investigate the possibility of a functional perception–production link to the extent that success in perceptual learning leads directly to an improvement in speech production by adult second-language learners.

Two recent studies provide some indication that transfer of perceptual learning to speech production can occur. For example, Rochet (1995) reported that after perceptual identification training with a synthetic French /bu/–/pu/ continuum, Mandarin speakers displayed more French-like voice onset time (VOT) perceptual categorization. Furthermore, production data from the Mandarin subjects showed a change in VOT durations in the direction of native French VOT durations. In several recent studies with children who have articulation disorders, Jamieson and Rvachew (Jamieson and Rvachew, 1992; Rvachew, 1994; Jamieson and Rvachew, 1994) found that speech perception training can facilitate sound production learning in children who exhibit both perception and production deficits. For instance, Rvachew (1994) found that subjects who received perception training in conjunction with traditional speech production therapy showed greater improvement in /ʃ/ production than control subjects who did not receive perception training. This result indicated that perception training can enhance the effectiveness of speech production therapy for phonologically delayed children. In the present study, we examined this perception–production link further by investigating the effects of perceptual learning on production of the /r/–/l/ contrast by adult native speakers of Japanese in the absence of any explicit production training, and across a wide range of phonetic contexts.

The general design of the present study had four phases: a pretest phase, a perceptual training phase, a post-test phase, and a production assessment phase. During the pretest phase, both perception and production data were collected from a group of adult Japanese speakers. In the perceptual training phase, the subjects were trained to identify English /r/ and /l/ minimal pairs using the high-variability training technique developed in earlier work (see Logan *et al.*, 1991; Lively *et al.*, 1993, 1994; Yamada, 1993 for details regarding the principal motivation behind this procedure). In the post-test phase, both perception and production data were once again collected from the Japanese listeners. Finally, during the production assessment phase, the pre- and post-test utterances were evaluated by a group of native American English speakers. Thus, in this study, we investigated the effect of perceptual learning on subsequent performance in both perception and production.

I. PERCEPTUAL LEARNING

A. Method

1. Subjects

The subjects were 11 adult, native speakers of Japanese (5 females and 6 males), ranging in age from 19 to 22 years. None had lived abroad or had any special training in English conversation. However, as is typical in Japan, all of the subjects had studied English since junior high school (from about age 12). The subjects were recruited from Doshisha University, Kyoto prefecture, Japan. A comparable group of 12 Japanese speakers (6 females and 6 males) served as control subjects. These control subjects were also drawn from the same population as the experimental subjects. None of the subjects reported any history of a speech or hearing impairment at the time of testing. A hearing screening performed at 15 dB hearing level (HL) for the frequencies 250–8000 Hz showed all subjects to have normal bilateral acuity. All subjects were paid for their participation.

2. Procedure

The perceptual training program followed the high-variability procedures first developed by Logan *et al.* (1991), and later extended by Yamada (1993). This procedure consisted of a pretest phase, a training phase, and post-test phase. The pretest phase consisted of a minimal pair identification task with naturally produced English /r/–/l/ minimal

word pairs produced by a native speaker of general American English. The perceptual learning phase involved 45 sessions (over a period of 3–4 weeks) of perceptual identification with feedback. The training stimuli consisted of a large number of naturally spoken /r/–/l/ minimal word pairs produced by five native speakers of general American English. Finally, the post-test phase included a perceptual identification post-test (identical to the pretest), and two tests of generalization. The tests of perceptual generalization consisted of a minimal word pair identification task with novel words spoken by a new speaker (test of generalization 1), and with novel words produced by one of the speakers used in creating the training stimuli (test of generalization 2). Control subjects performed the pretest, post-test, and two tests of generalization; however, these subjects did not go through the perceptual identification training program. For the control group, the time lag between the pretest and post-test phase was equal to the time it took for the trained subjects to participate in the entire 45-session training program (i.e., 3–4 weeks).

All perception training and testing was carried out at ATR Human Information Processing Research Laboratories in Kyoto, Japan. For all four perception tests (pretest, post-test, two tests of generalization) the same two-alternative forced choice minimal word pair identification procedure was used. Subjects were tested individually in a sound-treated room where they sat in a cubicle equipped with headphones (STAX-SR-Lambda Signature) and a NeXT workstation. Each trial began with a 500-ms presentation on the computer monitor of the standard English orthographies for an /r/–/l/ minimal pair. One member of the minimal pair appeared in the lower left corner of the screen; the other appeared in the lower right corner. The spoken test word was then presented at a comfortable listening level through the subjects' headphones. Subjects had 10 s to respond by pressing ''1'' to identify the spoken word as the orthographic word on the left of the screen, or ''2'' for the word on the right of the screen. For half the trials, a response of ''1'' corresponded to an /r/ identification label and a response of ''2'' corresponded to an /l/ identification label; for the other half of the trials, the order of identification labels was reversed. During the training trials, feedback was given in the form of a chime signaling a correct response and a buzzer signaling an incorrect response. After the buzzer for an incorrect response, the test word was repeated. As an additional motivation, each correct response received a 1 yen (approximately 1 cent) reward over and above the regular subject payment. There was no feedback in the pretest, post-test, or tests of generalization.

3. Stimuli

A large digital database of spoken words for the perception tests was originally recorded and compiled in the Speech Research Laboratory at Indiana University (see Logan *et al.*, 1991 for additional details). All stimuli were recorded in an IAC sound-attenuated booth. The utterances were low-pass filtered at 4.8 kHz and digitized at 10 kHz using a 12-bit analog-to-digital converter. The waveform files were then equated for rms amplitude using software developed in the Speech Research Laboratory. The files were then digitally transferred to ATR Human Information Processing Research Laboratories where they were upsampled to 22.05 kHz and rescaled to 16-bit resolution for presentation on the NeXT workstations.

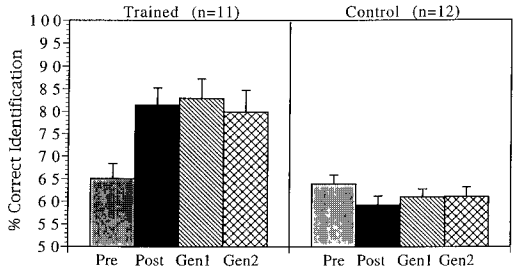

FIG. 1. Percent correct perceptual identification performance for trained (left panel) and control (right panel) subjects at pretest, post-test, and the two tests of generalization. The error bars represent one standard error from the mean.

The pretest and post-test stimuli were the same words as those used by Strange and Dittmann (1984). This set of stimuli consisted of 16 minimal pairs that contrasted /r/ and /l/ in four phonetic environments: initial singleton, initial cluster, intervocalic, and final cluster. There were also four minimal pairs that contrasted other English phonemes. These stimuli were recorded by a male speaker of general American English. The training stimuli consisted of 68 minimal pairs that contrasted /r/ and /l/ in five phonetic environments: 12 initial singleton pairs, 25 initial cluster pairs, 5 intervocalic pairs, 15 final singleton pairs, and 11 final cluster pairs. These stimuli were recorded by 5 speakers of general American English (3 males and 2 females). The stimuli for the first test of generalization consisted of an additional 96 words with /r/ or /l/ in five phonetic environments spoken by a new talker (i.e., new words by a new talker). The stimuli for the second test of generalization consisted of an additional 99 /r/–/l/ words (5 environments) spoken by one of the talkers in the training set (i.e., new words by an old talker).

B. Results of Perceptual Learning

Figure 1 shows the results of perceptual identification training for the experimental (left panel) and the control (right panel) groups. This figure displays the percentage of correct identifications for all four of the perceptual tests: the pretest, post-test, and the two tests of generalization. As shown in the left panel, the experimental (trained) group of subjects showed an improvement in their identification scores from pretest (65% correct identification) to post-test (81% correct identification), and this increase in performance was maintained for the two tests of generalization (83% and 80% correct identification for gen1 and gen2, respectively). Thus, on average, the trained subjects showed substantial gains in /r/–/l/ identification accuracy (16 percentage points). Nevertheless, it is important to note that this post-test level of identification accuracy is still substantially poorer than the near-perfect identification accuracy achieved by native English speakers.

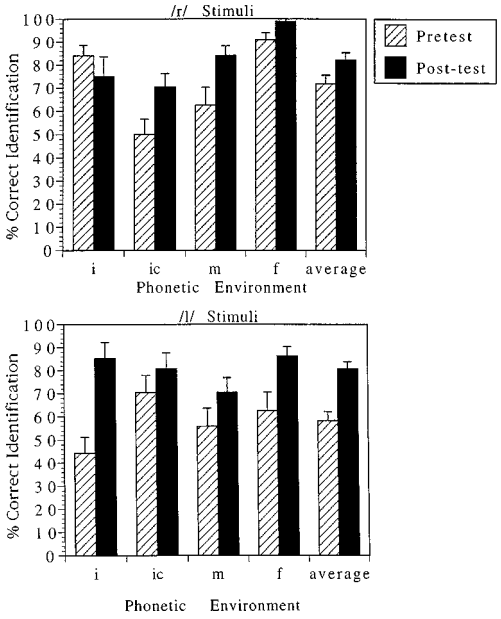

FIG. 2. Distribution of the Japanese trainees' identification responses at pretest and at post-test by phonetic environment. The upper panel shows the /r/ stimuli; the lower panel shows the /l/ stimuli. The environments are: i=initial, ic=initial cluster, m=medial, f=final. The error bars represent one standard error from the mean.

A two-factor analysis of variance (ANOVA) with group (trained, control) and test (pre, post, gen1, gen2) as factors showed a significant main effect of group [$F(1,84)=52.258$, $p<0.0001$], and a significant group×test interaction [$F(3,84)=5.136$, $p=0.0026$]. *Post hoc* pairwise comparisons (Fisher's PLSD) showed no difference between the trained and control groups' pretest accuracies. However, the trained group performed significantly better than the control group ($p<0.001$) on the post-test, as well as on both generalization tests. Furthermore, there was a significant improvement for the trained group from pretest to post-test ($p=0.0074$), pretest to gen1 ($p=0.0037$), and pretest to gen2 ($p=0.0141$). There was no difference between the post-test and either of the tests of generalization scores for the trained group, and no difference between the scores on all four tests for the control group.

In order to gain some insight into the perceptual reorganization that resulted from the perceptual learning task, we examined the pre- and post-test identification accuracies for the /r/ and /l/ stimuli separately for the trained subjects (see Fig. 2). A three-factor repeated measures ANOVA was performed with test (pre or post) as the repeated measure, and phoneme (/r/ or /l/) and environment (four levels) as within-groups factors.

This analysis revealed three main findings. First, the main effect of test was highly significant [$F(1,80)=40.369$, $p<0.0001$], due to the overall improvement in identification accuracy from pretest to post-test. Second, the main effect of phoneme was also significant [$F(1,80)=4.215$, $p=0.043$], with /r/ being generally more accurately identified than /l/. Finally, there was a significant interaction between test and phoneme [$F(1,80)=5.644$, $p=0.012$]: /l/ tokens showed more overall improvement from pretest to post-test than /r/ tokens. This change from an asymmetrical distribution of /r/–/l/ identification accuracy at pretest to a more symmetrical distribution at post-test suggests that, after training, subjects show signs of developing perceptual categories that correspond more closely to the target English /r/ and /l/ categories.

There was also a main effect of phonetic environment [$F(3,80)=4.603$, $p<0.005$], indicating that the accuracy for the various phonetic environments increased from initial cluster position to medial to initial singleton to final. This dependency on phonetic context replicates earlier findings reported by Gillette (1980) and Mochizuki (1981), as well as Sheldon and Strange (1982). The interaction between phoneme and environment was significant [$F(3,80)=4.647$, $p<0.005$], due to the high identification accuracy of /l/ in initial cluster position relative to /r/ in that environment. Finally, the three-way interaction (test×phoneme ×environment) [$F(3,80)=7.272$, $p<0.0002$] was also significant indicating that the perceptual learning of /r/ and /l/ was highly context-dependent.

In summary, these perceptual learning data provide a further replication of the findings of our earlier studies that used the high-variability perceptual training procedure to modify the acquisition of the English /r/–/l/ contrast by adult Japanese speakers (Logan *et al.*, 1991; Lively *et al.*, 1993; Lively *et al.*, 1994; Yamada, 1993). Having demonstrated significant perceptual learning for these Japanese adults, we now turn to the main concern of this study, that is, an assessment of the effects of perceptual learning on the production of English /r/–/l/ minimal word pairs by these subjects. Our goal here was to assess the extent to which the phonetic knowledge acquired during perceptual learning transferred to the production domain.

II. EFFECTS OF PERCEPTUAL LEARNING ON SPEECH PRODUCTION

A. Japanese /r/–/l/ productions

1. Procedure

During the pretest and post-test phases, audio recordings were made of the Japanese subjects producing English words that contrast /r/ and /l/. The pre- and post-test recordings were made directly before and after the perception pretest and post-test, respectively. The speech production task used a repetition procedure in which the subject read a set of English /r/–/l/ minimal pairs from a list of randomly ordered words. The subjects were provided with both visual and auditory prompts. The visual prompts consisted of a list of words written in standard English orthography. The auditory prompts consisted of a digital recording of the words spoken by a male speaker of general American English. This speaker was not one of the speakers that produced the stimuli for the perceptual identification tasks. The purpose of the auditory prompt was to provide the speakers with a model of how to pronounce the entire word aside from the target /r/ or /l/ segments. Because Japanese subjects have great difficulty with the /r/–/l/ perceptual contrast, we assumed that the subjects would not simply imitate the auditory model without relying on the printed word to inform them whether the word

was the /r/ or /l/ member of the minimal pair. In this way, this task was not simply a direct imitation task, but rather was a repetition task that was mediated by linguistic intention. The printed prompts provided the subjects with the abstract linguistic-phonetic information they needed to guide their productions of the /r/ and /l/ phonemes, and the auditory prompts helped ensure that the rest of the words remained relatively stable across subjects. Since the main concern of this study was the change in /r/ and /l/ production due to perceptual identification training, this task was deemed appropriate for a pre- and post-test measure of production ability. Nevertheless, it is important to note that this production task was not a measure of spontaneous speech production. It remains for future research to determine the relationship between pre- and post-test performance on our repetition task and on more naturalistic measures of production ability.

The recordings were made in an anechoic chamber at ATR Human Information Processing Research Laboratories. The recordings were digitized at a sampling rate of 22.05 kHz with 16-bit resolution through DAT (Sony PCM-2500 or 2600) and a DAT interface, DAT-Link+ (Townshend Computer Tools., Inc.). The speech files were stored on the hard disk of a Sun Sparc workstation and were then digitally transferred to the Speech Research Laboratory at Indiana University where they were rescaled to 12-bit resolution for later presentation to native speakers of English using a PDP-11 laboratory computer.

2. Stimuli

The stimuli obtained from the pretest and post-test recordings consisted of 55 English words containing /r/ and /l/, giving a total of 110 words. These stimuli for the production tests included /r/–/l/ minimal pairs with the target phoneme in seven phonetic environments. The breakdown of the word-pairs by phonetic environment was as follows: 10 with initial singletons, 10 with initial clusters, 10 with medial singletons, 10 with final singletons, 10 with final clusters, 2 with medial clusters, and 3 with initial triple clusters (e.g., ''splint-sprint''). Of these minimal pairs, half in each of the first five environments listed above came from the set of minimal pairs that were included in the earlier perceptual training stimuli, the other half were ''new,'' that is, they were not used in any of the perception tests. None of the perceptual stimulus sets included minimal pairs with /r/ and /l/ in the last two environments listed above: these were all ''new'' word pairs for our subjects.

B. American English listeners' preference judgments

To assess the transfer of the Japanese trainees' perceptual learning to production, a group of native speakers of American English performed a paired comparison task using each Japanese trainee's pretest and post-test productions. The purpose of this procedure was to assess whether native speakers of American English could reliably discriminate between the trainees' pre- and post-test productions. If the perceptual learning procedure is effective in producing changes in control over speech production, then the native English listeners should display a consistent preference for the post-test tokens over the pretest tokens. This paired-comparison method of judging the trainees' improvement in production was selected as an initial test because it was expected to be sensitive to small differences in articulation. Our rationale was that if the Japanese trainees' post-test productions were indeed reliably preferred over the pretest productions, then we would have a reason to submit the pre- and post-test productions to additional tests of perceptual analysis. The initial paired-comparison task provides information about the degree and direction of change between the pretest and post-test tokens. The subsequent minimal pair identification task provides information about a change in speech intelligibility specifically related to improved /r/ and /l/ articulation.

1. Procedure

Each trial began with a visual presentation of the target word in standard English orthography centered on a CRT monitor. The listeners then heard a single Japanese trainee's pretest and post-test productions of this word over headphones. The two versions of the target word were separated by 500 ms of silence. The listeners then had to decide which version of the target word was ''better,'' that is, which version was ''a clearer and more intelligible pronunciation of the word shown on the screen.'' The judges responded on a seven-button response box which was labeled using a seven-point scale where ''1'' indicated that the first version was ''much better'' than the second version, ''4'' indicated no noticeable difference between the two versions, and ''7'' indicated that the second version was much better than the first. Each pair of utterances was presented twice: once with the pretest version first and the post-test version second, and once in the reverse order. There were 110 pre-post pairs in each of the two presentation orders, plus 10 practice trials at the start of the session, for a total of 230 trials per session. The initial practice trials were excluded from the final data analysis. Each listener judged the full set of pre- and post-test productions from a single Japanese speaker. Ten listeners were assigned to each of the 23 Japanese speakers. Because there were 11 Japanese trained subjects and 12 Japanese control subjects, a total of 230 native English speakers participated as subjects. No American listener judged more than one Japanese subjects' productions. In the final data analysis, the responses were recorded so that a response of ''5'' or higher always corresponded to a preference for the post-test version, and a response of ''3'' or lower always corresponded to a preference for the pretest version. This recoding simply takes into account the counterbalanced order of stimulus presentation.

2. Subjects

The American English listeners were all students at Indiana University. None reported any history of speech or hearing impairment at the time of testing, and all were monolingual native speakers of general American English. All received one hour of course credit for their participation.

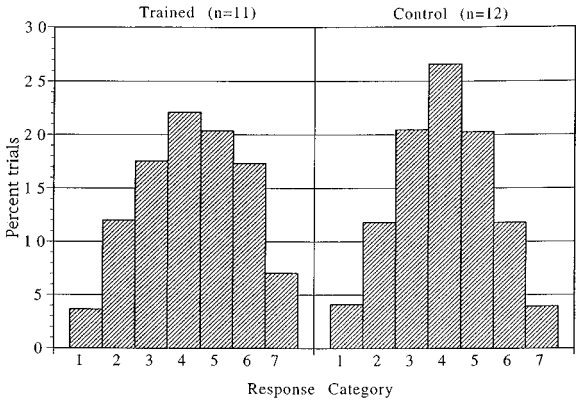

FIG. 3. Distribution of preference ratings across all seven response categories by the American English listeners for the Japanese trained (left panel) and control (right panel) subjects' pre- and post-test productions. A response of ''1'' indicated that the pretest version was ''much better'' than the post-test version, ''4'' indicated no noticeable difference between the pre- and post-test versions, and ''7'' indicated that the post-test token was ''much better'' than the pretest version.

3. Results

In the analysis of the data from the paired-comparison task, we examined the distribution of subjects' responses across the seven response categories for both the trained subjects (Fig. 3, left panel) and the control subjects (Fig. 3, right panel). The data shown in Fig. 3 are represented as proportions of the total number of responses from all listeners for each of the two groups of Japanese subjects.

As shown in Fig. 3, the distribution of ratings for the trained subjects' tokens (left panel) was skewed in favor of higher ratings, indicating a preference for the post-test tokens over the pretest tokens. In contrast, the native English speakers' ratings of the control subjects' tokens (right panel) were normally distributed across the seven response categories, indicating no systematic preference for either the pretest or the post-test tokens. The native English speakers' preference for the trained subjects' post-test productions over their pretest productions was confirmed by a highly significant chi square statistic, using the distribution of ratings for the control subjects' productions as the expected distribution [chi square$=1639.4$, $p(6)<0.001$]. This analysis was performed across all 24 200 trials for the trained subjects (220 trials$\times$11 trainees$\times$10 American listeners). Additionally, the Pearson coefficient of skewness for the trained subjects was negative (-0.527), indicating a greater median than mean; whereas for the control subjects, the mean and median were very close (Pearson coefficient of skewness$=0.090$). Finally, the frequency of ''post=pre'' responses (response category 4) was lower for the trained subjects than for the control subjects [$t(21)=-7.297$, $p<0.0001$], also indicating the increased discriminability of the trained subjects' pre- and post-test productions relative to those of the control subjects.

Taken together, these analyses of the preference data for the tokens produced by the trained and control Japanese subjects demonstrate reliable transfer of learning from perception to production for the trained subjects. Native speakers of English were able to reliably detect an improvement from the pretest to the post-test productions for the trained subjects; whereas, no reliable difference was observed for the tokens produced by the control subjects. Given that native speakers can discriminate the trained subjects' pre- and post-test tokens, our next step was to assess the extent to which the improvement in these utterances was due to improved /r/ and /l/ articulation; that is, whether American English listeners can identify the post-test productions more accurately than the pretest productions in a minimal pair identification task.

C. American English listeners' identification data

1. Procedure

The procedure for the minimal pair identification task was closely modeled after the task that the Japanese trainees performed during perceptual testing and training. In each experimental session, English listeners identified the full set of pre- and post-test productions from a single Japanese trainee. Each trial began with the two members of an English /r/–/l/ minimal pair appearing in standard English orthography on a CRT monitor in front of the subjects. One member of the minimal pair produced by a Japanese trainee was then presented over headphones. The listeners identified the word by pushing the left button on a two-button response box to select the word on the left of the CRT monitor, or the right button for the word on the right. Within a single experimental session, the complete set of pre- and post-test production tokens from a single Japanese trainee was presented in random order with each word presented twice, once with the correct response as a left button and once with the correct response as a right button. This arrangement resulted in a total of 440 experimental trials plus 10 practice trials at the beginning of the session, for a total of 450 trials. The productions of each of the 11 Japanese trainees and each of the 12 Japanese control subjects was identified in this manner by an independent panel of 10 English listeners, for a total of 230 listeners (10 different listeners for each of the 23 Japanese subjects). No American listener judged more than one Japanese subjects' productions.

2. Subjects

The English listeners were recruited from the university community in Bloomington, Indiana. None reported any history of speech or hearing impairment at the time of testing, and all were monolingual speakers of general American English. All were paid for their participation.

3. Results

Figure 4 shows percent correct identification of tokens from the trained (left panel) and control (right panel) Japanese subjects' productions as judged by the English listeners. Each panel shows the pretest level of performance along with the identification accuracy of the Japanese productions at the post-test phase for the ''old'' words (words that were included in the perceptual training stimulus set) and for the ''new'' words (novel words that the Japanese subjects had not been exposed to in any of the perceptual identification tests). The data shown here are averaged across the five phonetic environments that were included in the perceptual training stimulus set. The remaining two phonetic environ-

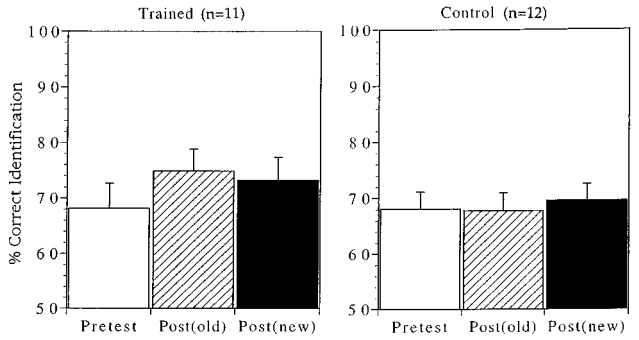

FIG. 4. Percent correct performance for trained (left panel) and control (right panel) subjects' productions as judged by American English listeners in the minimal pair identification task. The open bar represents the full set of pretest tokens, the slashed bar represents the post-test tokens that were included in the perceptual training set, and the solid bar represents the post-tokens that were not included in the perceptual training set. The error bars represent one standard error from the mean.

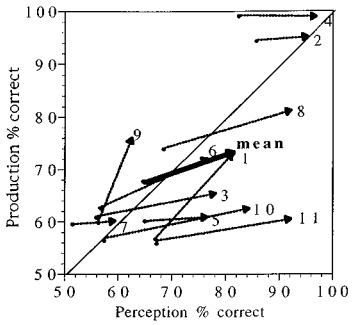

FIG. 5. Vector plot of individual Japanese subjects' perceptual identification accuracy (x axis) and production identification accuracy (y axis) from pre-test to post-test. Each individual subject's performance is indicated by a numbered vector. The mean performance is represented by the bold arrow. The diagonal represents the hypothetical vector location and orientation for a perfect correlation between perception and production.

ments that were included in the production pre- and post-test set (medial clusters and initial triple clusters) were omitted from this ''old'' versus ''new'' analysis because there were no ''old'' stimuli for these two environments.

As shown in Fig. 4, utterances from the trained subjects displayed significant improvement in identification from pre-test to post-test. Moreover, this improvement was consistent across both the ''old'' and the ''new'' items. A one-factor repeated measures ANOVA showed a significant effect of test [$F(2,20)=8.857$, $p=0.0018$]. Paired t tests established a significant difference between pretest and ''old'' post-test items [$t(10)=-3.321$, $p=0.0077$], between pretest and ''new'' post-test items [$t(10)=-2.809$, $p=0.0185$], but no difference between ''old'' post-test and ''new'' post-test items [$t(10)=1.705$, $p=0.1189$]. In contrast, for the control subjects there was no difference in identification across pre-test, ''new'' post-test or ''old'' post-test items. These data demonstrate that the identifiability of the Japanese trainees' productions in a two-alternative forced-choice task improved as a result of the perceptual training program, and that this improvement generalized to both ''old'' and ''new'' tokens.

Table I gives the identification accuracy scores averaged across all 11 trained subjects at pretest and at post-test broken down by phonetic environment and by phoneme (/r/ or /l/). A three-factor repeated measures ANOVA was performed with test (pre or post) as the repeated measure, and phoneme and phonetic environment as the within-groups factors. In this analysis, we found a highly significant main effect of the repeated measure factor (i.e., test) [$F(1,140)=21.850$, $p<0.001$] indicating a strong overall improvement in performance from pre- to post-test. There was also a highly significant main effect of phoneme [$F(1,140)=19.951$, $p<0.001$], due to the generally higher identification accuracy of the /r/ tokens relative to the /l/ tokens at both pre- and post-test. There was no main effect of phonetic environment. There were also no significant interactions between test and either phoneme or environment, indicating that the degree of improvement in speech production was consistent across these factors. Thus, the results show that the Japanese trainees' post-test productions were more accurately identified by native English listeners than their pretest productions. Additionally, these minimal-pair identification data indicate that, at both pretest and post-test, the /r/ tokens were more accurately identified than the /l/ tokens.

TABLE I. Pretest and post-test identification accuracies by environment for the Japanese trainee productions as judged by American English listeners.

	/r/		/l/	
Environment	Pretest	Post-test	Pretest	Post-test
Initial	68.29	81.29	60.46	68.29
Initial cluster	72.83	77.08	49.33	54.92
Medial	74.83	77.50	48.00	57.96
Final	84.38	82.13	66.54	73.54
Final cluster	78.25	81.92	70.29	77.04
Initial triple cluster	76.26	84.03	43.47	49.18
Medial cluster	68.96	70.63	51.25	59.17
Totals	74.83	79.22	55.62	62.87

The results of the two production evaluation tests (the paired comparison and the minimal pair identification task) clearly demonstrate significant improvements in the Japanese trainees' productions of /r/ and /l/ as a result of perceptual learning. The English listeners consistently judged the post-test utterances to be ''better'' tokens than the pre-test tokens, and they were more accurate in identifying the post-test tokens in an /r/–/l/ minimal-pair identification task. Furthermore, this improvement in production was robust in that it occurred across a variety of phonetic environments and it even generalized to novel words, i.e., words that the trainees had not been exposed to at all during perceptual learning. In contrast, the control subjects' productions showed no evidence of any change or improvement across any of these conditions. Having established that the perception training was effective in facilitating improvements in speech production, we now turn to an examination of the relationship between perception and production for individual subjects.

III. RELATION BETWEEN PERCEPTION AND PRODUCTION

Figure 5 displays the amount of learning observed in perception and production for each of the 11 Japanese train-

TABLE II. Individual Japanese trainee perception and production accuracy scores at pretest and at post-test. These data are averaged across /r/ and /l/, as well as across all phonetic environments.

	Perception			Production		
Trainee	Pretest	Post-test	Difference	Pretest	Post-test	Difference
1	67.19	81.25	14.06	57.18	73.00	15.82
2	85.94	95.31	9.37	94.59	95.18	0.59
3	56.25	78.13	21.88	61.18	65.41	4.23
4	82.81	96.88	14.07	99.18	98.95	−0.23
5	65.63	76.56	10.93	60.27	60.91	0.64
6	56.25	76.56	20.31	62.64	72.14	9.50
7	51.56	59.38	7.82	59.64	60.18	0.54
8	68.75	92.19	23.44	74.27	81.32	7.05
9	56.25	62.50	6.25	60.00	76.09	16.09
10	57.81	84.38	26.57	57.00	62.55	5.55
11	67.18	92.18	25.00	56.50	60.55	4.05
Totals	65.06	81.39	16.33	67.50	73.30	5.80

ees. This figure shows a ''perception–production space'' where the *x* axis represents each trainee's accuracy in perceptual identification of /r/ and /l/ minimal pairs, and the *y* axis represents accuracy in the identification of each trainee's productions by American English listeners. Thus, each trainee's performance is represented by a vector whose starting point corresponds to the trainee's pretest performance, and whose ending point corresponds to the trainee's post-test performance within this space. The group mean performance is indicated by the bold arrow, and the diagonal is the hypothesized vector that would indicate a perfect correlation between perception and production. The individual subjects' scores are given in Table II.

In perception, even though each subject showed some improvement from pretest to post-test, there was considerable individual variation across subjects in pretest accuracy, in post-test accuracy, as well as in the percentage change from pretest to post-test (see Table II). For instance, for the two subjects who performed well in the perception pretest (subjects 2 and 4), the training program was effective in enhancing their abilities to identify English /r/ and /l/ such that at post-test they approached native levels of performance. In contrast, for the poorest performer in the perception pretest (subject 7), the training program was only moderately effective. It is as if the two high performers used the training sessions to ''fine-tune'' an already well-defined preexisting two-way perceptual contrast. In contrast, even after 45 sessions of minimal-pair identification training, the poorest performer showed almost no evidence of learning to split a single perceptual category into two new categories. A striking individual difference that emerges from this perceptual identification data can be seen in the comparison between subjects 9 and 10. These two subjects performed at comparable levels at pretest; however, at post-test a difference of more than 20 percentage points was observed.

This wide range of individual performance is consistent with previous findings reported in other cross-language studies of /r/–/l/ perception (e.g., Goto, 1971; Mochizuki, 1981; MacKain *et al.*, 1981; Sheldon and Strange, 1982; Yamada *et al.*, 1994), nevertheless, is it still unclear what specific factors determine individual performance. Here we simply note the strong positive rank-order correlation (Spearman rho $=0.730$, $p=0.021$) between pretest level of performance and relative perceptual improvement, where relative perceptual improvement is defined as post-test accuracy minus pretest accuracy divided by 100 minus pretest accuracy. This is a measure of improvement as a proportion of the ''room for improvement.'' This correlation indicates that pretest level of performance is a fairly good predictor of the effectiveness of the perceptual training program for individual subjects; however, as demonstrated by subjects 9 and 10, there are other factors at work here too.

We also observed considerable variation across individual subjects' production performance at pretest and post-test (Fig. 5 and Table II). Subjects 2 and 4 produced highly intelligible /r/'s and /l/'s at pretest, and therefore had very little room for any improvement to be observed in production. Several of the other subjects' pretest productions were identified at a level around 60% accuracy; however, there were also large differences in the degree of production improvement across these subjects. For example, the pretest productions of subjects 3 and 9 were identified at comparable levels of accuracy; however, subject 9's post-test productions were identified far more accurately than those of subject 3.

The results from the present investigation allowed us to extend these findings on individual variation in perception and production by looking at the relationship between changes in one domain (speech perception) and changes in the other domain (speech production). It is clear from the data shown in Fig. 5 and Table II that at the post-test phase, perception performance generally exceeded production performance. This is not surprising since the trainees had extensive training in speech perception, whereas there was no explicit training in speech production. Any improvement observed in speech production was a result of transfer of knowledge gained in perceptual learning to the production domain. By comparing the degrees of improvement in perception and production across the individual trainees, we can obtain additional insight into the underlying basis for the learning in the two domains. In this analysis, we examined the rank-order correlation between improvement in perception and production across all subjects to test the hypothesis that subjects who show the most perceptual learning also

show the most improvement in production. However, as shown in the figure, there is no such correlation (Spearman rho=0.202, $p=0.522$). In other words, it is not the case that improvement in perception and production proceeded in parallel within individual subjects. Rather, it appears that, although perceptual learning generally transferred to improved production of this non-native contrast, as indicated by the positive slope of the mean vector, the two processes proceeded at different rates within individual subjects.

A more detailed examination of specific subjects' data revealed two kinds of situations that led to the lack of correlation between degrees of learning in perception and production that we observed in the present data. The first is illustrated by a comparison of subjects 9 and 10. These two subjects performed at a similar low level of performance in the perception pretest; however, at post-test, subject 10 performed considerably better than subject 9. However, in production, subject 9 showed a larger change than subject 10. A possible explanation for this discrepancy between learning in perception and production is that subject 9 continued to focus on perceptual cues that are not relevant for /r/–/l/ identification throughout the perceptual training program. However, in the production post-test, this subject was able to implement cues that were effective for improved /r/–/l/ identification in a two-alternative forced-choice identification task with native English listeners. For example, this subject may have focused on durational cues rather than spectral cues, and these attributes were sufficient to signal an /r/–/l/ contrast in production but were ineffective for the perceptual identification of /r/ and /l/ by native English speakers. In other words, for this subject, an apparent improvement in production was, in fact, a result of inappropriate, yet consistent, perception and production.

A second situation that could lead to a lack of correlation between learning in perception and production is illustrated by a comparison of subjects 6 and 3. These subjects show that production improvement can vary across individuals, even when initial performance and the degree of learning in perception are comparable. These two subjects performed at similar levels at the pretest phase in both perception and production. They also showed similar degrees of improvement in perceptual accuracy. Nevertheless, subject 6's post-test productions were identified more accurately by English listeners than subject 3's post-test productions. In other words, although subjects 3 and 6 showed comparable gain in perception, the transfer of perceptual learning to production was more effective for subject 6 than it was for subject 3 within the time frame of the present study. It is conceivable that, given more time to acquire the motor skills required for accurate /r/ and /l/ articulation, subject 3 would begin to show production improvement that is comparable to that of subject 6.

In summary, our investigation into the relationship between learning in perception and changes in production within individual subjects showed three main results. First, we found considerable variation across subjects in initial performance in both perception and production. Second, we observed a link between perception and production to the extent that perceptual learning generally transferred to improved production. This is seen by the positive slope of the mean vector in Fig. 5. Finally, we found little correlation between degrees of learning in perception and production after training in perception, due to the wide range of individual variation in learning strategies. This is seen by the deviation of the mean vector from the diagonal in Fig. 5. Taken together these findings support the hypothesis that learning in perception and production are closely linked, since perceptual learning generally transferred to improvement in production. However, learning in the perceptual domain is not a necessary or sufficient condition for learning in the production domain: the processes of learning in the two domains appear to be distinct within individual subjects.

IV. GENERAL DISCUSSION

The main goal of this study was to investigate the effects of perceptual learning on the production of non-native phonetic contrasts, and in so doing, to provide new data concerning the relationship between speech perception and production. First, we replicated earlier findings regarding the effectiveness of the high-variability perceptual training program for the acquisition of the English /r/–/l/ perceptual contrast by Japanese adults. Then, we showed that the knowledge gained about the non-native contrast from perceptual learning transferred to production of English /r/–/l/ words by the Japanese trainees. This improvement in production using a high-variability training procedure in perception was revealed by the results of two separate, but complementary, perceptual evaluation procedures using American English listeners as judges. The initial direct-comparison test demonstrated that the words produced by the Japanese trainees improved, in a general sense, from pretraining to post-training. The second two-alternative forced-choice identification test then showed, in a more specific sense, that the improvement in production resulted in better /r/–/l/ minimal pair intelligibility. This result was obtained for seven of the eleven individual subjects. Of the remaining subjects, the lack of improvement in production was due to a ceiling effect (subjects 2 and 4), or to consistently poor performance in perception (subject 7). Only one subject showed substantial improvement in perception, but consistently poor production (subject 5). Finally, a close examination of the degrees of improvement in perception and production within the individual Japanese trainees showed that, although initial performance in perception and production are well correlated, there is substantial individual variation in the degrees of learning in the two domains.

Having observed transfer of perceptual learning to aspects of speech production, we can now speculate as to the mechanisms that are responsible for this transfer, and what this tells us about the relationship between speech perception and production. A first possible account, along the lines of auditory-acoustic theories of speech perception (e.g., Stevens and Blumstein, 1981; Diehl and Kluender, 1989), would suppose that the learning in production involves a mechanism by which articulatory commands are tuned to internal acoustic representations. By this view, perceptual learning leads to more accurate internal acoustic representations of the target speech sounds, and these improved representations function

as acoustic templates that play an important role in monitoring the articulatory output. Thus, the learning in production occurs during production *per se*, that is, there is no change in the articulatory commands until they are actually activated during articulation. An alternative possibility, along the lines of the motor theory (e.g., Liberman *et al.*, 1967; Liberman and Mattingly, 1985; Liberman and Mattingly, 1989) would suppose that it is the articulatory commands that are modified during perceptual training. Under this view, the changes that result from perceptual training constitute permanent changes in the internal representation that is common to both perception and production. Thus, according to this view, learning results in changes in a single, domain-independent, phonetic representation, and as such, accounts for the apparent transfer of learning in perception to improvement in production. A direct-realist approach (e.g., Fowler, 1986; Best, 1995) would posit that during the perceptually oriented training, the trainees become perceptually attuned to the invariant gestural features of English /r/ and /l/. The subsequent transfer of this perceptual learning to production occurs as a result of the post-test productions being guided by the now more accurate, gesturally defined /r/ and /l/ phonetic categories. According to this account, the /r/ and /l/ phonetic categories were modified on the basis of input from the auditory mode, but the effects of their modification are observed in both the perceptual and the production domains due to their integrated communicative function.

The present data do not provide conclusive evidence to support any one of these theoretical accounts regarding the underlying mechanisms that facilitate the transfer of perceptual learning to speech production. However, the finding that the transfer of perceptual learning to improvement in production occurred in the absence of any explicit instruction in /r/–/l/ production leads us to believe that there is a unified, common mental representation that underlies both speech perception and speech production. This claim is consistent with both the motor theory and direct-realist approach, which suppose that units of speech perception and production are integrally defined in terms of articulatory gestures, and therefore that changes in the one domain have concomitant changes in the other. This view is not inconsistent with the notion that the modified acoustic-perceptual representations function as ''output monitors'' during speech production. However, the fact that most subjects showed some improvement immediately after the perceptually oriented training program seems to provide evidence against the idea that the changes in production occurred *only* during production *per se*. Nevertheless, due to the lack of correlation between the degrees of learning in the two domains, it appears that the specific motor commands necessary for improved /r/–/l/ production may be acquired at different rates for different subjects. This suggests that modification of an underlying perceptuomotor, phonetic representation is not sufficient on its own to result in corresponding modifications in speech production.

From an applied point of view, this study provides very encouraging new data regarding the acquisition of non-native speech contrasts in laboratory settings. Our findings show very clearly that the high-variability perceptual training procedure is robust: it is not only effective in training Japanese adults to perceive the English /r/–/l/ contrast, as we have shown in several previous studies, but this training program is also effective in improving the pronunciation of these non-native speech sounds without any explicit training or feedback in speech production. This result is consistent with the recent findings of Rochet (1995) who reported that a change in VOT categorization was accompanied by a change in VOT production for Mandarin speakers exposed to a synthetic French VOT continuum. Additionally, the present results are compatible with the recent findings on phonologically delayed children reported by Jamieson and Rvachew (Jamieson and Rvachew, 1992; Rvachew, 1994; Jamieson and Rvachew, 1994), which showed clear benefits of perception training in conjunction with traditional speech production therapy for that population.

The research by Jamieson and Rvachew as well as the present study focused on cases where the observed pretraining phoneme inventory is reduced relative to the non-native target inventory, and where difficulties in both perception and production are known to occur. Similarly, the research by Rochet focused on a case where the trainees' native categories differed phonetically from the target categories in both perception and production. This situation, where there is a clear match between perception and production characteristics, is likely to be the case where transfer of perceptual learning to speech production will be observed. Recent models, such as Best's ''Perceptual Assimilation Model'' (PAM) (Best *et al.*, 1988; Best, 1994; Best, 1995) and Flege's ''Speech Learning Model'' (SLM) (Flege, 1987, 1992, 1995), provide theoretical frameworks within which we can consider further which non-native contrasts are likely to show transfer of perceptual learning to production and which ones will not.

Both of these models propose that non-native phoneme perception abilities can be explained, at least in part, by reference to the native phonetic space. For example, in the case of the perception of English /r/ and /l/ by Japanese speakers, the observed difficulties can be explained in these models by the fact that Japanese has no such contrast in its native inventory. The most similar native Japanese phoneme is /ɾ/, which is described as an alveolar flap or stop depending on the phonetic context. Thus, with respect to the native Japanese phoneme inventory, English /r/ and /l/ are equally categorizable as this Japanese phoneme, and the contrast is therefore not supported by the native system in either perception or production. Whereas Best's PAM model makes predictions about the initial difficulty that a given non-native contrast proposes to listeners from a given native language background, Flege's SLM also makes several specific predictions about the persistence of foreign-accented production of a non-native contrast. SLM predicts that as long as native categories subsume non-native categories, accurate perception and production of the target categories will be blocked. Thus, in SLM, it is assumed that improvement in speech production as a consequence of perceptual learning is due to a reorganization of the auditory-acoustic phonetic space which is the underlying system used for both speech perception and production. Thus, SLM would predict that, with

respect to adult second-language learning, changes in perception will transfer to changes in production, and these changes will proceed in parallel. Although PAM is not a model of speech learning, it would make similar predictions regarding the transfer of perceptual learning to speech production. PAM would predict that as the listener becomes more ''attuned'' to the gestural constellation that characterizes a nonnative phoneme, he/she should learn to produce the required gestures for the target phonetic segment.

Although both models account for the main findings of the present study showing transfer of perceptual learning to speech production, neither model includes a mechanism to account for the observed lack of correlation between degrees of learning in the two domains. This reflects the main focus of these models on the relationship between the pretraining and the target phonetic categories. However, the present data indicate that more comprehensive models of second-language phonetic acquisition will need to address some of the specific characteristics of the relationship between learning in perception and production, as well as their variability across individual subjects.

In conclusion, we would like to emphasize that our goal in this research was to develop new techniques for the modification of the structure of the trainee's phonetic system, and in so doing, to investigate the nature of the relationship between learning in speech perception and production. In developing the perceptual training program, rather than explicitly focusing the trainee's attention on the detailed physical attributes of the perception and production of the target contrast, our approach has been to present the trainee with many exemplars of the target categories so that he or she can learn to integrate the exemplars into a linguistically meaningful phonetic space. The present study replicated earlier studies that showed the effectiveness of this ''high-variability'' approach to the acquisition of a non-native perceptual contrast. More importantly, however, this study has now extended these results by demonstrating that the changes produced by this approach to non-native phoneme acquisition occur at a level beyond the perceptual domain, that is, the modification of phonetic perception and the knowledge gained from this domain transferred to promote changes in speech production and motor control of these phonetic contrasts.

ACKNOWLEDGMENTS

We are grateful to Luis Hernandez and Takahiro Adachi for technical support, and to Fernando Vanegas for subject running. We also thank Bernard Rochet, Catherine Best, and Winifred Strange for many helpful comments and suggestions. This work was supported by NIDCD Training Grant No. DC-00012 and by NIDCD Research Grant No. DC-00111 to Indiana University.

Best, C. T., McRoberts, G. W., and Sithole, N. M. (**1988**). ''Examination of perceptual reorganization for nonnative speech contrasts: Zulu click discrimination by English-speaking adults and infants,'' J. Exp. Psychol. Hum. Percept. Perform. **14,** 345–360.

Best, C. T. (**1994**). ''Learning to perceive the sound pattern of English,'' in *Advances in Infancy Research*, edited by C. Rovee-Collier and L. Lipsitt (Ablex, Norwood, NJ). Also in Haskins Laboratories Status Report on Speech Research **SR-114**, 31–80.

Best, C. T. (**1995**). ''A direct-realist view of cross-language speech perception,'' in *Speech Perception and Linguistic Experience: Issues in Cross-Language Speech Research*, edited by W. Strange (York, Timonium, MD), pp. 171–206.

Diehl, R. L., and Kluender, K. R. (**1989**). ''On the objects of speech perception,'' Ecol. Psychol. **1**, 1–45.

Flege, J. E. (**1987**). ''The production of ''new'' and ''similar'' phones in a foreign language: Evidence for the effect of equivalence classification,'' J. Phonetics **15**, 47–65.

Flege, J. E. (**1988**). ''The production and perception of foreign language speech sounds,'' in *Human Communication and its Disorders: A Review*, edited by H. Winitz (Ablex, Norwood, NJ), pp. 224–401.

Flege, J. E. (**1992**). ''Speech learning in a second language,'' in *Phonological Development: Models, Research, and Implications*, edited by C. Ferguson, L. Menn, and C. Stoel-Gammon (York, Timonium, MD), pp. 565–604.

Flege, J. E. (**1995**). ''Second language speech learning: Theory, findings and problems,'' in *Speech Perception and Linguistic Experience: Issues in Cross-Language Research* edited by W. Strange (York, Timonium, MD), pp. 233–272.

Flege, J. E., and Hillenbrand, J. (**1987**). ''Limits on phonetic accuracy in foreign language speech production,'' in *Interlanguage Phonology: The Acquisition of a Second Language Sound System*, edited by G. Ioup and S. Weinberger (Newbury House, Cambridge), pp. 176–201.

Fowler, C. A. (**1986**). ''An event approach to the study of speech perception from a direct-realist perspective,'' J. Phonetics **14**, 3–28.

Gillette, S. (**1980**). ''Contextual variation in the perception of *L* and *R* by Japanese and Korean speakers,'' Minn. Papers Ling. Philos. Lang. **6**, 59–72.

Goto, H. (**1971**). ''Auditory perception by normal Japanese adults of the sounds 'l' and 'r','' Neuropsychologia **9**, 317–323.

Jamieson, D. G., and Rvachew, S. (**1992**). ''Remediating speech production errors with sound identification training,'' J. Speech-Lang. Pathol. Audiol. **16**, 201–210.

Jamieson, D. G., and Rvachew, S. (**1994**). ''Perception, production and training of new consonant contrasts in children with articulation disorders,'' *Proceedings of the International Conference on Spoken Language Processing* (Acoustical Society of Japan, Yokohama), pp. 199–1202.

Liberman, A. M., Cooper, F. S., Shankweiler, D. P., and Studdert-Kennedy, M. (**1967**). ''Perception of the speech code,'' Psychol. Rev. **74,** 431–461.

Liberman, A. M., and Mattingly, I. G. (**1985**). ''The motor theory of speech perception revised,'' Cognition **21**, 1–36.

Liberman, A. M., and Mattingly, I. G. (**1989**). ''A specialization for speech perception,'' Science **245,** 489–494.

Lively, S. E., Logan, J. D., and Pisoni, D. B. (**1993**). ''Training Japanese listeners to identify English /r/ ad /l/: II. the role of phonetic environment and talker variability in learning new perceptual categories,'' J. Acoust. Soc. Am. **94,** 1242–1255.

Lively, S. E., Pisoni, D. B., Yamada, R. A., Tohkura, Y., and Yamada, T. (**1994**). ''Training Japanese listeners to identify English /r/ and /l/: III. Long-term retention of new phonetic categories,'' J. Acoust. Soc. Am. **96,** 2076–2087.

Logan, J. D., Lively, S. E., and Pisoni, D. B. (**1991**). ''Training Japanese listeners to identify English /r/ and /l/: A first report,'' J. Acoust. Soc. Am. **89,** 874–886.

MacKain, K. S., Best, C. T., and Strange, W. (**1981**). ''Categorical perception of English /r/ and /l/ by Japanese bilinguals,'' Appl. Psycholinguistics **2**, 369–390.

Mochizuki, M. (**1981**). ''The identification of /r/ and /l/ in natural and synthesized speech,'' J. Phonetics **9**, 283–303.

Rochet, B. L. (**1995**). ''Perception and production of second-language speech sounds by adults,'' in *Speech Perception and Linguistic Experience: Issues in Cross-Language Research*, edited by W. Strange (York, Timonium, MD), pp. 379–410.

Rvachew, S. (**1994**). ''Speech perception training can facilitate sound production learning,'' J. Speech Hearing Res. **37,** 347–357.

Sheldon, A., and Strange, W. (**1982**). ''The acquisition of /r/ and /l/ by Japanese learners of English: Evidence that speech production can precede speech perception,'' Appl. Psycholinguistics **3**, 243–261.

Stevens, K. N., and Blumstein, S. E. (**1981**). ''The search for invariant acoustic correlates of phonetic features,'' in *Perspectives on the Study of Speech*, edited by P. D. Eimas and J. L. Miller (Erlbaum, Hillsdale, NJ), pp. 1–38.

Strange, W., and Dittmann, S. (**1984**). ''Effects of discrimination training on

the perception of /r/–/l/ by Japanese adults learning English,'' Percept. Psychophys. **36,** 131–145.
Tahta, S., Wood, M., and Loewenthal, K. (**1981**). ''Foreign accents: Factors relating to transfer of accent from the first language to a second language,'' Lang. Speech **24**, 265–272.
Yamada, R. A. (**1993**). ''Effects of extended training on /r/ and /l/ identification by native speakers of Japanese,'' J. Acoust. Soc. Am. **93,** 2391(A).
Yamada, R. A., Strange, W., Magnuson, J. S., Pruitt, J. S., and Clarke III, W. D. (**1994**). ''The intelligibility of Japanese speakers' productions of American English /r/, /l/, and /w/, as evaluated by native speakers of American English,'' *Proceedings of the International Conference of Spoken Language Processing* (Acoustical Society of Japan, Yokohama), pp. 2023–2026.

Acceptability for temporal modification of consecutive segments in isolated words[a)]

Hiroaki Kato[b)] and Minoru Tsuzaki
ATR Human Information Processing Research Laboratories, Hikaridai 2-2, Seikacho, Kyoto, 619-02, Japan

Yoshinori Sagisaka
ATR Interpreting Telecommunications Research Laboratories, Hikaridai 2-2, Seikacho, Kyoto, 619-02, Japan

(Received 1 February 1996; accepted for publication 26 November 1996)

Perceptual sensitivity to temporal modification in two consecutive speech segments was measured in word contexts to explore the following two questions: (1) whether there is an interaction between multiple segmental durations, and (2) what aspect of the stimulus context determines the perceptually salient temporal markers? Experiment 1 obtained acceptability ratings for words with temporal modifications. The results showed that the compensatory change in duration of a vowel (V) and its adjacent consonant (C) is not perceptually so salient as expected for the simultaneous modifications in the two segments. This finding suggests the presence of a time perception range wider than a single segment (V or C). The results of experiment 1 also showed that rating scores for compensatory modification between V and C do not depend on the temporal order of modified pairs (VC or CV), but rather on the loudness difference between V and C; the acceptability decreased when the loudness difference between V and C became high. This suggests that perceptually salient markers locate around major jumps in loudness. The second finding, the dependence on the loudness jump, was replicated in experiment 2, which utilized a detection task for temporal modifications on nonspeech stimuli modeling the time-loudness features of the speech stimuli. Experiment 3 further investigated the influence of the temporal order of V and C by utilizing the detection task for the speech stimuli instead of the acceptability ratings. [S0001-4966(97)01904-8]

PACS numbers: 43.72.Ja, 43.71.Gv, 43.66.Mk [JS]

INTRODUCTION

Rules to assign segmental duration have been proposed for speech synthesis to replicate the segmental durations found in natural speech (Allen *et al.*, 1987; Campbell, 1992; Fant and Kruckenberg, 1989; Higuchi *et al.*, 1993; Kaiki and Sagisaka, 1992; Klatt, 1979; Sagisaka and Tohkura, 1984; van Santen, 1994). Each of the segmental durations produced by such durational rules will have a certain amount of error compared with the corresponding naturally spoken duration. The effectiveness of a durational rule should be evaluated by how much these errors are acceptable to human listeners, who are the final recipients of synthesized speech in general. While some of the durational rules have been perceptually evaluated (Carlson *et al.*, 1979; Sagisaka and Tohkura, 1984), in almost all previous cases, the average of the durational errors has been adopted as the measure for evaluation. Although we will not deny the effectiveness of this traditional approach, i.e., the effort to minimize the average acoustic error, we also find it crucial to investigate the ''perceptual'' basis to the evaluation of durational modification and to test the validity of the implicit premise in the traditional approach.

The implicit premise of this approach is that the sum of the perceived distortion corresponding to each segmental error becomes equal to the perceptual distortion for the entire speech. There are two possible problems with this premise. The first problem is in its giving every segment the same weighting in error summation. In other words, it neglects segment attributes capable of affecting perceptual sensitivity to durational modification. For example, both Huggins (1972a) and Carlson and Granström (1975) reported that their subjects were more sensitive to durational changes of vowel (V) segments than to those of consonant (C) segments. The results of perceptual studies by Kato *et al.* (1992) and Klatt and Cooper (1975) also suggested that durational modifications in word initial syllables are more critical than those in word medial or word final syllables. The second problem with the traditional premise is that it neglects dependencies among multiple errors. Relation factors between errors in adjacent segments, e.g., differences in relative directions of deviations (the same or opposite), may affect the total impression of the perceived distortions, even when the average amounts of errors remain the same. If such a contextual effect on perceptual evaluation could be specified quantitatively, we could obtain a more valid (closer to human evaluation) measure than the traditional simple average of acoustic errors in evaluating durational rules. While the first problem can be addressed by perceptual studies for temporal modifications of single segments, the second problem needs to be addressed by studies for simultaneous modifica-

[a)]Part of this work was presented at the Third International Conference on Spoken Language Processing in 1994. [*Re*: Proceedings of ICSLP-94, pp. 1979–1982.]

[b)]Electronic-mail: kato@hip.atr.co.jp

tions of multiple segments. However, only few studies have so far been made on the latter topic. In the current study, therefore, we have focused on this second problem, and have conducted experiments to examine perceptual sensitivity to modifications made onto two consecutive segmental durations in a word.

The current study utilized two measures for perceptual sensitivity, i.e., detectability and acceptability. The detectability is fairly intuitive and psychophysically well-defined. The acceptability is, on the other hand, not generally defined and may be evaluated based on different norms. A word can have many quite different emotional or emphatic realizations which are judged to be equally acceptable according to the speakers intention. We, therefore, limited the material to normally pronounced word samples without any special emotional or emphatic intention from the speaker and measured the rate of acceptability for each manipulated stimulus as a normally stated exemplar of that token, focusing on the temporal aspect of the stimulus. In all of this, we have tried to explore two questions concerning contextual effect on perceptual evaluation for temporal modification of speech segments: (1) whether there is an interaction between multiple segmental durations, and (2) what aspect of the stimulus context determines the perceptual salience of temporal markers?

A. Processing range in perceptual evaluation of temporal modifications

The first purpose of the current study was to explore whether there is a processing range wider than a single segment, i.e., a phoneme, in the perceptual evaluation of temporal modifications in speech. A number of acoustic studies have pointed out that the duration of a given segment may depend on the surrounding contexts at various levels (Campbell, 1992; Fant and Kruckenberg, 1989; Hiki, 1967; Kaiki *et al.*, 1992; Takeda *et al.*, 1989; van Santen, 1992). Hiki (1967), for example, measured segmental durations in running speech comprising 424-mora text data and found a compensatory inclination between C durations and V durations within a mora. Also the effect of the number of morae in an utterance group on segmental durations has been reported at the word level (Takeda *et al.*, 1989) and at the sentence level (Kaiki *et al.*, 1992), as the tendency of each segmental duration to be inversely proportional to the number of morae. These results are consistent with the assumption that there are processing ranges wider than a single segment, i.e., a mora, a word, or a sentence, in the domain of speech production. However, these studies did not provide direct evidence for such a wide processing range in the domain of speech perception, because their studies were limited to the description of naturally spoken speech.

Perceptual studies, on the other hand, have looked at the perceptual consequence of temporal modifications in speech segments (Carlson and Granstrom, 1975; Fujisaki *et al.*, 1975; Huggins, 1972a, b; Klatt, 1976), but only a few have addressed perceptual phenomena caused by interactions among multiple modifications. Several studies have shown results suggesting the presence of perceptual compensation between V durations and their adjacent C durations. Huggins (1972b), Hoshino and Fujisaki (1983), and Sagisaka and Tohkura (1984) each reported that speech stimuli with multiple durational modifications in opposite directions between V and C tend to be heard as more natural than those with multiple durational modifications in the same direction. Sato (1977) moreover found that a lengthening of a consonant duration may cancel out the unnaturalness brought by the same amount of shortening of the adjacent vowel. A preliminary study by Carlson and Granstrom (1975), however, contrast with these studies. Carlson and Granstrom employed a discrimination task and found that listeners' sensitivity to a change in the duration of a vowel was not affected by the presence of a compensatory change in the duration of the succeeding fricative. Discrepancies among these studies may be attributed to differences in the speech utterances employed. However, one has yet to obtain sufficient information for deciding whether such temporal compensation between V and C is common because each of the previous studies employed a fairly small number of speech samples; i.e., two sentences in Sagisaka *et al.*'s study, three nonsense words in Hoshino *et al.*'s, one sentence in Huggins', the first to third syllables of one word *sakanayasan* (a fishmonger) in Sato's, and one word *plasta* in Carlson *et al.*'s.

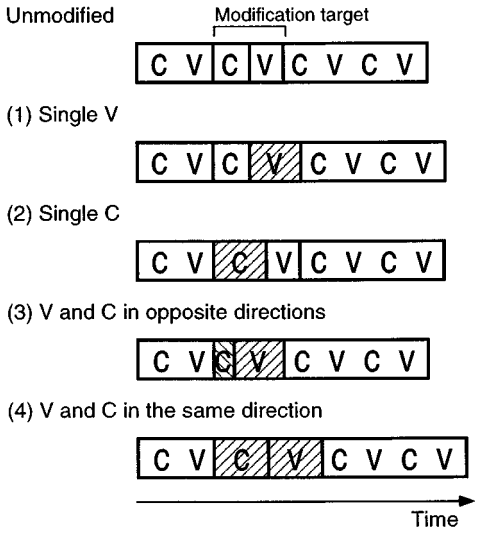

FIG. 1. Schematic examples of different modification types performed on each of the selected word samples: (1) single V, (2) single C, (3) V and C in opposite directions (compensatory modification), and (4) V and C in the same direction. Each C or V stands for a consonant segment or a vowel segment respectively, comprising a four-mora word. In the examples, the second consonant and the second vowel were chosen as the modification target. The hatched segments were temporally modified.

In the current study, therefore, we tried to provide a direct test of the hypothesis that there is a wider processing range than a single segment in the perceptual evaluation of temporal modifications in speech, by collecting a sufficient number of subjective responses using a sufficient number of stimulus samples. For this purpose, we measured perceptual compensation effects in accordance with the following procedure. First, we chose 30 V and C pairs from 15 four-mora Japanese words. Each of the chosen pairs was then temporally modified in four ways: (1) single V, (2) single C, (3) V and C in opposite directions, and (4) V and C in the same direction, as shown in Fig. 1. Secondly, temporal acceptabil-

ity was rated for each of the modified words by human listeners. The obtained rating scores were processed and mapped on an interval scale using a psychological scaling method, then pooled for each of the four modification conditions. If the traditional premise, i.e., adopting the average acoustic error as the evaluation measure of durational rules, was valid in terms of perception, then the estimation score for multiple modifications as a whole would be the same as the sum of the estimation scores for each of the single modifications. Thus, the estimation scores for both ''double modified'' conditions [Fig. 1, (3) and (4)], would each be expected to become equal to the sum of the scores for the ''single modified'' conditions [Fig. 1, (1) and (2)]. Otherwise, it would be suggested that the contextual factor among multiple modifications had affected the perceptual evaluation; this supports the presence of a wider processing range than a single segment in the time perception of speech. In particular, if the average estimation score for condition (3) was significantly lower than that for condition (4), this would imply a general tendency of the perceptual compensation effect (Hoshino and Fujisaki, 1983; Sagisaka and Tohkura, 1984). Although the stimuli were click sequences and the results may not be directly generalized for speech studies, Schulze (1978) did an experiment analogous to the current design. He reported results supporting the existence of such perceptual compensation effect, or the existence of a processing level that can cope with patterns distributed in a wide time span, involving multiple click intervals, rather than just a local dispersion, within a single interval.

B. Contextual effect on perceptual salience of temporal markers in speech

As temporal structures such as rhythm or tempo can be perceived in speech, there should be temporal markers giving us reference points for such temporal structures of speech. Therefore, one can deal with issues on the time perception of speech by considering these temporal markers. Problems then arising from this standpoint are that one cannot explicitly specify the locations of such temporal markers and that the markers do not necessarily have the same perceptual salience.

Numerous attempts have been made to specify temporal markers in speech perception. The following serve as examples: (1) earlier studies have assumed a perceptual beat to be located at vowel onsets or release points of a consonant into the succeeding vowel (Allen, 1972a, b; Rapp, 1971; Sato, 1977), (2) studies for ''perceptual centers (P-centers)'' have tried to calculate the precise location of the stress beat (Barbosa and Bailly, 1994; Fowler, 1979; Morton *et al.*, 1976; Scott, 1993); an analogous idea has been examined for the beat location of mora timing in Japanese (Kato and Hashimoto, 1992), and (3) another group of studies has attempted to find connections between the perceptual beat and production information such as the beginning of vowel articulations or the timing of motor commands (Fowler, 1983; Fujisaki and Higuchi, 1980; Tuller and Fowler, 1980). These studies have commonly assumed the presence of perceptual beats each of which has a one-to-one correspondence with some linguistic unit such as a syllable, stress, or mora and/or assumed the presence of perceptual isochronism of the beat sequence. Naturally, major interests of these studies have been centered on the acoustic/articulatory features or contexts affecting beat locations and on the degree of isochronism of the predicted beat locations; little attention has been given to the perceptual salience of each temporal marker, i.e., the susceptibility of each marker to temporal displacement. However, the perceptual salience of each marker seems to be of practical importance in evaluating durational rules because it can serve as an inherent perceptual weighting for individual temporal markers. In the current study, therefore, we first defined temporal markers as rapidly changing parts of speech in between steady-state parts and assumed, as a first-order approximation, that their locations were to be at both the V-to-C and C-to-V boundaries. The markers are not necessarily a single point in time but can be a part having a certain duration, e.g., a burst part of a stop or affricate consonant in a CV sequence is included into the temporal marker at the C-to-V boundary. Then, we tried to explore what aspect of stimulus context determines the perceptual salience of temporal markers without any assumption about the isochronous beat.

As shown in Fig. 1(3), the compensatory modification of two consecutive segments does not destroy the temporal structure outside the modified pair. Therefore, if each modification were made on stable parts, such as vowel plateaus, fricatives, nasals, or preburst closures, then generally speaking only the boundary between the two modified segments would be temporally displaced. In such a case, if the boundary part contains a perceptually salient temporal marker, this modification would have a strong effect on the perceptual evaluation such as a rating magnitude of perceptual distortion. In this way, any change in perceptual evaluation caused by the compensatory modification can be a measure for the perceptual salience of the temporal markers located between the two modified segments. Utilizing this measure, the current study tested the following two possible models for predicting the perceptual salience of temporal markers in speech.

The first model is called the CV model; ''CV'' stands for a pair of a consonant and its succeeding vowel. This model assumes that the consonant onset is perceptually the most salient and tries to explain the difference of perceptual effects such as the acceptability of temporal modifications mainly by this factor. Thus, the model assumes that the difference arises after the processes of segmentation and categorization which utilize speech-specific knowledge. The model is likely to be supported by linguistic considerations because a CV unit usually forms a mora, a phonological segmentation unit in Japanese. Several studies have repeatedly mentioned the importance of CV units in the domain of speech production (e.g., Campbell and Sagisaka, 1991; Sagisaka and Tohkura, 1984); the compensatory relation between a C duration and its succeeding V duration was observed in both Sagisaka *et al.*'s and also Campbell *et al.*'s studies that performed acoustical analyses on a large database of spoken Japanese. These previous studies apparently support the CV model. However, these studies could not directly support the dominance of the CV unit in speech

perception, because they are based on the observation of physical characteristics of ''naturally spoken'' speech and do not make an empirical assessment in the subjective evaluation for these stimuli.

On the other hand, in the domain of speech perception, several pioneering studies by Hoshino and Fujisaki (1983) and Sato (1977) have so far looked into the temporal compensation between V and its adjacent C. Although both studies suggested the presence of the compensation effect, they seem to disagree in results for the compensation unit. Hoshino and Fujisaki investigated the tolerability of changes in durations of V and C in nonsense words. Their results showed that the tolerability is higher for complementary duration changes of a C and its succeeding V than for those of a C and its preceding V. Sato, on the other hand, found that the decrease of naturalness caused by the lengthening of the first or the third vowel in the word *sakanayasan* (a fishmonger) could be recovered more by the shortening of its succeeding consonant than by the shortening of its preceding consonant. The former study supports the advantage of CV-unit compensation over VC-unit compensation, while the latter supports the advantage of VC-unit compensation. Thus, it is still an open question whether CV is a more significant unit for perceptual compensation than VC; the CV model therefore needs to be tested. Using a relatively large number of speech samples, the current study compared the perceptual evaluations for compensatory modifications on VC and on CV. If the compensatory modification on CV made a smaller perceptual effect than that on VC, then the CV model would be supported.

The second model is called the loudness model. This model assumes that the perceptual salience of a temporal marker would correlate with the amount of change in perceived intensity, i.e., loudness,[1] before and after the marker in question. Thus, the second model focuses on the psychophysical property of speech sound, while the first model is based on the linguistic property of speech, i.e., the mora. In the current study, we chose the magnitude of the loudness difference or jump between two modified segments from among various psychophysical variables, because previous studies have shown that perceptual sensitivity to durational modification on a single segment is correlated with the loudness of the modified segments relative to their surrounding segments (Kato *et al.*, 1993; Kato and Tsuzaki, 1994). If the temporal modification on the segment boundary having a larger loudness jump made a larger effect on the perceptual evaluation, then the loudness model would be supported.

I. EXPERIMENT 1

In experiment 1, the acceptability for temporal modification of V, C, or both V and C within a four-mora word was measured to test whether two consecutive temporal modifications interact with each other and to test the two models (CV and loudness) each describing a stimulus context that possibly correlates with the perceptual salience of temporal markers in speech.

TABLE I. Speech tokens selected in experiment 1. The underlined CVC sequences are the target parts. The left column shows the temporal positions of targets in a word, where C_i or V_i stands for the *i*th consonant or *i*th vowel in a word.

Target position	Roman transcription				
$C_1V_1C_2$	bakugeki	gakureki	hanareru	nagedasu	sakasama
$C_2V_2C_3$	hanahada	imasara	kasanaru	katameru	mikakeru
$C_3V_3C_4$	hanahada	korogasu	rokugatsu	tachimachi	tamatama

A. Method

1. Subjects

Six adults with normal hearing participated in experiment 1. All of them were native speakers of Japanese.

2. Stimuli

Fifteen words were selected from the ATR speech database (Kurematsu *et al.*, 1990) as the original material (Table I). All of them were commonly used four-mora Japanese words, excluding words with doubled vowels, geminated consonants, or moraic nasals[2] which may disturb the temporal regularities observed in open syllable sequences. The selected words were spoken naturally by one male speaker and were digitized at a 12-kHz sampling frequency and with 16-bit precision. One of the V segments in each of the selected words and either the preceding or succeeding C segment were chosen as the targets of durational modification. Thus, a set of target segments in experiment 1 comprised 15 CV pairs and 15 VC pairs. All the target vowels were /ɑ/ and their temporal positions in a word were chosen from the first three out of four morae.

Each of the paired target segments was temporally modified in four ways: (1) single V, (2) single C, (3) V and C in opposite directions, and (4) V and C in the same direction, as shown in Fig. 1. Each modification was either to lengthen or to shorten the segment(s). The size of a modification was either 15 or 30 ms. When two segments were modified, i.e., (3) or (4), the absolute modification size of one segment was equal to the other. The modifications were made by a cepstral analysis and resynthesis technique with the log magnitude approximation (LMA) filter (Imai and Kitamura, 1978), and were carried out at a 2.5-ms frame interval. The duration change was achieved by deleting or doubling the synthesis parameters frame by frame; the frames of interests were evenly chosen from an entire target part of each segment to be modified. The target parts were carefully trimmed out so as to exclude the transient parts at both ends of the vowels and the on-and-after burst parts of plosives or affricates. That is, since the temporal markers were assumed to be at the VC or CV boundaries, the editing procedures modified durations at locations remote from these boundaries. In addition to the above modified stimuli, we prepared unmodified stimuli for reference. In total, 435 word stimuli were prepared.[3]

3. Procedure

The stimuli were randomized and fed diotically to the subjects through a D/A converter (MD-8000 mkII, PAVEC),

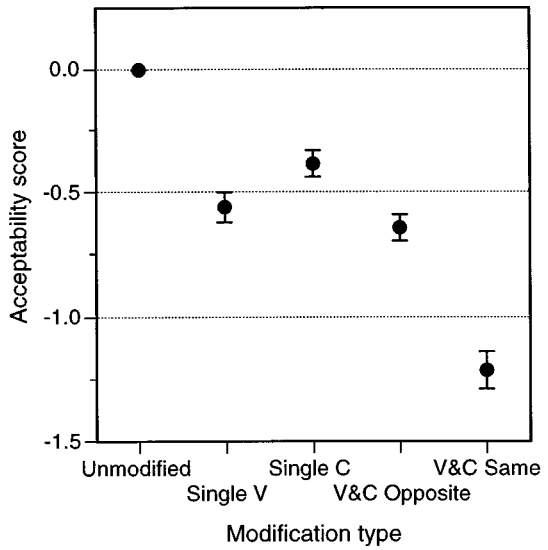

FIG. 2. Estimated acceptability scores pooled over 15 word stimuli for each type of temporal modification. The dots and error bars show the group averages and the standard errors, respectively.

a low-pass filter (FV-665, NF Electronic Instruments, f_c $=5700$ Hz, -96 dB/octave), and headphones (SR-Λ Professional, driven by SRM-1/MkII ATR Version, STAX) in a sound-treated room. The average presentation level was 73 dB (A-weighted) which was measured with a sound level meter (type 2231, Brüel & Kjær) mounted on an artificial ear (type 4153, Brüel & Kjær). A four-second interval was inserted after each presentation for subjects' response.

The subjects were told that each stimulus word was possibly subjected to a temporal modification. Their task was to rate how acceptable each stimulus was, as an exemplar of that token on a scale of seven subjective categories ranging from -3 to 3, where -3 corresponds to ''quite acceptable'' and 3 corresponds to ''unacceptable.''[4] The subjects were asked to respond regarding only the temporal aspect of the stimuli, as much as possible. Each subject rated each stimulus eight times in total. The obtained raw scores were pooled over all subjects for each category, then each stimulus was mapped on a unidimensional psychometric scale to assure an interval scale in accordance with Torgerson's law of categorical judgment[5] (Torgerson, 1958). The scaled estimation score of each ''modified'' stimulus was then adjusted by subtracting the scaled estimation score of its corresponding ''unmodified'' stimulus. Thus, the score finally obtained for each stimulus corresponded to the difference in acceptability from the unmodified reference stimulus.

B. Results and discussion

Figure 2 shows the estimated acceptability scores pooled over the 15 stimulus words for each of the four types of temporal modification, i.e., single V, single C, V and C in opposite directions (V and C opposite), and V and C in the same direction (V and C same). Multiple comparisons among these four modification conditions using Tukey–Kramer's HSD (the honestly significant difference) (SAS Institute Inc., 1990) indicated the differences between ''V and C same'' and the other three conditions, and between the conditions of ''single C'' and ''V and C opposite'' to be significant [$p<0.05$]. If the two single modifications of each ''double modified'' condition were to undergo the acceptability evaluation independently of the other, then no difference should be observed between the decreases in acceptability score for the two ''double modified'' conditions, i.e., ''V and C opposite'' and ''V and C same.'' This, however, was not the case. The acceptability score for ''V and C same'' decreased more drastically than that for ''V and C opposite'' as clearly shown in the figure.

These results mean that, simultaneous modifications in a V duration and its adjacent C duration are not independent of the other in terms of the acceptability evaluation. They seem to either perceptually compensate each other when in opposite directions or perceptually enhance each other when in the same direction. This suggests that a process having a time span wider than a single segment (V or C) is involved in the time perception of speech.

To test the two models (CV and loudness) each predicting a stimulus context that correlates with the perceptual salience of temporal markers, the following analyses focused on the modification type of ''V and C opposite,'' the compensatory modification. If a large amount of decrease in acceptability was observed for this type of modification, this would mean that a perceptually salient temporal marker was located at the boundary of modified V and C. This is because the compensatory modification does not change the temporal structures outside of the target V and C, but mainly displaces the part between the two target segments. According to the CV model, a lower acceptability would be predicted for VC pair modifications than for CV pair modifications because the latter case preserves the duration of CV which is assumed to be a perceptual unit in the model while the former case changes the unit duration. According to the loudness model, on the other hand, a lower acceptability would be predicted for a stimulus with a large loudness jump between modified V and C than for a stimulus with a small loudness jump between modified V and C. The temporal order between V and C does not have any constraints in this model.

To quantify the explanatory variable of the loudness model, the loudness contour was calculated for each of the 15 original word samples in accordance with ISO 532B (ISO, 1975) using Zwicker *et al.*'s (1991) algorithm. Figure 3 shows the examples of the obtained loudness contours and their corresponding waveforms. We then obtained the ''loudness jump'' by subtracting the median loudness of the C part from that of the V part. As every V target in this experiment was louder than its adjacent C parts, the employed loudness jumps were always positive. These obtained loudness jumps and the temporal order of modified V and C were adopted as the explanatory variables for the two models considered. Although we could not evaluate whether the populations of these two explanatory variables are independent of each other, the original word samples of the current experiment were selected so that these two variables were as little correlated with each other as possible, in order to make the subsequent statistical analyses reliable. Figure 4 shows the calculated loudness jumps as a function of the temporal order

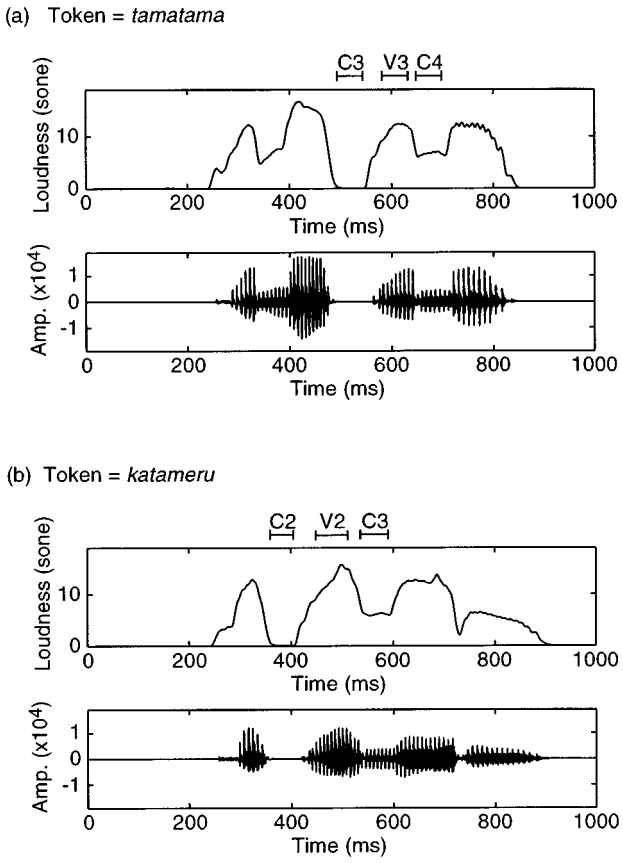

FIG. 3. Time waveforms and loudness contours of the word stimuli used in experiment 1. The horizontal bars at the top of each figure indicate the target parts to be modified. The sampled tokens are *tamatama* (''by accident'') and *katameru* (''to make hard'').

of modified V and C. A t test did not indicate the difference between the average loudness jump at VC boundaries and that at CV boundaries to be significant [$t(28)=0.28$, $p=0.80$].

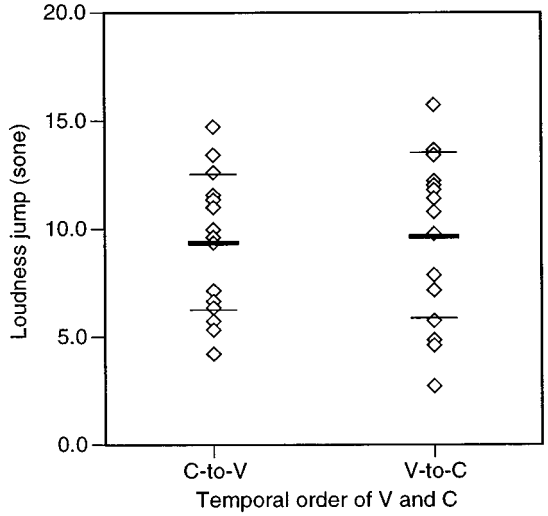

FIG. 4. Loudness jump as a function of the temporal order of V and C. The thick and thin lines show the group averages and standard deviations of loudness jump.

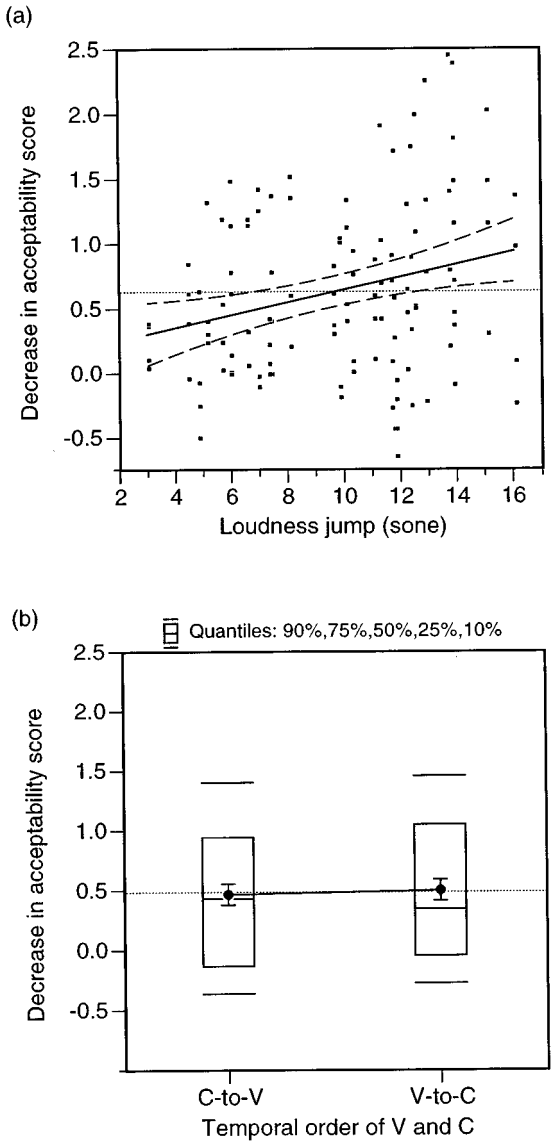

FIG. 5. Decrease in acceptability caused by compensatory modification as a function of the loudness jump between V and C (panel a) or the temporal order of V and C (panel b). In panel a, the thick solid line and dashed lines show the regression line and its 95% confidence curves. In panel b, the dots and error bars show the group averages and the standard errors, respectively. Quantile boxes are also shown in the figure. The horizontal thin dotted line in both panels marks the average of all samples.

In addition to the factors of loudness jump and temporal order of V and C, we included the following two factors which may affect the acceptability evaluation into a statistical test: the mora position of the modified vowel (1, 2, or 3), and the size of each single modification (15 or 30 ms). The effects of the above four factors and their interactions on the decrease in acceptability were tested by a four-way factorial general linear model (GLM)[6] (SAS Institute Inc., 1990). The main effect of the loudness jump was significant [$F(1,96)=10.5$, $p<0.005$]. The acceptability decreased with increasing loudness jump as shown in Fig. 5(a). The interaction between the loudness jump and the amount of modification was significant [$F(1,96)=4.15$, $p<0.05$]. The effect of loudness jump was stronger for the longer (30 ms) modification condition. The temporal order of V and C was not

significant [$F(1,96)=0.087$, $p=0.77$] as shown in Fig. 5(b). No other main effect or interaction was significant.

There was no evidence for the CV model within the scope of experiment 1. On the contrary, the results of the GLM analysis supported the loudness model; a large amount of loudness jump between modified segments generally caused a considerable decrease in acceptability. This suggests that perceptually salient temporal markers tend to locate around major loudness jumps. Note, however, that several factors capable of affecting the perception of temporal aspects of speech were not included in the current analysis; e.g., temporal discriminability is higher around phoneme boundaries when the phonemic distinction depends on the durational cue (Fujisaki *et al.*, 1975). Although we selected the stimulus tokens of experiment 1 so as to balance such factors, they were not completely factored out. Furthermore, we should not overlook the possibility that the effect observed might depend on the particular language of the material or the subjects because the prosodic pattern, in general, carriers different loads in different languages. Experiment 2 was therefore designed to test whether the factor of loudness jump really affects time perception, using nonspeech stimuli replicating the time-loudness features found in the speech stimuli of experiment 1. Although language factors cannot be completely eliminated provided the subjects are the native speakers of a single language, such nonspeech studies minimize the influence of both speech-related and language-specific factors. If the effectiveness of the loudness jump were to be confirmed in this nonspeech experiment, it would suggest that the effect found was based on general perceptual processes instead of speech-related or language-specific ones.

II. EXPERIMENT 2

The purpose of experiment 2 was to test the effect of loudness jump on the perceptual sensitivity to the displacement of temporal markers under controlled experimental conditions.

A. Method

1. Subject

Six adults with normal hearing participated in experiment 2. All subjects also participated in experiment 1, and, therefore, there was a period of one month between experiment 1 and experiment 2 to prevent the carry-over of judgment strategies as much as possible.

2. Design

The experiment was designed as a four-way factorial one. The first factor was the loudness jump between two modified segments (large jump or small jump). The other three factors were included mainly to test their interactions with the first factor; they were, the direction of the marker slope (rising or falling), the steepness of the marker slope (steep or broad), and the temporal position of the marker in a sequence (first half or second half).

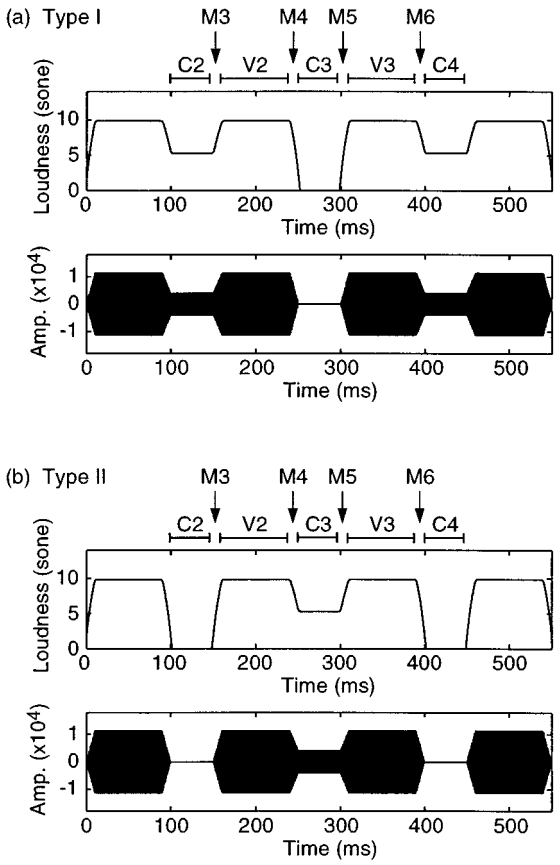

FIG. 6. Time waveforms and loudness contours of the two types of stimuli used in experiment 2. Each ''V'' or ''C'' indicates a target part to be modified. Each ''M'' indicates the location of a temporal marker considered. The level of V is 73 dB SPL (=9.85 sone), the level of louder C is 64 dB SPL (=5.28 sone), and that of softer C is ''silence.'' All signals are 1-kHz pure tones. The eight markers in the figures (type I and type II) comprise an orthogonal set for three (loudness jump, slope direction, temporal position) of the four factors considered. The fourth factor (slope steepness) is included by considering another set of type I and II stimuli of which the slope duration is 20 ms (broad slope); that of the above stimuli is 10 ms (steep slope).

3. Stimuli

Each stimulus was a 1-kHz tone with one of two types of overall amplitude contours as shown in Fig. 6. These two types (types I and type II) were modeled on typical loudness contours of four-mora word stimuli (see Fig. 3), and enabled us to complete the factorial design described above. Each stimulus comprised the alternation of slope and steady parts. As in experiment 1, temporal markers were defined in experiment 2 as rapidly changing parts of signal in between steady-state (either silence or sounding) parts; i.e., only the slope parts could become temporal markers. The steady parts each had one of the following three levels: 73 dB SPL (9.85 sone), 64 dB SPL (5.28 sone), or silence, where each was employed as an approximation for the average loudness of vowels, nasals, and preburst closures found in the speech stimuli used in experiment 1. The duration of the slope was 10 ms (steep) or 20 ms (broad). The duration of the loud part (V part in Fig. 6) including rise-fall slopes and the soft or silent part (C part in Fig. 6) were 100 and 50 ms, for the standard stimuli. One of the V durations in each of the com-

parison stimuli and either its preceding or succeeding C duration were modified in the opposite directions with 30 ms for each. The modification target was limited to the steady part in the second V (V2) or the third V (V3) and either of its adjacent C's (Fig. 6). Thus, the marker (transient part) between the modified segments was solely displaced forward or backward by 30 ms from the standard. In total, 32 stimuli were prepared.[7]

4. Procedure

The detectability index (d') was measured for the difference between each pair of standard and comparison stimuli by the method of constant stimuli. The experimental apparatus was the same as in experiment 1. The subjects listened to the standard and comparison stimuli and were asked to rate the difference between them using eight numerical categories: ''0'' to ''7,'' the larger number corresponding to a larger subjective difference. Since the stimuli were complex and unfamiliar to the subjects, the experimental trials were preceded by a 1-h practice session to familiarize the subjects with the stimuli. In each experimental trial, the subjects listened to the presentation of four successive stimuli, the first three each being the standard and the last one being a comparison. This repetition of standard stimuli served to effectively familiarize the subjects with the stimuli. The inter-onset interval of four stimulus sequences was 1400 ms each which was chosen so as to prevent temporal markers in the standard sequences coinciding to a perfect isochronous rhythm. Twenty percent of the trials were control trials in which each comparison stimulus was the same as the standard stimulus. Twelve judgments were collected from each subject for each stimulus. The obtained responses were pooled over all subjects for each category, then the detectability index, d', for each comparison stimulus was estimated in accordance with the theory of signal detection (Green and Swets, 1966).

B. Results and discussion

A four-way completely randomized factorial analysis of variance (ANOVA) was performed for the obtained detectability indices d'. The factor of loudness jump was significant [$F(1,16)=99.5$, $p<0.0001$]. The other three factors also turned out to be significant; they were, the direction of the slope [$F(1,16)=52.2$, $p<0.0001$], the steepness of the slope [$F(1,16)=6.30$, $p<0.05$], and the temporal position [$F(1,16)=36.7$, $p<0.0001$]. Besides these main effects, a significant interaction was observed between the factors of loudness jump and slope direction [$F(1,16)=7.88$, $p<0.05$]. No other interaction was significant.

Figure 7 shows d' for each combination of marker conditions pooled over the marker displacement directions as a function of the loudness jump. As clearly shown in the figure, the effect of loudness jump agrees with the observed one in experiment 1; i.e., a larger loudness jump causes a higher sensitivity. The effect of temporal position in a sequence was significant; i.e., displacements of the markers in the first half were detected more easily than those of the markers in the second half. This effect is consistent with the finding reported by Tanaka *et al.* (1994) that the temporal discrimination for the initial interval is easier than that for the succeeding intervals in a click sequence.

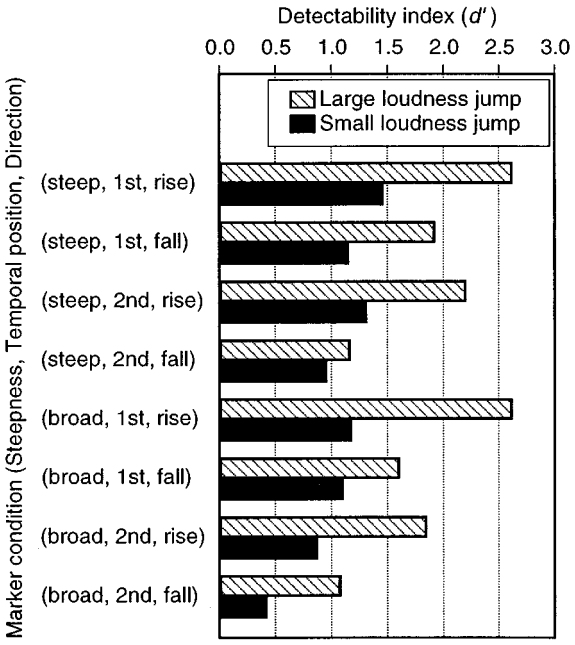

FIG. 7. Detectability index d' for a 30-ms displacement of a temporal marker in each combination of the marker conditions, as a function of the loudness jump between both sides of the marker. A larger d' implies easier detection.

The detectability of temporal displacement on a rising marker was significantly higher than that on a falling marker. Therefore, we thought that by applying this effect directly to experiment 1, the displacements of the C-to-V transition (always a rising slope) would have a greater effect on the perception than the displacements of the V-to-C transition (always falling one). However, this was not the case. So what brought about such an inconsistency between the factors of marker direction and the temporal order of V and C? Two major differences existed between experiment 1 and experiment 2. The first one was a physical difference between the speech stimuli and the pure-tone stimuli. While the rising and falling slopes compared in experiment 2 were the exact mirror images of each other in the time axis, experiment 1 used 30 different slopes (V-to-C or C-to-V transitions). Such a wide stimulus variation in experiment 1 possibly obscured the effect of marker direction.

The second difference was in the experimental procedure; experiment 1 employed the acceptability rating of single stimuli while experiment 2 used a detection task. The task in experiment 1 could be broken down, from an analytical viewpoint, into the following two stages: (1) a detection stage—each subject had to detect the difference between the temporal structure of the presented stimulus and that of his/her internal exemplar of that token even though a single stimulus was presented in each trial, and (2) a rating stage—the degree of acceptability was rated. That is, experiment 1 required the subjects to do a rather central or higher level process in addition to a simple detection task similar to the

one used in experiment 2. Therefore, even though the displacements of the C-to-V transition were detected more easily than those of the V-to-C transition, the rated score possibly showed no difference with regard to the temporal order of V and C if the subjects were more tolerant of the former displacements than the latter ones owing to any factor related to central processes. The influence of the mora unit is likely to be a candidate for such factors. Because a mora unit is usually comprised of a consonant and its succeeding vowel, a displacement of the C-to-V transition (rising marker) preserves the unit duration while that of the V-to-C transition (falling marker) changes it. Consequently, if the mora were a significant unit for the acceptability rating, a displacement of the V-to-C transition should be regarded as more critical than the displacement of the C-to-V transition was.

Experiment 3 was therefore designed to test the second possibility: whether the difference in task between experiment 1 and experiment 2 yielded the inconsistency between the factors of temporal order of V and C and marker direction. This experiment adopted the same task as experiment 2 and employed stimuli similar to experiment 1's, i.e., we tried to separate out the influence of the central processes possibly functioning at the rating stage. If the displacements of the C-to-V transition were detected more easily than those of the V-to-C transition, the hypothesis that the inconsistency between the results of experiment 1 and those of experiment 2 was due to the difference in task between these experiments would be supported. This would suggest the possibility that the CV unit (mora) functioned at the stage of the acceptability rating in experiment 1.

III. EXPERIMENT 3

The purpose of experiment 3 was to test whether the difference between the results of experiment 1 and those of experiment 2 had been produced by the difference in task between these experiments.

A. Method

1. Subject

Six adults with normal hearing participated in experiment 3. All subjects participated in all three experiments, and, therefore, there was a period of one month between two experiments to prevent the carry-over of judgment strategies as much as possible.

2. Stimuli

The stimuli were a reduced set of those used in experiment 1; the modification type was compensatory and the amount of each modification was 30 ms. In total, 60 word stimuli were employed (15 tokens×2 temporal orders×2 modification directions of vowel).

3. Procedure

The experimental apparatus was the same as in experiments 1 and 2. The experimental procedure and detectability calculation were the same as in experiment 2 except that a standard stimulus was presented once in each trial.

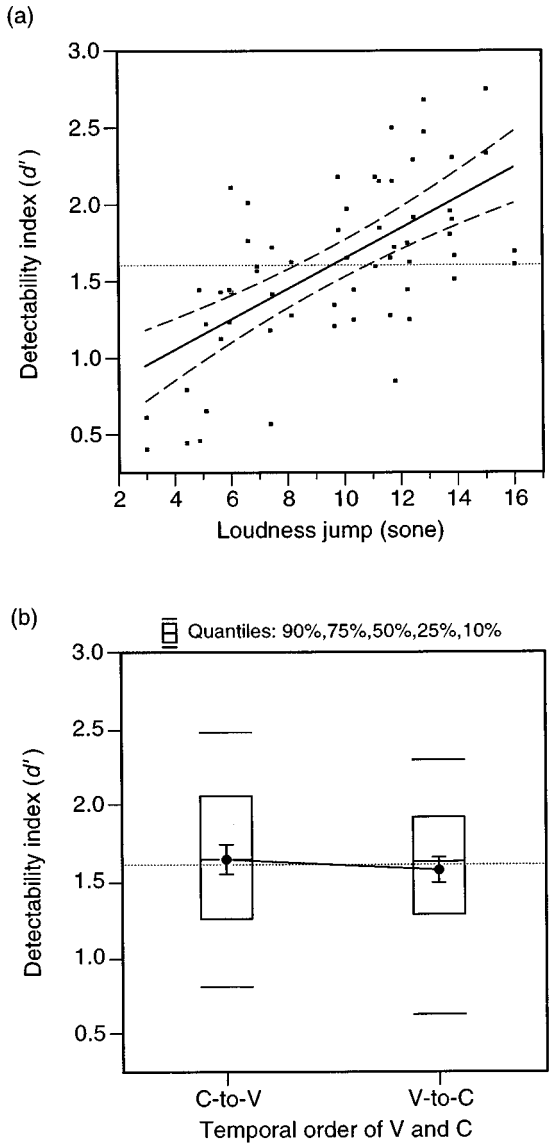

FIG. 8. Detectability index d' for a 30-ms compensatory modification as a function of the loudness jump between V and C (panel a) or the temporal order of V and C (panel b). In panel a, the thick solid line and dashed lines show the regression line and its 95% confidence curves. In panel b, the dots and error bars show the group averages and the standard errors, respectively. Quantile boxes are also shown in the figure. The horizontal thin dotted line in both panels marks the average of all samples.

B. Results and discussion

The effects of the following three factors: the loudness jump, the temporal order of V and C, and the temporal position of the modified vowel, and their interactions on the obtained detectability indices, d', were tested by a three-way factorial general linear model (GLM). The main effect of the loudness jump was significant [$F(1,48)=33.1$, $p<0.0001$]. On the other hand, the main effect of the temporal order of V and C was not significant [$F(1,48)=0.65$, $p=0.42$]. No other main effect or interaction was significant. Figure 8 shows the obtained d' as a function of the loudness jump (panel a) and the temporal order of V and C (panel b).

These results are in good agreement with those obtained in experiment 1. Even though the detection task of experiment 2 was adopted in experiment 3, there was no significant

effect for the temporal order of V and C. Thus, we can safely state that the inconsistency between the results of experiment 1 and those of experiment 2 was not due to the difference in experimental task but to the difference in stimuli. This finding, therefore, does not support the hypothesis that the mora unit functioned as a factor cancelling the effect of slope direction at the acceptability rating stage. Yet, we cannot exclude the possibility that the mora unit functioned in experiment 3 even though the task was of the detection type. We are, however, willing to say in a practical sense that such influence of the mora unit should be taken as a secondary effect preceded by more general processes based on the loudness jump.

Note that we adopted the loudness jump as a representative of the psychophysical auditory basis in contrast with more central or speech-specific ones. We should do further investigation to explore whether the loudness jump has an advantage or not over other psychoacoustical indices, e.g., the change in an auditory spectrum. In addition, the acoustic microstructures at the segmental boundaries such as the presence or magnitude of explosions or aspirations possibly affect the perceptual salience of temporal markers. The effect of such detailed differences should also be explored in further investigation, probably by means of psychoacoustical indices which can deal with fine temporal and spectral changes.

IV. GENERAL DISCUSSION

A. Possible evidence for the universality of the effect of loudness jumps

The results of both experiment 1 and experiment 3 demonstrated that the listeners were generally more sensitive to compensatory modifications of paired segments having a large loudness jump than to those having a small loudness jump. A similar effect of loudness jump was also observed for nonspeech stimuli in experiment 2. These observations suggest that the effect found is not a speech-specific one. Naturally, the effect must be independent of the variation of languages. Although such language independently cannot be proven by the current monolingual study, a phenomenon possibly reflecting the effect of loudness jump can be found in the previous study where English materials and English listeners were employed.

Huggins (1972b) has investigated perceptual compensation between a vowel duration and its adjacent consonant duration using the sentence ''the hostel for paupers strives for perfection'' which was spoken by a single male. His results showed that the vowel duration in the unstressed syllable ''per'' in the phrase ''for perfection'' was successfully compensated by the preburst closure duration of preceding consonant ''p'' while this was not the case for the vowel duration in the stressed syllable ''pau'' in the phrase ''for pauper.'' Huggins gave two ways to account for the observed inconsistency; i.e., perceptual compensation was not observed for ''paupers'' but it was for ''perfection.'' One was to reject the data from the case of ''perfection'' because the compensation found was highly dependent on a single pair of data points. The second was to argue that the compensation had the effect of not restoring the duration of the unstressed first vowel but of restoring the onset of the stressed second vowel in ''perfection.''

Both ways ignored the presence of perceptual compensation in the first syllable of ''perfection.'' However, we can give an alternative explanation. Although high intensity does not seem to be the primary requirement for the presence of syllable stress in English (Lehiste, 1970), a nucleus vowel in a stressed syllable generally has a greater intensity than that in an unstressed syllable (Fry, 1955; Lieberman, 1960). In addition, the intrinsic intensity of vowel /ɔ/ has been reported to be greater than that of vowel /ə/ (Lehiste and Peterson, 1959). Furthermore, the initial /p/ in a stressed syllable tends to be solidly unvoiced while the initial /p/ in an unstressed syllable can be pronounced weakly, sometimes reducing to a fricative. In the case of Huggins' study, therefore, it can plausibly be assumed that the difference in loudness, which is highly correlated with intensity, between C (preburst p-closure) and V was larger in the stressed /pɔ/ of ''paupers'' than in the unstressed /pə/ of ''perfection.'' This assumption is reinforced by the fact that both syllable materials were obtained from a single token uttered without any special emphasis, i.e., the conditions capable of affecting syllable intensity, other than the presence of stress and the intrinsic intensity, were almost the same for both materials.

Our loudness model predicts a high sensitivity to the temporal displacement of a C-to-V transition having a large loudness jump even though the C duration and the V duration had been complementarily modified. Taking this model into account, it is predicted that Huggins' listeners perceived the temporal displacement of the p-to-V transition in the first syllable of ''paupers'' to be larger than that of ''perfection.'' This difference in sensitivity to the temporal displacement possibly yielded the difference in significance level of the compensation effect. More specifically, in the case of ''paupers,'' the compensation effect did not turn out to be significant because the perceptual salience of the boundary part between the two modified segments was relatively high. In the case of ''perfection,'' on the other hand, the compensation effect could be observed because the boundary part was not so perceptually salient.

This is merely an example possibly demonstrating the language-independency of the effect of loudness jump. However, the effect observed in the current paper would lend support for the presence of language-independent universal rules in evaluating the temporal modification of speech segments.

B. Validity of judgments based on energy differences

The stimulus modification in the current study changes not only the segmental duration but also the overall energy of the stimulus. Therefore, one could claim that the listeners' strategy to distinguish stimuli was not based on differences in the temporal structure but on differences in the overall energy. This claim appears to be consistent with the current experimental results, i.e., the listeners are more sensitive to temporal modifications of markers having large loudness jumps than those having small loudness jumps, because a compensatory temporal modification brings a larger energy

change for a temporal marker having a large loudness jump than for a marker having a small loudness jump.

First, let us reexamine the results of experiment 2 under the assumption that the listeners did not process the differences between the standard and comparison stimuli in terms of temporal differences but differences in the overall energy. The ratio of the energy difference between the standard and comparison stimuli to the overall energy of the standard stimulus, i.e., the Weber fraction, was 8.42% or 0.367 dB when modified markers had the larger jump. This difference is equivalent to or smaller than the just noticeable differences (JND's) for energy differences[8] found in former psychophysical studies, i.e., approximately 10%–20% (Florentine, 1983; Green, 1993; Jesteadt *et al.*, 1977; Rabinowitz *et al.*, 1976; Riesz, 1928; Schroder *et al.*, 1994). Nevertheless, our listeners could achieve an average d' of 1.89. Assuming the standard score of the listeners' response were linear to the energy difference, the Weber fraction of the energy difference required for our listeners to produce a d' of unity would be 4.46%. This is, indeed, fairly smaller than formerly published JND's of auditory energy. Such high discriminability was also obtained for many of the speech stimuli in experiments 1 and 3.

In addition, the explanation based on comparisons of overall energy values does not predict many of the results in experiment 2. The experiment showed that the listeners' performance was significantly affected by at least three attributes of the displaced temporal markers, i.e., the slope direction (rising or falling), the steepness of the slope (steep or broad), and the temporal position in a sequence (first half or second half). However, none of these three attributes are dependent on differences in the overall energy between the standard and comparison stimuli. These results could hardly be obtained if the listeners did not pay attention to the temporal markers and did not consider them as cues of distinction.

Therefore, we should state that the claim that listeners can distinguish the stimuli by differences in the energy without processing temporal information is not plausible. It is reasonable to assume that the listeners made judgments by taking advantage of the differences in temporal structures of the stimuli.

V. CONCLUSIONS

The experimental results showed that the temporal modifications of two consecutive segments (V and C) are more acceptable when they are made in opposite directions than when they are made in the same direction. This suggests that a range having a wider time span, corresponding to a moraic range or wider, than a single segment (V or C) functions in the perceptual evaluation of temporal modifications in speech. The results additionally showed that the listeners' perceptual sensitivity to the compensatory modifications between V and C does not depend on the temporal order of V and C but rather on the loudness difference or jump between V and C; the sensitivity increased when the loudness jump between V and C became high. This suggests that the perceptual salience of temporal markers in speech is more closely related to an acoustic-based psychophysical feature (the loudness jump) than to a phonological or phonetical feature (the level of CV or VC). Large jumps in loudness generally coincide with the V-to-C and C-to-V transitions. This is probably one reason why previous studies where they assume a unit comprising CV or VC have, to some extent, succeeded in explaining perceptual phenomena. However, the current study implies that general auditory perception principles should be reexamined, as well as linguistic information, as efficient variables to explain the temporal aspects of speech perception. The important and practical suggestion of the current research is that when evaluating a durational rule objectively, the traditional measure, the average of acoustic errors, is not sufficient from a perceptual viewpoint. A measure more valid (closer to human evaluation) than the traditional average acoustic error could be expected by taking into account the perceptual effect described above.

ACKNOWLEDGMENTS

We would like to thank Noriko Yoshikawa and Masako Tanaka for their assistance in running the experiments, and the listeners involved in the experiments. We are also grateful to Nick Campbell, Alain de Cheveigné, and Hideki Kawahara, who gave many helpful comments on early versions of this paper, and to the reviewers who made themselves known (Rolf Carlson and Jan van Santen) who gave very valuable and detailed suggestions. One anonymous reviewer was particularly helpful by pointing out many ambiguous or misleading statements in addition to general criticisms, which resulted in a considerable improvement. We would also thank Yoh'ichi Tohkura for his continuous encouragement and the initial impetus for this study.

[1]Any usage of the word ''loudness'' in the current study means the loudness calculated by ISO-532 method B, unless otherwise stated. ISO-532B provides a loudness level or its equivalence in loudness as an instantaneous one. Although ISO-532B does not always provide excellent approximations for nonsteady-state signals like speech, we adopted this method due to the advantage of its psychophysical basis instead of adopting power or intensity which incorporates no psychophysical consideration.

[2]In the orthography, they each have a separate character with the same status as the CV units.

[3]They were, 15 CVC's×29 variations of modifications; i.e., 2 modification sizes (=15 ms, 30 ms)×2 modification directions (=lengthening, shortening)×7 modification types (=single V, single C succeeded by the target V, single C preceded by the target V, V and the preceding C in the same direction, V and the succeeding C in the same direction, V and the preceding C in opposite directions, and V and the succeeding C in opposite directions)+1 (=unmodified for reference).

[4]If listeners were asked to estimate ''naturalness,'' they would tend to use such a strict criterion that the range of temporal modifications having informative estimation results would be very restricted. To obtain information for a reasonably wide range of modifications, we chose the ''rating of acceptability'' over the ''rating of naturalness.''

[5]A method of psychological scaling using outputs of a rating scale method. Each of the categorical boundaries and the stimuli used in the rating are mapped on a unidimensional interval scale by the method.

[6]An extended version of the analysis of variance or ANOVA. GLM copes with continuous values as explanatory variables as well as nominal values.

[7]They were, 2 types of amplitude contours (=type I, type II, ×2 steepness conditions (=steep, broad)×2 slope directions (=rising, falling)×2 target positions (=first half, second half)×2 displacement directions (=forward, backward).

[8]We actually referred to studies of intensity discrimination because energy comparisons can be interchangeable with intensity comparisons when the stimuli involved are the same in terms of duration, and a lot of reliable jnd data can be obtained from studies on intensity comparisons.

Allen, G. D. (**1972a**). ''The location of rhythmic stress beats in English: An experimental study I,'' Lang. Speech **15**, 72–100.
Allen, G. D. (**1972b**). ''The location of rhythmic stress beats in English: An experimental study II,'' Lang. Speech **15**, 179–195.
Allen, J., Hunnicutt, M. S., and Klatt, D. H. (**1987**). *From Text to Speech: The MITalk System* (Cambridge U.P., Cambridge, UK).
Barbosa, P., and Bailly, G. (**1994**). ''Characterisation of rhythmic patterns for text-to-speech synthesis,'' Speech Commun. **15**, 127–137.
Campbell, W. N. (**1992**). ''Multi-level timing in speech,'' doctoral dissertation, University of Sussex, Brighton, UK.
Campbell, W. N., and Sagisaka, Y. (**1991**). ''Moraic and syllable-level effects on speech timing,'' Acoustical Society of Japan, Trans. Tech. Committee Speech SP90-107, 35–40.
Carlson, R., and Granström, B. (**1975**). ''Perception of segmental duration,'' in *Structure and Process in Speech Perception*, edited by A. Cohen and S. G. Nooteboom (Springer-Verlag, Berlin), pp. 90–106.
Carlson, R., Granström, B., and Klatt, D. H. (**1979**). ''Some notes on the perception of temporal patterns in speech,'' in *Frontiers of Speech Communication Research*, edited by B. Lindblom and S. Öhman (Academic, London), pp. 233–243.
Fant, G., and Kruckenberg, A. (**1989**). ''Preliminaries to the study of Swedish prose reading and reading style,'' Royal Institute of Technology, Speech Transmission Lab. Q. Prog. Status Report 2/1989, 1–83.
Florentine, M. (**1983**). ''Intensity discrimination as a function of level and frequency and its relation to high-frequency hearing,'' J. Acoust. Soc. Am. **74,** 1375–1379.
Fowler, C. A. (**1979**). ''Perceptual centers' in speech production and perception,'' Percept. Psychophys. **25,** 375–388.
Fowler, C. A. (**1983**). ''Converging sources of evidence on spoken and perceived rhythms of speech: Cyclic production of vowels in monosyllabic stress feet,'' J. Exp. Psychol. Gen. **112,** 386–412.
Fry, D. B. (**1955**). ''Duration and intensity as physical correlates of linguistic stress,'' J. Acoust. Soc. Am. **27,** 765–768.
Fujisaki, H., and Higuchi, N. (**1980**). ''Temporal organization of segmental features in Japanese disyllable,'' J. Acoust. Soc. Jpn. (E) **1**, 25–30.
Fujisaki, H., Nakamura, K., and Imoto, T. (**1975**). ''Auditory perception of duration of speech and non-speech stimuli,'' in *Auditory Analysis and Perception of Speech*, edited by G. Fant and M. A. A. Tatham (Academic, London), pp. 197–219.
Green, D. M. (**1993**). ''Auditory intensity discrimination,'' in *Human Psychophysics*, edited by W. A. Yost, A. N. Popper, and R. R. Fay (Springer-Verlag, New York), pp. 13–55.
Green, D. M., and Swets, J. A. (**1966**). *Signal Detection Theory and Psychophysics* (Wiley, New York).
Higuchi, N., Shimizu, T., Kawai, H., and Yamamoto, S. (**1993**). ''Control of phoneme duration based on the movement of speech organs,'' J. Acoust. Soc. Jpn. (E) **14**, 281–283.
Hiki, S., (**1967**). ''Effects of the context on the duration of phoneme segment,'' J. Acoust. Soc. Jpn. **23**, 317–318.
Hoshino, M., and Fujisaki, H. (**1983**). ''A study on perception of changes in segmental durations,'' Acoustical Society of Japan, Trans. Tech. Committee Speech H83-8/S82-75, 593–599 (in Japanese with English abstract and English figure captions).
Huggins, A. W. F. (**1972a**). ''Just noticeable differences for segment duration in natural speech,'' J. Acoust. Soc. Am. **51,** 1270–1278.
Huggins, A. W. F. (**1972b**). ''On the perception of temporal phenomena in speech,'' J. Acoust. Soc. Am. **51,** 1279–1290.
Imai, S., and Kitamura, T. (**1978**). ''Speech analysis synthesis system using the log magnitude approximation filter,'' Trans. Inst. Electron. Commun. Eng. Jpn. **J61-A**, 527–534 (in Japanese with English figure captions).
ISO (**1975**). ''Acoustics—Method for calculating loudness level,'' ISO 532-1975 (E) (International Organization for Standardization, Geneva).
Jesteadt, W., Wier, C. C., and Green, D. M. (**1977**). ''Intensity discrimination as a function of frequency and sensation level,'' J. Acoust. Soc. Am. **61,** 169–177.
Kaiki, N., and Sagisaka, Y. (**1992**). ''The control of segmental duration in speech synthesis using statistical methods,'' in *Speech Perception, Production and Linguistic Structure*, edited by Y. Tohkura, E. Vatikiotis-Bateson, and Y. Sagisaka (IOS, Amsterdam), pp. 391–402.
Kaiki, N., Takeda, K., and Sagisaka, Y. (**1992**). ''Linguistic properties in the control of segmental duration for speech synthesis,'' in *Talking Machines: Theories, Models, and Designs*, edited by G. Bailly, C. Benoît, and T. R. Sawallis (Elsevier, Amsterdam), pp. 255–263.
Kato, H., and Tsuzaki, M. (**1994**). ''Intensity effect on discrimination of auditory duration flanked by preceding and succeeding tones,'' J. Acoust. Soc. Jpn. (E) **15**, 349–351.
Kato, H., Tsuzaki, M., and Sagisaka, Y. (**1992**). ''Acceptability and discrimination threshold for distortion of segmental duration in Japanese words,'' in *Proceedings of International Conference on Spoken Language Processing* (University of Alberta, Edmonton, AB), pp. 507–510.
Kato, H., Tsuzaki, M., and Sagisaka, Y. (**1993**). ''Acceptability for durational modification of segments in words,'' Acoustical Society of Japan, Trans. Tech. Committee Speech SP92-145, 65–72 (in Japanese with English abstract and English figure captions).
Kato, M., and Hashimoto, S. (**1992**). ''Rhythm rules in Japanese based on the center of energy gravity of vowels,'' in *Proceedings of International Conference on Spoken Language Processing* (University of Alberta, Edmonton, AB), pp. 1139–1142.
Klatt, D. H. (**1976**). ''Linguistic uses of segmental duration in English: Acoustic and perceptual evidence,'' J. Acoust. Soc. Am. **59,** 1208–1221.
Klatt, D. H. (**1979**). ''Synthesis by rule of segmental durations in English sentences,'' in *Frontiers of Speech Communication Research*, edited by B. Lindblom and S. Öhman (Academic, London), pp. 287–299.
Klatt, D. H., and Cooper, W. E. (**1975**). ''Perception of segment duration in sentence contexts,'' in *Structure and Process in Speech Perception*, edited by A. Cohen and S. G. Nooteboom (Springer-Verlag, Berlin), pp. 69–89.
Kurematsu, A., Takeda, K., Sagisaka, Y., Katagiri, S., Kuwabara, H., and Shikano, K. (**1990**). ''ATR Japanese speech database as a tool of speech recognition and synthesis,'' Speech Commun. **9,** 357–363.
Lehiste, I. (**1970**). *Suprasegmentals* (MIT, Cambridge).
Lehiste, I., and Peterson, G. E. (**1959**). ''Vowel amplitude and phonemic stress in American English,'' J. Acoust. Soc. Am. **31,** 428–435.
Lieberman, P. (**1960**). ''Some acoustic correlates of word stress in American English,'' J. Acoust. Soc. Am. **32,** 451–454.
Morton, J., Marcus, S., and Frankish, C. (**1976**). ''Perceptual centers,'' Psychol. Rev. **83,** 405–408.
Rabinowitz, W. M., Lim, J. S., Braida, L. D., and Durlach, N. I. (**1976**). ''Intensity perception. VI Summary of recent data on deviations from Weber's law for 1000-Hz tone pulses,'' J. Acoust. Soc. Am. **59,** 1506–1509.
Rapp, K. (**1971**). ''A study of syllable timing,'' Royal Institute of Technology Speech Transmission Lab. Q. Prog. Status Report 1/1971, 14–19.
Riesz, R. R. (**1928**). ''Differential intensity sensitivity of the ear for pure tones,'' Phys. Rev. **31,** 867–875.
Sagisaka, Y., and Tohkura, Y. (**1984**). ''Phoneme duration control for speech synthesis by rule,'' Trans. Inst. Electron. Commun. Eng. Jpn. **J67-A**, 629–636 (in Japanese with English figure captions).
SAS Institute, Inc. (**1990**). *SAS/STAT User's Guide, Version 6* (SAS, Cary, NC), 4th ed., Vol. 2.
Sato, H. (**1977**). ''Segmental duration and timing location in speech,'' Acoustical Society of Japan, Trans. Tech. Committee Speech S77-31, 1–8 (in Japanese with English abstract).
Schroder, A. C., Viemeister, N. F., and Nelson, D. A. (**1994**). ''Intensity discrimination in normal-hearing and hearing-impaired listeners,'' J. Acoust. Soc. Am. **96,** 2683–2693.
Schulze, H.-H. (**1978**). ''The detectability of local and global displacements in regular rhythmic patterns,'' Psychol. Res. **40**, 173–181.
Scott, S. K. (**1993**). ''P-centres in speech—An acoustic analysis,'' doctoral dissertation, University College London, London, UK.
Takeda, K., Sagisaka, Y., and Kuwabara, H. (**1989**). ''On sentence-level factors governing segmental duration in Japanese,'' J. Acoust. Soc. Am. **86,** 2081–2087.
Tanaka, M., Tsuzaki, M. and Kato, H. (**1994**). ''Discrimination of empty duration in the click sequence simulating a mora structure,'' J. Acoust. Soc. Jpn. (E) **15**, 191–192.
Torgerson, W. S. (**1958**). *Theory and Methods of Scaling* (Wiley, New York).
Tuller, B., and Fowler, C. A. (**1980**). ''Some articulatory correlates of perceptual isochrony,'' Percept. Psychophys. **27,** 277–283.
van Santen, J. P. H. (**1992**). ''Contextual effects on vowel duration,'' **11,** 513–546.
van Santen, J. P. H. (**1994**). ''Assignment of segmental duration in text-to-speech synthesis,'' Comput. Speech Lang. **8**, 95–128.
Zwicker, E., Fastl, H., Widmann, U., Kurakata, K., Kuwano, S., and Namba, S. (**1991**). ''Program for calculating loudness according to DIN 45631 (ISO 532B),'' J. Acoust. Soc. Jpn. (E) **12**, 39–42.

Segment-based automatic language identification

Timothy J. Hazen and Victor W. Zue
Spoken Language Systems Group, Laboratory for Computer Science, Massachusetts Institute of Technology, Cambridge, Massachusetts 02139

(Received 15 April 1996; accepted for publication 25 November 1996)

This paper discusses the formulation, development and analysis of a segment-based approach to the automatic language identification (LID) problem. This system utilizes phonotactic, acoustic-phonetic, and prosodic information within a unified probabilistic framework. The implementation of this framework allows the relative contributions of different sources of information to be determined empirically, as well as providing the mechanism for combining them within one system. The system has been evaluated using the Oregon Graduate Institute (OGI) multi-language telephone speech corpus and the results are competitive with other current LID systems. The results have also indicated that, while the phontotactic information of a spoken utterance is the most useful information for LID, acoustic-phonetic and prosodic information can be useful for increasing a system's accuracy, especially when the utterance is short. © *1997 Acoustical Society of America.* [S0001-4966(97)02304-7]

PACS numbers: 43.72.Ne [JS]

INTRODUCTION

Automatic language identification (or LID) refers to the task of identifying the language being spoken by a person. For more than 20 years, interests and needs in the intelligence community have provided a major impetus for research in LID (Leonard and Doddington, 1974, 1975, 1978; Leonard, 1980). More recently, LID research has been enjoying a renaissance, spurred by research activities in multilingual speech recognition and understanding for which an efficient means for identifying the language being spoken has definite benefits. For example, telephone companies can provide better services to customers speaking different languages if an LID front-end can route calls to the appropriate operators. Similarly, a multilingual spoken language system (Glass *et al.*, 1993; Flammia *et al.*, 1994) can understand and respond in the user's native language if it can first identify the language being spoken. Machine translation systems can utilize LID to relieve the burden of requiring users to specify the language they are speaking before each turn. For a thorough summary of the research that has been performed in automatic language identification over the last 20 years, please refer to Zissman (1996).

Because languages of the world can be distinguished amongst one another by their own unique vocabulary and linguistic constructs, a spoken language can be identified, in principle, by passing the speech signal through a set of speech recognition/understanding systems running in parallel, each capable of deciphering a particular language of interest. Language identification can then be achieved implicitly by choosing the language of the system that yields the best score. Viewed in this manner, a reliable speech recognition/understanding system for all spoken languages should provide near perfect language identification when these systems are used jointly.

However, there are several reasons why such an approach may be impractical. Building a multilingual recognition/understanding system as described above requires extensive knowledge about the acoustic-phonetic, lexical, and linguistic rules for each of the languages of interest. Even for restricted domains, this knowledge may require a tremendous effort to acquire. The resulting systems may not be easily portable, since they will only perform well when the vocabulary and linguistic rules of the languages in question are well-specified. As such, porting such systems to new languages would be laborious and time consuming. Furthermore, it may be too computationally expensive to incorporate all of this knowledge even if it were available. Thus, the goal of LID research to date has generally been to develop dependable language identification methods which do not rely upon higher-level knowledge of the languages involved, but rather utilize only the information that is available directly from the waveform.

It has been observed that humans often can identify the language of an utterance even when they have no working linguistic knowledge of that language (Muthusamy and Cole, 1992), suggesting that they are able to learn and recognize language-specific patterns directly from the signal. In the absence of higher-level knowledge of a language, a listener presumably relies on lower-level constraints such as acoustic phonetics (i.e., the inventory and characteristics of sound units), phonotactics (i.e., the sequential constraints on sound patterns), and prosody (i.e., the suprasegmental properties).

The constraining power of these low-level characteristics for LID was first demonstrated in a feasibility study by House and Neuburg (1977). Their results offered the hope that very simple phonetic language models can be powerful tools for language identification. In this paper, we describe a LID system that is primarily built upon House and Neuburg's initial ideas. The speech signal is first segmented and classified into sequences of phonetic classes and the phonotactic properties of the resulting sequences are modeled statistically. Since other information besides phonotactics may also be useful for language identification, as has been demonstrated by other investigators (Muthusamy *et al.*, 1991;

Muthusamy and Cole, 1992; Itahashi *et al.*, 1994) our system will supplement the phonotactic information with prosodic and acoustic-phonetic information, all within one unified framework.

In this paper, we will first derive the theoretical framework for our LID system. This will be followed by a description of the system architecture and the resulting implementation. We contrast this system's design with the current state-of-the-art systems. Performance of our system on the Oregon Graduate Institute (OGI) multi-language telephone speech corpus (Muthusamy *et al.*, 1992; Cole *et al.*, 1994) under varying parameter settings will be presented and analyzed.

I. THEORY

A. Overview

An understanding of the characteristics of spoken language which are most useful for discriminating among languages is essential to the development of an LID system. An LID system must exploit the primary differences which exist among languages while still being robust in the face of speaker, channel, and vocabulary variability. However, the system also needs to be computationally efficient. Thus, it is desirable to discover language discriminating characteristics which are relatively easy to extract from the acoustic signal, do not require complex methodologies to model, and are relatively free of noise from speaker, channel, and vocabulary dependencies.

The language-discriminating information contained in the signal can be segmental and prosodic (e.g., suprasegmental). The segmental information can be acoustic-phonetic, which relates to the manner in which phones are realized acoustically by a speaker, or phonotactic, which relates to the higher-level rules governing the sequences of phones which are allowed within a language. Prosodic information is encoded in the fundamental frequency, intensity, and duration variations that span across segments. While the segmental and prosodic information may also carry higher-level linguistic constraints, our working assumption is that knowledge of this higher-level information will not be needed to identify the language of the utterance. In this section, we will briefly outline the theoretical framework for our LID system. Interested readers are referred to Hazen (1993) for a more detailed treatment.

B. Probabilistic framework

The system described in this paper utilizes a segment-based probabilistic framework. To begin, let $\mathbf{L}=\{L_1,L_2,\ldots,L_n\}$ represent the language set of n different languages. When an utterance is presented to the LID system, the system must use the acoustic information to decide which of the n languages in $\mathbf{L}$ was spoken.

Typically, the acoustic information of a spoken utterance is represented as a sequence of feature vectors representing the acoustic information at a fixed frame rate. For this derivation, we will assume that two specific types of information are extracted from the waveform for each time frame: the wideband spectral information and the voicing information. The wideband spectral information is the most useful information for determining the underlying phonetic sequence of a spoken utterance. The voicing information, i.e., the $F0$ contour, is primarily used when describing the prosody of an utterance. Because of the separate natures of the two types of information, it is useful to represent them as two separate sequences of vectors. Therefore, let $\mathbf{a}=\{\mathbf{a}_1,\mathbf{a}_2,\ldots,\mathbf{a}_m\}$ be the sequence of m vectors which represent the wideband spectral information of a spoken utterance and let $\mathbf{f}=\{\mathbf{f}_1,\mathbf{f}_2,\ldots,\mathbf{f}_m\}$ be the sequence of m vectors which represent the voicing information of a spoken utterance. Throughout this paper, the wideband spectral information contained in $\mathbf{a}$ will be referred to as the acoustic information and the information in $\mathbf{f}$ will be referred to as the $F0$ information.

Next, assume that we can utilize a phonetic speech recognizer to extract the most likely sequence of phonetic elements contained in the utterance. Let the recognized phonetic sequence, containing p phonetic elements, be represented as $C=\{c_1,c_2,\ldots,c_p\}$ where each c is represented with a specific phonetic element. For a segment-based approach, as is being pursued in our group, the concept of segmentation of the input speech must be incorporated into the probabilistic framework. Thus, let $S=\{s_1,s_2,\ldots,s_{p+1}\}$ represent the segmentation for the phonetic string C where each s represents the location of a segment boundary.

Given the acoustic information $\mathbf{a}$, the fundamental frequency $\mathbf{f}$, the most likely phonetic sequence C, and the segmentation S the most likely language is found using the following expression:

$$\arg\max_i \Pr(L_i|C,S,\mathbf{a},\mathbf{f}). \tag{1}$$

Using standard probability theory, this expression can be equivalently written as

$$\arg\max_i \Pr(\mathbf{a}|C,S,\mathbf{f},L_i)\Pr(S,\mathbf{f}|C,L_i)\Pr(C|L_i)\Pr(L_i). \tag{2}$$

The four probability expressions in (2) are organized in such a way that prosodic and phonetic information are contained in separate terms. In modeling, these terms become known as

(1) $\Pr(\mathbf{a}|C,S,\mathbf{f},L_i)\rightarrow$the phonetic acoustic model.
(2) $\Pr(S,\mathbf{f}|C,L_i)\rightarrow$the prosodic model.
(3) $\Pr(C|L_i)\rightarrow$the phonetic language model.
(4) $\Pr(L_i)\rightarrow$the *a priori* language probability.

The phonetic information is contained in two separate models: the phonetic acoustic model and the phonetic language model. In subsequent sections these models will simply be referred to as the acoustic model and the language model. The acoustic model accounts for the different acoustic realizations of the phonetic elements that may occur across languages, whereas the language model accounts for the probability distributions of the phonetic elements and the phonotactic constraints within each language. The prosodic model captures the differences that can occur in prosodic structures of different languages due to the stress or tone patterns created by variations in the phone durations and $F0$ contour. This organization provides a useful structure for

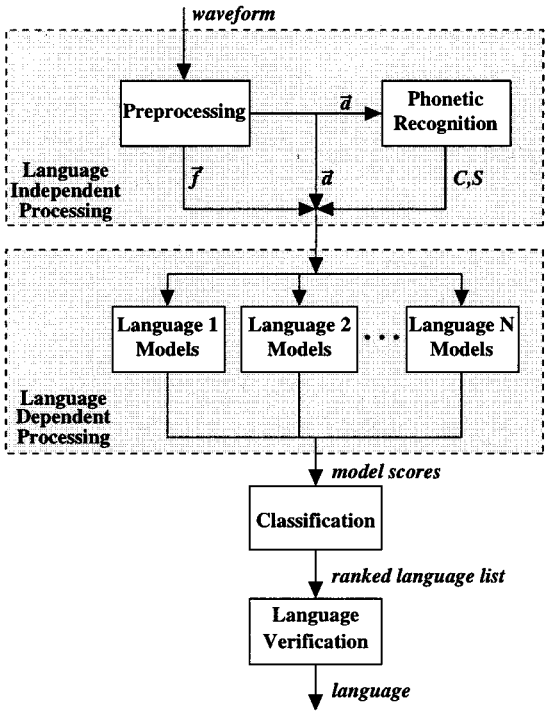

FIG. 1. System architecture.

evaluating the relative contributions towards language identification that phonotactic, acoustic-phonetic, and prosodic information provide.

II. SYSTEM DESIGN AND IMPLEMENTATION

A. General system architecture

The architecture of our LID system implementing the segment-based probabilistic framework described in Sec. II is shown in Fig. 1. It is realized as a series of four components a preprocessor, a phonetic recognizer, a fast match language identifier, and a language verifier. The preprocessor receives the raw acoustic waveform as its input and transforms it into the frame-based feature vectors **a** and **f**. The phonetic recognizer receives the acoustic information in **a** as its input and finds the best phonetic hypothesis and segmentation, C and S. The language identifier uses **a**, **f**, C, and S to construct a candidate list of the most likely languages. The language verifier then utilizes language-dependent speech recognizers to verify the languages provided by the language identifier. In this section we summarize the design choices made for each of the language identification components. Interested readers are referred to Hazen (1993) and Hazen and Zue (1994) for a more detailed description.

Our approach differs from similar approaches taken by Zissman (Zissman and Singer, 1994; Zissman, 1995) and by Kadambe and Hieronymus (1994, 1995) in that our system uses one language-*independent* phonetic recognizer instead of a set of language-*dependent* phonetic recognizers. Zissman has shown empirically that increasing the number of language-dependent recognizers increases performance in his system (Zissman, 1995). However, the increased performance comes at the expense of increased computation. It is for computational efficiency that we have adopted this simpler architecture.

B. Preprocessing

The acoustic vector **a** is represented with mel-frequency cepstral coefficients (MFCC's) (Mermelstein and Davis, 1980). A set of 14 MFCC's (including the energy term) are computed for each utterance every 5 ms using a 25.6-ms Hamming window and a 256-point discrete Fourier transform. To compensate for the varying acoustic properties of the different channels encountered in the OGI data, a blind deconvolution channel normalization scheme is also employed. For each utterance, the average value of each of the 14 MFCC's is computed over the length of the utterance. This average is then subtracted from the MFCC value of each frame in the utterance. In addition to the MFCC's, 14 delta MFCC's are also computed.

The voicing information contained in the vector **f** is extracted from the acoustic signal using a pitch detector originally devised by Secrest and Doddington (1983) and incorporated as part of the FORMANT program in Entropic's ESPS package. For each frame, a fundamental frequency ($F0$) and a probability of voicing parameter are estimated. In an attempt to eliminate speaker dependencies a two-step transformation is applied to the $F0$ values. First, the logarithm (base 2) of $F0$ is taken for all voiced frames (i.e., frames whose voicing probability is greater than 0.5). Second, again in the logarithm domain, the mean $F0$ value for each utterance is computed and subtracted from each $F0$ value. Additionally, a delta $F0$ value is calculated (also in the logarithm domain) for each voiced frame.

C. Phonetic recognition

The phonetic recognition component decodes the acoustic information into a string of phonetic events. In our system, phonetic recognition is performed by SUMMIT, a segment-based speech recognition system developed in our group (Zue *et al.*, 1989, 1990). SUMMIT utilizes a hierarchical segmentation algorithm to provide the segmentation search space. An ordered list of potential phone candidates and their respective likelihoods are produced for each potential segment. The phone likelihoods are obtained from mixture Gaussian density functions for each phone which model segment-based feature vectors. A search algorithm is applied to the segmentation and phone search space to find the most likely strings of phones. In our implementation, we used 87 language-independent phonetic units. Included in this set are several different silence and noise units. The 87 phones were the result of hand clustering over 900 unique labels which exist in the transcriptions of the training data. Similar phones, such as [iː] and [i], were collapsed into a single class to ensure an adequate amount of training data for each class while still maintaining a richness in phonetic description. The complete set of phonetic units used by the system is shown in Table I. To prevent the recognizer from being biased towards the phones of particular languages, no phonetic language model was used by SUMMIT (i.e., the *a priori* probabilities of the phones were presumed to be uniform).

TABLE I. List of phones and nonlinguistic descriptors most accurately describing the 87 phonetic units used within the language-independent phonetic recognizer.

Monothong vowels (16)	[i], [ɪ], [ɨ], [e], [æ], [ɛ], [a], [ɑ], [ʌ], [ɔ], [o], [ɤ], [ʊ], [u], [ɜ˞], [ɯᵻ]
Diphthongs (6)	[ei], [oʊ], [ɔɪ], [aʊ], [aɪ], [ai]
Semivowels (5)	[w], [j], [y], [l], [ɹ]
Flaps and taps (4)	[ɾ], [ɾ̃], [ɾʲ], [ɽ]
Nasals (4)	[m], [n̩], [n], [ŋ]
Fricatives (14)	[β], [f], [v], [θ], [ð], [s], [s̬], [z], [š], [ç], [x], [ʁ], [h], [ɦ]
Affricates (4)	[ts], [tʃ], [dʒ], [cç]
Stops (12)	[b], [p], [pʰ], [d], [d̪], [dʲ], [tʰ], [t̪], [tʲ], [g], [k], [kʰ]
Closures (11)	[b□], [p□], [d□], [d̪□], [d□], [t□], [t̪□], [tʲ□], [c□], [g□], [k□]
Nonphonetic units (11)	background noise, filled pause, pause, breath noise, line noise, nonspeech, post-vocalic glottalization, onset glottalization, lip smack, unintelligible speech, epinthetic closure

One primary difference between the training of the standard SUMMIT system and the system used in these experiments lies in the manner in which the segment boundary scoring parameters were selected. During standard training of the SUMMIT phonetic recognizer, the segment boundary scoring parameters are chosen to optimize the phonetic recognition performance on development data. For our experiments, these parameters were chosen to optimize the language identification accuracy of the language model which utilizes the output of the phonetic recognizer. This optimization process favored the removal of deletion errors at the expense of increased insertion errors, suggesting that segment deletion, which removes information, can be more harmful than the insertion of either extraneous information or additional noise.

D. Language identification

1. General framework

Using the framework discussed in Sec. II, the language identification component of the system models the expression:

$$\arg\max_i \Pr(\mathbf{a}|C,S,\mathbf{f},L_i)\Pr(S,\mathbf{f}|C,L_i)\Pr(C|L_i)\Pr(L_i). \quad (3)$$

For our experiments, the *a priori* language probability distribution was assumed to be uniform and hence ignored. As is standard, the expression was realized using its logarithmic form as follows:

$$\arg\max_i (\log \Pr(\mathbf{a}|C,S,\mathbf{f},L_i) + \log \Pr(S,\mathbf{f}|C,L_i) + \log \Pr(C|L_i)). \quad (4)$$

Figure 2 illustrates the components which are utilized in the realization of the expression in Eq. (4). Essentially, each language has its own language, acoustic, and prosodic models. The incoming utterance is scored by the models of each language and the candidate languages are then ranked by their respective scores. Figure 2 also shows one additional component not represented in Eq. (4). This component is the set of model weights w_1, w_2, and w_3. Ideally, these weights should all simply be set to one. However, as will be discussed later, these weights are necessary to avoid having one model dominate the total score for each language.

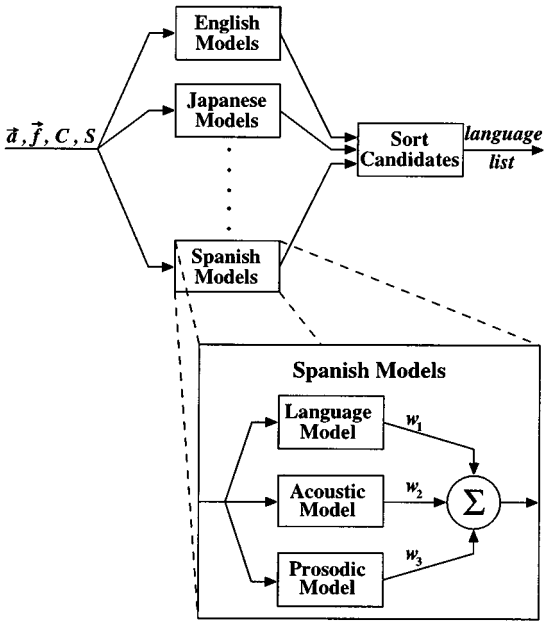

FIG. 2. Illustration of the language identification component of the system.

2. System training

Each term in Eq. (4) must be modeled using the transcription of the utterance as represented by the phonetic string C and the segmentation S. Standard speech recognition techniques which require a transcription for supervised training, such as n-gram and mixture Gaussians, are used to model the terms. To provide this transcription each training utterance is passed through the phonetic recognizer to produce an automatically generated transcription. The primary deviation from the ways these models are usually trained stems from the fact that, in our case, C and S do not represent the actual transcription of the underlying string of phones, but rather the output of a recognizer which is prone to errors. Thus the language, acoustic, and prosodic models which are eventually generated do not model the actual characteristics of each language, but rather the characteristics of each language after its utterances have been corrupted by the noise from the imperfect recognizer. For accurate language identification to occur, it is necessary for the noise generated by the phonetic recognizer to be accounted for in the modeling process since it will exist in the test data.

3. Language model

The language model refers to the expression $\Pr(C|L_i)$. The language model is potentially the most important ele-

ment of the system. House and Neuburg showed that simple n-gram language models applied to error-free sequences of phonetic elements as general as broad phonetic classes can reliably identify the language of an utterance (House and Neuburg, 1977). However, the language identification capabilities of an n-gram are degraded when the actual string of phonetic events is corrupted with errors.

The language model used for our experiments was an interpolated trigram model (Jelinek, 1990). The interpolated trigram can be expressed as

$$\hat{P}(c_i|c_{i-1},c_{i-2}) = \lambda_2 \Pr(c_i|c_{i-1},c_{i-2}) + (1-\lambda_2) \times [\lambda_1 \Pr(c_i|c_{i-1}) - (1-\lambda_1)\Pr(c_i)], \quad (5)$$

where λ_1 and λ_2 are weights which depend on the phones preceding c_i. Specifically, λ_1 is expressed as

$$\lambda_1 = \frac{k_{c_{i-1}}}{k_{c_{i-1}} + K_1}, \quad (6)$$

where $k_{c_{i-1}}$ is the number of exemplars of c_{i-1} in the training set and K_1 is a constant. Similarly, λ_2 is expressed as

$$\lambda_2 = \frac{k_{c_{i-1},c_{i-2}}}{k_{c_{i-1},c_{i-2}} + K_2}. \quad (7)$$

The constants K_1 and K_2 were chosen empirically to optimize the language identification performance of the interpolated trigram model on development test data extracted from the training set. The optimization process set the values of K_1 and K_2 to 350 and 800, respectively.

4. Acoustic model

The expression $\Pr(\mathbf{a}|\mathbf{f},S,C,L_i)$ is called the acoustic model, which is used to capture information about the acoustic realizations of each of the phones used in each language. To simplify the modeling, the acoustic information **a** is assumed to be independent of the fundamental frequency information **f**, and each segment is considered to be independent of all other segments. Like others before us, we make the statistical independence assumption realizing that it is, in all likelihood, difficult to justify. However, it is our belief that such an assumption will be less troublesome for us because we are dealing with segments rather than frames. With these assumptions, the acoustic model can be expressed as

$$\Pr(\mathbf{a}|\mathbf{f},S,C,L_i) = \Pr(\mathbf{a}|S,C,L_i) = \prod_{k=1}^{m} \Pr(\mathbf{a}_k|c_k,L_i), \quad (8)$$

where m is the number of segments in the utterance, and $\mathbf{a}_k$ is a segment-based feature vector describing the acoustics of the kth segment. In our case, each $\mathbf{a}_k$ contains 14 MFCC's and 14 delta MFCC's as averaged over the length of the segment.

Using the above assumptions, continuous probability density functions which model the segment-based acoustic feature vectors for each phone in each language can be used for the acoustic model. The acoustic feature vectors are modeled with mixtures of diagonal Gaussian density functions. To create the mixture Gaussian model for each phone in each language, the set of Gaussian density functions within each mixture are initialized from a set of clusters found with the k-means clustering algorithm. The Gaussians in each mixture are then iteratively reestimated to maximize the average likelihood score of the vectors in the training set. To ensure proper amounts of training data for each mixture of Gaussians, the number of Gaussians used to model each phonetic class is determined from the equation

$$n_g = \begin{cases} n_{\max}, & \text{if } k/100 > n_{\max}, \\ [k/100], & \text{otherwise}, \end{cases} \quad (9)$$

where n_g is the number of Gaussians used in the mixture Gaussian model of a particular phonetic class for a particular language, $n_{\max}$ is the maximum number of Gaussians allowed in each mixture, and k is the number of training vectors for the phonetic class in that particular language. The value of $n_{\max}$ was chosen to be 16 based upon prior experiments (Hazen, 1993).

5. Prosodic model

The prosodic model refers to the expression $\Pr(S,\mathbf{f}|C,L_i)$. Ideally, this model can be used to capture the differences among languages that exist in the prosodic structure of utterances. While useful and reliable methodologies are available for modeling acoustic and phonetic information, well-developed techniques for automatically capturing and understanding word- and sentence-level prosodic information remains elusive. Therefore, our prosodic model only captures simple statistical information about the fundamental frequency and segment duration information of an utterance.

To help simplify the modeling, the expression for the prosodic model can be expanded as follows

$$\Pr(S,\mathbf{f}|C,L_i) = \Pr(\mathbf{f}|S,C,L_i)\Pr(S|C,L_i). \quad (10)$$

With this expansion the prosodic model can be expressed as the product of two separate models: a fundamental frequency model and a segment duration model. This simplification and the independence assumptions which will further be made clearly ignore much of the information that should be captured by the prosodic model. An early experiment combining the fundamental frequency and segment duration models into a single segment-based prosodic model did not produce satisfactory results (Hazen and Zue, 1994). One potential way to improve these models is to consider more descriptive measurements such as those proposed in Muthusamy and Cole (1992) and Itahashi *et al.* (1994).

a. Fundamental frequency model. The expression $\Pr(\mathbf{f}|S,C,L_i)$ captures the information available in the $F0$ contour of an utterance. While there may be correlation between the $F0$ contour and the durations of the segments in the utterance, this correlation is ignored in order to simplify the modeling of the $F0$ contour. Thus **f** will be considered independent of S and C. With these assumptions the fundamental frequency model can be simplified as follows:

$$\Pr(\mathbf{f}|S,C,L_i) = \Pr(\mathbf{f}|L_i). \quad (11)$$

While there may be useful information available in the dynamics of the $F0$ contour, a method for modeling these

dynamics over time for the purpose of language identification is not yet obvious. Some of this dynamic information is presumably captured in the delta $F0$ values contained in $\mathbf{f}$. To simplify the modeling, each frame is considered to be statistically independent. With this assumption the $F0$ model can be written as

$$\Pr(\mathbf{f}|L_i)=\prod_{k=1}^{m}\Pr(\mathbf{f}_k|L_i), \tag{12}$$

where m is the number of frames in the utterance and $\mathbf{f}_k$ is a feature vector representing the $F0$ and delta $F0$ values for the kth frame. It should be mentioned that the computation in Eq. (12) only includes the frames which are voiced. The expression in Eq. (12) can be modeled with a mixture of full covariance Gaussian probability density functions. Based on prior experiments (Hazen, 1993), the number of full covariance density functions utilized in the mixture Gaussian model for each language was chosen to be 9.

b. Segment duration model. The expression $\Pr(S|C,L_i)$ captures the segment duration information in a utterance. While there may be very useful information contained in S regarding the stress patterns of the syllables, words, and sentences in each utterance, this information could require fairly complex modeling and as such will be ignored for these experiments in deference to simplicity. As a simplifying assumption each segment will be considered independent of all other segments. With this independence assumption, the segment duration model can be rewritten as

$$\Pr(S|C,L_i)=\prod_{k=1}^{m}\Pr(d_k|c_k,L_i), \tag{13}$$

where m is the number of segments in the utterance and d_k is the duration of the kth segment.

The expression $\Pr(d_k|c_k,L_i)$ can be modeled with a mixture of Gaussian models. As with the acoustic model, the number of Gaussians used to model each phone in each language is determined by the equation

$$n_g=\begin{cases} n_{\max}, & \text{if } k/30>n_{\max}, \\ \lceil k/30\rceil, & \text{otherwise}, \end{cases} \tag{14}$$

where n_g is the number of Gaussians used in the mixture Gaussian model of a particular phone for a particular language, $n_{\max}$ is the maximum number of Gaussians allowed in each mixture, and k is the number of training vectors available for the phone in that particular language. Based on prior experiments (Hazen, 1993), the value of $n_{\max}$ was chosen to be 4.

6. System integration

Finally, each of the individual models must be integrated into the complete LID system, i.e., the likelihood scores from each individual model for an utterance must be combined to provide one likelihood score for each language. Using the probabilistic framework, this can is accomplished with the following expression:

$$\arg\max_i(\log\Pr(\mathbf{a}|C,S,\mathbf{f},L_i)+\log\Pr(S,\mathbf{f}|C,L_i)$$

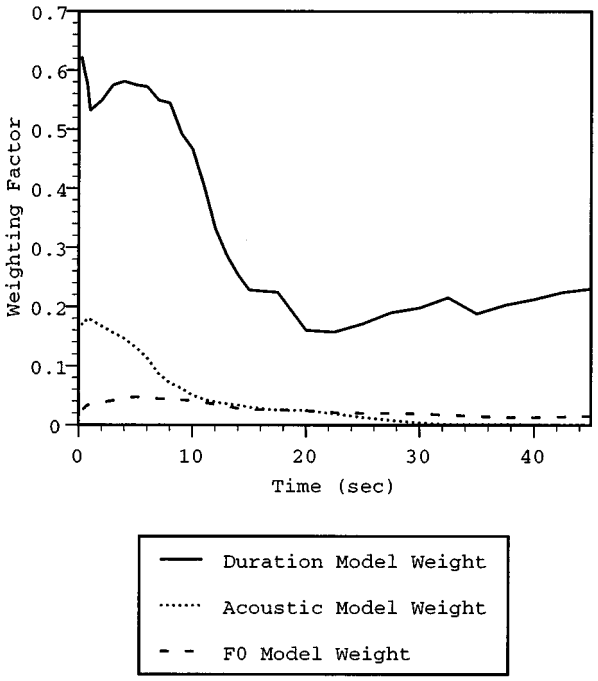

FIG. 3. Weighting factors of models over varying utterance length.

$$+\log\Pr(C|L_i)). \tag{15}$$

However, as documented in Hazen (1993), when the final system uses the simple addition of log likelihood scores with equal weights as described above, the final log likelihood score for each language is dominated by the acoustic model score. To compensate for this effect, the score from each model is multiplied by a weighting factor, as shown in Fig. 2. A hill-climbing optimization procedure is utilized to find an adequate set of weighting factors. This procedure adjusts the weights for the various models to optimize the language identification performance of the system on development data jackknifed from the training set. Because the weighting factors only need to provide a means of adjusting the *relative* scores of each model and not the absolute scores, the weight of the language model was pinned to a value of one while the weights for the acoustic, duration, and $F0$ models were allowed to vary during the iterative optimization process. The weighting factors were also optimized for different test utterance lengths. Figure 3 shows the weighting factors found by the hill-climbing procedures for the acoustic, duration, and $F0$ models. Note that as the test utterance length increases, the weights of the acoustic, duration, and prosodic models generally decrease. This effectively gives the language model more weight for longer utterances. Additionally it should be noted that, while the duration and prosodic model contribute to the total score even as the utterance length increases, the acoustic model effectively contributes nothing to the total score for longer utterances.

III. EXPERIMENTAL RESULTS AND DISCUSSION

The effectiveness of our LID system is empirically determined using the OGI multi-language telephone speech corpus (Muthusamy *et al.*, 1992; Cole *et al.*, 1994). This corpus contains utterances collected over the telephone lines

TABLE II. Language ID performance of the interpolated n-gram language model using varying n on the 45 s utterances.

n	Lang. ID accuracy (%)	Rank-order statistic
1	68.5	1.73
2	74.3	1.49
3	77.5	1.44

from native speakers of 11 different languages. For our experiments, we used a training set containing 5 987 topic-specific as well as unconstrained utterances. Of these, 471 utterances were accompanied by time-aligned phonetic transcriptions. The primary test set for our experiments contained 187 utterances as selected by The National Institute of Standards and Technology (NIST) for their March 1994 LID evaluation. These utterances were all a minimum of 30 s in length and contained completely unconstrained spontaneous speech from the 11 different languages. This test set is often referred to as the *45 second utterances* of NIST's 1994 test set. NIST also created a second test set by extracting 614 10-s segments of speech from the original 187 45-s utterances. This test set is referred to as the *10 second utterances*. Results using both test sets will be reported here.

There are many ways to measure the performance of an LID system, including its accuracy and computational efficiency. Computational efficiency is often difficult to compare across systems, since it depends on the specific implementation and computing platform. Therefore, we will focus only on our system's language identification accuracy, as measured by its top-choice accuracy and the rank-order statistics. The latter statistic measures the average rank of the correct language within the list of 11, which is indicative of how far down the correct language is from the top-choice answer.

In keeping with House and Neuburg's initial findings, we begin our analysis by focusing on the performance of the system using only the language model for language classification. House and Neuburg's approach suggested that broad phonetic analysis would be less error-prone than detailed classification while still providing reliable LID performance (House and Neuburg, 1977). However, our experiments showed that, despite poor recognition rates, detailed phonetic class representations provide more information than broad classes, and hence yield higher LID accuracy (Hazen, 1993; Hazen and Zue, 1993). Muthusamy *et al.* also concluded that fine phonetic classes were superior for language identification (Muthusamy *et al.*, 1993). Experiments have also shown that the exact choice of phones used in the set of fine phonetic units is not critical. We have observed empirically that our LID system achieved only a modest performance improvement when the inventory of phone units was increased to 87 from 59, the number of units used when the phonetic recognizer was trained on English utterances from the NTIMIT corpus (Hazen and Zue, 1994).

Because the language model is the primary component of the system, we decided to investigate in greater detail how the complexity of this component affects performance. Table II shows the language identification performance of a unigram, interpolated bigram, and interpolated trigram language model on the NIST test set. Judging from the trend shown in this table, it is conceivable that a further increase in accuracy could be realized by using a higher-order n-gram. However, the memory requirement of storing these n-grams for the set of 87 different phones would be prohibitive. An earlier study (Hazen and Zue, 1993) has shown that decreasing the number of phonetic classes helps improve the language identification accuracy of standard (noninterpolated) n-gram models when n is increased. This suggests that the investigation of interpolated class n-grams should be the next step toward improving upon the language model.

TABLE III. Performance of complete system and individual components on NIST 1994 test sets using language identification accuracy (''ACC'' in table) and rank-order statistic (''ROS'' in table).

	10 s utterances		45 s utterances	
Set of models	ACC	ROS	ACC	ROS
Complete system	65.3%	1.83	78.1%	1.43
Language model	62.7%	1.90	77.5%	1.44
Acoustic model	49.0%	2.70	53.5%	2.43
Duration model	31.7%	3.51	44.4%	3.00
$F0$ model	12.4%	5.31	20.9%	4.05

To assess the contributions made by each of the individual components, we also measured system performance under conditions in which only one of the components is used at a time as well as when the system utilizes all four components. The results are shown in Table III. At first glance, it would appear that most of the performance gain in the overall system is contributed by the language model. Closer examination, however, reveals that the contribution made by each individual component depends highly on the length of the utterances. This is shown in Fig. 4, in which the top-choice accuracy is plotted against utterance length. As can be seen in these figures, the acoustic model outperforms the language model for shorter utterances. As test utterances get longer, the performance of the language model eventually surpasses and greatly exceeds the performance of the other models. For utterances of 10 s or longer, as is the case with all the utterances in the official test set, the language model alone can achieve a performance comparable to that of the complete system. However, this figure shows that additional information beyond the phonotactic information can be useful for increasing language identification accuracy, especially when the utterance is short ($<$10 s).

As indicated in Table III, the overall system achieved a top-choice accuracy of 78.1% on the NIST test set, with a rank-order statistic of 1.43. For comparison, the best results to data are achieved by systems utilizing Zissman's basic design, which uses a bank of language-dependent phonetic recognizers instead of a single language-independent recognizer. On the same task Zissman's system achieved a top-choice accuracy of 88.8% (Zissman, 1995). However, Zissman's baseline system, which utilizes only phonotactic information (making it comparable to the language model component of our system), achieved an accuracy 79.7%. Because our language model accuracy was 77.5% (see Table

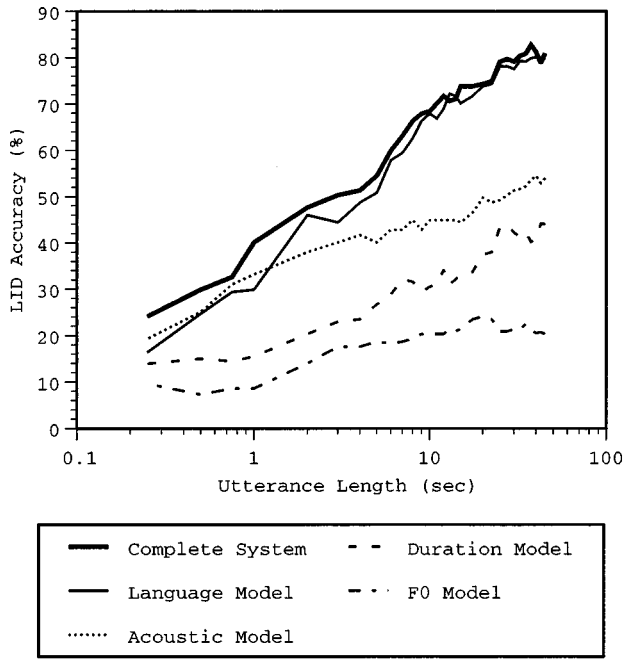

FIG. 4. Performance of system components over varying utterance length as tested on the 1994 NIST 45 s utterance test set.

III); this suggests that our system's performance is quite competitive. Zissman's improvement to 88.8% can be attributed to the addition of two new components: (1) gender specific phonetic recognizers, and (2) the incorporation of quantized duration information directly into the phonotactic model. Yan and Barnard made further modeling and classification refinements to Zissman's basic design to achieve an accuracy of 90.8% (Yan and Barnard, 1995). We believe similar refinements to our modeling techniques should result in performance improvements on the order of those encountered by Zissman and by Yan and Barnard.

In examining the overall performance of the system it is important to examine how the system performs on each individual test language. Table IV shows the performance of the system as broken down by language. The table also shows the amount of training data available for each language as well as whether or not time-aligned phonetic transcriptions were available for any of the training data in each language. As seen in the table, the availability of transcriptions for a particular language appears positively correlated with the system's accuracy for that language. The language-independent phonetic recognizer used by our system is only trained on data from the six languages which have transcriptions available. Thus, if a particular language utilizes a phone that is not utilized by one of the six languages used to train the phonetic recognizer, than that phone will never be identified correctly within the hypothesized string of phones generated by the phonetic recognizer.

TABLE IV. Relationship of the language identification accuracy of the system for particular languages to the size of the language's training set and the availability of transcribed data for that language.

Language	Test set 10 s	Test set 45 s	No. of training utterances	Transcriptions available?
Hindi	88%	95%	797	yes
English	87%	89%	1021	yes
Tamil	70%	71%	525	no
Farsi	67%	79%	438	no
Mandarin	67%	76%	481	yes
Japanese	66%	79%	408	yes
French	65%	82%	473	no
German	63%	89%	488	yes
Spanish	60%	71%	509	yes
Vietnamese	34%	60%	443	no
Korean	33%	50%	404	no

As seen in Table IV, the performance on Hindi and English utterances is significantly superior to the system's performance at identifying utterances from any other language. This result seems likely to be related to the fact that far more training data was available for training the models of these languages than the other languages. Hindi and English also had transcriptions available for portions of their training sets thus allowing all of their phones to be trained and utilized within the language-independent phonetic recognizer. Likewise, the two languages which performed the worst were Korean and Vietnamese. Neither of these two languages had transcriptions available to be used in training the phonetic recognizer. The fact that both languages contained phones not represented within the multilanguage phonetic recognizer, as well as the fact that the two languages had amongst the smallest amounts of training data, probably contributed to the poor performance on these languages. Of the remaining languages, French, Farsi, and Tamil also did not have transcriptions available but did have performances significantly higher than either Korean or Vietnamese. This is probably due in part to the fact that the phone sets of these languages were sufficiently covered by the languages which did possess transcriptions. These results indicate the need for ample, transcribed data from as many of the languages of interest as possible in order to perform highly accurate language identification.

IV. SUMMARY

In this paper, we describe a segment-based language identification system motivated by the ideas proposed by House and Neuburg. We formulated the problem into a probabilistic framework, reducing it to four separate components. The system was implemented with a single language-independent phonetic front-end for all languages. This novel approach differs from the most common approaches which utilize multiple single-language phonetic recognizers in the front-end. Using only one phonetic front-end allows the system to be more computationally efficient than the approaches using multiple recognizers in the front-end. Additionally, when using phonetic information only and gender-independent phonetic recognition, the system is competitive with other state-of-the-art systems. Although the system can achieve good performance based on the phonological language model alone, as suggested by House and Neuburg, other sources of information provide additional performance gain, especially when the system is tested on short utterances.

ACKNOWLEDGMENTS

This research was supported by ARPA under Contract No. N0014-89-J-1332 monitored through the Office of Naval Research and by a grant from Texas Instruments.

Cole, R., Fanty, M., Noel, M., and Lander, T. (**1994**). ''Telephone speech corpus development at CSLU,'' in *Proceedings of the 1994 International Conference on Spoken Language Processing* (Acoustical Society of Japan), pp. 1815–1818.

Flammia, G., Glass, J., Phillips, M., Polifroni, J., Seneff, S., and Zue, V. (**1994**). ''Porting the bilingual VOYAGER system to Italian,'' in *Proceedings of the 1994 International Conference on Spoken Language Processing* (Acoustical Society of Japan), pp. 911–914.

Glass, J., Goodine, D., Phillips, M., Sakai, S., Seneff, S., and Zue, V. (**1993**). ''A bilingual VOYAGER system,'' in *Proceedings of the 3rd European Conference on Speech Communication and Technology* (European Speech Commun. Assoc., Grenoble, France), pp. 2063–2066.

Hazen, T. J. (**1993**). ''Automatic language identification using a segment-based approach,'' Master's thesis, Massachusetts Institute of Technology.

Hazen, T. J., and Zue, V. W. (**1993**). ''Automatic language identification using a segment-based approach,'' in *Proceedings of the 3rd European Conference on Speech Communication and Technology* (European Speech Commun. Assoc., Grenoble, France), pp. 1307–1310.

Hazen, T. J., and Zue, V. W. (**1994**). ''Recent improvements in an approach to segment-based automatic language identification,'' in *Proceedings of the 1994 International Conference on Spoken Language Processing* (Acoustical Society of Japan), pp. 1883–1886.

House, A. S., and Neuburg, E. P. (**1977**). ''Toward automatic identification of the language of an utterance. I. Preliminary methodological considerations,'' J. Acoust. Soc. Am. **62,** 708–713.

Itahashi, S., Zhou, J. X., and Tanaka, K. (**1994**). ''Spoken language discrimination using speech fundamental frequency,'' in *Proceedings of the 1994 International Conference on Spoken Language Processing* (Acoustical Society of Japan), pp. 1899–1902.

Jelinek, F. (**1990**). ''Self-organized language modeling for speech recognition,'' in *Readings in Speech Recognition*, edited by Alex Waibel and Kai-Fu Lee (Morgan Kaufmann, San Mateo, CA), Chap. 8, pp. 450–506.

Kadambe, S., and Hieronymus, J. L. (**1994**). ''Spontaneous speech language identification with a knowledge of linguistics,'' in *Proceedings of the 1994 International Conference on Spoken Language Processing* (Acoustical Society of Japan), pp. 1879–1882.

Kadambe, S., and Hieronymus, J. L. (**1995**). ''Language identification with phonological and lexical models,'' in *Proceedings of the 1995 International Conference on Acoustics, Speech, and Signal Processing* (IEEE, Piscataway, NJ), pp. 3507–3510.

Leonard, R. G. (**1980**). ''Language recognition test and evaluation,'' Air Force Rome Air Development Center Technical Report No. RADC-TR-80-83.

Leonard, R. G., and Doddington, G. R. (**1974**). ''Automatic language identification,'' Air Force Rome Air Development Center Technical Report No. RADC-TR-74-200.

Leonard, R. G., and Doddington, G. R. (**1975**). ''Automatic language identification,'' Air Force Rome Air Development Center Technical Report No. RADC-TR-75-264.

Leonard, R. G., and Doddington, G. R. (**1978**). ''Automatic language discrimination,'' Air Force Rome Air Development Center Technical Report No. RADC-TR-78-5.

Mermelstein, P., and Davis, S. (**1980**). ''Comparison of parametric representations for monosyllabic word recognition in continuously spoken sentences,'' IEEE Trans. Acoust. Speech Signal Process. **28,** 357–366.

Muthusamy, Y., Berkling, K., Arai, T., Cole, R., and Barnard, E. (**1993**). ''A comparison of approaches to automatic language identification using telephone speech,'' in *Proceedings of the 3rd European Conference on Speech Communication and Technology* (European Speech Commun. Assoc., Grenoble, France), pp. 1307–1310.

Muthusamy, Y. K., and Cole, R. A. (**1992**). ''Automatic segmentation and identification of ten languages using telephone speech,'' in *Proceedings of the 1992 International Conference on Spoken Language Processing* (Univ. of Alberta, Edmonton, Canada), pp. 1007–1010.

Muthusamy, Y. K., Cole, R. A., and Gopalakrishnan, M. (**1991**). ''A segment-based approach to automatic language identification,'' in *Proceedings of the 1991 International Conference on Acoustics, Speech, and Signal Processing* (IEEE, Piscataway, NJ), pp. 353–356.

Muthusamy, Y. K., Cole, R. A., and Oshika, B. T. (**1992**). ''The OGI multilanguage telephone speech corpus,'' in *Proceedings of the 1992 International Conference on Spoken Language Processing* (Univ. of Alberta, Edmonton, Canada), pp. 895–898.

Secrest, B. G., and Doddington, G. R. (**1983**). ''An integrated pitch tracking algorithm for speech systems,'' in *Proceedings of the 1983 International Conference on Acoustics, Speech, and Signal Processing* (IEEE, Piscataway, NJ), pp. 1352–1355.

Yan, Y., and Barnard, E. (**1995**). ''An approach to language identification with enhanced language model,'' in *Proceedings of the 4th European Conference on Speech Communication and Technology* (European Speech Commun. Assoc., Grenoble, France), pp. 1351–1354.

Zissman, M. A. (**1995**). ''Language identification using phoneme recognition and phonotactic language modeling,'' in *Proceedings of the 1995 International Conference on Acoustics, Speech, and Signal Processing* (IEEE, Piscataway, NJ), pp. 3503–3506.

Zissman, M. A. (**1996**). ''Comparison of four approaches to automatic language identification of telephone speech,'' IEEE Trans. Speech Audio Process. **4**, 31–44.

Zissman, M. A., and Singer, E. (**1994**). ''Automatic language identification of telephone speech messages using phoneme recognition and *n*-gram models,'' in *Proceedings of the 1994 International Conference on Acoustics, Speech, and Signal Processing* (IEEE, Piscataway, NJ), pp. 305–308.

Zue, V., Glass, J., Goodine, D., Leung, H., Phillips, M., Polifroni, J., and Seneff, S. (**1990**). ''Recent progress on the SUMMIT system,'' in *Proceedings of the Third DARPA Speech and Natural Language Workshop* (Morgan Kaufmann, San Mateo, CA), pp. 380–384.

Zue, V., Glass, J., Phillips, M., and Seneff, S. (**1989**). ''The MIT SUMMIT speech recognition system: A progress report,'' in *Proceedings of the DARPA Speech and Natural Language Workshop* (Morgan Kaufmann, San Mateo, CA), pp. 179–189.

A consonance-based approach to the harpsichord tuning of Domenico Scarlatti

John Sankey
1369 Matheson Road, Gloucester, Ontario K1J 8B5, Canada

William A. Sethares
University of Wisconsin, Madison, Wisconsin 53706-1691

(Received 16 August 1995; revised 28 October 1996; accepted 29 October 1996)

This paper discusses a quantitative method for the study of historical keyboard instrument tunings that is based on a measure of the perceived dissonance of the intervals in a tuning and their frequency of occurrence in the compositions of Domenico Scarlatti (1685–1757). We conclude that the total dissonance of a large volume of music is a useful tool for studies of keyboard instrument tuning in a historical musical context, although it is insufficient by itself. Its use provides significant evidence that Scarlatti used French tunings of his period during the composition of his sonatas. Use of total dissonance to optimize a 12-tone tuning for a historical body of music can produce musically valuable results, but must at present be tempered with musical judgment, in particular to prevent overspecialization of the intervals. © *1997 Acoustical Society of America.*
[S0001-4966(97)03603-5]

PACS numbers: 43.75.Bc [WJS]

INTRODUCTION

Numerous musical scales have been used over the years for Western music, with the aim of maximizing the quality of sound produced by fixed-pitch 12-note instruments such as the harpsichord. The principal musical interval in this tradition is the octave, which is defined as a factor of 2 in frequency. Other ''pure'' intervals are defined as those formed by small integer ratios; such intervals have maximum overlap of harmonic partials of these instruments and hence tend to minimize beating. Given that the octaves are to be exactly in tune, only a few of the other intervals can be pure in a single fixed tuning.

The modern preference is to make all intervals somewhat ''impure'' by using 12 equal semitones. There is then no difference between various musical keys and there are no restrictions on modulation. Unfortunately, this also removes key tonality as a significant structure in music. Three hundred years ago this was not the case. Until about 1780, the preference was to tune keyboard instruments so that commonly used intervals were purer than those less used. The resulting nonequal semitones gave a different harmonic ''color'' to each musical key. These harmonic colors were part of the musical language of the time, philosophically and practically. If one wishes to understand the musical language of early keyboard composers, the tuning in which their music was conceived and heard is important.

However, few composers documented the exact tunings used in their music. Although there is sufficient historical evidence that the period and nationality of a composer can narrow the choice considerably, there are often significant variances between historically justifiable tunings for any specific piece of music. One of us (JS) has recorded the complete harpsichord works of Domenico Scarlatti (1685–1757) in the style of his time. Scarlatti's tuning preferences are particularly uncertain, since he was born and trained in Italy, but spent most of his career in Portugal and Spain, and did all of his significant composing while clearly under strong Spanish influence. A method which might infer information concerning his tuning preferences solely from his surviving music would therefore be of value to musicians and musicologists.

This paper discusses a quantitative method that is based on a measure of the perceived consonance of the intervals in a tuning and their frequency of occurrence in the compositions of Scarlatti. Its presumption is that Scarlatti would avoid passages using intervals that were markedly out-of-tune or dissonant in his tuning (such as wolf fifths) except in passing, and would tend on average to emphasize those intervals and keys which were relatively pure. Unlike traditional approaches to this question,[1] which are based on the same assumption, but rely upon culture-dependent interval selection and classification, this method is based directly upon experimentally determined psychoacoustic properties of human hearing.

Sethares[2] introduced a parameterization of the perceptual data of Plomp and Levelt[3] that can be used to calculate the perceived dissonance (or equivalently, the perceived consonance) of an interval given the spectrum of a sound. It can be used to relate the timbre of a musical sound to a set of intervals (or scale) in which the sound can be played most consonantly. This paper reports on the results of applying this approach to investigate harpsichord tunings of Domenico Scarlatti, by finding tunings which minimize the dissonance over all intervals actually used by Scarlatti in his sonatas. The resulting tunings are then compared both theoretically and using informal listener tests to several well known historical tunings. The method should be applicable to other early keyboard composers.

I. METHODOLOGY

There are four basic steps to find the most consonant tuning for a piece (or collection of pieces) of music. These are:

(1) Specify the timbre (spectrum) of each sound.
(2) Find (or count) the number of occurrences of each interval class, and weight by their duration.
(3) Choose an initial ''guess'' for the optimization algorithm.
(4) Implement a gradient descent (or other local optimization algorithm) to find the nearest ''least dissonant'' set of intervals.

The bulk of this section describes these four steps in detail. Since the Scarlatti sonatas were composed mostly for harpsichord, a spectrum was chosen that approximates an idealized harpsichord string. The tone was assumed to contain 32 harmonic partials at frequencies

$$(w,2w,3w,\ldots,32w), \tag{1}$$

where w is the fundamental. The amplitude of the partials was assumed to decrease by a factor of 0.75 (2.5 dB) per partial. Surviving historical harpsichords vary considerably in these parameters. The low strings of some have many more than 32 discernable partials, decreasing by a factor as high as 0.9, while the high strings of others display as few as 8 partials. The amplitudes of partials also have periodicities arising from the position at which the string is plucked, which varies widely, and room acoustics of the time also vary. We consider that the spectrum chosen is a reasonable approximation to the sounds of the harpsichords on which Scarlatti most likely played, in the portion of their range in which a musician is most sensitive to questions of tuning.

The Scarlatti recordings are in MIDI file format,[4] which is a widely accepted standard for encoding the finger motions of a keyboard player as a function of time. These finger motions are then transformed by a ''patch,'' a representation of the sound produced by the instrument used for the recording, to synthesize a performance similar to that heard in the recording studio. A program was written to parse these MIDI files and to collate the required information about frequency of occurrence of intervals and their duration in actual performance.

The dissonance between any two partials (pure tones) at frequencies $f1$ and $f2$, with amplitudes $v1$ and $v2$ can be calculated as

$$d(f1,f2,v1,v2)=v1v2(e^{-ax}-e^{-bx}), \tag{2}$$

where

$$x=0.24|f1-f2|/[0.021\ \min(f1,f2)+19],$$

$$a=3.5,\ \text{and}\ \ b=5.75. \tag{3}$$

The dissonance D( ) of a pair of notes $n1$ and $n2$ with fundamentals $w1$ and $w2$ is obtained by summing all the dissonances of all the partials to give

$$\mathbf{D}(n1,n2)=\sum_{i=0}^{31-k}\sum_{j=i+k}^{31} d((i+1)w1,(j+1)w2,0.75^i,0.75^j), \tag{4}$$

where $k=1$ to exclude unisons, which cannot be produced on a single manual harpsichord. This parameterization of the Plomp and Levelt psychoacoustic data was presented in Sethares,[2] where typical forms of the functions $d(\ )$ and D( ) are shown. The total dissonance (TD) of a musical passage of m notes is defined to be the sum of the dissonances weighted by the duration over which the intervals overlap in time, thus

$$\mathrm{TD}=\sum_{i=1}^{m-1}\sum_{j=i+1}^{m} D(i,j)t(i,j), \tag{5}$$

where $t(i,j)$ is the total time during which notes i and j sound simultaneously. Since d is always positive, D( ) and TD are always positive as well. Although the amplitude of a single held note of a harpsichord decreases with time, it increases significantly each time a succeeding note is played due to coupling via their shared soundboard. Given the high note rates in the sonatas, the rectangular sound intensity distribution implied by (5) is a reasonable approximation to make.

We define a ''tuning'' to be a set of 11 distinct intervals between 1:1 and 2:1. Then the TD for a musical composition differs depending on the tuning chosen since the different intervals have different values of $\mathrm{D}(i,j)$. By choosing the tuning properly, the total dissonance of the passage can be minimized, or equivalently, the consonance can be maximized. Thus the problem of choosing the tuning that maximizes consonance can be stated as an optimization problem: minimize the ''cost'' (the TD of the composition) by choice of the intervals that define the tuning. This optimization problem can be solved using a variety of techniques; we chose a gradient descent method similar to that of Sethares.[5] Indeed, the adaptive tuning method can be considered a special (instantaneous) case of the present method, which maintains a history of the piece via the $t(i,j)$ terms.

Let I_0 be the initial ''tuning vector'' containing a list of the intervals that define the tuning. A (locally) optimal I_* can be found by iterating

$$I_{k+1}=I_k-\mu\frac{d\mathrm{TD}}{dI_k}, \tag{6}$$

until convergence, where μ is a small positive step size and k is the iteration counter. The algorithm is said to have converged when $\Delta\mathrm{TD}/\Delta I_k$ is positive for all $\Delta I_k=\pm 0.025$ cents. (0.025 cents is the default pitch resolution of systems meeting the general Midi specification.) D( ) is a symmetric matrix with dimension equal to the number of notes of Scarlatti's harpsichords (up to 60), but since all tunings use pure octaves, the D( ) map into tuning vectors I_k and I_* of exactly 11 elements. Calculation is straightforward, although rather tedious. In most cases, the algorithm was initialized at the 12-tone equal tempered scale, that is, I_0 was a vector in which all adjacent intervals are equal to the twelfth root of 2,

TABLE I. Total dissonances relative to 12 tet for various tunings.

Historical tunings:	TD	s	Cents ($C\equiv 0$)										
12 tet	0	0	100.0	200.0	300.0	400.0	500.0	600.0	700.0	800.0	900.0	1000.0	1100.0
Bethisy	−0.4	4.1	86.8	193.2	288.9	386.3	496.3	586.6	696.6	787.0	889.7	992.6	1086.5
Rameau b	−0.5	7.1	92.5	193.2	304.8	386.3	503.4	582.2	696.6	800.0	889.7	1006.8	1082.9
Werckmeister 5	−0.6	2.6	96.1	203.9	300.0	396.1	503.9	600.0	702.0	792.2	900.0	1002.0	1098.0
d'Alembert	−0.8	4.1	86.8	193.2	290.2	386.3	496.7	586.6	696.6	787.0	889.7	993.5	1086.5
Barca	−1.0	2.4	92.2	196.7	296.1	393.5	498.0	590.2	698.4	794.1	895.1	996.1	1091.9
Marpourg	−1.3	6.1	84.3	193.2	293.8	386.3	503.4	579.5	696.6	789.1	889.7	998.6	1082.9
Werckmeister 4	1.4	5.2	82.4	196.1	294.1	392.2	498.0	588.3	694.1	784.4	890.2	1003.9	1086.3
Vallotti	−1.6	2.9	90.2	196.1	294.1	392.2	498.0	588.3	698.0	792.2	894.1	996.1	1090.2
Barca A	−1.7	2.4	92.2	200.3	296.1	397.1	498.0	593.8	702.0	794.1	898.7	998.0	1095.4
Werckmeister 3	−1.9	3.1	90.2	192.2	294.1	390.2	498.0	588.3	696.1	792.2	888.3	996.1	1092.2
Kirnberger 3	−1.9	3.4	90.2	193.2	294.1	386.3	498.0	590.2	696.6	792.2	889.7	996.1	1088.3
Corrette	−2.2	6.8	76.0	193.2	288.8	386.3	503.4	579.5	696.6	783.4	889.7	996.1	1082.9
Vallotti A	−2.5	2.9	90.2	200.0	294.1	396.1	498.0	592.2	702.0	792.2	898.0	996.1	1094.1
Chaumont	−3.3	7.7	76.0	193.2	288.8	386.3	503.4	579.5	696.6	772.6	889.7	996.1	1082.9
Rameau #	−4.0	7.1	76.0	193.2	285.6	386.3	497.9	579.5	696.6	775.4	889.7	993.2	1082.9
1/4 comma A	−5.8	10.3	76.1	193.2	310.3	386.3	503.4	579.5	696.6	772.6	889.7	1006.8	1082.9
Kirnberger 2	−6.0	4.5	90.2	203.9	294.1	386.3	498.0	590.2	702.0	792.2	895.1	996.1	1088.1
derived tunings:													
TDE	−1.6	2.2	98.0	200.0	302.0	402.1	505.5	605.3	698.1	800.0	900.2	1003.9	1104.1
TDA1	−2.3	4.6	85.6	193.4	291.4	386.3	498.0	584.8	696.8	787.5	888.7	994.9	1086.5
TDA2	−7.1	5.6	87.8	200.1	294.1	386.3	498.0	586.4	698.2	789.7	884.4	996.1	1084.5
K828 LS.27			86.3	192.4	289.7	385.2	495.8	585.8	695.8	785.9	888.9	993.0	1086.2
Minimum-TD tunings of individual sonatas:													
K1 L366			85.3	197.1	⋯	401.0	512.7	583.4	695.1	787.3	899.0	1010.7	1102.9
K6 L479			111.7	203.9	315.6	386.3	498.0	582	702.0	813.7	884.4	996.1	1088.3
K11 L352			⋯	203.9	315.7	384.6	498.0	583.2	702.0	813.7	905.8	1017.6	1088.3
K20 L375			104.8	216.5	287.2	398.9	517.6	602.8	714.6	785.2	897.0	989.1	1100.9

defined as 100 cents, about 1.059. In all cases in this paper, C is defined as 0 cents.

A tuning for which a desired composition (or collection of compositions) has smaller TD is to be preferred as far as consonance is concerned. In the context of attempting to draw historical implications, the measure of TD may provide reason for rejecting tunings (those which are overly dissonant) or reconsidering tunings (those with near-optimal values of TD). As we shall argue, such judgments cannot yet be made mechanically, but must still be tempered with musical insight. The variation in values of the TD for different tunings are quite small, less than 1‰ between musically useful tunings, and are therefore expressed in parts per thousand (‰) difference from 12-tone equal-tempered (12-tet) tuning. A difference of 1‰ is clearly audible to a trained musical ear in typical musical contexts. (For this reason, a numerical precision of nine decimal places or greater is advisable for the calculations of TD.)

Music of course does not consist solely of consonances. Baroque music is full of trills and similar features which involve overlapped seconds in real performance, and Scarlatti made heavy use of solidly overlapped seconds, deliberate dissonances, as a rhythmic device. We therefore omitted all intervals smaller than 3 semitones from the calculations of the TD, that is we used $k=3$ in (4). Thus, the consonance of large intervals occurring during periods of small-interval dissonance were still counted. We note that this had surprisingly little effect on the values of the convergent tunings; the precaution is probably unnecessary with other composers. The contrast between dissonance and consonance, sometimes useful musically, is not dealt with by the consonance method, but it is also not dealt with by that of Barnes.[1]

II. RESULTS AND DISCUSSIONS

Since harpsichords (in contrast with organs) were tuned very frequently, usually by the performer, one assumes that composers might have changed their preferred tuning over the course of their lifetime, or used more than one type of tuning depending upon the music to be played. In fact, both of these are well documented in the case of Rameau. So, we began the analysis by initializing the tuning vector I_k to the intervals of 12-tet, and found the optimum tunings I_*, those that minimize the TD for each of the 536 harpsichord sonatas individually, in the hope of discerning any such changes. A few example results are included in Table I. (Throughout, K numbers are those of the chronological Kirkpatrick catalogue,[6] L numbers those of the widely available Longo edition.) A histogram of all the tunings thus obtained is shown in Fig. 1. In this graph, the height of a bar shows for how many sonatas the optimum tuning contained a note of the pitch shown. As can be seen, for most of the 11 pitches, there were two strong preferences. Below the frequency bars is shown the location of the pure fifths (3:2, 701.955 cents) ascending and descending from C, e.g., $701.995n \bmod 1200$ for $n=-11$ to $+11$, the well-known enharmonic pitches. The minimization process for samples as small as one sonata thus for the most part ''locks on'' to the predominate non-

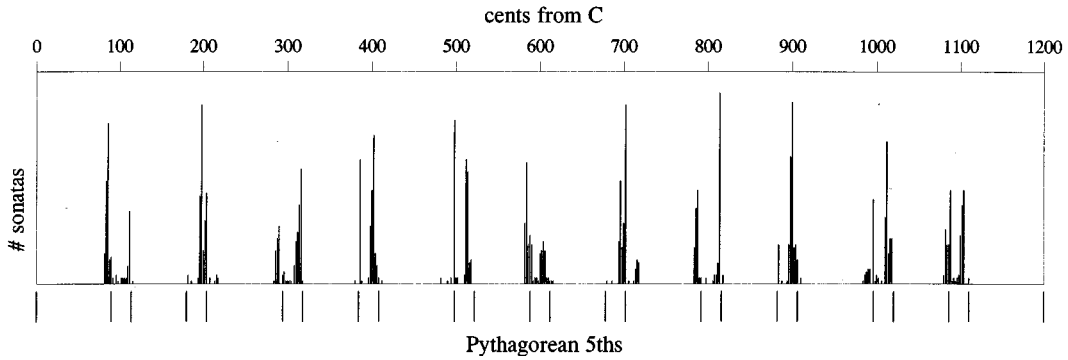

FIG. 1. Showing the relative distribution of optimal (TD minimized) tunings for each of the sonatas individually in relation to the Pythagorean cycle of pure fifths.

unison minimum in D( ), that at pure fifths.[7] This effect continued to dominate even when groups of up to ten sonatas were evaluated. Although Baroque harpsichordists would have refined the tuning of their instruments before performing suites of pieces using a consistent tonality set, just as harpsichordists do today, it is quite impractical to completely retune an instrument every 10 min (the length of a typical sonata pair with repeats and variations).

The primary formal structure of almost all of the sonatas follows two symmetries: tonalities are mirrored about a central double bar, and thematic material repeats after the double bar (although not always in exactly the same order). For example, K1 begins in D minor, progresses to A major at the double bar 14, and ends in D minor bar 31; thematically, bar 1 matches bar 14; 2–5, 22–25; 7, 17; 9, 18; 13, 31. One expects that Scarlatti's tuning(s) would have complemented and been consistent with these symmetries. Many of the single-sonata tunings found by this optimization method are not. For example, bars 9 and 18 in K1 are symmetrically designed to strongly establish the tonalities D minor and F major, respectively, but the pure D-A 5th on which bar 9 is based is inconsistent with the F-C 5th of bar 18, a very audible 15 cents smaller than pure in this tuning. By comparison, these intervals differ by only 4 cents in the Vallotti A tuning. Using optimized tunings to retune sections of music of sonata length does not, therefore, seem to be a reliable guide to the practice of Domenico Scarlatti, nor to be useful in detecting changes in tuning preferences over his oeuvre.

We then evaluated the relative TD of a number of tunings that are documented in the musical literature of Scarlatti's time. Meantone tuning, in which all fifths are equal excepting one ''wolf'' fifth G♯-E♭, was the commonest tuning at the close of the Middle Ages. It was considered to be in the key of D, and was modified steadily towards equal tempering by increasing the size of the equal fifths as time progressed. However, since only one note needs to be retuned in order to transpose any meantone tuning into the tuning for an adjacent fifth (e.g., to add or subtract one sharp or flat from the key signature), many performers did so to improve the sound of their favourite keys. The ''consonance'' (negative of TD, so that the minima are visible as peaks) relative to 12 tet for the set of all the Scarlatti sonatas is shown in Fig. 2 versus the size of the equal fifths and the position of the wolf fifth. There is a sharp minimum of TD with fifths 3.42 cents less than 12-tet when the wolf is between E♭ and B♭ or between E♭ and G♯, precisely the medieval 1/4-comma tunings in the keys of A and D. There is another broader minimum with fifths 1.8 cents larger than 12 tet, which is close to the ancient Pythagorean tuning with pure fifths. The general shape of the meantone TD of the entire keyboard oeuvre of Scarlatti is therefore in accord with historical musical practice.

Many historical harpsichord tunings have been quantified by Asselin;[8] the tunings used in this study are shown in Table I. Since the harpsichord scale has 11 degrees of freedom, it is desirable to characterize each tuning by a smaller number of musically useful parameters in order to clarify the results of the analysis. We have chosen for this purpose the mean absolute difference between the various tunings and 12 tet as a strength parameter s, i.e.,

$$s(t)=\overline{|c(k,e)-c(k,t)|}, \tag{7}$$

where $c(k,e)$ is the pitch in cents of note k from note 1 of the 12-tet scale, $c(k,t)$ the corresponding pitch of tuning t, and

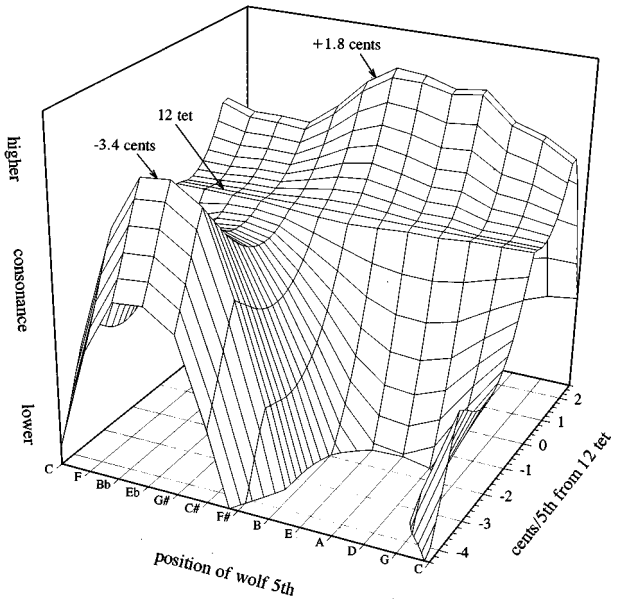

FIG. 2. Showing the relation between consonance (the negative of TD) relative to 12 tet, size of equal fifths in a meantone-type tuning and position of the unequal ''wolf'' fifth, for all the sonatas as one unit.

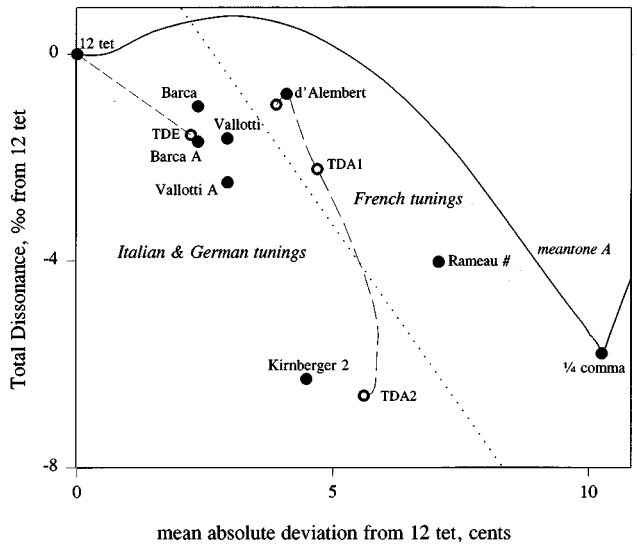

FIG. 3. Showing the total dissonance (TD) relative to the equal-tempered tuning (12 tet) of all the sonatas as one unit versus the mean absolute deviation from 12 tet for some tunings of Table I.

$$\overline{c(k,e)} = \overline{c(k,t)} \tag{8}$$

to remove the pitch scale dependence of the dissonance function d. Historically, the value of $s(t)$ has decreased with time, from 10 cents for the medieval 1/4-comma meantone tuning to essentially zero for modern piano tunings. In general, a low value of s is associated with tunings that work in a wide variety of keys, a high value with tunings placing many restrictions on modulation.

The values of the TD (5) for the recorded sonatas for these tunings are shown by solid circles in Fig. 3 versus the strength of the tuning (7). If a series of meantone-type tunings in A is constructed, with the size of the equal fifths decreasing from 12 tet (100 cents) to 96 cents, the locus of TD and s is the solid line shown. (It is the same curve as that for the wolf between E♭ and B♭ in Fig. 2.) In Fig. 3, a decrease of both the TD and s should be an improvement both in consonance and in modulatability. A decrease in the TD associated with an increase in s will however involve a choice based on musical context, since any improvement in consonance may be offset by a reduction in the range of keys in which the consonance will be useful.

In general, French tunings sought to purify the sound of major thirds, whereas Italian and German tunings were more closely derived from the fifth-based meantone. The two schools may be separated by the dotted line in Fig. 3; again the TD is in accordance with historical knowledge. Both Italian tunings in A show superior consonance to those in D, and Rameau's ''sharp'' tuning has greater consonance than that in Bb. (Modulated versions of any tuning have the same strength s.) The expectation from this figure is that Kirnberger 2 should be by far the best tuning for the sonatas, with meantone (1/4 comma) second except perhaps in some remote tonalities due to its strength. Next should be the sharp tuning of Rameau (again with possible difficulties in some tonalities), followed by Vallotti A, then Barca A. Unfortunately, other factors intervene.

A primary phrase pattern widely used in Western music, and particularly by Scarlatti in the sonatas, is a gradual increase of musical tension culminating in a musical steady state (stasis) or a release of tension (resolution). Increasing pitch, volume, rapidity, harmonic density, and harmonic dissonance are techniques of increasing musical tension. A skilled composer will use these various techniques in a mutually supporting way, in consistent patterns. If, therefore, use of a particular tuning enhances the ebb and flow of musical tension, it may be the tuning that the composer used to hear music. Since only a small proportion of potential intervals can be simultaneously in perfect tune in one tuning, it is likely that an erroneous tuning at least occasionally results in a glaring mismatch of musical shape.

The TD predictions fail badly with the tuning 2 of Kirnberger when this tension structure is taken into account; the consonances in this tuning generally fall in Scarlatti's relatively long tonal transition passages and all too frequently come to abrupt halts with unacceptably dissonant stases. For example, sonata K1 begins the second section with an A major triad ascent to an E in the treble, then repeats the figure in the bass under the sustained E. With Kirnberger 2, A-E is almost 11 cents smaller than pure, one of the most dissonant 5ths in the tuning. In both the Vallotti A and d'Alembert tunings, by comparison, A-E is a bit less than 1/4 comma smaller than pure, precisely right for an interim pause in the overall upward passage of which the A to E phrase forms a part. Beside frequently failing the tension-topology criterion, and the symmetry criteria discussed earlier, the 1/4-comma meantone tuning too often produces phrases that stay consistently out of tune for too long at a time for the ear (although obviously not long enough to affect the TD sufficiently), for example, the chromatic passages in bars 10–14 and 35–38 of K3 L378. In fact, these bars together with their symmetric pair 58–63 and 84–87 cannot be played in consistent tune with any placement of a 1/4-comma tuning wolf fifth.

However, although the tonal colours of Rameau are clearly in evidence to the modern ear, so are the consonances, which fall in the right places, and the tuning is particularly evocative in many of Scarlatti's slow plaintive melodic passages (K11, for example). The smooth matches of the Vallotti A tonal structure with those implicit in the music are very consistent, if unremarkable. The French tunings do indeed mostly have problems with dissonances in many places (the chromatic passages of K3, for example). However, the tuning of d'Alembert, despite its height on the graph, is a good overall musical match to the music, although few of its consonances seem really pure using the values of Asselin.

To quantify these judgments a bit better, a sample of 10% of the sonatas (every tenth) was used for a comparative listening test with the most promising tunings. The question asked for each of the 50 sonatas in the sample was: given that the tuning in question was the normal tuning colour of the culture, would a good composer have written this way for it? Since these tunings are rooted in history and, as a soloist, Scarlatti was free to tune his own instrument and to control his own sounds, this form of question is, we submit, appropriate to the purpose of this paper. (One would expect quite

TABLE II. Aural ranking of some tunings (see text for details).

Barca A	50
Vallotti A	46
TDA1	44
Werckmeister 3	39
Rameau #	34
Kirnberger 2	15
Meantone A	<0

different answers from musically naive listeners of the time, or of today, as well as from modern musicians unsteeped in baroque culture.) A single really unmusical dissonance, or serious mismatch between consonance shape and phrase shape rated a minus 1, more than a few awkward-sounding phrases rated a zero, while sonatas encountering no significant difficulties received +1. 12 tet is, of course, degenerate with respect to this question, and tunings that approach it would, in the limit, have a score of 50. Thus, a ''mild'' tuning will automatically receive a higher score than a strong tuning, which must be taken into account when comparing ratings. All the ratings were done by one person (JS) under consistent listening conditions. The results are shown in Table II. Although the rating is in the conventional form of a hypothesis to be disproven, it has a second interpretation—the fact that a tuning as strong as that of Rameau encounters so few difficulties must be considered as evidence on its own that Scarlatti had French tunings in mind as he composed. Original artists like Scarlatti often bend conventional notions to their limit, so the most likely tunings are not those with a perfect score, but rather the strongest ones that still have good scores. This suggests that the tuning of d'Alembert, descended from the earlier tuning of Rameau, is a very likely historically documented candidate for the tuning that Scarlatti used as he composed his music. We note that this is unexpected based upon historical evidence.

The historical instructions for some tunings are uncertain, even deliberately ambiguous, so modern numeric reconstructions may be slightly in error. This is almost certainly the case for the tuning of d'Alembert, which was described and redescribed in remarkably varied terms by several authors (e.g., Bethisy) of the time. We again applied the gradient algorithm with several cost functions to successively reduce the TD in small steps for the set of all the sonatas, beginning with this tuning (instead of initializing with 12 tet), with the hope that this might correct minor errors in what is basically a good tuning. We found that the routes of the optimizations as well as the final points were affected very little by step size below 0.5 cent, and also affected little by the number of harmonics in the timbre above 8, so computation time was reasonable (a weekend on a PC for the longest). Two routes the algorithm took are shown by dashed lines in Fig. 3. The longest (right) curve shows the route when the only criteria for the change in I was lower TD, the shortest (left) when I was optimized for lower s and lower TD simultaneously. The first minimization proceeded well beyond the best-sounding point along the path, ending up at a tuning (TDA2 in Fig. 3) that made the commonest intervals perfectly consonant but far too many lesser-used musically important ones unacceptably dissonant (for example, the repeated high D-A fifths of K1, 17 cents flat). A selection of the tunings along this path were listened to, and the musically most promising one (TDA1) chosen for a full listening test. It is an excellent tuning for the oeuvre. In fact, when all the 536 recorded sonatas were subjected to the criteria used for Table II with it, not a single sonata was rated −1, and only about 5% rated a 0.

Furthermore, if this small-step optimization from the d'Alembert tuning is applied individually to the few sonatas where the TDA1 tuning has residual difficulties, a similar behavior is observed. At first, the sound improves, and then, with further iteration, the tuning becomes ''overspecialized.'' For example, the 5ths ending many phrases of K328, and the chords closing each half, are a bit more discordant with TDA1 than one would wish, although consistently so. Applying the small-step refinement procedure for just this sonata produces the tuning included in Table I—the 5ths and chords all improve in consonance compared to TDA1, without changing the sound of the rest of the sonata adversely or changing the basic colour of the tuning. This is in accordance with historical practise, where a basic tuning would be ''touched up'' for a while to play a group of pieces that benefited from it (as opposed to the minimum-TD tunings which vary too much between sonatas to be practical).

We also applied this small-step optimization beginning with other tunings, to the set of all sonatas and to some individual sonatas. The qualitative pattern observed with the d'Alembert tuning—that the overall musical quality of the tuning first improved, and then declined as the TD approached its minimum—was also observed with most other tunings. However, none improved to anything like the same extent nor with the same consistency as did the d'Alembert tuning.

III. CONCLUSIONS

In summary, the total dissonance of a large volume of music is a useful tool for studies of 12-tone keyboard instrument tuning in a historical musical context, although it is insufficient by itself. Its use provides significant evidence that Domenico Scarlatti used the French tunings of his period during the period of composition of his sonatas. Use of total dissonance to optimize a 12-tone tuning for a historical body of music can produce musically valuable results, but must at present be tempered with musical judgment, in particular to prevent overspecialization of the intervals.

[1] J. Barnes, ''Bach's keyboard temperament; Internal evidence from the Well-Tempered Clavier,'' Early Music **7**, 236–249 (1979).
[2] W. A. Sethares, ''Local consonance and the relationship between tuning and timbre,'' J. Acoust. Soc. Am. **94**, 1218–1228 (1993).
[3] R. Plomp and W. J. M. Levelt, ''Tonal consonance and critical bandwidth,'' J. Acoust. Soc. Am. **38**, 548–560 (1965).
[4] The files are currently available on the Internet at ftp://ftp.cs.ruu.nl/pub/MIDI/SONGS/CLASSICAL/SCARLATTI/.
[5] W. A. Sethares, ''Adaptive tunings for musical scales,'' J. Acoust. Soc. Am. **96**, 10–18 (1994).
[6] R. Kirkpatrick, *Domenico Scarlatti* (Princeton U.P., Princeton, NJ, 1953).
[7] See Fig. 3 in Sethares (Ref. 2).
[8] P-Y. Asselin, *Musique et tempérament* (Éditions Costallat, Paris, 1985).

Directional tone color

Gabriel Weinreich
Randall Laboratory of Physics, University of Michigan, Ann Arbor, Michigan 48109-1120

(Received 23 August 1996; revised 11 December 1996; accepted 16 December 1996)

Above about 1 kHz, the angular radiation pattern of a violin begins to vary rapidly not only with direction but also with frequency, typically changing drastically from one semitone to the next. In an enclosed space, this characteristic, which we have named ''directional tone color,'' can sometimes produce the illusion that each note played by a solo violin comes from a different direction, endowing fast passages with a special flashing brilliance. It also has important consequences for the perception of vibrato, for the difference in sound between a solo violin and an orchestral section playing in unison, for the problem of reproducing violin sounds through a loudspeaker, and possibly for the mysterious quality called ''projection.'' This paper introduces the theoretical basis of directional tone color, presents data to support its existence, and discusses the various ways in which it can be musically important. © *1997 Acoustical Society of America.* [S0001-4966(97)05804-9]

PACS numbers: 43.75.De, 43.20.Rz [WJS]

I. THEORY

Except at the lowest frequencies, a violin radiates sound primarily through the vibration of its wooden shell. (It has been suggested[1] that air modes may possibly again become important at very high frequencies, where their density becomes larger than that of wood modes; but that would, in any case, not greatly affect the argument of this paper.) Accordingly, we begin by discussing the nature of the modes of such a shell.

A. Density of wood modes in frequency

If the elastic properties of the shell were isotropic, the frequency density of wood modes would be easy to compute.[2] First, we note that the density of such modes in the **k** plane is approximately constant and equal to $A/(2\pi)^2$, where A is the area of the shell. Second, we relate the absolute value of **k** to the frequency of a bending wave, which is proportional to k^2; hence, the area of the circle in the **k** plane containing modes up to a certain frequency is proportional to that frequency. Third, by multiplying this area by the density of modes, we obtain the total number of modes with frequencies up to any specified value; it, too, is proportional to the maximum frequency. Finally, the amount by which the maximum frequency changes when the number of modes is incremented by 1 is the average spacing Δf between them. The foregoing argument shows that it is constant; a simple calculation gives its value as

$$\Delta f = a c_W / A\sqrt{3}, \tag{1}$$

where c_W is the speed of compressional waves in the wood, and a is the thickness of the shell.

Unfortunately, the problem is made very much more complicated by the anisotropy of the wood. Not only are the speeds of compressional waves drastically different along and across the grain, but the effective Young's modulus for compressions in a direction making an angle α with the grain of the wood has the form

$$Y(\alpha) = L\cos^4\alpha + 2M\cos^2\alpha\sin^2\alpha + N\sin^4\alpha, \tag{2}$$

where L, M, N are three independent elastic constants. We see from this that the wave speeds in two mutually perpendicular directions still do not provide a sufficient specification of everything that we need to know. Further serious complications are introduced by the arching of the plates.

On the other hand, the fact that the average spacing of modes approaches constancy at high frequencies remains true even in these more complicated cases. We follow Cremer[2] in estimating it by replacing c_W in Eq. (1) with the mean proportional of the wave speeds in the two principal directions, resulting in values of Δf of 73 Hz for the top plate and 108 Hz for the back plate; the two then combine to give an overall average spacing for the instrument of about 44 Hz.

B. Distribution of radiation from a shell mode

In general, the angular distribution of radiation from a radiating system, or ''antenna,'' is governed above all by the relation of the size of the antenna to the radiated wavelength λ, or rather to $\lambda\!\!\!^{-} \equiv \lambda/2\pi$. If the antenna is much smaller than $\lambda\!\!\!^{-}$, the details of its structure become unimportant. The radiated sound is then isotropic, and its amplitude is determined by the net amplitude of pulsating volume, with parts of the surface that move outward being compensated by others which, at the same moment, move inward. (An exception occurs if the net pulsating volume is zero. This happens for a violin at very low frequencies,[3] an effect that we shall mention again in Sec. II G).

If, on the contrary, the antenna is large, individual regions of approximate size $\lambda\!\!\!^{-}$ will radiate more or less independently, producing ''beams'' which do, however, spread out with distance and hence interfere with each other (somewhat the way the two slits in a double-slit diffraction experiment do). The result is an angular distribution of radiation which becomes progressively more complex with increasing number of independently radiating regions.

 0001-4966/97/101(4)/2338/9/$10.00

To estimate the frequency at which a violin might be expected to pass from the ''small antenna'' to the ''large antenna'' regime, we note that for a spherical radiator this transition occurs when its radius is equal to λ. Taking the ''radius'' of a violin to be 7 cm, we then obtain a transition frequency of approximately 800 Hz. (We use a rather small value of radius, corresponding to a path that connects top and back via the C-bouts, since that is where the ''short-circuiting'' of the air flow, which defines the long-wavelength regime, will first occur.) Accordingly, we expect the radiation of a violin to be roughly isotropic below 800 Hz, becoming progressively more anisotropic above.

The next question is: To what degree, and beginning at what frequency, does the detailed pattern of a shell mode affect the directional distribution of radiation? In other words, are the sizes of the regions that move independently sufficiently large compared to an air wavelength to be individually effective? If we think of each of those regions as a rigid piston whose size is half a wavelength of the bending wave, we obtain as the corresponding transition frequency f_c/π^2, where f_c is the so-called *coincidence frequency*, the frequency at which the wavelength of a bending wave is equal to the wavelength of an air wave. For the violin top, for example, Cremer[4] estimates f_c as 4.87 kHz for waves along the grain and 18.42 kHz for waves perpendicular to it, which would give us transition frequencies of about 500 Hz and 2 kHz, respectively. Without attempting too detailed an interpretation, it is clear that the individual modes are apt to influence the radiation pattern at all frequencies that are of interest to us.

C. Excitation of individual modes

A driving force of a certain frequency, such as is provided by a steadily bowed string, will, in principle, put each mode of the violin into vibration; quantitatively, however, this excitation will be appreciable only for modes whose normal frequency is within a resonance width of a strong Fourier component of the driving signal. It is not always easy to determine, by simple inspection of radiativity curves, whether the individual peaks and valleys of the response are produced by single modes or by statistical combinations of many; knowing, however, that the modes have an average spacing of around 45 Hz (Sec. I A), it becomes clear that the observed peaks correspond either to single modes or, at most, to combinations of a small number of them (see Sec. II H). Accordingly, we would expect the angular pattern of violin radiation, once it begins to change at all, to change fairly drastically every 50 Hz or so.

We remind the reader that, by our definition, it is this very rapid variation of directivity with frequency that constitutes ''directional tone color.''

II. EXPERIMENT

All of our measurements are based on the principle of reciprocity, which relates the *outgoing* acoustic field radiated per unit transverse force on the bridge (the radiativity) to the motion of the bridge that results from a corresponding *incoming* unit acoustic field applied to the violin. In the original application of the principle to violin physics,[3] it was desired to obtain the radiativity as an expansion in multipole moments, which required the angular dependence of the corresponding incoming fields to have a controlled multipole nature as well. In the present work, the situation is conceptually much simpler: In order to measure the radiativity for outgoing waves in a particular direction, we need to expose the violin to an incoming plane wave *from* the same direction, and normalize the signal by the pressure amplitude as measured by a microphone in the same location as the violin is going to be.

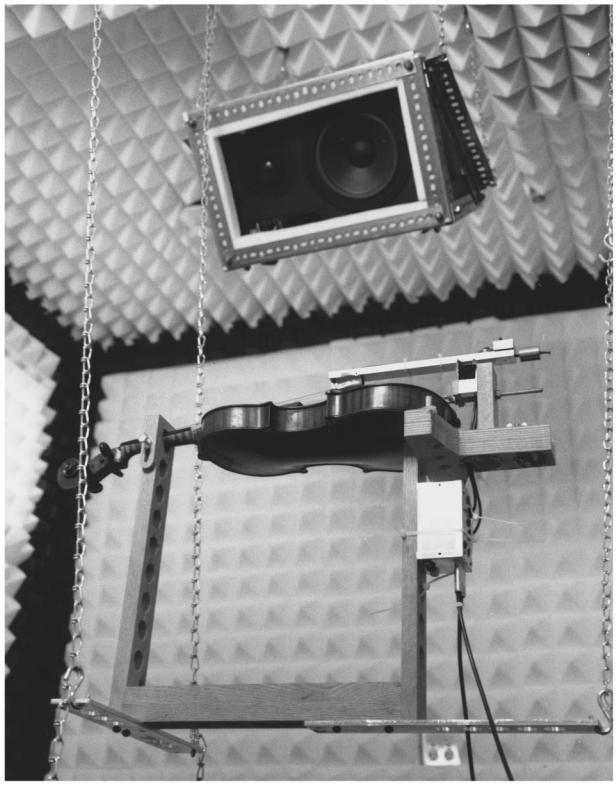

FIG. 1. Violin on its frame suspended in the Sonex-lined chamber. The ''tone arm'' holding the phonograph pickup is seen extending over the violin. ''Speaker 1'' is overhead; ''speaker 2,'' pointed to by the neck of the violin, is not visible.

Since our aim is to search for strong directional dependence, we have arbitrarily chosen two directions in which to compare the radiativity, namely, (1) more or less normal to the top plate of the violin, and (2) outward in the direction of the neck.

A. Transducers and electronics

The two necessary stimulus waves are generated by a pair of identical JBL model 4408 loudspeakers placed in our quasi-anechoic chamber, which is an approximately rectangular space $10\times12\times10$ ft high fully lined with 4-in. Sonex.

The velocity of the violin bridge is sensed by a standard magnetic phonograph pickup whose stylus rests on the bridge halfway between the D and A notches. The violin is loosely held in a horizontal position by a padded wooden frame which is in turn suspended from the ceiling of the chamber by three metal chains (Fig. 1). The phonograph pickup is mounted on a ''tone arm'' which rests on a knife

edge attached to the frame so as to allow it to pivot freely around a horizontal axis, maintaining the stylus at the correct vertical force. This force is adjusted by a counterweight attached to the arm.

The normalizing signal is measured by an inexpensive electret microphone at the end of a thin boom which is introduced when the violin is removed; it, too, then occupies what would otherwise be the midpoint between D and A notches of the bridge. (The choice of microphone position is discussed in Sec. II C.)

The speakers are driven by a signal comprised of a repetitive series of 8192 digital values generated at a 50-kHz sampling rate by the 12-bit D/A converter of a Data Translation DT2821 board controlled by a Pentium 100-MHz desk computer. It has the form of a Schroeder chirp[5] that covers the range from 122 Hz to 24.4 kHz in steps of 6.2 Hz. In synchronism with it, the 12-bit A/D converter of the same board receives the response signal, accumulating the sum of 16 passes after first allowing four passes (about two-thirds of a second) for the violin to reach steady state.

The driving voltage is filtered by an eight-pole Butterworth anti-alias filter with an 18-kHz cutoff before being applied to the voice coil of the appropriate speaker by a Crown D-150 power amplifier. The return signal—whether from the phonograph pickup or the microphone—is amplified by a low-noise preamplifier before leaving the chamber, and enters the A/D input of the DT2821 after being filtered by a second identical anti-alias filter.

B. Frequency limitations

Even though the computer-generated driving signals can easily cover a range of 18 kHz or more, the properties of our system are such as to make the data at very high frequencies undependable. The chief limitations come from (a) the phonograph pickup and the properties of the tone arm, whose own resonances appear clearly in the high-frequency data, especially when stylus motion is examined in the vertical direction; and (b) direct electromagnetic coupling between the speaker cable and the cable that connects the magnetic pickup to the preamplifier, since the signal level decreases at higher frequencies while capacitative coupling increases.

Although it is possible to address these factors, we decided that, for an investigation whose basic aim is the demonstration of directional tone color, it is sufficient to limit ourselves to the region up to 5 kHz, where (to the best of our knowledge) the data can be taken at face value.

C. Choice of microphone position

In order to obtain a valid measurement of radiativity, the complex velocity of the bridge must, at each frequency, be divided by the complex pressure amplitude of the incoming wave. Now it is, of course, a property of a pure traveling plane wave that its amplitude has the same value regardless of where it is measured, only the phase changing as a function of position. Therefore, a displacement of the microphone that provides the normalizing signal would merely change the phase of the measured radiativity; in other words, the choice of microphone position corresponds simply to a choice of origin with respect to which the radiativity will finally be specified. As explained in Sec. II A, we chose this origin to be, for simplicity, at the same place where the bridge velocity will be measured, but in fact it could just as well be anywhere else (although it is, naturally, important to keep it consistent between measurements).

Of course the situation changes if, as must be true in real life, the incoming-signal is *not* a pure traveling plane wave. Accordingly, we cannot interpret our results before carefully examining our stimulus waves.

D. Characterization of the stimulus waves

In order to test the degree to which sound waves generated by the speakers in our chamber conform to the above requirements, we compared the two complex amplitudes received from a given speaker when the microphone is displaced a few inches in a direction away from the speaker. As indicated in the previous section, (a) the magnitude of this ratio should be unity independent of frequency, and (b) its phase should be linear in frequency, changing by 2π when the frequency increases by $c/\Delta L$, where ΔL is the displacement and c the speed of sound.

Figure 2 shows the experimental value of this ratio plotted for each of the two speakers. It is clear that, although the overall behavior resembles what is expected, deviations do exist, indicating the presence of residual reflections; under such circumstances, our experimentally deduced radiativity in a particular direction will contain a coherent admixture of the radiativity in the reflected direction. We discuss the implications of this separately for the regions below and above 1 kHz.

Above 1 kHz, the directivity data are, as discussed in Sec. I C, expected to vary rapidly with frequency by considerably larger amounts, and on a finer frequency scale, than the driving signals of Fig. 2, an expectation which will be born out by our results (Sec. II F). So long as our purpose is to establish the existence of strong directional tone color, rather than investigate its precise fine details, a small amount of directional mixing is not important.

Below 1 kHz, the deviation from wave purity shown in Fig. 2 becomes worse, which is not surprising in view of the decreasing absorptivity of Sonex in this range. On the other hand, our expectation is, as discussed in Sec. I B, to see a more or less isotropic radiativity here; this expectation, too, will be born out by our data. But if the radiativity is truly the same in all directions, then the admixture of two directions should, in principle, make no difference, regardless of how large it is.

This reasoning assumes that the violin is sensitive only to the pressure (that being what the microphone measures), and not, for example, to its gradient. Since we know that in the long-wavelength region the monopole radiativity of the violin is much larger than $1/\lambda$ times its dipole radiativity,[3] the assumption of pure monopole sensitivity is valid as long as we do not place the violin too near a node of the field, which we have taken care not to do. (Another possible exception, also discussed in Ref. 3, will be taken up in Sec. II G below.)

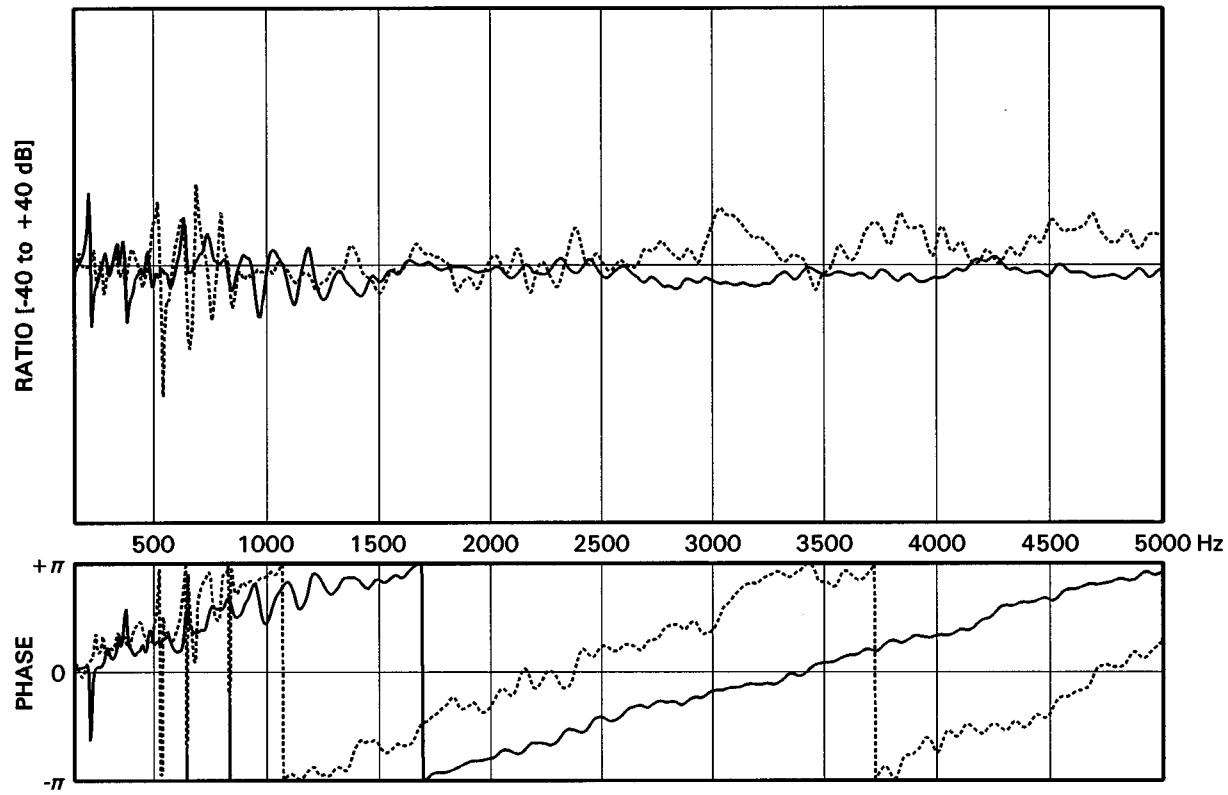

FIG. 2. Complex ratio by which the microphone's signal is multiplied when it is moved away from the speaker by a few inches. Solid curve: ''speaker 1;'' dotted curve: ''speaker 2.'' Top: amplitude of ratio; bottom: phase of ratio. (The amount by which the microphone was moved is not the same in the two cases.)

We conclude that, in either frequency region, the stimulus signals produced by our two speakers are sufficiently close to pure traveling waves for the purposes of this investigation.

E. Results for the radiativity

As already indicated, our aim in the present work is to compare the radiativities of a violin in two arbitrarily chosen directions, by first obtaining the response of the bridge stylus to a signal from each of the loudspeakers, then dividing by the microphone signal from the same speaker. Of course the data consist, after Fourier transformation, of a complex amplitude for each of 4096 frequencies, so that ''dividing one signal by another'' means performing one complex division at each frequency.

Figure 3 shows a comparison of the two radiativities so obtained for two frequency ranges: 150–1000 Hz (top) and 1500–3500 Hz (bottom). It will be seen from the top graph that, except for an unusual feature at about 230 Hz to be discussed in Sec. II G, the radiativities are pretty much the same up to about 800 Hz, in agreement with our expectations of isotropy (Sec. I B).

The situation is, however, radically different at higher frequencies, as shown in the bottom graph of Fig. 3. We note that the *frequency placement* of peaks and valleys which characterize the radiativities in the two directions are very similar—which is, of course, exactly what one would expect, since the same normal modes are represented in both cases. The magnitudes and phases of the two curves are, however, quite different from each other, and that in a completely irregular manner—again in agreement with our theoretical discussion.

F. Results for the directivity

Our four violins were picked to sample a large range, the purpose being to demonstrate a property which, we claim, is a necessary consequence of the instrument's structure. We identify them as follows:

LAB: A very ordinary student instrument;
MEL: A high-quality student instrument;
DAN: A modern professional instrument;
COM: A violin made of laminated synthetic material.

In each case, we obtain a measure of the directivity by dividing the radiativity along the neck (''direction 2'') by that perpendicular to the top plate (''direction 1''). Figure 4 shows the results of performing this division for the four violins, plotted on a log–log scale, and omitting the phase to simplify the graphs. Here the ratio is specified in decibels where, of course, 0 dB denotes isotropy (at least with regard to the two chosen directions), and positive values mean that the radiativity in ''direction 2'' exceeds the one in ''direction 1.'' The four graphs are offset vertically for clarity.

The frequency axis in Fig. 4 is also logarithmic, so that equal horizontal displacements mean equal musical intervals. In fact, this axis is labeled, in addition to the logarithmic frequency scale at the bottom, with steps of one-third octave, or four semitones, at the top, using the conventional musical notation in which A_4 corresponds to a frequency of 440 Hz.

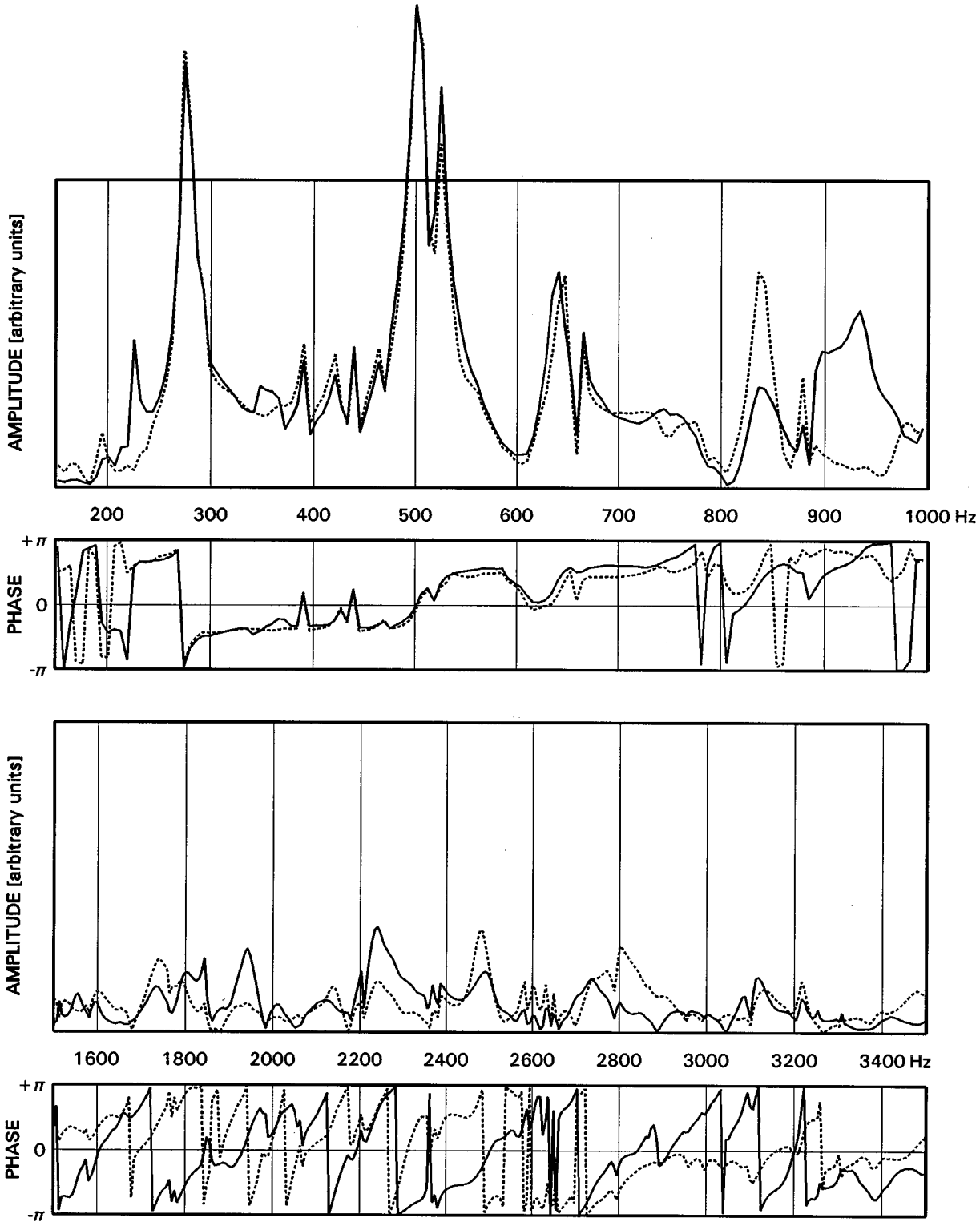

FIG. 3. Two frequency ranges of the radiativity amplitude and phase of violin ''DAN'' (linear scale) measured in two directions. Solid curves: ''direction 1;'' dotted curves: ''direction 2.'' The vertical scales are the same for both ranges.

We observe the following features in all four graphs:
(a) Except for the peculiar phenomenon around A3, all four violins exhibit a fair degree of isotropy up to about A_5, as expected.
(b) Above that frequency, the patterns become wildly irregular, jumping up and down by amounts that sometimes exceed 40 dB peak-to-peak; this is, of course, precisely the quality of ''directional tone color'' that we defined at the beginning of the paper. We also note that, as expected from the discussion of Sec. I C, the spacing of these peaks and valleys is in

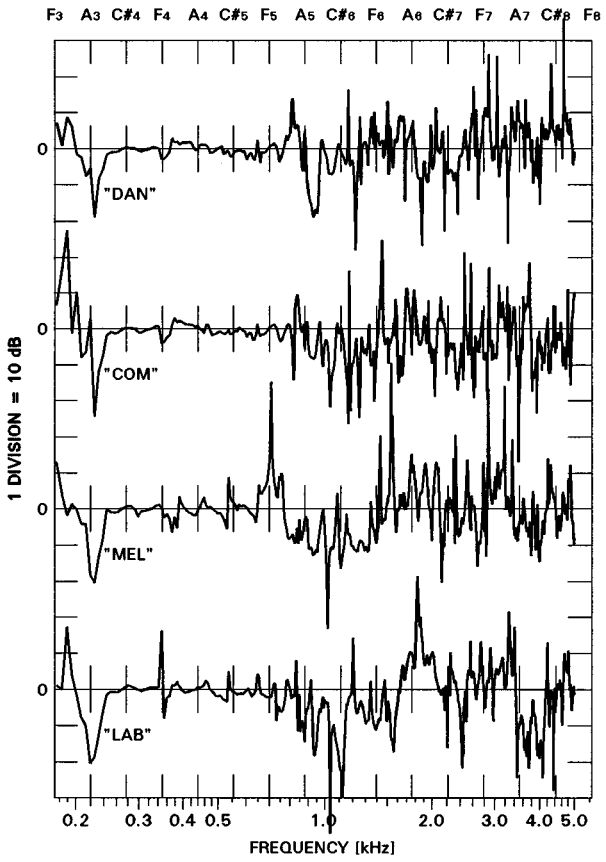

FIG. 4. Ratio of radiativity in ''direction 2'' to that in ''direction 1'' for four violins. The phases are not shown.

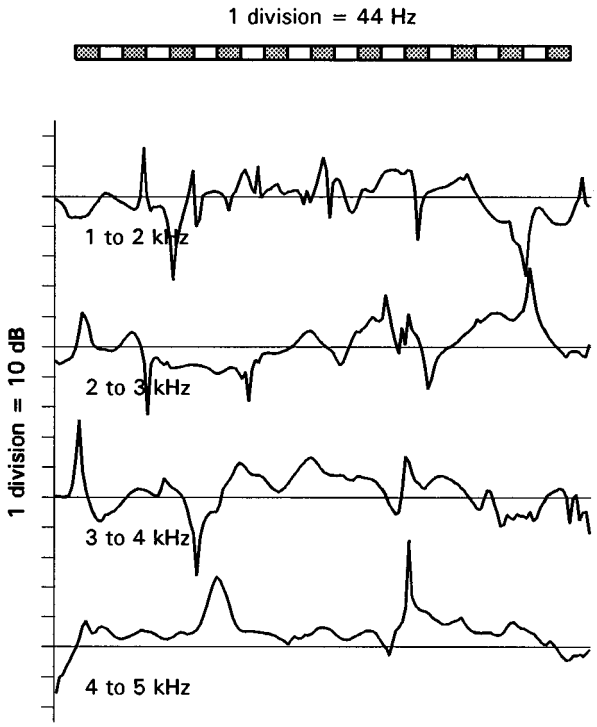

FIG. 5. Ratio of radiativity in ''direction 2'' to that in ''direction 1'' for violin ''DAN'' plotted against linear frequency. The scale above shows the expected density of wood modes.

the vicinity of one semitone where they first begin, with some tendency to become progressively finer as the frequency rises.

Our results appear to be generally consistent with those of Meyer[6] and of Saldner *et al.*,[7] neither one of whom, however, used the close frequency spacing required to detect the directional tone color phenomenon.

G. The feature around low A

As indicated in Sec. II D, the stimulus signals tend to deviate appreciably from pure traveling waves below about 1 kHz. Although this makes it difficult to interpret anisotropy data in detail in that band, it is nonetheless true, as we mentioned, that if the radiativity were truly isotropic such a deviation ought not to make any difference. Accordingly, even if a quantitative characterization is risky, one may state with some assurance that *below about 250 Hz the radiativity of our violins again begins to deviate from isotropy*. Indeed, the patterns in which they do so are rather similar (although by no means identical) for the four instruments.

In fact, this behavior appears precisely in the frequency region where the dipole moment of the violin begins to dominate.[3] That is, in our opinion, the most probable reason for the low-frequency anisotropy, which seems otherwise difficult to explain.

H. To what degree do the modes overlap?

Figure 5 repeats, for one of the violins (''DAN''), the same directional characteristic already shown in Fig. 4; this time, however, the frequency axis is linear instead of logarithmic, and the region from 1 to 5 kHz is stretched out into four sections so as to make its details more visible. For reference, we also show, at the top of the diagram, a scale whose divisions are 44 Hz, equal to the estimated average spacing of wood modes (Sec. I A). It appears that the first range of the graph, from 1 to 2 kHz, has a structure whose frequency scale is reasonably well described by this estimate; but the directivity becomes successively more ''washed out'' as we go toward higher frequencies (although not on a logarithmic scale!).

The most likely explanation of this behavior is, of course, that in the range of a few kHz the damping of modes increases so that they begin to overlap each other. It should be noted, however, that there may well be an additional factor contributing to this effect, namely the gradual appearance of air modes, whose density will be approaching that of the wood modes in the same approximate region.[1]

III. DISCUSSION

The phrase ''directional tone color'' in the sense of this paper was first introduced[8] in 1993. In this section we outline some of its consequences from the point of view of musical performance.

A. ''Flashing brilliance''

This phrase, also first introduced in Ref. 8, describes the fact that, in an enclosed space large enough for the ear to perceive the timing of separate reflections, the way that the radiation pattern of a violin changes drastically from one semitone to the next can confuse the common psychoacoustic directional cues, thus endowing the sound of the instrument with a characteristically striking spatial sense. Although, as always with subjective perceptions, it is difficult to find a verbal description that satisfies all listeners, we have heard comments that range from ''every note appears to be coming from a different direction'' to the much less specific ''the sound of a violin seems to be disembodied in mysterious and fascinating ways.''

The perception of this property of ''flashing brilliance'' is, of course, made especially complex (and, we suspect, especially brilliant) by the fact that the directional cues can be quite different for different harmonics of the same note. It should be noted here that, according to the discussion of Secs. I B and II F, the effect we are talking about will be strong for all partials of notes above the bottom of the E-string; but even for the lowest notes of the G-string it will be present starting with about the fourth partial.

B. Vibrato

As discussed in detail by Meyer,[9] vibrato on a violin—executed by a motion of the left wrist that causes the fingertip to roll forward and back on the fingerboard, thus causing an oscillatory variation of the string length—is reflected not only in frequency modulation but also in amplitude modulation of the played note, because of the way that the normal frequency of the string moves with respect to the peaks and valleys that characterize the instrument's radiativity. Since the peak-to-peak frequency range covered by a typical vibrato can exceed three-quarters of a semitone, we now see that the result will be a strong modulation of the directional radiation pattern as well.

The effect can be visualized in terms of a number of highly directional sound beacons, all of which the vibrato causes to undulate back and forth in a coherent and highly organized fashion. It is obvious that such a phenomenon will help immensely in fusing sounds of the ''differently directed'' partials into a single auditory stream; one may even speculate that it is a reason why vibrato is used so universally by violinists—as compared to wind players, from the sound of whose instruments directional tone color is generally absent. The reason is not, of course, that wind instruments lack directivity, but that they are unlikely to show a variation in their directivity which is anywhere near as large in amplitude or as dense in frequency.

C. *Solo* versus *tutti*

Although various explanations have been given[10] of the striking way in which a solo violin can be clearly heard above an orchestra even when the latter contains two dozen violins playing at more or less the same dynamic level, directional tone color may well, in fact, be the major factor contributing to this phenomenon. The point is, of course, that

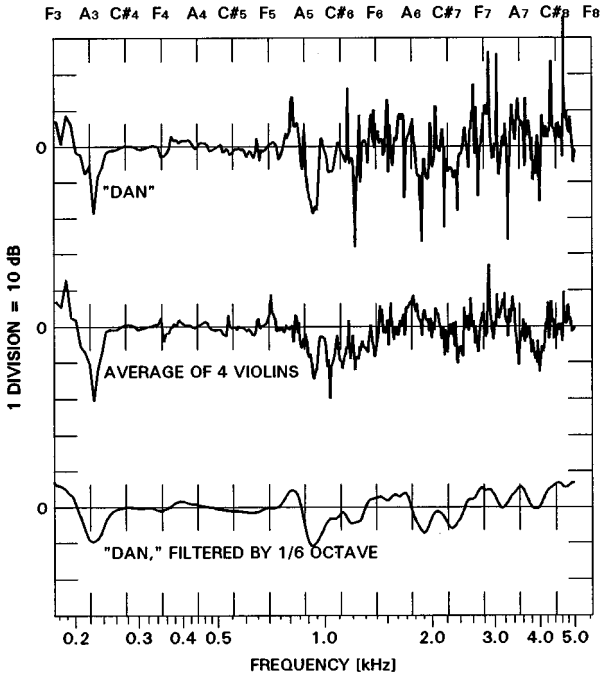

FIG. 6. Top: directivity amplitude of violin ''DAN,'' repeated from Fig. 4. Center: average of directivity amplitudes of the four violins of Fig. 4. Bottom: Directivity amplitude of ''DAN,'' as shown in the top graph, but filtered through a one-sixth octave filter.

even though the *presence* of large and closely spaced variations in the instrument's directivity, which is what ''directional tone color'' means, appears to be characteristic of every violin, the *exact placement* of these maxima and minima has no detailed correlation among different instruments. As a result, the process of summing a number of them will strongly diminish the variability of the total.

This effect is demonstrated in Fig. 6, which shows three different directivity curves. On top, we repeat the characteristic for one of the violins (''DAN'') that was already shown in Fig. 4; in the middle, the average of all four of our violins is plotted; and finally, the bottom curve shows the one for ''DAN'' digitally filtered through a one-sixth octave filter, which might be considered a reasonable estimate for what happens when 10 or 12 violins are playing together (on the assumption that the frequency scale on which any one violin changes its directivity is in the vicinity of a semitone). It is clear that averaging as few as four violins diminishes the directional tone color considerably, while the one-sixth octave filter essentially eliminates it entirely. Under such circumstances it is not surprising that a single solo violin, with a good vibrato to consolidate its auditory stream, can musically soar with ease above its orchestral environment.

In this connection it is interesting to note a curious situation that occurs in the fourth movement of the Sixth Symphony of Tchaikovski, the score of the first few measures of which (string parts only) is shown in Fig. 7. In this case the theme has its notes alternating between the first and second violins, so that the first note is played by the second violins, the next note by the first violins, and so on (a similar alter-

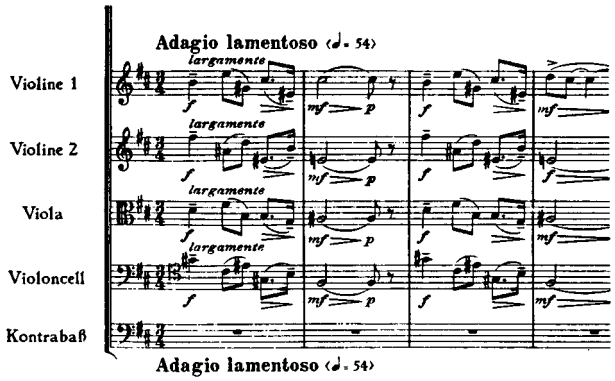

FIG. 7. Opening of the fourth movement of Tchaikovski's Sixth Symphony (string parts only). The well-known descending scale theme is heard as an alternation of notes between first and second violins.

nation appears in the two lower parts as well). Remembering that the normal way for an orchestra to be seated was, at that time, to have the first violins at the left of the stage and the second violins at the right, such an orchestration results in alternate notes of the same theme coming from radically different directions. It is hard to avoid the speculation that Tchaikovski, perhaps unconsciously, chose this unusual voice leading in order to give the violin sections a kind of artificial directional tone color, thus endowing a *tutti* passage with some of the tonal quality of solo instruments.

D. ''Projection''

Violinists place an attribute which they call ''projection'' of an instrument high on their list of desirable qualities; it seems to refer to an ability for its sound to fill a hall, although its adherents will emphasize that this does not just mean generating a lot of power but something rather different. If one tries to paraphrase such a quasi-definition by saying that ''projection'' refers not so much to the ability to permeate an auditorium with decibels as to *command attention* from listeners in various parts of it, then the physical quality of directional tone color immediately comes to mind. It might be, for example, that for a given individual instrument there are bands in which the variation of directivity is relatively weak or relatively slow, in which case that instrument might be observed to ''lack projection'' for frequencies that have important harmonic content in those bands. We emphasize that this hypothesis is, at the present moment, entirely speculative.

E. Electronic reproduction

Pierre Boulez has observed[11] that loudspeakers have the property of ''anonymizing'' the sound of musical instruments, that is, of making them all sound the same. Given the superb objective specifications of good modern loudspeakers, it is hard to put physical meaning to such a statement in terms of qualities such as frequency response or distortion. Yet there is one attribute of a loudspeaker which it does, indeed, impose upon all sounds that it generates, and that is its own directivity. Specifically, when music is played through a loudspeaker the quality of directional tone color is instantly and totally obliterated.

The damage is, perhaps, not excessively serious for wind instruments, and especially for the brasses, whose live sound is projected through a circular bell of a size not too radically different from that of a typical loudspeaker. As a result, the directional properties of this sound, essentially those of a circular piston of comparable diameter, remain—by coincidence, to be sure—relatively faithful. But when violin music undergoes the same process, the result is similar to what one would hear if the violinist were on the other side of a solid wall in which a circular hole the size of the speaker had been cut: none of the effects that we have enumerated in Secs. III A–D can any longer occur.

Indeed, a number of music lovers with whom the author has spoken are of the opinion that separating the sound of a solo violin from an accompanying orchestra is much easier to do in a concert hall than when listening to a recording, although others strongly disagree. Unfortunately, the question is complicated on the one hand by the presence of visual cues in a live performance, and on the other by the ability of recording engineers to enhance whatever part they wish to emphasize.

ACKNOWLEDGMENTS

This project benefitted enormously from the talent and expertise of Colin Holmes, who designed and built most of the electronics; from the help of Maureen Mellody, who together with him did most of the data collecting; and from the support of Joseph Curtin, who (among other things) lent us some of the violins that were used. The manuscript was critically read by Xavier Boutillon, Judith Brown, René Caussé, Joseph Curtin, Carleen Hutchins, Juergen Meyer, Thomas Rossing, Robert Schumacher, Olivier Warusfel, and James Woodhouse, every one of whom provided interesting and helpful comments (it goes without saying that all remaining blunders are the author's). Last but by no means least, the support of the National Science Foundation under Grant No. PHY-9319567 is gratefully acknowledged.

[1] G. Weinreich, ''Sound radiation from boxes with tone holes,'' J. Acoust. Soc. Am. **99**, 2502(A) (1996); see also G. Weinreich, ''Vibration and radiation of structures with application to string and percussion instruments,'' in *Mechanics of Musical Instruments*, edited by A. Hirschberg, J. Kergomard, and G. Weinreich (Springer-Verlag, New York, 1995).
[2] L. Cremer, *The Physics of the Violin*, transtated by J. S. Allen (MIT, Cambridge, MA, 1984), pp. 284–292.
[3] G. Weinreich, ''Sound hole sum rule and the dipole moment of the violin,'' J. Acoust. Soc. Am. **77**, 710–718 (1985).
[4] L. Cremer, *loc. cit.*, p. 315.
[5] M. Schroeder, ''Synthesis of low peak factor signals and binary signals with low autocorrelation,'' IEEE Trans. Inf. Theory **16**, 85–89 (1970).
[6] J. Meyer, ''Directivity of bowed string instruments and its effect on orchestral sound in concert halls,'' J. Acoust. Soc. Am. **51**, 1994–2009 (1972).
[7] H. O. Saldner, N.-E. Molin, and E. V. Jansson, ''Measurements of the sound distribution from vibration modes of a violin using reciprocity and electronic holography,'' in *Proceedings International Symposium on Musical Acoustics*, Catgut Acoustical Society/Société française d'Acoustique, 1995, pp. 413–419.
[8] G. Weinreich, ''Radiativity revisited: theory and experiment ten years

later,'' in SMAC 93: Proceedings of the Stockholm Music Acoustics Conference, edited by A. Friberg, J. Iwarsson, E. Jansson, and J. Sundberg (Royal Swedish Academy of Music, Stockholm, 1994), p. 436.
[9] J. Meyer, ''Zur klanglichen Wirkung des Streicher-Vibratos,'' Acustica **76**, 283–291 (1992).
[10] See, for example, J. Backus, *The Acoustical Foundations of Music* (Norton, New York, 1977), 2nd ed., p. 121.
[11] P. Boulez, ''Le haut-parleur anonymise la source réelle,'' Proc. 11th International Congress on Acoustics, Paris **8**, 216 (1983), and private communications.

Echolocation signals of the Greater Horseshoe bat *(Rhinolophus ferrumequinum)* in transfer flight and during landing

Biao Tian[a] and Hans-Ulrich Schnitzler
Lehrstuhl Tierphysiologie, Universität Tübingen, Auf der Morgenstelle 28, D-72076 Tübingen, Germany

(Received 27 March 1996; accepted for publication 6 October 1996)

Echolocation signals of horseshoe bats (*Rhinolophidae*) consist of a relatively long component of constant frequency (CF) which is preceded by an initial frequency-modulated (iFM) component and followed by a terminal frequency-modulated (tFM) component. To examine the role of these components in echolocation, four bats were trained to fly from a perch to a landing bar. A dual camera system allowed reconstruction of the flight paths in three dimensions. Echolocation signals were recorded, analyzed, and correlated with the flight behavior of the bats. It was confirmed that during flight the bats compensate the Doppler shifts which are produced by their own flight movement. In free flight they emit per wing beat one single signal of long duration, with little variation in the three signal components. In approach flight the bats reduce pulse duration and interval with decreasing target range. The iFM is not varied with respect to target range, suggesting that this component plays little role in the processing of echolocating a target of interest. The bandwidth of the tFM component is increased while its duration is shortened in proportion to decreasing target range, so that the signal–echo overlap of the FM component is avoided down to a target distance of 15 cm. These concurrent changes suggest that the tFM component is used for ranging. During the last 60 cm of the approach the bats compensated for the increase of echo SPL by lowering the emission level of the CF component by 6–9 dB and that of the tFM component by 9–11 dB per halving of range. The specific signal structure of horseshoe bats is discussed as an adaptation for the hunting of fluttering insects in highly cluttered environments. [S0001-4966(97)01903-6]

PACS numbers: 43.80.Ev, 43.80.Lb, 43.80.Ka, 43.70.Aj [FD]

INTRODUCTION

During evolution the echolocation systems of bats have been adapted to solve species-specific echolocation tasks. Different species of bats use different echolocation signals consisting either of constant frequency (CF) signals, quasi-constant frequency (QCF), or downward frequency-modulated (FM) elements or combinations of these. These signals differ in absolute frequency, bandwidth, harmonic structure, duration, and sound-pressure level (SPL), creating a variety of signal types found in echolocating bats (Schnitzler and Henson, 1980; Schnitzler and Kalko, 1997). In each species signal structure is furthermore varied, depending on the echolocation task which has to be solved. In search flight bats normally emit per respiratory cycle and wing beat one single signal with maximal duration and pulse interval (Schnitzler, 1971; Suthers *et al.*, 1972). When approaching a target, the bats change the pulse structure, reduce the pulse duration, the pulse interval and also often change the SPL (Schnitzler and Henson, 1980; Jen and Kamada, 1982; Kobler *et al.*, 1985; Neuweiler *et al.*, 1987).

Several hypotheses have been proposed to explain the above-mentioned changes in echolocation signals. Search signals are adapted for long-range detection and evaluation of targets, whereas approach signals are adapted for improving localization and tracking of a target of interest (Schnitzler, 1973b; Simmons, 1973; Simmons *et al.*, 1979; Schnitzler and Henson, 1980). During flight the change of the frequency of the CF portion in CF-FM bats compensates for Doppler shifts and keeps the echo frequency constant (Schnitzler, 1968; Schnitzler, 1970a, b; Gustafson and Schnitzler, 1979; Konstantinov *et al.*, 1978; Schuller, 1980). The reduction of the duration of FM signals or the FM portion in CF-FM signals prevents the overlap of the outgoing signal with the returning echo from the target of interest (which would otherwise disturb the determination of the time delay between outgoing pulse and returning echo) (Cahlander *et al.*, 1964; Schnitzler, 1968; Schnitzler *et al.*, 1987; Kalko and Schnitzler, 1989). The reduction of SPL is interpreted as part of a gain control mechanism which keeps the echo SPL constant (Jen and Kamada, 1982; Kobler *et al.*, 1985). The increased repetition rate increases the information flow (Simmons *et al.*, 1979; Schnitzler and Henson, 1980). The pulse interval is kept long enough that the echo of a pulse returns before the next pulse is started (Schnitzler, 1968; Schnitzler and Henson, 1980).

Horseshoe bats use signals which consist of an initial FM (iFM), a CF, and a terminal FM (tFM) portion (Schnitzler, 1968; Vogler and Neuweiler, 1983; Schnitzler *et al.*, 1985; Neuweiler *et al.*, 1987). The CF portion is adapted for fluttering target evaluation (Emde v.d., 1987; Emde v.d. and Menne, 1989). Analysis of insect echoes with 80-kHz tones shows that information on wing beat frequency, wing length, wing beat type, and probably wing structure is available from these echoes (Schnitzler *et al.*, 1983; Kober, 1988a, b;

[a]Present address: Georgetown University, Institute for Cognitive and Computational Sciences, The Research Building WP22A, 3970 Reservoir Road NW, Washington, DC 20007-2197.

Kober and Schnitzler, 1990). Behavioral studies show that *Rhinolophus ferrumequinum* can discriminate insects with different wing beat rates (Emde v.d., 1987, 1988; Emde v.d. and Menne, 1989) and classify insects with similar wingbeat rates according to their flutter signature (Emde v.d. and Schnitzler, 1990). An overrepresentation of frequencies around the frequency of the CF portion has been found in different stations of the auditory pathway of horseshoe bats including the basilar membrane (Bruns, 1976), the spiral ganglion (Bruns and Schmiezek, 1980), the cochlear nucleus (Feng and Vater, 1985), the inferior colliculus (Schuller and Pollak, 1979), and the auditory cortex (Ostwald, 1980, 1984). This overrepresentation builds the so-called ''auditory fovea'' which can precisely evaluate detailed information conveyed by the CF portion of the echolocation signal (Schuller and Pollak, 1979). Studies have shown that certain neurons in inferior colliculus (Schuller, 1984) and auditory cortex of the Greater Horseshoe bat (Ostwald, 1980, 1988) respond to natural ultrasonic echoes from fluttering insects. The tFM portion is adapted for a precise localization of a target (Schnitzler, 1973b; Simmons, 1973). The significance of the iFM is unclear. The change in signal SPL and its spectral content, which may play a role in distance determination, has not been studied so far in detail (Vogler and Neuweiler, 1983; Neuweiler *et al.*, 1987).

The measurement of all these parameters and the description of their change is very difficult, when a bat approaches a target. Only the change in frequency of the CF portion has been studied in detail (Schnitzler, 1968, 1970a, b). We have developed a new indoor recording system which allows us to measure all parameters, so that we can now address the question of what determines the structure of echolocation signals in the Greater Horseshoe bat.

I. MATERIALS AND METHODS

A. Subjects, training, and apparatus

Four adult Greater Horseshoe bats (*Rhinolophus ferrumequinum*, referred to as RF 1–RF 4) weighing about 30 g were used in the experiment. The animals had lived in the lab for at least 5 years, and were previously used in two-alternative-forced-choice studies. Before training they were housed in a large flight cage and fed with mealworms and water.

The flight room measured 4.7×4.7×2.9 m, and was divided into flight and recording areas. The recording equipment, except for two microphones and their stands, remained outside of the flight area. The walls in the flight area were covered with black velvet to improve the contrast for filming. ''Pass-point'' marks on the walls, providing a scale for the three-dimensional reconstruction of flight paths, were arranged in 3 horizontal and 12 vertical rows (Fig. 1). The distance between horizontal rows was 50 cm, and the distance between vertical rows was either 50 or 100 cm. The lower corner where wall 1 and wall 2 met was defined as the origin of the pass-point system. Marks on wall 1 lay in the *XZ* plane, marks on wall 2 in the *YZ* plane. A perch attached to wall 1 was 2 m high. A 20-cm-long landing bar, covered with sandpaper to make it an easy target for the bats, was

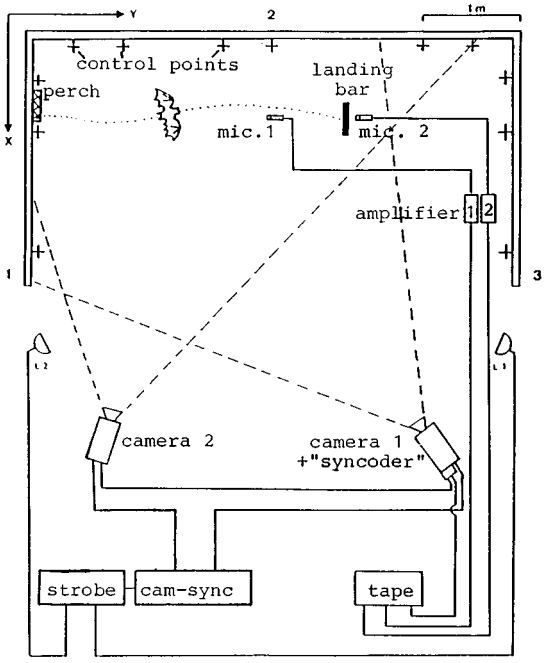

FIG. 1. Schematic overview of the flight chamber 4.7×4.7×2.15 m in size. The distance between the perch and the landing bar is 3 m. The walls in flight area are covered with black velvet. The crosses symbolize the markers of the pass-point system on the wall. The dotted line symbolizes the flight path of the bat. P: perch; L: landing bar; L1, L2: strobe lights; mic1, mic2: microphones.

mounted on a stand at a height of 1.5 m (Fig. 1). The horizontal distance between the perch and landing bar was 3 m. The stands for the landing bar and the microphones were also covered with black velvet to improve the contrast for filming.

We trained the bats to fly from the perch to the landing bar in the flight room. After each successful landing on the landing bar, bats were rewarded with mealworms. On average each individual received 15–20 mealworms per day. At the beginning of the training the bats seemed to be disturbed by the broadband noise pulses (about 85 dB at peak) generated by the strobe lights (see below). However, they soon adapted to the noise and assumed normal flights. During training, the bats sometimes started flights before the strobes were turned on, and echolocations sounds could be recorded over the monitoring microphones. The echolocation sounds recorded during these flights did not show any difference to the sounds recorded when the strobes were turned on. This suggested that the bats were not using visual cues for navigation to the landing bar. A recording session began only after the bats had learned to fly consistently along the same flight path and had adapted to the light flashes and camera noises.

The flights of bats were filmed with two 16-mm high-speed cameras (Arriflex 16 SR, high speed), which were phase synchronized (Arnold & Richter) (Fig. 1). Each camera was equipped with a wide angle objective (Zeiss Distagon 9.5 mm, f 1.2). At each frame the bats were illuminated with two strobe lights (Weinberger, strobe 1018 So 9), providing synchronized flashes of 30-μs duration. The short flash time ensured that the images of the bats were free of

smear caused by motion. Echolocation sounds were picked up by two condenser microphones (B & K, $\frac{1}{4}$ in., type 4135), amplified by two B & K amplifiers (B & K precision impulse sound level measure instrument 2209) and recorded on an ultrasound high-speed tape recorder (Racal Store 4 DS, tape speed 60 in./s). A synchronization unit at the master camera (syncoder) generated at each frame a synchronization signal which was recorded on the edge of the master and slave films, and also onto the sound track of the tape recorder so that the timing of sound emission could be exactly matched with the bat's position during flight. The equipment was calibrated with a B & K sound level calibrator (4230).

B. Recordings

Bat flights were filmed with the two cameras at 50 frames per second. According to the three-dimensional reconstruction (see below), the only restriction for camera placement was that both cameras had to catch at least four common pass-points in the pass-point system. In our experiment, the two cameras stood at a height of 1.6 m, about 4 m away from the recording area, so that whole flight area was covered by both cameras.

Since both the bat's sound emission (Schnitzler and Grinnell, 1977; Hartley, 1989) and the microphone (Kinsler and Frey, 1962) are highly directional, we chose microphone positions and orientations so that during each of the rather stereotyped flights a part of the whole sequence of echolocation signals was directed to the microphone.

C. Three-dimensional reconstruction

The three-dimensional reconstruction is based on photogrammetry (Finsterwalder and Hofmann, 1968; Schwidefsky and Ackermann, 1976). With this method the size and position of an object can be determined by the images of the object taken by two well-separated cameras. This method only requires that a number of defined points in space should also be on the images as reference whereas the positions and orientations of the cameras can be chosen arbitrarily as long as they can image the same reference points on the corresponding pictures. The pass-points mentioned above, which were placed with exact measurements, served here as the reference system. With the known coordinates of the reference points the positions and orientations of the cameras can be calculated backwards. Using the identified camera positions and orientations, the space coordinates of a flying bat and other objects were computed from the coordinates of the bat image on corresponding pictures. The tip of the bat nose was used as the visual reference point for the bat. The whole system was calibrated with exactly measured objects. It had a precision from 1 to 10 mm, depending on the position of the bat within the frames of the films. At the chosen camera positions in this paper the precision of spatial reconstruction was mostly under 5 mm.

Single frames of the films were projected (Vanguard/Weinberger, projection head M-16C) onto a digitizing tablet (Summagraphics, Bitpad). Corresponding frames from the two cameras were identified with the synchronization code recorded on the edge of each frame. The image coordinates

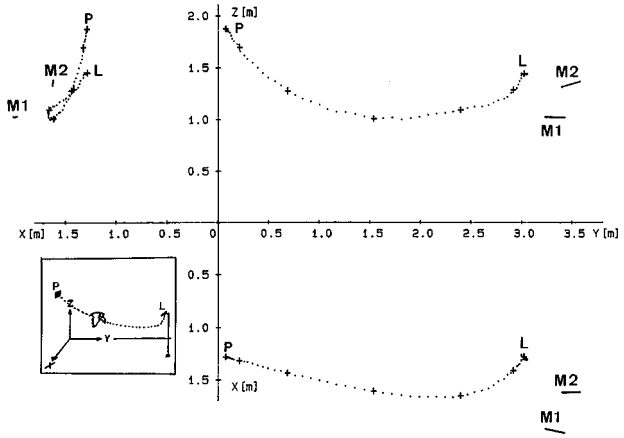

FIG. 2. A three-dimensional reconstruction of the flight path of RF 3. The actual flight positions of the bat are marked by the dots (time interval between two dots: 20 ms). Every tenth point is symbolized by a cross. *XZ* plane: frontal view (front view); *YZ* plane: lateral view (side view); *XY* plane: dorsal view (overview). P: perch; L: landing bar; M1, M2: microphones. The inset at lower left provides the orientation of the coordinate system.

of the objects of interest, such as pass-points, bat (tip of the nose), and microphones, were digitized and stored in an IBM-compatible personal computer. The space coordinates of the bat were computed with programs developed in the lab. The reconstructed flight path was then plotted on a three view plot (Fig. 2). The microphone positions and orientations were determined by the same procedure and were also plotted in Fig. 2.

The bat was filmed at 50 frames/s, i.e., at a frame interval of 20 ms. The bat's position was determined for each frame and the flight speed was calculated from the change in position from frame to frame. We also determined the bat's position at the instant of each sound emission by interpolation.

D. Sound analysis

The sounds were played back at $\frac{1}{32}$ of the recording speed and analyzed with a digital FFT frequency analyzer (Modular Signal Processing System, MOSIP, Medav) with a dynamic range of 80 dB. Because of background noise we had to limit the dynamic range to 50 dB. Time and frequency parameters were analyzed in the spectrogram mode. Within the displayed frequency range of 160 kHz the frequency resolution, Δf, was 400 Hz. With interpolation we reached a time resolution, Δt, of 0.2 ms. We measured the beginning and end of a signal where it dropped to 45 dB under the maximal level. The end of the iFM and the beginning of the tFM component were defined as the point 0.8 kHz under the frequency of the second harmonic of the CF component. The amplitude of the time signal was measured in the oscillogram mode, in order to determine the absolute sound-pressure level and calculate power ratios between the different components of the pulses. To estimate the sound-pressure ratio between harmonics, the peak amplitudes of the three harmonics of the CF component were also measured in the spectrum mode. The following parameters were computed by a custom computer program: target distance (the distance

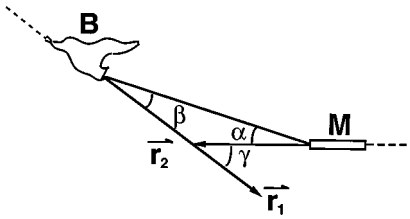

FIG. 3. The angles between the bat and the microphone. Angle α is the angle of the incidence of the echolocation sound, which means it is the angle between the microphone direction r_2 and the combination line BM between the bat and the microphone; angle β is the angle between the bat flight direction r_1 and the combination line BM between the bat and the microphone; angle γ is the angle between the bat flight direction r_1 and the microphone direction r_2.

from the bat's nose to the target), the bat's actual position, its flight velocity, the pulse duration, the duration of each pulse component, the interpulse interval (IPI, interval between the end of one pulse and the beginning of the next), the repetition rate, the duty cycle, the frequency of the second harmonic of the CF component, the bandwidth of the FM components, the maximal and mean amplitude of the CF component, the mean power ratio of iFM/CF and tFM/CF, and the sound-pressure ratios, the first to the second (1.h/2.h) and the third to the second harmonic (3.h/2.h). The target was defined as the point midway between the bat's feet on the landing bar.

Only sounds emitted within an angle of 5° from the microphone orientation axis (angle α in Fig. 3) and within an angle of 20° from the bat's flight direction (angle β) were used in the statistical evaluation. These limits ensure that the data were not substantially biased by the directional limits of both the bat's sound emission and the microphone. All the parameters listed above were plotted in relation to target distance.

The SPL of an emitted signal (RMS *re*: 20 μPa) (10 cm in front of the bat's nose) was calculated from the voltage of the recorded signal using the formula:

$$p_{10} = p_{\mathrm{ref}} + 20\log(U_x/U_{\mathrm{ref}}) + 20\log(D_x/D_{10}) + a(f)D_x + p_m(f),$$

where p_{10}=the SPL 10 cm in front of the bat's nose, p_{ref}=74 dB, the reference sound-pressure level, U_x=the voltage of the signal as measured with the MOSIP, U_{ref}=the voltage of the reference signal as measured with the MOSIP, D_x=the distance between bat and microphone, D_{10}=the reference distance (i.e., 10 cm in front of the bat's nose), $a(f)$=the frequency-dependent atmospheric attenuation, and $p_m(f)$=the frequency-dependent correction factor. Units are in dB.

This formula treats the bat's sound emission as a point source and follows the inverse-square law. The atmospheric attenuation is a function of frequency (Griffin, 1971; Lawrence and Simmons, 1982). At 80 kHz, which is near the most intense second harmonic, atmospheric attenuation is 3 dB/m. Because the sensitivity of the microphone attenuates at higher frequencies (>70 kHz), a correction factor is added. At 80 kHz, the correction factor is 14.5 dB.

We used the maximal voltage to calculate the maximal SPL and the mean voltage (rms value) to calculate the mean SPL.

To address the question whether in different echolocation situations the energy of the FM component is changed in relation to the energy of the CF component, the mean power ratio was introduced.

The voltages of consecutive signal sections were measured. Signal sections were 0.2 ms wide for the FM components and up to 5 ms wide for the CF components. The voltages were squared, multiplied by the time window, then divided by the number of time windows. To compare results for CF and FM components, the result for CF component was normalized to a 0.2-ms time window.

The following formulas were applied:

$$E = 0.2(U_{xi}{}^2(t_{i+1} - t_i))/(t_n - t_1),$$

$$R = 10\log(E_{\mathrm{fm}}/E_{\mathrm{cf}}),$$

where E=the mean energy of the pulse component, iFM, CF, and tFM, respectively; U_x=the measured voltage; t_i=the time at each measured point, R=the mean power ratio, and n=the number of windows.

The sound-pressure levels of the first three harmonics, measured in spectrum mode, were corrected with the atmospheric attenuation and transmission correction factors of the microphone. The ratios of the first/second harmonics and of the third/second were calculated.

II. RESULTS

A. Behavior during start, flight, and landing

The bats flew in stereotyped flight paths from the perch to the landing bar. After leaving the perch, they flew down to a height of about 1 m from the ground, then turned upward to the landing bar (Fig. 2). In the last 10–15 cm they turned over and landed on the landing bar with their back to the perch [Fig. 4(b)]. Most bats deviated somewhat to the right side (Fig. 2), although one bat (RF 1) turned to left or simply flew straight. During the recording sessions the flight path of each individual bat was relatively stable. Still, it appeared that the bats treated the recording microphones positioned along the flight path as obstacles, so that they varied their flight paths somewhat. This made recording much more difficult, since the flight path could not be predicted precisely each time the microphone positions were changed. We have also filmed bats in close-up range with higher speed (150 frames/s) and confirmed that the plane of the horseshoe was perpendicular to the flight direction and the bats did not turn their heads during the flight (Schnitzler and Grinnell, 1977).

B. Echolocation behavior during start, flight, and landing

The emitted echolocation sound sequences can be separated in three stages: free flight, approach, and terminal phase (Griffin *et al.*, 1960; Schnitzler, 1968). A complete flight from the perch to the landing bar is shown in Fig. 4(a), and the corresponding sound sequence during the three light flight stages is shown in Fig. 5.

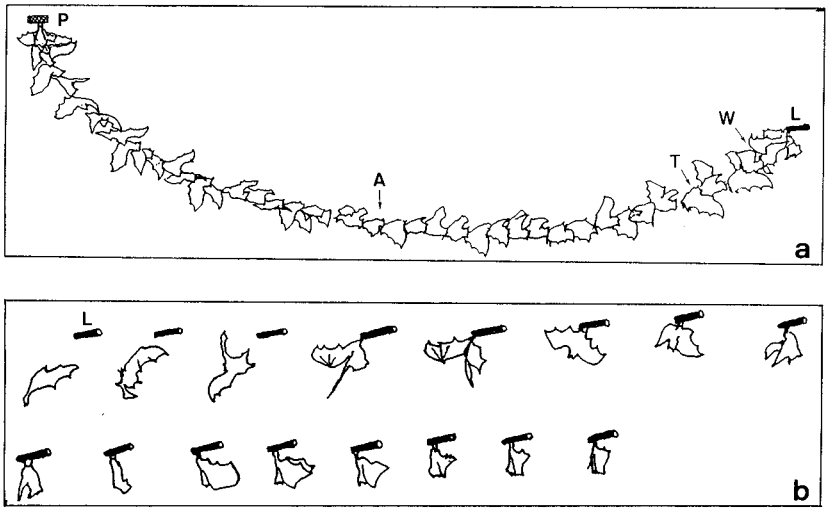

FIG. 4. A whole flight of RF 1 from the perch to the landing bar. The bat positions were drawn after consecutive pictures of a film recording. The time interval between two pictures was 20 ms. (a) The whole flight; (b) turning and landing. P: perch; L: landing bar; P-A: free flight; A-T: approach phase; T-L: terminal phase; W: begin of turning.

In free flight the bats emitted single sounds with a duration of about 50–60 ms [Fig. 6(a)]. The approach phase began with the emission of a sound group with two sounds [Fig. 6(b)] which was followed by further groups with 2–4 sounds [Fig. 6(b) and (c)]. Sometimes in the approach phase a single sound also appeared between the sound groups. The terminal phase was characterized by a group with many (in this case 14) short sounds [Fig. 6(d)]. The duration of the entire terminal group could exceed 200 ms.

The distances to the landing bar at which the approach phase started varied between 70 and 200 cm among the four bats, but it remained relatively constant for numerous flights

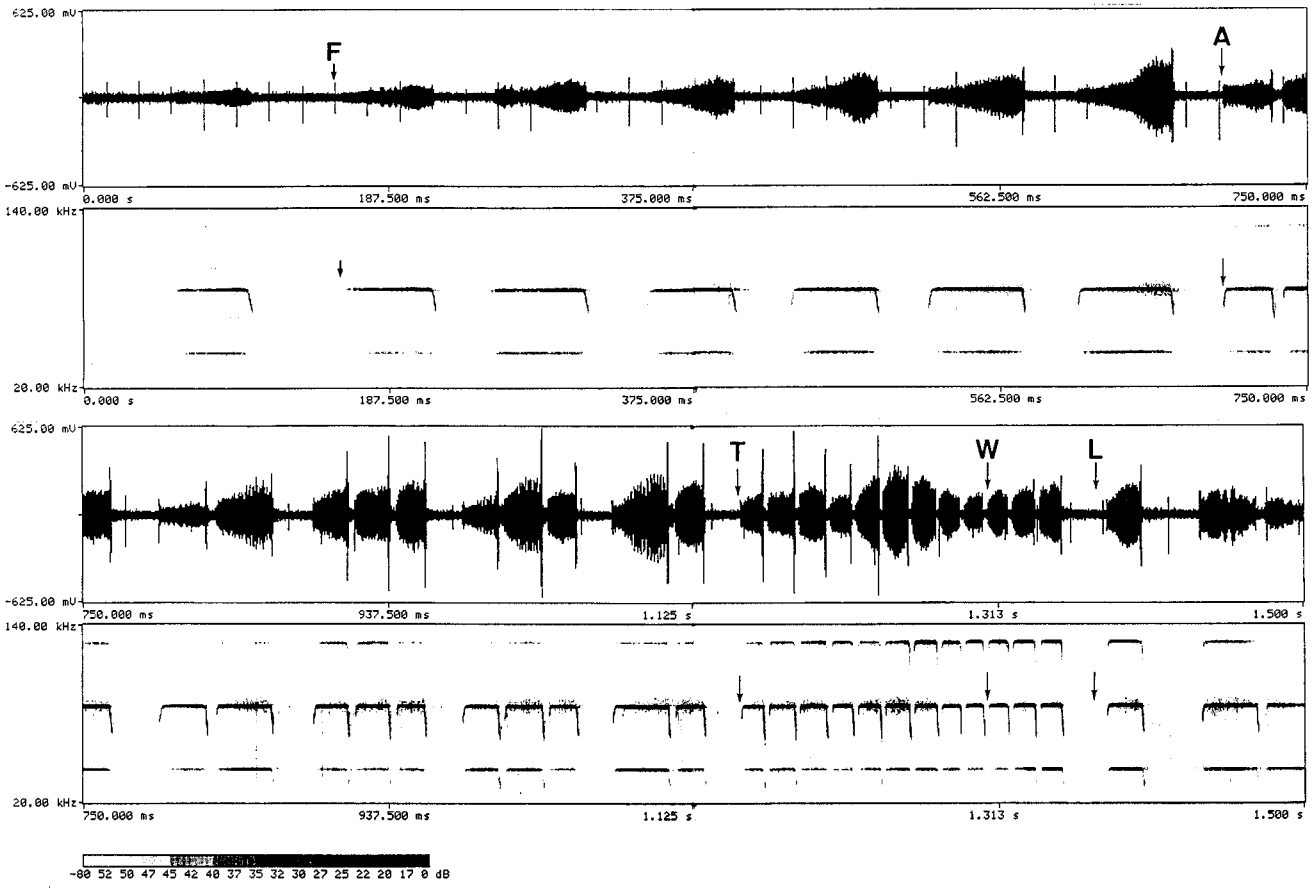

FIG. 5. The whole sequence of echolocation signals during the flight in Fig. 4. Upper row: oscillogram; lower row: spectrogram. The flight phases are marked as in Fig. 4 in the oscillogram. F-A: free flight; A-T: approach phase; T-L: terminal phase; W: begin of turning.

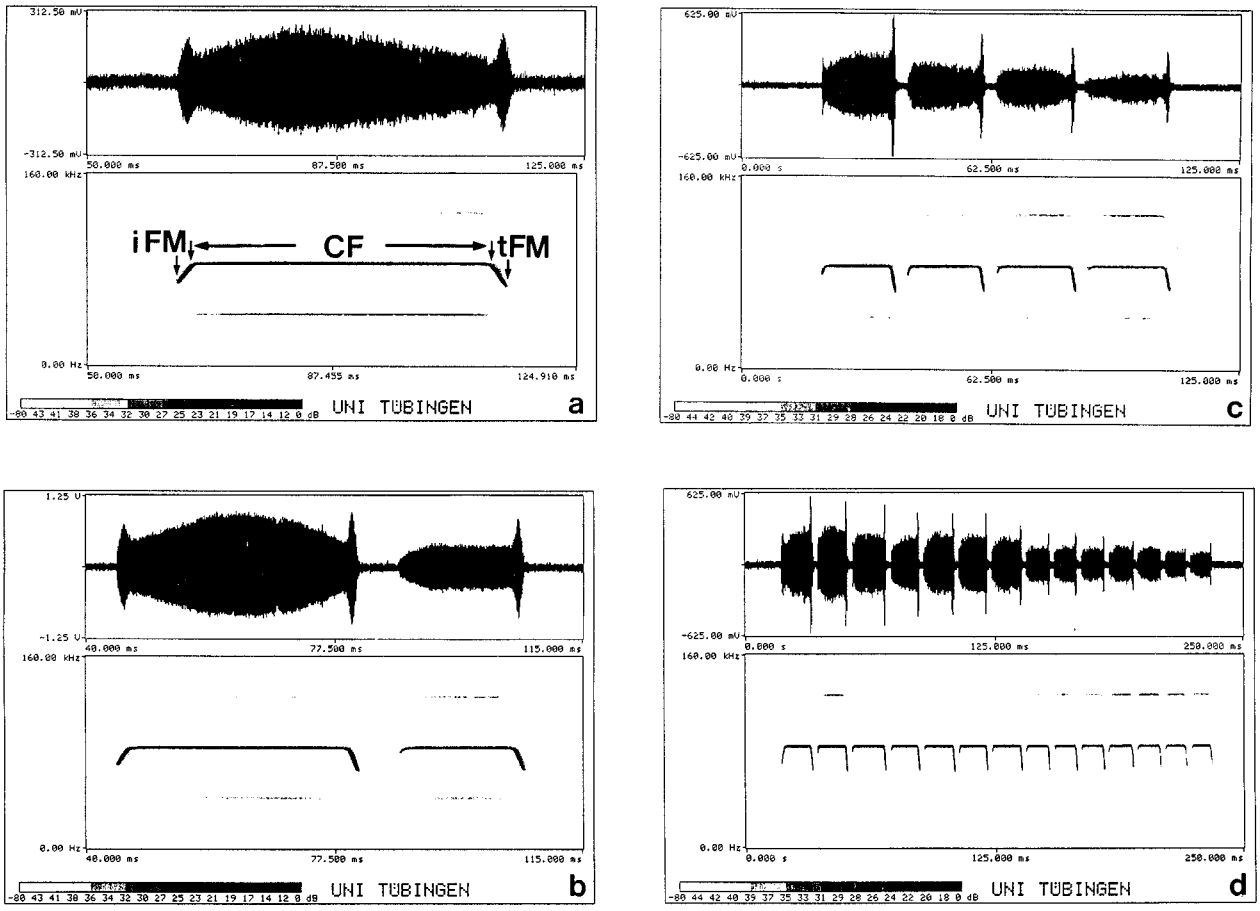

FIG. 6. Typical examples of the echolocation signals of *Rhinolophus ferrumequinum* in free flight (a), during approach [(b) and (c)], and during terminal phase (d). The upper part of each panel represents the time signal, and the lower part represents the spectrogram. In (a), the beginning and end of the initial upward frequency modulated component (iFM), the constant frequency component (CF), and the downward frequency modulated component (tFM) are measured and marked in the spectrogram. The beginning of the iFM and end of the tFM component were set at 45 dB under the maximal control level. The end of iFM and beginning of tFM were set at 0.8 kHz under the CF. During approach phase, the bat typically sends sound groups of 2 (b) to 4 (c) sounds per group. During terminal phase the bat sends usually a sound group with many short sounds [(d), here 14]. The sound has four harmonics. The fourth harmonic is out of the measuring range of the apparatus. The second one is the most prominent.

of each bat. Most commonly the approach phase began at a distance of 1.6 m. In RF 4 the approach phase started closer to the landing bar (0.7–1.3 m), while RF 1 normally switched to the approach phase at a distance of 2 m.

The terminal phase began at a distance of 30–50 cm from the target, depending on the flight speed and the number of sounds emitted in the terminal group. The faster the bat flew or the more sounds the bat emitted, the greater was the target distance at the beginning of the terminal phase. Late in the terminal phase the bat began to turn over, then landed, hanging on the landing bar [Fig. 4(b)]. In the course of this turn, the bats' echolocation signals were not directed towards the landing bar. This occurred most often during the final three pulses in the terminal phase call, at a distance about 10–15 cm to the target. Therefore, these last three pulses were not used in our study where we relate the signal structure to the target distance. After landing, the bats again emitted long single pulses, essentially identical to those before starting.

C. Analysis of pulse parameters

The echolocation signal of the Greater Horseshoe bat (*Rhinolophus ferrumequinum*) contains three parts [Fig. 6(a)]: the initial component (iFM), which is upward frequency modulated; the constant frequency (CF) component; and the terminal component (tFM), which is downward frequency modulated. The CF component has four harmonics with the second harmonic being most prominent (Fig. 6). The fourth harmonic is not shown here since it is beyond the recording range of the microphone. The amplitude course of the various components is shown in Fig. 6.

In single pulses emitted in free flight each of the components (iFM, CF, and tFM component) was characterized by an amplitude maximum [Fig. 6(a)]. This also held true for the first pulse in a pulse group, but the subsequent pulses in a group routinely failed to show the maximum in the iFM component [compare Fig. 6(b), (c), and (d)].

1. Time domain parameters

The average pulse duration in free flight was between 50 and 60 ms for all animals [Fig. 7(a) and (b)]. Immediately prior to the start of a flight, the bats emitted longer pulses, generally over 60 ms. RF 1 even emitted pulses lasting over 80 ms. After these long pulses, a pulse was sometimes omitted by RF 1 just after start. During free flight, two animals

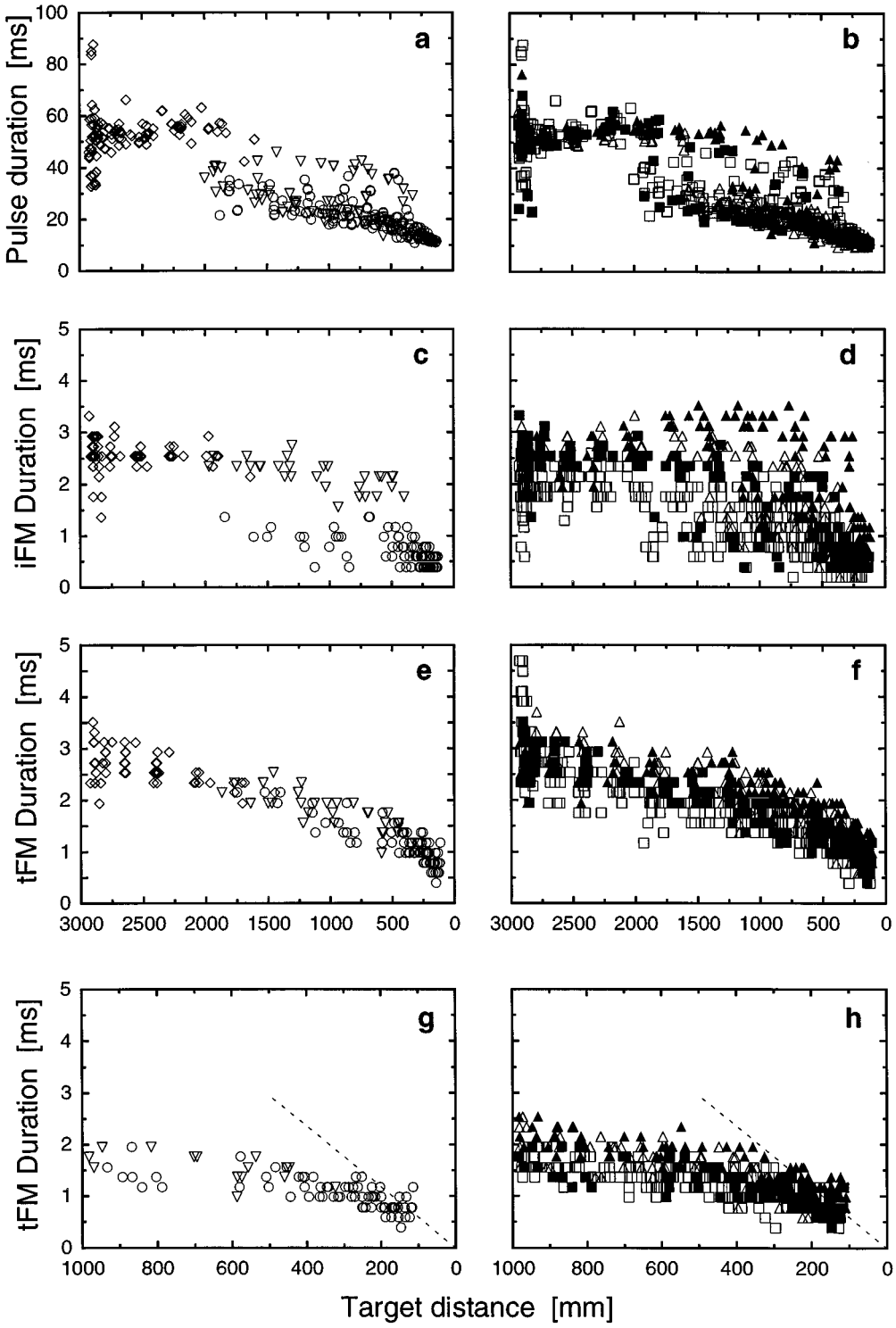

FIG. 7. Pulse duration [(a) and (b)], duration of iFM [(c) and (d)], and tFM component [(e) and (f)]. Left panels: examples from a single bat (a: RF 1; c,e,g: RF 2); right panels: data from all four bats. In (c) and (d) the durations of the iFM component of the subsequent sounds in a group separate from those of the single sounds or the first sounds in a group. The last 1 m of (e) and (f) is plotted in (g) and (h) to achieve a better resolution. The dotted line is the overlap line over which the outgoing pulse overlaps with its returning echo from the target. Left panels: rhombus: single pulse in free flight; triangle: first pulse of sound group; circle: subsequent pulses of a sound group. Right panels: open square: RF 1; filled square: RF 2; open triangle: RF 3; filled triangle: RF 4. If not especially remarked, these symbols are valid for all the following figures.

(RF 1 and RF 2) sometimes emitted a group of two sounds, each with a duration of 30–40 ms each [Fig. 7(a) and (b)]. In the approach and terminal phase the pulse duration changed depending on the target distance. In RF 1, the approach phase began at a target distance of about 2 m. Generally, the approach phase was characterized by pulse groups, with 2–4 pulses in each group, and each pulse lasting between 20 and 40 ms. Sometimes a single pulse of 40–50 ms in duration was also emitted during this phase. The terminal phase, characterized by one or more pulse groups with many short,

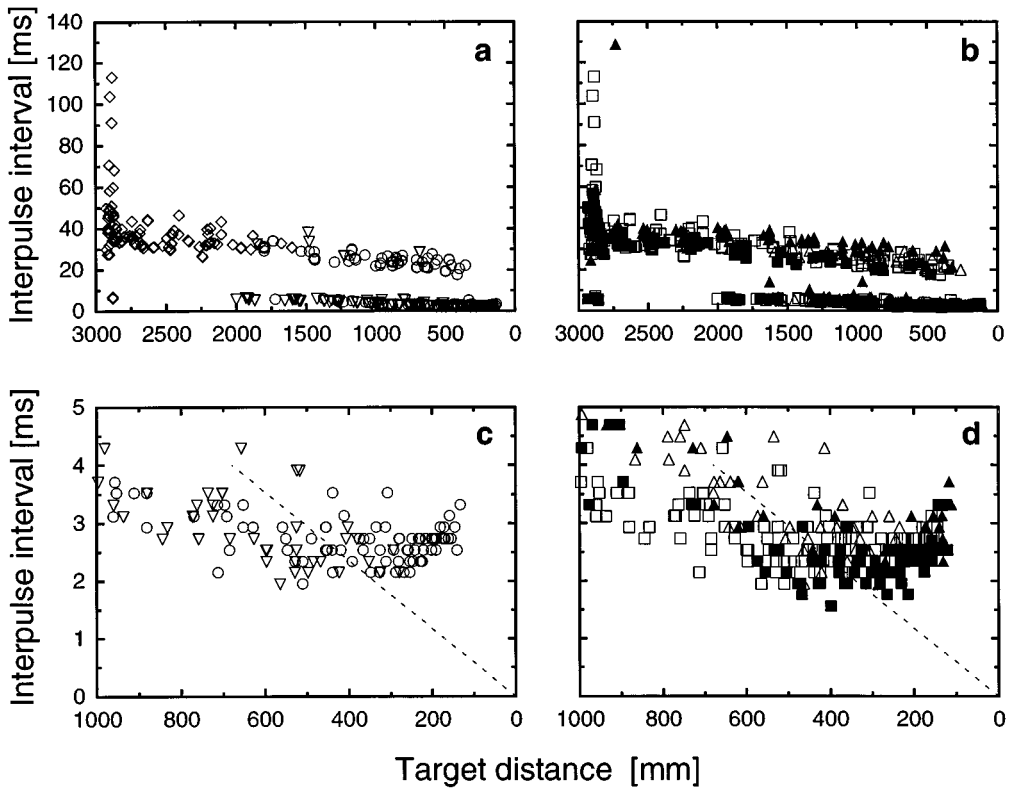

FIG. 8. Interpulse interval during the whole flight [(a) and (b)] and in last 1 m to the target [(c) and (d)]. Left panels: RF 2; right panels: all four animals. The dotted line is the overlap line. Under this line, an overlap between the returning echo and the next pulse occurs.

closely spaced pulses, began about 50 cm away from the target. In this phase, the pulse duration was reduced from 20 ms to about 10 ms [Fig. 7(a) and (b)].

In free flight, the iFM component was on average about 2–3 ms long for all animals observed (range=1.97–2.74 ms). During the approach and terminal phase the duration of the iFM component of the first pulse in a group had about the same length as those of single pulses in free flight, however, in subsequent pulses of a group it was much shorter [$t(df) > 20.9$, $df < 373$, $p < 0.001$] [Fig. 7(c) and (d)].

In free flight, the duration of the tFM component [Fig. 7(e) and (f)] varied between 2 and 3.7 ms with means between 2.5 and 3 ms for each animal. In all but one animal (RF 4), tFM was longer than the mean duration of iFM component in free flight. The duration of the tFM component was systematically shortened as the target distance decreased [Fig. 7(e) and (f)]. With very few exceptions, the outgoing tFM components did not overlap with their returning echoes from the target [Fig. 7(g) and (h)].

The interpulse interval is defined here as the time interval between the end of a pulse and the beginning of the next pulse. The average interpulse intervals were 35–40 ms during free flight (Fig. 8). Occasionally this interpulse interval was very long when one pulse was ''omitted'' [Fig. 8(a) and (b)]. Because the gaps between pulses in a group are shorter than those between the single pulses or between the last pulse of a group and the first one of the following group, two clusters emerged in the approach and terminal phase. The interpulse interval was successively reduced with decreasing target distance, but still remained longer than 2 ms.

When the bat was more than 40 cm away from the target, the interpulse interval was not long enough so that the returning echo from the target overlapped with the next outgoing pulse, shorter than this distance such an overlap did not occur, i.e., the bat did not emit a pulse until the echo of the last call had been received [Fig. 8(c) and (d)]. This suggests that the beginning of a new pulse does not interfere with the tFM component of the echo of the preceding pulse in the last 40 cm to the target.

The repetition rate and duty cycle (defined as percentage of time filled with sound) are shown in Fig. 9. They are also split into two clusters because of the different interpulse intervals within a pulse group and between pulse groups. The repetition rate increased from about 11 Hz in free flight to over 80 Hz during the terminal phase [Fig. 9(a) and (b)], while the duty cycle increased from about 60% to maximal 90% during the terminal phase [Fig. 9(c) and (d)].

2. Frequency domain parameters

The four animals had resting frequencies of the CF component between 83.9 and 85.6 kHz. During flight *Rhinolophus ferrumequinum* lowered the emission frequency depending on its flight speed. The emission frequency reached a minimum [Fig. 10(a) and (b)] when the flight speed reached its maximum of about 4.5 m/s. By lowering the emission frequency *Rhinolophus ferrumequinum* compensates for Doppler shifts to keep the echo frequency constant.

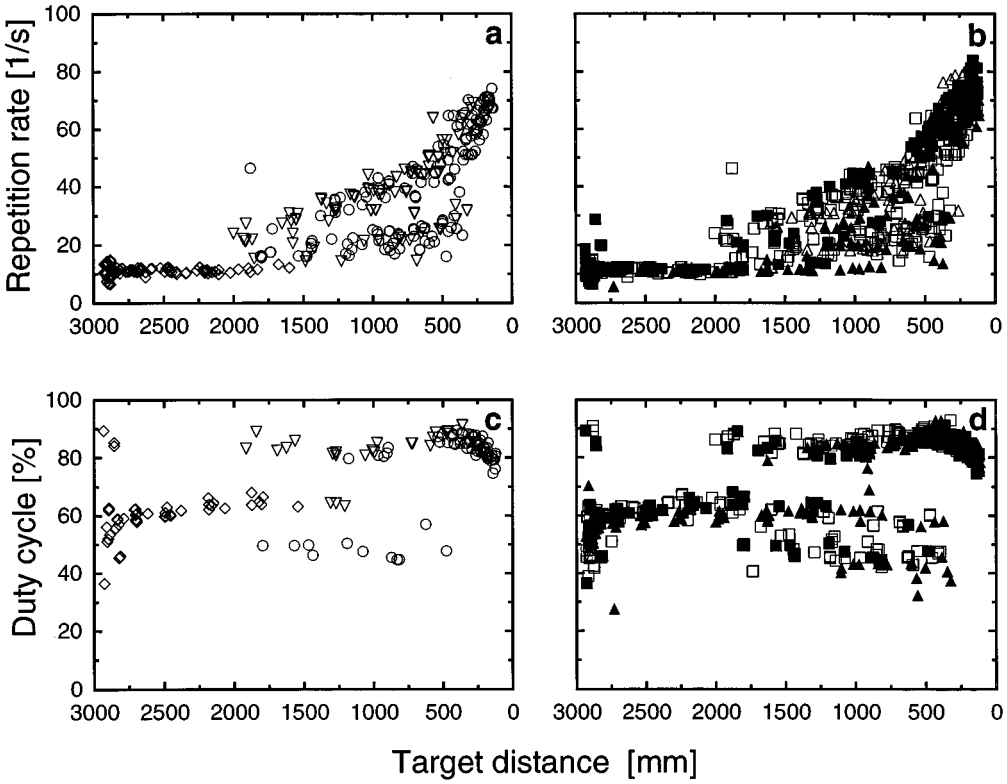

FIG. 9. Repetition rate of RF 1 (a) and all four animals (b) and duty cycle of RF 2 (c) and all four animals (d) during the whole flight.

This behavior has been termed Doppler shift compensation and has been described in detail (Schnitzler, 1968; Schnitzler and Henson, 1980).

The iFM component was well developed in pulses in free flight and in the first pulses of the pulse groups in the approach and terminal phase [Fig. 10(c) and (d)]. In the four bats we determined for these pulses the average bandwidths between 10.3 and 14.7 kHz. In subsequent pulses of pulse groups it was less prominent (bandwidth mostly below 5 kHz) or the iFM component was absent. Similar to the bandwidth, the duration of the iFM component of the single pulses and the first pulses in the groups was longer than the duration of the iFM component of the subsequent pulses in the groups [$t(df)>17.35$, $df<373$, $p<0.001$]. In fact, bandwidth and duration of the iFM component are positively correlated [correlation coeff.: $r>0.87$, mean $r=0.91$, $t(df)\geqslant 26.9$, $df>116$, $p<0.001$] [Fig. 11(a) and (b)].

The bandwidth of the tFM component ranged from 10–22 kHz [Fig. 10(e) and (f)]. In free flight we determined average bandwidths of 12.5–15.3 kHz in the four bats. In the approach and terminal phase the bandwidth of the tFM component was increased up to maximal values of 22 kHz [Fig. 10(e) and (f)]. No differences between the first pulse and subsequent pulses in a group were found. There seems only a weak negative correlation between pulse duration and bandwidth of the tFM component [Fig. 11(c) and (d)].

In signals where the iFM and the tFM showed a clear peak in the oscillogram we also determined the peak frequency. In all bats the peak frequency was about the same in the iFM and in the tFM. Furthermore, the peak frequency was mostly about 8.0–8.5 kHz below the emission frequency of the CF component.

3. Intensity domain parameters

The sound pressure level of the emitted signals (10 cm in front of the bat's nose) was changed during the flight from the perch to the landing bar. In free flight the maximal SPL of the CF component was between 115 and 125 dB SPL [Fig. 12(a) and (b)]. The average maximal SPL ranged from 117.6–120.4 dB in the four bats. The loudest signals were emitted at the beginning of the approach phase, with a maximum at 130 dB. During the terminal phase the maximal SPL was clearly reduced to about 95 dB [Fig. 12(a) and (b)].

Figure 12(c) and (d) (where distance was plotted logarithmically for the last meter to the target) show that in the last 60 cm of flight the bats reduced the SPL with a constant rate at each halving target distance. The rates were 6.1 dB in RF 1 ($r=0.76$, $p<0.001$, $n=107$), 8.8 dB in RF 2 ($r=0.95$, $p<0.001$, $n=68$), 9.4 dB in RF 3 ($r=0.78$, $p<0.001$, $n=54$), and 8.6 dB in RF 4 ($r=0.84$, $p<0.001$, $n=39$). Mean SPL followed a pattern similar to the maximal SPL.

Similar to the intensity change of the CF component, the intensity of tFM component also changed in different orientation situations. In free flight, the maximal SPL of the tFM component was between 102 and 128 dB [Fig. 12(e) and (f)]. The average maximal SPL ranged from 112.5–115.1 dB. In the approach phase, the maximal SPL could reach 128 dB. In the terminal phase the maximal SPL decreased to about 95 dB. In the last 60 cm of the flight the rates of the intensity reduction per each halving target distance were 9.6 dB in RF 1 ($r=0.81$, $p<0.001$, $n=107$), 11.1 dB in RF 2 ($r=0.95$, $p<0.001$, $n=68$), 9.6 dB in RF 3 ($r=0.73$, $p<0.001$, $n=54$), and 10.1 dB in RF 4 ($r=0.88$, $p<0.001$, $n=39$) [Fig. 12(g) and (h)].

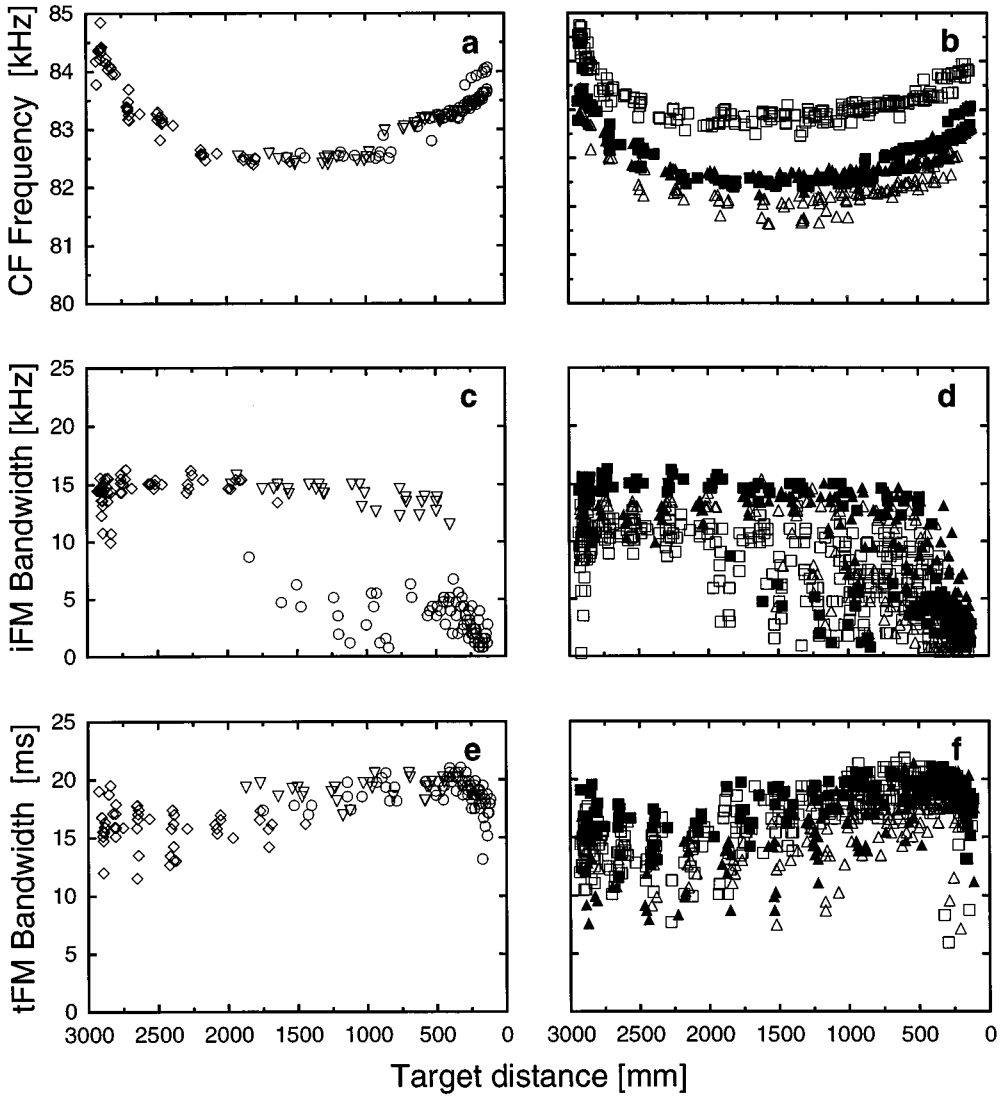

FIG. 10. Emission frequency of CF component [(a) and (b)], bandwidth of iFM [(c) and (d)], and tFM component [(e) and (f)] during the whole flight. Left panels: RF 2; right panels: all four animals. In (c) and (d) the data points of the iFM component of the subsequent sounds in a sound group separate from those of the single sound or the first sounds in a group.

Since the energy of an FM signal is distributed over a range of frequencies, the mean power ratio FM/CF was introduced to examine whether the intensity of the FM component changed in relationship to the CF component in different echolocation situations (Fig. 13). The mean power ratio iFM/CF of single pulses in free flight and the first pulse in a group varied in a range of ± 15 dB at the 0-dB line, while the values of the subsequent pulses in a group are clearly below the 0-dB line [Fig. 13(a) and (b)]. There is no systematic change in dependence on the target distance.

In free flight the mean power ratio of the tFM/CF fluctuated between -10 and $+5$ dB [Fig. 13(c) and (d)]. During the approach phase, i.e., about 1.5 m from the target, it increased to a maximum of $+10$ dB. When the bat was within about 0.5 m of the target, the tFM/CF power ratio declined to less than 0 dB. However, unlike the mean power ratio of the iFM/CF, the power ratio of the tFM component in all pulses remained above 0 dB at a target distance below 2 m, and declined only in the very last 50 cm of flight below 0 dB. There is an evident change of the mean power ratio tFM/CF here dependent on the target distance.

The sound-pressure level ratios of the harmonics were also compared (Fig. 14). The ratio of the first/second harmonics remained in a range of -45 to -15 dB during the entire flight, with no apparent systematic changes [Fig. 14(a) and (b)]. The ratio of third/second harmonics ranged from -35 to -15 dB at a distance of 0.5–3 m to target [Fig. 14(c) and (d)]. However, during the last 50 cm of flight, this ratio increased to over 0 dB, and higher values were routinely found in the last pulses of the terminal group.

III. DISCUSSION

A. Echolocation behavior of captive bats

Under laboratory conditions, i.e., in a confined space, bats have to cope with clutter of echoes from the walls, the ground, and the ceiling. Therefore they emit signals typical

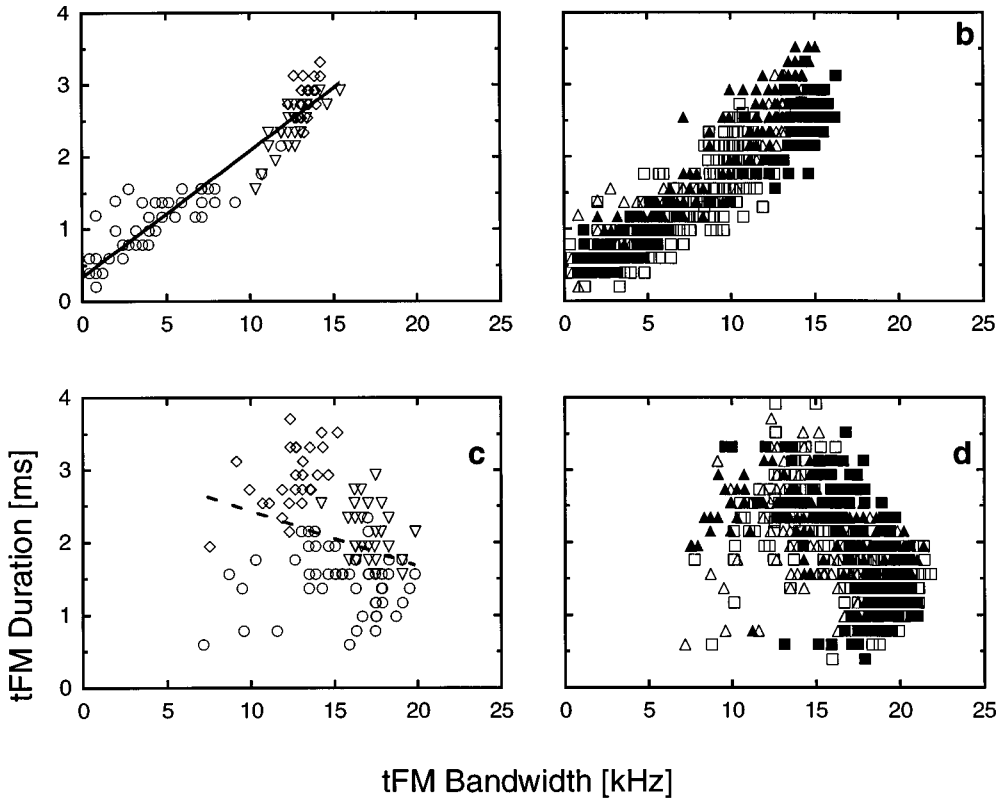

FIG. 11. Correlation between bandwidth and duration of iFM component of RF 3 (a) and all four animals (b) is plotted, the solid line is the correlation line. For comparison, the same scatter plots duration versus bandwidth of the tFM component were also plotted here for RF 3 (c) and all four animals (d). Only a weak but negative correlation was found.

for cluttered situations. *Eptesicus fuscus*, for example, emits up to 20-ms-long pulses in the open (Schnitzler, unpublished), but produces in the laboratory signals lasting only 3–5 ms. A similar tendency has been described for many other bats hunting for insects in open space.

However, rhinolophids and other bats that normally hunt close to surfaces and obstacles (Griffin and Simmons, 1974; Schnitzler *et al.*, 1985) are used to a cluttered background. For those bats the echolocation situation in the laboratory is comparable to some natural conditions. Therefore it is not surprising that *Rhinolophus ferrumequinum* can successfully pursue and catch flying prey in a cramped flight room (Trappe and Scnitzler, 1982), and that the duration of signals recorded in the field (Griffin and Simmons, 1974) is similar to that under laboratory conditions. In both situations the horseshoe bats have to solve similar echolocation tasks.

In our experiment, the Greater Horseshoe bats had learned to fly in a familiar environment from a perch to a landing bar. They had to solve an echolocation task which is similar to that of a wild bat making a transfer flight within the roost or within a well-known environment outside the roost. The given echolocation task is not comparable to a situation where a bat hunts for insects in the field. There it does not know where it will encounter the target it is searching for. This may result in differences in echolocation behavior between bats making transfer flights and bats hunting for insects.

B. Pulse parameters which are dependent on flight speed

Bats with long CF-FM signals such as the rhinolophids, hipposiderids, and the mustache bat *Pteronotus parnellii* lower their emission frequency to compensate for Doppler shifts in the echoes, and to uncouple the echo frequency from their own flight speed (Schnitzler, 1968, 1970a, b; Trappe and Schnitzler, 1982). Because the wings of fluttering insects are moving reflectors, they impose a rhythmical pattern of amplitude and frequency modulations on the CF component of the echo (Schnitzler *et al.*, 1983; Schnitzler, 1987; Kober and Schnitzler, 1990). The Greater Horseshoe bats evaluate this flutter information not only to discriminate insects with different wing beat frequencies (Emde v.d., 1987; Emde v.d. and Menne, 1989), but also to classify insect species according to their specific flutter signature (Emde v.d. and Schnitzler, 1990). This behavior has been described before and will therefore not be discussed here in detail.

C. Pulse parameters with a clear change in relation to the target

According to definition, the beginning of the approach phase is characterized by the first reaction to a target of interest (Griffin *et al.*, 1960; Schnitzler and Henson, 1980). Therefore, only pulse changes in the approach and terminal phase can be related to the target in a systematic way.

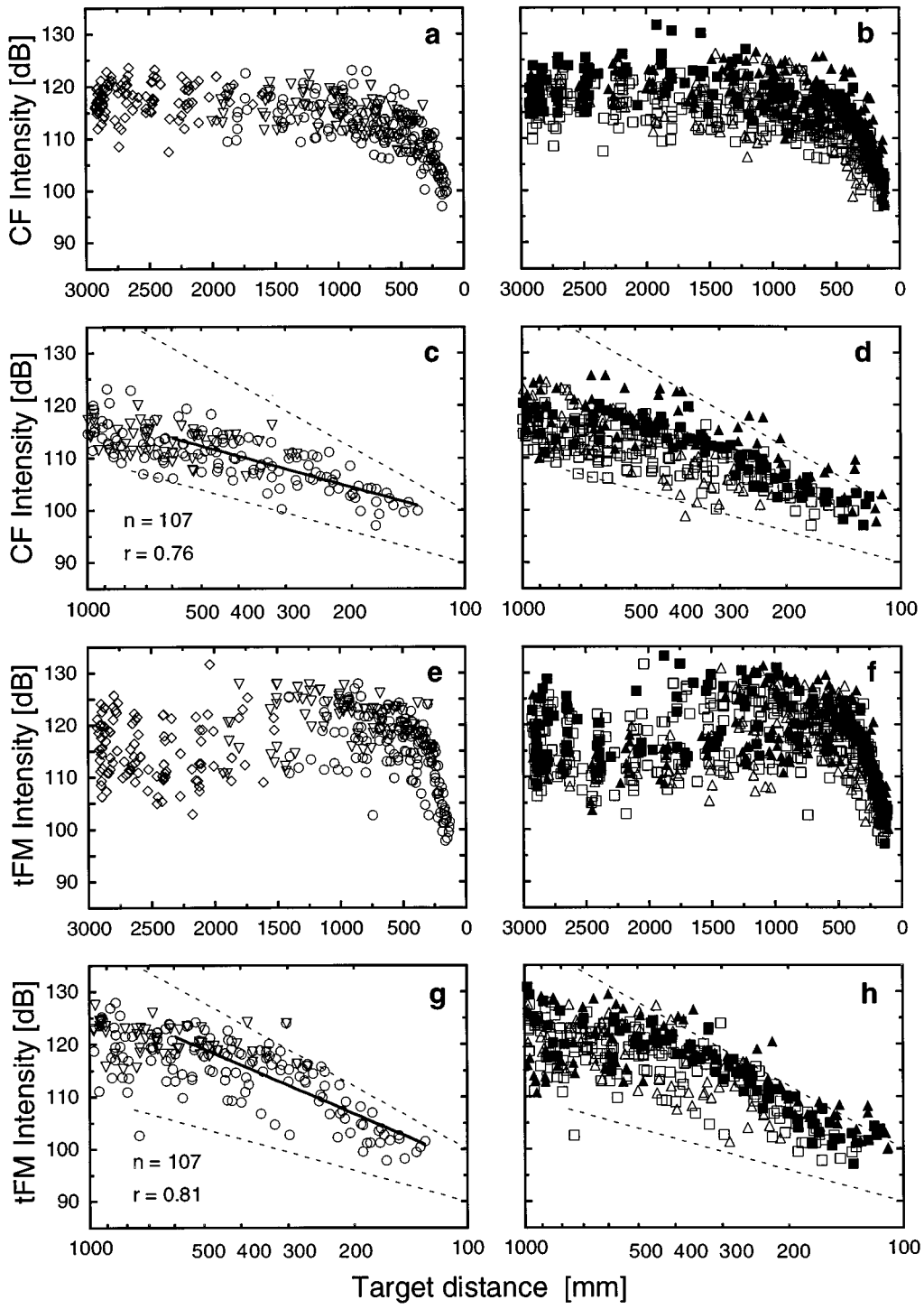

FIG. 12. Maximal intensity of CF [(a) and (b)] component and tFM component [(e) and (f)] in whole flight. Left panels: RF 1; right panels: all four animals. If the abscissa is plotted logarithmically, there is a decline of maximal intensity in RF 1 at 6.1 dB in CF component (c) and 9.6 dB in tFM component (g) at each halving of the last 60-cm target distance. The slope varied in different animals and was at 6–9 dB for CF component (d) and 9–11 for tFM component (h) per each halving of last 60-cm target distance. The dashed lines indicate the slope of 6 and 12 dB each halving of target distance, respectively. The atmospheric attenuation and geometric spreading are corrected with the correction factor at 80 kHz.

In our experiments the repetition rate increased from about 11 Hz in free flight to 20–50 Hz in approach phase, and reaches a maximum at about 70 Hz during the terminal phase (Fig. 9). We assume that bats increase the repetition rate with decreasing target distance to improve the information flow. The increase in repetition rate in CF-FM bats is not as much as that found in pure FM bats which reach maximal repetition rates of up to 210 Hz (Schnitzler, 1987; Kalko and Schnitzler, 1989). The reason could be that Greater Horseshoe bats approaching a target are still interested in the echo information carried by the CF component of the signal. Therefore, they have to use longer signals than FM bats, resulting in a lower repetition rate. Similar behavior has been observed in other bats with long CF-FM signals,

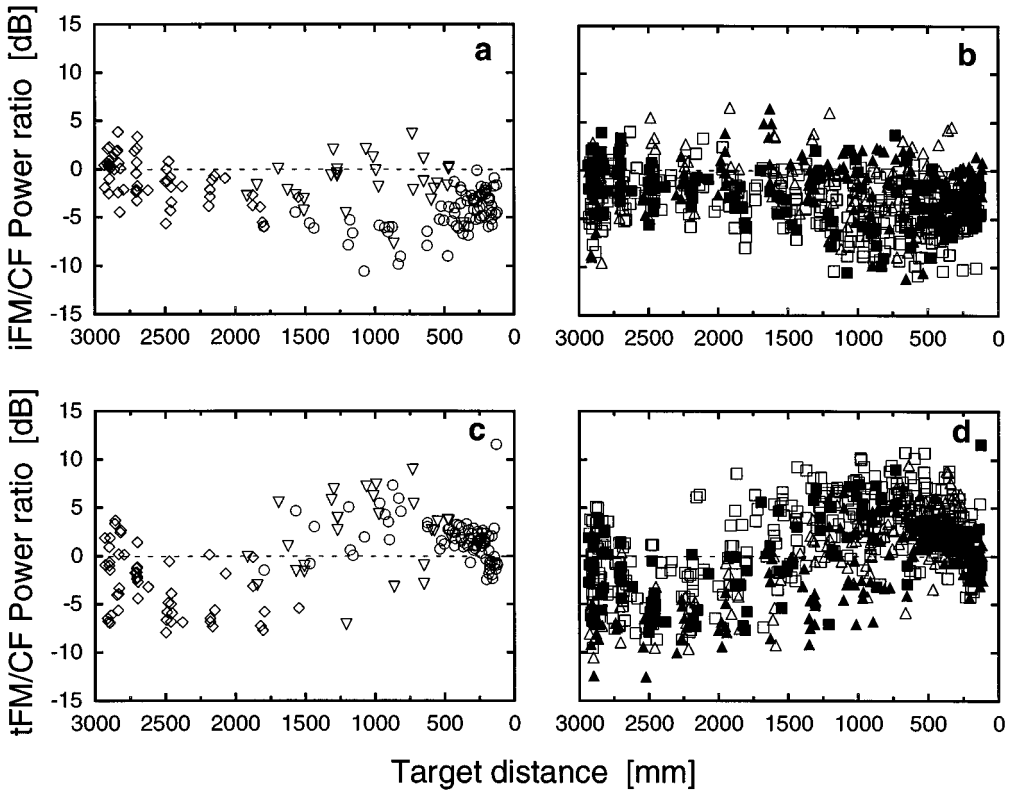

FIG. 13. Mean power ratios of iFM/CF [(a) and (b)] and tFM/CF [(c) and (d)]. Left panels: RF 2; right panels: all four animals. The dashed line is the 0-dB line. On the oscillogram the amplitude of the FM components was measured in consecutive time windows of 0.2 ms, the amplitude of the CF component was measured in variable time windows, but always smaller than 5 ms. The average amplitude of each component was calculated and compared with each other.

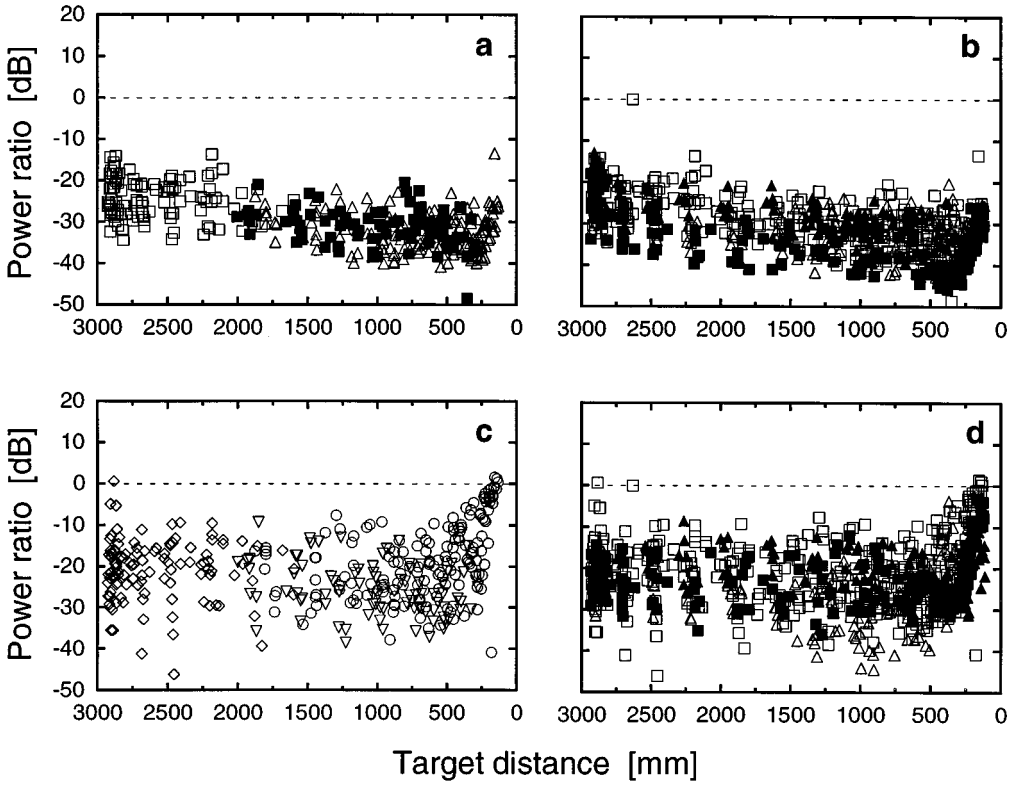

FIG. 14. Power ratio of first harmonic to second harmonic [(a) and (b)] and third to second harmonic [(c) and (d)]. Left panels: RF 1; right panels: all four animals. The amplitude of each harmonic was measured in spectrum and compared. The atmospheric attenuation was corrected with the value from Fig. 1 in Lawrence and Simmons' (1982) paper at 40, 80, and 120 kHz, respectively.

such as *Rhinolophus rouxi* (Schnitzler *et al.*, 1985; Neuweiler *et al.*, 1987), and *Pteronotus parnellii* (Schnitzler, 1970a, b; Jen and Kamada, 1982). The fish-catching bat *Noctilio leporinus*, a bat that produces CF-FM signals of intermediate length, changes from CF-FM signals in free flight and in most parts of the approach phase to a few short, pure FM signals in the terminal phase of an approach (Schnitzler *et al.*, 1994).

It is assumed that in CF-FM bats the time delay between the outgoing tFM component and its echo encodes range in a similar way as in FM bats where the time delay is measured between the FM signal and its echo (Schnitzler, 1968, 1970b, 1973a, b; Simmons, 1973). In *Rhinolophus ferrumequinum* the duration of the tFM component decreases systematically in relation to the target distance, so that the bats avoid the overlap of the outgoing tFM component with its echo from the target of interest (Fig. 7). A similar overlap avoidance was also found in bats with pure FM signals such as *Myotis lucifugus* (Cahlander *et al.*, 1964), *Myotis daubentoni* (Kalko and Schnitzler, 1989), and *Pipistrellus kuhli* (Schnitzler *et al.*, 1987; Kalko and Schnitzler, 1993). For FM bats it is assumed that avoiding the pulse–echo overlap prevents forward masking of the echo by the emitted signal and thus allows a good determination of range (Kalko and Schnitzler, 1989). We assume in *Rhinolophus ferrumequinum* a similar mechanism but only for the tFM components of emitted signal and echo. In some bats an overlap may occur within the last 20 cm before the bat reaches a target, for example, in *Eptesicus fuscus*, when tracking a target moving rapidly towards it (Hartley, 1992b). As the reaction time of bats is too long to react at such a close distance this overlap seems no more relevant for the tracking process. In the fishing bat *Noctilio leporinus* an overlap also occurs in the terminal phase of an approach (Hartley *et al.*, 1989). Schnitzler *et al.* (1994) suggest that this overlap may be explained by the specific fishing behavior of *Noctilio leporinus*. Since these bats hunt for targets that are often only detectable for a short instant, the FM portion of their signals may be optimized for the tracking of the target during the brief time when the prey can be localized by echolocation.

The interpulse interval between pulses within a pulse group in the approach phase or in the terminal group is rather small ($<$10 ms, Fig. 8). We showed for such pulses that at target ranges larger than 50 cm the echoes of the tFM component of the preceding pulse overlap with that of the following emitted pulse. This overlap seems to be not disturbing for *Rhinolophus ferrumequinum*, which suggests that there is no interference between the tFM echo of the preceding pulse and the less prominent iFM and well-developed CF component of the following pulse, and indicates separate information processing for the different components.

In free flight the maximal SPL of the CF component is close to 120 dB SPL in all four animals (Fig. 12). In this phase *Rhinolophus ferrumequinum* is in a mode where it uses echolocation signals with a relative high SPL to search the space for the target of interest. Our data in free flight match well with Schnitzler's (1968) results of 123 dB SPL of a free hanging *Rhinolophus ferrumequinum*. However, they are much higher than the results of Vogler and Neuweiler (1983), who measured 105–115 dB SPL in free flight and 70–90 dB SPL during the terminal phase. The different values may be due to the different recording conditions between these experiments. In our experiment, the microphones were placed optimally to match the actual bat position during the whole flight, whereas the microphone was set at a fixed position in Vogler and Neuweiler's experiment (1983).

When entering the approach phase after detection of a target, *Rhinolophus ferrumequinum* even increases the maximal SPL of the CF component up to 130 dB SPL (Fig. 12). As the bat gets closer to the target (under 0.6 m), the SPL decreased gradually to 90 dB at a rate of 6–9 dB for each halving of the target distance.

The SPL of the tFM component changes in a similar way (Fig. 12). It is increased after entering the approach phase, and when the bat comes closer to the target (under 0.6 m), the SPL is decreased with a rate of 9–11 dB per halving target range. These values are higher than the reduction rates of the CF component. This is consistent with the fact that the mean power ratio tFM/CF increases in the approach, but decreases in the last few sounds in the terminal phase (Fig. 13).

Vogler and Neuweiler (1983) found that for *Rhinolophus ferrumequinum* catching insects the echolocation sounds became fainter in the terminal phase. Similar results were also found in *Pteronotus parnellii* and *Eptesicus fuscus* avoiding obstacles (Jen and Kamada, 1982) and in *Noctilio leporinus* approaching a target (Hartley *et al.*, 1989). In more controlled experiments Hartley (1992b) showed that *Eptesicus fuscus* reduced the SPL of the emitted signals with 6 dB per halving of target range in the last 80–100 cm of an approach to a moving target, and Kobler *et al.* (1985) found that *Pteronotus parnellii* sitting on a pendulum decreased the SPL of the echolocation sounds during a forward sweep and increased it during a backward sweep. The change in SPL was about 6 dB for each halving or doubling of the target distance, respectively. Therefore, our data are consistent with the previous findings.

If a bat kept the signal SPL constant while approaching a target, the echo SPL would increase rapidly, since the transmission loss is reduced with decreasing target range. Bats could compensate for this increase of echo SPL with lowering of the signal SPL accordingly. Kobler *et al.* (1985) dubbed this phenomenon ''intensity compensation.''

The two-way transmission loss is the sum of spreading loss and loss due to atmospheric attenuation (Møhl, 1988). At small targets the spreading loss reduces the strength of echoes by a total of 12 dB for every doubling of target range due to spherical spreading. The additional effects of atmospheric attenuation can be neglected when target distance is small. For larger targets such as a wall in the experiments of Kobler *et al.* (1985) and the landing bar in our experiments, it is difficult to judge the spreading loss as the law of spherical spreading is not applicable in the rather large near field of such targets. Therefore it may well be that at least near the target the transmission loss may have been a few dB smaller than the 12 dB per doubling of distance in spherical spreading, but it can never be smaller than 6 dB per doubling of range, the minimum rendered by an ideal, planar reflecting surface (Simmons *et al.*, 1992).

The reduction of emission level with 6 dB per halving of target range during the last 80–100 cm of an approach in *Eptesicus fuscus* (Hartley, 1992b), with 6 dB during the last 150 cm in *Noctilio leporinus* (Hartley *et al.*, 1989), with 6 dB at a distance of 6–300 cm to the wall in a *Pteronotus parnellii* sitting on a pendulum (Kobler *et al.*, 1985), and with 6–9 dB at the CF component and 9–11 dB at the tFM component during the last 60 cm of an approach to a landing bar in *Rhinolophus ferrumequinum* (present study) suggests that these bats compensate at least for a substantial part of the increase in echo SPL due to the reduced spreading loss to keep the echo SPL within a certain, maybe physiologically optimal range. At large targets the reduction of spreading loss may be even in the same range as the reduction of the emission level. This would mean that the SPL of the returning echoes at the bat's ears may be kept constant in the final part of the approach.

Kick and Simmons (1984) showed that in *Eptesicus fuscus* the perceived echo SPL is influenced by an additional mechanism which they called automatic gain control. They tested the hearing threshold in a two-forced-choice echo discrimination task and found that it increased at a rate of 11 dB for each halving of echo delay within a target range of 1.1 m. In contrast to the data discussed above, the emission SPL was the same at different target ranges. They pointed out that the measured change in auditory sensitivity is very close to the spreading loss of 12 dB for each doubling distance, and as the emission level was the same at all tested ranges these bats should perceive the echo from targets within the tested range of 1.1 m at about the same sensation level. Kick and Simmons (1984) and Simmons *et al.* (1992) discussed possible mechanisms for the measured range-dependent change in auditory threshold and concluded that the contractions of the bat's middle-ear muscles synchronized to transmissions may account for the observed change in auditory sensitivity. They also suggested that forward masking by the sonar transmissions may contribute to the threshold shift. If in *Eptesicus fuscus* the described change of sensitivity of 11 dB per halving of range can be applied to a flying bat and if these bats also lower the emission level with 6 dB per halving of distance within the last 80–100 cm of an approach (Hartley, 1992b), the bats would overcompensate the spherical spreading loss of maximal 12 dB per doubling of range with an overall reduction of perceived echo SPL of 17 dB per halving of distance. In an experiment where the perception of echoes at different target ranges was tested in *Eptesicus fuscus* and *Noctilio leporinus*, Hartley (1992a) found that the loudness (perceived SPL) of echoes decreased about 6 dB per halving of target range. As these bats also lower the emission level with about 6 dB per halving of target range (Hartley, 1989, 1992b), the perceived echo SPL should be kept about constant throughout the final part of an approach. The presented data do not suffice to determine the degree to which bats compensate for the decrease in spherical loss when approaching a target by lowering the emission level and by an additional reduction in auditory sensitivity. Nevertheless, it can be assumed that both effects allow bats to regulate the perceived echo SPL in such a way that it is kept within a certain optimal range. This should improve the ability of the bat to extract behaviorally relevant information from the echoes.

We do not know whether *Rhinolophus ferrumequinum* also has some kind of automatic gain control mechanism which produces an additional attenuation of the perceived echo SPL. The proposed mechanisms in FM bats, namely middle ear attenuation and forward masking, cannot be applied in a similar way for CF-FM bats because of their long signals. Therefore we have no reason to assume that horseshoe bats have a mechanism similar to the automatic gain control mechanism postulated for FM bats. If we assume that bats pursuing an insect also lower the emission level by about 6–9 dB for the CF component and 9–11 dB for the tFM component in the final 60 cm of an approach, they would compensate at least for a substantial part of the increase in echo SPL due to the reduced spherical spreading loss. By this reduction they would keep the echo SPL within a certain range which could help to optimize the extraction of behaviorally relevant information from the echoes.

During the approach and terminal phase, the amplitude of the tFM component increases compared to the CF component (compare Figs. 5 and 6). The mean power ratio is between 0 and 10 dB (Fig. 13), and is much higher than in free flight. The systematic increase in emphasis on the tFM component indicates that this component plays an important role when *Rhinolophus ferrumequinum* approaches a target. As suggested before, we assume that the FM component is used to determine target range. As the exact localization of a target gets more important when a bat approaches the landing bar, this component gets more prominent.

During insect catching, *Rhinolophus ferrumequinum* emitted sounds whose tFM components were fainter than the CF components (Vogler and Neuweiler, 1983). Vogler and Neuweiler (1983) concluded that this cast some doubts onto the assumption of the tFM component being the carrier for range information. However, they did not mention how they determined the amplitude relationship between the FM and CF components. Again, it could be that the fixed position of the microphone had caused the different results. Another possibility is that they compared the averaged spectra. This may be misleading as in a CF signal the energy is concentrated in a small frequency band, thus producing a large peak, whereas in a FM signal the energy is distributed over many frequencies, thus producing a smaller peak even when both have the same SPL. Our data confirm previous findings where the tFM component was always present, e.g., in the recordings of *Rhinolophus ferrumequinum* (Trappe, 1982) and *Rhinolophus rouxi* (Schnitzler *et al.*, 1985). Moreover, Schnitzler (1968) found that the amplitude of the tFM component is additionally increased in the approach and terminal phase. We do not share the doubts of Vogler and Neuweiler (1983), and we assume that the tFM component is used for ranging.

The importance of the tFM component is also reflected in the increase of its bandwidth in the approach and terminal phase (Fig. 10). In free flight the bandwidth is kept between 12–16 kHz, whereas throughout the whole approach and terminal phase it is a kept between 15–22 kHz. Schnitzler (1968) found that the bandwidth of the tFM component is

between 13 and 16 kHz in all orientation situations. Trappe (1982) and Vogler and Neuweiler (1983) found that the bandwidth of the tFM component can be as much as 23–26 kHz during the approach phase, respectively. Our data confirm these early results. It is generally accepted that the accuracy of range determination increases with increasing bandwidth. Therefore the observed increase of the bandwidth of the tFM component also indicates that this component is used for ranging.

D. Pulse parameters which are not changed in relation to the target

The iFM component is always present in single pulses and in the first pulse of a pulse group but only weakly developed or absent in subsequent pulses in a pulse group. The duration is between 1.7 and 4.5 ms (Fig. 7), and the bandwidth varies between 10 and 16 kHz (Fig. 10). The mean power ratio iFM/CF is under 0 dB (Fig. 13). None of these parameters is changed systematically in relation to target range as it is the case with the tFM component. This suggests that the iFM component is not used to determine range in a similar way as it is assumed for the tFM component.

Schnitzler (1968) found that the duration of the iFM component of *Rhinolophus ferrumequinum* did not change in relation to different orientation situations. He described that its bandwidth varied widely between 1 and 12 kHz and that its amplitude was very low in comparison with other components. Therefore he concluded that the iFM component is not likely an important component for ranging. Vogler and Neuweiler (1983) found that *Rhinolophus ferrumequinum* typically emits FM-CF-FM sounds when catching flying prey under laboratory condition. In obstacle avoidance flights the bandwidth of the iFM component increased from 3.5 to 12 kHz. Except for the last two sounds during approach and terminal phase, the iFM component was fainter than the CF component. In obstacle avoidance flights the iFM component was prominent and louder than the CF component. But again, the methods to estimate the amplitude relationship between FM and CF components were not presented. From their results they concluded that the iFM component is an information carrying part of the echolocation signal. Our data, which compare favorably to the results and conclusion of Schnitzler (1968), do not support this assumption. We suggest that the iFM component does not carry relevant information and is not used for range determination.

We assume that the iFM component is the by-product of intonation. One argument for this assumption is that the duration of the iFM component is correlated with its bandwidth in all orientation situations, i.e., the FM rate remains constant [Fig. 11(a) and (b)], in contrast to the tFM component whose FM rate increases when the bat approaches a target [Fig. 11(c) and (d)]. This indicates that in all pulses the bat contracts its vocal cords in a similar way but opens the air stream which activates the oscillation of the vocal cords in a different way at single pulses or the first pulse of a group and at the subsequent pulses of a group. In single pulses and the first pulse of each group the air stream starts early during the stereotyped contraction process so that long iFM components of high bandwidth are produced. In the subsequent pulses of a group the air stream comes rather late so that short iFM components with narrow bandwidth are emitted.

There is no systematic change in ratios of the first and the third harmonic to the second harmonic during the whole flight except that only the third harmonic increased in the last few pulses of the terminal group (Fig. 14). Neuweiler *et al.* (1987) found that in *Rhinolophus rouxi* the first harmonic could sometimes be as strong as or even stronger than the second one. They suggested that the first harmonic may be an important component for echo processing in horseshoe bats. However, such a reversal of the normal amplitude relationship was not found in our results.

In well-developed iFM and tFM components, the highest amplitude found was always about 8 kHz below the emission frequency of the CF component (Figs. 5 and 6). This may be explained by the fact that the transfer function for the vocal tract often has a second peak below the maximum peak at the second harmonic (Hartley and Suthers, 1988). This best amplitude may reflect some specialization in this frequency range for the evaluation of range information.

E. Comparison with the echolocation behavior of bats hunting for insects

In our experiment, all four Greater Horseshoe bats exhibited echolocation behavior with three distinct phases: free flight, approach, and terminal phase. *Rhinolophus ferrumequinum* emits long, single pulses in free flight, pulse groups with 2–4 pulses in the approach phase, and a ''buzz'' group in the terminal phase. Only in RF 4 the approach phase was sometimes shorter than the others. RF 3 emitted once two terminal buzzes instead of one. However, in insect-catching *Rhinolophus ferrumequinum*, the approach phase can be reduced drastically or even skipped, i.e., the bat may switch directly from search flight to terminal phase, because of the unexpected appearance of the target of interest in space (Trappe, 1982; Trappe and Schnitzler, 1982). Sometimes, the terminal phase is prolonged to two or even three buzz groups because of the escape maneuver of the prey insect. Similar behavior was also observed in *Rhinolophus rouxi* in the field (Schnitzler *et al.*, 1985).

F. What determines pulse structure

In free or search flight, the iFM component seems to be a byproduct of the vocalization. It is stereotyped and appears in each single echolocation sound. The CF component delivers the information on a moving target, such as fluttering insects. The CF component also delivers some angular information, especially in combination with ear movements (Schnitzler and Henson, 1980). In transfer flight the acoustic flow field information in the CF components of echoes may also be used to avoid obstacles and to control the flight in the vicinity of ground and vegetation. Therefore, the CF component is more pronounced. The long duration and high intensity of the CF component allow the maximal scan time to detect and evaluate the changes in the echo frequency caused by the Doppler shifts at the maximal range. The tFM component allows precise ranging, which is impossible with the CF pulse and may also improve angular precision.

Once a target is detected by the bat, the sound duration is reduced to allow a higher repetition rate which is needed to increase the information flow. As the bat is approaching the target, more information about the location of the target becomes necessary for the flight course correction. During this phase, the iFM component has no importance since it does not change in a systematic relation to the target. Furthermore, it is largely reduced or even disappears in the subsequent pulses in a pulse group. The CF component is still needed to track and verify the identity of the target. The tFM component becomes more important as it is more pronounced compared with the CF component, to gain more information about range and direction. Its duration is reduced to avoid overlap with its returning echo from the target.

When the Greater Horseshoe bat comes close to a target, both the CF and tFM components are reduced in SPL, so that they are compensated at least for a substantial part of the increase in echo SPL due to the reduction in spreading loss. By this intensity compensation the horseshoe bats keep the echo SPL within a certain range, which may improve the extraction of relevant information from the echoes.

Our experiments provide support for the idea that the CF and the FM components are used to collect separate kinds of information. The CF component delivers Doppler-shift information, which allows the sensing of relative motion between the bat and a target and the evaluation of the flutter information produced in the echo by the rhythmical wing movements of prey insects. The tFM component is used in a similar way as in pure FM bats mainly for the localization of targets. This specific echolocation signal is an adaptation for the detection, classification, and localization of fluttering insects in highly cluttered environments.

ACKNOWLEDGMENTS

We wish to thank D. Menne for providing three-dimensional reconstruction programs and helping BT to write custom programs, J. Ostwald for valuable discussion, and K. Heblich and I. Kaipf for introducing BT into the methods. We also thank A. Mitz and J. Olsen for helpful comments and critical reviews and L. Crepeau, A. Kile, and E. Strohm for correcting English in early versions of the manuscript. The research was supported by the Deutsche Forschungsgemeinschaft (SFB 307).

Bruns, V. (**1976**). ''Peripheral auditory tuning for fine frequency analysis by the cf-fm bat, *Rhinolophus ferrumequinum*. II. Frequency mapping in the cochlea,'' J. Comp. Physiol. **106,** 87–97.

Bruns, V., and Schmieszek, E. (**1980**). ''Cochlea innervation in the Greater Horseshoe Bat: Demonstration of an acoustic fovea,'' Hear. Res. **3,** 27–43.

Cahlander, D. A., McCue, J. J. G., and Webster, F. A. (**1964**). ''The determination of distance by echolocating bats,'' Nature **201,** 544–546.

Emde, G. v.d. (**1987**). ''Die Klassifizierung von Insekten durch Echoortung bei der Gro*ß*en Hufeisennase (*Rhinolophus ferrumequinum*),'' Dissertation, Fakultät für Biologie, Eberhard-Karls-Universität, Tübingen.

Emde, G. v.d., and Menne, D. (**1989**). ''Discrimination of insect wing-beat-frequencies by the bat *Rhinolophus ferrumequinum*,'' J. Comp. Physiol. **164,** 663–671.

Emde, G. v.d., and Schnitzler, H.-U. (**1990**). ''Classification of insects by echolocating greater horseshoe bats,'' J. Comp. Physiol. **167,** 423–430.

Feng, A. S., and Vater, M. (**1985**). ''Functional organization of the cochlear nucleus of rufous horseshoe bats (*Rhinolophus rouxi*): Frequencies and internal connections are arranged in slabs,'' J. Comp. Neurol. **235,** 529–553.

Finsterwalder, R., and Hofmann, W. (**1968**). *Photogrammetrie* (Walter de Gruyter, Berlin).

Griffin, D. R. **(1971)**. ''The importance of atmospheric attenuation for the echolocation of bats (Chiroptera),'' Anim. Behav. **19**, 55–61.

Griffin, D. R., and Simmons, J. A. (**1974**). ''Echolocation of insects by horseshoe bats,'' Nature **250,** 731–732.

Griffin, D. R., Webster, F. A., and Michael, C. R. (**1960**). ''The echolocation of flying insects by bats,'' Anim. Behav. **8**, 141–154.

Gustafson, Y., and Schnitzler, H.-U. (**1979**). ''Echolocation and obstacle avoidance in the hipposiderid bat, *Asellia tridens*,'' J. Comp. Physiol. **131,** 161–167.

Hartley, D. J. (**1989**). ''The effect of atmospheric sound absorption on signal bandwidth and energy and some consequences for bat echolocation,'' J. Acoust. Soc. Am. **85,** 1338–1347.

Hartley, D. J. (**1992a**). ''Stabilization of perceived echo amplitude in echolocating bats. I. Echo detection and automatic gain control in the big brown bat, *Eptesicus fuscus*, and the fishing bat, *Noctilio leporinus*,'' J. Acoust. Soc. Am. **91,** 1120–1132.

Hartley, D. J. (**1992b**). ''Stabilization of perceived echo amplitude in echolocating bats. II. The acoustic behavior of the big brown bat, *Eptesicus fuscus*, when tracking moving prey,'' J. Acoust. Soc. Am. **91,** 1133–1149.

Hartley, D. J., and Suthers, R. A. (**1988**). ''The acoustics of the vocal tract in the horseshoe bat, *Rhinolophus hildebrandti*,'' J. Acoust. Soc. Am. **84,** 1201–1213.

Hartley, D. J., Campbell, K. A., and Suthers, R. A. (**1989**). ''The acoustic behavior of the fish-catching bat, *Noctilio leporinus*,'' J. Acoust. Soc. Am. **86,** 8–27.

Jen, P. H.-S., and Kamada, T. (**1982**). ''Analysis of orientation signals emitted by the CF-FM bat, *Pteronotus p. parnellii* and the FM bat, *Eptesicus fuscus*, during avoidance of moving and stationary obstacles,'' J. Comp. Physiol. **148,** 389–398.

Kalko, E. K. V., and Schnitzler, H.-U. (**1989**). ''The echolocation and hunting behavior of Daubenton's bat, *Myotis daubentoni*,'' Behav. Ecol. Sociobiol. **24**, 225–238.

Kalko, E. K. V., and Schnitzler, H.-U. (**1993**). ''Plasticity in echolocation signals of European pipistrelle bats in search flight: implications for habitat use and prey detection,'' Behav. Ecol. Sociobiol. **33**, 415–428.

Kick, S. A., and Simmons, J. A. (**1984**). ''Automatic gain control in the bat's receiver and the neuroethologogy of echolocation,'' J. Neurosci. **4,** 2725–2737.

Kinsler, L. E., and Frey, A. R. (**1962**). *Fundamentals of Acoustics* (Wiley, New York).

Kober, R. (**1988a**). ''Echoes of fluttering insects,'' in *Animal Sonar Processes and Performance*, edited by P. E. Nachtigall and P. W. B. Moore (Plenum, New York), pp. 477–481.

Kober, R. (**1988b**). ''Informationsgehalt der Ultraschallechos von Insekten,'' Dissertation, Fakultät für Biologie, Eberhard-Karls-Universität, Tübingen, Germany.

Kober, R., and Schnitzler, H.-U. (**1990**). ''Information in sonar echoes of fluttering insects available for echolocating bats,'' J. Acoust. Soc. Am. **87,** 882–896.

Kobler, J. B., Wilson, B. S., Henson, O. W., Jr., and Bishop, A. L. (**1985**). ''Echo intensity compensation by echolocating bats,'' Hear. Res. **20**, 99–108.

Konstantinov, A. I., Makarov, A. K., and Skolov, B. V. (**1978**). ''Doppler-pulse sonar system in *Rhinolophus ferrumequinum*,'' Kenya National Academy for Advancement of Arts and Science, pp. 155–163.

Lawrence, B. D., and Simmons, J. A. (**1982**). ''Measurements of atmospheric attenuation at ultrasonic frequencies and the significance for echolocation by bat,'' J. Acoust. Soc. Am. **71,** 585–590.

M*ø*hl, B. (**1988**). ''Target detection by echolocating bats,'' in *Animal Sonar Processes and Performance*, edited by P. E. Nachtigall and P. W. B. Moore (Plenum, New York), pp. 435–450.

Neuweiler, G., Metzner, W., Heilmann, U., Rübsamen, R., Eckrich, M., and Costa, H. H. (**1987**). ''Foraging behaviour and echolocation in the rufous horseshoe bat (*Rhinolophus rouxi*) of Sri Lanka,'' Behav. Ecol. Sociobiol. **20**, 53–67.

Ostwald, J. (**1980**). ''The functional organization of the auditory cortex in the CF-FM bat *Rhinolophus ferrumequinum*,'' in *Animal Sonar Systems*,

edited by R. G. Busnel and J. F. Fish (Plenum, New York), pp. 953–955.
Ostwald, J. (**1984**). ''Tonotopical organization and pure tone response characteristics of single units in the auditory cortex of the Greater Horseshoe Bat,'' J. Comp. Physiol. **155,** 821–834.
Ostwald, J. (**1988**). ''Encoding of natural insect echoes and sinusoidally modulated stimuli by neurons in the auditory cortex of the Greater Horseshoe Bat, *Rhinolophus ferrumequinum*,'' in *Animal Sonar Processes and Performance*, edited by P. E. Nachtigall and P. W. B. Moore (Plenum, New York), pp. 483–487.
Schnitzler, H.-U. (**1968**). ''Die Ultraschall-Ortungslaute der Hufeisen-Fledermäuse (*Chiroptera-Rhinolophidae*) in verschiedenen Orientierungssituationen,'' Z. Vergl. Physiol. **57**, 376–408.
Schnitzler, H.-U. (**1970a**). ''Echoortung bei der Fledermaus *Chilonycteris rubiginosa*,'' Z. Vergl. Physiol. **68**, 25–39.
Schnitzler, H.-U. (**1970b**). ''Comparison of the echolocation behavior in *Rhinolophus ferrumequinum* and *Chilonycteris rubiginosa*,'' Bijdr. Dierk. **40**, 77–80.
Schnitzler, H.-U. (**1971**). ''Fledermäuse im Windkanal,'' Z. Verlag. Physiol. **73**, 209–221.
Schnitzler, H.-U. (**1973a**). ''Control of Doppler shift compensation in the greater horseshoe bat, *Rhinolophus ferrumequinum*.,'' J. Comp. Physiol. **82,** 79–92.
Schnitzler, H.-U. (**1973b**). ''Die Echoortung der Fledermäuse und ihre hörphysiologischen Grundlagen,'' Fortschr. Zool. **21**, 136–189.
Schnitzler, H.-U. (**1987**). ''Echos of fluttering insects: information for echolocating bats,'' in *Recent Advances in the Study of Bats*, edited by M. B. Fenton, P. Racey, and J. M. V. Rayner (Cambridge U.P., Cambridge), pp. 226–243.
Schnitzler, H.-U., and Grinnell, A. D. (**1977**). ''Directional Sensitivity of Echolocation in the Horseshoe Bat, *Rhinolophus ferrumequinum.* I. Directionality of Sound Emission,'' J. Comp. Physiol. **116,** 51–61.
Schnitzler, H.-U., and Henson, O. W., Jr. (**1980**). ''Performance of airborne animal sonar systems: I. Microchiroptera,'' in *Animal Sonar Systems*, edited by R. G. Busnel and J. F. Fish (Plenum, New York), pp. 109–181.
Schnitzler, H.-U., and Kalko, E. K. V. (**1997**). ''Echolocation behavior of foraging bats,'' BioScience (in press).
Schnitzler, H.-U., Hackbarth, H., Heilmann, U., and Herbert, H. (**1985**). ''Echolocation behavior of rufous horseshoe bats hunting for insects in the flycatcher-style,'' J. Comp. Physiol. **157,** 39–46.
Schnitzler, H.-U., Kalko, E. K. V., Kaipf, I., and Grinnell, A. D. (**1994**). ''Fishing and echolocation behavior of the greater bulldog bat, *Noctilio leporinus*, in the field,'' Behav. Ecol. Sociobiol. **35**, 327–345.
Schnitzler, H.-U., Kalko, E. K. V., Miller, L., and Surlykke, A. (**1987**). ''The echolocation and hunting behavior of the bat, *Pipistrellus kuhli*,'' J. Comp. Physiol. **161,** 267–274.
Schnitzler, H.-U., Menne, D., Kober, R., and Heblich, K. (**1983**). ''The Acoustical Image of Fluttering Insects in Echolocating Bats,'' in *Neuroethology and Behavioral Physiology*, edited by F. Huber and H. Markl (Springer-Verlag, Berlin), pp. 235–250.
Schuller, G. (**1980**). ''Hearing characteristics and Doppler shift compensation in South Indian cf-fm bats,'' J. Comp. Physiol. **139,** 349–356.
Schuller, G. (**1984**). ''Natural ultrasonic echoes from wing beating insects are encoded by collicular neurons in the CF-FM bat, *Rhinolophus ferrumequinum*,'' J. Comp. Physiol. **155,** 121–128.
Schuller, G., and Pollak, G. (**1979**). ''Disproportionate frequency representation in the inferior colliculus of Doppler-compensating Greater Horseshoe Bats: Evidence for an acoustic fovea,'' J. Comp. Physiol. **132,** 47–54.
Schwidefsky, K., and Ackermann, F. (**1976**). *Photogrammetrie. Grundlagen, Verfahren, Anwendungen* (Teubner, Stuttgart).
Simmons, J. A. (**1973**). ''The resolution of target range by echolocation bats,'' J. Acoust. Soc. Am. **54,** 157–173.
Simmons, J. A., Fenton, M. B., and O'Farrell, M. J. (**1979**). ''Echolocation and pursuit of prey by bats,'' Science **203,** 16–21.
Simmons, J. A., Moffat, A. J. M., and Masters, W. M. (**1992**). ''Sonar gain control and echo detection thresholds in the echolocating bat, *Eptesicus fuscus*,'' J. Acoust. Soc. Am. **91,** 1150–1163.
Suthers, R. A., Thomas, S. P., and Suthers, B. J. (**1972**). ''Respiration, wing beat and ultrasonic pulse emission in an echolocating bat,'' J. Exp. Zool. **56**, 37–48.
Trappe, M. (**1982**). ''Verhalten und Echoortung der Großen Hufeisennase (*Rhinolophus ferrumequinum*) beim Insektenfang,'' Ph.D. thesis, University of Tübingen.
Trappe, M., and Schnitzler, H.-U. (**1982**). ''Doppler-Shift Compensation in Insect-Catching Horseshoe Bats,'' Naturwissenschaften **69,** 193–194.
Vogler, B., and Neuweiler, G. (**1983**). ''Echolocation in the noctule (*Nyctalus noctula*) and horseshoe bat (*Rhinolophus ferrumequinum*),'' J. Comp. Physiol. **152,** 421–432.

Measurements of ultrasonic pulse distortion produced by human chest wall

Laura M. Hinkelman[a)]
Department of Electrical Engineering, University of Rochester, Rochester, New York 14627

Thomas L. Szabo
Hewlett–Packard Imaging Systems, Andover, Massachusetts 01810

Robert C. Waag
Departments of Radiology and Electrical Engineering, University of Rochester, Rochester, New York 14627

(Received 26 May 1996; accepted for publication 26 November 1996)

Ultrasonic wavefront distortion produced by transmission through human chest wall specimens was measured over a two-dimensional aperture. Measured pulse wavefronts were sometimes disrupted by secondary wavefronts produced by interaction between the transmitted pulses and the bone and cartilage structures of the rib cage. The secondary wavefronts produced large distortions in the received waveforms and interfered with the determination of the wavefront distortion caused by soft-tissue inhomogeneities. The effects of secondary wavefronts were minimized by reducing the region of analysis. Differences in arrival time and energy level between these restricted regions and references that account for geometric delay and spreading were computed. Spectral changes were assessed by calculating a waveform similarity factor that is decreased from 1.0 by changes in waveform shape. For 16 different intercostal spaces, the arrival time fluctuations of the measured waveforms had an average ($\pm$s.d.) rms value of 21.3 ($\pm$8.4) ns and an average correlation length of 2.50 ($\pm$0.62) mm. The energy level fluctuations had an average rms value of 1.57 ($\pm$0.45) dB and an average correlation length of 1.98 ($\pm$0.33) mm, and the average waveform similarity factor was 0.964 ($\pm$0.012). For soft-tissue inhomogeneities in chest wall specimens, the average rms arrival time and energy level fluctuations were less than half those measured for the abdominal wall. However, although the average correlation length of the arrival time fluctuations was less than half that found for the abdominal wall, the average correlation length of the energy level fluctuations was similar to that of the abdominal wall.
[S0001-4966(97)04404-4]

PACS numbers: 43.80.Vj, 43.80.Ev, 43.80.Jz [FD]

INTRODUCTION

Transthoracic echocardiography has long been used to evaluate the size, shape, position, and motion of structures within the heart, particularly since the development of commercial dynamic cross-sectional imaging systems in the early 1970s. As in other clinical ultrasonic imaging applications, however, the tissues between the transducer and the target can degrade image quality. Transesophageal echocardiography was developed partly to avoid the influence of the ribs and soft tissues of the chest wall,[1] but is an invasive procedure that requires special skill to administer and is accompanied by some risk compared to conventional transthoracic echocardiographic imaging.[2,3] Nevertheless, transesophageal echocardiography has become increasingly popular because it provides superior images.[4,5]

Researchers in other areas of ultrasonic imaging have recently attempted to quantify and eliminate the effects of ultrasonic wavefront degradation caused by propagation through tissue inhomogeneities. Direct measurements of the distortion produced by the abdominal wall[6–8] and breast[9–12] have been made, and methods for the correction of this distortion have been investigated.[13–19] These measurements and techniques could provide a foundation from which diffraction-limited images of abdominal and breast structures may be obtained.

Not much information, however, appears to be available about the wavefront distortion produced by transmission through chest wall. A literature search found only one report on this subject. This report[20] describes a study in which the beams from single-element, unfocused transducers were measured after passage through rib cage specimens and compared to water path references. Propagation through the rib cage was found to cause loss of beam cross-sectional symmetry, increased beam diameter, deflection of the beam from its original trajectory, and division of the beam into two components. The distortion was most severe for transducers with diameters larger than the intercostal spaces and for large deviations of the incident angle from normal to the chest wall. However, little attempt was made to differentiate between the effects produced by inhomogeneities in the soft tissue of the rib cage and those caused by the ribs. Additional information about ultrasonic propagation through chest wall is needed to assess further the severity of wavefront distortion in transthoracic echocardiography and to evaluate the potential of wavefront distortion correction techniques for

[a)]Current affiliation: Department of Meteorology, The Pennsylvania State University, University Park, PA 16802.

 0001-4966/97/101(4)/2365/9/$10.00

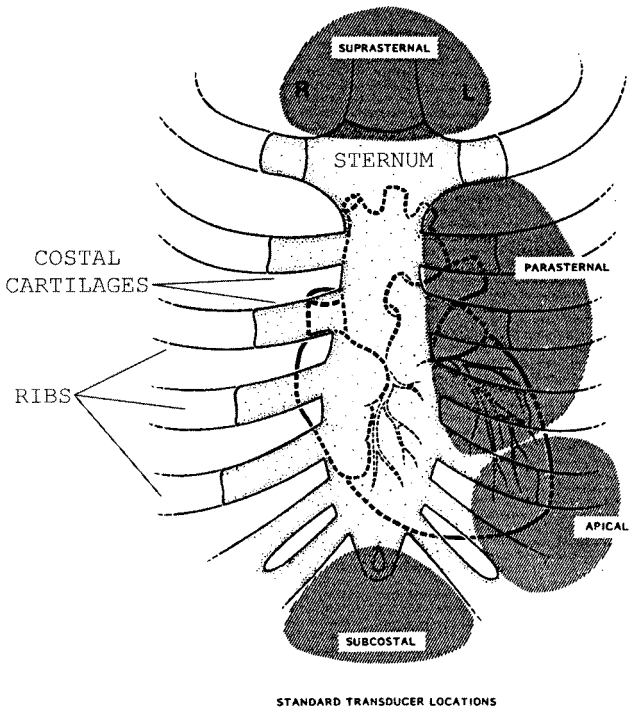

FIG. 1. Parasternal measurement location anatomy (adapted from Ref. 4, p. 81).

improving the quality of transthoracic cardiac b-scan images.

This study was undertaken to determine the ultrasonic propagation characteristics of intercostal chest wall sites commonly used for transthoracic cardiac imaging. Wavefronts were recorded over a two-dimensional aperture after transmission through human chest wall specimens. Statistics that describe arrival time fluctuations, energy level variations, and wave shape distortion produced by inhomogeneities in the soft tissues were calculated and compared to values from similar measurements using abdominal walls.[8,12] Distortion caused by the bones and cartilage of the rib cage was also considered.

I. METHOD

Complete unfixed breast plates were obtained during autopsy and stored frozen. The breast plates were then cut into approximately 10×10-cm^2 sections that were only minimally curved. Each section consisted of skin, subcutaneous fat, various muscle layers, connective tissues, and the internal membrane (parietal pleura) supported by two to four 7- to 10-cm lengths of costal cartilage and rib connected to a portion of the sternum. The 12 specimens used in this study came from seven donors who ranged in age from 79 to 96 with a mean age of 87. (The age at time of death of one donor was unknown.) Three of the donors were female and four were male. All of the six donors for whom cause of death was known died of cardiac or pulmonary ailments. The measurements reported here were made in parasternal locations within the 2nd, 3rd, or 4th intercostal spaces that are identified along with other transthoracic locations in Fig. 1. However, sections were taken without preference from both the right and left sides of the chest because the chest wall is morphologically symmetric. The average thickness of the measurement locations was 20.8 mm.

The measurement procedure was similar to that described in Refs. 8 and 12, but the measurement apparatus was modified somewhat for use with the chest wall specimens. The hemispheric source was replaced by a 0.5-in.-diam piston transducer fitted with a diverging lens, and a custom-made broadband cardiac array consisting of 96 elements with a pitch of 0.21 mm and an active elevation dimension of 0.40 mm was used as the receiver. The measurement spot size (0.084 mm^2) was more than 12 times smaller than that (1.04 mm^2) used in the previous abdominal wall and breast studies. A separate preamplifier was included in each of the channels. Software improvements allowed data to be collected at 4800 positions (all 96 elements at each of 50 mechanically scanned elevation positions) over an area of 20.16×20.00 mm^2 in about 10 min. At each position, 19 repetitions of the received signal were digitized into 12-bit samples at 20 MHz for an interval at of 23.8 μs each. The system had a center frequency of 2.3 MHz and a -6-dB bandwidth of 1.2 MHz. The measurement signal-to-noise ratio was about 50 dB.

Measurements were made in a tank filled with distilled water that had been degassed at 37 °C for a period of at least 12 h. The transducers were mounted approximately 185 mm apart in the tank. The face of the receiving array was centered over the source perpendicular to the source axis by iteratively moving the center array element to the position in the receiving plane with maximum received signal and then tilting the array to equalize the travel time of a pulse from the source to each corner of the two-dimensional receiving aperture. After this, the gain was adjusted so that the full range of the 12-bit A/D converter would be used and a water path data set was collected.

A specimen holder, containing saline solution and a chest wall section that had been pressurized at 500 psi for 30 min to force into solution any gas bubbles in the tissue, was positioned in the tank immediately in front of the receiving array with the skin surface facing the transmitter and the ribs running approximately parallel to the receiving array. In this position, the skin surface of the specimen was slightly compressed but no pressure was applied to the interior surface. The interior surface was smoothed by the parietal pleura, which stretches between the framework of the rib cage. As a result, no artificial surface irregularities that could influence the measurement results were introduced. A measurement window was located by moving the specimen laterally within the holder until a significant signal was received at each corner of the receiving area. The gain was adjusted to compensate for attenuation, the position of the specimen with respect to the receiver was recorded, and data were collected. This procedure was repeated for as many as four positions of the specimen at one or more intercostal spaces. A second water path measurement was made after removal of the chest wall specimen and readjustment of the gain.

Distortion characteristics were calculated for an 11.60×14.28-mm^2 subaperture selected from each data set to minimize the influence of secondary wavefronts that often

disrupted the main wavefront in regions of the full $20.16 \times 20.00\text{-mm}^2$ aperture. Variations in pulse arrival time energy level, and shape were computed as described in Ref. 12 with the exception that, because the region over which the distortion was computed was much smaller for the chest wall data, a second-order polynomial fit was substituted for the fourth-order polynomial fit in the determination of reference surfaces throughout the calculation. The calculation procedures are outlined below for convenient reference.

Pulse arrival times were estimated using the reference waveform method.[19] A reference waveform was created for each set of data by averaging those waveforms that met a cross-correlation criterion for similarity. Cross correlation of the reference pulse with all the measured waveforms yielded an arrival time surface that was smoothed to eliminate questionable outlying points. A two-dimensional second-order polynomial fit to the arrival time surface was used to position a window on the original waveforms. A new arrival time surface was then calculated by repeating the arrival time estimation procedure using the windowed data. The effects of geometry were removed by subtracting a best-fit two-dimensional, second-order polynomial from the new arrival time surface to obtain the arrival time fluctuations across the aperture. Energy level variations were calculated by integrating the squared amplitudes of the samples in each windowed waveform, converting the results to decibel units, and subtracting a fitted two-dimensional, second-order polynomial from the result. The arrival time and energy level variations determined for each data set were displayed as two-dimensional grey-scale plots and statistics characterizing their features were calculated. These statistics included the rms value and the 99.5% value, which defines the upper boundary of an interval containing 99.5% of the variation magnitudes. The spatial variability of the maps was described by the effective correlation length defined as the geometric mean of the interval between the half maximum amplitude points of the autocorrelation function in the array and elevation directions. In addition, the waveform similarity factor, which was introduced in Ref. 19 and ranges from a minimum of 0 to an ideal value of 1, was computed for all the windowed waveforms throughout the aperture to provide a measure of the variability in waveform shape.

High-resolution, cross-sectional ultrasonic images of the specimens were also obtained at a sequence of locations both perpendicular to and parallel to the measurement scan direction.

II. RESULTS

Waveforms measured over a $20.16 \times 20.00\text{-mm}^2$ aperture and compensated for geometric path for intercostal space 7L-2 appear in Fig. 2. These waveforms illustrate extreme levels of the distortion encountered when using the full measurement aperture. The main wavefront is highly distorted in panels (b)–(d), and a secondary wavefront approaches from a distance and eventually interferes with the main wavefront in panels (h)–(l). Such effects made the calculation of the arrival time of the main pulse difficult.

Ultrasonic images of specimen cross sections are shown in Fig. 3. The image in (a) shows a region of soft tissue having low attenuation. In (b), the ultrasonic pulse is highly attenuated and shadowing occurs. The b-scan in (c) illustrates imaging through a costal cartilage and demonstrates that intercostal spaces can be as narrow as approx. 1 cm.

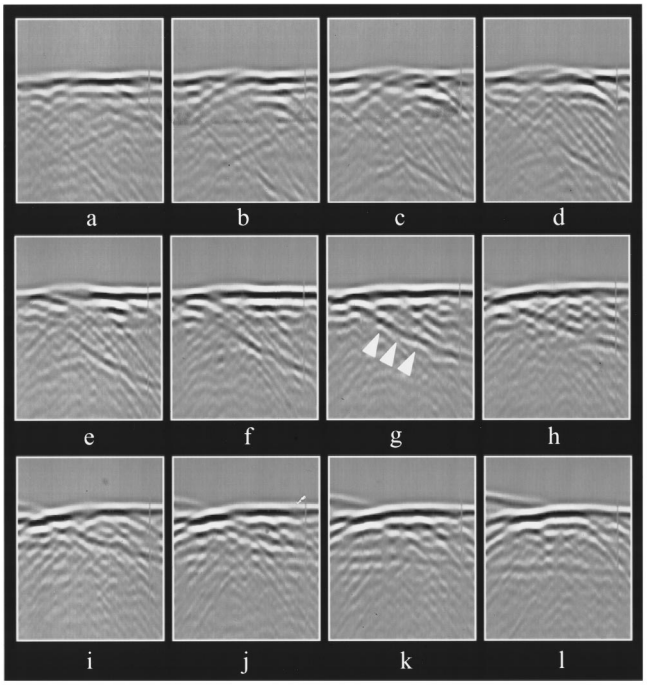

FIG. 2. Intercostal space 7L-2 waveforms compensated for geometric travel time. From left to right and top to bottom, each panel shows waveforms at sequential increments of 0.80 mm in elevation across the central region of the 20.00-mm aperture. At each elevation, the horizontal coordinate is the array direction and spans a distance of 20.16 mm in 0.21-mm increments while the vertical coordinate is time and spans an interval of 6.0 μs in 0.05-μs increments. Signal amplitude is shown linearly on a grey scale with the maximum signal in the two-dimensional aperture represented by white and the corresponding negative value by black. The approaching secondary wavefront is indicated by the arrows in panel g.

Representative $11.60 \times 14.28\text{-mm}^2$ subaperture waveforms compensated for geometric path and temporally windowed are shown in Fig. 4. The waveforms in (a) are for a representative water path while those in (b)–(d) are for three chest wall specimens that, respectively, illustrate low, medium, and high levels of the distortion measured for specimens in this study. The variability evident in the specimen results contrasts with the nearly uniform arrival time, energy level, and shape of the water path pulses.

Arrival time and energy level fluctuations throughout the aperture for two representative water paths and 16 different intercostal spaces of the seven chest wall specimens are arranged as side-by-side pairs of greyscale pictures in Fig. 5. The water path results indicate that system effects were minimal for these measurements. For individual specimen measurements, the energy level fluctuation patterns closely resemble those of the arrival time fluctuations. In addition, the characteristics of the arrival time and energy level fluctuation maps are similar for all the chest wall measurements except those of intercostal space 7L-3 shown in (o).

Statistics that describe the distortion produced by the 16 intercostal spaces are summarized in Table I. In addition to the rms values of the arrival time and energy level fluctua-

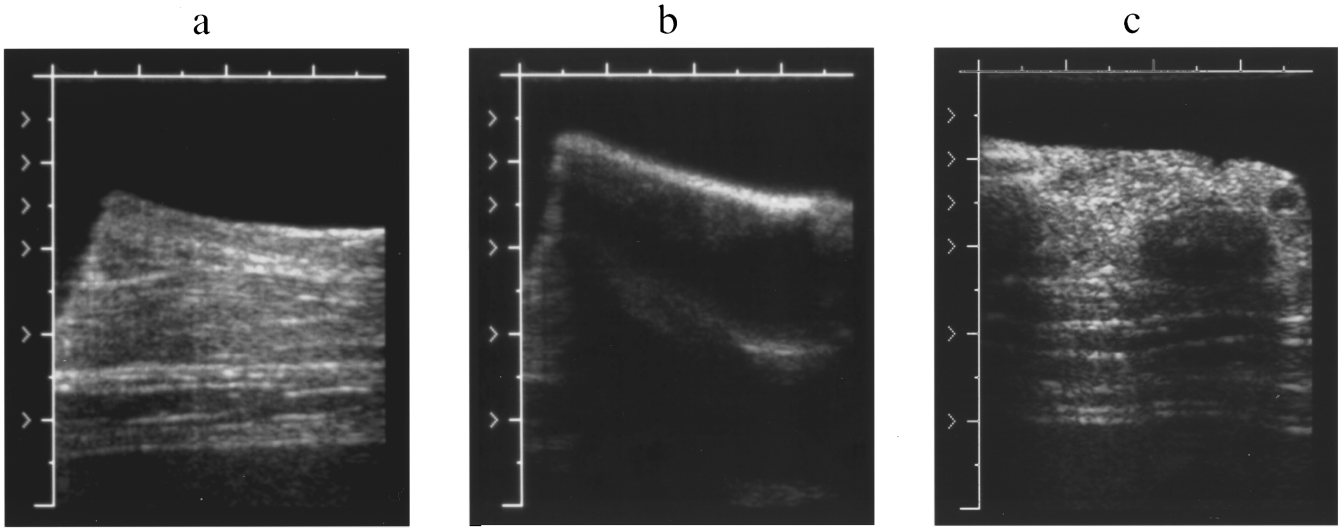

FIG. 3. 7.0-MHz linear array b-scan images of chest wall cross sections. (a) Scan through intercostal space 7L-2 in a region of soft tissue. (b) Scan along a rib or cartilage next to intercostal space 7L-2. (c) Scan perpendicular to costal cartilages of chest wall specimen 8L. In each image, the major divisions marked on the axes are spaced at 1-cm intervals.

tions, correlation lengths calculated for these fluctuations and the waveform similarity factor are given for each of the chest wall measurements. Results for five representative water path measurements are summarized in Table II for comparison.

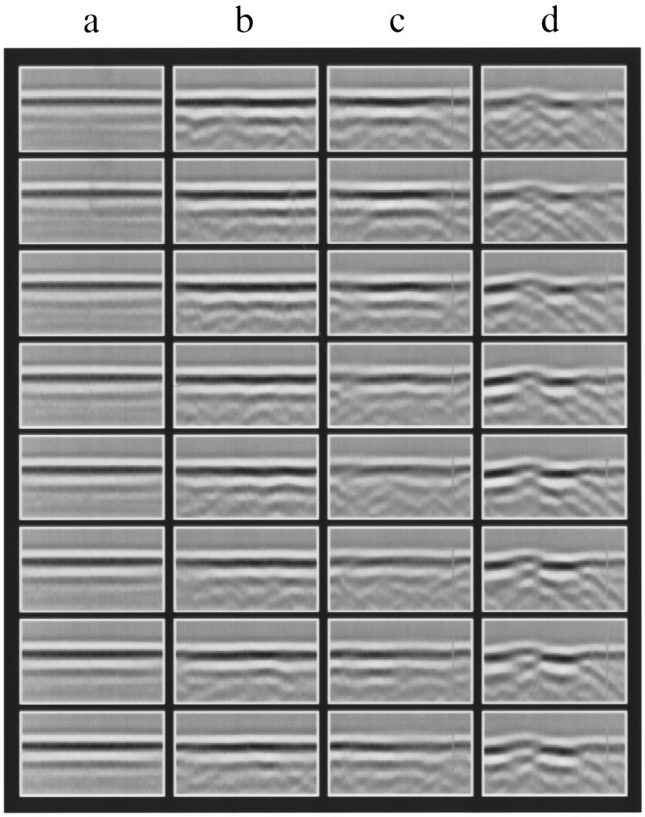

FIG. 4. Representative waveforms compensated for geometric travel time. (a) H_2O-46. (b) 2L-1. (c) 7R-2 (d) 7L-3. Each column of panels shows waveforms at sequential increments of 0.80 mm in elevation across the first half of the 11.60-mm aperture. At each elevation, the horizontal coordinate is the array direction and spans a distance of 14.28 mm in 0.21-mm increments while the vertical coordinate is time and spans an interval of 2.0 μs in 0.05-μs increments. Signal amplitude is shown linearly on a grey scale with the maximum signal in the two-dimensional aperture for each measurement represented by white and the corresponding negative value by black.

The quantitative results verify that system effects in these measurements were small and that the features of the arrival time and energy level fluctuation maps have similar spatial characteristics.

III. DISCUSSION

The parasternal windows are comprised of skin, fat, fascia, and muscle layers through which acoustic waves pass easily. These soft tissues are bordered by the sternum on one side and by the ribs and/or costal cartilages to the top and bottom, as shown in Fig. 1. Most of the measurements reported here were made close to the sternum and were thus bordered by costal cartilages rather than ribs. Costal cartilage begins as a softer and more homogeneous material than bone, but becomes ossified with age. The sternum, ribs, and costal cartilages limit the acoustic window because their sound speeds, impedances, and attenuation levels are much higher than those of the soft tissues, as indicated by the data in Table III.

A good acoustic window between the ribs or costal cartilages is needed to obtain high–quality parasternal echocardiograms in clinical practice.[5] Similarly, a good acoustic window was necessary in this study to obtain transmission data relatively free of secondary wavefronts. Relative to this study, however, the clinician has several advantages in this regard. First, because hand-held probes and real-time imaging systems are used in the clinic, the echocardiographer can make a rapid search over an extended area of the patient's rib cage to locate optimal imaging locations quickly. In the measurement configuration used here, acoustic windows are located by repeatedly repositioning the specimen between the source and receiver and using the amplitude of the received signal at various points in the aperture to assess the suitability of the position for measurements. Next, where the clinician is generally able to select a transducer with a footprint that fits within the available window, a standard aperture size of 20.16×20.00 mm^2 was used in these measurements in order to obtain uniform data sets covering a reasonably large

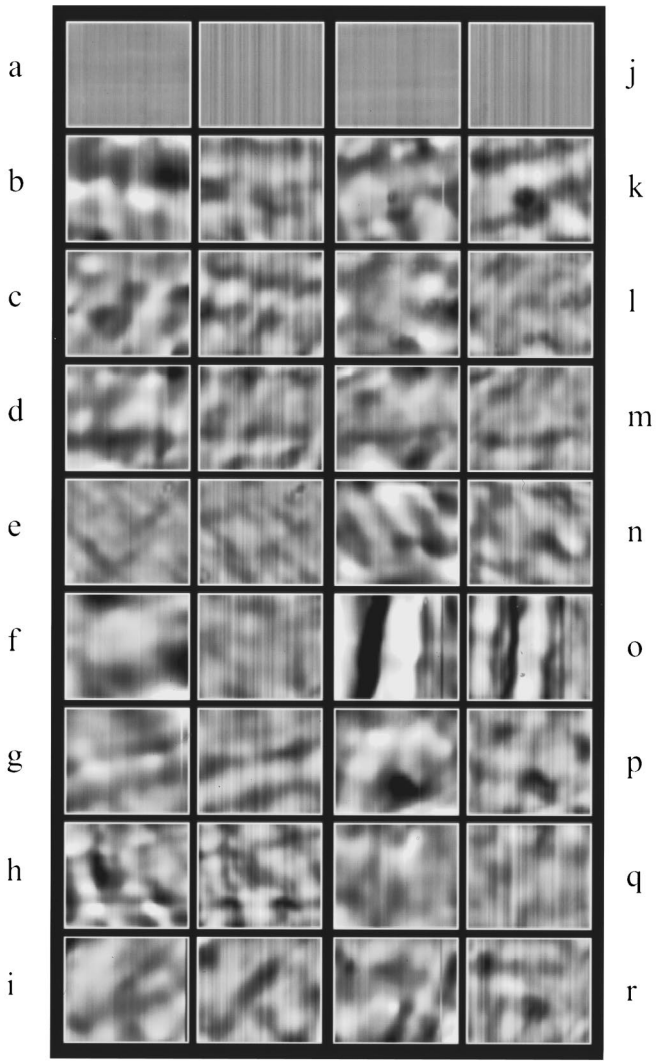

FIG. 5. Arrival time and energy level fluctuations for two water paths and 16 intercostal spaces. (a) H_2O-46. (b) 1L-1. (c) 1R-1. (d) 1R-2. (e) 2L-1. (f) 3L-2. (g) 4L-1. (h) 4R-2. (i) 5L-1, (j) H_2O-59. (k) 5L-2. (l) 6L-1. (m) 6L-2. (n) 7L-1 (o) 7L-3. (p) 7R-1. (q) 7R-2. (r) 7R-3. In the left panel of each pair, arrival time difference is shown on a linear scale with a maximum arrival time fluctuation of +50 ns represented by white and a minimum arrival time fluctuation of −50 ns represented by black. In the right panel of each pair, energy level fluctuations are shown on a logarithmic scale with a maximum positive excursion of +5 dB represented by white and a maximum negative excursion of −5 dB represented by black. In all panels, the horizontal coordinate is the array direction and spans a distance of 14.28 mm in 0.21-mm increments while the vertical coordinate corresponds to position of the array in elevation and spans a distance of 11.60 mm with points interpolated from measurements at 0.40-mm intervals to produce data at 0.20-mm increments.

area. The clinician applies pressure to the probe to push it between the ribs, widening the intercostal space by displacing the flexible rib structures, but in the measurements, some separation between the specimen and the receiving transducer was required in order to prevent movement or deformation of the specimen as the transducer was physically scanned across it to create the two-dimensional receiving aperture. Finally, the intercostal spaces of the chest wall specimens used here were narrower than those of the general population because of the age of the donors and muscle stiffness inherent to *post-mortem* specimens. This resulted in some of the measurement apertures being near or partly over the boney or cartilaginous parts of the rib cage.

The effects of various acoustic paths on the measurements are apparent in the original 20.16×20.00-mm^2 data sets and are illustrated by the wavefronts in Fig. 2 as well as by the b-scans in Fig. 3. For the data in Fig. 2, the measurement aperture was positioned about 2 cm from the sternum with the array approximately parallel to the ribs. However, the last several elevations fell directly over an area of rib cartilage. These elevations have been omitted from Fig. 2.

Representative paths are diagramed in Fig. 6. In some cases, such as path C in Fig. 6, the window is good because relatively homogeneous soft-tissue layers are traversed. Panel (a) in Fig. 2, which corresponds to the position of the b-scan in Fig. 3(a), illustrates this situation. Some regions include greater amounts of muscle and connective tissue that may speed up and refract the main wavefront, as in path B. Secondary wavefronts may be caused by pulses that glance off of or are diffracted by rib or cartilage, as in path D, and arrive in the aperture after the main wavefront. Secondary wavefronts may also come from refraction through cartilage as in path A, but would be attenuated to a lower level. Evidence of such reflected or refracted secondary wavefronts at an angle to the main wavefront can be seen in panels (d)–(l) of Fig. 2. Finally, if the receiver is placed directly over a rib, the wavefront will be highly attenuated, as in panel (b) of Fig. 3.

Isolation of the distortion caused by inhomogeneities in the soft tissues, therefore, required minimizing the effects of the secondary wavefronts in the measured data. Fortunately, because the measurements were made near the center of the intercostal spaces, the secondary wavefronts were generally restricted to the outer portions of the aperture and could be reduced by restricting the size of the region over which the ultrasonic field was analyzed. A standard 11.60×14.28-mm^2 area was selected because this area was sufficiently small to minimize secondary wavefront effects in a substantial number of measurements but large enough to retain relevancy to the clinical situation. Sixteen 11.60×14.28-mm^2 data sets, each from a different intercostal space from among the seven rib cages, were analyzed to determine the distortion produced by soft-tissue inhomogeneities. Data sets with significant secondary wavefronts throughout the aperture, such as that shown in Fig. 2, were not suitable for analysis by the protocol described here and so were not included in the final analysis.

Fitted curves were used in the distortion estimation procedure to remove the effects of measurement geometry and to define reference surfaces for calculation of arrival time and energy level fluctuations. In earlier work with abdominal wall and breast specimens (Refs. 7, 8, and 12), a two-dimensional fourth-order polynomial was used for these purposes. The degree of smoothing caused by this fit can be estimated based on the observation that the fourth-order polynomial has 15 zero crossings over the aperture area of 46.08×92.16 mm^2 used in these measurements, so that the highest spatial frequency removed by this fit is on the order of 0.03 mm^{-1}. Had a fourth-order polynomial been applied over the 11.60×14.28-mm^2 aperture of this study, the high-

TABLE I. Statistics of wavefront distortion produced by 16 different intercostal spaces.

		Arrival time fluctuations			Energy level fluctuations			
Intercostal space	Tissue thickness (mm)	rms value (ns)	99.5% value (ns)	Effective corr. len. (mm)	rms value (dB)	99.5% value (dB)	Effective corr. len. (mm)	Waveform similarity factor
1L-1	22	26.5	88.8	2.74	1.49	3.76	1.89	0.955
1R-1	28	16.0	43.5	1.96	1.64	4.47	1.95	0.968
1R-2	20	21.0	61.0	2.57	1.49	4.22	1.75	0.964
2L-1	23	8.7	25.6	1.90	0.94	2.59	1.68	0.980
3L-2	22	24.3	90.7	3.10	1.00	2.81	1.94	0.978
4L-1	18	15.5	46.7	2.40	1.48	3.91	2.21	0.965
4R-2	22	22.5	74.2	1.84	1.97	5.94	1.73	0.956
5L-1	14	17.0	64.4	2.37	1.71	4.77	1.99	0.970
5L-2	18	18.5	48.2	2.10	2.17	5.92	2.52	0.961
6L-1	15	18.7	60.0	2.23	1.22	3.53	1.68	0.973
6L-2	21	18.4	51.9	2.42	1.22	3.85	1.74	0.966
7L-1	25	23.6	60.6	2.25	1.58	4.26	1.79	0.957
7L-3	19	47.5	119.1	4.33	2.75	7.03	2.90	0.927
7R-1	22	26.7	86.5	3.14	1.72	5.04	1.97	0.968
7R-2	23	20.3	52.5	2.19	1.50	4.56	1.92	0.961
7R-3	20	15.3	47.0	2.46	1.24	3.97	1.97	0.969
mean	20.8	21.3	63.8	2.50	1.57	4.41	1.98	0.964
s.d.	3.5	8.4	23.1	0.62	0.45	1.15	0.33	0.012

est spatial frequency removed would have been about 0.15 mm^{-1}. A two-dimensional second-order polynomial was, therefore, substituted in the processing reported here to bring the resolution of the fit closer to that used in the previous reports. For the current aperture, the six roots of the second-order polynomial correspond to a smaller maximum spatial frequency of about 0.095 mm^{-1}.

The data within the 11.60×14.28-mm^2 regions analyzed for wavefront distortion were of high quality. On average, 95% of the 1972 waveforms in each of these 16 data sets were similar enough to be included in the final reference waveform. The arrival time of each waveform in the aperture was determined from the time position of its maximum correlation with the reference waveform. The value of this cross-correlation maximum averaged 0.938 for all the waveforms in the 16 data sets. Fewer than 1% of the calculated arrival times were discarded because they deviated significantly from the surrounding region of the calculated arrival time surface. These values indicate that the accuracy of the arrival times calculated for the reduced data sets is excellent. However, the degree to which restriction of the analysis window may alter values reported here relative to those encountered in apertures employed for clinical echocardiography requires further investigation.

Despite reduction of the measurement window size, distortion of all types, represented by the different acoustic paths in Fig. 6, was included to some degree in the 16 final data sets. For example, images columns (b) and (c) of Fig. 4 contain mainly paths through soft tissue (Fig. 6, path C) and paths through thicker muscle and connective tissue (Fig. 6, path B), while images in column (d) of Fig. 4 show contributions from other types of acoustic paths. In addition, as shown in Fig. 2, the structures of the chest wall can produce significant secondary scattering that arrives behind the main wavefront. Thus correction of the distortion caused by interaction of the ultrasonic pulses and rib cage structures may be required in addition to reduction of time shifts, amplitude changes, and waveform shape changes caused in the primary wavefront by soft-tissue inhomogeneities if the quality of transthoracic cardiac images is to be improved.

The arrival time and energy level fluctuations obtained for intercostal space 7L-3 in panel (o) of Fig. 5 merit special

TABLE II. Statistics of wavefront distortion measured for five water paths.

	Arrival time fluctuations			Energy level fluctuations			
Run number	rms value (ns)	99.5% value (ns)	Effective corr. len. (mm)	rms value (dB)	99.5% value (dB)	Effective corr. len. (mm)	Waveform similarity factor
36	2.33	6.93	1.56	0.36	0.94	1.46	0.993
37	1.78	5.12	1.68	0.38	0.92	1.51	0.992
46	2.10	6.53	0.99	0.36	0.94	1.44	0.989
51	2.79	7.69	2.01	0.36	0.89	1.68	0.993
59	2.05	6.17	1.19	0.35	0.89	1.45	0.990
mean	2.21	6.49	1.49	0.36	0.92	1.46	0.991
s.d.	0.38	0.95	0.40	0.01	0.03	0.03	0.002

TABLE III. Sound speed, attenuation, and acoustic impedance values for fat, muscle, cartilage, and bone. Speeds and attenuations compiled by Goss, Johnson, and Dunn (Refs. 21 and 22). Acoustic impedance values from Duck (Ref. 23).

Tissue	Sound speed (m/s)	Attenuation at 2.3 MHz (dB/cm)	Acoustic impedance (MRayl)
Fat	1480	1	1.38
Muscle	1550	2	1.63
Cartilage	1650	10	1.82
Bone	>2500	45	>5

comment. This measurement was made in the region of the internal mammary artery, which runs along the side of the sternum. Arterial walls are composed of muscle and connective tissue, and, in these experiments, blood was replaced by water. Since the donor of this specimen was an 85-year-old who died of a stroke, the artery may have been atherosclerotic, i.e., lined with fibrous plaque composed of muscle, collagen, cholesterol, and possibly calcium or other deposits.[24] For these or other reasons, the artery had a higher average speed of sound than either the surrounding tissue or water so that the wavefront was advanced by about 120 ns as it passed this location. This advance is apparent in the received wavefronts shown in Fig. 4(d) and appears as the vertical black stripe in the left panel of Fig. 5(o). The sound speed and density contrasts between the arterial wall and the surrounding tissues also cause scattering, that along with the higher absorption of this tissue, reduce the amplitude of the pulse. The resulting fluctuations in received energy are evident in the right panel of Fig. 5(o) as well as in the waveforms of Fig. 4(d). These fluctuations are consistent with acoustic shadowing artifacts commonly observed in b-scans of calcified plaques.[25] The rms arrival time fluctuation of 47.5 ns and the rms energy level fluctuation of 2.75 dB obtained for this measurement are about twice the average of these values for the other specimens, while the waveform

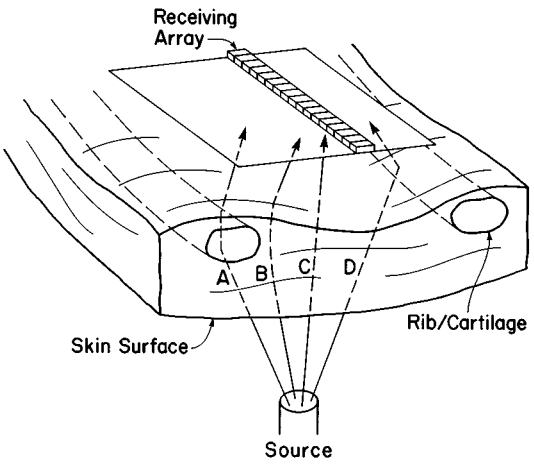

FIG. 6. Measurement configuration and possible acoustic paths. Path A illustrates refraction through cartilage. Signals following path B are refracted and sped up by the muscle and connective tissue at the marginal intercostal region. Path C passes entirely through soft tissue. Path D shows a glancing reflection from a rib or costal cartilage.

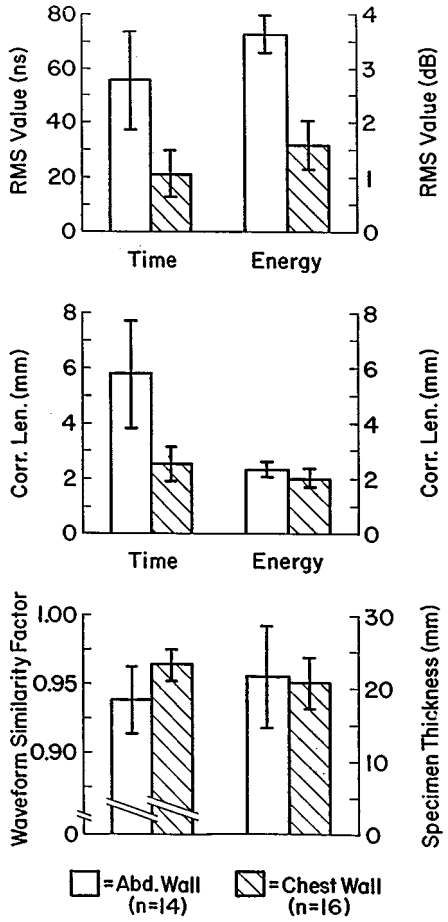

FIG. 7. Comparison of chest wall and abdominal wall wavefront distortion statistics. In each chart, the average and standard deviation of the measurements within each group are shown.

similarity factor is three standard deviations lower than the mean of the other specimens. The arrival time and energy level fluctuation correlation lengths are increased because the artery extends across the entire aperture. Thus, awareness of the location of specific anatomical features may help the echocardiographer minimize the effects of wavefront distortion in clinical images.

A comparison of the numerical results for the chest wall data given in Table I and values calculated from earlier measurements using abdominal wall specimens[8,12] reveals that the distortion produced by the chest wall is appreciably less severe. The bar charts in Fig. 7 show that the average rms arrival time fluctuation of 21.3 ($\pm$8.4) ns obtained for the chest wall specimens is only about one third of the 55.5 ($\pm$18.8) ns measured for the abdominal walls. Likewise, the average rms energy level fluctuation of 1.57 ($\pm$0.45) dB for the chest wall measurements is less than half of the 3.47 ($\pm$0.32) dB determined for the abdominal wall specimens. The average waveform similarity factor is correspondingly higher for the chest wall specimens than for the abdominal wall specimens.

The spatial characteristics of the arrival time and energy level fluctuations produced by the chest wall also differ from those measured for the abdominal wall. The arrival time and energy level fluctuation patterns for individual chest wall

specimens shown in Fig. 5 are more obviously correlated than were the arrival time and energy level fluctuation maps of the abdominal wall specimens in Ref. 8. The correlation lengths of the arrival time and energy level fluctuation maps calculated for the chest wall specimens, at 2.50 ($\pm$0.62) mm and 1.98 ($\pm$0.33) mm, respectively, are also more similar than the corresponding values of 5.78 ($\pm$1.99) mm and 2.31 ($\pm$0.26) mm obtained for the abdominal wall. However, although the average effective arrival time fluctuation correlation length computed for the chest wall is less than half of that obtained for the abdominal wall specimens, the average energy level fluctuation correlation lengths calculated for both the chest and abdominal wall specimens are nearly the same.

The arrival time and energy level fluctuation maps for the chest wall specimens appear to vary less from specimen to specimen than do the abdominal wall distortion maps. For example, the features in the chest wall fluctuation maps are frequently linear; where more than one feature exists, they are often parallel. This increase in similarity is reflected in the much smaller standard deviation in the arrival time fluctuation correlation lengths calculated for the chest wall specimens as compared to the abdominal wall specimens.

The differences between the wavefront distortion measured for the chest and abdominal wall are attributed primarily to differences in the morphology of the two types of specimens as well as to differences in the measurement configurations used. The presence of rib cage structures in the chest wall causes major artifacts, such as secondary wavefronts, not seen in abdominal wall measurements. The similarity of the fluctuation maps obtained for different chest wall specimens suggest that the anatomy of intercostal spaces near the sternum is relatively uniform compared to the structure throughout the upper half of the abdominal wall. Variations in overall thickness of the specimens did not contribute to these differences because the mean thickness of the measurement locations was nearly the same for both types of specimens (20.8$\pm$3.5 mm for the chest wall and 21.6$\pm$6.8 mm for the abdominal wall). However, the 2.3-MHz center-frequency pulses in this study would tend to interact less strongly with small-scale inhomogeneities than would the 3.75-MHz center-frequency pulses used in the abdominal wall study. The significantly reduced aperture size may have limited the correlation length of arrival time and energy level features measured here. In the case of abdominal wall measurements, tests indicate that when data sets are reduced from their original 92.16$\times$46.08-mm^2 size to 11$\times$14 mm^2 and processed by the method employed in this study, the calculated arrival time and energy level fluctuation correlation lengths can decrease to values less than 2 mm. However, since large aperture measurements have not been made for the chest wall, current data cannot be employed to infer that chest wall distortion measurements are similarly affected by aperture size. The 3.5$\times$ decrease in receiver element size in both the array and elevation directions in this study may also have had some bearing on the differences between the two types of data sets. Nevertheless, the major differences between the experimental systems were motivated by the use of receiving transducers appropriate to the two applications. Therefore, the measured differences in distortion between the chest and abdominal walls should be typical of the differences encountered clinically for the two types of ultrasonic imaging.

IV. CONCLUSION

Ultrasonic wavefront distortion produced by transmission through human chest wall specimens has been investigated by recording and analyzing pulse waveforms over a two-dimensional aperture. Secondary wavefronts produced by reflection or refraction at the surface of the bone and cartilage structures of the rib cage were observed in measurements for which the receiving aperture was as wide as or wider than the intercostal space. The degradation of wavefronts due to these effects was much more severe than that typically produced by soft-tissue inhomogeneities.

The effect of the soft-tissue inhomogeneities was investigated by processing waveforms received over a smaller area in which the presence of secondary wavefronts was minimized to obtain maps and statistics of arrival time and energy level fluctuations as well as a measure of the similarity of the waveforms throughout the subaperture. The variations in arrival time, energy level, and waveform shape produced by soft-tissue regions of the chest wall specimens were significantly smaller than the fluctuations measured for abdominal wall specimens in a previous study. The average correlation length of the arrival time fluctuations was less than half of that found for the abdominal wall while the average correlation length of the energy level fluctuations was similar to that for the abdominal wall, so that the average arrival time and energy level fluctuation correlation lengths for chest walls were about the same. The arrival time and energy level fluctuation maps for individual chest wall measurements were consequently more similar in appearance than the corresponding maps for abdominal wall measurements. As a group, the arrival time and energy level fluctuation maps for the 16 different intercostal spaces were also less variable than those of the 14 abdominal wall specimens.

The degree of wavefront distortion produced by propagation through the chest wall is critically dependent on both the size of the transducer aperture and its position. The reduced area measurements indicate that, for regions smaller than the typical cardiac transducer aperture size and away from bone or cartilage structures, distortion is much less than that found for the abdominal wall. However, if the transducer is placed near a rib or cartilage, severe distortion caused by secondary wavefronts can be present.

The results of this study provide new information about the characteristics of ultrasonic wavefront distortion produced by transmission through the chest wall for the development of next-generation cardiac imaging systems.

ACKNOWLEDGMENTS

The authors thank Roger Faison for his assistance in obtaining chest wall specimens from autopsy and Dr. Leon Metlay for inspecting and characterizing the specimens. Dong-Lai Liu is thanked for providing the original version of the wavefront distortion analysis software and improving the

data collection software. Special thanks also go to Michael Orr for assisting with the measurements and data analysis. Useful discussions with T. Douglas Mast are acknowledged with appreciation. We are grateful to James Fearnside, Matthew Mooney, and Donald Orofino in the Advanced Projects Group, Imaging Systems Division, of the Hewlett–Packard Corporation for providing the source transducer, receiving array, preamplifiers, and multiplexor used in the measurement system. Funding for this investigation was provided by the University of Rochester Diagnostic Ultrasound Research Laboratory Industrial Associates, NIH Grant Nos. DK 45533 and HL 50855, and U.S. Army Medical Research & Development Command Grant No. DAMD 17-94-J-4384. Computations were performed at the Cornell National Supercomputing Facility, which is supported, in part, by the National Science Foundation, New York State, and the IBM Corporation.

[1] J. Fearnside, ''Design Considerations for a Transesophageal Probe,'' in *Cardiovascular Imaging by Ultrasound*, edited by P. Hanrath, R. Uebis, and W. Krebs (Kluwer Academic, Boston, 1993).

[2] K.-L. Chan, G. I. Cohen, R. A. Sochowski, and M. G. Baird, ''Complications of Transesophageal Echocardiography in Ambulatory Adult Patients: Analysis of 1500 Consecutive Examinations,'' J. Am. Soc. Echocardiogr. **4**, 577–582 (1991).

[3] W. G. Daniel *et al.*, ''Safety of Transesophageal Echocardiography: A Multicenter Survey of 10,419 Examinations,'' Circulation **83**, 817–821 (1991).

[4] H. Feigenbaum, *Echocardiography* (Lea and Febiger, Philadelphia, 1994), Chap. 2.

[5] A. E. Weyman, *Principles and Practice of Echocardiography* (Lea and Febiger, Philadelphia, 1994).

[6] P. Krämmer and D. Hassler, ''Measurement of Spatial Time-of-Flight Fluctuations of Ultrasound Pulses Passing through Inhomogeneous Layers,'' Proc. IEEE 1987 Ultrason. Symp. **2**, 939–942 (1987).

[7] Y. Sumino and R. C. Waag, ''Measurements of Ultrasonic Pulse Arrival Time Differences Produced by Abdominal Wall Specimens,'' J. Acoust. Soc. Am. **90**, 2924–2930 (1991).

[8] L. M. Hinkelman, D.-L. Liu, L. A. Metlay, and R. C. Waag, ''Measurements of Ultrasonic Pulse Arrival Time and Energy Level Variations Produced by Propagation through Abdominal Wall,'' J. Acoust. Soc. Am. **95**, 530–541 (1994).

[9] G. E. Trahey, P. D. Freiburger, L. F. Nock, and D. C. Sullivan, ''*In Vivo* Measurements of Ultrasonic Beam Distortion in the Breast,'' Ultrason. Imag. **13**, 71–90 (1991).

[10] P. D. Freiburger, D. C. Sullivan, B. H. LeBlane, S. W. Smith, and G. E. Trahey, ''Two Dimensional Ultrasonic Beam Distortion in the Breast: *In Vivo* Measurements and Effects,'' Ultrason. Imag. **14**, 398–414(1992).

[11] Q. Zhu and B. D. Steinberg, ''Large-Transducer Measurements of Wavefront Distortion in the Female Breast,'' Ultrason. Imag. **14**, 276–299 (1992).

[12] L. M. Hinkelman, D.-L. Liu, R. C. Waag, Q. Zhu, and B. D. Steinberg, ''Measurement and Correction of Ultrasonic Pulse Distortion Produced by the Human Breast,'' J. Acoust. Soc. Am. **97**, 1958–1969 (1995).

[13] S. W. Flax and M. O'Donnell, ''Phase-Aberration Correction Using Signals from Point Reflectors and Diffuse Scatterers: Basic Principles,'' IEEE Trans. Ultrason. Ferroelectr. Freq. Control **35**, 758–767 (1988).

[14] M. O'Donnell and S. W. Flax, ''Phase-Aberration Correction Using Signals from Point Reflectors and Diffuse Scatterers: Measurements,'' IEEE Trans. Ultrason. Ferroelectr. Freq. Control **35**, 768–774 (1988).

[15] L. Nock, G. E. Trahey, and S. W. Smith, ''Phase Aberration Correction in Medical Ultrasound Using Speckle Brightness as a Quality Factor,'' J. Acoust. Soc. Am. **85**, 1819–1833 (1989).

[16] M. Fink, ''Time Reversal of Ultrasonic Fields—Part I: Basic Principles,'' IEEE Trans. Ultrason. Ferroelectr. Freq. Control **39**, 555–566 (1992).

[17] F. W. Wu, J.-L. Thomas, and M. Fink, ''Time Reversal of Ultrasonic Fields—Part II: Experimental Results,'' IEEE Trans. Ultrason. Ferroelectr. Freq. Control **39**, 567–578 (1992).

[18] D.-L. Liu and R. C. Waag, ''Time-Shift Compensation of Ultrasonic Pulse Focus Degradation Using Least-Mean-Square Error Estimates of Arrival Time,'' J. Acoust. Soc. Am. **95**, 542–555 (1994).

[19] D.-L. Liu and R. C. Waag, ''Correction of Ultrasonic Wavefront Distortion Using Backpropagation and a Reference Waveform Method for Time-Shift Compensation,'' J. Acoust. Soc. Am. **96**, 649–660 (1994).

[20] A. D. Savakur, K. K. Shung, and N. B. Miller, ''Distortions of Ultrasonic Field Introduced by the Rib Cage in Echocardiography,'' J. Clin. Ultrasound **10**, 413–419(1982).

[21] S. A. Goss, R. L. Johnston, and F. Dunn, ''Comprehensive Compilation of Empirical Ultrasonic Properties of Mammalian Tissues,'' J. Acoust. Soc. Am. **64**, 423–457 (1978).

[22] S. A. Goss, R. L. Johnston, and F. Dunn, ''Compilation of Empirical Ultrasonic Properties of Mammalian Tissues II,'' J. Acoust. Soc. Am. **68**, 93–108 (1980).

[23] F. A. Duck, *Physical Properties of Tissue* (Academic, New York, 1990).

[24] R. Ross, ''The Pathogenesis of Atherosclerosis—An Update,'' New Eng. J. Med. **314**, 488–500 (1986).

[25] A. J. Gerlock, Jr., V. L. Giyanani, and C. Krebs, *Applications of Noninvasive Vascular Techniques* (Saunders, Philadelphia, 1988), pp. 64–65.

LETTERS TO THE EDITOR

Comments on "Elastic wave radiation and diffraction of a piston source" [J. Acoust. Soc. Am. 87, 1894 (1990)]

Enyu Wang[a] and Gonghuan Du
Institute of Acoustics, Nanjing University, Nanjing 210093, People's Republic of China

(Received 14 August 1996; accepted for publication 28 August 1996)

It is noted that the second item in Eq. (12) [J. Acoust. Soc. Am. **87**, 1894 (1990)] could not be ignored at low frequencies. Meanwhile, a precise solution for Eq. (1) without overflow problems is proposed at high frequencies. © *1997 Acoustical Society of America.* [S0001-4966(97)01603-2]

PACS numbers: 43.20.Fn, 43.20.Rz [ANN]

LIST OF SYMBOLS

a	source radius
σ	source stress
α	compressional velocity
$k_\alpha=\omega/\alpha$	
$\nu=\sqrt{k^2-k_\alpha^2}$	
$F(k)=(2k^2-k_\beta^2)^2-4\nu\nu' k^2$	
μ	Lamé constant
ω	angular frequency
β	shear velocity
$k_\beta=\omega/\beta$	
$\nu'=\sqrt{k^2-k_\beta^2}$	

X. M. Tang *et al.* (1990) formulated the diffraction effects in radiated fields for both shear and compressional circular piston sources and calculated their average fields incident on a receiver that is coaxially aligned with the source. Their study is quite useful in application of piston source, particularly in solids. For a receiver transducer with the same radius as that of the compressional source, the average field is given by

$$\langle u_1\rangle=0, \quad \langle u_2\rangle=0, \tag{1}$$

$$\langle u_3\rangle=-\frac{a\sigma_{33}(\omega)}{\mu}\int_0^\infty \frac{2k^2-k_\beta^2}{F(k)}\,\nu e^{-\nu z}\,\frac{[J_1(ka)]^2}{ka}\,dk + \frac{a\sigma_{33}(\omega)}{\mu}\int_0^\infty \frac{2k^2}{F(k)}\,\nu e^{-\nu' z}\,\frac{[J_1(ka)]^2}{ka}\,dk.$$

Here u_1, u_2, u_3 are the displacements along the x, y, z directions, respectively.

To circumvent singularities along the integral path, Tang *et al.* substituted the integral variable k with $\overline{\gamma}=\sqrt{k^2-k_\gamma^2}z-ik_\gamma z$ to yield

$$\langle u_3\rangle=I\times a\sigma_{33}(\omega)/\mu, \quad I=I_\alpha+I_\beta,$$

where

$$I_\gamma=e^{-k_\gamma z}\,\frac{z}{a}\int_0^\infty \overline{f_\gamma}(\overline{\gamma}) \times\frac{\{J_1[(a/z)\sqrt{\overline{\gamma}^2+2i\overline{\gamma k}_\gamma z}]\}^2}{\overline{\gamma}^2+2i\overline{\gamma k}_\gamma z}\,e^{-\overline{\gamma}}d\overline{\gamma}, \quad \gamma=\alpha,\beta. \tag{2}$$

The first term in Eq. (1) represents the compressional signal, while the second term represents the shear signal. Both items were evaluated in Tang's paper. Here, we have two comments on their evaluation.

First, Tang *et al.* indicated in their paper that the first item is of limited value at zero frequency, while the second is singular, then with increasing frequency, the second decays rapidly. Therefore, they judged that the second term, a so-called ''time integral,'' can be ignored because the amplitude of the time integral is very small.

Through careful research, we find that it is not reasonable to ignore the second item when it constitutes a large part

[a]Current address: Institute of Ocean Sciences, Sidney, BC V8L 4B2, Canada.

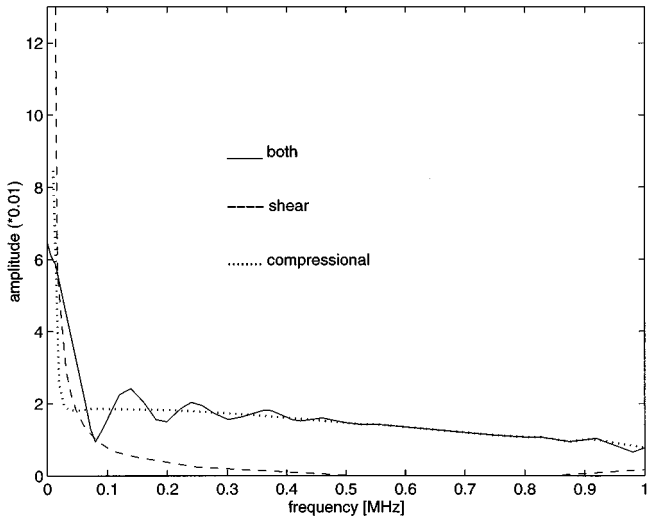

FIG. 1. Numerical evaluation of Eq. (2) for $a=10$ mm, $z=50$ mm, $\alpha=3.5$ km/s, $\beta=2.2$ km/s. The dotted, dashed, solid curves correspond to the first item, the second item, and both items, respectively.

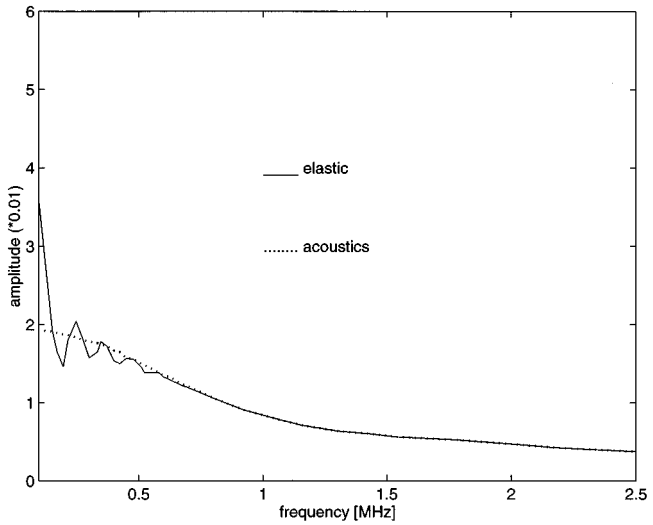

FIG. 2. Evaluation of Eq. (4) using the same parameters as those in Fig. 1. The solid and dotted curves correspond to the elastic and acoustic waves. The acoustic curve is multiplied by a factor of β^2/α^2. The beginning frequency is 0.1 MHz.

of Eq. (1) at low frequencies. Using the same Gauss–Laguerre algorithm as in Tang's paper, we get different results from theirs. Not only the shear but also the compressional signals are singular at zero frequency. However, these two items in Eq. (2) add up to a limited value at that frequency (Fig. 1). Hence, the second item could only be ignored at high frequencies, but at low frequencies, we should consider the contributions of both items.

In addition, Eq. (1) can be simplified to a closed form as follows for $\omega=0$:

$$I=a\int_0^\infty \frac{kz(\beta^2-\alpha^2)-\alpha^2}{2(\beta^2-\alpha^2)}\,e^{-kz}\,\frac{[J_1(ka)]^2}{(ka)^2}\,dk$$

$$=\frac{a}{8z}\sum_{m=0}^{\infty}\left(2m-\frac{\beta^2-2\alpha^2}{\beta^2-\alpha^2}\right)$$

$$\times\frac{\Gamma(2m+1)\Gamma(2m+3)}{m!\Gamma^2(m+2)\Gamma^2(m+3)}\left(-\frac{a^2}{4z^2}\right)^m,\quad z\neq 0. \tag{3}$$

Our evaluation of Eq. (2) is equal to the result of Eq. (3) at zero frequency. This special case has proved our calculation to be correct.

Second, overflow problems occur for Eq. (2) at very high frequencies. To solve the problem, Tang *et al.* first used Bass's numerical solution for the acoustic case. Then, through describing I_γ with Bass's acoustic solution by means of asymptotic method, they did an approximate calculation for the elastic case.

We find that, by substituting the integral variable k in Eq. (1) with $\zeta=\sqrt{k^2+k_\gamma^2}$ and changing Eq. (1) into

$$\langle u_3\rangle = I\times a\sigma_{33}(\omega)/\mu,\quad I=I_\alpha+I_\beta,$$

where

$$I_\gamma=\int_0^{ik_\gamma} f_\gamma(\zeta)e^{-\zeta z}\,\frac{[J_1(a\sqrt{\zeta^2+k_\gamma^2})]^2}{a^2(\zeta^2+k_\gamma^2)}\,d\zeta$$

$$+\int_0^\infty f_\gamma(\zeta)e^{-\zeta z}\,\frac{[J_1(a\sqrt{\zeta^2+k_\gamma^2})]^2}{a^2(\zeta^2+k_\gamma^2)}\,d\zeta,\quad \gamma=\alpha,\ \beta, \tag{4}$$

overflow problems can be avoided at high frequencies and a precise solution is obtained (Fig. 2). However, singularities at zero frequency can not be circumvented for Eq. (4).

Therefore, Eq. (4) makes it possible to avoid the trouble in matching the results of the numerical and asymptotic methods at certain frequencies (indicated by arrows in Fig. 3 in Tang *et al.*'s paper). Especially for the acoustic case, as there is no singularity at low frequencies, a precise solution for Eq. (4) can be obtained from zero frequency to very high frequency.

Gradshteyn, I. S., and Ryzhik, I. M. (**1980**). *Table of Integrals, Series, and Products* (Academic, New York), 4th ed., pp. 715, 1042.

Tang, X. M., Toksoz, M. N., and Cheng, C. H. (**1990**). ''Elastic wave radiation and diffraction of a piston source,'' J. Acoust. Soc. Am. **87**, 1894–1902.

Response to "Comments on 'Elastic wave radiation and diffraction of a piston source'" [J. Acoust. Soc. Am. 101, 2374 (1997)]

X. M. Tang
Western Atlas Logging Services, 10201 Westheimer, Houston, Texas 77251-1407

M. N. Toksoz and C. H. Cheng
Earth Resources Laboratory, Department of Earth, Atmospheric, and Planetary Sciences, Massachusetts Institute of Technology, Cambridge, Massachusetts 02139

(Received 28 August 1996; accepted for publication 28 August 1996)

The authors respond to the comments of Wang and Du. [S0001-4966(97)01703-7]

PACS numbers: 43.20.Fn, 43.20.Rz [ANN]

We thank Enyu Wang and Gonghuan Du of the Institute of Acoustics, Nanjing University, China, for their interest in our study on the elastic wave diffraction of a piston source (see Tang *et al.*[1]), and for pointing out an error in our calculation of the diffraction effect in the zero frequency limit. This error was due to a negligence of the zero-frequency singularity in the compressional-wave term [see Eq. (1) of Wang and Du]. The diffraction effect was calculated at discrete frequencies and the low-frequency values were incorrectly extrapolated to zero frequency when making the plots. Their comments not only preserve the integrity of the theory, but also point to the strong coupling between compressional and shear waves in the near field of a piston source.

We agree with Wang and Du that the compressional term must be singular at zero frequency. This singularity cancels that of the shear term in Eq. (1), because the total wavefield remains finite at zero frequency, as shown by Fig. 1 and Eq. (3) of Wang and Du. However, the series summation in their Eq. (3) is not valid in the limit as $z \to 0$. This summation converges for $z \geqslant (a/2)$, which applies to the value of z used in Fig. 1. This condition should be mentioned.

We also agree that the shear term in Eq. (1) cannot be ignored in the near field or at low frequencies. In fact, combining both compressional and shear terms in the near field of a piston source can make useful applications of the elastic wave diffraction theory in the near-source region. For example, by setting $z=0$ in Eq. (1), the following expression can be obtained

$$\langle u_3(\omega)\rangle = -\frac{a\sigma_{33}(\omega)}{\mu} \times \int_0^\infty \frac{k_\beta^2\sqrt{k^2-k_\alpha^2}}{(k^2-k_\beta^2)^2-4k^2\sqrt{k^2-k_\alpha^2}\,\sqrt{k^2-k_\beta^2}} \times \frac{[J_1(ka)]^2}{ka}\,dk.$$

This expression was applied by Tang[2] to evaluate the dynamic surface flow impedance of a porous medium as a function of frequency. Furthermore, by setting $\omega=0$ in the above expression, one gets

$$\langle u_3\rangle = -\frac{4a\sigma_{33}(1-\nu)}{3\pi\mu},$$

where ν is Poisson's ratio of an elastic half-space. This gives the average displacement at the contact between the half space and a circular disk of radius a on which a static pressure σ_{33} is acting. This result can also be derived from the theory of elasticity.[3] However, this result cannot be derived from Eq. (1) if the shear term is not included.

There exist different methods for evaluating the near-field diffraction effect. Our original method was to formulate the wavefield in the form of Eq. (2) of Wang and Du. The limitation of this formulation is that the Bessel function will overflow when the complex argument becomes large in the far field. The formulation proposed by Wang and Du [see their Eq. (4)] overcomes this problem. However, the integrand of the first integral in their Eq. (4) becomes rapidly oscillatory in the far field. Special care must be taken to ensure proper evaluation of this integral. Here, the use of asymptotic solutions becomes advantageous. Formulating the wavefield in either Eq. (2) or (4) has the advantage that it facilitates the comparison between acoustic and elastic diffraction theories, so that Bass'[4] asymptotic solution for the acoustic case can be readily applied to evaluate elastic wave diffraction in the far field.

In the far field of a piston source, as is the case for many practical applications, the second term of Eq. (1) can indeed be ignored. Even in the transition region between near and far field, this term may be ignored as long as the compressional and shear waves separate from each other and one is dealing with the compressional wave only. In this case the curve corresponding to the compressional wave (dotted curve in Fig. 1) should be used, instead of the solid curve (Figs. 1 and 2) which corresponds to the diffraction effect of the total wavefield. Using the results from our previous study, Tang *et al.*[5] showed that in the far field the radiated elastic wavefield separates into individual compressional and shear waves and that the in the axial region of a piston source the wavefield represented by the second term of Eq. (1) indeed vanishes.

[1] X. M. Tang, M. N. Toksoz, and C. H. Cheng, ''Elastic wave radiation and diffraction of a piston source,'' J. Acoust. Soc. Am. **87**, 1894–1902 (1990).
[2] X. M. Tang, ''Effects of mudcake on the measurement of fluid flow properties using borehole acoustic waves,'' 64th Annual Meeting, Society of Exploration Geophysicists, Los Angeles, Expanded Abstracts (1994), pp. 78–81.
[3] S. Timoshenko and J. N. Goodier, *Theory of Elasticity* (McGraw-Hill, New York, 1970).
[4] R. Bass, ''Diffraction effects in the ultrasonic field of a piston source,'' J. Acoust. Soc. Am. **30**, 602–605 (1958).
[5] X. M. Tang, Z. Y. Zhu, and M. N. Toksoz, ''Radiation patterns of compressional and shear transducers at the surface of an elastic half-space,'' J. Acoust. Soc. Am. **95**, 71–76 (1994).

Use of a power law relation to describe field measurements of compressional and shear velocity in a sediment

Harumi Endo
Department of Applied Physics, National Defense Academy, Yokosuka, 239 Japan

(Received 1 May 1996; accepted for publication 19 November 1996)

A sediment is assumed as a percolation network described by a ''Swiss cheese'' continuum model. A scaling law for a sediment is applicable to describe field measurements of compressional and shear velocity with porosity. The experimental data obtained by Deep Sea Drilling Project of three sites 288, 289, and 316 on the Ontong–Java Plateau in the western Pacific Ocean is available for calculations. The approximate expression of the variation of sound velocity with porosity (p) obtains when satisfied with the conditions of $p_c > p$, where p_c is the critical porosity. This expression is analogous to that of the frame bulk modulus obtained by Hamilton. © *1997 Acoustical Society of America.* [S0001-4966(97)01604-4]

PACS numbers: 43.20.Jr, 43.30.Ma [MAB]

INTRODUCTION

The study of sound velocity for a sediment is basic underwater acoustics. The sound velocity for a sediment can be calculated from the thermodynamics or elastic theory in a physical model, respectively. The thermodynamic model is based on the additivity laws of compressibility,[1] of the reciprocal of sound velocity[2,3] and the conservation law of internal energy,[4] respectively. On the other hand, the best-known example of an elastic model is the so-called Biot model,[5–9] which is explained with the elasticity of skeltal framework and pore fluid.

The diversity of circumstances of a real sediment makes it difficult to estimate its sound velocity. A sediment consists of a porous cluster of grains whose interconnected pores fill out with seawater. The grains as mixtures of rigid media consist of the biological and terrestrial debris with wide distributions of size. The mechanical and physical properties in porous media such as sintered powders,[10,11] brittle solids,[12] colloid particle aggregators,[13] and aerogels,[14,15] etc. have an influence on the disordered porous structures, where the connectivity of networks for clusters is of importance. The idea of percolation and fractal for the disordered porous structure such as a sediment is available for the investigation of mechanical and physical properties. A study[10,15–18] on percolation and fractal in acoustic processes is one of considerable current interest.

The object of this study is to find a percolational expression to describe field measurements of compressional and shear velocity in a sediment. First we show that the sound velocity is expressible with the porosity according to a power law. Next we derive an approximate expression for velocity variation with porosity.

I. BASIC RELATIONS

Assuming isotropic force constants between the nearest-neighbor sites in a percolating system, the Young's modulus (E) and the density (ρ) are described by the power laws,[19–21] $E \propto (f - f_c)^{\varepsilon}$, and $\rho \propto (f - f_c)^{l}$, where f is the occupied volume fraction of network sites, f_c is the critical volume fraction of network sites, and ε and l are the scaling exponents, respectively. The idea of percolation is applicable to a sediment with a percolated skeleton. A sediment can be treated by a ''Swiss cheese'' continuum model,[22–24] where spherical empty holes are randomly distributed in a uniform elastic medium. In this model the quantity of $(f - f_c)$ is assumed to be directly linked to that of $(p_c - p)$. In this model the expression of the variations of the velocity (v) and density with porosity is as follows:

$$v = v^0 (p_c - p)^{\delta} \tag{1}$$

and

$$\rho = \rho^0 (p_c - p)^{\gamma}, \tag{2}$$

where the superscript 0 indicates a value of the solid where p is zero, and δ and γ are the exponents of sound velocity and density, respectively. While the Young's modulus can be related to the sound velocity and the density, the following relation[14,25] can be derived:

$$E \propto \rho v^2 \propto \rho^{1+2\alpha} \tag{3}$$

and

$$v \propto \rho^{\alpha}, \tag{4}$$

where α is a thermodynamic Grüneisen's constant.[26]

II. CURVE FITTING

Unfortunately the auther is unable to find the data sets of sound velocity, density, and porosity of sediments in field measurements. The data sets used were obtained from Hurley and Mangnani[7] who had tabulated these values for carbonate sediments in the Deep Sea Drilling Project (DSDP) of three sites 288, 289, and 316 on the Ontong–Java Plateau in the western Pacific Ocean.

Let us suppose that the value of p_c is an approximation from the data of field measurements for the DSDP. Nobes[27] had exhibited the plot of sound velocity versus porosity on the basis of the data sets of DSDP. This is illustrated in Fig. 1 of Ref. 27 and describes that the sound velocity decreases with an increase in porosity and eventually approaches unity.

 0001-4966/97/101(4)/2378/3/$10.00

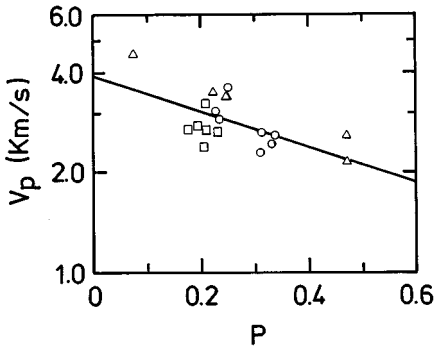

FIG. 1. The plot of v_p vs p for DSDP sites 288 (○), 289 (△), and 316 (□) from Table IV by Hurley and Manghnani.[7] The straight line shows the approximate expression of Eq. (9). The unit of v_p is km/s.

In the theoretical calculation of percolation threshold, Kertesz[28] and Elam *et al.*[29] had obtained the value of $p_c \simeq 0.97$, respectively, from the study of the critical properties of the void percolation problem for spheres while Woignier *et al.*[23] have experimentally found $p_c = 0.99 \pm 0.01$ from the analysis of elastic behavior of silica aerogels of a percolating system. In what follows, we assume that the porosity at a critical porosity should be defined as an approximation $p_c = 1$. By use of Table IV in Ref. 7, the scaling expressions of sound velocity and density become

$$v_p = 3.65(1-p)^{0.802}, \quad \text{s.d.} = 1.44 \times 10^{-1}, \tag{5}$$

$$v_s = 2.53(1-p)^{1.52}, \quad \text{s.d.} = 1.68 \times 10^{-1}, \tag{6}$$

and

$$\rho = 2.56(1-p)^{0.469}, \quad \text{s.d.} = 4.21 \times 10^{-2}, \tag{7}$$

where v_p and v_s are compressional and shear velocity, respectively. The units of density and sound velocity are g/cm^3 and km/s, respectively, and sd is the standard deviation.

The proportional constant shows the value at $p = 0$.

Next we obtain an approximate expression to the sound velocity and density. After taking the logarithms of Eq. (1), we will find the approximate expression of sound velocity to porosity,

$$\ln v = C - \delta p, \tag{8}$$

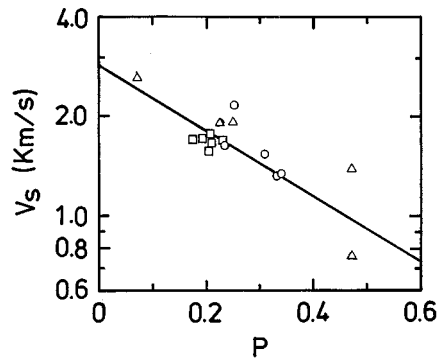

FIG. 2. The plot of v_s vs p for DSDP sites 288 (○), 289 (△), and 316 (□) from Table IV by Hurley and Manghnani.[7] The straight line shows the approximate expression of Eq. (10). The unit of v_s is km/s.

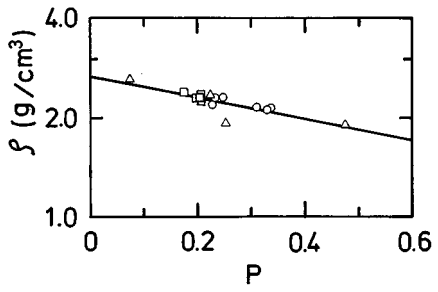

FIG. 3. The plot of ρ vs p for DSDP sites 288 (○), 289 (△), and 316 (□) from Table IV by Hurley and Manghnani.[7] The straight line shows the approximate expression of Eq. (11). The unit ρ is g/cm^3.

because $\ln(p_c - p) \simeq -p$ at $p_c = 1$ and $p_c > p$, and $C = \ln v^0$. With Table IV in Ref. 7, the approximate expressions of sound velocity and density to porosity are given by

$$\log v_p = 0.591 - 0.527p, \quad \text{s.d.} = 1.41 \times 10^{-1}, \tag{9}$$

$$\log v_s = 0.450 - 0.968p, \quad \text{s.d.} = 1.66 \times 10^{-1}, \tag{10}$$

and

$$\log \rho = 0.422 - 0.299p, \quad \text{s.d.} = 4.10 \times 10^{-2}, \tag{11}$$

where $v_p^0 = 3.90$ (km/s), $v_s^0 = 2.82$ (km/s), and $\rho^0 = 2.63$ (g/cm^3). The results show in Figs. 1–3, respectively, where the upper limit of porosity must not exceed $p > 0.5$, because the approximate of $\ln(1-p) \simeq -p$ fails.

The relationship between sound velocity and density can be derived as follows:

$$v_p = 0.772\rho^{1.60}, \quad \text{s.d.} = 8.59 \times 10^{-2}, \tag{12}$$

and

$$v_s = 0.102\rho^{3.37}, \quad \text{s.d.} = 1.69 \times 10^{-1}, \tag{13}$$

where both Tables (site 288) and (site 289) in Ref. 7 are available for the calculation of Eq. (4). The results are shown in Figs. 4 and 5, respectively.

III. CONSIDERATION

Hamilton[30] has found an empirical expression, where the logarithm of a frame bulk modulus is expressible in

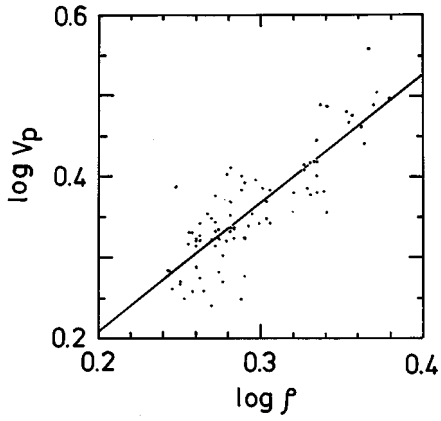

FIG. 4. The plot of log v_p vs log ρ for DSDP sites 288 and 289 from Tables I and II of Hurley and Manghnani.[7] The units of v_p and ρ are km/s and g/cm^3, respectively. The solid line shows Eq. (12).

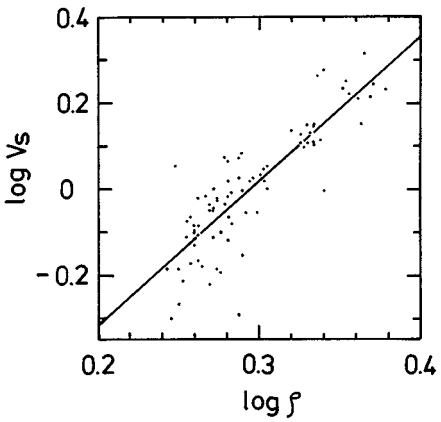

FIG. 5. The plot of log v_s vs log ρ for DSDP sites 288 and 289 from Tables I and II by Hurley and Manghnani.[7] The units of v_s and ρ are km/s and g/cm^3, respectively. The solid line shows Eq. (13).

terms of porosity. His expression is analogous to that of Eq. (8) which is the approximation of a power law. This is one of the strongest pieces of evidence in support of the power law for the frame bulk modulus of a sediment.

We have a relation among the exponents of Eqs. (1), (2), and (4), i.e., $\delta=\gamma\alpha$. The exponent value of δ obtains $\delta_p=0.802$ from Eq. (5) for compressional velocity and $\delta_s=1.52$ from Eq. (6) for shear velocity. By use of the relation of $\delta=\gamma\alpha$, we can derive the values of $\delta_p=0.750$ for compressional velocity and $\delta_s=1.58$ for shear velocity from Eqs. (7), (12), and (13). As can be seen from the fact that the calculated values of δ are in fair agreement with the observed exponent values of Eqs. (5) and (6), respectively, the assumption of $p_c=1$ is found to be reasonable.

Our expression for the field data of sound velocity has several advantages, compared with a thermodynamic or a Biot model. One of the principal advantages is that the resulting expression for the velocity variation as a function of porosity is very simple, although the constitution of a sediment is very complex. Consequently, it is instructive to consider that the derived exponents are available for only the sites 288, 289, and 316 of DSDP, because the sound velocity in field measurements depends on the diversity of circumstance of sediments.

In the studies of elastic properties of percolation systems, noted by de Gennes,[19] the elastic behavior of percolation lattice is an approximation, assuming isotropic force constances. However, the percolation model as an application for a sediment is only an approximation but is nevertheless useful for the description with a great variety of a sediment. Our expression is strictly empirical, but is straightforward and simple to use.

[1] A. B. Wood, *A Textbook of Sound* (MacMillan, New York, 1941).
[2] M. R. J. Wyllie, H. R. Gregory, and L. W. Gardner, ''Elastic waves in heterogeneous and porous media,'' Geophysics **21**, 41–70 (1956).
[3] D. C. Nobes, H. Villinger, E. E. Davis, and L. K. Law, ''Estimation of Marine Sediment Bulk Physical Properties at Depth From Seafloor Geophysical Measurements,'' J. Geophys. Res. **91**, 14 033–14 043 (1986).
[4] J. E. Nafe and C. L. Drake, ''Variation with depth in shallow and deep water marine sediments of porosity density and the velocities of compressional and shear waves,'' Geophysics **22**, 523–547 (1957).
[5] M. A. Biot, ''Theory of propagation of elastic waves in a fluid saturated porous solid. I. Low frequency range,'' J. Acoust. Soc. Am. **28**, 168–178 (1956).
[6] M. A. Biot, ''Theory of propagation of elastic waves in a fluid saturated porous solid. II. High frequency range,'' J. Acoust. Soc. Am. **28**, 178–191 (1956).
[7] M. T. Hurley and M. H. Manghnani, ''Modeling compressional wave velocity and attenuation in carbonate sediments,'' J. Acoust. Soc. Am. **89**, 2689–2695 (1991).
[8] J. G. Berryman, ''Confirmation of Biot's theory,'' Appl. Phys. Lett. **37**, 382–384 (1980).
[9] P. R. Ogushwith, ''Applicability of the Biot theory. I. Low-porosity materials,'' J. Acoust. Soc. Am. **77**, 429–440 (1985).
[10] M. C. Maliepaard, J. H. Page, J. P. Harrison, and R. J. Stubbs, ''Ultrasonic study of the vibrational modes of sintered metal powders,'' Phys. Rev. B **32**, 6261–6271 (1985).
[11] D. Deptuck, J. P. Harrison, and P. Zawadzki, ''Measurement of Elasticity and Conductivity of a Three-Dimensional Percolation System,'' Phys. Rev. Lett. **54**, 913–916 (1985).
[12] P. Ray and B. K. Chakrabarti, ''The critical behaviour of fracture properties of dilute brittle solid near the percolation threshold,'' J. Phys. C **18**, L185–L188 (1985).
[13] D. A. Weitz and M. Oliveria, ''Fractal Structures Formed by Kinetic Aggregation of Aqueous Gold Colloids,'' Phys. Rev. Lett. **52**, 1433–1436 (1984).
[14] E. Courtens and R. Vacher, ''Structure and Dynamics of Fractal Aerogels,'' Z. Phys. B **68**, 355–361 (1987).
[15] J. Gross, J. Fricke, and L. W. Hrubesh, ''Sound propagation in SiO_2 aerogel,'' J. Acoust. Soc. Am. **91**, 2004–2006 (1992).
[16] T. J. Plona, ''Observation of a second bulk compressional wave in a porous medium at ultrasonic frequencies,'' Appl. Phys. Lett. **36**, 259–261 (1980).
[17] M. Bernard and G. A. Williams, ''Surface and Bulk Tortuosity of Porous Ceramics near Percolation Threshold,'' Phys. Rev. Lett. **67**, 2585–2588 (1991).
[18] V. V. Zosimov and L. M. Lyamshev, ''Fractals and Scaling in Acoustics,'' Sov. Phys. Acoust. **40**, 627–653 (1994).
[19] P. G. de Gennes, ''On a relation between percolation theory and the elasticity of gels,'' J. Phys. (France) Lett. **37**, L1–L2 (1976).
[20] S. Feng and P. N. Sen, ''Percolation on Elastic Networks: New Exponent and Threshold,'' Phys. Rev. Lett. **52**, 216–219 (1984).
[21] Y. Kantor and I. Webman, ''Elastic Properties of Random Percolating Systems,'' Phys. Rev. Lett. **52**, 1891–1894 (1984).
[22] B. I. Halperin and S. Feng, ''Differences between Lattice and Continuum Percolation Transport Exponents,'' Phys. Rev. Lett. **54**, 2391–2394 (1985).
[23] T. Woignier, J. Phalippou, R. Sempere, and J. Pelous, ''Analysis of the elastic behaviour of silica aerogels taken as a percolating system,'' J. Phys. (France) **49**, 289–293 (1988).
[24] S. Miyazima, K. Maruyama, and K. Okumura, ''Critical Exponent of Bulk Conductivity in Swiss Cheese Model,'' J. Phys. Soc. Jpn. **60**, 2805–2807 (1991).
[25] J. K. Kjems and D. Posselt, ''Structure, elasticity and thermal properties of silica networks,'' in *Random Fluctuations and Pattern Growth: Experiments and Models*, edited by H. E. Stanley and N. Ostrowsky (Kluwer, Dordrecht, 1988), pp. 7–14.
[26] H. E. Bömmel and K. Dransfeld, ''Excitation and Attenuation of Hypersonic Waves in Quartz,'' Phys. Rev. **117**, 1245–1252 (1960).
[27] D. C. Nobes, ''A test of a simple model of acoustic velocity in marine sediments,'' J. Acoust. Soc. Am. **86**, 290–294 (1989).
[28] J. Kertesz, ''Percolation of holes between overlapping spheres: Monte Carlo calculation of the critical volume fraction,'' J. Phys. (France) Lett. **42**, L393–L395 (1981).
[29] W. T. Elam, A. R. Kerstein, and J. J. Rehr, ''Critical Properties of the Void Percolation Problem for Spheres,'' Phys. Rev. Lett. **52**, 1516–1519 (1984).
[30] E. L. Hamilton, ''Elastic Properties of Marine Sediments,'' J. Geophys. Res. **76**, 579–604 (1971).

Shape of the acoustic slowness surface of anisotropic solids near points of conical degeneracy

A. L. Shuvalov[a] and A. G. Every
Department of Physics, University of the Witwatersrand, P.O. Wits 2050, Johannesburg, South Africa

(Received 31 January 1996; accepted for publication 27 September 1996)

Phase-speed degeneracy results in striking distortions in the shape of the acoustic slowness surface of anisotropic solids. It is shown here that in the general case of conical degeneracy, there can be up to three pairs of lines of zero Gaussian curvature passing between the two adjacent slowness sheets through the point of degeneracy. © *1997 Acoustical Society of America.* [S0001-4966(97)05203-X]

PACS numbers: 43.35.Pt [HEB]

The shape of the slowness (inverse phase velocity) surface plays a crucial role in the interpretation of acoustic-wave phenomena and ballistic-phonon transport in anisotropic solids. Near directions of phase-speed degeneracy (acoustic axes) the slowness surface can display striking distortion, with lines of zero Gaussian curvature (parabolic lines) radiating outwards from the degeneracy point. This has profound consequences for phonon focusing,[1] wave-arrival singularities in dynamical response functions,[2] beam divergence,[3] and many other acoustic phenomena.

Barring accidental coincidences of elastic moduli, the generically possible types of degeneracy between slowness sheets are: conical contact occurring at threefold symmetry axes and in nonsymmetry directions of degeneracy, tangency at fourfold axes and axes of transverse isotropy, and line intersection in transversely isotropic media. Degeneracies pertaining to hexagonal crystals do not have any impact on the curvature of the slowness surface that requires special analytical treatment. The singular curvature patterns of slowness sheets near degeneracy points on threefold and fourfold axes are studied in Ref. 4. The object of the present communication is to analyze the curvature of the degenerate slowness sheets in the vicinity of a conical-type acoustical axis located in an arbitrary nonsymmetry direction.

Consider a crystal of density ρ and elastic modulus tensor c_{ijkl} of unrestricted anisotropy. The phase speeds v_α of the three wave branches $\alpha=1,2,3$, are determined by the secular equation

$$\det(m_i c_{ijkl} m_l - \lambda_\alpha \delta_{jk}) = 0, \tag{1}$$

where the unit vector $\mathbf{m}$ is the wave normal, $\lambda_\alpha=\rho v_\alpha^2$, and δ_{ij} is the Kronecker delta. The cubic equation (1), applied to an arbitrary acoustic axis $\mathbf{m}_0$, splits into a quadratic and a linear equation, yielding simple analytical solutions[5] for the degenerate and nondegenerate eigenvalues $\lambda_{01}=\lambda_{02}\equiv\lambda_{0d}$ and λ_{03}, where $\lambda_{0\alpha}\equiv\lambda_\alpha(\mathbf{m}_0)$.

In order to represent the approximate solution of Eq. (1) near $\mathbf{m}_0$, we introduce the polar angle θ measured from $\mathbf{m}_0$ taken parallel to the axis X_3, and denote the variation of propagation direction $\delta\mathbf{m}$ near $\mathbf{m}_0$ in leading order as $\delta\mathbf{m}\equiv\theta\mathbf{e}$, where $\theta\ll 1$ and

$$\mathbf{e}=\begin{pmatrix}\cos\varphi\\ \sin\varphi\\ 0\end{pmatrix} \tag{2}$$

is the running unit vector specified in the plane orthogonal to $\mathbf{m}_0$ by the azimuthal angle φ measured from the arbitrary chosen axis X_1 (see Fig. 1). Bearing in mind that generic (stable) phase-speed degeneracy at the $\mathbf{m}_0$ under consideration belongs to the conical type, and following the perturbation procedure of Ref. 6, we obtain the expansion of the eigenvalues $\lambda_\alpha(\mathbf{m})$ for the slow and fast ($\alpha=s$ and f) degenerate branches up to terms in θ^2 in the form

$$\lambda_\alpha=\lambda_{0d}+\beta_\alpha\theta+\gamma_\alpha\theta^2, \quad \alpha=s,f, \tag{3}$$

where

$$\beta_\alpha(\varphi)=\mathbf{1}\cdot\mathbf{e}\mp[(\mathbf{p}\cdot\mathbf{e})^2+(\mathbf{q}\cdot\mathbf{e})^2]^{1/2}, \tag{4}$$

$$\gamma_\alpha(\varphi)=\frac{1}{2}\left\{\mathbf{eHe}\mp\frac{(\mathbf{p}\cdot\mathbf{e})(\mathbf{eFe})+(\mathbf{q}\cdot\mathbf{e})(\mathbf{eGe})}{[(\mathbf{p}\cdot\mathbf{e})^2+(\mathbf{q}\cdot\mathbf{e})^2]^{1/2}}\right\}, \tag{5}$$

upper and lower signs corresponding to $\alpha=s$ and f, respectively; and

$$\mathbf{1}=[(A_{01}A_{01})+(A_{02}A_{02})]\mathbf{m}_0,$$

$$\mathbf{p}=[(A_{01}A_{01})-(A_{02}A_{02})]\mathbf{m}_0,$$

$$\mathbf{q}=[(A_{01}A_{02})+(A_{02}A_{01})]\mathbf{m}_0,$$

$$\mathbf{H}=(A_{01}A_{01})+(A_{02}A_{02})-2\lambda_{0d}+\frac{1}{\lambda_{0d}-\lambda_{03}}\times(\mathbf{q}^{(1)}\otimes\mathbf{q}^{(1)}+\mathbf{q}^{(2)}\otimes\mathbf{q}^{(2)}),$$

$$\mathbf{F}=(A_{01}A_{01})-(A_{02}A_{02})+\frac{1}{\lambda_{0d}-\lambda_{03}}\times(\mathbf{q}^{(1)}\otimes\mathbf{q}^{(1)}-\mathbf{q}^{(2)}\otimes\mathbf{q}^{(2)}),$$

[a]Permanent address: Institute of Crystallography, Russian Academy of Sciences, Moscow 117333, Russia.

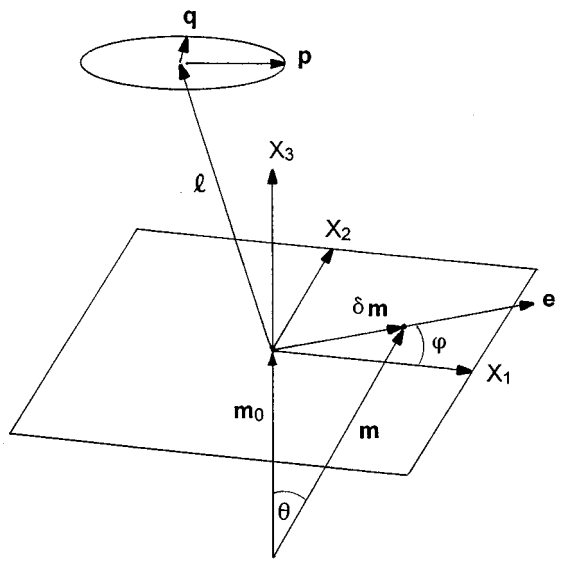

FIG. 1. Geometry of the conical degeneracy.

$$\mathbf{G}=(A_{01}A_{02})+(A_{02}A_{01})+\frac{1}{\lambda_{0d}-\lambda_{03}}\times(\mathbf{q}^{(1)}\otimes\mathbf{q}^{(2)}+\mathbf{q}^{(2)}\otimes\mathbf{q}^{(1)}),$$

$$\mathbf{q}^{(a)}=[(A_{0a}A_{03})+(A_{03}A_{0a})]\mathbf{m}_0,\quad a=1,2. \tag{6}$$

In Eqs. (4), (5), and (6) the dot between vectors and the symbol $\otimes$ imply scalar and dyadic products, respectively; $\mathbf{eHe}=e_iH_{ij}e_j$, $\mathbf{eFe}=e_iF_{ij}e_j$, $\mathbf{eGe}=e_iG_{ij}e_j$; and we use notations $(ab)\equiv a_ic_{ijkl}b_l$ for the matrices obtained by contracting the elastic modulus tensor with mutually orthogonal unit vectors $\mathbf{A}_{01}$, $\mathbf{A}_{02}$, $\mathbf{A}_{03}$, among which $\mathbf{A}_{03}\equiv\mathbf{A}_3(\mathbf{m}_0)$ is the polarization of the nondegenerate mode traveling along $\mathbf{m}_0$ and the orientation of the rectangular frame $\mathbf{A}_{01}$, $\mathbf{A}_{02}$ in the plane orthogonal to $\mathbf{A}_{03}$ is arbitrary. We note that vectors $\mathbf{l},\mathbf{p},\mathbf{q}$ (see Fig. 1) are directly related to the orientation of the cone of internal refraction: $\mathbf{l}$ connects the cone's axis with the center of its elliptical lid, while $\mathbf{p}$ and $\mathbf{q}$, which lie in the (X_1,X_2) plane and are hence orthogonal to $\mathbf{m}_0$, determine the semiaxes of this ellipse.[5]

Principal curvatures $K_1^{(\alpha)},K_2^{(\alpha)}$ of the slowness sheets $S_\alpha\ni\mathbf{s}_\alpha=\mathbf{m}\sqrt{\rho/\lambda_\alpha}$, $\alpha=s,f$, in the infinitesimal neighborhood of their joint conical point $\mathbf{s}_{0d}=\mathbf{m}_0\sqrt{\rho/\lambda_{0d}}$ may be obtained by using standard equations of differential geometry, as described in Ref. 4 for the case of acoustic axes along symmetry directions. Calculation in leading order in $\theta\ll 1$ yields the following expressions:

$$K_1^{(\alpha)}(\varphi)=\frac{1}{\sqrt{\rho\lambda_{0d}[1+(\beta_0^2+\beta_0'^2)/4\lambda_{0d}^2]}(1+\beta_\alpha^2/4\lambda_{0d}^2)}\times\left(\lambda_{0d}-\frac{\beta_\alpha^2}{4\lambda_{0d}}+\gamma_\alpha\right),\quad \alpha=s,f, \tag{7}$$

$$K_2^{(\alpha)}(\theta,\varphi)=\frac{1}{\theta}\frac{(1+\beta_0^2/4\lambda_{0d}^2)}{2\sqrt{\rho\lambda_{0d}}[1+(\beta_\alpha^2+\beta_\alpha'^2)/4\lambda_{0d}^2]^{3/2}}\times(\beta_\alpha+\beta_\alpha''),\quad \alpha=s,f \tag{8}$$

(prime implies derivative with respect to φ). Here the principal curvature $K_1^{(\alpha)}(\varphi)$ at a point $\mathbf{s}_\alpha(\theta,\varphi)_{|\theta\to 0}$ is the curvature of the curve in the cross-sectioning plane containing the normal $\nu_\alpha(\theta,\varphi)$ to the sheet S_α and parallel to the axis $\mathbf{m}_0$, and $K_2^{(\alpha)}(\theta,\varphi)$ is the curvature of the curve in the other (orthogonal) principal cut containing the normal $\nu_\alpha(\theta,\varphi)$ at the given point. In leading order the relation for the normal ν_α does not depend on θ and may be written in the adopted base (see Fig. 1) as

$$\nu_\alpha=\frac{1}{\sqrt{4\lambda_{0d}^2+\beta_\alpha^2+\beta_\alpha'^2}}\begin{pmatrix}-\beta_\alpha'\sin\varphi+\beta_\alpha\cos\varphi\\ \beta_\alpha'\cos\varphi+\beta_\alpha\sin\varphi\\ 2\lambda_{0d}\end{pmatrix}. \tag{9}$$

Note that vectors $\mathbf{m}_0$, ν_α, and $\mathbf{e}$ are not coplanar, which is in contrast to the case of conical degeneracy along a threefold symmetry axis where β_α is constant.

According to (8), the divergence of the principle curvature $K_2^{(\alpha)}$ proportional to θ^{-1} entails an energy flux anticaustic.[7] In view of (4),

$$\beta_\alpha+\beta_\alpha''=\mp\frac{[(\mathbf{p}\cdot\mathbf{e}')(\mathbf{q}\cdot\mathbf{e})-(\mathbf{q}\cdot\mathbf{e}')(\mathbf{p}\cdot\mathbf{e})]^2}{[(\mathbf{p}\cdot\mathbf{e})^2+(\mathbf{q}\cdot\mathbf{e})^2]^{3/2}},\quad \alpha=s,f. \tag{10}$$

Equations (8) and (10) confirm that near an arbitrary conical degeneracy the quantities $K_2^{(\alpha)}(\theta,\varphi)$ depend on φ but remain sign-definite:

$$\operatorname{sgn}K_2^{(s)}\langle 0,\operatorname{sgn}K_2^{(f)}\rangle 0\quad\text{for all }\varphi. \tag{11}$$

Note also that by Eqs. (2), (4), and (10), $\beta_s(\varphi)=-\beta_f(\varphi+\pi)$, $\beta_s'(\varphi)=-\beta_f'(\varphi+\pi)$, and $\beta_s(\varphi)+\beta_s''(\varphi)=-[\beta_f(\varphi+\pi)+\beta_f''(\varphi+\pi)]$, and hence by virtue of Eq. (8)

$$K_2^{(s)}(0,\varphi)=-K_2^{(f)}(\theta,\varphi+\pi). \tag{12}$$

Substitution of Eqs. (4) and (5) into (7) reveals that the sign of the curvature $K_1^{(\alpha)}(\varphi)$ is determined as follows

$$\operatorname{sgn}K_1^{(\alpha)}(\varphi)=\operatorname{sgn}[C(\varphi)\mp D(\varphi)],\quad \alpha=s,f, \tag{13}$$

where

$$C(\varphi)=[(\mathbf{p}\cdot\mathbf{e})^2+(\mathbf{q}\cdot\mathbf{e})^2]^{1/2}[4\lambda_{0d}^2+2\lambda_{0d}\mathbf{eHe}-(\mathbf{l}\cdot\mathbf{e})^2-(\mathbf{p}\cdot\mathbf{e})^2-(\mathbf{q}\cdot\mathbf{e})^2], \tag{14}$$

$$D(\varphi)=2\lambda_{0d}[(\mathbf{p}\cdot\mathbf{e})(\mathbf{eFe})+(\mathbf{q}\cdot\mathbf{e})(\mathbf{eGe})]-2(\mathbf{l}\cdot\mathbf{e})[(\mathbf{p}\cdot\mathbf{e})^2+(\mathbf{q}\cdot\mathbf{e})^2].$$

Evidently the fractional cofactor in the right-hand side of Eq. (7) skips from one branch to the other as $\varphi\to-\varphi$, for which $C(\varphi)=C(\varphi+\pi)$, $D(\varphi)=-D(\varphi+\pi)$, and therefore

$$K_1^{(s)}(\varphi)=K_1^{(f)}(\varphi+\pi). \tag{15}$$

There are various options for the curvatures $K_1^{(s)},K_1^{(f)}$. They may both be positive for all φ, which in view of (11) implies saddle and convex shape of slowness sheets S_s and S_f in the domain surrounding the conical point $\mathbf{s}_{0d}$, or they may both be negative for all φ, which implies concave and saddle shape in the domain surrounding $\mathbf{s}_{0d}$. (Note that the latter option is excluded for the case of conical degeneracy along a

threefold axis.) The third option is that there are parabolic lines, separating segments of negative and positive Gaussian curvature, which radiate outwards from the conical point $\mathbf{s}_{0d}$. The equation $K_1^{(\alpha)}(\varphi)=0$, defining the possible orientations φ of the parabolic lines, may be cast in the form

$$C^2(\varphi)=D^2(\varphi). \tag{16}$$

By appeal to (13) it follows that Eq. (16) represents an algebraic equation of 6th order in $x\equiv\tan\varphi$ with real coefficients. It may have no real solutions, or yield one, two, or three pairs of real roots x_i. Each root x_i, $i=1,...,6$, determines a parabolic line which passes from one degenerate sheet to the other through the point $\mathbf{s}_{0d}$ in accordance with Eq. (15).

Let us specify the form of Eq. (16) for the case of a conical acoustic axis $\mathbf{m}_0$ lying in a symmetry plane m. Taking the X_3 axis along $\mathbf{m}_0$ and measuring the angle φ from the X_1 axis orthogonal to m, we arrive at the equation

$$\begin{aligned}(p^2\tan^2\varphi+q^2)&[(4\lambda_{0d}^2+2\lambda_{0d}H_{22}-l^2-p^2)\tan^2\varphi\\&+4\lambda_{0d}^2+2\lambda_{0d}H_{11}-q^2]^2\\&=4\tan^2\varphi[(lp^2-\lambda_{0d}pF_{22})\tan^2\varphi+lq^2\\&\quad-\lambda_{0d}(pF_{11}+2qG_{12})]^2,\end{aligned} \tag{17}$$

where vectors $\mathbf{l}=(0,l,0)^T$; $\mathbf{p}=(0,p,0)^T$; $\mathbf{q}=(q,0,0)^T$ and components of matrices $\mathbf{H}$, $\mathbf{F}$, $\mathbf{G}$ are determined by Eqs. (6), in which with no loss of generality we assume $\mathbf{A}_{01}\|X_1$. Equation (17) is cubic in $(\tan^2\varphi)$, and so pairs of its solutions conform to the mirror plane symmetry. Clearly, a threefold axis may radiate parabolic lines solely in the form of three pairs.

The analysis presented here yields the following conclusions. A conical point $\mathbf{s}_{0d}$ in the slowness surface which is associated with an acoustic axes of arbitrary nonsymmetrical orientation is either embraced by a ''homogeneous'' curvature domain (saddle or concave for S_s, convex or saddle for S_f), or it emits one, two, or three pairs of parabolic lines which separate alternating segments of different curvature (saddle and concave regions on S_s, convex and saddle regions on S_f) and pass from the one slowness sheet to the other at $\mathbf{s}_{0d}$. The number of parabolic lines stemming from $\mathbf{s}_{0d}$ and their orientation near $\mathbf{s}_{0d}$ may be determined from Eqs. (16) and (17).

These conclusions have a number of observable consequences. Particularly noteworthy is that the collision between phonon focusing caustics and anticaustics, which has been so strikingly demonstrated for symmetry axis conical points by Hurley *et al.*,[8] can also exist in various forms for conical points not located along threefold symmetry axes. There remain a number of challenging problems, such as determining the analytical form of the wave arrival singularity in the elastodynamic Green's function in the neighborhood of a conical point intersected by parabolic lines in the slowness surface.

ACKNOWLEDGMENTS

Financial support for this project has been provided by the South African Foundation for Research Development, the University of the Witwatersrand, and the Russian Foundation for Basic Research.

[1] H. J. Maris, in *Nonequilibrium Phonons in Nonmetallic Crystals*, edited by W. Eisenmenger and A. A. Kaplyanskii (North-Holland, Amsterdam, 1986), p. 51.
[2] A. G. Every and K. Y. Kim, J. Acoust. Soc. Am. **95**, 2505 (1994).
[3] B. P. Newberry and R. B. Thompson, J. Acoust. Soc. Am. **85**, 2290 (1989).
[4] A. L. Shuvalov and A. G. Every, Phys. Rev. B **53**, 14906 (1996).
[5] F. I. Fedorov, *Theory of Elastic Waves in Crystals* (Plenum, New York, 1968).
[6] V. I. Alshits, A. V. Sarychev, and A. L. Shuvalov, Sov. Phys. JETP **62**, 531 (1985).
[7] A. G. Every, Phys. Rev. B **34**, 2852 (1986).
[8] D. C. Hurley, M. T. Ramsbey, and J. P. Wolfe, in *Phonon Scattering in Condensed Matter V*, edited by A. C. Anderson and J. P. Wolfe (Springer-Verlag, Berlin, 1986), p. 299.

An adaptive decentralized multiuser receiver for deep-water acoustic telemetry

Zoran Zvonar
Analog Devices, Communications Division, Wilmington, Massachusetts 01887

David Brady
Department of Electrical and Computer Engineering, Northeastern University, Boston, Massachusetts 02115

Josko Catipovic
Woods Hole Oceanographic Institution, Woods Hole, Massachusetts 02543

(Received 15 July 1995; accepted for publication 1 October 1996)

An acoustic local area network has been deployed for multipoint-to-point telemetry between ocean bottom sensors and a surface receiver in deep-water areas. A major obstacle for coherent communications in this channel is strong multiple-access interference from other acoustic modems, which affects a common narrowband request channel of the network protocol. The network throughput and packet delay depend on the capability of the receiver to resolve collisions between request packets. In this paper a multiuser receiver for joint channel parameter estimation, multiple-access interference suppression and signal detection is proposed. The receiver is fully adaptive, requiring no side information about the channel conditions or the signal parameters of the interfering users in the network. Receiver performance is demonstrated through experiments in a deep-water acoustic channel. © *1997 Acoustical Society of America.* [S0001-4966(97)02704-5]

PACS numbers: 43.60.Dh, 43.60.Lq, 43.30.Pc [JLK]

INTRODUCTION

Recent advances in underwater acoustic telemetry[1] permit long-term, real-time data acquisition in deep-water areas, allowing adaptive sampling and interactive experiment control. An Acoustic Local Area Network (ALAN), presently deployed in the Monterey Canyon, has the operational range of 5–10 km from the central controller, which is located at a surface buoy and communicates with ocean bottom nodes.[2,3] Telemetry is supported from various data acquisition instruments, as depicted in Fig. 1, such as low-rate thermistors or current meters to high data rate sources such as imaging systems or ocean-bottom seismometers. The ALAN protocol selection was influenced by characteristics of underwater acoustic communication channel, such as a long (compared to the packet length) propagation delay and relatively infrequent access to the central controller. The finite-energy constraints for battery-powered transmitters require efficient protocol with minimal packet retransmissions.[2]

Although some obstacles to coherent communications in a deep-water channel are phase fluctuations, Doppler effects and possible multipath due to surface reflections or reflection from topographic sources (hills, cliffs, hollows, etc.), experimental work has demonstrated that strong multiple-access interference from other acoustic modems is the dominant interference source in the network scenario.[3] This is especially detrimental to the ALAN protocol which uses a narrowband request channel to initiate the packet-forwarding process. Since all request packets overlap in time and frequency, network performance depends on the receiver capability to resolve collisions between packets from several asynchronous acoustic modems. Bandwidth constraints in the ALAN request channel preclude the use of standard multiple-access techniques. To achieve a sufficiently high data rate on the request channel, ALAN employs bandwidth-efficient signature waveforms, which yield substantial multiple-access interference. The most difficult scenario arises when the interfering signal is much stronger than the desired one, and is referred to as the near-far problem.

This paper focuses on an adaptive decentralized minimum mean squared error (MMSE) receiver which jointly estimates the desired signal parameters (bit-timing, carrier phase), suppresses multiple-access interference, performs equalization in the presence of eventual intersymbol interference (ISI) and recombines multipath arrivals resulting in an implicit diversity improvement. Previous theoretical work on MMSE multiuser receivers[4–6] is extended to a realistic underwater communication scenario by incorporating estimation and tracking of the desired signal parameters in the presence of interference and by validating the proposed algorithm on experimental data. The proposed adaptive receiver achieves the performance of the centralized multiuser detector[3] and preserves the near-far resistance, while requiring only the knowledge of a unique training sequence for the user of interest.

I. SYSTEM MODEL

Assuming the same carrier frequency for all active users in the system, the transmitted signal of the kth user is represented in complex baseband form as

$$u_k(t)=\sum_i b_k(i)s_k(t-iT), \tag{1}$$

where $\{b_k(i)\}$ is the sequence of independent M-ary data symbols, $s_k(t)$ is the unique signature waveform of user k,

 0001-4966/97/101(4)/2384/4/$10.00

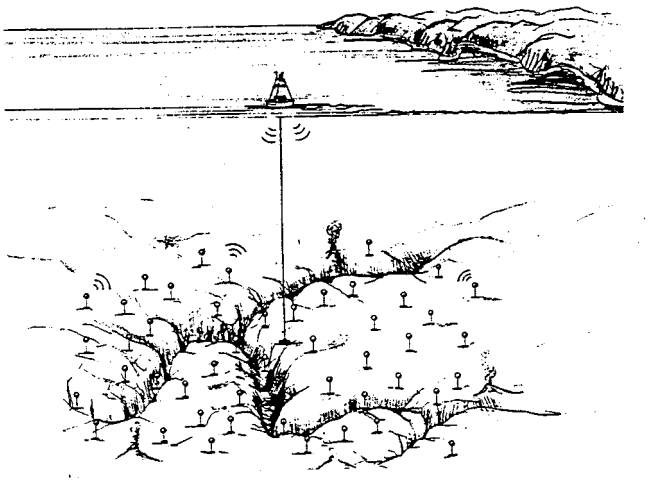

FIG. 1. Deep-water ALAN in Monterey Canyon.

and T is the common symbol duration. The transmitted signal of each user in the network consists of a packet header followed by a silence period and a data block. The packet header consists of frequency tones of predetermined duration, whose frequencies are selected outside the data band. It is used for packet source identification and coarse time synchronization (obtained by cross-correlation with packet header).

A multiuser receiver observes the superposition of distorted signals from all the users corrupted by the additive noise. After downconversion and lowpass filtering the received signal is represented by

$$r(t)=\sum_i \sum_{k=1}^{K} b_k(i)h_k(t-iT-\tau_k,t)e^{j\theta_k(t)}+n(t), \qquad (2)$$

where $h_k(\tau,t)$ is the overall channel response, representing the convolution of the signature waveform, the physical channel impulse response and the receiving filter impulse response. τ_k and $\theta_k(t)$ denote the delay and the carrier phase for user k, and $n(t)$ is additive noise. The carrier phase $\theta_k(t)$ models both constant phase offset and Doppler frequency shift.

An adaptive linear multiuser receiver consists of a fractionally spaced transversal filter with tap spacing T_s, followed by the phase recovery circuit as depicted in Fig. 2. In contrast to the classical approach in spread spectrum systems, there is no explicit matched filtering to the signature sequence, and the signal is sampled directly at time intervals $T_s \leq 1/(2*BW)$, where BW is the highest bandwidth of the baseband signature waveforms employed in the system. The fractionally spaced transversal filter performs several functions: adaptive matched filtering, multiple-access interference suppression, linear equalization of ISI and timing error compensation (effectively eliminating the need for a symbol timing loop[7]).

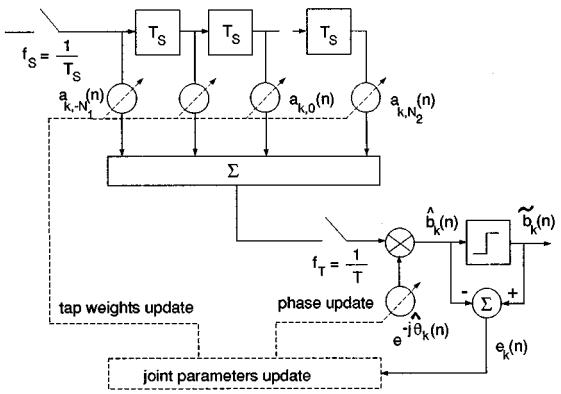

FIG. 2. Adaptive multiuser receiver for deep-water acoustic telemetry.

In the presence of large Doppler shifts associated with telemetry platforms, the adaptive receiver may suffer from tap rotation.[7] To alleviate this problem, carrier phase recovery is performed jointly with the adaptation of the filter taps. Carrier recovery is achieved via a second order decision-directed stochastic gradient algorithm.[1] The transversal filter and the carrier phase updates are performed once per symbol interval. The adaptive algorithm for joint estimation of the filter taps and carrier phase is presented in the following section.

II. ADAPTIVE MULTIUSER RECEIVER

Assuming the constant channel impulse response and constant carrier phase within the coherence time of the channel, the optimal values of equalization and synchronization parameters for the receiver in Fig. 2 are derived using the mean-squared error (MSE) optimization criterion.

The tap weight vector for the kth user is defined as $\mathbf{a}_k=[a_{k,-N_1}\cdots a_{k,N_2}]^T$, with $a_{k,0}$ being the central reference tap. The transversal filter spans both precursors and postcursors. The input signal, sampled at the rate $f_s=1/T_s$, is stored in the delay-line and represented at time instant nT by a vector

$$\mathbf{r}(n)=[r(nT+N_1T_s)\cdots r(nT-N_2T_s)]^T. \qquad (3)$$

The estimate of the data symbol at time instant nT is formed at the phase-corrected output of transversal filter

$$\hat{b}_k(n)=\mathbf{a}_k^H\mathbf{r}(n)e^{-j\hat{\theta}_k}, \qquad (4)$$

where H denotes the conjugate transpose and $\hat{\theta}_k$ is the phase estimate for the user k. From the symbol estimate the binary decision $\tilde{b}_k(n)$ is obtained as the closest signal point and the complex valued decision error is defined as $e_k(n)=\tilde{b}_k(n)-\hat{b}_k(n)$. We concentrate on the direct adaptation of the transversal filter coefficients driven by the output error, using either known data in the training period or decisions in the decision-directed mode.

The receiver parameters are optimized based on joint minimization of the MSE

$$\mathrm{MSE}=E\{|\mathbf{e}_k(n)|^2\}=E\{|b_k(n)-\mathbf{a}_k^H\mathbf{r}(n)e^{-j\hat{\theta}_k}|^2\} \qquad (5)$$

with respect to the filter tap weights $\mathbf{a}_k$ and the carrier phase $\hat{\theta}_k$, resulting in a coupled system of equations. The optimal values of the filter coefficients are obtained as the solution of the finite-order Wiener-filtering problem

$$\mathbf{a}_k=\mathbf{R}_{\mathbf{u}_k\mathbf{u}_k}^{-1}\mathbf{R}_{\mathbf{u}_k b_k}, \qquad (6)$$

where $\mathbf{u}_k(n)=\mathbf{r}(n)e^{-j\hat{\theta}_k}$ and cross-correlations are defined as $\mathbf{R}_{xy}=E\{\mathbf{x}(n)\mathbf{y}^H(n)\}$. The optimal value of the phase estimate satisfies the equation

$$\frac{\partial \mathrm{MSE}}{\partial \hat{\theta}_k}=-2\,\mathrm{Im}\{\mathbf{a}_k^H\mathbf{r}(n)e^{-j\hat{\theta}_k}e_k^*(n)\}=0. \tag{7}$$

While MSE optimization provides optimal parameters within the coherence time of the channel, practical receiver parameters should be evaluated recursively in order to track the time variations of the underwater channel. Previous work has established that the simplest form of an adaptive algorithm which uses the combination of a least mean squares (LMS) algorithm for the equalizer coefficients update, and the first order digital phase locked loop (DPLL) exhibits poor phase-tracking capabilities in time-varying ocean channels.[1] Alternatively, a second order DPLL is introduced into the process of joint synchronization and equalization. Using the analogy between the phase detector output of a classical DPLL and the instantaneous estimate of the MSE gradient with respect to $\hat{\theta}_k$,

$$\Phi_k(n)=\mathrm{Im}\{\hat{b}_k(n)e_k^*(n)\} \tag{8}$$

is defined as the equivalent output of the phase detector. The second order phase update equation is given by

$$\hat{\theta}_k(n+1)=\hat{\theta}_k(n)+A_k\Phi_k(n)+B_k\sum_{m=0}^{n-1}\Phi_k(m), \tag{9}$$

where A_k and B_k are proportional and integral tracking constants, respectively.

The transversal filter taps are updated using the recursive least-squares (RLS) algorithm due to its superior convergence properties compared to the LMS algorithm and insensitivity to the eigenvalue spread of the correlation matrix. The solution for the tap weight vector is given by

$$\mathbf{a}_k(n)=\hat{\mathbf{R}}^{-1}_{\mathbf{u}_k\mathbf{u}_k}(n)\hat{\mathbf{R}}_{\mathbf{u}_k b_k}(n), \tag{10}$$

where $\mathbf{u}_k(n)=\mathbf{r}(n)e^{-j\hat{\theta}_k(n)}$, estimated cross-correlation matrices are

$$\hat{\mathbf{R}}_{\mathbf{xy}}(n)=\sum_{m=0}^{\infty}\lambda^n\mathbf{x}(n-m)\mathbf{y}'(n-m), \tag{11}$$

and λ is a forgetting factor which accounts for the exponential windowing of the past data. The adaptive solution provides the multiple-access interference suppression capability to the receiver by finding the component of the desired signal vector that is orthogonal to the interference vectors.

III. EXPERIMENTAL RESULTS

In this section the performance of the proposed adaptive multiuser receiver is demonstrated on experimental data collected by the Woods Hole Oceanographic Institution south of Martha's Vineyard. In the experiment, two acoustic modems transmitted data packets of 700 bits using BPSK modulation at a data rate of 1 kbit/sec with spreading factor of 3 at a 15 KHz carrier frequency. The modems were deployed at a depth of 2500 m. Both the transmitters and the ship-based receiver were omnidirectional. The difference in received power between the packets was on the order of 10 dB. It should be noted that spread spectrum reception using matched filter would provide unacceptable performance for the weak signal in this case due to extremely small processing gain.

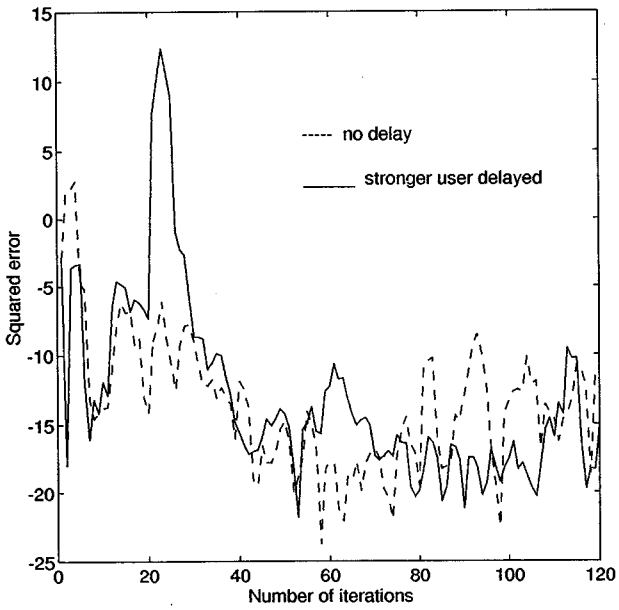

FIG. 3. Convergence characteristics of adaptive multiuser receiver in deep-water 2500 m experiment. Receiver parameters: transversal filter with 12 taps, training length 36 symbols, $\lambda=0.99$, $A_1=0.08$, $B_1=A_1/10$.

Fractionally spaced transversal filter is designed to span two data symbols in order to cover the overlapping interfering symbols in asynchronous case and to compensate for moderate ISI. The squared error of the weaker user is presented in Fig. 3 for two scenarios: 1) collision occurs at the beginning of the training block and 2) collision occurs later during adaptation. Training length was equal to $3N_f$, where N_f is the number of filter taps. Although in the second case we observe a sharp increase of the squared error due to the presence of 10 dB stronger interference, readaptation was fast and receiver performance was not affected, i.e., there were no demodulation errors in the data block of the weaker user.

In Fig. 4 we present the results obtained using a $T/6$ fractionally spaced linear receiver with 12 taps, for the case when the collision of two packets occurred at the very beginning of the transmission. The total averaged squared error of two users indicates convergence within the training period of 36 bits as shown in Fig. 4(a). The phase estimates indicate Doppler shifts due to relative motion between transmitter and receiver. The estimated Doppler shifts for the deep-water channel range from 1.5–7 Hz depending on the receiver depth and experiment realization. No errors were detected in the data block despite the presence of a strong interfering signal. The same conclusions were obtained for other data sets, corresponding to various transmitter depths and different near-far scenarios.

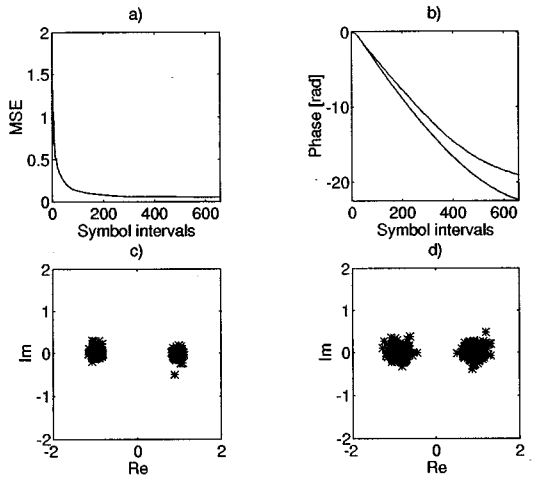

FIG. 4. Experimental results for linear adaptive receiver with 12 taps for transmitter depth of 2500 m: (a) total averaged squared error, (b) frequency estimates, (c) output scatter plot of user 1, (d) output scatter plot of user 2.

IV. CONCLUDING REMARKS

Fully adaptive multiuser receiver has been presented for the deep-water ALAN applications. Previous theoretical work has been extended by incorporating channel estimation, frequency and bit timing tracking to insure reliable underwater modem operation. This allows the network modem to operate in realistic channel conditions with large multiple-access interference, significant Doppler shift, channel time-variations and possible multipath propagation. Rapid convergence of the algorithm and low complexity allow simple real-time implementation on the programmable DSP platforms. The efficiency of the algorithm has been demonstrated on the experimental data. Adaptive multiuser receiver benefits communication scenarios where minimal knowledge is provided on the receiver side (training sequence of the desired user) and increase the network throughput by resolving the collisions between the transmitted packets. These features could significantly benefit future ALAN deployments.

ACKNOWLEDGMENTS

The ALAN project is supported by the National Science Foundation, Oceanographic Technology Division, Grant No. OCE-92-01191. The authors would like to thank Steve Merriam and Lee Freitag of the Woods Hole Oceanographic Institution for the data acquisition.

[1] M. Stojanovic, J. Catipovic, and J. Proakis, ''Adaptive multichannel combining and equalization for underwater acoustic communications,'' J. Acoust. Soc. Am. **94**, 1621–1631 (1993).
[2] J. Catipovic, D. Brady, and S. Etchemendy, ''Development of Underwater Acoustic Modems and Networks,'' Oceanography **3**, 112–119 (1993).
[3] D. Brady and J. Catipovic, ''Adaptive Multiuser Detection for Underwater Acoustical Channels,'' IEEE J. Ocean. Eng. **19**, 158–165 (1994).
[4] S. Miller, ''An Adaptive Direct-Sequence Code-Division Multiple-Access Receiver for Multiuser Interference Rejection,'' IEEE Trans. Commun. **43**, 1764–1765 (1995).
[5] U. Madhow and M. Honig, ''MMSE Interference Suppression for Direct-Sequence Spread Spectrum CDMA,'' IEEE Trans. Commun. **42**, 3178–3188 (1994).
[6] P. Rapajic and B. Vucetic, ''Adaptive Receiver Structures for Asynchronous CDMA System,'' IEEE J. Sel. Areas Commun. **12**, 685–697 (1994).
[7] R. Gitlin, J. Hayes, and S. Weinstein, *Data Communications Principles* (Plenum, New York, 1992).

Relating change in signal-to-noise ratio to array gain for microphone arrays used in rooms

James M. Kates[a)]
Center for Research in Speech and Hearing Sciences, City University of New York, Graduate Center, Room 901, 33 West 42nd Street, New York, New York 10036

(Received 25 June 1996; accepted for publication 21 October 1996)

Microphone arrays have proven effective in improving speech intelligibility in noise for the hearing impaired. Two different acoustic performance metrics have been proposed for evaluating the performance of microphone arrays in reverberant rooms. The signal-to-noise ratio (SNR) metric uses the improvement in SNR at the microphone output relative to the microphone input, and includes the reverberant speech as part of the desired speech signal. The array-gain metric, on the other hand, ignores the reverberant speech and measures the degree to which the noise in the room has been suppressed. An approximate relationship between these two metrics is derived so that results using one metric can be compared to results using the other even when the signal and noise correlation matrices are not available. © *1997 Acoustical Society of America.* [S0001-4966(97)04803-0]

PACS numbers: 43.66.Ts, 43.60.Gk, 43.38.Hz [JWH]

INTRODUCTION

Multimicrophone arrays are among the few techniques that have been shown to improve speech intelligibility in noise for the hearing impaired. The data of Soede *et al.* (1993a,b) demonstrated a significant benefit in speech intelligibility for hearing-impaired subjects using a five-microphone array in a diffuse noise field, and recent experiments (Kates *et al.*, 1996; Saunders and Kates, 1996) have demonstrated significant benefits for hearing-impaired listeners using microphone arrays in reverberant rooms.

Acoustic performance metrics have also been introduced (Greenberg and Zurek, 1992; Greenberg *et al.*, 1993; Stadler and Rabinowitz, 1993; Hoffman *et al.*, 1994; Kates and Weiss, 1996) for calculating the anticipated improvement in speech intelligibility resulting from arrays used in rooms. The intelligibility-weighted signal-to-noise ratio (SNR) metric (Greenberg and Zurek, 1992; Greenberg *et al.*, 1993) uses the improvement in SNR at the microphone output relative to the microphone input and includes the reverberant speech as part of the desired speech signal. The articulation-index (AI)-weighted array-gain metric (Stadler and Rabinowitz, 1993; Kates and Weiss, 1996), on the other hand, ignores the reverberant speech and measures the degree to which the noise in the room has been suppressed. Both metrics are based on the steady-state array input and output power, and therefore ignore the temporal structure of the room reflections and the effects that the reflection timing, amplitude, and direction of arrival could have on speech intelligibility.

Comparing results calculated with the two different performance metrics can be difficult because of the difference in the treatment of the reverberant speech. In an anechoic environment the two metrics are identical since there is no reverberant field and hence no reverberant speech power. The array directivity attenuates the noise while leaving the speech from the specified look direction unaffected. In a room, however, the metrics will differ, and this difference increases as the reverberant speech power increases relative to the direct speech power at the array input. The array directivity leaves the direct speech from the source unaffected at the array output, but reduces the amplitude of both the noise and the reverberant speech passed by the array. Thus the greatest difference between the two performance metrics occurs at low direct-to-reverberant speech ratios, a condition under which adaptive array processing has shown little improvement in SNR (Hoffman *et al.*, 1994) but where large values of array gain have been reported (Kates and Weiss, 1996). An approximate relationship between the two performance metrics is derived so that results using one metric can be compared to results using the other even when the signal and noise correlation matrices are not available.

I. ACOUSTIC PERFORMANCE METRICS

Two acoustic performance metrics have been proposed for arrays being used for hearing aids. One metric is the AI-weighted array gain (Stadler and Rabinowitz, 1993; Kates and Weiss, 1996). The AI-weighted array gain is calculated from the array gain computed at each frequency of the Fourier-transformed data, and the array gains are combined using weights for each frequency band derived from the articulation index importance function given by Kryter (1962). The array gain (Cox *et al.*, 1987) for the kth fast Fourier transform (FET) bin is given by

$$G(k)=\frac{|\mathbf{w}^*(k)\mathbf{d}(k)|^2}{\mathbf{w}^*(k)\mathbf{Q}(k)\mathbf{w}(k)}, \tag{1}$$

where $\mathbf{d}(k)$ is the steering vector, $\mathbf{w}(k)$ the array weight vector, and $\mathbf{Q}(k)$ is the noise-alone correlation matrix normalized so that $\mathrm{Tr}[\mathbf{Q}(k)]=M$, the number of microphones in the array. The array gain depends on the array weights and on the spatial distribution of the noise, but is independent of the actual signal and noise powers. An array consisting of a single omnidirectional microphone has an array gain of 1. Since both the speech and noise are measured in a reverber-

[a)]New affiliation: Audiologic, 6655 Lookout Rd., Suite 200, Boulder, CO 80301, E-mail: jim@audiologic.com

ant room, this metric gives the ratio of the power in the direct portion of the speech signal to the total direct-plus-reverberant noise power at the array output, normalized by the SNR at the array input. This measure thus represents the directional gain of the array in the noise field found in the room.

The AI-weighted array gain is then given by

$$G_{\mathrm{AI}}=\sum_{k=0}^{K} a(k)[10\log_{10} G(k)] \ \mathrm{dB}, \tag{2}$$

where the set of weights $\{a(k)\}$ is the AI importance function weights given by Kryter (1962) reinterpolated for the FFT band edges. Spread of masking effects are ignored in this metric. The AI-weighted array gain G_{AI} is expressed in dB regarding the array gain for a single omnidirectional microphone.

The array gain given in Eq. (1) differs from the ratio of intelligibility-weighted array output SNR to input SNR that has also been proposed as the basis of the performance metric (Greenberg *et al.*, 1993). The array output SNR is the ratio of the total speech power to the total noise power at the output of the array. The speech and noise powers both include the reverberated as well as the direct components. The change in SNR due to the array is given by

$$\Delta\mathrm{SNR}(k)=\frac{\mathbf{w}^*(k)\mathbf{P}(k)\mathbf{w}(k)}{\mathbf{w}^*(k)\mathbf{Q}(k)\mathbf{w}(k)}, \tag{3}$$

where $\mathbf{P}(k)$ is the speech-alone correlation matrix normalized so that $\mathrm{Tr}[\mathbf{P}(k)]=M$, and $\mathbf{Q}(k)$ is the normalized noise-alone correlation matrix. The two metrics given by Eqs. (1) and (3) thus have the same denominators, and differ only in the numerators. The processing benefit using the ΔSNR metric would then be calculated as the ratio of the array output SNR to the array input SNR as given by Eq. (3), converted to dB and summed over frequency using the AI weights. Greenberg *et al.* (1993) use the notation G_I to represent this AI-weighted sum.

In much of the literature on arrays, the array gain and the ratio of array output to input SNR are used interchangeably (Monzingo and Miller, 1980). An anechoic environment is assumed for most radar and sonar problems, and under anechoic conditions the only signal power is that coming directly from the source. Since there is no reverberation, the numerator of Eq. (3) reduces to that of Eq. (1) and the metrics become identical. The distinction between the metrics in estimating array performance is due to the signal reverberation present in the room.

II. RELATING ΔSNR TO ARRAY GAIN

The speech power at the input to the array can be expressed as $S=D+R$, where D is the speech power arriving directly from the sound source and R is the power in the reverberant speech field. The noise field power is N, so the SNR at the array input is given by

$$\mathrm{SNR}_{\mathrm{IN}}=\frac{D+R}{N}. \tag{4}$$

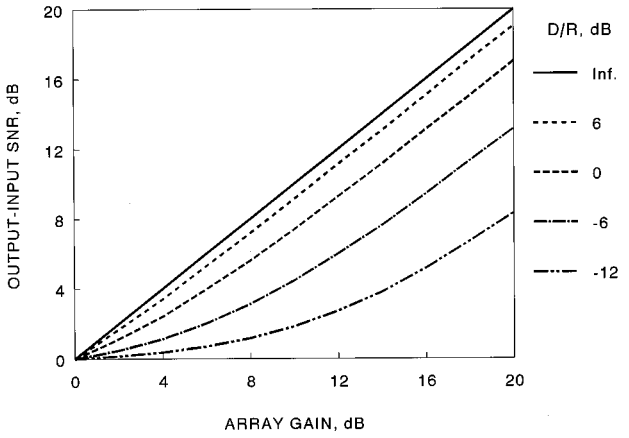

FIG. 1. SNR improvement for a microphone array as a function of the array gain. The curve parameter D/R is the direct-to-reverberant ratio for the speech measured at the array location.

The array gain is G, so the SNR at the array output including the reverberant speech is given by

$$\mathrm{SNR}_{\mathrm{OUT}}=\frac{D+(R/G)}{(N/G)}, \tag{5}$$

assuming that the array gain has attenuated the reverberant speech field by the same amount as the noise field. Another way of stating this assumption is that the reverberant speech is assumed to have the same spatial distribution as the noise at the array location. This assumption will be valid if the power in the reverberant noise field is greater than the direct noise power at the array location, and if the set of reflections for the speech and noise are similar at the array location. If there are a small number of noise sources very close to the array, resulting in the direct noise power from a limited set of directions dominating the reverberated noise power, then Eq. (5) may not be accurate.

The change in SNR due to the array is then

$$\Delta\mathrm{SNR}=\frac{G(D/R)+1}{(D/R)+1}, \tag{6}$$

where D/R is the ratio of the direct to reverberant speech at the input to the array. Equation (6) thus relates the change in SNR given by Eq. (3) to the array gain given by Eq. (1). The range of ΔSNR given by Eq. (6) is thus $1\leqslant\Delta\mathrm{SNR}\leqslant G$ as D/R goes from 0 to ∞. For the more typical case of $D/R=1$, the result is $\Delta\mathrm{SNR}=(G+1)/2$.

Conversely, given ΔSNR, the equivalent array gain can be computed as

$$G=\frac{[\Delta\mathrm{SNR}(D/R+1)]-1}{(D/R)}. \tag{7}$$

The range of G given by Eq. (7) is thus $\Delta\mathrm{SNR}\leqslant G\leqslant\infty$ as D/R goes from ∞ to 0. For the case of $D/R=1$, the result is $G=2(\Delta\mathrm{SNR})-1$.

The relationship between ΔSNR and the array gain is plotted in Fig. 1 with the speech direct/reverberant ratio D/R as the parameter. In an anechoic environment D/R approaches infinity, and the two metrics are identical. For a D/R of 6 dB, which represents a room with very little rever-

TABLE I. ΔSNR from the Table III data of Hoffman *et al.* (1994) converted to equivalent AI-weighted array gain using Eq. (7). The test condition is the five-microphone array using 16-tap adaptive filters at the output of each microphone ($m=5$, $l=16$), in simulated conference room environments.

D/R, dB	ΔSNR, dB	Equivalent array gain, dB
−3.97	3.40	7.1
−8.43	2.83	9.2

beration or a speech source close to the array, the two metrics are still quite similar. Reducing D/R to 0 dB, which places the speech source-to-array separation at the critical distance for the room, results in an asymptotic reduction of 3 dB in ΔSNR as the array gain increases. Increasing the separation between the speech source and the array to greater than the critical distance results in large reductions in ΔSNR relative to the array gain.

The results plotted in Fig. 1 indicate that the ΔSNR performance metric will deviate substantially from the array gain when the reverberant speech power exceeds the direct speech power. For normal conversations, with the two parties relatively close together, the two metrics will give similar results since it is assumed that $(D/R)>0$ dB. When the speech source is far from the array, resulting in $(D/R)<0$ dB, ΔSNR can be much lower than the array gain. The two performance metrics will therefore differ substantially for typical conference room or lecture hall conditions, and the ΔSNR metric will predict much less array benefit than will the array gain. The difference in performance predictions at low values of D/R applies to any form of array processing, including delay-and-sum beamforming and superdirective array processing as well as adaptive systems.

This difference in metrics, rather than any inherent difference in the adaptive array processing algorithms, may explain the poorer performance results reported by Hoffman *et al.* (1994) using the ΔSNR metric in comparison with Kates and Weiss (1996) using the array gain metric for $D/R<0$ dB. Table I presents two entries from Table III of Hoffman *et al.* (1994) for a five-microphone adaptive array using 16-tap adaptive filters at the output of each microphone. The data are for a simulated conference room environment. Converting the intelligibility-weighted ΔSNR values given by Hoffman *et al.* (1994) into the equivalent AI-weighted array gain using Eq. (7) results in an array gain of 9.2 dB for $D/R=-8.4$ dB, which is consistent with the 9–11 dB found by Kates and Weiss (1996) for a five-microphone adaptive array using 16-tap filters at D/R values of −6 to −10 dB.

III. CONCLUSIONS

The results presented herein allow a direct transformation between array results using the array gain and ΔSNR performance metrics even when the signal and noise correlation matrices are not available. The relationship has the greatest validity at low values of the speech direct-to-reverberant ratio and when the noise sources are far from the array in a reverberant room. These, however, are the conditions under which the performance metrics show the greatest disparity and a transformation is most needed. If AI-weighted values are being transformed, the most accurate relationship requires performing the transformation at each frequency separately and then summing across frequency using the intelligibility weights. If D/R is independent of frequency, the AI-weighted values can be transformed directly. A comparison of two sets of adaptive array data, superficially different and from two separate published studies, showed that the results are actually quite similar when the same performance metric is used for both experiments.

The relationship between ΔSNR and array gain does not address the issue of which metric is more accurate in predicting improvements in speech intelligibility when an array is used in a room. An improved performance metric, taking into account how reverberation affects speech intelligibility, is needed. In a related experiment involving hearing-impaired subjects listening through a microphone array, Saunders and Kates (1996) found that a weighted average of the ΔSNR and array gain metrics, modified to include a simplified model of upward spread of masking, was much more accurate than either metric alone in predicting the improvement in speech intelligibility in rooms.

ACKNOWLEDGMENTS

The work presented in this paper was supported by research Grant No. 5 R01 DC01915-03 from the National Institute on Deafness and Other Communication Disorders, National Institutes of Health.

Cox, H., Zeskind, R. M., and Owen, M. M. (**1987**). ''Robust adaptive beamforming,'' IEEE Trans. Acoust. Speech Signal Process. **ASSP-35,** 1365–1376.

Greenberg, J. E., and Zurek, P. M. (**1992**). ''Evaluation of an adaptive beamforming method for hearing aids,'' J. Acoust. Soc. Am. **91,** 1662–1676.

Greenberg, J. E., Peterson, P. M., and Zurek, P. M. (**1993**). ''Intelligibility-weighted measures of speech-to-interference ratio and speech system performance,'' J. Acoust. Soc. Am. **94,** 3009–3010.

Hoffman, M. W., Trine, T. D., Buckley, K. M., and van Tasell, D. J. (**1994**). ''Robust adaptive microphone array processing for hearing aids: Realistic speech enhancement,'' J. Acoust. Soc. Am. **96,** 759–770.

Kates, J. M., and Weiss, M. R. (**1996**). ''A comparison of hearing-aid array-processing techniques,'' J. Acoust. Soc. Am. **99,** 3138–3148.

Kates, J. M., Saunders, G. H., and Weiss, M. R. (**1996**). ''An evaulation of hearing-aid array processing techniques,'' Issues in Advanced Hearing Aid Research Conference, Lake Arrowhead, CA, May (unpublished).

Kryter, K. D. (**1962**). ''Methods for calculation and use of the Articulation Index,'' J. Acoust. Soc. Am. **34,** 1689–1697.

Monzingo, R. A., and Miller, T. W. (**1980**). *Introduction to Adaptive Arrays* (Wiley, New York), pp. 78–105.

Saunders, G. H., and Kates, J. M. (**1996**). ''Speech intelligiblity enhancement using hearing-aid array processing'' (unpublished).

Soede, W., Berkhout, A. J., and Bilsen, F. A. (**1993a**). ''Development of a directional hearing instrumenet based on array technology,'' J. Acoust. Soc. Am. **94,** 785–798.

Soede, W., Bilsen, F. A., and Berkhout, A. J. (**1993b**). ''Assessment of a directional microphone array for hearing-imparied listeners,'' J. Acoust. Soc. Am. **94,** 799–808.

Stadler, R. W., and Rabinowitz, W. M. (**1993**). ''On the potential of fixed arrays for hearing aids,'' J. Acoust. Soc. Am. **94,** 1332–1342.

Calibration methods of voltage-to-distance function for an electromagnetic articulometer (EMA) system

Tokihiko Kaburagi and Masaaki Honda
Information Science Research Laboratory, NTT Basic Research Laboratories, 3-1 Morinosato-Wakamiya, Atsugi, Kanagawa, 243-01 Japan

(Received 14 June 1996; accepted for publication 13 November 1996)

In electromagnetic articulometer (EMA) systems, the relationship between the voltage of the received signal and the distance between the transmitter and receiver coils is represented by a voltage-to-distance (VD) function. This paper describes an adaptive calibration method for determining unknown parameters in the VD function in which the parameters are determined using automatically selected local calibration data. This method is compared with the conventional fixed method in which the parameters are computed from calibration data covering the entire measurement area. Experimental results show that the measurement error of the adaptive method is 0.106 mm for a 14×14-cm measurement area and is less than half of that in the fixed method. In addition, this error is the same as that when the region of the receiver position is restricted to a 4×4-cm local area in the fixed method. [S0001-4966(97)00704-2]

PACS numbers: 43.70.Aj, 43.70.Jt [AL]

INTRODUCTION

Electromagnetic articulometer (EMA) systems are useful tools for monitoring the movements of speech articulators with fine spatial and temporal resolutions (Hixon, 1971; Schönle *et al.*, 1987; Perkell *et al.*, 1992). The EMA system employs three transmitter coils driven by alternating currents of different frequencies. The voltage of received signals, which are electromagnetically induced in the receiver coil, is measured for each transmitter. The relationship between the voltage in the receiver and its distance from the transmitter is given by a voltage-to-distance (VD) function, and this function is used to calculate the transmitter–receiver distance from the measured voltage. Finally, the position of the receiver coil is determined as the crossing point of three circles, the center and radius of that given by each transmitter position and corresponding transmitter–receiver distance (Schönle *et al.*, 1987).

Prior to the experiment, a calibration is required to determine the unknown parameters in the VD function. Conventionally, a set of parameters is determined using calibration data measured at multiple points in a measurement area (Perkell *et al.*, 1992; Gracco and Nye, 1993; Hoole, 1993). Alternatively, we propose a new method which adaptively determines the parameters according to the position of the receiver coil. In this paper, we describe two types of calibration methods, i.e., conventional (fixed) and adaptive methods, and compare them quantitatively by evaluating the measurement accuracy.

I. HARDWARE AND FORM OF VD FUNCTION

The EMA system used in this study (Carstens Articulograph AG100, Germany) has three transmitter coils positioned at vertices P_1, P_2, and P_3 of a regular triangle with side lengths of 64.18 cm. By denoting the distance between ith transmitter and the receiver coil as d_i and the voltage of the received signal for ith transmitter as v_i, VD function is expressed as

$$v_i = \frac{a_i}{d_i^{b_i}} \cos\theta \qquad \text{for } i = 1,2,3, \tag{1}$$

where a_i and b_i are unknown parameters to be determined. The tilt of the receiver is represented by θ.

II. CALIBRATION METHODS FOR VD FUNCTION

A. Fixed calibration method

The fixed calibration method is performed by (1) measuring the calibration data and (2) determining the optimal parameters.

In the first step, the voltage of the received signal is measured at known transmitter-receiver distances. We examine four types of fixed method in terms of the sampling point assignment of the calibration data.

Method I

As illustrated in Fig. 1, a rectangular measurement area inside the triangle $P_1P_2P_3$ covers the entire range of multiple points on the articulators. In this method, calibration data are measured at each point assigned along each line passing through a transmitter position P_i and the center of the measurement area P_c.

Method II

Sampling points of the calibration data are assigned at each crossing point of grids drawn at equal intervals in the horizontal and vertical directions (Fig. 2) so that the sampling points can cover the entire measurement area.

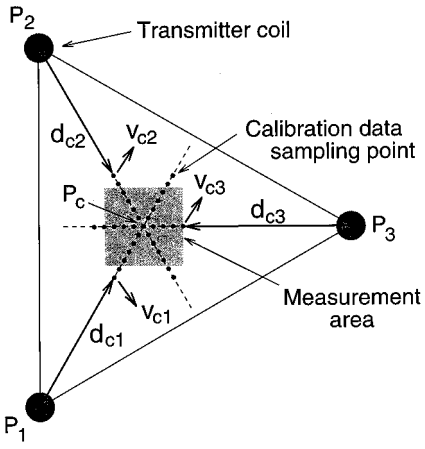

FIG. 1. Sampling point assignment of calibration data in fixed method I.

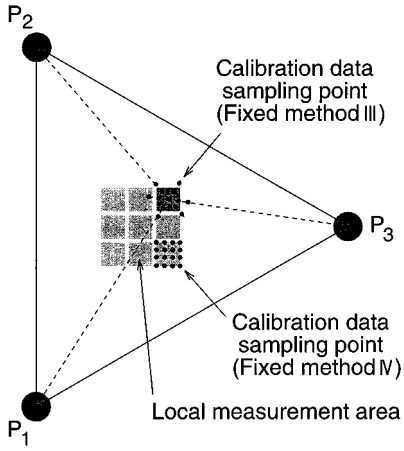

FIG. 3. Sampling point assignment of calibration data in fixed methods III and IV.

Method III

If it is possible to know *a priori* the region of each receiver coil during the experiment, it can help to reduce the measurement error by sampling the calibration data from that local region (Perkell *et al.*, 1992). In this method, sampling points are assigned along each line passing through a transmitter P_i and the center of the local measurement area (Fig. 3).

Method IV

Sampling points are assigned at each crossing point of grids drawn at equal intervals in the local measurement area (Fig. 3).

In the second step, we define a calibration error in terms of the logarithmic value of the voltage as

$$e_n = \ln v_{ci}(n) - \ln \frac{a_i}{d_{ci}^{bi}(n)} \quad \text{for } n = 1,2,3,\ldots,N_i, \tag{2}$$

where $v_{ci}(n)$ and $d_{ci}(n)$ represent the voltage and transmitter-receiver distance in the calibration data and N_i is the number of calibration data for the transmitter i. It should be noted that the tilt of the receiver coil is set at zero. Then, a_i and b_i in Eq. (1) are determined as the parameter combination that delivers a minimum for the sum over the squares of all calibration errors

$$a_i^*, b_i^* = \arg \min_{a_i, b_i} \sum_{n=1}^{N_i} e_n^2. \tag{3}$$

This problem can be solved explicitly by expressing the right-hand side of Eq. (2) as a linear function of $\ln a_i$ and b_i.

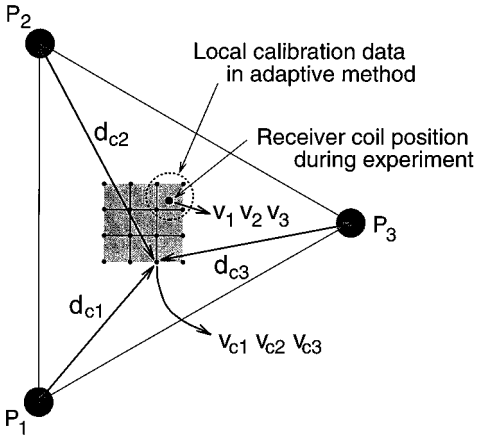

FIG. 2. Sampling point assignment of calibration data in fixed method II and adaptive method.

B. Adaptive calibration method

The adaptive calibration method is performed by (1) measuring the calibration data, (2) selecting the local calibration data that are possibly neighboring the receiver position in the experiment, and (3) determining the parameters for local calibration data. Only the first step precedes the experiment. The second and third steps are applied to each sample of experimental data (voltage). In the second step, the location of the receiver coil is *a priori* unknown.

First, the entire calibration data are taken at each crossing point as shown in Fig. 2. Next, the selection of local data is automatically performed by comparing the experimental and calibration data using a distance measure:

$$D_n = \sum_{i=1}^{3} w_i \left(\frac{v_i}{\Sigma_{j=1}^{3} v_j} - \frac{v_{ci}(n)}{\Sigma_{j=1}^{3} v_{cj}(n)} \right)^2, \tag{4}$$

where v_i represents the voltage in the experimental data, $v_{ci}(n)$ represents the voltage in the nth calibration data, and w_i is a weighting coefficient. In this measure, each voltage is divided by the sum over three transmitters. This normalization cancels the influence of the tilt of the receiver coil between the numerator and the denominator. When the receiver coil is moved away from transmitter i, the corresponding voltage v_i becomes small and its contribution to the computation of D_n is consequently reduced. The weight w_i is, therefore, set as $w_i = v_i^{-1}/\Sigma_{i=1}^{3} v_i^{-1}$. After computing D_n for every piece of calibration data, the distance measurements D_n are sorted in ascending order and the local calibration data are found by examining the first M indices of those distance measurements. M is the number of the local calibration data, and parameters in Eq. (1) are determined for them

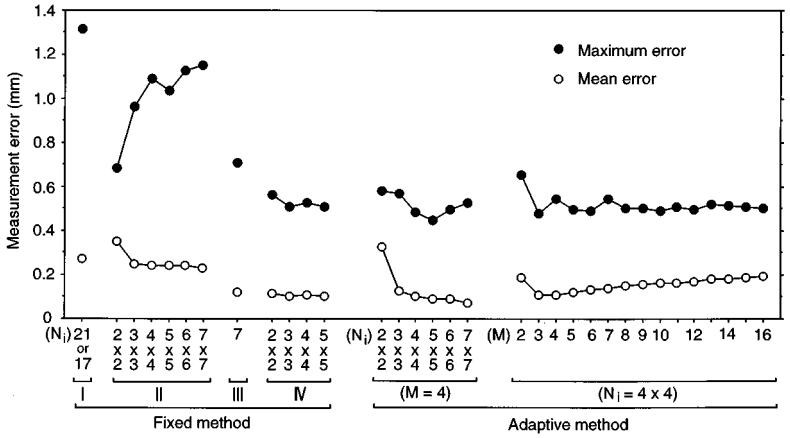

FIG. 4. Measurement error (the Euclidian distance between the actual and measured positions) observed at $15\times15=225$ locations spaced at 1-cm intervals over a 14×14-cm area. Mean and maximum errors are plotted for each calibration method while varying the number of total calibration data N_i and local calibration data M.

by finding the weighted mean-square-error solutions of $\ln a_i$ and b_i as

$$a_i^*, b_i^* = \arg\min_{a_i, b_i} \sum_{m=1}^{M} v_m e_m^2, \tag{5}$$

where m represents the index of the local calibration data. When the distance measure D_m is small, this calibration point is possibly closer to the receiver position in the experiment. Such calibration data are heavily weighted in Eq. (5) by setting v_m as $v_m = D_m^{-1}/\Sigma_{m=1}^{M} D_m^{-1}$.

III. COMPARISON OF MEASUREMENT ACCURACY

In this section, we compare the fixed and adaptive calibration methods by evaluating the measurement accuracy of the receiver position.

A. Measurement accuracy in each calibration method

The measurement accuracy of each calibration method was assessed based on the errors observed at $15\times15=225$ locations spaced at 1-cm intervals over a 14×14-cm measurement area. The off-center misalignment and tilt of the receiver coil, which may be the source of measurement errors in the experiment, was fixed at zero in this study. At each location, the error was evaluated as the Euclidian distance $\sqrt{(x_m-x)^2+(y_m-y)^2}$ between the actual position (x,y) and the measured position (x_m,y_m). Measurement errors obtained for the fixed and adaptive calibration methods are plotted in Fig. 4.

In fixed method I, calibration data were sampled at 1-cm intervals and the sample number N_i was 21 for transmitters 1 and 2 and 17 for transmitter 3.[1] In fixed method II, the sample number N_i ranged from 2×2 to 7×7. The samples were taken from the four extreme corners of the measurement area for $N_i=2\times2$. When N_i was increased, the interval between sample points was set at $14/(N_i-1)$ cm. As a result, the measurement error in method II was smaller than that in method I: for the sample number of 7×7, the mean and maximum error was 0.230 and 1.150 mm. The standard deviation (s.d.) was 0.175 mm.

In fixed methods III and IV, we assumed that the size of the local measurement area was 4×4 cm. As shown in Fig. 3, nine local areas were set in the entire area with a spacing of 1 cm. A different set of parameters a_i and b_i was determined for each local area. In evaluating the measurement error, the parameter set was selected according to the actual position of the receiver coil. The error was slightly smaller in method IV: the mean (maximum) error was 0.106 (0.508) mm for a sample number of 5×5 per local area; s.d. was 0.058 mm.

In the adaptive method, we first examined the effect of N_i, the total number of the calibration data. The number of local calibration data was fixed at $M=4$. The measurement error, which decreased as the sample number N_i increased, reached a saturation level at $N_i=4\times4$ or 5×5. Next, the total number was fixed at $N_i=4\times4$ and the number of local calibration data M was varied over a range from 2 to 16. The relationship between the sample number and the error was not monotonic: when M was increased, the error first decreased and then slightly increased. The smallest error was found for $M=4$. The mean (maximum) error was 0.106 (0.485) mm and s.d. was 0.082 mm.

B. Measurement accuracy as a function of receiver position

Next, we examined the measurement accuracy at different receiver positions in the 14×14-cm measurement area. We set the origin of the x and y axes at the center of the measurement area. As shown in the upper part of Fig. 5, the receiver coil was moved at 1-mm intervals along lines $x=0$, 23.3, 46.6, and 70.0 mm for a range of $-70\leqslant y\leqslant70$ mm. The measurement error was evaluated for fixed method II ($N_i=7\times7$), fixed method IV ($N_i=5\times5$), and the adaptive method ($N_i=4\times4$, $M=4$). Calibration data employed in fixed method IV were measured in a local area around the center ($-20\leqslant x\leqslant20, -20\leqslant y\leqslant20$ mm).

In Fig. 5, the measurement error is plotted as a function of the actual position. The results show that, in fixed method II, the measurement error was almost at the same level independent of the receiver position except for the results taken

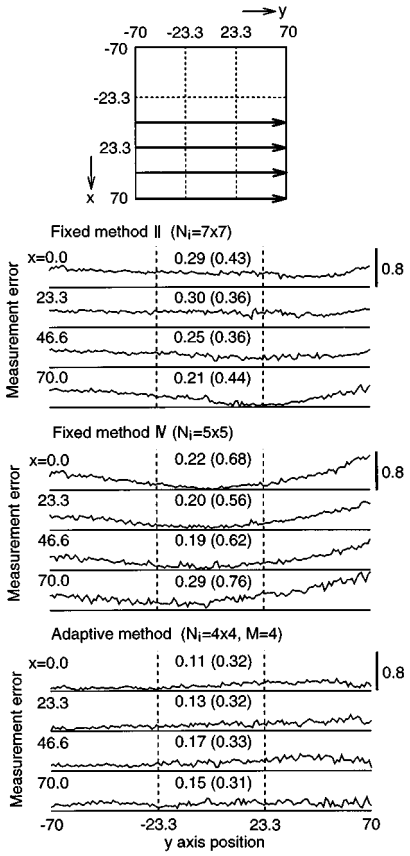

FIG. 5. Measurement error depending on the receiver position in a 14 $\times$14-cm measurement area. As illustrated in the upper part of the figure, a receiver coil was moved parallel to the y axis at 1-mm intervals, and the measurement error, the Euclidian distance between the actual and measured positions, was measured at each point. Traces show the measurement error as a function of the y axis position for fixed methods II and IV and the adaptive method. Numerals at the center of each trace show the mean and maximum errors. The unit of all the numerals is mm.

at $x=70$ mm. In fixed method IV, the error was very small in the local area where the calibration data were taken. However, the measurement error increased rapidly as the receiver moved away from the local area. In the adaptive method, the measurement error was almost at the same level independent of the receiver position. In addition, the average error along the y axis was smaller than that obtained by the fixed methods.

C. Measurement accuracy for a different VD function

The measurement accuracy was examined for another type of the VD function given as $v = a/d^{(b_1 d^2 + b_2 d + b_3)}$ (Perkell *et al.*, 1992). In fixed method IV and the adaptive method, the measurement error was the same as that for the VD function given in Eq. (1). In fixed method II, the mean error reduced slightly from 0.230 to 0.224 mm.

IV. SUMMARY AND CONCLUSIONS

We have described calibration methods for determining unknown parameters in the voltage-to-distance function. In the conventional fixed method, parameters are determined for all the calibration data that cover the entire or explicitly specified local measurement area. In the adaptive method, parameters are determined for local calibration data selected automatically depending on the receiver position in the experiment. The main results are as follows:

(1) In the fixed calibration method, the mean measurement error of the receiver position is 0.230 mm for a 14 $\times$14-cm measurement area.

(2) This error is reduced to 0.106 mm by restricting the region of the receiver coil to a 4$\times$4-cm local area. The measurement error increases rapidly when the receiver moves away from this local area.

(3) In the adaptive calibration method, mean measurement error (0.106 mm) is the same as that in the fixed method where the receiver location is restricted to the local area. In addition, the error is almost at the same level independent of the receiver position in the measurement area.

These results show that the adaptive calibration method can make the experimental procedure very simple because we do not need to specify *a priori* the local region in which each receiver coil is expected to be located, and at the same time, measurement accuracy remains high.

[1]The sampling points were determined so that (1) the center P_c was sampled and (2) the measurement area was inside a circle, the radius of which corresponds to the distance of the farthest sample from the transmitter, and outside a circle, the radius of which corresponds to the distance of the nearest sample from the transmitter.

Gracco, V. L., and Nye, P. W. (**1993**). ''Magnetometry in speech articulation research: Some misadventures on the road to enlightenment,'' Proc. ACCOR Workshop on Electromagnetic Articulography in Phonetic Research (FIPKM **31**, der Universität München), pp. 91–104.

Hixon, T. J. (**1971**). ''An electromagnetic method for transducing jaw movements during speech,'' J. Acoust. Soc. Am. **49,** 603–606.

Hoole, P. (**1993**). ''Methodological considerations in the use of electromagnetic articulography in phonetic research,'' Proc. ACCOR Workshop on Electromagnetic Articulography in Phonetic Research (FIPKM **31**, der Universität München), pp. 43–64.

Perkell, J. S., Cohen, M. H., Svirsky, M. A., Matthies, M. L., Garabieta, I., and Jackson, M. T. T. (**1992**). ''Electromagnetic midsagittal articulometer (EMMA) systems for transducing speech articulatory movements,'' J. Acoust. Soc. Am. **92,** 3078–3096.

Schönle, P. W., Gräbe, K., Wenig, P., Höhne, J., Schrader, J., and Conrad, B. (**1987**). ''Electromagnetic articulography: use of alternating magnetic fields for tracking movements of multiple points inside and outside the vocal tract,'' Brain Lang. **31**, 26–35.

Erratum: Analysis of the numerically implemented angular spectrum approach based on the evaluation of two-dimensional acoustic fields. Part I. Errors due to the discrete Fourier transform and discretization [J. Acoust. Soc. Am. 99, 1339–1348 (1996)]

Ping Wu, Rymantas Kazys, and Tadeusz Stepinski
Uppsala University, Department of Technology, Circuits and Systems, Box 534, S-751 21 Uppsala, Sweden

(Received 15 September 1996; accepted for publication 14 October 1996)

[S0001-4966(97)00104-5]

PACS numbers: 43.20.Rz, 43.20.Bi, 43.10.Vx [JEG]

The index $-L/2+1, \ldots, -2, -1, 0, 1, 2, \ldots, L/2$ in Fig. 1 should read $-L/2, \ldots, -2, -1, 0, 1, 2, \ldots, L/2-1$ and $x=\Delta d/2$ in the sentence ''When L is even, the center of source at $x=\Delta d/2$'' below Fig. 1 should read $x=-\Delta d/2$.

In Eq. (8), the exponential on the right-hand side should read

$$\exp\left[j2\pi\left(\frac{i_x m_x}{N} + z\sqrt{1/\lambda^2-(m_x\Delta f)^2} \right) \right].$$

In Eq. (16), the first exponential factor on the right-hand side should read

$$\exp\left(\frac{-j2\pi m_x \phi}{N} \right).$$

Figures 8(a), (c), and 9(a) should be replaced by the following ones, and in the caption of Fig. 9, ''(c) the zooming-in of (a) and (d) the zooming-in of (b)'' should be deleted.

The statements for analyzing the effect of the half-sample phase shift in Sec. IV B should be modified by the following:

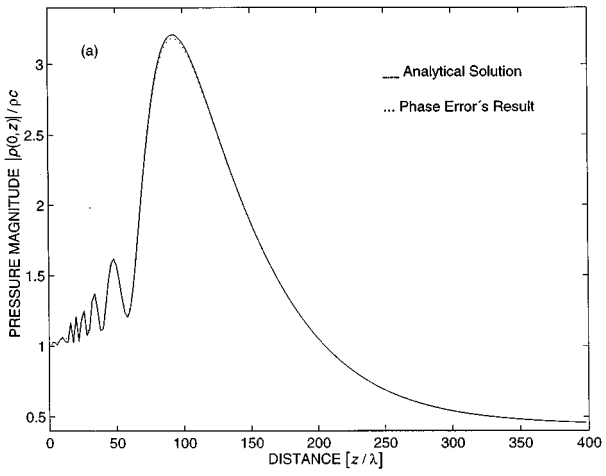

FIG. 9. The DFT's-spectra based results. Analytical solution's pressure magnitude (solid curves) versus ASA's pressure magnitude (dotted curves) which are normalized by ρc on the z axis $x/A=0$ for the array having 32 elements with width $2a=\lambda$ and focusing the field at point $x=0, z=100\lambda$. (a) $x/A=0$.

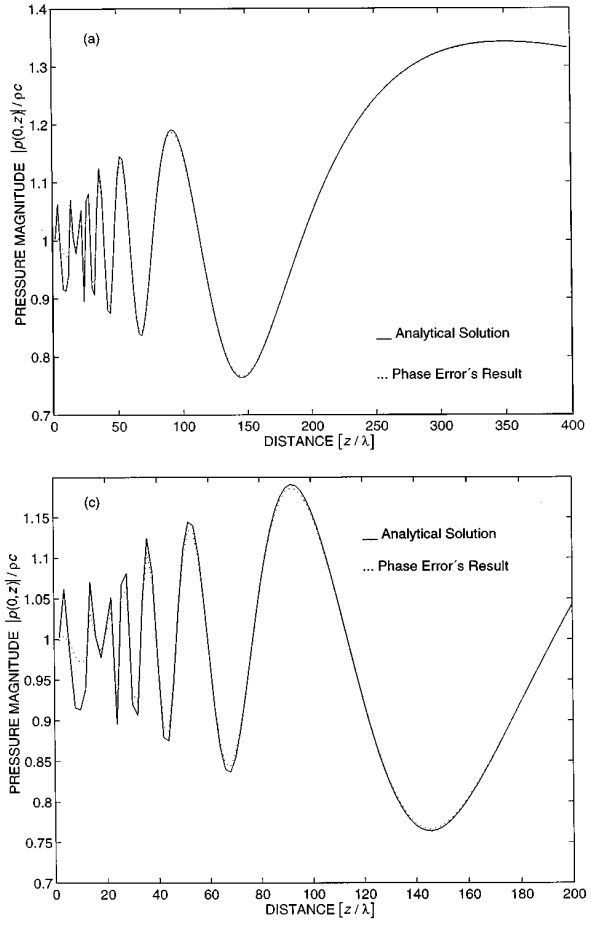

FIG. 8. The DFT's-spectra-based results. Analytical solution's pressure magnitude (solid curves) versus ASA's pressure magnitude (dotted curves) which are normalized by ρc on the z axis $x/A=0$ for the transducer with $2A=32\lambda$. (a) $x/A=0$, and (c) the zooming-in of (a).

 0001-4966/97/101(4)/2395/2/$10.00

B. Effect of the half-sample phase shift

. . . Applying this angular spectrum to the computation of the field produces the results shown in Fig. 8. In these figures the analytical solution and the phase error's results on the z axis [Fig. 8(a) and (c)] show small difference and those off the z axis [Fig. 8(b) and (d)] show larger difference. Figure 9 is the field which is supposed to be focused at 100λ, and it also shows the situation similar to that in Fig. 8. The differences caused by the phase error are easily understood. Because the discretized source is shifted by a half-sample length $\Delta d/2$, an extra phase term $e^{j2\pi m_x/N}$ is induced into the angular spectrum of the source and the field from the shifted source is also shifted by $\Delta d/2$. Take Figs. 8 and 9 as examples, the phase error's fields on the z axis [Figs. 8(a) and 9(a)] are actually the analytical ones off the z axis at $x=\Delta d/2$, and the fields off the z axis at $x=2A$ [Figs. 8(b) and 9(b)] are actually the analytical ones off the z axis at $x=2A+\Delta d/2$ instead of $x=2A$.

ACKNOWLEDGMENT

The authors would like to thank Dr. Jamal Assaad from University of Valenciennes, Valenciennes, France, for his attention to find out some of the errors.

Erratum: Analysis of the numerically implemented angular spectrum approach based on the evaluation of two-dimensional acoustic fields. Part II. Characteristics as a function of angular range [J. Acoust. Soc. Am. 99, 1349–1359 (1996)]

Ping Wu, Rymantas Kazys, and Tadeusz Stepinski

Uppsala University, Department of Technology, Circuits and Systems, Box 534, S-751 21 Uppsala, Sweden

(Received 15 September 1996; accepted for publication 14 October 1996)

[S0001-4966(97)00204-X]

PACS numbers: 43.20.Rz, 43.20.Bi, 43.10.Vx [JEG]

In the caption of Fig. 9, Eq. (26) should read Eq. (8).

TECHNICAL NOTES AND RESEARCH BRIEFS

Paul B. Ostergaard
10 Glenwood Way, West Caldwell, New Jersey 07006

Editor's Note: *Original contributions to the Technical Notes and Research Briefs section are always welcome. Manuscripts should be double-spaced, and ordinarily not longer than about 1500 words. There are no publication charges, and consequently, no free reprints; however, reprints may be purchased at the usual prices.*

Advanced-degree dissertations in acoustics

Editor's note: Abstracts of Doctoral and Master's theses will be welcomed at all times. Please note that they must be double spaced, limited to 200 words, must include the appropriate PACS classification numbers, and be formatted as shown below (don't make the editor retype them, please!). The address for obtaining a copy of the thesis is helpful. Please submit two copies.

The parabolic equation method for outdoor sound propagation [43.28.Fp, 43.20.Bi]—Marta Galindo Arranz, *Dept. of Acoustic Technology, Technical University of Denmark, DK-2800 Lyngby, Denmark 1996 (Ph.D.).* The parabolic equation method (abbreviated PE) transforms the elliptic Helmholtz equation into a parabolic wave equation, which solves an initial value problem. Solving an initial value problem is desirable in the study of propagation of waves through complex environments, where the closed solutions of boundary value problems turn out to be too complex. Three different applications of the Crank–Nicolson parabolic equation method, CNPE, are presented. The first two applications study variations of the ground in a homogeneous atmosphere. Propagation of the sound above a mixed impedance ground and up-slope sound propagation are investigated. In the third application, the influence of the atmosphere is studied, characterized, and implemented in the CNPE method. The refraction of the sound due to the wind and temperature gradients, and the scattering due to the turbulence of the atmosphere is taken into account in the calculations. The flexibility and powerfulness of the PE method are demonstrated in the report. In several aspects of PE the report presents important new ideas.

Thesis advisor: Karsten B. Rasmussen.

Development of methods for evaluation of pitch strength in musical tones [43.75.Mn, 43.66.Hg]—Alexander Galembo, *St. Petersburg Institute of Cinema and Television, Ul. Pravdy 13, St. Petersburg 191126, Russia, February 1995 (Ph.D.).* The work is based on acoustic analyses and perceptual evaluations of real and synthesized piano tones. In the first part, psychological factors which limit the reliability of judgments of tone quality, such as terminology, cross-modal masking (hearing–tactile feedback), and prejudices were analyzed, and recommendations given for how to limit the effects of such factors. In the second part, dealing with the perceptual evaluation and acoustical analysis of treble tones in the piano, it was experimentally demonstrated that a prominent noise component is present, mainly due to structure-borne sound following the blow of the hammer. For quantifying the influence on the perceived pitch strength, a measurement of the harmonic-to-noise ratio, using a method with adjustable comb filtering of short time segments of the signal was proposed. In a third part, the characteristic stretching of the partial frequencies in piano tones due to string stiffness was analyzed. It was shown that cepstral analysis, as well as the concept of harmonic product spectrum, can be used to visualize and measure inharmonicity. A new algorithm, ''the inharmonic product spectrum,'' was designed for more accurate measurements of the inharmonicity coefficient, using a method of parameter variation. In a generalized approach a tunable ''inharmonic comb filter'' was developed, giving fast and accurate measurements of inharmonicity as well as a new convenient way of visualizing tones from musical instruments.

Thesis advisor: Prof. Y. Vakhitov.

 0001-4966/97/101(4)/2397/1/$10.00